NASA/TP–2014-218256

Supersonic Retropropulsion Test 1853 in NASA LaRC Unitary Plan Wind Tunnel Test Section 2

Scott A. Berry and Matthew N. Rhode
Langley Research Center, Hampton, Virginia

April 2014

NASA STI Program . . . in Profile

Since its founding, NASA has been dedicated to the advancement of aeronautics and space science. The NASA scientific and technical information (STI) program plays a key part in helping NASA maintain this important role.

The NASA STI program operates under the auspices of the Agency Chief Information Officer. It collects, organizes, provides for archiving, and disseminates NASA's STI. The NASA STI program provides access to the NASA Aeronautics and Space Database and its public interface, the NASA Technical Report Server, thus providing one of the largest collections of aeronautical and space science STI in the world. Results are published in both non-NASA channels and by NASA in the NASA STI Report Series, which includes the following report types:

- TECHNICAL PUBLICATION. Reports of completed research or a major significant phase of research that present the results of NASA Programs and include extensive data or theoretical analysis. Includes compilations of significant scientific and technical data and information deemed to be of continuing reference value. NASA counterpart of peer-reviewed formal professional papers, but having less stringent limitations on manuscript length and extent of graphic presentations.

- TECHNICAL MEMORANDUM. Scientific and technical findings that are preliminary or of specialized interest, e.g., quick release reports, working papers, and bibliographies that contain minimal annotation. Does not contain extensive analysis.

- CONTRACTOR REPORT. Scientific and technical findings by NASA-sponsored contractors and grantees.

- CONFERENCE PUBLICATION. Collected papers from scientific and technical conferences, symposia, seminars, or other meetings sponsored or co-sponsored by NASA.

- SPECIAL PUBLICATION. Scientific, technical, or historical information from NASA programs, projects, and missions, often concerned with subjects having substantial public interest.

- TECHNICAL TRANSLATION. English-language translations of foreign scientific and technical material pertinent to NASA's mission.

Specialized services also include organizing and publishing research results, distributing specialized research announcements and feeds, providing information desk and personal search support, and enabling data exchange services.

For more information about the NASA STI program, see the following:

- Access the NASA STI program home page at *http://www.sti.nasa.gov*

- E-mail your question to help@sti.nasa.gov

- Fax your question to the NASA STI Information Desk at 443-757-5803

- Phone the NASA STI Information Desk at 443-757-5802

- Write to:
  STI Information Desk
  NASA Center for AeroSpace Information
  7115 Standard Drive
  Hanover, MD 21076-1320

NASA/TP–2014-218256

Supersonic Retropropulsion Test 1853 in NASA LaRC Unitary Plan Wind Tunnel Test Section 2

Scott A. Berry and Matthew N. Rhode
Langley Research Center, Hampton, Virginia

National Aeronautics and
Space Administration

Langley Research Center
Hampton, Virginia 23681-2199

April 2014

Acknowledgments

The authors would like to acknowledge the support of NASA's Exploration Technology Development and Demonstration (ETDD) Program and Fundamental Aeronautics Program (FAP). ETDD's Entry, Descent, and Landing (EDL) Technology Development Project and FAP's Hypersonics Project, both managed at NASA Langley Research Center, jointly supported the work documented herein. The experimental model was manufactured at Modern Machine and Tool Company with support from the following individuals: Doug Bach, Tim Britt, Ron Dupont, Danny Boulais, Gene Pantaleo, Steve Robinette, Jim Rupp, Max Ward, Ken Woodman, Howard Walls, Joe Hudson, Richard Vest, Jerry Moore, David Winebarger, David Leatherman, Brian Petritsch, Bill Bent, Tim White, Mel Ashley, J.C. Lane, Rex Gay, Brent Meadors, Dennis Yates. The experimental test campaign was conducted with the help from the following: Karl Edquist, Chuck Player, Chris Laws, Courtney Spells, Andrew McCrea, Bil Kleb, Guy Schauerhamer, Kerry Trumble, Bill Oberkampf, Ashley Korzun, Aaron Fuchs, Bryan Falman, Ricky Hall, Paul Bagby, and Steve Jones. Posttest analysis support was provided by the following: Josh Cordoni (UVA), Juan Cruz (Georgia Tech), Patrick Schultz (UNCC), Mike Kegerise, Shann Rufer, and Brett Bathel. Finally, the review committee, consisting of Khaled Abdol-Hamid, Bil Kleb, Kelly Murphy, Rob Bauerle, and Diego Capriotti, and editorial staff, consisting of Kay Forrest and Staci Altizer, were critical to the completion of this report. Thanks for your support!

The use of trademarks or names of manufacturers in this report is for accurate reporting and does not constitute an official endorsement, either expressed or implied, of such products or manufacturers by the National Aeronautics and Space Administration.

Available from:

NASA Center for AeroSpace Information
7115 Standard Drive
Hanover, MD 21076-1320
443-757-5802

Abstract

A supersonic retropropulsion experiment was conducted in the Langley Research Center Unitary Plan Wind Tunnel Test Section 2 at Mach numbers of 2.4, 3.5, and 4.6. Intended as a code validation effort, this study used pretest computations to size and refine the model such that tunnel blockage and internal flow separations were minimized. A 5-in diameter 70 degree sphere-cone forebody, which can accommodate up to four 4:1 area ratio nozzles, followed by a 9.55 inches long cylindrical aft body was selected for this test after computational maturation. The primary measurements for this experiment were high spatial-density surface pressures. In addition, high speed schlieren video and internal pressures and temperatures were acquired. The test included parametric variations in the number of nozzles utilized, thrust coefficients (roughly 0 to 4), and angles of attack (–8 to 20 degrees). The run matrix was developed to also allow quantification of various sources of experimental uncertainty, such as random errors due to run-to-run variations and systematic errors due to flowfield or model misalignments. To accommodate the uncertainty assessment, many runs and replicates were conducted with the model at various locations within the tunnel and with model roll angles of 0, 60, 120, and 180 degrees. This test report is intended to provide comprehensive details of the experiment as a reference for future computational comparisons and as such contains a review of key observations, as well as all schlieren and pressure results within appendices.

THIS PAGE INTENTIONALLY LEFT BLANK

TABLE OF CONTENTS

SECTION 1: INTRODUCTION 1

SECTION 2: APPARATUS AND METHODS 4
2.1 Facility 4
2.2 Model 7
2.3 Instrumentation 10
2.4 Test Conditions and Run Matrix 12
2.5 Data Acquisition & Reduction 13

SECTION 3: TEST SET UP AND EXECUTION 15

SECTION 4: DISCUSSION OF RESULTS 19
4.1 Baseline 19
4.2 Center Nozzle 22
4.3 Tri-Nozzle 32
4.4 Quad-nozzle 41
4.5 High Frequency Analysis 48
4.6 Uncertainty Analysis 48

SECTION 5: SUMMARY 50

SECTION 6: REFERENCES 52

APPENDIX A: MODEL DRAWINGS 55

APPENDIX B: TEST DETAILS 124

APPENDIX C: SCHLIEREN RESULTS 145

APPENDIX D: PRESSURE DATA LINE PLOTS 226

APPENDIX E: PRESSURE CONTOUR PLOTS 720

LIST OF TABLES

Table 1. Extracted flow features and properties for the center nozzle for α = 0°.30
Table 2. Summary of the pressure coefficient uncertainties at one standard deviation. 49

Table A-1. As-built surface pressure port locations. 56
Table A-2. Parameter list and definitions. 61

Table B-1. Notional run matrix. 124
Table B-2. Notational trust coefficients. 130
Table B-3. Chronological run log. 132
Table B-4. Angle of attack sweep schedule. 142
Table B-5. Statistical analysis of as-tested flow conditions. 143

Table C-1. Schlieren video acquisition information in run chronological order.. 146
Table C-2. Schlieren cases rearranged by configuration. 148

LIST OF FIGURES

Figure 1. Conceptual sketch of SRP flow features..... 2
Figure 2. The Unitary Plan Wind Tunnel complex in Building 1251 at NASA Langley Research Center. 4
Figure 3. Schematic of the NASA LaRC Unitary Plan Wind Tunnel complex. . 5
Figure 4. Schematic of the UPWT Test Section 2 nozzle block. 5
Figure 5. Test Section 2 model support system..... 6
Figure 6. Simplified schematic of the UPWT high pressure system. 7
Figure 7. Oblique view of UPWT SRP model assembly. 8
Figure 8. Major components of UPWT SRP model assembly. 8
Figure 9. Oblique view of insulator saddle block. 9
Figure 10. Close up of the instrumented center nozzle. 10
Figure 11. Forebody surface instrumentation layout for the baseline configuration. 11
Figure 12. Test conditions within operating envelope for UPWT Test Section 2. 13
Figure 13. The SRP model installed in the UPWT Test Section 2. 15
Figure 14. The internal pressure lines and instrumentation wiring. 15
Figure 15. The baseline model installed in Test Section 2. 17
Figure 16. The baseline model installed in the UPWT. 17
Figure 17. The center nozzle configuration installed in the UPWT. 18
Figure 18. The tri-nozzle configuration installed in the UPWT. 18
Figure 19. The effect of Mach number for the baseline configuration at α = 0°. 20
Figure 20. The effect of angle of attack for the baseline configuration at M_∞ = 4.6 (Run 283). 21
Figure 21. Contour maps showing the effect of angle of attack for the baseline configuration at M_∞ = 2.4 (Run 274). 22
Figure 22. The effect of Mach number for the center nozzle at α = 0° and C_T = 2. 23
Figure 23. The effect of thrust coefficient for the center nozzle at M_∞ = 4.6 and α = 0°. 24
Figure 24. Comparison of contour maps to Schlieren for a range of thrust cases for the center nozzle configuration at M_∞ = 2.4 and α = 0° (Runs 319, 139, 141, 137, and 136, respectively). 25
Figure 25. The effect of angle of attack for the center nozzle at M_∞ = 4.6 and C_T = 2 (Run 165). 26
Figure 26. Contour maps showing the effect of angle of attack for the center nozzle configuration at M_∞ = 2.4 and C_T = 2.0, and ϕ = 0° (Run 141). 27
Figure 27. Relevant dimensions to be extracted from the Schlieren data. 28
Figure 28. Center nozzle shock and plume tracings for all three Mach numbers at α = 0°. 29

Figure 29. Flow feature standoff distance versus nozzle pressure ratio for $\alpha = 0°$. 31
Figure 30. Bow shock and plume shapes as a function of α for Mach 4.6, $C_T = 2$. 32
Figure 31. The effect of Mach number for the tri-nozzle at $\alpha = 0°$ and $C_T = 2$. . 33
Figure 32. The effect of thrust coefficient for the tri-nozzle at $M\infty = 4.6$ and $\alpha = 0°$. 34
Figure 33. Comparison of contour maps to schlieren images for a range of thrust cases for tri-nozzle configuration at $M\infty = 2.4$ and $\alpha = 0°$ (Runs 180, 221, 202, 198, 194, and 190, respectively). 35
Figure 34. Comparison of contour maps for complete range of thrust cases for tri-nozzle configuration at $M\infty = 2.4$ and $\alpha = 0°$ (Run 179). 35
Figure 35. The effect of angle of attack for the tri-nozzle at $M\infty = 4.6$ and $C_T = 2$ (Run 248). 36
Figure 36. Comparison of contour maps for a range of angle of attack and roll cases for the tri-nozzle configuration at $M\infty = 4.6$ and $C_T = 2$. 38
Figure 37. Tri nozzle shock and plume tracings for $M\infty = 3.5$ at $\alpha = 0$. 39
Figure 38. Comparison of center and tri nozzle bow shocks for $M\infty = 3.5$ at $\alpha = 0$. 40
Figure 39. The effect of Mach number for the quad-nozzle at $\alpha = 0°$ and $C_T = 2$. 41
Figure 40. The effect of thrust coefficient for the quad-nozzle at $M\infty = 2.4$ and $\alpha = 0°$. 42
Figure 41. The effect of model roll for the quad-nozzle at $M\infty = 2.4$, $\alpha = 0°$, and $C_T = 3$. 43
Figure 42. The effect of angle of attack for the quad-nozzle at $M\infty = 2.4$, $\phi = 0°$, and $C_T = 2$ (Run 288). 44
Figure 43. The effect of angle of attack for the quad-nozzle at $M\infty = 2.4$, $\phi = 180°$, and $C_T = 2$ (Run 291). 45
Figure 44. Comparison of contour maps for a range of angle of attack and roll cases for the quad-nozzle configuration at $M\infty = 2.4$, and $C_T = 1$. .. 47

Figure A-1. View from the front of the model. 55
Figure A-2. View from the port side of the model. 56
Figure A-3. SRP model sting showing high pressure air supply port. 110
Figure A-4. ULTEM insulator saddle block. 110
Figure A-5. Manifold assembly. 111
Figure A-6. Initial assembly of forebody and manifold. 111
Figure A-7. Forebody assembly with baseline inserts installed. 112
Figure A-8. Six of eight baseline and nozzle inserts. 112
Figure A-9. Instrumented half aft shell. 113
Figure A-10. Rear cover support plate showing wiring access hole. 113
Figure A-11. Assembly of sting and rear cover support plate. 114

Figure A-12. Backside of forebody showing pressure tube port posts and shims for inserts..... 114
Figure A-13. Sting assembly with Kulite pressure transducers installed. 115
Figure A-14. Insulator saddle block with one ESP module attached. 115
Figure A-15. Installation of the double O-rings for each insert. 116
Figure A-16. Center plug installation prior to seating the insert past the O-rings. 116
Figure A-17. All four baseline plug inserts in the proper (seated) position..... 117
Figure A-18. Forebody guide posts used for proper alignment of manifold during assembly. 117
Figure A-19. Installation of bolts that hold forebody in place..... 118
Figure A-20. O-ring between manifold and sting/plenum..... 118
Figure A-21. Installation of bolts that hold manifold to sting. 119
Figure A-22. Installation of saddle block with one ESP module attached. 119
Figure A-23. Close-up of a saddle block thermocouple for monitoring ESP module temperatures..... 120
Figure A-24. Installation of the aft cover plates. 120
Figure A-25. View showing model internal volume before installation of pressure tubes. 121
Figure A-26. Close-up showing clearance between ESP module and aft cover plate..... 121
Figure A-27. Installation of second aft cover plate. 122
Figure A-28. Fully assembled model with baseline inserts..... 122
Figure A-29. All four nozzle inserts in the proper (seated) position..... 123
Figure A-30. Assembly of the forebody and manifold with nozzle inserts. 123

Figure C-1. Run 58: baseline schlieren video images for range of α_τ at $M\infty$ = 3.5, C_T = 0.0, and ϕ = 60 deg. 151
Figure C-2. Run 67: baseline Schlieren video images for range of α_τ = at $M\infty$ = 3.5, C_T = 0.0, and ϕ = 60 deg. 152
Figure C-3. Run 86: baseline Schlieren video images for range of α_τ = at $M\infty$ = 4.6, C_T = 0.0, and ϕ = 0 deg. 154
Figure C-4. Run 106: baseline Schlieren video images for range of α_τ at $M\infty$ = 4.6, C_T = 0.0, and ϕ = 120 deg. 156
Figure C-5. Run 136: center nozzle schlieren video images for range of α_τ at $M\infty$ = 2.4, C_T = 4.0, and ϕ = 0 deg. 158
Figure C-6. Run 137: center nozzle schlieren video images for range of α_τ at $M\infty$ = 2.4, C_T = 3.0, and ϕ = 0 deg. 159
Figure C-7. Run 139: center nozzle schlieren video images for range of α_τ at $M\infty$ = 2.4, C_T = 1.0, and ϕ = 180 deg. 160
Figure C-8. Run 141: center nozzle schlieren video images for range of α_τ at $M\infty$ = 2.4, C_T = 2.0, and ϕ = 180 deg. 161
Figure C-9. Run 150: center nozzle schlieren video images for range of α_τ at $M\infty$ = 3.5, C_T = 3.0, and ϕ = 0 deg. 162

Figure C-10. Run 153: center nozzle schlieren video images for range of α_τ at $M\infty$ = 3.5, C_T = 2.0, and ϕ = 0 deg. 163
Figure C-11. Run 154: center nozzle schlieren video images for range of α_τ at $M\infty$ = 3.5, C_T = 1.0, and ϕ = 0 deg. 164
Figure C-12. Run 157: center nozzle schlieren video images for range of α_τ at $M\infty$ = 3.5, C_T = 0.5, and ϕ = 0 deg. 165
Figure C-13. Run 158: center nozzle schlieren video images for range of α_τ at $M\infty$ = 3.5, C_T = 0.2, and ϕ = 0 deg. 166
Figure C-14. Run 163: center nozzle schlieren video images for range of α_τ at $M\infty$ = 4.6, C_T = 3.0, and ϕ = 0 deg. 167
Figure C- 15. Run 165: center nozzle schlieren video images for range of α_τ at $M\infty$ = 4.6, C_T = 2.0, and ϕ = 0 deg. 168
Figure C-16. Run 167: center nozzle schlieren video images for range of α_τ at $M\infty$ = 4.6, C_T = 1.0, and ϕ = 0 deg. 169
Figure C-17. Run 169: center nozzle schlieren video images for range of α_τ at $M\infty$ = 4.6, C_T = 0.5, and ϕ = 180 deg. 170
Figure C-18. Run 171: center nozzle schlieren video images for range of α_τ at $M\infty$ = 4.6, C_T = 0.2, and ϕ =180 deg. 171
Figure C-19. Run 180: tri-nozzle schlieren video images for range of α_τ at $M\infty$ = 2.4, C_T = 0.0, and ϕ = 0 deg. 171
Figure C-20. Run 185: tri-nozzle schlieren video images for range of α_τ at $M\infty$ = 3.5, C_T = 0.0, and ϕ = deg. 172
Figure C-21. Run 190: tri-nozzle schlieren video images for range of α_τ at $M\infty$ = 2.4, C_T = 3.0, and ϕ = 0 deg. 174
Figure C-22. Run 192: tri-nozzle schlieren video images for range of α_τ at $M\infty$ = 2.4, C_T = 3.0, and ϕ = 120 deg. 175
Figure C-23. Run 194: tri-nozzle schlieren video images for range of α_τ at $M\infty$ = 2.4, C_T = 2.0, and ϕ = 180 deg. 175
Figure C-24. Run 198: tri-nozzle schlieren video images for range of α_τ at $M\infty$ = 2.4, C_T = 1.0, and ϕ = 0 deg. 176
Figure C-25. Run 202: tri-nozzle schlieren video images for range of α_τ at $M\infty$ = 2.4, C_T = 0.43, and ϕ = 180 deg. 177
Figure C-26. Run 206: tri-nozzle schlieren video images for range of α_τ at $M\infty$ = 2.4, C_T = 0.43, and ϕ = 0 deg. 178
Figure C-27. Run 212: tri-nozzle schlieren video images for range of α_τ at $M\infty$ = 4.6, C_T = 2.93, and ϕ = 60 deg. 179
Figure C-28. Run 214: tri-nozzle schlieren video images for range of α_τ at $M\infty$ = 4.6, C_T = 2.95, and ϕ = 180 deg. 180
Figure C-29. Run 221: tri-nozzle schlieren video images for range of α_τ at $M\infty$ = 2.4, C_T = 0.24, and ϕ = 0 deg. 182
Figure C-30. Run 222: tri-nozzle schlieren video images for range of α_τ at $M\infty$ = 3.5, C_T = 2.96, and ϕ = 0 deg. 182

Figure C-31. Run 225: tri-nozzle schlieren video images for range of α_τ at $M\infty$ = 3.5, C_T = 2.99, and ϕ = 180 deg. 184
Figure C-32. Run 226: tri-nozzle schlieren video images for range of α_τ at $M\infty$ = 3.5, C_T = 1.96, and ϕ = 180 deg. 185
Figure C-33. Run 247: tri-nozzle schlieren video images for range of α_τ at $M\infty$ = 4.6, C_T = 1.92, and ϕ = 0 deg. 186
Figure C-34. Run 248: tri-nozzle schlieren video images for range of α_τ at $M\infty$ = 4.6, C_T = 1.93, and ϕ = 180 deg. 188
Figure C-35. Run 249: tri-nozzle schlieren video images for range of α_τ at $M\infty$ = 4.6, C_T = 0.90, and ϕ = 180 deg. 189
Figure C-36. Run 253: tri-nozzle schlieren video images for range of α_τ at $M\infty$ = 4.6, C_T = 0.43, and ϕ = 0 deg. 190
Figure C-37. Run 257: tri-nozzle schlieren video images for range of α_τ at $M\infty$ = 4.6, C_T = 0.20, and ϕ = 0 deg. 191
Figure C-38. Run 262: tri-nozzle schlieren video images for range of α_τ at $M\infty$ = 4.6, C_T = 2.94, and ϕ = 0 deg. 192
Figure C-39. Run 263: tri-nozzle schlieren video images for range of α_τ at $M\infty$ = 4.6, C_T = 2.94, and ϕ = 180 deg. 193
Figure C-40. Run 264: tri-nozzle schlieren video images for range of α_τ at $M\infty$ = 4.6, α = 0 deg, and ϕ = 60 deg. 194
Figure C-41. Run 264: tri-nozzle schlieren video images for range of α_τ at $M\infty$ = 4.6, α = 12 deg, and ϕ = 60 deg. 195
Figure C-42. Run 265: tri-nozzle schlieren video images for range of α_τ at $M\infty$ = 3.5, C_T = 0.91, and ϕ = 0 deg. 195
Figure C-43. Run 266: tri-nozzle schlieren video images for range of α_τ at $M\infty$ = 3.5, C_T = 0.83, and ϕ = 0 deg. 196
Figure C-44. Run 267: tri-nozzle schlieren video images for range of α_τ at $M\infty$ = 3.5 and α = 0 deg. 197
Figure C-45. Run 274: baseline schlieren video images for range of α_τ at $M\infty$ = 2.4, C_T = 0.0, and ϕ = 180 deg. 200
Figure C-46. Run 276: baseline schlieren video images for range of α_τ at $M\infty$ = 3.5, C_T = 0.0, and ϕ = 180 deg. 202
Figure C-47. Run 283: baseline schlieren video images for range of α_τ at $M\infty$ = 4.6, C_T = 0.0, and ϕ = 180 deg. 204
Figure C-48. Run 288: quad-nozzle schlieren video images for range of α_τ at $M\infty$ = 2.4, C_T = 1.93, and ϕ = 0 deg. 206
Figure C-49. Run 291: quad-nozzle schlieren video images for range of α_τ at $M\infty$ = 2.4, C_T = 1.94, and ϕ = 180 deg. 208
Figure C-50. Run 292: quad-nozzle schlieren video images for range of model positions at $M\infty$ = 2.4, α_τ = 0 deg, and C_T = 1.93. 209
Figure C-51. Run 293: quad-nozzle schlieren video images for range of α_τ at $M\infty$ = 2.4, C_T = 0.94, and ϕ = 180 deg. 210

Figure C-52. Run 297: quad-nozzle schlieren video images for range of model positions at $M\infty = 2.4$, $\alpha_\tau = 0$ deg, and $C_T = 2.95$. 211
Figure C-53. Run 298: quad-nozzle schlieren video images for range of α_τ at $M\infty = 3.5$, $C_T = 1.91$, and $\phi = 0$ deg. 212
Figure C-54. Run 301: quad-nozzle schlieren video images for range of α_τ at $M\infty = 3.5$, $C_T = 1.92$, and $\phi = 180$ deg. 213
Figure C-55. Run 305: quad-nozzle schlieren video images for range of α_τ at $M\infty = 3.5$, $C_T = 0.90$, and $\phi = 0$ deg. 214
Figure C-56. Run 306: quad-nozzle schlieren video images for range of model positions at $M\infty = 3.5$ and $\alpha_\tau = 0$ deg. 215
Figure C-57. Run 307: quad-nozzle schlieren video images for range of α_τ at $M\infty = 4.6$, $C_T = 1.92$, and $\phi = 0$ deg. 216
Figure C-58. Run 311: quad-nozzle schlieren video images for range of α_τ at $M\infty = 4.6$, $C_T = 1.93$, and $\phi = 180$ deg. 217
Figure C-59. Run 315: quad-nozzle schlieren video images for range of α_τ at $M\infty = 4.6$, $C_T = 0.91$, and $\phi = 0$ deg. 218
Figure C-60. Run 318: center nozzle schlieren video images for range of α_τ at $M\infty = 2.4$, $C_T = 1.98$, and $\phi = 0$ deg. 219
Figure C-61. Run 319: center nozzle schlieren video images for range of α_τ at $M\infty = 2.4$, $C_T = 0.46$, and $\phi = 0$ deg. 221
Figure C-62. Run 320: center nozzle schlieren video images for range of α_τ at $M\infty = 3.5$, $C_T = 1.96$, and $\phi = 0$ deg. 222
Figure C-63. Run 321: center nozzle schlieren video images for range of α_τ at $M\infty = 4.6$, $C_T = 1.96$, and $\phi = 0$ deg. 223

Figure D-1. Baseline configuration, Run 013, $M\infty = 2.4$, $Re_\infty = 1.0\text{x}10^6$/ft, $\phi = 0.03°$, $X_S = 25.16$ in, $Y_S = 0.03$ in, $C_T = 0.00$. 227
Figure D-2. Baseline configuration, Run 014, $M\infty = 2.4$, $Re_\infty = 1.0\text{x}10^6$/ft, $\phi = 59.97°$, $X_S = 25.16$ in, $Y_S = 0.00$ in, $C_T = 0.00$..... 229
Figure D-3. Baseline configuration, Run 016, $M\infty = 2.4$, $Re_\infty = 1.0\text{x}10^6$/ft, $\phi = 0.05°$, $X_S = 25.16$ in, $Y_S = 0.00$ in, $C_T = 0.00$..... 231
Figure D-4. Baseline configuration, Run 017, $M\infty = 2.4$, $Re_\infty = 1.0\text{x}10^7$/ft, $\phi = 59.86°$, $X_S = 25.16$ in, $Y_S = 0.00$ in, $C_T = 0.00$..... 233
Figure D-5. Baseline configuration, Run 018, $M\infty = 2.4$, $Re_\infty = 1.0\text{x}10^6$/ft, $\phi = 119.96°$, $X_S = 25.16$ in, $Y_S = 0.00$ in, $C_T = 0.00$..... 235
Figure D-6. Baseline configuration, Run 019, $M\infty = 2.4$, $Re_\infty = 1.0\text{x}10^6$/ft, $\phi = 179.91°$, $X_S = 25.16$ in, $Y_S = 0.00$ in, $C_T = 0.00$..... 237
Figure D-7. Baseline configuration, Run 020, $M\infty = 2.4$, $Re_\infty = 1.0\text{x}10^6$/ft, $\phi = 0.01°$, $X_S = 39.93$ in, $Y_S = 0.00$ in, $C_T = 0.00$..... 239
Figure D-8. Baseline configuration, Run 021, $M\infty = 2.4$, $Re_\infty = 1.0\text{x}10^7$/ft, $\phi = 59.88°$, $X_S = 39.93$ in, $Y_S = 0.00$ in, $C_T = 0.00$..... 241
Figure D-9. Baseline configuration, Run 022, $M\infty = 2.4$, $Re_\infty = 1.0\text{x}10^6$/ft, $\phi = 120.06°$, $X_S = 39.93$ in, $Y_S = 0.00$ in, $C_T = 0.00$..... 243

Figure D-10. Baseline configuration, Run 023, $M\infty = 2.4$, $Re_\infty = 1.0x10^6$/ft, $\phi = 179.99°$, $X_S = 39.93$ in, $Y_S = 0.00$ in, $C_T = 0.00$..... 245
Figure D-11. Baseline configuration, Run 024, $M\infty = 2.4$, $Re_\infty = 1.0x10^6$/ft, $\phi = 0.01°$, $X_S = 39.93$ in, $Y_S = 0.00$ in, $C_T = 0.00$..... 247
Figure D-12. Baseline configuration, Run 025, $M\infty = 2.4$, $Re_\infty = 1.0x10^6$/ft, $\phi = 60.08°$, $X_S = 39.93$ in, $Y_S = 0.00$ in, $C_T = 0.00$..... 249
Figure D-13. Baseline configuration, Run 026, $M\infty = 2.4$, $Re_\infty = 1.0x10^6$/ft, $\phi = 0.03°$, $X_S = 50.17$ in, $Y_S = 0.00$ in, $C_T = 0.00$..... 251
Figure D-14. Baseline configuration, Run 027, $M\infty = 2.4$, $Re_\infty = 1.0x10^6$/ft, $\phi = 60.08°$, $X_S = 50.17$ in, $Y_S = 0.00$ in, $C_T = 0.00$..... 253
Figure D-15. Baseline configuration, Run 028, $M\infty = 2.4$, $Re_\infty = 1.0x10^6$/ft, $\phi = 120.06°$, $X_S = 50.17$ in, $Y_S = 0.00$ in, $C_T = 0.00$..... 255
Figure D-16. Baseline configuration, Run 029, $M\infty = 2.4$, $Re_\infty = 1.0x10^6$/ft, $\phi = 179.91°$, $X_S = 50.17$ in, $Y_S = 0.00$ in, $C_T = 0.00$..... 257
Figure D-17. Baseline configuration, Run 030, $M\infty = 2.4$, $Re_\infty = 1.0x10^6$/ft, $\phi = 179.91°$, $X_S = 25.18$ in, $Y_S = 0.00$ in, $C_T = 0.00$..... 259
Figure D-18. Baseline configuration, Run 031, $M\infty = 2.4$, $Re_\infty = 1.0x10^6$/ft, $\phi = 119.92°$, $X_S = 25.18$ in, $Y_S = 0.00$ in, $C_T = 0.00$..... 261
Figure D-19. Baseline configuration, Run 032, $M\infty = 2.4$, $Re_\infty = 1.0x10^6$/ft, $\phi = 59.98°$, $X_S = 25.18$ in, $Y_S = 0.00$ in, $C_T = 0.00$..... 263
Figure D-20. Baseline configuration, Run 033, $M\infty = 2.4$, $Re_\infty = 1.0x10^6$/ft, $\phi = 0.05°$, $X_S = 25.18$ in, $Y_S = 0.00$ in, $C_T = 0.00$..... 265
Figure D-21. Baseline configuration, Run 034, $M\infty = 2.4$, $Re_\infty = 1.0x10^6$/ft, $\phi = 0.05°$, $X_S = 25.18$ in, $Y_S = 7.99$ in, $C_T = 0.00$..... 267
Figure D-22. Baseline configuration, Run 035, $M\infty = 2.4$, $Re_\infty = 1.0x10^6$/ft, $\phi = 60.08°$, $X_S = 25.18$ in, $Y_S = 7.99$ in, $C_T = 0.00$..... 269
Figure D-23. Baseline configuration, Run 036, $M\infty = 2.4$, $Re_\infty = 1.0x10^6$/ft, $\phi = 119.90°$, $X_S = 25.18$ in, $Y_S = 7.99$ in, $C_T = 0.00$..... 271
Figure D-24. Baseline configuration, Run 037, $M\infty = 2.4$, $Re_\infty = 1.0x10^6$/ft, $\phi = 179.95°$, $X_S = 25.18$ in, $Y_S = 7.99$ in, $C_T = 0.00$..... 273
Figure D-25. Baseline configuration, Run 038, $M\infty = 2.4$, $Re_\infty = 1.0x10^6$/ft, $\phi = 179.95°$, $X_S = 40.19$ in, $Y_S = 7.99$ in, $C_T = 0.00$..... 275
Figure D-26. Baseline configuration, Run 039, $M\infty = 2.4$, $Re_\infty = 1.0x10^6$/ft, $\phi = 119.90°$, $X_S = 40.19$ in, $Y_S = 7.99$ in, $C_T = 0.00$..... 277
Figure D-27. Baseline configuration, Run 040, $M\infty = 2.4$, $Re_\infty = 1.0x10^6$/ft, $\phi = 59.92°$, $X_S = 40.19$ in, $Y_S = 7.99$ in, $C_T = 0.00$..... 279
Figure D-28. Baseline configuration, Run 041, $M\infty = 2.4$, $Re_\infty = 1.0x10^6$/ft, $\phi = 0.05°$, $X_S = 40.19$ in, $Y_S = 7.99$ in, $C_T = 0.00$..... 281
Figure D-29. Baseline configuration, Run 042, $M\infty = 2.4$, $Re_\infty = 1.0x10^6$/ft, $\phi = -0.05°$, $X_S = 40.19$ in, $Y_S = -8.00$ in, $C_T = 0.00$. 283
Figure D-30. Baseline configuration, Run 043, $M\infty = 2.4$, $Re_\infty = 1.0x10^6$/ft, $\phi = 59.92°$, $X_S = 40.19$ in, $Y_S = -8.00$ in, $C_T = 0.00$. 285
Figure D-31. Baseline configuration, Run 044, $M\infty = 2.4$, $Re_\infty = 1.0x10^6$/ft, $\phi = 119.90°$, $X_S = 40.19$ in, $Y_S = –8.00$ in, $C_T = 0.00$..... 287

Figure D-32. Baseline configuration, Run 045, $M\infty = 2.4$, $Re_\infty = 1.0x10^6$/ft, $\phi = 179.95°$, $X_S = 40.19$ in, $Y_S = –8.00$ in, $C_T = 0.00$..... 289
Figure D-33. Baseline configuration, Run 046, $M\infty = 2.4$, $Re_\infty = 1.0x10^6$/ft, $\phi = 179.95°$, $X_S = 50.16$ in, $Y_S = –8.00$ in, $C_T = 0.00$..... 291
Figure D-34. Baseline configuration, Run 047, $M\infty = 2.4$, $Re_\infty = 1.0x10^6$/ft, $\phi = 119.98°$, $X_S = 50.16$ in, $Y_S = –8.00$ in, $C_T = 0.00$..... 293
Figure D-35. Baseline configuration, Run 048, $M\infty = 2.4$, $Re_\infty = 1.0x10^6$/ft, $\phi = 59.98°$, $X_S = 50.16$ in, $Y_S = –8.00$ in, $C_T = 0.00$..... 295
Figure D-36. Baseline configuration, Run 049, $M\infty = 2.4$, $Re_\infty = 1.0x10^6$/ft, $\phi = 0.05°$, $X_S = 50.16$ in, $Y_S = –8.00$ in, $C_T = 0.00$..... 297
Figure D-37. Baseline configuration, Run 050, $M\infty = 3.5$, $Re_\infty = 1.0x10^7$/ft, $\phi = 59.96°$, $X_S = 50.16$ in, $Y_S = 0.00$ in, $C_T = 0.00$..... 299
Figure D-38. Baseline configuration, Run 051, $M\infty = 3.5$, $Re_\infty = 1.0x10^6$/ft, $\phi = 119.94°$, $X_S = 50.16$ in, $Y_S = 0.00$ in, $C_T = 0.00$..... 301
Figure D-39. Baseline configuration, Run 052, $M\infty = 3.5$, $Re_\infty = 1.0x10^6$/ft, $\phi = 179.99°$, $X_S = 50.16$ in, $Y_S = 0.00$ in, $C_T = 0.00$..... 303
Figure D-40. Baseline configuration, Run 053, $M\infty = 3.5$, $Re_\infty = 1.0x10^6$/ft, $\phi = 0.01°$, $X_S = 39.93$ in, $Y_S = 0.00$ in, $C_T = 0.00$..... 305
Figure D-41. Baseline configuration, Run 054, $M\infty = 3.5$, $Re_\infty = 1.0x10^6$/ft, $\phi = 120.06°$, $X_S = 40.17$ in, $Y_S = 0.00$ in, $C_T = 0.00$..... 307
Figure D-42. Baseline configuration, Run 055, $M\infty = 3.5$, $Re_\infty = 1.0x10^6$/ft, $\phi = 59.98°$, $X_S = 40.17$ in, $Y_S = 0.00$ in, $C_T = 0.00$..... 309
Figure D-43. Baseline configuration, Run 056, $M\infty = 3.5$, $Re_\infty = 1.0x10^6$/ft, $\phi = −0.07°$, $X_S = 40.17$ in, $Y_S = 0.00$ in, $C_T = 0.00$. 311
Figure D-44. Baseline configuration, Run 057, $M\infty = 3.5$, $Re_\infty = 1.0x10^7$/ft, $\phi = −0.07°$, $X_S = 25.16$ in, $Y_S = 0.00$ in, $C_T = 0.00$. 313
Figure D-45. Baseline configuration, Run 058, $M\infty = 3.5$, $Re_\infty = 1.0x10^7$/ft, $\phi = 59.98°$, $X_S = 25.16$ in, $Y_S = 0.00$ in, $C_T = 0.00$..... 315
Figure D-46. Baseline configuration, Run 059, $M\infty = 3.5$, $Re_\infty = 1.0x10^7$/ft, $\phi = 120.12°$, $X_S = 25.16$ in, $Y_S = 0.00$ in, $C_T = 0.00$..... 317
Figure D-47. Baseline configuration, Run 060, $M\infty = 3.5$, $Re_\infty = 1.0x10^6$/ft, $\phi = 179.95°$, $X_S = 25.16$ in, $Y_S = 0.00$ in, $C_T = 0.00$..... 319
Figure D-48. Baseline configuration, Run 065, $M\infty = 3.5$, $Re_\infty = 1.0x10^7$/ft, $\phi = −0.01°$, $X_S = 25.16$ in, $Y_S = −8.00$ in, $C_T = 0.00$. 321
Figure D-49. Baseline configuration, Run 067, $M\infty = 3.5$, $Re_\infty = 1.0x10^7$/ft, $\phi = 60.00°$, $X_S = 25.16$ in, $Y_S = –8.00$ in, $C_T = 0.00$..... 323
Figure D-50. Baseline configuration, Run 068, $M\infty = 3.5$, $Re_\infty = 1.0x10^6$/ft, $\phi = 120.02°$, $X_S = 25.16$ in, $Y_S = –8.00$ in, $C_T = 0.00$..... 325
Figure D-51. Baseline configuration, Run 069, $M\infty = 3.5$, $Re_\infty = 1.0x10^7$/ft, $\phi = 179.95°$, $X_S = 25.16$ in, $Y_S = –8.00$ in, $C_T = 0.00$..... 327
Figure D-52. Baseline configuration, Run 070, $M\infty = 3.5$, $Re_\infty = 1.0x10^6$/ft, $\phi = 179.95°$, $X_S = 40.16$ in, $Y_S = –8.00$ in, $C_T = 0.00$..... 329
Figure D-53. Baseline configuration, Run 073, $M\infty = 3.5$, $Re_\infty = 1.0x10^6$/ft, $\phi = 119.98°$, $X_S = 40.18$ in, $Y_S = –8.00$ in, $C_T = 0.00$..... 331

Figure D-54. Baseline configuration, Run 074, $M\infty = 3.5$, $Re_\infty = 1.0x10^7$/ft, $\phi = 59.96°$, $X_S = 40.18$ in, $Y_S = –8.00$ in, $C_T = 0.00$..... 333
Figure D-55. Baseline configuration, Run 075, $M\infty = 3.5$, $Re_\infty = 1.0x10^6$/ft, $\phi = 0.03°$, $X_S = 40.18$ in, $Y_S = –8.00$ in, $C_T = 0.00$..... 335
Figure D-56. Baseline configuration, Run 076, $M\infty = 3.5$, $Re_\infty = 1.0x10^7$/ft, $\phi = 0.03°$, $X_S = 40.18$ in, $Y_S = 7.99$ in, $C_T = 0.00$..... 337
Figure D-57. Baseline configuration, Run 077, $M\infty = 3.5$, $Re_\infty = 1.0x10^7$/ft, $\phi = 59.93°$, $X_S = 40.16$ in, $Y_S = 7.99$ in, $C_T = 0.00$..... 339
Figure D-58. Baseline configuration, Run 078, $M\infty = 3.5$, $Re_\infty = 1.0x10^6$/ft, $\phi = 119.98°$, $X_S = 40.16$ in, $Y_S = 7.95$ in, $C_T = 0.00$..... 341
Figure D-59. Baseline configuration, Run 079, $M\infty = 3.5$, $Re_\infty = 1.0x10^7$/ft, $\phi = −179.99°$, $X_S = 40.16$ in, $Y_S = 7.95$ in, $C_T = 0.00$. 343
Figure D-60. Baseline configuration, Run 080, $M\infty = 3.5$, $Re_\infty = 1.0x10^7$/ft, $\phi = −179.99°$, $X_S = 50.15$ in, $Y_S = 7.95$ in, $C_T = 0.00$. 345
Figure D-61. Baseline configuration, Run 081, $M\infty = 3.5$, $Re_\infty = 1.0x10^7$/ft, $\phi = 119.98°$, $X_S = 50.15$ in, $Y_S = 7.95$ in, $C_T = 0.00$..... 347
Figure D-62. Baseline configuration, Run 082, $M\infty = 3.5$, $Re_\infty = 1.0x10^7$/ft, $\phi = 59.94°$, $X_S = 50.15$ in, $Y_S = 7.95$ in, $C_T = 0.00$..... 349
Figure D-63. Baseline configuration, Run 083, $M\infty = 3.5$, $Re_\infty = 1.0x10^7$/ft, $\phi = 0.01°$, $X_S = 50.15$ in, $Y_S = 7.95$ in, $C_T = 0.00$..... 351
Figure D-64. Baseline configuration, Run 086, $M\infty = 4.6$, $Re_\infty = 1.1x10^7$/ft, $\phi = 0.01°$, $X_S = 25.17$ in, $Y_S = 0.00$ in, $C_T = 0.00$..... 353
Figure D-65. Baseline configuration, Run 087, $M\infty = 4.6$, $Re_\infty = 1.1x10^7$/ft, $\phi = 59.98°$, $X_S = 25.17$ in, $Y_S = 0.00$ in, $C_T = 0.00$..... 355
Figure D-66. Baseline configuration, Run 088, $M\infty = 4.6$, $Re_\infty = 1.1x10^7$/ft, $\phi = 119.96°$, $X_S = 25.17$ in, $Y_S = 0.00$ in, $C_T = 0.00$..... 357
Figure D-67. Baseline configuration, Run 089, $M\infty = 4.6$, $Re_\infty = 1.1x10^7$/ft, $\phi = 179.91°$, $X_S = 25.17$ in, $Y_S = 0.00$ in, $C_T = 0.00$..... 359
Figure D-68. Baseline configuration, Run 090, $M\infty = 4.6$, $Re_\infty = 1.1x10^7$/ft, $\phi = 0.01°$, $X_S = 40.15$ in, $Y_S = 0.00$ in, $C_T = 0.00$..... 361
Figure D-69. Baseline configuration, Run 091, $M\infty = 4.6$, $Re_\infty = 1.1x10^7$/ft, $\phi = 59.94°$, $X_S = 40.18$ in, $Y_S = 0.00$ in, $C_T = 0.00$..... 363
Figure D-70. Baseline configuration, Run 092, $M\infty = 4.6$, $Re_\infty = 1.1x10^7$/ft, $\phi = 119.98°$, $X_S = 40.18$ in, $Y_S = 0.00$ in, $C_T = 0.00$..... 365
Figure D-71. Baseline configuration, Run 093, $M\infty = 4.6$, $Re_\infty = 1.1x10^7$/ft, $\phi = 179.91°$, $X_S = 40.18$ in, $Y_S = 0.00$ in, $C_T = 0.00$..... 367
Figure D-72. Baseline configuration, Run 094, $M\infty = 4.6$, $Re_\infty = 1.1x10^7$/ft, $\phi = 179.91°$, $X_S = 50.14$ in, $Y_S = 0.00$ in, $C_T = 0.00$..... 369
Figure D-73. Baseline configuration, Run 095, $M\infty = 4.6$, $Re_\infty = 1.1x10^7$/ft, $\phi = 119.96°$, $X_S = 50.14$ in, $Y_S = 0.00$ in, $C_T = 0.00$..... 371
Figure D-74. Baseline configuration, Run 096, $M\infty = 4.6$, $Re_\infty = 1.1x10^7$/ft, $\phi = 59.90°$, $X_S = 50.14$ in, $Y_S = 0.00$ in, $C_T = 0.00$..... 373
Figure D-75. Baseline configuration, Run 097, $M\infty = 4.6$, $Re_\infty = 1.1x10^7$/ft, $\phi = −0.07°$, $X_S = 50.14$ in, $Y_S = 0.00$ in, $C_T = 0.00$. 375

Figure D-76. Baseline configuration, Run 098, $M\infty = 4.6$, $Re_\infty = 1.1x10^7$/ft, $\phi = -0.07°$, $X_S = 50.14$ in, $Y_S = 7.99$ in, $C_T = 0.00$. 377
Figure D-77. Baseline configuration, Run 099, $M\infty = 4.6$, $Re_\infty = 1.1x10^7$/ft, $\phi = 59.86°$, $X_S = 50.14$ in, $Y_S = 7.99$ in, $C_T = 0.00$..... 379
Figure D-78. Baseline configuration, Run 100, $M\infty = 4.6$, $Re_\infty = 1.1x10^7$/ft, $\phi = 120.06°$, $X_S = 50.14$ in, $Y_S = 7.99$ in, $C_T = 0.00$..... 381
Figure D-79. Baseline configuration, Run 101, $M\infty = 4.6$, $Re_\infty = 1.1x10^7$/ft, $\phi = 179.97°$, $X_S = 50.14$ in, $Y_S = 7.99$ in, $C_T = 0.00$..... 383
Figure D-80. Baseline configuration, Run 104, $M\infty = 4.6$, $Re_\infty = 1.5x10^7$/ft, $\phi = -0.03°$, $X_S = 25.19$ in, $Y_S = 0.00$ in, $C_T = 0.00$. 384
Figure D-81. Baseline configuration, Run 105, $M\infty = 4.6$, $Re_\infty = 1.5x10^7$/ft, $\phi = 59.94°$, $X_S = 25.19$ in, $Y_S = 0.00$ in, $C_T = 0.00$..... 386
Figure D-82. Baseline configuration, Run 106, $M\infty = 4.6$, $Re_\infty = 1.5x10^7$/ft, $\phi = 120.02°$, $X_S = 25.19$ in, $Y_S = 0.00$ in, $C_T = 0.00$..... 388
Figure D-83. Baseline configuration, Run 107, $M\infty = 4.6$, $Re_\infty = 1.5x10^7$/ft, $\phi = 179.93°$, $X_S = 25.19$ in, $Y_S = 0.00$ in, $C_T = 0.00$..... 390
Figure D-84. Baseline configuration, Run 108, $M\infty = 4.6$, $Re_\infty = 1.5x10^7$/ft, $\phi = 179.93°$, $X_S = 40.15$ in, $Y_S = 0.00$ in, $C_T = 0.00$..... 392
Figure D-85. Baseline configuration, Run 109, $M\infty = 4.6$, $Re_\infty = 1.5x10^7$/ft, $\phi = 119.98°$, $X_S = 40.15$ in, $Y_S = 0.00$ in, $C_T = 0.00$..... 394
Figure D-86. Baseline configuration, Run 110, $M\infty = 4.6$, $Re_\infty = 1.5x10^7$/ft, $\phi = 59.88°$, $X_S = 40.15$ in, $Y_S = 0.00$ in, $C_T = 0.00$..... 396
Figure D-87. Baseline configuration, Run 111, $M\infty = 4.6$, $Re_\infty = 1.5x10^7$/ft, $\phi = -0.01°$, $X_S = 40.09$ in, $Y_S = 0.00$ in, $C_T = 0.00$. 398
Figure D-88. Baseline configuration, Run 112, $M\infty = 4.6$, $Re_\infty = 1.5x10^7$/ft, $\phi = -0.01°$, $X_S = 50.19$ in, $Y_S = 0.00$ in, $C_T = 0.00$. 400
Figure D-89. Baseline configuration, Run 113, $M\infty = 4.6$, $Re_\infty = 1.5x10^7$/ft, $\phi = 59.96°$, $X_S = 50.19$ in, $Y_S = 0.00$ in, $C_T = 0.00$..... 402
Figure D-90. Baseline configuration, Run 114, $M\infty = 4.6$, $Re_\infty = 1.5x10^7$/ft, $\phi = 120.10°$, $X_S = 50.19$ in, $Y_S = 0.00$ in, $C_T = 0.00$..... 404
Figure D-91. Baseline configuration, Run 115, $M\infty = 4.6$, $Re_\infty = 1.5x10^7$/ft, $\phi = 179.97°$, $X_S = 50.19$ in, $Y_S = 0.00$ in, $C_T = 0.00$..... 406
Figure D-92. Baseline configuration, Run 116, $M\infty = 4.6$, $Re_\infty = 1.5x10^7$/ft, $\phi = 179.97°$, $X_S = 50.19$ in, $Y_S = 8.00$ in, $C_T = 0.00$..... 408
Figure D- 93. Baseline configuration, Run 117, $M\infty = 4.6$, $Re_\infty = 1.5x10^7$/ft, $\phi = 119.98°$, $X_S = 50.19$ in, $Y_S = 8.00$ in, $C_T = 0.00$..... 410
Figure D-94. Baseline configuration, Run 118, $M\infty = 4.6$, $Re_\infty = 1.5x10^7$/ft, $\phi = 59.90°$, $X_S = 50.19$ in, $Y_S = 8.00$ in, $C_T = 0.00$..... 412
Figure D-95. Baseline configuration, Run 119, $M\infty = 4.6$, $Re_\infty = 1.5x10^7$/ft, $\phi = 0.03°$, $X_S = 50.19$ in, $Y_S = 8.00$ in, $C_T = 0.00$..... 414
Figure D-96. Baseline configuration, Run 120, $M\infty = 4.6$, $Re_\infty = 1.5x10^7$/ft, $\phi = 0.03°$, $X_S = 25.16$ in, $Y_S = -8.00$ in, $C_T = 0.00$..... 416
Figure D-97. Baseline configuration, Run 121, $M\infty = 4.6$, $Re_\infty = 1.5x10^7$/ft, $\phi = 60.00°$, $X_S = 25.16$ in, $Y_S = -8.00$ in, $C_T = 0.00$..... 418

Figure D-98. Baseline configuration, Run 122, $M\infty$ = 4.6, Re_∞ = 1.5x10^7/ft, ϕ = 120.06°, X_S = 25.16 in, Y_S = –8.00 in, C_T = 0.00..... 420
Figure D-99. Baseline configuration, Run 123, $M\infty$ = 4.6, Re_∞ = 1.5x10^7/ft, ϕ = 179.93°, X_S = 25.16 in, Y_S = –8.00 in, C_T = 0.00..... 422
Figure D-100. Center nozzle configuration, Run 136, $M\infty$ = 2.4, Re_∞ = 1.0x10^7/ft, ϕ = −0.01°, X_S = 40.16 in, Y_S = 0.00 in, C_T = 3.96. 424
Figure D-101. Center nozzle configuration, Run 137, $M\infty$ = 2.4, Re_∞ = 1.0x10^7/ft, ϕ = −0.03°, X_S = 40.15 in, Y_S = 0.00 in, C_T = 3.01. 426
Figure D-102. Center nozzle configuration, Run 138, $M\infty$ = 2.4, Re_∞ = 1.0x10^7/ft, ϕ = 179.97°, X_S = 40.15 in, Y_S = 0.00 in, C_T = 3.02..... 428
Figure D-103. Center nozzle configuration, Run 139, $M\infty$ = 2.4, Re_∞ = 1.0x10^7/ft, ϕ = 179.97°, X_S = 40.15 in, Y_S = 0.00 in, C_T = 0.97..... 430
Figure D-104. Center nozzle configuration, Run 140, $M\infty$ = 2.4, Re_∞ = 1.0x10^6/ft, ϕ = −0.03°, X_S = 40.15 in, Y_S = 0.00 in, C_T = 0.97. 432
Figure D-105. Center nozzle configuration, Run 141, $M\infty$ = 2.4, Re_∞ = 1.0x10^7/ft, ϕ = −0.03°, X_S = 40.15 in, Y_S = 0.00 in, C_T = 1.98. 434
Figure D-106. Center nozzle configuration, Run 142, $M\infty$ = 2.4, Re_∞ = 1.0x10^6/ft, ϕ = −179.91°, X_S = 40.15 in, Y_S = 0.00 in, C_T = 1.97. 436
Figure D-107. Center nozzle configuration, Run 143, $M\infty$ = 2.4, Re_∞ = 1.0x10^6/ft, ϕ = −179.91°, X_S = 40.15 in, Y_S = 0.00 in, C_T = 0.47. 438
Figure D-108. Center nozzle configuration, Run 144, $M\infty$ = 2.4, Re_∞ = 1.0x10^6/ft, ϕ = 0.01°, X_S = 40.15 in, Y_S = 0.00 in, C_T = 0.46..... 440
Figure D-109. Center nozzle configuration, Run 145, $M\infty$ = 2.4, Re_∞ = 1.0x10^7/ft, ϕ = 0.01°, X_S = 40.15 in, Y_S = 0.00 in, C_T = 0.23..... 442
Figure D-110. Center nozzle configuration, Run 146, $M\infty$ = 2.4, Re_∞ = 1.0x10^7/ft, ϕ = 179.99°, X_S = 40.15 in, Y_S = 0.00 in, C_T = 0.23..... 444
Figure D-111. Center nozzle configuration, Run 148, $M\infty$ = 2.4, Re_∞ = 1.0x10^6/ft, ϕ = 179.99°, X_S = 40.15 in, Y_S = 0.00 in, C_T = 0.00..... 446
Figure D-112. Center nozzle configuration, Run 149, $M\infty$ = 2.4, Re_∞ = 1.0x10^6/ft, ϕ = −0.03°, X_S = 40.15 in, Y_S = 0.00 in, C_T = 0.00. 448
Figure D-113. Center nozzle configuration, Run 150, $M\infty$ = 3.5, Re_∞ = 1.0x10^7/ft, ϕ = −0.03°, X_S = 40.17 in, Y_S = 0.00 in, C_T = 2.99. 450
Figure D-114. Center nozzle configuration, Run 151, $M\infty$ = 3.5, Re_∞ = 1.0x10^6/ft, ϕ = −179.97°, X_S = 40.17 in, Y_S = 0.00 in, C_T = 2.98. 452
Figure D-115. Center nozzle configuration, Run 152, $M\infty$ = 3.5, Re_∞ = 1.0x10^7/ft, ϕ = −179.97°, X_S = 40.17 in, Y_S = 0.00 in, C_T = 1.97. 454
Figure D-116. Center nozzle configuration, Run 153, $M\infty$ = 3.5, Re_∞ = 1.0x10^6/ft, ϕ = −0.09°, X_S = 40.17 in, Y_S = 0.00 in, C_T = 1.96. 456
Figure D-117. Center nozzle configuration, Run 154, $M\infty$ = 3.5, Re_∞ = 1.0x10^7/ft, ϕ = −0.09°, X_S = 40.17 in, Y_S = 0.00 in, C_T = 0.92. 458
Figure D-118. Center nozzle configuration, Run 155, $M\infty$ = 3.5, Re_∞ = 1.0x10^7/ft, ϕ = 179.91°, X_S = 40.17 in, Y_S = 0.00 in, C_T = 0.94..... 460
Figure D-119. Center nozzle configuration, Run 156, $M\infty$ = 3.5, Re_∞ = 1.0x10^7/ft, ϕ = 179.93°, X_S = 40.17 in, Y_S = 0.00 in, C_T = 0.46..... 462

Figure D-120. Center nozzle configuration, Run 157, M_∞ = 3.5, Re_∞ = 1.0x10^6/ft, ϕ = 0.07°, X_S = 40.17 in, Y_S = 0.00 in, C_T = 0.45..... 464
Figure D-121. Center nozzle configuration, Run 159, M_∞ = 3.5, Re_∞ = 1.0x10^7/ft, ϕ = −0.01°, X_S = 40.17 in, Y_S = 0.00 in, C_T = 0.21. 466
Figure D-122. Center nozzle configuration, Run 160, M_∞ = 3.5, Re_∞ = 1.0x10^6/ft, ϕ = 179.93°, X_S = 40.17 in, Y_S = 0.00 in, C_T = 0.21..... 468
Figure D-123. Center nozzle configuration, Run 161, M_∞ = 3.5, Re_∞ = 1.0x10^6/ft, ϕ = 179.93°, X_S = 40.17 in, Y_S = 0.00 in, C_T = 0.00..... 470
Figure D-124. Center nozzle configuration, Run 162, M_∞ = 3.5, Re_∞ = 1.0x10^6/ft, ϕ = 0.03°, X_S = 40.17 in, Y_S = 0.00 in, C_T = 0.00..... 472
Figure D-125. Center nozzle configuration, Run 163, M_∞ = 4.6, Re_∞ = 1.5x10^7/ft, ϕ = 0.03°, X_S = 40.17 in, Y_S = 0.00 in, C_T = 2.97..... 474
Figure D-126. Center nozzle configuration, Run 164, M_∞ = 4.6, Re_∞ = 1.5x10^7/ft, ϕ = 179.93°, X_S = 40.17 in, Y_S = 0.00 in, C_T = 2.95..... 476
Figure D-127. Center nozzle configuration, Run 165, M_∞ = 4.6, Re_∞ = 1.5x10^7/ft, ϕ = 179.93°, X_S = 40.15 in, Y_S = 0.00 in, C_T = 1.98..... 478
Figure D-128. Center nozzle configuration, Run 166, M_∞ = 4.6, Re_∞ = 1.5x10^7/ft, ϕ = 0.03°, X_S = 40.15 in, Y_S = 0.00 in, C_T = 1.97..... 480
Figure D-129. Center nozzle configuration, Run 167, M_∞ = 4.6, Re_∞ = 1.5x10^7/ft, ϕ = 0.03°, X_S = 40.15 in, Y_S = 0.00 in, C_T = 0.96..... 482
Figure D-130. Center nozzle configuration, Run 168, M_∞ = 4.6, Re_∞ = 1.5x10^7/ft, ϕ = 179.95°, X_S = 40.15 in, Y_S = 0.00 in, C_T = 0.93..... 484
Figure D-131. Center nozzle configuration, Run 169, M_∞ = 4.6, Re_∞ = 1.5x10^7/ft, ϕ = 179.95°, X_S = 40.15 in, Y_S = 0.00 in, C_T = 0.46..... 486
Figure D-132. Center nozzle configuration, Run 170, M_∞ = 4.6, Re_∞ = 1.5x10^7/ft, ϕ = 0.03°, X_S = 40.15 in, Y_S = 0.00 in, C_T = 0.46..... 488
Figure D-133. Center nozzle configuration, Run 171, M_∞ = 4.6, Re_∞ = 1.5x10^7/ft, ϕ = 0.03°, X_S = 40.15 in, Y_S = 0.00 in, C_T = 0.22..... 490
Figure D-134. Center nozzle configuration, Run 172, M_∞ = 4.6, Re_∞ = 1.5x10^7/ft, ϕ = 179.91°, X_S = 40.15 in, Y_S = 0.00 in, C_T = 0.22..... 492
Figure D-135. Center nozzle configuration, Run 173, M_∞ = 4.6, Re_∞ = 1.5x10^7/ft, ϕ = 179.91°, X_S = 40.15 in, Y_S = 0.00 in, C_T = 0.00..... 494
Figure D-136. Center nozzle configuration, Run 174, M_∞ = 4.6, Re_∞ = 1.5x10^7/ft, ϕ = −0.07°, X_S = 40.15 in, Y_S = 0.00 in, C_T = 0.00. 496
Figure D-137. Tri-nozzle configuration, Run 180, M_∞ = 2.4, Re_∞ = 1.0x10^7/ft, ϕ = −0.01°, X_S = 40.15 in, Y_S = 0.00 in, C_T = 0.00. 498
Figure D-138. Tri-nozzle configuration, Run 181, M_∞ = 2.4, Re_∞ = 1.0x10^7/ft, ϕ = 179.97°, X_S = 40.15 in, Y_S = 0.00 in, C_T = 0.00..... 500
Figure D-139. Tri-nozzle configuration, Run 182, M_∞ = 2.4, Re_∞ = 1.0x10^6/ft, ϕ = 120.02°, X_S = 40.15 in, Y_S = 0.00 in, C_T = 0.00..... 502
Figure D-140. Tri-nozzle configuration, Run 183, M_∞ = 2.4, Re_∞ = 1.0x10^6/ft, ϕ = 59.98°, X_S = 40.15 in, Y_S = 0.00 in, C_T = 0.00..... 504
Figure D-141. Tri-nozzle configuration, Run 184, M_∞ = 3.5, Re_∞ = 1.0x10^7/ft, ϕ = 0.05°, X_S = 40.15 in, Y_S = 0.00 in, C_T = 0.00..... 506

Figure D-142. Tri-nozzle configuration, Run 185, M_∞ = 3.5, Re_∞ = 1.0x10^7/ft, ϕ = 59.88°, X_S = 40.15 in, Y_S = 0.00 in, C_T = 0.00..... 508
Figure D-143. Tri-nozzle configuration, Run 186, M_∞ = 3.5, Re_∞ = 1.0x10^7/ft, ϕ = 120.00°, X_S = 40.15 in, Y_S = 0.00 in, C_T = 0.00..... 510
Figure D-144. Tri-nozzle configuration, Run 187, M_∞ = 3.5, Re_∞ = 1.0x10^6/ft, ϕ = 179.95°, X_S = 40.15 in, Y_S = 0.00 in, C_T = 0.00..... 512
Figure D-145. Tri-nozzle configuration, Run 190, M_∞ = 2.4, Re_∞ = 1.0x10^7/ft, ϕ = −0.01°, X_S = 40.15 in, Y_S = 0.00 in, C_T = 2.94. 514
Figure D-146. Tri-nozzle configuration, Run 191, M_∞ = 2.4, Re_∞ = 1.0x10^6/ft, ϕ = 59.88°, X_S = 40.15 in, Y_S = 0.00 in, C_T = 2.92..... 516
Figure D-147. Tri-nozzle configuration, Run 192, M_∞ = 2.4, Re_∞ = 1.0x10^6/ft, ϕ = 120.00°, X_S = 40.15 in, Y_S = 0.00 in, C_T = 2.94..... 518
Figure D-148. Tri-nozzle configuration, Run 193, M_∞ = 2.4, Re_∞ = 1.0x10^6/ft, ϕ = −179.97°, X_S = 40.15 in, Y_S = 0.00 in, C_T = 2.96. 520
Figure D-149. Tri-nozzle configuration, Run 194, M_∞ = 2.4, Re_∞ = 1.0x10^7/ft, ϕ = −179.97°, X_S = 40.15 in, Y_S = 0.00 in, C_T = 1.94. 522
Figure D-150. Tri-nozzle configuration, Run 195, M_∞ = 2.4, Re_∞ = 1.0x10^7/ft, ϕ = 120.02°, X_S = 40.15 in, Y_S = 0.00 in, C_T = 1.93..... 524
Figure D-151. Tri-nozzle configuration, Run 196, M_∞ = 2.4, Re_∞ = 1.0x10^6/ft, ϕ = 59.88°, X_S = 40.15 in, Y_S = 0.00 in, C_T = 1.93..... 526
Figure D-152. Tri-nozzle configuration, Run 197, M_∞ = 2.4, Re_∞ = 1.0x10^6/ft, ϕ = −0.01°, X_S = 40.15 in, Y_S = 0.00 in, C_T = 1.94. 528
Figure D-153. Tri-nozzle configuration, Run 198, M_∞ = 2.4, Re_∞ = 1.0x10^7/ft, ϕ = −0.01°, X_S = 40.15 in, Y_S = 0.00 in, C_T = 0.94. 530
Figure D-154. Tri-nozzle configuration, Run 199, M_∞ = 2.4, Re_∞ = 1.0x10^6/ft, ϕ = 59.92°, X_S = 40.15 in, Y_S = 0.00 in, C_T = 0.94..... 532
Figure D-155. Tri-nozzle configuration, Run 200, M_∞ = 2.4, Re_∞ = 1.0x10^7/ft, ϕ = 120.00°, X_S = 40.15 in, Y_S = 0.00 in, C_T = 0.94..... 534
Figure D-156. Tri-nozzle configuration, Run 201, M_∞ = 2.4, Re_∞ = 1.0x10^7/ft, ϕ = 179.99°, X_S = 40.15 in, Y_S = 0.00 in, C_T = 0.94..... 536
Figure D-157. Tri-nozzle configuration, Run 202, M_∞ = 2.4, Re_∞ = 1.0x10^7/ft, ϕ = 179.99°, X_S = 40.15 in, Y_S = 0.00 in, C_T = 0.43..... 538
Figure D-158. Tri-nozzle configuration, Run 203, M_∞ = 2.4, Re_∞ = 1.0x10^7/ft, ϕ = −179.97°, X_S = 40.15 in, Y_S = 0.00 in, C_T = 0.44. 540
Figure D-159. Tri-nozzle configuration, Run 204, M_∞ = 2.4, Re_∞ = 1.0x10^6/ft, ϕ = 120.04°, X_S = 40.15 in, Y_S = 0.00 in, C_T = 0.43..... 542
Figure D-160. Tri-nozzle configuration, Run 205, M_∞ = 2.4, Re_∞ = 1.0x10^6/ft, ϕ = 59.88°, X_S = 40.15 in, Y_S = 0.00 in, C_T = 0.44..... 544
Figure D-161. Tri-nozzle configuration, Run 206, M_∞ = 2.4, Re_∞ = 1.0x10^7/ft, ϕ = −0.05°, X_S = 40.15 in, Y_S = 0.00 in, C_T = 0.43. 546
Figure D-162. Tri-nozzle configuration, Run 211, M_∞ = 4.6, Re_∞ = 1.5x10^7/ft, ϕ = −0.03°, X_S = 40.15 in, Y_S = 0.00 in, C_T = 2.93. 548
Figure D-163. Tri-nozzle configuration, Run 212, M_∞ = 4.6, Re_∞ = 1.5x10^7/ft, ϕ = 59.96°, X_S = 40.15 in, Y_S = 0.00 in, C_T = 2.94..... 550

Figure D-164. Tri-nozzle configuration, Run 213, M_∞ = 4.6, Re_∞ = 1.5x10^7/ft, ϕ = 120.04°, X_S = 40.15 in, Y_S = 0.00 in, C_T = 2.87..... 552
Figure D-165. Tri-nozzle configuration, Run 214, M_∞ = 4.6, Re_∞ = 1.5x10^7/ft, ϕ = 179.99°, X_S = 40.15 in, Y_S = 0.00 in, C_T = 2.96..... 554
Figure D-166. Tri-nozzle configuration, Run 217, M_∞ = 2.4, Re_∞ = 1.0x10^6/ft, ϕ = −0.03°, X_S = 40.15 in, Y_S = 0.00 in, C_T = 0.47. 556
Figure D-167. Tri-nozzle configuration, Run 218, M_∞ = 2.4, Re_∞ = 1.0x10^6/ft, ϕ = 59.88°, X_S = 40.15 in, Y_S = 0.00 in, C_T = 0.48..... 558
Figure D-168. Tri-nozzle configuration, Run 219, M_∞ = 2.4, Re_∞ = 1.0x10^7/ft, ϕ = 120.02°, X_S = 40.15 in, Y_S = 0.00 in, C_T = 0.47..... 560
Figure D-169. Tri-nozzle configuration, Run 220, M_∞ = 2.4, Re_∞ = 1.0x10^6/ft, ϕ = 179.95°, X_S = 40.15 in, Y_S = 0.00 in, C_T = 0.48..... 562
Figure D-170. Tri-nozzle configuration, Run 221, M_∞ = 2.4, Re_∞ = 1.0x10^6/ft, ϕ = −0.01°, X_S = 40.15 in, Y_S = 0.00 in, C_T = 0.24. 564
Figure D-171. Tri-nozzle configuration, Run 222, M_∞ = 3.5, Re_∞ = 1.0x10^6/ft, ϕ = −0.01°, X_S = 40.15 in, Y_S = 0.00 in, C_T = 2.94. 566
Figure D-172. Tri-nozzle configuration, Run 223, M_∞ = 3.5, Re_∞ = 1.0x10^7/ft, ϕ = 59.90°, X_S = 40.15 in, Y_S = 0.00 in, C_T = 2.95..... 568
Figure D-173. Tri-nozzle configuration, Run 224, M_∞ = 3.5, Re_∞ = 1.0x10^7/ft, ϕ = 120.06°, X_S = 40.15 in, Y_S = 0.00 in, C_T = 2.97..... 570
Figure D-174. Tri-nozzle configuration, Run 225, M_∞ = 3.5, Re_∞ = 1.0x10^6/ft, ϕ = 179.97°, X_S = 40.15 in, Y_S = 0.00 in, C_T = 2.97..... 572
Figure D-175. Tri-nozzle configuration, Run 226, M_∞ = 3.5, Re_∞ = 1.0x10^6/ft, ϕ = 179.97°, X_S = 40.15 in, Y_S = 0.00 in, C_T = 1.96..... 574
Figure D-176. Tri-nozzle configuration, Run 227, M_∞ = 3.5, Re_∞ = 1.0x10^6/ft, ϕ = 120.04°, X_S = 40.15 in, Y_S = 0.00 in, C_T = 1.95..... 576
Figure D-177. Tri-nozzle configuration, Run 228, M_∞ = 3.5, Re_∞ = 1.0x10^7/ft, ϕ = 59.96°, X_S = 40.15 in, Y_S = 0.00 in, C_T = 1.94..... 578
Figure D-178. Tri-nozzle configuration, Run 229, M_∞ = 3.5, Re_∞ = 1.0x10^7/ft, ϕ = −0.01°, X_S = 40.15 in, Y_S = 0.00 in, C_T = 1.94. 580
Figure D-179. Tri-nozzle configuration, Run 230, M_∞ = 3.5, Re_∞ = 1.0x10^7/ft, ϕ = −0.03°, X_S = 40.15 in, Y_S = 0.00 in, C_T = 0.96. 582
Figure D-180. Tri-nozzle configuration, Run 233, M_∞ = 3.5, Re_∞ = 1.0x10^6/ft, ϕ = 59.90°, X_S = 40.15 in, Y_S = 0.00 in, C_T = 0.97..... 584
Figure D-181. Tri-nozzle configuration, Run 234, M_∞ = 3.5, Re_∞ = 1.0x10^7/ft, ϕ = −0.05°, X_S = 40.15 in, Y_S = 0.00 in, C_T = 0.96. 586
Figure D-182. Tri-nozzle configuration, Run 235, M_∞ = 3.5, Re_∞ = 1.0x10^7/ft, ϕ = 120.06°, X_S = 40.15 in, Y_S = 0.00 in, C_T = 0.96..... 588
Figure D-183. Tri-nozzle configuration, Run 236, M_∞ = 3.5, Re_∞ = 1.0x10^6/ft, ϕ = 179.95°, X_S = 40.15 in, Y_S = 0.00 in, C_T = 0.97..... 590
Figure D-184. Tri-nozzle configuration, Run 237, M_∞ = 3.5, Re_∞ = 1.0x10^7/ft, ϕ = 179.95°, X_S = 40.15 in, Y_S = 0.00 in, C_T = 0.48..... 592
Figure D-185. Tri-nozzle configuration, Run 238, M_∞ = 3.5, Re_∞ = 1.0x10^6/ft, ϕ = 120.00°, X_S = 40.15 in, Y_S = 0.00 in, C_T = 0.47..... 594

Figure D-186. Tri-nozzle configuration, Run 239, M_∞ = 3.5, Re_∞ = 1.0x10^7/ft, ϕ = 59.94°, X_S = 40.15 in, Y_S = 0.00 in, C_T = 0.46..... 596
Figure D-187. Tri-nozzle configuration, Run 240, M_∞ = 3.5, Re_∞ = 1.0x10^6/ft, ϕ = −0.05°, X_S = 40.15 in, Y_S = 0.00 in, C_T = 0.46. 598
Figure D-188. Tri-nozzle configuration, Run 241, M_∞ = 3.5, Re_∞ = 1.0x10^7/ft, ϕ = −0.05°, X_S = 40.15 in, Y_S = 0.00 in, C_T = 0.23. 600
Figure D-189. Tri-nozzle configuration, Run 242, M_∞ = 4.6, Re_∞ = 1.5x10^7/ft, ϕ = −0.05°, X_S = 40.15 in, Y_S = 0.00 in, C_T = 1.96. 602
Figure D-190. Tri-nozzle configuration, Run 243, M_∞ = 4.6, Re_∞ = 1.5x10^7/ft, ϕ = 59.94°, X_S = 40.15 in, Y_S = 0.00 in, C_T = 1.96..... 604
Figure D-191. Tri-nozzle configuration, Run 244, M_∞ = 4.6, Re_∞ = 1.5x10^7/ft, ϕ = 120.06°, X_S = 40.15 in, Y_S = 0.00 in, C_T = 1.96..... 606
Figure D-192. Tri-nozzle configuration, Run 245, M_∞ = 4.6, Re_∞ = 1.5x10^7/ft, ϕ = −179.99°, X_S = 40.15 in, Y_S = 0.00 in, C_T = 1.96. 608
Figure D-193. Tri-nozzle configuration, Run 247, M_∞ = 4.6, Re_∞ = 1.5x10^7/ft, ϕ = −0.03°, X_S = 40.15 in, Y_S = 0.00 in, C_T = 1.92. 610
Figure D-194. Tri-nozzle configuration, Run 248, M_∞ = 4.6, Re_∞ = 1.5x10^7/ft, ϕ = 179.99°, X_S = 40.15 in, Y_S = 0.00 in, C_T = 1.93..... 612
Figure D-195. Tri-nozzle configuration, Run 249, M_∞ = 4.6, Re_∞ = 1.5x10^7/ft, ϕ = 179.99°, X_S = 40.15 in, Y_S = 0.00 in, C_T = 0.90..... 614
Figure D-196. Tri-nozzle configuration, Run 250, M_∞ = 4.6, Re_∞ = 1.5x10^7/ft, ϕ = 120.04°, X_S = 40.15 in, Y_S = 0.00 in, C_T = 0.90..... 616
Figure D-197. Tri-nozzle configuration, Run 251, M_∞ = 4.6, Re_∞ = 1.5x10^7/ft, ϕ = 59.98°, X_S = 40.15 in, Y_S = 0.00 in, C_T = 0.89..... 618
Figure D-198. Tri-nozzle configuration, Run 252, M_∞ = 4.6, Re_∞ = 1.5x10^7/ft, ϕ = −0.03°, X_S = 40.15 in, Y_S = 0.00 in, C_T = 0.90. 620
Figure D-199. Tri-nozzle configuration, Run 253, M_∞ = 4.6, Re_∞ = 1.5x10^7/ft, ϕ = −0.03°, X_S = 40.15 in, Y_S = 0.00 in, C_T = 0.43. 622
Figure D-200. Tri-nozzle configuration, Run 254, M_∞ = 4.6, Re_∞ = 1.5x10^7/ft, ϕ = 59.94°, X_S = 40.15 in, Y_S = 0.00 in, C_T = 0.43..... 624
Figure D-201. Tri-nozzle configuration, Run 255, M_∞ = 4.6, Re_∞ = 1.5x10^7/ft, ϕ = 120.02°, X_S = 40.15 in, Y_S = 0.00 in, C_T = 0.42..... 626
Figure D-202. Tri-nozzle configuration, Run 256, M_∞ = 4.6, Re_∞ = 1.5x10^7/ft, ϕ = 179.95°, X_S = 40.15 in, Y_S = 0.00 in, C_T = 0.43..... 628
Figure D-203. Tri-nozzle configuration, Run 257, M_∞ = 4.6, Re_∞ = 1.5x10^7/ft, ϕ = −0.03°, X_S = 40.15 in, Y_S = 0.00 in, C_T = 0.20. 630
Figure D-204. Tri-nozzle configuration, Run 258, M_∞ = 4.6, Re_∞ = 1.5x10^7/ft, ϕ = −0.03°, X_S = 40.15 in, Y_S = 0.00 in, C_T = 0.00. 632
Figure D-205. Tri-nozzle configuration, Run 259, M_∞ = 4.6, Re_∞ = 1.5x10^7/ft, ϕ = 59.90°, X_S = 40.15 in, Y_S = 0.00 in, C_T = 0.00..... 634
Figure D-206. Tri-nozzle configuration, Run 260, M_∞ = 4.6, Re_∞ = 1.5x10^7/ft, ϕ = 120.00°, X_S = 40.15 in, Y_S = 0.00 in, C_T = 0.00..... 636
Figure D-207. Tri-nozzle configuration, Run 261, M_∞ = 4.6, Re_∞ = 1.5x10^7/ft, ϕ = 179.95°, X_S = 40.15 in, Y_S = 0.00 in, C_T = 0.00..... 638

Figure D-208. Tri-nozzle configuration, Run 262, M_∞ = 4.6, Re_∞ = 1.5x10^7/ft, ϕ = 0.01°, X_S = 40.15 in, Y_S = 0.00 in, C_T = 2.92..... 640
Figure D-209. Tri-nozzle configuration, Run 263, M_∞ = 4.6, Re_∞ = 1.5x10^7/ft, ϕ = −179.95°, X_S = 40.15 in, Y_S = 0.00 in, C_T = 2.94. 642
Figure D-210. Tri-nozzle configuration, Run 265, M_∞ = 3.5, Re_∞ = 1.0x10^6/ft, ϕ = −0.05°, X_S = 40.15 in, Y_S = 0.00 in, C_T = 0.91. 644
Figure D-211. Tri-nozzle configuration, Run 266, M_∞ = 3.5, Re_∞ = 1.0x10^6/ft, ϕ = −0.05°, X_S = 40.15 in, Y_S = 0.00 in, C_T = 0.44. 646
Figure D-212. Baseline configuration, Run 271, M_∞ = 2.4, Re_∞ = 1.0x10^6/ft, ϕ = −0.03°, X_S = 40.16 in, Y_S = 0.00 in, C_T = 0.00. 648
Figure D-213. Baseline configuration, Run 272, M_∞ = 2.4, Re_∞ = 1.0x10^6/ft, ϕ = 59.92°, X_S = 40.16 in, Y_S = 0.00 in, C_T = 0.00..... 650
Figure D-214. Baseline configuration, Run 273, M_∞ = 2.4, Re_∞ = 1.0x10^7/ft, ϕ = 120.00°, X_S = 40.16 in, Y_S = 0.00 in, C_T = 0.00..... 652
Figure D-215. Baseline configuration, Run 0274, M_∞ = 2.4, Re_∞ = 1.0x10^6/ft, ϕ = 179.99°, X_S = 40.16 in, Y_S = 0.00 in, C_T = 0.00..... 654
Figure D-216. Baseline configuration, Run 276, M_∞ = 3.5, Re_∞ = 1.0x10^7/ft, ϕ = 179.99°, X_S = 40.16 in, Y_S = 0.00 in, C_T = 0.00..... 656
Figure D-217. Baseline configuration, Run 277, M_∞ = 3.5, Re_∞ = 1.0x10^6/ft, ϕ = 120.00°, X_S = 40.16 in, Y_S = 0.00 in, C_T = 0.00..... 658
Figure D-218. Baseline configuration, Run 278, M_∞ = 3.5, Re_∞ = 1.0x10^7/ft, ϕ = 59.96°, X_S = 40.16 in, Y_S = 0.00 in, C_T = 0.00..... 660
Figure D-219. Baseline configuration, Run 279, M_∞ = 3.5, Re_∞ = 1.0x10^7/ft, ϕ = −0.05°, X_S = 40.16 in, Y_S = 0.00 in, C_T = 0.00. 662
Figure D-220. Baseline configuration, Run 280, M_∞ = 4.6, Re_∞ = 1.5x10^7/ft, ϕ = −0.05°, X_S = 40.16 in, Y_S = 0.00 in, C_T = 0.00. 664
Figure D-221. Baseline configuration, Run 281, M_∞ = 4.6, Re_∞ = 1.5x10^7/ft, ϕ = 59.92°, X_S = 40.16 in, Y_S = 0.00 in, C_T = 0.00..... 666
Figure D-222. Baseline configuration, Run 282, M_∞ = 4.6, Re_∞ = 1.5x10^7/ft, ϕ = 120.02°, X_S = 40.16 in, Y_S = 0.00 in, C_T = 0.00..... 668
Figure D-223. Baseline configuration, Run 283, M_∞ = 4.6, Re_∞ = 1.5x10^7/ft, ϕ = 179.95°, X_S = 40.16 in, Y_S = 0.00 in, C_T = 0.00..... 670
Figure D-224. Quad-nozzle configuration, Run 288, M_∞ = 2.4, Re_∞ = 1.0x10^7/ft, ϕ = −0.03°, X_S = 40.17 in, Y_S = 0.00 in, C_T = 1.92. 672
Figure D-225. Quad-nozzle configuration, Run 289, M_∞ = 2.4, Re_∞ = 1.0x10^7/ft, ϕ = 59.98°, X_S = 40.17 in, Y_S = 0.00 in, C_T = 1.93..... 674
Figure D-226. Quad-nozzle configuration, Run 290, M_∞ = 2.4, Re_∞ = 1.0x10^7/ft, ϕ = 120.04°, X_S = 40.17 in, Y_S = 0.00 in, C_T = 1.94..... 676
Figure D-227. Quad-nozzle configuration, Run 291, M_∞ = 2.4, Re_∞ = 1.0x10^6/ft, ϕ = −179.95°, X_S = 40.17 in, Y_S = 0.00 in, C_T = 1.93. 678
Figure D-228. Quad-nozzle configuration, Run 293, M_∞ = 2.4, Re_∞ = 1.0x10^7/ft, ϕ = 179.97°, X_S = 40.16 in, Y_S = 0.00 in, C_T = 0.94..... 680
Figure D-229. Quad-nozzle configuration, Run 294, M_∞ = 2.4, Re_∞ = 1.0x10^6/ft, ϕ = 120.02°, X_S = 40.16 in, Y_S = 0.00 in, C_T = 0.95..... 682

Figure D-230. Quad-nozzle configuration, Run 295, $M\infty$ = 2.4, Re_∞ = 1.0x10^7/ft, ϕ = 59.96°, X_S = 40.16 in, Y_S = 0.00 in, C_T = 0.95..... 684
Figure D-231. Quad-nozzle configuration, Run 296, $M\infty$ = 2.4, Re_∞ = 1.0x10^7/ft, ϕ = −0.05°, X_S = 40.16 in, Y_S = 0.00 in, C_T = 0.94. 686
Figure D-232. Quad-nozzle configuration, Run 298, $M\infty$ = 3.5, Re_∞ = 1.0x10^7/ft, ϕ = 0.01°, X_S = 40.16 in, Y_S = 0.00 in, C_T = 1.92..... 688
Figure D-233. Quad-nozzle configuration, Run 299, $M\infty$ = 3.5, Re_∞ = 1.0x10^7/ft, ϕ = 59.92°, X_S = 40.16 in, Y_S = 0.00 in, C_T = 1.92..... 690
Figure D-234. Quad-nozzle configuration, Run 300, $M\infty$ = 3.5, Re_∞ = 1.0x10^6/ft, ϕ = 120.02°, X_S = 40.16 in, Y_S = 0.00 in, C_T = 1.92..... 692
Figure D-235. Quad-nozzle configuration, Run 301, $M\infty$ = 3.5, Re_∞ = 1.0x10^7/ft, ϕ = 179.95°, X_S = 40.16 in, Y_S = 0.00 in, C_T = 1.93..... 694
Figure D-236. Quad-nozzle configuration, Run 302, $M\infty$ = 3.5, Re_∞ = 1.0x10^7/ft, ϕ = 179.95°, X_S = 40.16 in, Y_S = 0.00 in, C_T = 0.91..... 696
Figure D-237. Quad-nozzle configuration, Run 303, $M\infty$ = 3.5, Re_∞ = 1.0x10^7/ft, ϕ = 120.08°, X_S = 40.16 in, Y_S = 0.00 in, C_T = 0.90..... 698
Figure D-238. Quad-nozzle configuration, Run 304, $M\infty$ = 3.5, Re_∞ = 1.0x10^7/ft, ϕ = 59.94°, X_S = 40.16 in, Y_S = 0.00 in, C_T = 0.90..... 700
Figure D-239. Quad-nozzle configuration, Run 305, $M\infty$ = 3.5, Re_∞ = 1.0x10^6/ft, ϕ = −0.03°, X_S = 40.16 in, Y_S = 0.00 in, C_T = 0.90. 702
Figure D-240. Quad-nozzle configuration, Run 307, $M\infty$ = 4.6, Re_∞ = 1.5x10^7/ft, ϕ = 0.05°, X_S = 40.17 in, Y_S = 0.00 in, C_T = 1.92..... 704
Figure D-241. Quad-nozzle configuration, Run 309, $M\infty$ = 4.6, Re_∞ = 1.5x10^7/ft, ϕ = 59.88°, X_S = 40.17 in, Y_S = 0.00 in, C_T = 1.92..... 706
Figure D-242. Quad-nozzle configuration, Run 310, $M\infty$ = 4.6, Re_∞ = 1.5x10^7/ft, ϕ = 120.02°, X_S = 40.17 in, Y_S = 0.00 in, C_T = 1.92..... 708
Figure D-243. Quad-nozzle configuration, Run 311, $M\infty$ = 4.6, Re_∞ = 1.5x10^7/ft, ϕ = −179.99°, X_S = 40.17 in, Y_S = 0.00 in, C_T = 1.93. 710
Figure D-244. Quad-nozzle configuration, Run 312, $M\infty$ = 4.6, Re_∞ = 1.5x10^7/ft, ϕ = −179.97°, X_S = 40.17 in, Y_S = 0.00 in, C_T = 0.92. 712
Figure D-245. Quad-nozzle configuration, Run 313, $M\infty$ = 4.6, Re_∞ = 1.5x10^7/ft, ϕ = 120.04°, X_S = 40.17 in, Y_S = 0.00 in, C_T = 0.92..... 714
Figure D-246. Quad-nozzle configuration, Run 314, $M\infty$ = 4.6, Re_∞ = 1.5x10^7/ft, ϕ = 59.98°, X_S = 40.17 in, Y_S = 0.00 in, C_T = 0.92..... 716
Figure D-247. Quad-nozzle configuration, Run 315, $M\infty$ = 4.6, Re_∞ = 1.5x10^7/ft, ϕ = 0.05°, X_S = 40.17 in, Y_S = 0.00 in, C_T = 0.91..... 718

Figure E-1. Baseline configuration, Run 013, $M\infty$ = 2.4, Re_∞ = 1.0x10^6/ft, ϕ = 0.03°, X_S = 25.16 in, Y_S = 0.04 in, C_T = 0.00..... 721
Figure E-2. Baseline configuration, Run 014, $M\infty$ = 2.4, Re_∞ = 1.0x10^6/ft, ϕ = 60.02°, X_S = 25.16 in, Y_S = 0.00 in, C_T = 0.00..... 722
Figure E-3. Baseline configuration, Run 016, $M\infty$ = 2.4, Re_∞ = 1.0x10^6/ft, ϕ = 0.05°, X_S = 25.16 in, Y_S = 0.00 in, C_T = 0.00..... 723
Figure E-4. Baseline configuration, Run 017, $M\infty$ = 2.4, Re_∞ = 1.0x10^6/ft, ϕ = 59.94°, X_S = 25.16 in, Y_S = 0.00 in, C_T = 0.00..... 724

Figure E-5. Baseline configuration, Run 018, $M\infty = 2.4$, $Re_\infty = 1.0x10^6$/ft, $\phi = 119.90°$, $X_S = 25.16$ in, $Y_S = 0.00$ in, $C_T = 0.00$ 725
Figure E-6. Baseline configuration, Run 019, $M\infty = 2.4$, $Re_\infty = 1.0x10^6$/ft, $\phi = 179.93°$, $X_S = 25.16$ in, $Y_S = 0.00$ in, $C_T = 0.00$ 726
Figure E-7. Baseline configuration, Run 020, $M\infty = 2.4$, $Re_\infty = 1.0x10^6$/ft, $\phi = 0.01°$, $X_S = 39.93$ in, $Y_S = 0.00$ in, $C_T = 0.00$ 727
Figure E-8. Baseline configuration, Run 021, $M\infty = 2.4$, $Re_\infty = 1.0x10^6$/ft, $\phi = 59.94°$, $X_S = 39.93$ in, $Y_S = 0.00$ in, $C_T = 0.00$ 728
Figure E-9. Baseline configuration, Run 022, $M\infty = 2.4$, $Re_\infty = 1.0x10^6$/ft, $\phi = 120.00°$, $X_S = 39.93$ in, $Y_S = 0.00$ in, $C_T = 0.00$ 729
Figure E-10. Baseline configuration, Run 023, $M\infty = 2.4$, $Re_\infty = 1.0x10^6$/ft, $\phi = 179.99°$, $X_S = 39.93$ in, $Y_S = 0.00$ in, $C_T = 0.00$ 730
Figure E-11. Baseline configuration, Run 024, $M\infty = 2.4$, $Re_\infty = 1.0x10^6$/ft, $\phi = 0.01°$, $X_S = 39.93$ in, $Y_S = 0.00$ in, $C_T = 0.00$ 731
Figure E-12. Baseline configuration, Run 025, $M\infty = 2.4$, $Re_\infty = 1.0x10^6$/ft, $\phi = 60.08°$, $X_S = 39.93$ in, $Y_S = 0.00$ in, $C_T = 0.00$ 732
Figure E-13. Baseline configuration, Run 026, $M\infty = 2.4$, $Re_\infty = 1.0x10^6$/ft, $\phi = 0.03°$, $X_S = 50.17$ in, $Y_S = 0.00$ in, $C_T = 0.00$ 733
Figure E-14. Baseline configuration, Run 027, $M\infty = 2.4$, $Re_\infty = 1.0x10^6$/ft, $\phi = 60.08°$, $X_S = 50.17$ in, $Y_S = 0.00$ in, $C_T = 0.00$ 734
Figure E-15. Baseline configuration, Run 028, $M\infty = 2.4$, $Re_\infty = 1.0x10^6$/ft, $\phi = 120.06°$, $X_S = 50.17$ in, $Y_S = 0.00$ in, $C_T = 0.00$ 735
Figure E-16. Baseline configuration, Run 029, $M\infty = 2.4$, $Re_\infty = 1.0x10^6$/ft, $\phi = 179.91°$, $X_S = 50.17$ in, $Y_S = 0.00$ in, $C_T = 0.00$ 736
Figure E-17. Baseline configuration, Run 030, $M\infty = 2.4$, $Re_\infty = 1.0x10^6$/ft, $\phi = 179.91°$, $X_S = 25.18$ in, $Y_S = 0.00$ in, $C_T = 0.00$ 737
Figure E-18. Baseline configuration, Run 031, $M\infty = 2.4$, $Re_\infty = 1.0x10^6$/ft, $\phi = 119.92°$, $X_S = 25.18$ in, $Y_S = 0.00$ in, $C_T = 0.00$ 738
Figure E-19. Baseline configuration, Run 032, $M\infty = 2.4$, $Re_\infty = 1.0x10^6$/ft, $\phi = 59.98°$, $X_S = 25.18$ in, $Y_S = 0.00$ in, $C_T = 0.00$ 739
Figure E-20. Baseline configuration, Run 033, $M\infty = 2.4$, $Re_\infty = 1.0x10^6$/ft, $\phi = 0.05°$, $X_S = 25.18$ in, $Y_S = 0.00$ in, $C_T = 0.00$ 740
Figure E-21. Baseline configuration, Run 034, $M\infty = 2.4$, $Re_\infty = 1.0x10^6$/ft, $\phi = 0.05°$, $X_S = 25.18$ in, $Y_S = 7.99$ in, $C_T = 0.00$ 741
Figure E-22. Baseline configuration, Run 035, $M\infty = 2.4$, $Re_\infty = 1.0x10^6$/ft, $\phi = 60.08°$, $X_S = 25.18$ in, $Y_S = 7.99$ in, $C_T = 0.00$ 742
Figure E-23. Baseline configuration, Run 036, $M\infty = 2.4$, $Re_\infty = 1.0x10^6$/ft, $\phi = 119.90°$, $X_S = 25.18$ in, $Y_S = 7.99$ in, $C_T = 0.00$ 743
Figure E-24. Baseline configuration, Run 037, $M\infty = 2.4$, $Re_\infty = 1.0x10^6$/ft, $\phi = 179.95°$, $X_S = 25.18$ in, $Y_S = 7.99$ in, $C_T = 0.00$ 744
Figure E-25. Baseline configuration, Run 038, $M\infty = 2.4$, $Re_\infty = 1.0x10^6$/ft, $\phi = 179.95°$, $X_S = 40.19$ in, $Y_S = 7.99$ in, $C_T = 0.00$ 745
Figure E-26. Baseline configuration, Run 039, $M\infty = 2.4$, $Re_\infty = 1.0x10^6$/ft, $\phi = 119.90°$, $X_S = 40.19$ in, $Y_S = 7.99$ in, $C_T = 0.00$ 746

Figure E-27. Baseline configuration, Run 040, $M\infty = 2.4$, $Re_\infty = 1.0x10^6$/ft, $\phi = 59.98°$, $X_S = 40.19$ in, $Y_S = 7.99$ in, $C_T = 0.00$..... 747
Figure E-28. Baseline configuration, Run 041, $M\infty = 2.4$, $Re_\infty = 1.0x10^6$/ft, $\phi = 0.05°$, $X_S = 40.19$ in, $Y_S = 7.99$ in, $C_T = 0.00$..... 748
Figure E-29. Baseline configuration, Run 042, $M\infty = 2.4$, $Re_\infty = 1.0x10^6$/ft, $\phi = -0.05°$, $X_S = 40.19$ in, $Y_S = -8.00$ in, $C_T = 0.00$. 749
Figure E-30. Baseline configuration, Run 043, $M\infty = 2.4$, $Re_\infty = 1.0x10^6$/ft, $\phi = 59.92°$, $X_S = 40.19$ in, $Y_S = -8.00$ in, $C_T = 0.00$. 750
Figure E-31. Baseline configuration, Run 044, $M\infty = 2.4$, $Re_\infty = 1.0x10^6$/ft, $\phi = 119.90°$, $X_S = 40.19$ in, $Y_S = –8.00$ in, $C_T = 0.00$..... 751
Figure E-32. Baseline configuration, Run 045, $M\infty = 2.4$, $Re_\infty = 1.0x10^6$/ft, $\phi = 179.95°$, $X_S = 40.19$ in, $Y_S = –8.00$ in, $C_T = 0.00$..... 752
Figure E-33. Baseline configuration, Run 046, $M\infty = 2.4$, $Re_\infty = 1.0x10^6$/ft, $\phi = 179.95°$, $X_S = 50.16$ in, $Y_S = –8.00$ in, $C_T = 0.00$..... 753
Figure E-34. Baseline configuration, Run 047, $M\infty = 2.4$, $Re_\infty = 1.0x10^6$/ft, $\phi = 119.92°$, $X_S = 50.16$ in, $Y_S = –8.00$ in, $C_T = 0.00$..... 754
Figure E-35. Baseline configuration, Run 048, $M\infty = 2.4$, $Re_\infty = 1.0x10^6$/ft, $\phi = 59.98°$, $X_S = 50.16$ in, $Y_S = –8.00$ in, $C_T = 0.00$..... 755
Figure E-36. Baseline configuration, Run 049, $M\infty = 2.4$, $Re_\infty = 1.0x10^6$/ft, $\phi = 0.05°$, $X_S = 50.16$ in, $Y_S = –8.00$ in, $C_T = 0.00$..... 756
Figure E-37. Baseline configuration, Run 050, $M\infty = 3.5$, $Re_\infty = 1.0x10^6$/ft, $\phi = 60.02°$, $X_S = 50.16$ in, $Y_S = 0.00$ in, $C_T = 0.00$..... 757
Figure E-38. Baseline configuration, Run 051, $M\infty = 3.5$, $Re_\infty = 1.0x10^6$/ft, $\phi = 119.94°$, $X_S = 50.16$ in, $Y_S = 0.00$ in, $C_T = 0.00$..... 758
Figure E-39. Baseline configuration, Run 052, $M\infty = 3.5$, $Re_\infty = 1.0x10^6$/ft, $\phi = 179.99°$, $X_S = 50.16$ in, $Y_S = 0.00$ in, $C_T = 0.00$..... 759
Figure E-40. Baseline configuration, Run 053, $M\infty = 3.5$, $Re_\infty = 1.0x10^6$/ft, $\phi = 0.01°$, $X_S = 39.93$ in, $Y_S = 0.00$ in, $C_T = 0.00$..... 760
Figure E-41. Baseline configuration, Run 054, $M\infty = 3.5$, $Re_\infty = 1.0x10^6$/ft, $\phi = 120.06°$, $X_S = 40.17$ in, $Y_S = 0.00$ in, $C_T = 0.00$..... 761
Figure E-42. Baseline configuration, Run 055, $M\infty = 3.5$, $Re_\infty = 1.0x10^6$/ft, $\phi = 59.98°$, $X_S = 40.17$ in, $Y_S = 0.00$ in, $C_T = 0.00$..... 762
Figure E-43. Baseline configuration, Run 056, $M\infty = 3.5$, $Re_\infty = 1.0x10^6$/ft, $\phi = -0.07°$, $X_S = 40.17$ in, $Y_S = 0.00$ in, $C_T = 0.00$. 763
Figure E-44. Baseline configuration, Run 057, $M\infty = 3.5$, $Re_\infty = 1.0x10^6$/ft, $\phi = -0.07°$, $X_S = 25.16$ in, $Y_S = 0.00$ in, $C_T = 0.00$. 764
Figure E-45. Baseline configuration, Run 058, $M\infty = 3.5$, $Re_\infty = 1.0x10^6$/ft, $\phi = 60.04°$, $X_S = 25.16$ in, $Y_S = 0.00$ in, $C_T = 0.00$..... 765
Figure E-46. Baseline configuration, Run 059, $M\infty = 3.5$, $Re_\infty = 1.0x10^6$/ft, $\phi = 120.06°$, $X_S = 25.16$ in, $Y_S = 0.00$ in, $C_T = 0.00$..... 766
Figure E-47. Baseline configuration, Run 060, $M\infty = 3.5$, $Re_\infty = 1.0x10^6$/ft, $\phi = 179.95°$, $X_S = 25.16$ in, $Y_S = 0.00$ in, $C_T = 0.00$..... 767
Figure E-48. Baseline configuration, Run 065, $M\infty = 3.5$, $Re_\infty = 1.0x10^6$/ft, $\phi = -0.01°$, $X_S = 25.16$ in, $Y_S = -8.00$ in, $C_T = 0.00$. 768

Figure E-49. Baseline configuration, Run 067, $M\infty = 3.5$, $Re_\infty = 1.0x10^6$/ft, $\phi = 60.06°$, $X_S = 25.16$ in, $Y_S = –8.00$ in, $C_T = 0.00$..... 769
Figure E-50. Baseline configuration, Run 068, $M\infty = 3.5$, $Re_\infty = 1.0x10^6$/ft, $\phi = 119.96°$, $X_S = 25.16$ in, $Y_S = –8.00$ in, $C_T = 0.00$..... 770
Figure E-51. Baseline configuration, Run 069, $M\infty = 3.5$, $Re_\infty = 1.0x10^6$/ft, $\phi = 179.95°$, $X_S = 25.16$ in, $Y_S = –8.00$ in, $C_T = 0.00$..... 771
Figure E-52. Baseline configuration, Run 070, $M\infty = 3.5$, $Re_\infty = 1.0x10^6$/ft, $\phi = 179.95°$, $X_S = 40.16$ in, $Y_S = –8.00$ in, $C_T = 0.00$..... 772
Figure E-53. Baseline configuration, Run 073, $M\infty = 3.5$, $Re_\infty = 1.0x10^6$/ft, $\phi = 119.92°$, $X_S = 40.18$ in, $Y_S = –8.00$ in, $C_T = 0.00$..... 773
Figure E-54. Baseline configuration, Run 074, $M\infty = 3.5$, $Re_\infty = 1.0x10^6$/ft, $\phi = 60.02°$, $X_S = 40.18$ in, $Y_S = –8.00$ in, $C_T = 0.00$..... 774
Figure E-55. Baseline configuration, Run 075, $M\infty = 3.5$, $Re_\infty = 1.0x10^6$/ft, $\phi = 0.03°$, $X_S = 40.18$ in, $Y_S = –8.00$ in, $C_T = 0.00$..... 775
Figure E-56. Baseline configuration, Run 076, $M\infty = 3.5$, $Re_\infty = 1.0x10^6$/ft, $\phi = 0.03°$, $X_S = 40.18$ in, $Y_S = 7.99$ in, $C_T = 0.00$..... 776
Figure E-57. Baseline configuration, Run 077, $M\infty = 3.5$, $Re_\infty = 1.0x10^6$/ft, $\phi = 59.98°$, $X_S = 40.16$ in, $Y_S = 7.99$ in, $C_T = 0.00$..... 777
Figure E-58. Baseline configuration, Run 078, $M\infty = 3.5$, $Re_\infty = 1.0x10^6$/ft, $\phi = 119.92°$, $X_S = 40.16$ in, $Y_S = 7.95$ in, $C_T = 0.00$..... 778
Figure E-59. Baseline configuration, Run 079, $M\infty = 3.5$, $Re_\infty = 1.0x10^6$/ft, $\phi = −179.99°$, $X_S = 40.16$ in, $Y_S = 7.95$ in, $C_T = 0.00$. 779
Figure E-60. Baseline configuration, Run 080, $M\infty = 3.5$, $Re_\infty = 1.0x10^6$/ft, $\phi = −179.99°$, $X_S = 50.15$ in, $Y_S = 7.95$ in, $C_T = 0.00$. 780
Figure E-61. Baseline configuration, Run 081, $M\infty = 3.5$, $Re_\infty = 1.0x10^6$/ft, $\phi = 119.92°$, $X_S = 50.15$ in, $Y_S = 7.95$ in, $C_T = 0.00$..... 781
Figure E-62. Baseline configuration, Run 082, $M\infty = 3.5$, $Re_\infty = 1.0x10^6$/ft, $\phi = 60.00°$, $X_S = 50.15$ in, $Y_S = 7.95$ in, $C_T = 0.00$..... 782
Figure E-63. Baseline configuration, Run 083, $M\infty = 3.5$, $Re_\infty = 1.0x10^6$/ft, $\phi = 0.01°$, $X_S = 50.15$ in, $Y_S = 7.95$ in, $C_T = 0.00$..... 783
Figure E-64. Baseline configuration, Run 086, $M\infty = 4.6$, $Re_\infty = 1.1x10^6$/ft, $\phi = 0.01°$, $X_S = 25.17$ in, $Y_S = 0.00$ in, $C_T = 0.00$..... 784
Figure E-65. Baseline configuration, Run 087, $M\infty = 4.6$, $Re_\infty = 1.1x10^6$/ft, $\phi = 60.04°$, $X_S = 25.17$ in, $Y_S = 0.00$ in, $C_T = 0.00$..... 785
Figure E-66. Baseline configuration, Run 088, $M\infty = 4.6$, $Re_\infty = 1.1x10^6$/ft, $\phi = 119.90°$, $X_S = 25.17$ in, $Y_S = 0.00$ in, $C_T = 0.00$..... 786
Figure E-67. Baseline configuration, Run 089, $M\infty = 4.6$, $Re_\infty = 1.1x10^6$/ft, $\phi = 179.91°$, $X_S = 25.17$ in, $Y_S = 0.00$ in, $C_T = 0.00$..... 787
Figure E-68. Baseline configuration, Run 090, $M\infty = 4.6$, $Re_\infty = 1.1x10^6$/ft, $\phi = 0.01°$, $X_S = 40.15$ in, $Y_S = 0.00$ in, $C_T = 0.00$..... 788
Figure E-69. Baseline configuration, Run 091, $M\infty = 4.6$, $Re_\infty = 1.1x10^6$/ft, $\phi = 60.00°$, $X_S = 40.18$ in, $Y_S = 0.00$ in, $C_T = 0.00$..... 789
Figure E-70. Baseline configuration, Run 092, $M\infty = 4.6$, $Re_\infty = 1.1x10^6$/ft, $\phi = 119.92°$, $X_S = 40.18$ in, $Y_S = 0.00$ in, $C_T = 0.00$..... 790

Figure E-71. Baseline configuration, Run 093, $M\infty = 4.6$, $Re_\infty = 1.1x10^6$/ft, $\phi = 179.91°$, $X_S = 40.18$ in, $Y_S = 0.00$ in, $C_T = 0.00$ 791
Figure E-72. Baseline configuration, Run 094, $M\infty = 4.6$, $Re_\infty = 1.1x10^6$/ft, $\phi = 179.91°$, $X_S = 50.14$ in, $Y_S = 0.00$ in, $C_T = 0.00$ 792
Figure E-73. Baseline configuration, Run 095, $M\infty = 4.6$, $Re_\infty = 1.1x10^6$/ft, $\phi = 119.90°$, $X_S = 50.14$ in, $Y_S = 0.00$ in, $C_T = 0.00$ 793
Figure E-74. Baseline configuration, Run 096, $M\infty = 4.6$, $Re_\infty = 1.1x10^6$/ft, $\phi = 59.96°$, $X_S = 50.14$ in, $Y_S = 0.00$ in, $C_T = 0.00$ 794
Figure E-75. Baseline configuration, Run 097, $M\infty = 4.6$, $Re_\infty = 1.1x10^6$/ft, $\phi = -0.07°$, $X_S = 50.14$ in, $Y_S = 0.00$ in, $C_T = 0.00$. 795
Figure E-76. Baseline configuration, Run 098, $M\infty = 4.6$, $Re_\infty = 1.1x10^6$/ft, $\phi = -0.07°$, $X_S = 50.14$ in, $Y_S = 7.99$ in, $C_T = 0.00$. 796
Figure E-77. Baseline configuration, Run 099, $M\infty = 4.6$, $Re_\infty = 1.1x10^6$/ft, $\phi = 59.92°$, $X_S = 50.14$ in, $Y_S = 7.99$ in, $C_T = 0.00$ 797
Figure E-78. Baseline configuration, Run 100, $M\infty = 4.6$, $Re_\infty = 1.1x10^6$/ft, $\phi = 120.00°$, $X_S = 50.14$ in, $Y_S = 7.99$ in, $C_T = 0.00$ 798
Figure E-79. Baseline configuration, Run 101, $M\infty = 4.6$, $Re_\infty = 1.1x10^6$/ft, $\phi = 179.97°$, $X_S = 50.14$ in, $Y_S = 7.99$ in, $C_T = 0.00$ 799
Figure E-80. Baseline configuration, Run 104, $M\infty = 4.6$, $Re_\infty = 1.5x10^6$/ft, $\phi = -0.03°$, $X_S = 25.19$ in, $Y_S = 0.00$ in, $C_T = 0.00$. 800
Figure E-81. Baseline configuration, Run 105, $M\infty = 4.6$, $Re_\infty = 1.5x10^6$/ft, $\phi = 60.00°$, $X_S = 25.19$ in, $Y_S = 0.00$ in, $C_T = 0.00$ 801
Figure E-82. Baseline configuration, Run 106, $M\infty = 4.6$, $Re_\infty = 1.5x10^6$/ft, $\phi = 119.96°$, $X_S = 25.19$ in, $Y_S = 0.00$ in, $C_T = 0.00$ 802
Figure E-83. Baseline configuration, Run 107, $M\infty = 4.6$, $Re_\infty = 1.5x10^6$/ft, $\phi = 179.93°$, $X_S = 25.19$ in, $Y_S = 0.00$ in, $C_T = 0.00$ 803
Figure E-84. Baseline configuration, Run 108, $M\infty = 4.6$, $Re_\infty = 1.5x10^6$/ft, $\phi = 179.93°$, $X_S = 40.15$ in, $Y_S = 0.00$ in, $C_T = 0.00$ 804
Figure E-85. Baseline configuration, Run 109, $M\infty = 4.6$, $Re_\infty = 1.5x10^6$/ft, $\phi = 119.92°$, $X_S = 40.15$ in, $Y_S = 0.00$ in, $C_T = 0.00$ 805
Figure E-86. Baseline configuration, Run 110, $M\infty = 4.6$, $Re_\infty = 1.5x10^6$/ft, $\phi = 59.94°$, $X_S = 40.15$ in, $Y_S = 0.00$ in, $C_T = 0.00$ 806
Figure E-87. Baseline configuration, Run 111, $M\infty = 4.6$, $Re_\infty = 1.5x10^6$/ft, $\phi = -0.01°$, $X_S = 40.09$ in, $Y_S = 0.00$ in, $C_T = 0.00$. 807
Figure E-88. Baseline configuration, Run 112, $M\infty = 4.6$, $Re_\infty = 1.5x10^6$/ft, $\phi = -0.01°$, $X_S = 50.19$ in, $Y_S = 0.00$ in, $C_T = 0.00$. 808
Figure E-89. Baseline configuration, Run 113, $M\infty = 4.6$, $Re_\infty = 1.5x10^6$/ft, $\phi = 60.02°$, $X_S = 50.19$ in, $Y_S = 0.00$ in, $C_T = 0.00$ 809
Figure E-90. Baseline configuration, Run 114, $M\infty = 4.6$, $Re_\infty = 1.5x10^6$/ft, $\phi = 120.04°$, $X_S = 50.19$ in, $Y_S = 0.00$ in, $C_T = 0.00$ 810
Figure E-91. Baseline configuration, Run 115, $M\infty = 4.6$, $Re_\infty = 1.5x10^6$/ft, $\phi = 179.97°$, $X_S = 50.19$ in, $Y_S = 0.00$ in, $C_T = 0.00$ 811
Figure E-92. Baseline configuration, Run 116, $M\infty = 4.6$, $Re_\infty = 1.5x10^6$/ft, $\phi = 179.97°$, $X_S = 50.19$ in, $Y_S = 8.00$ in, $C_T = 0.00$ 812

Figure E-93. Baseline configuration, Run 117, $M\infty = 4.6$, $Re_\infty = 1.5x10^6$/ft, $\phi = 119.92°$, $X_S = 50.19$ in, $Y_S = 8.00$ in, $C_T = 0.00$..... 813
Figure E-94. Baseline configuration, Run 118, $M\infty = 4.6$, $Re_\infty = 1.5x10^6$/ft, $\phi = 59.96°$, $X_S = 50.19$ in, $Y_S = 8.00$ in, $C_T = 0.00$..... 814
Figure E-95. Baseline configuration, Run 119, $M\infty = 4.6$, $Re_\infty = 1.5x10^6$/ft, $\phi = 0.03°$, $X_S = 50.19$ in, $Y_S = 8.00$ in, $C_T = 0.00$..... 815
Figure E-96. Baseline configuration, Run 120, $M\infty = 4.6$, $Re_\infty = 1.5x10^6$/ft, $\phi = 0.03°$, $X_S = 25.16$ in, $Y_S = –8.00$ in, $C_T = 0.00$..... 816
Figure E-97. Baseline configuration, Run 121, $M\infty = 4.6$, $Re_\infty = 1.5x10^6$/ft, $\phi = 60.06°$, $X_S = 25.16$ in, $Y_S = –8.00$ in, $C_T = 0.00$..... 817
Figure E-98. Baseline configuration, Run 122, $M\infty = 4.6$, $Re_\infty = 1.5x10^6$/ft, $\phi = 120.00°$, $X_S = 25.16$ in, $Y_S = –8.00$ in, $C_T = 0.00$..... 818
Figure E-99. Baseline configuration, Run 123, $M\infty = 4.6$, $Re_\infty = 1.5x10^6$/ft, $\phi = 179.91°$, $X_S = 25.16$ in, $Y_S = –8.00$ in, $C_T = 0.00$..... 819
Figure E-100. Center nozzle configuration, Run 136, $M\infty = 2.4$, $Re_\infty = 1.0x10^6$/ft, $\phi = –0.01°$, $X_S = 40.16$ in, $Y_S = 0.00$ in, $C_T = 4.03$..... 820
Figure E-101. Center nozzle configuration, Run 137, $M\infty = 2.4$, $Re_\infty = 1.0x10^6$/ft, $\phi = −0.03°$, $X_S = 40.15$ in, $Y_S = 0.00$ in, $C_T = 2.99$. 821
Figure E-102. Center nozzle configuration, Run 138, $M\infty = 2.4$, $Re_\infty = 1.0x10^6$/ft, $\phi = 179.97°$, $X_S = 40.15$ in, $Y_S = 0.00$ in, $C_T = 3.01$..... 822
Figure E-103. Center nozzle configuration, Run 139, $M\infty = 2.4$, $Re_\infty = 1.0x10^6$/ft, $\phi = 179.97°$, $X_S = 40.15$ in, $Y_S = 0.00$ in, $C_T = 0.97$..... 823
Figure E-104. Center nozzle configuration, Run 140, $M\infty = 2.4$, $Re_\infty = 1.0x10^6$/ft, $\phi = –0.03°$, $X_S = 40.15$ in, $Y_S = 0.00$ in, $C_T = 0.97$..... 824
Figure E-105. Center nozzle configuration, Run 141, $M\infty = 2.4$, $Re_\infty = 1.0x10^6$/ft, $\phi = −0.03°$, $X_S = 40.15$ in, $Y_S = 0.00$ in, $C_T = 1.98$. 825
Figure E-106. Center nozzle configuration, Run 142, $M\infty = 2.4$, $Re_\infty = 1.0x10^6$/ft, $\phi = −179.91°$, $X_S = 40.15$ in, $Y_S = 0.00$ in, $C_T = 1.99$. 826
Figure E-107. Center nozzle configuration, Run 143, $M\infty = 2.4$, $Re_\infty = 1.0x10^6$/ft, $\phi = −179.91°$, $X_S = 40.15$ in, $Y_S = 0.00$ in, $C_T = 0.46$. 827
Figure E-108. Center nozzle configuration, Run 144, $M\infty = 2.4$, $Re_\infty = 1.0x10^6$/ft, $\phi = 0.01°$, $X_S = 40.15$ in, $Y_S = 0.00$ in, $C_T = 0.47$..... 828
Figure E-109. Center nozzle configuration, Run 145, $M\infty = 2.4$, $Re_\infty = 1.0x10^6$/ft, $\phi = 0.01°$, $X_S = 40.15$ in, $Y_S = 0.00$ in, $C_T = 0.23$..... 829
Figure E-110. Center nozzle configuration, Run 146, $M\infty = 2.4$, $Re_\infty = 1.0x10^6$/ft, $\phi = 179.99°$, $X_S = 40.15$ in, $Y_S = 0.00$ in, $C_T = 0.23$..... 830
Figure E-111. Center nozzle configuration, Run 147, $M\infty = 2.4$, $Re_\infty = 1.0x10^6$/ft, $\phi = −180.00°$, $X_S = 40.15$ in, $Y_S = 0.00$ in, $C_T = 0.19$. 831
Figure E-112. Center nozzle configuration, Run 148, $M\infty = 2.4$, $Re_\infty = 1.0x10^6$/ft, $\phi = 179.99°$, $X_S = 40.15$ in, $Y_S = 0.00$ in, $C_T = 0.00$..... 832
Figure E-113. Center nozzle configuration, Run 149, $M\infty = 2.4$, $Re_\infty = 1.0x10^6$/ft, $\phi = −0.03°$, $X_S = 40.15$ in, $Y_S = 0.00$ in, $C_T = 0.00$. 833
Figure E-114. Center nozzle configuration, Run 150, $M\infty = 3.5$, $Re_\infty = 1.0x10^6$/ft, $\phi = −0.03°$, $X_S = 40.17$ in, $Y_S = 0.00$ in, $C_T = 2.99$. 834

Figure E-115. Center nozzle configuration, Run 151, $M\infty = 3.5$, $Re_\infty = 1.0x10^6$/ft, $\phi = -179.97°$, $X_S = 40.17$ in, $Y_S = 0.00$ in, $C_T = 3.01$. 835
Figure E-116. Center nozzle configuration, Run 152, $M\infty = 3.5$, $Re_\infty = 1.0x10^6$/ft, $\phi = -179.97°$, $X_S = 40.17$ in, $Y_S = 0.00$ in, $C_T = 1.95$. 836
Figure E-117. Center nozzle configuration, Run 153, $M\infty = 3.5$, $Re_\infty = 1.0x10^6$/ft, $\phi = -0.09°$, $X_S = 40.17$ in, $Y_S = 0.00$ in, $C_T = 1.96$. 837
Figure E-118. Center nozzle configuration, Run 154, $M\infty = 3.5$, $Re_\infty = 1.0x10^6$/ft, $\phi = -0.09°$, $X_S = 40.17$ in, $Y_S = 0.00$ in, $C_T = 0.94$. 838
Figure E-119. Center nozzle configuration, Run 155, $M\infty = 3.5$, $Re_\infty = 1.0x10^6$/ft, $\phi = 179.91°$, $X_S = 40.17$ in, $Y_S = 0.00$ in, $C_T = 0.95$..... 839
Figure E-120. Center nozzle configuration, Run 156, $M\infty = 3.5$, $Re_\infty = 1.0x10^6$/ft, $\phi = 179.93°$, $X_S = 40.17$ in, $Y_S = 0.00$ in, $C_T = 0.45$..... 840
Figure E-121. Center nozzle configuration, Run 157, $M\infty = 3.5$, $Re_\infty = 1.0x10^6$/ft, $\phi = 0.07°$, $X_S = 40.17$ in, $Y_S = 0.00$ in, $C_T = 0.45$..... 841
Figure E-122. Center nozzle configuration, Run 159, $M\infty = 3.5$, $Re_\infty = 1.0x10^6$/ft, $\phi = -0.01°$, $X_S = 40.17$ in, $Y_S = 0.00$ in, $C_T = 0.21$. 842
Figure E-123. Center nozzle configuration, Run 160, $M\infty = 3.5$, $Re_\infty = 1.0x10^6$/ft, $\phi = 179.93°$, $X_S = 40.17$ in, $Y_S = 0.00$ in, $C_T = 0.21$..... 843
Figure E-124. Center nozzle configuration, Run 161, $M\infty = 3.5$, $Re_\infty = 1.0x10^6$/ft, $\phi = 179.93°$, $X_S = 40.17$ in, $Y_S = 0.00$ in, $C_T = 0.00$..... 844
Figure E-125. Center nozzle configuration, Run 162, $M\infty = 3.5$, $Re_\infty = 1.0x10^6$/ft, $\phi = 0.03°$, $X_S = 40.17$ in, $Y_S = 0.00$ in, $C_T = 0.00$..... 845
Figure E-126. Center nozzle configuration, Run 163, $M\infty = 4.6$, $Re_\infty = 1.5x10^6$/ft, $\phi = 0.03°$, $X_S = 40.17$ in, $Y_S = 0.00$ in, $C_T = 2.92$..... 846
Figure E-127. Center nozzle configuration, Run 164, $M\infty = 4.6$, $Re_\infty = 1.5x10^6$/ft, $\phi = 1479.91°$, $X_S = 40.17$ in, $Y_S = 0.00$ in, $C_T = 2.91$..... 847
Figure E-128. Center nozzle configuration, Run 165, $M\infty = 4.6$, $Re_\infty = 1.5x10^6$/ft, $\phi = 179.93°$, $X_S = 40.15$ in, $Y_S = 0.00$ in, $C_T = 1.93$..... 848
Figure E-129. Center nozzle configuration, Run 166, $M\infty = 4.6$, $Re_\infty = 1.5x10^6$/ft, $\phi = 0.03°$, $X_S = 40.15$ in, $Y_S = 0.00$ in, $C_T = 1.96$..... 849
Figure E-130. Center nozzle configuration, Run 167, $M\infty = 4.6$, $Re_\infty = 1.5x10^6$/ft, $\phi = 0.03°$, $X_S = 40.15$ in, $Y_S = 0.00$ in, $C_T = 0.94$..... 850
Figure E-131. Center nozzle configuration, Run 168, $M\infty = 4.6$, $Re_\infty = 1.5x10^6$/ft, $\phi = 179.95°$, $X_S = 40.15$ in, $Y_S = 0.00$ in, $C_T = 0.96$..... 851
Figure E-132. Center nozzle configuration, Run 169, $M\infty = 4.6$, $Re_\infty = 1.5x10^6$/ft, $\phi = 179.95°$, $X_S = 40.15$ in, $Y_S = 0.00$ in, $C_T = 0.45$..... 852
Figure E-133. Center nozzle configuration, Run 170, $M\infty = 4.6$, $Re_\infty = 1.5x10^6$/ft, $\phi = 0.03°$, $X_S = 40.15$ in, $Y_S = 0.00$ in, $C_T = 0.46$..... 853
Figure E-134. Center nozzle configuration, Run 171, $M\infty = 4.6$, $Re_\infty = 1.5x10^6$/ft, $\phi = 0.03°$, $X_S = 40.15$ in, $Y_S = 0.00$ in, $C_T = 0.22$..... 854
Figure E-135. Center nozzle configuration, Run 172, $M\infty = 4.6$, $Re_\infty = 1.5x10^6$/ft, $\phi = 179.91°$, $X_S = 40.15$ in, $Y_S = 0.00$ in, $C_T = 0.22$..... 855
Figure E-136. Center nozzle configuration, Run 173, $M\infty = 4.6$, $Re_\infty = 1.5x10^6$/ft, $\phi = 179.91°$, $X_S = 40.15$ in, $Y_S = 0.00$ in, $C_T = 0.00$..... 856

Figure E-137. Center nozzle configuration, Run 174, M_∞ = 4.6, Re_∞ = 1.5x10^6/ft, ϕ = −0.07°, X_S = 40.15 in, Y_S = 0.00 in, C_T = 0.00. 857
Figure E-138. Tri-nozzle configuration, Run 179, M_∞ = 2.4, Re_∞ = 1.0x10^6/ft, ϕ = 0.09°, X_S = 40.15 in, Y_S = 0.00 in, C_T = 2.95..... 858
Figure E-139. Tri-nozzle configuration, Run 180, M_∞ = 2.4, Re_∞ = 1.0x10^6/ft, ϕ = −0.01°, X_S = 40.15 in, Y_S = 0.00 in, C_T = 0.00. 859
Figure E-140. Tri-nozzle configuration, Run 181, M_∞ = 2.4, Re_∞ = 1.0x10^6/ft, ϕ = 179.97°, X_S = 40.15 in, Y_S = 0.00 in, C_T = 0.00..... 860
Figure E-141. Tri-nozzle configuration, Run 182, M_∞ = 2.4, Re_∞ = 1.0x10^6/ft, ϕ = 119.96°, X_S = 40.15 in, Y_S = 0.00 in, C_T = 0.00..... 861
Figure E-142. Tri-nozzle configuration, Run 183, M_∞ = 2.4, Re_∞ = 1.0x10^6/ft, ϕ = 60.04°, X_S = 40.15 in, Y_S = 0.00 in, C_T = 0.00..... 862
Figure E-143. Tri-nozzle configuration, Run 184, M_∞ = 3.5, Re_∞ = 1.0x10^6/ft, ϕ = 0.05°, X_S = 40.15 in, Y_S = 0.00 in, C_T = 0.00..... 863
Figure E-144. Tri-nozzle configuration, Run 185, M_∞ = 3.5, Re_∞ = 1.0x10^6/ft, ϕ = 59.94°, X_S = 40.15 in, Y_S = 0.00 in, C_T = 0.00..... 864
Figure E-145. Tri-nozzle configuration, Run 186, M_∞ = 3.5, Re_∞ = 1.0x10^6/ft, ϕ = 119.94°, X_S = 40.15 in, Y_S = 0.00 in, C_T = 0.00..... 865
Figure E-146. Tri-nozzle configuration, Run 187, M_∞ = 3.5, Re_∞ = 1.0x10^6/ft, ϕ = 179.97°, X_S = 40.15 in, Y_S = 0.00 in, C_T = 0.00..... 866
Figure E-147. Tri-nozzle configuration, Run 190, M_∞ = 2.4, Re_∞ = 1.0x10^6/ft, ϕ = −0.03°, X_S = 40.15 in, Y_S = 0.00 in, C_T = 2.95. 867
Figure E-148. Tri-nozzle configuration, Run 191, M_∞ = 2.4, Re_∞ = 1.0x10^6/ft, ϕ = 58.37°, X_S = 40.15 in, Y_S = 0.00 in, C_T = 2.95..... 868
Figure E-149. Tri-nozzle configuration, Run 192, M_∞ = 2.4, Re_∞ = 1.0x10^6/ft, ϕ = 119.94°, X_S = 40.15 in, Y_S = 0.00 in, C_T = 2.93..... 869
Figure E-150. Tri-nozzle configuration, Run 193, M_∞ = 2.4, Re_∞ = 1.0x10^6/ft, ϕ = −179.97°, X_S = 40.15 in, Y_S = 0.00 in, C_T = 2.95. 870
Figure E-151. Tri-nozzle configuration, Run 194, M_∞ = 2.4, Re_∞ = 1.0x10^6/ft, ϕ = −179.97°, X_S = 40.15 in, Y_S = 0.00 in, C_T = 1.94. 871
Figure E-152. Tri-nozzle configuration, Run 195, M_∞ = 2.4, Re_∞ = 1.0x10^6/ft, ϕ = 119.96°, X_S = 40.15 in, Y_S = 0.00 in, C_T = 1.93..... 872
Figure E-153. Tri-nozzle configuration, Run 196, M_∞ = 2.4, Re_∞ = 1.0x10^6/ft, ϕ = 59.94°, X_S = 40.15 in, Y_S = 0.00 in, C_T = 1.93..... 873
Figure E-154. Tri-nozzle configuration, Run 197, M_∞ = 2.4, Re_∞ = 1.0x10^6/ft, ϕ = −0.01°, X_S = 40.15 in, Y_S = 0.00 in, C_T = 1.93. 874
Figure E-155. Tri-nozzle configuration, Run 198, M_∞ = 2.4, Re_∞ = 1.0x10^6/ft, ϕ = −0.01°, X_S = 40.15 in, Y_S = 0.00 in, C_T = 0.95. 875
Figure E-156. Tri-nozzle configuration, Run 199, M_∞ = 2.4, Re_∞ = 1.0x10^6/ft, ϕ = 59.98°, X_S = 40.15 in, Y_S = 0.00 in, C_T = 0.94..... 876
Figure E-157. Tri-nozzle configuration, Run 200, M_∞ = 2.4, Re_∞ = 1.0x10^6/ft, ϕ = 119.94°, X_S = 40.15 in, Y_S = 0.00 in, C_T = 0.94..... 877
Figure E-158. Tri-nozzle configuration, Run 201, M_∞ = 2.4, Re_∞ = 1.0x10^6/ft, ϕ = 179.99°, X_S = 40.15 in, Y_S = 0.00 in, C_T = 0.94..... 878

Figure E-159. Tri-nozzle configuration, Run 202, M_∞ = 2.4, Re_∞ = 1.0x10^6/ft, ϕ = 179.99°, X_S = 40.15 in, Y_S = 0.00 in, C_T = 0.43..... 879
Figure E-160. Tri-nozzle configuration, Run 203, M_∞ = 2.4, Re_∞ = 1.0x10^6/ft, ϕ = −179.97°, X_S = 40.15 in, Y_S = 0.00 in, C_T = 0.44. 880
Figure E-161. Tri-nozzle configuration, Run 204, M_∞ = 2.4, Re_∞ = 1.0x10^6/ft, ϕ = 119.98°, X_S = 40.15 in, Y_S = 0.00 in, C_T = 0.44..... 881
Figure E-162. Tri-nozzle configuration, Run 205, M_∞ = 2.4, Re_∞ = 1.0x10^6/ft, ϕ = 59.94°, X_S = 40.15 in, Y_S = 0.00 in, C_T = 0.43..... 882
Figure E-163. Tri-nozzle configuration, Run 206, M_∞ = 2.4, Re_∞ = 1.0x10^6/ft, ϕ = −0.05°, X_S = 40.15 in, Y_S = 0.00 in, C_T = 0.43. 883
Figure E-164. Tri-nozzle configuration, Run 211, M_∞ = 4.6, Re_∞ = 1.5x10^6/ft, ϕ = −0.03°, X_S = 40.15 in, Y_S = 0.00 in, C_T = 2.94. 884
Figure E-165. Tri-nozzle configuration, Run 212, M_∞ = 4.6, Re_∞ = 1.5x10^6/ft, ϕ = 60.02°, X_S = 40.15 in, Y_S = 0.00 in, C_T = 2.93..... 885
Figure E-166. Tri-nozzle configuration, Run 213, M_∞ = 4.6, Re_∞ = 1.5x10^6/ft, ϕ = 119.98°, X_S = 40.15 in, Y_S = 0.00 in, C_T = 2.95..... 886
Figure E-167. Tri-nozzle configuration, Run 214, M_∞ = 4.6, Re_∞ = 1.5x10^6/ft, ϕ = 179.99°, X_S = 40.15 in, Y_S = 0.00 in, C_T = 2.95..... 887
Figure E-168. Tri-nozzle configuration, Run 217, M_∞ = 2.4, Re_∞ = 1.0x10^6/ft, ϕ = −0.03°, X_S = 40.15 in, Y_S = 0.00 in, C_T = 0.48. 888
Figure E-169. Tri-nozzle configuration, Run 218, M_∞ = 2.4, Re_∞ = 1.0x10^6/ft, ϕ = 59.94°, X_S = 40.15 in, Y_S = 0.00 in, C_T = 0.48..... 889
Figure E-170. Tri-nozzle configuration, Run 219, M_∞ = 2.4, Re_∞ = 1.0x10^6/ft, ϕ = 119.96°, X_S = 40.15 in, Y_S = 0.00 in, C_T = 0.48..... 890
Figure E-171. Tri-nozzle configuration, Run 220, M_∞ = 2.4, Re_∞ = 1.0x10^6/ft, ϕ = 179.95°, X_S = 40.15 in, Y_S = 0.00 in, C_T = 0.48..... 891
Figure E-172. Tri-nozzle configuration, Run 221, M_∞ = 2.4, Re_∞ = 1.0x10^6/ft, ϕ = −0.01°, X_S = 40.15 in, Y_S = 0.00 in, C_T = 0.23. 892
Figure E-173. Tri-nozzle configuration, Run 222, M_∞ = 3.5, Re_∞ = 1.0x10^6/ft, ϕ = −0.01°, X_S = 40.15 in, Y_S = 0.00 in, C_T = 2.95. 893
Figure E-174. Tri-nozzle configuration, Run 223, M_∞ = 3.5, Re_∞ = 1.0x10^6/ft, ϕ = 59.96°, X_S = 40.15 in, Y_S = 0.00 in, C_T = 2.94..... 894
Figure E-175. Tri-nozzle configuration, Run 224, M_∞ = 3.5, Re_∞ = 1.0x10^6/ft, ϕ = 120.00°, X_S = 40.15 in, Y_S = 0.00 in, C_T = 3.00..... 895
Figure E-176. Tri-nozzle configuration, Run 225, M_∞ = 3.5, Re_∞ = 1.0x10^6/ft, ϕ = 179.97°, X_S = 40.15 in, Y_S = 0.00 in, C_T = 2.98..... 896
Figure E-177. Tri-nozzle configuration, Run 226, M_∞ = 3.5, Re_∞ = 1.0x10^6/ft, ϕ = 179.97°, X_S = 40.15 in, Y_S = 0.00 in, C_T = 1.96..... 897
Figure E-178. Tri-nozzle configuration, Run 227, M_∞ = 3.5, Re_∞ = 1.0x10^6/ft, ϕ = 119.98°, X_S = 40.15 in, Y_S = 0.00 in, C_T = 1.94..... 898
Figure E-179. Tri-nozzle configuration, Run 228, M_∞ = 3.5, Re_∞ = 1.0x10^6/ft, ϕ = 60.02°, X_S = 40.15 in, Y_S = 0.00 in, C_T = 1.94..... 899
Figure E-180. Tri-nozzle configuration, Run 229, M_∞ = 3.5, Re_∞ = 1.0x10^6/ft, ϕ = −0.03°, X_S = 40.15 in, Y_S = 0.00 in, C_T = 1.95. 900

Figure E-181. Tri-nozzle configuration, Run 230, M_∞ = 3.5, Re_∞ = 1.0x10^6/ft, ϕ = −0.03°, X_S = 40.15 in, Y_S = 0.00 in, C_T = 0.97. 901
Figure E-182. Tri-nozzle configuration, Run 233, M_∞ = 3.5, Re_∞ = 1.0x10^6/ft, ϕ = 59.96°, X_S = 40.15 in, Y_S = 0.00 in, C_T = 0.96..... 902
Figure E-183. Tri-nozzle configuration, Run 234, M_∞ = 3.5, Re_∞ = 1.0x10^6/ft, ϕ = −0.05°, X_S = 40.15 in, Y_S = 0.00 in, C_T = 0.97. 903
Figure E-184. Tri-nozzle configuration, Run 235, M_∞ = 3.5, Re_∞ = 1.0x10^6/ft, ϕ = 120.00°, X_S = 40.15 in, Y_S = 0.00 in, C_T = 0.96..... 904
Figure E-185. Tri-nozzle configuration, Run 236, M_∞ = 3.5, Re_∞ = 1.0x10^6/ft, ϕ = 179.95°, X_S = 40.15 in, Y_S = 0.00 in, C_T = 0.96..... 905
Figure E-186. Tri-nozzle configuration, Run 237, M_∞ = 3.5, Re_∞ = 1.0x10^6/ft, ϕ = 179.95°, X_S = 40.15 in, Y_S = 0.00 in, C_T = 0.47..... 906
Figure E-187. Tri-nozzle configuration, Run 238, M_∞ = 3.5, Re_∞ = 1.0x10^6/ft, ϕ = 119.94°, X_S = 40.15 in, Y_S = 0.00 in, C_T = 0.47..... 907
Figure E-188. Tri-nozzle configuration, Run 239, M_∞ = 3.5, Re_∞ = 1.0x10^6/ft, ϕ = 60.00°, X_S = 40.15 in, Y_S = 0.00 in, C_T = 0.00..... 908
Figure E-189. Tri-nozzle configuration, Run 240, M_∞ = 3.5, Re_∞ = 1.0x10^6/ft, ϕ = −0.05°, X_S = 40.15 in, Y_S = 0.00 in, C_T = 0.46. 909
Figure E-190. Tri-nozzle configuration, Run 241, M_∞ = 3.5, Re_∞ = 1.0x10^6/ft, ϕ = −0.05°, X_S = 40.15 in, Y_S = 0.00 in, C_T = 0.22. 910
Figure E-191. Tri-nozzle configuration, Run 242, M_∞ = 4.6, Re_∞ = 1.5x10^6/ft, ϕ = −0.05°, X_S = 40.15 in, Y_S = 0.00 in, C_T = 1.96. 911
Figure E-192. Tri-nozzle configuration, Run 243, M_∞ = 4.6, Re_∞ = 1.5x10^6/ft, ϕ = 60.00°, X_S = 40.15 in, Y_S = 0.00 in, C_T = 1.95..... 912
Figure E-193. Tri-nozzle configuration, Run 244, M_∞ = 4.6, Re_∞ = 1.5x10^6/ft, ϕ = 120.00°, X_S = 40.15 in, Y_S = 0.00 in, C_T = 1.96..... 913
Figure E-194. Tri-nozzle configuration, Run 245, M_∞ = 4.6, Re_∞ = 1.5x10^6/ft, ϕ = −179.99°, X_S = 40.15 in, Y_S = 0.00 in, C_T = 1.97. 914
Figure E-195. Tri-nozzle configuration, Run 247, M_∞ = 4.6, Re_∞ = 1.5x10^6/ft, ϕ = −0.03°, X_S = 40.15 in, Y_S = 0.00 in, C_T = 1.92. 915
Figure E-196. Tri-nozzle configuration, Run 248, M_∞ = 4.6, Re_∞ = 1.5x10^6/ft, ϕ = 179.99°, X_S = 40.15 in, Y_S = 0.00 in, C_T = 1.93..... 916
Figure E-197. Tri-nozzle configuration, Run 249, M_∞ = 4.6, Re_∞ = 1.5x10^6/ft, ϕ = 179.99°, X_S = 40.15 in, Y_S = 0.00 in, C_T = 0.90..... 917
Figure E-198. Tri-nozzle configuration, Run 250, M_∞ = 4.6, Re_∞ = 1.5x10^6/ft, ϕ = 119.96°, X_S = 40.15 in, Y_S = 0.00 in, C_T = 0.90..... 918
Figure E-199. Tri-nozzle configuration, Run 251, M_∞ = 4.6, Re_∞ = 1.5x10^6/ft, ϕ = 60.04°, X_S = 40.15 in, Y_S = 0.00 in, C_T = 0.90..... 919
Figure E-200. Tri-nozzle configuration, Run 252, M_∞ = 4.6, Re_∞ = 1.5x10^6/ft, ϕ = −0.03°, X_S = 40.15 in, Y_S = 0.00 in, C_T = 0.90. 920
Figure E-201. Tri-nozzle configuration, Run 253, M_∞ = 4.6, Re_∞ = 1.5x10^6/ft, ϕ = −0.03°, X_S = 40.15 in, Y_S = 0.00 in, C_T = 0.42. 921
Figure E-202. Tri-nozzle configuration, Run 254, M_∞ = 4.6, Re_∞ = 1.5x10^6/ft, ϕ = 60.00°, X_S = 40.15 in, Y_S = 0.00 in, C_T = 0.42..... 922

Figure E-203. Tri-nozzle configuration, Run 255, M_∞ = 4.6, Re_∞ = 1.5x10^6/ft, ϕ = 119.96°, X_S = 40.15 in, Y_S = 0.00 in, C_T = 0.42..... 923
Figure E-204. Tri-nozzle configuration, Run 256, M_∞ = 4.6, Re_∞ = 1.5x10^6/ft, ϕ = 179.95°, X_S = 40.15 in, Y_S = 0.00 in, C_T = 0.43..... 924
Figure E-205. Tri-nozzle configuration, Run 257, M_∞ = 4.6, Re_∞ = 1.5x10^6/ft, ϕ = −0.03°, X_S = 40.15 in, Y_S = 0.00 in, C_T = 0.20. 925
Figure E-206. Tri-nozzle configuration, Run 258, M_∞ = 4.6, Re_∞ = 1.5x10^6/ft, ϕ = −0.03°, X_S = 40.15 in, Y_S = 0.00 in, C_T = 0.00. 926
Figure E-207. Tri-nozzle configuration, Run 259, M_∞ = 4.6, Re_∞ = 1.5x10^6/ft, ϕ = 59.96°, X_S = 40.15 in, Y_S = 0.00 in, C_T = 0.00..... 927
Figure E-208. Tri-nozzle configuration, Run 260, M_∞ = 4.6, Re_∞ = 1.5x10^6/ft, ϕ = 119.94°, X_S = 40.15 in, Y_S = 0.00 in, C_T = 0.00..... 928
Figure E-209. Tri-nozzle configuration, Run 261, M_∞ = 4.6, Re_∞ = 1.5x10^6/ft, ϕ = 179.95°, X_S = 40.15 in, Y_S = 0.00 in, C_T = 0.00..... 929
Figure E-210. Tri-nozzle configuration, Run 262, M_∞ = 4.6, Re_∞ = 1.5x10^6/ft, ϕ = 0.01°, X_S = 40.15 in, Y_S = 0.00 in, C_T = 2.94..... 930
Figure E-211. Tri-nozzle configuration, Run 263, M_∞ = 4.6, Re_∞ = 1.5x10^6/ft, ϕ = −179.99°, X_S = 40.15 in, Y_S = 0.00 in, C_T = 2.93. 931
Figure E-212. Tri-nozzle configuration, Run 264, M_∞ = 4.6, Re_∞ = 1.5x10^6/ft, ϕ = 179.99°, X_S = 40.15 in, Y_S = 0.00 in, C_T = 5.95..... 932
Figure E-213. Tri-nozzle configuration, Run 265, M_∞ = 3.5, Re_∞ = 1.0x10^6/ft, ϕ = −0.05°, X_S = 40.15 in, Y_S = 0.00 in, C_T = 0.91. 933
Figure E-214. Tri-nozzle configuration, Run 266, M_∞ = 3.5, Re_∞ = 1.0x10^6/ft, ϕ = −0.05°, X_S = 40.15 in, Y_S = 0.00 in, C_T = 0.45. 934
Figure E-215. Tri-nozzle configuration, Run 267, M_∞ = 3.5, Re_∞ = 1.0x10^6/ft, ϕ = −0.05°, X_S = 40.15 in, Y_S = 0.00 in, C_T = 4.95. 935
Figure E-216. Baseline configuration, Run 271, M_∞ = 2.4, Re_∞ = 1.0x10^6/ft, ϕ = −0.03°, X_S = 40.16 in, Y_S = 0.00 in, C_T = 0.00. 936
Figure E-217. Baseline configuration, Run 272, M_∞ = 2.4, Re_∞ = 1.0x10^6/ft, ϕ = 59.98°, X_S = 40.16 in, Y_S = 0.00 in, C_T = 0.00..... 937
Figure E-218. Baseline configuration, Run 273, M_∞ = 2.4, Re_∞ = 1.0x10^6/ft, ϕ = 119.94°, X_S = 40.16 in, Y_S = 0.00 in, C_T = 0.00..... 938
Figure E-219. Baseline configuration, Run 0274, M_∞ = 2.4, Re_∞ = 1.0x10^6/ft, ϕ = 179.99°, X_S = 40.16 in, Y_S = 0.00 in, C_T = 0.00..... 939
Figure E-220. Baseline configuration, Run 276, M_∞ = 3.5, Re_∞ = 1.0x10^6/ft, ϕ = 179.99°, X_S = 40.16 in, Y_S = 0.00 in, C_T = 0.00..... 940
Figure E-221. Baseline configuration, Run 277, M_∞ = 3.5, Re_∞ = 1.0x10^6/ft, ϕ = 119.94°, X_S = 40.16 in, Y_S = 0.00 in, C_T = 0.00..... 941
Figure E-222. Baseline configuration, Run 278, M_∞ = 3.5, Re_∞ = 1.0x10^6/ft, ϕ = 60.00°, X_S = 40.16 in, Y_S = 0.00 in, C_T = 0.00..... 942
Figure E-223. Baseline configuration, Run 279, M_∞ = 3.5, Re_∞ = 1.0x10^6/ft, ϕ = −0.05°, X_S = 40.16 in, Y_S = 0.00 in, C_T = 0.00. 943
Figure E-224. Baseline configuration, Run 280, M_∞ = 4.6, Re_∞ = 1.5x10^6/ft, ϕ = −0.05°, X_S = 40.16 in, Y_S = 0.00 in, C_T = 0.00. 944

Figure E-225. Baseline configuration, Run 281, $M\infty$ = 4.6, Re_∞ = 1.5x10^6/ft, ϕ = 59.98°, X_S = 40.16 in, Y_S = 0.00 in, C_T = 0.00..... 945
Figure E-226. Baseline configuration, Run 282, $M\infty$ = 4.6, Re_∞ = 1.5x10^6/ft, ϕ = 119.96°, X_S = 40.16 in, Y_S = 0.00 in, C_T = 0.00..... 946
Figure E-227. Baseline configuration, Run 283, $M\infty$ = 4.6, Re_∞ = 1.5x10^6/ft, ϕ = 179.97°, X_S = 40.16 in, Y_S = 0.00 in, C_T = 0.00..... 947
Figure E-228. Quad-nozzle configuration, Run 288, $M\infty$ = 2.4, Re_∞ = 1.0x10^6/ft, ϕ = −0.03°, X_S = 40.17 in, Y_S = 0.00 in, C_T = 1.92. 948
Figure E-229. Quad-nozzle configuration, Run 289, $M\infty$ = 2.4, Re_∞ = 1.0x10^6/ft, ϕ = 59.98°, X_S = 40.17 in, Y_S = 0.00 in, C_T = 1.93..... 949
Figure E-230. Quad-nozzle configuration, Run 290, $M\infty$ = 2.4, Re_∞ = 1.0x10^6/ft, ϕ = 119.98°, X_S = 40.17 in, Y_S = 0.00 in, C_T = 1.93..... 950
Figure E-231. Quad-nozzle configuration, Run 291, $M\infty$ = 2.4, Re_∞ = 1.0x10^6/ft, ϕ = −179.95°, X_S = 40.17 in, Y_S = 0.00 in, C_T = 1.94. 951
Figure E-232. Quad-nozzle configuration, Run 292, $M\infty$ = 2.4, Re_∞ = 1.0x10^6/ft, ϕ = 149.95°, X_S = 40.16 in, Y_S = 0.00 in, C_T = 1.93..... 952
Figure E-233. Quad-nozzle configuration, Run 293, $M\infty$ = 2.4, Re_∞ = 1.0x10^6/ft, ϕ = 179.97°, X_S = 40.16 in, Y_S = 0.00 in, C_T = 0.94..... 953
Figure E-234. Quad-nozzle configuration, Run 294, $M\infty$ = 2.4, Re_∞ = 1.0x10^6/ft, ϕ = 119.96°, X_S = 40.16 in, Y_S = 0.00 in, C_T = 0.95..... 954
Figure E-235. Quad-nozzle configuration, Run 295, $M\infty$ = 2.4, Re_∞ = 1.0x10^6/ft, ϕ = 60.02°, X_S = 40.16 in, Y_S = 0.00 in, C_T = 0.94..... 955
Figure E-236. Quad-nozzle configuration, Run 296, $M\infty$ = 2.4, Re_∞ = 1.0x10^6/ft, ϕ = −0.05°, X_S = 40.16 in, Y_S = 0.00 in, C_T = 0.95. 956
Figure E-237. Quad-nozzle configuration, Run 297, $M\infty$ = 2.4, Re_∞ = 1.0x10^6/ft, ϕ = 30.03°, X_S = 40.15 in, Y_S = 0.00 in, C_T = 2.95..... 957
Figure E-238. Quad-nozzle configuration, Run 298, $M\infty$ = 3.5, Re_∞ = 1.0x10^6/ft, ϕ = 0.01°, X_S = 40.16 in, Y_S = 0.00 in, C_T = 1.91..... 958
Figure E-239. Quad-nozzle configuration, Run 299, $M\infty$ = 3.5, Re_∞ = 1.0x10^6/ft, ϕ = 59.98°, X_S = 40.16 in, Y_S = 0.00 in, C_T = 1.92..... 959
Figure E-240. Quad-nozzle configuration, Run 300, $M\infty$ = 3.5, Re_∞ = 1.0x10^6/ft, ϕ = 119.96°, X_S = 40.16 in, Y_S = 0.00 in, C_T = 1.92..... 960
Figure E-241. Quad-nozzle configuration, Run 301, $M\infty$ = 3.5, Re_∞ = 1.0x10^6/ft, ϕ = 179.95°, X_S = 40.16 in, Y_S = 0.00 in, C_T = 1.92..... 961
Figure E-242. Quad-nozzle configuration, Run 302, $M\infty$ = 3.5, Re_∞ = 1.0x10^6/ft, ϕ = 179.95°, X_S = 40.16 in, Y_S = 0.00 in, C_T = 0.90..... 962
Figure E-243. Quad-nozzle configuration, Run 303, $M\infty$ = 3.5, Re_∞ = 1.0x10^6/ft, ϕ = 120.02°, X_S = 40.16 in, Y_S = 0.00 in, C_T = 0.89..... 963
Figure E-244. Quad-nozzle configuration, Run 304, $M\infty$ = 3.5, Re_∞ = 1.0x10^6/ft, ϕ = 60.00°, X_S = 40.16 in, Y_S = 0.00 in, C_T = 0.90..... 964
Figure E-245. Quad-nozzle configuration, Run 305, $M\infty$ = 3.5, Re_∞ = 1.0x10^6/ft, ϕ = −0.03°, X_S = 40.16 in, Y_S = 0.00 in, C_T = 0.90. 965
Figure E-246. Quad-nozzle configuration, Run 306, $M\infty$ = 3.5, Re_∞ = 1.0x10^6/ft, ϕ = 29.99°, X_S = 40.17 in, Y_S = 0.00 in, C_T = 2.92..... 966

Figure E-247. Quad-nozzle configuration, Run 307, M_∞ = 4.6, Re_∞ = 1.5x10^6/ft, ϕ = 0.05°, X_S = 40.17 in, Y_S = 0.00 in, C_T = 1.93..... 967
Figure E-248. Quad-nozzle configuration, Run 309, M_∞ = 4.6, Re_∞ = 1.5x10^6/ft, ϕ = 59.94°, X_S = 40.17 in, Y_S = 0.00 in, C_T = 1.92..... 968
Figure E-249. Quad-nozzle configuration, Run 310, M_∞ = 4.6, Re_∞ = 1.5x10^6/ft, ϕ = 119.96°, X_S = 40.17 in, Y_S = 0.00 in, C_T = 1.92..... 969
Figure E-250. Quad-nozzle configuration, Run 311, M_∞ = 4.6, Re_∞ = 1.5x10^6/ft, ϕ = −179.97°, X_S = 40.17 in, Y_S = 0.00 in, C_T = 1.92. 970
Figure E-251. Quad-nozzle configuration, Run 312, M_∞ = 4.6, Re_∞ = 1.5x10^6/ft, ϕ = −179.97°, X_S = 40.17 in, Y_S = 0.00 in, C_T = 0.91. 971
Figure E-252. Quad-nozzle configuration, Run 313, M_∞ = 4.6, Re_∞ = 1.5x10^6/ft, ϕ = 119.98°, X_S = 40.17 in, Y_S = 0.00 in, C_T = 0.92..... 972
Figure E-253. Quad-nozzle configuration, Run 314, M_∞ = 4.6, Re_∞ = 1.5x10^6/ft, ϕ = 60.04°, X_S = 40.17 in, Y_S = 0.00 in, C_T = 0.91..... 973
Figure E-254. Quad-nozzle configuration, Run 315, M_∞ = 4.6, Re_∞ = 1.5x10^6/ft, ϕ = 0.05°, X_S = 40.17 in, Y_S = 0.00 in, C_T = 0.92..... 974
Figure E-255. Center nozzle configuration, Run 319, M_∞ = 2.4, Re_∞ = 1.0x10^6/ft, ϕ = 0.01°, X_S = 37.47 in, Y_S = 0.00 in, C_T = 0.45..... 975
Figure E-256. Center nozzle configuration, Run 320, M_∞ = 3.5, Re_∞ = 1.0x10^6/ft, ϕ = 0.01°, X_S = 43.35 in, Y_S = 0.00 in, C_T = 1.96..... 976
Figure E-257. Center nozzle configuration, Run 321, M_∞ = 4.6, Re_∞ = 1.5x10^6/ft, ϕ = 0.01°, X_S = 42.98 in, Y_S = 0.00 in, C_T = 1.96..... 977

NOMENCLATURE

Symbols

A_{ref}	forebody reference area, ft^2
C_p	pressure coefficient
C_T	thrust coefficient
D	diameter, in
L	model length used to normalize longitudinal distance on the model, in
M	Mach number
P	pressure, psia or psf
q	dynamic pressure, psf
Re	unit Reynolds number, ft^{-1}
R	forebody radius used to normalize radial distance on the model, in
r, θ	model polar coordinates, defined in figure 11
T	temperature, deg F or R
V	velocity, ft/sec
x, y, z	model Cartesian coordinates
X, Y, Z	tunnel Cartesian coordinates, defined in figure 5
α	model angle of attack, deg
β	model angle of yaw, deg
ϕ	model roll angle, deg
ρ	density, slug/ft3

Subscripts

j	conditions within the nozzle jet
S	strut position
T	stagnation
∞	free-stream conditions

Acronyms

A/D	analog-to-digital
AMS	angle measurement system
CFD	computational fluid dynamics
DCV	digital control valve
DWG	drawing
EDL	entry, descent, and landing
ESP	electronically scanned pressure
fps	frames per second
LaRC	Langley Research Center
NASA	National Aeronautics and Space Administration
RTD	resistance temperature detector
SRP	supersonic retropropulsion
UPWT	Unitary Plan Wind Tunnel
ViDI	Virtual Diagnostics Interface

SECTION 1
INTRODUCTION

Present capability for entry, descent, and landing (EDL) of small robotic missions to Mars, typified by a landed mass less than a metric ton, is predicated on the use of parachutes for a significant portion of the deceleration required to safely reach the surface. Practically speaking, this approach is not scalable to larger payloads because of physical limits with parachute size, materials, and testing capabilities. A proposed alternate approach is to use propulsive deceleration earlier in the trajectory, taking advantage of engines, typically required for landing, while still flying supersonically. Thus, supersonic retropropulsion (SRP), or the use of engine thrust directed towards the oncoming supersonic free-stream flow to slow down, is deemed a potentially enabling technology for future large payload missions to Mars (such as human exploration missions that would be on the order of tens of metric tons) and is a present focus of the EDL community. For further discussions of SRP from a systems analysis and performance perspective (see ref. 1–5). A broader survey of the literature is provided in reference 6.

To date, only a handful of studies have been conducted for understanding the fluid dynamics phenomena associated with the use of SRP, and most of those were performed decades ago, for an example see reference 7. These older studies were typically exploratory in nature, designed to investigate the aerodynamic behavior of various representative Mars EDL SRP configurations. While useful for providing insights into the complex interaction between a supersonic free stream and an opposing rocket plume, shown notionally in figure 1 for a single nozzle, the historical reports have not retained enough detail for meaningful comparisons against modern computational fluid dynamics (CFD) codes (ref. 8). For instance, while static aerodynamic response characteristics are reported, the dynamics of the interactions are often neither discussed nor captured in the still images and time averaged data. Thus, there is a need for modern SRP experiments, designed to provide higher fidelity datasets specifically for CFD comparisons. With potential for multi-phased and unsteady plumes, and large scale separations and turbulence, SRP represents an extremely complex and challenging problem for use as a test case for assessing CFD modeling strengths and weaknesses, as discussed in references 8 and 9. Other recent reports that also provide comparisons of computational solutions against the historical data include references 10–15.

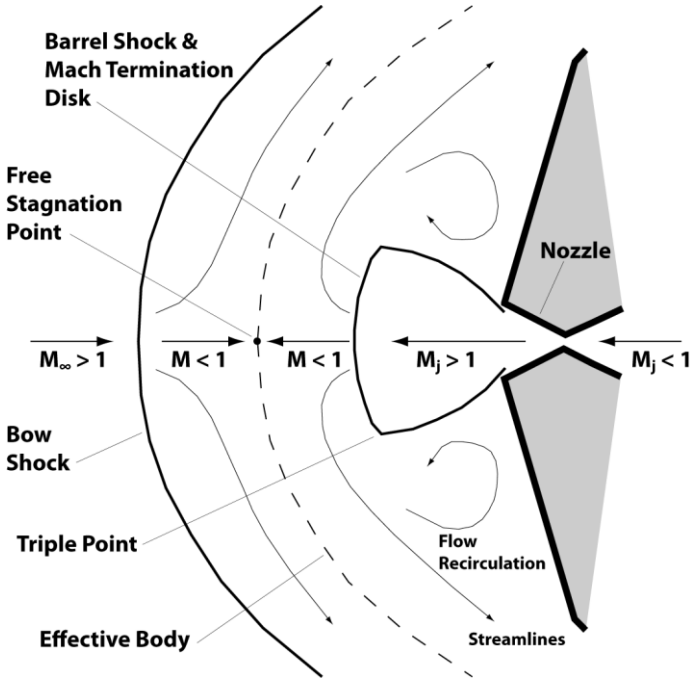

Figure 1. Conceptual sketch of SRP flow features.

Figure 1 provides the salient flowfield features associated with supersonic retropropulsion, which is characterized by a bow shock that is pushed further away from the body via the addition of the jet flow emanating from the nozzles. For the simple case of a single nozzle with sufficient backpressure, the exiting supersonic jet forms a barrel shock and corresponding shear layer that is terminated by a Mach disk as the jet flow decelerates to subsonic conditions because of the oncoming flow. The intersection of the barrel shock and Mach disk forms the triple point, an annular region that represents the terminus of the jet plume. The boundary between the two flowfields, the oncoming free stream and opposing jet flow, establishes an "effective body" that represents a new "virtual" entry body shape. A point exists on this effective body at which both flowfields stagnate typically just in front of the Mach disk. The fluidic nature of the effective body suggests dynamic behavior, but the level of unsteadiness and/or impact for a future flight system is not established by the historical data.

Past SRP experiments have established that for a given configuration two distinct flowfield modes can result, depending on the nozzle backpressure. For high nozzle chamber pressures, a short, wide jet plume (as depicted in figure 1) is formed that tends to be fairly stable. This case is typically referred to as *blunt penetration mode*, resulting in jet plumes that globally push the bow shock away from the body. The other end of the backpressure spectrum results in narrow and elongated plumes that appear to penetrate the bow shock. In this case, typically referred to as *long penetration mode*, the jet plumes only locally displace the bow shock, resulting in a more dynamic and unstable flowfield. Reference 16 provides further discussion of the transition between these two regimes. From a future flight system perspective, high mass missions would likely require high thrust and thus high nozzle chamber pressures, taking advantage of the relative stability of the blunt penetration mode.

The present report provides details of an experimental SRP study conducted in 2010 in the National Aeronautics and Space Administration (NASA) Langley Research Center (LaRC) Unitary Plan Wind Tunnel (UPWT). The primary objective of this study was to conduct a validation experiment in support of improved CFD models and capabilities. Thus, both experimentalists and computationalists were heavily engaged in all aspects of the design of the wind tunnel model and execution of the experiment, a recommendation of reference 17. As a validation experiment, the forebody was heavily instrumented with surface pressure ports, with modules internal to the model to minimize pressure response issues. Also, a few fast response pressure gages were included to monitor forebody surface pressure fluctuations. A high speed video camera was used to capture the dynamics of the interactions between the bow shock and jet plume. Pretest CFD solutions were used to size the model within the test core to minimize tunnel interference effects. Internal flow computations also pointed to concerns over potential liquefaction within the nozzle plumes. To mitigate the need for computing multiphase flows, the decision was made to preheat the high pressure air leading into the plenum. This necessitated a heat conduction analysis of the model assembly to insure the internal pressure modules did not exceed their safe operating conditions and led to the addition of an insulating barrier between the plenum and modules. In addition, Virtual Diagnostics Interface (ViDI) simulations (ref. 18) were conducted of the movement of the tunnel's angle of attack mechanism in pitch, yaw, roll, and translation within the tunnel. These simulations were completed to assess the allowable range of the model (with a notional plume structure) movement within the tunnel test core in support of the run matrix development. The widest reasonable range of movement was required to allow quantification of measurement uncertainty (in a manner similar to ref. 17). Model design and test development aspects are also discussed in reference 19, and preliminary experimental results are presented in reference 20. The present report provides details of the experiment, a discussion of the trends observed, as well as a compendium of the schlieren and surface pressure results. High frequency results and analysis are presented in reference 21. The derived uncertainty results and analysis are presented in reference 22.

SECTION 2
APPARATUS AND METHODS

2.1 Facility

The NASA LaRC UPWT is a closed circuit continuous flow pressure tunnel with two test sections that are nominally 4-ft by 4-ft in cross section and 7 feet long. A photograph of the building that houses this test complex is shown in figure 2 (ref. 23). The primary elements of the UPWT are a 100,000-horsepower compressor-drive system, a dry air supply and evacuating system, a cooling system, and interconnecting tubes that allow air circulation through either of the two test sections. A general layout that highlights these facility elements is illustrated in figure 3 (ref. 23). The Mach number range is 1.50 to 2.86 in Test Section 1 and 2.30 to 4.63 in Test Section 2. The stagnation pressure can be varied up to a maximum of 50 psia in Test Section 1 and 100 psia in Test Section 2. Each test section has an asymmetric sliding-block type nozzle that accelerates the flow to supersonic conditions within the test section. The Mach number within the test section is varied by moving the lower sliding block, which alters the nozzle-throat-to-test-section area ratio. Figure 4 provides a sketch of the sliding-block nozzle concept, while the test section and model support system are shown in figure 5 (ref. 23). The second minimum area downstream of the test section is controlled by hinged sidewalls that provide the required constriction for stabilizing the posttest section normal shock for the various operating Mach numbers. The most recent calibration of the tunnel (from 1981) is provided in reference 24 while reference 25 provides details for planning a test within the UPWT.

Figure 2. The Unitary Plan Wind Tunnel complex in Building 1251 at NASA Langley Research Center (ref. 23).

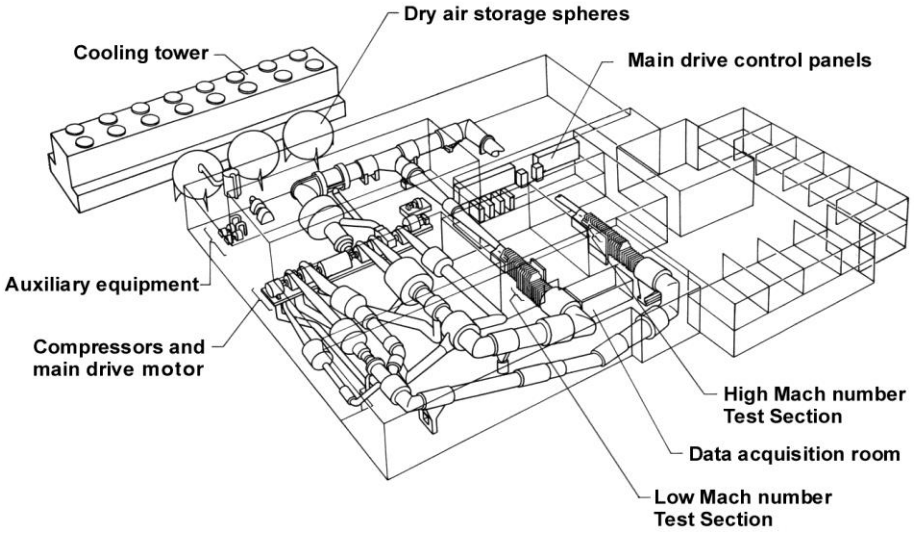

Figure 3. Schematic of the NASA LaRC Unitary Plan Wind Tunnel complex (ref. 23).

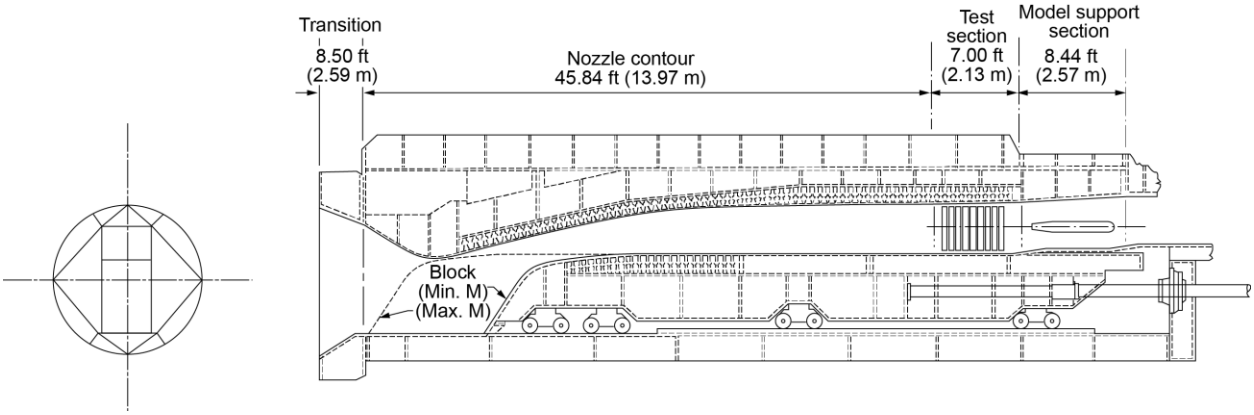

Figure 4. Schematic of the UPWT Test Section 2 nozzle block (ref. 23).

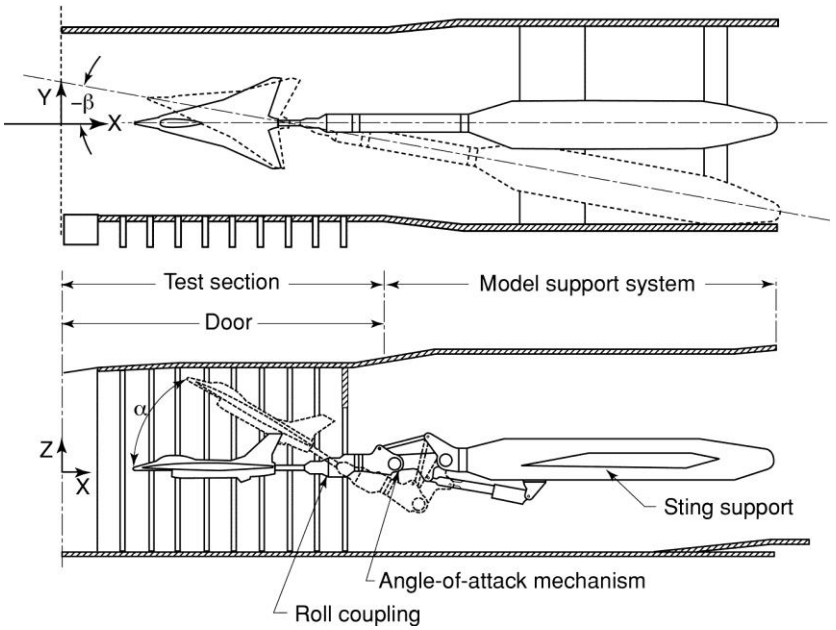

Figure 5. Test Section 2 model support system (ref. 23).

Test Section 2 was used exclusively for this study, as this leg provided the Mach numbers of interest identified by recent system level trade studies (ref. 3 and 5). Thus, all subsequent facility discussion will focus on the capabilities of the higher Mach number leg. The facility has six centrifugal compressors that are used in specific combinations, or modes, depending on the desired Mach number. For each mode, or Mach number range, the upper limit of the operating envelope is established by the drive system power and the stagnation pressure limit, while the lower limit is dictated by the supersonic-flow stability characteristics at reduced pressure. Typical unit Reynolds numbers for testing in the UPWT Test Section 2 are 1 to 5 million per foot. The tunnel stagnation temperatures are typically 125 or 150°F depending on the mode of operation.

The standard Test Section 2 model mounting hardware was used for this test, as shown in figure 5. The basic mechanism is the horizontal wall mounted strut that is capable of forward and aft travel (in the *x* direction) of up to 36.25 in. Attached to this strut is a sting support that allows lateral traverse (in the *y* direction) of ±20 in and sideslip motion ±12 degrees. Forward of the sting support are the angle of attack (α) and roll mechanisms, which provide a pitch range of –15 to 30 degrees and a range of roll of up to 357 degrees.

An upgraded capability for supplying high pressure air to the model has recently been completed for the UPWT. As shown in figure 6, high pressure air at nearly 5,000 psi is controlled and fed to the model through a digital control valve (DCV). The DCV provides manual control of both temperature (by using an inline heater) and pressure over the ranges of ambient to 275°F and 50 psi to 3,800 psi, respectively. The mass flow control range is 0.02 to 30 lbm/s at these conditions. Control accuracy is better than ±2 percent for the pressure range of 50–250 psi, ±1 percent for the pressure range of 250–3,800 psi, and ±5°F in temperature.

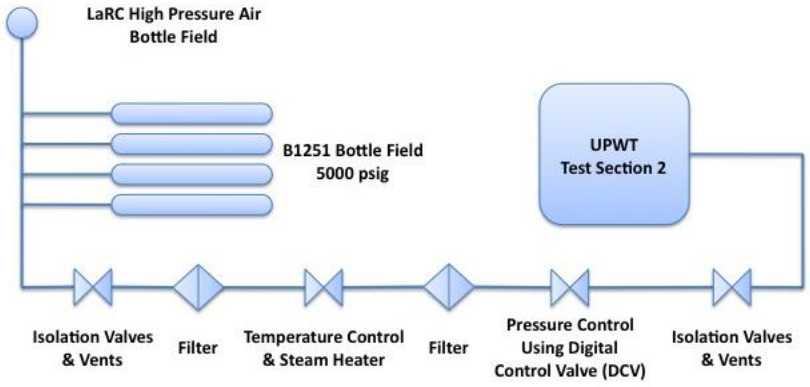

Figure 6. Simplified schematic of the UPWT high pressure system.

2.2 Model

The issues that affected the design of this model are discussed in detail in reference 19. A sketch of the final design is provided in figure 7. After refinement based on pretest computations, a 5 in diameter SRP model was selected. The model includes a highly instrumented 70 degree sphere-cone forebody with locations for four nozzle or plug inserts, followed by a 9.55 in long cylindrical aftbody. A cutaway sketch is provided in figure 8, showing that the assembled model was designed with a partially hollow sting that feeds an internal plenum connected to each nozzle location via a four-port manifold. The plenum is a constant diameter pipe with a 5 degrees flare leading to the manifold. The predicted Mach number within the main plenum is on the order of 0.1 for worst-case conditions (highest mass flow rate). The sting and manifold assembly provides the structural load path to hold the forebody with either plugs or nozzles in place. The aftbody, comprised of two half-cylindrical shells, provides a non-load bearing enclosure intended to protect the internal instrumentation (also shown in figure 8). One nozzle/plug location is on the model centerline, while the other three are located at a radial distance midway between the centerline and maximum forebody radius and spaced 120 degrees apart. These locations can accommodate either a nozzle or a plug. The nozzles built for this study had a 4:1 exit-to-throat area ratio. The plugs provide a baseline forebody surface with no steps or gaps. The model was not designed to replicate any current configuration or full-scale system but rather to provide generic CFD validation data for a range of jet configurations and conditions. The design drawings for the as-built model are provided in Appendix A. Photographs of the individual components and partial assemblies obtained during the model acceptance fit-check review are also provided in Appendix A.

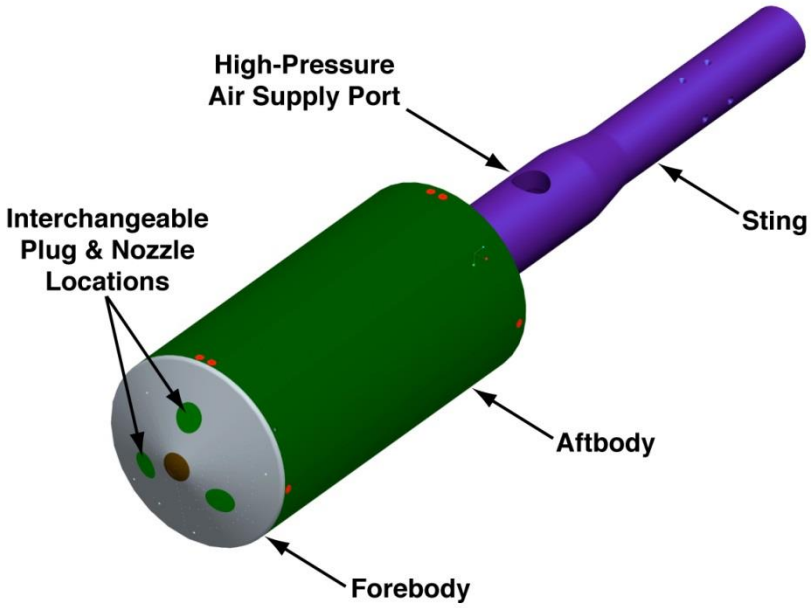

Figure 7. Oblique view of UPWT SRP model assembly.

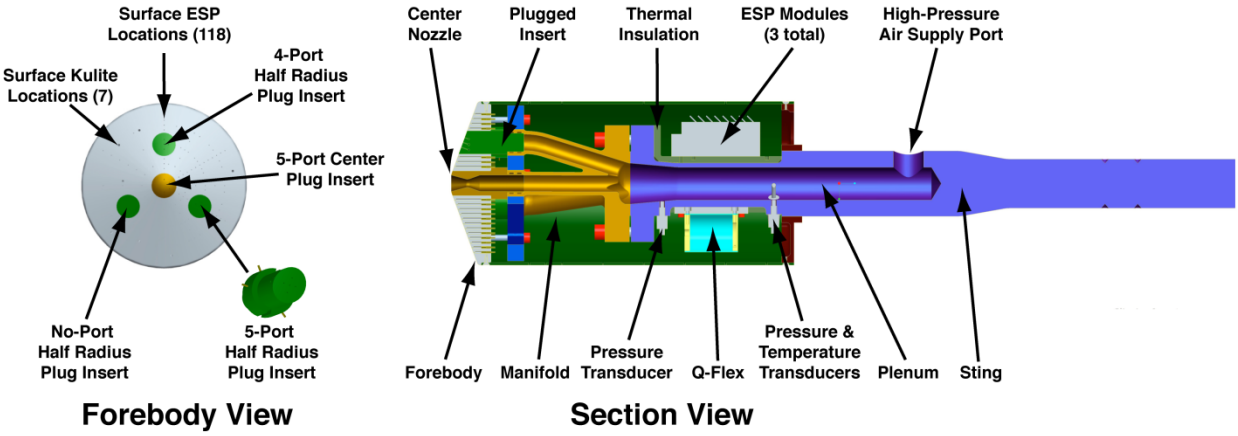

Figure 8. Major components of UPWT SRP model assembly.

One unique component of this model that warrants further discussion is the manifold assembly design and fabrication. The manifold encloses the main plenum and provides the ports to each individual nozzle. This part consists of a laser-sintered stainless steel front plenum (see DWG 1168292 in Appendix A) and a Type–304 stainless steel nozzle interface plate (DWG 1168293) that together hold the inserts and forebody in place. These two components were brazed together, and this assembly was inspected and qualified prior to final machining (see DWG 1168298). Once the manifold assembly was completed, a hydrostatic pressure vessel bench test was conducted to 3,750 psi (or 150 percent of the maximum planned pressure, 2,500 psi) prior to initiation of the wind tunnel test.

The use of heated high pressure air induced concern regarding the internal temperature of the model where the pressure instrumentation would reside (ref. 19. An insulating barrier was added to the model to reduce conduction heating of the instrumentation modules. For the insulating

barrier between the plenum/sting and the pressure modules, a tough, machinable thermoplastic material called ULTEM® 1000 was used. This high performance polymer maintains its high strength and rigidity even at elevated temperatures, thus providing an excellent platform with which to attach and isolate the modules. This piece is shown in light green of the cutaway of figure 8. This insulating barrier was sufficient to maintain the pressure instrumentation within acceptable temperatures during the test. Figure 9 provides an oblique view of the final design of the insulator saddle block showing the mounting holes for assembly. The saddle block provides attachment surfaces for three pressure modules.

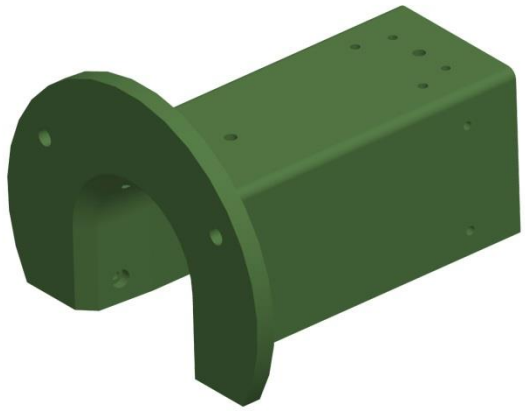

Figure 9. Oblique view of insulator saddle block.

The model was also designed to minimize down time for configuration changes. The design included small, easily replaceable inserts for the nozzles and plugs. The use of inserts was preferable to reduce impact on planned surface pressure taps on the forebody. The pressure tubes were installed with slack to allow the swap-out of inserts with pressure tubing connections left intact, minimizing the number of leak checks during the test campaign. In addition, the pressure tubing was installed with quick disconnects, in case either the forebody or pressure modules needed removal for any reason. Configuration changes were initiated by removing the uninstrumented cylindrical shell, allowing access to the bolts that secure the forebody. Sliding the forebody forward a few inches on the long bolts provided enough clearance to remove and replace the inserts. Three out of four baseline plug inserts had built-in surface pressure taps (see DWG 1168294 & 1168295), which required additional tubes to be connected to the pressure modules. Two of the four nozzle inserts (one on centerline, also shown in figure 10, and one on the periphery) had internal high pressure and temperature instrumentation (for measuring pressure losses between the main plenum and the nozzle throats) that required connection to the data acquisition system.

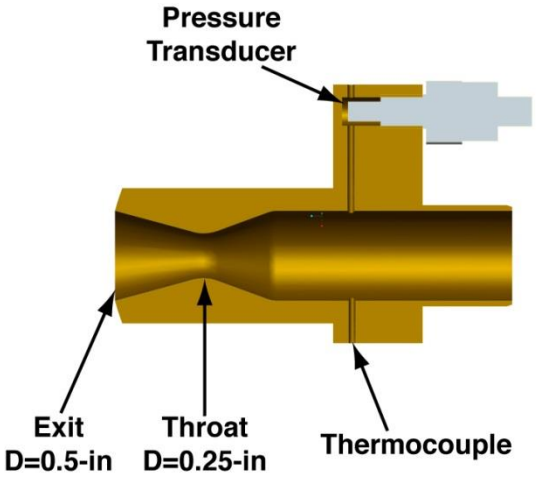

Figure 10. Close up of the instrumented center nozzle.

2.3 Instrumentation

The primary measurements on the model was 167 surface pressure ports connected via 0.040 inch diameter flexible urethane tubing to three Pressure Systems, Inc. (currently owned by Measurement Specialties™) electronically scanned pressure (ESP) transducer modules located within the model. Two 64-port modules (0–5 ± 0.005 psid) were used to measure surface static pressures at 118 locations on the model forebody, as well as 4 locations on the aftbody, while a 48-port (0–2.5 ± 0.003 psid) module was used to measure pressures at the remaining 45 locations on the aftbody. A sketch of the surface port locations is provided in figure 11. Note that on the aftbody, all instrumentation was placed on the portside shell (θ = 180° to 360°) to allow easier access to the internal compartment. A high number of pressure ports were desired to provide data for CFD validation and to aid posttest experimental uncertainty analysis. Table A-1 provides the locations for all surface pressure measurements. All three modules were teed to a common reference pressure that was pulled down to a hard vacuum to provide absolute pressure measurements. Three separate known pressures were supplied by Ruska Model 6211–801 pressure gages (0–38 ± 0.004 psia) to transducers on each ESP module and were monitored to check for drift in the ESP pressure measurements. In-situ ESP calibrations were performed using the system Model 8432–15A pressure calibration unit (PCU, 0–15 ± 0.003 psia) when the drift exceeded 2.5 psf.

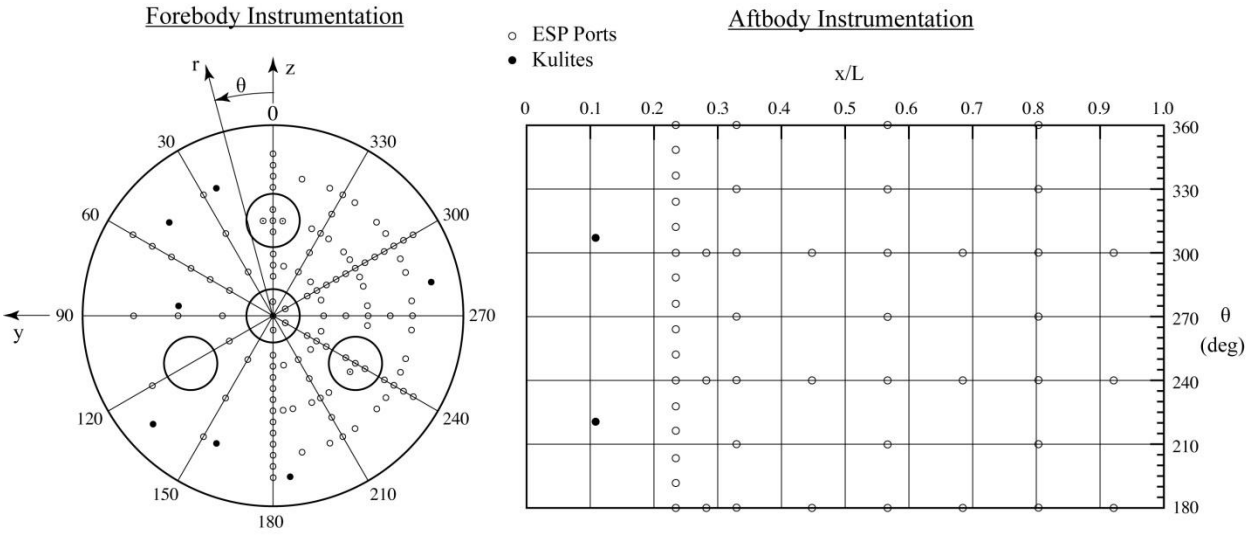

Figure 11. Forebody surface instrumentation layout for the baseline configuration.

Seven 0.0625-inch diameter Kulite XCS–062–5A pressure transducers (0–5 ± 0.013 psia) were mounted flush to the surface of the model forebody, also shown in figure 11, with an adhesive potting material and used for measuring fluctuating surface pressures. The Kulites were included to monitor and measure any high frequency oscillations arising from the jet/free-stream interactions. Two additional Kulite transducers were mounted in the model aft shell just behind the shoulder but were unfortunately damaged during model assembly. The output signals from the Kulite gages were split to both the standard and high speed data acquisition systems to provide simultaneous time-averaged and unsteady pressure measurements.

Pressures were measured in the model at different locations along the high pressure airflow path using up to four Kulite XT–190–2000A pressure transducers (0–2000 ± 2 psia). Two transducers were located at different stations in the model plenum (see figure 8), with the gages mounted flush to the inside surface of the plenum chamber. The remaining two pressure transducers were connected and used for measuring internal pressure losses between plenum and nozzle. These ports were located 0.417 inches upstream of the nozzles for both the center and a periphery nozzle. Figure 10 provides a representative sketch of the center nozzle, showing the location of the pressure and temperature instrumentation just ahead of the nozzle. These transducers were active only when their respective nozzles were installed in the model. Plenum temperatures were measured using a 6 mm diameter Omega RTD–NPT–72–A platinum resistance temperature detector (RTD) probe (132–910 ± 1°R) embedded 0.5 inches into the high pressure airflow. Additionally, each of the two instrumented nozzles contained a Type K thermocouple (132–2,742 ± 4°R) mounted flush to the inside surface and opposite of the plenum pressure port (shown in figure 10).

A NASA Langley built accelerometer was installed internal to the model (noted as Q-Flex in figure 8) and used to directly measure model pitch angle during the test. The device was calibrated in place as a function of pitch and roll angles using a multi-axis Langley Angle

Measurement System (AMS) (ref. 26) installed on the model during setup. The resultant calibration accuracy was approximately ±0.01 degrees.

Eight Type K thermocouples (132–2,742 ± 4°R) were installed to monitor and measure the thermal environment inside the model during the test. One thermocouple was mounted underneath each ESP module as well as the accelerometer, while the remaining four thermocouples were mounted to the inside surface of the aft shell at a location of approximately half the model length and every 90 degrees around the circumference.

A calibrated Flow–Dyne Engineering subsonic venturi flow meter with a 1.503 inch diameter inlet and 0.695 inch diameter throat was installed in the high pressure air line just outside of the test section and used to measure the mass flow rate of air exhausting through the model nozzles. The venturi inlet pressure was measured using a Druck PDCR 4060 pressure transducer (0–3,000 ± 2.4 psia), while the inlet temperature was measured using a 0.25-inch diameter Type T shielded thermocouple probe (132–1,122 ± 2 R). The pressure drop across the venturi throat was determined with a Bell & Howell Model 4–351–0004 differential pressure transducer (0–100 ± 0.05 psid) that was calibrated in one direction to increase accuracy.

To capture the dynamics of flowfield interactions between the bow and barrel shocks, a high speed digital camera was used to record the schlieren video. The Phantom 12, from Vision Research, is a 1 megapixel camera capable of taking more than 6,200 frames per second (fps) at full 1280 x 800 resolution and up to 1,000,000 fps at reduced resolution. For the present test, framing rates between 5,000 and 10,000 fps were used.

2.4 Test Conditions and Run Matrix

Table A-2 provides a complete list of parameters for this test. Table B-1 provides the notional run matrix and shows the key parameters of importance such as the configuration (number of nozzles), model attitude and location (angle of attack, roll, and position within the tunnel), free-stream conditions (Mach and Reynolds numbers), and nozzle conditions (thrust coefficient, and plenum pressure and temperature). The run matrix provides the pretest plan for sequencing the test in that it reflects the intended order for varying the key parameters. For instance, for any given configuration, an angle of attack sequence is obtained prior to changing the roll angle, strut position, plenum condition, or Mach number, in that order. To limit the scope of the present study, only a single low Reynolds number condition was considered for each Mach number of interest, as shown in figure 12. The lower Reynolds numbers allowed for the highest range of thrust coefficients obtainable for the study, as thrust coefficients are inversely proportional to the tunnel dynamic pressure. To summarize, the tunnel test conditions for this study include Mach numbers of 2.4 and 3.5 at a Reynolds number of 1.0×10^6/ft, and 4.6 at a Reynolds number of 1.5×10^6/ft; model positional settings for angles of attack of 0, ±4, ±8, 12, 16, and 20 degrees, roll angles of 0, 60, 120, and 180 degrees, model *x* positions of 25, 40, and 50 inches, and *y* positions of 0 and ±8 inches; and high pressure air conditions of pressures ranging from 0 to 1,500 psi and temperatures ranging from 120°F to 170°F.

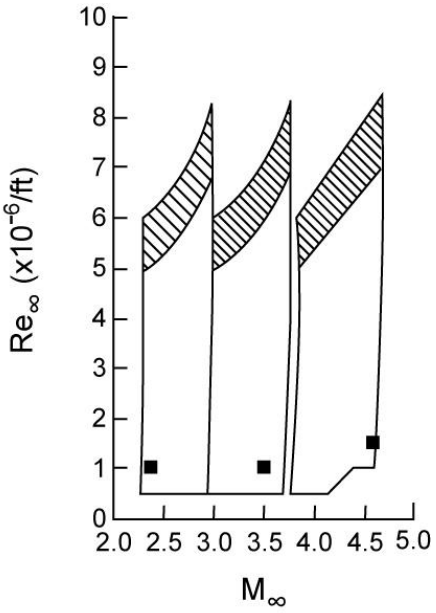

Figure 12. Test conditions within operating envelope for UPWT Test Section 2.

2.5 Data Acquisition & Reduction

The parameter list provided in Table A-2 also lists the equations used for data reduction for this test. The ESP surface pressure measurements were acquired with the Esterline 8400 System at 10 samples/sec. Remaining data channels were acquired at 30 samples/sec through a NEFF 620 signal conditioner/multiplexer system. The NEFF channels were processed through analog 1 Hz, low pass, four-pole Butterworth filters and recorded using a MODCOMP 88100 computer at 16 bit analog-to-digital (A/D) conversion. Both systems used a sampling period of 2.5 seconds. The unsteady pressure data from the Kulite transducers were sampled at 40,000 samples/sec for a 2.5 second sampling period using a National Instruments/Labview-based high speed data system synchronized to the standard data system. These data were processed through a 20 kHz low pass filter and recorded at 16-bit A/D conversion.

Raw voltages from the instrumentation were recorded and processed in real time through respective calibration functions into engineering unit values for real-time display, monitoring, and plotting. Facility flow conditions were calculated via standard gas dynamic equations using measured tunnel stagnation conditions and calibrated values of free-stream Mach number. These flow conditions were then used to compute parameters such as the surface pressure coefficients, nozzle pressure ratios, nozzle exit-to-static pressure ratios, and nozzle thrust coefficients.

The measured plenum static pressures were corrected to total pressure values using total-to-static pressure ratios calculated from estimates of the plenum Mach number. These estimates were computed from a binomial approximation of the mass flow rate equation using the measured mass flow rates, plenum temperatures, and plenum cross section areas, and are valid for small values of Mach number. Nozzle exit conditions were calculated based on the plenum total conditions and the nozzle exit-to-throat area ratios. The thrust of each nozzle was computed

from the total measured mass flow rates and the ratio of the individual nozzle throat area to the total nozzle throat area.

The model nose position relative to the test section coordinate system was computed for each data point based on the axial and lateral movements of the model support system as well as the pitch and yaw angles of the model. Positional information was then used during the uncertainty assessment phase of the data analysis process. No attempt was made to correct the model angle of attack for noted flow angularity for this facility. Instead, any tunnel flow angularity was to be captured as part of the uncertainty assessment (ref. 22).

SECTION 3
TEST SET UP AND EXECUTION

Model installation into the tunnel began early in July 2010. Figure 13 provides a photograph of the model installed within the UPWT. A few days were required to install the model and high pressure air supply line, along with a careful installation and systematic leak checking of each pressure tube connection between the surface pressure ports and the ESP modules, (see figure 14). In situ calibrations of the ESP modules and the air supply venturi were also conducted using the facility as a vacuum chamber prior to the start of the test in order to insure systems were behaving as expected.

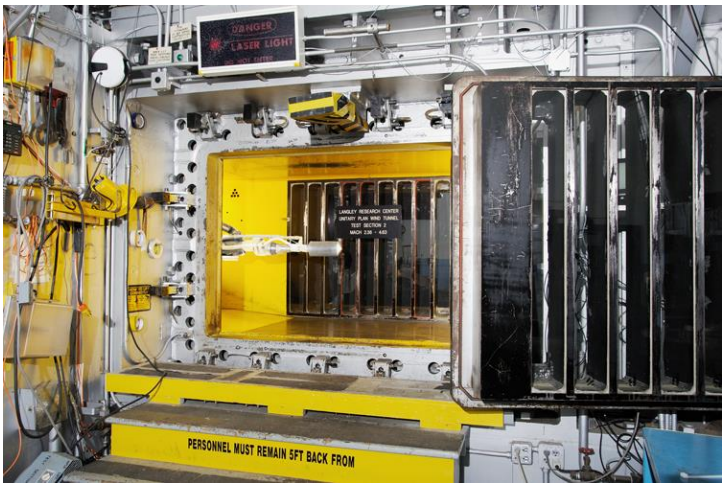

Figure 13. The SRP model installed in the UPWT Test Section 2.

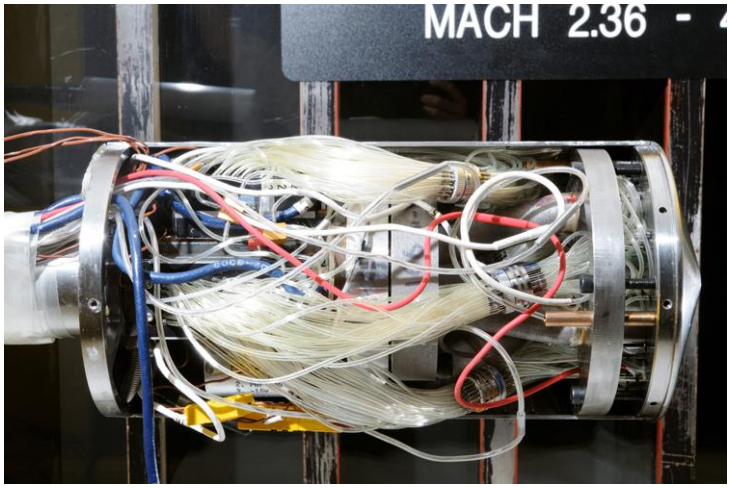

Figure 14. The internal pressure lines and instrumentation wiring.

The test team held a prioritization meeting the week preceding test initiation to revise the run matrix, allowing for lower priority objectives to be omitted if testing appeared behind schedule. The matrix was updated to include a three tiered priority system: 1 being the highest priority, 2 being cases that should be obtained, time permitting, and 3 being cases only considered if ahead

of schedule. Table B-1 provides the run matrix as laid out by the pretest prioritization meeting with the sequence of parametric variation from first to last; however, the actual run numbers obtained for each case replace the prioritization numbers that would have been listed in the three right-most columns. In the cases where a lower priority item was dropped from the test, the table cell is left blank with a gray filler. Table B-2 provides corresponding plenum conditions for nominal thrust coefficients that were planned for during the test. The actual run-averaged tunnel and nozzle flow conditions obtained for each run are provided in the run log listed in Table B-3. The angle of attack pitch pause schedule for each run is provided in Table B-4. Statistical analyses of all test points obtained for a given flow condition are provided in Table B-5. Schlieren video data was not acquired for every run and angle of attack because of file memory and transfer constraints. Table C-1 provides a summary of the schlieren video data obtained during the test.

The model provided for four configurations: (1) the baseline model, with plug inserts in all four locations, (2) the center nozzle, with plug inserts in the three peripheral locations, (3) the tri-nozzle, with a plug insert in only the center location, and (4) the quad-nozzle, with no plug inserts. The first three configurations were considered Priority 1, while the quad configuration was considered Priority 2. In the end, all four configurations were tested. For the angle of attack sweep, the tunnel pitch mechanism was programmed to pause at –8, –4, 0, 4, 8, 12, 16, and 20 degrees and a repeat of 0 degrees, in that order. This sweep sequence was used for most of the test. (There were a few cases at the highest angle of attack and thrust coefficients in which the tunnel seemed close to tunnel unstart, so these cases were omitted.) To extend the spatial coverage of the clustered instrumentation, model roll angles of 0, 60, 120, and 180 degrees were used. Model roll also provided repeatability data with select angle of attack cases (e.g., $\alpha = -4$ degrees with 0 degree roll is a repeat of $\alpha = 4$ degrees with 180 degrees roll). A full range of streamwise (*X*) and lateral (*Y*) model translations were considered important for the uncertainty estimation, especially for the baseline configuration, to provide repeatability data from different stations within the tunnel. For the baseline configuration, independent translations in either the *X* or *Y* directions were considered Priority 1 and combined *X* and *Y* translations were considered Priority 2. For the nozzle configurations, only *X* translations were considered as Priority 2, while *X* and *Y* translations were considered Priority 3. When nozzles were installed in the model, the plenum pressure was controlled and adjusted via the DCV, with a fixed temperature near 170°F to provide the thrust coefficients listed in Table B-2. A broad range of thrust coefficients was considered Priority 1, although additional cases were captured as part of the pretest matrix as Priority 2. For tunnel operating conditions, the widest possible range of Mach numbers for Test Section 2 at a single unit Reynolds number case was considered a top priority. Mach numbers of 2.4 and 3.5 at a Reynolds number of 1.0×10^6/ft, and 4.6 at a Reynolds number of 1.5×10^6/ft were used. To reduce likelihood for tunnel unstarts, these conditions were selected to be a safe margin above the lower limit of the operating envelope of the tunnel, as shown in figure 12.

The baseline configuration is shown in figure 15, which also shows some of the port side instrumentation bundles strapped to the outside of the tunnel hardware. In this photo, the model has been rolled to the 180 degrees position such that the air supply feed line is at the bottom. Figure 16 provides a sequence of starboard side photos showing the location of the instrumentation and high pressure lines for each roll increment of zero (with the air supply line on top) to 180 degrees. The baseline runs were primarily intended for quantifying various

sources of experimental uncertainty. The lateral and streamwise translations to various stations within the tunnel coupled with the model rolls allows for sensor-to-senor comparisons such that instrumentation and flowfield uniformity uncertainties can be estimated. In the streamwise direction, the model translations are notionally 15 in forward and 10 in back. In the lateral direction, the model translations are ±8 in.

Figure 15. The baseline model installed in Test Section 2.

(a) Roll = 0 degrees.

(b) Roll = 60 degrees.

(c) Roll = 120 degrees.

(d) Roll = 180 degrees.

Figure 16. The baseline model installed in the UPWT.

Figure 17 provides another starboard side photo of the center nozzle configuration showing the downstream attachment points for the instrumentation bundle and air supply line. The center configuration represents the simplest nozzle case for CFD comparisons and the data most similar to historical results. In reference to the run matrix shown in Table B-1, a few streamwise translation cases were planned but not performed because of time constraints. In addition, many of the 60 and 120 degrees roll cases were omitted also because of time constraints, as they were considered redundant for this axisymmetric case.

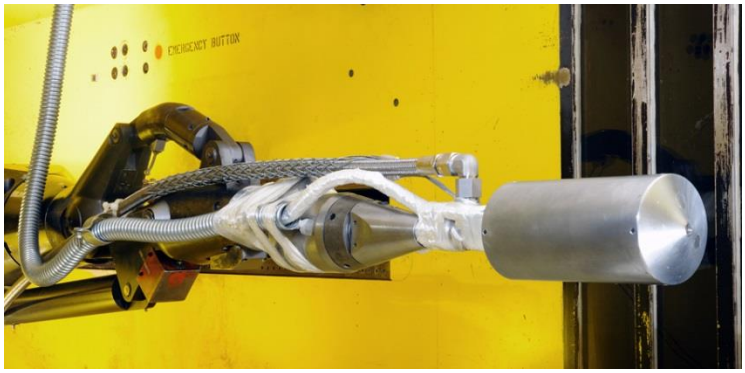

Figure 17. The center nozzle configuration installed in the UPWT.

The tri-nozzle configuration, shown in figure 18, was also deemed important for comparison against historical data, as there have been previous studies that looked at multiple nozzles located towards the model periphery. The location of these nozzles, at the midpoint of the radius of the forebody, is unique, however, closer inboard than all previous studies. During the test, most Priority 1 cases were acquired with the exception of the highest thrust coefficient and late repeat cases. Priority 2 and 3 cases planned to acquire model translation data on the tri nozzle were not acquired due to time constraints.

Figure 18. The tri-nozzle configuration installed in the UPWT.

The quad-nozzle configuration was originally Priority 2; however, a real-time team decision was made during the test that this data would be unique due to the addition of the center nozzle, which had not been studied before. Due to time constraints, the range of thrust coefficients acquired for the quad configuration was reduced to only a few cases.

SECTION 4
DISCUSSION OF RESULTS

The following figures and discussion provide a review of key observations from the test. These figures include schlieren still frame images (extracted from the high speed videos) and corresponding forebody surface pressure coefficient data (line plots and contour maps) to illustrate trends. The schlieren images used within figures included in this section have been zoomed and cropped to enlarge the details of interest. The original full frame images can be found within the schlieren appendix. Note that in the pressure data line plots to follow, polar coordinates are used for axisymmetric data ($\alpha = 0°$) with a ray emanating from the model centerline, and Cartesian coordinates are used for nonaxisymmetric data ($\alpha \neq 0°$) with a ray of data across the width of the model. For completeness, all results are contained within appendices in run chronological order: schlieren images, including representative still frames and time averaged and standard deviation results, in Appendix C surface pressure data in line plot format for select rays on the forebody and aftbody in Appendix D; and forebody contour maps derived from the pressure data in Appendix E. The high frequency data analysis and uncertainty assessment are to be published separately, although preliminary results have been published in references 21 and 22, respectively. In the discussion to follow, observations of unsteadiness are qualitatively assigned based on a review of the video data. In these cases, the "unsteadiness" can be seen through bow shocks and/or plumes that appear irregular in shape in the still frame images, or blurry in the time averaged images captured in the appendix.

4.1 Baseline

Figure 19 provides the effect of Mach number for the baseline configuration at $\alpha = 0°$. As expected, the bow shock moves closer to the forebody, and the pressure coefficient increases as the Mach number increases. Note that the distance between the slats in the schlieren window is 5.5 in, with each slat measuring 1.25 in. These can be used as scales to roughly estimate bow shock location as a function of Mach number, with the standoff distance decreasing by an approximate factor of two when going from Mach 2.4 to 4.6. The stagnation pressure coefficient increases by roughly 5 percent between Mach 2.4 and 3.5, but less than 1 percent going to Mach 4.6. The smaller increase in pressure between the two highest Mach numbers is indicative of Mach number independence, as the stagnation point pressure coefficient asymptotes to a value near 1.8 as Mach number increases.

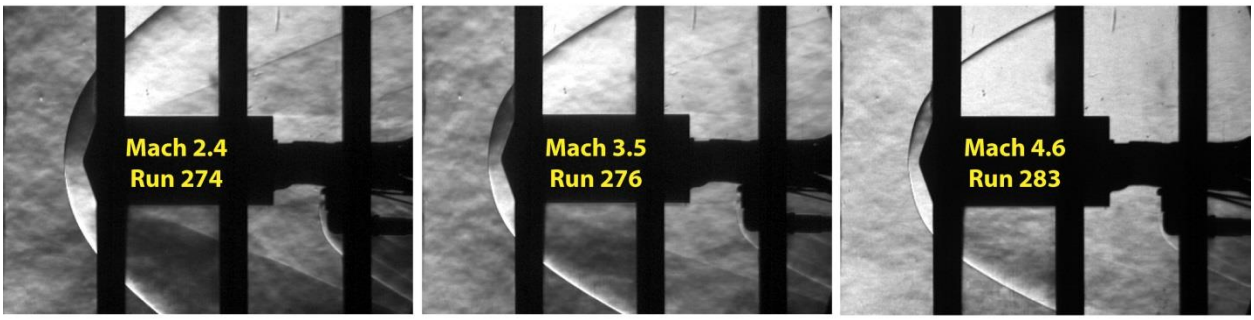

(a) Schlieren.

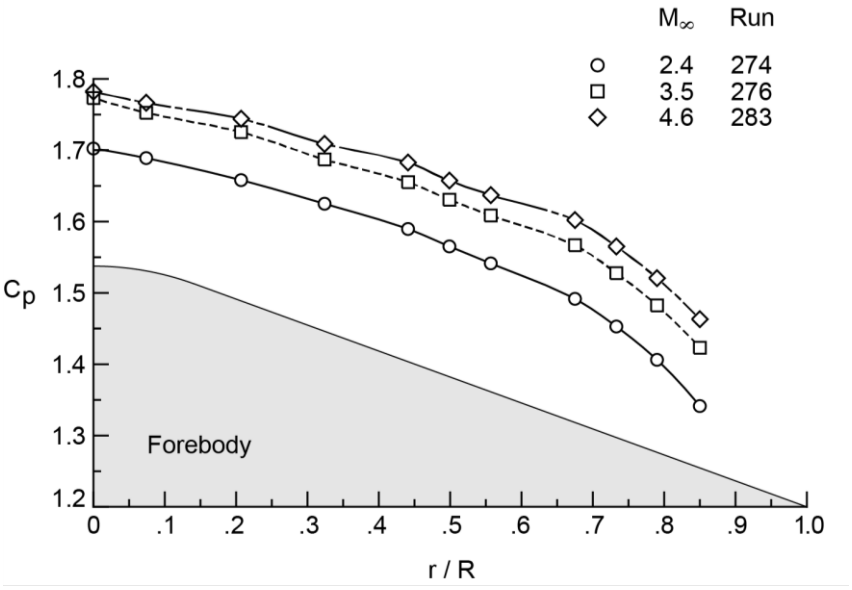

(b) Surface pressure.

Figure 19. The effect of Mach number for the baseline configuration at $\alpha = 0°$.

Figure 20 provides the effect of angle of attack for the baseline configuration at $M\infty = 4.6$. These results are representative of all three Mach numbers. The flowfield is very steady for all angles of attack (see Appendix C). The pressure data, shown for a ray from top to bottom for this orientation, shows the stagnation point peak moving off the center nose radius onto the flatter cone region for the higher angles of attack. Also note in the schlieren images that the model translates downstream with increasing angle of attack due to the design of the model pitch mechanism.

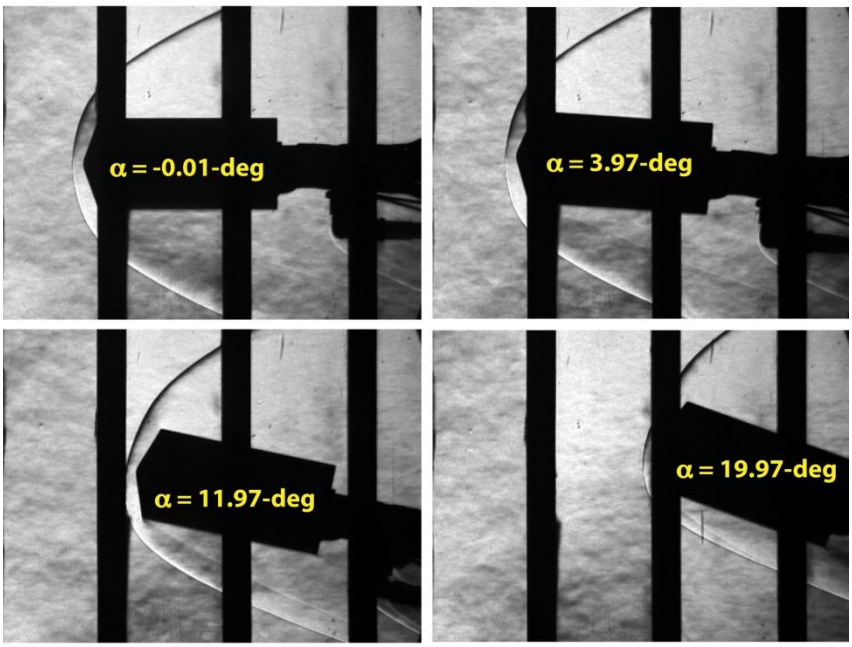

(a) Schlieren.

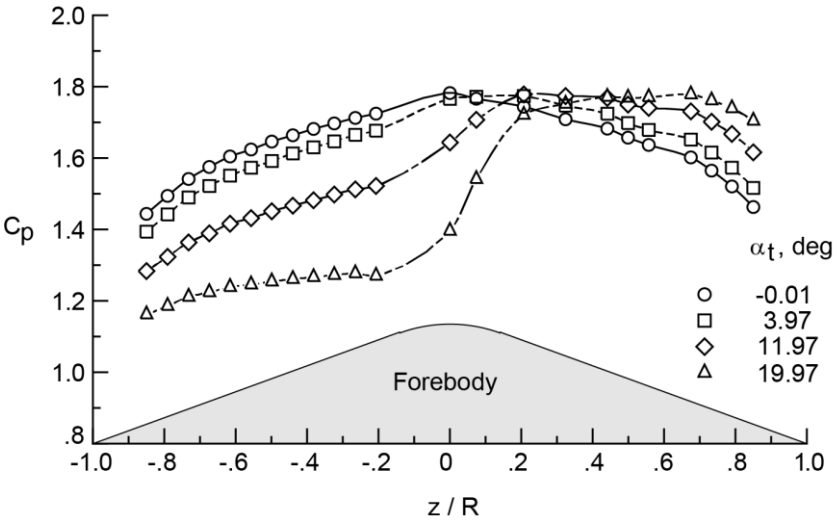

(b) Surface pressure.

Figure 20. The effect of angle of attack for the baseline configuration at M_∞ = 4.6 (Run 283).

Figure 21 provides forebody pressure coefficient contour maps for the range of angles of attack at Mach 2.4 showing the global movement of the surface pressure for each test point. These global maps were interpolated from the pointwise measurements, as represented by the black dots for each sensor. All faulty sensors were omitted from the data file prior to the generation of the contour maps. It should be noted that these images are based on a body-fixed coordinate system. For the case shown here, Run 274, the model was rolled to ϕ =180° so that an upward pitch movement (i.e., α = 20°) corresponds to decreased pressure on the lower half. These trends

are representative of the effect of angle of attack on the baseline configuration for all Mach numbers. All contour maps are contained within Appendix E along with a description of how they were generated.

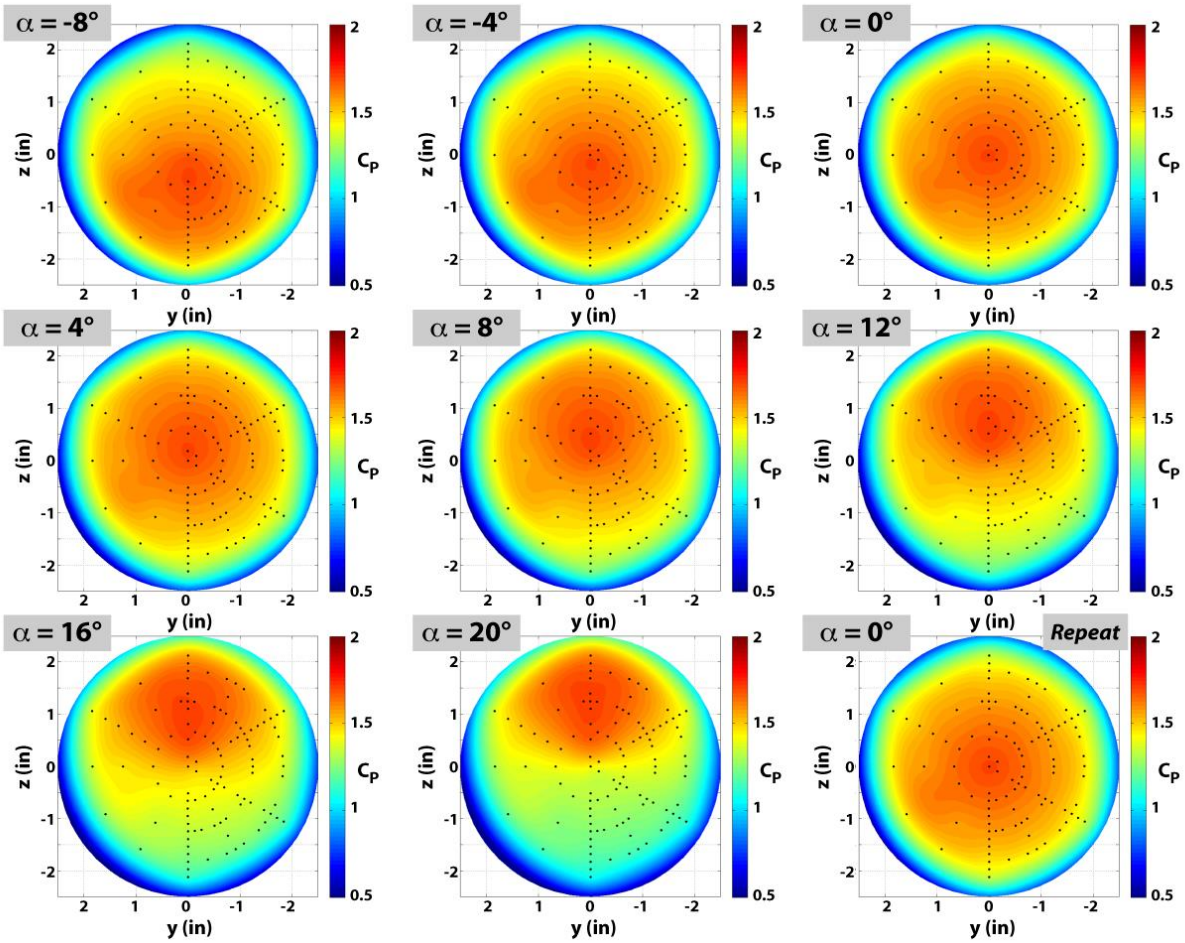

Figure 21. Contour maps showing the effect of angle of attack for the baseline configuration at M_∞ = 2.4 (Run 274).

4.2 Center Nozzle

The effect of Mach number for the center nozzle configuration at $\alpha = 0°$ and $C_T = 2$ is shown in figure 22. The flow emanating from the center nozzle forms a barrel shock that is even wider (for these conditions) at the jet terminus (or triple point) than the model. The curved jet terminus, or Mach termination disk, is partially obscured by the window slats for this model location. However, there are other model positions contained in Appendix C that provide a better view of this region. Aside from the increased bow shock standoff distance due to the plume, the bow shock shapes are quite similar to those shown for the baseline configuration. The nozzle flow does induce a small amount of flow unsteadiness, in the annular triple point region, as can be seen by reviewing the standard deviation images of Appendix C. Aside from the slight triple-point "flapping," the rest of the flowfield is quite steady for all Mach numbers at

$\alpha = 0°$. The pressure data on the forebody, shown for a ray from the centerline to the shoulder are relatively flat, indicative of a large flow separation zone due to the annular recirculation of the nozzle plume. Note that the pressure taps from r/R of 0 to 0.2 are located on the center plug, which is not installed for this configuration.

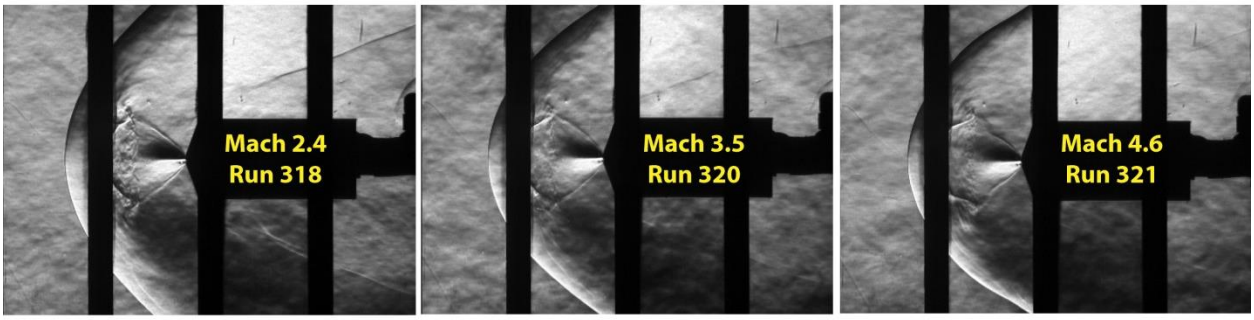

(a) Schlieren.

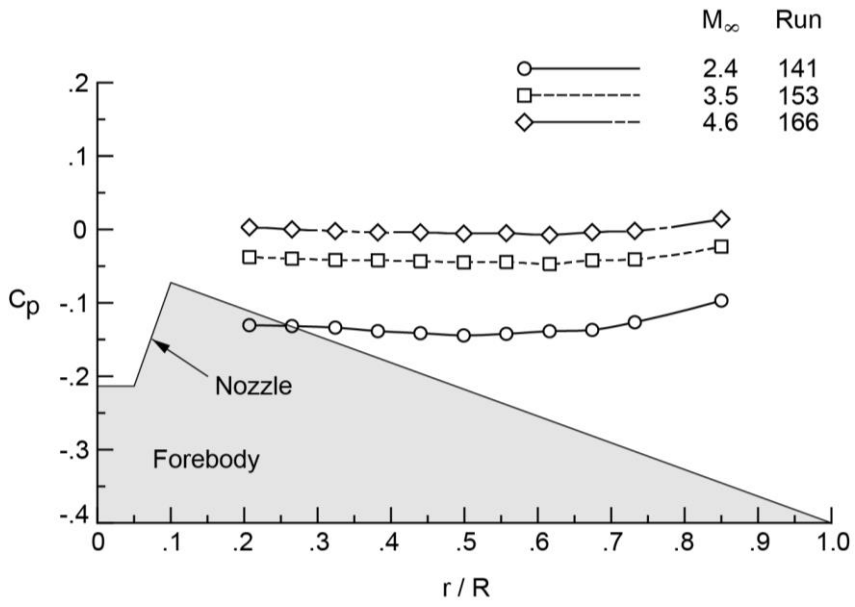

(b) Surface pressure.

Figure 22. The effect of Mach number for the center nozzle at $\alpha = 0°$ and $C_T = 2$.

The effect of increasing thrust coefficient for the center nozzle at $M\infty = 4.6$ and $\alpha = 0°$ is shown in figure 23. The bow shock standoff, as well as the maximum width of the barrel shock, is directly affected by the thrust coefficient. Note that, for the images of figure 19 and figure 23, the model is in the same location, nearly aligned with the third window slat from the right. For the lowest thrust coefficient ($C_T = 0.5$), the bow shock stand off distance is significantly increased from just in front of slat #3 for the baseline case (shown in figure 19) to almost touching slat #4 (the distance between the slats is roughly 5.5 in). Further increase of the thrust to $C_T = 3.0$ resulted in further increase of the stand off distance (now ahead of slat #4). Extraction of the standoff distances will be further examined and discussed at the end of this section. The video data (see Appendix C) reveals, as with the previous example, that the

flowfield is steady, with the exception of the triple point region, for the range of thrust cases acquired. The pressure data suggests that the forebody is mostly separated, with the shoulder region being most affected by the changing thrust levels. The pressure coefficient at the shoulder drops from 1.48 for the baseline no blowing result (shown previously) to roughly 0.29 at C_T = 0.5 and then down to just below zero at C_T = 3.0.

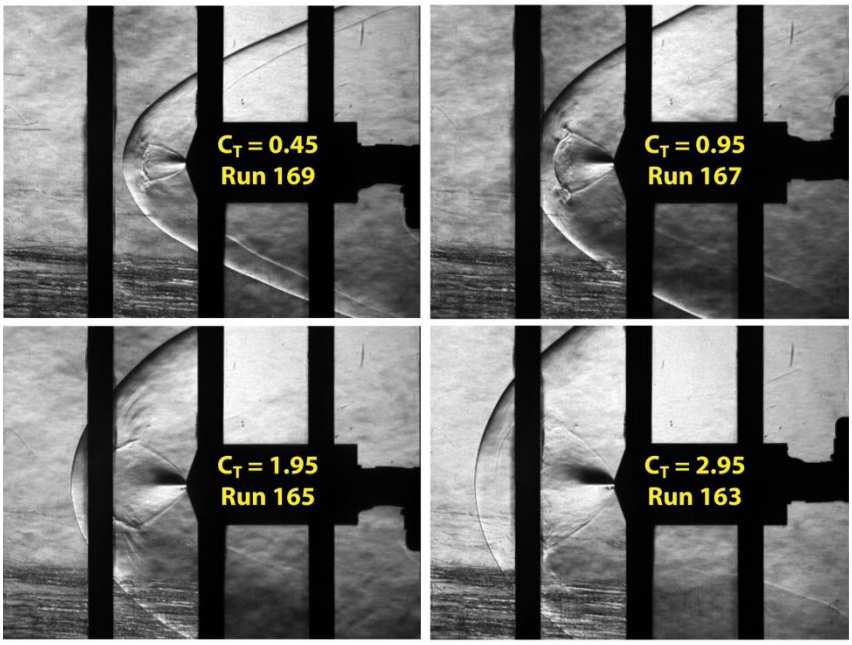

(a) Schlieren.

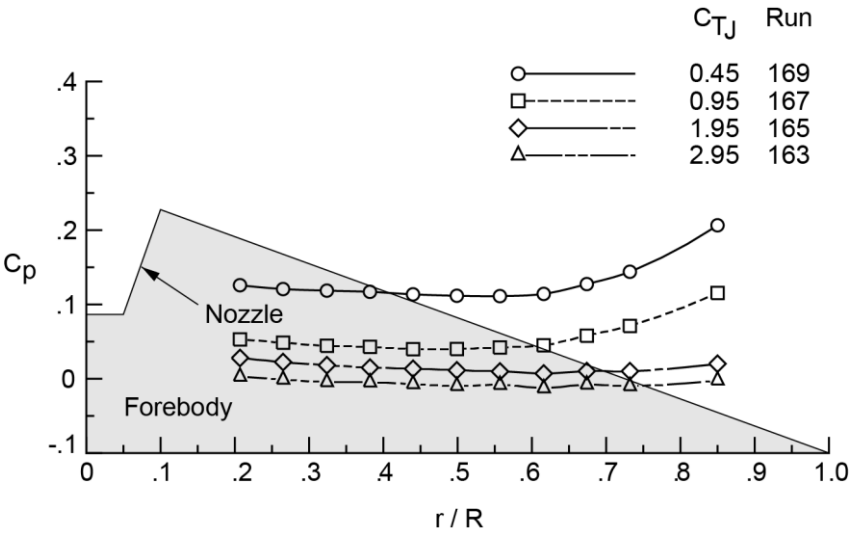

(b) Surface pressure.

Figure 23. The effect of thrust coefficient for the center nozzle at $M\infty$ = 4.6 and α = 0°.

The contour maps can also be used to visualize the global effect of the increasing thrust or plume size. Figure 24 provides a comparison of the contour maps to the corresponding schlieren images for a range of thrust cases at Mach 2.4 and $\alpha = 0°$. For the higher thrust cases, the size of the Mach disk at the end of the plume is greater than the forebody diameter, effectively shielding the forebody from the oncoming flow. For thrust coefficients less than or equal to one, the plume only partially shields the forebody, thus the shoulder region sees an increase in pressure as a result. At the lowest thrust case, the schlieren image suggests a new compression shock ahead of the forebody shoulder, indicating supersonic flow in that region. The trends shown here for Mach 2.4 are representative of those observed for other Mach numbers.

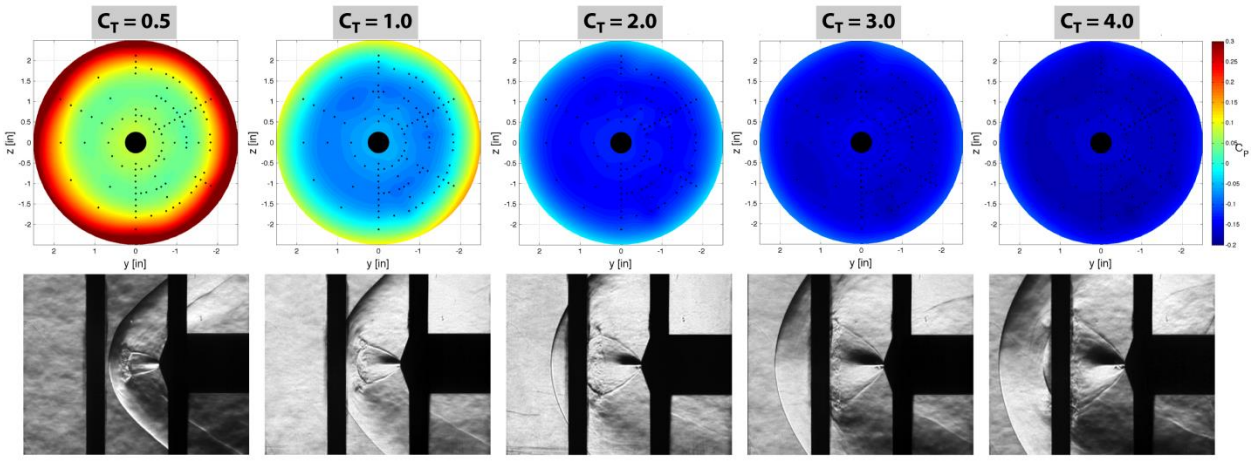

Figure 24. Comparison of contour maps to Schlieren for a range of thrust cases for the center nozzle configuration at $M_\infty = 2.4$ and $\alpha = 0°$ (Runs 319, 139, 141, 137, and 136, respectively).

Figure 25 provides the effect of angle of attack for the center nozzle configuration at $M_\infty = 4.6$ and $C_T = 2$. As mentioned earlier, irregular bow shocks and plumes can be used as a gross indicator of unsteadiness and this is evident in the image shown for the highest angle of attack. However, at moderate angles of attack the observed unsteadiness is more localized to the windward triple point region and thus the still frame image shown for $\alpha = 12°$ does not appear irregular, although a slight bulge in the bow shock is seen. Thus, the jet interaction region flowfield becomes increasingly unsteady for the center nozzle at angles of attack greater than 10 degrees, first emanating in the triple point region and then encompassing the entire flowfield. Appendix C provides additional processing that allows assessment of the unsteadiness observed from the schlieren video. The forebody pressure data, shown for a ray from top to bottom for this orientation, indicate that the windward surface pressure increases while the leeward decreases as the angle of attack is increased. The trends shown here for $M_\infty = 4.6$ and $C_T = 2$ are fairly typical of those observed with the other Mach and thrust cases.

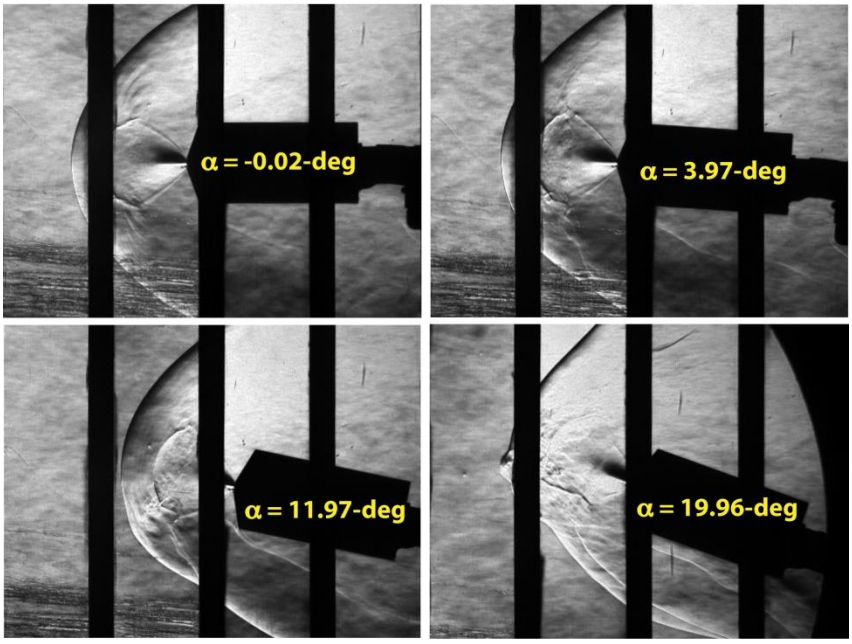

(a) Schlieren.

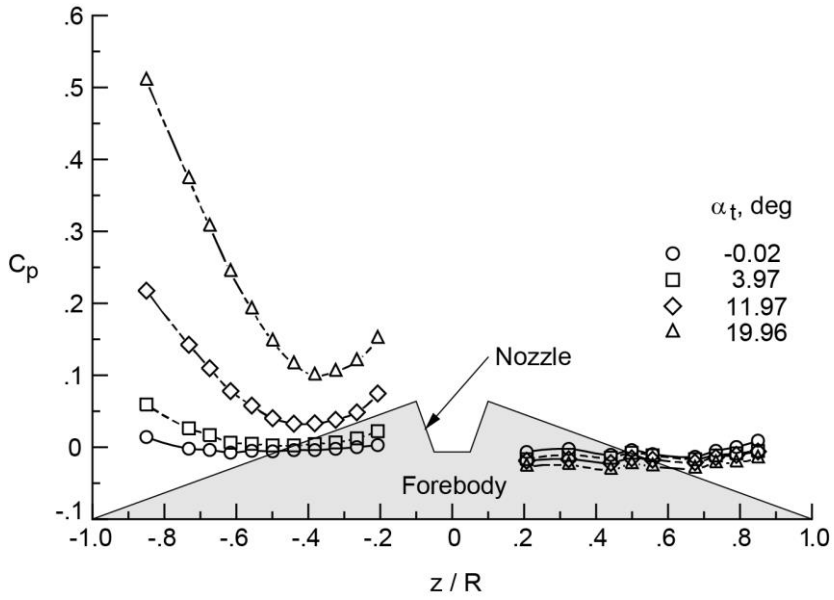

(b) Surface pressure.

Figure 25. The effect of angle of attack for the center nozzle at M_∞ = 4.6 and C_T = 2 (Run 165).

Figure 26 provides the forebody pressure contour maps for the complete range of angles of attack obtained during Run 141, which is for the center nozzle configuration at Mach 2.4 with a thrust coefficient of two and a roll angle of zero. Elevated pressures are evident on the windward side of the forebody (the lower portion for positive angles of attack), specifically on the forebody shoulder and a small region nearer to the nozzle, perhaps due to a horseshoe vortex. The results

shown here are fairly typical of the other Mach and thrust cases for the center nozzle, with the exception of the highest thrust case (Run 136). For Run 136, at Mach 2.4 and C_T = 4, the bow shock could be seen to be interacting with the tunnel sidewalls (the downstream bow shock "shadow" seen most clearly in the standard deviation images, the right-most column in Appendix C) for all angles of attack. When the model was pitched up to 12 degrees during Run 136, the flow became highly unsteady in contrast to the lower thrust cases, and the higher angle of attack cases were dropped from the run. The corresponding contour maps (see Appendix E) for this run reveal an asymmetric pattern that also suggests the possibility of a tunnel interference effect.

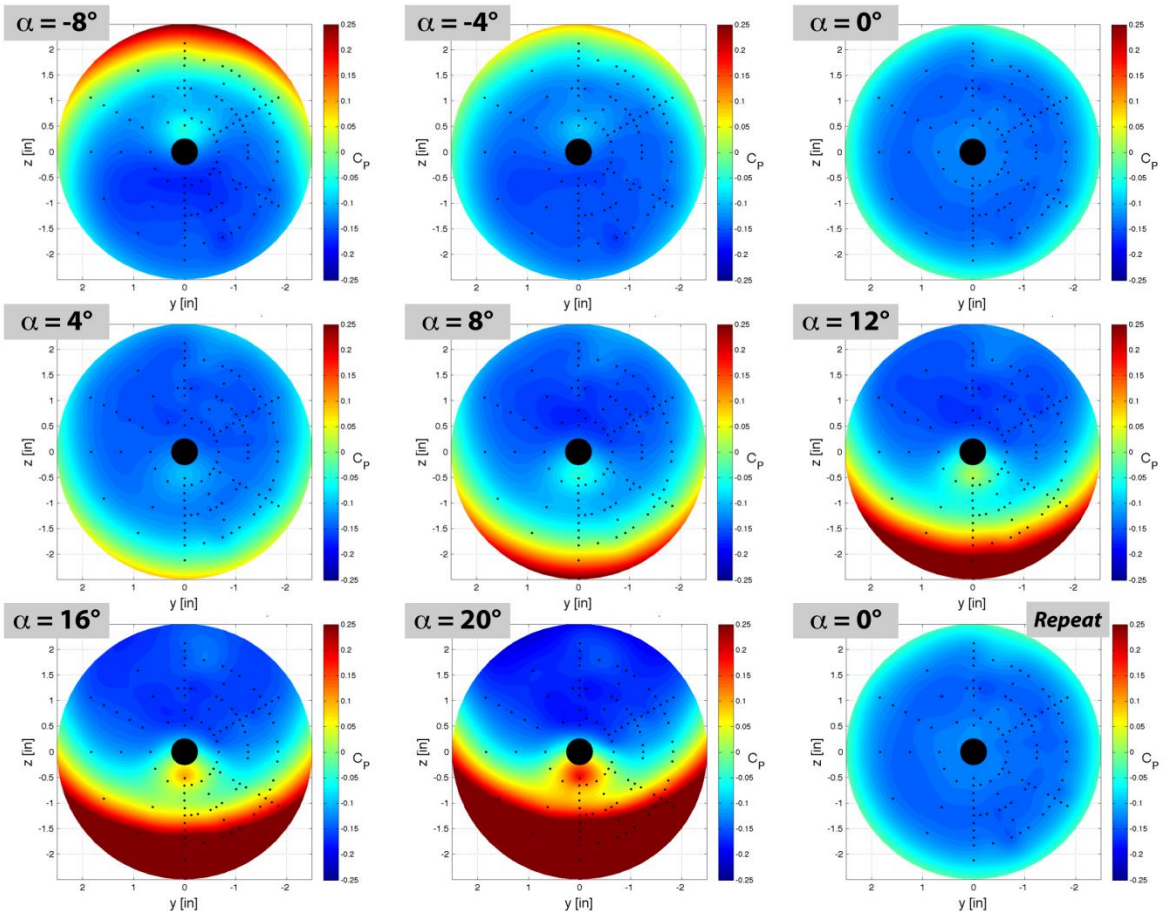

Figure 26. Contour maps showing the effect of angle of attack for the center nozzle configuration at M_∞ = 2.4 and C_T = 2.0, and ϕ = 0° (Run 141).

The schlieren data were used to extract the dimensions of relevant flow features for the center nozzle case, specifically the shock stand off distance and radius, and the jet plume length and radius, as shown in figure 27. These dimensions are intended as scaling parameters to assist in the development of engineering relations for predicting SRP thrust behavior. The extraction was performed from scaled tracings of the steady state flow features using Adobe Illustrator. First the schlieren images, including the still, average intensity, and standard deviation images captured in Appendix C, were imported onto different layers within Illustrator and aligned to overlay each other. Then, on a fourth layer, the relevant features were traced to fit all three

sources of information. Each "data" layer could be made visible or invisible as needed to compare the tracing to all three images. In certain cases, when a flow feature was hidden behind one of the window slats, an alternate run, where the model was physically moved to a different location within the tunnel, was used to assure that the tracing was correctly captured. For all cases, the schlieren images were aligned with the model as the reference point. This process was completed for the range of thrust cases for each Mach number, and also one angle of attack sweep. The model width (diameter of 5 inches) was then used to scale the entire ensemble of tracings, and the feature lengths and radii were extracted.

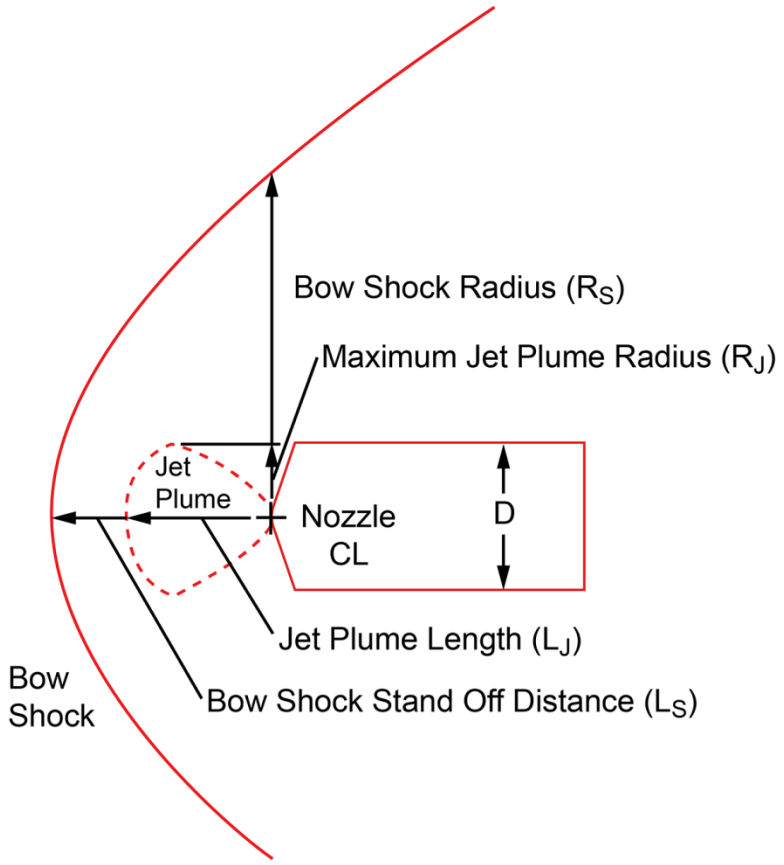

Figure 27. Relevant dimensions to be extracted from the Schlieren data.

The center nozzle shock and plume tracings are shown in figure 28 for all three Mach numbers at $\alpha = 0°$, each for the acquired range of thrust coefficients. The extracted dimensions, as well as corresponding pressure and mass flow ratios for each run, are listed in Table 1. The ratios chosen to reflect the nozzle performance for each run are the ratio of jet static exit pressure to free-stream, post shock total pressure (P_J/P_{T2}) and jet mass flow rate to tunnel mass flow rate (m_J/m_∞) ratios.

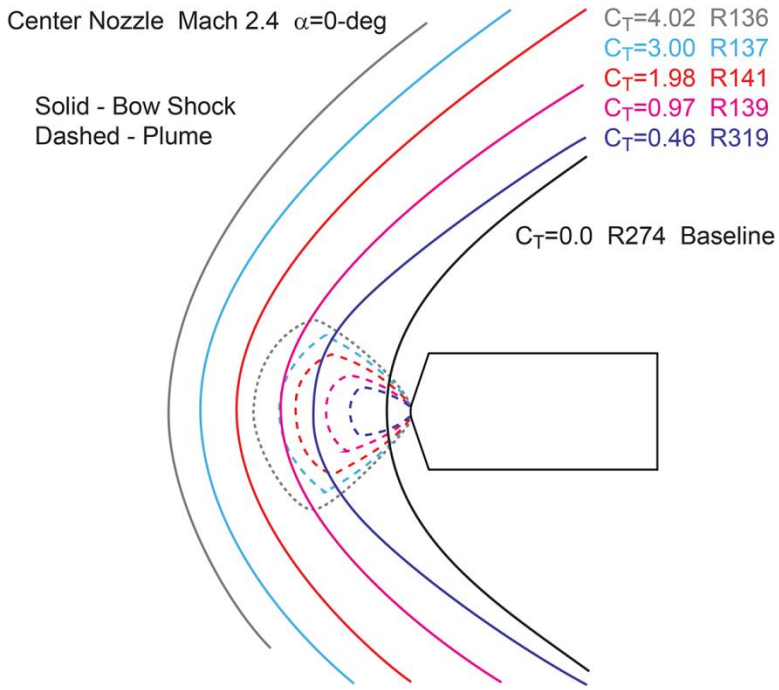

(a) Bow shock and plume shapes as a function of C_T for Mach 2.4.

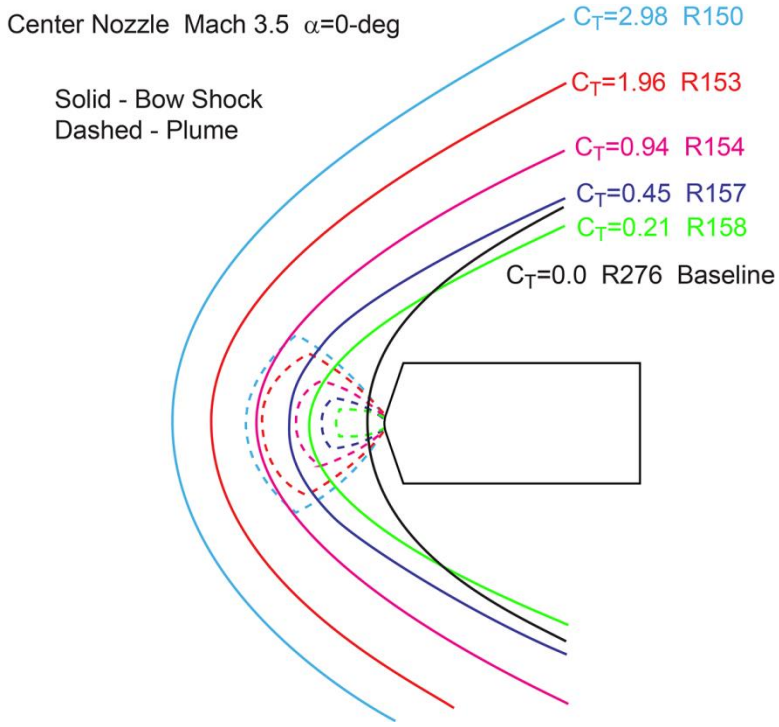

(b) Bow shock and plume shapes as a function of C_T for Mach 3.5.

Figure 28. Center nozzle shock and plume tracings for all three Mach numbers at $\alpha = 0°$.

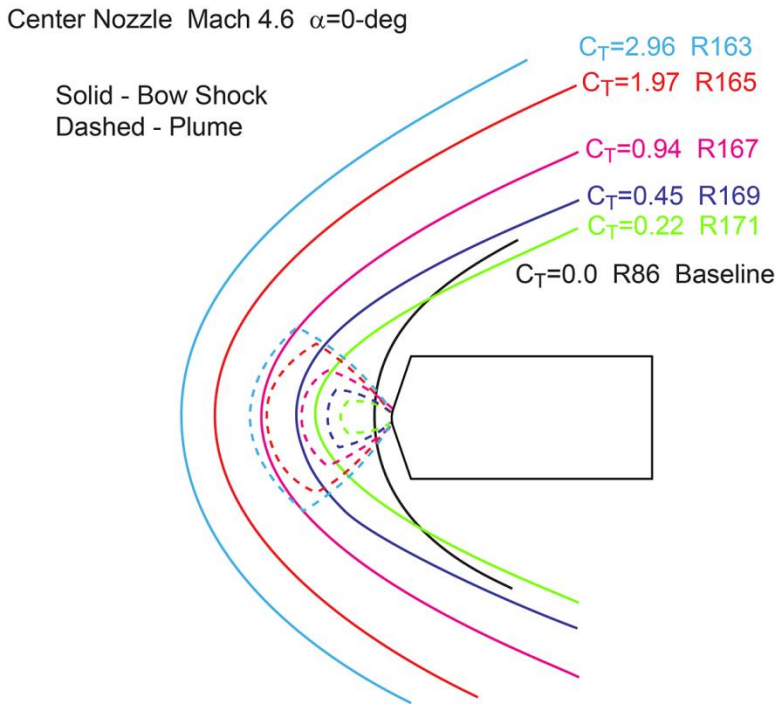

(c) Bow shock and plume shapes as a function of C_T for Mach 4.6.

Figure 28. Concluded.

Table 1. Extracted flow features and properties for the center nozzle for $\alpha = 0°$.

M_∞	C_T	Test/Run	P_J/P_{T2}	m_J/m_∞	L_S (in)	R_S (in)	L_J (in)	R_J (in)
2.4	0	T1853/274	–	–	1.04	3.92	–	–
	0.46	319	1.9	0.0017	4.18	6.61	2.59	1.06
	0.97	139	3.8	0.0036	5.63	8.81	3.66	1.64
	1.98	141,318	7.5	0.0074	7.54	11.79	4.99	2.59
	3.00	137	11.2	0.0113	9.10	14.10	5.69	3.37
	4.02	136	14.7	0.0150	10.47	16.31	6.81	4.10
3.5	0	T1853/276	–	–	0.71	2.97	–	–
	0.22	158	1.0	0.0009	3.14	4.21	1.99	0.56
	0.45	157	2.0	0.0020	3.98	5.44	2.59	1.06
	0.94	154	4.0	0.0042	5.35	7.21	3.67	1.77
	1.97	153,320	7.8	0.0087	7.24	9.83	5.09	2.95
	2.96	150	11.7	0.0132	8.86	12.40	5.78	3.70
4.6	0	T1853/86	–	–	0.68	2.93	–	–
	0.22	171	1.0	0.0011	3.10	3.98	2.07	0.64
	0.45	169	2.0	0.0022	3.91	5.22	2.62	1.17
	0.94	167	4.0	0.0047	5.34	6.97	3.70	1.95
	1.97	165,321	8.0	0.0095	7.22	9.67	5.09	3.04
	2.96	163	11.8	0.0145	8.58	11.52	5.78	3.75

From the tabulated data, one can surmise that the plume shape is primarily driven by the ratio of the jet static pressure to the post shock total pressure, as the plume dimensions are largely consistent between the three Mach numbers. On the other hand, the shock standoff distance varies with Mach number. An effective body, which represents the fluid boundary between the two flowfields (the jet plume on the model side and the free stream on the other) is of interest, but is not easily seen in the schlieren imagery. The difference between the shock standoff distance for the blowing and nonblowing cases ($L_S - L_{S0}$) can be used as an estimate of the effective body length. Doing this also shows a direct relation between the effective body and the jet pressure ratio (P_J/P_{T2}), regardless of Mach number. The dependence of the standoff distances (referenced to the nozzle exit diameter) to the jet pressure ratio are shown in figure 29. Note that the jet plume and effective body standoffs are largely independent of Mach number.

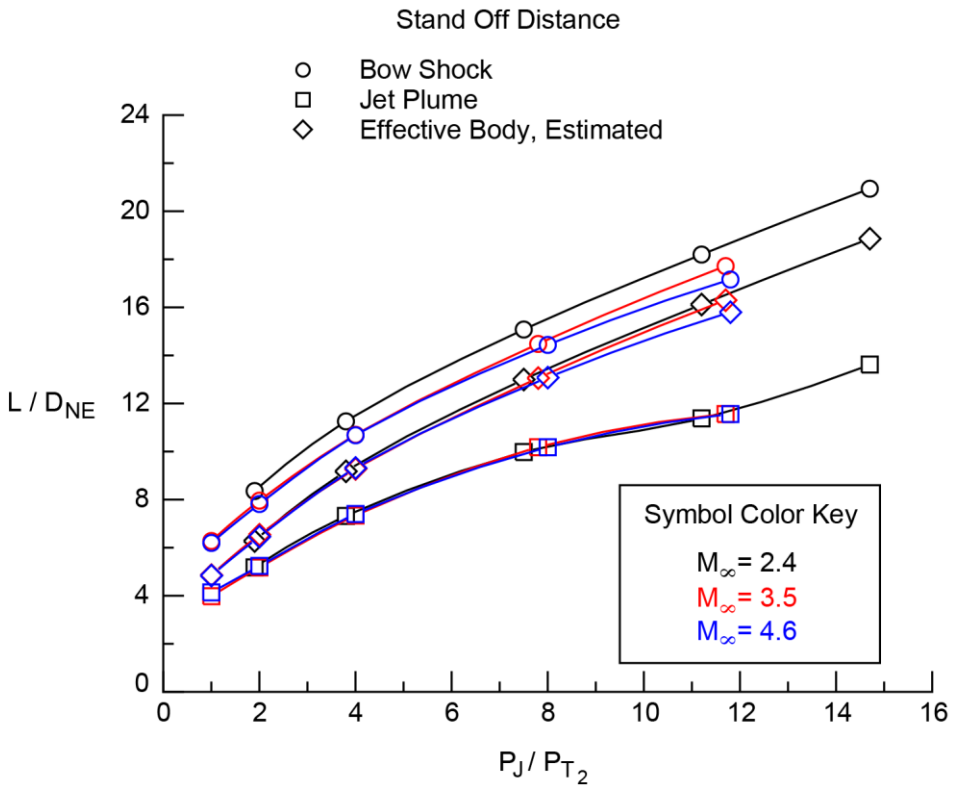

Figure 29. Flow feature stand off distance versus nozzle pressure ratio for $\alpha = 0°$.

The effect of angle of attack was looked at for the center nozzle at Mach 4.6 and $C_T = 2$, including comparison of repeat runs. The angle of attack tracing results are shown in figure 30. With the model as the point of reference and C_T held constant, the plume shape can be seen to be fairly invariant to angle of attack. The bow shock pivots around the plume as angle of attack changes. For cases where blunt, stable plumes are established, the bow shock and plume regions behave independently with the effective body as the interface boundary.

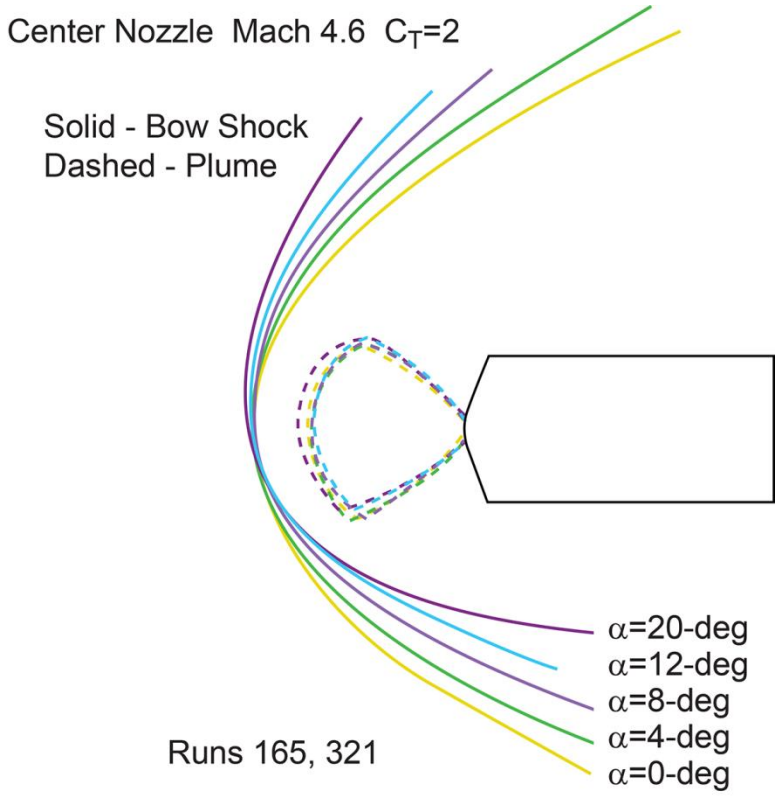

Figure 30. Bow shock and plume shapes as a function of α for Mach 4.6, C_T = 2.

4.3 Tri-Nozzle

Figure 31 provides the effect of Mach number for the tri-nozzle configuration at $\alpha = 0°$ and $C_T = 2$. As shown by the irregular shape captured in these single frame images, the bow shocks are unsteady, making it more difficult to accurately estimate stand off distances. In general, the tri-nozzle was the least steady configuration of the four tested across the spectrum of Mach, thrust, and angle of attack cases acquired during this test. The pressure data on the forebody, shown for a ray from the centerline to the shoulder, is relatively flat for $M_\infty = 2.4$, indicative of a large flow separation zone due to recirculation around the periphery of the nozzle jets, while the higher Mach numbers show increased pressure in the center plug region. Note the pressure taps from r/R of 0.4 to 0.6 are located on the peripheral plug, which is removed for this configuration.

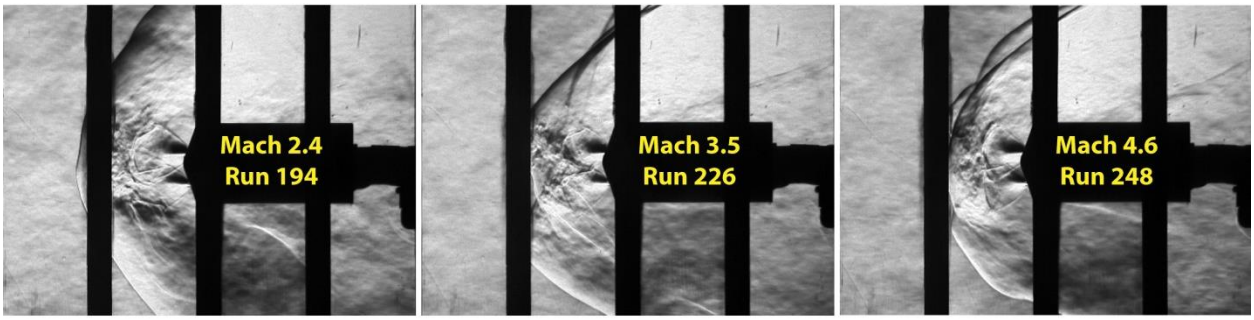

(a) Schlieren.

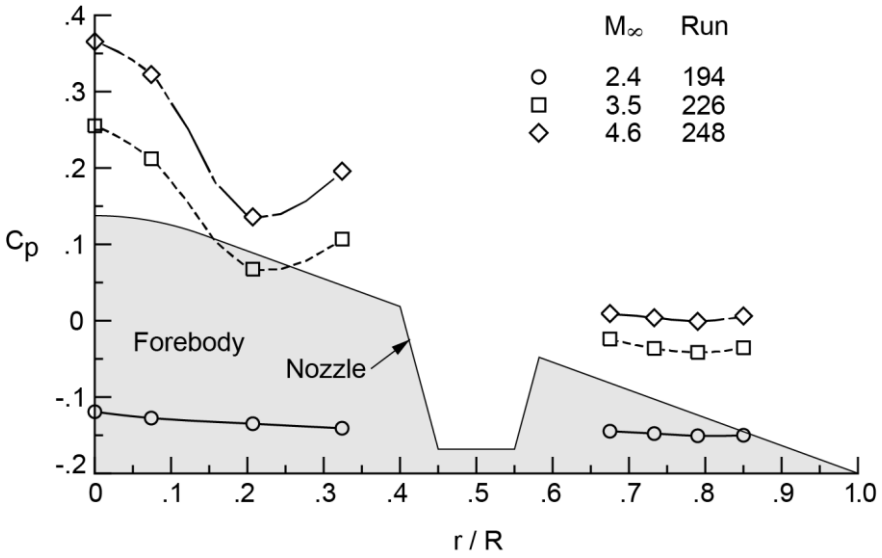

(b) Surface pressure.

Figure 31. The effect of Mach number for the tri-nozzle at $\alpha = 0°$ and $C_T = 2$.

The effect of increasing thrust coefficient is shown in figure 32 for the tri-nozzle configuration at $M\infty = 4.6$ and $\alpha = 0°$. At the lowest thrust coefficient ($C_T = 0.5$), the jet plumes independently protrude through the bow shock and are unsteady. As shown, this lower thrust case also corresponds with the higher measured forebody pressures. This particular case is likely an example of the unstable long penetration mode discussed earlier. As thrust is increased, the individual jets broaden and coalesce, forcing the bow shock further away from the forebody and lowering the measured surface pressure. The bow shock structure for these higher thrusting cases is mostly steady with periodic perturbations emanating from a region in front of the three jets (see Appendix C), although the level of unsteadiness appears to increase slightly for the highest thrust cases acquired.

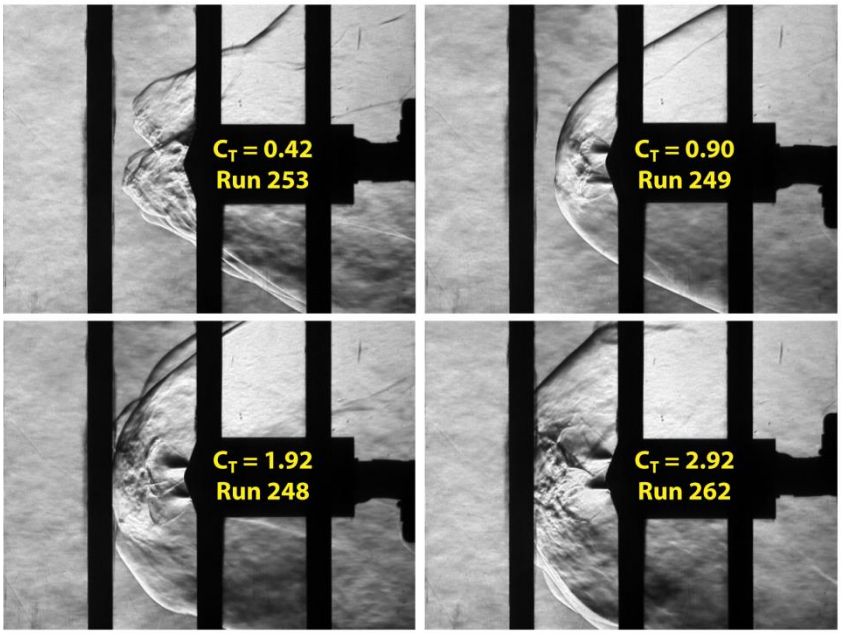

(a) Schlieren.

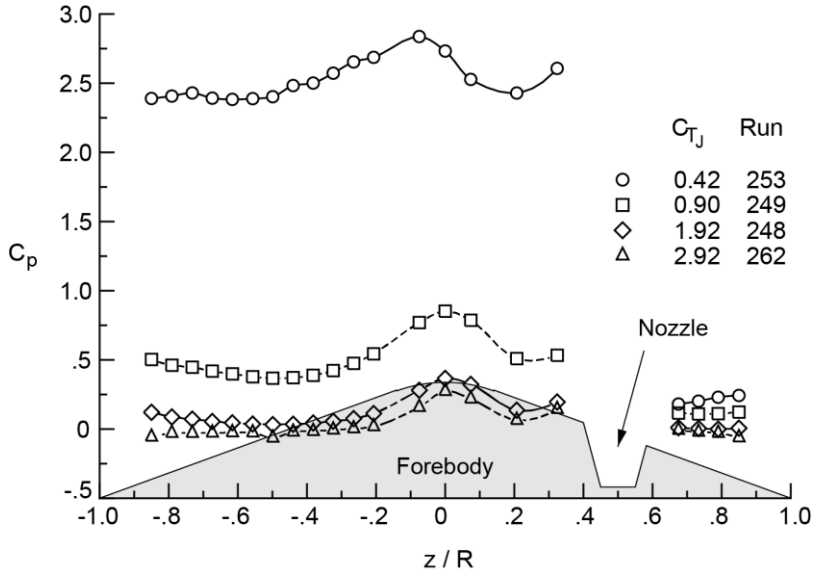

(b) Surface pressure.

Figure 32. The effect of thrust coefficient for the tri-nozzle at $M\infty$ = 4.6 and α = 0°.

Figure 33 provides a comparison of the contour maps to the corresponding schlieren images for a range of thrust cases at Mach 2.4 and α = 0°. For the higher thrust cases, the size of the merged Mach disks at the end of the plumes is greater than the model diameter, effectively shielding the forebody from the oncoming flow. For a thrust coefficient of one, the plumes appear blunt, displacing the bow shock globally, but are not totally merged as some aerodynamic pressure is seen in the boundaries between the three nozzles. For thrust coefficients less than one, the plumes are completely independent, thus, exposing the forebody to a significant increase in

aerodynamic pressure. For the two lowest thrust cases, the schlieren images show the plumes protruding through the bow shock and from the videos one can see the protrusions as highly dynamic. Figure 34 provides just the contour maps for the entire range of thrust cases for the tri-nozzle at Mach 2.4 and $\alpha = 0°$. The trends shown here for Mach 2.4 are representative of those observed for the other two Mach numbers.

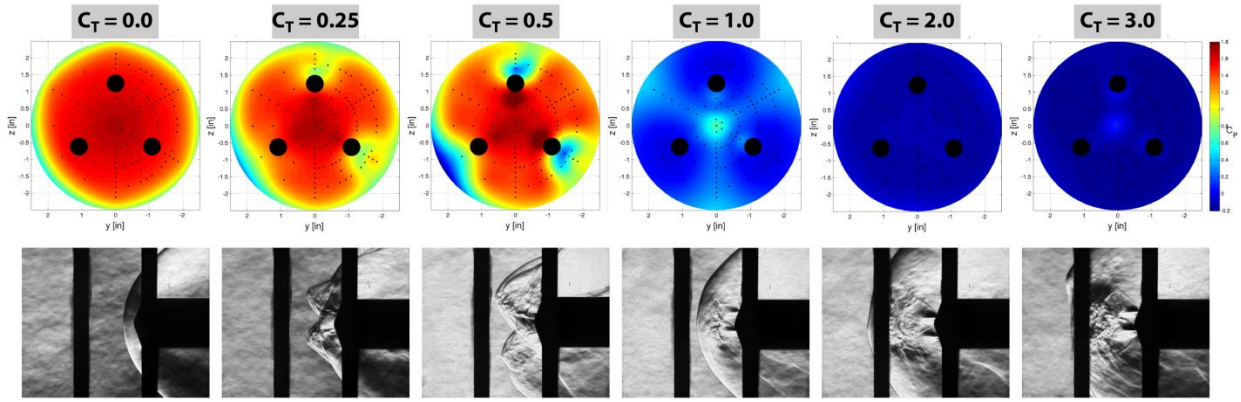

Figure 33. Comparison of contour maps to schlieren images for a range of thrust cases for tri-nozzle configuration at $M\infty = 2.4$ and $\alpha = 0°$ (Runs 180, 221, 202, 198, 194, and 190, respectively).

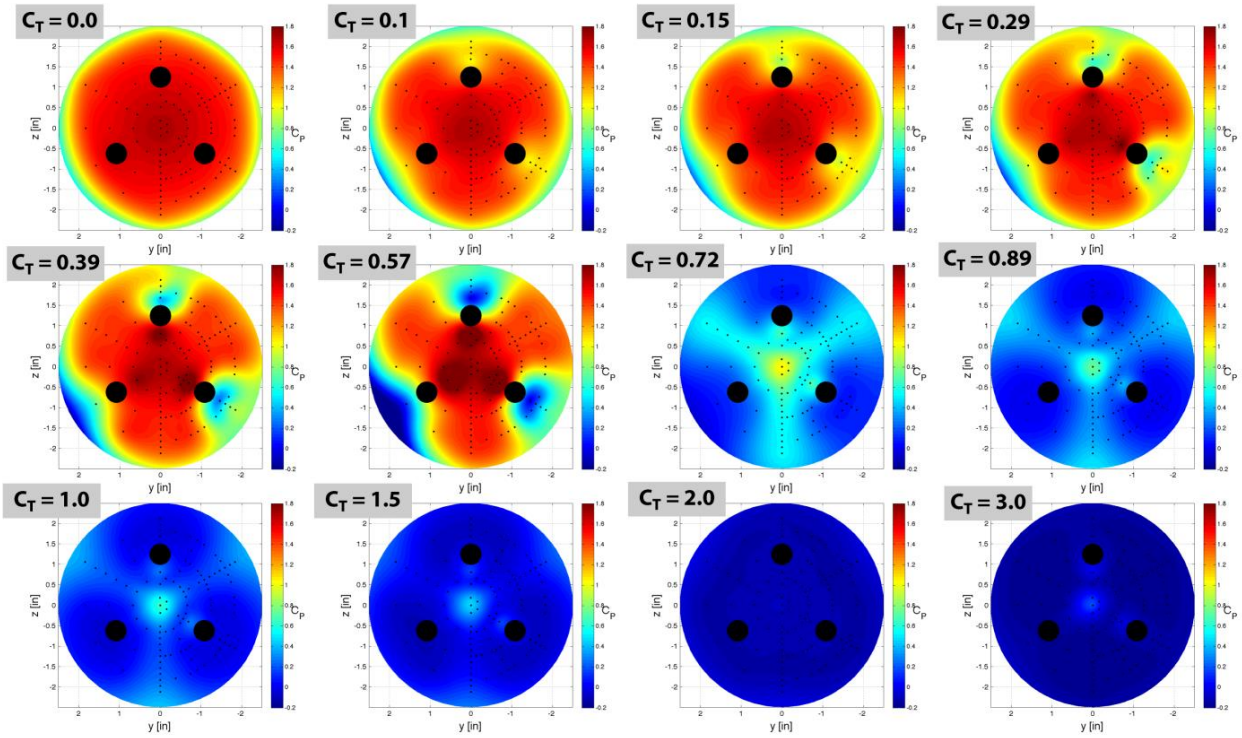

Figure 34. Comparison of contour maps for complete range of thrust cases for tri-nozzle configuration at $M\infty = 2.4$ and $\alpha = 0°$ (Run 179).

Figure 35 provides the effect of angle of attack for the tri-nozzle configuration at $M\infty$ = 4.6, ϕ = 180° and C_T = 2. For the thrust case shown, the effect of increasing angle of attack serves to increase the overall level of unsteadiness. This observation holds true for both model orientations of ϕ = 0° and 180° at this thrust level (see schlieren for Runs 247 and 248, pages 180 and 182). However, at higher thrust coefficients, model orientation plays a role in whether the flowfield is steady or not when the model is at angle of attack. For instance, at C_T = 3, when the model is rolled to ϕ = 180° the flowfield becomes steady as angle of attack increases, while at ϕ = 0° the flowfield remains unsteady. To see this in the schlieren results, please compare Runs 262 and 263 in Appendix C (pages 186 and 187). This mode switching behavior was also seen with the quad nozzle configuration and thus will be discussed further in the next section. In terms of the pressure data trends, shown for a ray from top to bottom with the peripheral plug centered on the windward side (ϕ = 180°), C_P increases on the windward ray with increasing angle of attack, while the centerline and leeward regions decrease.

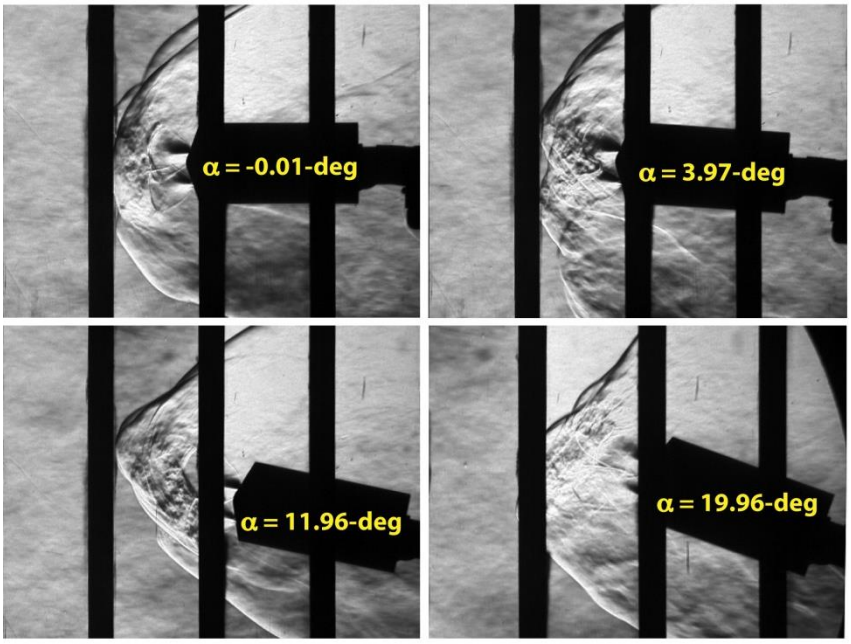

(a) Schlieren.

Figure 35. The effect of angle of attack for the tri-nozzle at $M\infty$ = 4.6 and C_T = 2 (Run 248).

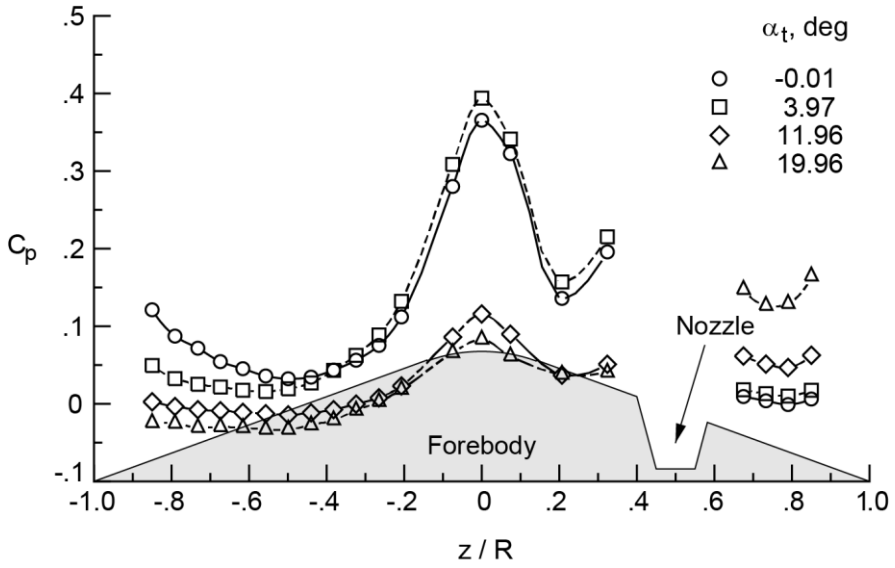

(b) Surface pressure.

Figure 35. Concluded

Figure 36 provides comparison of forebody C_P contours for the range of angles of attack and roll at Mach 2.4 and C_T = 1. For angles of attack of 16 degrees and higher, the orientation of the nozzles significantly affect the forebody flow, with the ϕ = 0° and 120° cases displaying the highest pressures. For these two cases, the windward side of the model has two nozzles on either side of centerline, allowing a high pressure region to form between the nozzles at high angles of attack. The other cases (ϕ = 60° and 180°) have just one nozzle bisecting the windward centerline, effectively diverting high pressure from the surface. The trends shown here for Mach 2.4 are representative of those observed for the other two Mach numbers.

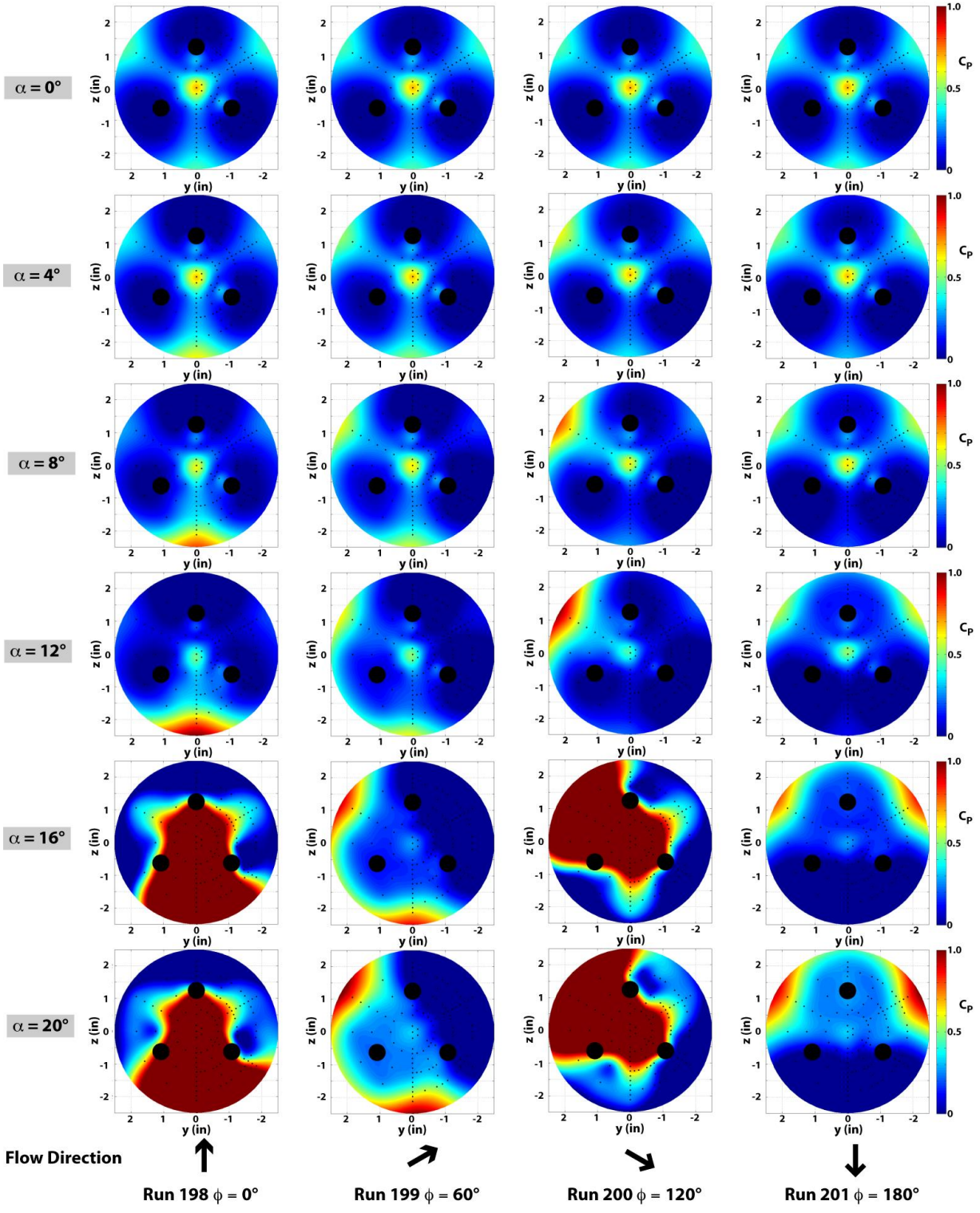

Figure 36. Comparison of contour maps for a range of angle of attack and roll cases for the tri-nozzle configuration at $M\infty = 4.6$ and $C_T = 2$.

Shock and plume tracings were also investigated for the multi nozzle cases, but the increased level of flowfield unsteadiness resulted in more subjective extraction of relevant dimensions. An example is provided in figure 37, which was completed for the tri nozzle configuration at Mach 3.5 and $\alpha = 0°$ providing shock and plume tracings for the range of acquired thrust coefficients. When possible, multiple cases were used to establish qualitative repeatability within a given thrust level. It is interesting to note that at the higher thrust coefficients, repeatability appears to be fairly good, likely an indication of the relatively stable and steady bow shock behavior. At C_T of 3 and below, the bow shocks and plumes were noticeably less steady, which is reflected in less repeatable tracings. Due to the subjective nature of the results obtained for this case, tracings were not attempted for the rest of the multi nozzle configurations and cases.

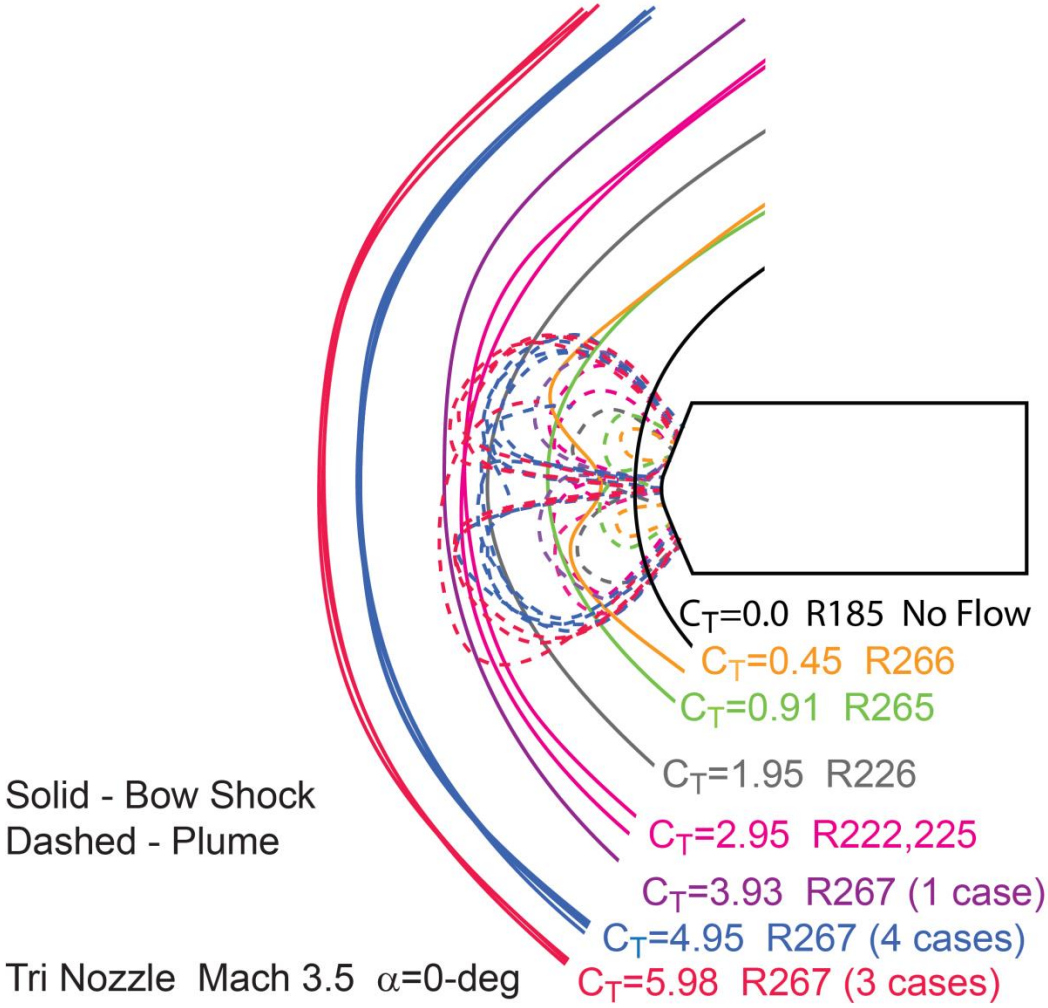

Figure 37. Tri nozzle shock and plume tracings for $M\infty = 3.5$ at $\alpha = 0$.

A comparison of the bow shock standoffs for the center and tri nozzle results at comparable thrust levels for Mach 3.5 and $\alpha = 0°$ is provided in figure 38, with the center nozzle shown by solid lines and the tri nozzle by dashed. As is illustrated in this figure, at equivalent thrust

coefficients, the center nozzle provides a greater displacement of the shock standoff distance than the tri nozzle. Also included are the corresponding jet pressure ratios for each case. Note, the 3 to 1 ratio in the difference in number of nozzles results in identical jet pressure ratios between the center nozzle with a $C_T = 1$ and a tri nozzle with $C_T = 3$. In the figure, this comparison is almost accommodated when comparing Run 154 for the center nozzle to Run 222 for the tri nozzle. Thus, jet pressure ratio appears to be a better indicator of bow shock displacement, although for equivalent P_J/P_{T2} the tri nozzle does provide for a wider bow shock than the center nozzle.

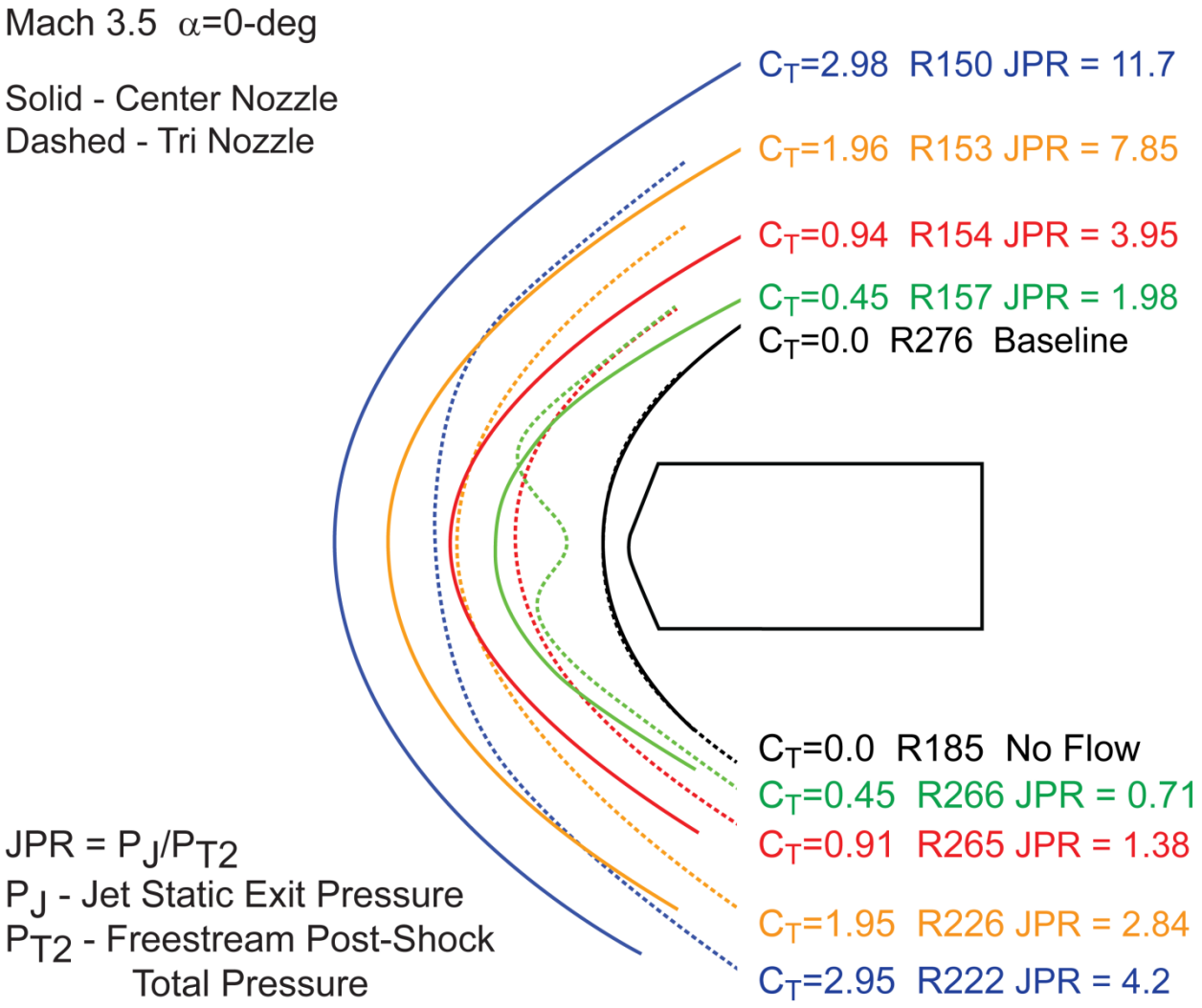

Figure 38. Comparison of center and tri nozzle bow shocks for $M_\infty = 3.5$ at $\alpha = 0$.

4.4 Quad-nozzle

The effect of Mach number on the quad-nozzle configuration at $\alpha = 0°$ and $C_T = 2$ is provided in figure 39. A general observation is that the extra nozzle on center tended to reduce the level of flowfield unsteadiness, when compared against the tri nozzle results, for the limited set of conditions studied here. Even so, the bow shock is somewhat unsteady at the highest Mach number (as indicated by the irregular bow shock in the $M\infty = 4.6$ image). The pressure data on the forebody, shown for a ray from bottom to top, is relatively flat, indicating a largely separated forebody, with the pressure coefficient level rising with increasing Mach number. Note the pressure taps from –0.2 to 0.2 and 0.4 to 0.6 are not installed for this configuration.

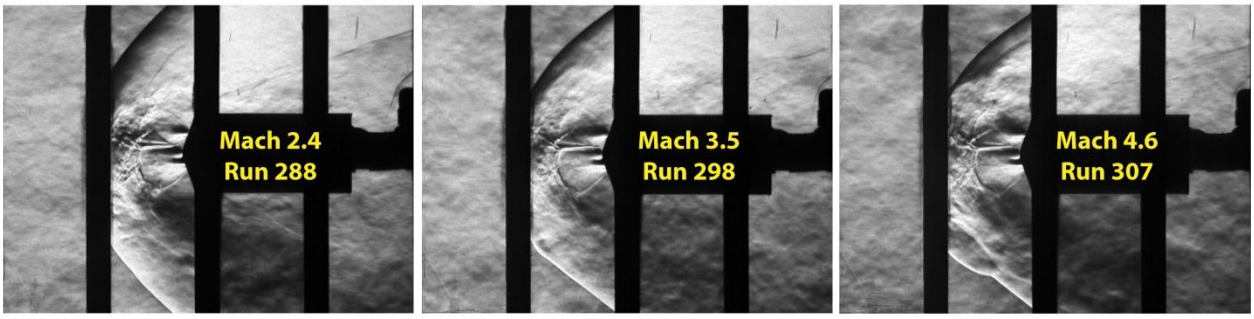

(a) Schlieren.

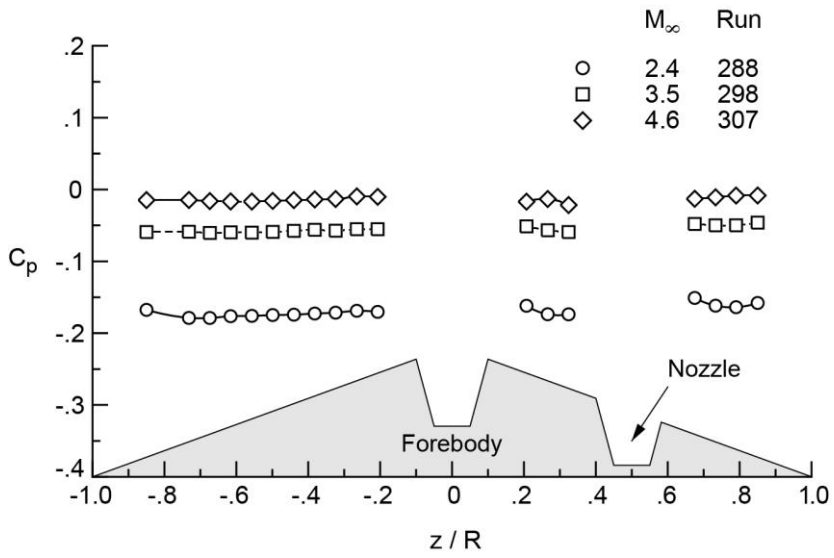

(b) Surface pressure.

Figure 39. The effect of Mach number for the quad-nozzle at $\alpha = 0°$ and $C_T = 2$.

The effect of increasing thrust coefficient is shown in figure 40 for the quad-nozzle configuration at $M\infty = 2.4$ and $\alpha = 0°$. Because of time constraints, only a limited set of thrust coefficients was acquired for the quad configuration. The Mach 2.4 case provides the widest range of C_T and thus is shown here. For an angle of attack of zero, the bow shock is generally steady over this thrust coefficient range, with only minor and infrequent perturbations observed in the video,

although the frequency of these perturbations do increase as Mach and thrust increases (as seen in Appendix C). As shown with the pressure plot, the initial effect of increasing thrust is to lower the measured forebody pressures. However, once a $C_T = 2$ is reached, there appears to be no further influence of thrusting on the measured pressure.

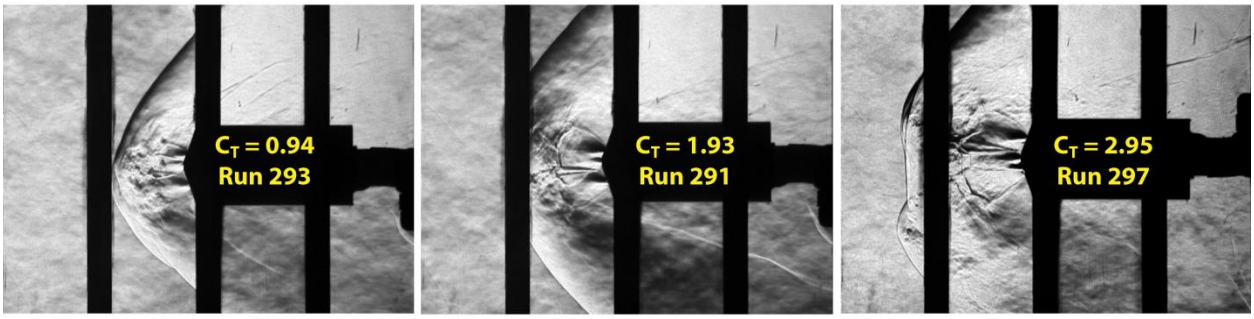

(a) Schlieren.

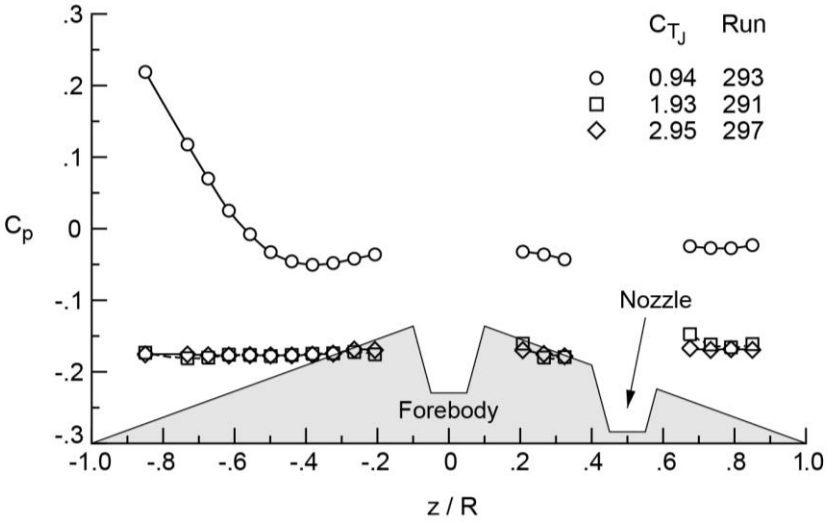

(b) Surface pressure.

Figure 40. The effect of thrust coefficient for the quad-nozzle at $M\infty$ = 2.4 and α = 0°.

An interesting feature was observed for the higher thrust cases on the quad nozzle configuration in the region of the virtual stagnation point, which was not seen previously with the tri nozzle. This feature, best described as a tripod with legs splayed out towards the bow shock, was revealed after rolling the model in 30 degree increments, see figure 40 as an example for the quad nozzle at $M\infty$ = 2.4, α = 0°, and C_T = 3. In these close-up comparisons of the plume region for the quad nozzle model rolled at ϕ = 0° and 30°, the "tripod" is more easily seen in the averaged intensity and standard deviation images for the ϕ = 30° case. At thrust levels sufficient to constrain and constrict the center plume, pressure relief is only allowed in a forward direction at each of the three interface boundaries between center and peripheral plumes (approximately the midpoint between any two peripheral nozzles).

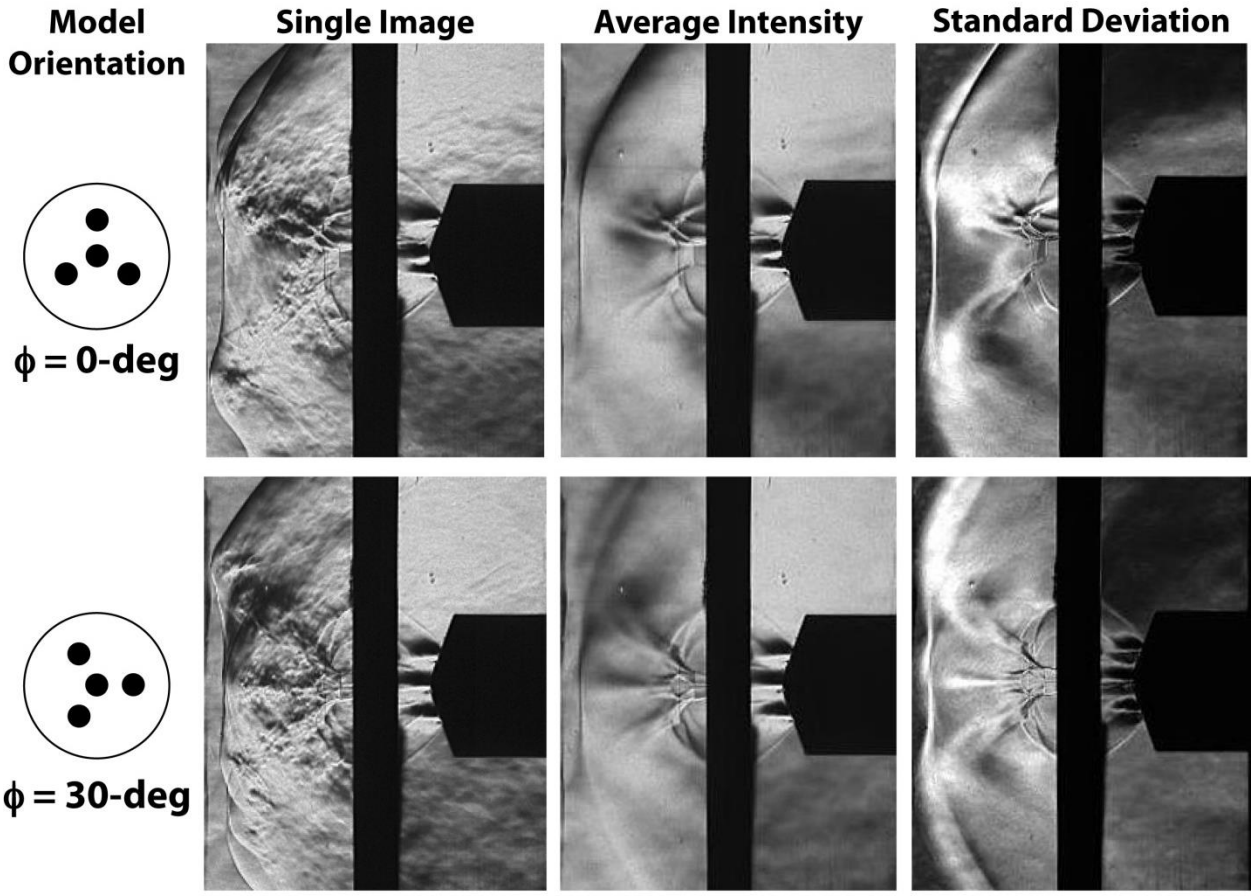

Figure 41. The effect of model roll for the quad-nozzle at $M\infty$ = 2.4, α = 0°, and C_T = 3.

Figure 42 provides the angle of attack effect for the quad-nozzle configuration. In general terms, the quad-nozzle was steadier for similar angles of attack and thrust coefficients than the tri-nozzle. As mentioned earlier with the tri nozzle results, the quad nozzle configuration also showed that while at angle of attack, the orientation of the nozzles is important for establishing the dynamics of the flowfield. For example, figure 42 provides the sweep of angles of attack for the case where two of the peripheral nozzles are opposed on either side of the model windward symmetry plane (ϕ = 0°). In this orientation, the nozzle/bow shock interaction region is fairly unstable and unsteady at angles of attack of 16 degrees and higher. When the model orientation is such that one nozzle is located on the windward symmetry plane, such as is shown in figure 43 (ϕ = 180°), the flowfield for these high angle of attack cases becomes very stable and steady (see also Appendix C). From the pressure data comparison, the unsteady case corresponds to a greater increase in forebody pressure at the higher angles of attack than the steady case. In the case on the steady orientation, the windward jet serves to dominate the forebody pressure field through the separations surrounding the jet.

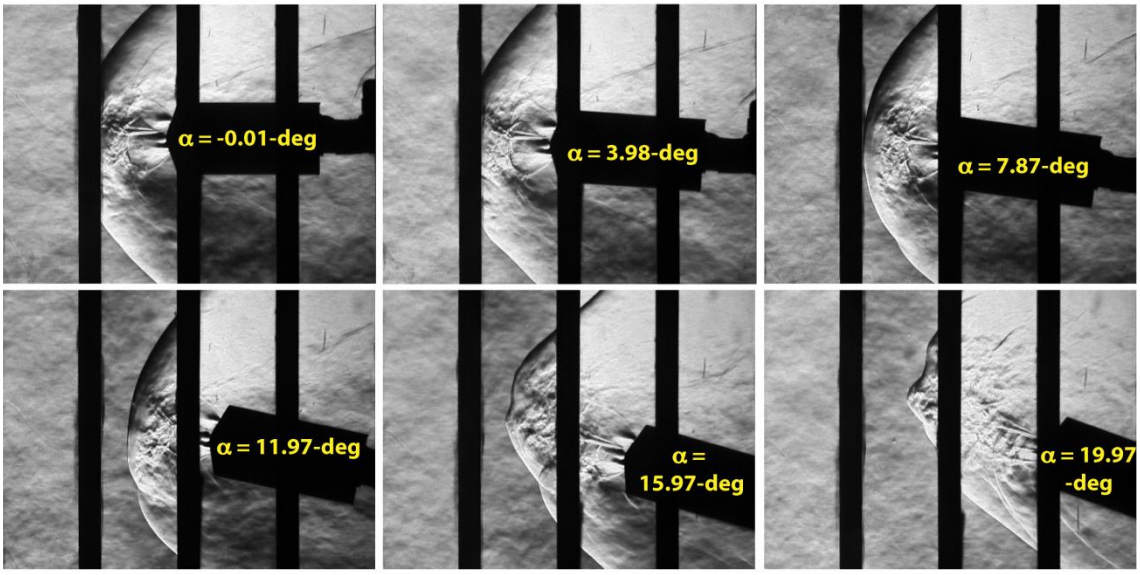

(a) Schlieren.

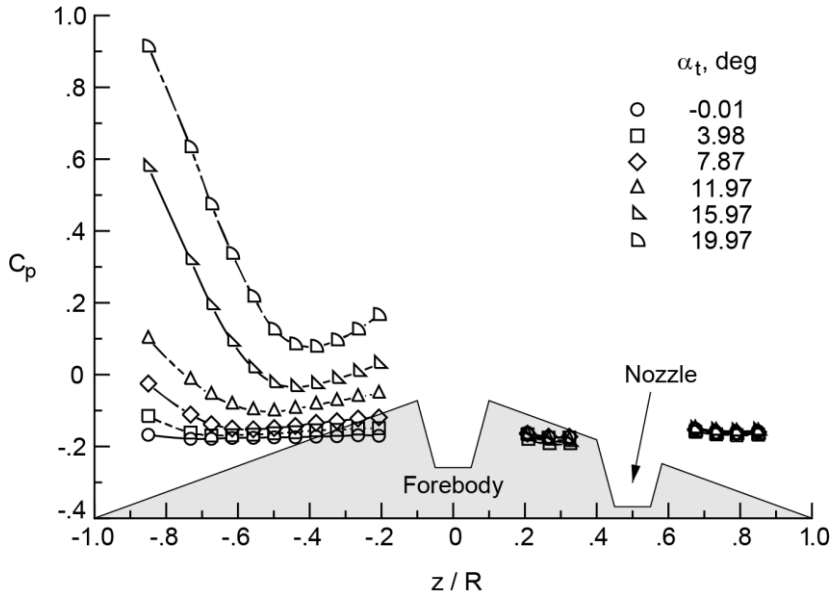

(b) Surface pressure.

Figure 42. The effect of angle of attack for the quad-nozzle at $M\infty = 2.4$, $\phi = 0°$, and $C_T = 2$ (Run 288).

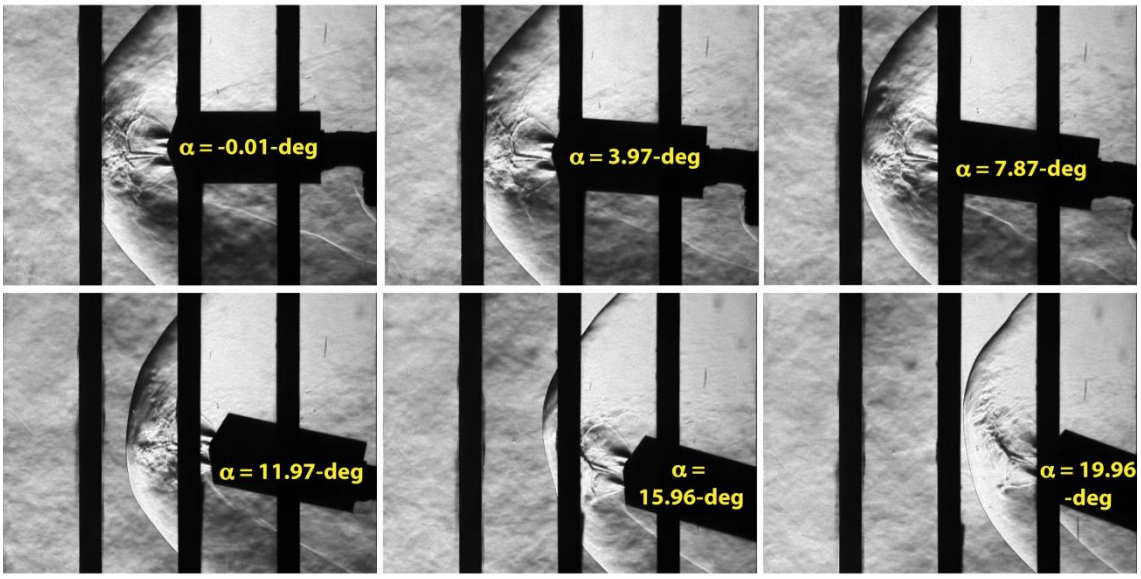

(a) Schlieren.

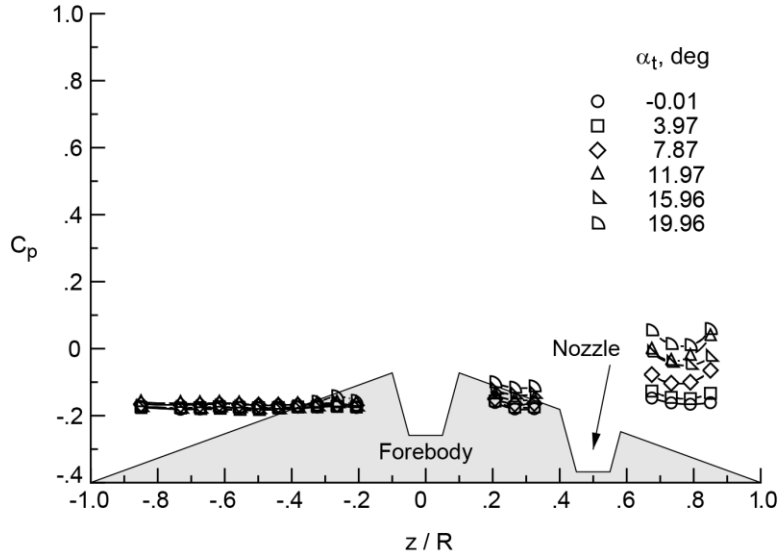

(b) Surface pressure.

Figure 43. The effect of angle of attack for the quad-nozzle at M_∞ = 2.4, ϕ = 180°, and C_T = 2 (Run 291).

Figure 44 provides contour maps for the same range of angle of attack and roll cases as discussed previously, except at Mach 2.4 and $C_T = 1$. For angles of attack of 16 degrees and higher, the orientation of the nozzles have a significant effect on the forebody flow, with the $\phi = 0°$ and 120° cases displaying the highest pressures. For these cases, the windward side of the model has two nozzles on either side of centerline, allowing a high pressure region to form between at high angles of attack. The other cases ($\phi = 60°$ and 180°) have the single nozzle bisecting the windward centerline, effectively diverting high pressure from the surface. The trends shown here for Mach 2.4 are representative of those observed for other Mach numbers.

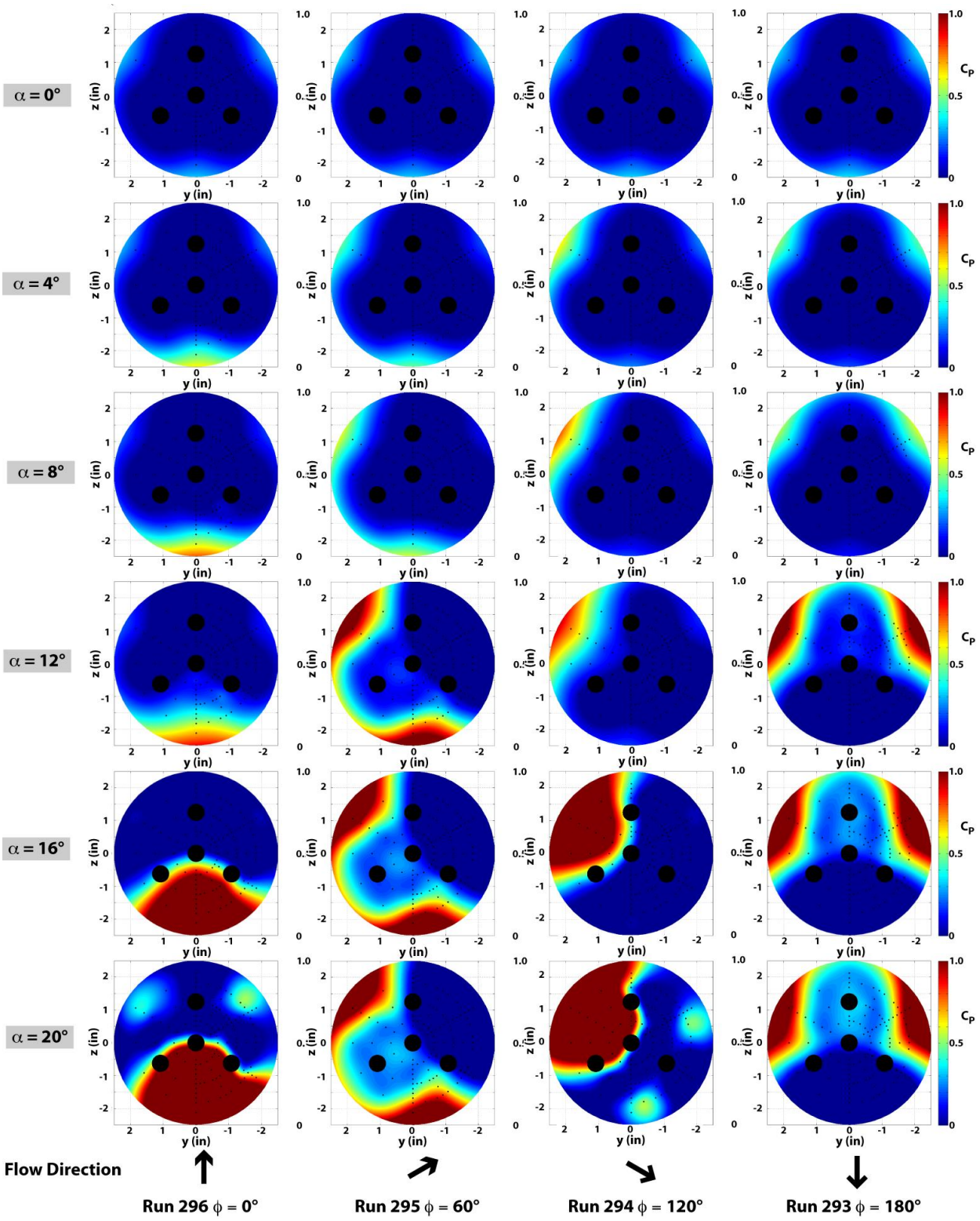

Figure 44. Comparison of contour maps for a range of angle of attack and roll cases for the quad-nozzle configuration at $M\infty = 2.4$ and $C_T = 1$.

4.5 High Frequency Analysis

While the high frequency sensors were an important element to this test, the magnitude of the dataset and analysis requires that these results be documented separately and by a different set of authors (ref. 27). Besides, from the context of the observations and conclusions reached within the present document, the high frequency results are ancillary. Quantitative observations of dynamic behavior will be most useful when compared against computational results, as was done in refs 28 and 29 based on the preliminary analysis of reference 21. From those published results, which only cover a subset of the Mach 4.6 data, the following observations were reached: (a) in the absence of retrorocket flow, no detectable periodic dynamics were observed on the forebody; (b) once plume flow was established, different dynamics were observed depending on the thrust levels; (c) angle of attack did not strongly affect the dynamics observed, only modifying the peak frequency slightly; (d) for the center nozzle configuration, a strong peak frequency was observed at roughly 2kHz (with harmonics) for the $C_T = 2$ case, which is consistent with published computational predictions (ref. 28); and (d) for the multi nozzle configurations, the measured frequency peaks become less distinct, an indication of the flow being less periodic (or more chaotic) in nature.

4.6 Uncertainty Analysis

A goal of this CFD validation experiment was to estimate the pressure coefficient uncertainties of the experimental data in order to provide a basis for comparison to CFD predictions. Data from the baseline non-thrusting model configuration were used to estimate separate components of uncertainty due to random error, flowfield nonuniformity, and model/instrumentation asymmetries over the full range of model angle of attack, roll angle, and test section axial and lateral locations. The components of uncertainty were estimated from the statistical analysis of residuals determined through the comparisons of measurements from certain parings of runs and pressure ports. For instance, a comparison of replicate runs at the same Mach number, test section location, and model angular orientation yields information about the random error component of uncertainty. Conversely, a comparison of runs at the same model orientation but different locations in the test section provides information about uncertainty due to flowfield nonuniformity. Similarly, a comparison of different pressure port measurements for the same location in the test section, and the same location in the blunt body flowfield, would provide information about uncertainty due to model geometry/instrumentation asymmetries. The test matrix given in Table B-1 was used to identify pairs of runs from which the residuals were calculated for each of the three components of uncertainties discussed above.

A summary of the pressure coefficient uncertainties at one standard deviation is given in Table 2. For each Mach number, the uncertainties are broken out into the individual components along with a total uncertainty computed as the root-sum-square of the component uncertainties. The table also provides information about the number of data records and residuals that were used in the calculation of each component uncertainty, as well as the percentage contribution to the total variance for each uncertainty component. As the table clearly illustrates, the flowfield nonuniformity contributes most significantly to the overall uncertainty, a finding in qualitative agreement with that from other experiments reported in the literature and using the same analysis methodology. A complete discussion of the details of the uncertainty analysis and results will be

provided in a separate report (ref. 30); however, preliminary results were previously published in reference 22.

Table 2. Summary of the pressure coefficient uncertainties at one standard deviation.

Mach	Uncertainty Source	# Records, *L*	# Residuals, *N*	s	% Total Variance
2.4	Random	210	31,544	0.00111	8
	Flowfield	830	126,108	0.00341	75
	Geometry	786	60,990	0.00160	17
	Total	1826	218,642	0.00394	100
3.5	Random	75	11,087	0.00183	10
	Flowfield	780	118,332	0.00531	80
	Geometry	528	37,720	0.00190	10
	Total	1383	167,139	0.00593	100
4.6	Random	68	10,016	0.00294	15
	Flowfield	410	62,010	0.00637	71
	Geometry	320	28,392	0.00276	13
	Total	798	100,418	0.00754	100

SECTION 5
SUMMARY

The present report provides details and results from Test 1853, which was conducted in UPWT Test Section 2 to provide code validation SRP data. This test, conducted in July 2010, accomplished 322 runs and 3669 test points, covering 4 model configurations, 3 Mach numbers, 8 angles of attack, 4 roll angles, multiple tunnel locations, and thrust coefficients up to and including 5. The SRP model consisted of a 5 in diameter 70 degree sphere-cone forebody followed by a 9.55 in long aftbody. The forebody was designed to allow placement of up to four 4:1 area ratio nozzles. The primary instrumentation for this test was 174 surface pressure ports, 125 of which were located on the forebody (including 7 dynamic data sensors), and high-speed schlieren video. SRP data was acquired at Mach numbers of 2.4, 3.5, and 4.6. Four model configurations were tested, a baseline (all locations plugged), center nozzle (periphery plugged), tri-nozzle (center plugged), and quad-nozzle (no plugs). The primary parametrics were a thrust coefficient range of 0 to 5 and angles of attack range of –8 to 20 degrees. The intent of this test was to generate validation quality data for comparison against CFD modeling techniques. Thus the run matrix for this study was carefully crafted to allow for quantification of various sources of experimental uncertainty, such as random errors due to run-to-run variations and bias errors due to flowfield or model misalignments. To accommodate the uncertainty assessment, many repeat runs were conducted with the model at various locations within the tunnel and with the model rolled 0, 60, 120, and 180 degrees. All of the schlieren and steady-state pressure data obtained during Test 1853 are contained within the appendices of this report. Separate papers are planned to cover the details of the high frequency data and uncertainty analysis, although some results are also contained herein.

Below is a review of the major findings from Test 1853:

For the baseline configuration,

- the results were as expected, showing a decrease in shock standoff and an increase in pressure coefficient as the Mach number is increased;
- the angle of attack effect is to increase windward forebody pressures while decreasing leeward;
- the translation and roll data were used as part of the uncertainty assessment.

For the center nozzle configuration,

- the largest forward displacement of the bow shock for a given thrust coefficient was provided;
- the thrust coefficients above one were sufficient to establish broad and steady jet plumes that mostly shielded the forebody surface from high aerodynamic pressures;
- for angles of attack of 12° and lower, the flowfield remained fairly steady. However, higher AOA resulted in highly chaotic plumes and bow shocks;

- jet plume dimensions were directly related to the jet pressure ratio and independent of Mach number and angle of attack.

For the tri nozzle configuration,

- the results, overall, were the least steady of the three blowing configurations;
- the thrust cases included unsteady long penetration mode results at the lower thrust range;
- at thrust coefficients of one and above, short, steady plumes associated with the blunt penetration mode largely shielded the forebody from aerodynamic pressure;
- at thrust coefficients above 2, model orientation affected flowfield stability at angles of attack greater than 12°;
- unsteady behavior at angle of attack appeared related to a buildup of surface pressure between the plumes; inversely, when a single nozzle bisected the windward forebody, aerodynamic pressure was diverted and the flow field was steady;
- the results provided for a wider displacement of the bow shock when compared to the center nozzle at equivalent jet pressure ratios.

For the quad nozzle configuration,

- the results were slightly less unsteady when compared to the tri nozzle, over the limited range of thrust coefficient results tested here;
- an interesting feature was observed just ahead of the jet plumes that were not seen with the other blowing configurations;
- the model orientation effects seen at angle of attack were similar to the previous observations with the tri nozzle.

SECTION 6
REFERENCES

1. Braun, R. D., and Manning, R. M., "Mars Exploration Entry, Descent, and Landing Challenges," *Journal of Spacecraft and Rockets*, Vol. 44, No. 2, 2007, pp. 310–323.

2. Steinfeldt, B. A., Theisinger, J. E., Korzun, A. M., Clark, I. G., Grant, M. J., and Braun, R. D., "High Mass Mars Entry, Descent, and Landing Architecture Assessment," AIAA Paper 2009–6684, Sept. 2009.

3. Dwyer Cianciolo, A. M., et al., "Entry, Descent and Landing Systems Analysis Study: Phase 1 Report," NASA TM 2010–216720, July 2010.

4. Edquist, K. T., Dyakonov, A. A., Korzun, A. M., Shidner, J. D., Studak, J. W., Tigges, M. A., Kipp, D. M., Prakash, R., Trumble, K. A., Dupzyk, I. C., "Development of Supersonic Retro-Propulsion for Future Mars Entry, Descent, and Landing Systems," AIAA Paper 2010–5046, June 2010.

5. Korzun, A. M., and Braun, R. D., "Performance Characterization of Supersonic Retropropulsion for High-Mass Mars Entry Systems," *Journal of Spacecraft and Rockets*, Vol. 47, No. 5, 2010, pp. 836–848.

6. Korzun, A. M., Braun, R. D., and Cruz, J. R., "Survey of Supersonic Retropropulsion Technology for Mars Entry, Descent, and Landing," *Journal of Spacecraft and Rockets*, Vol. 46, No. 5, 2009, pp. 929–937.

7. Jarvinen, P. O., and Adams, R. H., "The Aerodynamic Characteristics of Large Angled Cones with Retrorockets," NASA CR NAS 7–576, Feb. 1970.

8. Trumble, K. A., Schauerhamer, D. G., Kleb, W. L., Carlson, J. R., Buning, P. G., Edquist, K. T., and Barnhardt, M. D., "An Initial Assessment of Navier–Stokes Codes Applied to Supersonic Retro-Propulsion," AIAA Paper 2010–5047, June 2010.

9. Trumble, K. A., Schauerhamer, D. G., Kleb, W. L., Carlson, J. R., and Edquist, K. T., "Analysis of Navier–Stokes Codes Applied to Supersonic Retro-Propulsion Wind Tunnel Test," IEEE Aerospace Conference Paper No.1471, March 2011.

10. Korzun, A. M., Cordell, Jr., C. E., and Braun, R. D., "Comparison of Inviscid and Viscous Aerodynamic Predictions of Supersonic Retropropulsion Flowfields," AIAA Paper 2010–5048, June 2010.

11. Cordell, Jr., C. E., Clark, I. G., and Braun, R. D., "CFD Verification of Supersonic Retropropulsion for a Central and Peripheral Configuration," to be published at IEEEAC, March 2011.

12. Daso, E. O., Pritchett, V. E., Wang, T. S., Ota, D. K., Blankson, I. M., and Auslender, A. H., "Dynamics of Shock Dispersion and Interactions in Supersonic Freestreams with Counterflowing Jets," *AIAA Journal*, Vol. 47, No. 6, 2009, pp. 1313–1326.

13. Chang, C. L., Venkatachari, B. S., and Cheng, G. C., "Effect of Counterflow Jet on a Supersonic Reentry Capsule," AIAA paper 2006–4776, 2006.

14. Bakhtian, N. M., and Aftosmis, M. J., "Parametric Study of Peripheral Nozzle Configurations for Supersonic Retropropulsion," AIAA Paper 2010–1238, 2010.

15. Nomura, H., Aso, S., and Nishida, M., "Numerical Simulation of Opposing Sonic Jets," *Computers and Fluids*, Vol. 21, No. 2, 1992, pp. 229–233.

16. Korzun, Ashley M., "Aerodynamic and Performance Characterization of Supersonic Retropropulsion for Application to Planetary Entry and Descent." Ph.D. Thesis, Georgia Institute of Technology, May 2012.

17. Aeschliman, D. P. and Oberkampf, W. L., "Experimental Methodology for Computational Fluid Dynamics Code Validation," *AIAA Journal*, Vol. 36, No. 5, 1998, pp. 733–741.

18. Schwartz, R., "ViDI: Virtual Diagnostics Interface, Volume 1 – The Future of Wind Tunnel Testing," NASA/CR–2003–212667, Dec. 2003.

19. Berry, S. A., Laws, C. T., Kleb, W. L., Rhode, M. N., Spells, C., Mccrea, A. C., Trumble, K. A., Schauerhamer, D. G., Oberkampf, W. L., "Supersonic Retro-Propulsion Experimental Design for Computational Fluid Dynamics Model Validation," IEEE Aerospace Conference Paper No.1499, March 2011.

20. Berry, S. A., Rhode, M. N., Edquist, K. T., and Player, C. J., "Supersonic Retropropulsion Experimental Results from the NASA Langley Unitary Plan Wind Tunnel," AIAA Paper 2011–3489, June 2011.

21. Codoni, J. R., and Berry, S. A., "Analysis of Dynamic Data from Supersonic Retropropulsion Experiments in NASA Langley's Unitary Plan Wind Tunnel," AIAA Paper 2012–2706, June 2012.

22. Rhode, M. N. and Oberkampf, W. L., "Estimation of Uncertainty for a Supersonic Retro-Propulsion Model Validation Experiment in a Wind Tunnel," AIAA Paper 2012–2707, June 2012.

23. Micol, J.R., "Langley Research Center's Unitary Plan Wind Tunnel: Testing Capabilities and Recent Modernization Activities", AIAA 2001-0456, 2001.

24. Jackson, Jr., C. M., Corlett, W. A., and Monta, W. J., "Description and Calibration of the Langley Unitary Plan Wind Tunnel," NASA TP 1905, Nov. 1981.

25. Wassum, D. L. and Hyman, Jr., C. E. "Procedures and Requirements for Testing in the Langley Research Center Unitary Plan Wind Tunnel," NASA TM 100529, Feb. 1988.

26. Crawford, B. L., "Angle Measurement System (AMS) for Establishing Model Pitch and Roll Zero, and Performing Single Axis Angle Comparisons," AIAA Paper 2007–1162, Jan. 2007.

27. Berry, S. A., and Codoni, J. R., "Dynamic Data Analysis of Supersonic Retropropulsion Results from NASA Langley's Unitary Plan Wind Tunnel," forthcoming NASA report.

28. Kleb, W. L., Carlson, J. R., Buning, P. G., Berry, S. A., Rhode, M. N., Edquist, K. T., Schauerhamer, D. G., Trumble, K. A., Sozer, E., "Toward Supersonic Retropropulsion CFD Validation," AIAA Paper 2011–3490, June 2011.

29. Schauerhamer, D.G., Trumble, K.A., Kleb, W.L., Carlson, J.R., Edquist, K.T., "Continuing Validation of Computational Fluid Dynamics For Supersonic Retropropulsion," AIAA Paper 2012-0864, Jan 2012.

30. Rhode, M. N. and Oberkampf, W. L., "Estimation of Uncertainty for a Supersonic Retro-Propulsion Model Validation Experiment in a Wind Tunnel," forthcoming NASA report.

APPENDIX A
MODEL DRAWINGS

A1.0 Model Details

This appendix contains details pertaining to the model, including figures and tables of the as-built port locations and parameter list definitions, the model drawings, and photos of the parts and assemblies taken during the model acceptance check out (6/24/10). The model drawings are provided courtesy of Chris Laws, Aeronautics Systems Engineering Branch.

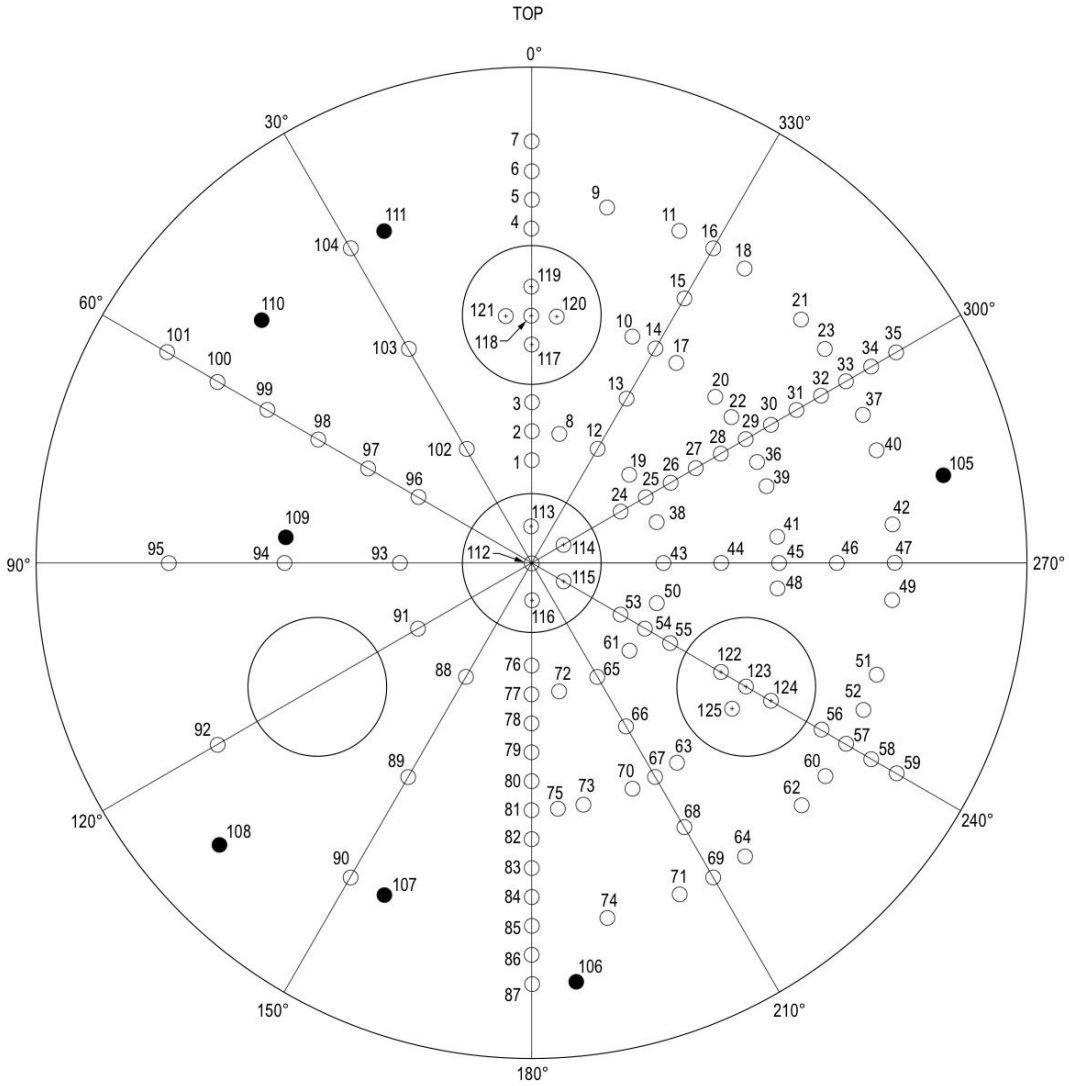

Figure A-1. View from the front of the model.

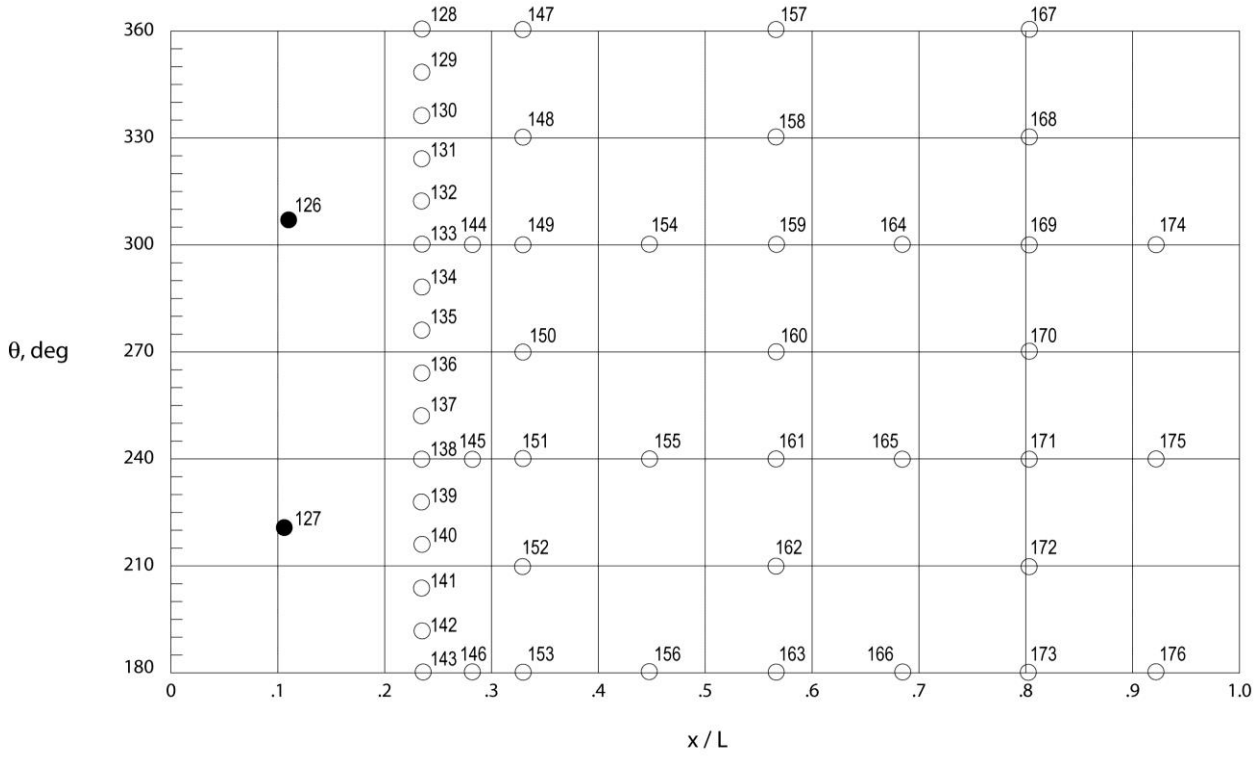

Figure A-2. View from the port side of the model.

Table A-1. As-built surface pressure port locations.

Port	Type	Dimensional					Nondimensional			
		r, in	*θ*, deg	*x*, in	*y*, in	*z*, in	*r*/*R*	*x*/*L*	*y*/*L*	*z*/*L*
P001	ESP	0.518	359.912	0.187	0.518	359.912	0.207	0.018	0.207	359.912
P002	ESP	0.665	359.882	0.241	0.665	359.882	0.266	0.023	0.266	359.882
P003	ESP	0.810	359.864	0.294	0.810	359.864	0.324	0.028	0.324	359.864
P004	ESP	1.687	0.053	0.612	1.687	0.053	0.675	0.058	0.675	0.053
P005	ESP	1.831	359.951	0.665	1.831	359.951	0.733	0.063	0.733	359.951
P006	ESP	1.976	359.988	0.718	1.976	359.988	0.790	0.068	0.790	359.988
P007	ESP	2.126	359.995	0.772	2.126	359.995	0.850	0.073	0.850	359.995
P008	ESP	0.665	347.880	0.241	0.665	347.880	0.266	0.023	0.266	347.880
P009	ESP	1.833	348.011	0.666	1.833	348.011	0.733	0.063	0.733	348.011
P010	ESP	1.249	336.009	0.454	1.249	336.009	0.500	0.043	0.500	336.009
P011	ESP	1.833	336.009	0.666	1.833	336.009	0.733	0.063	0.733	336.009
P012	ESP	0.665	329.935	0.241	0.665	329.935	0.266	0.023	0.266	329.935
P013	ESP	0.957	329.965	0.347	0.957	329.965	0.383	0.033	0.383	329.965
P014	ESP	1.249	329.993	0.453	1.249	329.993	0.499	0.043	0.499	329.993
P015	ESP	1.541	329.982	0.560	1.541	329.982	0.616	0.053	0.616	329.982
P016	ESP	1.833	330.001	0.666	1.833	330.001	0.733	0.063	0.733	330.001
P017	ESP	1.245	324.091	0.452	1.245	324.091	0.498	0.043	0.498	324.091

Table A-1. Continued.

Port	Type	Dimensional					Nondimensional			
		r, in	θ, deg	*x*, in	*y*, in	*z*, in	*r*/*R*	*x*/*L*	*y*/*L*	*z*/*L*
P018	ESP	1.832	324.105	0.666	1.832	324.105	0.733	0.063	0.733	324.105
P019	ESP	0.664	312.096	0.241	0.664	312.096	0.265	0.023	0.265	312.096
P020	ESP	1.249	312.109	0.451	1.249	312.109	0.500	0.043	0.500	312.109
P021	ESP	1.831	312.080	0.666	1.831	312.080	0.733	0.063	0.733	312.080
P022	ESP	1.248	306.113	0.453	1.248	306.113	0.499	0.043	0.499	306.113
P023	ESP	1.831	306.105	0.665	1.831	306.105	0.732	0.063	0.732	306.105
P024	ESP	0.518	299.970	0.188	0.518	299.970	0.207	0.018	0.207	299.970
P025	ESP	0.664	299.952	0.241	0.664	299.952	0.266	0.023	0.266	299.952
P026	ESP	0.810	299.961	0.294	0.810	299.961	0.324	0.028	0.324	299.961
P027	ESP	0.956	299.983	0.347	0.956	299.983	0.382	0.033	0.382	299.983
P028	ESP	1.102	299.998	0.400	1.102	299.998	0.441	0.038	0.441	299.998
P029	ESP	1.247	300.033	0.453	1.247	300.033	0.499	0.043	0.499	300.033
P030	ESP	1.394	299.984	0.508	1.394	299.984	0.558	0.048	0.558	299.984
P031	ESP	1.543	300.006	0.553	1.543	300.006	0.617	0.052	0.617	300.006
P032	ESP	1.686	300.006	0.613	1.686	300.006	0.675	0.058	0.675	300.006
P033	ESP	1.832	300.010	0.666	1.832	300.010	0.733	0.063	0.733	300.010
P034	ESP	1.978	300.025	0.719	1.978	300.025	0.791	0.068	0.791	300.025
P035	ESP	2.124	300.009	0.772	2.124	300.009	0.850	0.073	0.850	300.009
P036	ESP	1.246	294.106	0.450	1.246	294.106	0.498	0.043	0.498	294.106
P037	ESP	1.831	294.085	0.665	1.831	294.085	0.732	0.063	0.732	294.085
P038	ESP	0.664	288.029	0.241	0.664	288.029	0.265	0.023	0.265	288.029
P039	ESP	1.247	288.087	0.453	1.247	288.087	0.499	0.043	0.499	288.087
P040	ESP	1.831	288.078	0.665	1.831	288.078	0.732	0.063	0.732	288.078
P041	ESP	1.247	276.082	0.453	–1.240	0.132	0.499	0.043	–0.117	0.013
P042	ESP	1.831	276.103	0.666	–1.821	0.195	0.732	0.063	–0.172	0.018
P043	ESP	0.665	269.952	0.241	–0.665	–0.001	0.266	0.023	–0.063	0.000
P044	ESP	0.956	269.997	0.347	–0.956	0.000	0.383	0.033	–0.091	0.000
P045	ESP	1.249	269.970	0.453	–1.249	–0.001	0.499	0.043	–0.118	0.000
P046	ESP	1.540	270.001	0.560	–1.540	0.000	0.616	0.053	–0.146	0.000
P047	ESP	1.832	270.019	0.666	–1.832	0.001	0.733	0.063	–0.174	0.000
P048	ESP	1.247	264.092	0.453	–1.240	–0.128	0.499	0.043	–0.118	–0.012
P049	ESP	1.829	264.118	0.664	–1.819	–0.187	0.731	0.063	–0.172	–0.018
P050	ESP	0.663	252.161	0.241	–0.631	–0.203	0.265	0.023	–0.060	–0.019
P051	ESP	1.830	252.076	0.665	–1.741	–0.563	0.732	0.063	–0.165	–0.053
P052	ESP	1.831	246.110	0.665	–1.674	–0.741	0.732	0.063	–0.159	–0.070
P053	ESP	0.518	239.848	0.188	–0.448	–0.260	0.207	0.018	–0.042	–0.025
P054	ESP	0.661	239.884	0.256	–0.571	–0.331	0.264	0.024	–0.054	–0.031
P055	ESP	0.807	239.948	0.293	–0.699	–0.404	0.323	0.028	–0.066	–0.038
P056	ESP	1.687	240.117	0.613	–1.463	–0.841	0.675	0.058	–0.139	–0.080
P057	ESP	1.831	240.119	0.665	–1.587	–0.912	0.732	0.063	–0.150	–0.086

Table A-1. Continued.

Port	Type	Dimensional					Nondimensional			
		r, in	θ, deg	*x*, in	*y*, in	*z*, in	*r*/*R*	*x*/*L*	*y*/*L*	*z*/*L*
P058	ESP	1.979	239.980	0.719	–1.714	–0.990	0.792	0.068	–0.162	–0.094
P059	ESP	2.126	240.055	0.773	–1.842	–1.061	0.850	0.073	–0.175	–0.101
P060	ESP	1.831	234.055	0.665	–1.482	–1.075	0.732	0.063	–0.140	–0.102
P061	ESP	0.663	228.121	0.240	–0.493	–0.442	0.265	0.023	–0.047	–0.042
P062	ESP	1.831	228.098	0.665	–1.362	–1.223	0.732	0.063	–0.129	–0.116
P063	ESP	1.246	216.050	0.452	–0.733	–1.007	0.498	0.043	–0.069	–0.095
P064	ESP	1.830	216.042	0.665	–1.077	–1.480	0.732	0.063	–0.102	–0.140
P065	ESP	0.663	209.938	0.241	–0.331	–0.575	0.265	0.023	–0.031	–0.054
P066	ESP	0.952	210.003	0.346	–0.476	–0.825	0.381	0.033	–0.045	–0.078
P067	ESP	1.246	209.964	0.452	–0.622	–1.080	0.498	0.043	–0.059	–0.102
P068	ESP	1.539	210.030	0.559	–0.770	–1.333	0.616	0.053	–0.073	–0.126
P069	ESP	1.832	210.012	0.665	–0.916	–1.586	0.733	0.063	–0.087	–0.150
P070	ESP	1.247	204.080	0.453	–0.509	–1.139	0.499	0.043	–0.048	–0.108
P071	ESP	1.831	204.086	0.665	–0.747	–1.672	0.732	0.063	–0.071	–0.158
P072	ESP	0.663	192.075	0.240	–0.139	–0.648	0.265	0.023	–0.013	–0.061
P073	ESP	1.247	192.088	0.453	–0.261	–1.219	0.499	0.043	–0.025	–0.116
P074	ESP	1.831	192.048	0.665	–0.382	–1.790	0.732	0.063	–0.036	–0.170
P075	ESP	1.247	186.098	0.453	–0.132	–1.239	0.499	0.043	–0.013	–0.117
P076	ESP	0.518	179.985	0.187	0.000	–0.517	0.207	0.018	0.000	–0.049
P077	ESP	0.663	179.928	0.240	0.001	–0.663	0.265	0.023	0.000	–0.063
P078	ESP	0.810	179.964	0.294	0.001	–0.810	0.324	0.028	0.000	–0.077
P079	ESP	0.955	179.946	0.346	0.001	–0.955	0.382	0.033	0.000	–0.090
P080	ESP	1.101	180.002	0.400	0.000	–1.101	0.440	0.038	0.000	–0.104
P081	ESP	1.247	179.986	0.453	0.000	–1.247	0.499	0.043	0.000	–0.118
P082	ESP	1.393	179.996	0.506	0.000	–1.393	0.557	0.048	0.000	–0.132
P083	ESP	1.539	180.011	0.559	0.000	–1.539	0.616	0.053	0.000	–0.146
P084	ESP	1.685	180.019	0.612	–0.001	–1.685	0.674	0.058	0.000	–0.160
P085	ESP	1.831	180.024	0.665	–0.001	–1.831	0.732	0.063	0.000	–0.173
P086	ESP	1.977	180.002	0.718	0.000	–1.976	0.791	0.068	0.000	–0.187
P087	ESP	2.124	180.062	0.772	–0.002	–2.124	0.850	0.073	0.000	–0.201
P088	ESP	0.663	150.006	0.240	0.332	–0.575	0.265	0.023	0.031	–0.054
P089	ESP	1.247	150.019	0.453	0.623	–1.080	0.499	0.043	0.059	–0.102
P090	ESP	1.831	150.057	0.665	0.914	–1.586	0.732	0.063	0.087	–0.150
P091	ESP	0.663	120.037	0.240	0.574	–0.332	0.265	0.023	0.054	–0.031
P092	ESP	1.831	120.081	0.665	1.584	–0.918	0.732	0.063	0.150	–0.087
P093	ESP	0.665	89.986	0.241	0.665	0.000	0.266	0.023	0.063	0.000
P094	ESP	1.247	90.011	0.453	1.247	0.000	0.499	0.043	0.118	0.000
P095	ESP	1.831	90.032	0.665	1.831	–0.001	0.732	0.063	0.173	0.000
P096	ESP	0.661	59.770	0.239	0.571	0.333	0.264	0.023	0.054	0.032
P097	ESP	0.953	60.019	0.352	0.825	0.476	0.381	0.033	0.078	0.045

Table A-1. Continued.

Port	Type	Dimensional					Nondimensional			
		r, in	θ, deg	*x*, in	*y*, in	*z*, in	*r*/*R*	*x*/*L*	*y*/*L*	*z*/*L*
P098	ESP	1.244	59.968	0.451	1.077	0.622	0.498	0.043	0.102	0.059
P099	ESP	1.541	59.927	0.560	1.333	0.772	0.616	0.053	0.126	0.073
P100	ESP	1.829	60.083	0.664	1.585	0.912	0.732	0.063	0.150	0.086
P101	ESP	2.125	59.963	0.772	1.840	1.064	0.850	0.073	0.174	0.101
P102	ESP	0.661	29.615	0.240	0.327	0.575	0.265	0.023	0.031	0.054
P103	ESP	1.245	29.845	0.452	0.619	1.080	0.498	0.043	0.059	0.102
P104	ESP	1.831	29.897	0.665	0.913	1.587	0.732	0.063	0.086	0.150
P105	Kulite	2.124	282.015	0.772	–2.078	0.442	0.850	0.073	–0.197	0.042
P106	Kulite	2.125	186.074	0.772	–0.225	–2.113	0.850	0.073	–0.021	–0.200
P107	Kulite	1.832	156.086	0.666	0.743	–1.675	0.733	0.063	0.070	–0.159
P108	Kulite	2.122	132.064	0.771	1.576	–1.422	0.849	0.073	0.149	–0.135
P109	Kulite	1.247	84.071	0.454	1.241	0.129	0.499	0.043	0.118	0.012
P110	Kulite	1.832	48.055	0.665	1.362	1.224	0.733	0.063	0.129	0.116
P111	Kulite	1.832	23.988	0.666	0.745	1.674	0.733	0.063	0.071	0.159
P112	ESP	0.003	193.032	0.064	–0.001	–0.003	0.001	0.006	0.000	0.000
P113	ESP	0.185	0.858	0.081	0.003	0.184	0.074	0.008	0.000	0.017
P114	ESP	0.184	299.589	0.081	–0.160	0.091	0.074	0.008	–0.015	0.009
P115	ESP	0.186	240.067	0.081	–0.161	–0.093	0.075	0.008	–0.015	–0.009
P116	ESP	0.189	180.584	0.082	–0.002	–0.189	0.075	0.008	0.000	–0.018
P117	ESP	1.102	0.008	0.400	0.000	1.102	0.441	0.038	0.000	0.104
P118	ESP	1.247	0.095	0.453	0.002	1.247	0.499	0.043	0.000	0.118
P119	ESP	1.393	0.077	0.506	0.002	1.393	0.557	0.048	0.000	0.132
P120	ESP	1.249	354.175	0.453	–0.127	1.242	0.499	0.043	–0.012	0.118
P121	ESP	1.252	5.978	0.456	0.130	1.245	0.501	0.043	0.012	0.118
P122	ESP	1.103	240.074	0.399	–0.956	–0.550	0.441	0.038	–0.091	–0.052
P123	ESP	1.248	240.024	0.452	–1.081	–0.624	0.499	0.043	–0.102	–0.059
P124	ESP	1.393	240.068	0.505	–1.207	–0.695	0.557	0.048	–0.114	–0.066
P125	ESP	1.250	234.004	0.453	–1.011	–0.735	0.500	0.043	–0.096	–0.070
P126	Kulite	2.500	307.062	1.162	–1.995	1.507	1.000	0.110	–0.189	0.143
P127	Kulite	2.500	220.768	1.119	–1.632	–1.893	1.000	0.106	–0.155	–0.179
P128	ESP	2.500	360.579	2.480	0.025	2.500	1.000	0.235	0.002	0.237
P129	ESP	2.500	348.440	2.478	–0.501	2.449	1.000	0.235	–0.047	0.232
P130	ESP	2.500	336.302	2.476	–1.005	2.289	1.000	0.235	–0.095	0.217
P131	ESP	2.500	324.184	2.477	–1.463	2.027	1.000	0.235	–0.139	0.192
P132	ESP	2.500	312.333	2.474	–1.848	1.684	1.000	0.234	–0.175	0.159
P133	ESP	2.500	300.226	2.479	–2.160	1.259	1.000	0.235	–0.205	0.119
P134	ESP	2.500	288.203	2.479	–2.375	0.781	1.000	0.235	–0.225	0.074
P135	ESP	2.500	276.125	2.478	–2.486	0.267	1.000	0.235	–0.235	0.025
P136	ESP	2.500	264.090	2.477	–2.487	–0.257	1.000	0.235	–0.236	–0.024
P137	ESP	2.500	252.130	2.474	–2.379	–0.767	1.000	0.234	–0.225	–0.073

Table A-1. Concluded.

Port	Type	Dimensional					Nondimensional			
		r, in	θ, deg	*x*, in	*y*, in	*z*, in	*r*/*R*	*x*/*L*	*y*/*L*	*z*/*L*
P138	ESP	2.500	239.942	2.477	–2.164	–1.252	1.000	0.235	–0.205	–0.119
P139	ESP	2.500	227.932	2.473	–1.856	–1.675	1.000	0.234	–0.176	–0.159
P140	ESP	2.500	216.069	2.479	–1.472	–2.021	1.000	0.235	–0.139	–0.191
P141	ESP	2.500	203.793	2.476	–1.009	–2.288	1.000	0.235	–0.096	–0.217
P142	ESP	2.500	191.795	2.480	–0.511	–2.447	1.000	0.235	–0.048	–0.232
P143	ESP	2.500	180.256	2.491	–0.011	–2.500	1.000	0.236	–0.001	–0.237
P144	ESP	2.500	300.113	2.977	–2.163	1.254	1.000	0.282	–0.205	0.119
P145	ESP	2.500	239.924	2.978	–2.163	–1.253	1.000	0.282	–0.205	–0.119
P146	ESP	2.500	180.294	2.977	–0.013	–2.500	1.000	0.282	–0.001	–0.237
P147	ESP	2.500	360.421	3.477	0.018	2.500	1.000	0.329	0.002	0.237
P148	ESP	2.500	330.250	3.477	–1.241	2.170	1.000	0.329	–0.118	0.206
P149	ESP	2.500	300.048	3.477	–2.164	1.252	1.000	0.329	–0.205	0.119
P150	ESP	2.500	269.957	3.477	–2.500	–0.002	1.000	0.329	–0.237	0.000
P151	ESP	2.500	240.105	3.477	–2.167	–1.246	1.000	0.329	–0.205	–0.118
P152	ESP	2.500	209.816	3.473	–1.243	–2.169	1.000	0.329	–0.118	–0.205
P153	ESP	2.500	180.200	3.479	–0.009	–2.500	1.000	0.330	–0.001	–0.237
P154	ESP	2.500	300.222	4.726	–2.160	1.258	1.000	0.448	–0.205	0.119
P155	ESP	2.500	239.994	4.729	–2.165	–1.250	1.000	0.448	–0.205	–0.118
P156	ESP	2.500	180.347	4.725	–0.015	–2.500	1.000	0.448	–0.001	–0.237
P157	ESP	2.500	360.411	5.977	0.018	2.500	1.000	0.566	0.002	0.237
P158	ESP	2.500	330.307	5.977	–1.238	2.172	1.000	0.566	–0.117	0.206
P159	ESP	2.500	300.190	5.982	–2.161	1.257	1.000	0.567	–0.205	0.119
P160	ESP	2.500	270.062	5.979	–2.500	0.003	1.000	0.566	–0.237	0.000
P161	ESP	2.500	240.009	5.977	–2.165	–1.250	1.000	0.566	–0.205	–0.118
P162	ESP	2.500	209.944	5.977	–1.248	–2.166	1.000	0.566	–0.118	–0.205
P163	ESP	2.500	180.240	5.979	–0.010	–2.500	1.000	0.566	–0.001	–0.237
P164	ESP	2.500	300.185	7.224	–2.161	1.257	1.000	0.684	–0.205	0.119
P165	ESP	2.500	239.951	7.224	–2.164	–1.252	1.000	0.684	–0.205	–0.119
P166	ESP	2.500	180.274	7.229	–0.012	–2.500	1.000	0.685	–0.001	–0.237
P167	ESP	2.500	360.478	8.481	0.021	2.500	1.000	0.803	0.002	0.237
P168	ESP	2.500	330.308	8.480	–1.238	2.172	1.000	0.803	–0.117	0.206
P169	ESP	2.500	300.032	8.478	–2.164	1.251	1.000	0.803	–0.205	0.119
P170	ESP	2.500	270.200	8.480	–2.500	0.009	1.000	0.803	–0.237	0.001
P171	ESP	2.500	239.946	8.478	–2.164	–1.252	1.000	0.803	–0.205	–0.119
P172	ESP	2.500	209.803	8.478	–1.243	–2.169	1.000	0.803	–0.118	–0.206
P173	ESP	2.500	180.183	8.470	–0.008	–2.500	1.000	0.802	–0.001	–0.237
P174	ESP	2.500	300.084	9.733	–2.163	1.253	1.000	0.922	–0.205	0.119
P175	ESP	2.500	240.005	9.732	–2.165	–1.250	1.000	0.922	–0.205	–0.118
P176	ESP	2.500	180.326	9.731	–0.014	–2.500	1.000	0.922	–0.001	–0.237

Table A-2. Parameter list and definitions.

(a) Logistical and reference.

#	NAME	VALUE	UNITS	DESCRIPTION	EQUATION
1	TEST	1853	–	Test number	constant
2	RUN		–	Run number	set value
3	POINT		–	Point number	set value
4	ACQDATE		–	Data acquisition date (yyyymmdd)	e.g., May 18, 2009 = 20090518
5	ACQTIME		–	Data acquisition time, CDT (hhmmss)	e.g. 2:54:32 PM = 145432
6	DATAREV		–	Data reduction revision number (beginning at 0)	set value
7	CONFIGCO		–	Model configuration ID	set value: 0 = no nozzles; 1 = Nozzle 1; 2 = Nozzles 2,3,4; 3 = Nozzles 1,2,3,4
8	FAC	8	–	Facility identifier number	constant
9	SREF	0.13635	ft^2	Aerodynamic reference area (A_{ref})	constant
10	LREF	0.41667	ft	Aerodynamic reference length	constant
11	THAFA		deg	Pitch plane flow angle w.r.t gravity axis system	facility method
12	PSIFA		deg	Yaw plane flow angle w.r.t gravity axis system	facility method

Table A-2. Continued.

(b) Model attitude and location.

#	NAME	VALUE	UNITS	DESCRIPTION	EQUATION
13	THASS		deg	Support system pitch angle w.r.t. gravity axis system	facility measurement
14	PSISS		deg	Support system yaw angle w.r.t. gravity axis system	facility measurement
15	PHISS		deg	Support system roll angle w.r.t. gravity axis system	facility measurement
16	QFLEX		deg	Measured model Q-Flex pitch angle	facility measurement
17	ALPHA		deg	Model angle of attack	facility method
18	BETA		deg	Model angle of sideslip	facility method
19	PHI		deg	Model angle of roll	PHI = atan(tan(BETA)/sin(ALPHA))
20	ALPHAT		deg	Total angle of attack	ALPHAT = acos(cos(ALPHA)*cos(BETA))
21	XSS		in	Test section *x* axis position of model nose at zero AOA, including axial movement of model support system	facility method
22	YSS		in	Test section *y* axis position of model nose at zero AOA, including lateral movement of model support system	facility method
23	ZSS		in	Test section *z* axis position of model nose at zero AOA	facility method
24	DXSS		in	Change in test section *x* axis position of model nose with pitch angle, relative to model support system	DXSS = XMODEL – XSS
25	DYSS		in	Change in test section *y* axis position of model nose with yaw angle, relative to model support system	DYSS = YMODEL – YSS
26	DZSS		in	Change in test section *z* axis position of model nose with pitch angle, relative to model support system	DZSS = ZMODEL – ZSS
27	XMODEL		in	Test section *x* axis position of model nose	facility method; Euler rotations
28	YMODEL		in	Test section *y* axis position of model nose	facility method; Euler rotations
29	ZMODEL		in	Test section *z* axis position of model nose	facility method; Euler rotations

Table A-2. Continued.

(c) Facility flow conditions and tunnel wall pressures.

#	NAME	VALUE	UNITS	DESCRIPTION	EQUATION
30	MACH		–	Free-stream Mach number	facility method
31	PTINF		psfa	Facility stilling chamber total pressure	facility measurement
32	TTINF		Rankine	Facility stilling chamber total temperature	facility measurement
33	DEWPOINT		Rankine	Dewpoint temperature measured in facility stilling chamber	facility measurement
34	SPHUMID		lbm H_20/lbm air	Free-stream specific humidity	facility method
35	PINF		psfa	Free-stream static pressure	facility method
36	TINF		Rankine	Free-stream static temperature	facility method
37	RHOINF		slug/ft^3	Free-stream density	facility method
38	QINF		psfa	Free-stream dynamic pressure	facility method
39	VINF		ft/sec	Free-stream velocity	facility method
40	REINF		1/ft	Free-stream unit Reynolds number	facility method
41	RED		–	Free-stream Reynolds number, based on reference length	RED = REINF*LREF
42	GAMMA	1.400	–	Ratio of specific heats	constant
43	RGAS	1716.59	ft-lbf/(slug-R)	Gas constant, air	constant
44	SPRINF		–	Free-stream normal shock static pressure ratio	SPRINF = 1 + 2*GAMMA/(GAMMA + 1)*(MACH^2 – 1)
45	SDRINF		–	Free-stream normal shock density ratio	SDRINF = (GAMMA + 1)*MACH^2/((GAMMA – 1) *MACH^2 + 2)
46	PT2		psfa	Free-stream post-normal-shock stagnation pressure	PT2 = PTINF*SPRINF^(–1/(GAMMA – 1)) *SDRINF^(GAMMA/(GAMMA – 1))
47	TT2		Rankine	Free-stream post-normal-shock stagnation temperature	TT2 = TTINF

Table A-2. Continued.
(c) Concluded.

#	NAME	VALUE	UNITS	DESCRIPTION	EQUATION
48	MACH2		–	Free-stream post-normal-shock Mach number	MACH2 = sqrt((1 + 0.5 *(GAMMA – 1)*MACH^2)/ (GAMMA*MACH^2 – 0.5*(GAMMA – 1))
49	P2		psfa	Free-stream post-normal-shock static pressure	P2 = PINF*SPRINF
50	T2		Rankine	Free-stream post-normal-shock static temperature	T2 = TINF*SPRINF/SDRINF
51	RHO2		slug/ft^3	Free-stream post-normal-shock density	RHO2 = RHOINF*SDRINF
52	V2		ft/sec	Free-stream post-normal-shock velocity	V2 = VINF/SDRINF
53	Q2		psfa	Free-stream post-normal-shock dynamic pressure	Q2 = 0.5*RHO2*V2^2
54	PWALL01		psia	Test section wall static pressure #76, X = 32.6875, Y = 3.0	facility measurement
55	PWALL02		psia	Test section wall static pressure #75, X = 39.6875, Y = 3.0	facility measurement
56	PWALL03		psia	Test section wall static pressure #74, X = 46.6875, Y = 3.0	facility measurement
57	PWALL04		psia	Test section wall static pressure #73, X = 53.6875, Y = 3.0	facility measurement
58	PWALL05		psia	Test section wall static pressure #72, X = 60.6875, Y = 3.0	facility measurement
59	PWALL06		psia	Test section wall static pressure #71, X = 67.1875, Y = 3.0	facility measurement
60	PWALL07		psia	Test section wall static pressure #70, X = 73.1875, Y = 3.0	facility measurement
61	PWALL08		psia	Test section wall static pressure #69, X = 92.7500, Y = 3.0	facility measurement
62	PWALL09		psia	Test section wall static pressure #68, X = 97.7500, Y = 3.0	facility measurement
63	PWALL10		psia	Test section wall static pressure #67, X = 109.8125, Y = 3.0	facility measurement

Table A-2. Continued.

(d) Model thermocouple temperatures.

#	NAME	VALUE	UNITS	DESCRIPTION	EQUATION
64	TMODEL1		deg F	Model temperature #1, Type K thermocouple, TOP	facility measurement
65	TMODEL2		deg F	Model temperature #2, Type K thermocouple, STARBOARD	facility measurement
66	TMODEL3		deg F	Model temperature #3, Type K thermocouple, BOTTOM	facility measurement
67	TMODEL4		deg F	Model temperature #4, Type K thermocouple, PORT	facility measurement
68	TQFLEX		deg F	Temperature beneath Q-Flex, Type K thermocouple	facility measurement

(e) Model plenum conditions.

#	NAME	VALUE	UNITS	DESCRIPTION	EQUATION
69	PPLENA		psia	Measured plenum static pressure A, plenum upstream (relative to HPA flow) Kulite XT–190–2000A, 7700–7–152	facility measurement
70	PPLENB		psia	Measured plenum static pressure B, plenum downstream (relative to HPA flow) Kulite XT–190–2000A, 7700–7–151	facility measurement
71	PPLEN1		psia	Measured plenum static pressure in Nozzle #1 (center nozzle)	facility measurement; PPLEN1 = IJ1*(transducer calibration function)
72	PPLEN2		psia	Measured plenum static pressure in Nozzle #2 (half radius nozzle, 0 deg orientation)	facility measurement; PPLEN2 = IJ2*(transducer calibration function)
73	TTJA		Rankine	Measured plenum total temperature A, RTD probe, plenum upstream (relative to HPA flow)	facility measurement
74	TTJ1		Rankine	Measured plenum total temperature in Nozzle #1, Type K thermocouple	facility measurement; TTJ1 = IJ1*(thermocouple calibration function)

Table A-2. Continued.
(e) Concluded.

#	NAME	VALUE	UNITS	DESCRIPTION	EQUATION
75	TTJ2		Rankine	Measured plenum total temperature in Nozzle #2, Type K thermocouple	facility measurement; TTJ2 = IJ2*(thermocouple calibration function)
76	GAMMAP		–	Ratio of specific heats evaluated at plenum static conditions	GASPROPS – user input method 3 (PTJ, TTJ); GASPROPS output variable = GAMMA1
77	APLENA	0.78540	in^2	Cross-sectional area of model plenum at station A	constant
78	APLENB	0.89185	in^2	Cross-sectional area of model plenum at station B	constant
79	APLEN1	0.19635	in^2	Cross-sectional area of model plenum in Nozzle #1	constant
80	APLEN2	0.19635	in^2	Cross-sectional area of model plenum in Nozzle #2	constant
81	MPLENA		–	Model plenum Mach number at station A	MPLENA = WVEN/GC *sqrt (TTJA*RGASJ/GAMMAP) /(PPLENA*APLENA)
82	MPLENB		–	Model plenum Mach number at station B	MPLENB = WVEN /GC* sqrt(TTJA*RGASJ/GAMMAP) /(PPLENB*APLENB)
83	MPLEN1		–	Model plenum Mach number in Nozzle #1	MPLEN1 = IJ1*WVEN/GC* ATHROTJ1/ATHROTJT*sqrt (TTJ1*RGASJ/GAMMAP) /(PPLEN1*APLEN1)
84	MPLEN2		–	Model plenum Mach number in Nozzle #2	MPLEN2 = IJ2*WVEN /GC*ATHROTJ2/ATHROTJT* sqrt(TTJ2*RGASJ/GAMMAP) /(PPLEN2 *APLEN2)
85	PTJA		psia	Plenum total pressure at station A	PTJA = PPLENA*(1 + 0.5 *(GAMMAP – 1) *MPLENA^2)^(GAMMAP /(GAMMAP – 1))
86	PTJB		psia	Plenum total pressure at station B	PTJB = PPLENB*(1 + 0.5 *(GAMMAP – 1) *MPLENB^2)^(GAMMAP /(GAMMAP – 1))
87	PTJ1		psia	Plenum total pressure in Nozzle #1	PTJ1 = IJ1*PPLEN1*(1 + 0.5 *(GAMMAP – 1) *MPLEN1^2)^(GAMMAP /(GAMMAP – 1))
88	PTJ2		psia	Plenum total pressure in Nozzle #2	PTJ2 = IJ2*PPLEN2*(1 + 0.5 *(GAMMAP – 1) *MPLEN2^2)^(GAMMAP /(GAMMAP – 1))

Table A-2. Continued.

(f) Facility venturi measurements.

#	NAME	VALUE	UNITS	DESCRIPTION	EQUATION
89	GC	32.17405	lbm/slug	Mass units conversion factor	constant
90	DVEN1	1.50300	in	Venturi upstream diameter	constant
91	DVEN2	0.69500	in	Venturi throat diameter	constant
92	AVEN1	1.77422	in^2	Venturi upstream area	constant
93	AVEN2	0.37937	in^2	Venturi throat area	constant
94	BETAVEN	0.46241	–	Venturi diameter ratio (BETAVEN = DVEN2/DVEN1)	constant
95	PVEN1		psia	Venturi upstream static pressure	facility measurement
96	TVEN1		Rankine	Venturi upstream static temperature	facility measurement
97	ZVEN1		–	Venturi upstream compressibility factor, evaluated at PVEN1 & TVEN3 conditions	GASPROPS–user input method 3 (PVEN1, TVEN1); GASPROPS output variable = Z1
98	RHOVEN1		slug/ft^3	Venturi upstream static density	GASPROPS–user input method 3 (PVEN1, TVEN1); GASPROPS output variable = RH1
99	MUVEN1		lbf-sec/ft^2	Venturi downstream viscosity	GASPROPS–user input method 3 (PVEN1, TVEN1); GASPROPS output variable = MU1
100	GAMMAVEN		–	Venturi ratio of specific heats evaluated at upstream conditions	GASPROPS–user input method 3 (PVEN1, TVEN1); GASPROPS output variable = GAMMA1
101	PVEN2		psia	Venturi throat static pressure	PVEN2 = PVEN1 - PDIFFVEN
102	PDIFFVEN		psia	Venturi upstream-to-throat static pressure differential (PVEN1–PVEN2)	facility measurement

Table A-2. Continued.

(f) Facility venturi measurements.

#	NAME	VALUE	UNITS	DESCRIPTION	EQUATION
103	PRATVEN		–	Venturi throat-to-upstream static pressure ratio	PRATVEN = PVEN2/PVEN1
104	WVENHYD		lbm/sec	Venturi incompressible mass flow rate (Hydraulic Equation)	WVENHYD = GC*AVEN2/144*sqrt(2*RHOVEN 1*144*PDIFFVEN /(1–BETAVEN^4))
105	YVEN		–	Venturi expansion factor	YVEN = sqrt(GAMMAVEN /(GAMMAVEN–1)*PRATVEN ^(2/GAMMAVEN)*(1–PRATVEN ^((GAMMAVEN–1) /GAMMAVEN))*(1–BETAVEN^4) /((1-PRATVEN)*(1–BETAVEN^4 *PRATVEN^(2/GAMMAVEN))))
106	WVENIDEL		lbm/sec	Venturi ideal mass flow rate	WVENIDEL = YVEN*WVENHYD
107	REVEN2		–	Venturi throat Reynolds number	REVEN2 = 4/GC*WVEN/(PI*DVEN2/12*MU VEN1)
108	CDVEN		–	Venturi discharge coefficient	CDVEN = b0 + b1*REVEN2 + b2/ sqrt(REVEN2); where 'b' coefficients are given in 'Venturi Cd Table' page
109	WVEN		lbm/sec	Venturi mass flow rate	WVEN = CDVEN*WVENIDEL
110	WDCV		lbm/sec	Digital control valve mass flow rate	facility method (from digital control valve)

(g) Model nozzle calculations.

#	NAME	VALUE	UNITS	DESCRIPTION	EQUATION
111	REALGAS		–	Flag to denote method used for calculation of nozzle exit conditions (IDEAL GAS = 0, REAL GAS = 1)	set value
112	IJ1		–	Flag to denote presence of nozzle #1 in model (OFF = 0, ON = 1)	set value

Table A-2. Continued.

(g) Continued.

#	NAME	VALUE	UNITS	DESCRIPTION	EQUATION
113	IJ2		–	Flag to denote presence of nozzle #2 in model (OFF = 0, ON = 1)	set value
114	IJ3		–	Flag to denote presence of nozzle #3 in model (OFF = 0, ON = 1)	set value
115	IJ4		–	Flag to denote presence of nozzle #4 in model (OFF = 0, ON = 1)	set value
116	DTHROTJ 1	0.2491	in	Nozzle throat diameter, nozzle #1	constant
117	DTHROTJ 2	0.2498	in	Nozzle throat diameter, nozzle #2	constant
118	DTHROTJ 3	0.2535	in	Nozzle throat diameter, nozzle #3	constant
119	DTHROTJ 4	0.2503	in	Nozzle throat diameter, nozzle #4	constant
120	DEXITJ1	0.5014	in	Nozzle virtual exit diameter, nozzle #1	constant
121	DEXITJ2	0.4965	in	Nozzle virtual exit diameter, nozzle #2	constant
122	DEXITJ3	0.4989	in	Nozzle virtual exit diameter, nozzle #3	constant
123	DEXITJ4	0.4996	in	Nozzle virtual exit diameter, nozzle #4	constant
124	ATHROTJ1	0.048735	in^2	Nozzle throat area, nozzle #1	constant
125	ATHROTJ2	0.049009	in^2	Nozzle throat area, nozzle #2	constant
126	ATHROTJ3	0.050471	in^2	Nozzle throat area, nozzle #3	constant
127	ATHROTJ4	0.049205	in^2	Nozzle throat area, nozzle #4	constant
128	AEXITJ1	0.197451	in^2	Nozzle virtual exit area, nozzle #1	constant
129	AEXITJ2	0.193610	in^2	Nozzle virtual exit area, nozzle #2	constant
130	AEXITJ3	0.195487	in^2	Nozzle virtual exit area, nozzle #3	constant
131	AEXITJ4	0.196036	in^2	Nozzle virtual exit area, nozzle #4	constant
132	ARATIOJ1	4.051550	–	Nozzle exit-to-throat area ratio, nozzle #1	constant

Table A-2. Continued.

(g) Continued.

#	NAME	VALUE	UNITS	DESCRIPTION	EQUATION
133	ARATIOJ2	3.950514	–	Nozzle exit-to-throat area ratio, nozzle #2	constant
134	ARATIOJ3	3.873210	–	Nozzle exit-to-throat area ratio, nozzle #3	constant
135	ARATIOJ4	3.984035	–	Nozzle exit-to-throat area ratio, nozzle #4	constant
136	THETAWJ 1	14.981	deg	Nozzle exit wall angle, nozzle #1	constant
137	THETAWJ 2	14.977	deg	Nozzle exit wall angle, nozzle #2	constant
138	THETAWJ 3	14.994	deg	Nozzle exit wall angle, nozzle #3	constant
139	THETAWJ 4	14.985	deg	Nozzle exit wall angle, nozzle #4	constant
140	LAMBDAJ1	0.98301	–	Streamline spreading momentum correction factor, nozzle #1	constant
141	LAMBDAJ2	0.98302	–	Streamline spreading momentum correction factor, nozzle #2	constant
142	LAMBDAJ3	0.98298	–	Streamline spreading momentum correction factor, nozzle #3	constant
143	LAMBDAJ4	0.98300	–	Streamline spreading momentum correction factor, nozzle #4	constant
144	ATHROTJ T		in^2	Total nozzle throat area of nozzles present in model	ATHROTJT = dotproduct(ATHROTJ(i),IJ(i))
145	RGASJ	1716.59	ft-lbf/ (slug-R)	Gas constant, air	constant
146	PTJ		psia	Average measured plenum total pressure	PTJ = average(PTJA:PTJB)
147	TTJ		Rankine	Average measured plenum total temperature	TTJ = TTJA
148	GAMMAT		–	Nozzle throat specific heat ratio (assumes choked flow at nozzle throat)	GASPROPS – user input method 1 (PTJ, TTJ, MACH = 1); GASPROPS output variable = GAMMA1
149	NPRJ		–	Nozzle pressure ratio	NPRJ = PTJ/PINF*144
150	NTRJ		–	Nozzle temperature ratio	NTRJ = TTJ/TINF
151	WTAPJ		–	Nozzle mass flow function (assumes choked flow at nozzle throat)	WTAPJ = sqrt (GAMMAT/RGASJ*(2/(GAMMAT + 1))^((GAMMAT + 1) /(GAMMAT – 1)))

Table A-2. Continued.

(g) Continued.

#	NAME	VALUE	UNITS	DESCRIPTION	EQUATION
152	WIDEALJ		lbm/sec	Nozzle net ideal mass flow (assumes choked flow at nozzle throat)	WIDEALJ = GC*WTAPJ*PTJ*ATHROTJT/ sqrt(TTJ)
153	CDISJ		–	Nozzle net discharge coefficient	CDISJ = WVEN/WIDEALJ
154	NPRJ_PT1		–	Nozzle pressure ratio, referenced to facility total pressure	NPRJ_PT1 = PTJ/PTINF*144
155	NRPJ_PT2		–	Nozzle pressure ratio, referenced to post-normal-shock stagnation pressure	NRPJ_PT2 = PTJ/PT2*144
156	NPRJ_P2		–	Nozzle pressure ratio, referenced to post-normal-shock static pressure	NPRJ_P2 = PTJ/P2*144
157	M0J1	2.9571	–	Ideal gas nozzle exit Mach number, nozzle #1	constant
158	M0J2	2.9305	–	Ideal gas nozzle exit Mach number, nozzle #2	constant
159	M0J3	2.9097	–	Ideal gas nozzle exit Mach number, nozzle #3	constant
160	M0J4	2.9394	–	Ideal gas nozzle exit Mach number, nozzle #4	constant
161	MEXITJ1		–	Nozzle exit Mach number, nozzle #1	MEXITJ1 = IJ1*M0J1*(A0 + A1*PTJ + A2*PTJ^2); “A” constants found in Nozzle Mexit Variation, cells K74:M77
162	MEXITJ2		–	Nozzle exit Mach number, nozzle #2	MEXITJ2 = IJ2*M0J2*(A0 + A1*PTJ + A2*PTJ^2); “A” constants found in Nozzle Mexit Variation, cells K74:M77
163	MEXITJ3		–	Nozzle exit Mach number, nozzle #3	MEXITJ3 = IJ3*M0J3*(A0 + A1*PTJ + A2*PTJ^2); “A” constants found in Nozzle Mexit Variation, cells K74:M77
164	MEXITJ4		–	Nozzle exit Mach number, nozzle #4	MEXITJ4 = IJ4*M0J4*(A0 + A1*PTJ + A2*PTJ^2); “A” constants found in Nozzle Mexit Variation, cells K74:M77

Table A-2. Continued.

(g) Continued.

#	NAME	VALUE	UNITS	DESCRIPTION	EQUATION
165	GAMMAJ1		–	Nozzle exit specific heat ratio, nozzle #1	GASPROPS – user input method 1 (PTJ, TTJ, MEXITJ1); GASPROPS output variable = GAMMA1; GAMMAJ1 = IJ1* (GASPROPS output)
166	GAMMAJ2		–	Nozzle exit specific heat ratio, nozzle #2	GASPROPS – user input method 1 (PTJ, TTJ, MEXITJ2); GASPROPS output variable = GAMMA1; GAMMAJ2 = IJ2* (GASPROPS output)
167	GAMMAJ3		–	Nozzle exit specific heat ratio, nozzle #3	GASPROPS – user input method 1 (PTJ, TTJ, MEXITJ3); GASPROPS output variable = GAMMA1; GAMMAJ3 = IJ3* (GASPROPS output)
168	GAMMAJ4		–	Nozzle exit specific heat ratio, nozzle #4	GASPROPS – user input method 1 (PTJ, TTJ, MEXITJ4); GASPROPS output variable = GAMMA1; GAMMAJ4 = IJ4* (GASPROPS output)
169	PJ1		psia	Nozzle exit static pressure, nozzle #1	GASPROPS – user input method 1 (PTJ, TTJ, MEXITJ1); GASPROPS output variable = P1; PJ1 = IJ1* (GASPROPS output)
170	PJ2		psia	Nozzle exit static pressure, nozzle #2	GASPROPS – user input method 1 (PTJ, TTJ, MEXITJ2); GASPROPS output variable = P1; PJ2 = IJ2* (GASPROPS output)
171	PJ3		psia	Nozzle exit static pressure, nozzle #3	GASPROPS – user input method 1 (PTJ, TTJ, MEXITJ3); GASPROPS output variable = P1; PJ3 = IJ3* (GASPROPS output)
172	PJ4		psia	Nozzle exit static pressure, nozzle #4	GASPROPS – user input method 1 (PTJ, TTJ, MEXITJ4); GASPROPS output variable = P1; PJ4 = IJ4* (GASPROPS output)

Table A-2. Continued.

(g) Continued.

#	NAME	VALUE	UNITS	DESCRIPTION	EQUATION
173	TJ1		Rankine	Nozzle exit static temperature, nozzle #1	GASPROPS – user input method 1 (PTJ, TTJ, MEXITJ1); GASPROPS output variable = T1; TJ1 = IJ1* (GASPROPS output)
174	TJ2		Rankine	Nozzle exit static temperature, nozzle #2	GASPROPS – user input method 1 (PTJ, TTJ, MEXITJ2); GASPROPS output variable = T1; TJ2 = IJ2* (GASPROPS output)
175	TJ3		Rankine	Nozzle exit static temperature, nozzle #3	GASPROPS – user input method 1 (PTJ, TTJ, MEXITJ3); GASPROPS output variable = T1; TJ3 = IJ3* (GASPROPS output)
176	TJ4		Rankine	Nozzle exit static temperature, nozzle #4	GASPROPS – user input method 1 (PTJ, TTJ, MEXITJ4); GASPROPS output variable = T1; TJ4 = IJ4* (GASPROPS output)
177	VJ1		ft/sec	Nozzle exit velocity, nozzle #1	GASPROPS – user input method 1 (PTJ, TTJ, MEXITJ1); GASPROPS output variable = U1; VJ1 = IJ1* (GASPROPS output)
178	VJ2		ft/sec	Nozzle exit velocity, nozzle #2	GASPROPS – user input method 1 (PTJ, TTJ, MEXITJ2); GASPROPS output variable = U1; VJ2 = IJ2* (GASPROPS output)
179	VJ3		ft/sec	Nozzle exit velocity, nozzle #3	GASPROPS – user input method 1 (PTJ, TTJ, MEXITJ3); GASPROPS output variable = U1; VJ3 = IJ3 *(GASPROPS output)
180	VJ4		ft/sec	Nozzle exit velocity, nozzle #4	GASPROPS–user input method 1 (PTJ, TTJ, MEXITJ4); GASPROPS output variable = U1; VJ4 = IJ4* (GASPROPS output)
181	WJ1		lbm/sec	Nozzle mass flow rate, nozzle #1	WJ1 = IJ1*WVEN *ATHROTJ1/ATHROTJT
182	WJ2		lbm/sec	Nozzle mass flow rate, nozzle #2	WJ2 = IJ2*WVEN *ATHROTJ2/ATHROTJT
183	WJ3		lbm/sec	Nozzle mass flow rate, nozzle #3	WJ3 = IJ3*WVEN *ATHROTJ3/ATHROTJT
184	WJ4		lbm/sec	Nozzle mass flow rate, nozzle #4	WJ4 = IJ4*WVEN *ATHROTJ4/ATHROTJT

Table A-2. Continued.
(g) Concluded.

#	NAME	VALUE	UNITS	DESCRIPTION	EQUATION
185	WVJ1		lbf	Nozzle momentum flux, nozzle #1	WVJ1 = WJ1/GC*VJ1
186	WVJ2		lbf	Nozzle momentum flux, nozzle #2	WVJ2 = WJ2/GC*VJ2
187	WVJ3		lbf	Nozzle momentum flux, nozzle #3	WVJ3 = WJ3/GC*VJ3
188	WVJ4		lbf	Nozzle momentum flux, nozzle #4	WVJ4 = WJ4/GC*VJ4
189	FVACJ1		lbf	Nozzle thrust, nozzle #1	FVACJ1 = LAMBDAJ1*WVJ1 + PJ1*AEXITJ1
190	FVACJ2		lbf	Nozzle thrust, nozzle #2	FVACJ2 = LAMBDAJ2*WVJ2 + PJ2*AEXITJ2
191	FVACJ3		lbf	Nozzle thrust, nozzle #3	FVACJ3 = LAMBDAJ3*WVJ3 + PJ3*AEXITJ3
192	FVACJ4		lbf	Nozzle thrust, nozzle #4	FVACJ4 = LAMBDAJ4*WVJ4 + PJ4*AEXITJ4
193	CTJ1		–	Nozzle thrust coefficient, nozzle #1	CTJ1 = FVACJ1/(QINF*SREF)
194	CTJ2		–	Nozzle thrust coefficient, nozzle #2	CTJ2 = FVACJ2/(QINF*SREF)
195	CTJ3		–	Nozzle thrust coefficient, nozzle #3	CTJ3 = FVACJ3/(QINF*SREF)
196	CTJ4		–	Nozzle thrust coefficient, nozzle #4	CTJ4 = FVACJ4/(QINF*SREF)
197	PRATJ1		–	Nozzle exit-to-free-stream static pressure ratio, nozzle #1	PRATJ1 = PJ1/PINF*144
198	PRATJ2		–	Nozzle exit-to-free-stream static pressure ratio, nozzle #2	PRATJ2 = PJ2/PINF*144
199	PRATJ3		–	Nozzle exit-to-free-stream static pressure ratio, nozzle #3	PRATJ3 = PJ3/PINF*144
200	PRATJ4		–	Nozzle exit-to-free-stream static pressure ratio, nozzle #4	PRATJ4 = PJ4/PINF*144
201	FVACJTOT		lbf	Total nozzle thrust	FVACJTOT = sum(FVACJ1:FVACJ4)
202	CTJTOT		lbf	Total nozzle thrust coefficient	CTJTOT = sum(CTJ1:CTJ4)

Table A-2. Continued.

(h) ESP auxiliary measurements.

#	NAME	VALUE	UNITS	DESCRIPTION	EQUATION
203	ESPREF		psia	Reference pressure supplied to ESP module in LAT	facility measurement
204	ESPTEMP2		deg F	Measured temperature from ESP module #1	facility measurement
205	ESPTEMP3		deg F	Measured temperature from ESP module #2	facility measurement
206	ESPTEMP4		deg F	Measured temperature from ESP module #3	facility measurement
207	PMON1		psia	Monitor pressure #1 from facility-supplied pressure standard	facility measurement
208	PMON2		psia	Monitor pressure #2 from facility-supplied pressure standard	facility measurement
209	PMON3		psia	Monitor pressure #3 from facility-supplied pressure standard	facility measurement
210	ESPMON21		psia	Measurement of PMON1 by ESP module #2	facility measurement
211	ESPMON22		psia	Measurement of PMON2 by ESP module #2	facility measurement
212	ESPMON23		psia	Measurement of PMON3 by ESP module #2	facility measurement
213	ESPMON31		psia	Measurement of PMON1 by ESP module #3	facility measurement
214	ESPMON32		psia	Measurement of PMON2 by ESP module #3	facility measurement
215	ESPMON33		psia	Measurement of PMON3 by ESP module #3	facility measurement
216	ESPMON41		psia	Measurement of PMON1 by ESP module #4	facility measurement
217	ESPMON42		psia	Measurement of PMON2 by ESP module #4	facility measurement
218	ESPMON43		psia	Measurement of PMON3 by ESP module #4	facility measurement
219	DESPM21		psia	Difference between measured ESP pressure in module #2 and supplied monitor pressure 1	DESPM21 = ESPMON21 – PMON1

Table A-2. Continued.
(h) Concluded.

#	NAME	VALUE	UNITS	DESCRIPTION	EQUATION
220	DESPM22		psia	Difference between measured ESP pressure in module #2 and supplied monitor pressure 2	DESPM22 = ESPMON22 – PMON2
221	DESPM23		psia	Difference between measured ESP pressure in module #2 and supplied monitor pressure 3	DESPM23 = ESPMON23 – PMON3
222	DESPM31		psia	Difference between measured ESP pressure in module #3 and supplied monitor pressure 1	DESPM31 = ESPMON31 –PMON1
223	DESPM32		psia	Difference between measured ESP pressure in module #3 and supplied monitor pressure 2	DESPM32 = ESPMON32 – PMON2
224	DESPM33		psia	Difference between measured ESP pressure in module #3 and supplied monitor pressure 3	DESPM33 = ESPMON33 – PMON3
225	DESPM41		psia	Difference between measured ESP pressure in module #4 and supplied monitor pressure 1	DESPM41 = ESPMON41 –PMON1
226	DESPM42		psia	Difference between measured ESP pressure in module #4 and supplied monitor pressure 2	DESPM42 = ESPMON42 – PMON2
227	DESPM43		psia	Difference between measured ESP pressure in module #4 and supplied monitor pressure 3	DESPM43 = ESPMON43 – PMON3

(i) Model surface static pressures.

#	NAME	VALUE	UNITS	DESCRIPTION	EQUATION
228	P001		psia	Model surface pressure – ESP	facility measurement
229	P002		psia	Model surface pressure – ESP	facility measurement
230	P003		psia	Model surface pressure – ESP	facility measurement
231	P004		psia	Model surface pressure – ESP	facility measurement
232	P005		psia	Model surface pressure – ESP	facility measurement
233	P006		psia	Model surface pressure – ESP	facility measurement

Table A-2. Continued.

(i) Continued.

#	NAME	VALUE	UNITS	DESCRIPTION	EQUATION
234	P007		psia	Model surface pressure – ESP	facility measurement
235	P008		psia	Model surface pressure – ESP	facility measurement
236	P009		psia	Model surface pressure – ESP	facility measurement
237	P010		psia	Model surface pressure – ESP	facility measurement
238	P011		psia	Model surface pressure – ESP	facility measurement
239	P012		psia	Model surface pressure – ESP	facility measurement
240	P013		psia	Model surface pressure – ESP	facility measurement
241	P014		psia	Model surface pressure – ESP	facility measurement
242	P015		psia	Model surface pressure – ESP	facility measurement
243	P016		psia	Model surface pressure – ESP	facility measurement
244	P017		psia	Model surface pressure – ESP	facility measurement
245	P018		psia	Model surface pressure – ESP	facility measurement
246	P019		psia	Model surface pressure – ESP	facility measurement
247	P020		psia	Model surface pressure – ESP	facility measurement
248	P021		psia	Model surface pressure – ESP	facility measurement
249	P022		psia	Model surface pressure – ESP	facility measurement
250	P023		psia	Model surface pressure – ESP	facility measurement
251	P024		psia	Model surface pressure – ESP	facility measurement
252	P025		psia	Model surface pressure – ESP	facility measurement
253	P026		psia	Model surface pressure – ESP	facility measurement
254	P027		psia	Model surface pressure – ESP	facility measurement
255	P028		psia	Model surface pressure – ESP	facility measurement
256	P029		psia	Model surface pressure – ESP	facility measurement
257	P030		psia	Model surface pressure – ESP	facility measurement
258	P031		psia	Model surface pressure – ESP	facility measurement
259	P032		psia	Model surface pressure – ESP	facility measurement
260	P033		psia	Model surface pressure – ESP	facility measurement
261	P034		psia	Model surface pressure – ESP	facility measurement
262	P035		psia	Model surface pressure – ESP	facility measurement
263	P036		psia	Model surface pressure – ESP	facility measurement
264	P037		psia	Model surface pressure – ESP	facility measurement
265	P038		psia	Model surface pressure – ESP	facility measurement
266	P039		psia	Model surface pressure – ESP	facility measurement
267	P040		psia	Model surface pressure – ESP	facility measurement
268	P041		psia	Model surface pressure – ESP	facility measurement
269	P042		psia	Model surface pressure – ESP	facility measurement
270	P043		psia	Model surface pressure – ESP	facility measurement
271	P044		psia	Model surface pressure – ESP	facility measurement

Table A-2. Continued.

(i) Continued.

#	NAME	VALUE	UNITS	DESCRIPTION	EQUATION
272	P045		psia	Model surface pressure – ESP	facility measurement
273	P046		psia	Model surface pressure – ESP	facility measurement
274	P047		psia	Model surface pressure – ESP	facility measurement
275	P048		psia	Model surface pressure – ESP	facility measurement
276	P049		psia	Model surface pressure – ESP	facility measurement
277	P050		psia	Model surface pressure – ESP	facility measurement
278	P051		psia	Model surface pressure – ESP	facility measurement
279	P052		psia	Model surface pressure – ESP	facility measurement
280	P053		psia	Model surface pressure – ESP	facility measurement
281	P054		psia	Model surface pressure – ESP	facility measurement
282	P055		psia	Model surface pressure – ESP	facility measurement
283	P056		psia	Model surface pressure – ESP	facility measurement
284	P057		psia	Model surface pressure – ESP	facility measurement
285	P058		psia	Model surface pressure – ESP	facility measurement
286	P059		psia	Model surface pressure – ESP	facility measurement
287	P060		psia	Model surface pressure – ESP	facility measurement
288	P061		psia	Model surface pressure – ESP	facility measurement
289	P062		psia	Model surface pressure – ESP	facility measurement
290	P063		psia	Model surface pressure – ESP	facility measurement
291	P064		psia	Model surface pressure – ESP	facility measurement
292	P065		psia	Model surface pressure – ESP	facility measurement
293	P066		psia	Model surface pressure – ESP	facility measurement
294	P067		psia	Model surface pressure – ESP	facility measurement
295	P068		psia	Model surface pressure – ESP	facility measurement
296	P069		psia	Model surface pressure – ESP	facility measurement
297	P070		psia	Model surface pressure – ESP	facility measurement
298	P071		psia	Model surface pressure – ESP	facility measurement
299	P072		psia	Model surface pressure – ESP	facility measurement
300	P073		psia	Model surface pressure – ESP	facility measurement
301	P074		psia	Model surface pressure – ESP	facility measurement
302	P075		psia	Model surface pressure – ESP	facility measurement
303	P076		psia	Model surface pressure – ESP	facility measurement
304	P077		psia	Model surface pressure – ESP	facility measurement
305	P078		psia	Model surface pressure – ESP	facility measurement
306	P079		psia	Model surface pressure – ESP	facility measurement
307	P080		psia	Model surface pressure – ESP	facility measurement
308	P081		psia	Model surface pressure – ESP	facility measurement
309	P082		psia	Model surface pressure – ESP	facility measurement

Table A-2. Continued.

(i) Continued.

#	NAME	VALUE	UNITS	DESCRIPTION	EQUATION
310	P083		psia	Model surface pressure – ESP	facility measurement
311	P084		psia	Model surface pressure – ESP	facility measurement
312	P085		psia	Model surface pressure – ESP	facility measurement
313	P086		psia	Model surface pressure – ESP	facility measurement
314	P087		psia	Model surface pressure – ESP	facility measurement
315	P088		psia	Model surface pressure – ESP	facility measurement
316	P089		psia	Model surface pressure – ESP	facility measurement
317	P090		psia	Model surface pressure – ESP	facility measurement
318	P091		psia	Model surface pressure – ESP	facility measurement
319	P092		psia	Model surface pressure – ESP	facility measurement
320	P093		psia	Model surface pressure – ESP	facility measurement
321	P094		psia	Model surface pressure – ESP	facility measurement
322	P095		psia	Model surface pressure – ESP	facility measurement
323	P096		psia	Model surface pressure – ESP	facility measurement
324	P097		psia	Model surface pressure – ESP	facility measurement
325	P098		psia	Model surface pressure – ESP	facility measurement
326	P099		psia	Model surface pressure – ESP	facility measurement
327	P100		psia	Model surface pressure – ESP	facility measurement
328	P101		psia	Model surface pressure – ESP	facility measurement
329	P102		psia	Model surface pressure – ESP	facility measurement
330	P103		psia	Model surface pressure – ESP	facility measurement
331	P104		psia	Model surface pressure – ESP	facility measurement
332	P105		psia	Model surface pressure – Kulite XCS–062–5A, 7822–7–336	facility measurement
333	P106		psia	Model surface pressure – Kulite XCS–062–5A, 7822–7–325	facility measurement
334	P107		psia	Model surface pressure – Kulite XCS–062–5A, 7822–7–329	facility measurement
335	P108		psia	Model surface pressure – Kulite XCS–062–5A, 7822–7–327	facility measurement
336	P109		psia	Model surface pressure – Kulite XCS–062–5A, 7822–7–324	facility measurement
337	P110		psia	Model surface pressure – Kulite XCS–062–5A, 7822–7–323	facility measurement
338	P111		psia	Model surface pressure – Kulite XCS–062–5A, 7822–7–322	facility measurement
339	P112		psia	Model surface pressure – ESP	facility measurement
340	P113		psia	Model surface pressure – ESP	facility measurement
341	P114		psia	Model surface pressure – ESP	facility measurement

Table A-2. Continued.

(i) Continued.

#	NAME	VALUE	UNITS	DESCRIPTION	EQUATION
342	P115		psia	Model surface pressure – ESP	facility measurement
343	P116		psia	Model surface pressure – ESP	facility measurement
344	P117		psia	Model surface pressure – ESP	facility measurement
345	P118		psia	Model surface pressure – ESP	facility measurement
346	P119		psia	Model surface pressure – ESP	facility measurement
347	P120		psia	Model surface pressure – ESP	facility measurement
348	P121		psia	Model surface pressure – ESP	facility measurement
349	P122		psia	Model surface pressure – ESP	facility measurement
350	P123		psia	Model surface pressure – ESP	facility measurement
351	P124		psia	Model surface pressure – ESP	facility measurement
352	P125		psia	Model surface pressure – ESP	facility measurement
353	P126	999	psia	Model surface pressure – Kulite XCS–062–5A, 7822–7–331	constant (since no longer operable as destroyed 7/2/10 during installation)
354	P127	999	psia	Model surface pressure – Kulite XCS–062–5A, 7822–7–328	constant (since no longer operable as destroyed 7/2/10 during installation)
355	P128		psia	Model surface pressure – ESP	facility measurement
356	P129		psia	Model surface pressure – ESP	facility measurement
357	P130		psia	Model surface pressure – ESP	facility measurement
358	P131		psia	Model surface pressure – ESP	facility measurement
359	P132		psia	Model surface pressure – ESP	facility measurement
360	P133		psia	Model surface pressure – ESP	facility measurement
361	P134		psia	Model surface pressure – ESP	facility measurement
362	P135		psia	Model surface pressure – ESP	facility measurement
363	P136		psia	Model surface pressure – ESP	facility measurement
364	P137		psia	Model surface pressure – ESP	facility measurement
365	P138		psia	Model surface pressure – ESP	facility measurement
366	P139		psia	Model surface pressure – ESP	facility measurement
367	P140		psia	Model surface pressure – ESP	facility measurement
368	P141		psia	Model surface pressure – ESP	facility measurement
369	P142		psia	Model surface pressure – ESP	facility measurement
370	P143		psia	Model surface pressure – ESP	facility measurement
371	P144		psia	Model surface pressure – ESP	facility measurement
372	P145		psia	Model surface pressure – ESP	facility measurement
373	P146		psia	Model surface pressure – ESP	facility measurement
374	P147		psia	Model surface pressure – ESP	facility measurement
375	P148		psia	Model surface pressure – ESP	facility measurement

Table A-2. Continued.
(i) Concluded.

#	NAME	VALUE	UNITS	DESCRIPTION	EQUATION
376	P149		psia	Model surface pressure – ESP	facility measurement
377	P150		psia	Model surface pressure – ESP	facility measurement
378	P151		psia	Model surface pressure – ESP	facility measurement
379	P152		psia	Model surface pressure – ESP	facility measurement
380	P153		psia	Model surface pressure – ESP	facility measurement
381	P154		psia	Model surface pressure – ESP	facility measurement
382	P155		psia	Model surface pressure – ESP	facility measurement
383	P156		psia	Model surface pressure – ESP	facility measurement
384	P157		psia	Model surface pressure – ESP	facility measurement
385	P158		psia	Model surface pressure – ESP	facility measurement
386	P159		psia	Model surface pressure – ESP	facility measurement
387	P160		psia	Model surface pressure – ESP	facility measurement
388	P161		psia	Model surface pressure – ESP	facility measurement
389	P162		psia	Model surface pressure – ESP	facility measurement
390	P163		psia	Model surface pressure – ESP	facility measurement
391	P164		psia	Model surface pressure – ESP	facility measurement
392	P165		psia	Model surface pressure – ESP	facility measurement
393	P166		psia	Model surface pressure – ESP	facility measurement
394	P167		psia	Model surface pressure – ESP	facility measurement
395	P168		psia	Model surface pressure – ESP	facility measurement
396	P169		psia	Model surface pressure – ESP	facility measurement
397	P170		psia	Model surface pressure – ESP	facility measurement
398	P171		psia	Model surface pressure – ESP	facility measurement
399	P172		psia	Model surface pressure – ESP	facility measurement
400	P173		psia	Model surface pressure – ESP	facility measurement
401	P174		psia	Model surface pressure – ESP	facility measurement
402	P175		psia	Model surface pressure – ESP	facility measurement
403	P176		psia	Model surface pressure – ESP	facility measurement

(j) Model surface static pressure coefficients.

#	NAME	VALUE	UNITS	DESCRIPTION	EQUATION
404	CP001		–	Model surface pressure coefficient – ESP	CP001 = (P001*144 – PINF)/QINF
405	CP002		–	Model surface pressure coefficient – ESP	CP002 = (P002*144 – PINF)/QINF
406	CP003		–	Model surface pressure coefficient – ESP	CP003 = (P003*144 – PINF)/QINF

Table A-2. Continued.

(j) Continued.

#	NAME	VALUE	UNITS	DESCRIPTION	EQUATION
407	CP004		–	Model surface pressure coefficient – ESP	CP004 = (P004*144 – PINF)/QINF
408	CP005		–	Model surface pressure coefficient – ESP	CP005 = (P005*144 – PINF)/QINF
409	CP006		–	Model surface pressure coefficient – ESP	CP006 = (P006*144 – PINF)/QINF
410	CP007		–	Model surface pressure coefficient – ESP	CP007 = (P007*144 – PINF)/QINF
411	CP008		–	Model surface pressure coefficient – ESP	CP008 = (P008*144 – PINF)/QINF
412	CP009		–	Model surface pressure coefficient – ESP	CP009 = (P009*144 – PINF)/QINF
413	CP010		–	Model surface pressure coefficient – ESP	CP010 = (P010*144 – PINF)/QINF
414	CP011		–	Model surface pressure coefficient – ESP	CP011 = (P011*144 – PINF)/QINF
415	CP012		–	Model surface pressure coefficient – ESP	CP012 = (P012*144 – PINF)/QINF
416	CP013		–	Model surface pressure coefficient – ESP	CP013 = (P013*144 – PINF)/QINF
417	CP014		–	Model surface pressure coefficient – ESP	CP014 = (P014*144 – PINF)/QINF
418	CP015		–	Model surface pressure coefficient – ESP	CP015 = (P015*144 – PINF)/QINF
419	CP016		–	Model surface pressure coefficient – ESP	CP016 = (P016*144 – PINF)/QINF
420	CP017		–	Model surface pressure coefficient – ESP	CP017 = (P017*144 – PINF)/QINF
421	CP018		–	Model surface pressure coefficient – ESP	CP018 = (P018*144 – PINF)/QINF
422	CP019		–	Model surface pressure coefficient – ESP	CP019 = (P019*144 – PINF)/QINF
423	CP020		–	Model surface pressure coefficient – ESP	CP020 = (P020*144 – PINF)/QINF
424	CP021		–	Model surface pressure coefficient – ESP	CP021 = (P021*144 – PINF)/QINF
425	CP022		–	Model surface pressure coefficient – ESP	CP022 = (P022*144 – PINF)/QINF
426	CP023		–	Model surface pressure coefficient – ESP	CP023 = (P023*144 – PINF)/QINF
427	CP024		–	Model surface pressure coefficient – ESP	CP024 = (P024*144 – PINF)/QINF

Table A-2. Continued.

(j) Continued.

#	NAME	VALUE	UNITS	DESCRIPTION	EQUATION
428	CP025		–	Model surface pressure coefficient – ESP	CP025 = (P025*144 – PINF)/QINF
429	CP026		–	Model surface pressure coefficient – ESP	CP026 = (P026*144 – PINF)/QINF
430	CP027		–	Model surface pressure coefficient – ESP	CP027 = (P027*144 – PINF)/QINF
431	CP028		–	Model surface pressure coefficient – ESP	CP028 = (P028*144 – PINF)/QINF
432	CP029		–	Model surface pressure coefficient – ESP	CP029 = (P029*144 – PINF)/QINF
433	CP030		–	Model surface pressure coefficient – ESP	CP030 = (P030*144 – PINF)/QINF
434	CP031		–	Model surface pressure coefficient – ESP	CP031 = (P031*144 – PINF)/QINF
435	CP032		–	Model surface pressure coefficient – ESP	CP032 = (P032*144 – PINF)/QINF
436	CP033		–	Model surface pressure coefficient – ESP	CP033 = (P033*144 – PINF)/QINF
437	CP034		–	Model surface pressure coefficient – ESP	CP034 = (P034*144 – PINF)/QINF
438	CP035		–	Model surface pressure coefficient – ESP	CP035 = (P035*144 – PINF)/QINF
439	CP036		–	Model surface pressure coefficient – ESP	CP036 = (P036*144 – PINF)/QINF
440	CP037		–	Model surface pressure coefficient – ESP	CP037 = (P037*144 – PINF)/QINF
441	CP038		–	Model surface pressure coefficient – ESP	CP038 = (P038*144 – PINF)/QINF
442	CP039		–	Model surface pressure coefficient – ESP	CP039 = (P039*144 – PINF)/QINF
443	CP040		–	Model surface pressure coefficient – ESP	CP040 = (P040*144 – PINF)/QINF
444	CP041		–	Model surface pressure coefficient – ESP	CP041 = (P041*144 – PINF)/QINF
445	CP042		–	Model surface pressure coefficient – ESP	CP042 = (P042*144 – PINF)/QINF
446	CP043		–	Model surface pressure coefficient – ESP	CP043 = (P043*144 – PINF)/QINF
447	CP044		–	Model surface pressure coefficient – ESP	CP044 = (P044*144 – PINF)/QINF
448	CP045		–	Model surface pressure coefficient – ESP	CP045 = (P045*144 – PINF)/QINF

Table A-2. Continued.

(j) Continued.

#	NAME	VALUE	UNITS	DESCRIPTION	EQUATION
449	CP046		–	Model surface pressure coefficient – ESP	CP046 = (P046*144 – PINF)/QINF
450	CP047		–	Model surface pressure coefficient – ESP	CP047 = (P047*144 – PINF)/QINF
451	CP048		–	Model surface pressure coefficient – ESP	CP048 = (P048*144 – PINF)/QINF
452	CP049		–	Model surface pressure coefficient – ESP	CP049 = (P049*144 – PINF)/QINF
453	CP050		–	Model surface pressure coefficient – ESP	CP050 = (P050*144 – PINF)/QINF
454	CP051		–	Model surface pressure coefficient – ESP	CP051 = (P051*144 – PINF)/QINF
455	CP052		–	Model surface pressure coefficient – ESP	CP052 = (P052*144 – PINF)/QINF
456	CP053		–	Model surface pressure coefficient – ESP	CP053 = (P053*144 – PINF)/QINF
457	CP054		–	Model surface pressure coefficient – ESP	CP054 = (P054*144 – PINF)/QINF
458	CP055		–	Model surface pressure coefficient – ESP	CP055 = (P055*144 – PINF)/QINF
459	CP056		–	Model surface pressure coefficient – ESP	CP056 = (P056*144 – PINF)/QINF
460	CP057		–	Model surface pressure coefficient – ESP	CP057 = (P057*144 – PINF)/QINF
461	CP058		–	Model surface pressure coefficient – ESP	CP058 = (P058*144 – PINF)/QINF
462	CP059		–	Model surface pressure coefficient – ESP	CP059 = (P059*144 – PINF)/QINF
463	CP060		–	Model surface pressure coefficient – ESP	CP060 = (P060*144 – PINF)/QINF
464	CP061		–	Model surface pressure coefficient – ESP	CP061 = (P061*144 – PINF)/QINF
465	CP062		–	Model surface pressure coefficient – ESP	CP062 = (P062*144 – PINF)/QINF
466	CP063		–	Model surface pressure coefficient – ESP	CP063 = (P063*144 – PINF)/QINF
467	CP064		–	Model surface pressure coefficient – ESP	CP064 = (P064*144 – PINF)/QINF
468	CP065		–	Model surface pressure coefficient – ESP	CP065 = (P065*144 – PINF)/QINF
469	CP066		–	Model surface pressure coefficient – ESP	CP066 = (P066*144 – PINF)/QINF

Table A-2. Continued.

(j) Continued.

#	NAME	VALUE	UNITS	DESCRIPTION	EQUATION
470	CP067		–	Model surface pressure coefficient – ESP	CP067 = (P067*144 – PINF)/QINF
471	CP068		–	Model surface pressure coefficient – ESP	CP068 = (P068*144 – PINF)/QINF
472	CP069		–	Model surface pressure coefficient – ESP	CP069 = (P069*144 – PINF)/QINF
473	CP070		–	Model surface pressure coefficient – ESP	CP070 = (P070*144 – PINF)/QINF
474	CP071		–	Model surface pressure coefficient – ESP	CP071 = (P071*144 – PINF)/QINF
475	CP072		–	Model surface pressure coefficient – ESP	CP072 = (P072*144 – PINF)/QINF
476	CP073		–	Model surface pressure coefficient – ESP	CP073 = (P073*144 – PINF)/QINF
477	CP074			Model surface pressure coefficient – ESP	CP074 = (P074*144 – PINF)/QINF
478	CP075			Model surface pressure coefficient – ESP	CP075 = (P075*144 – PINF)/QINF
479	CP076			Model surface pressure coefficient – ESP	CP076 = (P076*144 – PINF)/QINF
480	CP077			Model surface pressure coefficient – ESP	CP077 = (P077*144 – PINF)/QINF
481	CP078			Model surface pressure coefficient – ESP	CP078 = (P078*144 – PINF)/QINF
482	CP079			Model surface pressure coefficient – ESP	CP079 = (P079*144 – PINF)/QINF
483	CP080			Model surface pressure coefficient – ESP	CP080 = (P080*144 – PINF)/QINF
484	CP081			Model surface pressure coefficient – ESP	CP081 = (P081*144 – PINF)/QINF
485	CP082			Model surface pressure coefficient – ESP	CP082 = (P082*144 – PINF)/QINF
486	CP083			Model surface pressure coefficient – ESP	CP083 = (P083*144 – PINF)/QINF
487	CP084			Model surface pressure coefficient – ESP	CP084 = (P084*144 – PINF)/QINF
488	CP085			Model surface pressure coefficient – ESP	CP085 = (P085*144 – PINF)/QINF
489	CP086			Model surface pressure coefficient – ESP	CP086 = (P086*144 – PINF)/QINF
490	CP087			Model surface pressure coefficient – ESP	CP087 = (P087*144 – PINF)/QINF

Table A-2. Continued.

(j) Continued.

#	NAME	VALUE	UNITS	DESCRIPTION	EQUATION
491	CP088			Model surface pressure coefficient – ESP	CP088 = (P088*144 – PINF)/QINF
492	CP089			Model surface pressure coefficient – ESP	CP089 = (P089*144 – PINF)/QINF
493	CP090			Model surface pressure coefficient – ESP	CP090 = (P090*144 – PINF)/QINF
494	CP091			Model surface pressure coefficient – ESP	CP091 = (P091*144 – PINF)/QINF
495	CP092			Model surface pressure coefficient – ESP	CP092 = (P092*144 – PINF)/QINF
496	CP093			Model surface pressure coefficient – ESP	CP093 = (P093*144 – PINF)/QINF
497	CP094			Model surface pressure coefficient – ESP	CP094 = (P094*144 – PINF)/QINF
498	CP095			Model surface pressure coefficient – ESP	CP095 = (P095*144 – PINF)/QINF
499	CP096			Model surface pressure coefficient – ESP	CP096 = (P096*144 – PINF)/QINF
500	CP097			Model surface pressure coefficient – ESP	CP097 = (P097*144 – PINF)/QINF
501	CP098			Model surface pressure coefficient – ESP	CP098 = (P098*144 – PINF)/QINF
502	CP099			Model surface pressure coefficient – ESP	CP099 = (P099*144 – PINF)/QINF
503	CP100			Model surface pressure coefficient – ESP	CP100 = (P100*144 – PINF)/QINF
504	CP101			Model surface pressure coefficient – ESP	CP101 = (P101*144 – PINF)/QINF
505	CP102			Model surface pressure coefficient – ESP	CP102 = (P102*144 – PINF)/QINF
506	CP103			Model surface pressure coefficient – ESP	CP103 = (P103*144 – PINF)/QINF
507	CP104			Model surface pressure coefficient – ESP	CP104 = (P104*144 – PINF)/QINF
508	CP105			Model surface pressure coefficient – Kulite	CP105 = (P105*144 – PINF)/QINF
509	CP106			Model surface pressure coefficient – Kulite	CP106 = (P106*144 – PINF)/QINF
510	CP107			Model surface pressure coefficient – Kulite	CP107 = (P107*144 – PINF)/QINF
511	CP108			Model surface pressure coefficient – Kulite	CP108 = (P108*144 – PINF)/QINF

Table A-2. Continued.

(j) Continued.

#	NAME	VALUE	UNITS	DESCRIPTION	EQUATION
512	CP109			Model surface pressure coefficient – Kulite	CP109 = (P109*144 – PINF)/QINF
513	CP110			Model surface pressure coefficient – Kulite	CP110 = (P110*144 – PINF)/QINF
514	CP111			Model surface pressure coefficient – Kulite	CP111 = (P111*144 – PINF)/QINF
515	CP112			Model surface pressure coefficient – ESP	CP112 = (P112*144 – PINF)/QINF
516	CP113			Model surface pressure coefficient – ESP	CP113 = (P113*144 – PINF)/QINF
517	CP114			Model surface pressure coefficient – ESP	CP114 = (P114*144 – PINF)/QINF
518	CP115			Model surface pressure coefficient – ESP	CP115 = (P115*144 – PINF)/QINF
519	CP116			Model surface pressure coefficient – ESP	CP116 = (P116*144 – PINF)/QINF
520	CP117			Model surface pressure coefficient – ESP	CP117 = (P117*144 – PINF)/QINF
521	CP118			Model surface pressure coefficient – ESP	CP118 = (P118*144 – PINF)/QINF
522	CP119			Model surface pressure coefficient – ESP	CP119 = (P119*144 – PINF)/QINF
523	CP120			Model surface pressure coefficient – ESP	CP120 = (P120*144 – PINF)/QINF
524	CP121			Model surface pressure coefficient – ESP	CP121 = (P121*144 – PINF)/QINF
525	CP122			Model surface pressure coefficient – ESP	CP122 = (P122*144 – PINF)/QINF
526	CP123			Model surface pressure coefficient – ESP	CP123 = (P123*144 – PINF)/QINF
527	CP124			Model surface pressure coefficient – ESP	CP124 = (P124*144 – PINF)/QINF
528	CP125			Model surface pressure coefficient – ESP	CP125 = (P125*144 – PINF)/QINF
529	CP126	999		Model surface pressure coefficient – Kulite	constant (since no longer operable)
530	CP127	999		Model surface pressure coefficient – Kulite	constant (since no longer operable)
531	CP128			Model surface pressure coefficient – ESP	CP128 = (P128*144 – PINF)/QINF
532	CP129			Model surface pressure coefficient – ESP	CP129 = (P129*144 – PINF)/QINF

Table A-2. Continued.

(j) Continued.

#	NAME	VALUE	UNITS	DESCRIPTION	EQUATION
533	CP130			Model surface pressure coefficient – ESP	CP130 = (P130*144 – PINF)/QINF
534	CP131			Model surface pressure coefficient – ESP	CP131 = (P131*144 – PINF)/QINF
535	CP132			Model surface pressure coefficient – ESP	CP132 = (P132*144 – PINF)/QINF
536	CP133			Model surface pressure coefficient – ESP	CP133 = (P133*144 – PINF)/QINF
537	CP134			Model surface pressure coefficient – ESP	CP134 = (P134*144 – PINF)/QINF
538	CP135			Model surface pressure coefficient – ESP	CP135 = (P135*144 – PINF)/QINF
539	CP136			Model surface pressure coefficient – ESP	CP136 = (P136*144 – PINF)/QINF
540	CP137			Model surface pressure coefficient – ESP	CP137 = (P137*144 – PINF)/QINF
541	CP138			Model surface pressure coefficient – ESP	CP138 = (P138*144 – PINF)/QINF
542	CP139			Model surface pressure coefficient – ESP	CP139 = (P139*144 – PINF)/QINF
543	CP140			Model surface pressure coefficient – ESP	CP140 = (P140*144 – PINF)/QINF
544	CP141			Model surface pressure coefficient – ESP	CP141 = (P141*144 – PINF)/QINF
545	CP142			Model surface pressure coefficient – ESP	CP142 = (P142*144 – PINF)/QINF
546	CP143			Model surface pressure coefficient – ESP	CP143 = (P143*144 – PINF)/QINF
547	CP144			Model surface pressure coefficient – ESP	CP144 = (P144*144 – PINF)/QINF
548	CP145			Model surface pressure coefficient – ESP	CP145 = (P145*144 – PINF)/QINF
549	CP146			Model surface pressure coefficient – ESP	CP146 = (P146*144 – PINF)/QINF
550	CP147			Model surface pressure coefficient – ESP	CP147 = (P147*144 – PINF)/QINF
551	CP148			Model surface pressure coefficient – ESP	CP148 = (P148*144 – PINF)/QINF
552	CP149			Model surface pressure coefficient – ESP	CP149 = (P149*144 – PINF)/QINF
553	CP150			Model surface pressure coefficient – ESP	CP150 = (P150*144 – PINF)/QINF

Table A-2. Continued.

(j) Continued.

#	NAME	VALUE	UNITS	DESCRIPTION	EQUATION
554	CP151			Model surface pressure coefficient – ESP	CP151 = (P151*144 – PINF)/QINF
555	CP152			Model surface pressure coefficient – ESP	CP152 = (P152*144 – PINF)/QINF
556	CP153			Model surface pressure coefficient – ESP	CP153 = (P153*144 – PINF)/QINF
557	CP154			Model surface pressure coefficient – ESP	CP154 = (P154*144 – PINF)/QINF
558	CP155			Model surface pressure coefficient – ESP	CP155 = (P155*144 – PINF)/QINF
559	CP156			Model surface pressure coefficient – ESP	CP156 = (P156*144 – PINF)/QINF
560	CP157			Model surface pressure coefficient – ESP	CP157 = (P157*144 – PINF)/QINF
561	CP158			Model surface pressure coefficient – ESP	CP158 = (P158*144 – PINF)/QINF
562	CP159			Model surface pressure coefficient – ESP	CP159 = (P159*144 – PINF)/QINF
563	CP160			Model surface pressure coefficient – ESP	CP160 = (P160*144 – PINF)/QINF
564	CP161			Model surface pressure coefficient – ESP	CP161 = (P161*144 – PINF)/QINF
565	CP162			Model surface pressure coefficient – ESP	CP162 = (P162*144 – PINF)/QINF
566	CP163			Model surface pressure coefficient – ESP	CP163 = (P163*144 – PINF)/QINF
567	CP164			Model surface pressure coefficient – ESP	CP164 = (P164*144 – PINF)/QINF
568	CP165			Model surface pressure coefficient – ESP	CP165 = (P165*144 – PINF)/QINF
569	CP166			Model surface pressure coefficient – ESP	CP166 = (P166*144 – PINF)/QINF
570	CP167			Model surface pressure coefficient – ESP	CP167 = (P167*144 – PINF)/QINF
571	CP168			Model surface pressure coefficient – ESP	CP168 = (P168*144 – PINF)/QINF
572	CP169			Model surface pressure coefficient – ESP	CP169 = (P169*144 – PINF)/QINF
573	CP170			Model surface pressure coefficient – ESP	CP170 = (P170*144 – PINF)/QINF
574	CP171			Model surface pressure coefficient – ESP	CP171 = (P171*144 – PINF)/QINF

Table A-2. Continued.
(j) Concluded.

#	NAME	VALUE	UNITS	DESCRIPTION	EQUATION
575	CP172			Model surface pressure coefficient – ESP	CP172 = (P172*144 – PINF)/QINF
576	CP173			Model surface pressure coefficient – ESP	CP173 = (P173*144 – PINF)/QINF
577	CP174			Model surface pressure coefficient – ESP	CP174 = (P174*144 – PINF)/QINF
578	CP175			Model surface pressure coefficient – ESP	CP175 = (P175*144 – PINF)/QINF
579	CP176			Model surface pressure coefficient – ESP	CP176 = (P176*144 – PINF)/QINF

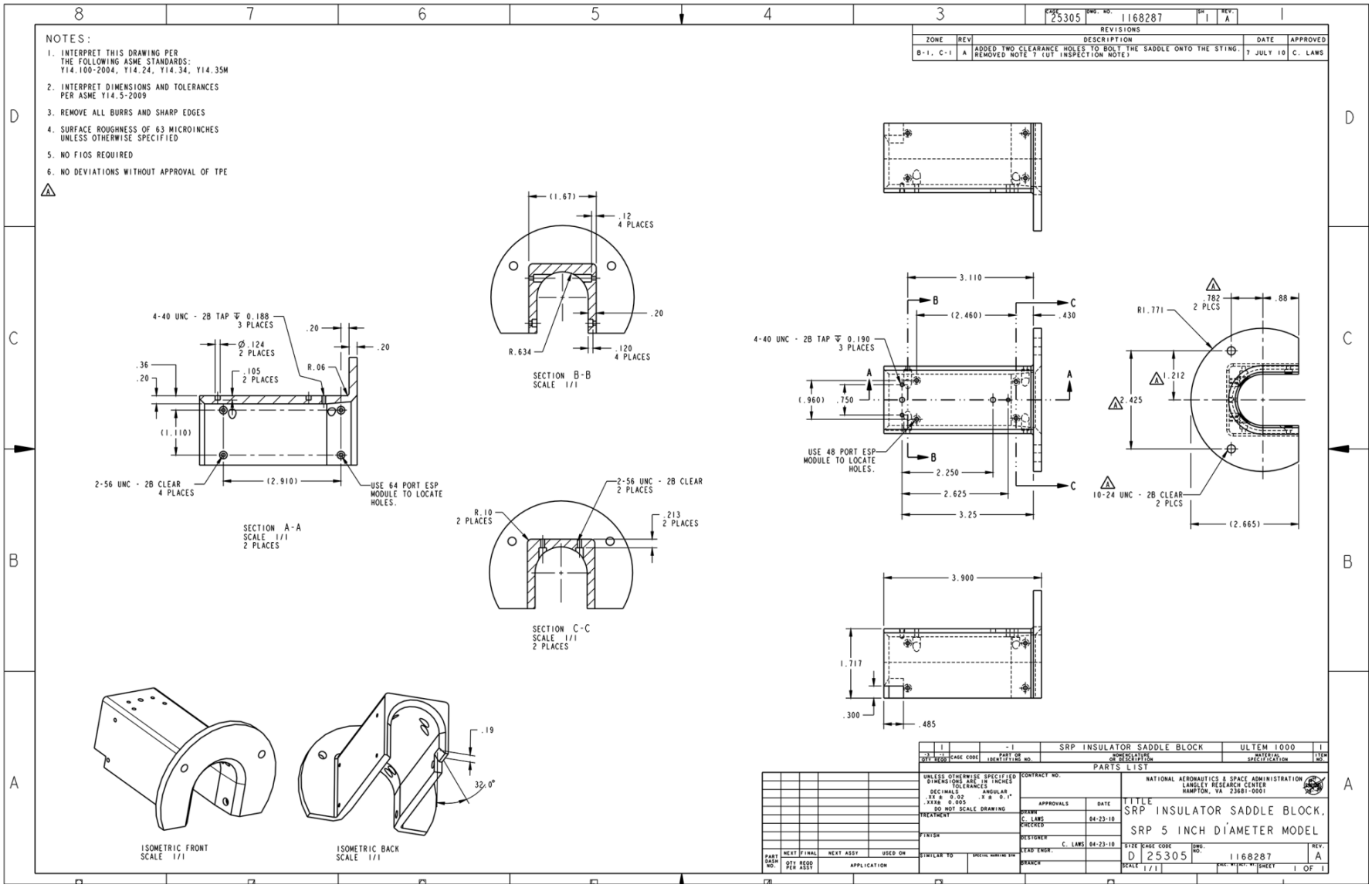
NOTES:
1. INTERPRET THIS DRAWING PER THE FOLLOWING ASME STANDARDS: Y14.100-2004, Y14.24, Y14.34, Y14.35M
2. INTERPRET DIMENSIONS AND TOLERANCES PER ASME Y14.5-2009
3. REMOVE ALL BURRS AND SHARP EDGES
4. SURFACE ROUGHNESS OF 63 MICROINCHES UNLESS OTHERWISE SPECIFIED
5. NO FIOS REQUIRED
6. NO DEVIATIONS WITHOUT APPROVAL OF TPE
REVISIONS
ZONE REV DESCRIPTION DATE APPROVED
B-1, C-1 A ADDED TWO CLEARANCE HOLES TO BOLT THE SADDLE ONTO THE STING. REMOVED NOTE 7 (UT INSPECTION NOTE) 7 JULY 10 C. LAWS
SECTION A-A
SECTION B-B
SECTION C-C
ISOMETRIC FRONT
ISOMETRIC BACK
USE 64 PORT ESP MODULE TO LOCATE HOLES.
USE 48 PORT ESP MODULE TO LOCATE HOLES.
SRP INSULATOR SADDLE BLOCK
ULTEM 1000
PARTS LIST
NATIONAL AERONAUTICS & SPACE ADMINISTRATION
LANGLEY RESEARCH CENTER
HAMPTON, VA 23681-0001
TITLE
SRP INSULATOR SADDLE BLOCK,
SRP 5 INCH DIAMETER MODEL
SIZE D
CAGE CODE 25305
DWG. NO. 1168287
REV. A
SCALE 1/1
SHEET 1 OF 1

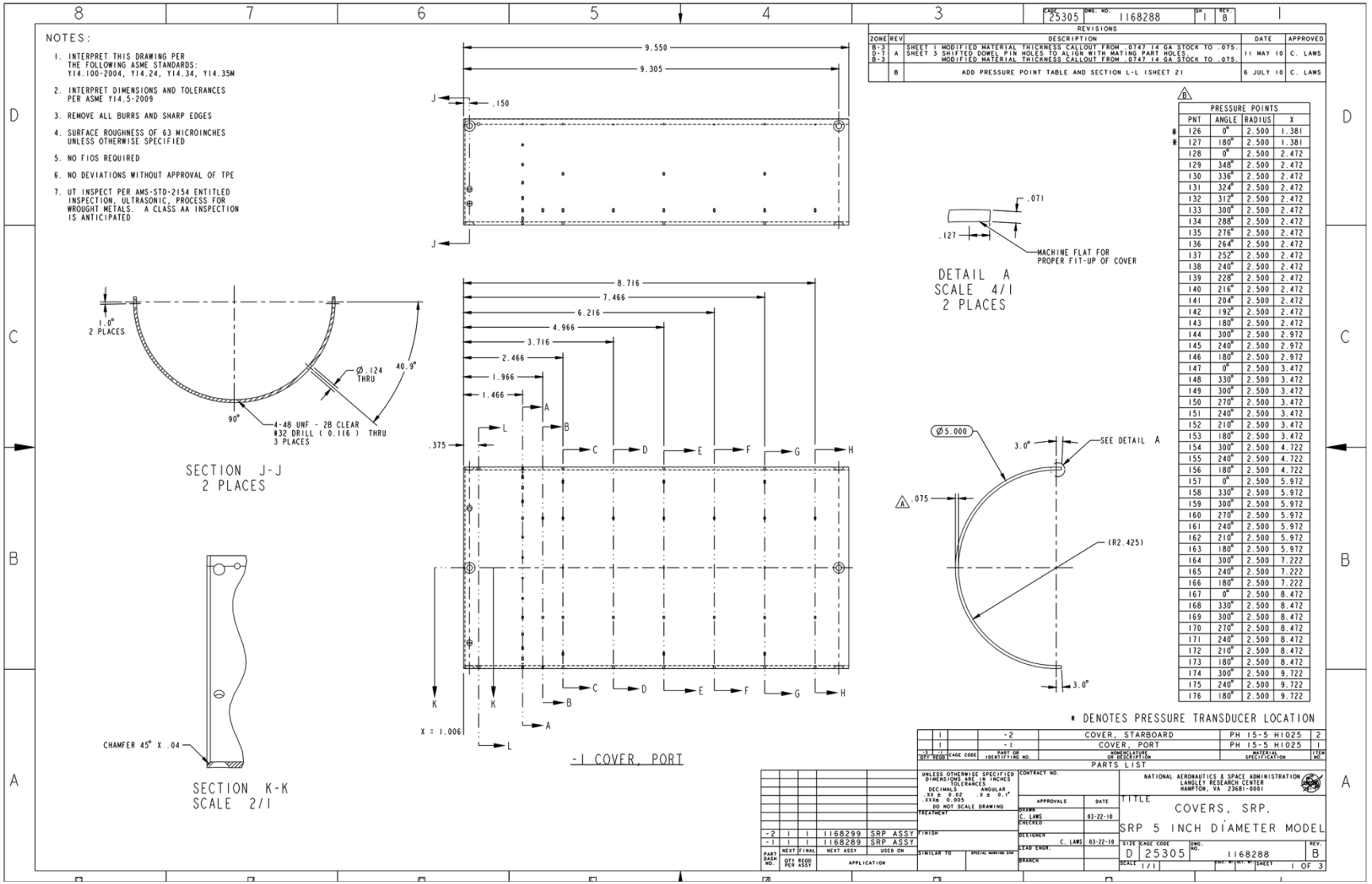
NOTES:
1. INTERPRET THIS DRAWING PER THE FOLLOWING ASME STANDARDS: Y14.100-2004, Y14.24, Y14.34, Y14.35M
2. INTERPRET DIMENSIONS AND TOLERANCES PER ASME Y14.5-2009
3. REMOVE ALL BURRS AND SHARP EDGES
4. SURFACE ROUGHNESS OF 63 MICROINCHES UNLESS OTHERWISE SPECIFIED
5. NO FIOS REQUIRED
6. NO DEVIATIONS WITHOUT APPROVAL OF TPE
7. UT INSPECT PER AMS-STD-2154 ENTITLED INSPECTION, ULTRASONIC, PROCESS FOR WROUGHT METALS. A CLASS AA INSPECTION IS ANTICIPATED
CAGE 25305 DWG. NO. 1168288 SH 1 REV. B
REVISIONS
ZONE REV DESCRIPTION DATE APPROVED
B-3 A SHEET 1 MODIFIED MATERIAL THICKNESS CALLOUT FROM .0747 14 GA STOCK TO .075. 11 MAY 10 C. LAWS
D-7 SHEET 3 SHIFTED DOWEL PIN HOLES TO ALIGN WITH MATING PART HOLES.
B-3 MODIFIED MATERIAL THICKNESS CALLOUT FROM .0747 14 GA STOCK TO .075.
B ADD PRESSURE POINT TABLE AND SECTION L-L (SHEET 2) 6 JULY 10 C. LAWS
9.550
9.305
.150
J
J
1.0° 2 PLACES
Ø.124 THRU
40.9°
90°
4-48 UNF - 2B CLEAR #32 DRILL (0.116) THRU 3 PLACES
SECTION J-J 2 PLACES
8.716
7.466
6.216
4.966
3.716
2.466
1.966
1.466
.375
A
B
C
D
E
F
G
H
K
K
X = 1.006
L
L
-1 COVER, PORT
.071
.127
MACHINE FLAT FOR PROPER FIT-UP OF COVER
DETAIL A SCALE 4/1 2 PLACES
Ø5.000
3.0°
SEE DETAIL A
.075
(R2.425)
3.0°
CHAMFER 45° X .04
SECTION K-K SCALE 2/1
PRESSURE POINTS
PNT ANGLE RADIUS X
* 126 0° 2.500 1.381
* 127 180° 2.500 1.381
128 0° 2.500 2.472
129 348° 2.500 2.472
130 336° 2.500 2.472
131 324° 2.500 2.472
132 312° 2.500 2.472
133 300° 2.500 2.472
134 288° 2.500 2.472
135 276° 2.500 2.472
136 264° 2.500 2.472
137 252° 2.500 2.472
138 240° 2.500 2.472
139 228° 2.500 2.472
140 216° 2.500 2.472
141 204° 2.500 2.472
142 192° 2.500 2.472
143 180° 2.500 2.472
144 300° 2.500 2.972
145 240° 2.500 2.972
146 180° 2.500 2.972
147 0° 2.500 3.472
148 330° 2.500 3.472
149 300° 2.500 3.472
150 270° 2.500 3.472
151 240° 2.500 3.472
152 210° 2.500 3.472
153 180° 2.500 3.472
154 300° 2.500 4.722
155 240° 2.500 4.722
156 180° 2.500 4.722
157 0° 2.500 5.972
158 330° 2.500 5.972
159 300° 2.500 5.972
160 270° 2.500 5.972
161 240° 2.500 5.972
162 210° 2.500 5.972
163 180° 2.500 5.972
164 300° 2.500 7.222
165 240° 2.500 7.222
166 180° 2.500 7.222
167 0° 2.500 8.472
168 330° 2.500 8.472
169 300° 2.500 8.472
170 270° 2.500 8.472
171 240° 2.500 8.472
172 210° 2.500 8.472
173 180° 2.500 8.472
174 300° 2.500 9.722
175 240° 2.500 9.722
176 180° 2.500 9.722
* DENOTES PRESSURE TRANSDUCER LOCATION
-2 COVER, STARBOARD PH 15-5 H1025 2
-1 COVER, PORT PH 15-5 H1025 1
QTY REQD CAGE CODE PART OR IDENTIFYING NO. NOMENCLATURE OR DESCRIPTION MATERIAL SPECIFICATION ITEM NO.
PARTS LIST
-2 1 1 1168299 SRP ASSY
-1 1 1 1168289 SRP ASSY
PART DASH NO. NEXT ASSY FINAL ASSY QTY REQD PER ASSY NEXT ASSY USED ON APPLICATION
UNLESS OTHERWISE SPECIFIED DIMENSIONS ARE IN INCHES TOLERANCES DECIMALS .XX ± 0.02 .XXX ± 0.005 ANGULAR .X ± 0.1° DO NOT SCALE DRAWING
TREATMENT FINISH
CONTRACT NO.
APPROVALS DATE
DRAWN C. LAWS 03-22-10
CHECKED
DESIGNER C. LAWS 03-22-10
LEAD ENGR.
BRANCH
SIMILAR TO SPECIAL MARKING DIM
NATIONAL AERONAUTICS & SPACE ADMINISTRATION LANGLEY RESEARCH CENTER HAMPTON, VA 23681-0001
TITLE COVERS, SRP, SRP 5 INCH DIAMETER MODEL
SIZE CAGE CODE DWG. NO. REV.
D 25305 1168288 B
SCALE 1/1 SHEET 1 OF 3

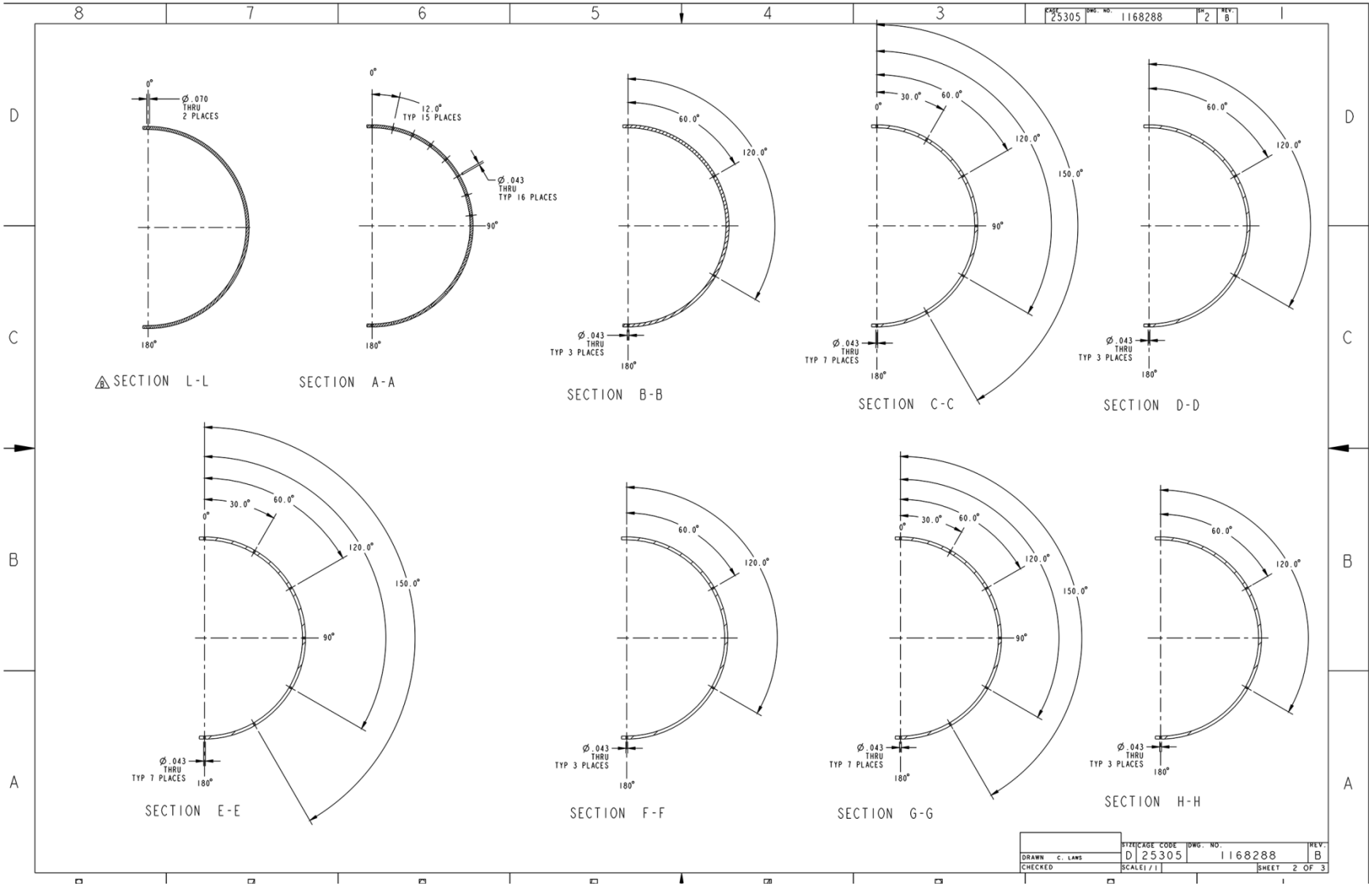
8
7
6
5
4
3
2
1
D
C
B
A
CAGE 25305
DWG. NO. 1168288
SH. 2
REV. B
0°
Ø.070 THRU 2 PLACES
180°
SECTION L-L
12.0° TYP 15 PLACES
Ø.043 THRU TYP 16 PLACES
90°
SECTION A-A
60.0°
120.0°
Ø.043 THRU TYP 3 PLACES
SECTION B-B
30.0°
150.0°
Ø.043 THRU TYP 7 PLACES
SECTION C-C
SECTION D-D
SECTION E-E
SECTION F-F
SECTION G-G
SECTION H-H
DRAWN C. LAWS
CHECKED
SIZE D
CAGE CODE 25305
DWG. NO. 1168288
REV. B
SCALE 1/1
SHEET 2 OF 3

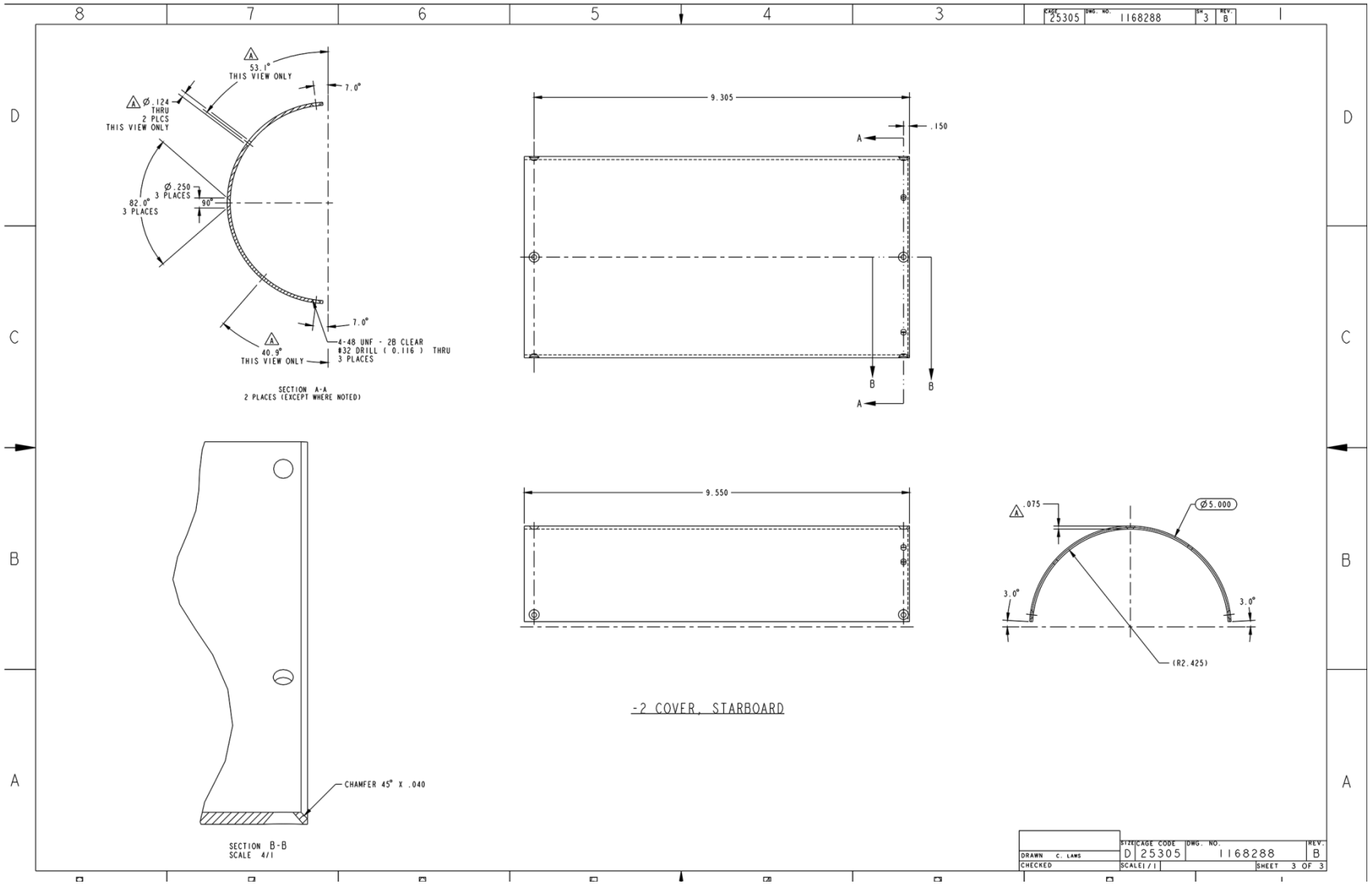
CAGE 25305
DWG. NO. 1168288
SH 3
REV. B
53.1° THIS VIEW ONLY
7.0°
Ø.124 THRU 2 PLCS THIS VIEW ONLY
Ø.250 3 PLACES
90°
82.0° 3 PLACES
7.0°
4-48 UNF - 2B CLEAR #32 DRILL (0.116) THRU 3 PLACES
40.9° THIS VIEW ONLY
SECTION A-A
2 PLACES (EXCEPT WHERE NOTED)
9.305
.150
A
B
B
A
9.550
.075
Ø5.000
3.0°
3.0°
(R2.425)
-2 COVER, STARBOARD
CHAMFER 45° X .040
SECTION B-B
SCALE 4/1
DRAWN C. LAWS
CHECKED
SIZE D
CAGE CODE 25305
DWG. NO. 1168288
REV. B
SCALE 1/1
SHEET 3 OF 3

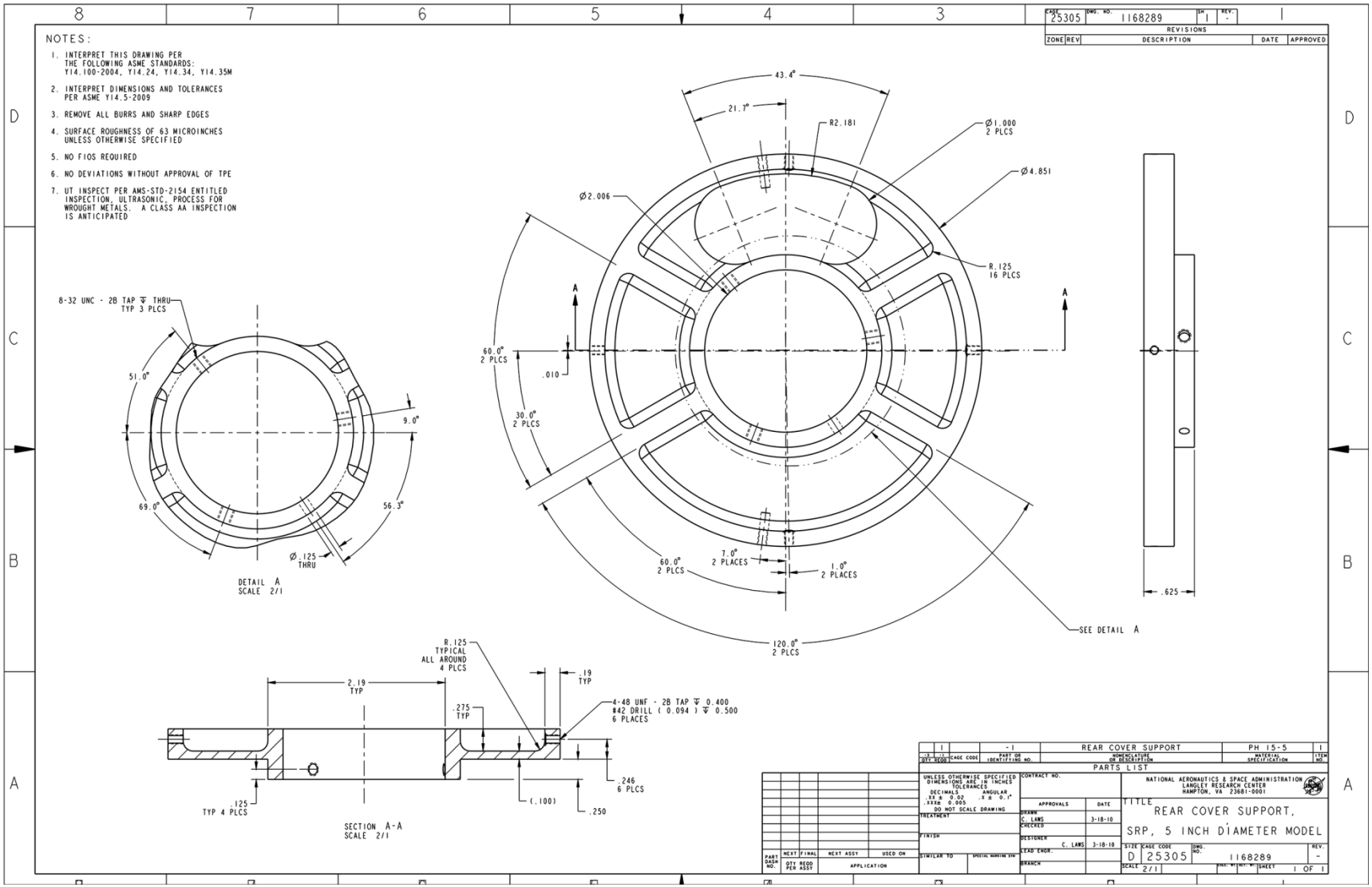
NOTES:
1. INTERPRET THIS DRAWING PER THE FOLLOWING ASME STANDARDS: Y14.100-2004, Y14.24, Y14.34, Y14.35M
2. INTERPRET DIMENSIONS AND TOLERANCES PER ASME Y14.5-2009
3. REMOVE ALL BURRS AND SHARP EDGES
4. SURFACE ROUGHNESS OF 63 MICROINCHES UNLESS OTHERWISE SPECIFIED
5. NO FIOS REQUIRED
6. NO DEVIATIONS WITHOUT APPROVAL OF TPE
7. UT INSPECT PER AMS-STD-2154 ENTITLED INSPECTION, ULTRASONIC, PROCESS FOR WROUGHT METALS. A CLASS AA INSPECTION IS ANTICIPATED
CAGE 25305 DWG. NO. 1168289 SH 1 REV. -
REVISIONS
ZONE REV DESCRIPTION DATE APPROVED
43.4°
21.7°
R2.181
Ø1.000 2 PLCS
Ø4.851
Ø2.006
R.125 16 PLCS
60.0° 2 PLCS
.010
30.0° 2 PLCS
7.0° 2 PLACES
1.0° 2 PLACES
60.0° 2 PLCS
120.0° 2 PLCS
SEE DETAIL A
.625
8-32 UNC - 2B TAP ↧ THRU TYP 3 PLCS
51.0°
9.0°
69.0°
56.3°
Ø.125 THRU
DETAIL A SCALE 2/1
R.125 TYPICAL ALL AROUND 4 PLCS
2.19 TYP
.19 TYP
.275 TYP
4-48 UNF - 2B TAP ↧ 0.400 #42 DRILL (0.094) ↧ 0.500 6 PLACES
.125 TYP 4 PLCS
(.100)
.246 6 PLCS
.250
SECTION A-A SCALE 2/1
QTY REQD | CAGE CODE | PART OR IDENTIFYING NO. | NOMENCLATURE OR DESCRIPTION | MATERIAL SPECIFICATION | ITEM NO.
1 | - 1 | REAR COVER SUPPORT | PH 15-5 | 1
PARTS LIST
UNLESS OTHERWISE SPECIFIED DIMENSIONS ARE IN INCHES TOLERANCES DECIMALS .XX ± 0.02 .XXX ± 0.005 DO NOT SCALE DRAWING ANGULAR ± ± 0.1°
TREATMENT
FINISH
CONTRACT NO.
APPROVALS DATE
DRAWN C. LAWS 3-18-10
CHECKED
DESIGNER C. LAWS 3-18-10
LEAD ENGR.
BRANCH
NEXT ASSY | USED ON
SIMILAR TO | SPECIAL MARKING SYM
PART DASH NO. | QTY REQD PER ASSY | APPLICATION
NASA NATIONAL AERONAUTICS & SPACE ADMINISTRATION LANGLEY RESEARCH CENTER HAMPTON, VA 23681-0001
TITLE
REAR COVER SUPPORT,
SRP, 5 INCH DIAMETER MODEL
SIZE D CAGE CODE 25305 DWG. NO. 1168289 REV. -
SCALE 2/1 SHEET 1 OF 1

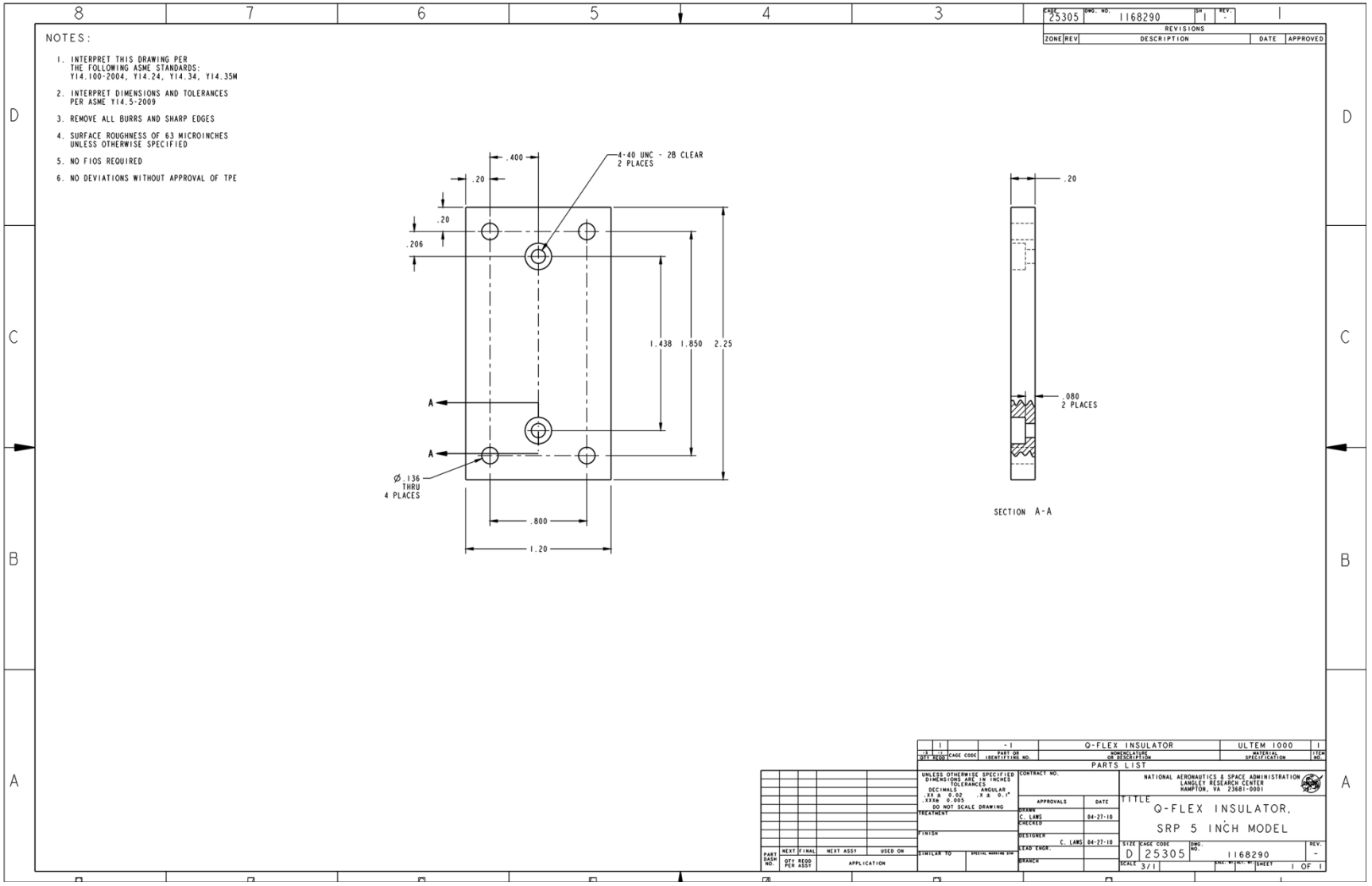
NOTES:
1. INTERPRET THIS DRAWING PER THE FOLLOWING ASME STANDARDS: Y14.100-2004, Y14.24, Y14.34, Y14.35M
2. INTERPRET DIMENSIONS AND TOLERANCES PER ASME Y14.5-2009
3. REMOVE ALL BURRS AND SHARP EDGES
4. SURFACE ROUGHNESS OF 63 MICROINCHES UNLESS OTHERWISE SPECIFIED
5. NO FIOS REQUIRED
6. NO DEVIATIONS WITHOUT APPROVAL OF TPE
.400
.20
.20
.206
4-40 UNC - 2B CLEAR 2 PLACES
1.438
1.850
2.25
Ø.136 THRU 4 PLACES
.800
1.20
.20
.080 2 PLACES
SECTION A-A
CAGE 25305
DWG. NO. 1168290
SH 1
REV. -
REVISIONS
ZONE REV DESCRIPTION DATE APPROVED
Q-FLEX INSULATOR
ULTEM 1000
PARTS LIST
UNLESS OTHERWISE SPECIFIED DIMENSIONS ARE IN INCHES TOLERANCES DECIMALS .XX ± 0.02 .XXX ± 0.005 ANGULAR .X ± 0.1°
DO NOT SCALE DRAWING
TREATMENT
FINISH
CONTRACT NO.
APPROVALS DATE
DRAWN C. LAWS 04-27-10
CHECKED
DESIGNER C. LAWS 04-27-10
LEAD ENGR.
BRANCH
NATIONAL AERONAUTICS & SPACE ADMINISTRATION LANGLEY RESEARCH CENTER HAMPTON, VA 23681-0001
TITLE
Q-FLEX INSULATOR, SRP 5 INCH MODEL
SIZE D CAGE CODE 25305 DWG. NO. 1168290 REV. -
SCALE 3/1 SHEET 1 OF 1

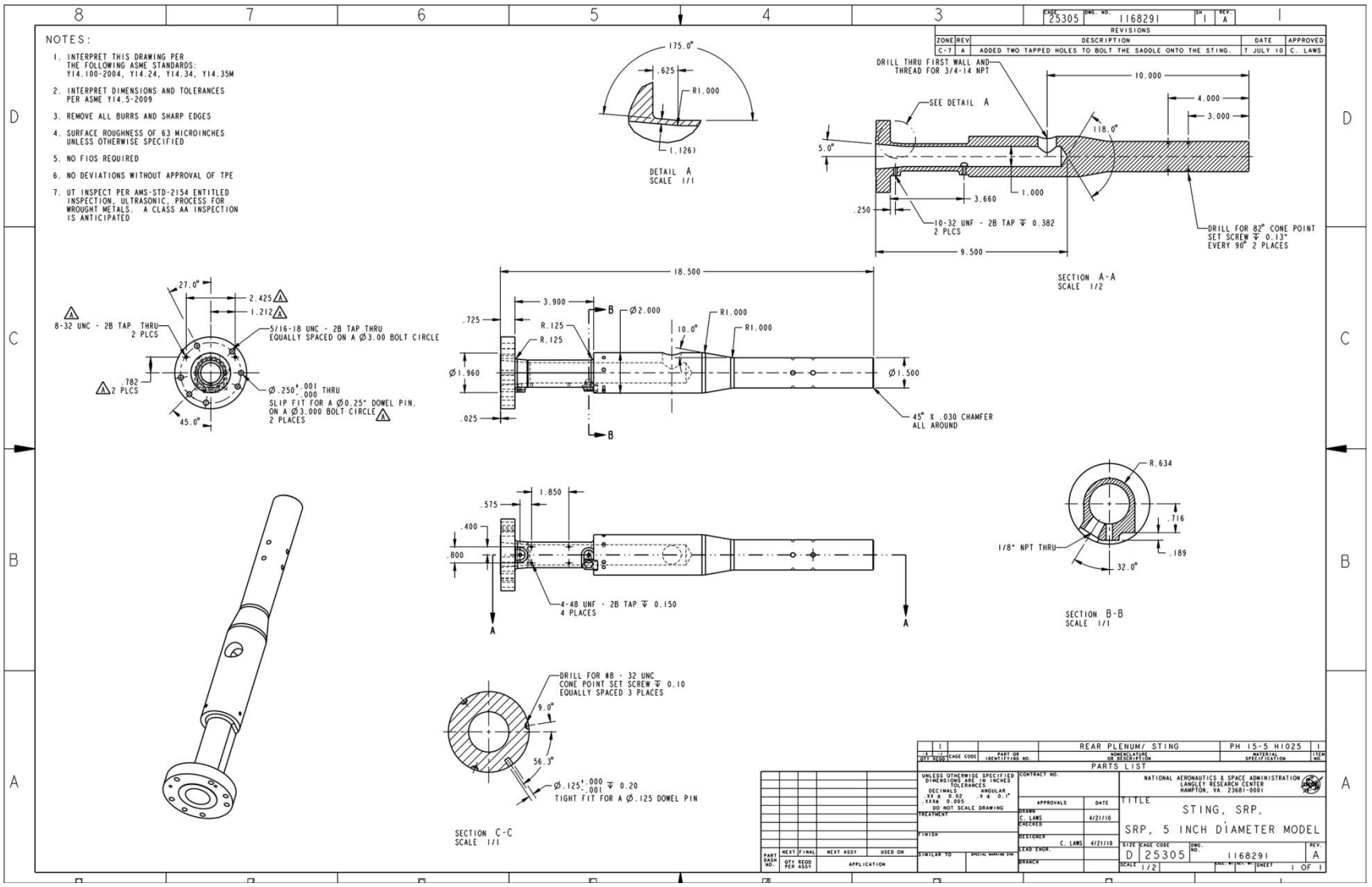
NOTES:
1. INTERPRET THIS DRAWING PER THE FOLLOWING ASME STANDARDS: Y14.100-2004, Y14.24, Y14.34, Y14.35M
2. INTERPRET DIMENSIONS AND TOLERANCES PER ASME Y14.5-2009
3. REMOVE ALL BURRS AND SHARP EDGES
4. SURFACE ROUGHNESS OF 63 MICROINCHES UNLESS OTHERWISE SPECIFIED
5. NO FIOS REQUIRED
6. NO DEVIATIONS WITHOUT APPROVAL OF TPE
7. UT INSPECT PER AMS-STD-2154 ENTITLED INSPECTION, ULTRASONIC, PROCESS FOR WROUGHT METALS. A CLASS AA INSPECTION IS ANTICIPATED
CAGE 25305 DWG. NO. 1168291 SH 1 REV. A
REVISIONS
ZONE REV DESCRIPTION DATE APPROVED
C-7 A ADDED TWO TAPPED HOLES TO BOLT THE SADDLE ONTO THE STING. 7 JULY 10 C. LAWS
DETAIL A SCALE 1/1
SECTION A-A SCALE 1/2
SECTION B-B SCALE 1/1
SECTION C-C SCALE 1/1
8-32 UNC - 2B TAP THRU 2 PLCS
5/16-18 UNC - 2B TAP THRU EQUALLY SPACED ON A Ø3.00 BOLT CIRCLE
Ø.250 +.001 -.000 THRU SLIP FIT FOR A Ø0.25" DOWEL PIN. ON A Ø3.000 BOLT CIRCLE 2 PLACES
45° X .030 CHAMFER ALL AROUND
4-48 UNF - 2B TAP ↧ 0.150 4 PLACES
DRILL FOR #8 - 32 UNC CONE POINT SET SCREW ↧ 0.10 EQUALLY SPACED 3 PLACES
Ø.125 +.000 -.001 ↧ 0.20 TIGHT FIT FOR A Ø.125 DOWEL PIN
DRILL THRU FIRST WALL AND THREAD FOR 3/4-14 NPT
10-32 UNF - 2B TAP ↧ 0.382 2 PLCS
DRILL FOR 82° CONE POINT SET SCREW ↧ 0.13" EVERY 90° 2 PLACES
1/8" NPT THRU
REAR PLENUM/ STING
PH 15-5 H1025
PARTS LIST
NATIONAL AERONAUTICS & SPACE ADMINISTRATION LANGLEY RESEARCH CENTER HAMPTON, VA 23681-0001
TITLE STING, SRP, SRP, 5 INCH DIAMETER MODEL
SIZE D CAGE CODE 25305 DWG. NO. 1168291 REV. A
SCALE 1/2 SHEET 1 OF 1

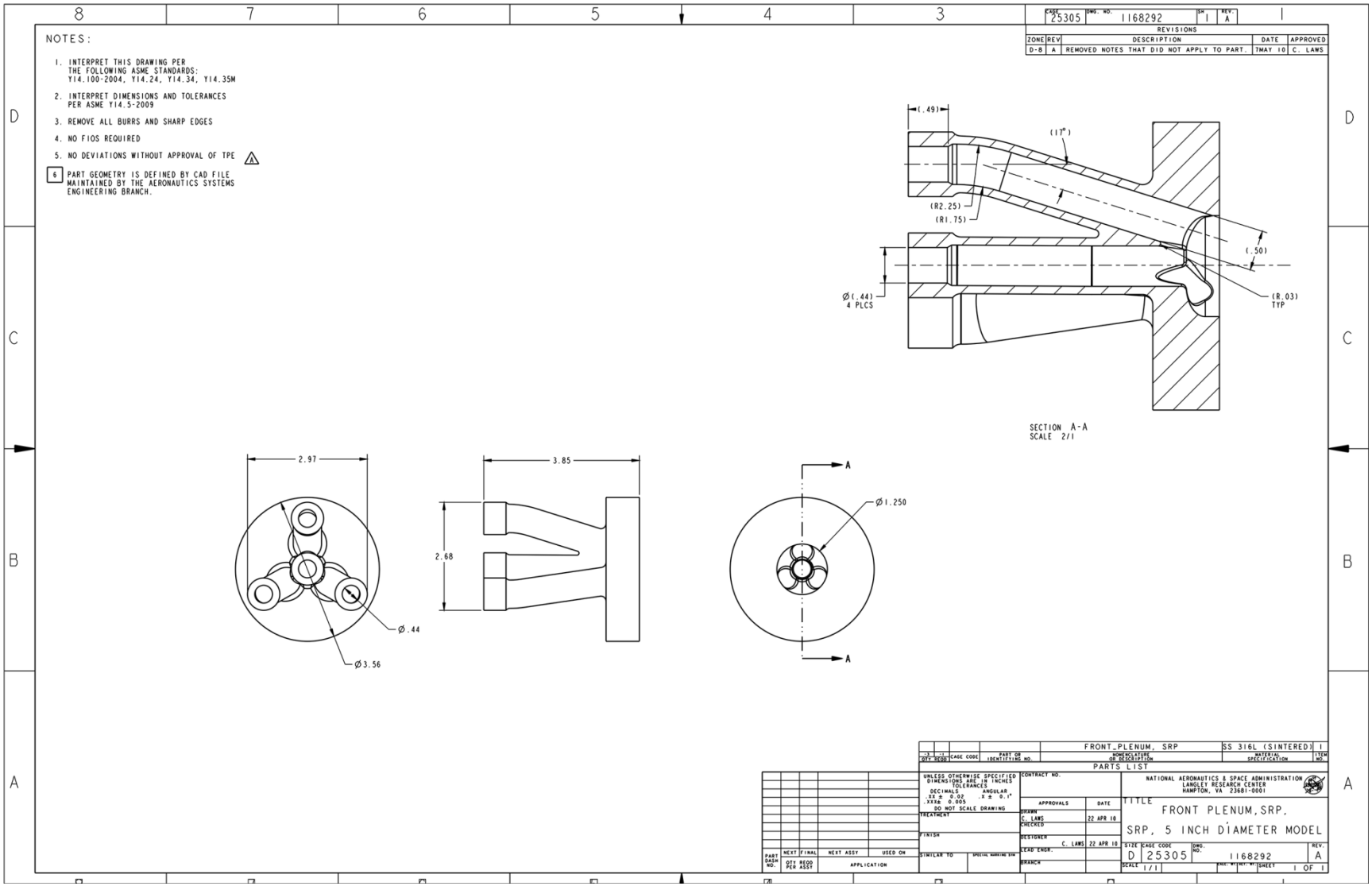
NOTES:
1. INTERPRET THIS DRAWING PER THE FOLLOWING ASME STANDARDS: Y14.100-2004, Y14.24, Y14.34, Y14.35M
2. INTERPRET DIMENSIONS AND TOLERANCES PER ASME Y14.5-2009
3. REMOVE ALL BURRS AND SHARP EDGES
4. NO FIOS REQUIRED
5. NO DEVIATIONS WITHOUT APPROVAL OF TPE
6 PART GEOMETRY IS DEFINED BY CAD FILE MAINTAINED BY THE AERONAUTICS SYSTEMS ENGINEERING BRANCH.
CAGE 25305 DWG. NO. 1168292 SH 1 REV. A
REVISIONS
ZONE REV DESCRIPTION DATE APPROVED
D-8 A REMOVED NOTES THAT DID NOT APPLY TO PART. 7MAY 10 C. LAWS
(.49)
(17°)
(R2.25)
(R1.75)
(.50)
Ø(.44) 4 PLCS
(R.03) TYP
SECTION A-A
SCALE 2/1
2.97
3.85
2.68
Ø.44
Ø3.56
A
Ø1.250
A
FRONT_PLENUM, SRP
SS 316L (SINTERED)
PARTS LIST
UNLESS OTHERWISE SPECIFIED DIMENSIONS ARE IN INCHES TOLERANCES DECIMALS .XX ± 0.02 .XXX ± 0.005 ANGULAR .X ± 0.1° DO NOT SCALE DRAWING
TREATMENT
FINISH
CONTRACT NO.
APPROVALS DATE
DRAWN C. LAWS 22 APR 10
CHECKED
DESIGNER C. LAWS 22 APR 10
LEAD ENGR.
BRANCH
NATIONAL AERONAUTICS & SPACE ADMINISTRATION LANGLEY RESEARCH CENTER HAMPTON, VA 23681-0001
TITLE
FRONT PLENUM, SRP,
SRP, 5 INCH DIAMETER MODEL
SIZE D CAGE CODE 25305 DWG. NO. 1168292 REV. A
SCALE 1/1 SHEET 1 OF 1

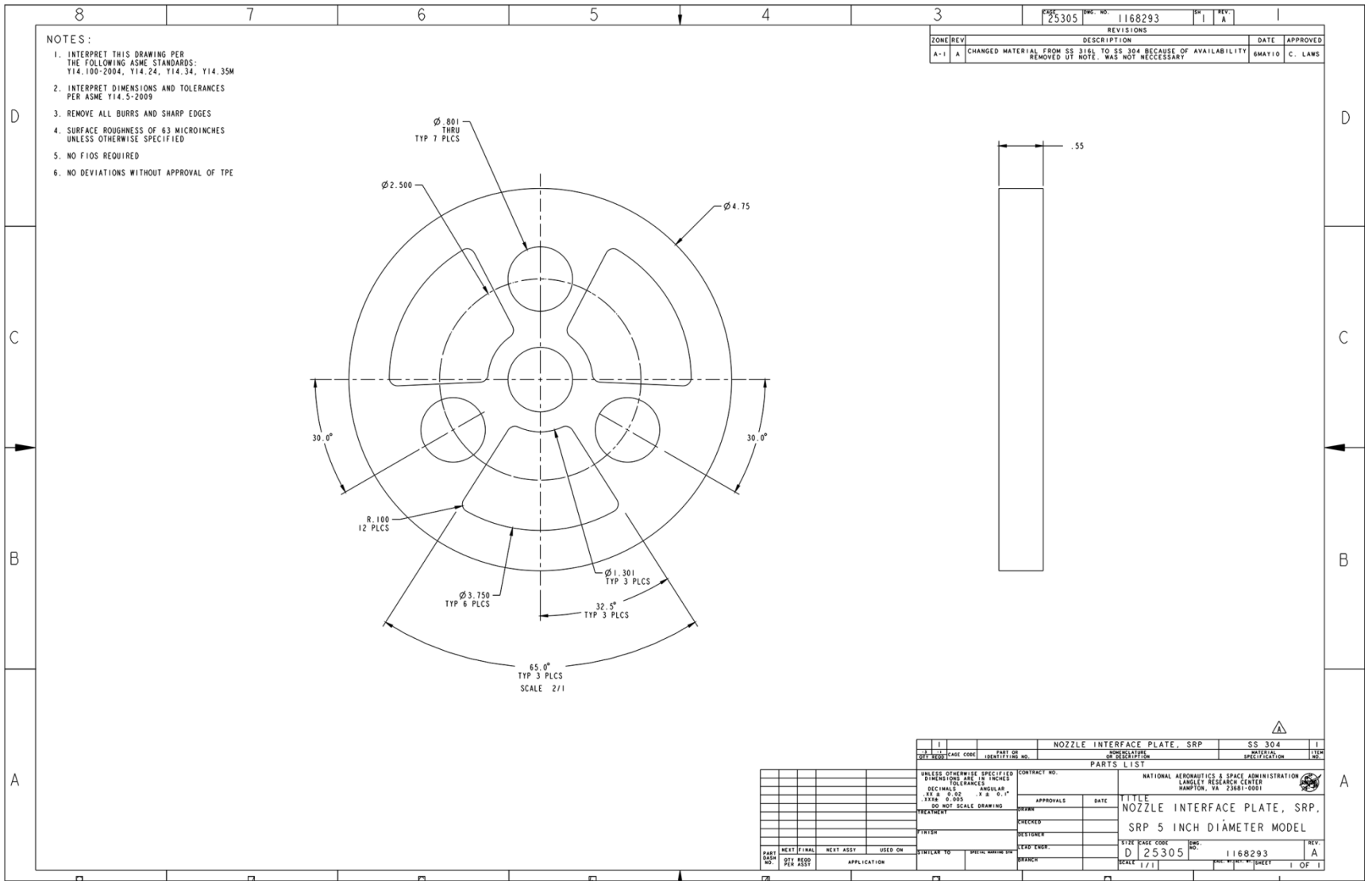
NOTES:
1. INTERPRET THIS DRAWING PER THE FOLLOWING ASME STANDARDS: Y14.100-2004, Y14.24, Y14.34, Y14.35M
2. INTERPRET DIMENSIONS AND TOLERANCES PER ASME Y14.5-2009
3. REMOVE ALL BURRS AND SHARP EDGES
4. SURFACE ROUGHNESS OF 63 MICROINCHES UNLESS OTHERWISE SPECIFIED
5. NO FIOS REQUIRED
6. NO DEVIATIONS WITHOUT APPROVAL OF TPE
Ø.801 THRU TYP 7 PLCS
Ø2.500
Ø4.75
30.0°
30.0°
R.100 12 PLCS
Ø1.301 TYP 3 PLCS
Ø3.750 TYP 6 PLCS
32.5° TYP 3 PLCS
65.0° TYP 3 PLCS
SCALE 2/1
.55
REVISIONS
ZONE REV DESCRIPTION DATE APPROVED
A-1 A CHANGED MATERIAL FROM SS 316L TO SS 304 BECAUSE OF AVAILABILITY REMOVED UT NOTE. WAS NOT NECCESSARY 6MAY10 C. LAWS
NOZZLE INTERFACE PLATE, SRP
SS 304
PARTS LIST
NATIONAL AERONAUTICS & SPACE ADMINISTRATION LANGLEY RESEARCH CENTER HAMPTON, VA 23681-0001
TITLE
NOZZLE INTERFACE PLATE, SRP,
SRP 5 INCH DIAMETER MODEL
SIZE D CAGE CODE 25305 DWG. NO. 1168293 REV. A
SCALE 1/1 SHEET 1 OF 1

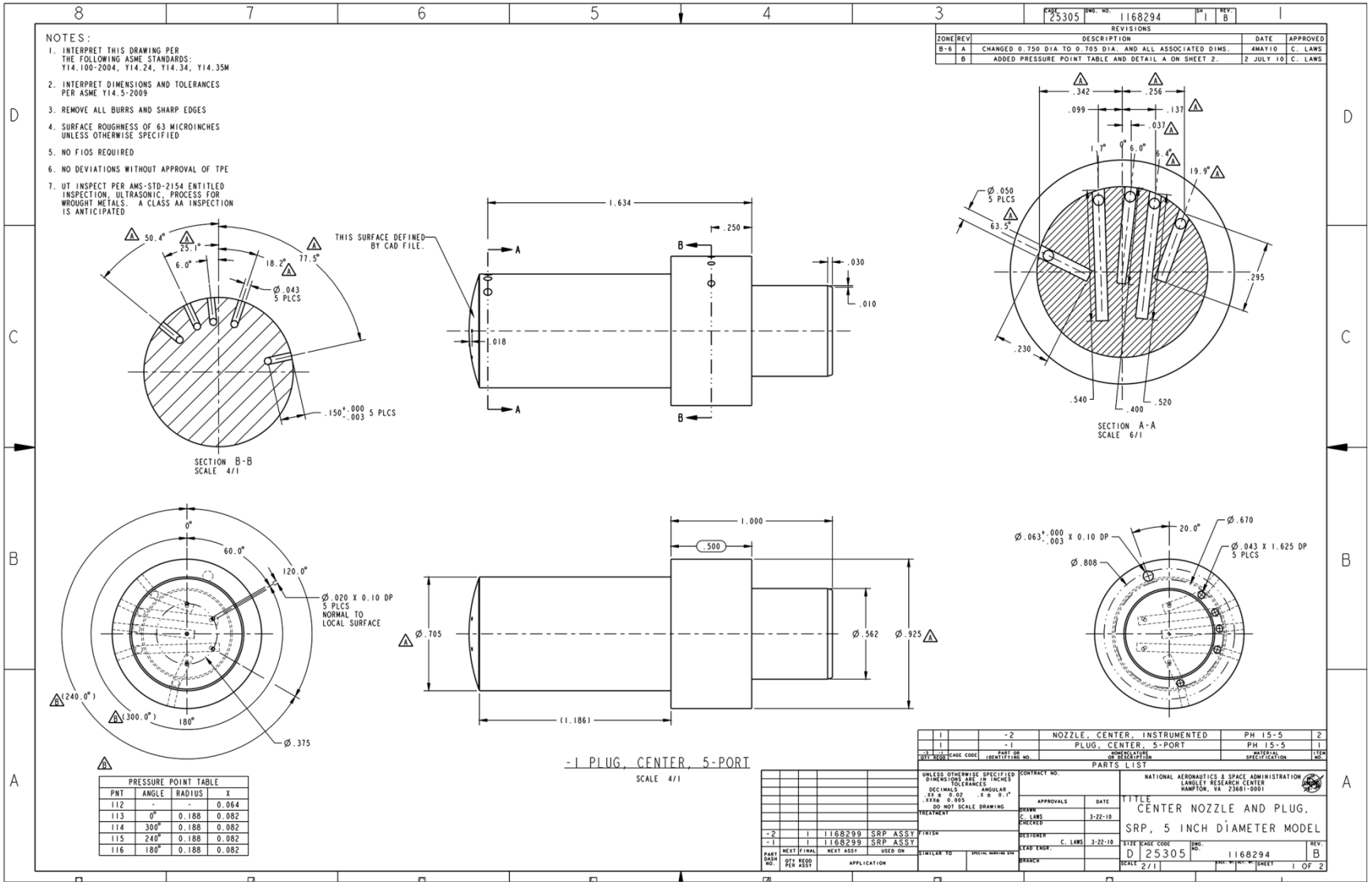
NOTES:
1. INTERPRET THIS DRAWING PER THE FOLLOWING ASME STANDARDS: Y14.100-2004, Y14.24, Y14.34, Y14.35M
2. INTERPRET DIMENSIONS AND TOLERANCES PER ASME Y14.5-2009
3. REMOVE ALL BURRS AND SHARP EDGES
4. SURFACE ROUGHNESS OF 63 MICROINCHES UNLESS OTHERWISE SPECIFIED
5. NO FIOS REQUIRED
6. NO DEVIATIONS WITHOUT APPROVAL OF TPE
7. UT INSPECT PER AMS-STD-2154 ENTITLED INSPECTION, ULTRASONIC, PROCESS FOR WROUGHT METALS. A CLASS AA INSPECTION IS ANTICIPATED
REVISIONS
ZONE REV DESCRIPTION DATE APPROVED
B-6 A CHANGED 0.750 DIA TO 0.705 DIA. AND ALL ASSOCIATED DIMS. 4MAY10 C. LAWS
B ADDED PRESSURE POINT TABLE AND DETAIL A ON SHEET 2. 2 JULY 10 C. LAWS
SECTION B-B SCALE 4/1
THIS SURFACE DEFINED BY CAD FILE.
SECTION A-A SCALE 6/1
PRESSURE POINT TABLE
PNT ANGLE RADIUS X
112 - - 0.064
113 0° 0.188 0.082
114 300° 0.188 0.082
115 240° 0.188 0.082
116 180° 0.188 0.082
-1 PLUG, CENTER, 5-PORT
SCALE 4/1
-2 NOZZLE, CENTER, INSTRUMENTED PH 15-5
-1 PLUG, CENTER, 5-PORT PH 15-5
PARTS LIST
UNLESS OTHERWISE SPECIFIED DIMENSIONS ARE IN INCHES
DO NOT SCALE DRAWING
NATIONAL AERONAUTICS & SPACE ADMINISTRATION LANGLEY RESEARCH CENTER HAMPTON, VA 23681-0001
TITLE CENTER NOZZLE AND PLUG, SRP, 5 INCH DIAMETER MODEL
DRAWN C. LAWS 3-22-10
DESIGNER C. LAWS 3-22-10
SIZE D CAGE CODE 25305 DWG. NO. 1168294 REV. B
SCALE 2/1 SHEET 1 OF 2

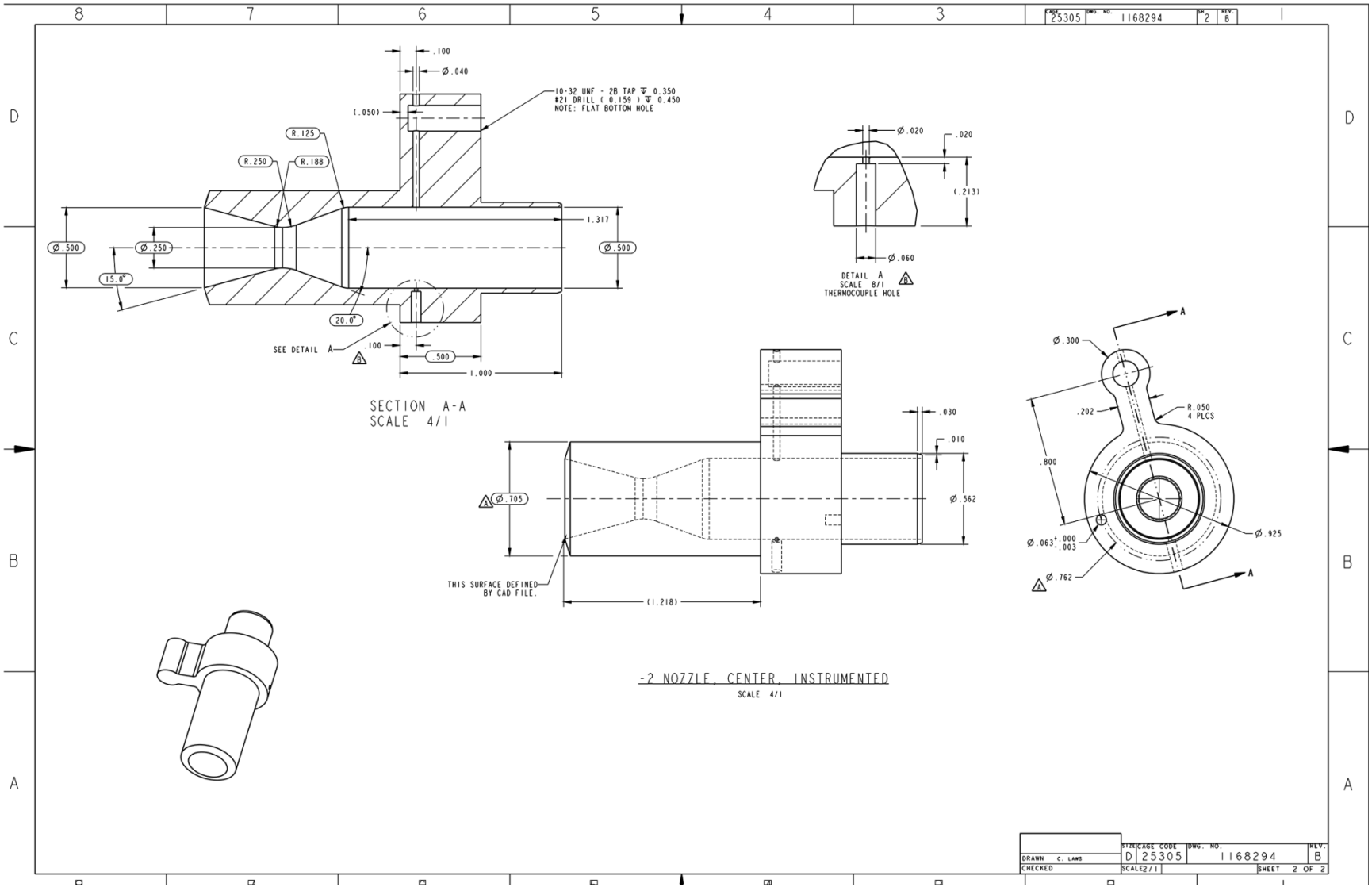
CAGE 25305 DWG. NO. 1168294 SH 2 REV. B
.100
Ø.040
(.050)
10-32 UNF - 2B TAP ↧ 0.350
#21 DRILL (0.159) ↧ 0.450
NOTE: FLAT BOTTOM HOLE
R.125
R.250
R.188
Ø.500
Ø.250
15.0°
1.317
Ø.500
20.0°
SEE DETAIL A
.100
.500
1.000
SECTION A-A
SCALE 4/1
Ø.020
.020
(.213)
Ø.060
DETAIL A
SCALE 8/1
THERMOCOUPLE HOLE
.030
.010
Ø.705
Ø.562
THIS SURFACE DEFINED BY CAD FILE.
(1.218)
-2 NOZZLE, CENTER, INSTRUMENTED
SCALE 4/1
Ø.300
.202
R.050
4 PLCS
.800
Ø.925
Ø.063 +.000 -.003
Ø.762
DRAWN C. LAWS
CHECKED
SIZE D CAGE CODE 25305 DWG. NO. 1168294 REV. B
SCALE 2/1
SHEET 2 OF 2

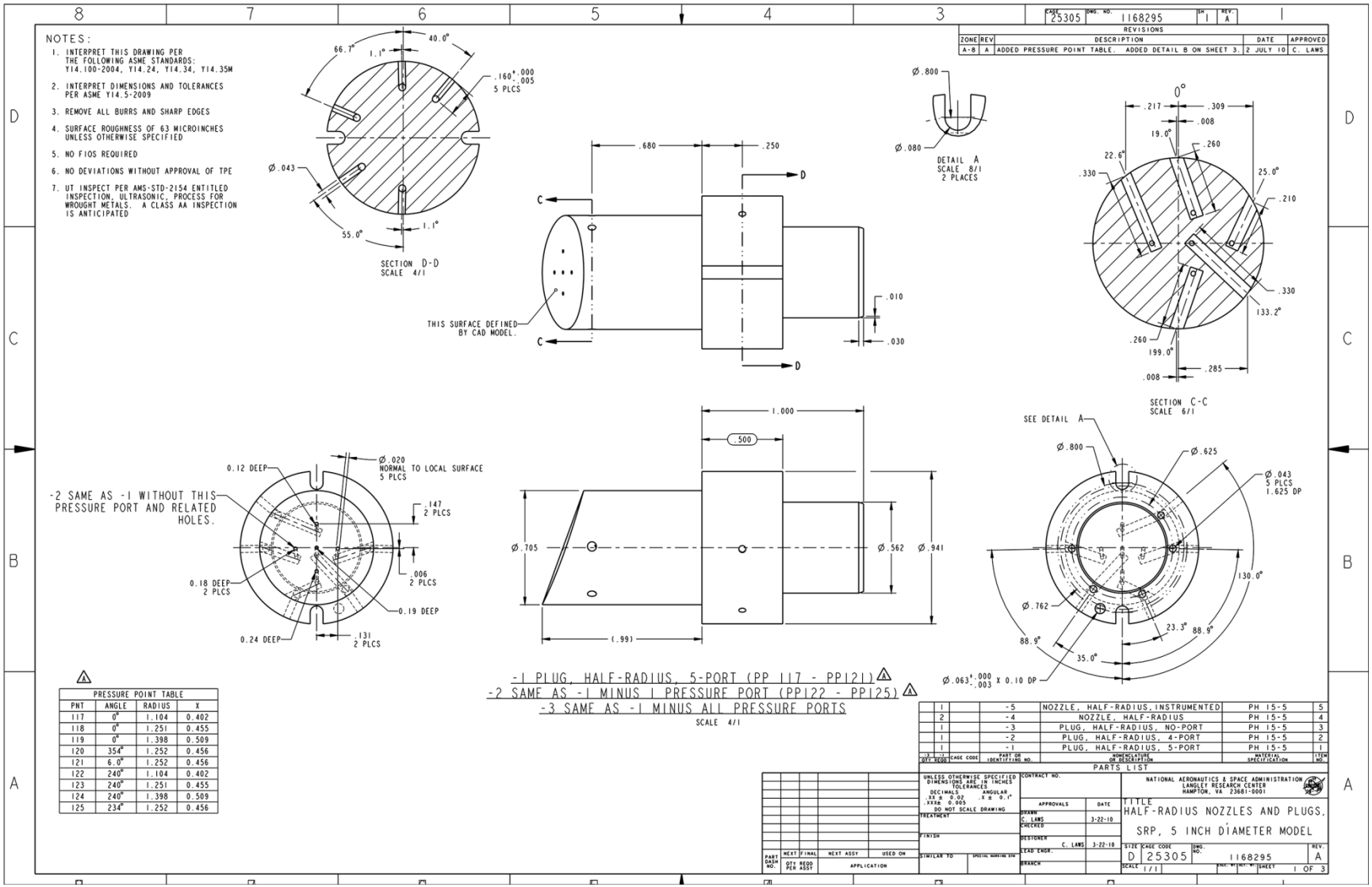
NOTES:
1. INTERPRET THIS DRAWING PER THE FOLLOWING ASME STANDARDS: Y14.100-2004, Y14.24, Y14.34, Y14.35M
2. INTERPRET DIMENSIONS AND TOLERANCES PER ASME Y14.5-2009
3. REMOVE ALL BURRS AND SHARP EDGES
4. SURFACE ROUGHNESS OF 63 MICROINCHES UNLESS OTHERWISE SPECIFIED
5. NO FIOS REQUIRED
6. NO DEVIATIONS WITHOUT APPROVAL OF TPE
7. UT INSPECT PER AMS-STD-2154 ENTITLED INSPECTION, ULTRASONIC, PROCESS FOR WROUGHT METALS. A CLASS AA INSPECTION IS ANTICIPATED
CAGE 25305 DWG. NO. 1168295 SH 1 REV. A
REVISIONS
ZONE REV DESCRIPTION DATE APPROVED
A-8 A ADDED PRESSURE POINT TABLE. ADDED DETAIL B ON SHEET 3. 2 JULY 10 C. LAWS
66.7°
40.0°
1.1°
.160 +.000 -.005 5 PLCS
Ø.043
55.0°
1.1°
SECTION D-D SCALE 4/1
Ø.800
Ø.080
DETAIL A SCALE 8/1 2 PLACES
.680
.250
C
D
THIS SURFACE DEFINED BY CAD MODEL.
.010
.030
0°
.217
.309
.008
19.0°
.260
22.6°
.330
25.0°
.210
.330
133.2°
.260
199.0°
.285
.008
SECTION C-C SCALE 6/1
0.12 DEEP
Ø.020 NORMAL TO LOCAL SURFACE 5 PLCS
-2 SAME AS -1 WITHOUT THIS PRESSURE PORT AND RELATED HOLES.
.147 2 PLCS
.006 2 PLCS
0.18 DEEP 2 PLCS
0.19 DEEP
0.24 DEEP
.131 2 PLCS
1.000
.500
Ø.705
Ø.562
Ø.941
(.99)
SEE DETAIL A
Ø.800
Ø.625
Ø.043 5 PLCS 1.625 DP
130.0°
Ø.762
23.3°
88.9°
88.9°
35.0°
Ø.063 +.000 -.003 X 0.10 DP
PRESSURE POINT TABLE
PNT ANGLE RADIUS X
117 0° 1.104 0.402
118 0° 1.251 0.455
119 0° 1.398 0.509
120 354° 1.252 0.456
121 6.0° 1.252 0.456
122 240° 1.104 0.402
123 240° 1.251 0.455
124 240° 1.398 0.509
125 234° 1.252 0.456
-1 PLUG, HALF-RADIUS, 5-PORT (PP 117 - PP121)
-2 SAME AS -1 MINUS 1 PRESSURE PORT (PP122 - PP125)
-3 SAME AS -1 MINUS ALL PRESSURE PORTS
SCALE 4/1
1 -5 NOZZLE, HALF-RADIUS, INSTRUMENTED PH 15-5 5
2 -4 NOZZLE, HALF-RADIUS PH 15-5 4
1 -3 PLUG, HALF-RADIUS, NO-PORT PH 15-5 3
1 -2 PLUG, HALF-RADIUS, 4-PORT PH 15-5 2
1 -1 PLUG, HALF-RADIUS, 5-PORT PH 15-5 1
-3 -1 QTY REQD CAGE CODE PART OR IDENTIFYING NO. NOMENCLATURE OR DESCRIPTION MATERIAL SPECIFICATION ITEM NO.
PARTS LIST
UNLESS OTHERWISE SPECIFIED DIMENSIONS ARE IN INCHES TOLERANCES DECIMALS ANGULAR .XX ± .02 ± 0.1° .XXX ± .005
DO NOT SCALE DRAWING
TREATMENT
FINISH
CONTRACT NO.
APPROVALS DATE
DRAWN C. LAWS 3-22-10
CHECKED
DESIGNER C. LAWS 3-22-10
LEAD ENGR.
BRANCH
NATIONAL AERONAUTICS & SPACE ADMINISTRATION LANGLEY RESEARCH CENTER HAMPTON, VA 23681-0001
TITLE
HALF-RADIUS NOZZLES AND PLUGS, SRP, 5 INCH DIAMETER MODEL
SIZE D CAGE CODE 25305 DWG. NO. 1168295 REV. A
SCALE 1/1 SHEET 1 OF 3
PART DASH NO. QTY REQD PER ASSY NEXT ASSY USED ON
APPLICATION
SIMILAR TO SPECIAL MARKING SYS

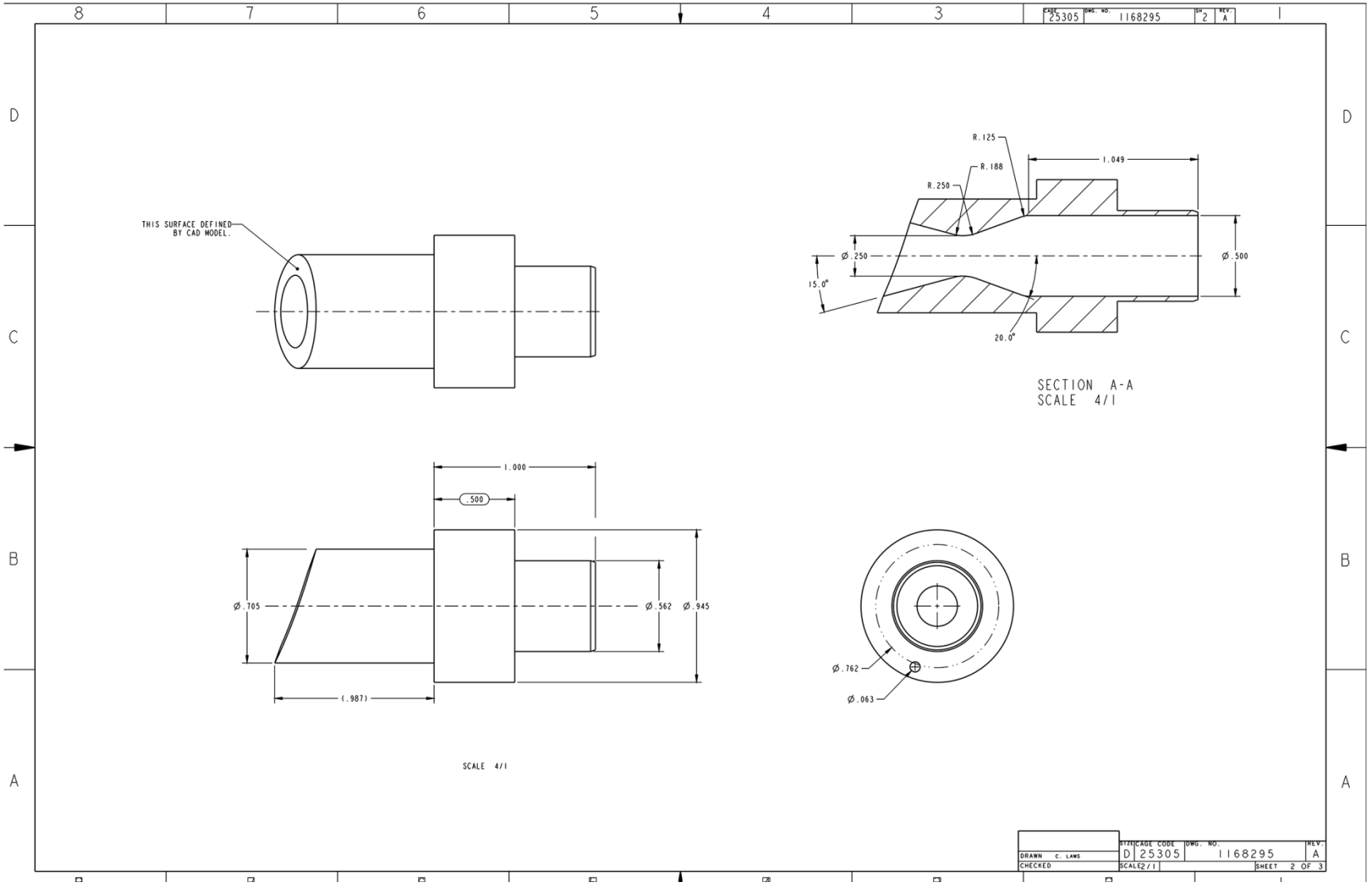
CAGE 25305
DWG. NO. 1168295
SH 2
REV. A
THIS SURFACE DEFINED BY CAD MODEL.
R.125
R.188
R.250
1.049
Ø.250
Ø.500
15.0°
20.0°
SECTION A-A
SCALE 4/1
1.000
.500
Ø.705
Ø.562
Ø.945
(.987)
SCALE 4/1
Ø.762
Ø.063
DRAWN C. LAWS
CHECKED
SIZE D
CAGE CODE 25305
DWG. NO. 1168295
REV. A
SCALE 2/1
SHEET 2 OF 3

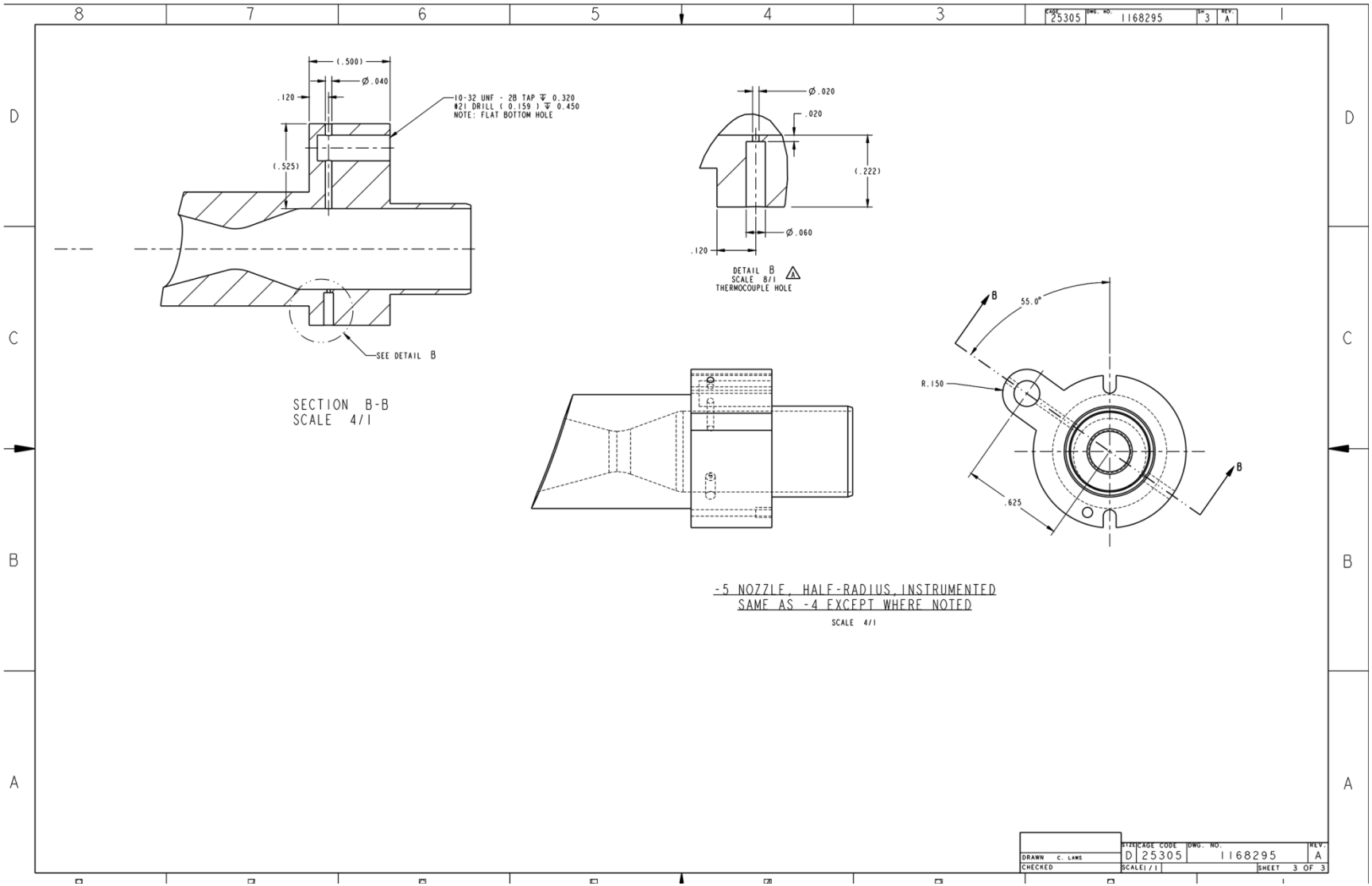
CAGE 25305
DWG. NO. 1168295
SH 3
REV. A
(.500)
Ø.040
.120
10-32 UNF - 2B TAP ↧ 0.320
#21 DRILL (0.159) ↧ 0.450
NOTE: FLAT BOTTOM HOLE
(.525)
SEE DETAIL B
SECTION B-B
SCALE 4/1
Ø.020
.020
(.222)
Ø.060
.120
DETAIL B
SCALE 8/1
THERMOCOUPLE HOLE
55.0°
R.150
.625
-5 NOZZLE, HALF-RADIUS, INSTRUMENTED
SAME AS -4 EXCEPT WHERE NOTED
SCALE 4/1
DRAWN C. LAWS
CHECKED
SIZE D
CAGE CODE 25305
DWG. NO. 1168295
REV. A
SCALE 1/1
SHEET 3 OF 3

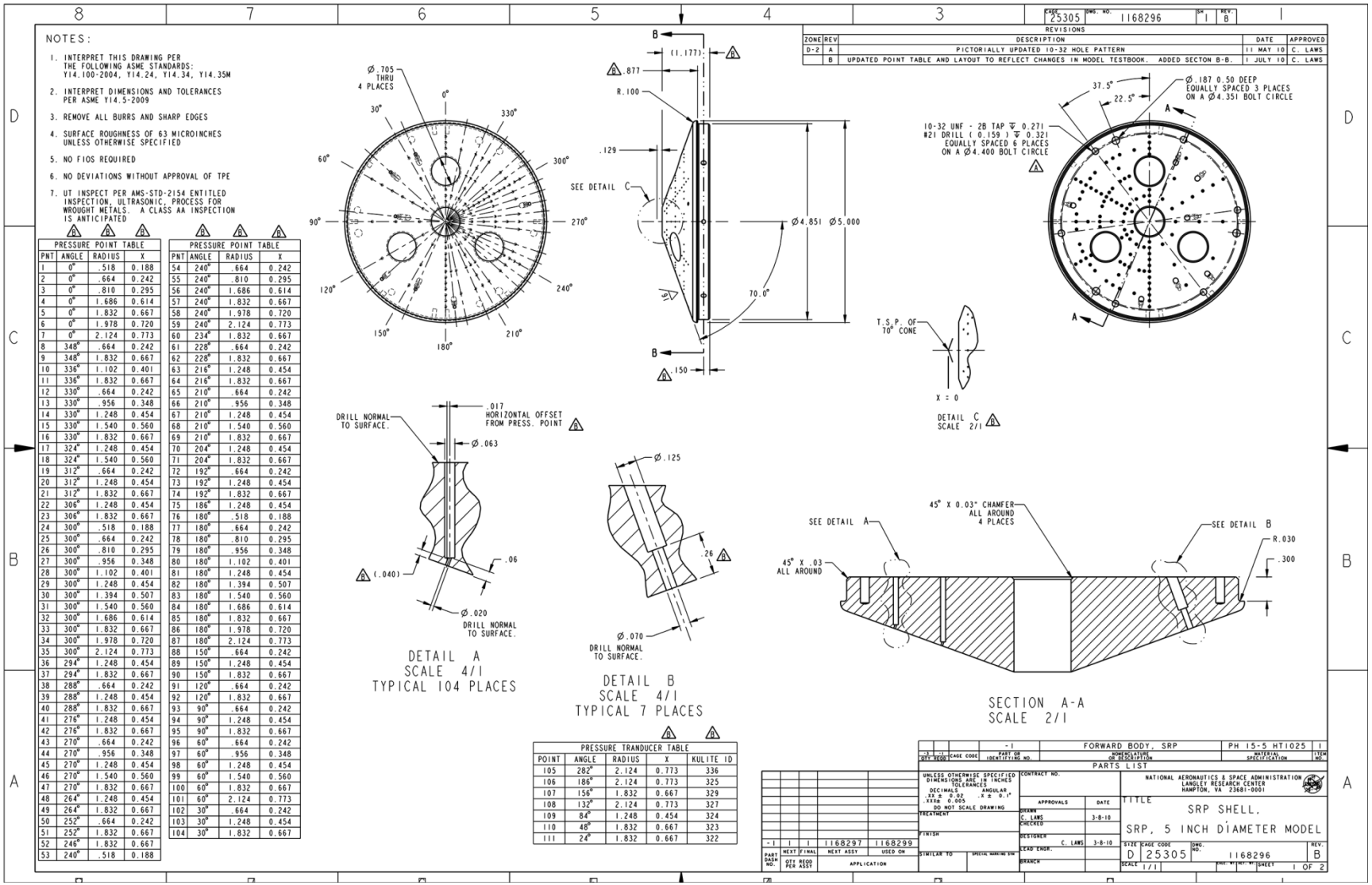
NOTES:
1. INTERPRET THIS DRAWING PER THE FOLLOWING ASME STANDARDS: Y14.100-2004, Y14.24, Y14.34, Y14.35M
2. INTERPRET DIMENSIONS AND TOLERANCES PER ASME Y14.5-2009
3. REMOVE ALL BURRS AND SHARP EDGES
4. SURFACE ROUGHNESS OF 63 MICROINCHES UNLESS OTHERWISE SPECIFIED
5. NO FIOS REQUIRED
6. NO DEVIATIONS WITHOUT APPROVAL OF TPE
7. UT INSPECT PER AMS-STD-2154 ENTITLED INSPECTION, ULTRASONIC, PROCESS FOR WROUGHT METALS. A CLASS AA INSPECTION IS ANTICIPATED
REVISIONS
ZONE REV DESCRIPTION DATE APPROVED
D-2 A PICTORIALLY UPDATED 10-32 HOLE PATTERN 11 MAY 10 C. LAWS
B UPDATED POINT TABLE AND LAYOUT TO REFLECT CHANGES IN MODEL TESTBOOK. ADDED SECTON B-B. 1 JULY 10 C. LAWS
CAGE 25305 DWG. NO. 1168296 SH 1 REV. B
PRESSURE POINT TABLE
PNT ANGLE RADIUS X
1 0° .518 0.188
2 0° .664 0.242
3 0° .810 0.295
4 0° 1.686 0.614
5 0° 1.832 0.667
6 0° 1.978 0.720
7 0° 2.124 0.773
8 348° .664 0.242
9 348° 1.832 0.667
10 336° 1.102 0.401
11 336° 1.832 0.667
12 330° .664 0.242
13 330° .956 0.348
14 330° 1.248 0.454
15 330° 1.540 0.560
16 330° 1.832 0.667
17 324° 1.248 0.454
18 324° 1.540 0.560
19 312° .664 0.242
20 312° 1.248 0.454
21 312° 1.832 0.667
22 306° 1.248 0.454
23 306° 1.832 0.667
24 300° .518 0.188
25 300° .664 0.242
26 300° .810 0.295
27 300° .956 0.348
28 300° 1.102 0.401
29 300° 1.248 0.454
30 300° 1.394 0.507
31 300° 1.540 0.560
32 300° 1.686 0.614
33 300° 1.832 0.667
34 300° 1.978 0.720
35 300° 2.124 0.773
36 294° 1.248 0.454
37 294° 1.832 0.667
38 288° .664 0.242
39 288° 1.248 0.454
40 288° 1.832 0.667
41 276° 1.248 0.454
42 276° 1.832 0.667
43 270° .664 0.242
44 270° .956 0.348
45 270° 1.248 0.454
46 270° 1.540 0.560
47 270° 1.832 0.667
48 264° 1.248 0.454
49 264° 1.832 0.667
50 252° .664 0.242
51 252° 1.832 0.667
52 246° 1.832 0.667
53 240° .518 0.188
PRESSURE POINT TABLE
PNT ANGLE RADIUS X
54 240° .664 0.242
55 240° .810 0.295
56 240° 1.686 0.614
57 240° 1.832 0.667
58 240° 1.978 0.720
59 240° 2.124 0.773
60 234° 1.832 0.667
61 228° .664 0.242
62 228° 1.832 0.667
63 216° 1.248 0.454
64 216° 1.832 0.667
65 210° .664 0.242
66 210° .956 0.348
67 210° 1.248 0.454
68 210° 1.540 0.560
69 210° 1.832 0.667
70 204° 1.248 0.454
71 204° 1.832 0.667
72 192° .664 0.242
73 192° 1.248 0.454
74 192° 1.832 0.667
75 186° 1.248 0.454
76 180° .518 0.188
77 180° .664 0.242
78 180° .810 0.295
79 180° .956 0.348
80 180° 1.102 0.401
81 180° 1.248 0.454
82 180° 1.394 0.507
83 180° 1.540 0.560
84 180° 1.686 0.614
85 180° 1.832 0.667
86 180° 1.978 0.720
87 180° 2.124 0.773
88 150° .664 0.242
89 150° 1.248 0.454
90 150° 1.832 0.667
91 120° .664 0.242
92 120° 1.832 0.667
93 90° .664 0.242
94 90° 1.248 0.454
95 90° 1.832 0.667
96 60° .664 0.242
97 60° .956 0.348
98 60° 1.248 0.454
99 60° 1.540 0.560
100 60° 1.832 0.667
101 60° 2.124 0.773
102 30° .664 0.242
103 30° 1.248 0.454
104 30° 1.832 0.667
Ø.705 THRU 4 PLACES
(1.177)
.877
R.100
.129
SEE DETAIL C
Ø4.851 Ø5.000
70.0°
.150
Ø.187 0.50 DEEP EQUALLY SPACED 3 PLACES ON A Ø4.351 BOLT CIRCLE
37.5°
22.5°
10-32 UNF - 2B TAP ↧ 0.271
#21 DRILL (0.159) ↧ 0.321
EQUALLY SPACED 6 PLACES ON A Ø4.400 BOLT CIRCLE
T.S.P. OF 70° CONE
X = 0
DETAIL C SCALE 2/1
DRILL NORMAL TO SURFACE.
.017 HORIZONTAL OFFSET FROM PRESS. POINT
Ø.063
(.040)
.06
Ø.020
DRILL NORMAL TO SURFACE.
DETAIL A SCALE 4/1 TYPICAL 104 PLACES
Ø.125
.26
Ø.070
DRILL NORMAL TO SURFACE.
DETAIL B SCALE 4/1 TYPICAL 7 PLACES
45° X 0.03" CHAMFER ALL AROUND 4 PLACES
SEE DETAIL A
SEE DETAIL B
45° X .03 ALL AROUND
R.030
.300
SECTION A-A SCALE 2/1
PRESSURE TRANDUCER TABLE
POINT ANGLE RADIUS X KULITE ID
105 282° 2.124 0.773 336
106 186° 2.124 0.773 325
107 156° 1.832 0.667 329
108 132° 2.124 0.773 327
109 84° 1.248 0.454 324
110 48° 1.832 0.667 323
111 24° 1.832 0.667 322
-1 FORWARD BODY, SRP PH 15-5 HT1025 1
UNLESS OTHERWISE SPECIFIED DIMENSIONS ARE IN INCHES TOLERANCES DECIMALS .XX ± 0.02 .XXX 0.005 ANGULAR .X ± 0.1° DO NOT SCALE DRAWING
TREATMENT
FINISH
APPROVALS DATE
DRAWN C. LAWS 3-8-10
CHECKED
DESIGNER C. LAWS 3-8-10
LEAD ENGR.
BRANCH
CONTRACT NO.
NATIONAL AERONAUTICS & SPACE ADMINISTRATION LANGLEY RESEARCH CENTER HAMPTON, VA 23681-0001
TITLE
SRP SHELL, SRP, 5 INCH DIAMETER MODEL
SIZE D CAGE CODE 25305 DWG. NO. 1168296 REV. B
SCALE 1/1 SHEET 1 OF 2
-1 1168297 1168299
PART DASH NO. NEXT FINAL QTY REQD PER ASSY NEXT ASSY USED ON APPLICATION
SIMILAR TO SPECIAL MARKING REQ

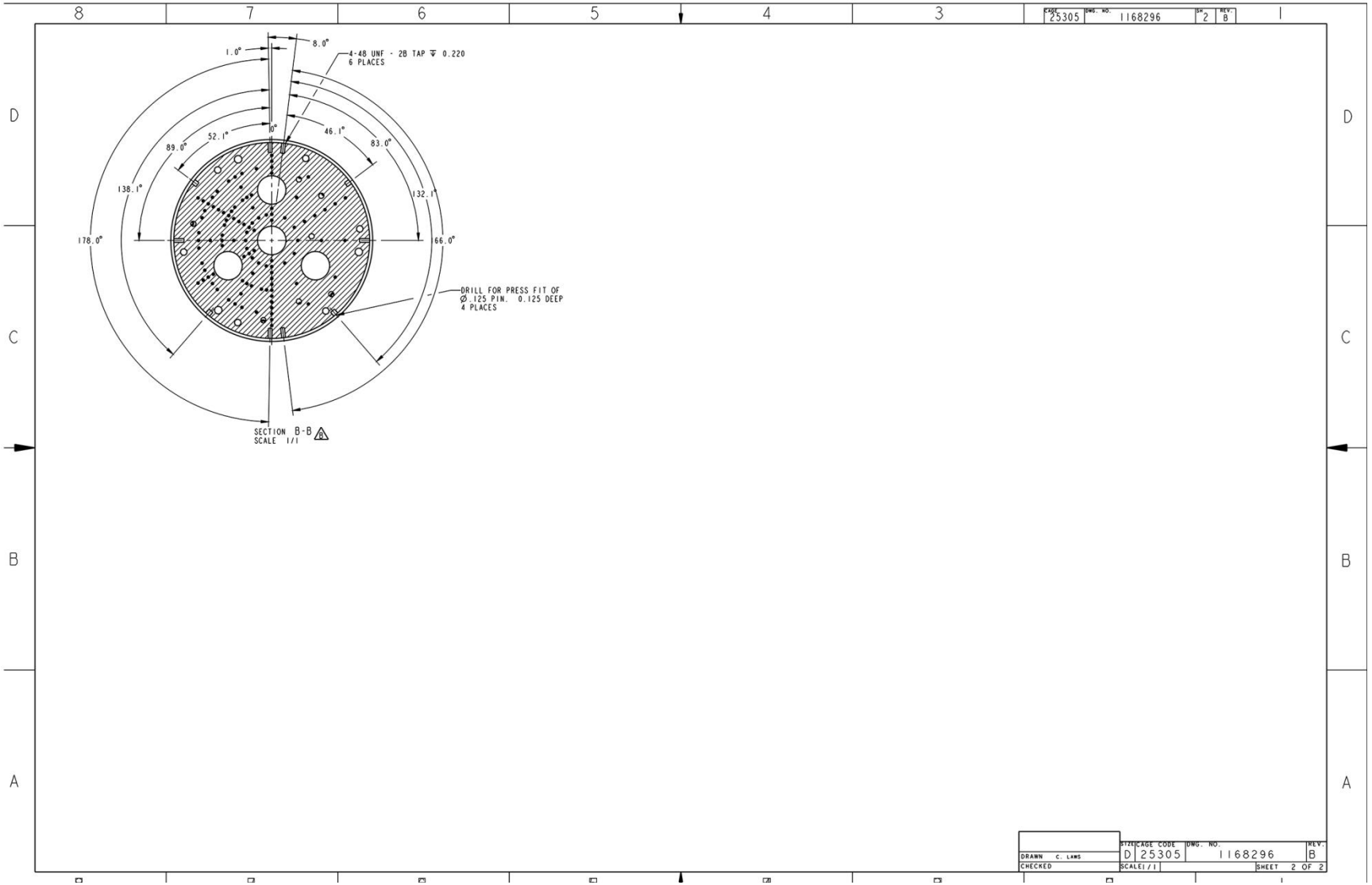
8
7
6
5
4
3
1
D
C
B
A
CAGE 25305
DWG. NO. 1168296
SH 2
REV. B
8.0°
1.0°
4-48 UNF - 2B TAP ↧ 0.220
6 PLACES
0°
46.1°
52.1°
83.0°
89.0°
132.1°
138.1°
178.0°
66.0°
DRILL FOR PRESS FIT OF
Ø.125 PIN. 0.125 DEEP
4 PLACES
SECTION B-B
SCALE 1/1
B
DRAWN C. LAWS
CHECKED
SIZE D
CAGE CODE 25305
DWG. NO. 1168296
REV. B
SCALE 1/1
SHEET 2 OF 2

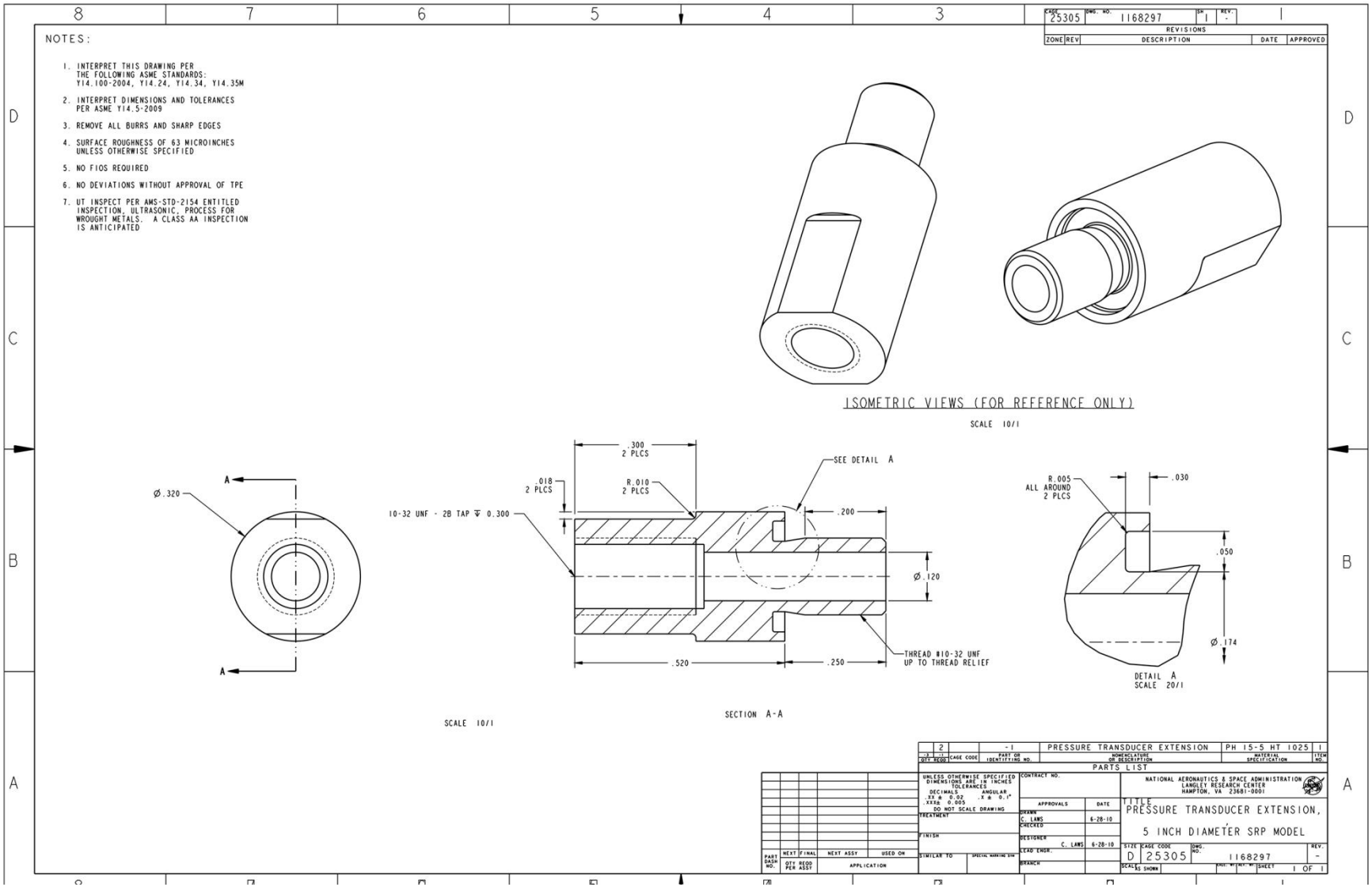
NOTES:
1. INTERPRET THIS DRAWING PER THE FOLLOWING ASME STANDARDS: Y14.100-2004, Y14.24, Y14.34, Y14.35M
2. INTERPRET DIMENSIONS AND TOLERANCES PER ASME Y14.5-2009
3. REMOVE ALL BURRS AND SHARP EDGES
4. SURFACE ROUGHNESS OF 63 MICROINCHES UNLESS OTHERWISE SPECIFIED
5. NO FIOS REQUIRED
6. NO DEVIATIONS WITHOUT APPROVAL OF TPE
7. UT INSPECT PER AMS-STD-2154 ENTITLED INSPECTION, ULTRASONIC, PROCESS FOR WROUGHT METALS. A CLASS AA INSPECTION IS ANTICIPATED
CAGE 25305 DWG. NO. 1168297 SH 1 REV. -
REVISIONS
ZONE REV DESCRIPTION DATE APPROVED
ISOMETRIC VIEWS (FOR REFERENCE ONLY)
SCALE 10/1
Ø.320
A
A
SCALE 10/1
.300 2 PLCS
.018 2 PLCS
R.010 2 PLCS
SEE DETAIL A
10-32 UNF - 2B TAP ↧ 0.300
.200
Ø.120
THREAD #10-32 UNF UP TO THREAD RELIEF
.520
.250
SECTION A-B
R.005 ALL AROUND 2 PLCS
.030
.050
Ø.174
DETAIL A SCALE 20/1
PRESSURE TRANSDUCER EXTENSION
PH 15-5 HT 1025
PARTS LIST
UNLESS OTHERWISE SPECIFIED DIMENSIONS ARE IN INCHES TOLERANCES DECIMALS .XX ± 0.02 .X ± 0.1° XXX± 0.005 DO NOT SCALE DRAWING
TREATMENT
FINISH
CONTRACT NO.
APPROVALS DATE
DRAWN C. LAWS 6-28-10
CHECKED
DESIGNER C. LAWS 6-28-10
LEAD ENGR.
BRANCH
NATIONAL AERONAUTICS & SPACE ADMINISTRATION LANGLEY RESEARCH CENTER HAMPTON, VA 23681-0001
TITLE PRESSURE TRANSDUCER EXTENSION, 5 INCH DIAMETER SRP MODEL
SIZE D CAGE CODE 25305 DWG. NO. 1168297 REV. -
SCALE AS SHOWN SHEET 1 OF 1

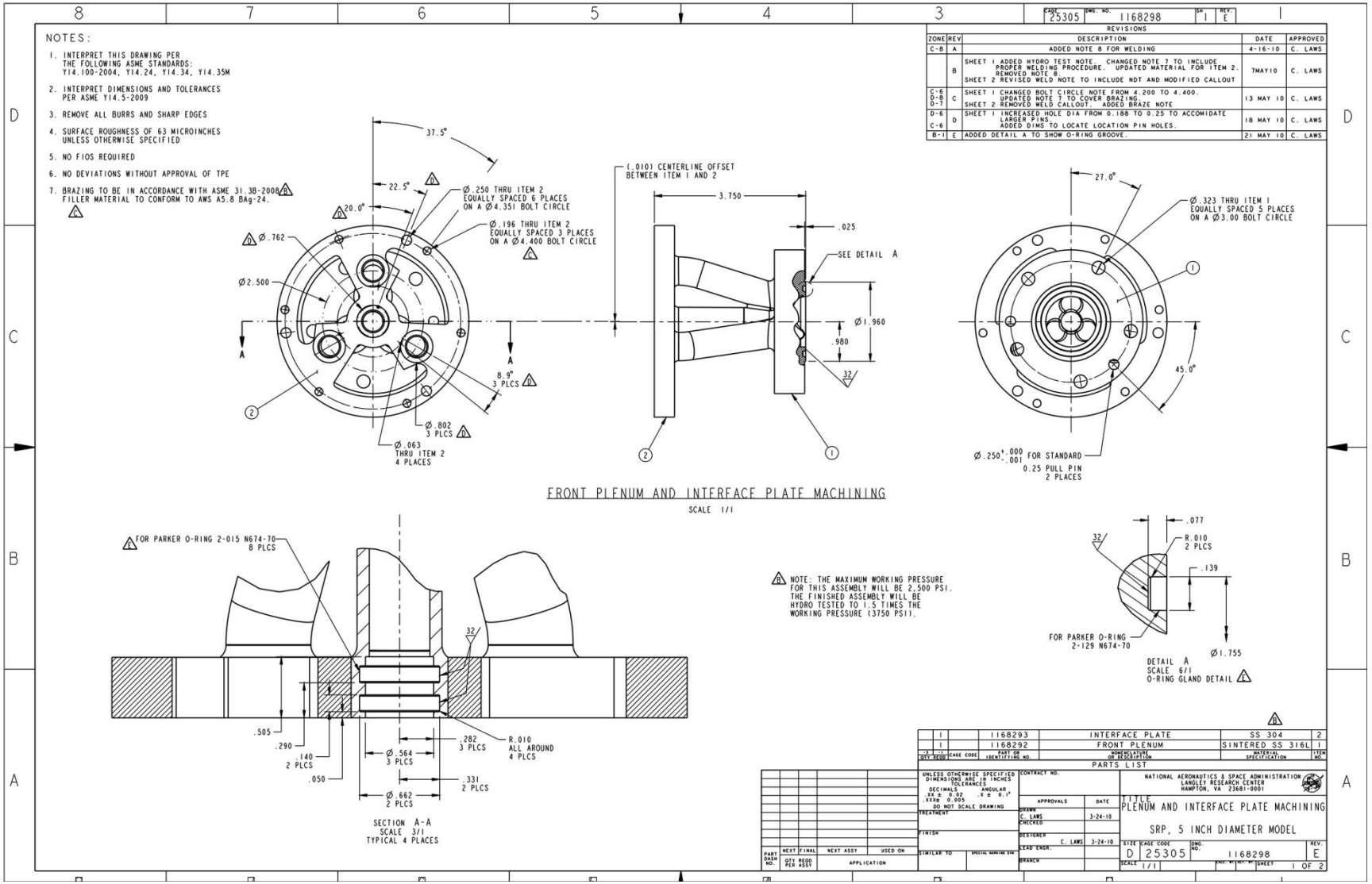
NOTES:
1. INTERPRET THIS DRAWING PER THE FOLLOWING ASME STANDARDS: Y14.100-2004, Y14.24, Y14.34, Y14.35M
2. INTERPRET DIMENSIONS AND TOLERANCES PER ASME Y14.5-2009
3. REMOVE ALL BURRS AND SHARP EDGES
4. SURFACE ROUGHNESS OF 63 MICROINCHES UNLESS OTHERWISE SPECIFIED
5. NO FIOS REQUIRED
6. NO DEVIATIONS WITHOUT APPROVAL OF TPE
7. BRAZING TO BE IN ACCORDANCE WITH ASME 31.3B-2008 FILLER MATERIAL TO CONFORM TO AWS A5.8 BAg-24.
REVISIONS
ZONE REV DESCRIPTION DATE APPROVED
C-8 A ADDED NOTE 8 FOR WELDING 4-16-10 C. LAWS
B SHEET 1 ADDED HYDRO TEST NOTE. CHANGED NOTE 7 TO INCLUDE PROPER WELDING PROCEDURE. UPDATED MATERIAL FOR ITEM 2. REMOVED NOTE 8. SHEET 2 REVISED WELD NOTE TO INCLUDE NDT AND MODIFIED CALLOUT 7MAY10 C. LAWS
C-6 D-8 D-7 C SHEET 1 CHANGED BOLT CIRCLE NOTE FROM 4.200 TO 4.400. UPDATED NOTE 7 TO COVER BRAZING. SHEET 2 REMOVED WELD CALLOUT. ADDED BRAZE NOTE 13 MAY 10 C. LAWS
D-6 C-6 D SHEET 1 INCREASED HOLE DIA FROM 0.188 TO 0.25 TO ACCOMIDATE LARGER PINS. ADDED DIMS TO LOCATE LOCATION PIN HOLES. 18 MAY 10 C. LAWS
B-1 E ADDED DETAIL A TO SHOW O-RING GROOVE. 21 MAY 10 C. LAWS
37.5°
22.5°
20.0°
Ø.250 THRU ITEM 2 EQUALLY SPACED 6 PLACES ON A Ø4.351 BOLT CIRCLE
Ø.196 THRU ITEM 2 EQUALLY SPACED 3 PLACES ON A Ø4.400 BOLT CIRCLE
Ø.762
Ø2.500
8.9° 3 PLCS
Ø.802 3 PLCS
Ø.063 THRU ITEM 2 4 PLACES
(.010) CENTERLINE OFFSET BETWEEN ITEM 1 AND 2
3.750
.025
SEE DETAIL A
Ø1.960
.980
32
27.0°
Ø.323 THRU ITEM 1 EQUALLY SPACED 5 PLACES ON A Ø3.00 BOLT CIRCLE
45.0°
Ø.250 +.000 -.001 FOR STANDARD 0.25 PULL PIN 2 PLACES
FRONT PLENUM AND INTERFACE PLATE MACHINING
SCALE 1/1
FOR PARKER O-RING 2-015 N674-70 8 PLCS
.505
.290
.140 2 PLCS
.050
Ø.564 3 PLCS
.282 3 PLCS
R.010 ALL AROUND 4 PLCS
.331 2 PLCS
Ø.662 2 PLCS
SECTION A-A SCALE 3/1 TYPICAL 4 PLACES
NOTE: THE MAXIMUM WORKING PRESSURE FOR THIS ASSEMBLY WILL BE 2,500 PSI. THE FINISHED ASSEMBLY WILL BE HYDRO TESTED TO 1.5 TIMES THE WORKING PRESSURE (3750 PSI).
.077
R.010 2 PLCS
.139
FOR PARKER O-RING 2-129 N674-70
Ø1.755
DETAIL A SCALE 6/1 O-RING GLAND DETAIL
1 1168293 INTERFACE PLATE SS 304 2
1 1168292 FRONT PLENUM SINTERED SS 316L 1
PARTS LIST
UNLESS OTHERWISE SPECIFIED DIMENSIONS ARE IN INCHES TOLERANCES DECIMALS .XX ± 0.02 .XXX ± 0.005 ANGULAR .X ± 0.1° DO NOT SCALE DRAWING
TREATMENT
FINISH
APPROVALS DATE
DRAWN C. LAWS 3-24-10
CHECKED
DESIGNER C. LAWS 3-24-10
LEAD ENGR.
BRANCH
CONTRACT NO.
NATIONAL AERONAUTICS & SPACE ADMINISTRATION LANGLEY RESEARCH CENTER HAMPTON, VA 23681-0001
TITLE PLENUM AND INTERFACE PLATE MACHINING
SRP, 5 INCH DIAMETER MODEL
SIZE D CAGE CODE 25305 DWG. NO. 1168298 REV. E
SCALE 1/1 SHEET 1 OF 2

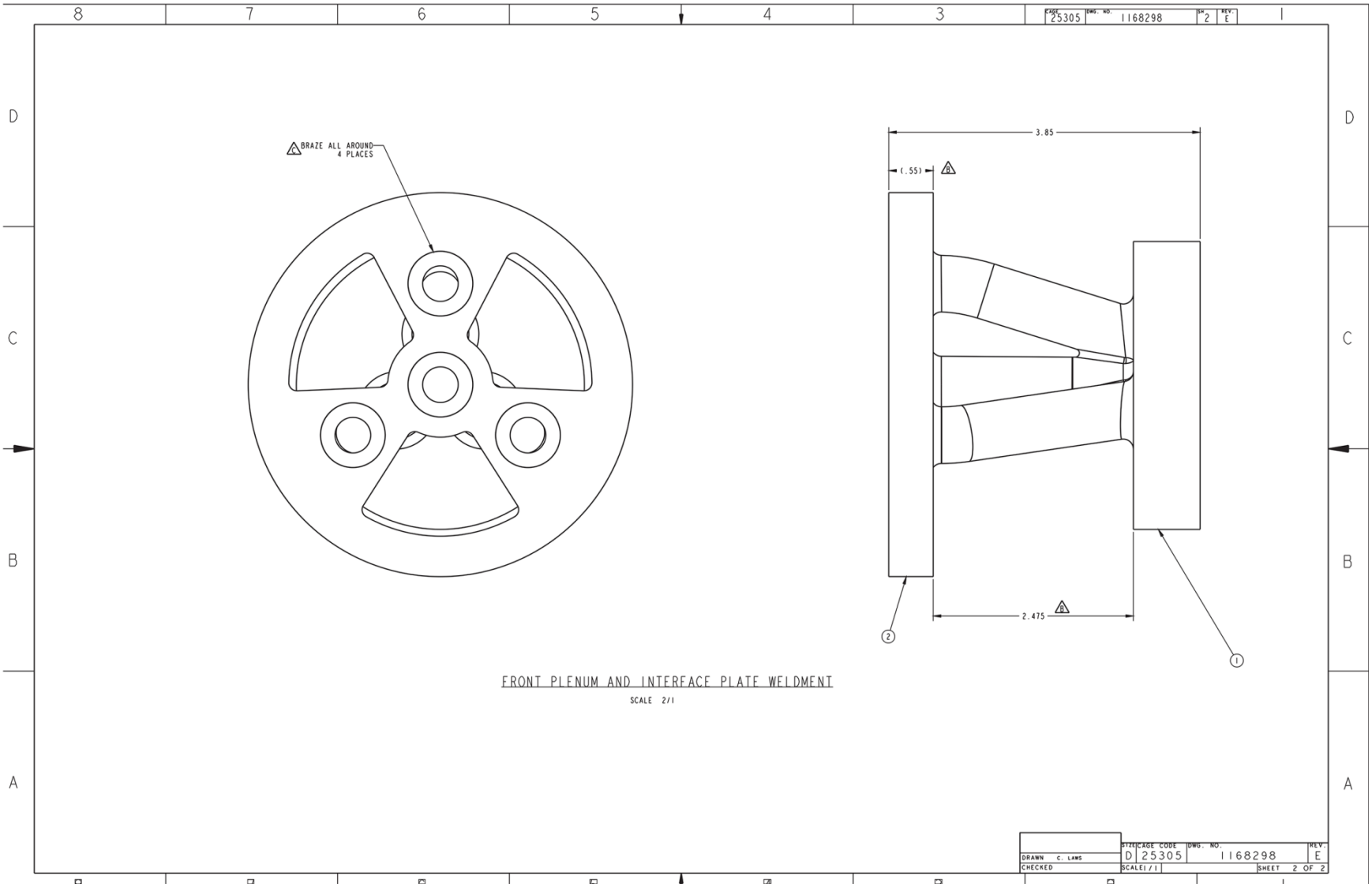
8
7
6
5
4
3
2
1
D
C
B
A
CAGE 25305
DWG. NO. 1168298
SH. 2
REV. E
BRAZE ALL AROUND
4 PLACES
3.85
(.55)
B
2.475
B
2
1
FRONT PLENUM AND INTERFACE PLATE WELDMENT
SCALE 2/1
DRAWN C. LAWS
CHECKED
SIZE D
CAGE CODE 25305
DWG. NO. 1168298
REV. E
SCALE 1/1
SHEET 2 OF 2

A2.0 Photos of Parts and Assembly Taken During Model Acceptance Fit Check (6/24/10)

Figure A-3. SRP model sting showing high pressure air supply port.

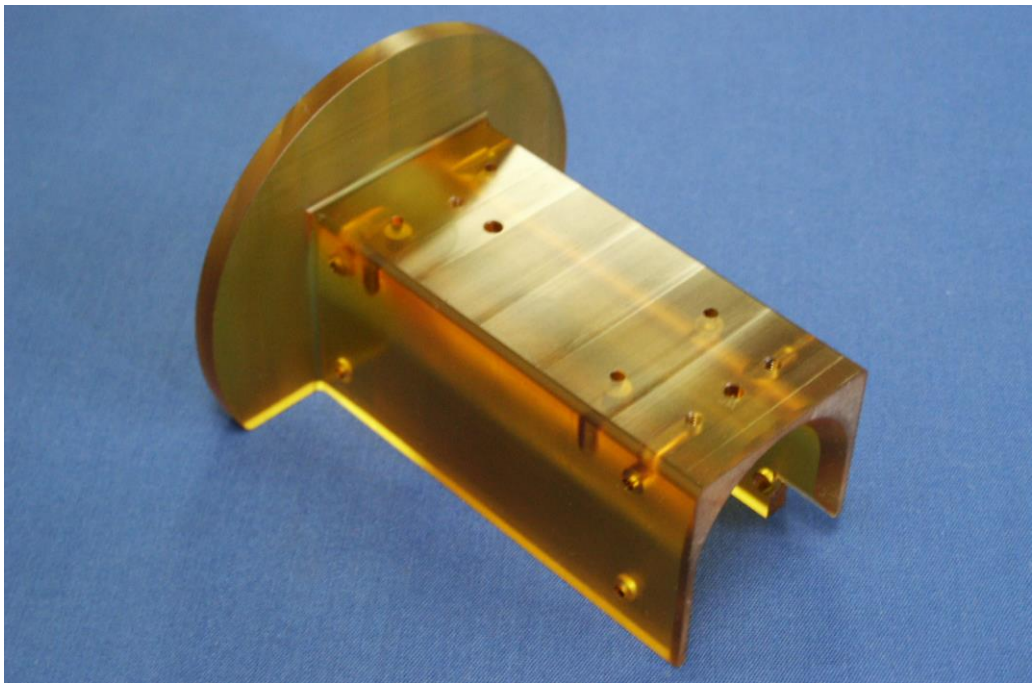

Figure A-4. ULTEM insulator saddle block.

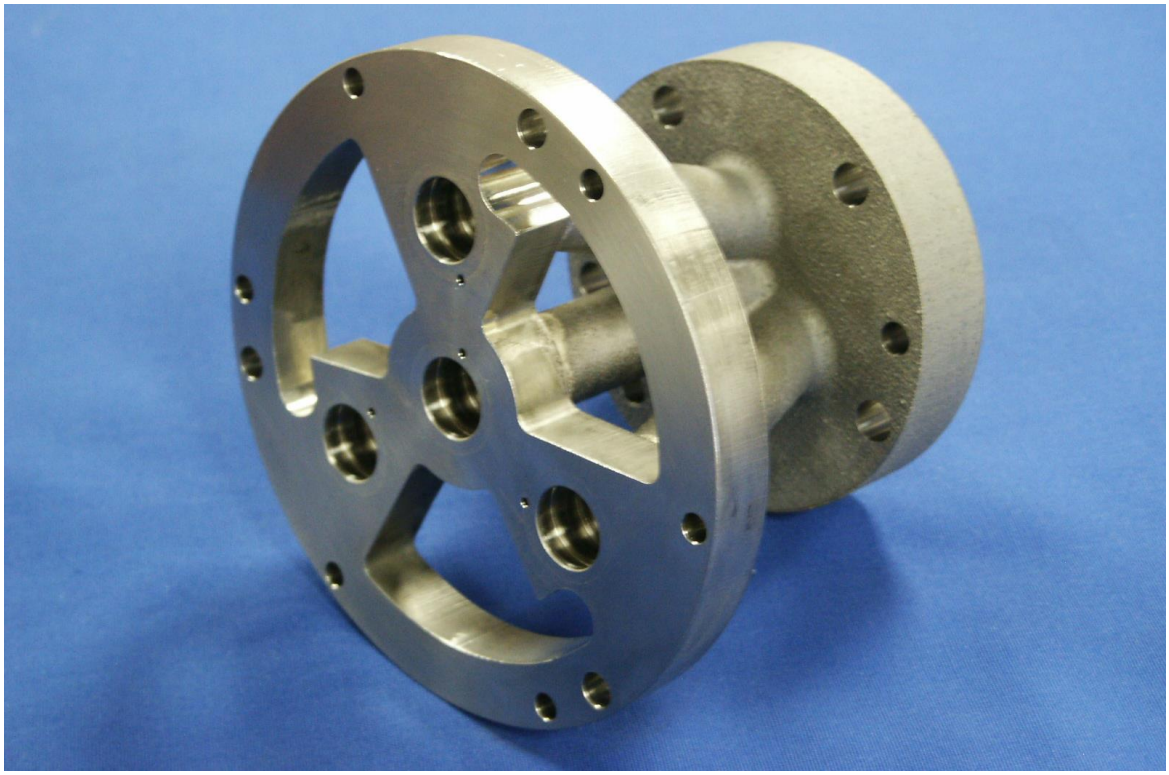

Figure A-5. Manifold assembly.

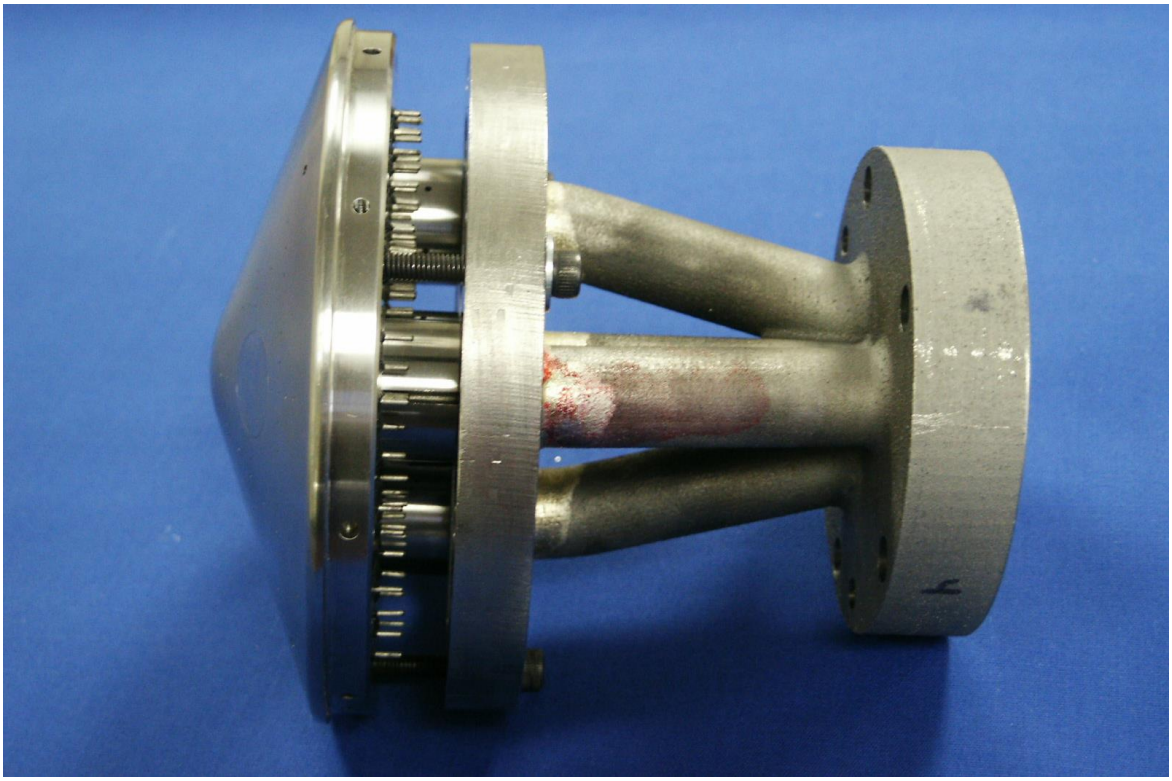

Figure A-6. Initial assembly of forebody and manifold.

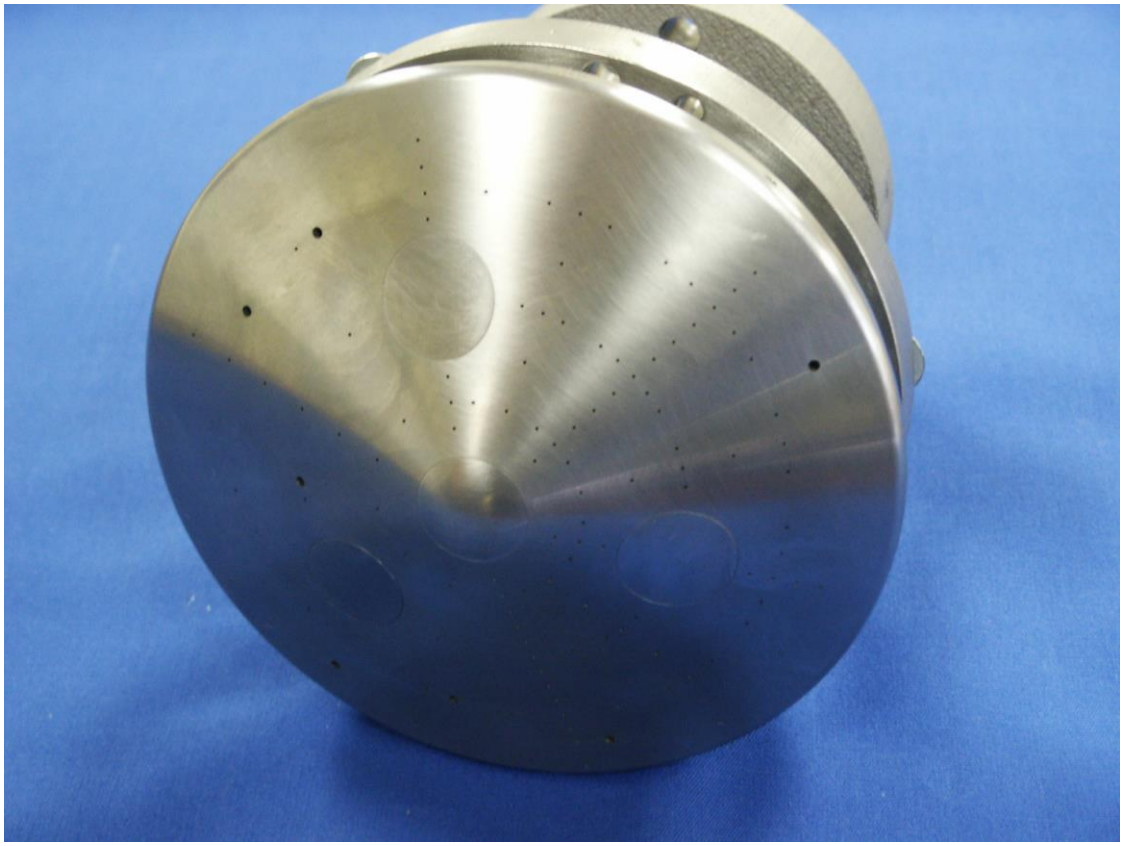

Figure A-7. Forebody assembly with baseline inserts installed.

Figure A-8. Six of eight baseline and nozzle inserts.

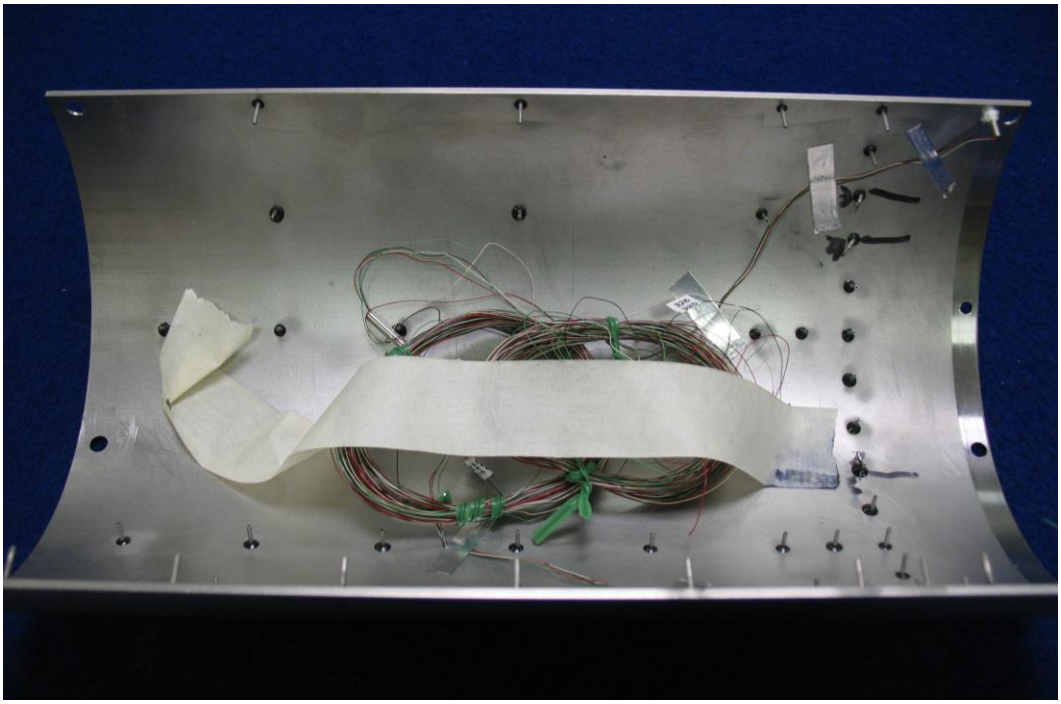

Figure A-9. Instrumented half aft shell.

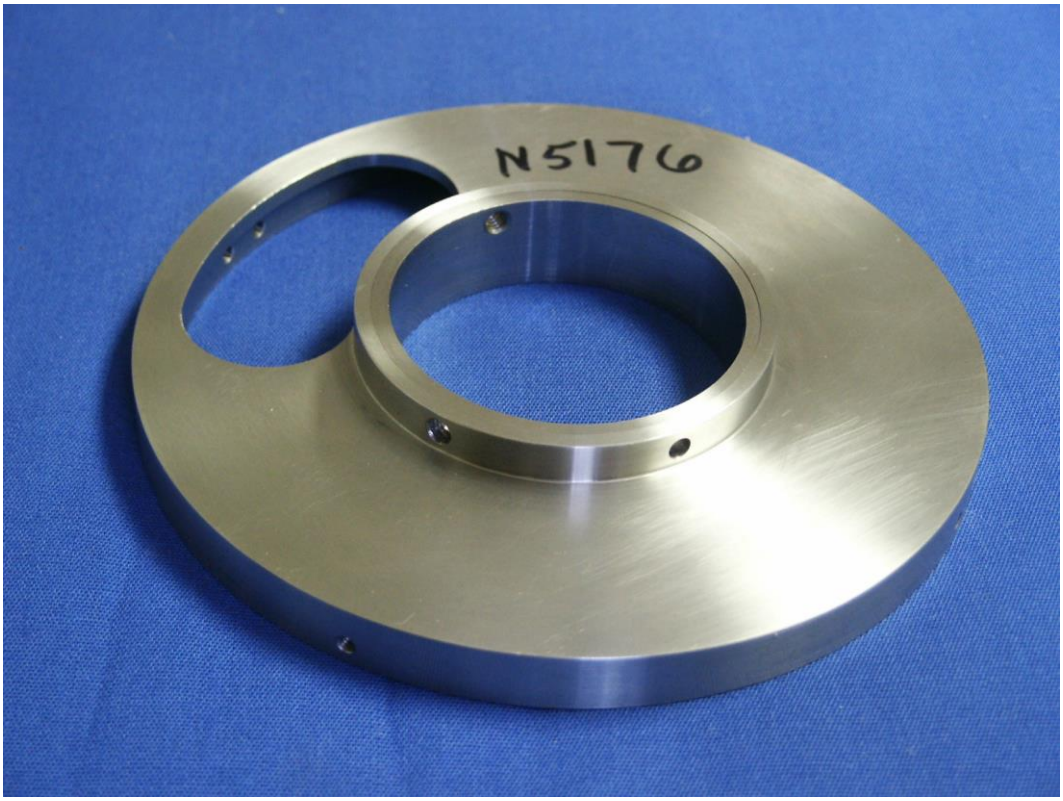

Figure A-10. Rear cover support plate showing wiring access hole.

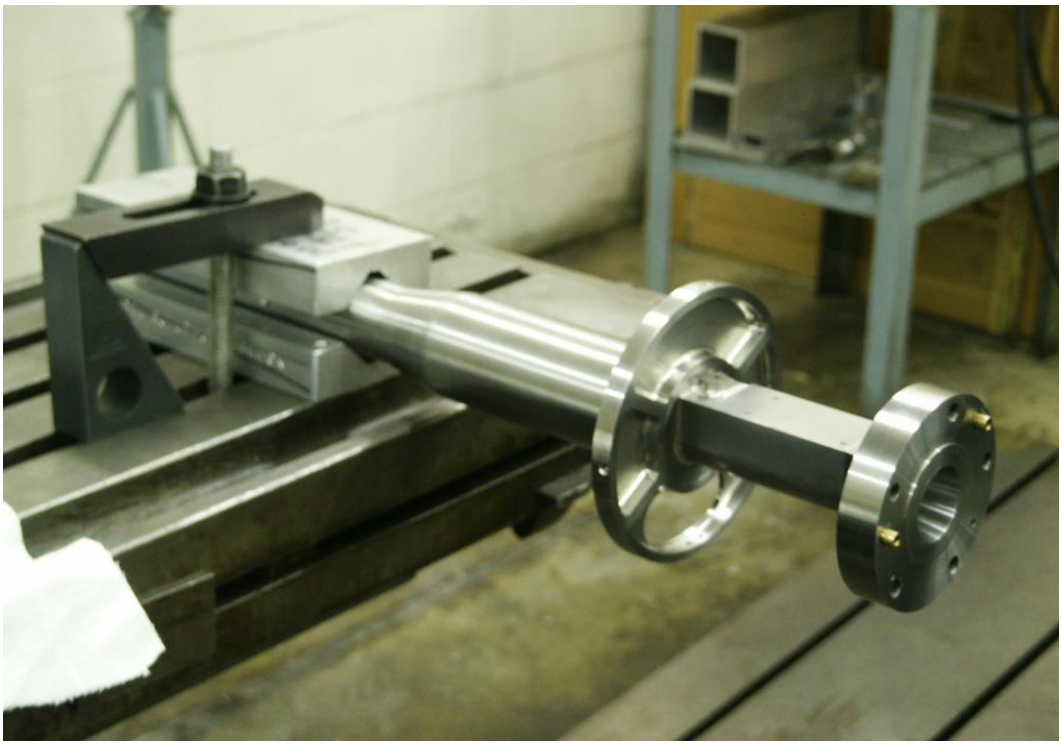

Figure A-11. Assembly of sting and rear cover support plate.

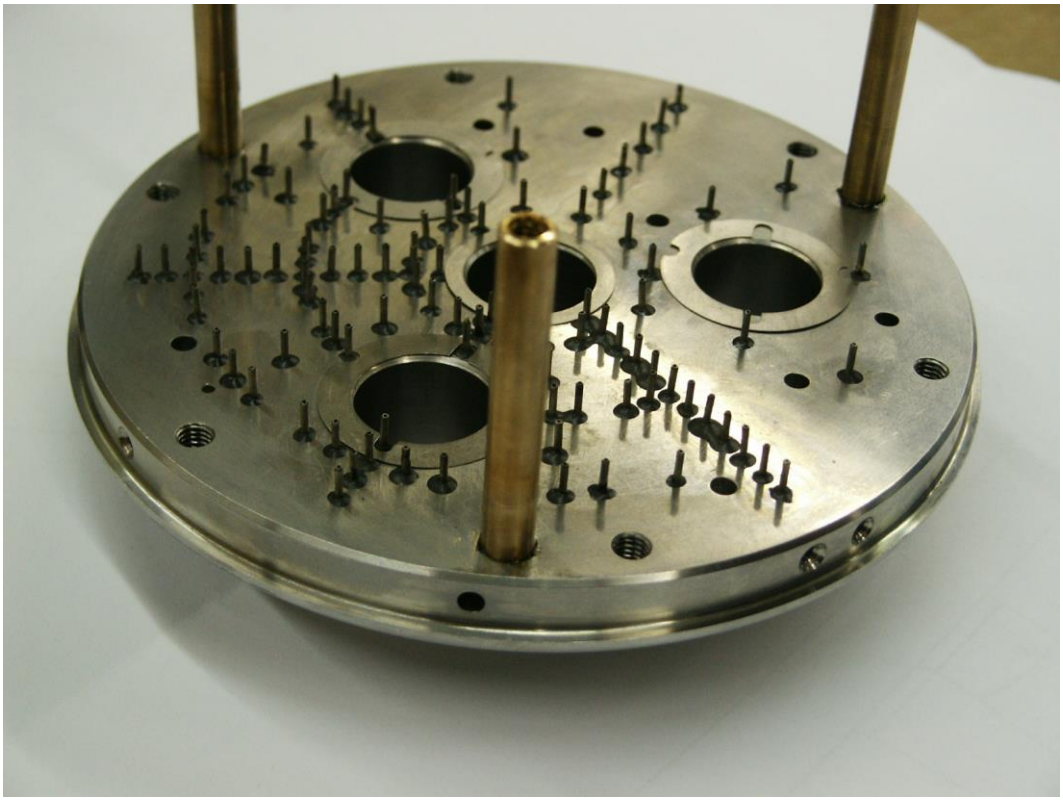

Figure A-12. Backside of forebody showing pressure tube port posts and shims for inserts.

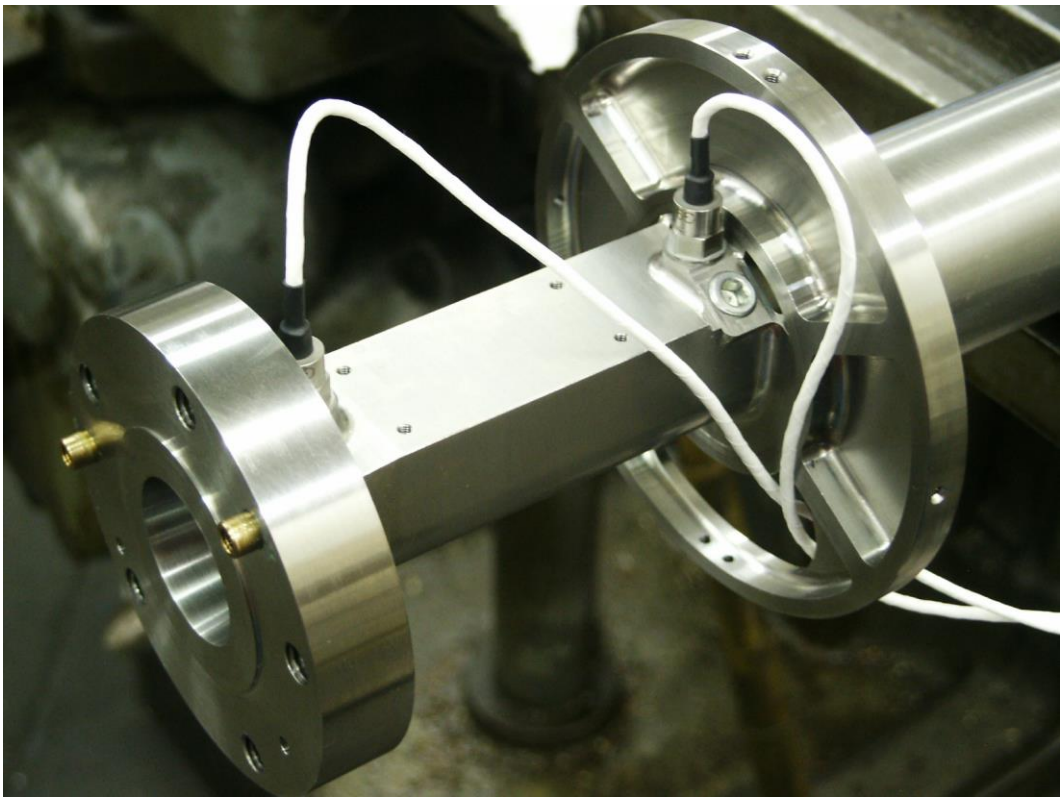

Figure A-13. Sting assembly with Kulite pressure transducers installed.

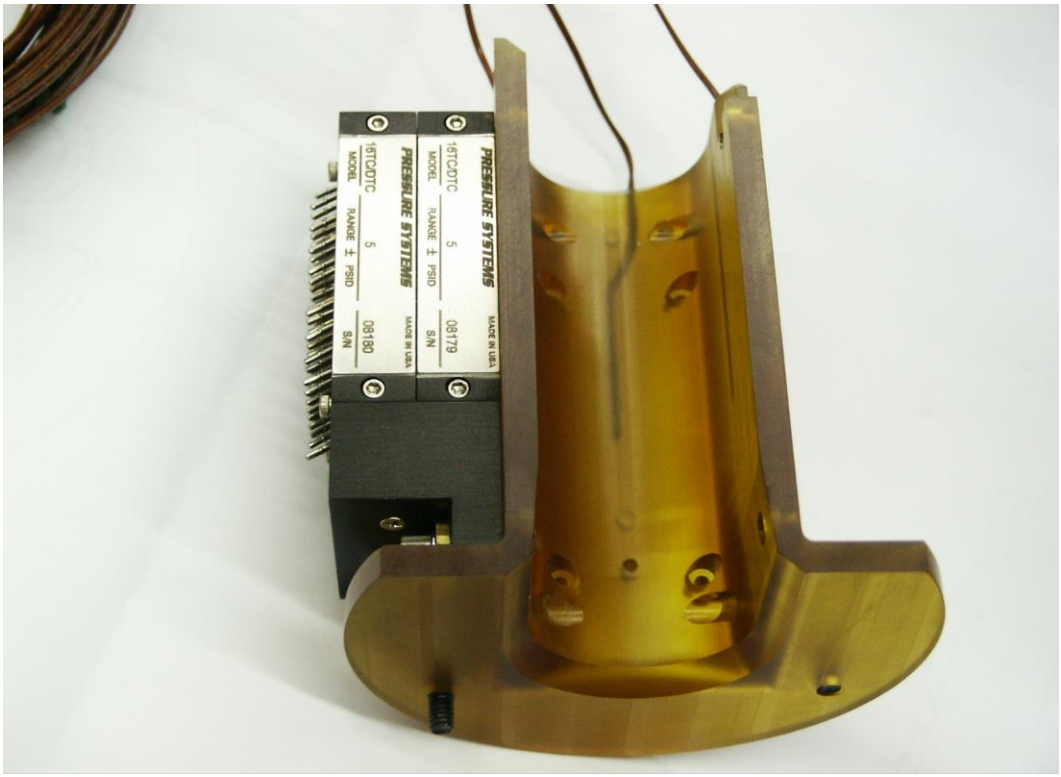

Figure A-14. Insulator saddle block with one ESP module attached.

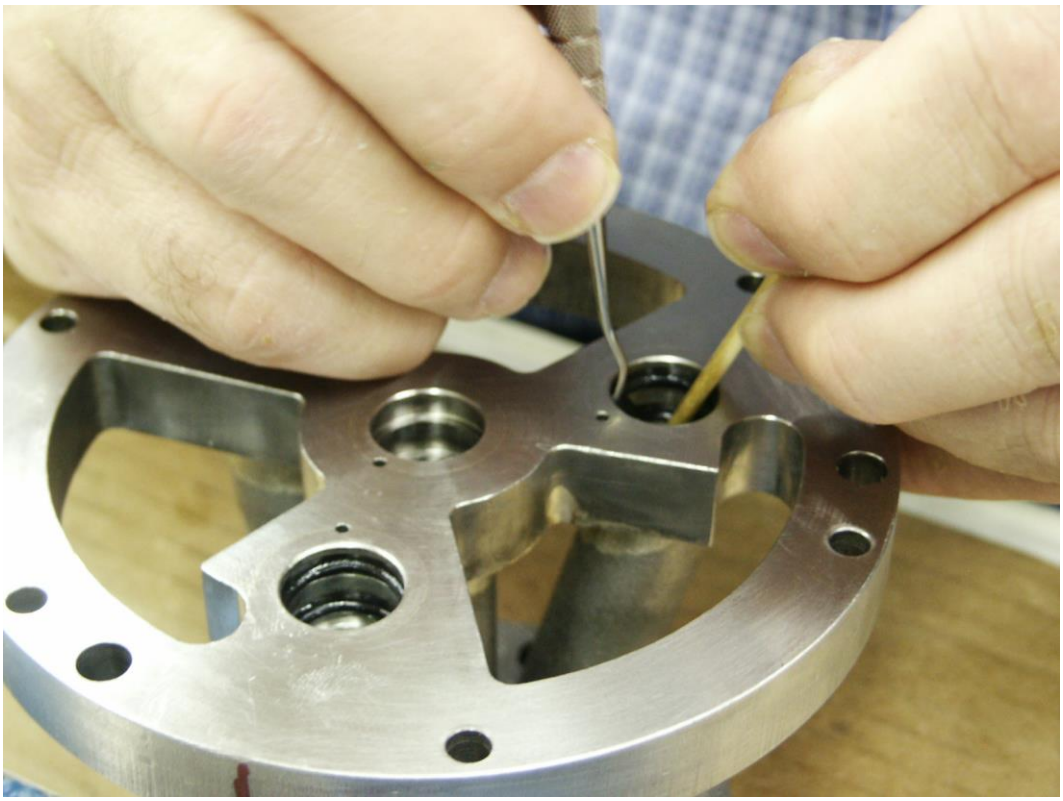

Figure A-15. Installation of the double O-rings for each insert.

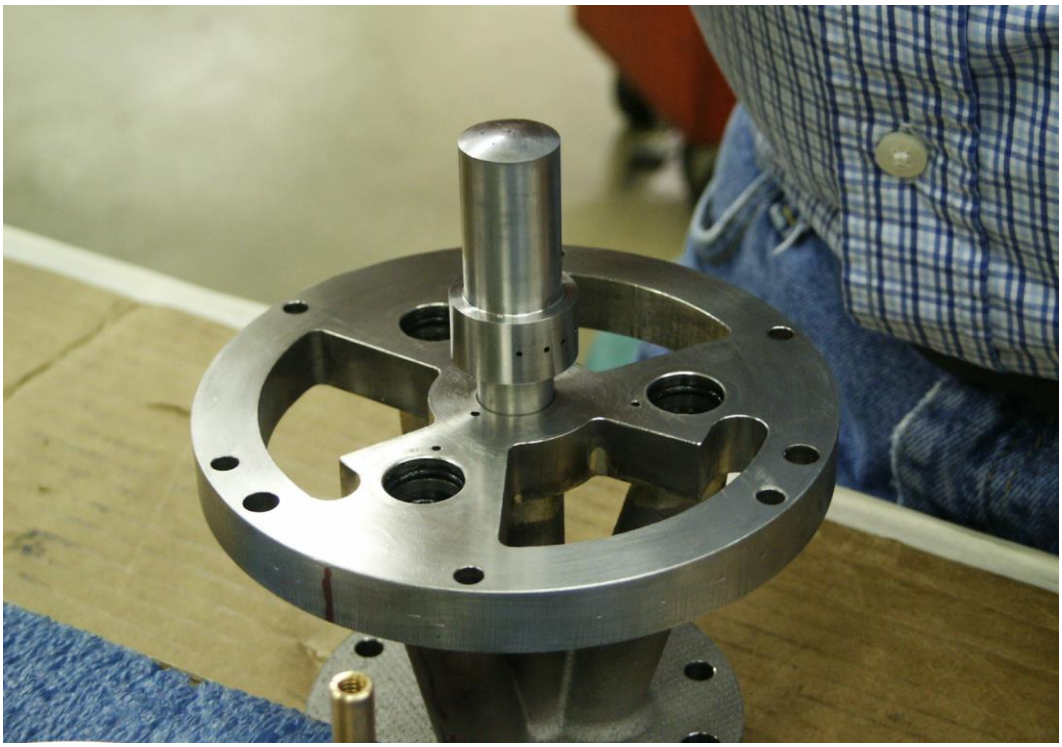

Figure A-16. Center plug installation prior to seating the insert past the O-rings.

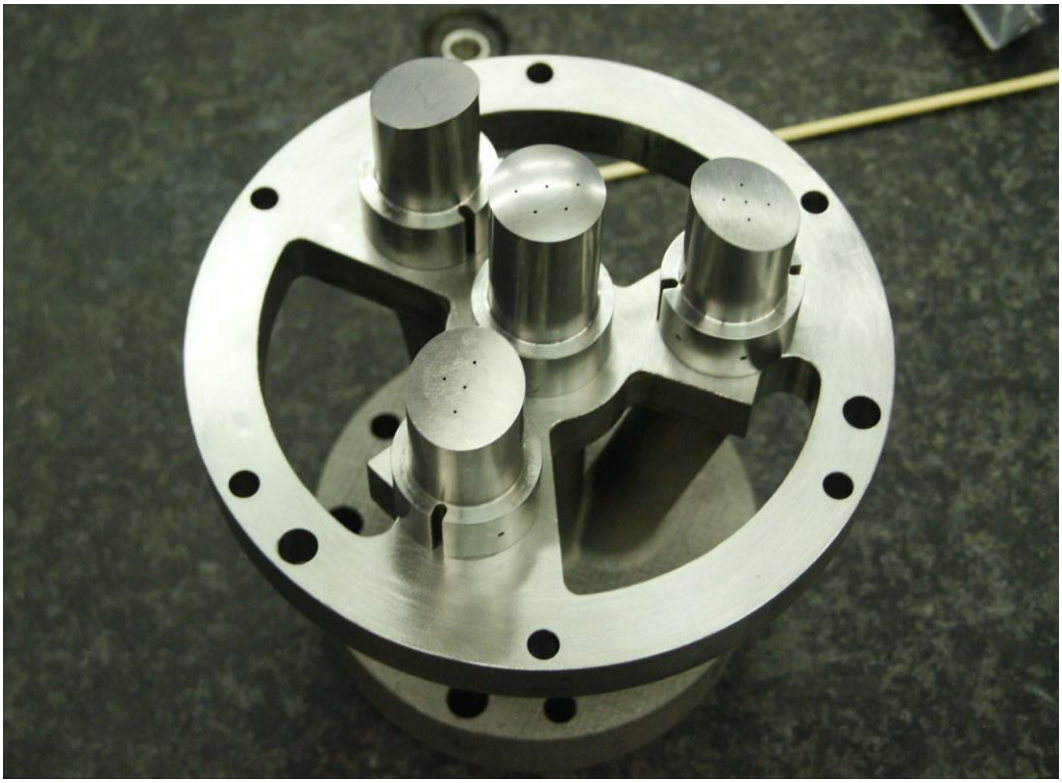

Figure A-17. All four baseline plug inserts in the proper (seated) position.

Figure A-18. Forebody guide posts used for proper alignment of manifold during assembly.

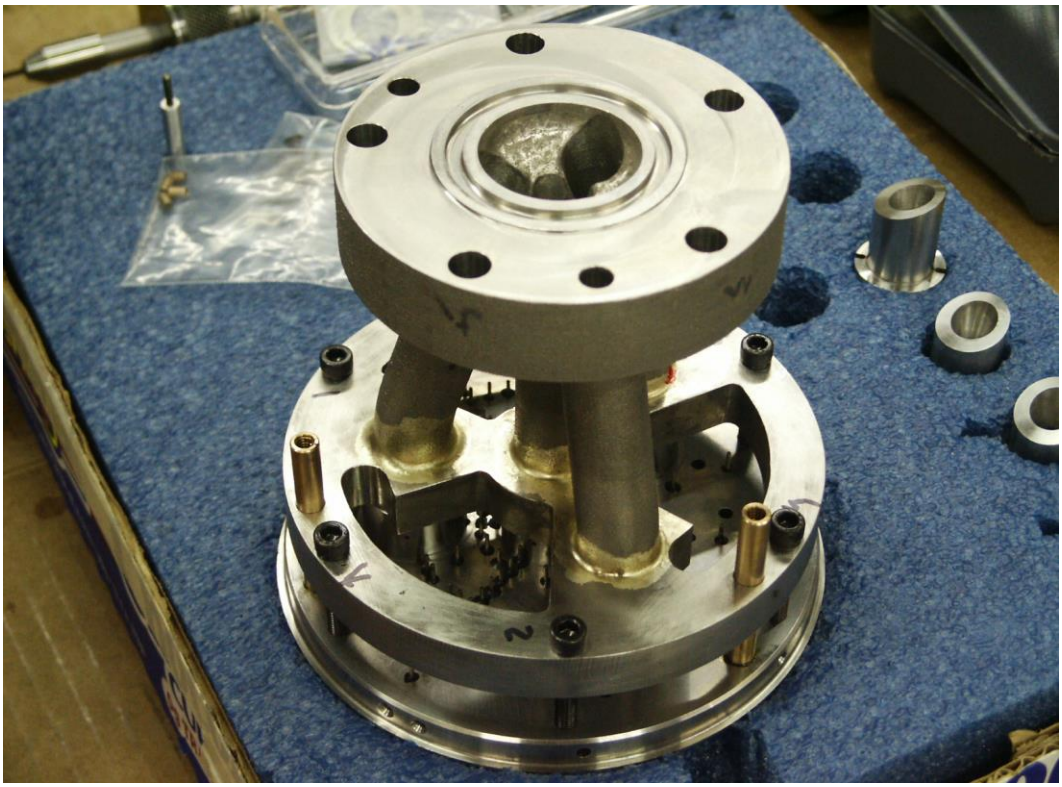

Figure A-19. Installation of bolts that hold forebody in place.

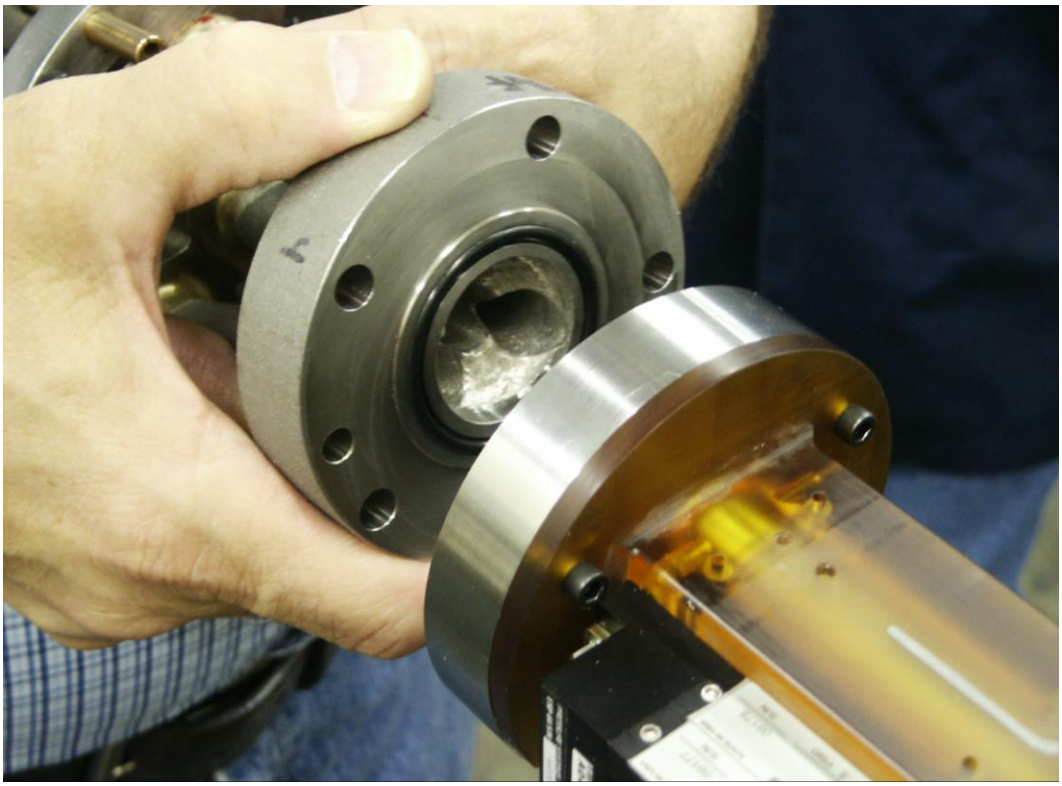

Figure A-20. O-ring between manifold and sting/plenum.

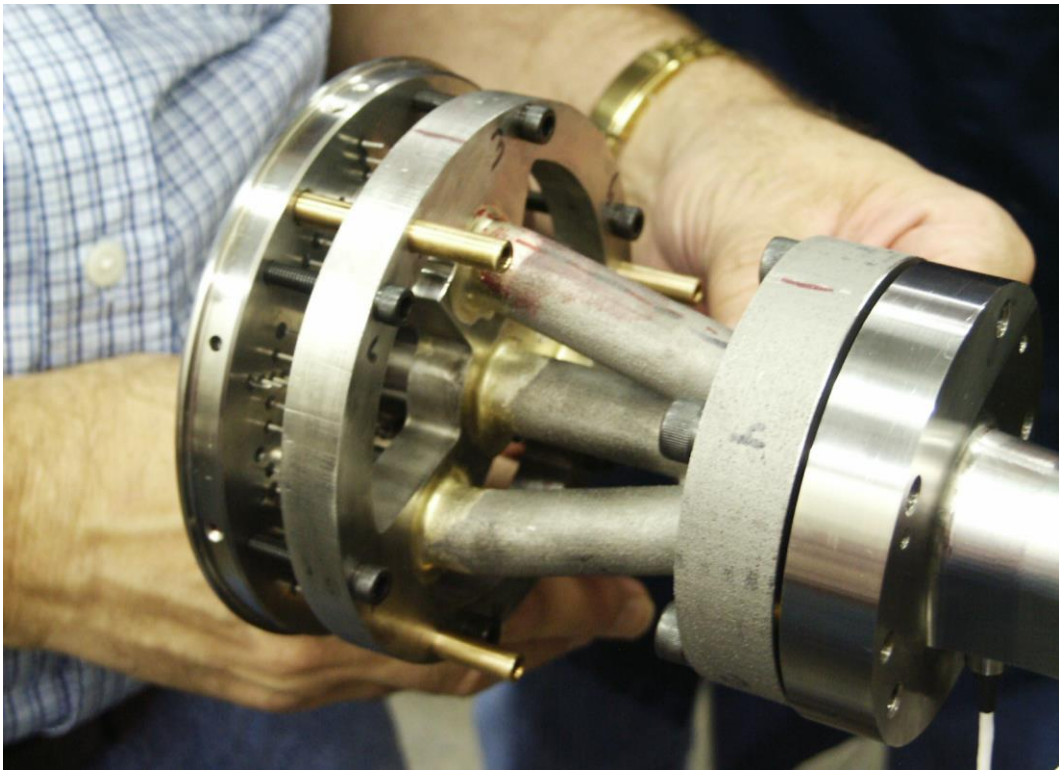

Figure A-21. Installation of bolts that hold manifold to sting.

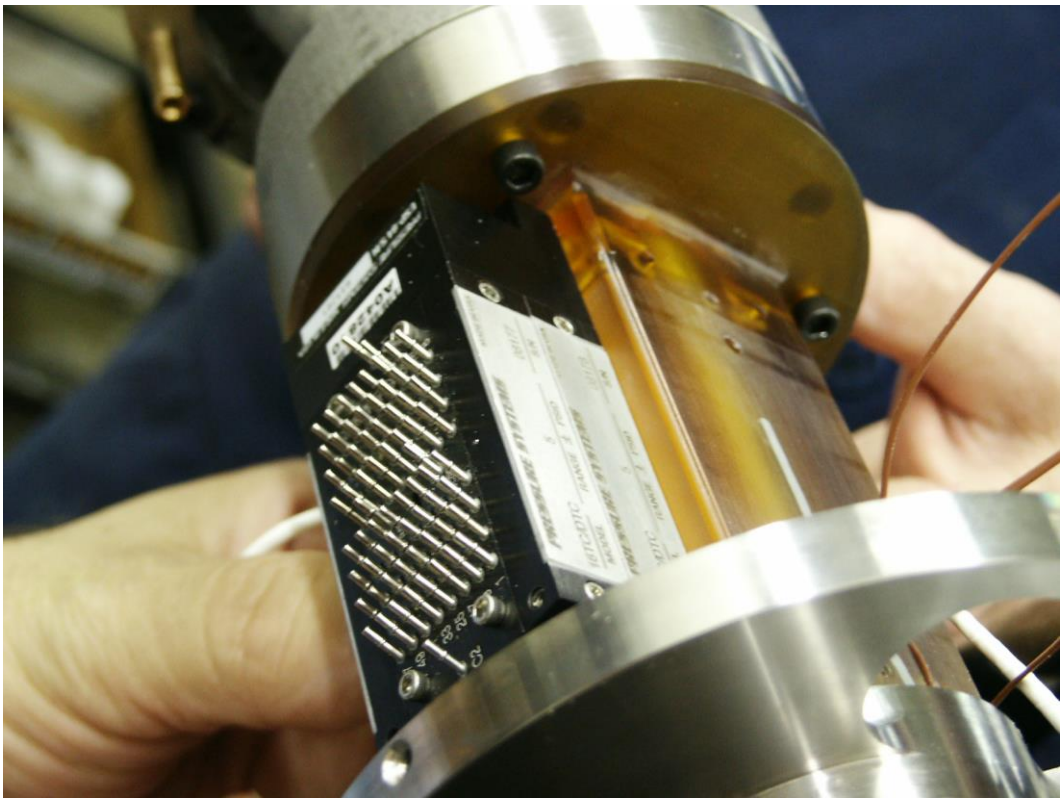

Figure A-22. Installation of saddle block with one ESP module attached.

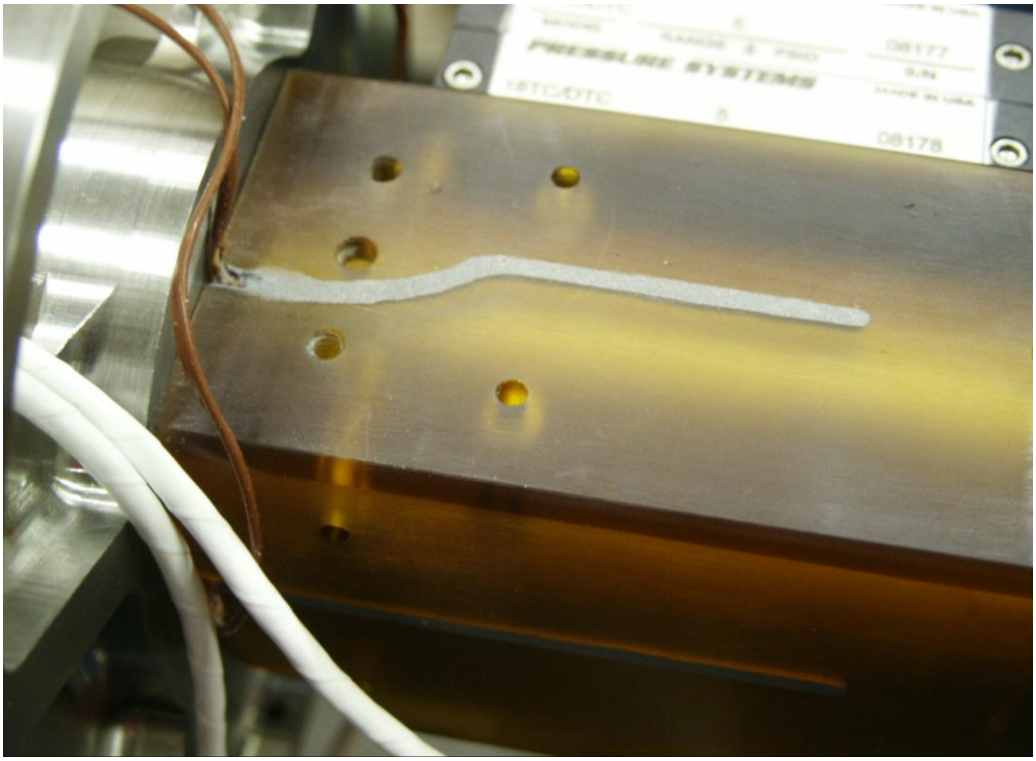

Figure A-23. Close-up of a saddle block thermocouple for monitoring ESP module temperatures.

Figure A-24. Installation of the aft cover plates.

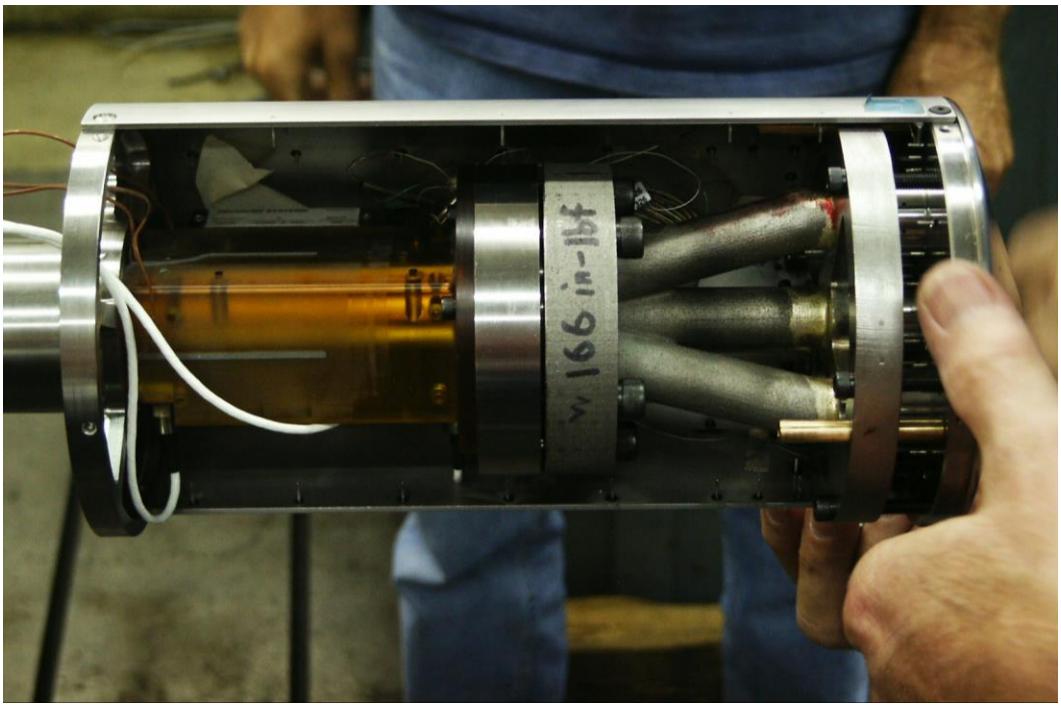

Figure A-25. View showing model internal volume before installation of pressure tubes.

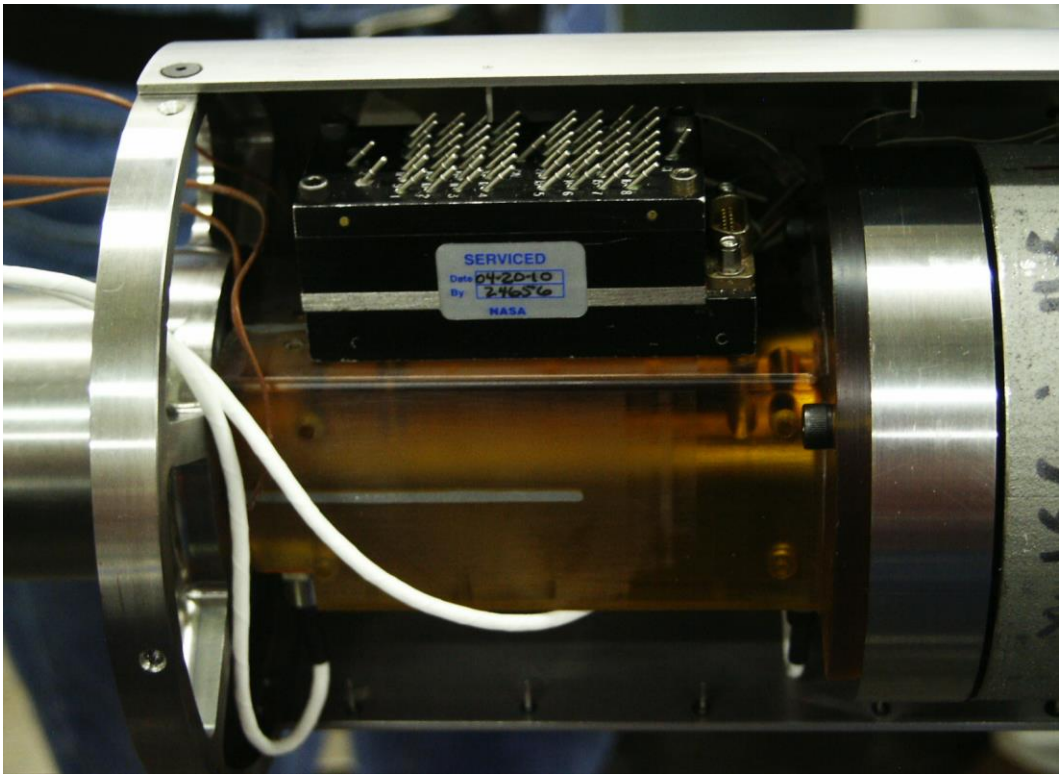

Figure A-26. Close-up showing clearance between ESP module and aft cover plate.

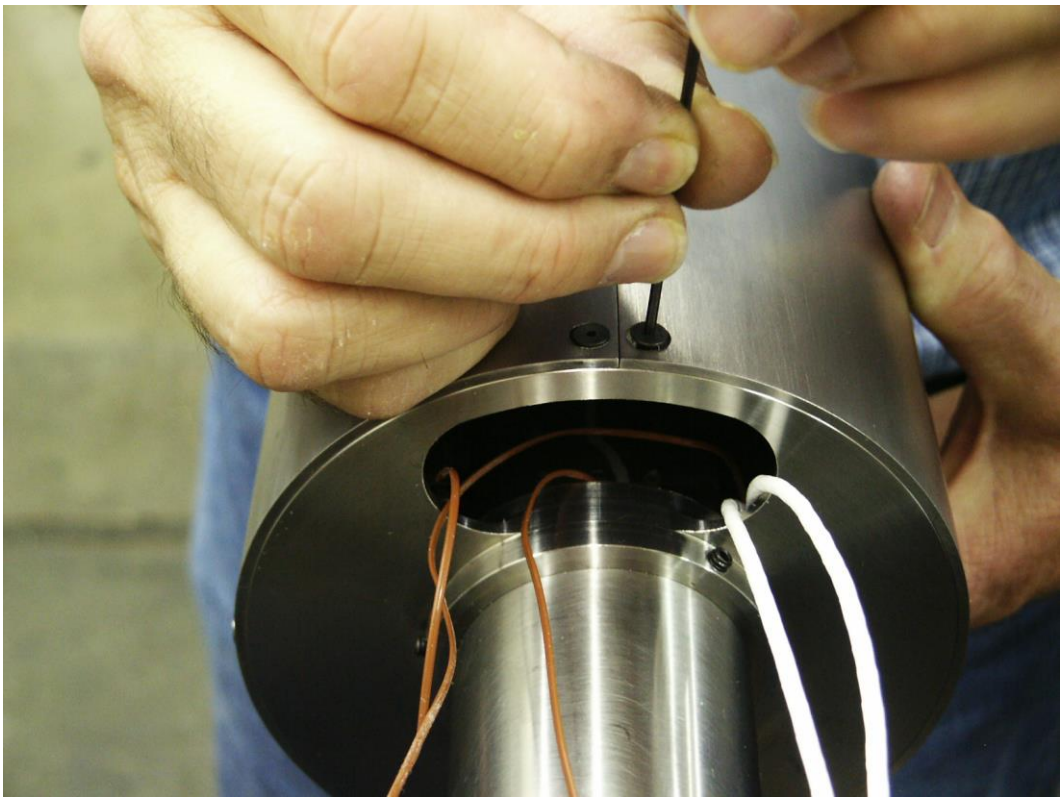

Figure A-27. Installation of second aft cover plate.

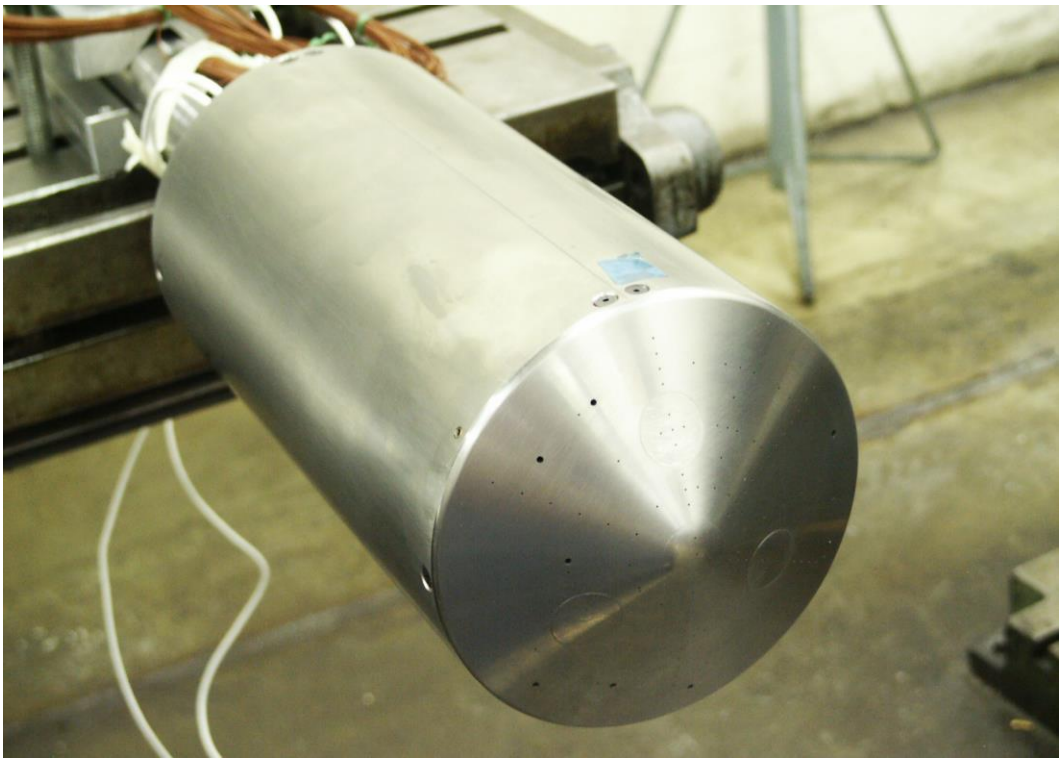

Figure A-28. Fully assembled model with baseline inserts.

Figure A-29. All four nozzle inserts in the proper (seated) position.

Figure A-30. Assembly of the forebody and manifold with nozzle inserts.

APPENDIX B
TEST DETAILS

This appendix contains details pertaining to the test, including tables of the notional run matrix, notional thrust coefficients, Test 11853 chronological run log, pitch sweep, and a statistical analysis of the resulting flow conditions.

Table B-1. Notional run matrix.

(a) Baseline: no nozzles test matrix.

# of Nozzles	Model Attitude & Location				Plenum Conditions			Mach Number / PT1 (psf)		
	Pitch	Roll	X_Strut	Y_Strut	CT	PTJ	TTJ	2.40	3.50	4.60
	{deg}	{deg}	{in}	{in}		{psia}	{R}	779.1	1442.5	2441.3
0	A1	0	40.163	0	0.0	0	0	20, 24	56	111
0	A1	60	40.163	0	0.0	0	0	21, 25	55	110
0	A1	120	40.163	0	0.0	0	0	22	54	109
0	A1	180	40.163	0	0.0	0	0	23	53	108
0	A1	0	25.163	0	0.0	0	0	33	57	104
0	A1	60	25.163	0	0.0	0	0	32	58	105
0	A1	120	25.163	0	0.0	0	0	31	59	106
0	A1	180	25.163	0	0.0	0	0	30	60	107
0	A1	0	50.163	0	0.0	0	0	26	49	112
0	A1	60	50.163	0	0.0	0	0	27	50	113
0	A1	120	50.163	0	0.0	0	0	28	51	114
0	A1	180	50.163	0	0.0	0	0	29	52	115
0	A1	0	40.163	8	0.0	0	0	41	76	
0	A1	60	40.163	8	0.0	0	0	40	77	
0	A1	120	40.163	8	0.0	0	0	39	78	
0	A1	180	40.163	8	0.0	0	0	38	79	
0	A1	0	40.163	–8	0.0	0	0	42	75	
0	A1	60	40.163	–8	0.0	0	0	43	74	
0	A1	120	40.163	–8	0.0	0	0	44	73	
0	A1	180	40.163	–8	0.0	0	0	45	70	
0	A1	0	25.163	8	0.0	0	0	34		
0	A1	60	25.163	8	0.0	0	0	35		
0	A1	120	25.163	8	0.0	0	0	36		
0	A1	180	25.163	8	0.0	0	0	37		
0	A1	0	50.163	–8	0.0	0	0	49		
0	A1	60	50.163	–8	0.0	0	0	48		
0	A1	120	50.163	–8	0.0	0	0	47		

Table B-1. Continued.

(a) Concluded

# of Nozzles	Model Attitude & Location				Plenum Conditions			Mach Number / PT1 (psf)		
	Pitch	Roll	X_Strut	Y_Strut	CT	PTJ	TTJ	2.40	3.50	4.60
	{deg}	{deg}	{in}	{in}		{psia}	{R}	779.1	1442.5	2441.3
0	A1	180	50.163	–8	0.0	0	0	46		
0	A1	0	25.163	–8	0.0	0	0		65	120
0	A1	60	25.163	–8	0.0	0	0		67	121
0	A1	120	25.163	–8	0.0	0	0		68	122
0	A1	180	25.163	–8	0.0	0	0		69	123
0	A1	0	50.163	8	0.0	0	0		83	119
0	A1	60	50.163	8	0.0	0	0		82	118
0	A1	120	50.163	8	0.0	0	0		81	117
0	A1	180	50.163	8	0.0	0	0		80	116

(b) Center nozzle-only test matrix.

# of Nozzles	Model Attitude & Location				Plenum Conditions			Mach Number / PT1 (psf)		
	Pitch	Roll	X_Strut	Y_Strut	CT	PTJ	TTJ	2.40	3.50	4.60
	{deg}	{deg}	{in}	{in}		{psia}	{R}	779.1	1442.5	2441.3
1	A1	0	40.163	0	0.0	0	0	149	162	174
1	A1	60	40.163	0	0.0	0	0			
1	A1	120	40.163	0	0.0	0	0			
1	A1	180	40.163	0	0.0	0	0	148	161	173
1	A1	0	40.163	0	0.25	table	640	145	159	171
1	A1	60	40.163	0	0.25	table	640			
1	A1	120	40.163	0	0.25	table	640			
1	A1	180	40.163	0	0.25	table	640	146	160	172
1	A1	0	40.163	0	0.5	table	640	144	157	170
1	A1	60	40.163	0	0.5	table	640			
1	A1	120	40.163	0	0.5	table	640			
1	A1	180	40.163	0	0.5	table	640	143	156	169
1	A1	0	40.163	0	1.0	table	640	140	154	167
1	A1	60	40.163	0	1.0	table	640			
1	A1	120	40.163	0	1.0	table	640			
1	A1	180	40.163	0	1.0	table	640	139	155	168
1	A1	0	40.163	0	2.0	table	640	141	153	166
1	A1	60	40.163	0	2.0	table	640			
1	A1	120	40.163	0	2.0	table	640			
1	A1	180	40.163	0	2.0	table	640	142	152	165

Table B-1. Continued.
(b) Concluded.

# of Nozzles	Model Attitude & Location				Plenum Conditions			Mach Number / PT1 (psf)		
	Pitch	Roll	X_Strut	Y_Strut	CT	PTJ	TTJ	2.40	3.50	4.60
	{deg}	{deg}	{in}	{in}		{psia}	{R}	779.1	1442.5	2441.3
1	A1	0	40.163	0	3.0	table	640	137	150	163
1	A1	60	40.163	0	3.0	table	640			
1	A1	120	40.163	0	3.0	table	640			
1	A1	180	40.163	0	3.0	table	640	138	151	164
1	A1	0	25.163	0	0.5	table	640			
1	A1	60	25.163	0	0.5	table	640			
1	A1	120	25.163	0	0.5	table	640			
1	A1	180	25.163	0	0.5	table	640			
1	A1	0	50.163	0	0.5	table	640			
1	A1	60	50.163	0	0.5	table	640			
1	A1	120	50.163	0	0.5	table	640			
1	A1	180	50.163	0	0.5	table	640			
1	A1	0	25.163	0	1.0	table	640			
1	A1	60	25.163	0	1.0	table	640			
1	A1	120	25.163	0	1.0	table	640			
1	A1	180	25.163	0	1.0	table	640			
1	A1	0	50.163	0	1.0	table	640			
1	A1	60	50.163	0	1.0	table	640			
1	A1	120	50.163	0	1.0	table	640			
1	A1	180	50.163	0	1.0	table	640			
1	A1	0	25.163	4	1.0	table	640			
1	A1	60	25.163	4	1.0	table	640			
1	A1	120	25.163	4	1.0	table	640			
1	A1	180	25.163	4	1.0	table	640			
1	A1	0	25.163	–4	1.0	table	640			
1	A1	60	25.163	–4	1.0	table	640			
1	A1	120	25.163	–4	1.0	table	640			
1	A1	180	25.163	–4	1.0	table	640			
1	A1	0	40.163	0	3.0	table	640			
1	A1	60	40.163	0	3.0	table	640			
1	A1	120	40.163	0	3.0	table	640			
1	A1	180	40.163	0	3.0	table	640			
1	A1	0	40.163	0	5.0	table	640			
1	A1	60	40.163	0	5.0	table	640			
1	A1	120	40.163	0	5.0	table	640			
1	A1	180	40.163	0	5.0	table	640			

Table B-1. Continued.
(c) Tri-nozzle test matrix.

# of Nozzles	Model Attitude & Location				Plenum Conditions			Mach Number / PT1 (psf)		
	Pitch	Roll	X_Strut	Y_Strut	CT	PTJ	TTJ	2.40	3.50	4.60
	{deg}	{deg}	{in}	{in}		{psia}	{R}	779.1	1442.5	2441.3
3	A1	0	40.163	0	0.0	0	0	180	184	258
3	A1	60	40.163	0	0.0	0	0	183	185	259
3	A1	120	40.163	0	0.0	0	0	182	186	260
3	A1	180	40.163	0	0.0	0	0	181	187	261
3	A1	0	40.163	0	0.25	table	640	221	241	257
3	A1	60	40.163	0	0.25	table	640			
3	A1	120	40.163	0	0.25	table	640			
3	A1	180	40.163	0	0.25	table	640			
3	A1	0	40.163	0	0.5	table	640	217	240,266	253
3	A1	60	40.163	0	0.5	table	640	218	239	254
3	A1	120	40.163	0	0.5	table	640	219	238	255
3	A1	180	40.163	0	0.5	table	640	220	237	256
3	A1	0	40.163	0	1.0	table	640	198	230,234,265	252
3	A1	60	40.163	0	1.0	table	640	199	233	251
3	A1	120	40.163	0	1.0	table	640	200	235	250
3	A1	180	40.163	0	1.0	table	640	201	236	249
3	A1	0	40.163	0	2.0	table	640	197	229	242,247
3	A1	60	40.163	0	2.0	table	640	196	228	243
3	A1	120	40.163	0	2.0	table	640	195	227	244
3	A1	180	40.163	0	2.0	table	640	194	226	245,248
3	A1	0	40.163	0	3.0	table	640	190	222	211,262
3	A1	60	40.163	0	3.0	table	640	191	223	212
3	A1	120	40.163	0	3.0	table	640	192	224	213
3	A1	180	40.163	0	3.0	table	640	193	225	214,263
3	A1	0	25.163	0	0.5	table	640			
3	A1	60	25.163	0	0.5	table	640			
3	A1	120	25.163	0	0.5	table	640			
3	A1	180	25.163	0	0.5	table	640			
3	A1	0	50.163	0	0.5	table	640			
3	A1	60	50.163	0	0.5	table	640			
3	A1	120	50.163	0	0.5	table	640			
3	A1	180	50.163	0	0.5	table	640			
3	A1	0	25.163	0	1.0	table	640			

Table B-1. Continued.

(c) Concluded.

# of Nozzles	Model Attitude & Location				Plenum Conditions			Mach Number / PT1 (psf)		
	Pitch	Roll	X_Strut	Y_Strut	CT	PTJ	TTJ	2.40	3.50	4.60
	{deg}	{deg}	{in}	{in}		{psia}	{R}	779.1	1442.5	2441.3
3	A1	60	25.163	0	1.0	table	640			
3	A1	120	25.163	0	1.0	table	640			
3	A1	180	25.163	0	1.0	table	640			
3	A1	0	50.163	0	1.0	table	640			
3	A1	60	50.163	0	1.0	table	640			
3	A1	120	50.163	0	1.0	table	640			
3	A1	180	50.163	0	1.0	table	640			
3	A1	0	25.163	4	1.0	table	640			
3	A1	60	25.163	4	1.0	table	640			
3	A1	120	25.163	4	1.0	table	640			
3	A1	180	25.163	4	1.0	table	640			
3	A1	0	25.163	–4	1.0	table	640			
3	A1	60	25.163	–4	1.0	table	640			
3	A1	120	25.163	–4	1.0	table	640			
3	A1	180	25.163	–4	1.0	table	640			
3	A1	0	40.163	0	3.0	table	640			
3	A1	60	40.163	0	3.0	table	640			
3	A1	120	40.163	0	3.0	table	640			
3	A1	180	40.163	0	3.0	table	640			
3	A1	0	40.163	0	5.0	table	640			
3	A1	60	40.163	0	5.0	table	640			
3	A1	120	40.163	0	5.0	table	640			
3	A1	180	40.163	0	5.0	table	640			

(d) Quad-nozzle test matrix.

# of Nozzles	Model Attitude & Location				Plenum Conditions			Mach Number / PT1 (psf)		
	Pitch	Roll	X_Strut	Y_Strut	CT	PTJ	TTJ	2.40	3.50	4.60
	{deg}	{deg}	{in}	{in}		{psia}	{R}	779.1	1442.5	2441.3
4	A1	0	40.163	0	0.0	0	0			
4	A1	60	40.163	0	0.0	0	0			
4	A1	120	40.163	0	0.0	0	0			
4	A1	180	40.163	0	0.0	0	0			
4	A1	0	40.163	0	0.25	table	640			

Table B-1. Continued

(d) Concluded.

# of Nozzles	Model Attitude & Location				Plenum Conditions			Mach Number / PT1 (psf)		
	Pitch	Roll	X_Strut	Y_Strut	CT	PTJ	TTJ	2.40	3.50	4.60
	{deg}	{deg}	{in}	{in}		{psia}	{R}	779.1	1442.5	2441.3
4	A1	60	40.163	0	0.25	table	640			
4	A1	120	40.163	0	0.25	table	640			
4	A1	180	40.163	0	0.25	table	640			
4	A1	0	40.163	0	0.5	table	640			
4	A1	60	40.163	0	0.5	table	640			
4	A1	120	40.163	0	0.5	table	640			
4	A1	180	40.163	0	0.5	table	640			
4	A1	0	40.163	0	1.0	table	640	296	305	315
4	A1	60	40.163	0	1.0	table	640	295	304	314
4	A1	120	40.163	0	1.0	table	640	294	303	313
4	A1	180	40.163	0	1.0	table	640	293	302	312
4	A1	0	40.163	0	2.0	table	640	288	298	307
4	A1	60	40.163	0	2.0	table	640	289	299	309
4	A1	120	40.163	0	2.0	table	640	290	300	310
4	A1	180	40.163	0	2.0	table	640	291	301	311
4	A1	0	40.163	0	3.0	table	640			
4	A1	60	40.163	0	3.0	table	640			
4	A1	120	40.163	0	3.0	table	640			
4	A1	180	40.163	0	3.0	table	640			

(e) Baseline: repeat at the end of the test.

# of Nozzles	Model Attitude & Location				Plenum Conditions			Mach Number / PT1 (psf)		
	Pitch	Roll	X_Strut	Y_Strut	CT	PTJ	TTJ	2.40	3.50	4.60
	{deg}	{deg}	{in}	{in}		{psia}	{R}	779.1	1442.5	2441.3
0	A1	0	40.163	0	0.0	0	0	271	279	280
0	A1	60	40.163	0	0.0	0	0	272	278	281
0	A1	120	40.163	0	0.0	0	0	273	277	282
0	A1	180	40.163	0	0.0	0	0	274	276	283
0	A1	0	25.163	–8	0.0	0	0			
0	A1	60	25.163	–8	0.0	0	0			
0	A1	120	25.163	–8	0.0	0	0			
0	A1	180	25.163	–8	0.0	0	0			
0	A1	0	50.163	8	0.0	0	0			
0	A1	60	50.163	8	0.0	0	0			
0	A1	120	50.163	8	0.0	0	0			
0	A1	180	50.163	8	0.0	0	0			

Table B-1. Continued.

(f) Tri-nozzle repeat at the end of the test.

# of Nozzles	Model Attitude & Location				Plenum Conditions			Mach Number / PT1 (psf)		
	Pitch	Roll	X_Strut	Y_Strut	CT	PTJ	TTJ	2.40	3.50	4.60
	{deg}	{deg}	{in}	{in}		{psia}	{R}	779.1	1442.5	2441.3
3	A1	0	40.163	0	0.5	table	640			
3	A1	60	40.163	0	0.5	table	640			
3	A1	120	40.163	0	0.5	table	640			
3	A1	180	40.163	0	0.5	table	640			
3	A1	0	40.163	0	1.0	table	640			
3	A1	60	40.163	0	1.0	table	640			
3	A1	120	40.163	0	1.0	table	640			
3	A1	180	40.163	0	1.0	table	640			
3	A1	0	40.163	0	2.0	table	640			
3	A1	60	40.163	0	2.0	table	640			
3	A1	120	40.163	0	2.0	table	640			
3	A1	180	40.163	0	2.0	table	640			

Table B-2. Notational trust coefficients.

(a) Center nozzle.

MACH	2.4	3.5	4.6
CT	PTJ, psia (TTJ = 180°F)		
0.25	96.97	70.48	74.75
0.5	193.94	140.95	149.50
1	387.89	281.90	299.00
2	775.77	563.80	598.00
3	1163.66	845.70	897.01
4	1551.55	1127.61	1196.01
5	1939.44	1409.51	1495.01
6	2327.32	1691.41	1794.01
7	2715.21	1973.31	2093.01
8	3103.10	2255.21	2392.01
9	3490.99	2537.11	2691.02
10	3878.87	2819.01	2990.02

Table B-2. Concluded.

(b) Tri-nozzle.

MACH	2.4	3.5	4.6
CT	PTJ, psia (TTJ = 180°F)		
0.25	32.32	23.49	24.92
0.5	64.65	46.98	49.83
1	129.30	93.97	99.67
2	258.59	187.93	199.33
3	387.89	281.90	299.00
4	517.18	375.87	398.67
5	646.48	469.84	498.34
6	775.77	563.80	598.00
7	905.07	657.77	697.67
8	1034.37	751.74	797.34
9	1163.66	845.70	897.01
10	1292.96	939.67	996.67

(c) Quad-nozzle.

MACH	2.4	3.5	4.6
CT	PTJ, psia (TTJ = 180°F)		
0.25	24.24	17.62	18.69
0.5	48.49	35.24	37.38
1	96.97	70.48	74.75
2	193.94	140.95	149.50
3	290.92	211.43	224.25
4	387.89	281.90	299.00
5	484.86	352.38	373.75
6	581.83	422.85	448.50
7	678.80	493.33	523.25
8	775.77	563.80	598.00
9	872.75	634.28	672.75
10	969.72	704.75	747.50

Table B-3. Chronological run log.

		RUN INFORMATION					MODEL ATTITUDE & LOCATION				RUN-AVERAGED FLOW CONDITIONS									NOZZLE EXIT CONDITIONS			
DATE	TIME	RUN	POINT		Key	#	PITCH	ROLL	X_STRUT	Y_STRUT	PTINF	TTINF	MACH	REINF	PINF	TINF	RHOINF	QINF	DEWPT	PTJ	TTJ	WJ	CT
2010			START	END		NOZ	{deg}	{deg}	{in}	{in}	{psf}	{R}		{1/ft}	{psf}	{R}	{slug/ft^3}	{psf}	{deg F}	{psia}	{R}	{lbm/sec}	
7/13	13:44	9	467	467	4	0	0.006	0.03	5.01	0.00	2115.71	539.47	0.0	0.00E+00	2115.7	539.5	2.28E–03	0.00	70.16	0.00	0.00	0.000	0.000
7/13	15:11	10	468	468	2	0	–0.005	0.01	25.72	0.00	2115.07	539.62	0.0	0.00E+00	2115.1	539.6	2.28E–03	0.00	70.16	0.00	0.00	0.000	0.000
7/13	17:19	10	469	477	1	0	B4–A1	0.01	40.16	0.00	778.31	595.24	2.4	9.98E+05	53.2	276.6	1.12E–04	214.65	–18.61	0.00	0.00	0.000	0.000
7/13	17:34	11	478	486	1	0	B4–A1	59.98	40.16	0.00	778.00	594.68	2.4	9.99E+05	53.2	276.3	1.12E–04	214.56	–13.73	0.00	0.00	0.000	0.000
7/13	17:43	11	487	488	3	0	–0.079	0.01	40.16	0.00	196.12	579.73	0.0	0.00E+00	196.1	579.7	2.90E–05	0.00	–13.59	0.00	0.00	0.000	0.000
7/13	17:47	11	489	489	3	0	–0.076	0.01	40.16	0.00	2108.16	610.54	0.0	0.00E+00	2108.2	610.5	2.01E–03	0.00	–29.68	0.00	0.00	0.000	0.000
7/14	7:44	12	490	490	2	0	–0.079	0.01	40.16	0.00	2117.23	549.43	0.0	0.00E+00	2117.2	549.4	2.24E–03	0.00	70.33	0.00	0.00	0.000	0.000
7/14	7:59	12	491	492	2	0	–0.072	0.01	40.16	0.00	380.37	522.86	0.0	0.00E+00	380.4	522.9	4.24E–04	0.00	–14.35	0.00	0.00	0.000	0.000
7/14	9:39	13	493	504	1	0	B4–A1	0.03	25.16	0.03	777.56	594.72	2.4	9.99E+05	53.2	276.4	1.12E–04	214.44	–23.89	16.26	580.89	0.000	0.000
7/14	9:49	14	505	516	1	0	B4–A1	59.71	25.16	–0.03	777.37	594.62	2.4	9.99E+05	53.2	276.3	1.12E–04	214.39	–24.07	16.29	580.78	0.000	0.000
7/14	9:52	15	517	517	5	0	B4–A1	119.90	25.16	0.00	776.95	594.67	2.4	9.98E+05	53.1	276.3	1.12E–04	214.27	–24.09	0.00	0.00	0.000	0.000
7/14	10:05	16	518	527	1	0	B4–A1	0.05	25.16	0.00	777.90	594.75	2.4	9.99E+05	53.2	276.4	1.12E–04	214.53	–24.18	16.28	580.86	0.000	0.000
7/14	10:11	17	528	536	1	0	B4–A1	59.53	25.16	0.00	777.38	594.45	2.4	9.99E+05	53.2	276.2	1.12E–04	214.39	–24.24	16.29	580.84	0.000	0.000
7/14	10:16	18	537	545	1	0	B4–A1	120.30	25.16	0.00	777.50	594.80	2.4	9.99E+05	53.2	276.4	1.12E–04	214.42	–24.29	16.32	580.90	0.000	0.000
7/14	10:21	19	546	554	1	0	B4–A1	179.92	25.16	0.00	777.48	594.73	2.4	9.99E+05	53.2	276.4	1.12E–04	214.42	–24.36	16.35	580.97	0.000	0.000
7/14	10:50	20	557	565	1	0	B4–A1	0.01	39.93	0.00	777.60	594.84	2.4	9.99E+05	53.2	276.4	1.12E–04	214.45	–22.45	16.28	580.53	0.000	0.000
7/14	11:28	21	566	574	1	0	B4–A1	59.53	39.93	0.00	777.50	594.33	2.4	1.00E+06	53.2	276.2	1.12E–04	214.42	–24.53	16.43	582.97	0.000	0.000
7/14	11:36	22	575	583	1	0	B4–A1	120.41	39.93	0.00	777.43	594.76	2.4	9.99E+05	53.2	276.4	1.12E–04	214.41	–24.45	16.43	582.62	0.000	0.000
7/14	11:42	23	584	592	1	0	B4–A1	179.99	39.93	0.00	777.70	594.74	2.4	9.99E+05	53.2	276.4	1.12E–04	214.48	–24.46	16.43	582.40	0.000	0.000
7/14	11:47	24	593	601	1	0	B4–A1	0.01	39.93	0.00	777.60	594.52	2.4	9.99E+05	53.2	276.3	1.12E–04	214.45	–24.53	16.38	582.08	0.000	0.000
7/14	11:53	25	602	610	1	0	B4–A1	59.67	39.93	0.00	777.46	594.79	2.4	9.99E+05	53.2	276.4	1.12E–04	214.41	–24.62	16.38	581.99	0.000	0.000
7/14	12:03	26	611	619	1	0	B4–A1	0.03	50.17	0.00	777.38	594.50	2.4	9.99E+05	53.2	276.3	1.12E–04	214.39	–24.70	16.39	582.28	0.000	0.000
7/14	12:08	27	620	628	1	0	B4–A1	59.67	50.17	0.00	777.50	594.75	2.4	9.99E+05	53.2	276.4	1.12E–04	214.42	–24.73	16.39	582.26	0.000	0.000
7/14	12:13	28	629	637	1	0	B4–A1	120.47	50.17	0.00	777.48	594.79	2.4	9.99E+05	53.2	276.4	1.12E–04	214.42	–24.72	16.41	582.25	0.000	0.000
7/14	12:19	29	638	646	1	0	B4–A1	179.91	50.17	0.00	776.98	594.37	2.4	9.99E+05	53.1	276.2	1.12E–04	214.28	–24.71	16.42	582.19	0.000	0.000
7/14	12:27	30	647	655	1	0	B4–A1	179.91	25.18	0.00	777.46	594.27	2.4	1.00E+06	53.2	276.1	1.12E–04	214.41	–24.83	16.40	581.99	0.000	0.000
7/14	12:32	31	656	664	1	0	B4–A1	120.33	25.18	0.00	777.74	595.02	2.4	9.98E+05	53.2	276.5	1.12E–04	214.49	–24.82	16.39	581.77	0.000	0.000
7/14	12:37	32	665	673	1	0	B4–A1	59.57	25.18	0.00	777.58	594.37	2.4	1.00E+06	53.2	276.2	1.12E–04	214.44	–24.77	16.37	581.80	0.000	0.000
7/14	12:44	33	674	682	1	0	B4–A1	0.05	25.18	0.00	777.46	594.75	2.4	9.99E+05	53.2	276.4	1.12E–04	214.41	–24.71	16.36	581.86	0.000	0.000
7/14	12:58	34	683	691	1	0	B4–A1	0.05	25.18	7.99	777.72	594.78	2.4	9.99E+05	53.2	276.4	1.12E–04	214.48	–24.71	16.38	582.35	0.000	0.000
7/14	13:04	35	692	700	1	0	B4–A1	59.67	25.18	7.99	777.46	594.58	2.4	9.99E+05	53.2	276.3	1.12E–04	214.41	–24.71	16.39	582.11	0.000	0.000

Table B-3. Continued.

		RUN INFORMATION					MODEL ATTITUDE & LOCATION				RUN-AVERAGED FLOW CONDITIONS									NOZZLE EXIT CONDITIONS			
DATE	TIME	RUN	POINT		Key	#	PITCH	ROLL	X_STRUT	Y_STRUT	PTINF	TTINF	MACH	REINF	PINF	TINF	RHOINF	QINF	DEWPT	PTJ	TTJ	WJ	CT
2010			START	END		NOZ	{deg}	{deg}	{in}	{in}	{psf}	{R}		{1/ft}	{psf}	{R}	{slug/ft^3}	{psf}	{deg F}	{psia}	{R}	{lbm/sec}	
7/14	13:09	36	701	709	1	0	B4–A1	120.31	25.18	7.99	777.46	594.52	2.4	9.99E+05	53.2	276.3	1.12E–04	214.41	–24.71	16.40	581.96	0.000	0.000
7/14	13:14	37	710	718	1	0	B4–A1	179.95	25.18	7.99	777.55	594.67	2.4	9.99E+05	53.2	276.3	1.12E–04	214.44	–24.71	16.40	581.80	0.000	0.000
7/14	13:22	38	719	727	1	0	B4–A1	179.95	40.19	7.99	777.72	594.74	2.4	9.99E+05	53.2	276.4	1.12E–04	214.48	–24.62	16.40	581.86	0.000	0.000
7/14	13:27	39	728	736	1	0	B4–A1	120.31	40.19	7.99	777.53	594.51	2.4	9.99E+05	53.2	276.3	1.12E–04	214.43	–24.54	16.40	581.86	0.000	0.000
7/14	13:32	40	737	745	1	0	B4–A1	59.57	40.19	7.99	777.36	594.53	2.4	9.99E+05	53.2	276.3	1.12E–04	214.39	–24.47	16.38	581.83	0.000	0.000
7/14	13:38	41	746	754	1	0	B4–A1	–0.05	40.19	7.99	777.65	594.63	2.4	9.99E+05	53.2	276.3	1.12E–04	214.46	–24.42	16.36	581.76	0.000	0.000
7/14	13:51	42	755	763	1	0	B4–A1	–0.05	40.19	–8.00	777.67	595.13	2.4	9.98E+05	53.2	276.5	1.12E–04	214.47	–23.39	16.40	582.34	0.000	0.000
7/14	14:05	43	764	772	1	0	B4–A1	59.51	40.19	–8.00	777.02	595.71	2.4	9.96E+05	53.1	276.8	1.12E–04	214.29	–18.12	16.43	582.91	0.000	0.000
7/14	14:10	44	773	781	1	0	B4–A1	120.31	40.19	–8.00	777.41	594.30	2.4	1.00E+06	53.2	276.2	1.12E–04	214.40	–18.29	16.43	582.41	0.000	0.000
7/14	14:15	45	782	790	1	0	B4–A1	179.95	40.19	–8.00	777.55	594.79	2.4	9.99E+05	53.2	276.4	1.12E–04	214.44	–18.97	16.44	582.30	0.000	0.000
7/14	14:24	46	791	799	1	0	B4–A1	179.95	50.16	–8.00	777.41	594.50	2.4	9.99E+05	53.2	276.3	1.12E–04	214.40	–25.57	16.42	582.08	0.000	0.000
7/14	14:29	47	800	808	1	0	B4–A1	120.33	50.16	–8.00	777.60	594.95	2.4	9.98E+05	53.2	276.5	1.12E–04	214.45	–25.30	16.42	582.00	0.000	0.000
7/14	14:34	48	809	817	1	0	B4–A1	59.57	50.16	–8.00	777.55	594.39	2.4	1.00E+06	53.2	276.2	1.12E–04	214.44	–25.45	16.40	582.16	0.000	0.000
7/14	14:39	49	818	826	1	0	B4–A1	–0.04	50.16	–8.00	777.48	595.01	2.4	9.98E+05	53.2	276.5	1.12E–04	214.42	–25.19	16.40	582.15	0.000	0.000
7/14	15:13	49	827	835	1	0	B4–A1	–0.04	50.16	–8.00	777.48	595.01	2.4	9.98E+05	53.2	276.5	1.12E–04	214.42	–25.19	16.40	582.15	0.000	0.000
7/14	15:19	50	836	844	1	0	B4–A1	59.61	50.16	0.00	1386.36	594.67	3.5	9.99E+05	18.2	172.4	6.14E–05	155.86	–16.04	16.34	580.96	0.000	0.000
7/14	15:33	51	847	855	1	0	B4–A1	120.35	50.16	0.00	1386.55	595.15	3.5	9.98E+05	18.2	172.5	6.14E–05	155.88	–13.60	16.31	579.80	0.000	0.000
7/14	15:38	52	856	864	1	0	B4–A1	179.99	50.16	0.00	1387.18	595.56	3.5	9.98E+05	18.2	172.6	6.14E–05	155.95	–12.40	16.31	579.53	0.000	0.000
7/14	15:50	53	865	873	1	0	B4–A1	179.99	40.17	0.00	1386.19	594.72	3.5	9.99E+05	18.2	172.4	6.14E–05	155.84	–20.34	16.26	578.99	0.000	0.000
7/14	16:20	54	874	882	1	0	B4–A1	120.47	40.17	0.00	1386.60	594.33	3.5	1.00E+06	18.2	172.3	6.15E–05	155.89	–22.28	16.20	578.45	0.000	0.000
7/14	16:25	55	883	891	1	0	B4–A1	59.57	40.17	0.00	1386.48	594.94	3.5	9.99E+05	18.2	172.4	6.14E–05	155.88	–22.02	16.17	578.16	0.000	0.000
7/14	16:30	56	892	900	1	0	B4–A1	–0.07	40.17	0.00	1386.65	595.21	3.5	9.98E+05	18.2	172.5	6.14E–05	155.90	–21.97	16.14	577.95	0.000	0.000
7/14	16:39	57	901	909	1	0	B4–A1	–0.07	25.16	0.00	1385.88	594.07	3.5	1.00E+06	18.2	172.2	6.15E–05	155.81	–19.64	16.12	577.70	0.000	0.000
7/14	16:44	58	910	918	1	0	B4–A1	59.63	25.16	0.00	1386.58	594.44	3.5	1.00E+06	18.2	172.3	6.15E–05	155.89	–19.46	16.11	577.40	0.000	0.000
7/14	16:49	59	919	927	1	0	B4–A1	120.47	25.16	0.00	1386.65	594.26	3.5	1.00E+06	18.2	172.2	6.15E–05	155.90	–19.79	16.14	577.35	0.000	0.000
7/14	16:55	60	928	936	1	0	B4–A1	179.95	25.16	0.00	1386.24	594.75	3.5	9.99E+05	18.2	172.4	6.14E–05	155.85	–19.45	16.16	577.23	0.000	0.000
7/14	17:02	61	937	939	3	0	0.031	179.95	25.16	0.00	193.10	585.20	0.0	0.00E+00	193.1	585.2	1.92E–04	0.00	–14.80	0.00	0.00	0.000	0.000
7/14	17:06	61	940	940	3	0	0.026	179.95	25.16	0.00	2117.44	614.60	0.0	0.00E+00	2117.4	614.6	2.01E–04	0.00	–14.72	0.00	0.00	0.000	0.000
7/15	7:13	64	941	941	2	0	0.014	179.95	25.16	0.00	2125.22	560.76	0.0	0.00E+00	2125.2	560.8	2.21E–03	0.00	70.17	0.00	0.00	0.000	0.000
7/15	7:52	64	942	943	2	0	0.016	179.95	25.16	0.00	365.58	538.63	0.0	0.00E+00	365.6	538.6	3.95E–04	0.00	38.48	0.00	0.00	0.000	0.000
7/15	8:55	65	944	952	1	0	B4–A1	–0.01	25.16	–8.00	1387.13	593.83	3.5	1.00E+06	18.2	172.1	6.16E–05	155.95	–24.87	–3.13	572.24	0.000	0.000
7/15	8:59	66	953	959	5	0	B4–A1	60.06	25.16	–8.00	1386.93	595.23	3.5	9.98E+05	18.2	172.5	6.13E–05	155.93	–17.72	0.00	0.00	0.000	0.000

Table B-3. Continued.

		RUN INFORMATION					MODEL ATTITUDE & LOCATION				RUN-AVERAGED FLOW CONDITIONS									NOZZLE EXIT CONDITIONS			
DATE	TIME	RUN	POINT		Key	#	PITCH	ROLL	X_STRUT	Y_STRUT	PTINF	TTINF	MACH	REINF	PINF	TINF	RHOINF	QINF	DEWPT	PTJ	TTJ	WJ	CT
2010			START	END		NOZ	{deg}	{deg}	{in}	{in}	{psf}	{R}		{1/ft}	{psf}	{R}	{slug/ft^3}	{psf}	{deg F}	{psia}	{R}	{lbm/sec}	
7/15	11:19	67	960	968	1	0	B4–A1	59.65	25.16	–8.00	1386.14	593.81	3.5	1.00E+06	18.2	172.1	6.15E–05	155.84	–24.22	–2.76	577.14	0.000	0.000
7/15	11:25	68	969	977	1	0	B4–A1	120.37	25.16	–8.00	1387.34	595.35	3.5	9.98E+05	18.2	172.6	6.14E–05	155.97	–23.69	–2.74	576.94	0.000	0.000
7/15	11:37	69	978	986	1	0	B4–A1	179.95	25.16	–8.00	1387.68	595.31	3.5	9.99E+05	18.2	172.6	6.14E–05	156.01	–23.85	–2.76	576.50	0.000	0.000
7/15	11:53	70	987	995	1	0	B4–A1	179.95	40.16	–8.00	1385.21	594.81	3.5	9.98E+05	18.2	172.4	6.14E–05	155.73	–22.63	–2.77	575.98	0.000	0.000
7/15	12:31	71	996	997	3	0	0.024	179.95	40.16	–8.00	184.57	584.11	0.0	0.00E+00	184.6	584.1	1.84E–04	0.00	–0.36	0.00	0.00	0.000	0.000
7/15	12:35	71	998	998	3	0	0.02	179.95	40.16	–8.00	2124.14	615.72	0.0	0.00E+00	2124.1	615.7	2.01E–03	0.00	–19.62	0.00	0.00	0.000	0.000
7/15	14:40	72	999	1000	2	0	0.236	179.95	41.22	–8.00	399.49	536.57	0.0	0.00E+00	399.5	536.6	4.34E–04	0.00	72.88	0.00	0.00	0.000	0.000
7/15	15:07	73	1001	1009	1	0	B4–A1	120.33	40.18	–8.00	1386.48	595.01	3.5	9.99E+05	18.2	172.5	6.14E–05	155.88	52.08	–3.13	571.26	0.000	0.000
7/15	15:12	74	1010	1018	1	0	B4–A1	59.61	40.18	–8.00	1386.19	594.63	3.5	9.99E+05	18.2	172.4	6.14E–05	155.84	–20.67	–3.11	571.93	0.000	0.000
7/15	15:17	75	1019	1027	1	0	B4–A1	0.03	40.18	–8.00	1386.29	594.87	3.5	9.99E+05	18.2	172.4	6.14E–05	155.86	–20.66	–3.08	572.50	0.000	0.000
7/15	15:27	76	1028	1036	1	0	B4–A1	0.03	40.18	7.99	1386.43	594.64	3.5	1.00E+06	18.2	172.4	6.14E–05	155.87	–23.11	–3.00	573.61	0.000	0.000
7/15	15:33	77	1037	1045	1	0	B4–A1	59.57	40.16	7.99	1386.67	594.55	3.5	1.00E+06	18.2	172.3	6.15E–05	155.90	–22.94	–2.97	573.96	0.000	0.000
7/15	15:38	78	1046	1054	1	0	B4–A1	120.33	40.16	7.95	1387.20	595.03	3.5	9.99E+05	18.2	172.5	6.14E–05	155.96	–23.00	–2.91	574.21	0.000	0.000
7/15	15:45	79	1055	1063	1	0	B4–A1	–179.99	40.16	7.95	1387.03	594.69	3.5	1.00E+06	18.2	172.4	6.15E–05	155.94	–22.39	–2.88	574.51	0.000	0.000
7/15	16:09	80	1064	1072	1	0	B4–A1	–179.99	50.15	7.95	1386.98	595.13	3.5	9.99E+05	18.2	172.5	6.14E–05	155.93	–20.60	–2.85	575.16	0.000	0.000
7/15	16:15	81	1073	1081	1	0	B4–A1	120.33	50.15	7.95	1385.47	594.15	3.5	1.00E+06	18.2	172.2	6.14E–05	155.76	–20.93	–2.82	575.56	0.000	0.000
7/15	16:20	82	1082	1090	1	0	B4–A1	59.59	50.15	7.95	1386.00	594.62	3.5	9.99E+05	18.2	172.4	6.14E–05	155.82	–20.88	–2.86	575.54	0.000	0.000
7/15	16:25	83	1091	1099	1	0	B4–A1	0.01	50.15	7.95	1386.05	594.78	3.5	9.99E+05	18.2	172.4	6.14E–05	155.83	–20.85	–2.87	575.62	0.000	0.000
7/15	16:32	84	1100	1101	3	0	–0.091	0.01	50.15	0.00	192.13	583.61	0.0	0.00E+00	192.1	583.6	1.92E+01	0.00	–21.95	0.00	0.00	0.000	0.000
7/16	6:52	85	1102	1102	2	0	–0.1	0.01	25.17	0.00	2124.57	560.47	0.0	0.00E+00	2124.6	560.5	2.21E–03	0.00	69.44	0.00	0.00	0.000	0.000
7/16	7:54	85	1103	1104	2	0	–0.1	0.01	25.17	0.00	318.06	554.58	0.0	0.00E+00	318.1	554.6	3.34E–04	0.00	–16.36	0.00	0.00	0.000	0.000
7/16	9:40	86	1105	1113	1	0	B4–A1	0.01	25.17	0.00	2600.06	610.78	4.6	1.06E+06	7.9	116.7	3.96E–05	117.56	–13.33	–2.77	578.16	0.000	0.000
7/16	9:49	87	1114	1122	1	0	B4–A1	59.63	25.17	0.00	2599.68	610.27	4.6	1.06E+06	7.9	116.6	3.96E–05	117.54	–13.33	–2.70	579.06	0.000	0.000
7/16	9:55	88	1123	1131	1	0	B4–A1	120.31	25.17	0.00	2599.73	610.22	4.6	1.06E+06	7.9	116.6	3.96E–05	117.55	–17.12	–2.63	579.56	0.000	0.000
7/16	10:00	89	1132	1140	1	0	B4–A1	179.91	25.17	0.00	2599.94	610.12	4.6	1.06E+06	7.9	116.6	3.96E–05	117.55	–19.18	–2.57	580.05	0.000	0.000
7/16	10:06	90	1141	1149	1	0	B4–A1	0.01	40.15	0.00	2599.51	610.16	4.6	1.06E+06	7.9	116.6	3.96E–05	117.54	–19.11	–2.62	580.52	0.000	0.000
7/16	10:12	91	1150	1158	1	0	B4–A1	59.59	40.18	0.00	2599.82	609.99	4.6	1.07E+06	7.9	116.6	3.97E–05	117.55	–19.12	–2.58	580.90	0.000	0.000
7/16	10:17	92	1159	1167	1	0	B4–A1	120.33	40.18	0.00	2599.56	610.06	4.6	1.06E+06	7.9	116.6	3.96E–05	117.54	–19.16	–2.54	581.18	0.000	0.000
7/16	10:22	93	1168	1176	1	0	B4–A1	179.91	40.18	0.00	2599.92	609.97	4.6	1.07E+06	7.9	116.6	3.97E–05	117.55	–19.22	–2.50	581.54	0.000	0.000
7/16	10:27	94	1177	1185	1	0	B4–A1	179.91	50.14	0.00	2599.54	610.02	4.6	1.06E+06	7.9	116.6	3.96E–05	117.54	–19.22	–2.48	581.87	0.000	0.000
7/16	10:32	95	1186	1194	1	0	B4–A1	120.31	50.14	0.00	2599.85	609.89	4.6	1.07E+06	7.9	116.6	3.97E–05	117.55	–19.23	–2.48	582.13	0.000	0.000
7/16	10:37	96	1195	1203	1	0	B4–A1	59.55	50.14	0.00	2599.22	609.82	4.6	1.07E+06	7.9	116.6	3.97E–05	117.52	–19.23	–2.50	582.37	0.000	0.000

Table B-3. Continued.

		RUN INFORMATION					MODEL ATTITUDE & LOCATION				RUN-AVERAGED FLOW CONDITIONS									NOZZLE EXIT CONDITIONS			
DATE	TIME	RUN	POINT		Key	#	PITCH	ROLL	X_STRUT	Y_STRUT	PTINF	TTINF	MACH	REINF	PINF	TINF	RHOINF	QINF	DEWPT	PTJ	TTJ	WJ	CT
2010			START	END		NOZ	{deg}	{deg}	{in}	{in}	{psf}	{R}		{1/ft}	{psf}	{R}	{slug/ft^3}	{psf}	{deg F}	{psia}	{R}	{lbm/sec}	
7/16	10:43	97	1204	1212	1	0	B4–A1	–0.07	50.14	0.00	2599.54	609.84	4. 6	1.07E+06	7.9	116.6	3.97E–05	117.54	–19.19	–2.50	582.56	0.000	0.000
7/16	11:17	98	1213	1221	1	0	B4–A1	–0.07	50.14	7.99	2599.73	609.53	4.6	1.07E+06	7.9	116.5	3.97E–05	117.55	–18.64	–2.38	584.64	0.000	0.000
7/16	11:24	99	1222	1231	1	0	B4–A1	59.51	50.14	7.99	2599.66	609.77	4.6	1.07E+06	7.9	116.5	3.97E–05	117.54	–17.99	–2.36	584.90	0.000	0.000
7/16	11:32	100	1232	1240	1	0	B4–A1	120.42	50.14	7.99	2599.80	609.55	4.6	1.07E+06	7.9	116.5	3.97E–05	117.55	–16.93	–2.32	585.11	0.000	0.000
7/16	11:36	101	1241	1244	1	0	B4–A1	179.97	50.14	7.99	2600.26	609.52	4.6	1.07E+06	7.9	116.5	3.97E–05	117.57	–15.94	–2.29	585.32	0.000	0.000
7/19	8:53	103	1245	1246	2	0	–0.027	–0.01	26.27	0.00	314.93	540.82	0.0	0.00E+00	314.9	540.8	3.39E–04	0.00	–26.18	0.00	0.00	0.000	0.000
7/19	10:21	104	1247	1255	1	0	B4–A1	–0.03	25.18	0.00	3657.65	611.33	4.6	1.49E+06	11.2	116.8	5.57E–05	165.38	–12.71	16.07	578.69	0.000	0.000
7/19	10:26	105	1256	1264	1	0	B4–A1	59.59	25.19	0.00	3657.58	610.78	4.6	1.50E+06	11.2	116.7	5.57E–05	165.38	–12.71	16.13	579.23	0.000	0.000
7/19	10:31	106	1265	1273	1	0	B4–A1	120.37	25.19	0.00	3657.55	610.74	4.6	1.50E+06	11.2	116.7	5.57E–05	165.37	–12.71	16.19	579.72	0.000	0.000
7/19	10:36	107	1274	1282	1	0	B4–A1	179.93	25.19	0.00	3657.43	610.30	4.6	1.50E+06	11.2	116.6	5.58E–05	165.37	–12.71	16.23	580.18	0.000	0.000
7/19	10:45	108	1283	1291	1	0	B4–A1	179.93	40.15	0.00	3657.60	610.14	4.6	1.50E+06	11.2	116.6	5.58E–05	165.38	–12.71	16.28	581.03	0.000	0.000
7/19	10:50	109	1292	1300	1	0	B4–A1	120.33	40.15	0.00	3657.72	610.24	4.6	1.50E+06	11.2	116.6	5.58E–05	165.38	–12.70	16.29	581.37	0.000	0.000
7/19	10:55	110	1301	1309	1	0	B4–A1	59.53	40.15	0.00	3657.74	610.16	4.6	1.50E+06	11.2	116.6	5.58E–05	165.38	–11.00	16.30	581.64	0.000	0.000
7/19	11:01	111	1310	1318	1	0	B4–A1	–0.01	40.09	0.00	3657.43	609.96	4.6	1.50E+06	11.2	116.6	5.58E–05	165.37	–11.46	16.30	582.06	0.000	0.000
7/19	11:08	112	1319	1327	1	0	B4–A1	–0.01	50.19	0.00	3657.48	610.01	4.6	1.50E+06	11.2	116.6	5.58E–05	165.37	–11.52	16.33	582.45	0.000	0.000
7/19	11:13	113	1328	1336	1	0	B4–A1	59.61	50.19	0.00	3657.77	610.04	4.6	1.50E+06	11.2	116.6	5.58E–05	165.38	–11.58	16.36	582.71	0.000	0.000
7/19	11:18	114	1337	1345	1	0	B4–A1	120.45	50.19	0.00	3657.67	610.01	4.6	1.50E+06	11.2	116.6	5.58E–05	165.38	–11.59	16.40	582.92	0.000	0.000
7/19	11:23	115	1346	1354	1	0	B4–A1	179.97	50.19	0.00	3657.77	609.83	4.6	1.50E+06	11.2	116.6	5.58E–05	165.38	–11.67	16.43	583.16	0.000	0.000
7/19	11:32	116	1355	1363	1	0	B4–A1	179.97	50.19	8.00	3657.65	609.98	4.6	1.50E+06	11.2	116.6	5.58E–05	165.38	–11.67	16.46	583.79	0.000	0.000
7/19	11:37	117	1364	1372	1	0	B4–A1	120.33	50.19	8.00	3657.55	609.80	4.6	1.50E+06	11.2	116.6	5.58E–05	165.37	–11.67	16.46	584.10	0.000	0.000
7/19	11:42	118	1373	1381	1	0	B4–A1	59.55	50.19	8.00	3657.41	609.98	4.6	1.50E+06	11.2	116.6	5.58E–05	165.37	–11.67	16.46	584.43	0.000	0.000
7/19	11:48	119	1382	1390	1	0	B4–A1	0.03	50.19	8.00	3657.89	609.84	4.6	1.50E+06	11.2	116.6	5.58E–05	165.39	–11.58	16.46	584.72	0.000	0.000
7/19	12:00	120	1391	1400	1	0	B4–A1	0.03	25.16	–8.00	3657.66	609.78	4.6	1.50E+06	11.2	116.5	5.58E–05	165.38	–11.49	16.49	585.37	0.000	0.000
7/19	12:05	121	1401	1409	1	0	B4–A1	59.65	25.16	–8.00	3657.62	609.90	4.6	1.50E+06	11.2	116.6	5.58E–05	165.38	–11.38	16.51	585.40	0.000	0.000
7/19	12:09	122	1410	1418	1	0	B4–A1	120.41	25.16	–8.00	3657.74	609.60	4.6	1.50E+06	11.2	116.5	5.58E–05	165.38	–11.35	16.54	585.34	0.000	0.000
7/19	12:14	123	1419	1427	1	0	B4–A1	179.93	25.16	–8.00	3657.65	609.62	4.6	1.50E+06	11.2	116.5	5.58E–05	165.38	–11.28	16.56	585.36	0.000	0.000
7/20	12:22	124	1431	1435	5	0	–0.014	49.73	27.56	0.00	0.00	552.30	0.0	0.00E+00	0.0	552.3	0.00E+00	0.00	65.91	0.00	0.00	0.000	0.000
7/20	13:26	125	1436	1437	2	0	B4–A1	26.64	33.85	0.00	2123.60	550.59	0.0	0.00E+00	2123.6	550.6	2.25E–03	0.00	64.76	0.00	0.00	0.000	0.000
7/20	15:25	129	1509	1946	4	0	B4–A1	–0.01	40.13	0.00	2130.49	547.97	0.0	0.00E+00	2130.5	548.0	2.26E–03	0.00	65.48	889.11	572.34	0.000	0.000
7/21	6:59	131	1947	1947	2	1	–0.054	–0.01	26.77	0.00	2123.92	545.84	0.0	0.00E+00	2123.9	545.8	2.27E–03	0.00	66.48	0.00	0.00	0.000	0.000
7/22	7:09	135	1951	1953	2	1	–0.057	–0.01	26.77	0.00	2123.49	543.50	0.0	0.00E+00	2123.5	543.5	2.28E–03	0.00	66.12	0.00	0.00	0.000	0.000
7/22	7:56	135	1954	1958	2	1	–0.056	–0.01	26.77	0.00	327.11	532.52	0.0	0.00E+00	327.1	532.5	3.58E–04	0.00	–26.19	0.00	0.00	0.000	0.000

Table B-3. Continued.

		RUN INFORMATION					MODEL ATTITUDE & LOCATION				RUN-AVERAGED FLOW CONDITIONS									NOZZLE EXIT CONDITIONS			
DATE	TIME	RUN	POINT		Key	#	PITCH	ROLL	X_STRUT	Y_STRUT	PTINF	TTINF	MACH	REINF	PINF	TINF	RHOINF	QINF	DEWPT	PTJ	TTJ	WJ	CT
2010			START	END		NOZ	{deg}	{deg}	{in}	{in}	{psf}	{R}		{1/ft}	{psf}	{R}	{slug/ft^3}	{psf}	{deg F}	{psia}	{R}	{lbm/sec}	
7/22	9:09	136	1959	1964	1	1	B4–A3	–0.01	40.16	0.00	778.03	594.64	2.4	1.00E+06	53.2	276.3	1.12E–04	214.57	–25.56	1551.23	637.33	1.642	4.024
7/22	9:38	137	1965	1970	1	1	B4–A3	–0.03	40.15	0.00	778.14	594.73	2.4	1.00E+06	53.2	276.4	1.12E–04	214.60	–25.40	1162.84	630.66	1.228	3.002
7/22	9:50	138	1971	1978	1	1	B4–A2	179.97	40.15	0.00	777.92	594.68	2.4	9.99E+05	53.2	276.3	1.12E–04	214.54	–25.36	1165.00	633.93	1.228	3.012
7/22	10:04	139	1979	1988	1	1	B4–A1	179.97	40.15	0.00	777.88	594.55	2.4	1.00E+06	53.2	276.3	1.12E–04	214.53	–25.36	388.43	624.75	0.393	0.968
7/22	10:11	140	1989	1997	1	1	B4–A1	–0.03	40.15	0.00	778.06	594.82	2.4	9.99E+05	53.2	276.4	1.12E–04	214.58	–25.11	387.98	624.28	0.393	0.967
7/22	10:22	141	1998	2006	1	1	B4–A1	–0.03	40.15	0.00	777.72	594.68	2.4	9.99E+05	53.2	276.3	1.12E–04	214.48	–24.96	775.00	638.08	0.801	1.982
7/22	10:27	142	2007	2015	1	1	B4–A1	–179.91	40.15	0.00	777.84	594.56	2.4	1.00E+06	53.2	276.3	1.12E–04	214.52	–25.18	776.77	643.54	0.798	1.983
7/22	10:55	143	2016	2024	1	1	B4–A1	–179.91	40.15	0.00	777.96	594.72	2.4	9.99E+05	53.2	276.4	1.12E–04	214.55	–24.82	194.06	620.04	0.190	0.468
7/22	11:00	144	2025	2033	1	1	B4–A1	0.01	40.15	0.00	777.96	594.61	2.4	1.00E+06	53.2	276.3	1.12E–04	214.55	–24.89	194.07	618.78	0.188	0.464
7/22	11:08	145	2034	2042	1	1	B4–A1	0.01	40.15	0.00	777.89	594.59	2.4	1.00E+06	53.2	276.3	1.12E–04	214.53	–24.89	96.65	606.25	0.093	0.228
7/22	11:14	146	2043	2051	1	1	B4–A1	60.00	40.15	0.00	778.08	594.67	2.4	1.00E+06	53.2	276.3	1.12E–04	214.58	–24.89	96.83	603.33	0.093	0.228
7/22	11:20	147	2052	2055	1	1	B4–A1	89.99	40.15	0.00	778.09	594.80	2.4	9.99E+05	53.2	276.4	1.12E–04	214.59	–24.89	86.21	600.43	0.083	0.201
7/22	11:31	148	2056	2064	1	1	B4–A1	60.00	40.15	0.00	777.74	594.65	2.4	9.99E+05	53.2	276.3	1.12E–04	214.49	–25.42	3.87	592.00	0.000	0.000
7/22	11:37	149	2065	2073	1	1	B4–A1	–0.03	40.15	0.00	778.58	594.95	2.4	1.00E+06	53.3	276.5	1.12E–04	214.72	–22.18	3.78	590.26	0.000	0.000
7/22	12:23	150	2074	2082	1	1	B4–A1	–0.03	40.17	0.00	1386.07	594.48	3.5	1.00E+06	18.2	172.3	6.14E–05	155.83	–21.75	848.84	639.79	0.873	2.978
7/22	12:29	151	2083	2091	1	1	B4–A1	–179.97	40.17	0.00	1386.19	594.84	3.5	9.99E+05	18.2	172.4	6.14E–05	155.84	–21.16	850.00	637.95	0.874	2.977
7/22	12:37	152	2092	2100	1	1	B4–A1	–179.97	40.17	0.00	1386.43	594.71	3.5	9.99E+05	18.2	172.4	6.14E–05	155.87	–21.19	562.87	630.63	0.577	1.960
7/22	12:42	153	2101	2109	1	1	B4–A1	–0.09	40.17	0.00	1386.58	594.86	3.5	9.99E+05	18.2	172.4	6.14E–05	155.89	–21.19	563.40	628.33	0.579	1.962
7/22	12:51	154	2110	2118	1	1	B4–A1	–0.09	40.17	0.00	1387.10	594.57	3.5	1.00E+06	18.2	172.3	6.15E–05	155.95	–20.20	281.32	621.69	0.276	0.938
7/22	13:21	155	2119	2127	1	1	B4–A1	179.92	40.17	0.00	1386.24	593.98	3.5	1.00E+06	18.2	172.2	6.15E–05	155.85	–21.94	282.60	617.63	0.281	0.950
7/22	13:31	156	2128	2136	1	1	B4–A1	179.93	40.17	0.00	1386.31	594.66	3.5	9.99E+05	18.2	172.4	6.14E–05	155.86	–21.72	139.65	609.19	0.134	0.452
7/22	13:36	157	2137	2145	1	1	B4–A1	0.07	40.17	0.00	1386.43	594.64	3.5	1.00E+06	18.2	172.4	6.14E–05	155.87	–21.62	140.12	607.70	0.133	0.448
7/22	13:45	158	2146	2154	5	1	B4–A1	0.07	40.17	0.00	1386.91	594.52	3.5	1.00E+06	18.2	172.3	6.14E–05	155.92	–18.42	70.02	597.83	0.063	0.210
7/22	14:32	159	2155	2163	1	1	B4–A1	0.00	40.17	0.00	1386.70	594.65	3.5	1.00E+06	18.2	172.4	6.14E–05	155.90	–21.22	69.88	605.89	0.062	0.210
7/22	14:37	160	2164	2172	1	1	B4–A1	179.93	40.17	0.00	1386.48	594.56	3.5	1.00E+06	18.2	172.3	6.14E–05	155.88	–21.15	69.75	601.42	0.062	0.210
7/22	14:43	161	2173	2181	1	1	B4–A1	179.93	40.17	0.00	1386.38	594.69	3.5	9.99E+05	18.2	172.4	6.14E–05	155.87	–21.06	3.29	594.81	0.000	0.000
7/22	14:49	162	2182	2190	1	1	B4–A1	0.03	40.17	0.00	1386.41	594.90	3.5	9.99E+05	18.2	172.4	6.14E–05	155.87	–20.96	3.08	591.54	0.000	0.000
7/22	15:53	163	2191	2199	1	1	B4–A1	0.03	40.17	0.00	3658.90	610.12	4.6	1.50E+06	11.2	116.6	5.58E–05	165.43	–6.33	896.53	634.14	0.926	2.959
7/22	16:00	164	2200	2208	1	1	B4–A1	179.93	40.17	0.00	3658.18	609.73	4.6	1.50E+06	11.2	116.5	5.58E–05	165.40	–9.80	900.08	628.66	0.931	2.960
7/22	16:11	165	2209	2217	1	1	B4–A1	179.93	40.15	0.00	3657.58	609.60	4.6	1.50E+06	11.2	116.5	5.58E–05	165.38	–10.81	598.93	622.08	0.620	1.968
7/22	16:17	166	2218	2226	1	1	B4–A1	0.03	40.15	0.00	3657.24	609.85	4.6	1.50E+06	11.2	116.6	5.58E–05	165.36	–10.81	598.09	621.86	0.619	1.966
7/22	16:25	167	2227	2235	1	1	B4–A1	0.03	40.15	0.00	3657.89	609.69	4.6	1.50E+06	11.2	116.5	5.58E–05	165.39	–10.81	298.58	617.13	0.296	0.943

Table B-3. Continued.

		RUN INFORMATION					MODEL ATTITUDE & LOCATION				RUN-AVERAGED FLOW CONDITIONS									NOZZLE EXIT CONDITIONS			
DATE	TIME	RUN	POINT		Key	#	PITCH	ROLL	X_STRUT	Y_STRUT	PTINF	TTINF	MACH	REINF	PINF	TINF	RHOINF	QINF	DEWPT	PTJ	TTJ	WJ	CT
2010			START	END		NOZ	{deg}	{deg}	{in}	{in}	{psf}	{R}		{1/ft}	{psf}	{R}	{slug/ft^3}	{psf}	{deg F}	{psia}	{R}	{lbm/sec}	
7/22	16:31	168	2236	2244	1	1	B4–A1	179.95	40.15	0.00	3657.53	609.60	4.6	1.50E+06	11.2	116.5	5.58E–05	165.37	–10.80	298.20	618.12	0.294	0.938
7/22	16:39	169	2245	2253	1	1	B4–A1	179.95	40.15	0.00	3657.58	609.82	4.6	1.50E+06	11.2	116.6	5.58E–05	165.38	–8.49	148.09	613.28	0.142	0.454
7/22	16:44	170	2254	2262	1	1	B4–A1	0.03	40.15	0.00	3658.18	609.52	4.6	1.50E+06	11.2	116.5	5.58E–05	165.40	–8.85	148.23	612.11	0.143	0.455
7/22	16:52	171	2263	2271	1	1	B4–A1	0.03	40.15	0.00	3657.91	609.60	4.6	1.50E+06	11.2	116.5	5.58E–05	165.39	–9.74	74.45	604.78	0.069	0.219
7/22	16:57	172	2272	2280	1	1	B4–A1	179.92	40.15	0.00	3657.55	609.74	4.6	1.50E+06	11.2	116.5	5.58E–05	165.37	–10.72	74.51	601.98	0.069	0.219
7/22	17:02	173	2281	2289	1	1	B4–A1	179.91	40.15	0.00	3657.14	609.86	4.6	1.50E+06	11.2	116.6	5.58E–05	165.36	–10.72	3.36	597.47	0.000	0.000
7/22	17:07	174	2290	2298	1	1	B4–A1	–0.07	40.15	0.00	3657.58	609.93	4.6	1.50E+06	11.2	116.6	5.58E–05	165.38	–10.72	3.20	594.66	0.000	0.000
7/22	17:16	175	2299	2300	3	1	0.022	–0.07	40.15	0.00	893.38	588.35	0.0	0.00E+00	893.4	588.4	8.85E–04	0.00	–19.25	0.00	0.00	0.000	0.000
7/22	17:18	175	2301	2301	3	1	–0.1	–0.07	40.15	0.00	2117.23	614.95	0.0	0.00E+00	2117.2	615.0	2.01E–03	0.00	–21.22	0.00	0.00	0.000	0.000
7/23	14:20	178	2305	2305	2	3	0.356	0.09	40.15	0.00	320.54	548.53	0.0	0.00E+00	320.5	548.5	3.40E–04	0.00	2.51	0.00	0.00	0.000	0.000
7/23	15:05	179	2307	2543	1	3	0.349	0.09	40.15	0.00	778.07	595.28	2.4	9.98E+05	53.2	276.6	1.12E–04	214.58	–23.91	vary	560.06	vary	vary
7/23	15:41	180	2544	2554	1	3	B4–A1	0.00	40.15	0.00	777.80	594.54	2.4	1.00E+06	53.2	276.3	1.12E–04	214.51	–28.15	3.93	588.07	0.000	0.000
7/23	15:49	181	2555	2563	1	3	B4–A1	179.97	40.15	0.00	778.32	594.47	2.4	1.00E+06	53.2	276.2	1.12E–04	214.65	–28.13	3.85	586.35	0.000	0.000
7/23	15:54	182	2564	2572	1	3	B4–A1	120.37	40.15	0.00	778.27	594.75	2.4	1.00E+06	53.2	276.4	1.12E–04	214.64	–27.80	3.85	585.87	0.000	0.000
7/23	15:59	183	2573	2581	1	3	B4–A1	59.63	40.15	0.00	777.96	594.74	2.4	9.99E+05	53.2	276.4	1.12E–04	214.55	–27.52	3.78	585.34	0.000	0.000
7/23	16:21	184	2582	2590	1	3	B4–A1	0.05	40.15	0.00	1387.15	593.53	3.5	1.00E+06	18.2	172.0	6.16E–05	155.95	–21.66	2.96	583.95	0.000	0.000
7/23	16:27	185	2591	2599	1	3	B4–A1	59.53	40.15	0.00	1387.13	594.97	3.5	9.99E+05	18.2	172.5	6.14E–05	155.95	–21.43	2.90	583.39	0.000	0.000
7/23	16:32	186	2600	2608	1	3	B4–A1	120.35	40.15	0.00	1387.08	594.58	3.5	1.00E+06	18.2	172.3	6.15E–05	155.94	–21.34	2.93	582.99	0.000	0.000
7/23	16:37	187	2609	2617	1	3	B4–A1	179.96	40.15	0.00	1386.84	594.75	3.5	1.00E+06	18.2	172.4	6.14E–05	155.92	–21.34	2.89	582.52	0.000	0.000
7/23	16:45	188	2618	2619	3	3	–0.056	–0.01	40.15	0.00	196.45	583.65	0.0	0.00E+00	196.4	583.6	1.96E–04	0.00	–21.34	0.00	0.00	0.000	0.000
7/23	16:49	188	2620	2620	3	3	–0.1	–0.01	40.15	0.00	2117.88	616.76	0.0	0.00E+00	2117.9	616.8	2.00E–03	0.00	–21.34	0.00	0.00	0.000	0.000
7/26	7:55	189	2621	2622	2	3	–0.124	–2.72	40.15	0.00	2125.43	546.27	0.0	0.00E+00	2125.4	546.3	2.27E–03	0.00	64.70	0.00	0.00	0.000	0.000
7/26	8:25	189	2623	2624	2	3	–0.124	–2.72	40.15	0.00	380.37	522.52	0.0	0.00E+00	380.4	522.5	4.24E–04	0.00	–22.60	0.00	0.00	0.000	0.000
7/26	9:26	190	2625	2633	1	3	B4–A1	–0.01	40.15	0.00	777.98	594.57	2.4	1.00E+06	53.2	276.3	1.12E–04	214.56	–27.60	391.69	633.39	1.186	2.939
7/26	9:31	191	2634	2641	1	3	B4–A1	59.48	40.15	0.00	777.82	594.57	2.4	1.00E+06	53.2	276.3	1.12E–04	214.51	–27.30	389.25	637.75	1.177	2.926
7/26	9:47	192	2642	2649	1	3	B4–A2	120.21	40.15	0.00	777.95	595.29	2.4	9.98E+05	53.2	276.6	1.12E–04	214.55	–23.28	391.13	635.92	1.185	2.943
7/26	10:09	193	2650	2657	1	3	B4–A2	–179.97	40.15	0.00	777.90	594.68	2.4	9.99E+05	53.2	276.3	1.12E–04	214.53	–26.04	392.77	638.96	1.185	2.950
7/26	10:24	194	2658	2666	1	3	B4–A1	–179.97	40.15	0.00	778.20	594.64	2.4	1.00E+06	53.2	276.3	1.12E–04	214.62	–26.04	260.46	623.73	0.788	1.940
7/26	10:29	195	2667	2675	1	3	B4–A1	120.37	40.15	0.00	777.86	594.57	2.4	1.00E+06	53.2	276.3	1.12E–04	214.52	–26.05	259.56	618.32	0.789	1.935
7/26	10:34	196	2676	2684	1	3	B4–A1	59.53	40.15	0.00	777.94	594.62	2.4	1.00E+06	53.2	276.3	1.12E–04	214.54	–26.05	258.82	617.07	0.787	1.929
7/26	10:39	197	2685	2693	1	3	B4–A1	–0.01	40.15	0.00	777.91	594.76	2.4	9.99E+05	53.2	276.4	1.12E–04	214.54	–26.25	259.10	617.30	0.788	1.931
7/26	10:48	198	2694	2702	1	3	B4–A1	–0.01	40.15	0.00	777.91	594.51	2.4	1.00E+06	53.2	276.3	1.12E–04	214.54	–24.46	130.51	615.45	0.384	0.944

Table B-3. Continued.

		RUN INFORMATION					MODEL ATTITUDE & LOCATION				RUN-AVERAGED FLOW CONDITIONS									NOZZLE EXIT CONDITIONS			
DATE	TIME	RUN	POINT		Key	#	PITCH	ROLL	X_STRUT	Y_STRUT	PTINF	TTINF	MACH	REINF	PINF	TINF	RHOINF	QINF	DEWPT	PTJ	TTJ	WJ	CT
2010			START	END		NOZ	{deg}	{deg}	{in}	{in}	{psf}	{R}		{1/ft}	{psf}	{R}	{slug/ft^3}	{psf}	{deg F}	{psia}	{R}	{lbm/sec}	
7/26	10:53	199	2703	2711	1	3	B4–A1	59.57	40.15	0.00	778.10	594.79	2.4	9.99E+05	53.2	276.4	1.12E–04	214.59	–21.69	130.11	616.73	0.382	0.939
7/26	10:58	200	2712	2720	1	3	B4–A1	120.35	40.15	0.00	778.06	594.66	2.4	1.00E+06	53.2	276.3	1.12E–04	214.58	–21.83	130.32	616.57	0.382	0.941
7/26	11:03	201	2721	2729	1	3	B4–A1	179.99	40.15	0.00	777.96	594.54	2.4	1.00E+06	53.2	276.3	1.12E–04	214.55	–22.17	130.87	617.04	0.384	0.946
7/26	11:17	202	2730	2738	1	3	B4–A1	179.99	40.15	0.00	777.89	594.58	2.4	1.00E+06	53.2	276.3	1.12E–04	214.53	–22.74	63.93	607.59	0.175	0.431
7/26	11:38	203	2739	2747	1	3	B4–A1	–179.97	40.15	0.00	778.01	594.64	2.4	1.00E+06	53.2	276.3	1.12E–04	214.56	–23.03	64.16	607.24	0.178	0.437
7/26	11:43	204	2748	2756	1	3	B4–A1	120.39	40.15	0.00	777.94	594.83	2.4	9.99E+05	53.2	276.4	1.12E–04	214.54	–23.03	63.88	606.28	0.177	0.436
7/26	11:48	205	2757	2765	1	3	B4–A1	59.53	40.15	0.00	778.13	594.80	2.4	9.99E+05	53.2	276.4	1.12E–04	214.60	–22.99	63.97	606.76	0.176	0.433
7/26	11:54	206	2766	2774	1	3	B4–A1	–0.05	40.15	0.00	778.01	594.44	2.4	1.00E+06	53.2	276.2	1.12E–04	214.56	–22.94	63.71	606.00	0.177	0.435
7/26	12:07	207	2775	2775	3	3	–0.121	–0.01	40.15	0.00	2126.51	614.20	0.0	0.00E+00	2126.5	614.2	2.97E–04	0.00	–0.61	0.00	0.00	0.000	0.000
7/26	12:48	208	2776	2776	2	3	–0.125	9.33	40.15	0.00	2127.60	579.24	0.0	0.00E+00	2127.6	579.2	2.14E–03	0.00	35.04	0.00	0.00	0.000	0.000
7/26	13:09	208	2777	2778	2	3	–0.124	9.33	40.15	0.00	331.34	564.63	0.0	0.00E+00	331.3	564.6	3.42E–04	0.00	–21.87	0.00	0.00	0.000	0.000
7/26	14:37	210	2780	2785	5	3	–0.137	–0.29	40.15	0.00	2143.08	584.51	0.0	4.12E+06	2143.1	584.5	2.14E–03	0.00	70.32	vary	601.83	vary	vary
7/26	16:40	211	2786	2793	1	3	B4–A2	–0.03	40.15	0.00	3658.04	609.79	4.6	1.50E+06	11.2	116.6	5.58E–05	165.40	–6.84	303.50	625.48	0.916	2.932
7/26	16:45	212	2794	2801	1	3	B4–A2	59.76	40.15	0.00	3657.91	609.84	4.6	1.50E+06	11.2	116.6	5.58E–05	165.39	–6.73	303.28	627.67	0.915	2.933
7/26	16:49	213	2802	2809	1	3	B4–A2	120.25	40.15	0.00	3657.85	609.73	4.6	1.50E+06	11.2	116.5	5.58E–05	165.39	–6.67	302.03	626.89	0.911	2.919
7/26	16:55	214	2810	2817	1	3	B4–A2	179.99	40.15	0.00	3657.93	609.76	4.6	1.50E+06	11.2	116.5	5.58E–05	165.39	–6.59	305.05	625.47	0.924	2.954
7/26	17:06	215	2818	2819	3	3	–0.126	–0.01	40.15	0.00	382.32	566.49	0.0	0.00E+00	382.3	566.5	3.93E–04	0.00	–6.63	0.00	0.00	0.000	0.000
7/26	17:12	215	2820	2820	3	3	–0.122	–0.01	40.15	0.00	2124.14	609.57	0.0	0.00E+00	2124.1	609.6	2.03E–03	0.00	–2.08	0.00	0.00	0.000	0.000
7/27	7:55	216	2821	2821	2	3	–0.115	–0.03	40.15	0.00	2131.05	562.34	0.0	0.00E+00	2131.1	562.3	2.21E–03	0.00	53.02	0.00	0.00	0.000	0.000
7/27	8:24	216	2822	2823	2	3	–0.109	–0.03	40.15	0.00	318.71	553.19	0.0	0.00E+00	318.7	553.2	3.36E–04	0.00	–20.13	0.00	0.00	0.000	0.000
7/27	9:18	217	2824	2832	1	3	B4–A1	–0.03	40.15	0.00	777.82	594.80	2.4	9.99E+05	53.2	276.4	1.12E–04	214.51	–26.81	69.29	608.03	0.193	0.474
7/27	9:23	218	2833	2841	1	3	B4–A1	59.53	40.15	0.00	777.91	594.77	2.4	9.99E+05	53.2	276.4	1.12E–04	214.54	–27.16	69.60	610.18	0.194	0.478
7/27	9:28	219	2842	2850	1	3	B4–A1	120.37	40.15	0.00	777.82	594.55	2.4	1.00E+06	53.2	276.3	1.12E–04	214.51	–27.28	69.58	609.56	0.193	0.476
7/27	9:33	220	2851	2859	1	3	B4–A1	179.95	40.15	0.00	777.77	594.65	2.4	9.99E+05	53.2	276.3	1.12E–04	214.50	–27.17	69.98	610.07	0.195	0.479
7/27	9:40	221	2860	2868	1	3	B4–A1	–0.01	40.15	0.00	777.48	594.68	2.4	9.99E+05	53.2	276.3	1.12E–04	214.42	–27.17	36.40	601.17	0.096	0.235
7/27	11:17	222	2869	2877	1	3	B4–A1	–0.01	40.15	0.00	1386.60	594.59	3.5	1.00E+06	18.2	172.3	6.14E–05	155.89	–16.75	288.71	623.35	0.874	2.963
7/27	11:22	223	2878	2886	1	3	B4–A1	59.55	40.15	0.00	1385.98	594.25	3.5	1.00E+06	18.2	172.2	6.15E–05	155.82	–16.53	289.79	623.22	0.876	2.971
7/27	11:26	224	2887	2895	1	3	B4–A1	120.41	40.15	0.00	1386.86	595.00	3.5	9.99E+05	18.2	172.5	6.14E–05	155.92	–16.09	288.61	622.75	0.876	2.966
7/27	11:34	225	2896	2904	1	3	B4–A1	179.97	40.15	0.00	1386.86	594.99	3.5	9.99E+05	18.2	172.5	6.14E–05	155.92	–15.84	290.89	622.12	0.882	2.985
7/27	11:56	226	2905	2913	1	3	B4–A1	179.97	40.15	0.00	1386.19	594.77	3.5	9.99E+05	18.2	172.4	6.14E–05	155.84	–14.89	192.86	619.18	0.578	1.956
7/27	12:05	227	2914	2922	1	3	B4–A1	120.39	40.15	0.00	1386.10	595.12	3.5	9.98E+05	18.2	172.5	6.14E–05	155.83	–15.03	192.14	619.05	0.575	1.948
7/27	12:10	228	2923	2934	1	3	B4–A1	59.61	40.15	0.00	1385.81	593.98	3.5	1.00E+06	18.2	172.2	6.15E–05	155.80	–14.72	191.76	619.68	0.574	1.944

Table B-3. Continued.

		RUN INFORMATION					MODEL ATTITUDE & LOCATION				RUN-AVERAGED FLOW CONDITIONS									NOZZLE EXIT CONDITIONS			
DATE	TIME	RUN	POINT		Key	#	PITCH	ROLL	X_STRUT	Y_STRUT	PTINF	TTINF	MACH	REINF	PINF	TINF	RHOINF	QINF	DEWPT	PTJ	TTJ	WJ	CT
2010			START	END		NOZ	{deg}	{deg}	{in}	{in}	{psf}	{R}		{1/ft}	{psf}	{R}	{slug/ft^3}	{psf}	{deg F}	{psia}	{R}	{lbm/sec}	
7/27	12:15	229	2935	2940	1	3	B4–A1	–0.02	40.15	0.00	1386.94	595.07	3.5	9.99E+05	18.2	172.5	6.14E–05	155.93	–14.75	191.94	619.60	0.575	1.947
7/27	12:28	230	2941	2949	1	3	B4–A1	–0.03	40.15	0.00	1387.32	594.47	3.5	1.00E+06	18.2	172.3	6.15E–05	155.97	–14.46	98.99	614.50	0.284	0.962
7/27	12:54	231	2950	2951	3	3	–0.122	–0.01	40.15	0.00	188.46	583.73	0.0	0.00E+00	188.5	583.7	1.88E–04	0.00	–16.38	0.00	0.00	0.000	0.000
7/27	13:07	231	2952	2952	3	3	–0.118	–0.01	40.15	0.00	2130.62	589.58	0.0	0.00E+00	2130.6	589.6	2.11E–03	0.00	5.68	0.00	0.00	0.000	0.000
7/27	14:43	232	2953	2954	2	3	–0.119	–0.01	40.15	0.00	340.52	566.09	0.0	0.00E+00	340.5	566.1	3.50E–04	0.00	–35.22	0.00	0.00	0.000	0.000
7/27	15:12	233	2955	2963	1	3	B4–A1	59.55	40.15	0.00	1386.79	594.65	3.5	1.00E+06	18.2	172.4	6.15E–05	155.91	–24.56	98.39	590.80	0.290	0.964
7/27	15:17	234	2964	2972	1	3	B4–A1	–0.05	40.15	0.00	1386.79	594.77	3.5	1.00E+06	18.2	172.4	6.14E–05	155.91	–24.32	98.58	593.97	0.291	0.968
7/27	15:22	235	2973	2981	1	3	B4–A1	120.41	40.15	0.00	1386.74	594.62	3.5	1.00E+06	18.2	172.4	6.15E–05	155.91	–24.06	98.45	596.85	0.288	0.960
7/27	15:27	236	2982	2990	1	3	B4–A1	179.95	40.15	0.00	1386.29	594.70	3.5	9.99E+05	18.2	172.4	6.14E–05	155.86	–23.96	99.16	599.79	0.289	0.967
7/27	15:41	237	2991	3001	1	3	B4–A1	179.95	40.15	0.00	1387.58	594.01	3.5	1.00E+06	18.2	172.2	6.16E–05	156.00	–21.66	50.14	597.64	0.137	0.461
7/27	15:47	238	3002	3010	1	3	B4–A1	120.35	40.15	0.00	1387.22	595.20	3.5	9.99E+05	18.2	172.5	6.14E–05	155.96	–18.03	50.64	597.72	0.138	0.465
7/27	15:55	239	3011	3019	1	3	B4–A1	59.59	40.15	0.00	1387.44	595.14	3.5	9.99E+05	18.2	172.5	6.14E–05	155.98	–15.92	50.70	598.96	0.137	0.463
7/27	16:01	240	3020	3028	1	3	B4–A1	–0.05	40.15	0.00	1386.50	594.27	3.5	1.00E+06	18.2	172.3	6.15E–05	155.88	–16.22	50.76	599.95	0.137	0.462
7/27	16:12	241	3029	3037	1	3	B4–A1	–0.05	40.15	0.00	1386.50	594.27	3.5	1.00E+06	18.2	172.3	6.15E–05	155.88	–18.72	26.62	593.41	0.067	0.225
7/27	16:42	242	3038	3046	1	3	B4–A1	–0.05	40.15	0.00	3657.74	609.76	4.6	1.50E+06	11.2	116.5	5.58E–05	165.38	–0.62	205.41	624.32	0.611	1.959
7/27	16:47	243	3047	3055	1	3	B4–A1	59.59	40.15	0.00	3657.96	609.60	4.6	1.50E+06	11.2	116.5	5.58E–05	165.39	–2.36	205.03	626.00	0.609	1.955
7/27	16:52	244	3056	3064	1	3	B4–A1	120.41	40.15	0.00	3657.86	609.79	4.6	1.50E+06	11.2	116.5	5.58E–05	165.39	–3.55	205.47	625.65	0.612	1.962
7/27	16:57	245	3065	3073	1	3	B4–A1	–179.99	40.15	0.00	3658.13	609.73	4.6	1.50E+06	11.2	116.5	5.58E–05	165.40	–3.69	206.20	624.94	0.615	1.970
7/27	17:05	246	3074	3075	3	3	–0.147	–0.03	40.15	0.00	388.15	571.36	0.0	0.00E+00	388.2	571.4	3.96E–04	0.00	–24.54	0.00	0.00	0.000	0.000
7/27	17:09	246	3076	3076	3	3	–0.144	–0.03	40.15	0.00	2127.16	619.12	0.0	0.00E+00	2127.2	619.1	2.00E–03	0.00	–27.46	0.00	0.00	0.000	0.000
7/28	8:36	247	3080	3089	1	3	B4–A1	–0.03	40.15	0.00	3658.01	610.37	4.6	1.50E+06	11.2	116.7	5.58E–05	165.39	–11.11	201.19	623.56	0.599	1.919
7/28	8:42	248	3090	3098	1	3	B4–A1	179.99	40.15	0.00	3657.94	610.45	4.6	1.50E+06	11.2	116.7	5.58E–05	165.39	–11.71	202.53	629.30	0.600	1.930
7/28	8:51	249	3099	3107	1	3	B4–A1	179.99	40.15	0.00	3657.94	610.08	4.6	1.50E+06	11.2	116.6	5.58E–05	165.39	–12.24	99.14	627.41	0.278	0.898
7/28	8:56	250	3108	3116	1	3	B4–A1	120.39	40.15	0.00	3657.60	610.25	4.6	1.50E+06	11.2	116.6	5.58E–05	165.38	–12.59	99.11	628.12	0.279	0.901
7/28	9:01	251	3117	3125	1	3	B4–A1	59.63	40.15	0.00	3658.51	610.21	4.6	1.50E+06	11.2	116.6	5.58E–05	165.42	–12.69	98.99	628.82	0.277	0.897
7/28	9:06	252	3126	3134	1	3	B4–A1	–0.03	40.15	0.00	3657.79	610.16	4.6	1.50E+06	11.2	116.6	5.58E–05	165.38	–12.81	99.16	628.48	0.277	0.898
7/28	9:16	253	3135	3143	1	3	B4–A1	–0.03	40.15	0.00	3657.98	609.88	4.6	1.50E+06	11.2	116.6	5.58E–05	165.39	–12.96	49.92	618.75	0.132	0.428
7/28	9:21	254	3144	3152	1	3	B4–A1	59.59	40.15	0.00	3657.96	609.94	4.6	1.50E+06	11.2	116.6	5.58E–05	165.39	–12.86	49.59	617.58	0.132	0.425
7/28	9:26	255	3153	3161	1	3	B4–A1	120.37	40.15	0.00	3657.86	609.99	4.6	1.50E+06	11.2	116.6	5.58E–05	165.39	–12.84	49.55	616.14	0.130	0.421
7/28	9:31	256	3162	3170	1	3	B4–A1	179.95	40.15	0.00	3657.96	609.90	4.6	1.50E+06	11.2	116.6	5.58E–05	165.39	–12.75	49.75	614.95	0.132	0.425
7/28	9:41	257	3171	3179	1	3	B4–A1	–0.03	40.15	0.00	3657.89	609.87	4.6	1.50E+06	11.2	116.6	5.58E–05	165.39	–12.65	25.29	604.69	0.062	0.199
7/28	9:49	258	3180	3188	1	3	B4–A1	–0.03	40.15	0.00	3658.37	609.63	4.6	1.50E+06	11.2	116.5	5.58E–05	165.41	–12.45	3.92	596.86	0.000	0.000

Table B-3. Continued.

		RUN INFORMATION					MODEL ATTITUDE & LOCATION				RUN-AVERAGED FLOW CONDITIONS									NOZZLE EXIT CONDITIONS			
DATE	TIME	RUN	POINT		Key	#	PITCH	ROLL	X_STRUT	Y_STRUT	PTINF	TTINF	MACH	REINF	PINF	TINF	RHOINF	QINF	DEWPT	PTJ	TTJ	WJ	CT
2010			START	END		NOZ	{deg}	{deg}	{in}	{in}	{psf}	{R}		{1/ft}	{psf}	{R}	{slug/ft^3}	{psf}	{deg F}	{psia}	{R}	{lbm/sec}	
7/28	9:55	259	3189	3197	1	3	B4–A1	59.55	40.15	0.00	3658.01	609.76	4.6	1.50E+06	11.2	116.5	5.58E–05	165.39	–12.27	3.75	594.76	0.000	0.000
7/28	10:05	260	3198	3215	1	3	B4–A1	120.35	40.15	0.00	3658.08	609.84	4.6	1.50E+06	11.2	116.6	5.58E–05	165.40	–11.73	3.72	593.30	0.000	0.000
7/28	10:10	261	3216	3224	1	3	B4–A1	179.95	40.15	0.00	3657.96	609.81	4.6	1.50E+06	11.2	116.6	5.58E–05	165.39	–10.97	3.65	592.50	0.000	0.000
7/28	10:23	262	3225	3233	1	3	B4–A2	0.01	40.15	0.00	3656.93	609.76	4.6	1.50E+06	11.2	116.5	5.58E–05	165.35	–10.73	302.81	624.18	0.919	2.937
7/28	10:30	263	3234	3241	1	3	B4–A2	–179.97	40.15	0.00	3657.85	609.99	4.6	1.50E+06	11.2	116.6	5.58E–05	165.39	–10.40	303.07	630.93	0.913	2.935
7/28	11:05	264	3242	3244	1	3	0.015	–60.00	40.16	0.00	3657.82	609.61	4.6	1.50E+06	11.2	116.5	5.58E–05	165.39	–9.37	vary	621.68	vary	vary
7/28	11:51	265	3245	3253	1	3	B4–A1	–0.05	40.15	0.00	1387.49	595.15	3.5	9.99E+05	18.2	172.5	6.14E–05	155.99	–25.33	93.69	604.90	0.271	0.912
7/28	12:10	266	3254	3262	1	3	B4–A1	–0.05	40.15	0.00	1386.46	594.96	3.5	9.99E+05	18.2	172.5	6.14E–05	155.87	–24.55	84.78	599.70	0.248	0.830
7/28	12:17	267	3263	3264	1	3	0.031	–0.05	40.15	0.00	1387.26	594.89	3.5	1.00E+06	18.2	172.4	6.14E–05	155.96	–20.23	vary	615.55	vary	vary
7/28	12:33	268	3265	3266	3	3	–0.141	–0.01	43.10	0.00	193.86	584.81	0.0	0.00E+00	193.9	584.8	1.93E–04	0.00	–16.55	0.00	0.00	0.000	0.000
7/28	12:36	268	3267	3267	3	3	–0.144	–0.01	43.10	0.00	2123.06	623.54	0.0	0.00E+00	2123.1	623.5	1.98E–03	0.00	–23.93	0.00	0.00	0.000	0.000
7/29	7:27	269	3268	3268	5	0	2.127	–2.76	43.10	0.00	0.00	558.53	0.0	0.00E+00	0.0	558.5	0.00E+00	0.00	59.85	0.00	0.00	0.000	0.000
7/29	15:48	269	3269	3272	2	0	0.278	–0.71	41.09	0.00	2112.53	553.82	0.0	0.00E+00	2112.5	553.8	2.22E–03	0.00	56.42	0.00	0.00	0.000	0.000
7/30	6:42	270	3273	3273	2	0	–0.107	–0.03	40.16	0.00	2113.12	548.57	0.0	0.00E+00	2113.1	548.6	2.24E–03	0.00	64.84	0.00	0.00	0.000	0.000
7/30	7:49	270	3274	3275	2	0	–0.114	–0.03	40.16	0.00	338.47	538.96	0.0	0.00E+00	338.5	539.0	3.66E–04	0.00	9.38	0.00	0.00	0.000	0.000
7/30	8:32	271	3276	3284	1	0	B4–A1	–0.03	40.16	0.00	778.01	594.74	2.4	9.99E+05	53.2	276.4	1.12E–04	214.56	–26.43	1.14	571.08	0.000	0.000
7/30	8:37	272	3285	3293	1	0	B4–A1	59.57	40.16	0.00	777.94	594.64	2.4	1.00E+06	53.2	276.3	1.12E–04	214.54	–26.14	1.19	572.52	0.000	0.000
7/30	8:42	273	3294	3302	1	0	B4–A1	120.35	40.16	0.00	777.98	594.53	2.4	1.00E+06	53.2	276.3	1.12E–04	214.56	–25.53	1.26	573.63	0.000	0.000
7/30	8:49	274	3303	3311	1	0	B4–A1	179.99	40.16	0.00	777.89	594.60	2.4	1.00E+06	53.2	276.3	1.12E–04	214.53	–25.70	1.32	574.73	0.000	0.000
7/30	9:28	276	3312	3321	1	0	B4–A1	179.99	40.16	0.00	1386.83	594.75	3.5	1.00E+06	18.2	172.4	6.14E–05	155.92	–19.86	1.32	576.02	0.000	0.000
7/30	9:33	277	3322	3330	1	0	B4–A1	120.35	40.16	0.00	1386.29	594.92	3.5	9.99E+05	18.2	172.4	6.14E–05	155.86	–20.54	1.28	575.80	0.000	0.000
7/30	9:38	278	3331	3339	1	0	B4–A1	59.61	40.16	0.00	1386.98	594.66	3.5	1.00E+06	18.2	172.4	6.15E–05	155.93	–20.37	1.25	575.91	0.000	0.000
7/30	9:43	279	3340	3348	1	0	B4–A1	–0.05	40.16	0.00	1386.58	594.79	3.5	9.99E+05	18.2	172.4	6.14E–05	155.89	–19.91	1.21	575.90	0.000	0.000
7/30	10:30	280	3349	3357	1	0	B4–A1	–0.05	40.16	0.00	3658.22	609.96	4.6	1.50E+06	11.2	116.6	5.58E–05	165.40	–7.76	1.36	577.72	0.000	0.000
7/30	10:35	281	3358	3366	1	0	B4–A1	59.57	40.16	0.00	3657.91	609.87	4.6	1.50E+06	11.2	116.6	5.58E–05	165.39	–9.96	1.38	578.58	0.000	0.000
7/30	10:40	282	3367	3375	1	0	B4–A1	120.37	40.16	0.00	3658.06	609.90	4.6	1.50E+06	11.2	116.6	5.58E–05	165.40	–10.36	1.39	579.29	0.000	0.000
7/30	10:46	283	3376	3384	1	0	B4–A1	179.96	40.16	0.00	3658.06	609.97	4.6	1.50E+06	11.2	116.6	5.58E–05	165.40	–10.98	1.42	580.20	0.000	0.000
7/30	10:55	283	3385	3386	3	0	–0.137	–0.03	40.16	0.00	373.46	570.50	0.0	0.00E+00	373.5	570.5	3.81E–04	0.00	–24.48	0.00	0.00	0.000	0.000
7/30	10:58	284	3387	3387	3	0	–0.137	–0.03	40.16	0.00	2116.79	614.35	0.0	0.00E+00	2116.8	614.4	2.01E–03	0.00	–29.02	0.00	0.00	0.000	0.000
7/30	14:42	285	3389	3389	5	4	–0.136	–2.76	40.16	0.00	2116.79	570.20	0.0	0.00E+00	2116.8	570.2	2.16E–03	0.00	46.40	0.00	0.00	0.000	0.000
7/30	15:14	285	3390	3391	5	4	–0.128	–2.78	40.16	0.00	357.37	551.56	0.0	0.00E+00	357.4	551.6	3.77E–04	0.00	69.94	0.00	0.00	0.000	0.000
7/30	17:02	286	3392	3392	4	4	–0.002	–0.05	29.69	0.00	1329.26	594.77	0.0	0.00E+00	1329.3	594.8	1.30E–03	0.00	–25.62	271.15	628.94	1.223	2.111

Table B-3. Continued.

		RUN INFORMATION					MODEL ATTITUDE & LOCATION				RUN-AVERAGED FLOW CONDITIONS									NOZZLE EXIT CONDITIONS			
DATE	TIME	RUN	POINT		Key	#	PITCH	ROLL	X_STRUT	Y_STRUT	PTINF	TTINF	MACH	REINF	PINF	TINF	RHOINF	QINF	DEWPT	PTJ	TTJ	WJ	CT
2010			START	END		NOZ	{deg}	{deg}	{in}	{in}	{psf}	{R}		{1/ft}	{psf}	{R}	{slug/ft^3}	{psf}	{deg F}	{psia}	{R}	{lbm/sec}	
7/30	17:47	286	3393	3393	4	4	0.006	–0.05	29.69	0.00	2115.93	575.92	0.0	0.00E+00	2115.9	575.9	2.14E–03	0.00	–7.40	0.00	0.00	0.000	0.000
7/31	6:55	287	3394	3395	2	4	0.007	–0.03	29.69	0.00	2119.17	555.46	0.0	0.00E+00	2119.2	555.5	3.63E–04	0.00	49.70	0.00	0.00	0.000	0.000
7/31	7:21	287	3396	3397	5	4	0.011	–0.03	29.69	0.00	339.23	543.88	0.0	0.00E+00	339.2	543.9	3.63E+02	0.00	69.94	0.00	0.00	0.000	0.000
7/31	8:02	288	3398	3398	5	4	0.002	–0.03	40.17	0.00	778.03	594.92	2.4	9.98E+05	53.2	276.5	1.12E–04	214.57	–23.42	0.00	0.00	0.000	0.000
7/31	8:35	288	3399	3408	1	4	B4–A1	–0.03	40.17	0.00	777.88	594.50	2.4	1.00E+06	53.2	276.3	1.12E–04	214.53	–26.12	195.76	630.23	0.777	1.928
7/31	8:41	289	3409	3417	1	4	B4–A1	59.62	40.17	0.00	778.10	594.56	2.4	1.00E+06	53.2	276.3	1.12E–04	214.59	–26.30	195.86	631.05	0.778	1.932
7/31	8:47	290	3418	3426	1	4	B4–A1	120.39	40.17	0.00	778.10	594.58	2.4	1.00E+06	53.2	276.3	1.12E–04	214.59	–26.52	195.83	629.57	0.778	1.930
7/31	8:54	291	3427	3435	1	4	B4–A1	–179.95	40.17	0.00	778.06	594.75	2.4	9.99E+05	53.2	276.4	1.12E–04	214.58	–26.58	196.12	628.78	0.781	1.935
7/31	9:10	292	3436	3438	1	4	0.002	vary	vary	0.00	777.89	594.50	2.4	1.00E+06	53.2	276.3	1.12E–04	214.53	–28.73	195.54	628.99	0.778	1.928
7/31	9:18	293	3439	3447	1	4	B4–A1	179.97	40.16	0.00	778.08	594.50	2.4	1.00E+06	53.2	276.3	1.12E–04	214.58	–29.02	98.91	623.07	0.380	0.941
7/31	9:23	294	3448	3456	1	4	B4–A1	120.37	40.16	0.00	778.06	594.90	2.4	9.99E+05	53.2	276.4	1.12E–04	214.58	–29.17	99.07	621.13	0.382	0.945
7/31	9:29	295	3457	3465	1	4	B4–A1	59.61	40.16	0.00	778.08	594.46	2.4	1.00E+06	53.2	276.2	1.12E–04	214.58	–29.29	99.21	621.13	0.383	0.947
7/31	9:33	296	3466	3474	1	4	B4–A1	–0.05	40.16	0.00	777.86	594.69	2.4	9.99E+05	53.2	276.3	1.12E–04	214.52	–29.51	98.97	621.00	0.382	0.944
7/31	9:46	297	3475	3478	1	4	0.047	vary	vary	0.00	778.09	594.63	2.4	1.00E+06	53.2	276.3	1.12E–04	214.59	–29.47	295.57	630.36	1.192	2.951
7/31	10:30	298	3479	3487	1	4	B4–A1	0.01	40.16	0.00	1386.98	594.59	3.5	1.00E+06	18.2	172.3	6.15E–05	155.93	–21.37	142.97	621.87	0.563	1.915
7/31	10:35	299	3488	3496	1	4	B4–A1	59.57	40.16	0.00	1385.95	593.61	3.5	1.00E+06	18.2	172.1	6.15E–05	155.82	–19.93	143.04	620.88	0.565	1.919
7/31	11:06	300	3497	3505	1	4	B4–A1	120.37	40.16	0.00	1387.75	595.35	3.5	9.99E+05	18.2	172.6	6.14E–05	156.02	–24.02	143.07	620.01	0.565	1.914
7/31	11:10	301	3506	3514	1	4	B4–A1	179.95	40.16	0.00	1386.67	594.66	3.5	1.00E+06	18.2	172.4	6.14E–05	155.90	–22.11	143.49	619.90	0.567	1.923
7/31	11:20	302	3515	3523	1	4	B4–A1	179.95	40.16	0.00	1386.72	594.42	3.5	1.00E+06	18.2	172.3	6.15E–05	155.90	–21.32	71.21	614.77	0.266	0.905
7/31	11:24	303	3524	3532	1	4	B4–A1	120.43	40.16	0.00	1386.29	594.45	3.5	1.00E+06	18.2	172.3	6.15E–05	155.86	–21.17	70.78	612.99	0.264	0.898
7/31	11:29	304	3533	3541	1	4	B4–A1	59.59	40.16	0.00	1386.67	594.94	3.5	9.99E+05	18.2	172.4	6.14E–05	155.90	–21.08	71.07	612.72	0.266	0.904
7/31	11:34	305	3542	3550	1	4	B4–A1	–0.03	40.16	0.00	1387.22	595.11	3.5	9.99E+05	18.2	172.5	6.14E–05	155.96	–20.92	71.10	612.45	0.266	0.902
7/31	11:45	306	3551	3555	1	4	0.004	vary	vary	0.00	1386.55	595.32	3.5	9.98E+05	18.2	172.6	6.14E–05	155.88	–18.81	vary	619.05	vary	vary
7/31	12:22	307	3556	3564	1	4	B4–A1	0.05	40.17	0.00	3657.79	609.68	4.6	1.50E+06	11.2	116.5	5.58E–05	165.38	–7.60	151.93	618.38	0.602	1.923
7/31	12:27	308	3565	3573	5	4	B4–A1	59.98	40.17	0.00	3657.96	609.66	4.6	1.50E+06	11.2	116.5	5.58E–05	165.39	–8.93	148.34	618.86	0.605	1.920
7/31	12:34	309	3574	3582	1	4	B4–A1	59.53	40.17	0.00	3658.01	609.80	4.6	1.50E+06	11.2	116.6	5.58E–05	165.39	–10.11	151.99	619.74	0.601	1.921
7/31	12:48	310	3583	3592	1	4	B4–A1	120.36	40.17	0.00	3658.13	609.85	4.6	1.50E+06	11.2	116.6	5.58E–05	165.40	–10.79	152.14	620.37	0.601	1.922
7/31	12:54	311	3593	3601	1	4	B4–A1	–179.98	40.17	0.00	3657.77	609.71	4.6	1.50E+06	11.2	116.5	5.58E–05	165.38	–11.29	152.41	620.71	0.602	1.926
7/31	13:09	312	3602	3610	1	4	B4–A1	–179.97	40.17	0.00	3658.25	609.21	4.6	1.50E+06	11.2	116.4	5.59E–05	165.41	–11.47	76.81	615.87	0.285	0.915
7/31	13:14	313	3611	3619	1	4	B4–A1	120.39	40.17	0.00	3657.70	609.69	4.6	1.50E+06	11.2	116.5	5.58E–05	165.38	–13.52	76.48	614.91	0.287	0.918
7/31	13:19	314	3620	3628	1	4	B4–A1	59.63	40.17	0.00	3658.10	609.95	4.6	1.50E+06	11.2	116.6	5.58E–05	165.40	–13.53	76.47	614.87	0.286	0.916
7/31	13:25	315	3629	3637	1	4	B4–A1	0.05	40.17	0.00	3658.20	609.35	4.6	1.50E+06	11.2	116.5	5.59E–05	165.40	–12.03	76.39	614.81	0.285	0.912

Table B-3. Concluded.

		RUN INFORMATION					MODEL ATTITUDE & LOCATION				RUN-AVERAGED FLOW CONDITIONS									NOZZLE EXIT CONDITIONS			
DATE	TIME	RUN	POINT		Key	# NOZ	PITCH	ROLL	X_STRUT	Y_STRUT	PTINF	TTINF	MACH	REINF	PINF	TINF	RHOINF	QINF	DEWPT	PTJ	TTJ	WJ	CT
2010			START	END			{deg}	{deg}	{in}	{in}	{psf}	{R}		{1/ft}	{psf}	{R}	{slug/ft^3}	{psf}	{deg F}	{psia}	{R}	{lbm/sec}	
7/31	13:38	316	3638	3639	3	4	0.015	0.05	40.17	0.00	378.65	565.79	0.0	0.00E+00	378.6	565.8	3.90E–04	0.00	–25.91	0.00	0.00	0.000	0.000
7/31	13:40	316	3640	3640	3	4	0.016	0.05	40.17	0.00	2114.20	617.80	0.0	0.00E+00	2114.2	617.8	1.99E–03	0.00	–32.68	0.00	0.00	0.000	0.000
7/31	15:04	317	3641	3641	2	1	–0.051	60.98	40.17	0.00	2118.09	585.01	0.0	0.00E+00	2118.1	585.0	2.11E–03	0.00	6.80	0.00	0.00	0.000	0.000
7/31	15:22	317	3642	3644	2	1	–0.052	60.98	40.17	0.00	357.05	570.67	0.0	0.00E+00	357.0	570.7	3.64E–04	0.00	–18.77	0.00	0.00	0.000	0.000
7/31	15:50	318	3645	3649	1	1	vary	0.01	vary	0.00	777.90	594.64	2.4	9.99E+05	53.2	276.3	1.12E–04	214.53	–16.12	777.49	595.24	0.833	1.985
7/31	15:58	319	3650	3655	1	1	vary	0.01	vary	0.00	777.85	594.69	2.4	9.99E+05	53.2	276.3	1.12E–04	214.52	–16.04	193.57	593.31	0.189	0.457
7/31	16:20	320	3656	3660	1	1	vary	0.01	vary	0.00	1386.38	594.07	3.5	1.00E+06	18.2	172.2	6.15E–05	155.86	–10.20	563.49	605.49	0.589	1.957
7/31	16:43	321	3661	3666	1	1	vary	0.01	vary	0.00	3659.15	609.91	4.6	1.50E+06	11.2	116.6	5.58E–05	165.45	0.86	599.91	611.34	0.622	1.956
7/31	16:52	322	3667	3668	3	1	–0.012	–0.01	40.17	0.00	373.35	564.90	0.0	0.00E+00	373.4	564.9	3.85E–04	0.00	–7.83	0.00	0.00	0.000	0.000
7/31	16:55	322	3669	3669	3	1	–0.01	–0.01	40.17	0.00	2106.86	616.44	0.0	0.00E+00	2106.9	616.4	1.99E–03	0.00	–7.78	0.00	0.00	0.000	0.000

Key	Run Condition
1	Normal Run
2	Pre-Run Wind-Off Zero
3	Post-Run Wind-Off Zero
4	Wind-Off Data Run or Checkout Run
5	Bad Data or Incorrect Operating Conditions

Table B-4. Angle of attack sweep schedule.

Pause Step	Schedule		
	A1	A2	A3
1	–8.0	–8.0	–8.0
2	–4.0	–4.0	–4.0
3	0.0	0.0	0.0
4	4.0	4.0	4.0
5	8.0	8.0	8.0
6	12.0	12.0	12.0
7	16.0	16.0	
8	20.0	0.0	
9	0.0		

Table B-5. Statistical analysis of as-tested flow conditions.

(a) M_∞ = 2.40.

Parameter	Units	Min	Max	Median	Mean	Std Dev	Std Err Mean
$P_{T,\infty}$	lbf/ft^2	774.360	780.840	777.816	777.844	0.58504	0.01813
$T_{T,\infty}$	R	593.780	597.760	594.690	594.806	0.47827	0.01482
Dew Point	deg F	–29.559	–15.969	–24.624	–24.693	2.14019	0.06633
P_∞	lbf/ft^2	52.966	53.409	53.202	53.204	0.04002	0.00124
T_∞	R	275.920	277.770	276.343	276.397	0.22224	0.00689
ρ_∞	slug/ft^3	1.1154E–04	1.1260E–04	1.1215E–04	1.1214E–04	1.1463E–07	3.5528E–09
q_∞	lbf/ft^2	213.558	215.345	214.511	214.519	0.16134	0.00500
V_∞	ft/sec	1954.350	1960.890	1955.840	1956.034	0.78602	0.02436
Re_∞	1/ft	992577	1003361	999175	998983	1273.90520	39.48315

(b) M_∞ = 3.50.

Parameter	Units	Min	Max	Median	Mean	Std Dev	Std Err Mean
$P_{T,\infty}$	lbf/ft^2	1375.270	1391.690	1386.720	1386.624	1.08953	0.04148
$T_{T,\infty}$	R	592.710	596.540	594.700	594.677	0.54294	0.02067
Dew Point	deg F	–28.120	–9.414	–21.068	–20.351	3.14173	0.12022
P_∞	lbf/ft^2	18.031	18.246	18.181	18.180	0.01428	0.00054
T_∞	R	171.800	172.910	172.377	172.370	0.15737	0.00599
ρ_∞	slug/ft^3	6.0992E–05	6.1650E–05	6.1438E–05	6.1441E–05	6.8395E–08	2.6038E–09
q_∞	lbf/ft^2	154.617	156.462	155.904	155.893	0.12249	0.00466
V_∞	ft/sec	2248.940	2256.200	2252.710	2252.671	1.02843	0.03915
Re_∞	1/ft	992826	1004777	999558	999659.75	1502.36120	57.19392

Table B-5. Concluded.

(c) M_∞ = 4.60.

Parameter	Units	Min	Max	Median	Mean	Std Dev	Std Err Mean
$P_{T,\infty}$	lbf/ft^2	3648.240	3660.980	3657.740	3657.843	0.83870	0.03326
$T_{T,\infty}$	R	609.060	611.590	609.850	609.910	0.33981	0.01347
Dew Point	deg F	–20.624	1.131	–11.342	–10.480	2.85393	0.11317
P_∞	lbf/ft^2	11.136	11.175	11.166	11.166	0.00256	0.00010
T_∞	R	116.411	116.894	116.562	116.573	0.06495	0.00258
ρ_∞	slug/ft^3	5.5634E–05	5.5890E–05	5.5803E–05	5.5789E–05	3.3875E–08	1.3432E–09
q_∞	lbf/ft^2	164.953	165.529	165.383	165.387	0.03792	0.00150
V_∞	ft/sec	2433.060	2438.110	2434.640	2434.755	0.67810	0.02689
Re_∞	1/ft	1491902	1502623	1499140	1498914.4	1410.09850	55.91404

APPENDIX C
SCHLIEREN RESULTS

Schlieren videos were acquired with a high speed digital camera, the Vision Research Phantom 12, to capture flow field dynamics resulting from jet/bow shock interactions. Due to data file storage constraints on the camera, only select test points within a run were captured to minimize the offload frequency. At times during the test when the camera storage was full, offloading of video files precluded capturing results for a few runs. Table C-1 provides a list of the schlieren videos captured in run chronological order, with an "X" to mark the specific angles of attack acquired. Also shown in Table C-1 are the video camera settings (camera resolution, framing rate, and total number of frames) for each run. The schlieren video cases are reorganized in Table C-2 to provide the matrix of cases captured for each configuration: the baseline model, and center, tri- and quad-nozzle cases. All schlieren results are provided in run chronological order following the tables. In some cases, extra videos were taken with the model translated or rolled to reveal hidden flow features. These cases do not show up specifically in the tables, but the uniqueness of these repeat cases is contained within the figure captions. For the multi-nozzle cases, roll increments of 30 degrees (as opposed the standard 60 degrees called out in the run matrix) allowed for the three peripheral nozzles to be out of phase, thereby showing flow from each nozzle independently in the schlieren.

Flow dynamics are difficult to capture with a single extracted image from the video file. To better represent the unsteadiness, video processing was employed. For each case, three images are provided in a row to illustrate the level of flow unsteadiness. The first image provides a single arbitrary frame extracted from the video file, showing specific flow features frozen in time. The second image provides the average intensity of all frames from the video file. This particular type of processing is suggestive of schlieren video taken with standard video framing rates (30 fps), which tends to blur out unsteadiness and accentuates only steady features. The last image provides the standard deviation of all the frames in the video. In this case, the whiter/brighter areas indicate where the fluctuations are most intense, identifying regions of flow unsteadiness. When flow is steady, the three images will look similar, such as seen with the baseline cases. Note that video processing was applied consistently for all runs, the varying results with the first few runs were due to a schlieren knife edge misalignment that could not be compensated for with posttest digital enhancement.

For those interested in viewing the videos, they have been compiled into three files according to Mach number, each lasting just under 18 minutes. These videos have been archived at NASA YouTube Links:

- SRP_m2.4.avi: http://youtu.be/-ezb03W6KCc
- SRP_m3.5.avi: http://youtu.be/fTmPc1olhiU
- SRP_m4.6.avi: http://youtu.be/i-coJg_vgxI

Table C-1. Schlieren video acquisition information in run chronological order.

Run	Nozzles	Mach	C_T	Alpha, deg								Resolution	Framing Rate	# Frames
				–8	–4	0	4	8	12	16	20		frames/sec	
58	0	3.50	0.000	X	X	X	X	X	X		X	1280 x 800	6245	2471
67	0	3.50	0.000	X	X	X	X	X	X	X	X	1280 x 800	6245	2471
86	0	4.60	0.000	X	X	X	X	X	X		X	1280 x 800	6245	2471
106	0	4.60	0.000	X	X	X	X	X	X	X	X	1024 x 800	6245	3090
136	1	2.40	4.024			X	X		X			1024 x 800	6245	1390
137	1	2.40	3.002			X	X		X			1024 x 800	6245	1390
139	1	2.40	0.968			X	X	X	X		X	1024 x 800	6245	1390
141	1	2.40	1.982			X	X	X	X			1024 x 800	6245	1390
150	1	3.50	2.978			X	X		X		X	1024 x 800	6245	695
153	1	3.50	1.962			X	X	X	X		X	1024 x 800	6245	695
154	1	3.50	0.938			X	X		X		X	1024 x 800	6245	695
157	1	3.50	0.448			X	X		X		X	1024 x 800	6245	695
158	1	3.50	0.210			X	X		X		X	1024 x 800	6245	695
163	1	4.60	2.959			X	X		X		X	1024 x 800	6245	695
165	1	4.60	1.968			X	X		X		X	1024 x 800	6245	695
167	1	4.60	0.943			X	X		X			1024 x 800	6245	695
169	1	4.60	0.454			X	X					1024 x 800	6245	695
171	1	4.60	0.219			X						1024 x 800	6245	695
180	3	2.40	0.000			X	X	X	X	X	X	896 x 704	5000	721
185	3	3.50	0.000			X	X	X	X	X	X	896 x 704	5000	721
190	3	2.40	2.939			X	X		X		X	896 x 704	5000	721
192	3	2.40	2.943					X				896 x 704	5000	721
194	3	2.40	1.940			X	X		X		X	896 x 704	5000	721

Table C-1. Continued.

Run	Nozzles	Mach	C_T	Alpha, deg								Resolution	Framing Rate	# Frames
				–8	–4	0	4	8	12	16	20		frames/sec	
198	3	2.40	0.944			X	X		X		X	896 x 704	5000	721
202	3	2.40	0.431			X	X		X		X	896 x 704	5000	721
206	3	2.40	0.435			X						896 x 704	5000	721
212	3	4.60	2.933			X	X	X	X	X		896 x 672	10000	598
214	3	4.60	2.954	X	X	X	X	X	X	X		896 x 672	10000	598
221	3	2.40	0.235			X	X		X			896 x 672	10000	598
222	3	3.50	2.963			X	X	X	X	X	X	896 x 672	10000	598
225	3	3.50	2.985			X	X	X	X	X	X	896 x 672	10000	598
226	3	3.50	1.956			X	X		X		X	896 x 672	10000	598
247	3	4.60	1.919			X	X	X	X		X	896 x 672	10000	598
248	3	4.60	1.930			X	X	X	X		X	896 x 672	10000	598
249	3	4.60	0.898			X	X		X		X	896 x 672	10000	598
253	3	4.60	0.428			X	X		X		X	896 x 672	10000	598
257	3	4.60	0.199			X	X		X	X		896 x 672	10000	598
262	3	4.60	2.937			X	X		X	X		896 x 672	10000	598
263	3	4.60	2.935			X	X		X	X		896 x 672	10000	598
264	3	4.60	vary			X			X			896 x 672	10000	598
265	3	3.50	0.912			X	X		X		X	896 x 672	10000	598
266	3	3.50	0.830			X	X		X		X	896 x 672	10000	598
267	3	3.50	vary			X						896 x 672	10000	598
274	0	2.40	0.000	X	X	X	X	X	X	X	X	896 x 672	10000	598
276	0	3.50	0.000	X	X	X	X	X	X	X	X	896 x 672	10000	598
283	0	4.60	0.000	X	X	X	X	X	X	X	X	896 x 672	10000	598
288	4	2.40	1.928	X	X	X	X	X	X	X	X	896 x 672	10000	598
291	4	2.40	1.935			X	X	X	X	X	X	896 x 672	10000	598

Table C-1. Concluded.

Run	Nozzles	Mach	C_T	Alpha, deg								Resolution	Framing Rate	# Frames
				–8	–4	0	4	8	12	16	20		frames/sec	
292	4	2.40	1.928			X						896 x 672	10000	598
293	4	2.40	0.941			X	X	X	X		X	896 x 672	10000	598
297	4	2.40	2.951			X						896 x 672	10000	598
298	4	3.50	1.915			X	X		X		X	896 x 672	10000	598
301	4	3.50	1.923			X	X		X		X	896 x 672	10000	598
305	4	3.50	0.902			X	X		X		X	896 x 672	10000	598
306	4	3.50	vary			X						896 x 672	10000	598
307	4	4.60	1.923			X	X		X		X	896 x 672	10000	598
311	4	4.60	1.926			X	X		X		X	896 x 672	10000	598
315	4	4.60	0.912			X	X		X		X	896 x 672	10000	598
318	1	2.40	1.985			X		X	X			896 x 672	10000	598
319	1	2.40	0.457			X	X	X	X		X	896 x 672	10000	598
320	1	3.50	1.957			X		X	X			896 x 672	10000	598
321	1	4.60	1.956			X		X	X			896 x 672	10000	598

Table C-2. Schlieren cases rearranged by configuration.
(a) Matrix of baseline schlieren cases.

	Mach 2.4									Mach 3.5									Mach 4.6								
CT	RUN	Alpha, deg								RUN	Alpha, deg								RUN	Alpha, deg							
		–8	–4	0	4	8	12	16	20		–8	–4	0	4	8	12	16	20		–8	–4	0	4	8	12	16	20
0.00	274	X	X	X	X	X	X	X	X	58	X	X	X	X	X	X		X	86	X	X	X	X	X	X		X
										67	X	X	X	X	X	X	X	X	106	X	X	X	X	X	X	X	X
										276	X	X	X	X	X	X	X	X	283	X	X	X	X	X	X	X	X

Table C-2. Continued.
(b) Matrix of center nozzle schlieren cases.

CT	Mach 2.4									Mach 3.5									Mach 4.6								
	RUN	Alpha, deg								RUN	Alpha, deg								RUN	Alpha, deg							
		–8	–4	0	4	8	12	16	20		–8	–4	0	4	8	12	16	20		–8	–4	0	4	8	12	16	20
0																											
0.25										158			X	X		X		X	171			X					
0.5	319			X	X	X	X		X	157			X	X		X		X	169			X	X				
1	139			X	X	X	X		X	154			X	X		X		X	167			X	X		X		
2	141			X	X	X	X			320			X		X	X			321			X		X	X		
3	318			X		X	X			153			X	X	X	X		X	165			X	X		X		X
4	137			X	X		X			150			X	X		X		X	163			X	X		X		X

(c) Matrix of tri-nozzle schlieren cases.

CT	Mach 2.4									Mach 3.5									Mach 4.6								
	RUN	Alpha, deg								RUN	Alpha, deg								RUN	Alpha, deg							
		–8	–4	0	4	8	12	16	20		–8	–4	0	4	8	12	16	20		–8	–4	0	4	8	12	16	20
0	180			X	X	X	X	X	X	185			X	X	X	X	X	X									
0.25	221			X	X		X												257			X	X		X	X	
0.5	202			X	X		X		X										253			X	X		X		X
0.5	206			X																							
1										265			X	X		X		X	249			X	X		X		X
1	198			X	X		X		X	266			X	X		X		X									
2	194			X	X		X		X	226			X	X		X		X	247			X	X	X	X		X
2																			248			X	X	X	X		X
3	190			X	X		X		X	222			X	X	X	X	X	X	212			X	X	X	X	X	
3	192					X				225			X	X	X	X	X	X	263			X	X		X	X	
3																			262			X	X		X	X	
3																			214	X	X	X	X	X	X	X	
Vary										267			X						264			X			X		

Table C-2. Concluded.
(d) Matrix of quad-nozzle schlieren cases.

CT	Mach 2.4									Mach 3.5									Mach 4.6								
	RUN	Alpha, deg								RUN	Alpha, deg								RUN	Alpha, deg							
		–8	–4	0	4	8	12	16	20		–8	–4	0	4	8	12	16	20		–8	–4	0	4	8	12	16	20
1	293			X	X	X	X		X	305			X	X		X		X	315			X	X		X		X
2	288	X	X	X	X	X	X	X	X	298			X	X		X		X	307			X	X		X		X
2	291			X	X	X	X	X	X	301			X	X		X		X	311			X	X		X		X
2	292			X																							
3	297			X																							
Vary										306			X														

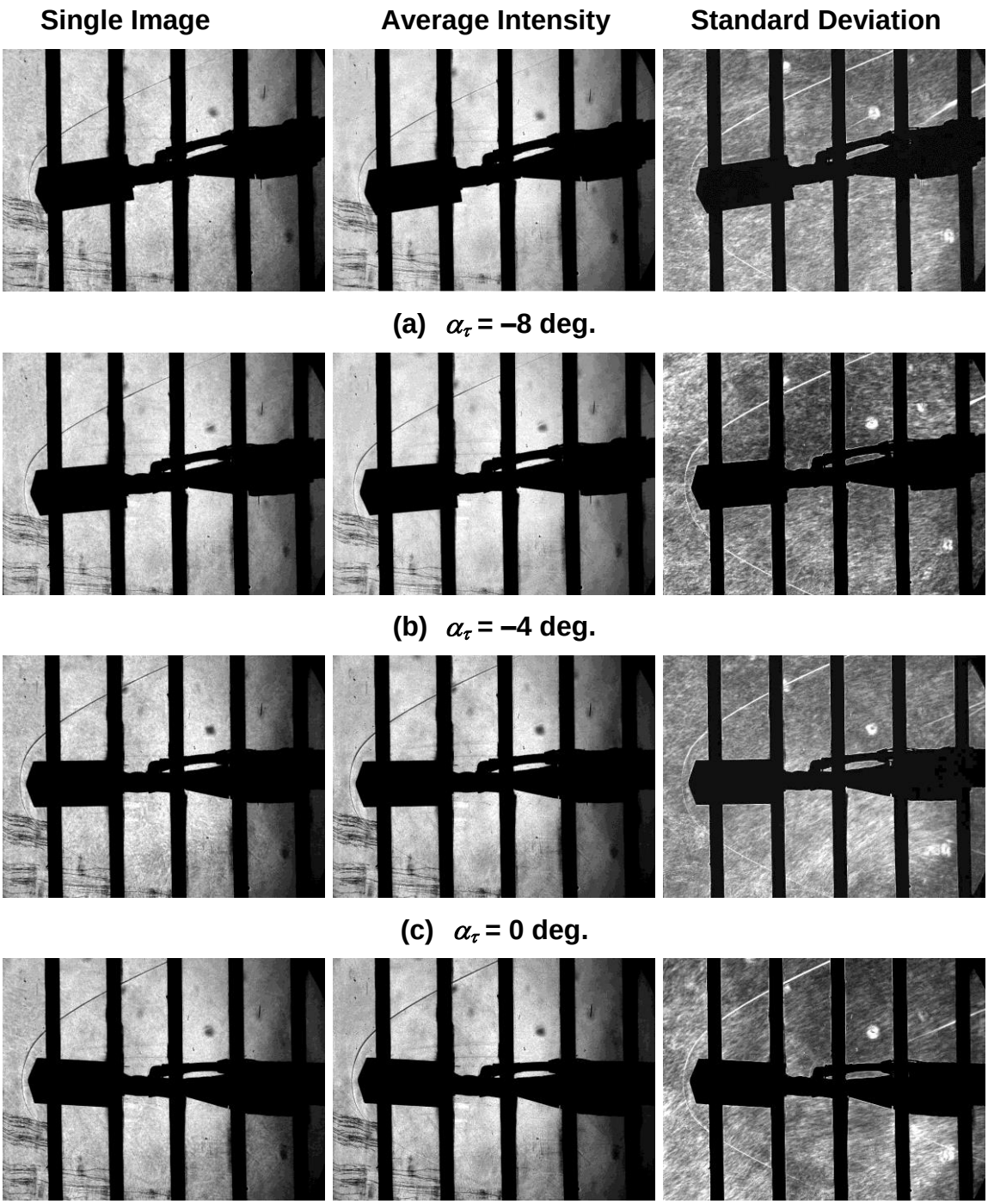

Figure C-1. Run 58: baseline schlieren video images for range of α_τ at M_∞ = 3.5, C_T = 0.0, and ϕ = 60 deg.

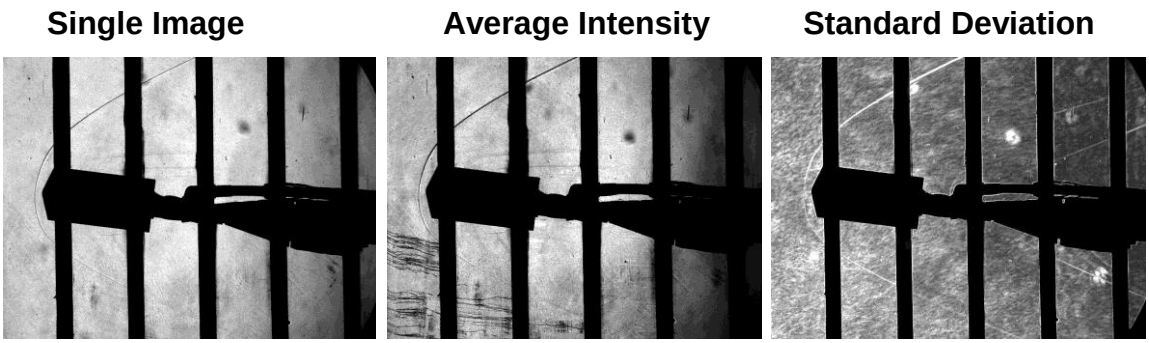

(e) α_τ = 8 deg.

(f) α_τ = 12 deg.

(g) α_τ = 20 deg.

Figure C-1. Concluded.

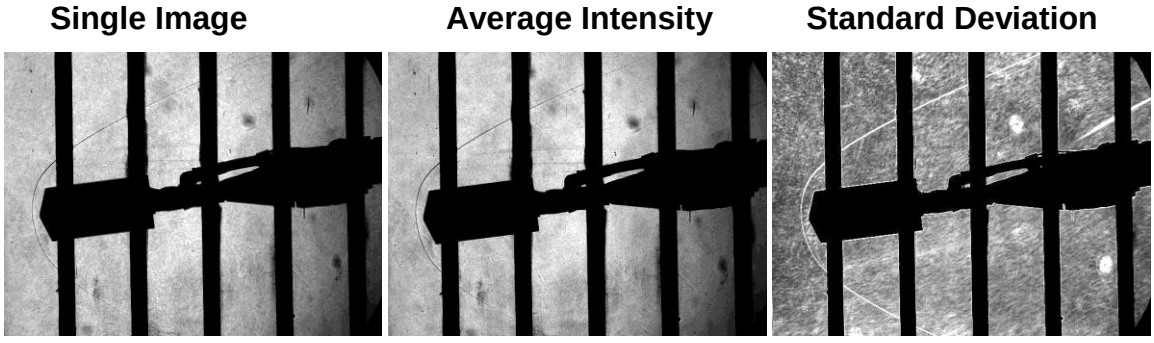

(a) α_τ = –8 deg.

Figure C-2. Run 67: baseline Schlieren video images for range of α_τ at $M\infty$ = 3.5, C_T = 0.0, and ϕ = 60 deg.

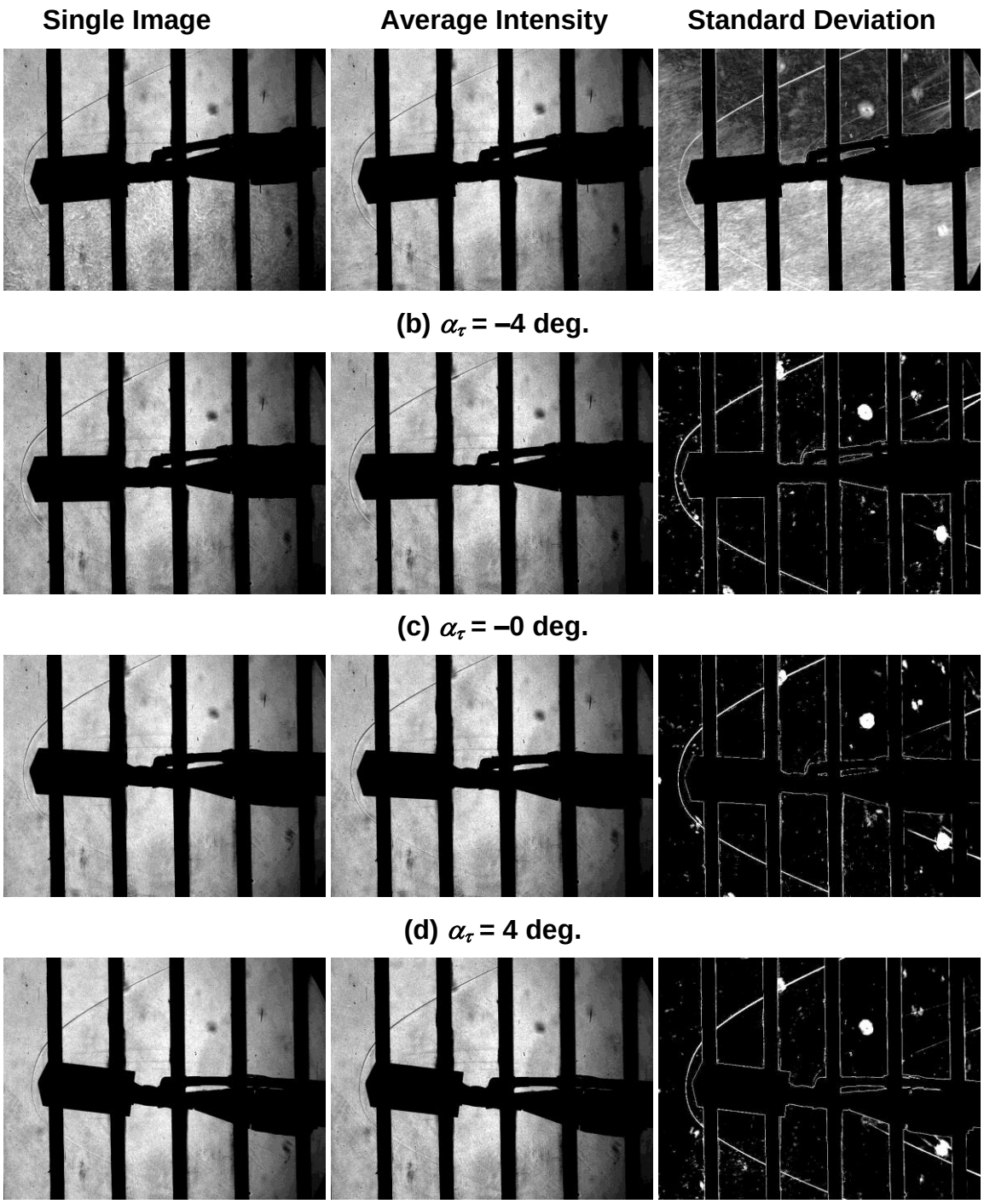

(b) α_τ = –4 deg.

(c) α_τ = –0 deg.

(d) α_τ = 4 deg.

(e) α_τ = 8 deg.

Figure C-2. Continued.

Single Image | Average Intensity | Standard Deviation

(f) α_τ = 12 deg.

(g) α_τ = 16 deg.

(h) α_τ = 20 deg.

Figure C-2. Concluded.

Single Image | Average Intensity | Standard Deviation

(a) α_τ = –8 deg.

Figure C-3. Run 86: baseline Schlieren video images for range of α_τ at $M\infty$ = 4.6, C_T = 0.0, and ϕ = 0 deg.

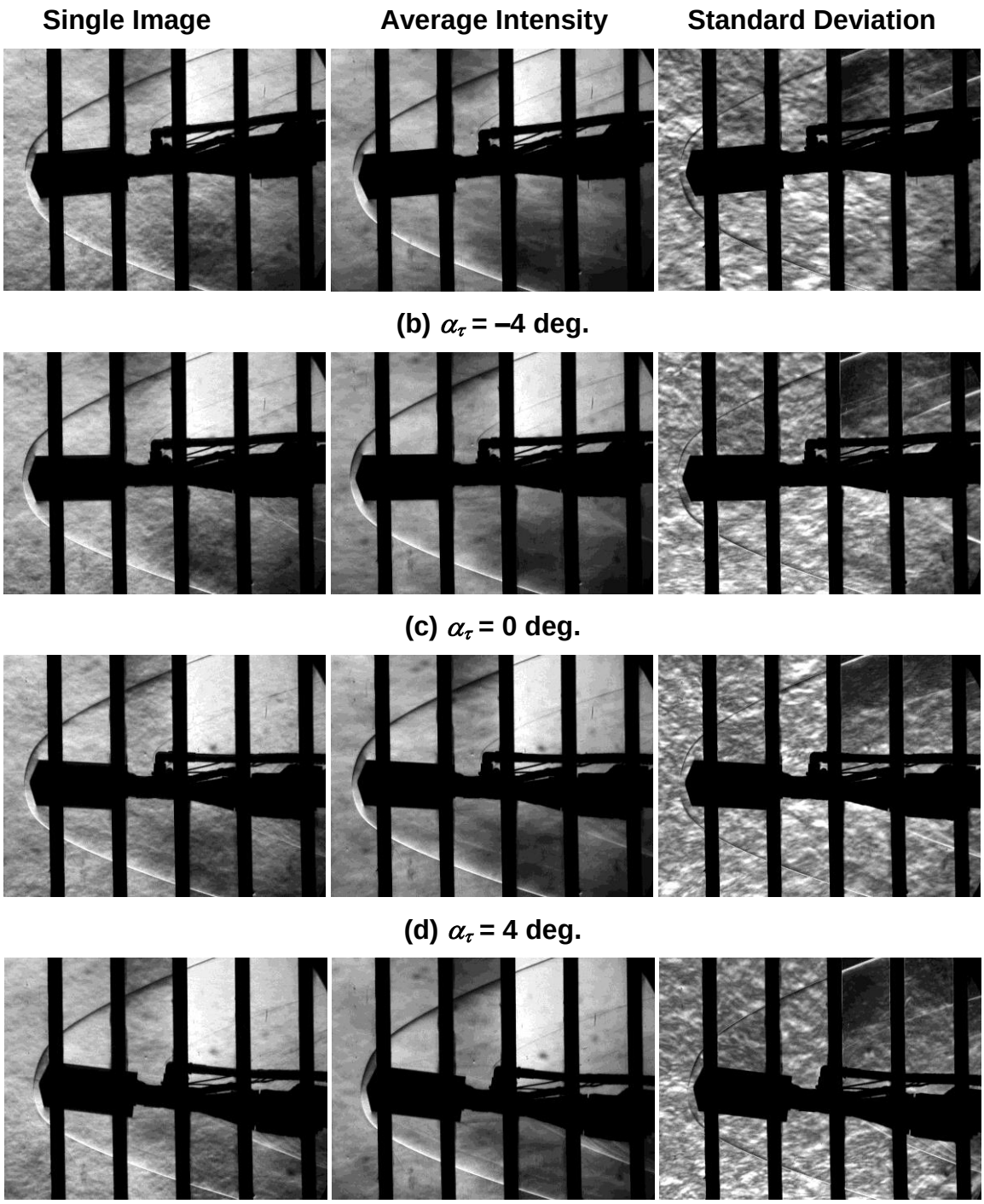

(b) α_τ = –4 deg.

(c) α_τ = 0 deg.

(d) α_τ = 4 deg.

(e) α_τ = 8 deg.

Figure C-3. Continued.

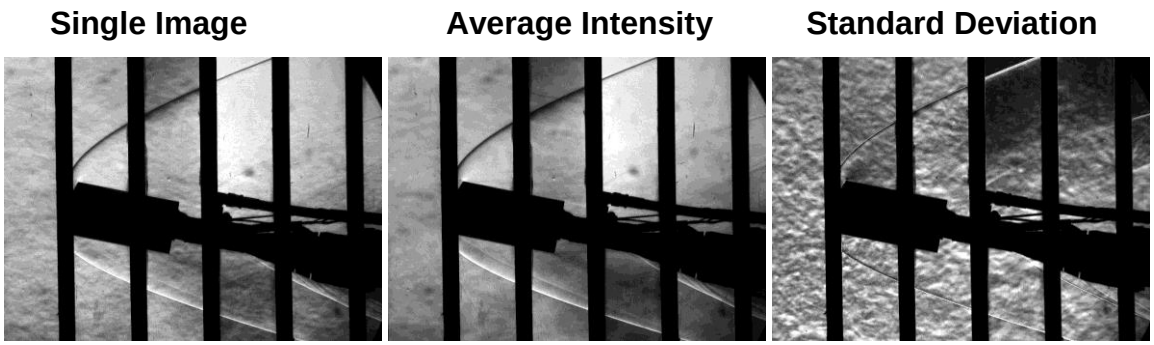

(f) α_τ = 12 deg.

(g) α_τ = 16 deg.

Figure C-3. Concluded.

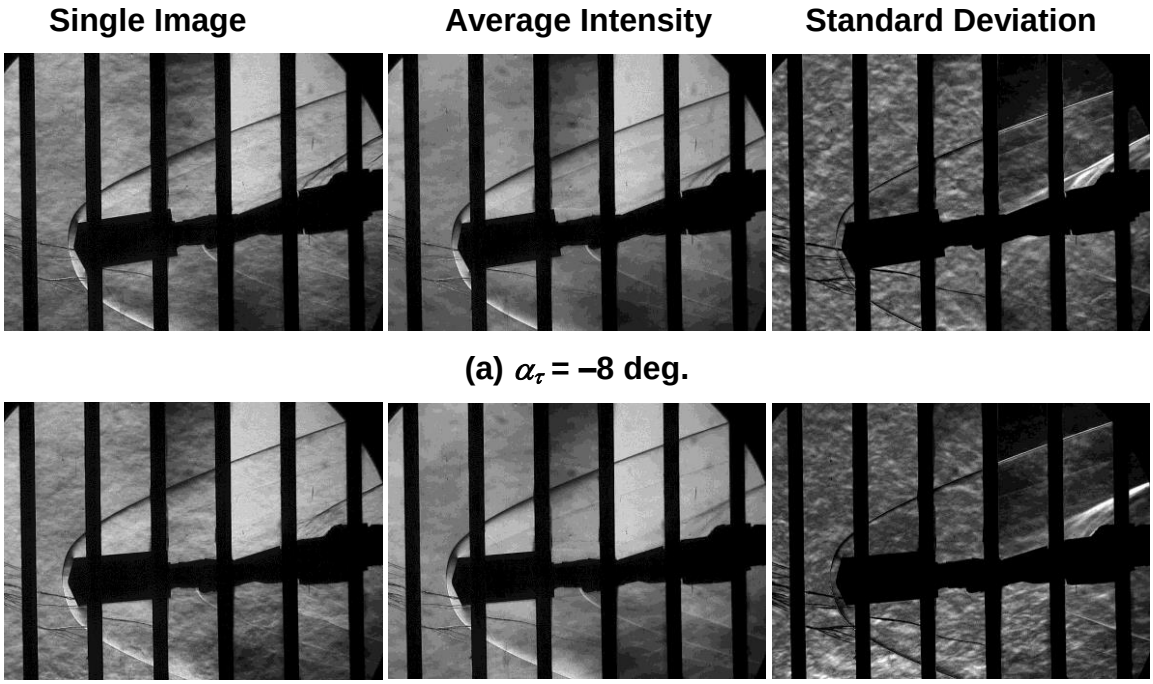

(a) α_τ = –8 deg.

(b) α_τ = –4 deg.

Figure C-4. Run 106: baseline Schlieren video images for range of α_τ at $M\infty$ = 4.6, C_T = 0.0, and ϕ = 120 deg.

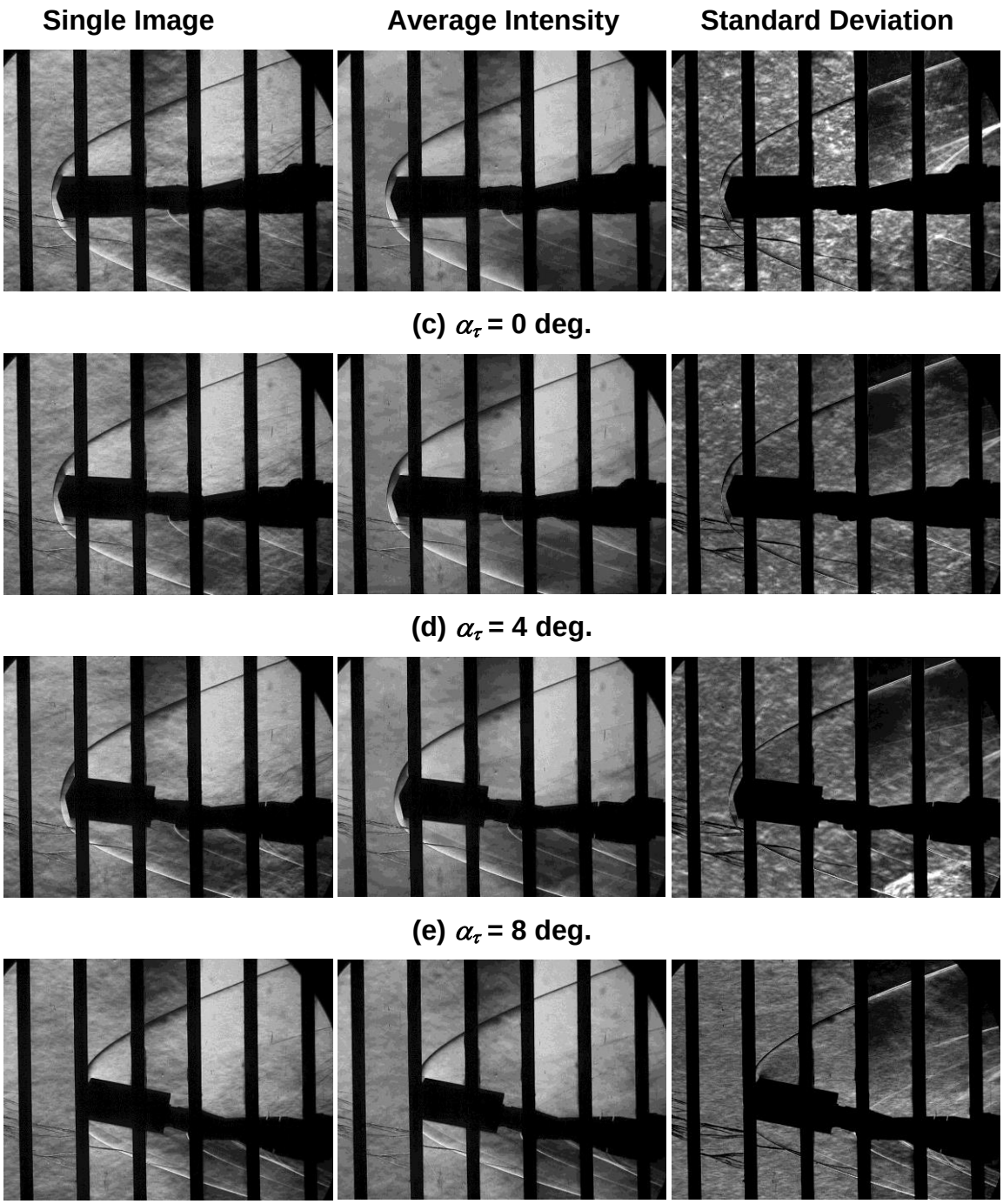

(c) α_τ = 0 deg.

(d) α_τ = 4 deg.

(e) α_τ = 8 deg.

(f) α_τ = 12 deg.

Figure C-4. Continued.

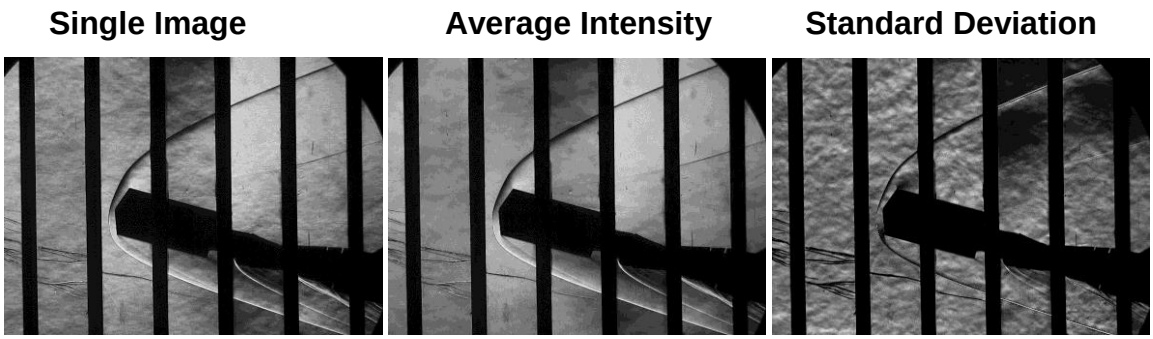

(g) α_τ = 16 deg.

(h) α_τ = 20 deg.

Figure C-4. Concluded.

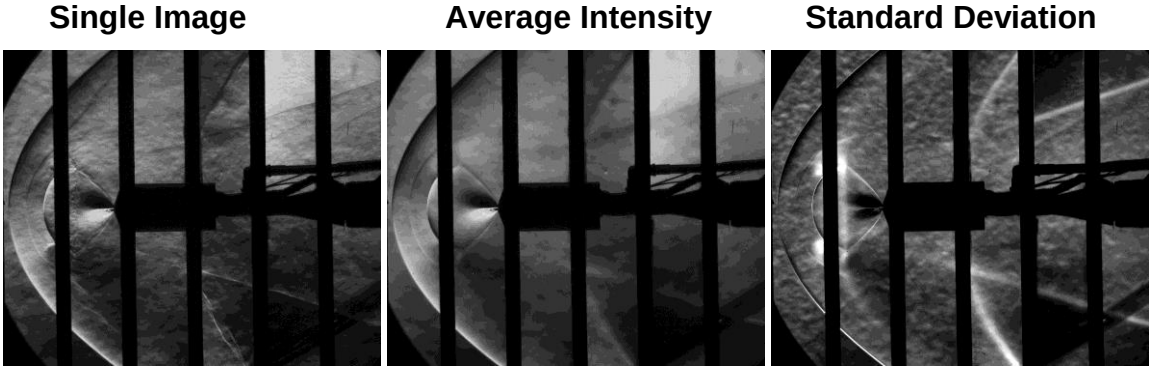

(a) α_τ = 0 deg, taken prior to the run with the model forward.

(b) α_τ = 0 deg.

Figure C-5. Run 136: center nozzle schlieren video images for range of α_τ at $M\infty$ = 2.4, C_T = 4.0, and ϕ = 0 deg.

(c) α_τ = 4 deg.

(d) α_τ = 12 deg.

Figure C-5. Concluded.

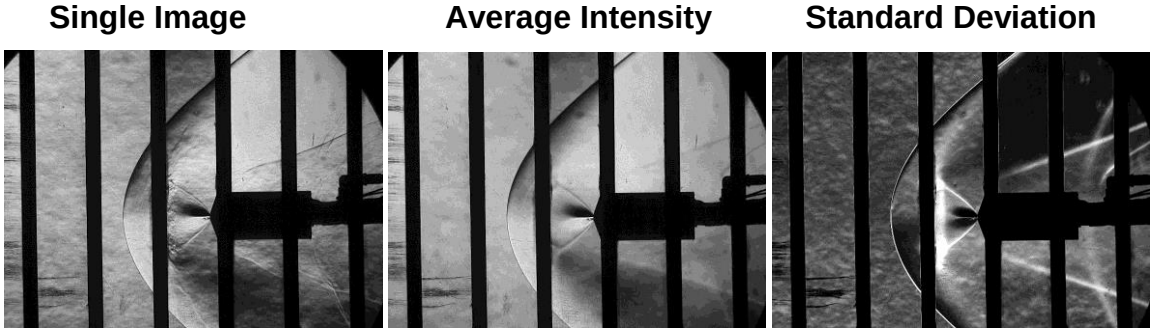

(a) α_τ = 0 deg.

(b) α_τ = 4 deg.

Figure C-6. Run 137: center nozzle schlieren video images for range of α_τ at $M\infty$ = 2.4, C_T = 3.0, and ϕ = 0 deg.

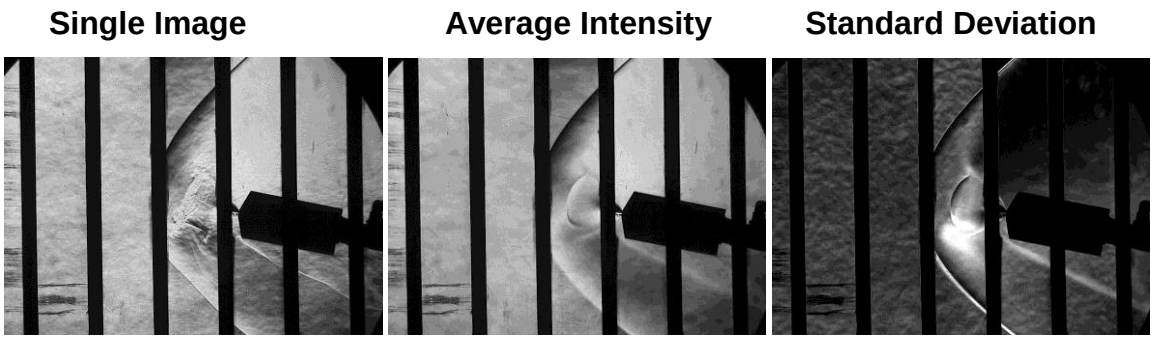

(c) α_τ = 12 deg.

Figure C-6. Concluded.

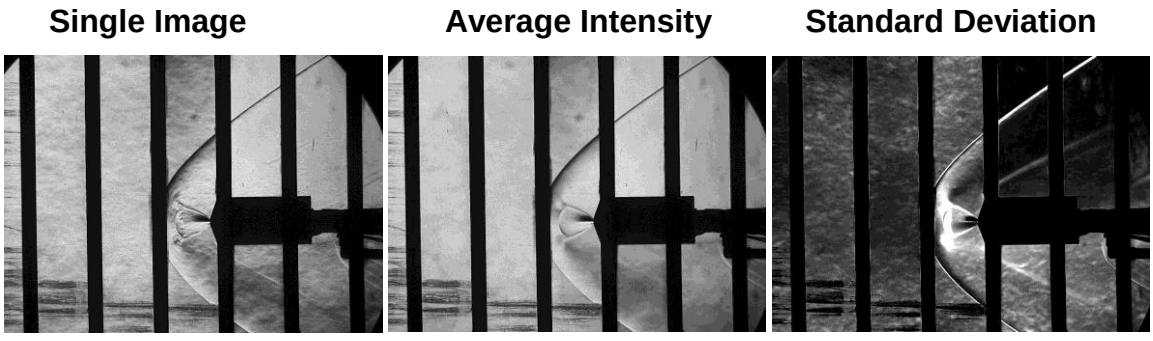

(a) α_τ = 0 deg.

(b) α_τ = 4 deg.

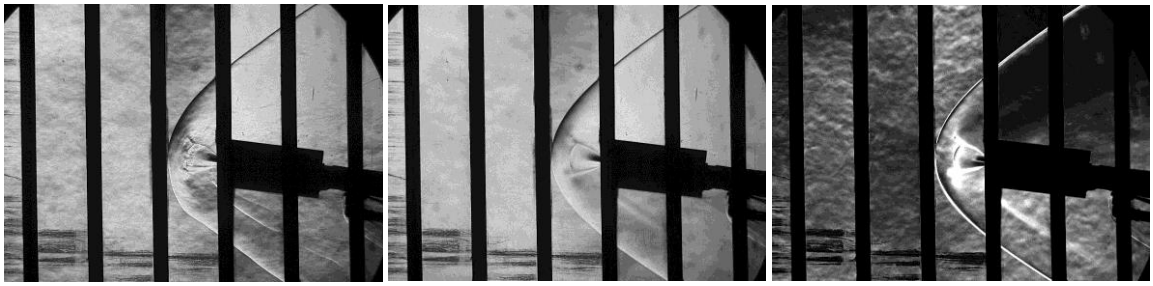

(c) α_τ = 8 deg.

Figure C-7. Run 139: center nozzle schlieren video images for range of α_τ at $M\infty$ = 2.4, C_T = 1.0, and ϕ = 180 deg.

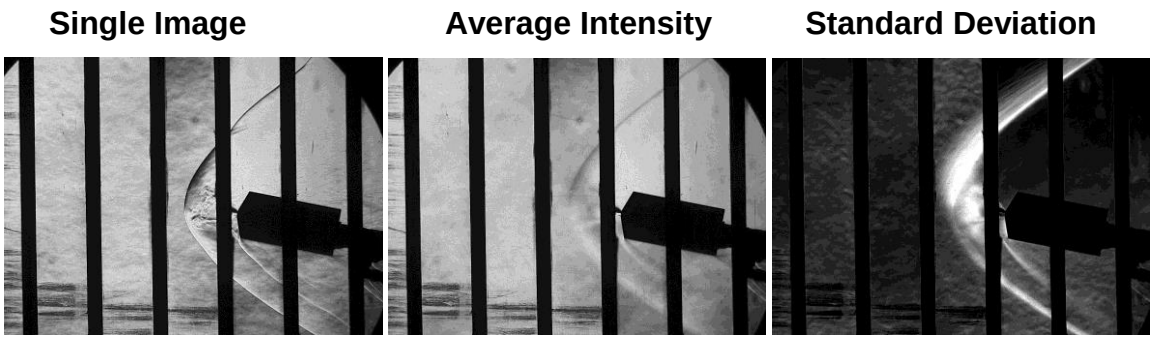

(d) α_τ = 12 deg.

(e) α_τ = 20 deg.

Figure C-7. Concluded.

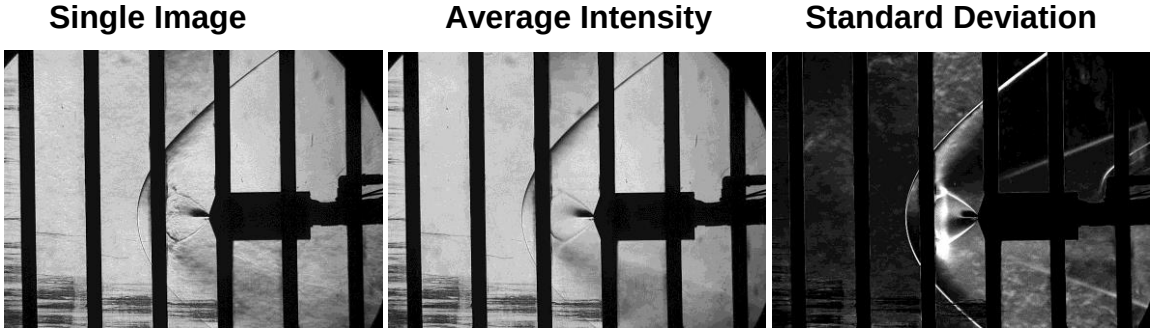

(a) α_τ = 0 deg.

(b) α_τ = 4 deg.

Figure C-8. Run 141: center nozzle schlieren video images for range of α_τ at $M\infty$ = 2.4, C_T = 2.0, and ϕ = 180 deg.

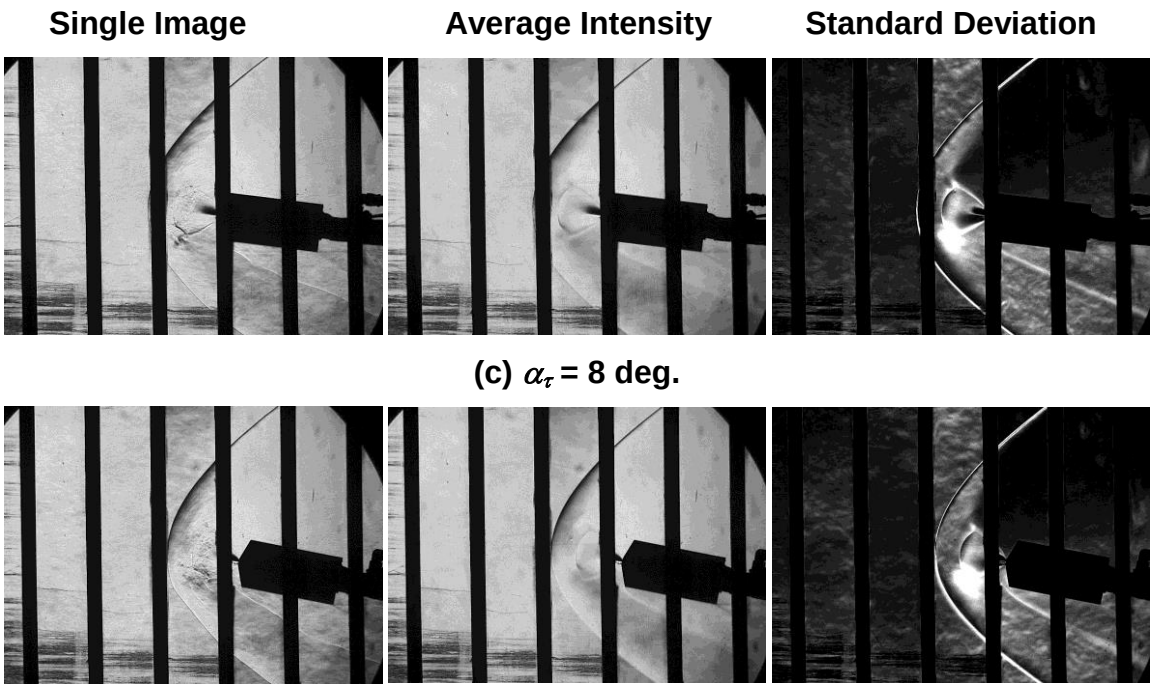

(c) α_τ = 8 deg.

(d) α_τ = 12 deg.

Figure C-8. Concluded.

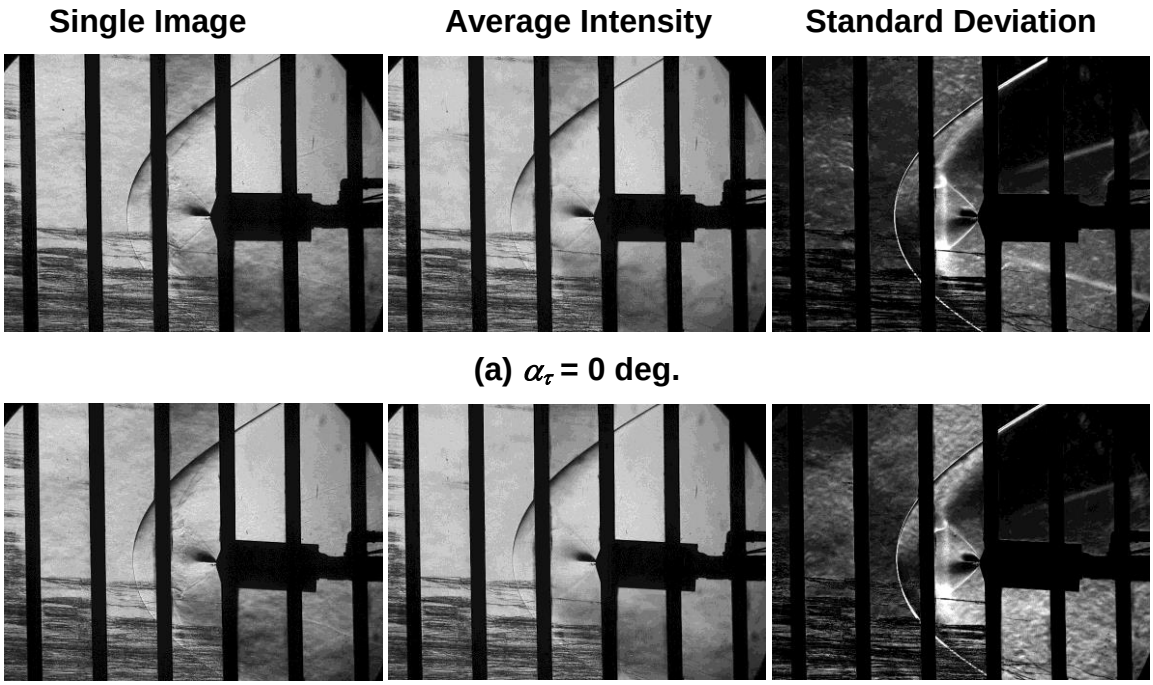

(a) α_τ = 0 deg.

(b) α_τ = 4 deg.

Figure C-9. Run 150: center nozzle schlieren video images for range of α_τ at $M\infty$ = 3.5, C_T = 3.0, and ϕ = 0 deg.

(c) α_τ = 12 deg.

(d) α_τ = 20 deg.

Figure C-9. Concluded.

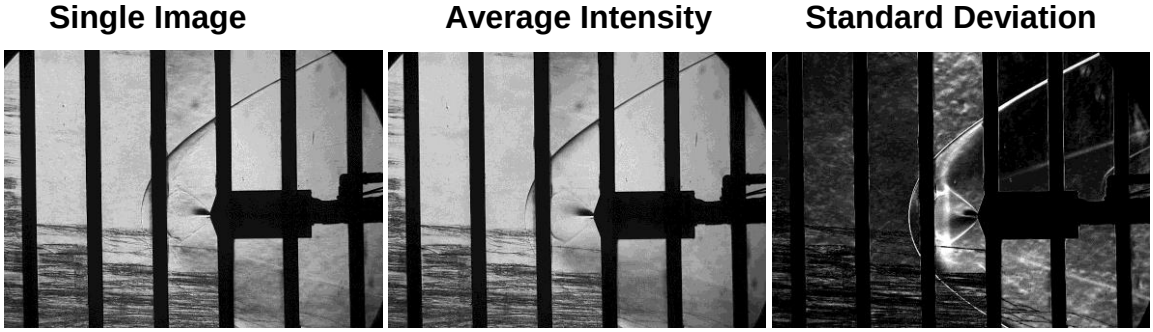

(a) α_τ = 0 deg.

(b) α_τ = 4 deg.

Figure C-10. Run 153: center nozzle schlieren video images for range of α_τ at $M\infty$ = 3.5, C_T = 2.0, and ϕ = 0 deg.

Single Image | Average Intensity | Standard Deviation

(c) α_τ = 8 deg.

(d) α_τ = 12 deg.

(e) α_τ = 20 deg.

Figure C-10. Concluded.

Single Image | Average Intensity | Standard Deviation

(a) α_τ = 0 deg.

Figure C-11. Run 154: center nozzle schlieren video images for range of α_τ at M_∞ = 3.5, C_T = 1.0, and ϕ = 0 deg.

Single Image | Average Intensity | Standard Deviation

(b) α_τ = 4 deg.

(c) α_τ = 12 deg.

d) α_τ = 20 deg.

Figure C-11. Concluded.

Single Image | Average Intensity | Standard Deviation

(a) α_τ = 0 deg.

Figure C-12. Run 157: center nozzle schlieren video images for range of α_τ at $M\infty$ = 3.5, C_T = 0.5, and ϕ = 0 deg.

Single Image | Average Intensity | Standard Deviation

(b) α_τ = 4 deg.

c) α_τ = 12 deg.

(d) α_τ = 20 deg.

Figure C-12. Concluded.

Single Image | Average Intensity | Standard Deviation

(a) α_τ = 0 deg.

Figure C-13. Run 158: center nozzle schlieren video images for range of α_τ at $M\infty$ = 3.5, C_T = 0.2, and ϕ = 0 deg.

Single Image | Average Intensity | Standard Deviation

(b) α_τ = 4 deg.

(c) α_τ = 12 deg.

(d) α_τ = 20 deg.

Figure C-13. Concluded.

Single Image | Average Intensity | Standard Deviation

(a) α_τ = 0 deg.

Figure C-14. Run 163: center nozzle schlieren video images for range of α_τ at M_∞ = 4.6, C_T = 3.0, and ϕ = 0 deg.

Single Image | Average Intensity | Standard Deviation

(b) α_τ = 4 deg.

(c) α_τ = 12 deg.

(d) α_τ = 20 deg.

Figure C-14. Concluded.

Single Image | Average Intensity | Standard Deviation

(a) α_τ = 0 deg.

Figure C- 15. Run 165: center nozzle schlieren video images for range of α_τ at M_∞ = 4.6, C_T = 2.0, and ϕ = 0 deg.

Single Image | Average Intensity | Standard Deviation

(b) α_τ = 4 deg.

(c) α_τ = 12 deg.

(d) α_τ = 20 deg.

Figure C-15. Concluded.

Single Image | Average Intensity | Standard Deviation

(a) α_τ = 0 deg.

Figure C-16. Run 167: center nozzle schlieren video images for range of α_τ at $M\infty$ = 4.6, C_T = 1.0, and ϕ = 0 deg.

(b) α_τ = 4 deg.

(c) α_τ = 12 deg.

Figure C-16. Concluded.

(a) α_τ = 0 deg.

(b) α_τ = 4 deg.

Figure C-17. Run 169: center nozzle schlieren video images for range of α_τ at $M\infty$ = 4.6, C_T = 0.5, and ϕ = 180 deg.

(a) α_τ = 0 deg.

Figure C-18. Run 171: center nozzle schlieren video images for range of α_τ at $M\infty$ = 4.6, C_T = 0.2, and ϕ =180 deg.

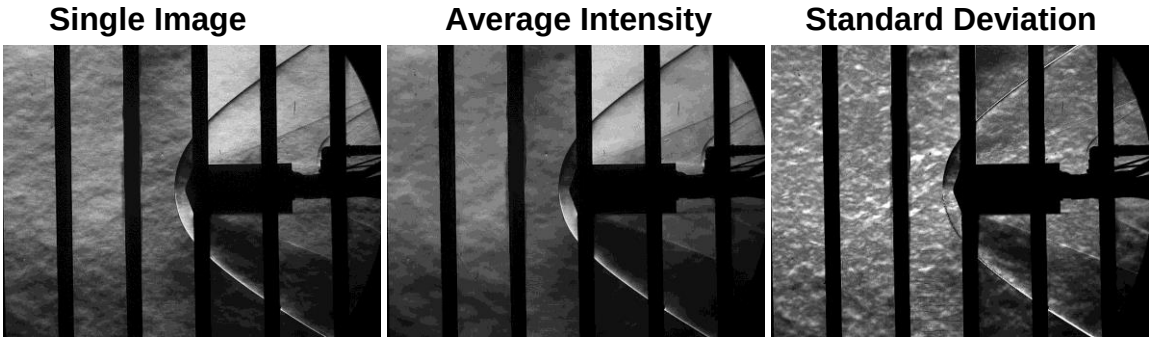

(a) α_τ = 0 deg.

(b) α_τ = 4 deg.

(c) α_τ = 8 deg.

Figure C-19. Run 180: tri-nozzle schlieren video images for range of α_τ at $M\infty$ = 2.4, C_T = 0.0, and ϕ = 0 deg.

Single Image | Average Intensity | Standard Deviation

(d) α_τ = 12 deg.

(e) α_τ = 16 deg.

(f) α_τ = 20 deg.

Figure C-19. Concluded.

Single Image | Average Intensity | Standard Deviation

(a) α_τ = 0 deg.

Figure C-20. Run 185: tri-nozzle schlieren video images for range of α_τ at $M\infty$ = 3.5, C_T = 0.0, and ϕ = deg.

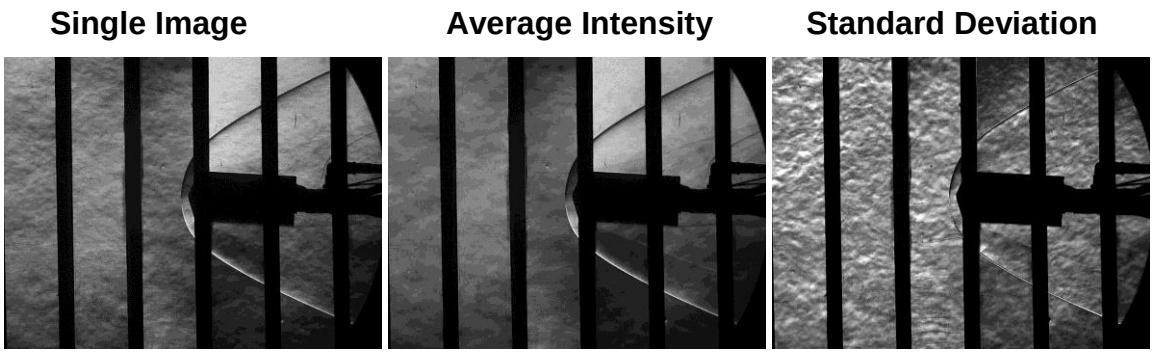

(b) α_τ = 4 deg.

(c) α_τ = 8 deg.

(d) α_τ = 12 deg.

(e) α_τ = 16 deg.

Figure C-20. Continued.

(f) α_τ = 20 deg.

Figure C-20. Concluded.

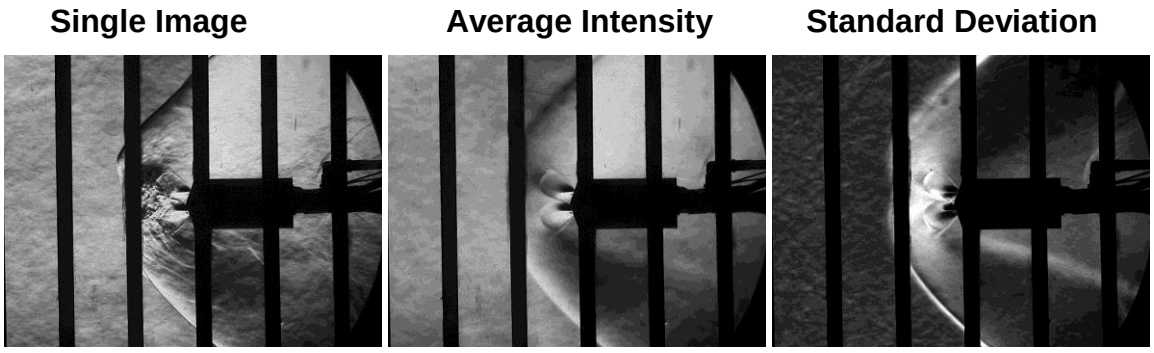

(a) α_τ = 0 deg.

(b) α_τ = 4 deg.

(c) α_τ = 12 deg.

Figure C-21. Run 190: tri-nozzle schlieren video images for range of α_τ at $M\infty$ = 2.4, C_T = 3.0, and ϕ = 0 deg.

(d) α_τ = 20 deg.

Figure C-21. Concluded.

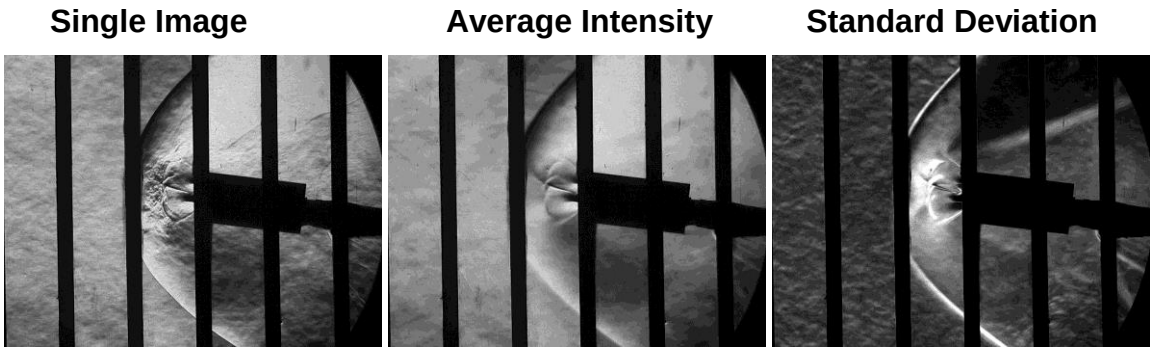

(a) α_τ = 8 deg.

Figure C-22. Run 192: tri-nozzle schlieren video images for range of α_τ at M_∞ = 2.4, C_T = 3.0, and ϕ = 120 deg.

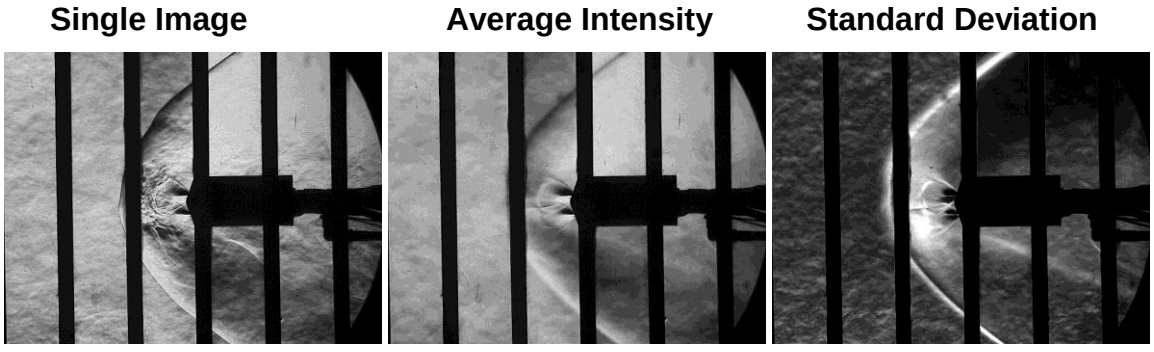

(a) α_τ = 0 deg.

Figure C-23. Run 194: tri-nozzle schlieren video images for range of α_τ at M_∞ = 2.4, C_T = 2.0, and ϕ = 180 deg.

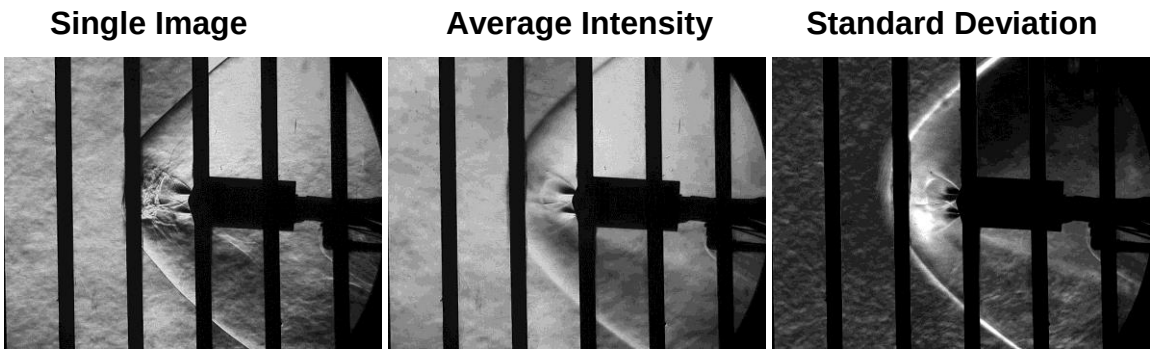

(b) α_τ = 4 deg.

(c) α_τ = 12 deg.

(d) α_τ = 20 deg.

Figure C-23. Concluded.

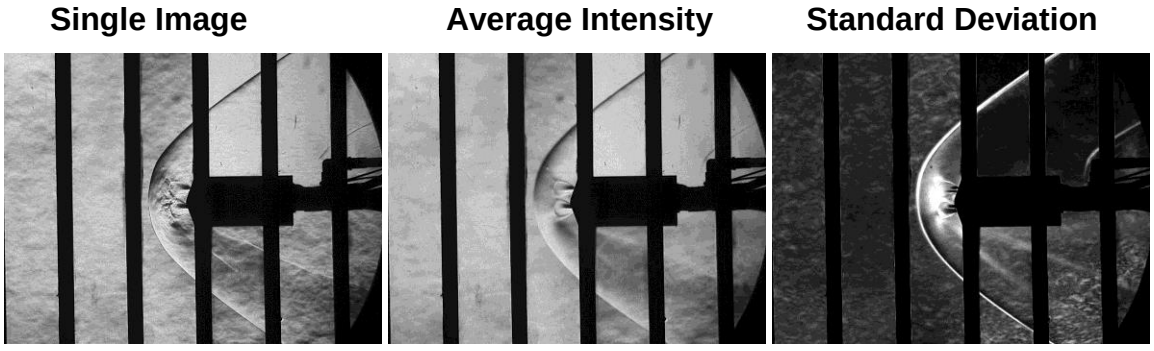

(a) α_τ = 0 deg.

Figure C-24. Run 198: tri-nozzle schlieren video images for range of α_τ at $M\infty$ = 2.4, C_T = 1.0, and ϕ = 0 deg.

(b) α_τ = 4 deg.

(c) α_τ = 12 deg.

(d) α_τ = 20 deg.

Figure C-24. Concluded.

(a) α_τ = 0 deg.

Figure C-25. Run 202: tri-nozzle schlieren video images for range of α_τ at $M\infty$ = 2.4, C_T = 0.43, and ϕ = 180 deg.

Single Image | Average Intensity | Standard Deviation

(b) α_τ = 4 deg.

(c) α_τ = 12 deg.

(d) α_τ = 20 deg.

Figure C-25. Concluded.

Single Image | Average Intensity | Standard Deviation

(a) α_τ = 0 deg.

Figure C-26. Run 206: tri-nozzle schlieren video images for range of α_τ at $M\infty$ = 2.4, C_T = 0.43, and ϕ = 0 deg.

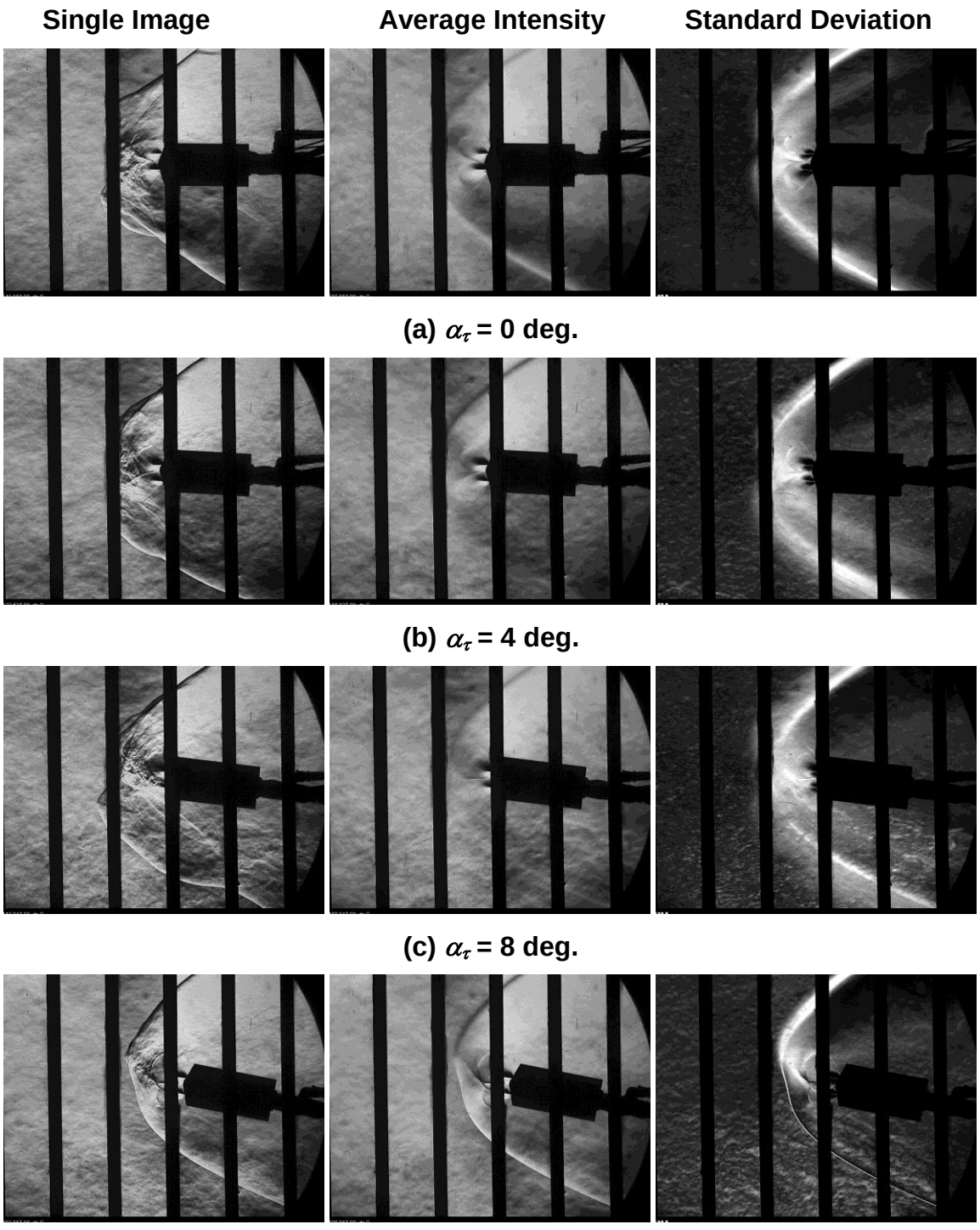

Figure C-27. Run 212: tri-nozzle schlieren video images for range of α_τ at M_∞ = 4.6, C_T = 2.93, and ϕ = 60 deg.

(e) α_τ = 16 deg.

Figure C-27. Concluded.

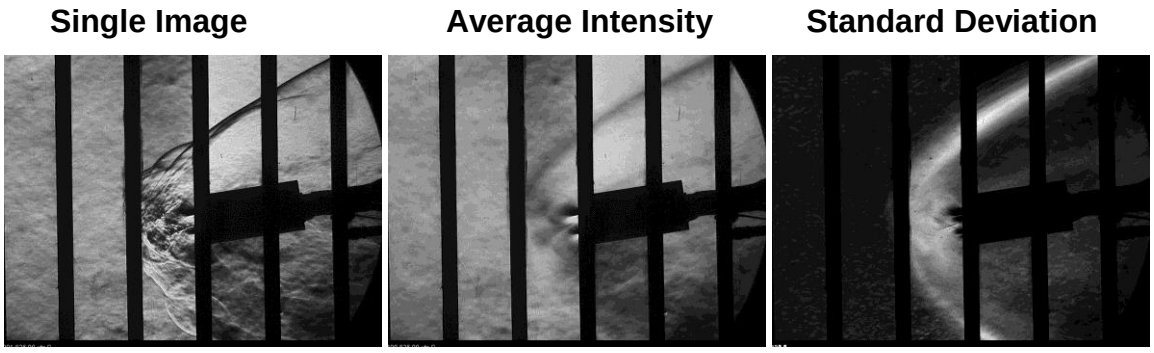

(a) α_τ = –8 deg.

(b) α_τ = –4 deg.

(c) α_τ = 0 deg.

Figure C-28. Run 214: tri-nozzle schlieren video images for range of α_τ at $M\infty$ = 4.6, C_T = 2.95, and ϕ = 180 deg.

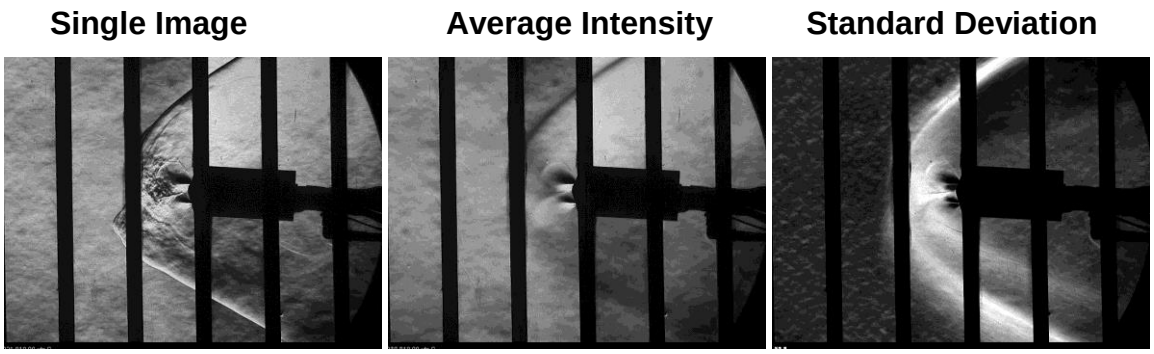

(d) α_τ = 4 deg.

(e) α_τ = 8 deg.

(f) α_τ = 12 deg.

(g) α_τ = 16 deg.

Figure C-28. Concluded.

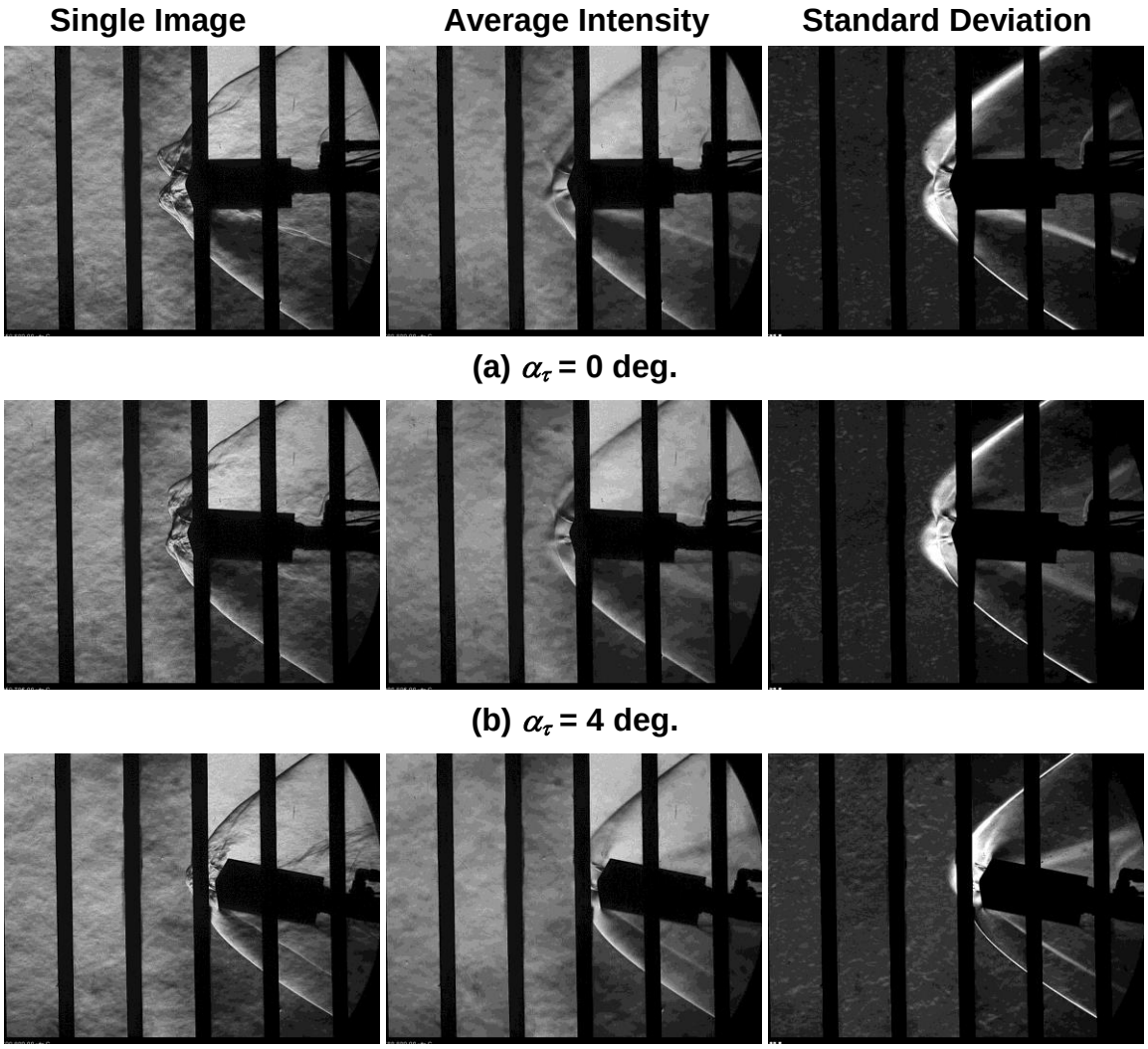

(a) α_τ = 0 deg.

(b) α_τ = 4 deg.

(c) α_τ = 12 deg.

Figure C-29. Run 221: tri-nozzle schlieren video images for range of α_τ at $M\infty$ = 2.4, C_T = 0.24, and ϕ = 0 deg.

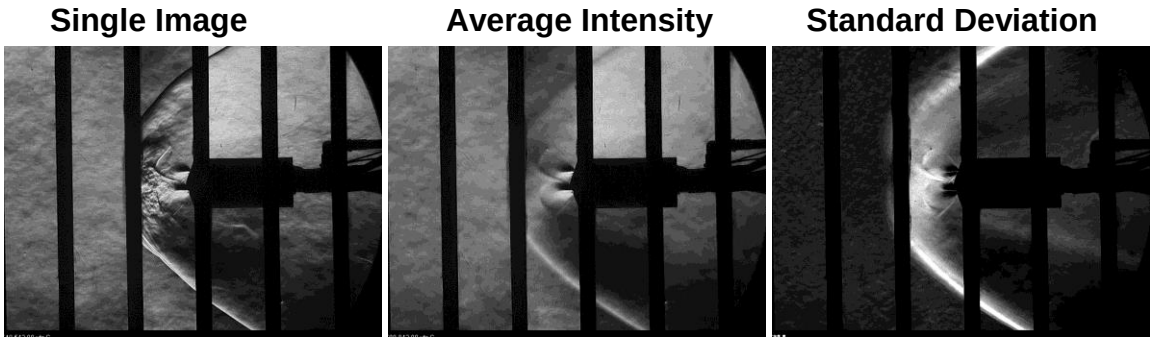

(a) α_τ = 0 deg.

Figure C-30. Run 222: tri-nozzle schlieren video images for range of α_τ at $M\infty$ = 3.5, C_T = 2.96, and ϕ = 0 deg.

(b) α_τ = 4 deg.

c) α_τ = 8 deg.

(d) α_τ = 12 deg.

(e) α_τ = 16 deg.

Figure C-30. Continued.

Single Image | Average Intensity | Standard Deviation

(f) α_τ = 20 deg.

Figure C-30. Concluded.

Single Image | Average Intensity | Standard Deviation

(a) α_τ = 0 deg.

(b) α_τ = 4 deg.

c) α_τ = 8 deg.

Figure C-31. Run 225: tri-nozzle schlieren video images for range of α_τ at $M\infty$ = 3.5, C_T = 2.99, and ϕ = 180 deg.

(d) α_τ = 12 deg.

(e) α_τ = 16 deg.

(f) α_τ = 20 deg.

Figure C-31. Concluded.

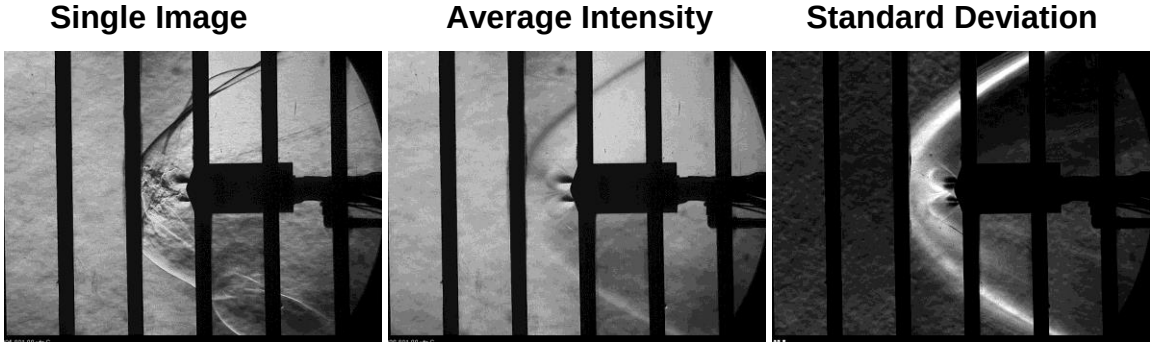

a) α_τ = 0 deg.

Figure C-32. Run 226: tri-nozzle schlieren video images for range of α_τ at $M\infty$ = 3.5, C_T = 1.96, and ϕ = 180 deg.

Single Image | Average Intensity | Standard Deviation

(b) α_τ = 4 deg.

(c) α_τ = 12 deg.

(d) α_τ = 20 deg.

Figure C-32. Concluded.

Single Image | Average Intensity | Standard Deviation

(a) α_τ = 0 deg.

Figure C-33. Run 247: tri-nozzle schlieren video images for range of α_τ at $M\infty$ = 4.6, C_T = 1.92, and ϕ = 0 deg.

Single Image | Average Intensity | Standard Deviation

(b) α_τ = 4 deg.

(c) α_τ = 8 deg.

(d) α_τ = 12 deg.

(e) α_τ = 20 deg.

Figure C-33. Concluded.

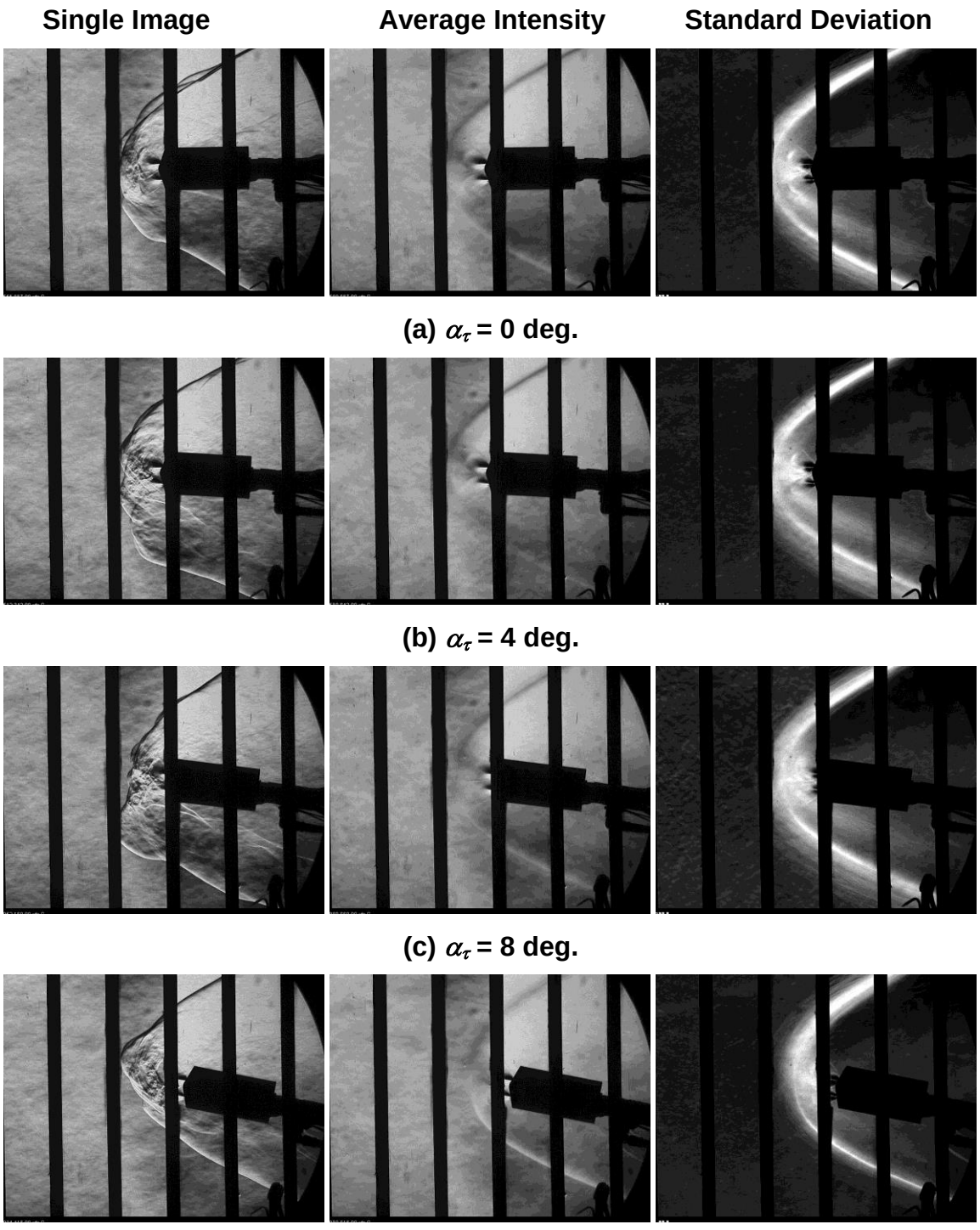

Figure C-34. Run 248: tri-nozzle schlieren video images for range of α_τ at M_∞ = 4.6, C_T = 1.93, and ϕ = 180 deg.

(e) α_τ = 20 deg.

Figure C-34. Concluded.

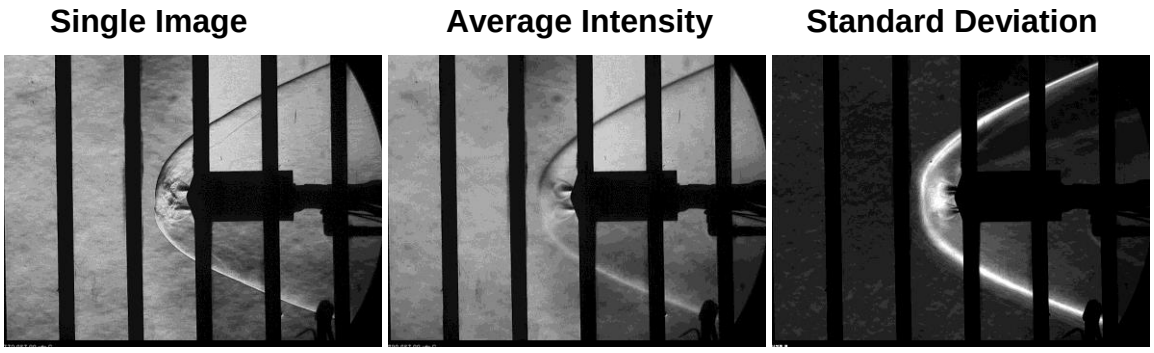

(a) α_τ = 0 deg.

(b) α_τ = 4 deg.

(c) α_τ = 12 deg.

Figure C-35. Run 249: tri-nozzle schlieren video images for range of α_τ at $M\infty$ = 4.6, C_T = 0.90, and ϕ = 180 deg.

(d) α_τ = 20 deg.

Figure C-35. Concluded.

(a) α_τ = 0 deg.

(b) α_τ = 4 deg.

(c) α_τ = 12 deg.

Figure C-36. Run 253: tri-nozzle schlieren video images for range of α_τ at $M\infty$ = 4.6, C_T = 0.43, and ϕ = 0 deg.

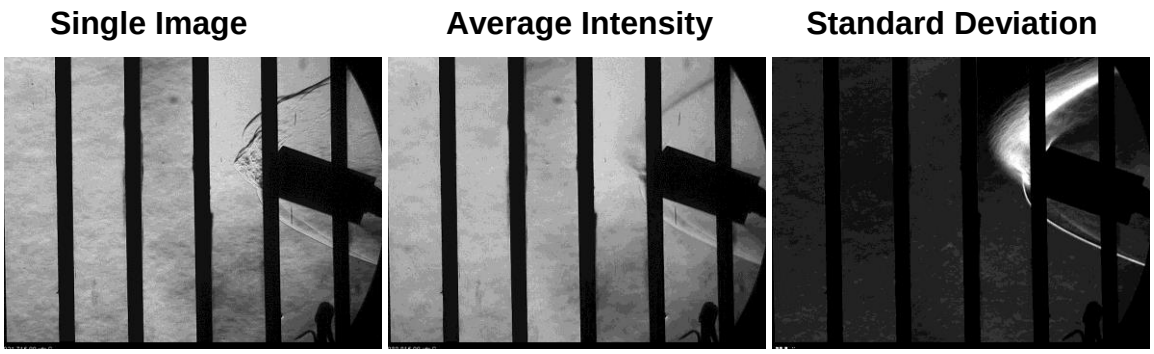

(d) α_τ = 20 deg.

Figure C-36. Concluded.

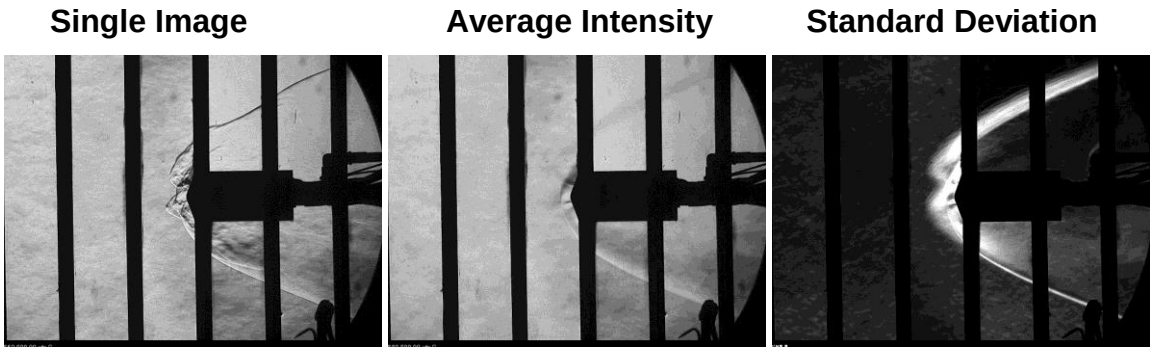

(a) α_τ = 0 deg.

(b) α_τ = 4 deg.

(c) α_τ = 12 deg.

Figure C-37. Run 257: tri-nozzle schlieren video images for range of α_τ at $M\infty$ = 4.6, C_T = 0.20, and ϕ = 0 deg.

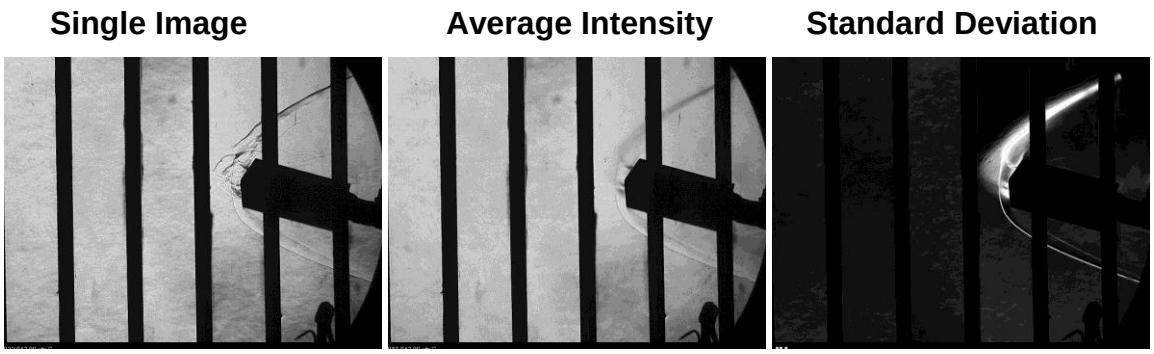

(d) α_τ = 16 deg.

Figure C-37. Concluded.

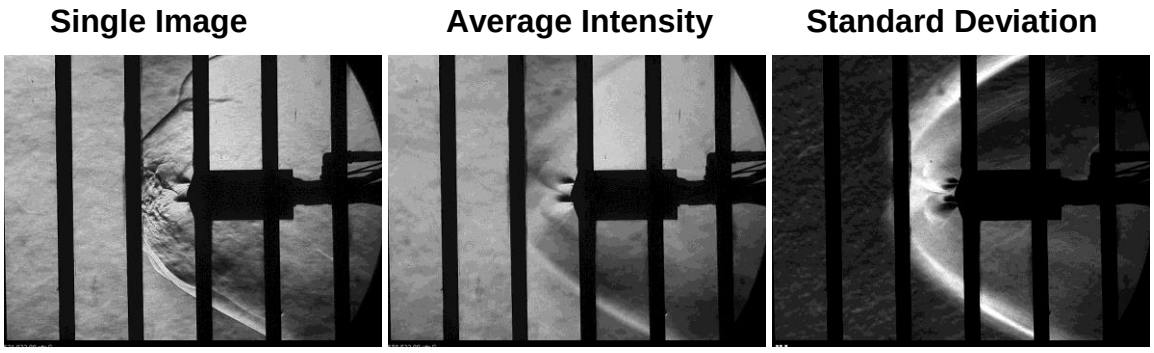

(a) α_τ = 0 deg.

(b) α_τ = 4 deg.

(c) α_τ = 12 deg.

Figure C-38. Run 262: tri-nozzle schlieren video images for range of α_τ at $M\infty$ = 4.6, C_T = 2.94, and ϕ = 0 deg.

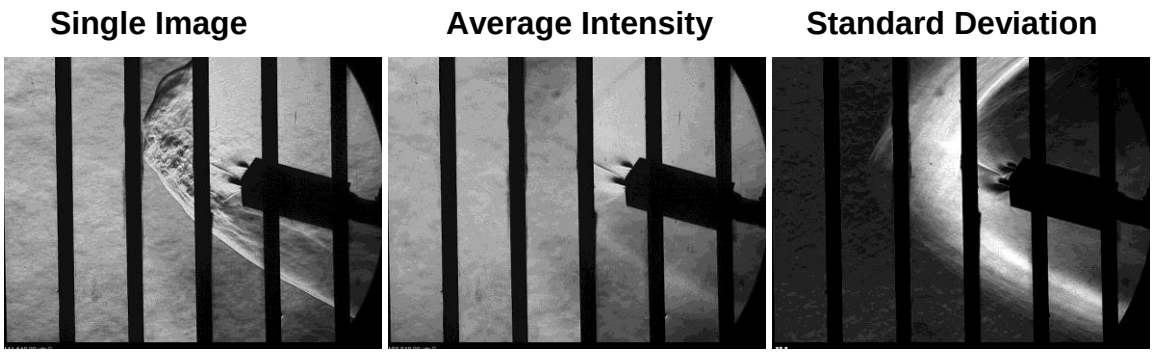

(d) α_τ = 16 deg.

Figure C-38. Concluded.

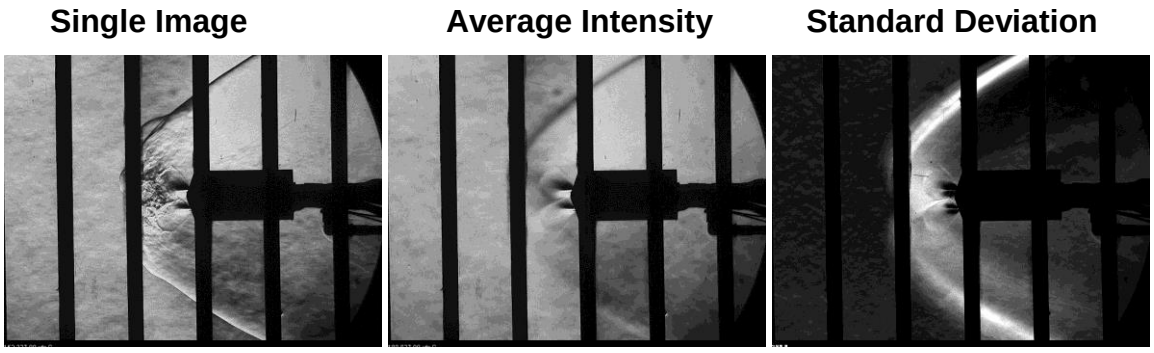

(a) α_τ = 0 deg.

(b) α_τ = 4 deg.

(c) α_τ = 12 deg.

Figure C-39. Run 263: tri-nozzle schlieren video images for range of α_τ at $M\infty$ = 4.6, C_T = 2.94, and ϕ = 180 deg.

Single Image | Average Intensity | Standard Deviation

(d) α_τ = 16deg.

Figure C-39. Concluded.

Single Image | Average Intensity | Standard Deviation

(a) C_T = 3.

(b) C_T = 4.

(c) C_T = 5.

Figure C-40. Run 264: tri-nozzle schlieren video images for range of α_τ at M_∞ = 4.6, α = 0 deg, and ϕ = 60 deg.

(d) C_T = 6.

Figure C-40. Concluded.

(a) C_T = 3.

Figure C-41. Run 264: tri-nozzle schlieren video images for range of α_τ at $M\infty$ = 4.6, α = 12 deg, and ϕ = 60 deg.

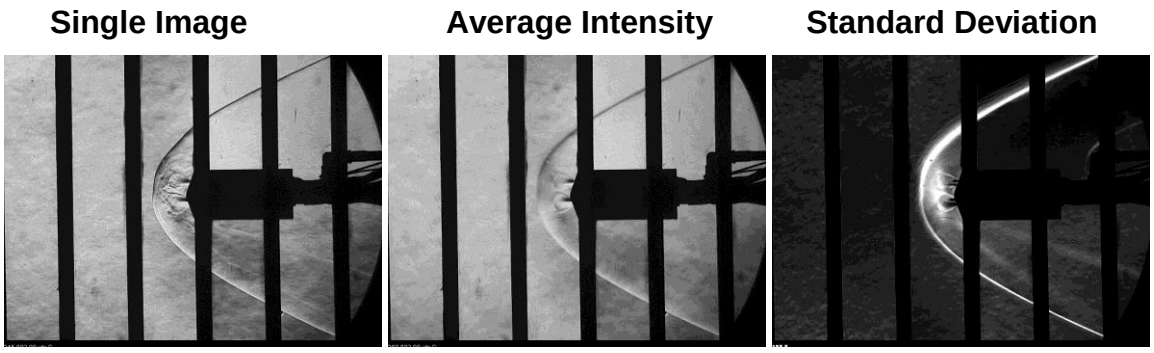

(a) α_τ = 0 deg.

Figure C-42. Run 265: tri-nozzle schlieren video images for range of α_τ at $M\infty$ = 3.5, C_T = 0.91, and ϕ = 0 deg.

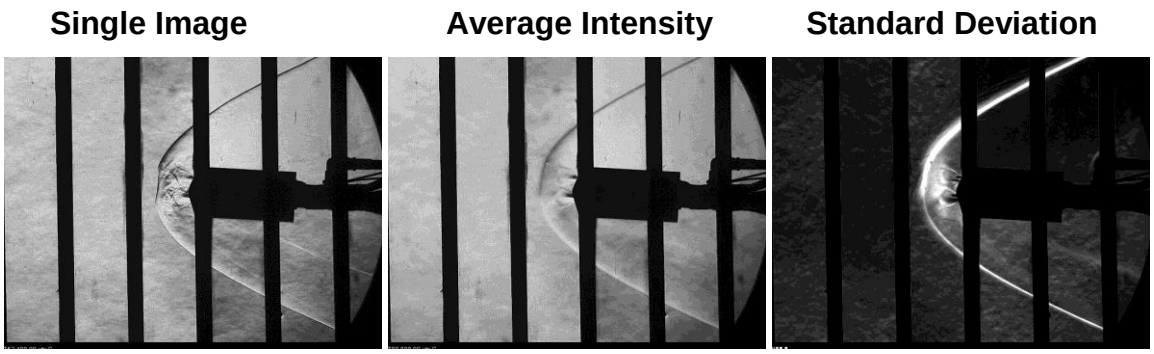

(b) α_τ = 4 deg.

(c) α_τ = 12 deg.

(d) α_τ = 20 deg.

Figure C-42. Concluded.

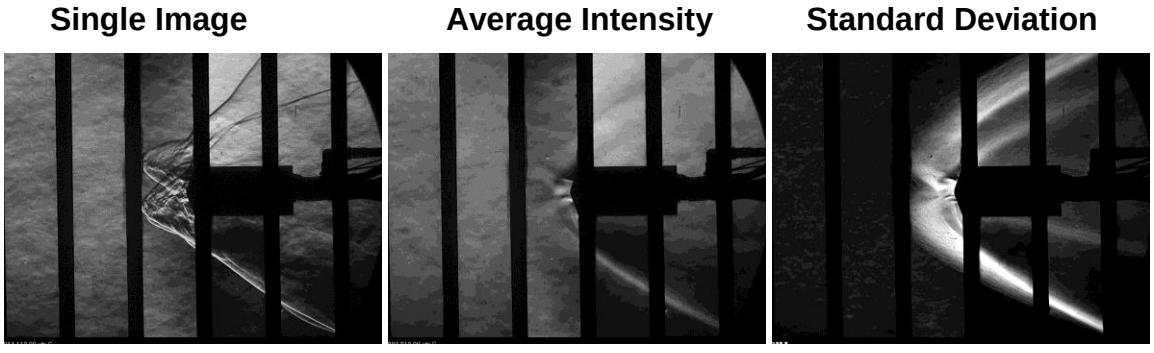

(a) α_τ = 0 deg.

Figure C-43. Run 266: tri-nozzle schlieren video images for range of α_τ at $M\infty$ = 3.5, C_T = 0.83, and ϕ = 0 deg.

Single Image | Average Intensity | Standard Deviation

(b) α_τ = 4 deg.

(c) α_τ = 12 deg.

(d) α_τ = 20 deg.

Figure C-43. Concluded.

Single Image | Average Intensity | Standard Deviation

(a) C_T = 4, X_S = 40", and ϕ = 0 deg.

Figure C-44. Run 267: tri-nozzle schlieren video images for range of α_τ at $M\infty$ = 3.5 and α = 0 deg.

Single Image | Average Intensity | Standard Deviation

(b) C_T = 5, X_S = 40”, and ϕ = 0 deg.

(c) C_T = 5, X_S = 40”, and ϕ = 30 deg.

(d) C_T = 5, X_S = 42”, and ϕ = 30 deg.

(e) C_T = 5, X_S = 42”, and ϕ = 0 deg.

Figure C-44. Continued.

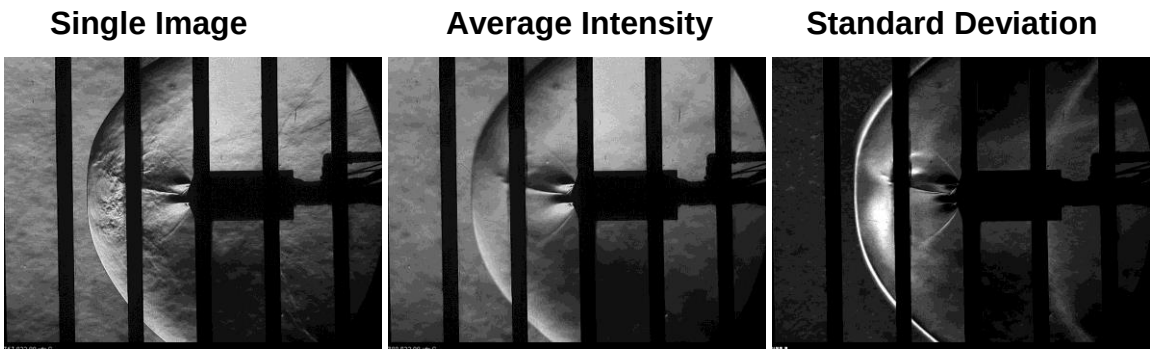

(f) C_T = 6, X_S = 40”, and ϕ = 0 deg.

(g) C_T = 6, X_S = 40”, and ϕ = 30 deg.

(h) C_T = 6, X_S = 44”, and ϕ = 30 deg.

(i) C_T = 6, X_S = 44”, and ϕ = 0 deg.

Figure C-44. Concluded.

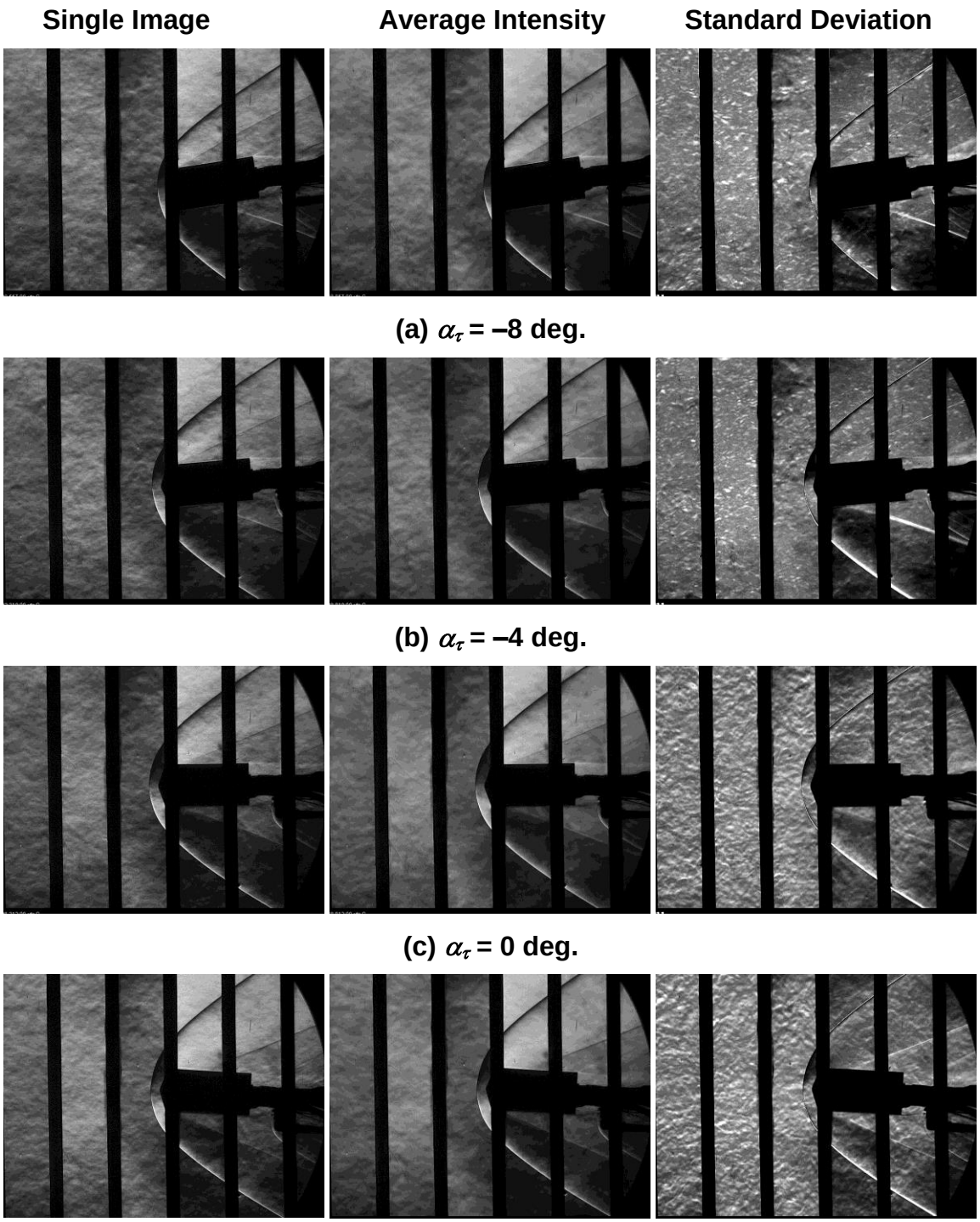

Figure C-45. Run 274: baseline schlieren video images for range of α_τ at M_∞ = 2.4, C_T = 0.0, and ϕ = 180 deg.

Single Image | Average Intensity | Standard Deviation

(e) α_T = 8 deg.

(f) α_T = 12 deg.

(g) α_T = 16 deg.

(h) α_T = 20 deg.

Figure C-45. Concluded.

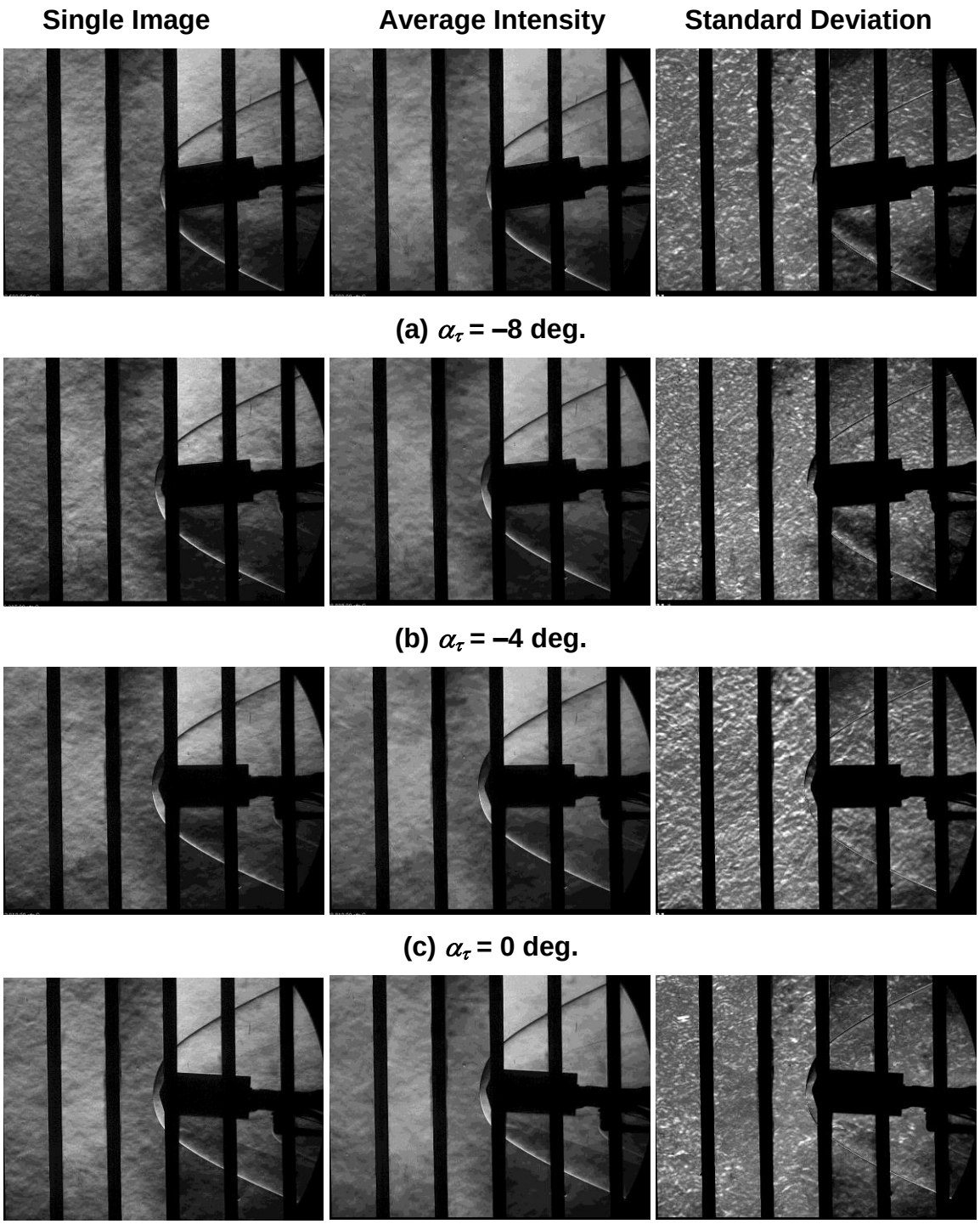

Figure C-46. Run 276: baseline schlieren video images for range of α_τ at M_∞ = 3.5, C_T = 0.0, and ϕ = 180 deg.

(e) α_τ = 8 deg.

(f) α_τ = 12 deg.

(g) α_τ = 16 deg.

(h) α_τ = 20 deg.

Figure C-46. Concluded.

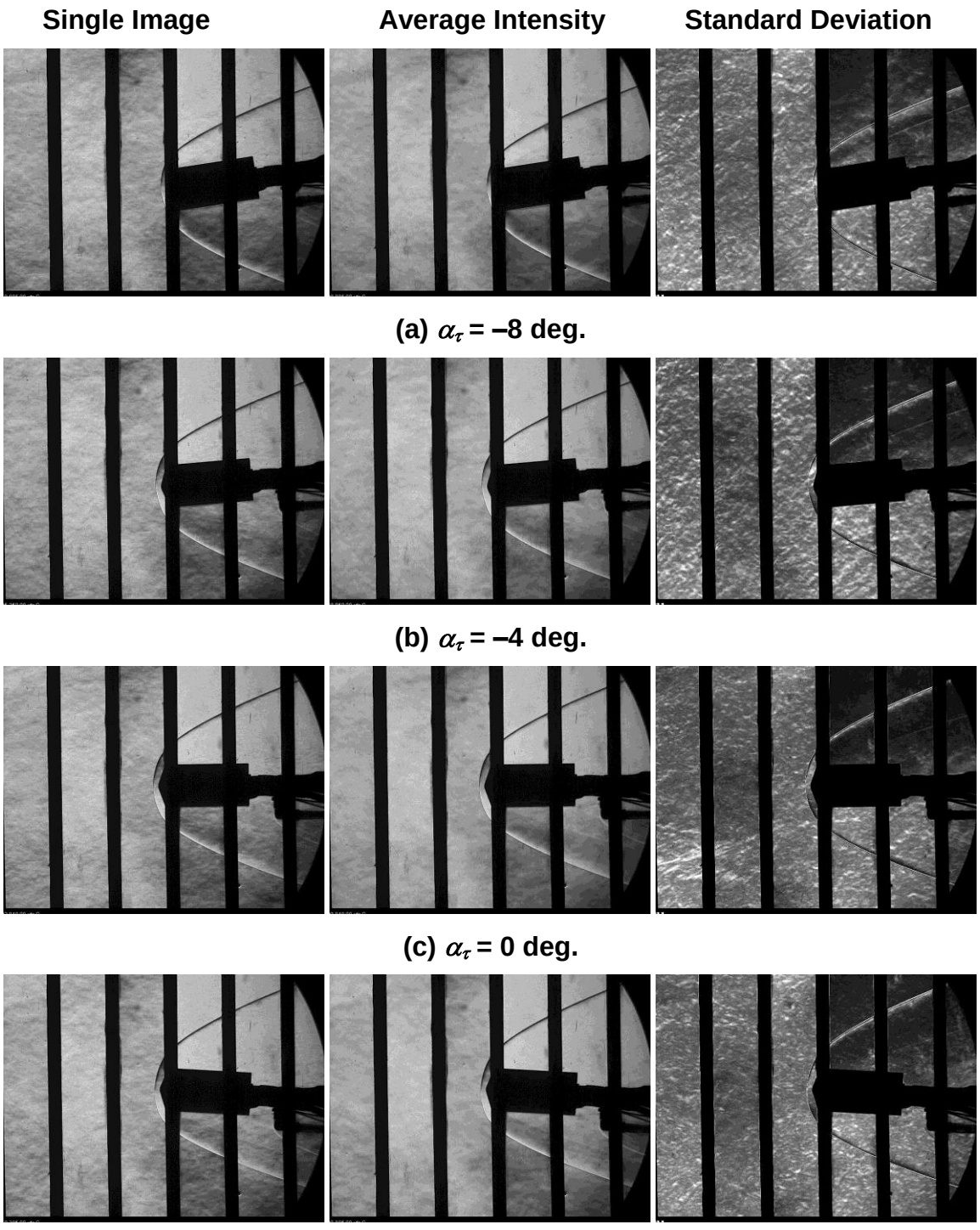

Figure C-47. Run 283: baseline schlieren video images for range of α_τ at M_∞ = 4.6, C_T = 0.0, and ϕ = 180 deg.

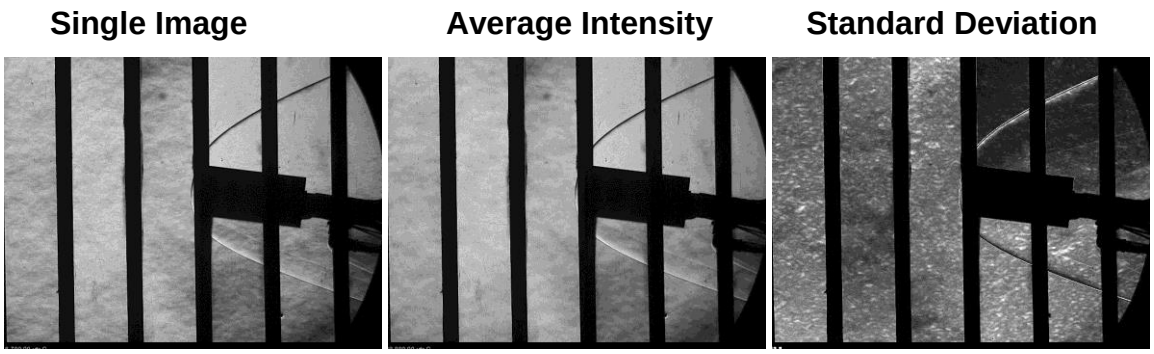

(e) α_τ = 8 deg.

(f) α_τ = 12 deg.

(g) α_τ = 16 deg.

(h) α_τ = 20 deg.

Figure C-47. Concluded.

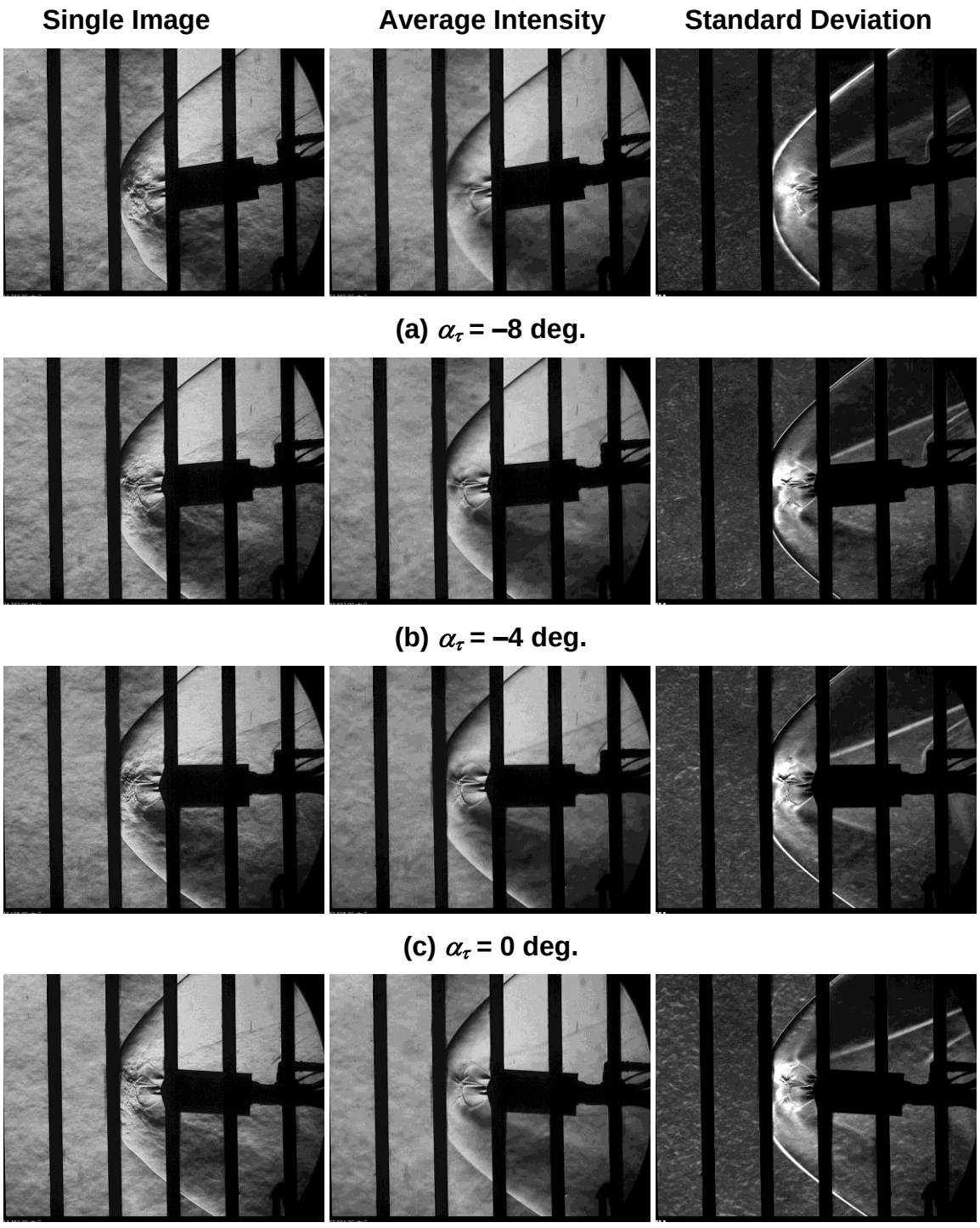

Figure C-48. Run 288: quad-nozzle schlieren video images for range of α_τ at M_∞ = 2.4, C_T = 1.93, and ϕ = 0 deg.

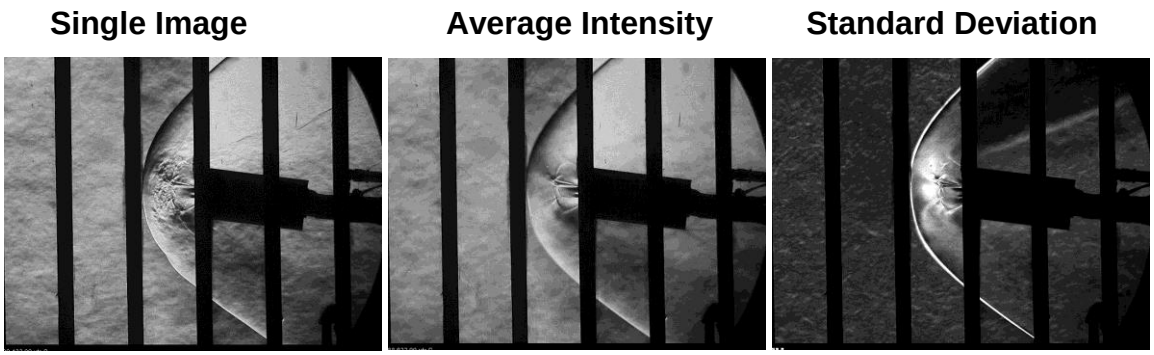

(e) α_τ = 8 deg.

(f) α_τ = 12 deg.

(g) α_τ = 16 deg.

(h) α_τ = 20 deg.

Figure C-48. Concluded.

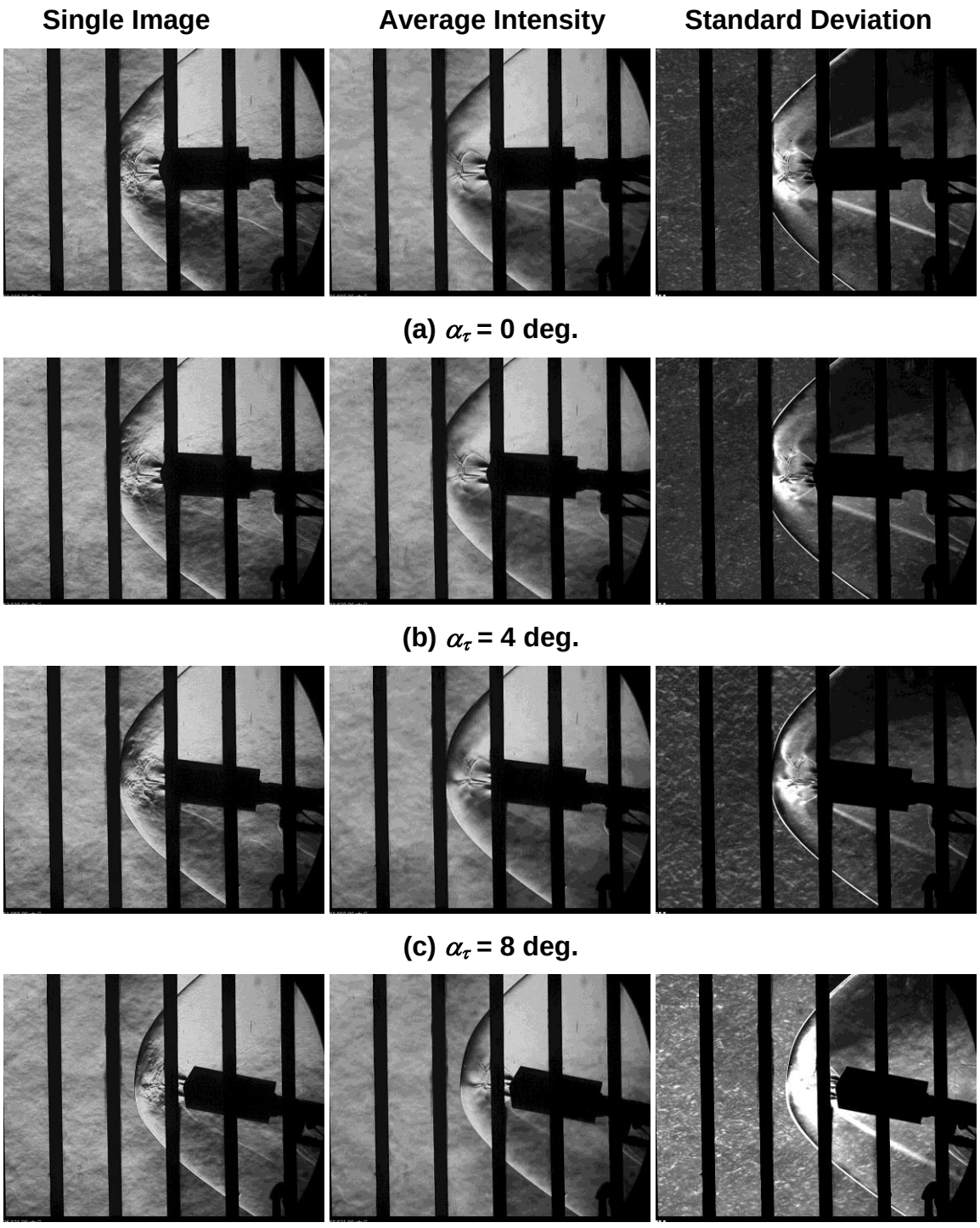

Figure C-49. Run 291: quad-nozzle schlieren video images for range of α_τ at M_∞ = 2.4, C_T = 1.94, and ϕ = 180 deg.

Single Image | Average Intensity | Standard Deviation

(e) α_τ = 16 deg.

(f) α_τ = 20 deg.

Figure C-49. Concluded.

Single Image | Average Intensity | Standard Deviation

(a) X_S = 40" and ϕ = 180 deg.

(b) X_S = 42" and ϕ = 180 deg.

Figure C-50. Run 292: quad-nozzle schlieren video images for range of model positions at $M\infty$ = 2.4, α_τ = 0 deg, and C_T = 1.93.

Single Image | Average Intensity | Standard Deviation

(c) X_S = 42" and ϕ = 150 deg.

Figure C-50. Concluded.

Single Image | Average Intensity | Standard Deviation

(a) α_τ = 0 deg.

(b) α_τ = 4 deg.

(c) α_τ = 8 deg.

Figure C-51. Run 293: quad-nozzle schlieren video images for range of α_τ at $M\infty$ = 2.4, C_T = 0.94, and ϕ = 180 deg.

Single Image | Average Intensity | Standard Deviation

(d) α_τ = 12 deg.

(e) α_τ = 20 deg.

Figure C-51. Concluded.

Single Image | Average Intensity | Standard Deviation

(a) X_S = 40” and ϕ = 0 deg.

(b) X_S = 40” and ϕ = 30 deg.

Figure C-52. Run 297: quad-nozzle schlieren video images for range of model positions at M_∞ = 2.4, α_τ = 0 deg, and C_T = 2.95.

(c) X_S = 43” and ϕ = 30 deg.

(d) X_S = 43” and ϕ = 0 deg.

Figure C-52. Concluded.

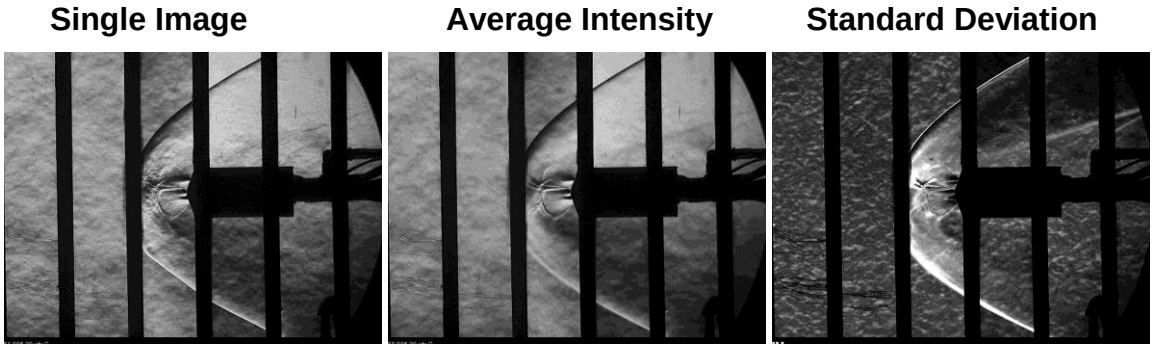

(a) α_τ = 0 deg.

(b) α_τ = 4 deg.

Figure C-53. Run 298: quad-nozzle schlieren video images for range of α_τ at $M\infty$ = 3.5, C_T = 1.91, and ϕ = 0 deg.

Single Image | Average Intensity | Standard Deviation

(c) α_τ = 12 deg.

(d) α_τ = 20 deg.

Figure C-53. Concluded.

Single Image | Average Intensity | Standard Deviation

(a) α_τ = 0 deg.

(b) α_τ = 4 deg.

Figure C-54. Run 301: quad-nozzle schlieren video images for range of α_τ at $M\infty$ = 3.5, C_T = 1.92, and ϕ = 180 deg.

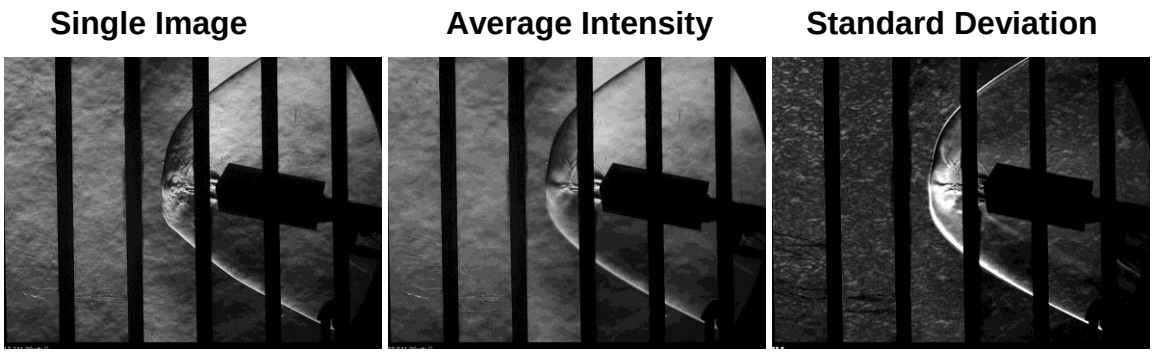

(c) α_τ = 12 deg.

(d) α_τ = 20 deg.

Figure C-54. Concluded.

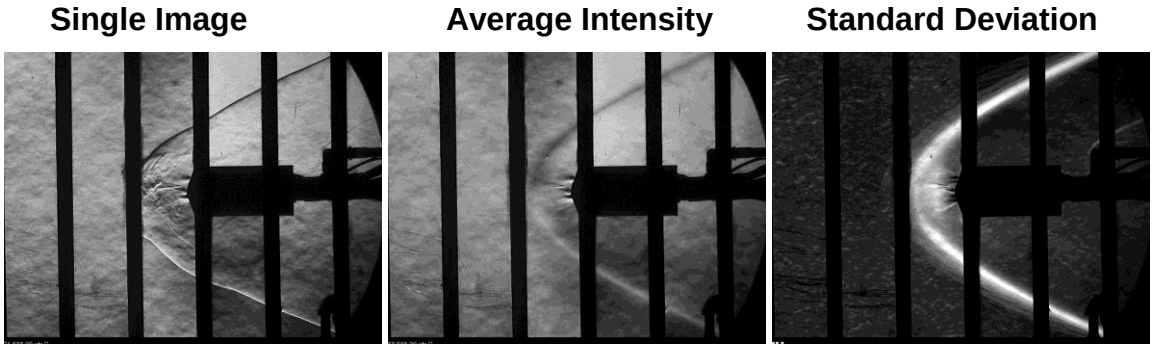

(a) α_τ = 0 deg.

(b) α_τ = 4 deg.

Figure C-55. Run 305: quad-nozzle schlieren video images for range of α_τ at $M\infty$ = 3.5, C_T = 0.90, and ϕ = 0 deg.

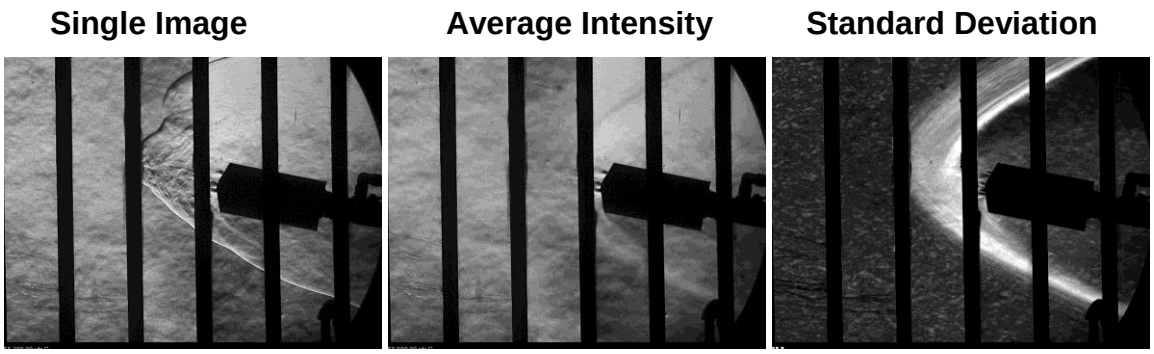

(c) α_τ = 12 deg.

(d) α_τ = 20 deg.

Figure C-55. Concluded.

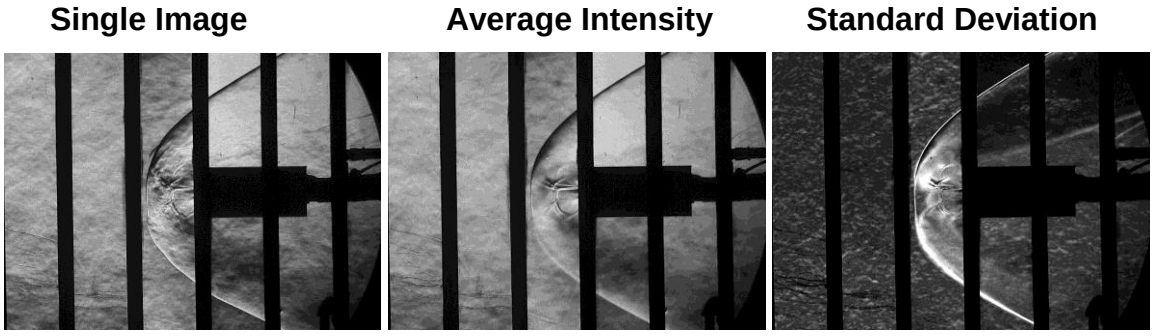

(a) X_S = 41”, C_T = 2, and ϕ = 0 deg.

(b) X_S = 40”, C_T = 3, and ϕ = 0 deg.

Figure C-56. Run 306: quad-nozzle schlieren video images for range of model positions at M_∞ = 3.5 and α_τ = 0 deg.

(c) X_S = 40”, C_T = 3, and ϕ = 30 deg.

(d) X_S = 43”, C_T = 3, and ϕ = 30 deg.

(e) X_S = 43”, C_T = 3, and ϕ = 0 deg.

Figure C-56. Concluded.

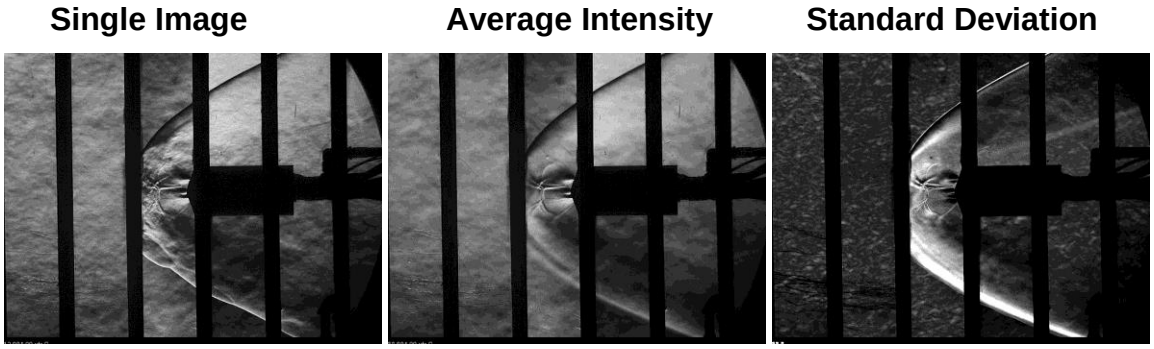

(a) α_τ = 0 deg.

Figure C-57. Run 307: quad-nozzle schlieren video images for range of α_τ at $M\infty$ = 4.6, C_T = 1.92, and ϕ = 0 deg.

Single Image | Average Intensity | Standard Deviation

(b) α_τ = 4 deg.

(c) α_τ = 12 deg.

(d) α_τ = 20 deg.

Figure C-57. Concluded.

Single Image | Average Intensity | Standard Deviation

(a) α_τ = 0 deg.

Figure C-58. Run 311: quad-nozzle schlieren video images for range of α_τ at $M\infty$ = 4.6, C_T = 1.93, and ϕ = 180 deg.

Single Image | Average Intensity | Standard Deviation

(b) α_τ = 4 deg.

(c) α_τ = 12 deg.

(d) α_τ = 20 deg.

Figure C-58. Concluded.

Single Image | Average Intensity | Standard Deviation

(a) α_τ = 0 deg.

Figure C-59. Run 315: quad-nozzle schlieren video images for range of α_τ at $M\infty$ = 4.6, C_T = 0.91, and ϕ = 0 deg.

Single Image | Average Intensity | Standard Deviation

(b) α_τ = 4 deg.

(c) α_τ = 12 deg.

(d) α_τ = 20 deg.

Figure C-59. Concluded.

Single Image | Average Intensity | Standard Deviation

(a) α_τ = 0 deg, X_S = 40".

Figure C-60. Run 318: center nozzle schlieren video images for range of α_τ at $M\infty$ = 2.4, C_T = 1.98, and ϕ = 0 deg.

Single Image	Average Intensity	Standard Deviation

(b) α_τ = 0 deg, X_S = 44”.

(c) α_τ = 8 deg, X_S = 40”.

(d) α_τ = 8 deg, X_S = 43”.

(e) α_τ = 12 deg, X_S = 40”.

Figure C-60. Concluded.

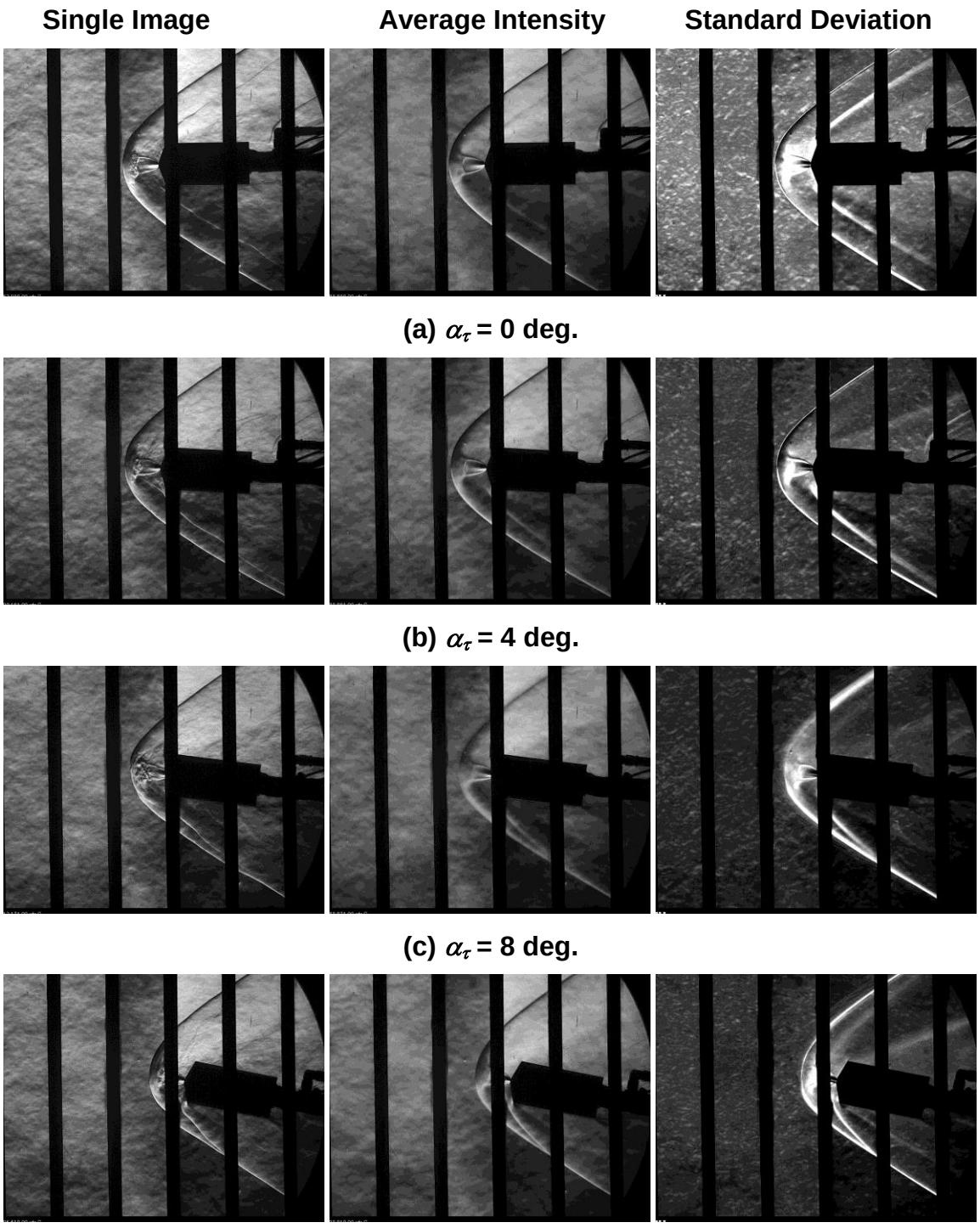

Figure C-61. Run 319: center nozzle schlieren video images for range of α_τ at M_∞ = 2.4, C_T = 0.46, and ϕ = 0 deg.

Single Image | Average Intensity | Standard Deviation

(e) α_τ = 12 deg, X_S = 40".

(f) α_τ = 20 deg.

Figure C-61. Concluded.

Single Image | Average Intensity | Standard Deviation

(a) α_τ = 0 deg, X_S = 40".

(b) α_τ = 0 deg, X_S = 43".

Figure C-62. Run 320: center nozzle schlieren video images for range of α_τ at $M\infty$ = 3.5, C_T = 1.96, and ϕ = 0 deg.

Single Image | Average Intensity | Standard Deviation

(c) α_τ = 8 deg, X_S = 40”.

(d) α_τ = 8 deg, X_S = 43”.

(e) α_τ = 12 deg, X_S = 40”.

Figure C-62. Concluded.

Single Image | Average Intensity | Standard Deviation

(a) α_τ = 0 deg, X_S = 40”.

Figure C-63. Run 321: center nozzle schlieren video images for range of α_τ at $M\infty$ = 4.6, C_T = 1.96, and ϕ = 0 deg.

(b) α_τ = 0 deg, X_S = 43”.

(c) α_τ = 8 deg, X_S = 40”.

(d) α_τ = 8 deg, X_S = 43”.

(e) α_τ = 12 deg, X_S = 40”.

Figure C-63. Continued.

Single Image	Average Intensity	Standard Deviation

(f) α_τ = 12 deg, X_S = 43".

Figure C-63. Concluded.

APPENDIX D
PRESSURE DATA LINE PLOTS

Plots of the pressure coefficients for selected pressure ports are given for each run performed during the wind tunnel experiment, with the exception of the six runs listed below. For each run, individual plots are provided for the both the forebody and aft body of the model at nominal angles of attack of –8, –4, 0, 4, 8, 12, 16, and 20 degrees, and labeled a–h, respectively, with the actual model angle of attack shown to the right of the label. The pressure coefficient data are plotted with respect to the cylindrical model coordinate system illustrated at the top of each page. Results are shown for arrays of pressure ports at six different azimuthal orientations around the body, as illustrated in the diagram and listed in the key at the upper right. These azimuths were chosen to provide good coverage of the forebody and because the azimuths are common to both the forebody and aft body. Note that there are no pressure ports on the aft body at the $\theta = 60°$ azimuth, however. Runs 292, 297, 306, 319, 320, and 321 were mainly repeat runs completed for the sake of obtaining additional schlieren locations and roll angles and, thus, did not follow the normal angle of attack sweep.

The plots are presented with one range of C_p on the ordinate for the aft body and four ranges of C_p on the ordinate for the forebody. The plot ordinate range on the forebody was chosen based on the maximum C_p values for a given model configuration and thrust coefficient. No error bars are shown to avoid cluttering the small plots. Information on the C_p uncertainties is provided in the main body of the paper. The model configuration is given in the information string at the bottom of each page and is also shown in the diagram at the upper left of each page. The four smaller circles within the forebody diagram represent the four nozzles, with a filled circle representing a powered nozzle for that particular run.

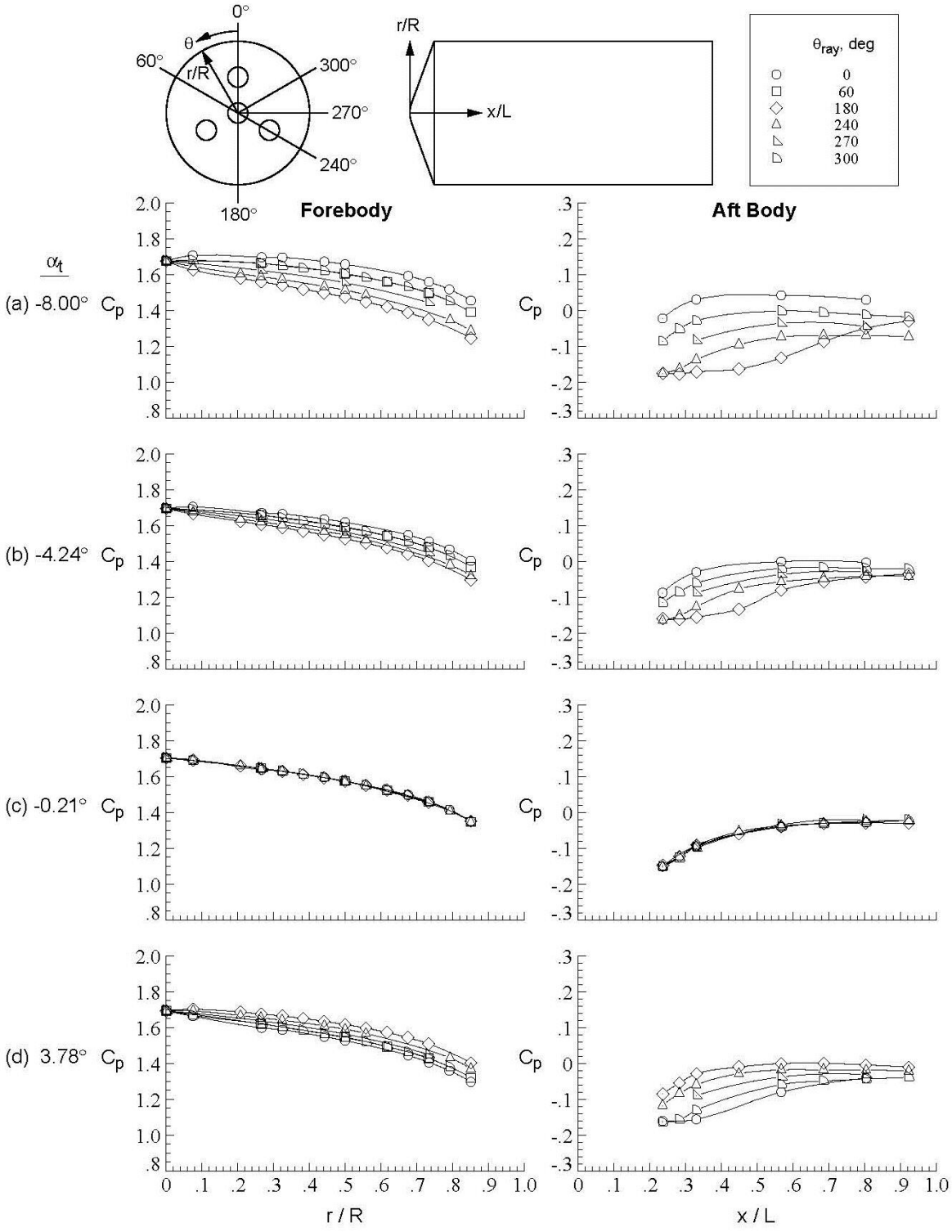

Figure D-1. Baseline configuration, Run 013, $M\infty = 2.4$, $Re_\infty = 1.0 \times 10^6$/ft, $\phi = 0.03°$, $X_S = 25.16$ in, $Y_S = 0.03$ in, $C_T = 0.00$.

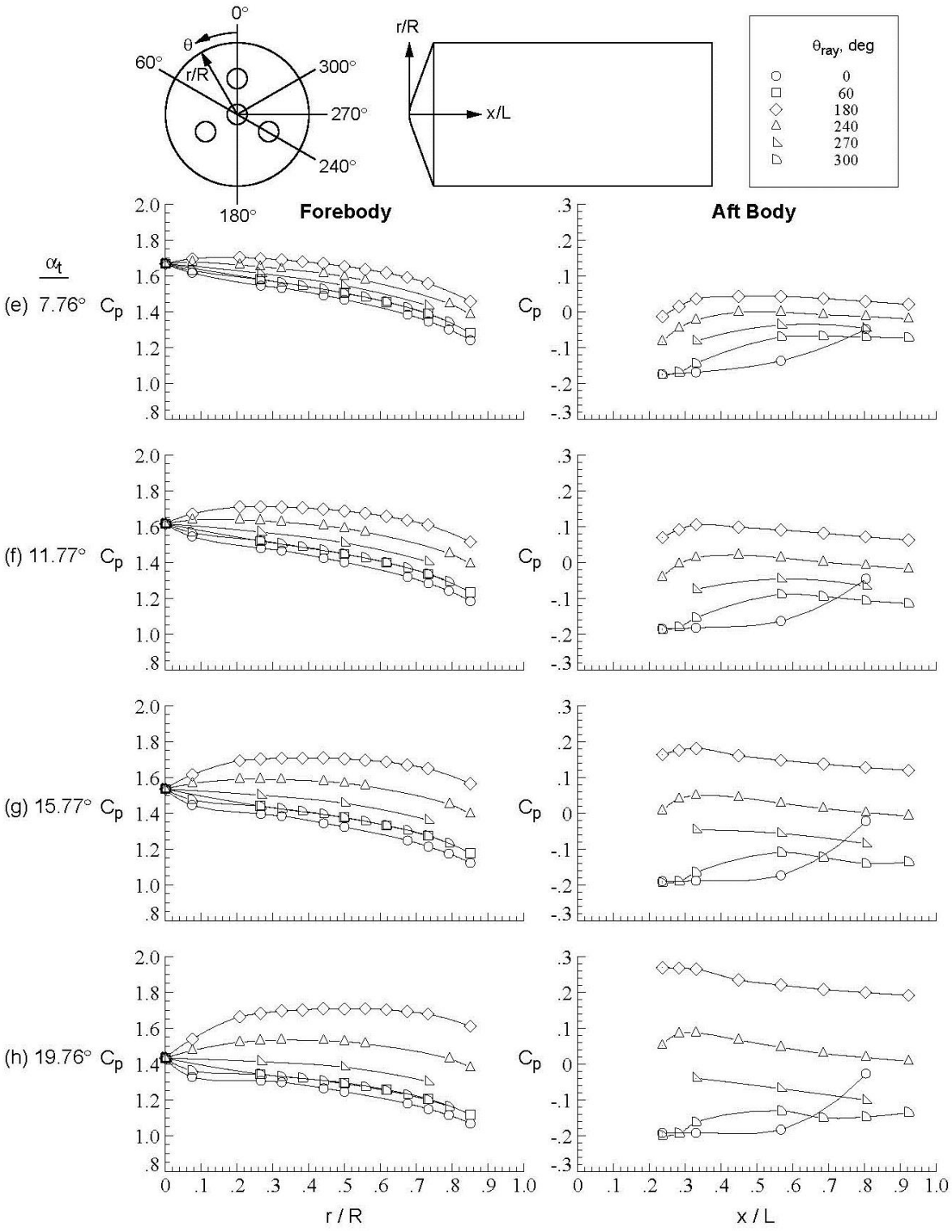

Figure D-1. Concluded.

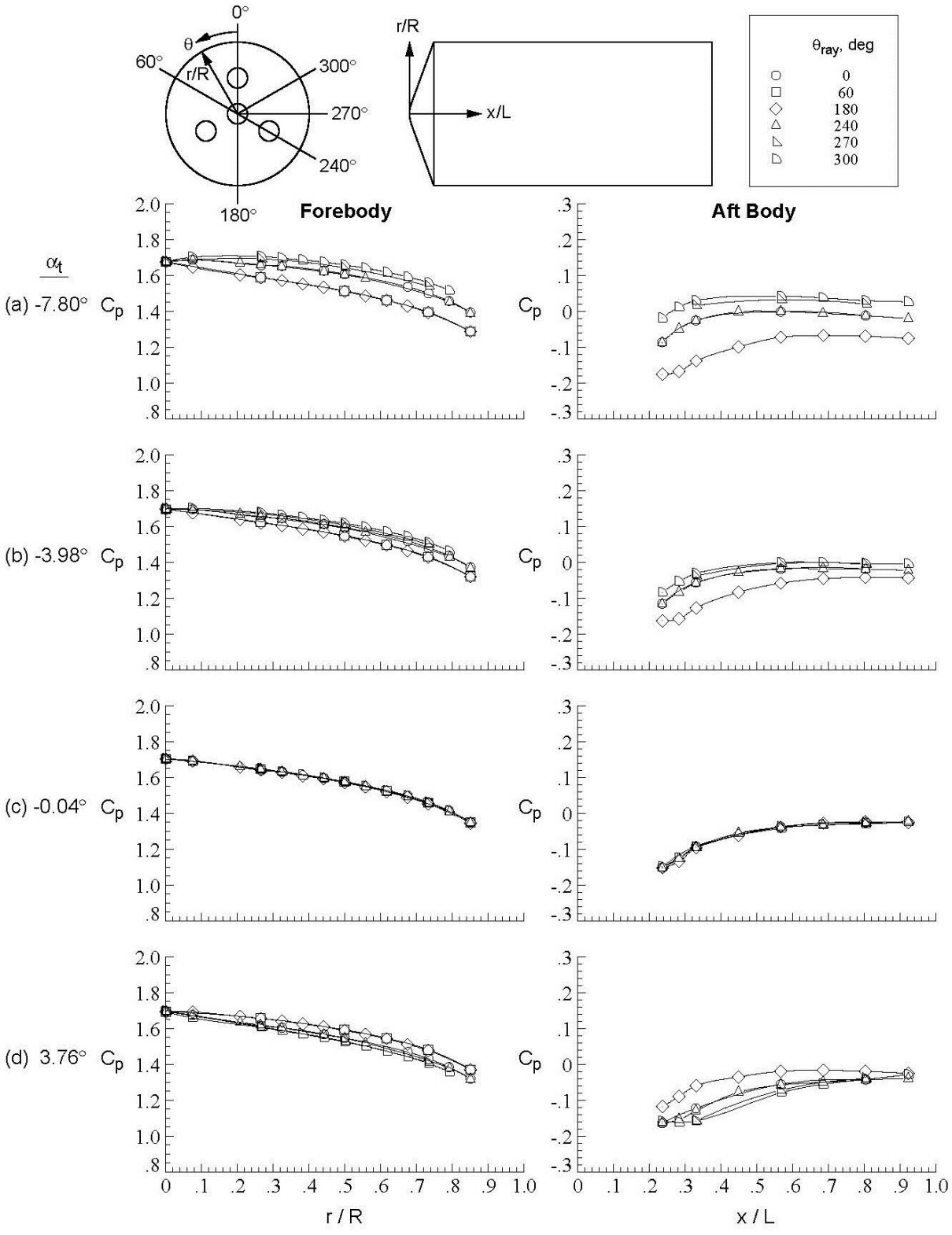

Figure D-2. Baseline configuration, Run 014, M_∞ = 2.4, Re_∞ = 1.0x10^6/ft, ϕ = 59.97°, X_S = 25.16 in, Y_S = 0.00 in, C_T = 0.00.

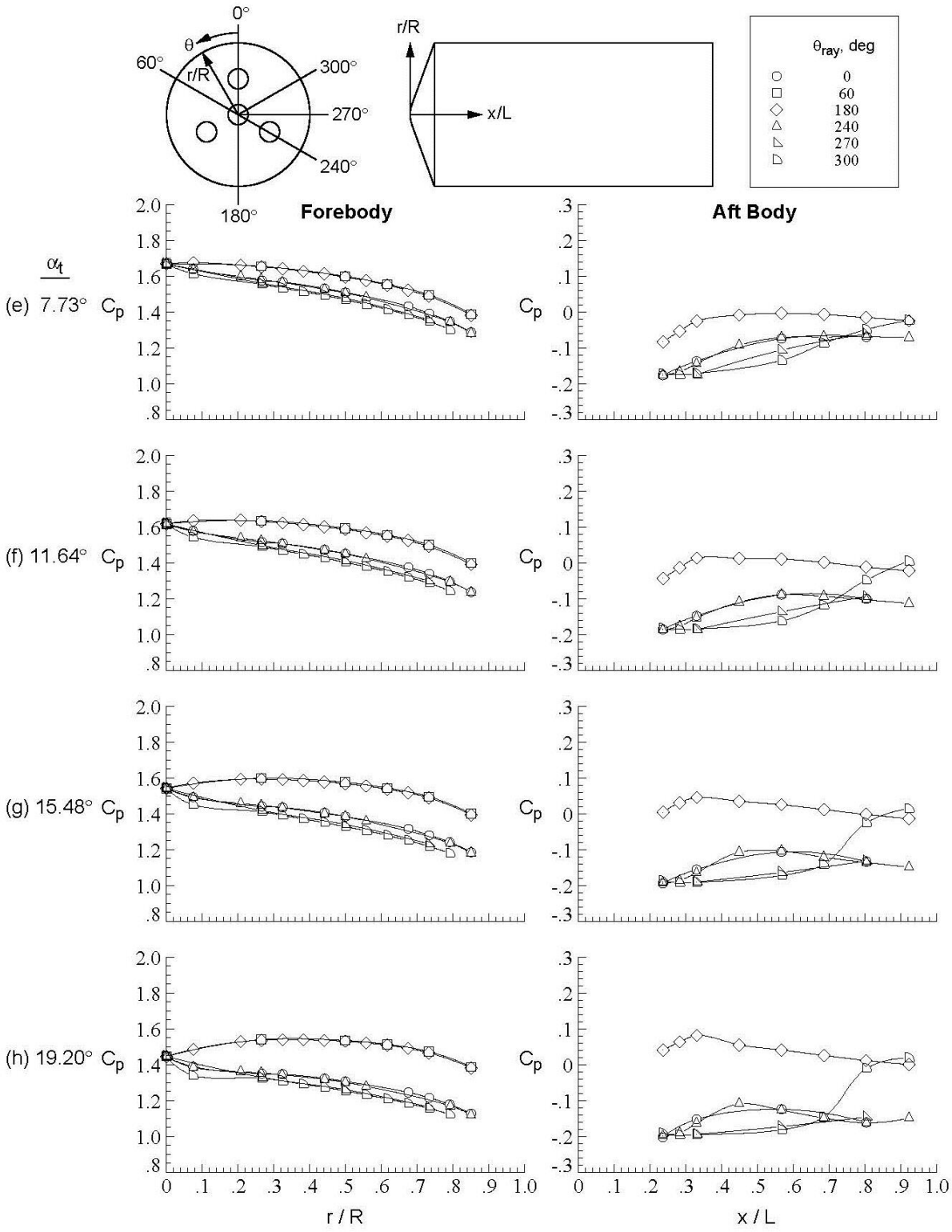

Figure D-2. Concluded.

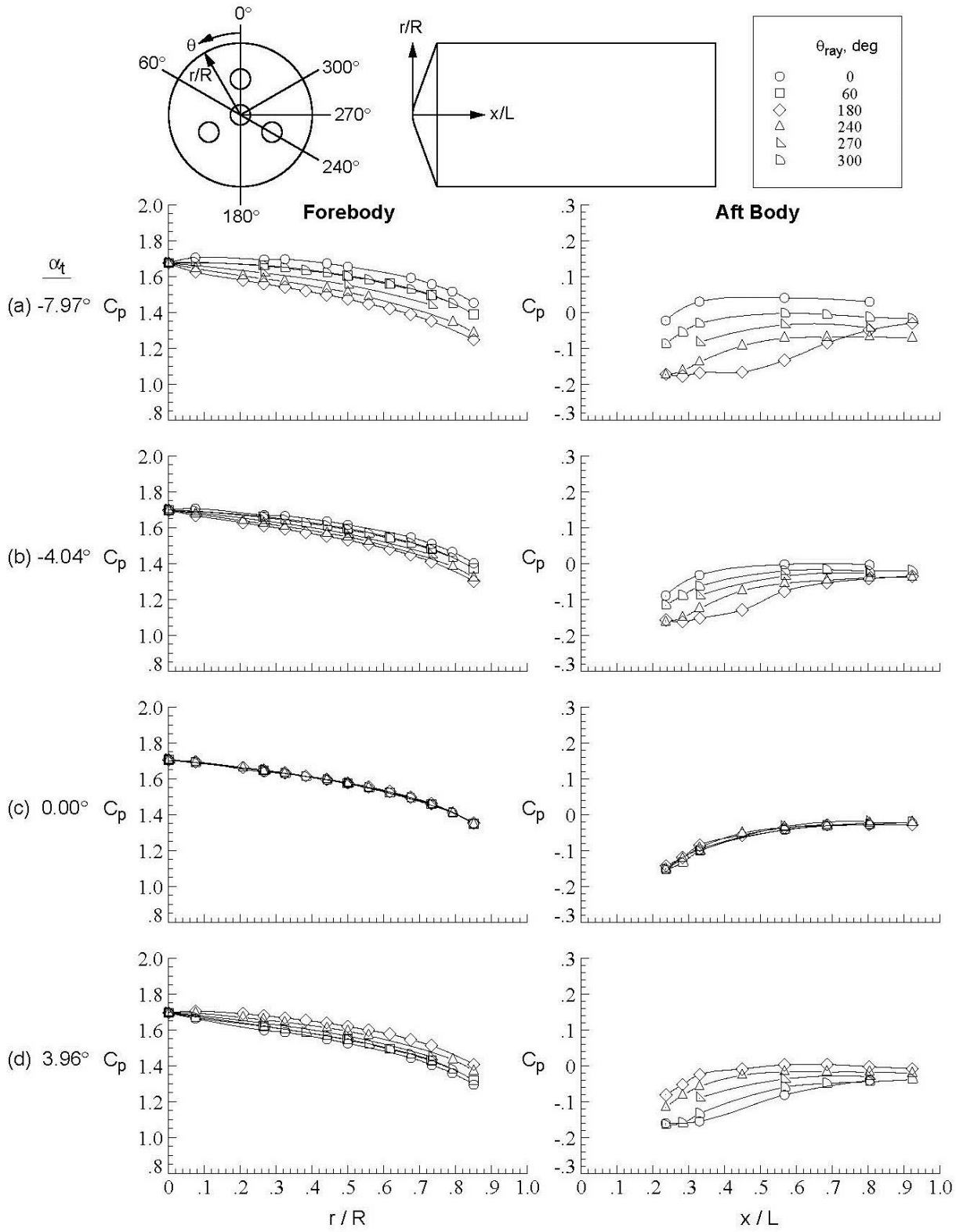

Figure D-3. Baseline configuration, Run 016, $M\infty$ = 2.4, Re_∞ = 1.0x10^6/ft, ϕ = 0.05°, X_S = 25.16 in, Y_S = 0.00 in, C_T = 0.00.

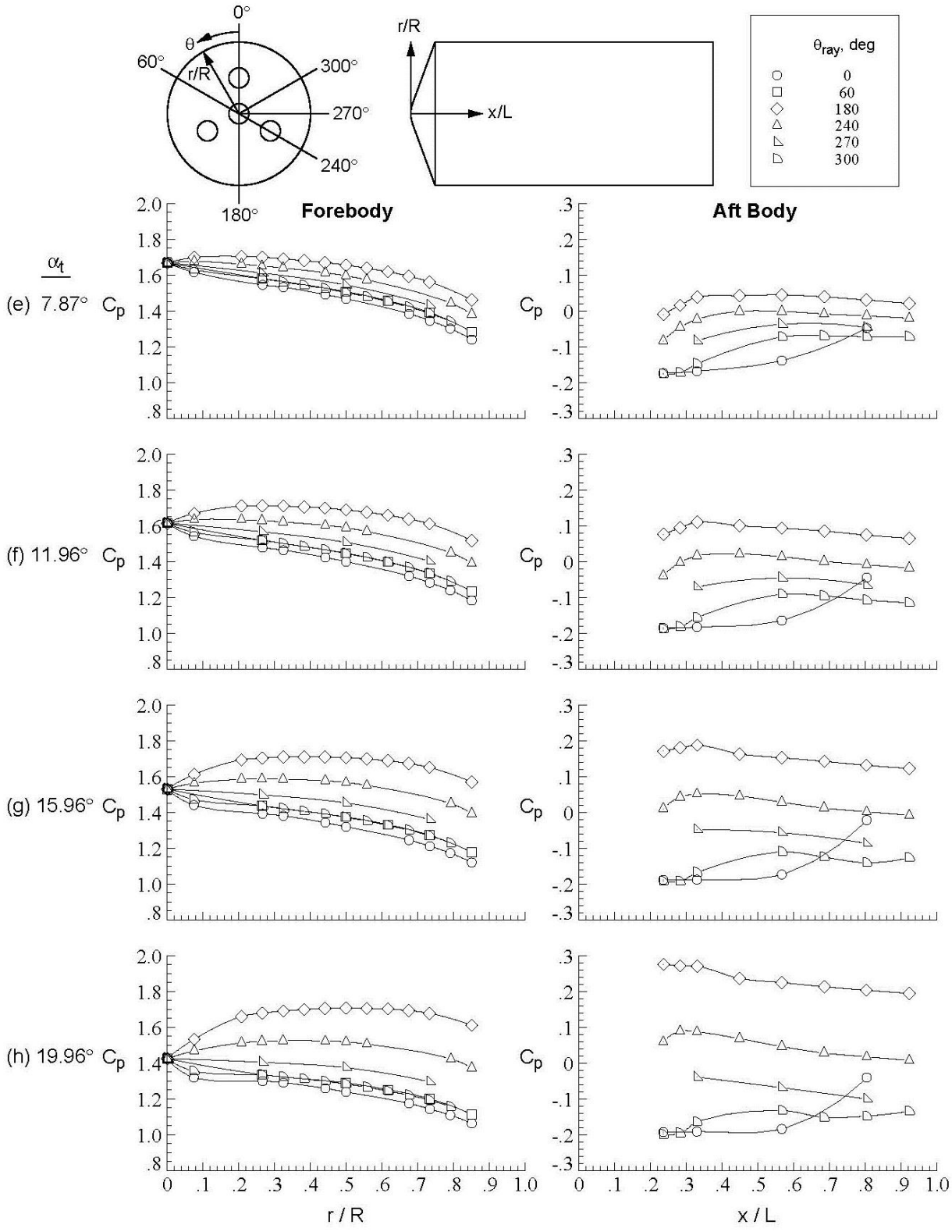

Figure D-3. Concluded.

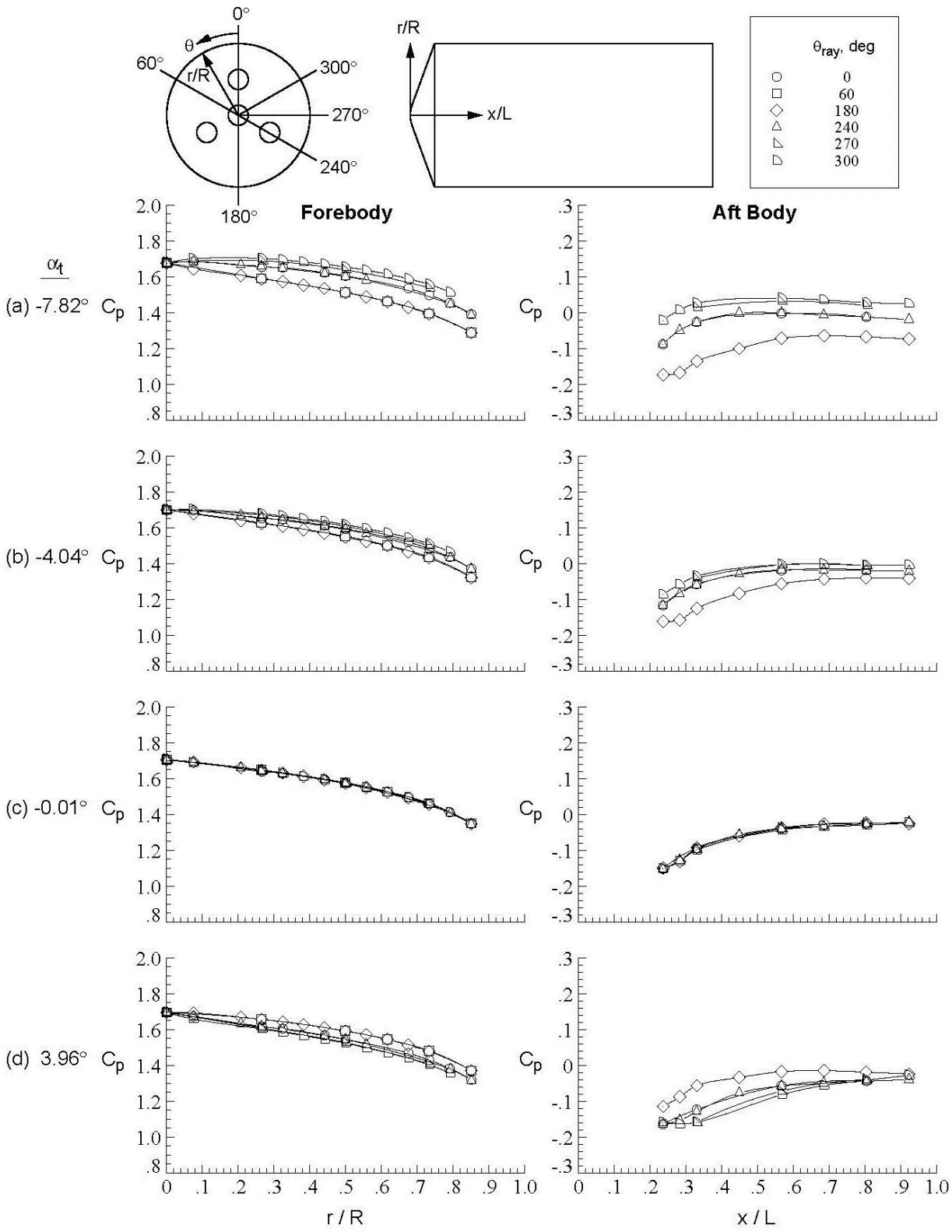

Figure D-4. Baseline configuration, Run 017, M_∞ = 2.4, Re_∞ = 1.0x10^7/ft, ϕ = 59.86°, X_S = 25.16 in, Y_S = 0.00 in, C_T = 0.00.

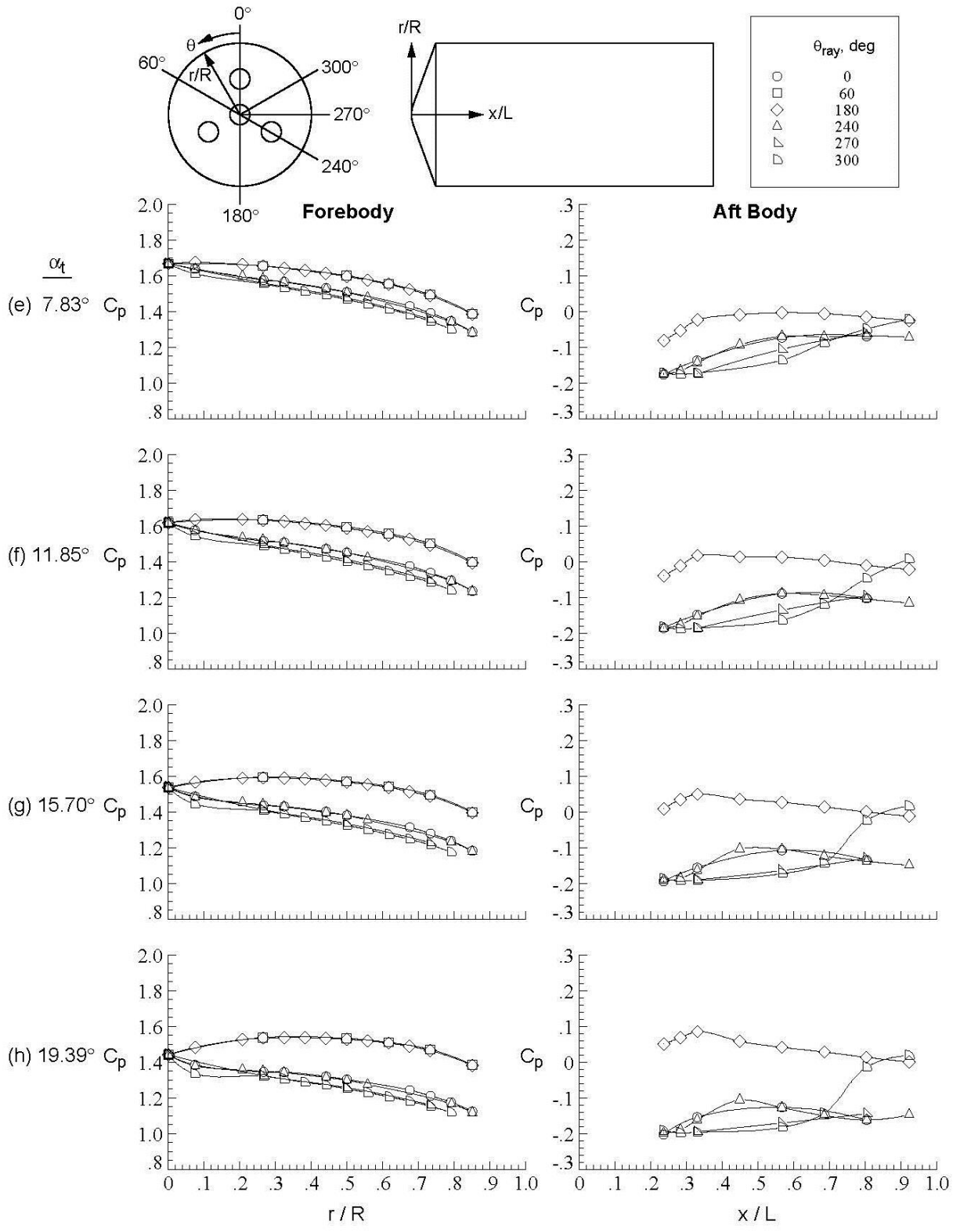

Figure D-4. Concluded.

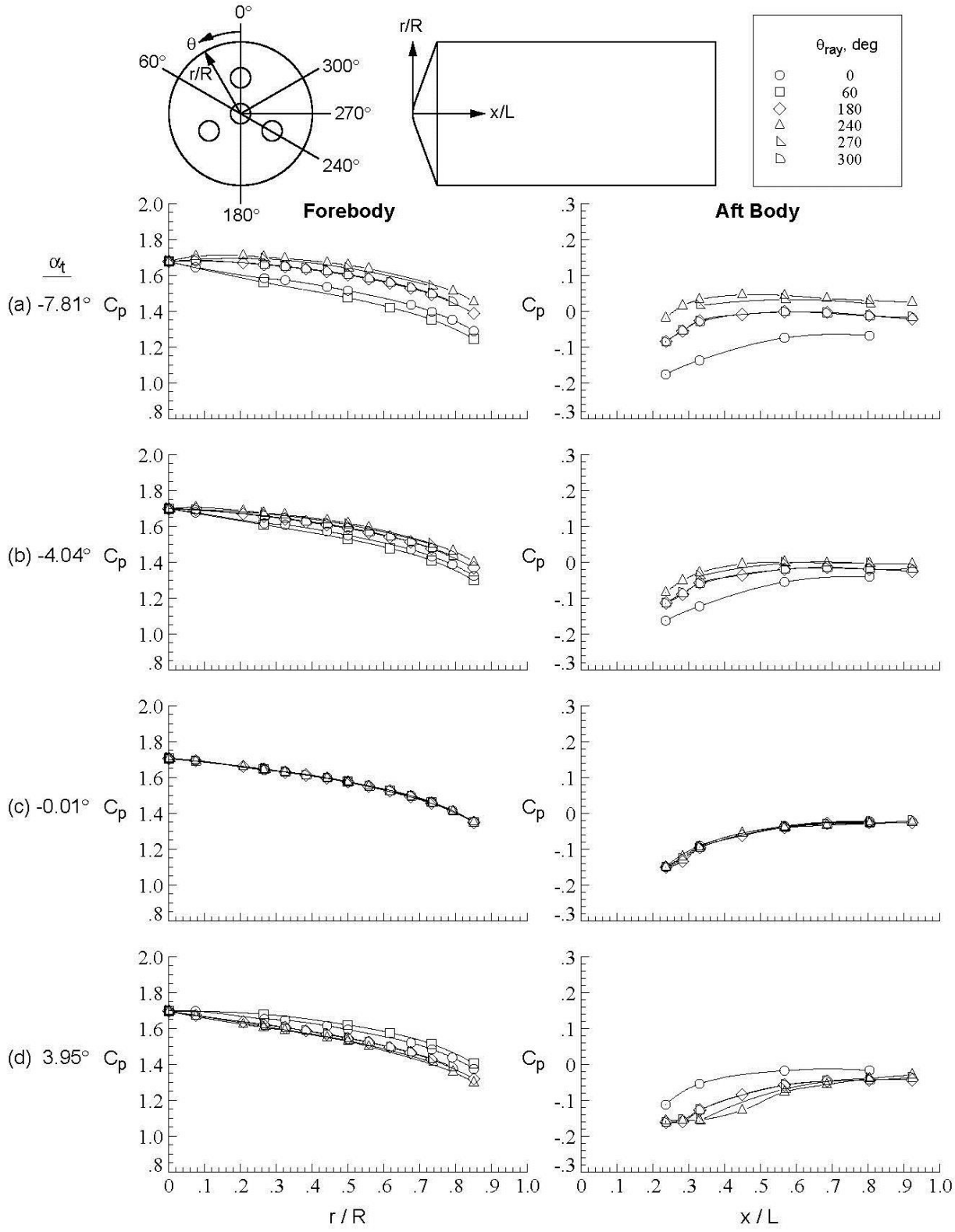

Figure D-5. Baseline configuration, Run 018, M_∞ = 2.4, Re_∞ = 1.0x10^6/ft, ϕ = 119.96°, X_S = 25.16 in, Y_S = 0.00 in, C_T = 0.00.

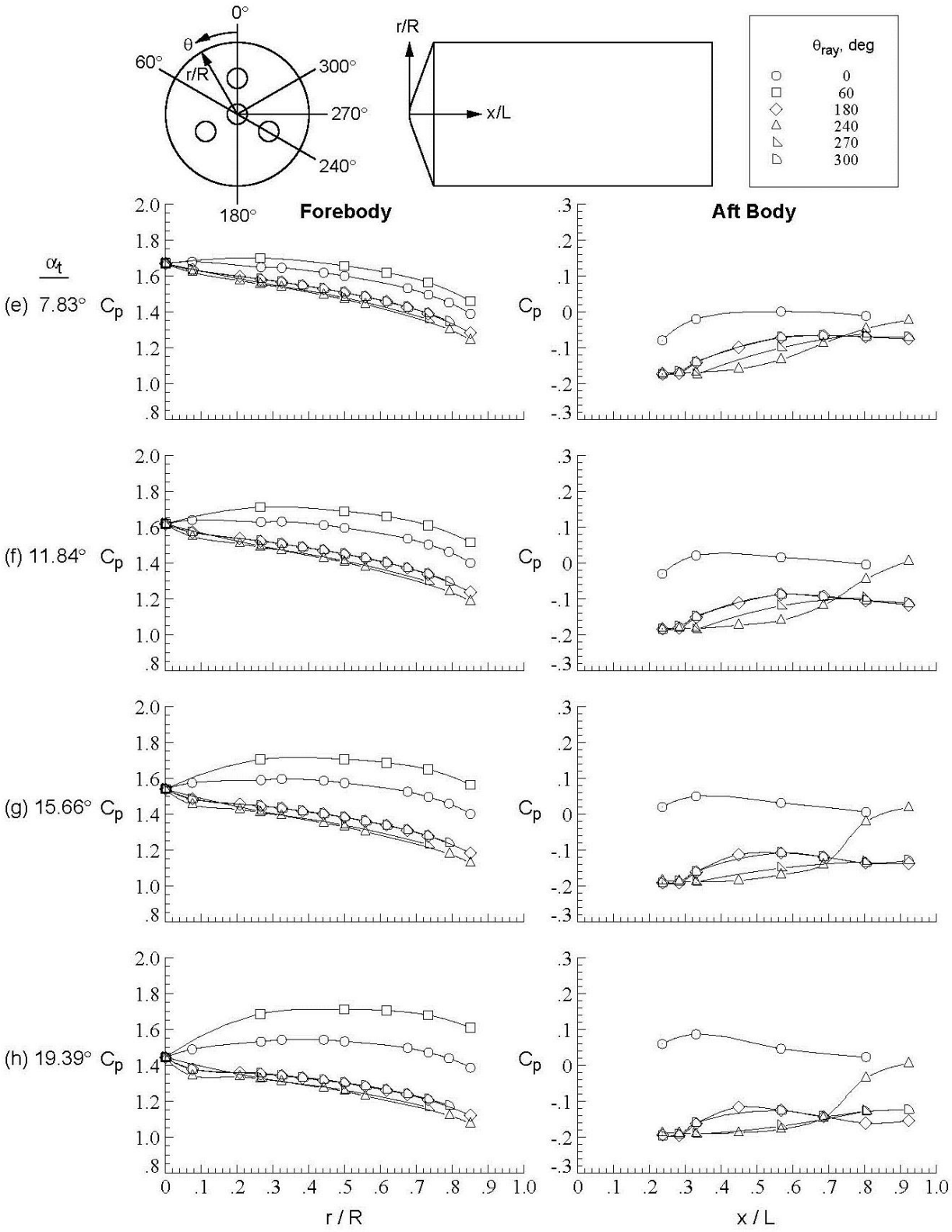

Figure D-5. Concluded.

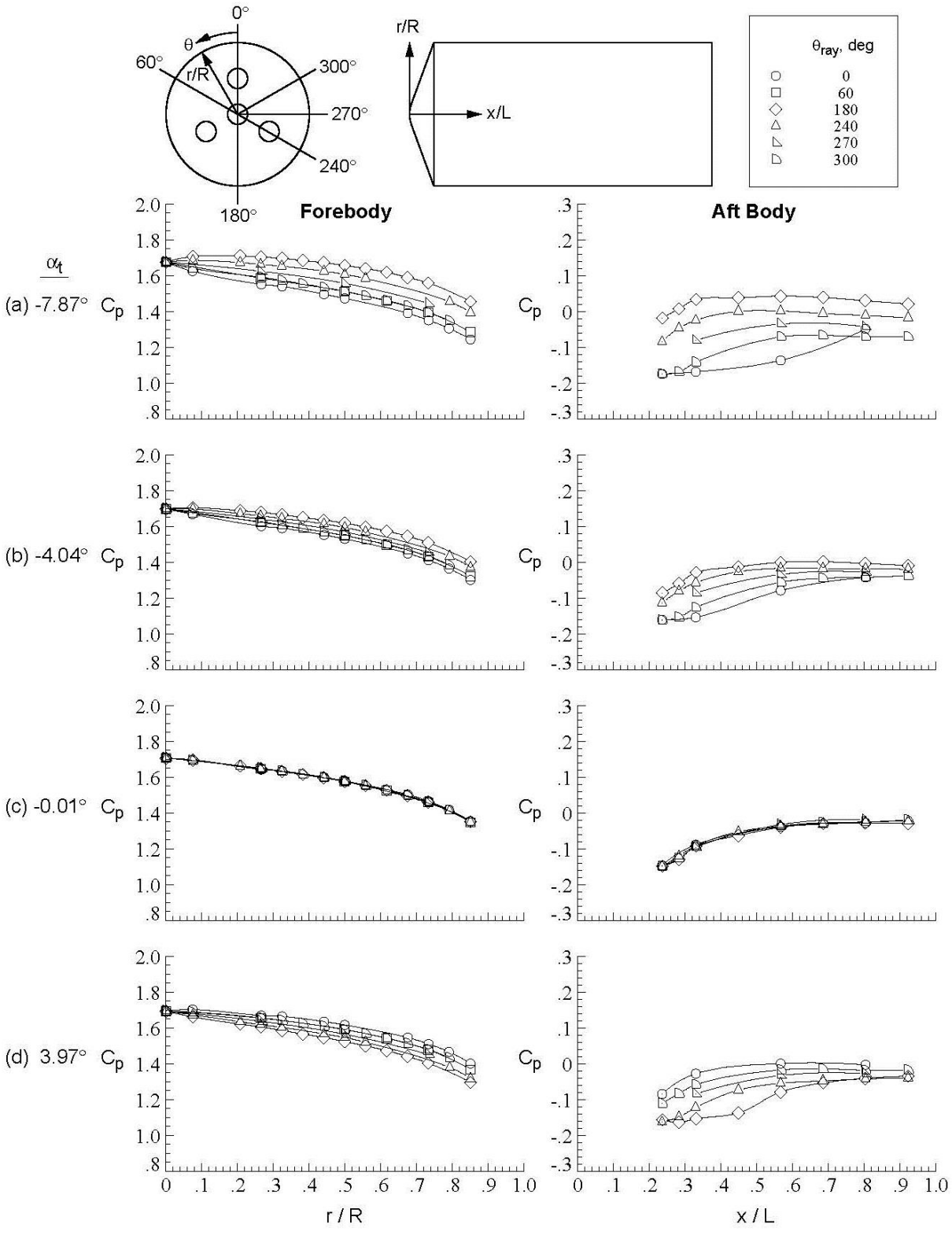

Figure D-6. Baseline configuration, Run 019, M_∞ = 2.4, Re_∞ = 1.0x10^6/ft, ϕ = 179.91°, X_S = 25.16 in, Y_S = 0.00 in, C_T = 0.00.

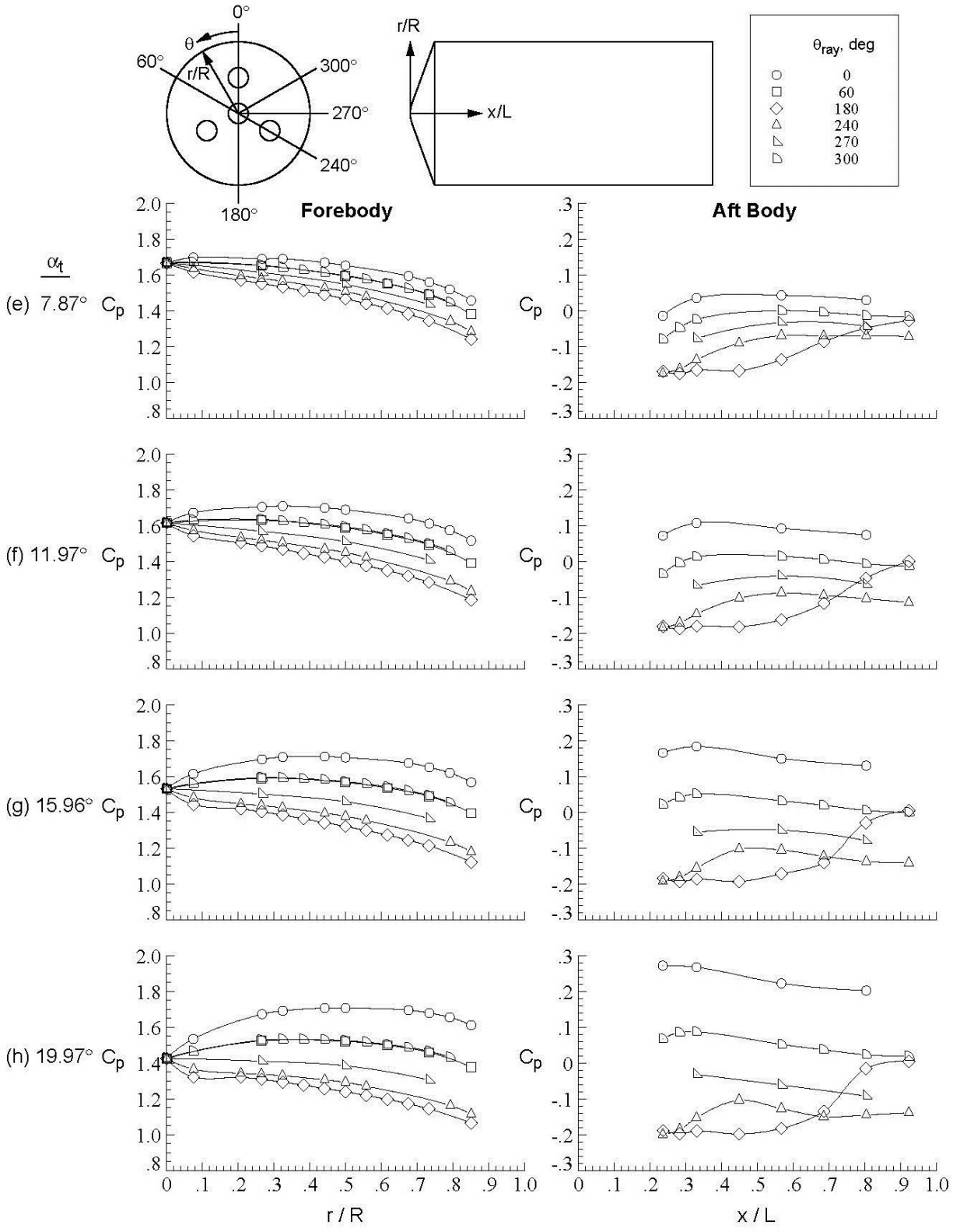

Figure D-6. Concluded.

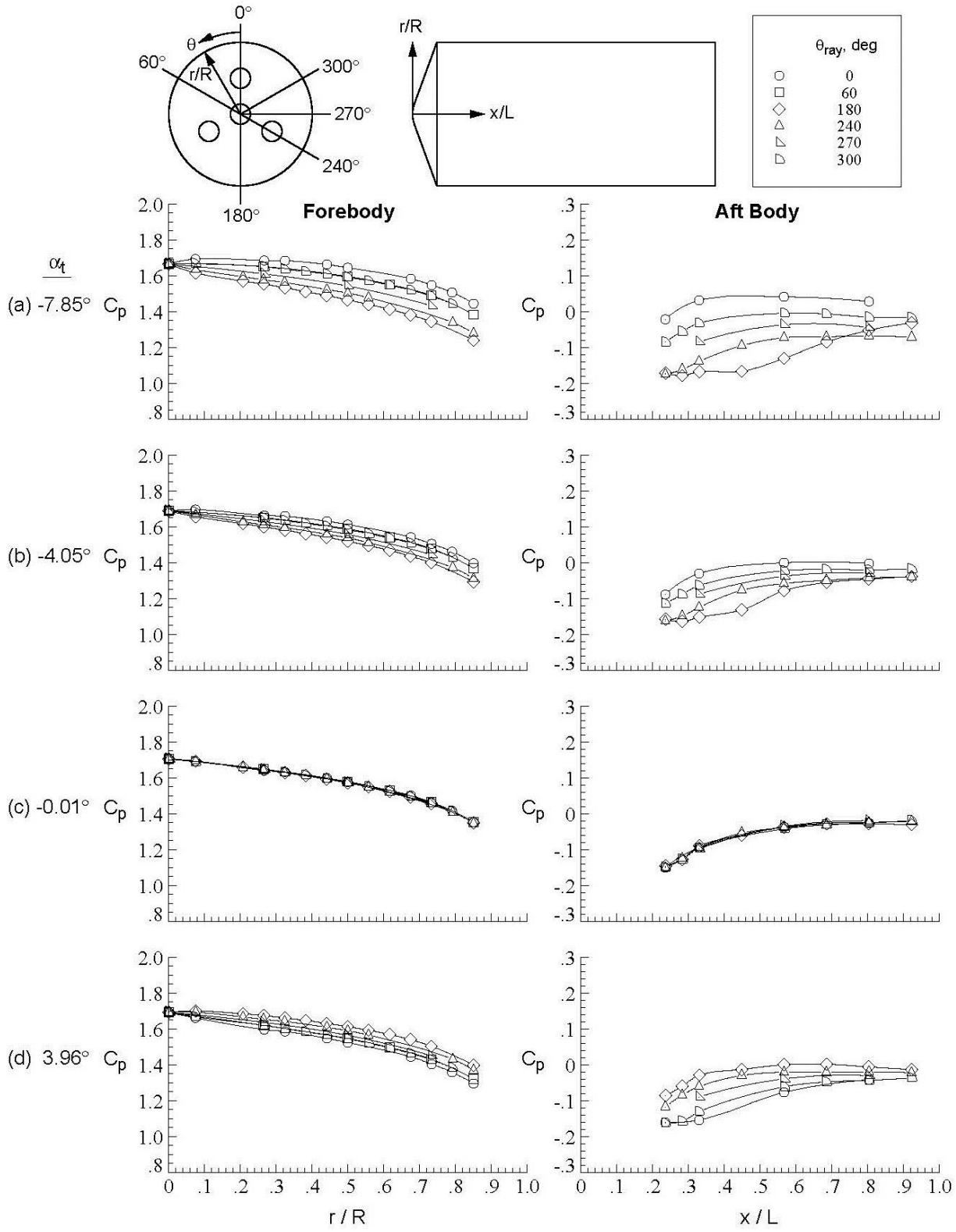

Figure D-7. Baseline configuration, Run 020, M_∞ = 2.4, Re_∞ = 1.0x10^6/ft, ϕ = 0.01°, X_S = 39.93 in, Y_S = 0.00 in, C_T = 0.00.

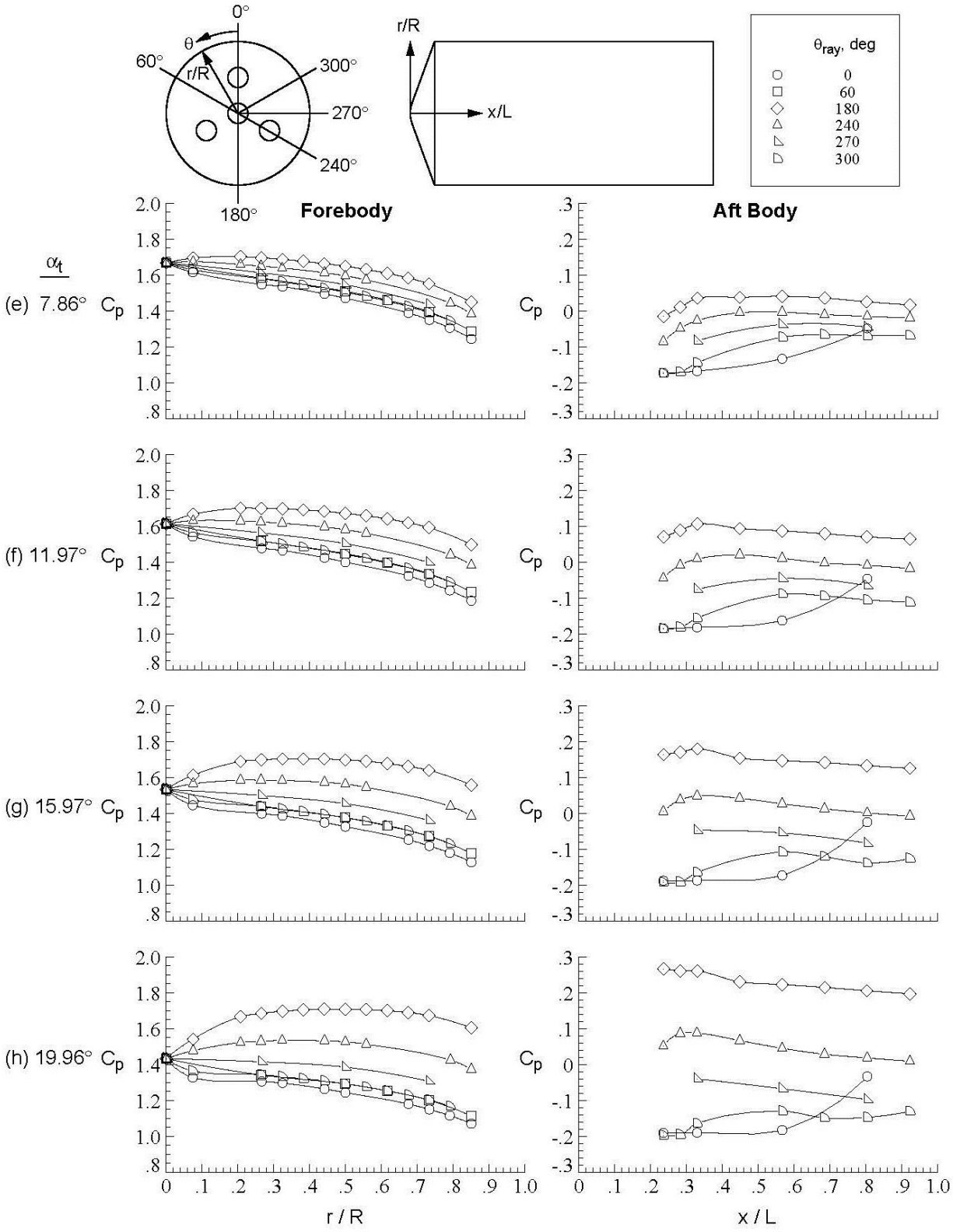

Figure D-7. Concluded.

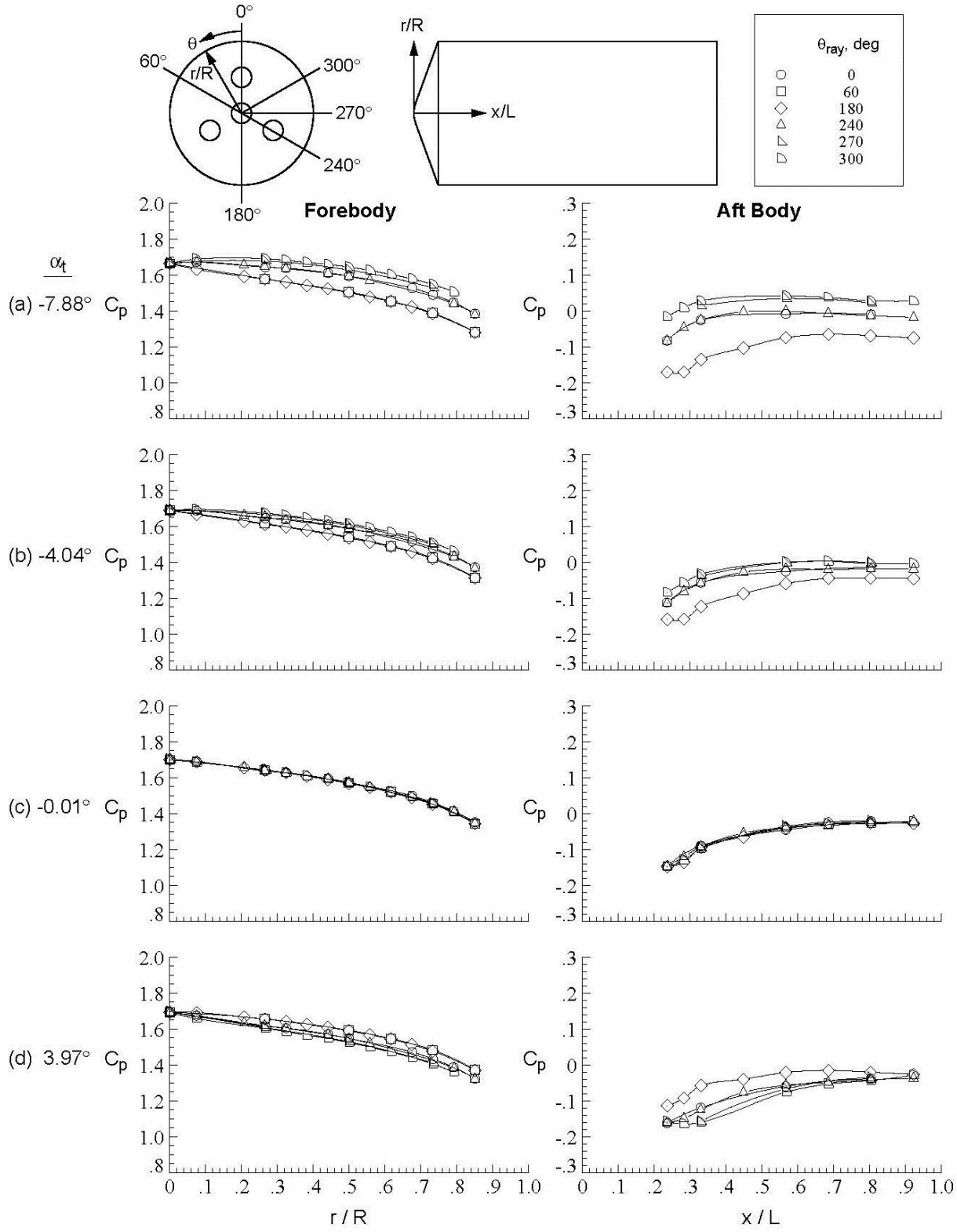

Figure D-8. Baseline configuration, Run 021, M_∞ = 2.4, Re_∞ = 1.0x10^7/ft, ϕ = 59.88°, X_S = 39.93 in, Y_S = 0.00 in, C_T = 0.00.

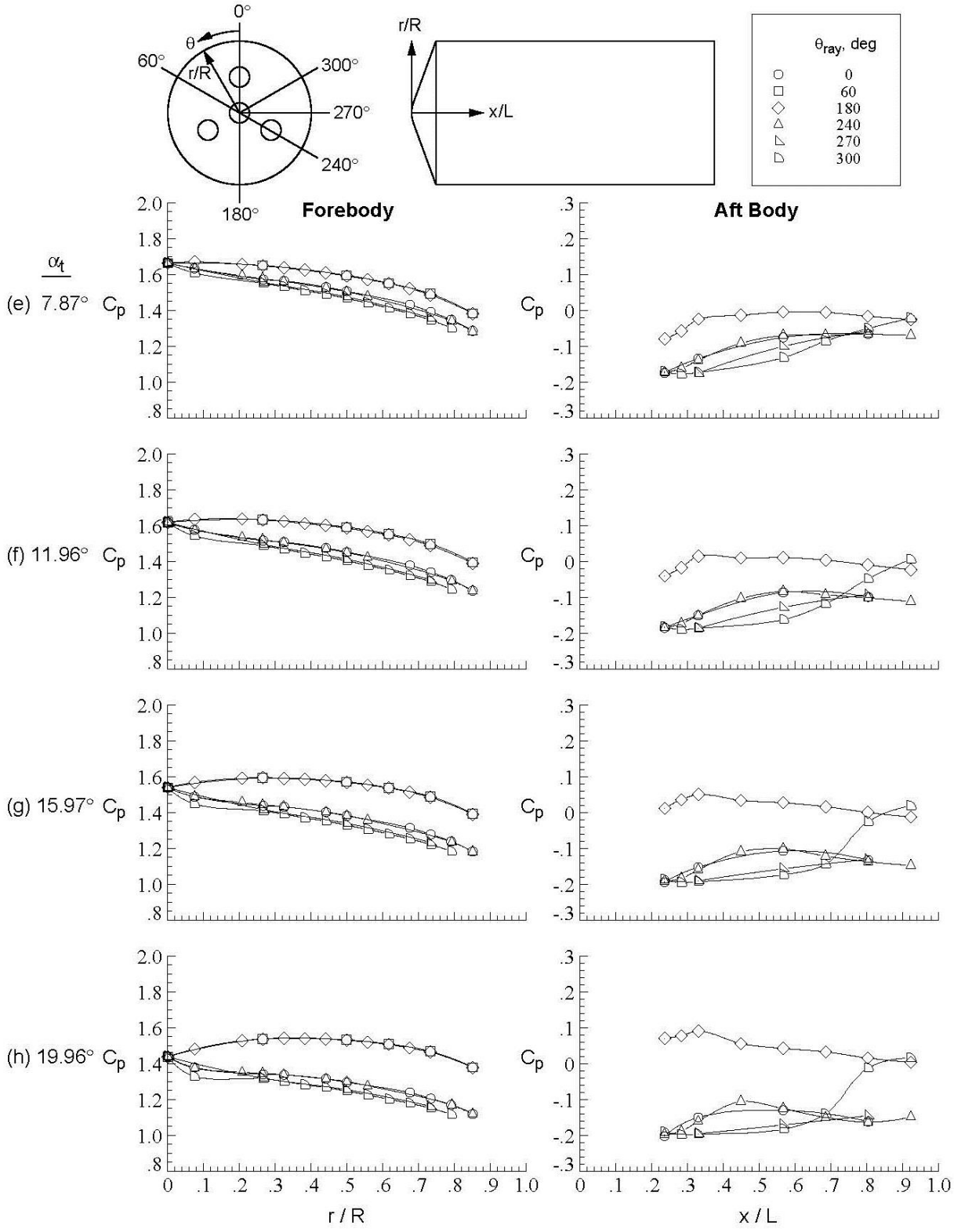

Figure D-8. Concluded.

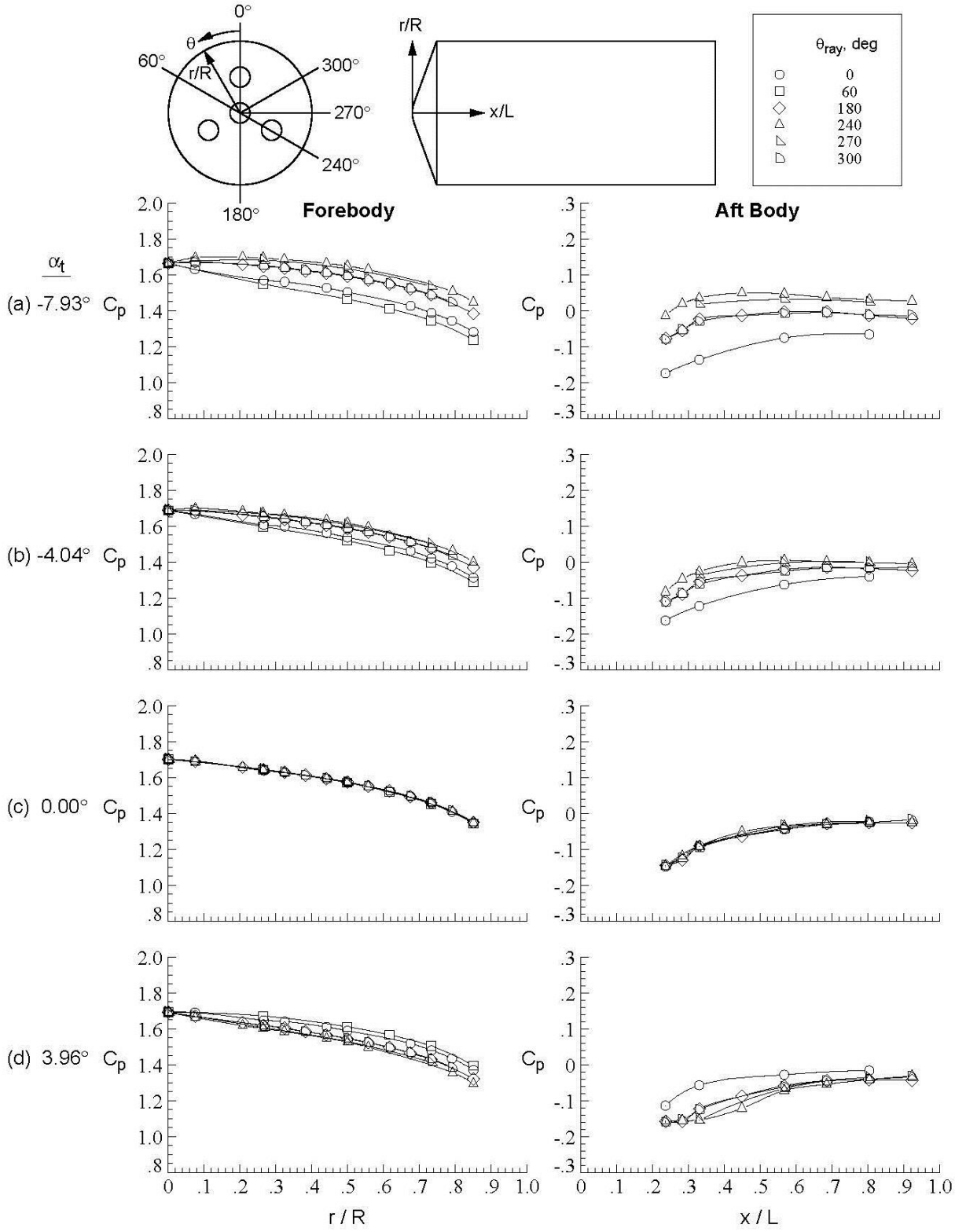

Figure D-9. Baseline configuration, Run 022, M_∞ = 2.4, Re_∞ = 1.0x10^6/ft, ϕ = 120.06°, X_S = 39.93 in, Y_S = 0.00 in, C_T = 0.00.

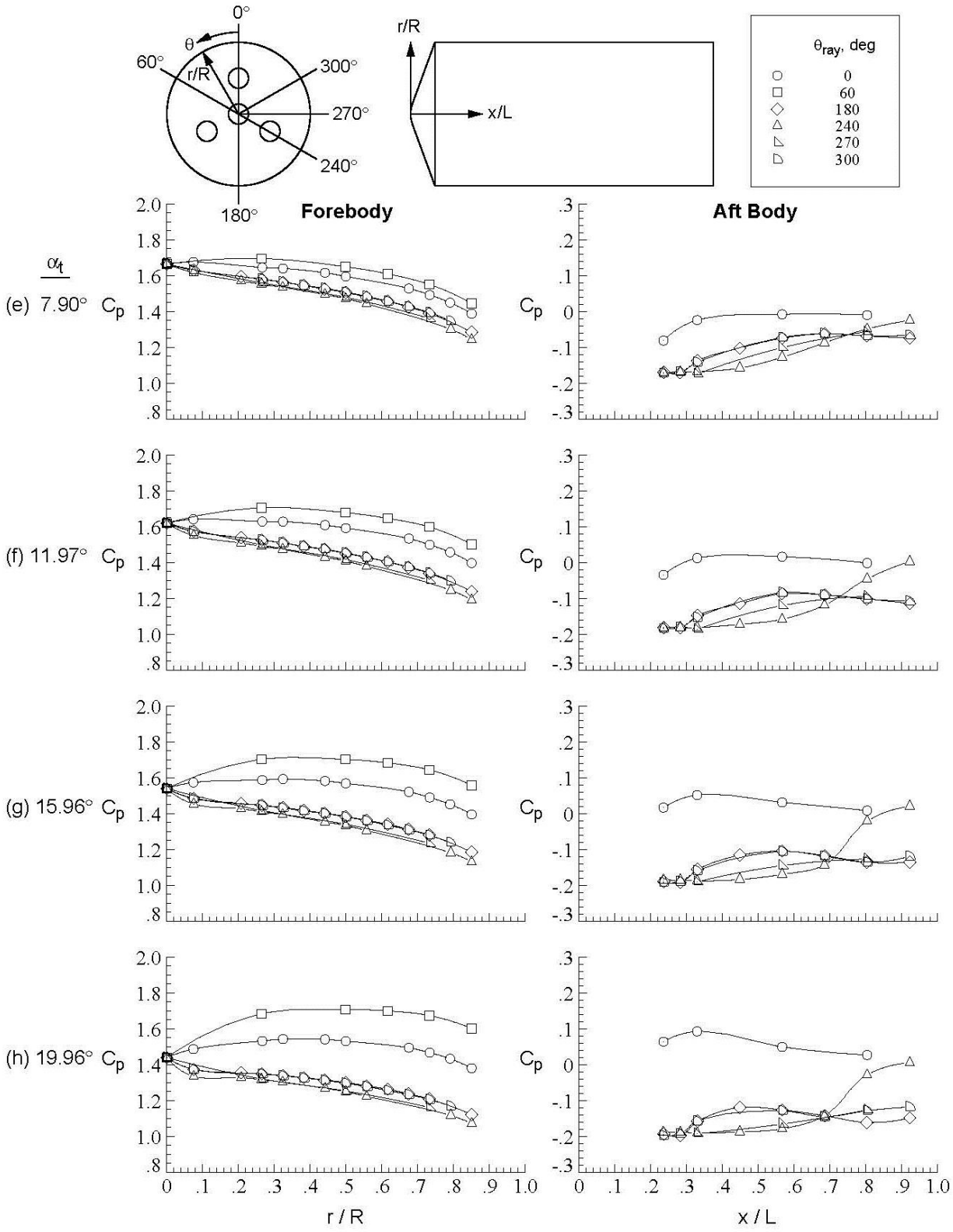

Figure D-9. Concluded.

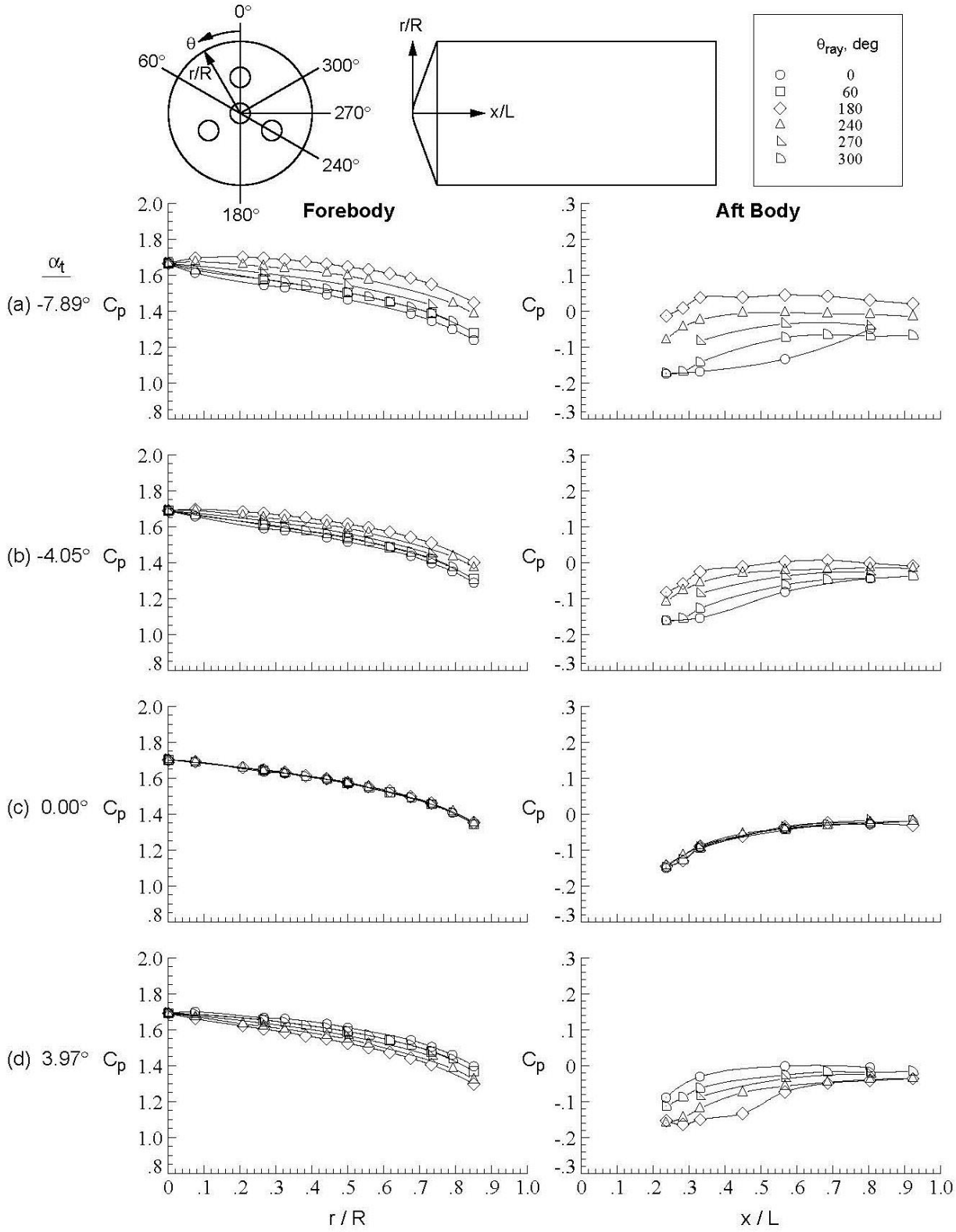

Figure D-10. Baseline configuration, Run 023, M_∞ = 2.4, Re_∞ = 1.0x10^6/ft, ϕ = 179.99°, X_S = 39.93 in, Y_S = 0.00 in, C_T = 0.00.

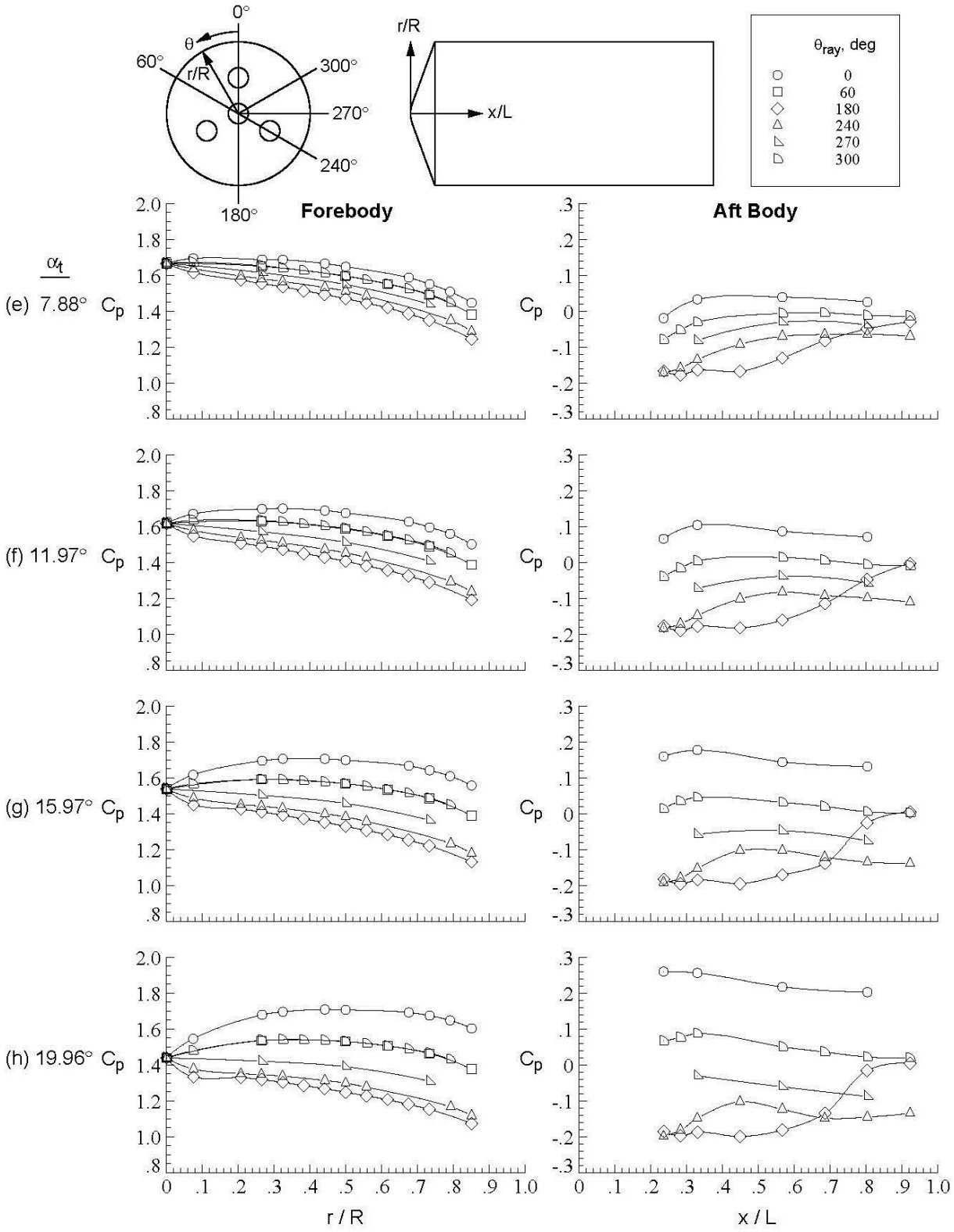

Figure D-10. Concluded.

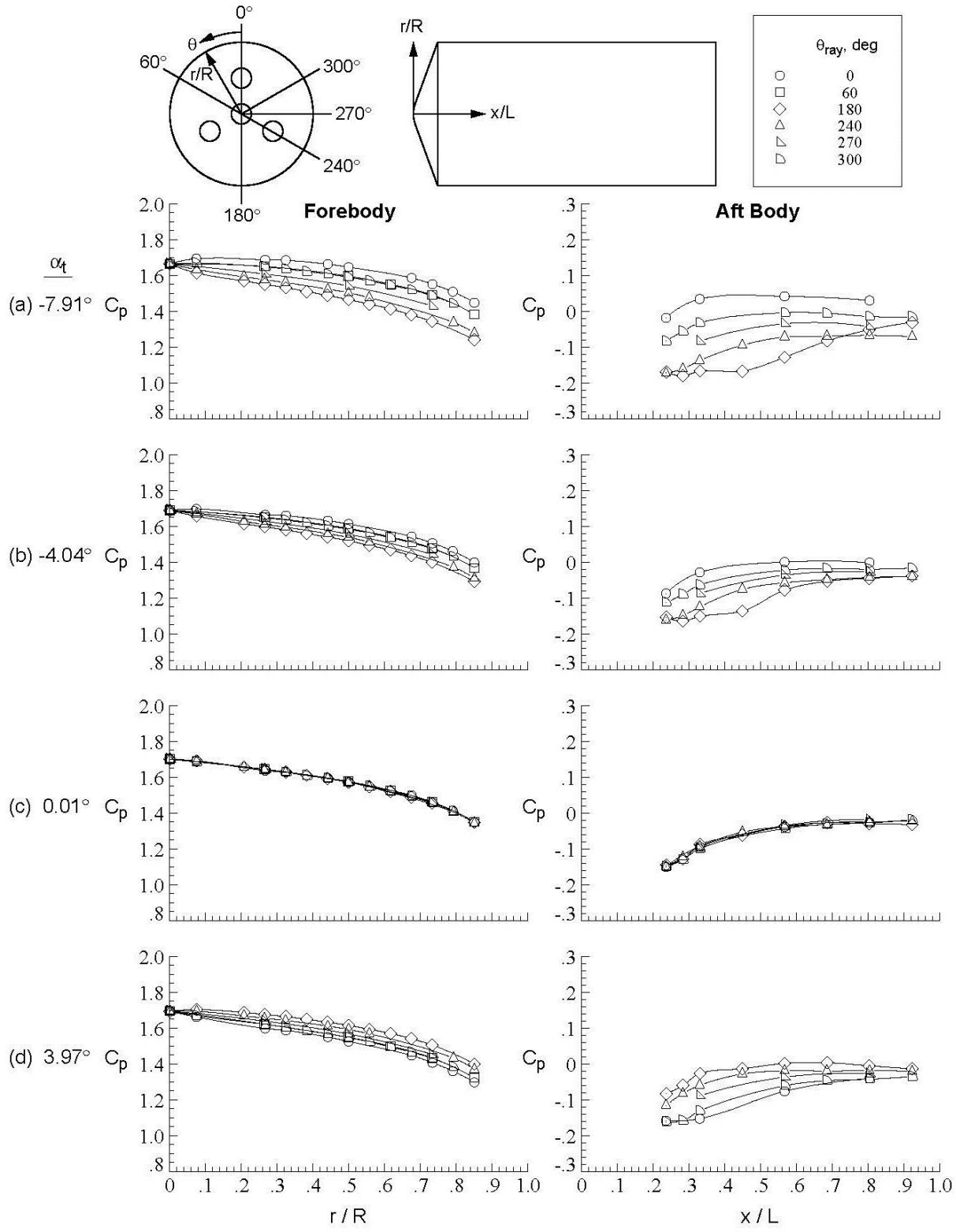

Figure D-11. Baseline configuration, Run 024, M_∞ = 2.4, Re_∞ = 1.0x10^6/ft, ϕ = 0.01°, X_S = 39.93 in, Y_S = 0.00 in, C_T = 0.00.

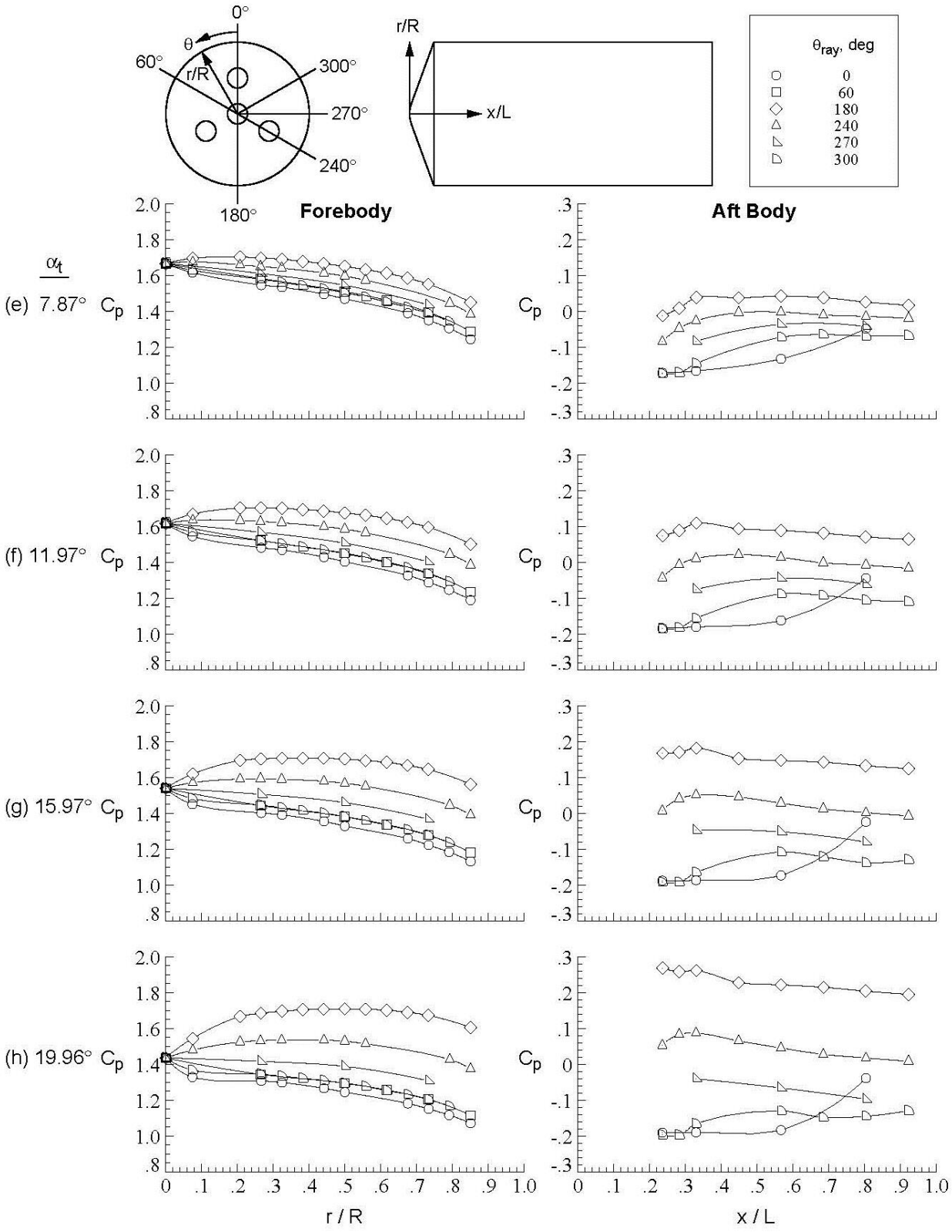

Figure D-11. Concluded.

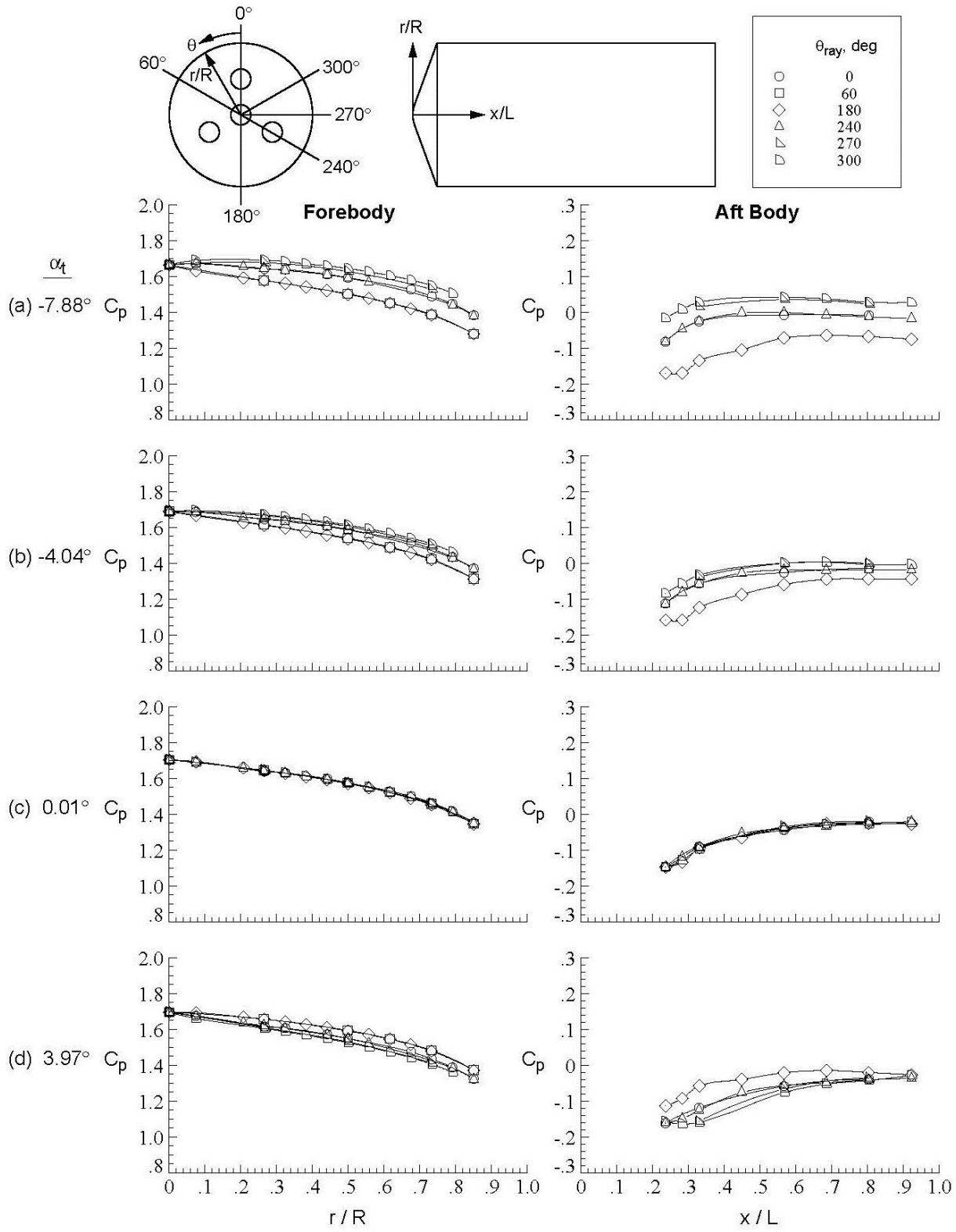

Figure D-12. Baseline configuration, Run 025, M_∞ = 2.4, Re_∞ = 1.0x10^6/ft, ϕ = 60.08°, X_S = 39.93 in, Y_S = 0.00 in, C_T = 0.00.

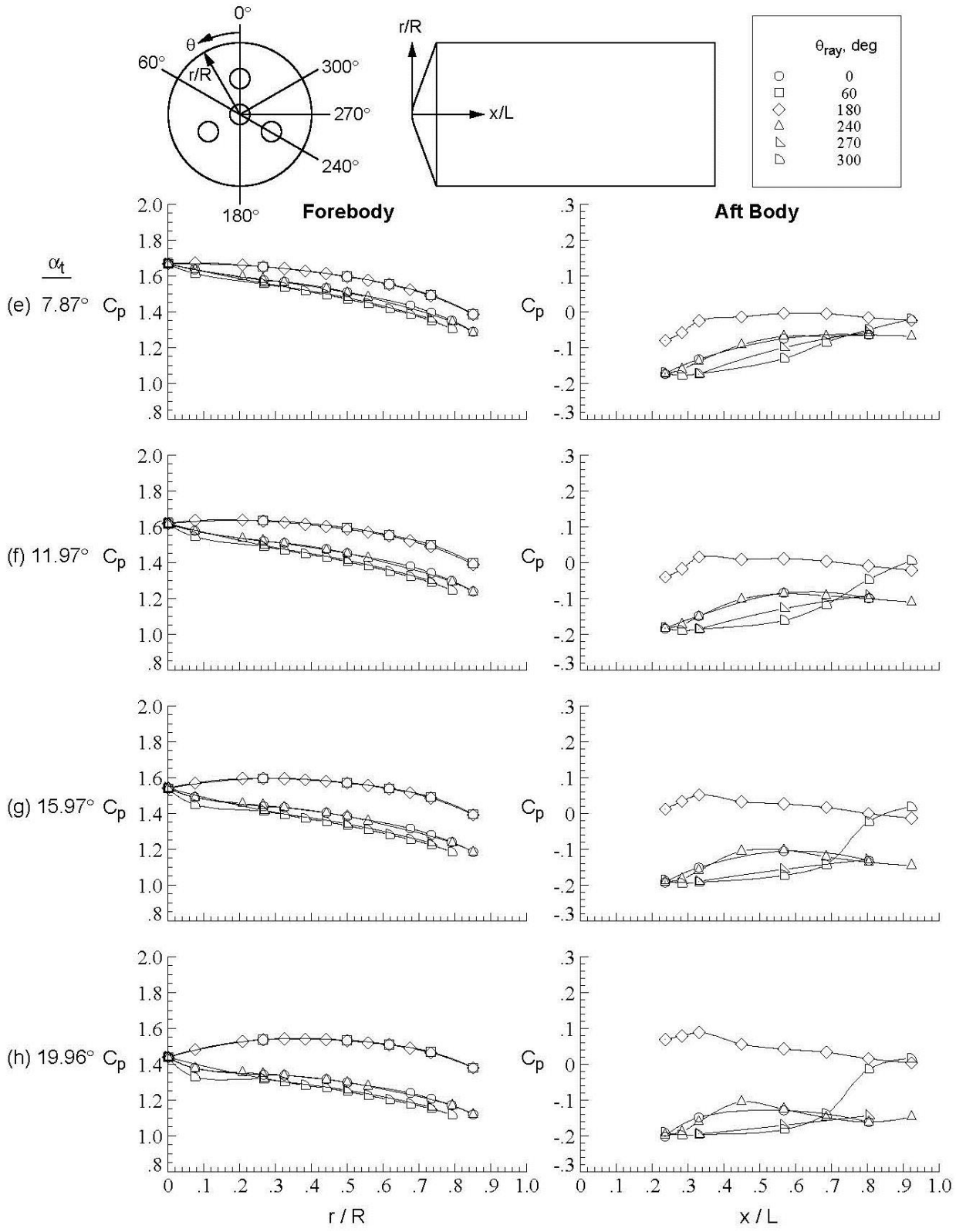

Figure D-12. Concluded.

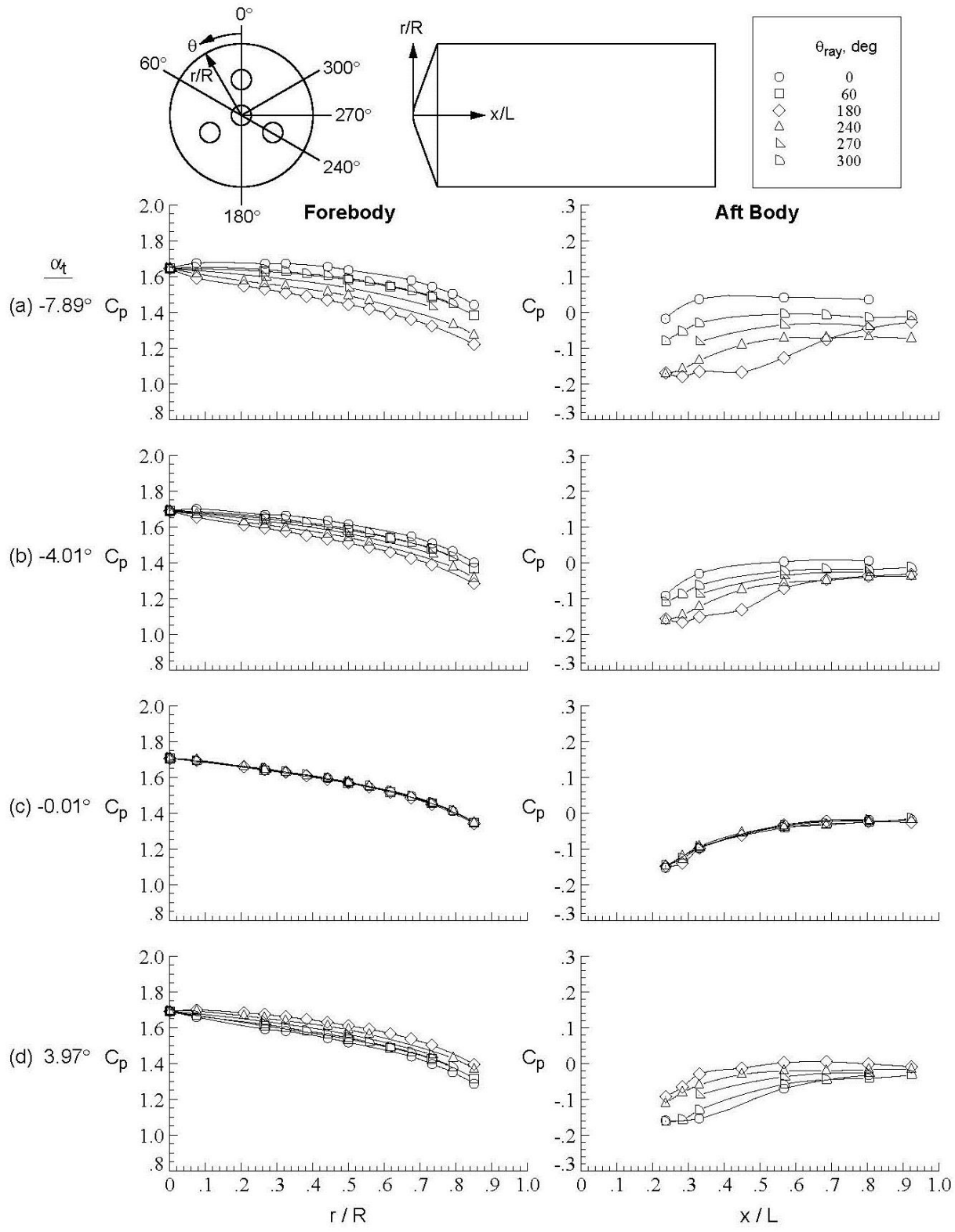

Figure D-13. Baseline configuration, Run 026, M_∞ = 2.4, Re_∞ = 1.0x10^6/ft, ϕ = 0.03°, X_S = 50.17 in, Y_S = 0.00 in, C_T = 0.00.

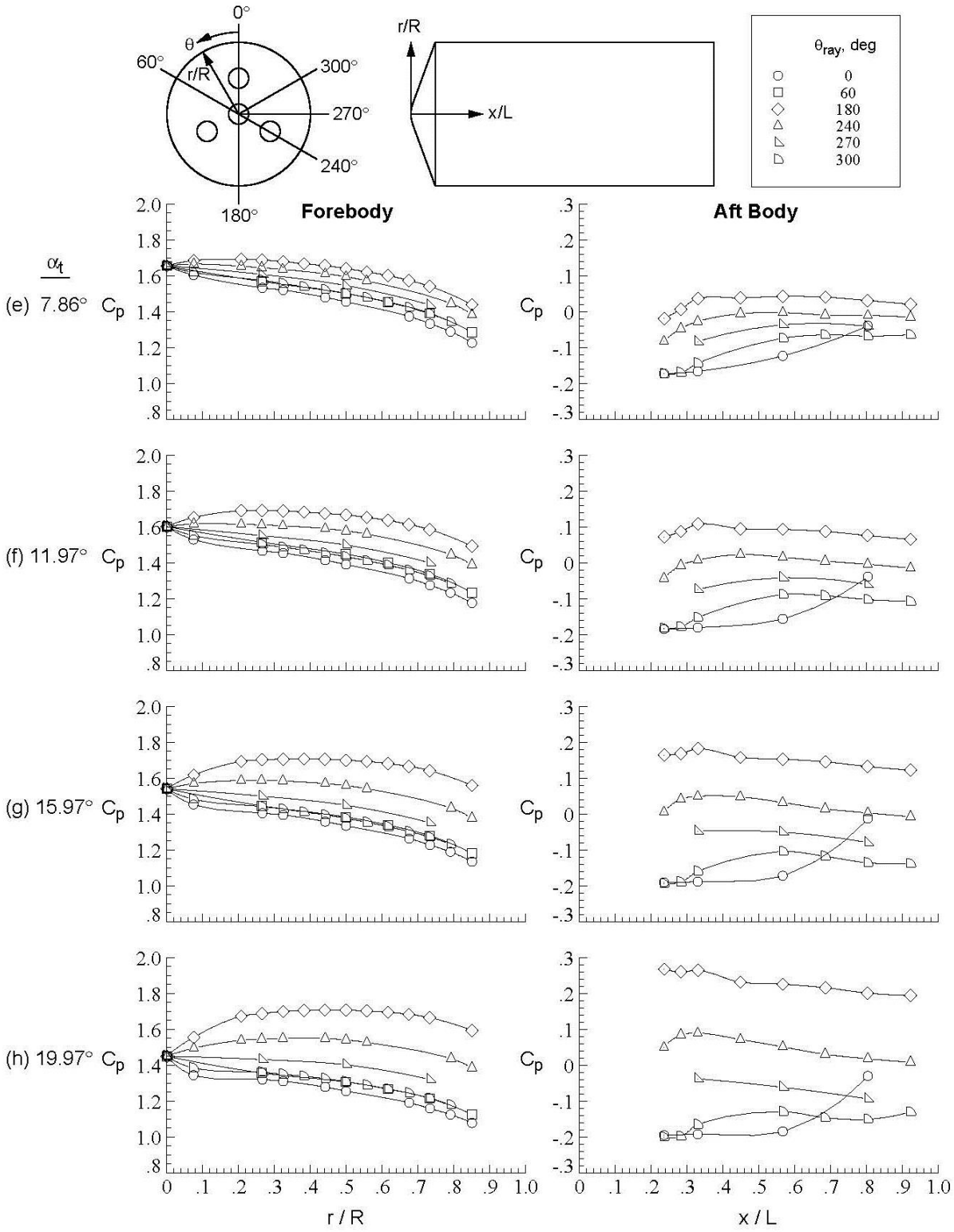

Figure D-13. Concluded.

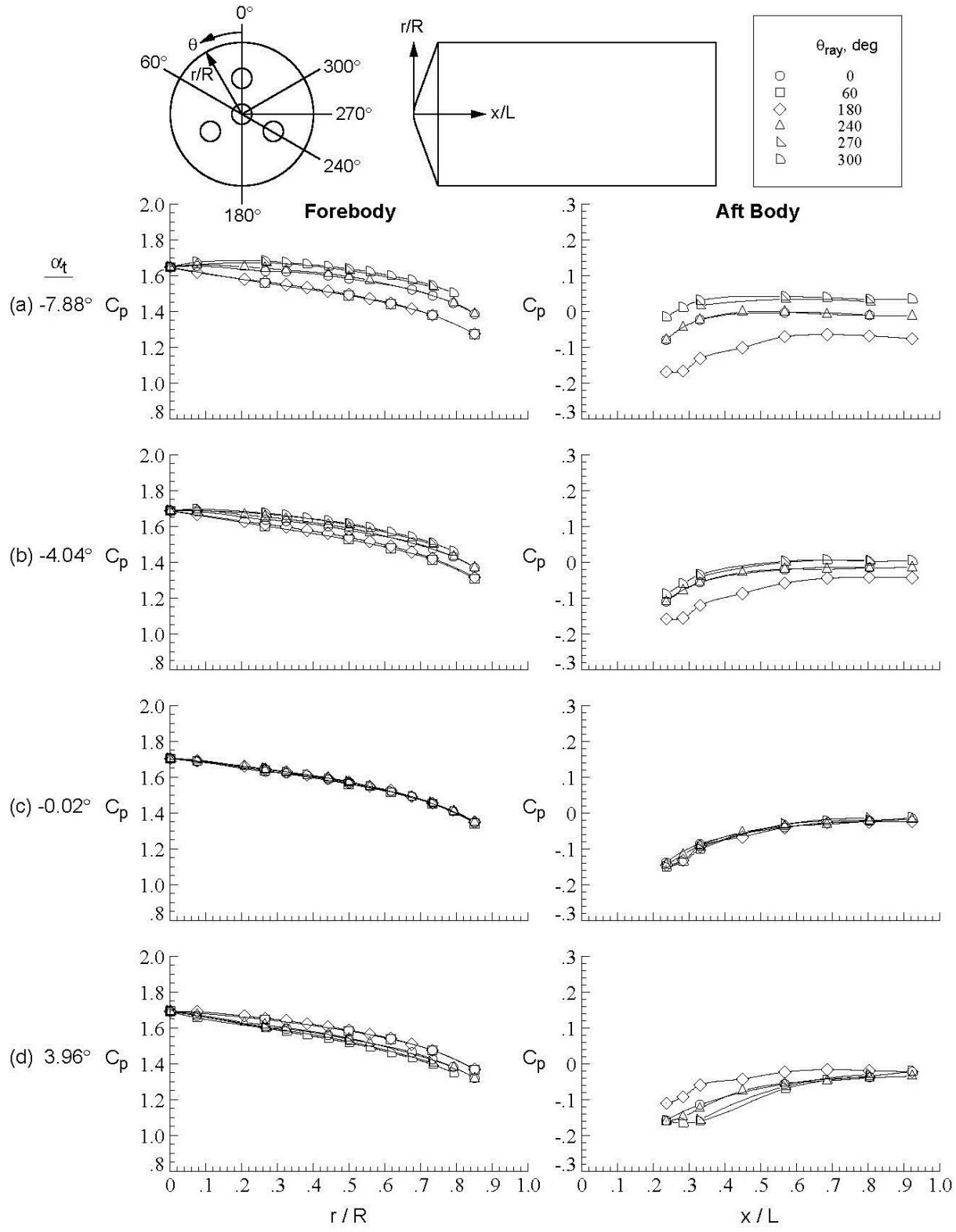

Figure D-14. Baseline configuration, Run 027, M_∞ = 2.4, Re_∞ = 1.0x10^6/ft, ϕ = 60.08°, X_S = 50.17 in, Y_S = 0.00 in, C_T = 0.00.

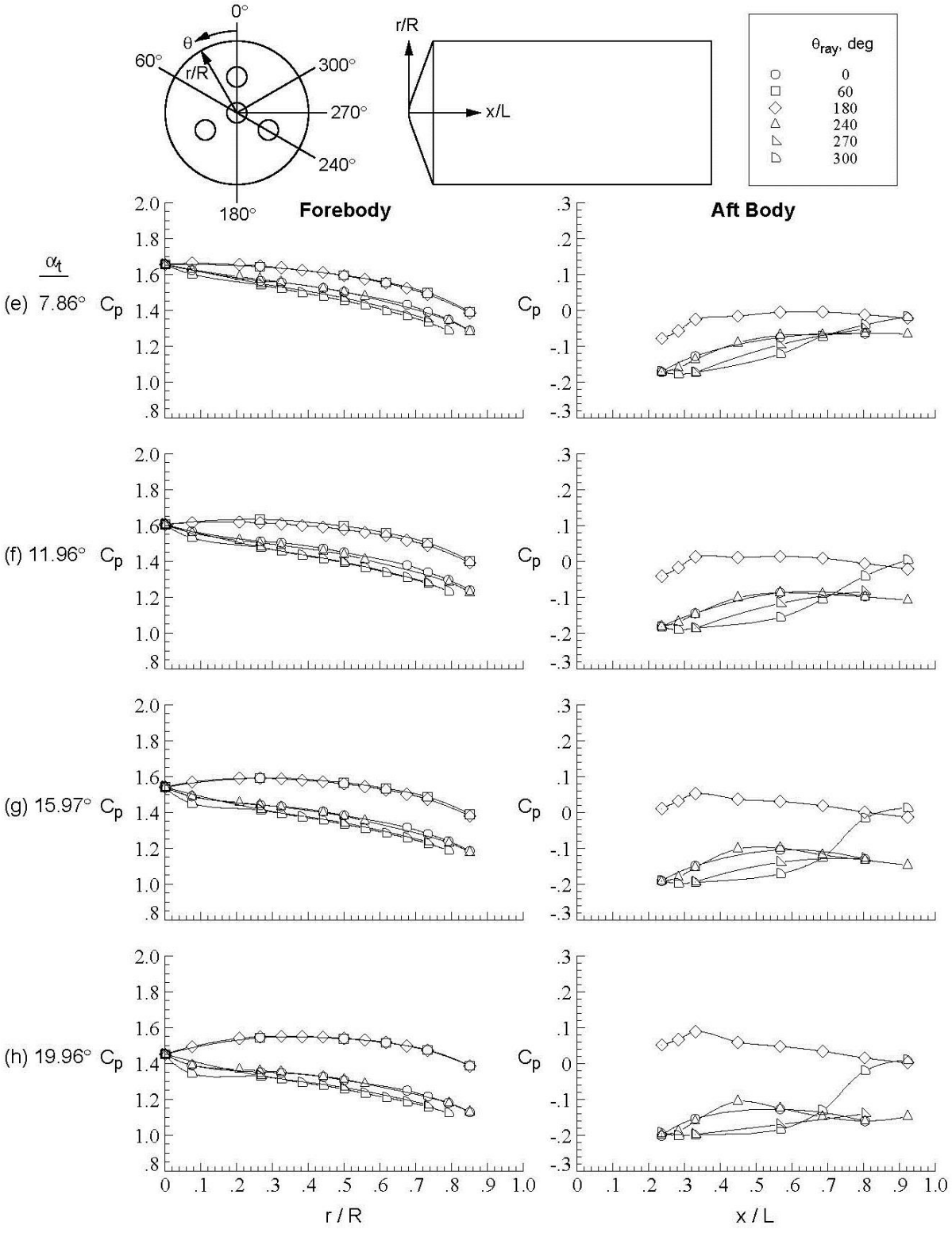

Figure D-14. Concluded.

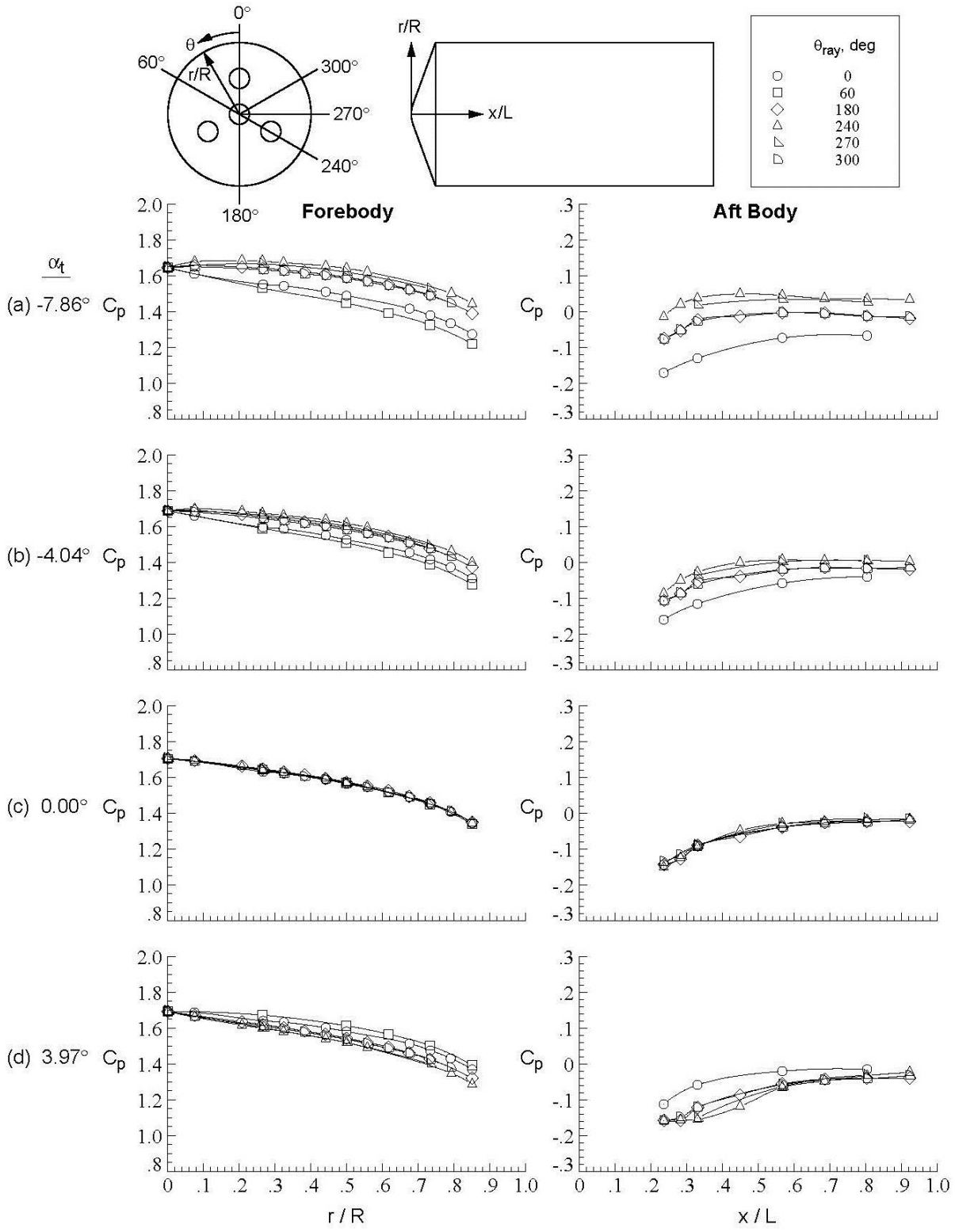

Figure D-15. Baseline configuration, Run 028, M_∞ = 2.4, Re_∞ = 1.0x10^6/ft, ϕ = 120.06°, X_S = 50.17 in, Y_S = 0.00 in, C_T = 0.00.

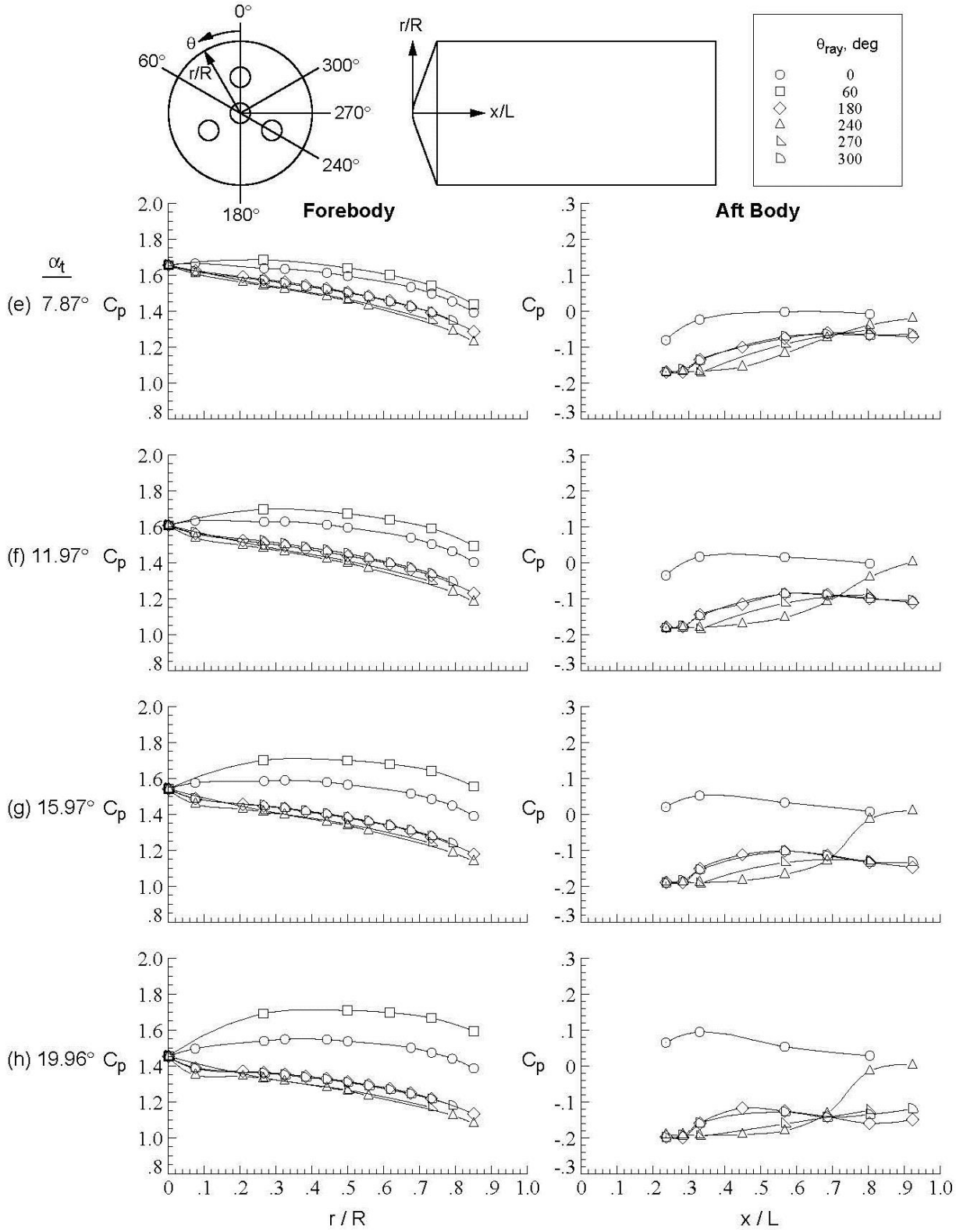

Figure D-15. Concluded.

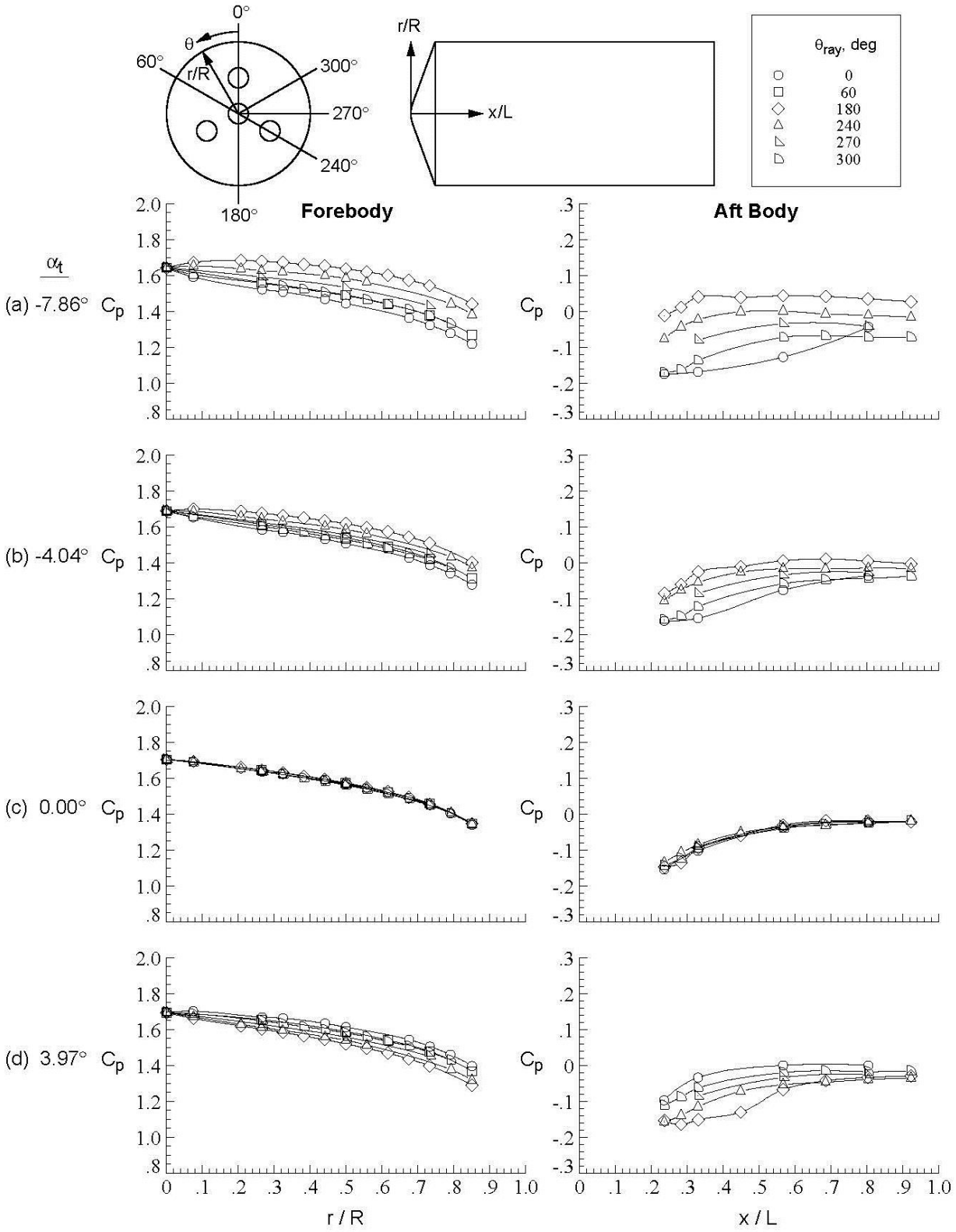

Figure D-16. Baseline configuration, Run 029, M_∞ = 2.4, Re_∞ = 1.0x10^6/ft, ϕ = 179.91°, X_S = 50.17 in, Y_S = 0.00 in, C_T = 0.00.

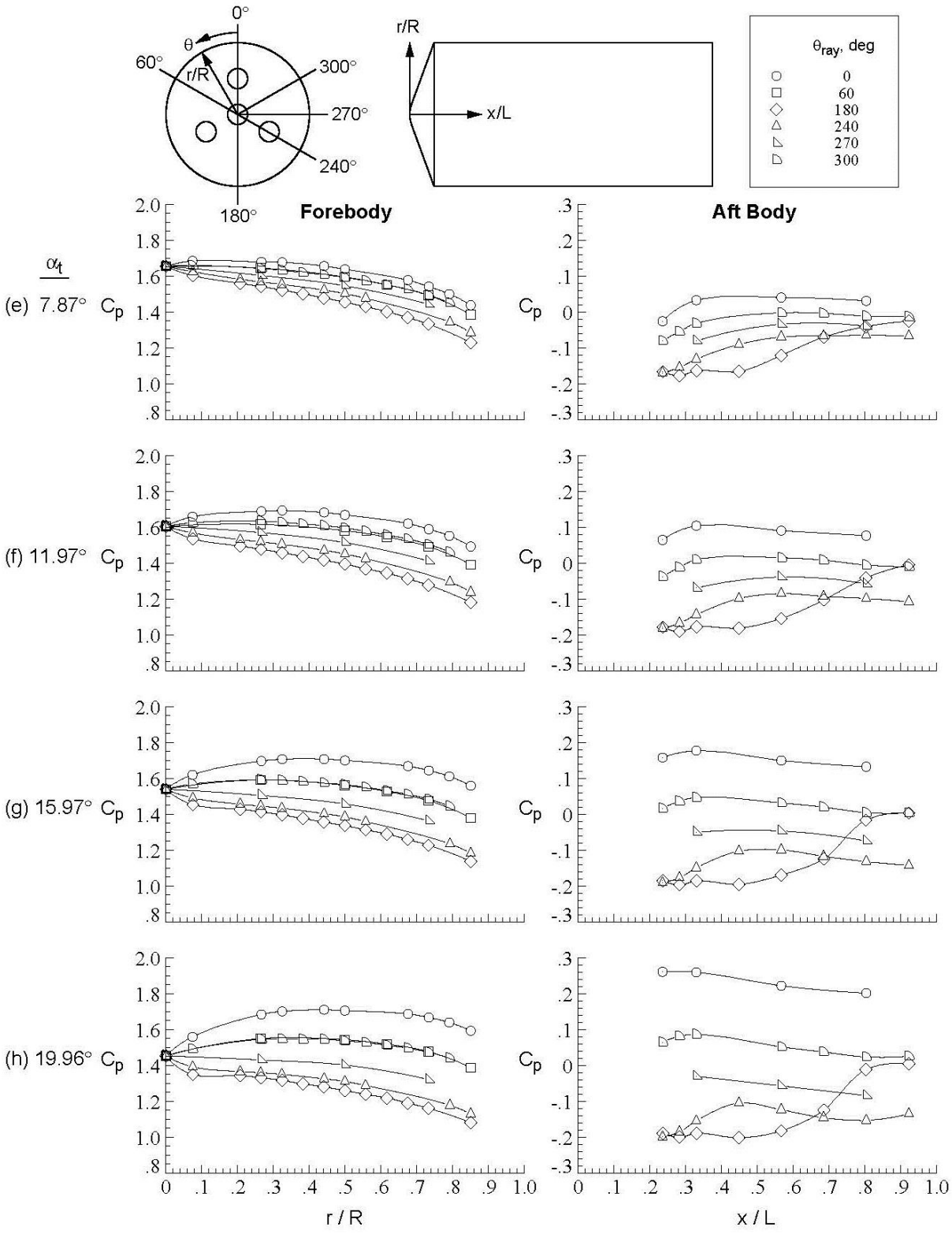

Figure D-16. Concluded.

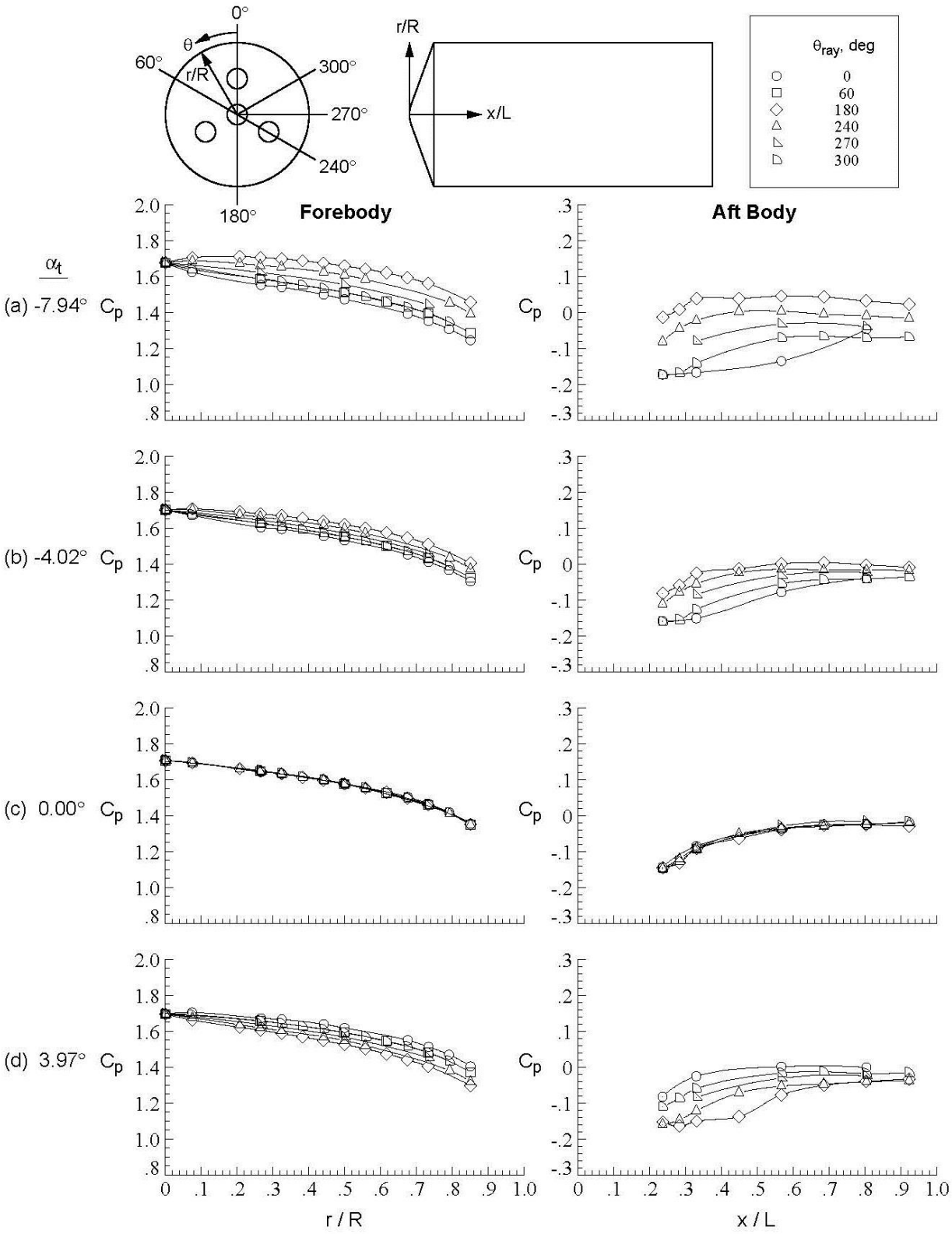

Figure D-17. Baseline configuration, Run 030, M_∞ = 2.4, Re_∞ = 1.0x10^6/ft, ϕ = 179.91°, X_S = 25.18 in, Y_S = 0.00 in, C_T = 0.00.

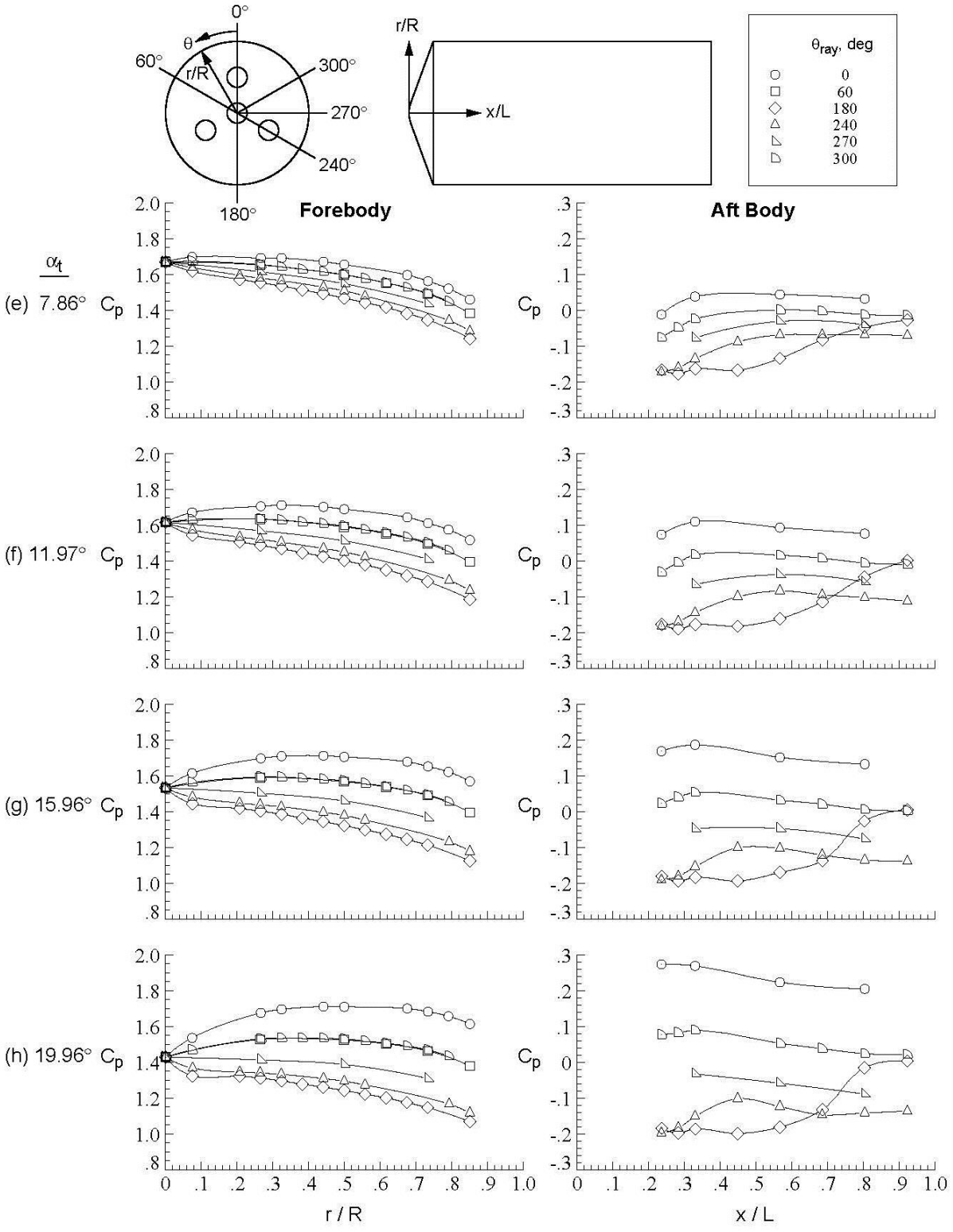

Figure D-17. Concluded.

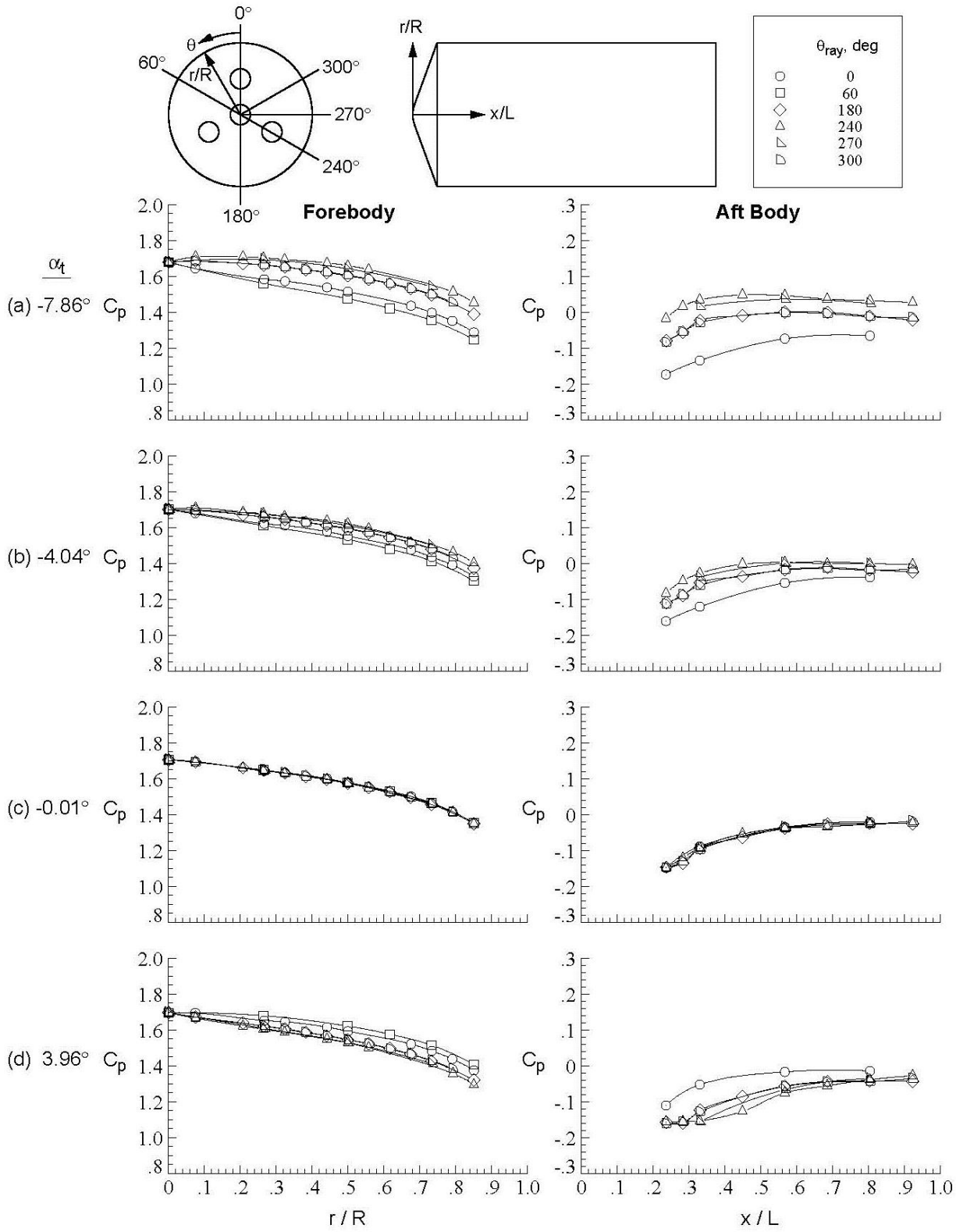

Figure D-18. Baseline configuration, Run 031, M_∞ = 2.4, Re_∞ = 1.0x10^6/ft, ϕ = 119.92°, X_S = 25.18 in, Y_S = 0.00 in, C_T = 0.00.

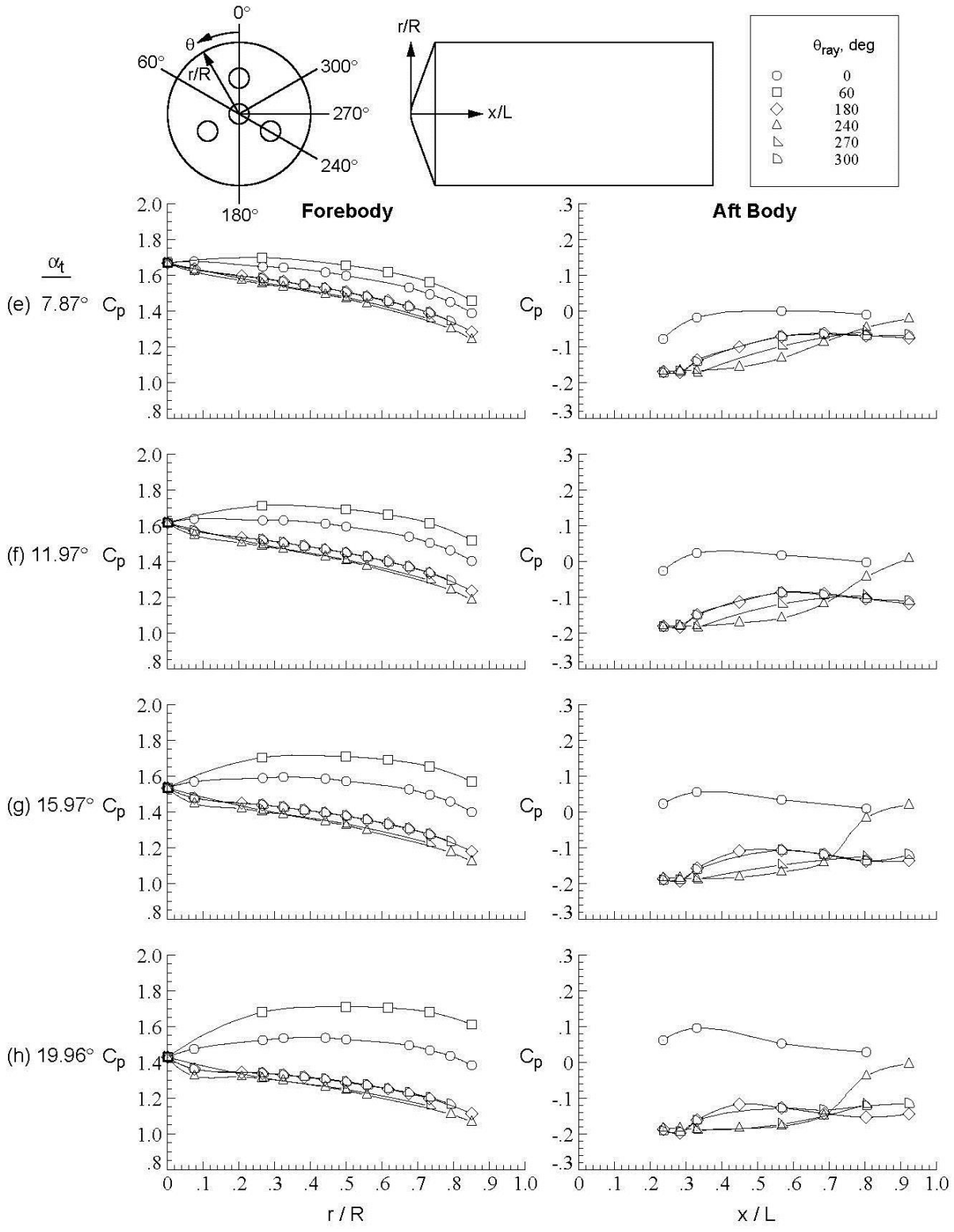

Figure D-18. Concluded.

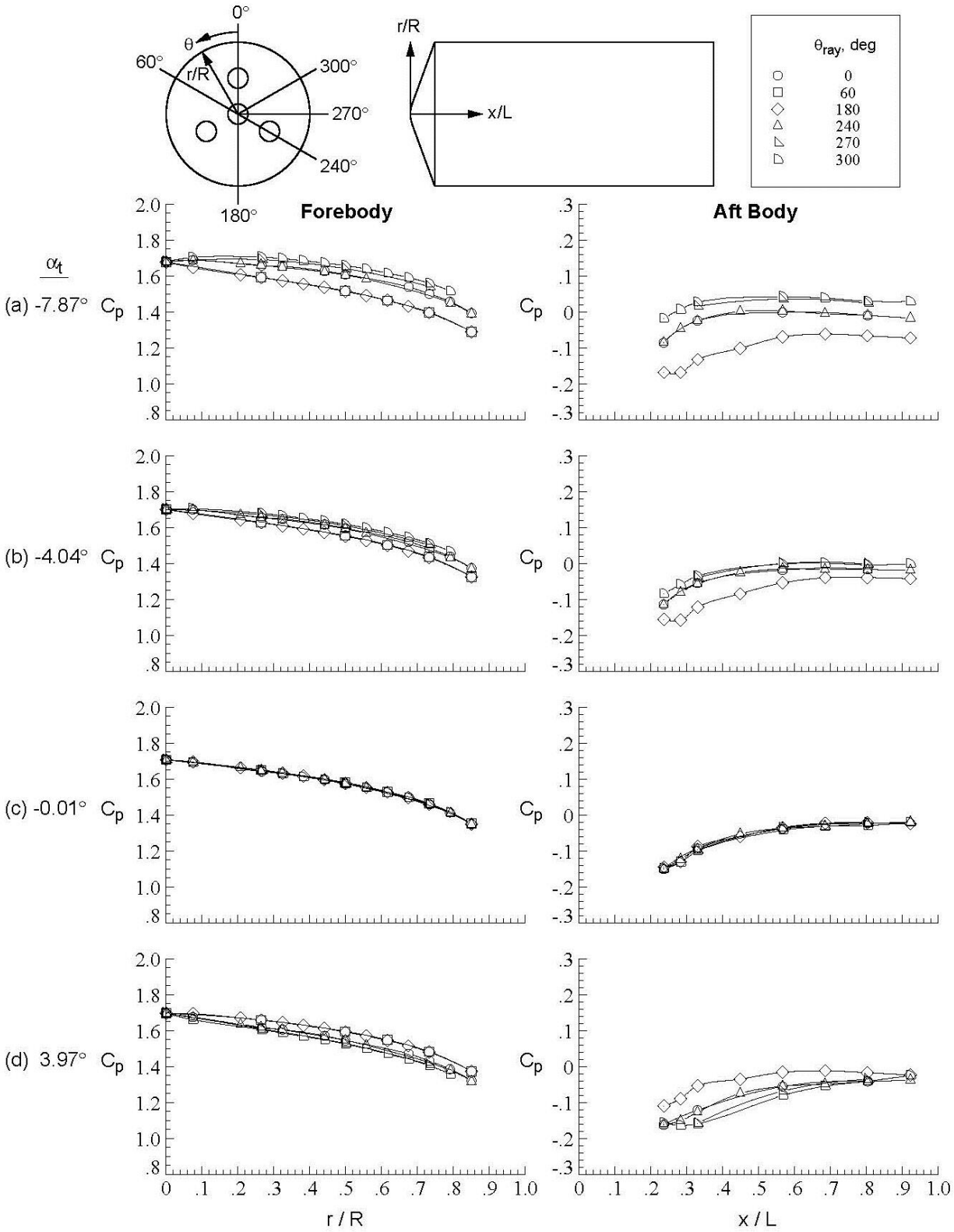

Figure D-19. Baseline configuration, Run 032, M_∞ = 2.4, Re_∞ = 1.0x10^6/ft, ϕ = 59.98°, X_S = 25.18 in, Y_S = 0.00 in, C_T = 0.00.

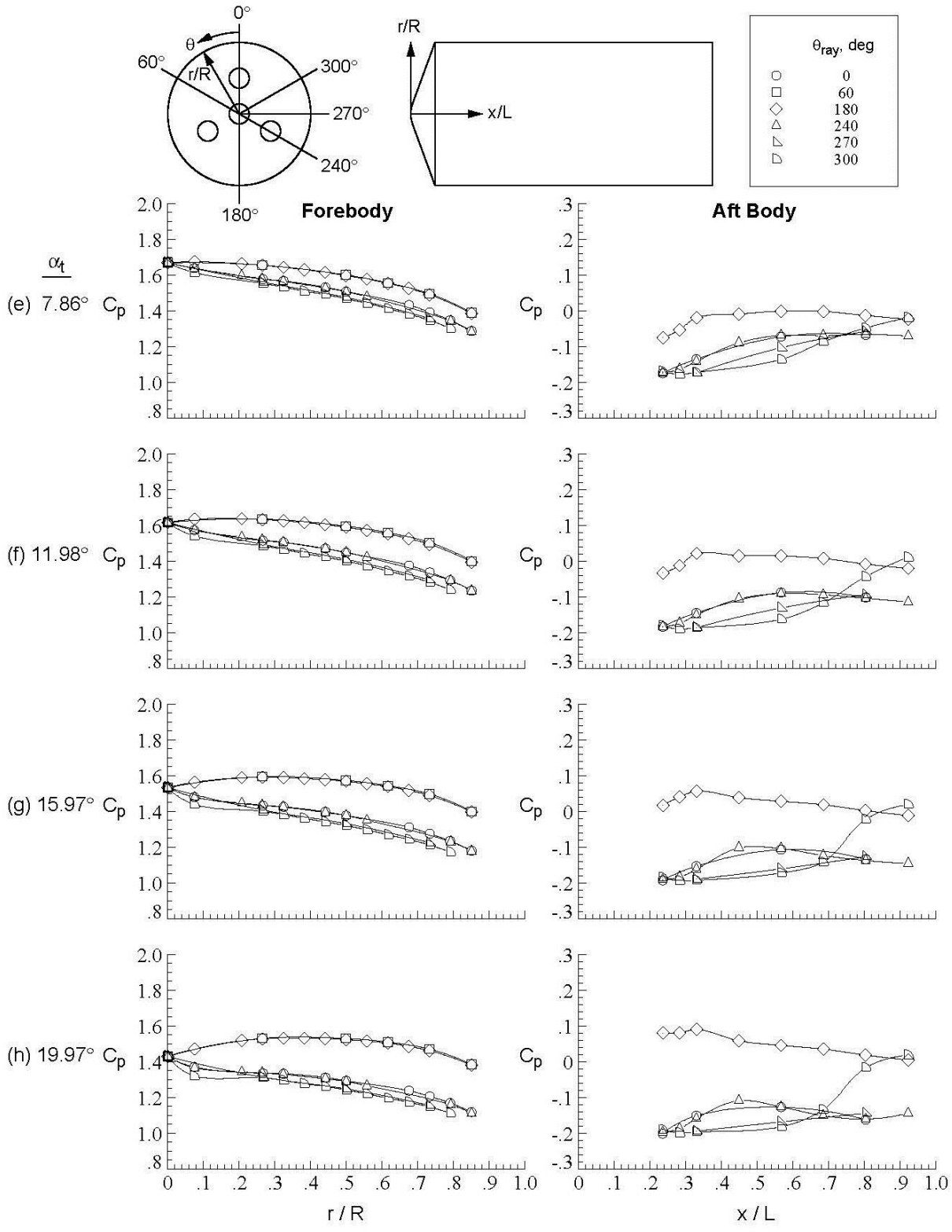

Figure D-19. Concluded.

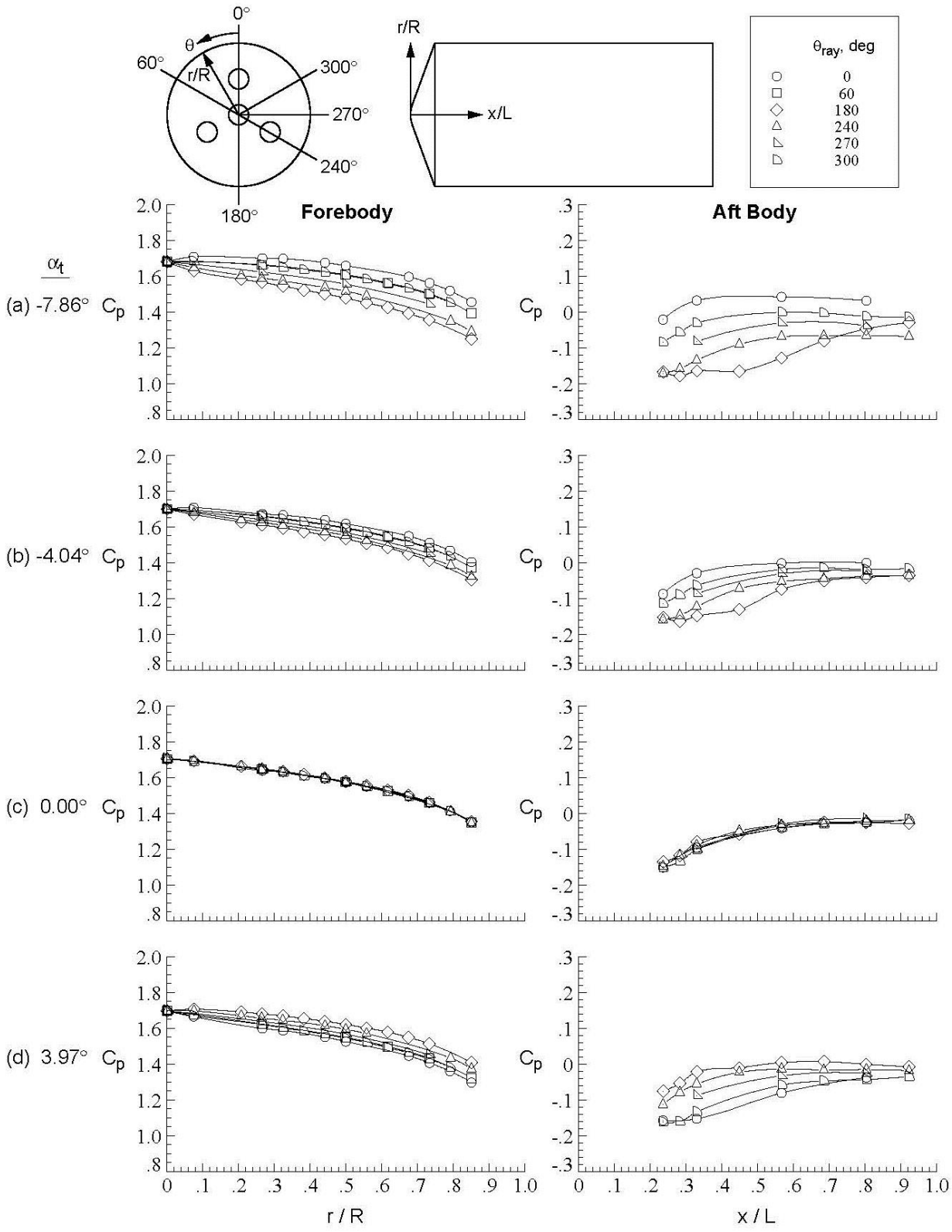

Figure D-20. Baseline configuration, Run 033, M_∞ = 2.4, Re_∞ = 1.0x10^6/ft, ϕ = 0.05°, X_S = 25.18 in, Y_S = 0.00 in, C_T = 0.00.

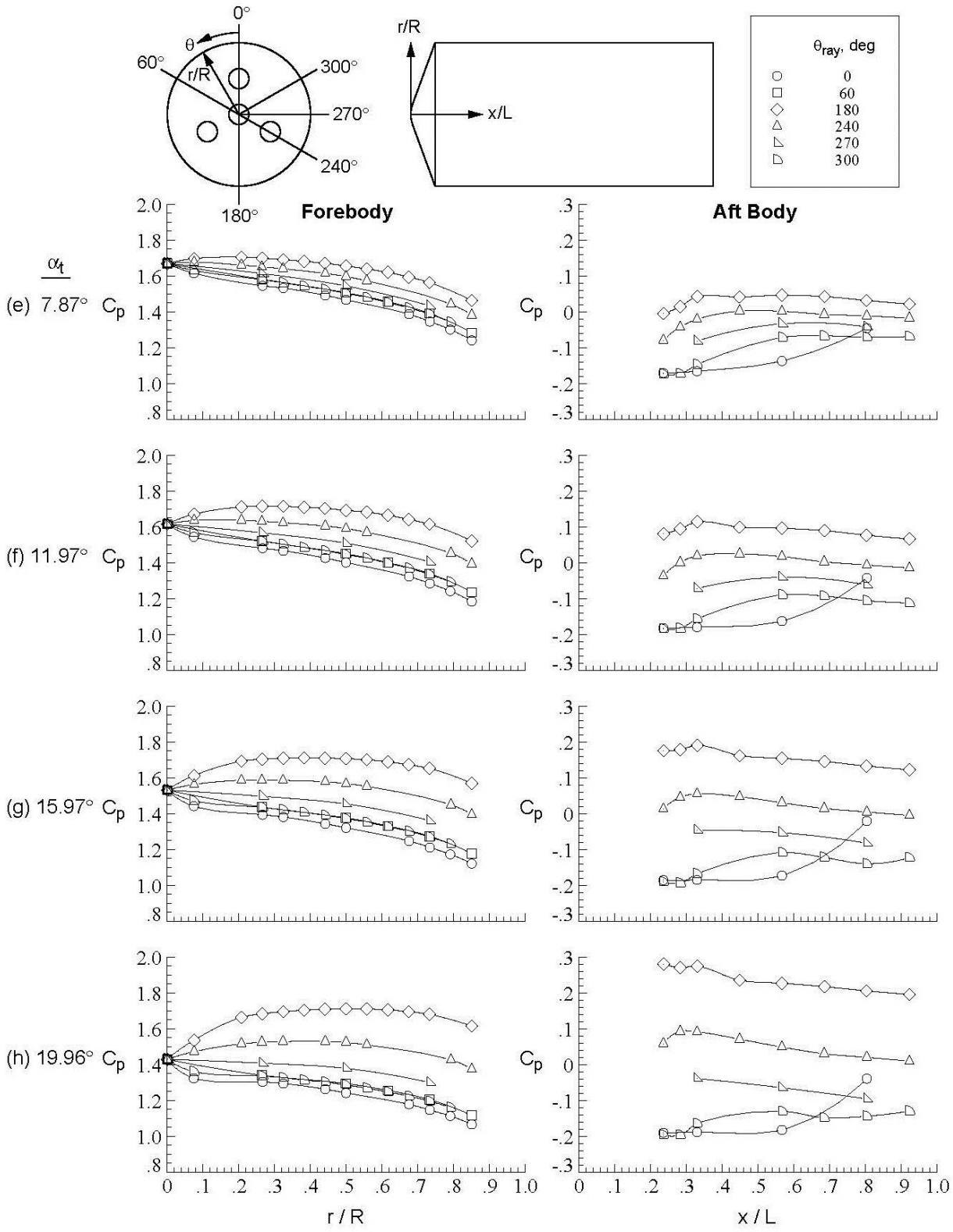

Figure D-20. Concluded.

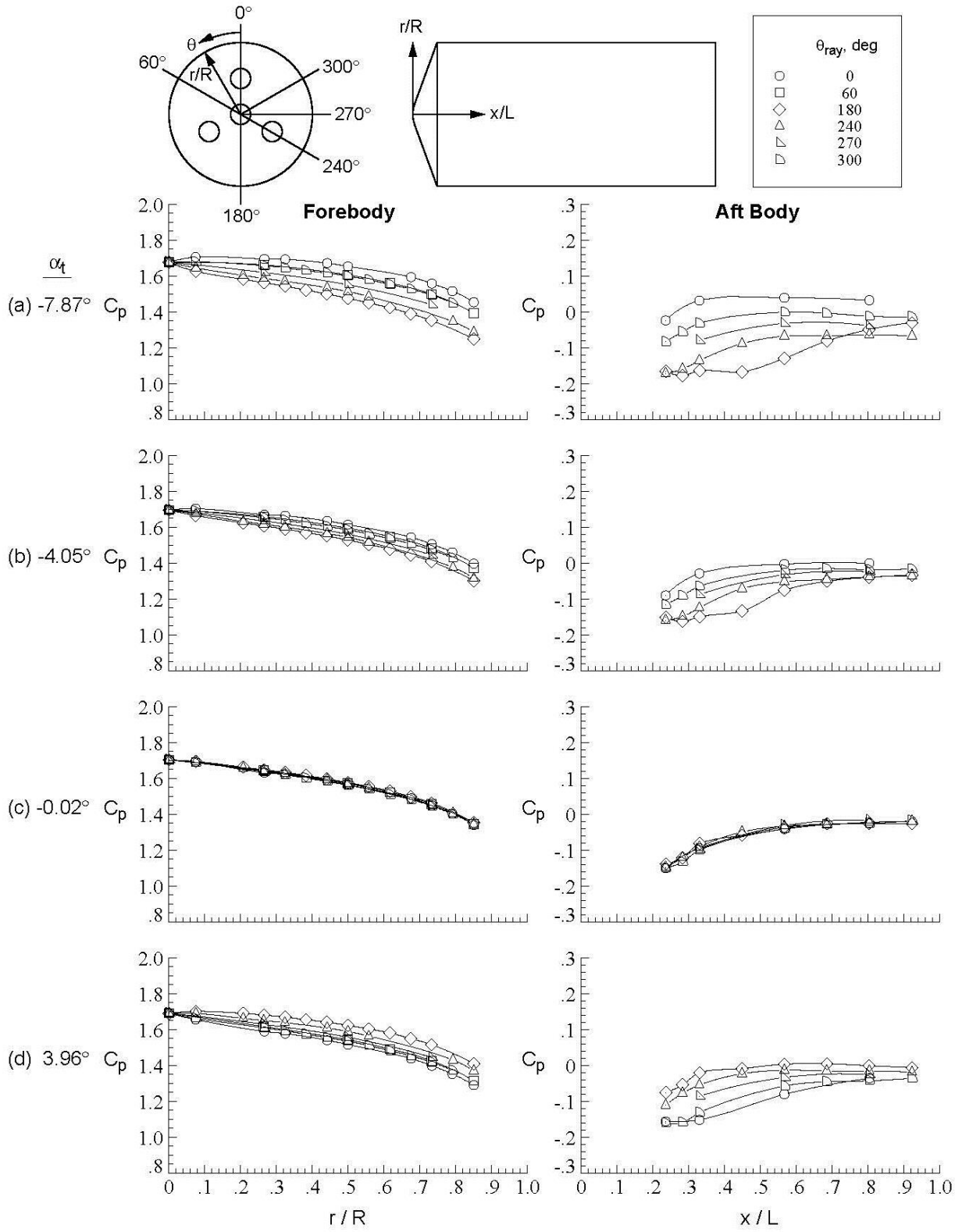

Figure D-21. Baseline configuration, Run 034, $M\infty$ = 2.4, Re_∞ = 1.0x10^6/ft, ϕ = 0.05°, X_S = 25.18 in, Y_S = 7.99 in, C_T = 0.00.

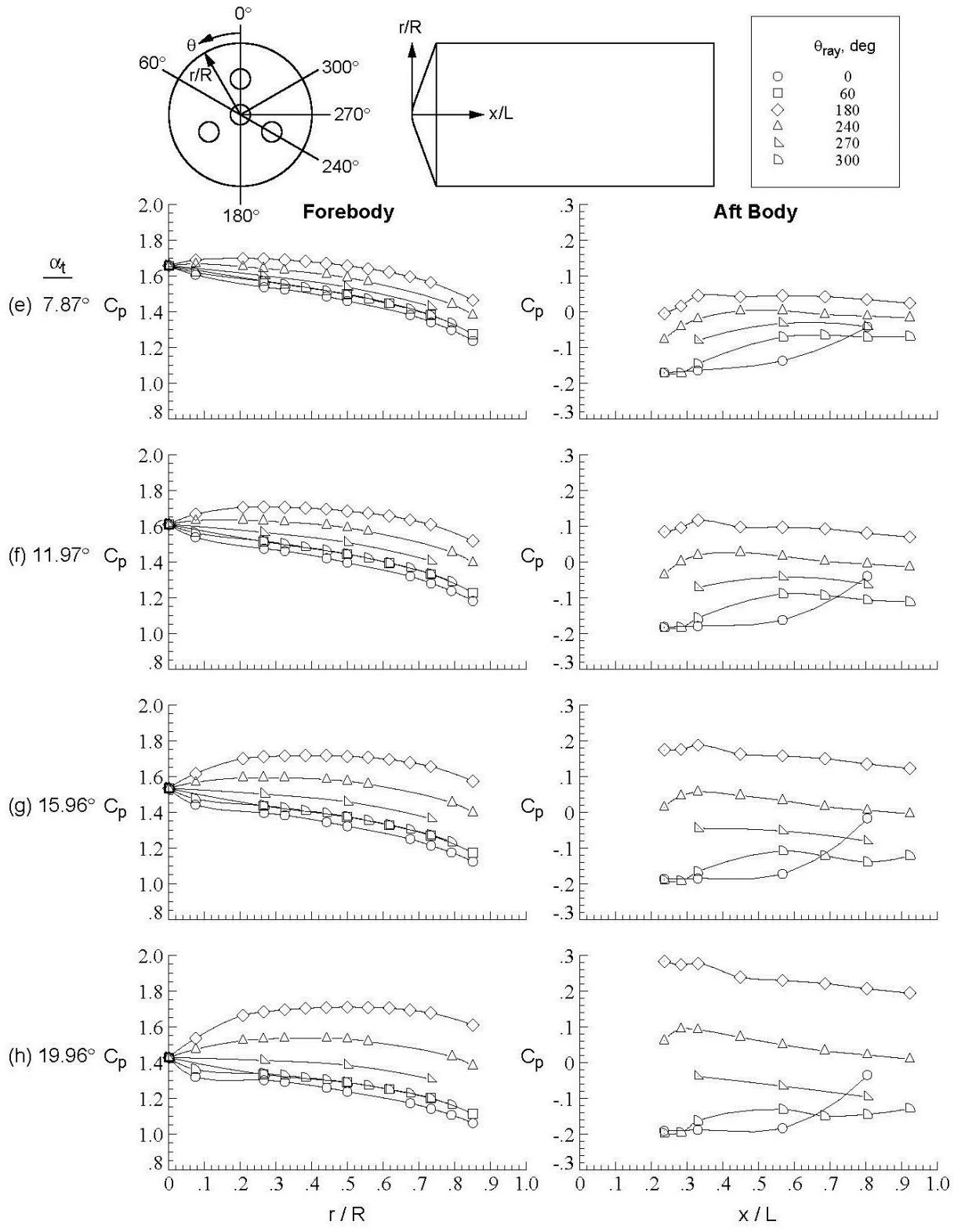

Figure D-21. Concluded.

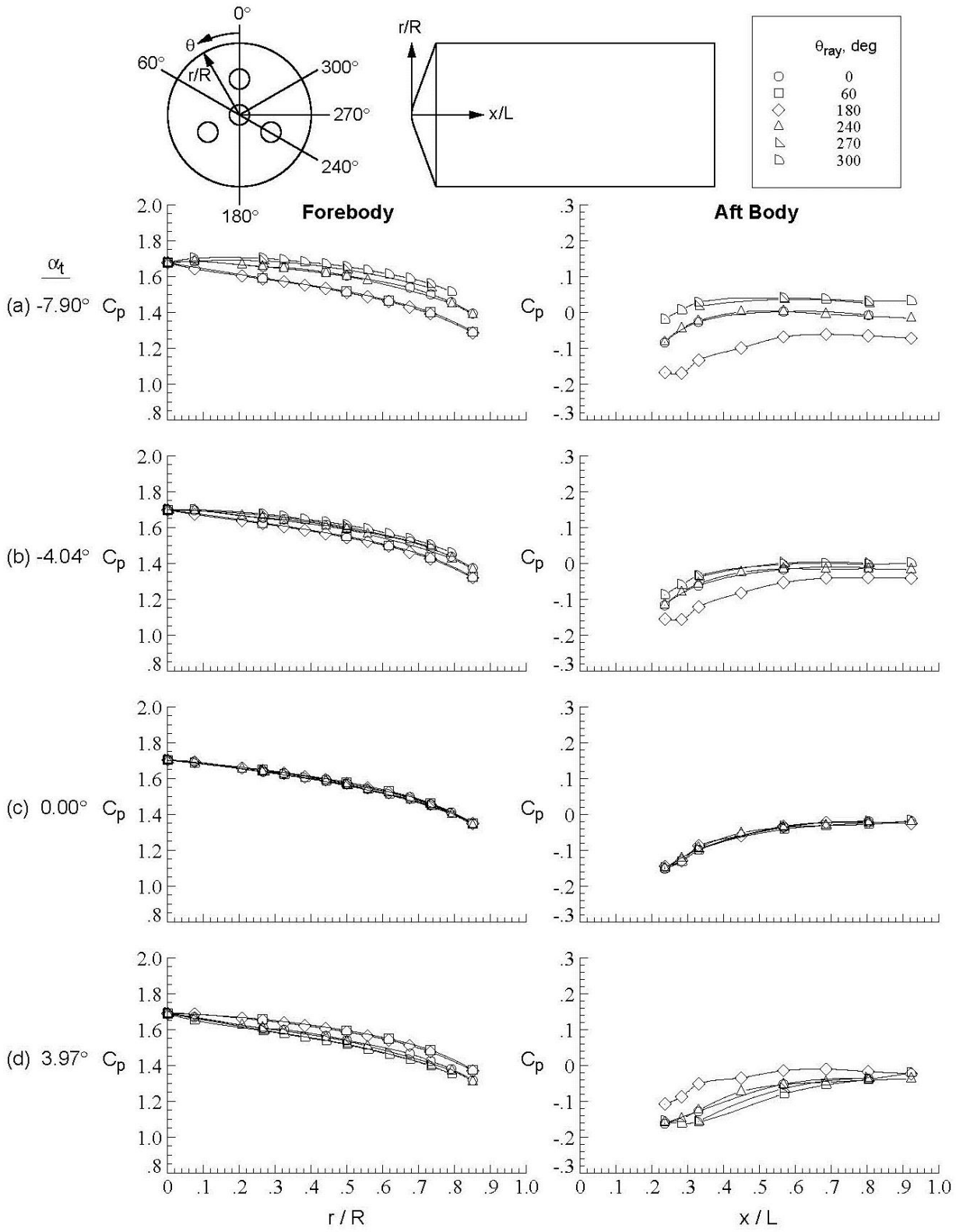

Figure D-22. Baseline configuration, Run 035, M_∞ = 2.4, Re_∞ = 1.0x10^6/ft, ϕ = 60.08°, X_S = 25.18 in, Y_S = 7.99 in, C_T = 0.00.

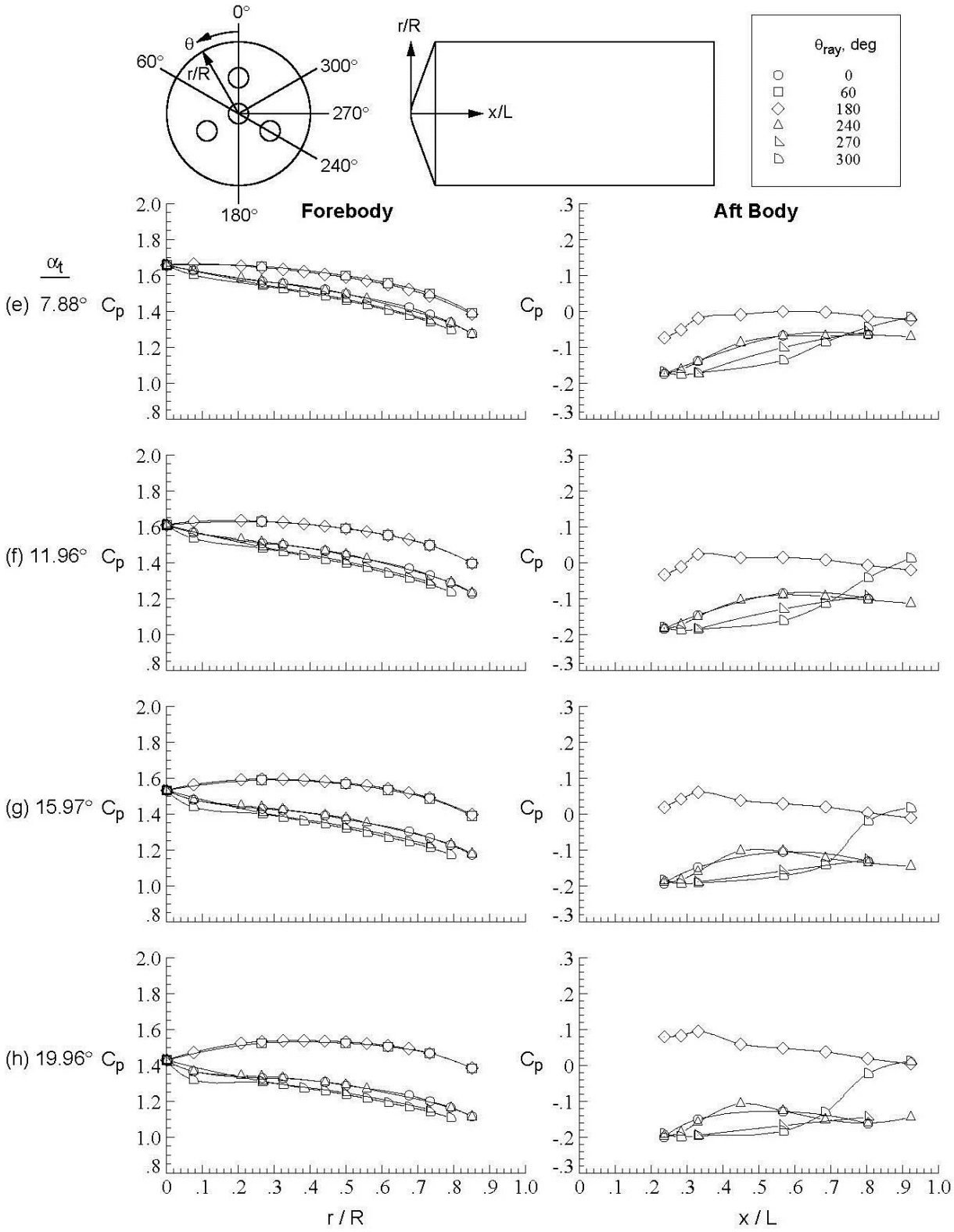

Figure D-22. Concluded.

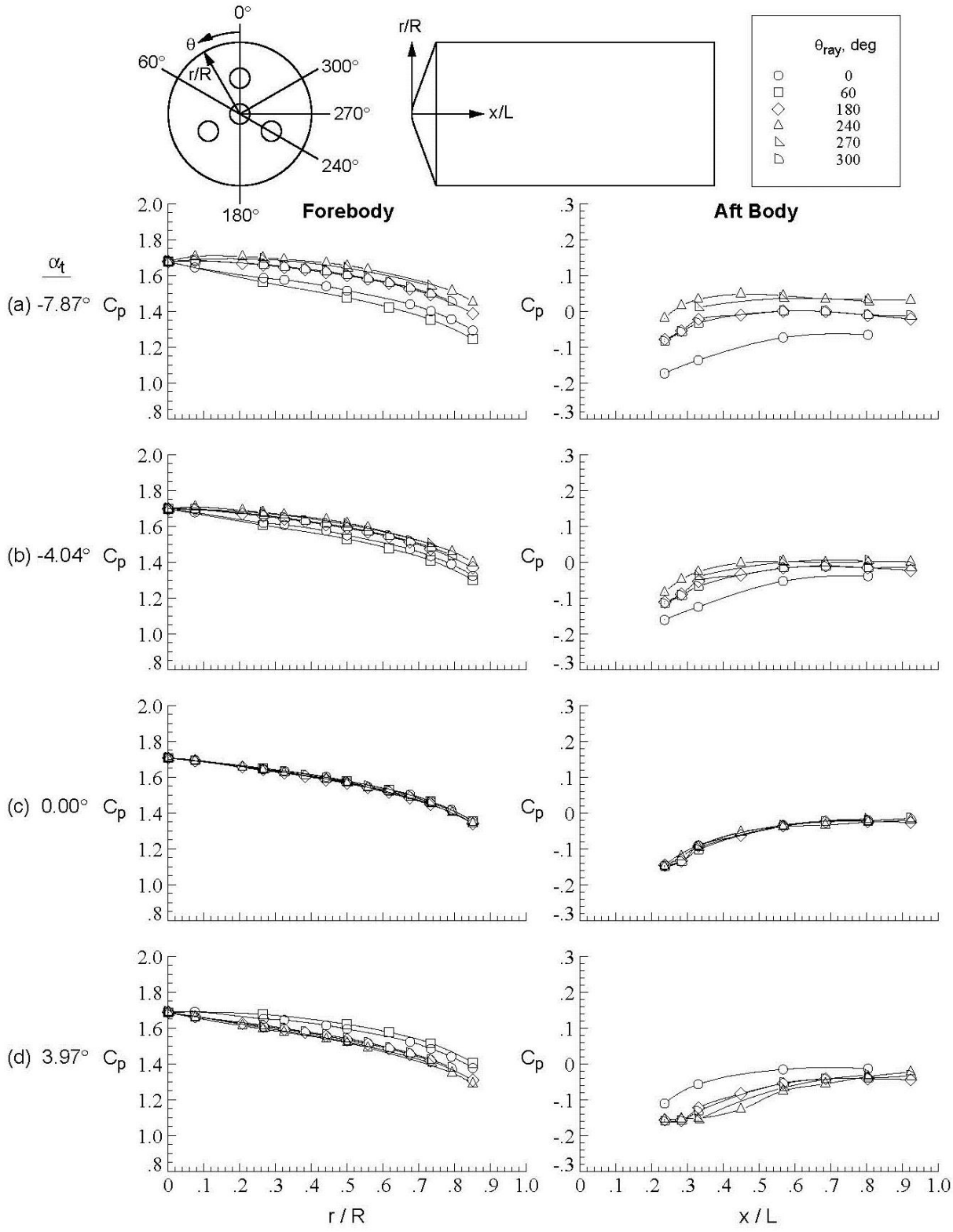

Figure D-23. Baseline configuration, Run 036, M_∞ = 2.4, Re_∞ = 1.0x10^6/ft, ϕ = 119.90°, X_S = 25.18 in, Y_S = 7.99 in, C_T = 0.00.

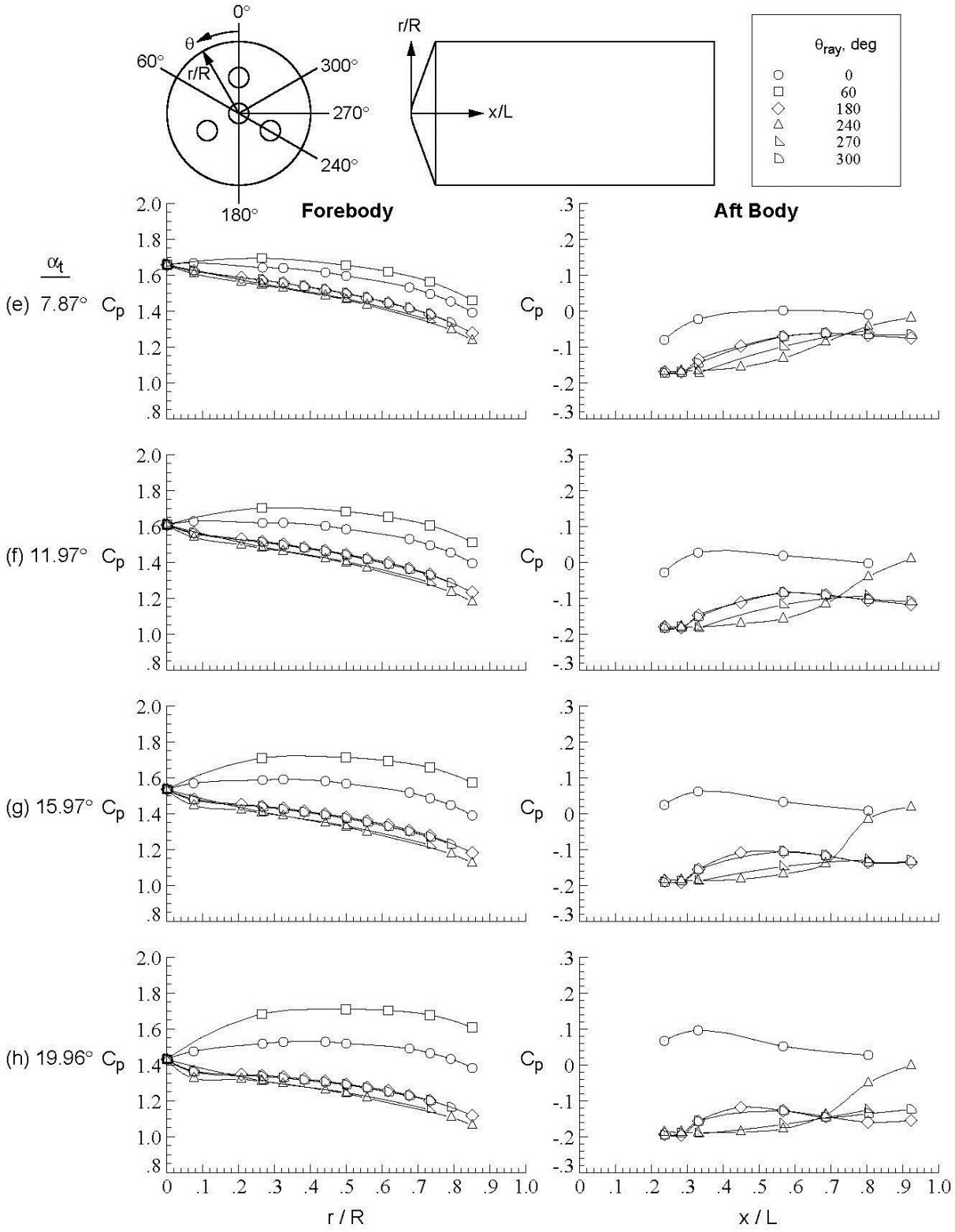

Figure D-23. Concluded.

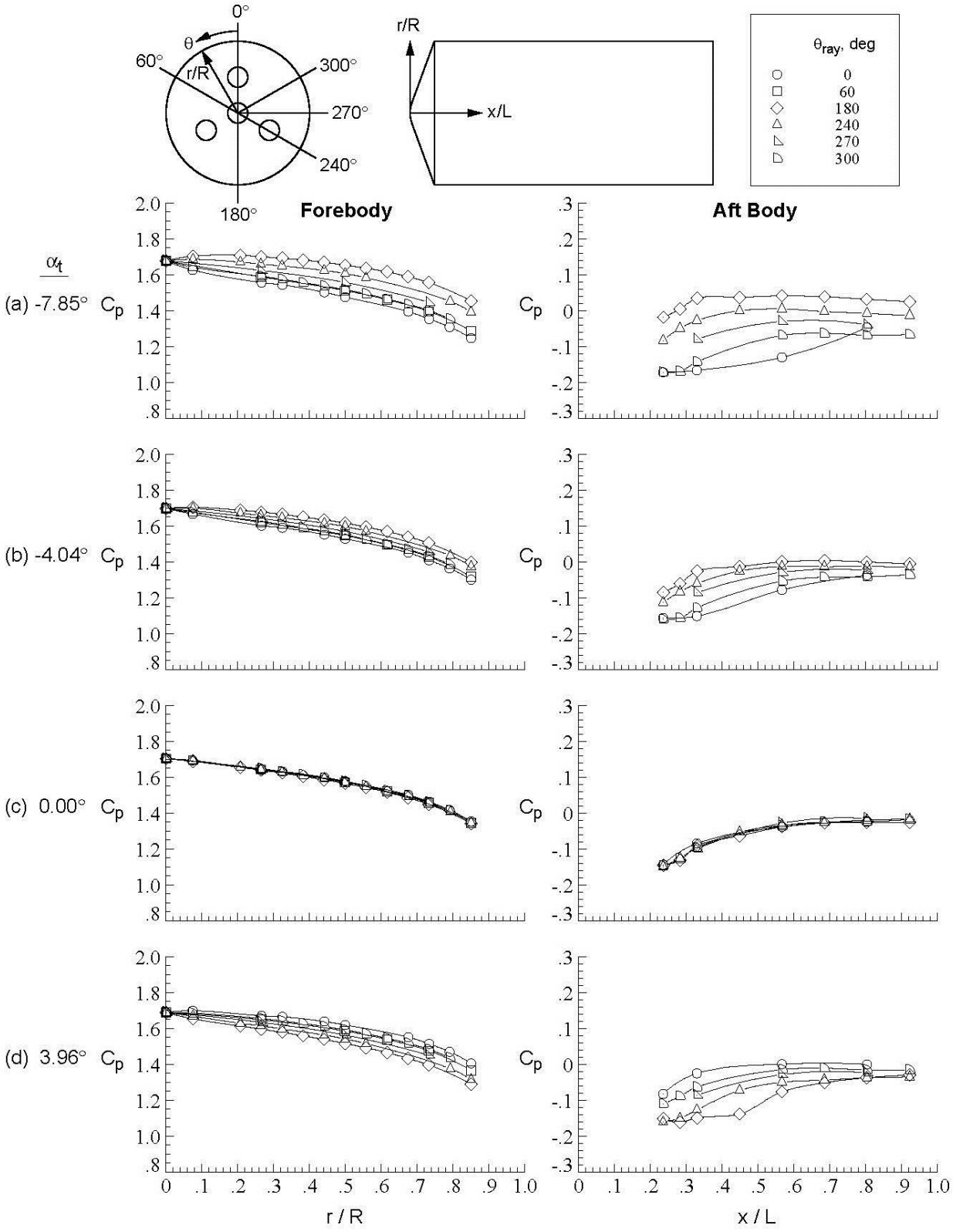

Figure D-24. Baseline configuration, Run 037, M_∞ = 2.4, Re_∞ = 1.0x10^6/ft, ϕ = 179.95°, X_S = 25.18 in, Y_S = 7.99 in, C_T = 0.00.

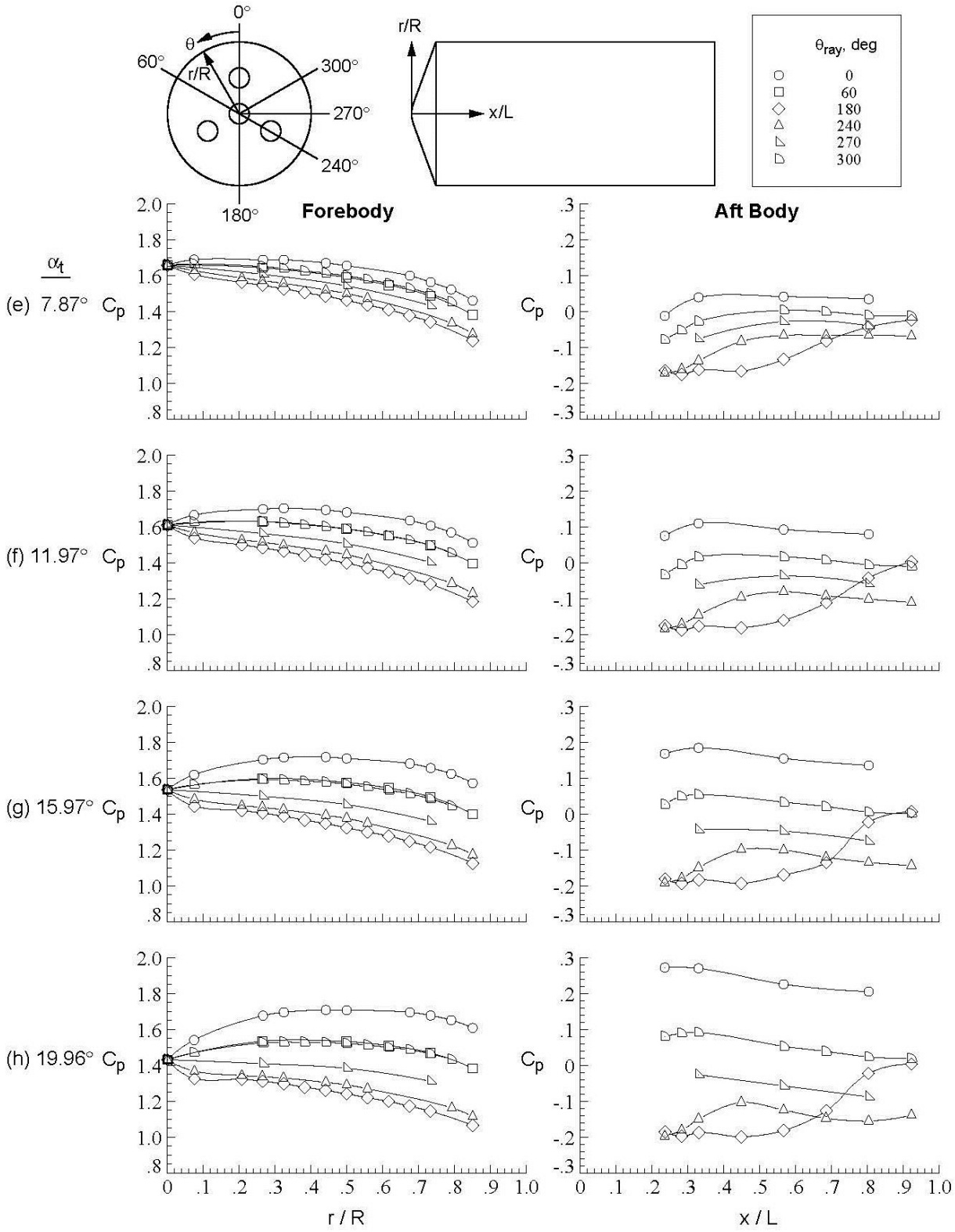

Figure D-24. Concluded.

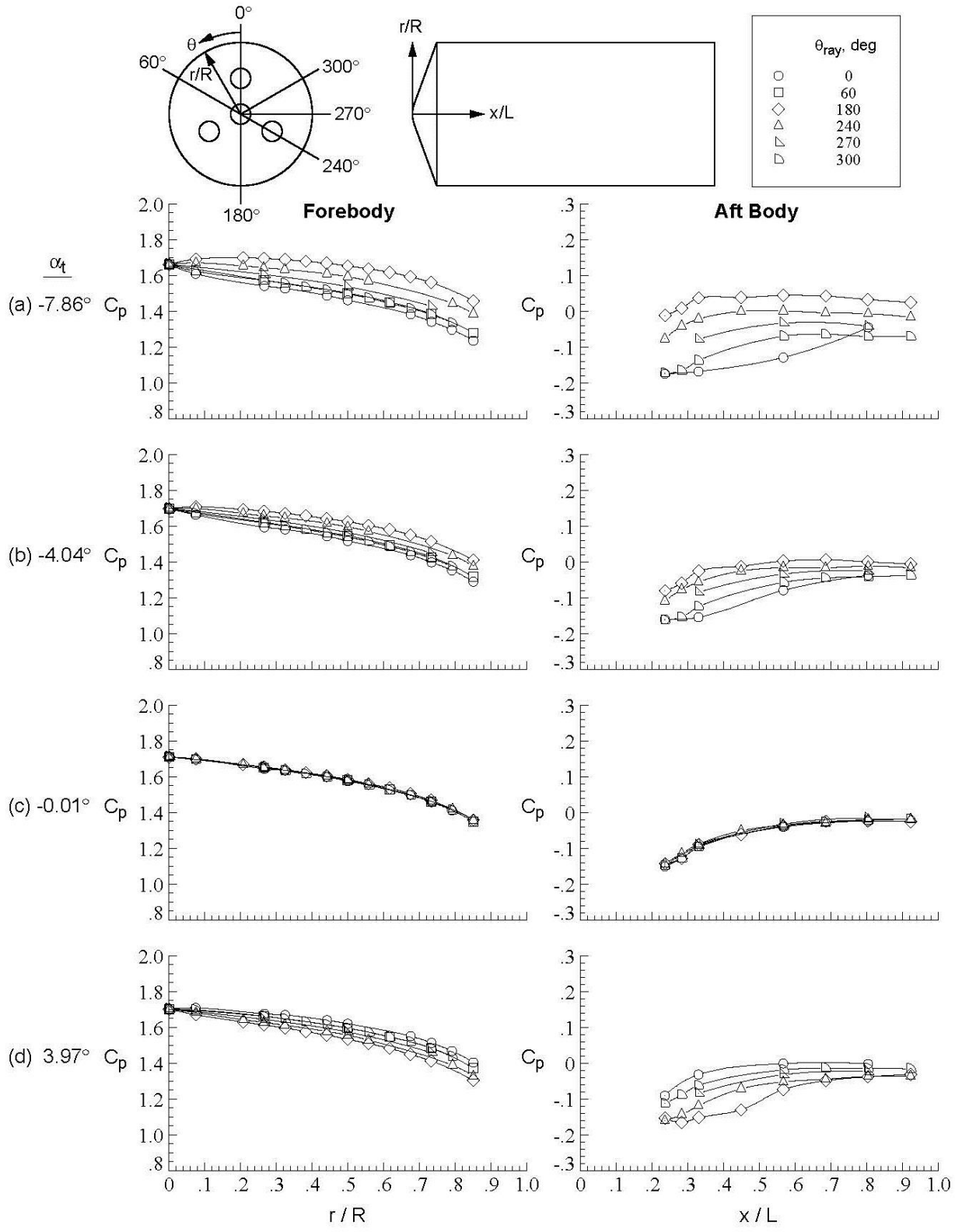

Figure D-25. Baseline configuration, Run 038, M_∞ = 2.4, Re_∞ = 1.0x10^6/ft, ϕ = 179.95°, X_S = 40.19 in, Y_S = 7.99 in, C_T = 0.00.

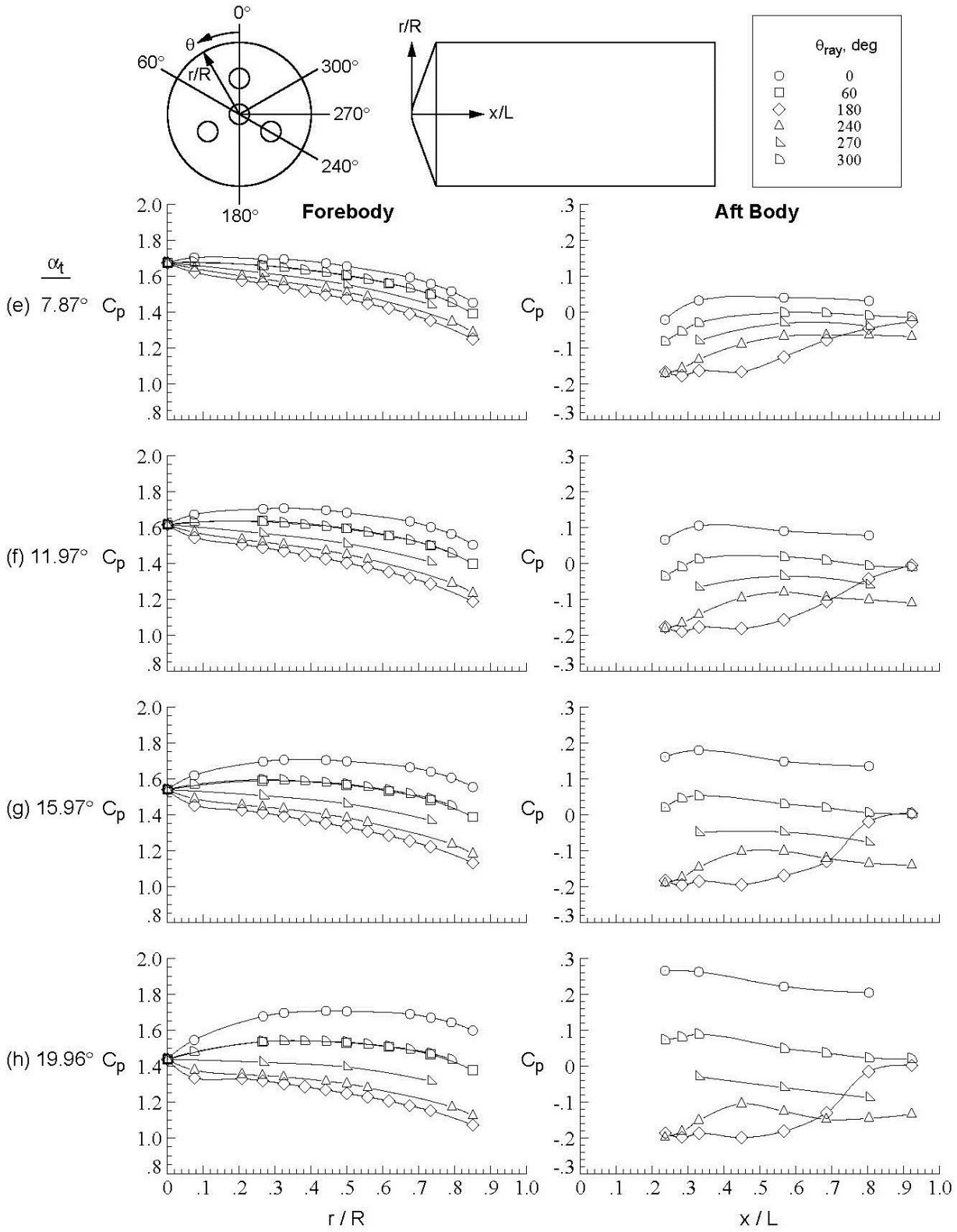

Figure D-25. Concluded.

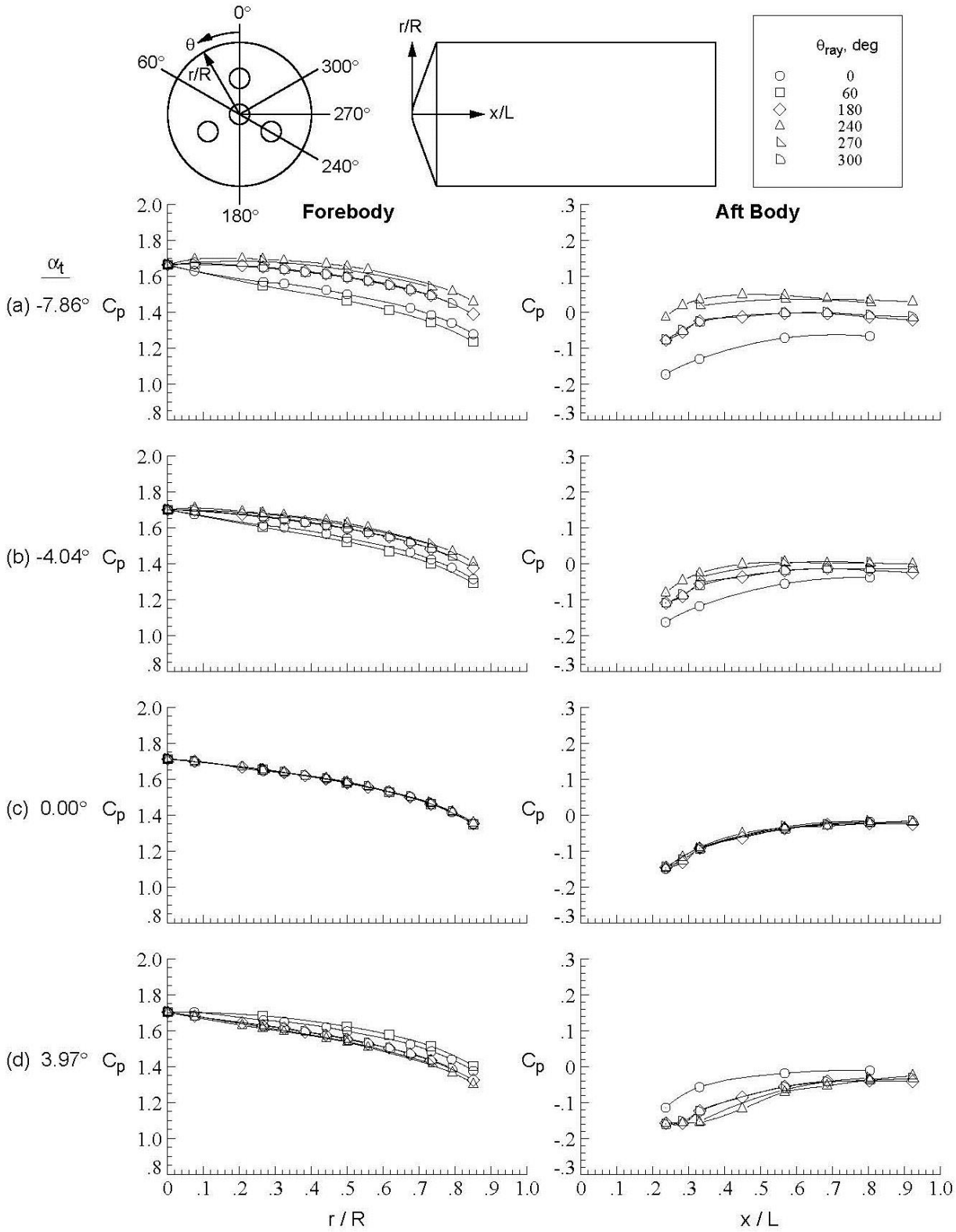

Figure D-26. Baseline configuration, Run 039, M_∞ = 2.4, Re_∞ = 1.0x10^6/ft, ϕ = 119.90°, X_S = 40.19 in, Y_S = 7.99 in, C_T = 0.00.

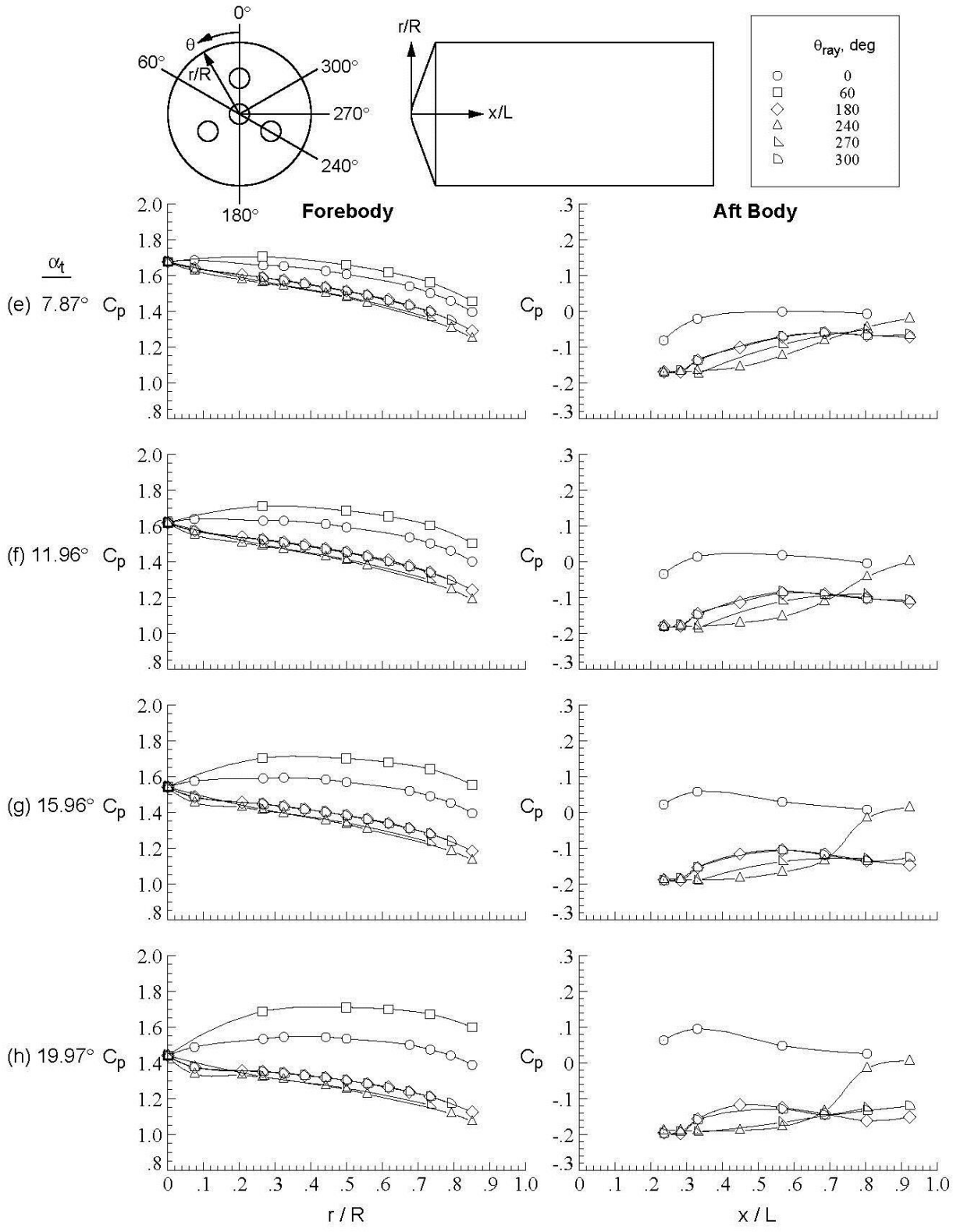

Figure D-26. Concluded.

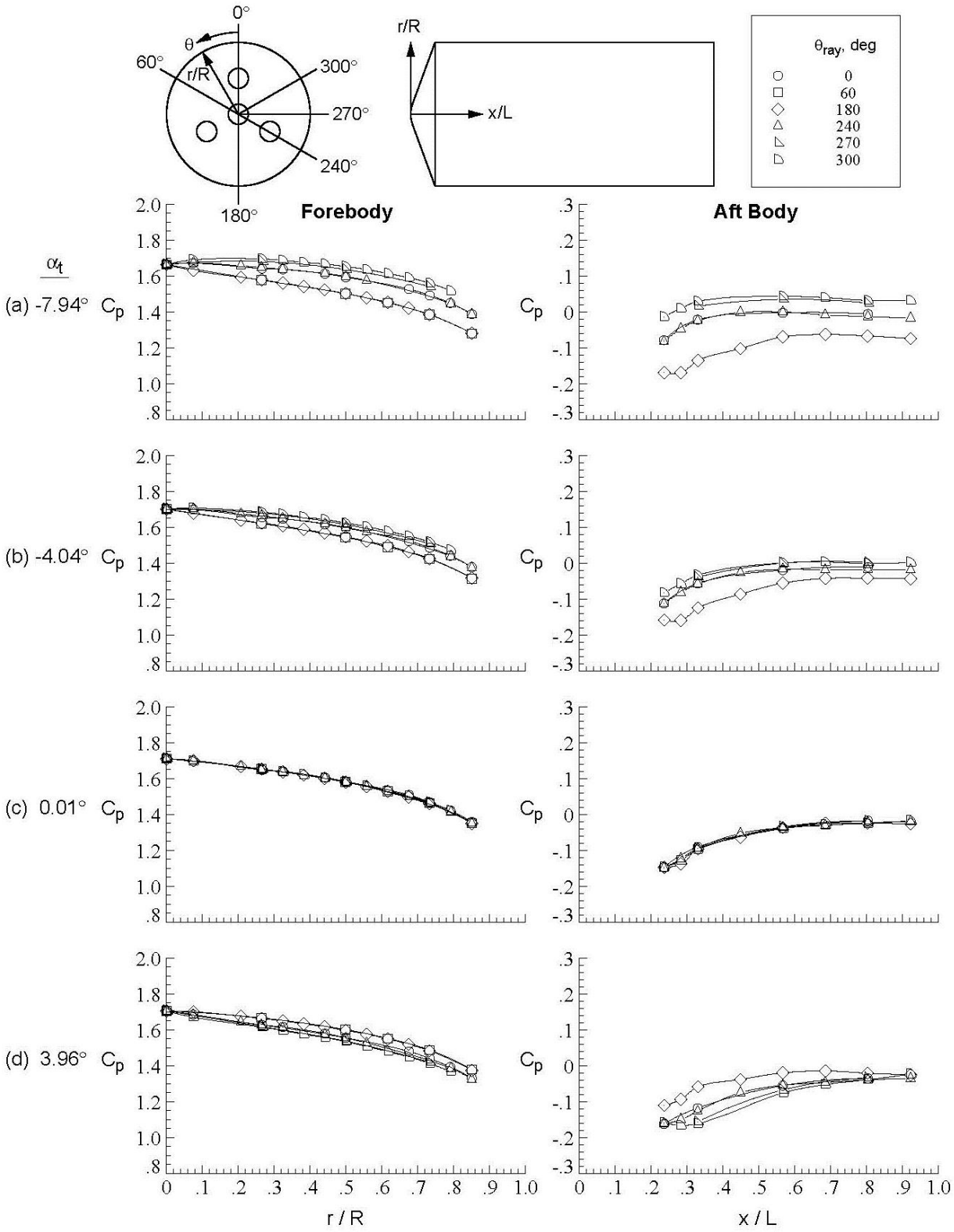

Figure D-27. Baseline configuration, Run 040, M_∞ = 2.4, Re_∞ = 1.0x10^6/ft, ϕ = 59.92°, X_S = 40.19 in, Y_S = 7.99 in, C_T = 0.00.

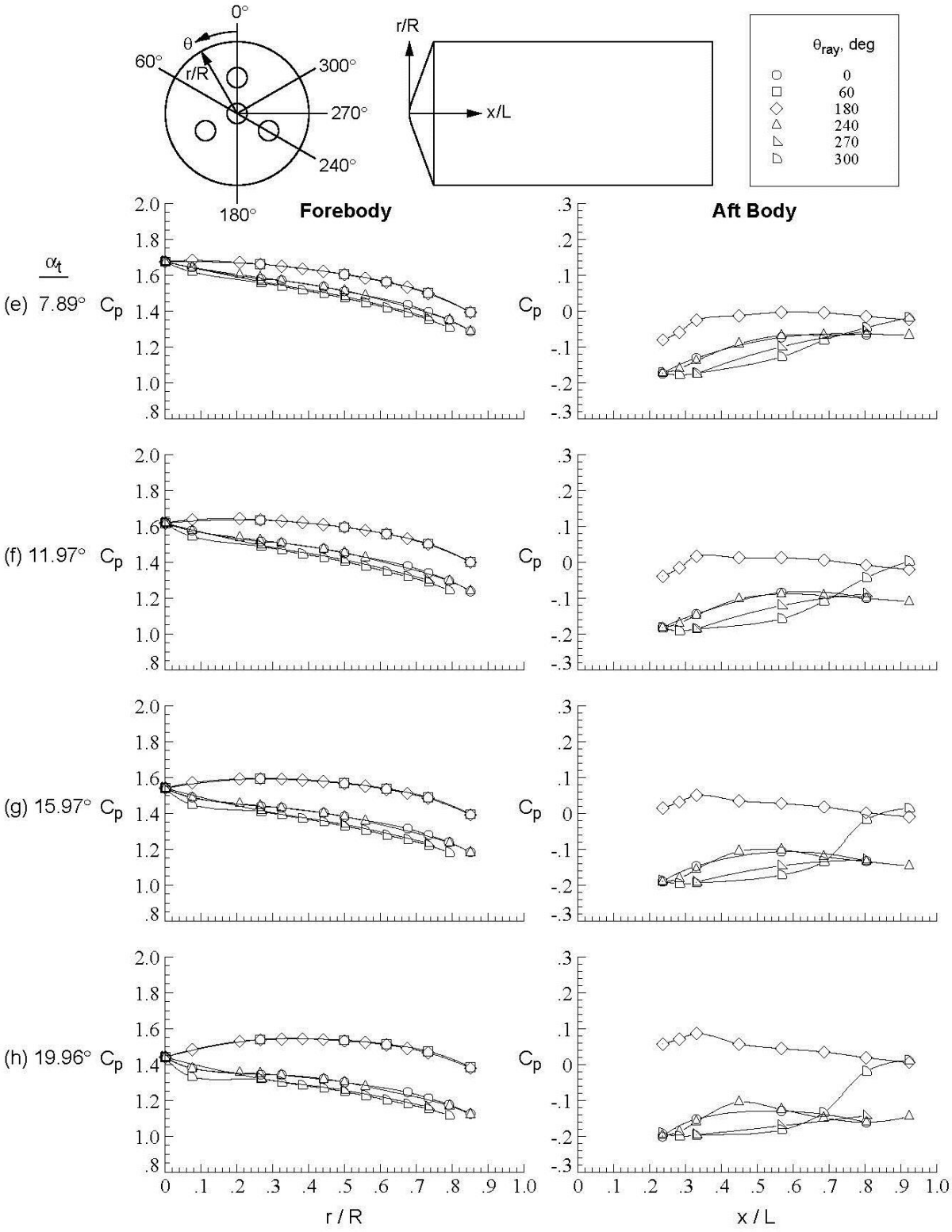

Figure D-27. Concluded.

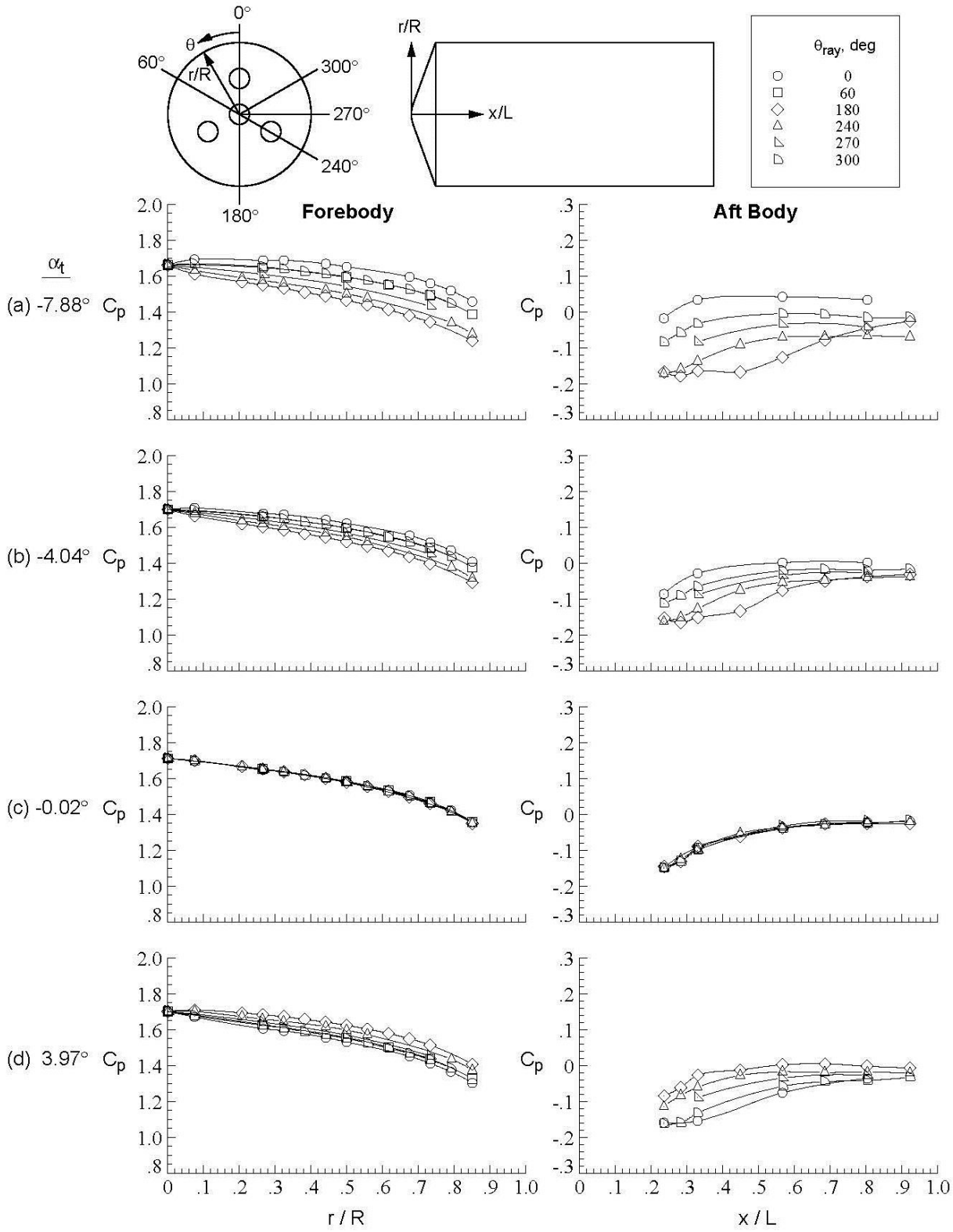

Figure D-28. Baseline configuration, Run 041, M_∞ = 2.4, Re_∞ = 1.0x10^6/ft, ϕ = 0.05°, X_S = 40.19 in, Y_S = 7.99 in, C_T = 0.00.

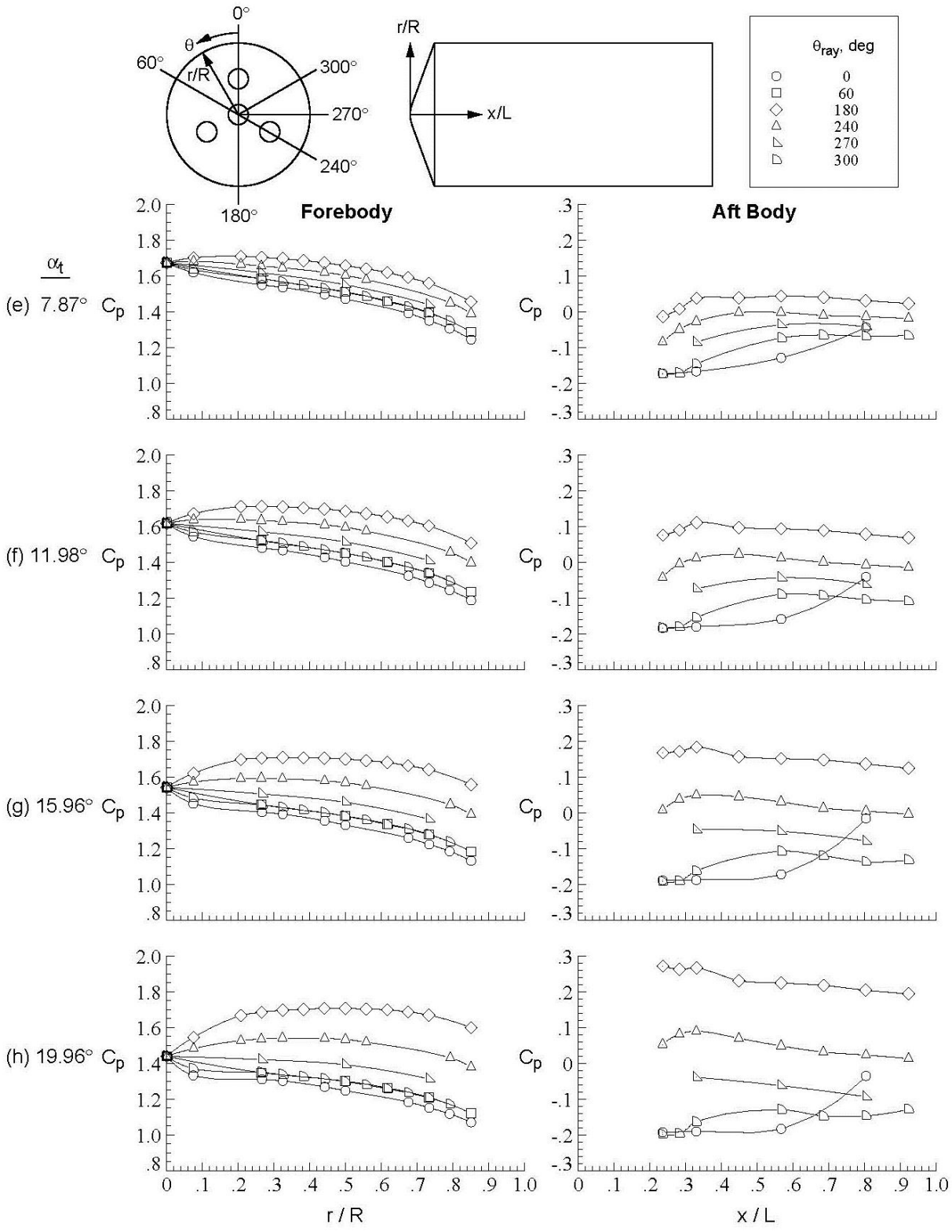

Figure D-28. Concluded.

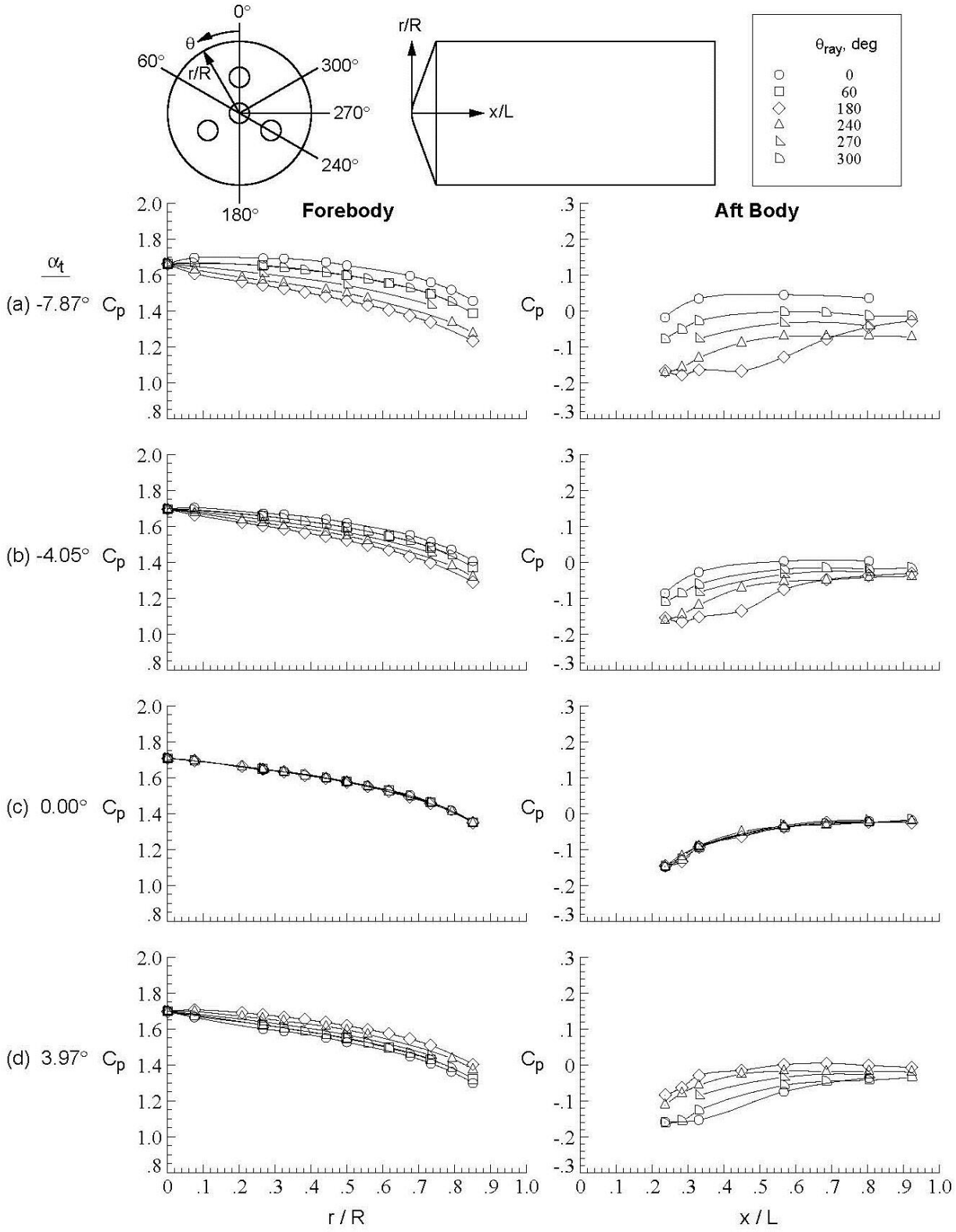

Figure D-29. Baseline configuration, Run 042, M_∞ = 2.4, Re_∞ = 1.0x10^6/ft, ϕ = −0.05°, X_S = 40.19 in, Y_S = −8.00 in, C_T = 0.00.

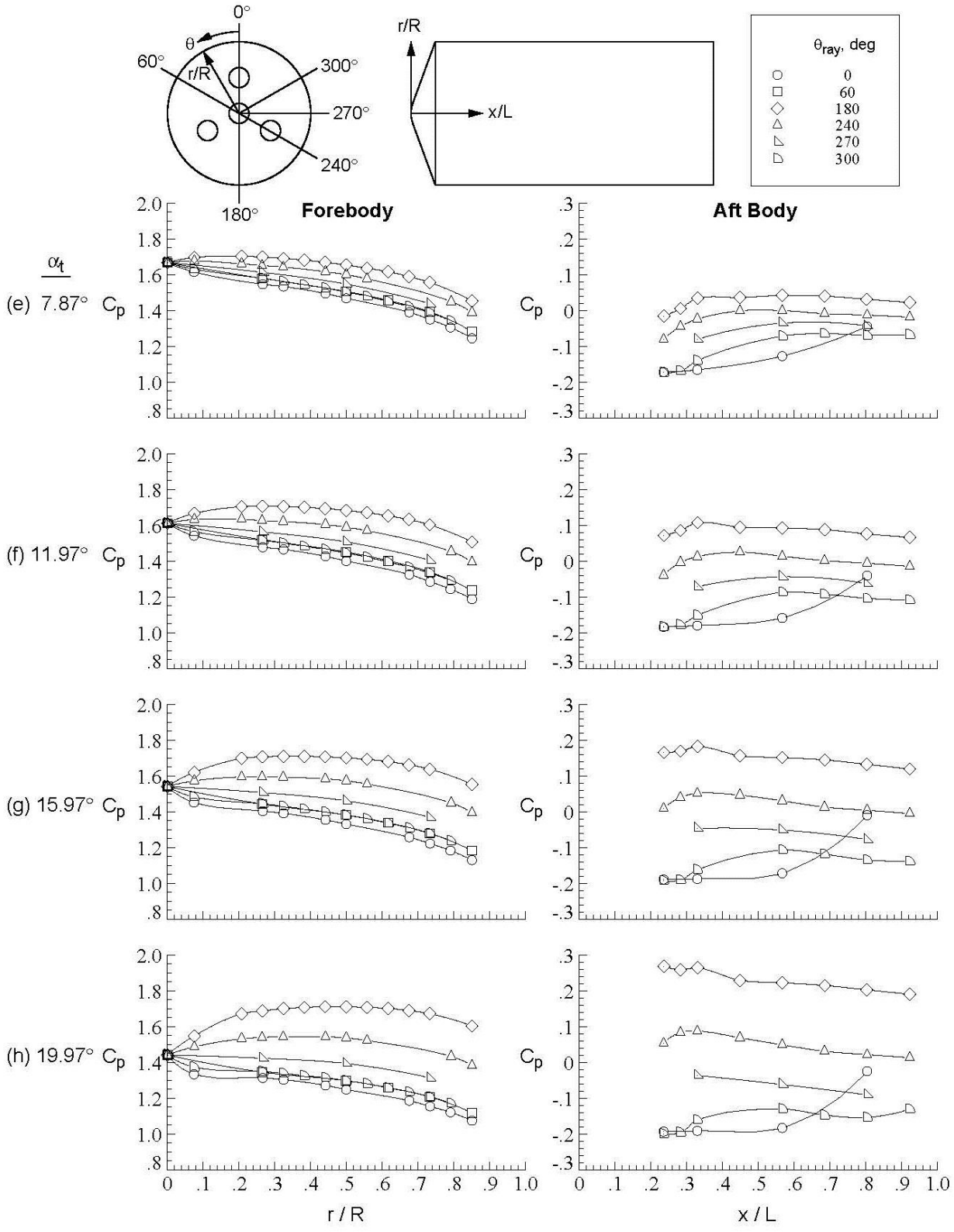

Figure D-29. Concluded.

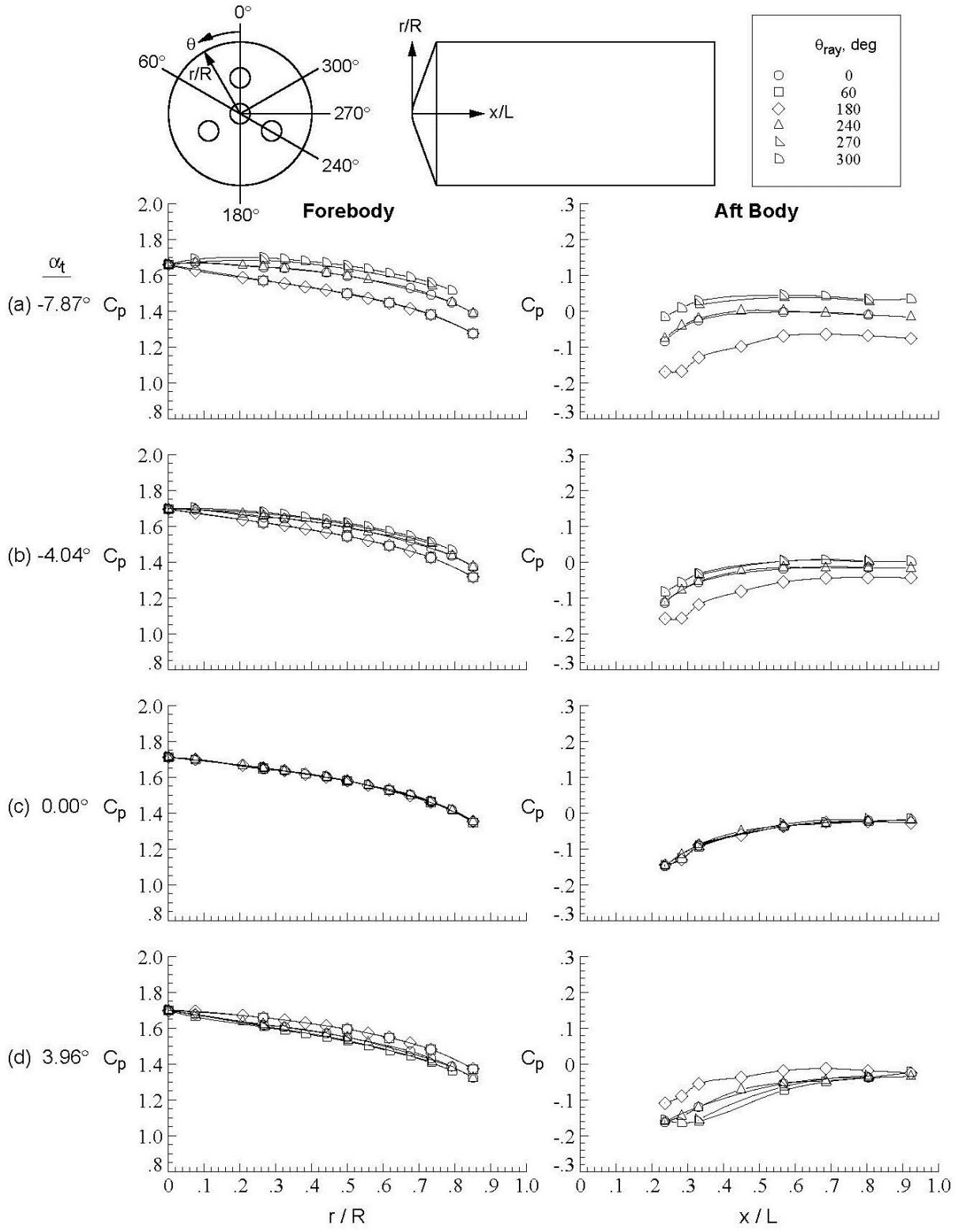

Figure D-30. Baseline configuration, Run 043, M_∞ = 2.4, Re_∞ = 1.0x10^6/ft, ϕ = 59.92°, X_S = 40.19 in, Y_S = −8.00 in, C_T = 0.00.

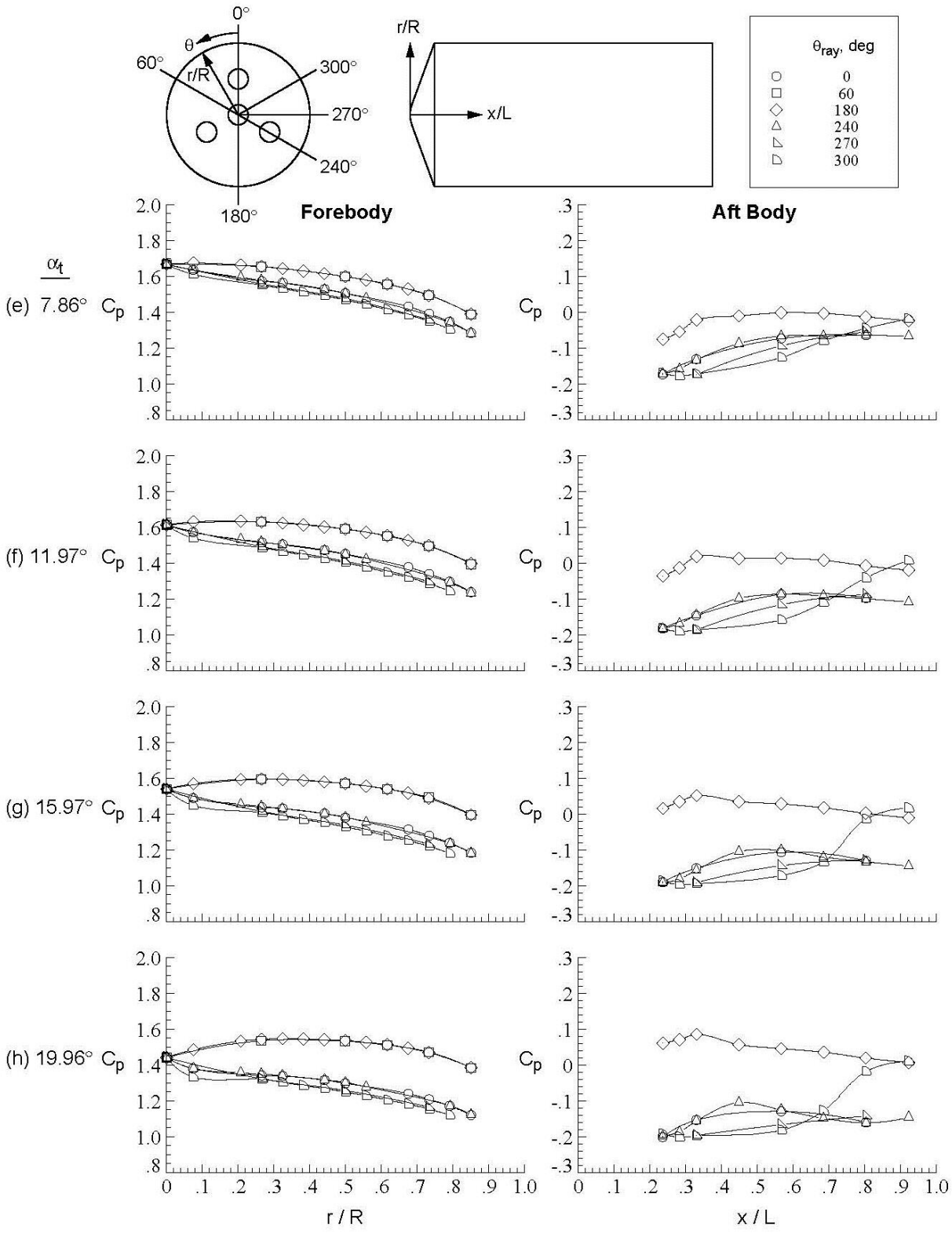

Figure D-30. Concluded.

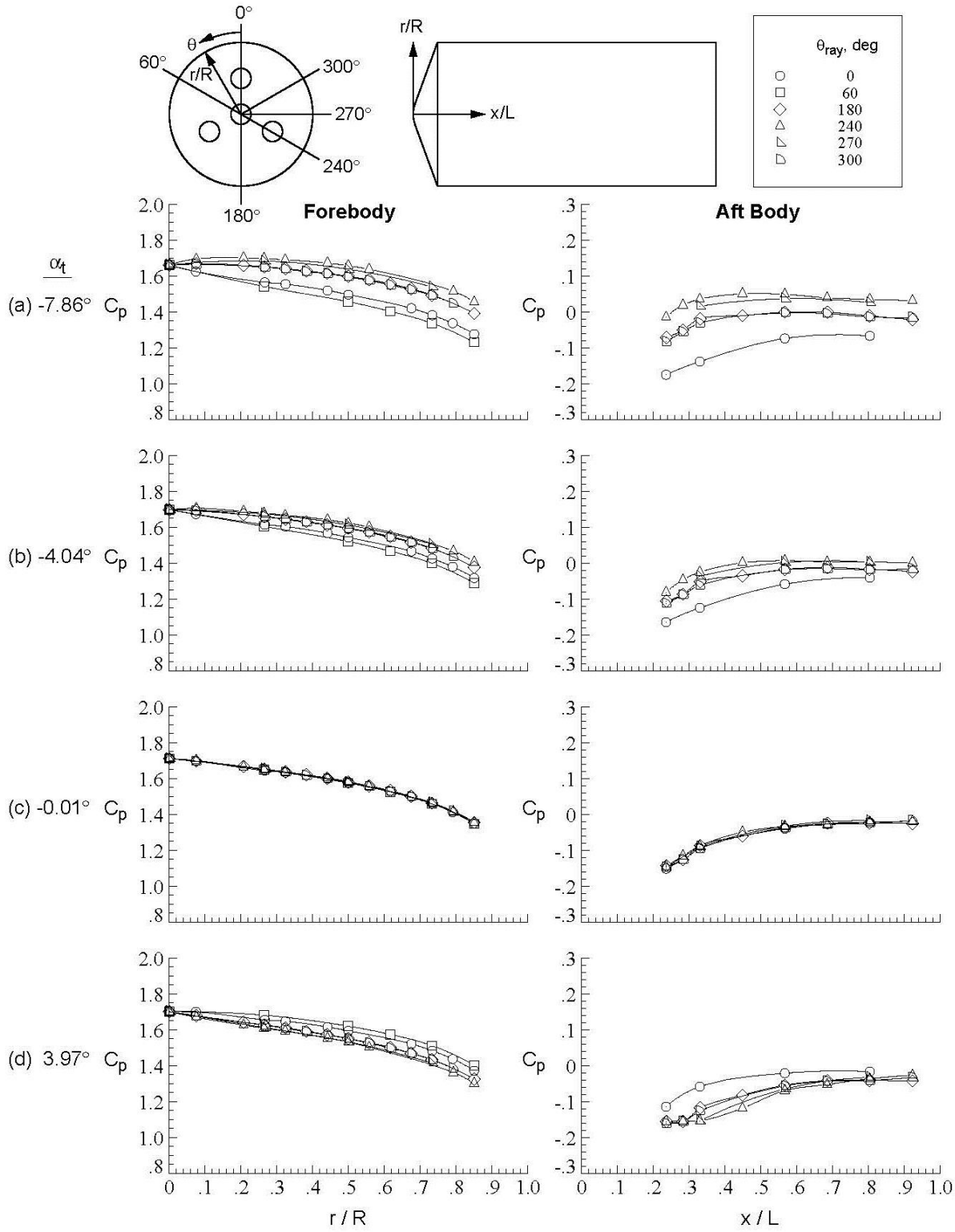

Figure D-31. Baseline configuration, Run 044, M_∞ = 2.4, Re_∞ = 1.0x10^6/ft, ϕ = 119.90°, X_S = 40.19 in, Y_S = –8.00 in, C_T = 0.00.

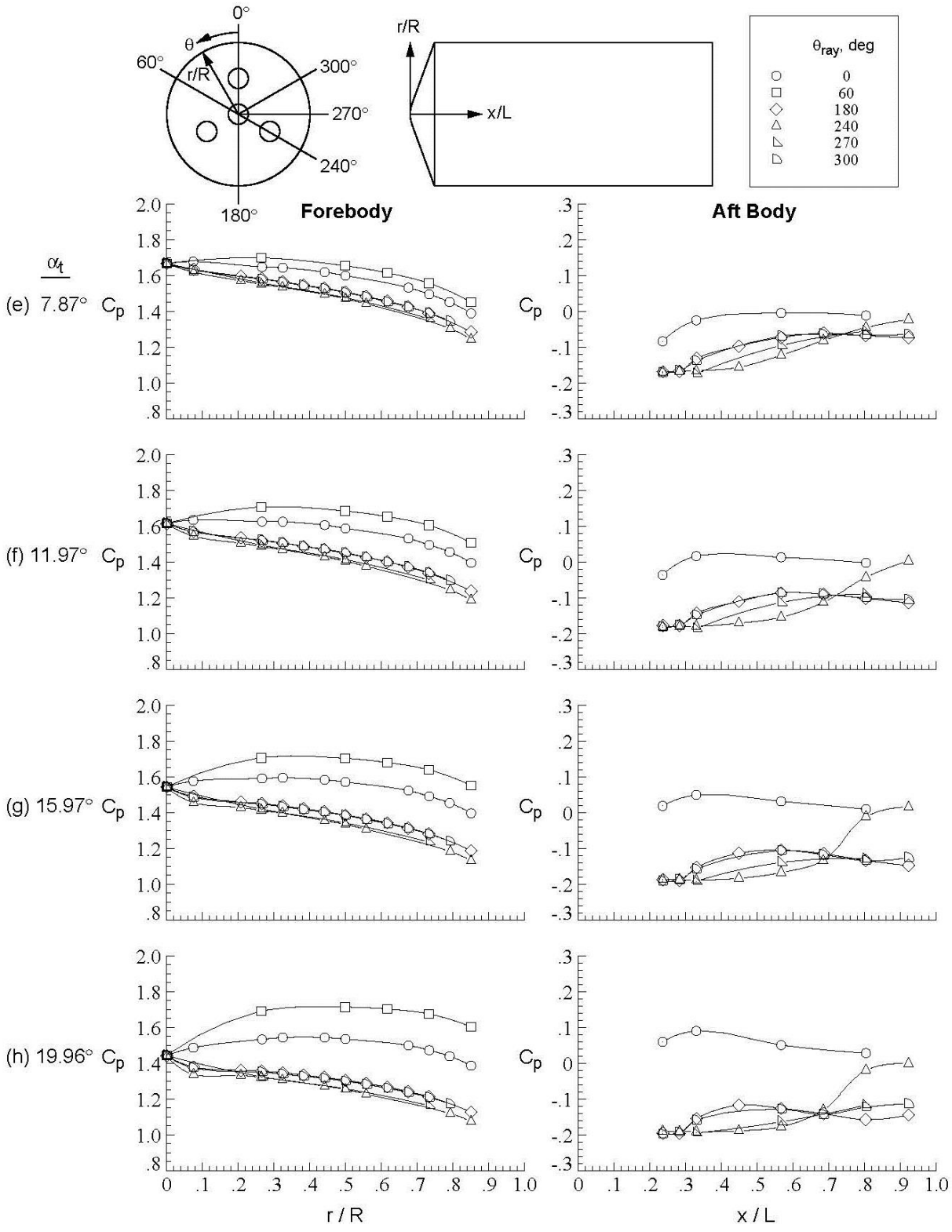

Figure D-31. Concluded.

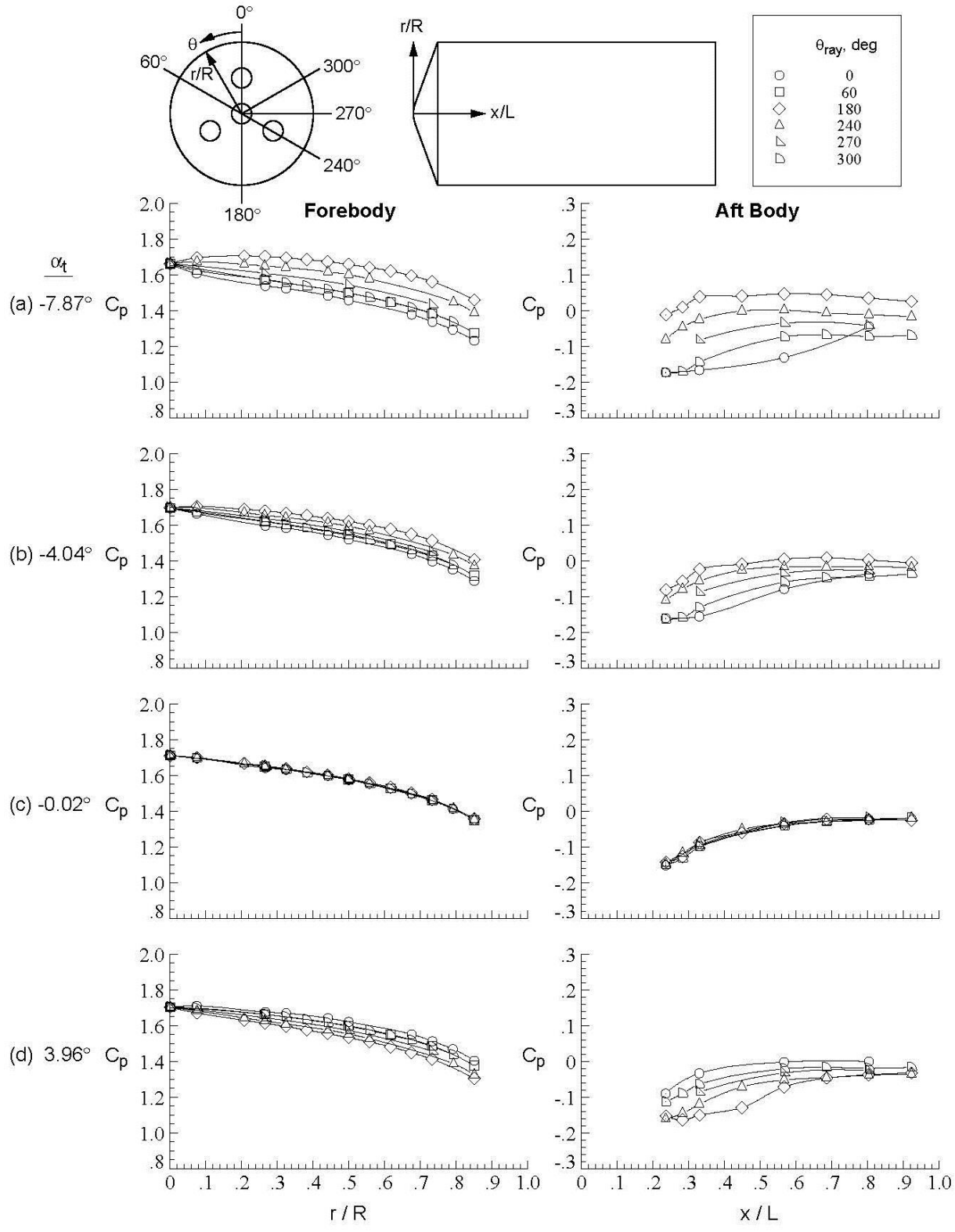

Figure D-32. Baseline configuration, Run 045, M_∞ = 2.4, Re_∞ = 1.0x10^6/ft, ϕ = 179.95°, X_S = 40.19 in, Y_S = –8.00 in, C_T = 0.00.

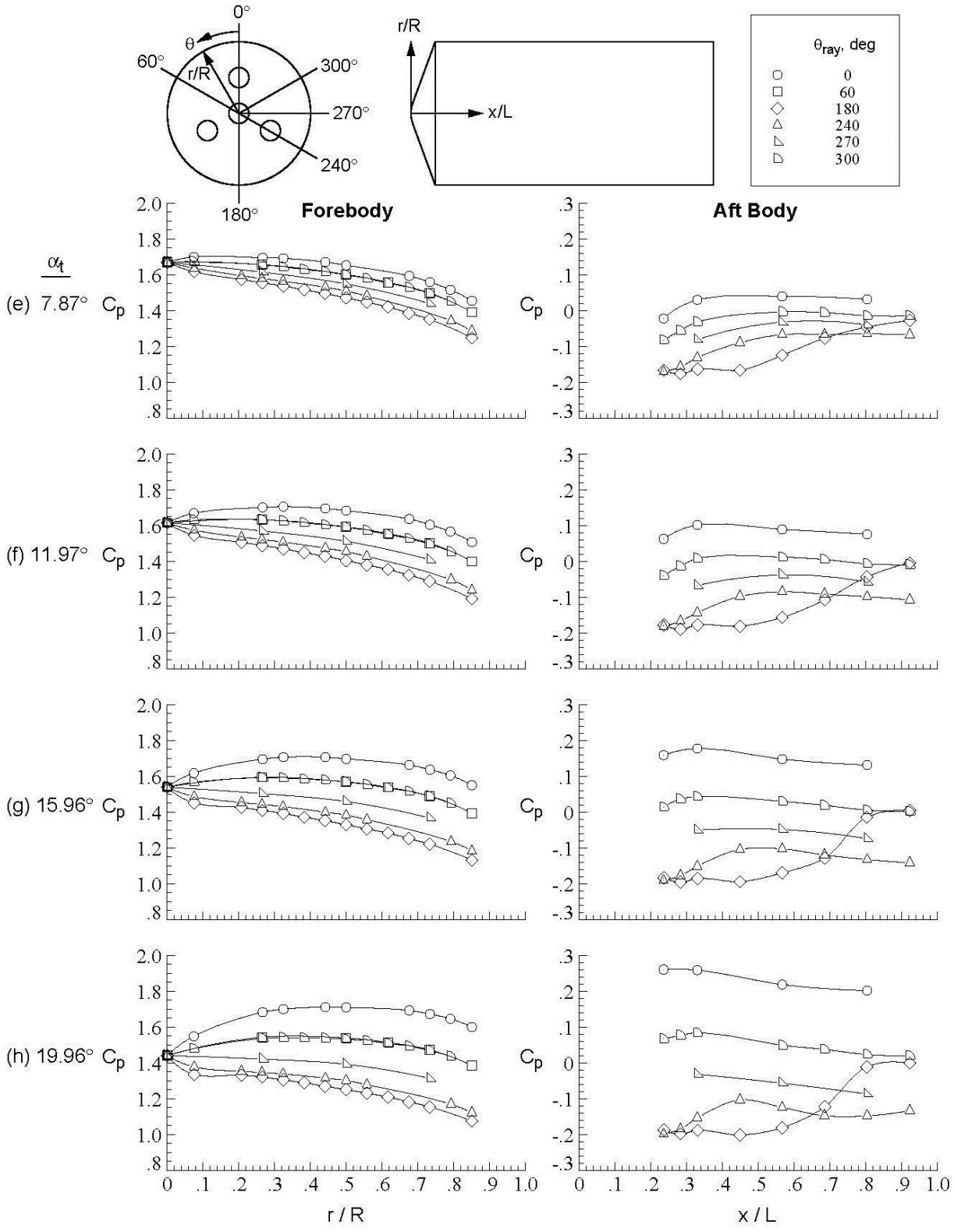

Figure D-32. Concluded.

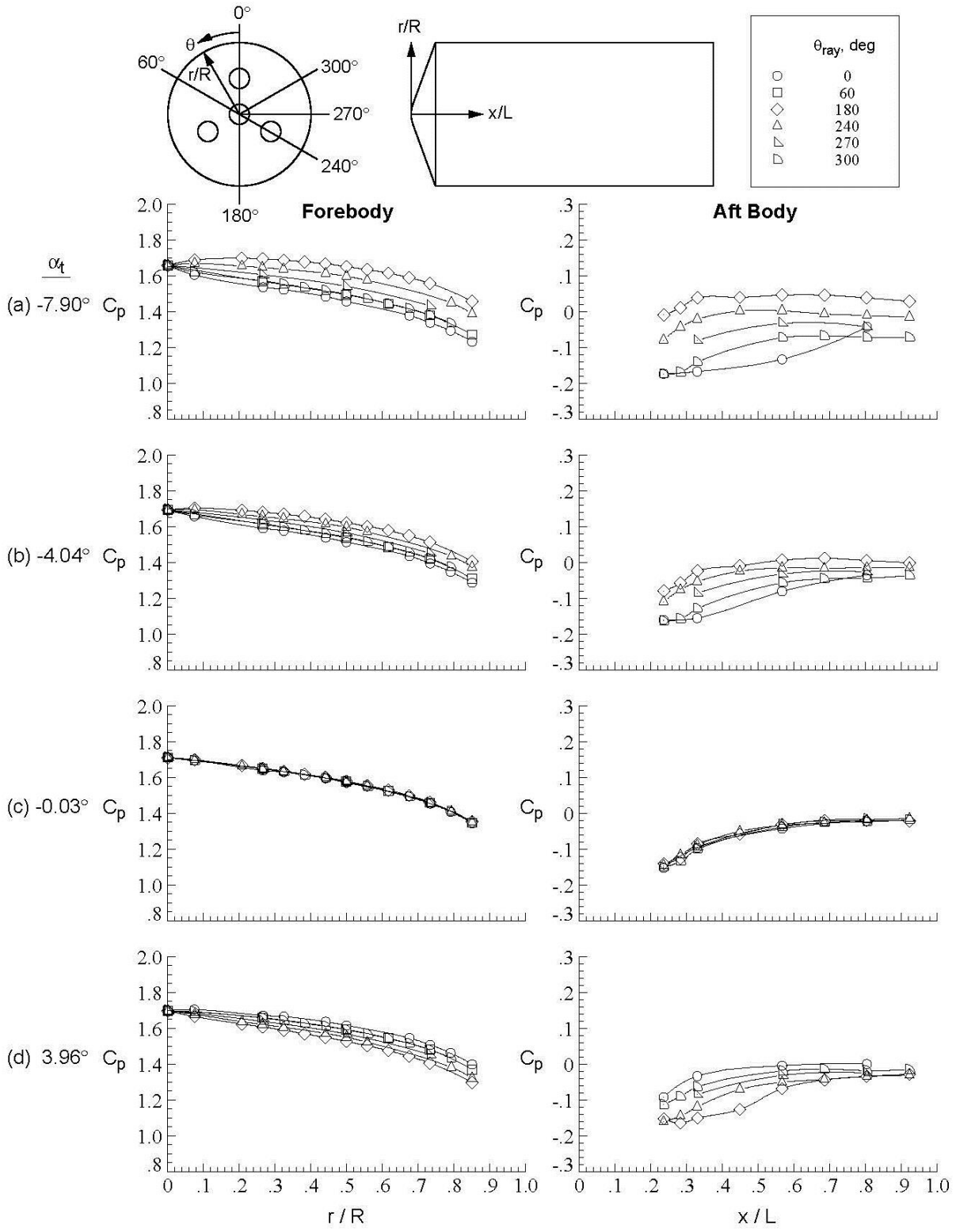

Figure D-33. Baseline configuration, Run 046, M_∞ = 2.4, Re_∞ = 1.0x10^6/ft, ϕ = 179.95°, X_S = 50.16 in, Y_S = –8.00 in, C_T = 0.00.

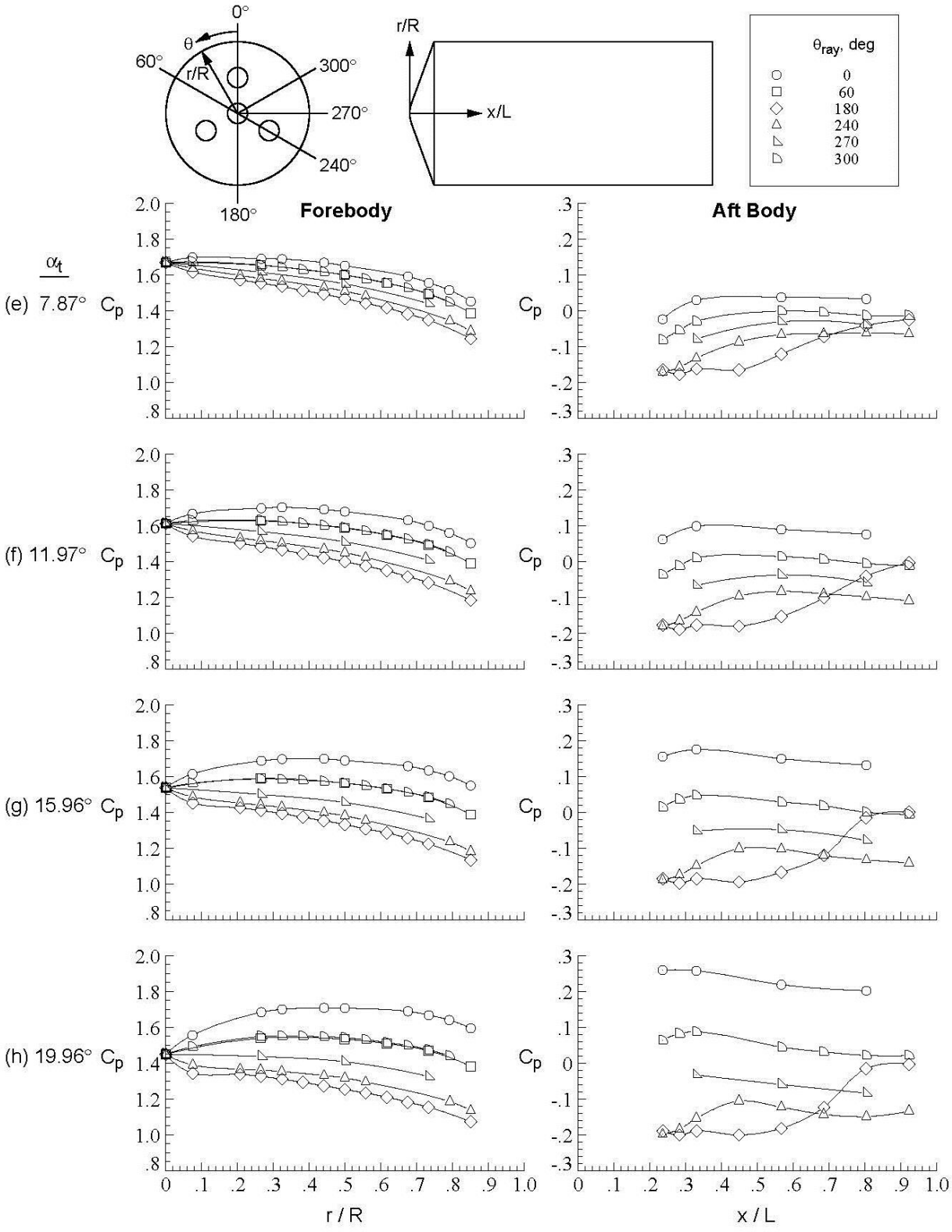

Figure D-33. Concluded.

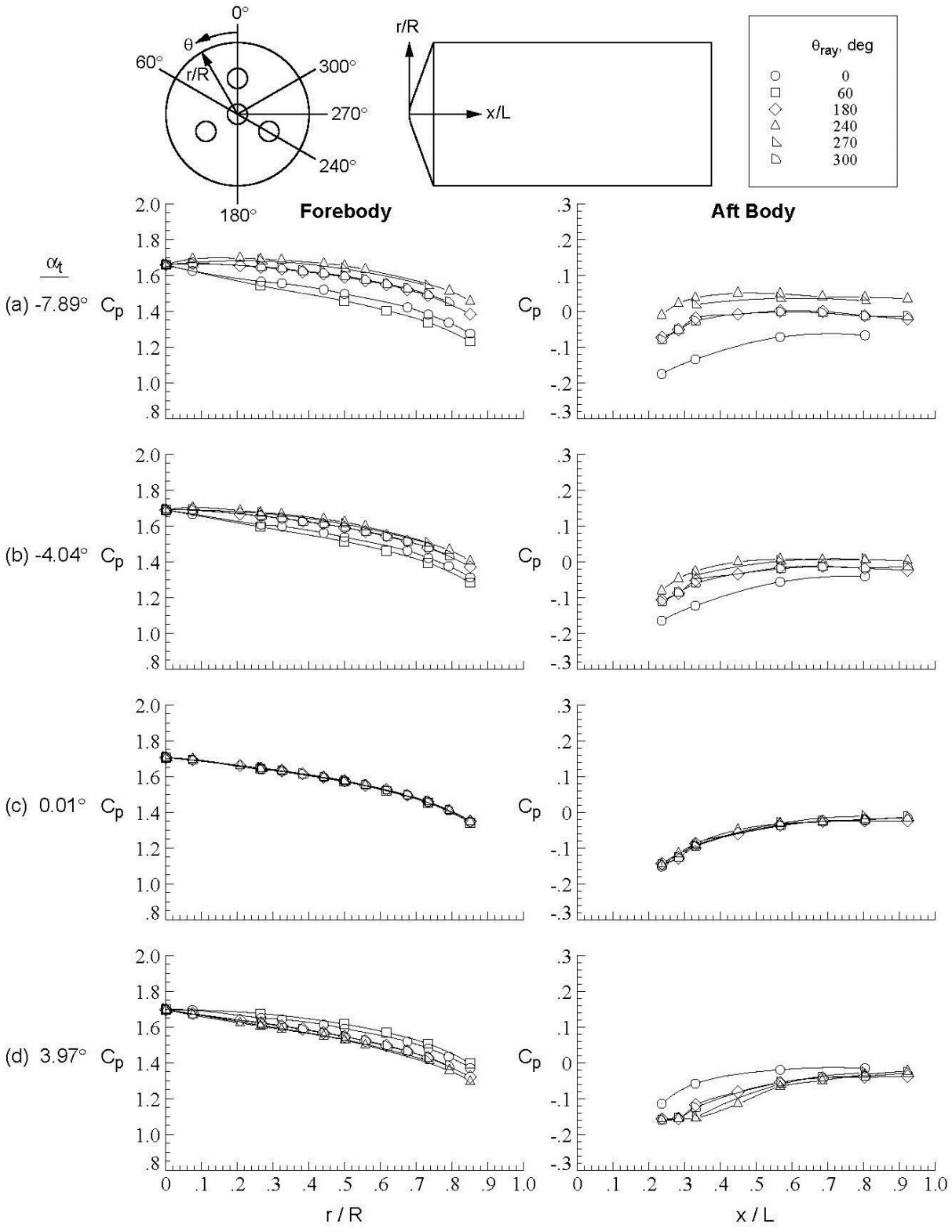

Figure D-34. Baseline configuration, Run 047, M_∞ = 2.4, Re_∞ = 1.0x10^6/ft, ϕ = 119.98°, X_S = 50.16 in, Y_S = –8.00 in, C_T = 0.00.

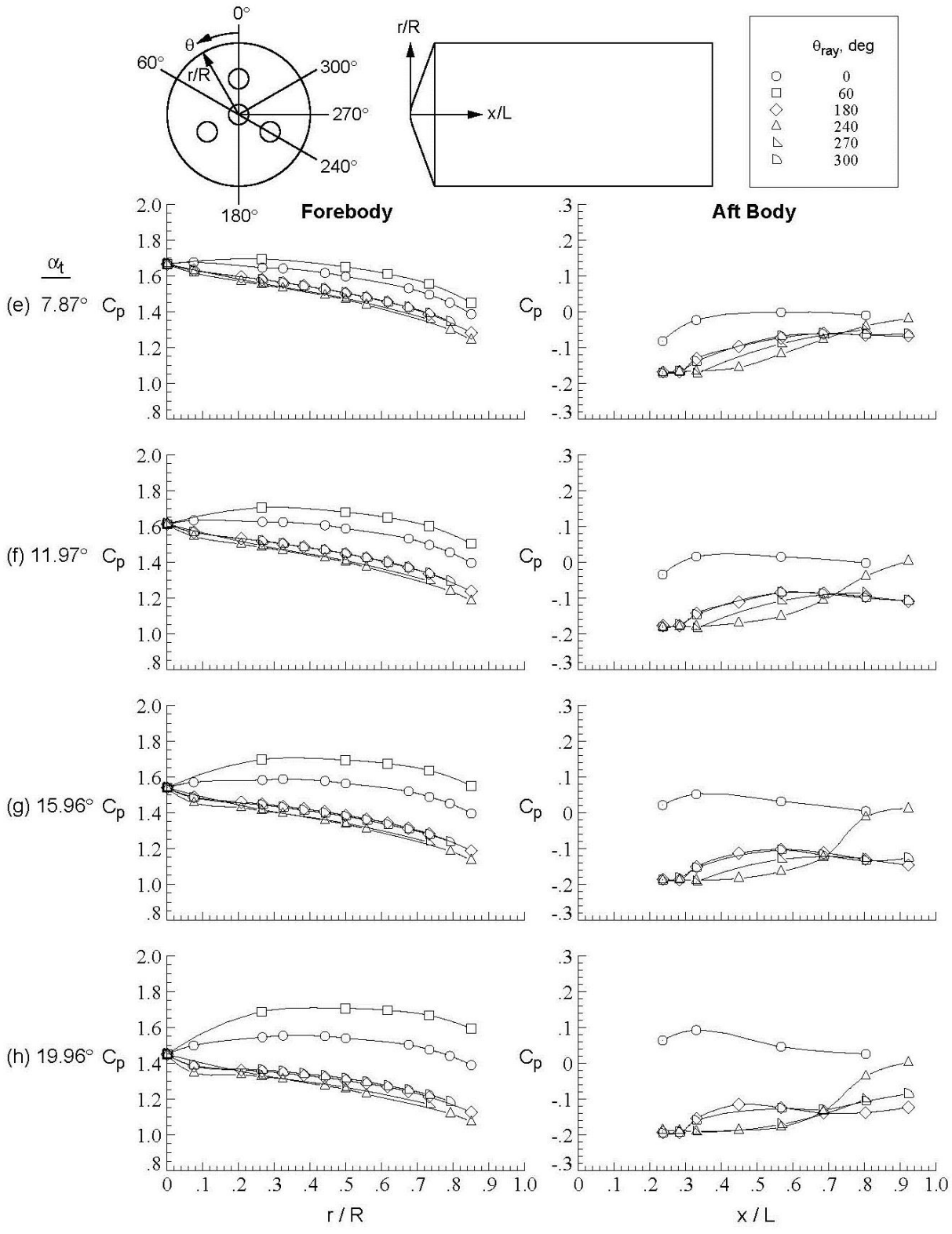

Figure D-34. Concluded.

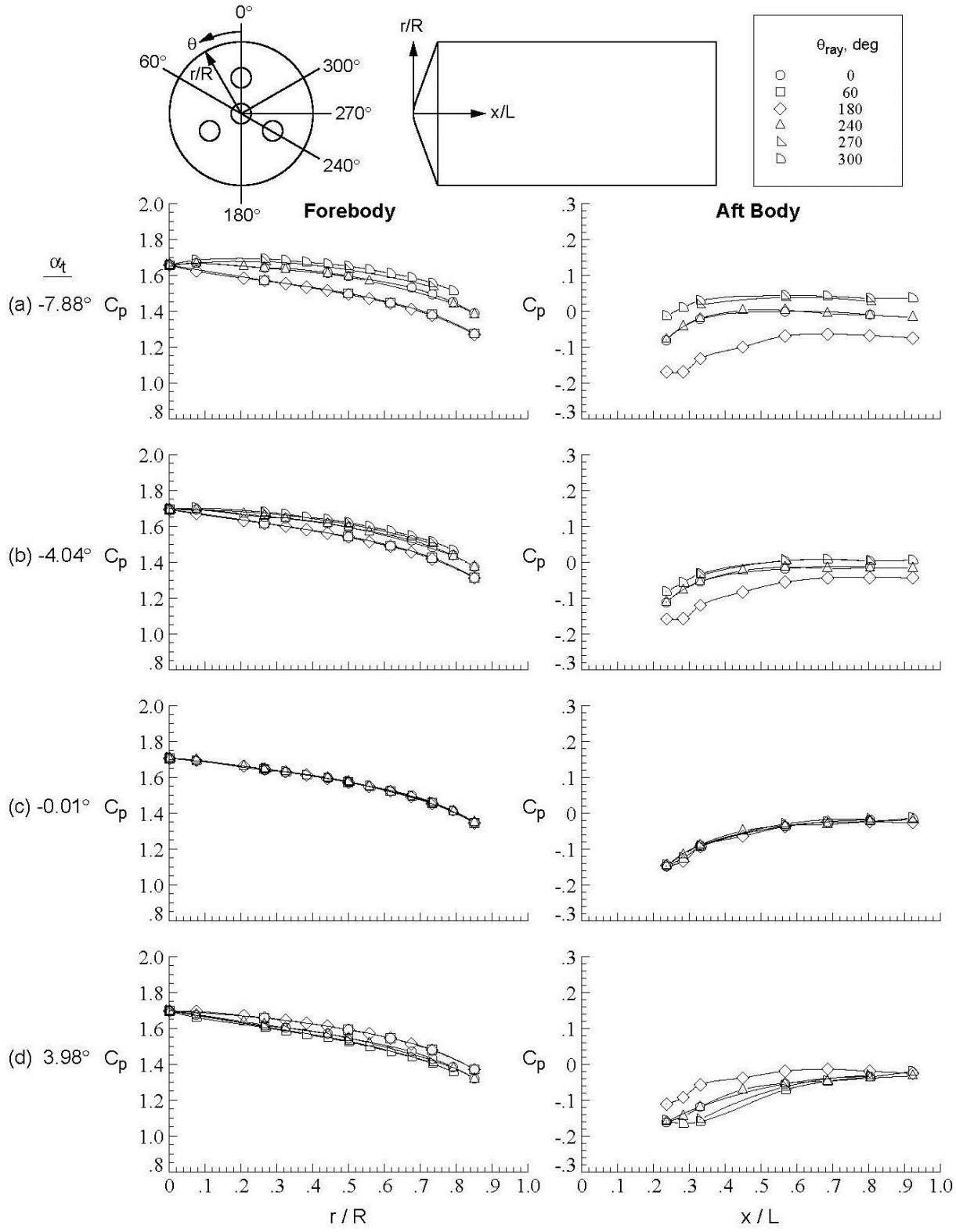

Figure D-35. Baseline configuration, Run 048, M_∞ = 2.4, Re_∞ = 1.0x10^6/ft, ϕ = 59.98°, X_S = 50.16 in, Y_S = –8.00 in, C_T = 0.00.

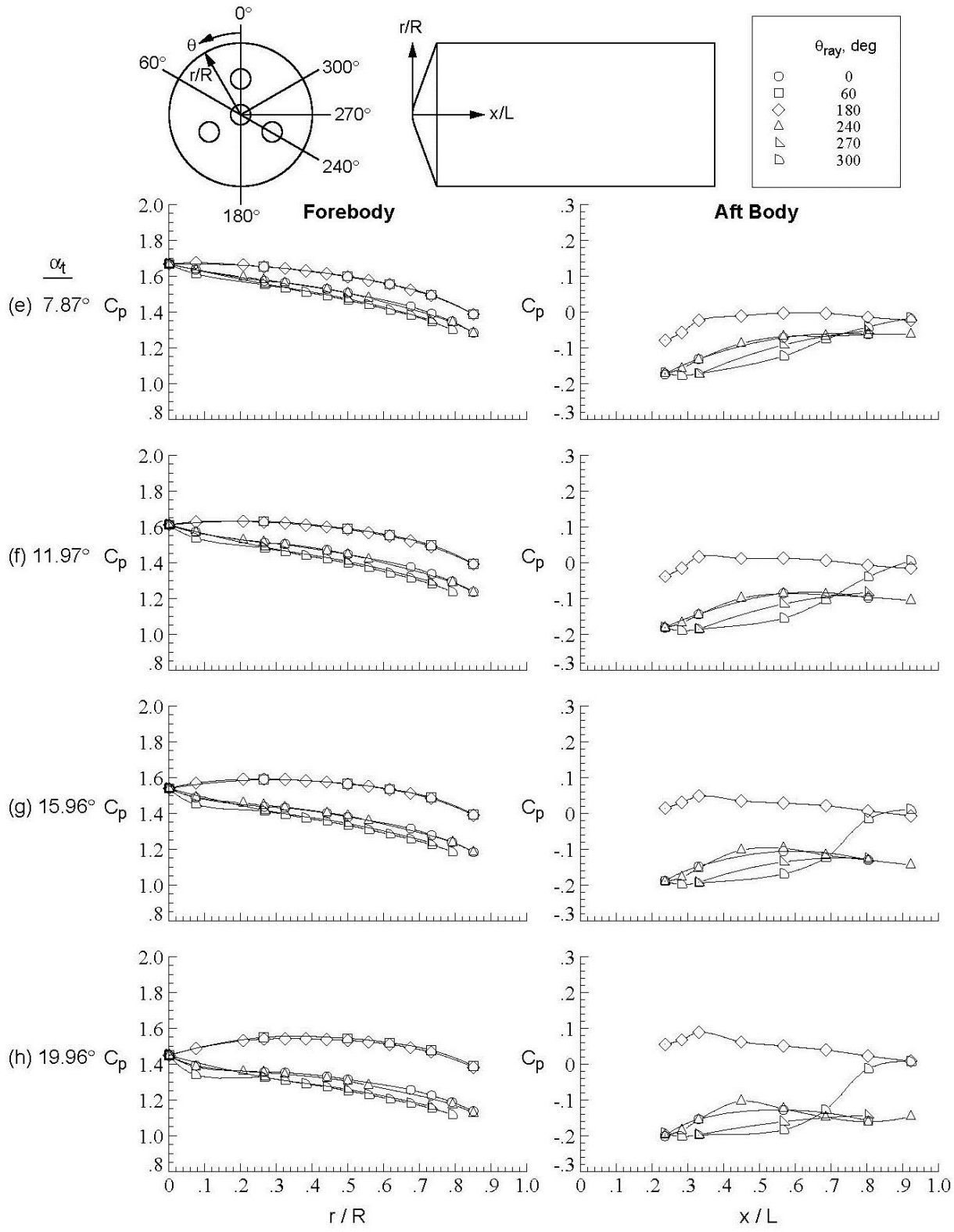

Figure D-35. Concluded.

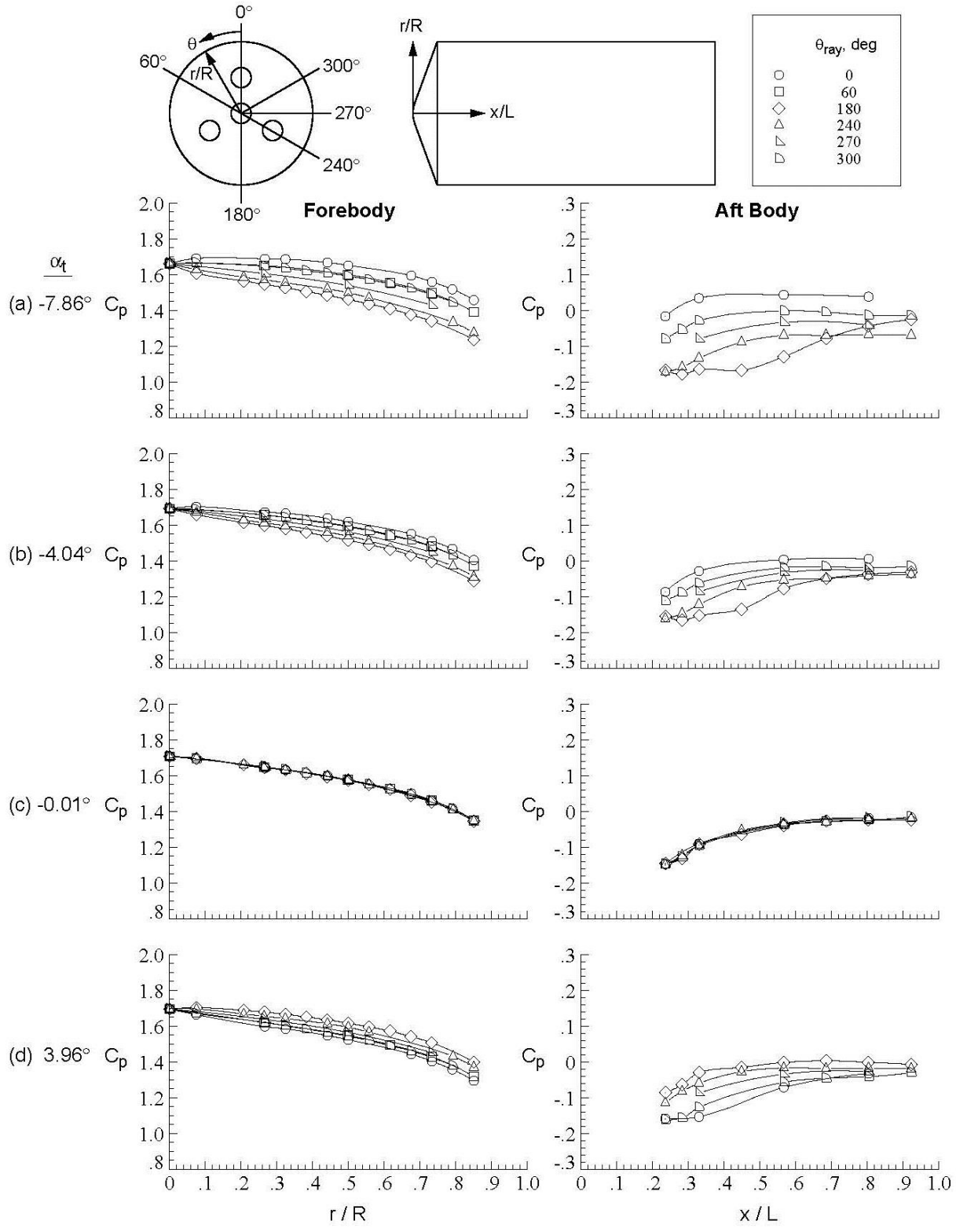

Figure D-36. Baseline configuration, Run 049, M_∞ = 2.4, Re_∞ = 1.0x10^6/ft, ϕ = 0.05°, X_S = 50.16 in, Y_S = –8.00 in, C_T = 0.00.

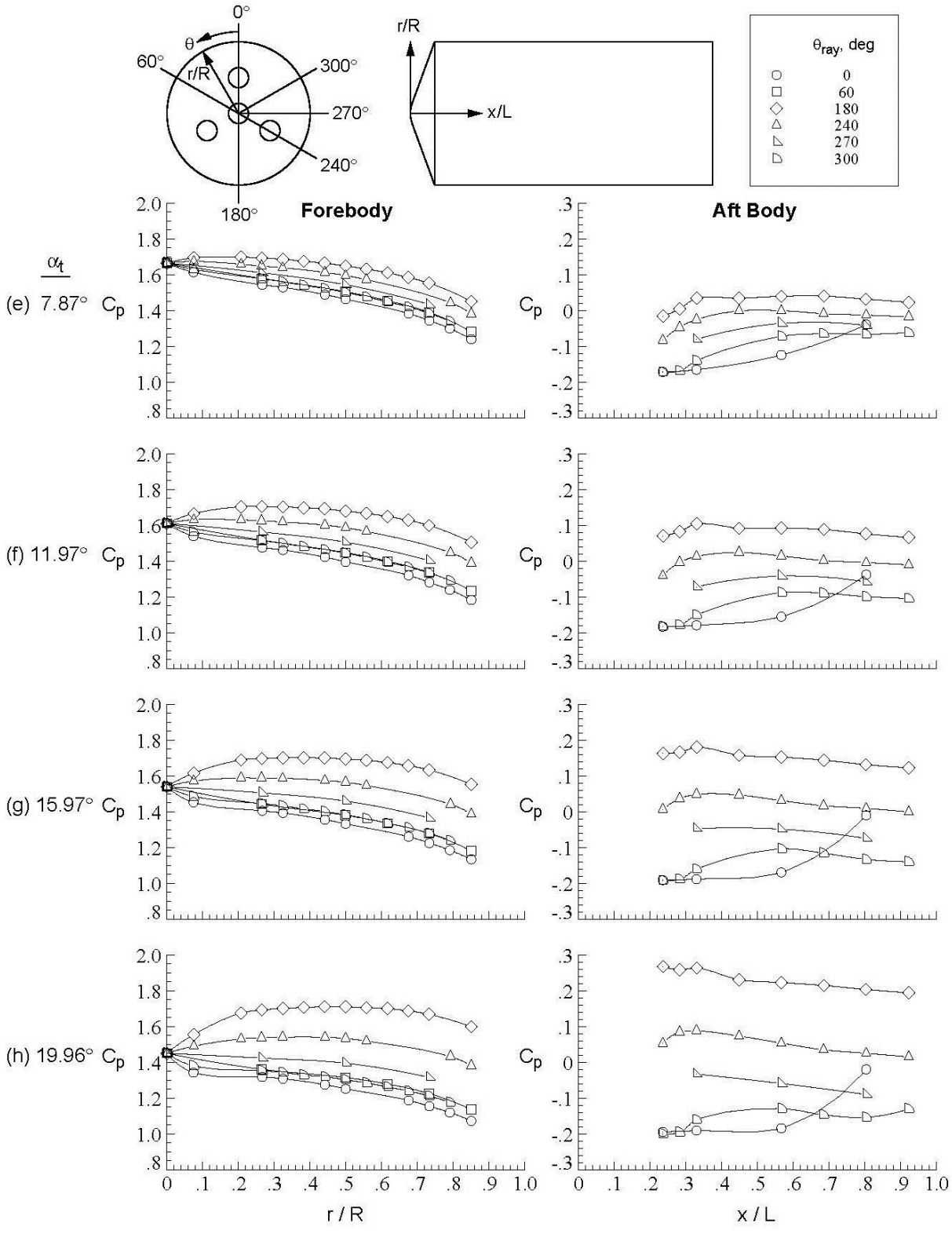

Figure D-36. Concluded.

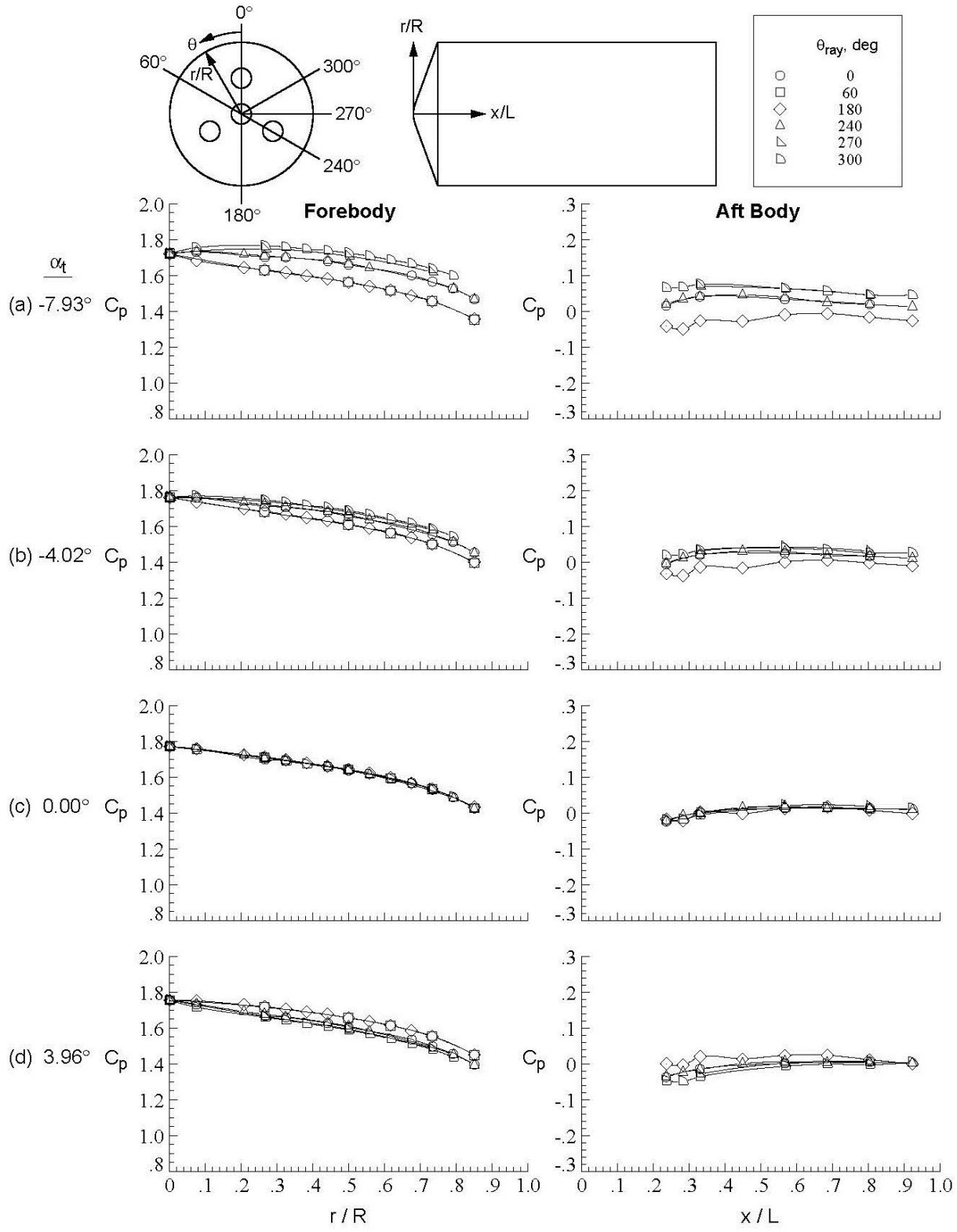

Figure D-37. Baseline configuration, Run 050, M_∞ = 3.5, Re_∞ = 1.0x10^7/ft, ϕ = 59.96°, X_S = 50.16 in, Y_S = 0.00 in, C_T = 0.00.

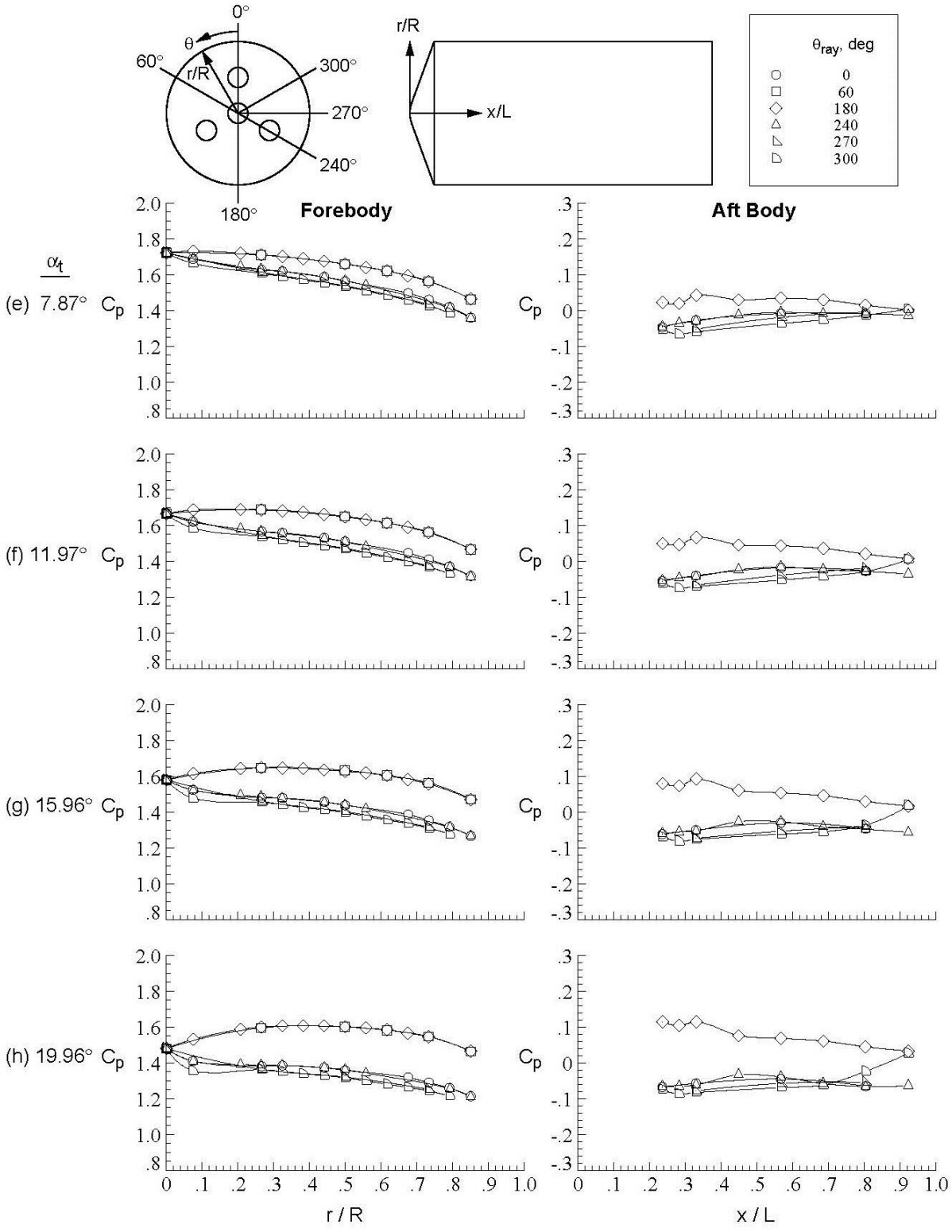

Figure D-37. Concluded.

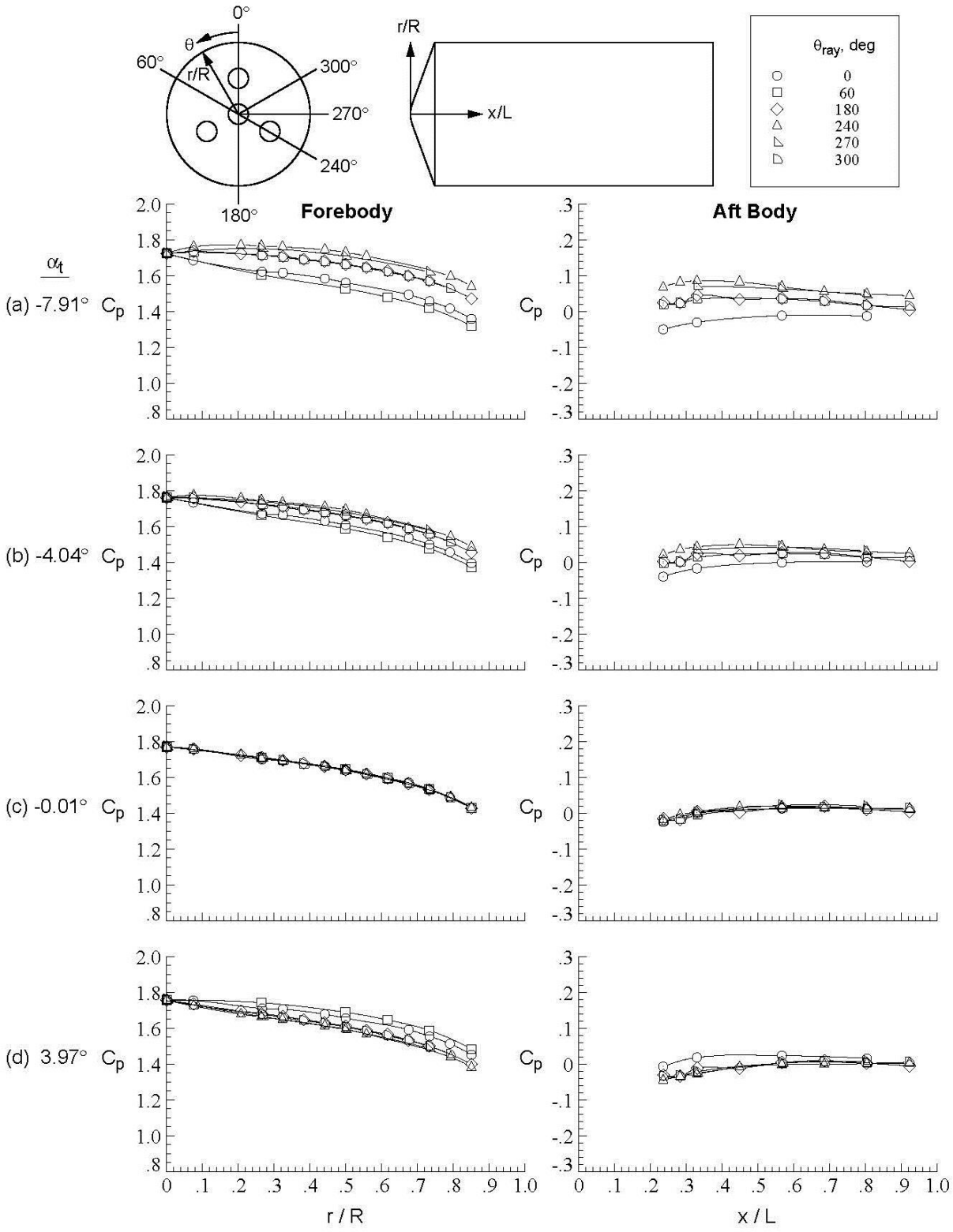

Figure D-38. Baseline configuration, Run 051, M_∞ = 3.5, Re_∞ = 1.0x10^6/ft, ϕ = 119.94°, X_S = 50.16 in, Y_S = 0.00 in, C_T = 0.00.

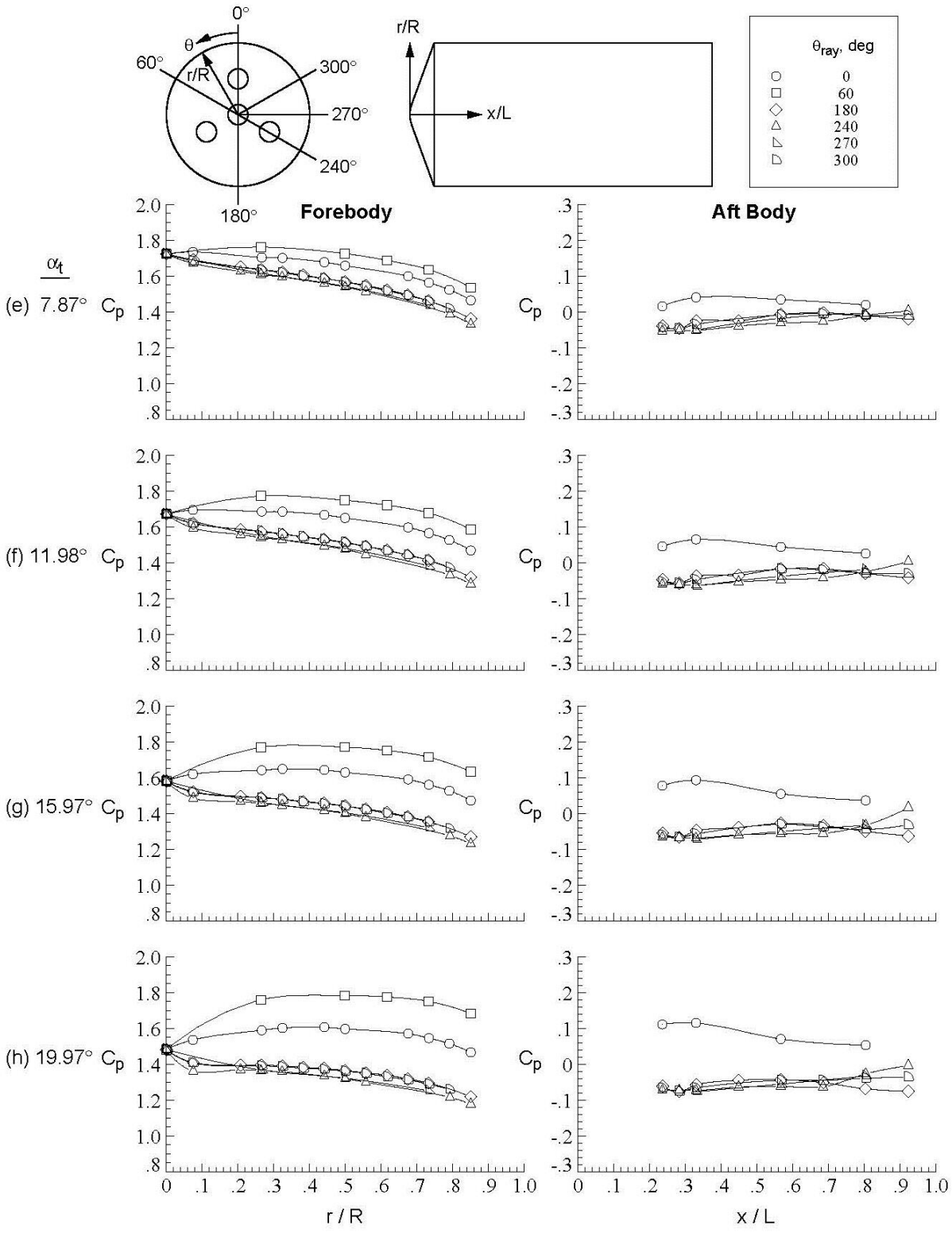

Figure D-38. Concluded.

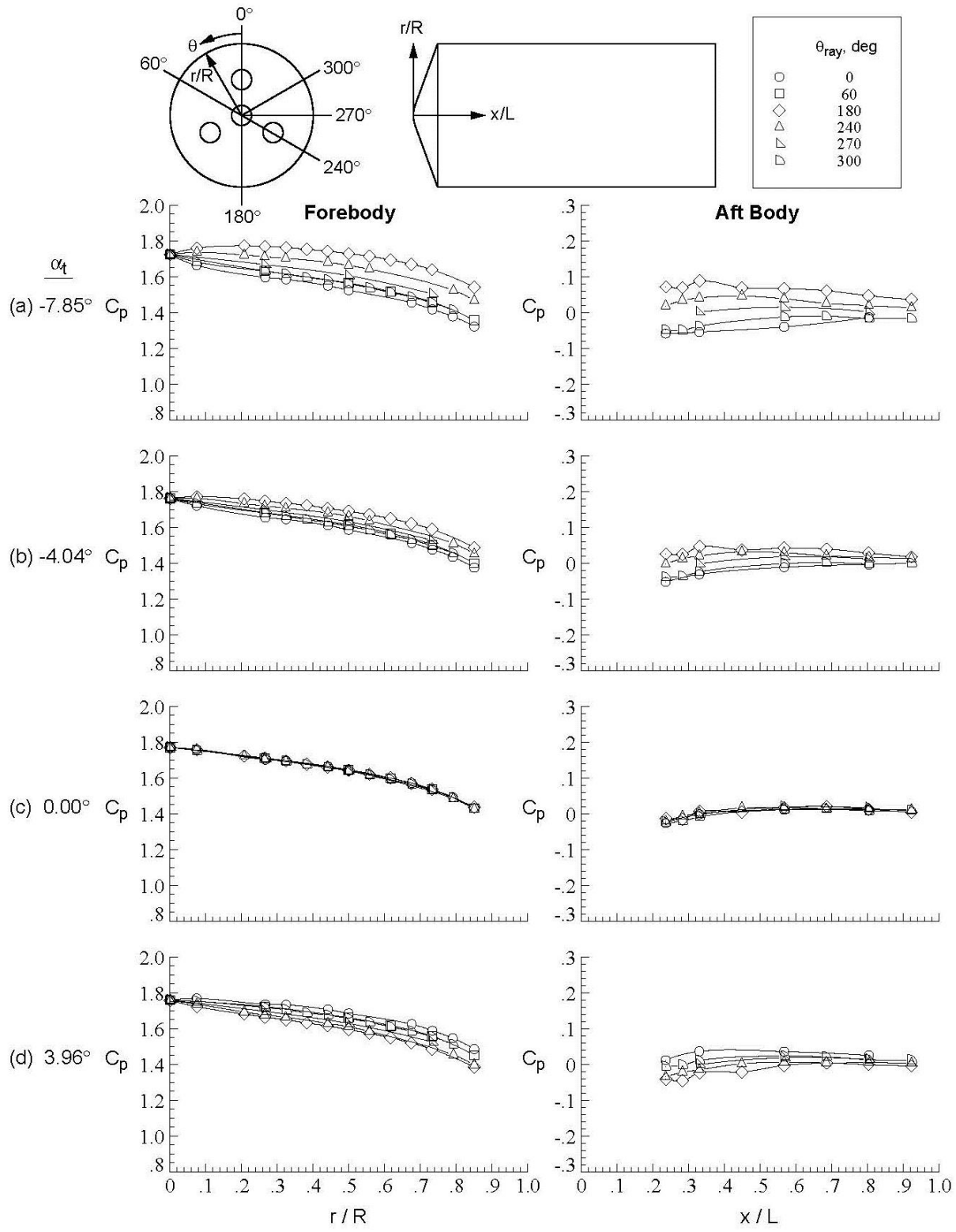

Figure D-39. Baseline configuration, Run 052, M_∞ = 3.5, Re_∞ = 1.0x10^6/ft, ϕ = 179.99°, X_S = 50.16 in, Y_S = 0.00 in, C_T = 0.00.

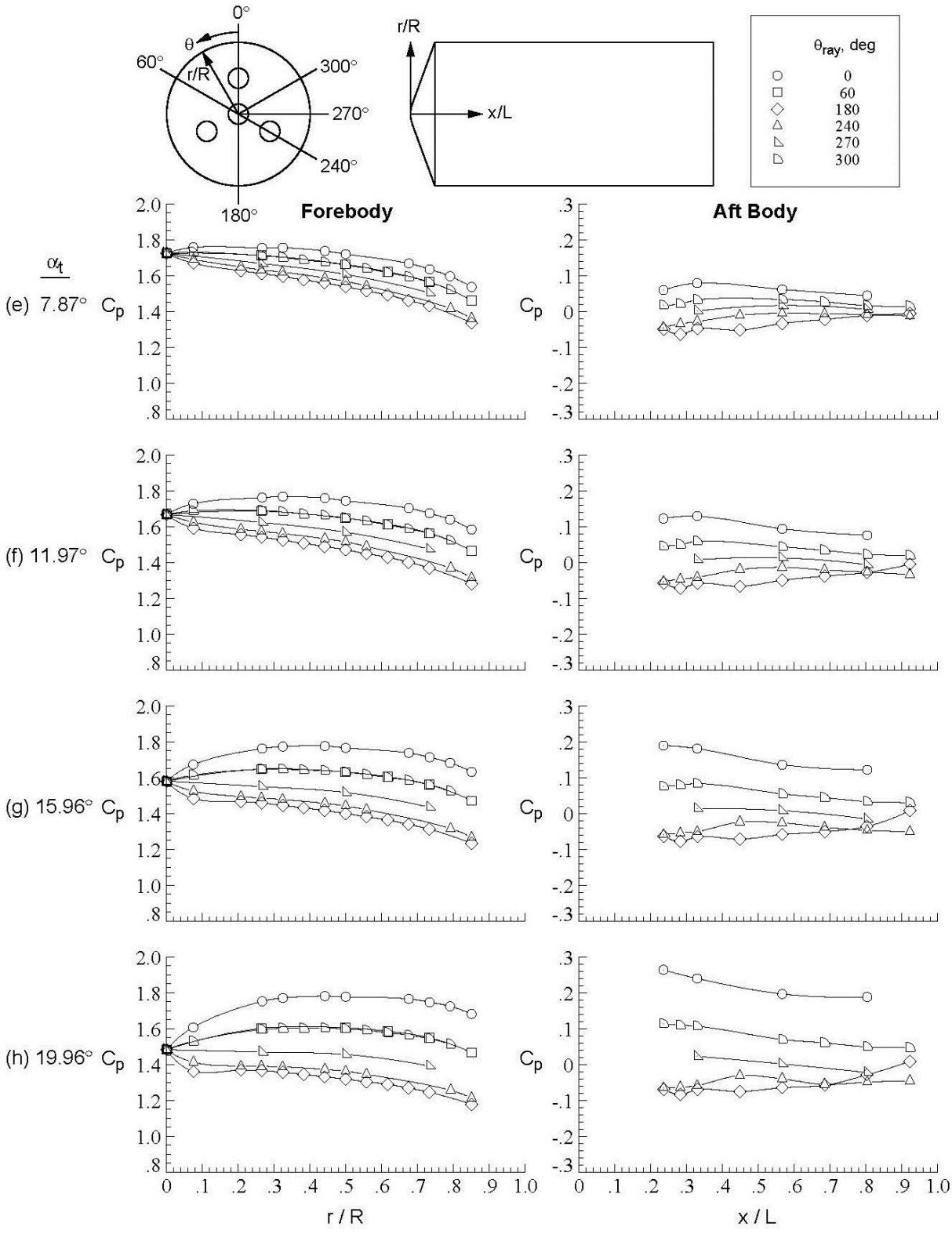

Figure D-39. Concluded.

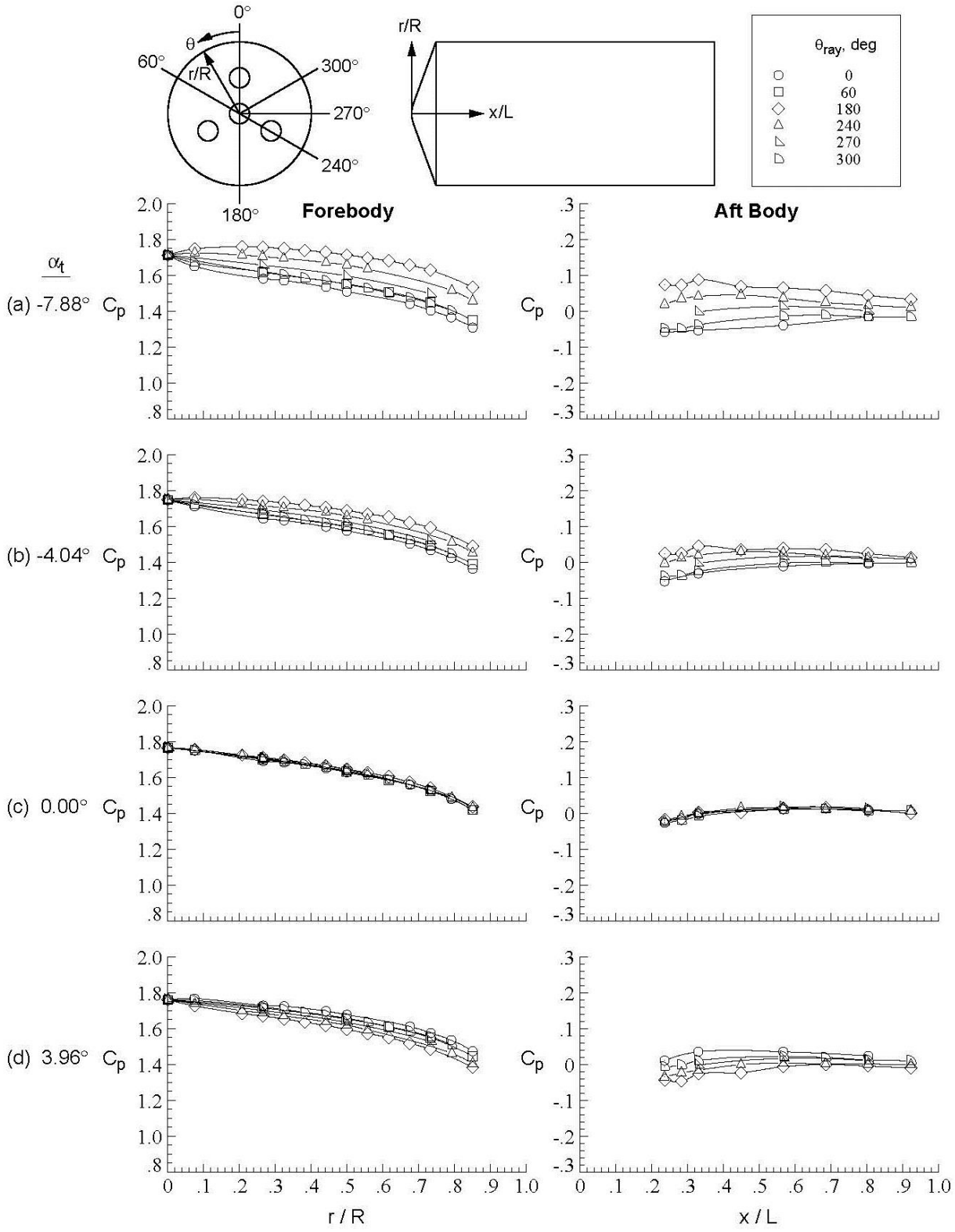

Figure D-40. Baseline configuration, Run 053, M_∞ = 3.5, Re_∞ = 1.0x10^6/ft, ϕ = 0.01°, X_S = 39.93 in, Y_S = 0.00 in, C_T = 0.00.

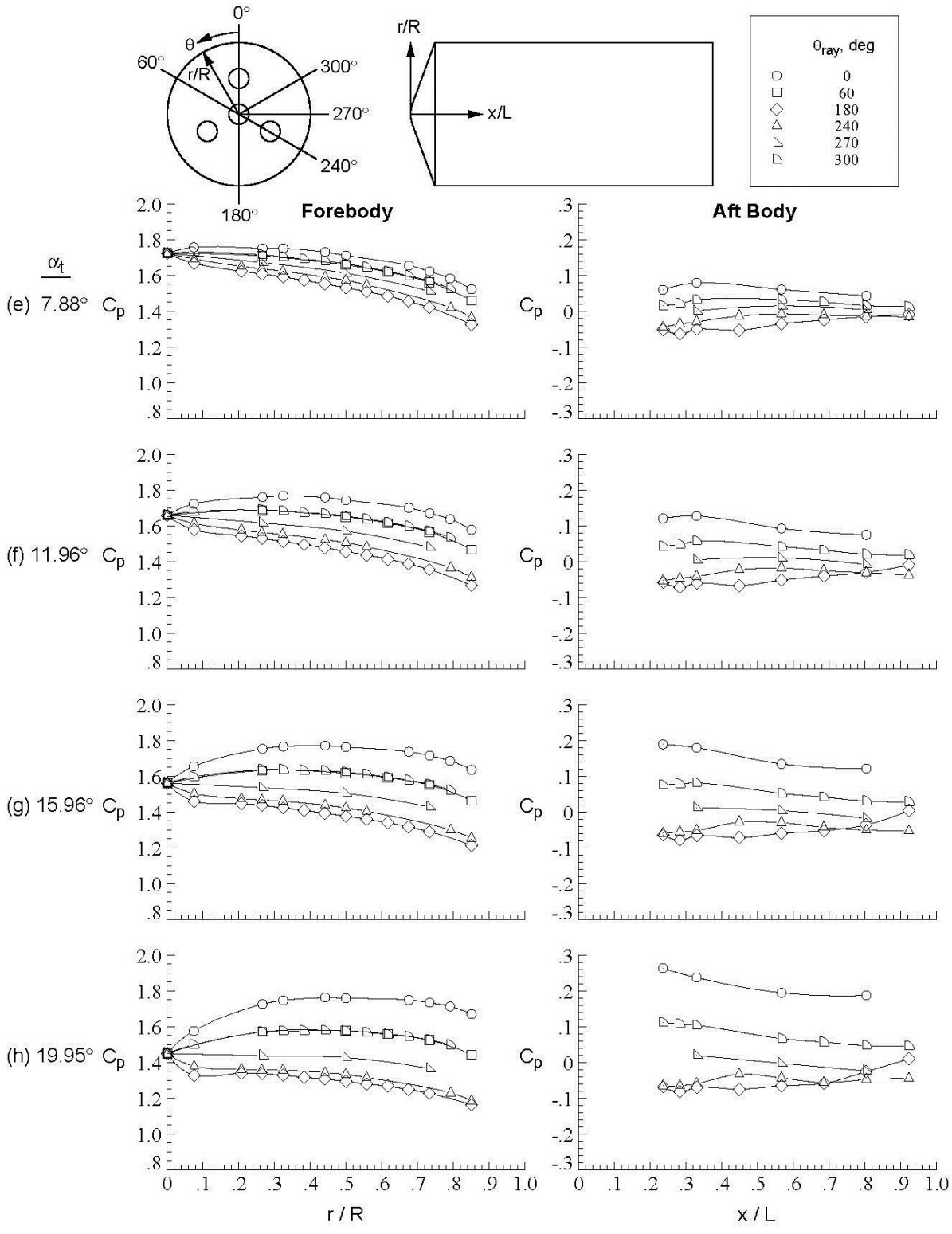

Figure D-40. Concluded.

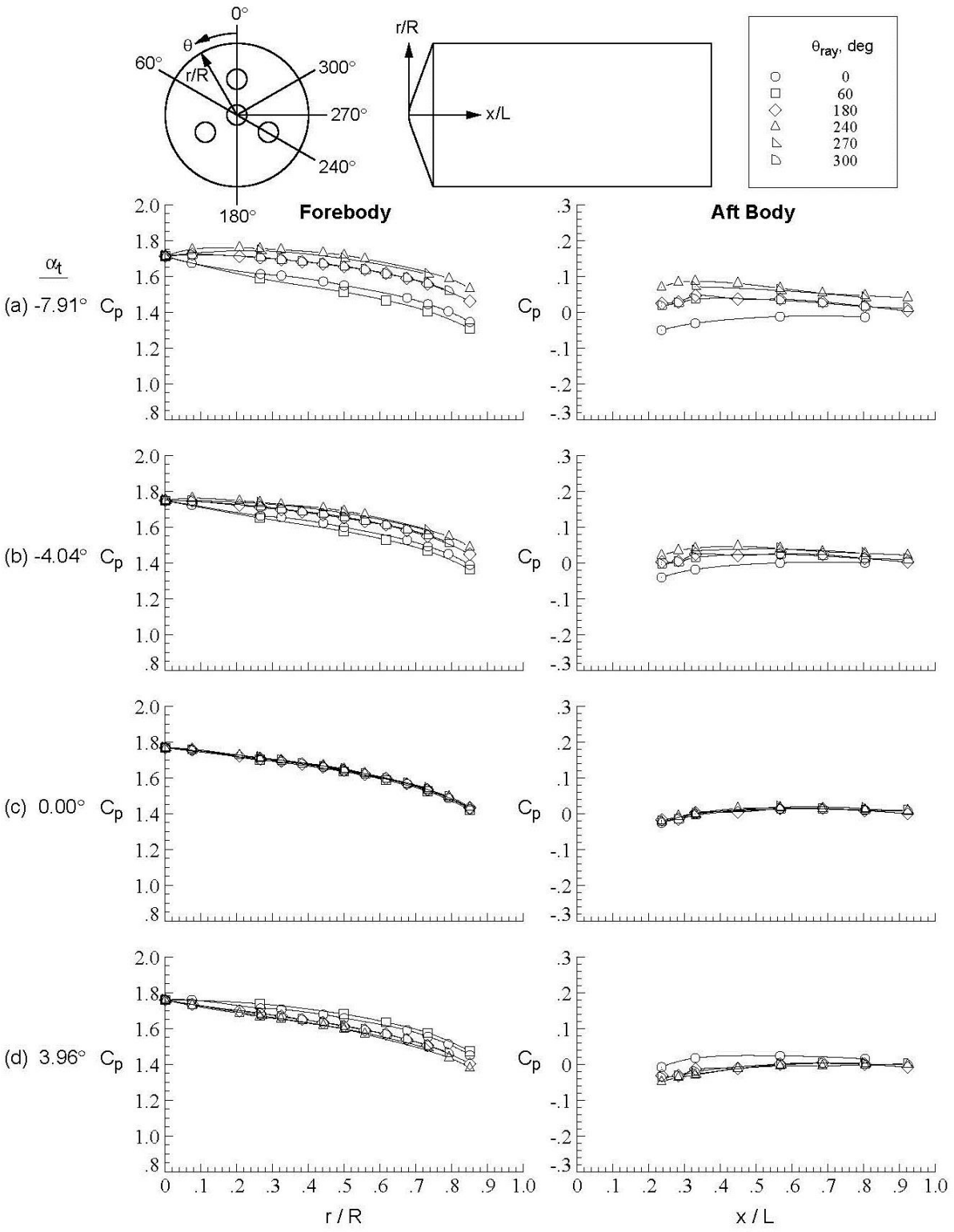

Figure D-41. Baseline configuration, Run 054, M_∞ = 3.5, Re_∞ = 1.0x10^6/ft, ϕ = 120.06°, X_S = 40.17 in, Y_S = 0.00 in, C_T = 0.00.

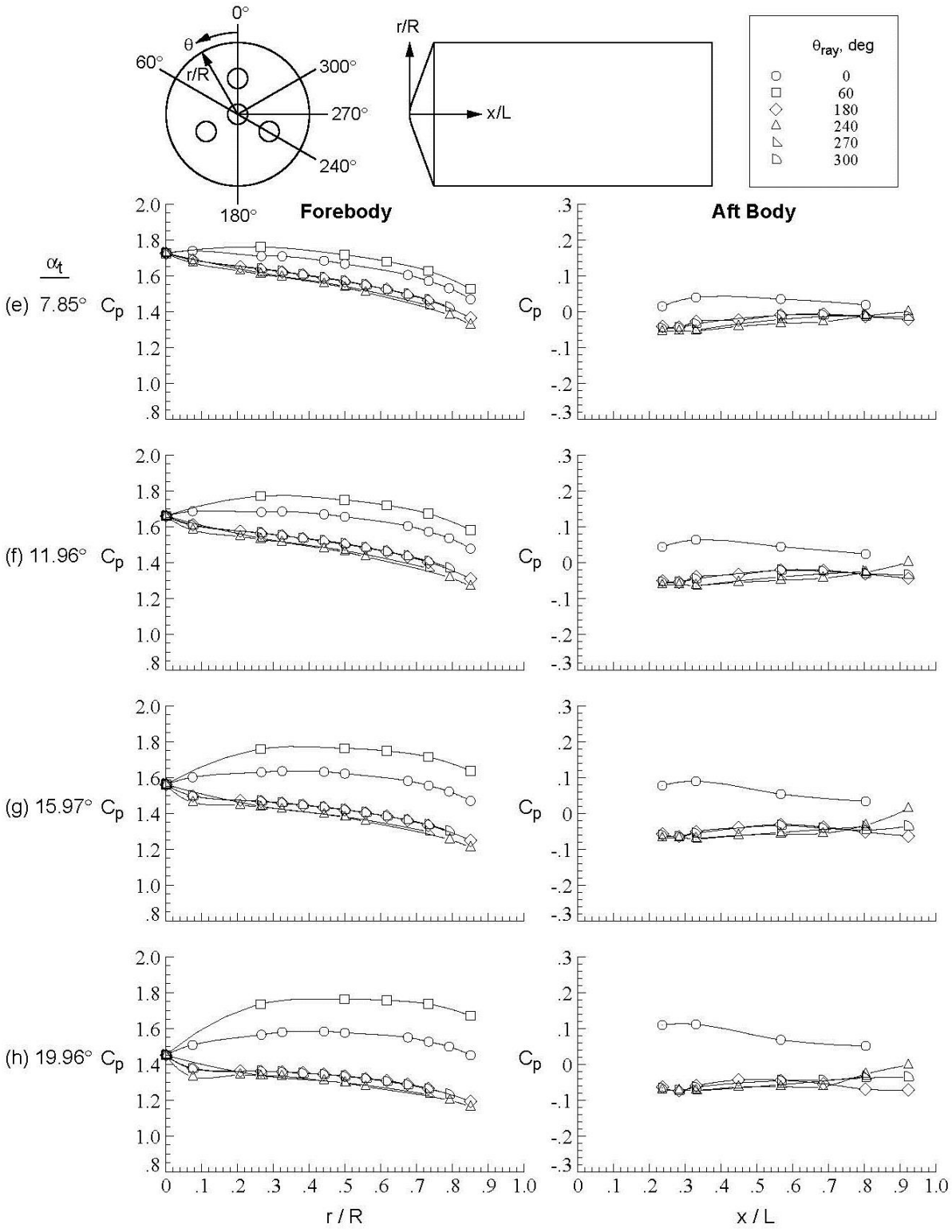

Figure D-41. Concluded.

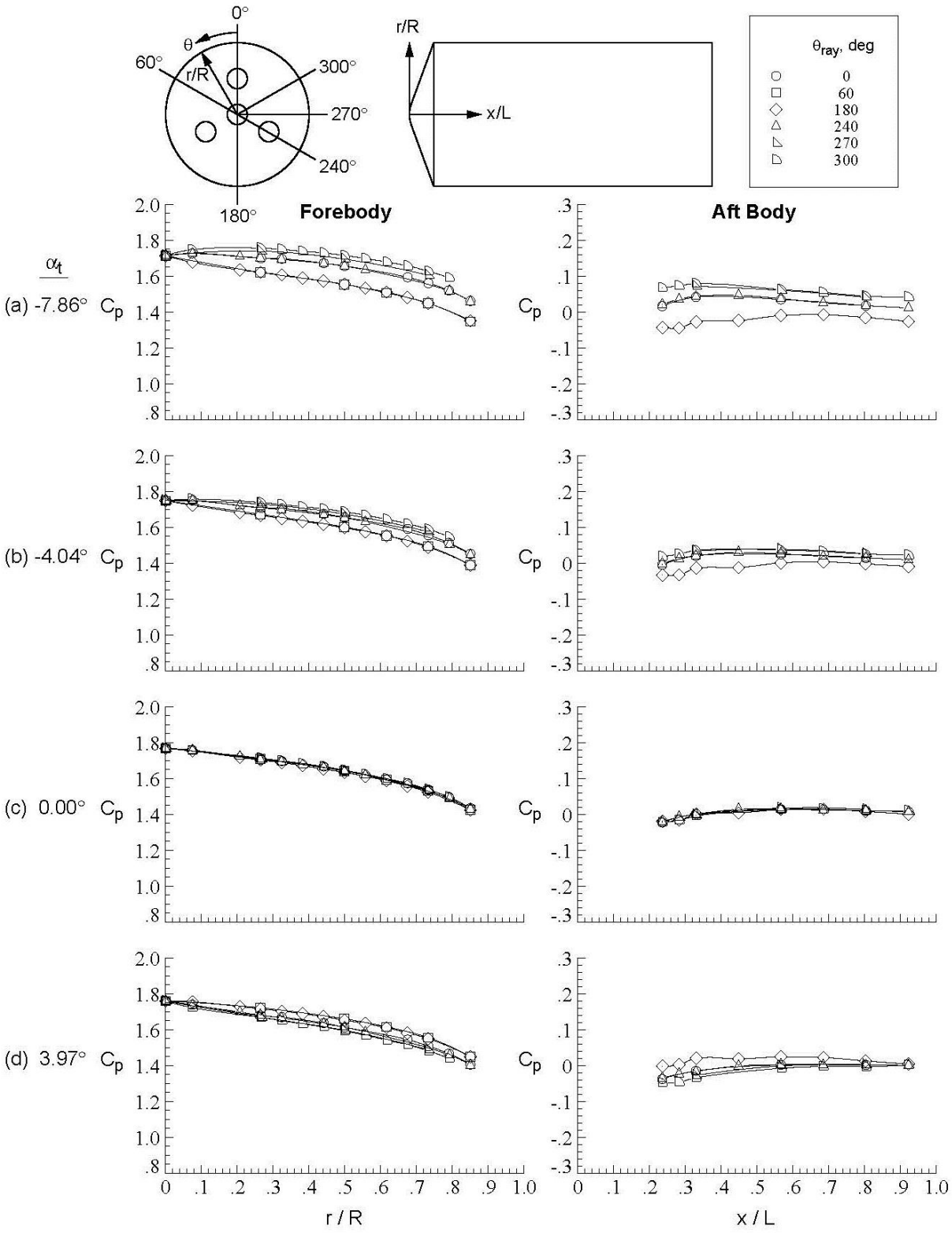

Figure D-42. Baseline configuration, Run 055, M_∞ = 3.5, Re_∞ = 1.0x10^6/ft, ϕ = 59.98°, X_S = 40.17 in, Y_S = 0.00 in, C_T = 0.00.

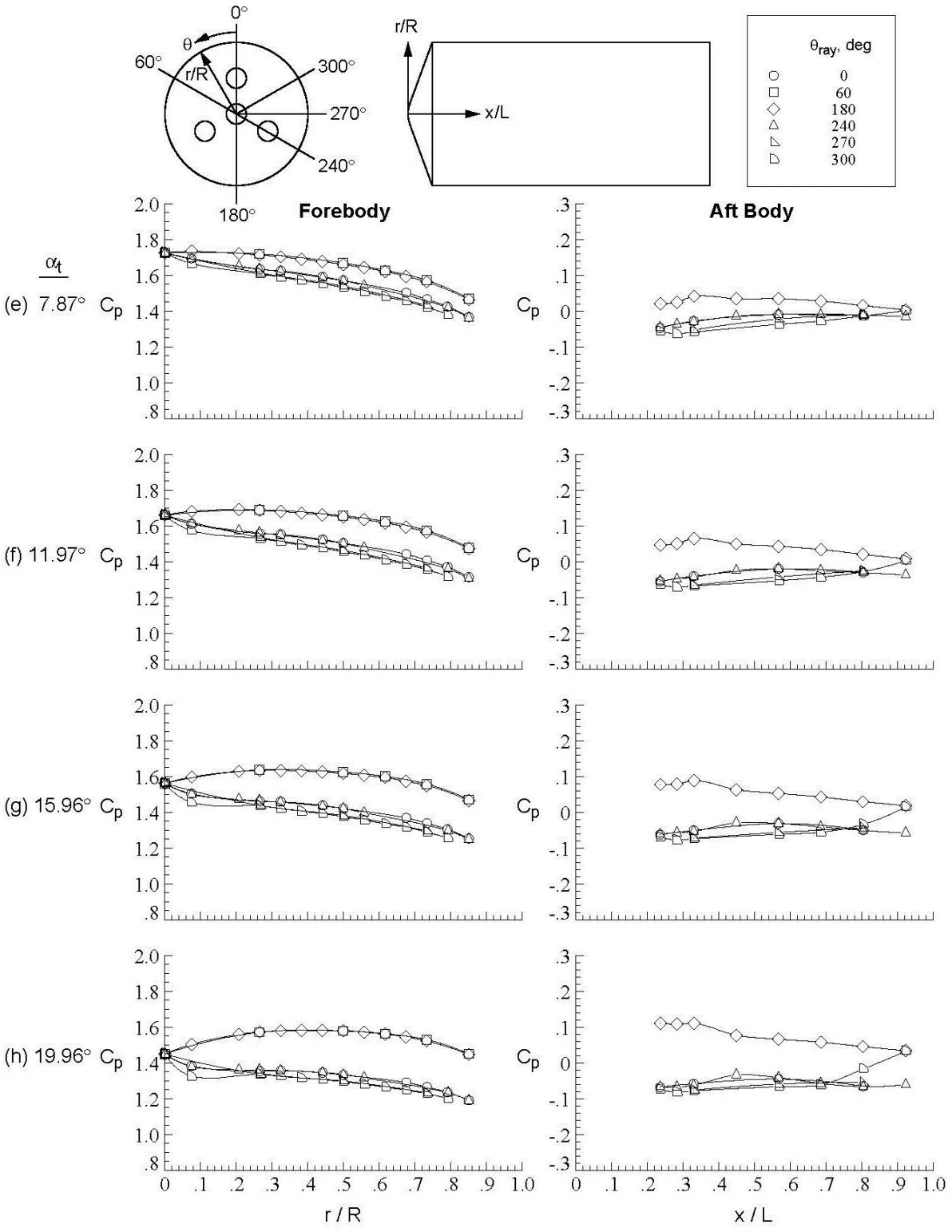

Figure D-42. Concluded.

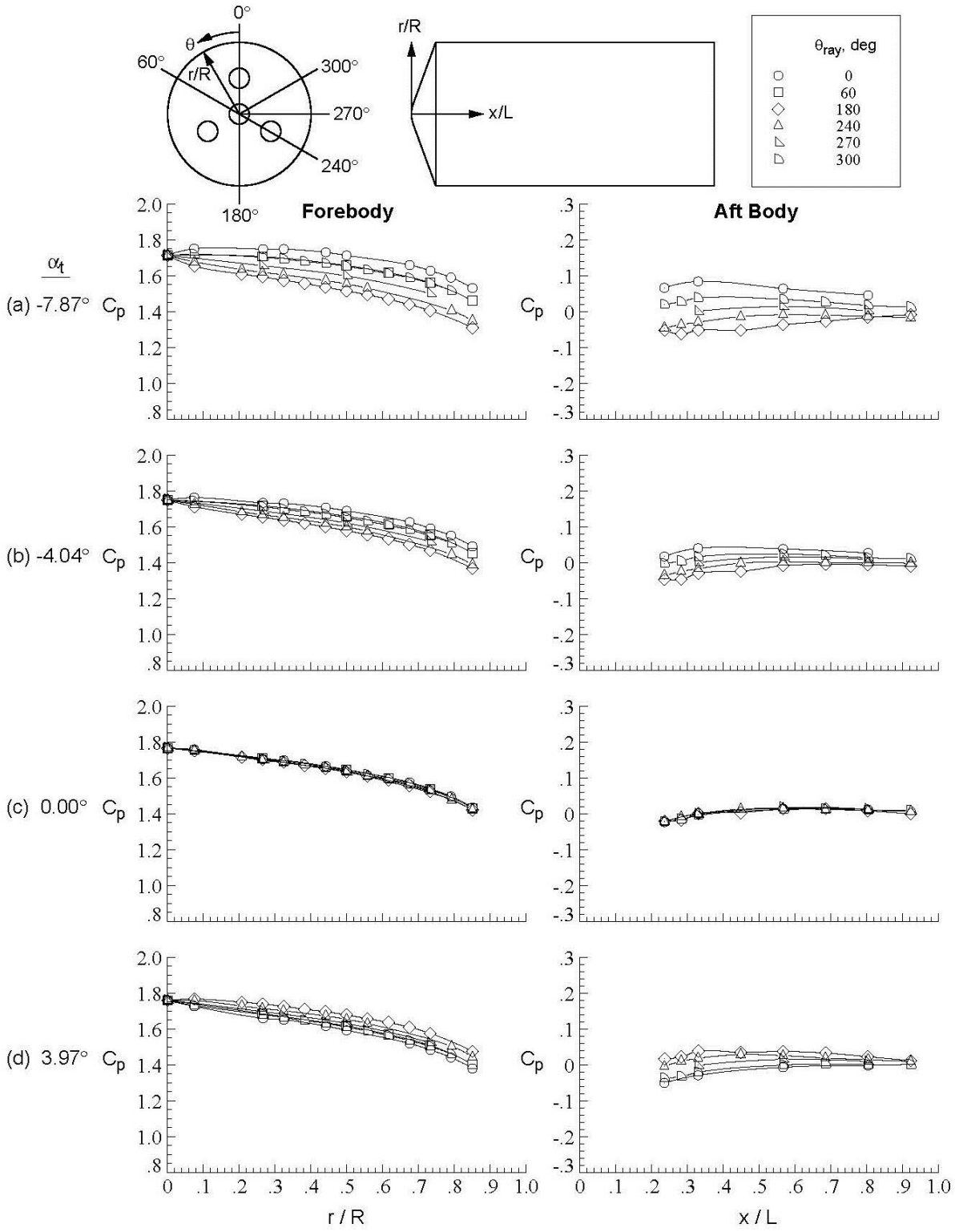

Figure D-43. Baseline configuration, Run 056, M_∞ = 3.5, Re_∞ = 1.0x10^6/ft, ϕ = −0.07°, X_S = 40.17 in, Y_S = 0.00 in, C_T = 0.00.

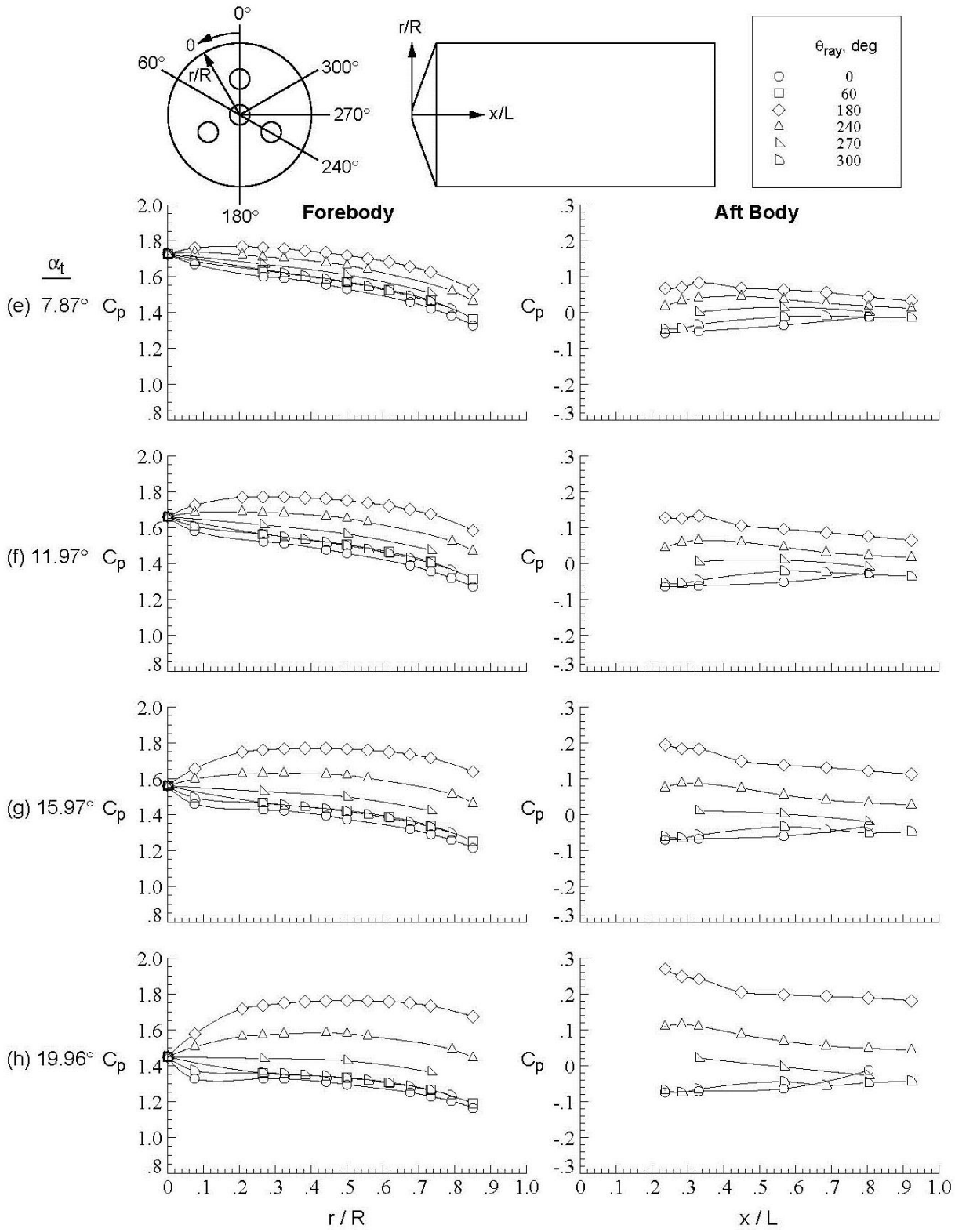

Figure D-43. Concluded.

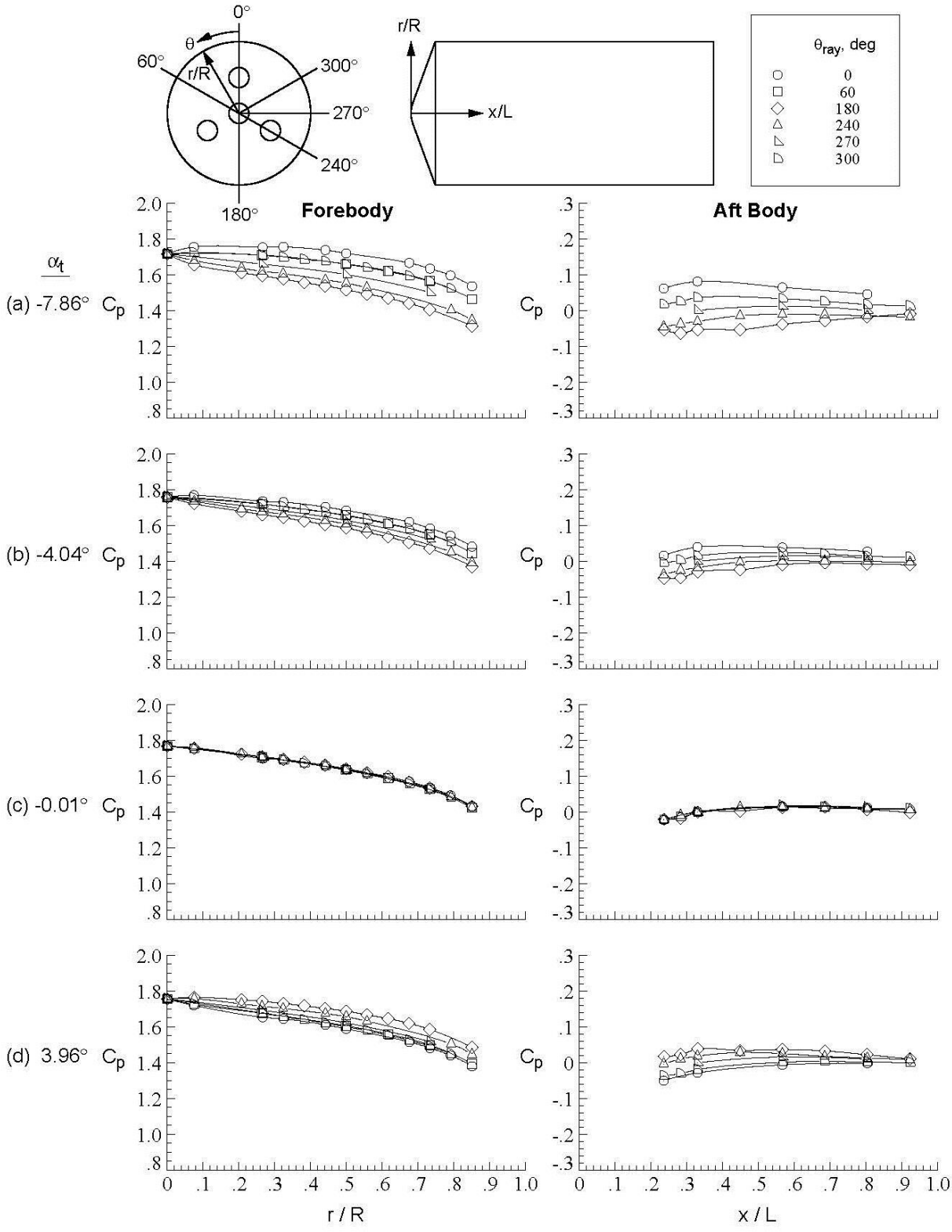

Figure D-44. Baseline configuration, Run 057, M_∞ = 3.5, Re_∞ = 1.0x10^7/ft, ϕ = −0.07°, X_S = 25.16 in, Y_S = 0.00 in, C_T = 0.00.

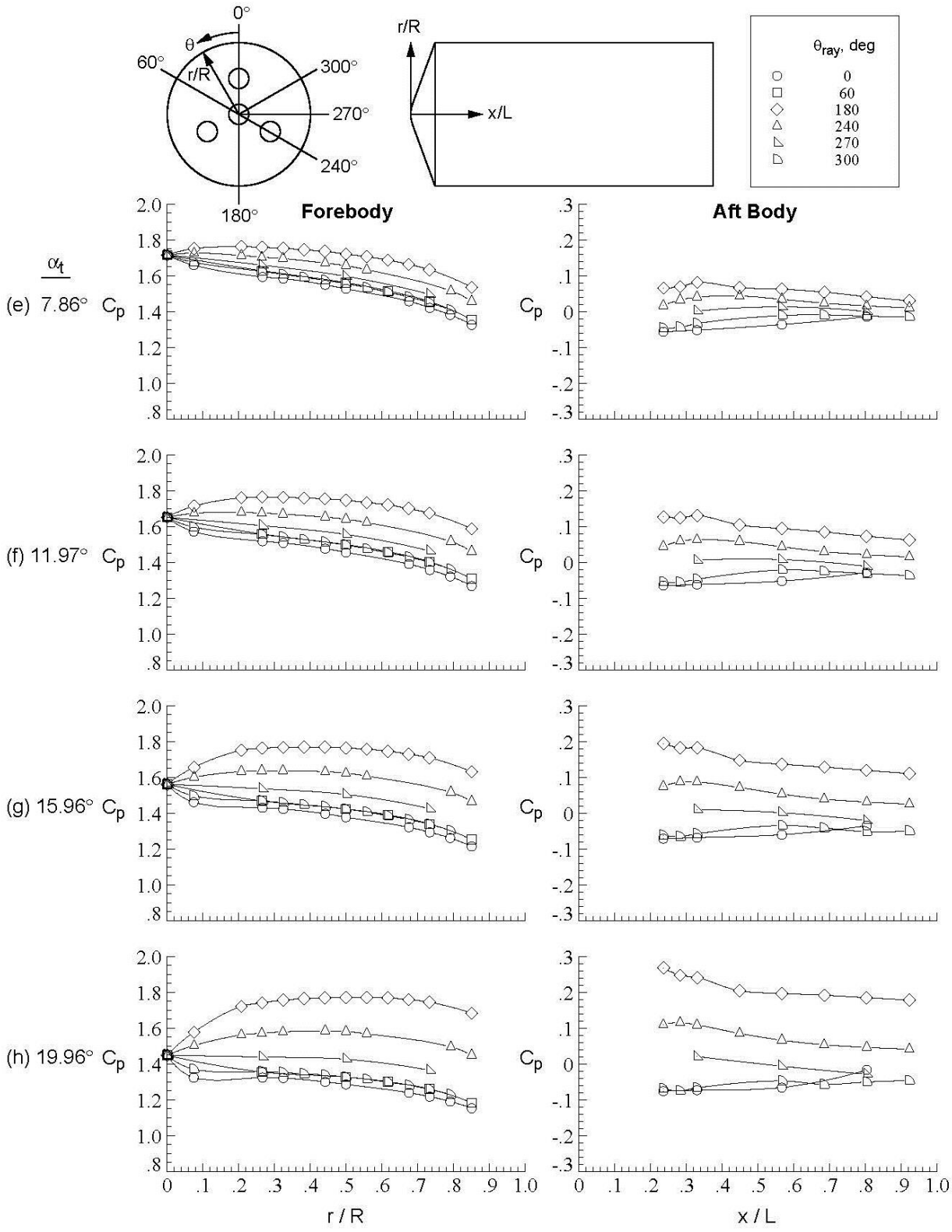

Figure D-44. Concluded.

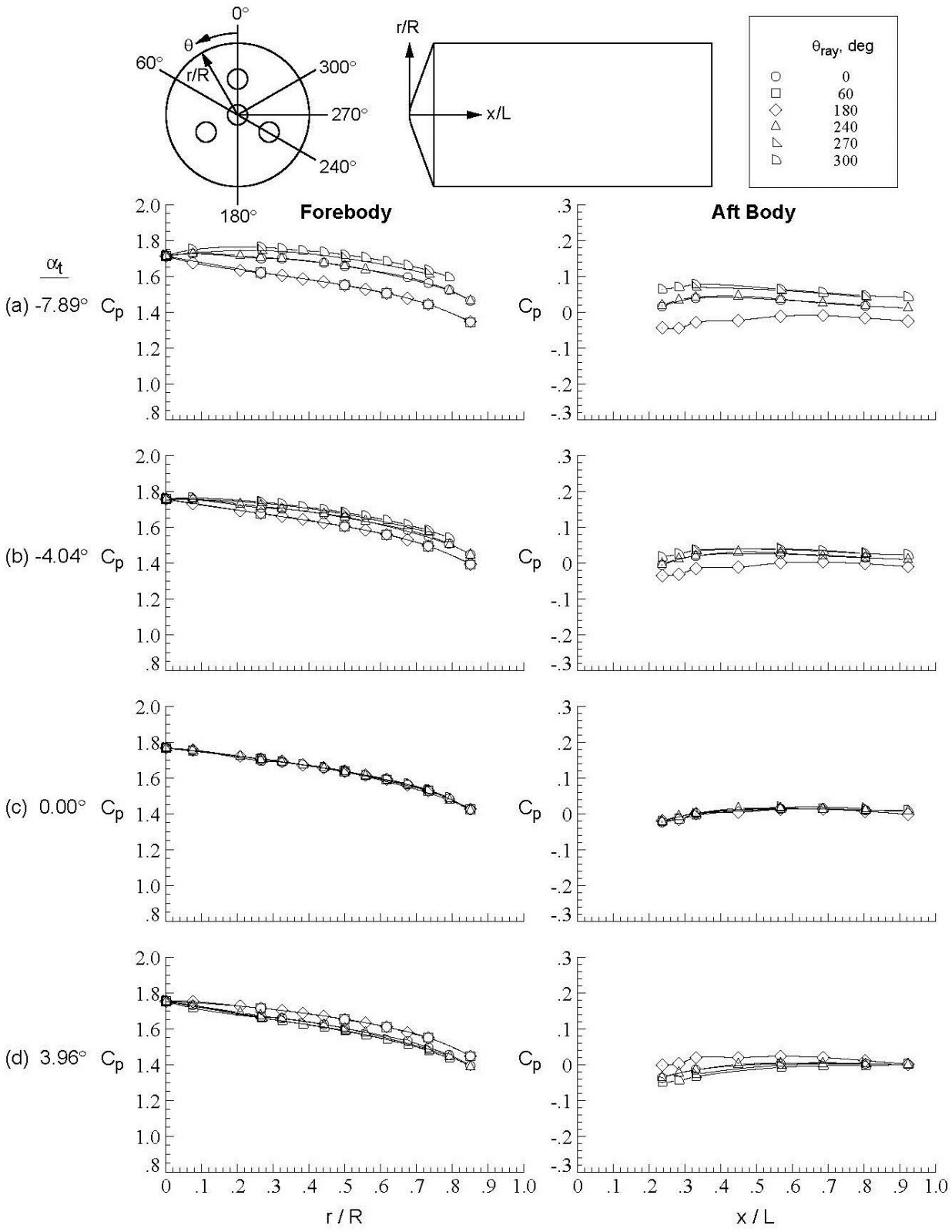

Figure D-45. Baseline configuration, Run 058, M_∞ = 3.5, Re_∞ = 1.0x10^7/ft, ϕ = 59.98°, X_S = 25.16 in, Y_S = 0.00 in, C_T = 0.00.

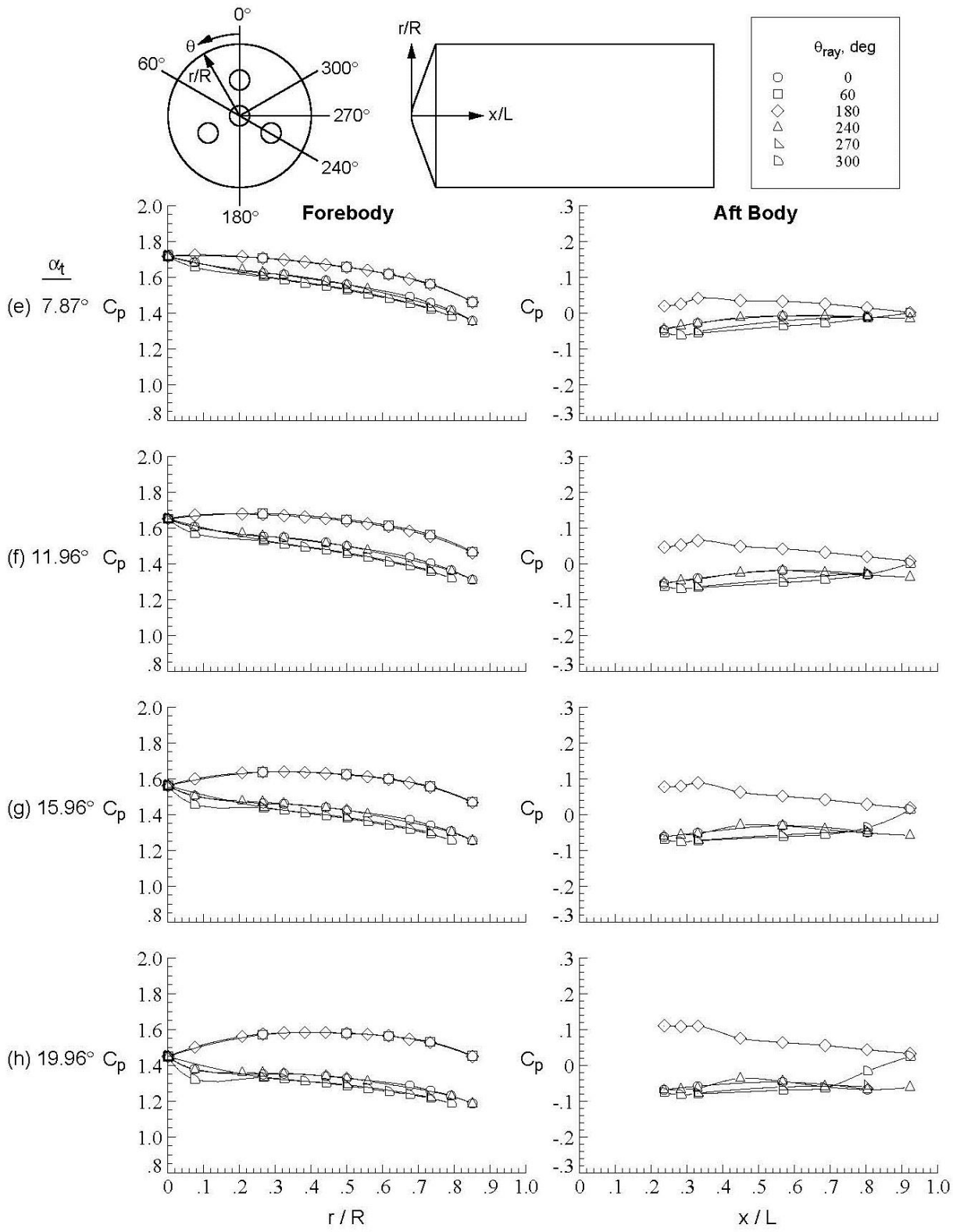

Figure D-45. Concluded.

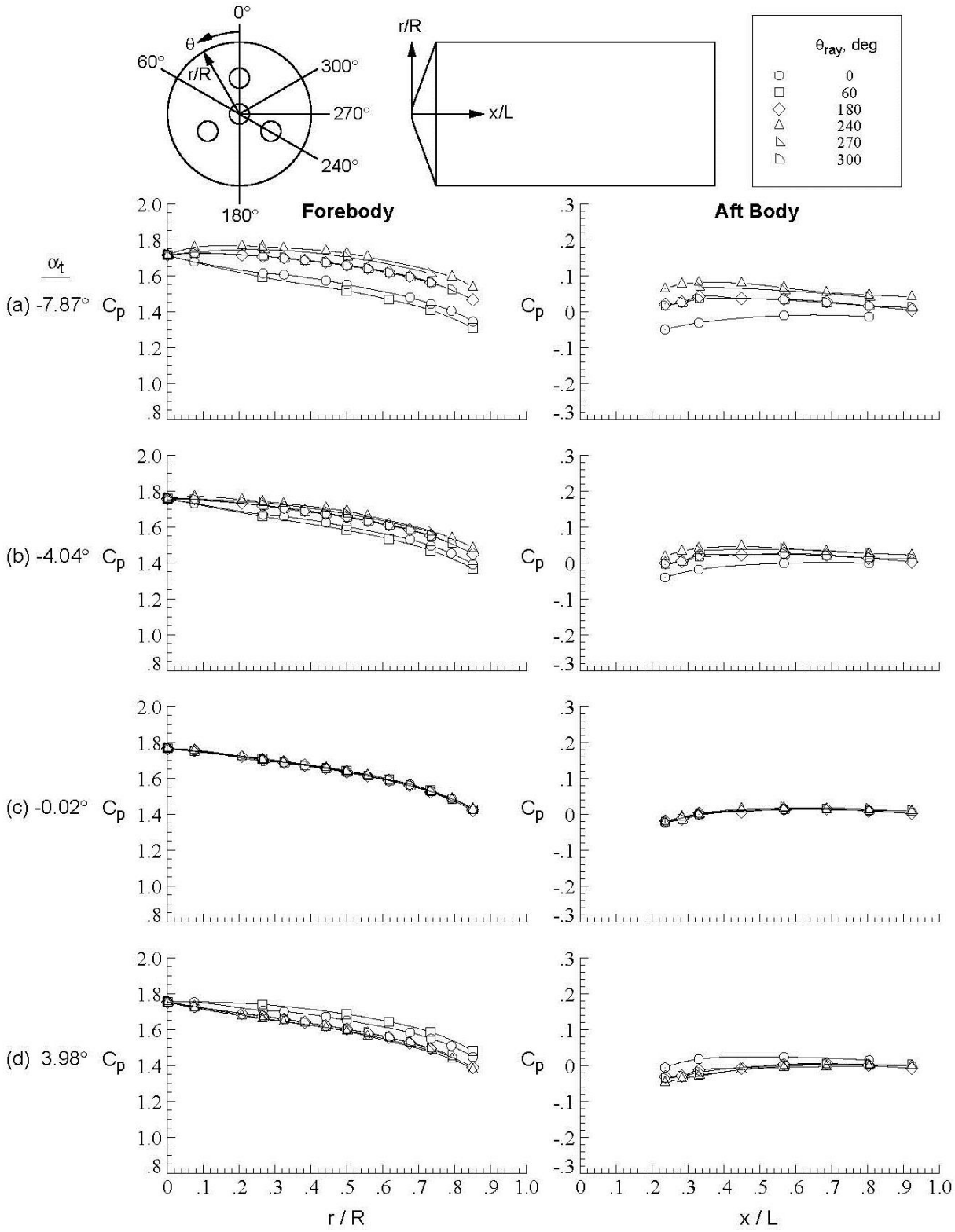

Figure D-46. Baseline configuration, Run 059, M_∞ = 3.5, Re_∞ = 1.0x10^7/ft, ϕ = 120.12°, X_S = 25.16 in, Y_S = 0.00 in, C_T = 0.00.

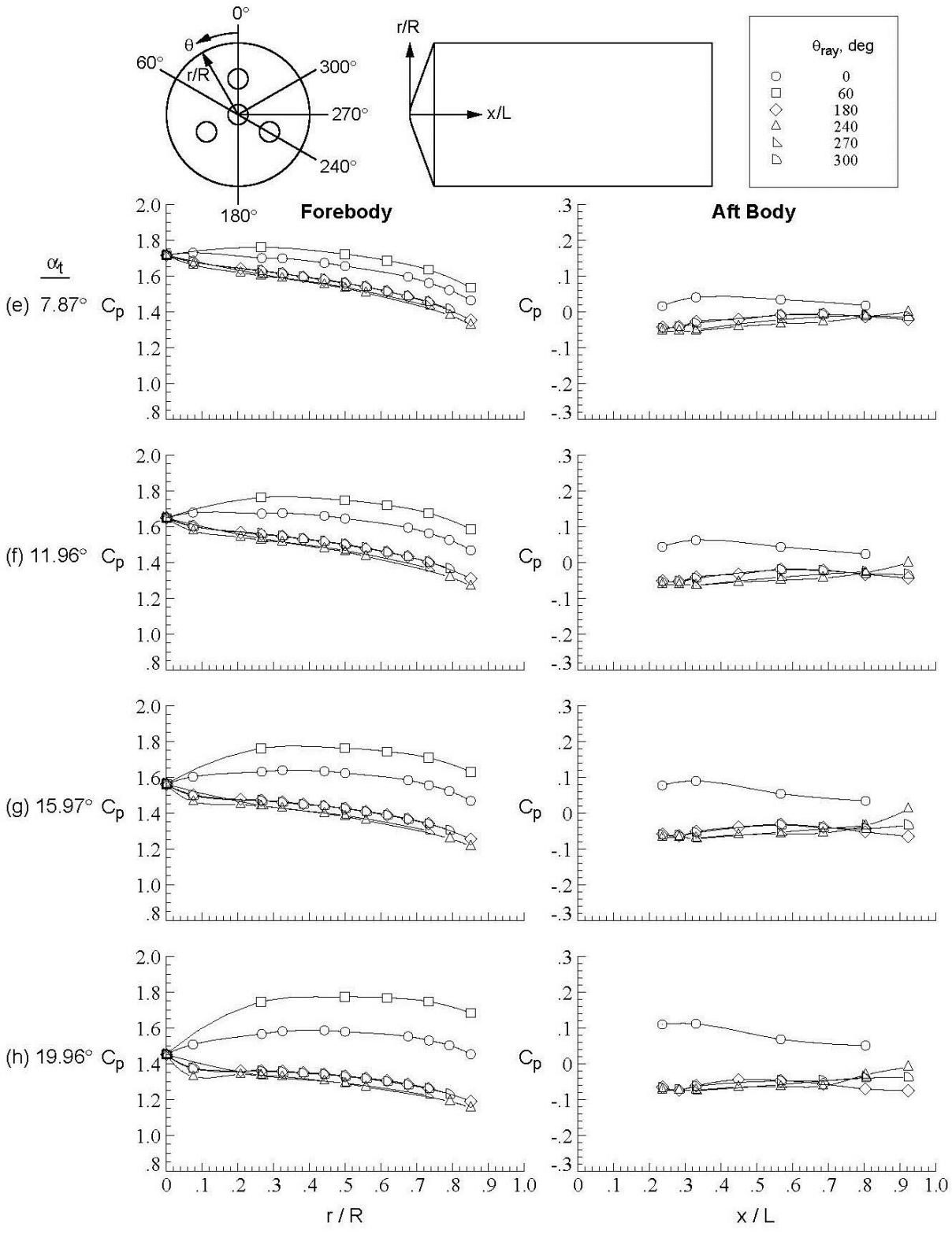

Figure D-46. Concluded.

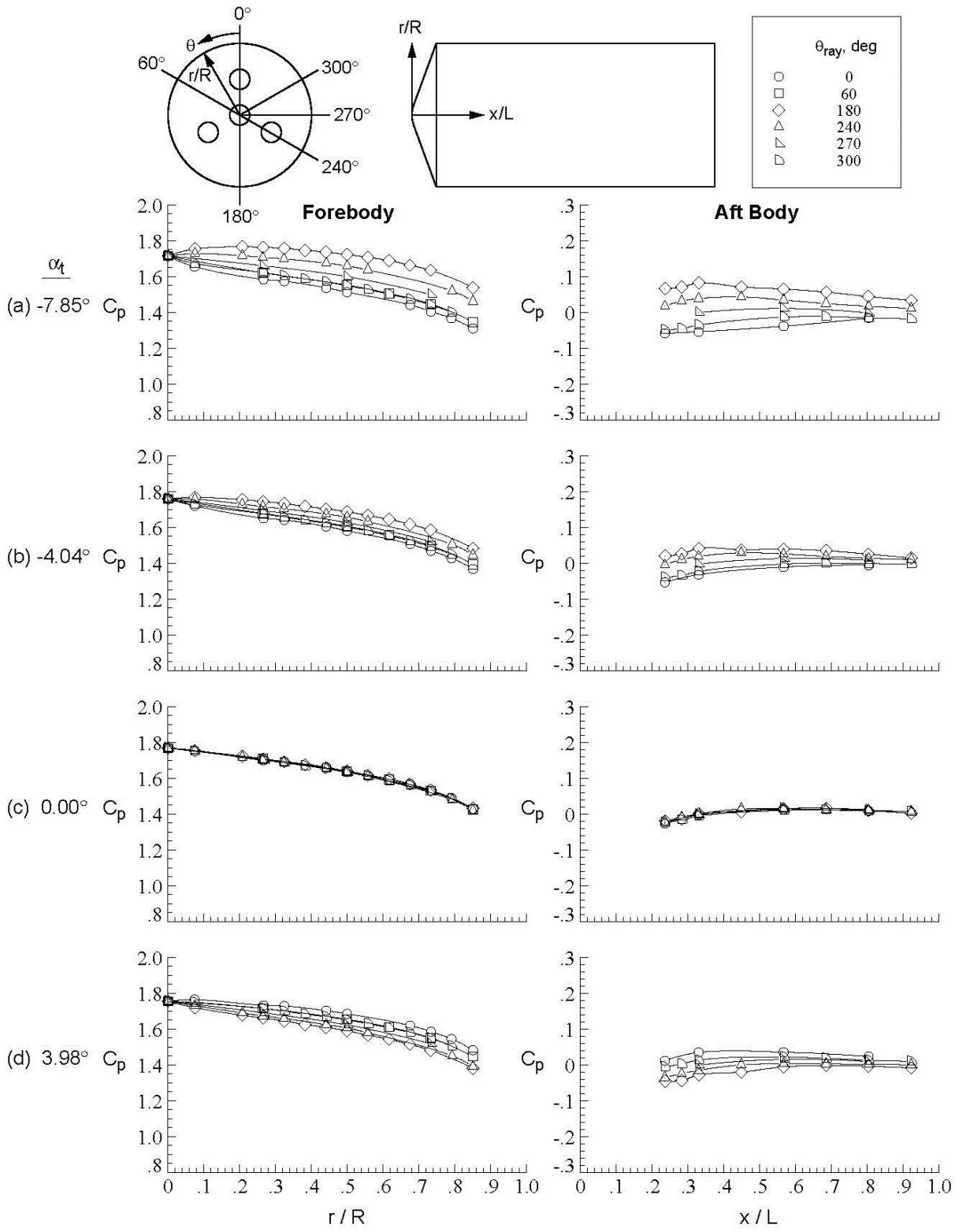

Figure D-47. Baseline configuration, Run 060, M_∞ = 3.5, Re_∞ = 1.0x10^6/ft, ϕ = 179.95°, X_S = 25.16 in, Y_S = 0.00 in, C_T = 0.00.

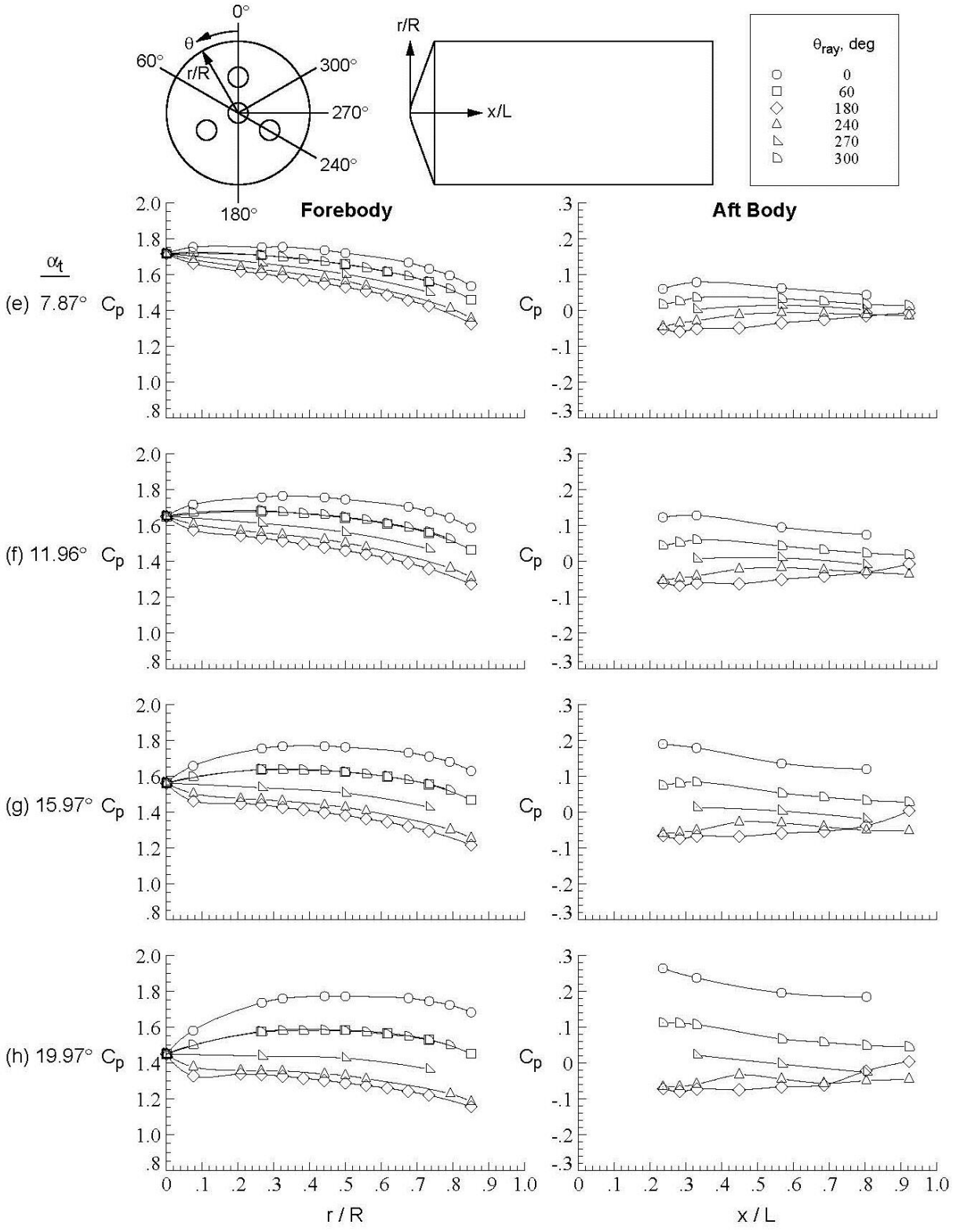

Figure D-47. Concluded.

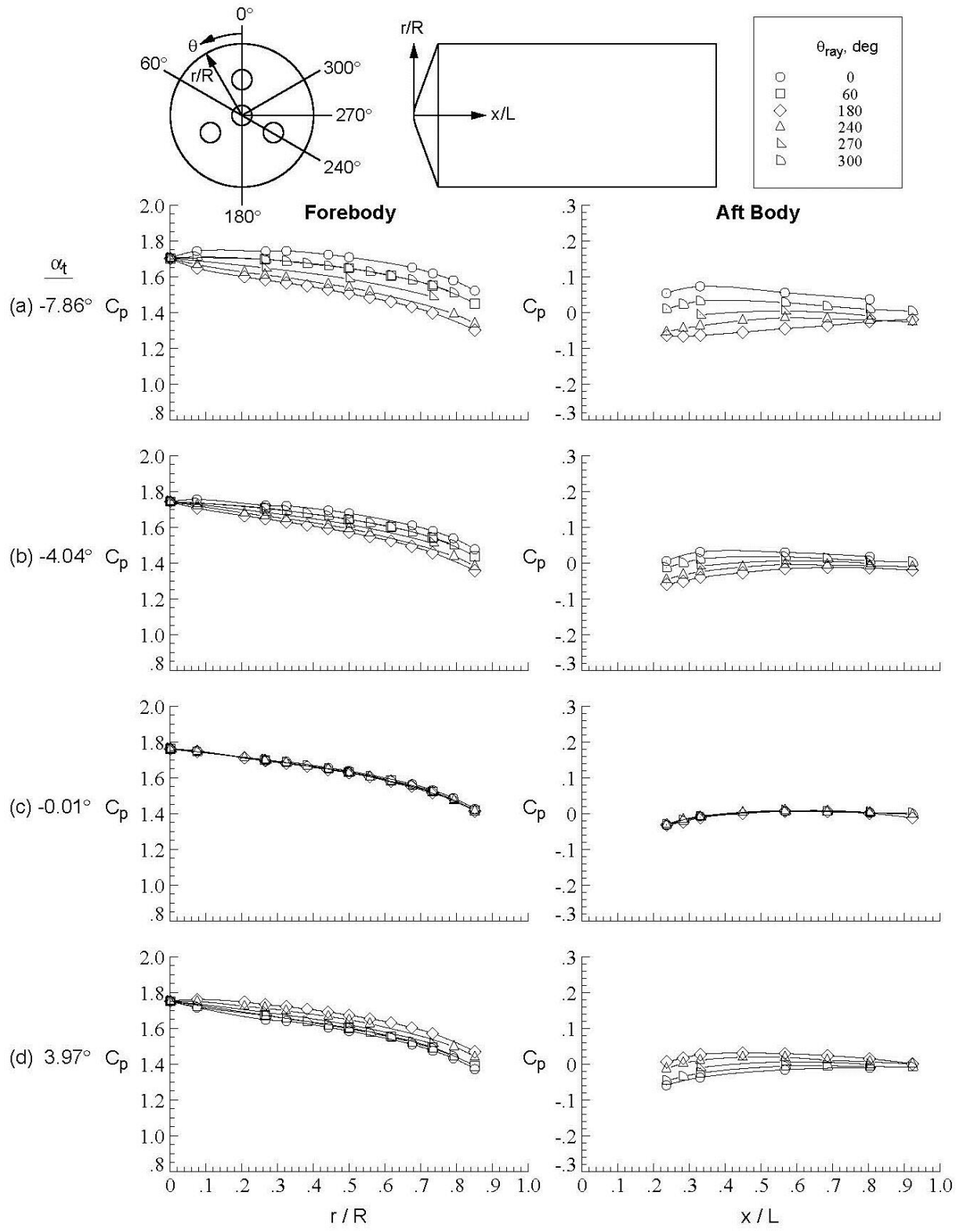

Figure D-48. Baseline configuration, Run 065, M_∞ = 3.5, Re_∞ = 1.0x10^7/ft, ϕ = −0.01°, X_S = 25.16 in, Y_S = −8.00 in, C_T = 0.00.

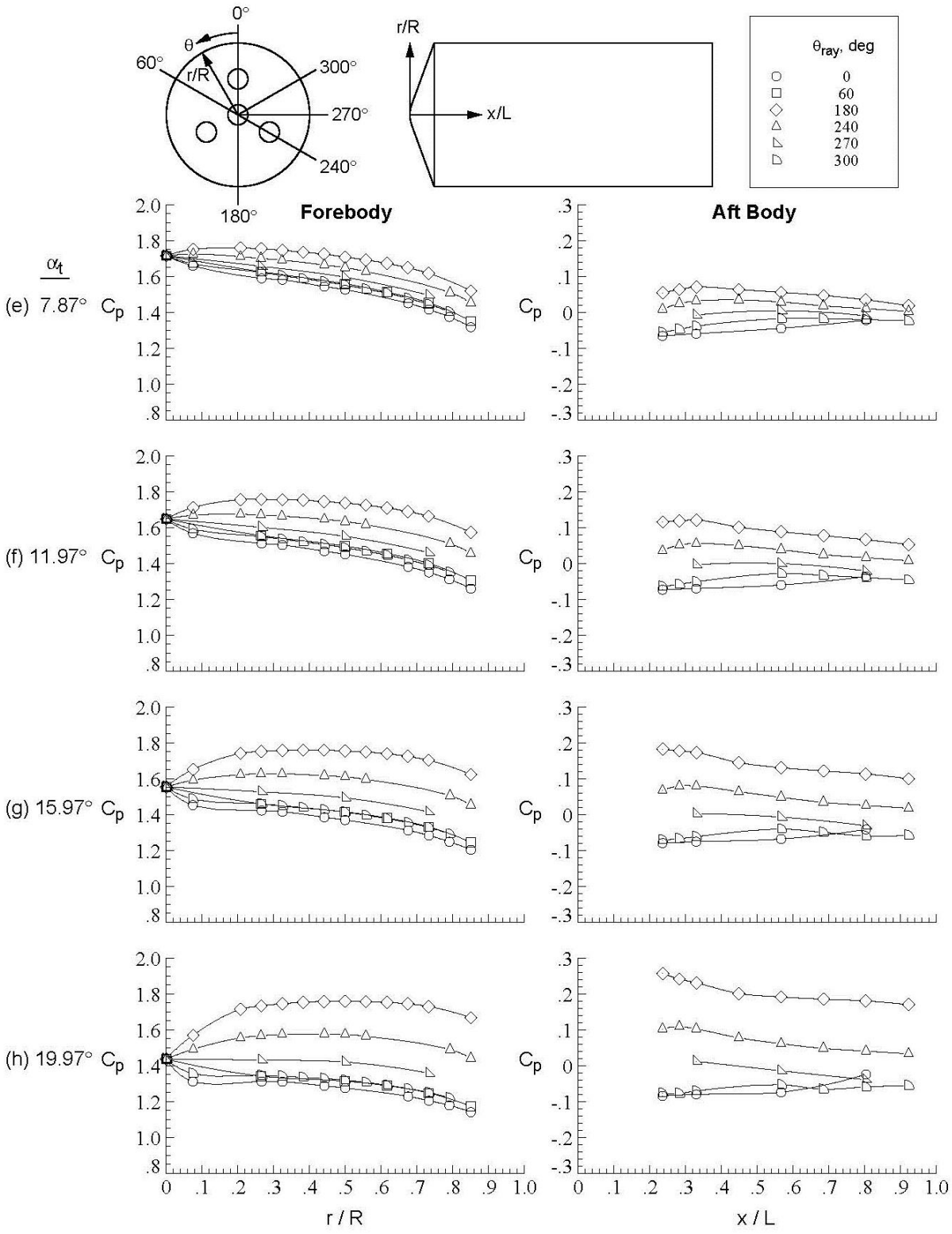

Figure D-48. Concluded.

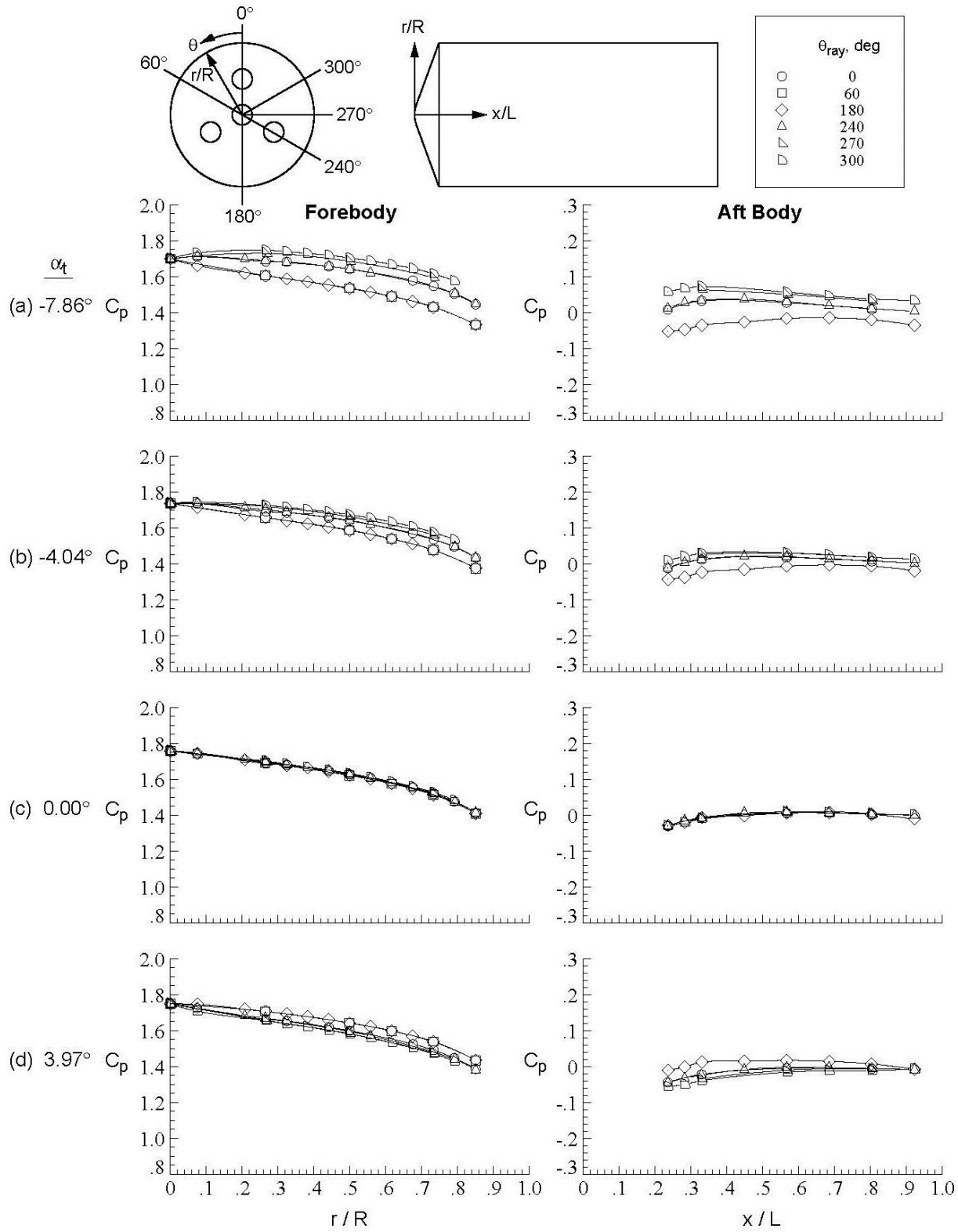

Figure D-49. Baseline configuration, Run 067, M_∞ = 3.5, Re_∞ = 1.0x10^7/ft, ϕ = 60.00°, X_S = 25.16 in, Y_S = –8.00 in, C_T = 0.00.

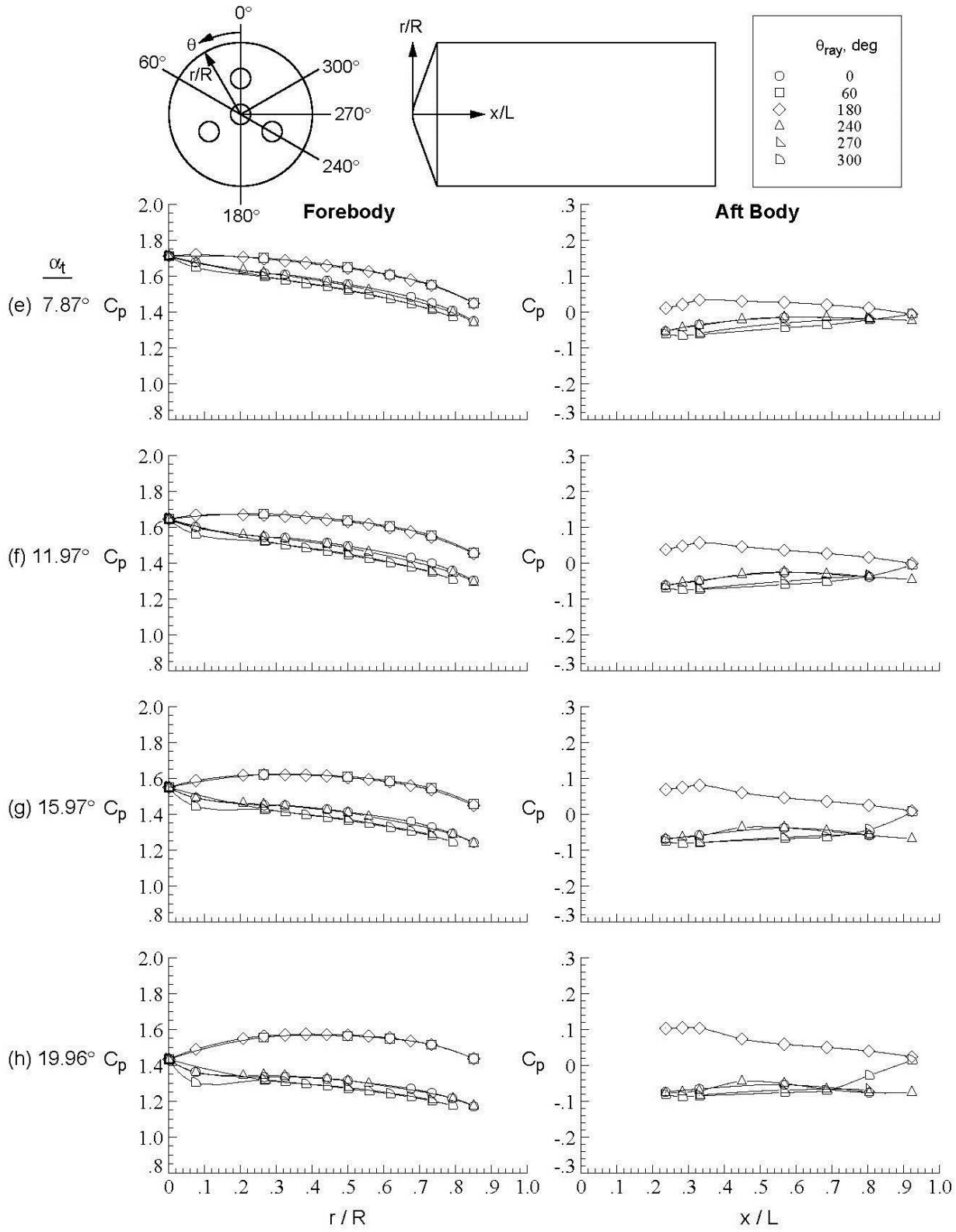

Figure D-49. Concluded.

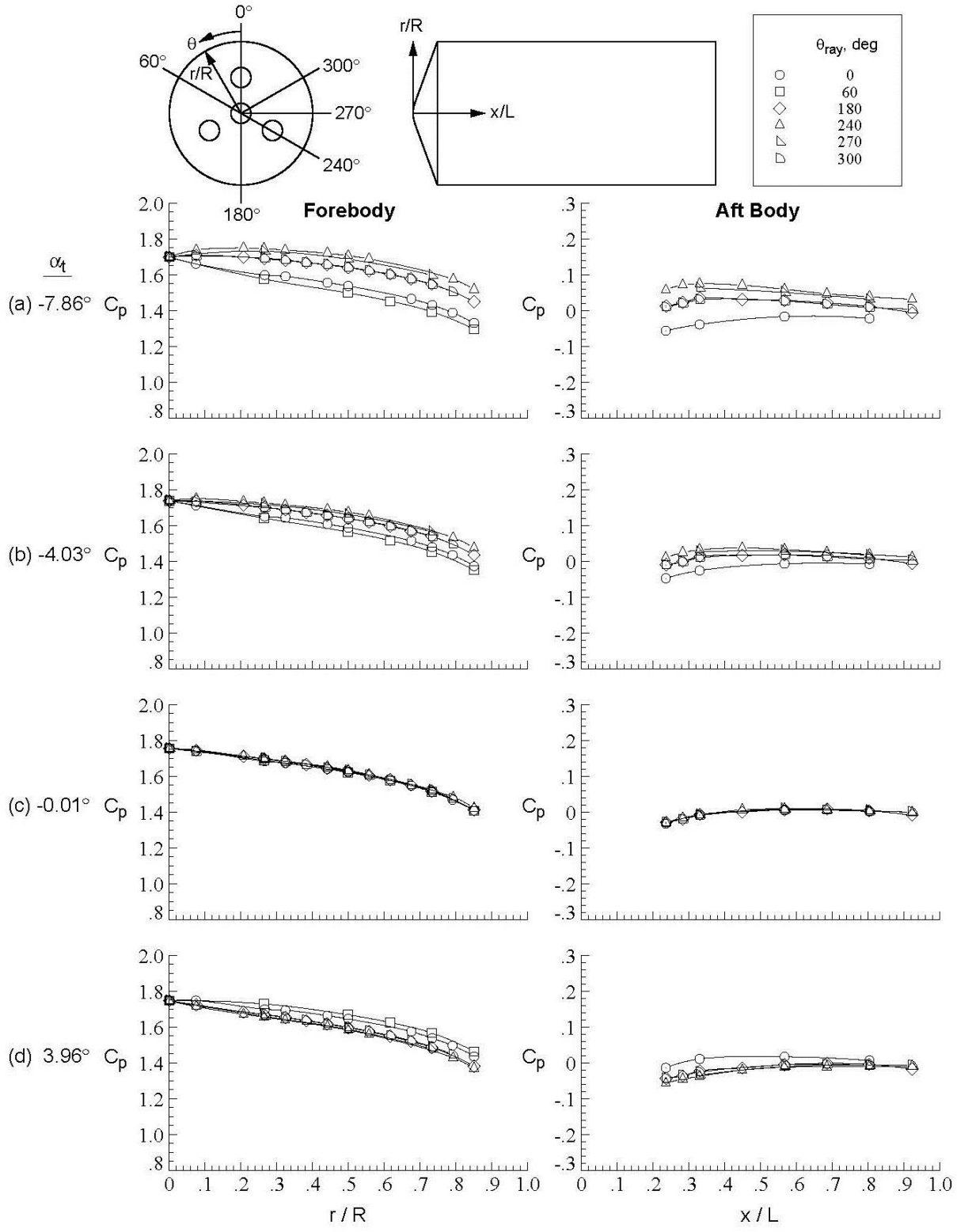

Figure D-50. Baseline configuration, Run 068, M_∞ = 3.5, Re_∞ = 1.0x10^6/ft, ϕ = 120.02°, X_S = 25.16 in, Y_S = –8.00 in, C_T = 0.00.

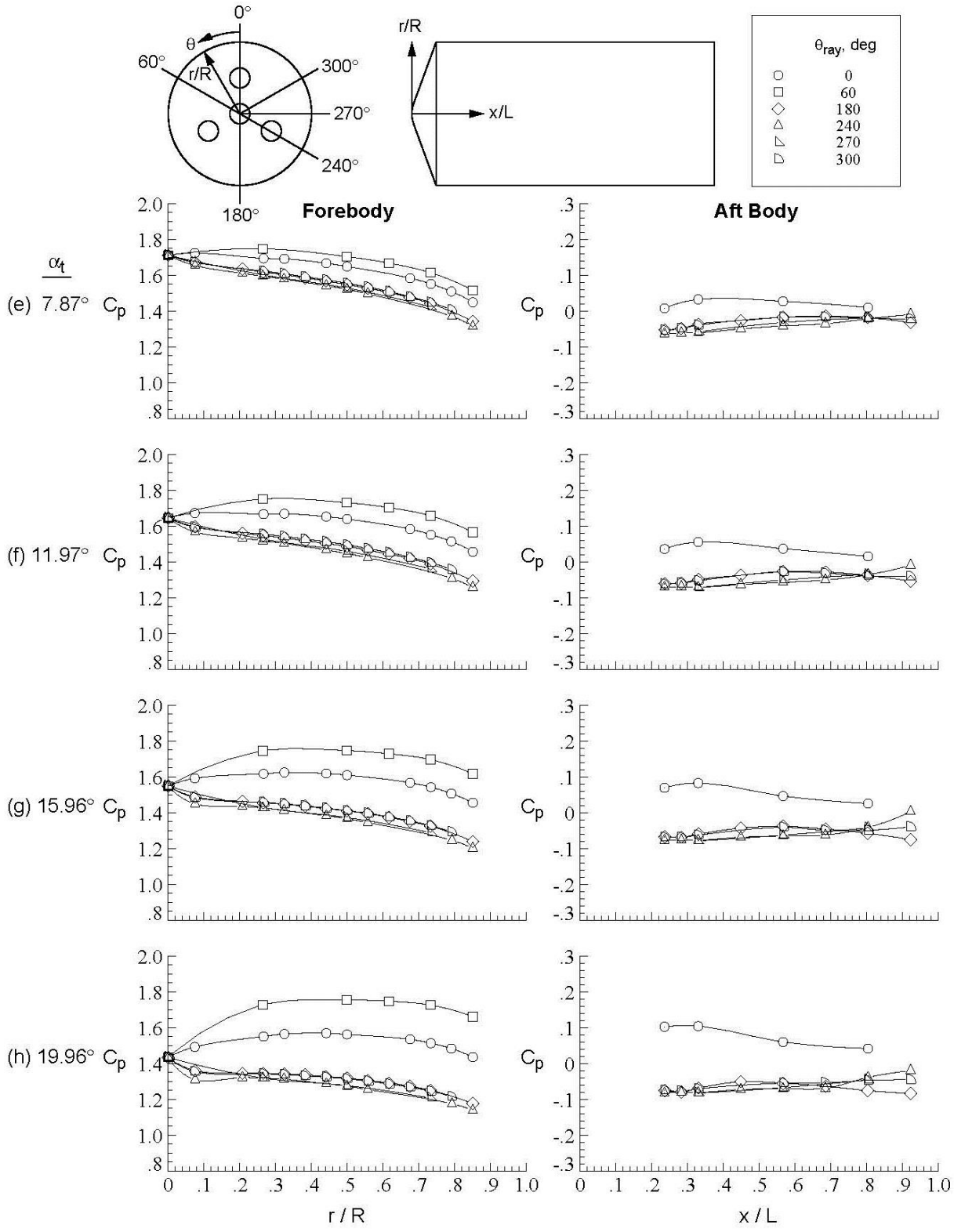

Figure D-50. Concluded.

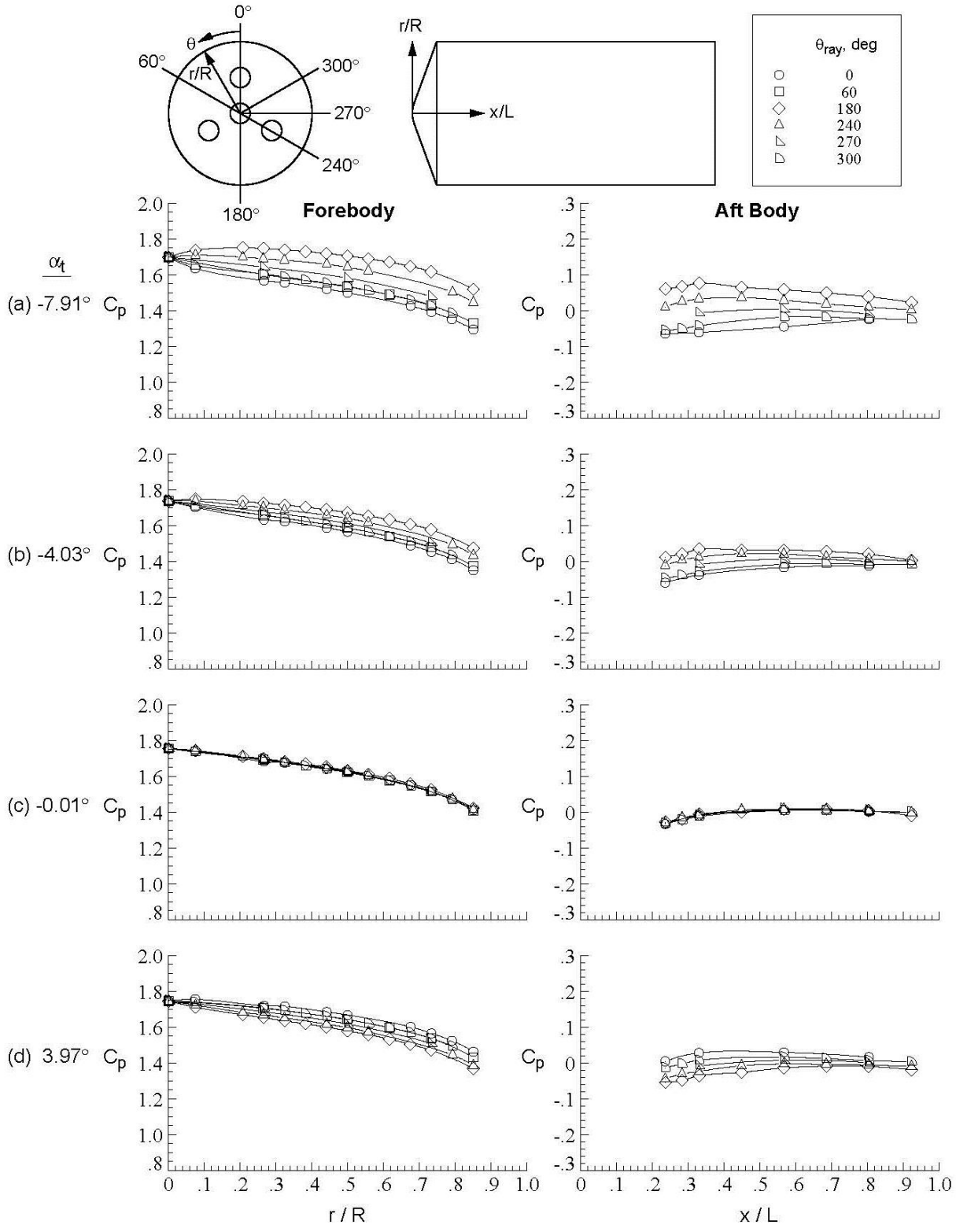

Figure D-51. Baseline configuration, Run 069, M_∞ = 3.5, Re_∞ = 1.0x10^7/ft, ϕ = 179.95°, X_S = 25.16 in, Y_S = –8.00 in, C_T = 0.00.

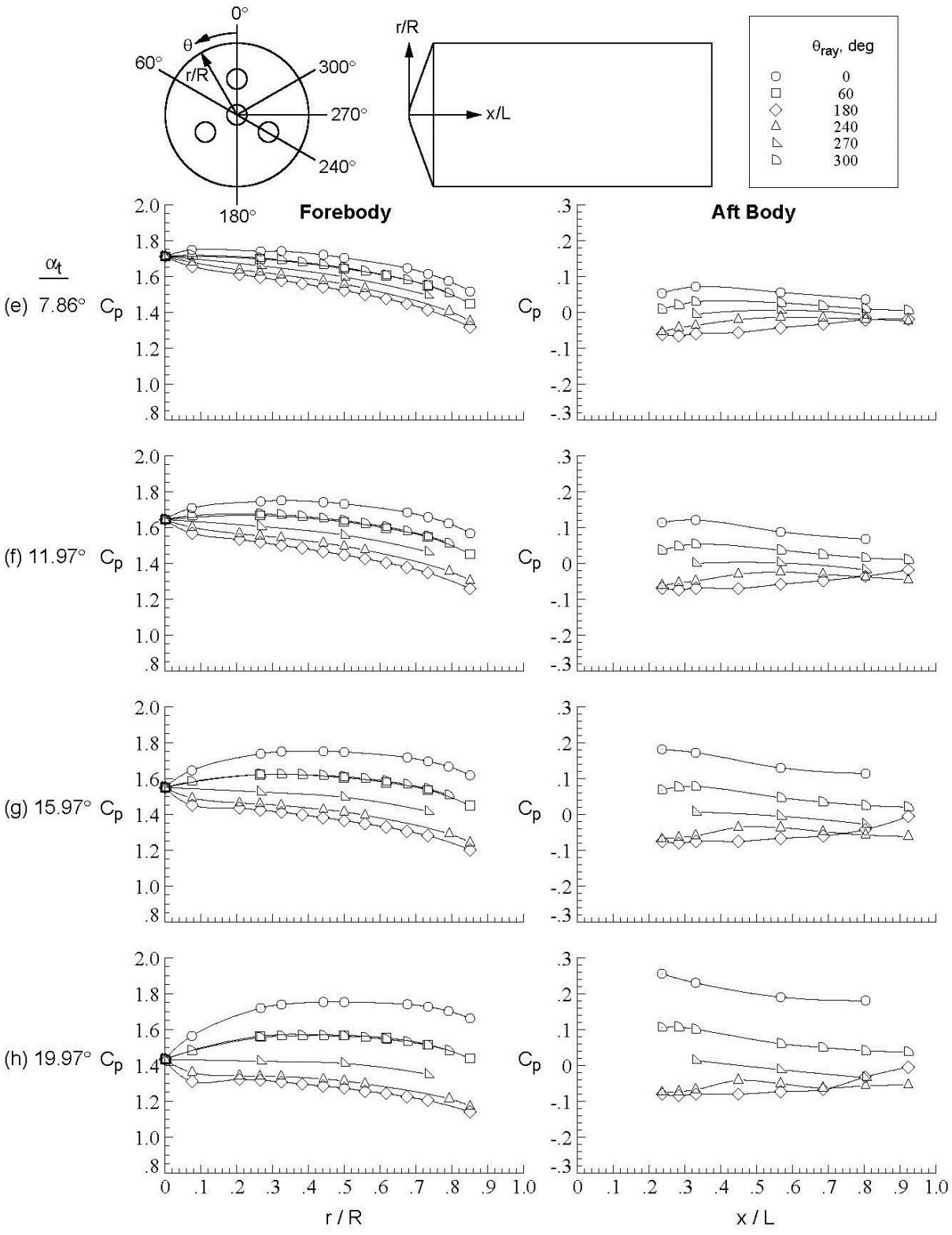

Figure D-51. Concluded.

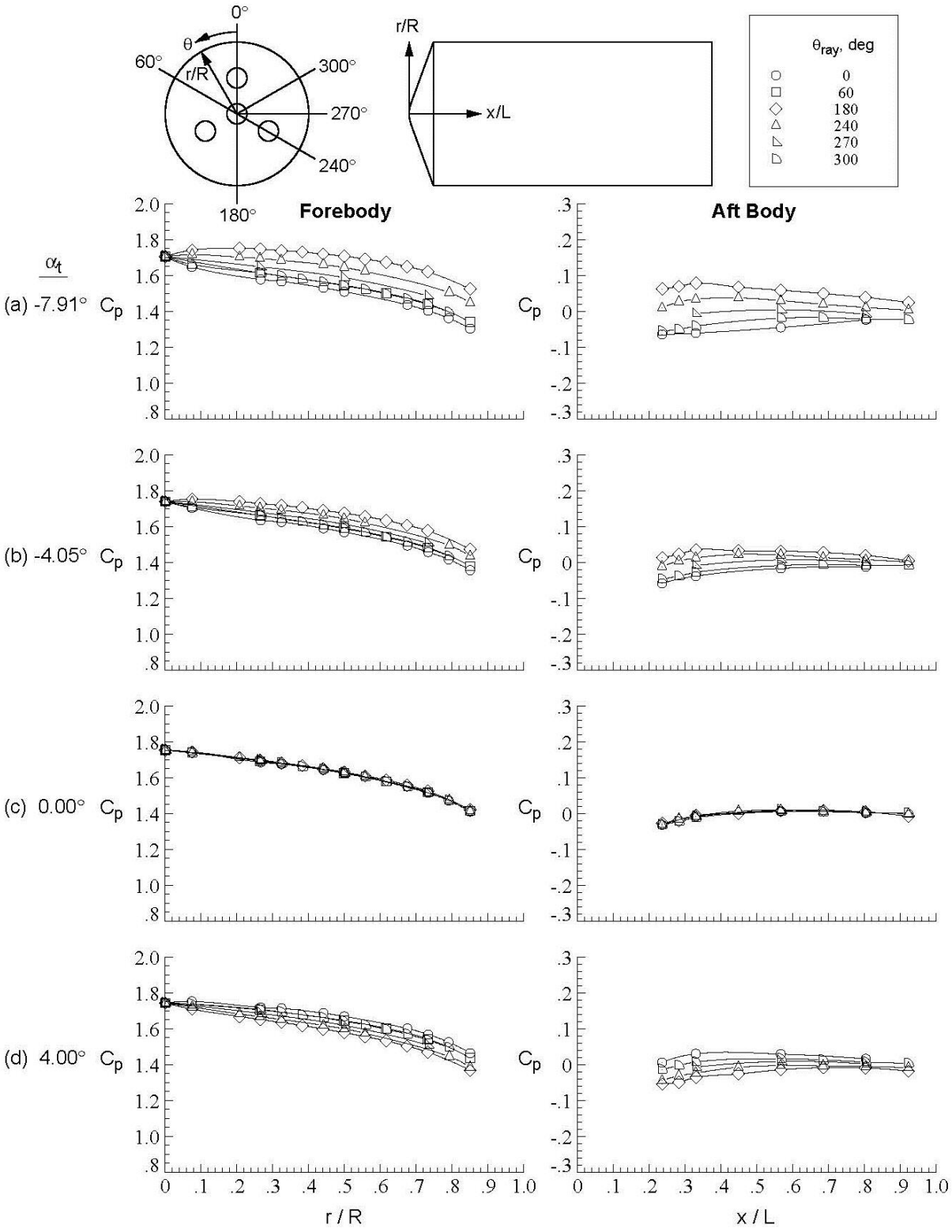

Figure D-52. Baseline configuration, Run 070, M_∞ = 3.5, Re_∞ = 1.0x10^6/ft, ϕ = 179.95°, X_S = 40.16 in, Y_S = –8.00 in, C_T = 0.00.

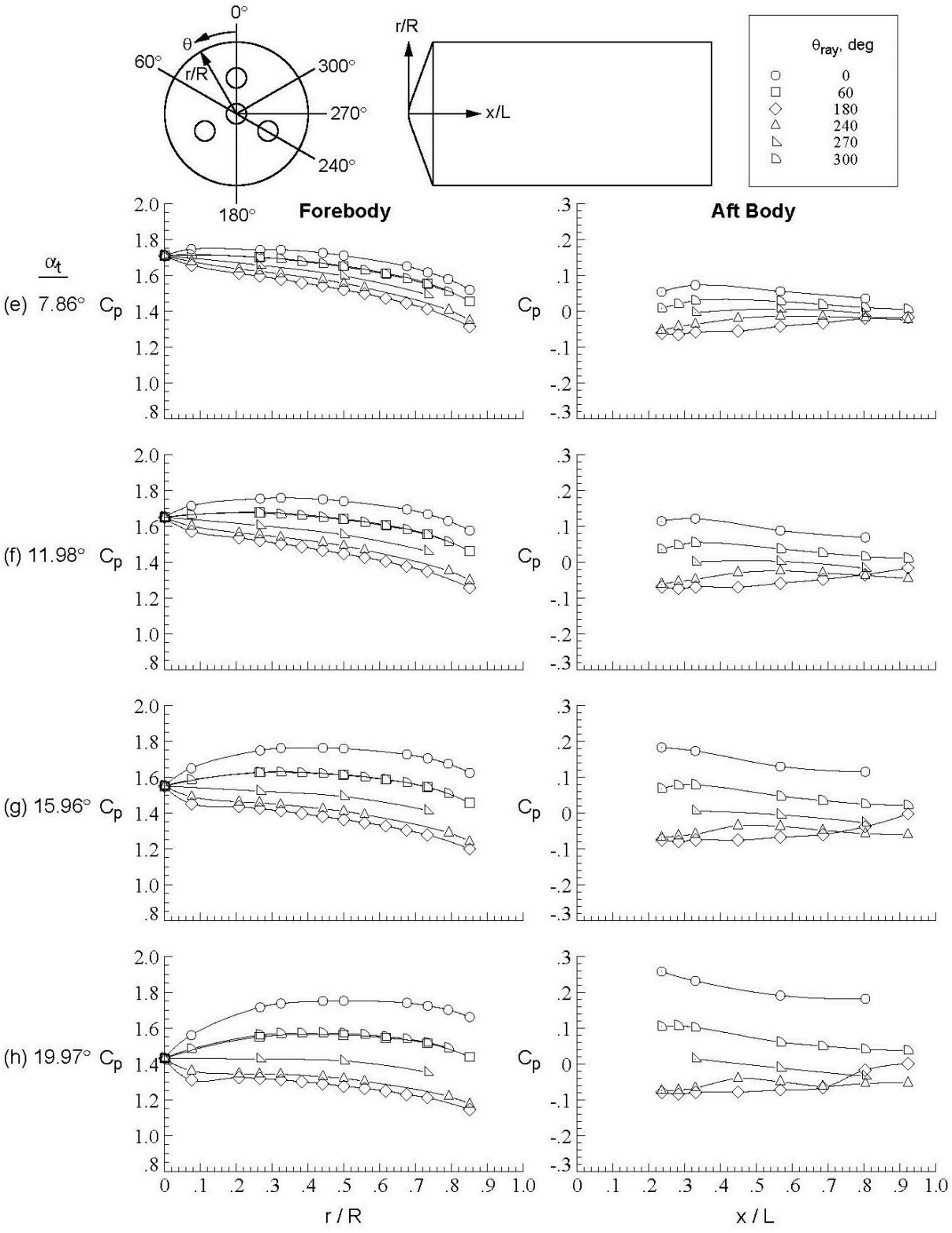

Figure D-52. Concluded.

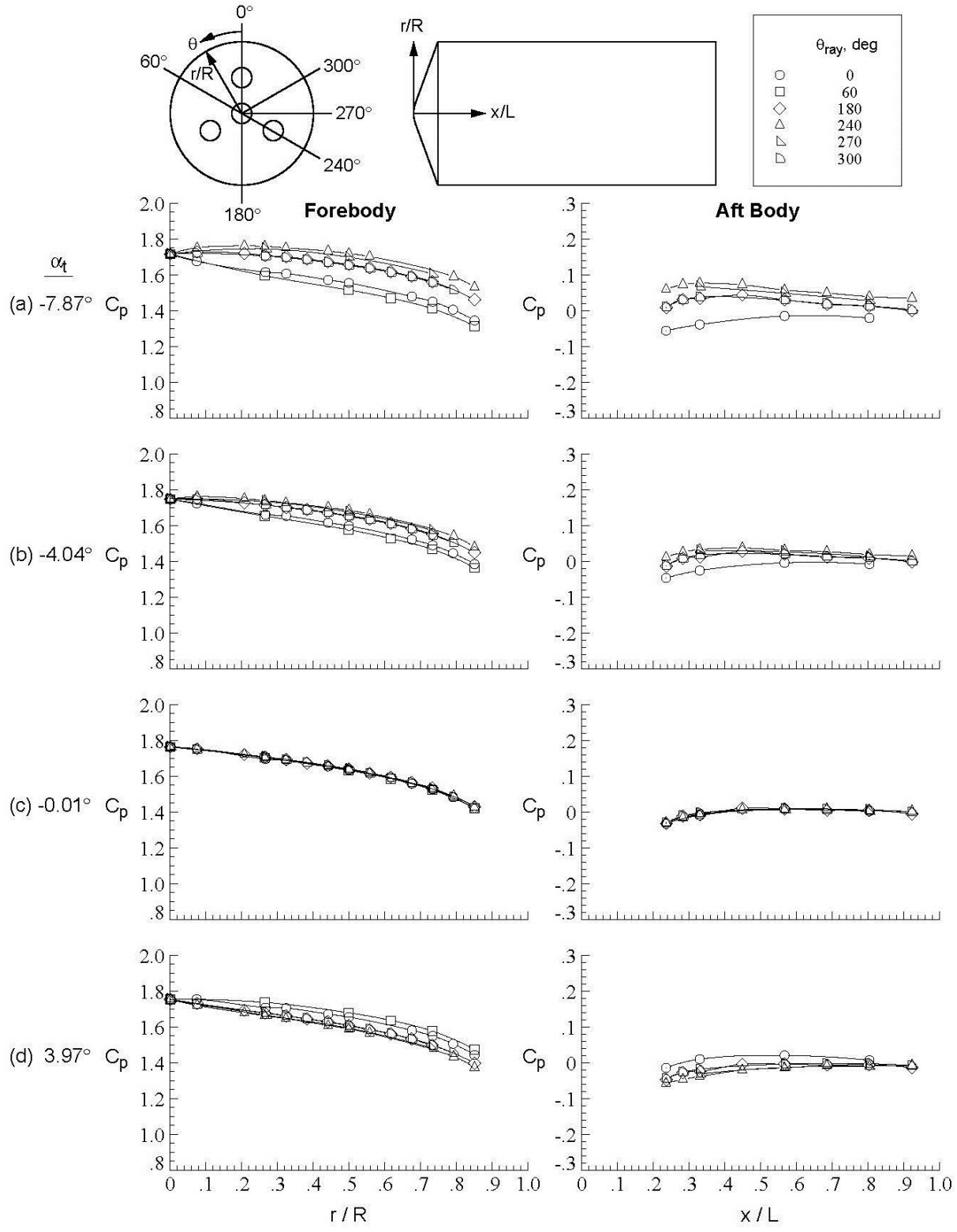

Figure D-53. Baseline configuration, Run 073, M_∞ = 3.5, Re_∞ = 1.0x10^6/ft, ϕ = 119.98°, X_S = 40.18 in, Y_S = –8.00 in, C_T = 0.00.

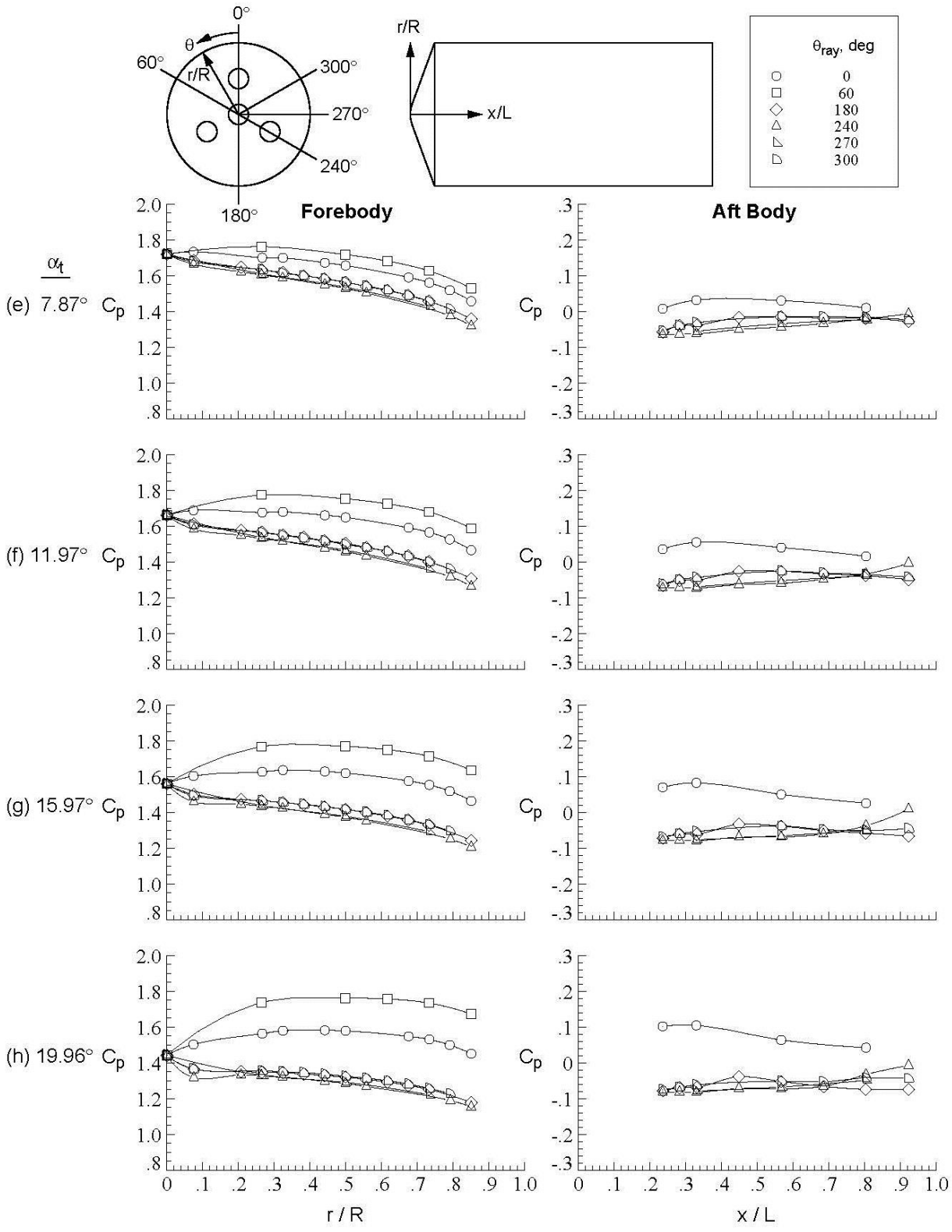

Figure D-53. Concluded.

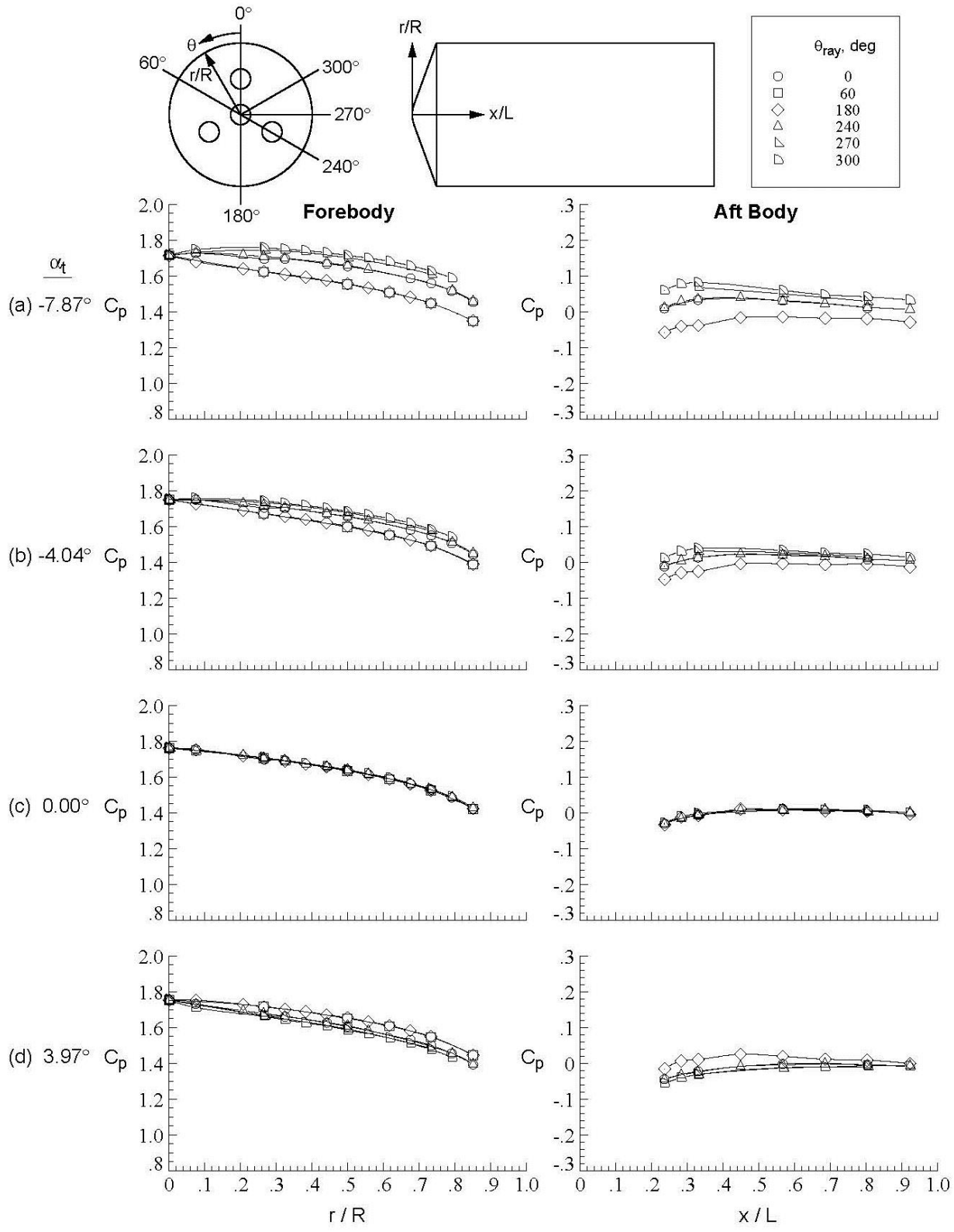

Figure D-54. Baseline configuration, Run 074, M_∞ = 3.5, Re_∞ = 1.0x10^7/ft, ϕ = 59.96°, X_S = 40.18 in, Y_S = –8.00 in, C_T = 0.00.

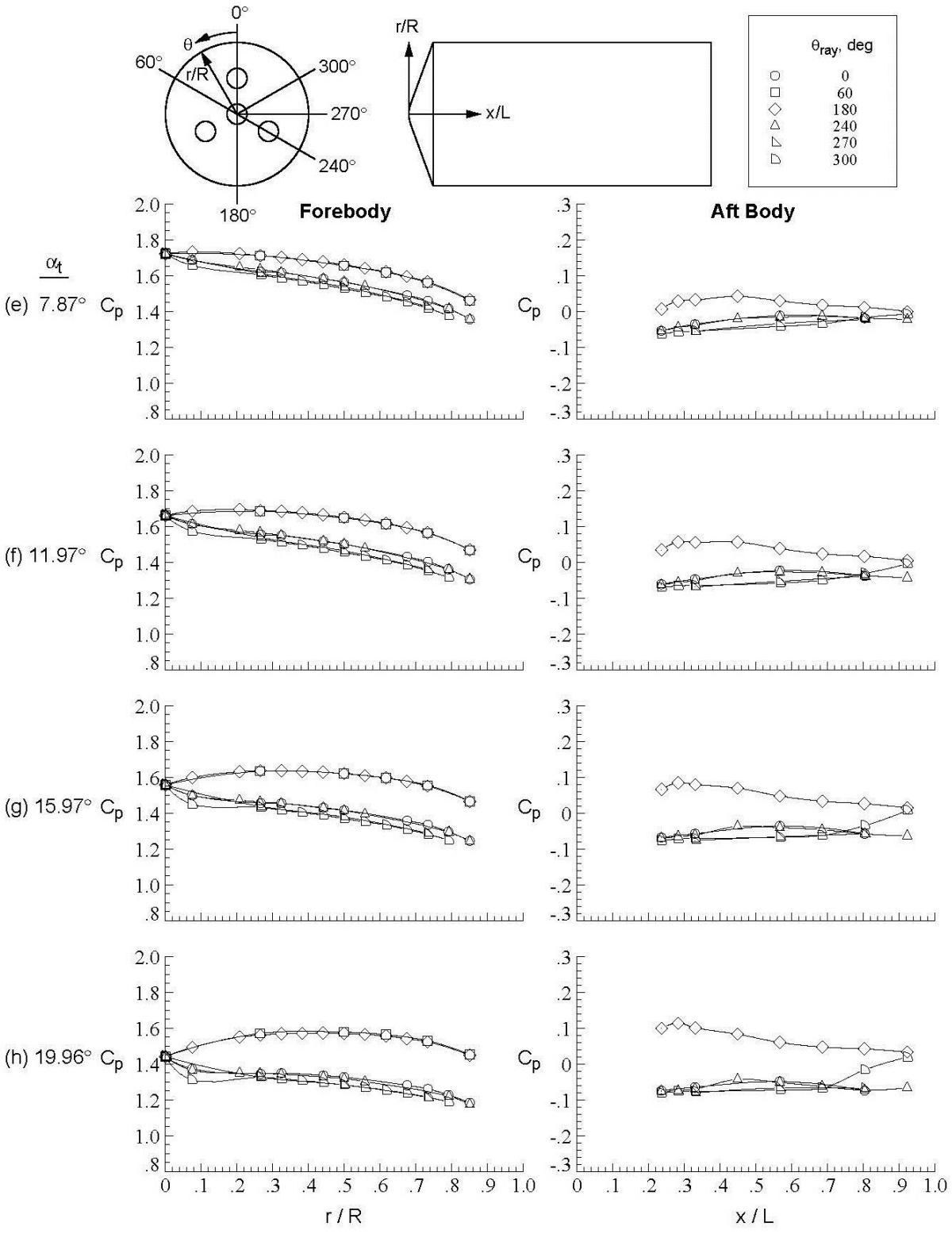

Figure D-54. Concluded.

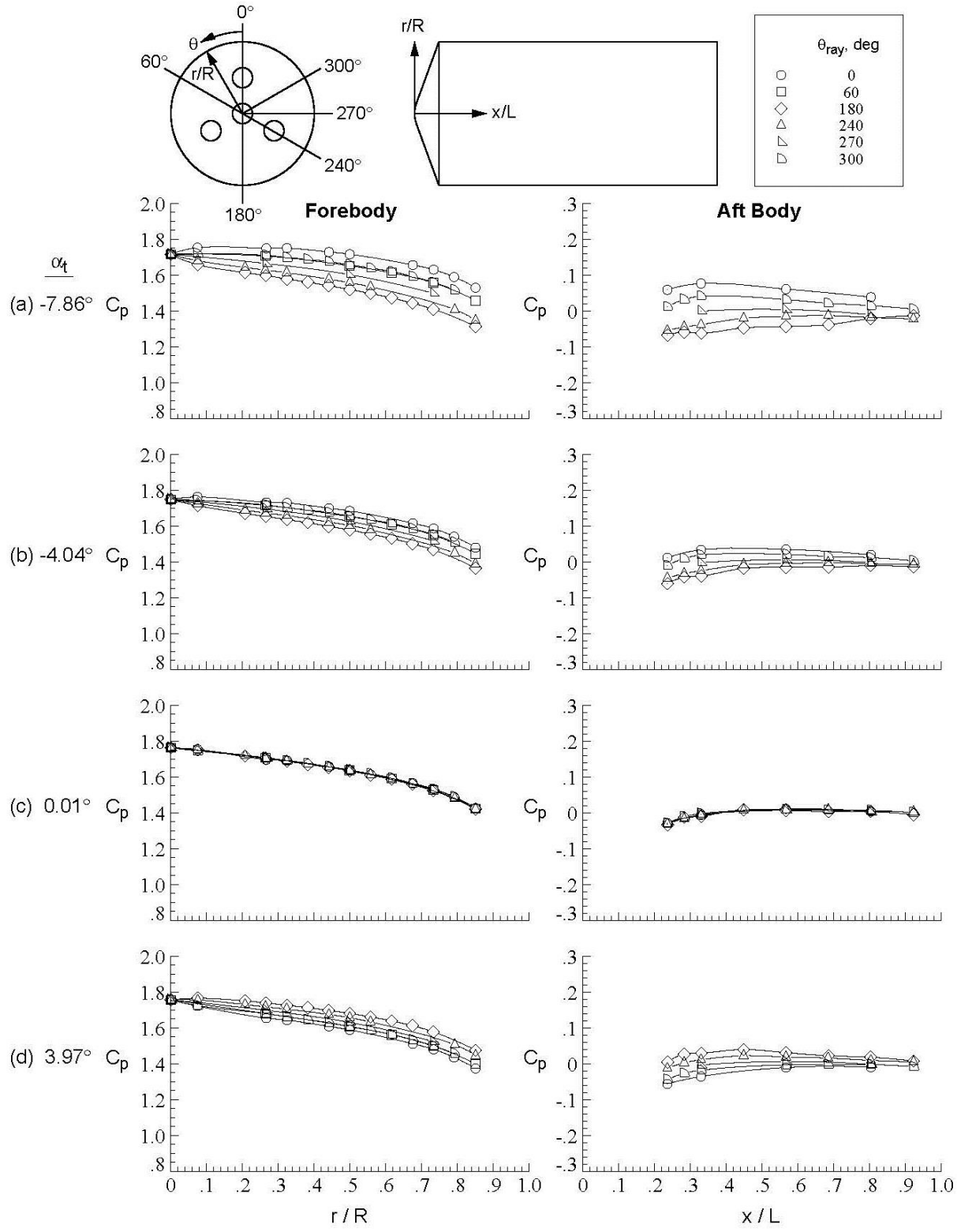

Figure D-55. Baseline configuration, Run 075, M_∞ = 3.5, Re_∞ = 1.0x10^6/ft, ϕ = 0.03°, X_S = 40.18 in, Y_S = –8.00 in, C_T = 0.00.

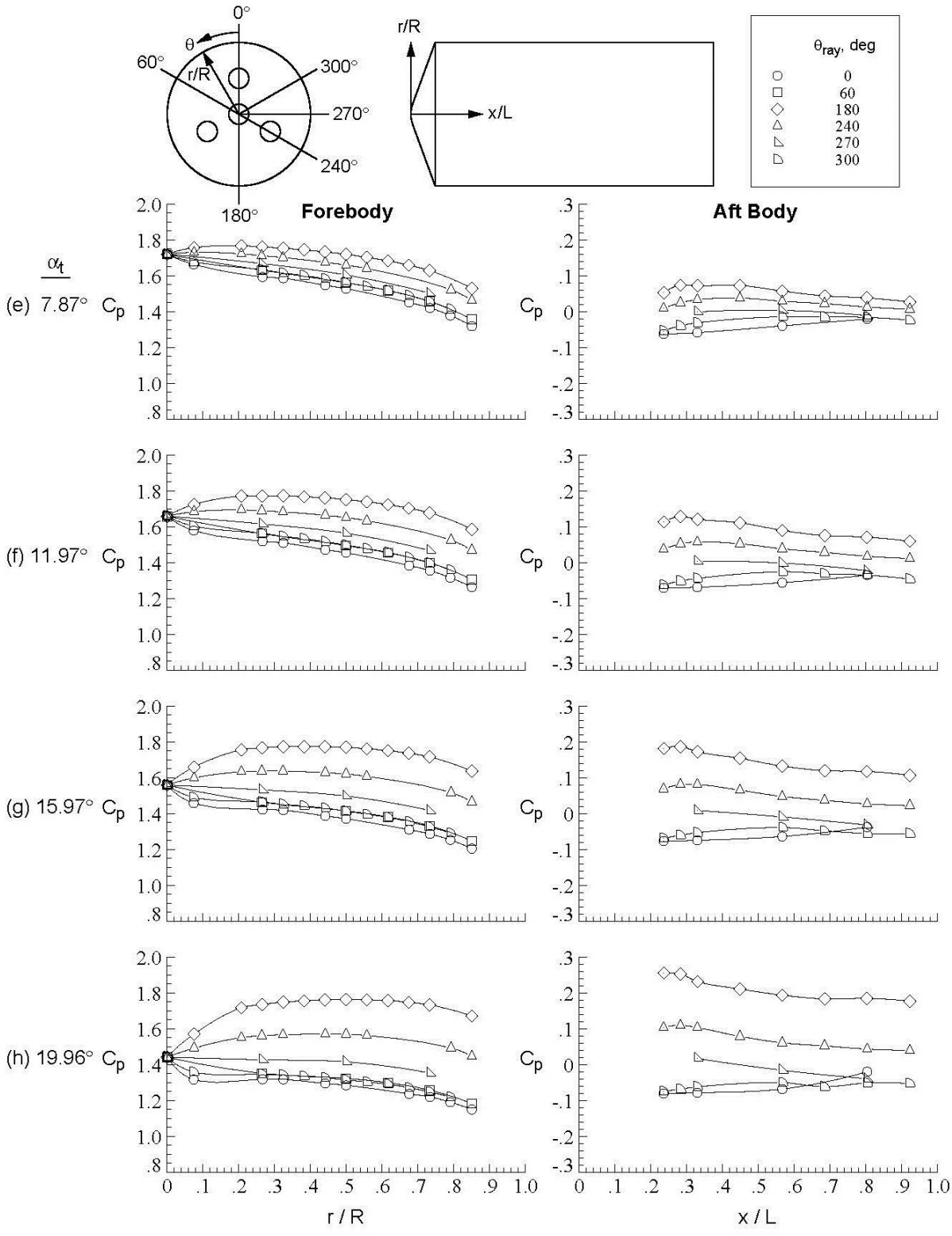

Figure D-55. Concluded.

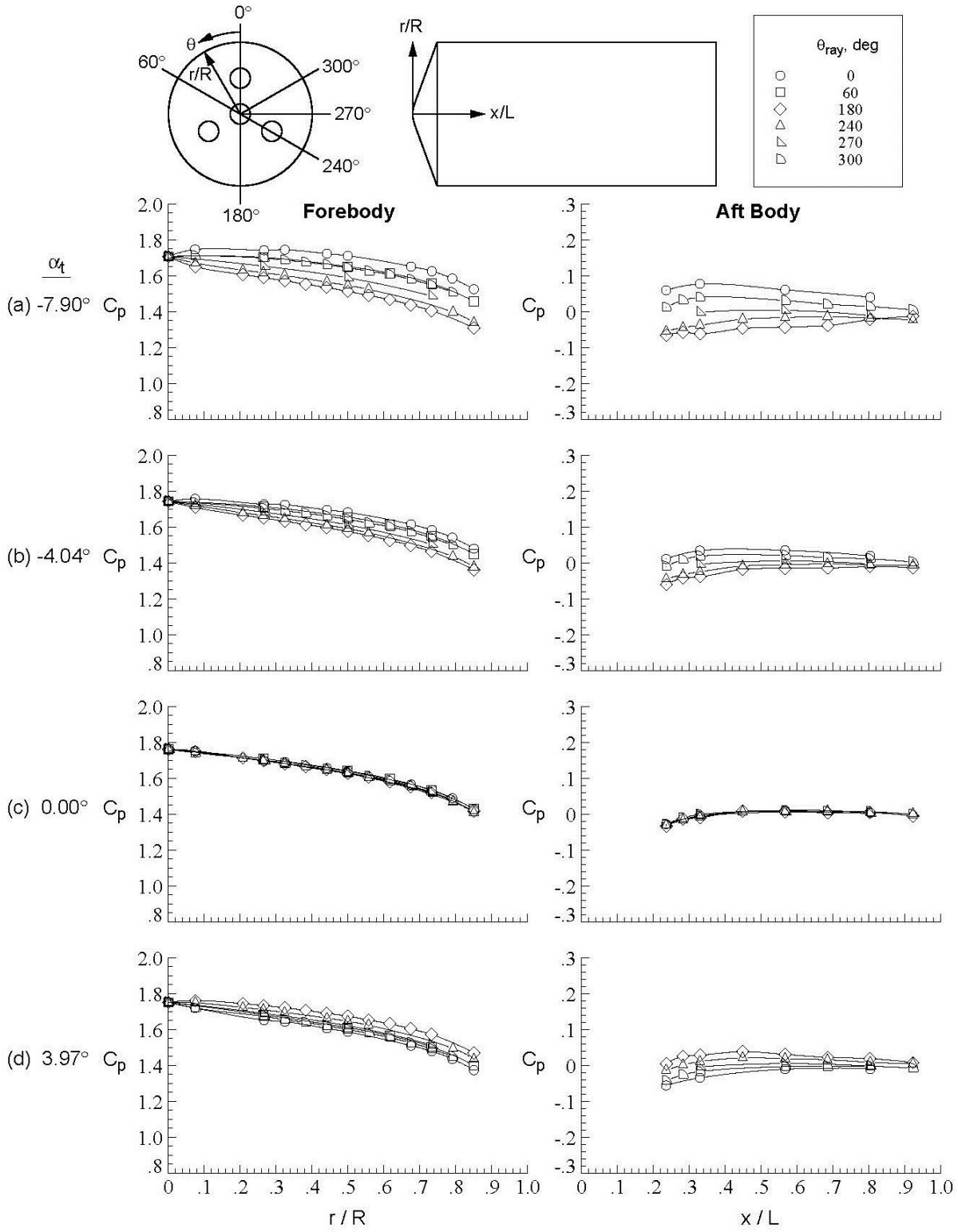

Figure D-56. Baseline configuration, Run 076, M_∞ = 3.5, Re_∞ = 1.0x10^7/ft, ϕ = 0.03°, X_S = 40.18 in, Y_S = 7.99 in, C_T = 0.00.

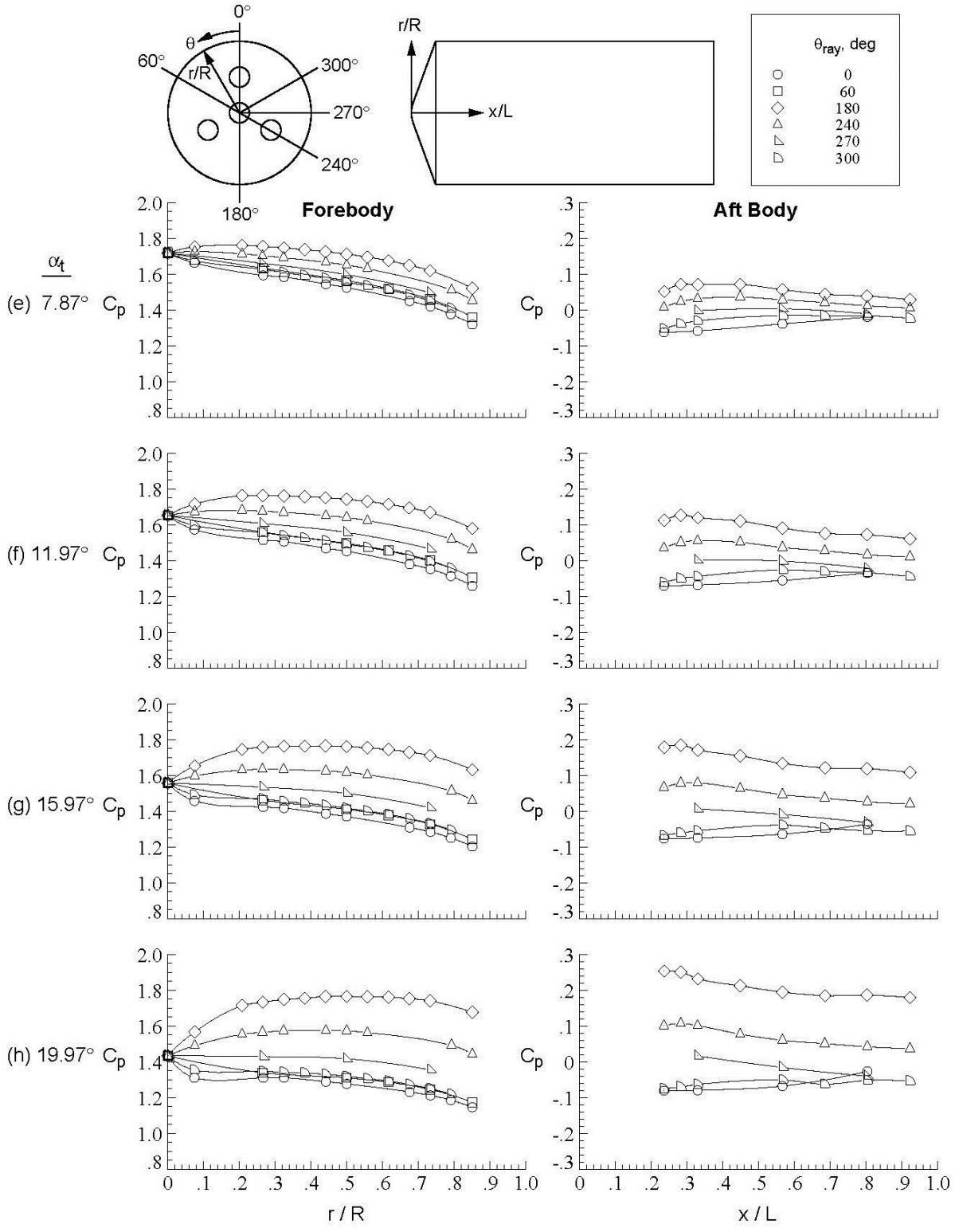

Figure D-56. Concluded.

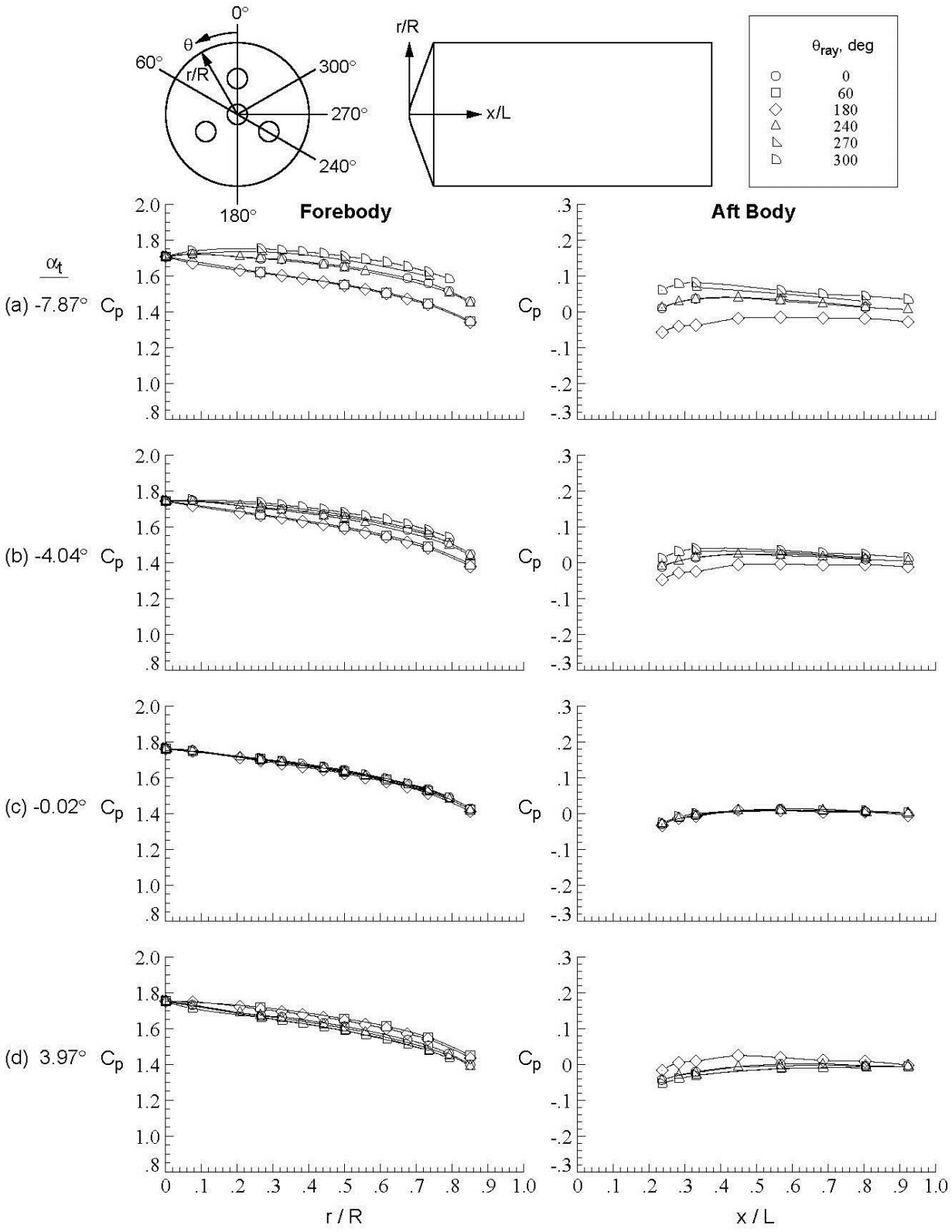

Figure D-57. Baseline configuration, Run 077, M_∞ = 3.5, Re_∞ = 1.0x10^7/ft, ϕ = 59.93°, X_S = 40.16 in, Y_S = 7.99 in, C_T = 0.00.

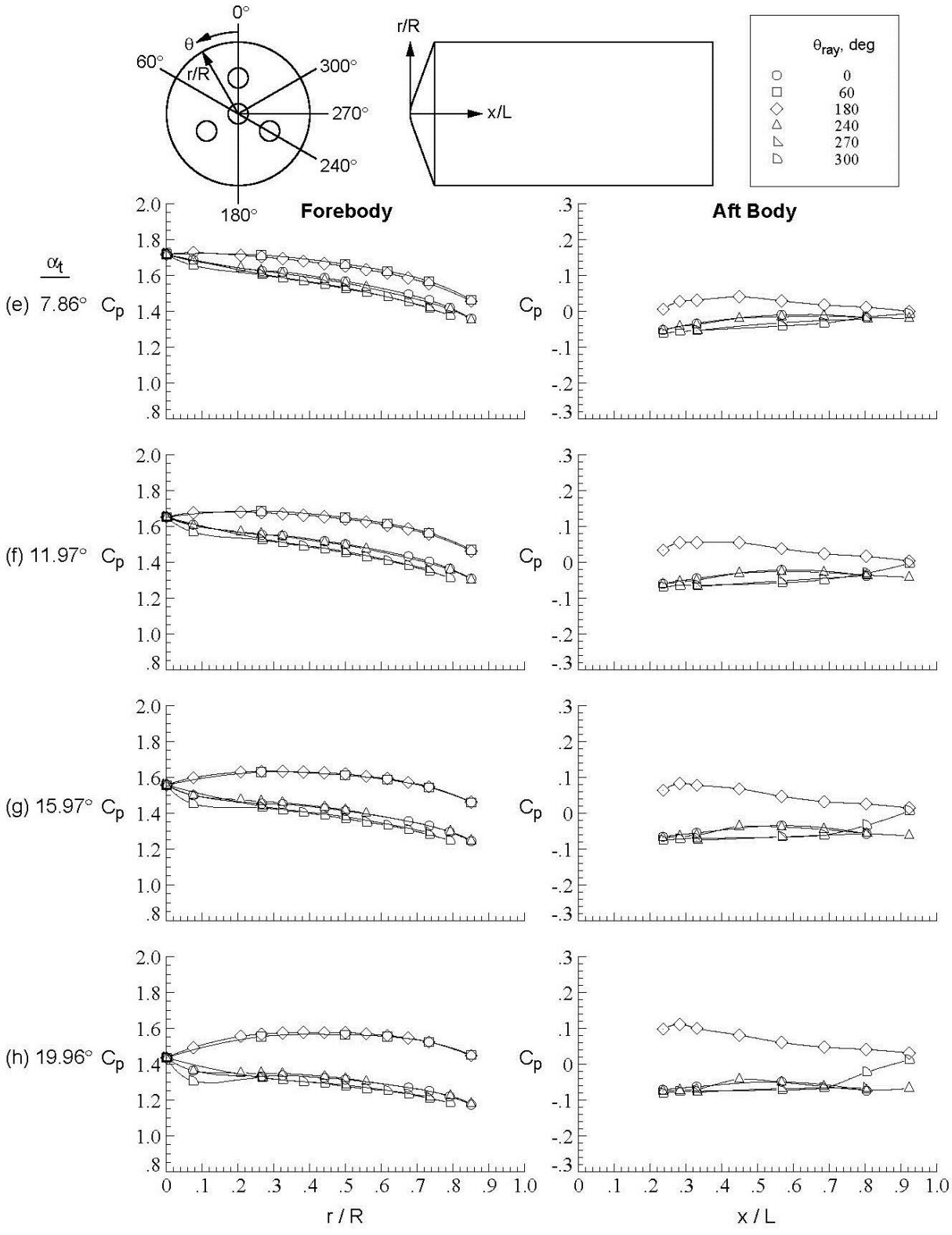

Figure D-57. Concluded.

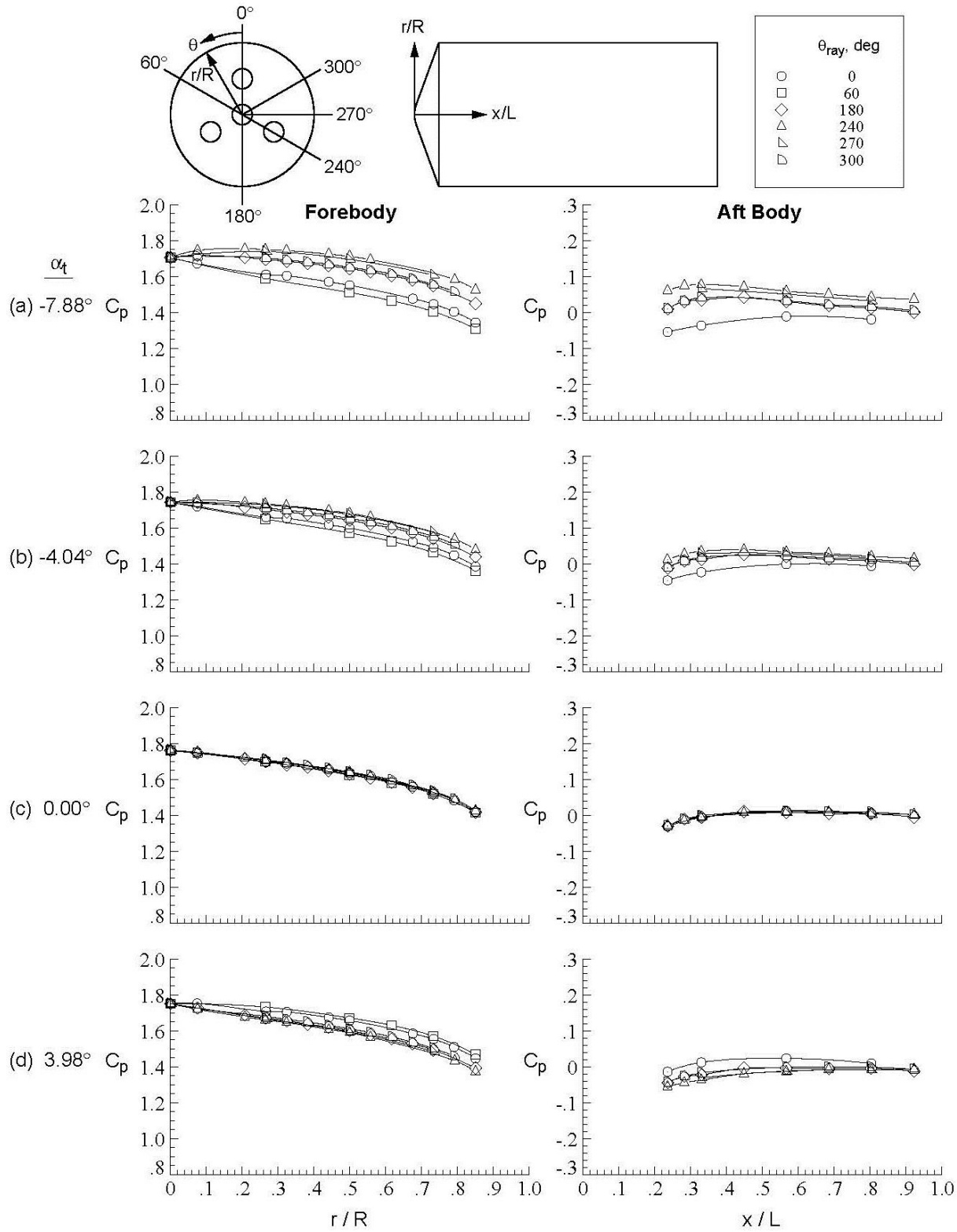

Figure D-58. Baseline configuration, Run 078, M_∞ = 3.5, Re_∞ = 1.0x10^6/ft, ϕ = 119.98°, X_S = 40.16 in, Y_S = 7.95 in, C_T = 0.00.

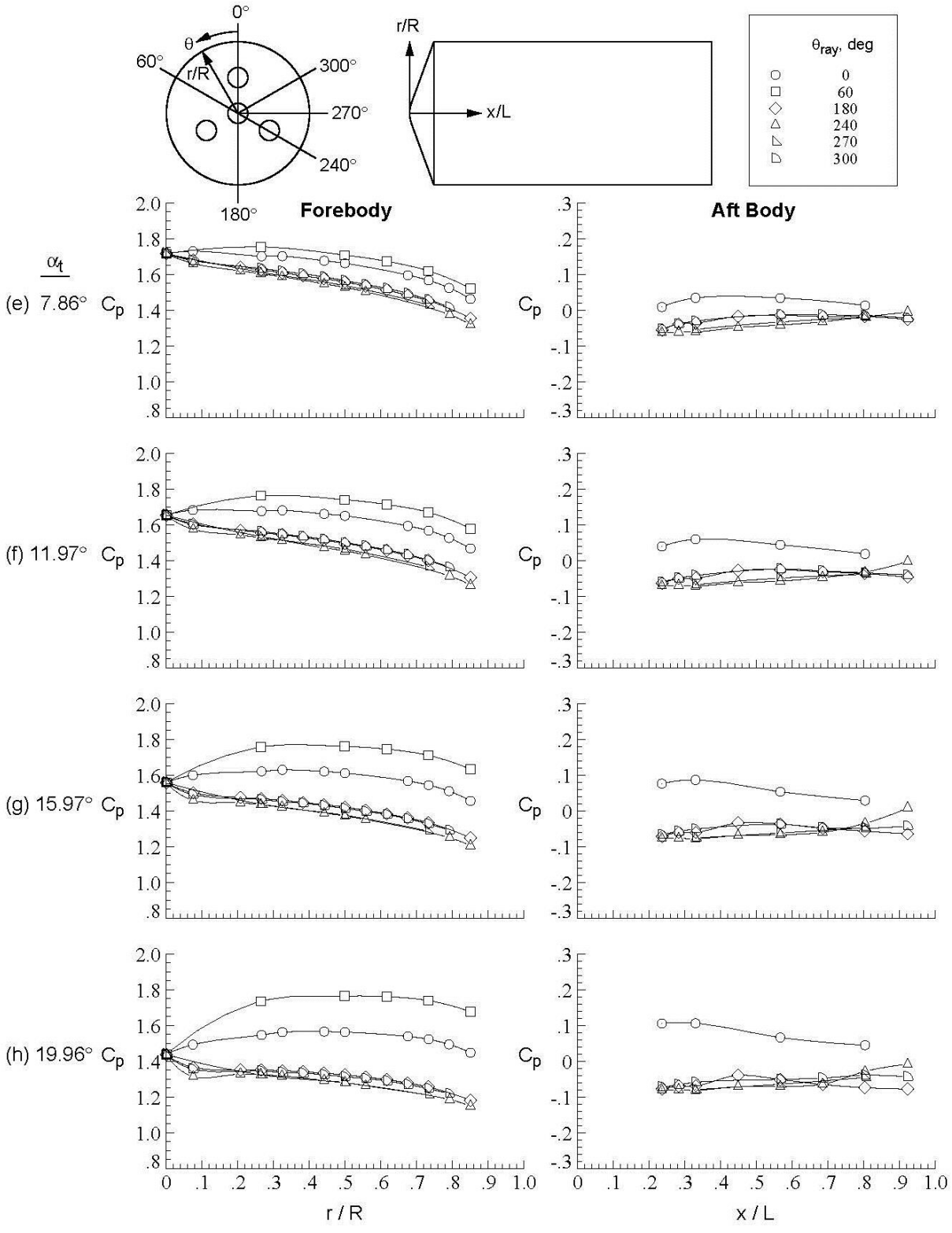

Figure D-58. Concluded.

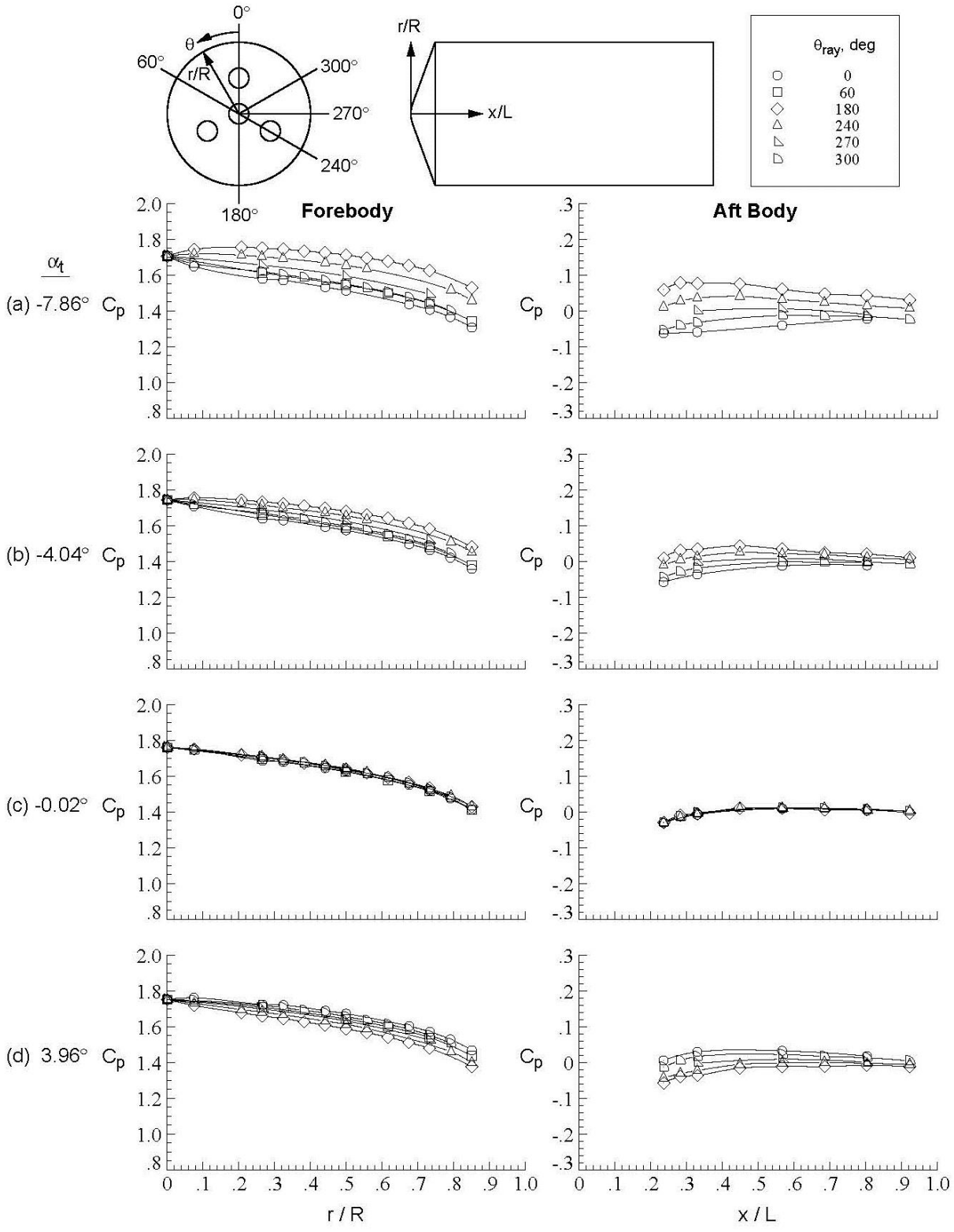

Figure D-59. Baseline configuration, Run 079, M_∞ = 3.5, Re_∞ = 1.0x10^7/ft, ϕ = −179.99°, X_S = 40.16 in, Y_S = 7.95 in, C_T = 0.00.

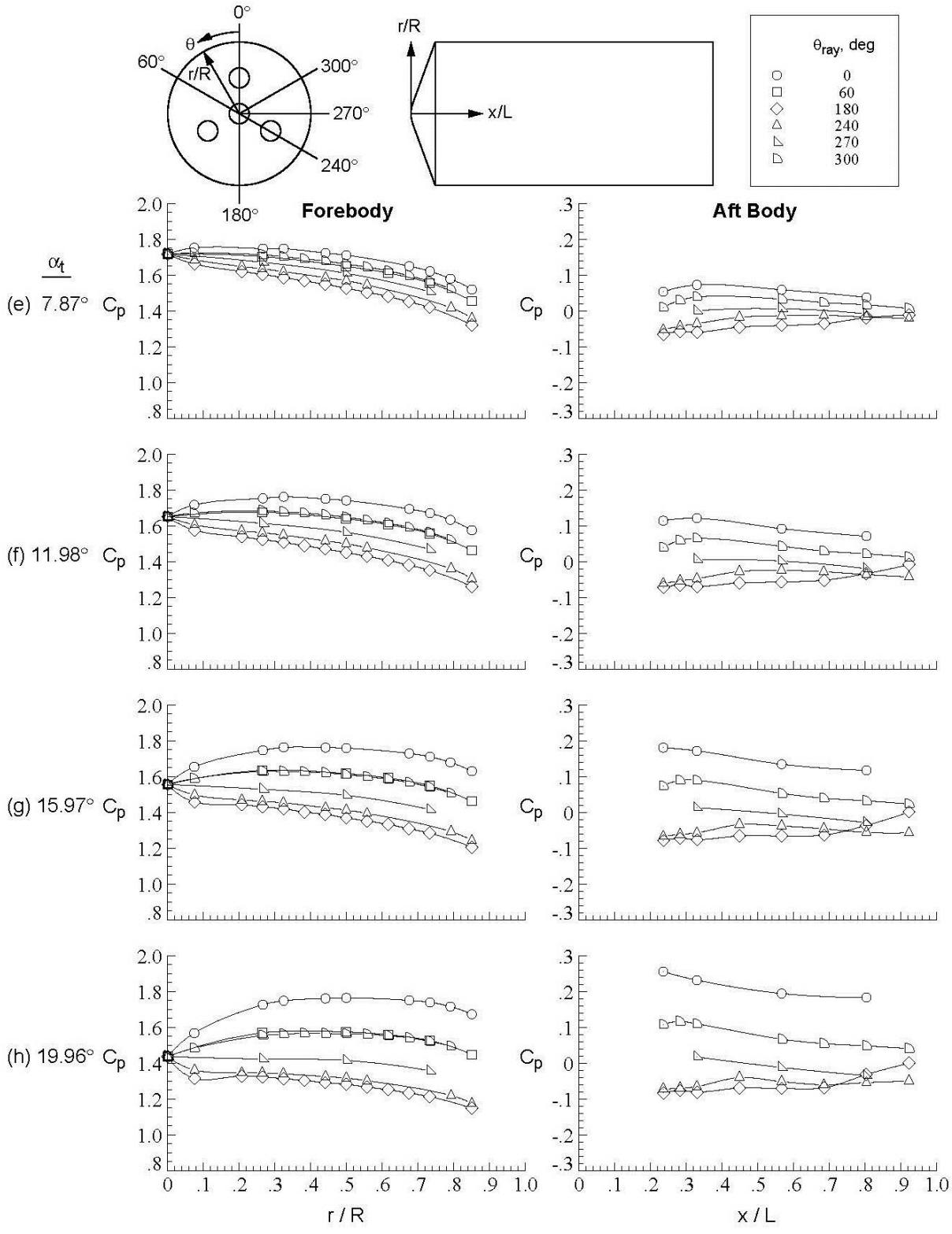

Figure D-59. Concluded.

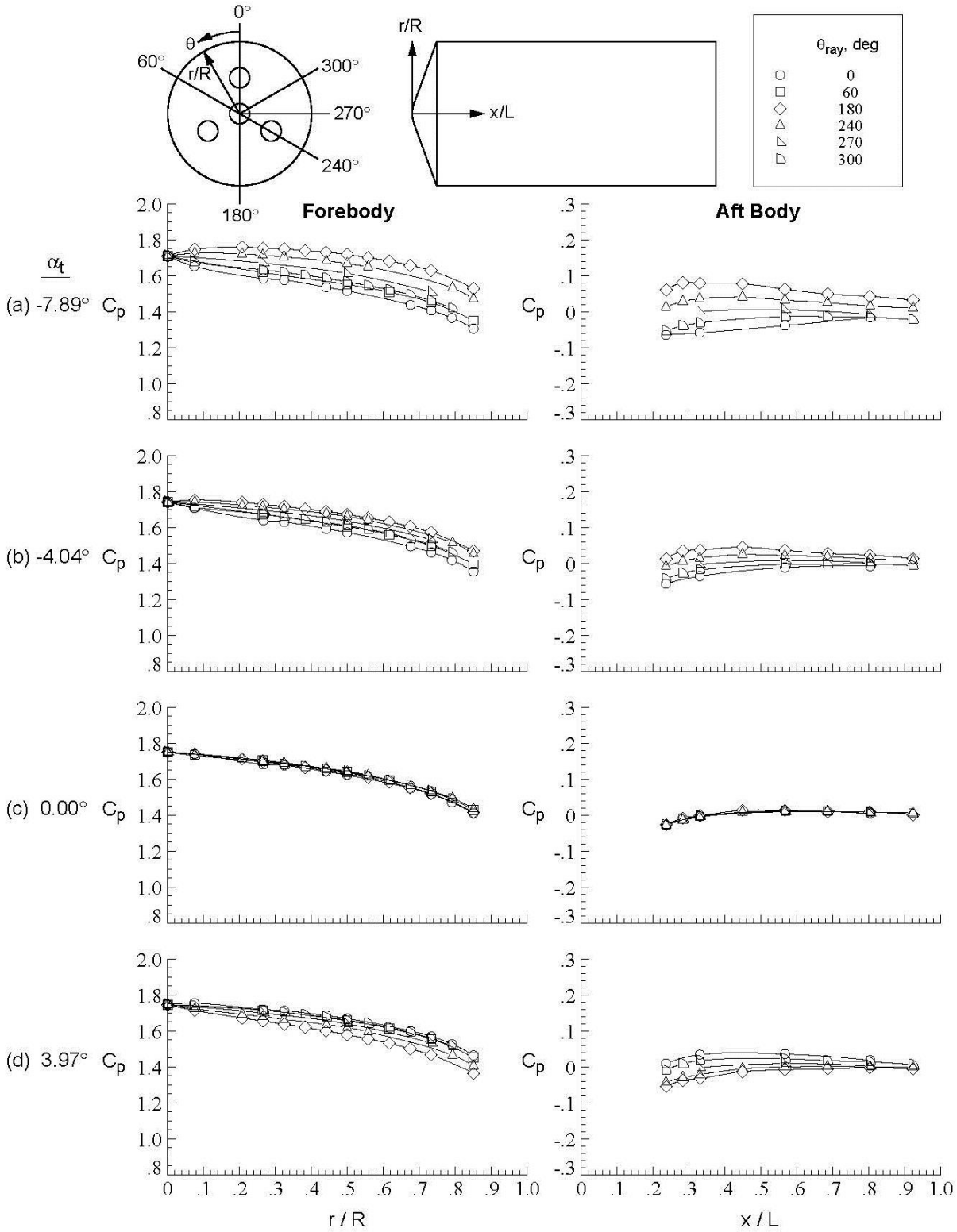

Figure D-60. Baseline configuration, Run 080, M_∞ = 3.5, Re_∞ = 1.0x10^7/ft, ϕ = −179.99°, X_S = 50.15 in, Y_S = 7.95 in, C_T = 0.00.

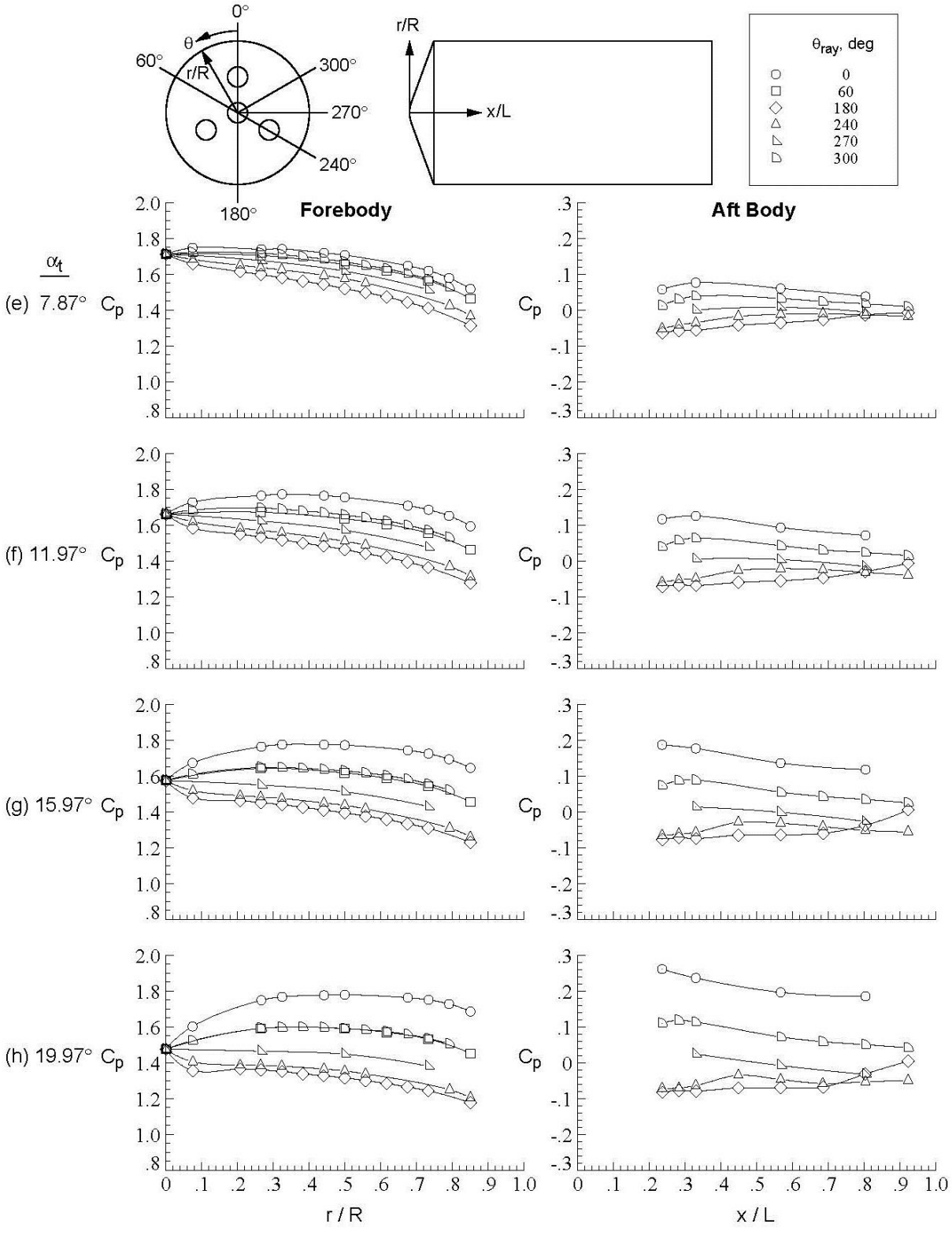

Figure D-60. Concluded.

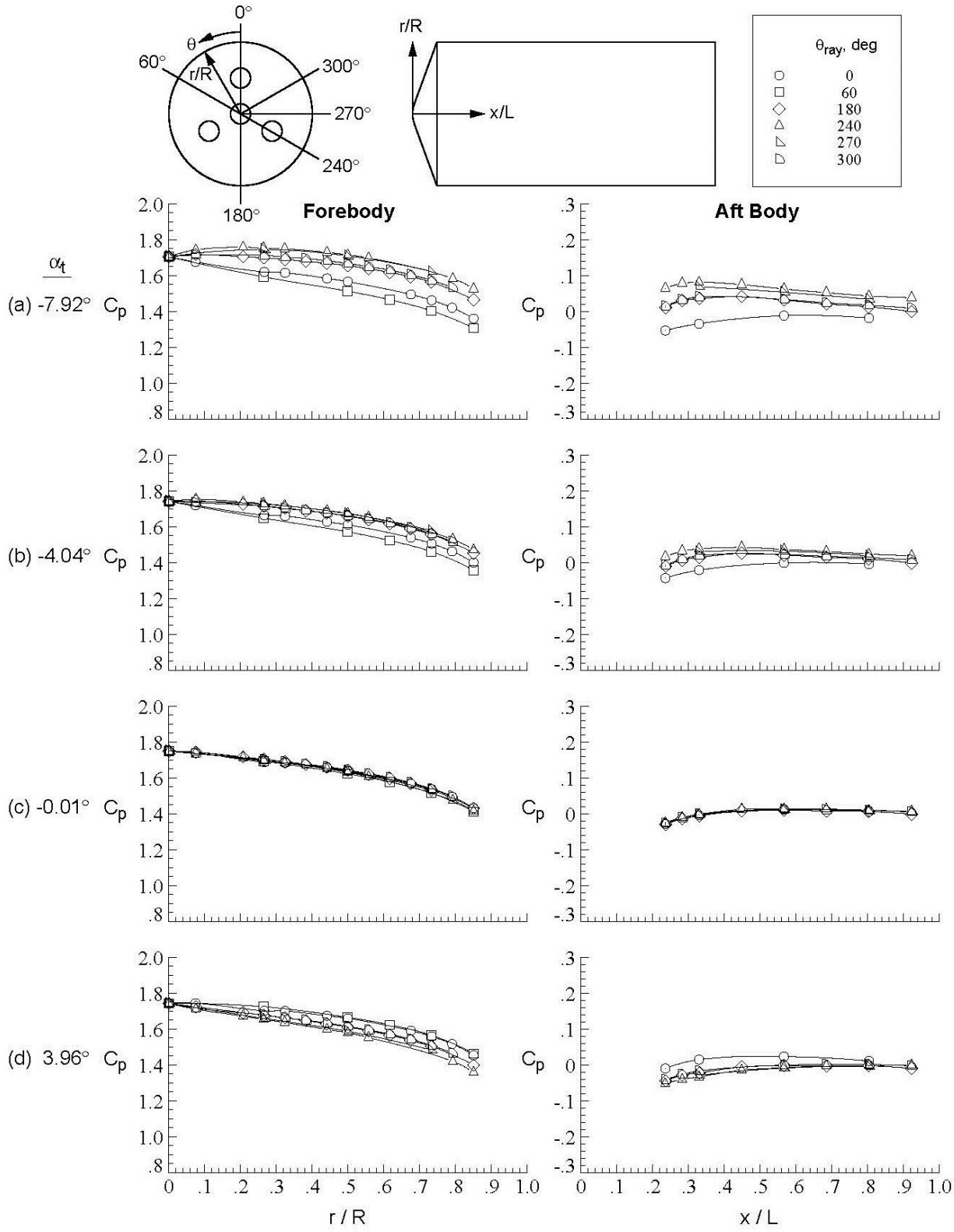

Figure D-61. Baseline configuration, Run 081, M_∞ = 3.5, Re_∞ = 1.0x10^7/ft, ϕ = 119.98°, X_S = 50.15 in, Y_S = 7.95 in, C_T = 0.00.

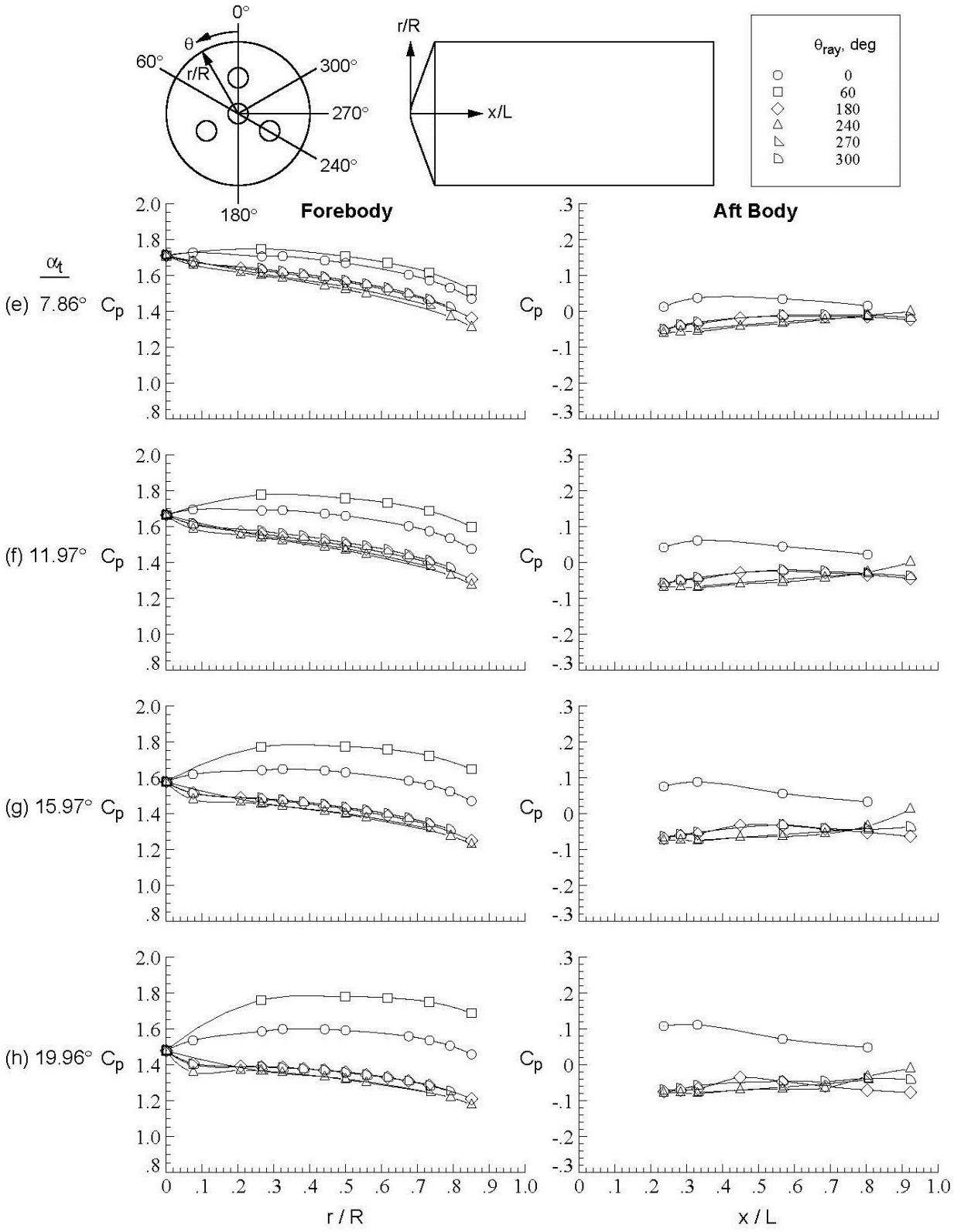

Figure D-61. Concluded.

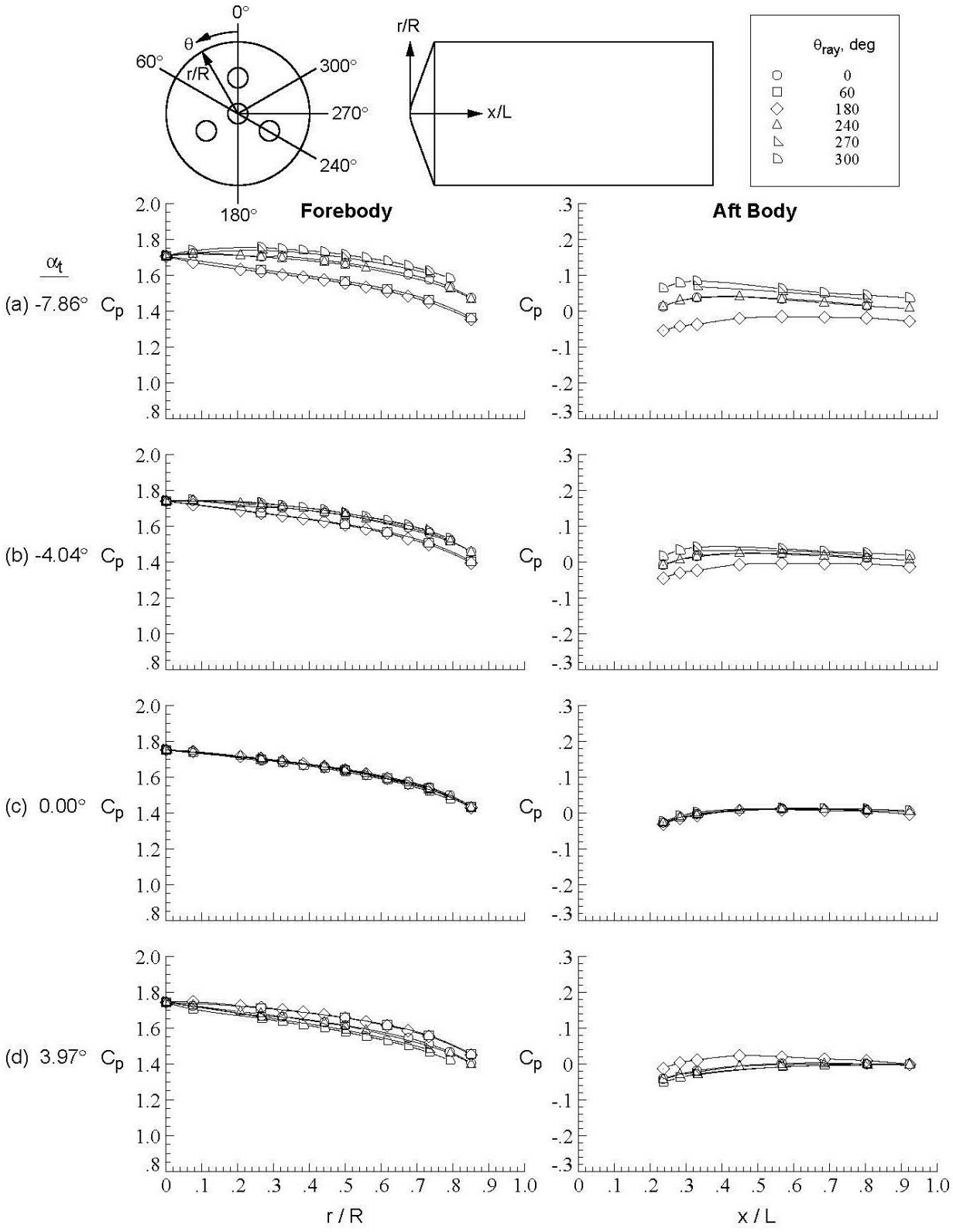

Figure D-62. Baseline configuration, Run 082, M_∞ = 3.5, Re_∞ = 1.0x10^7/ft, ϕ = 59.94°, X_S = 50.15 in, Y_S = 7.95 in, C_T = 0.00.

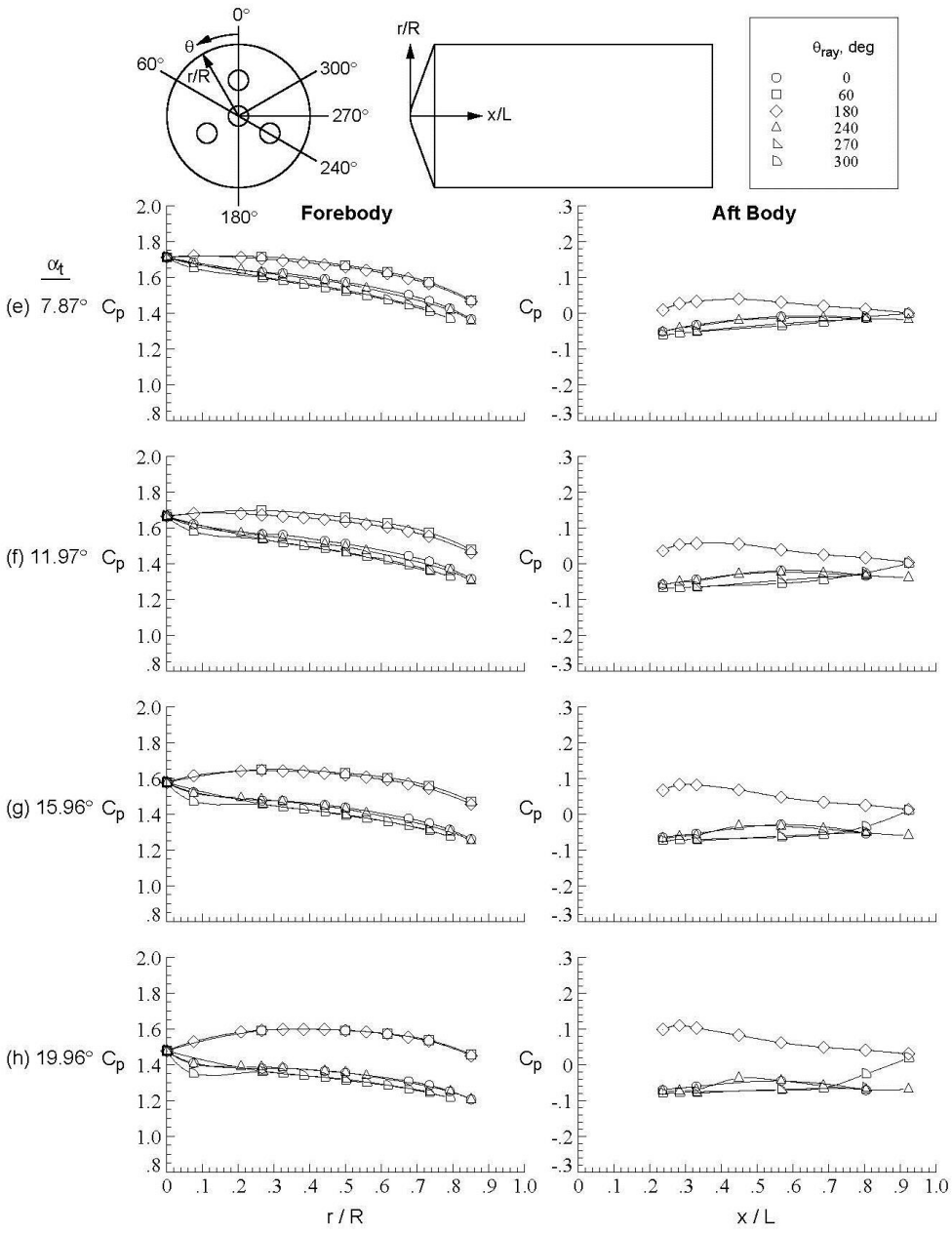

Figure D-62. Concluded.

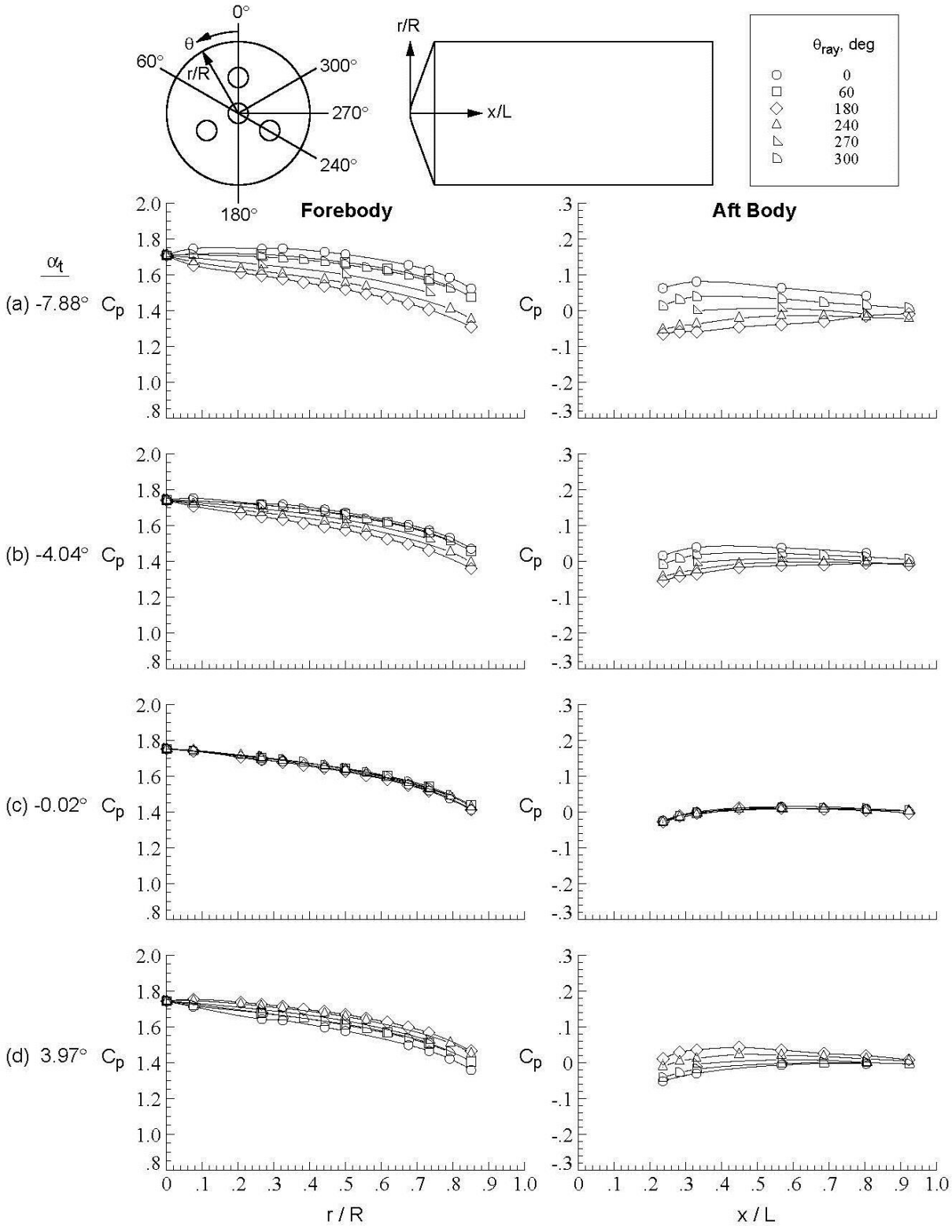

Figure D-63. Baseline configuration, Run 083, M_∞ = 3.5, Re_∞ = 1.0x10^7/ft, ϕ = 0.01°, X_S = 50.15 in, Y_S = 7.95 in, C_T = 0.00.

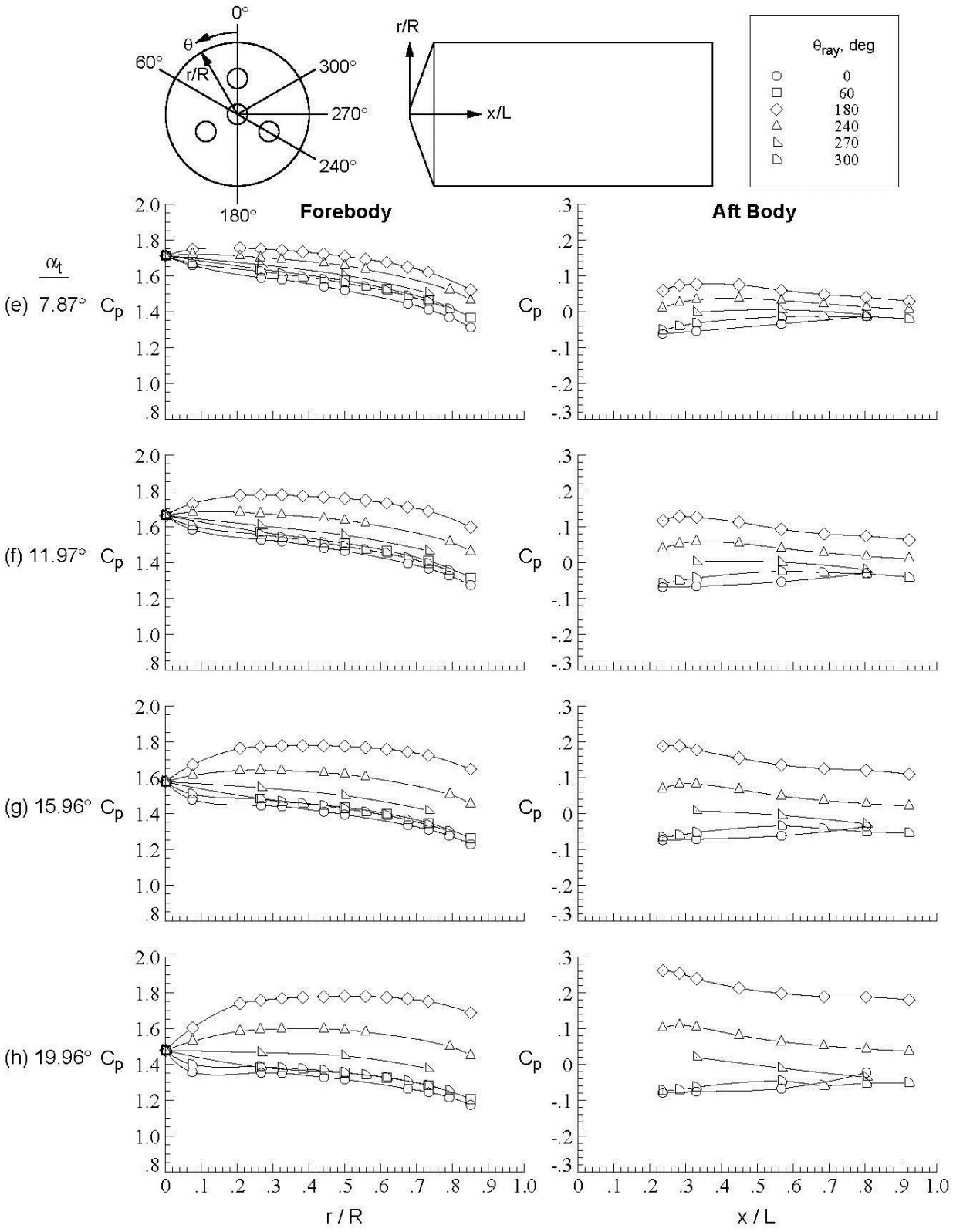

Figure D-63. Concluded.

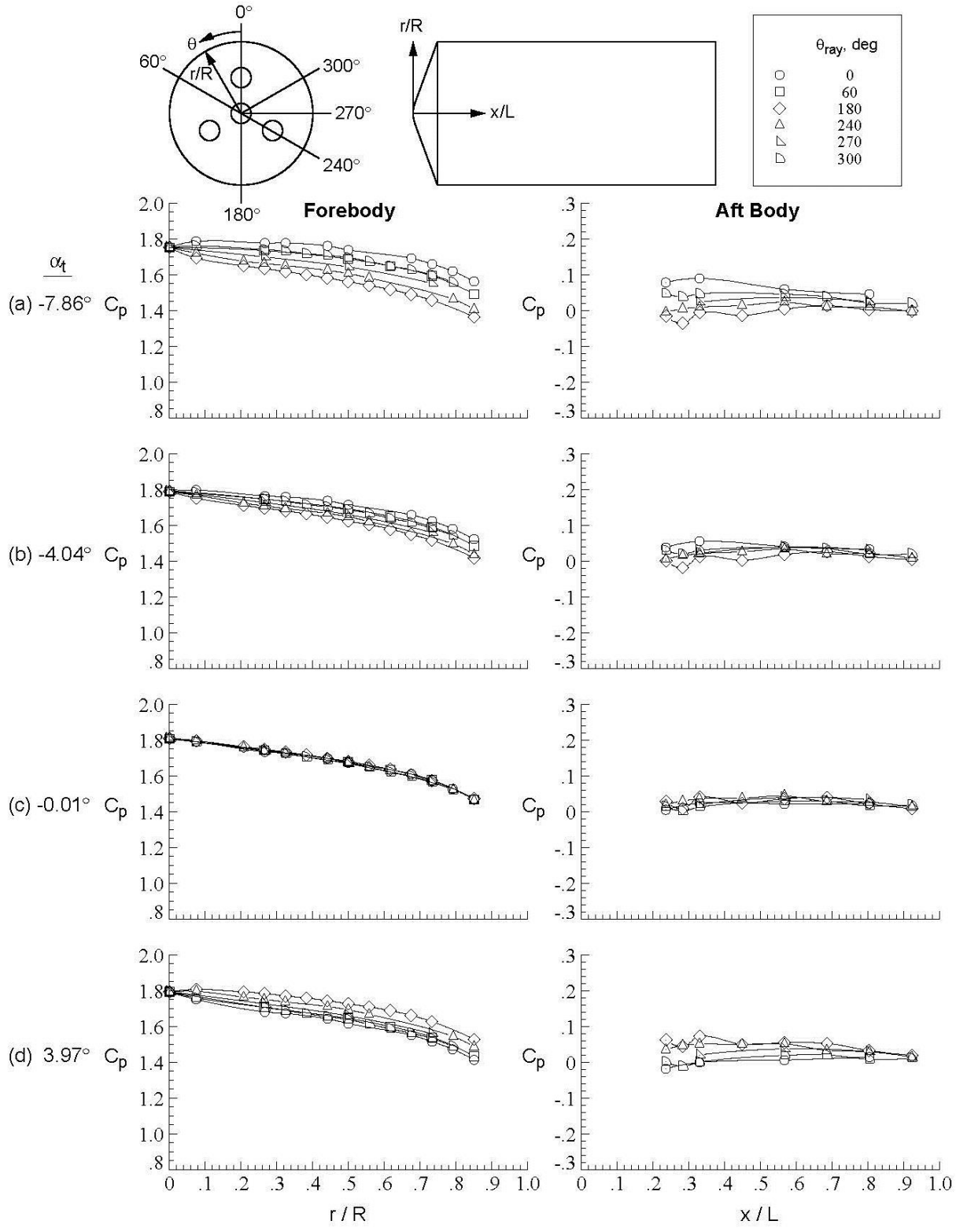

Figure D-64. Baseline configuration, Run 086, M_∞ = 4.6, Re_∞ = 1.1x10^7/ft, ϕ = 0.01°, X_S = 25.17 in, Y_S = 0.00 in, C_T = 0.00.

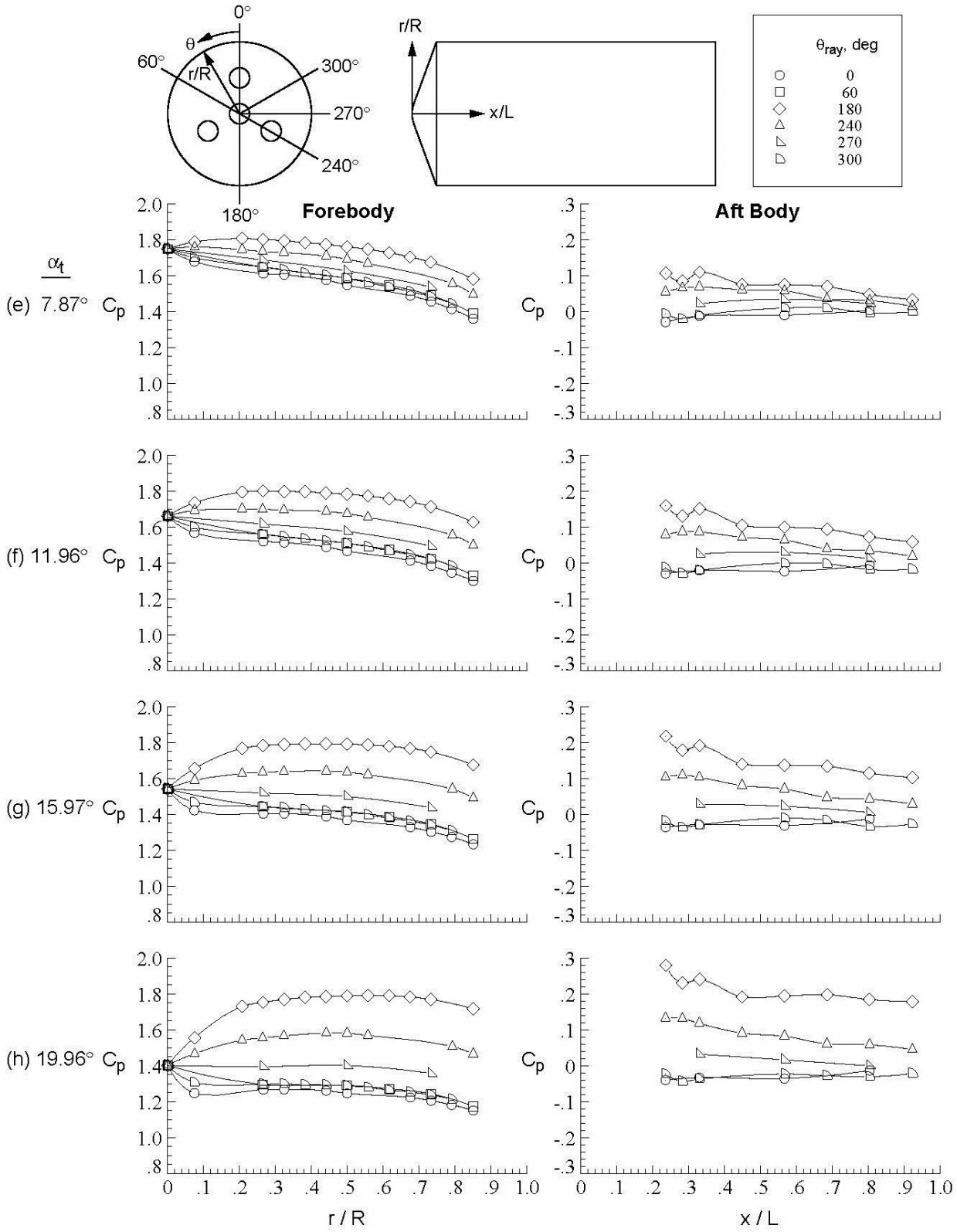

Figure D-64. Concluded.

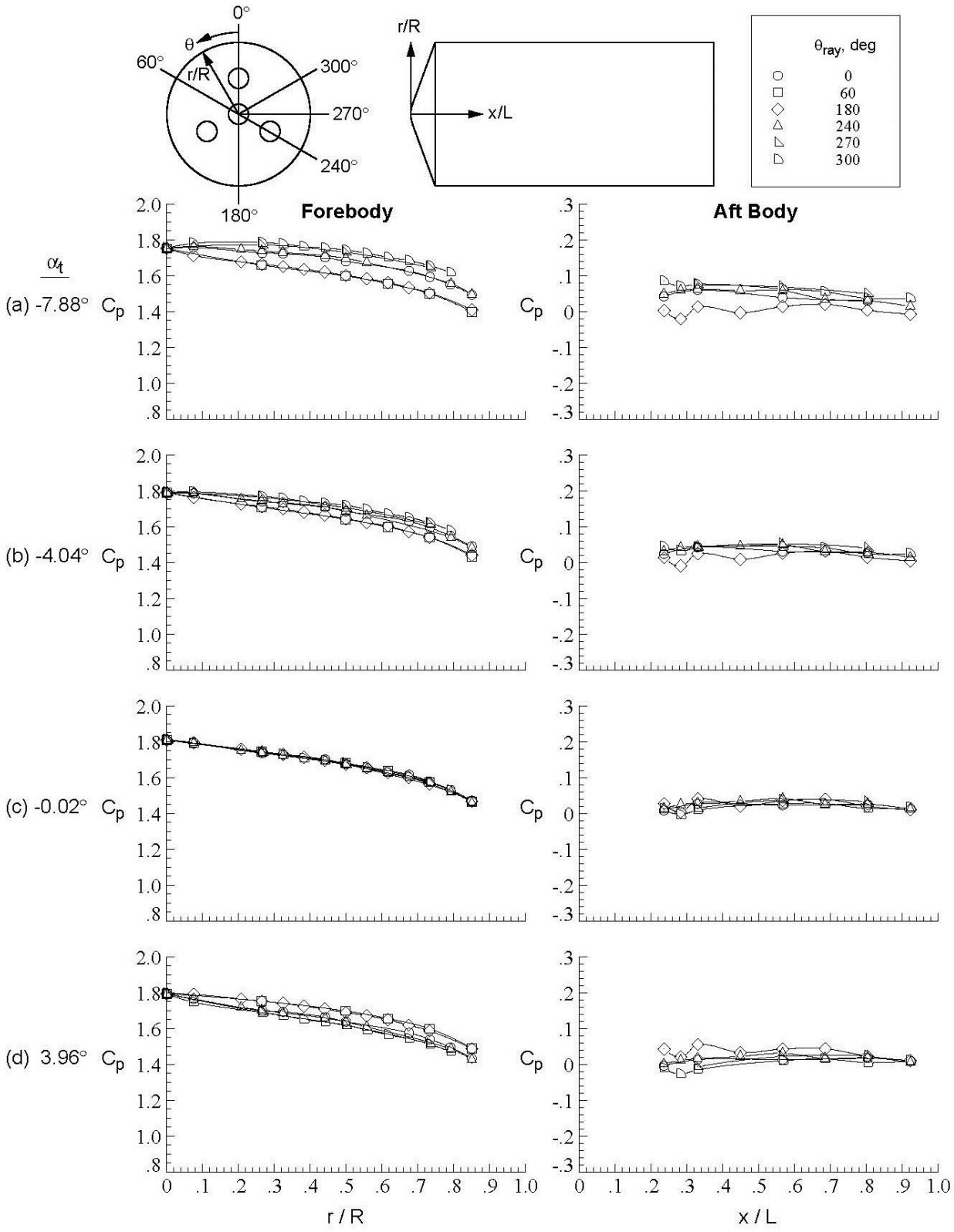

Figure D-65. Baseline configuration, Run 087, M_∞ = 4.6, Re_∞ = 1.1x10^7/ft, ϕ = 59.98°, X_S = 25.17 in, Y_S = 0.00 in, C_T = 0.00.

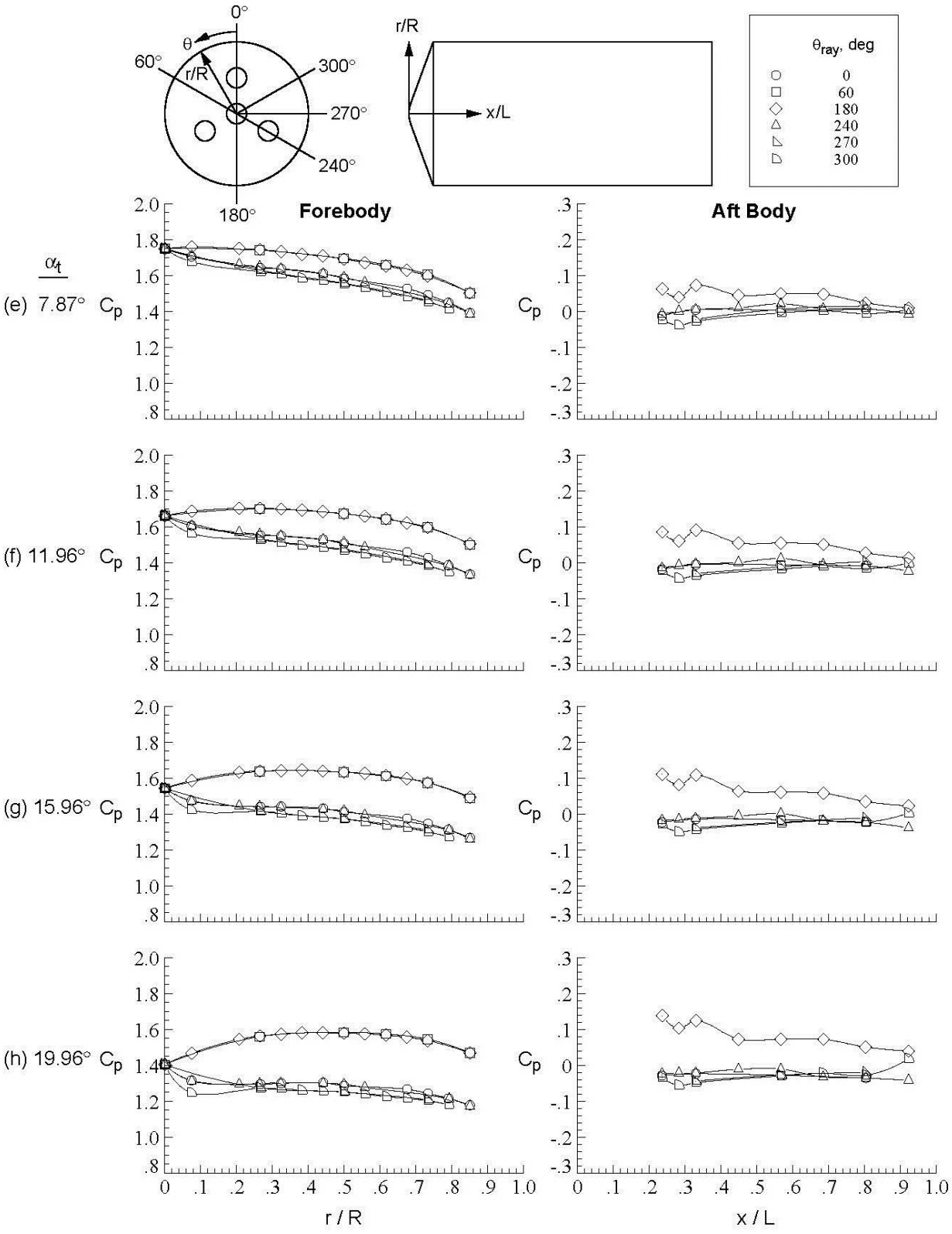

Figure D-65. Concluded.

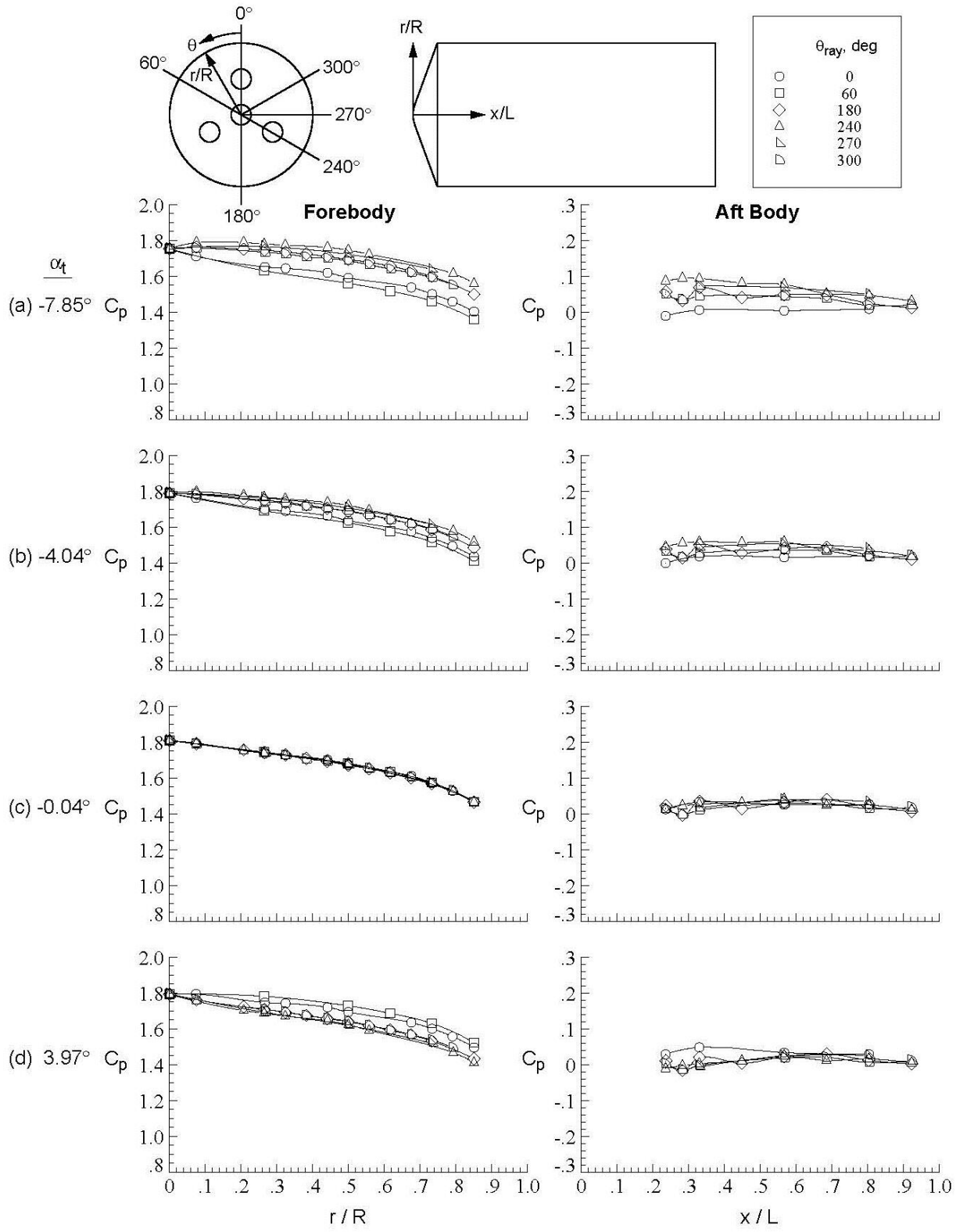

Figure D-66. Baseline configuration, Run 088, M_∞ = 4.6, Re_∞ = 1.1x10^7/ft, ϕ = 119.96°, X_S = 25.17 in, Y_S = 0.00 in, C_T = 0.00.

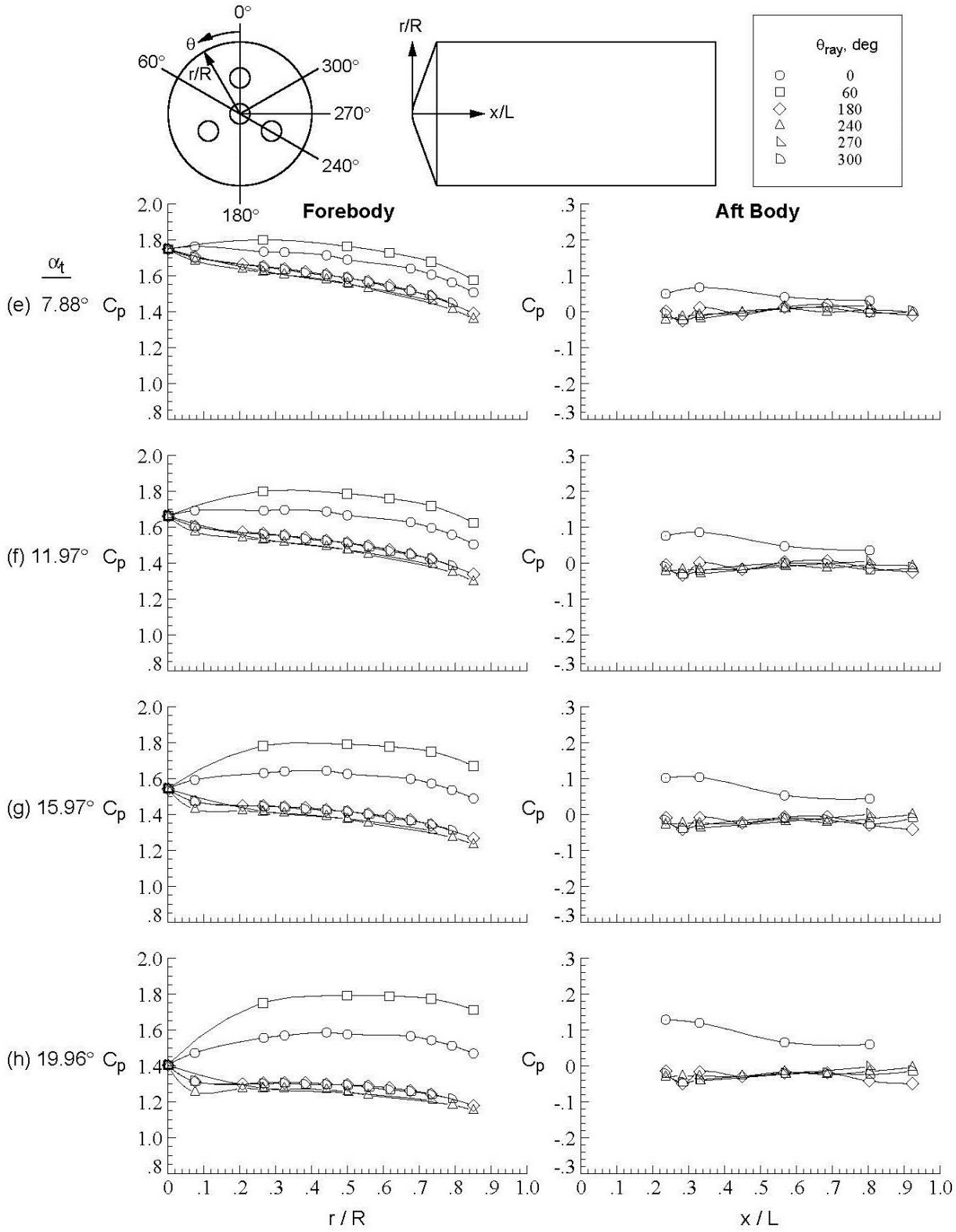

Figure D-66. Concluded.

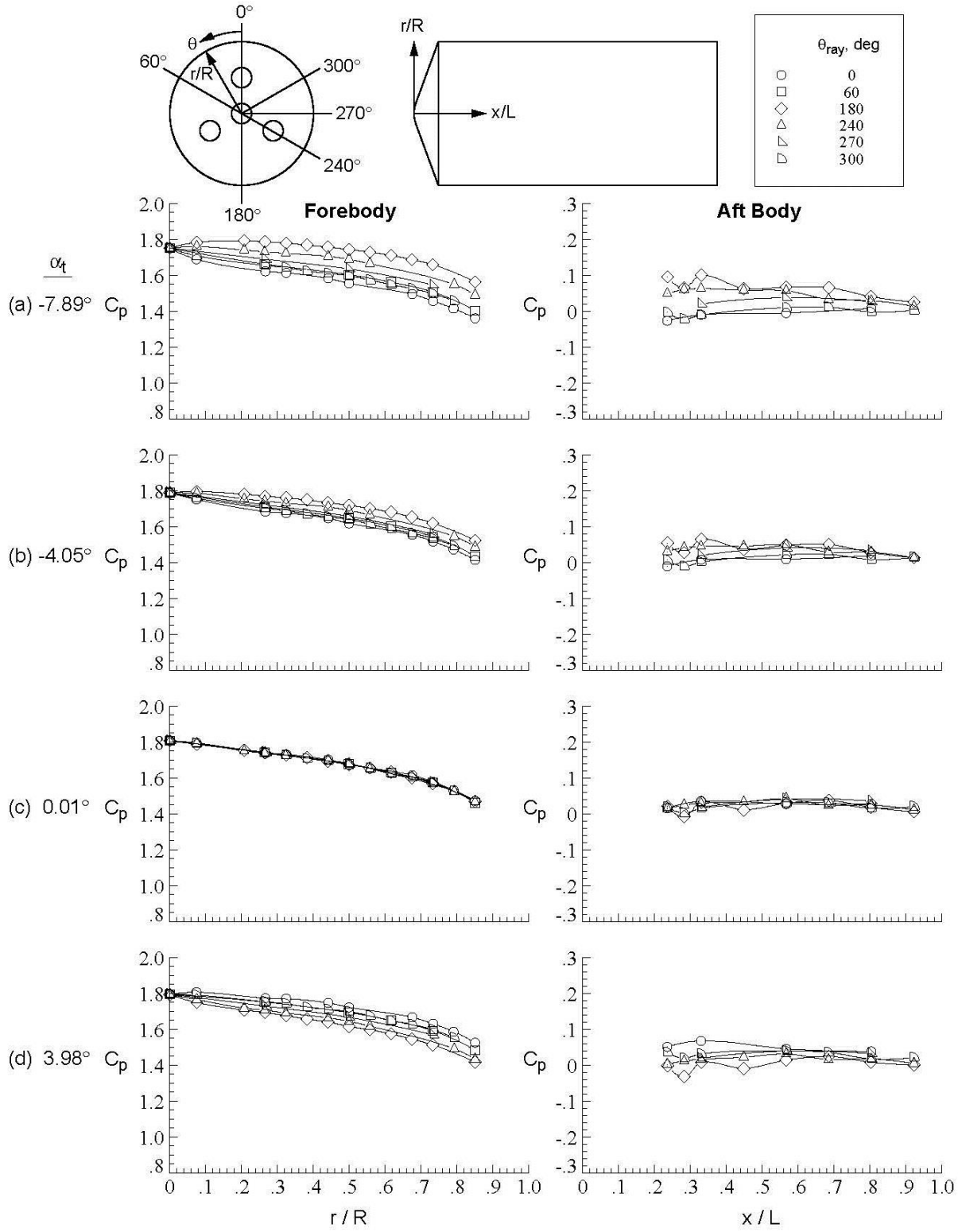

Figure D-67. Baseline configuration, Run 089, M_∞ = 4.6, Re_∞ = 1.1x10^7/ft, ϕ = 179.91°, X_S = 25.17 in, Y_S = 0.00 in, C_T = 0.00.

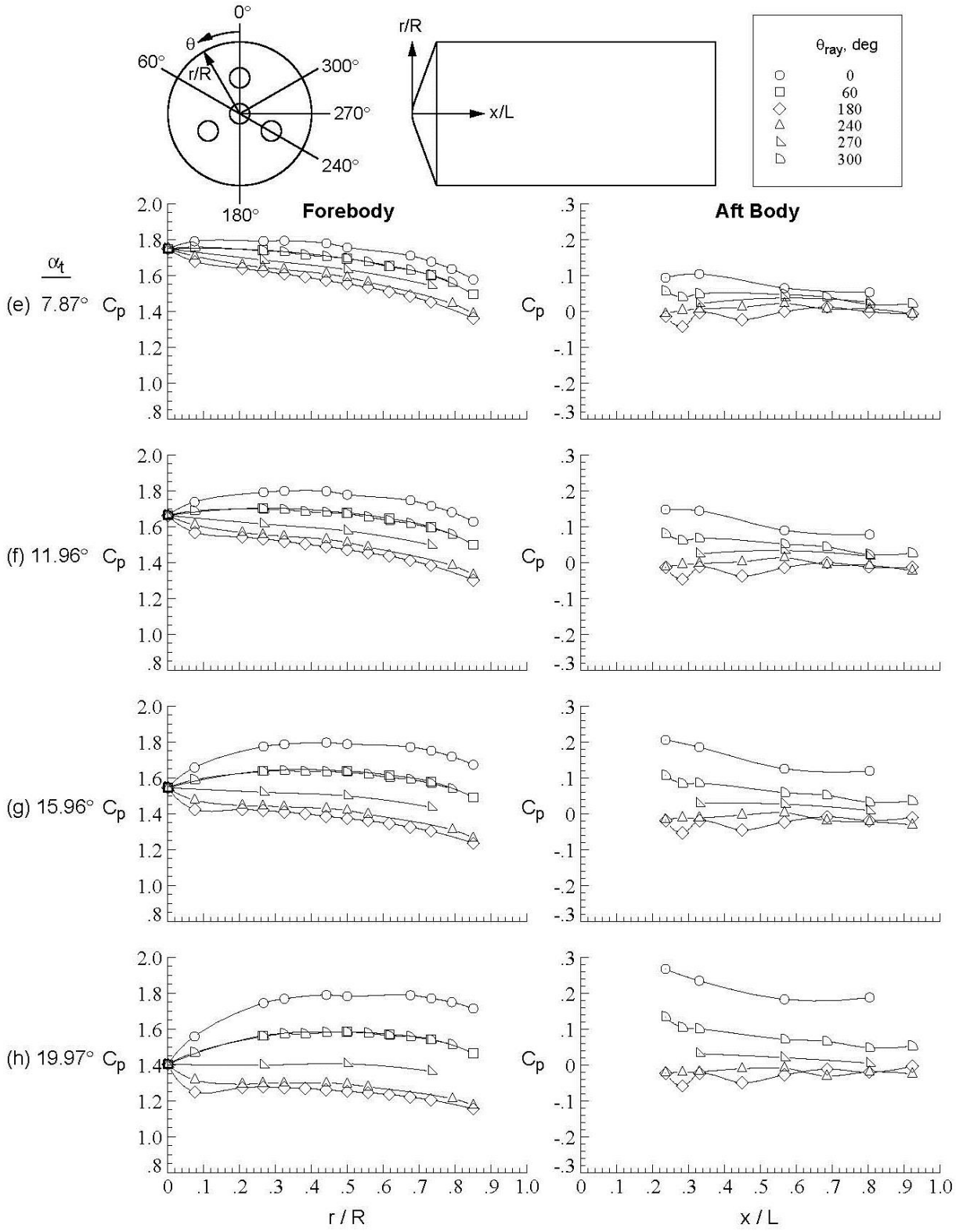

Figure D-67. Concluded.

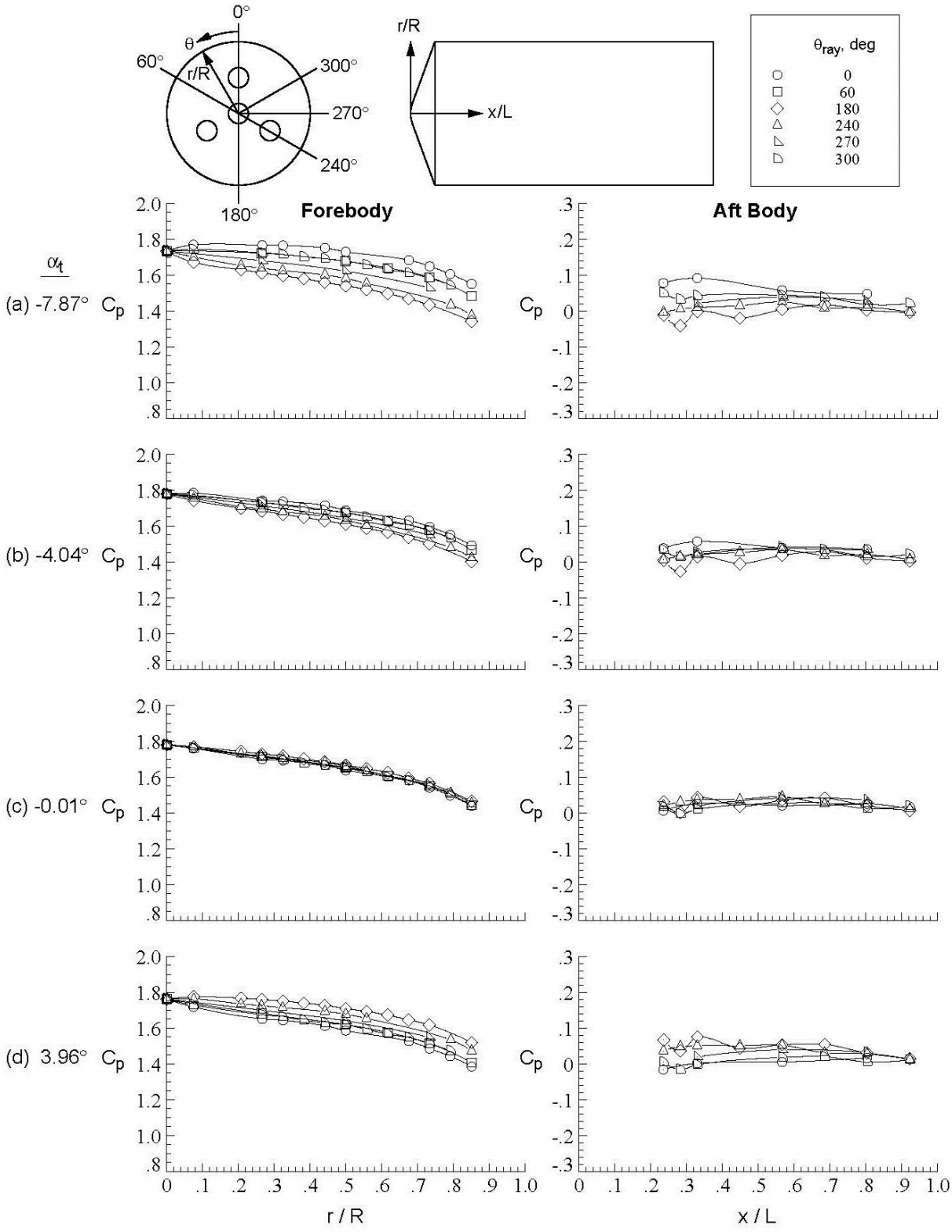

Figure D-68. Baseline configuration, Run 090, M_∞ = 4.6, Re_∞ = 1.1x10^7/ft, ϕ = 0.01°, X_S = 40.15 in, Y_S = 0.00 in, C_T = 0.00.

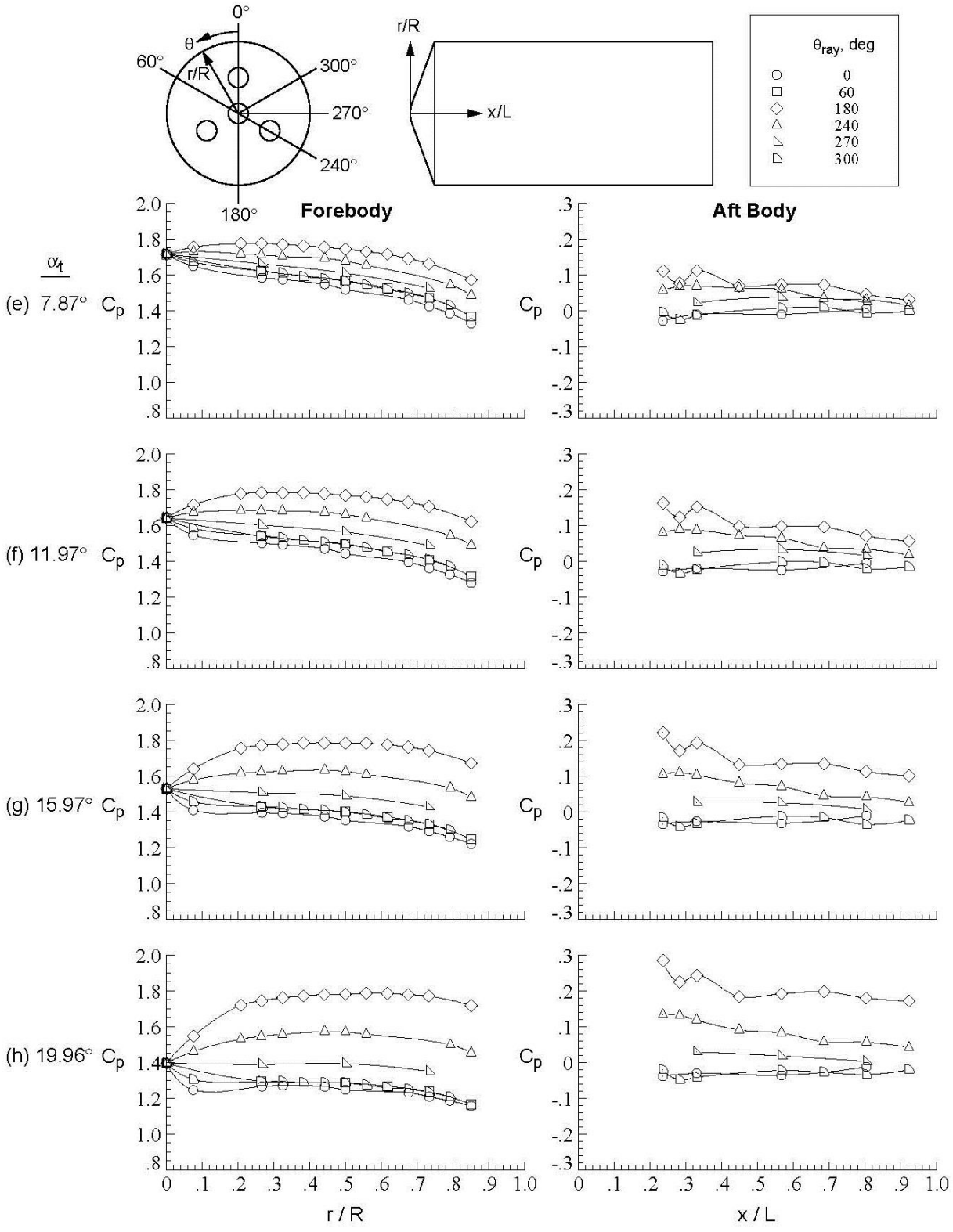

Figure D-68. Concluded.

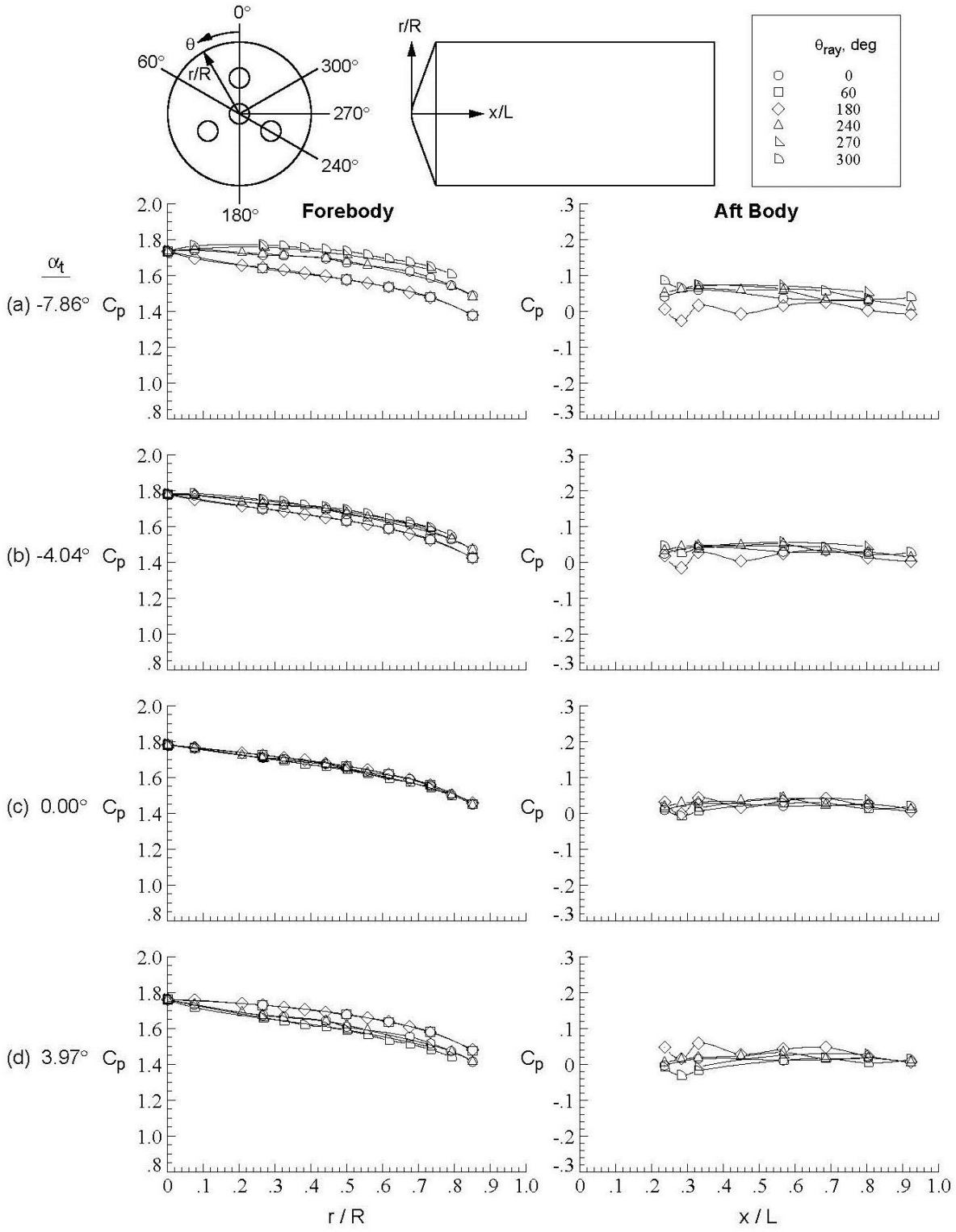

Figure D-69. Baseline configuration, Run 091, M_∞ = 4.6, Re_∞ = 1.1x10^7/ft, ϕ = 59.94°, X_S = 40.18 in, Y_S = 0.00 in, C_T = 0.00.

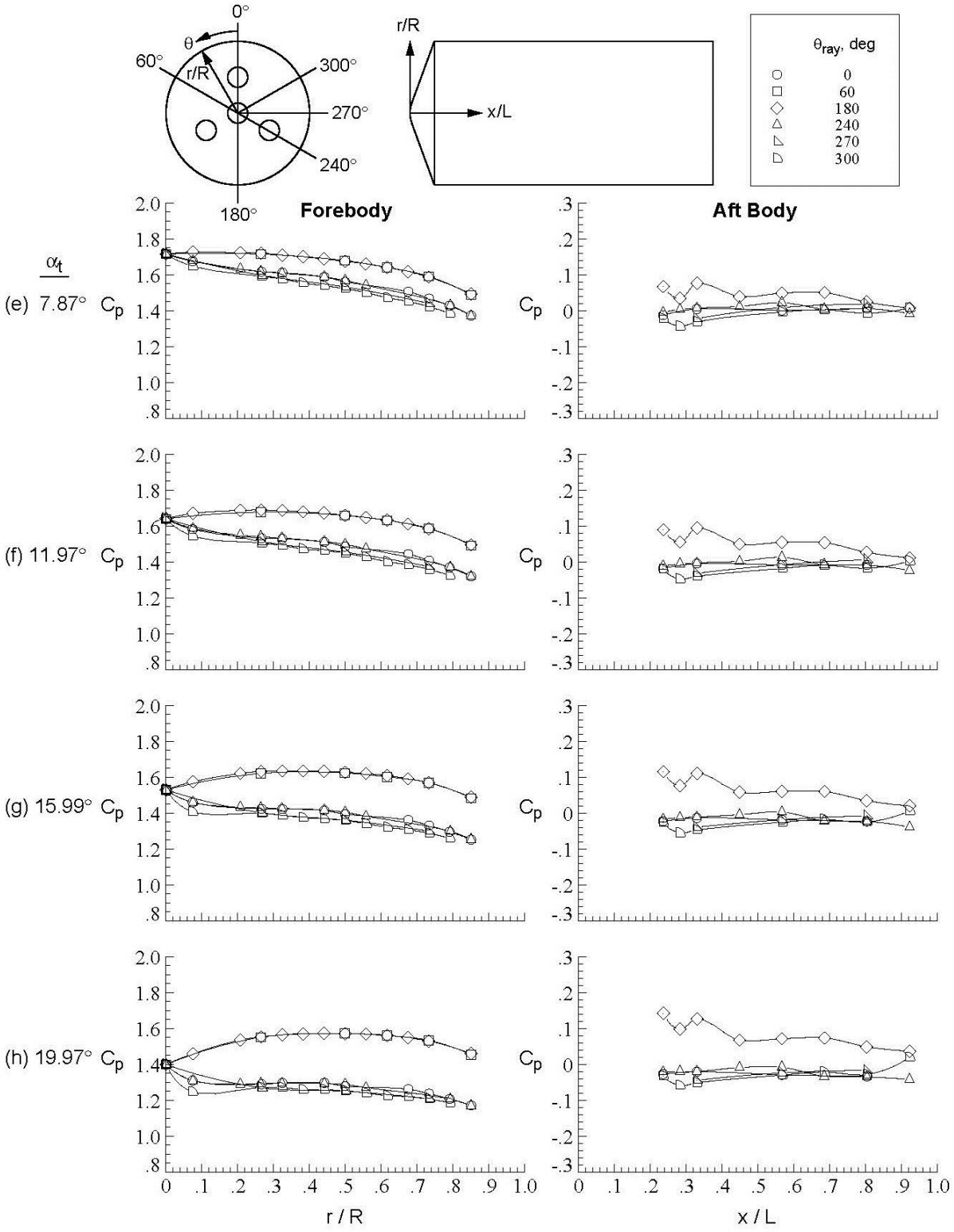

Figure D-69. Concluded.

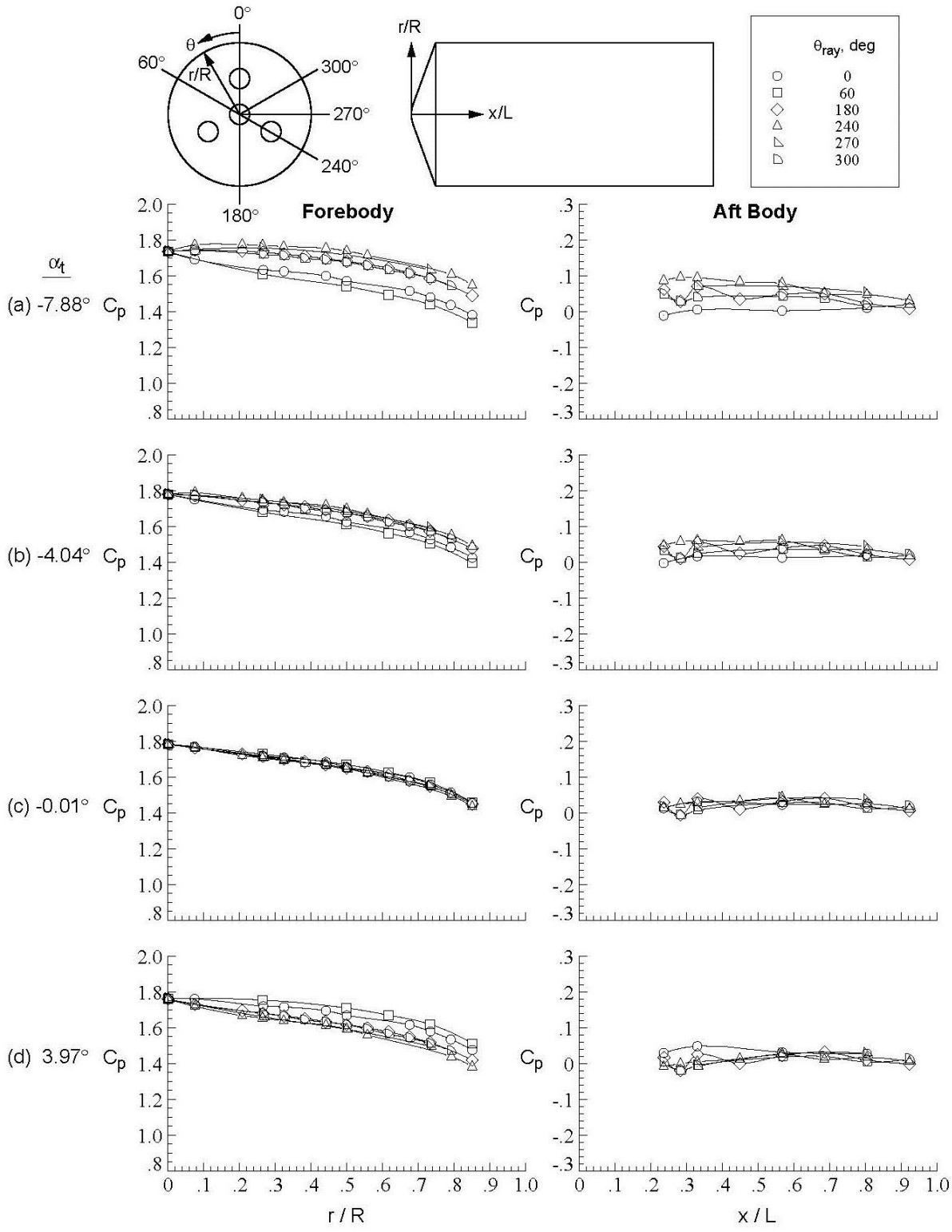

Figure D-70. Baseline configuration, Run 092, M_∞ = 4.6, Re_∞ = 1.1x10^7/ft, ϕ = 119.98°, X_S = 40.18 in, Y_S = 0.00 in, C_T = 0.00.

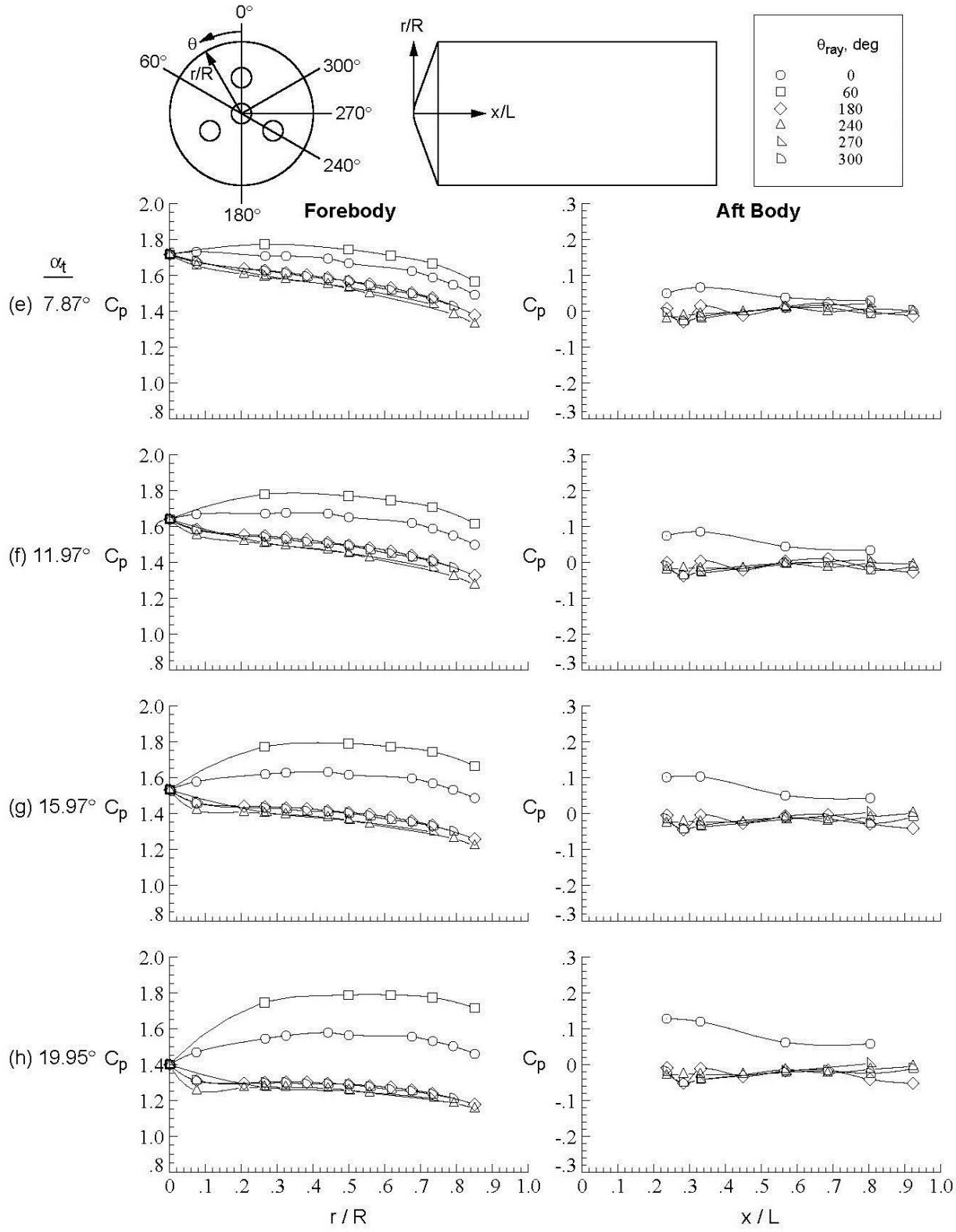

Figure D-70. Concluded.

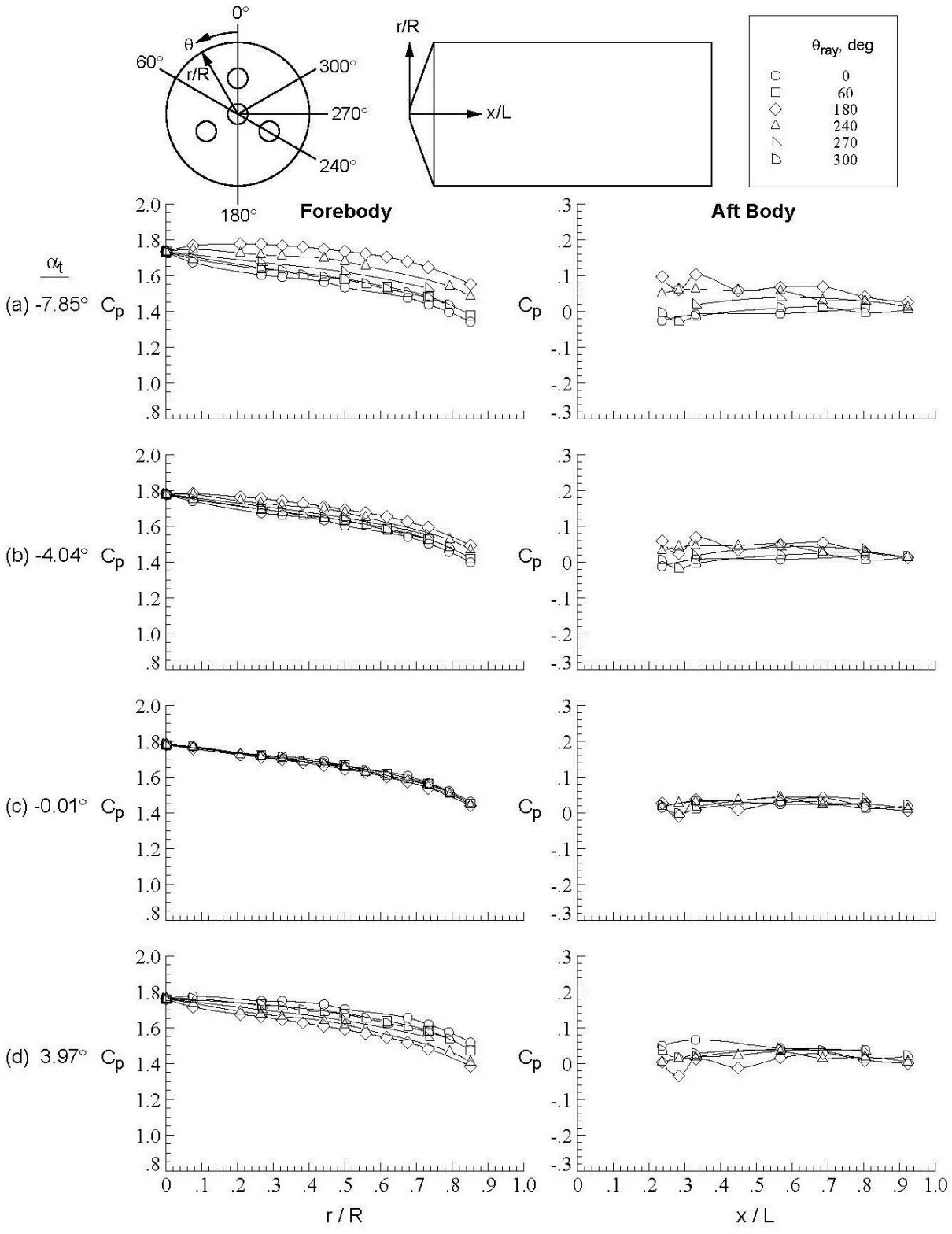

Figure D-71. Baseline configuration, Run 093, M_∞ = 4.6, Re_∞ = 1.1x10^7/ft, ϕ = 179.91°, X_S = 40.18 in, Y_S = 0.00 in, C_T = 0.00.

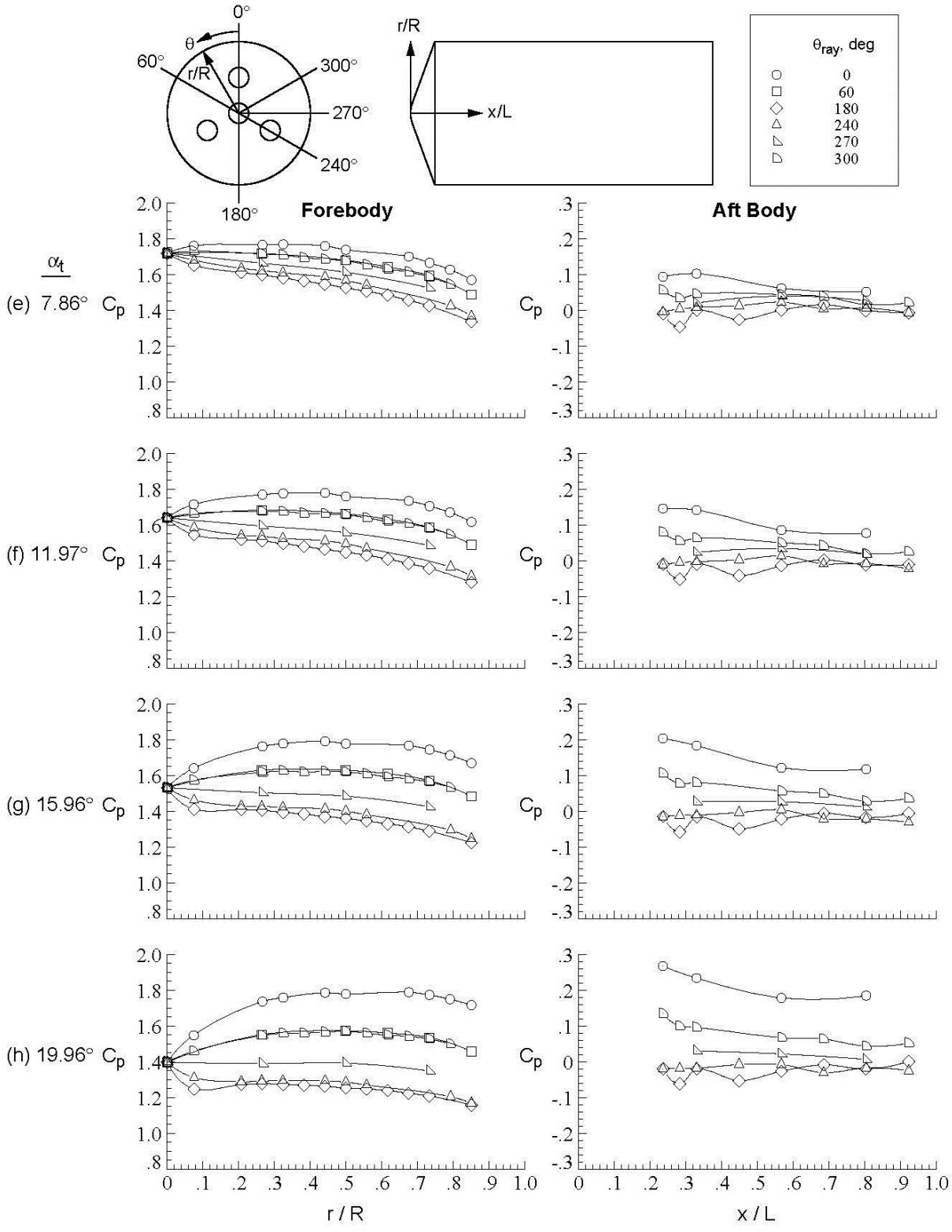

Figure D-71. Concluded.

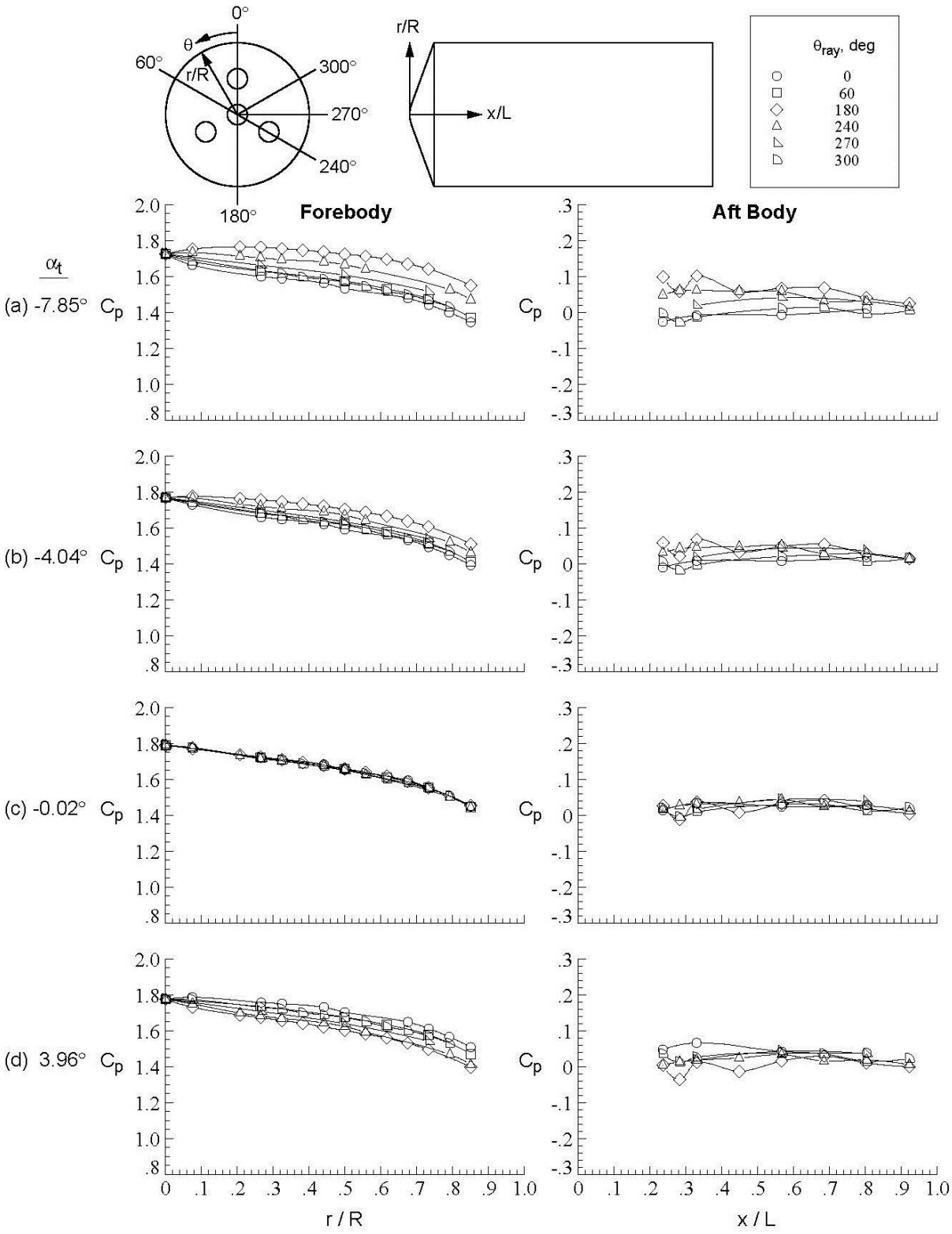

Figure D-72. Baseline configuration, Run 094, M_∞ = 4.6, Re_∞ = 1.1x10^7/ft, ϕ = 179.91°, X_S = 50.14 in, Y_S = 0.00 in, C_T = 0.00.

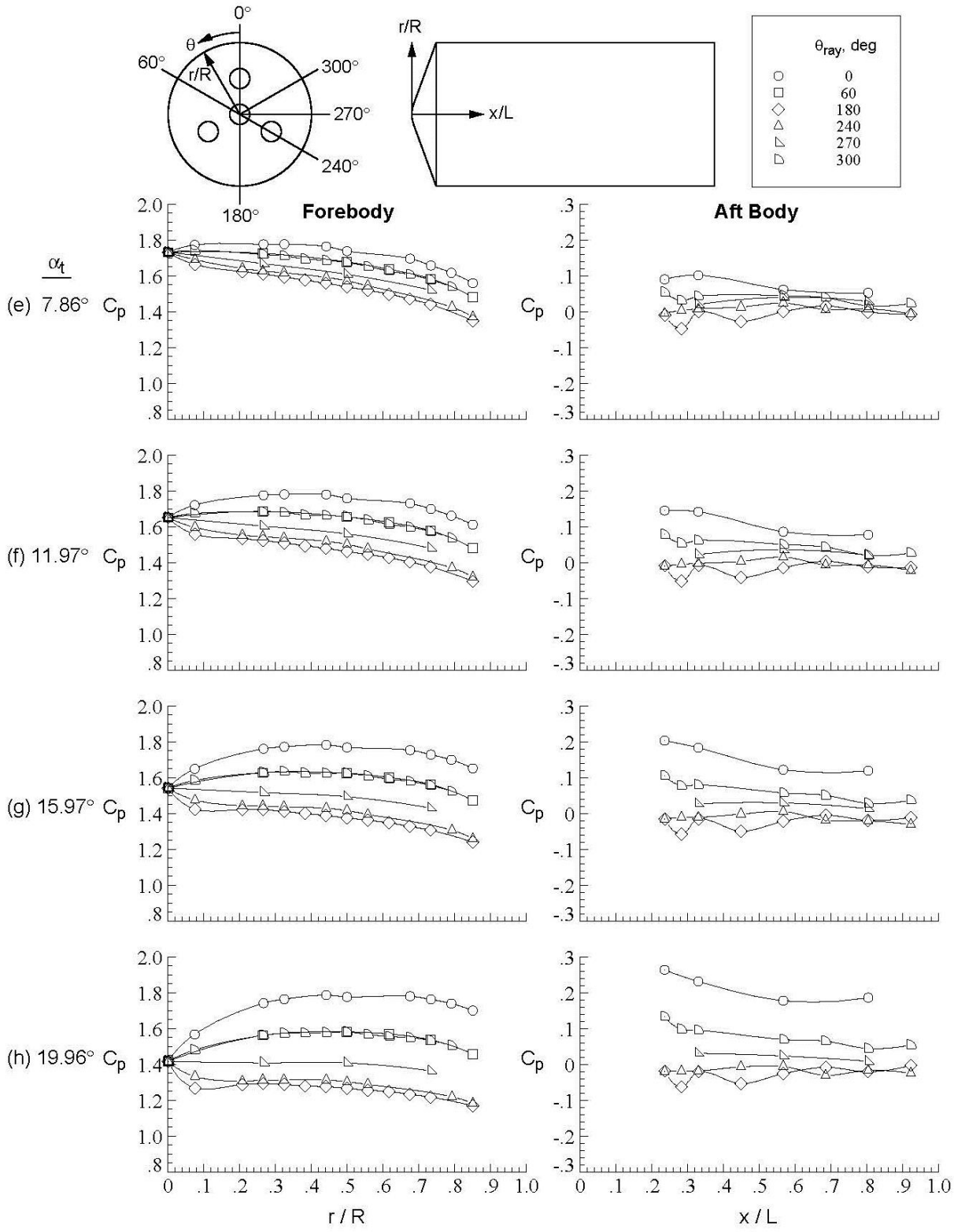

Figure D-72. Concluded.

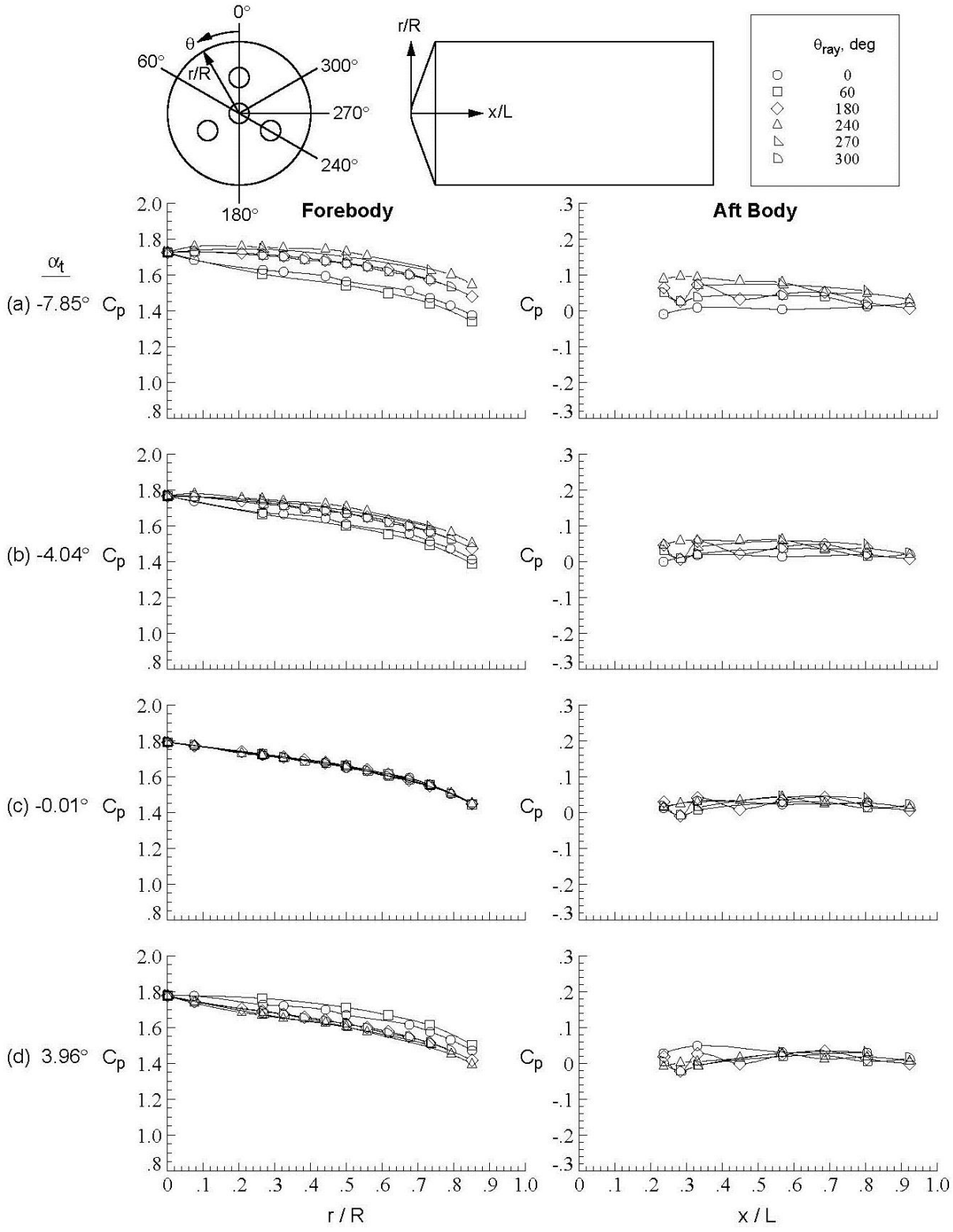

Figure D-73. Baseline configuration, Run 095, M_∞ = 4.6, Re_∞ = 1.1x10^7/ft, ϕ = 119.96°, X_S = 50.14 in, Y_S = 0.00 in, C_T = 0.00.

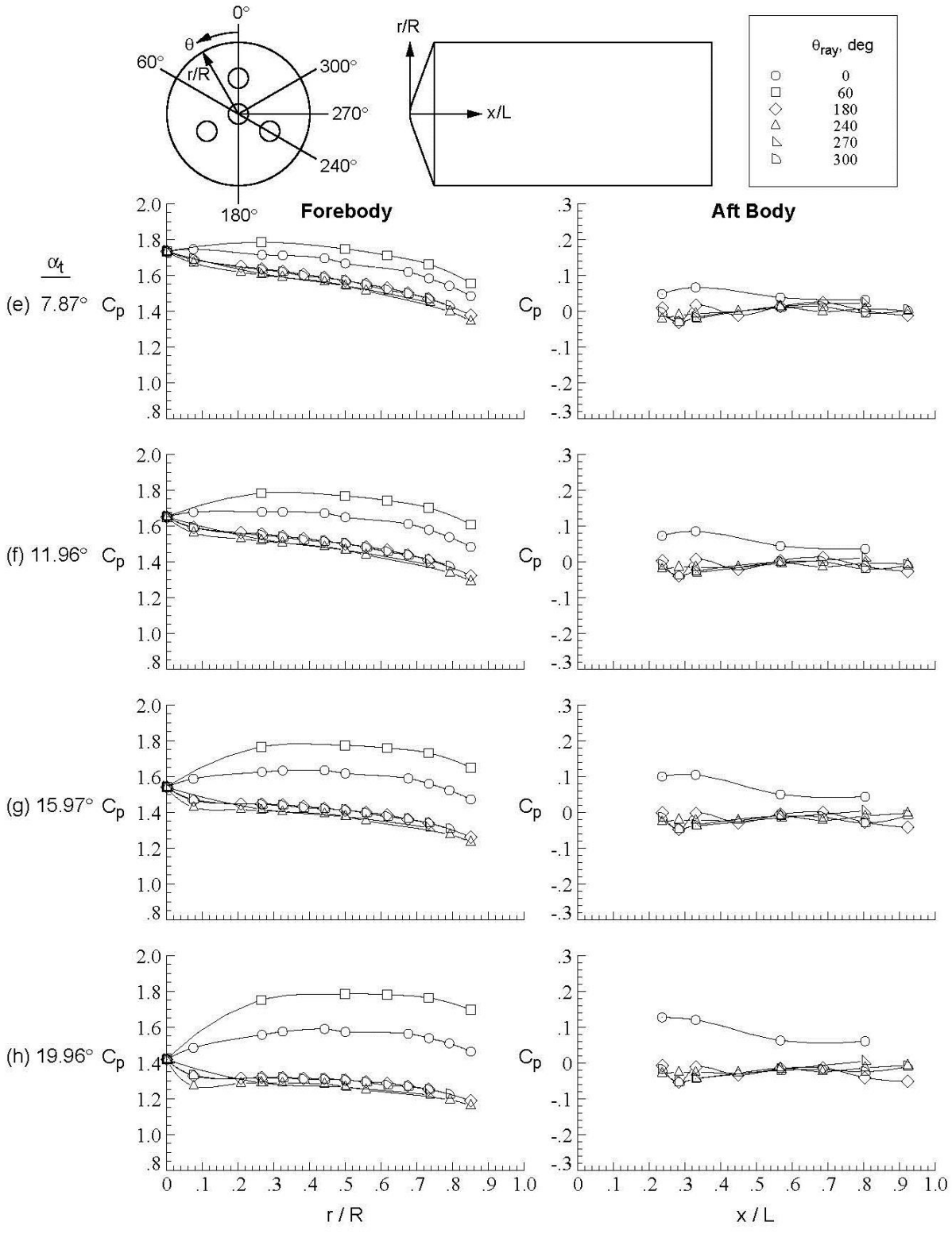

Figure D-73. Concluded.

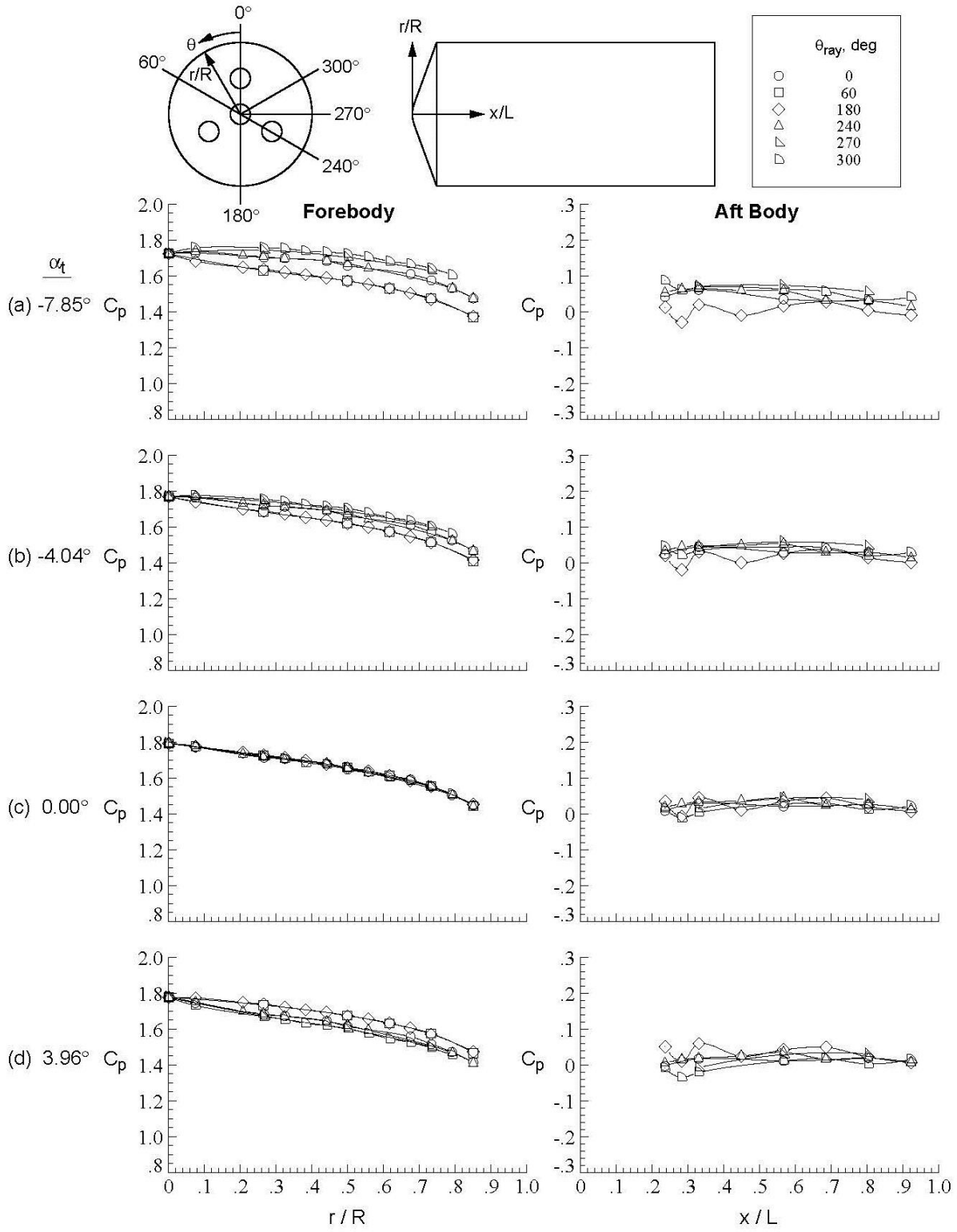

Figure D-74. Baseline configuration, Run 096, M_∞ = 4.6, Re_∞ = 1.1x10^7/ft, ϕ = 59.90°, X_S = 50.14 in, Y_S = 0.00 in, C_T = 0.00.

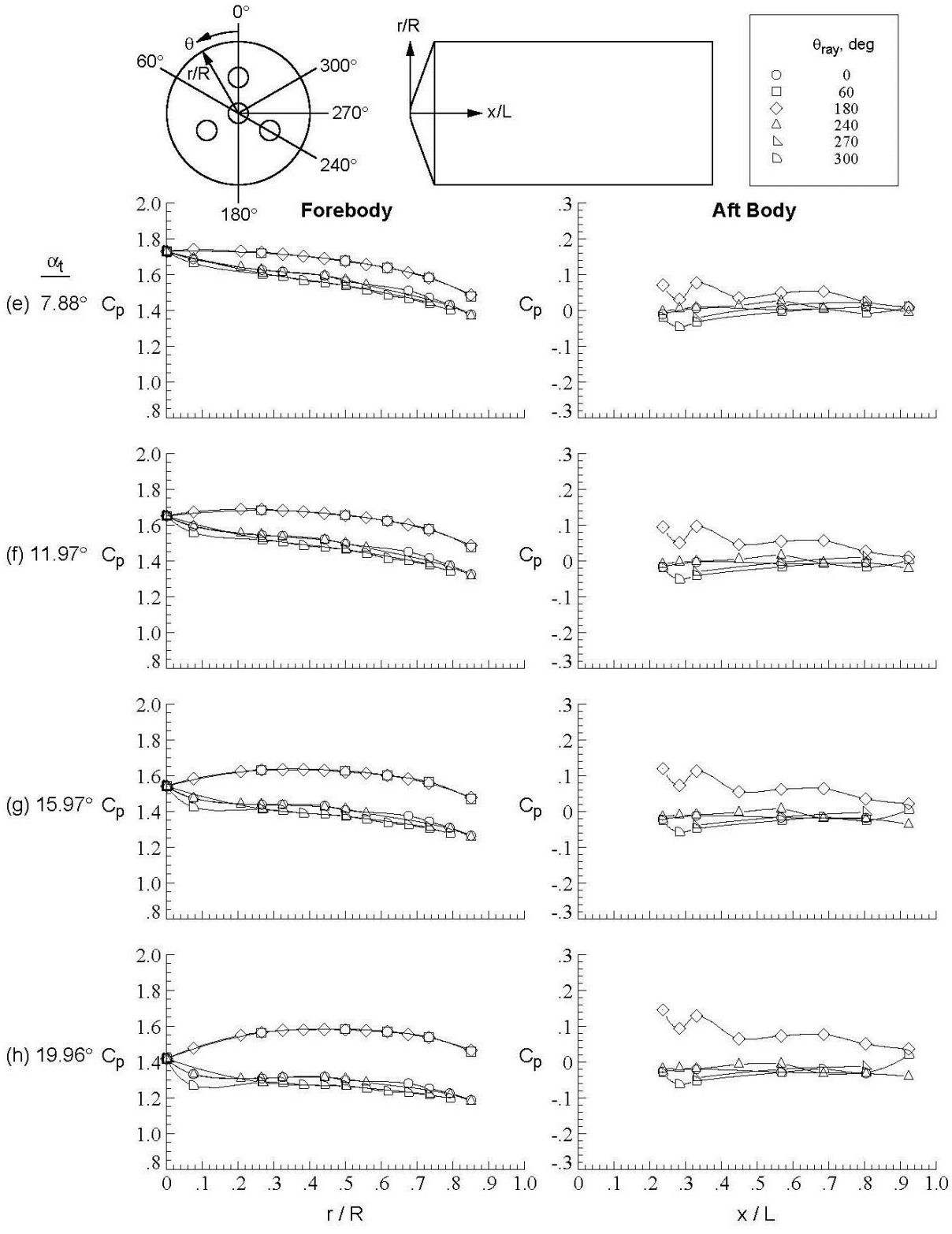

Figure D-74. Concluded.

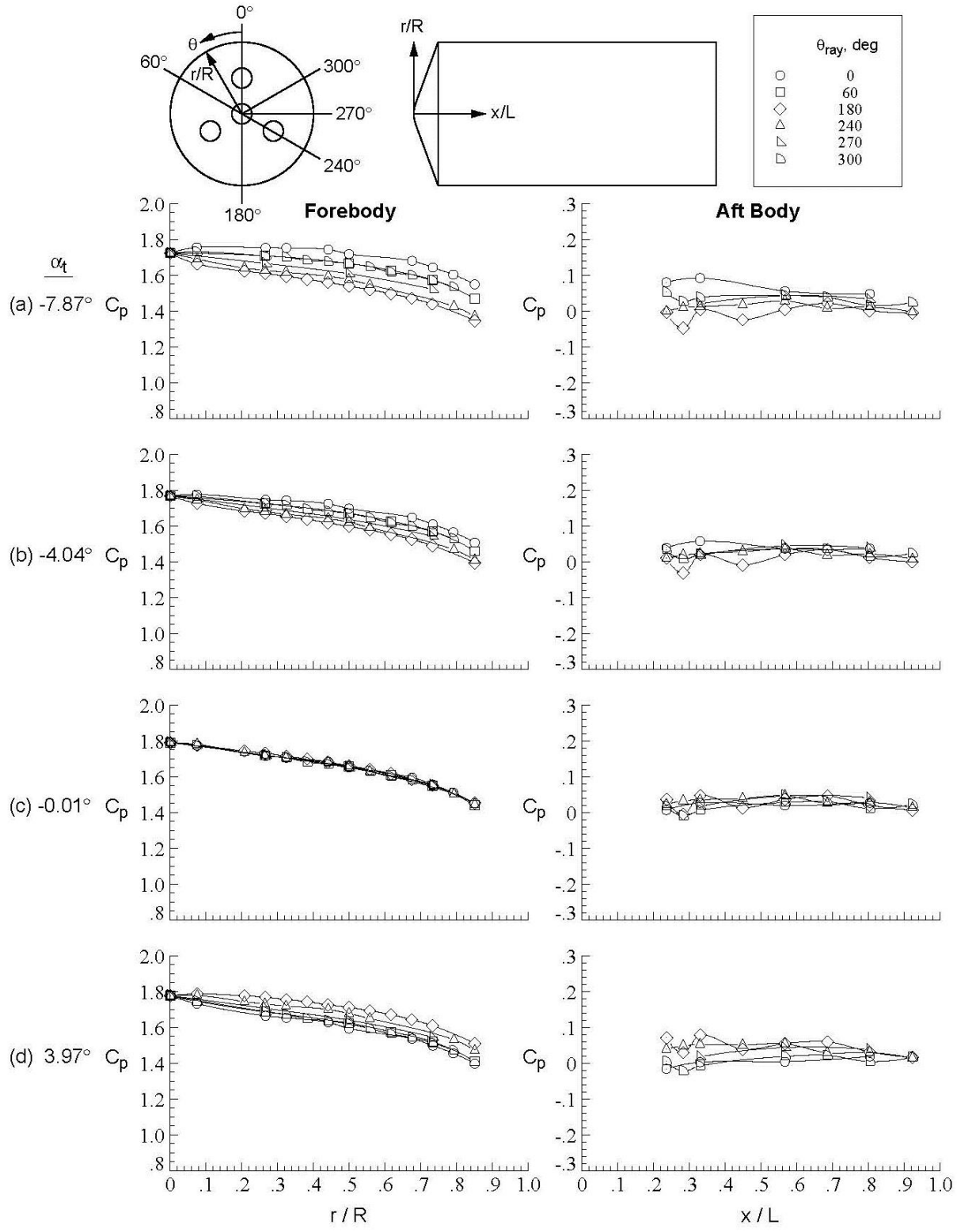

Figure D-75. Baseline configuration, Run 097, M_∞ = 4.6, Re_∞ = 1.1x10^7/ft, ϕ = −0.07°, X_S = 50.14 in, Y_S = 0.00 in, C_T = 0.00.

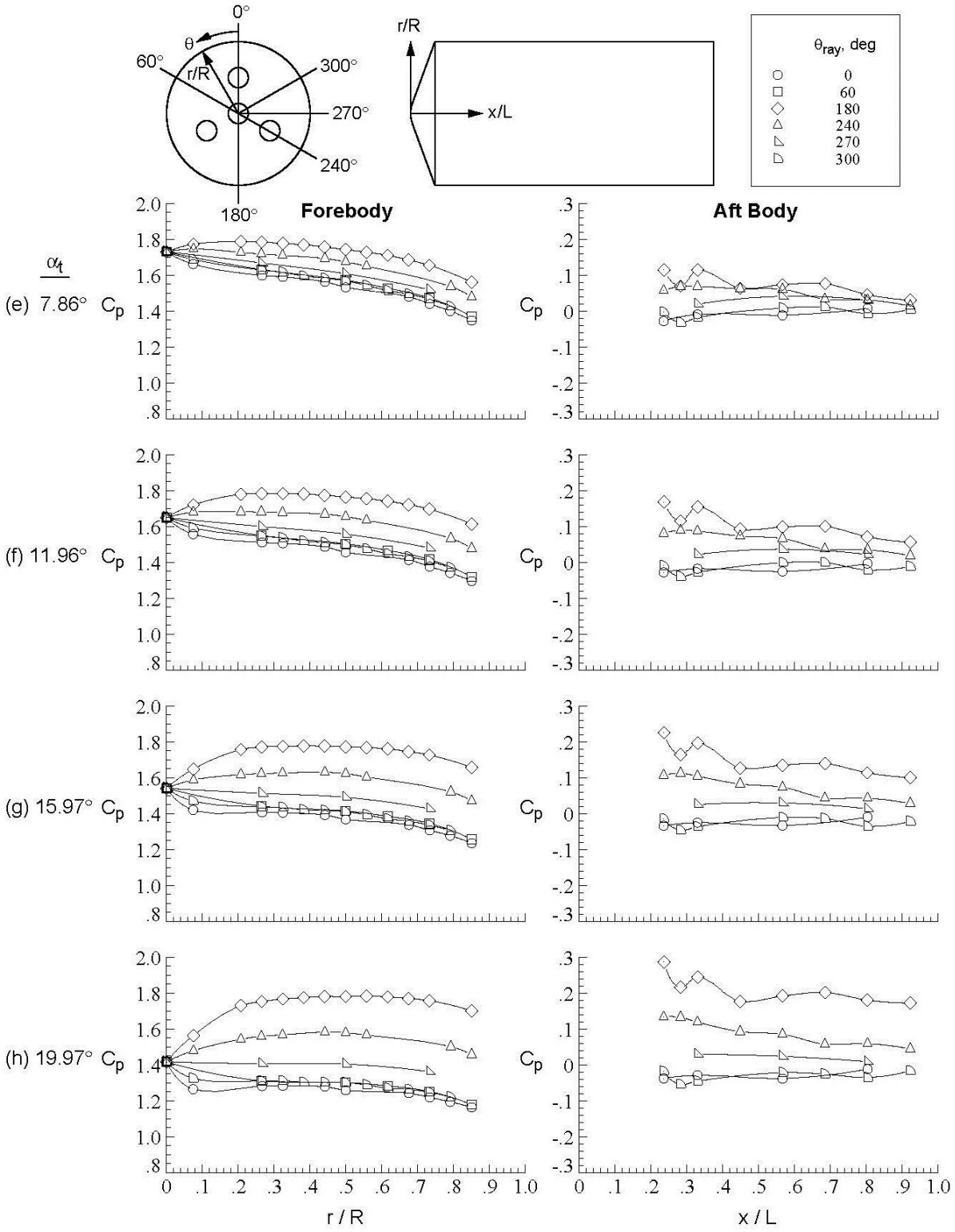

Figure D-75. Concluded.

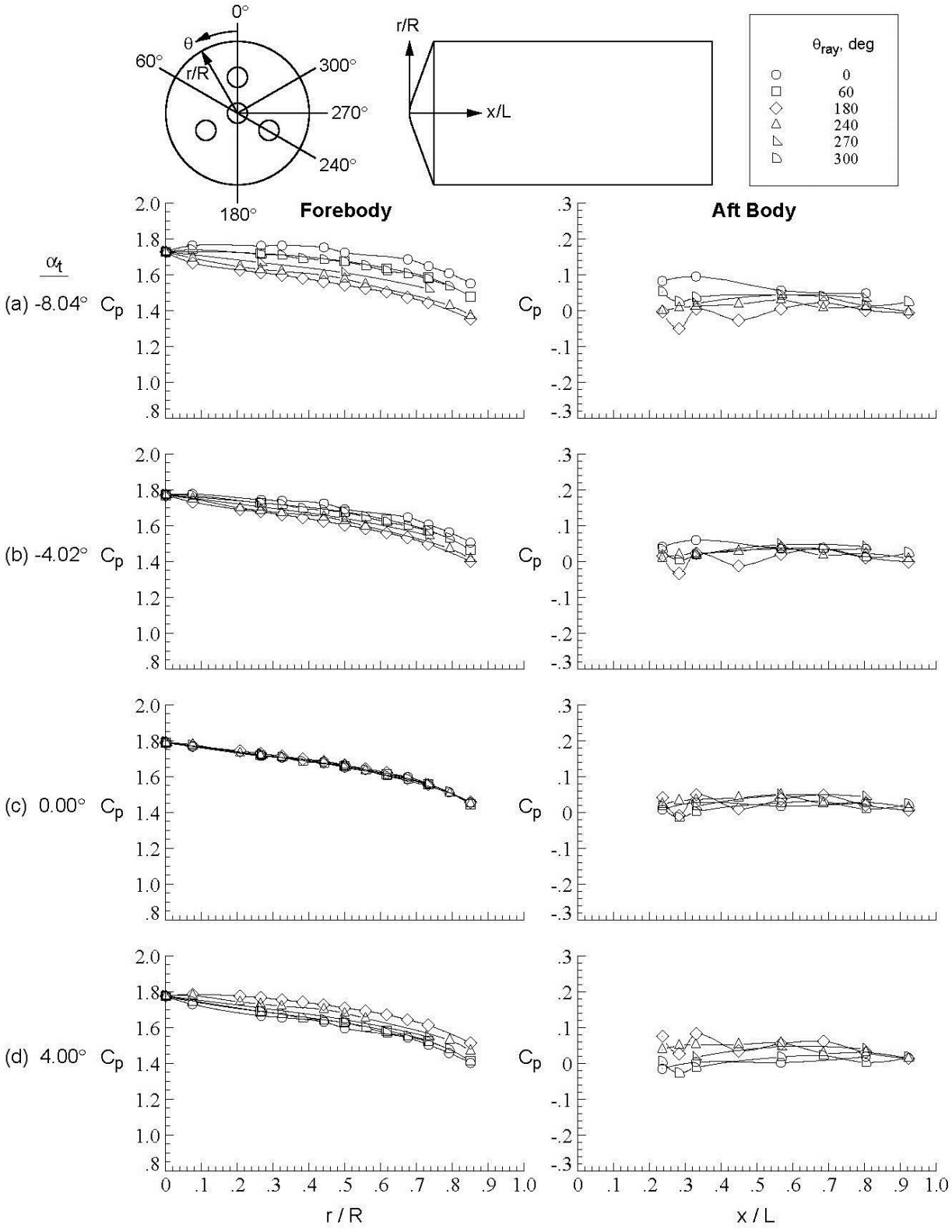

Figure D-76. Baseline configuration, Run 098, M_∞ = 4.6, Re_∞ = 1.1x10^7/ft, ϕ = −0.07°, X_S = 50.14 in, Y_S = 7.99 in, C_T = 0.00.

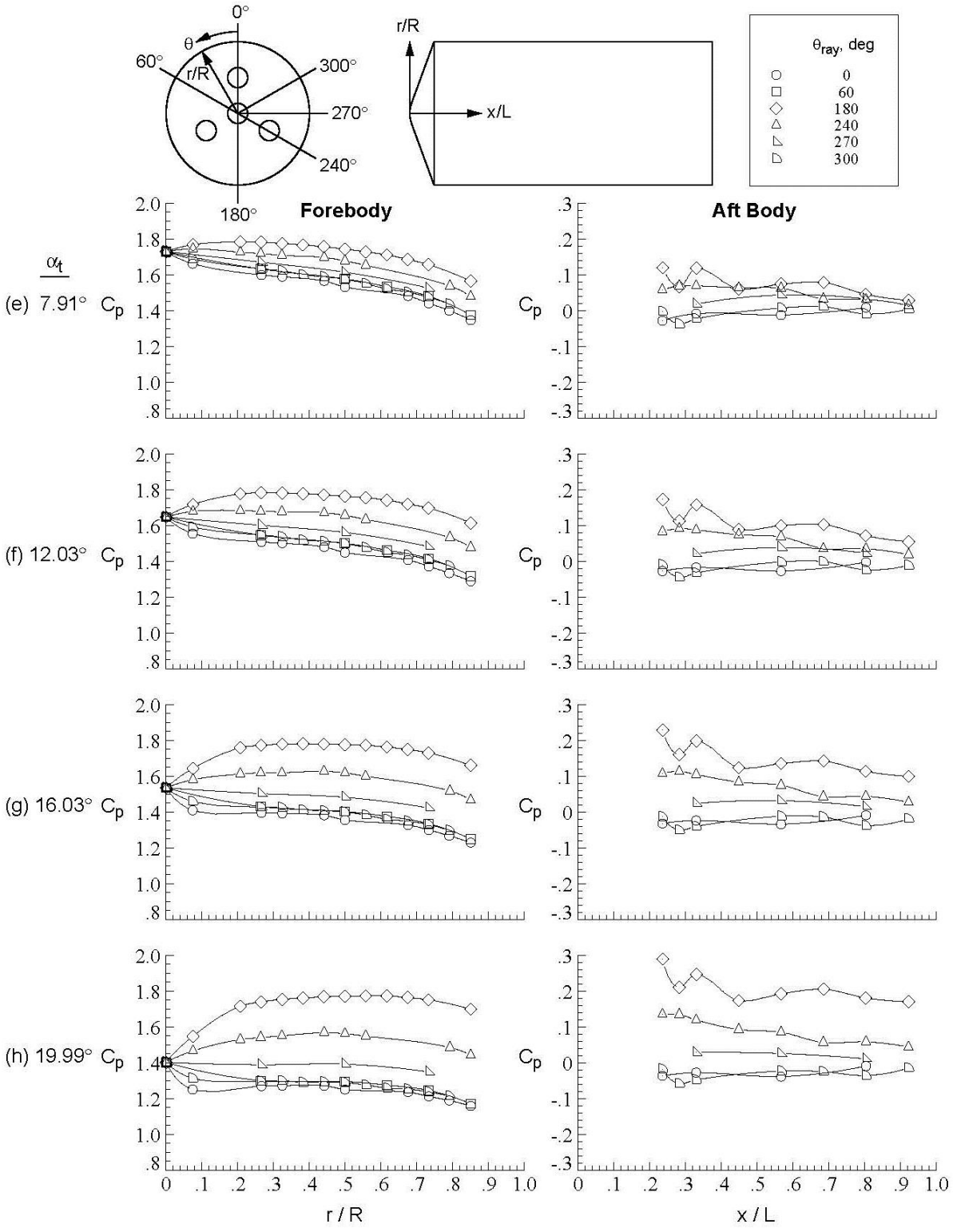

Figure D-76. Concluded.

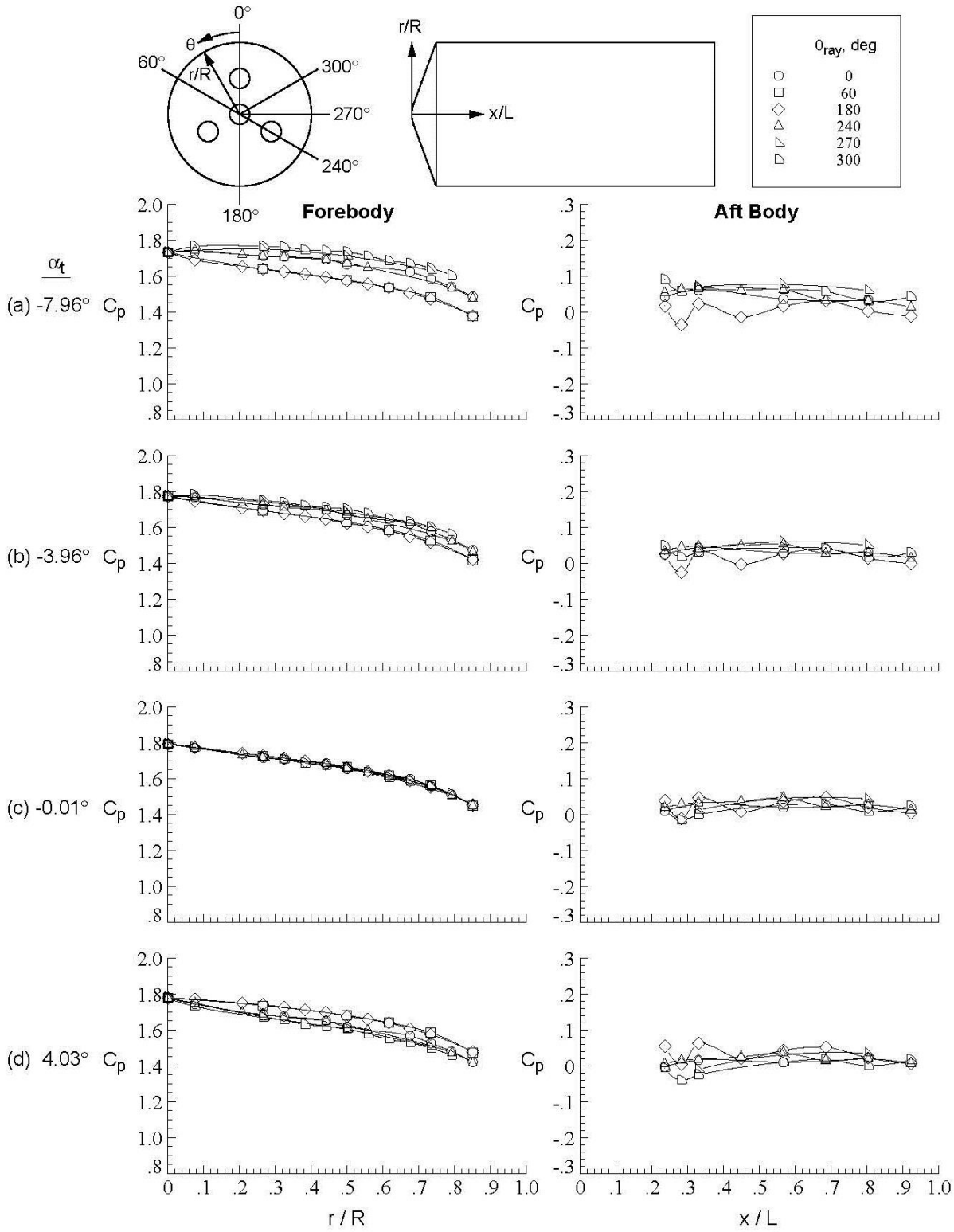

Figure D-77. Baseline configuration, Run 099, M_∞ = 4.6, Re_∞ = 1.1x10^7/ft, ϕ = 59.86°, X_S = 50.14 in, Y_S = 7.99 in, C_T = 0.00.

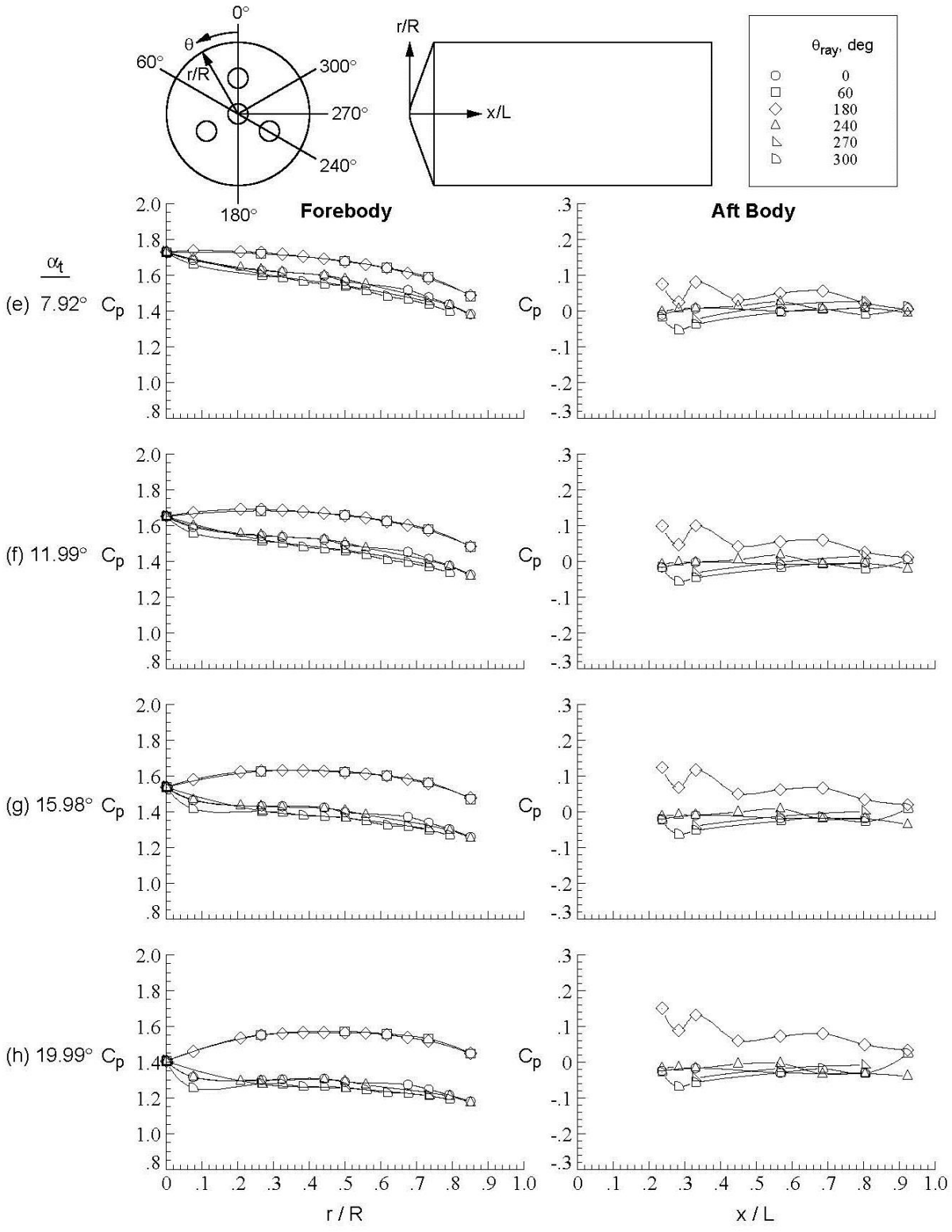

Figure D-77. Concluded.

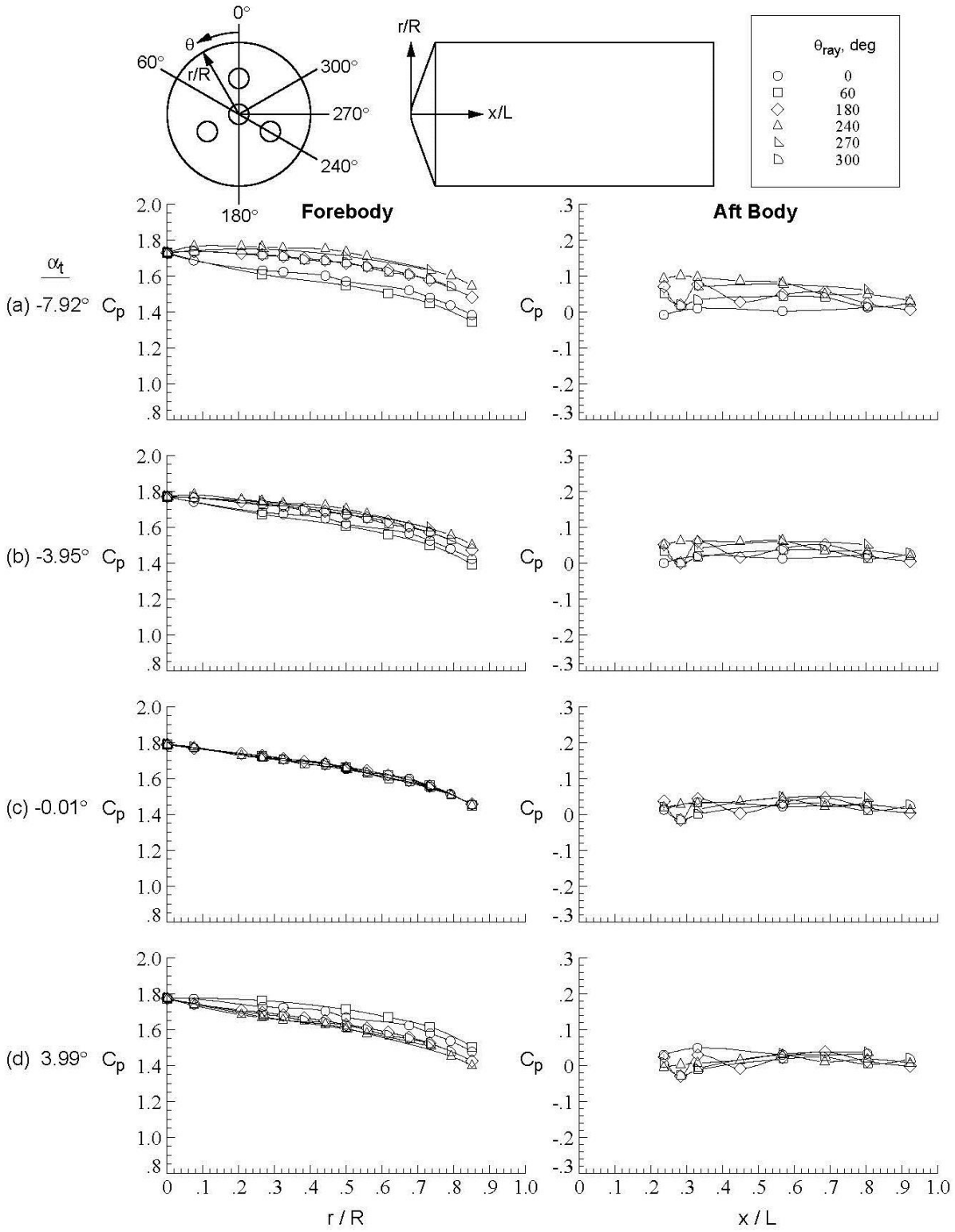

Figure D-78. Baseline configuration, Run 100, M_∞ = 4.6, Re_∞ = 1.1x10^7/ft, ϕ = 120.06°, X_S = 50.14 in, Y_S = 7.99 in, C_T = 0.00.

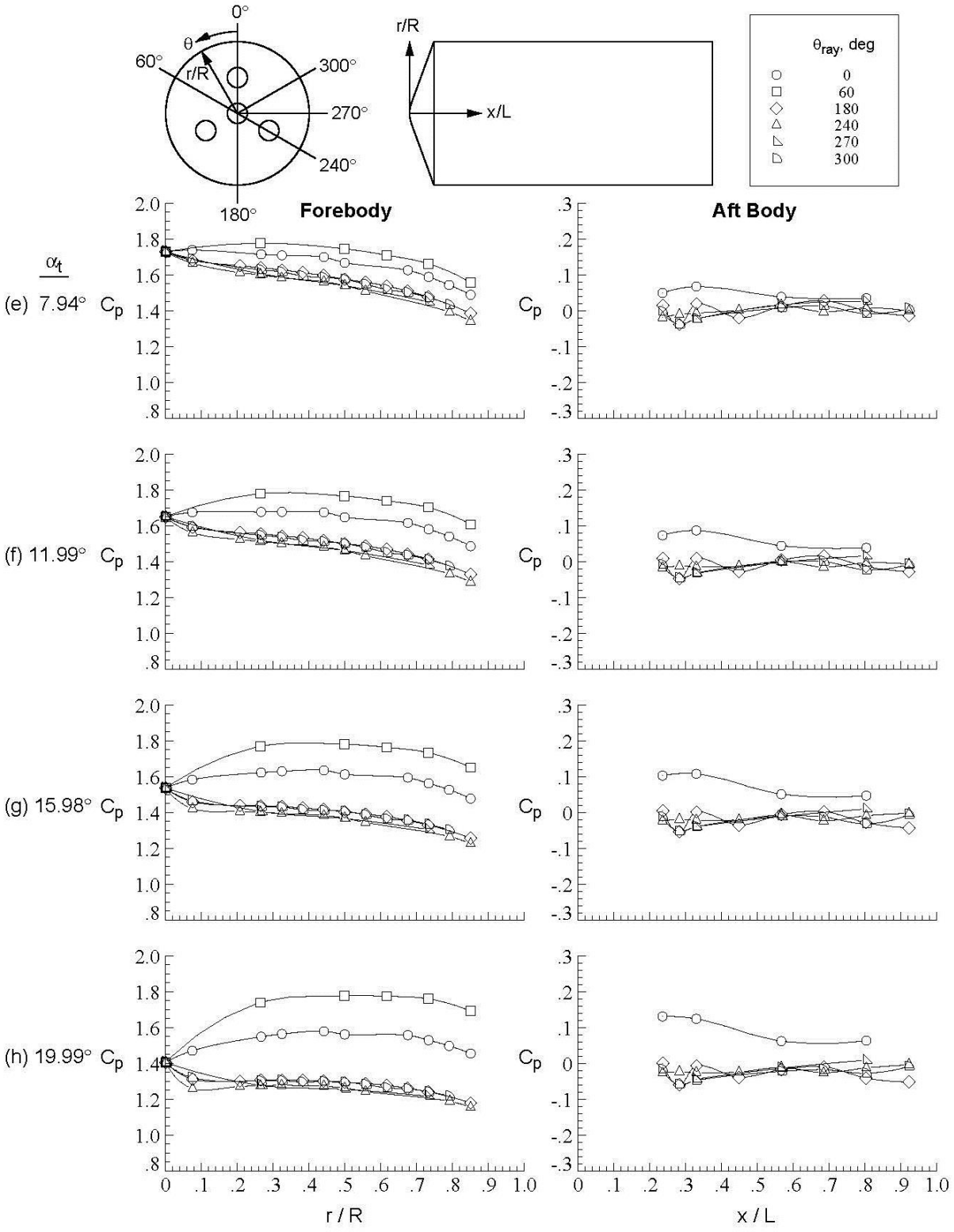

Figure D-78. Concluded.

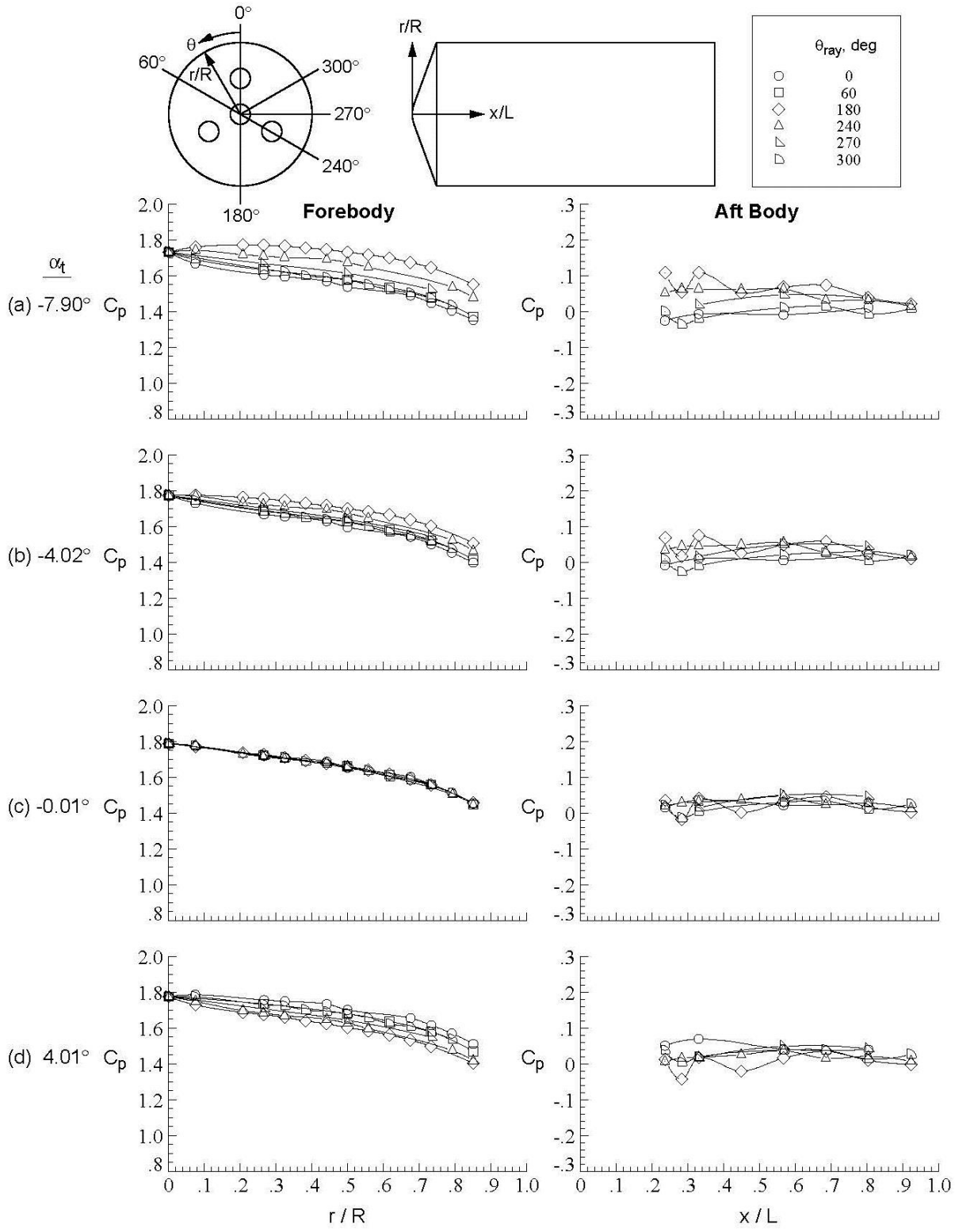

Figure D-79. Baseline configuration, Run 101, M_∞ = 4.6, Re_∞ = 1.1x10^7/ft, ϕ = 179.97°, X_S = 50.14 in, Y_S = 7.99 in, C_T = 0.00.

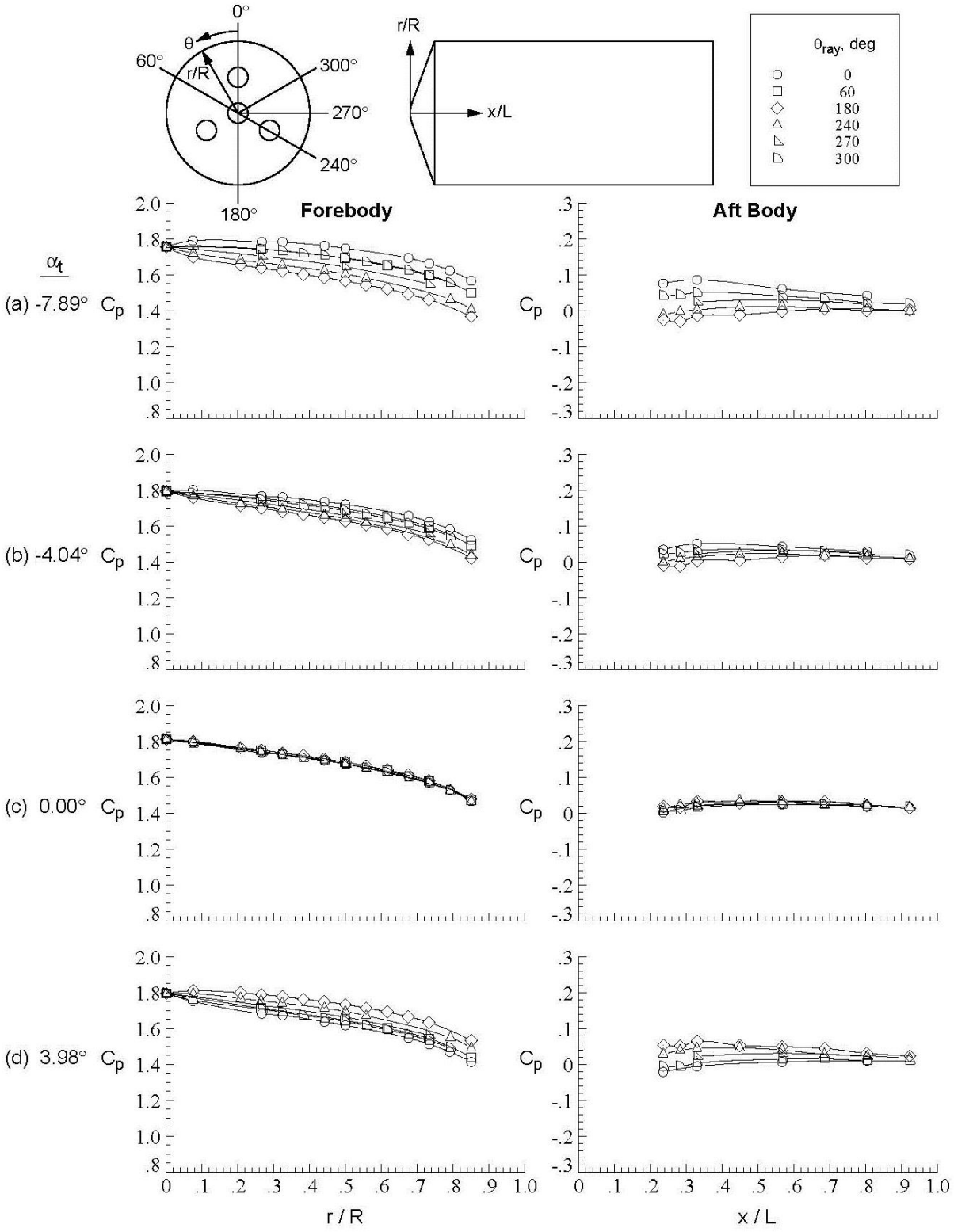

Figure D-80. Baseline configuration, Run 104, M_∞ = 4.6, Re_∞ = 1.5x10^7/ft, ϕ = −0.03°, X_S = 25.19 in, Y_S = 0.00 in, C_T = 0.00.

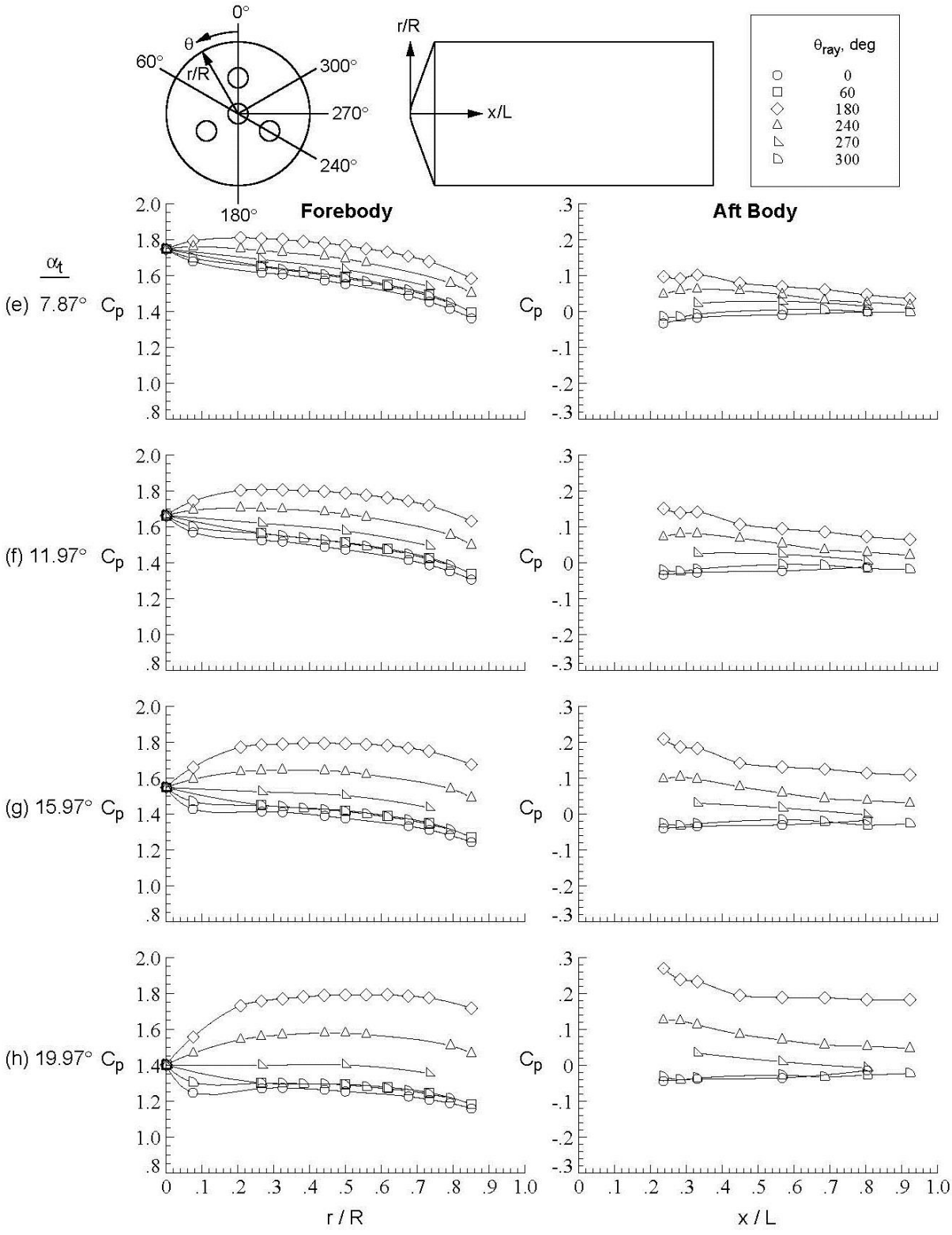

Figure D-80. Concluded.

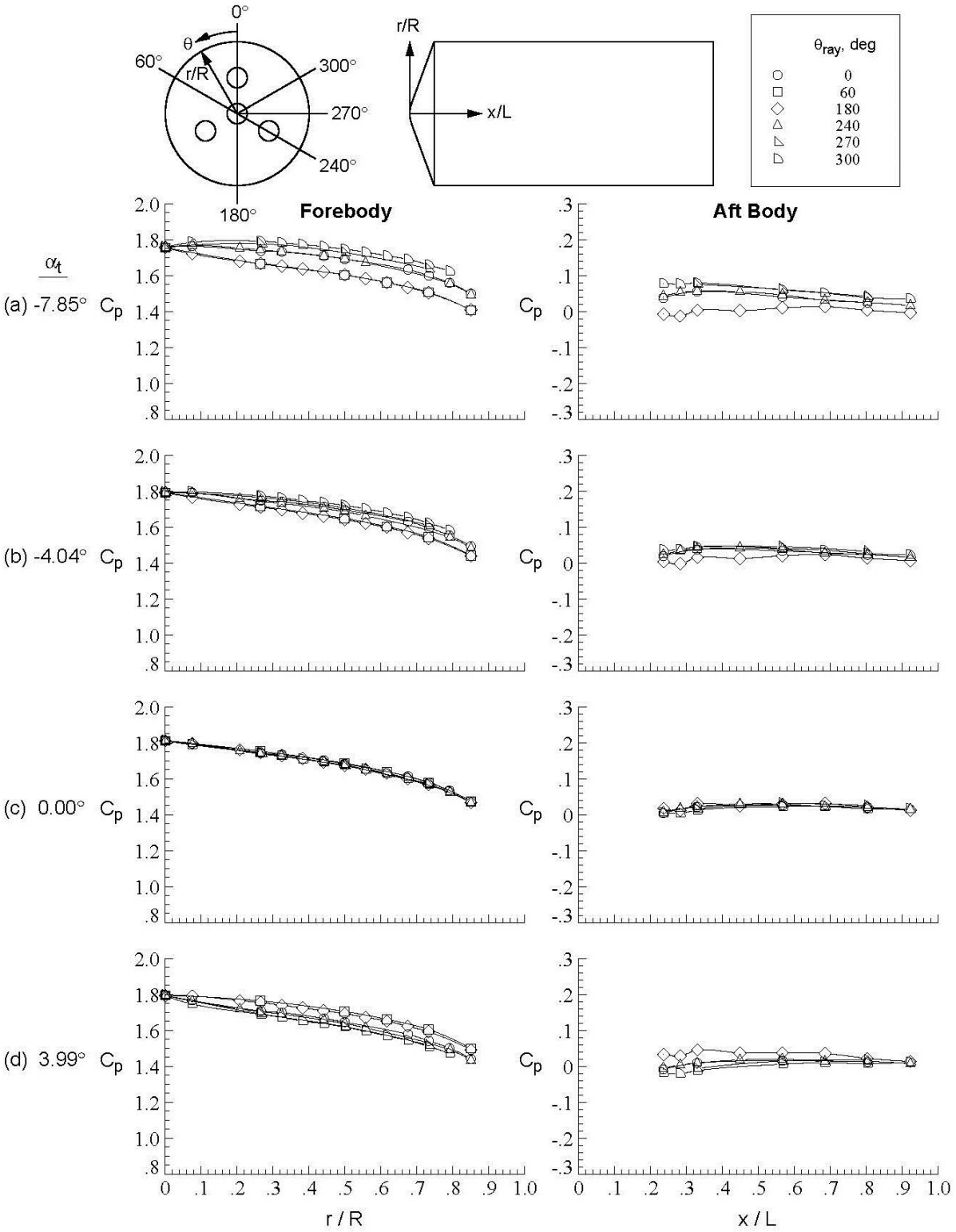

Figure D-81. Baseline configuration, Run 105, M_∞ = 4.6, Re_∞ = 1.5x10^7/ft, ϕ = 59.94°, X_S = 25.19 in, Y_S = 0.00 in, C_T = 0.00.

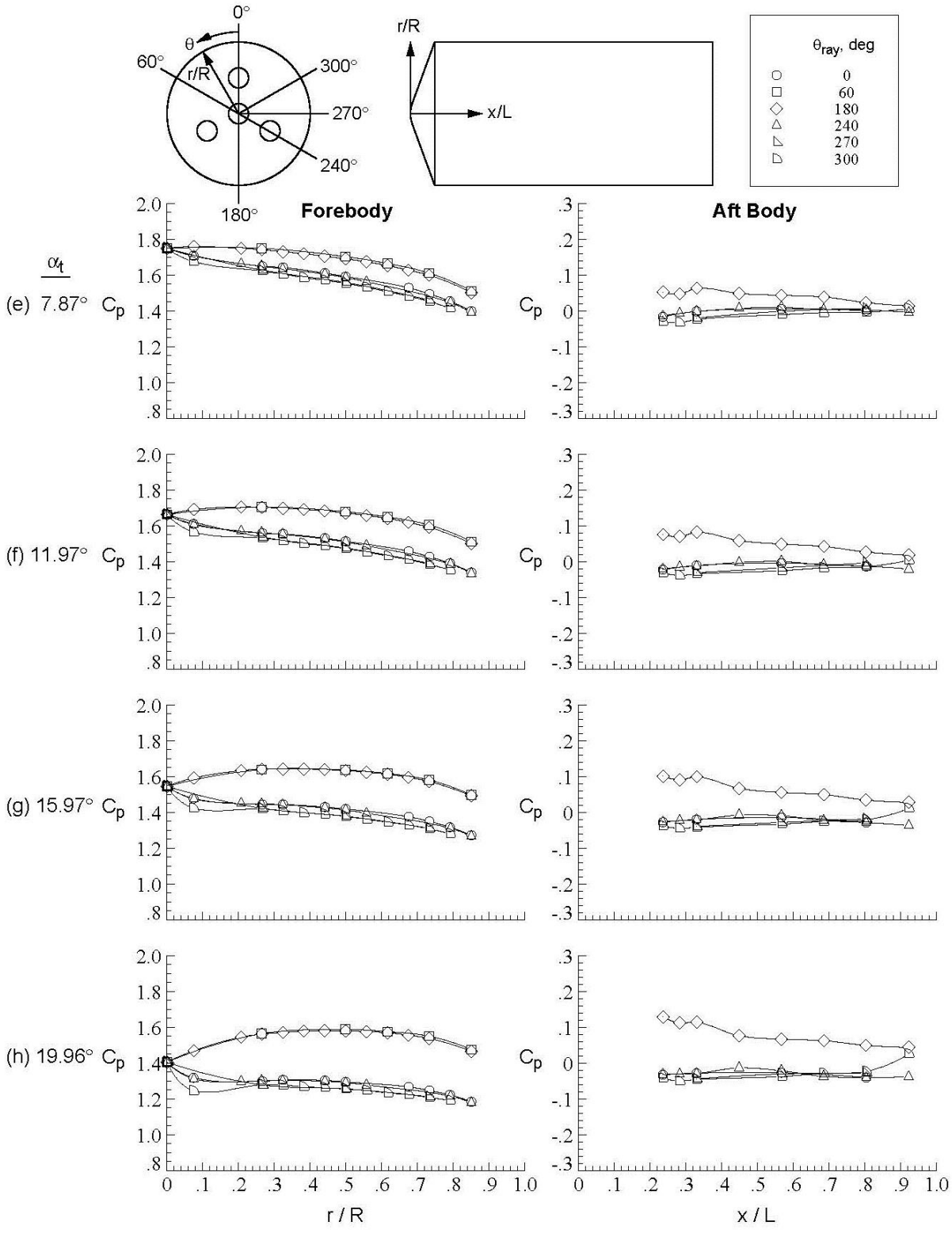

Figure D-81. Concluded.

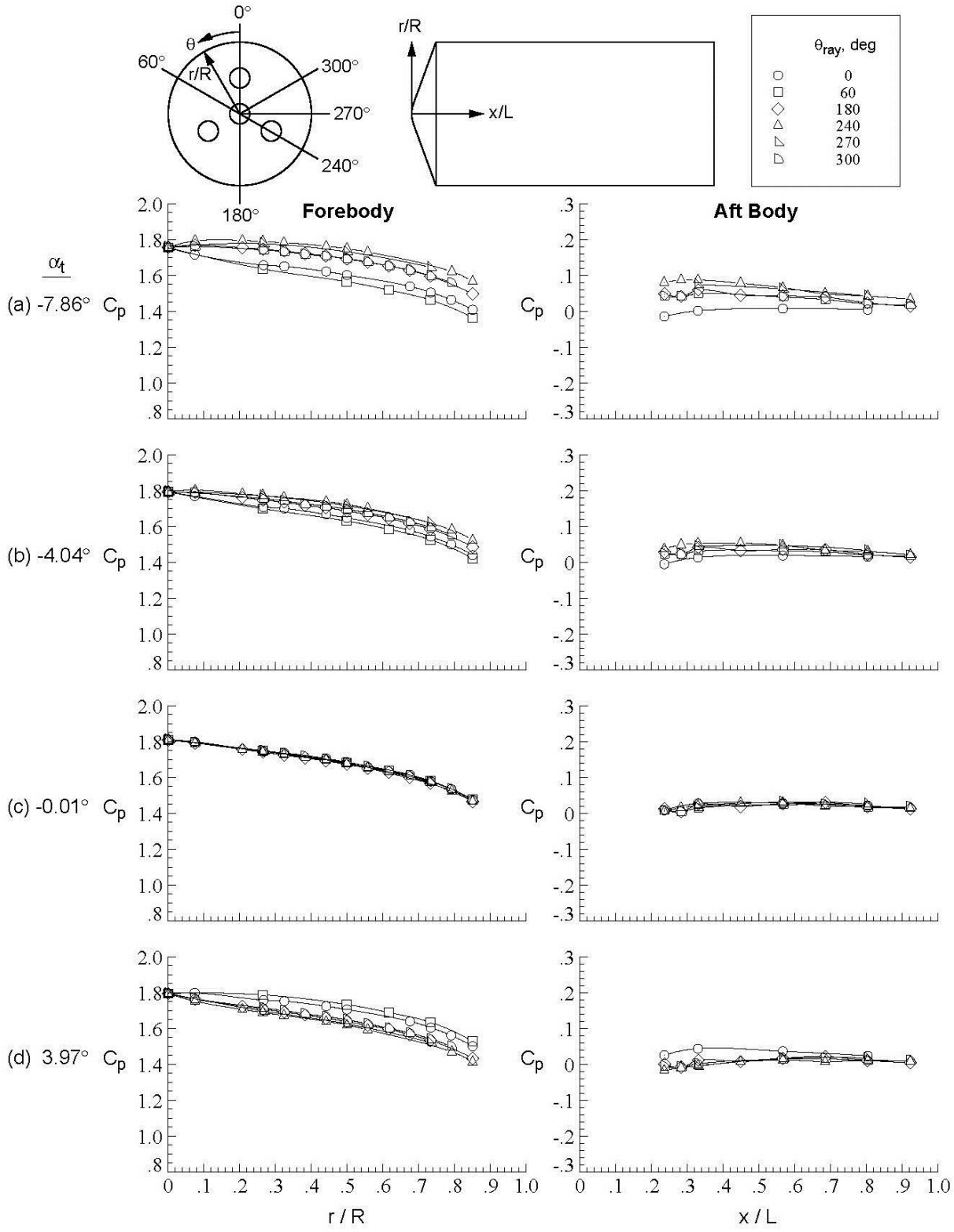

Figure D-82. Baseline configuration, Run 106, M_∞ = 4.6, Re_∞ = 1.5x10^7/ft, ϕ = 120.02°, X_S = 25.19 in, Y_S = 0.00 in, C_T = 0.00.

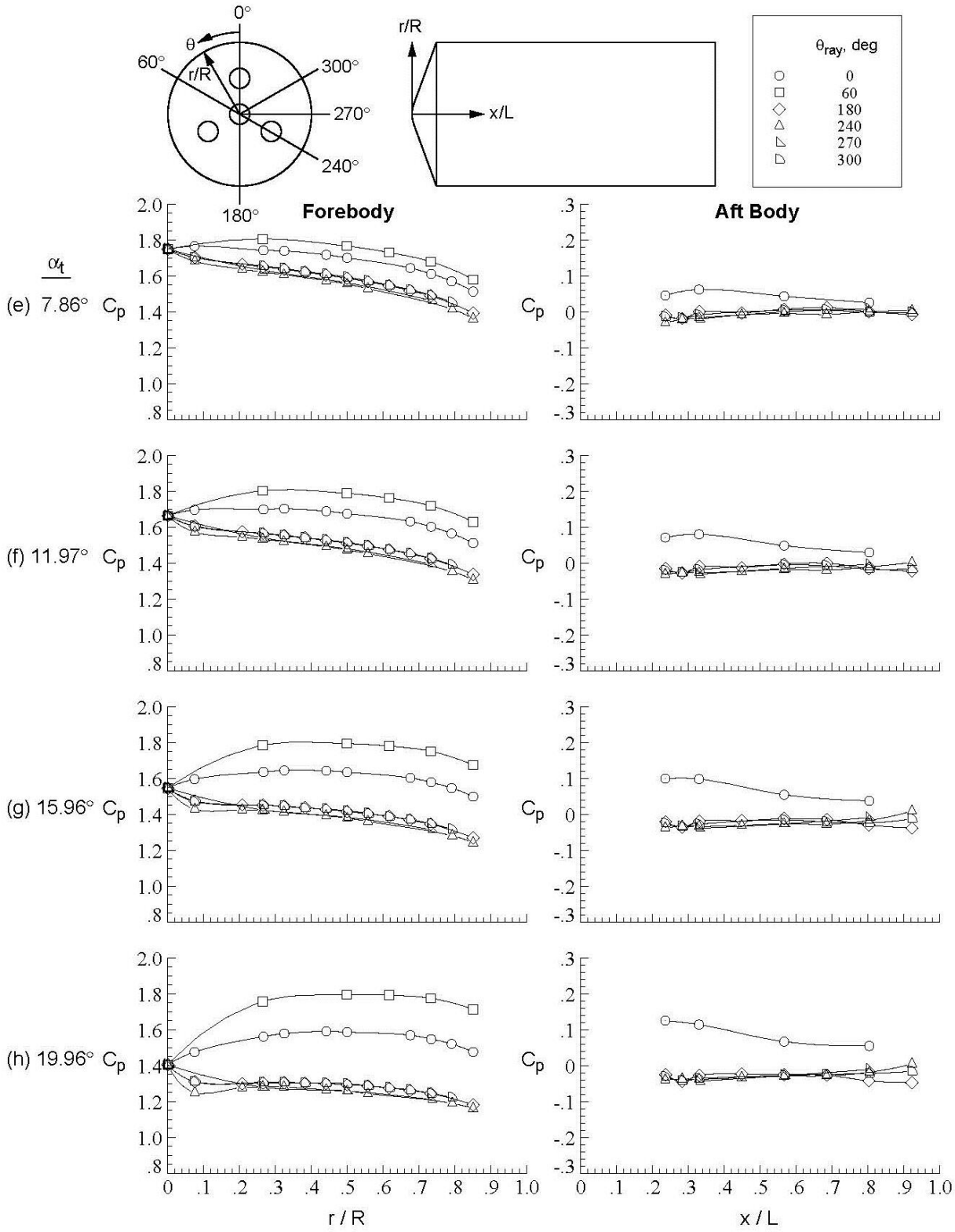

Figure D-82. Concluded.

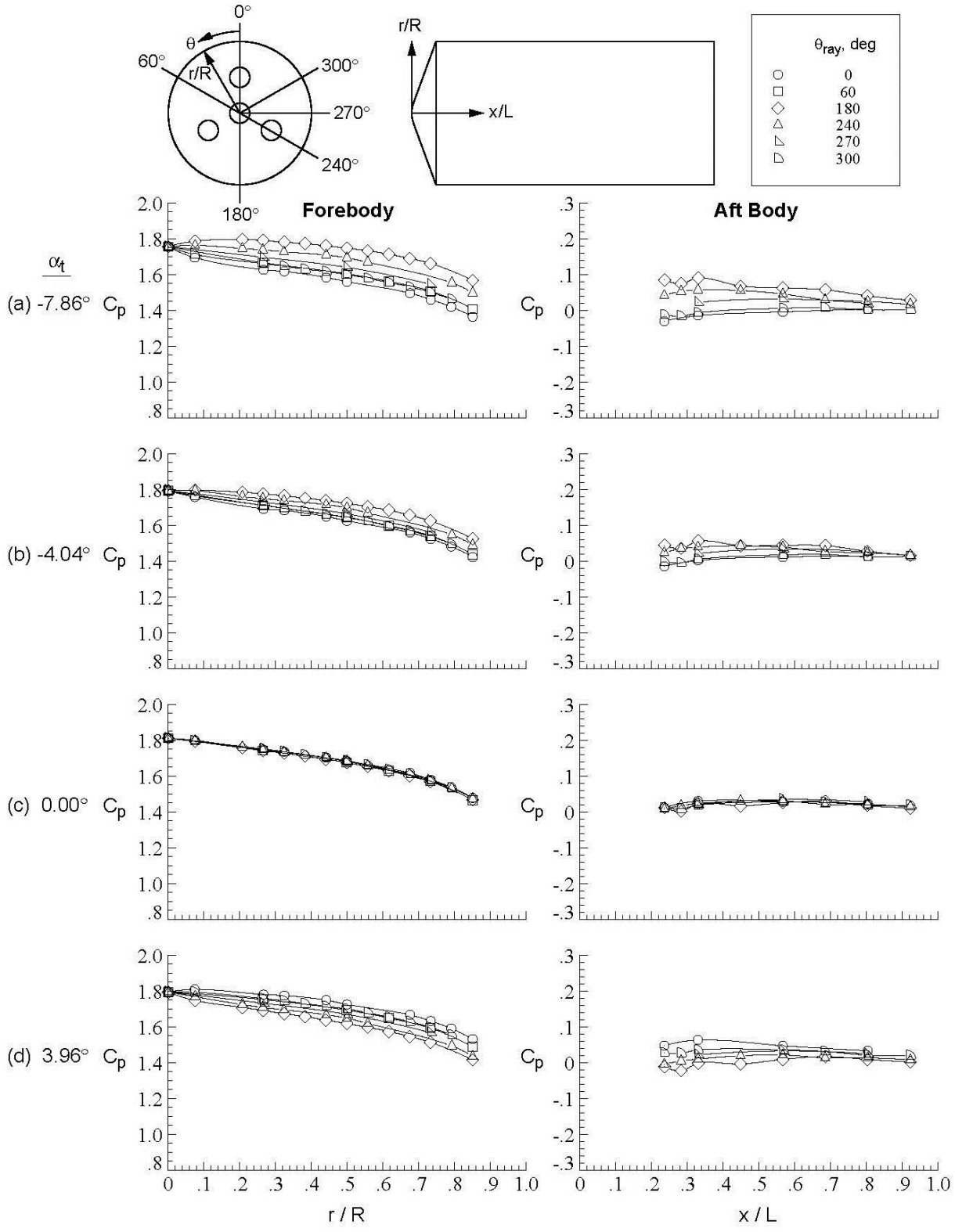

Figure D-83. Baseline configuration, Run 107, M_∞ = 4.6, Re_∞ = 1.5x10^7/ft, ϕ = 179.93°, X_S = 25.19 in, Y_S = 0.00 in, C_T = 0.00.

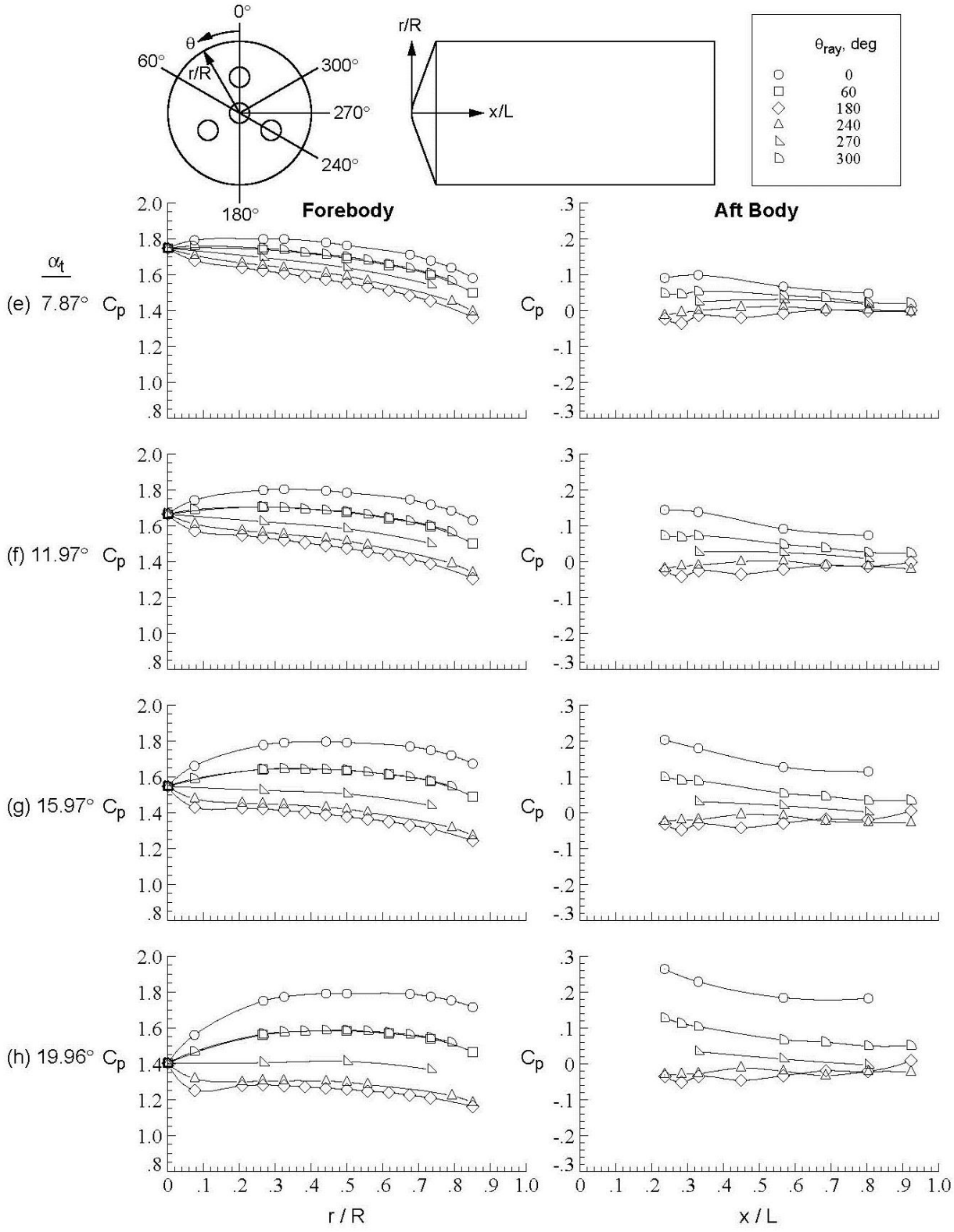

Figure D-83. Concluded.

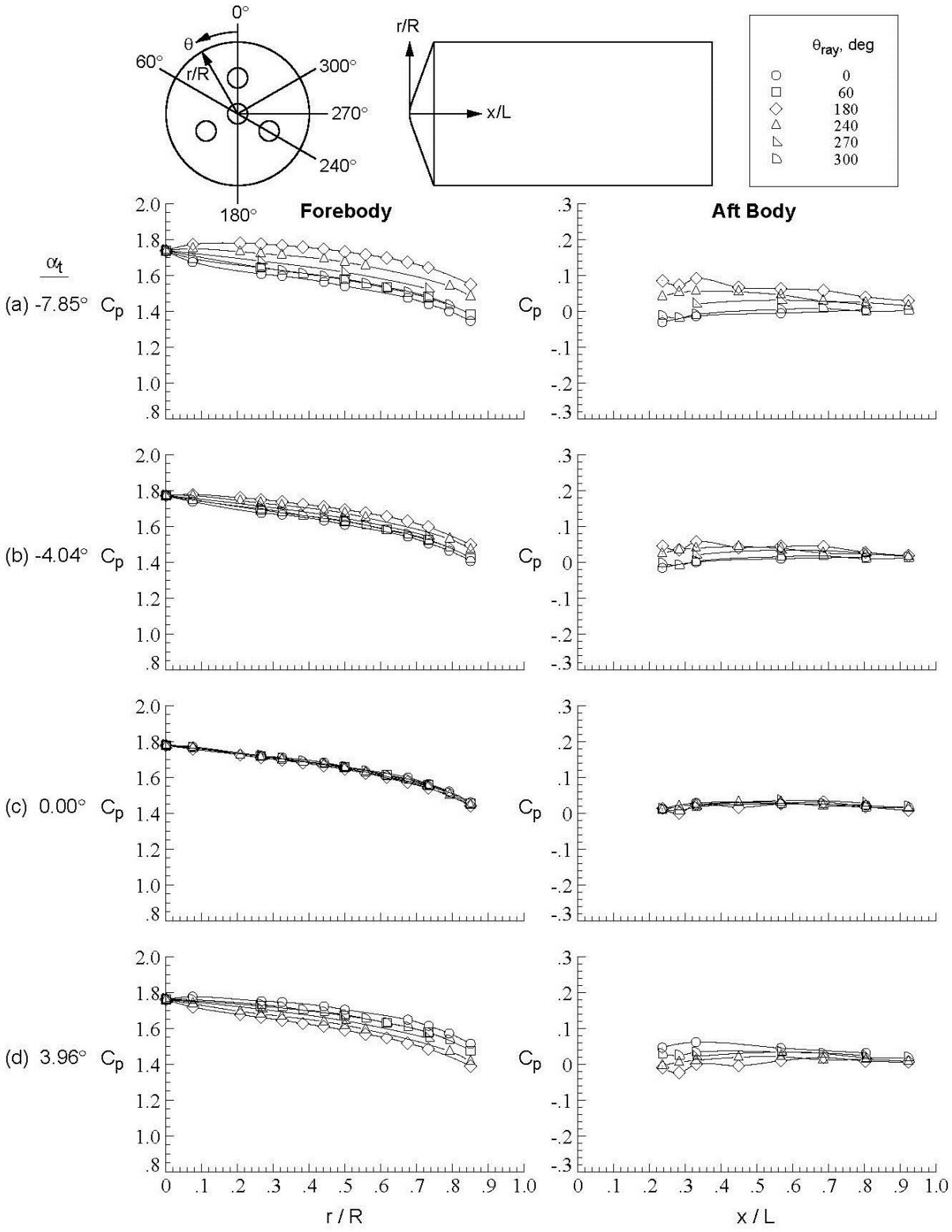

Figure D-84. Baseline configuration, Run 108, M_∞ = 4.6, Re_∞ = 1.5x10^7/ft, ϕ = 179.93°, X_S = 40.15 in, Y_S = 0.00 in, C_T = 0.00.

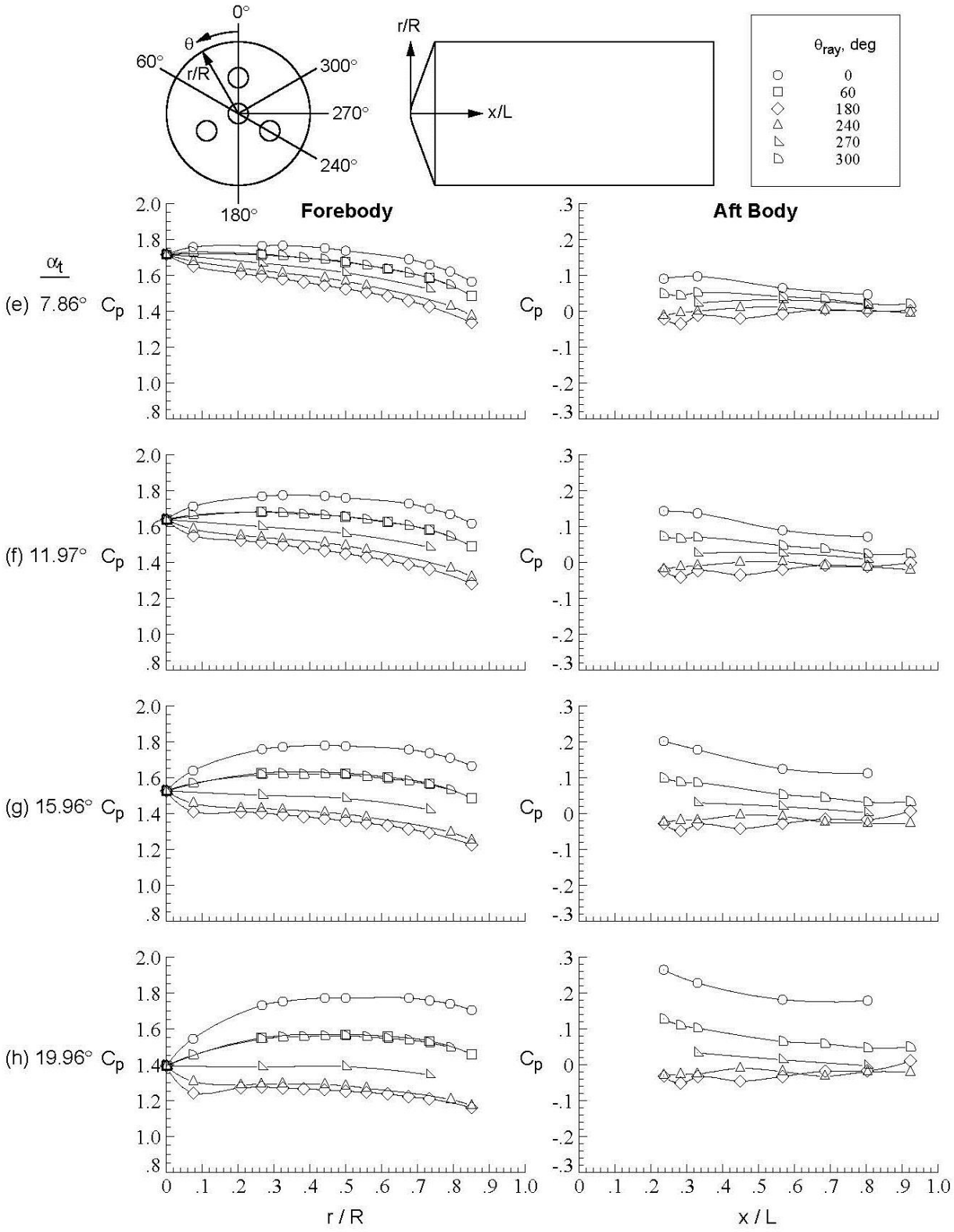

Figure D-84. Concluded.

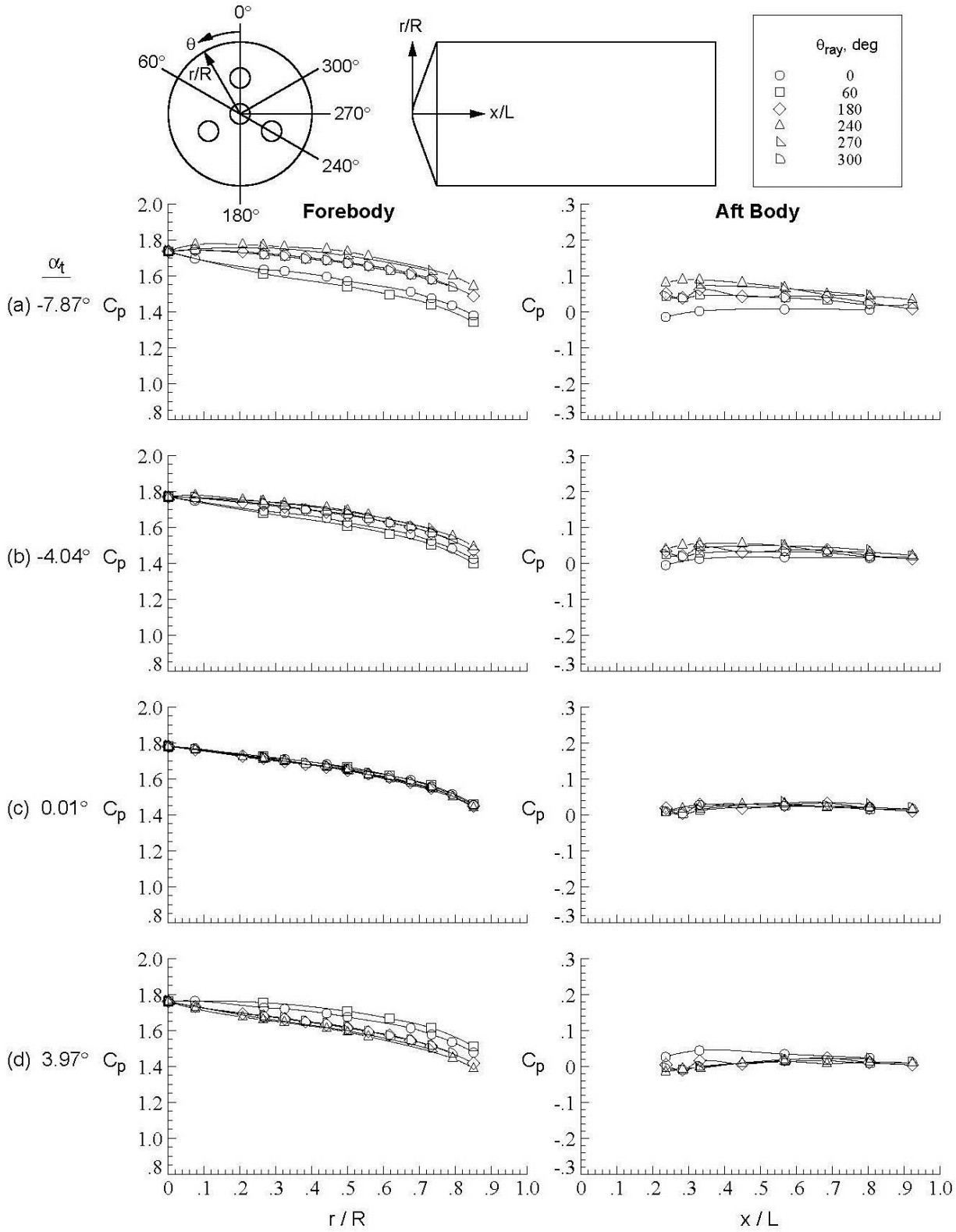

Figure D-85. Baseline configuration, Run 109, M_∞ = 4.6, Re_∞ = 1.5x10^7/ft, ϕ = 119.98°, X_S = 40.15 in, Y_S = 0.00 in, C_T = 0.00.

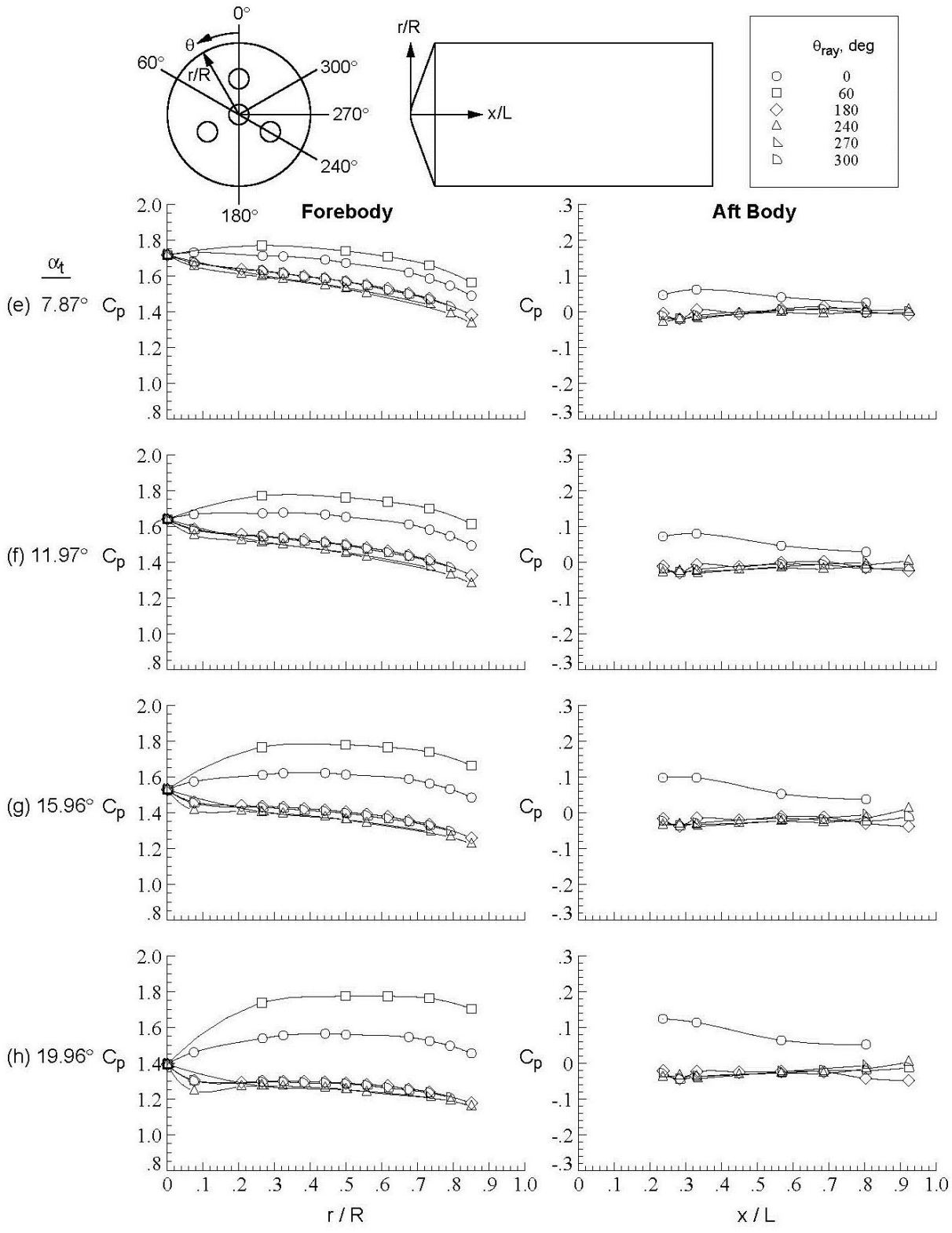

Figure D-85. Concluded.

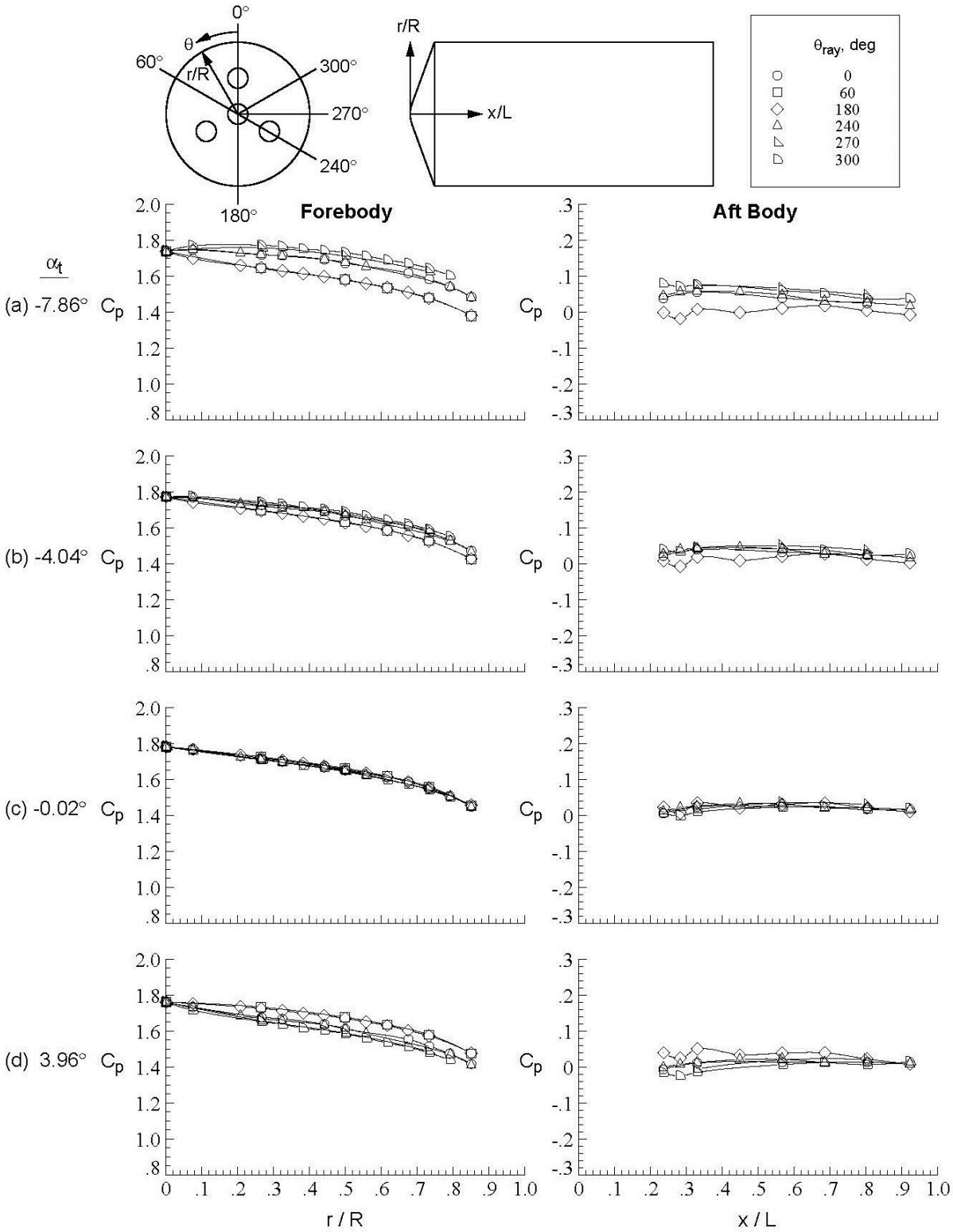

Figure D-86. Baseline configuration, Run 110, M_∞ = 4.6, Re_∞ = 1.5x10^7/ft, ϕ = 59.88°, X_S = 40.15 in, Y_S = 0.00 in, C_T = 0.00.

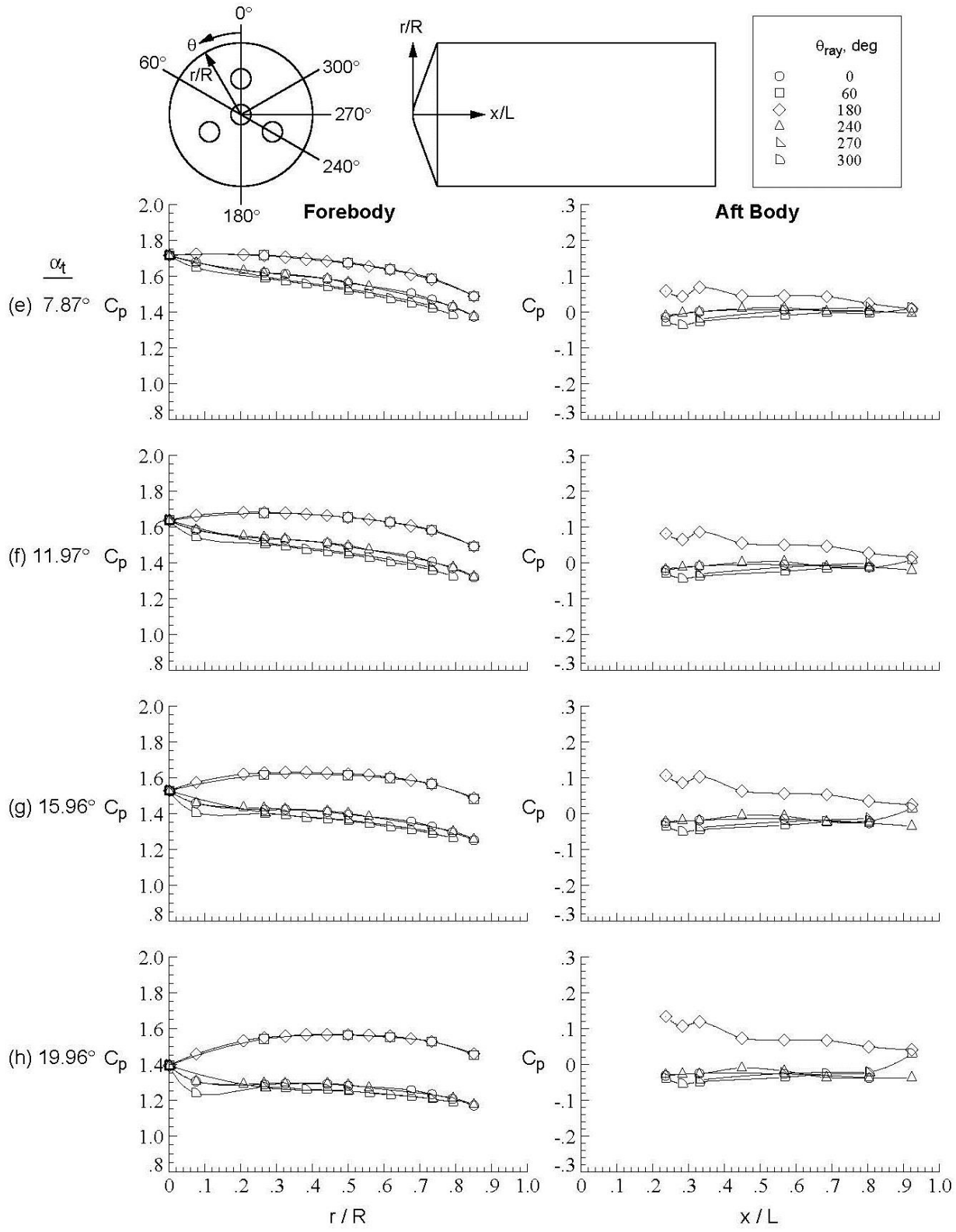

Figure D-86. Concluded.

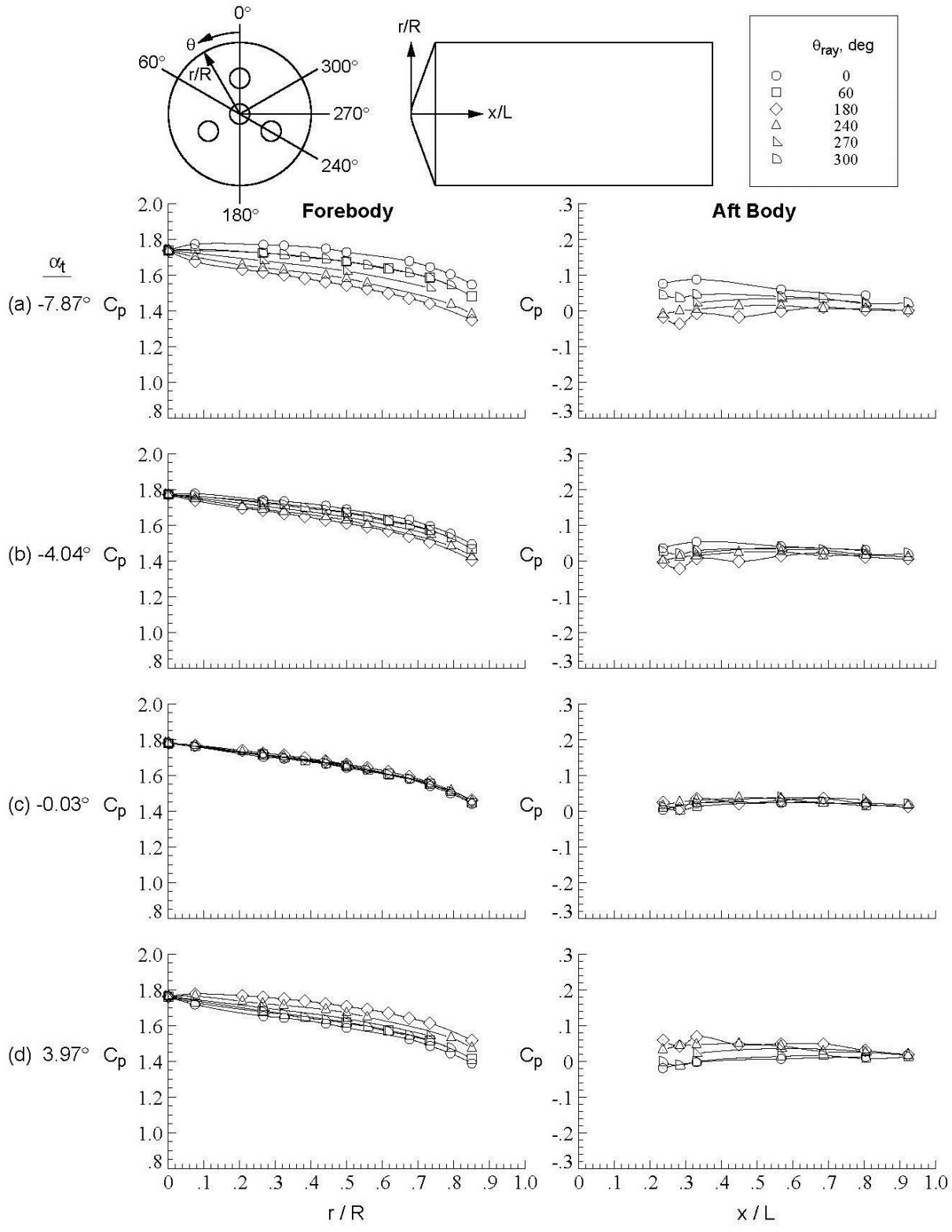

Figure D-87. Baseline configuration, Run 111, M_∞ = 4.6, Re_∞ = 1.5x10^7/ft, ϕ = −0.01°, X_S = 40.09 in, Y_S = 0.00 in, C_T = 0.00.

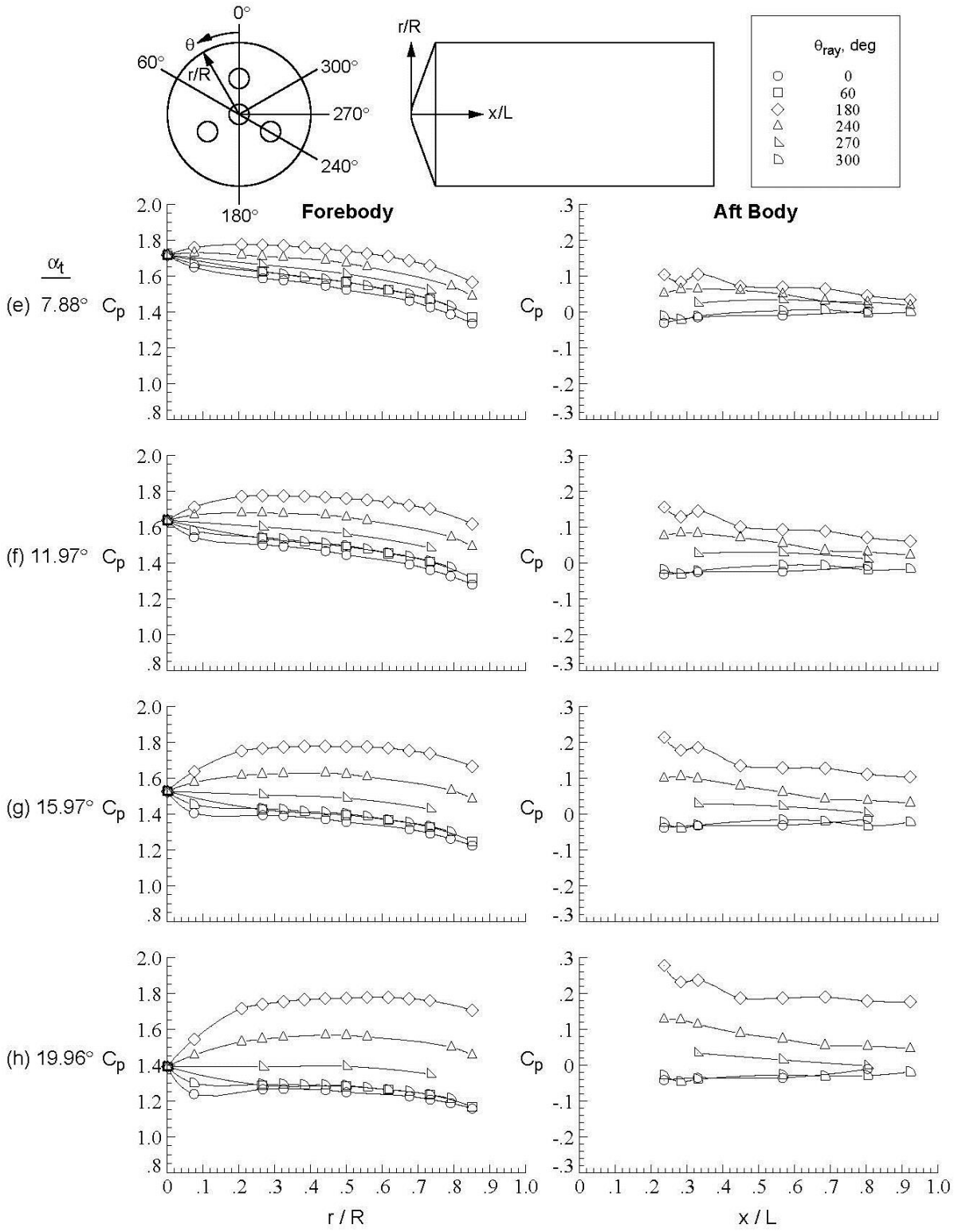

Figure D-87. Concluded.

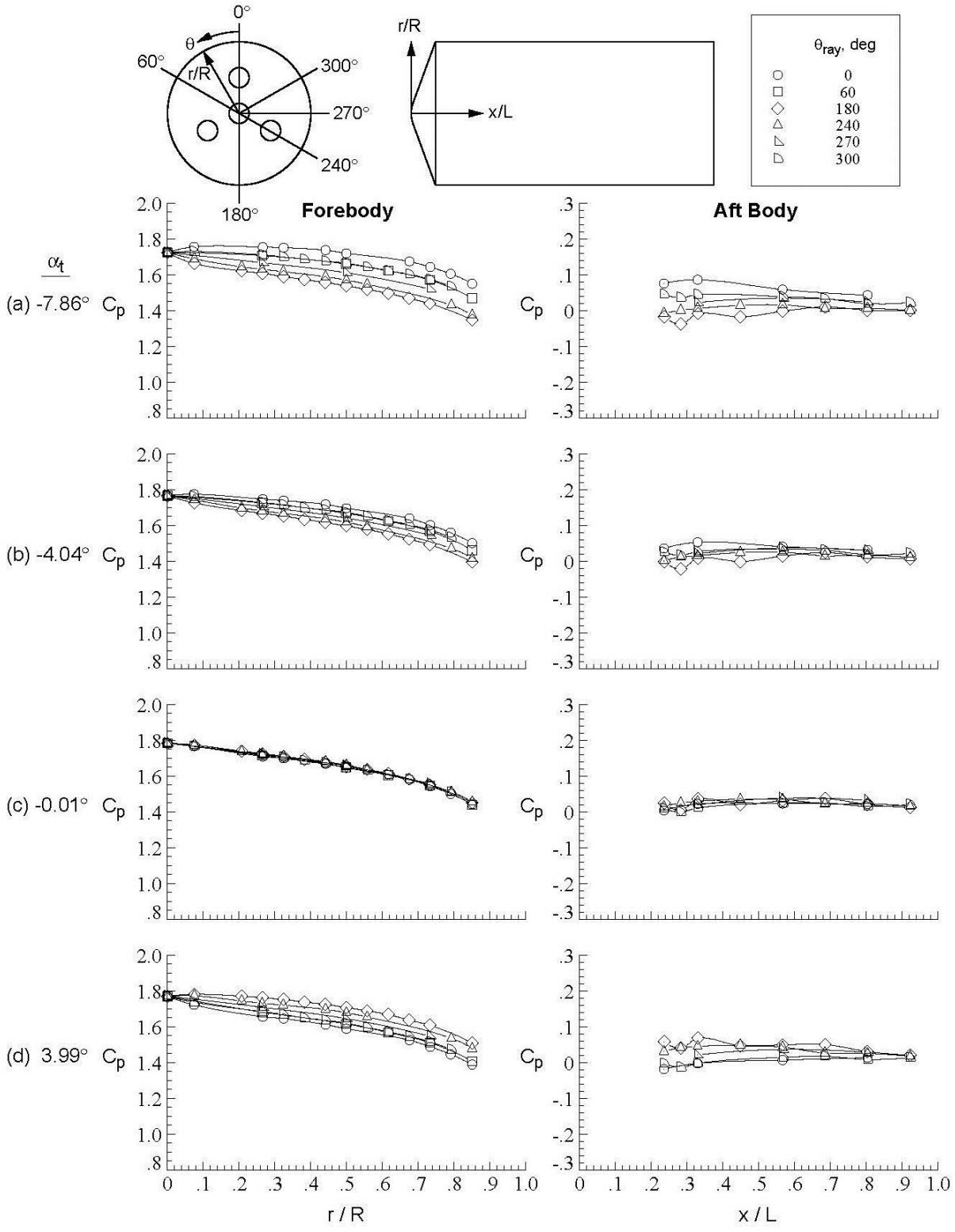

Figure D-88. Baseline configuration, Run 112, M_∞ = 4.6, Re_∞ = 1.5x10^7/ft, ϕ = −0.01°, X_S = 50.19 in, Y_S = 0.00 in, C_T = 0.00.

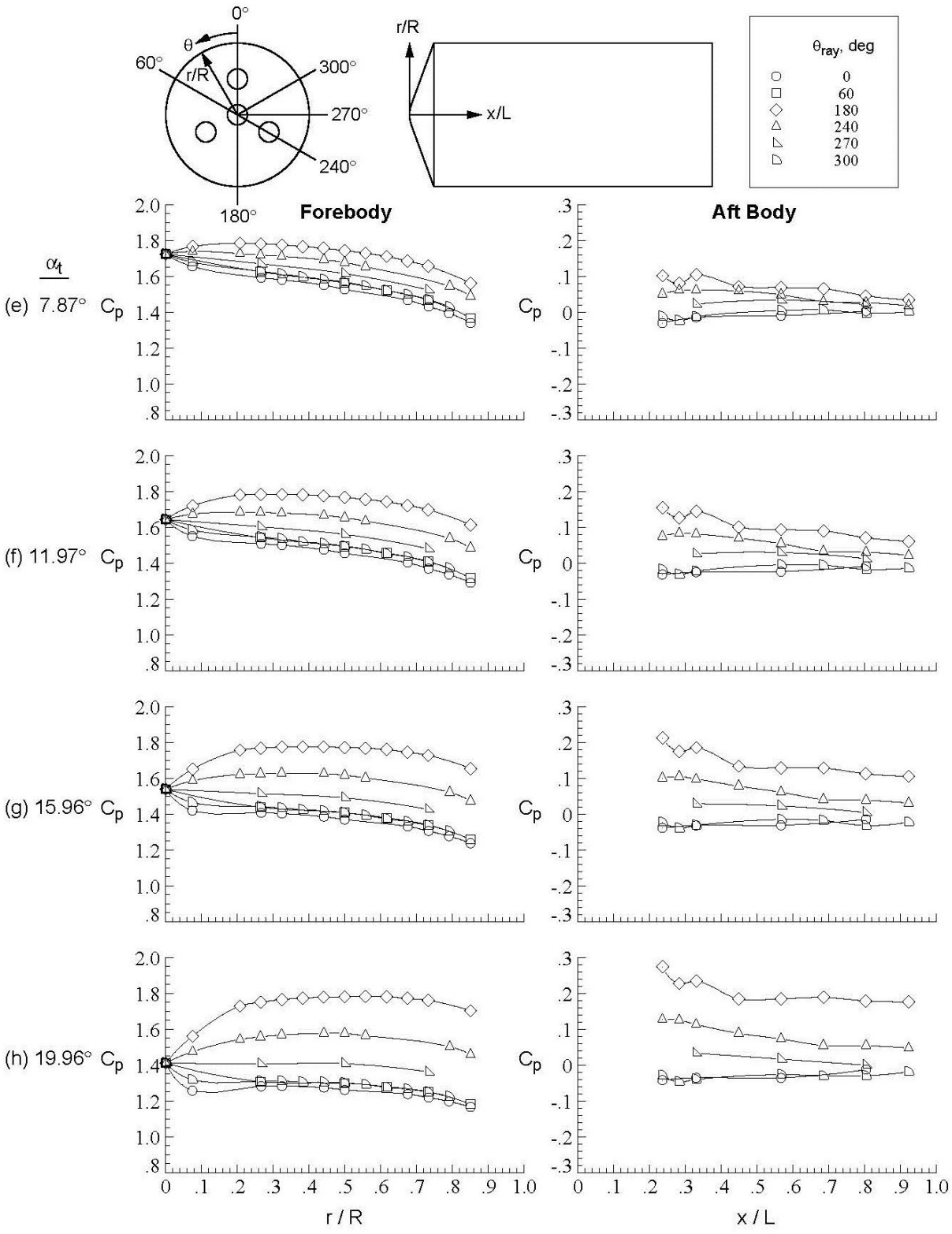

Figure D-88. Concluded.

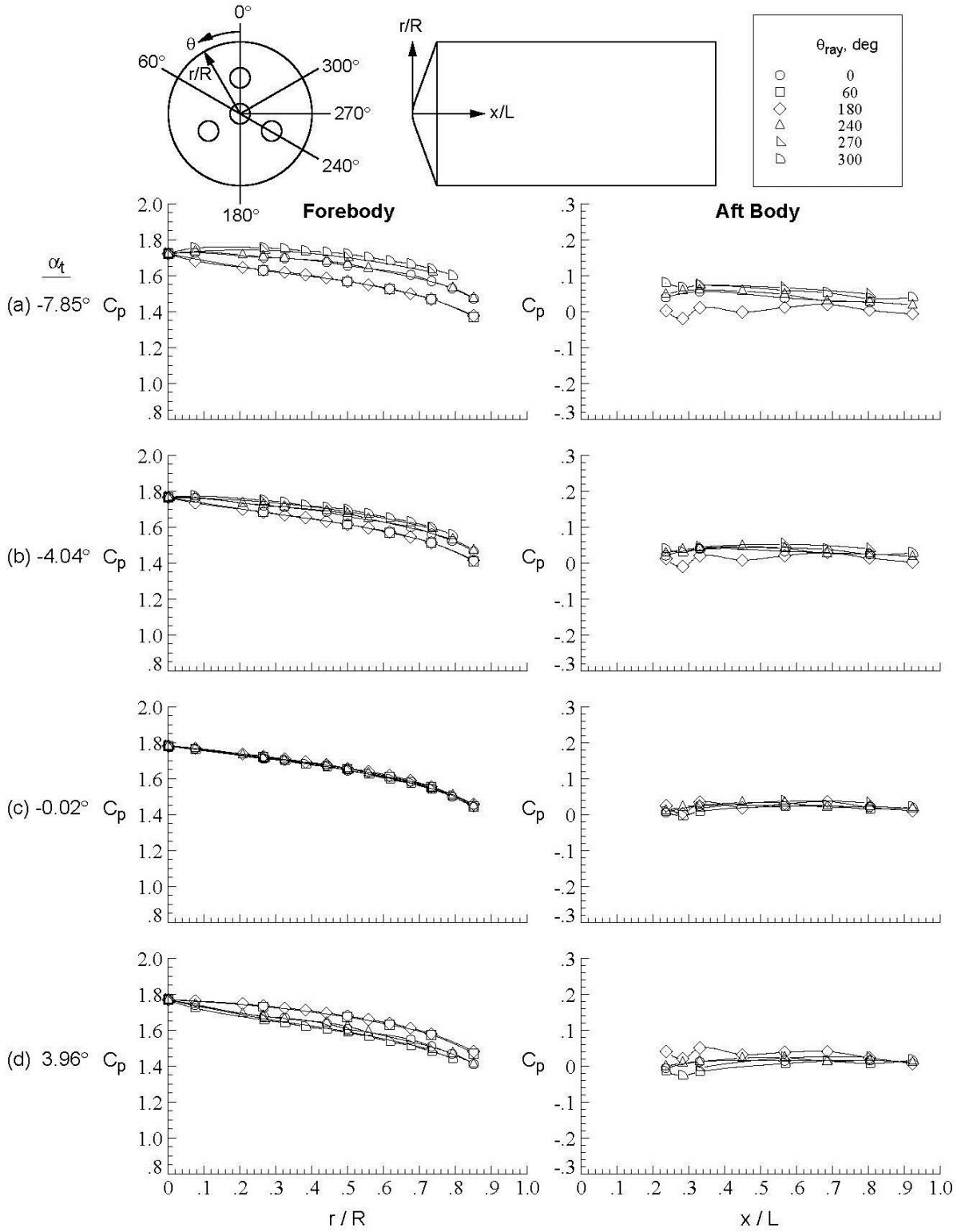

Figure D-89. Baseline configuration, Run 113, M_∞ = 4.6, Re_∞ = 1.5x10^7/ft, ϕ = 59.96°, X_S = 50.19 in, Y_S = 0.00 in, C_T = 0.00.

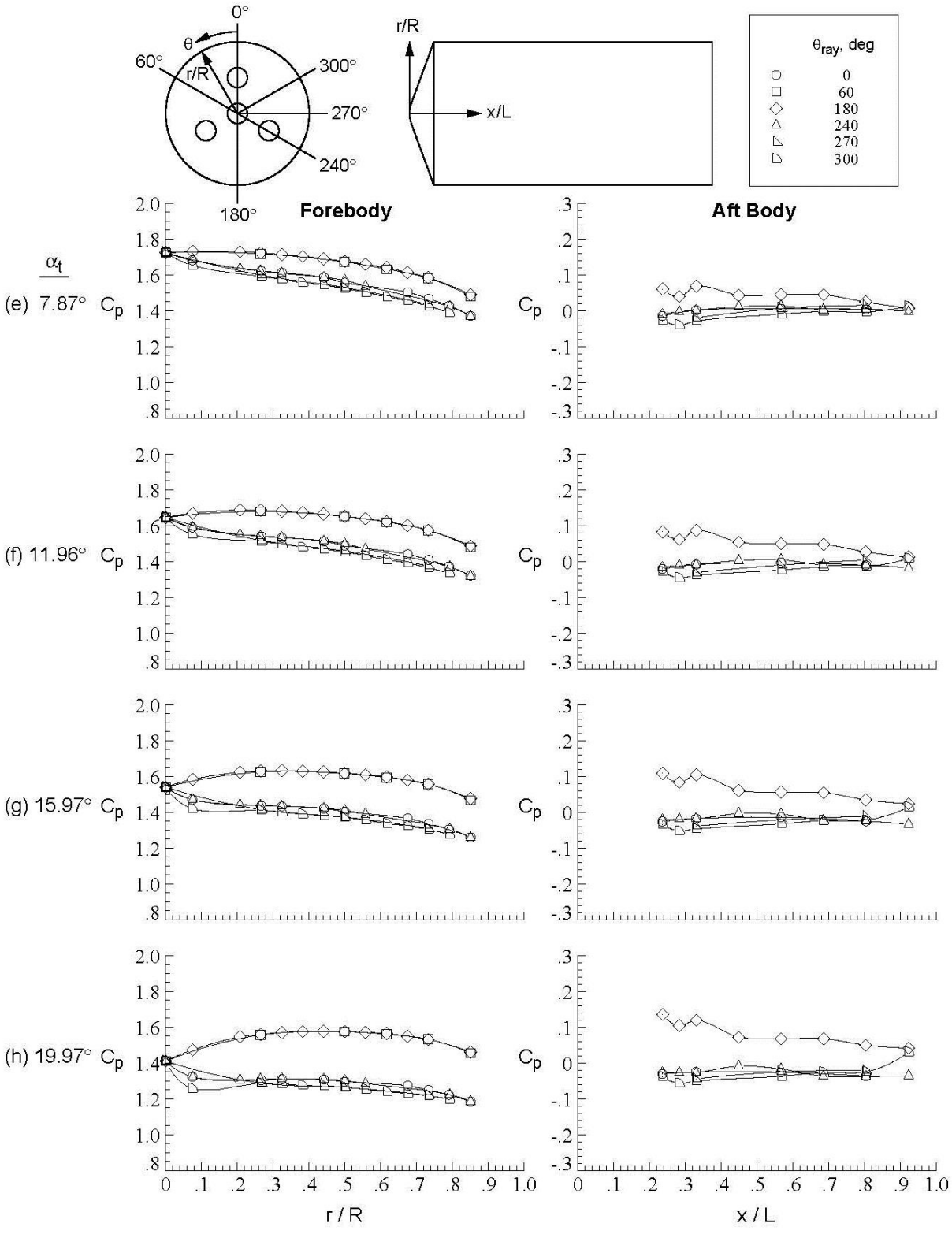

Figure D-89. Concluded.

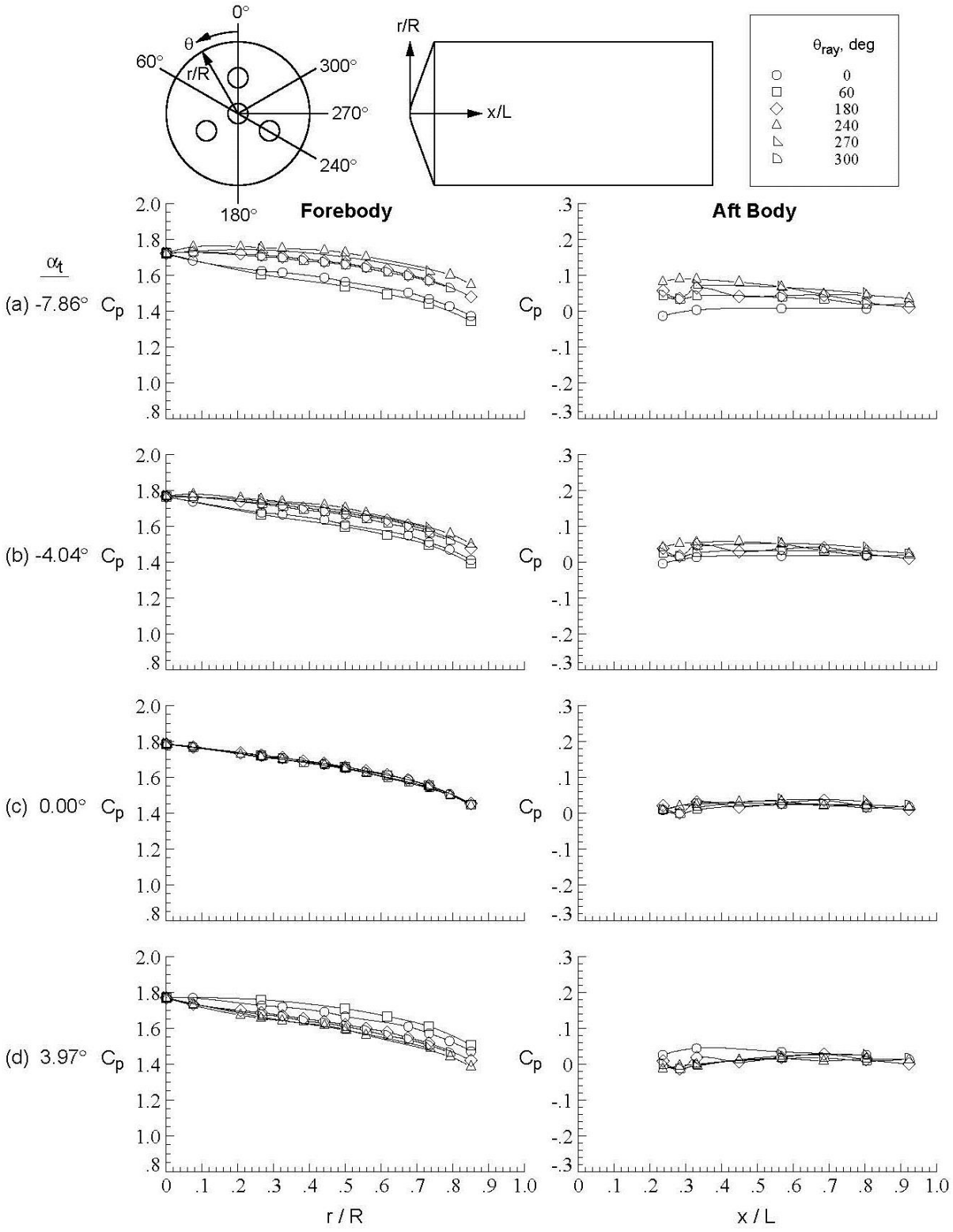

Figure D-90. Baseline configuration, Run 114, M_∞ = 4.6, Re_∞ = 1.5x10^7/ft, ϕ = 120.10°, X_S = 50.19 in, Y_S = 0.00 in, C_T = 0.00.

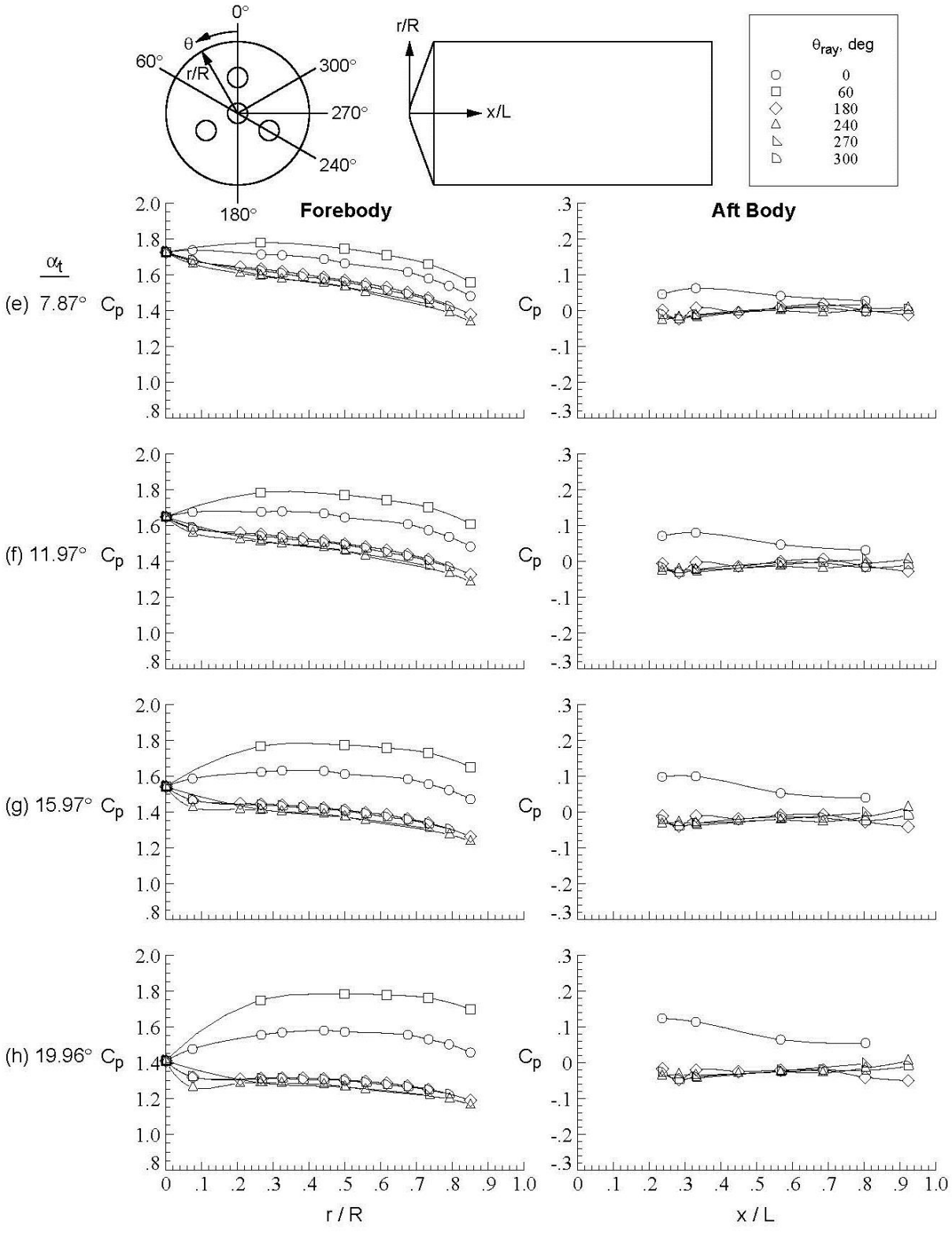

Figure D-90. Concluded.

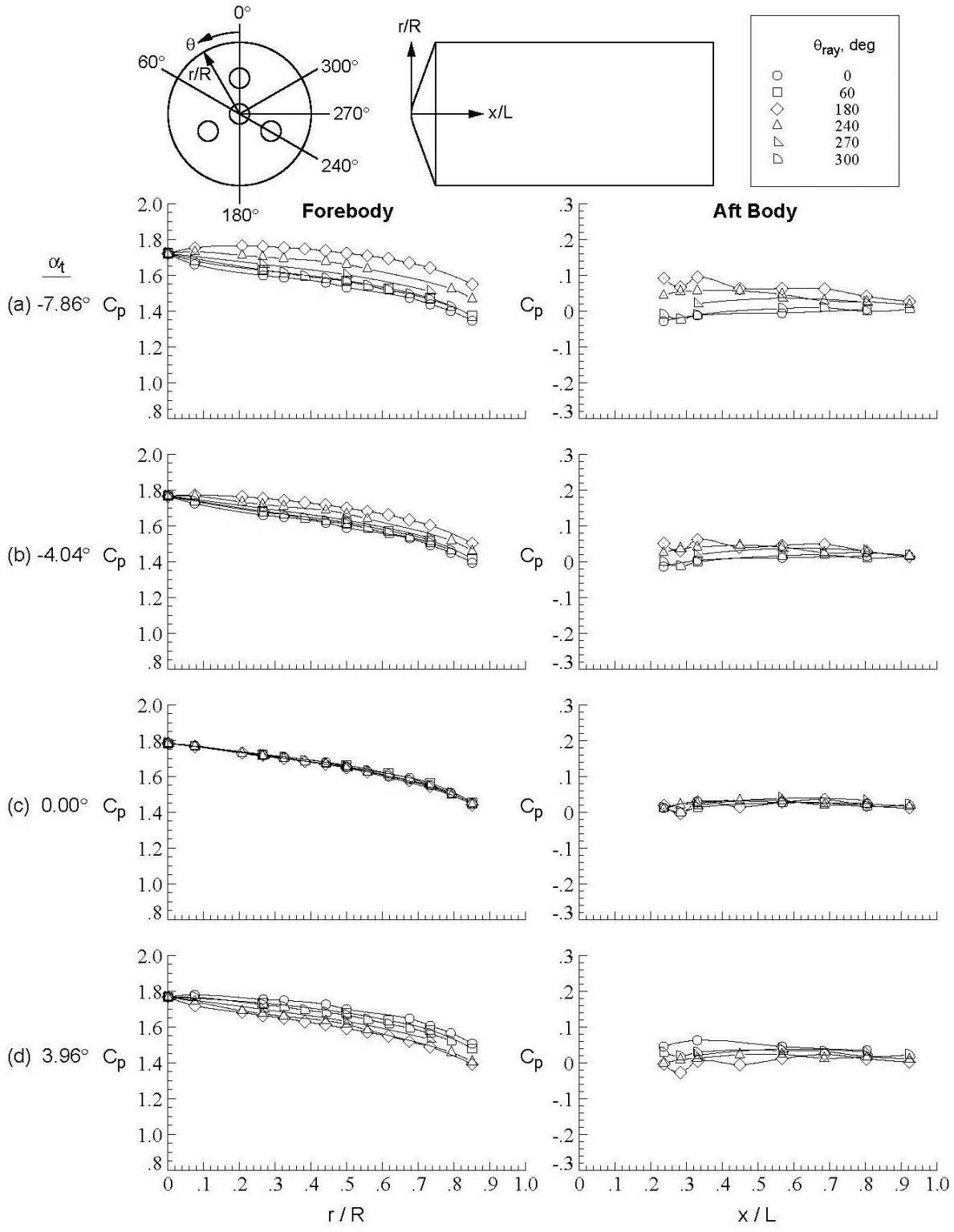

Figure D-91. Baseline configuration, Run 115, M_∞ = 4.6, Re_∞ = 1.5x10^7/ft, ϕ = 179.97°, X_S = 50.19 in, Y_S = 0.00 in, C_T = 0.00.

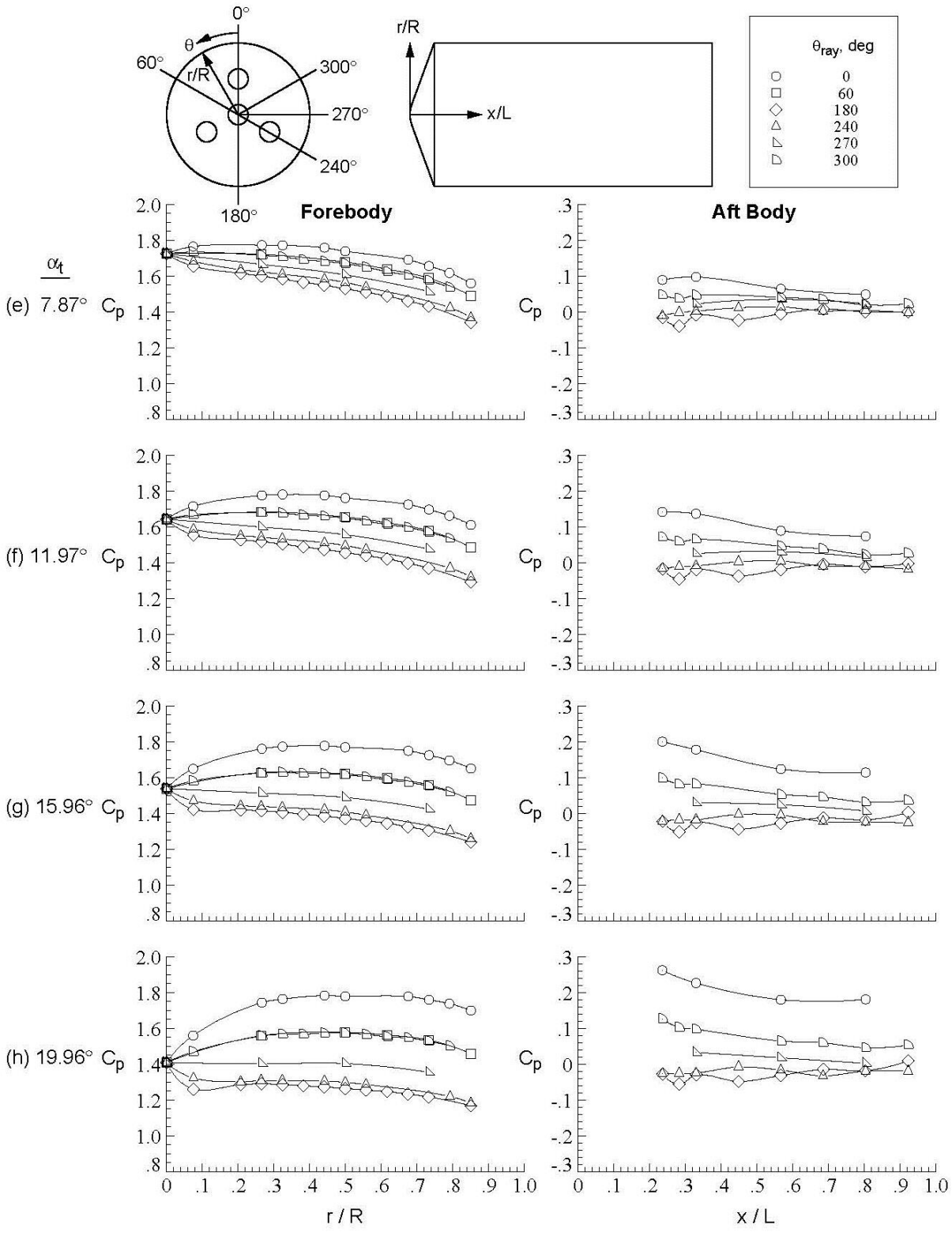

Figure D-91. Concluded.

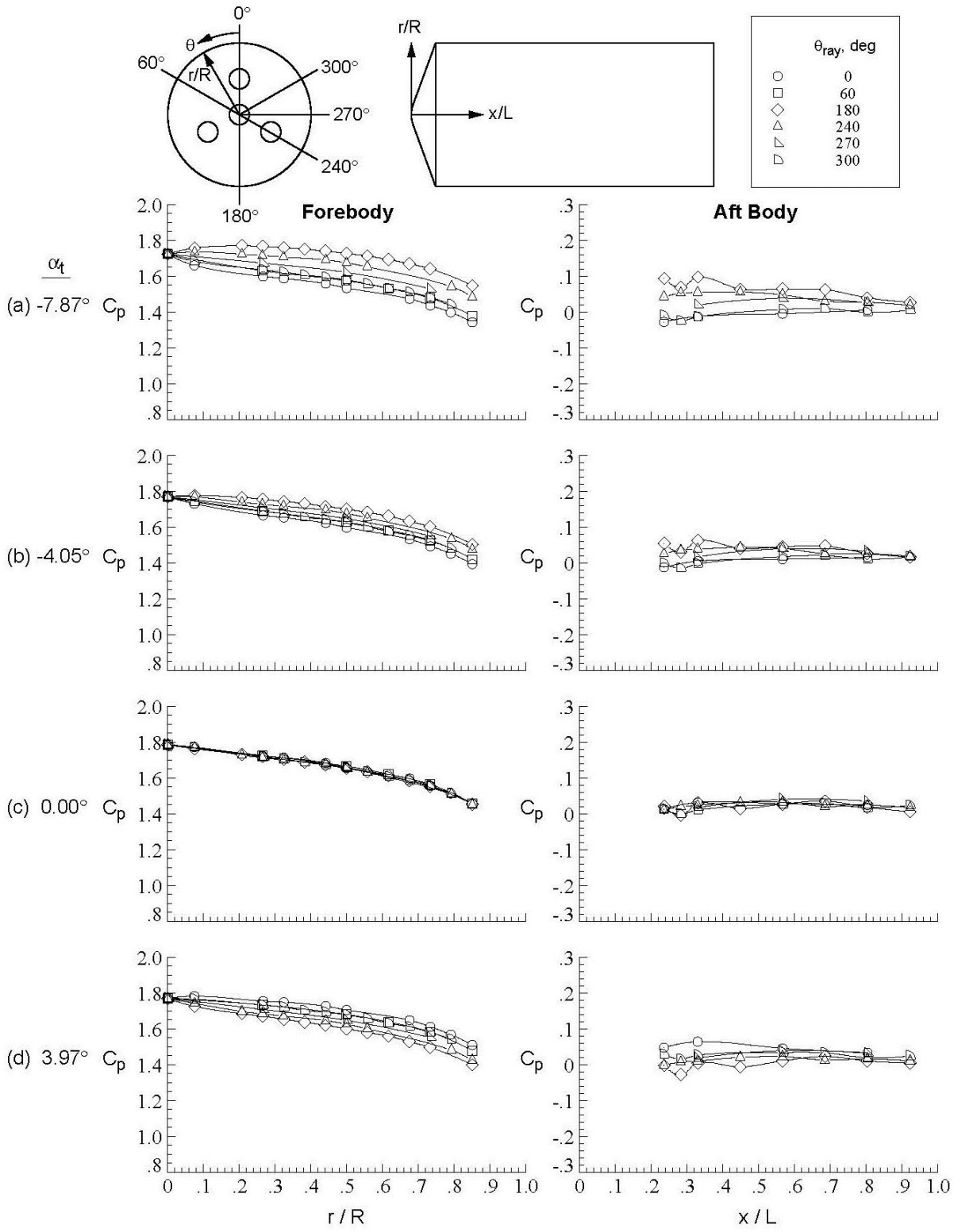

Figure D-92. Baseline configuration, Run 116, M_∞ = 4.6, Re_∞ = 1.5x10^7/ft, ϕ = 179.97°, X_S = 50.19 in, Y_S = 8.00 in, C_T = 0.00.

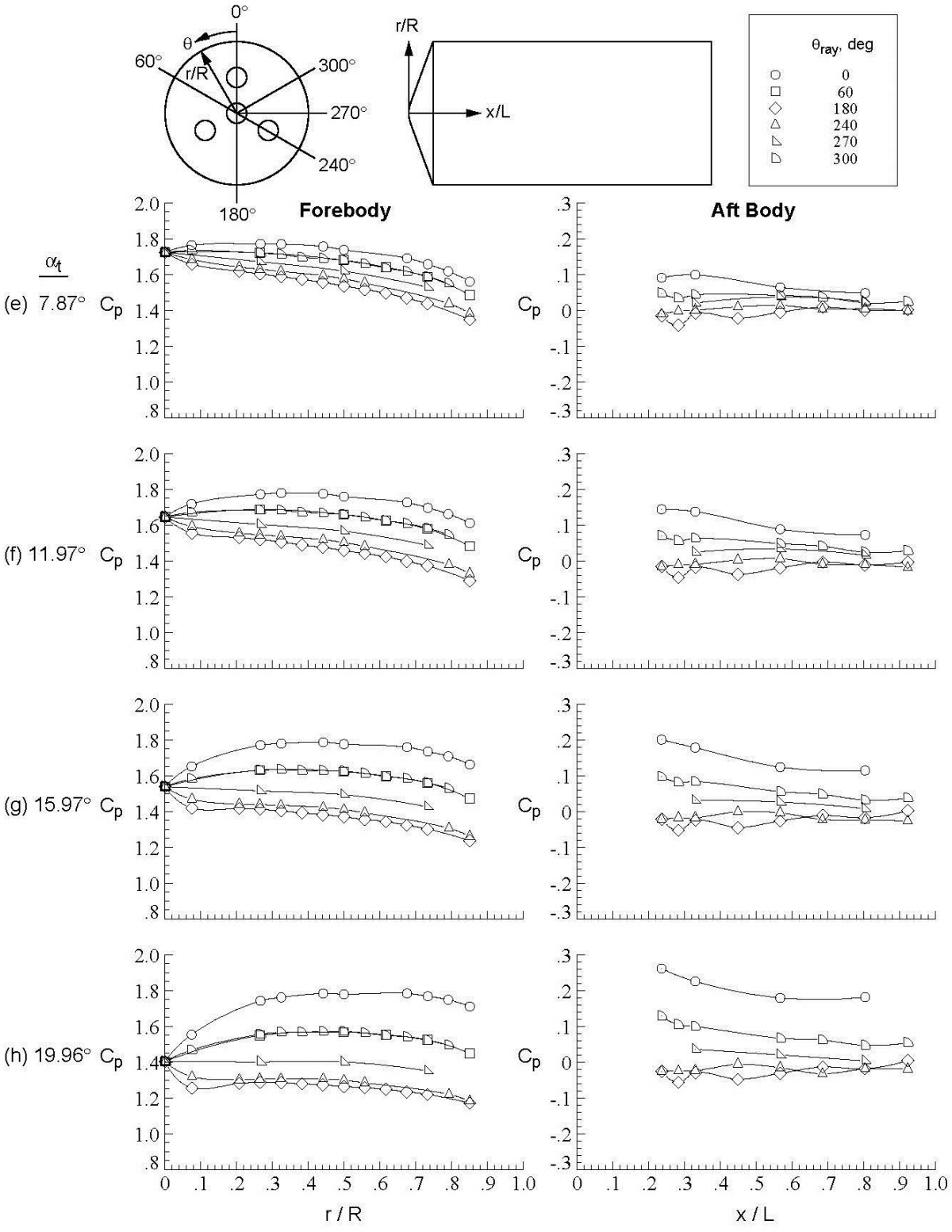

Figure D-92. Concluded.

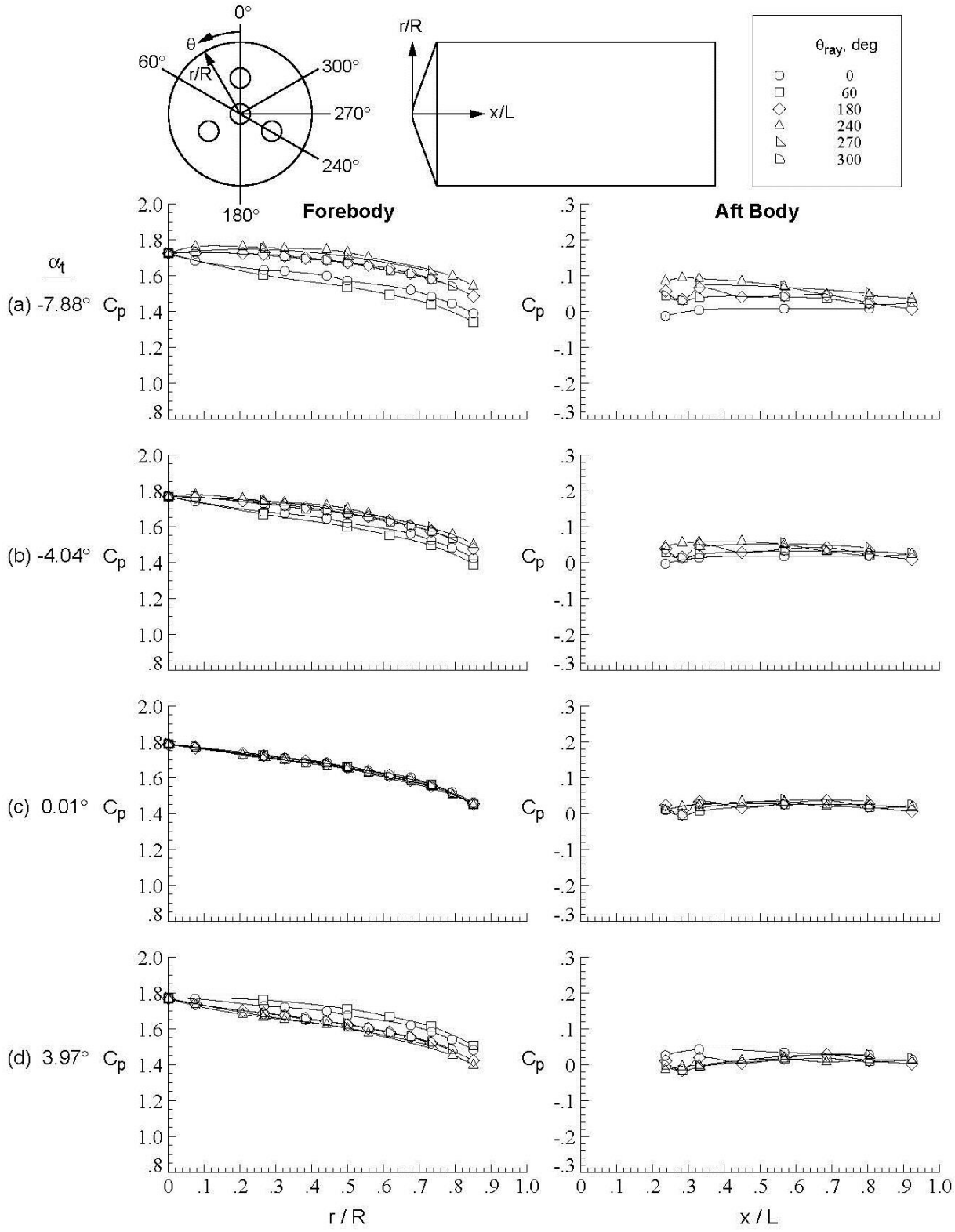

Figure D- 93. Baseline configuration, Run 117, M_∞ = 4.6, Re_∞ = 1.5x10^7/ft, ϕ = 119.98°, X_S = 50.19 in, Y_S = 8.00 in, C_T = 0.00.

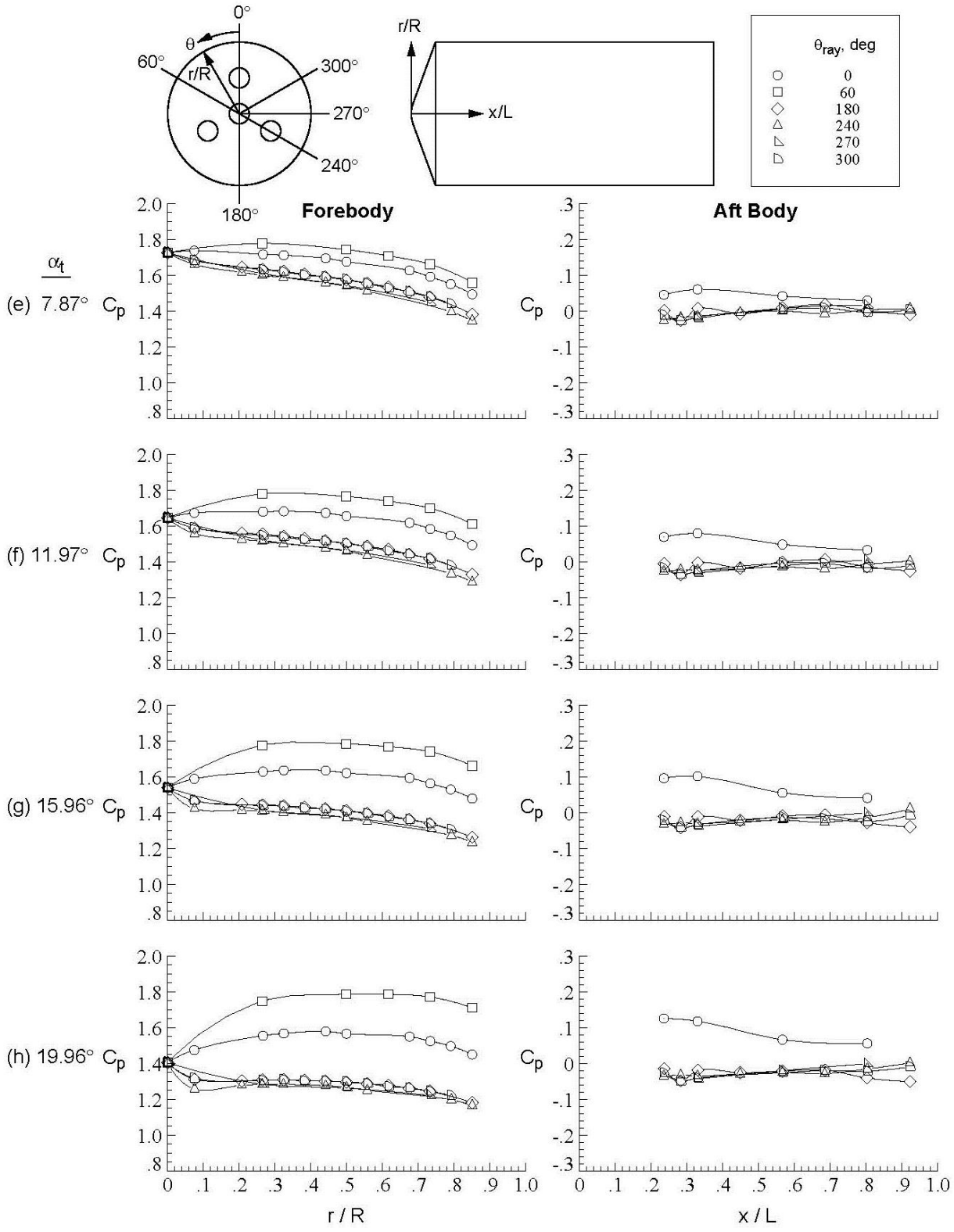

Figure D-93. Concluded.

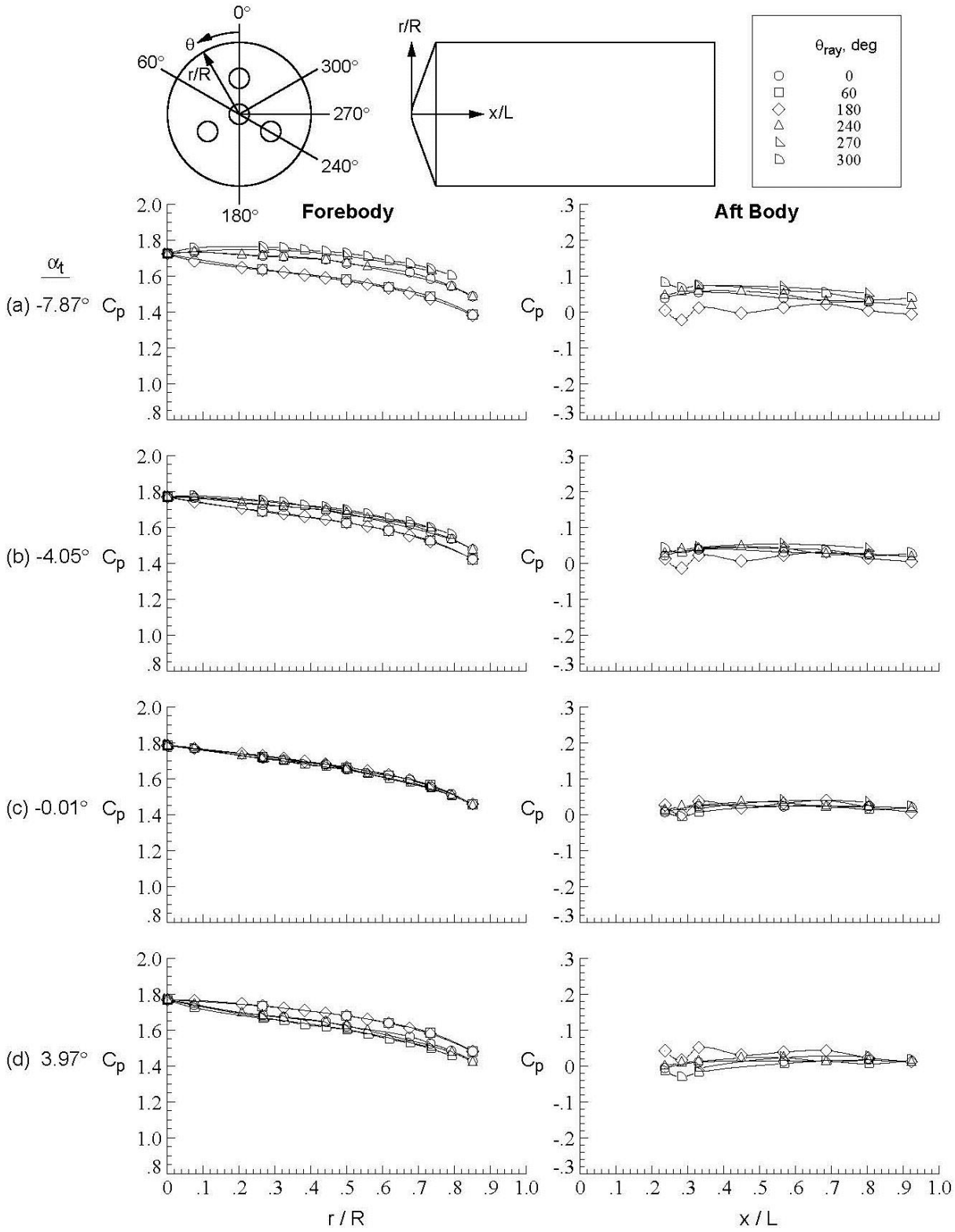

Figure D-94. Baseline configuration, Run 118, M_∞ = 4.6, Re_∞ = 1.5x10^7/ft, ϕ = 59.90°, X_S = 50.19 in, Y_S = 8.00 in, C_T = 0.00.

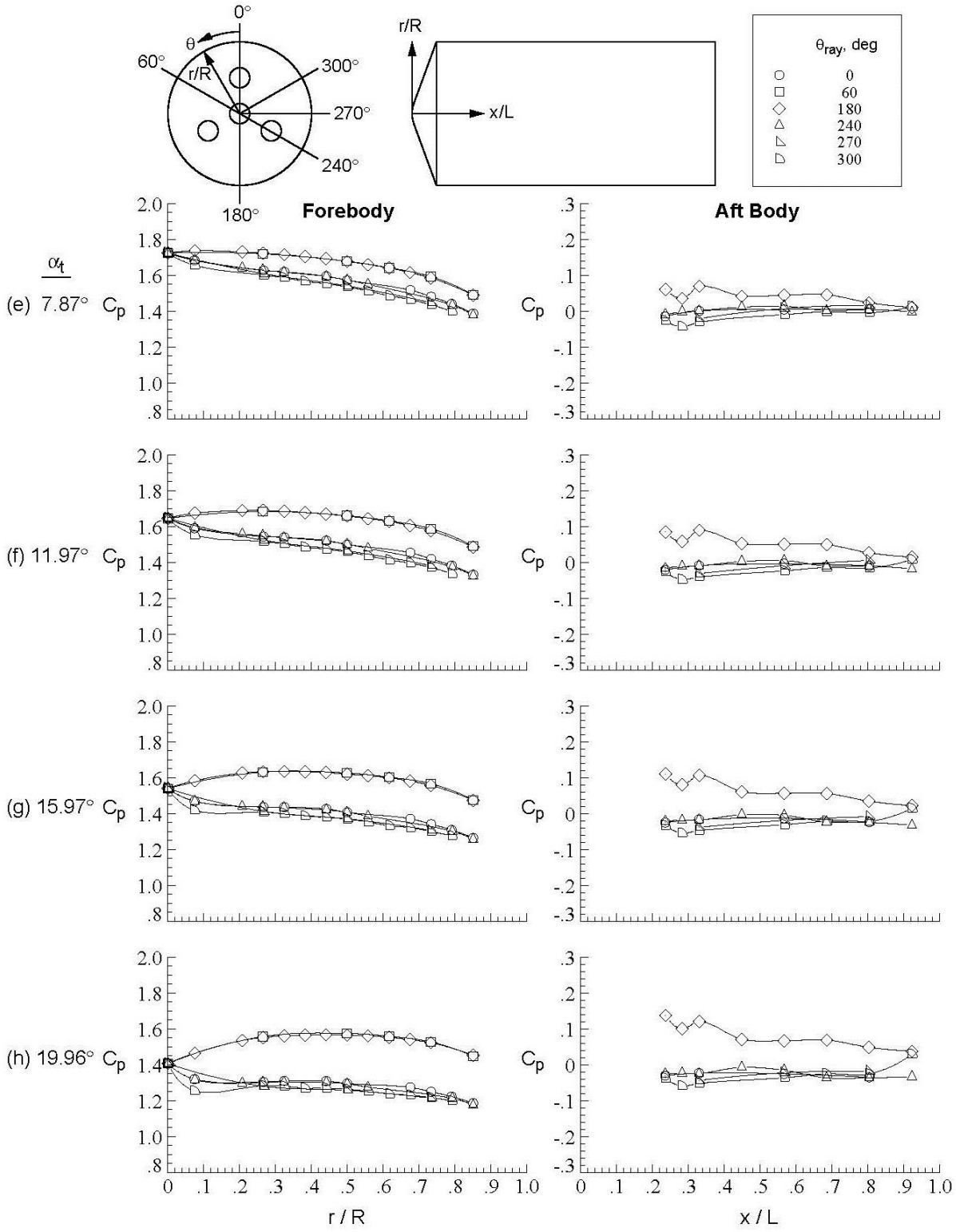

Figure D-94. Concluded.

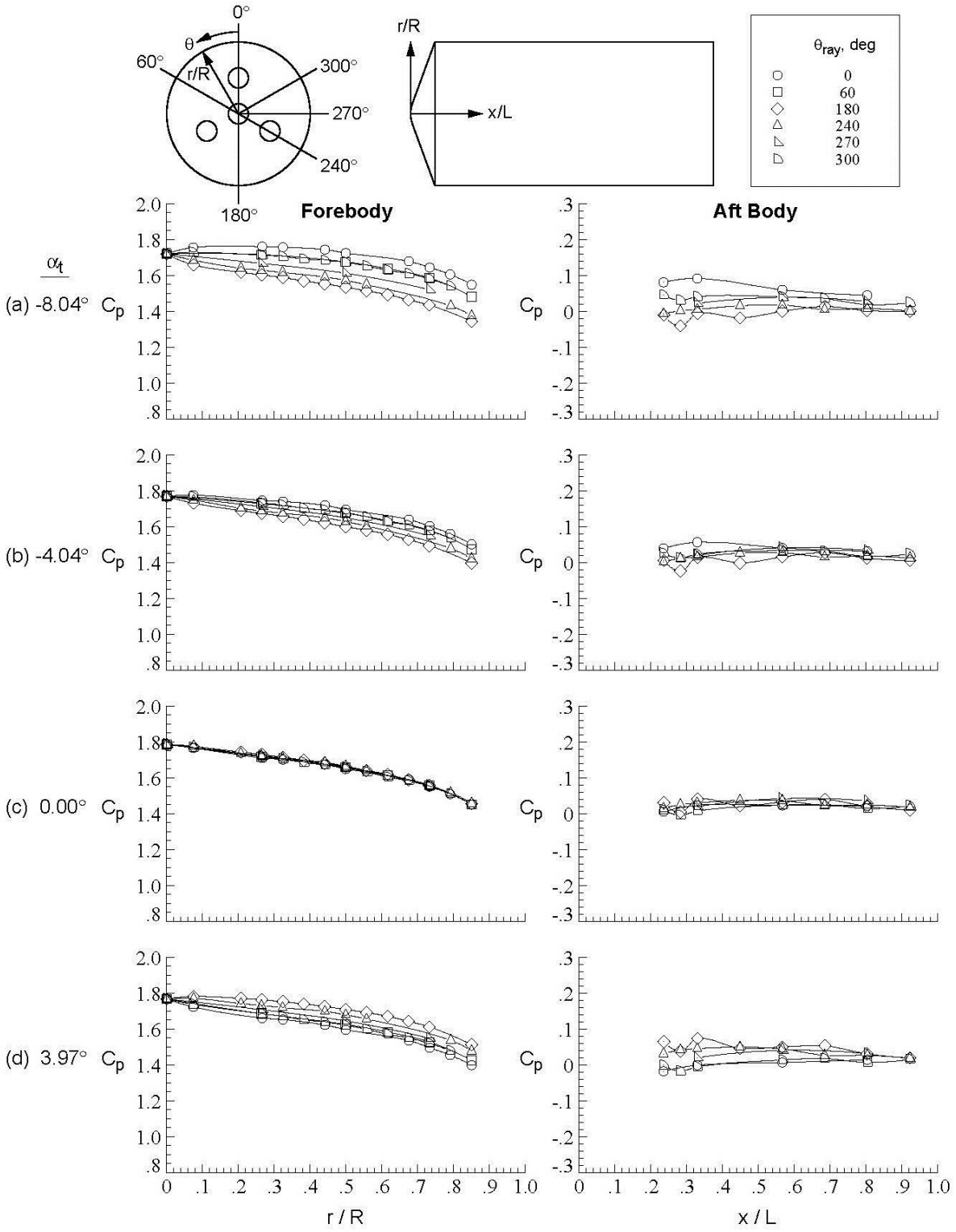

Figure D-95. Baseline configuration, Run 119, M_∞ = 4.6, Re_∞ = 1.5x10^7/ft, ϕ = 0.03°, X_S = 50.19 in, Y_S = 8.00 in, C_T = 0.00.

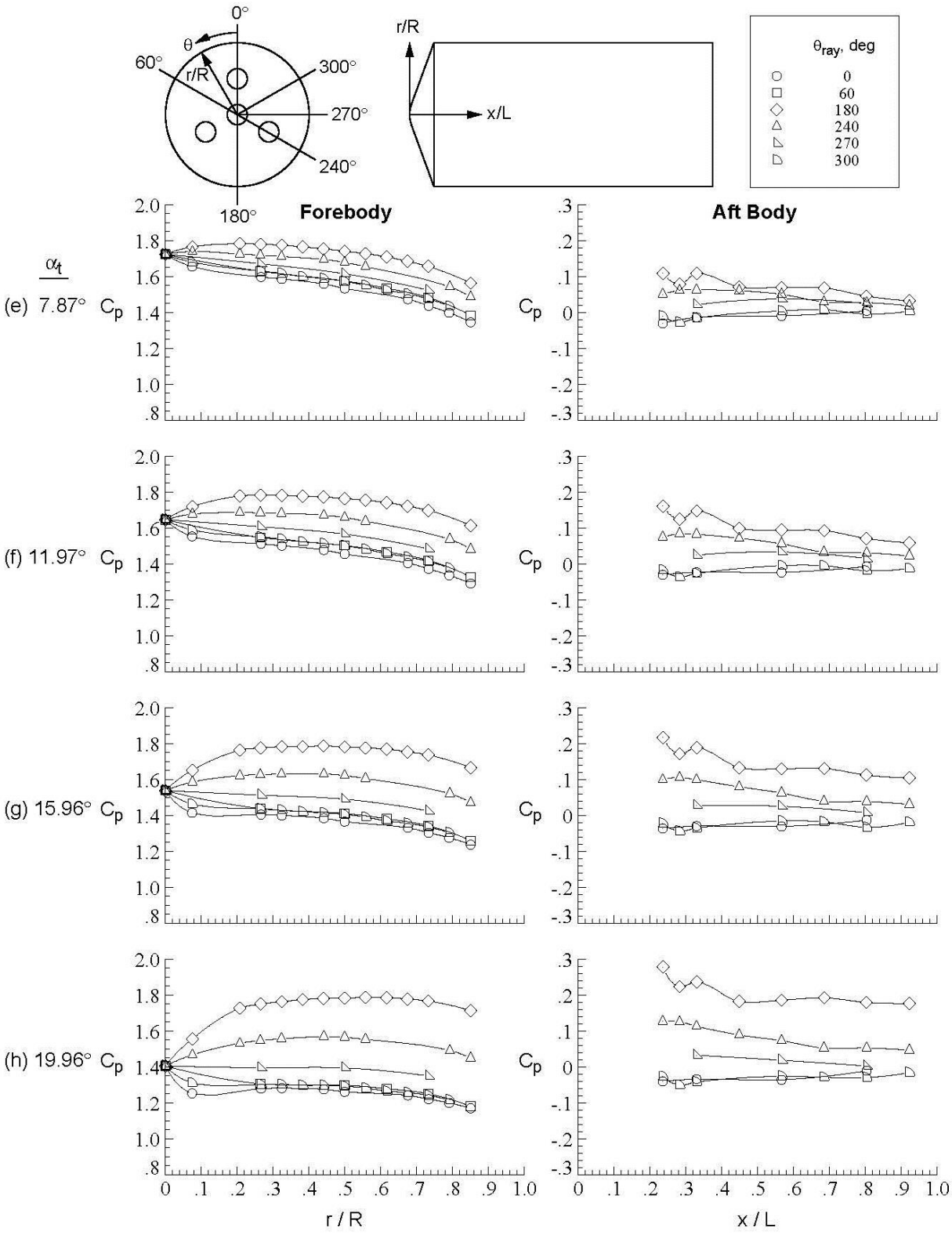

Figure D-95. Concluded.

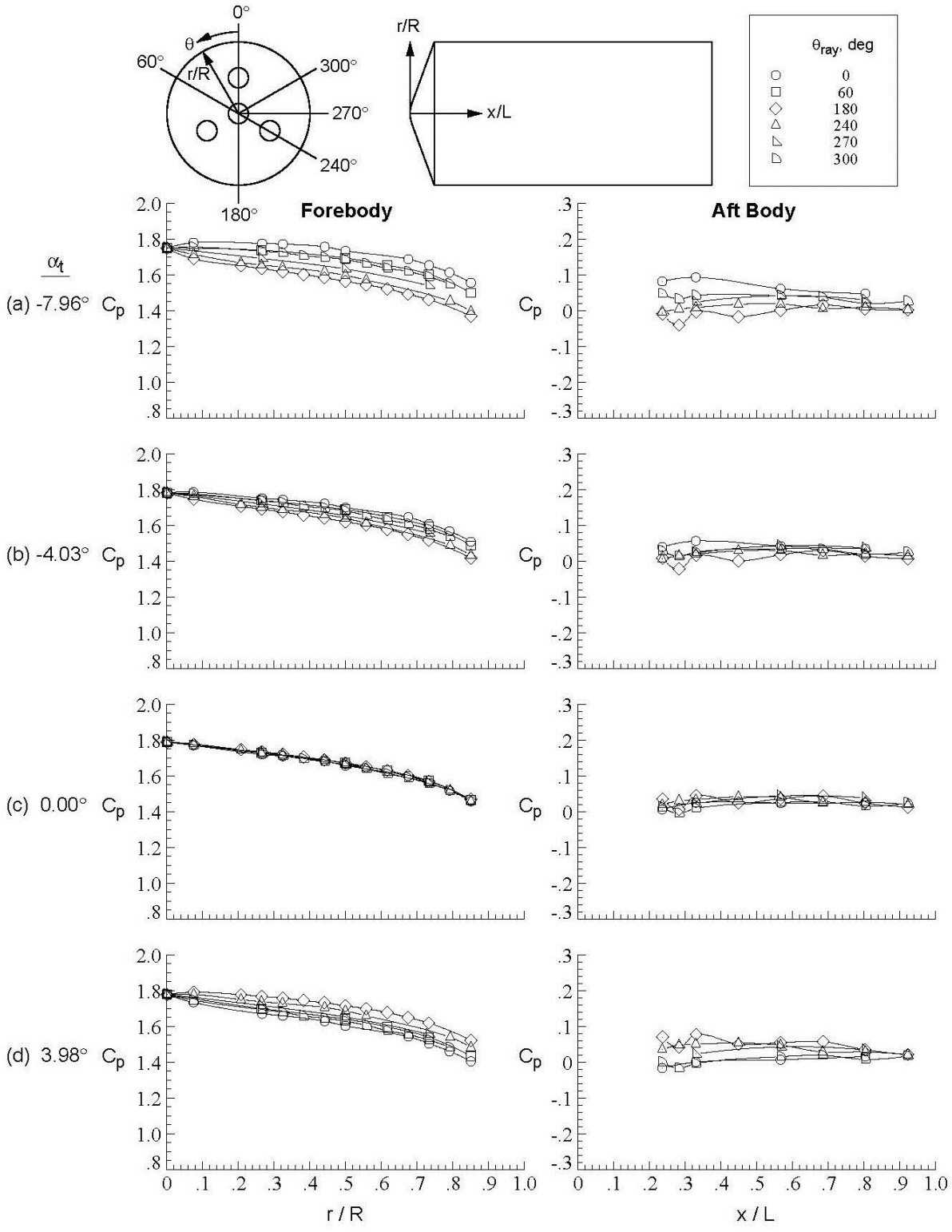

Figure D-96. Baseline configuration, Run 120, M_∞ = 4.6, Re_∞ = 1.5x10^7/ft, ϕ = 0.03°, X_S = 25.16 in, Y_S = –8.00 in, C_T = 0.00.

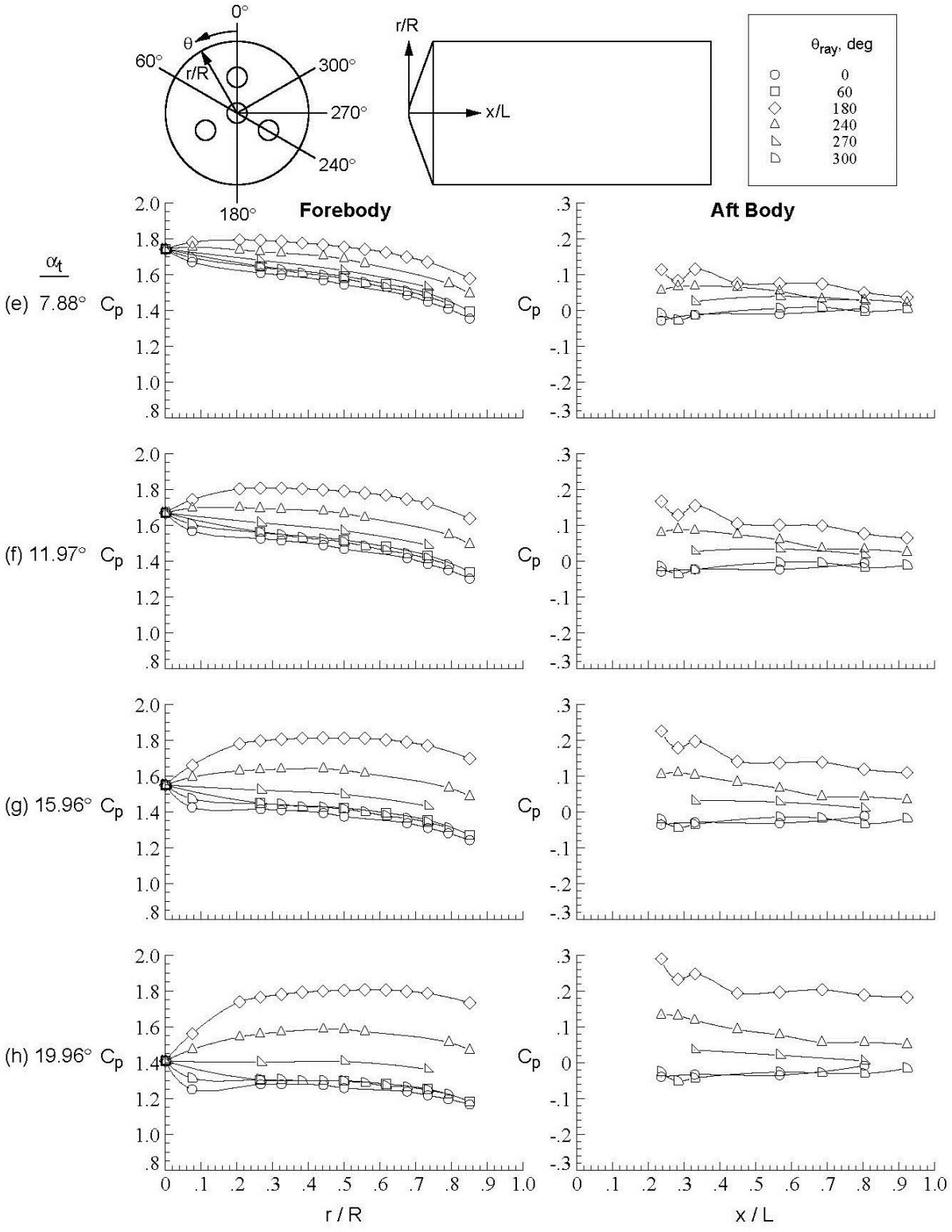

Figure D-96. Concluded.

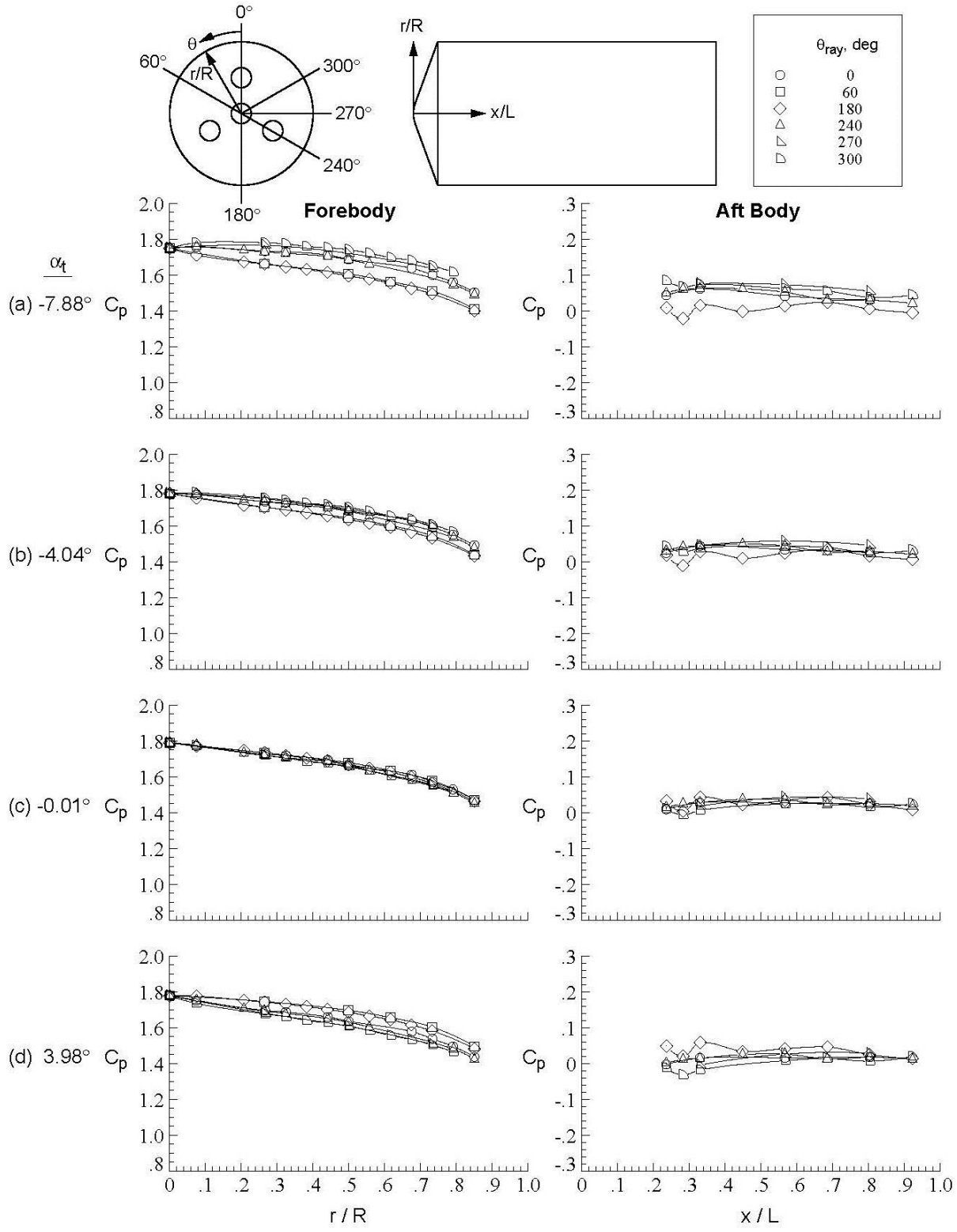

Figure D-97. Baseline configuration, Run 121, M_∞ = 4.6, Re_∞ = 1.5x10^7/ft, ϕ = 60.00°, X_S = 25.16 in, Y_S = –8.00 in, C_T = 0.00.

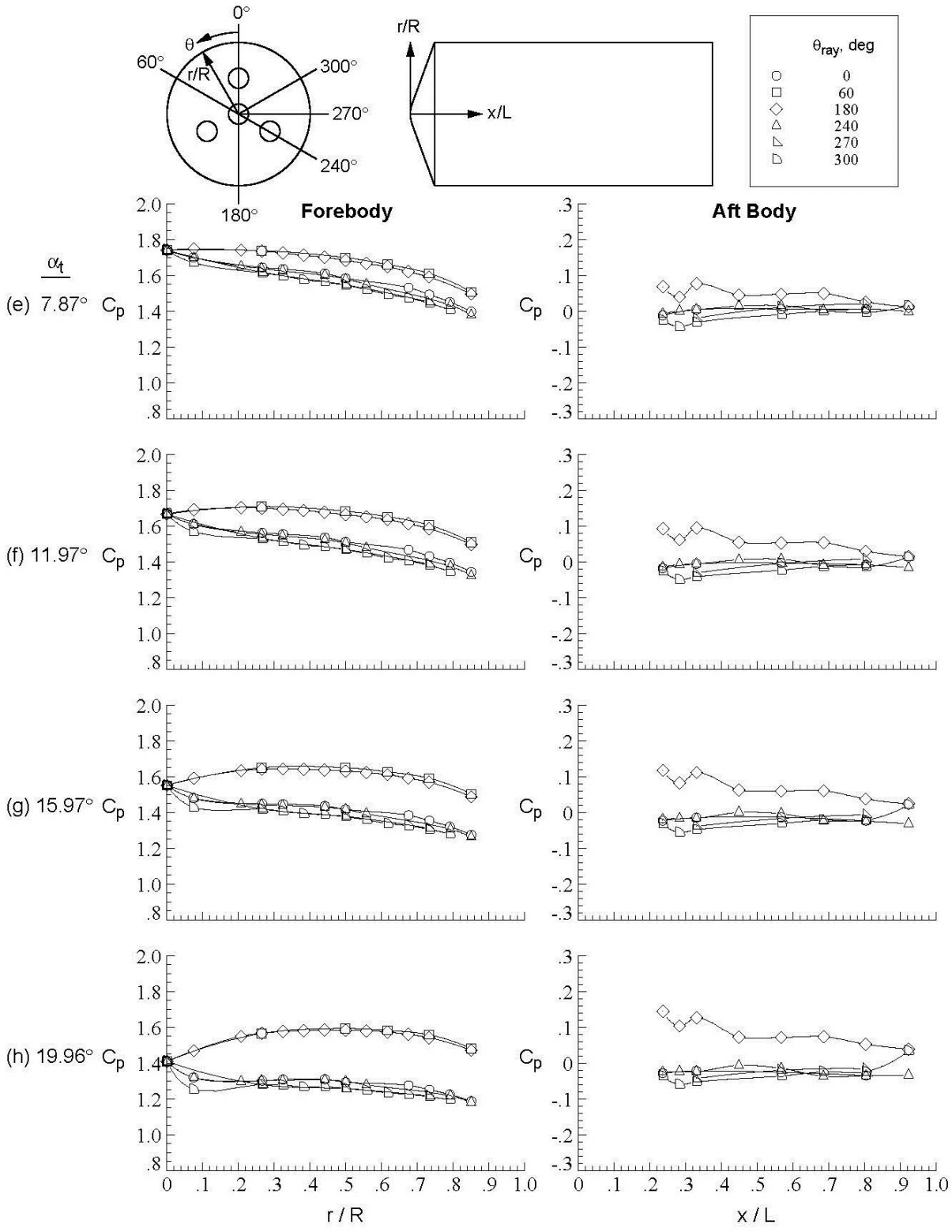

Figure D-97. Concluded.

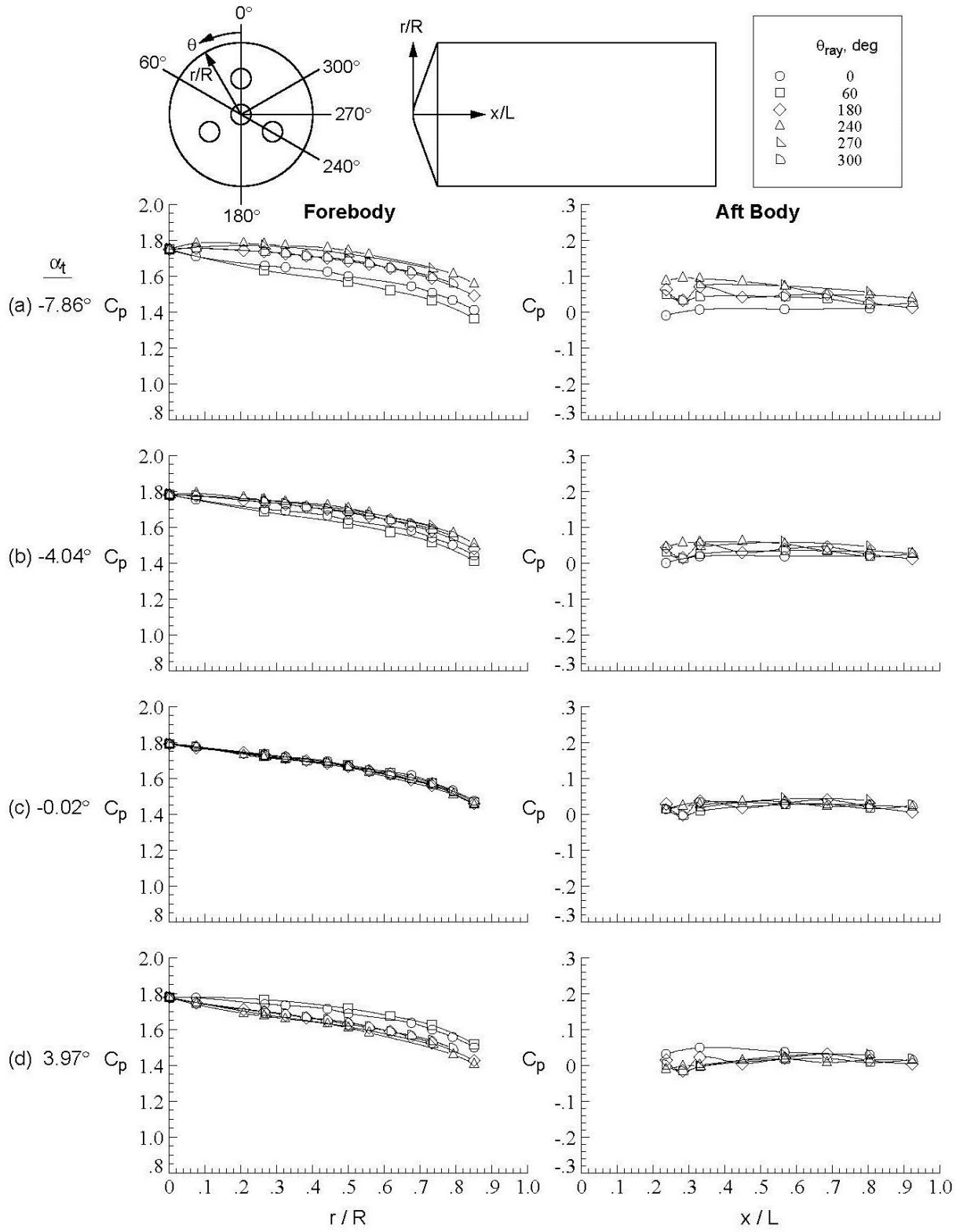

Figure D-98. Baseline configuration, Run 122, M_∞ = 4.6, Re_∞ = 1.5x10^7/ft, ϕ = 120.06°, X_S = 25.16 in, Y_S = –8.00 in, C_T = 0.00.

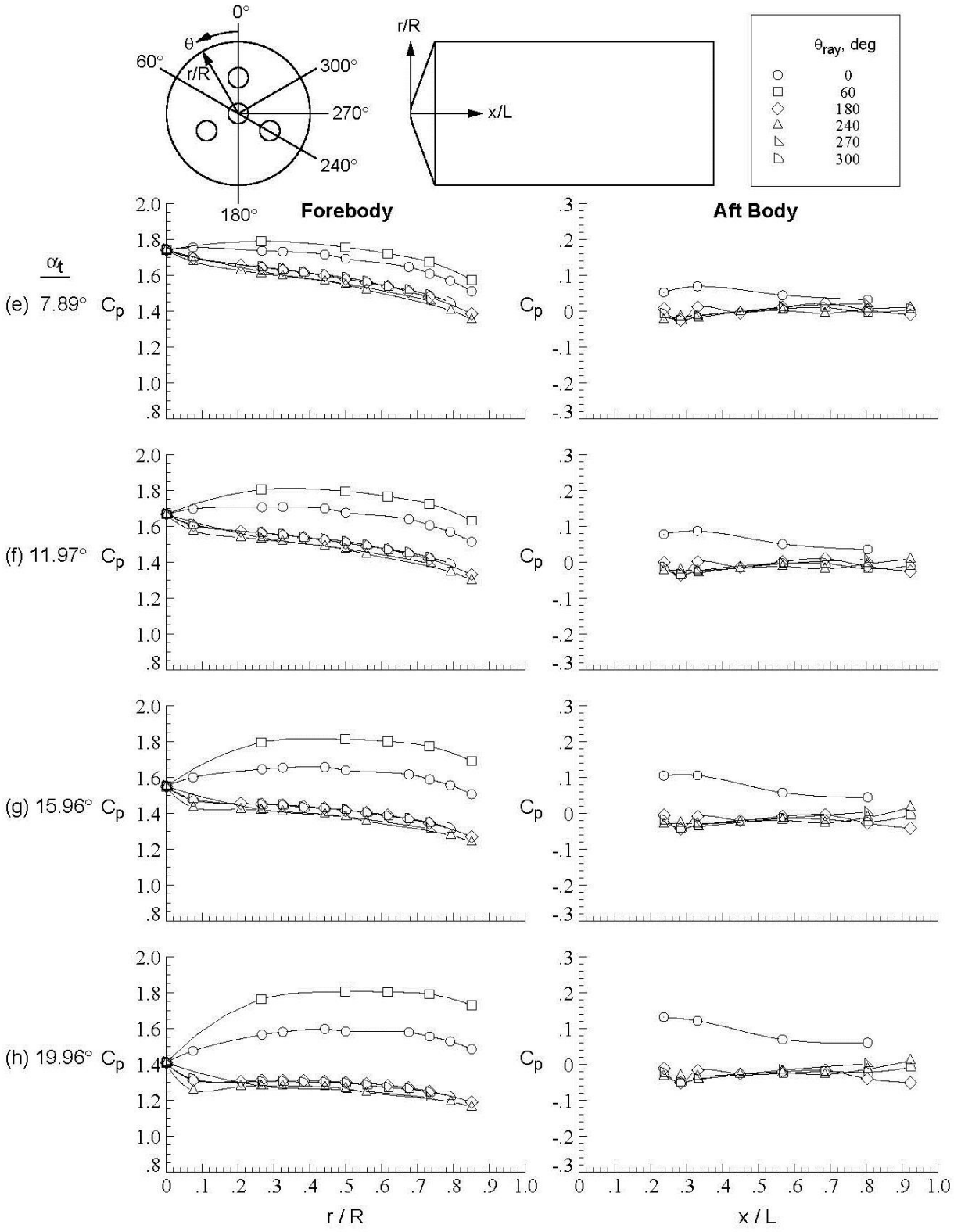

Figure D-98. Concluded.

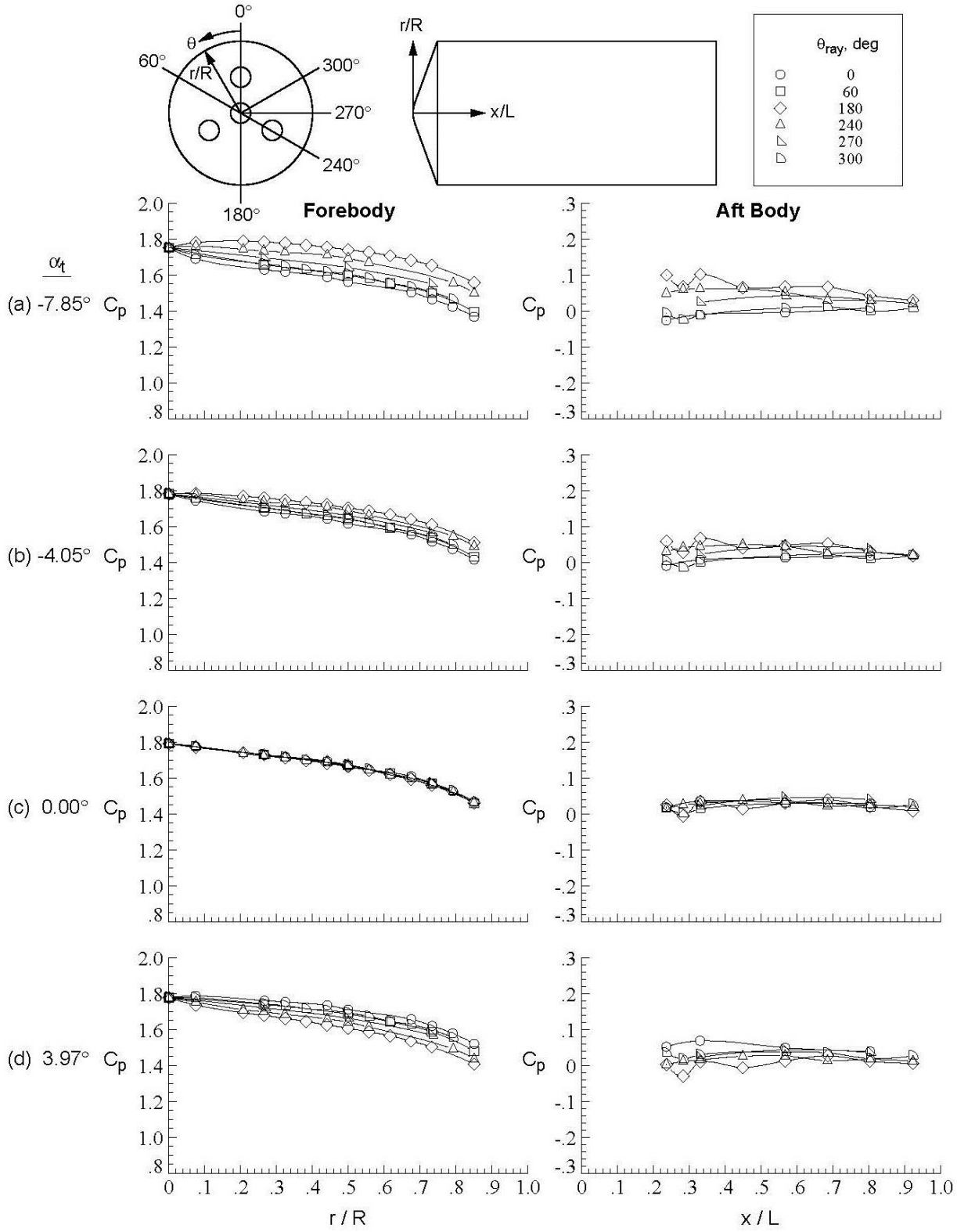

Figure D-99. Baseline configuration, Run 123, M_∞ = 4.6, Re_∞ = 1.5x10^7/ft, ϕ = 179.93°, X_S = 25.16 in, Y_S = –8.00 in, C_T = 0.00.

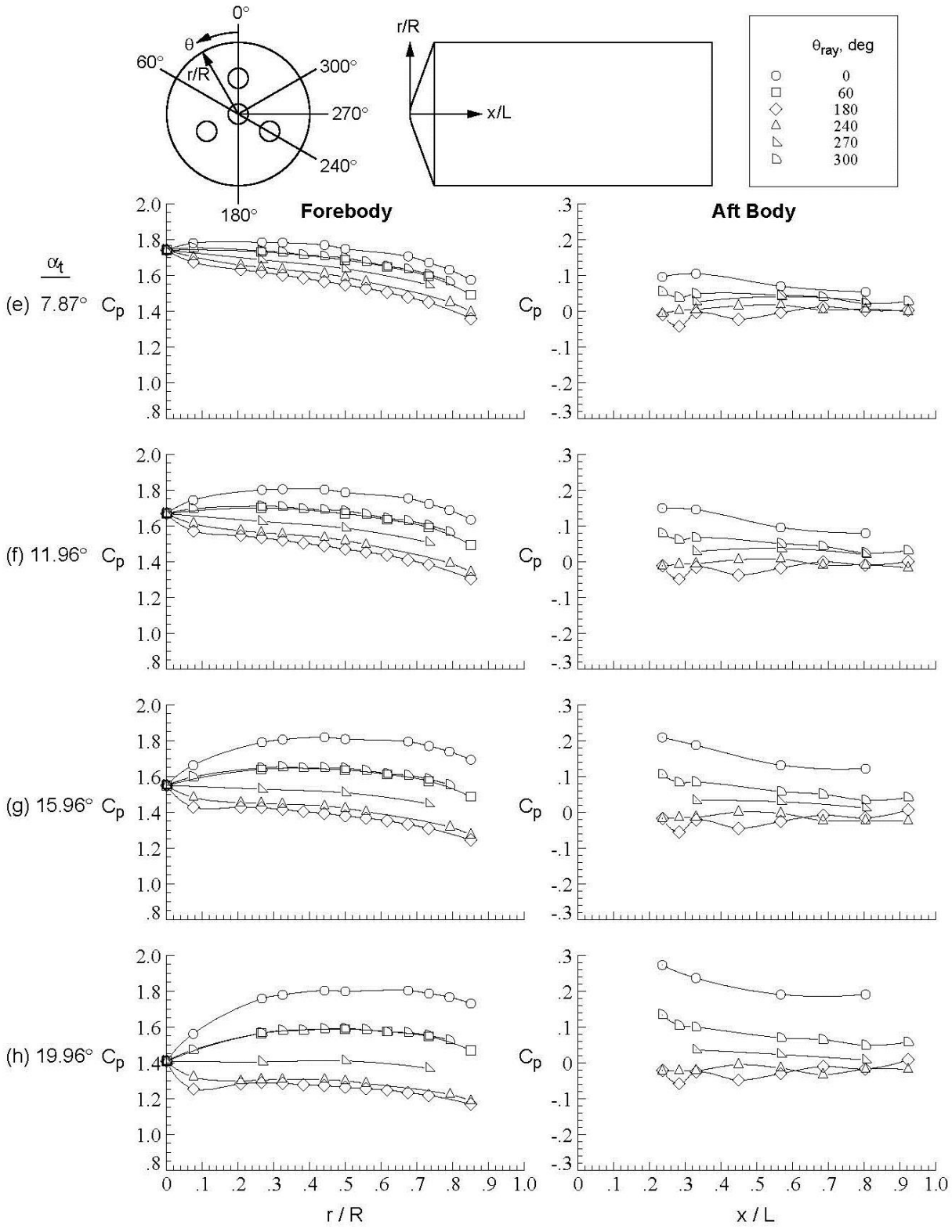

Figure D-99. Concluded.

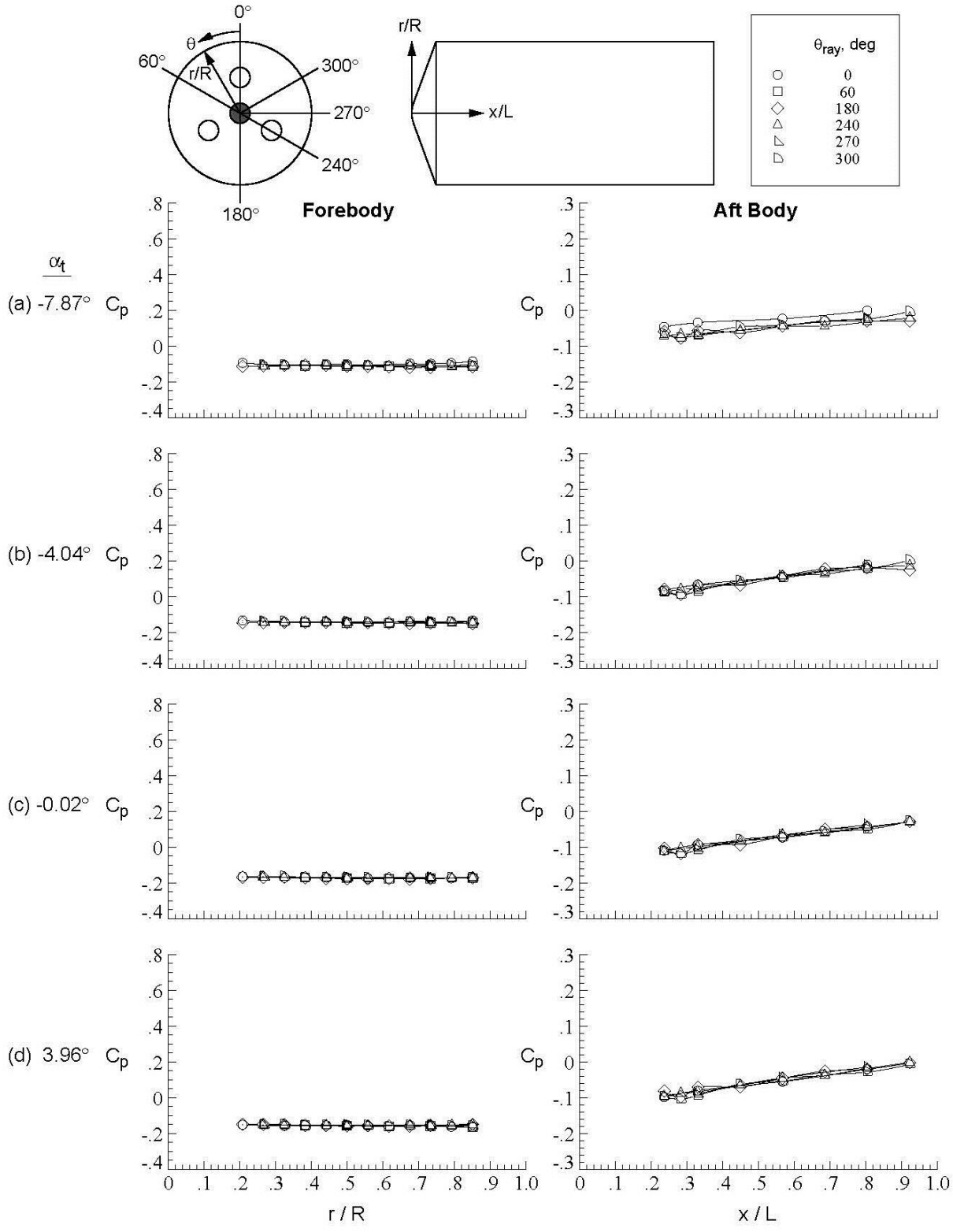

Figure D-100. Center nozzle configuration, Run 136, M_∞ = 2.4, Re_∞ = 1.0x10^7/ft, ϕ = −0.01°, X_S = 40.16 in, Y_S = 0.00 in, C_T = 3.96.

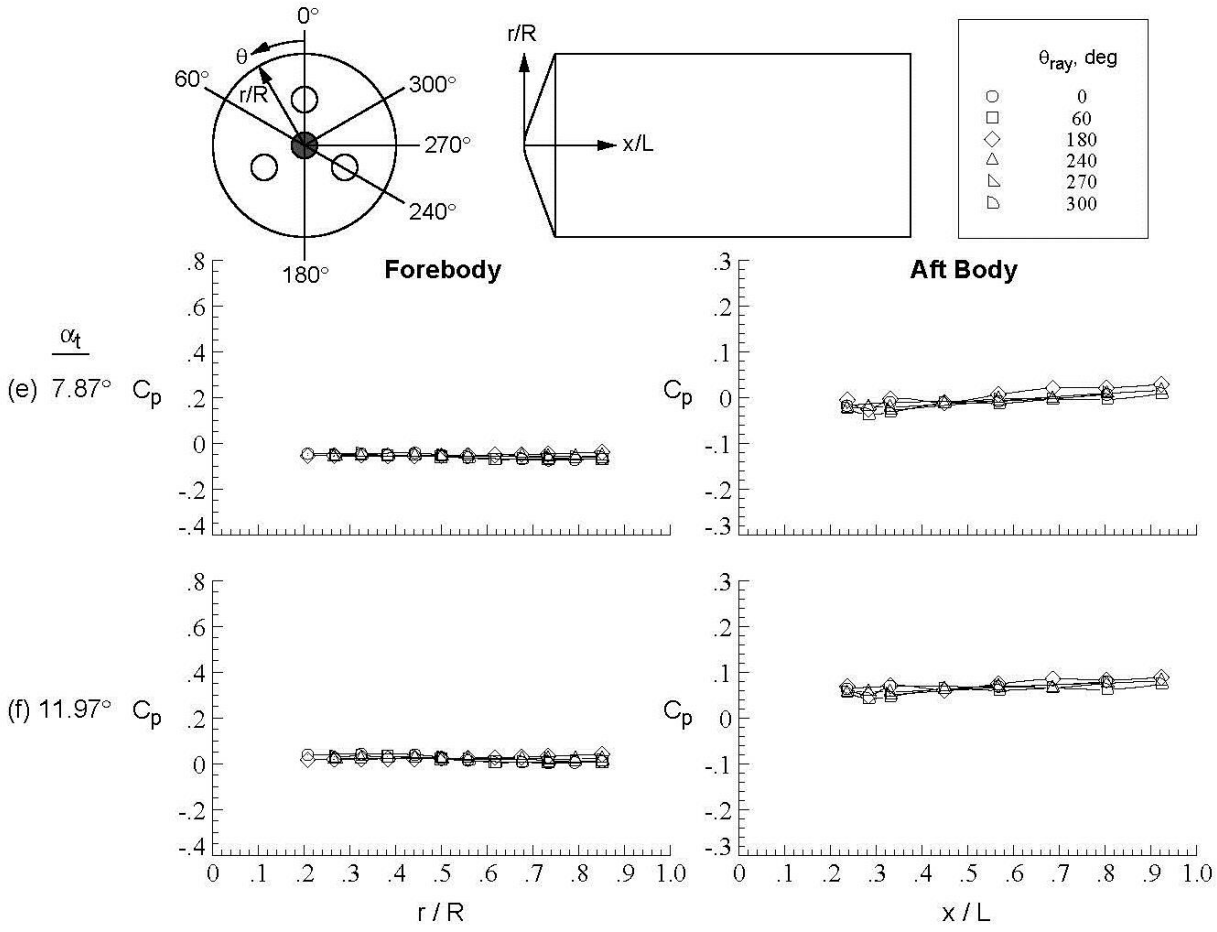

Figure D-100.Concluded.

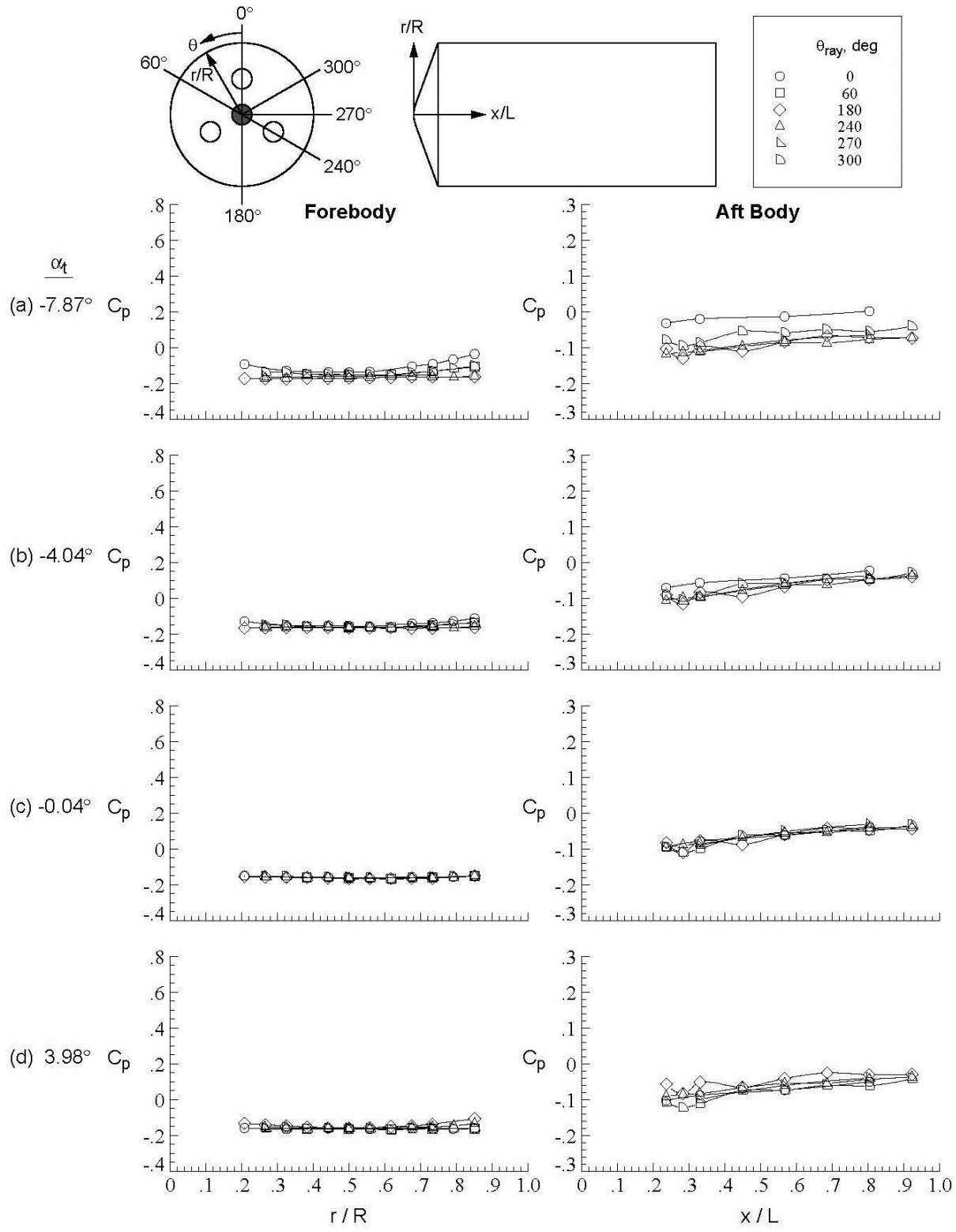

Figure D-101. Center nozzle configuration, Run 137, $M\infty = 2.4$, $Re_\infty = 1.0 \times 10^7$/ft, $\phi = -0.03°$, $X_S = 40.15$ in, $Y_S = 0.00$ in, $C_T = 3.01$.

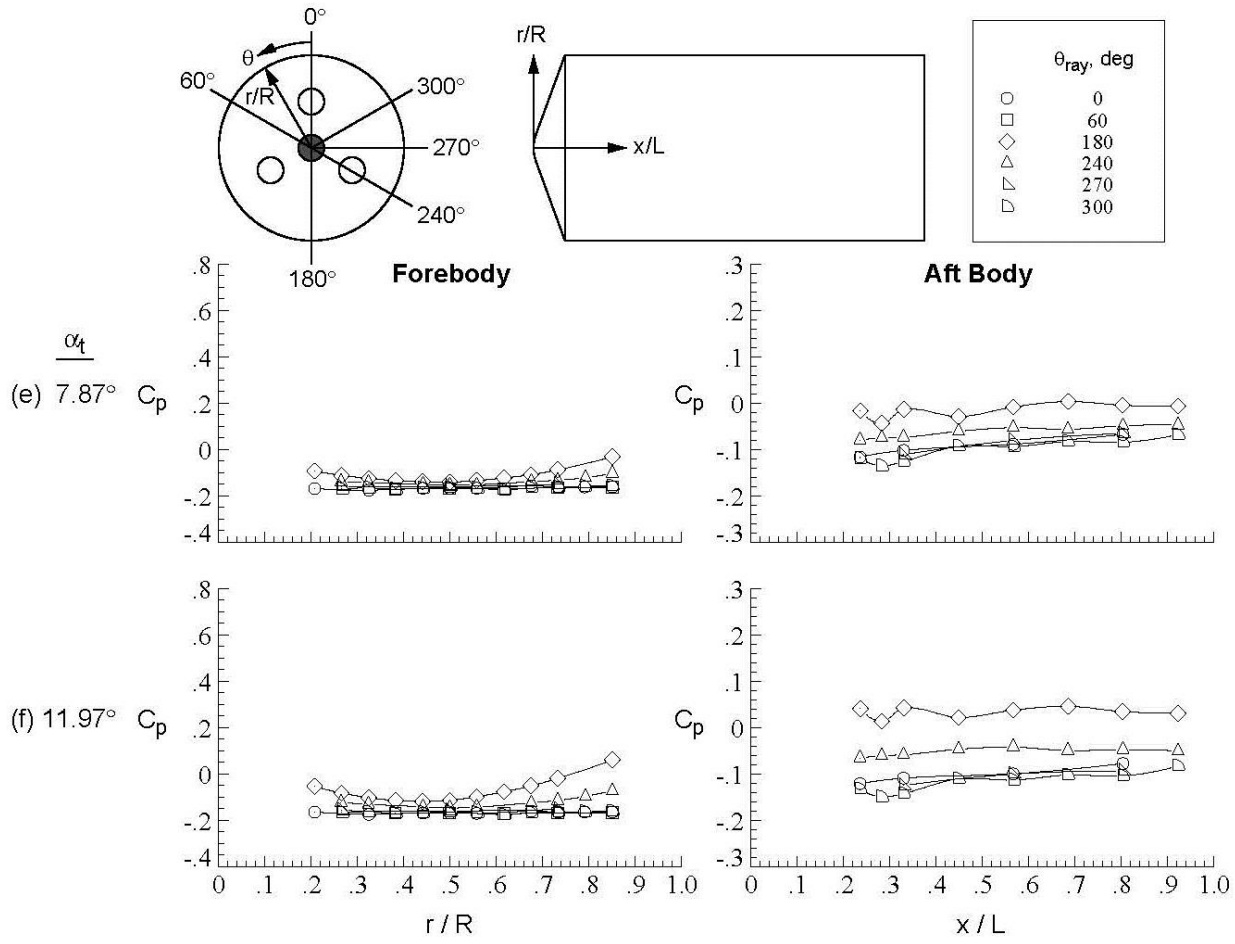

Figure D-101.Concluded.

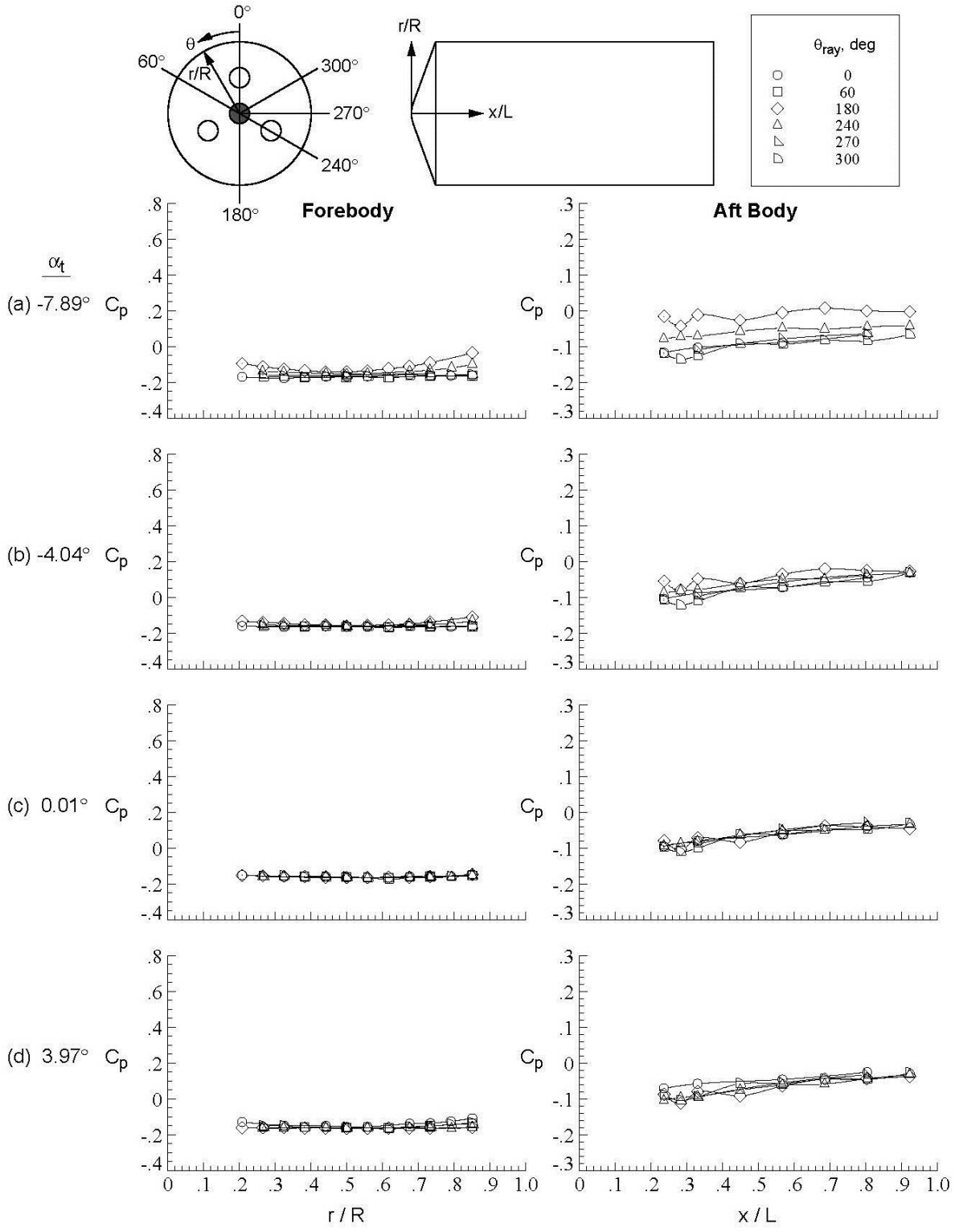

Figure D-102. Center nozzle configuration, Run 138, M_∞ = 2.4, Re_∞ = 1.0x10^7/ft, ϕ = 179.97°, X_S = 40.15 in, Y_S = 0.00 in, C_T = 3.02.

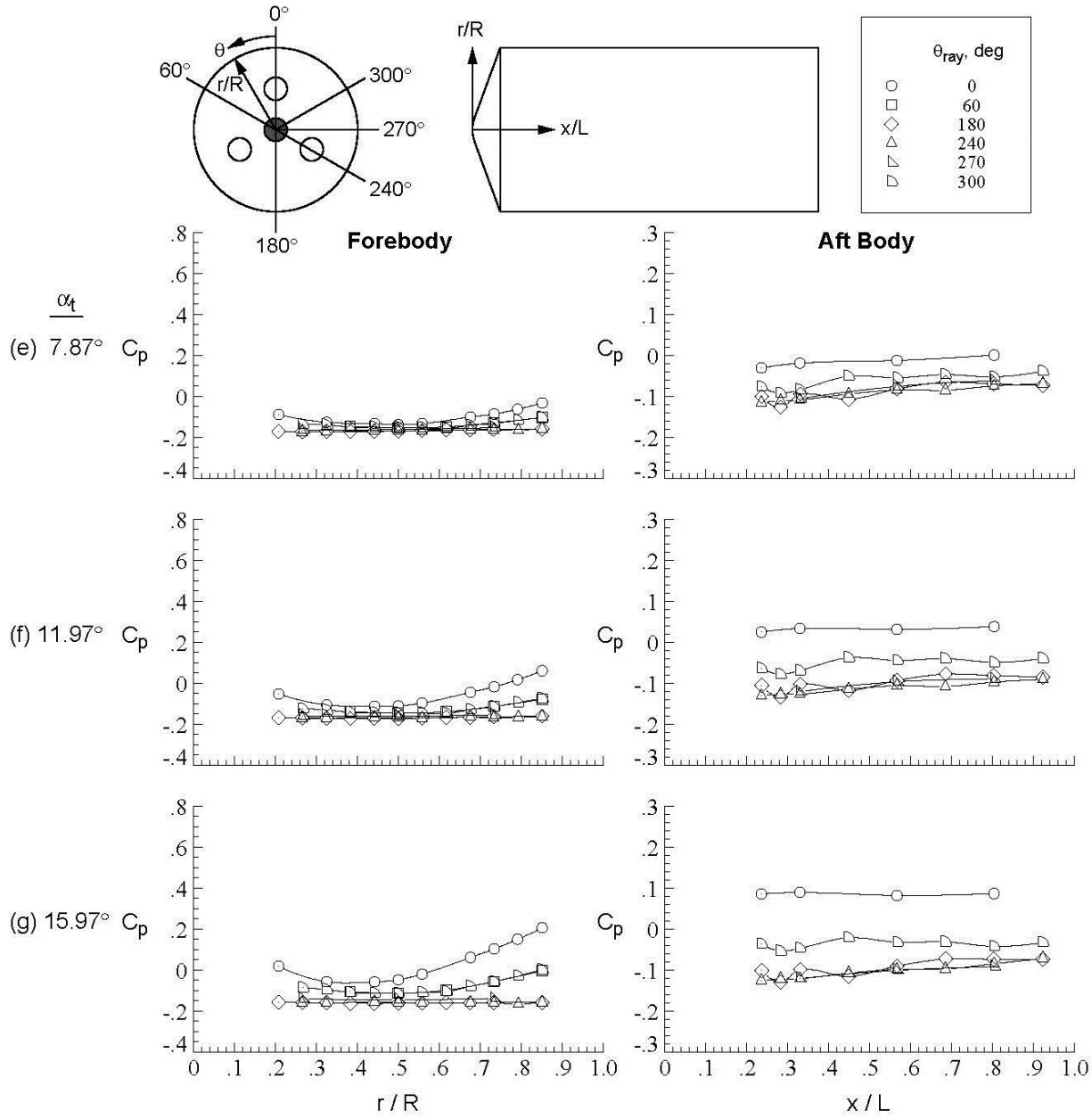

Figure D-102.Concluded.

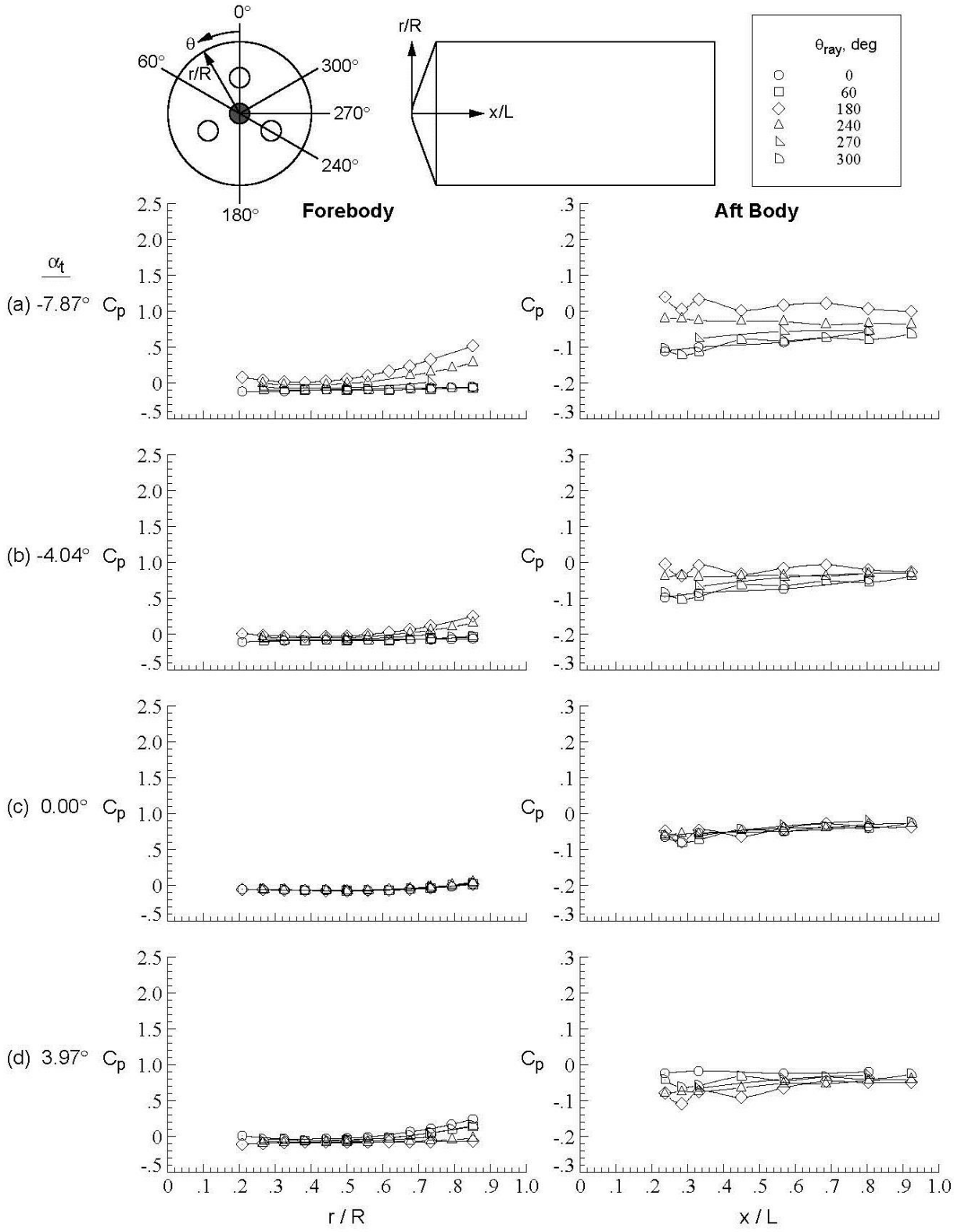

Figure D-103. Center nozzle configuration, Run 139, M_∞ = 2.4, Re_∞ = 1.0x10^7/ft, ϕ = 179.97°, X_S = 40.15 in, Y_S = 0.00 in, C_T = 0.97.

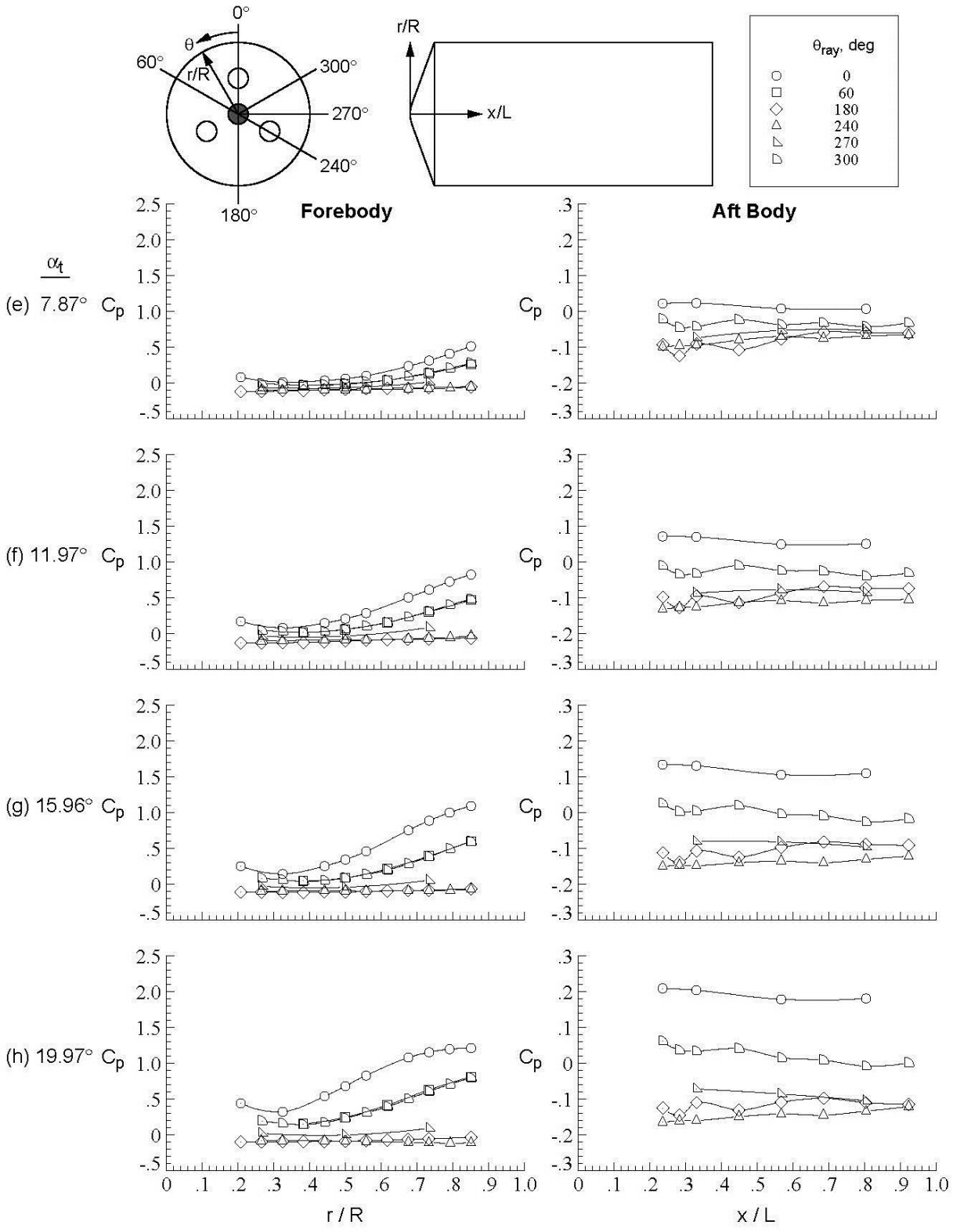

Figure D-103.Concluded.

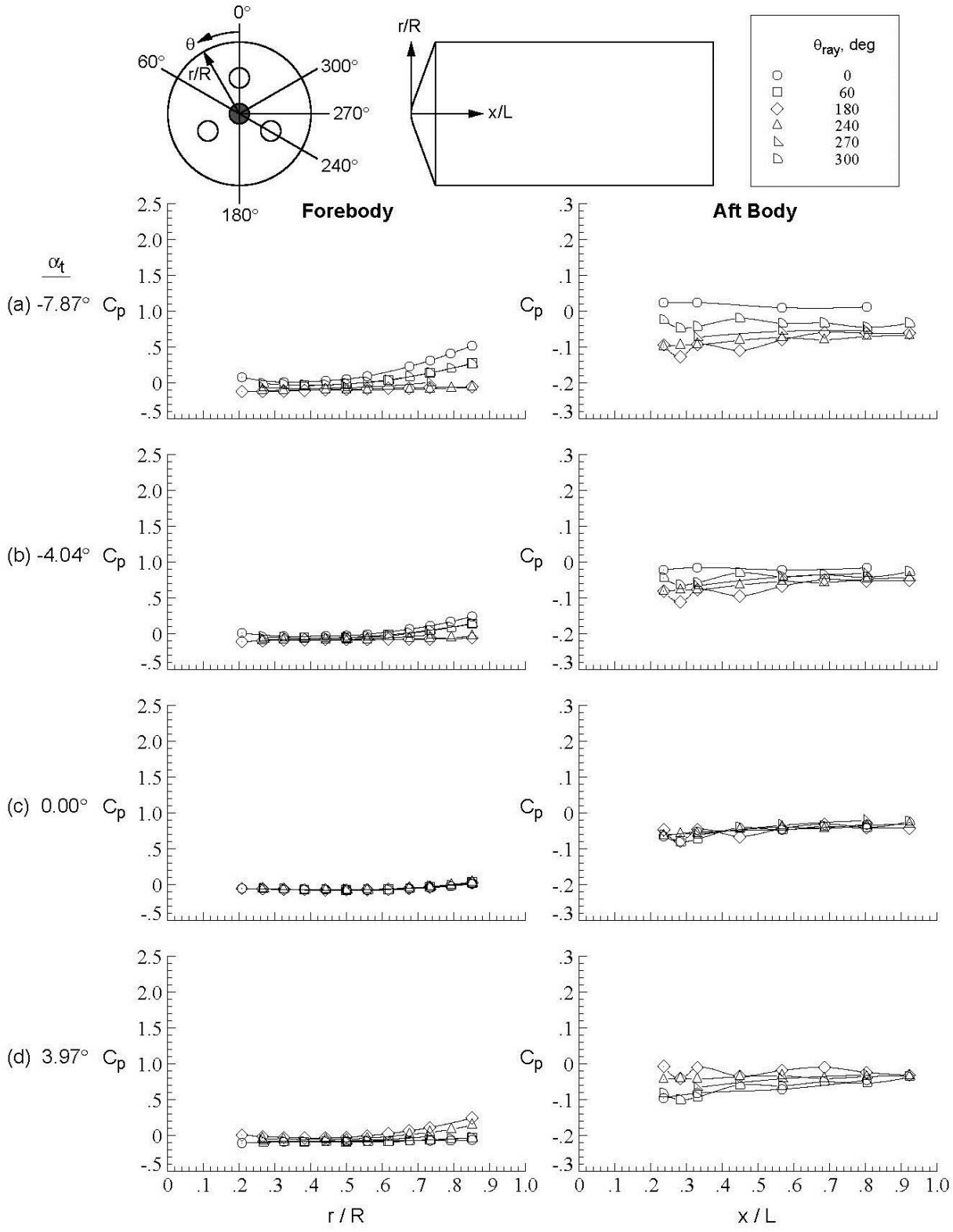

Figure D-104. Center nozzle configuration, Run 140, M_∞ = 2.4, Re_∞ = 1.0x10^6/ft, ϕ = −0.03°, X_S = 40.15 in, Y_S = 0.00 in, C_T = 0.97.

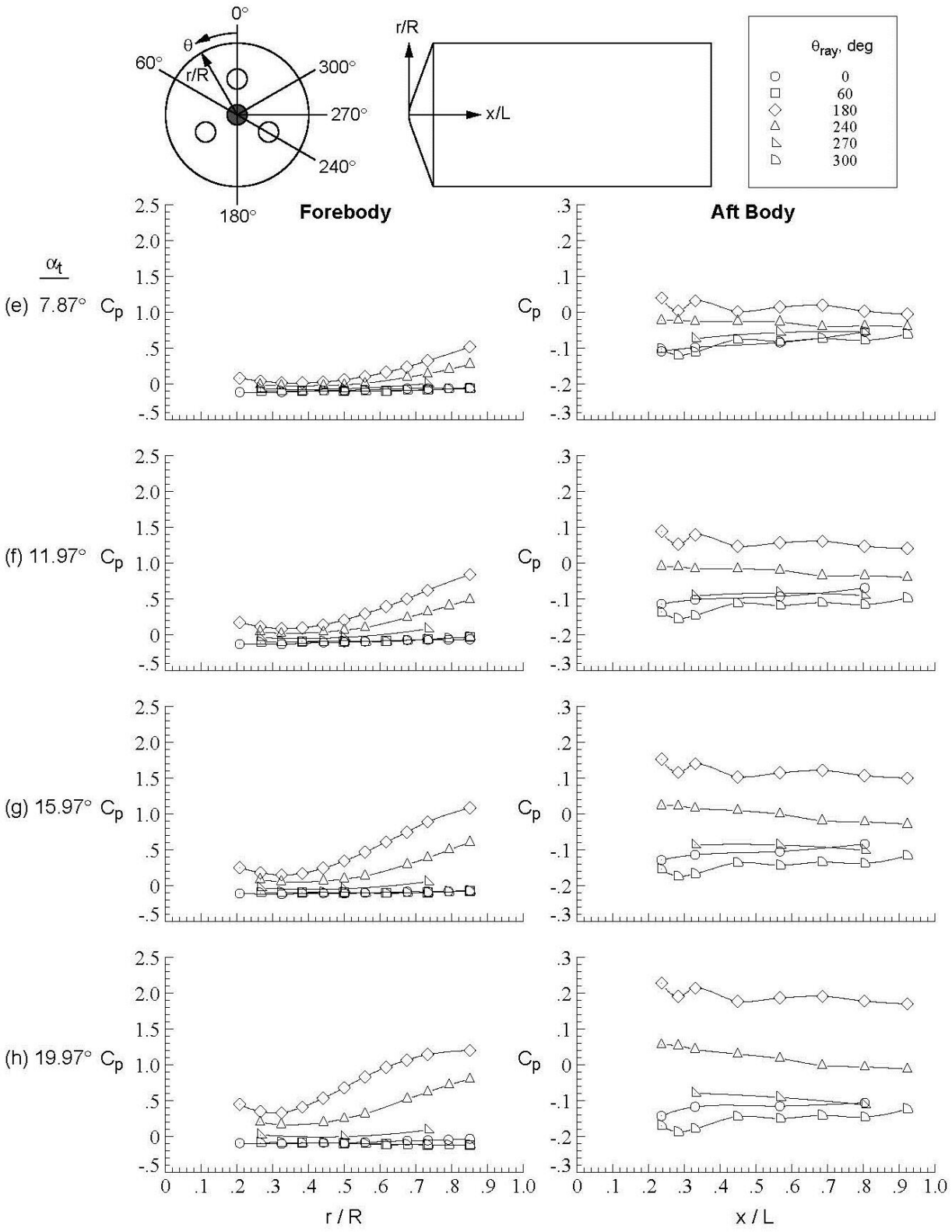

Figure D-104.Concluded.

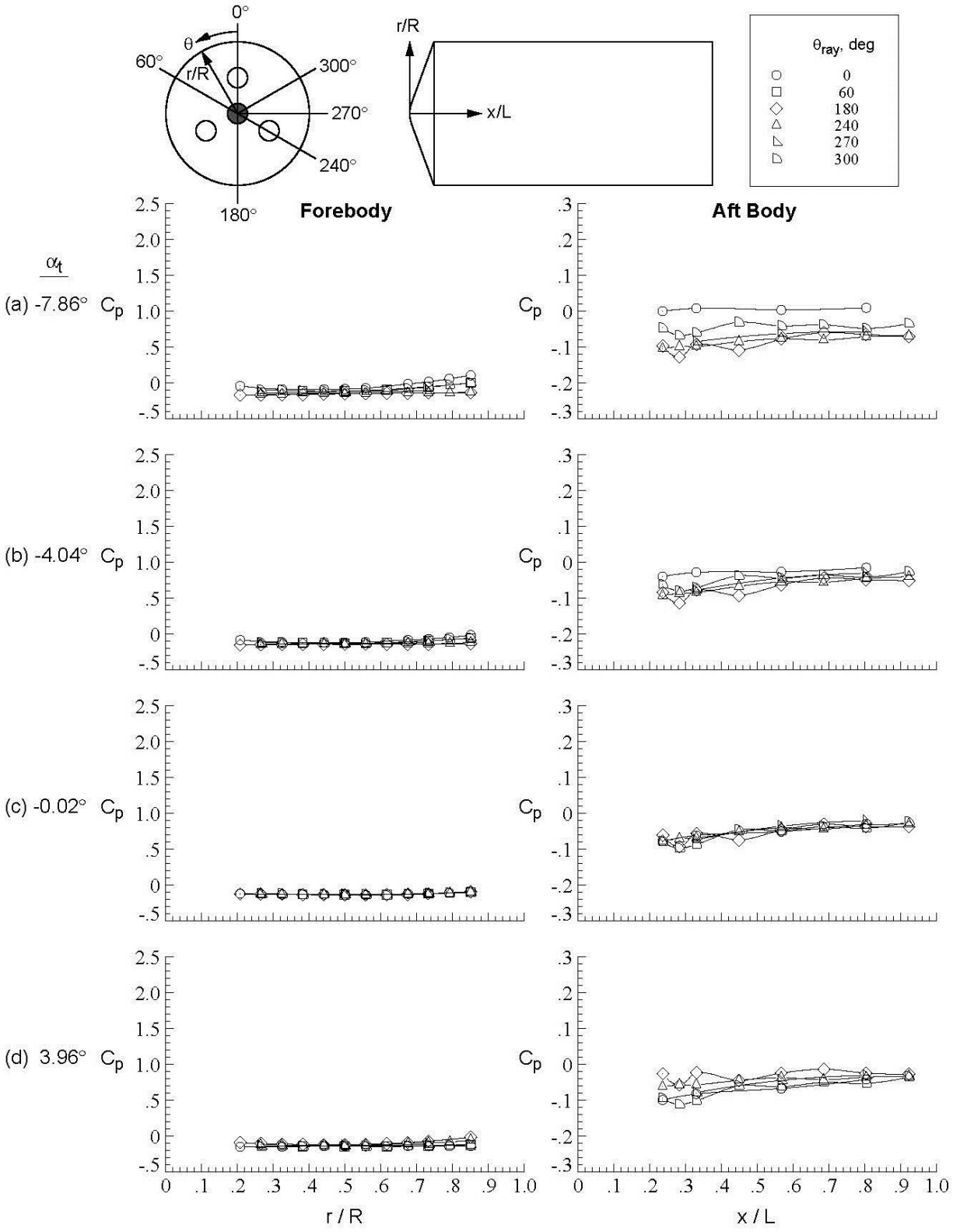

Figure D-105. Center nozzle configuration, Run 141, M_∞ = 2.4, Re_∞ = 1.0x10^7/ft, ϕ = −0.03°, X_S = 40.15 in, Y_S = 0.00 in, C_T = 1.98.

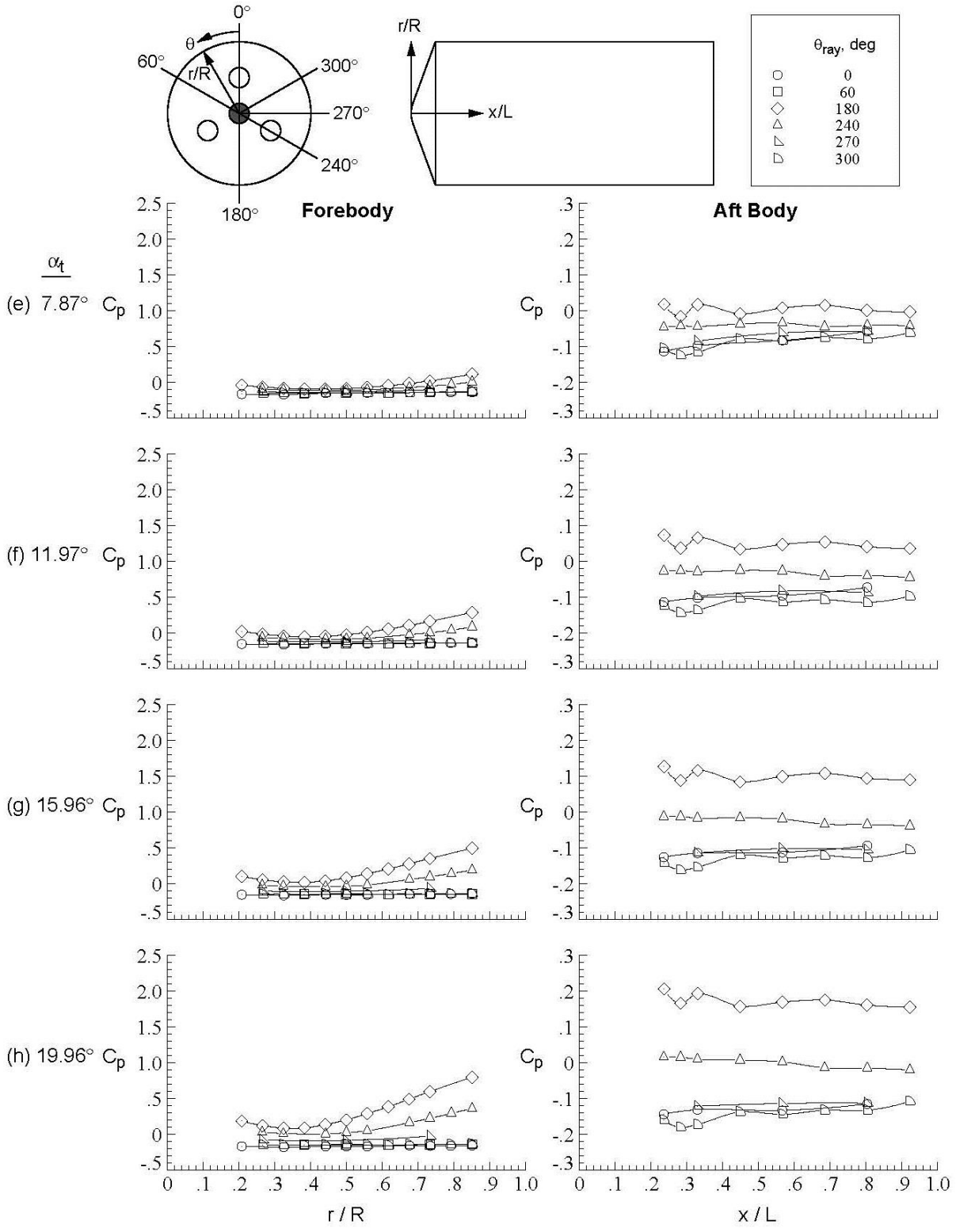

Figure D-105.Concluded.

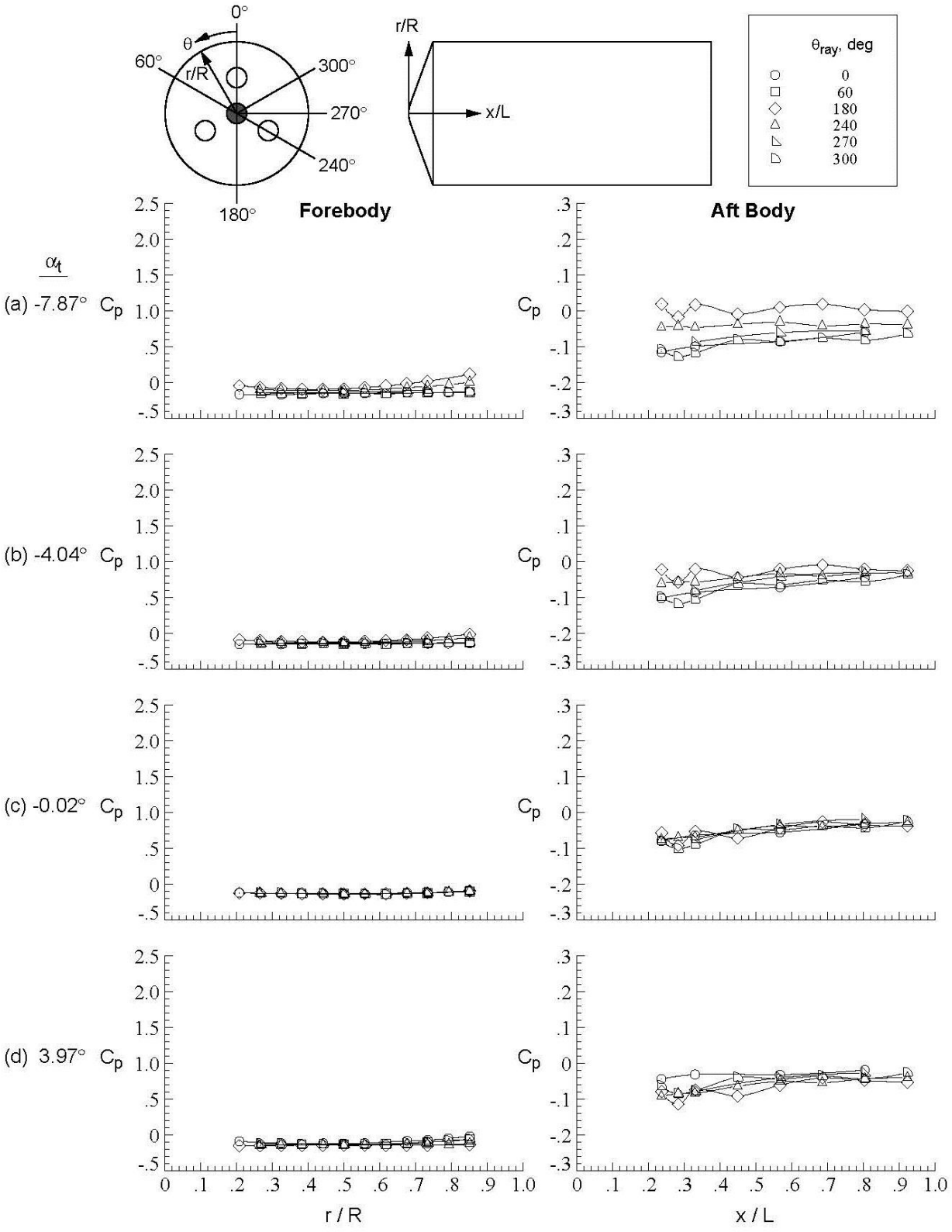

Figure D-106. Center nozzle configuration, Run 142, M_∞ = 2.4, Re_∞ = 1.0x10^6/ft, ϕ = −179.91°, X_S = 40.15 in, Y_S = 0.00 in, C_T = 1.97.

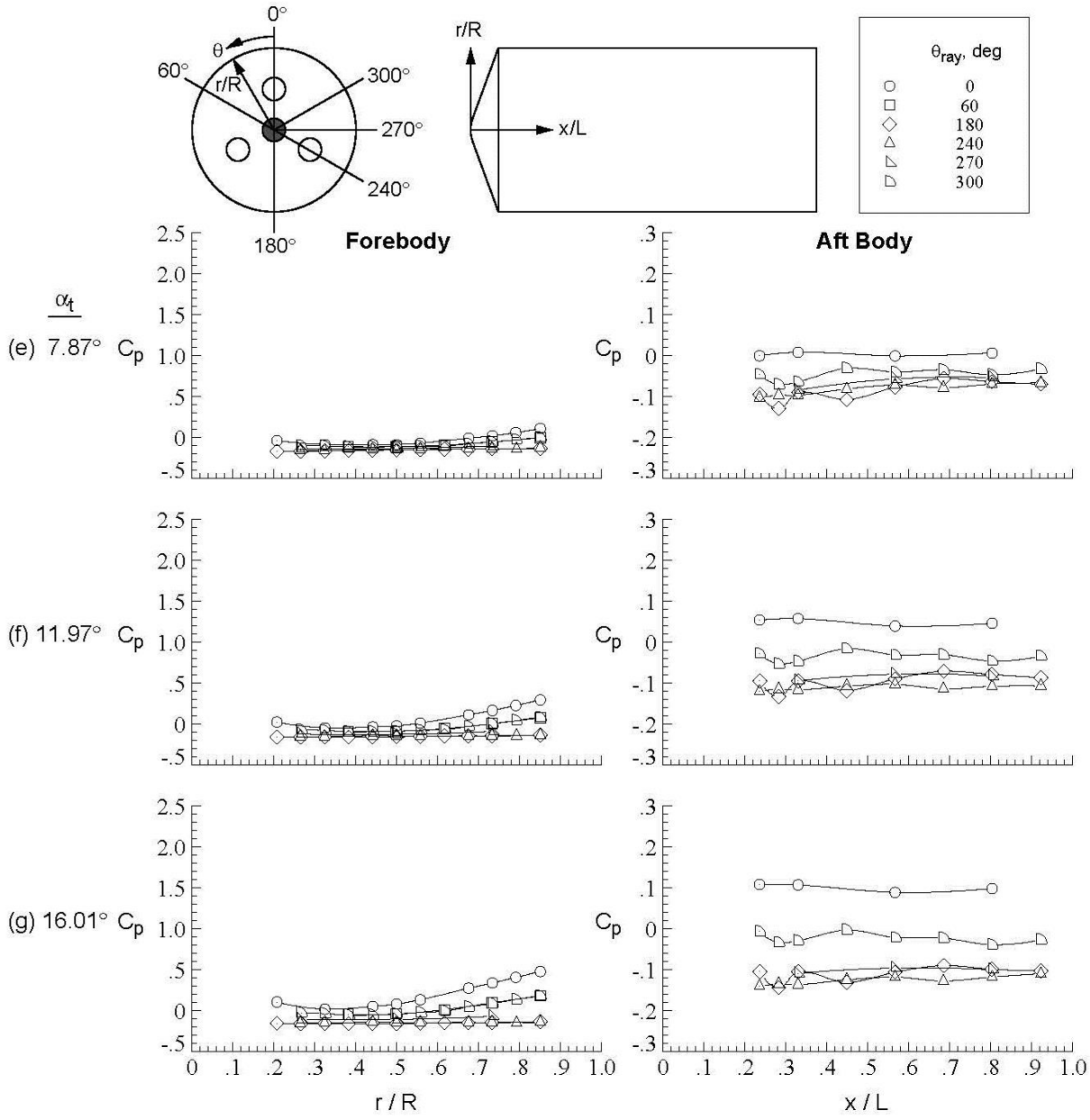

Figure D-106.Concluded.

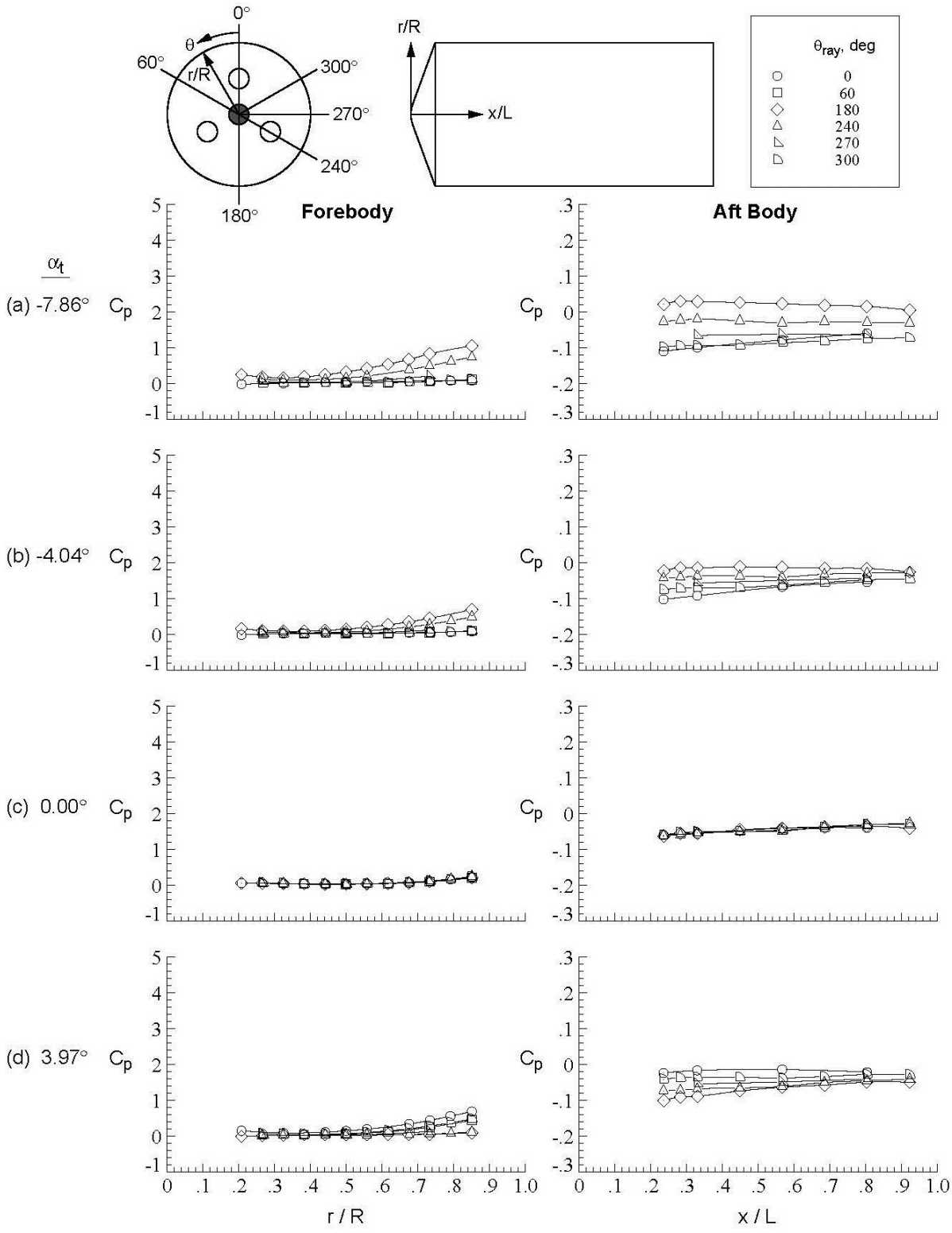

Figure D-107. Center nozzle configuration, Run 143, M_∞ = 2.4, Re_∞ = 1.0x10^6/ft, ϕ = −179.91°, X_S = 40.15 in, Y_S = 0.00 in, C_T = 0.47.

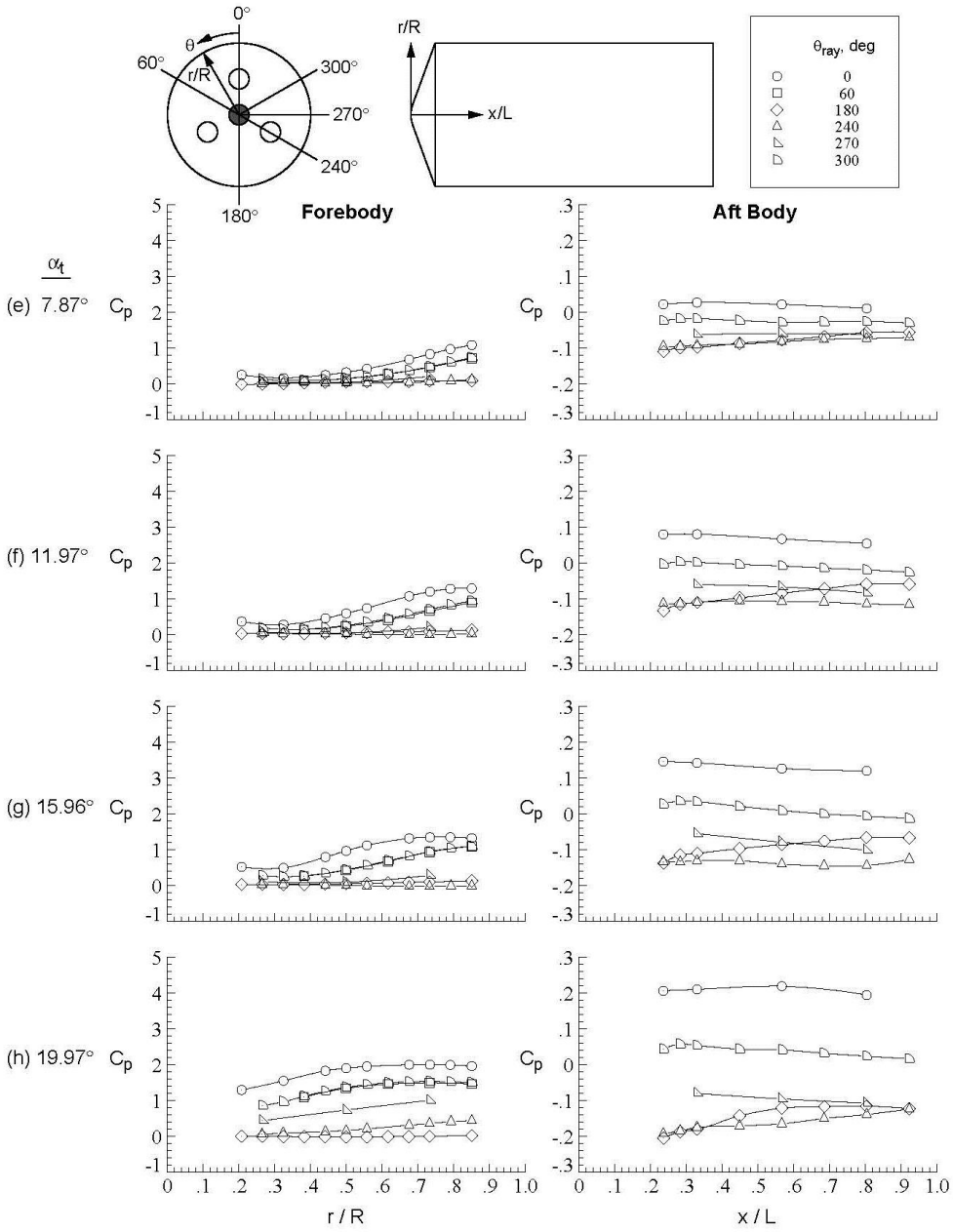

Figure D-107.Concluded.

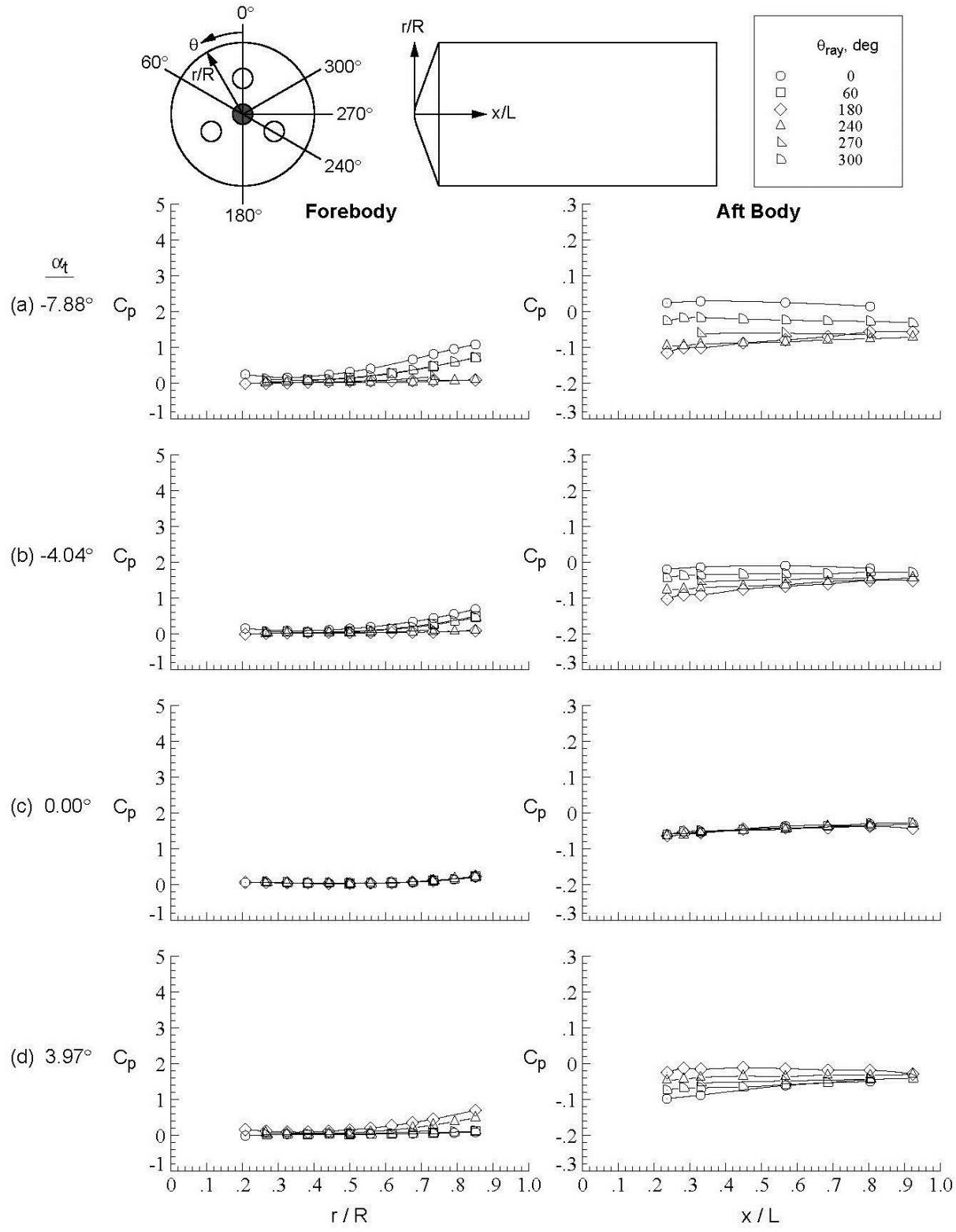

Figure D-108. Center nozzle configuration, Run 144, $M\infty$ = 2.4, Re_∞ = 1.0x10^6/ft, ϕ = 0.01°, X_S = 40.15 in, Y_S = 0.00 in, C_T = 0.46.

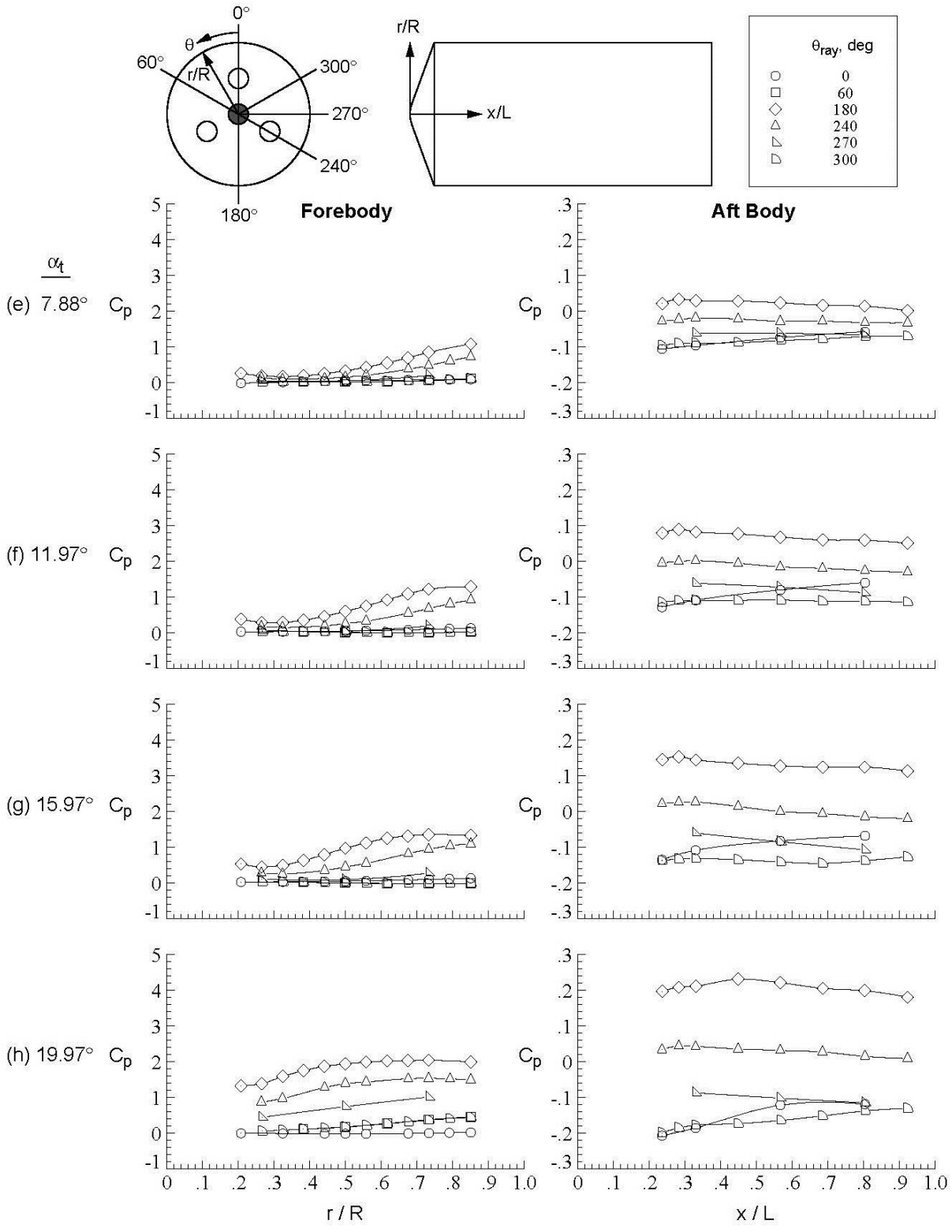

Figure D-108.Concluded.

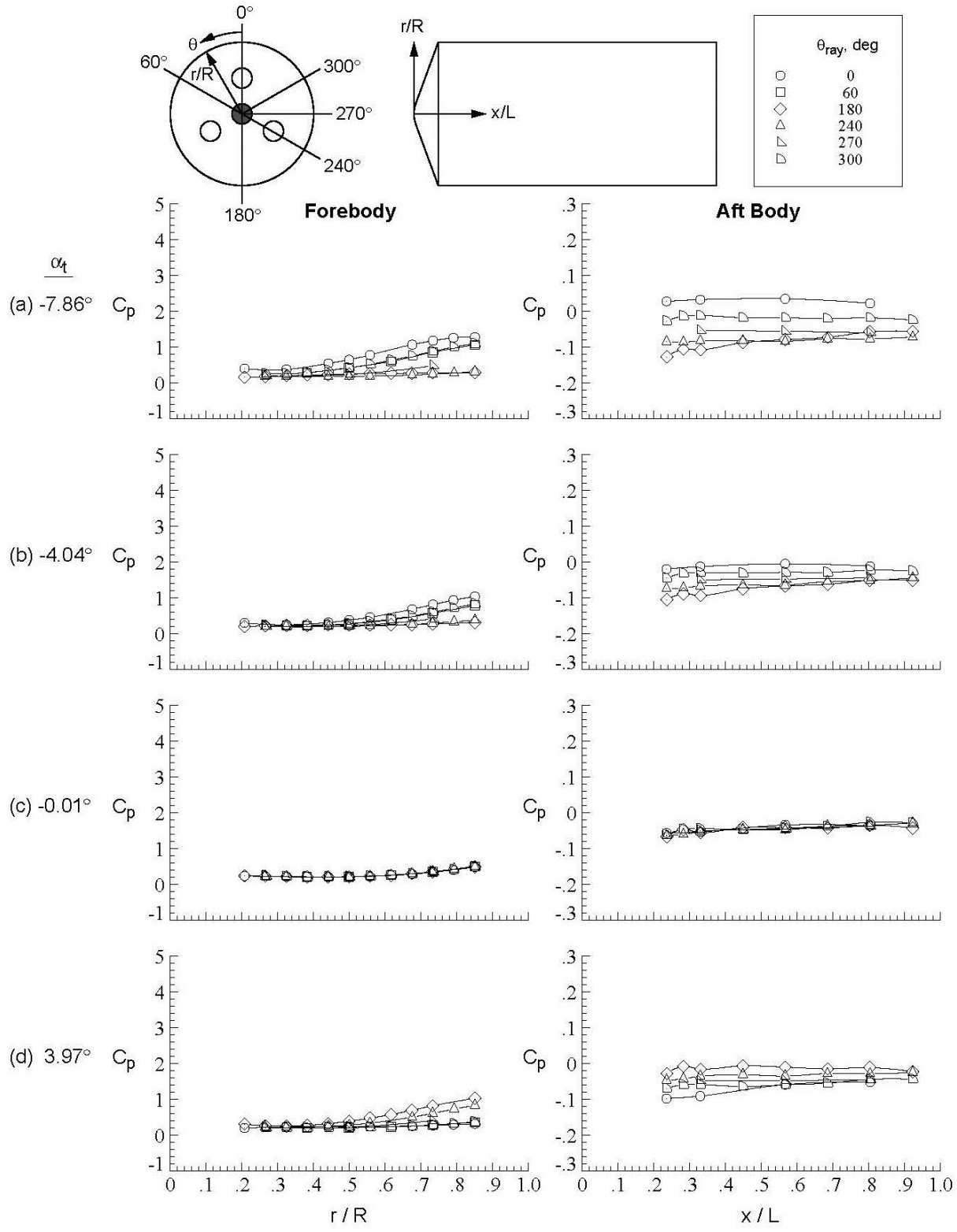

Figure D-109. Center nozzle configuration, Run 145, M_∞ = 2.4, Re_∞ = 1.0x10^7/ft, ϕ = 0.01°, X_S = 40.15 in, Y_S = 0.00 in, C_T = 0.23.

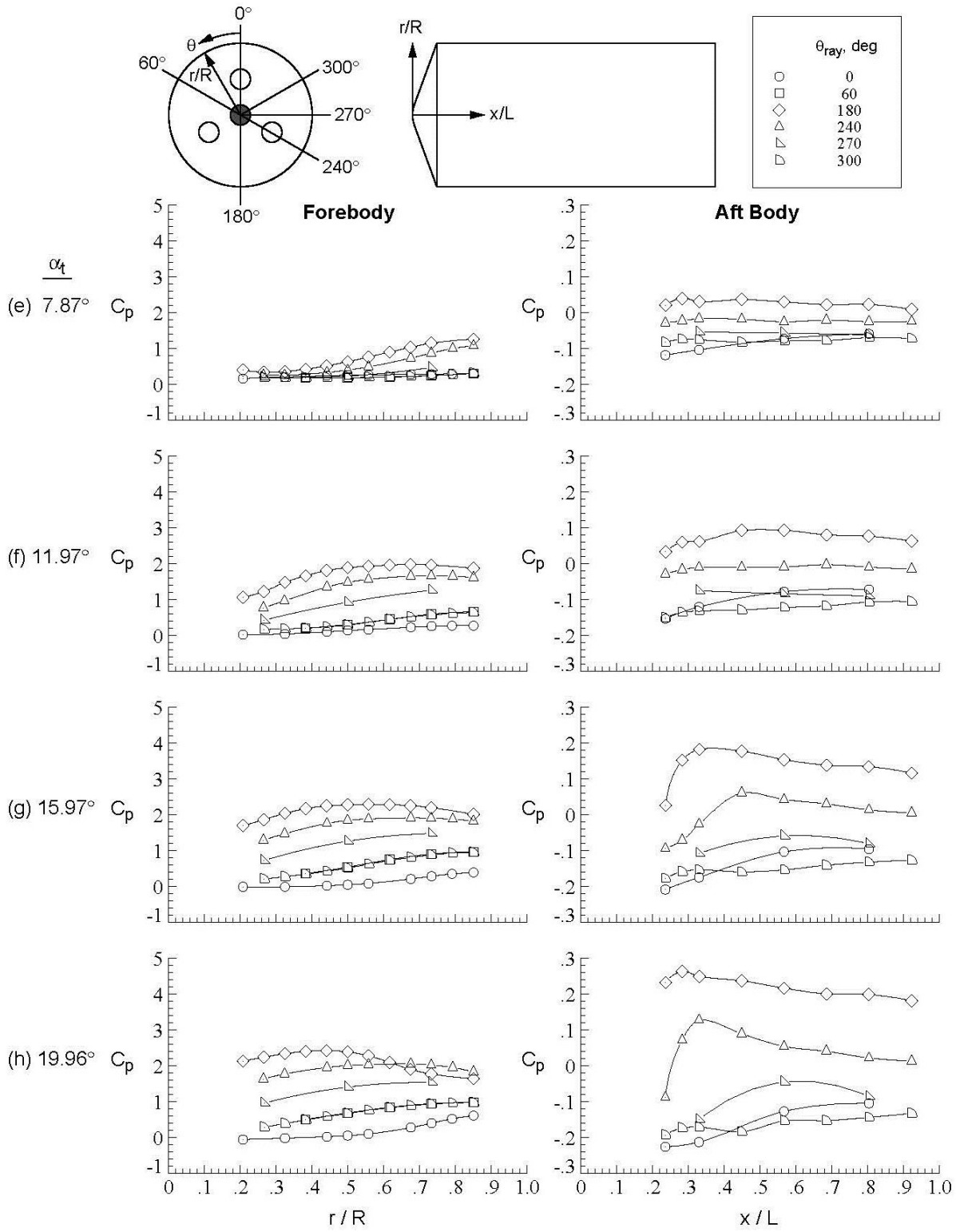

Figure D-109.Concluded.

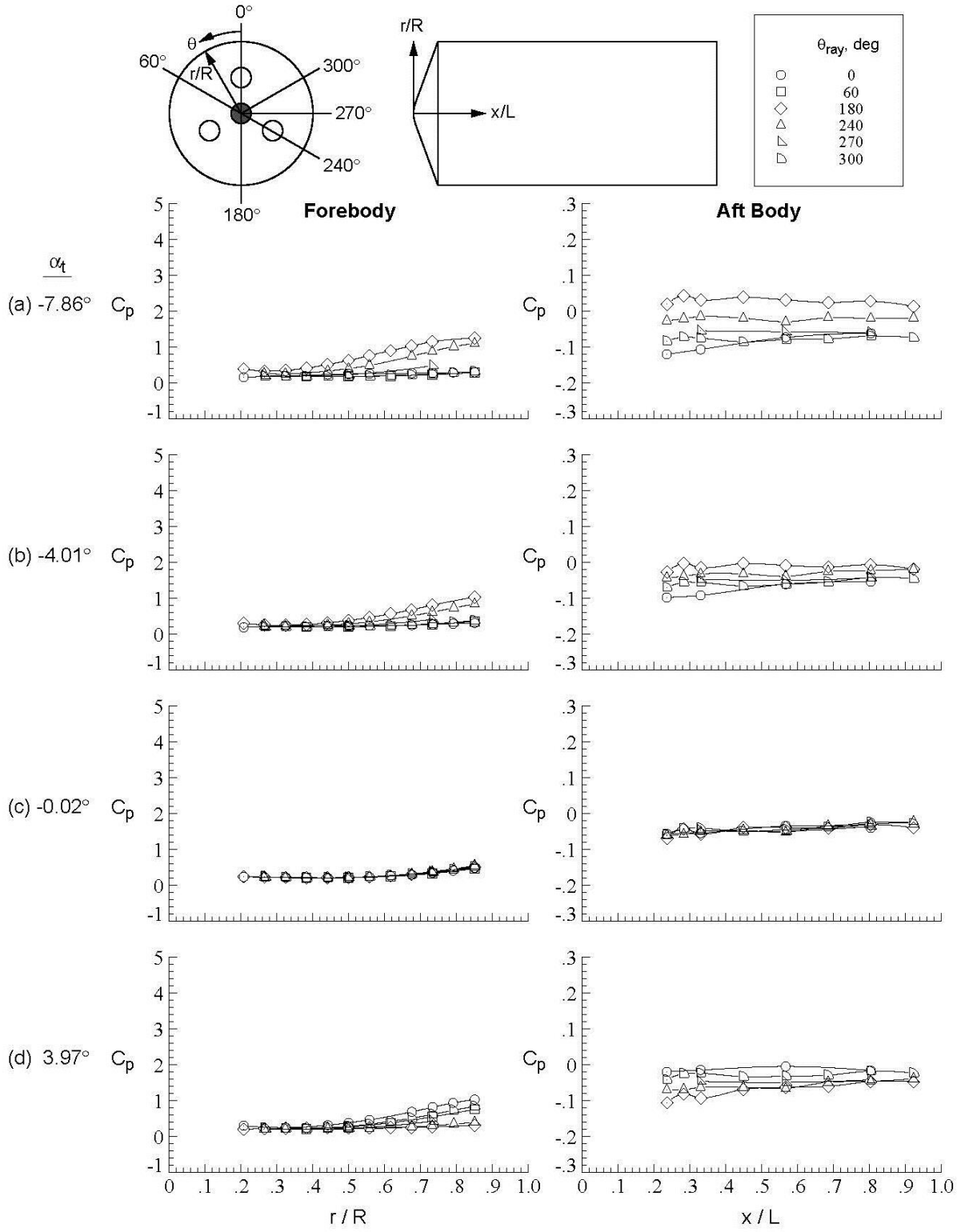

Figure D-110. Center nozzle configuration, Run 146, $M\infty = 2.4$, $Re_\infty = 1.0 \times 10^7$/ft, $\phi = 179.99°$, $X_S = 40.15$ in, $Y_S = 0.00$ in, $C_T = 0.23$.

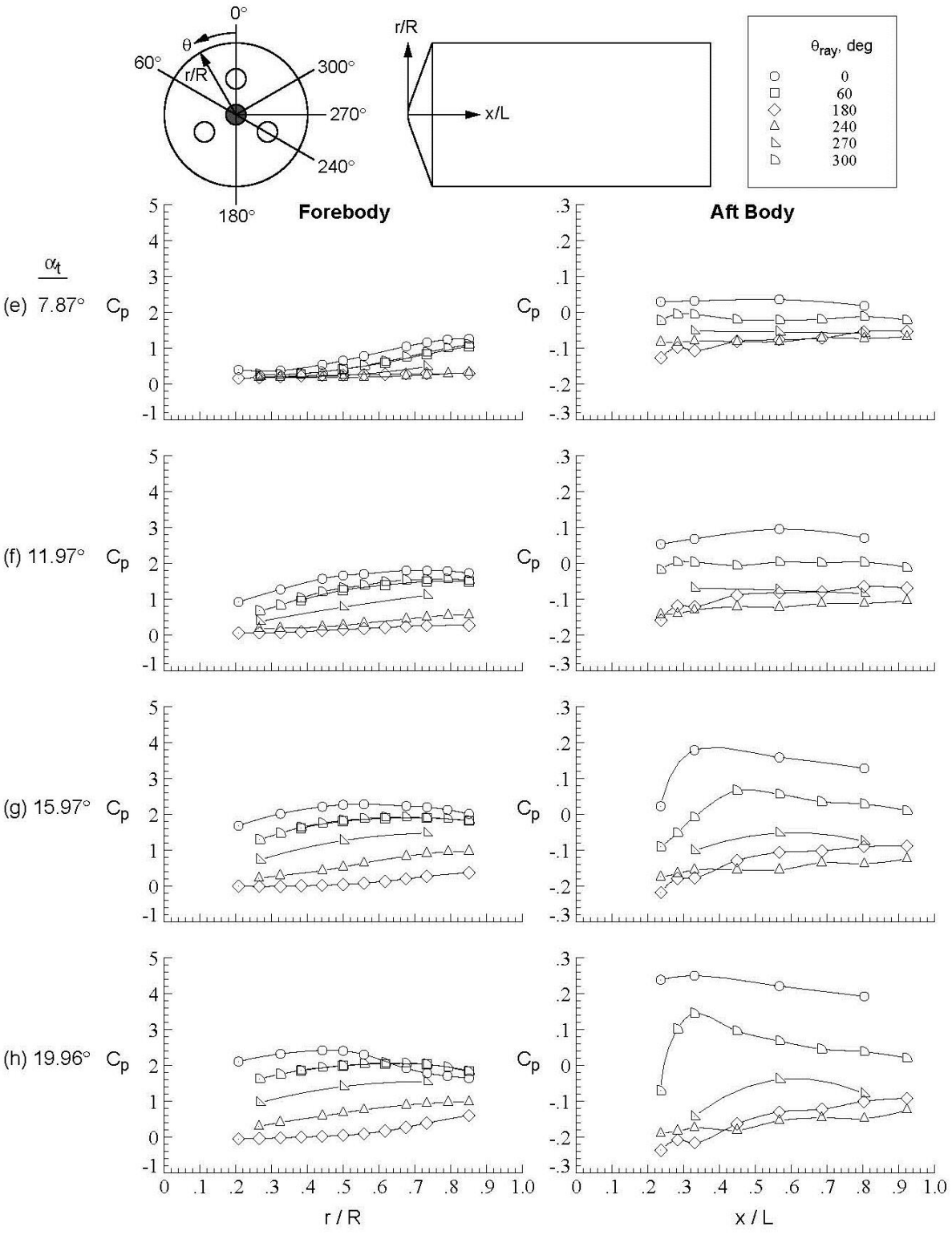

Figure D-110.Concluded.

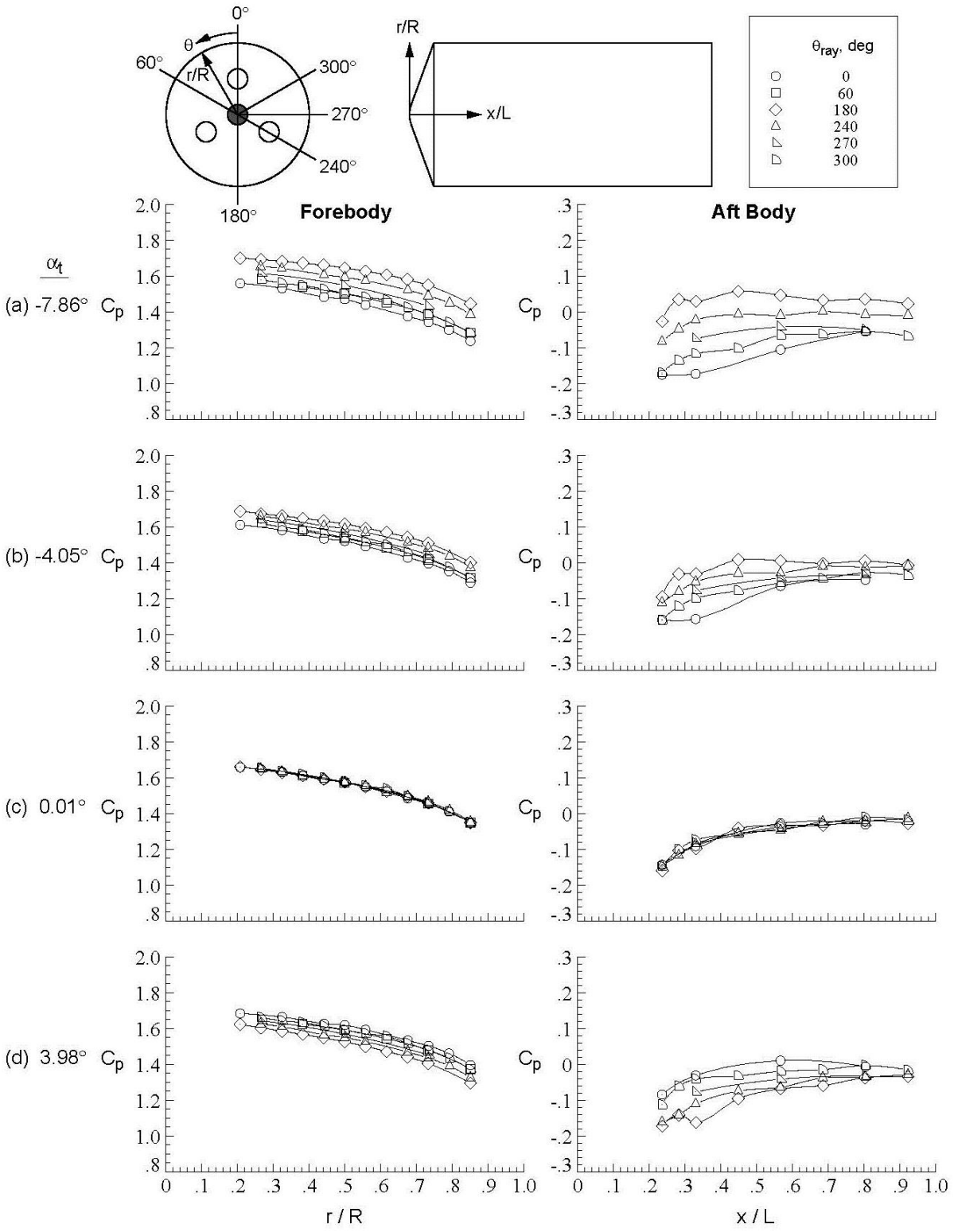

Figure D-111. Center nozzle configuration, Run 148, M_∞ = 2.4, Re_∞ = 1.0x10^6/ft, ϕ = 179.99°, X_S = 40.15 in, Y_S = 0.00 in, C_T = 0.00.

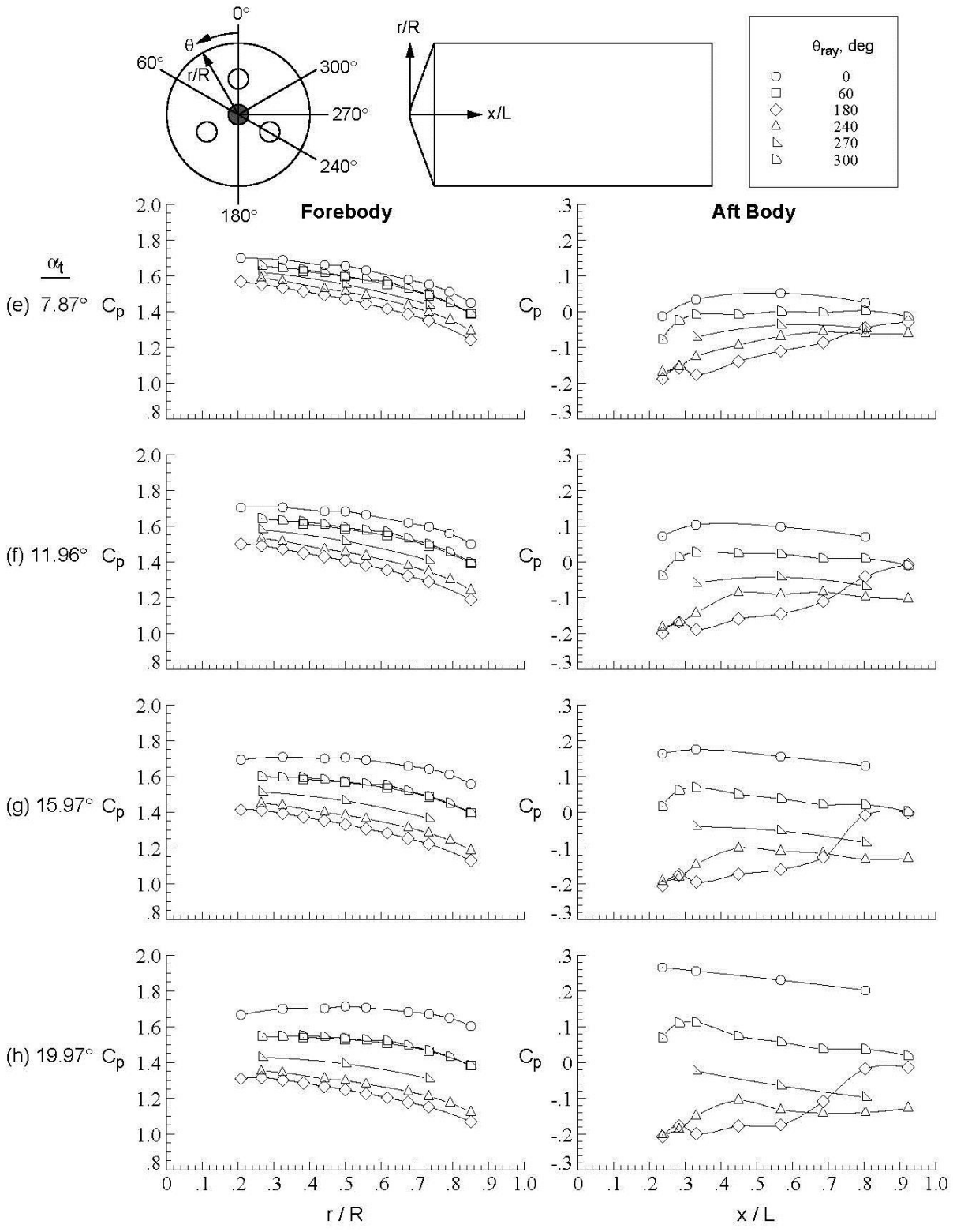

Figure D-111.Concluded.

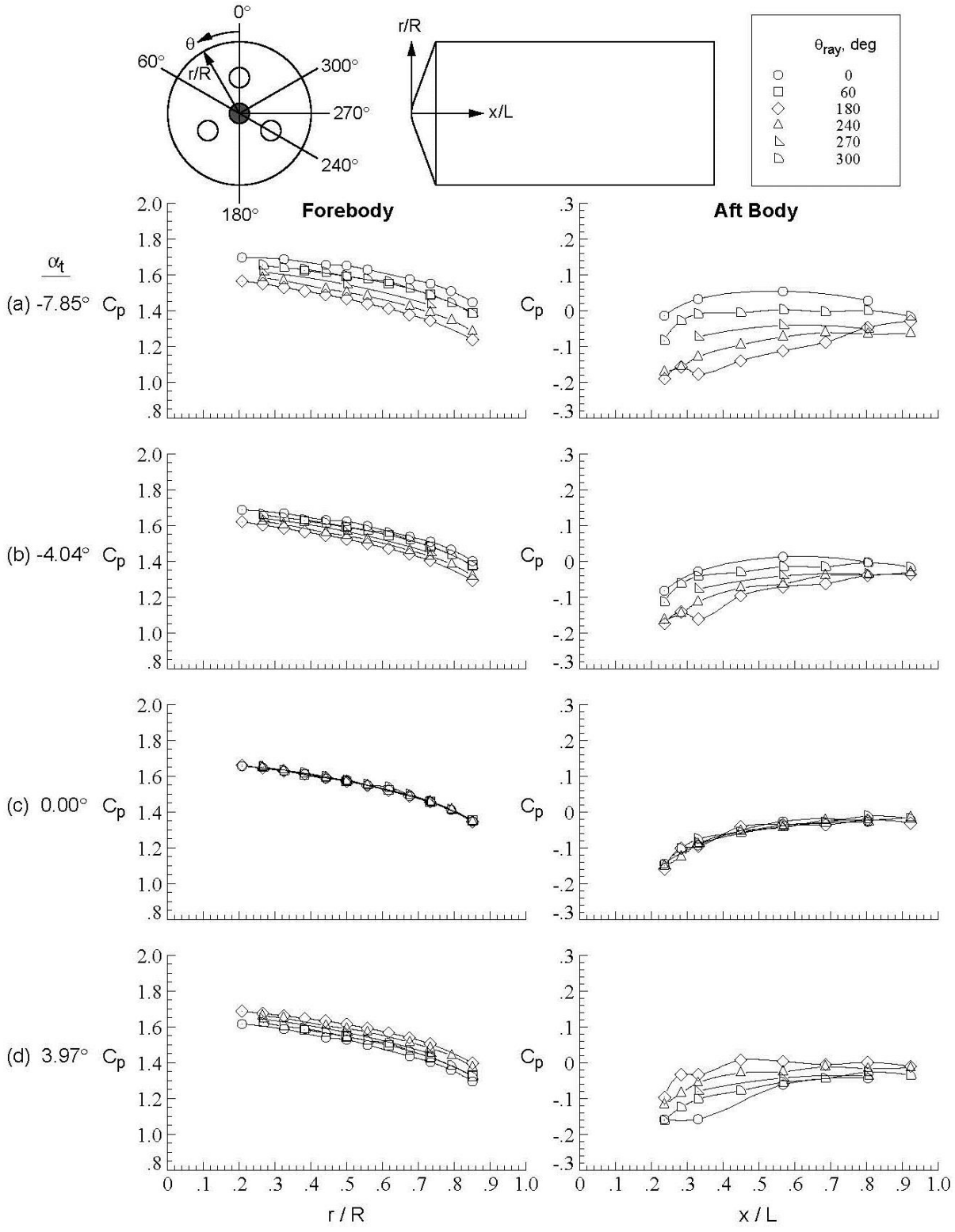

Figure D-112. Center nozzle configuration, Run 149, $M\infty = 2.4$, $Re_\infty = 1.0 \times 10^6$/ft, $\phi = -0.03°$, $X_S = 40.15$ in, $Y_S = 0.00$ in, $C_T = 0.00$.

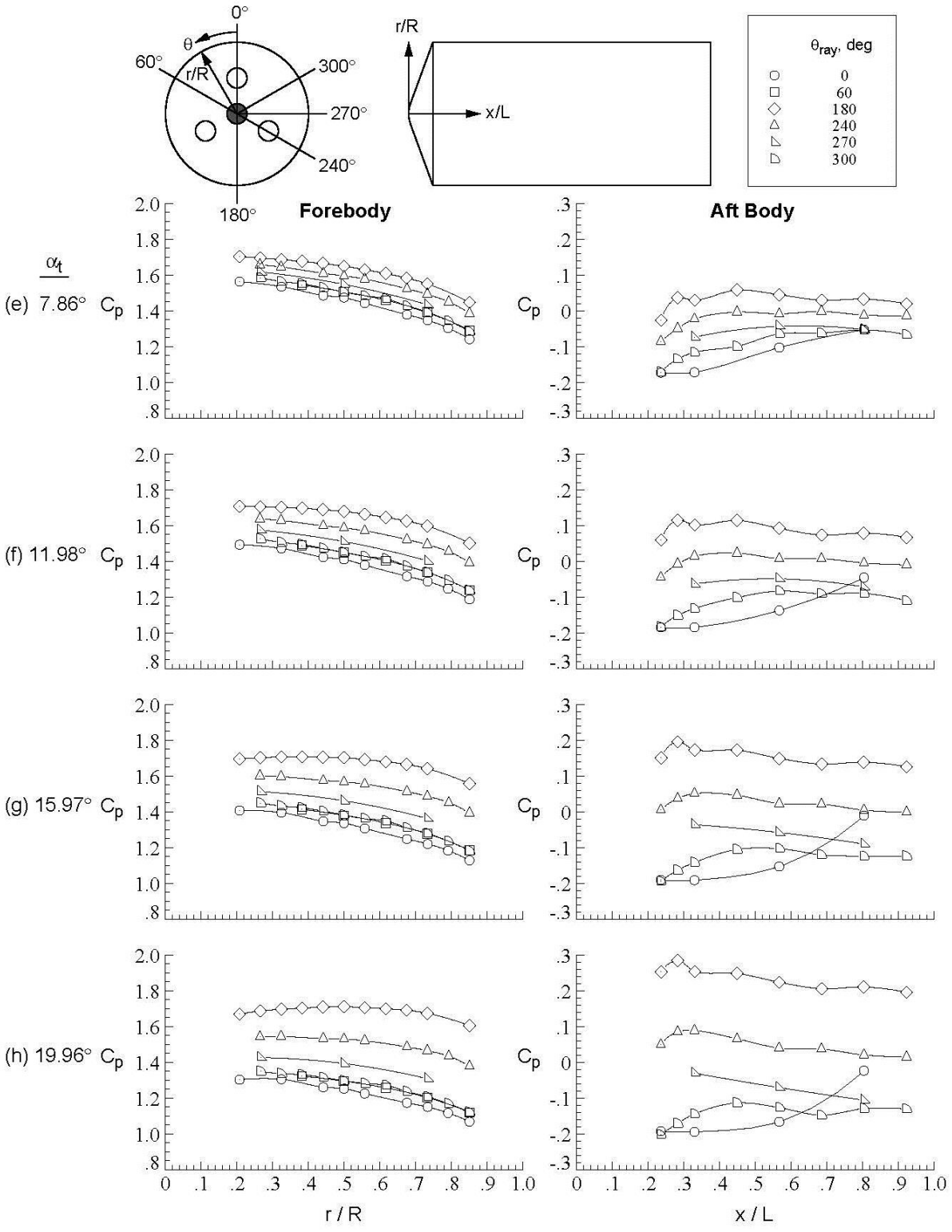

Figure D-112.Concluded.

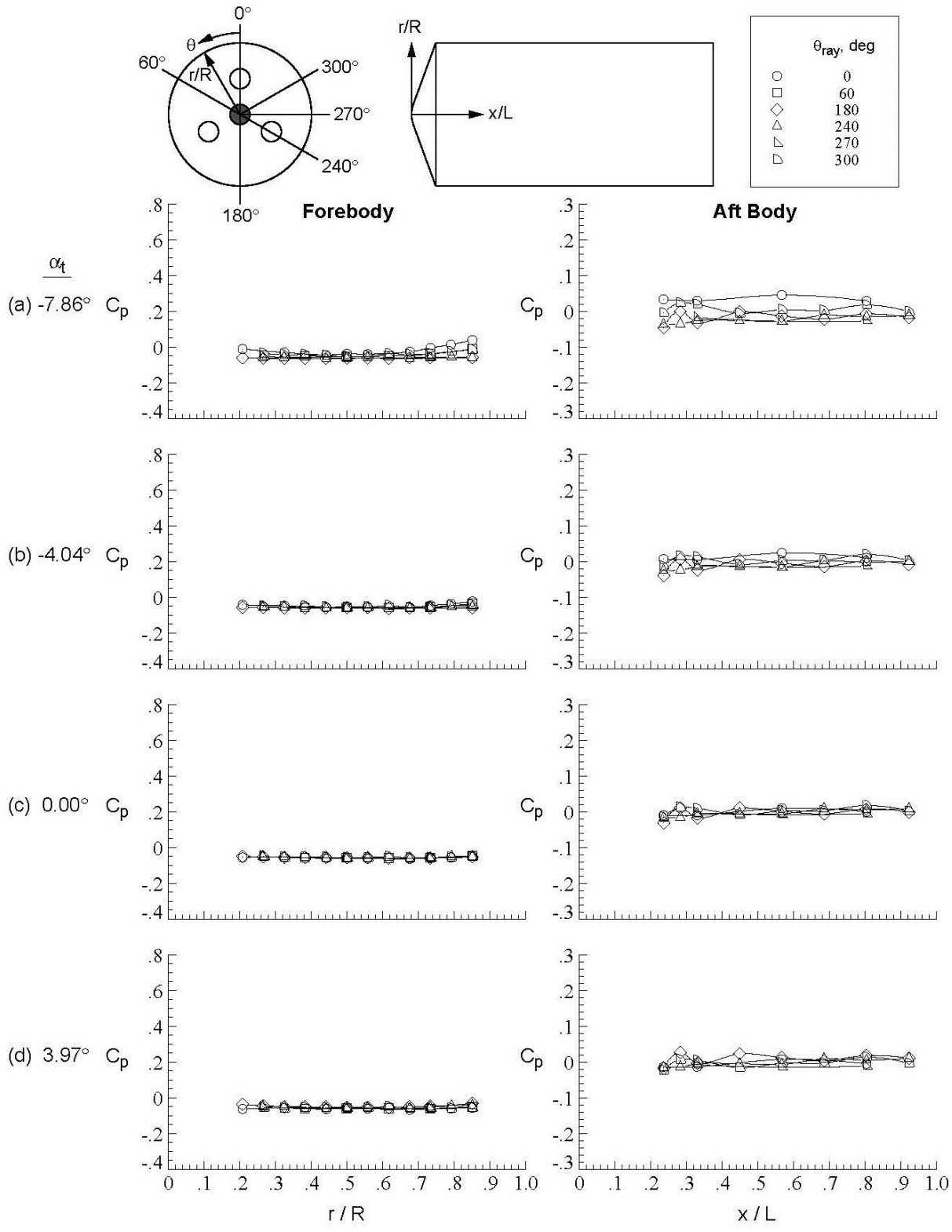

Figure D-113. Center nozzle configuration, Run 150, M_∞ = 3.5, Re_∞ = 1.0x10^7/ft, ϕ = −0.03°, X_S = 40.17 in, Y_S = 0.00 in, C_T = 2.99.

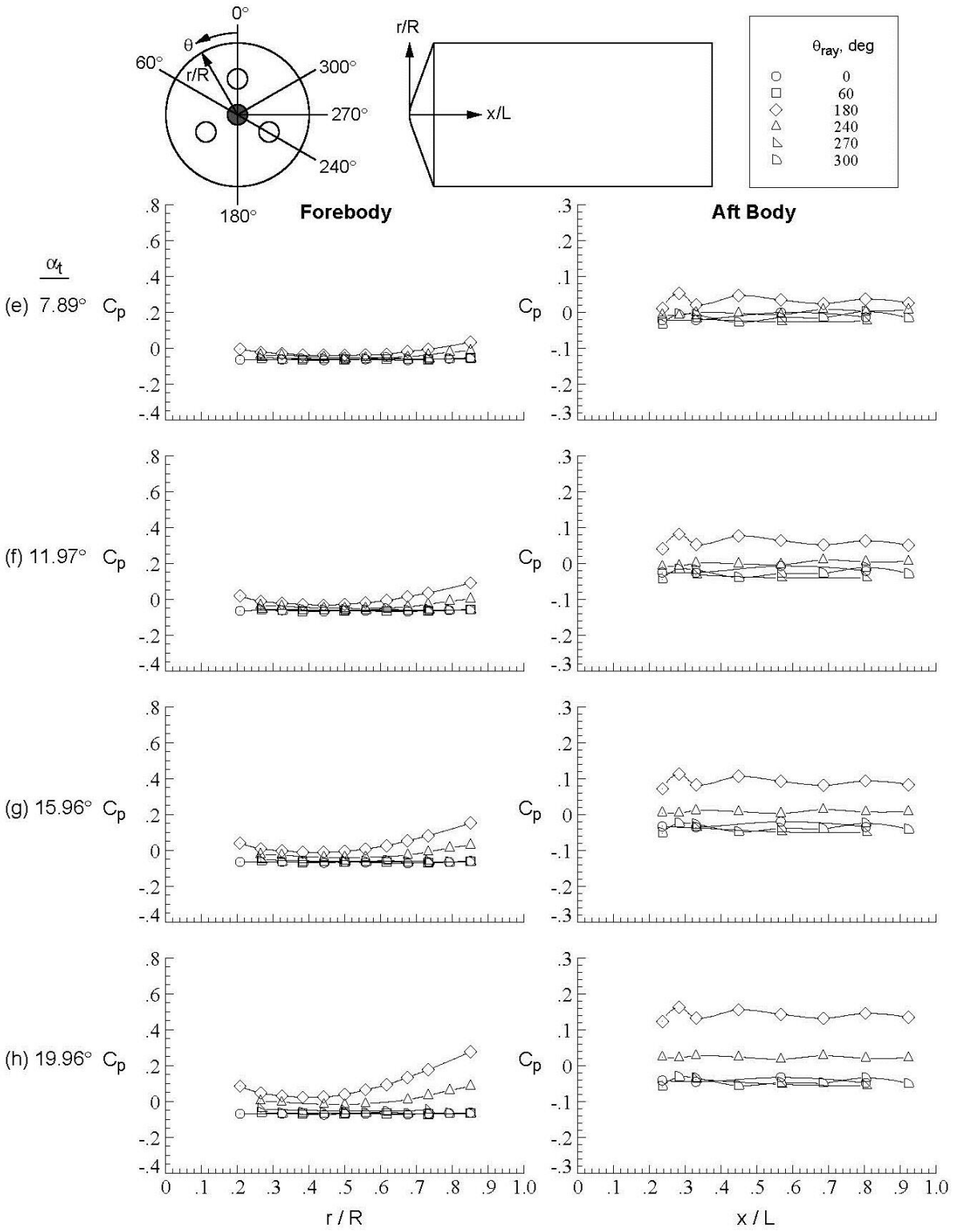

Figure D-113.Concluded.

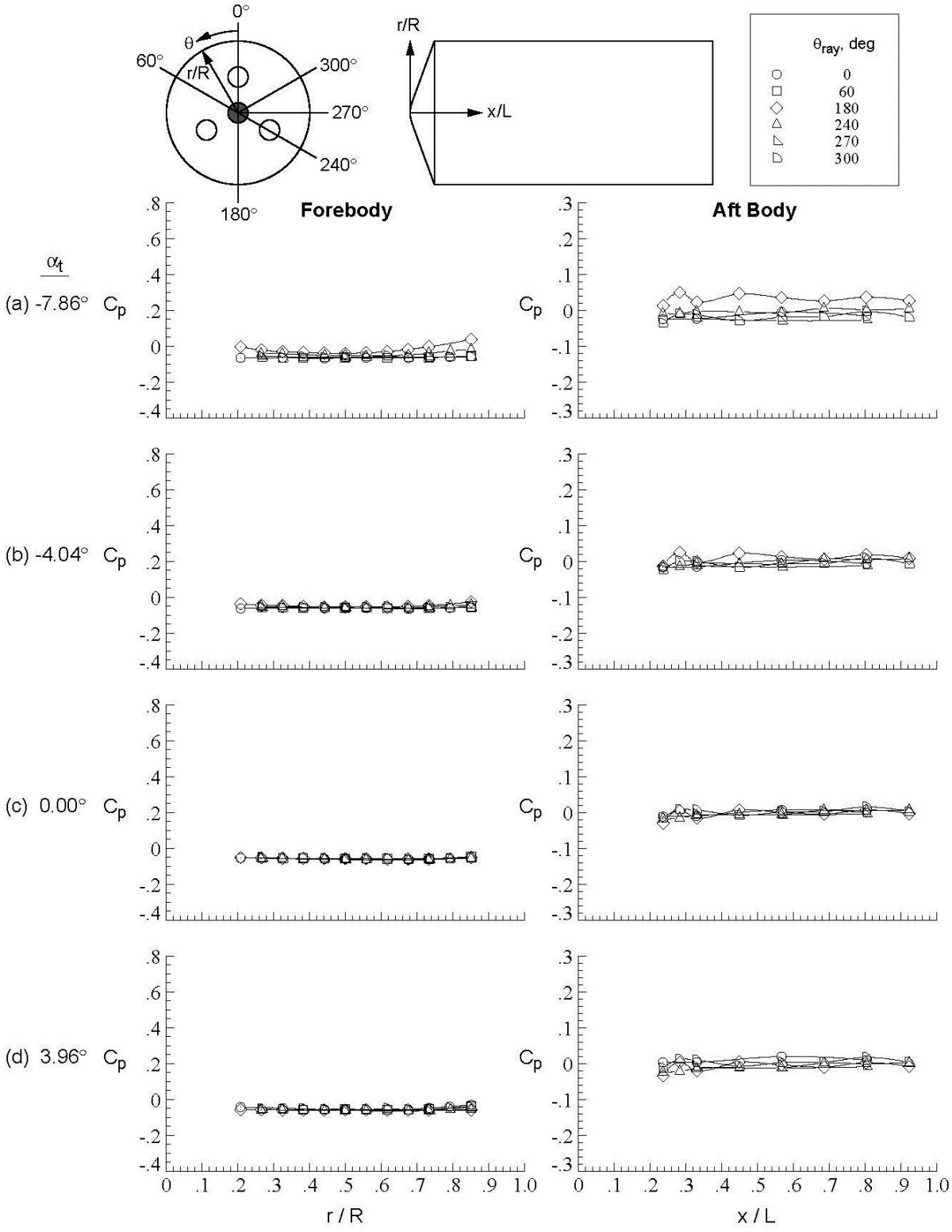

Figure D-114. Center nozzle configuration, Run 151, M_∞ = 3.5, Re_∞ = 1.0x10^6/ft, ϕ = −179.97°, X_S = 40.17 in, Y_S = 0.00 in, C_T = 2.98.

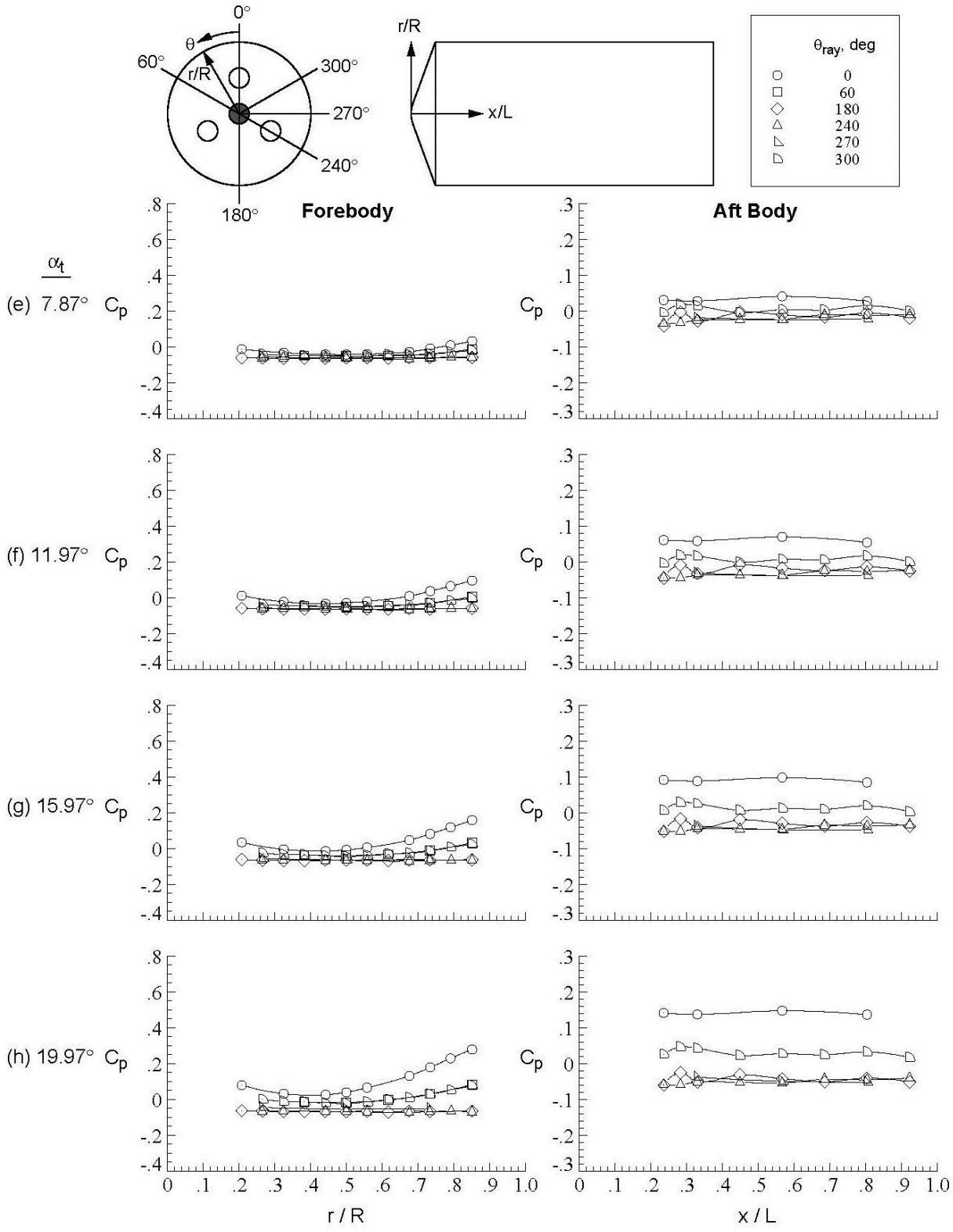

Figure D-114.Concluded.

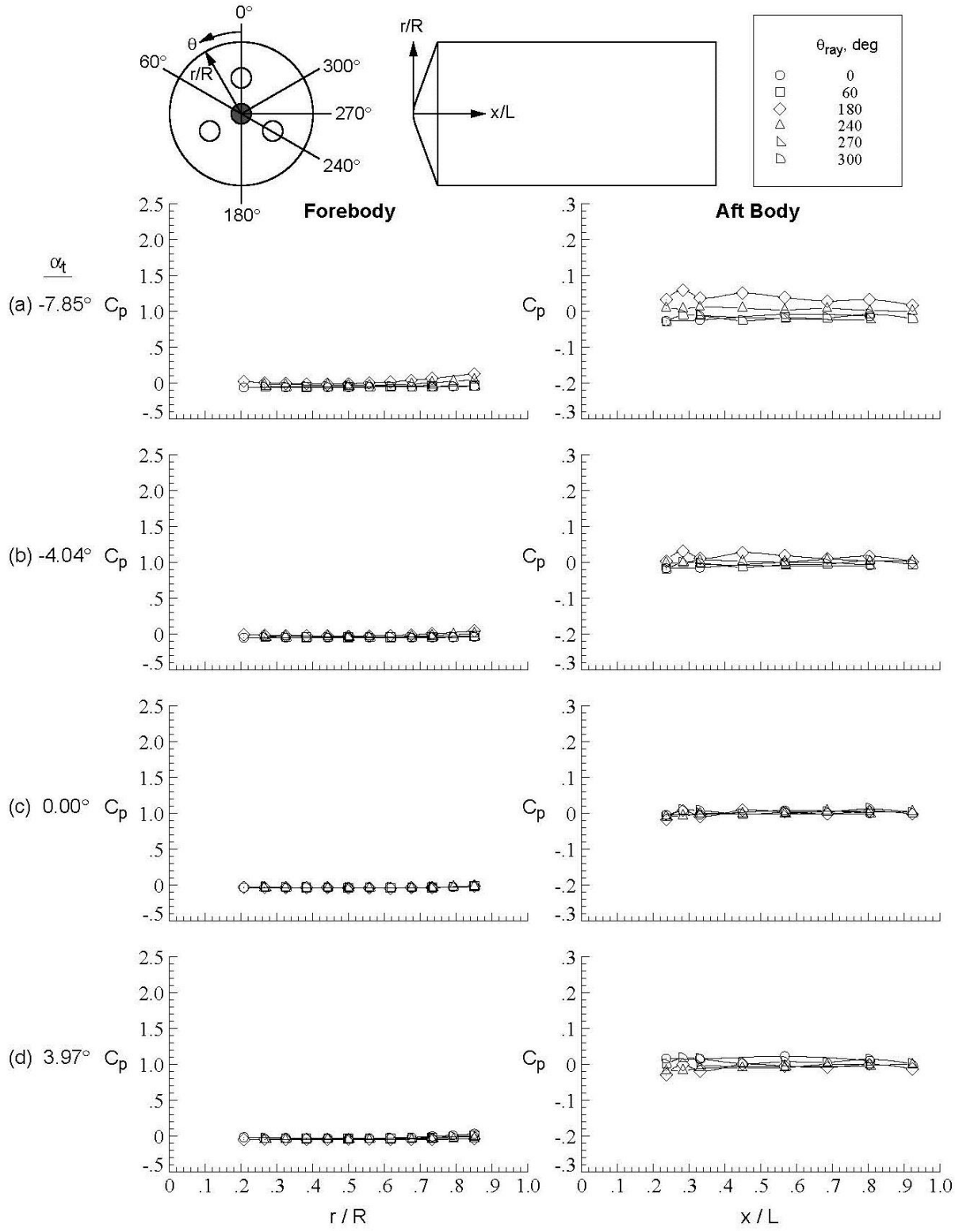

Figure D-115. Center nozzle configuration, Run 152, M_∞ = 3.5, Re_∞ = 1.0x10^7/ft, ϕ = −179.97°, X_S = 40.17 in, Y_S = 0.00 in, C_T = 1.97.

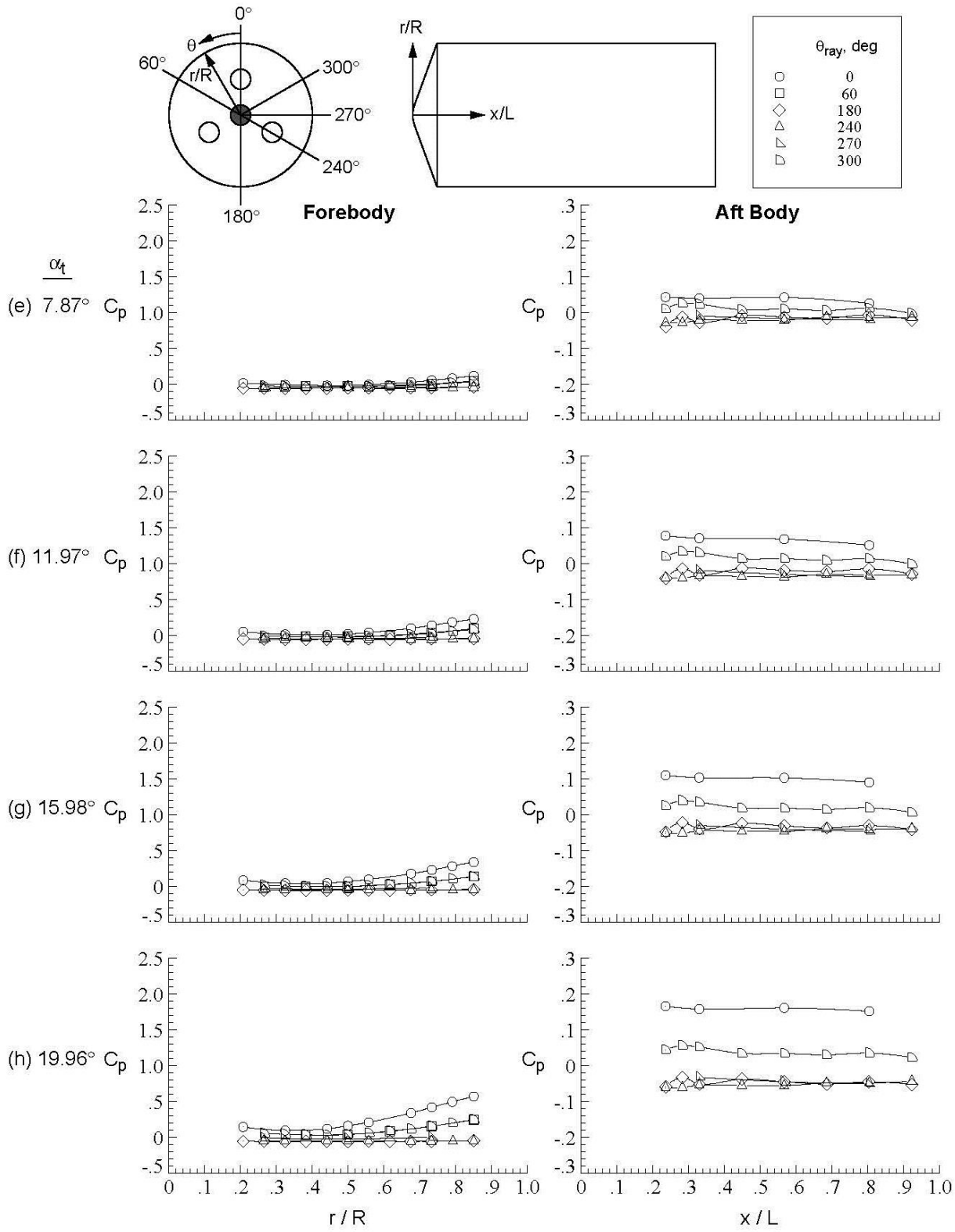

Figure D-115.Concluded.

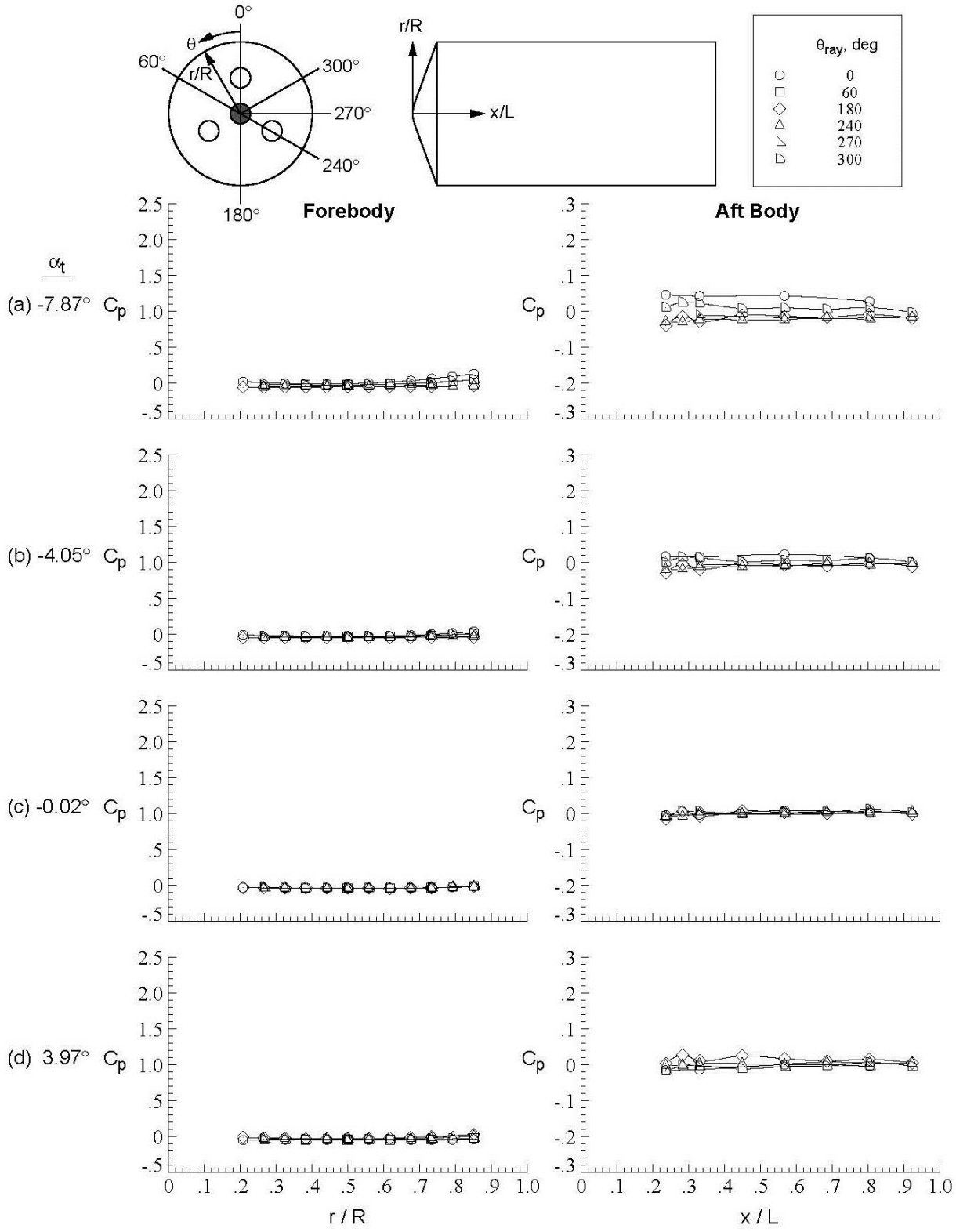

Figure D-116. Center nozzle configuration, Run 153, M_∞ = 3.5, Re_∞ = 1.0x10^6/ft, ϕ = −0.09°, X_S = 40.17 in, Y_S = 0.00 in, C_T = 1.96.

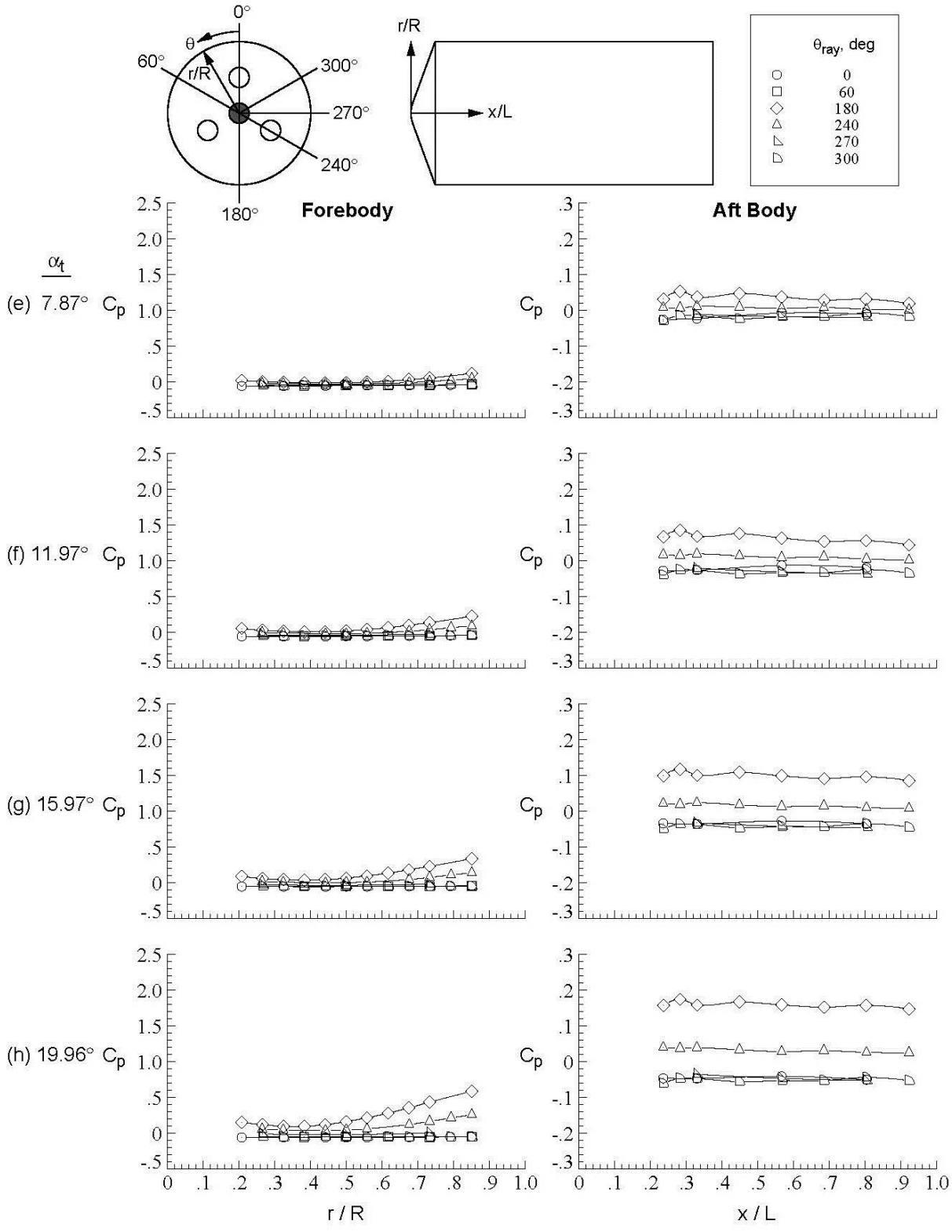

Figure D-116.Concluded.

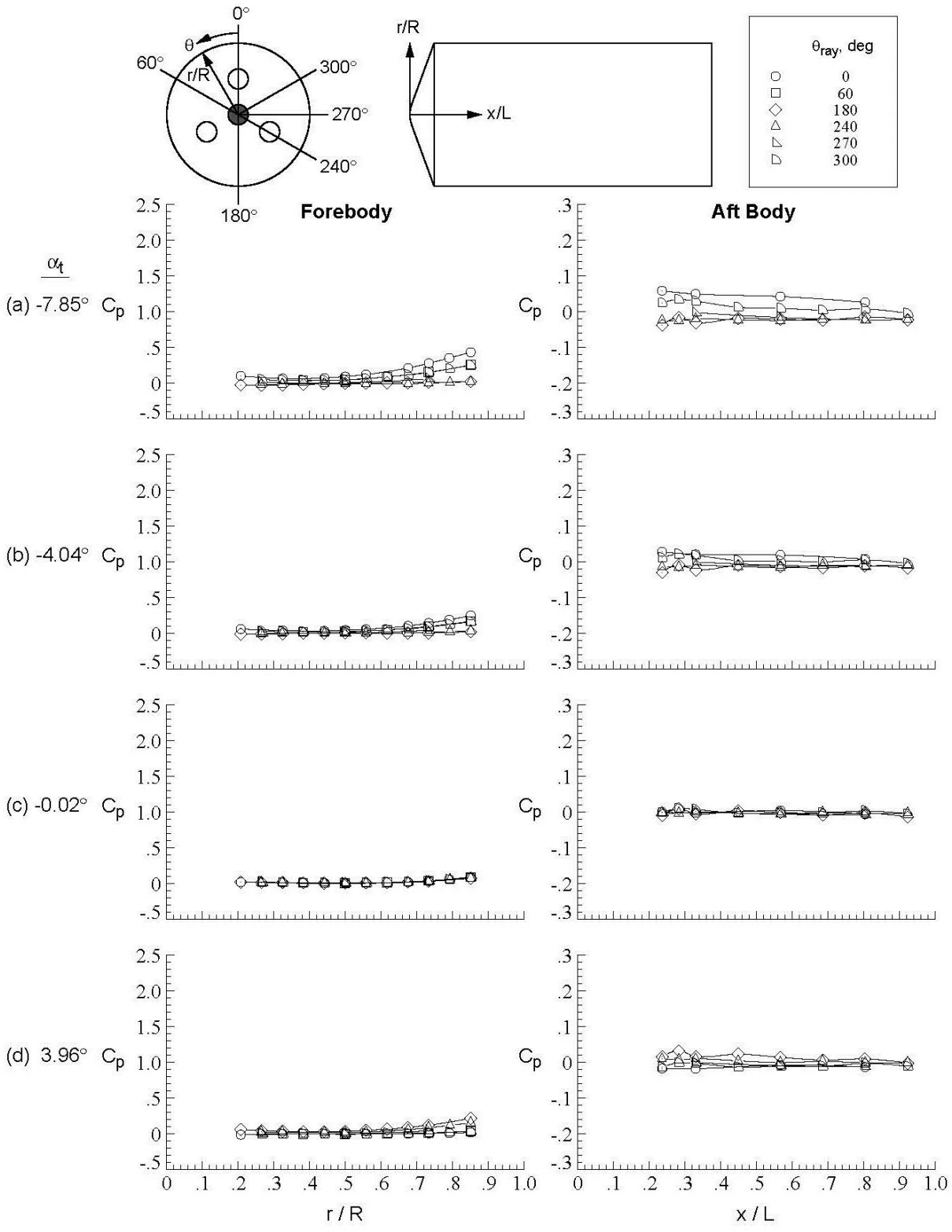

Figure D-117. Center nozzle configuration, Run 154, M_∞ = 3.5, Re_∞ = 1.0x10^7/ft, ϕ = −0.09°, X_S = 40.17 in, Y_S = 0.00 in, C_T = 0.92.

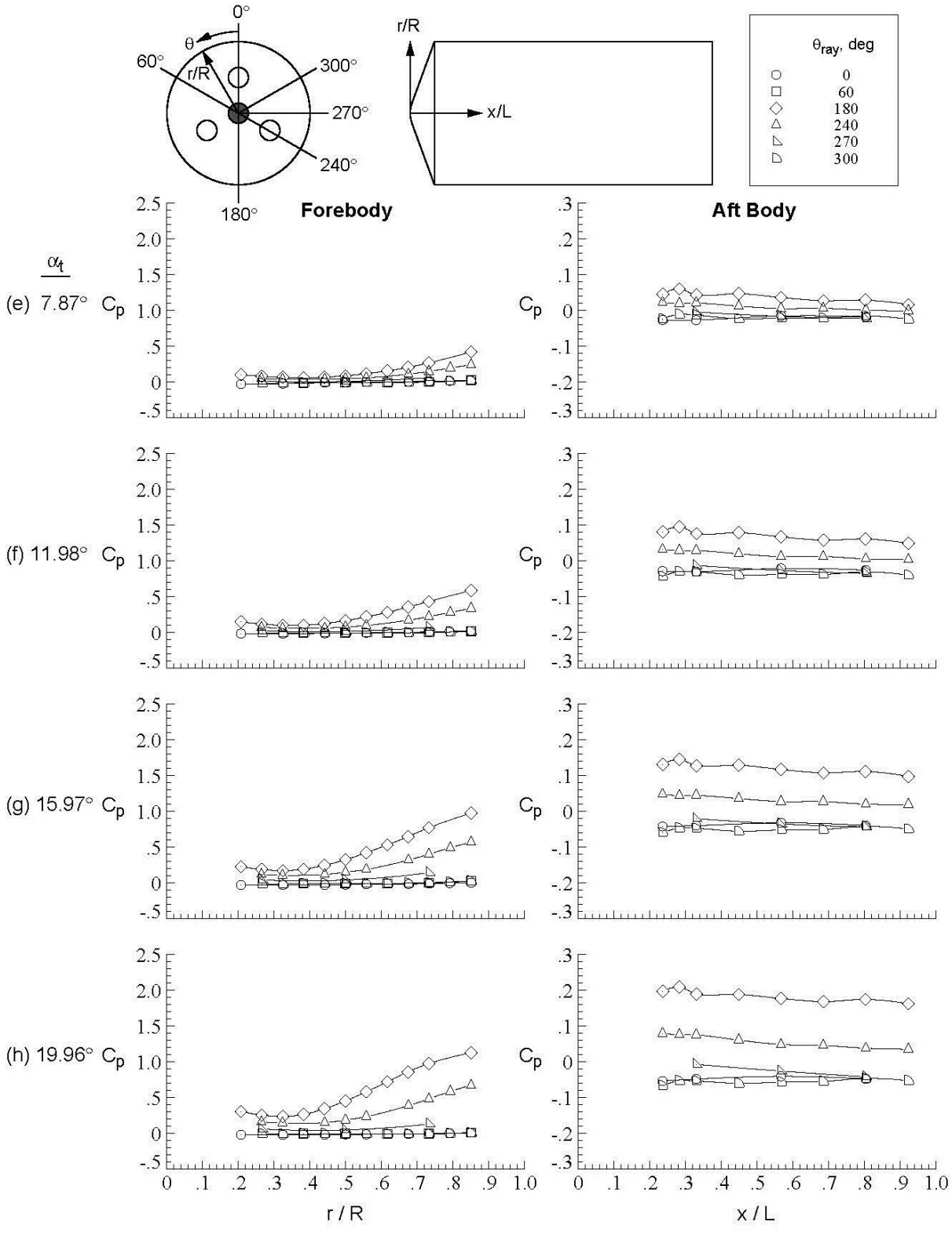

Figure D-117.Concluded.

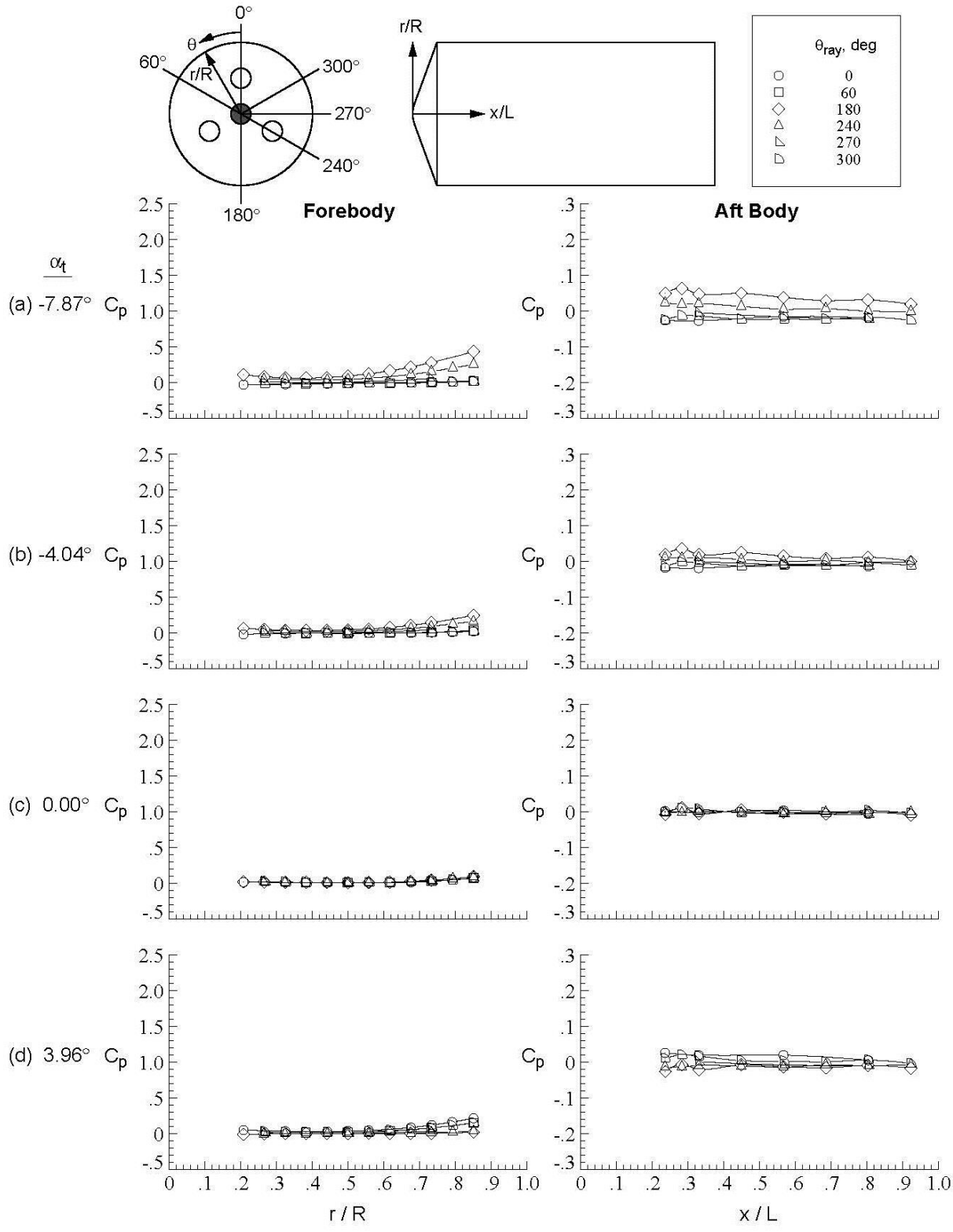

Figure D-118. Center nozzle configuration, Run 155, $M\infty = 3.5$, $Re_\infty = 1.0 \times 10^7$/ft, $\phi = 179.91°$, $X_S = 40.17$ in, $Y_S = 0.00$ in, $C_T = 0.94$.

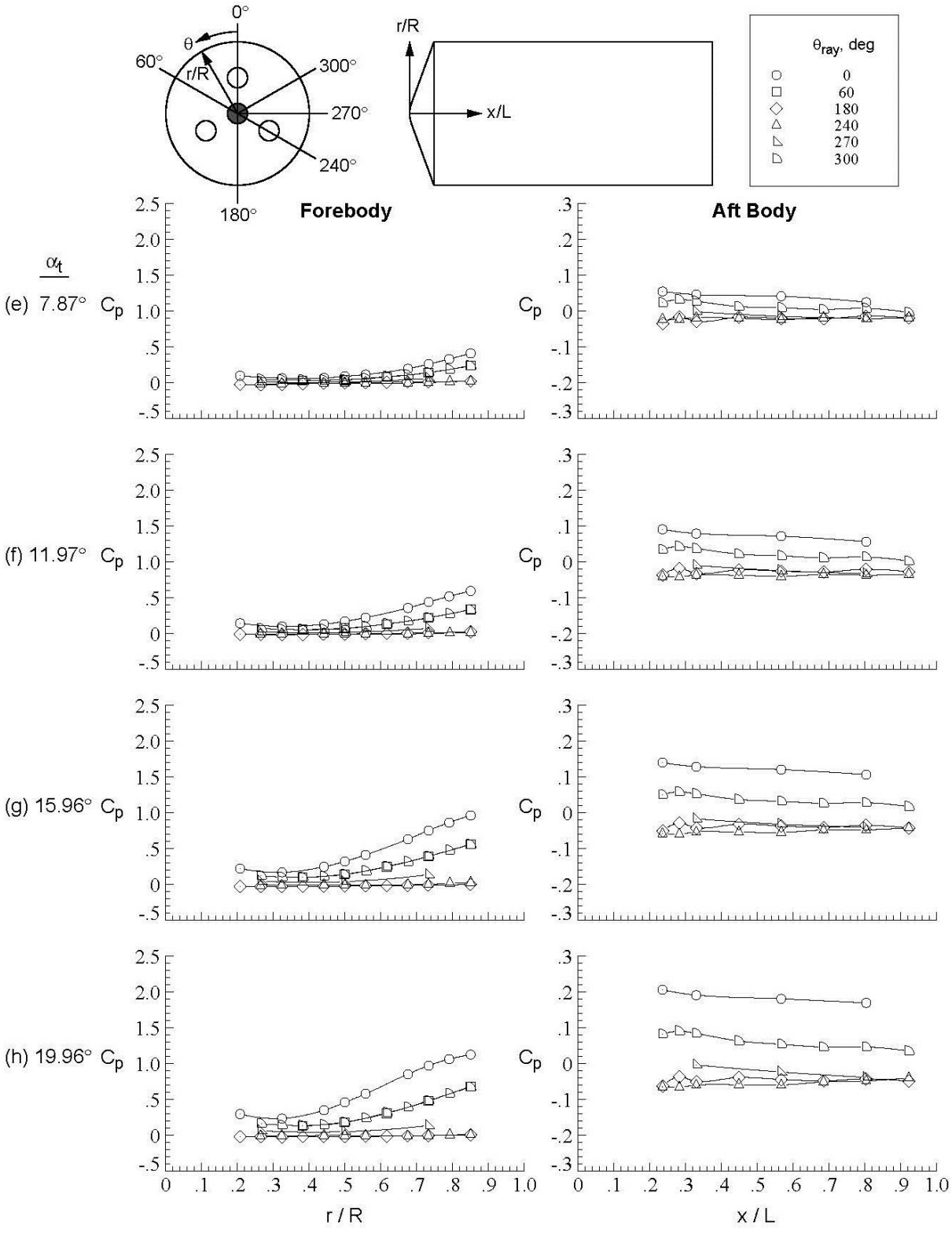

Figure D-118.Concluded.

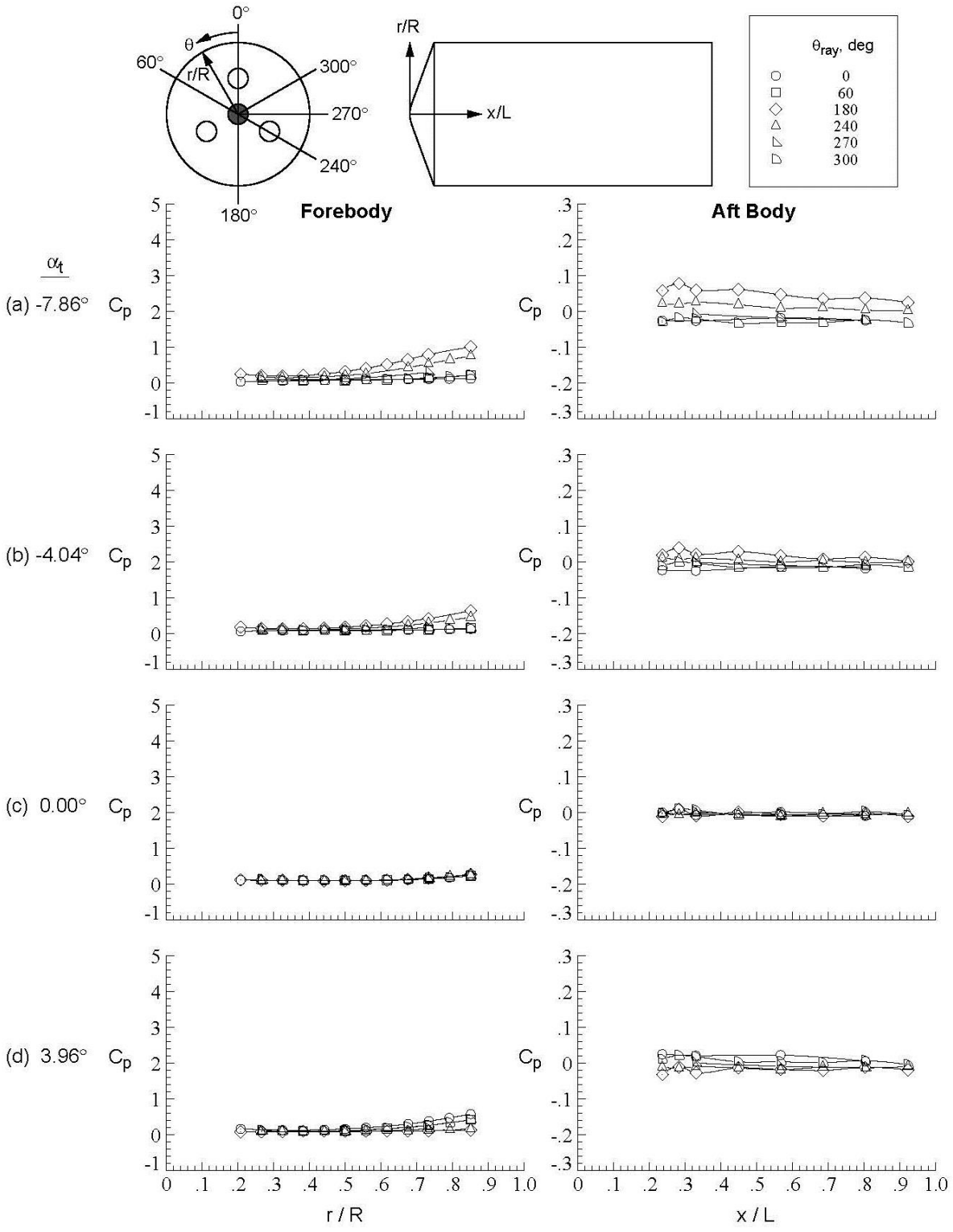

Figure D-119. Center nozzle configuration, Run 156, M_∞ = 3.5, Re_∞ = 1.0x10^7/ft, ϕ = 179.93°, X_S = 40.17 in, Y_S = 0.00 in, C_T = 0.46.

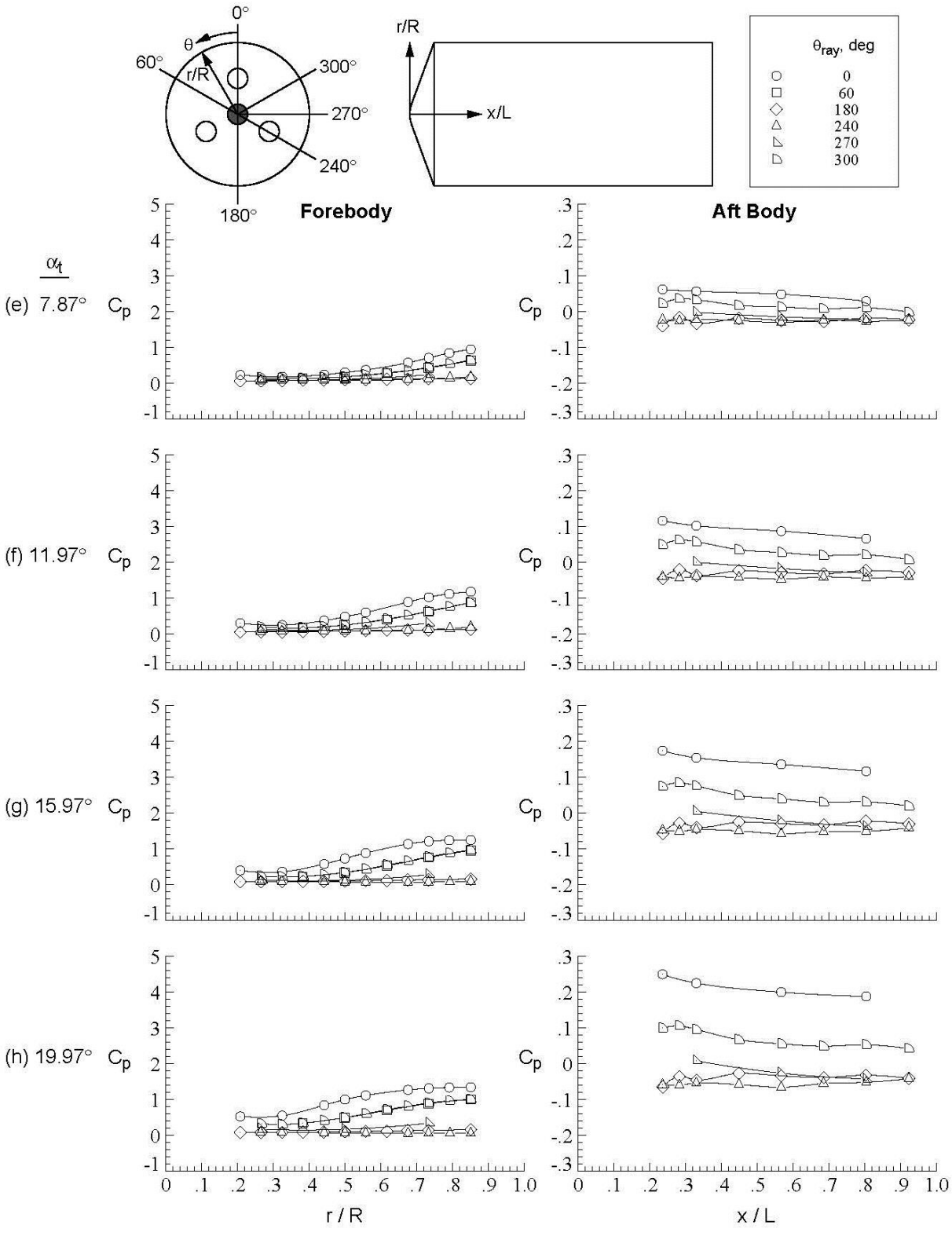

Figure D-119.Concluded.

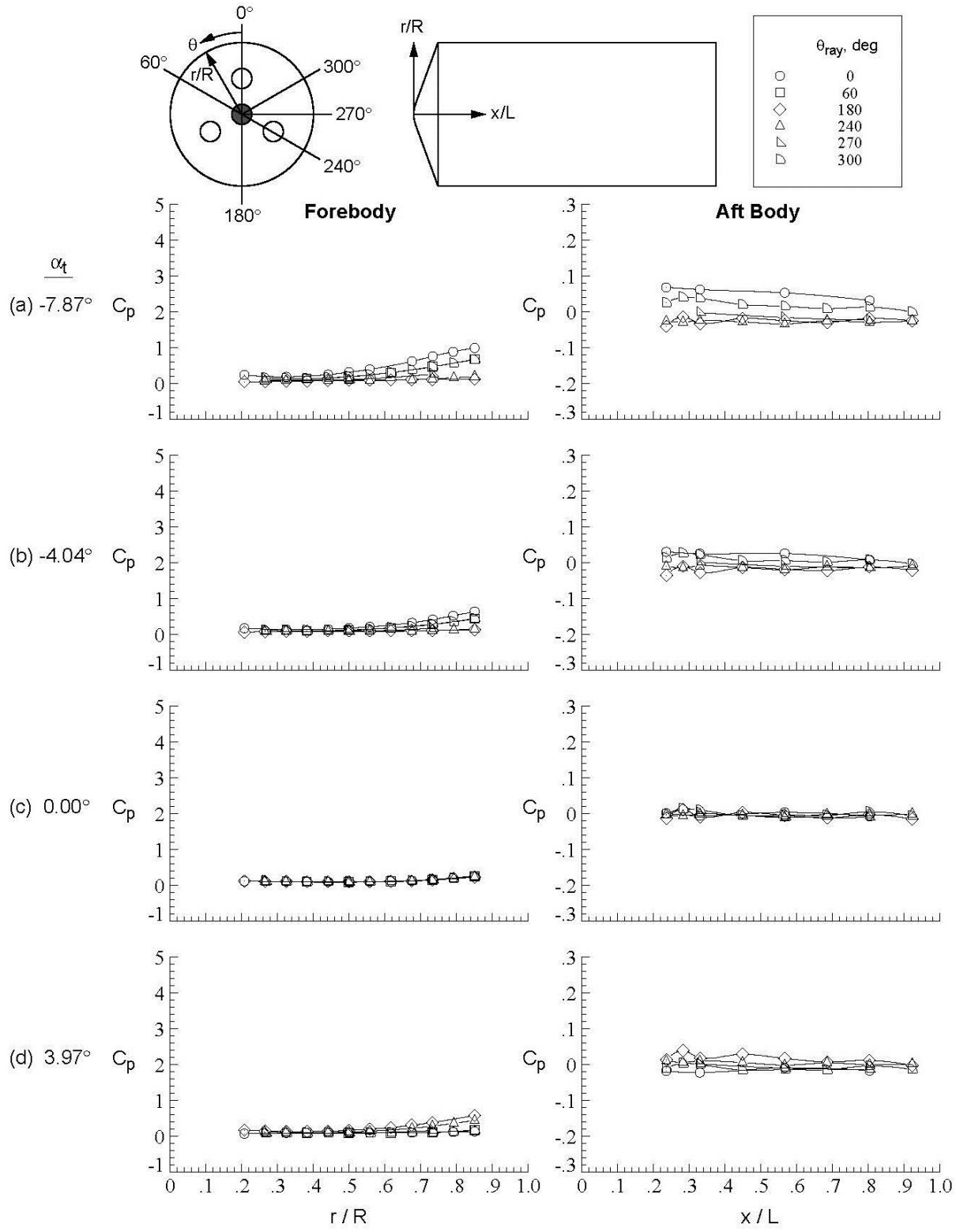

Figure D-120. Center nozzle configuration, Run 157, $M\infty$ = 3.5, Re_∞ = 1.0x10^6/ft, ϕ = 0.07°, X_S = 40.17 in, Y_S = 0.00 in, C_T = 0.45.

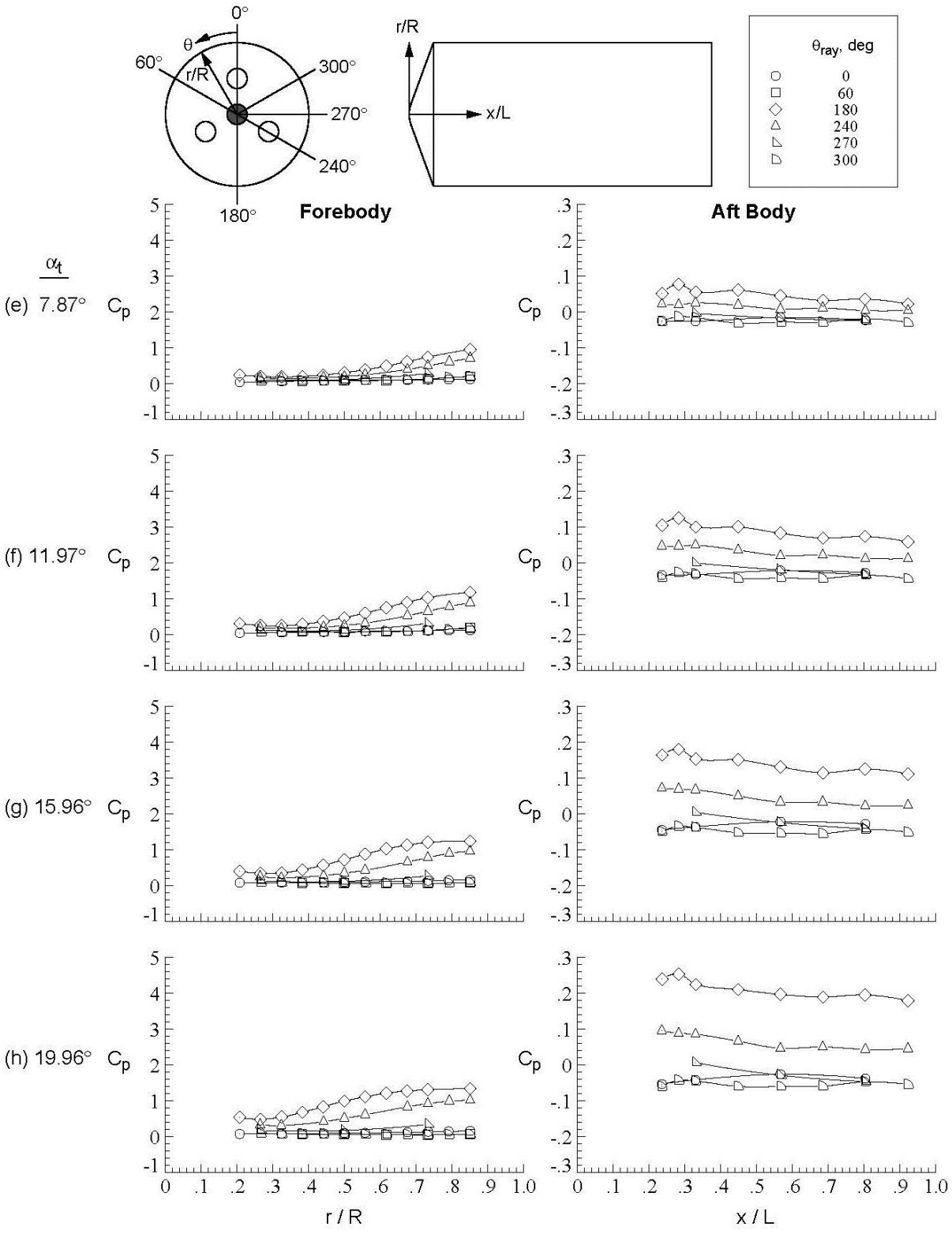

Figure D-120.Concluded.

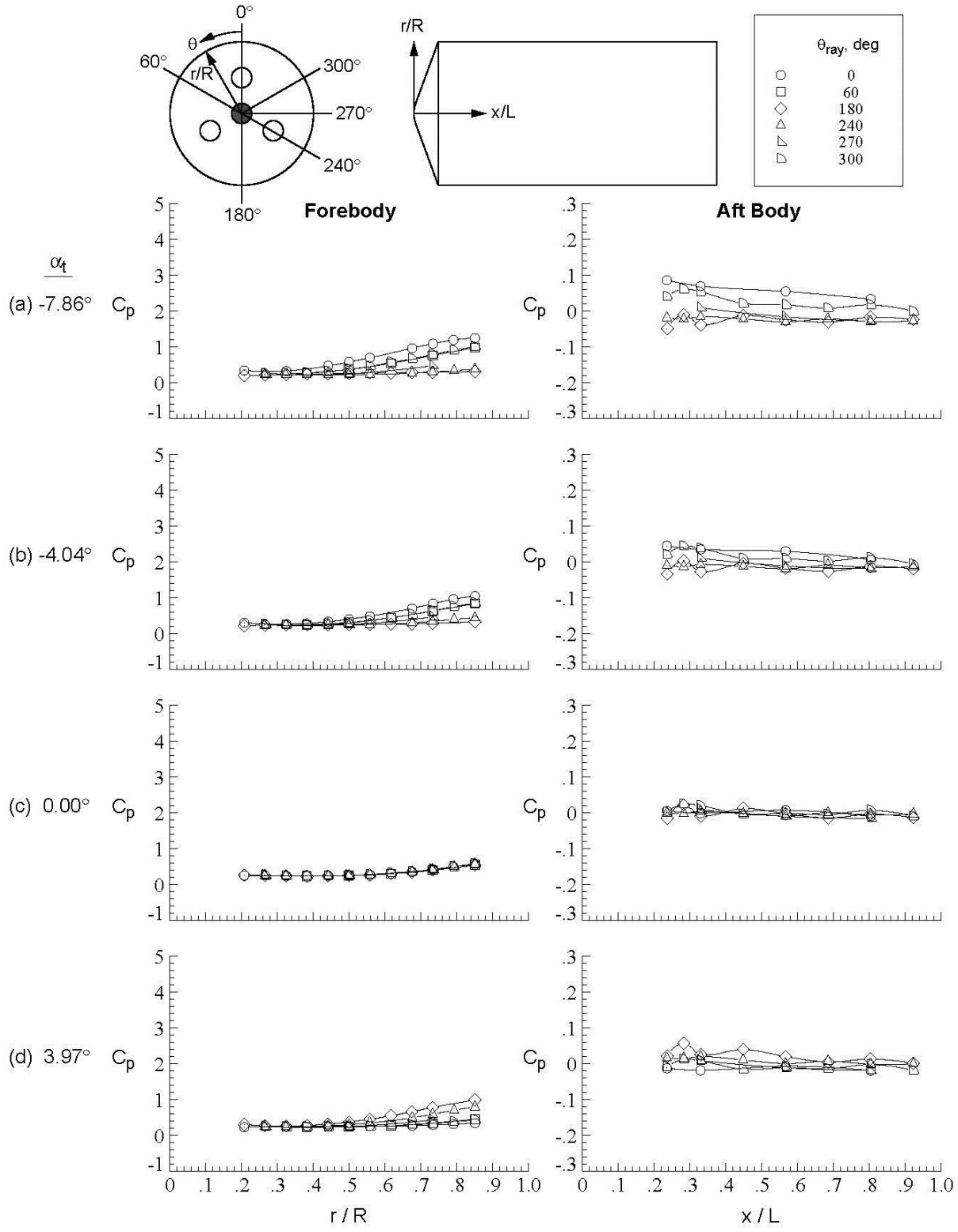

Figure D-121. Center nozzle configuration, Run 159, M_∞ = 3.5, Re_∞ = 1.0x10^7/ft, ϕ = −0.01°, X_S = 40.17 in, Y_S = 0.00 in, C_T = 0.21.

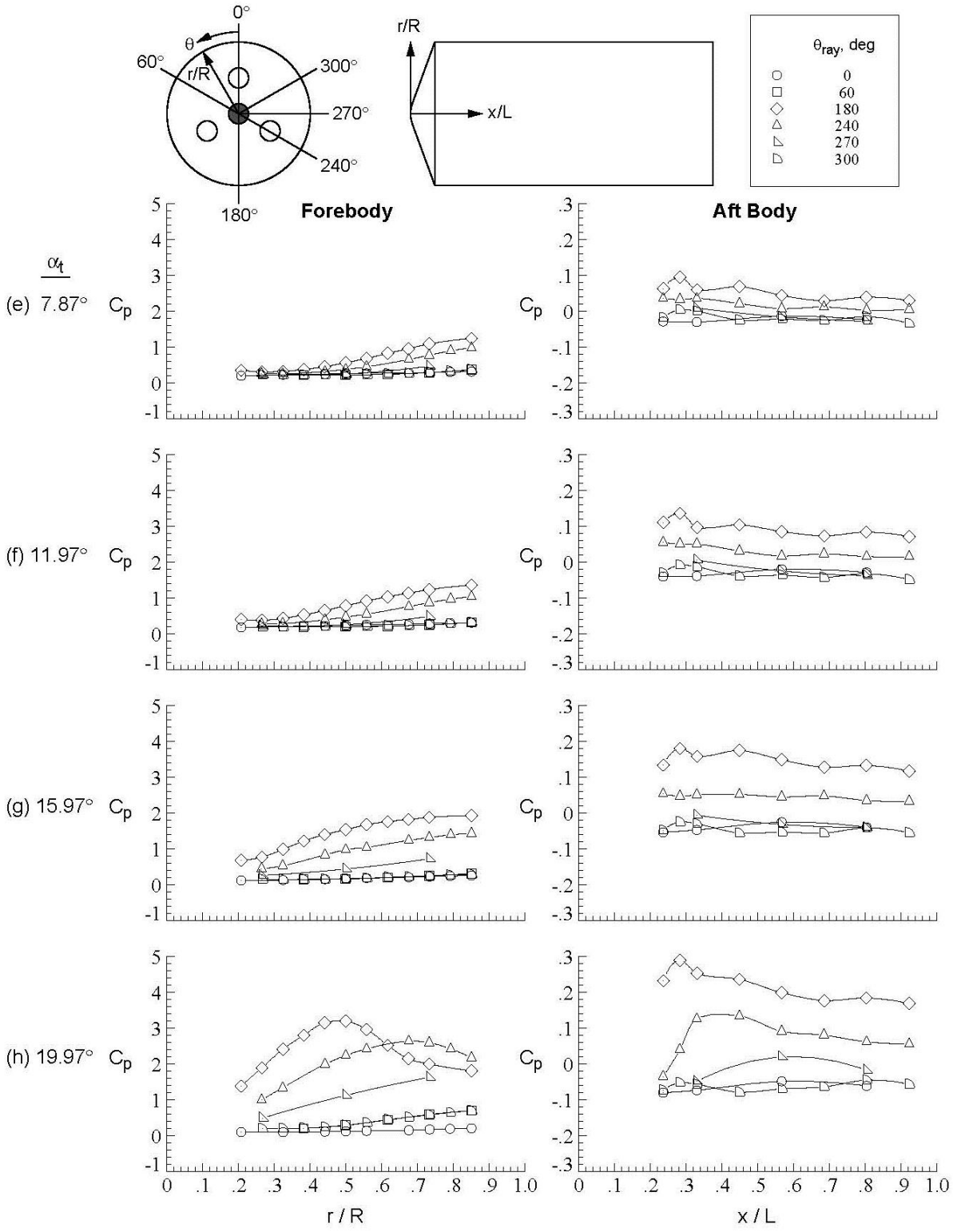

Figure D-121.Concluded.

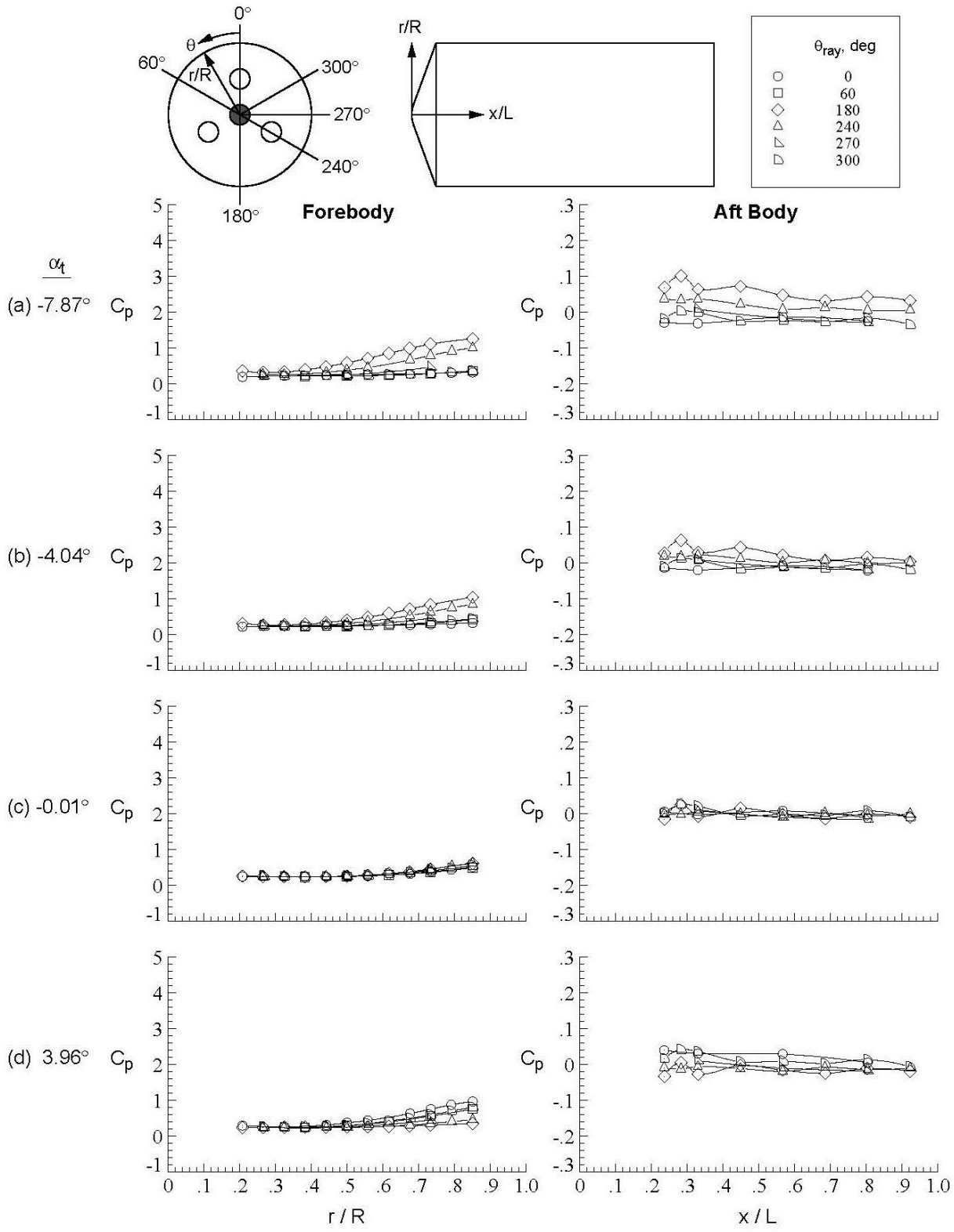

Figure D-122. Center nozzle configuration, Run 160, $M\infty$ = 3.5, Re_∞ = 1.0x10^6/ft, ϕ = 179.93°, X_S = 40.17 in, Y_S = 0.00 in, C_T = 0.21.

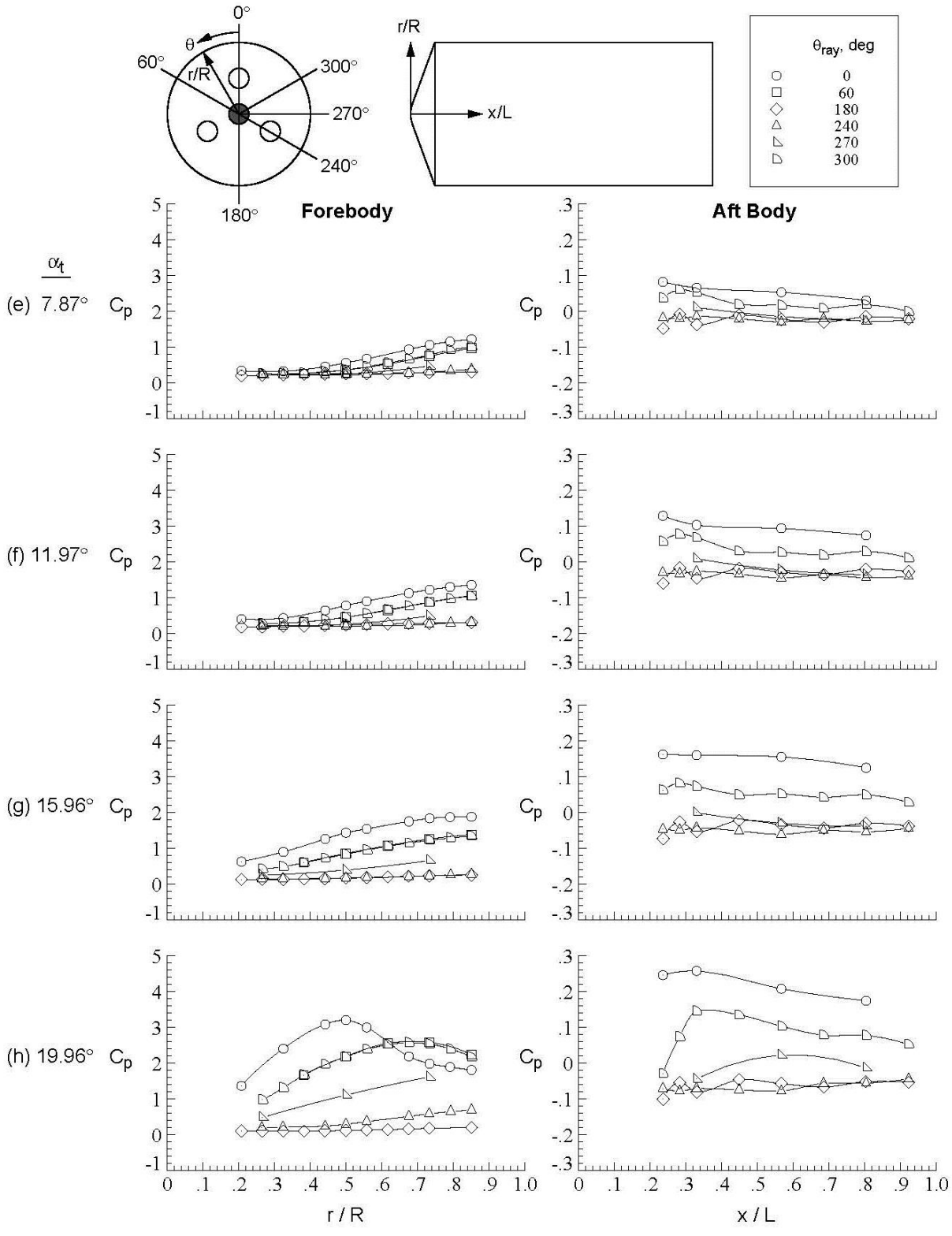

Figure D-122.Concluded.

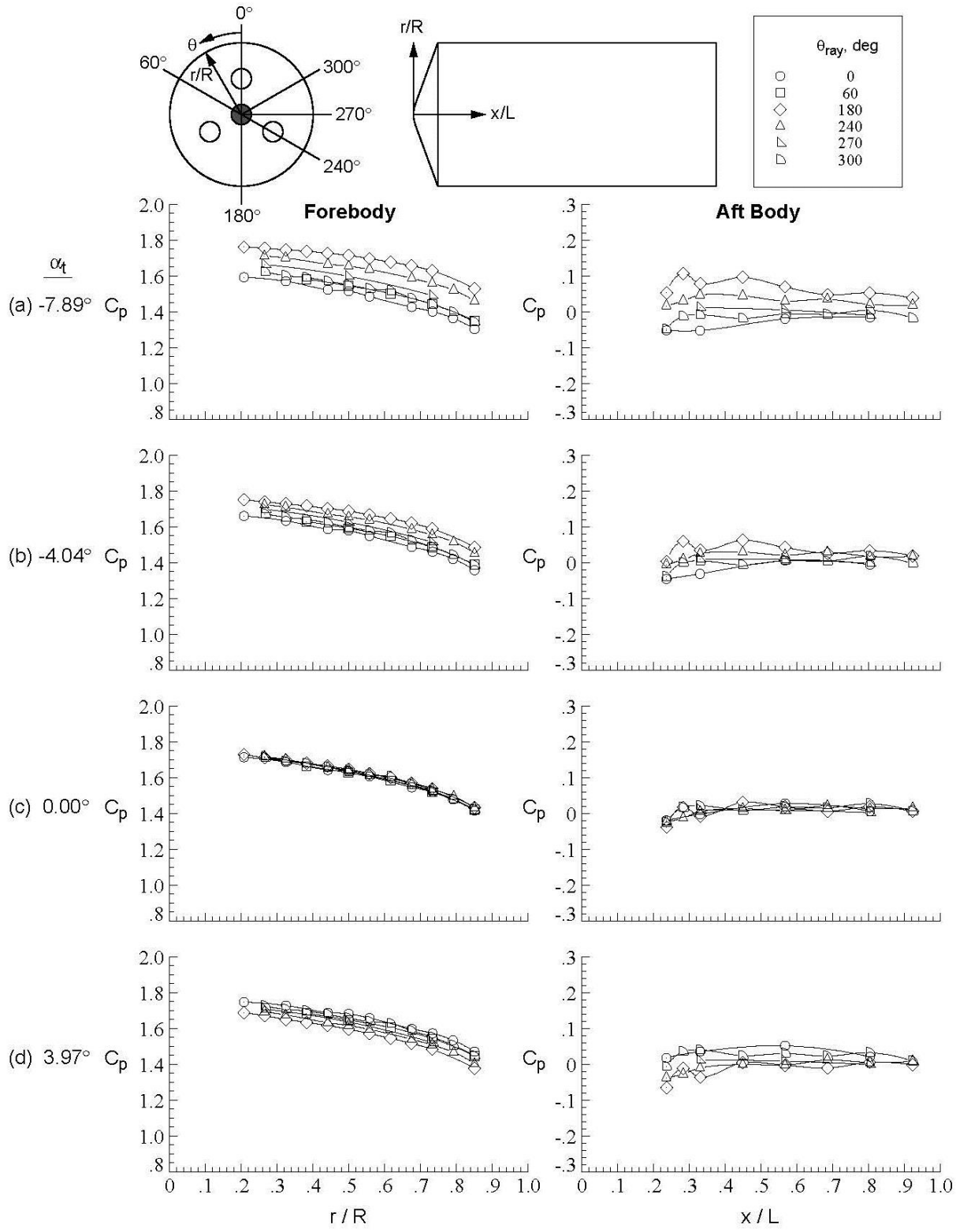

Figure D-123. Center nozzle configuration, Run 161, M_∞ = 3.5, Re_∞ = 1.0x10^6/ft, ϕ = 179.93°, X_S = 40.17 in, Y_S = 0.00 in, C_T = 0.00.

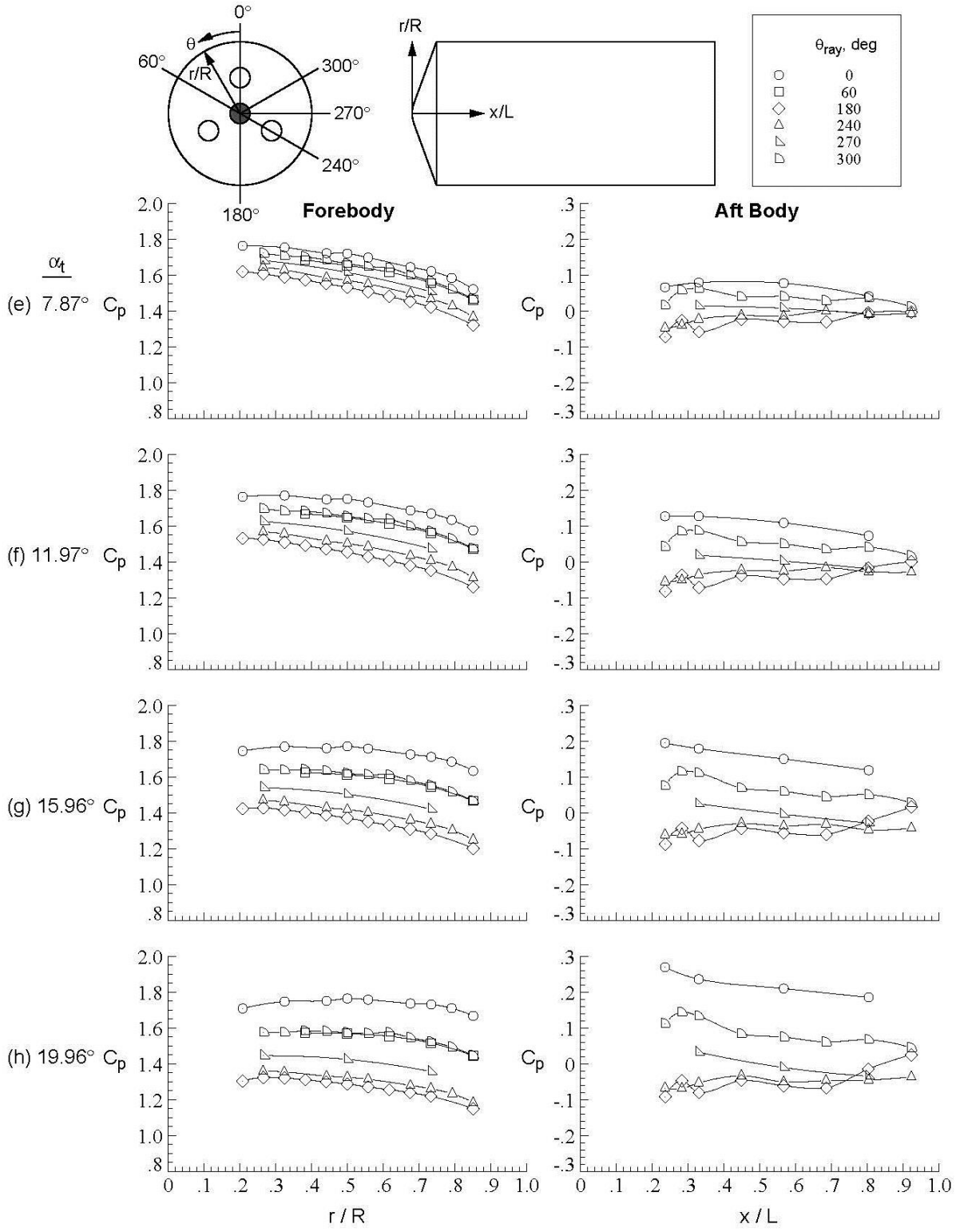

Figure D-123.Concluded.

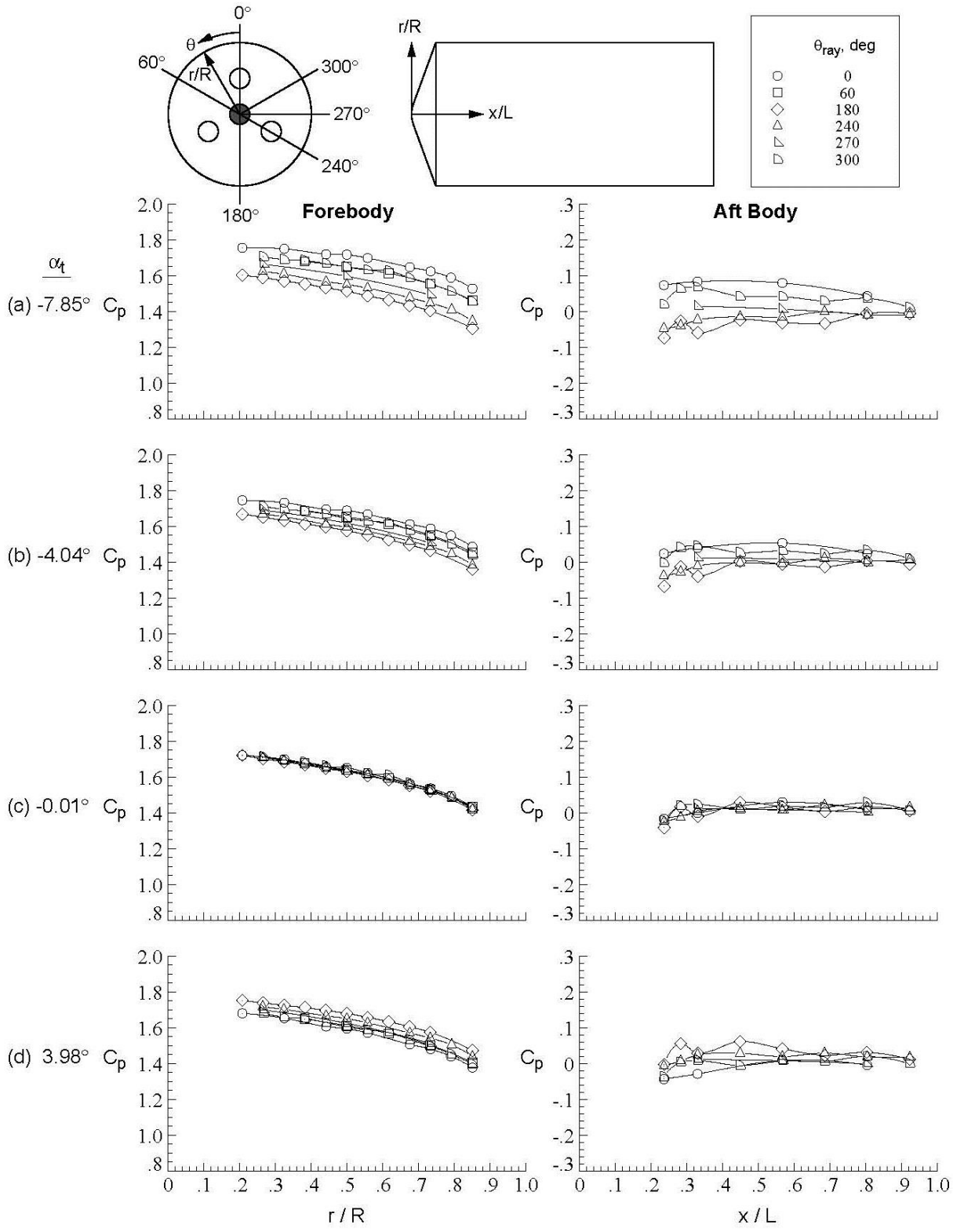

Figure D-124. Center nozzle configuration, Run 162, M_∞ = 3.5, Re_∞ = 1.0x10^6/ft, ϕ = 0.03°, X_S = 40.17 in, Y_S = 0.00 in, C_T = 0.00.

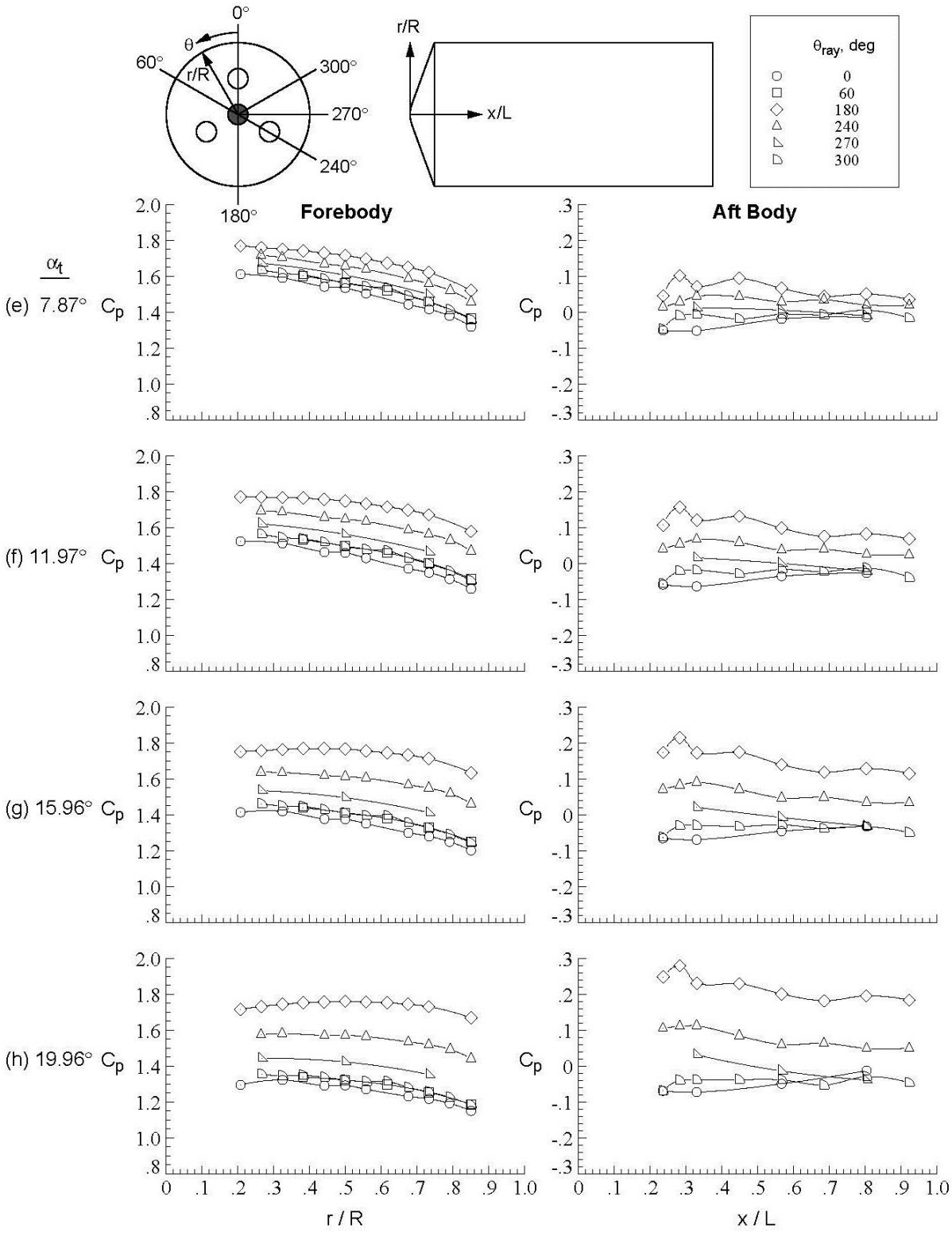

Figure D-124.Concluded.

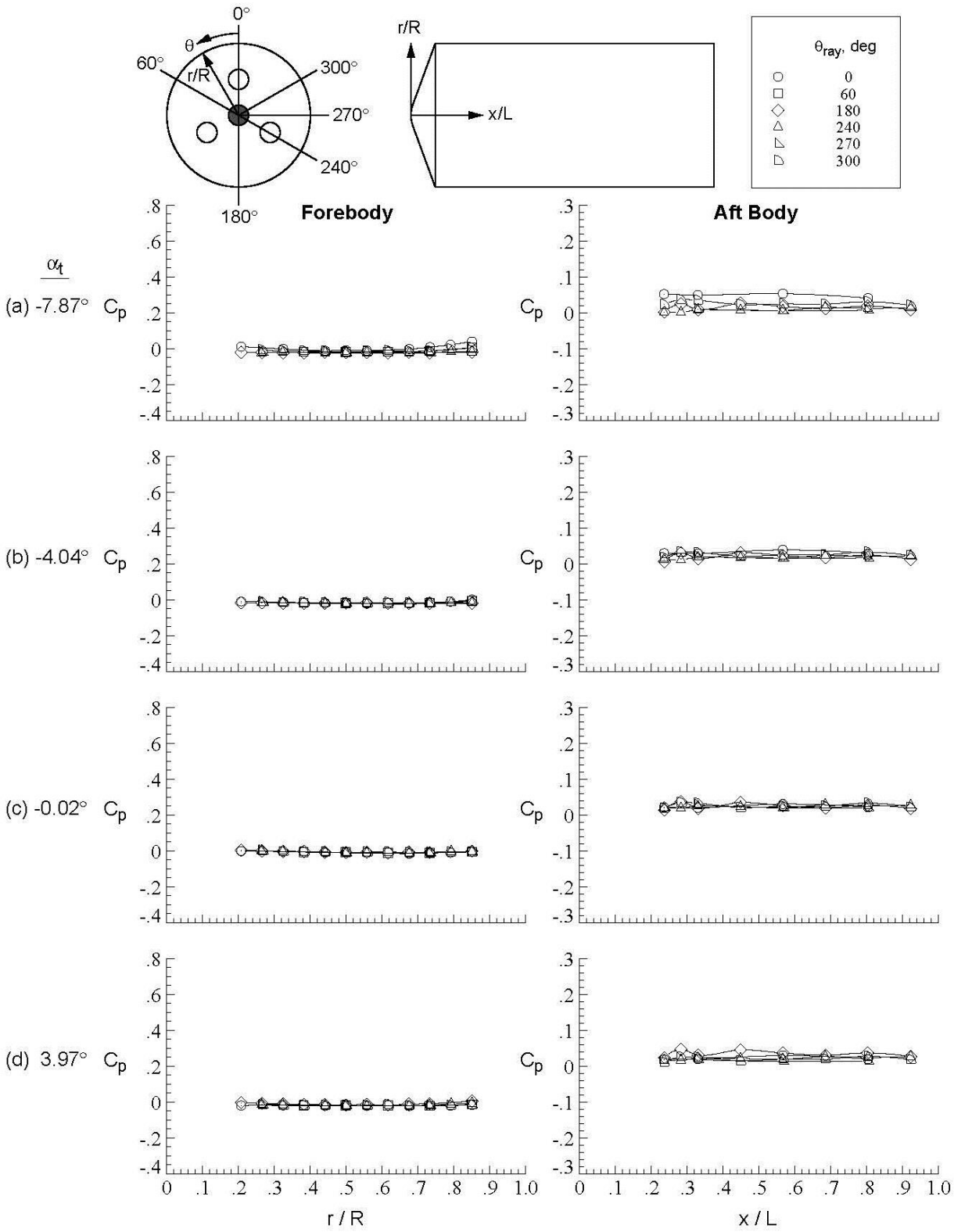

Figure D-125. Center nozzle configuration, Run 163, M_∞ = 4.6, Re_∞ = 1.5x10^7/ft, ϕ = 0.03°, X_S = 40.17 in, Y_S = 0.00 in, C_T = 2.97.

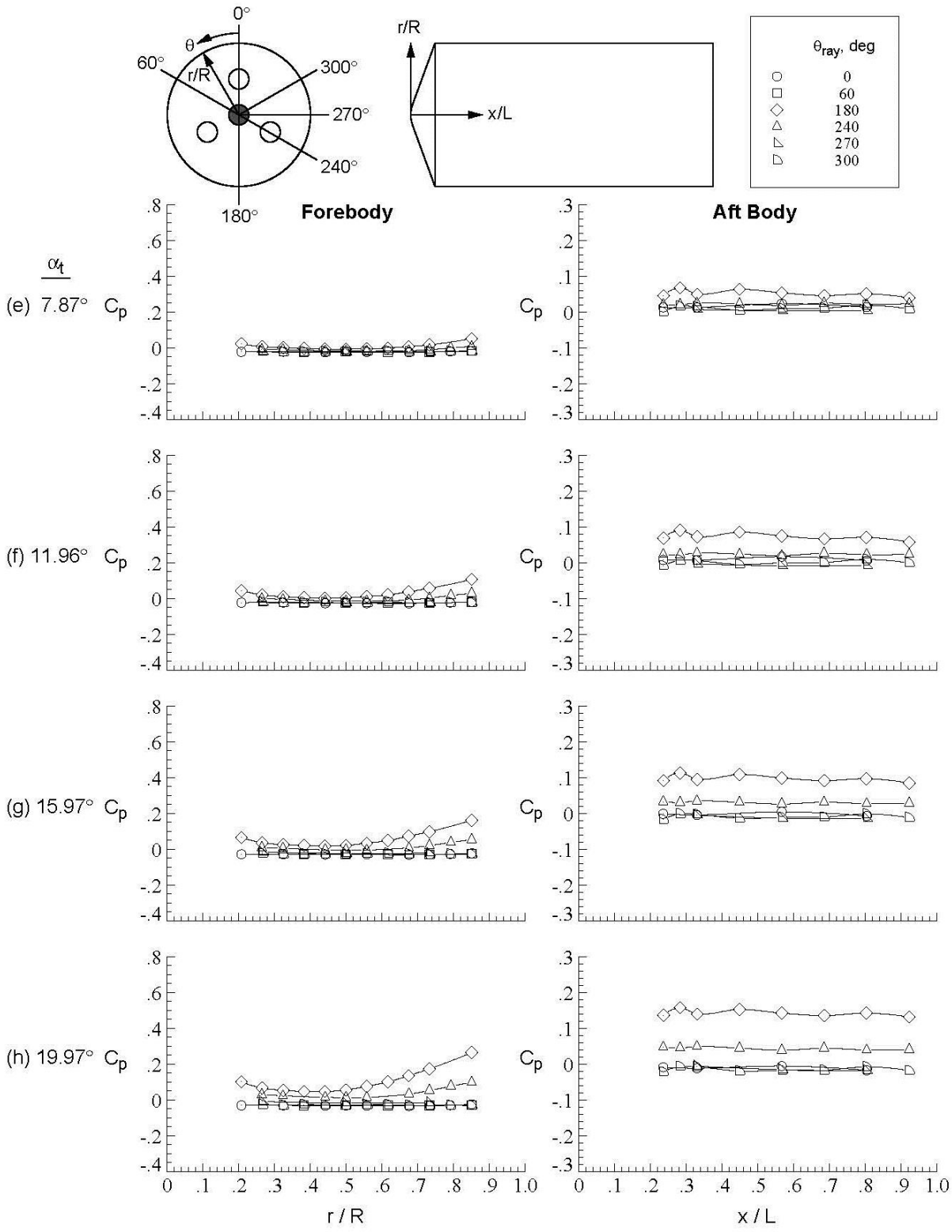

Figure D-125.Concluded.

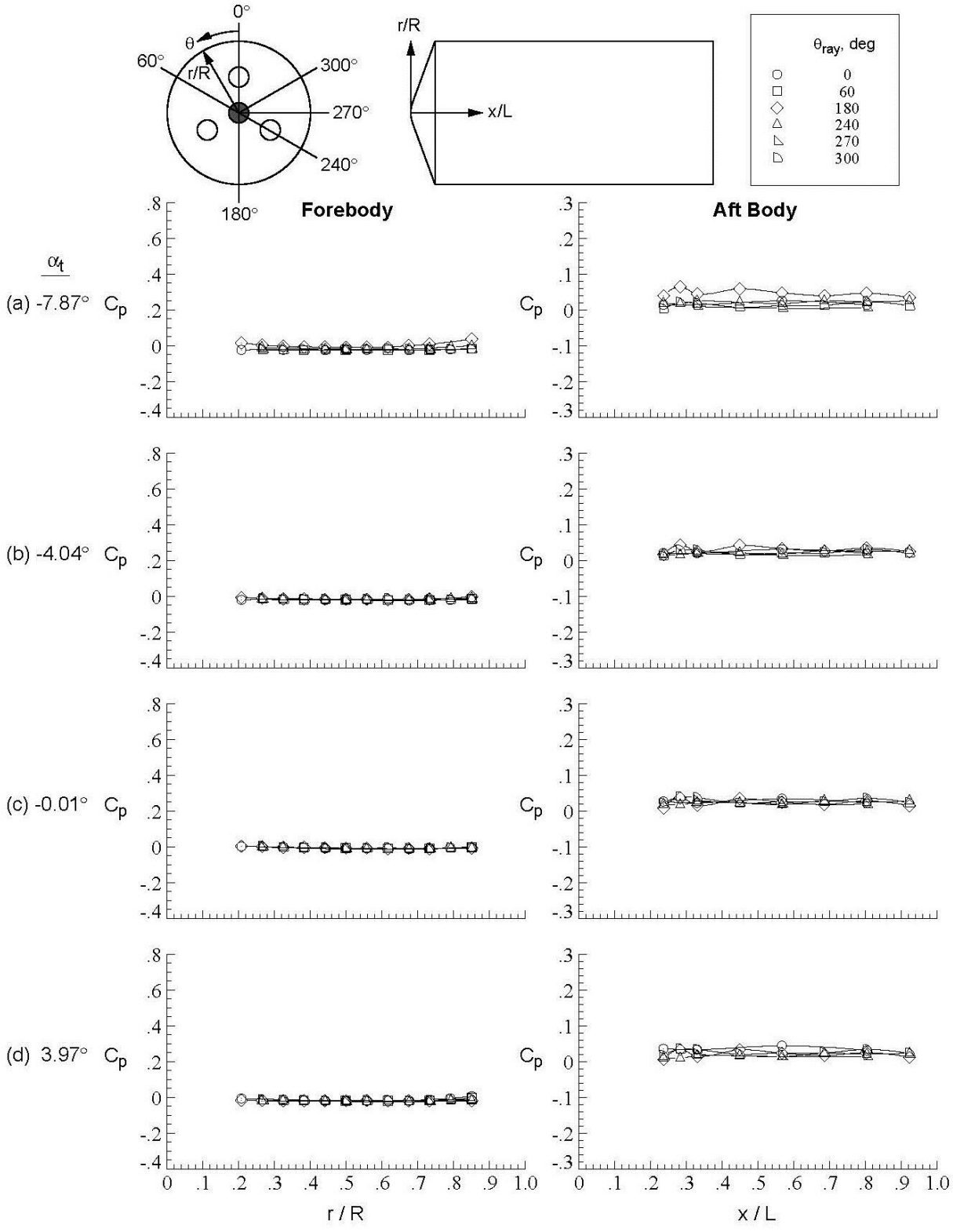

Figure D-126. Center nozzle configuration, Run 164, M_∞ = 4.6, Re_∞ = 1.5x10^7/ft, ϕ = 179.93°, X_S = 40.17 in, Y_S = 0.00 in, C_T = 2.95.

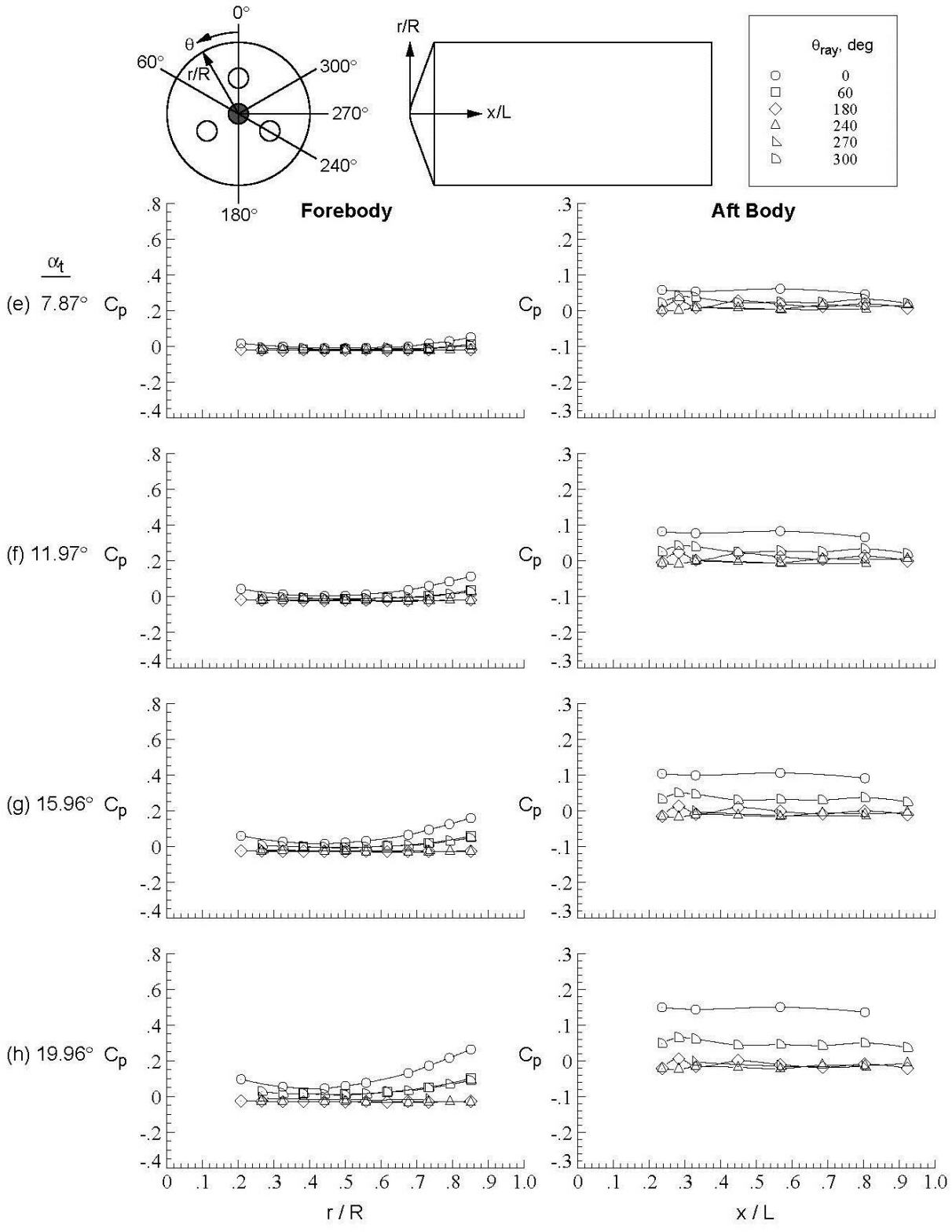

Figure D-126.Concluded.

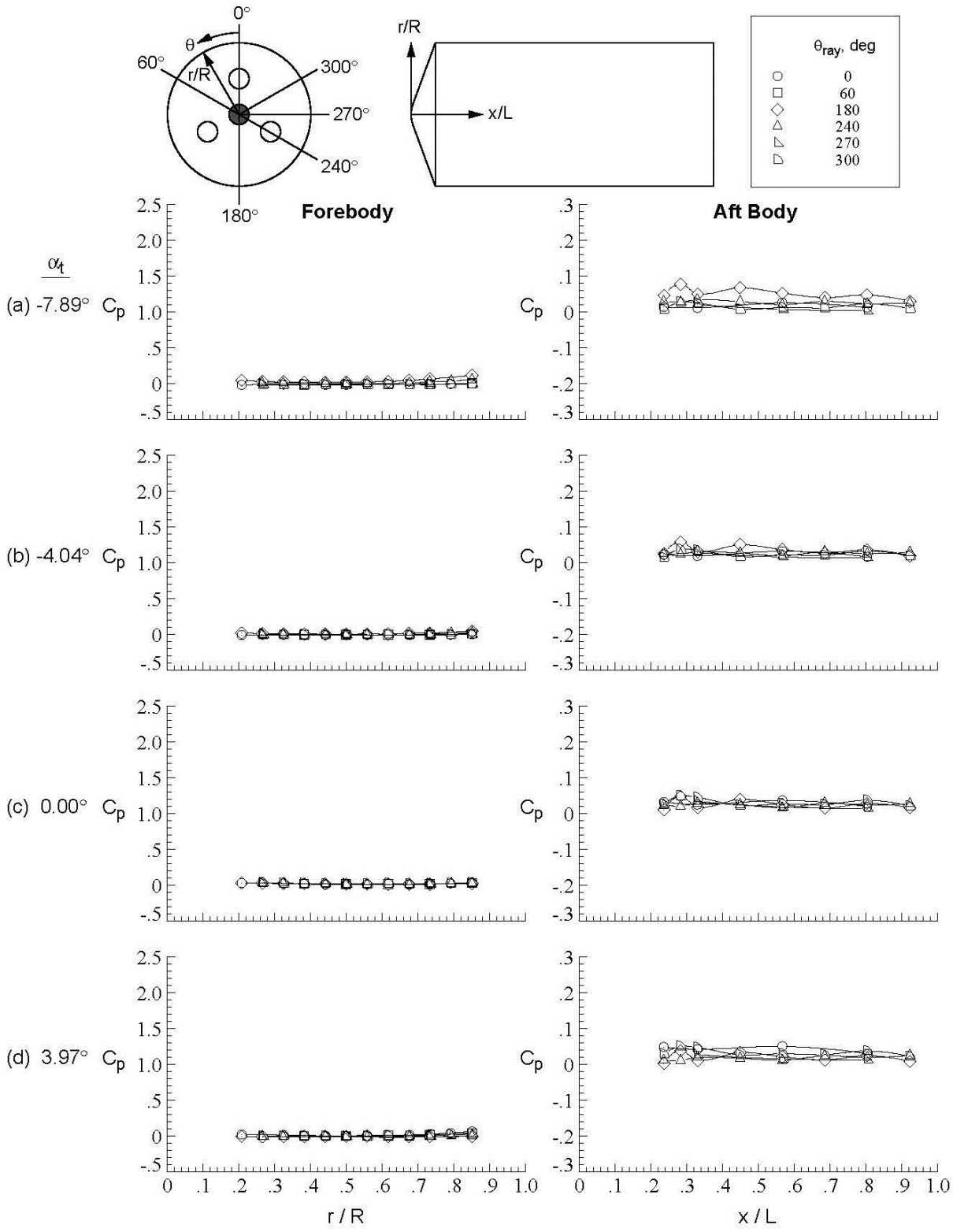

Figure D-127. Center nozzle configuration, Run 165, M_∞ = 4.6, Re_∞ = 1.5x10^7/ft, ϕ = 179.93°, X_S = 40.15 in, Y_S = 0.00 in, C_T = 1.98.

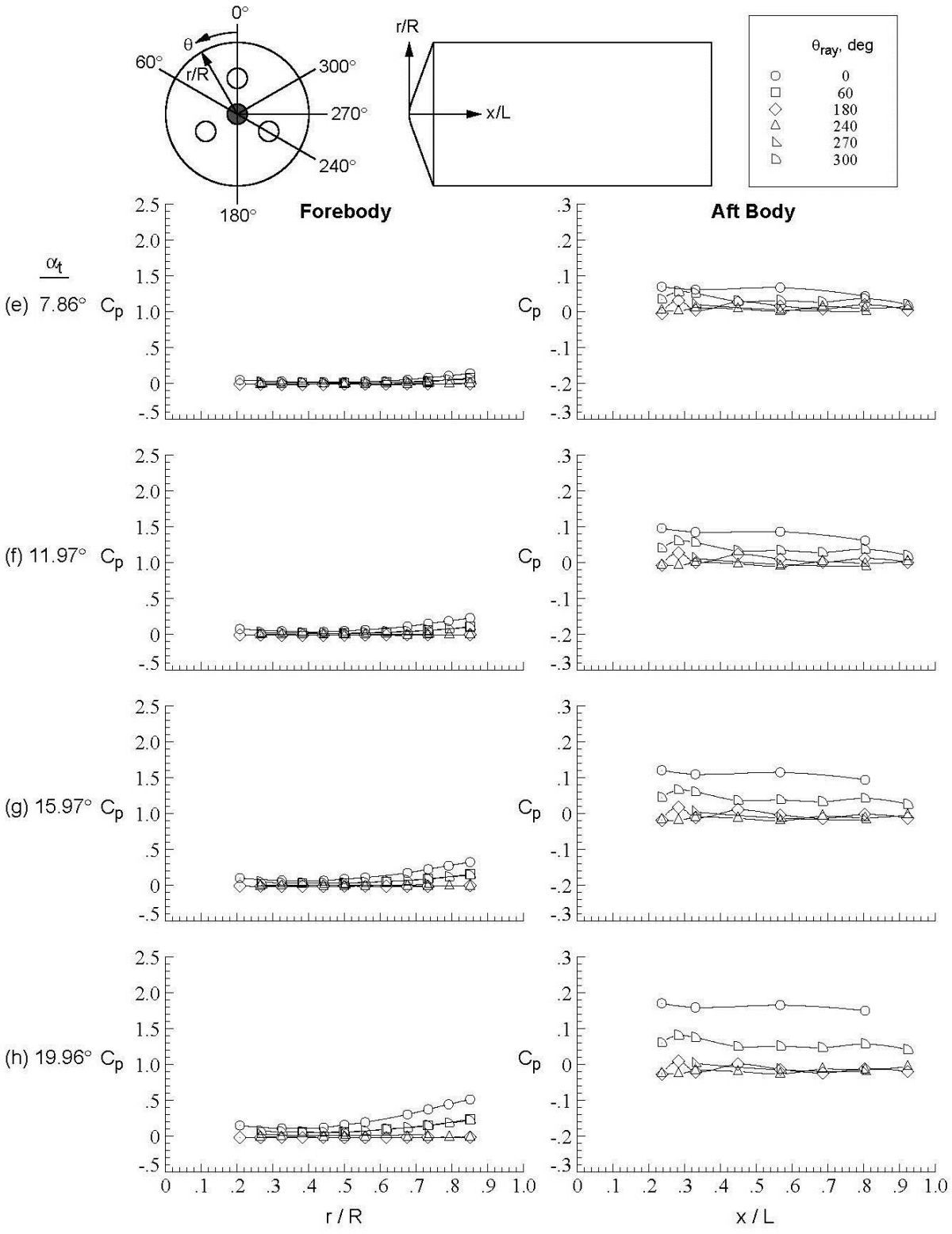

Figure D-127.Concluded.

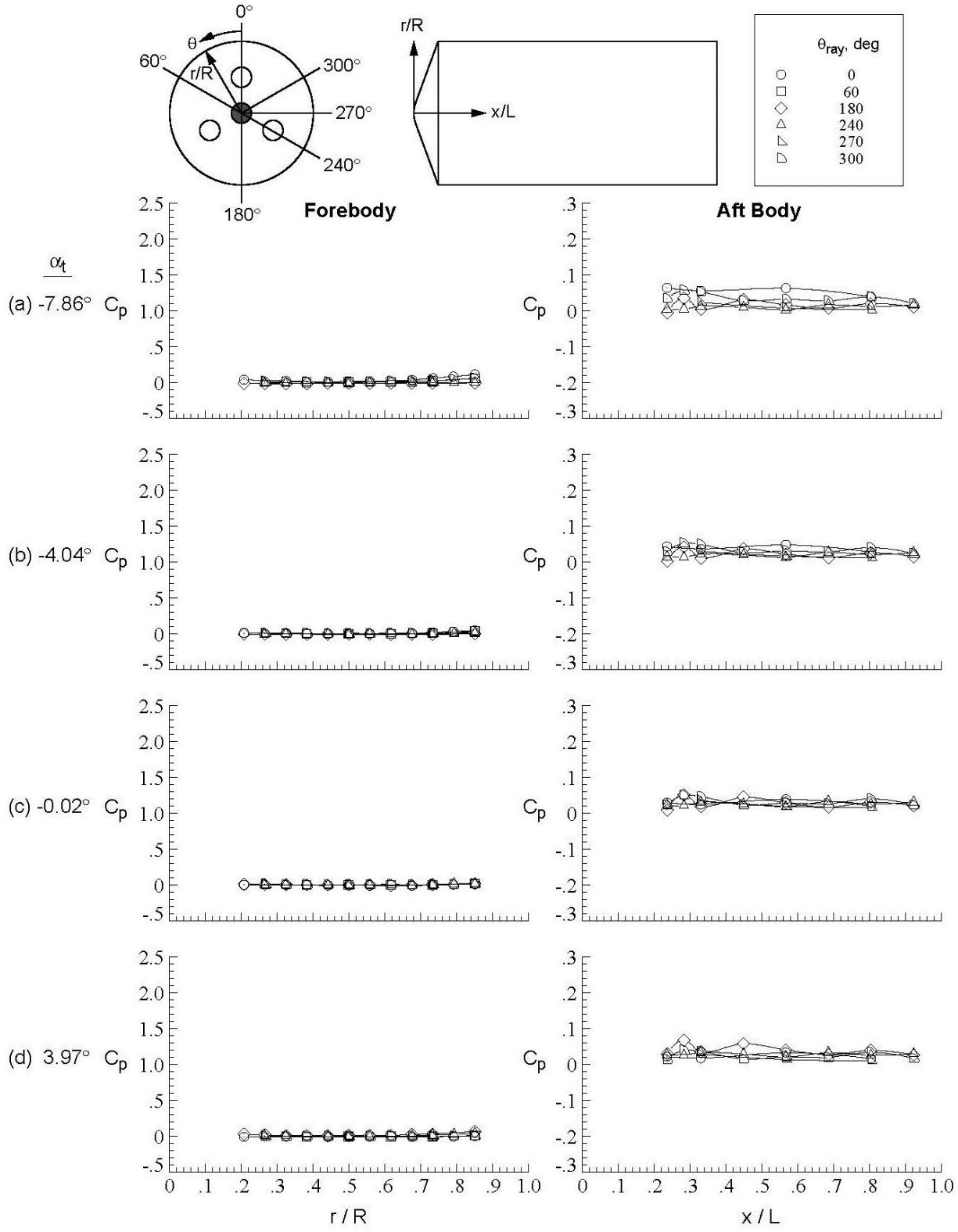

Figure D-128. Center nozzle configuration, Run 166, M_∞ = 4.6, Re_∞ = 1.5x10^7/ft, ϕ = 0.03°, X_S = 40.15 in, Y_S = 0.00 in, C_T = 1.97.

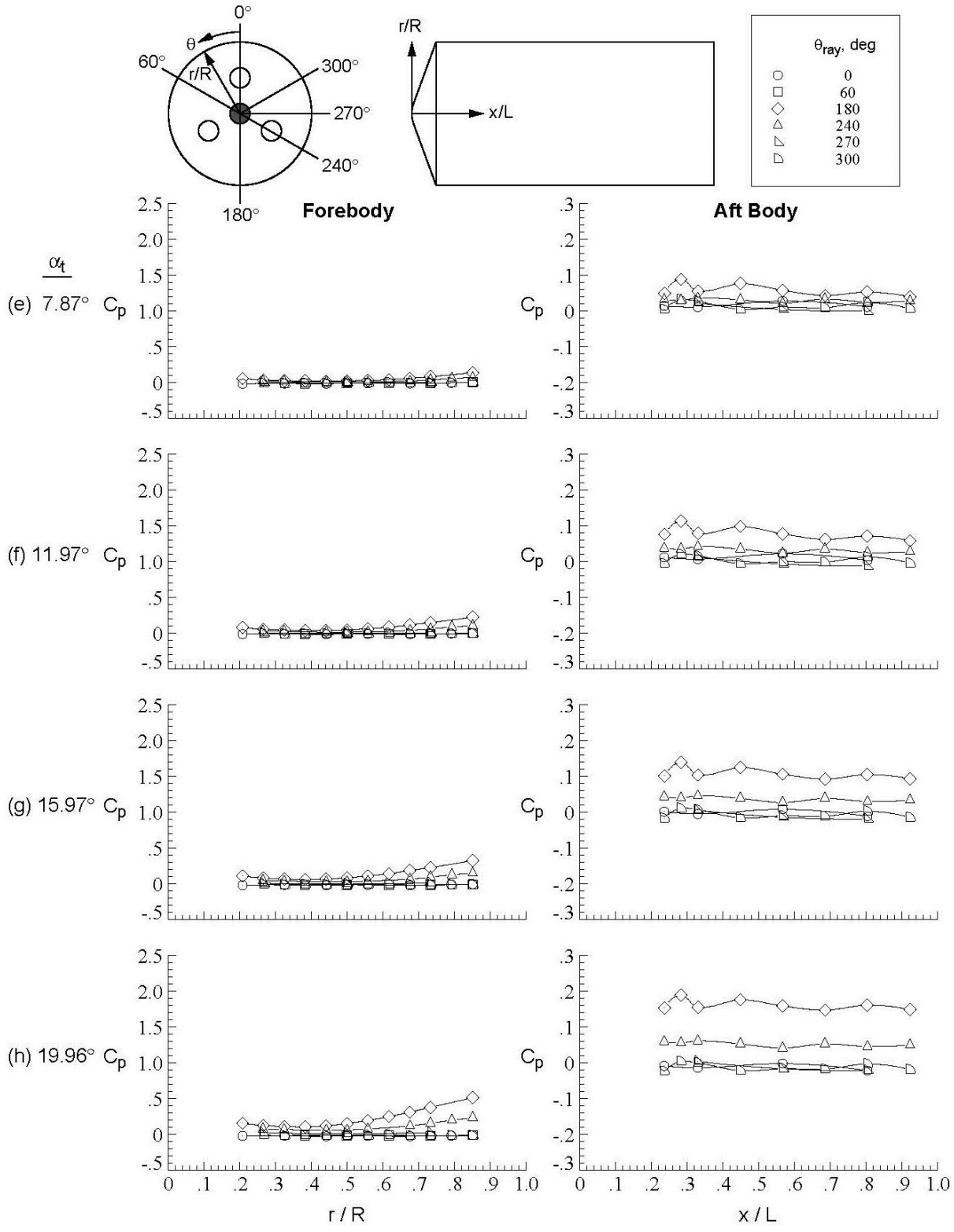

Figure D-128.Concluded.

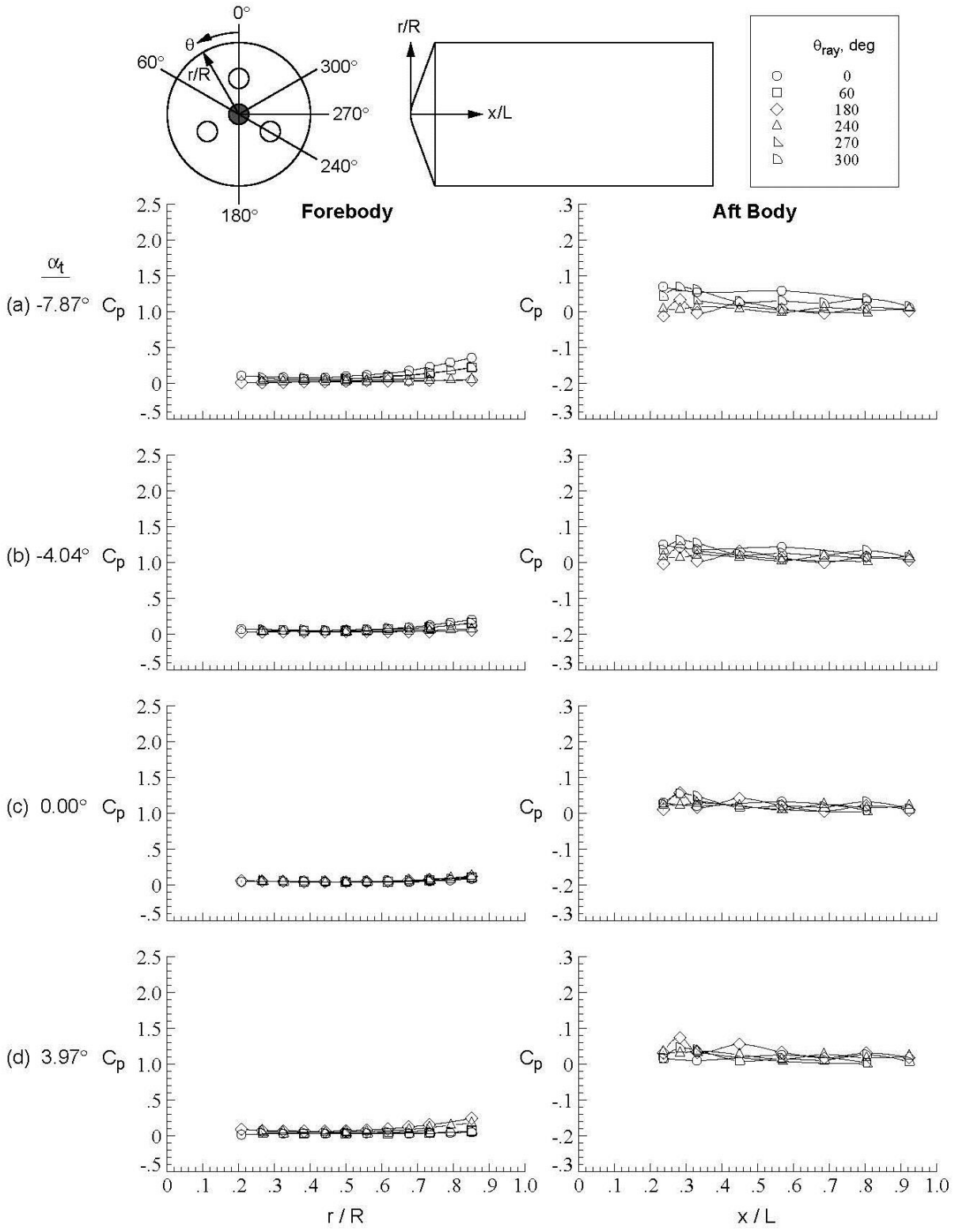

Figure D-129. Center nozzle configuration, Run 167, M_∞ = 4.6, Re_∞ = 1.5x10^7/ft, ϕ = 0.03°, X_S = 40.15 in, Y_S = 0.00 in, C_T = 0.96.

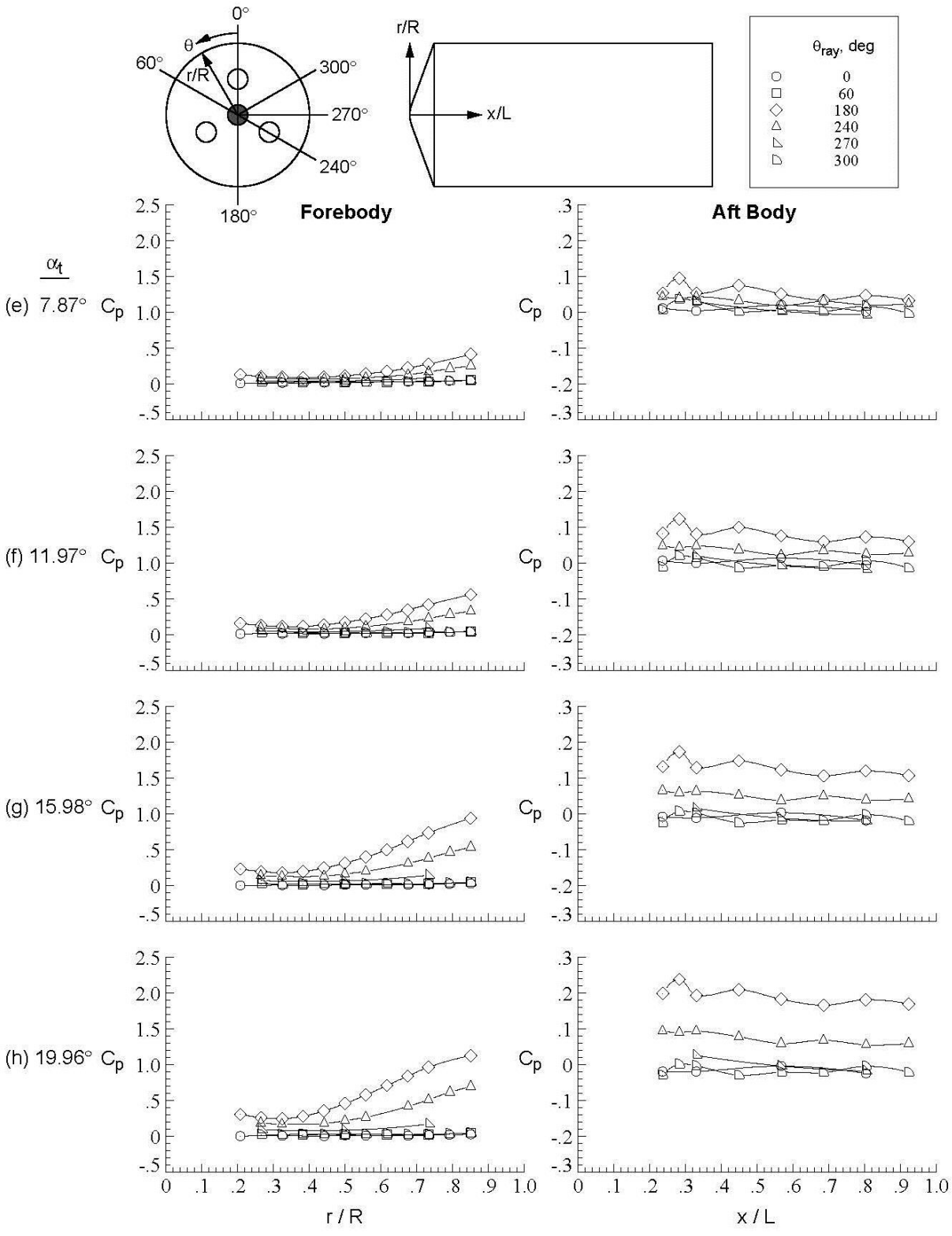

Figure D-129.Concluded.

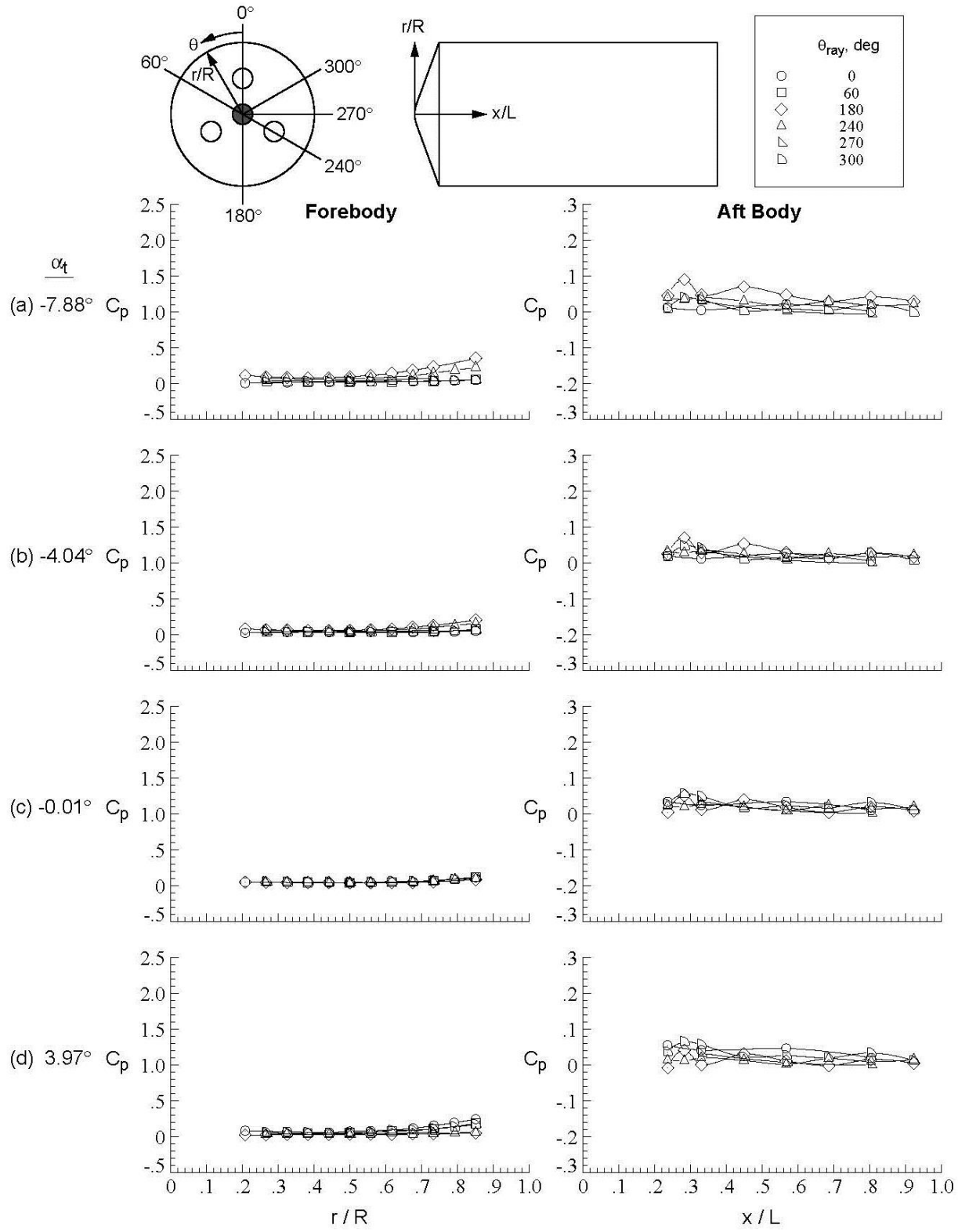

Figure D-130. Center nozzle configuration, Run 168, M_∞ = 4.6, Re_∞ = 1.5x10^7/ft, ϕ = 179.95°, X_S = 40.15 in, Y_S = 0.00 in, C_T = 0.93.

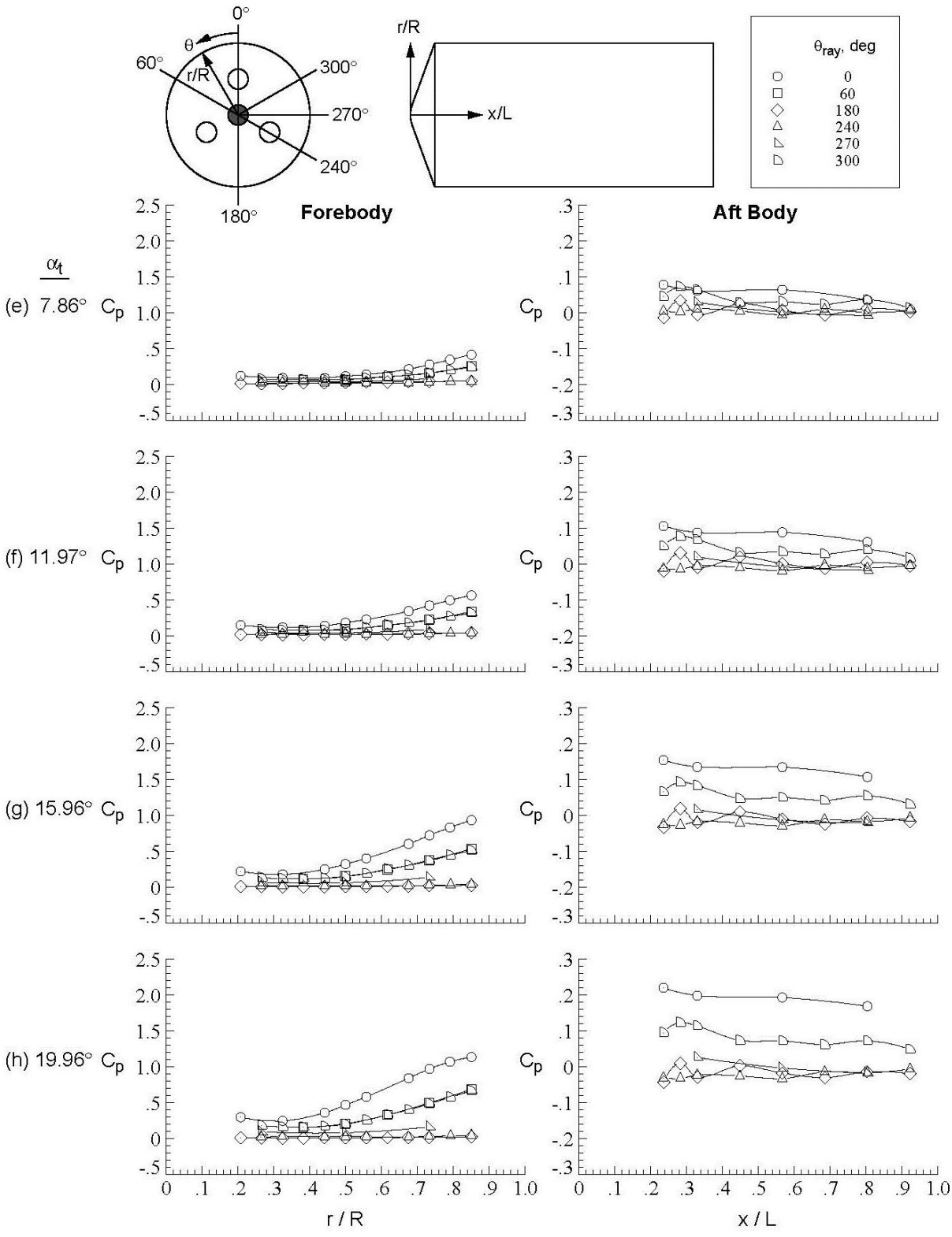

Figure D-130.Concluded.

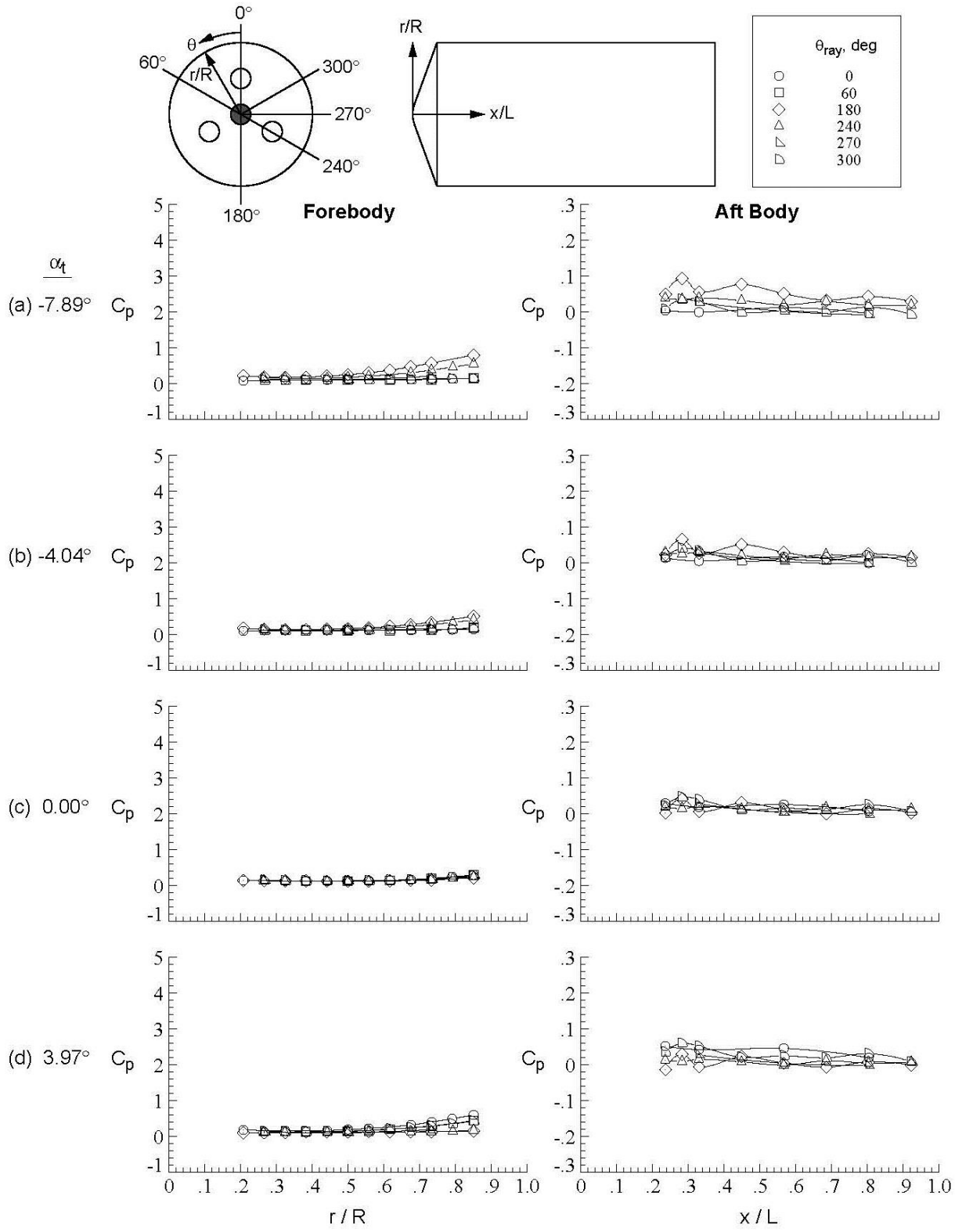

Figure D-131. Center nozzle configuration, Run 169, M_∞ = 4.6, Re_∞ = 1.5x10^7/ft, ϕ = 179.95°, X_S = 40.15 in, Y_S = 0.00 in, C_T = 0.46.

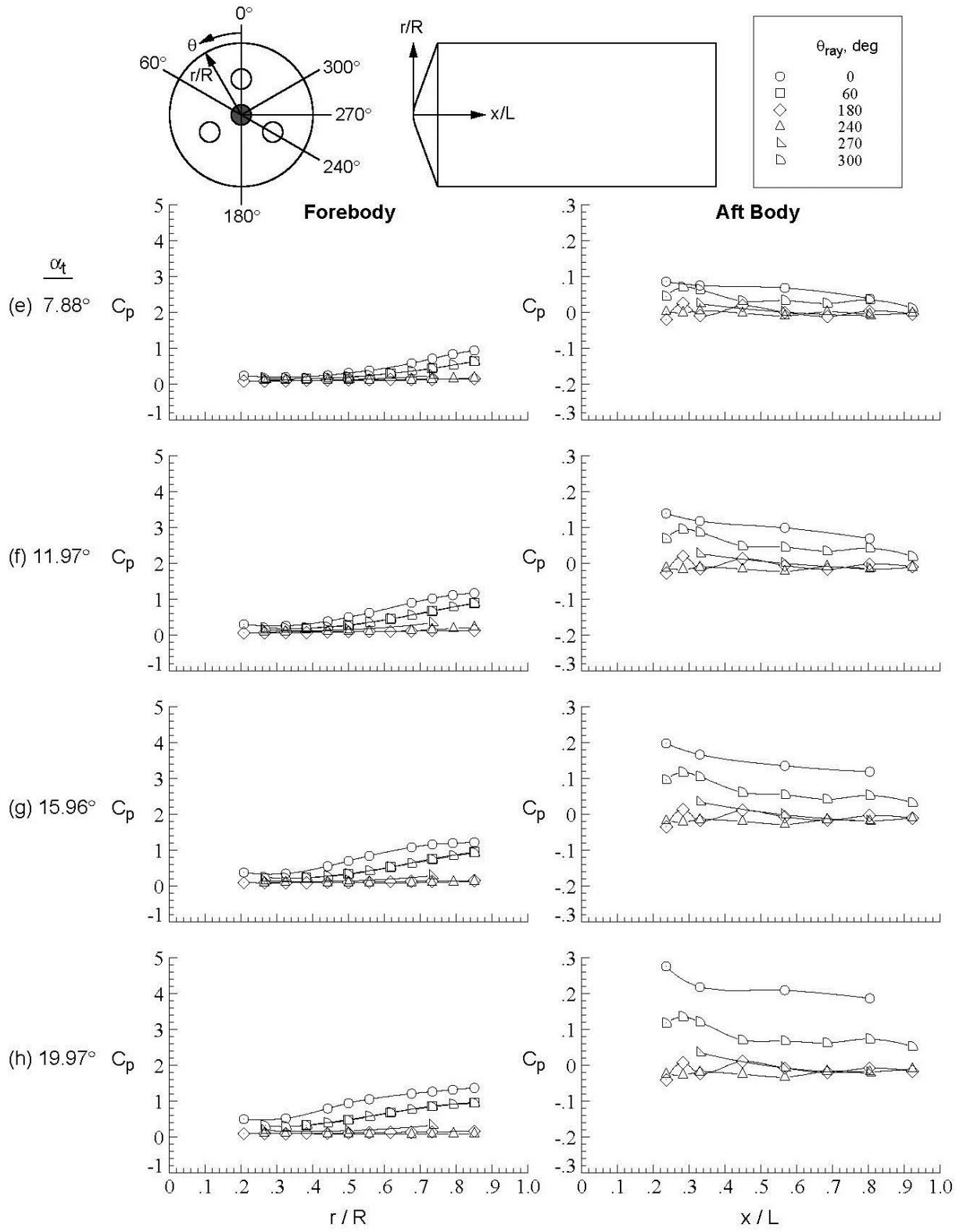

Figure D-131.Concluded.

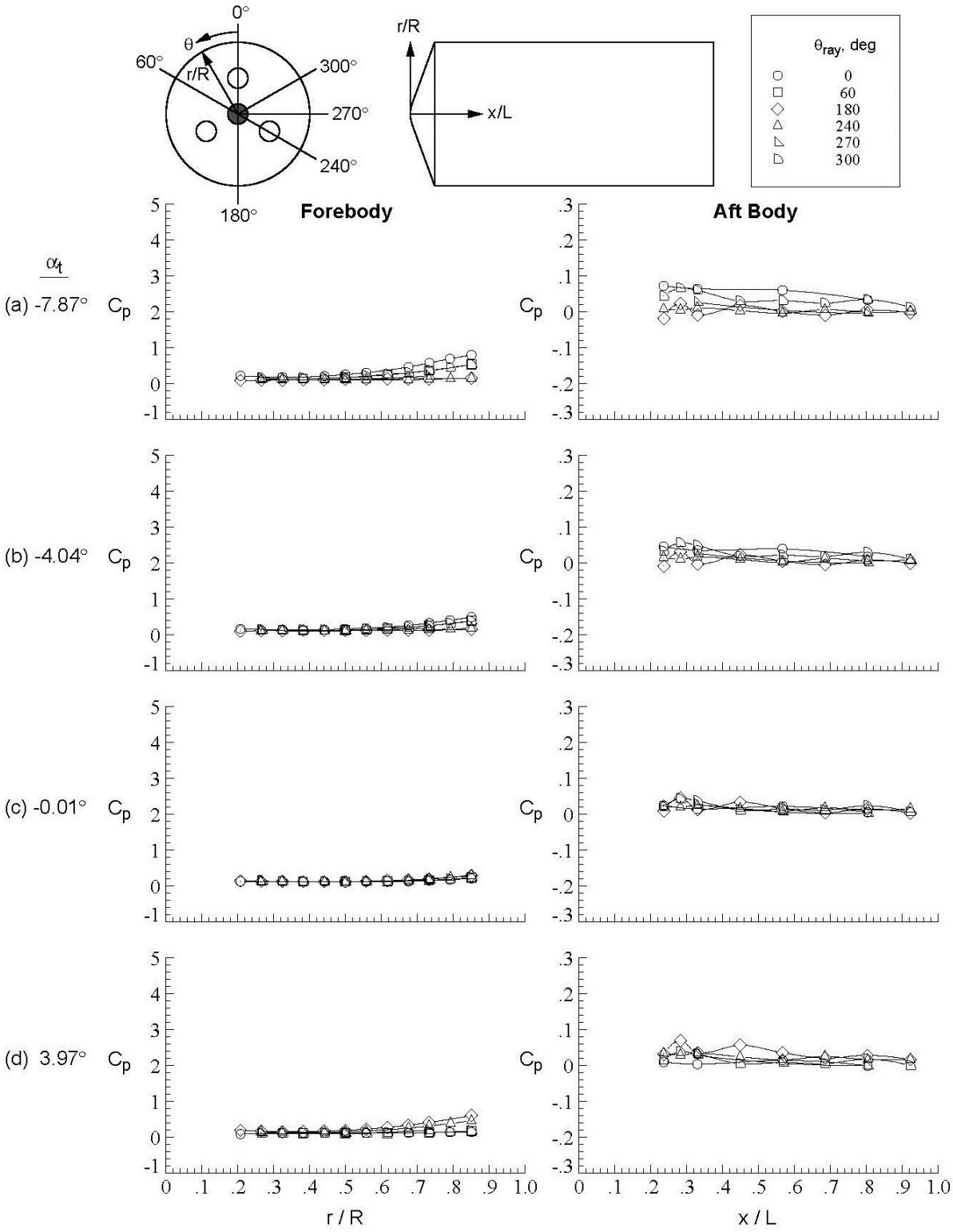

Figure D-132. Center nozzle configuration, Run 170, M_∞ = 4.6, Re_∞ = 1.5x10^7/ft, ϕ = 0.03°, X_S = 40.15 in, Y_S = 0.00 in, C_T = 0.46.

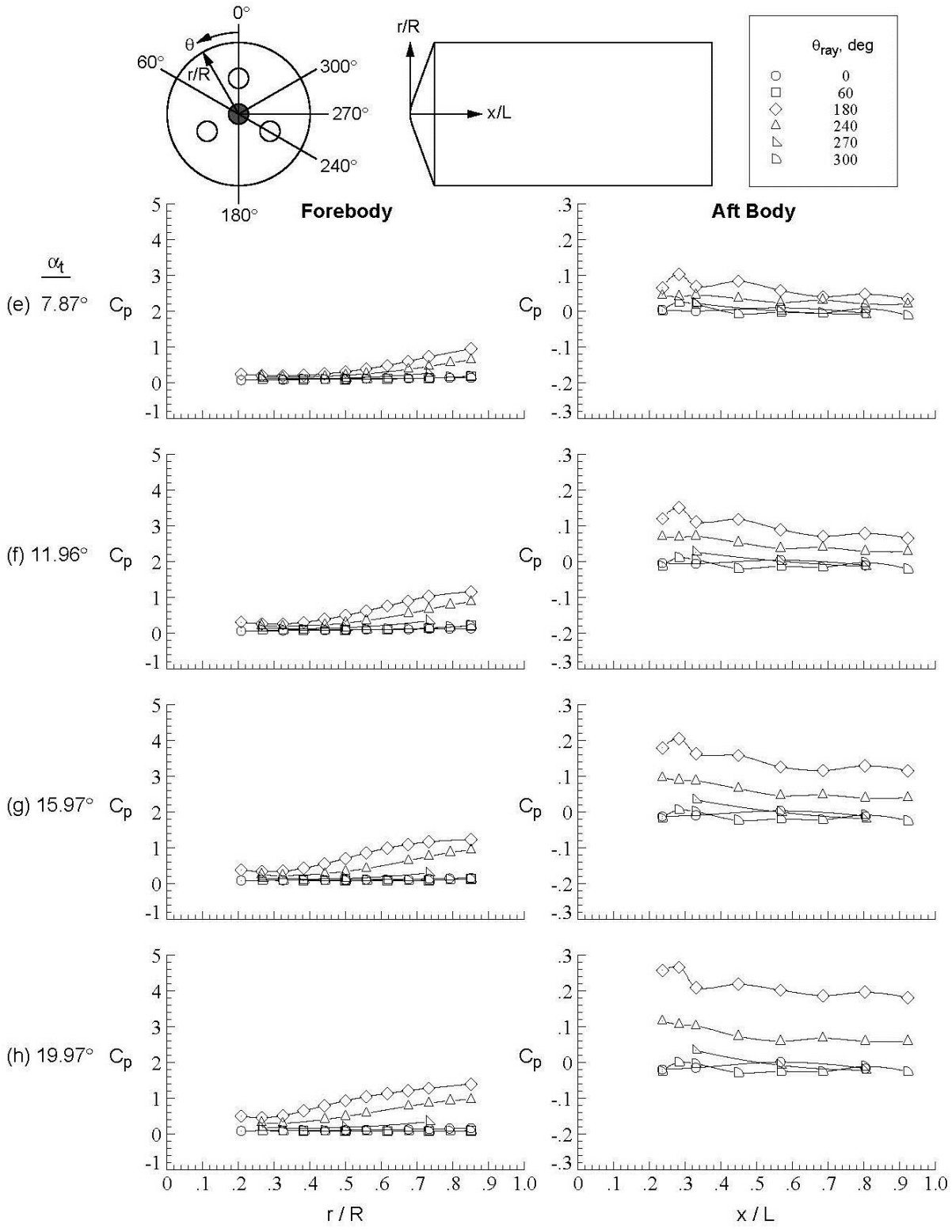

Figure D-132.Concluded.

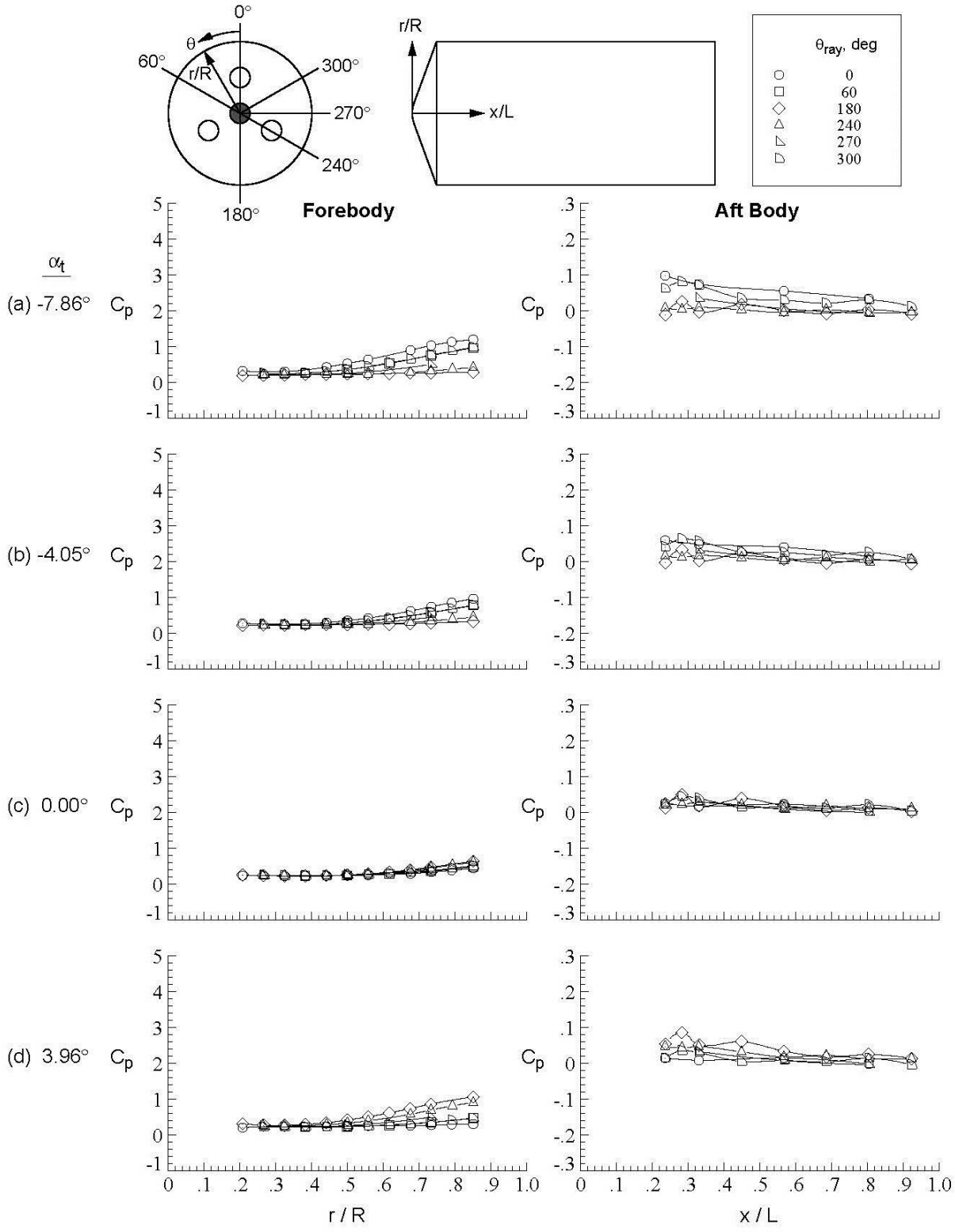

Figure D-133. Center nozzle configuration, Run 171, M_∞ = 4.6, Re_∞ = 1.5x10^7/ft, ϕ = 0.03°, X_S = 40.15 in, Y_S = 0.00 in, C_T = 0.22.

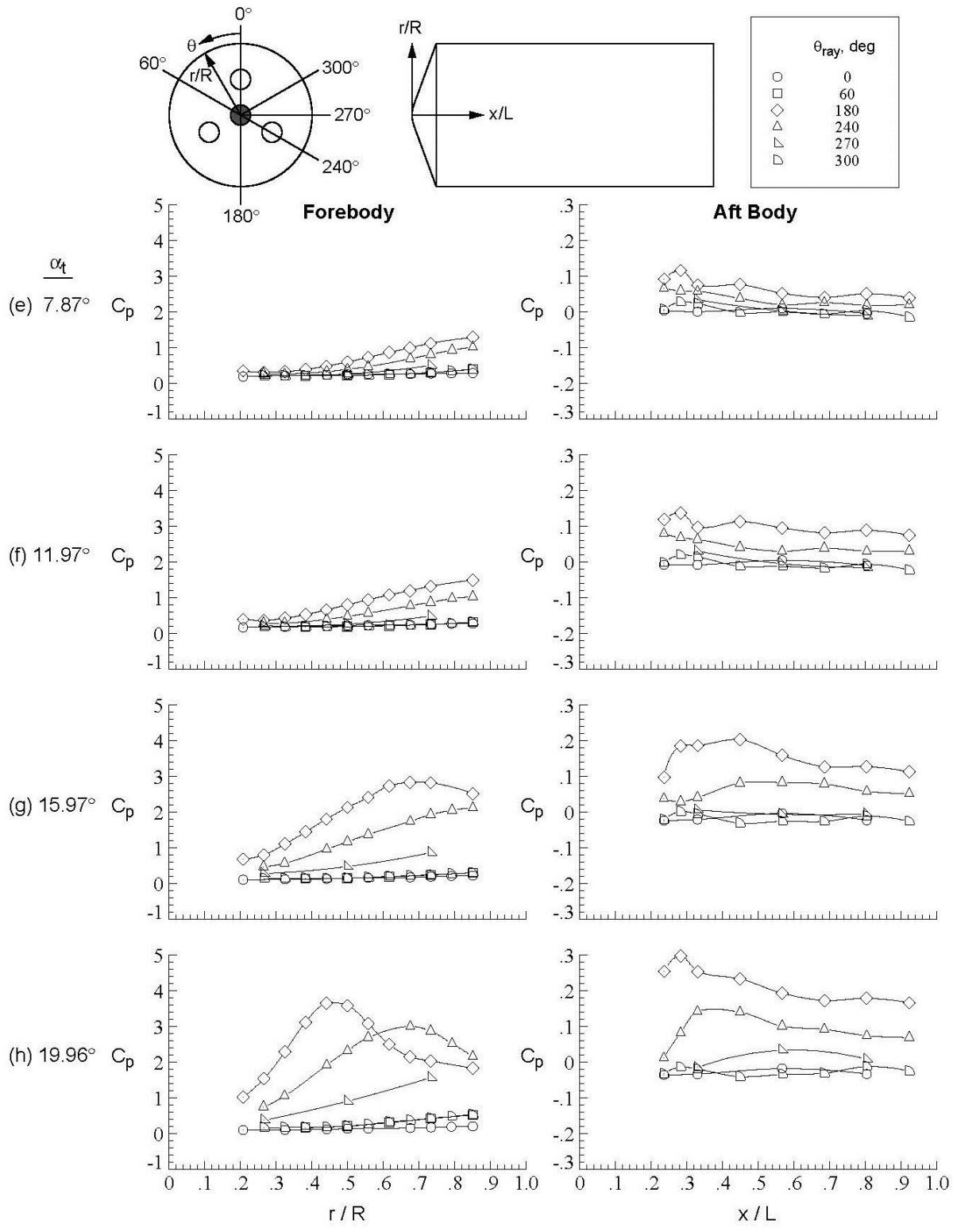

Figure D-133.Concluded.

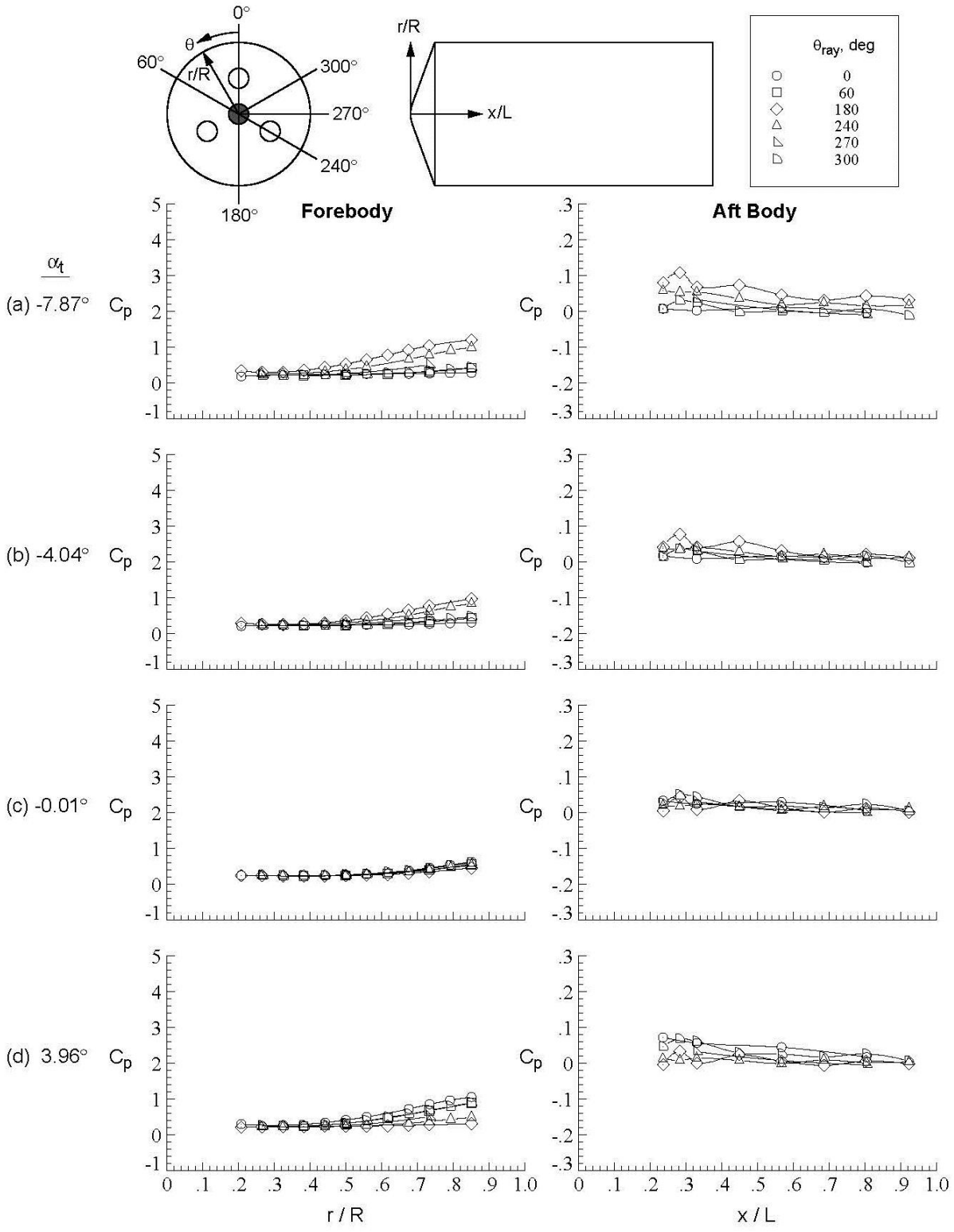

Figure D-134. Center nozzle configuration, Run 172, M_∞ = 4.6, Re_∞ = 1.5x10^7/ft, ϕ = 179.91°, X_S = 40.15 in, Y_S = 0.00 in, C_T = 0.22.

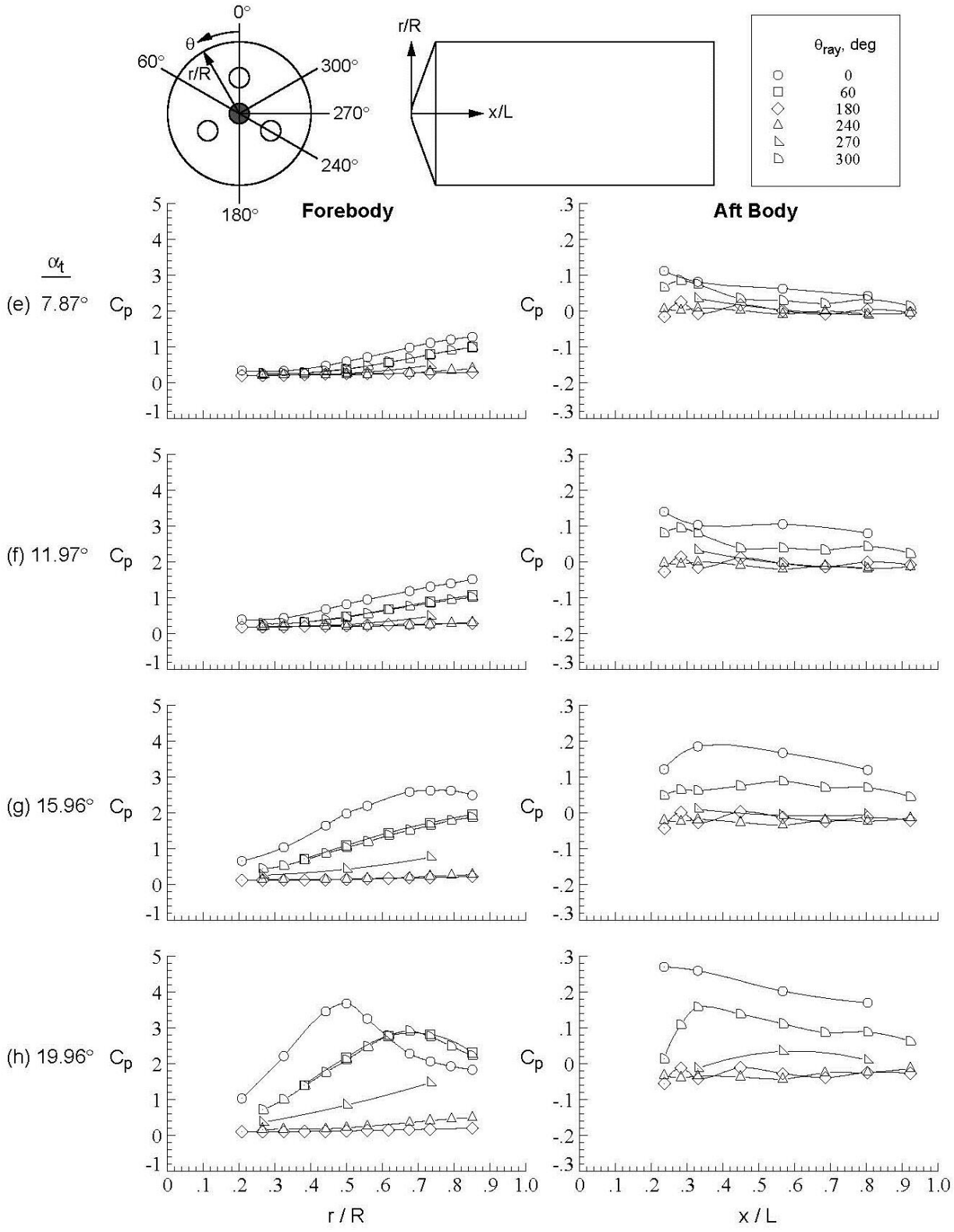

Figure D-134.Concluded.

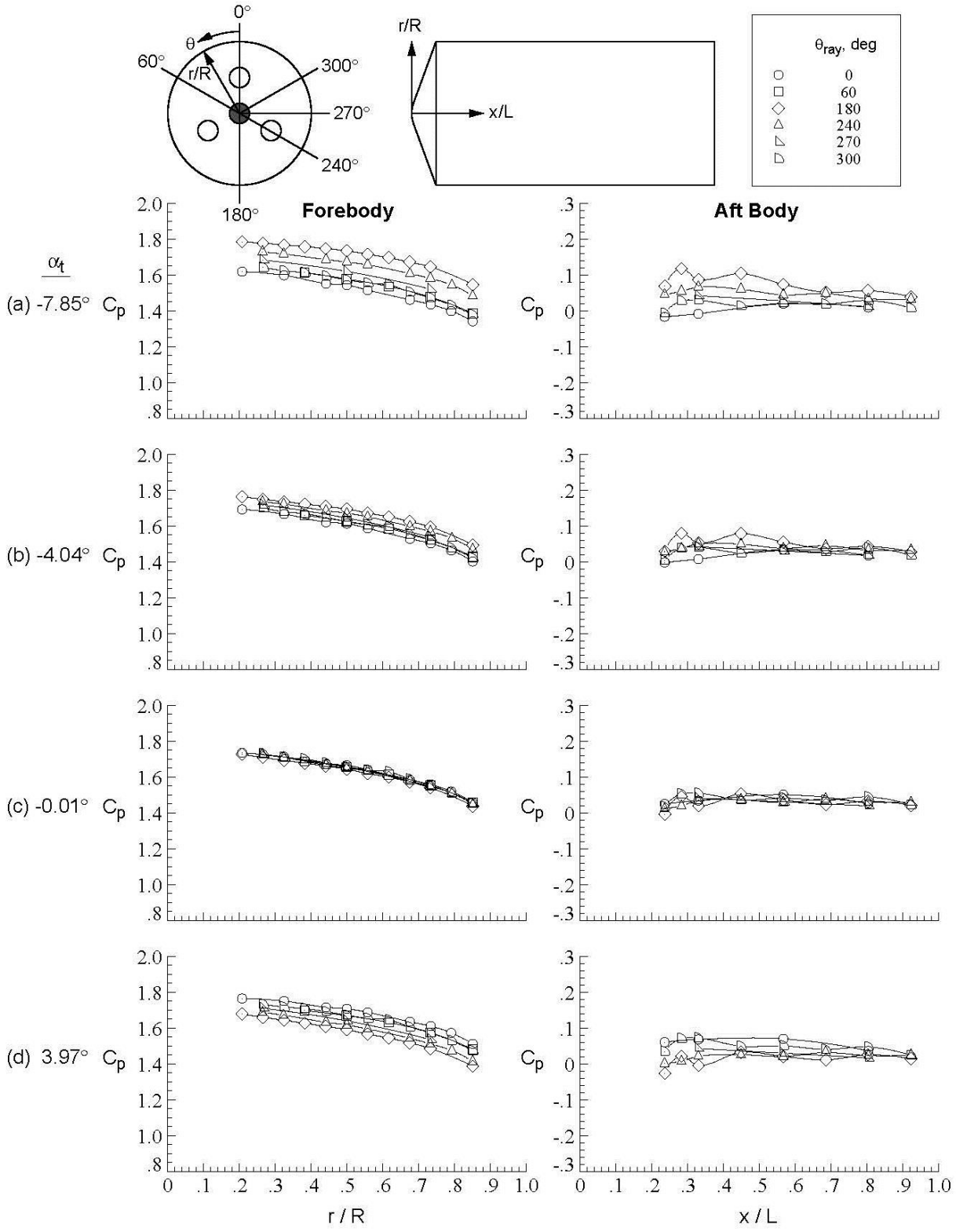

Figure D-135. Center nozzle configuration, Run 173, M_∞ = 4.6, Re_∞ = 1.5x10^7/ft, ϕ = 179.91°, X_S = 40.15 in, Y_S = 0.00 in, C_T = 0.00.

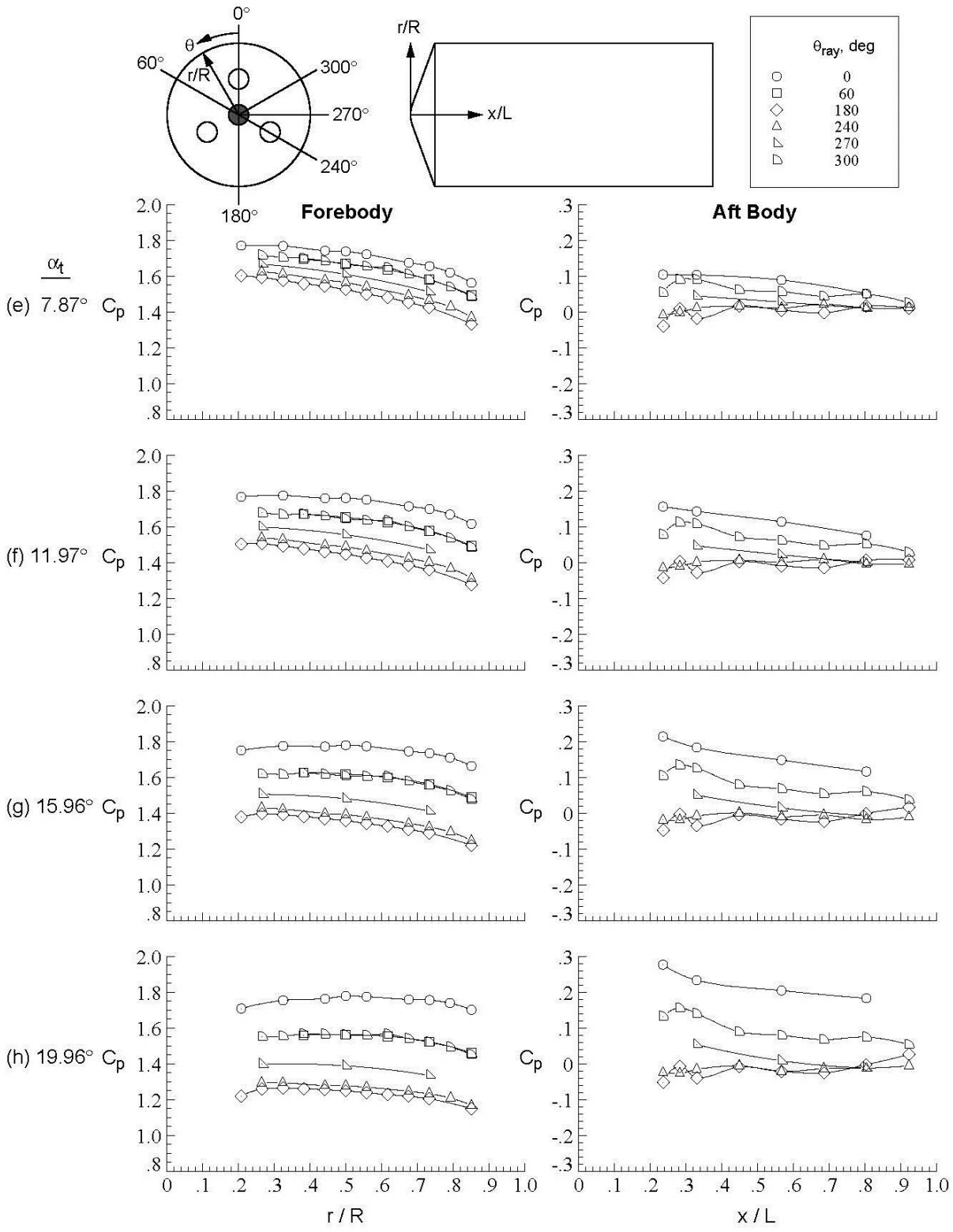

Figure D-135.Concluded.

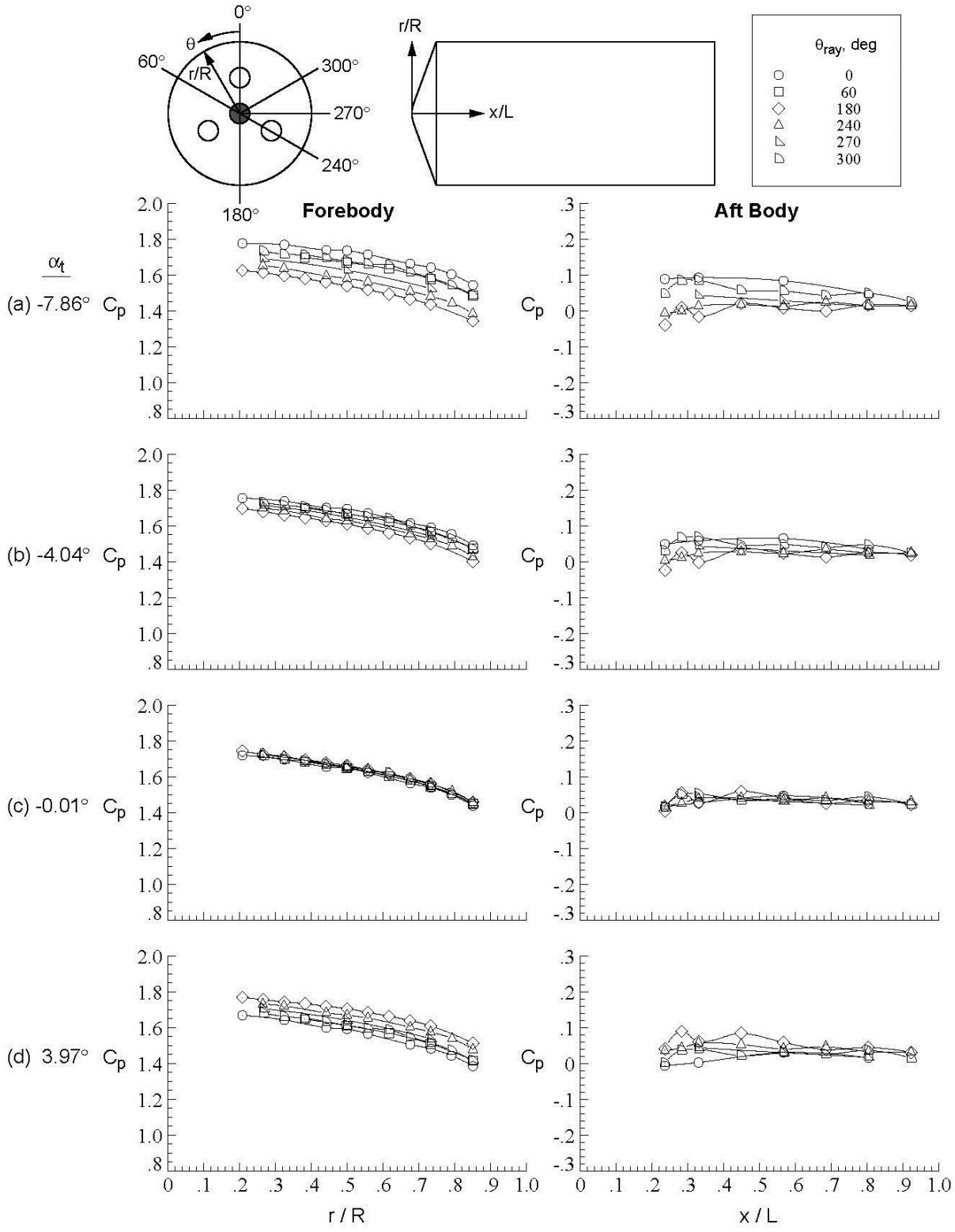

Figure D-136. Center nozzle configuration, Run 174, M_∞ = 4.6, Re_∞ = 1.5x10^7/ft, ϕ = −0.07°, X_S = 40.15 in, Y_S = 0.00 in, C_T = 0.00.

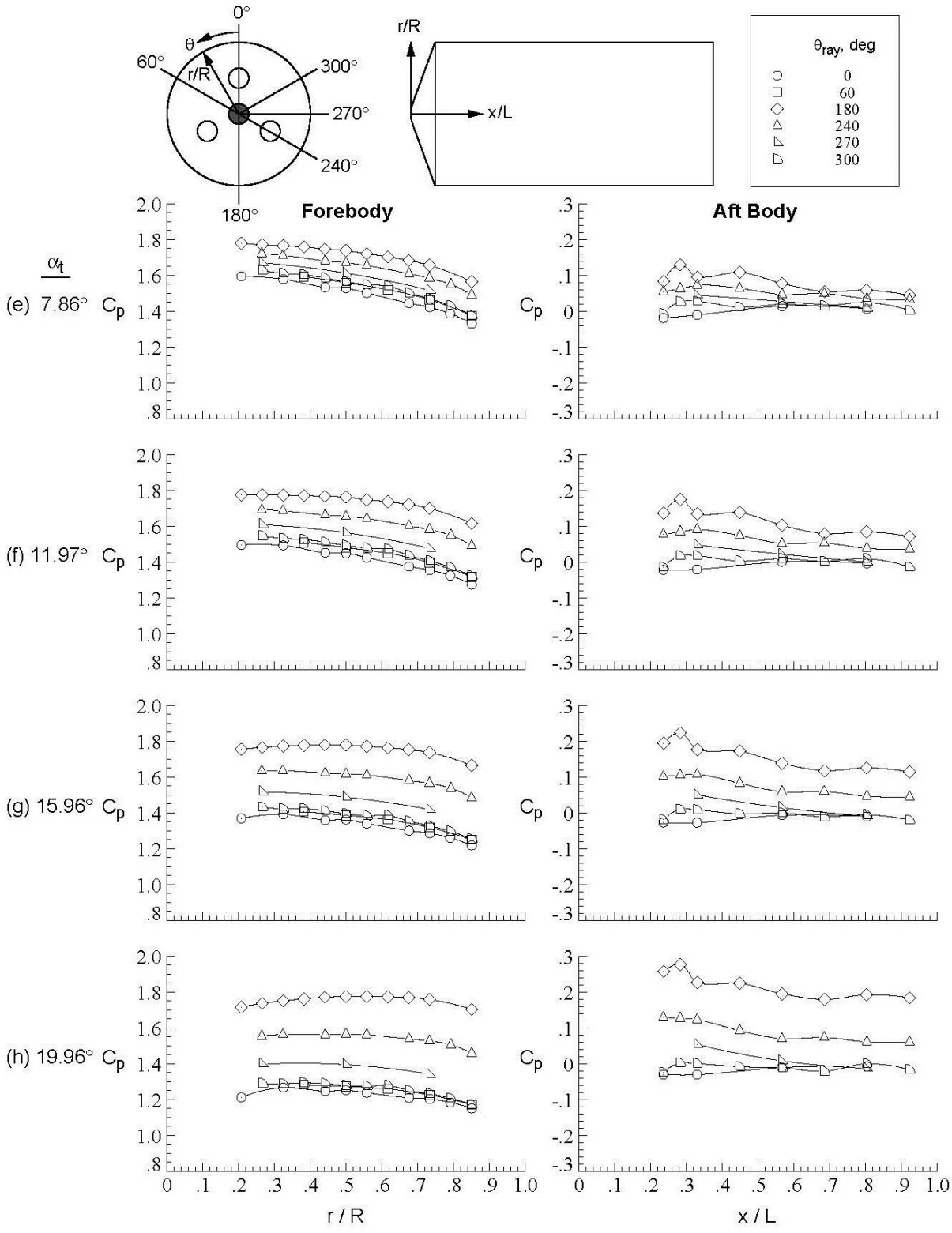

Figure D-1361. Concluded.

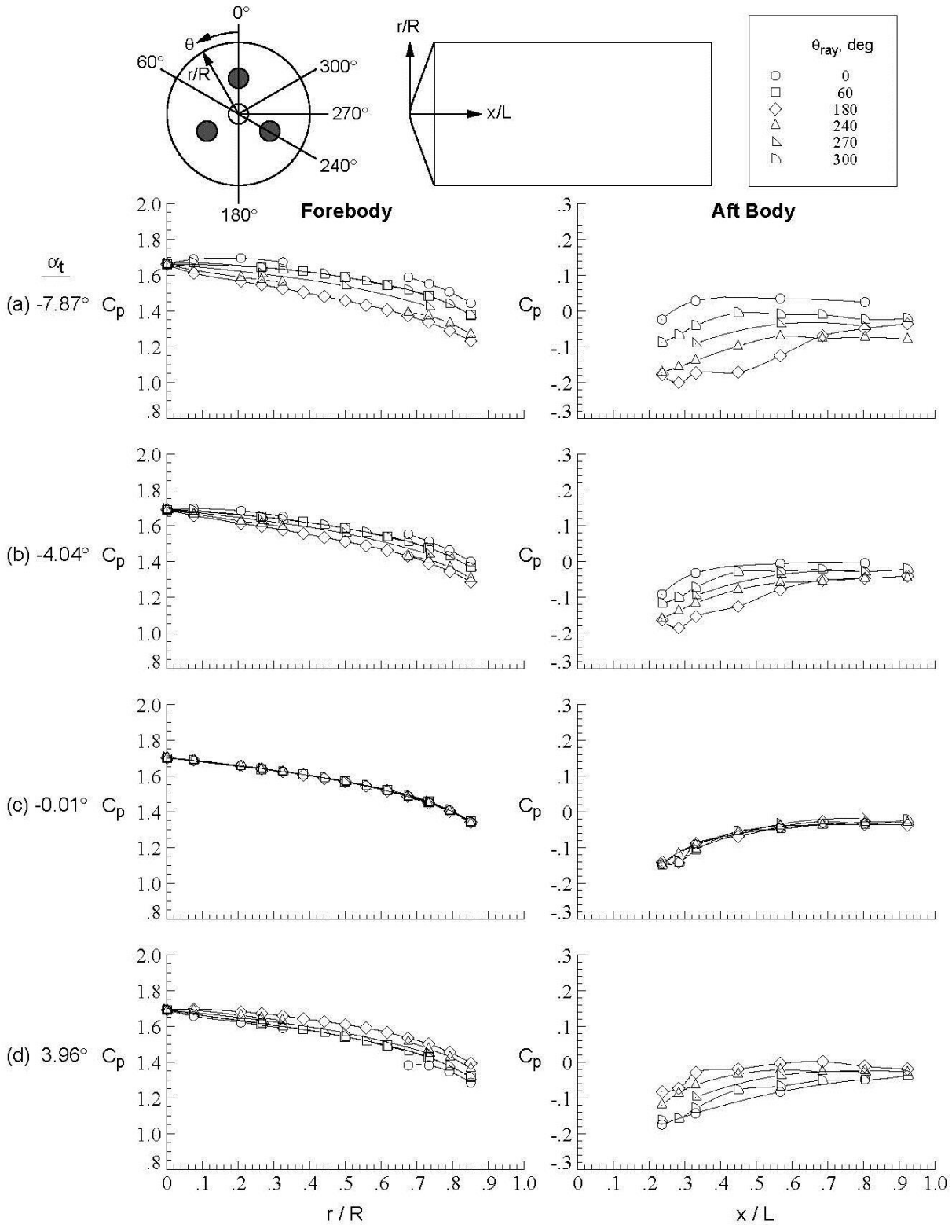

Figure D-137.Tri-nozzle configuration, Run 180, M_∞ = 2.4, Re_∞ = 1.0x10^7/ft, ϕ = −0.01°, X_S = 40.15 in, Y_S = 0.00 in, C_T = 0.00.

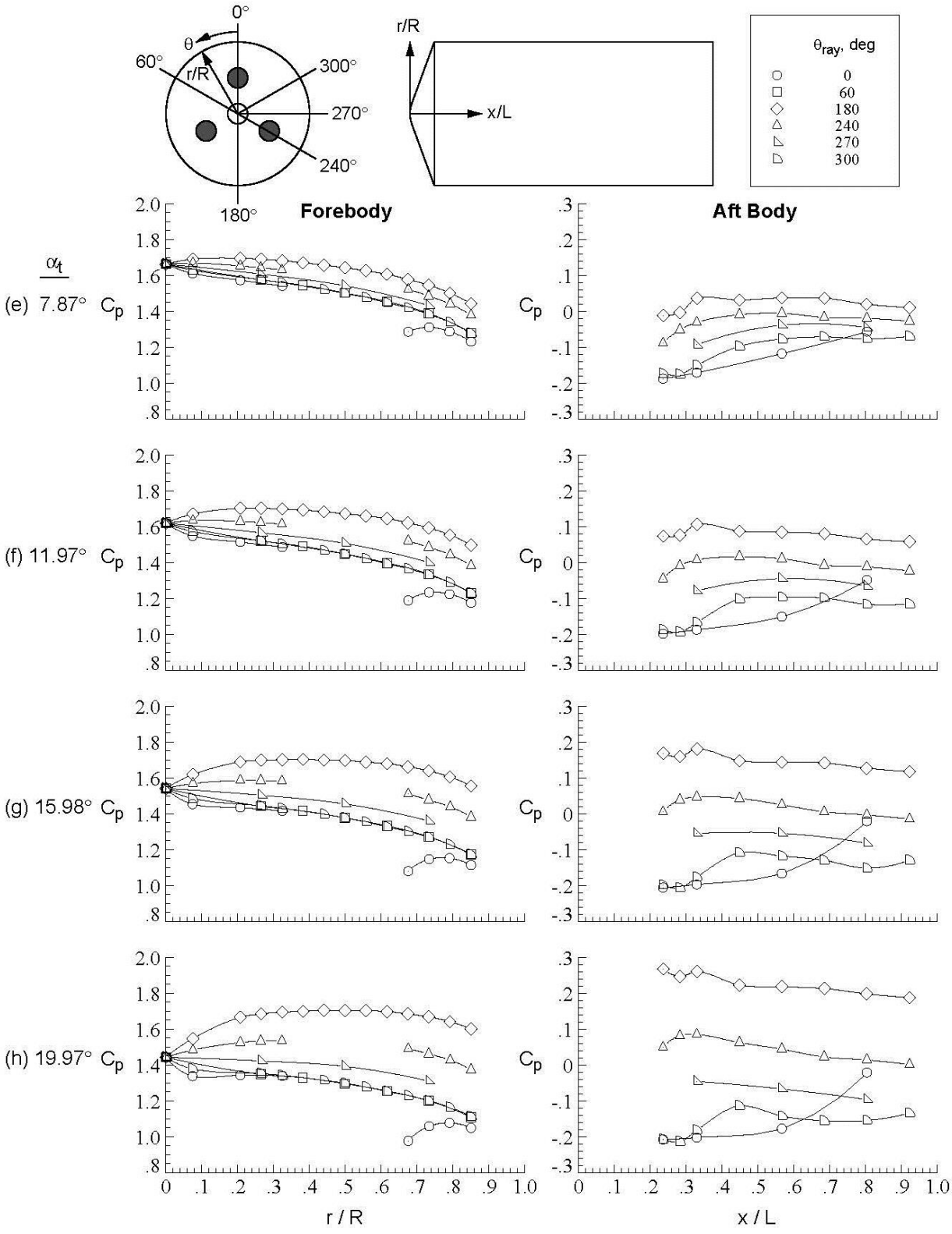

Figure D-137.Concluded.

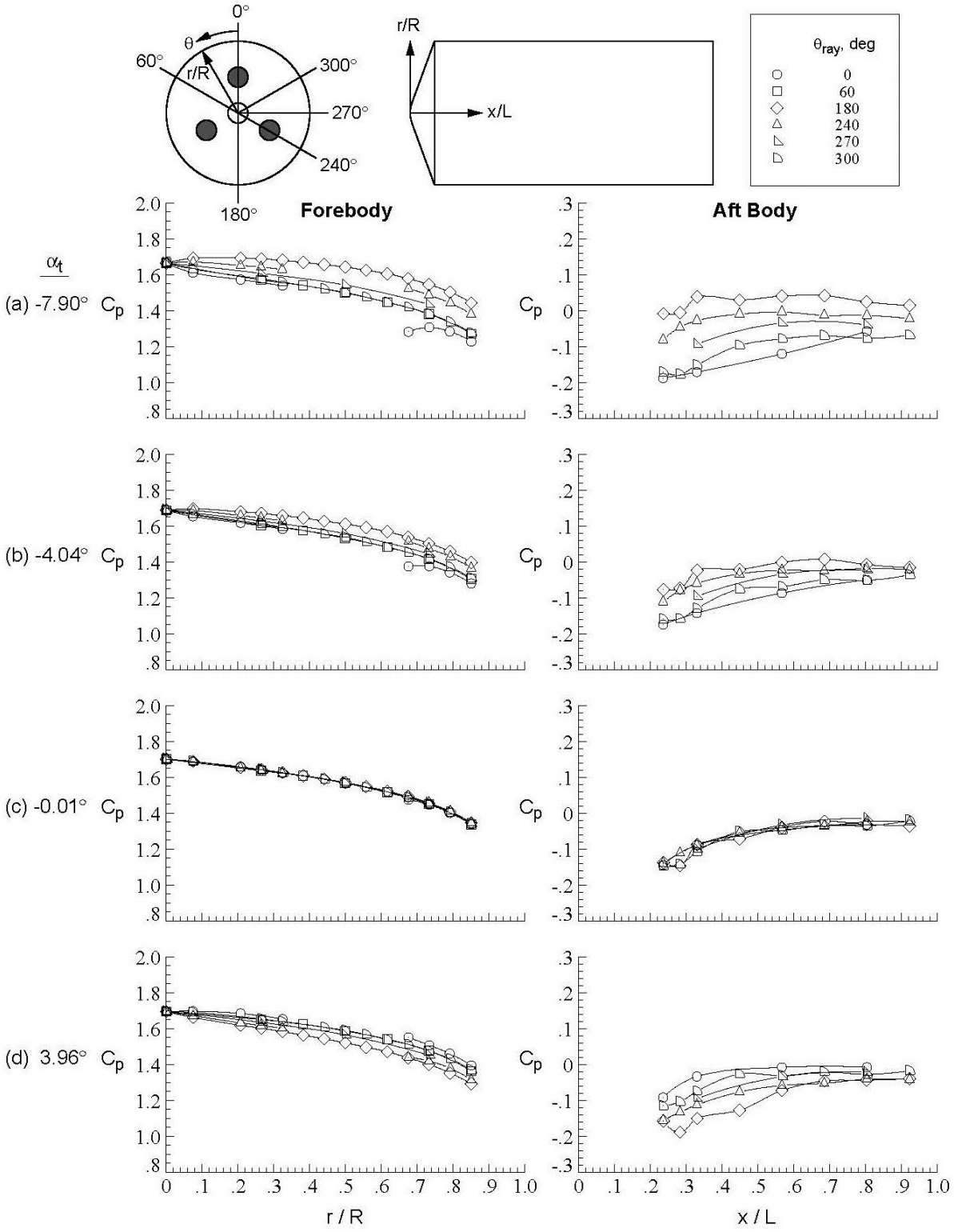

Figure D-138.Tri-nozzle configuration, Run 181, $M\infty$ = 2.4, Re_∞ = 1.0x10^7/ft, ϕ = 179.97°, X_S = 40.15 in, Y_S = 0.00 in, C_T = 0.00.

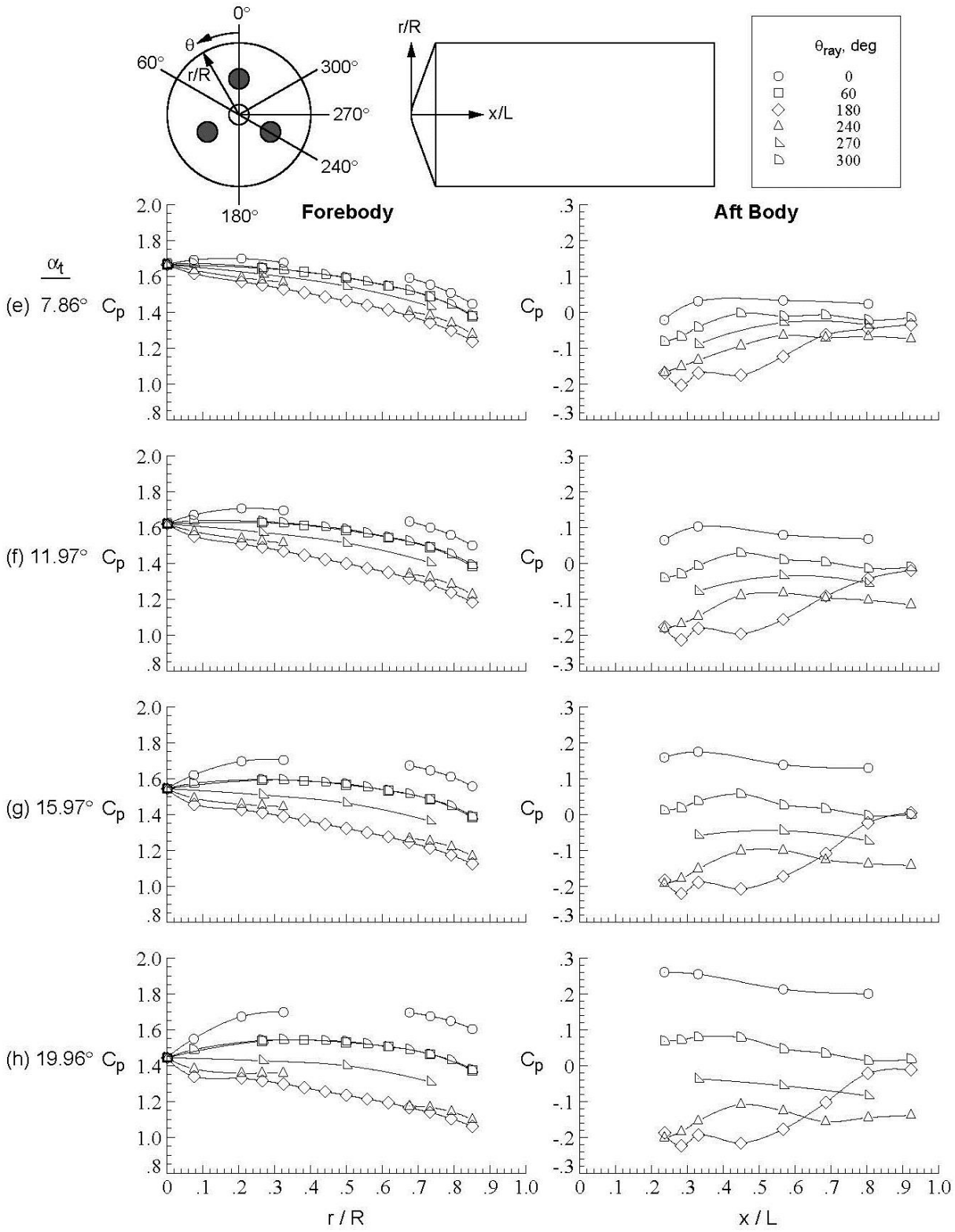

Figure D-138.Concluded.

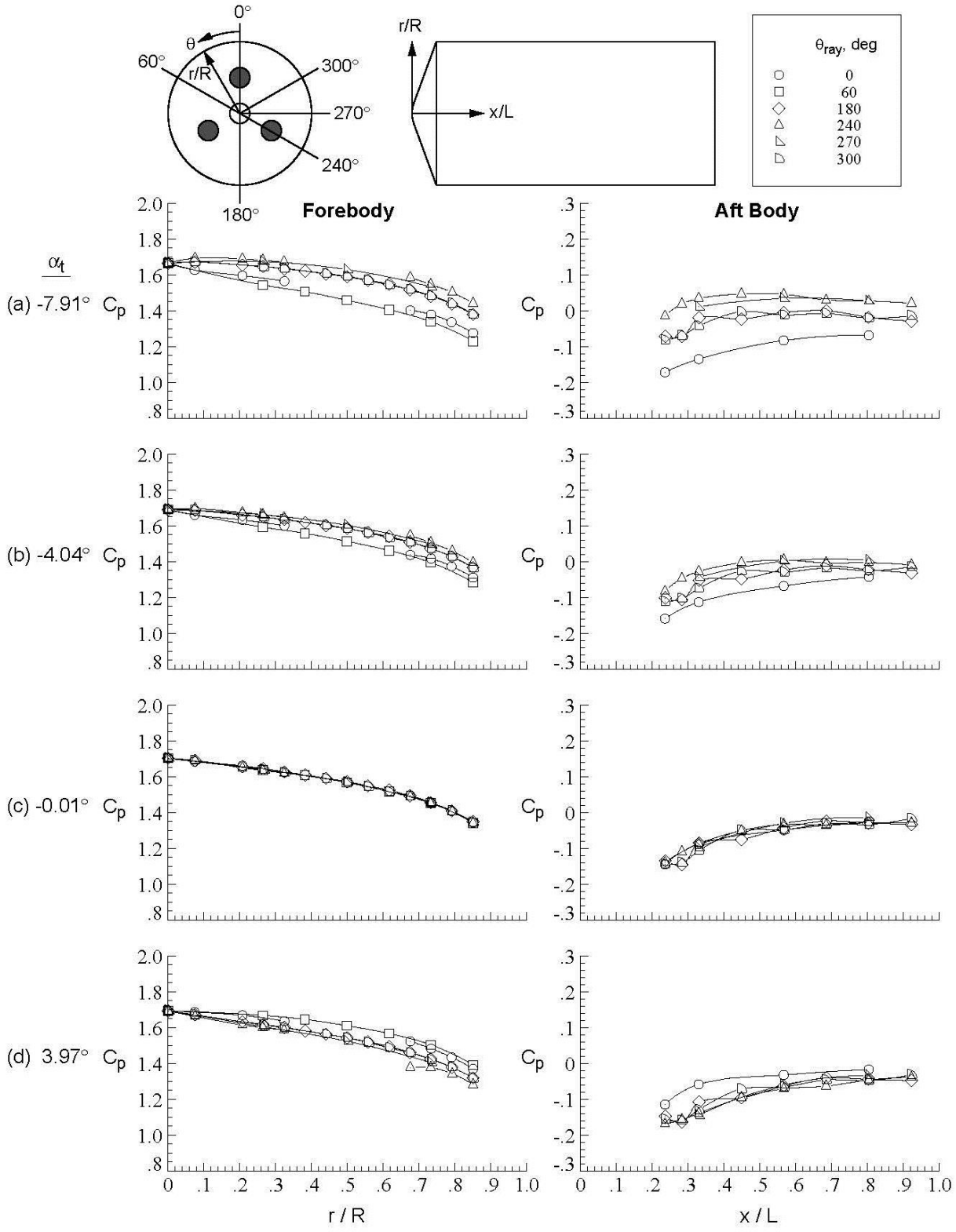

Figure D-139.Tri-nozzle configuration, Run 182, M_∞ = 2.4, Re_∞ = 1.0x10^6/ft, ϕ = 120.02°, X_S = 40.15 in, Y_S = 0.00 in, C_T = 0.00.

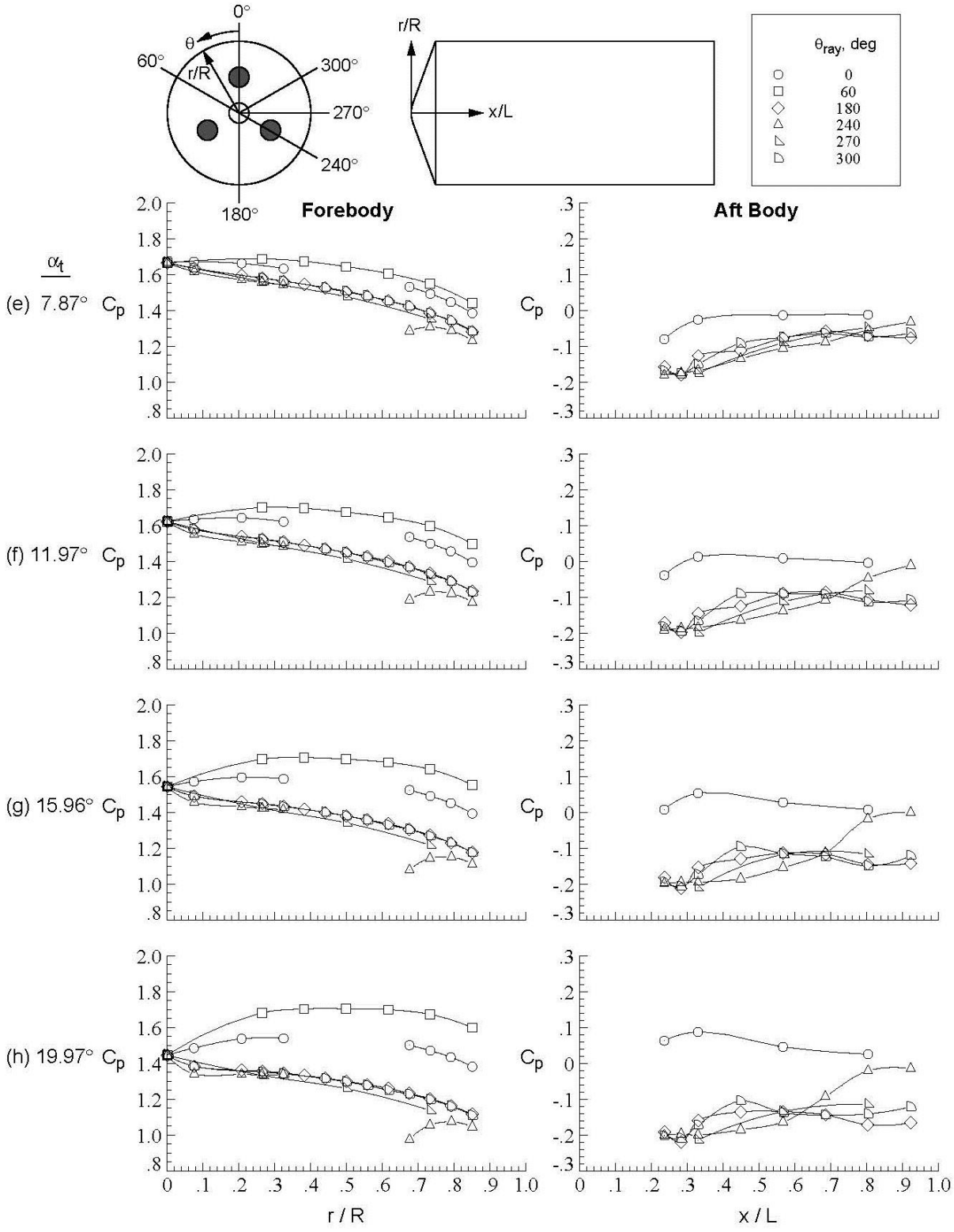

Figure D-139.Concluded.

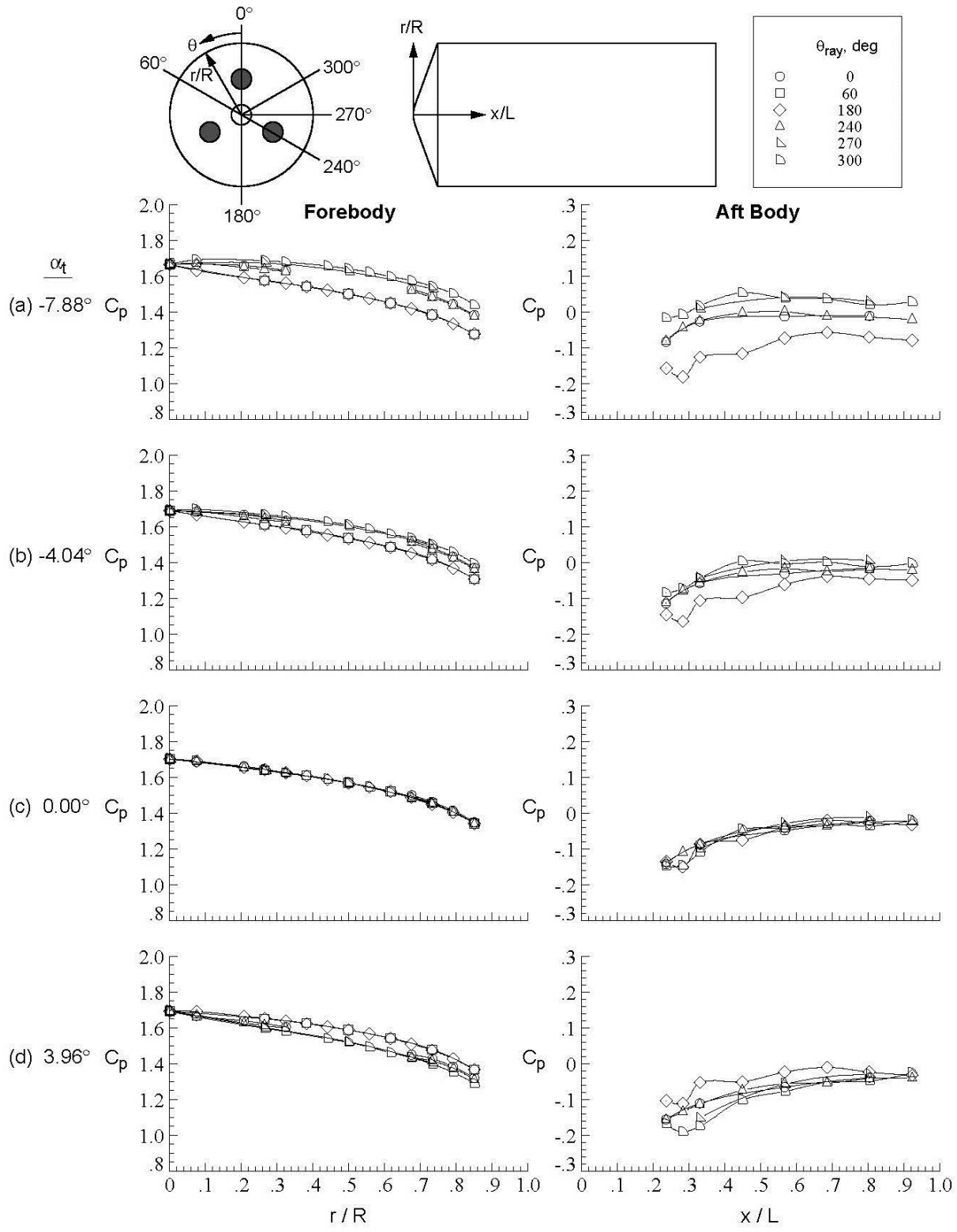

Figure D-140.Tri-nozzle configuration, Run 183, M_∞ = 2.4, Re_∞ = 1.0x10^6/ft, ϕ = 59.98°, X_S = 40.15 in, Y_S = 0.00 in, C_T = 0.00.

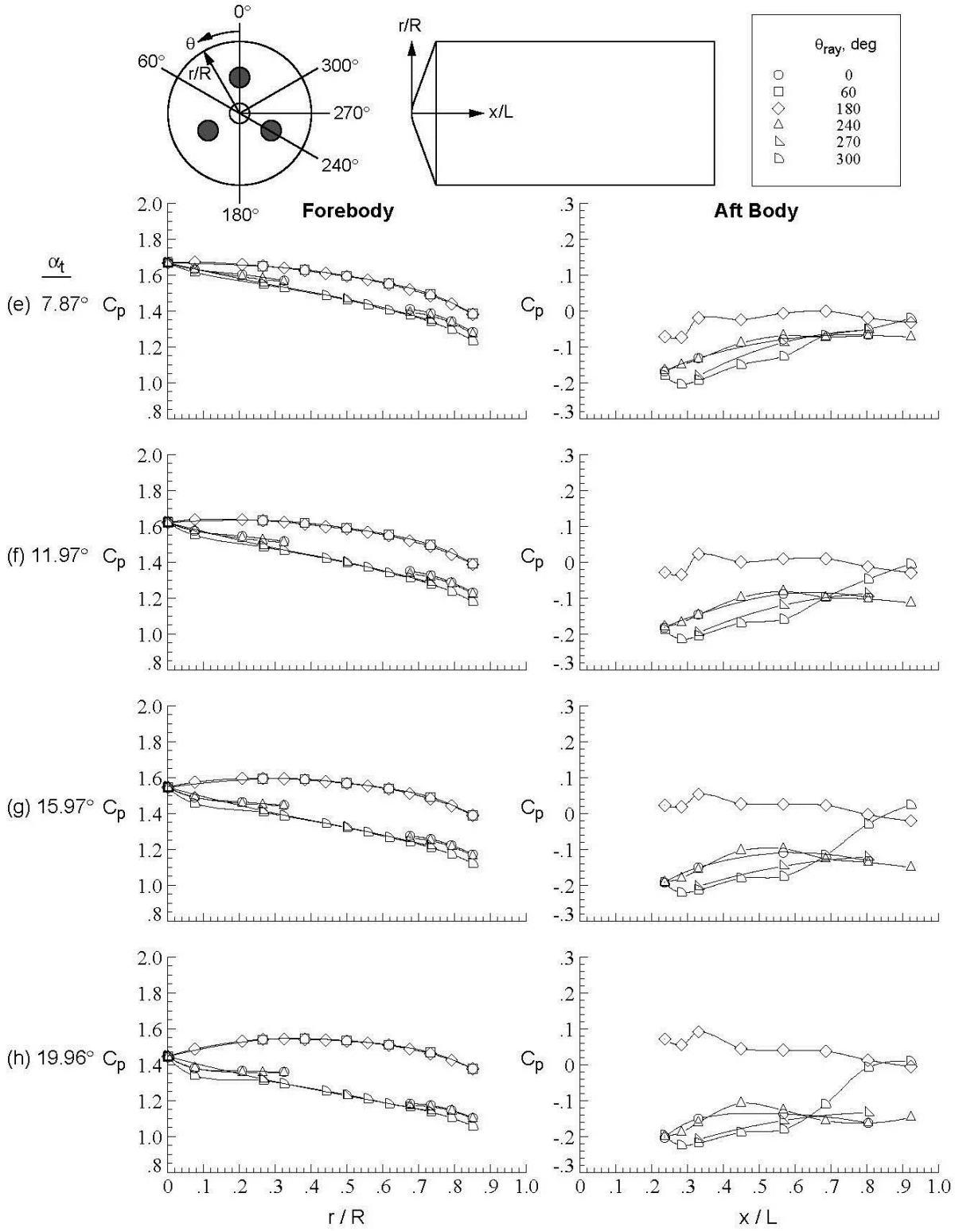

Figure D-140.Concluded.

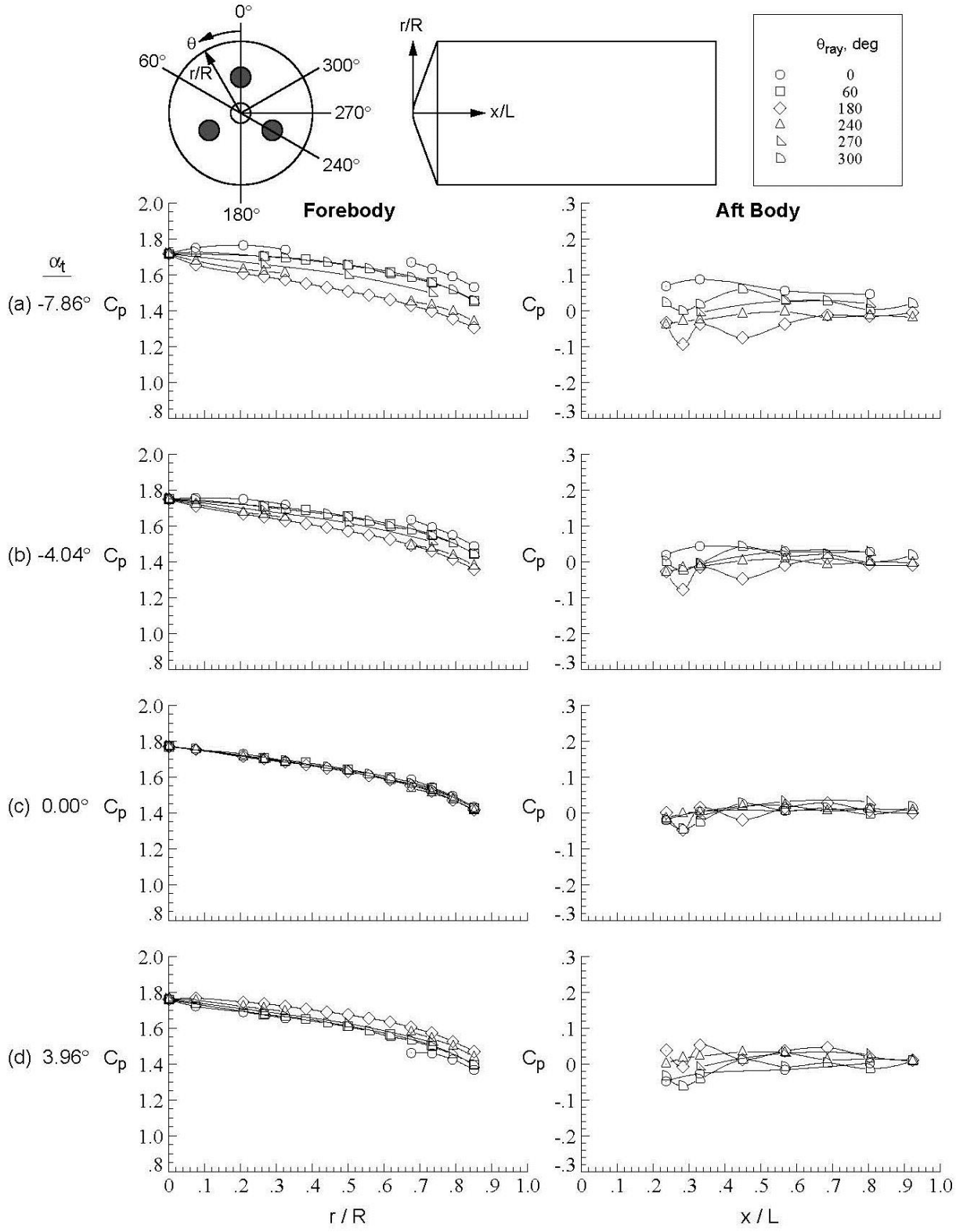

Figure D-141.Tri-nozzle configuration, Run 184, M_∞ = 3.5, Re_∞ = 1.0x10^7/ft, ϕ = 0.05°, X_S = 40.15 in, Y_S = 0.00 in, C_T = 0.00.

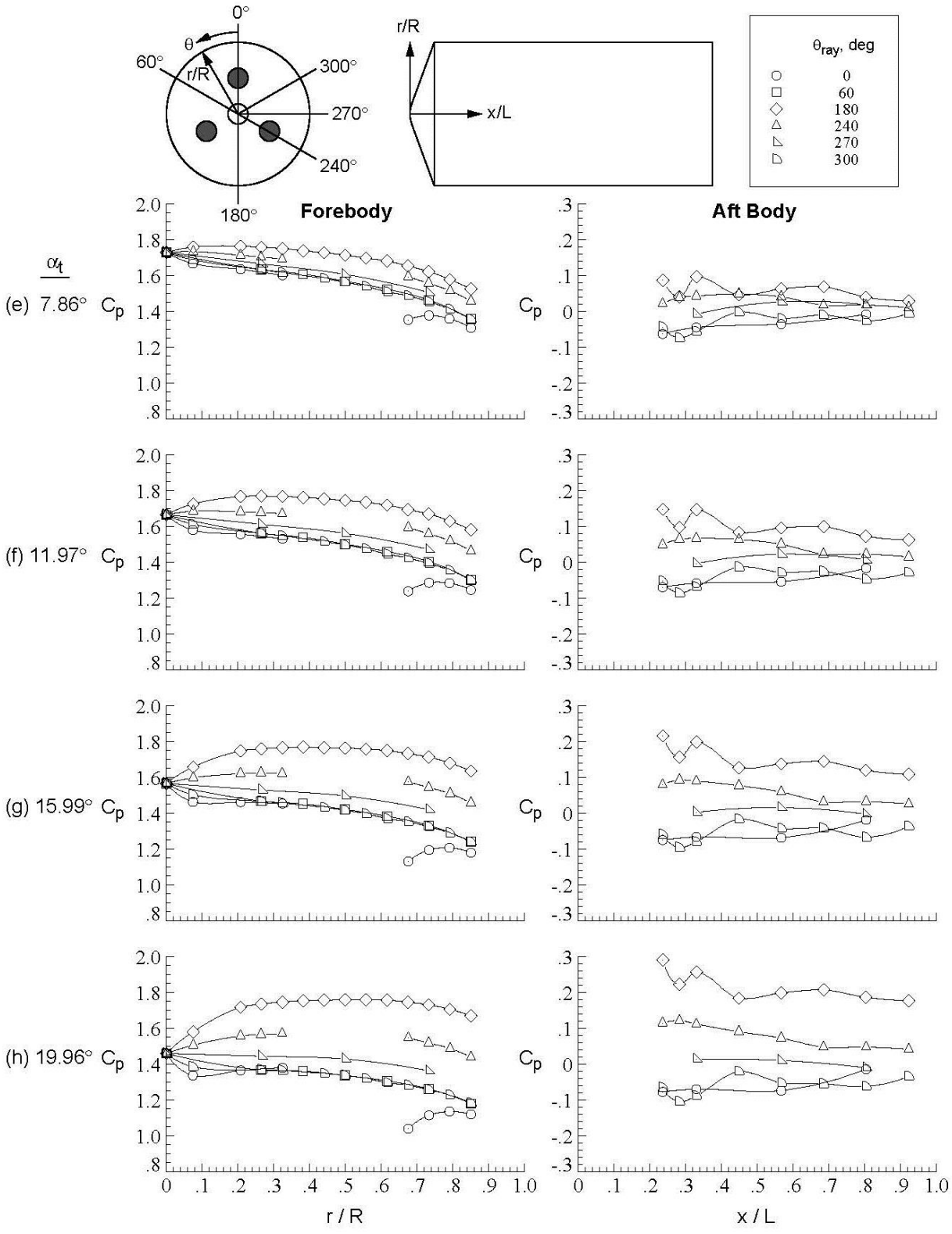

Figure D-141.Concluded.

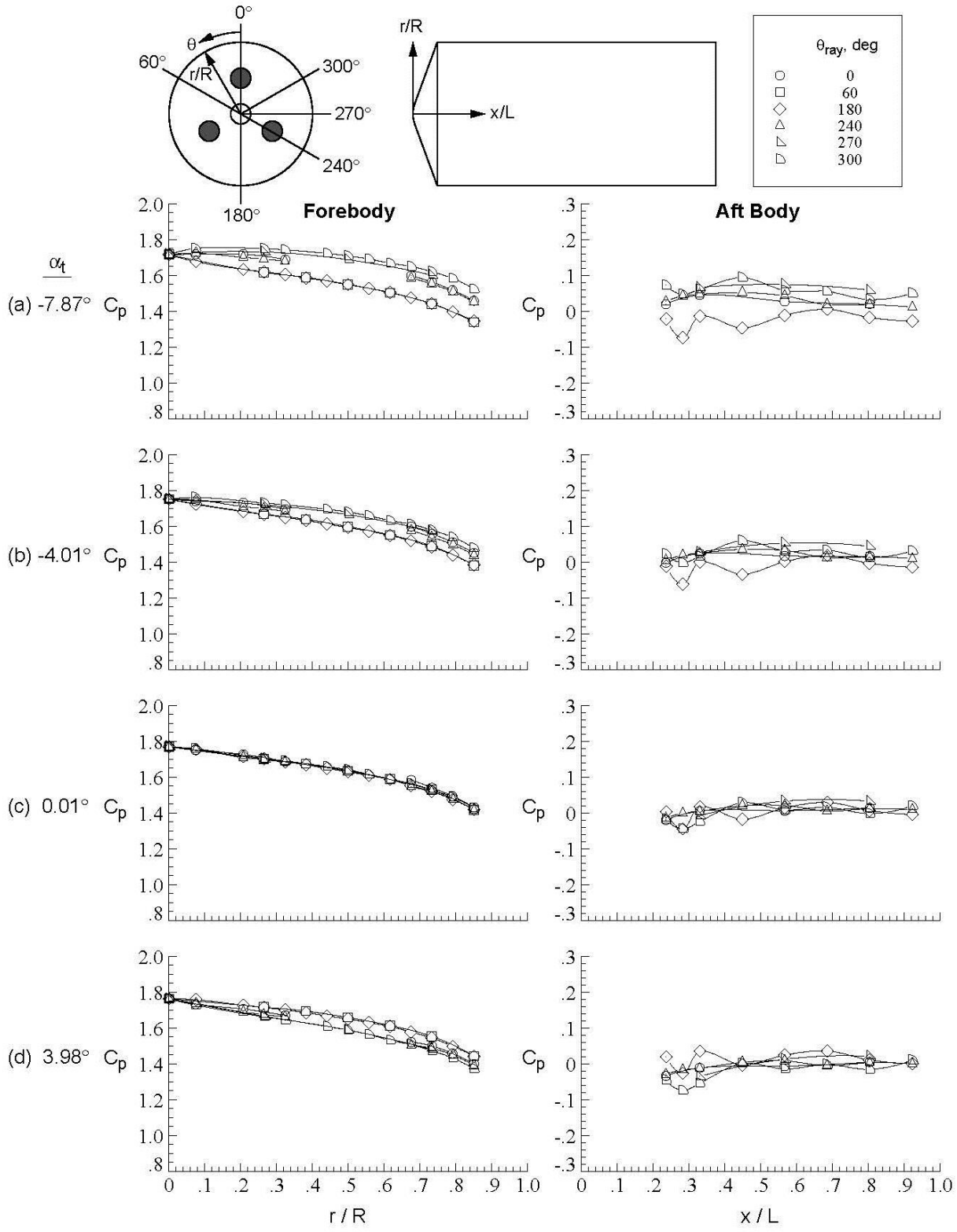

Figure D-142.Tri-nozzle configuration, Run 185, M_∞ = 3.5, Re_∞ = 1.0x10^7/ft, ϕ = 59.88°, X_S = 40.15 in, Y_S = 0.00 in, C_T = 0.00.

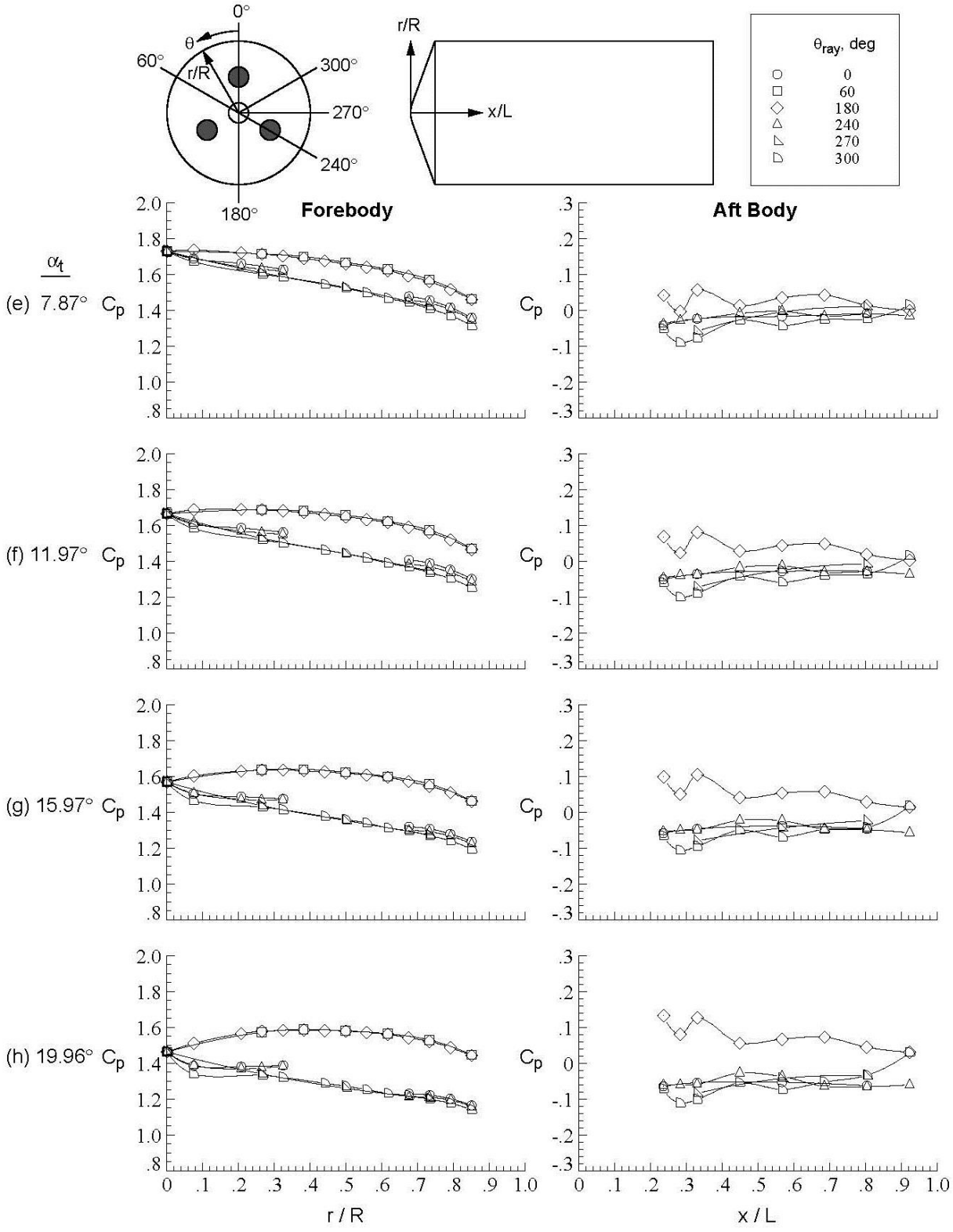

Figure D-142.Concluded.

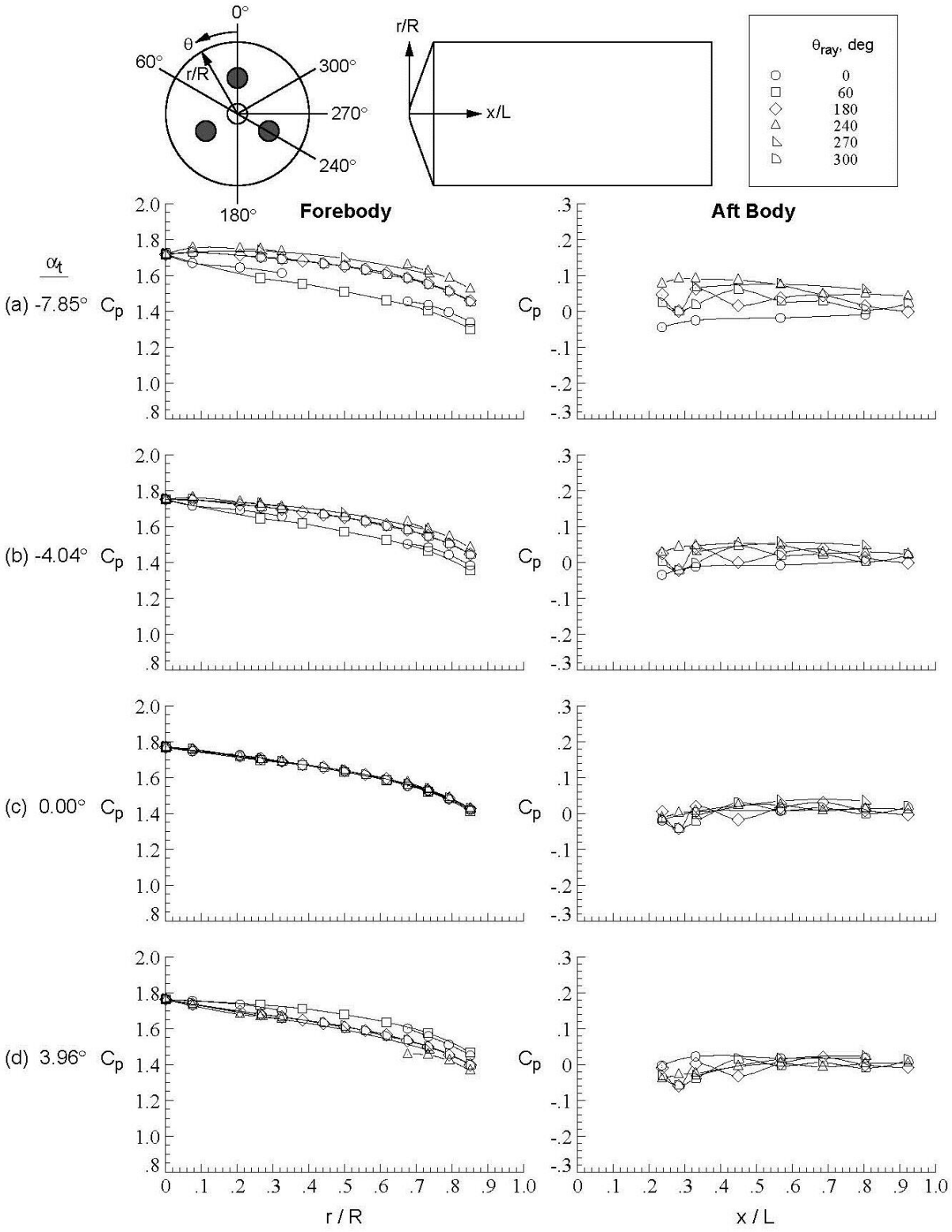

Figure D-143.Tri-nozzle configuration, Run 186, M_∞ = 3.5, Re_∞ = 1.0x10^7/ft, ϕ = 120.00°, X_S = 40.15 in, Y_S = 0.00 in, C_T = 0.00.

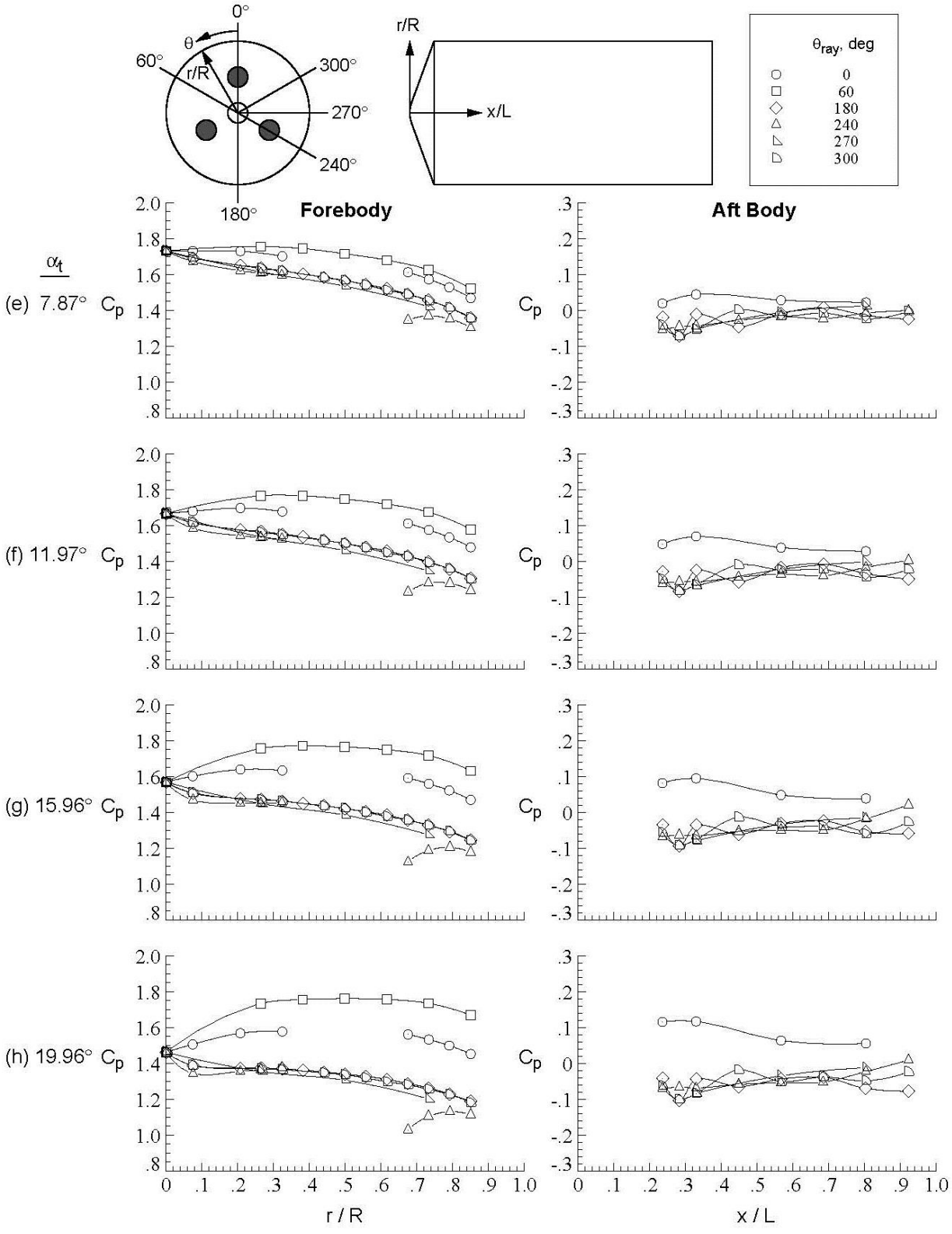

Figure D-143.Concluded.

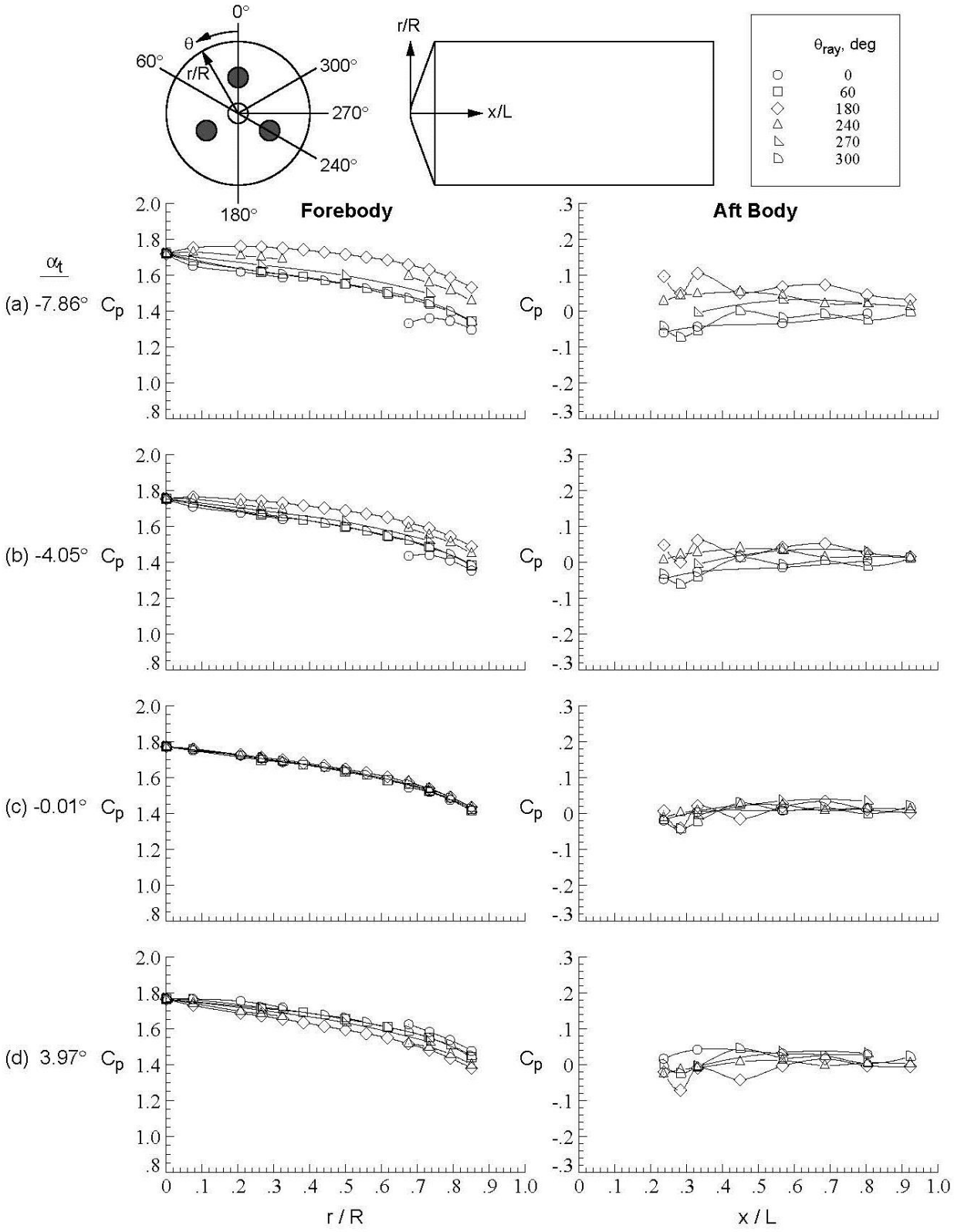

Figure D-144.Tri-nozzle configuration, Run 187, M_∞ = 3.5, Re_∞ = 1.0x10^6/ft, ϕ = 179.95°, X_S = 40.15 in, Y_S = 0.00 in, C_T = 0.00.

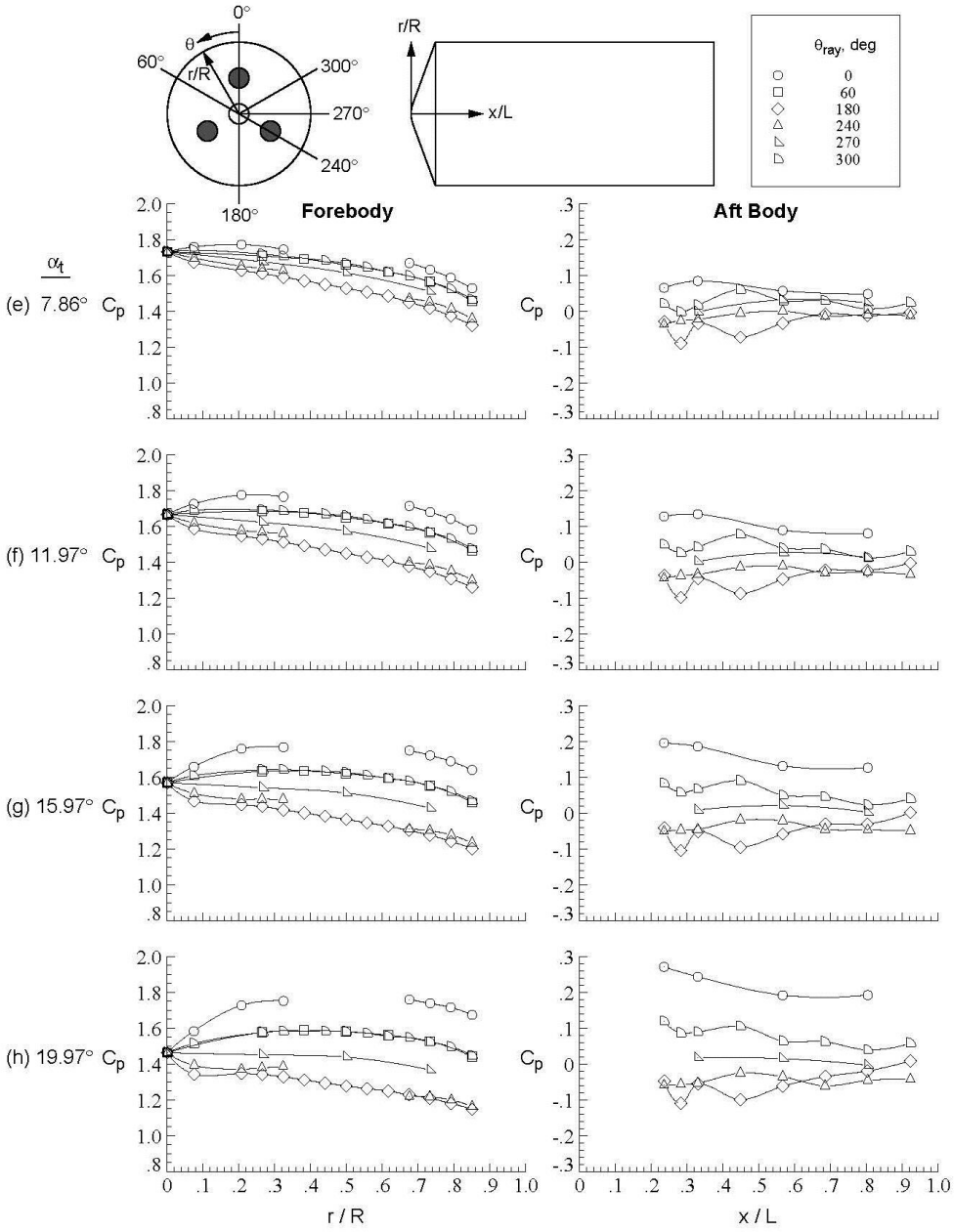

Figure D-144.Concluded.

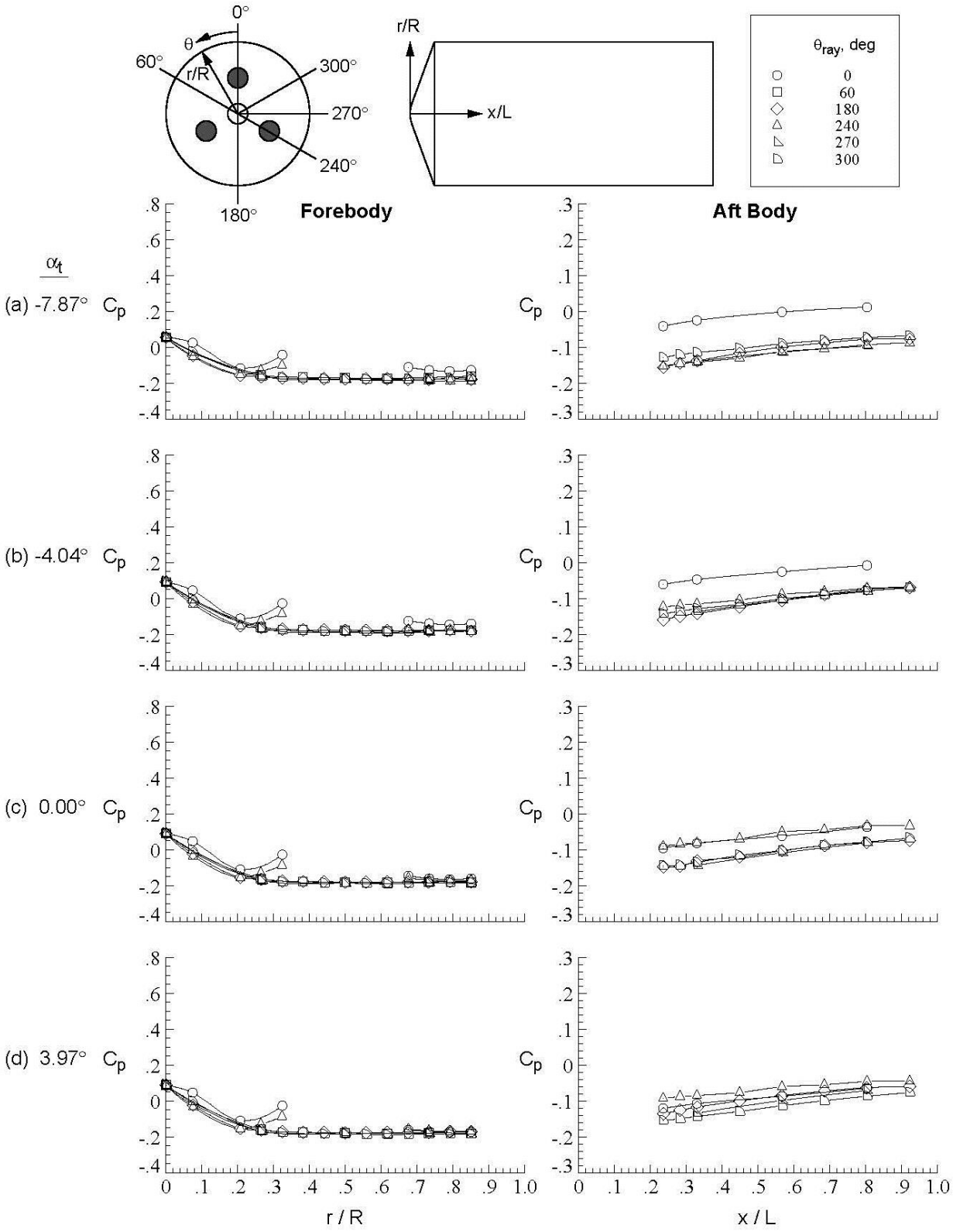

Figure D-145.Tri-nozzle configuration, Run 190, M_∞ = 2.4, Re_∞ = 1.0x10^7/ft, ϕ = −0.01°, X_S = 40.15 in, Y_S = 0.00 in, C_T = 2.94.

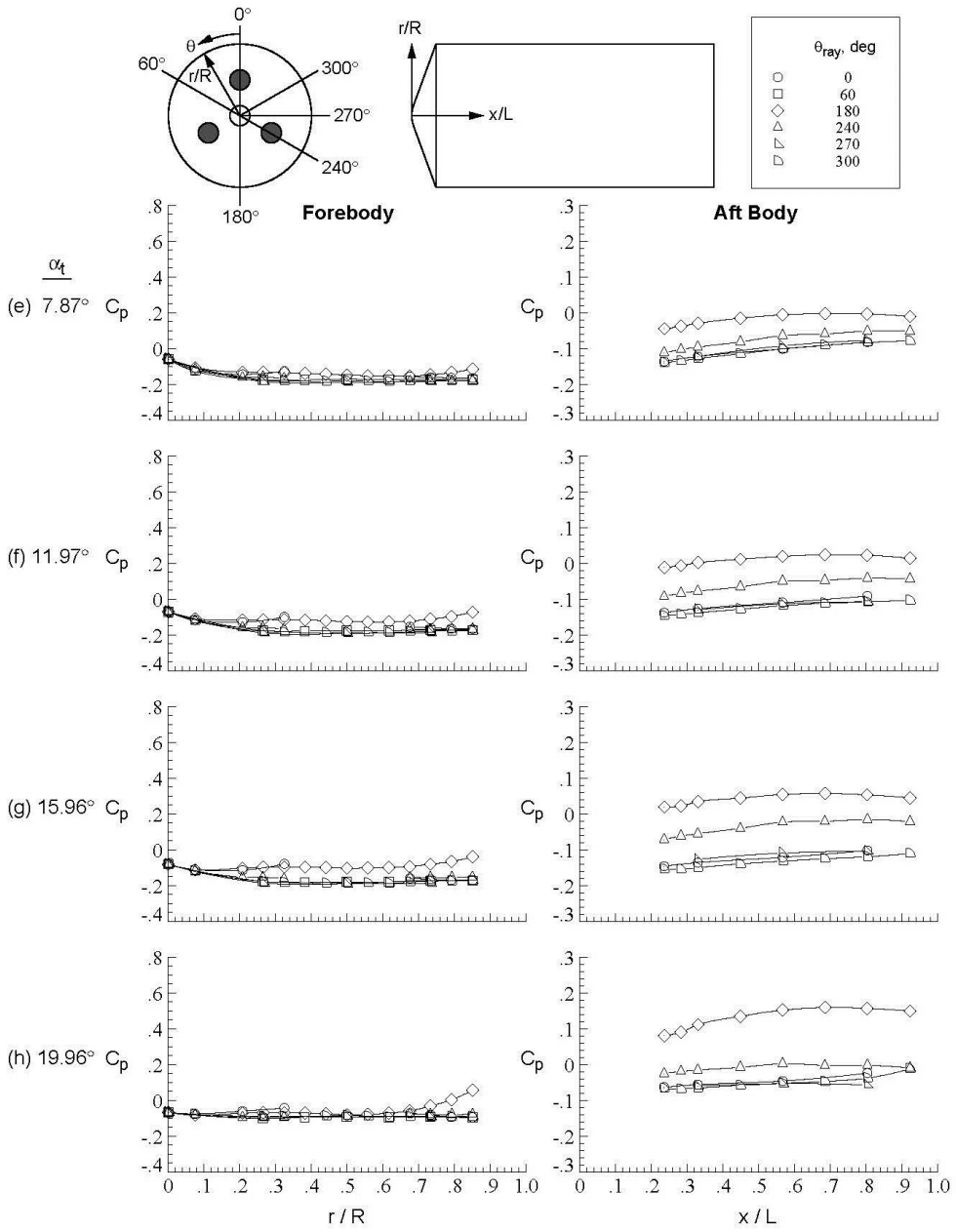

Figure D-145.Concluded.

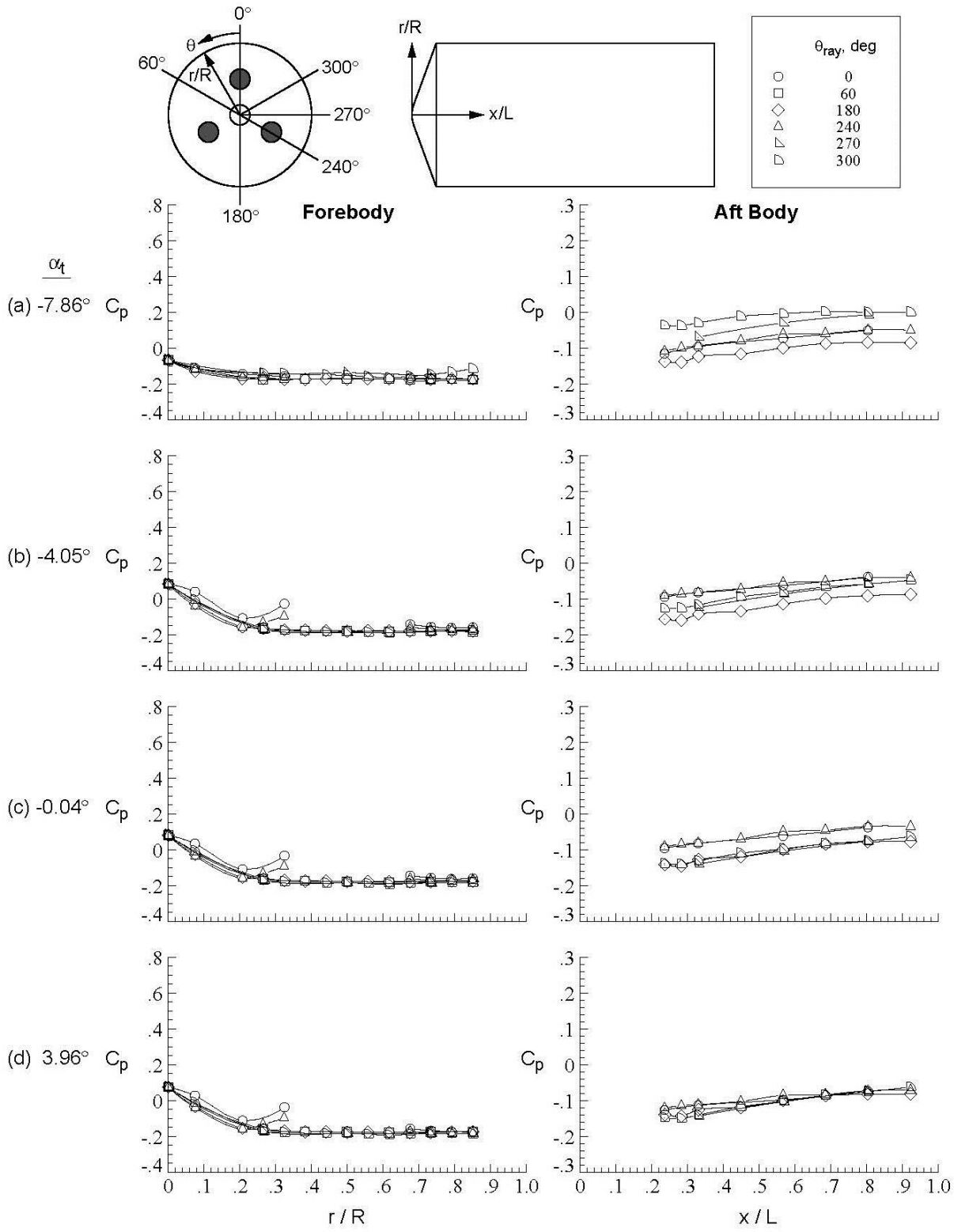

Figure D-146.Tri-nozzle configuration, Run 191, $M\infty$ = 2.4, Re_∞ = 1.0x10^6/ft, ϕ = 59.88°, X_S = 40.15 in, Y_S = 0.00 in, C_T = 2.92.

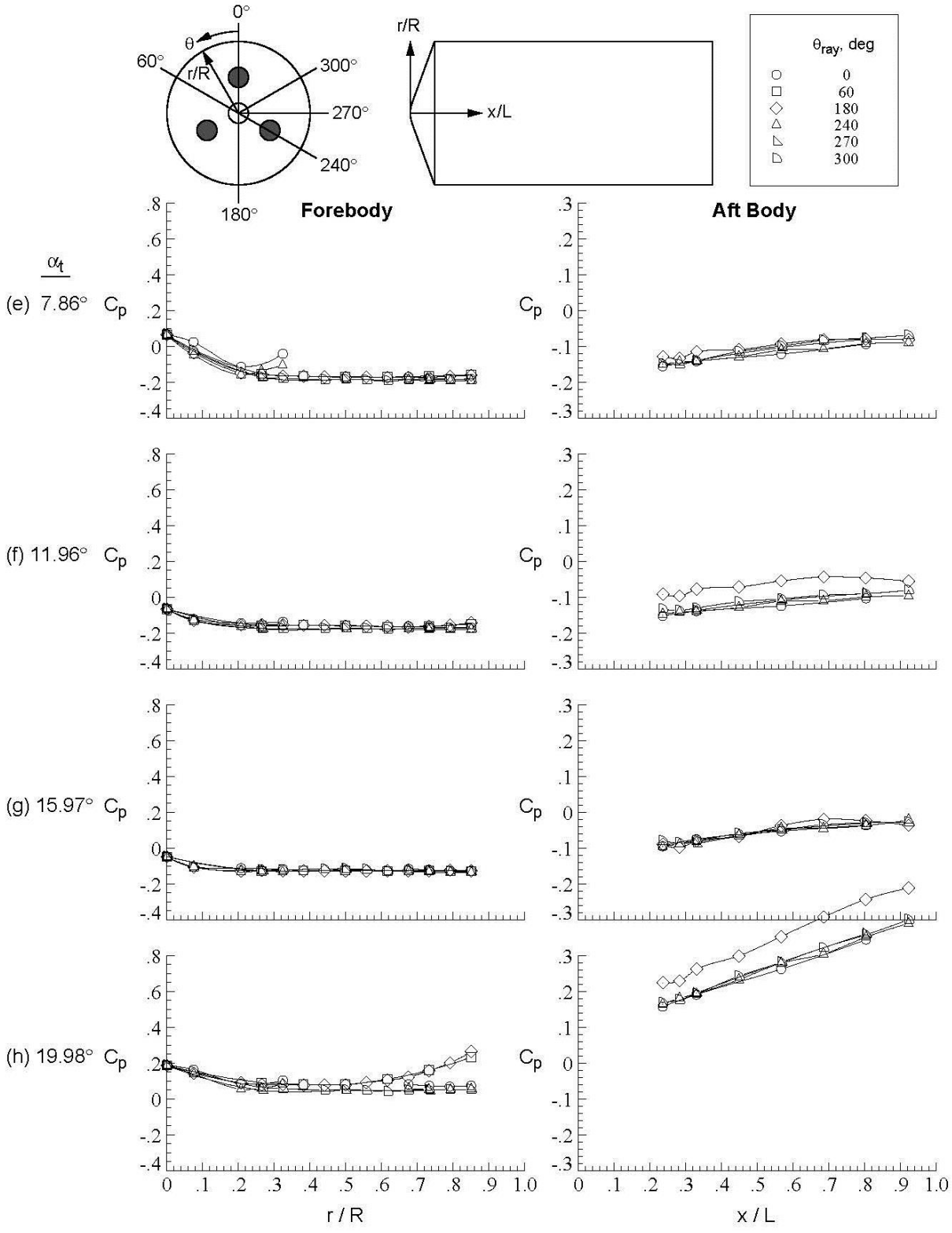

Figure D-146.Concluded.

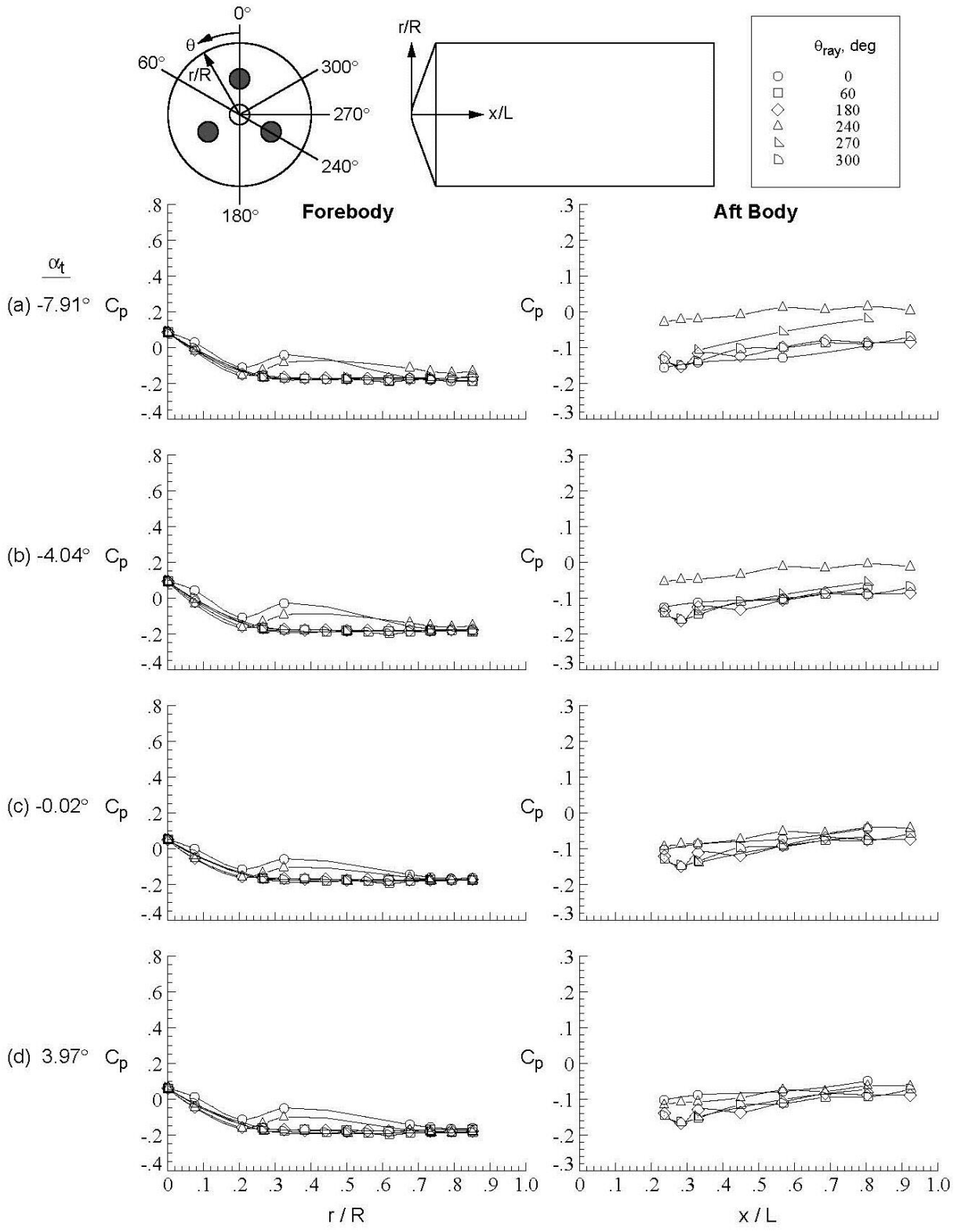

Figure D-147.Tri-nozzle configuration, Run 192, M_∞ = 2.4, Re_∞ = 1.0x10^6/ft, ϕ = 120.00°, X_S = 40.15 in, Y_S = 0.00 in, C_T = 2.94.

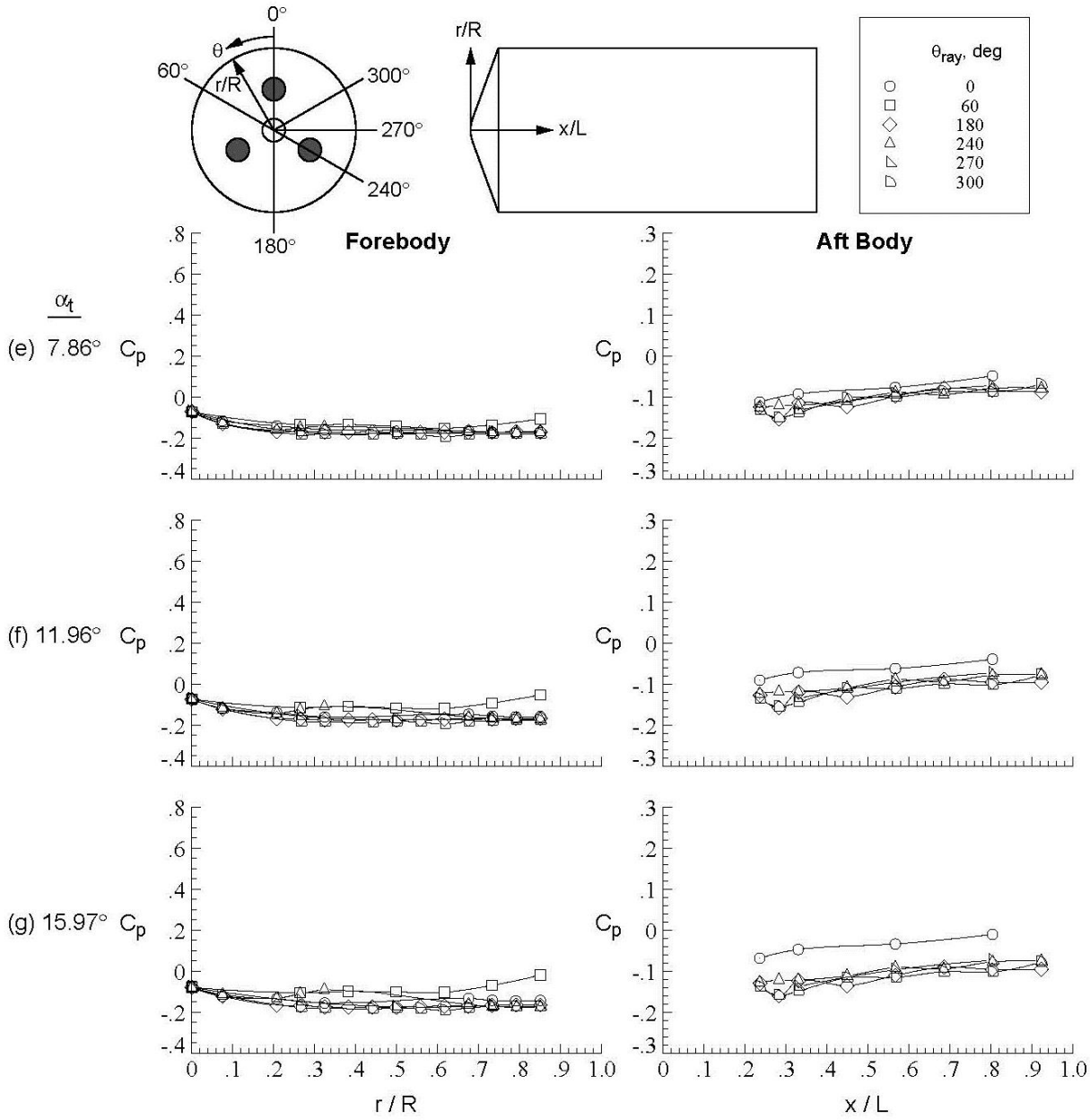

Figure D-147.Concluded.

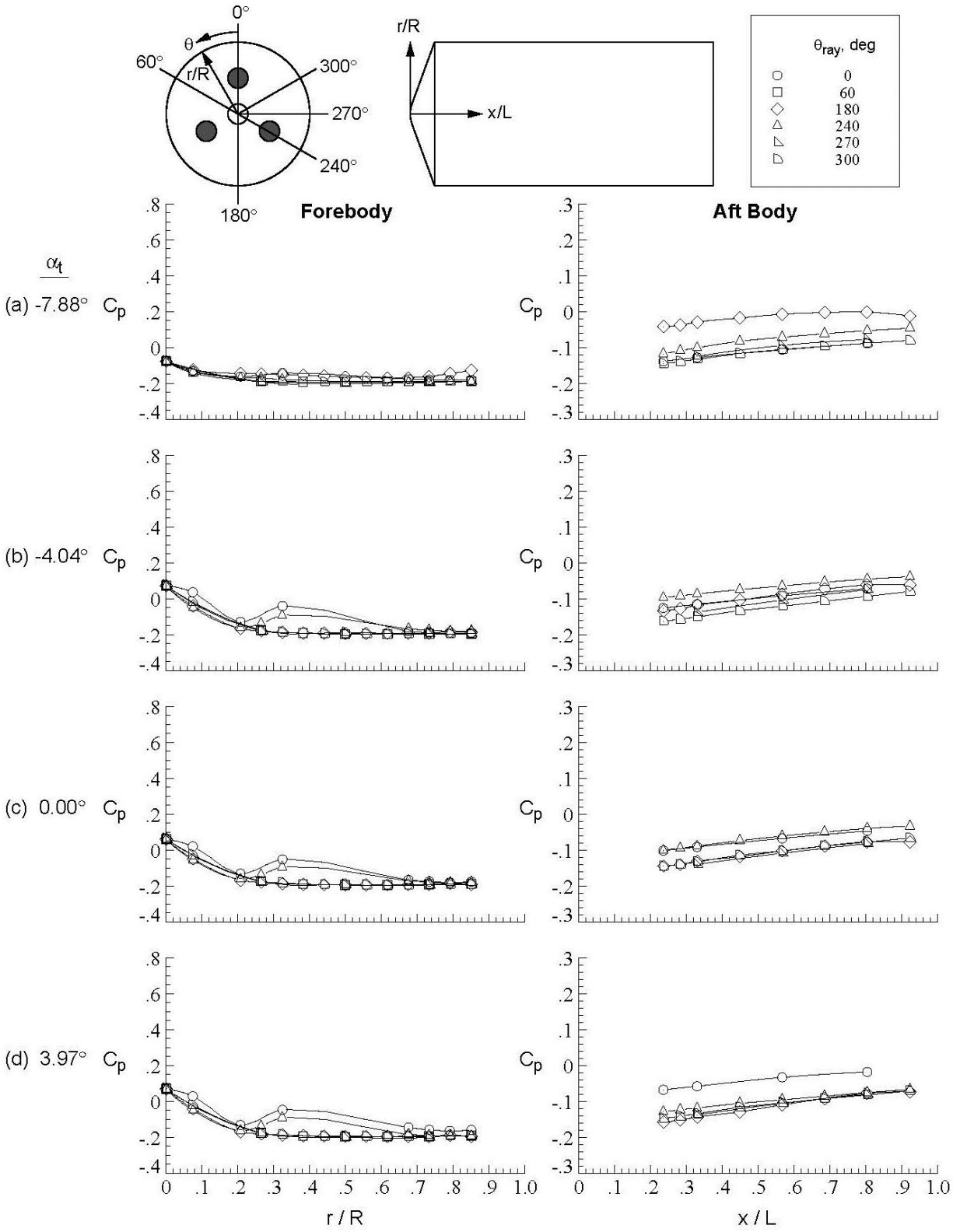

Figure D-148.Tri-nozzle configuration, Run 193, M_∞ = 2.4, Re_∞ = 1.0x10^6/ft, ϕ = −179.97°, X_S = 40.15 in, Y_S = 0.00 in, C_T = 2.96.

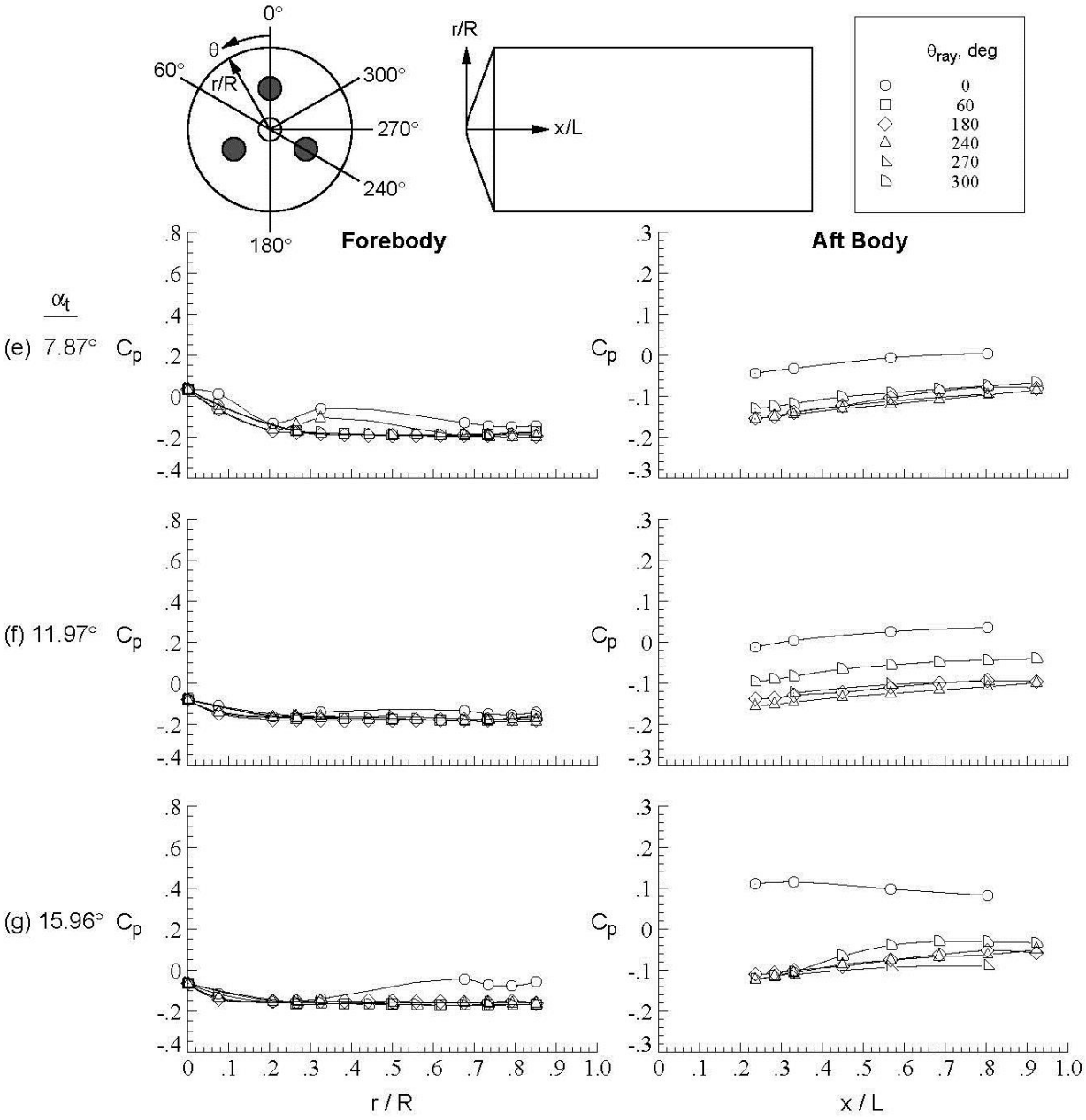

Figure D-148.Concluded.

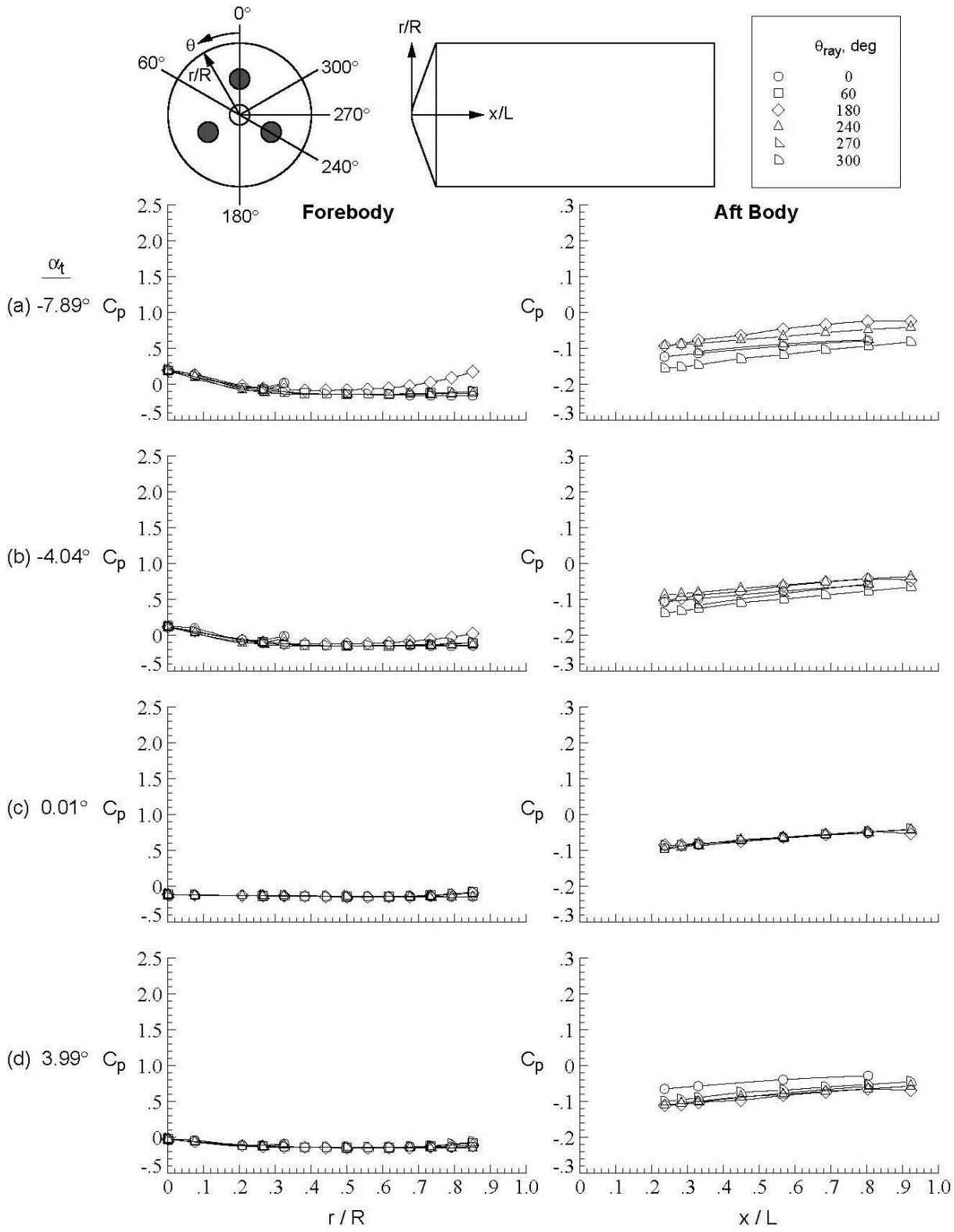

Figure D-149.Tri-nozzle configuration, Run 194, $M\infty$ = 2.4, Re_∞ = 1.0x10^7/ft, ϕ = −179.97°, X_S = 40.15 in, Y_S = 0.00 in, C_T = 1.94.

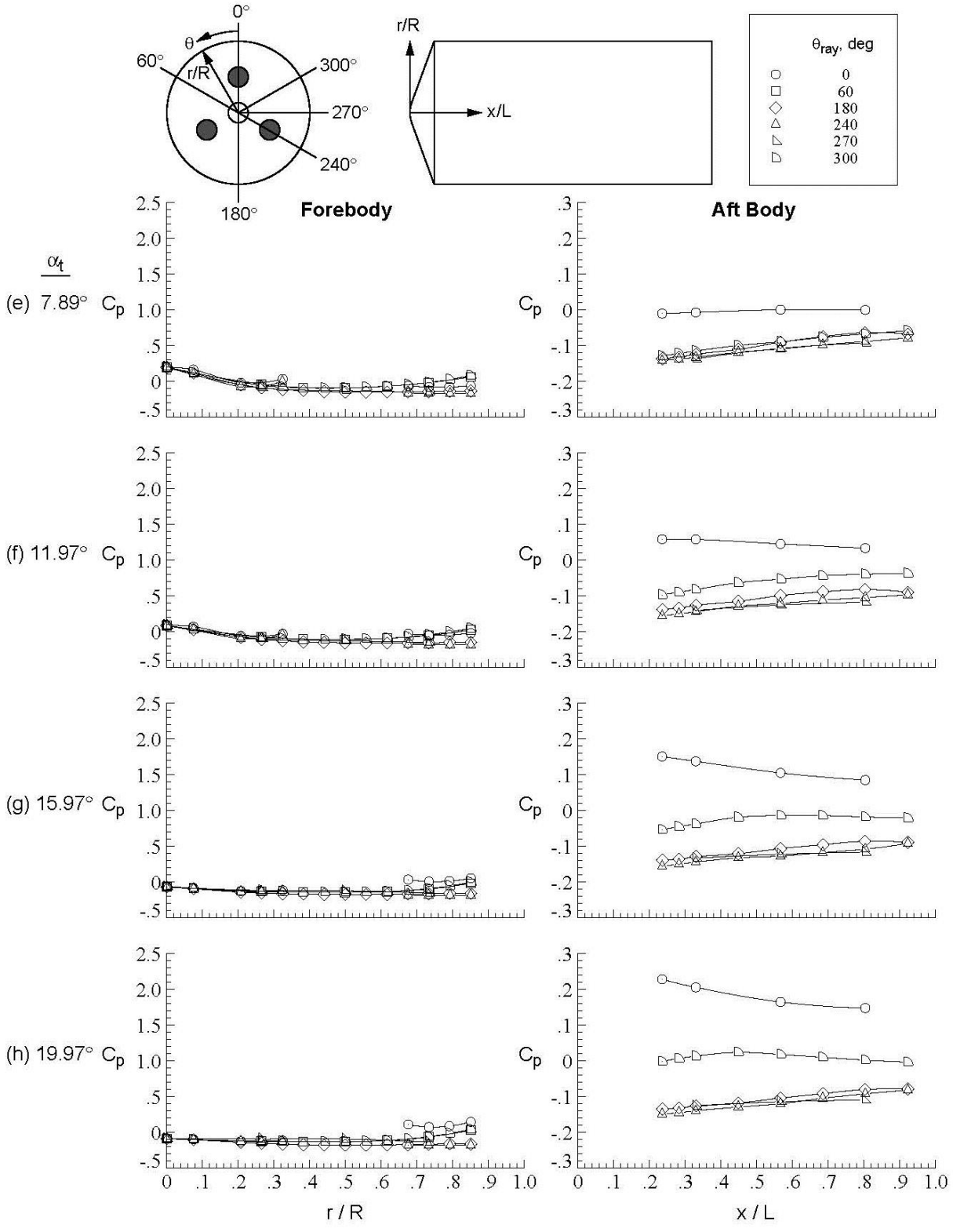

Figure D-149.Concluded.

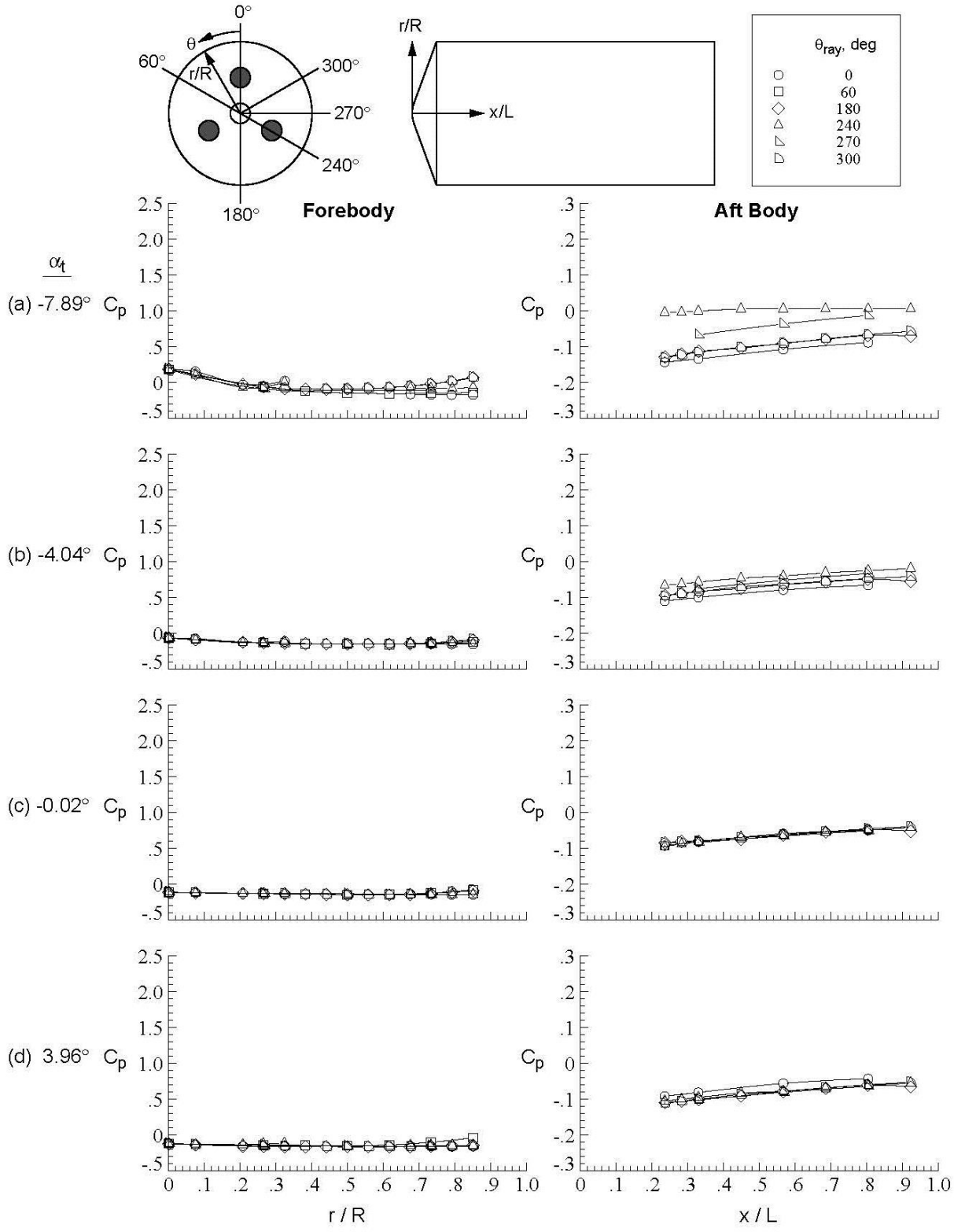

Figure D-150.Tri-nozzle configuration, Run 195, $M\infty$ = 2.4, Re_∞ = 1.0x10^7/ft, ϕ = 120.02°, X_S = 40.15 in, Y_S = 0.00 in, C_T = 1.93.

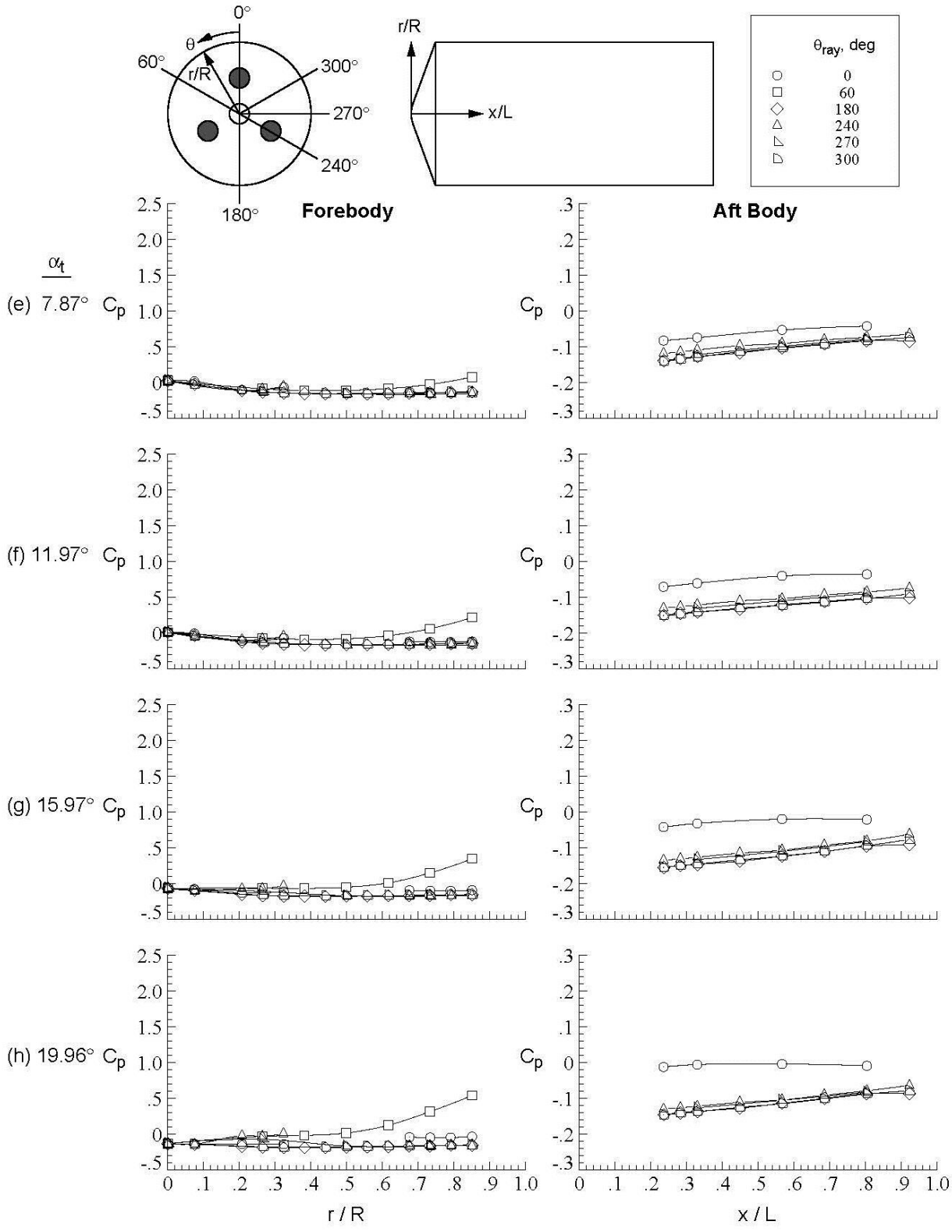

Figure D-150.Concluded.

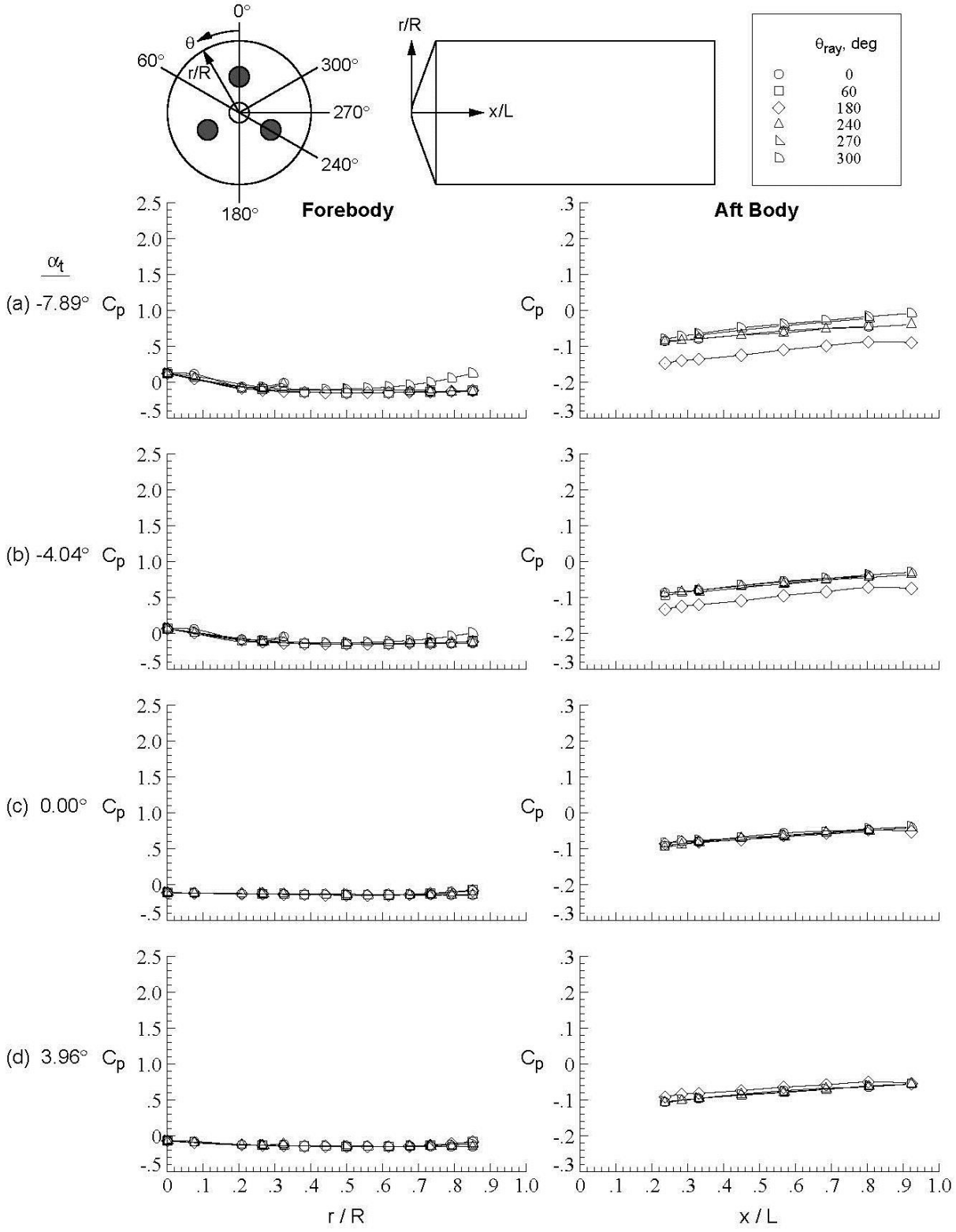

Figure D-151.Tri-nozzle configuration, Run 196, M_∞ = 2.4, Re_∞ = 1.0x10^6/ft, ϕ = 59.88°, X_S = 40.15 in, Y_S = 0.00 in, C_T = 1.93.

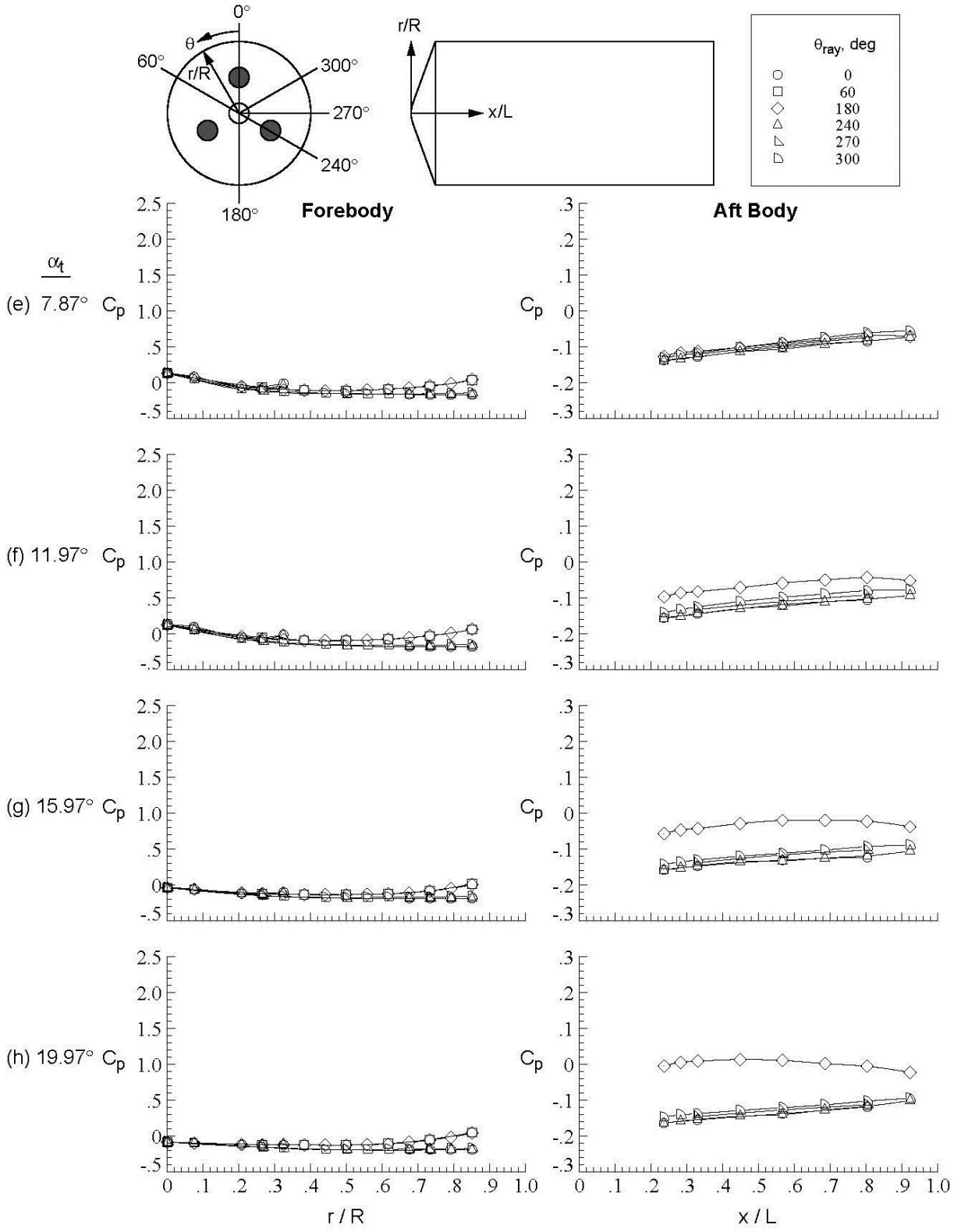

Figure D-151.Concluded.

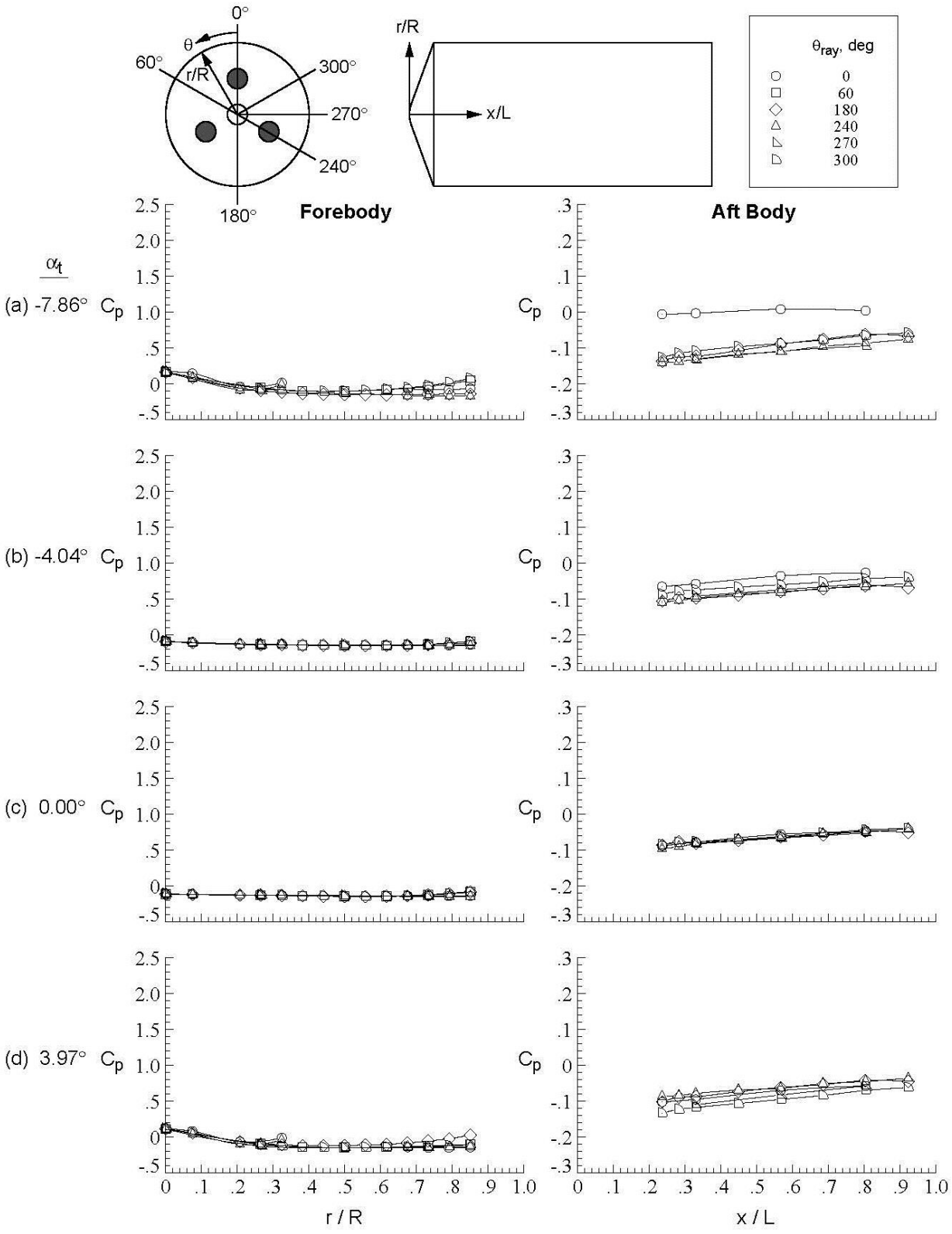

Figure D-152.Tri-nozzle configuration, Run 197, M_∞ = 2.4, Re_∞ = 1.0x10^6/ft, ϕ = −0.01°, X_S = 40.15 in, Y_S = 0.00 in, C_T = 1.94.

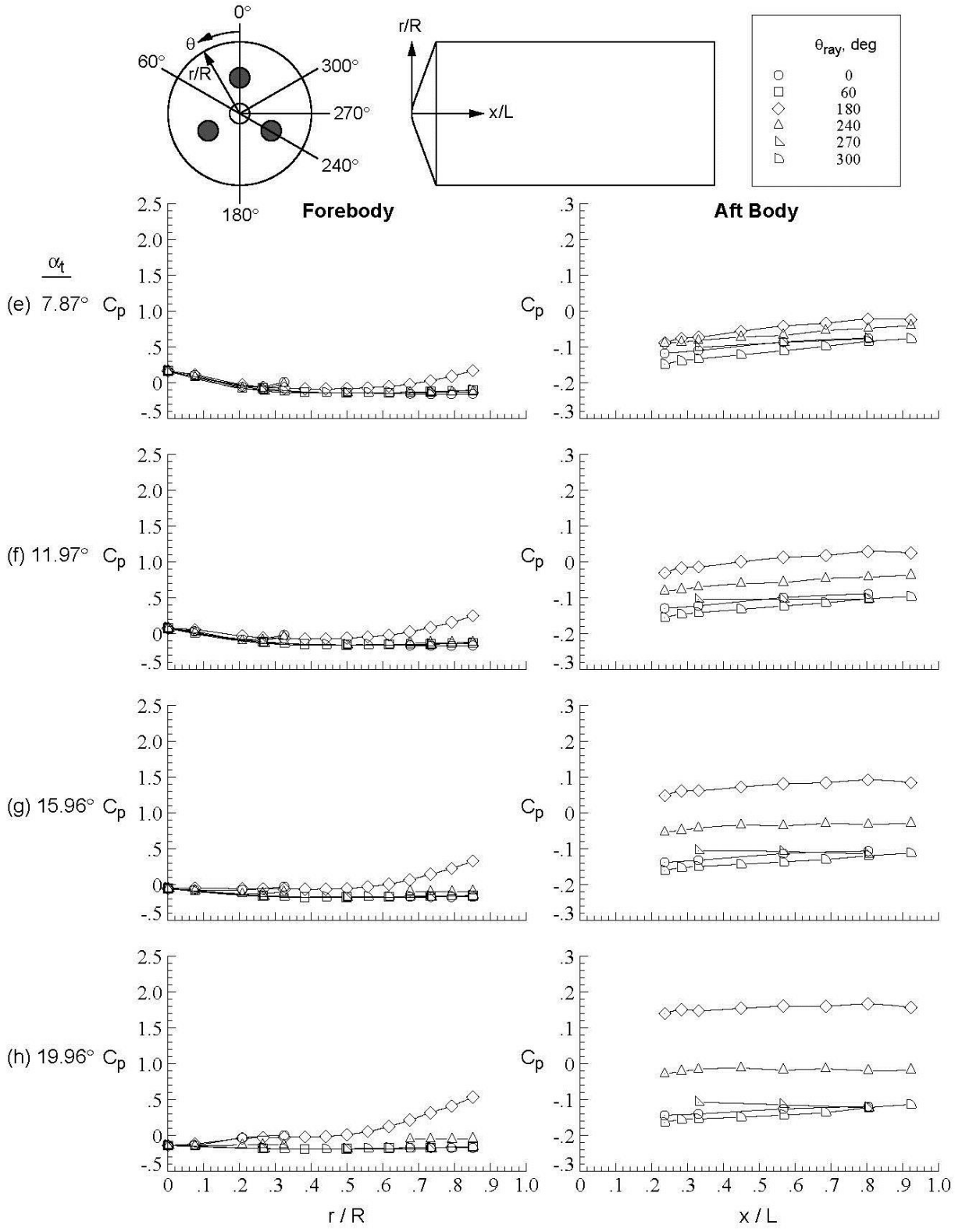

Figure D-152.Concluded.

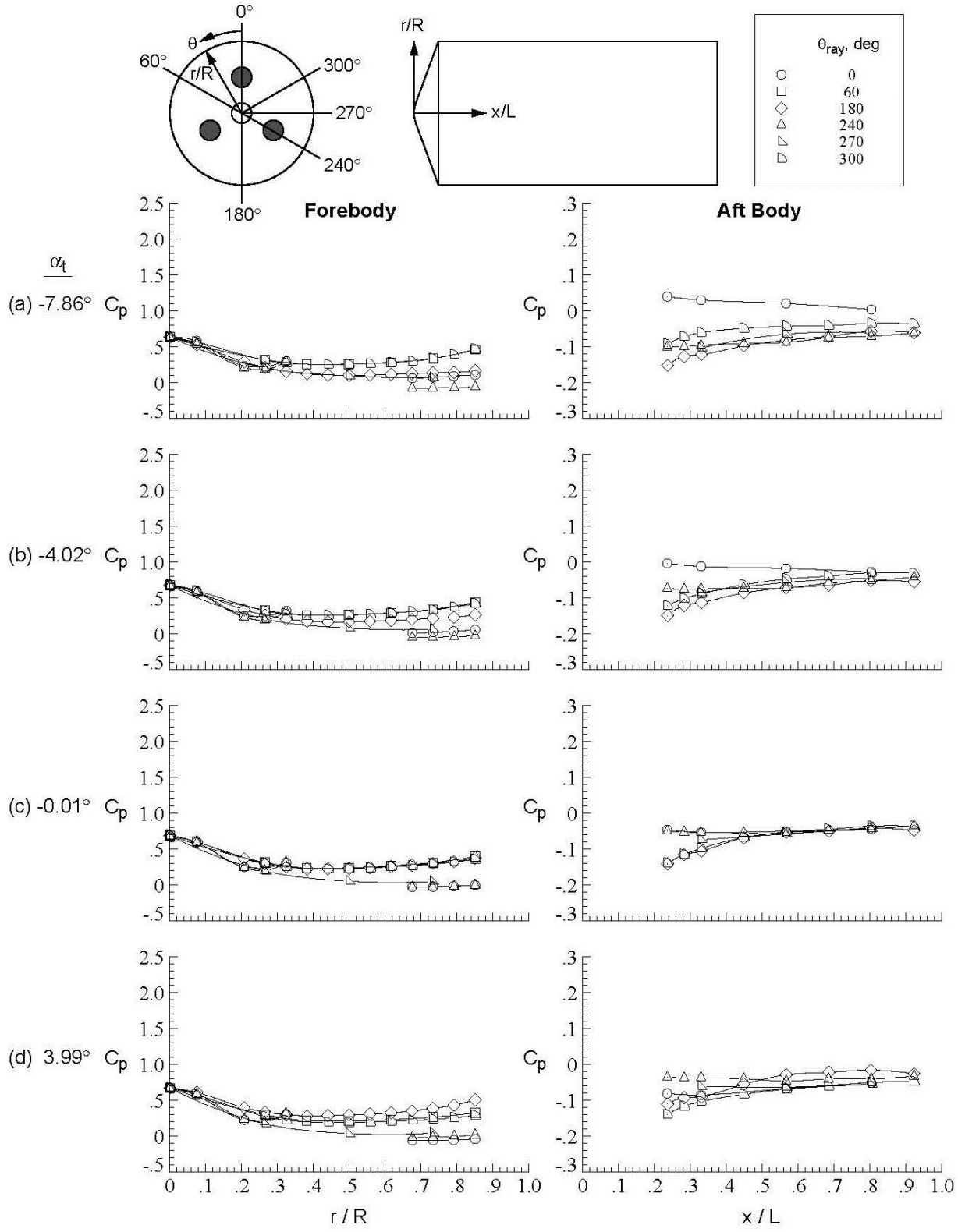

Figure D-153. Tri-nozzle configuration, Run 198, M_∞ = 2.4, Re_∞ = 1.0x10^7/ft, ϕ = −0.01°, X_S = 40.15 in, Y_S = 0.00 in, C_T = 0.94.

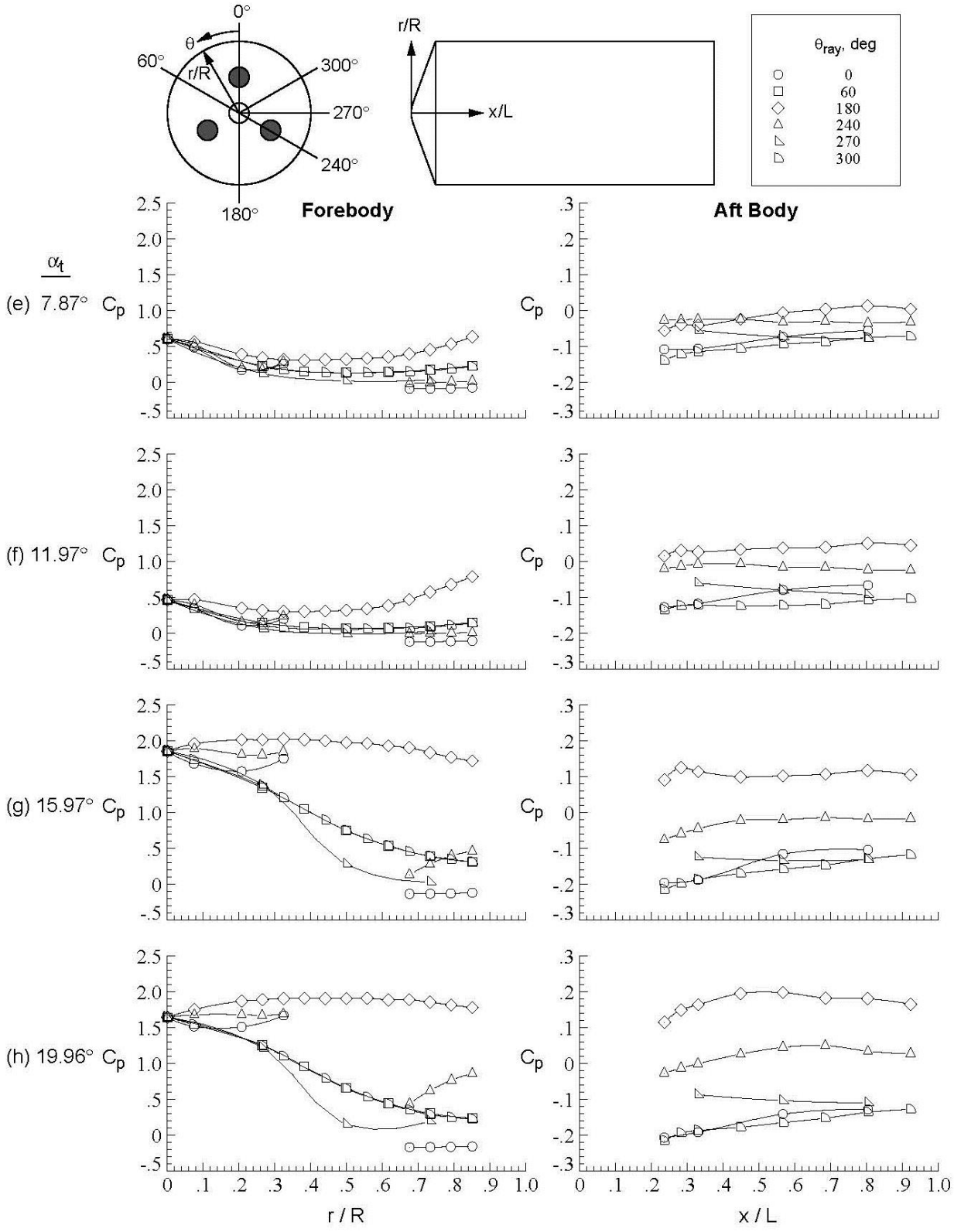

Figure D-153.Concluded.

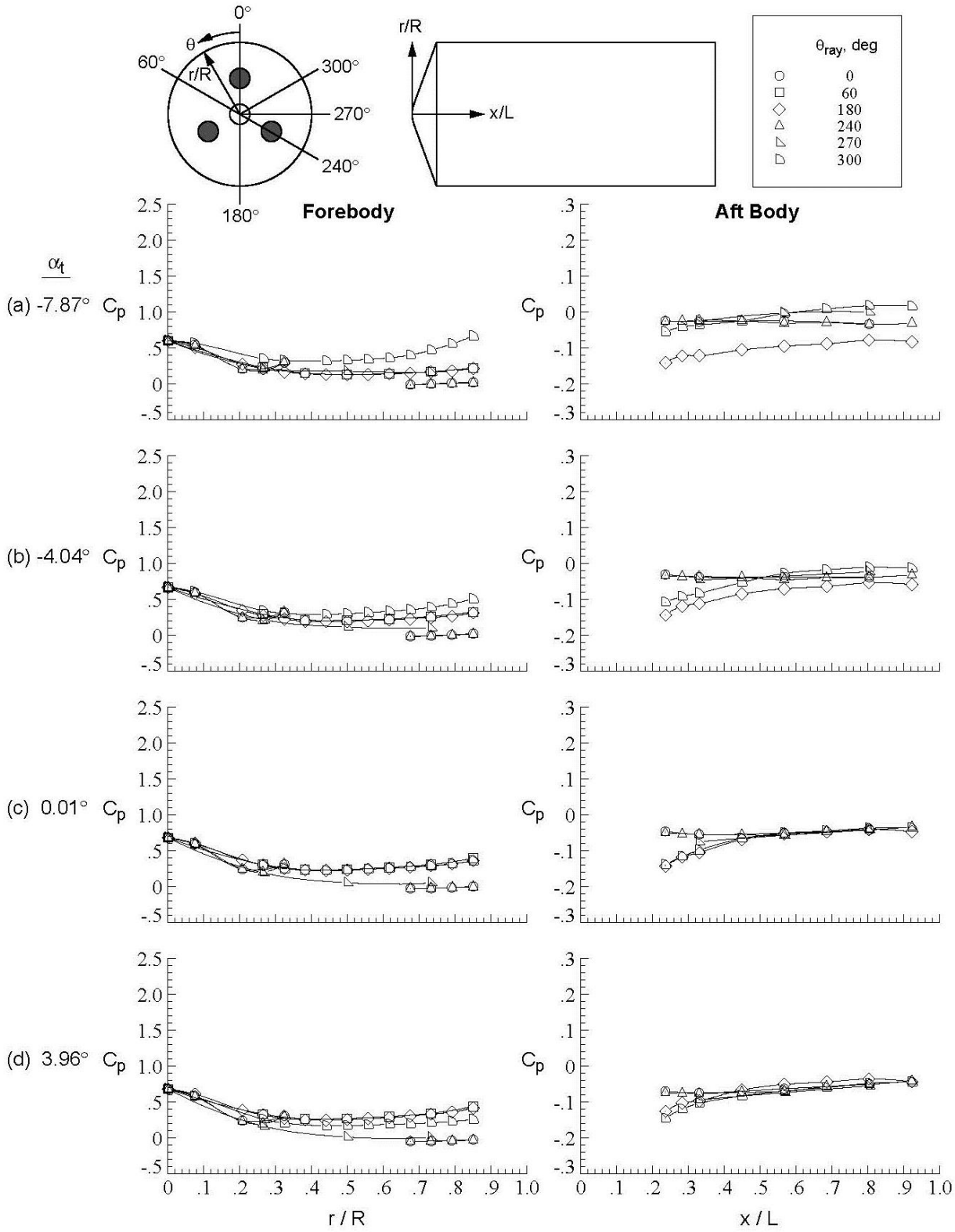

Figure D-154. Tri-nozzle configuration, Run 199, M_∞ = 2.4, Re_∞ = 1.0x10^6/ft, ϕ = 59.92°, X_S = 40.15 in, Y_S = 0.00 in, C_T = 0.94.

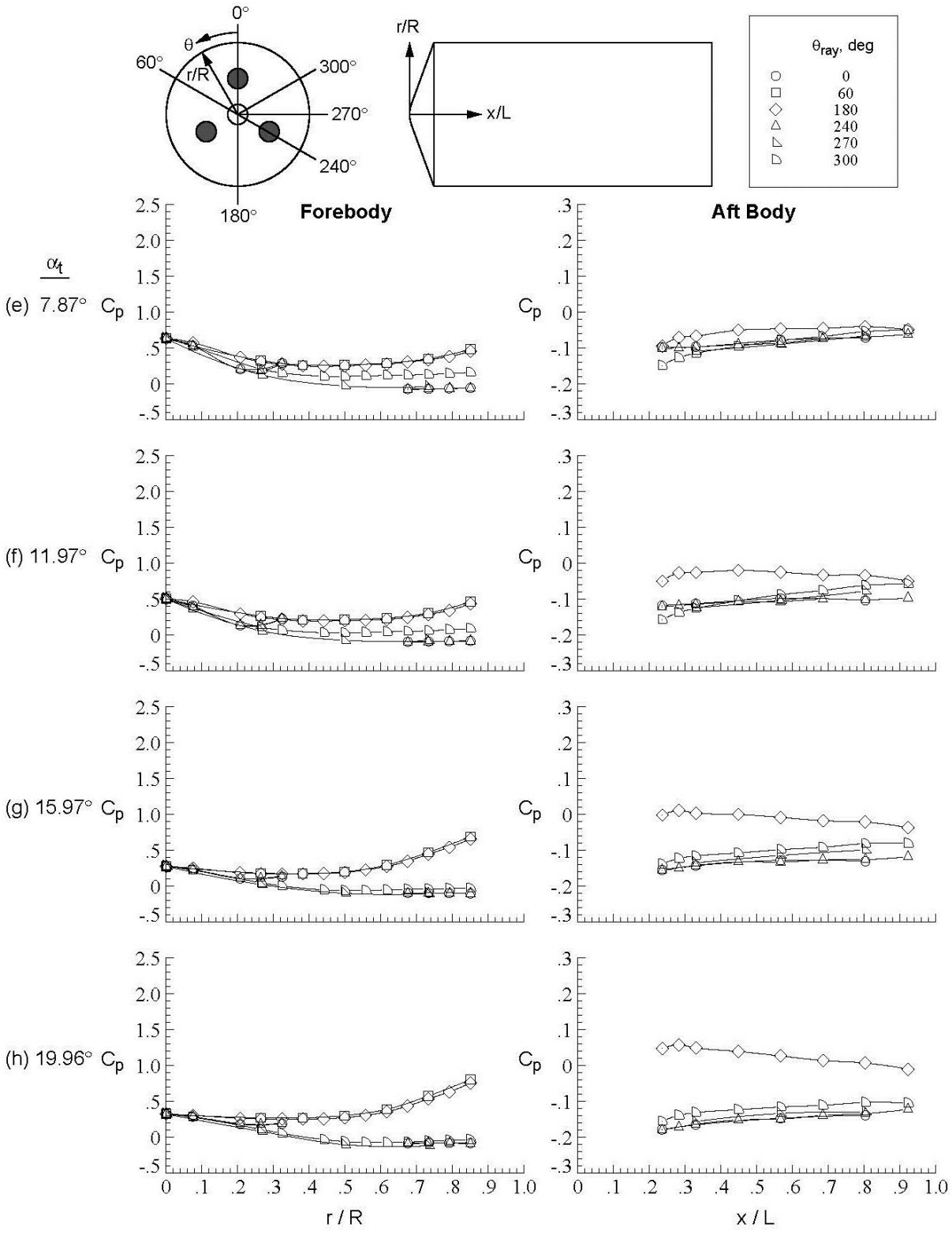

Figure D-154.Concluded.

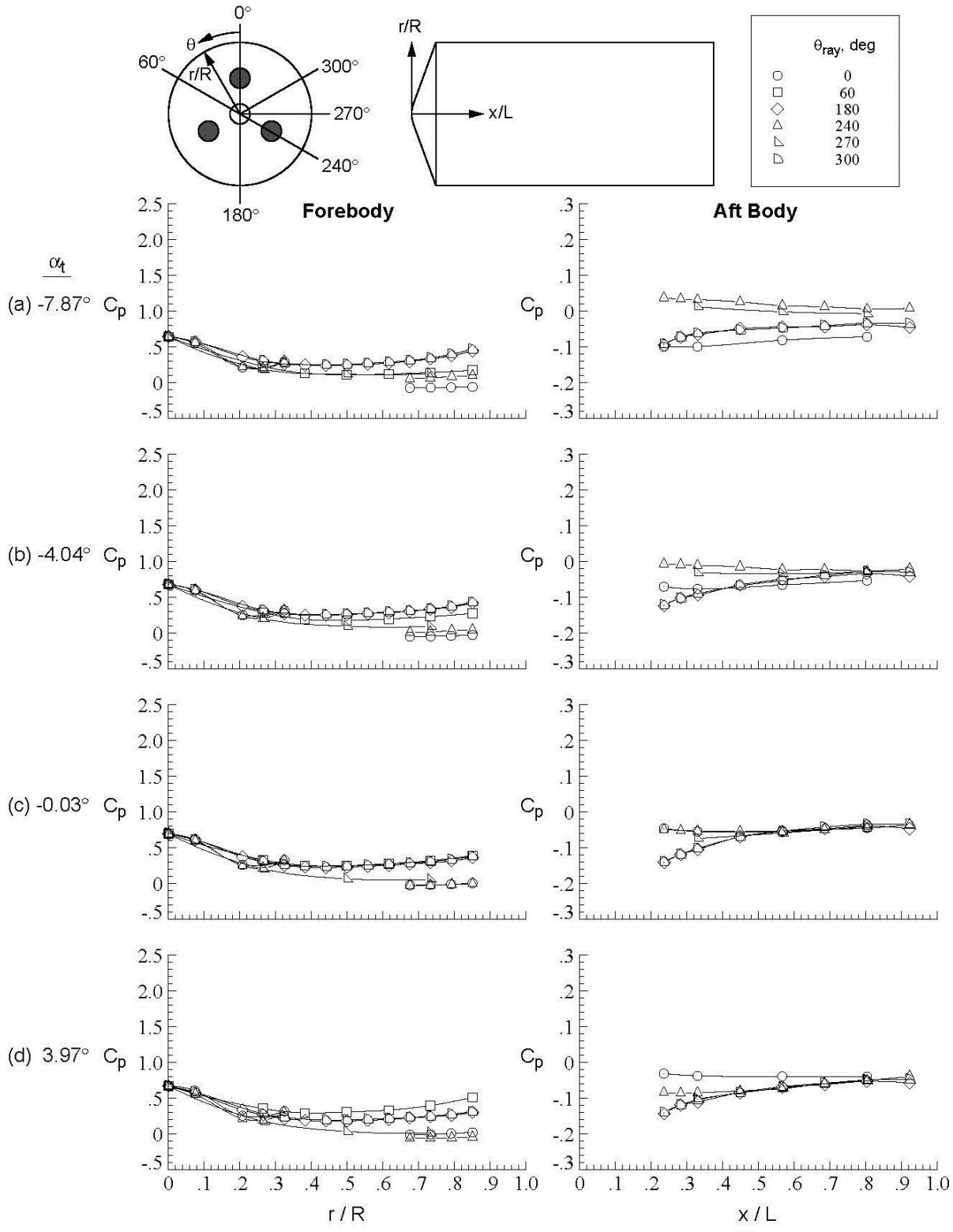

Figure D-155. Tri-nozzle configuration, Run 200, M_∞ = 2.4, Re_∞ = 1.0x10^7/ft, ϕ = 120.00°, X_S = 40.15 in, Y_S = 0.00 in, C_T = 0.94.

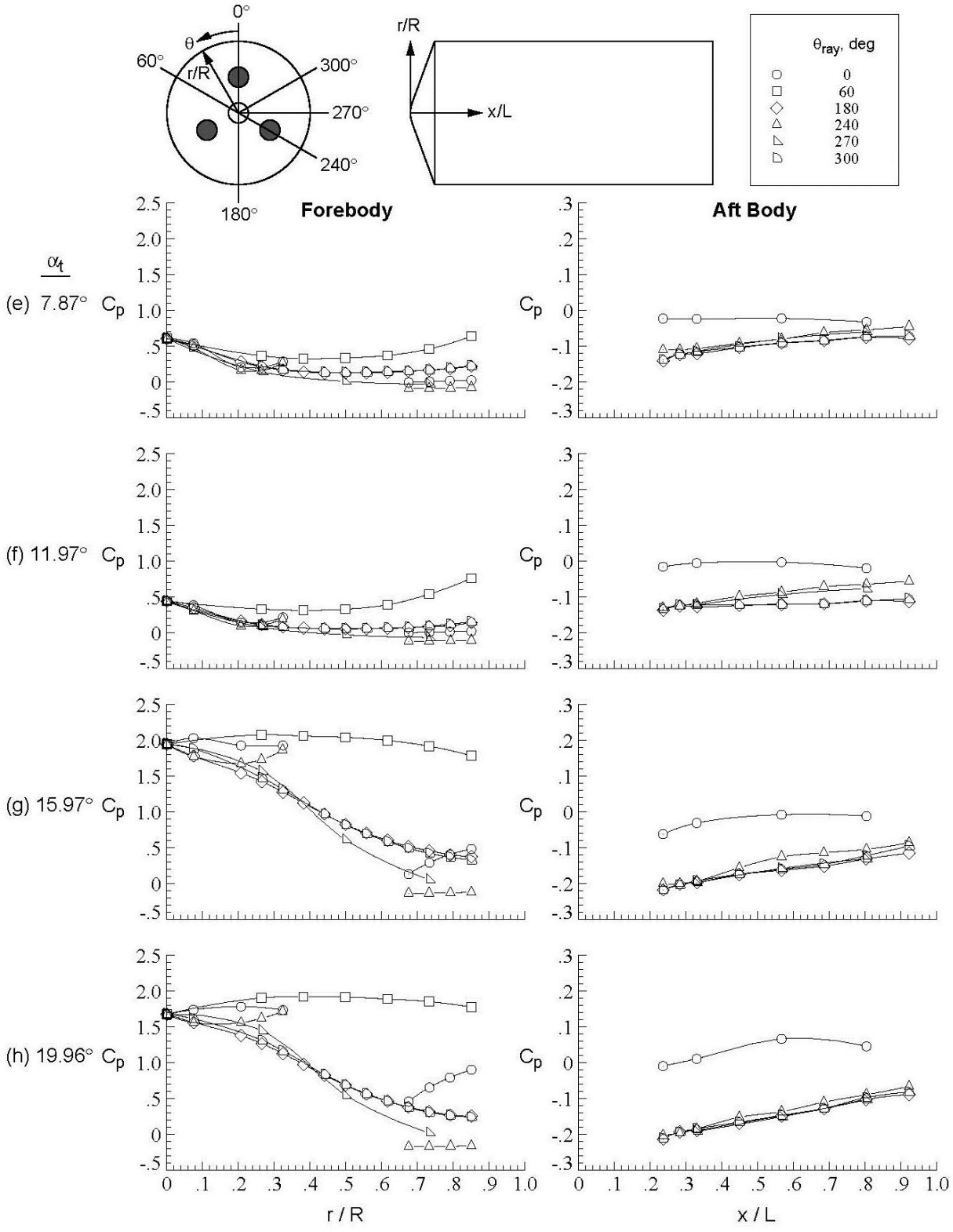

Figure D-155.Concluded.

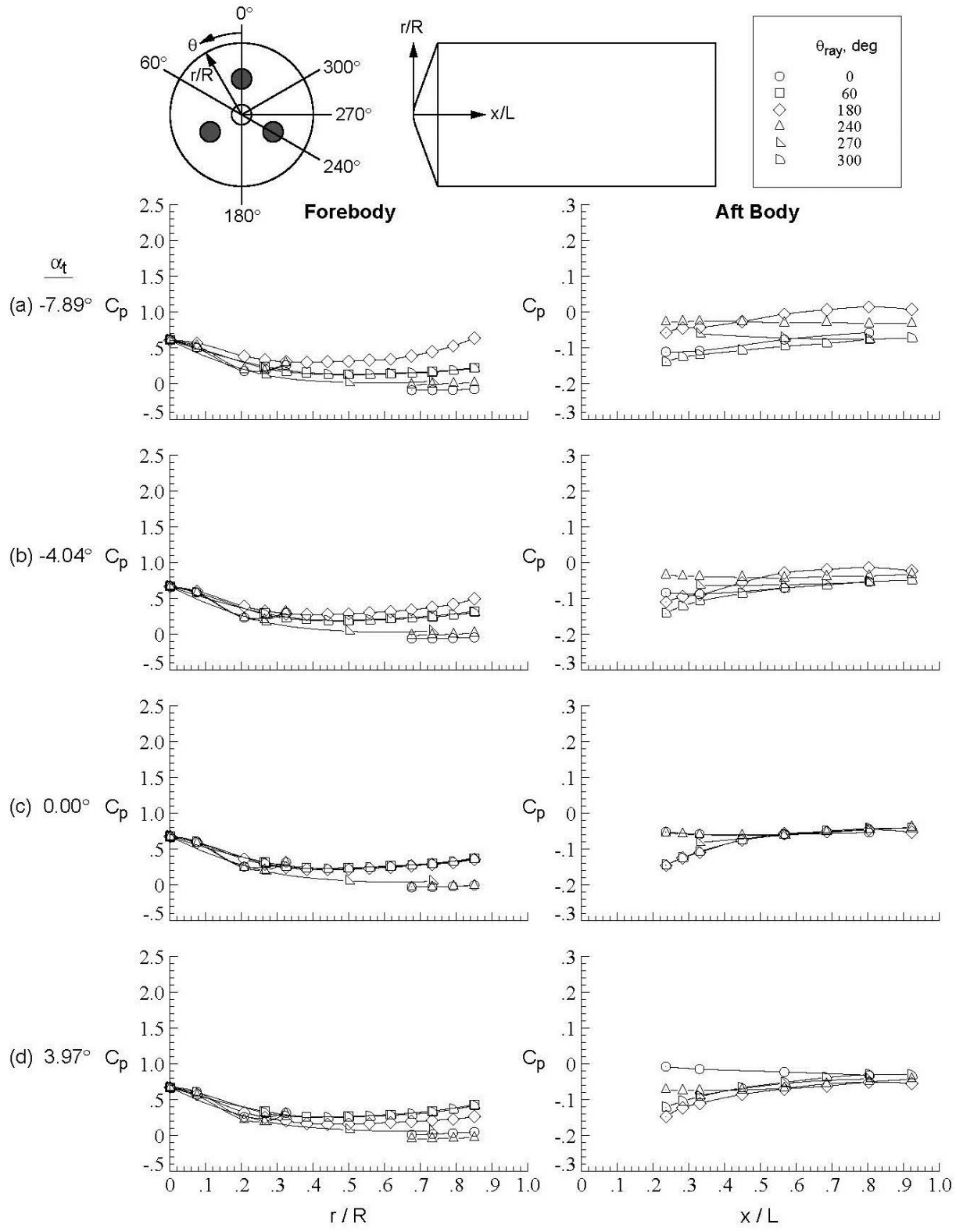

Figure D-156. Tri-nozzle configuration, Run 201, M_∞ = 2.4, Re_∞ = 1.0x10^7/ft, ϕ = 179.99°, X_S = 40.15 in, Y_S = 0.00 in, C_T = 0.94.

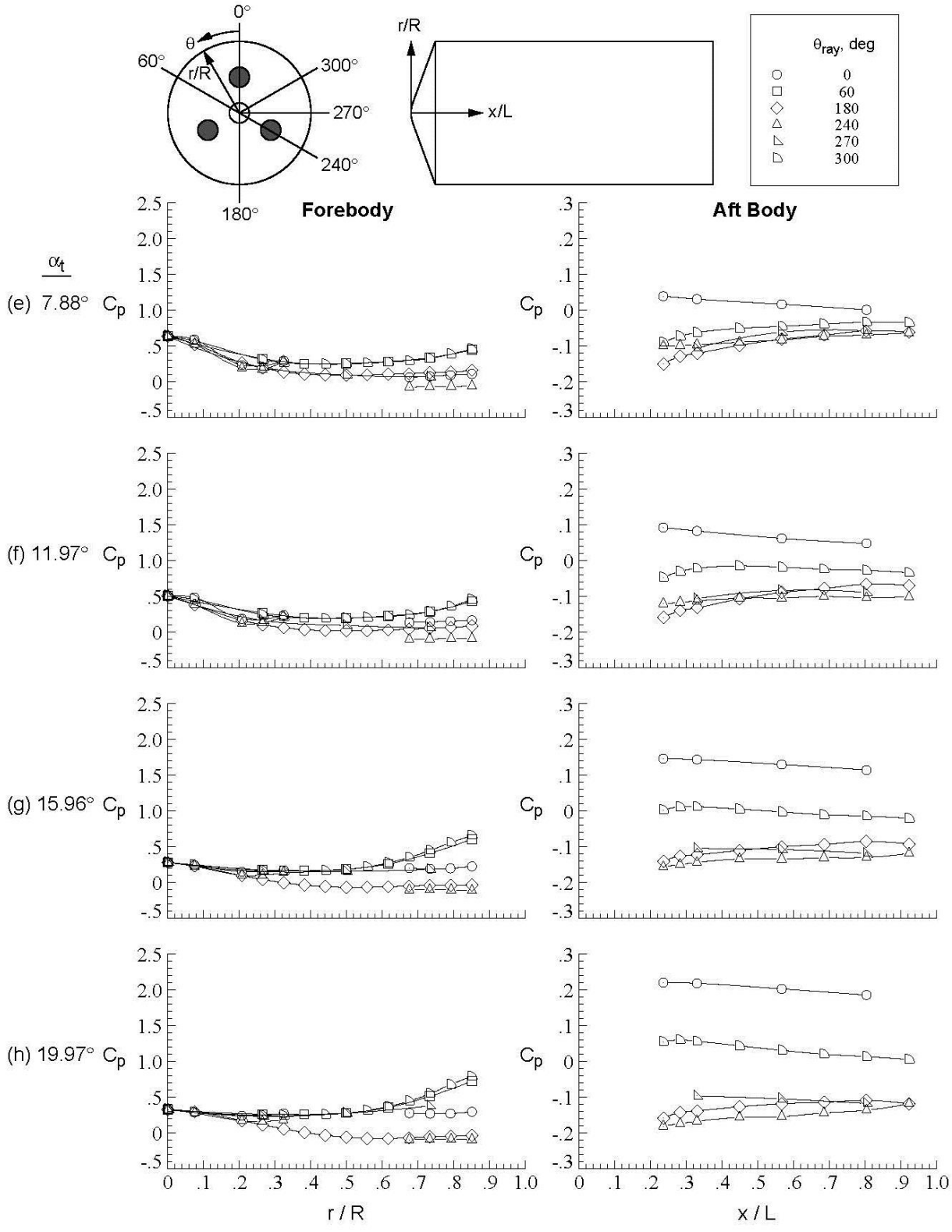

Figure D-156.Concluded.

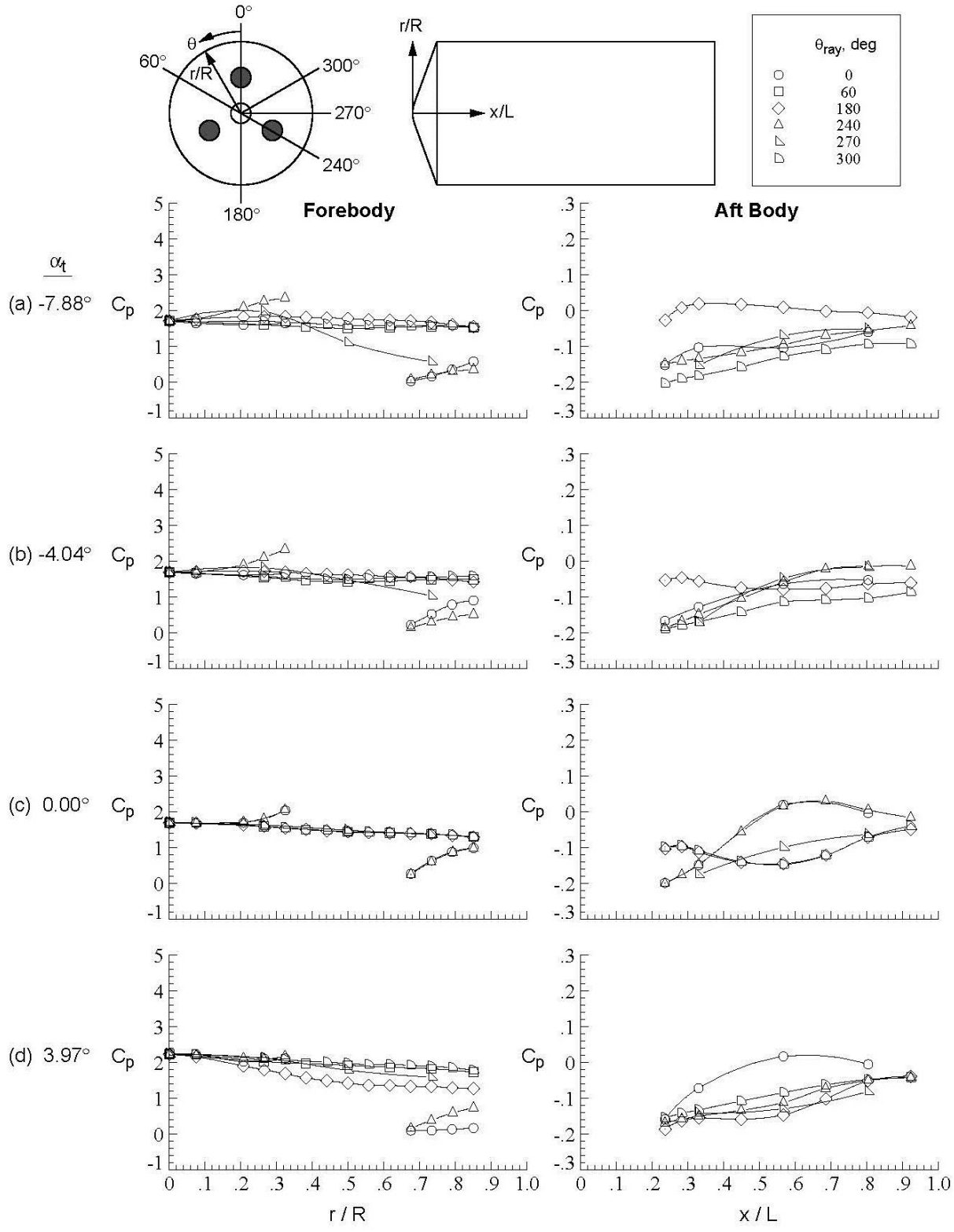

Figure D-157. Tri-nozzle configuration, Run 202, M_∞ = 2.4, Re_∞ = 1.0x10^7/ft, ϕ = 179.99°, X_S = 40.15 in, Y_S = 0.00 in, C_T = 0.43.

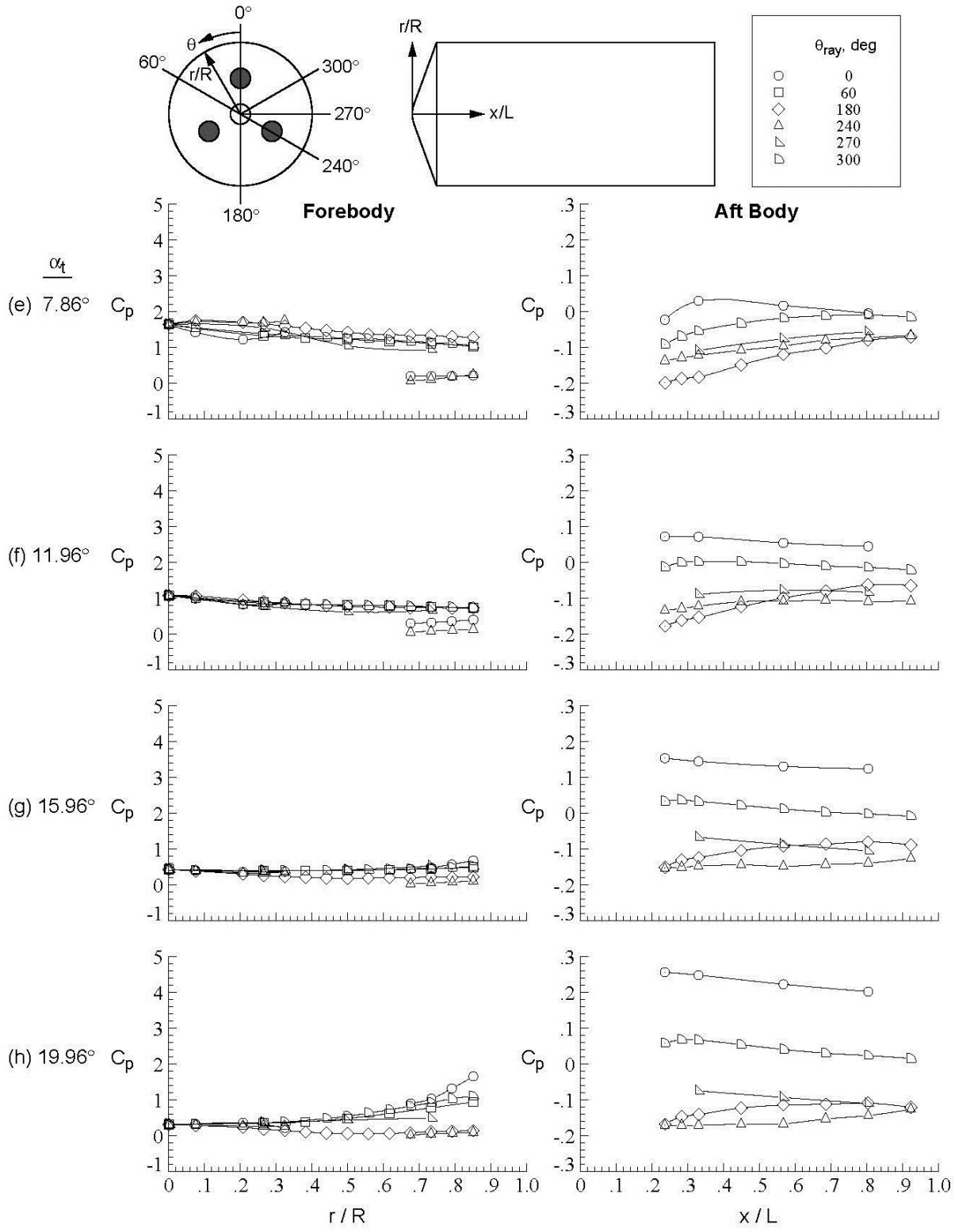

Figure D-157.Concluded.

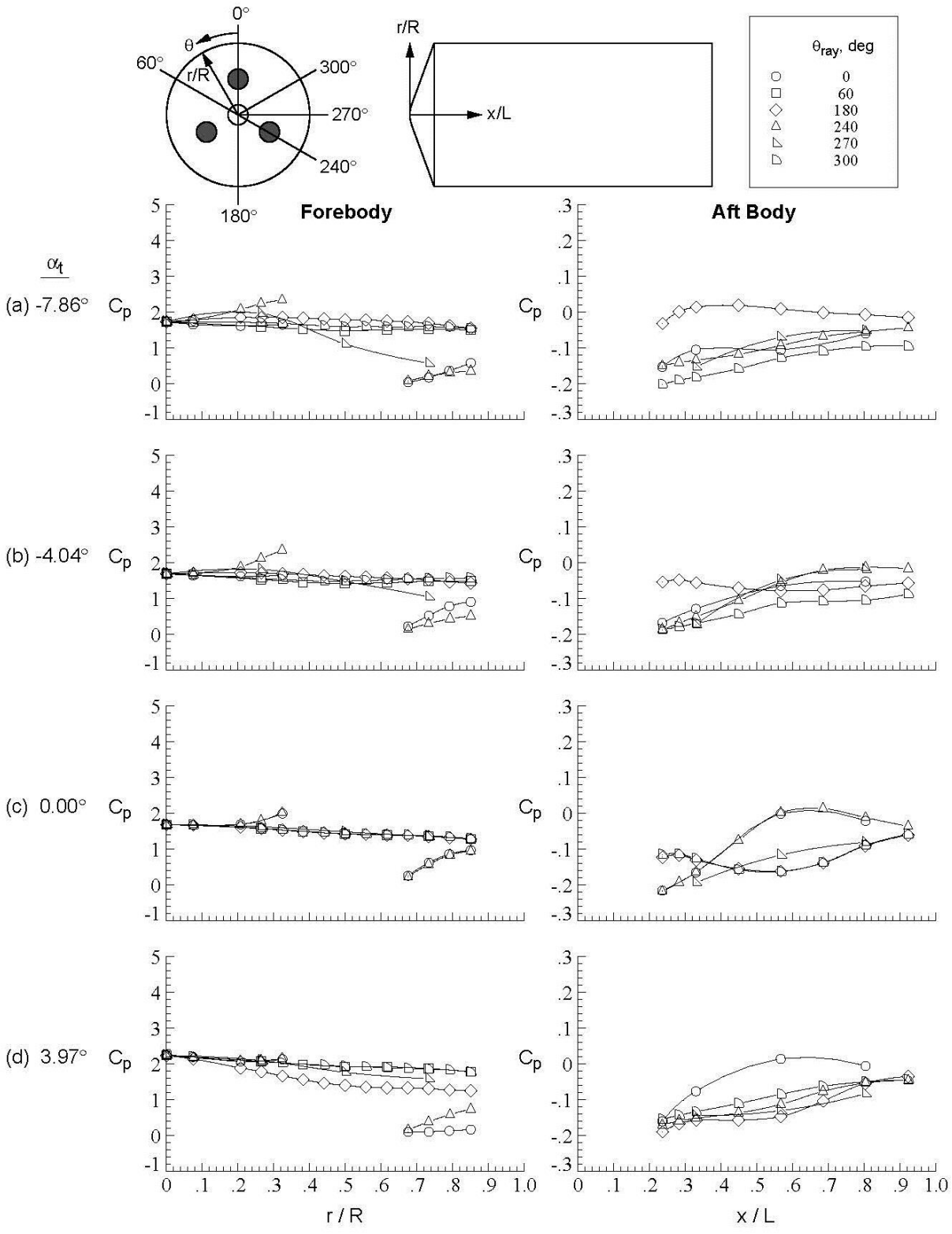

Figure D-158. Tri-nozzle configuration, Run 203, M_∞ = 2.4, Re_∞ = 1.0x10^7/ft, ϕ = −179.97°, X_S = 40.15 in, Y_S = 0.00 in, C_T = 0.44.

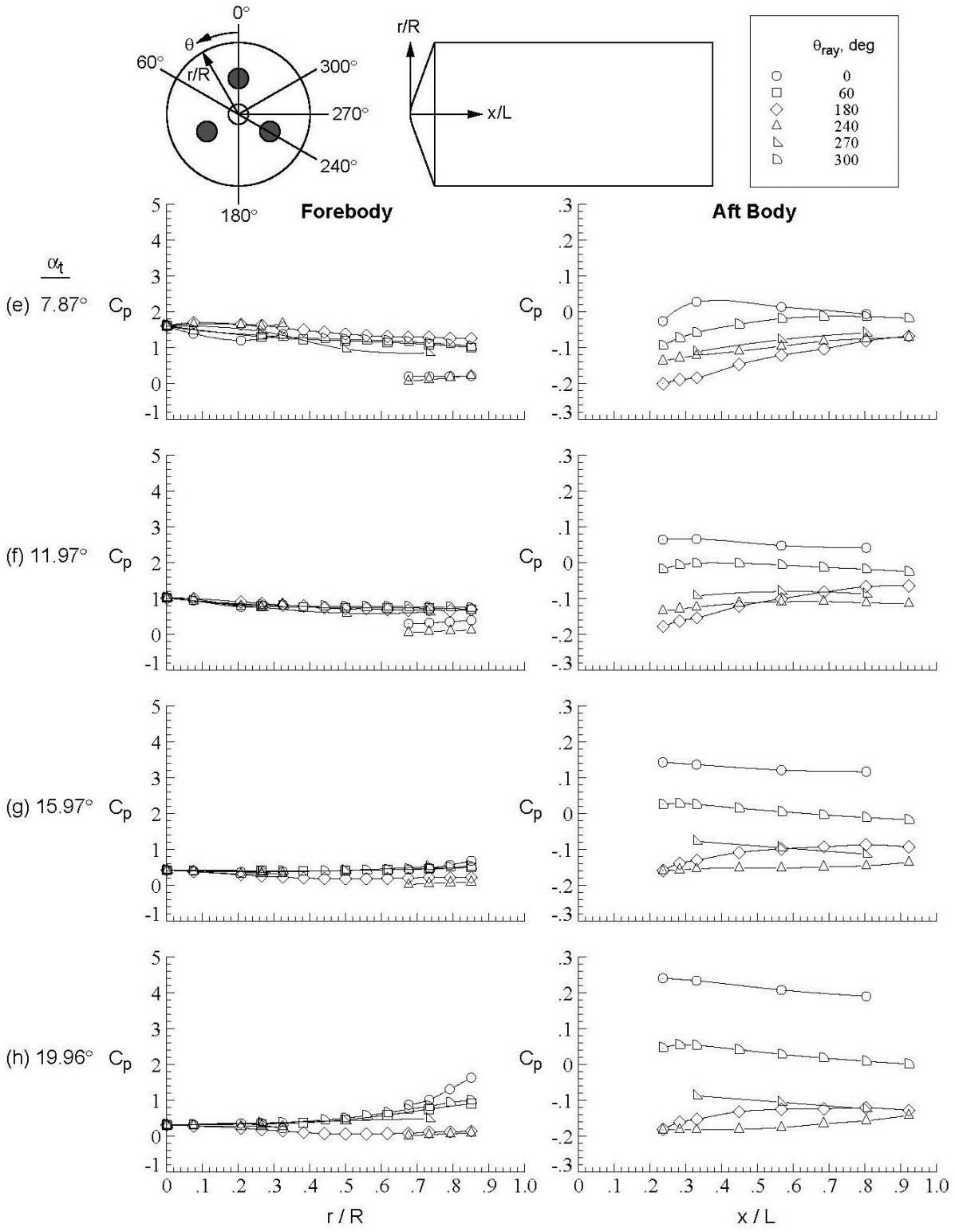

Figure D-158.Concluded.

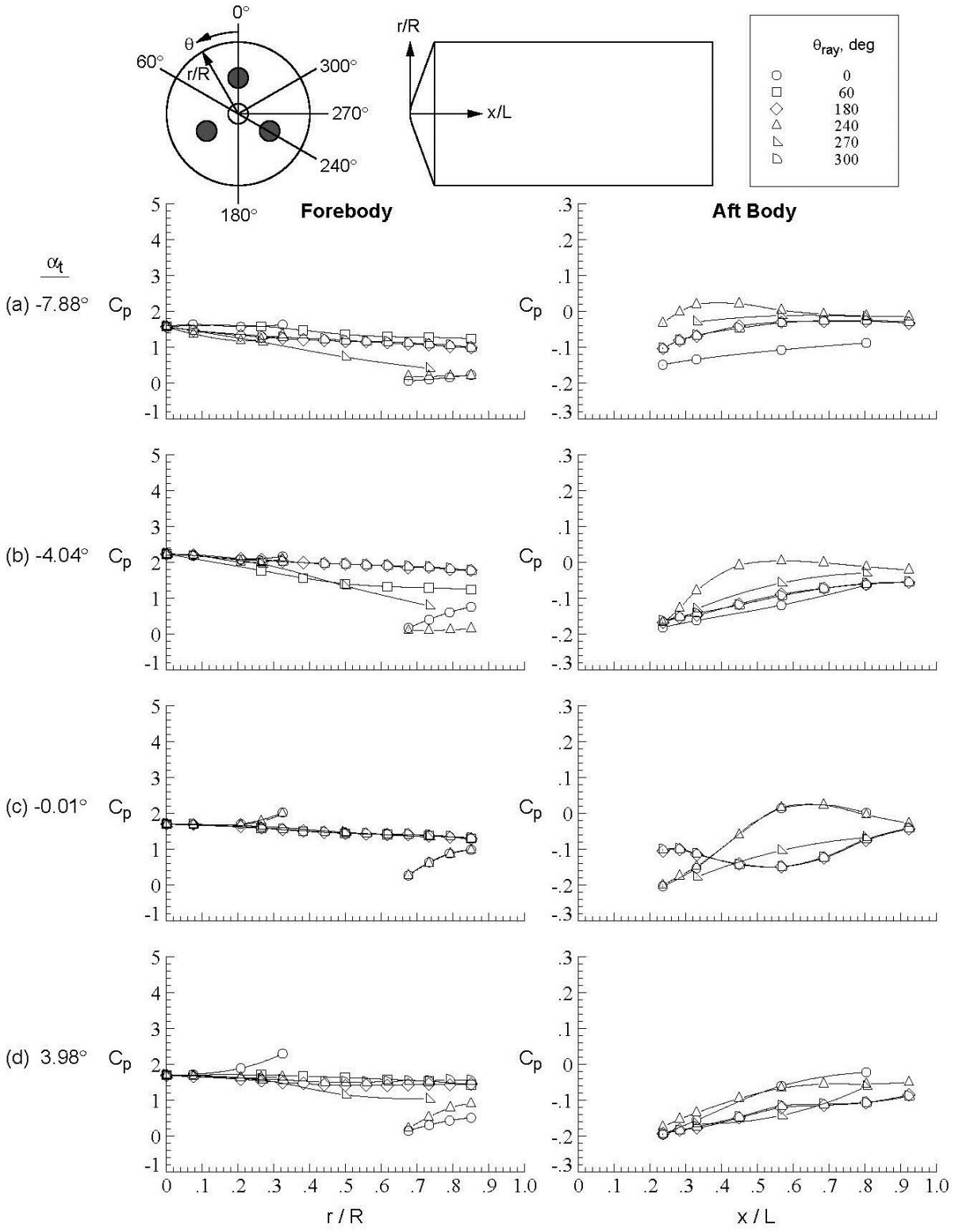

Figure D-159. Tri-nozzle configuration, Run 204, $M\infty$ = 2.4, Re_∞ = 1.0x10^6/ft, ϕ = 120.04°, X_S = 40.15 in, Y_S = 0.00 in, C_T = 0.43.

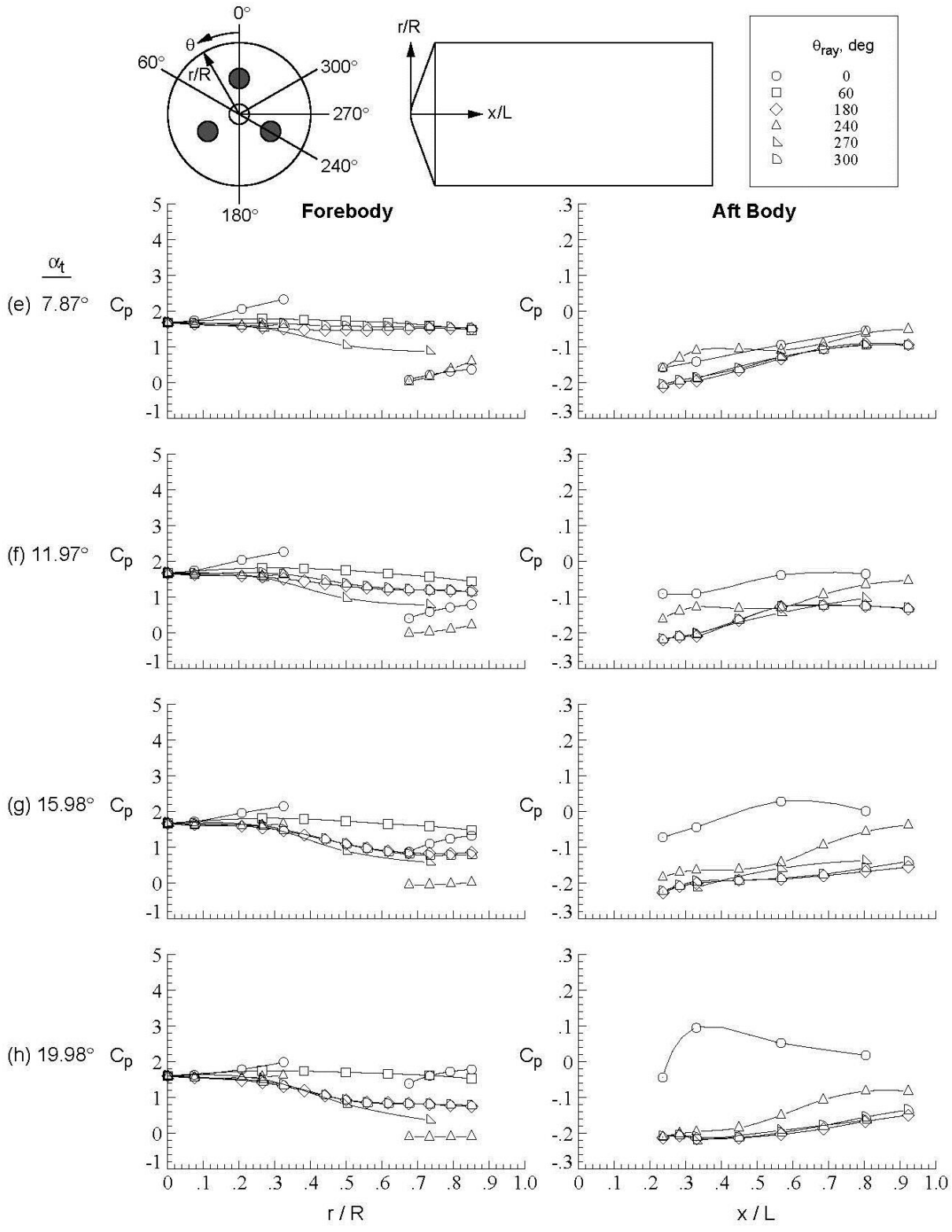

Figure D-159.Concluded.

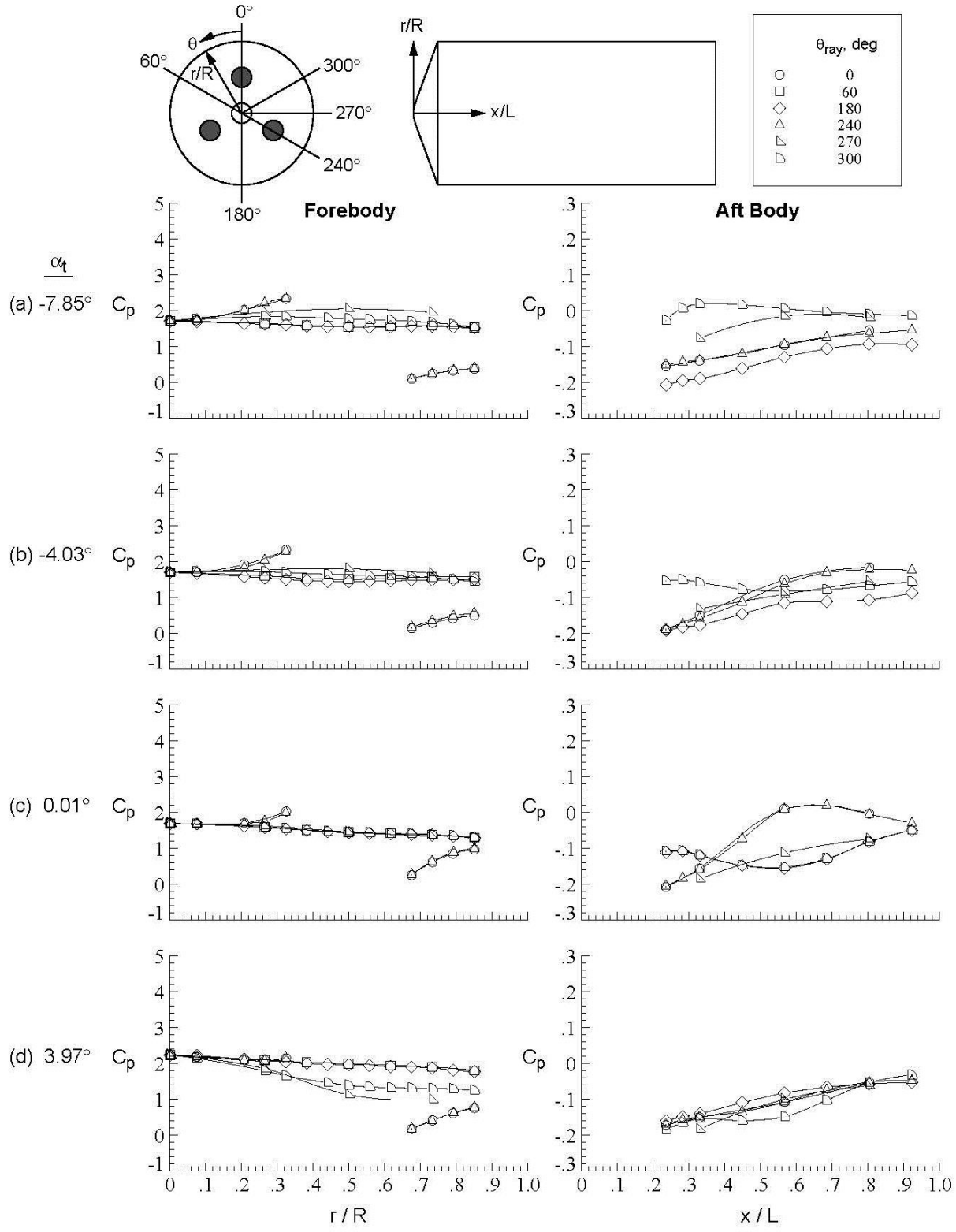

Figure D-160. Tri-nozzle configuration, Run 205, M_∞ = 2.4, Re_∞ = 1.0x10^6/ft, ϕ = 59.88°, X_S = 40.15 in, Y_S = 0.00 in, C_T = 0.44.

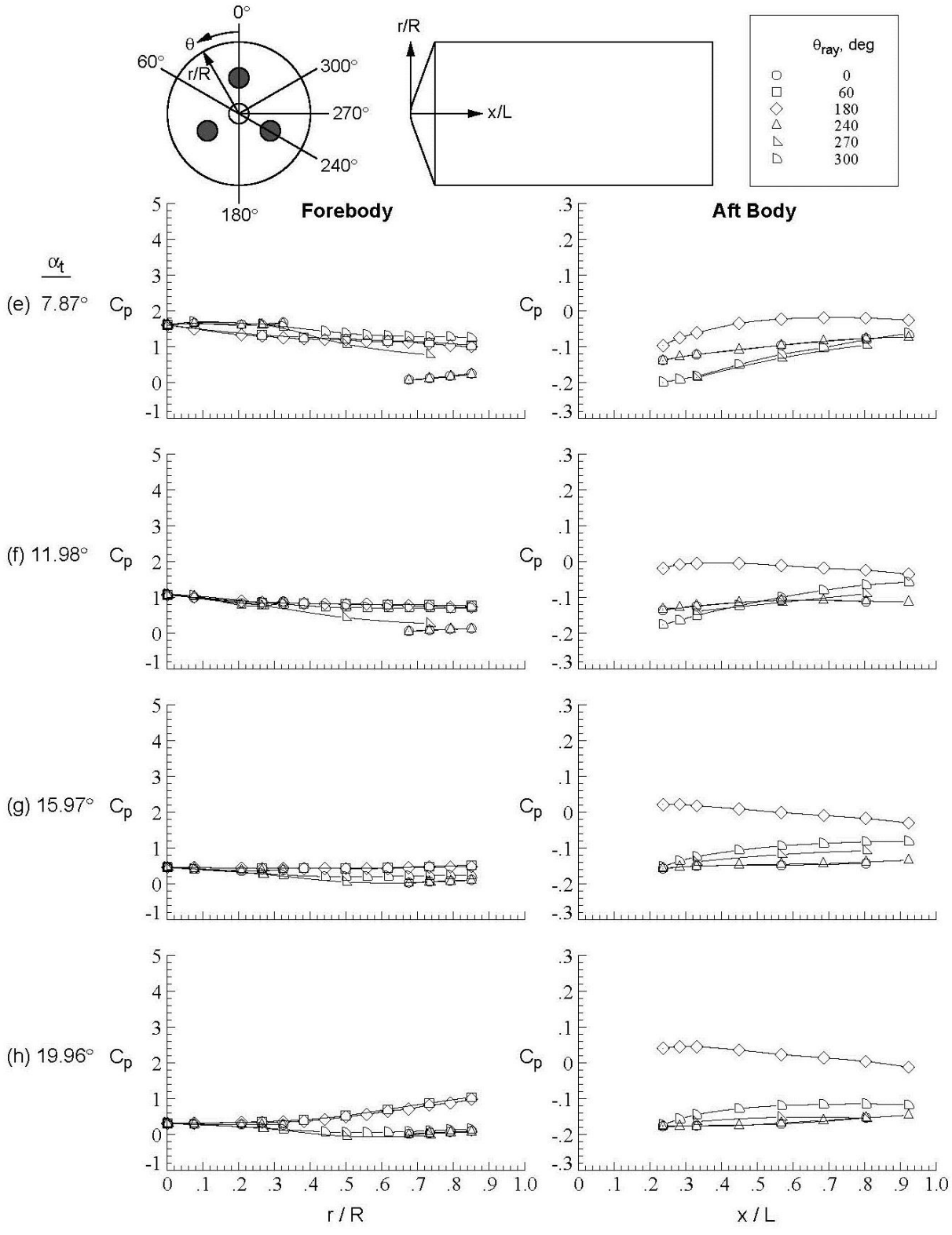

Figure D-160.Concluded.

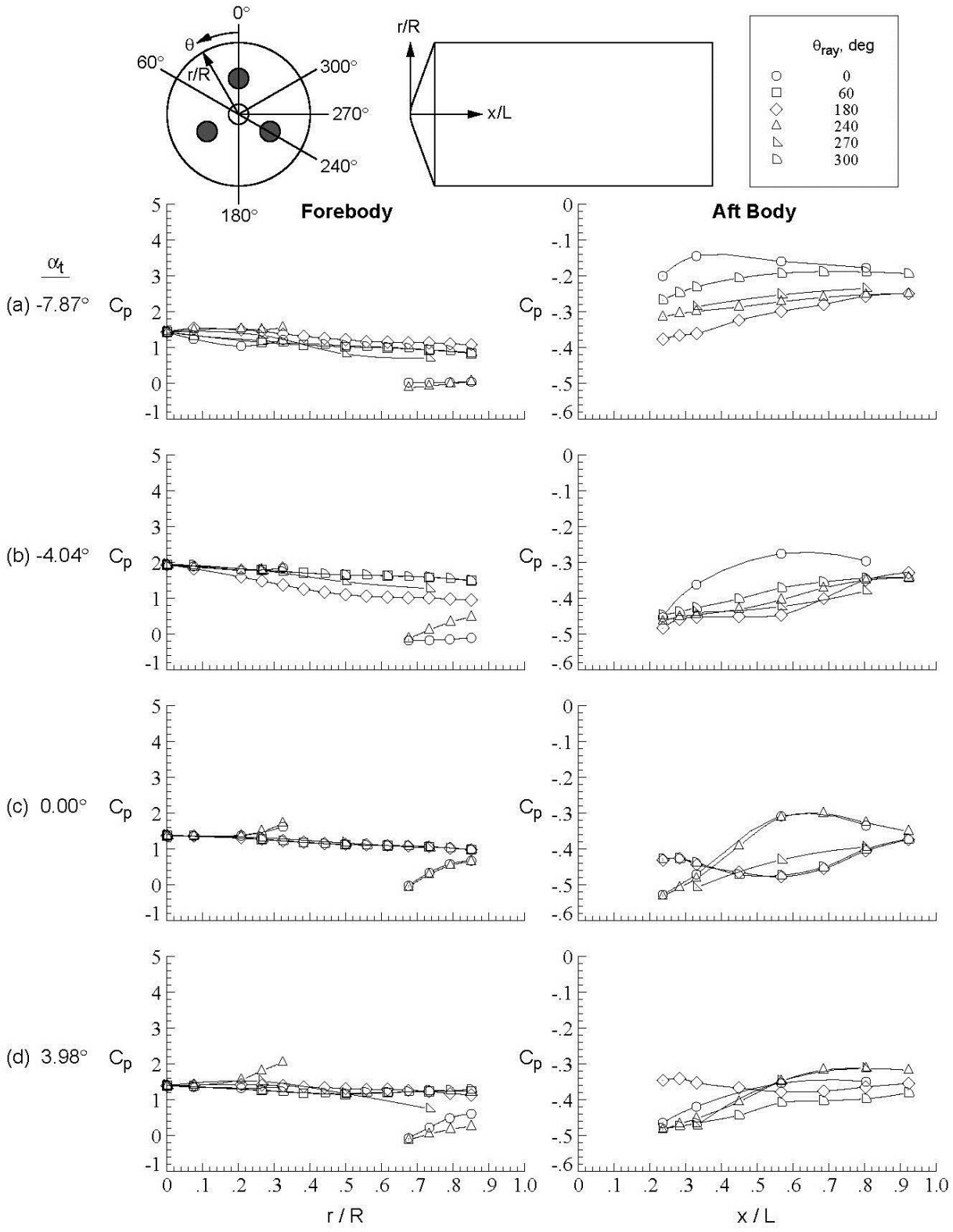

Figure D-161. Tri-nozzle configuration, Run 206, M_∞ = 2.4, Re_∞ = 1.0x10^7/ft, ϕ = −0.05°, X_S = 40.15 in, Y_S = 0.00 in, C_T = 0.43.

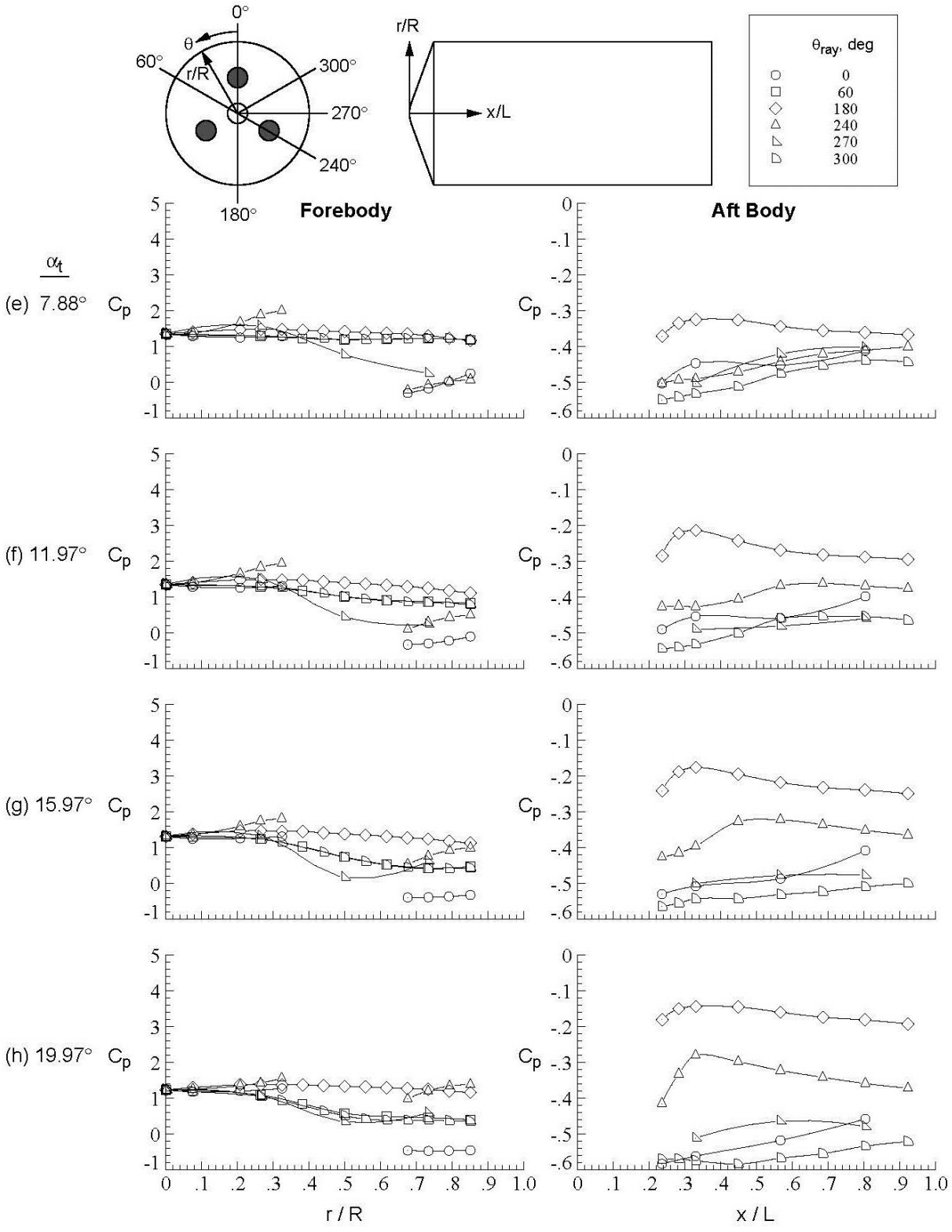

Figure D-161.Concluded.

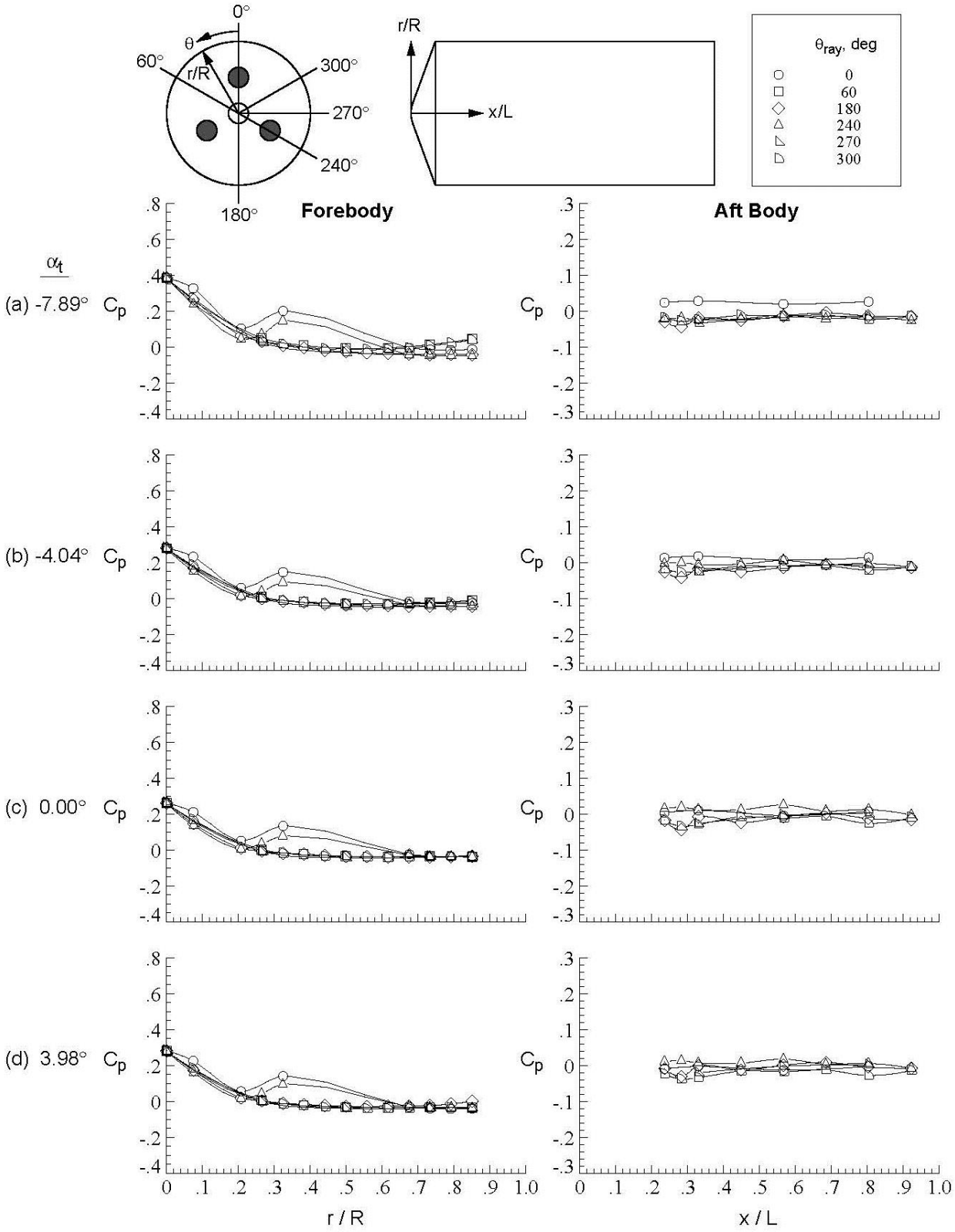

Figure D-162. Tri-nozzle configuration, Run 211, M_∞ = 4.6, Re_∞ = 1.5x10^7/ft, ϕ = −0.03°, X_S = 40.15 in, Y_S = 0.00 in, C_T = 2.93.

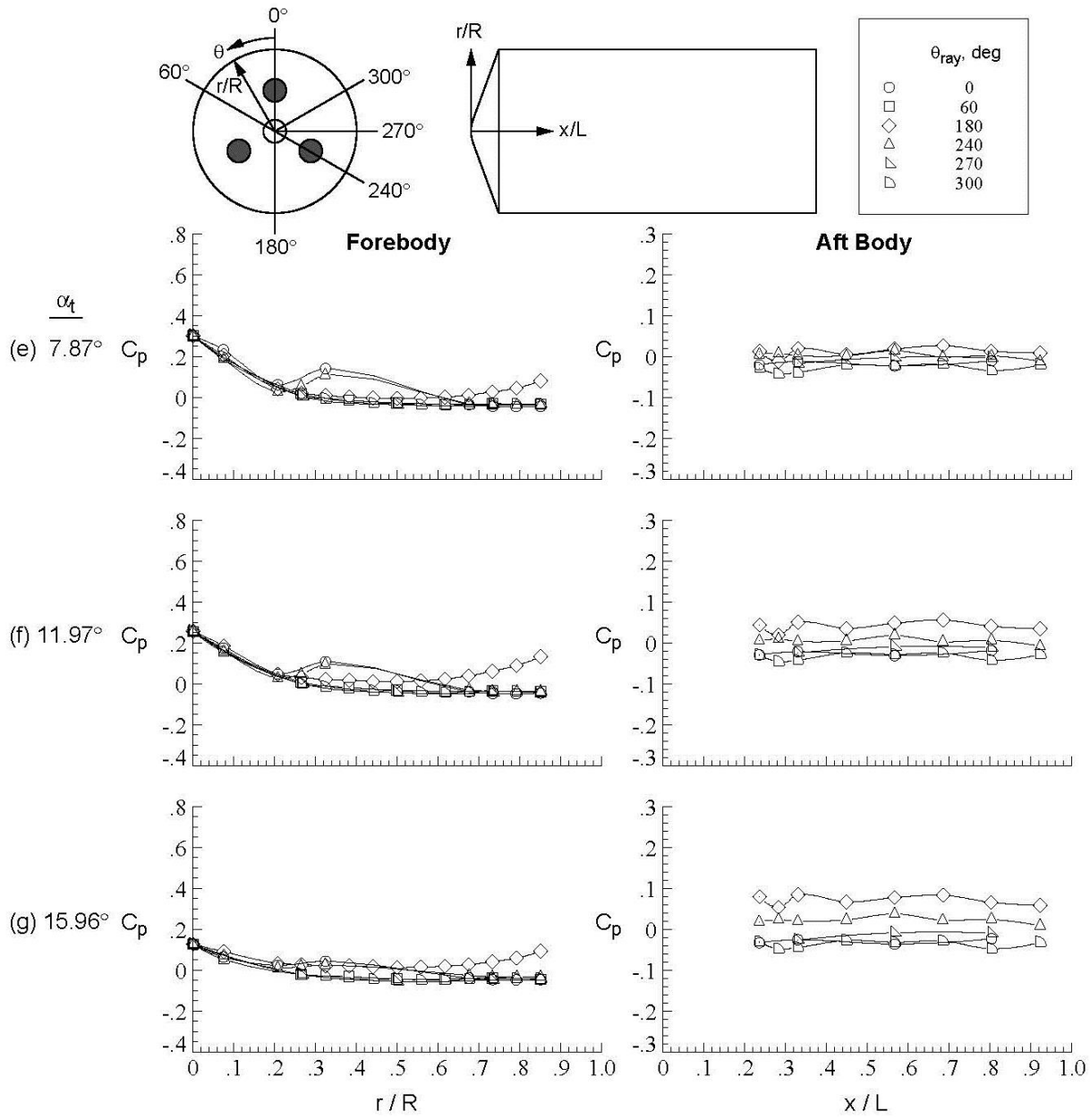

Figure D-162.Concluded.

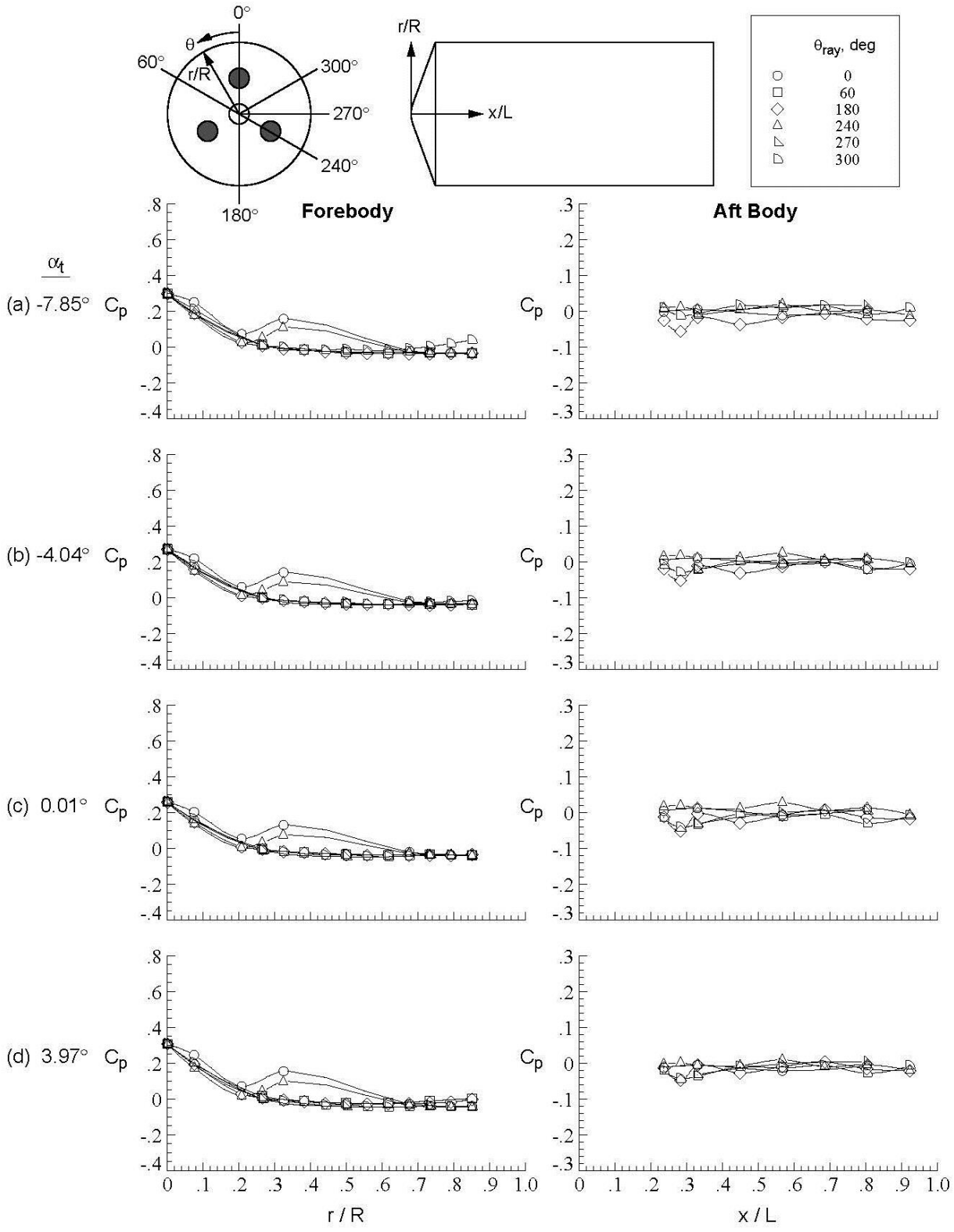

Figure D-163. Tri-nozzle configuration, Run 212, M_∞ = 4.6, Re_∞ = 1.5x10^7/ft, ϕ = 59.96°, X_S = 40.15 in, Y_S = 0.00 in, C_T = 2.94.

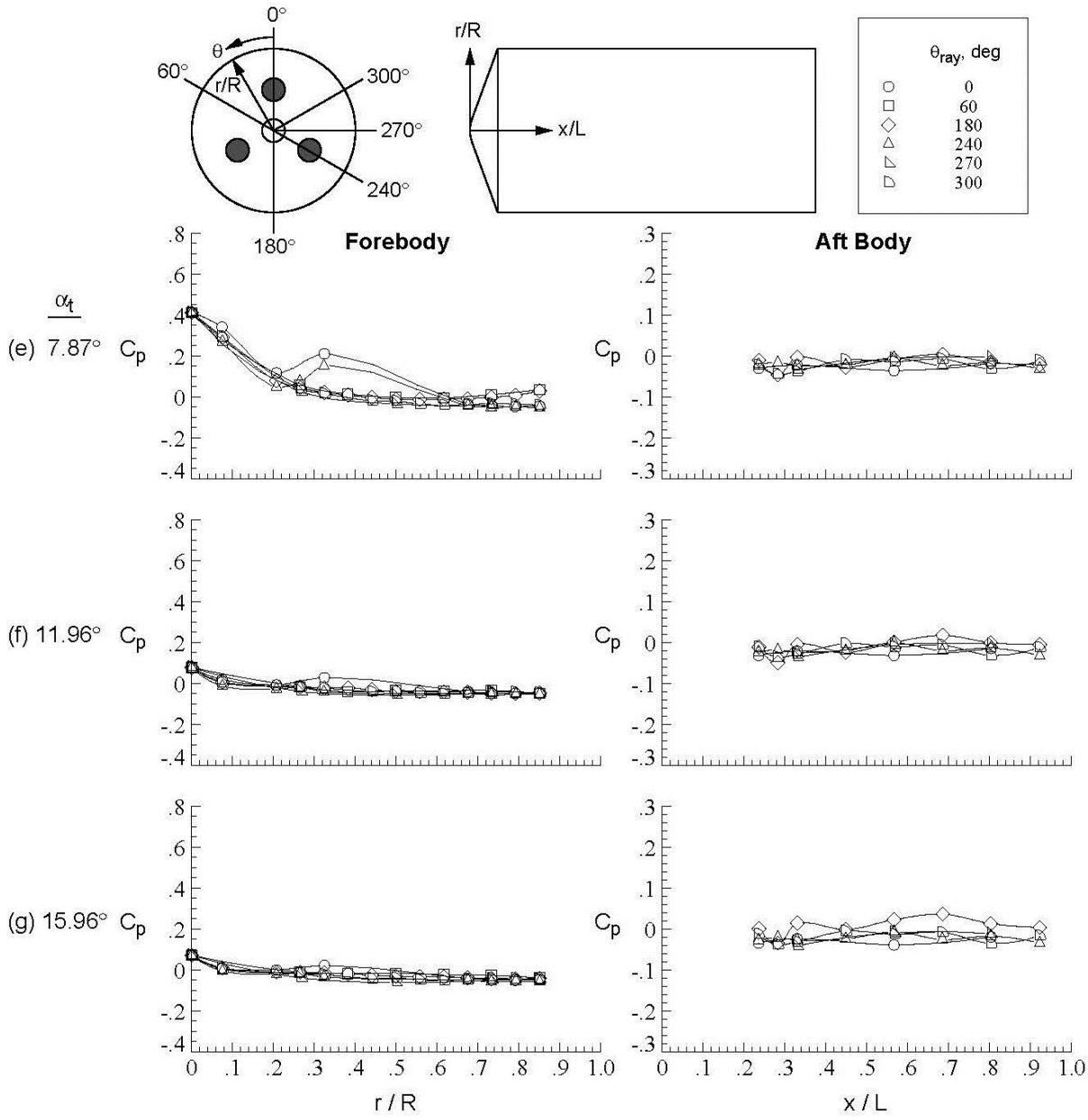

Figure D-163.Concluded.

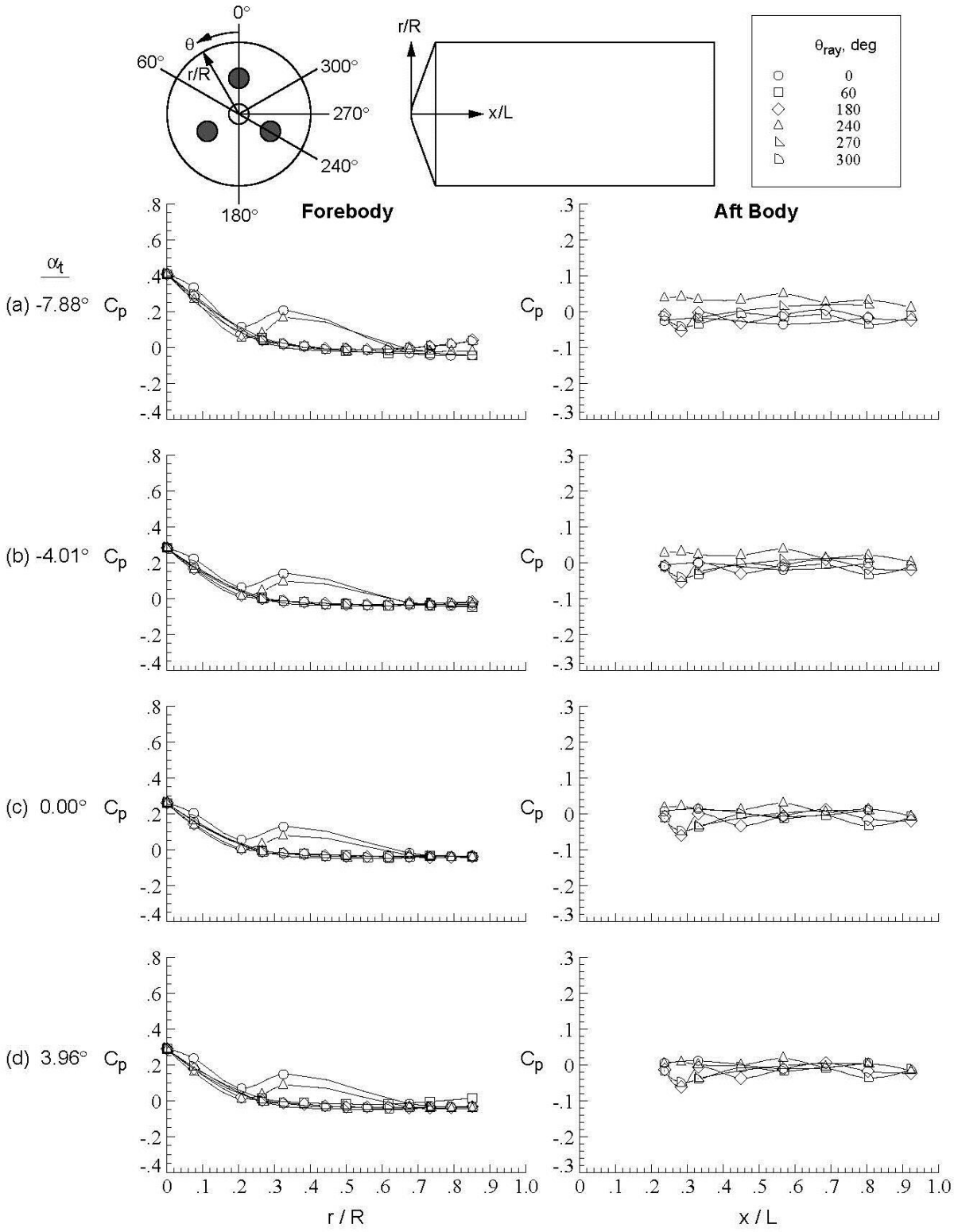

Figure D-164. Tri-nozzle configuration, Run 213, M_∞ = 4.6, Re_∞ = 1.5x10^7/ft, ϕ = 120.04°, X_S = 40.15 in, Y_S = 0.00 in, C_T = 2.87.

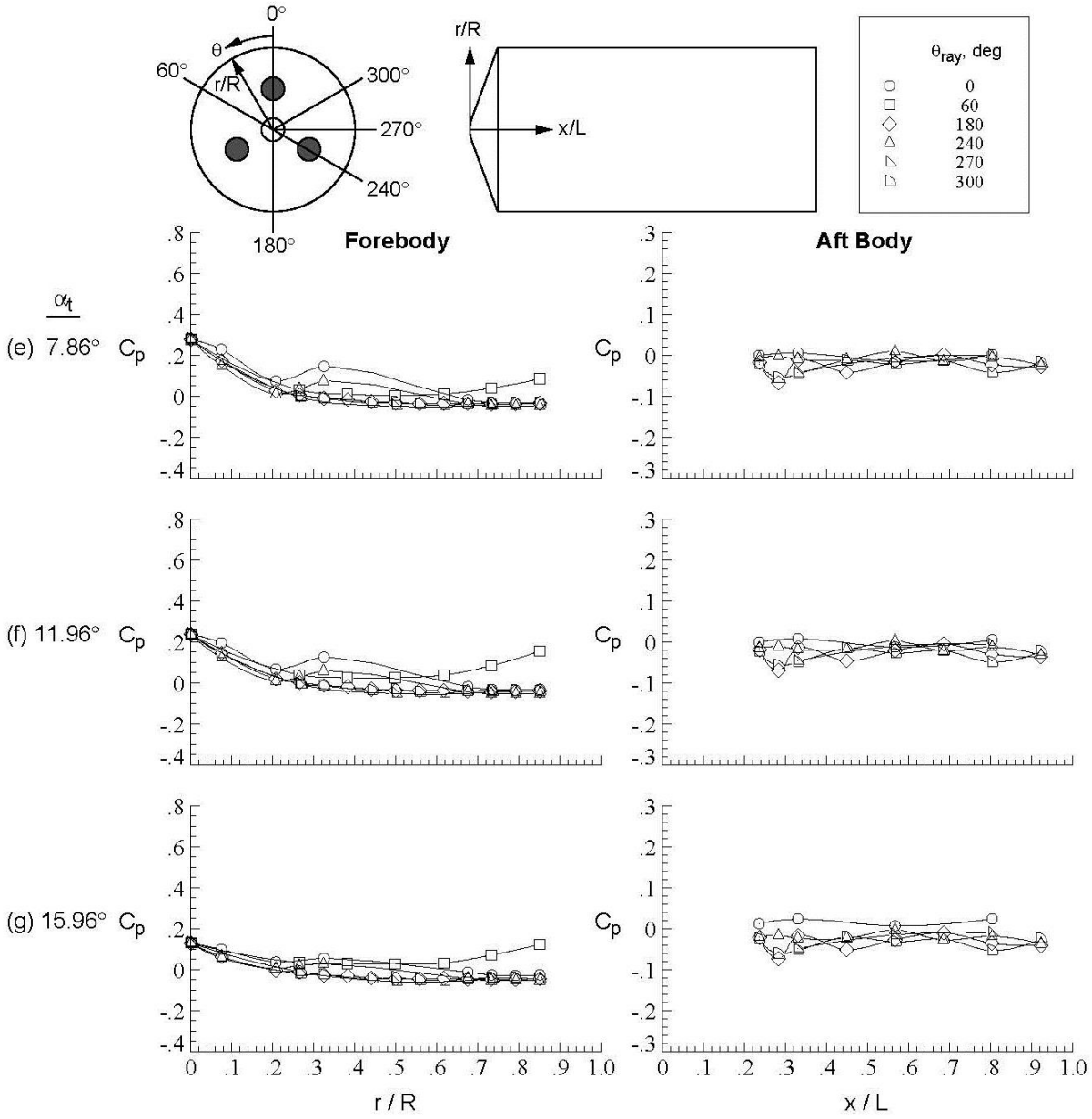

Figure D-164.Concluded.

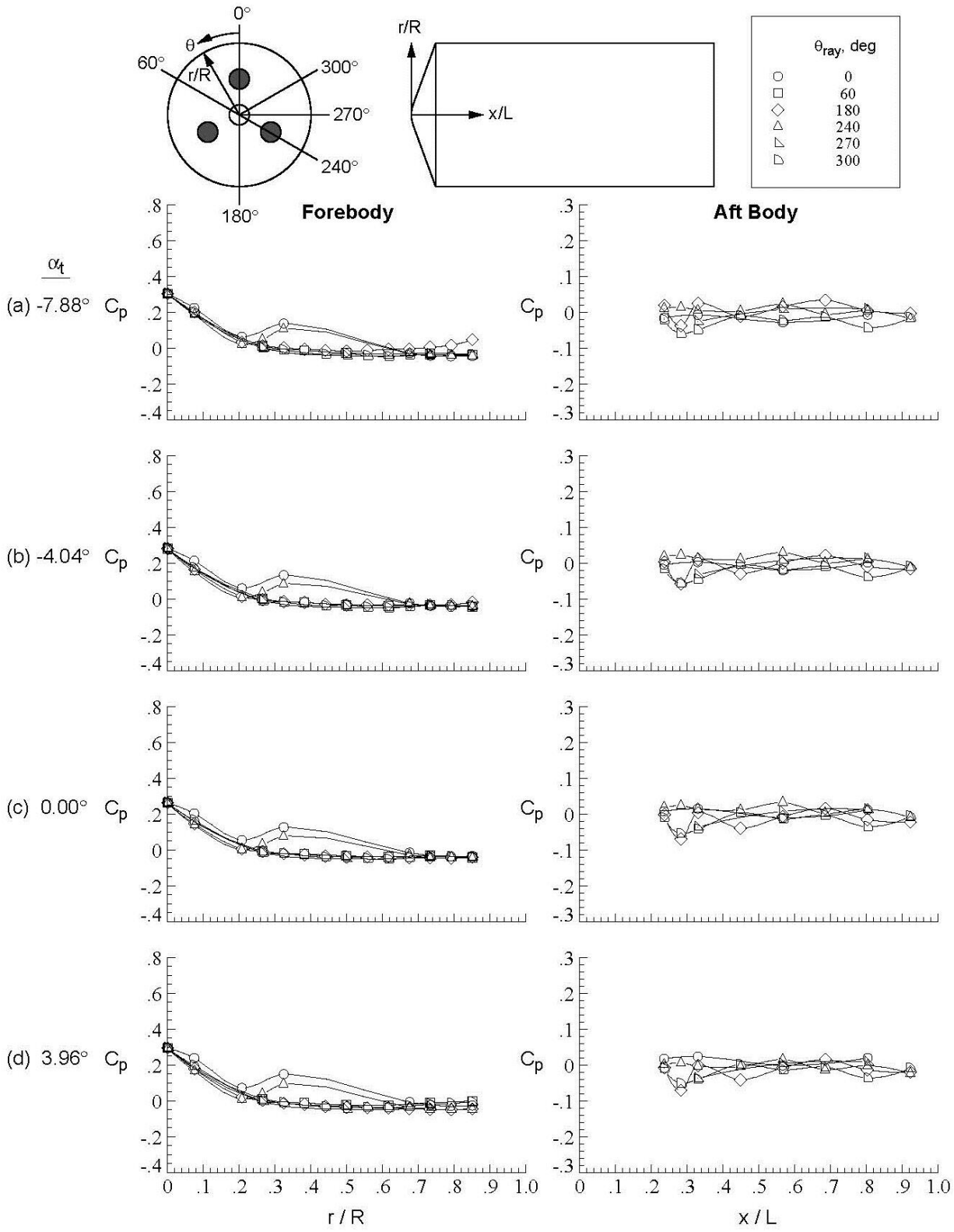

Figure D-165. Tri-nozzle configuration, Run 214, M_∞ = 4.6, Re_∞ = 1.5x10^7/ft, ϕ = 179.99°, X_S = 40.15 in, Y_S = 0.00 in, C_T = 2.96.

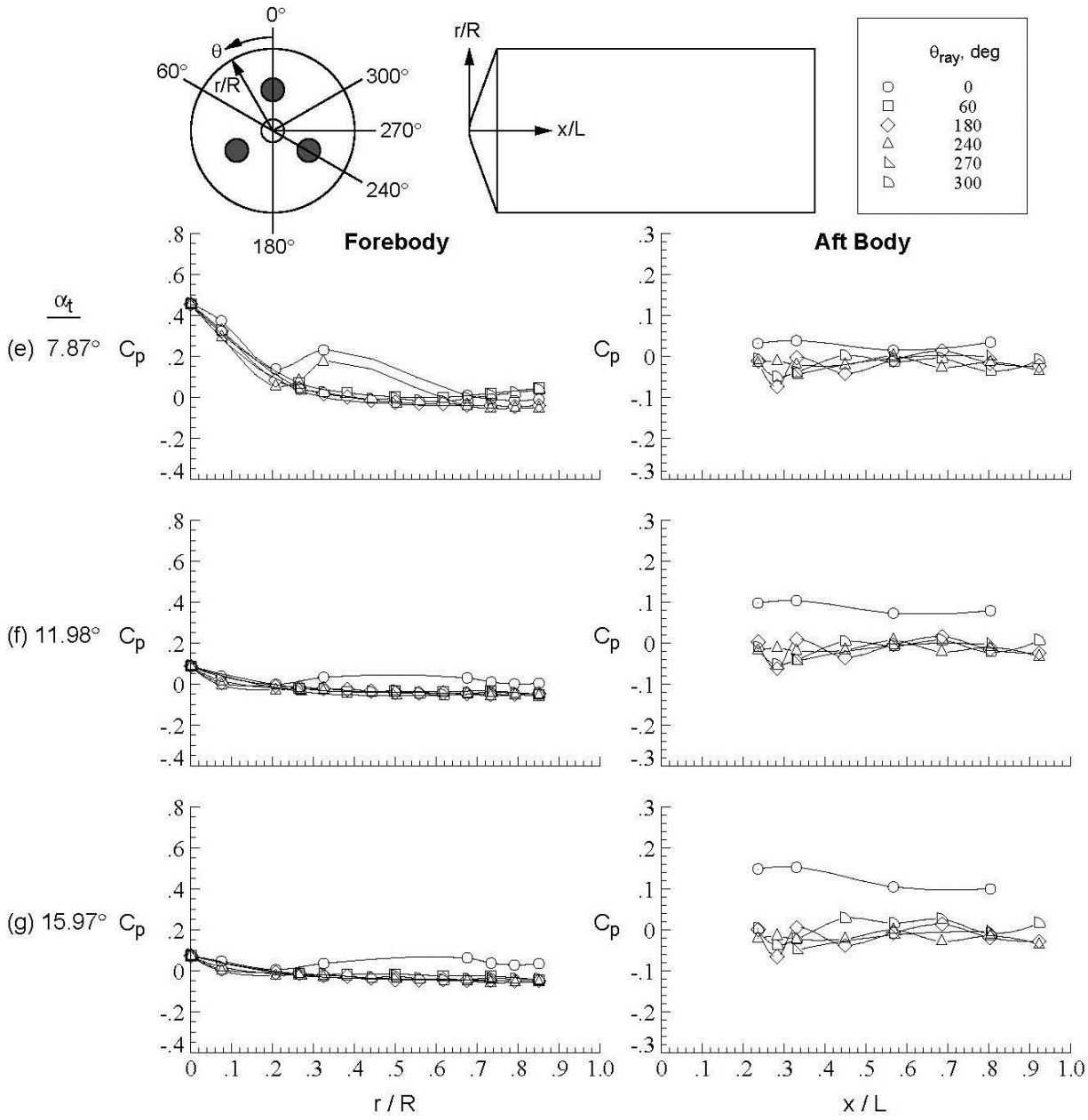

Figure D-165.Concluded.

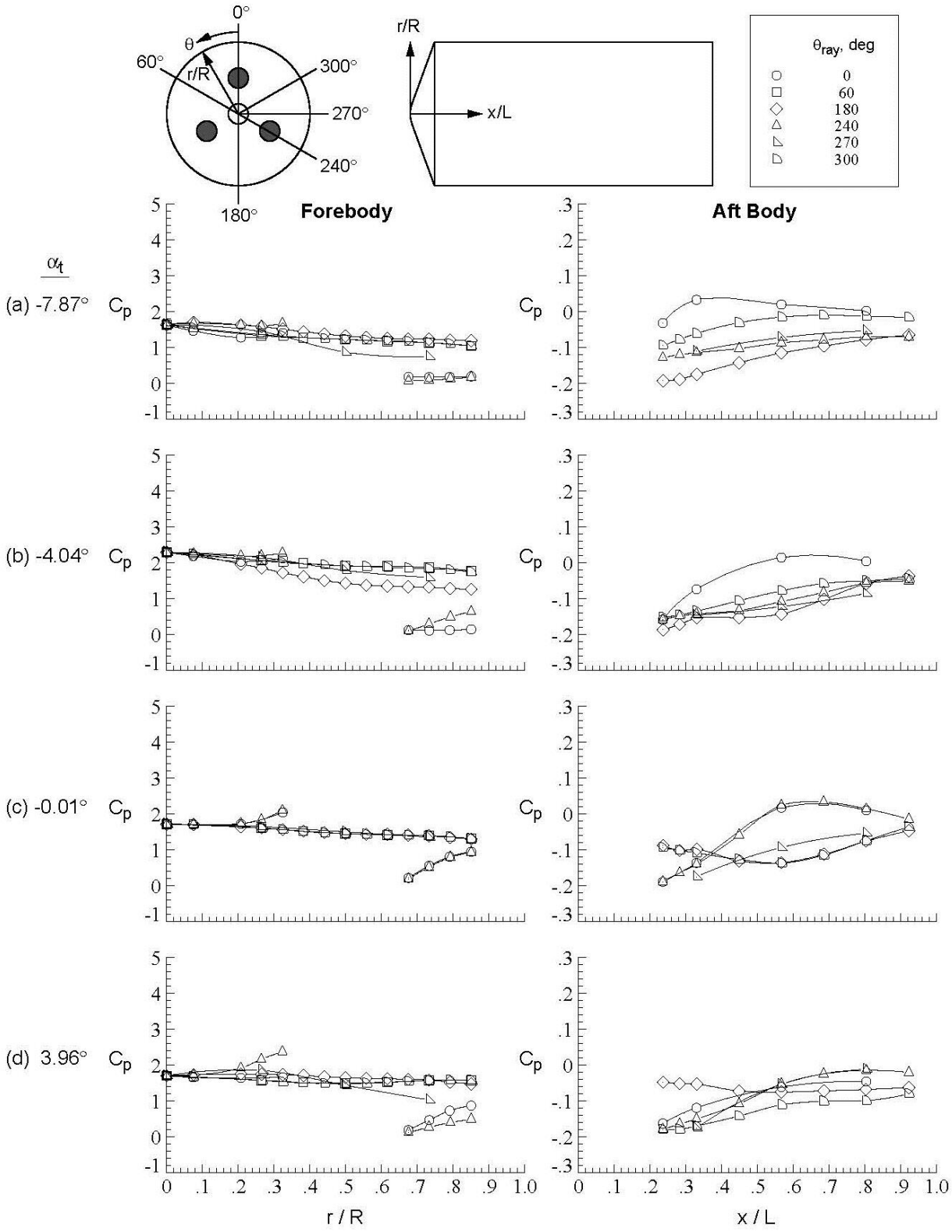

Figure D-166. Tri-nozzle configuration, Run 217, $M\infty = 2.4$, $Re_\infty = 1.0 \times 10^6$/ft, $\phi = -0.03°$, $X_S = 40.15$ in, $Y_S = 0.00$ in, $C_T = 0.47$.

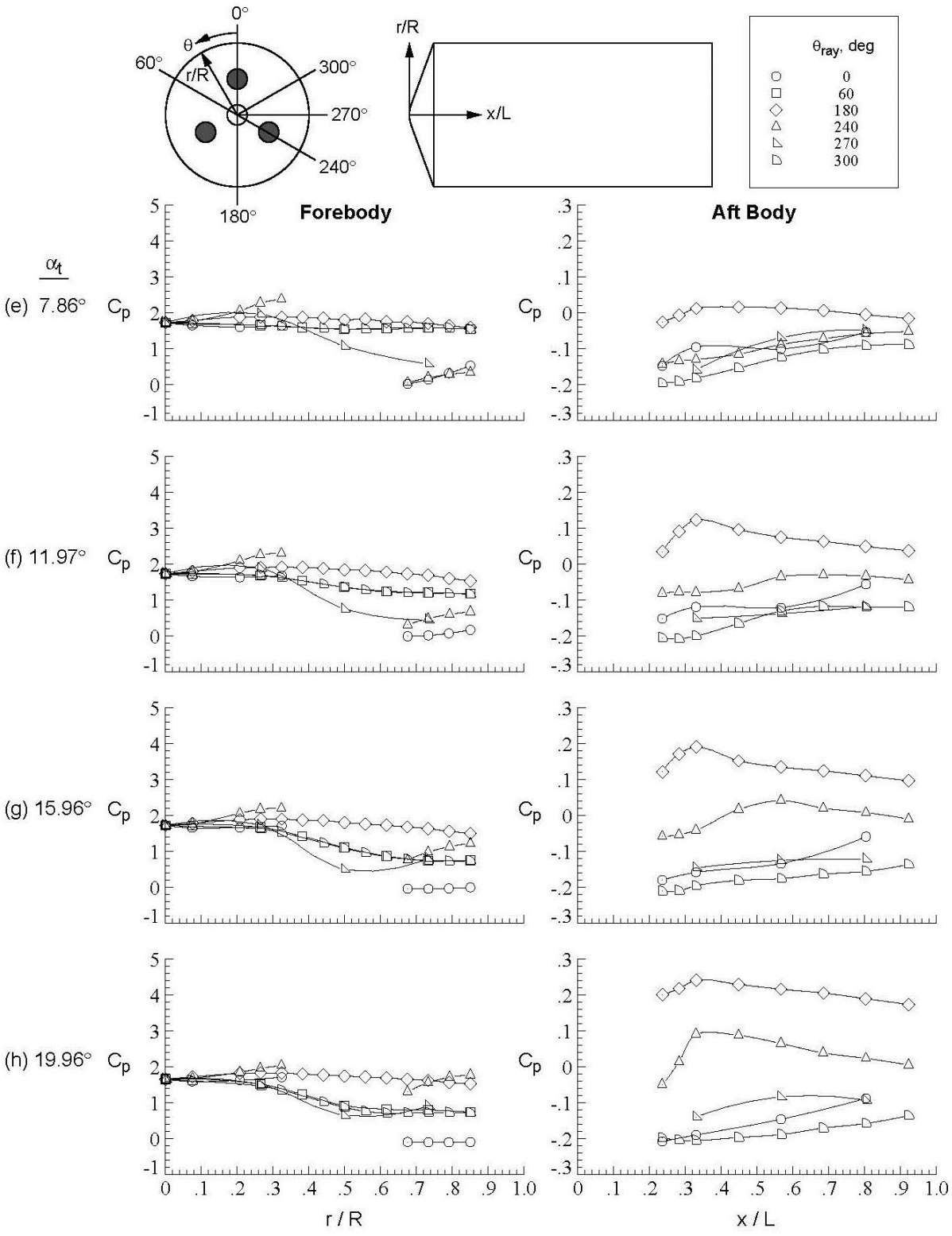

Figure D-166.Concluded.

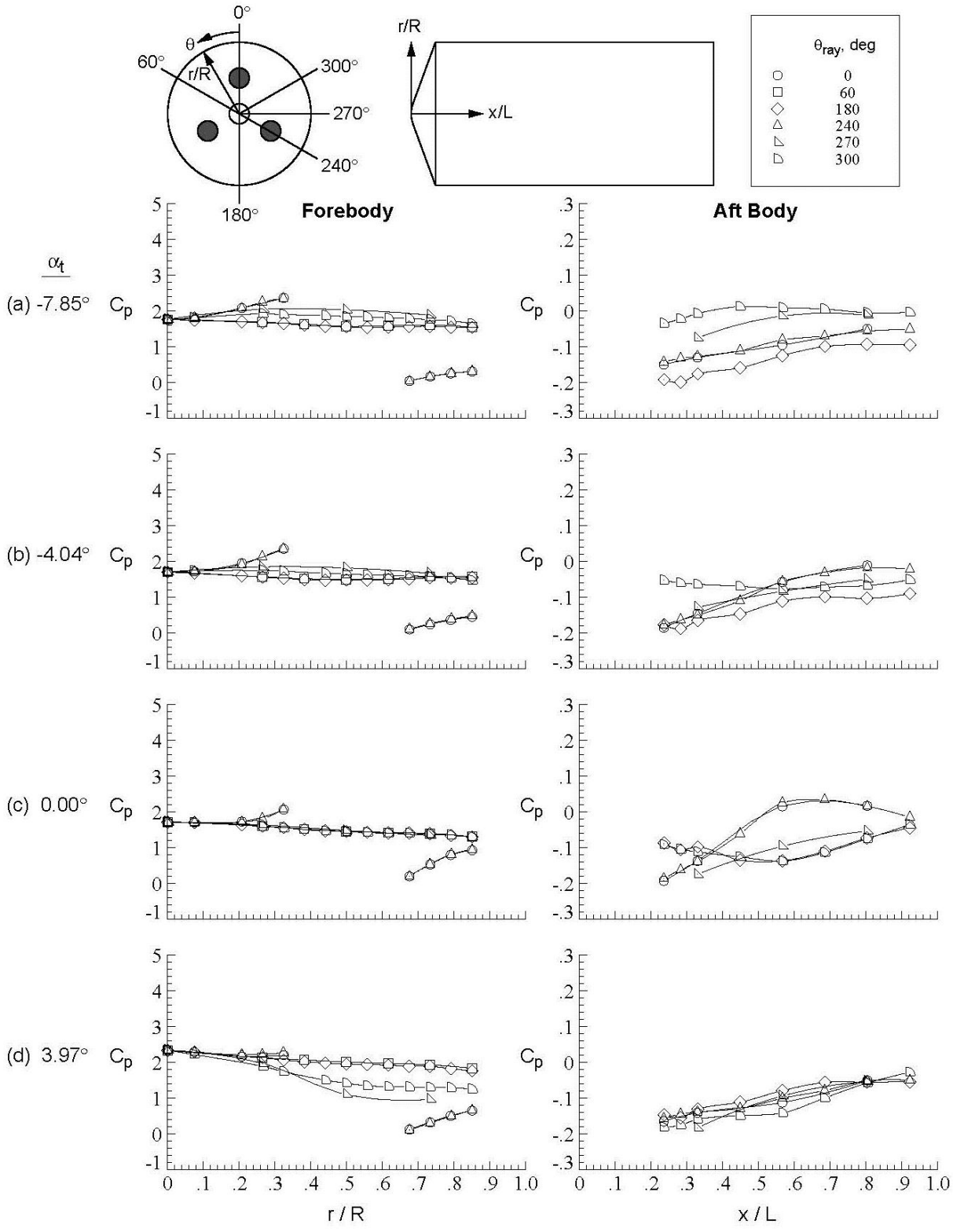

Figure D-167. Tri-nozzle configuration, Run 218, M_∞ = 2.4, Re_∞ = 1.0x10^6/ft, ϕ = 59.88°, X_S = 40.15 in, Y_S = 0.00 in, C_T = 0.48.

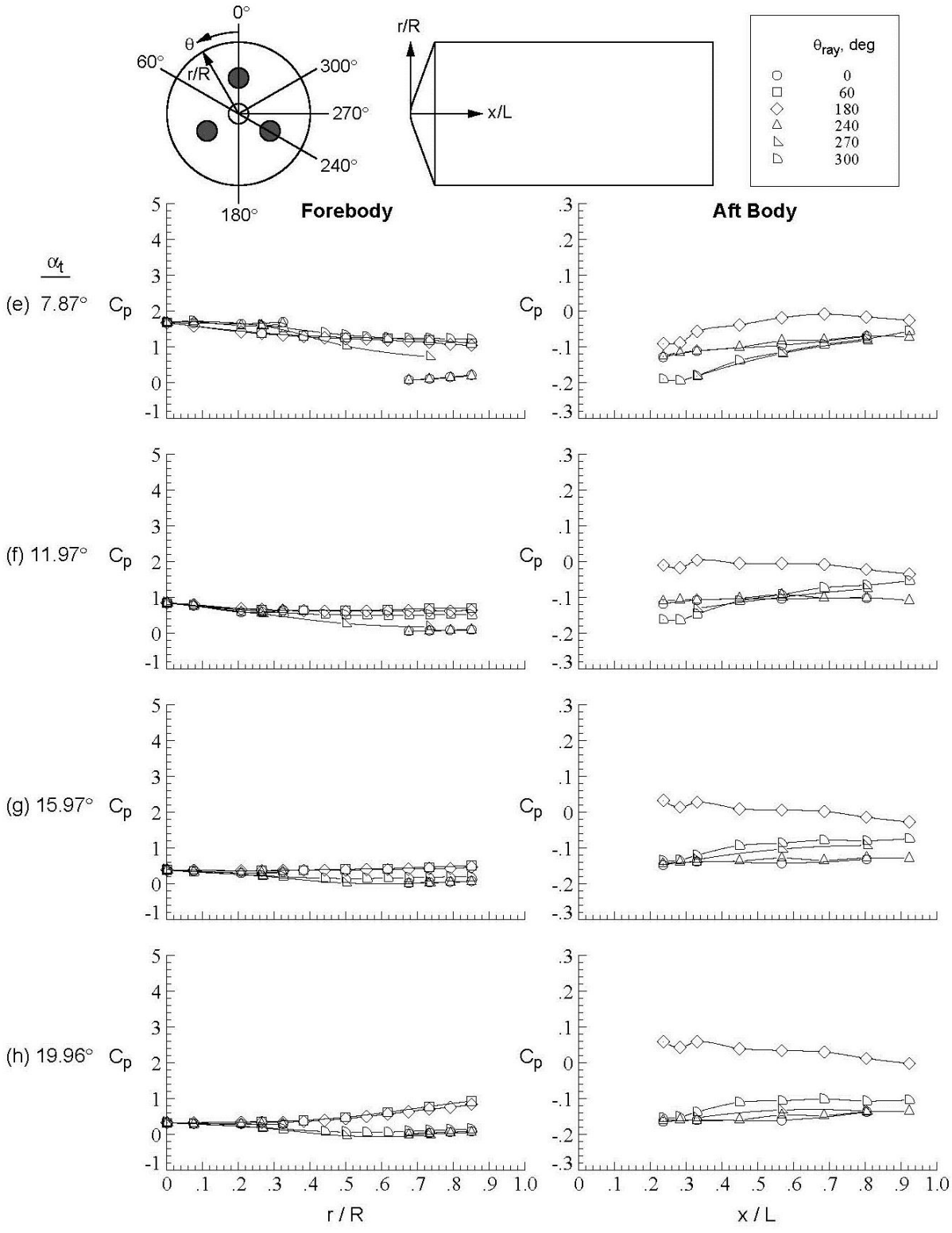

Figure D-167.Concluded.

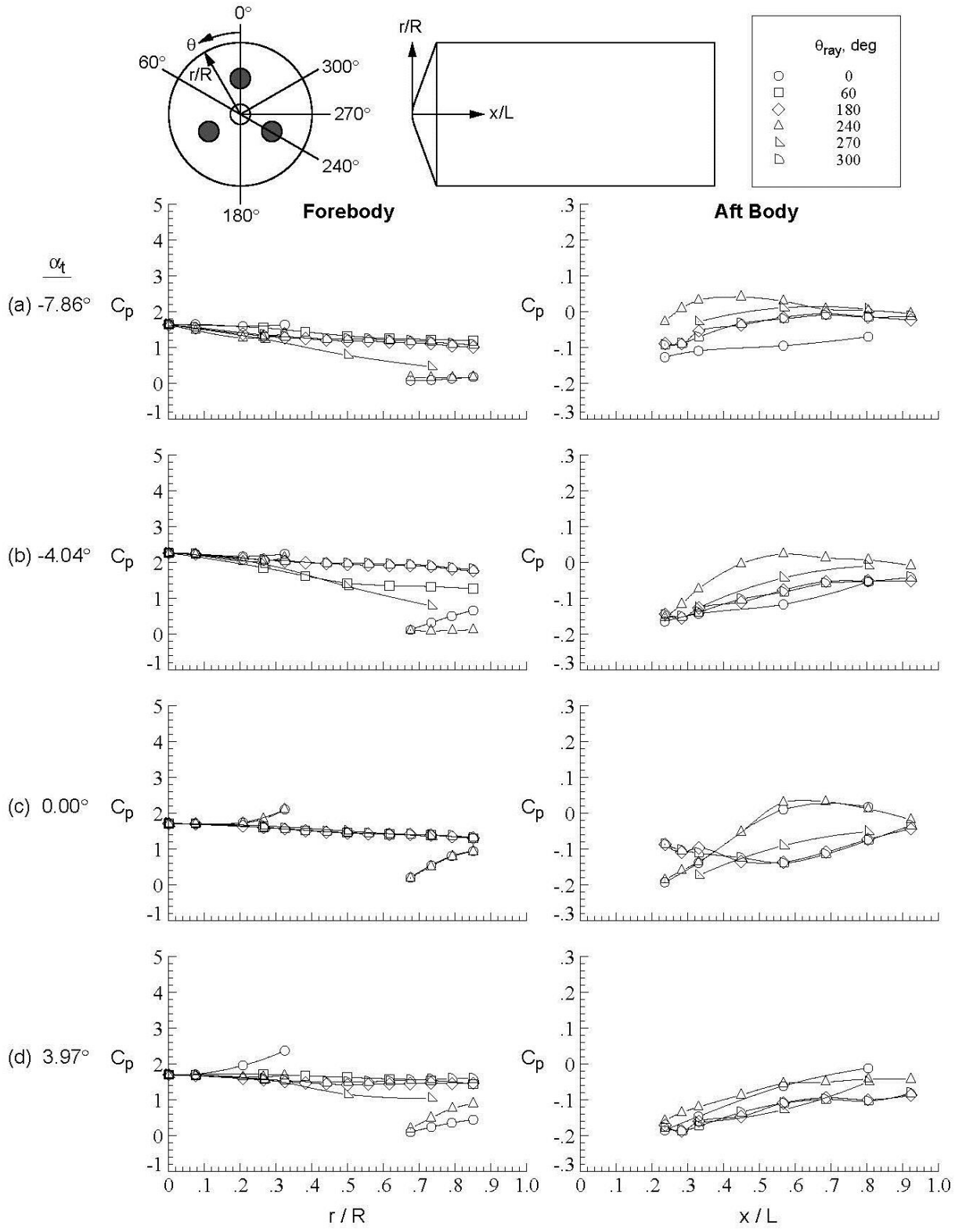

Figure D-168. Tri-nozzle configuration, Run 219, $M\infty$ = 2.4, Re_∞ = 1.0x10^7/ft, ϕ = 120.02°, X_S = 40.15 in, Y_S = 0.00 in, C_T = 0.47.

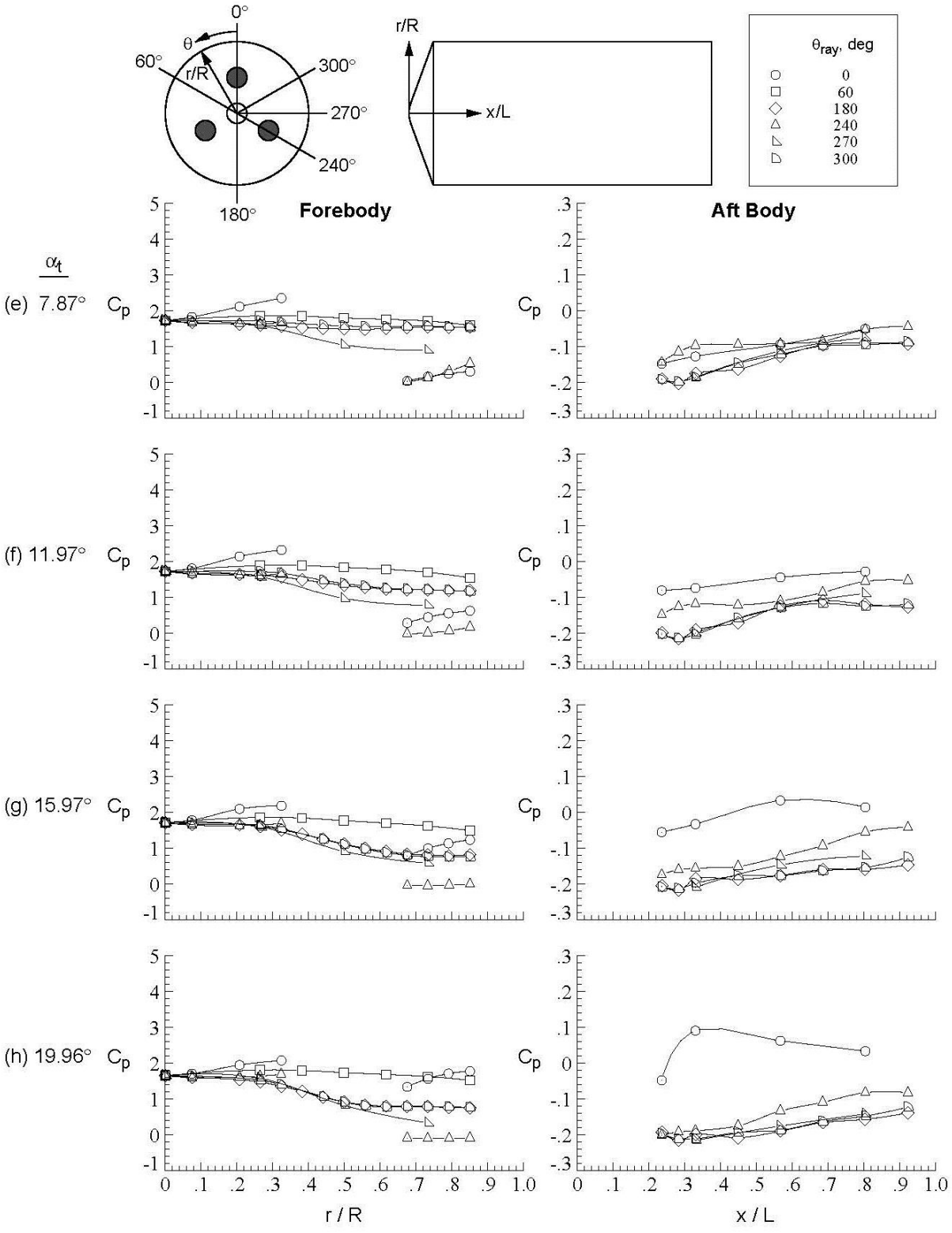

Figure D-168.Concluded.

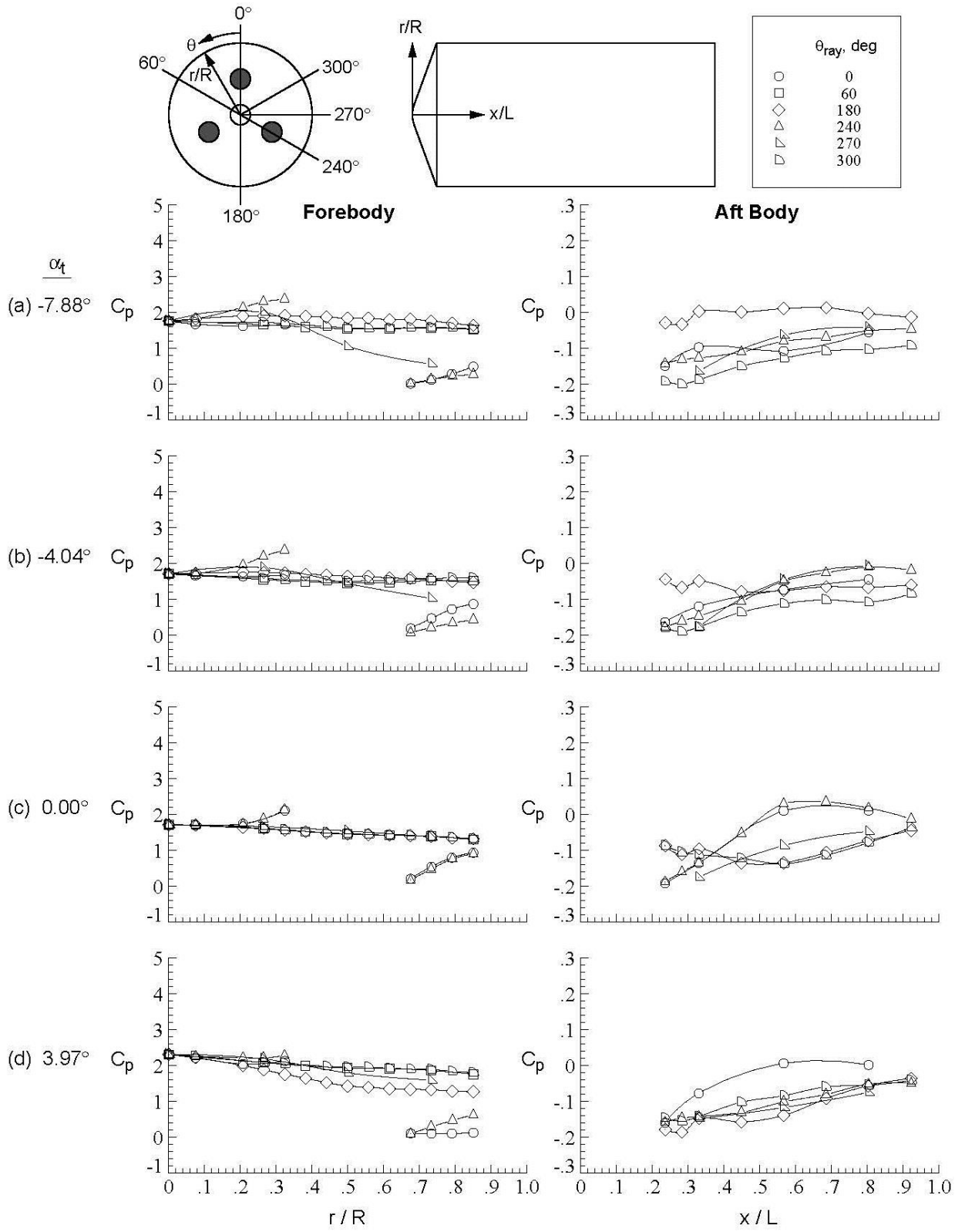

Figure D-169. Tri-nozzle configuration, Run 220, M_∞ = 2.4, Re_∞ = 1.0x10^6/ft, ϕ = 179.95°, X_S = 40.15 in, Y_S = 0.00 in, C_T = 0.48.

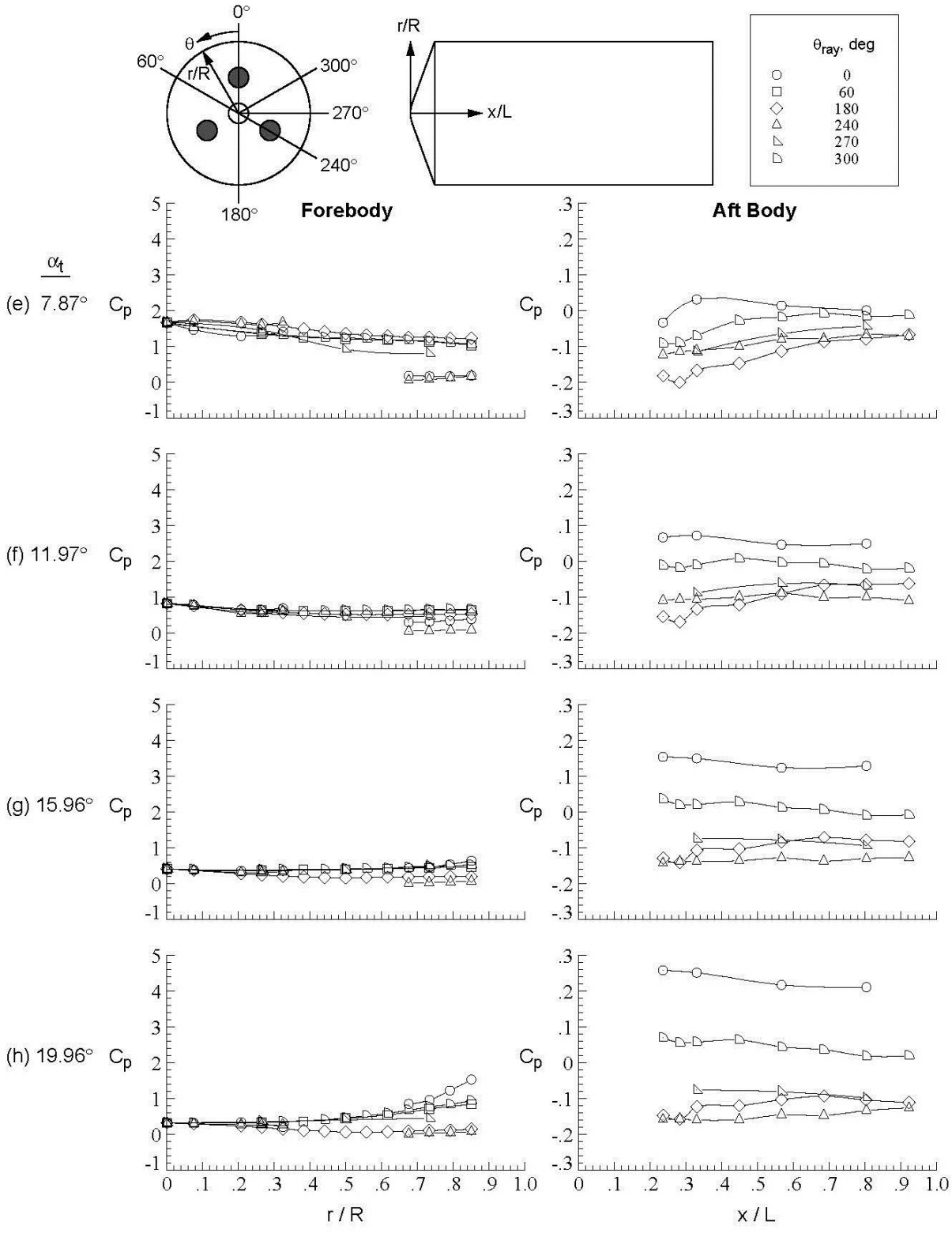

Figure D-169.Concluded.

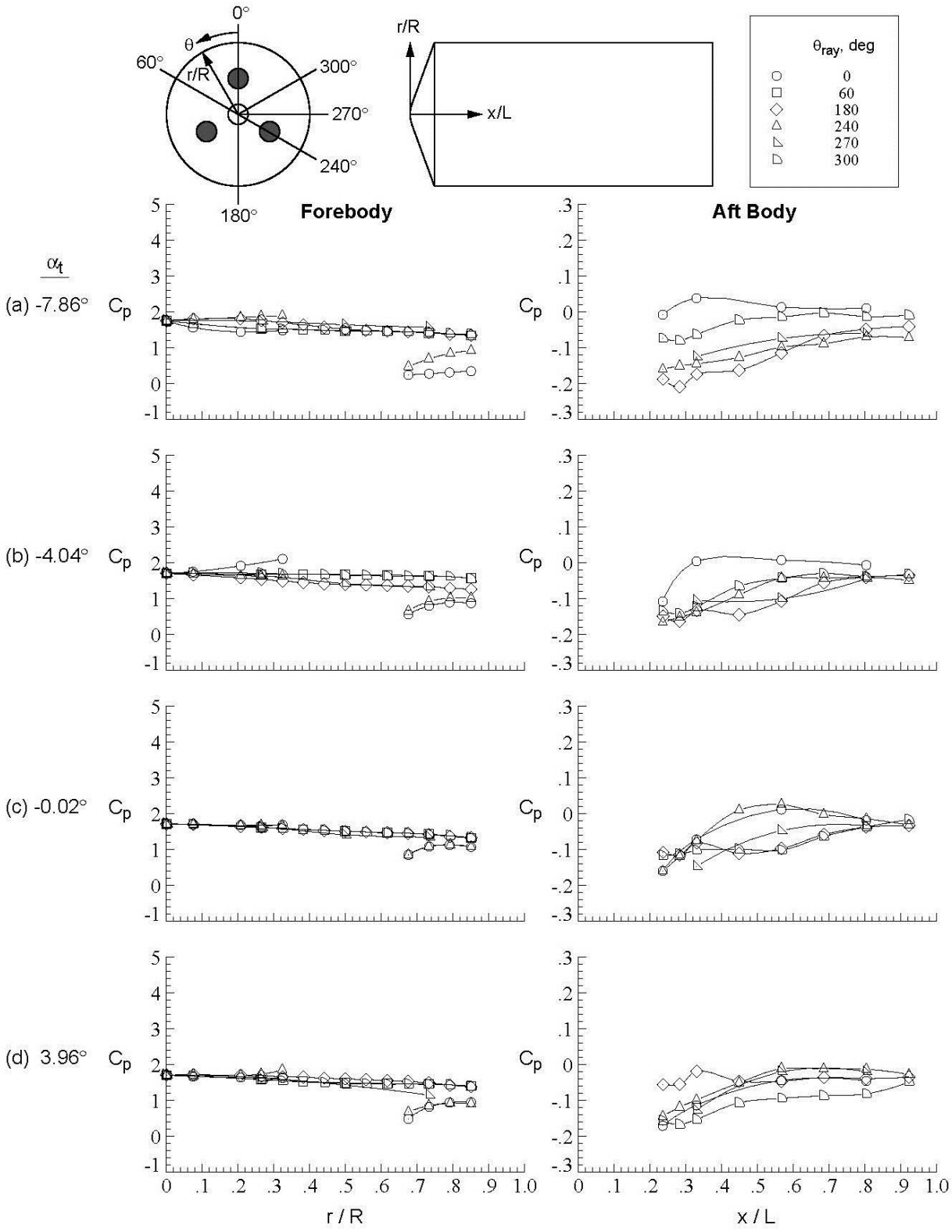

Figure D-170. Tri-nozzle configuration, Run 221, M_∞ = 2.4, Re_∞ = 1.0x10^6/ft, ϕ = −0.01°, X_S = 40.15 in, Y_S = 0.00 in, C_T = 0.24.

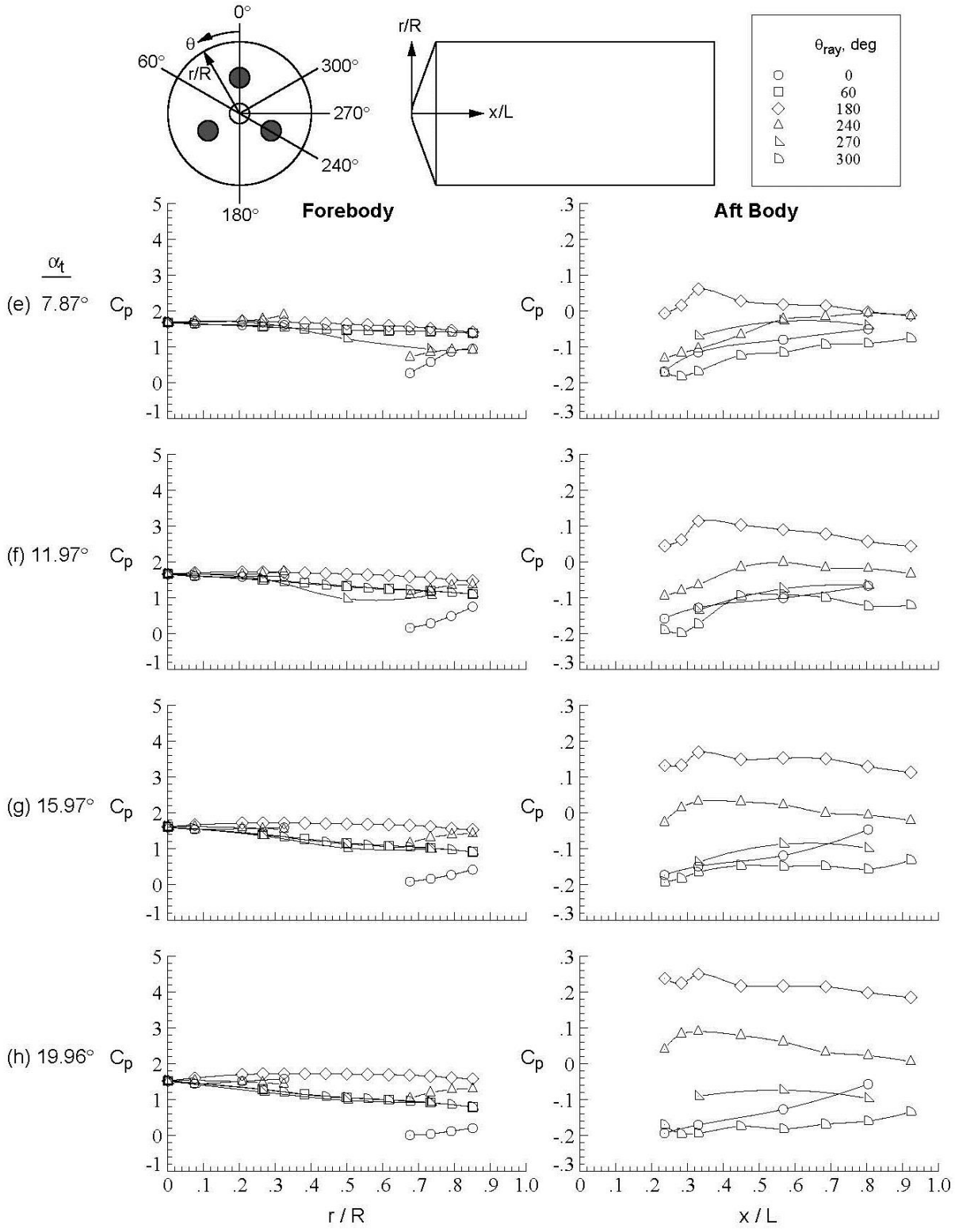

Figure D-170.Concluded.

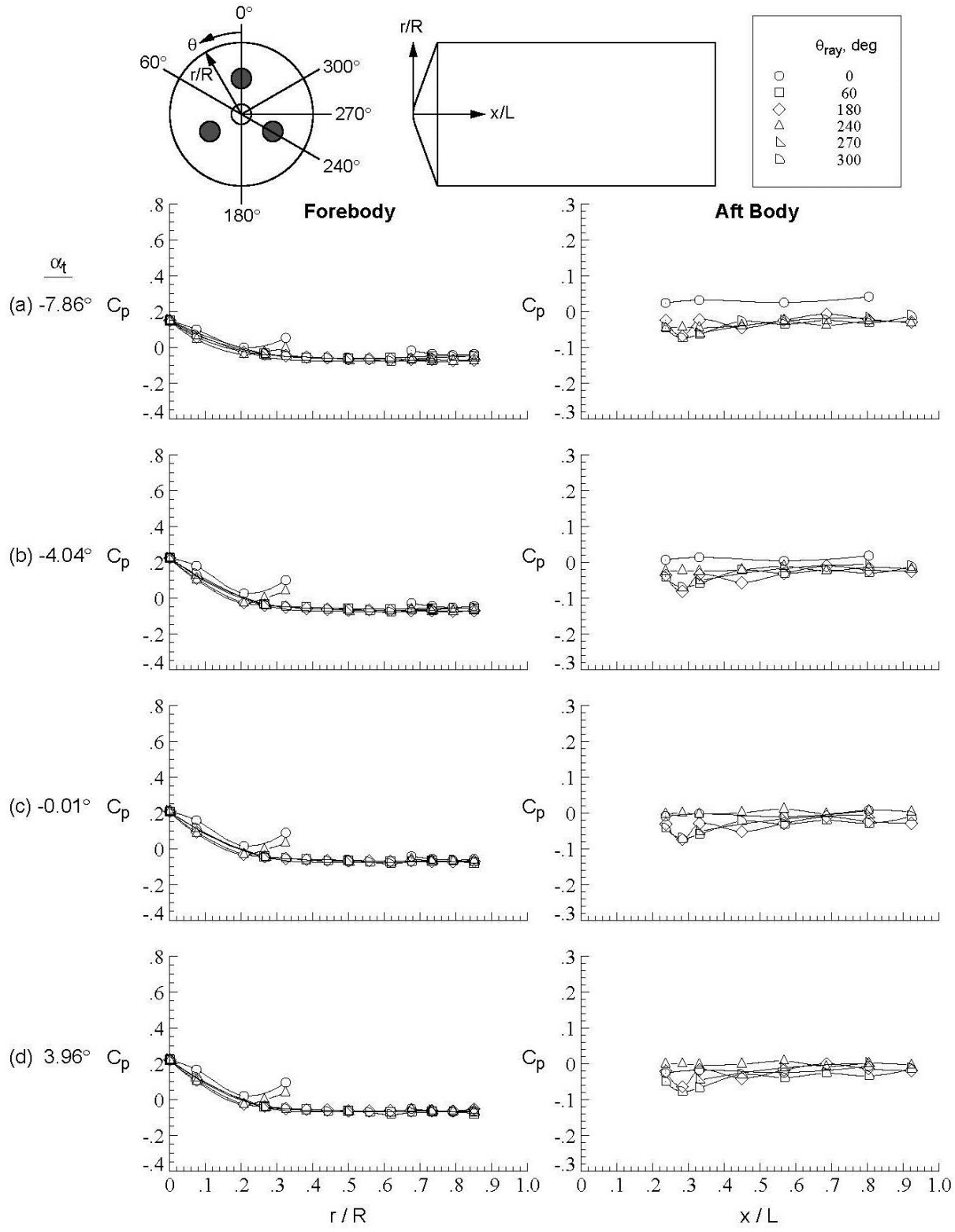

Figure D-171. Tri-nozzle configuration, Run 222, M_∞ = 3.5, Re_∞ = 1.0x10^6/ft, ϕ = −0.01°, X_S = 40.15 in, Y_S = 0.00 in, C_T = 2.94.

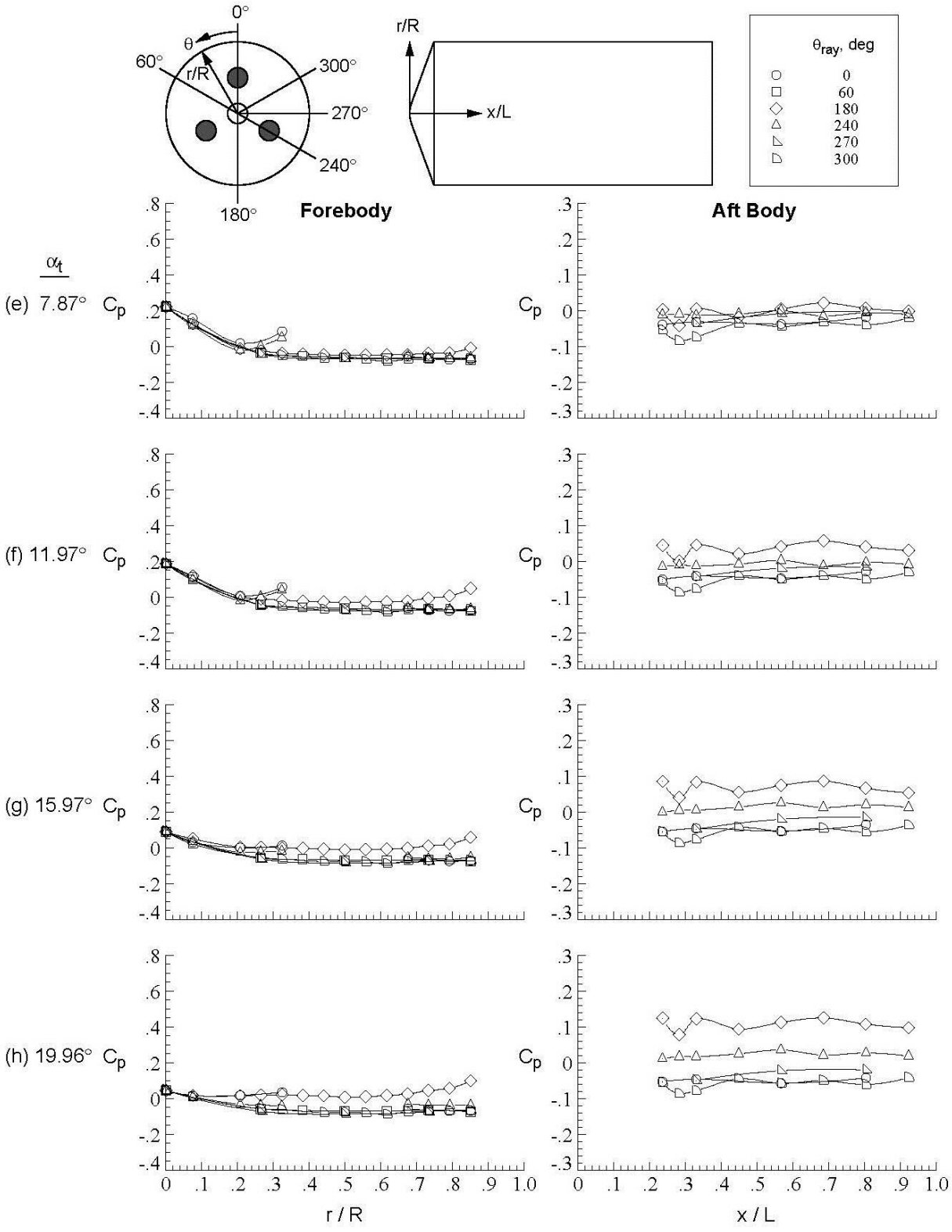

Figure D-171.Concluded.

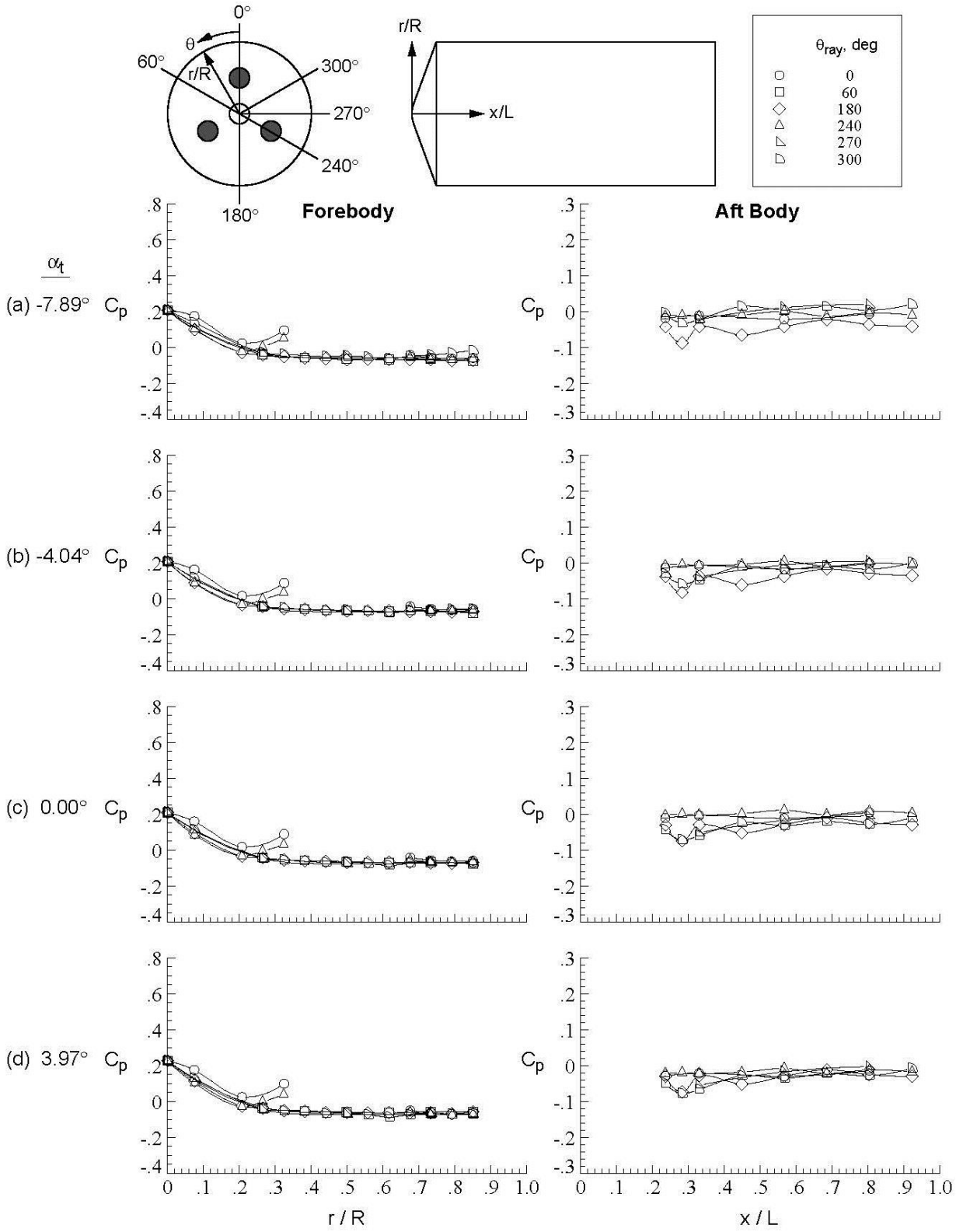

Figure D-172. Tri-nozzle configuration, Run 223, $M\infty$ = 3.5, Re_∞ = 1.0x10^7/ft, ϕ = 59.90°, X_S = 40.15 in, Y_S = 0.00 in, C_T = 2.95.

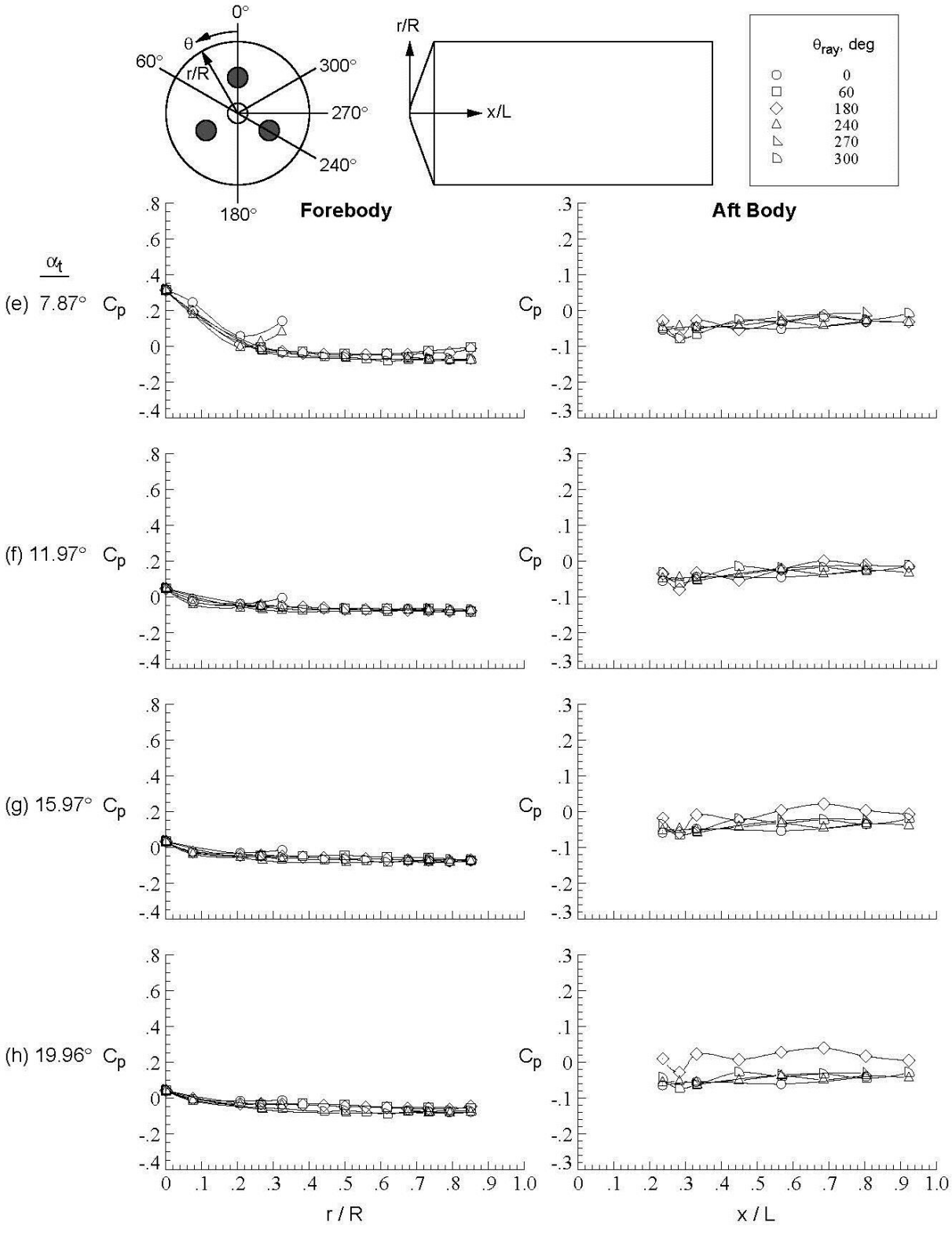

Figure D-172.Concluded.

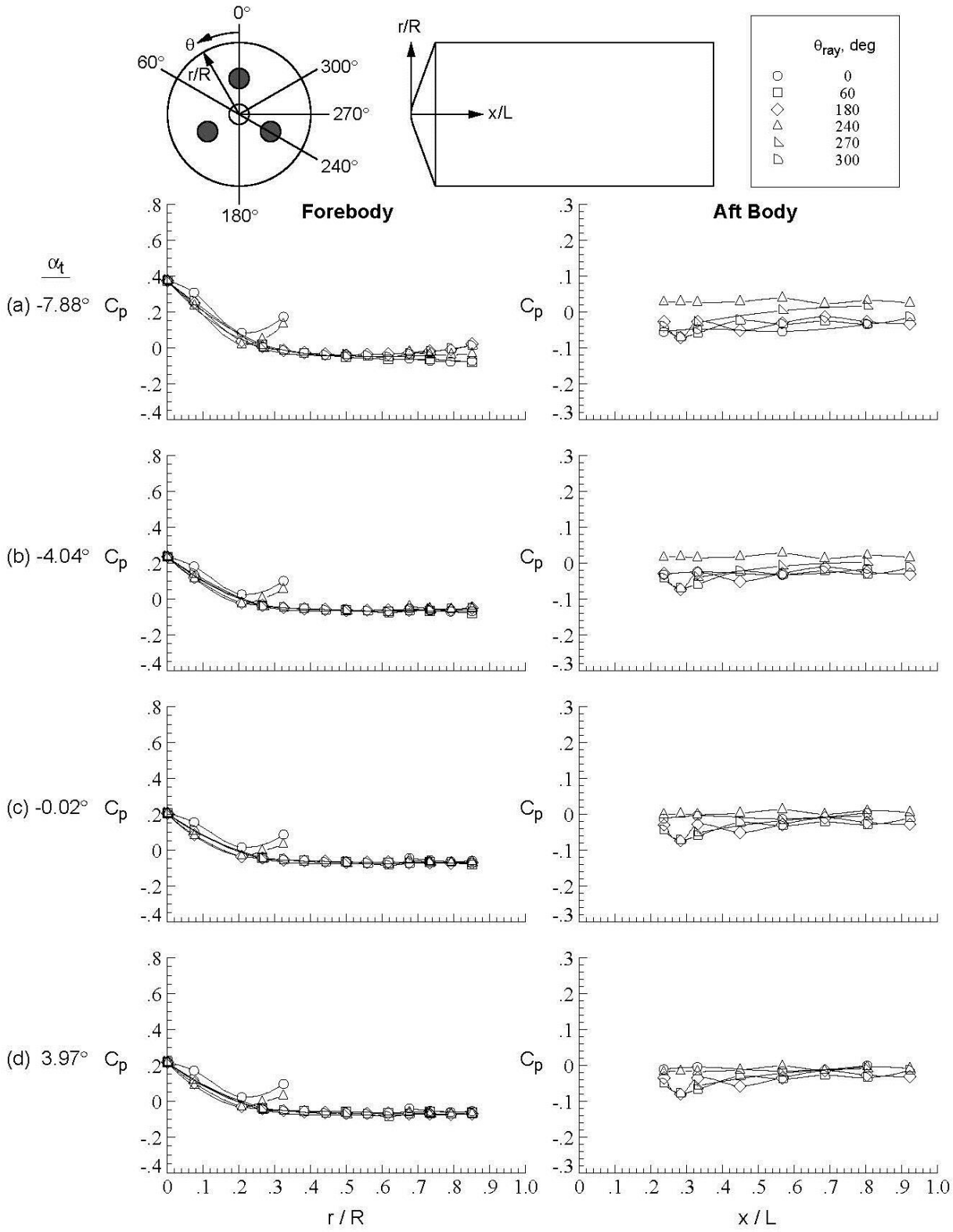

Figure D-173. Tri-nozzle configuration, Run 224, M_∞ = 3.5, Re_∞ = 1.0x10^7/ft, ϕ = 120.06°, X_S = 40.15 in, Y_S = 0.00 in, C_T = 2.97.

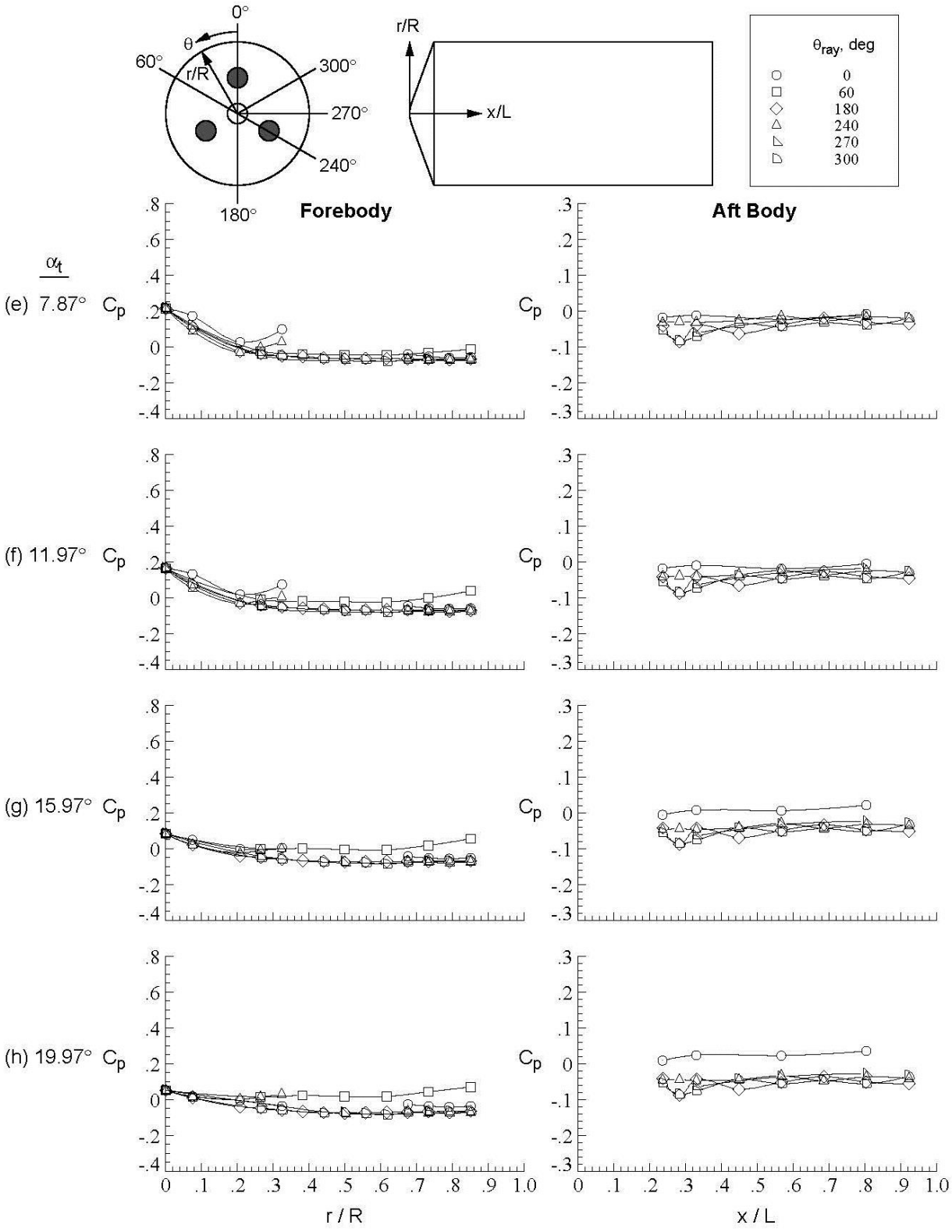

Figure D-173.Concluded.

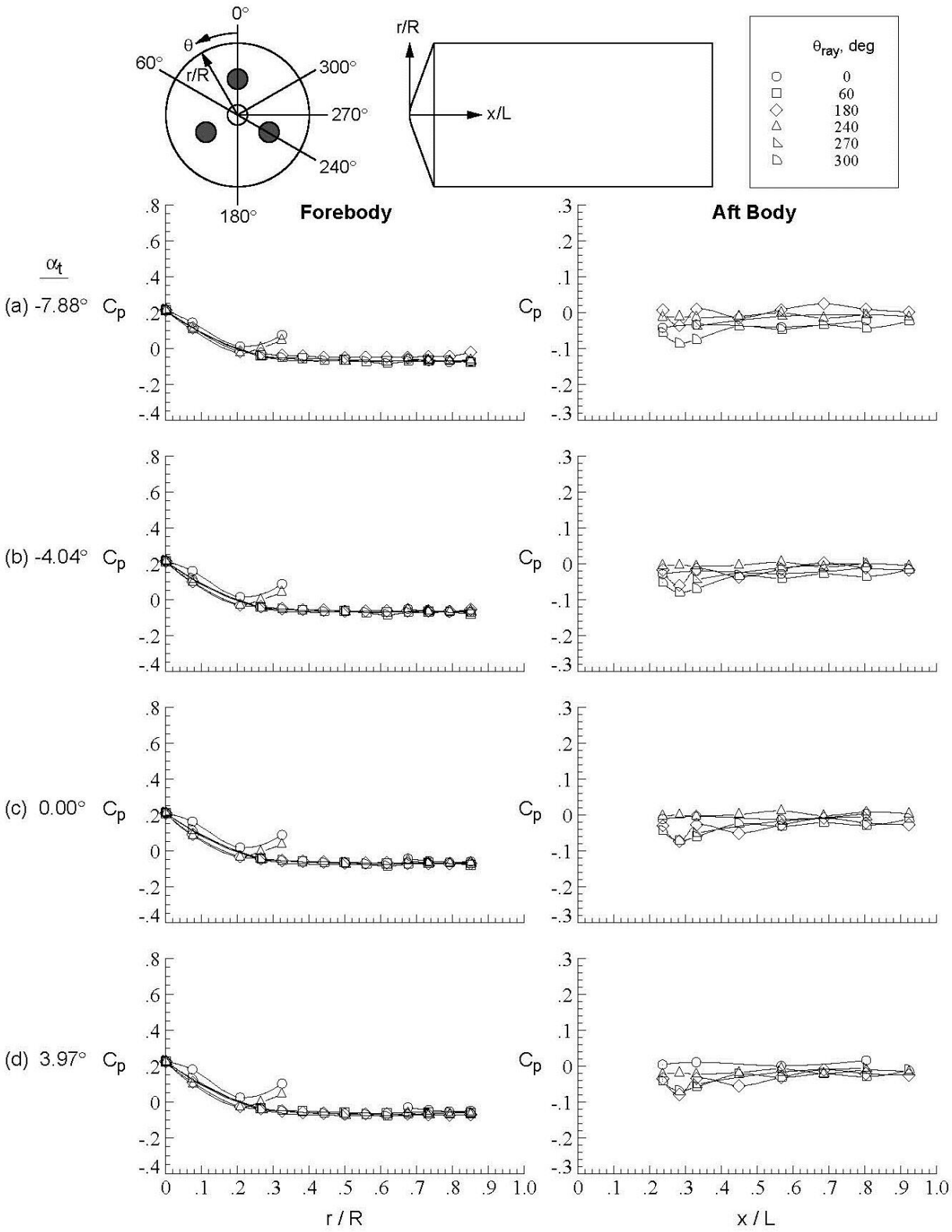

Figure D-174. Tri-nozzle configuration, Run 225, M_∞ = 3.5, Re_∞ = 1.0x10^6/ft, ϕ = 179.97°, X_S = 40.15 in, Y_S = 0.00 in, C_T = 2.97.

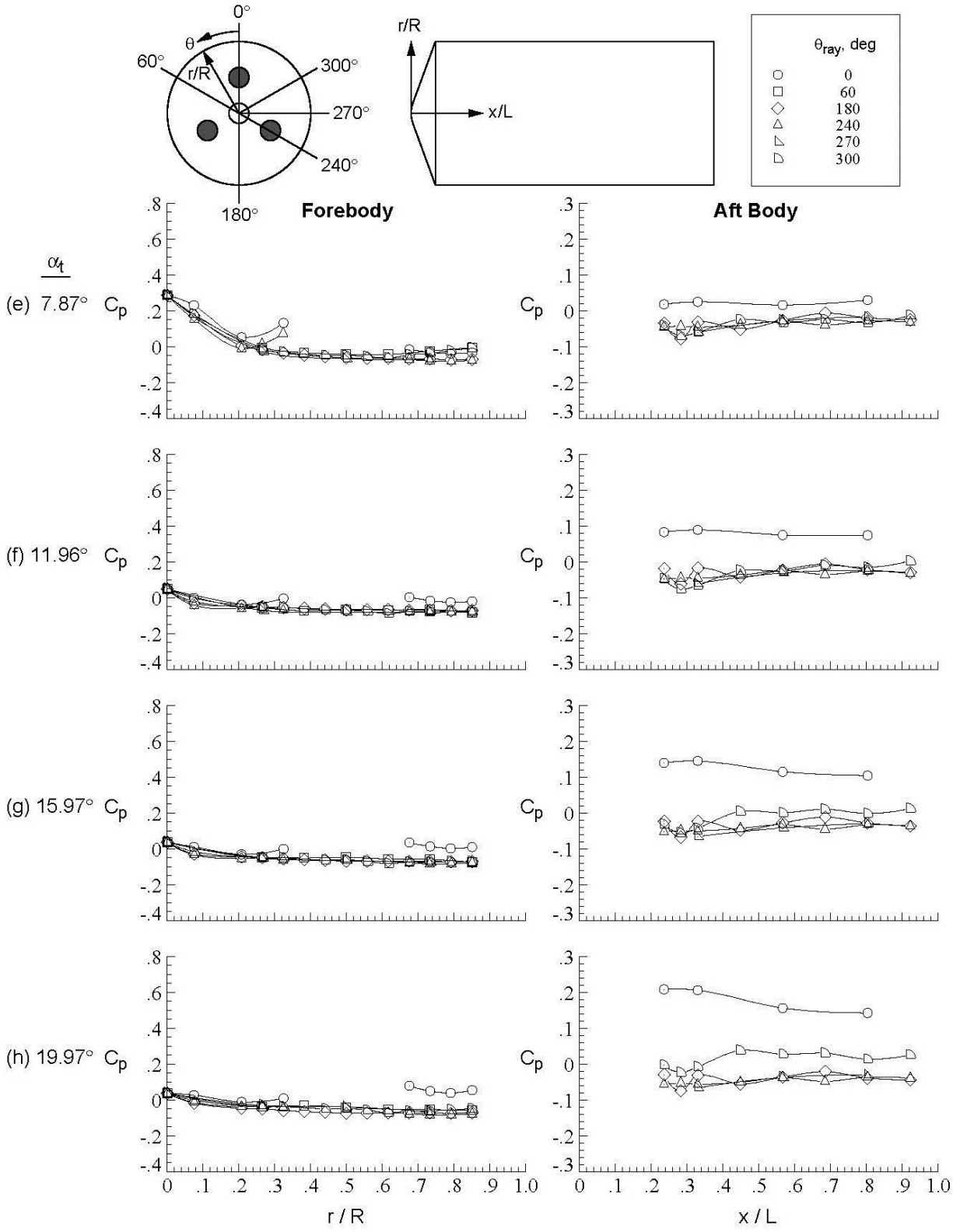

Figure D-174.Concluded.

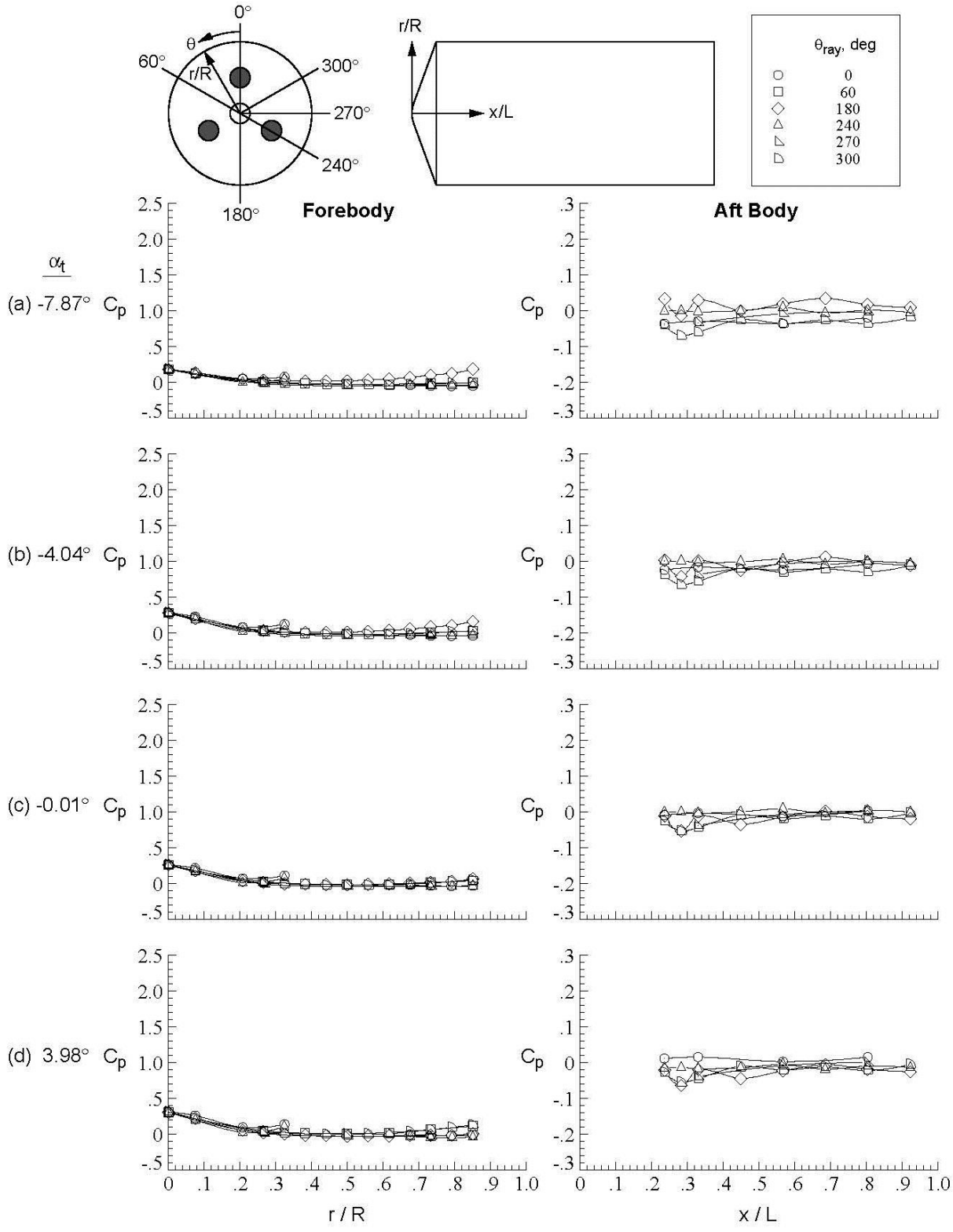

Figure D-175. Tri-nozzle configuration, Run 226, M_∞ = 3.5, Re_∞ = 1.0x10^6/ft, ϕ = 179.97°, X_S = 40.15 in, Y_S = 0.00 in, C_T = 1.96.

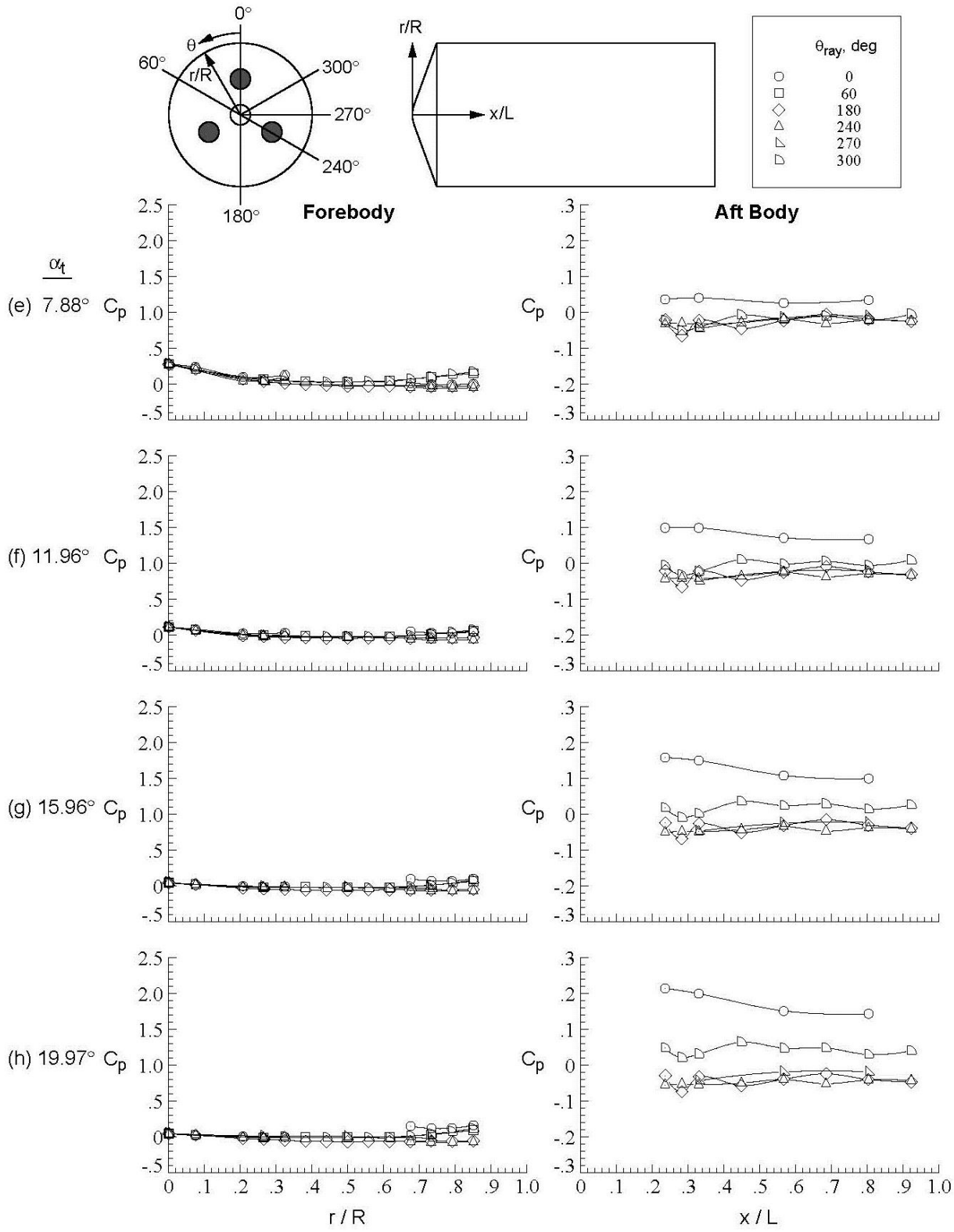

Figure D-175.Concluded.

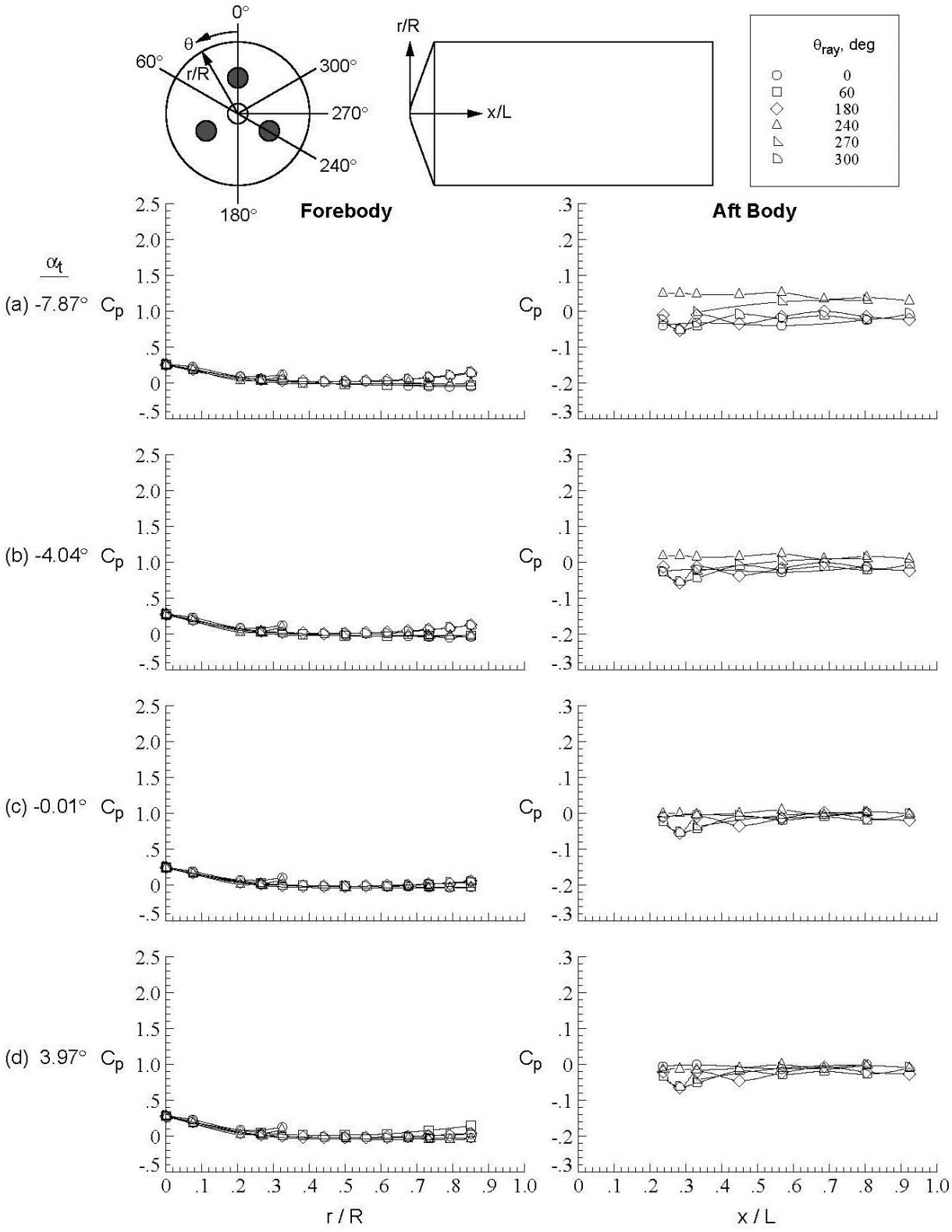

Figure D-176. Tri-nozzle configuration, Run 227, M_∞ = 3.5, Re_∞ = 1.0x10^6/ft, ϕ = 120.04°, X_S = 40.15 in, Y_S = 0.00 in, C_T = 1.95.

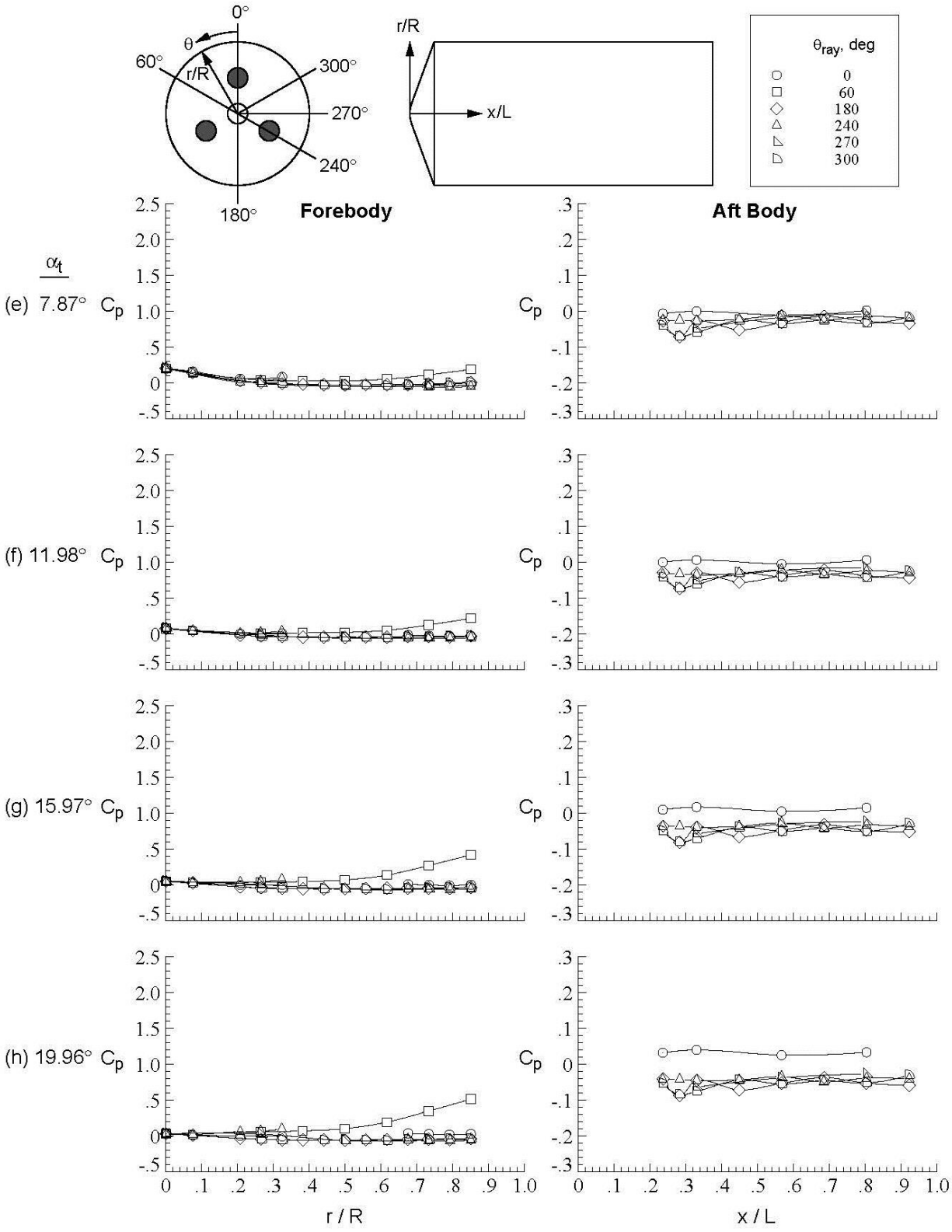

Figure D-176.Concluded.

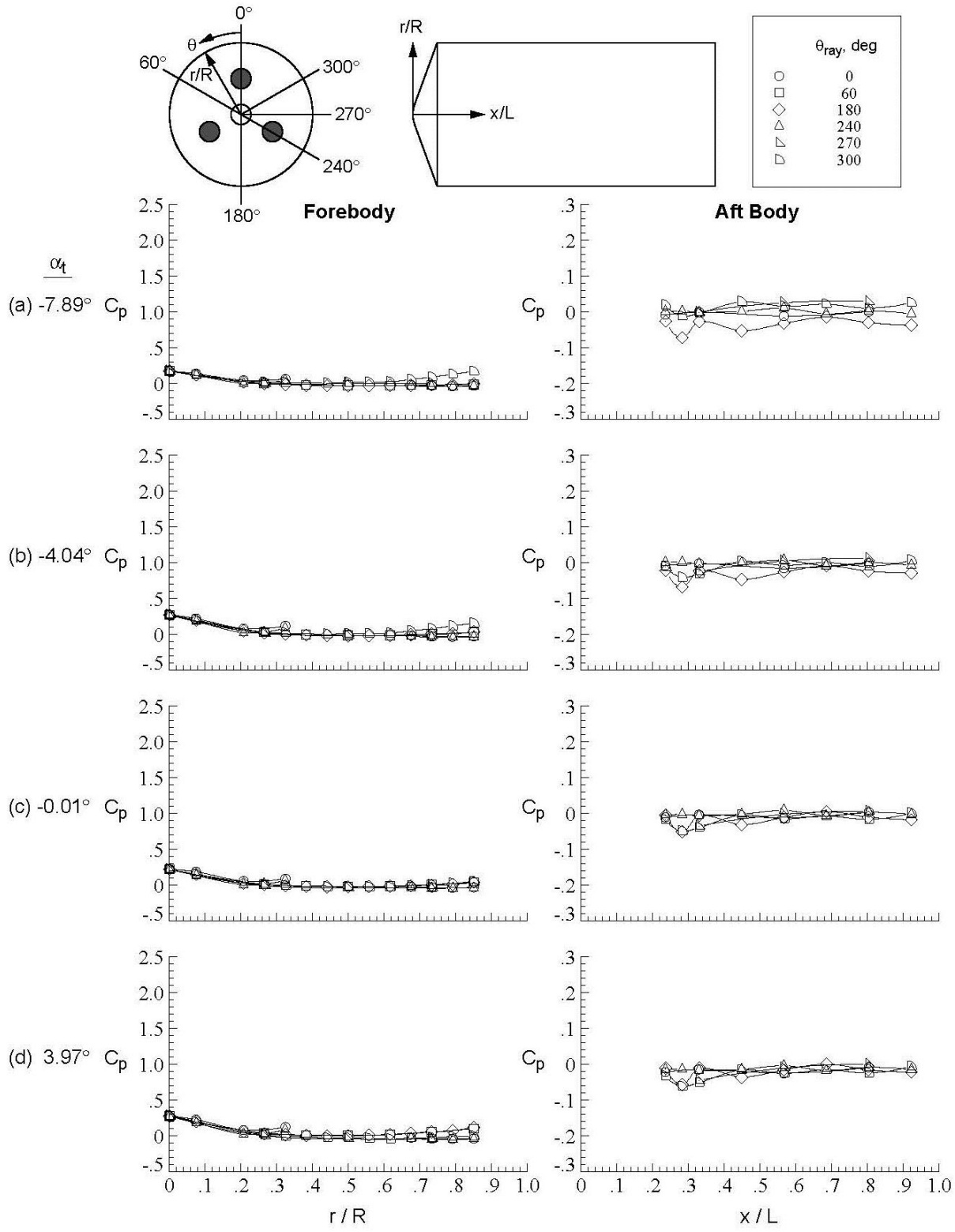

Figure D-177. Tri-nozzle configuration, Run 228, M_∞ = 3.5, Re_∞ = 1.0x10^7/ft, ϕ = 59.96°, X_S = 40.15 in, Y_S = 0.00 in, C_T = 1.94.

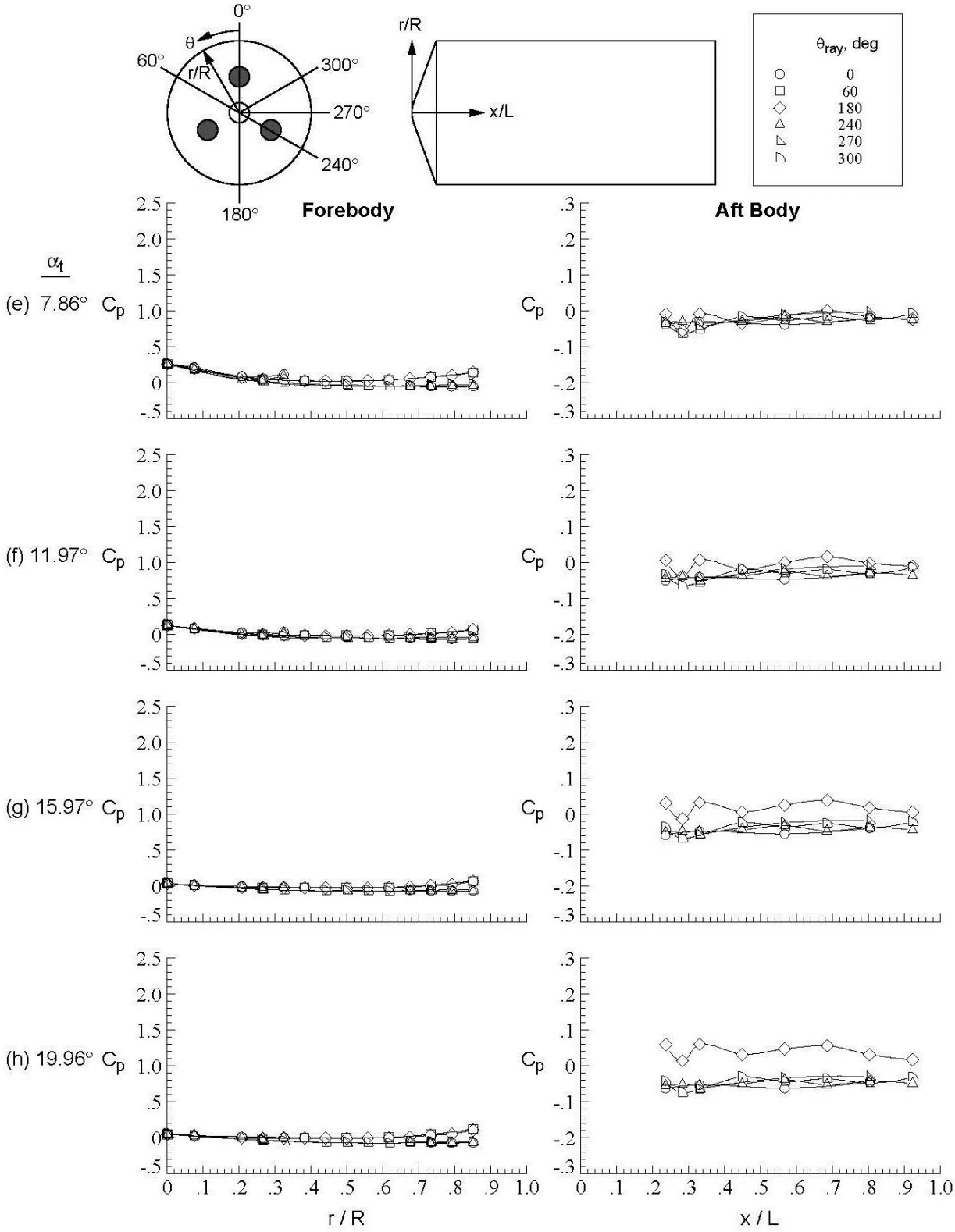

Figure D-177.Concluded.

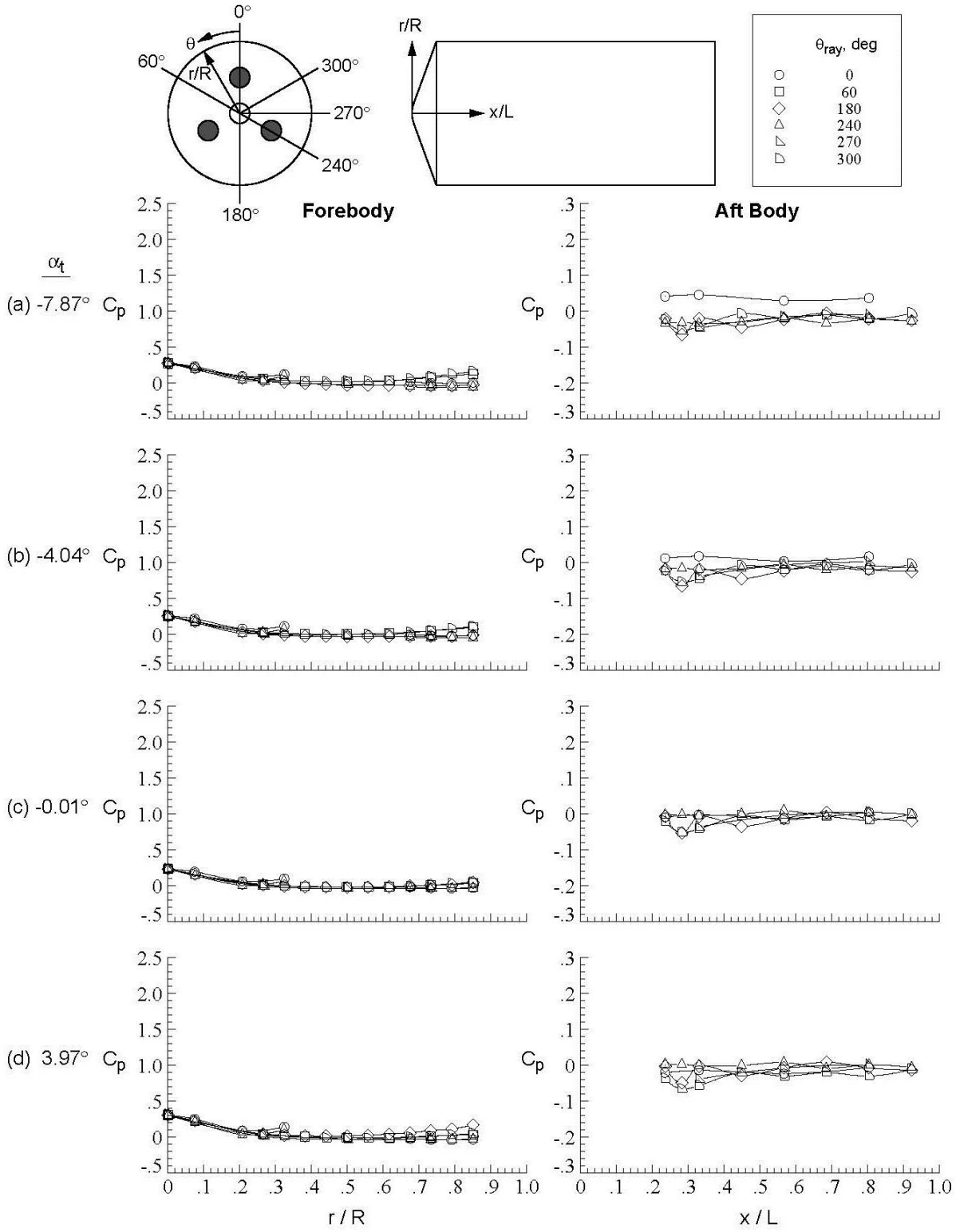

Figure D-178. Tri-nozzle configuration, Run 229, M_∞ = 3.5, Re_∞ = 1.0x10^7/ft, ϕ = −0.01°, X_S = 40.15 in, Y_S = 0.00 in, C_T = 1.94.

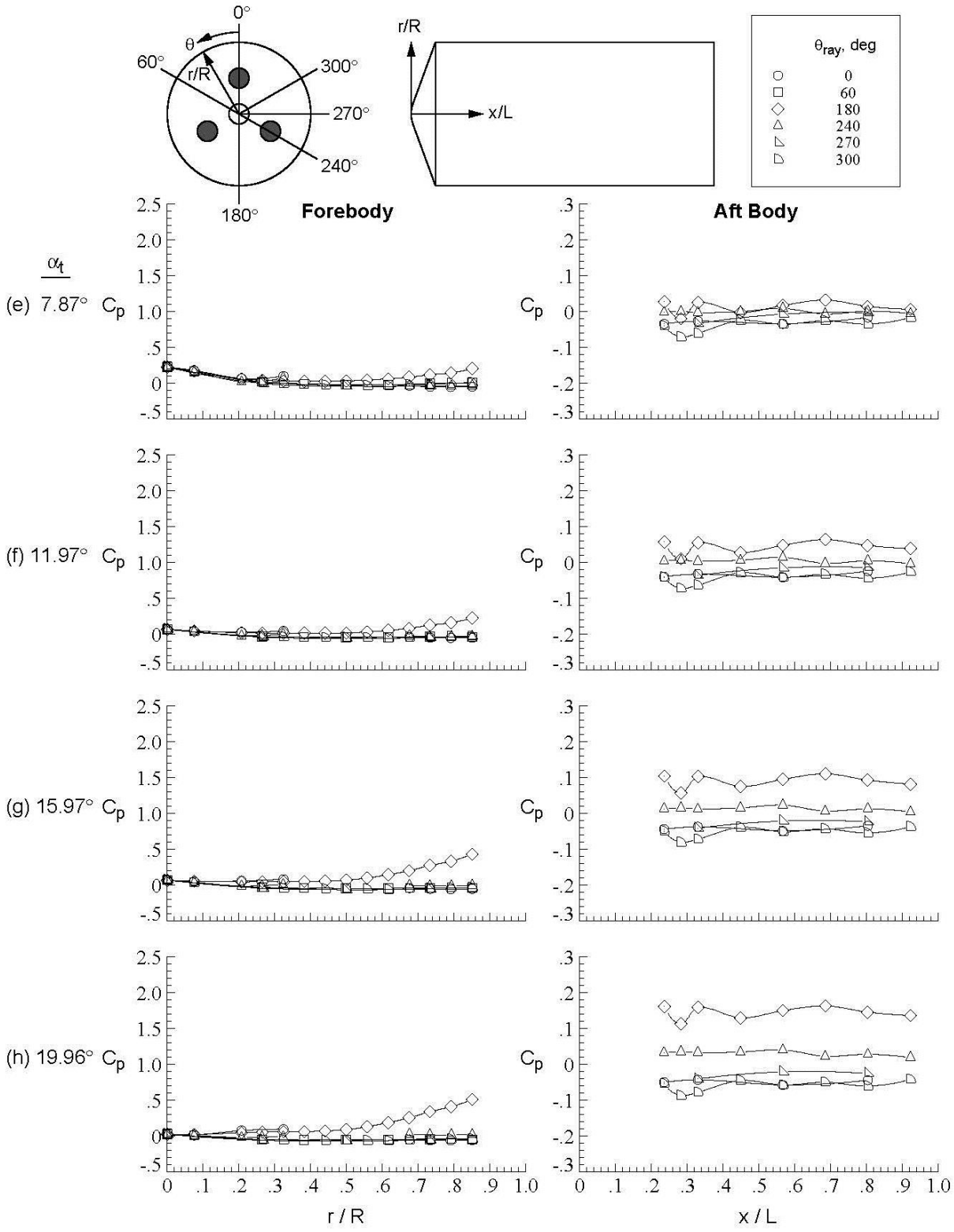

Figure D-178.Concluded.

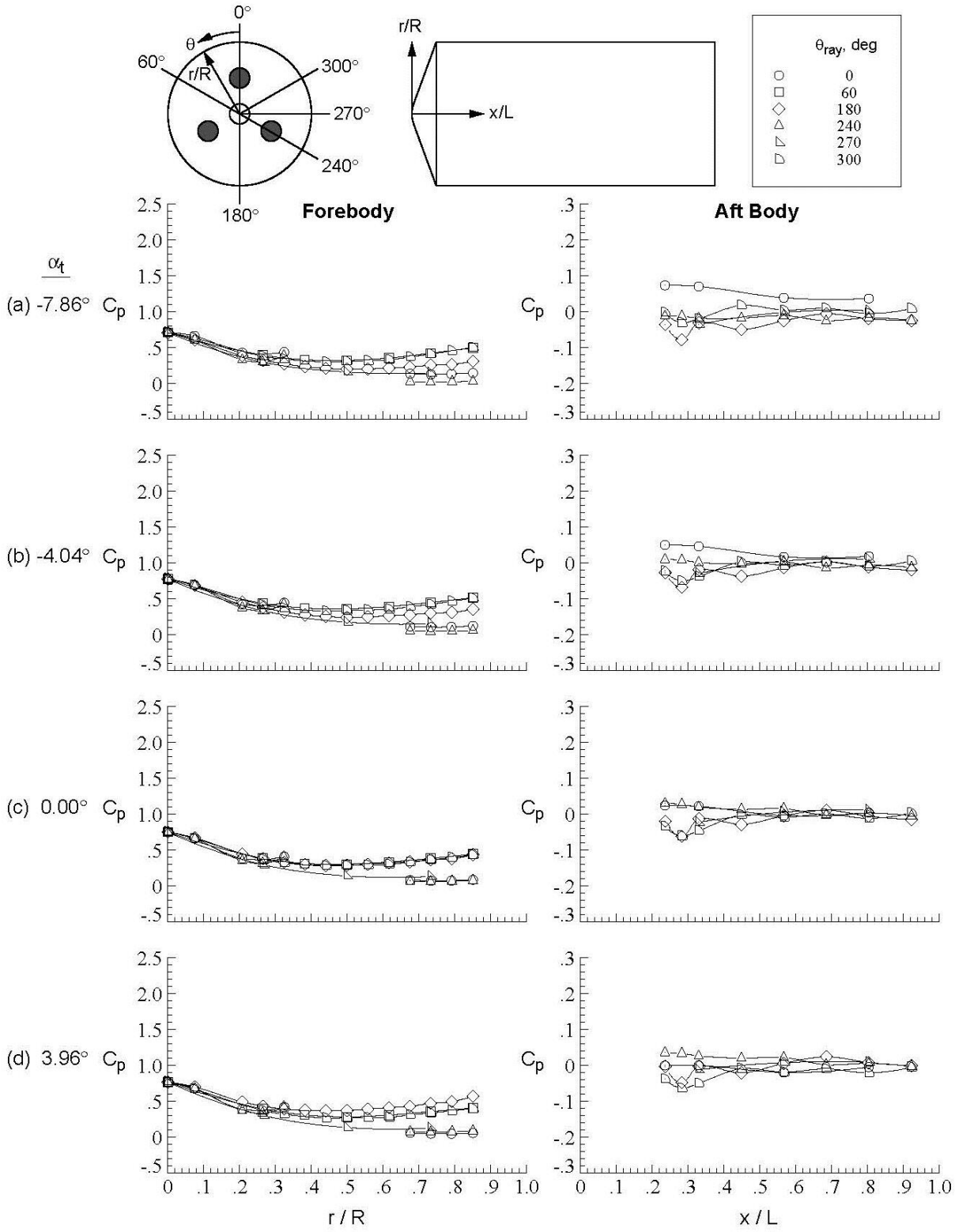

Figure D-179. Tri-nozzle configuration, Run 230, M_∞ = 3.5, Re_∞ = 1.0x10^7/ft, ϕ = −0.03°, X_S = 40.15 in, Y_S = 0.00 in, C_T = 0.96.

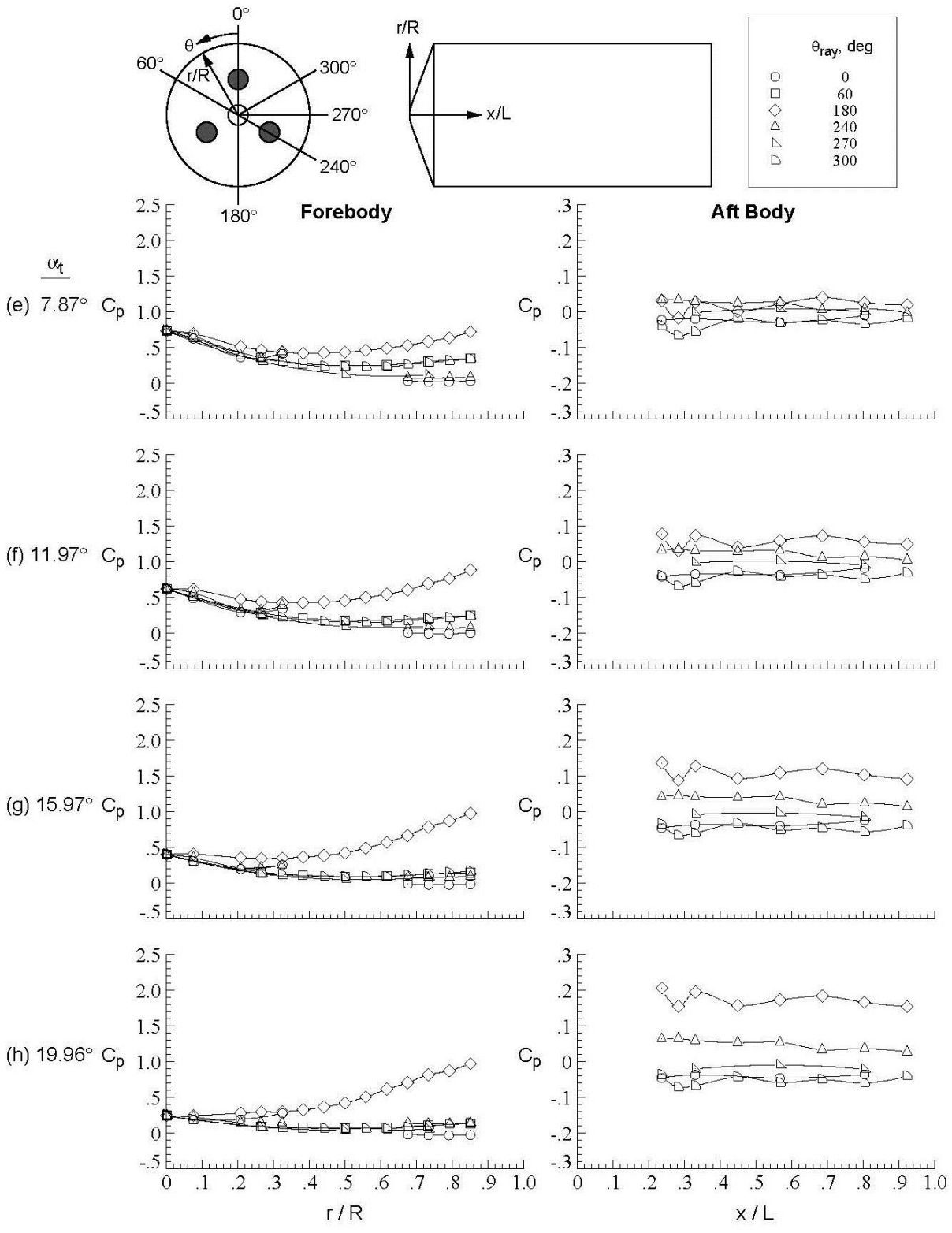

Figure D-179.Concluded.

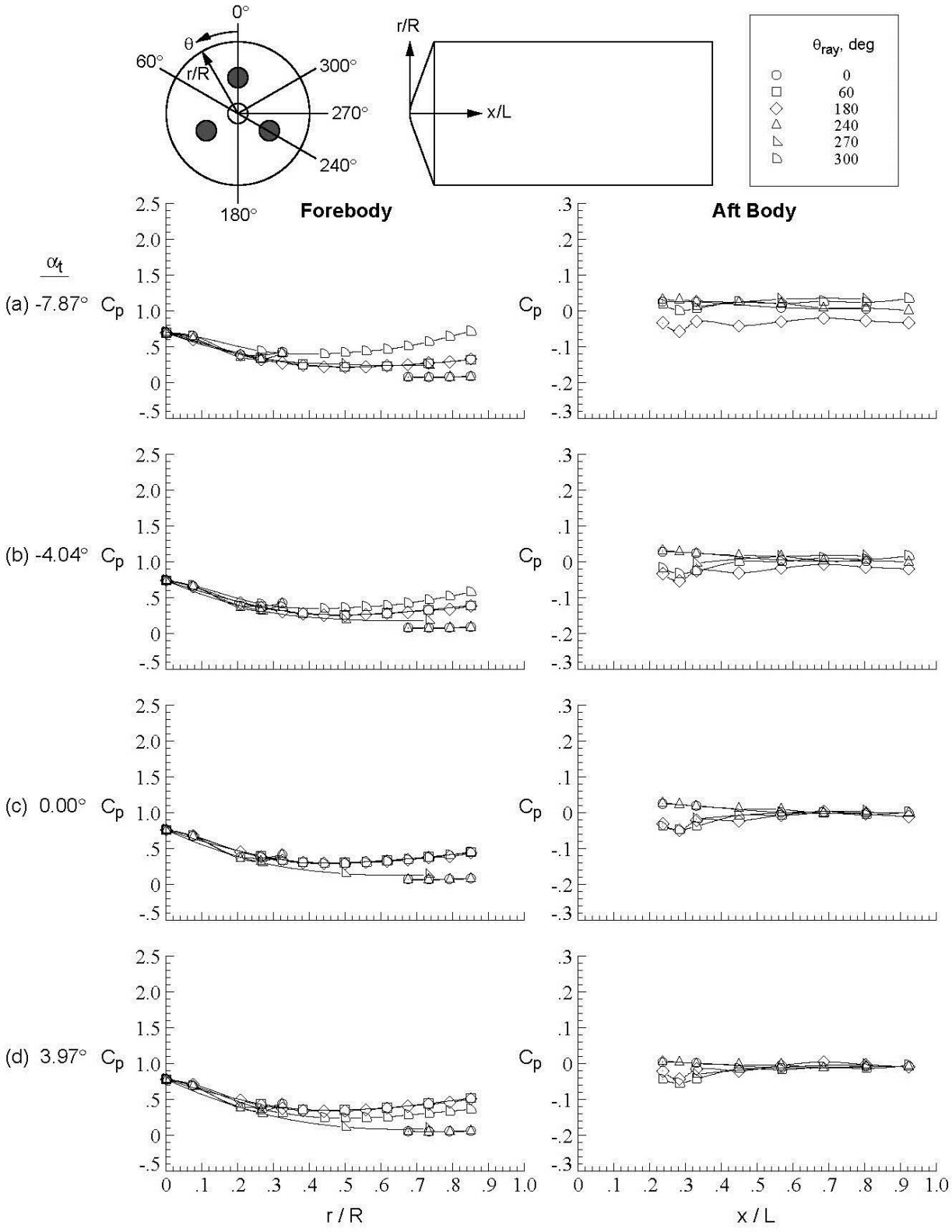

Figure D-180. Tri-nozzle configuration, Run 233, M_∞ = 3.5, Re_∞ = 1.0x10^6/ft, ϕ = 59.90°, X_S = 40.15 in, Y_S = 0.00 in, C_T = 0.97.

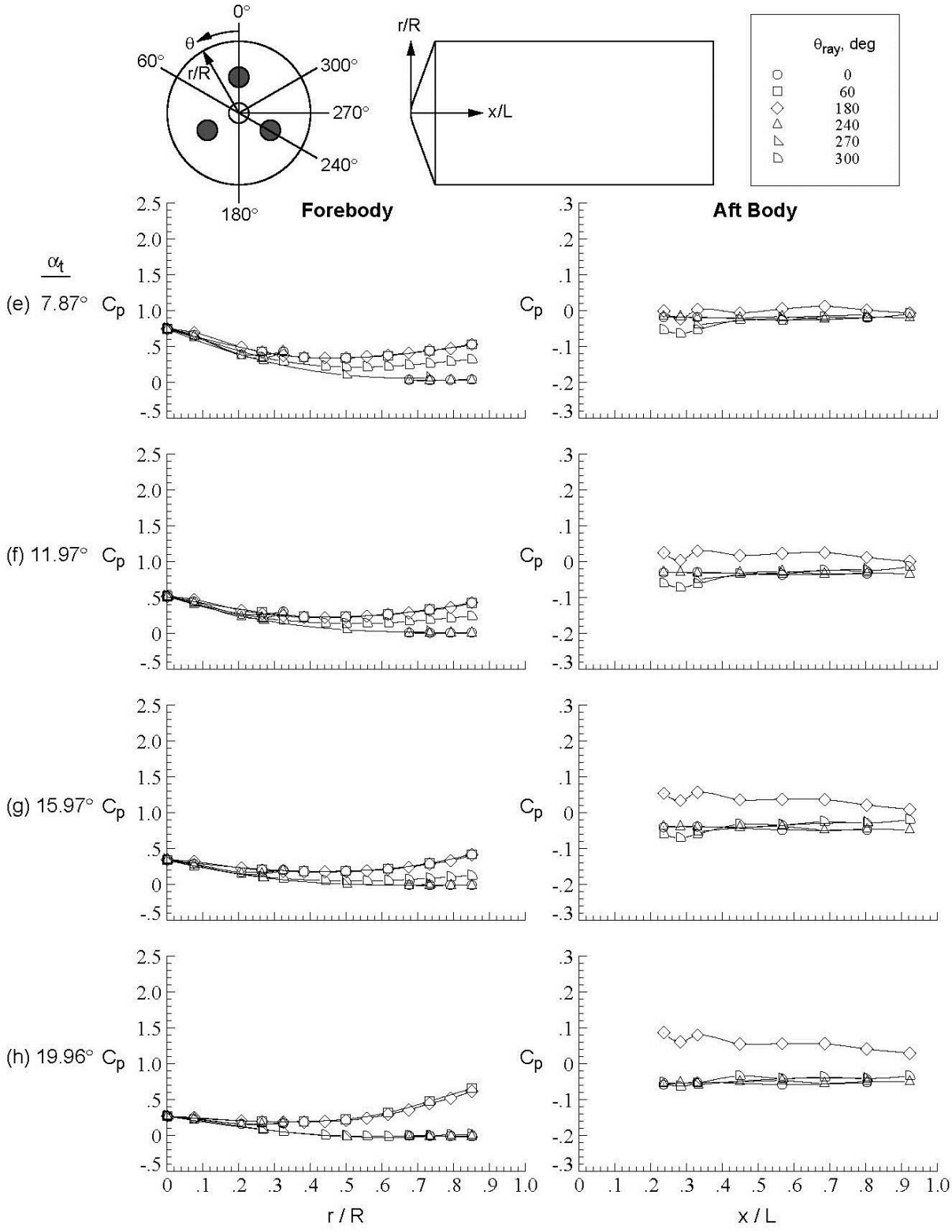

Figure D-180.Concluded.

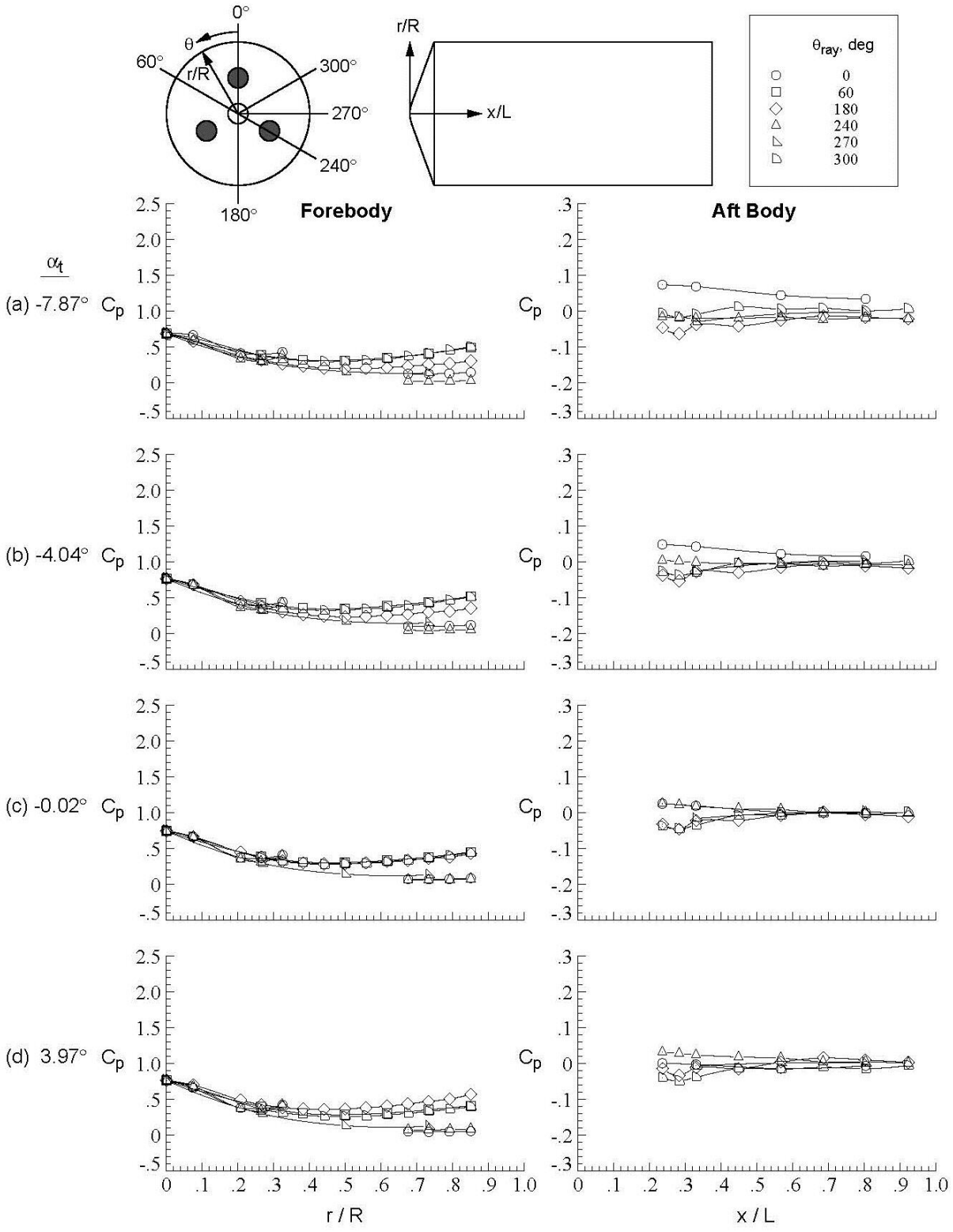

Figure D-181. Tri-nozzle configuration, Run 234, M_∞ = 3.5, Re_∞ = 1.0x10^7/ft, ϕ = −0.05°, X_S = 40.15 in, Y_S = 0.00 in, C_T = 0.96.

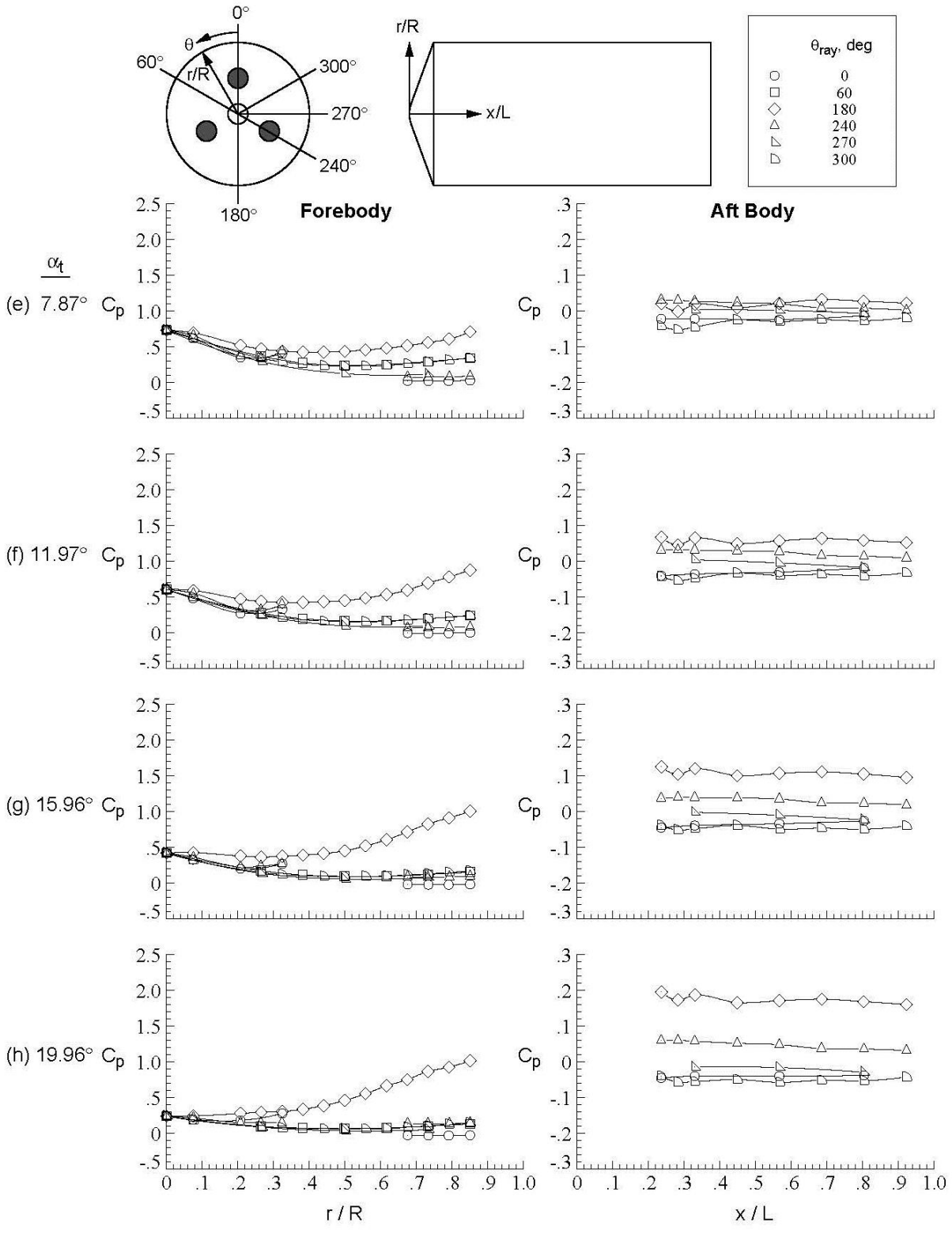

Figure D-181.Concluded.

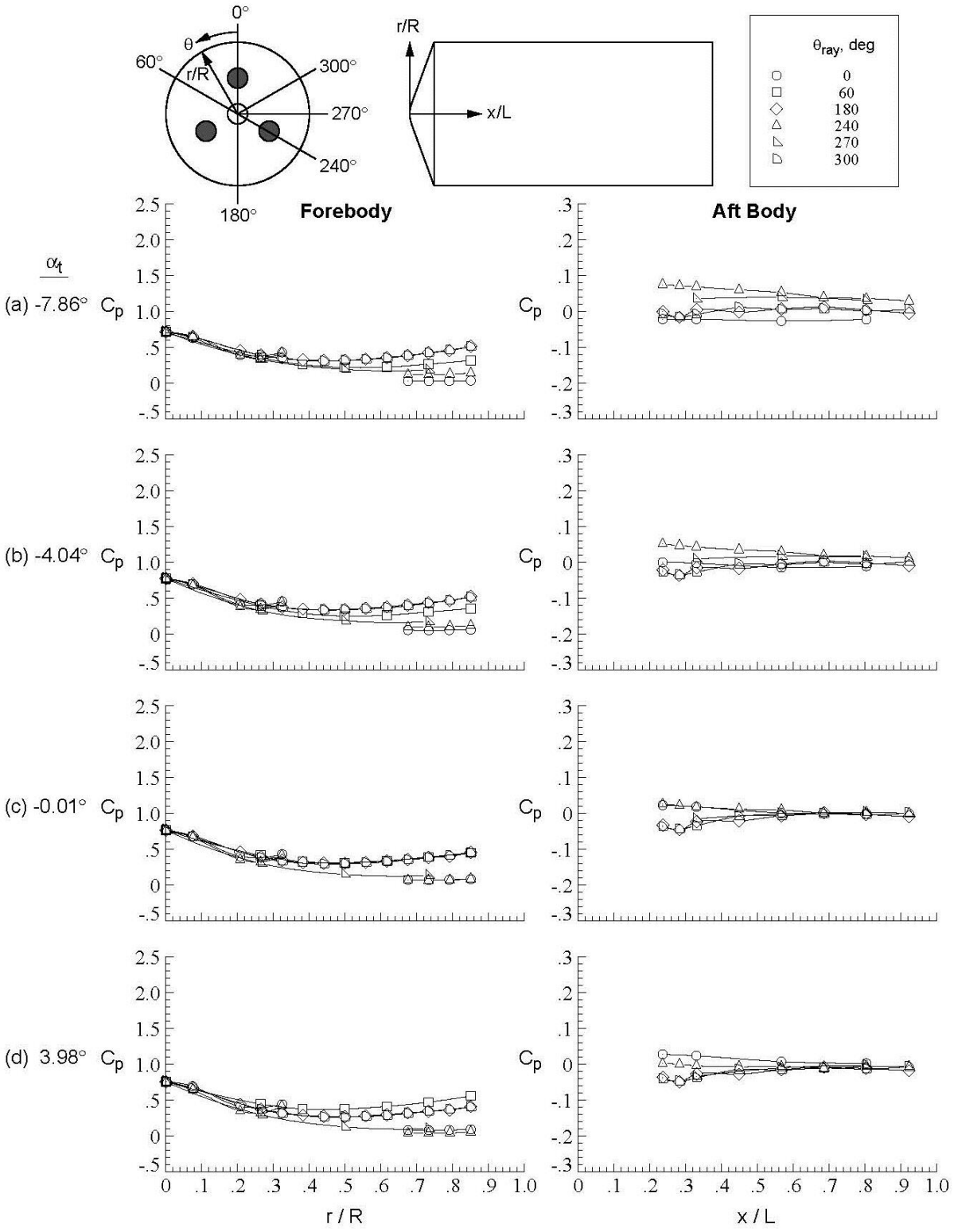

Figure D-182. Tri-nozzle configuration, Run 235, M_∞ = 3.5, Re_∞ = 1.0x10^7/ft, ϕ = 120.06°, X_S = 40.15 in, Y_S = 0.00 in, C_T = 0.96.

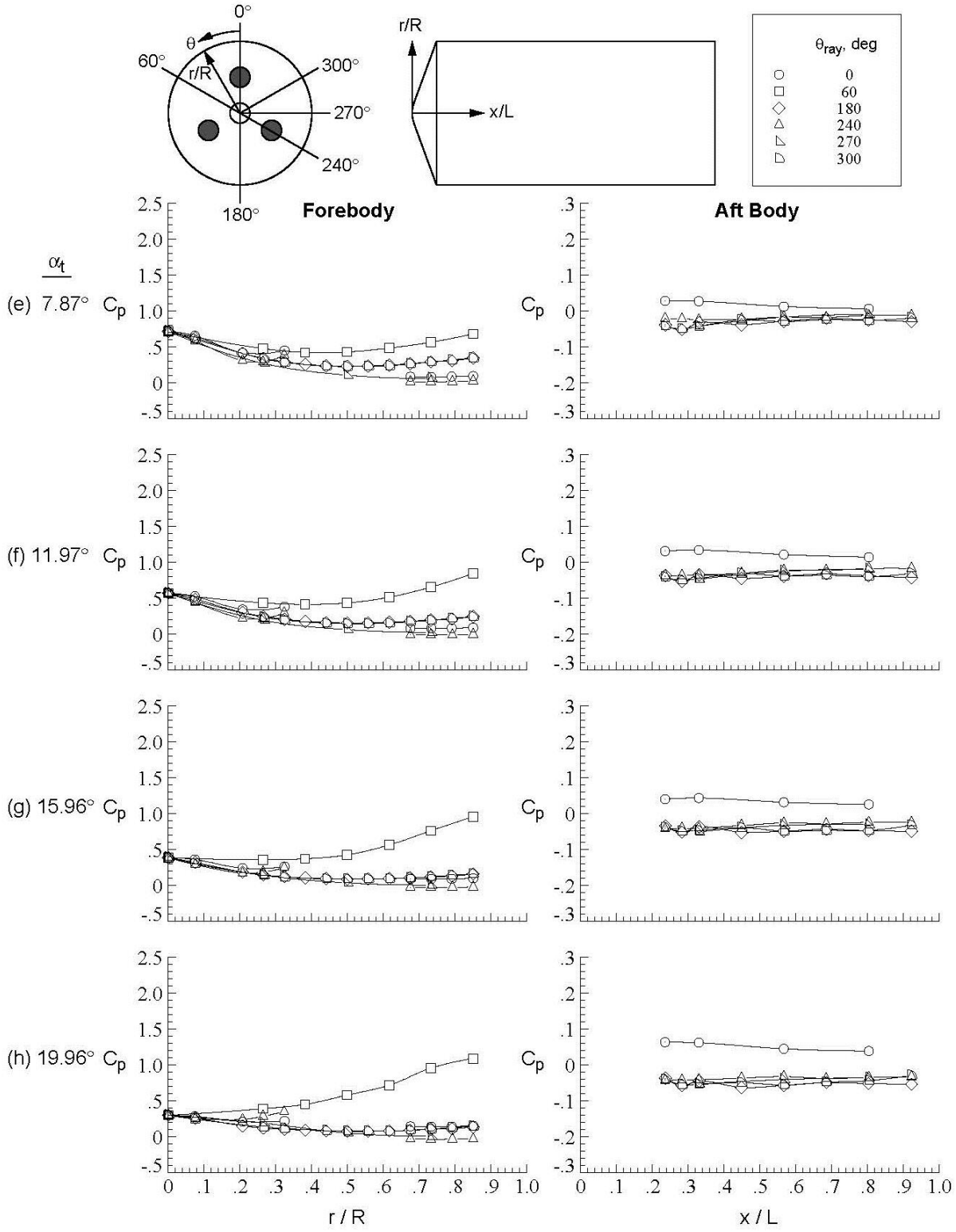

Figure D-182.Concluded.

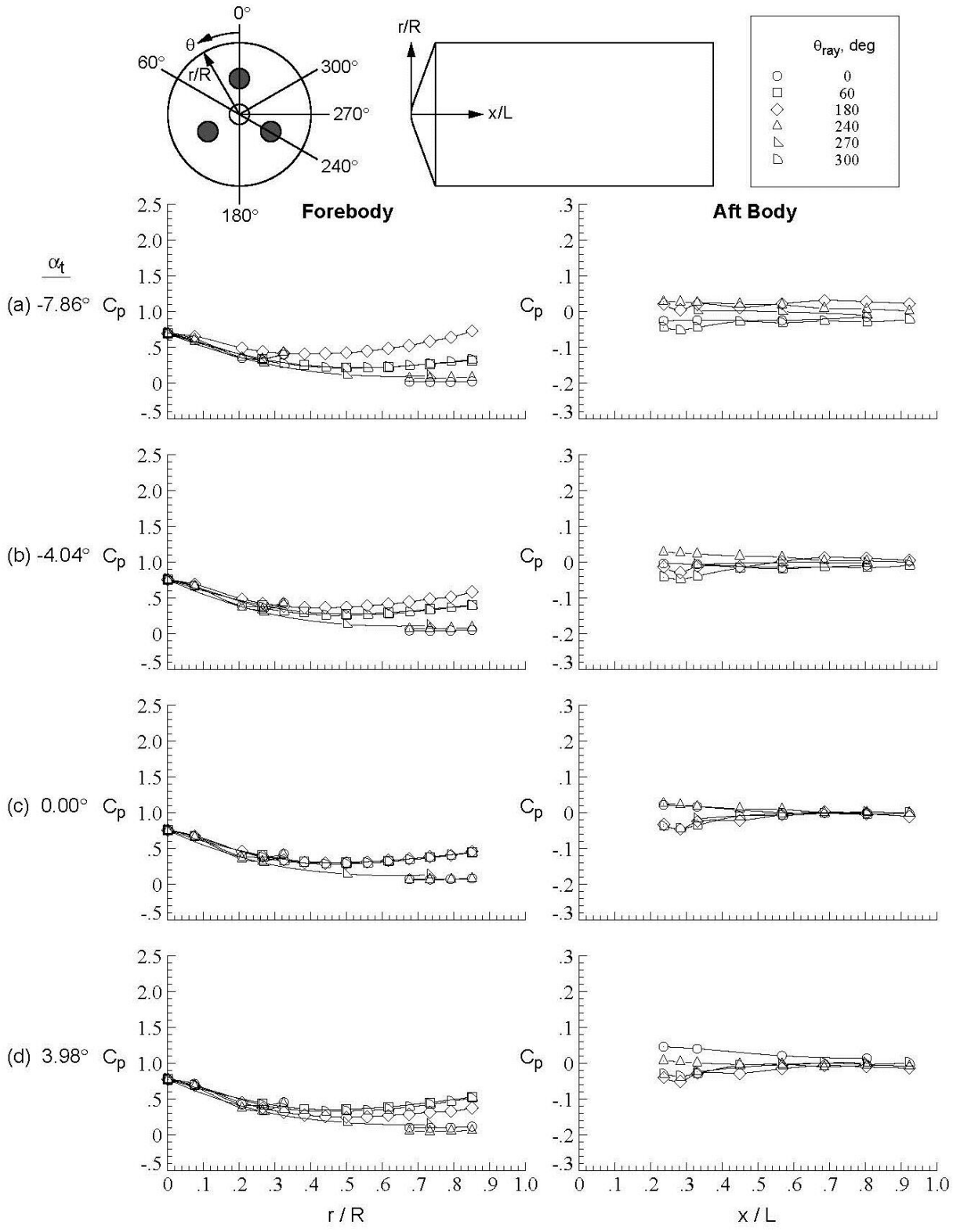

Figure D-183. Tri-nozzle configuration, Run 236, M_∞ = 3.5, Re_∞ = 1.0x10^6/ft, ϕ = 179.95°, X_S = 40.15 in, Y_S = 0.00 in, C_T = 0.97.

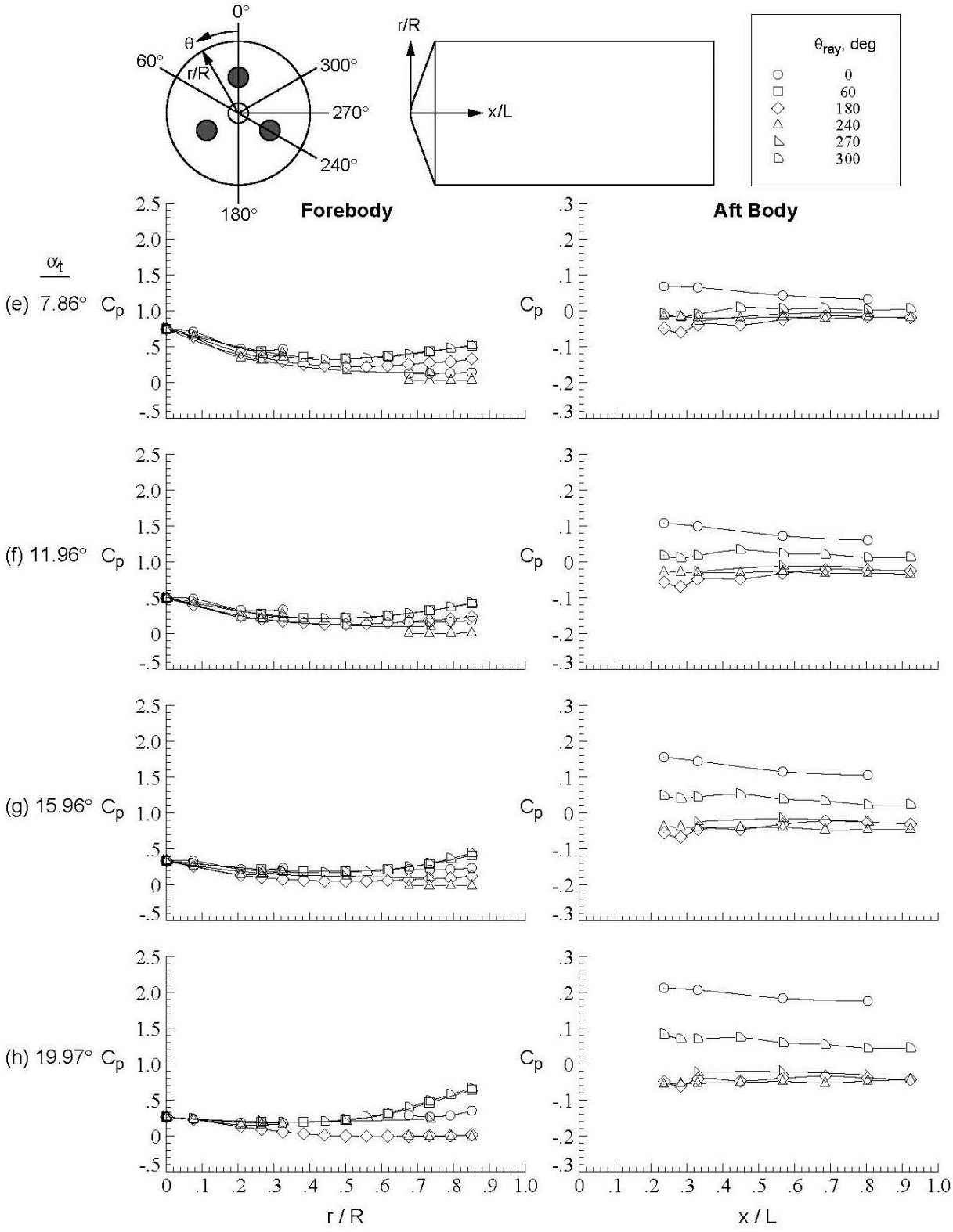

Figure D-183.Concluded.

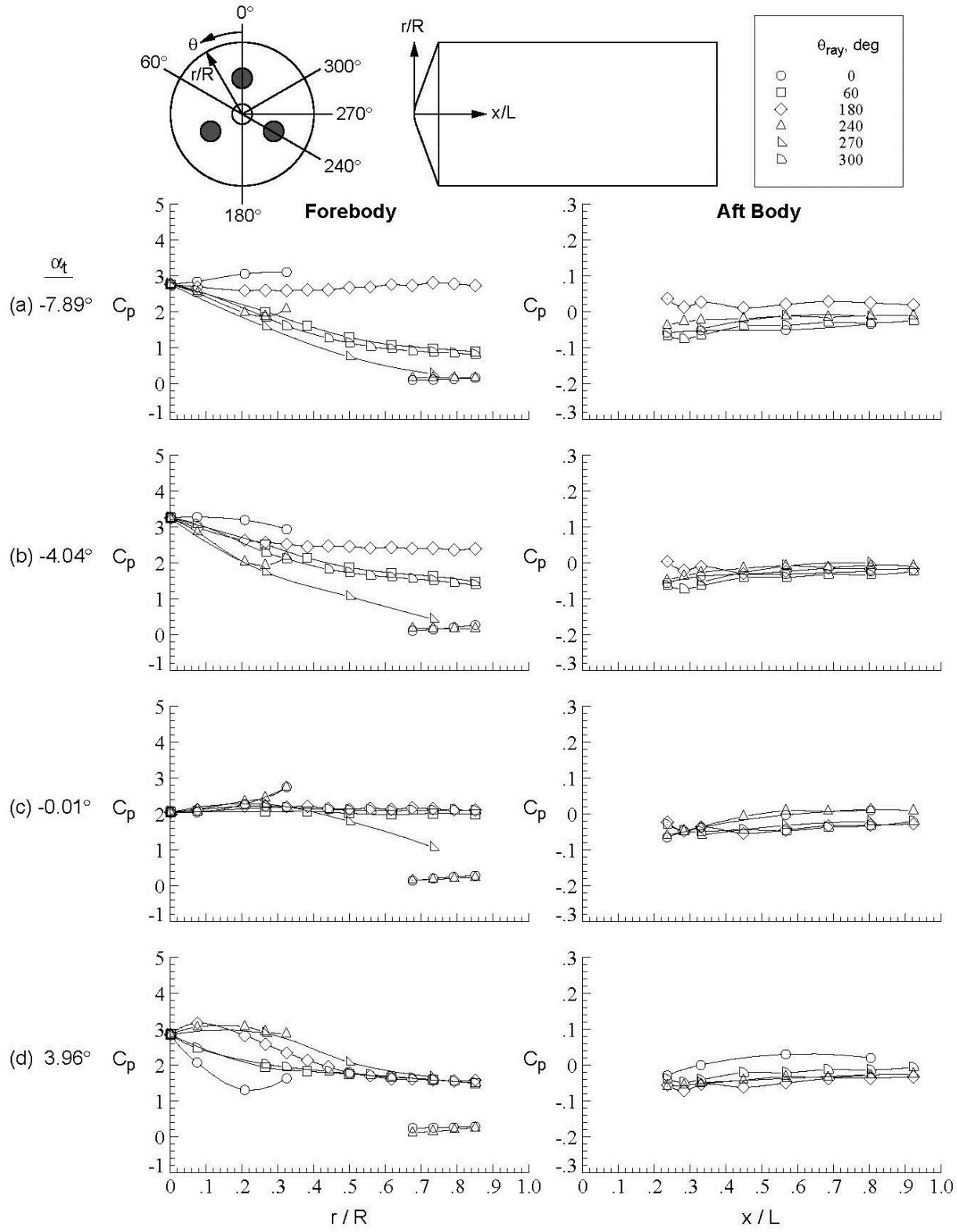

Figure D-184. Tri-nozzle configuration, Run 237, M_∞ = 3.5, Re_∞ = 1.0x10^7/ft, ϕ = 179.95°, X_S = 40.15 in, Y_S = 0.00 in, C_T = 0.48.

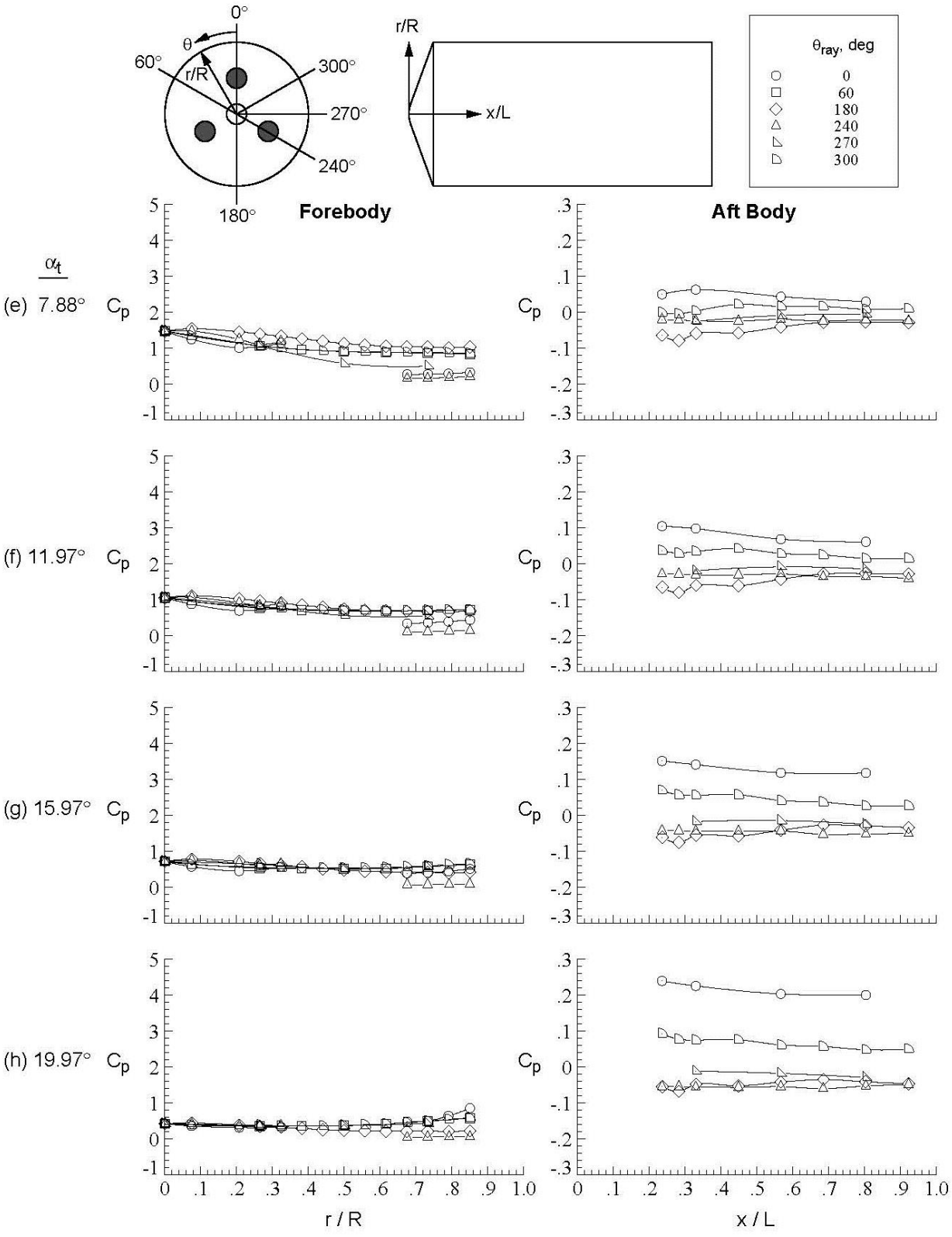

Figure D-184.Concluded.

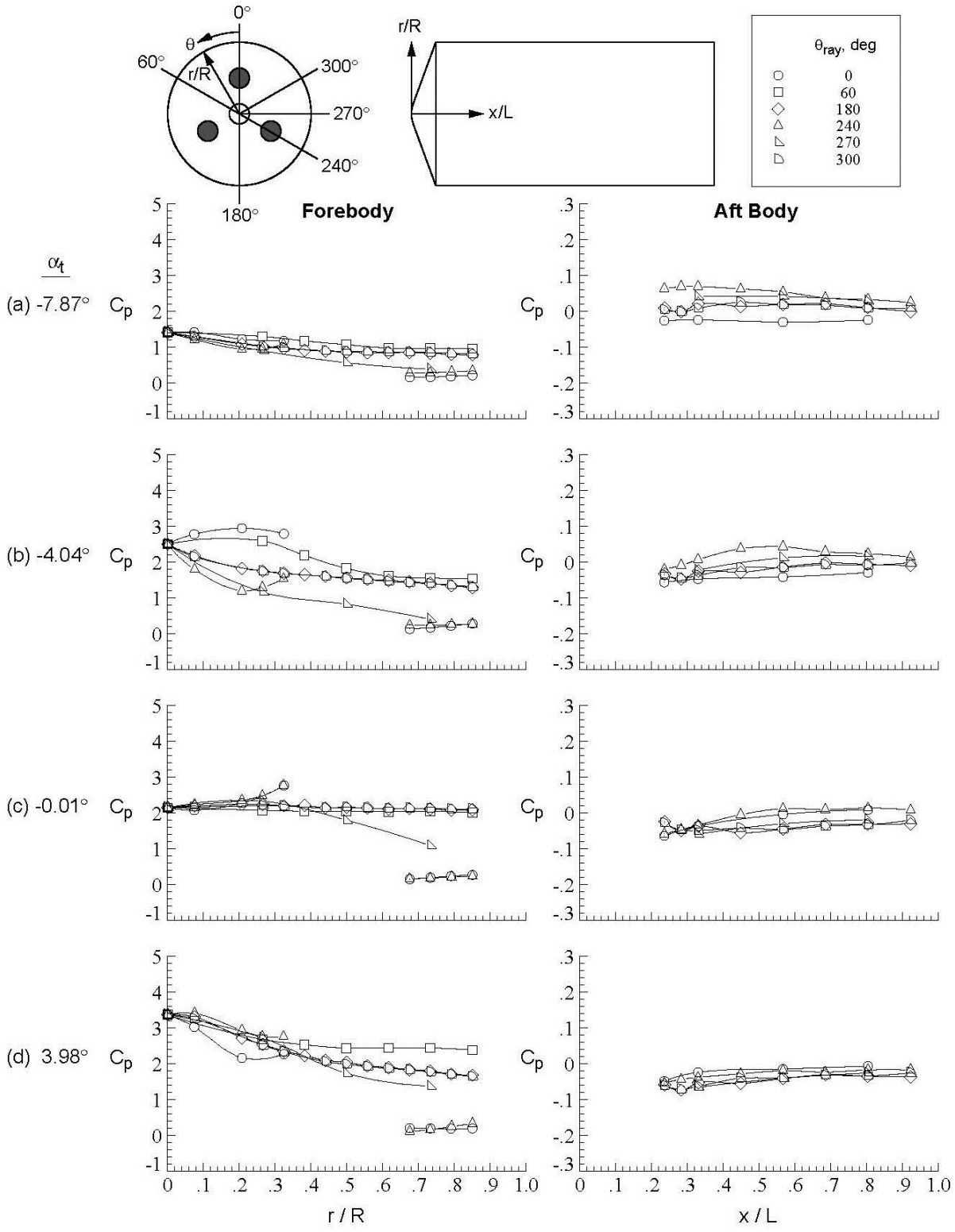

Figure D-185. Tri-nozzle configuration, Run 238, M_∞ = 3.5, Re_∞ = 1.0x10^6/ft, ϕ = 120.00°, X_S = 40.15 in, Y_S = 0.00 in, C_T = 0.47.

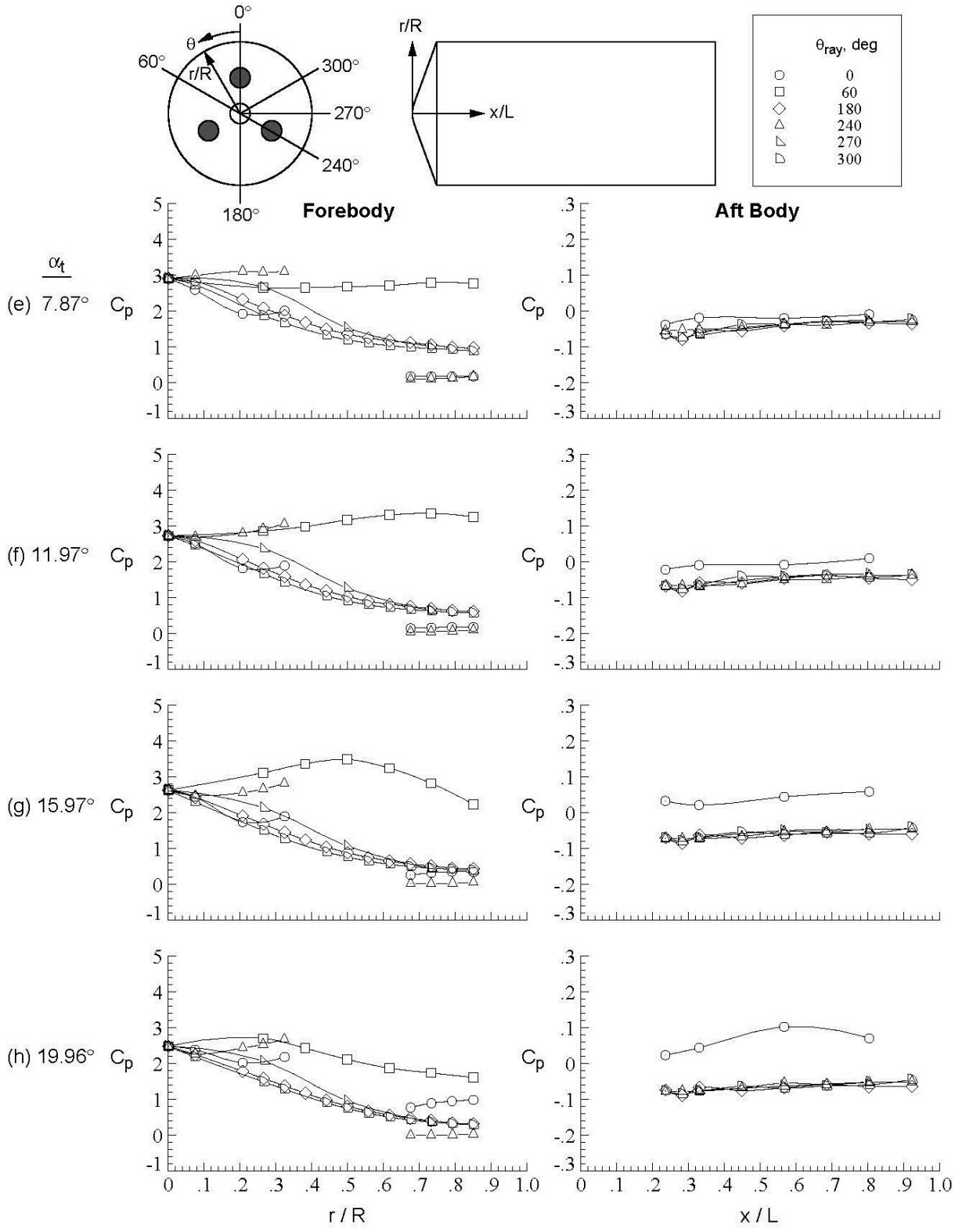

Figure D-185.Concluded.

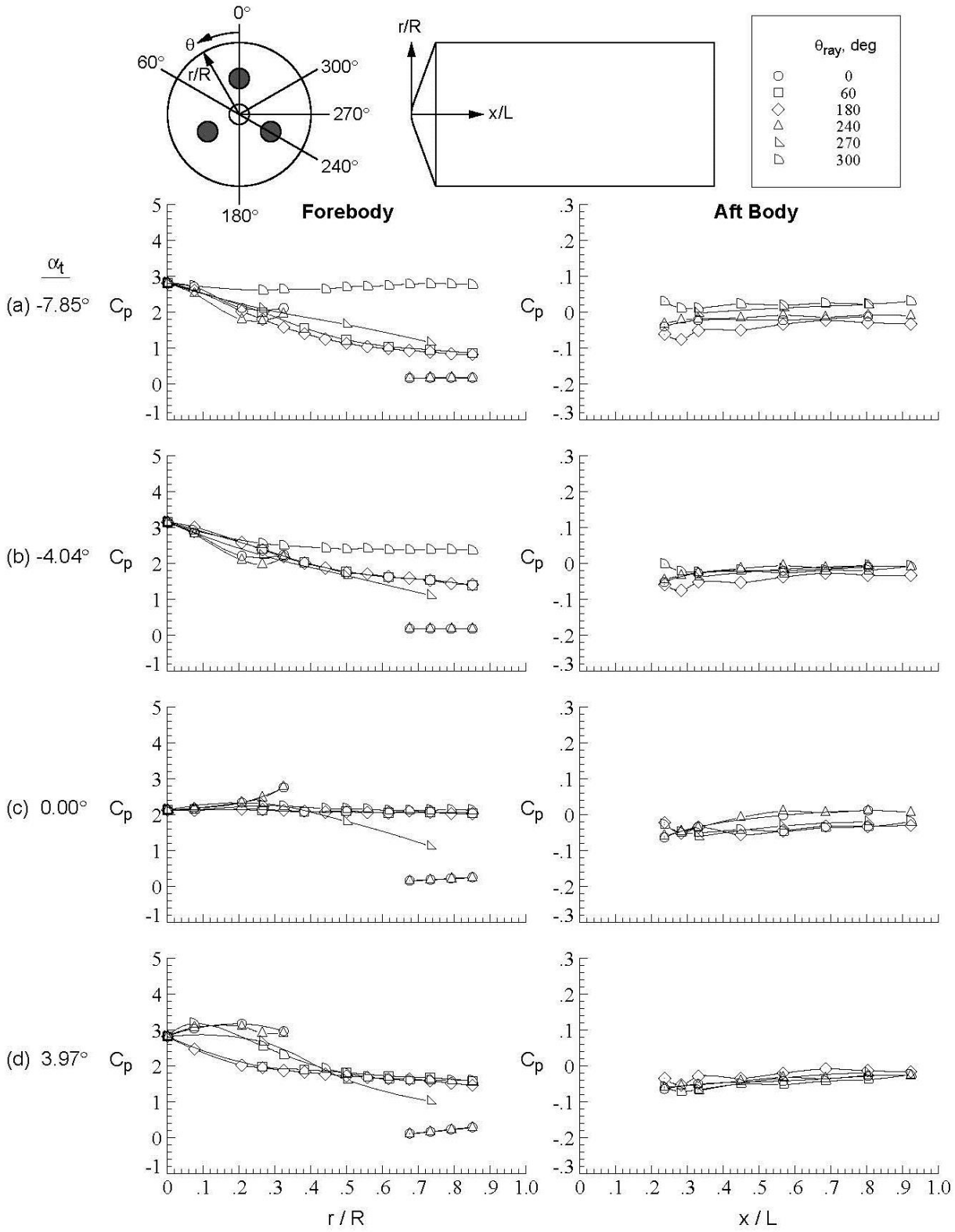

Figure D-186. Tri-nozzle configuration, Run 239, M_∞ = 3.5, Re_∞ = 1.0x10^7/ft, ϕ = 59.94°, X_S = 40.15 in, Y_S = 0.00 in, C_T = 0.46.

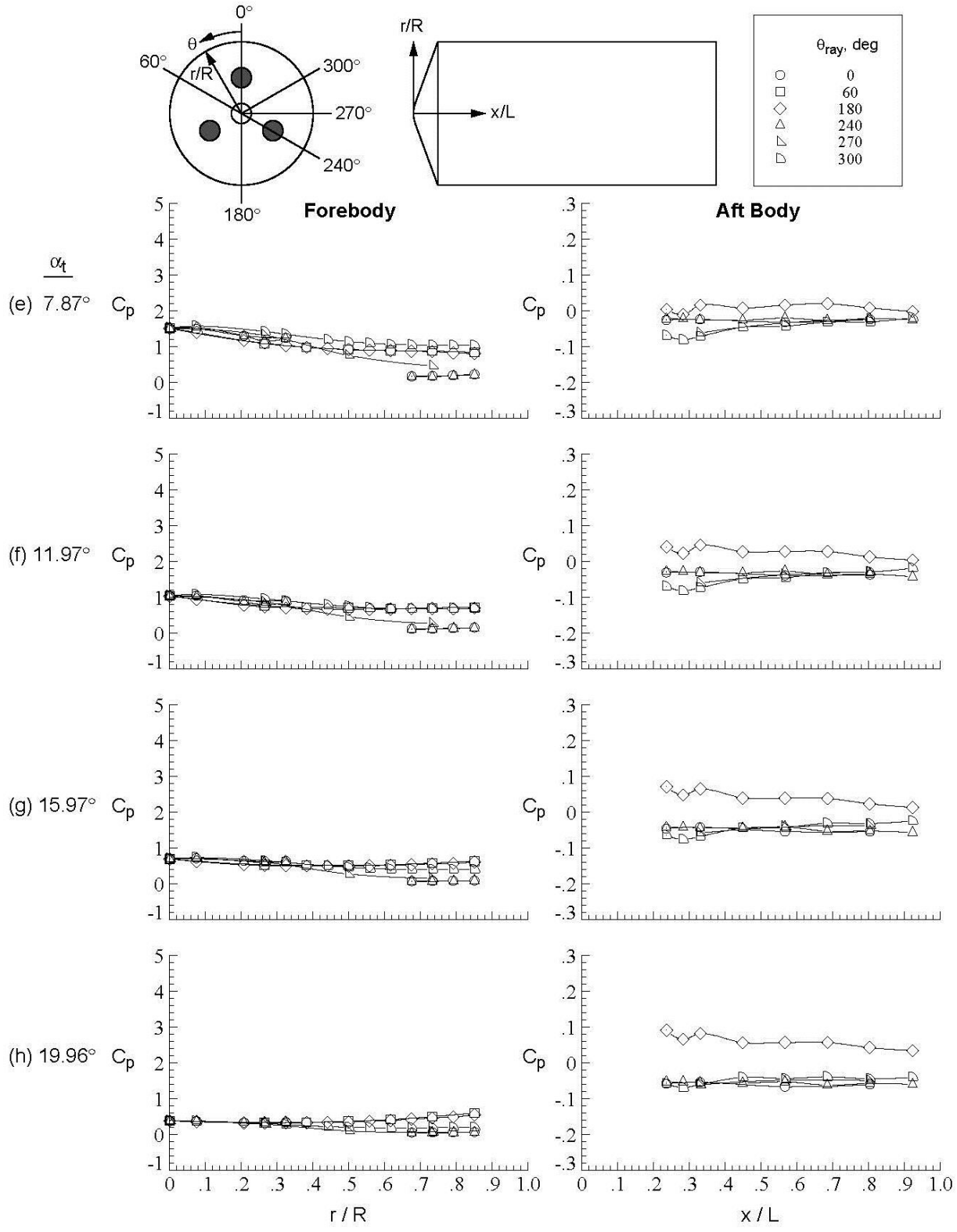

Figure D-186.Concluded.

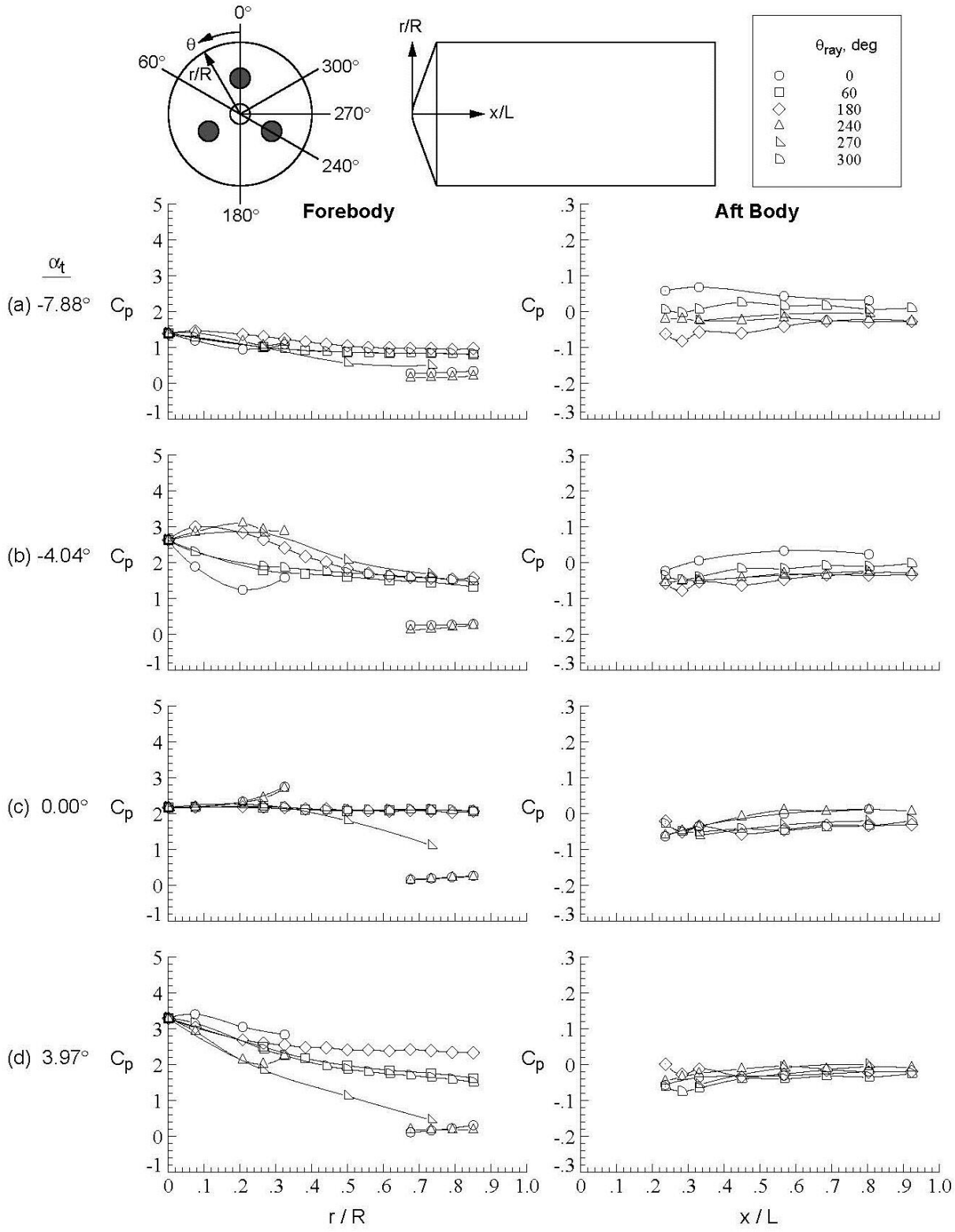

Figure D-187. Tri-nozzle configuration, Run 240, M_∞ = 3.5, Re_∞ = 1.0x10^6/ft, ϕ = −0.05°, X_S = 40.15 in, Y_S = 0.00 in, C_T = 0.46.

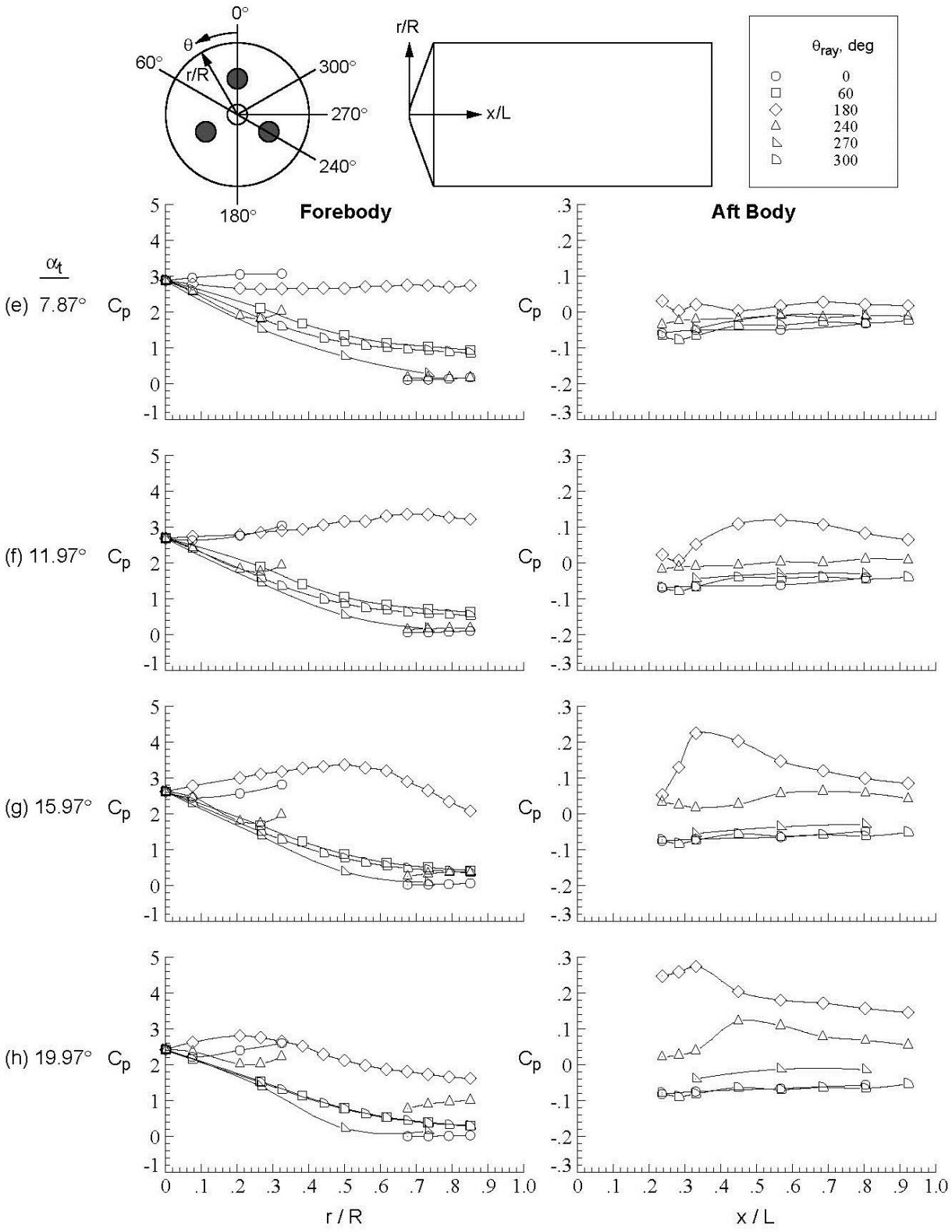

Figure D-187.Concluded.

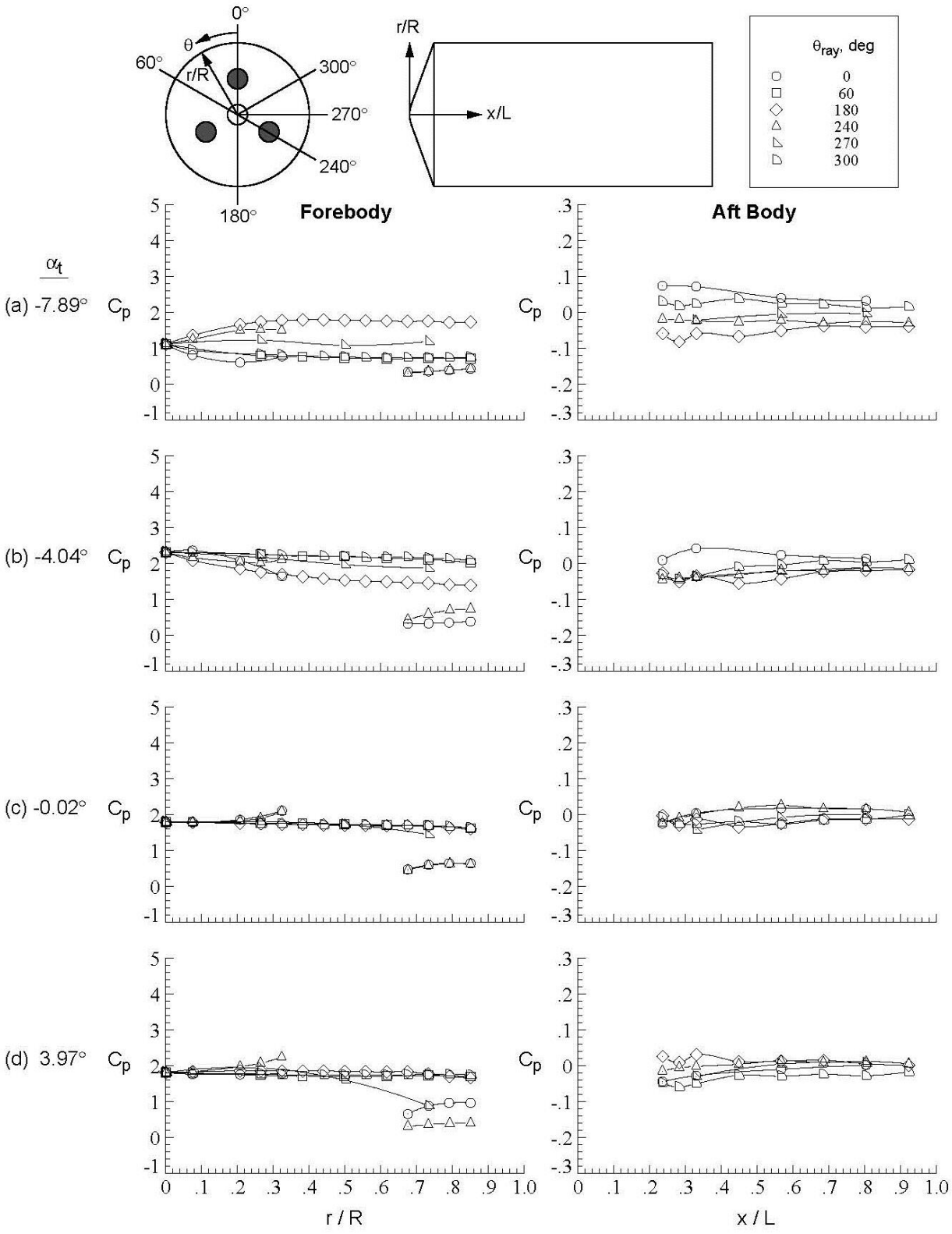

Figure D-188. Tri-nozzle configuration, Run 241, M_∞ = 3.5, Re_∞ = 1.0x10^7/ft, ϕ = −0.05°, X_S = 40.15 in, Y_S = 0.00 in, C_T = 0.23.

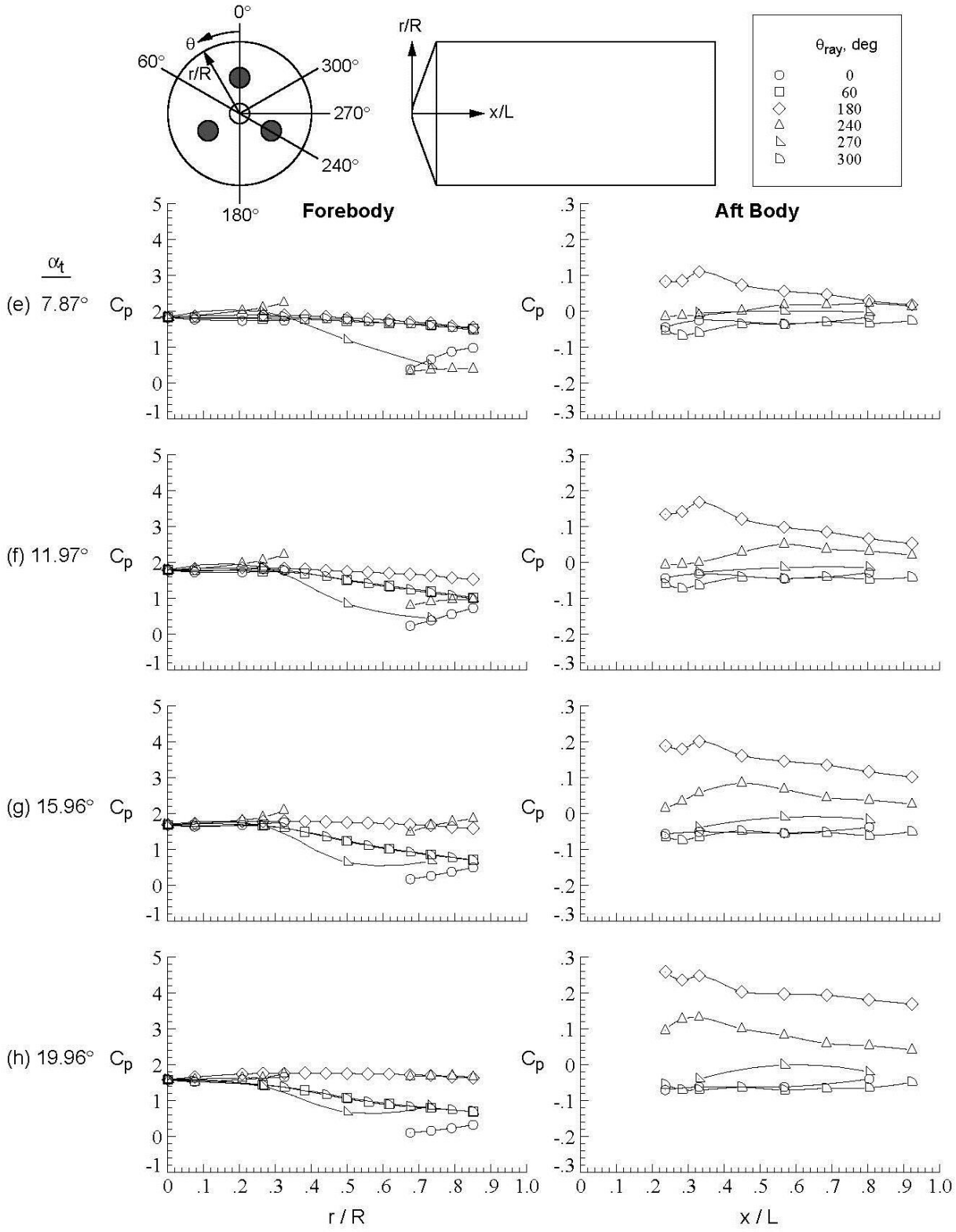

Figure D-188.Concluded.

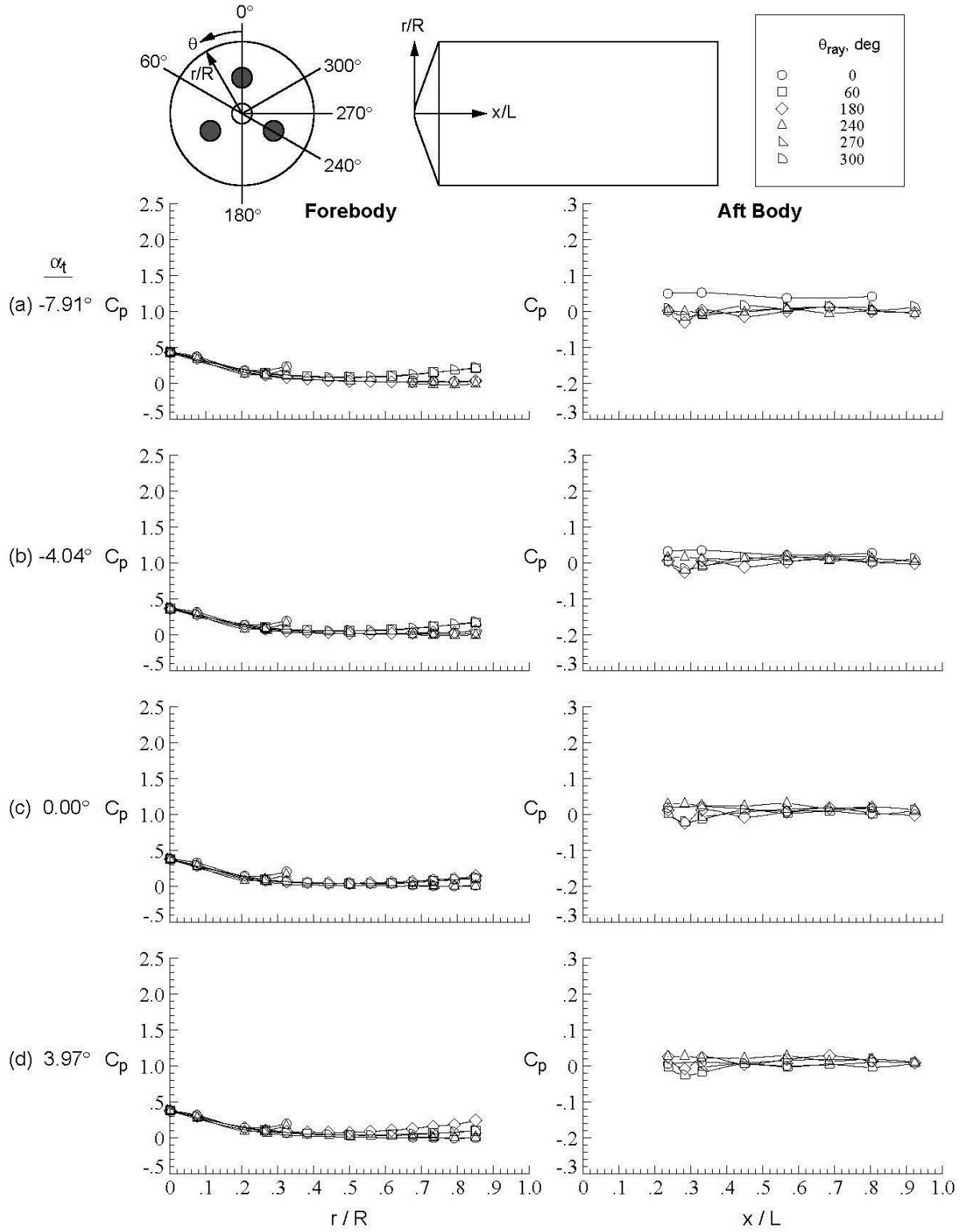

Figure D-189. Tri-nozzle configuration, Run 242, M_∞ = 4.6, Re_∞ = 1.5x10^7/ft, ϕ = −0.05°, X_S = 40.15 in, Y_S = 0.00 in, C_T = 1.96.

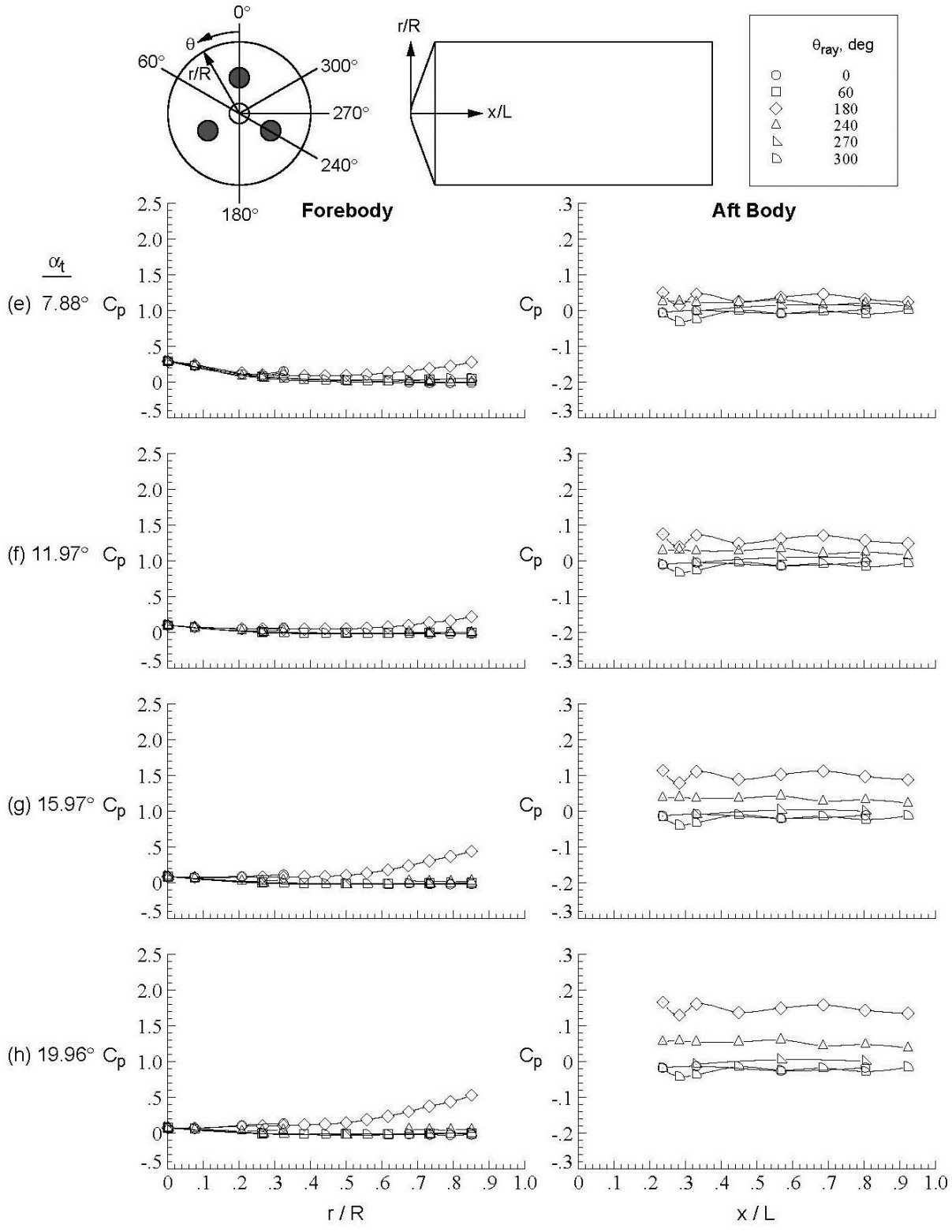

Figure D-189.Concluded.

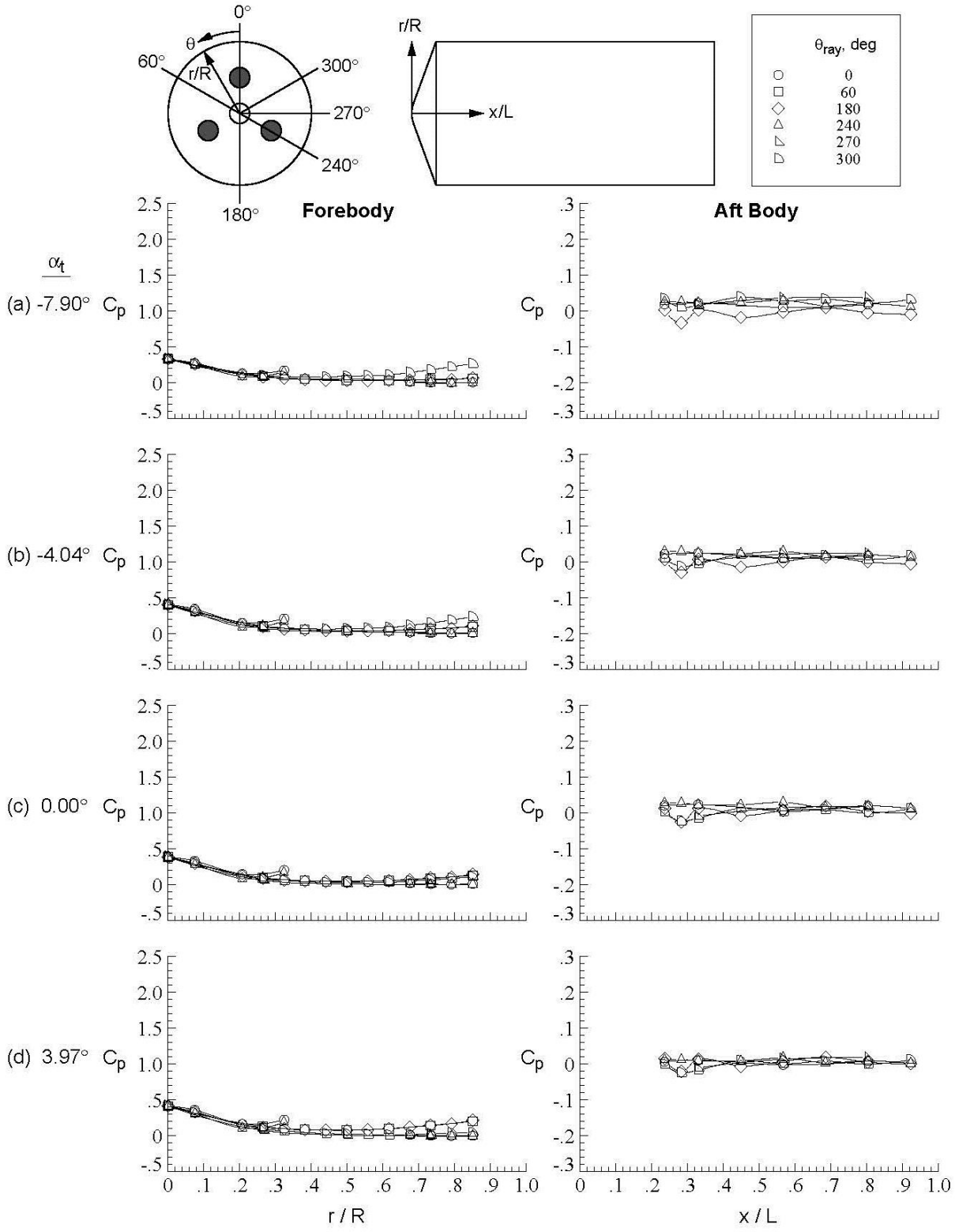

Figure D-190. Tri-nozzle configuration, Run 243, M_∞ = 4.6, Re_∞ = 1.5x10^7/ft, ϕ = 59.94°, X_S = 40.15 in, Y_S = 0.00 in, C_T = 1.96.

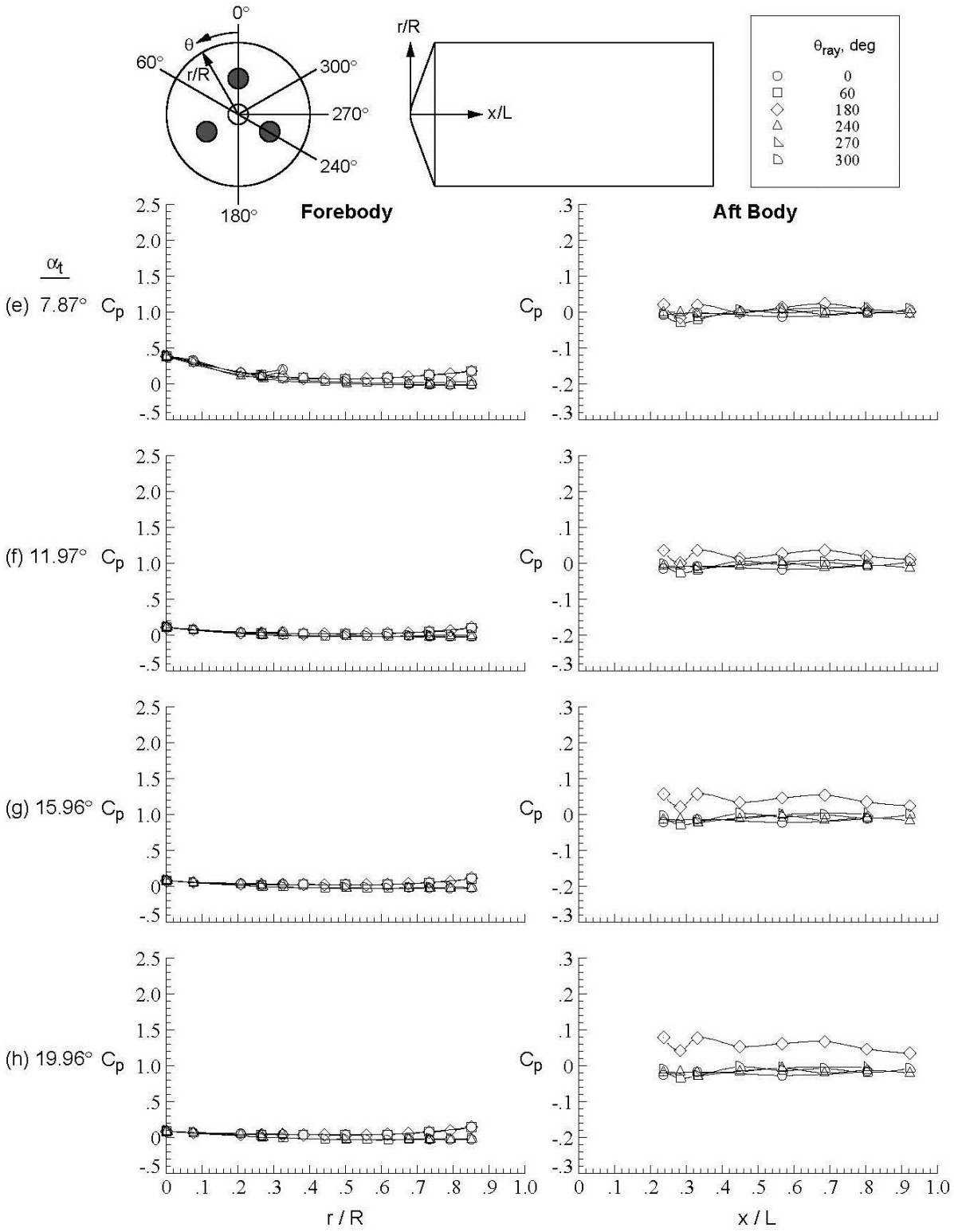

Figure D-190.Concluded.

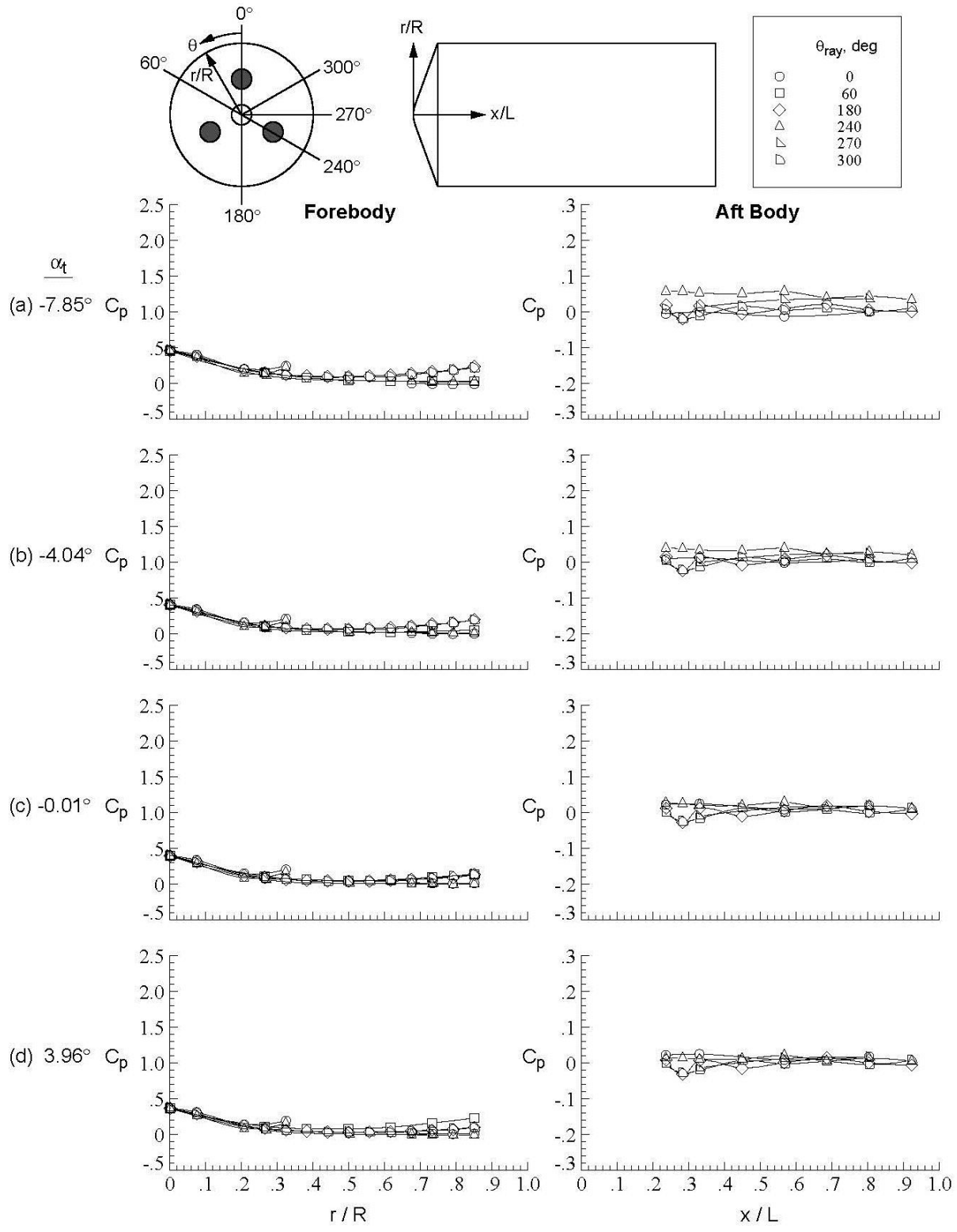

Figure D-191. Tri-nozzle configuration, Run 244, M_∞ = 4.6, Re_∞ = 1.5x10^7/ft, ϕ = 120.06°, X_S = 40.15 in, Y_S = 0.00 in, C_T = 1.96.

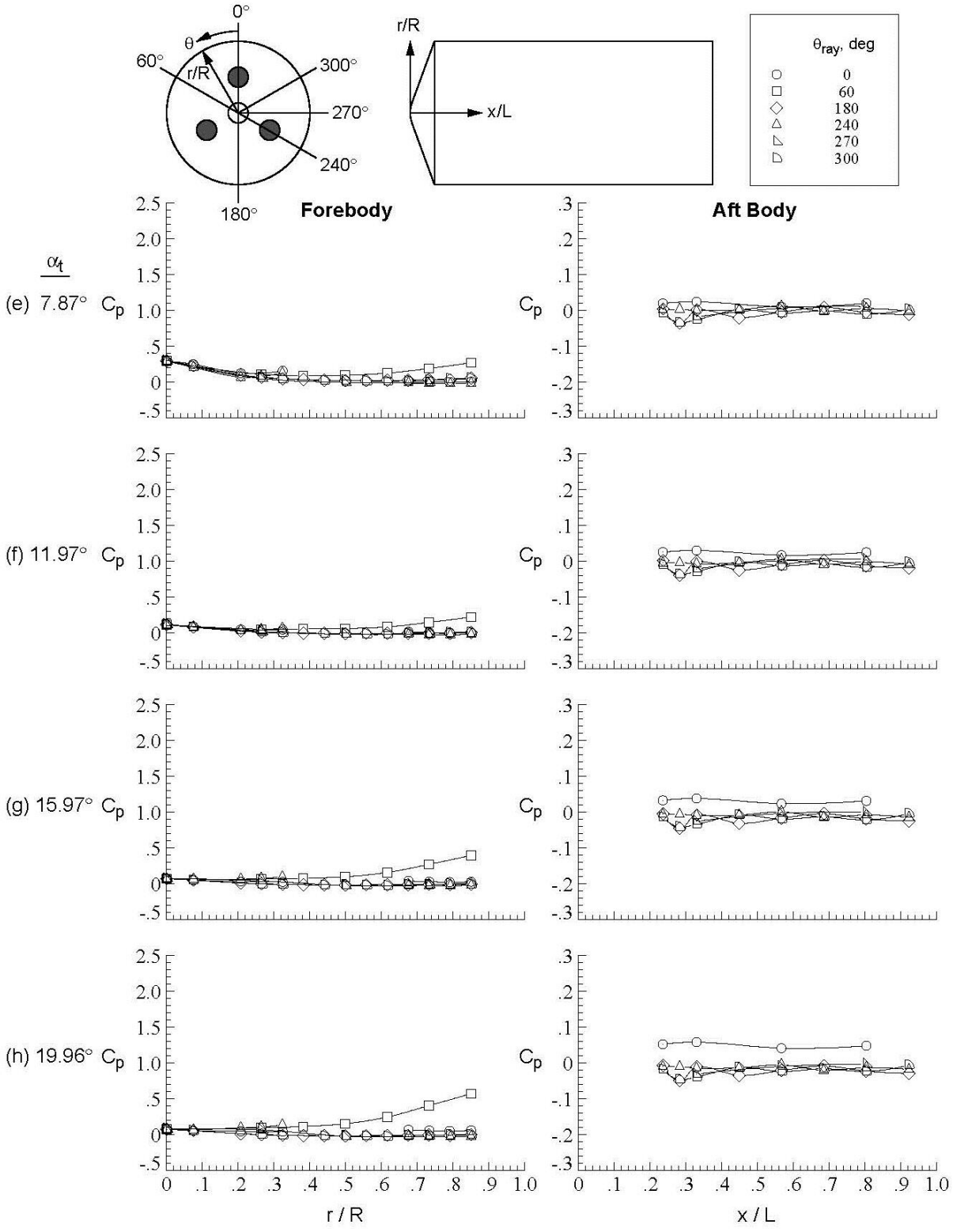

Figure D-191.Concluded.

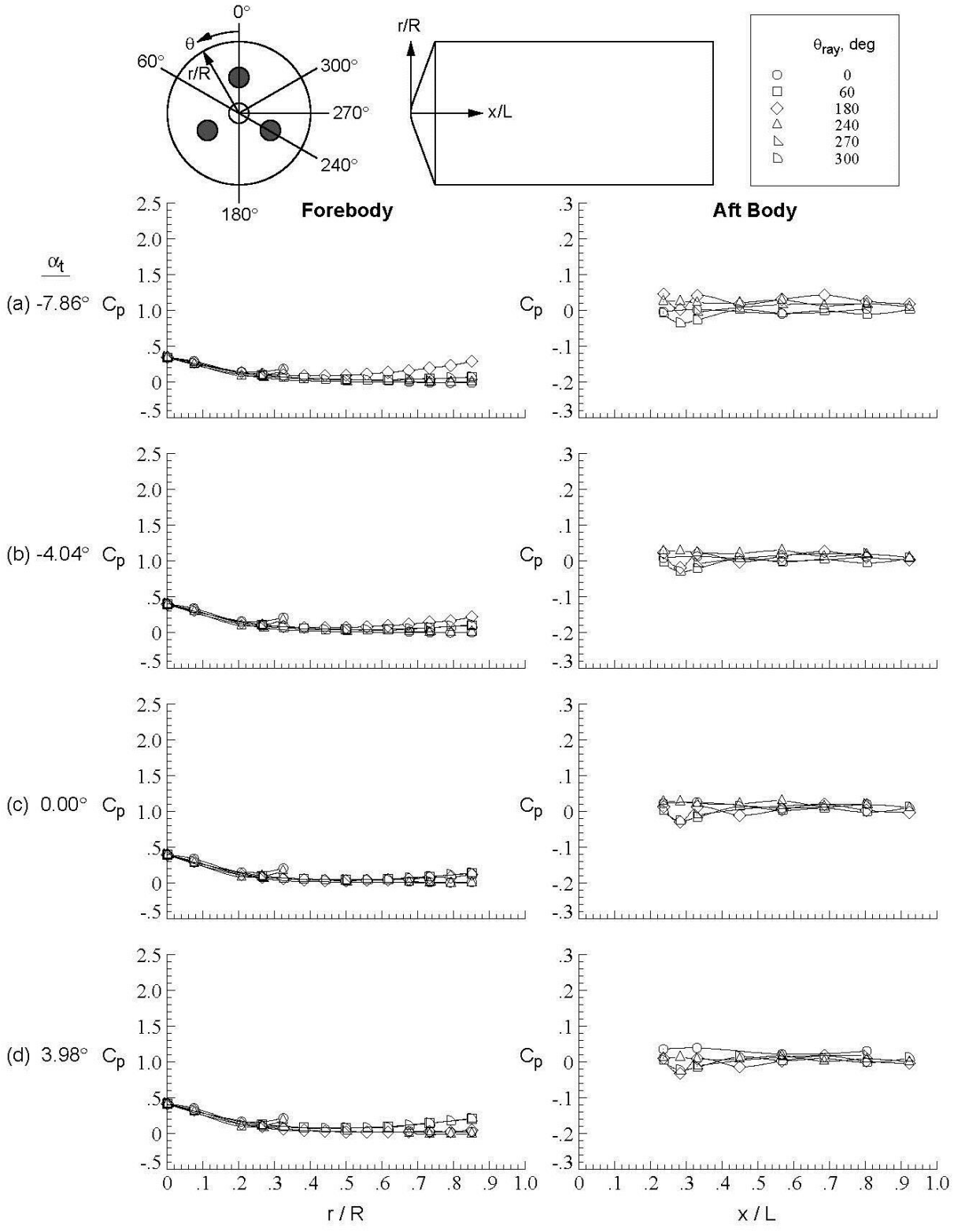

Figure D-192. Tri-nozzle configuration, Run 245, M_∞ = 4.6, Re_∞ = 1.5x10^7/ft, ϕ = −179.99°, X_S = 40.15 in, Y_S = 0.00 in, C_T = 1.96.

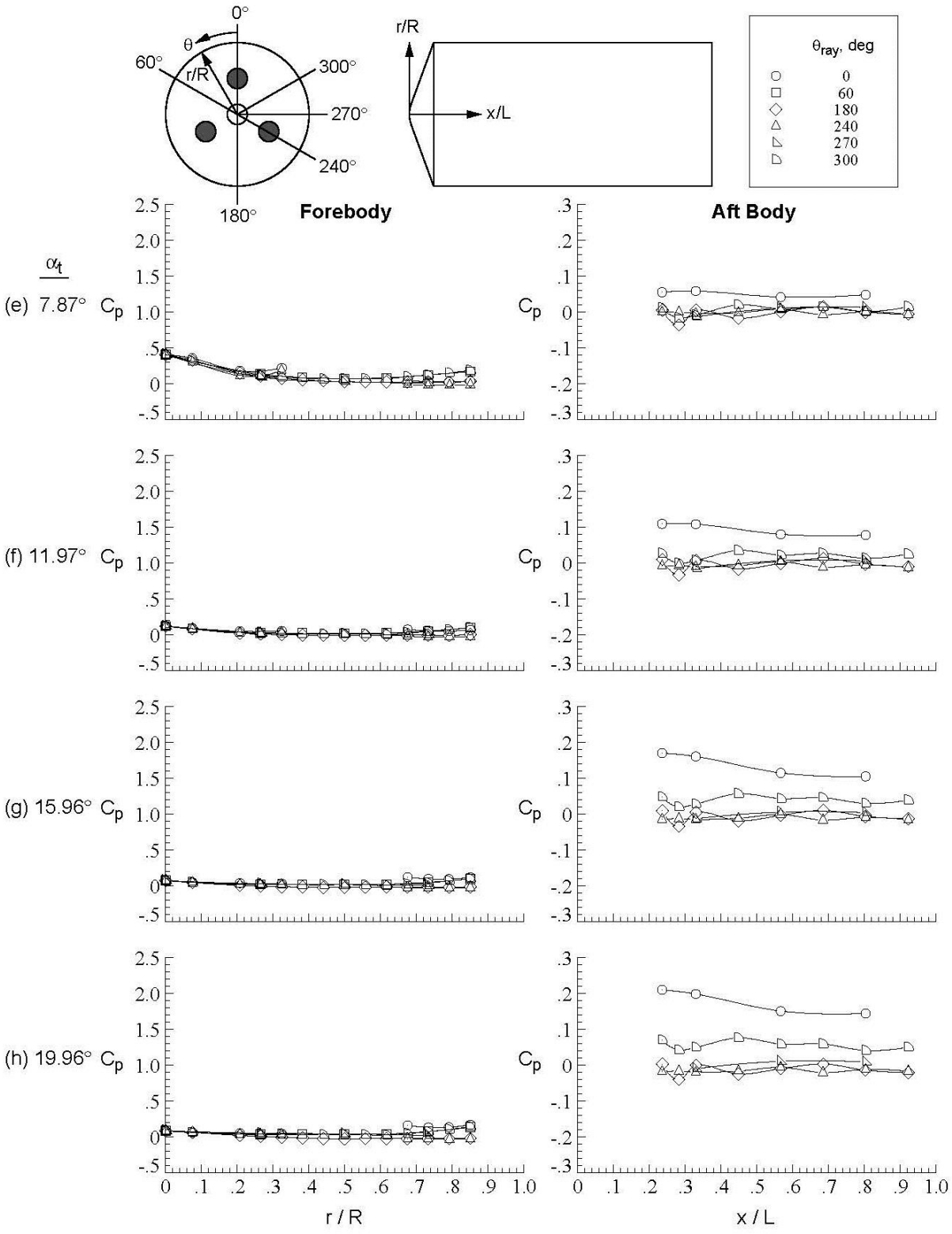

Figure D-192.Concluded.

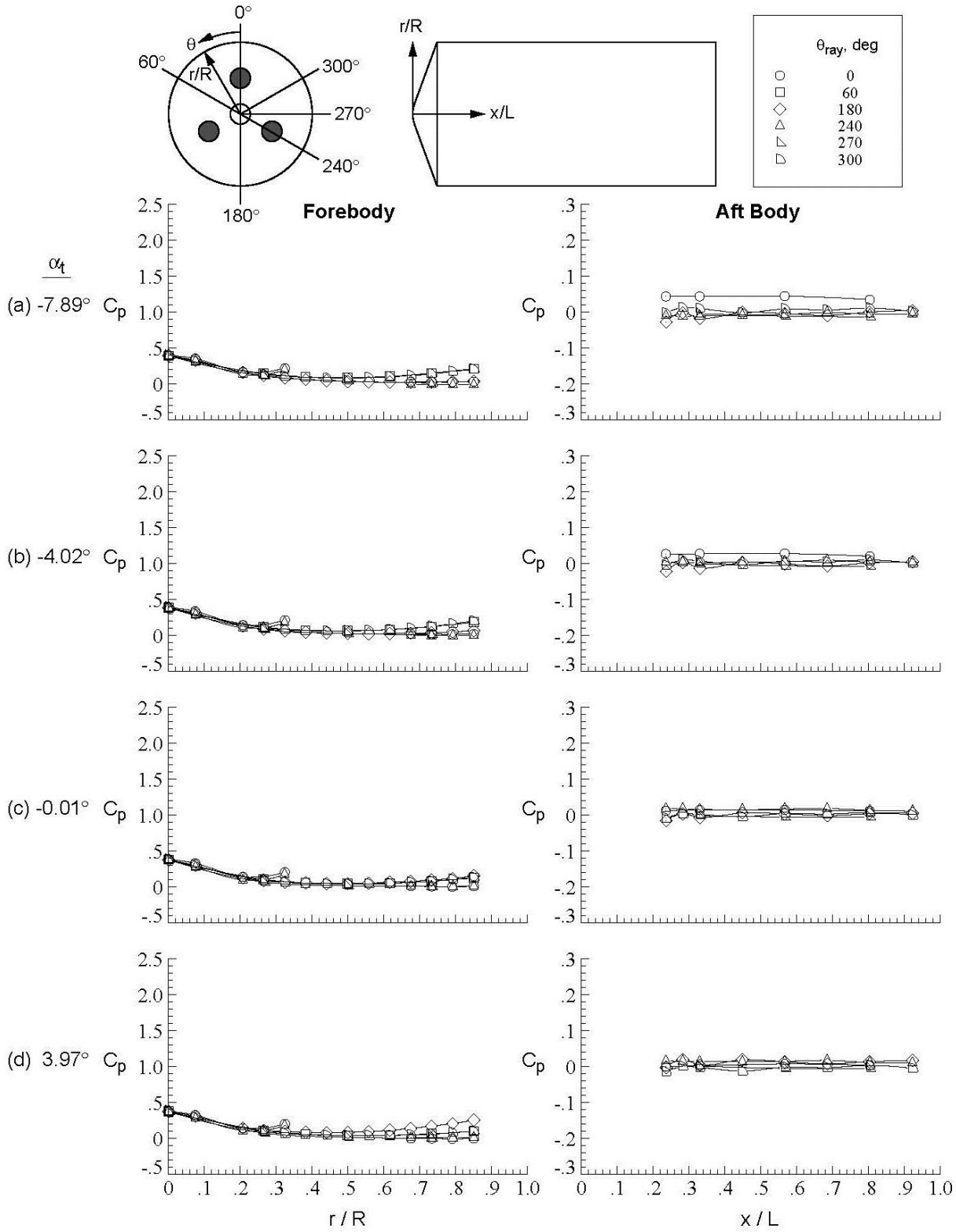

Figure D-193. Tri-nozzle configuration, Run 247, M_∞ = 4.6, Re_∞ = 1.5x10^7/ft, ϕ = −0.03°, X_S = 40.15 in, Y_S = 0.00 in, C_T = 1.92.

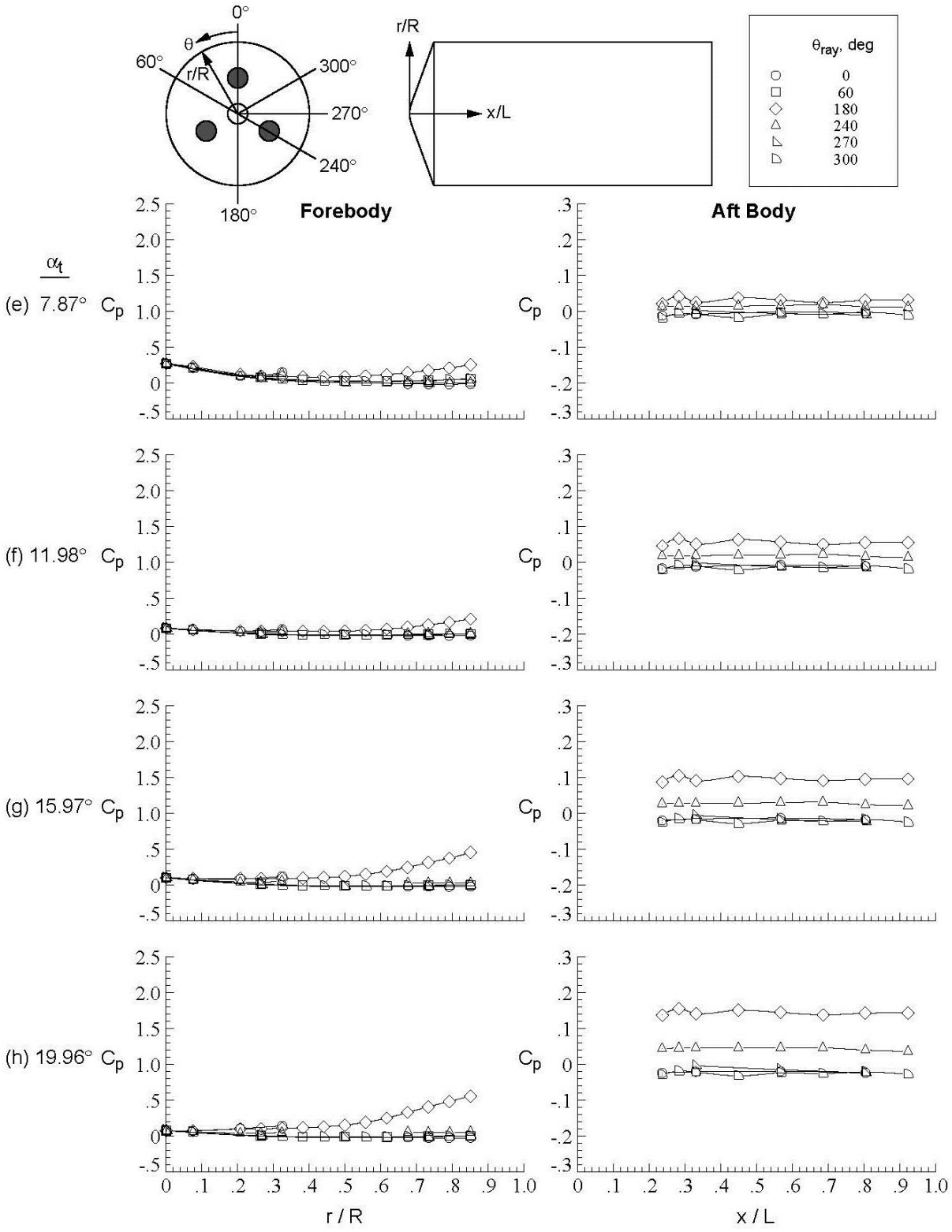

Figure D-193.Concluded.

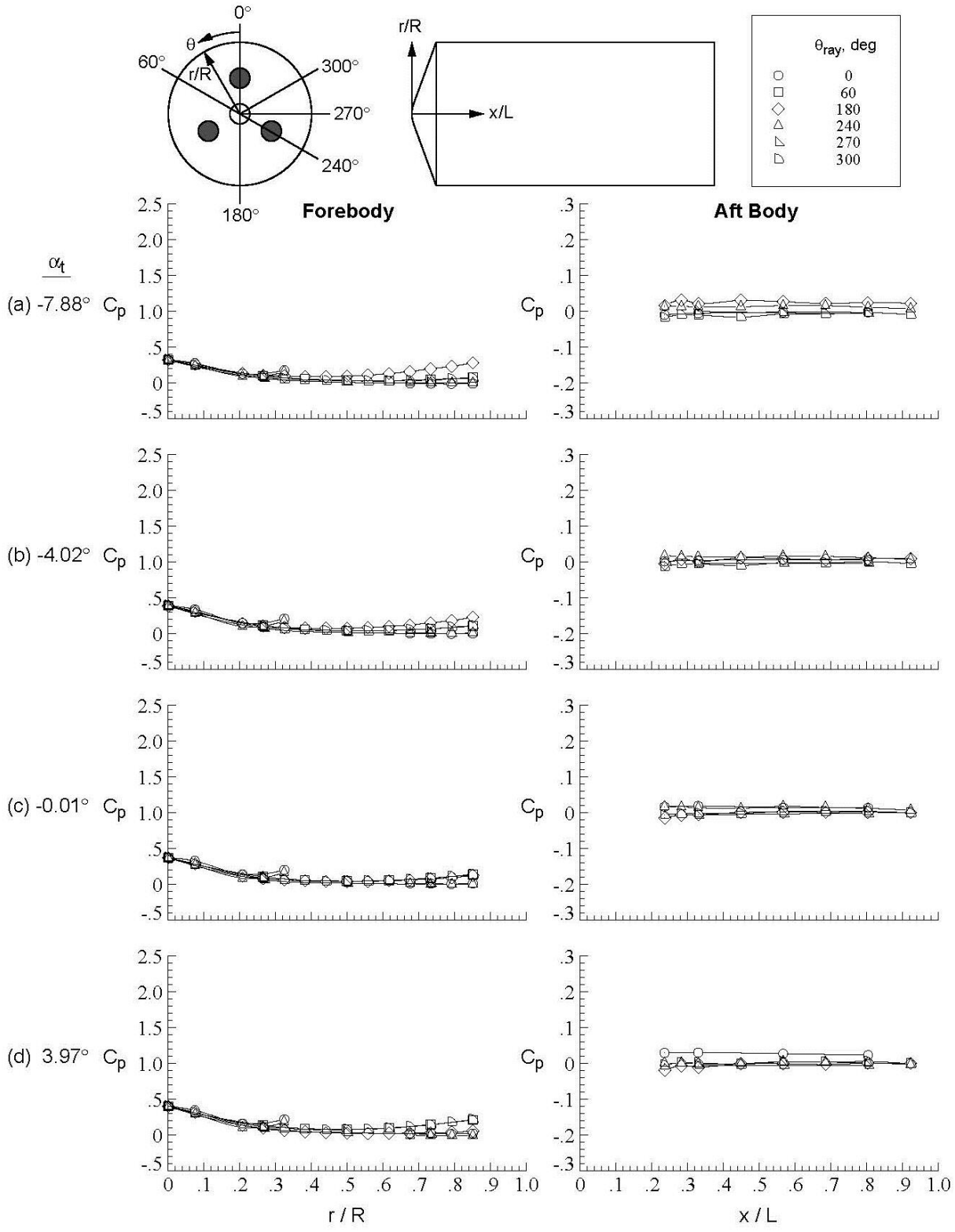

Figure D-194. Tri-nozzle configuration, Run 248, M_∞ = 4.6, Re_∞ = 1.5x10^7/ft, ϕ = 179.99°, X_S = 40.15 in, Y_S = 0.00 in, C_T = 1.93.

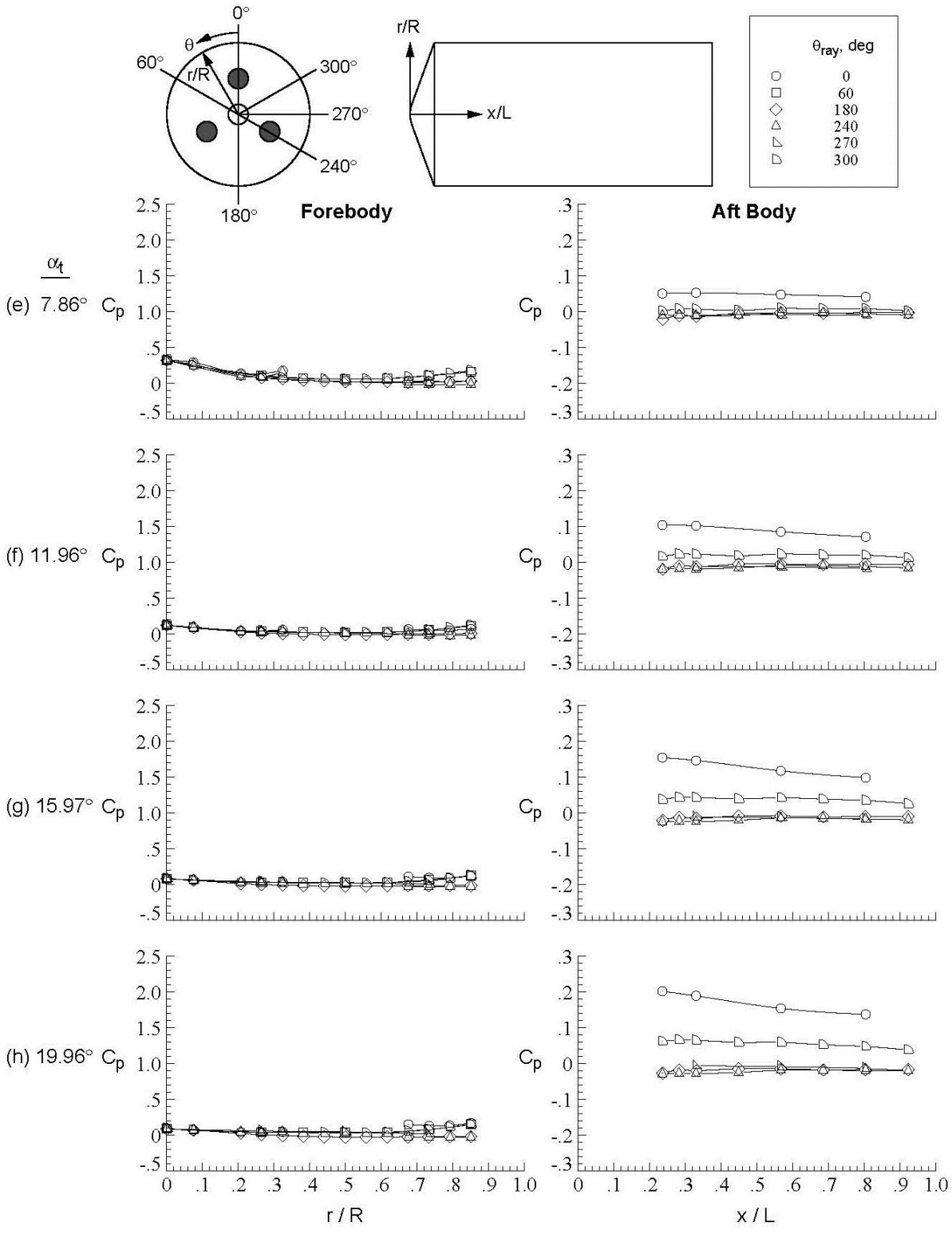

Figure D-194.Concluded.

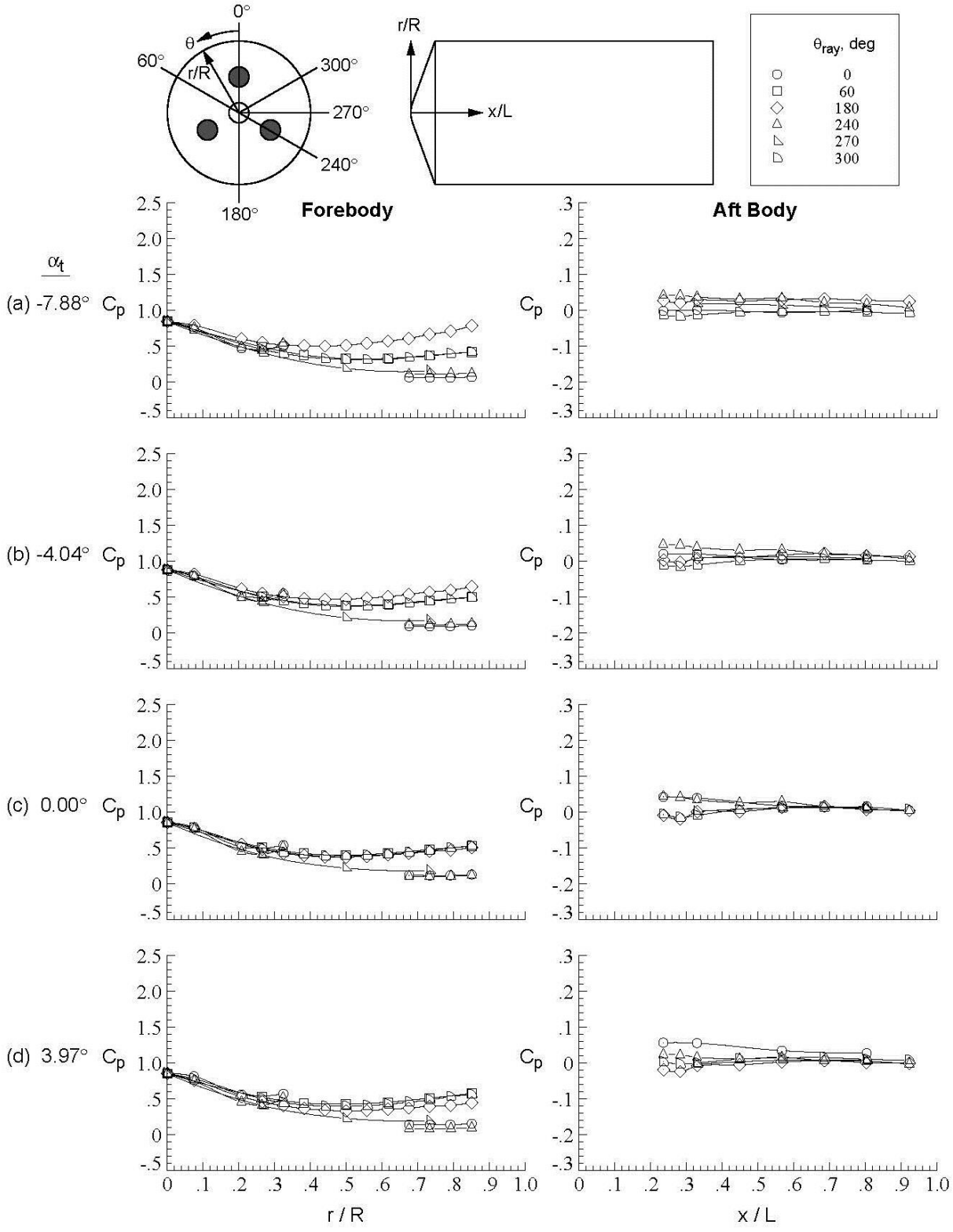

Figure D-195. Tri-nozzle configuration, Run 249, M_∞ = 4.6, Re_∞ = 1.5x10^7/ft, ϕ = 179.99°, X_S = 40.15 in, Y_S = 0.00 in, C_T = 0.90.

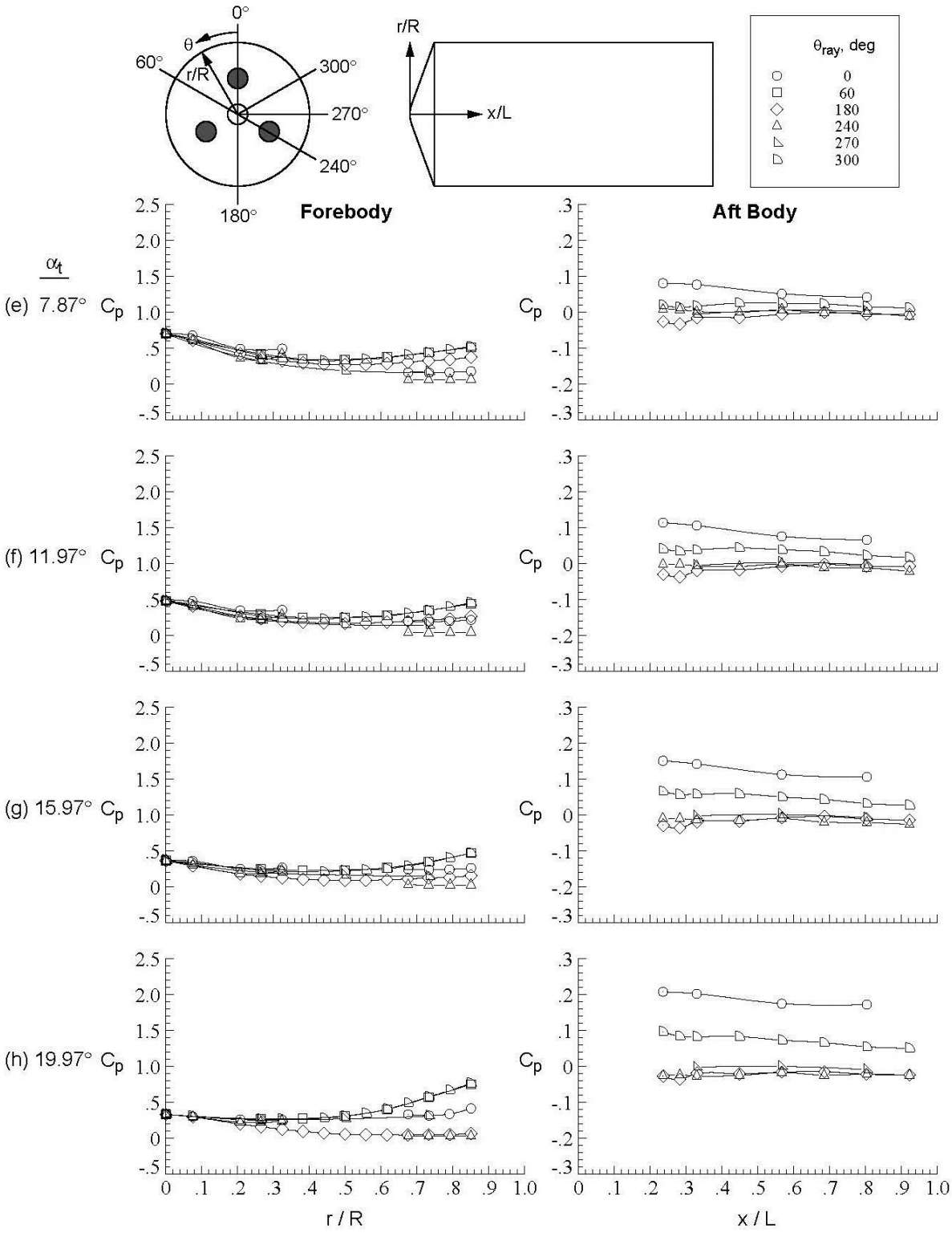

Figure D-195.Concluded.

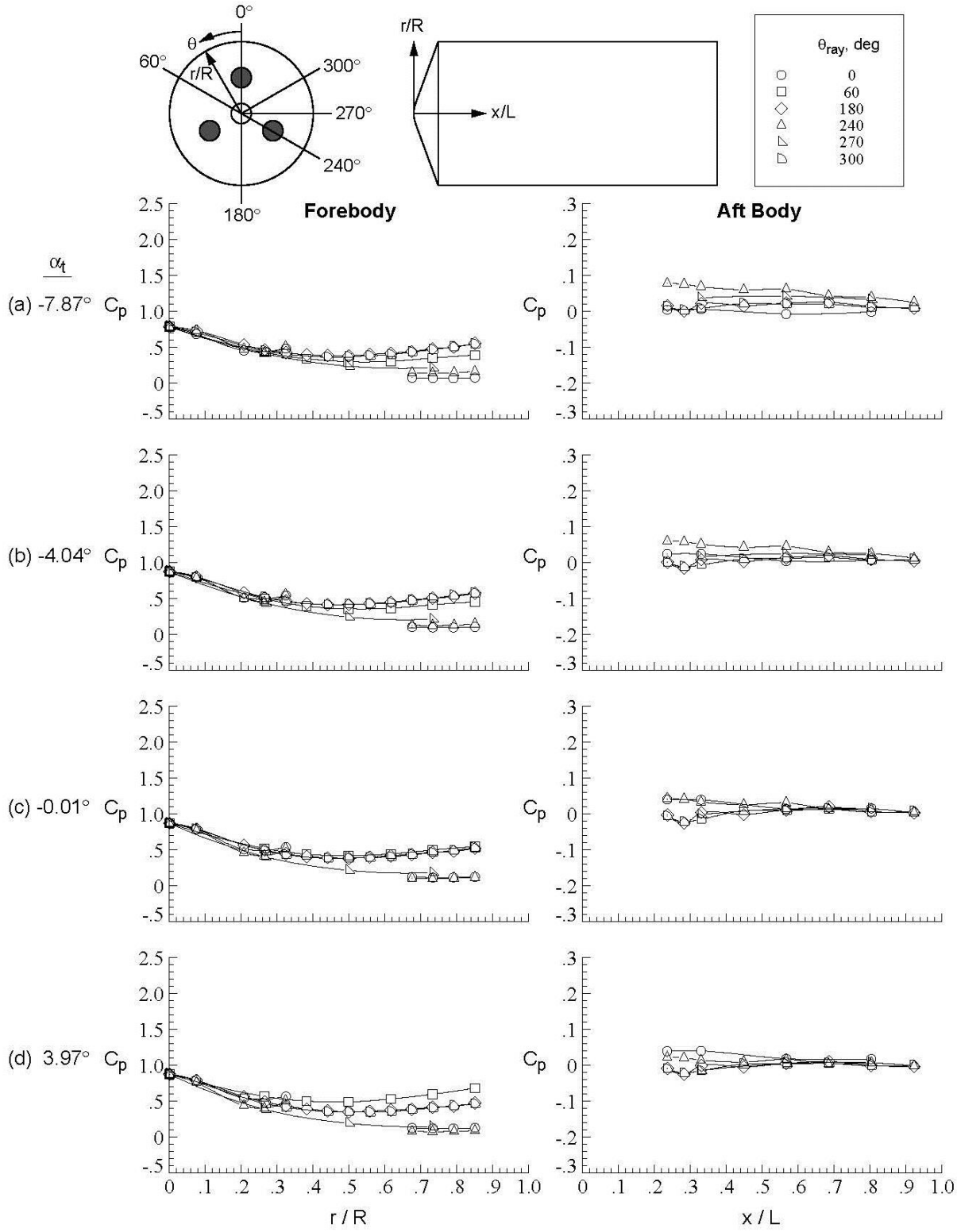

Figure D-196. Tri-nozzle configuration, Run 250, M_∞ = 4.6, Re_∞ = 1.5x10^7/ft, ϕ = 120.04°, X_S = 40.15 in, Y_S = 0.00 in, C_T = 0.90.

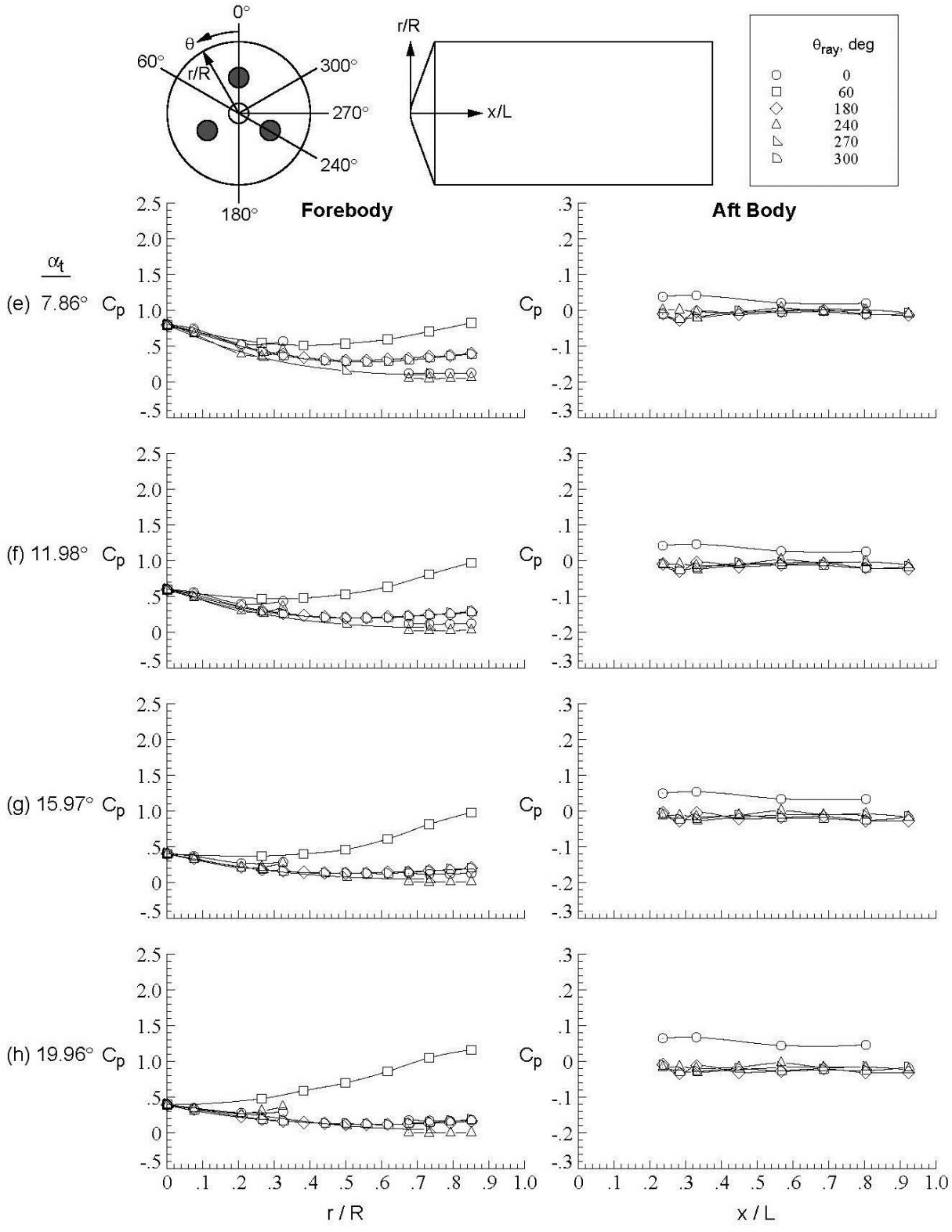

Figure D-196.Concluded.

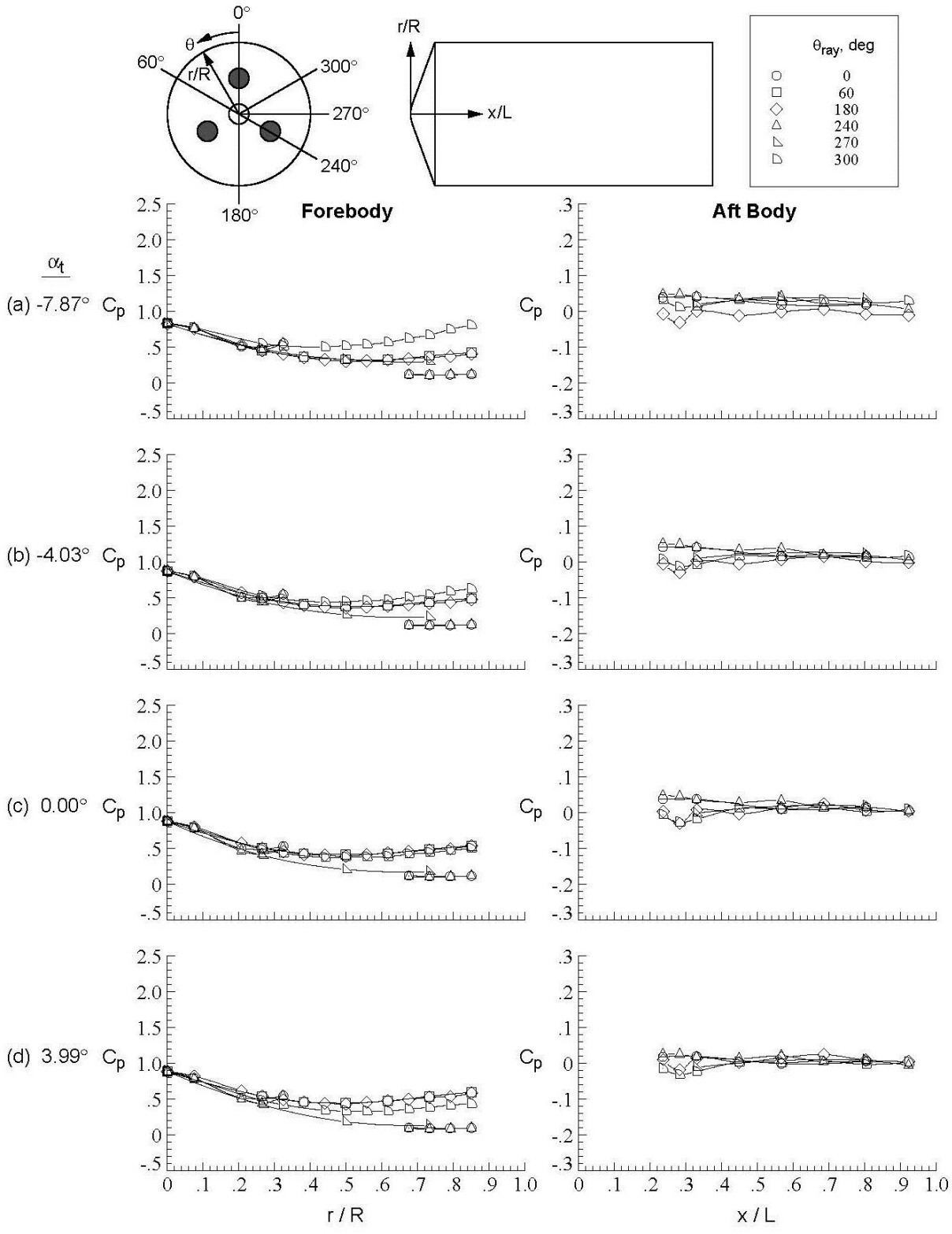

Figure D-197. Tri-nozzle configuration, Run 251, M_∞ = 4.6, Re_∞ = 1.5x10^7/ft, ϕ = 59.98°, X_S = 40.15 in, Y_S = 0.00 in, C_T = 0.89.

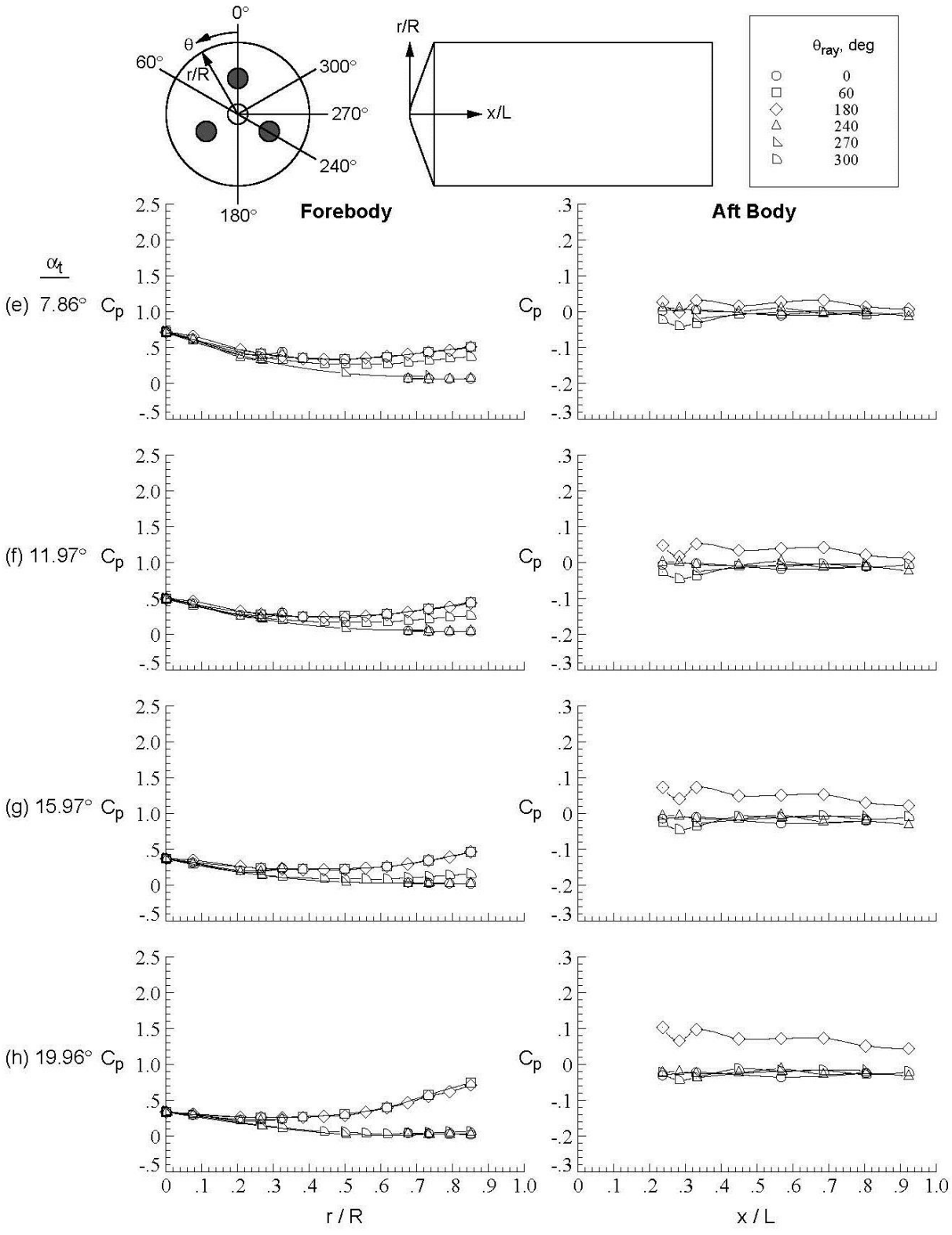

Figure D-197.Concluded.

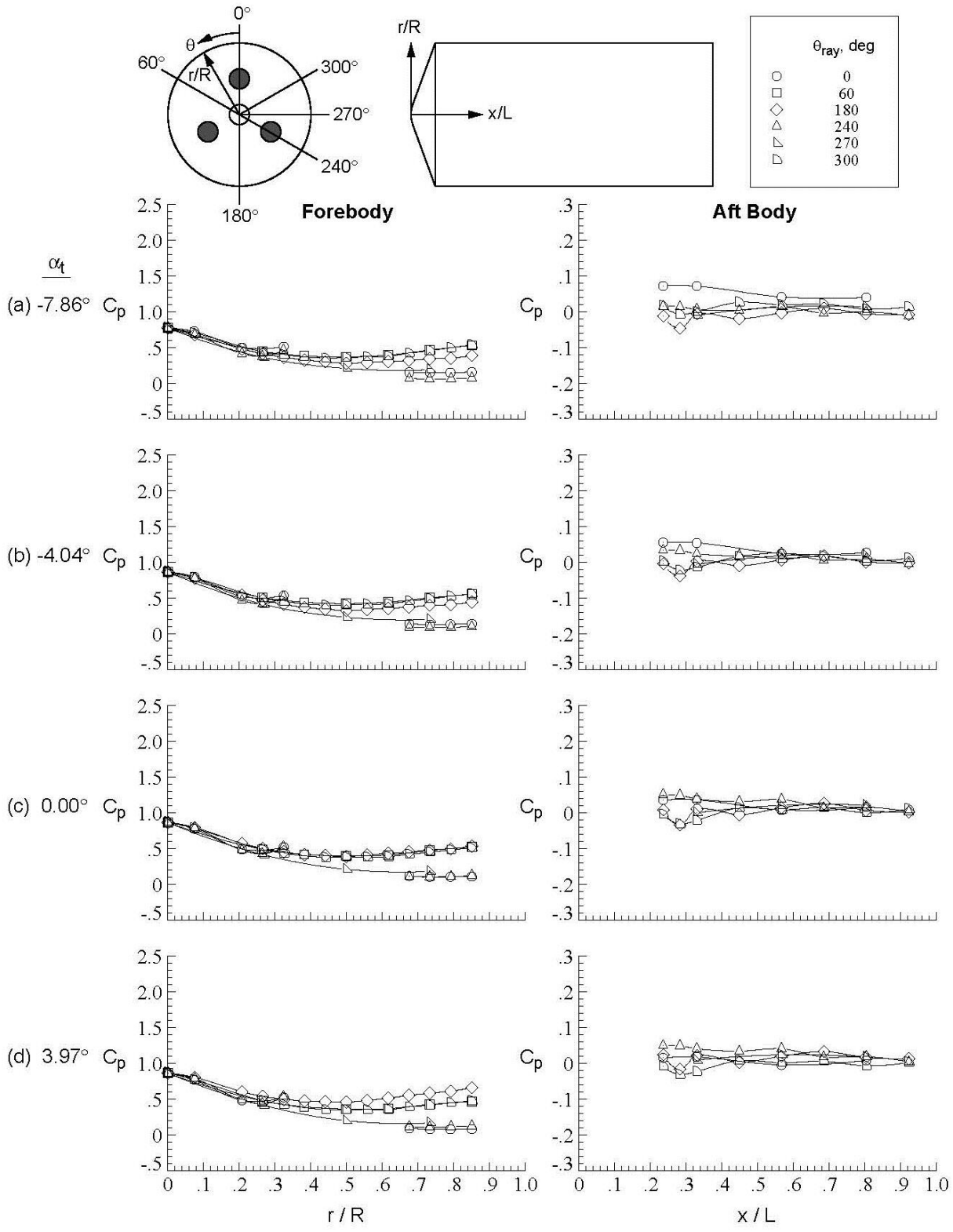

Figure D-198. Tri-nozzle configuration, Run 252, $M\infty = 4.6$, $Re_\infty = 1.5 \times 10^7$/ft, $\phi = -0.03°$, $X_S = 40.15$ in, $Y_S = 0.00$ in, $C_T = 0.90$.

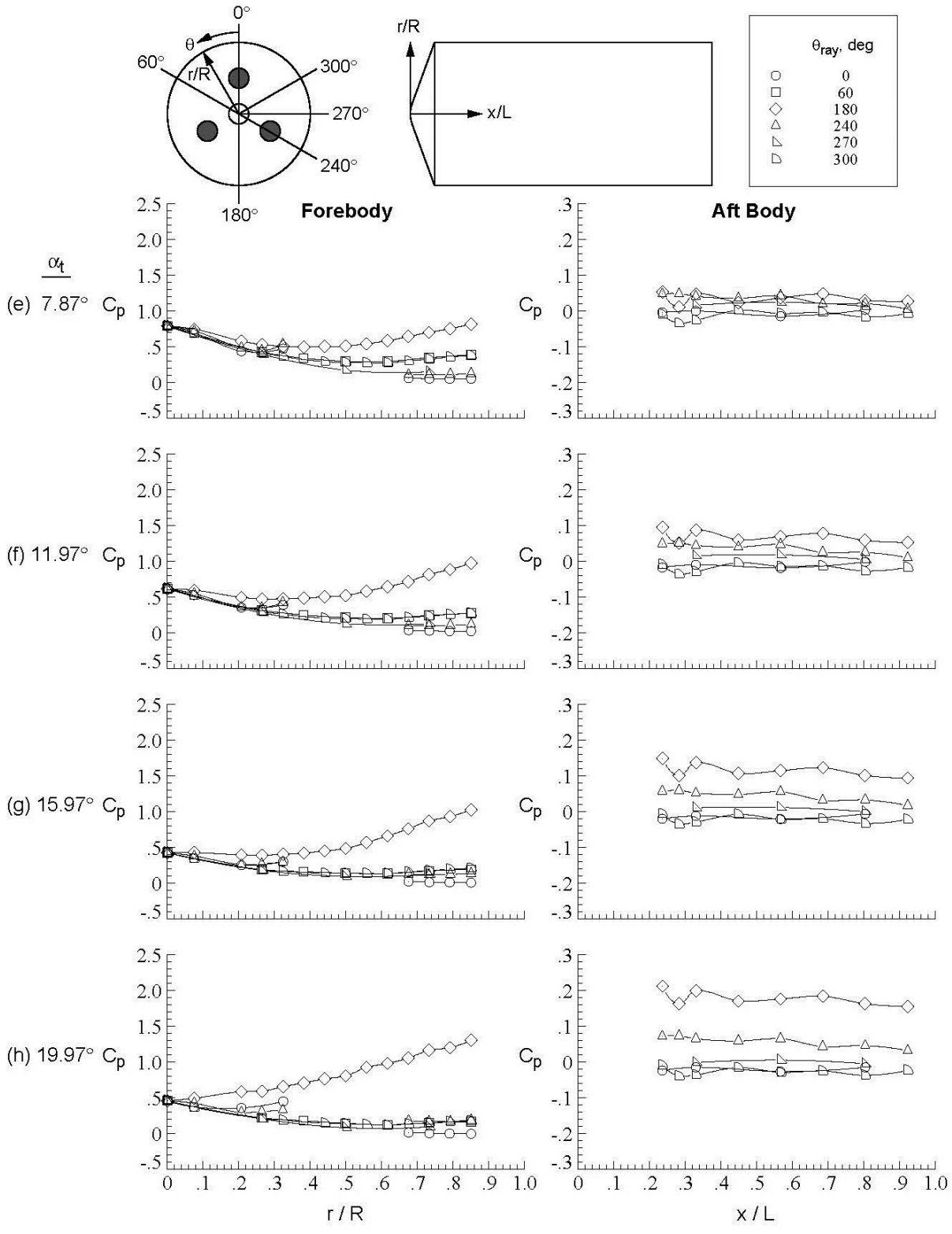

Figure D-198.Concluded.

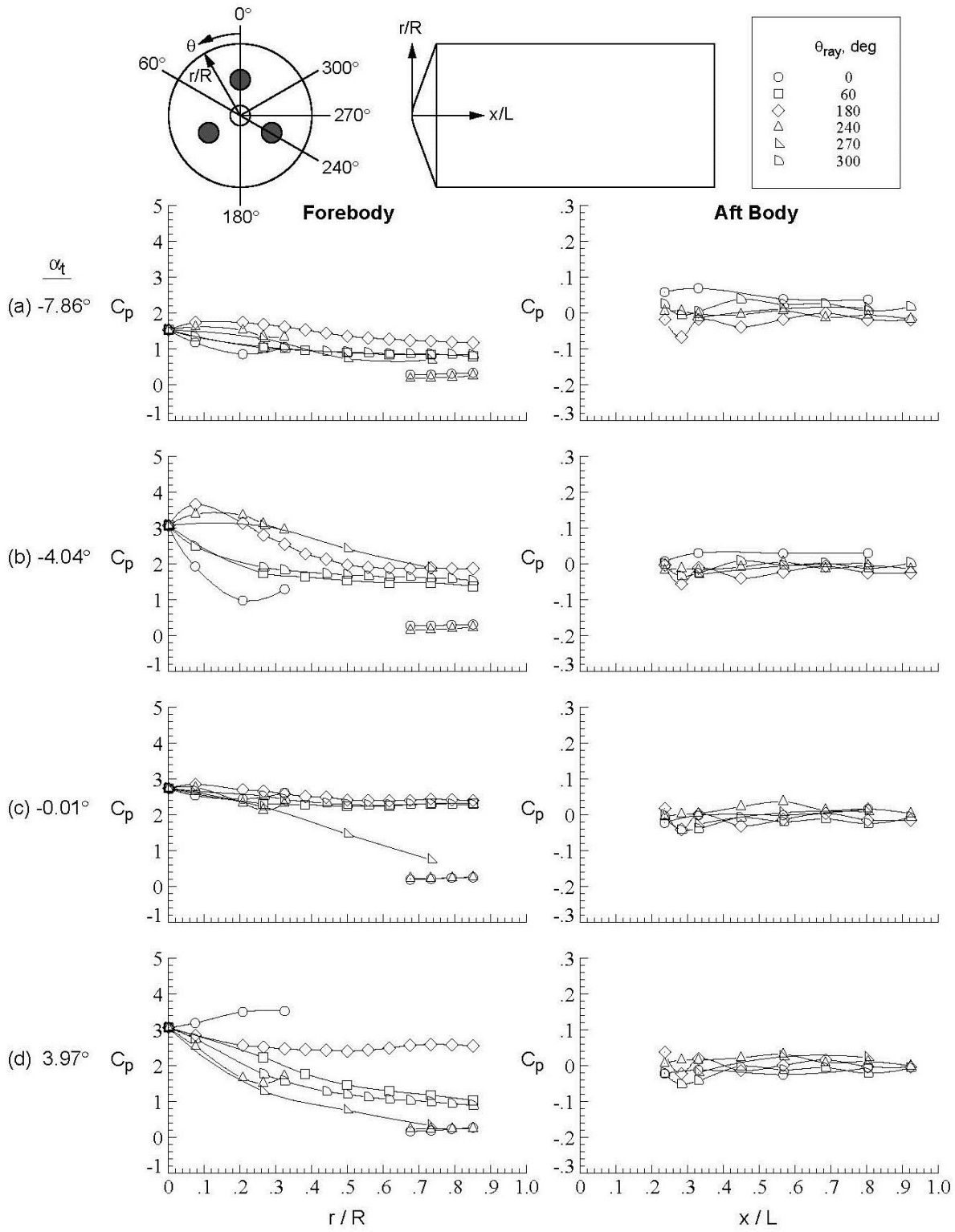

Figure D-199. Tri-nozzle configuration, Run 253, M_∞ = 4.6, Re_∞ = 1.5x10^7/ft, ϕ = −0.03°, X_S = 40.15 in, Y_S = 0.00 in, C_T = 0.43.

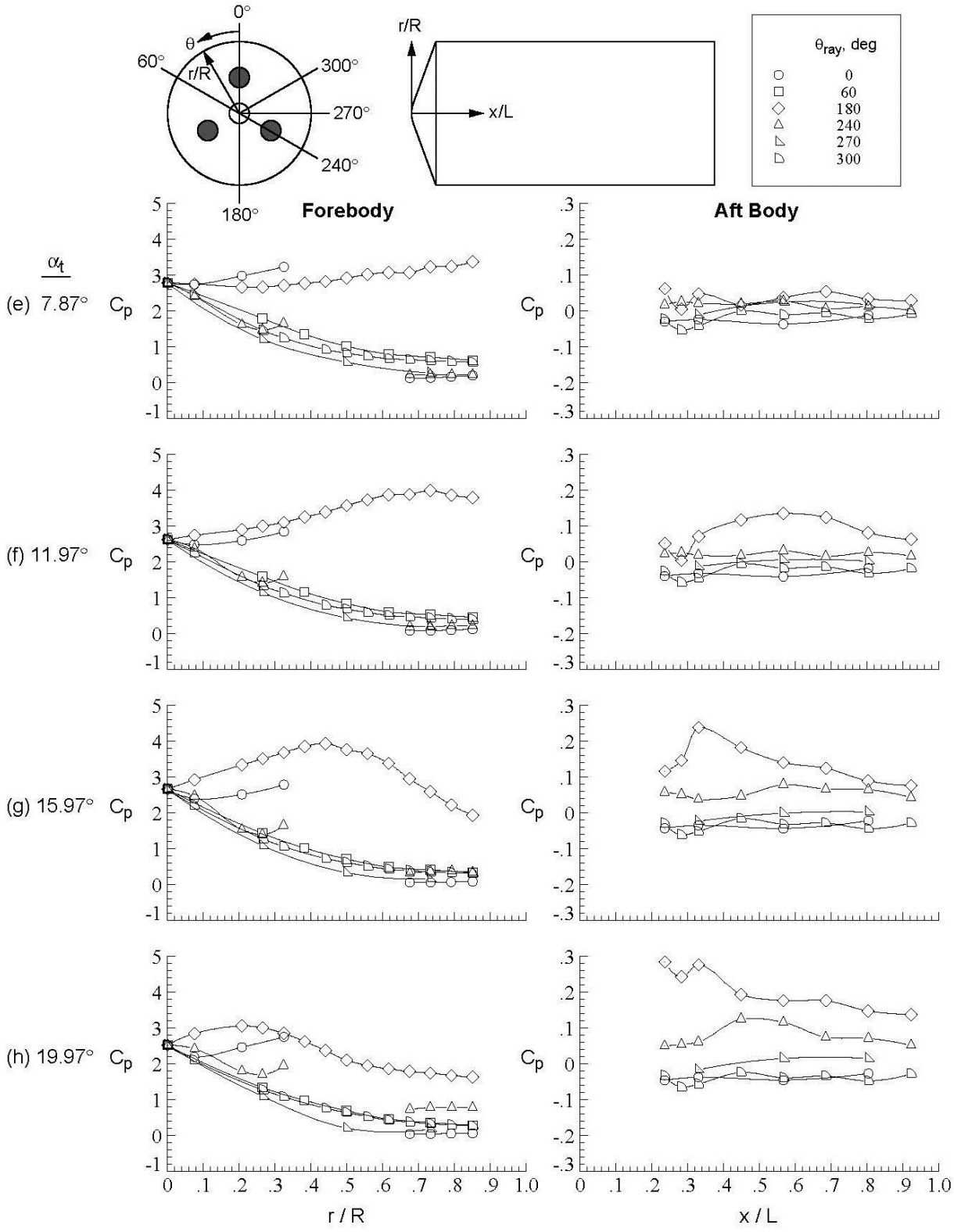

Figure D-199.Concluded.

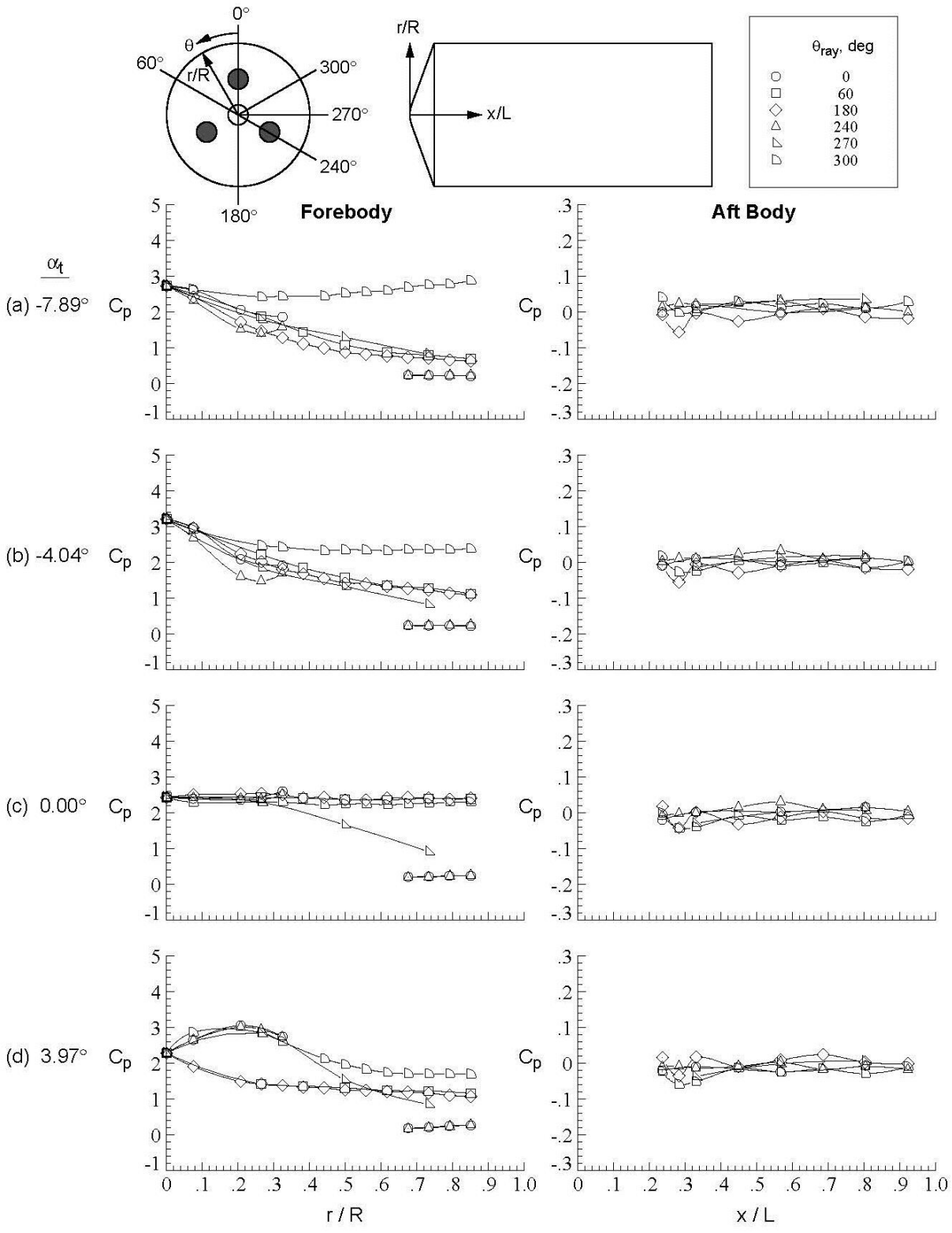

Figure D-200. Tri-nozzle configuration, Run 254, $M\infty$ = 4.6, Re_∞ = 1.5x10^7/ft, ϕ = 59.94°, X_S = 40.15 in, Y_S = 0.00 in, C_T = 0.43.

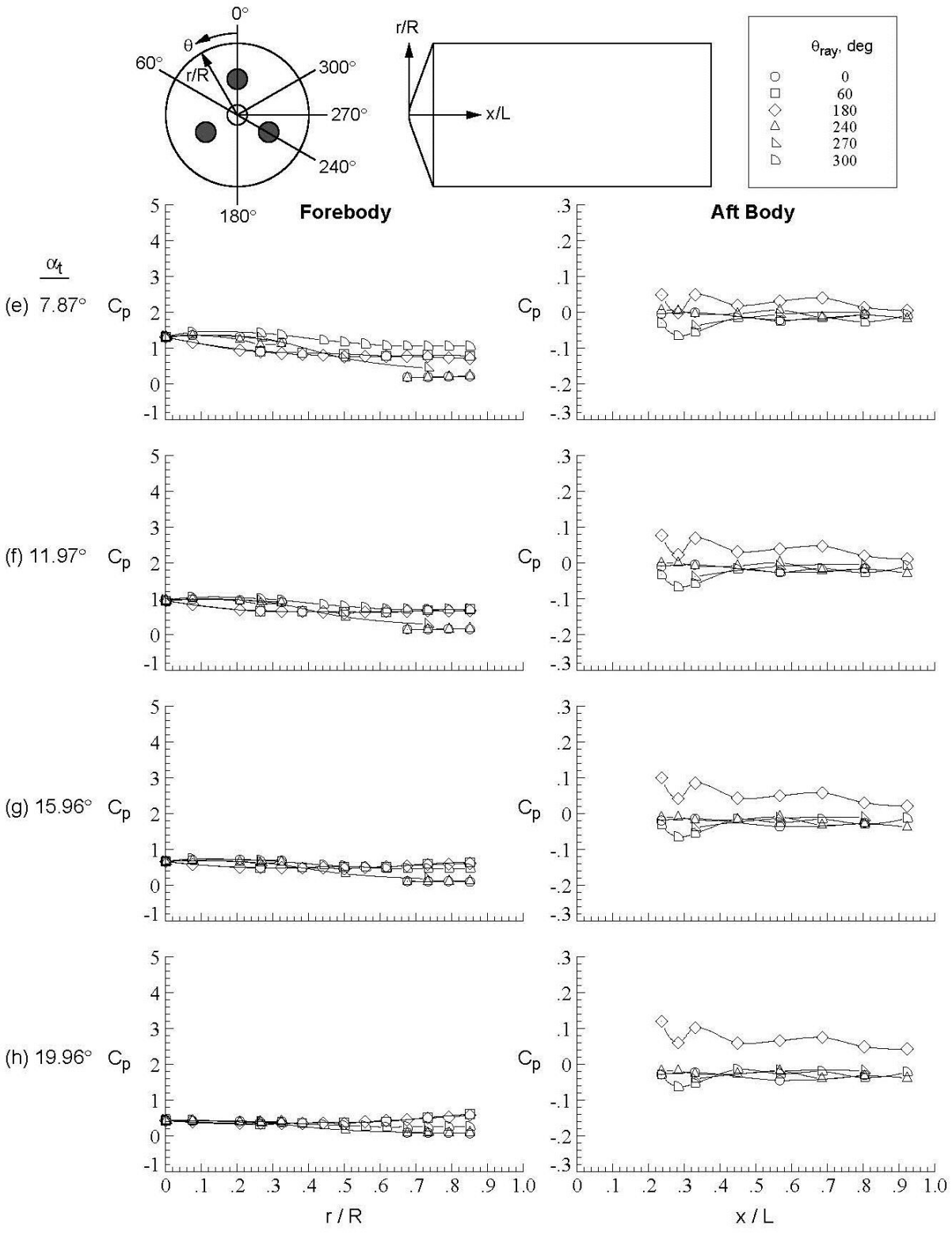

Figure D-200.Concluded.

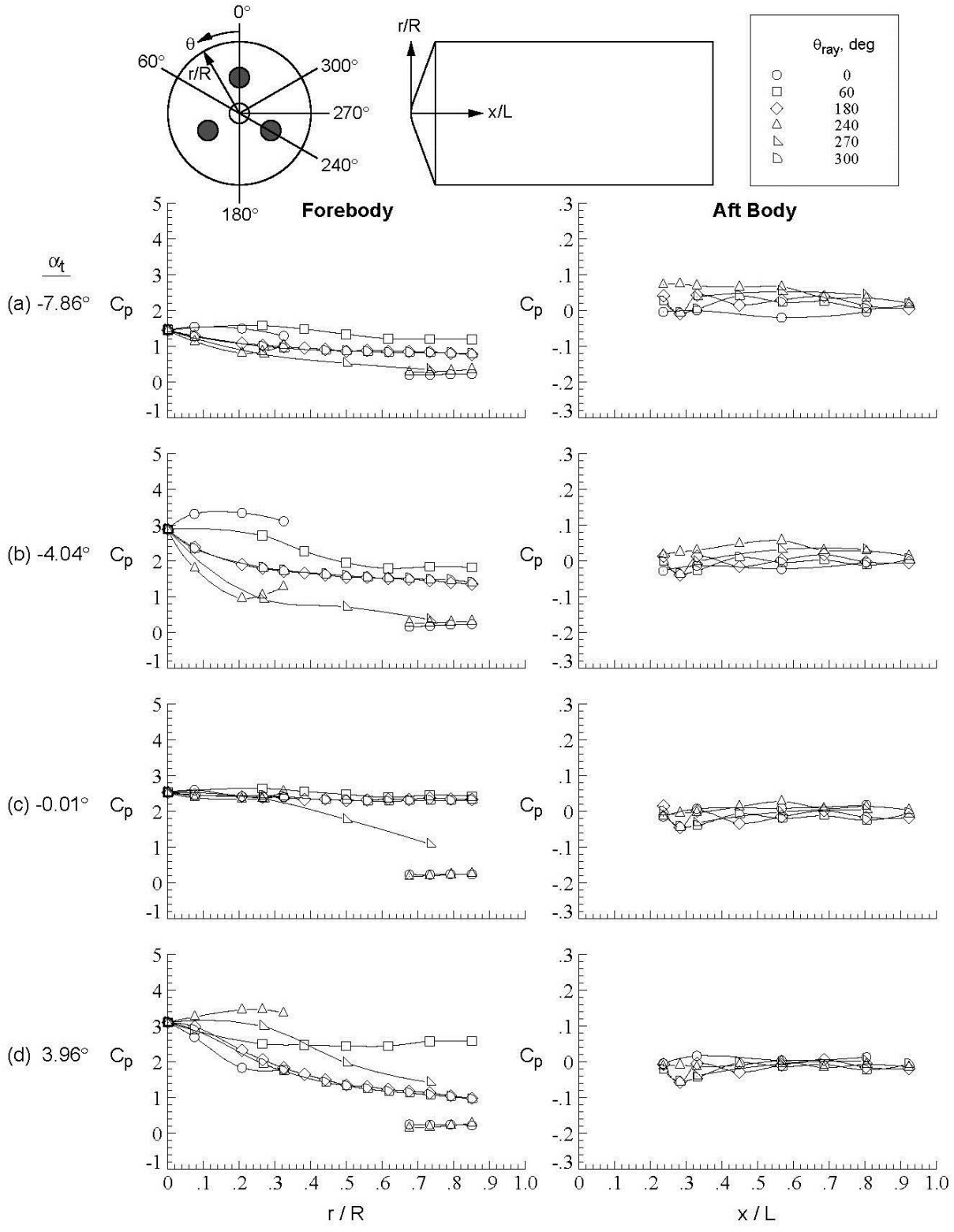

Figure D-201. Tri-nozzle configuration, Run 255, M_∞ = 4.6, Re_∞ = 1.5x10^7/ft, ϕ = 120.02°, X_S = 40.15 in, Y_S = 0.00 in, C_T = 0.42.

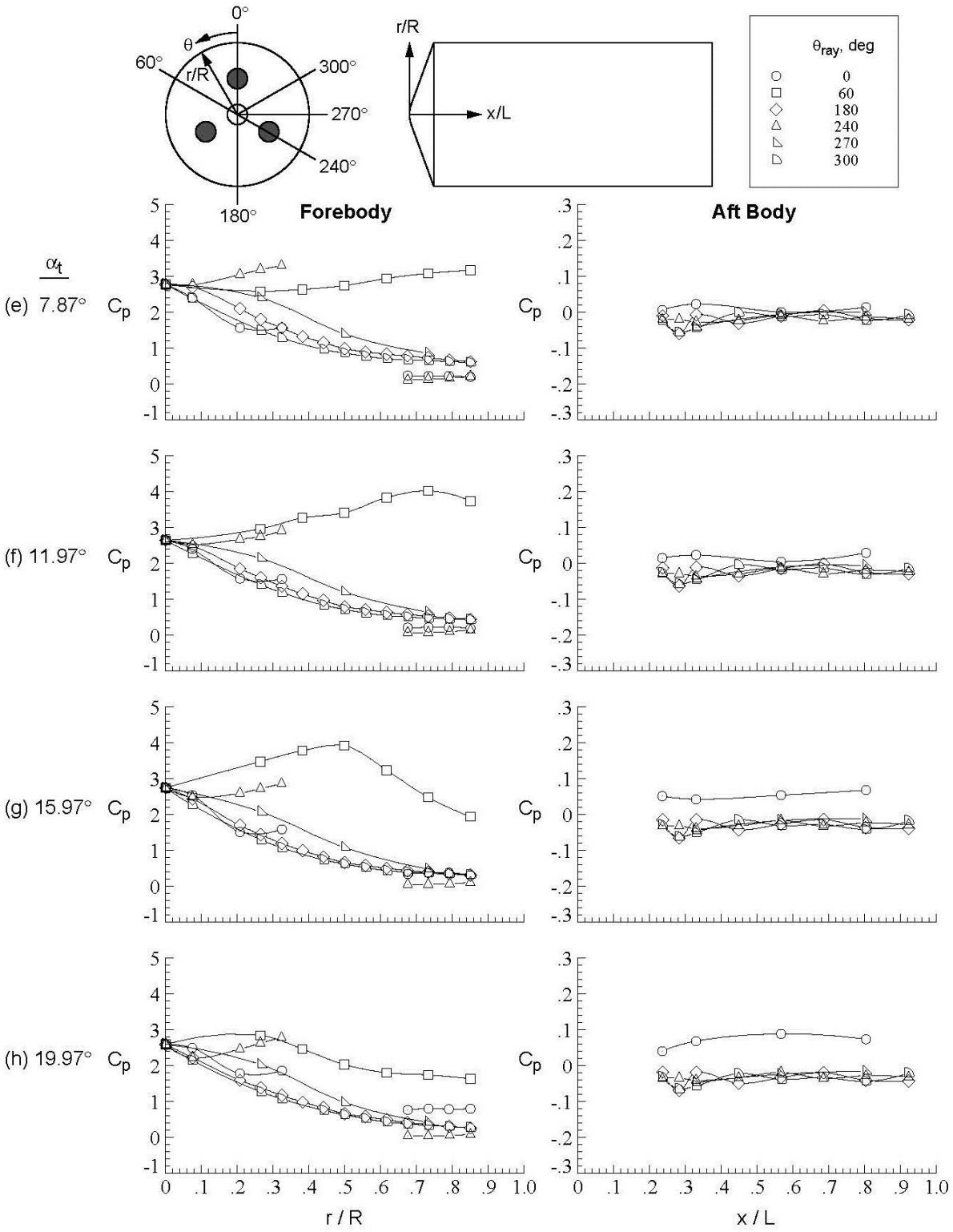

Figure D-201.Concluded.

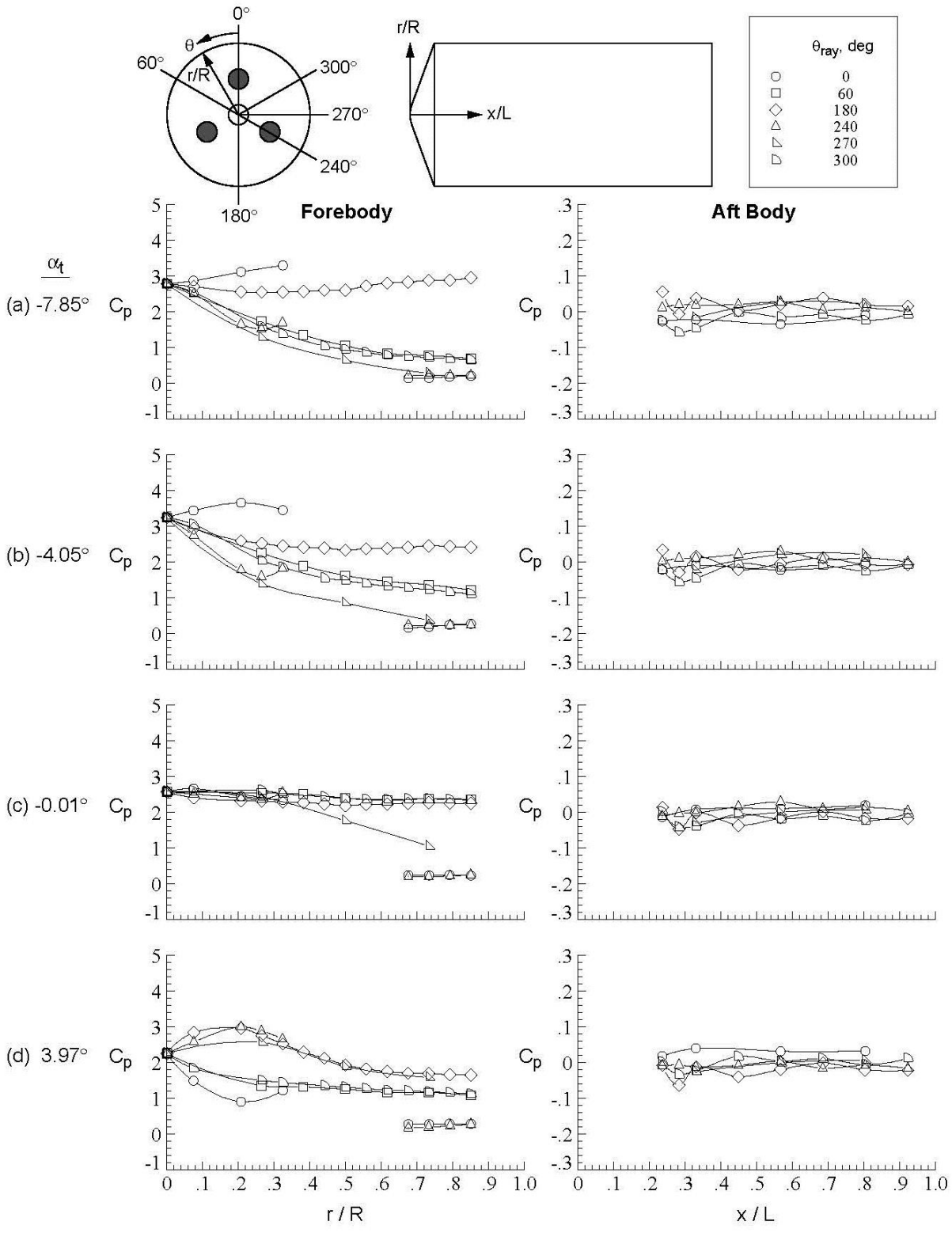

Figure D-202. Tri-nozzle configuration, Run 256, M_∞ = 4.6, Re_∞ = 1.5x10^7/ft, ϕ = 179.95°, X_S = 40.15 in, Y_S = 0.00 in, C_T = 0.43.

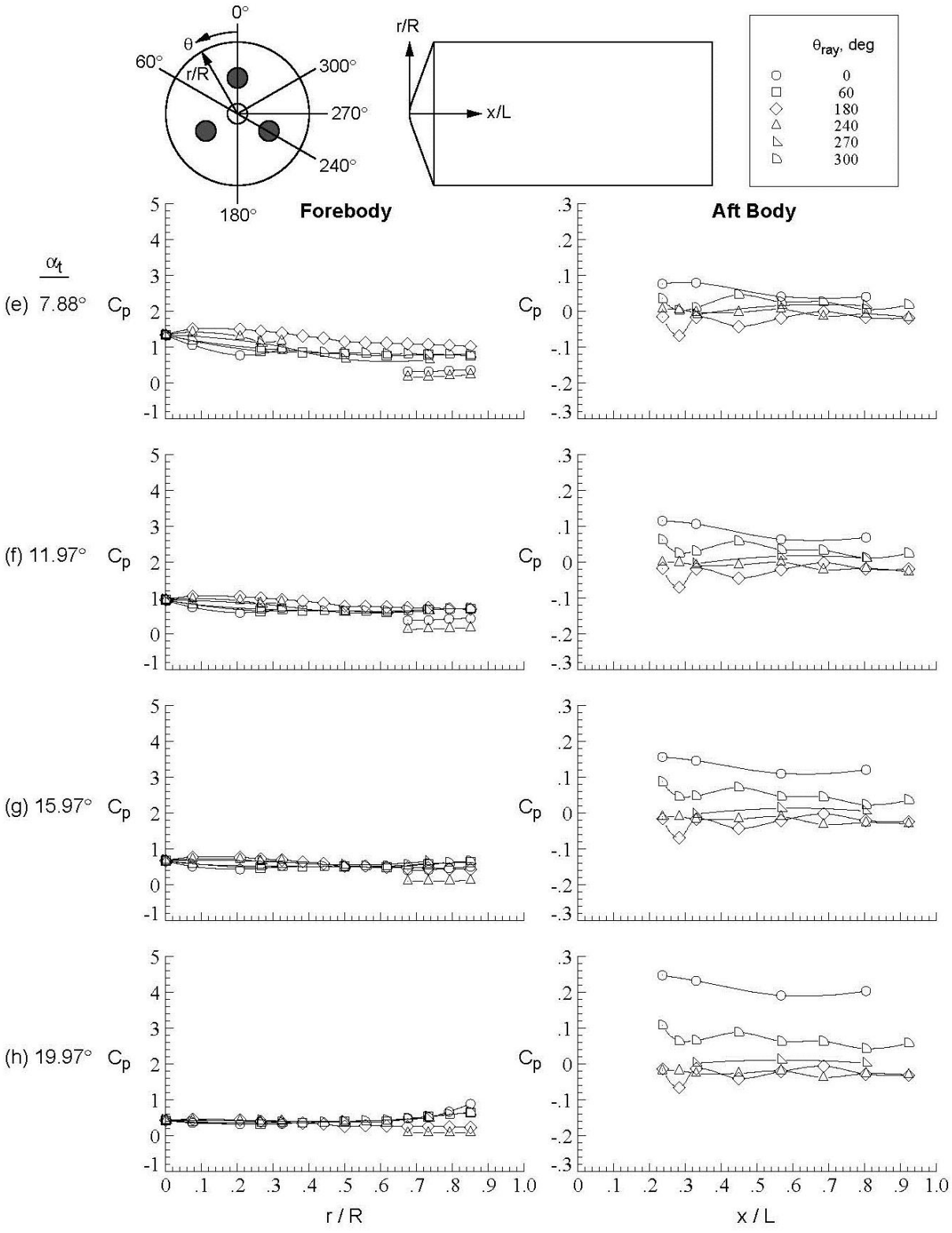

Figure D-202.Concluded.

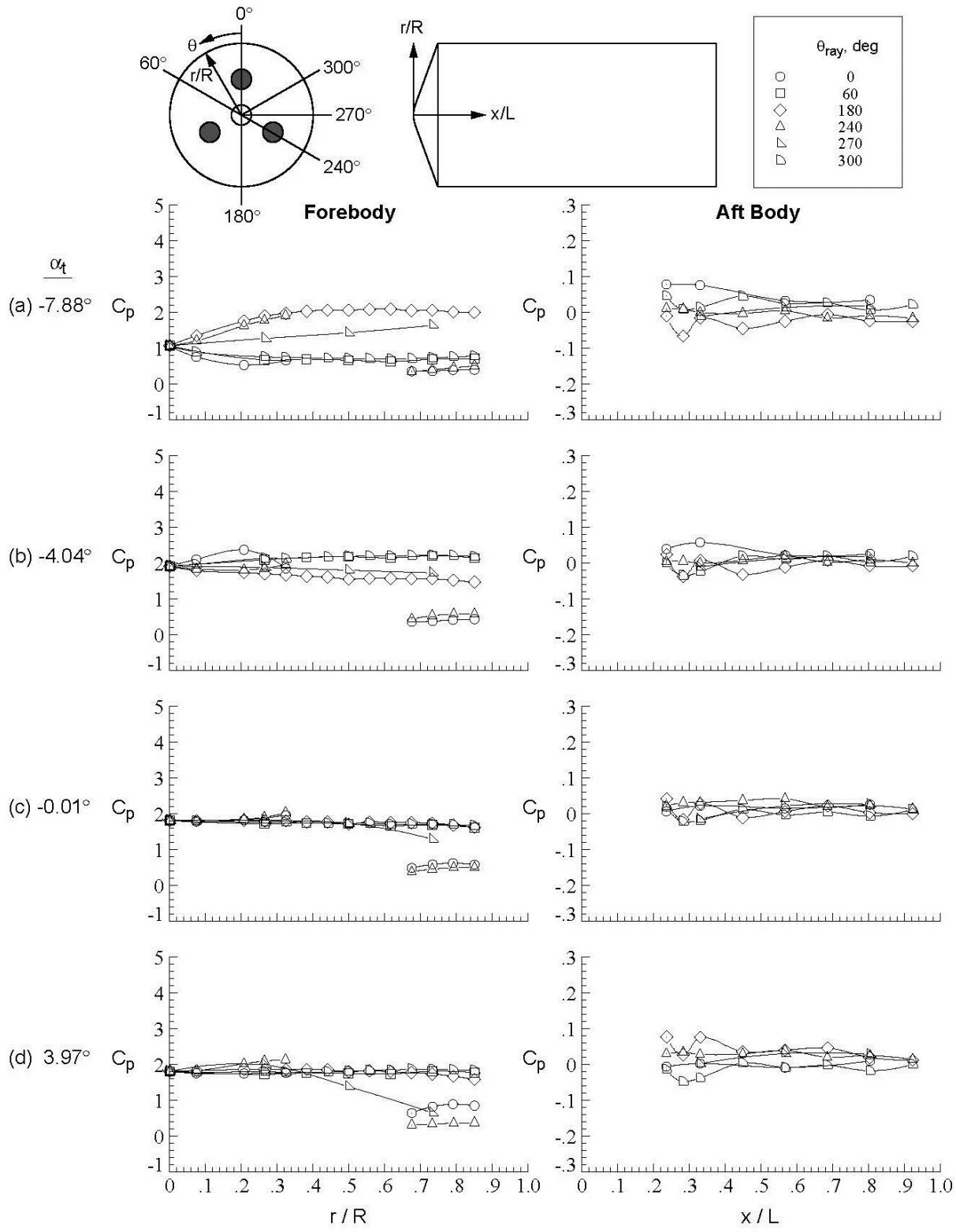

Figure D-203. Tri-nozzle configuration, Run 257, M_∞ = 4.6, Re_∞ = 1.5x10^7/ft, ϕ = −0.03°, X_S = 40.15 in, Y_S = 0.00 in, C_T = 0.20.

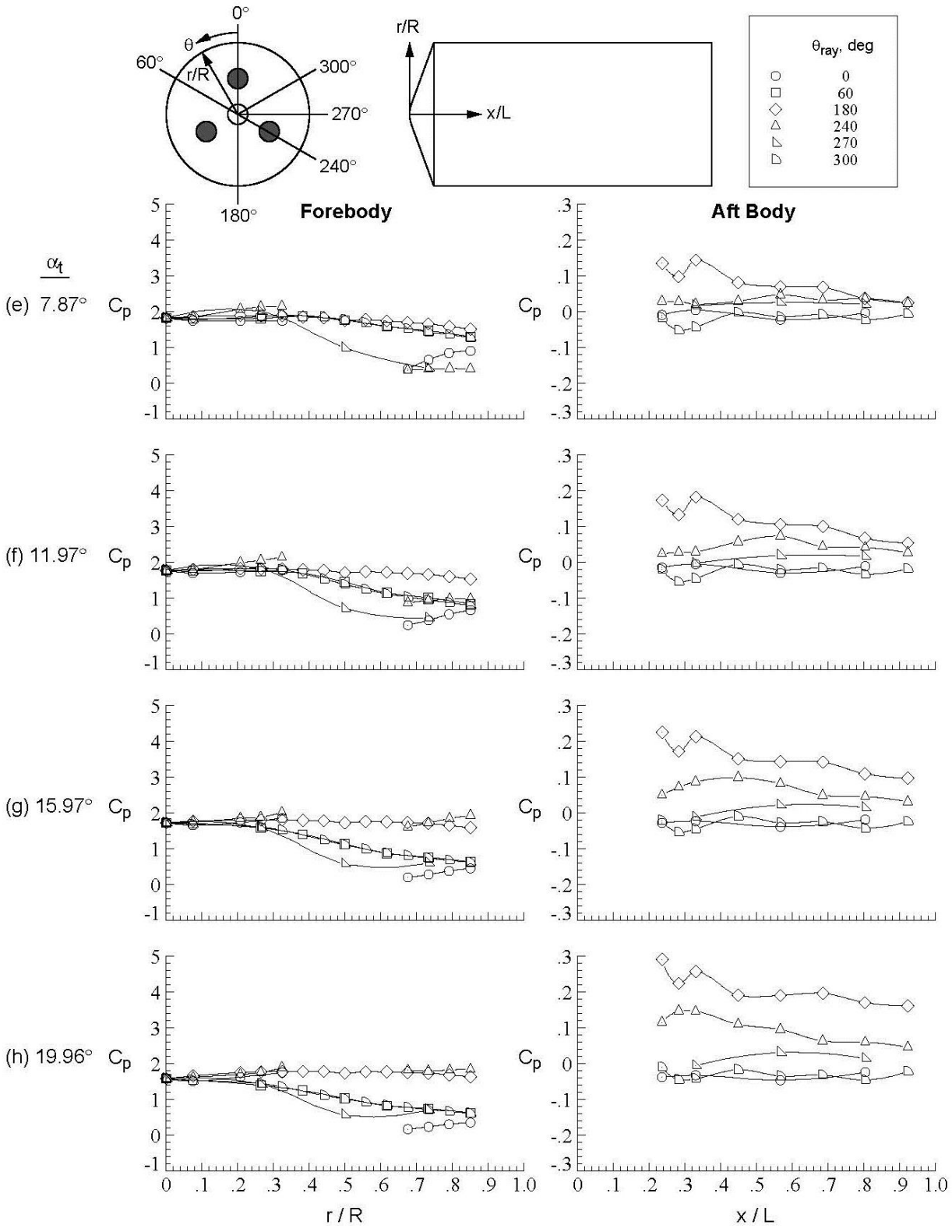

Figure D-203.Concluded.

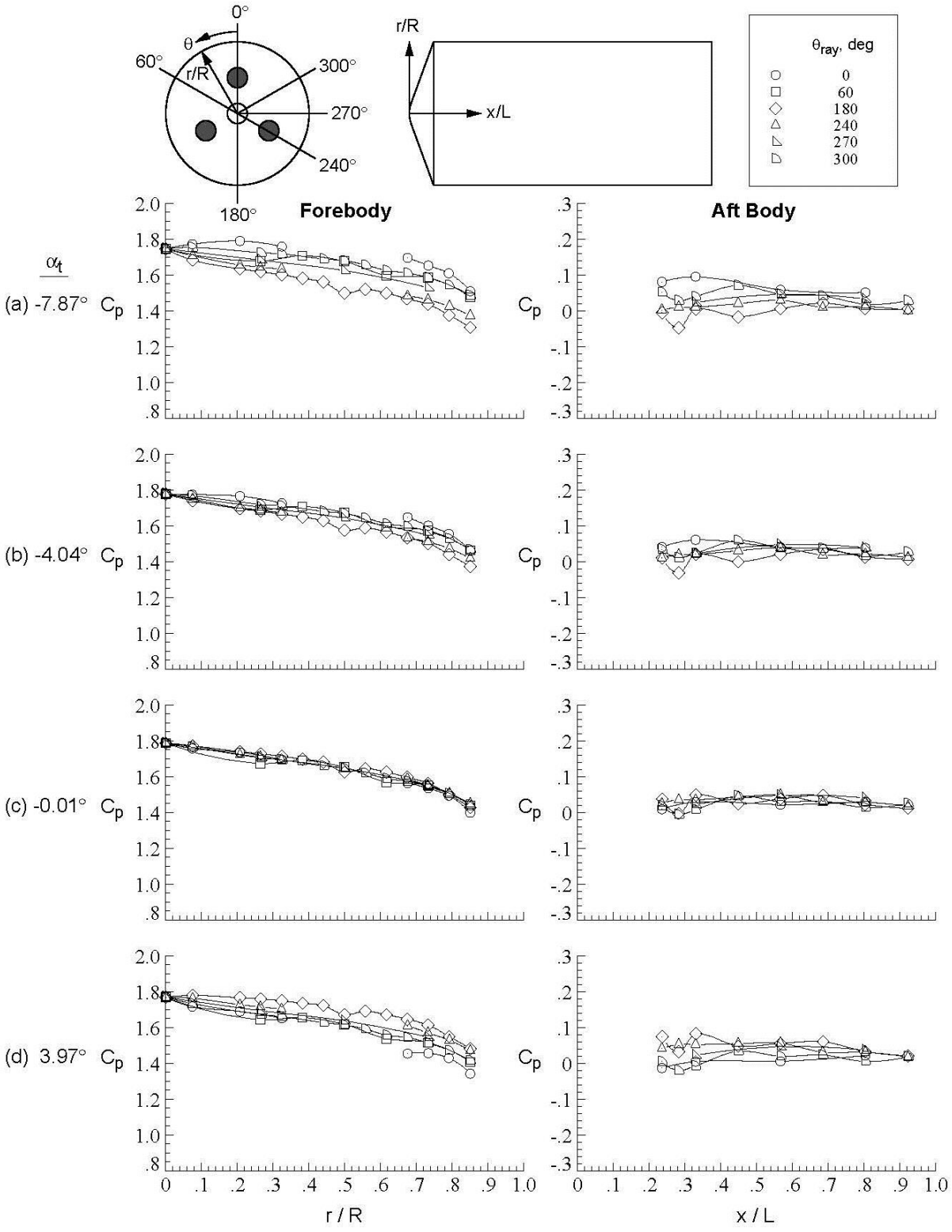

Figure D-204. Tri-nozzle configuration, Run 258, M_∞ = 4.6, Re_∞ = 1.5x10^7/ft, ϕ = −0.03°, X_S = 40.15 in, Y_S = 0.00 in, C_T = 0.00.

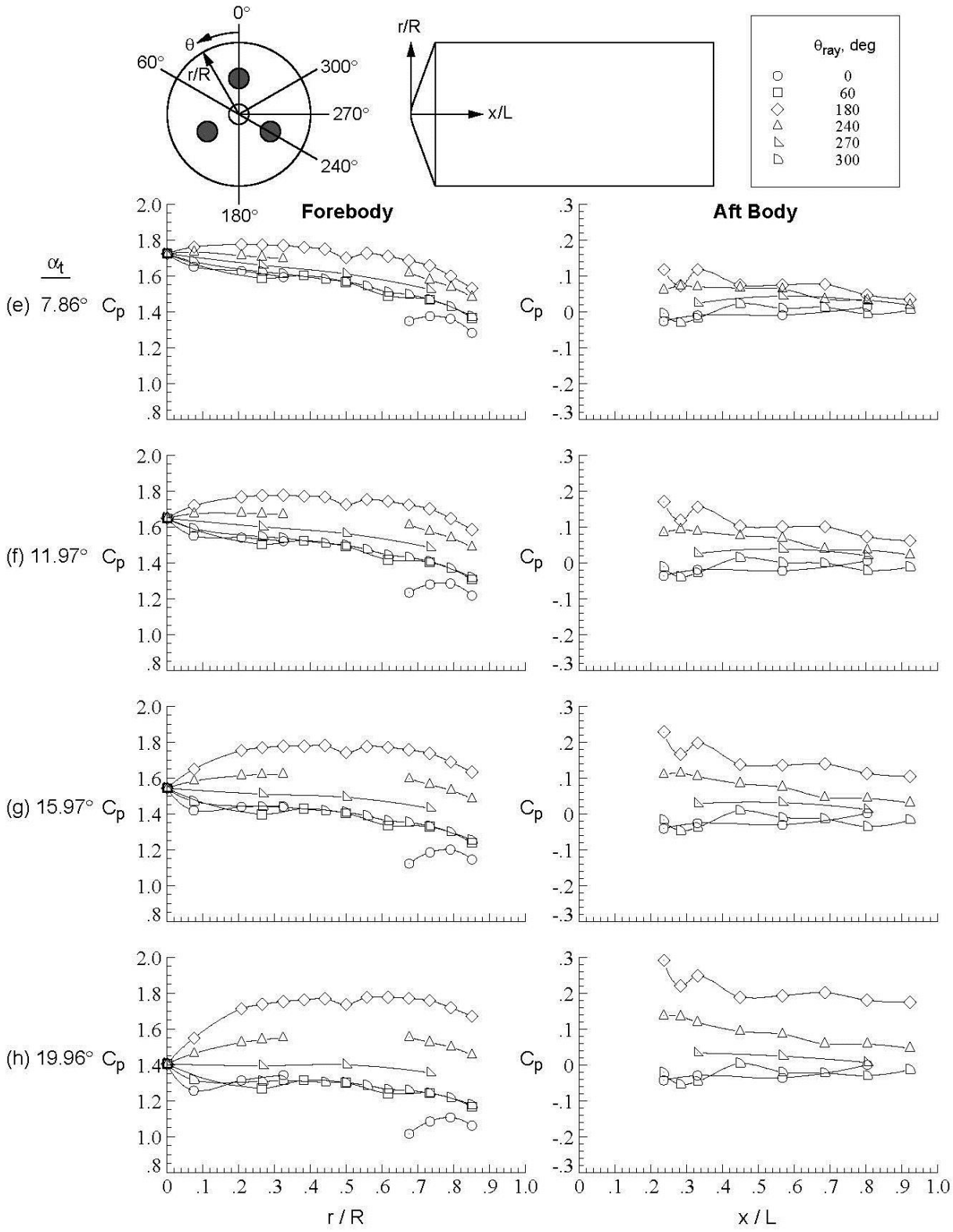

Figure D-204.Concluded.

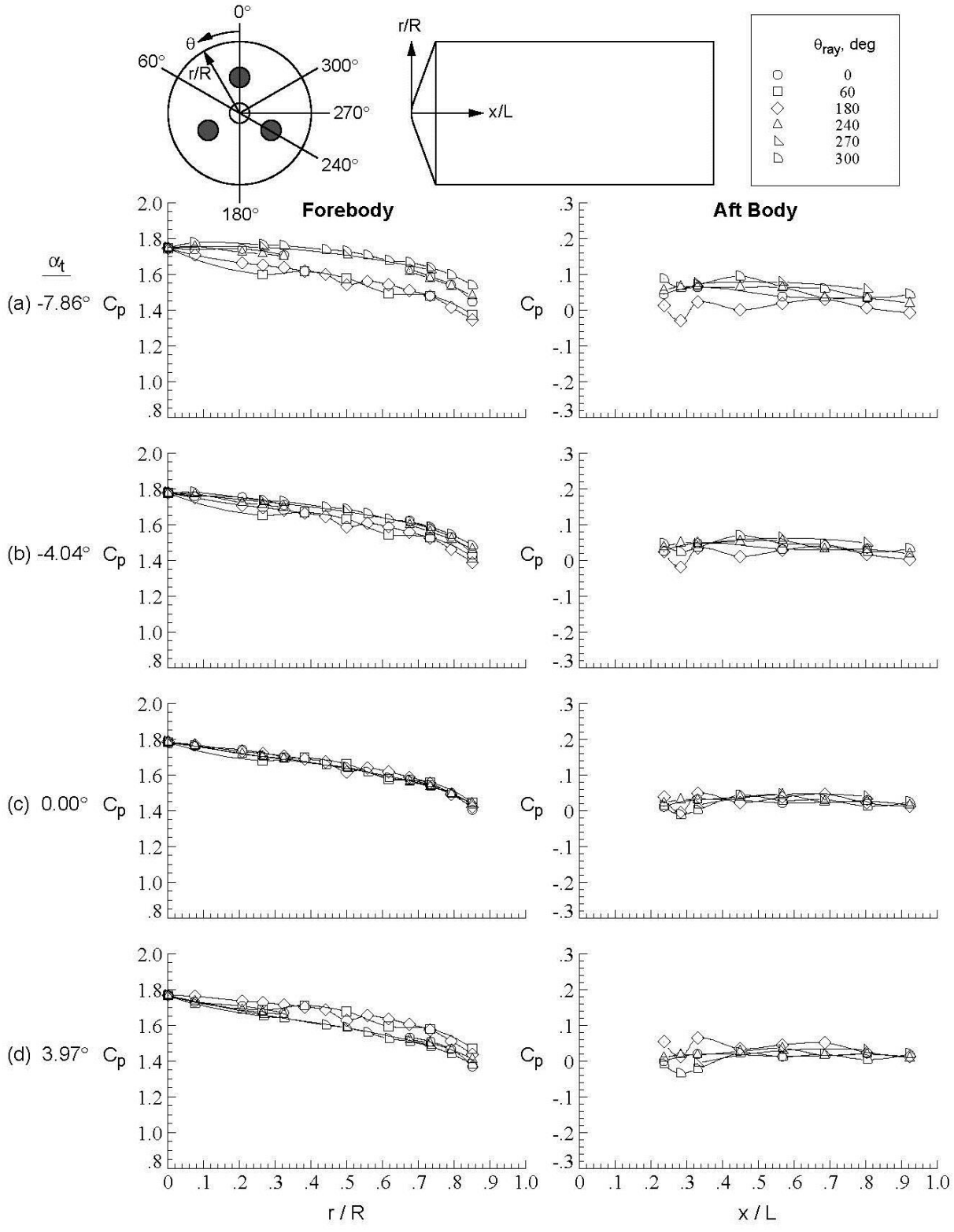

Figure D-205. Tri-nozzle configuration, Run 259, M_∞ = 4.6, Re_∞ = 1.5x10^7/ft, ϕ = 59.90°, X_S = 40.15 in, Y_S = 0.00 in, C_T = 0.00.

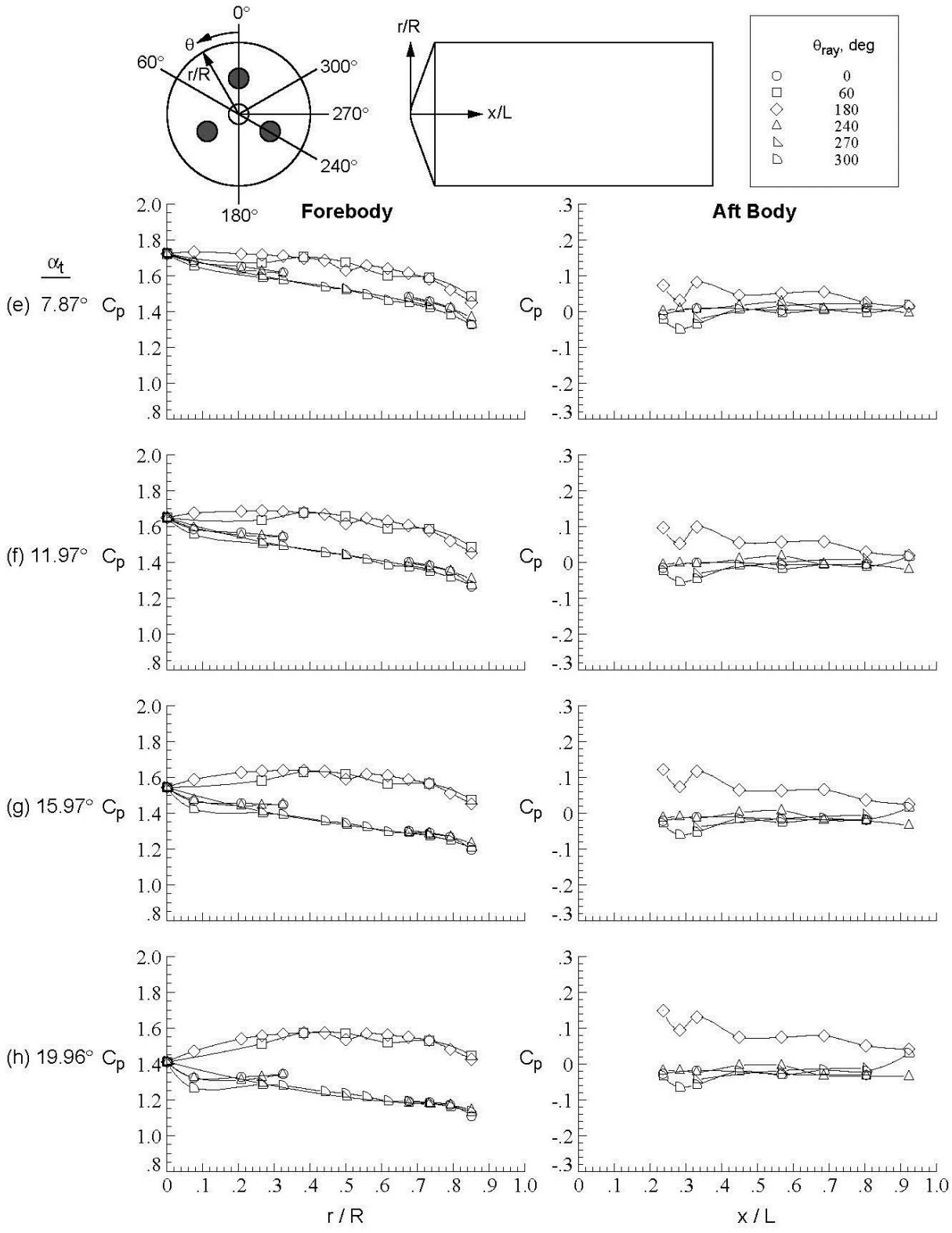

Figure D-205.Concluded.

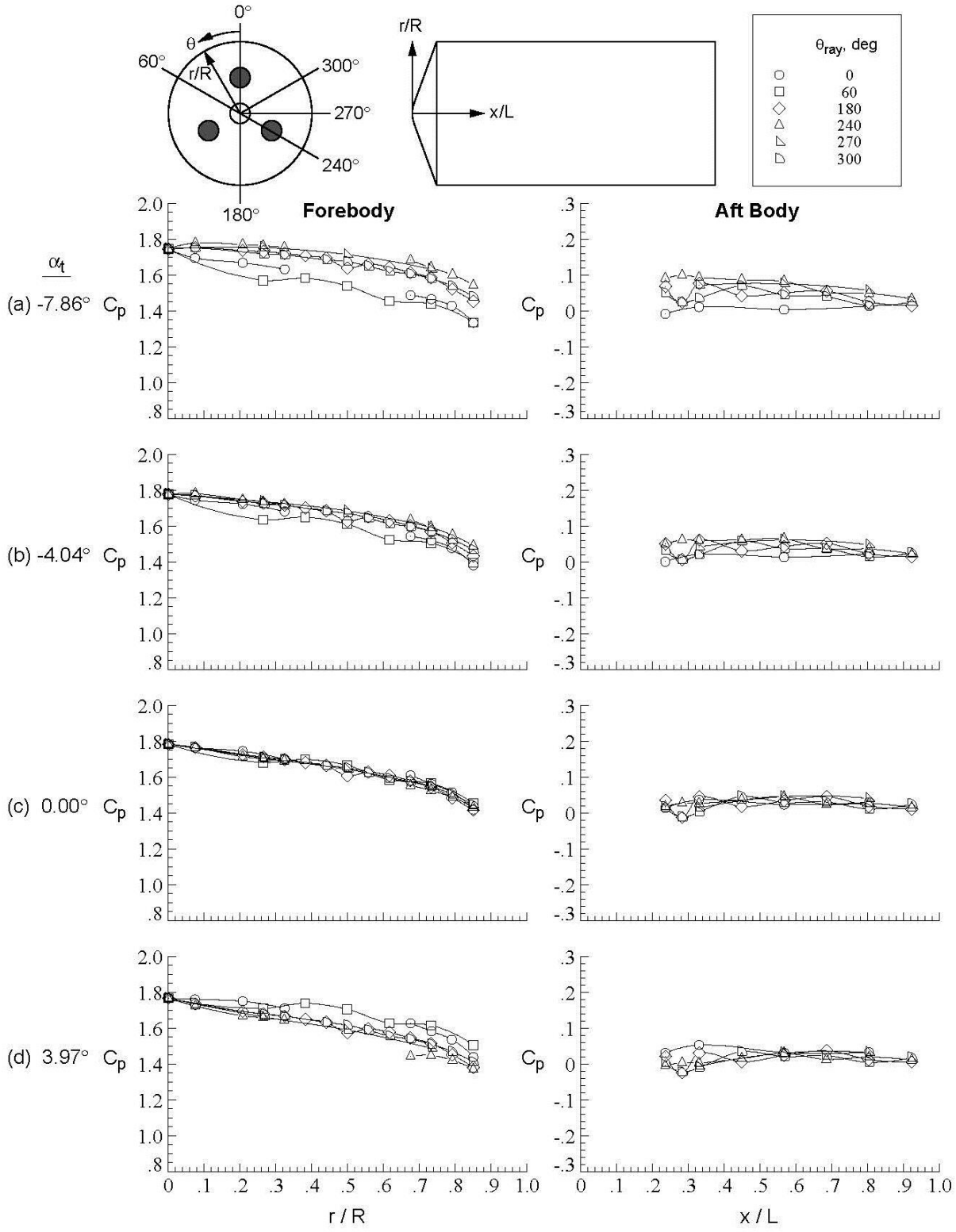

Figure D-206. Tri-nozzle configuration, Run 260, $M\infty$ = 4.6, Re_∞ = 1.5x10^7/ft, ϕ = 120.00°, X_S = 40.15 in, Y_S = 0.00 in, C_T = 0.00.

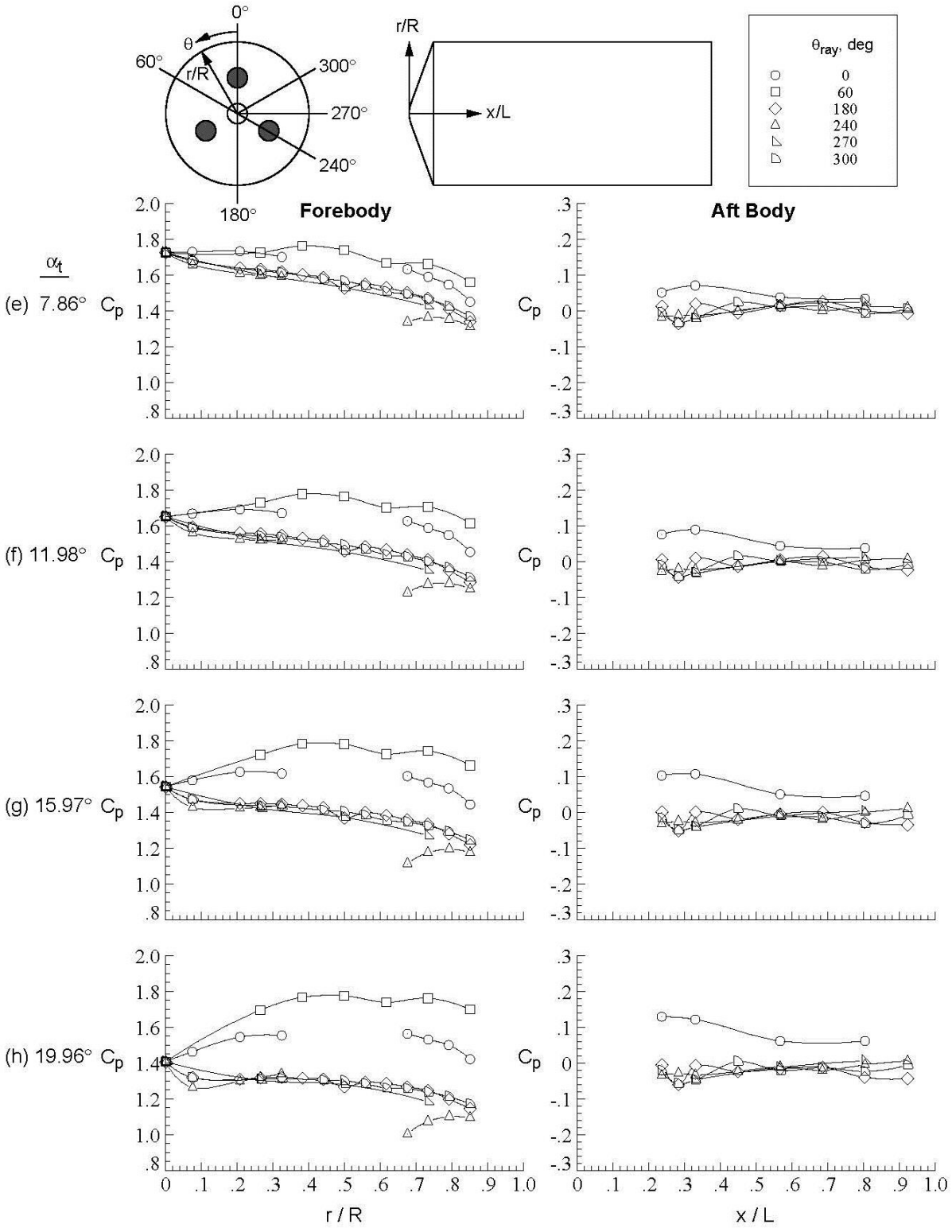

Figure D-206.Concluded.

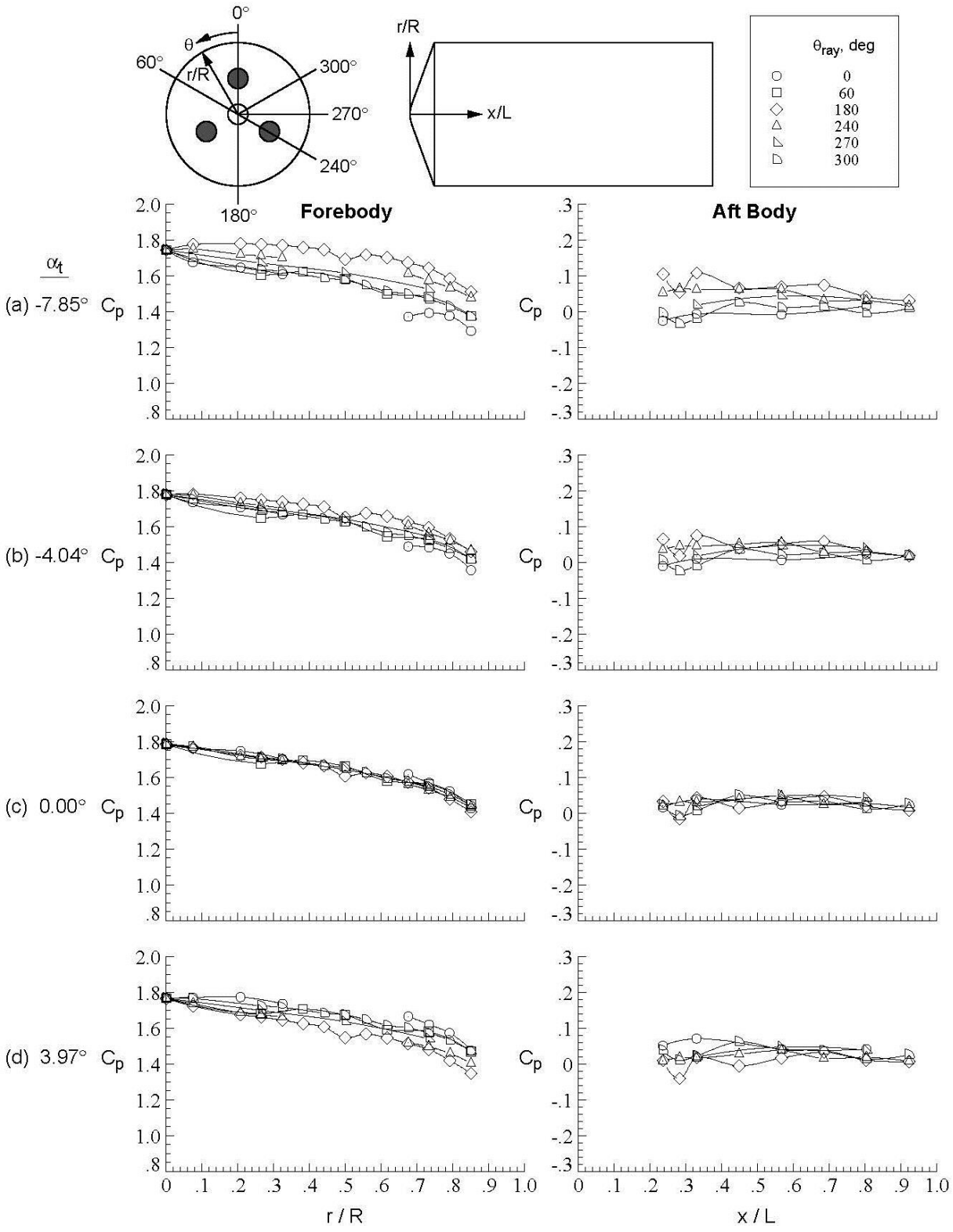

Figure D-207. Tri-nozzle configuration, Run 261, M_∞ = 4.6, Re_∞ = 1.5x10^7/ft, ϕ = 179.95°, X_S = 40.15 in, Y_S = 0.00 in, C_T = 0.00.

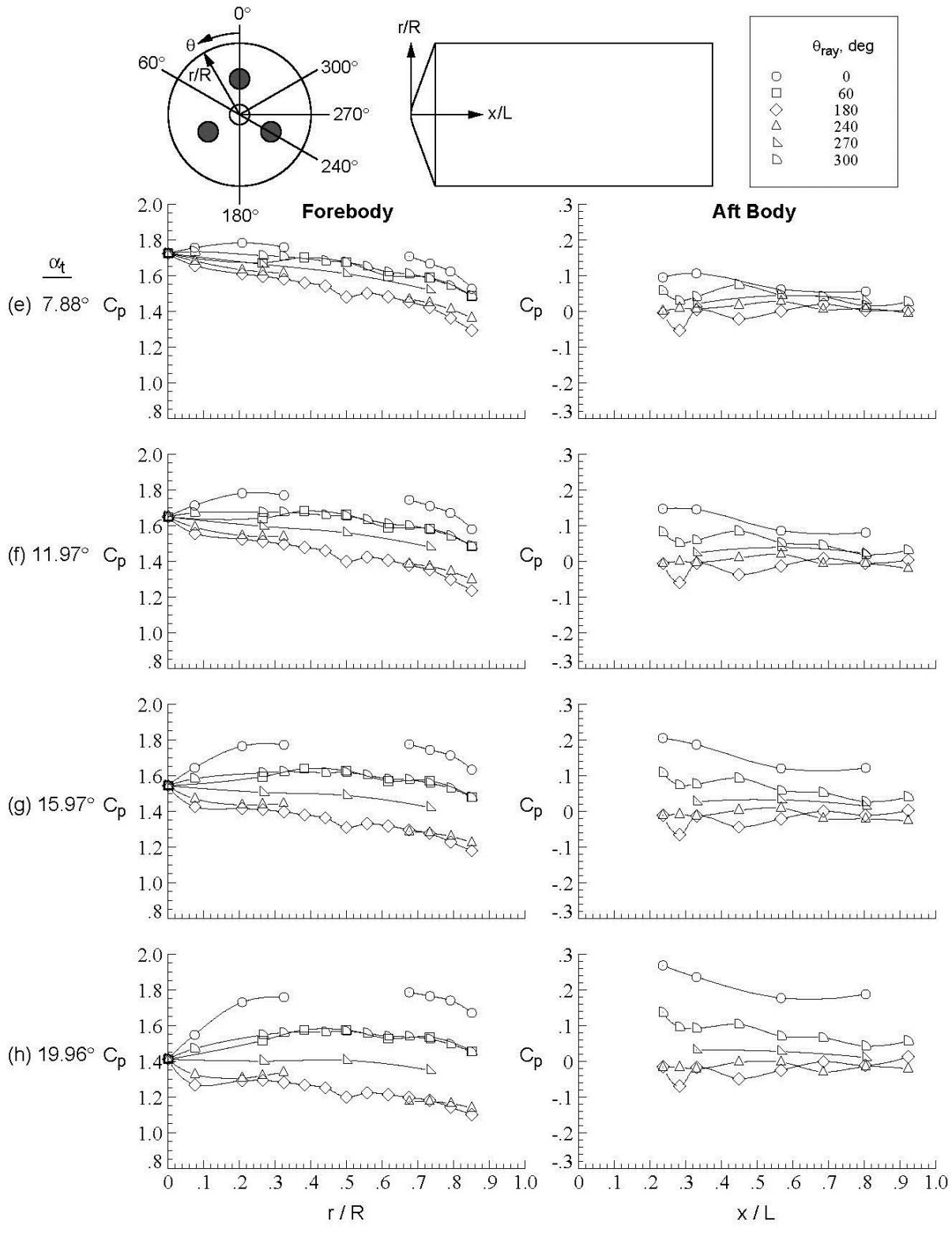

Figure D-207.Concluded.

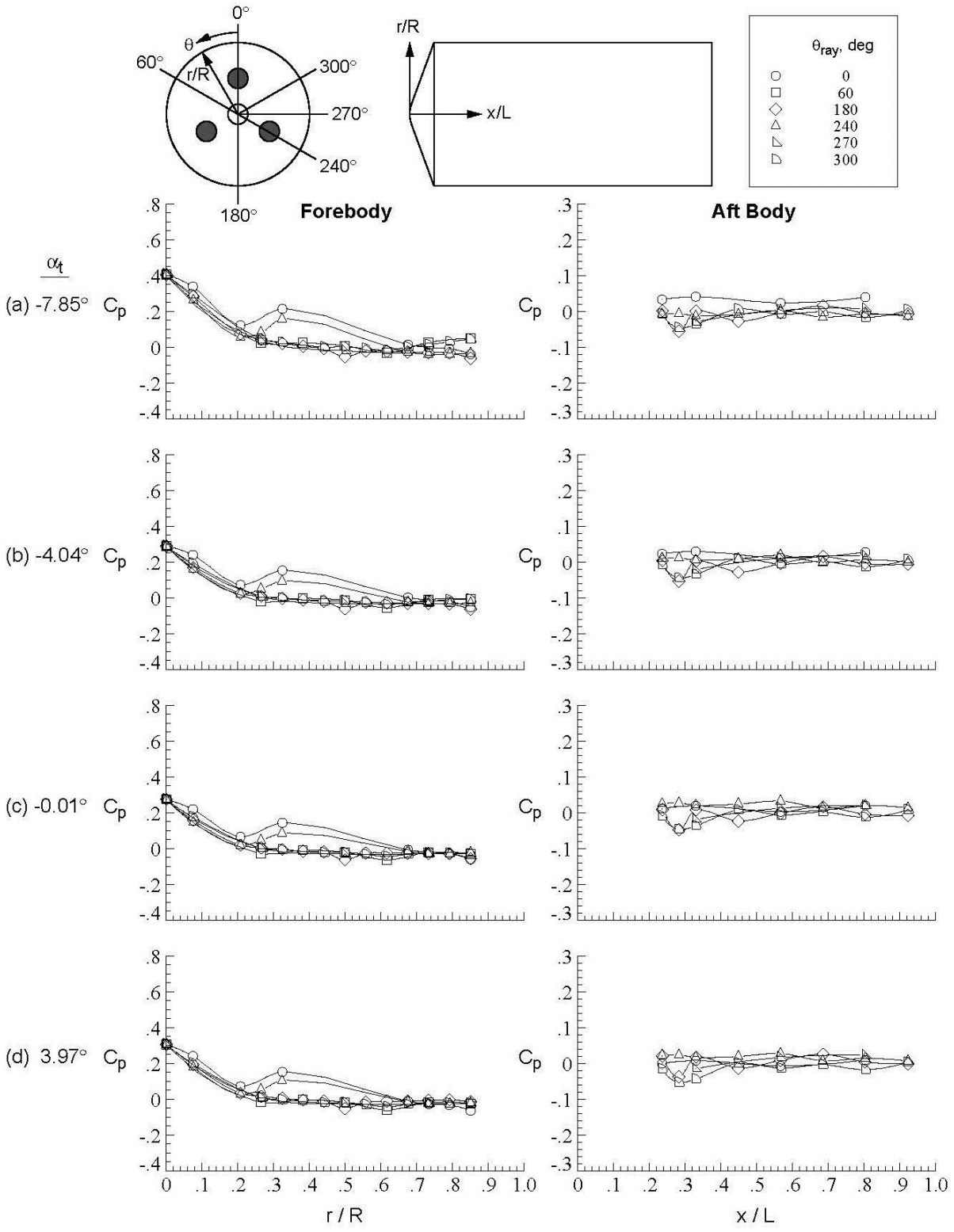

Figure D-208. Tri-nozzle configuration, Run 262, $M\infty$ = 4.6, Re_∞ = 1.5x10^7/ft, ϕ = 0.01°, X_S = 40.15 in, Y_S = 0.00 in, C_T = 2.92.

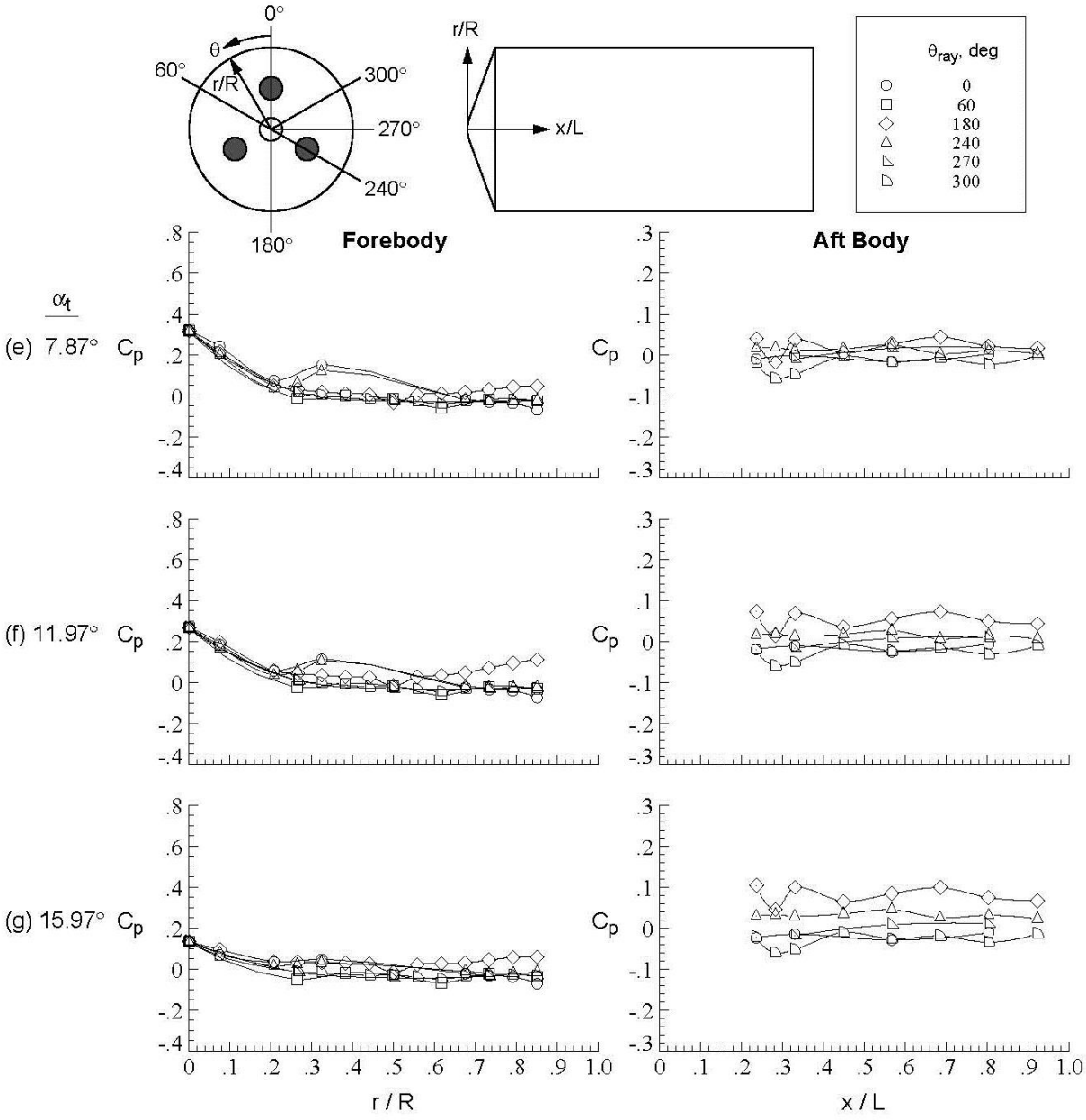

Figure D-208.Concluded.

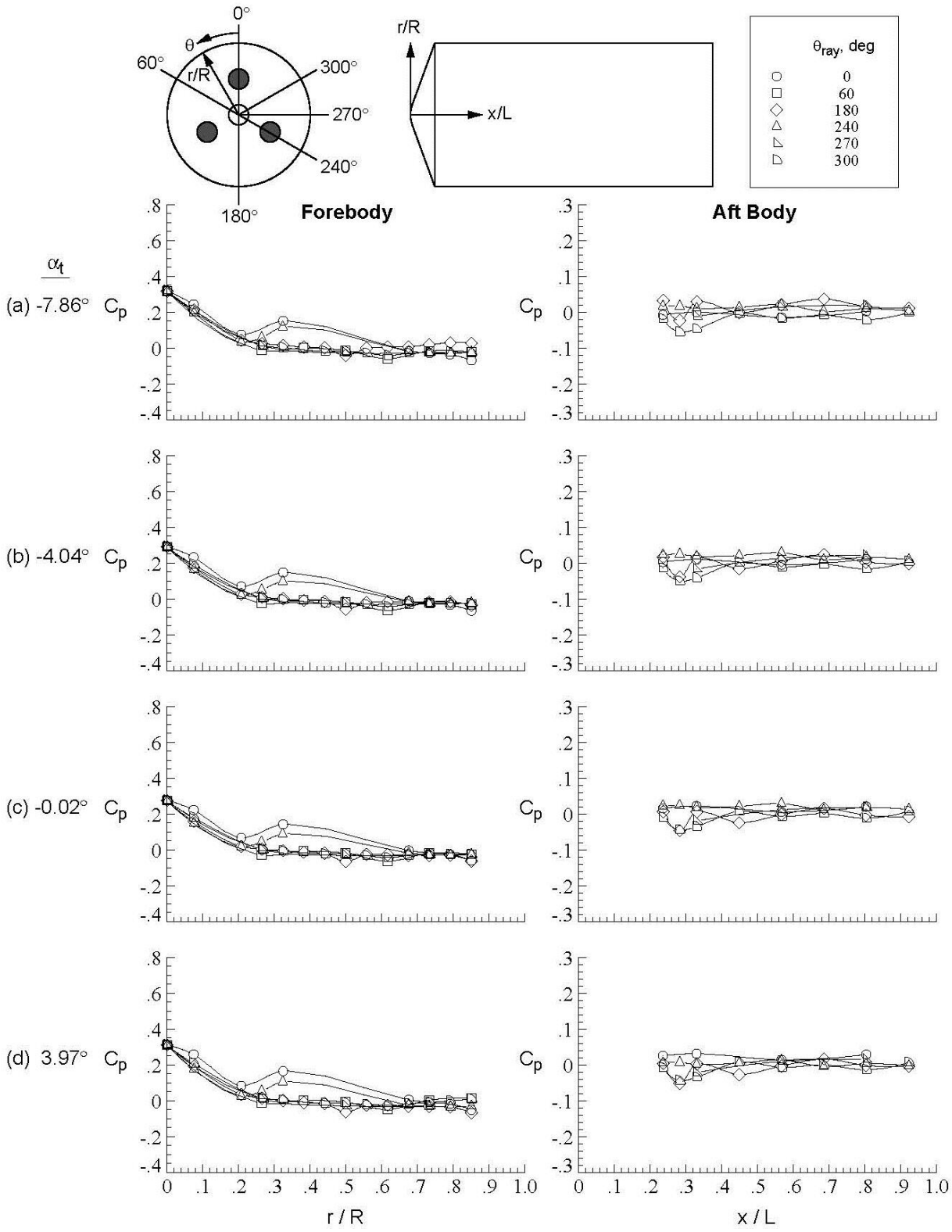

Figure D-209. Tri-nozzle configuration, Run 263, $M\infty = 4.6$, $Re_\infty = 1.5 \times 10^7$/ft, $\phi = -179.95°$, $X_S = 40.15$ in, $Y_S = 0.00$ in, $C_T = 2.94$.

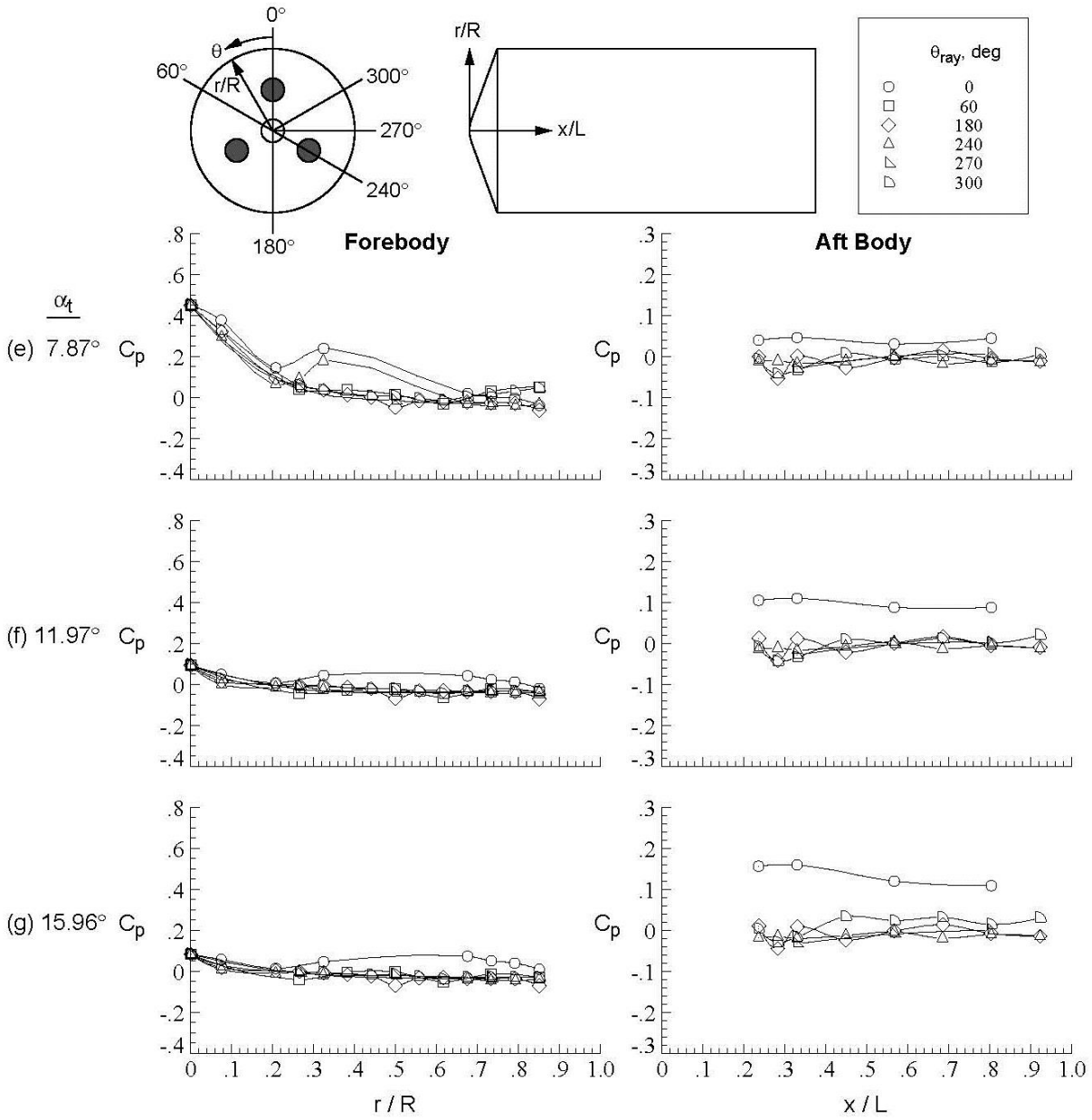

Figure D-209.Concluded.

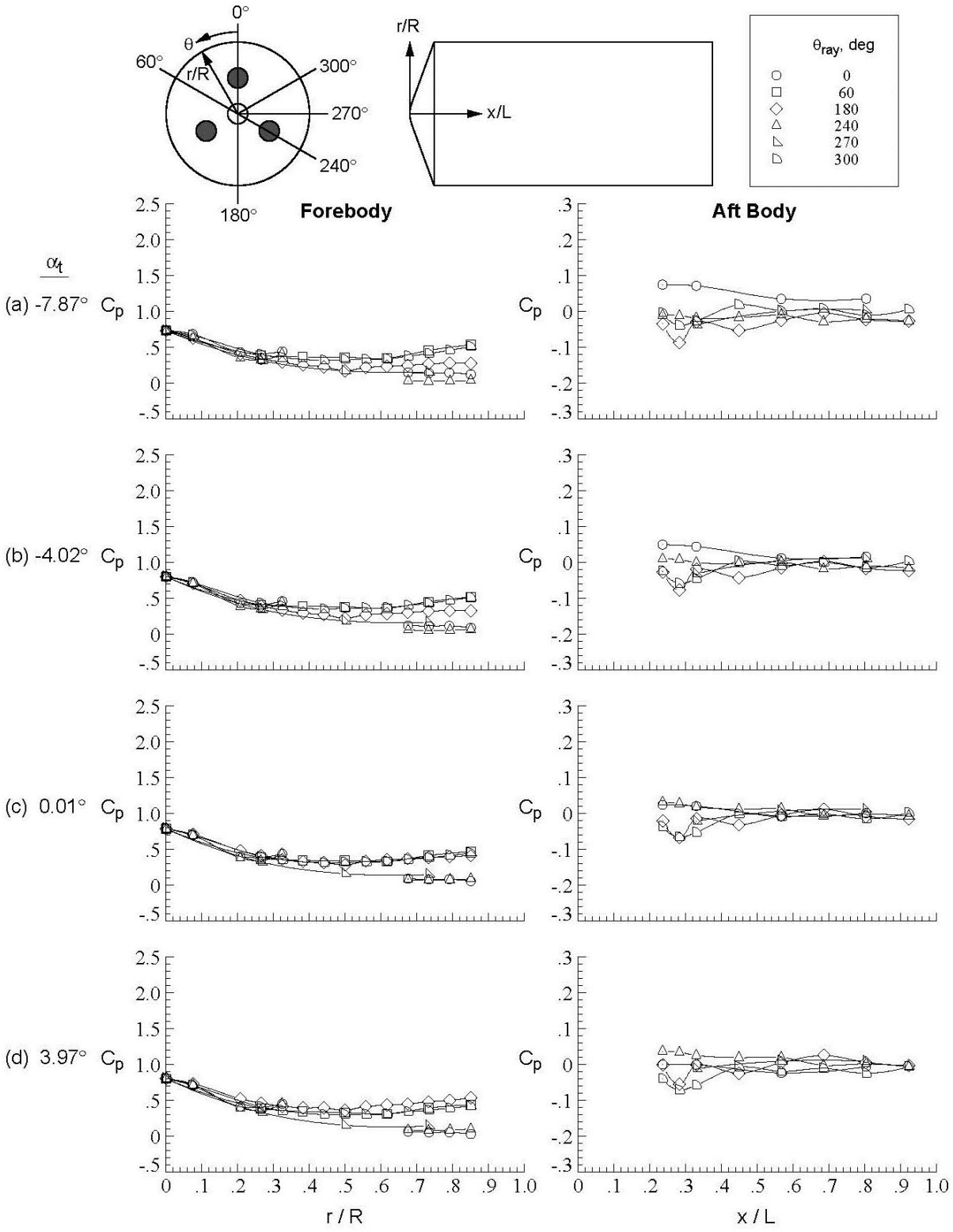

Figure D-210. Tri-nozzle configuration, Run 265, M_∞ = 3.5, Re_∞ = 1.0x10^6/ft, ϕ = −0.05°, X_S = 40.15 in, Y_S = 0.00 in, C_T = 0.91.

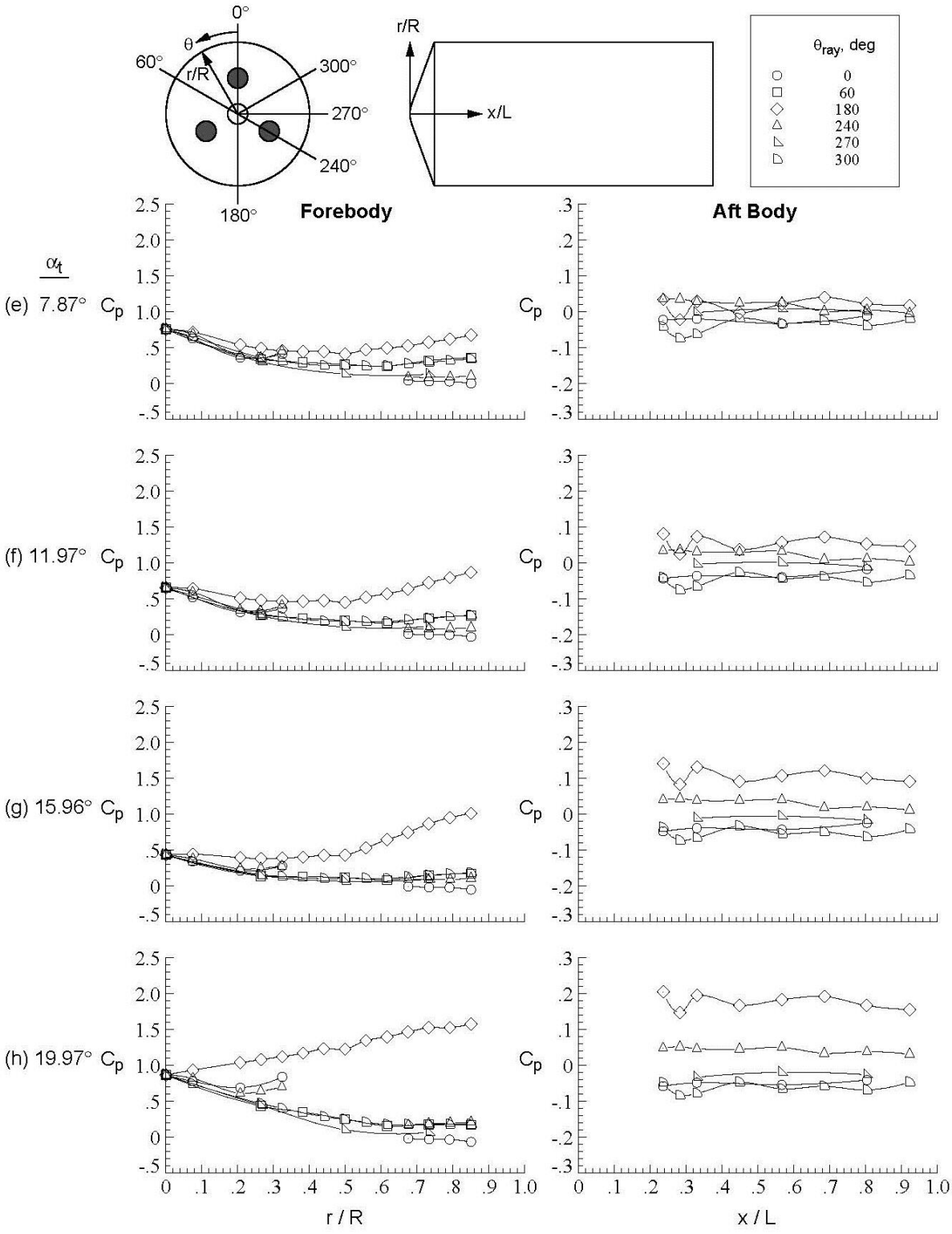

Figure D-210.Concluded.

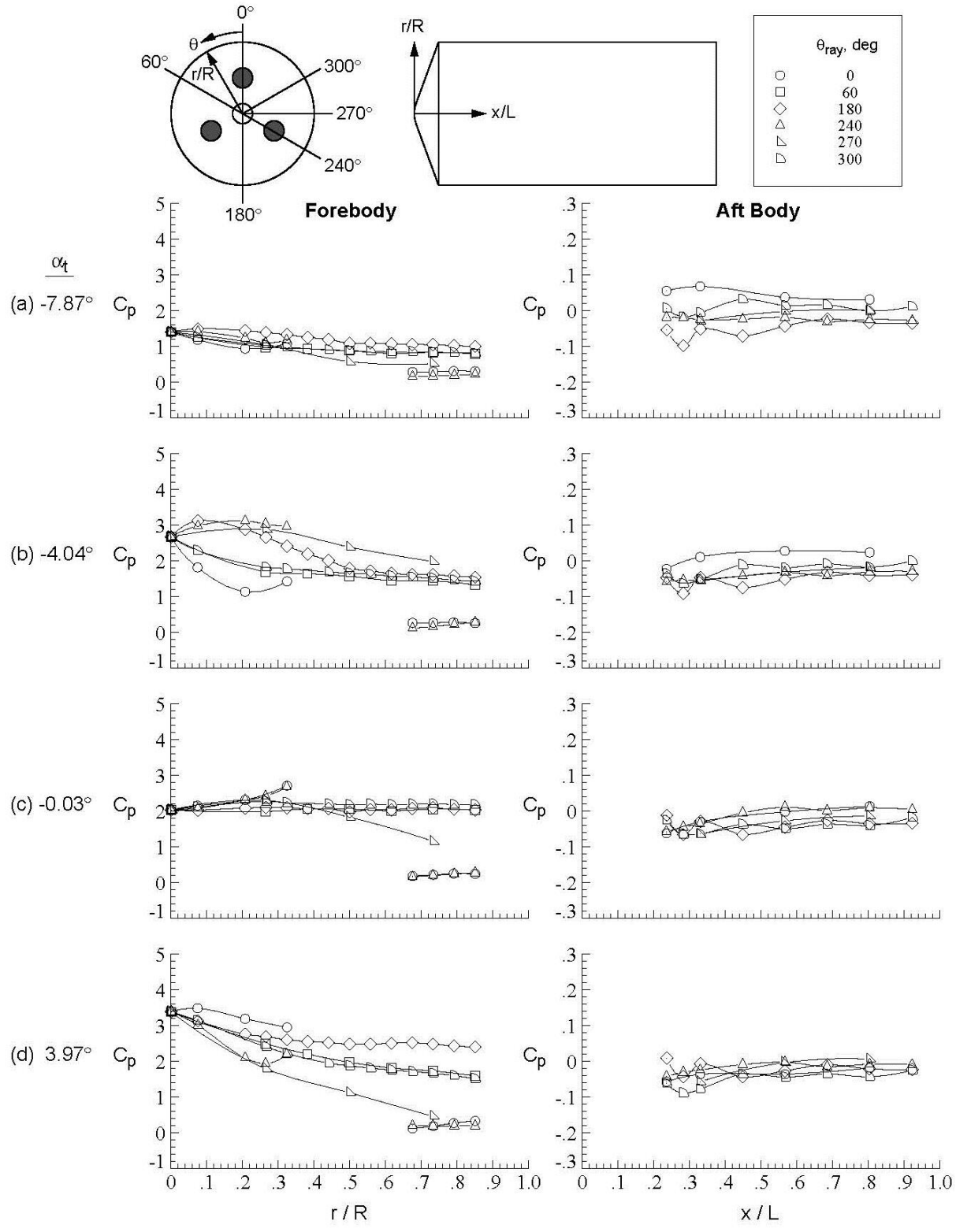

Figure D-211. Tri-nozzle configuration, Run 266, M_∞ = 3.5, Re_∞ = 1.0x10^6/ft, ϕ = −0.05°, X_S = 40.15 in, Y_S = 0.00 in, C_T = 0.44.

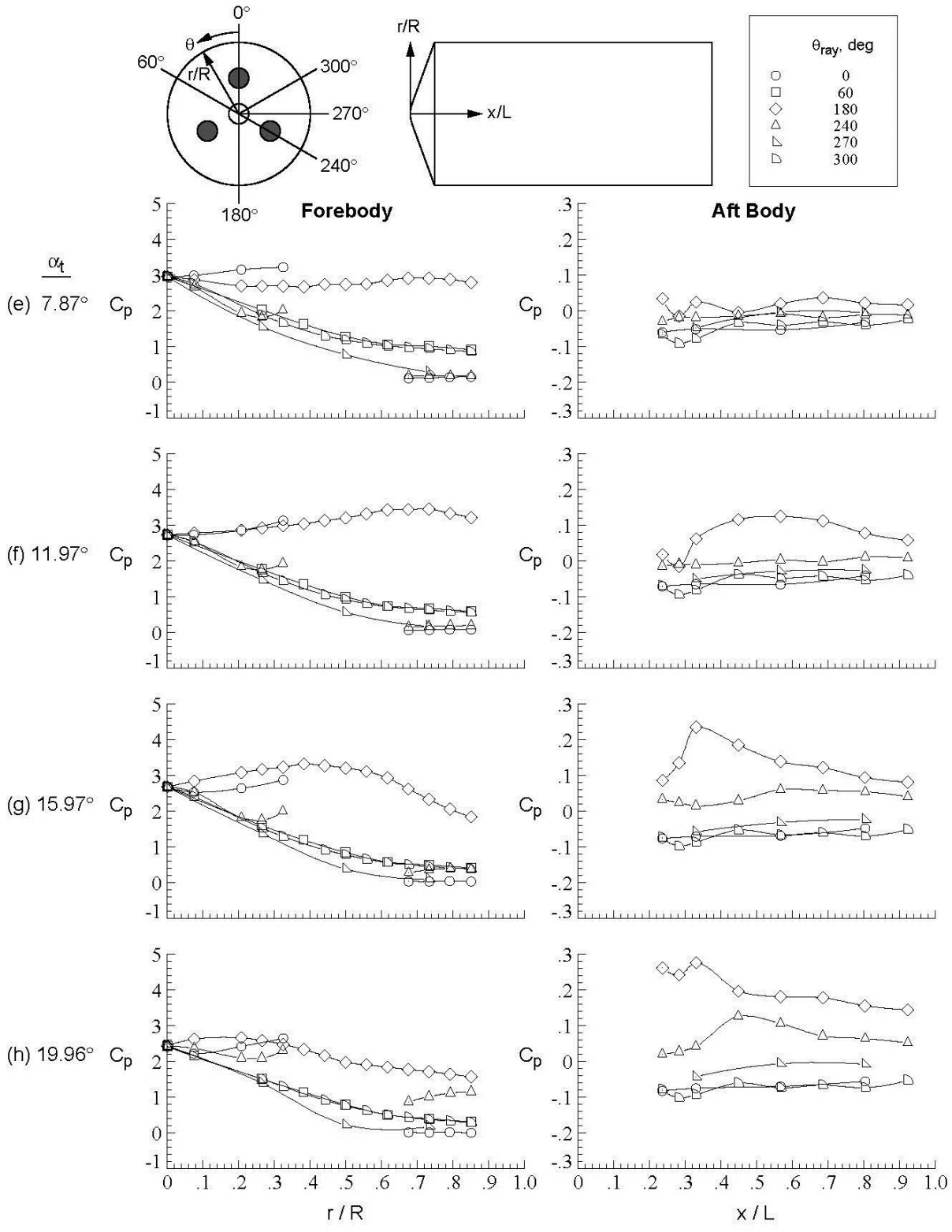

Figure D-211.Concluded.

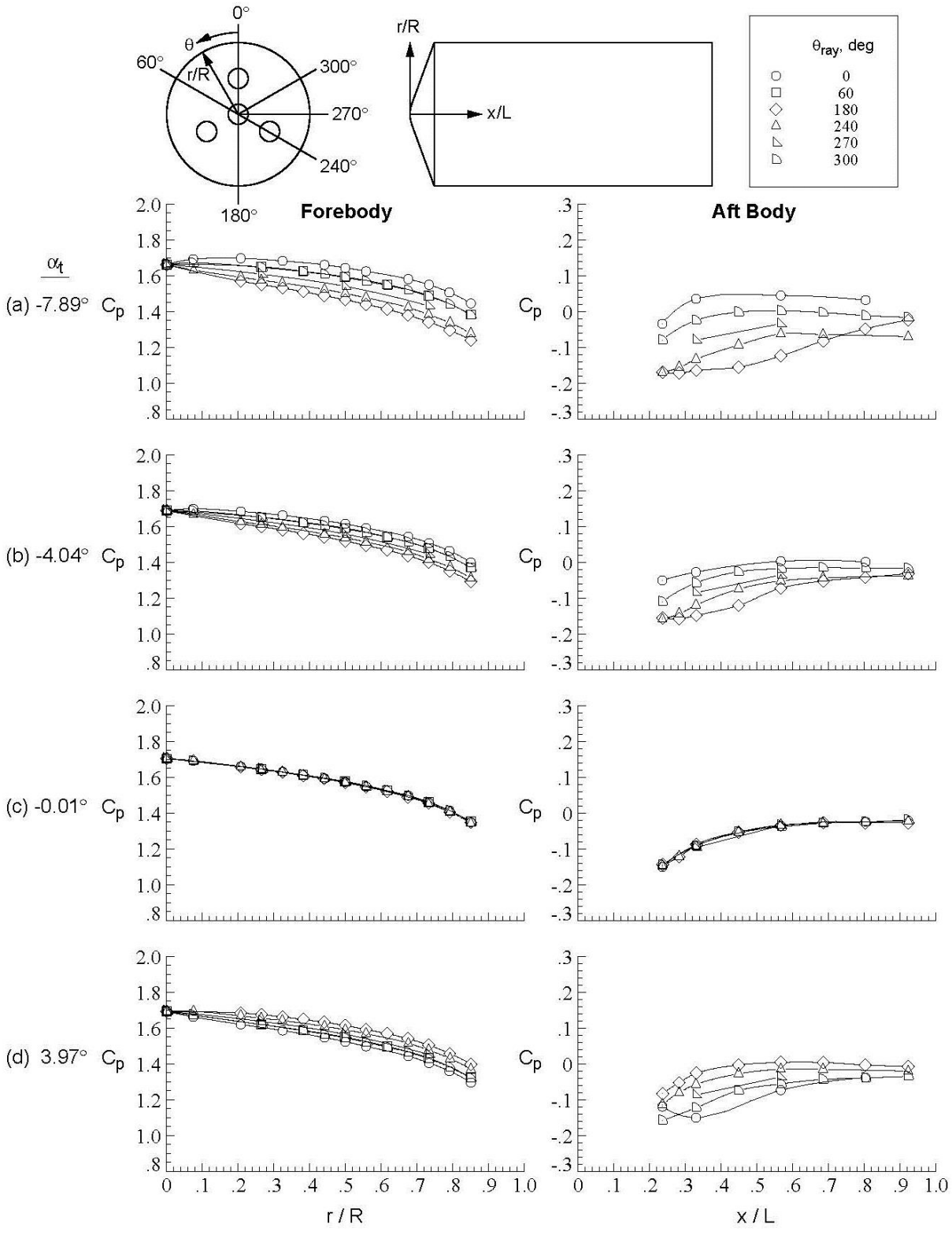

Figure D-212. Baseline configuration, Run 271, M_∞ = 2.4, Re_∞ = 1.0x10^6/ft, ϕ = −0.03°, X_S = 40.16 in, Y_S = 0.00 in, C_T = 0.00.

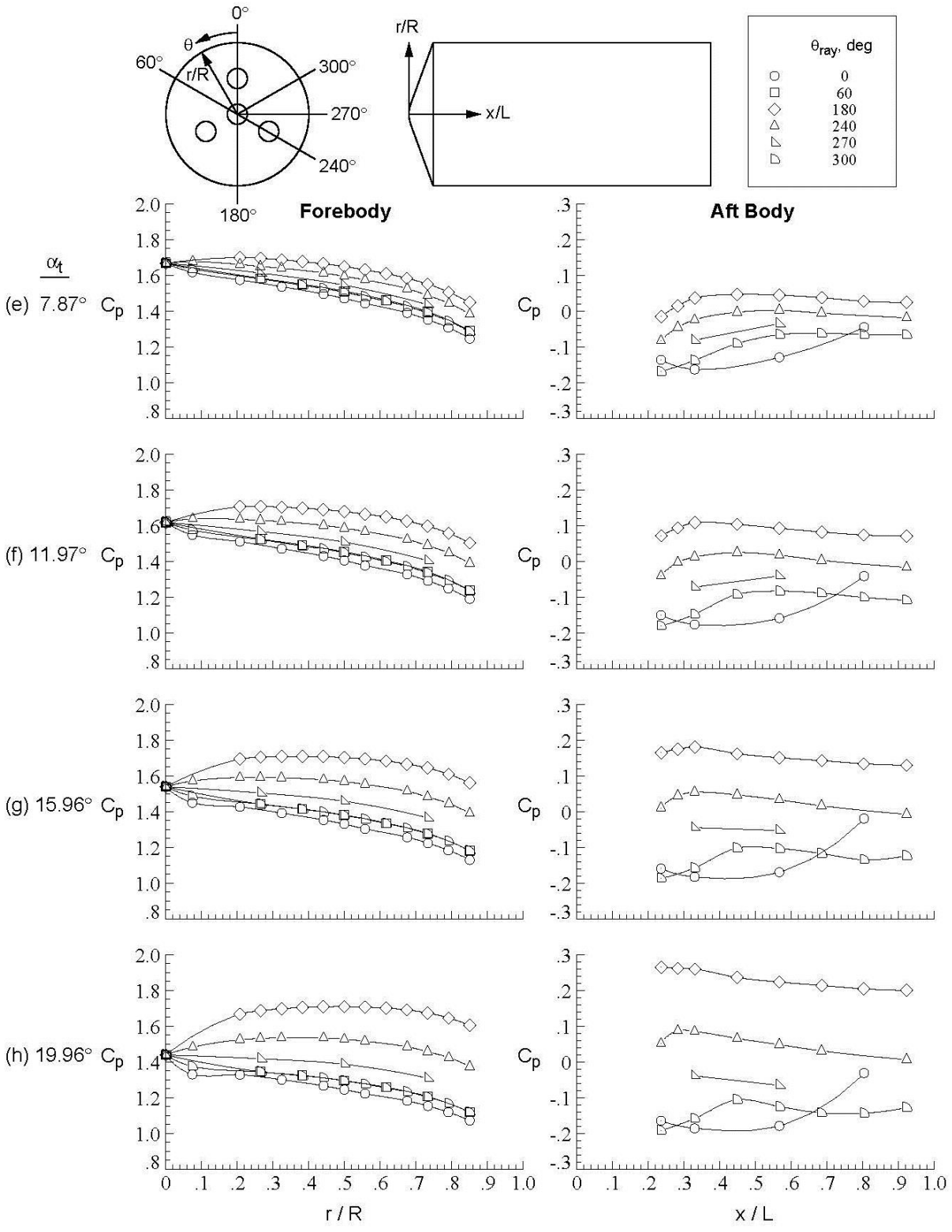

Figure D-212.Concluded.

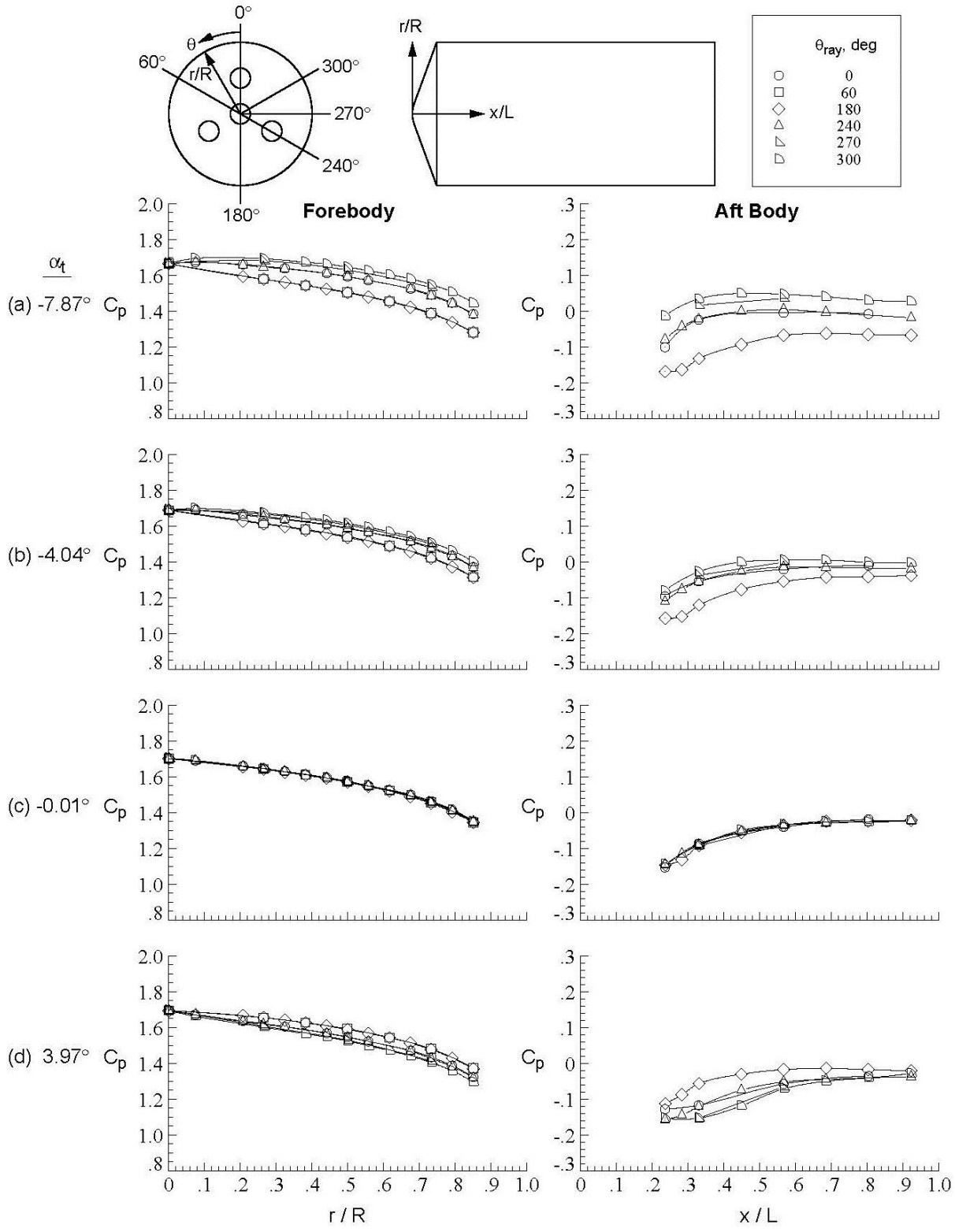

Figure D-213. Baseline configuration, Run 272, M_∞ = 2.4, Re_∞ = 1.0x10^6/ft, ϕ = 59.92°, X_S = 40.16 in, Y_S = 0.00 in, C_T = 0.00.

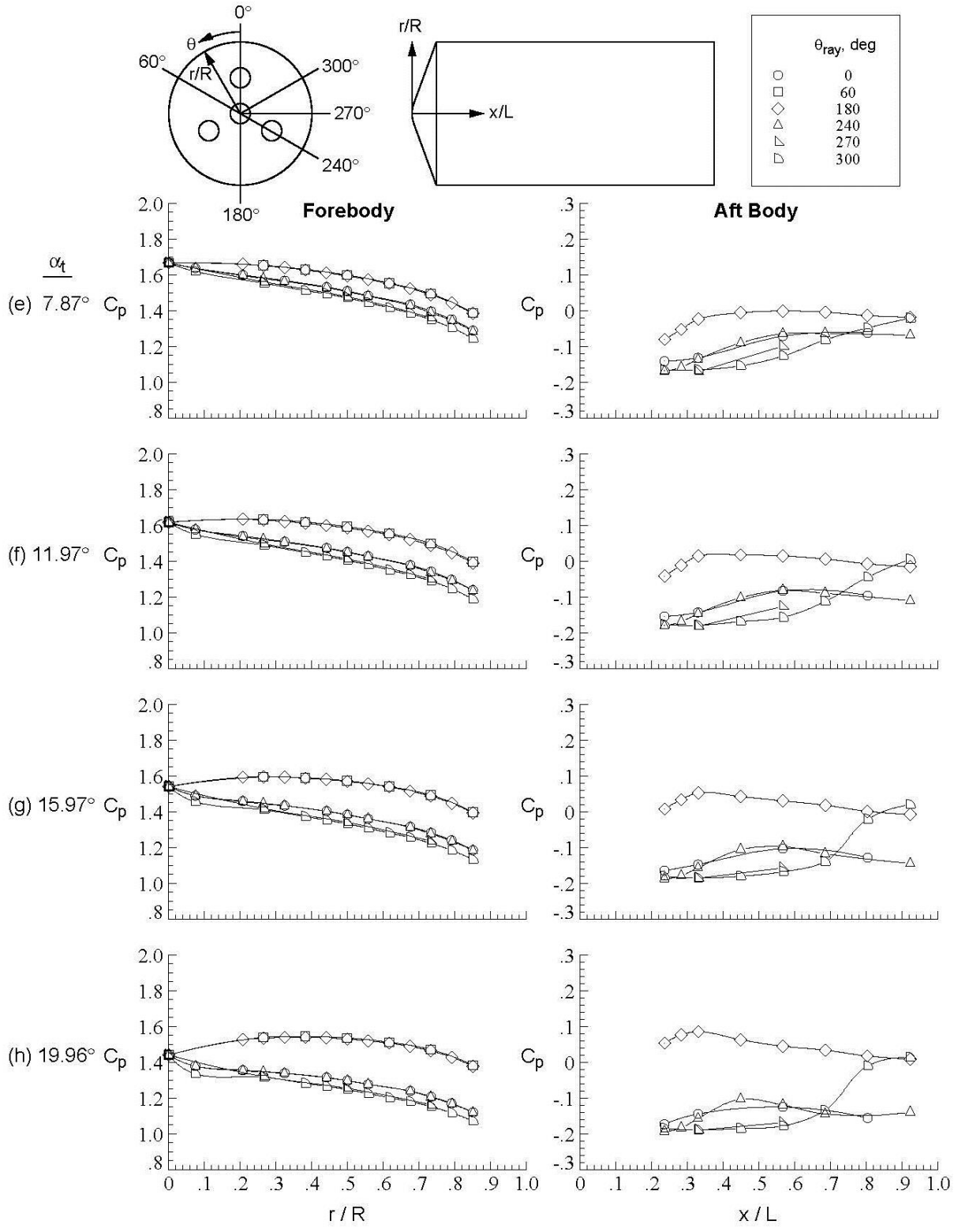

Figure D-213.Concluded.

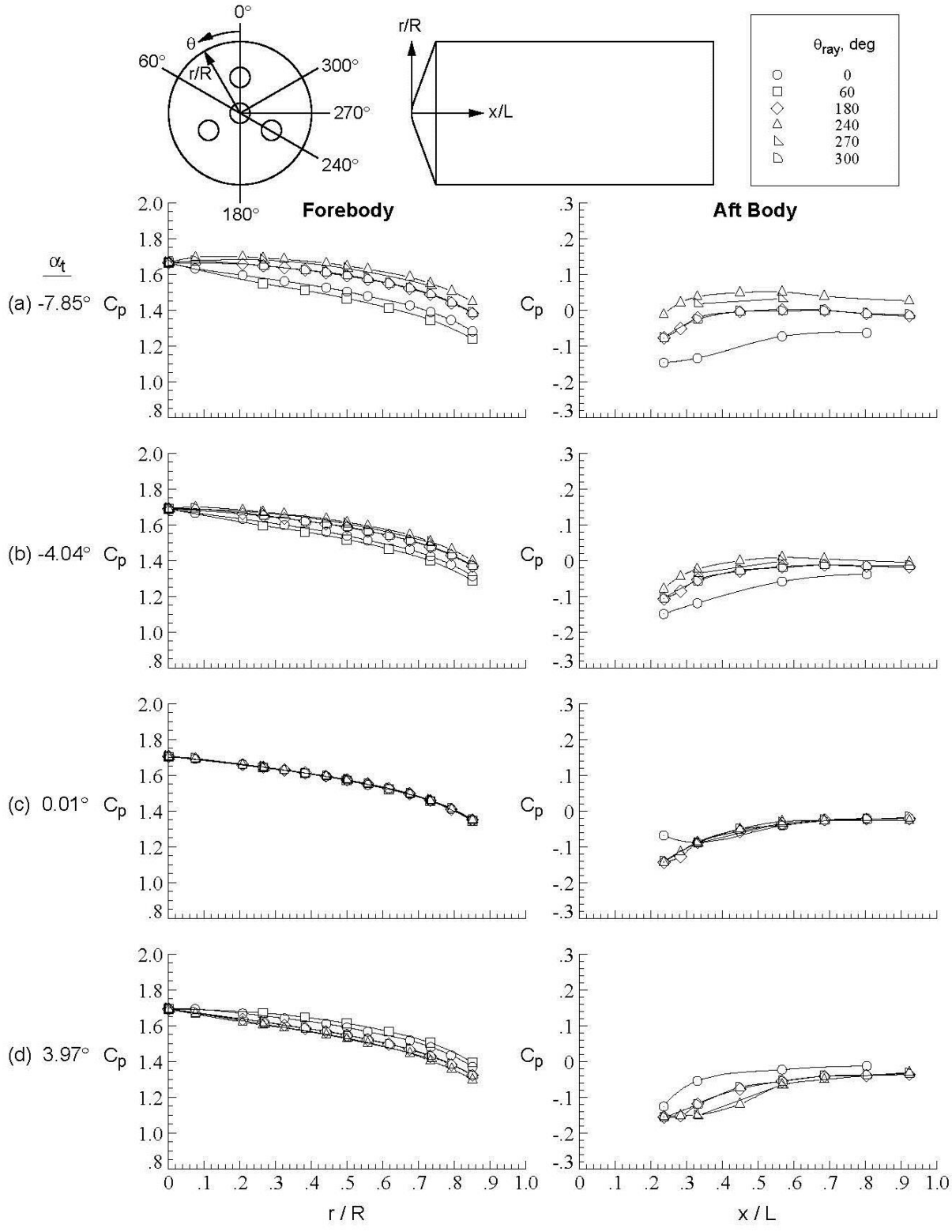

Figure D-214. Baseline configuration, Run 273, M_∞ = 2.4, Re_∞ = 1.0x10^7/ft, ϕ = 120.00°, X_S = 40.16 in, Y_S = 0.00 in, C_T = 0.00.

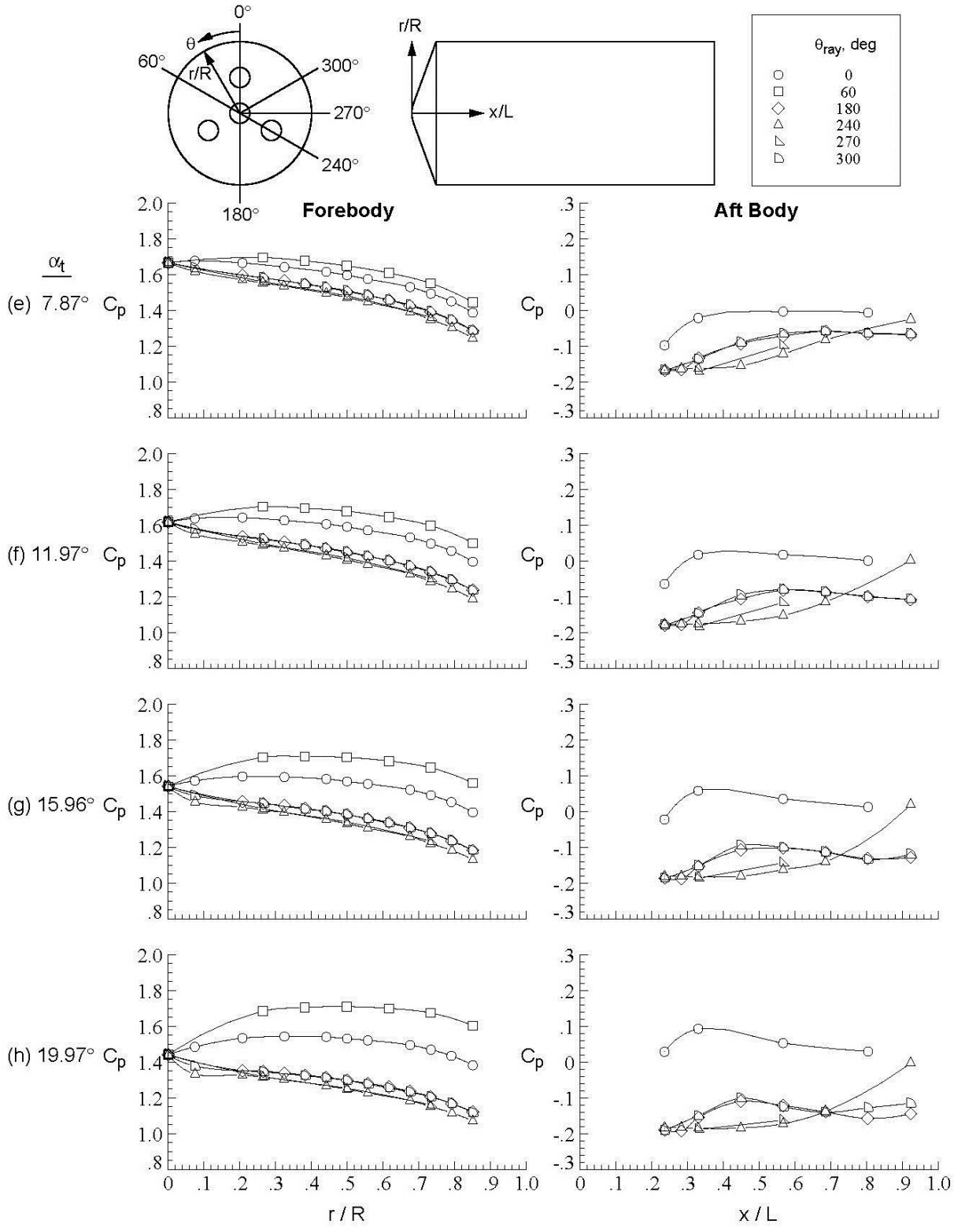

Figure D-214.Concluded.

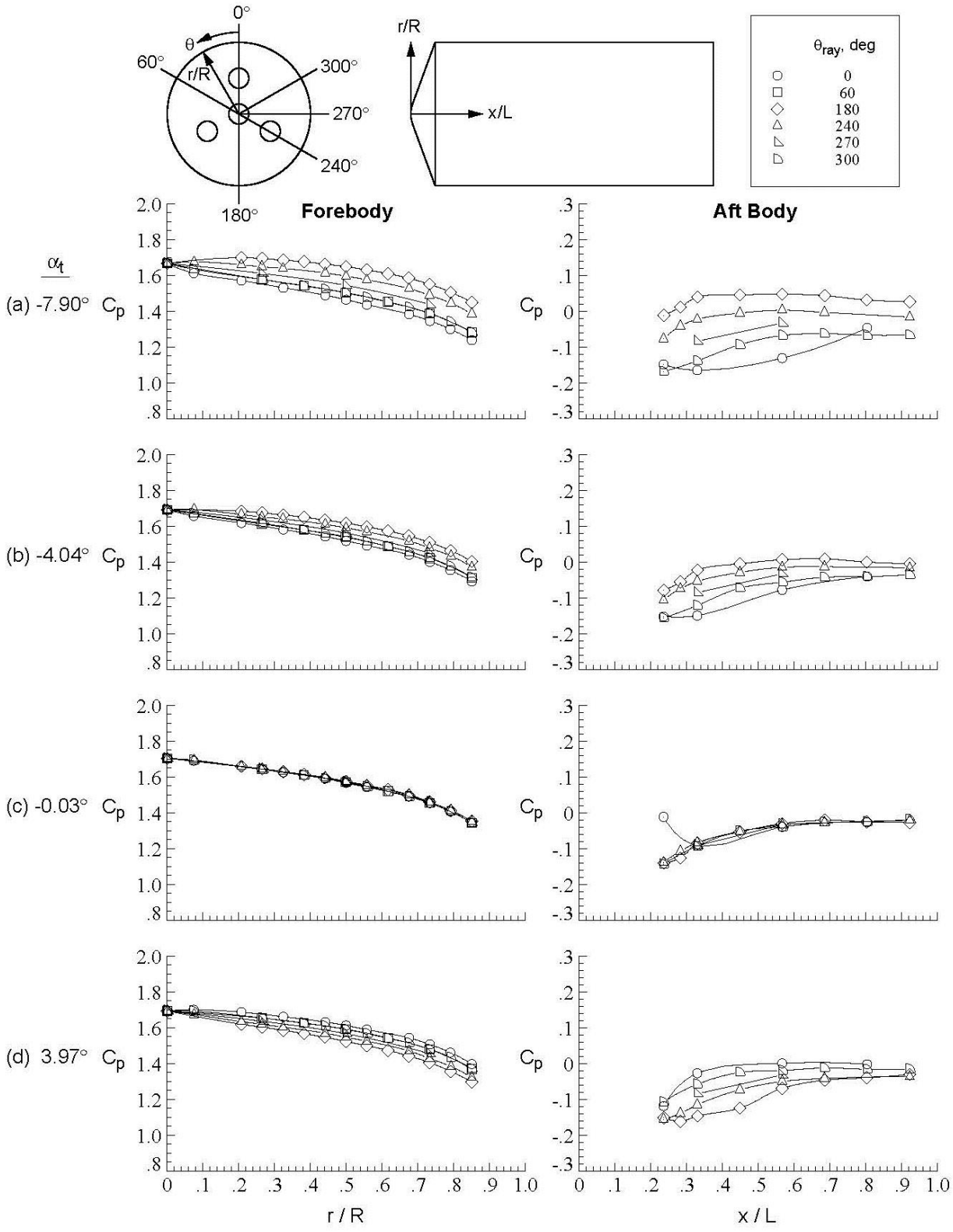

Figure D-215. Baseline configuration, Run 0274, M_∞ = 2.4, Re_∞ = 1.0x10^6/ft, ϕ = 179.99°, X_S = 40.16 in, Y_S = 0.00 in, C_T = 0.00.

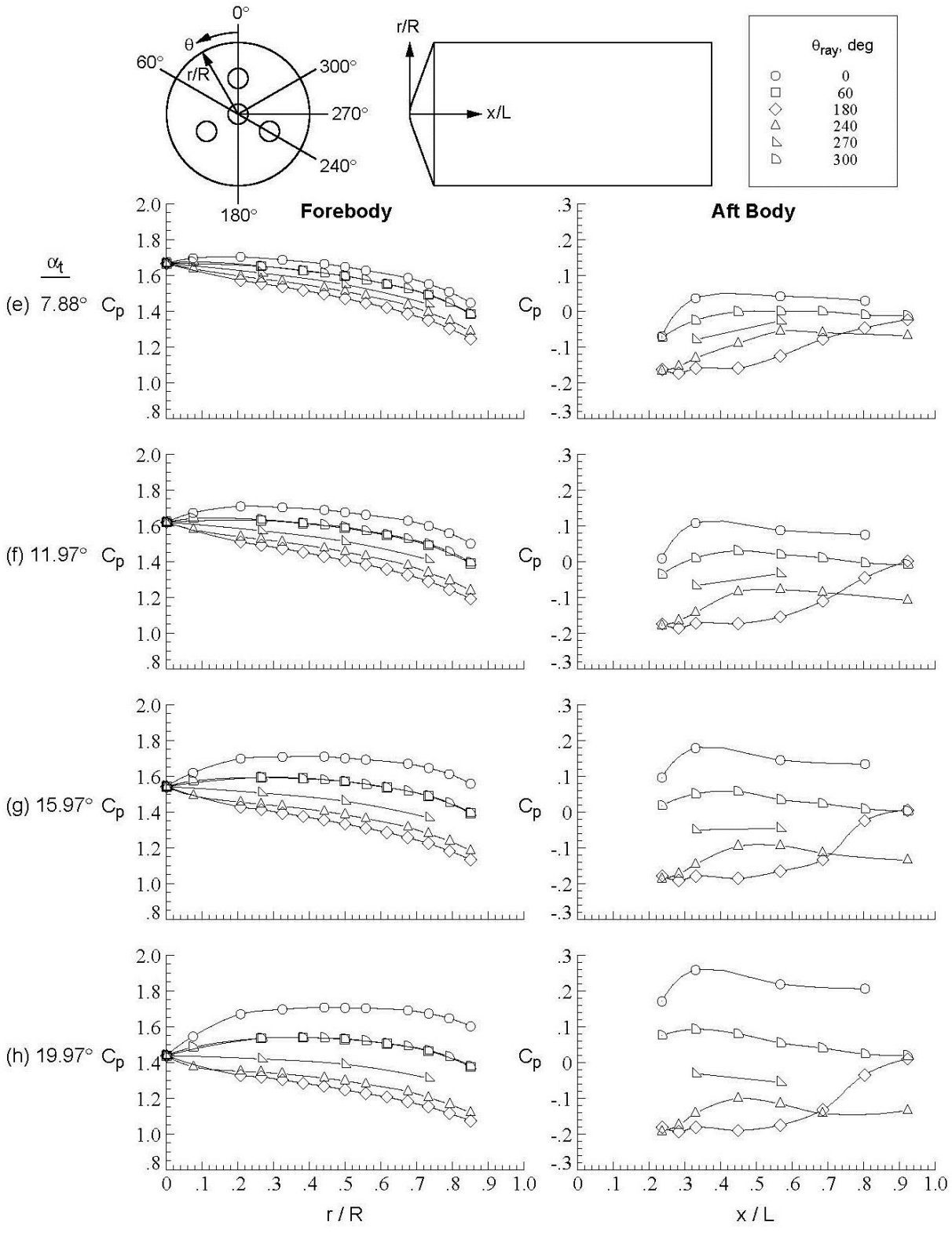

Figure D-215.Concluded.

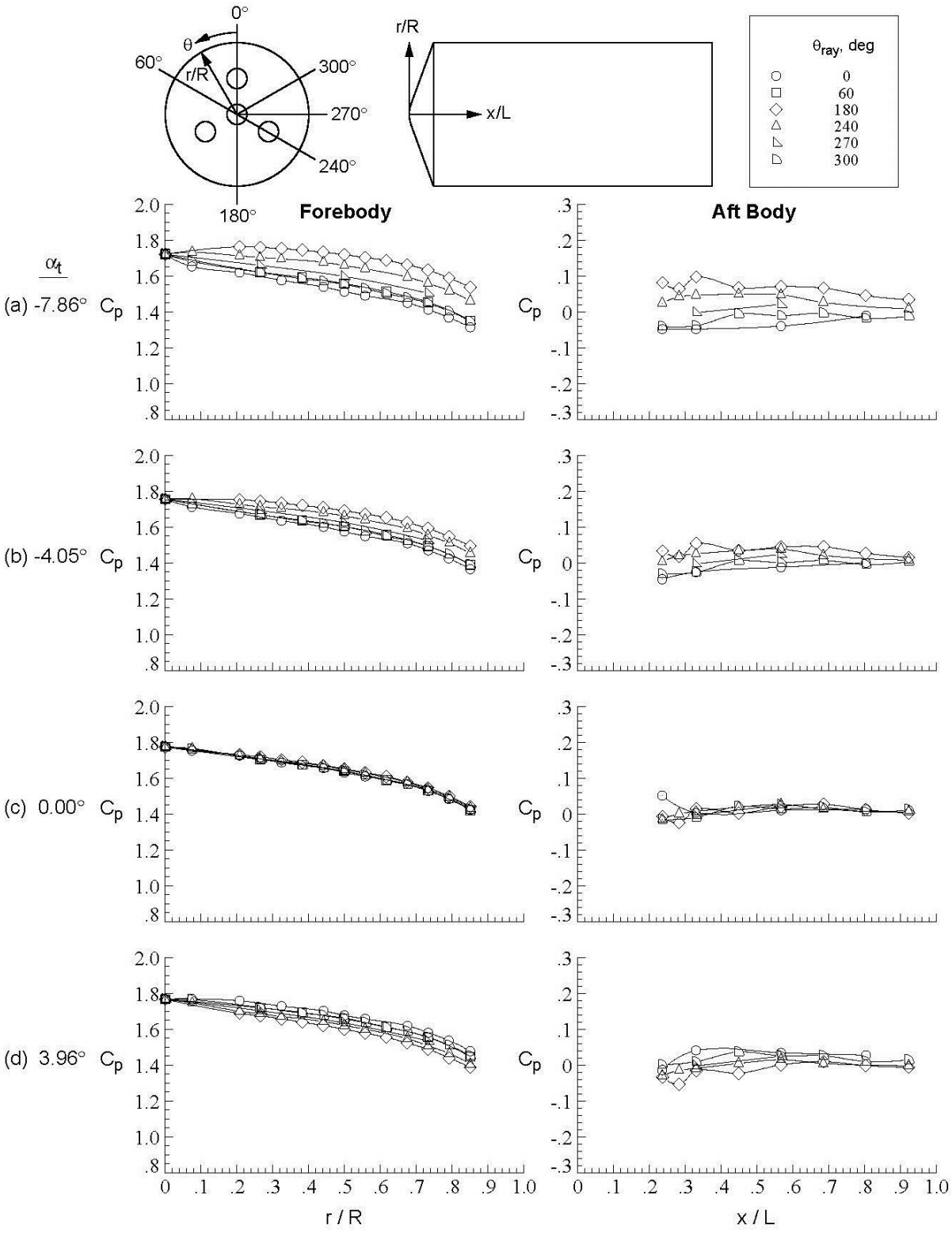

Figure D-216. Baseline configuration, Run 276, M_∞ = 3.5, Re_∞ = 1.0x10^7/ft, ϕ = 179.99°, X_S = 40.16 in, Y_S = 0.00 in, C_T = 0.00.

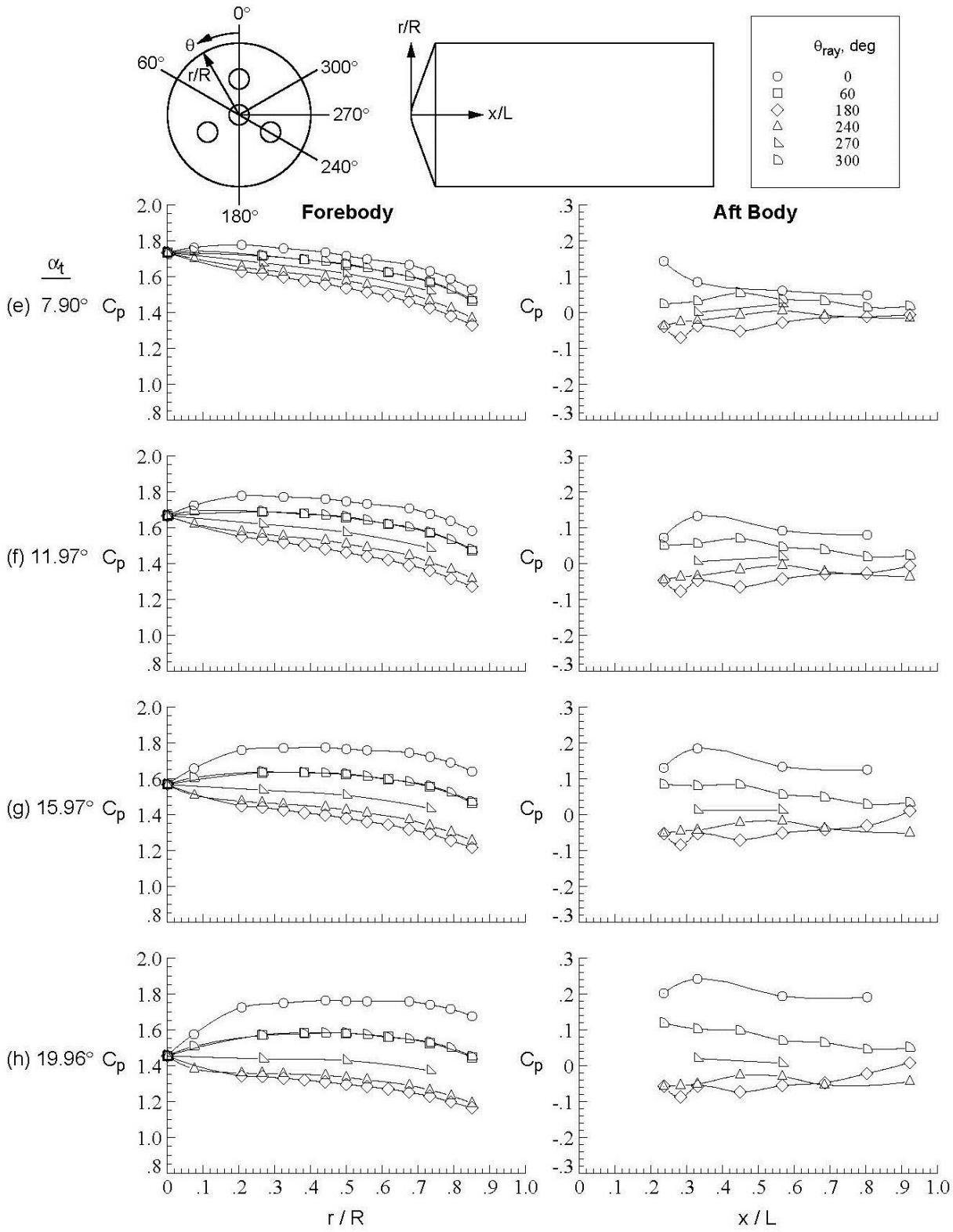

Figure D-216.Concluded.

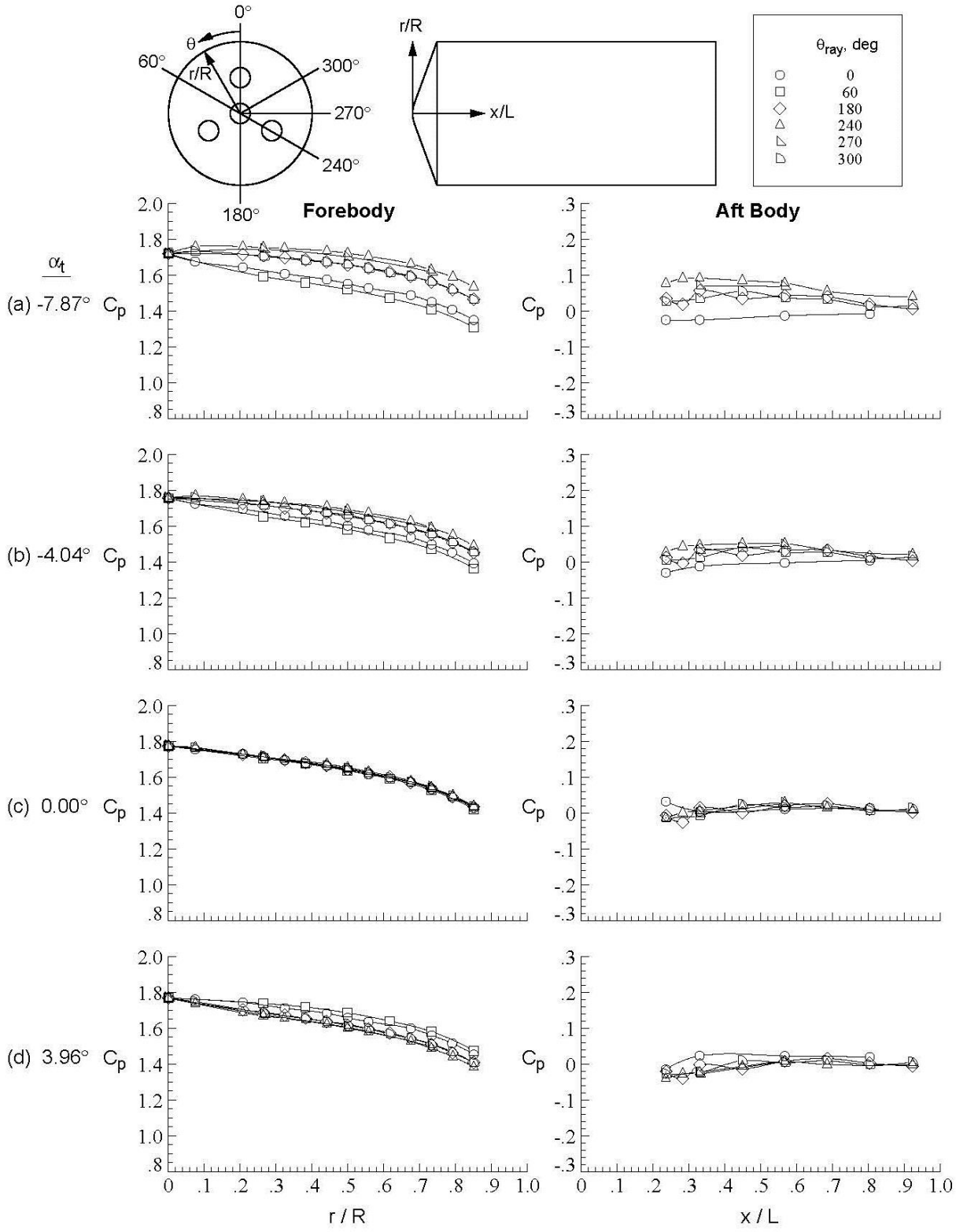

Figure D-217. Baseline configuration, Run 277, M_∞ = 3.5, Re_∞ = 1.0x10^6/ft, ϕ = 120.00°, X_S = 40.16 in, Y_S = 0.00 in, C_T = 0.00.

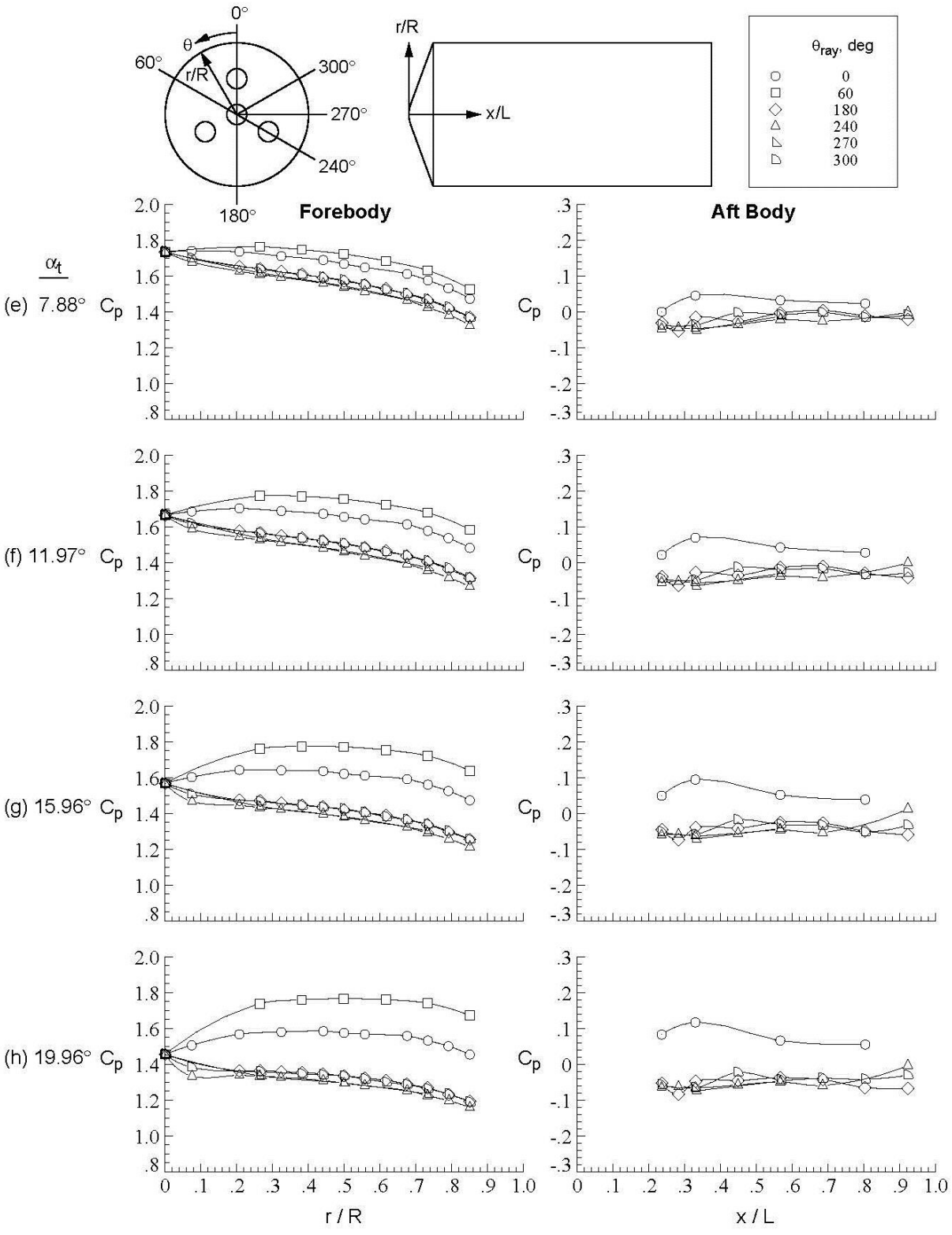

Figure D-217.Concluded.

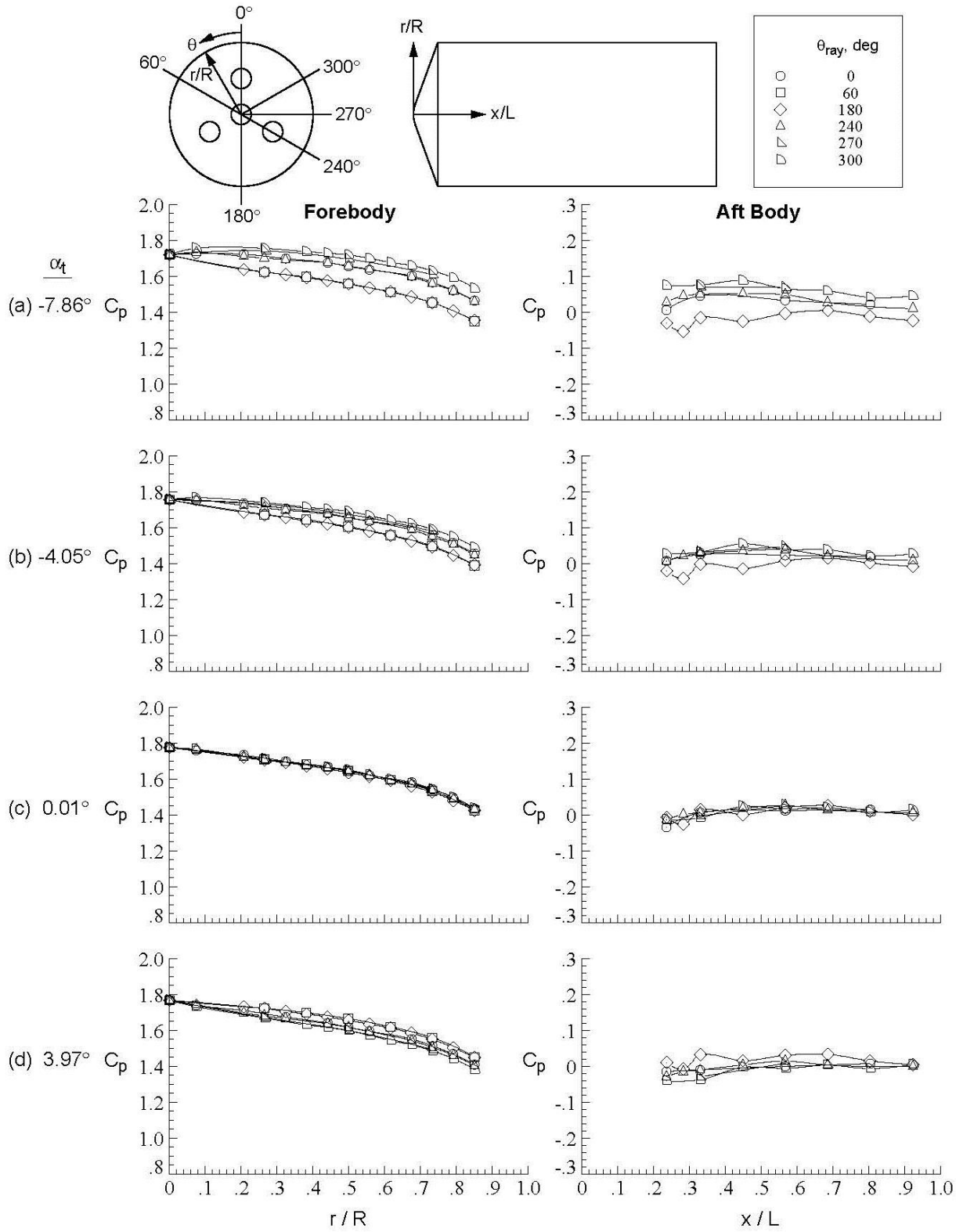

Figure D-218. Baseline configuration, Run 278, M_∞ = 3.5, Re_∞ = 1.0x10^7/ft, ϕ = 59.96°, X_S = 40.16 in, Y_S = 0.00 in, C_T = 0.00.

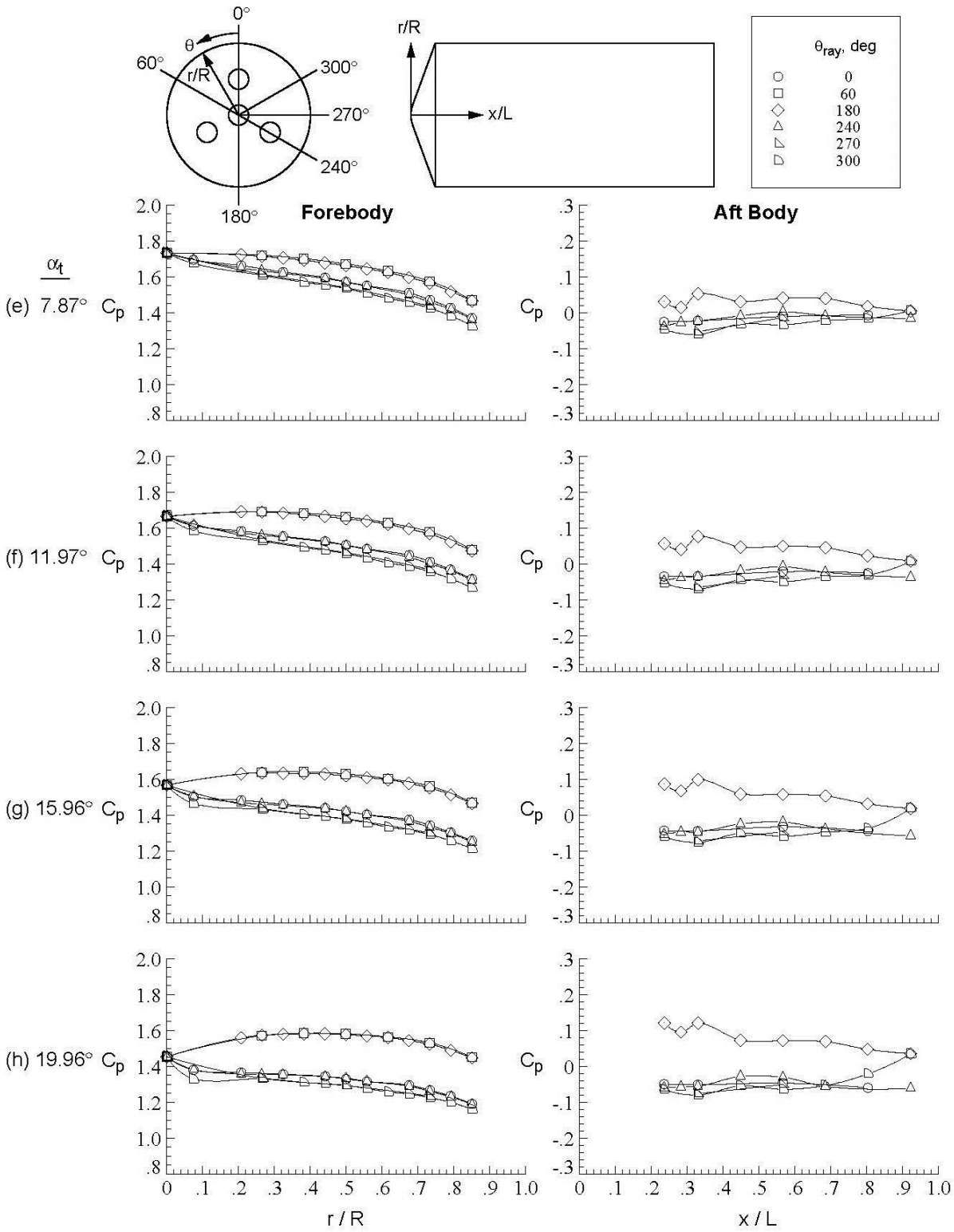

Figure D-218.Concluded.

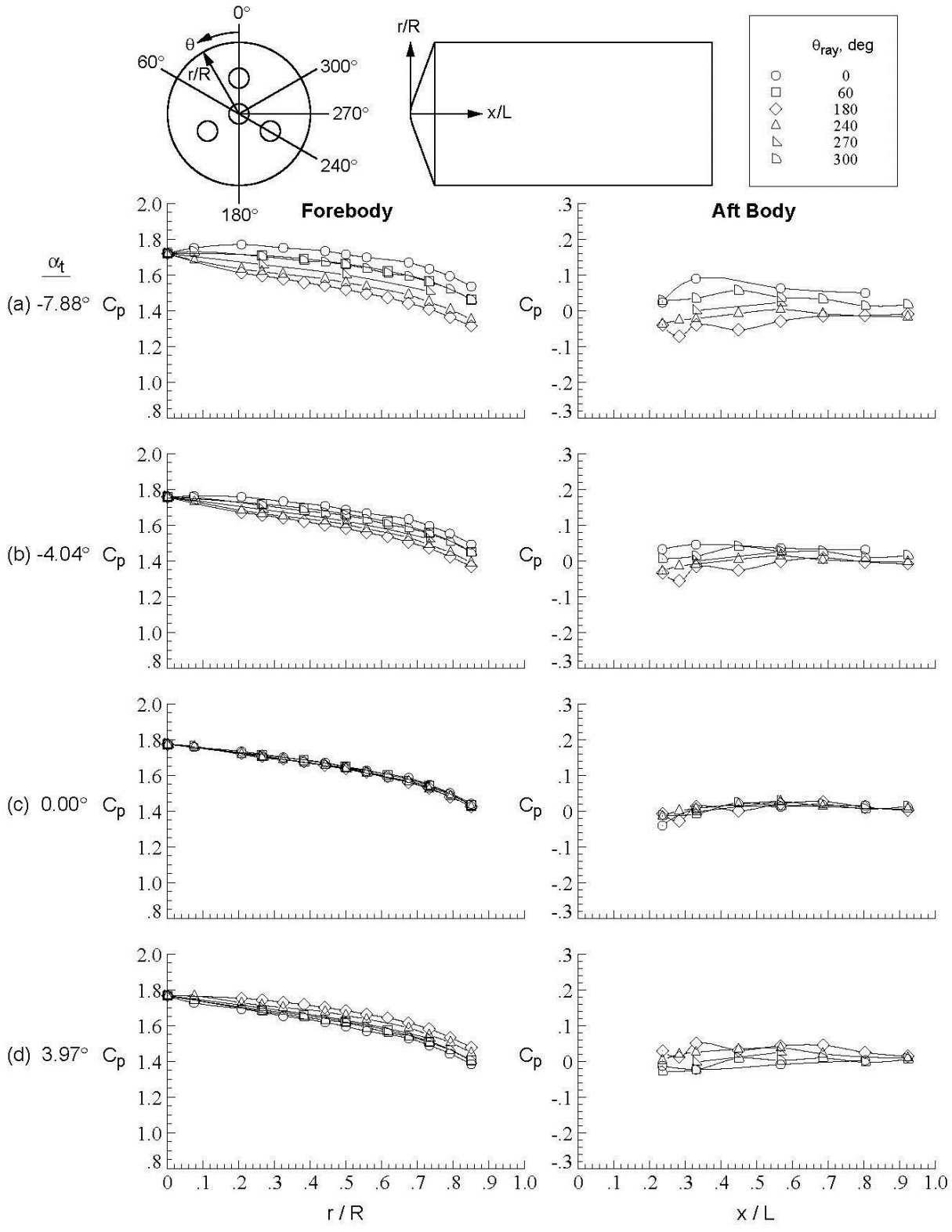

Figure D-219. Baseline configuration, Run 279, M_∞ = 3.5, Re_∞ = 1.0x10^7/ft, ϕ = −0.05°, X_S = 40.16 in, Y_S = 0.00 in, C_T = 0.00.

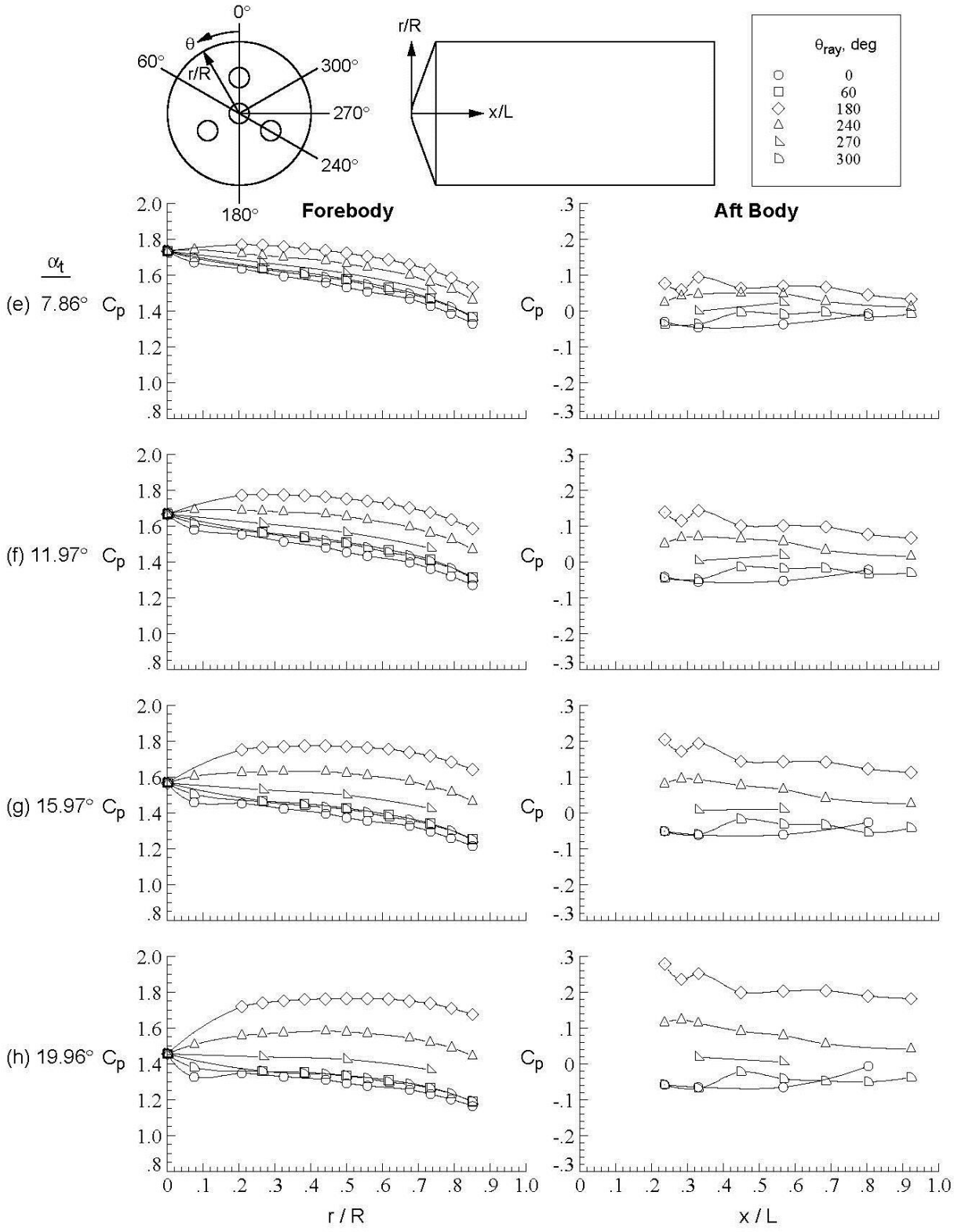

Figure D-219.Concluded.

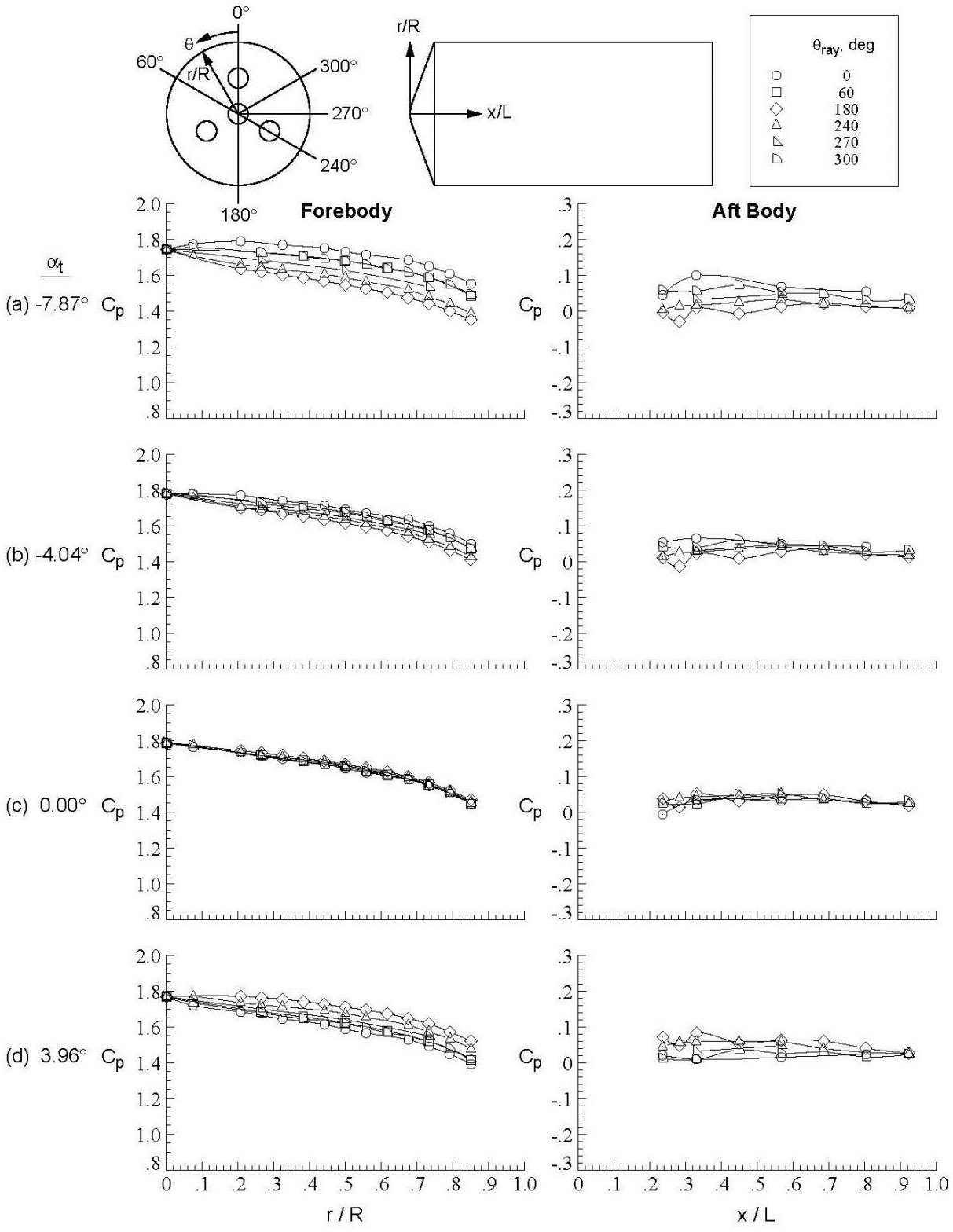

Figure D-220. Baseline configuration, Run 280, M_∞ = 4.6, Re_∞ = 1.5x10^7/ft, ϕ = −0.05°, X_S = 40.16 in, Y_S = 0.00 in, C_T = 0.00.

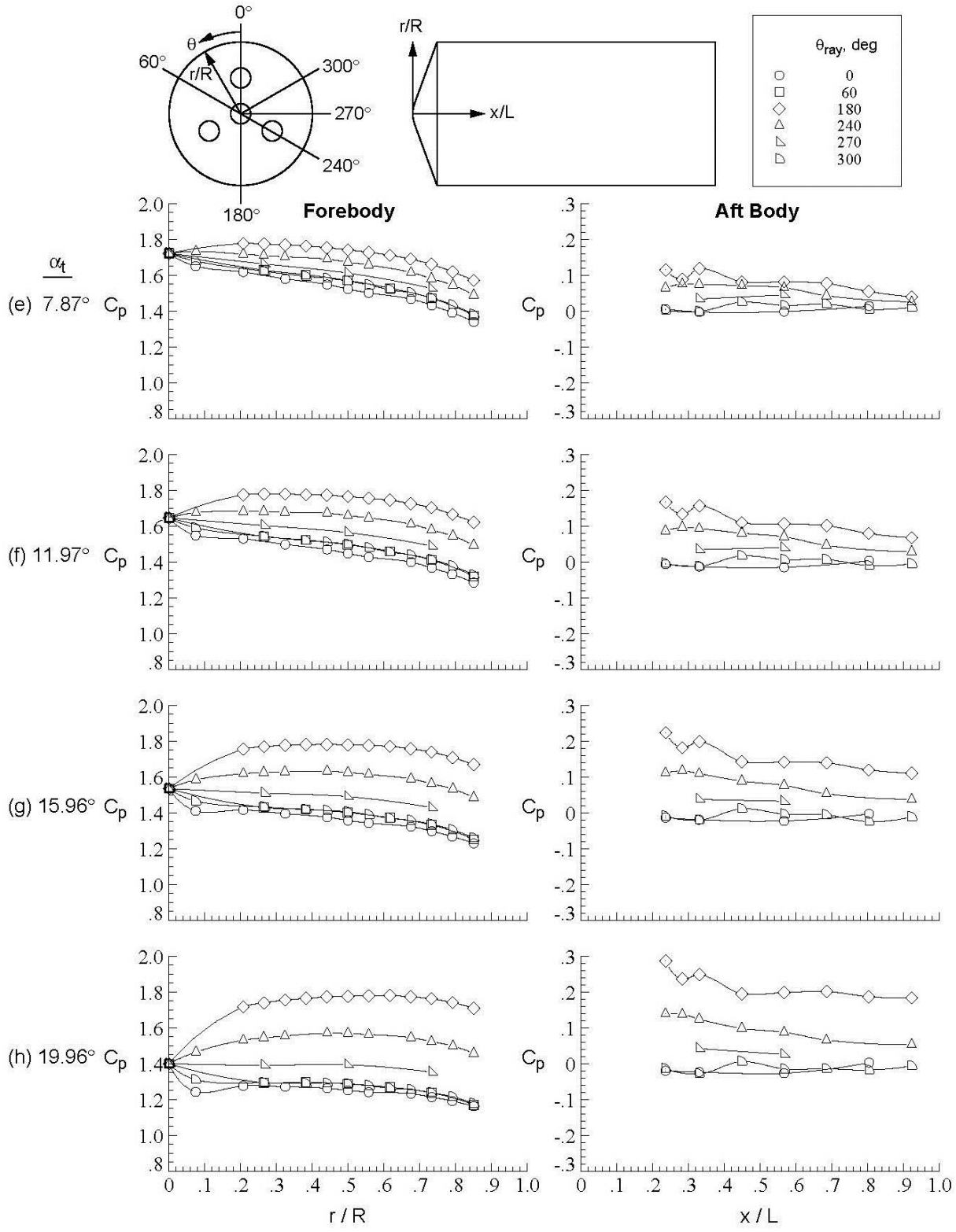

Figure D-220.Concluded.

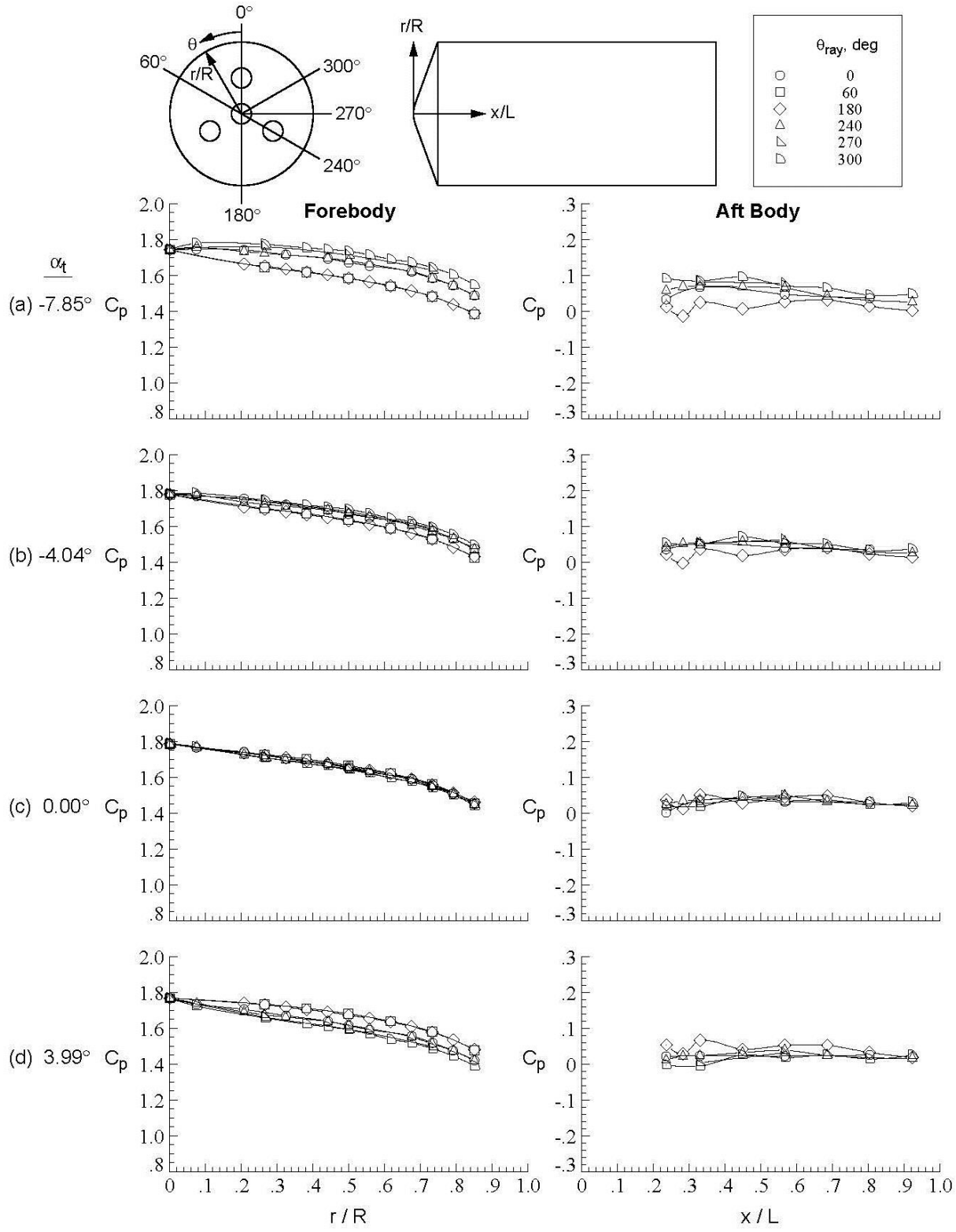

Figure D-221. Baseline configuration, Run 281, M_∞ = 4.6, Re_∞ = 1.5x10^7/ft, ϕ = 59.92°, X_S = 40.16 in, Y_S = 0.00 in, C_T = 0.00.

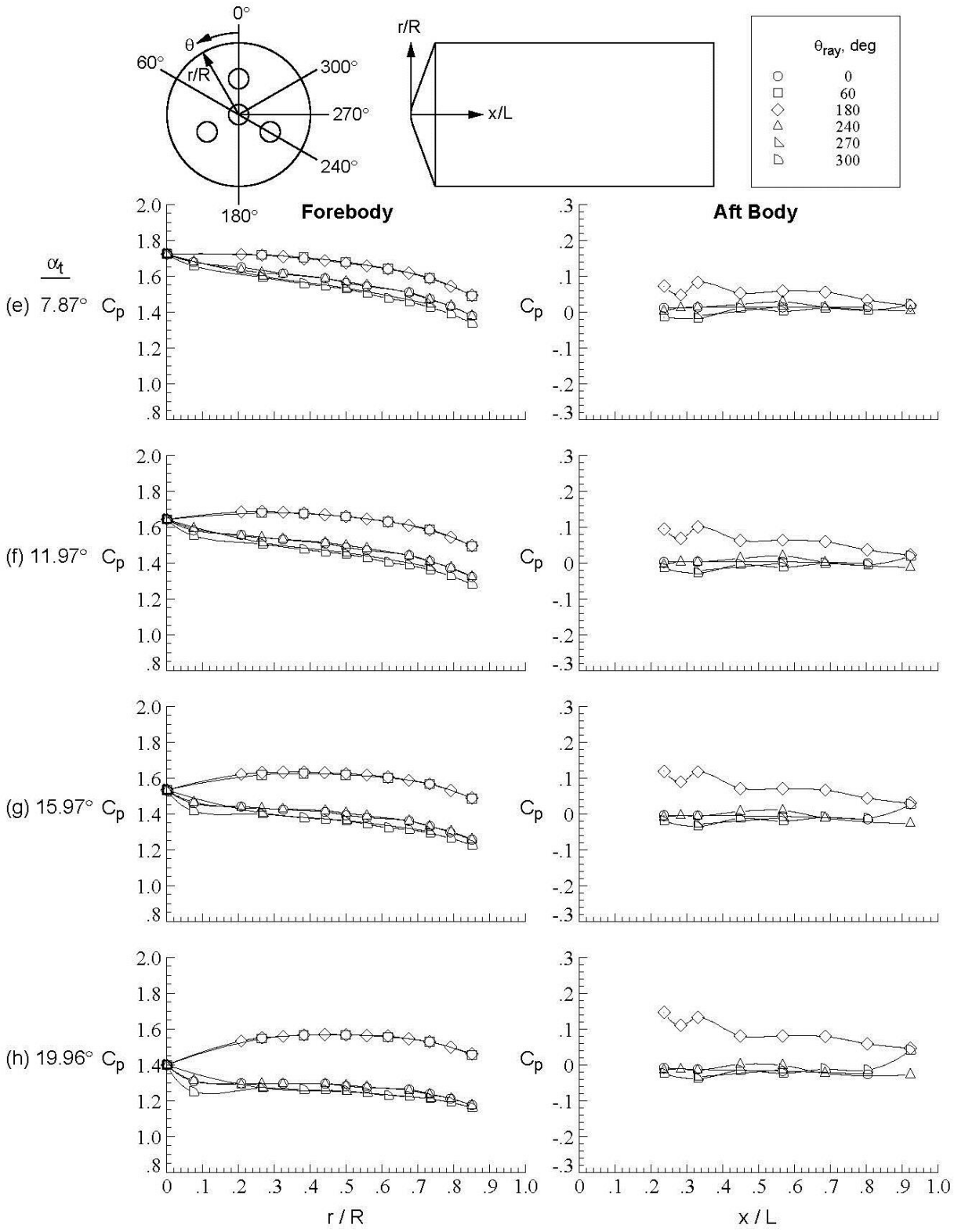

Figure D-221.Concluded.

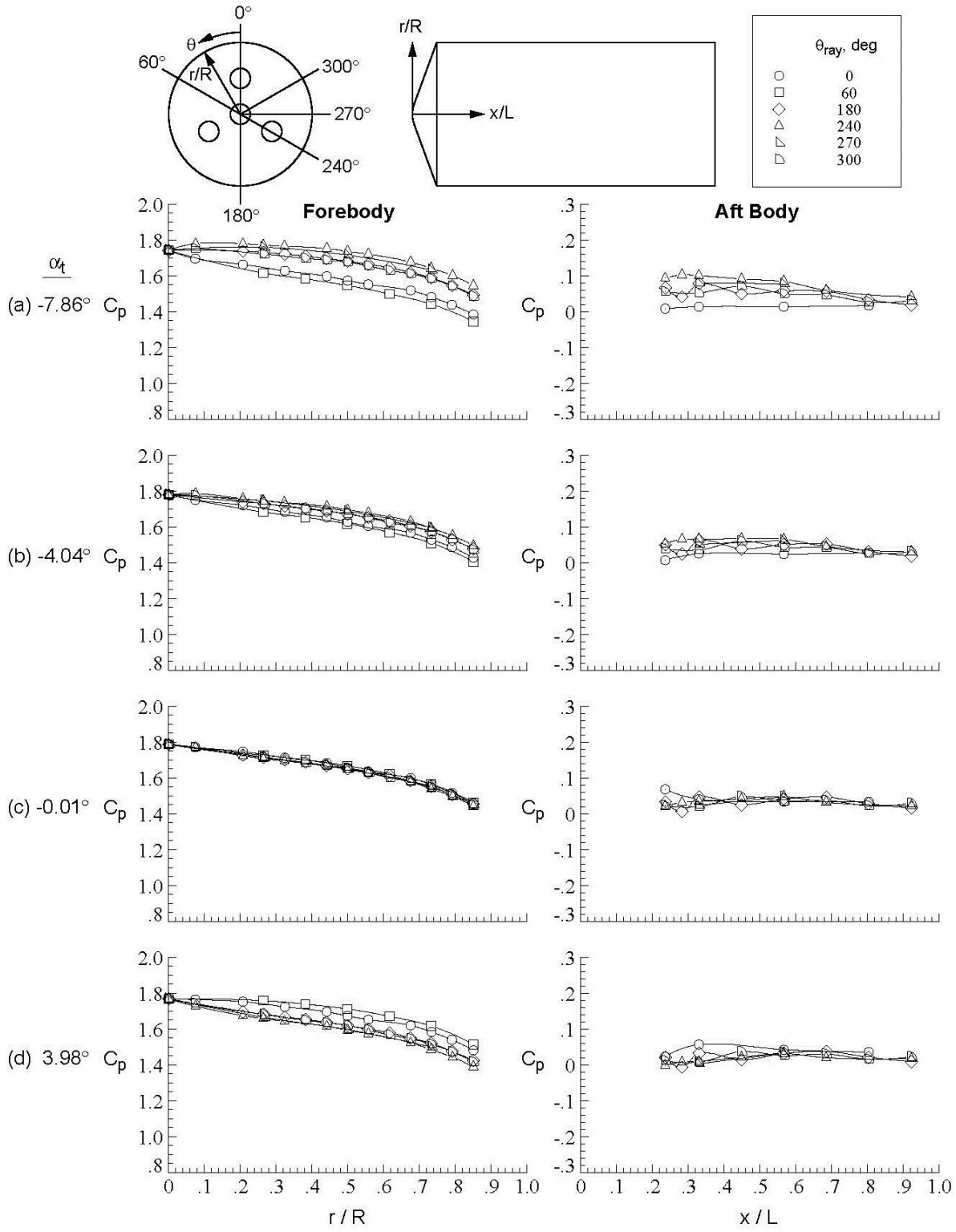

Figure D-222. Baseline configuration, Run 282, M_∞ = 4.6, Re_∞ = 1.5x10^7/ft, ϕ = 120.02°, X_S = 40.16 in, Y_S = 0.00 in, C_T = 0.00.

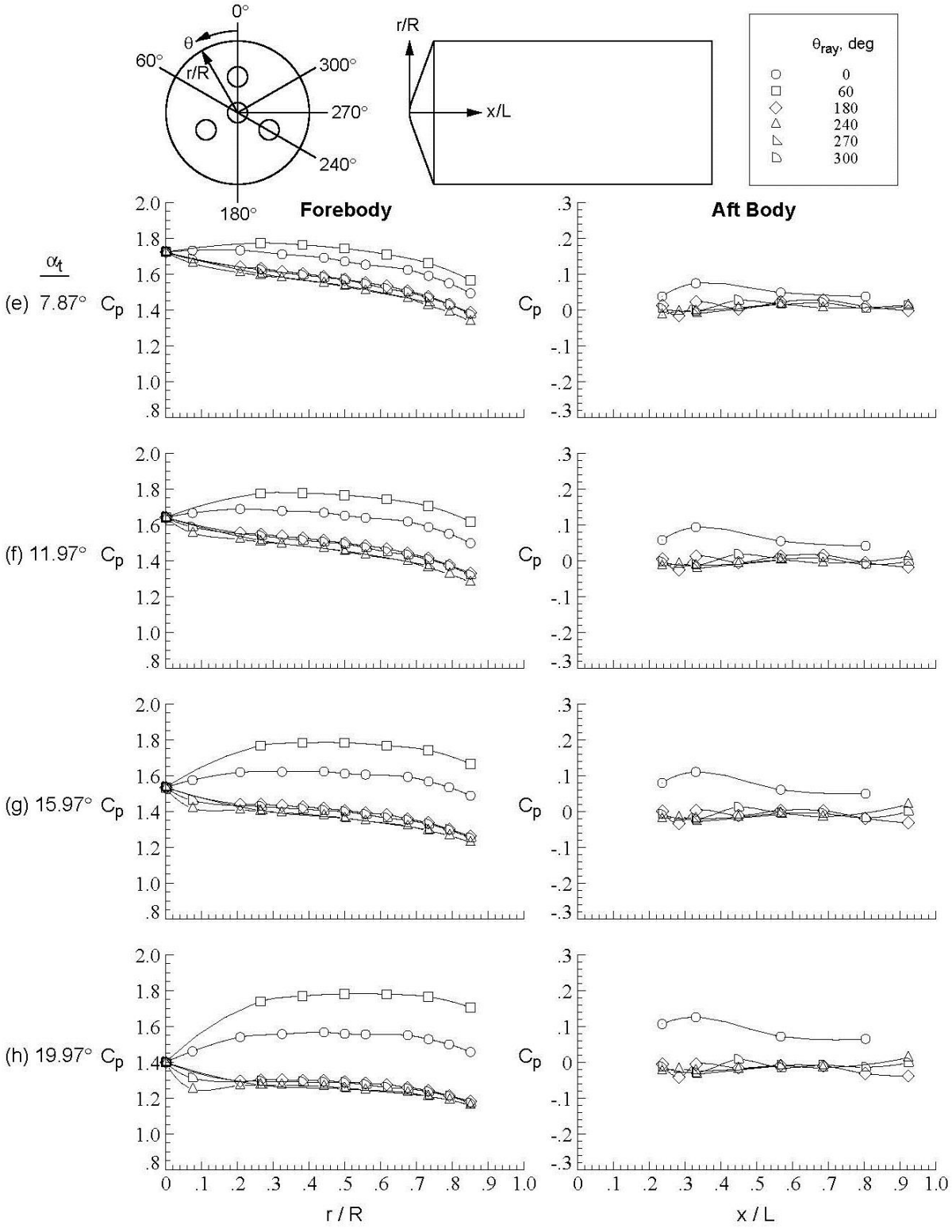

Figure D-222.Concluded.

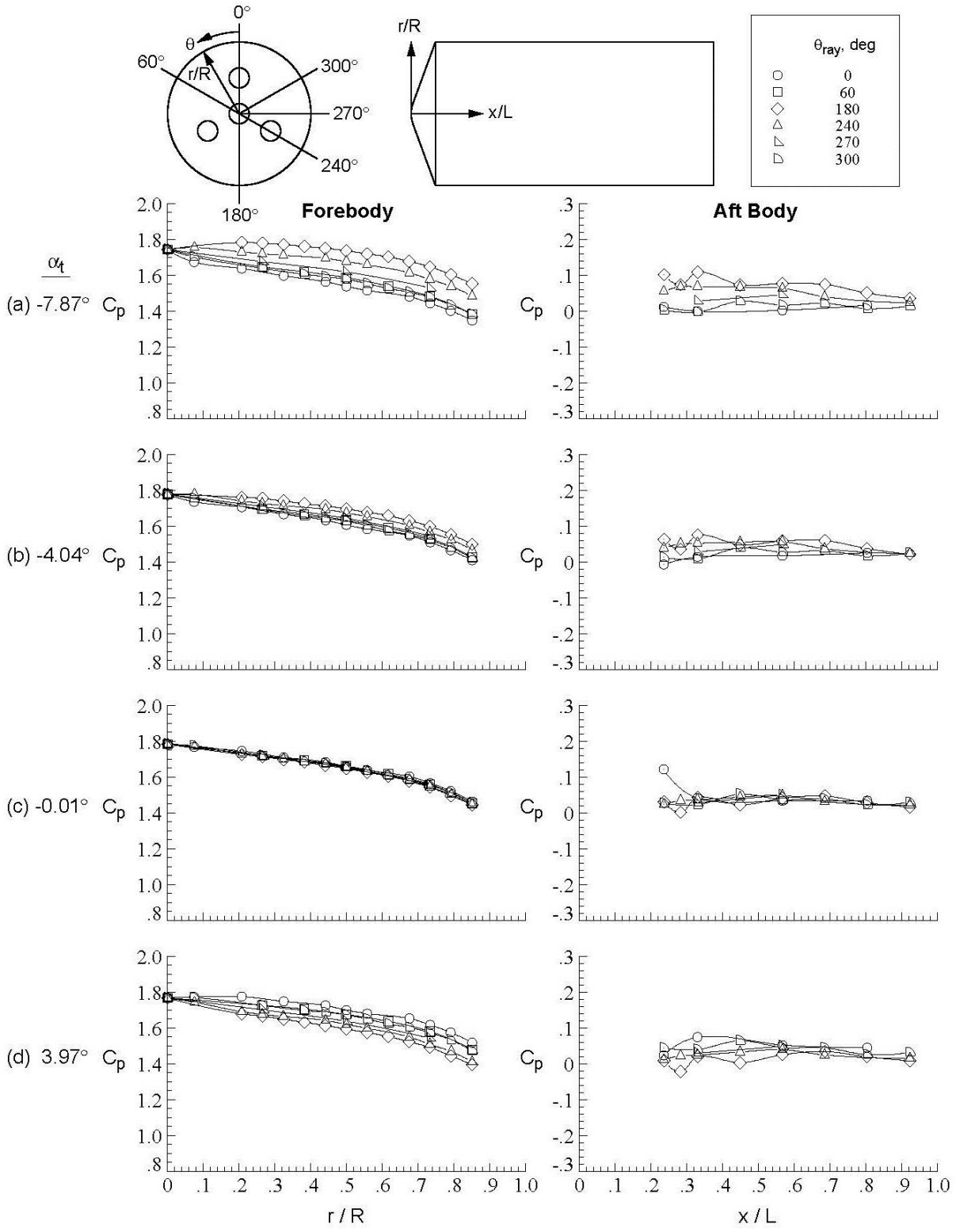

Figure D-223. Baseline configuration, Run 283, M_∞ = 4.6, Re_∞ = 1.5x10^7/ft, ϕ = 179.95°, X_S = 40.16 in, Y_S = 0.00 in, C_T = 0.00.

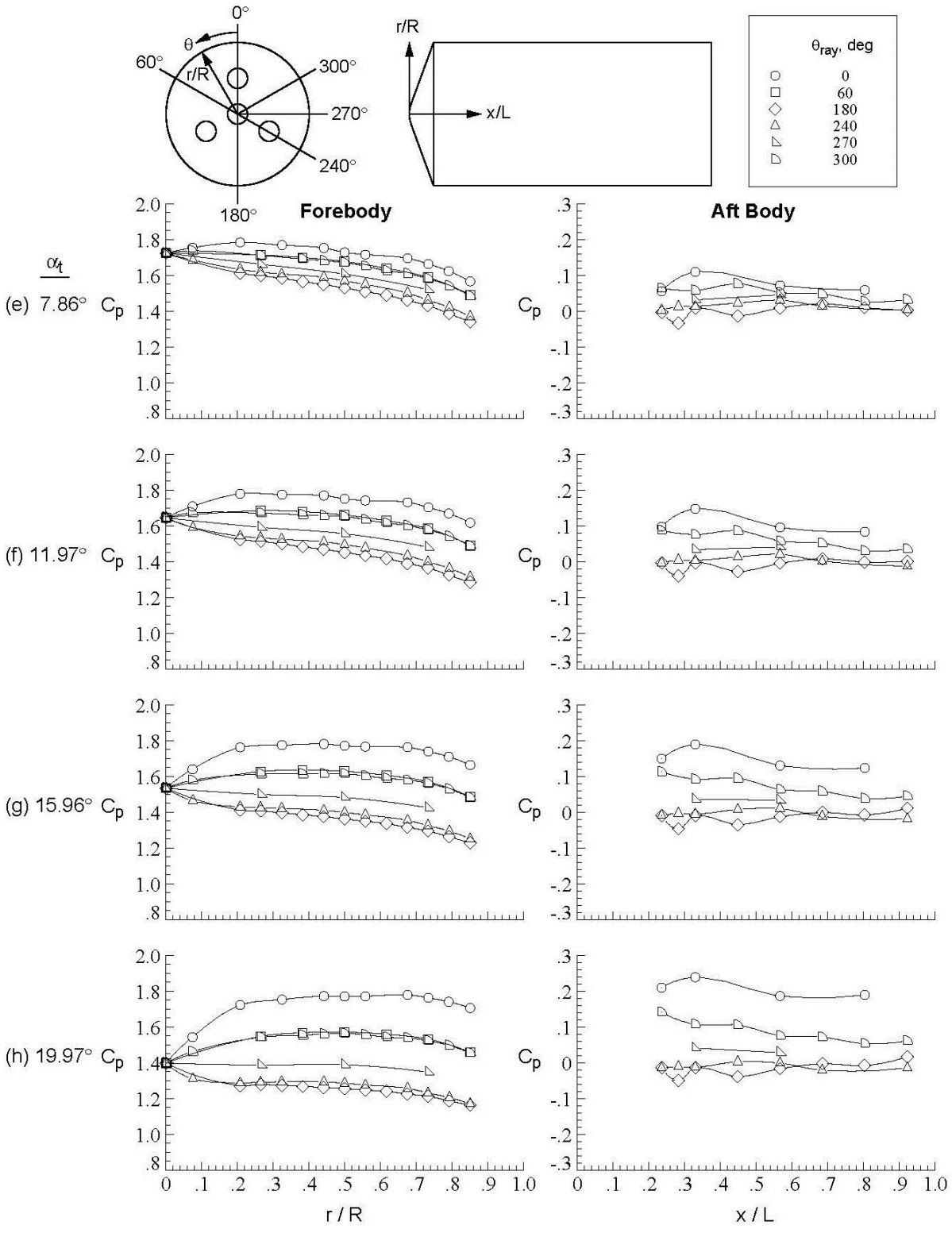

Figure D-223.Concluded.

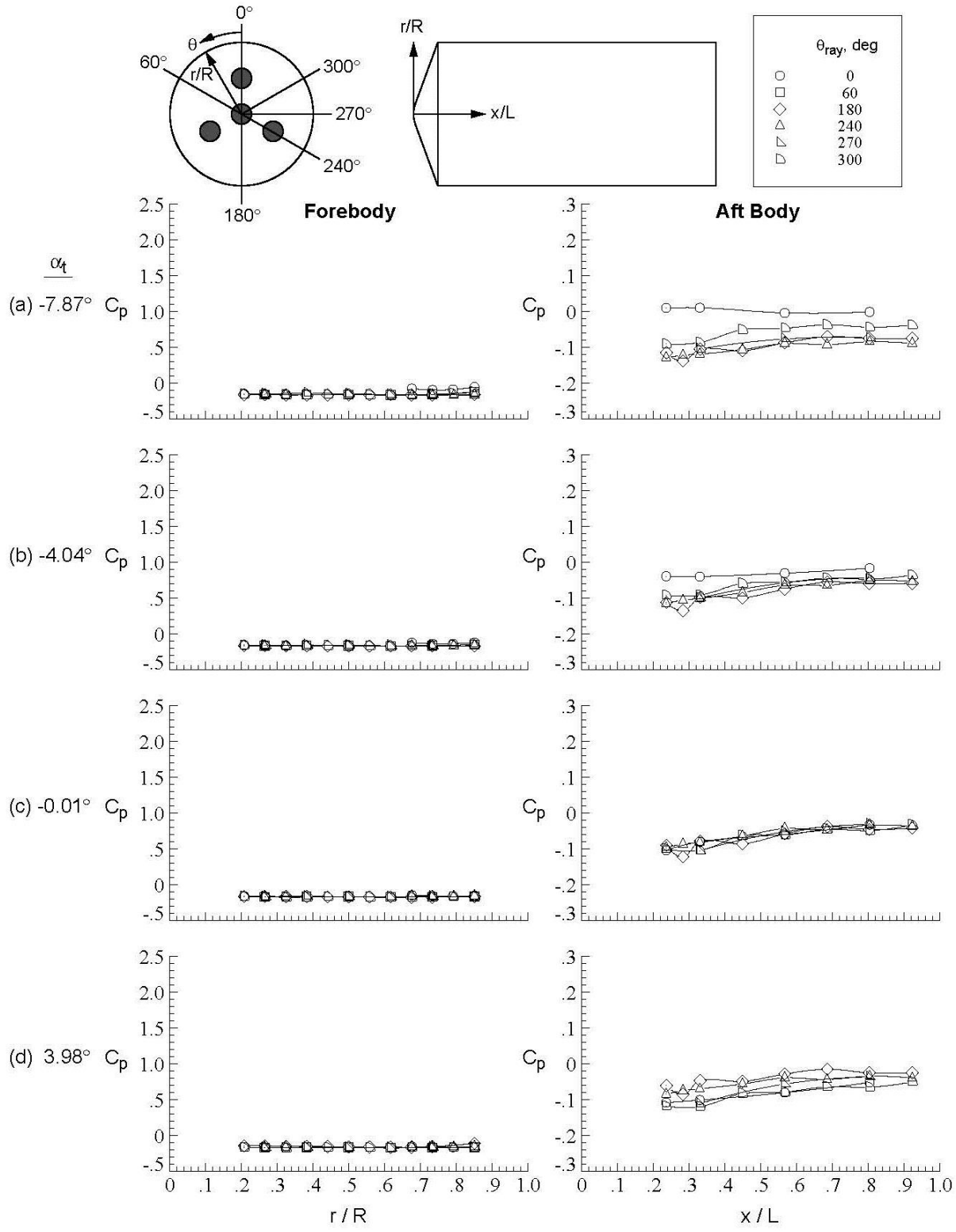

Figure D-224. Quad-nozzle configuration, Run 288, M_∞ = 2.4, Re_∞ = 1.0x10^7/ft, ϕ = −0.03°, X_S = 40.17 in, Y_S = 0.00 in, C_T = 1.92.

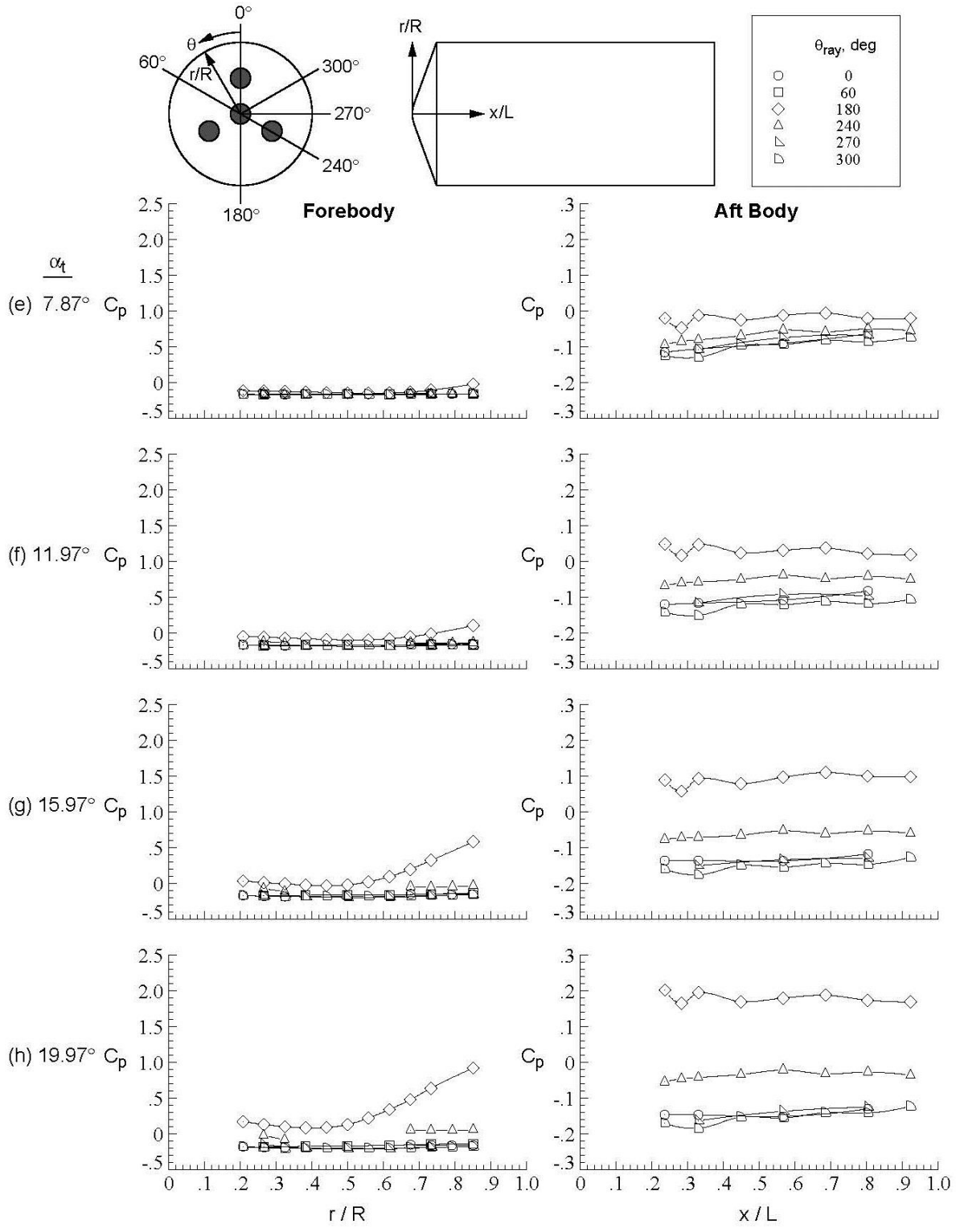

Figure D-224.Concluded.

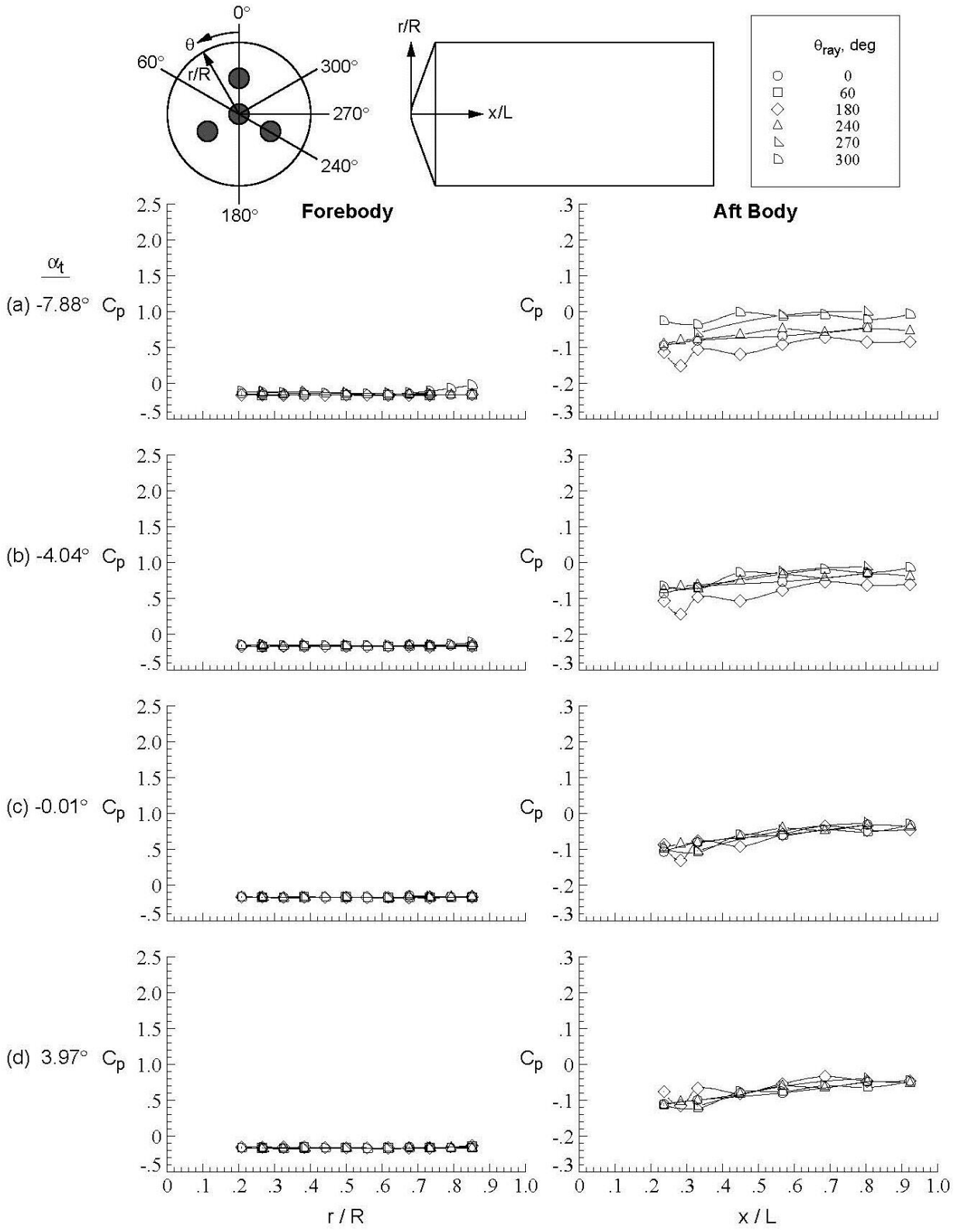

Figure D-225. Quad-nozzle configuration, Run 289, M_∞ = 2.4, Re_∞ = 1.0x10^7/ft, ϕ = 59.98°, X_S = 40.17 in, Y_S = 0.00 in, C_T = 1.93.

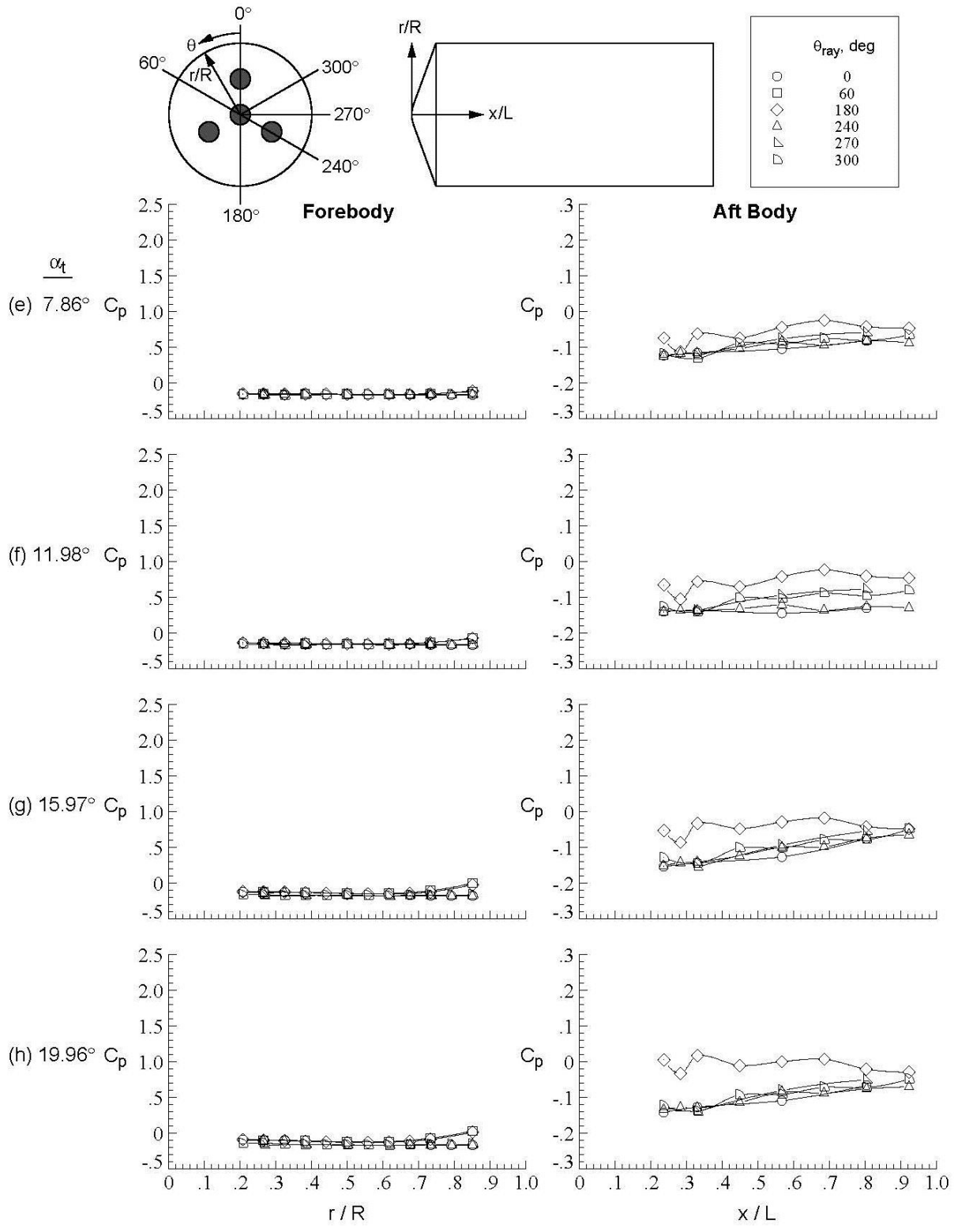

Figure D-225.Concluded.

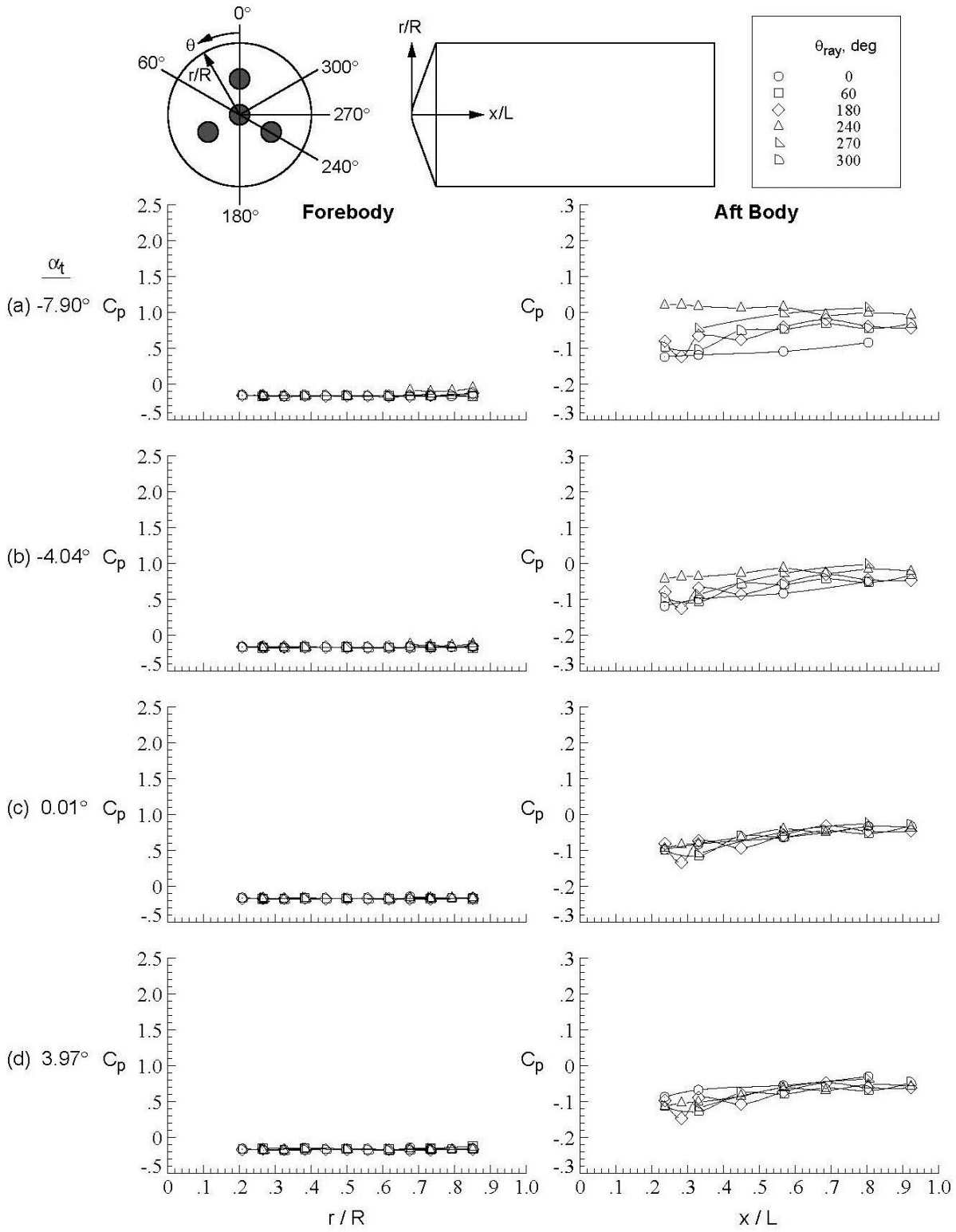

Figure D-226. Quad-nozzle configuration, Run 290, M_∞ = 2.4, Re_∞ = 1.0x10^7/ft, ϕ = 120.04°, X_S = 40.17 in, Y_S = 0.00 in, C_T = 1.94.

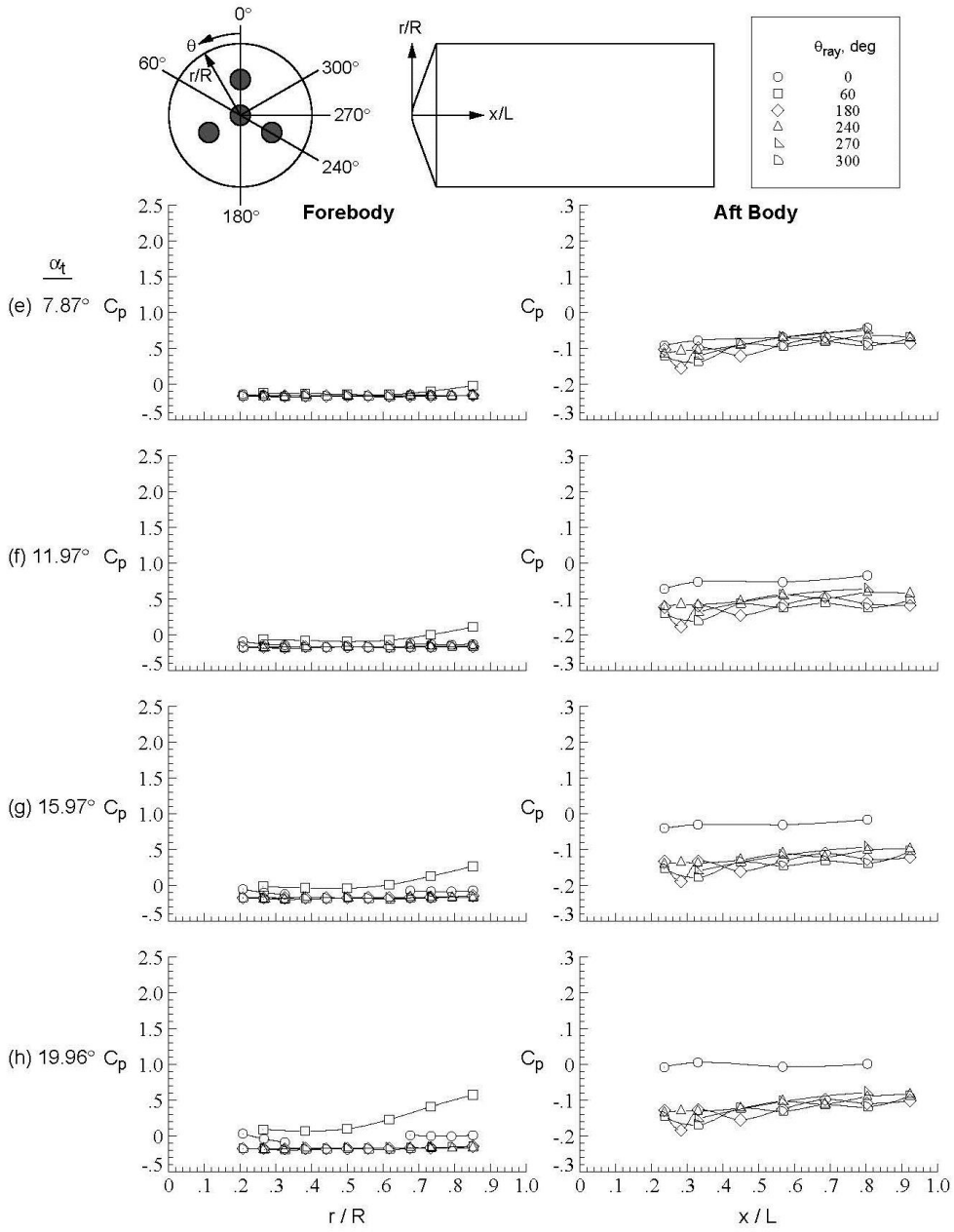

Figure D-226.Concluded.

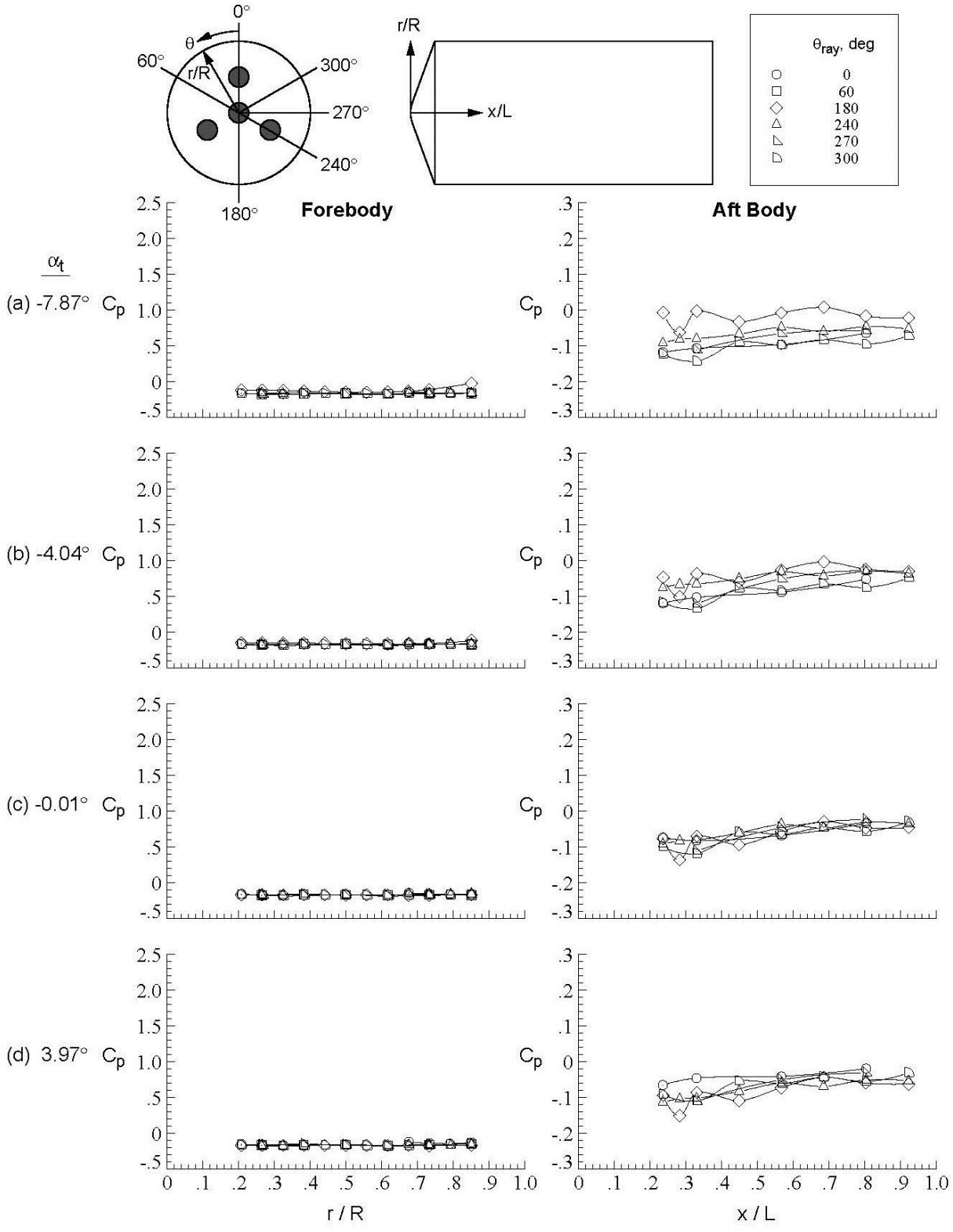

Figure D-227. Quad-nozzle configuration, Run 291, M_∞ = 2.4, Re_∞ = 1.0x10^6/ft, ϕ = −179.95°, X_S = 40.17 in, Y_S = 0.00 in, C_T = 1.93.

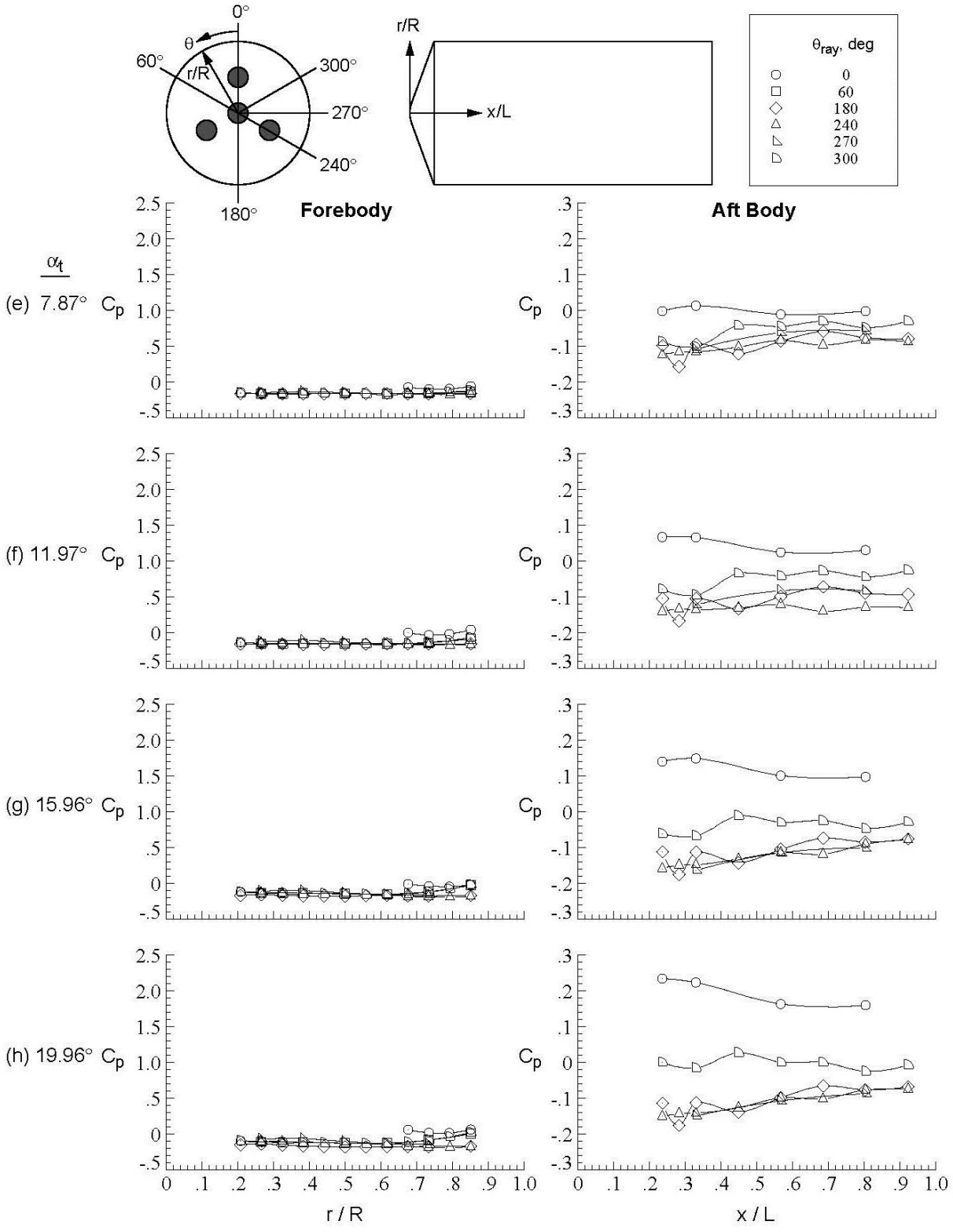

Figure D-227.Concluded.

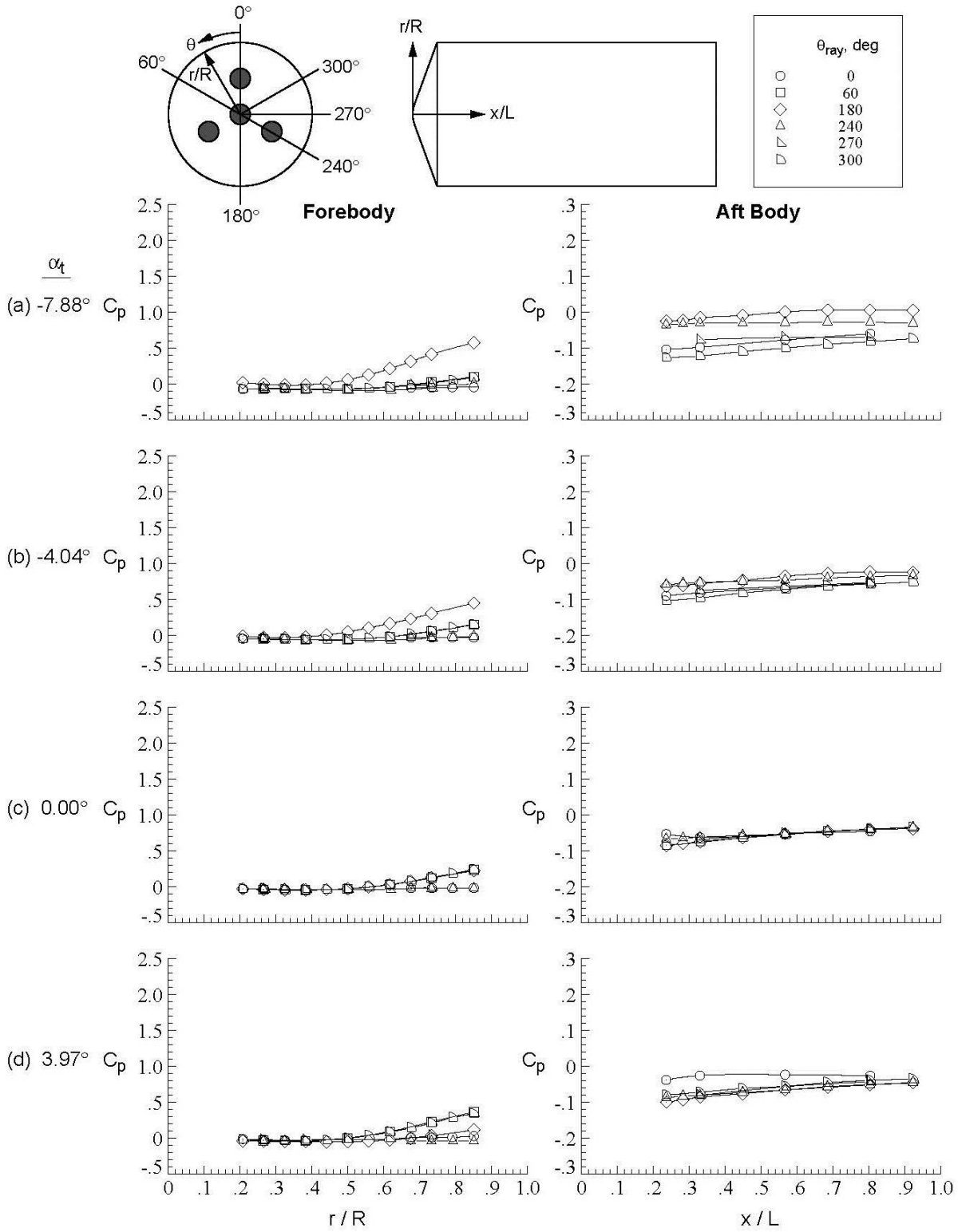

Figure D-228. Quad-nozzle configuration, Run 293, M_∞ = 2.4, Re_∞ = 1.0x10^7/ft, ϕ = 179.97°, X_S = 40.16 in, Y_S = 0.00 in, C_T = 0.94.

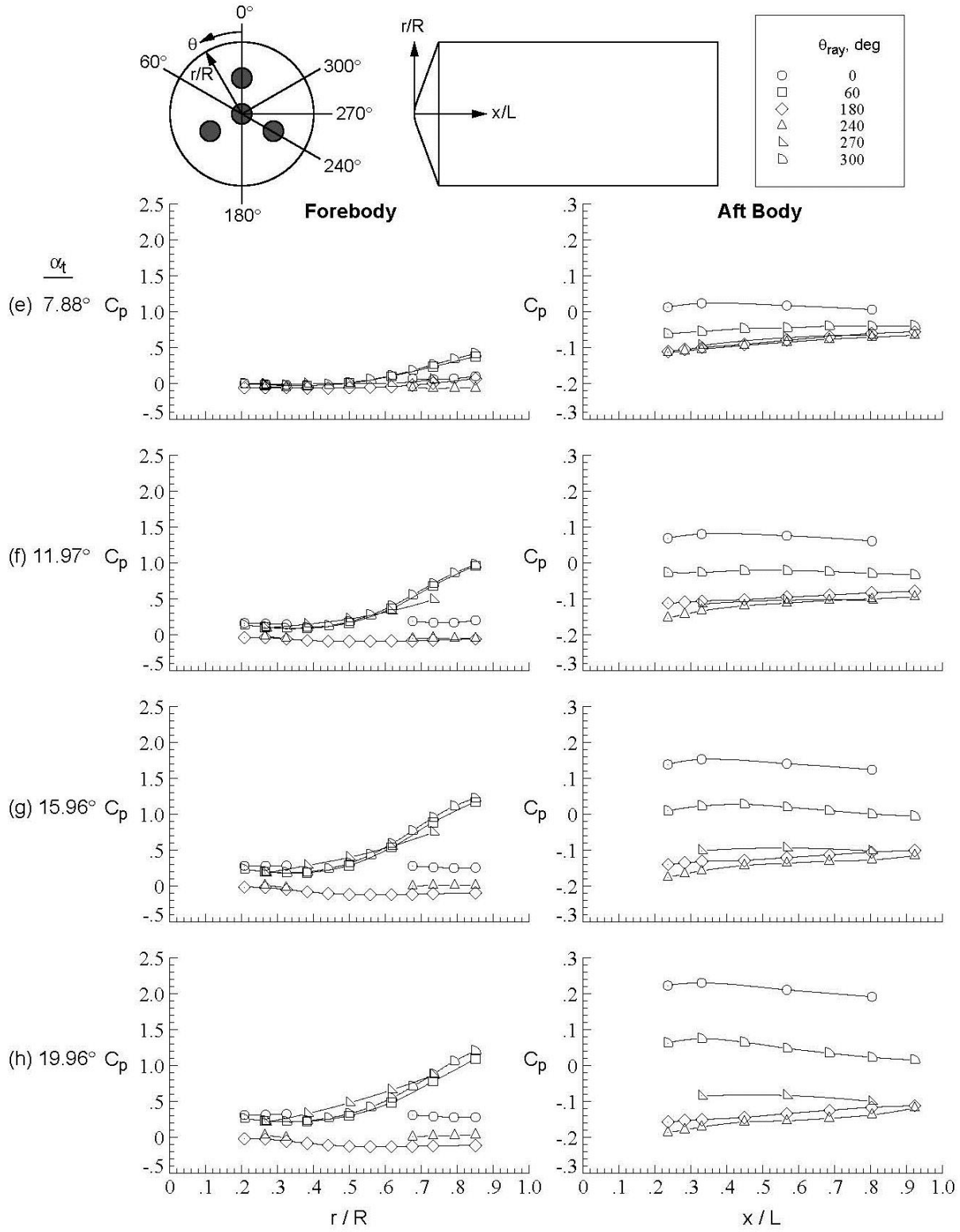

Figure D-228.Concluded.

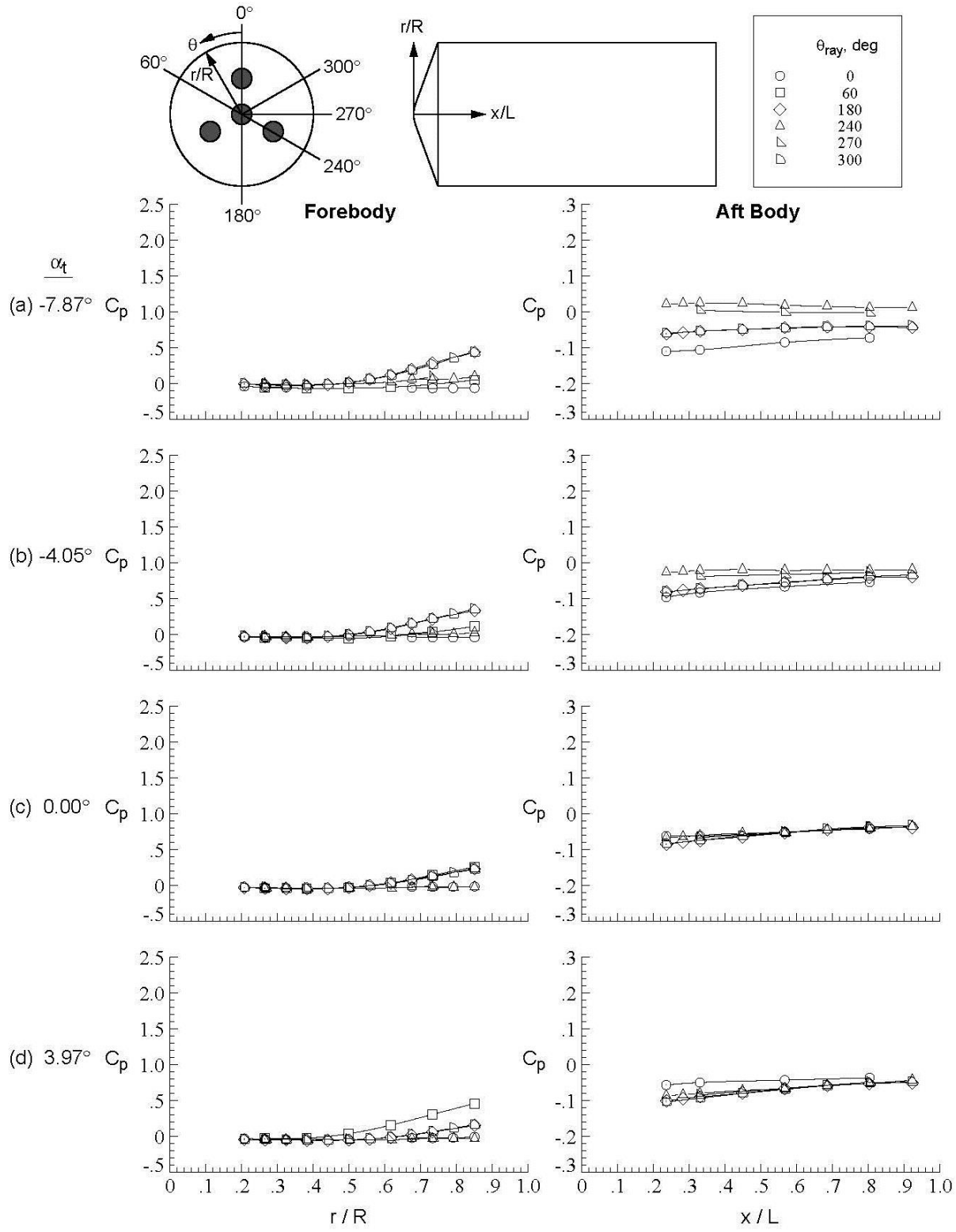

Figure D-229. Quad-nozzle configuration, Run 294, M_∞ = 2.4, Re_∞ = 1.0x10^6/ft, ϕ = 120.02°, X_S = 40.16 in, Y_S = 0.00 in, C_T = 0.95.

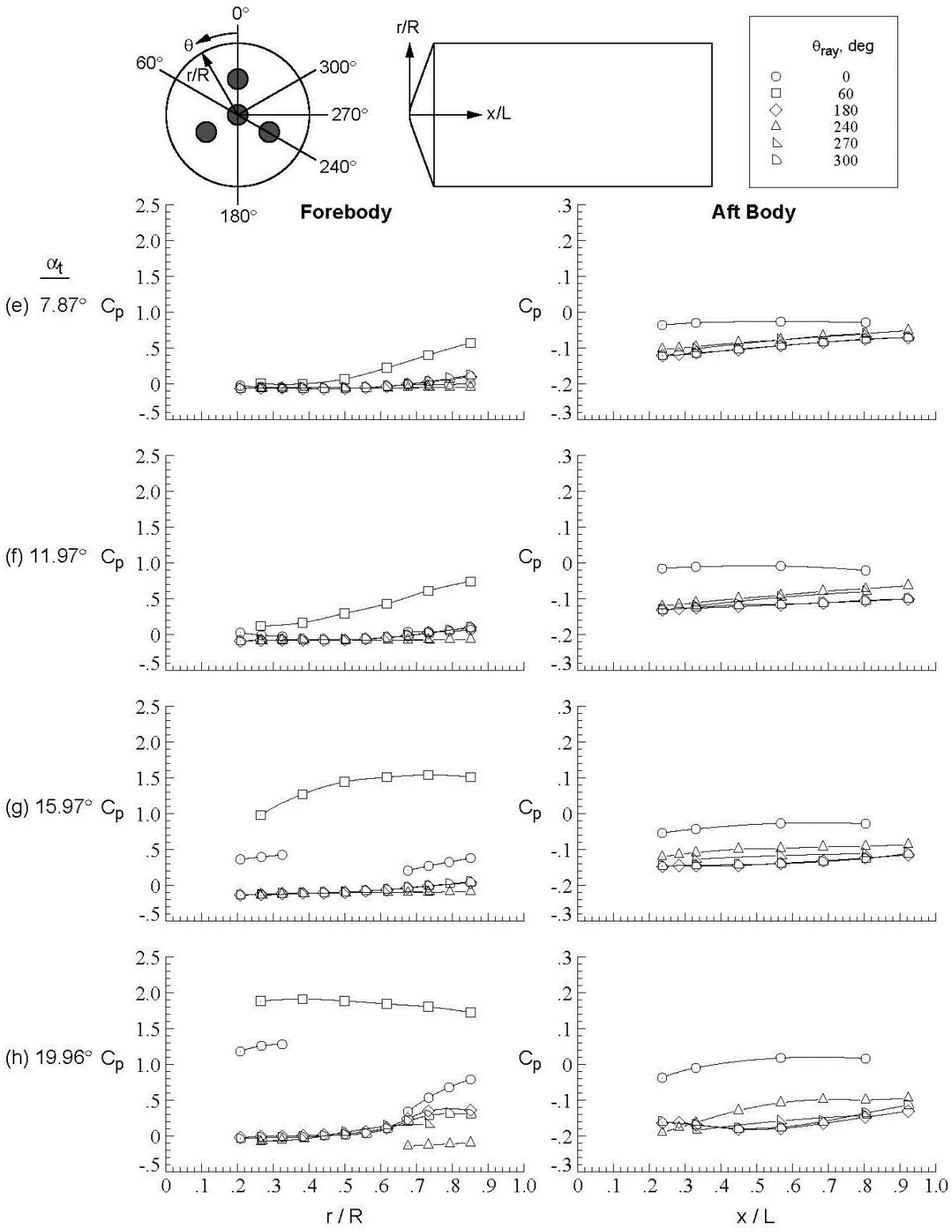

Figure D-229.Concluded.

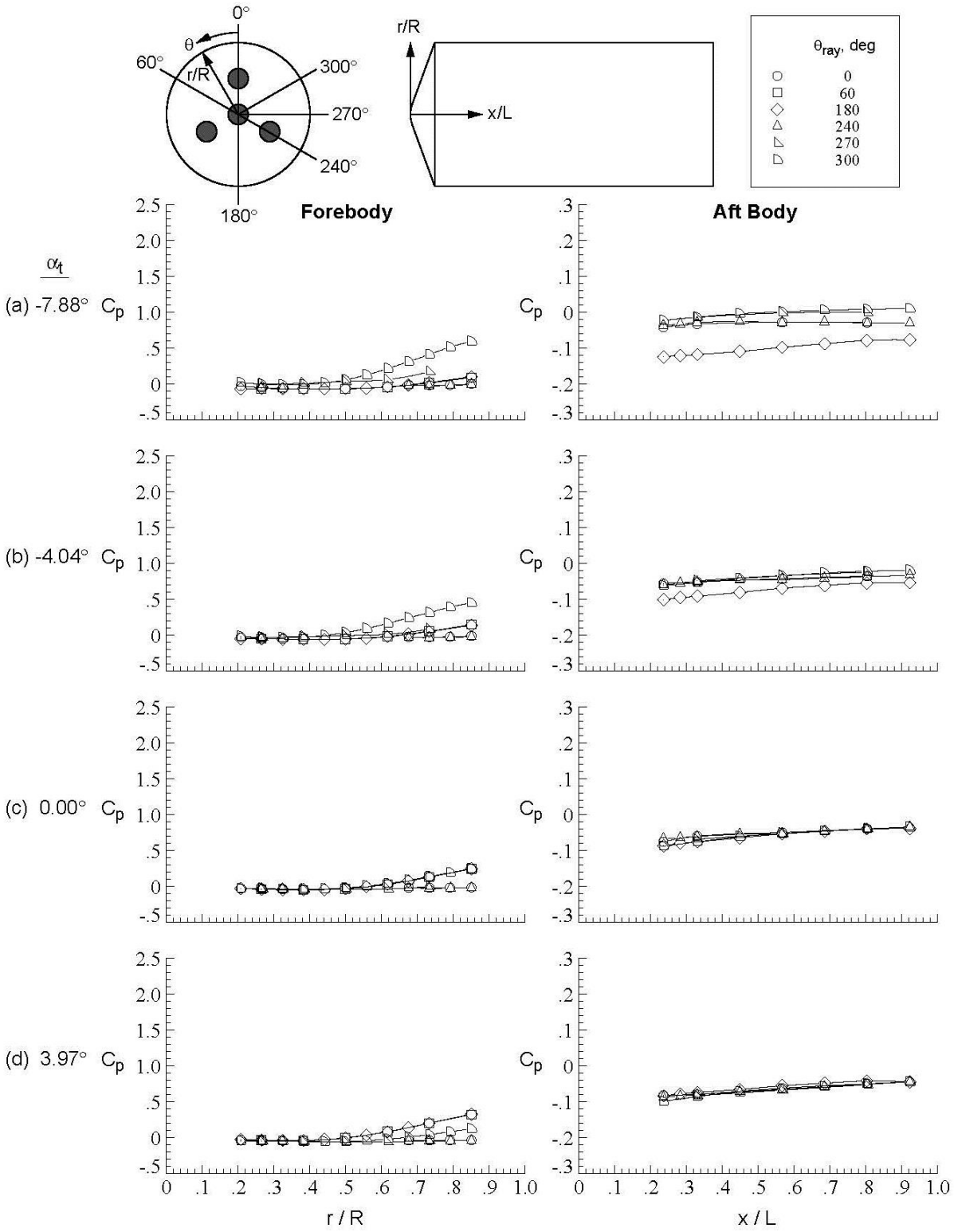

Figure D-230. Quad-nozzle configuration, Run 295, M_∞ = 2.4, Re_∞ = 1.0x10^7/ft, ϕ = 59.96°, X_S = 40.16 in, Y_S = 0.00 in, C_T = 0.95.

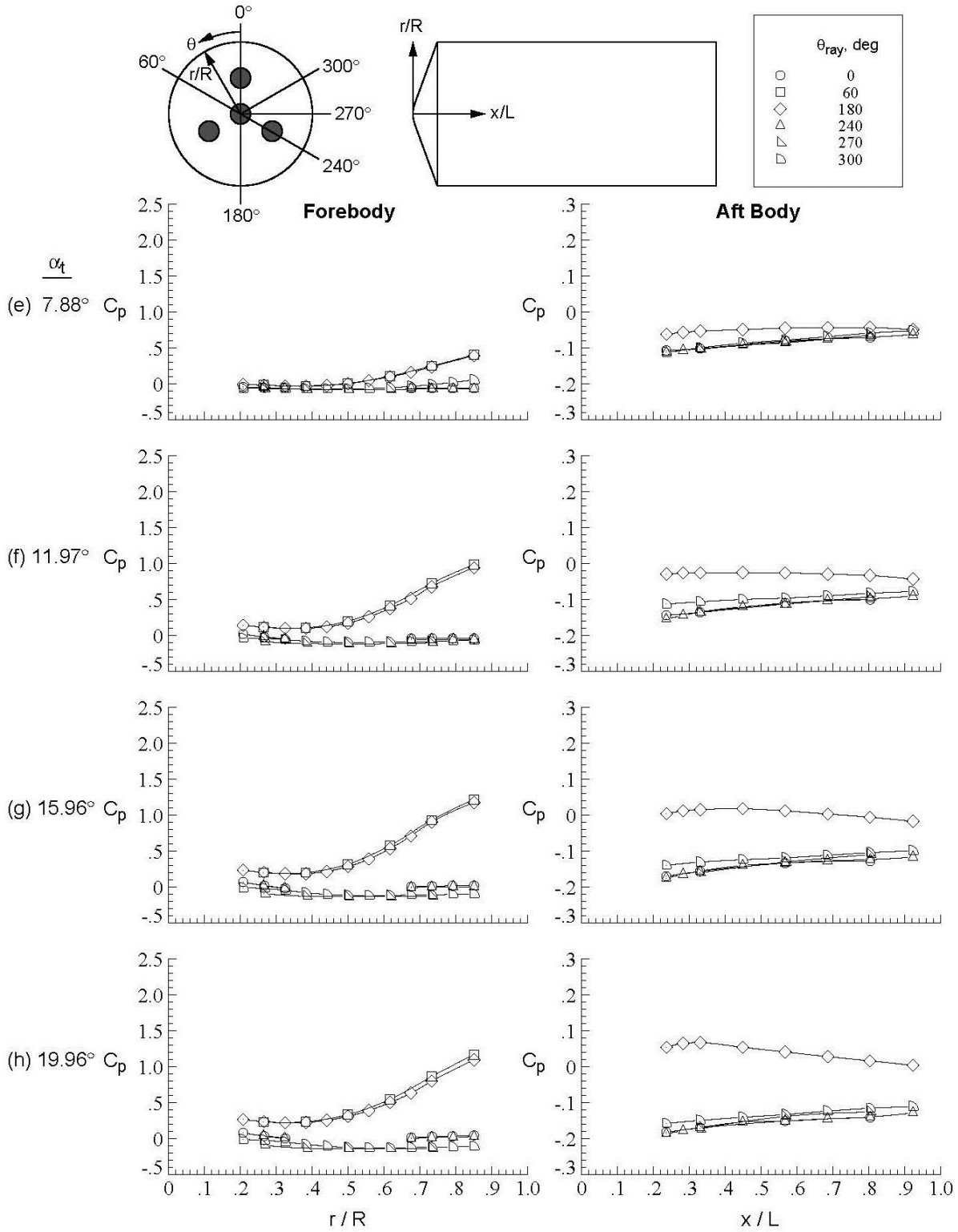

Figure D-230.Concluded.

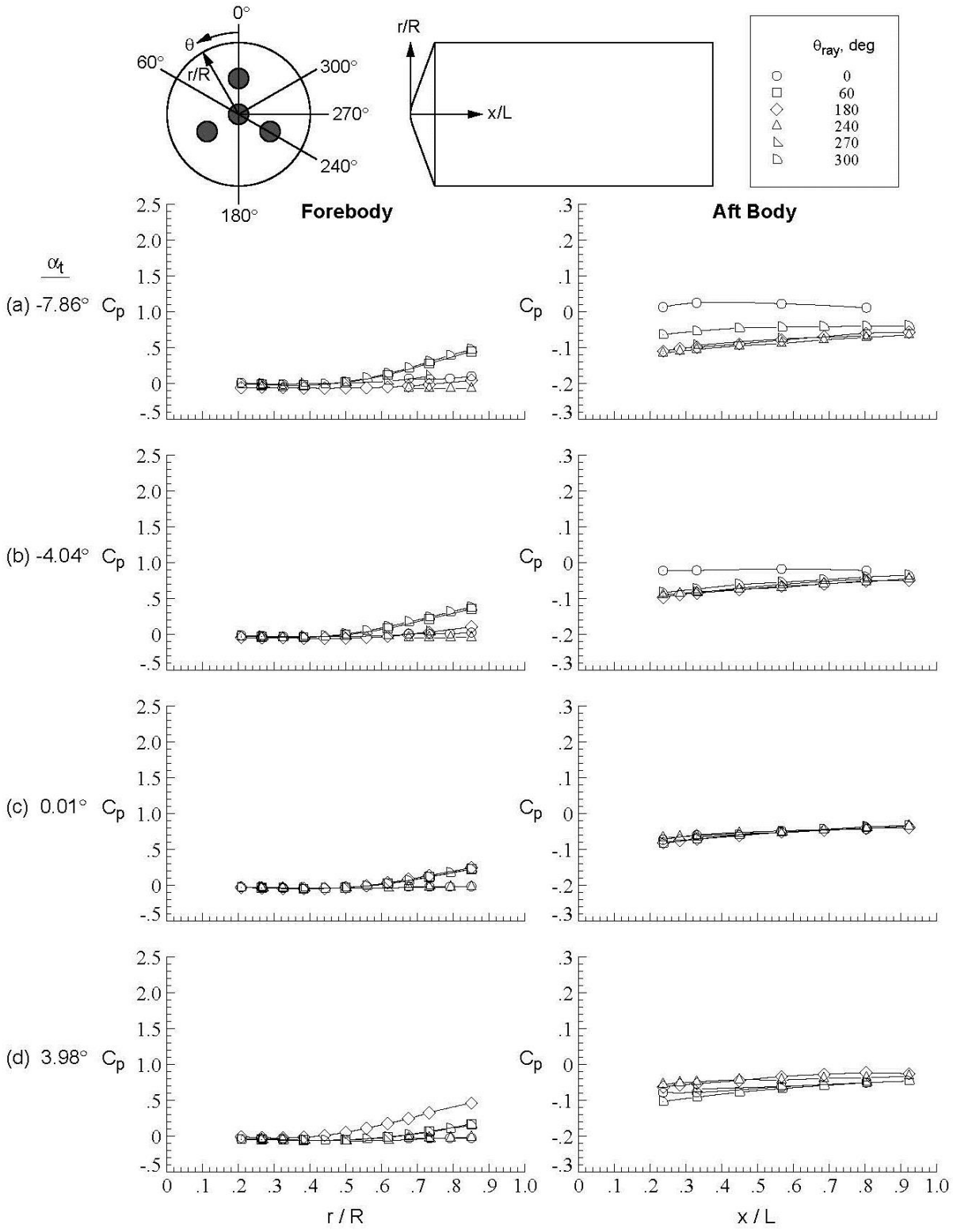

Figure D-231. Quad-nozzle configuration, Run 296, M_∞ = 2.4, Re_∞ = 1.0x10^7/ft, ϕ = −0.05°, X_S = 40.16 in, Y_S = 0.00 in, C_T = 0.94.

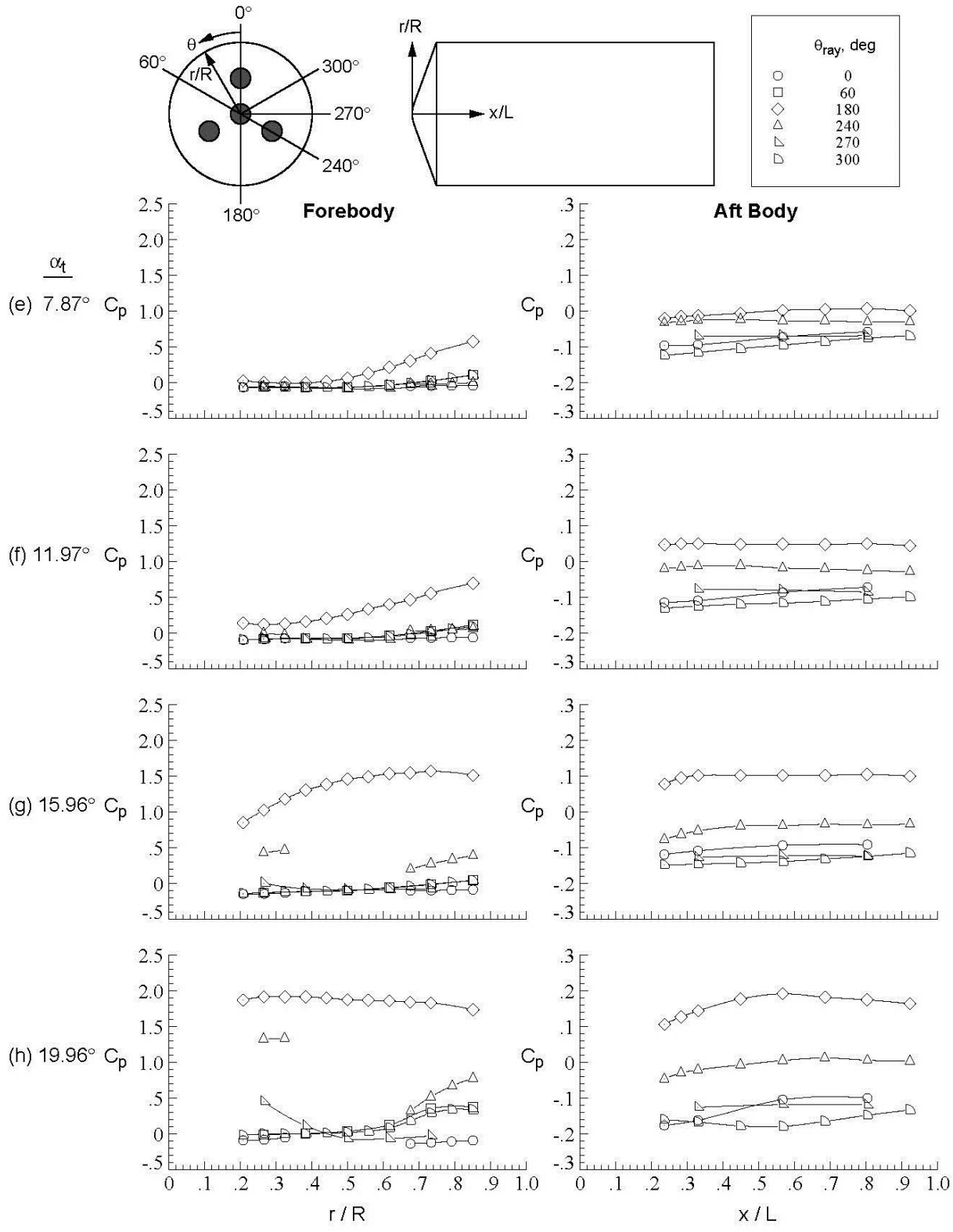

Figure D-231.Concluded.

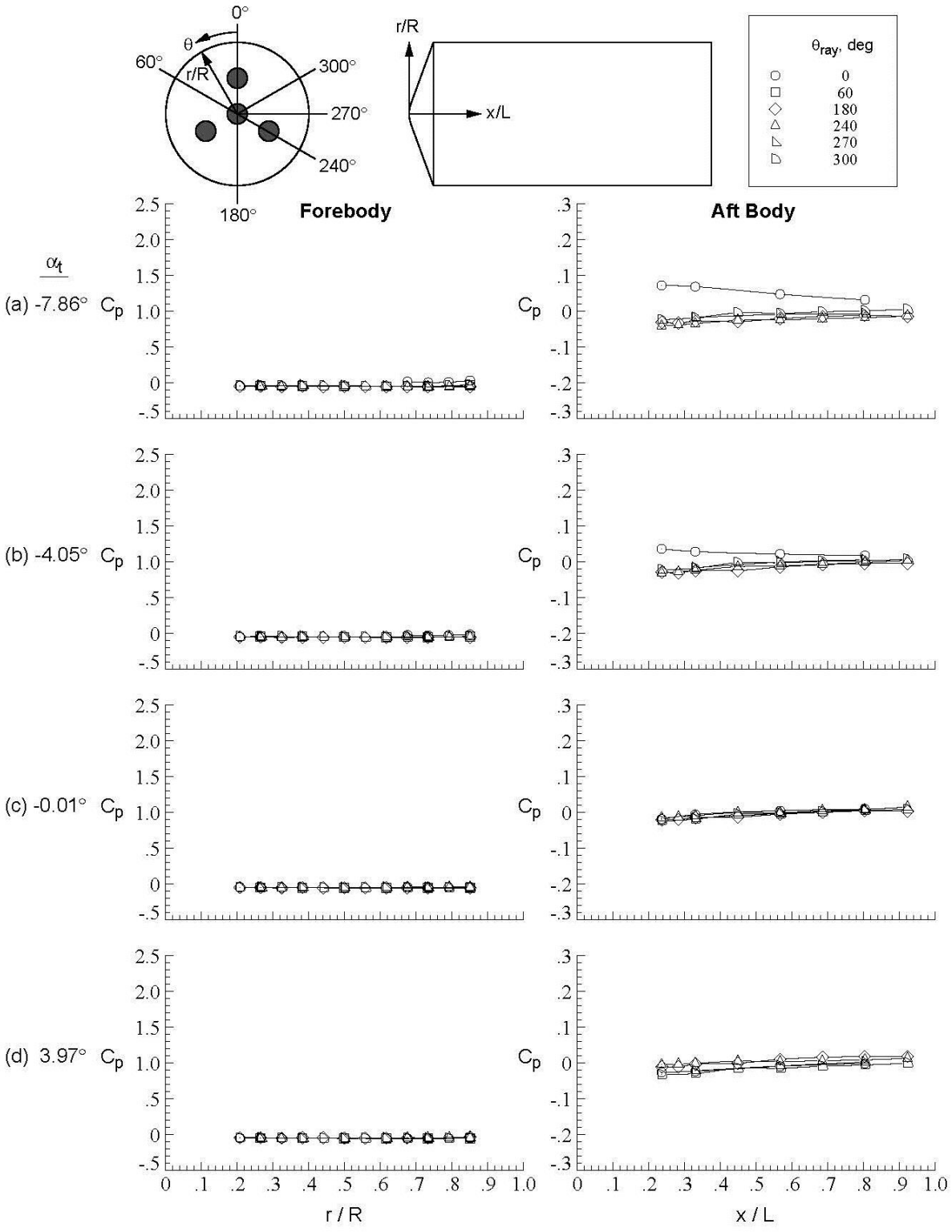

Figure D-232. Quad-nozzle configuration, Run 298, M_∞ = 3.5, Re_∞ = 1.0x10^7/ft, ϕ = 0.01°, X_S = 40.16 in, Y_S = 0.00 in, C_T = 1.92.

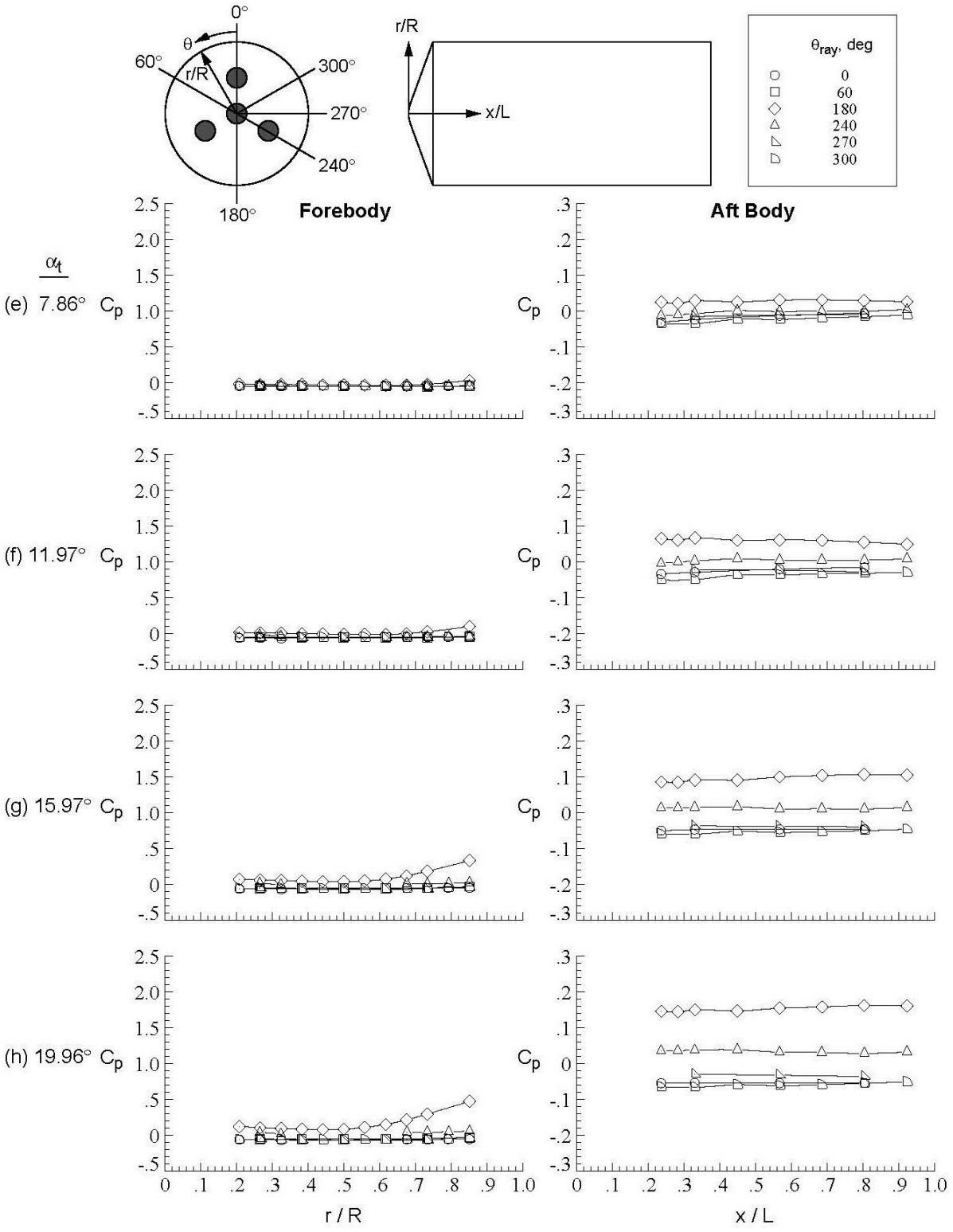

Figure D-232.Concluded.

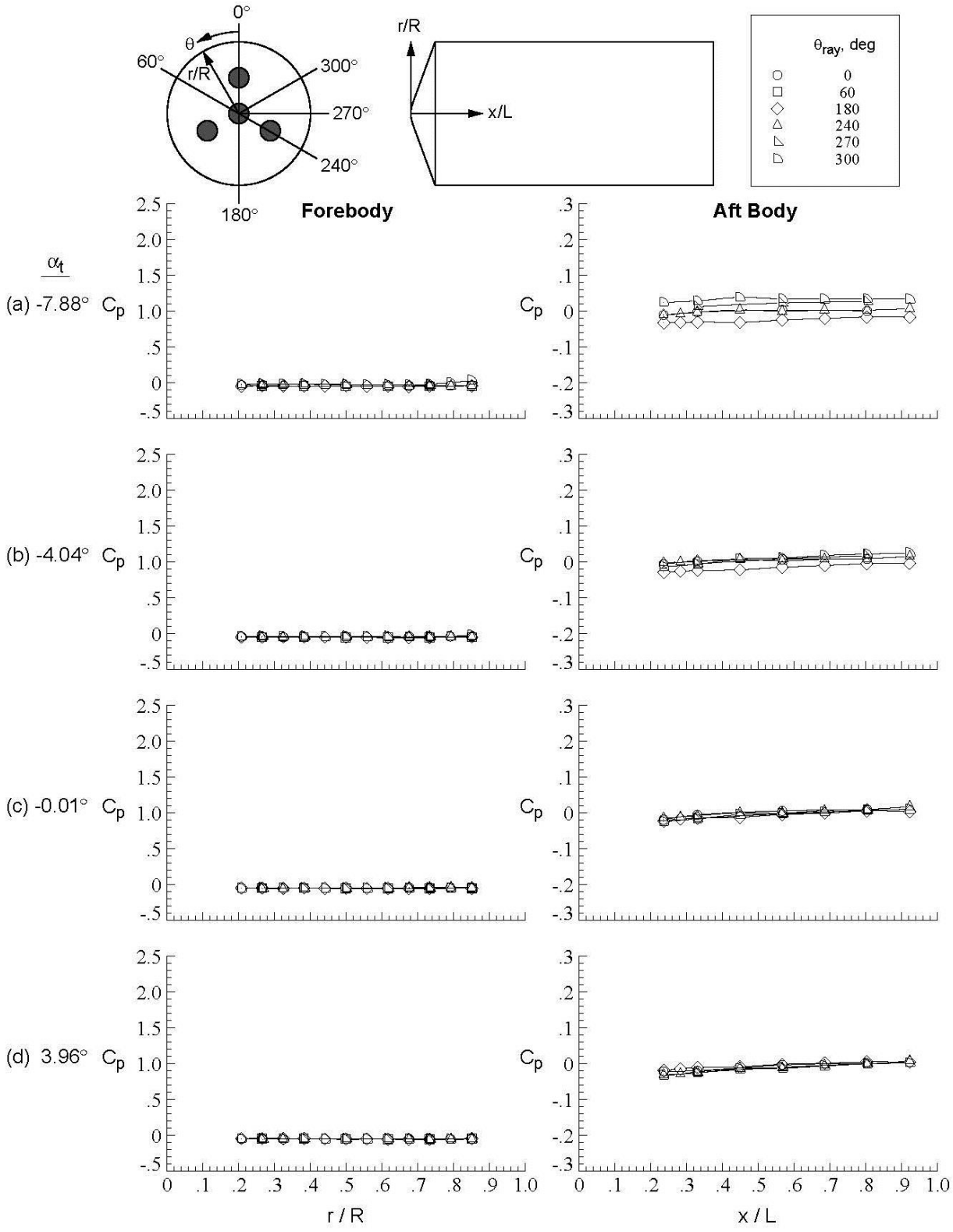

Figure D-233. Quad-nozzle configuration, Run 299, M_∞ = 3.5, Re_∞ = 1.0x10^7/ft, ϕ = 59.92°, X_S = 40.16 in, Y_S = 0.00 in, C_T = 1.92.

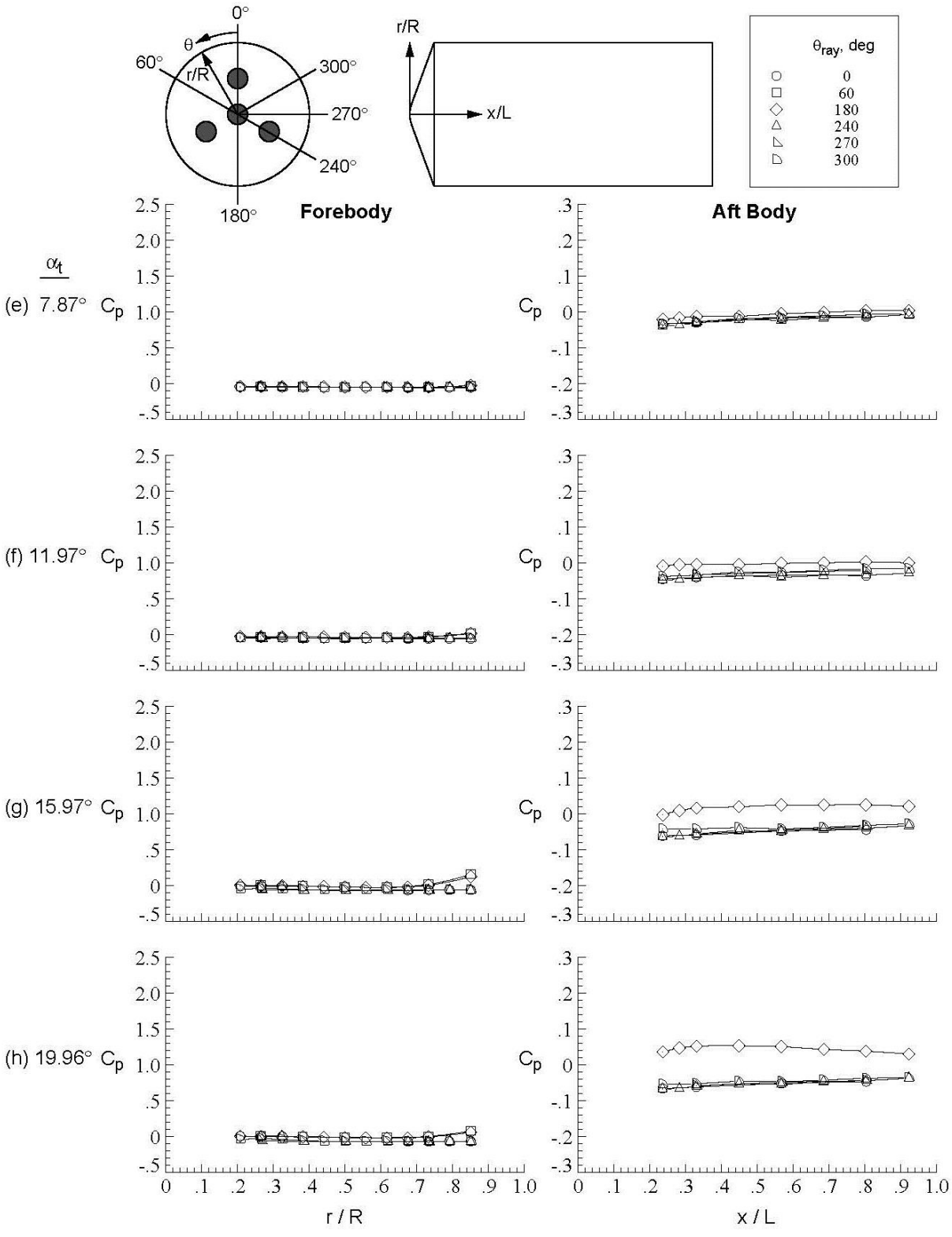

Figure D-233.Concluded.

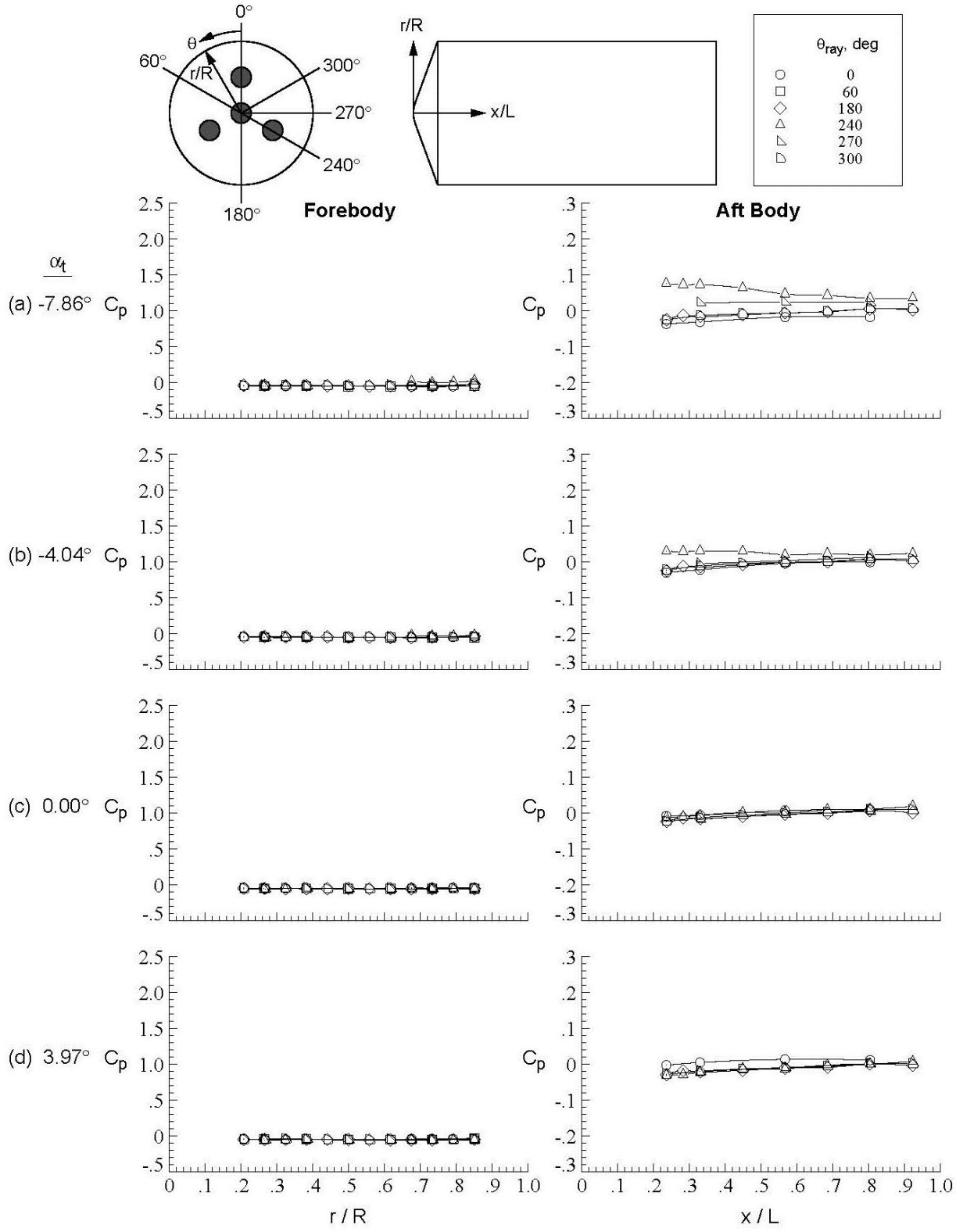

Figure D-234. Quad-nozzle configuration, Run 300, M_∞ = 3.5, Re_∞ = 1.0x10^6/ft, ϕ = 120.02°, X_S = 40.16 in, Y_S = 0.00 in, C_T = 1.92.

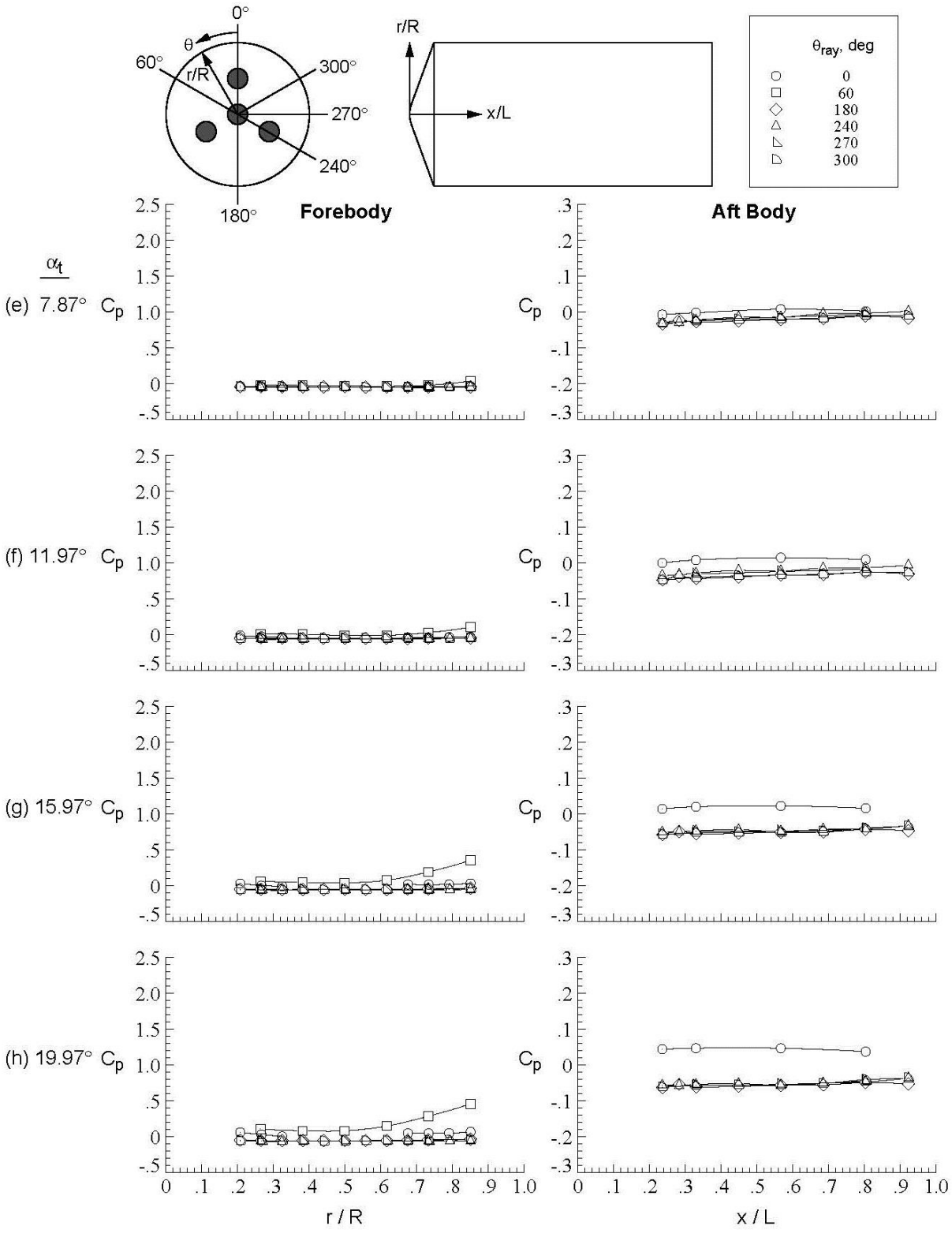

Figure D-234.Concluded.

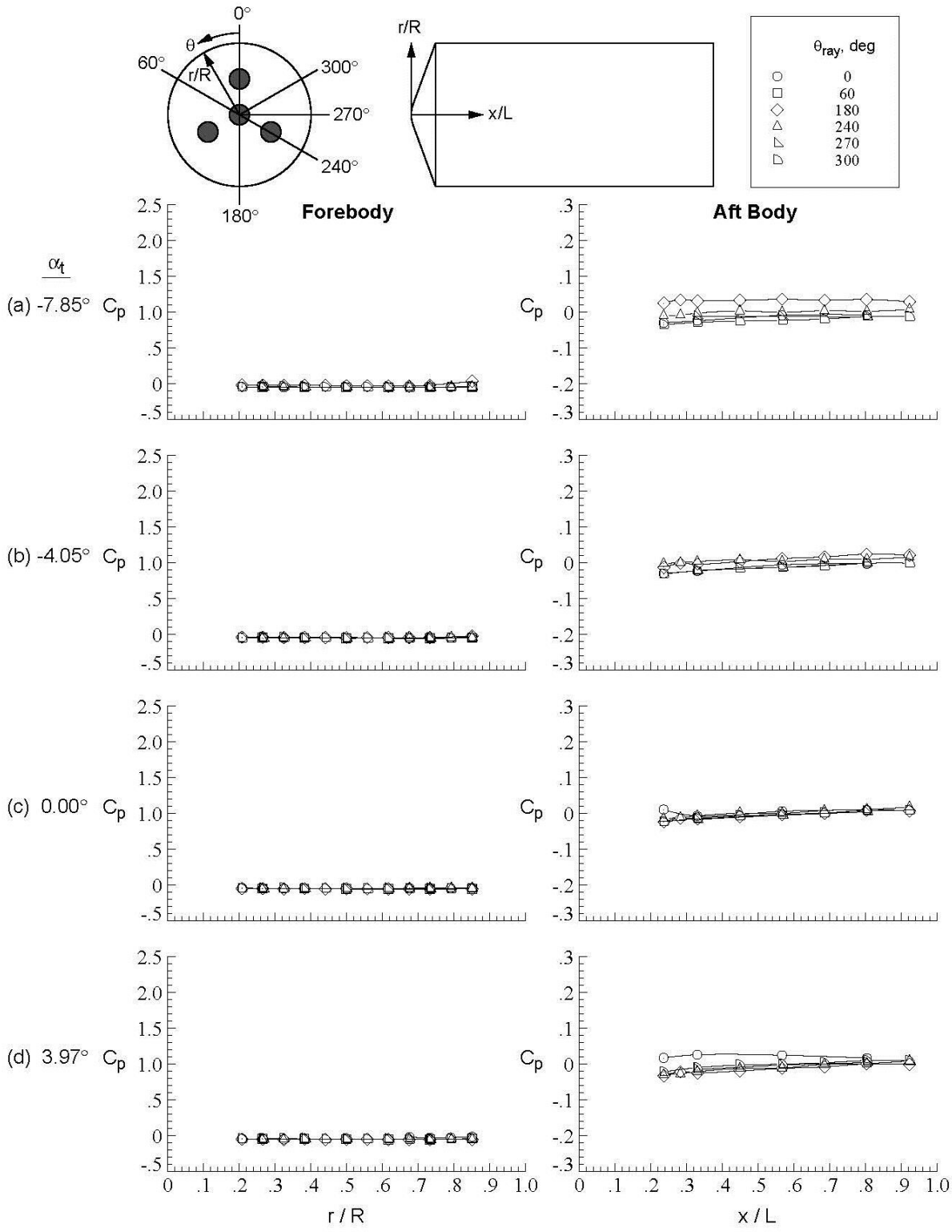

Figure D-235. Quad-nozzle configuration, Run 301, M_∞ = 3.5, Re_∞ = 1.0x10^7/ft, ϕ = 179.95°, X_S = 40.16 in, Y_S = 0.00 in, C_T = 1.93.

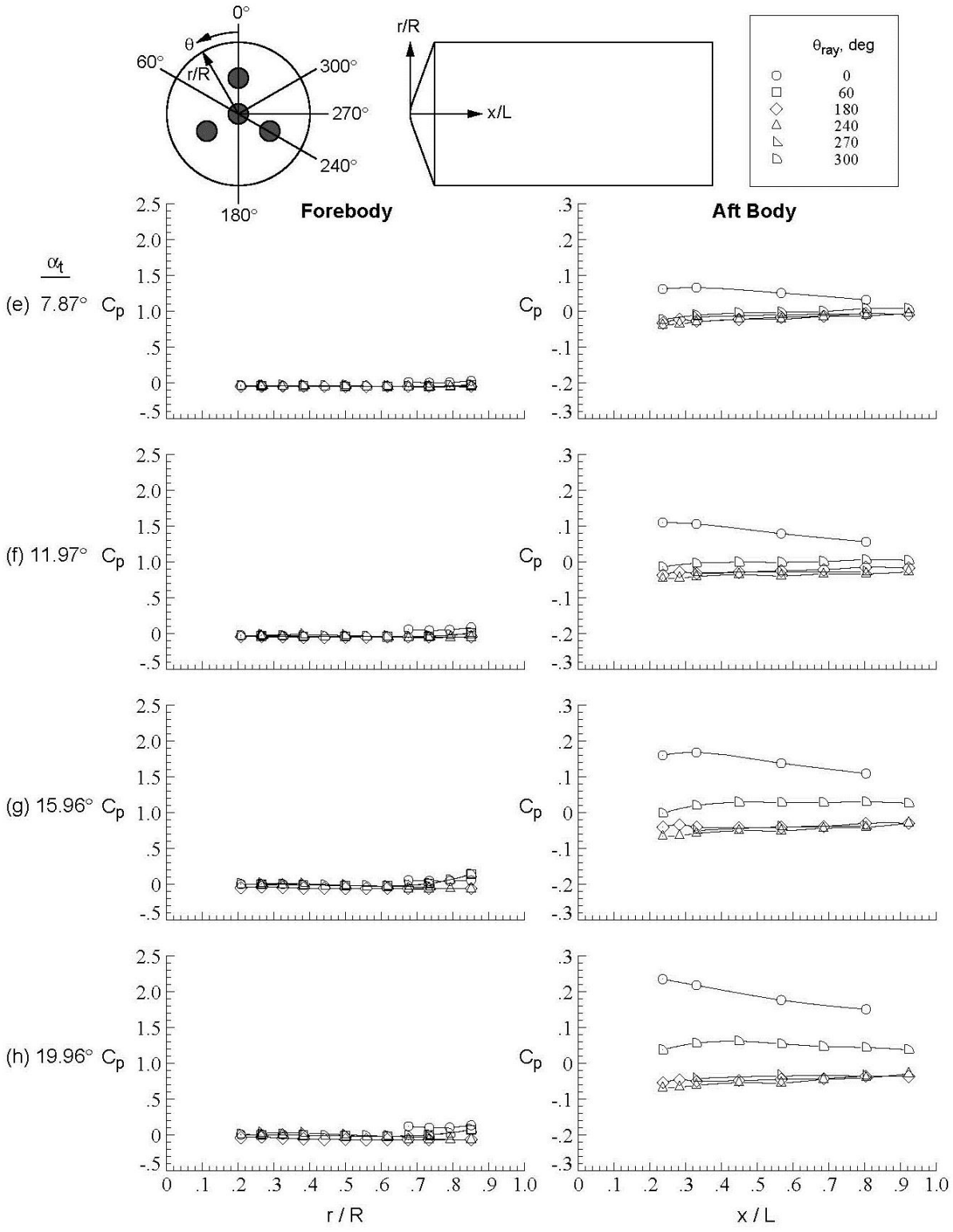

Figure D-235.Concluded.

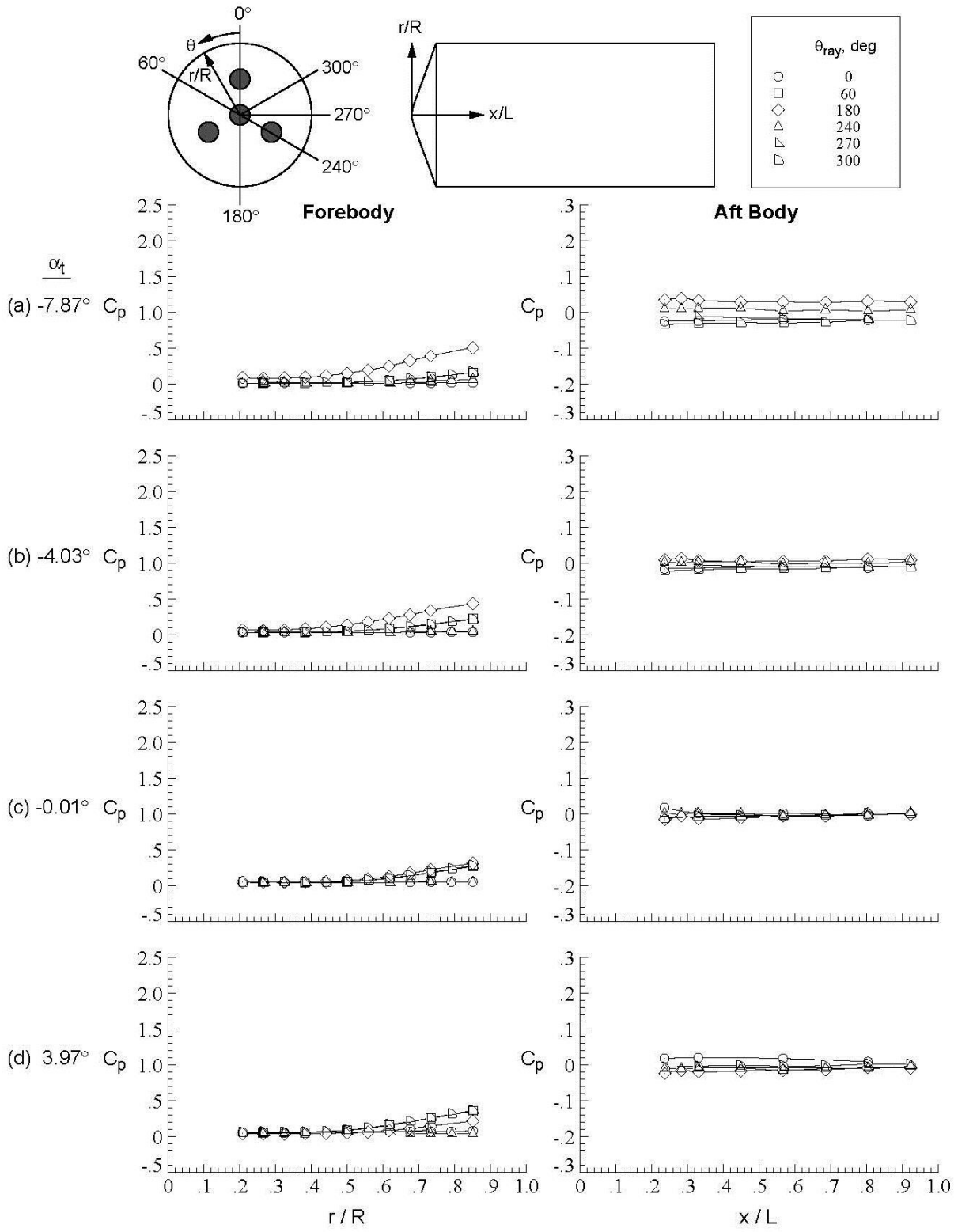

Figure D-236. Quad-nozzle configuration, Run 302, M_∞ = 3.5, Re_∞ = 1.0x10^7/ft, ϕ = 179.95°, X_S = 40.16 in, Y_S = 0.00 in, C_T = 0.91.

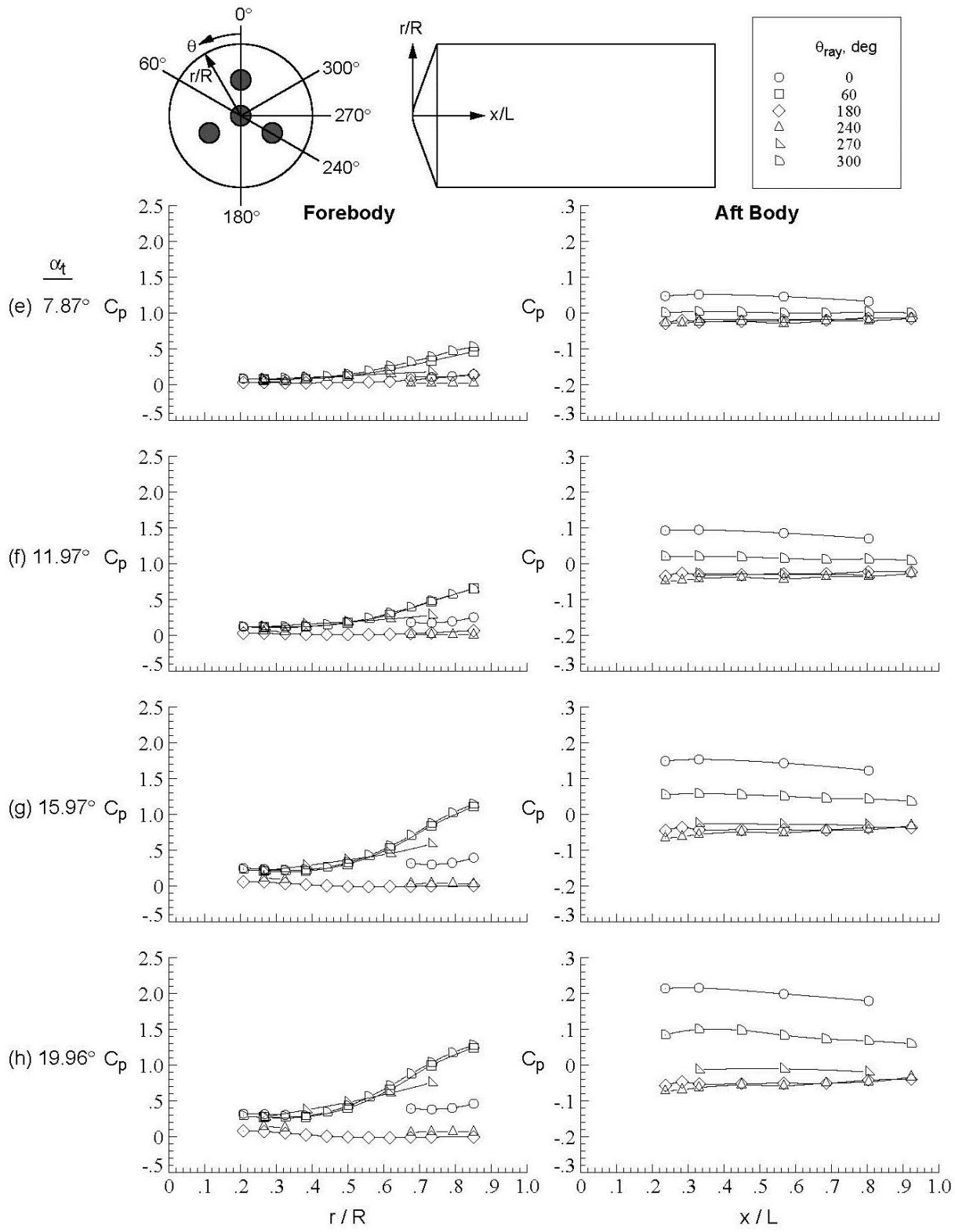

Figure D-236.Concluded.

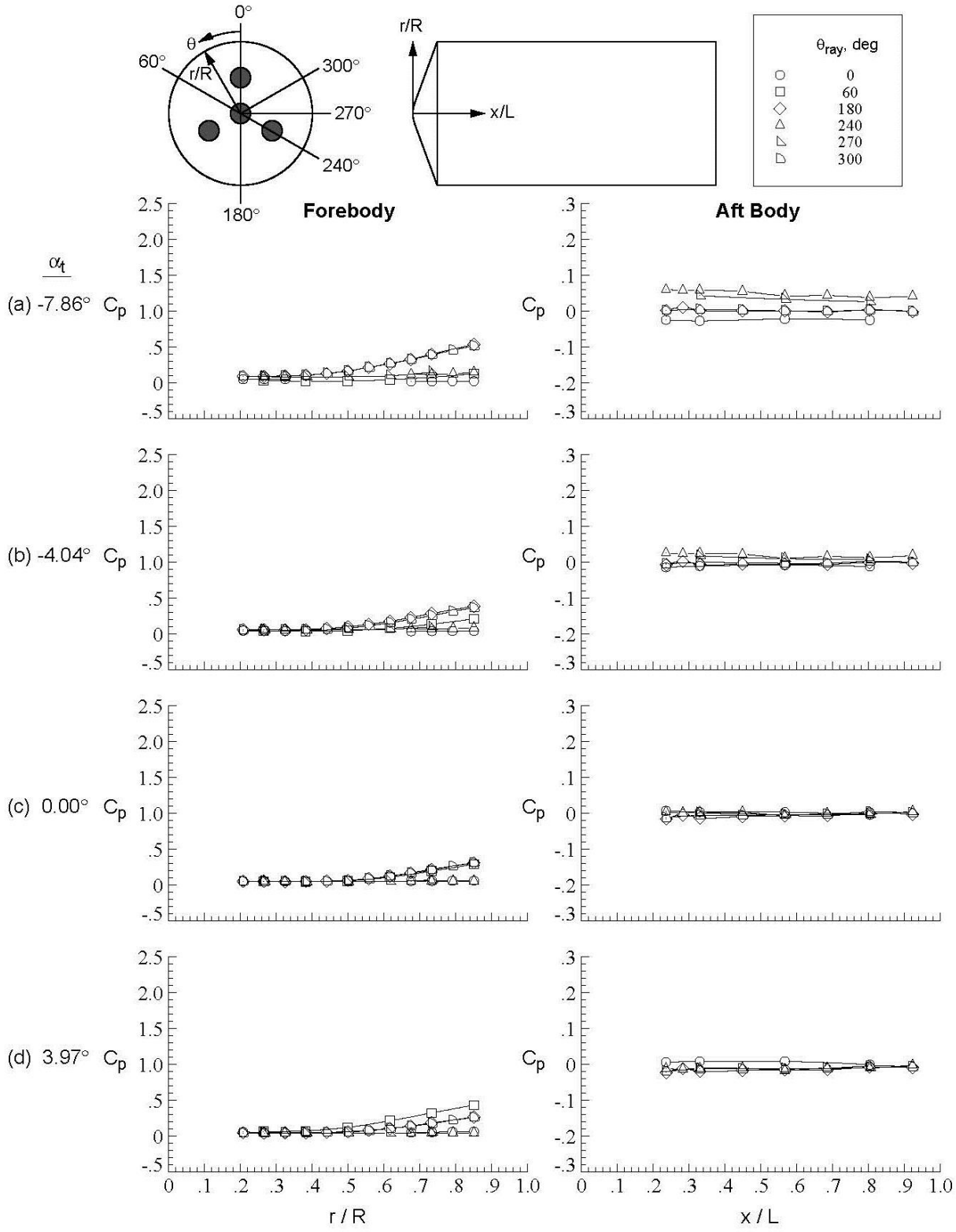

Figure D-237. Quad-nozzle configuration, Run 303, M_∞ = 3.5, Re_∞ = 1.0x10^7/ft, ϕ = 120.08°, X_S = 40.16 in, Y_S = 0.00 in, C_T = 0.90.

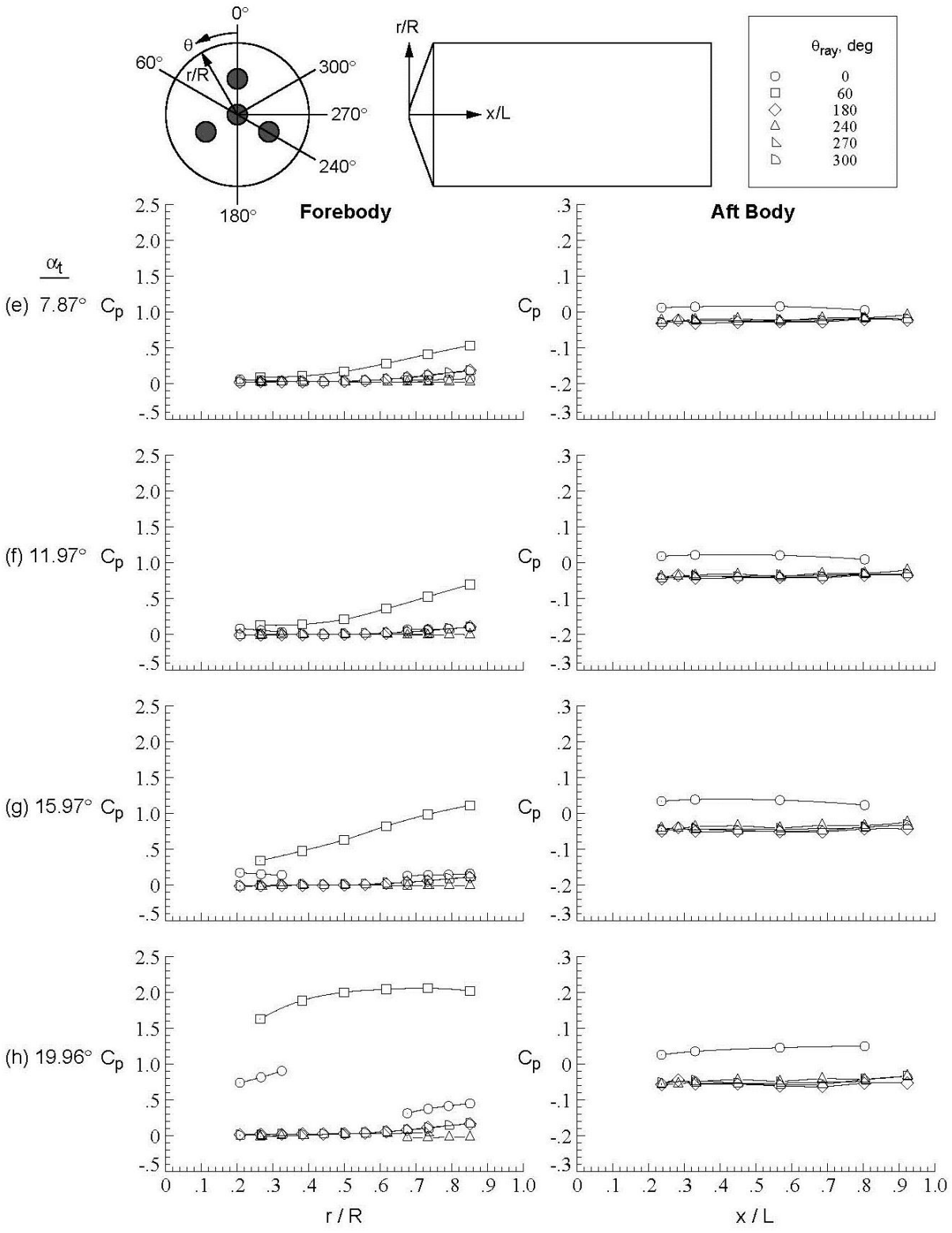

Figure D-237.Concluded.

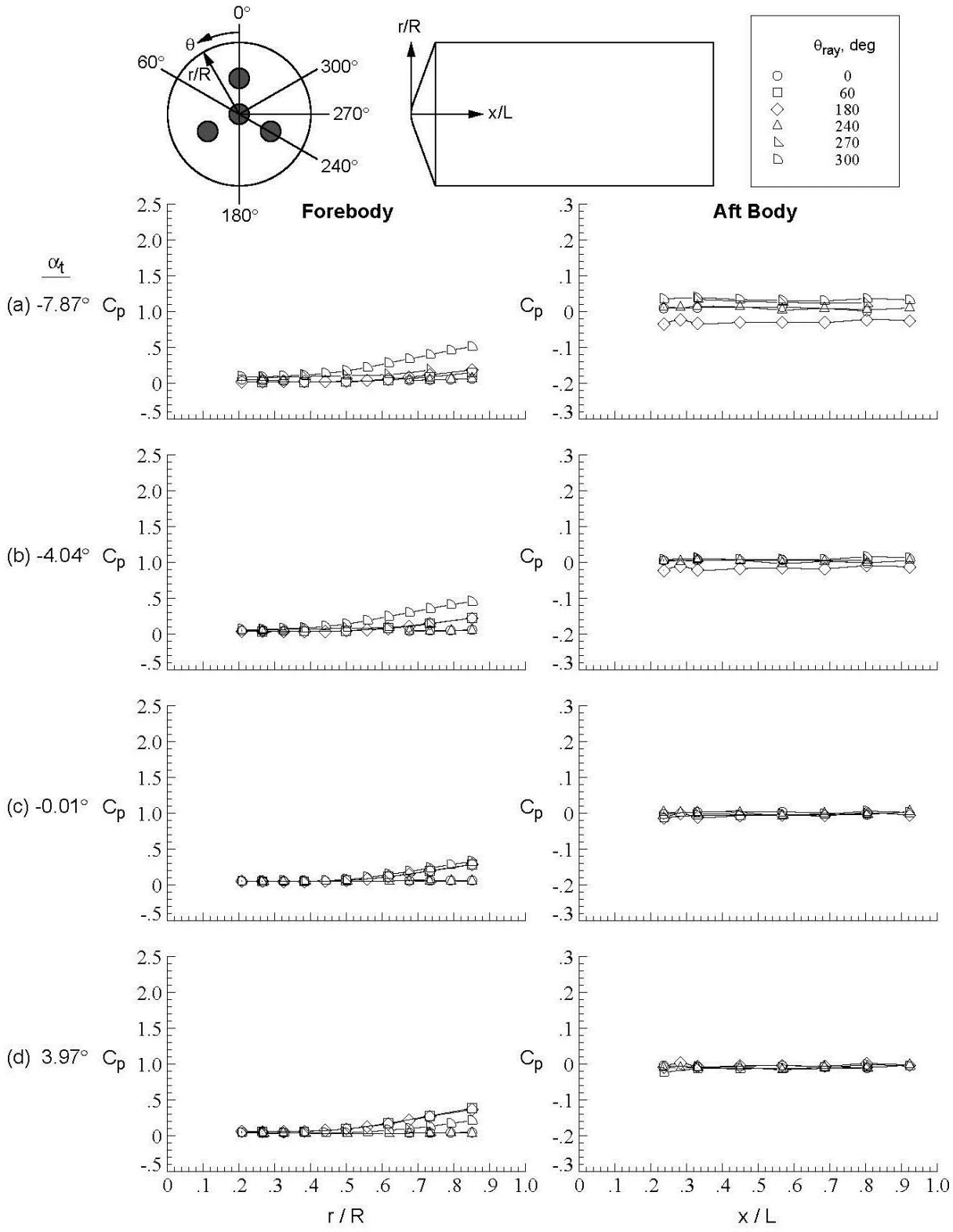

Figure D-238. Quad-nozzle configuration, Run 304, M_∞ = 3.5, Re_∞ = 1.0x10^7/ft, ϕ = 59.94°, X_S = 40.16 in, Y_S = 0.00 in, C_T = 0.90.

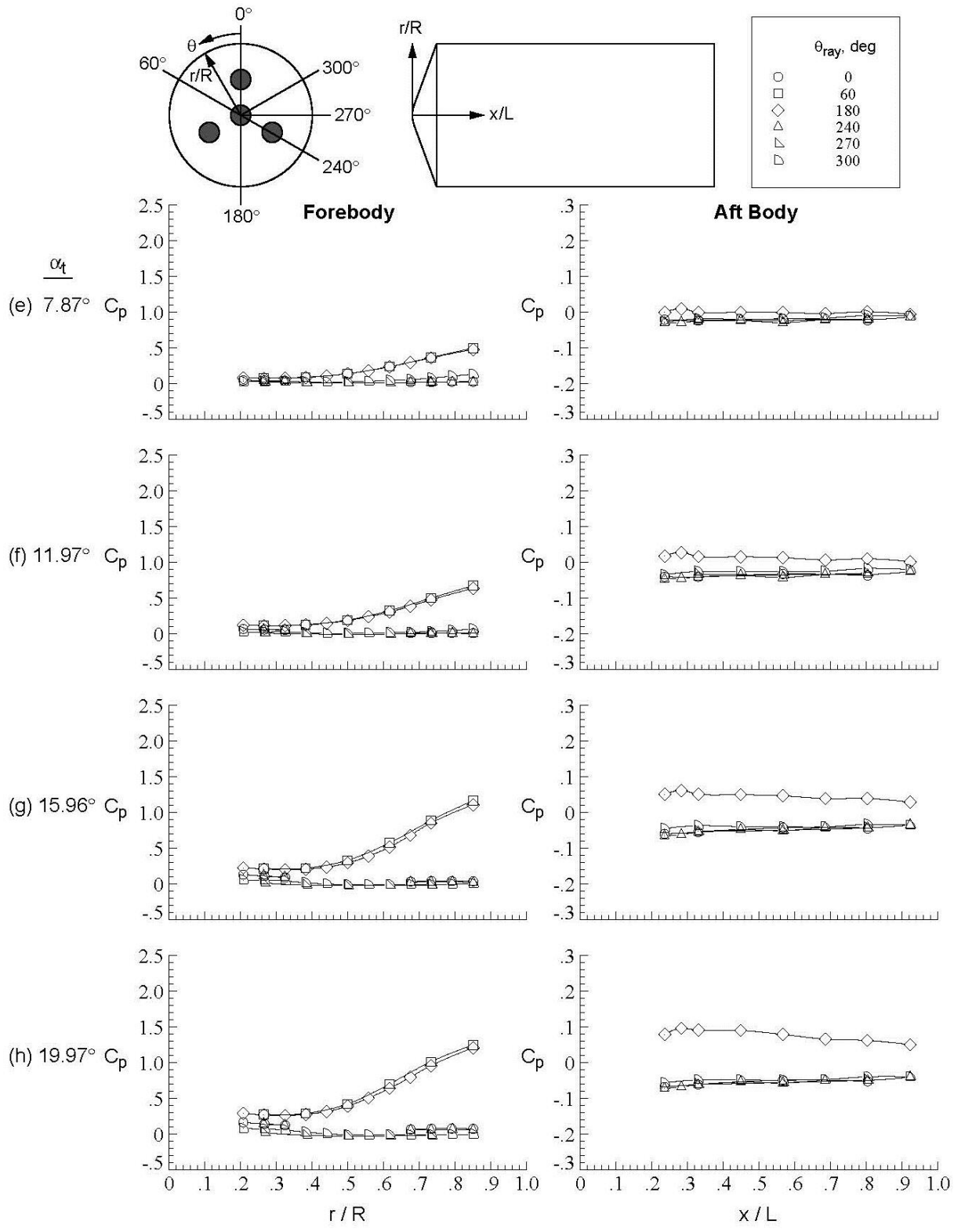

Figure D-238.Concluded.

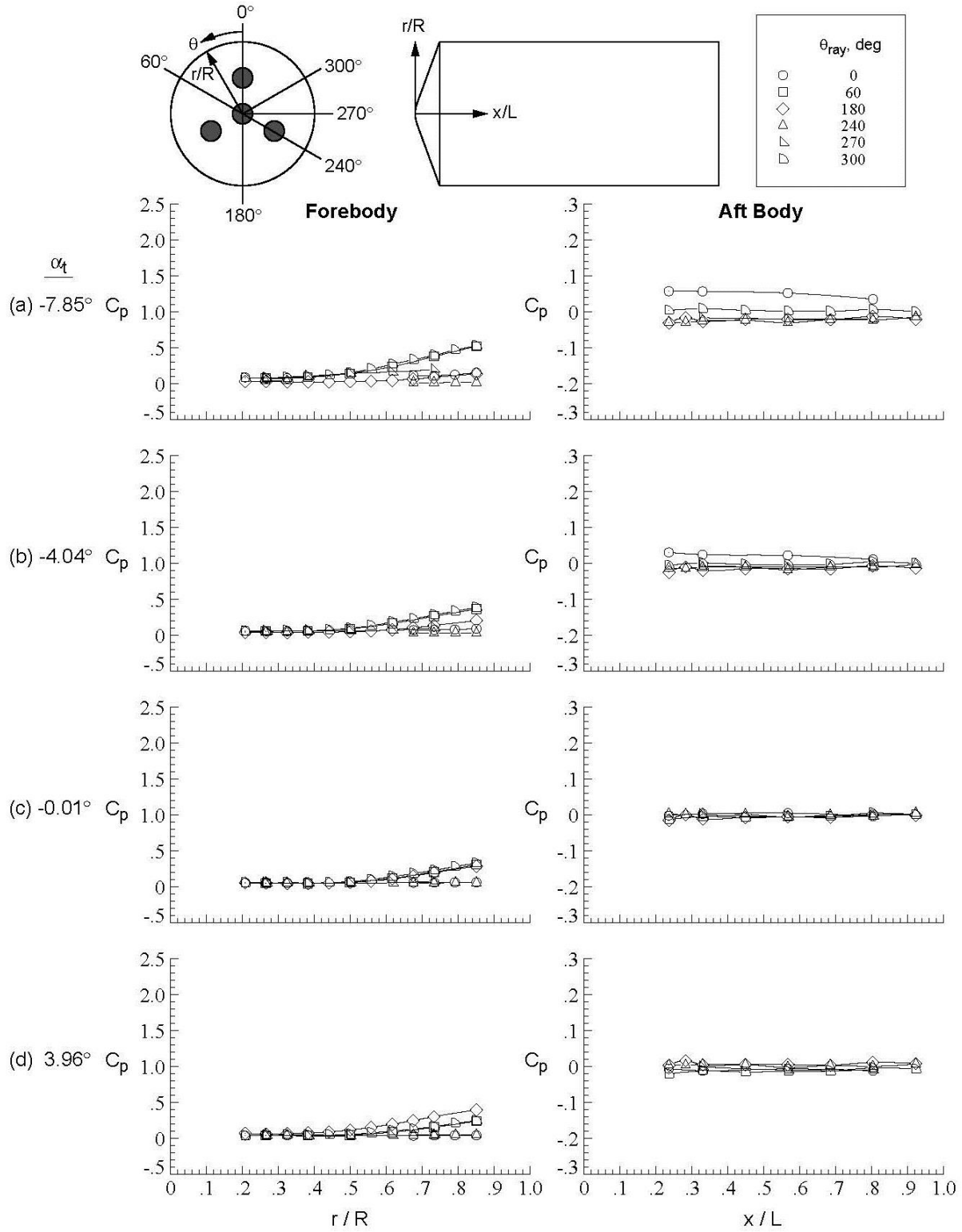

Figure D-239. Quad-nozzle configuration, Run 305, M_∞ = 3.5, Re_∞ = 1.0x10^6/ft, ϕ = −0.03°, X_S = 40.16 in, Y_S = 0.00 in, C_T = 0.90.

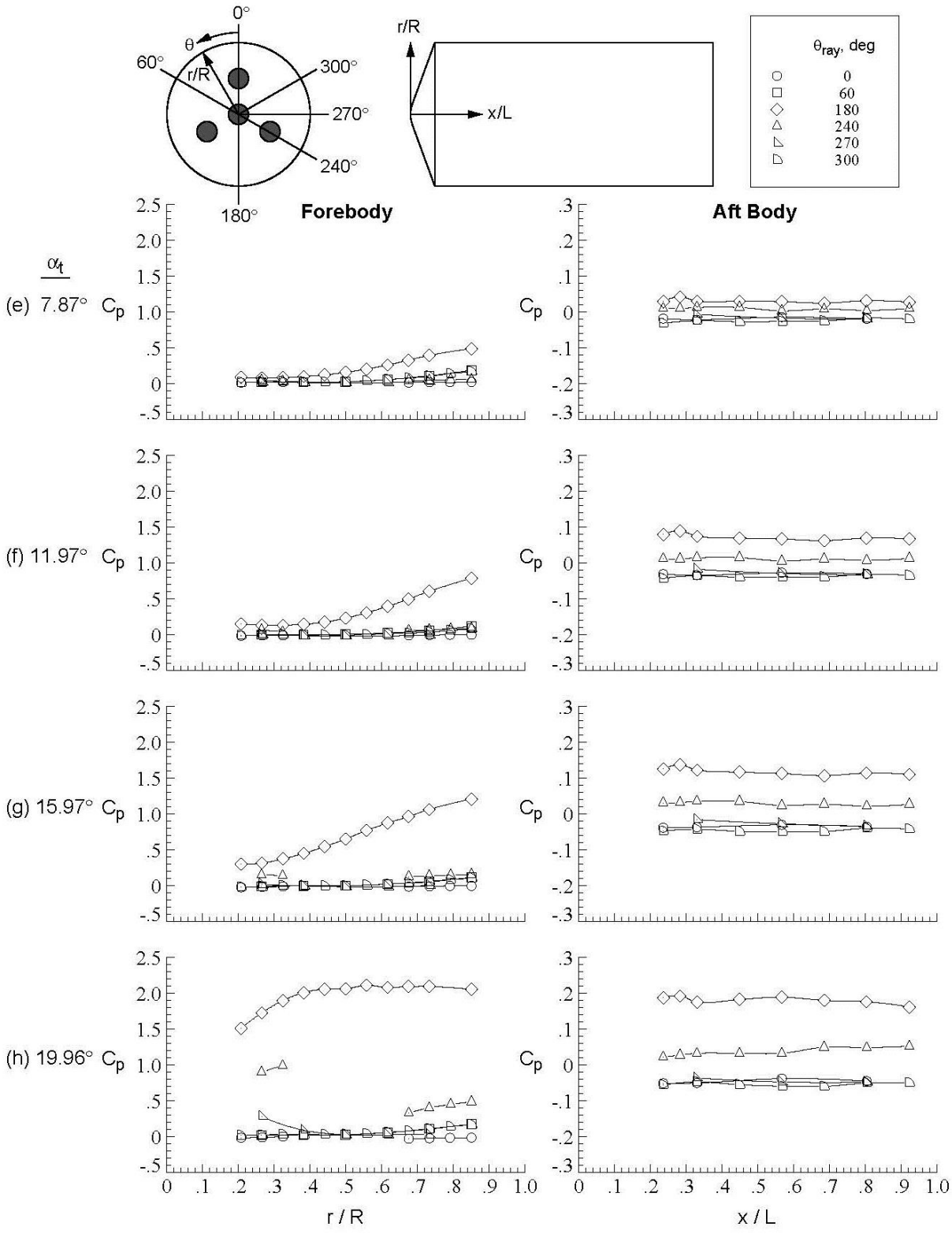

Figure D-239.Concluded.

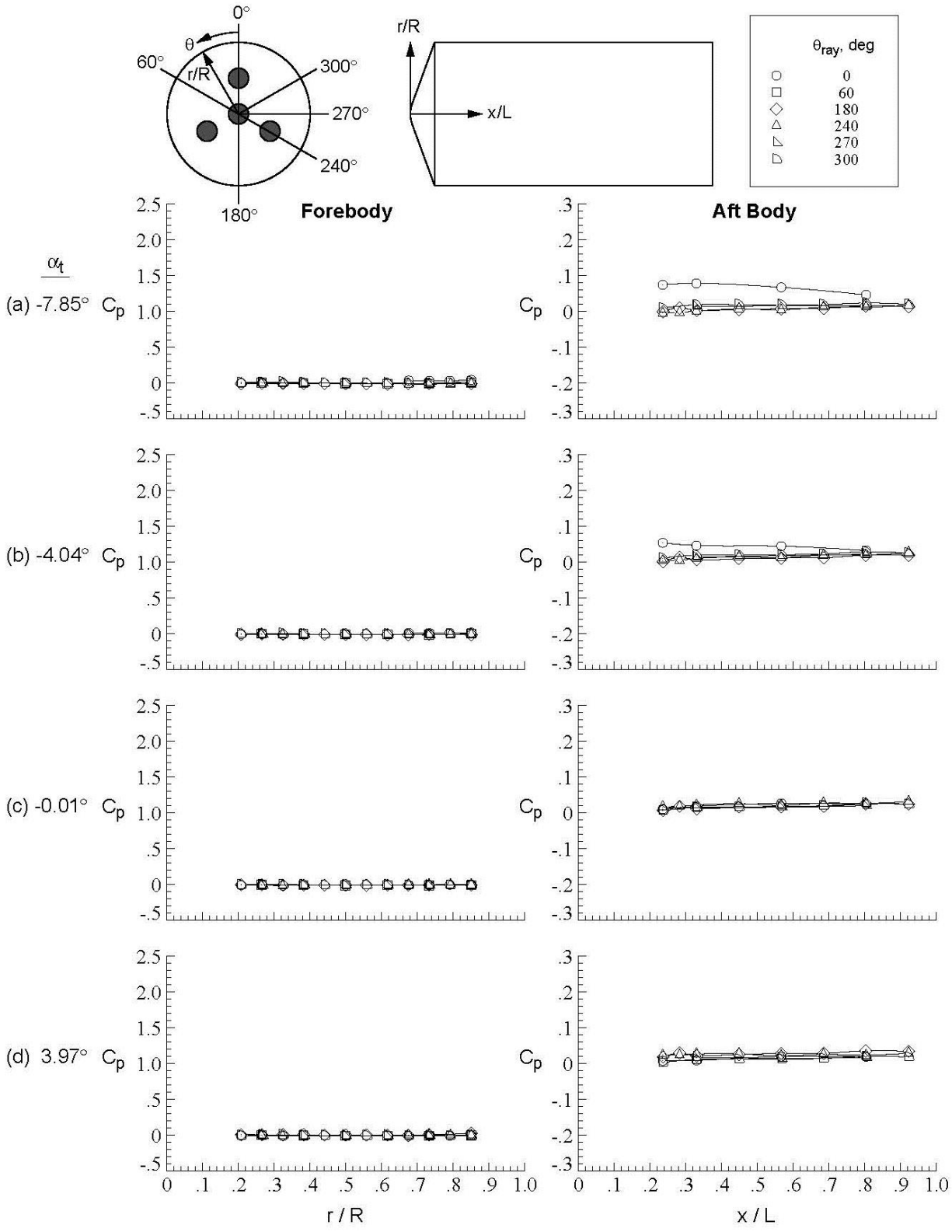

Figure D-240. Quad-nozzle configuration, Run 307, M_∞ = 4.6, Re_∞ = 1.5x10^7/ft, ϕ = 0.05°, X_S = 40.17 in, Y_S = 0.00 in, C_T = 1.92.

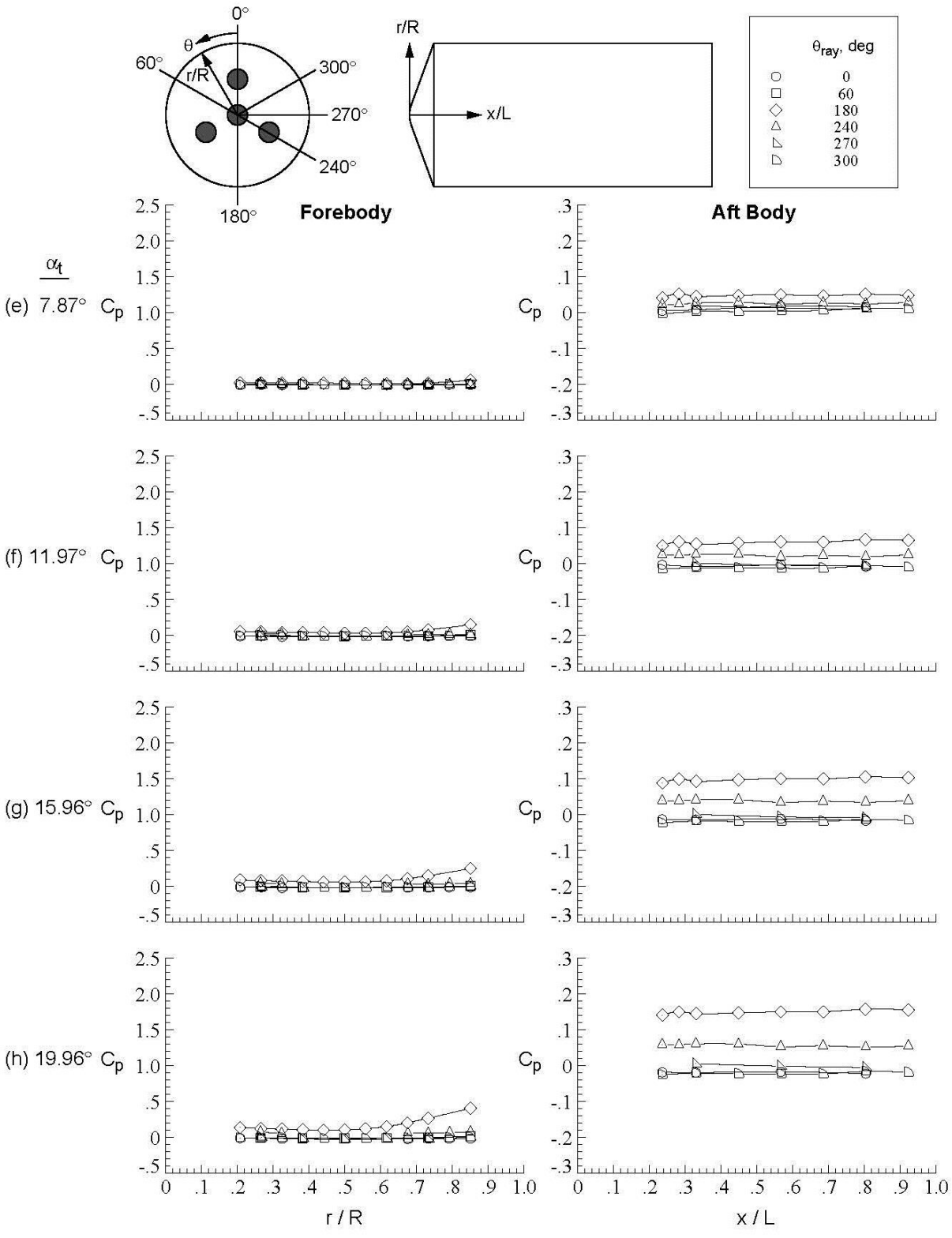

Figure D-240.Concluded.

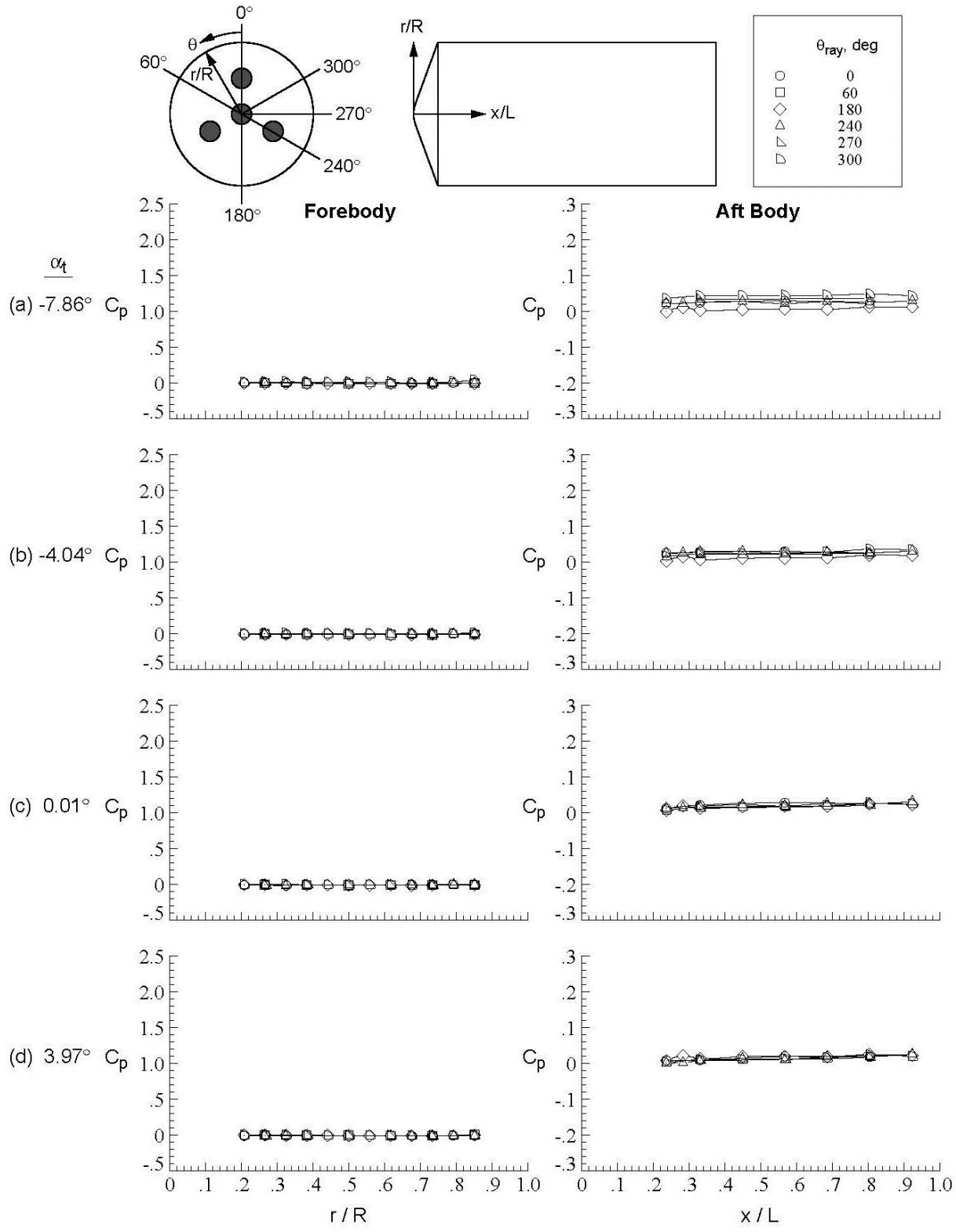

Figure D-241. Quad-nozzle configuration, Run 309, M_∞ = 4.6, Re_∞ = 1.5x10^7/ft, ϕ = 59.88°, X_S = 40.17 in, Y_S = 0.00 in, C_T = 1.92.

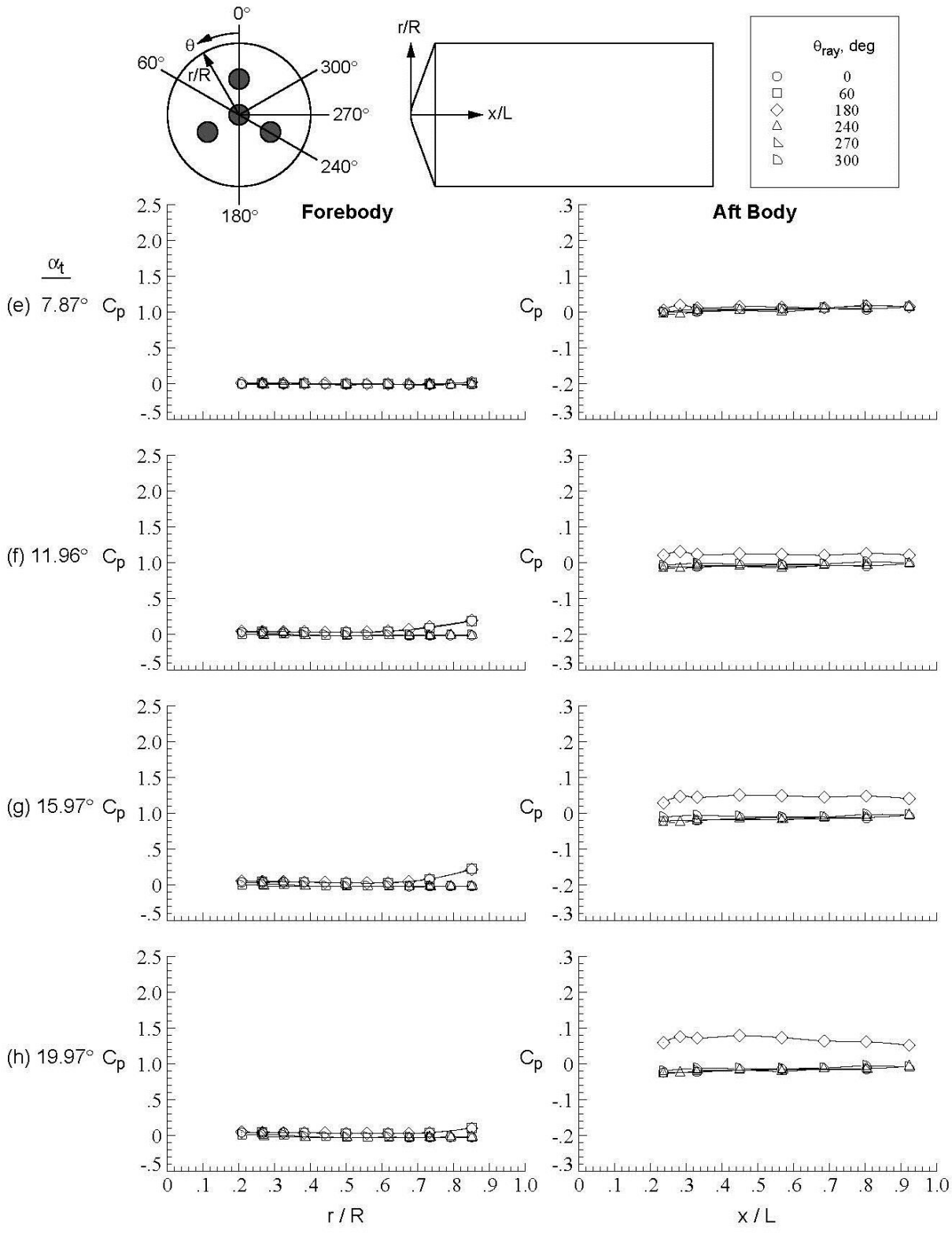

Figure D-241.Concluded.

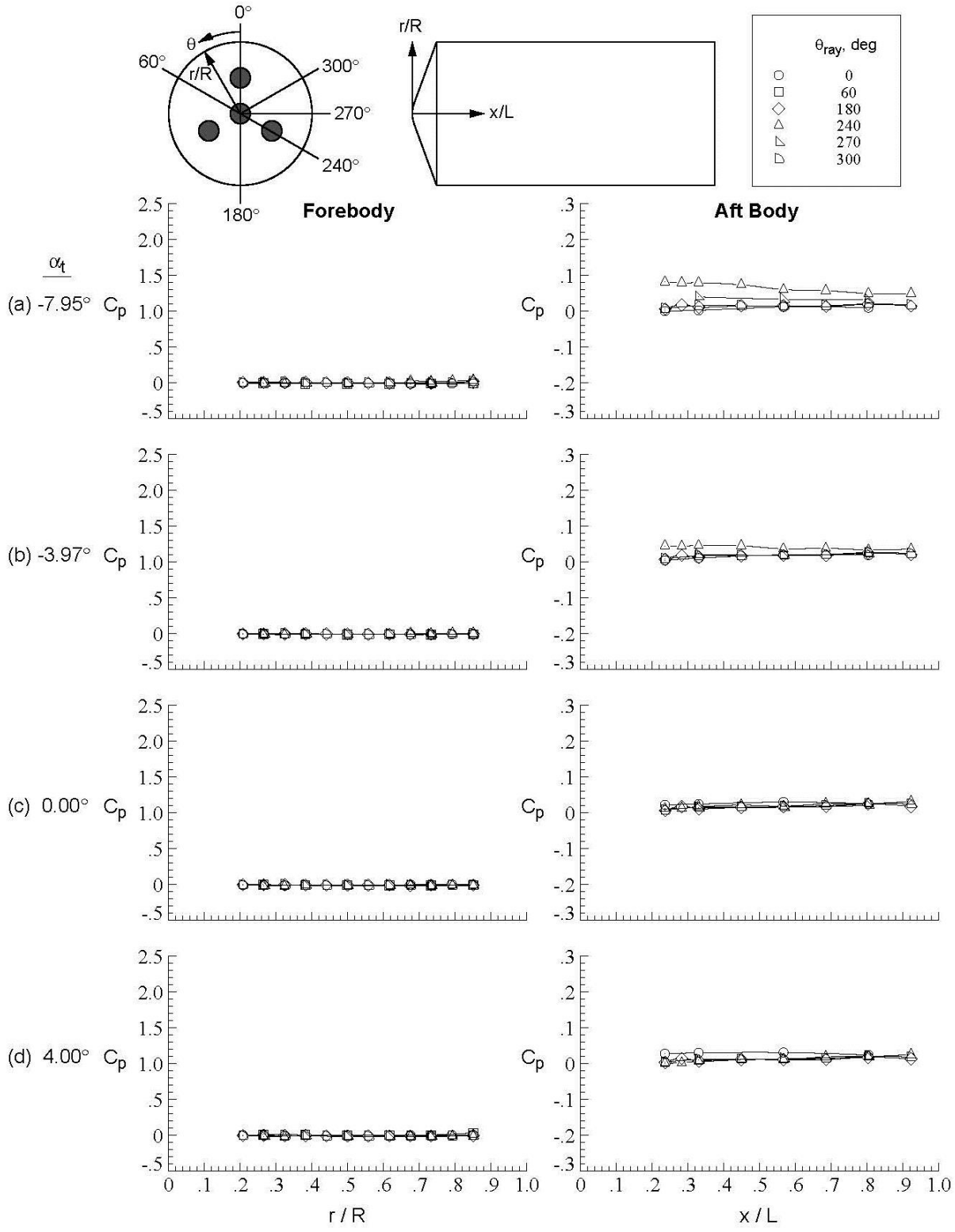

Figure D-242. Quad-nozzle configuration, Run 310, M_∞ = 4.6, Re_∞ = 1.5x10^7/ft, ϕ = 120.02°, X_S = 40.17 in, Y_S = 0.00 in, C_T = 1.92.

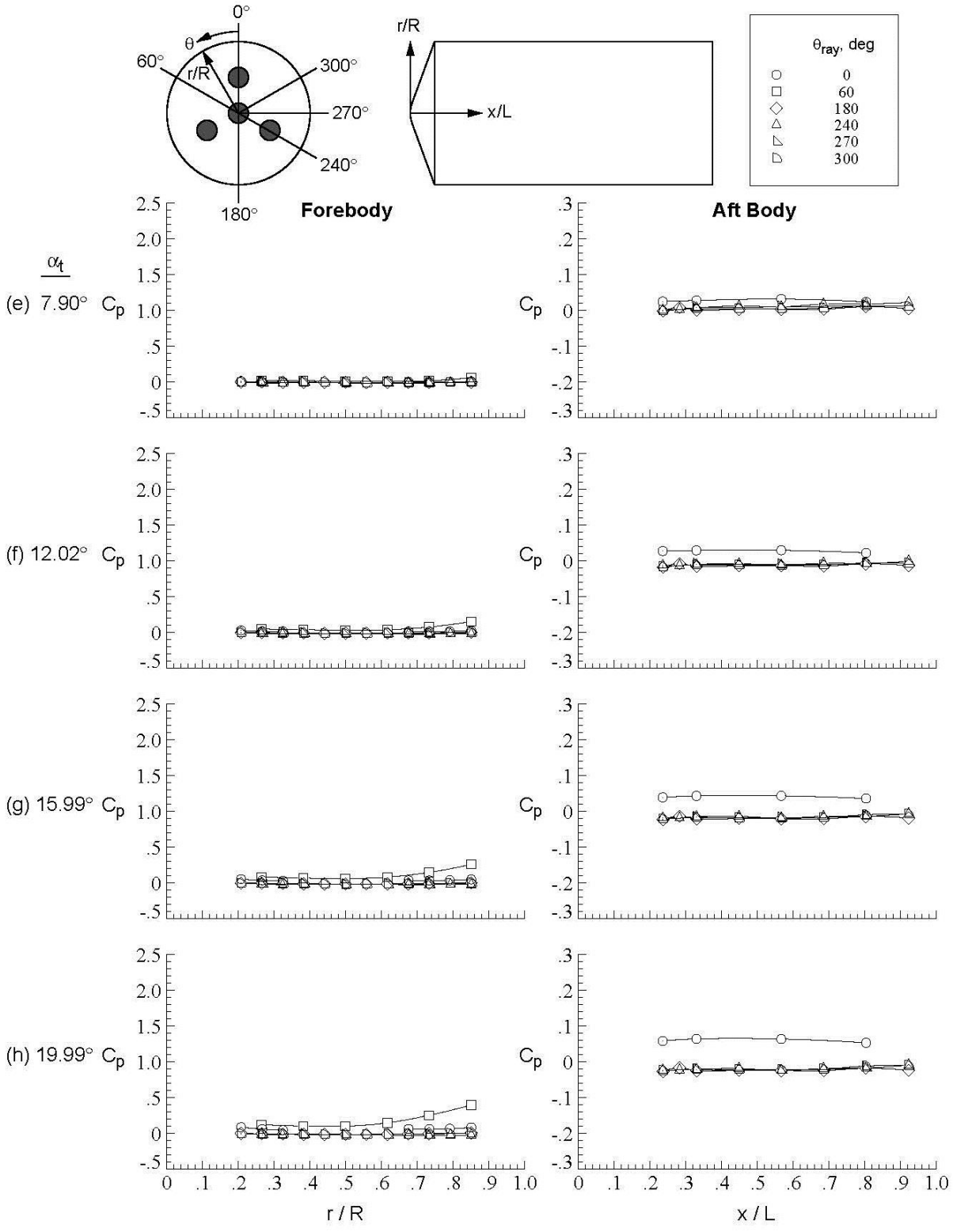

Figure D-242.Concluded.

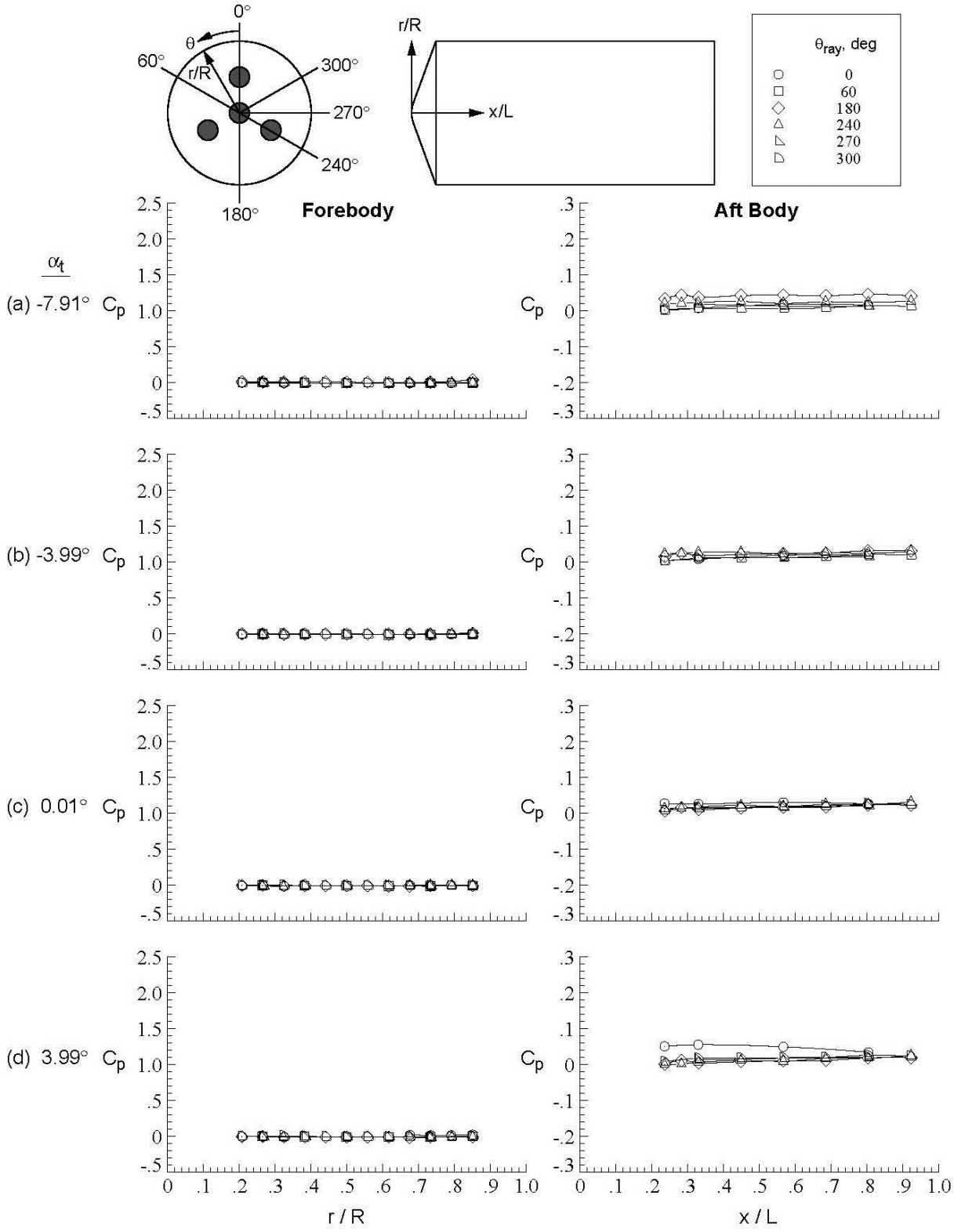

Figure D-243. Quad-nozzle configuration, Run 311, M_∞ = 4.6, Re_∞ = 1.5x10^7/ft, ϕ = −179.99°, X_S = 40.17 in, Y_S = 0.00 in, C_T = 1.93.

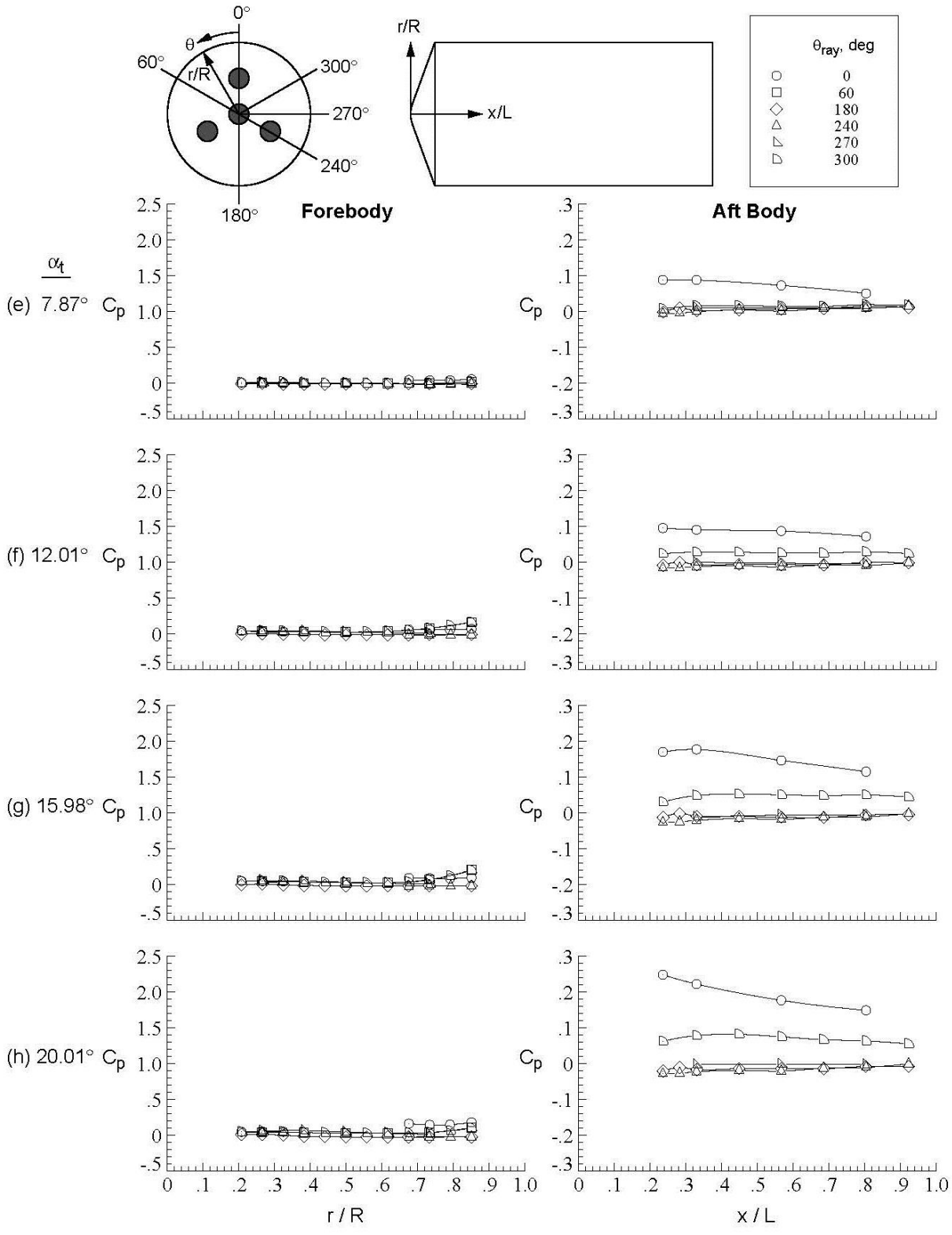

Figure D-243.Concluded.

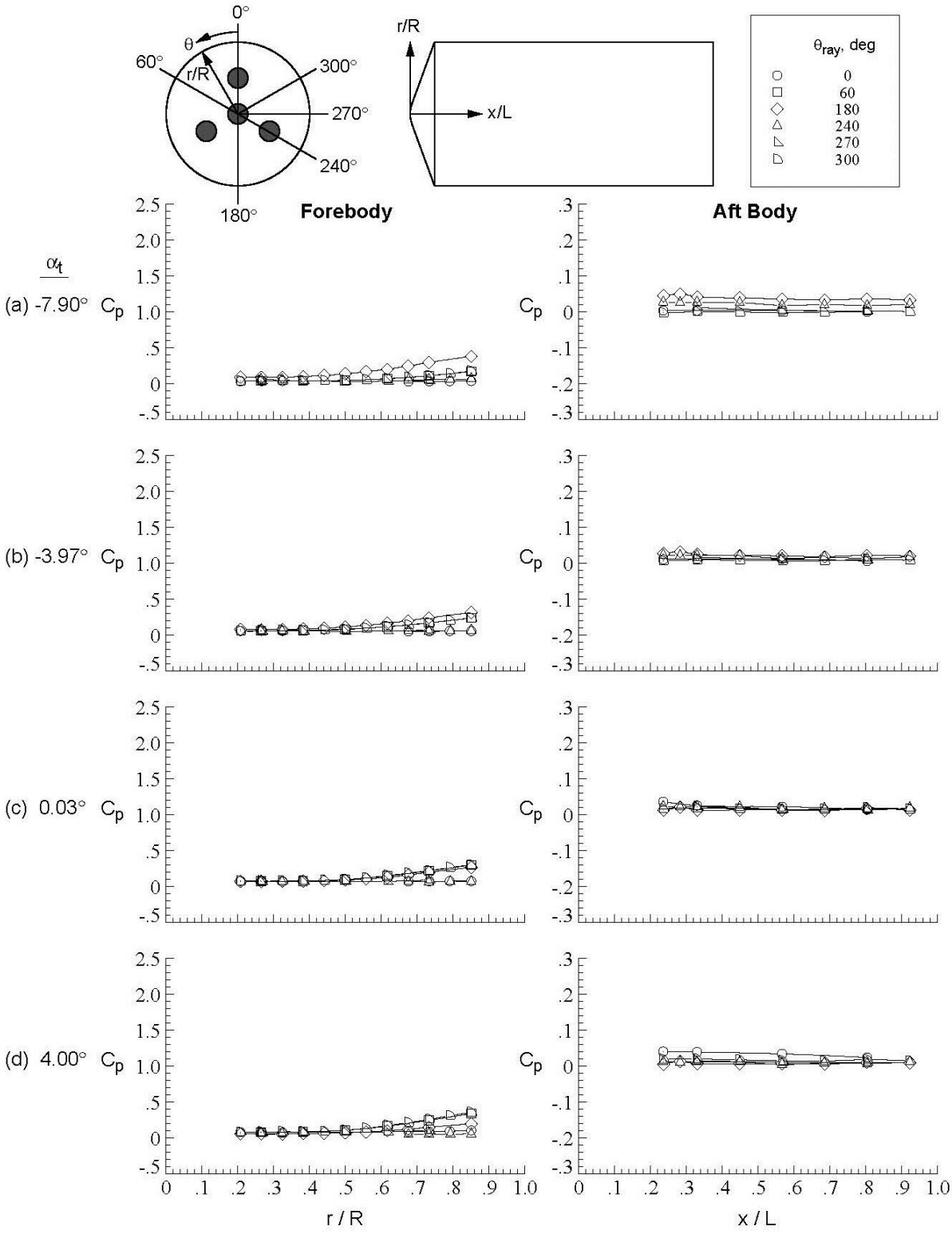

Figure D-244. Quad-nozzle configuration, Run 312, M_∞ = 4.6, Re_∞ = 1.5x10^7/ft, ϕ = −179.97°, X_S = 40.17 in, Y_S = 0.00 in, C_T = 0.92.

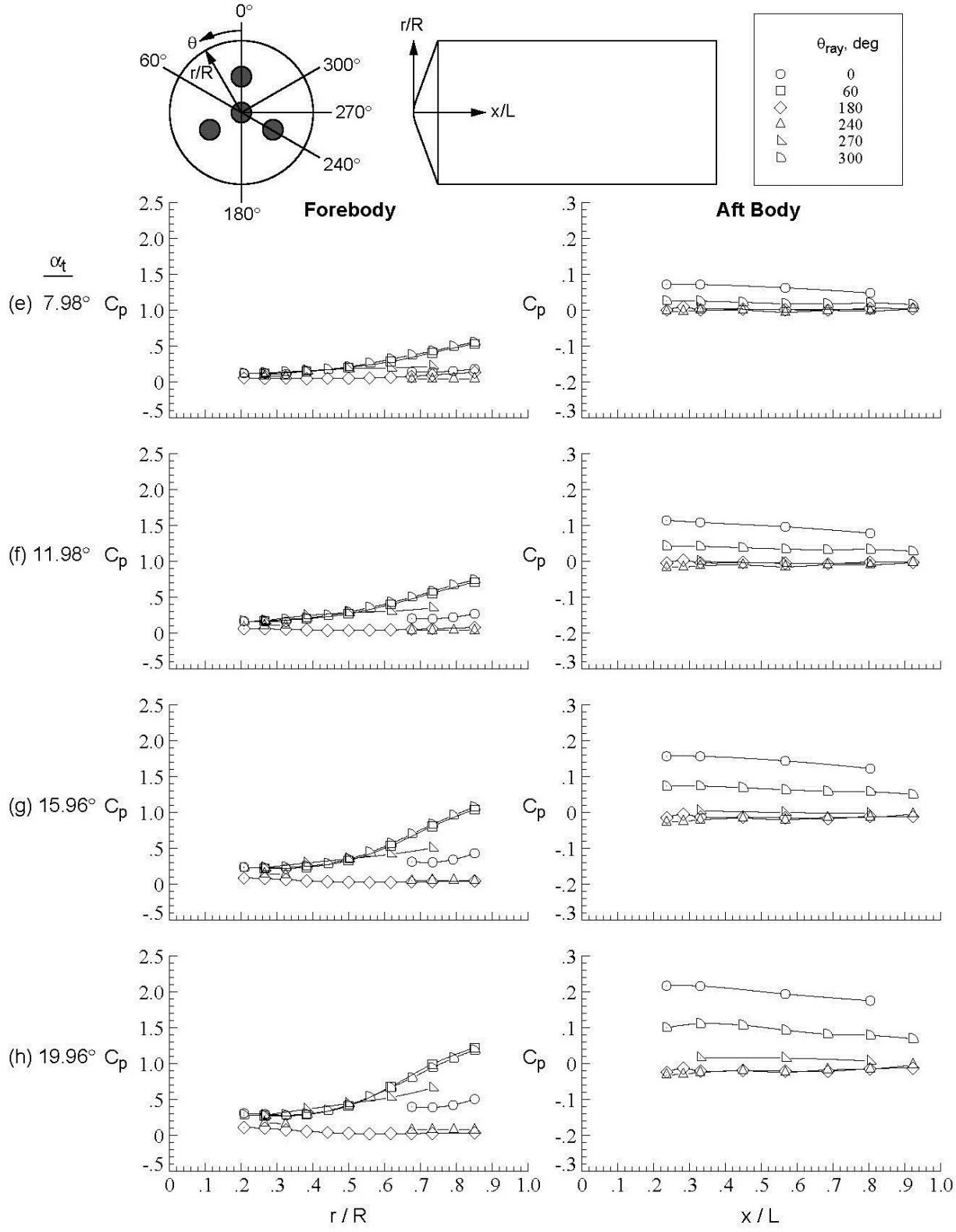

Figure D-244.Concluded.

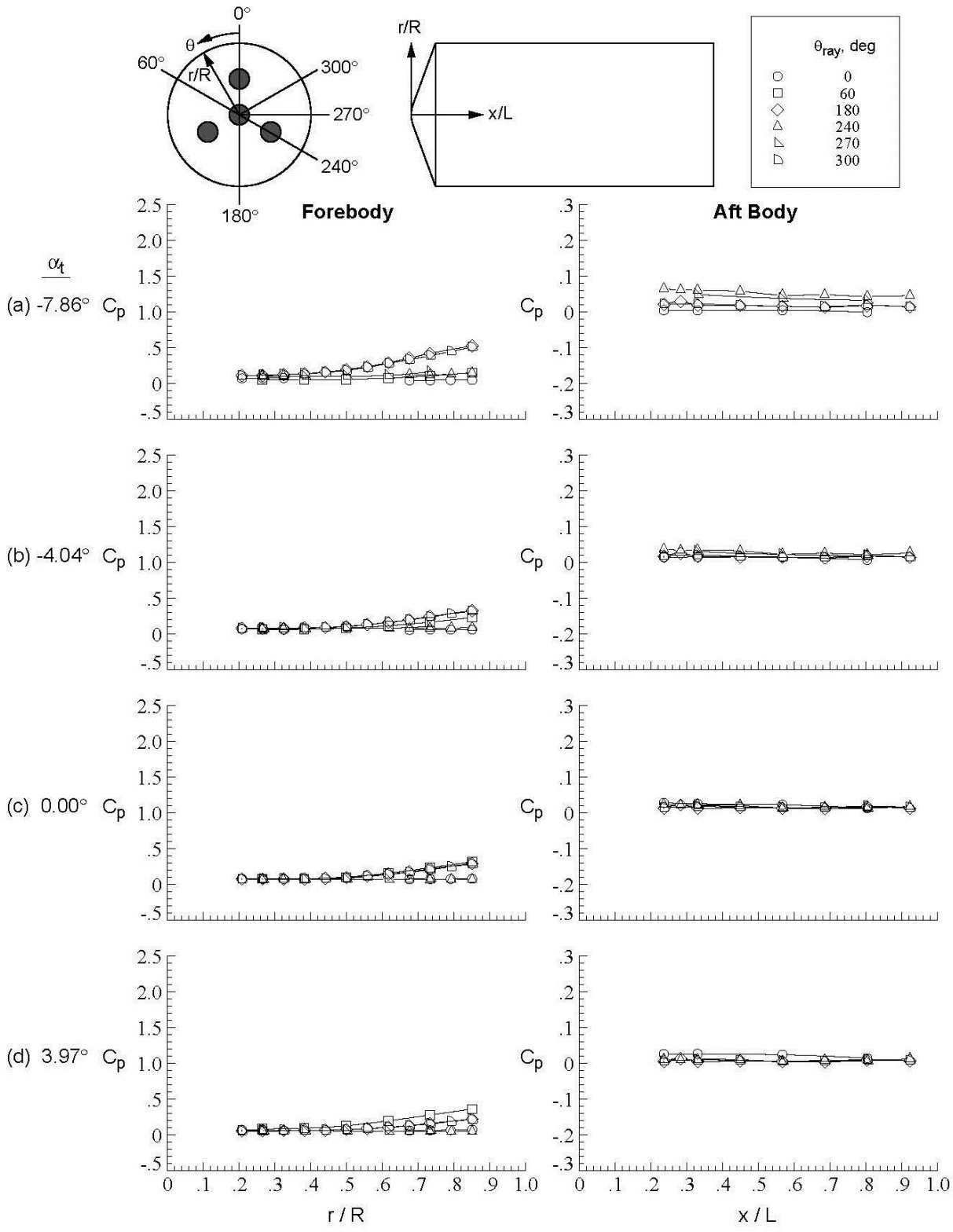

Figure D-245. Quad-nozzle configuration, Run 313, M_∞ = 4.6, Re_∞ = 1.5x10^7/ft, ϕ = 120.04°, X_S = 40.17 in, Y_S = 0.00 in, C_T = 0.92.

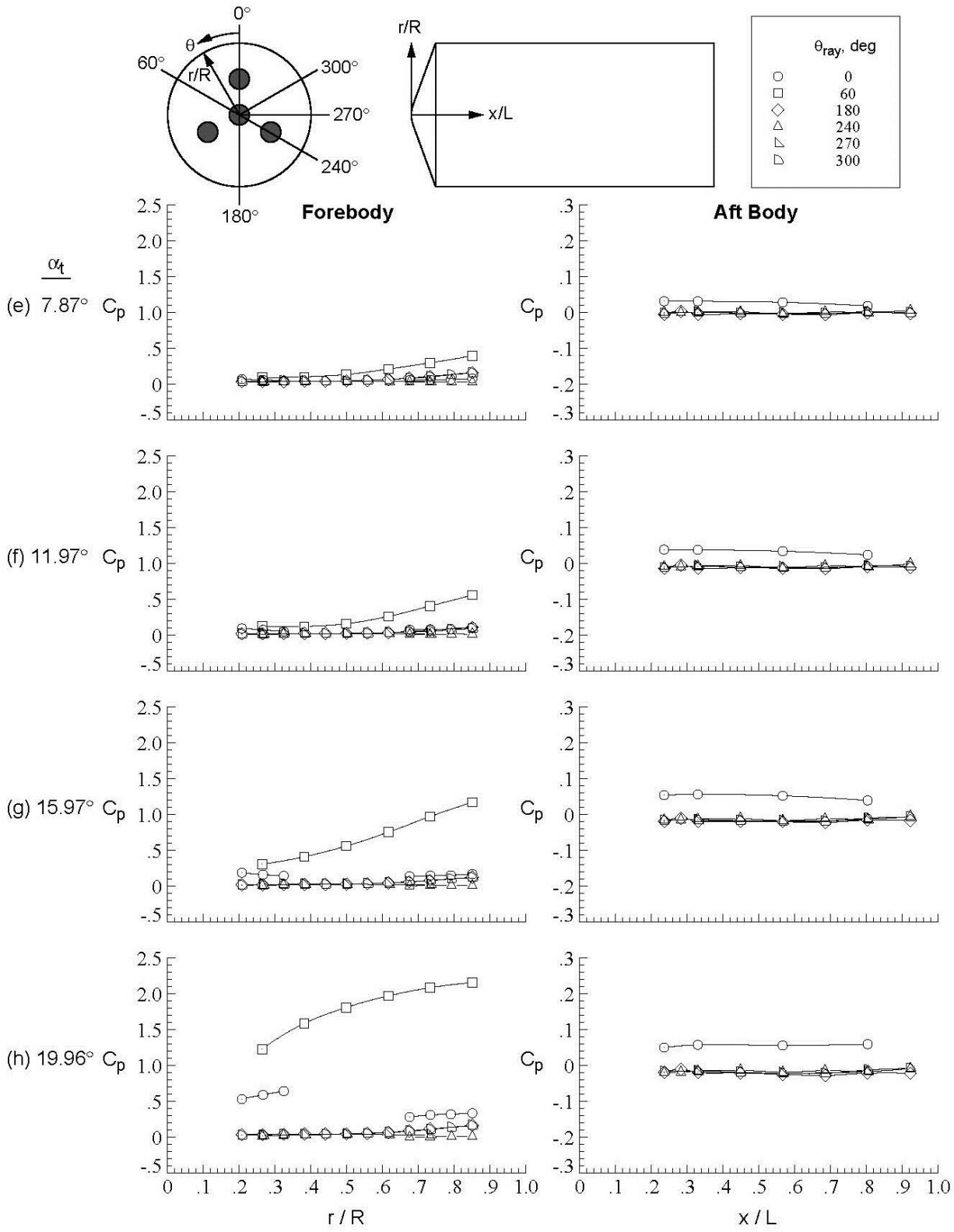

Figure D-245.Concluded.

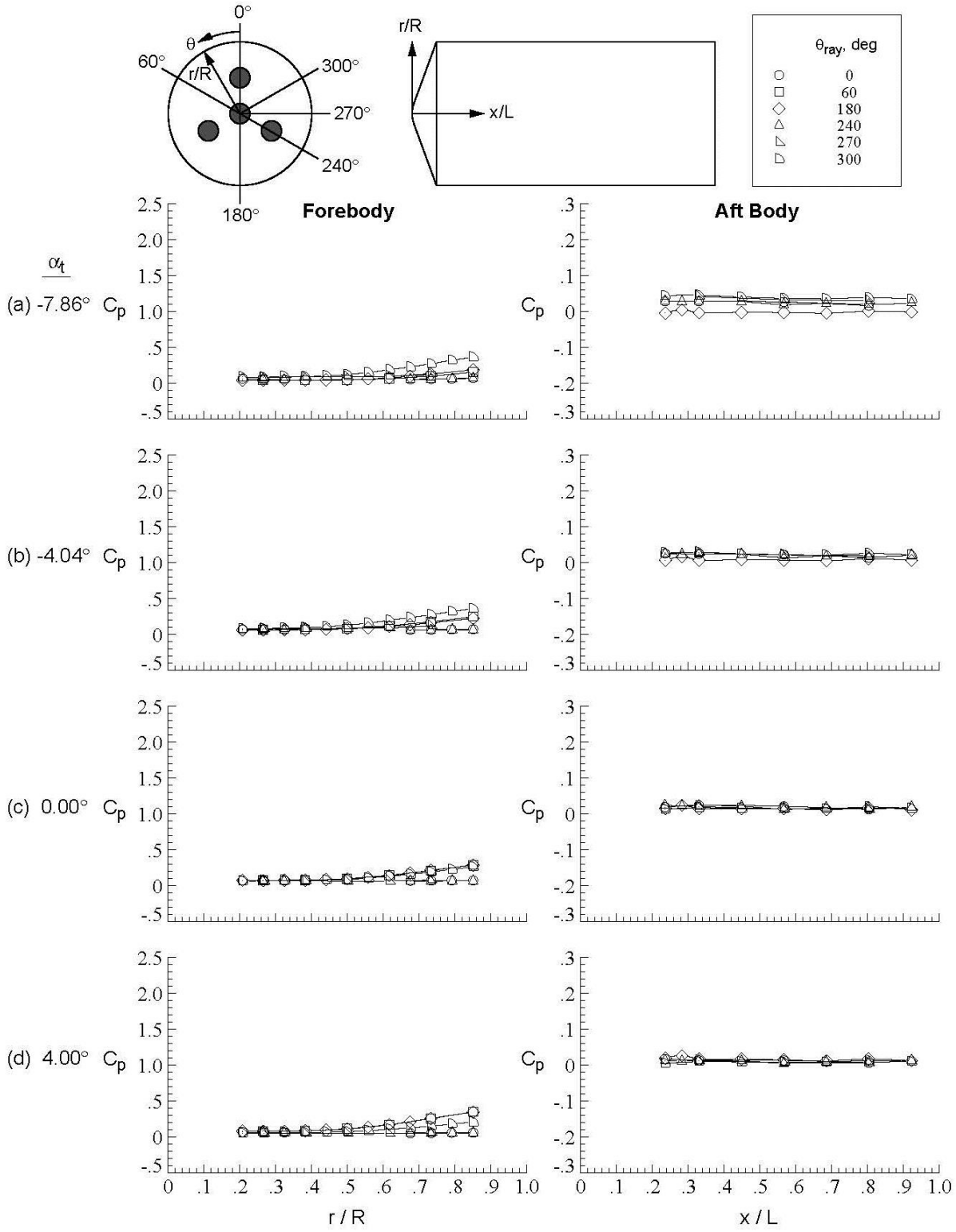

Figure D-246. Quad-nozzle configuration, Run 314, M_∞ = 4.6, Re_∞ = 1.5x10^7/ft, ϕ = 59.98°, X_S = 40.17 in, Y_S = 0.00 in, C_T = 0.92.

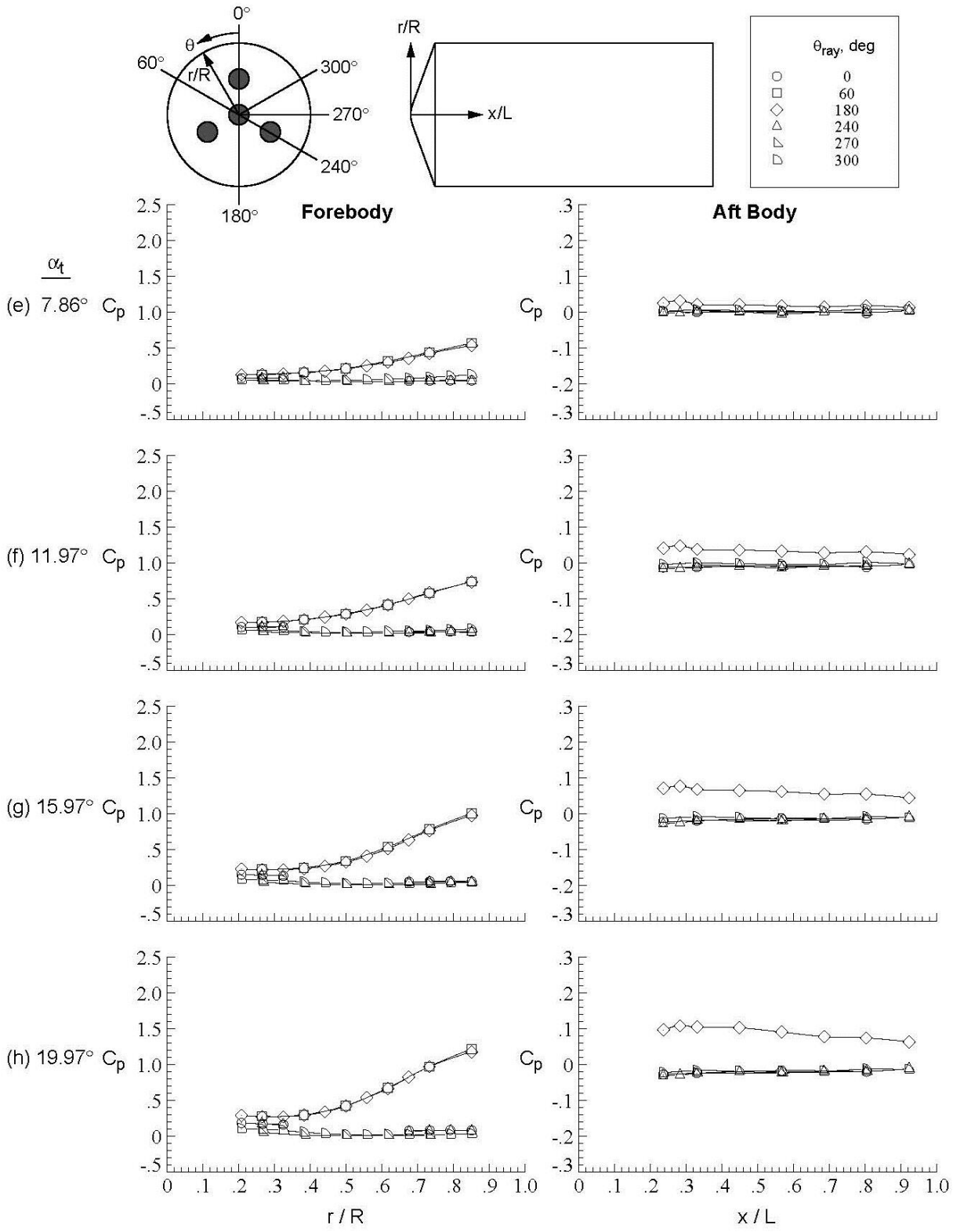

Figure D-246.Concluded.

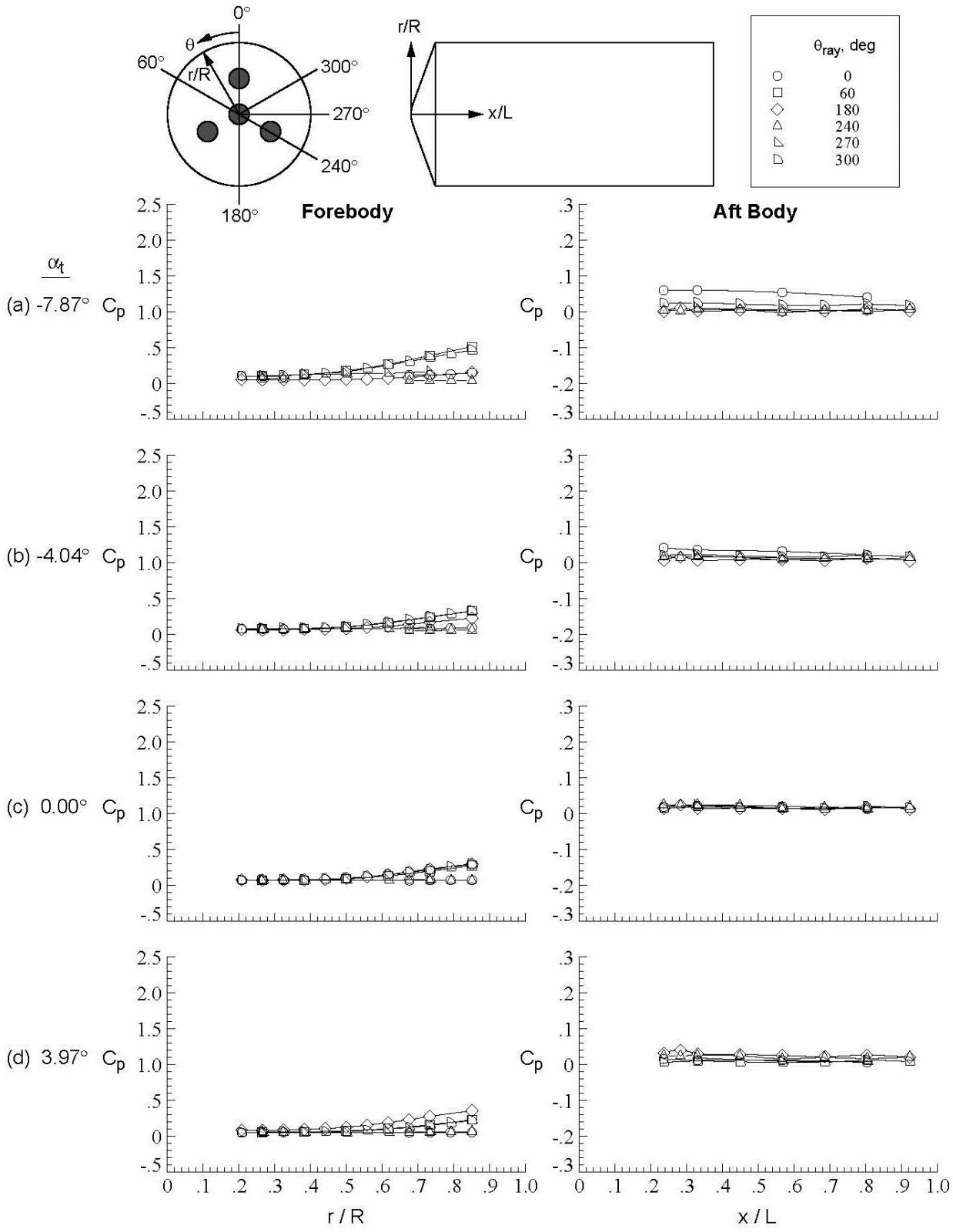

Figure D-247. Quad-nozzle configuration, Run 315, M_∞ = 4.6, Re_∞ = 1.5x10^7/ft, ϕ = 0.05°, X_S = 40.17 in, Y_S = 0.00 in, C_T = 0.91.

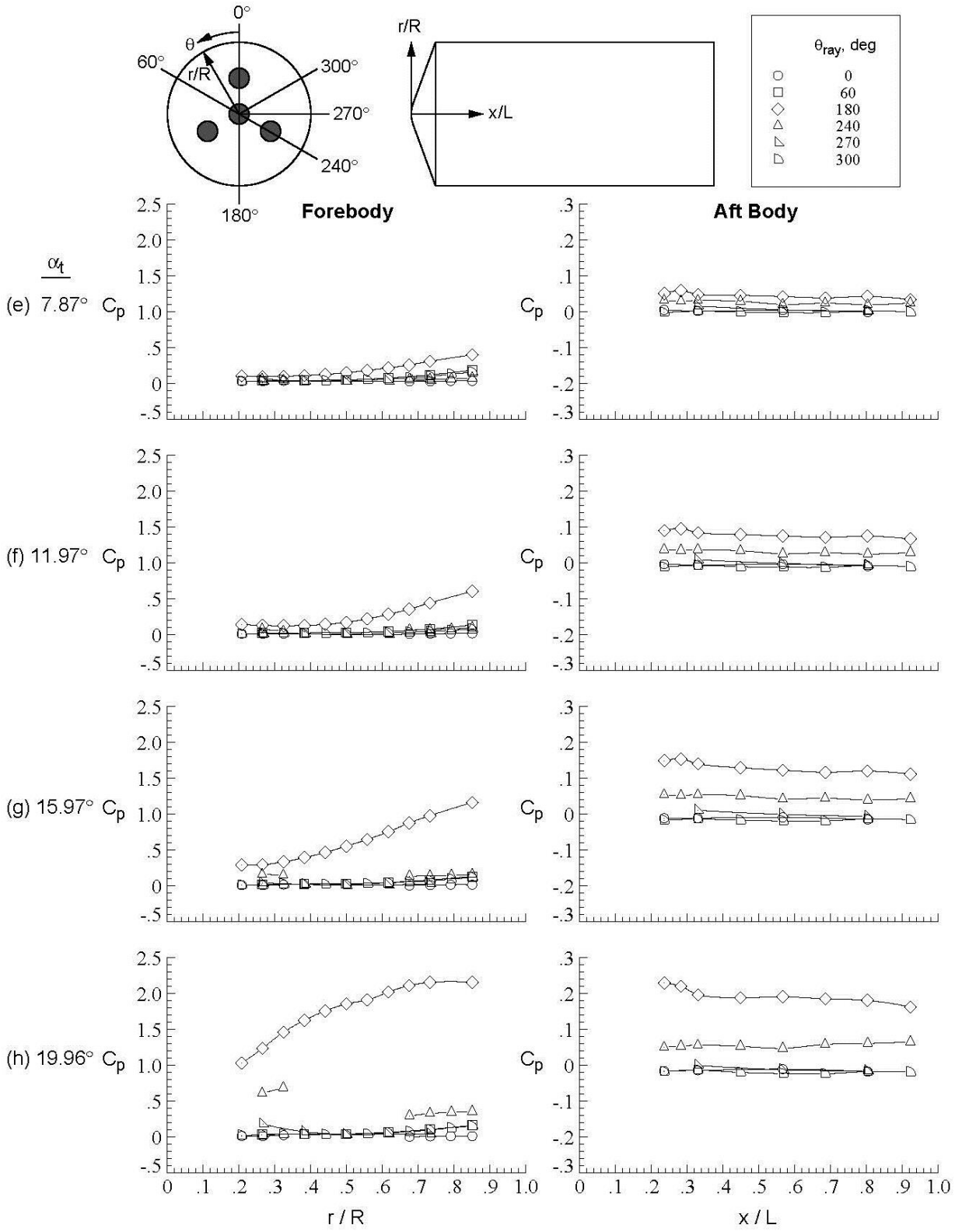

Figure D-247. Concluded.

APPENDIX E
PRESSURE CONTOUR PLOTS

The pressure data was also used to develop contour maps of the forebody for every test point within a run. The contour maps were generated with MatLab based on 2D interpolation/extrapolation of the test data, using the *griddata* function assuming a biharmonic spline fit on a 2D polar grid. Known faulty ports were not utilized during the mapping process. Mapping the data in this manner was helpful for double-checking the list of faulty ports as part of the data analysis process. The contour maps could also be used to calculate a rough-order force coefficient for comparison against computational results if needed. The following pages, one per run, provide the resulting contour maps for each unique test point (redundant points were omitted to reduce the page count). The plots were allowed to auto scale so that the global trends could be observed. Direct comparisons between runs can best be accomplished using the line plots in the previous appendix.

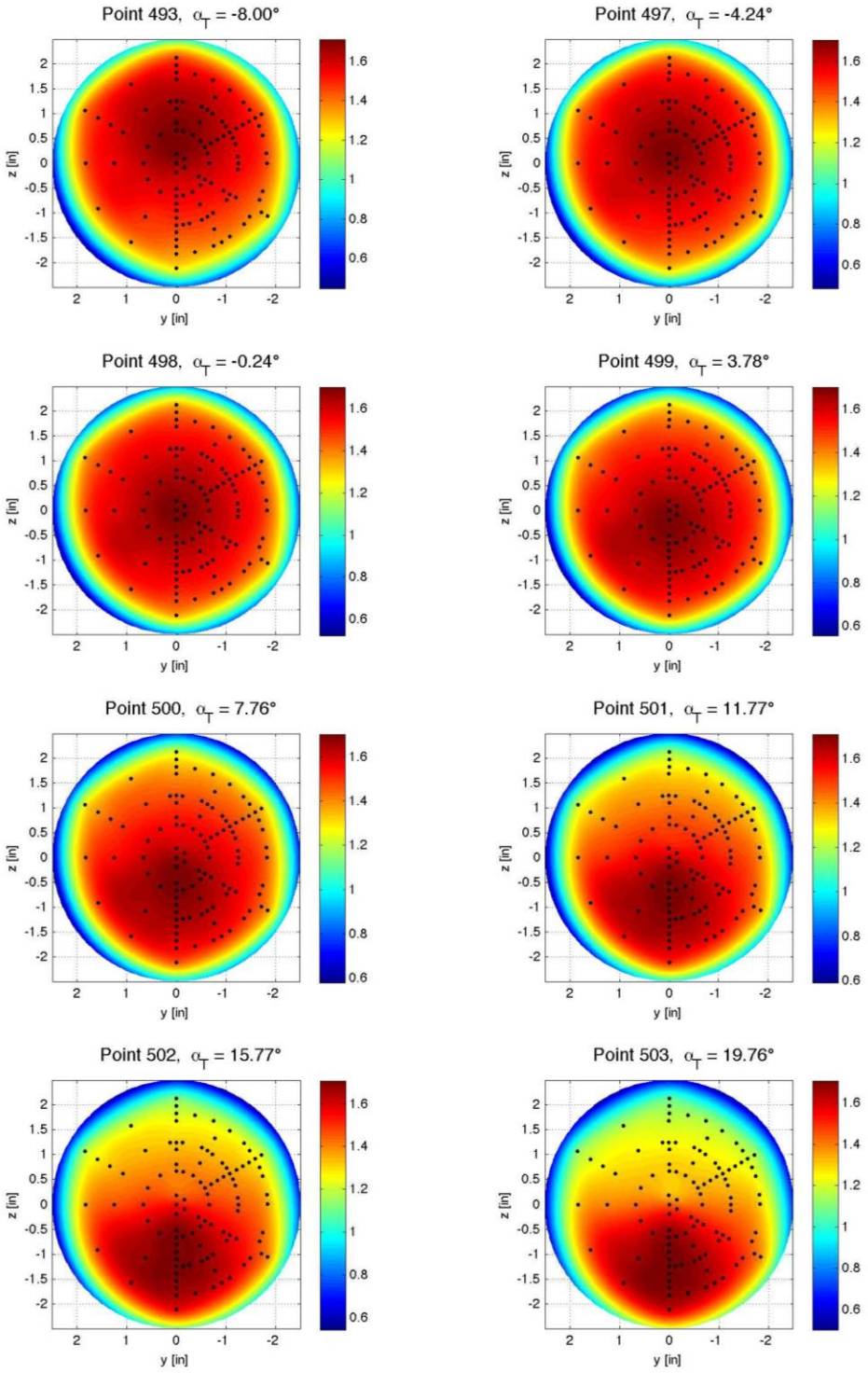

Figure E-1. Baseline configuration, Run 013, $M\infty$ = 2.4, Re_∞ = 1.0x10^6/ft, ϕ = 0.03°, X_S = 25.16 in, Y_S = 0.04 in, C_T = 0.00.

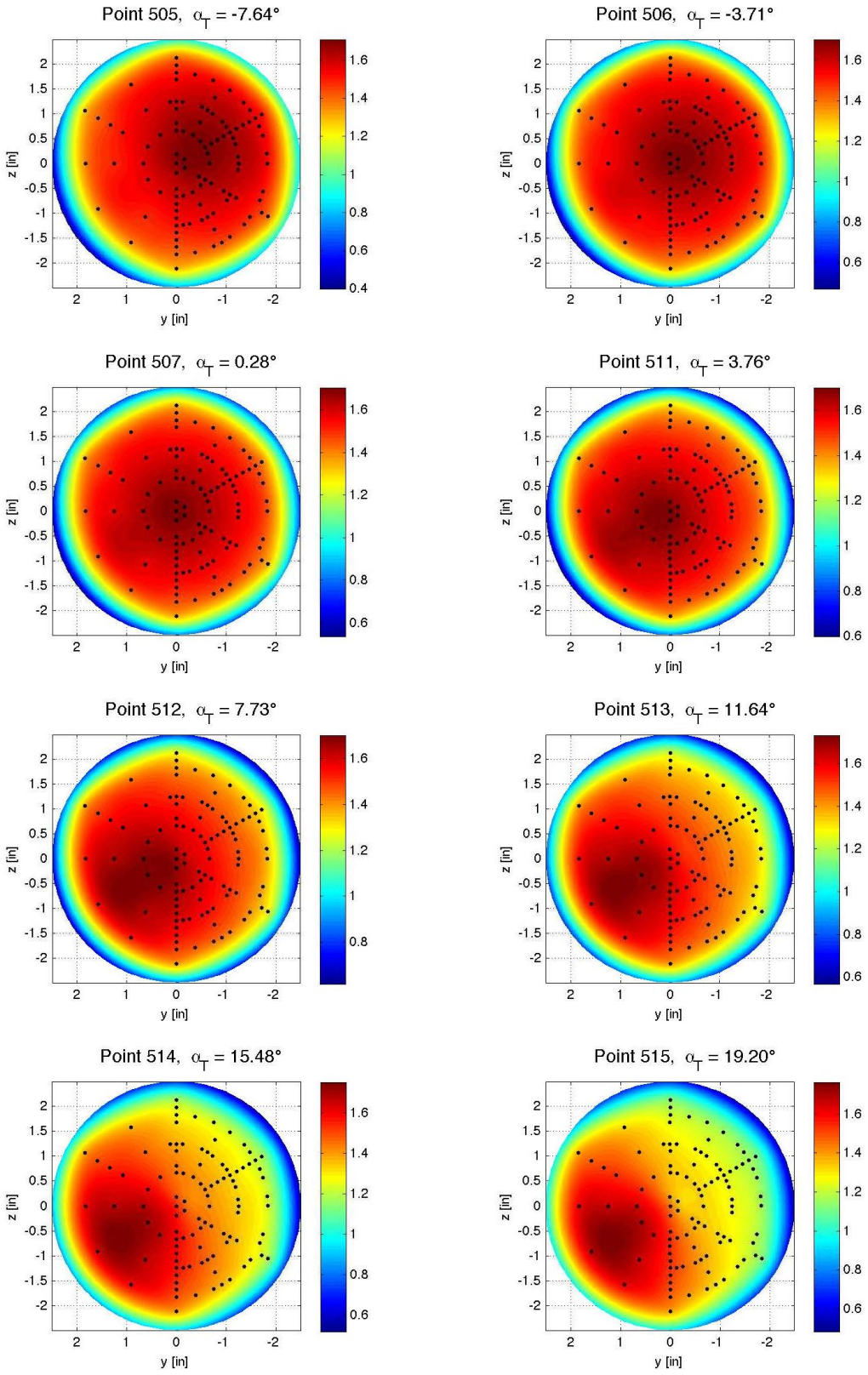

Figure E-2. Baseline configuration, Run 014, $M\infty$ = 2.4, Re_∞ = 1.0x10^6/ft, ϕ = 60.02°, X_S = 25.16 in, Y_S = 0.00 in, C_T = 0.00.

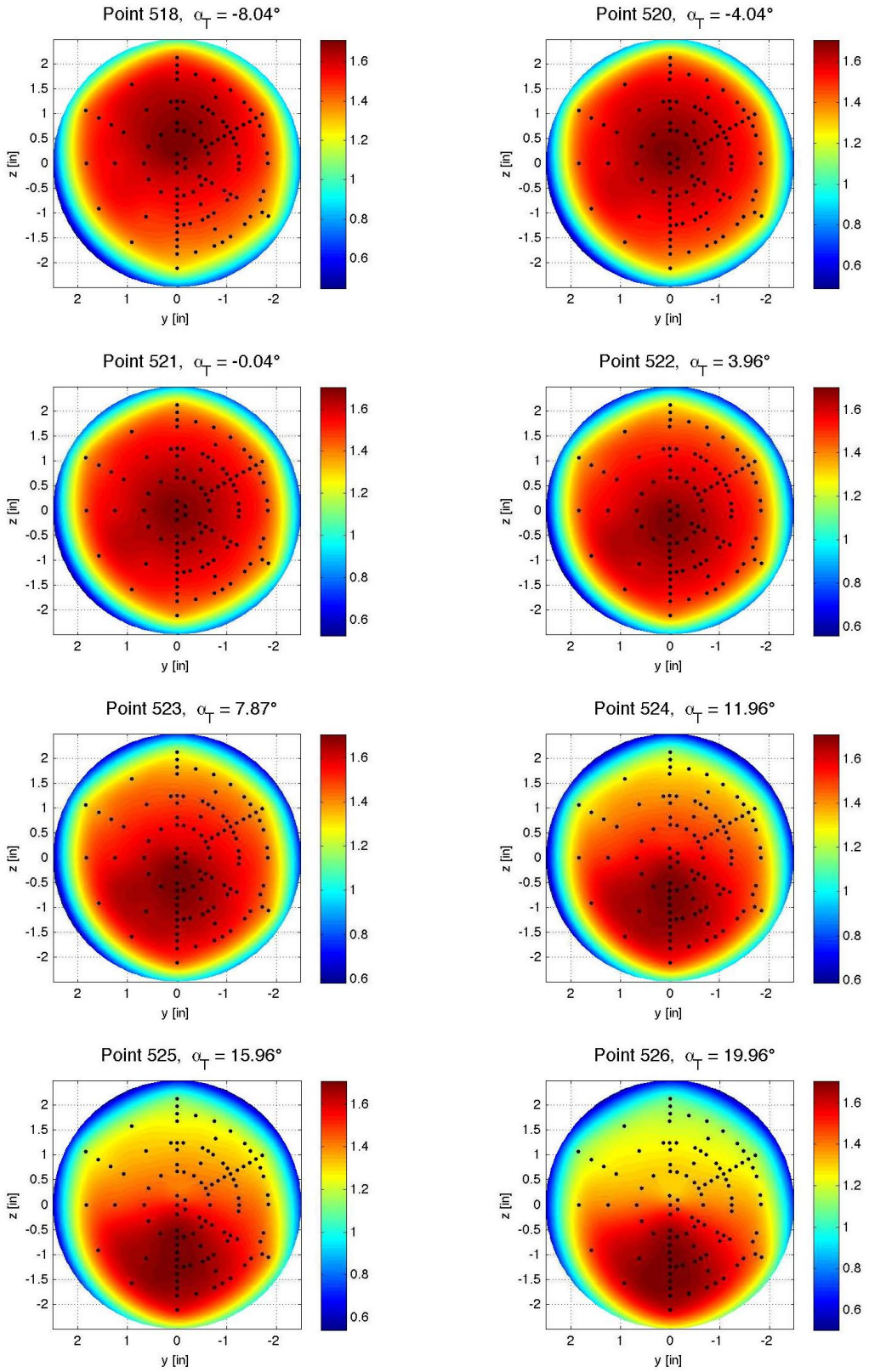

Figure E-3. Baseline configuration, Run 016, $M\infty$ = 2.4, Re_∞ = 1.0x10^6/ft, ϕ = 0.05°, X_S = 25.16 in, Y_S = 0.00 in, C_T = 0.00.

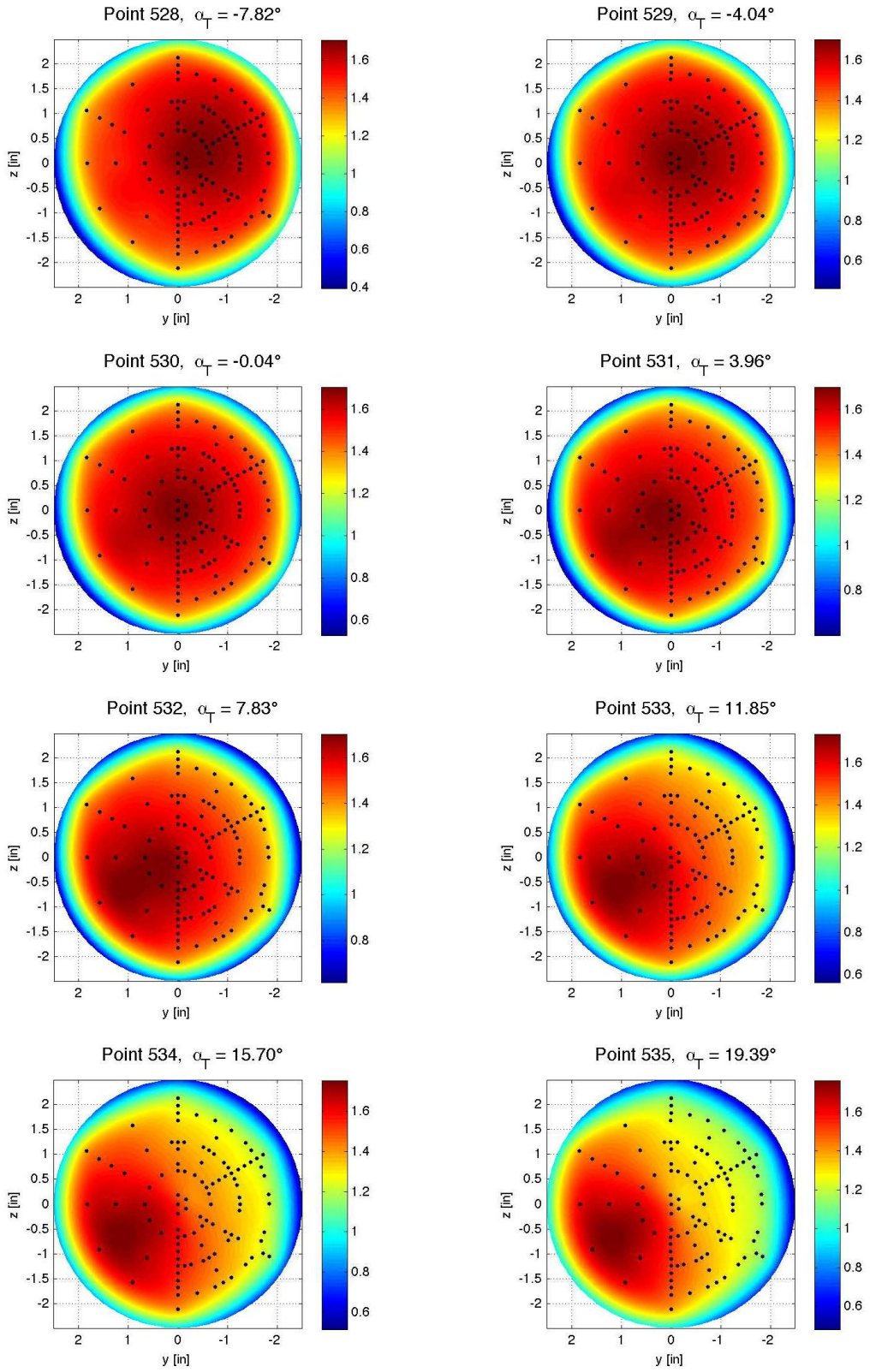

Figure E-4. Baseline configuration, Run 017, $M\infty$ = 2.4, Re_∞ = 1.0x10^6/ft, ϕ = 59.94°, X_S = 25.16 in, Y_S = 0.00 in, C_T = 0.00.

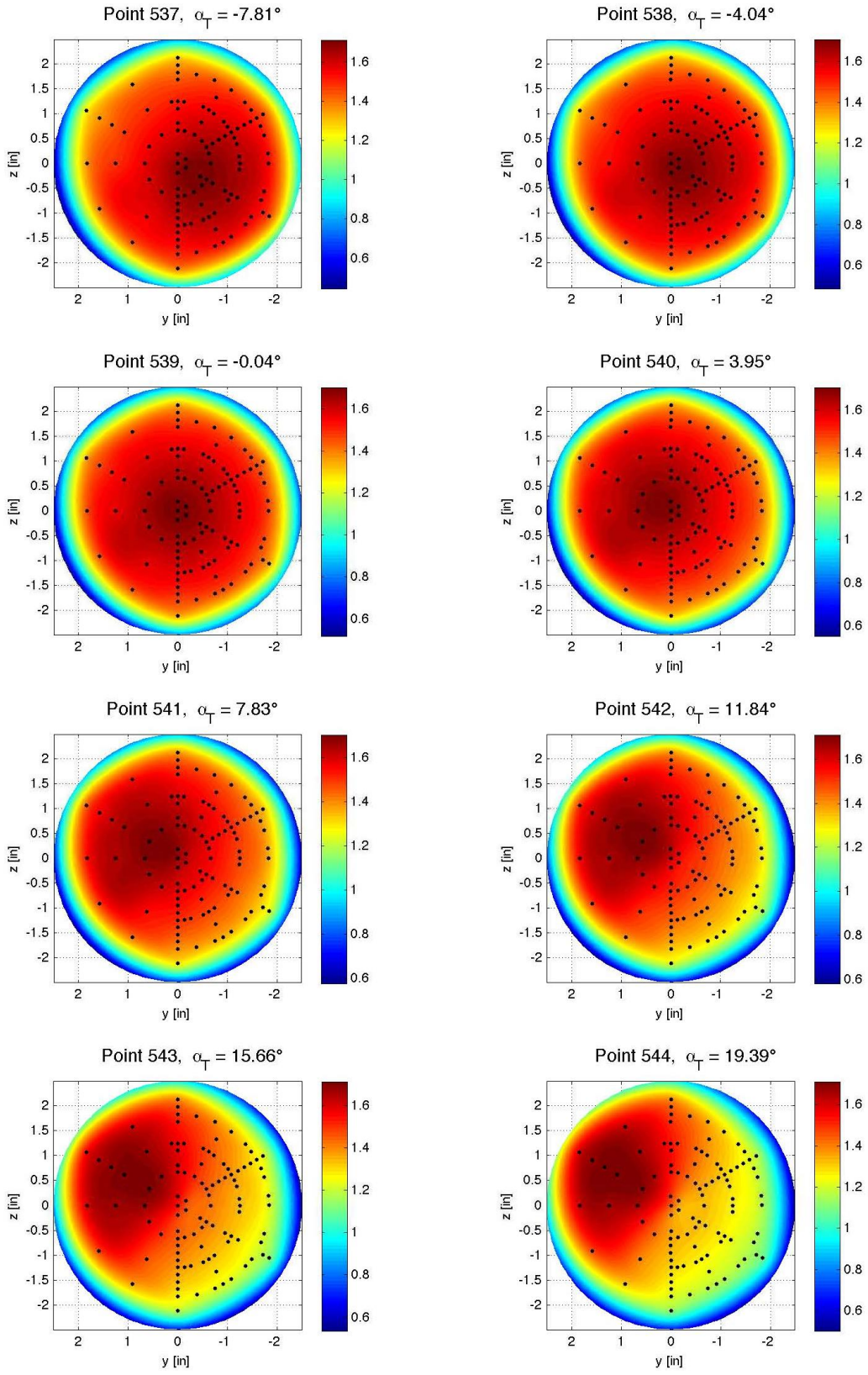

Figure E-5. Baseline configuration, Run 018, $M\infty$ = 2.4, Re_∞ = 1.0x10^6/ft, ϕ = 119.90°, X_S = 25.16 in, Y_S = 0.00 in, C_T = 0.00.

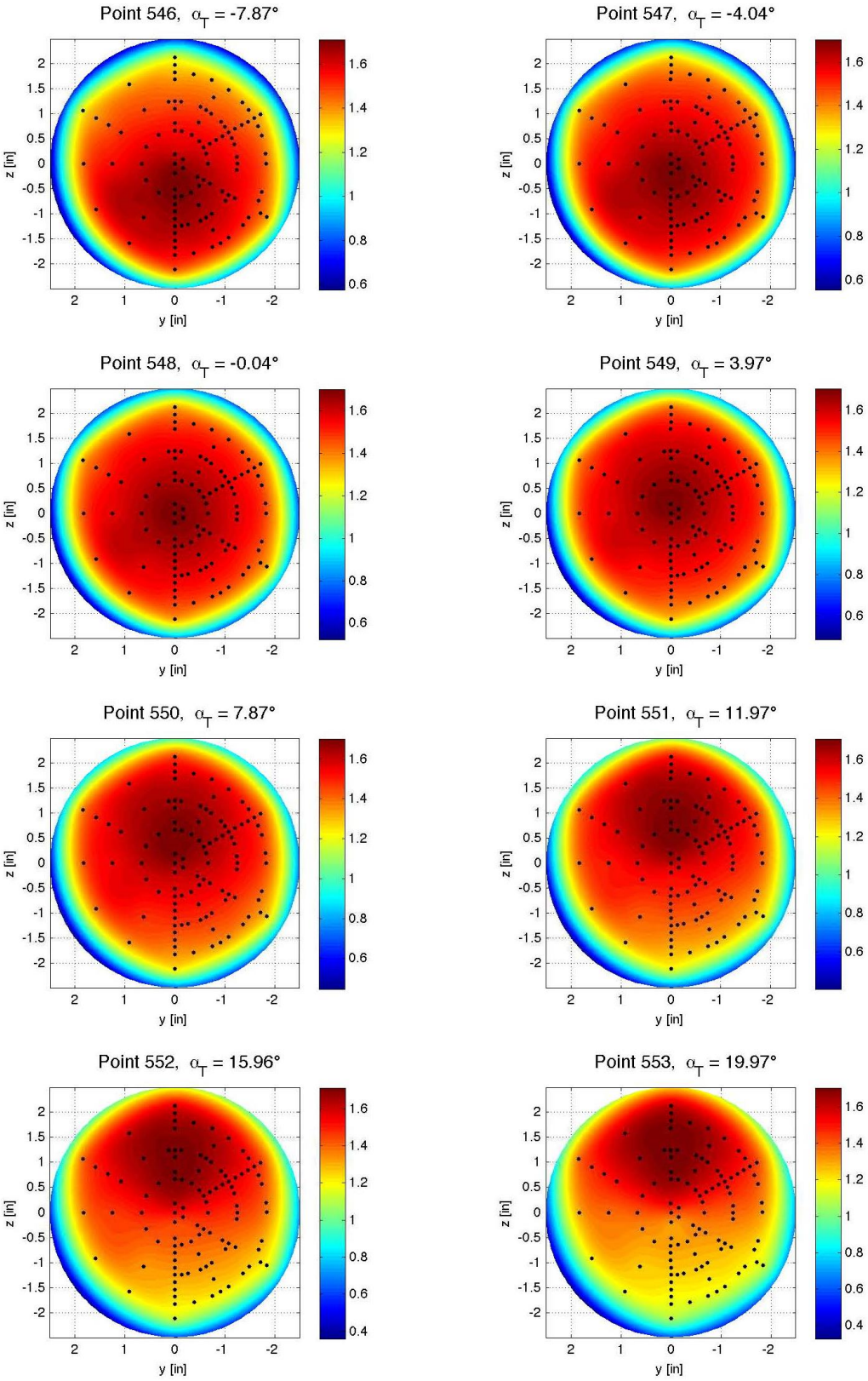

Figure E-6. Baseline configuration, Run 019, $M\infty$ = 2.4, Re_∞ = 1.0x10^6/ft, ϕ = 179.93°, X_S = 25.16 in, Y_S = 0.00 in, C_T = 0.00.

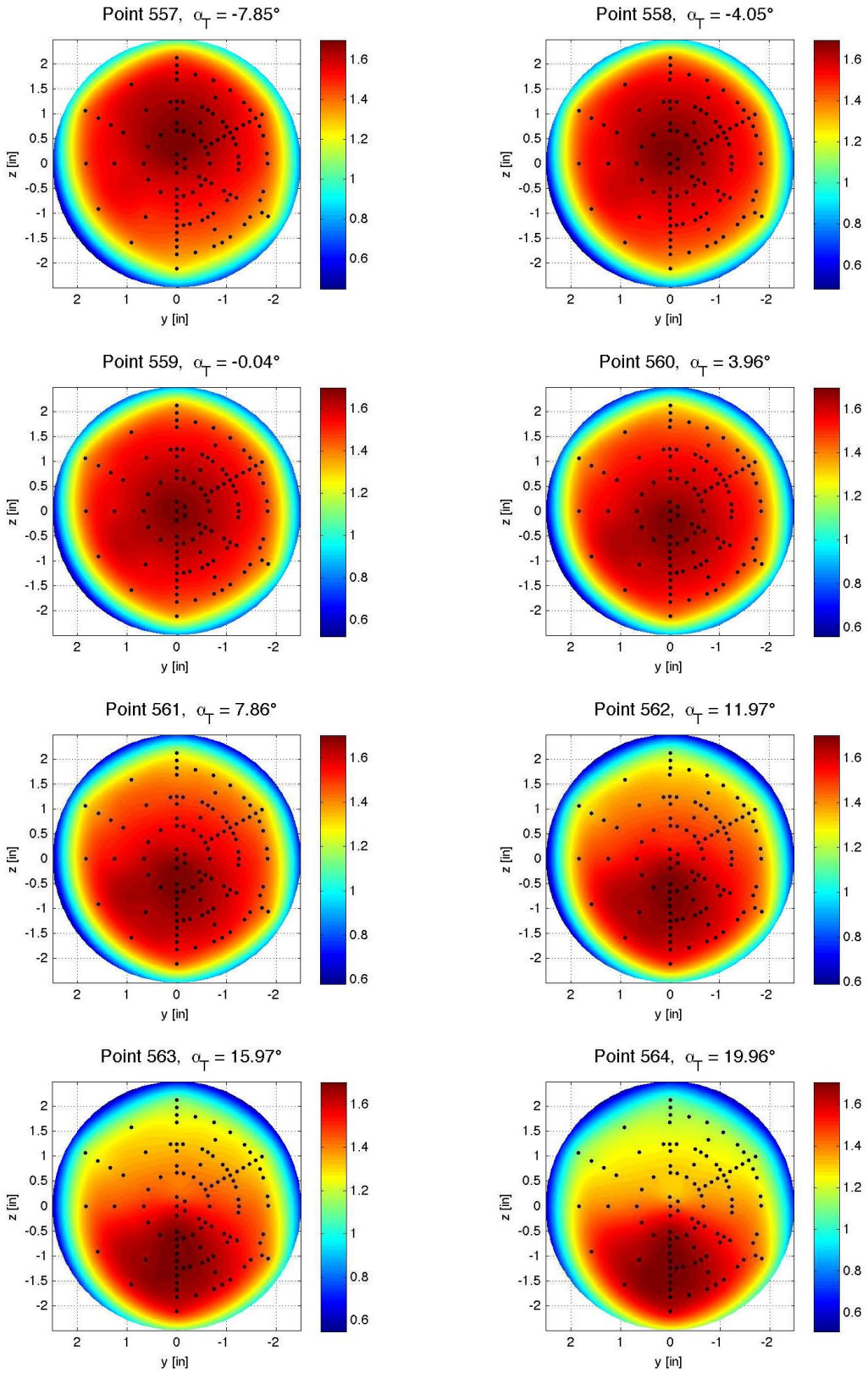

Figure E-7. Baseline configuration, Run 020, $M\infty$ = 2.4, Re_∞ = 1.0x10^6/ft, ϕ = 0.01°, X_S = 39.93 in, Y_S = 0.00 in, C_T = 0.00.

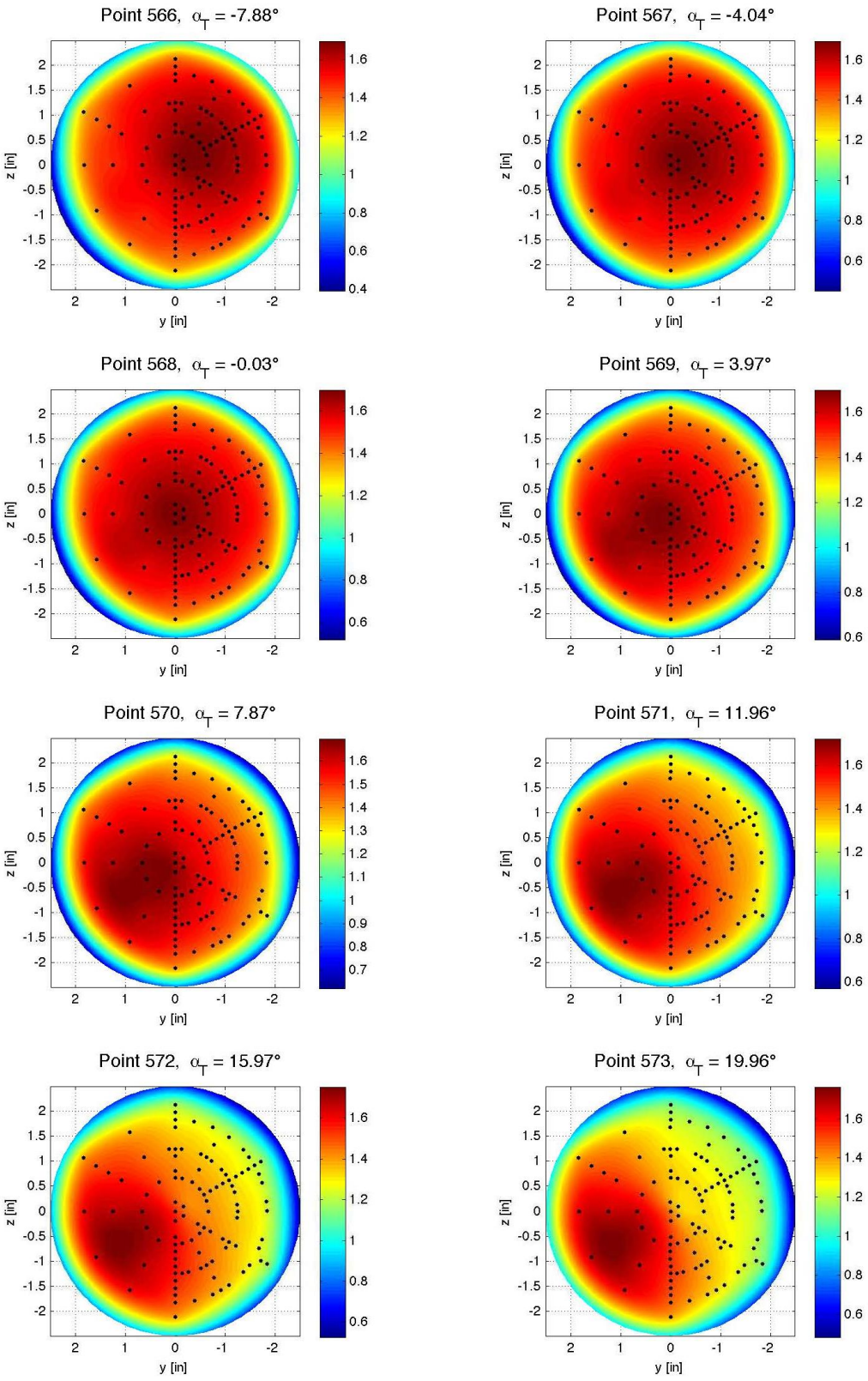

Figure E-8. Baseline configuration, Run 021, $M\infty$ = 2.4, Re_∞ = 1.0x10^6/ft, ϕ = 59.94°, X_S = 39.93 in, Y_S = 0.00 in, C_T = 0.00.

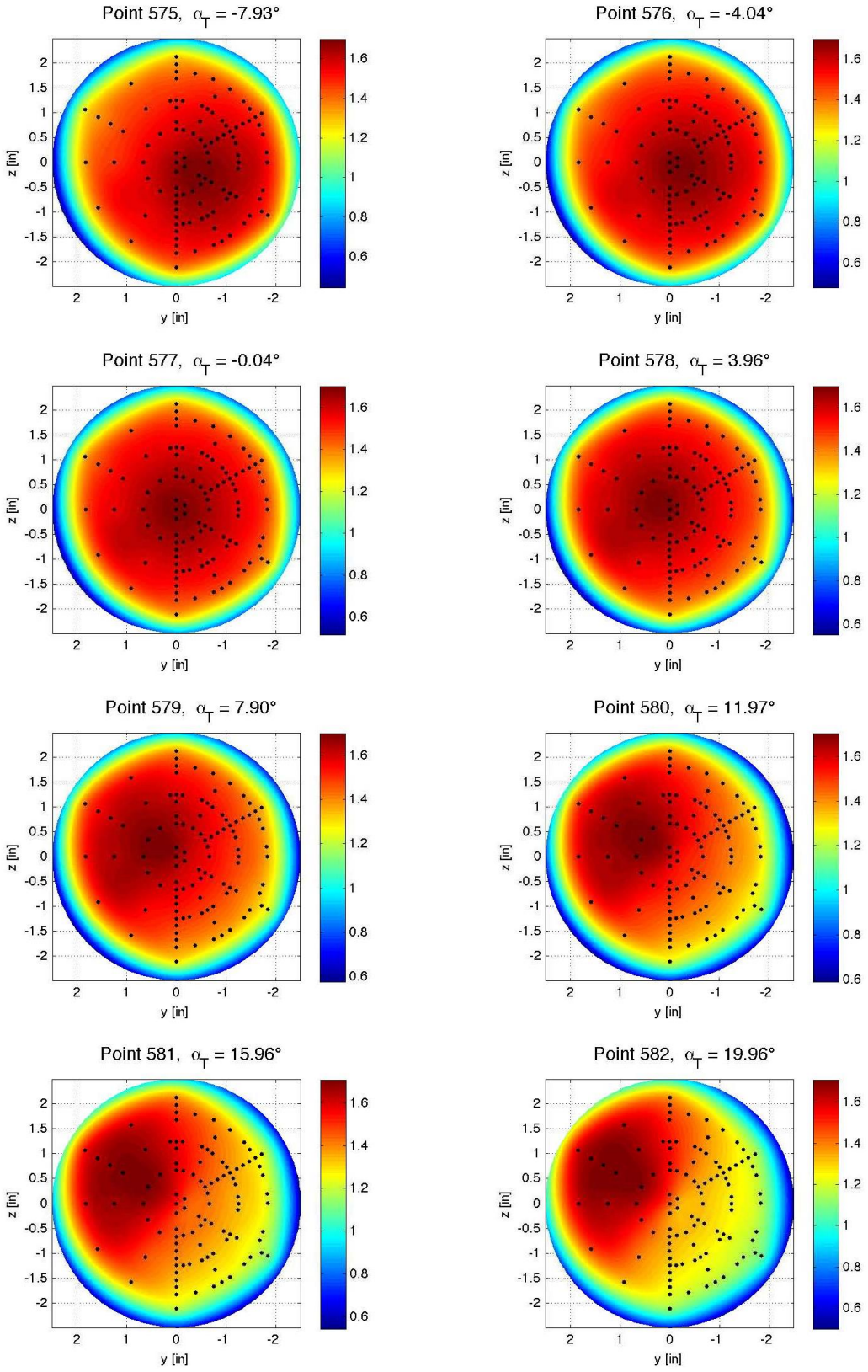

Figure E-9. Baseline configuration, Run 022, M_∞ = 2.4, Re_∞ = 1.0x10^6/ft, ϕ = 120.00°, X_S = 39.93 in, Y_S = 0.00 in, C_T = 0.00.

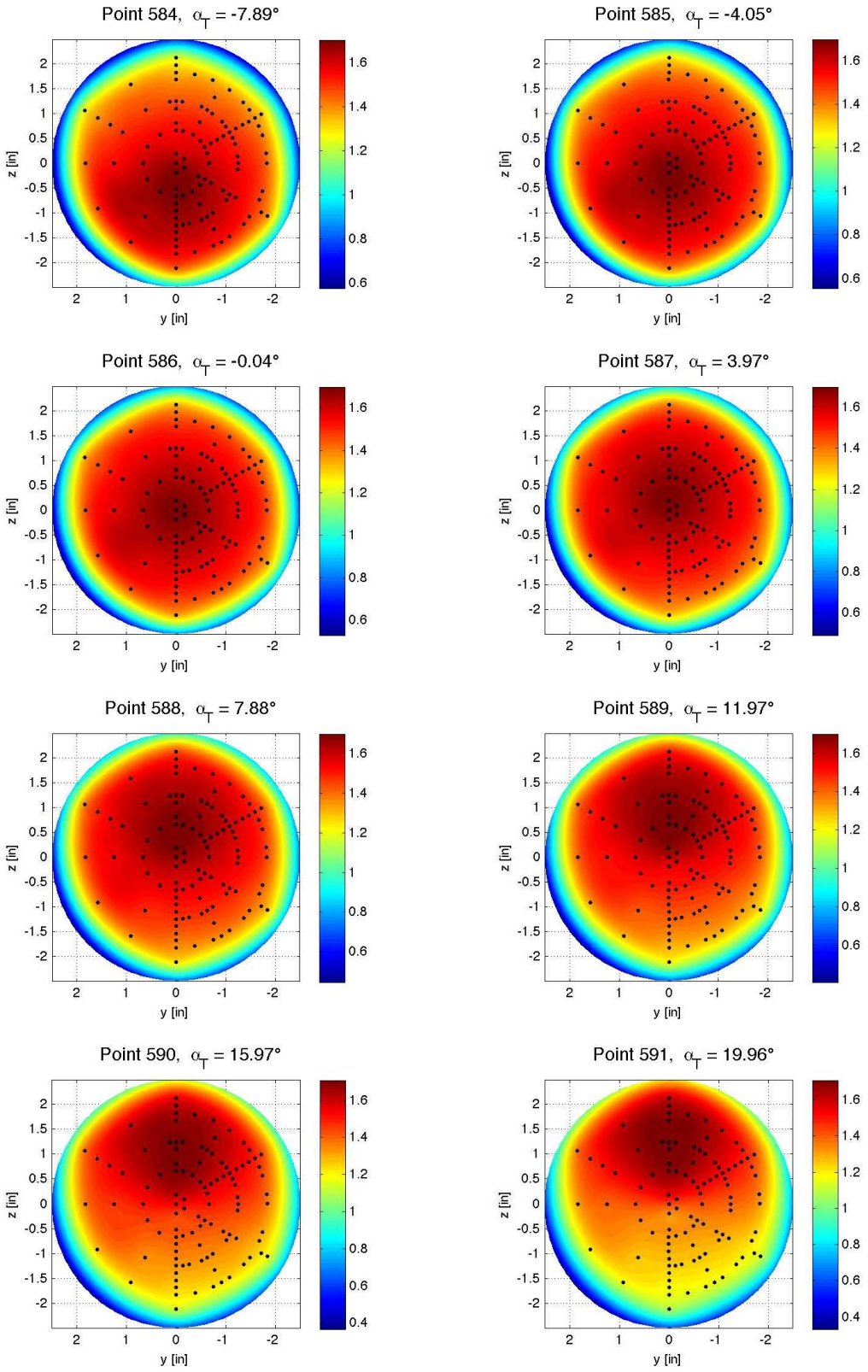

Figure E-10. Baseline configuration, Run 023, M_∞ = 2.4, Re_∞ = 1.0x10^6/ft, ϕ = 179.99°, X_S = 39.93 in, Y_S = 0.00 in, C_T = 0.00.

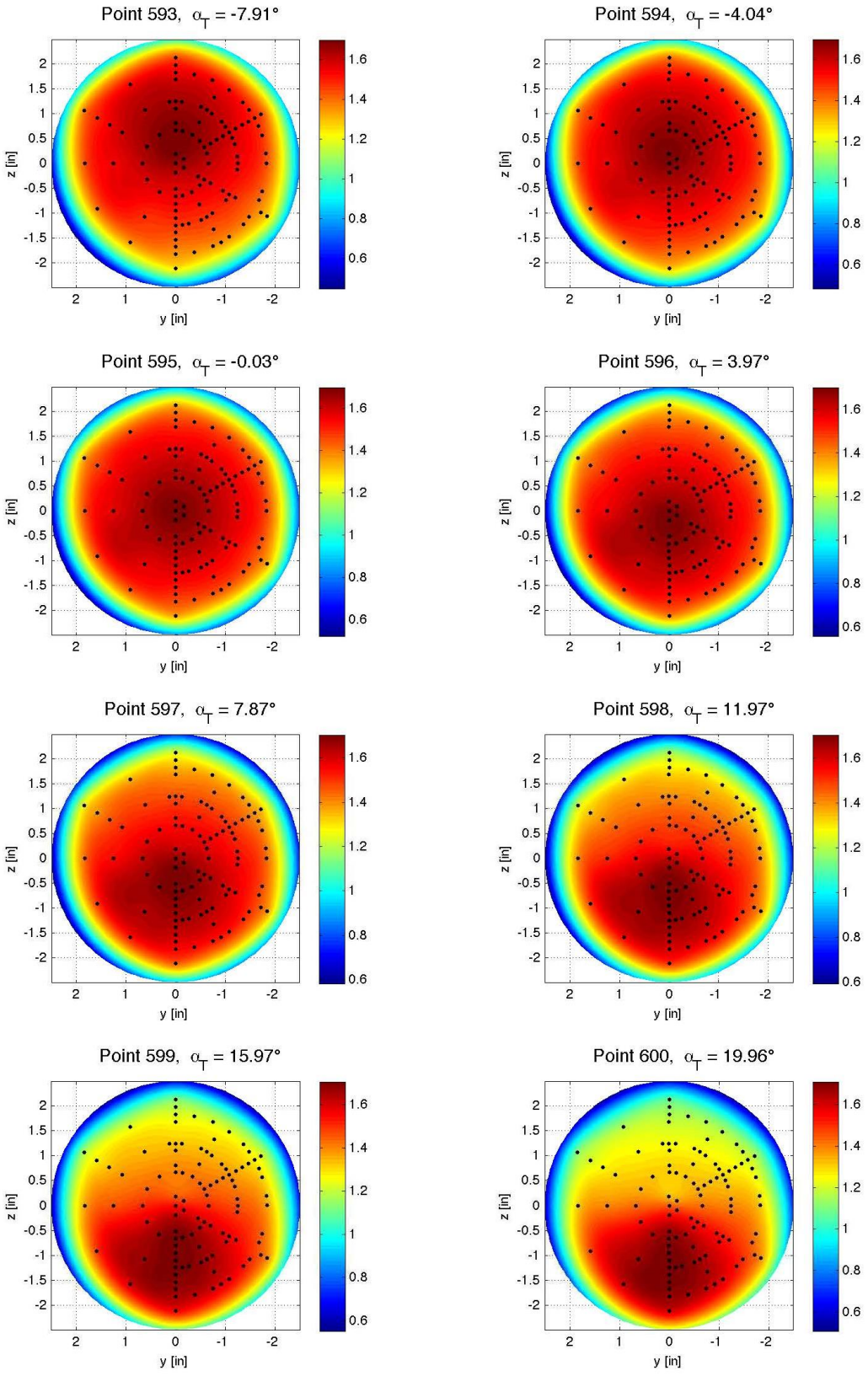

Figure E-11. Baseline configuration, Run 024, $M\infty$ = 2.4, Re_∞ = 1.0x10^6/ft, ϕ = 0.01°, X_S = 39.93 in, Y_S = 0.00 in, C_T = 0.00.

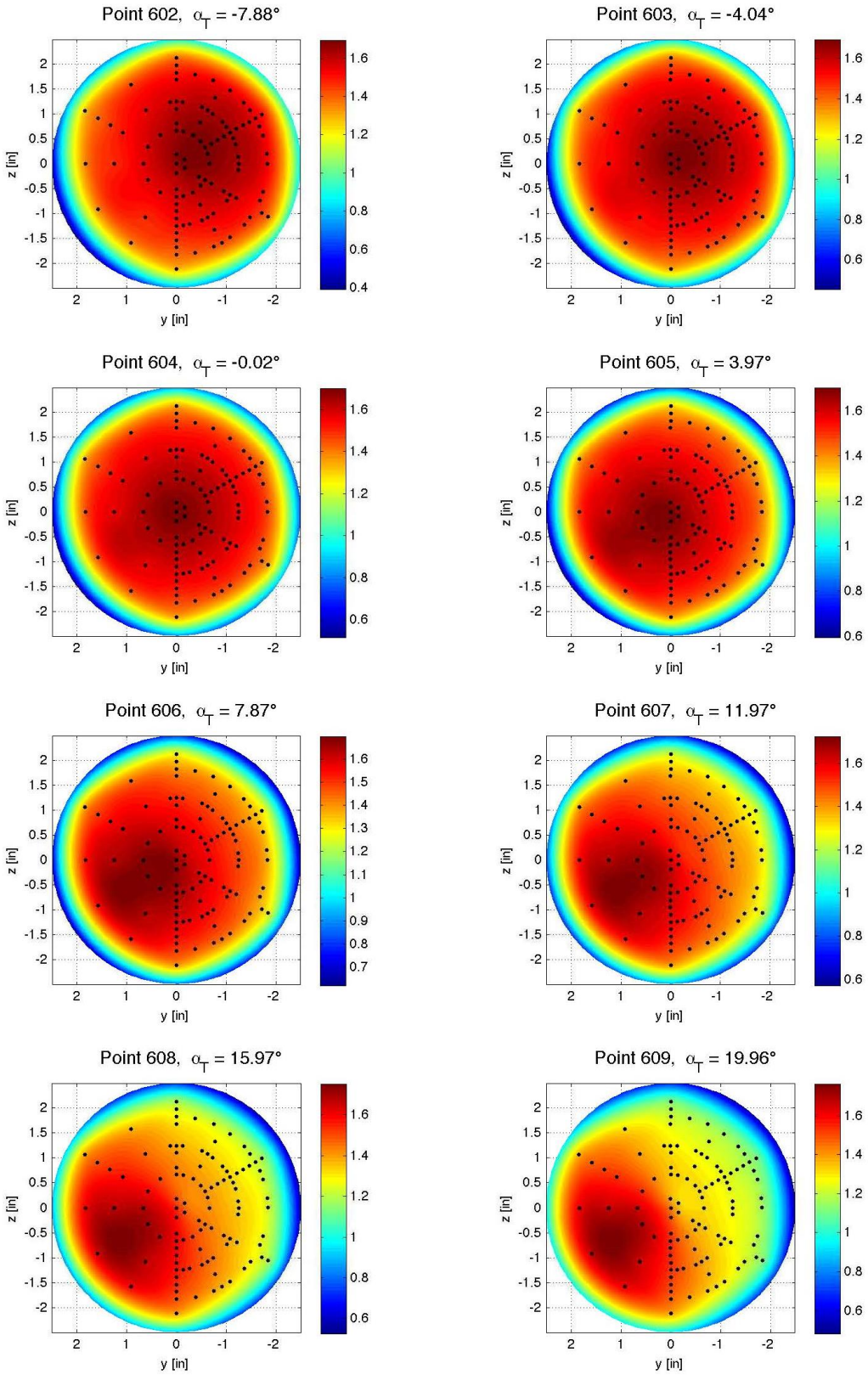

Figure E-12. Baseline configuration, Run 025, M_∞ = 2.4, Re_∞ = 1.0x10^6/ft, ϕ = 60.08°, X_S = 39.93 in, Y_S = 0.00 in, C_T = 0.00.

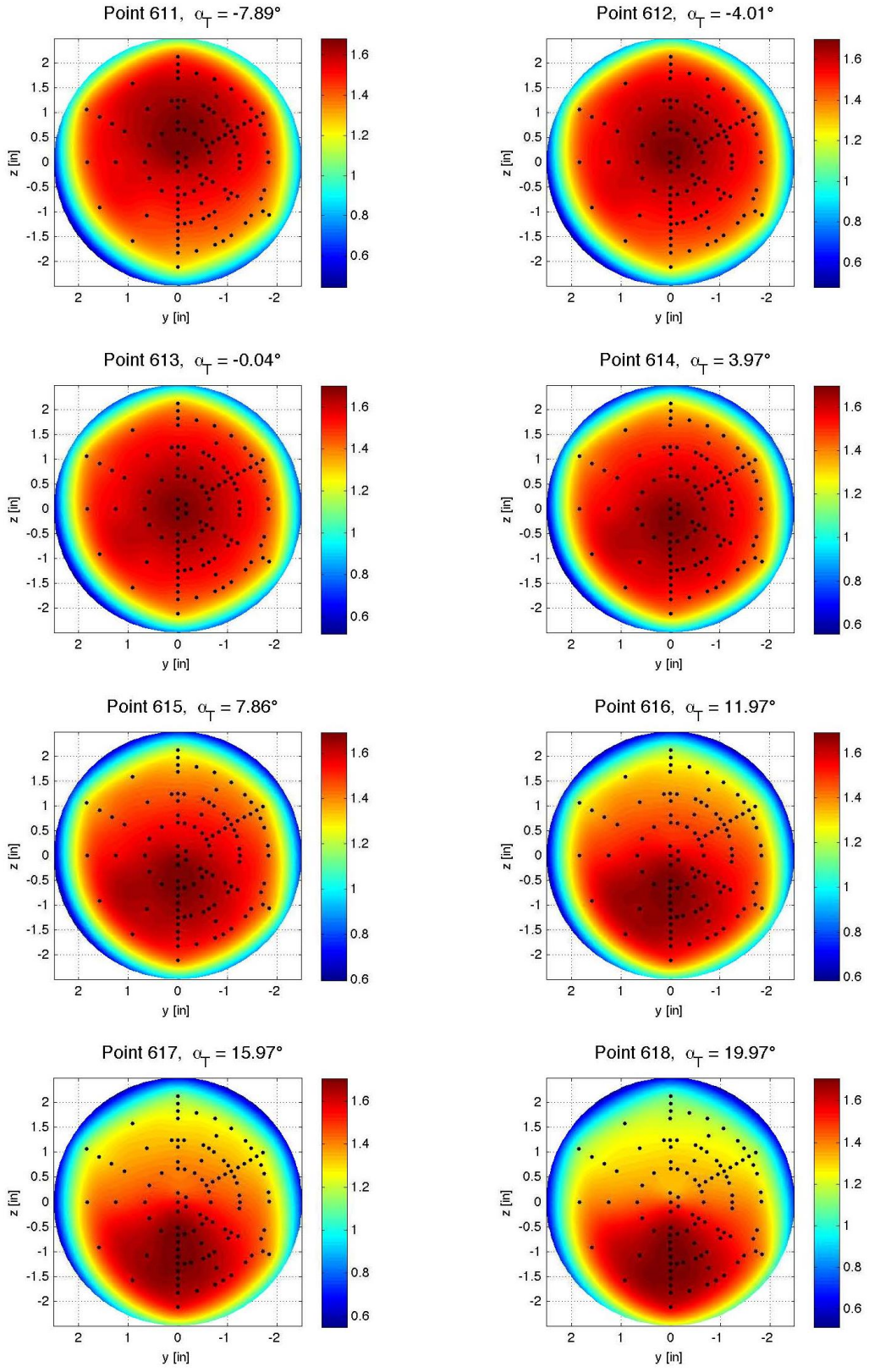

Figure E-13. Baseline configuration, Run 026, M_∞ = 2.4, Re_∞ = 1.0x10^6/ft, ϕ = 0.03°, X_S = 50.17 in, Y_S = 0.00 in, C_T = 0.00.

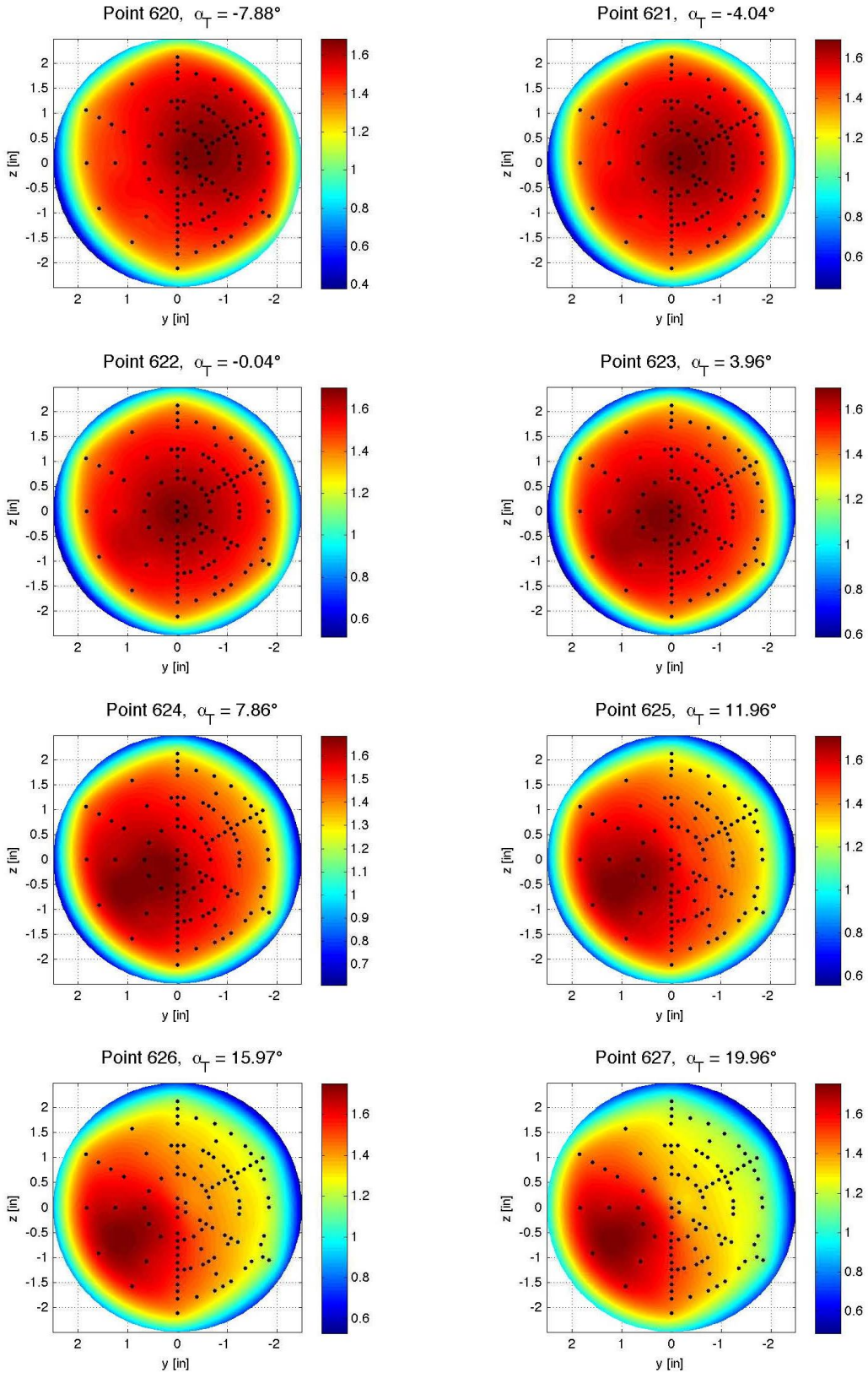

Figure E-14. Baseline configuration, Run 027, M_∞ = 2.4, Re_∞ = 1.0x10^6/ft, ϕ = 60.08°, X_S = 50.17 in, Y_S = 0.00 in, C_T = 0.00.

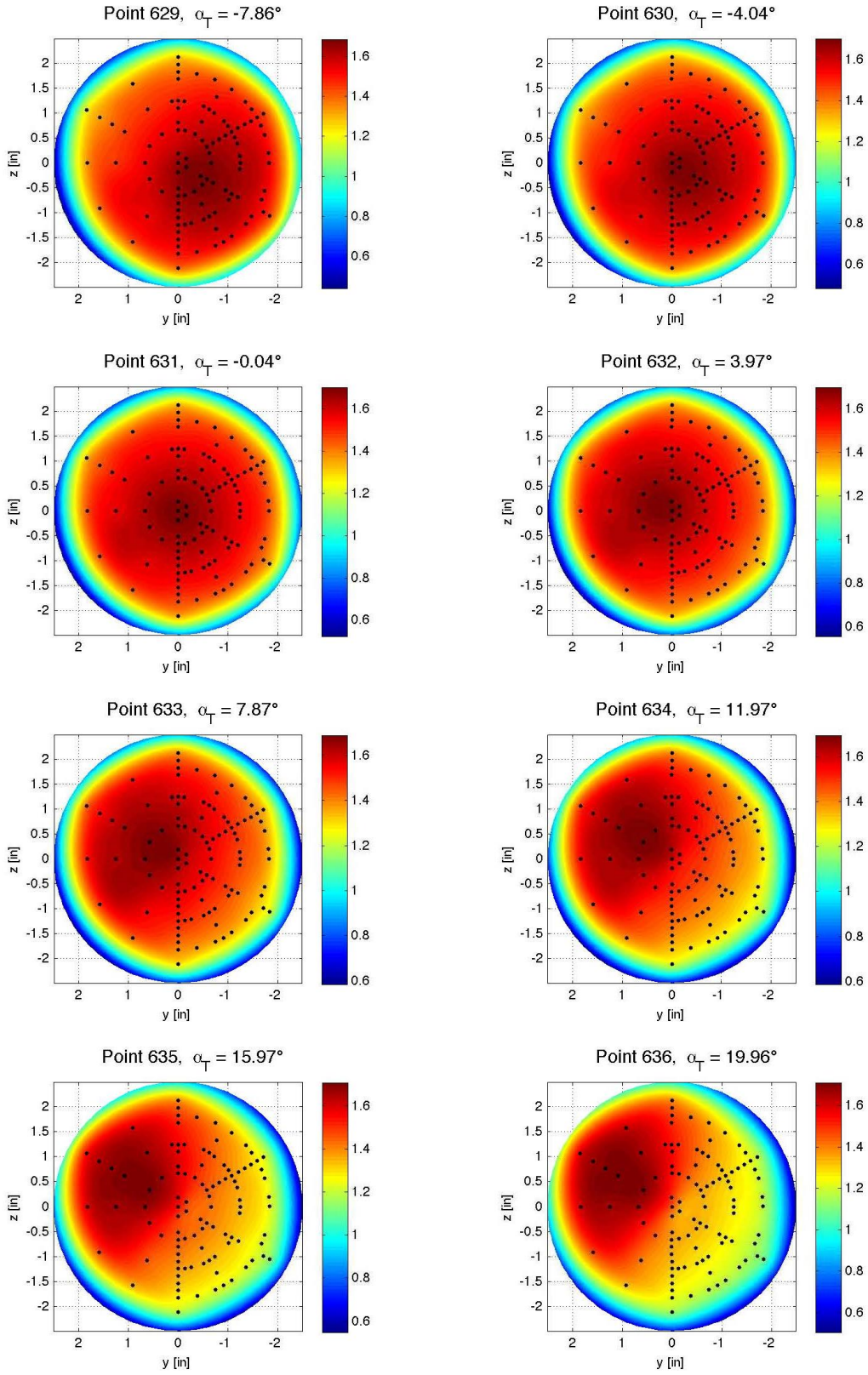

Figure E-15. Baseline configuration, Run 028, M_∞ = 2.4, Re_∞ = 1.0x10^6/ft, ϕ = 120.06°, X_S = 50.17 in, Y_S = 0.00 in, C_T = 0.00.

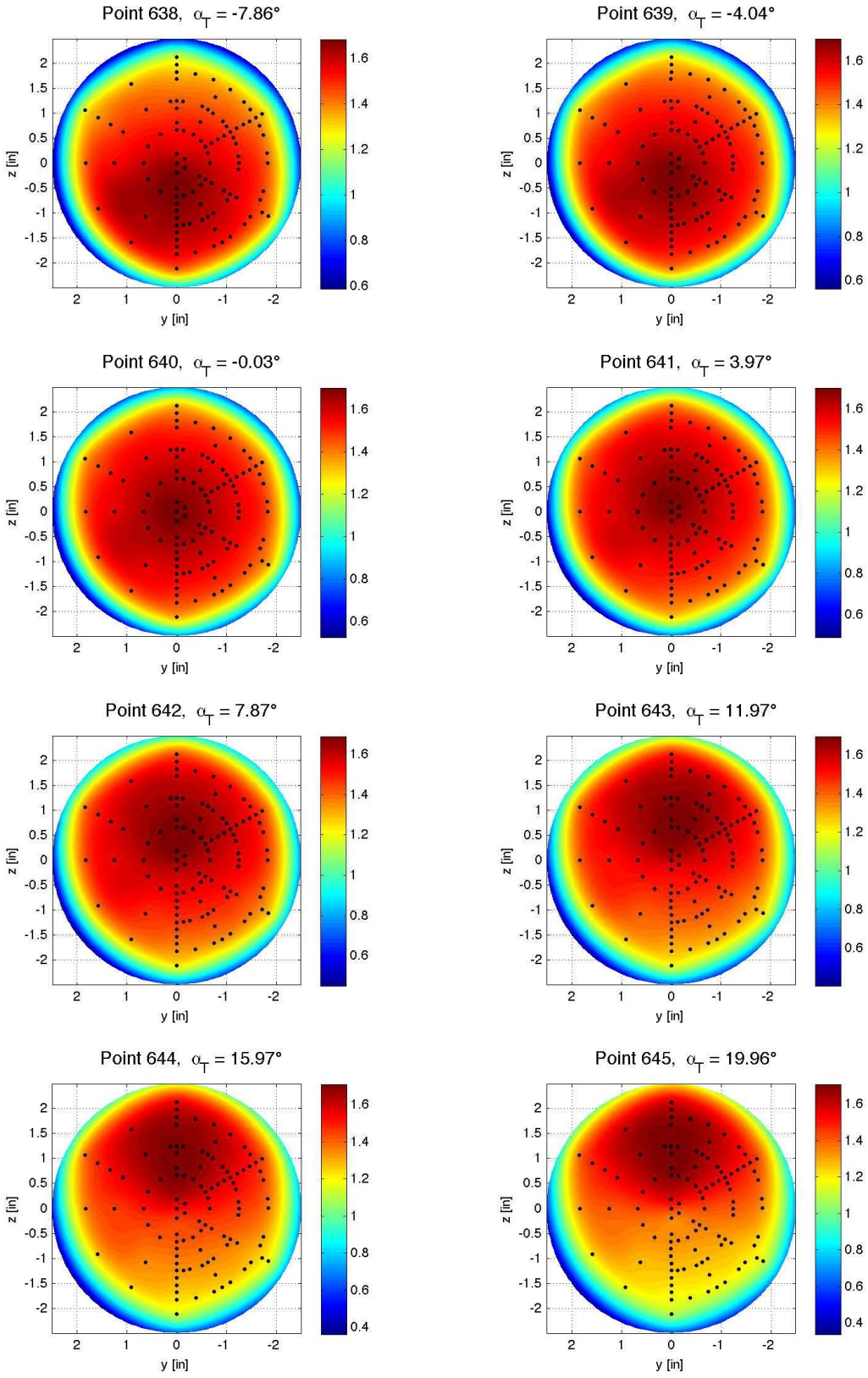

Figure E-16. Baseline configuration, Run 029, M_∞ = 2.4, Re_∞ = 1.0x10^6/ft, ϕ = 179.91°, X_S = 50.17 in, Y_S = 0.00 in, C_T = 0.00.

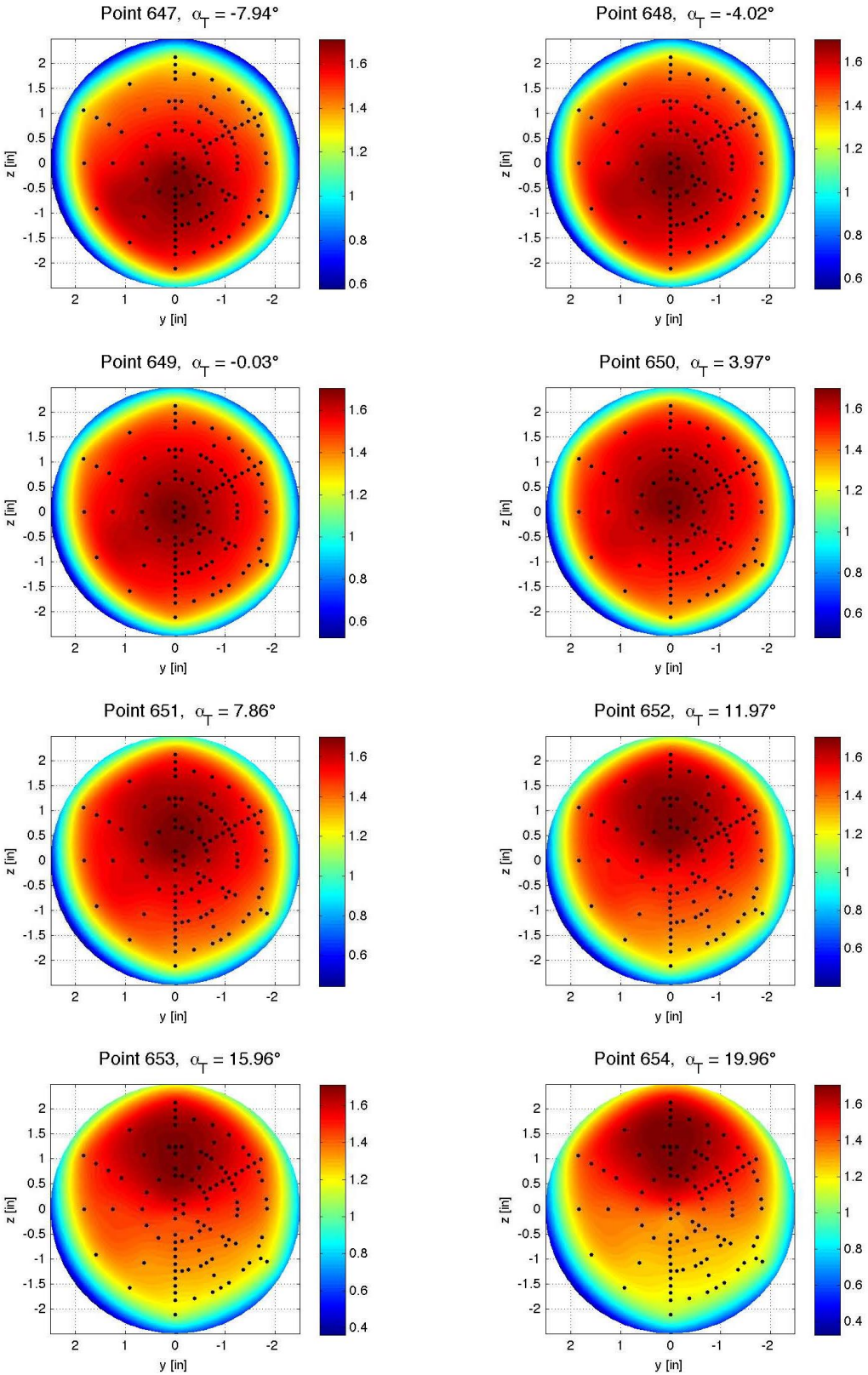

Figure E-17. Baseline configuration, Run 030, M_∞ = 2.4, Re_∞ = 1.0x10^6/ft, ϕ = 179.91°, X_S = 25.18 in, Y_S = 0.00 in, C_T = 0.00.

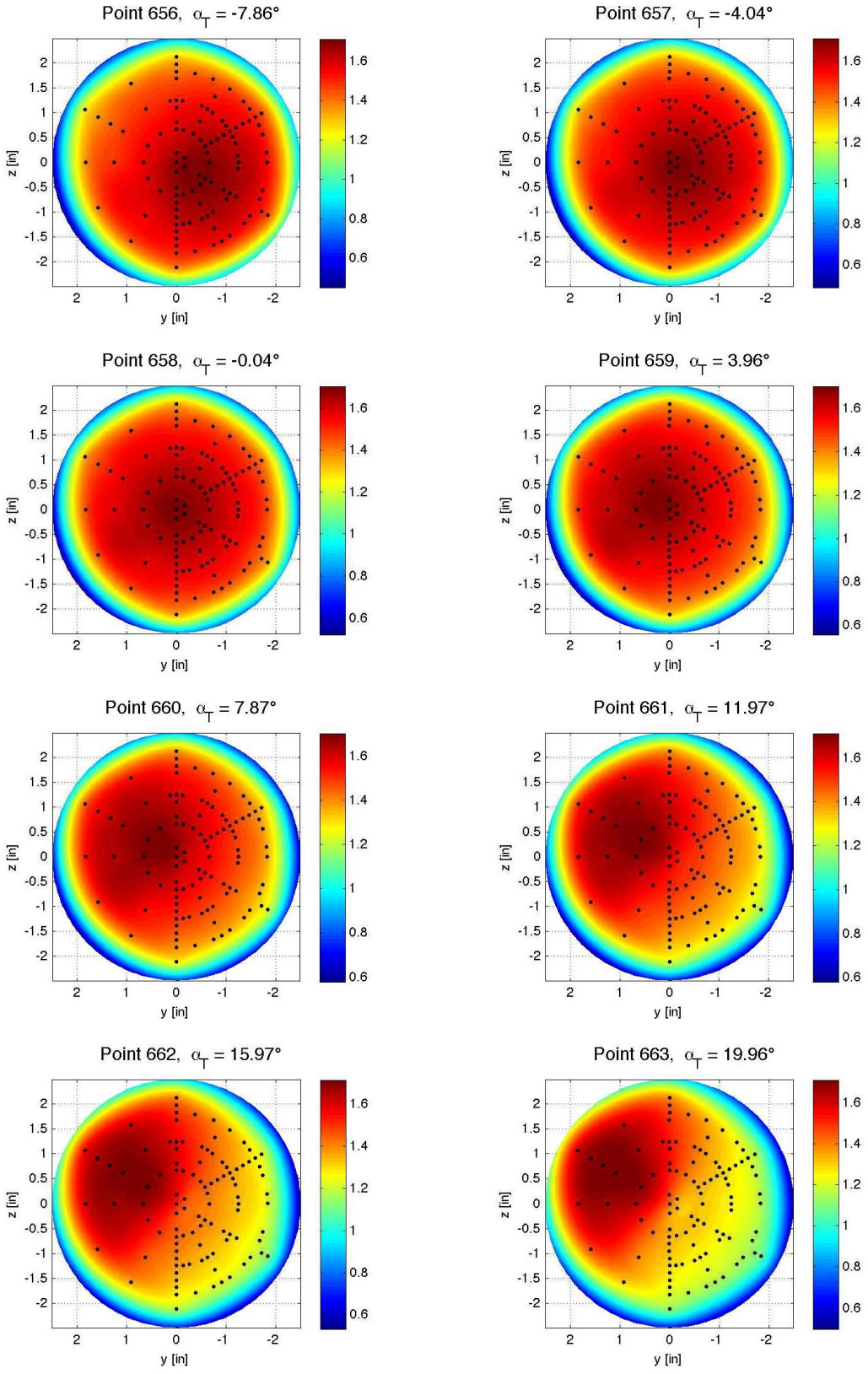

Figure E-18. Baseline configuration, Run 031, M_∞ = 2.4, Re_∞ = 1.0x10^6/ft, ϕ = 119.92°, X_S = 25.18 in, Y_S = 0.00 in, C_T = 0.00.

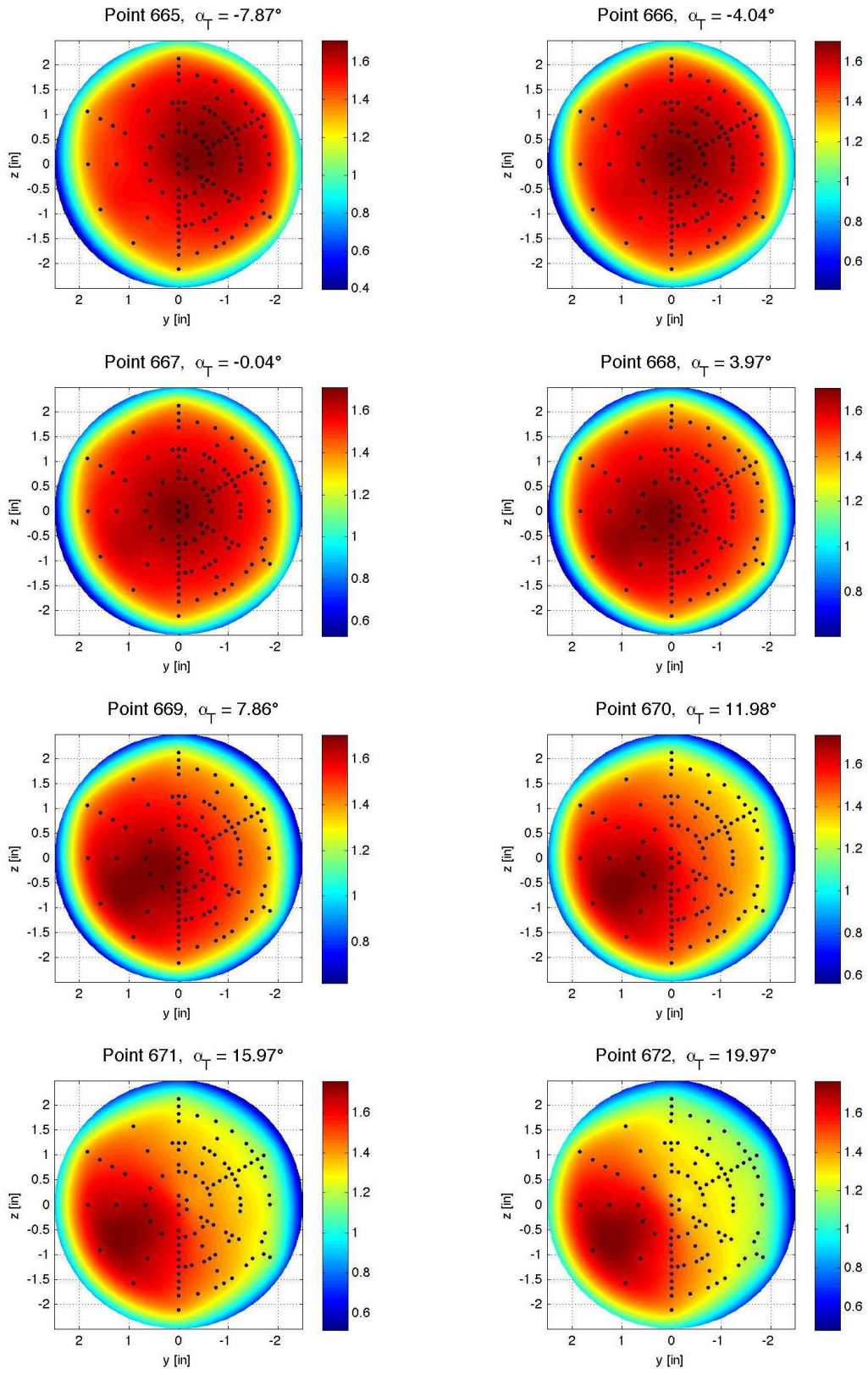

Figure E-19. Baseline configuration, Run 032, M_∞ = 2.4, Re_∞ = 1.0x10^6/ft, ϕ = 59.98°, X_S = 25.18 in, Y_S = 0.00 in, C_T = 0.00.

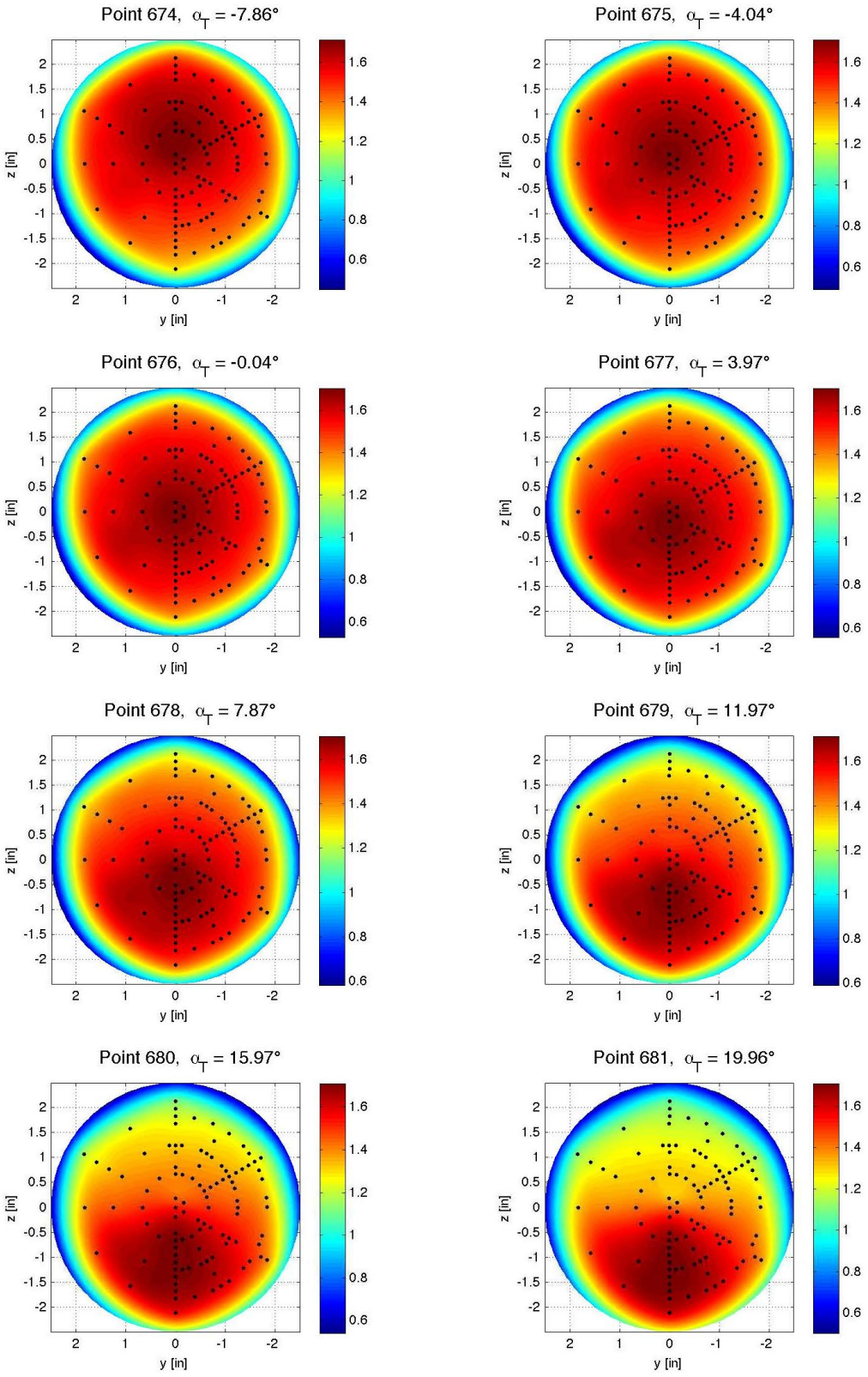

Figure E-20. Baseline configuration, Run 033, M_∞ = 2.4, Re_∞ = 1.0x10^6/ft, ϕ = 0.05°, X_S = 25.18 in, Y_S = 0.00 in, C_T = 0.00.

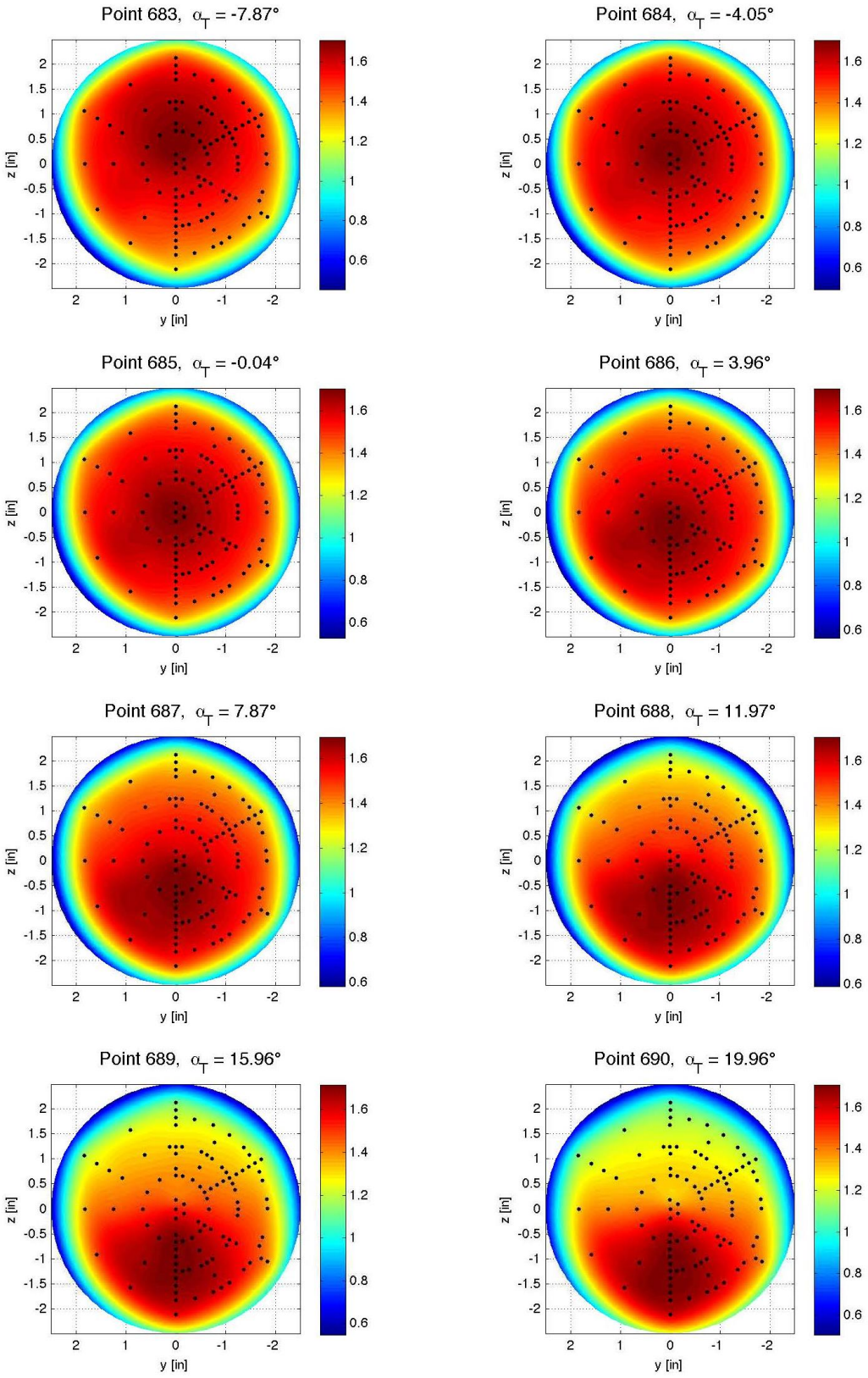

Figure E-21. Baseline configuration, Run 034, M_∞ = 2.4, Re_∞ = 1.0x10^6/ft, ϕ = 0.05°, X_S = 25.18 in, Y_S = 7.99 in, C_T = 0.00.

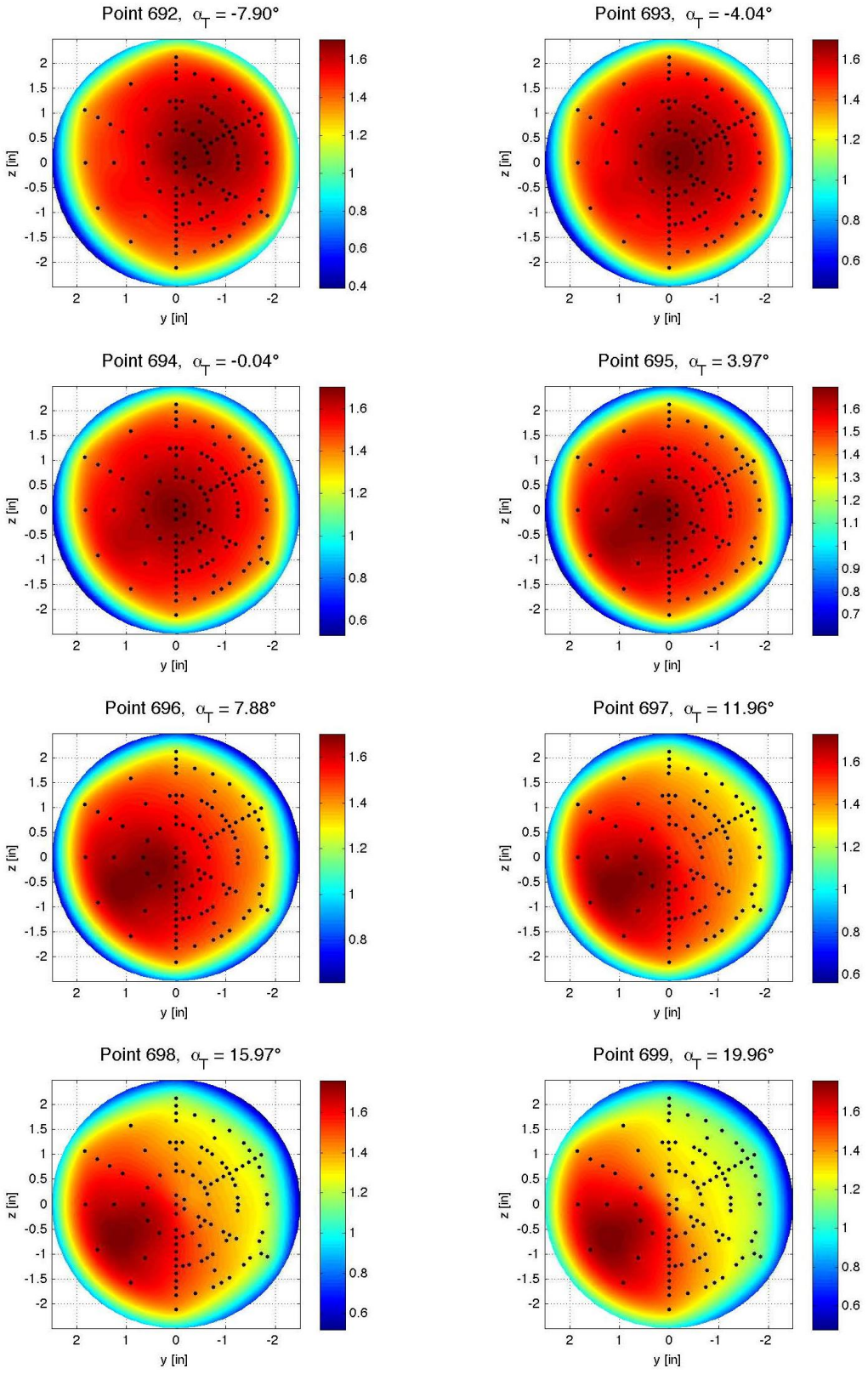

Figure E-22. Baseline configuration, Run 035, $M\infty$ = 2.4, Re_∞ = 1.0x10^6/ft, ϕ = 60.08°, X_S = 25.18 in, Y_S = 7.99 in, C_T = 0.00.

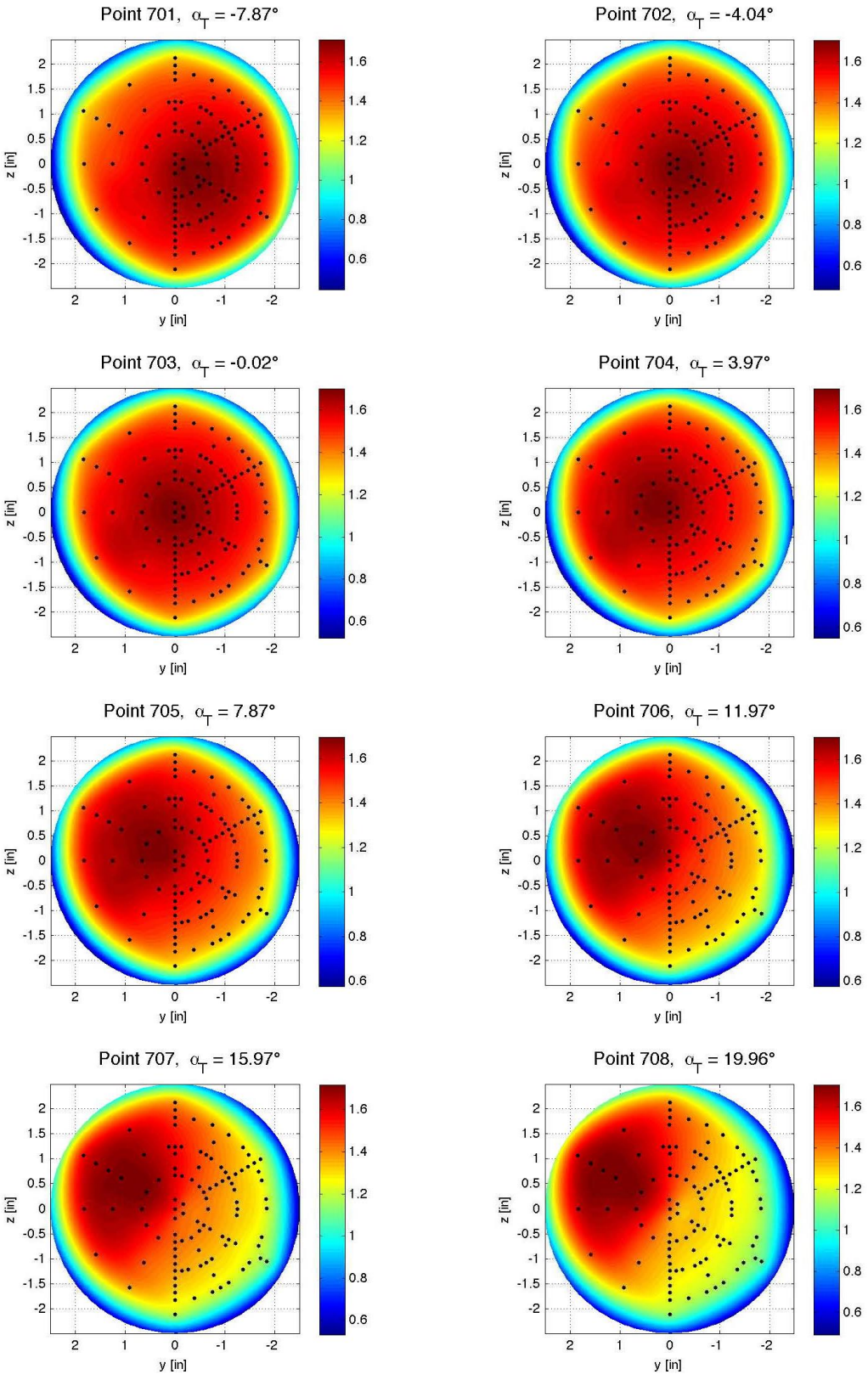

Figure E-23. Baseline configuration, Run 036, M_∞ = 2.4, Re_∞ = 1.0x10^6/ft, ϕ = 119.90°, X_S = 25.18 in, Y_S = 7.99 in, C_T = 0.00.

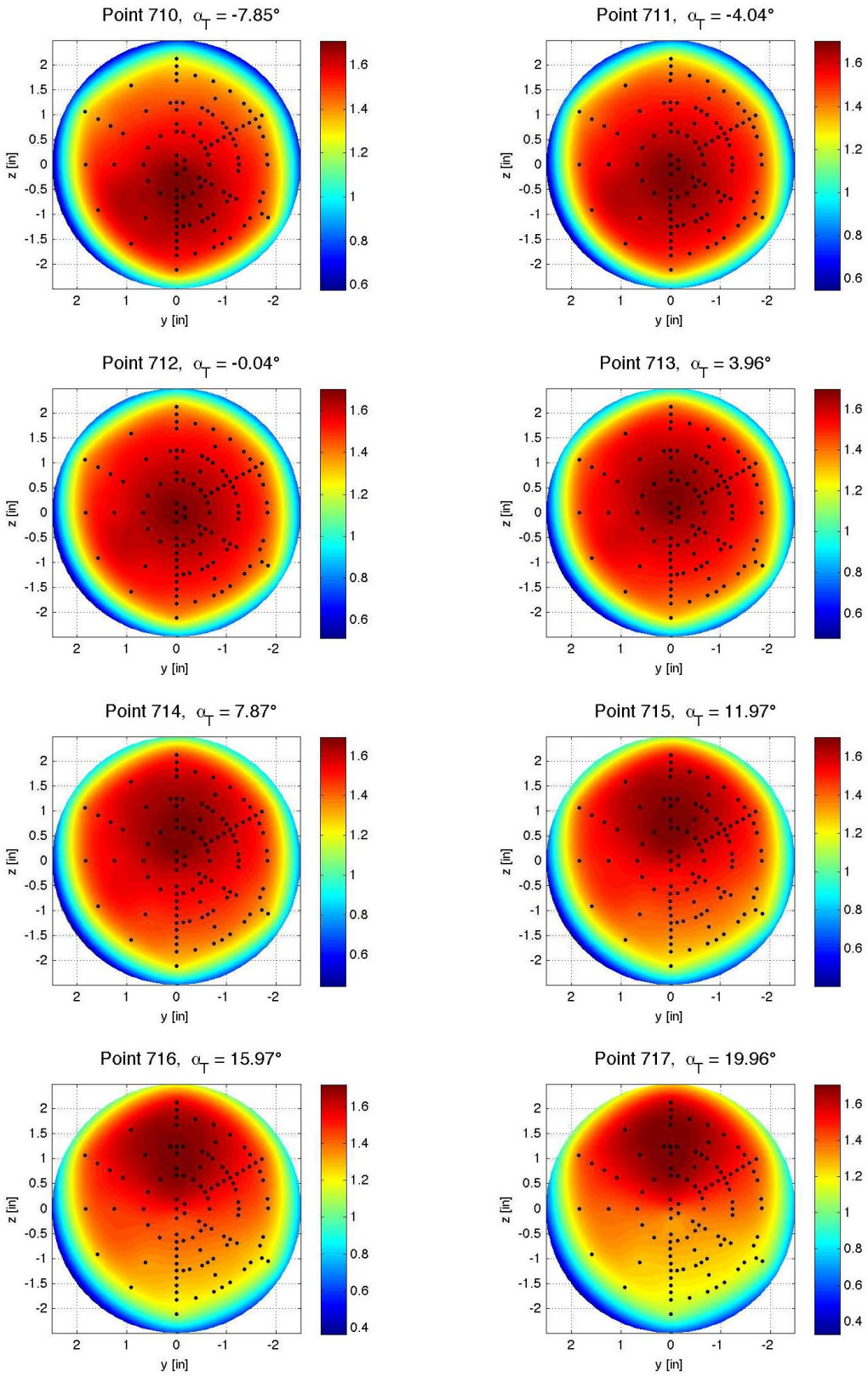

Figure E-24. Baseline configuration, Run 037, M_∞ = 2.4, Re_∞ = 1.0x10^6/ft, ϕ = 179.95°, X_S = 25.18 in, Y_S = 7.99 in, C_T = 0.00.

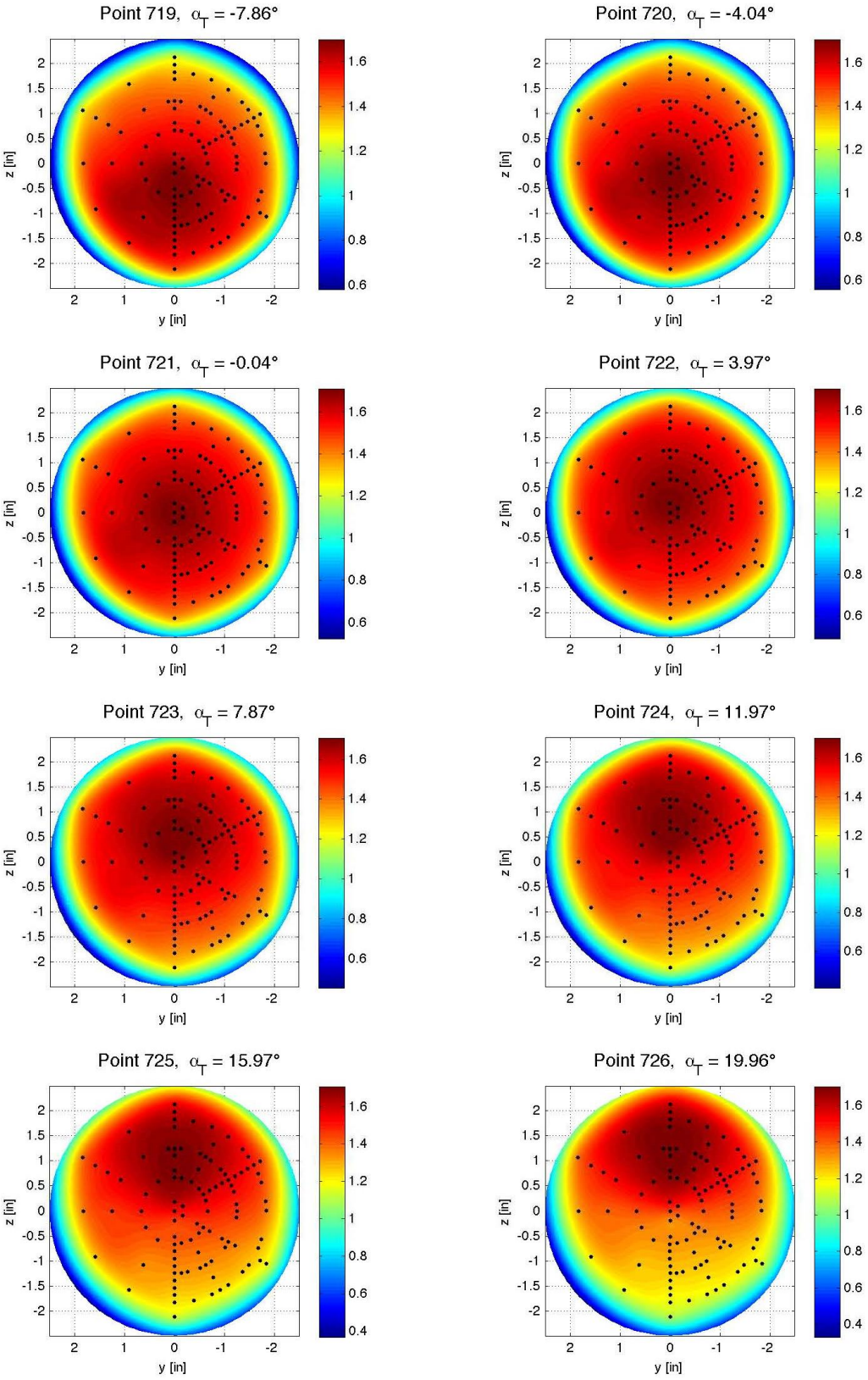

Figure E-25. Baseline configuration, Run 038, M_∞ = 2.4, Re_∞ = 1.0x10^6/ft, ϕ = 179.95°, X_S = 40.19 in, Y_S = 7.99 in, C_T = 0.00.

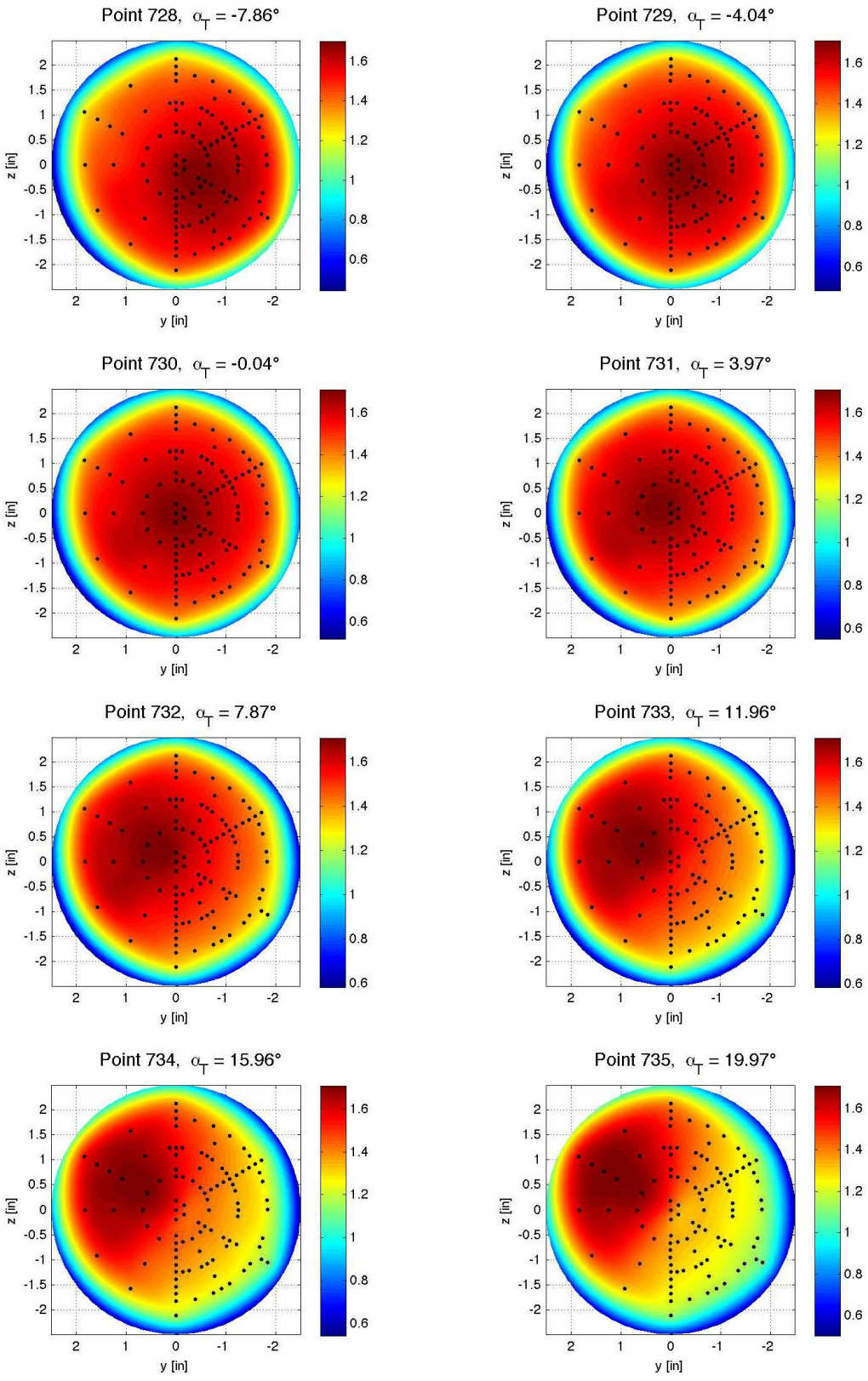

Figure E-26. Baseline configuration, Run 039, M_∞ = 2.4, Re_∞ = 1.0x10^6/ft, ϕ = 119.90°, X_S = 40.19 in, Y_S = 7.99 in, C_T = 0.00.

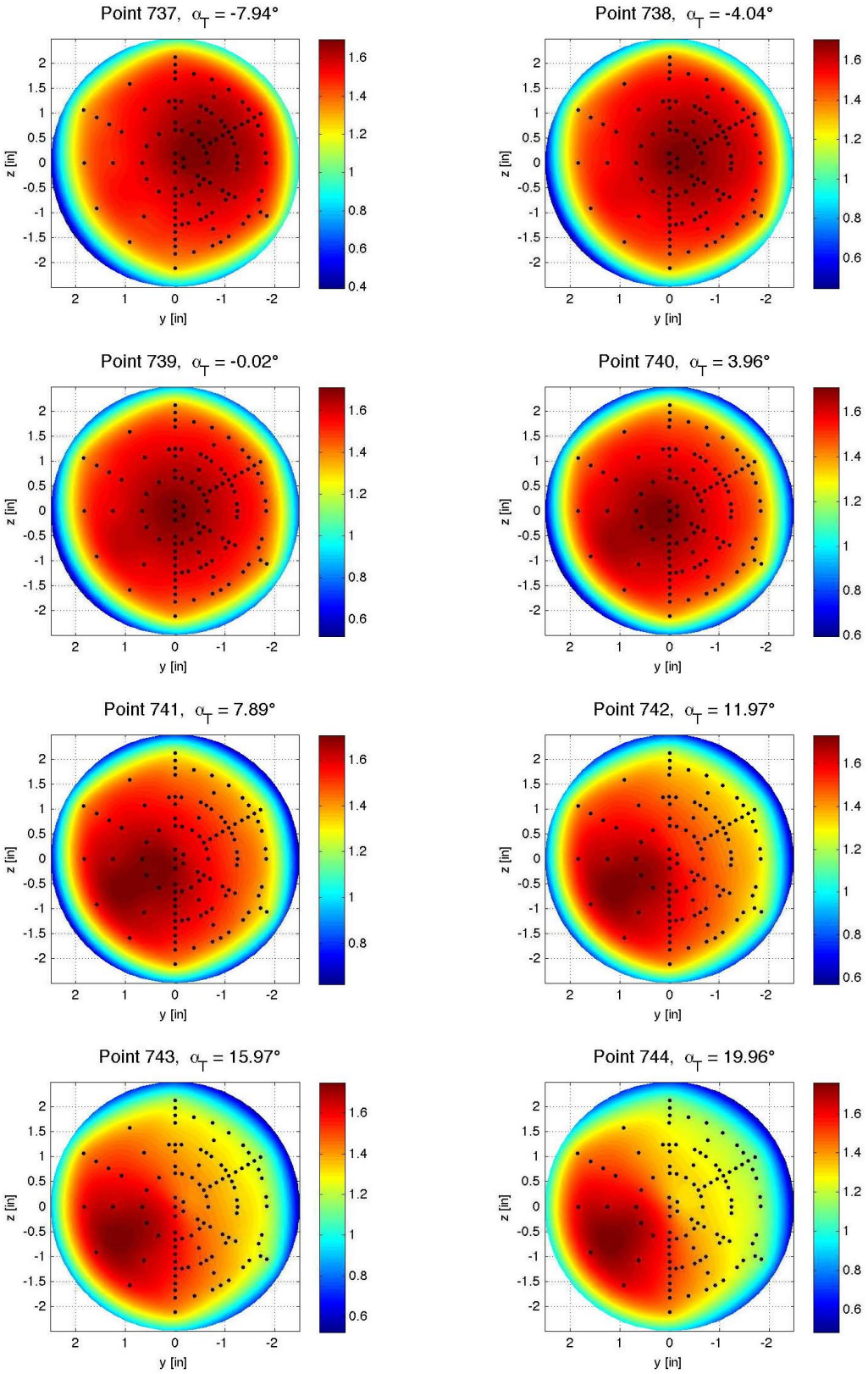

Figure E-27. Baseline configuration, Run 040, M_∞ = 2.4, Re_∞ = 1.0x10^6/ft, ϕ = 59.98°, X_S = 40.19 in, Y_S = 7.99 in, C_T = 0.00.

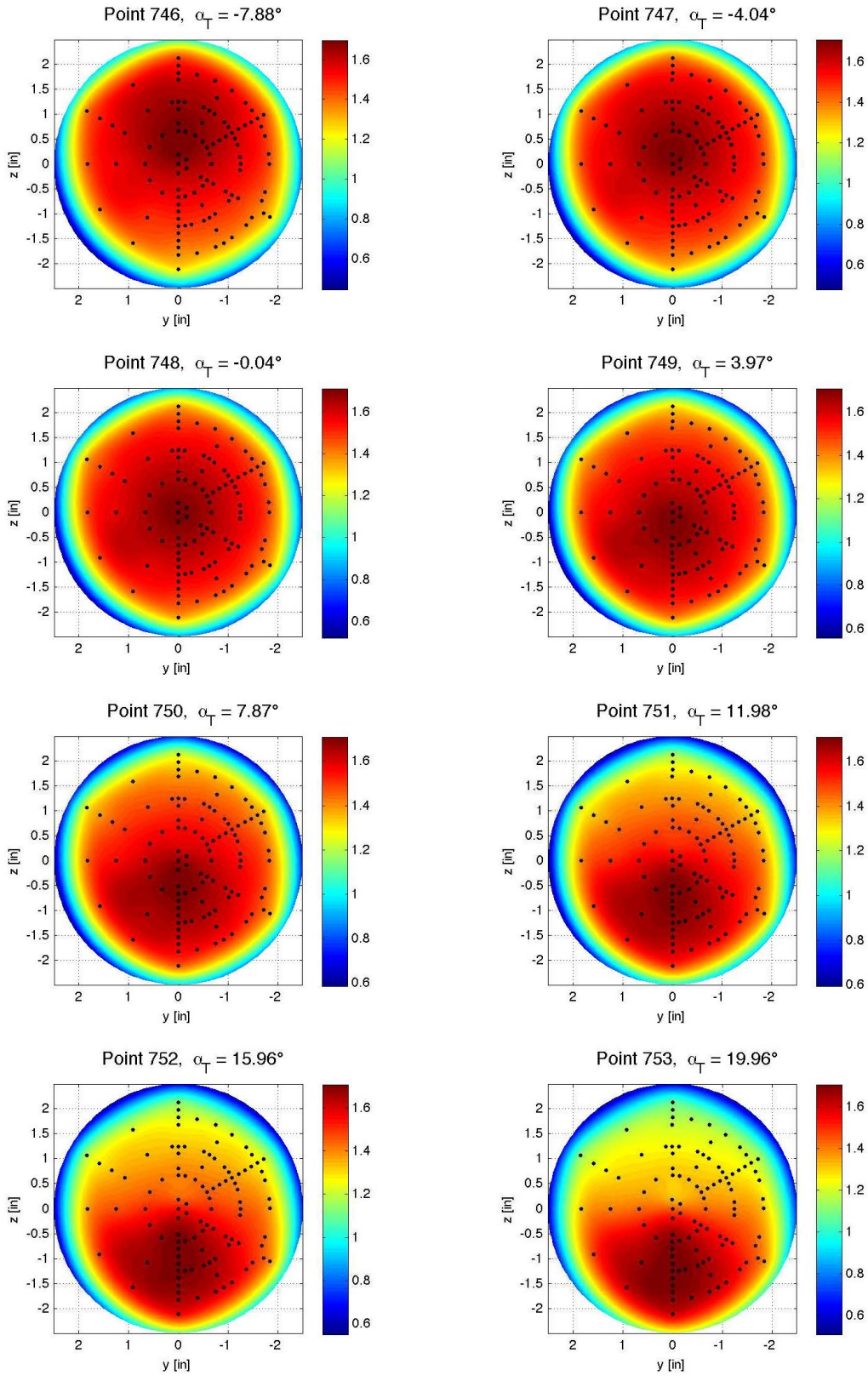

Figure E-28. Baseline configuration, Run 041, M_∞ = 2.4, Re_∞ = 1.0x10^6/ft, ϕ = 0.05°, X_S = 40.19 in, Y_S = 7.99 in, C_T = 0.00.

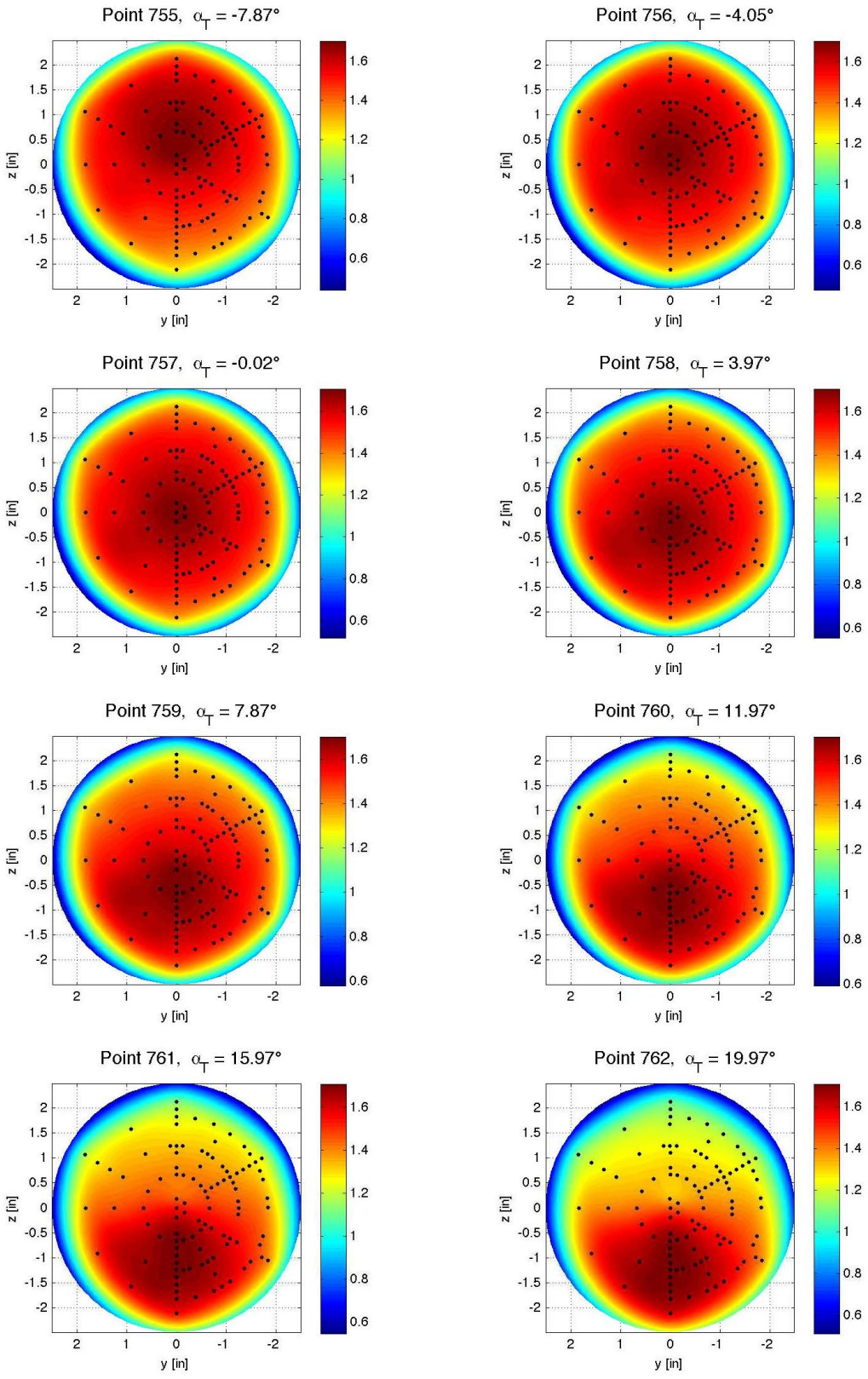

Figure E-29. Baseline configuration, Run 042, M_∞ = 2.4, Re_∞ = 1.0x10^6/ft, ϕ = −0.05°, X_S = 40.19 in, Y_S = −8.00 in, C_T = 0.00.

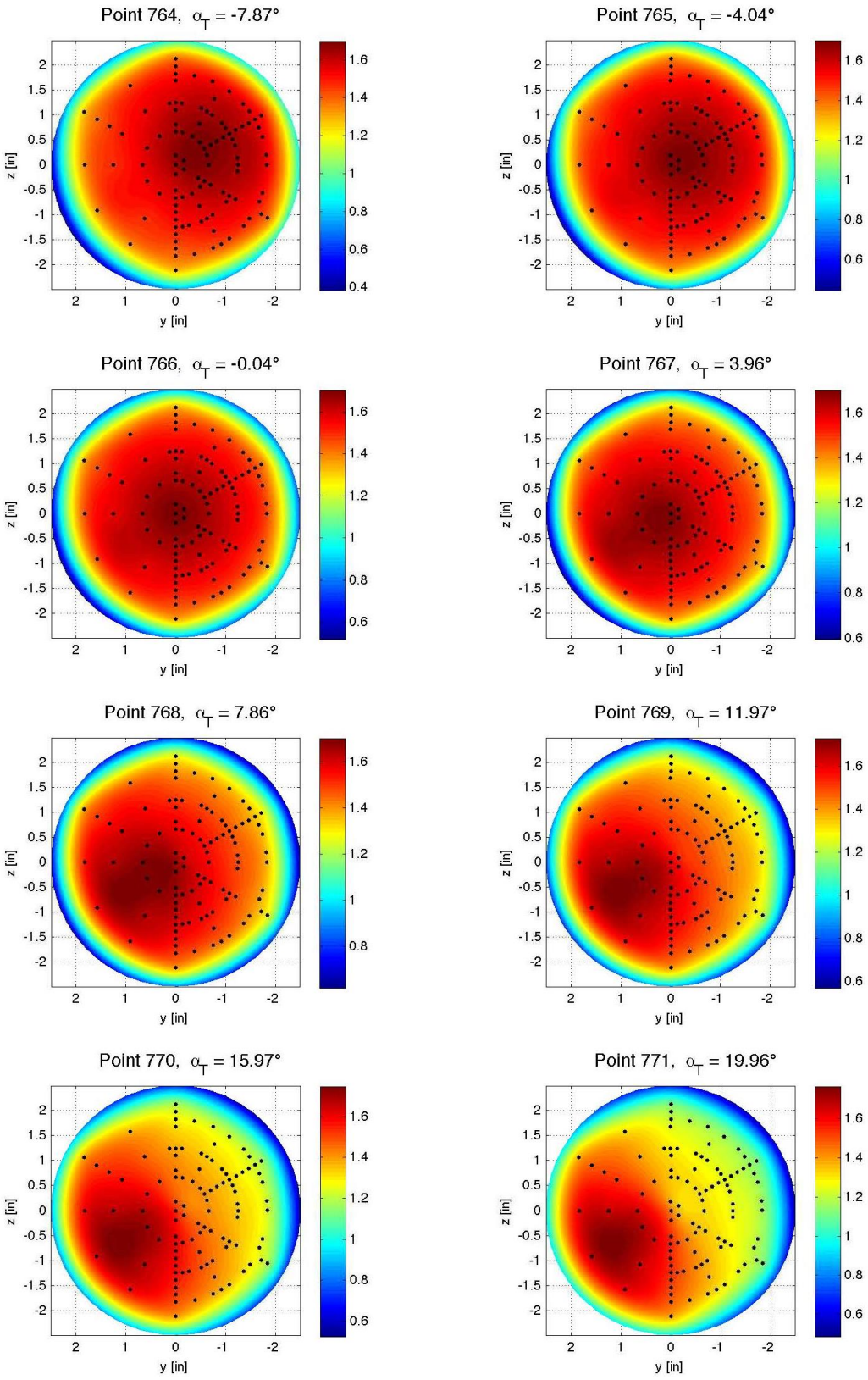

Figure E-30. Baseline configuration, Run 043, M_∞ = 2.4, Re_∞ = 1.0x10^6/ft, ϕ = 59.92°, X_S = 40.19 in, Y_S = −8.00 in, C_T = 0.00.

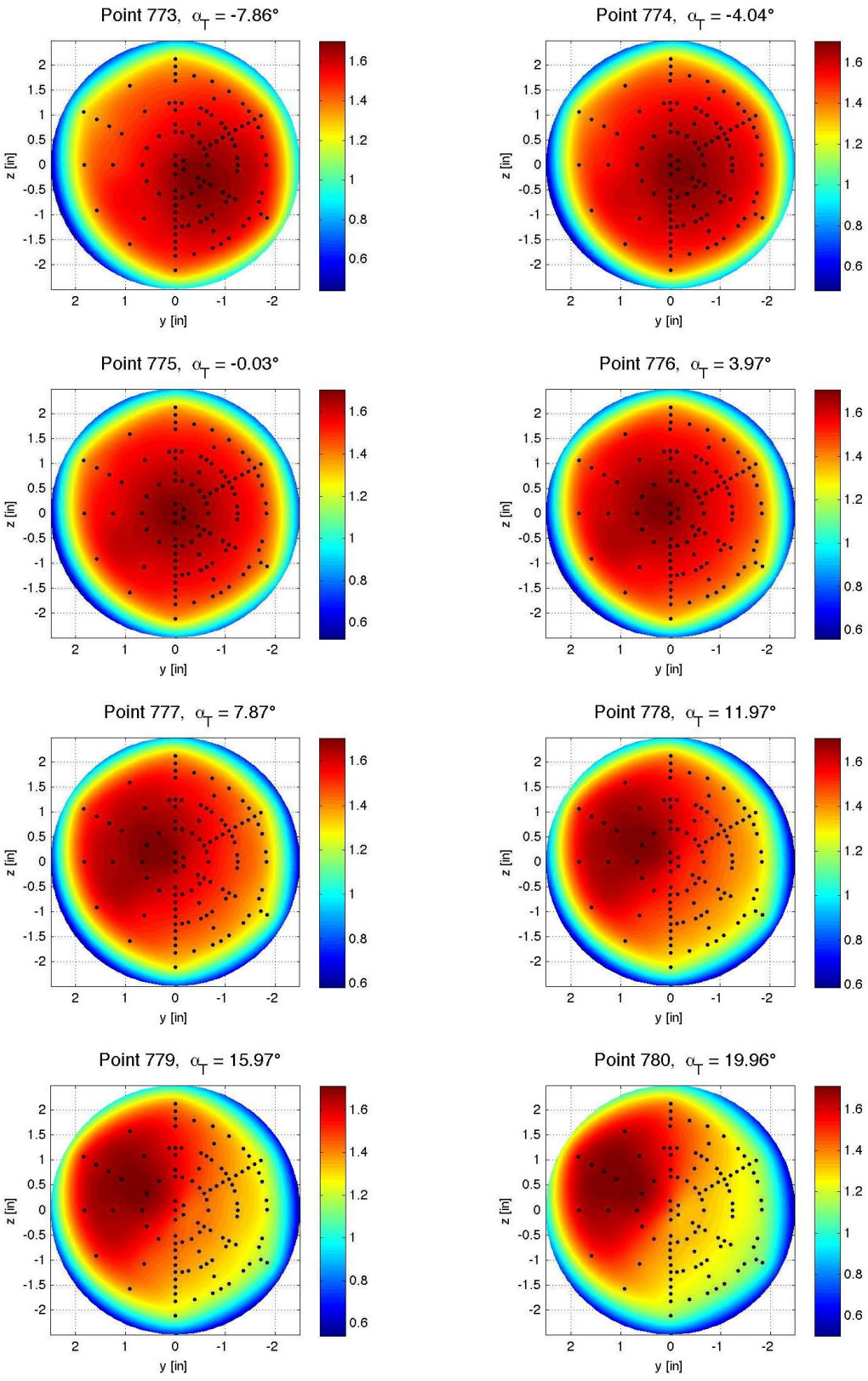

Figure E-31. Baseline configuration, Run 044, M_∞ = 2.4, Re_∞ = 1.0x10^6/ft, ϕ = 119.90°, X_S = 40.19 in, Y_S = –8.00 in, C_T = 0.00.

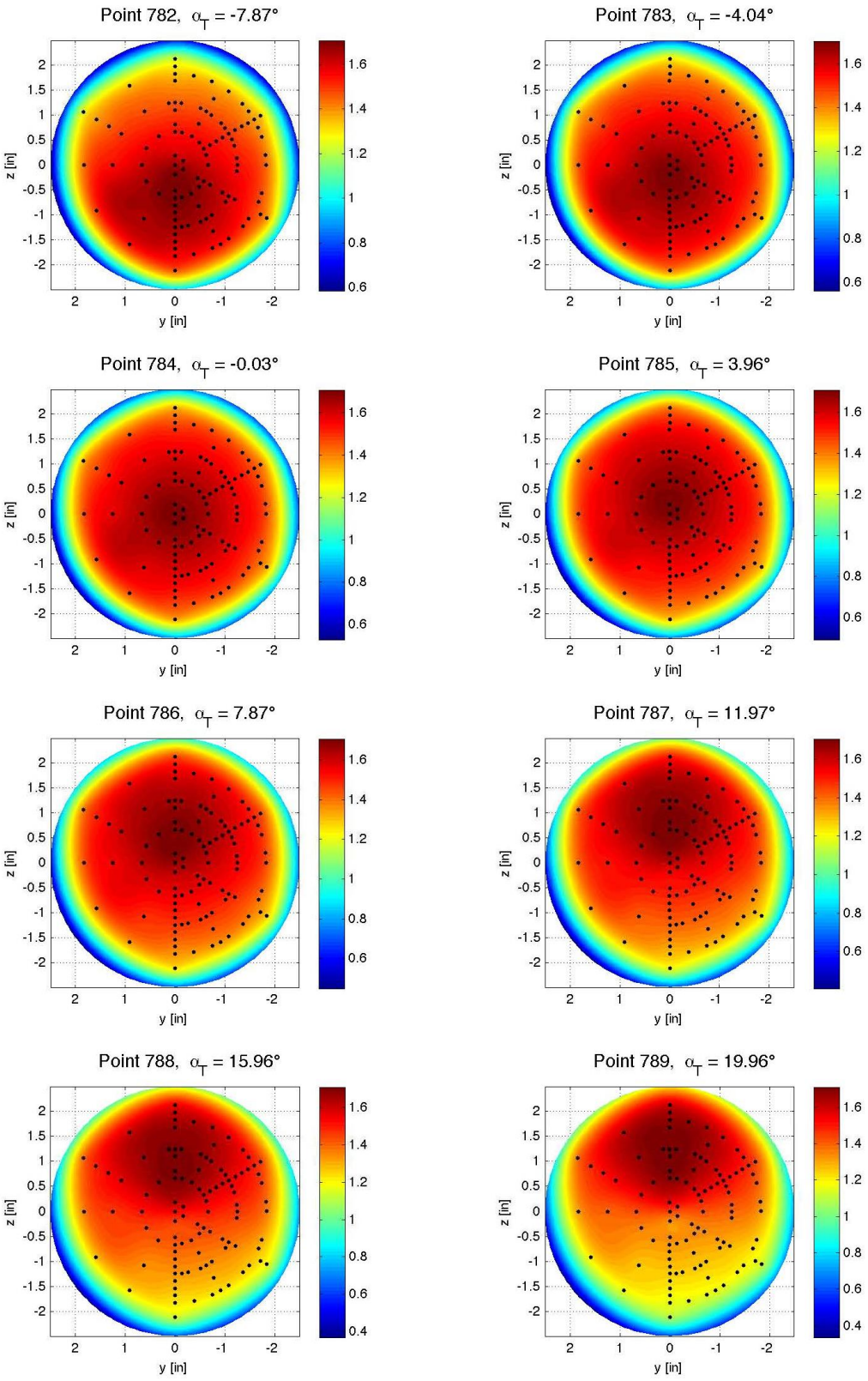

Figure E-32. Baseline configuration, Run 045, M_∞ = 2.4, Re_∞ = 1.0x10^6/ft, ϕ = 179.95°, X_S = 40.19 in, Y_S = –8.00 in, C_T = 0.00.

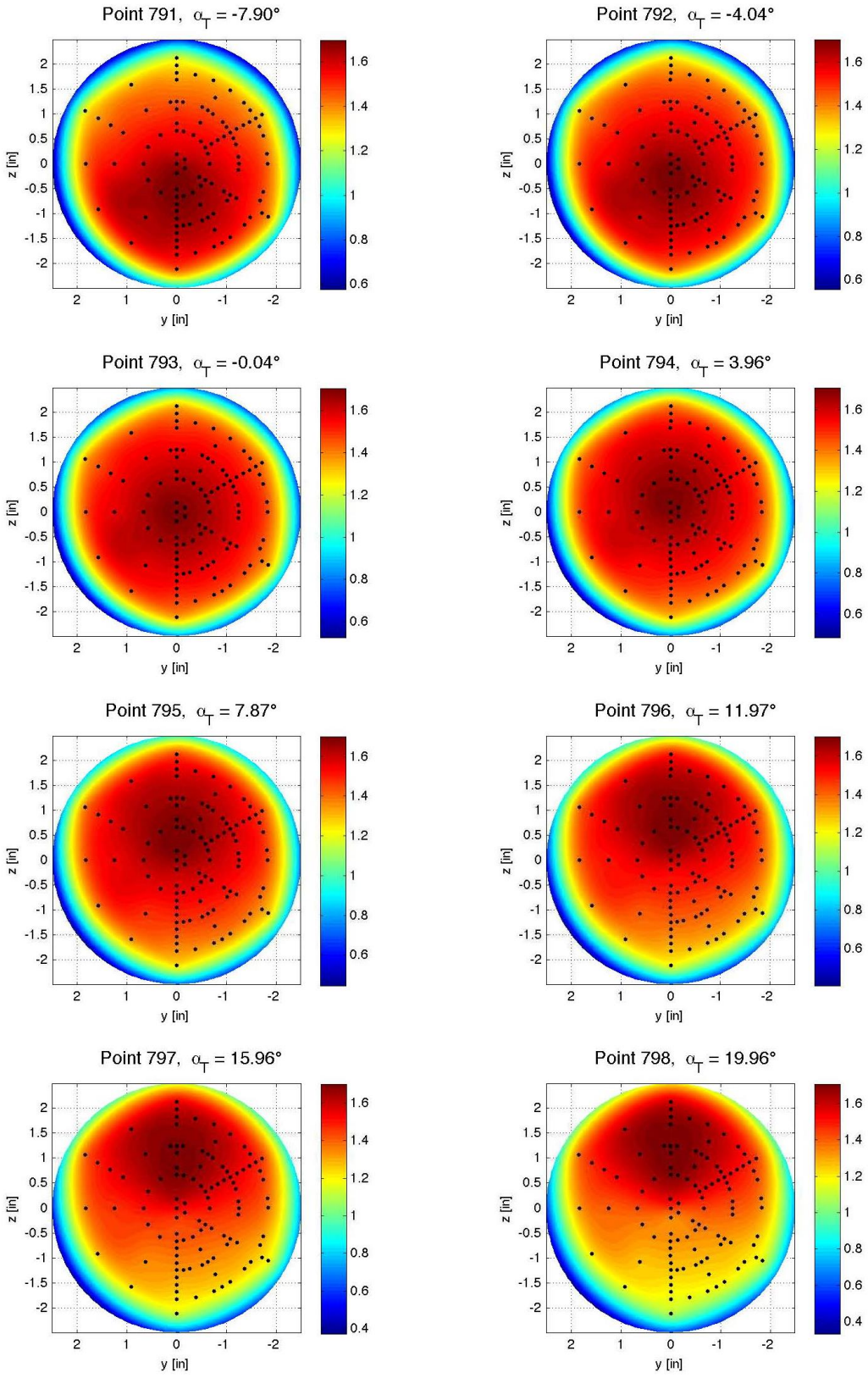

Figure E-33. Baseline configuration, Run 046, M_∞ = 2.4, Re_∞ = 1.0x10^6/ft, ϕ = 179.95°, X_S = 50.16 in, Y_S = –8.00 in, C_T = 0.00.

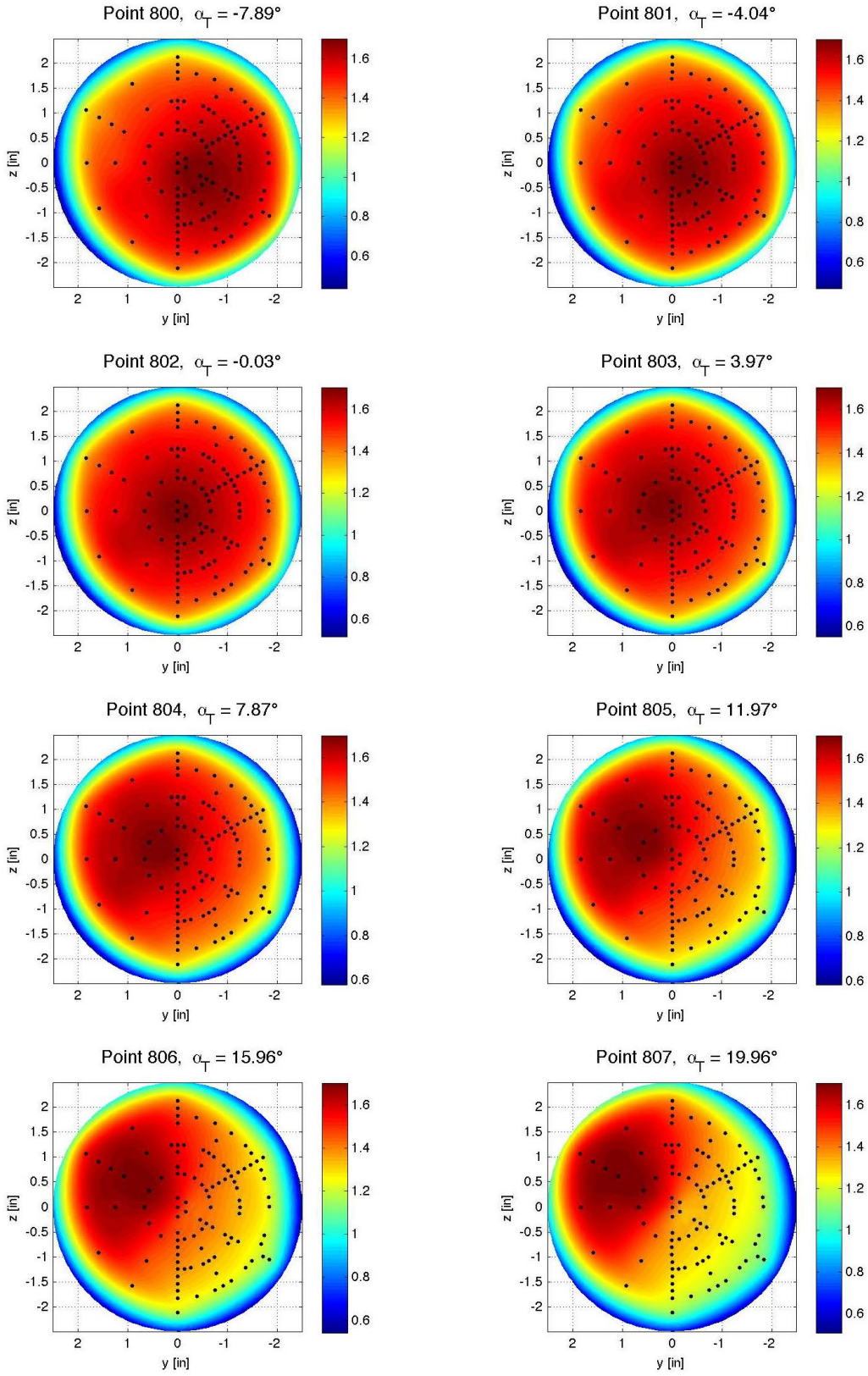

Figure E-34. Baseline configuration, Run 047, M_∞ = 2.4, Re_∞ = 1.0x10^6/ft, ϕ = 119.92°, X_S = 50.16 in, Y_S = –8.00 in, C_T = 0.00.

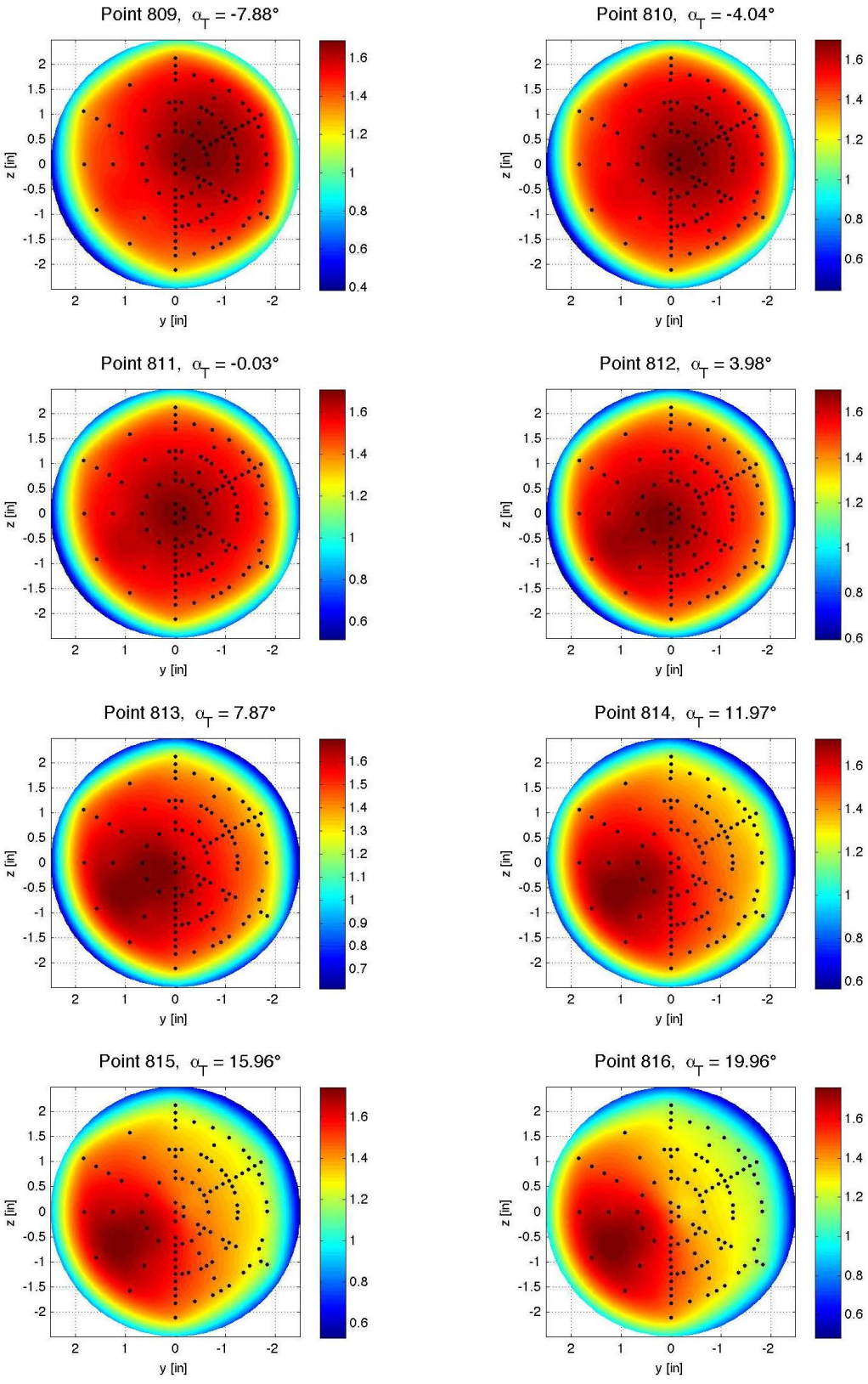

Figure E-35. Baseline configuration, Run 048, M_∞ = 2.4, Re_∞ = 1.0x10^6/ft, ϕ = 59.98°, X_S = 50.16 in, Y_S = –8.00 in, C_T = 0.00.

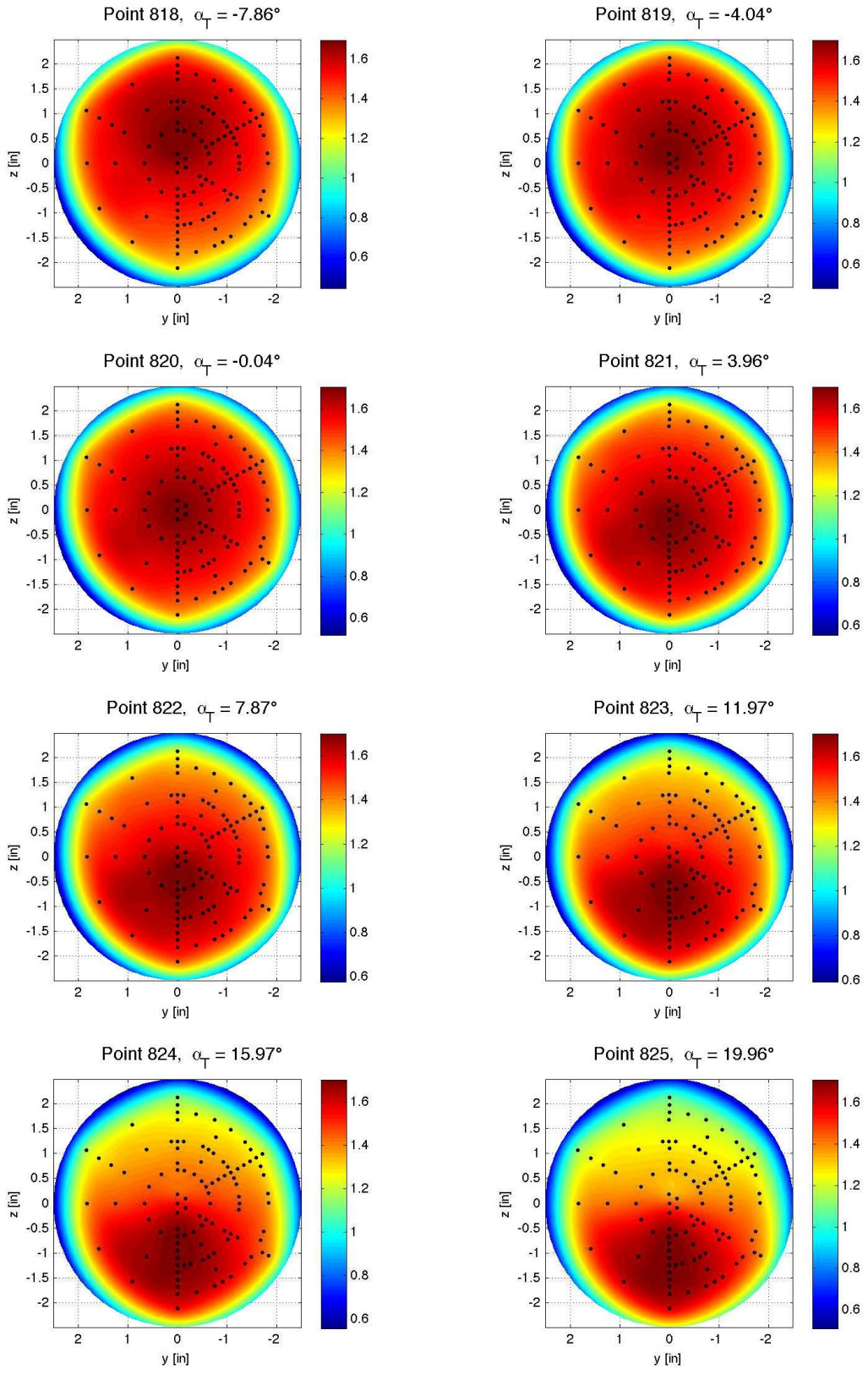

Figure E-36. Baseline configuration, Run 049, $M\infty$ = 2.4, Re_∞ = 1.0x10^6/ft, ϕ = 0.05°, X_S = 50.16 in, Y_S = –8.00 in, C_T = 0.00.

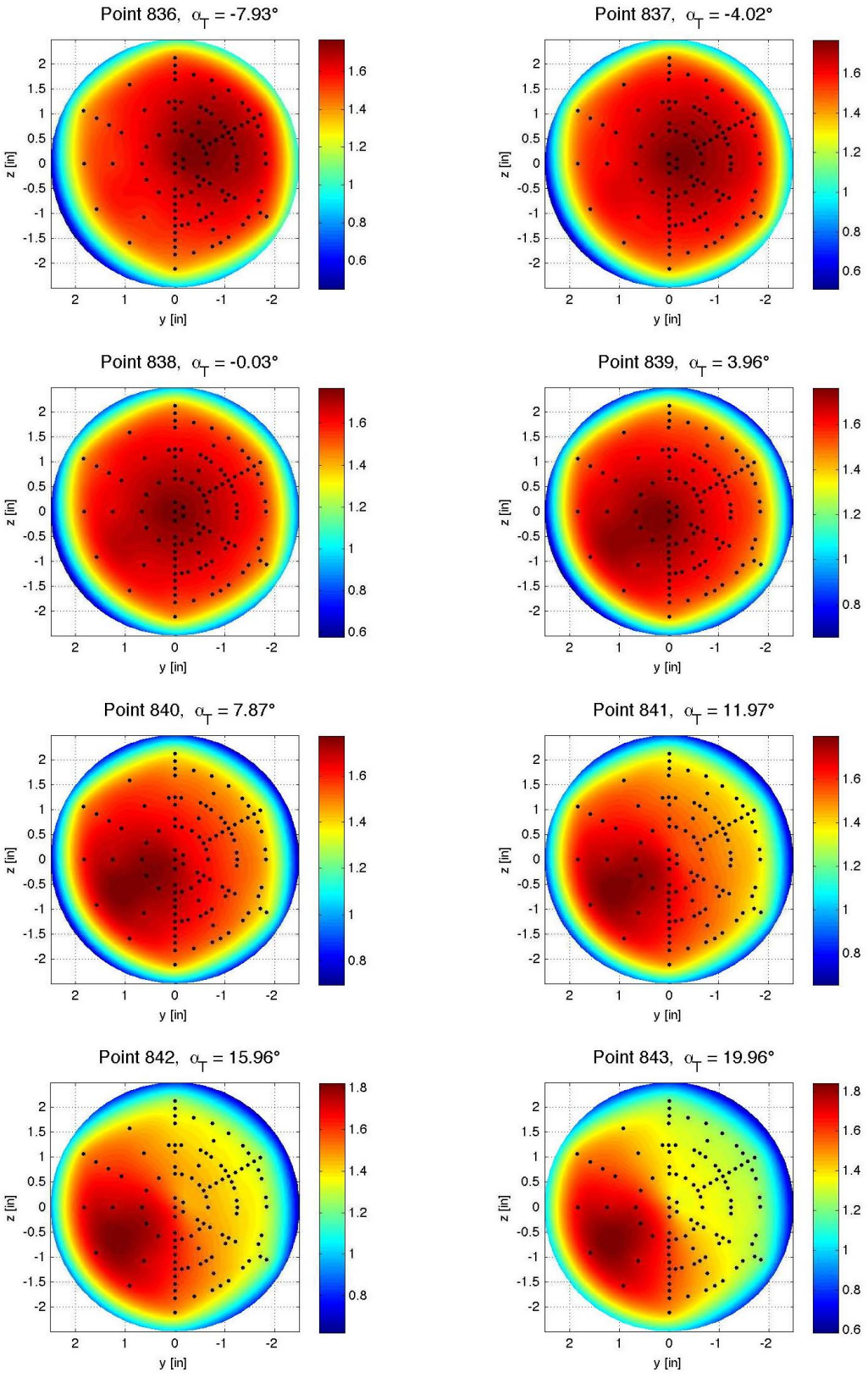

Figure E-37. Baseline configuration, Run 050, M_∞ = 3.5, Re_∞ = 1.0x10^6/ft, ϕ = 60.02°, X_S = 50.16 in, Y_S = 0.00 in, C_T = 0.00.

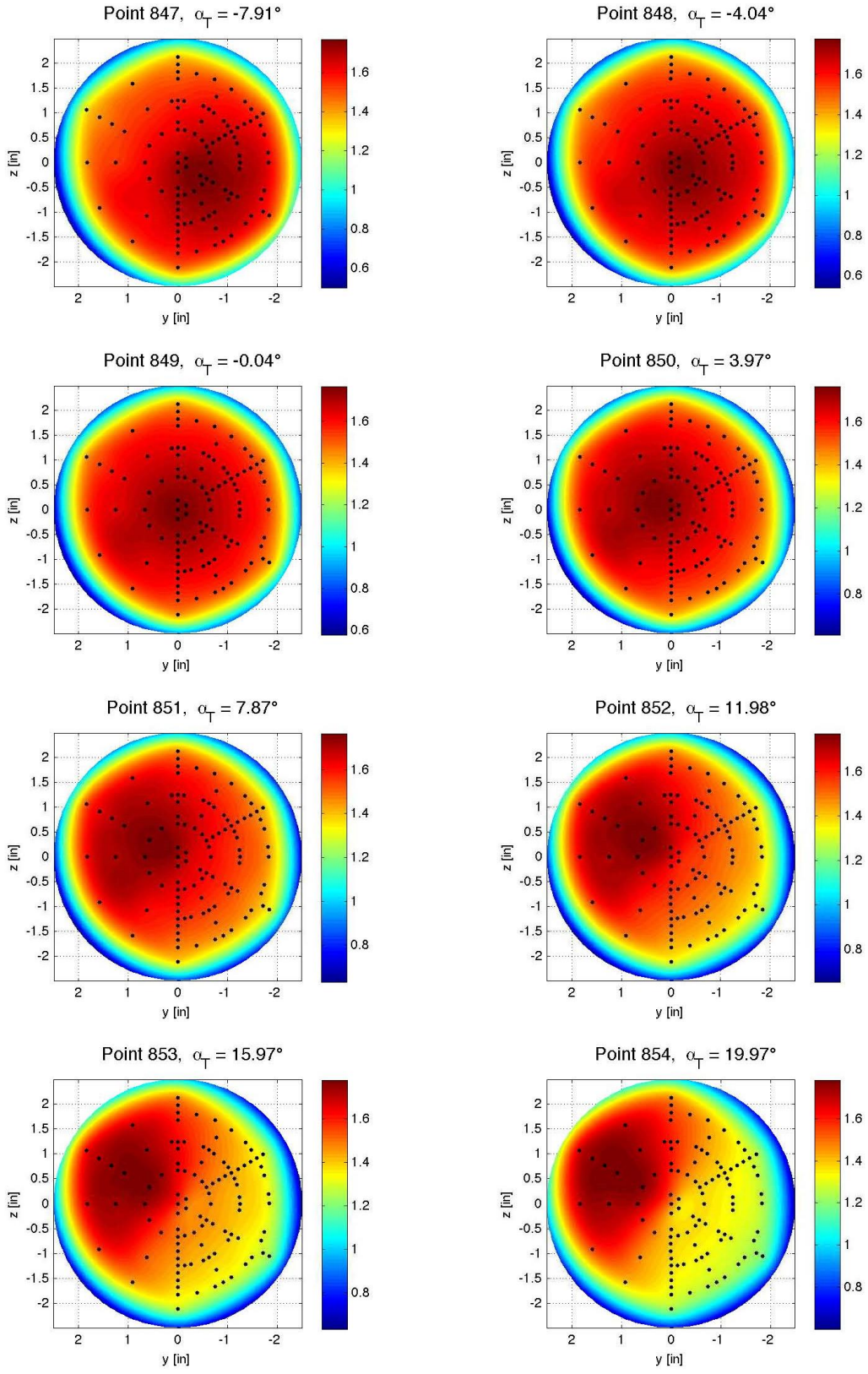

Figure E-38. Baseline configuration, Run 051, M_∞ = 3.5, Re_∞ = 1.0x10^6/ft, ϕ = 119.94°, X_S = 50.16 in, Y_S = 0.00 in, C_T = 0.00.

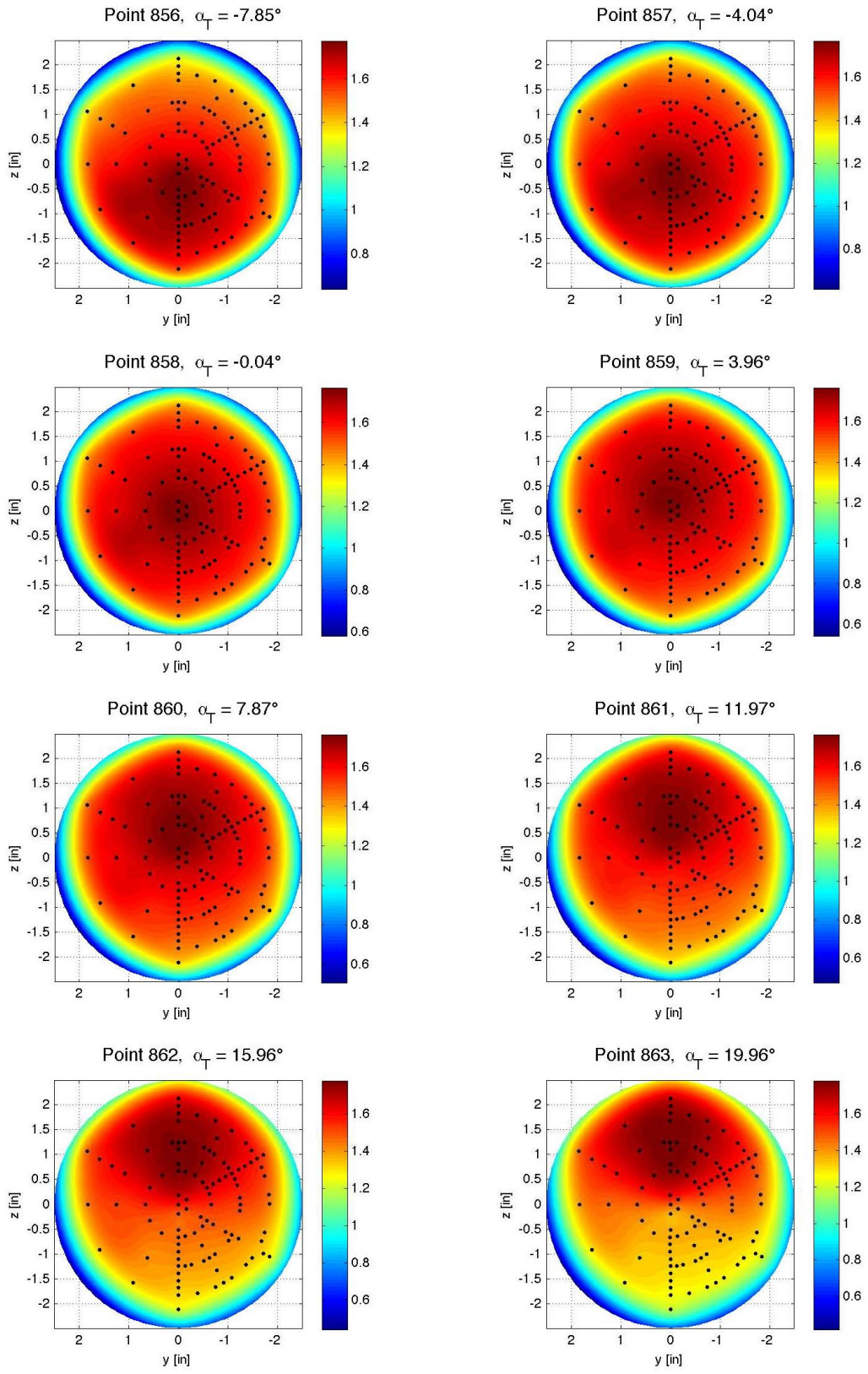

Figure E-39. Baseline configuration, Run 052, M_∞ = 3.5, Re_∞ = 1.0x10^6/ft, ϕ = 179.99°, X_S = 50.16 in, Y_S = 0.00 in, C_T = 0.00.

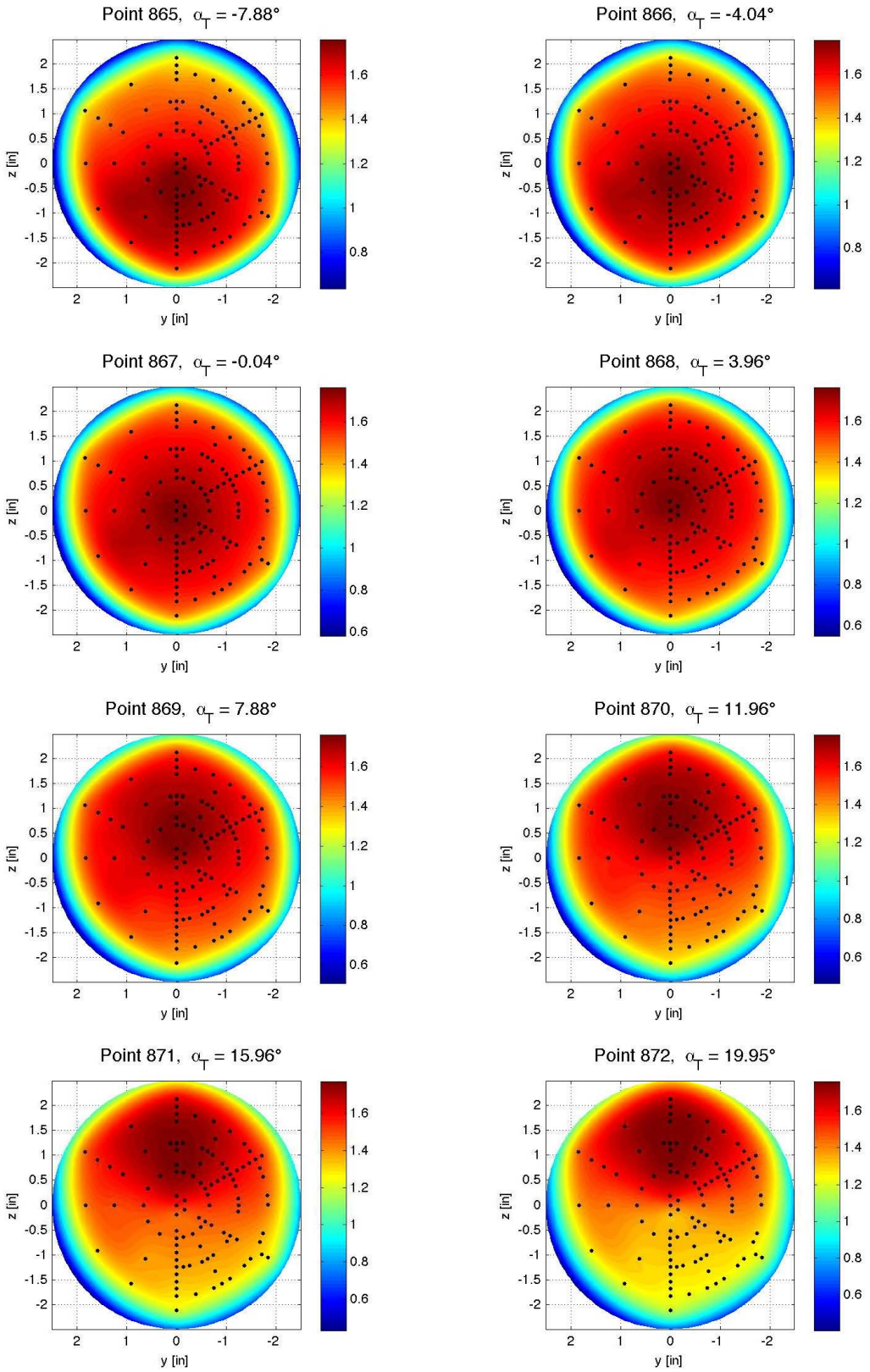

Figure E-40. Baseline configuration, Run 053, $M\infty$ = 3.5, Re_∞ = 1.0x10^6/ft, ϕ = 0.01°, X_S = 39.93 in, Y_S = 0.00 in, C_T = 0.00.

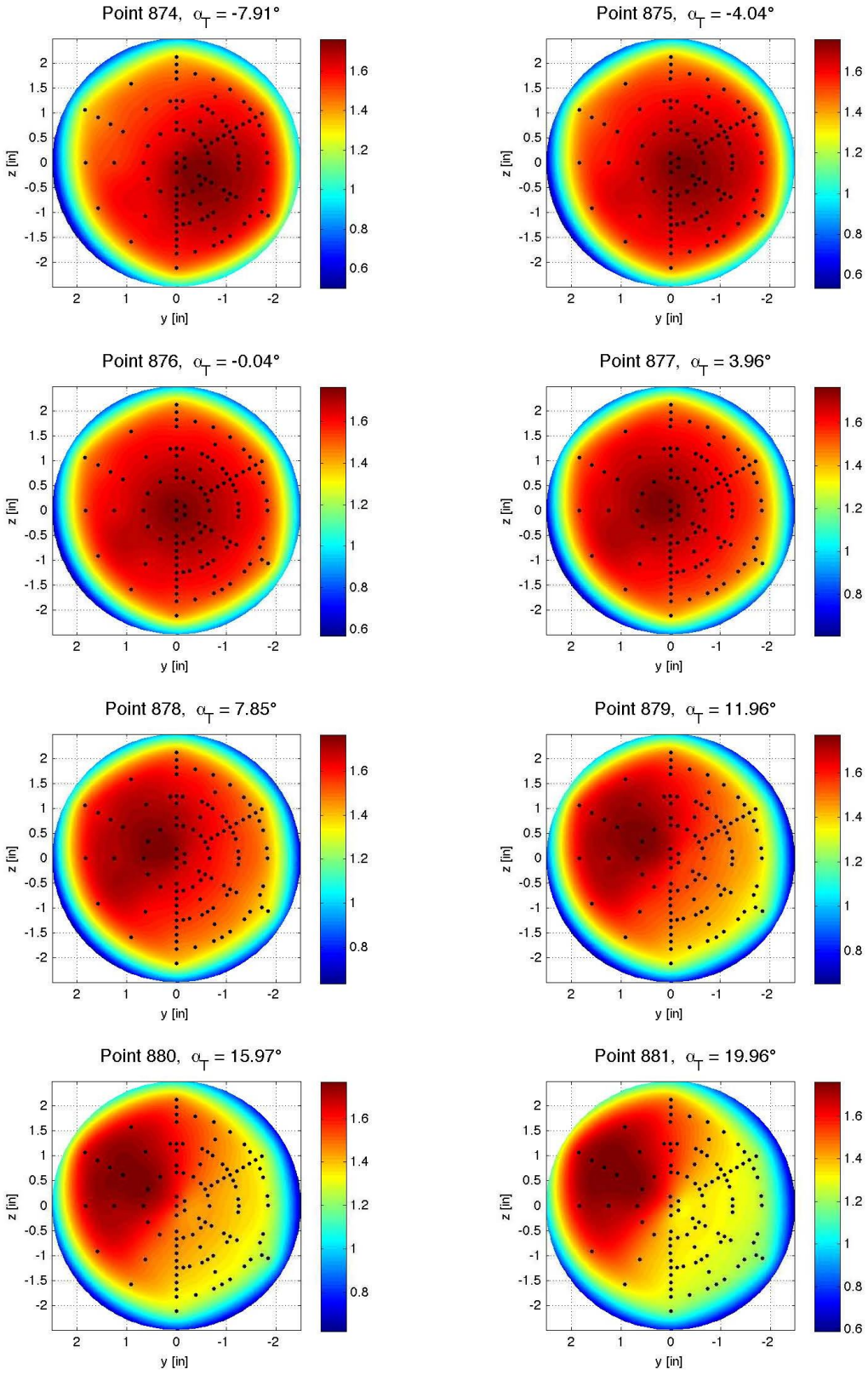

Figure E-41. Baseline configuration, Run 054, M_∞ = 3.5, Re_∞ = 1.0x10^6/ft, ϕ = 120.06°, X_S = 40.17 in, Y_S = 0.00 in, C_T = 0.00.

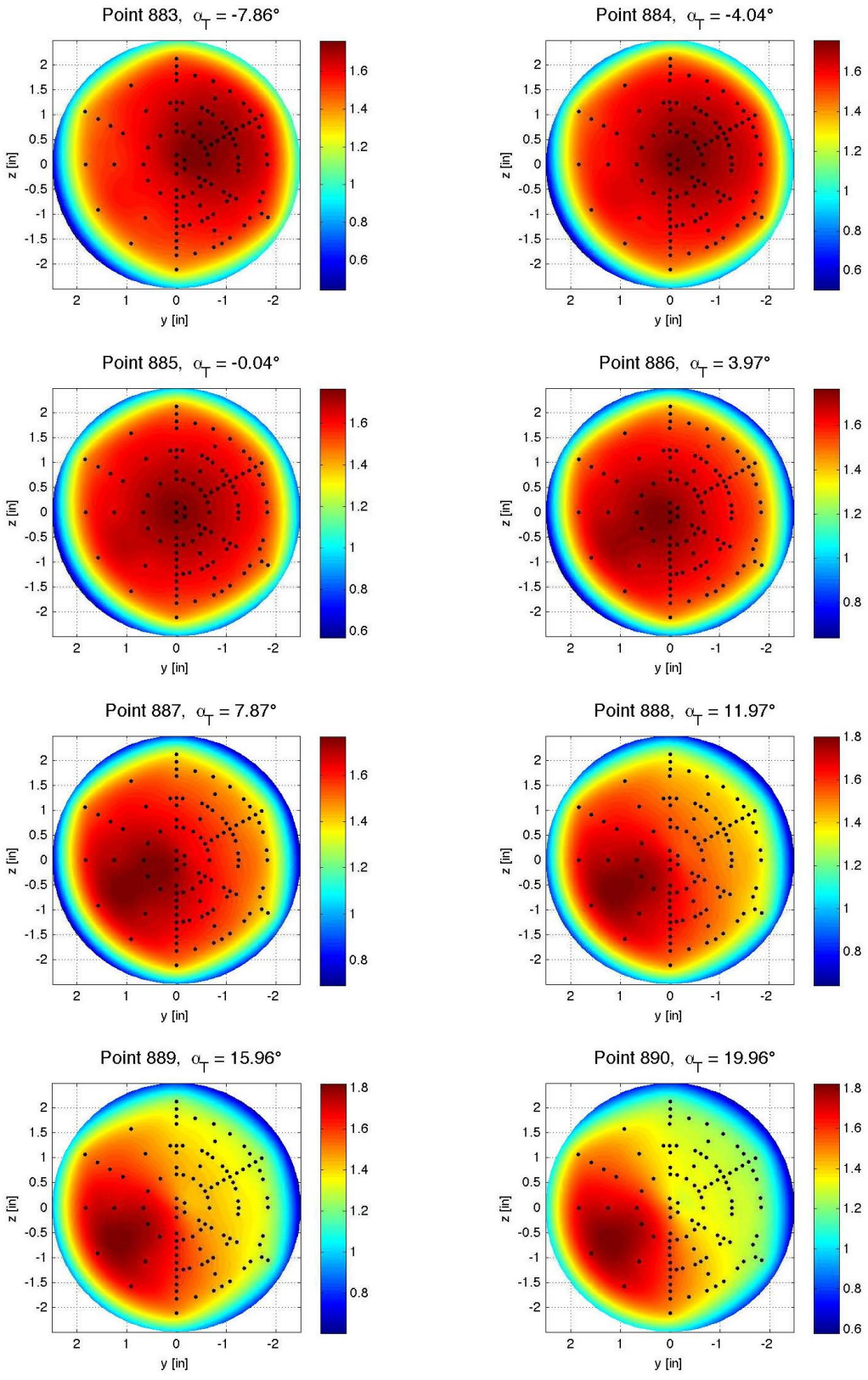

Figure E-42. Baseline configuration, Run 055, M_∞ = 3.5, Re_∞ = 1.0x10^6/ft, ϕ = 59.98°, X_S = 40.17 in, Y_S = 0.00 in, C_T = 0.00.

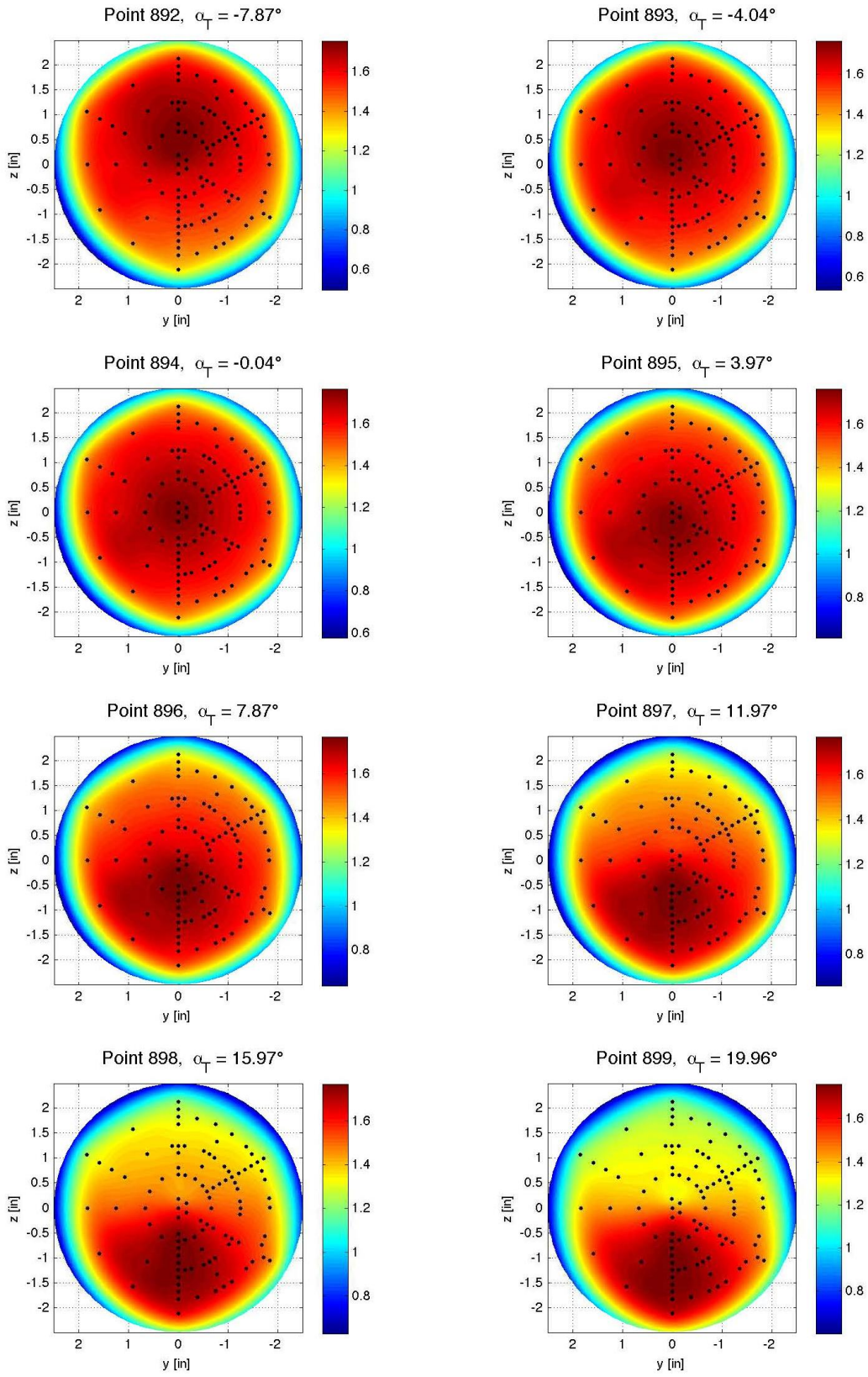

Figure E-43. Baseline configuration, Run 056, M_∞ = 3.5, Re_∞ = 1.0x10^6/ft, ϕ = −0.07°, X_S = 40.17 in, Y_S = 0.00 in, C_T = 0.00.

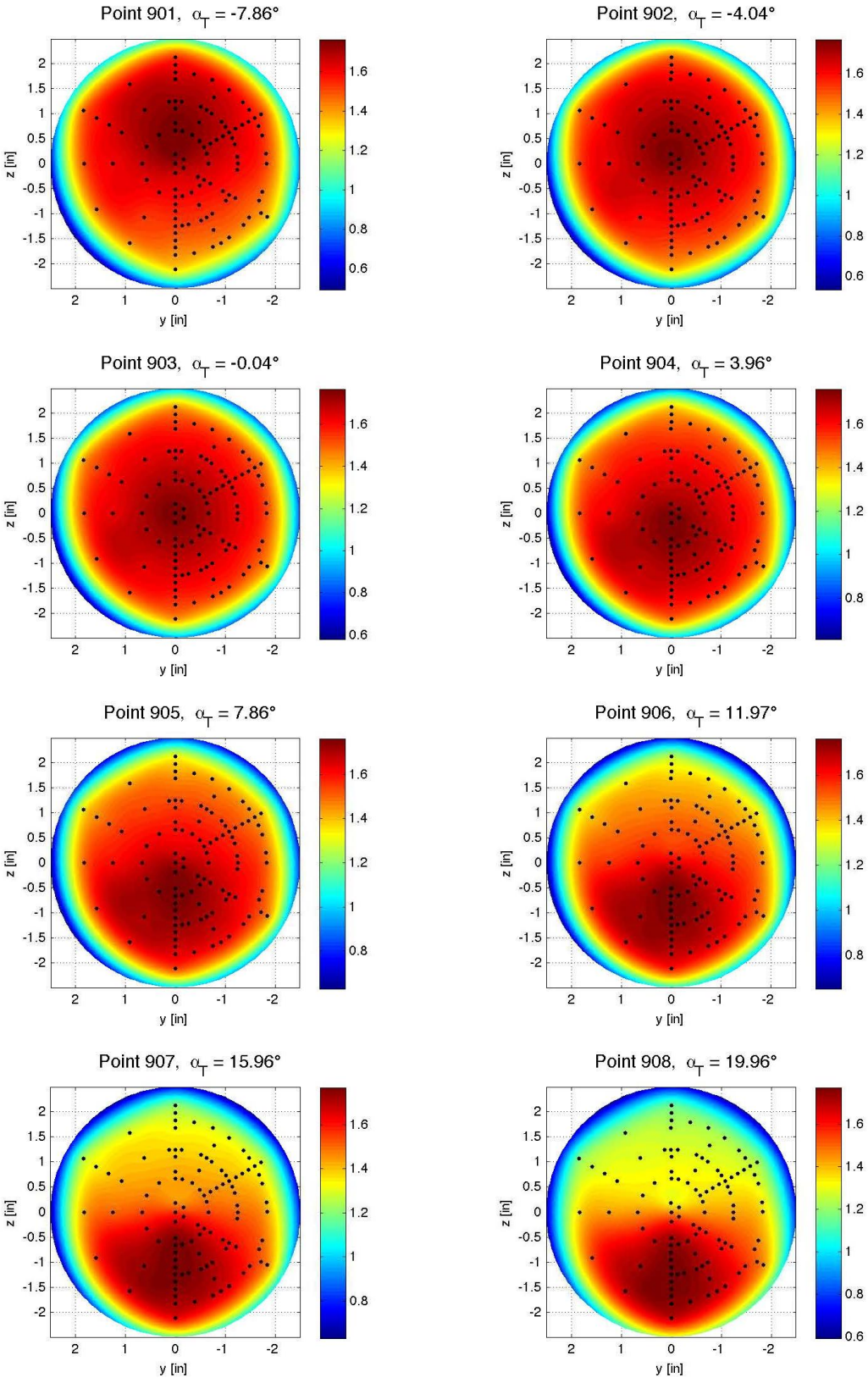

Figure E-44. Baseline configuration, Run 057, M_∞ = 3.5, Re_∞ = 1.0x10^6/ft, ϕ = −0.07°, X_S = 25.16 in, Y_S = 0.00 in, C_T = 0.00.

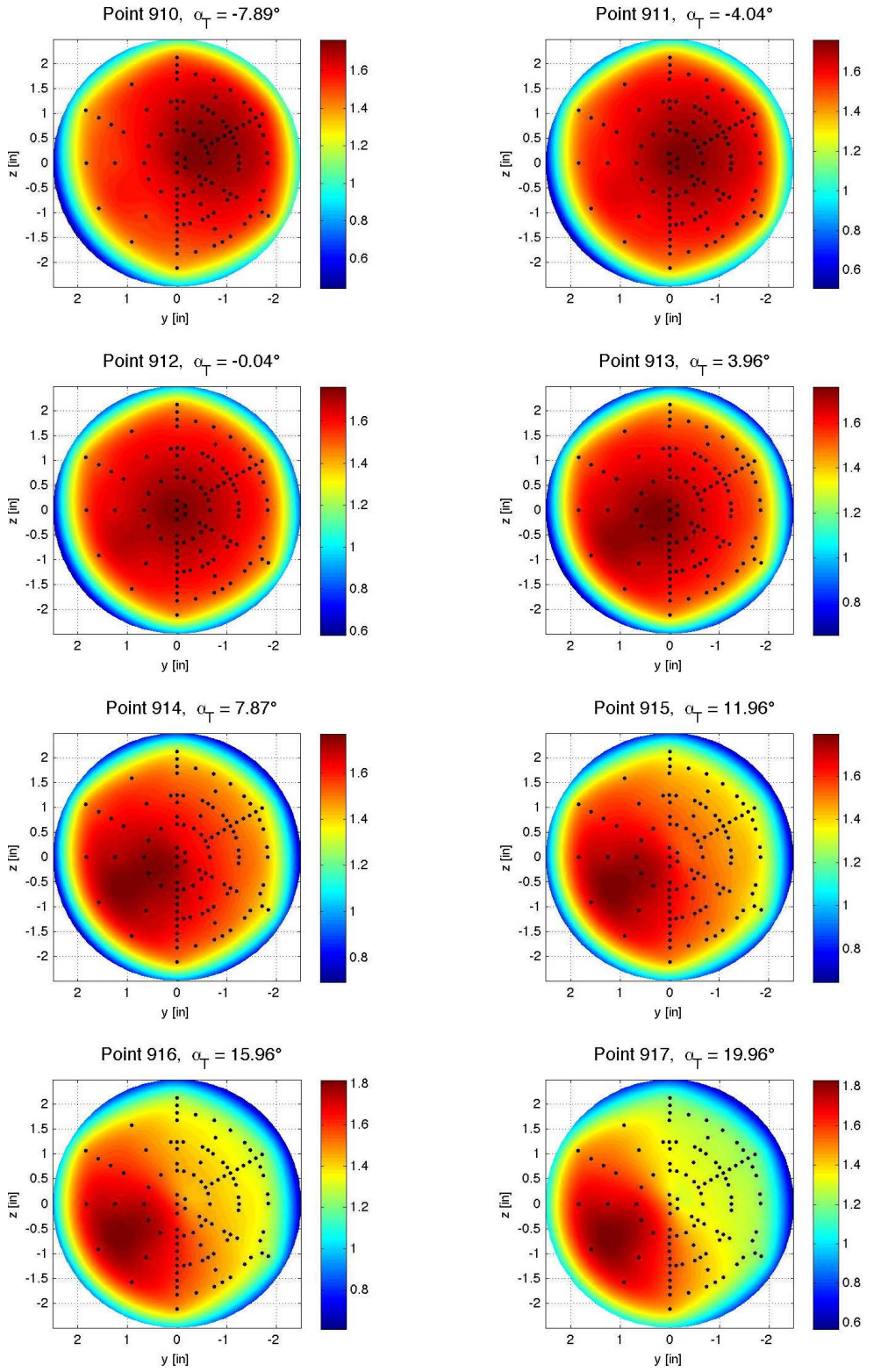

Figure E-45. Baseline configuration, Run 058, $M\infty$ = 3.5, Re_∞ = 1.0x10^6/ft, ϕ = 60.04°, X_S = 25.16 in, Y_S = 0.00 in, C_T = 0.00.

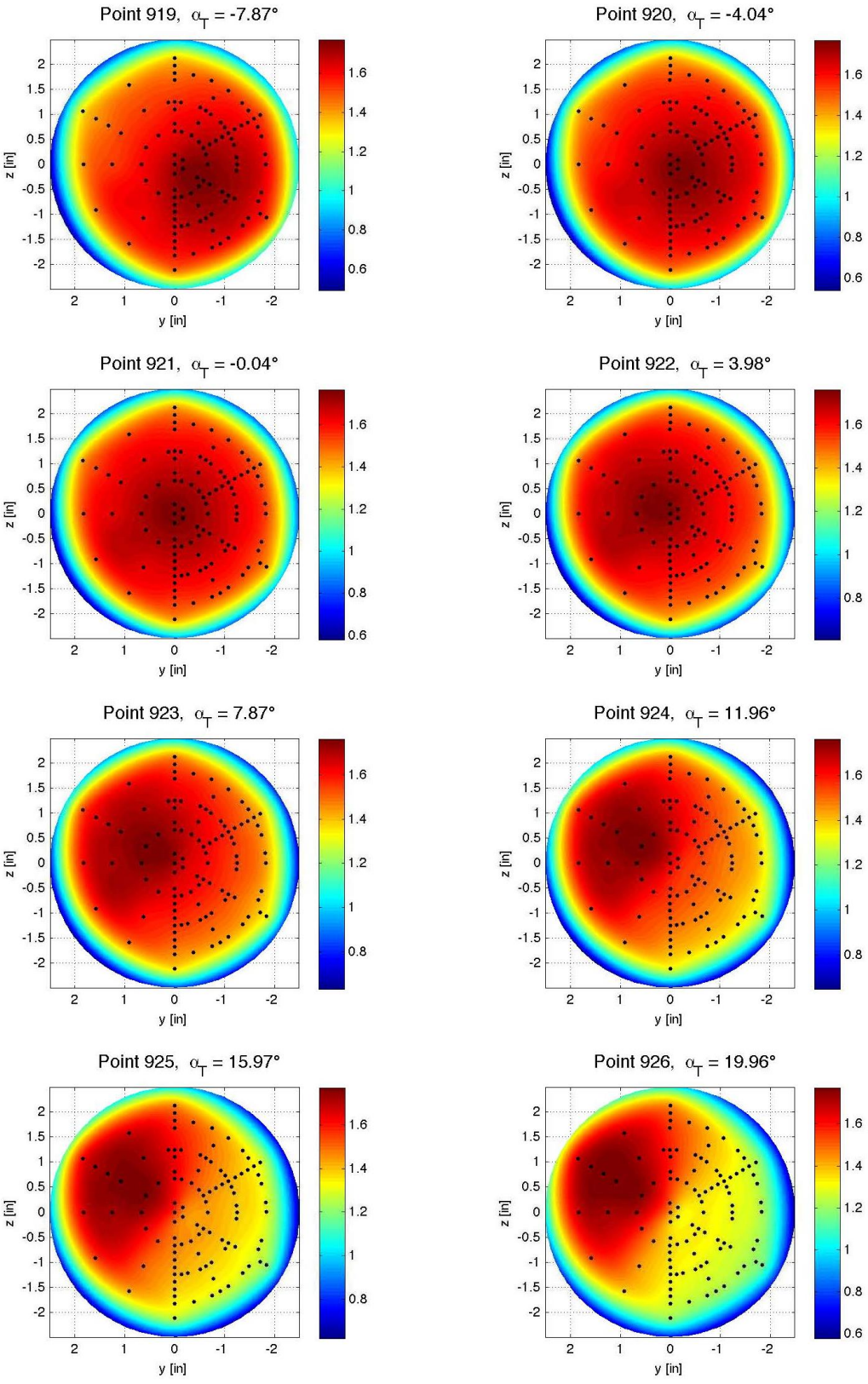

Figure E-46. Baseline configuration, Run 059, M_∞ = 3.5, Re_∞ = 1.0x10^6/ft, ϕ = 120.06°, X_S = 25.16 in, Y_S = 0.00 in, C_T = 0.00.

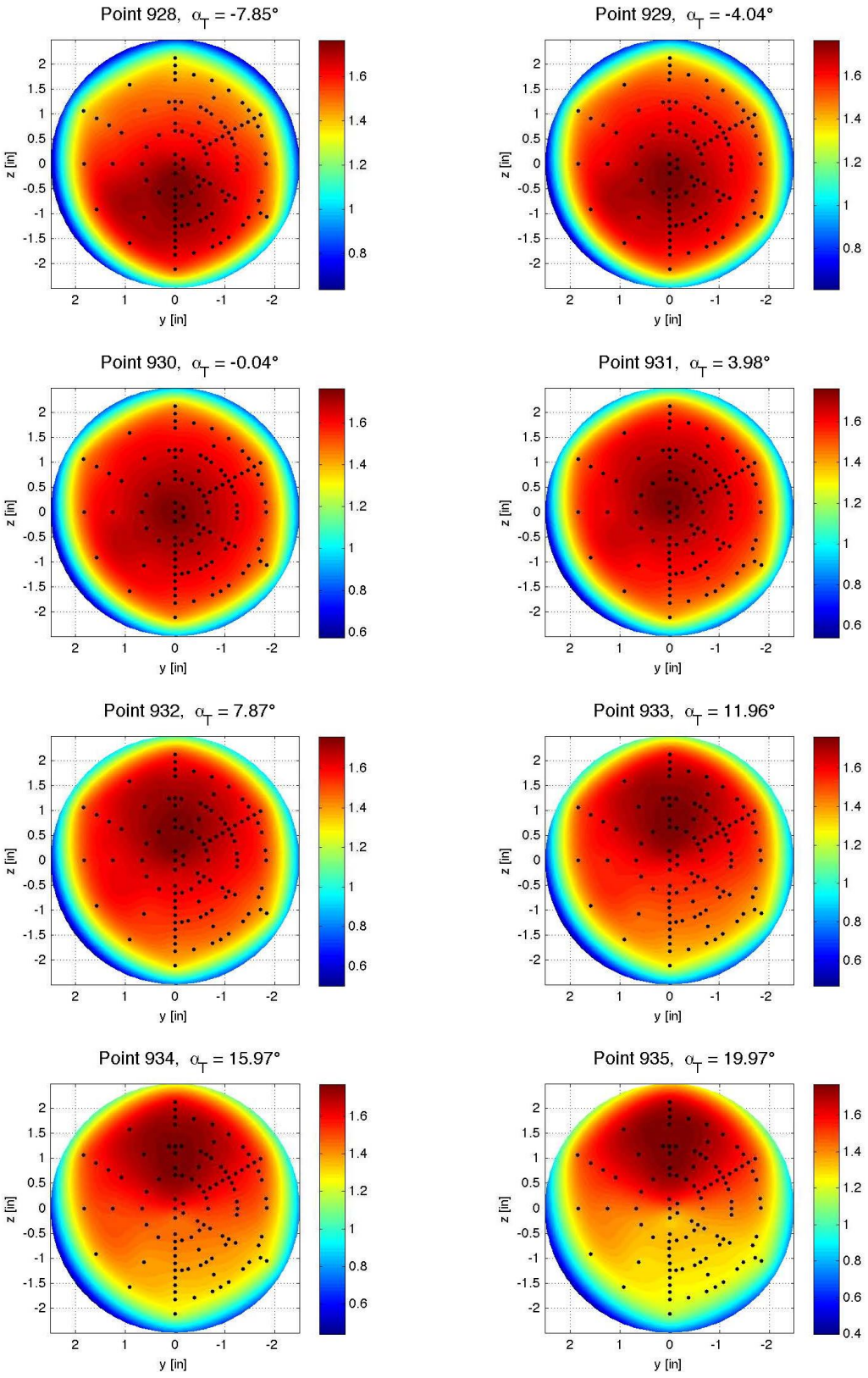

Figure E-47. Baseline configuration, Run 060, M_∞ = 3.5, Re_∞ = 1.0x10^6/ft, ϕ = 179.95°, X_S = 25.16 in, Y_S = 0.00 in, C_T = 0.00.

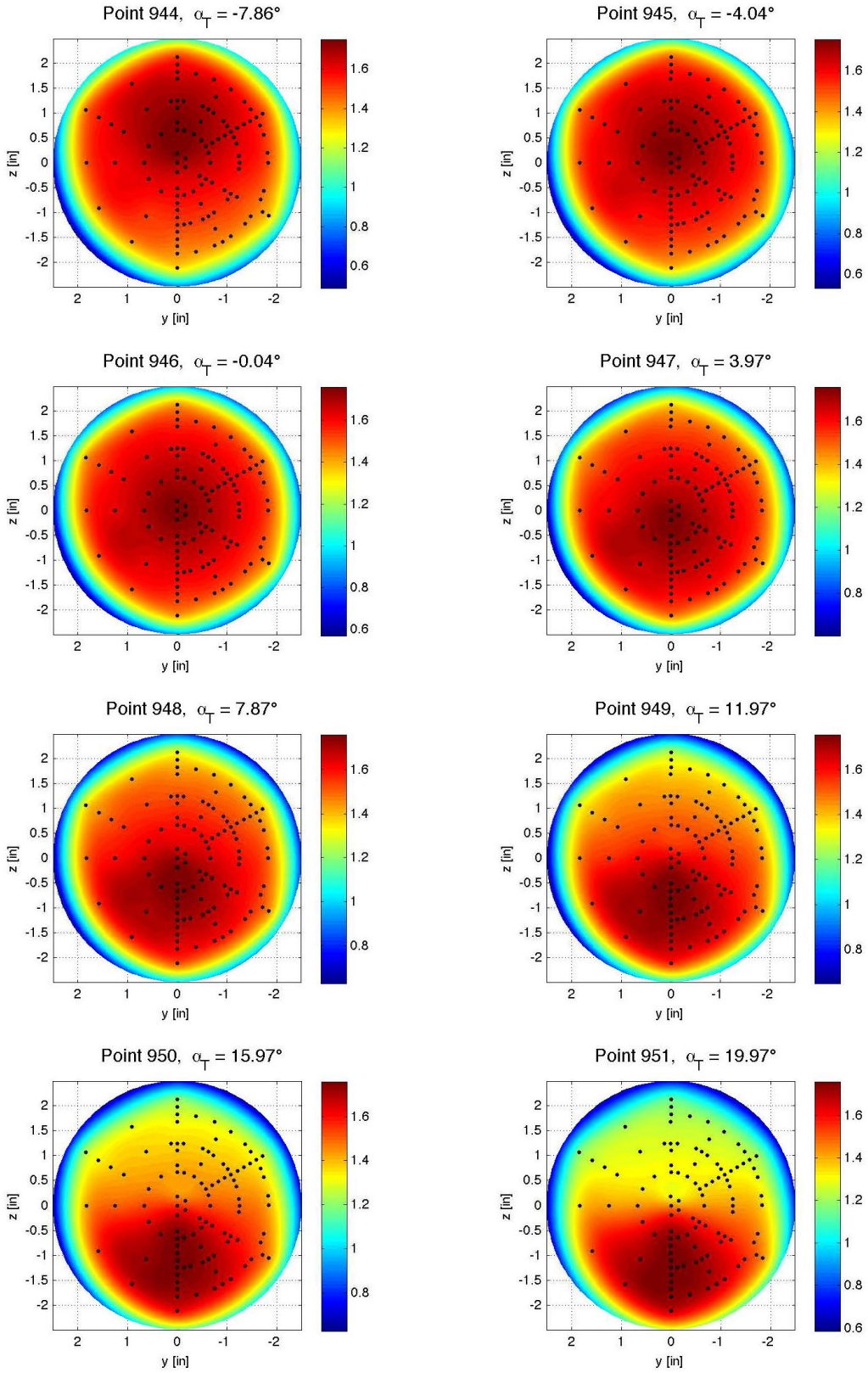

Figure E-48. Baseline configuration, Run 065, M_∞ = 3.5, Re_∞ = 1.0x10^6/ft, ϕ = −0.01°, X_S = 25.16 in, Y_S = −8.00 in, C_T = 0.00.

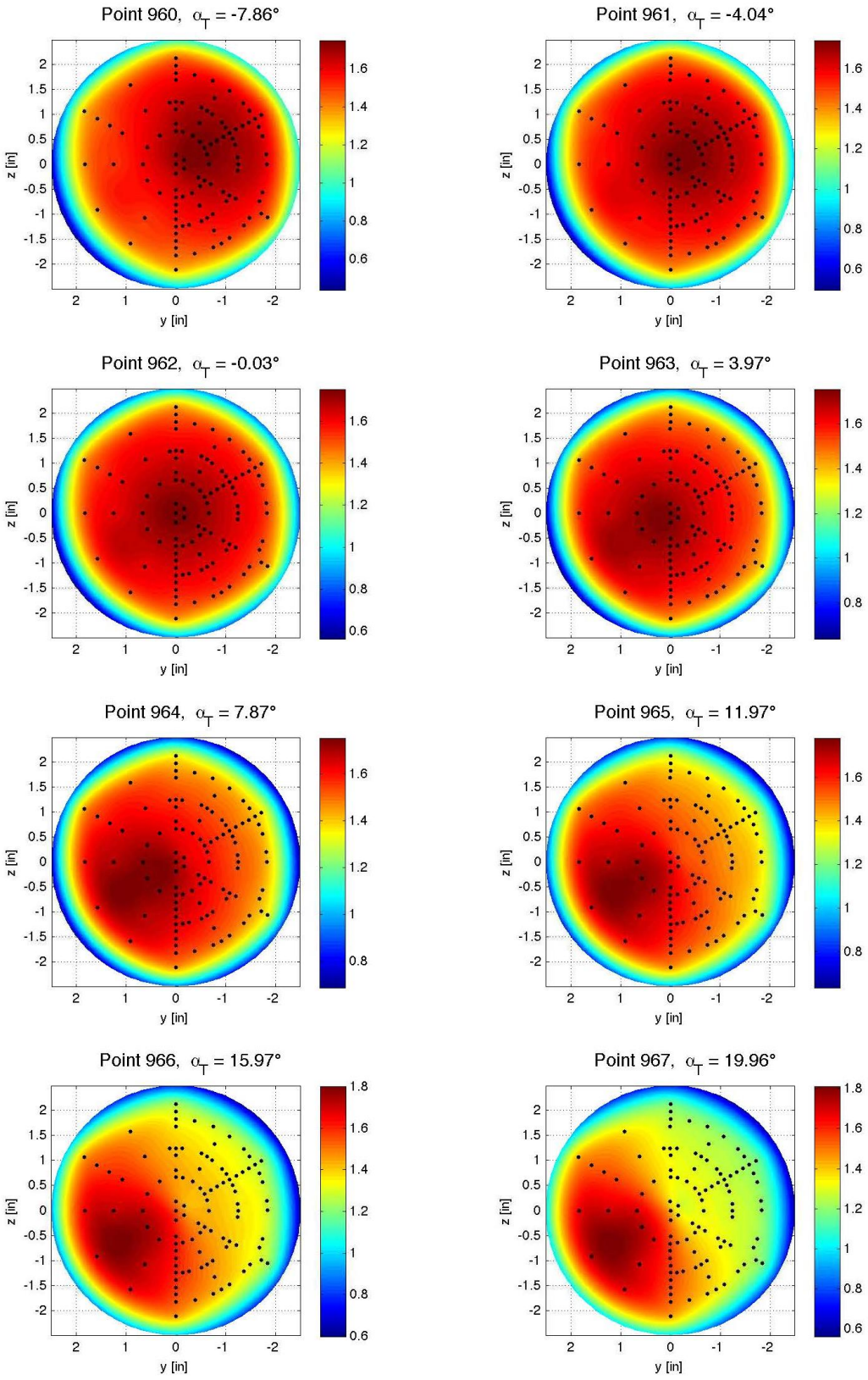

Figure E-49. Baseline configuration, Run 067, M_∞ = 3.5, Re_∞ = 1.0x10^6/ft, ϕ = 60.06°, X_S = 25.16 in, Y_S = –8.00 in, C_T = 0.00.

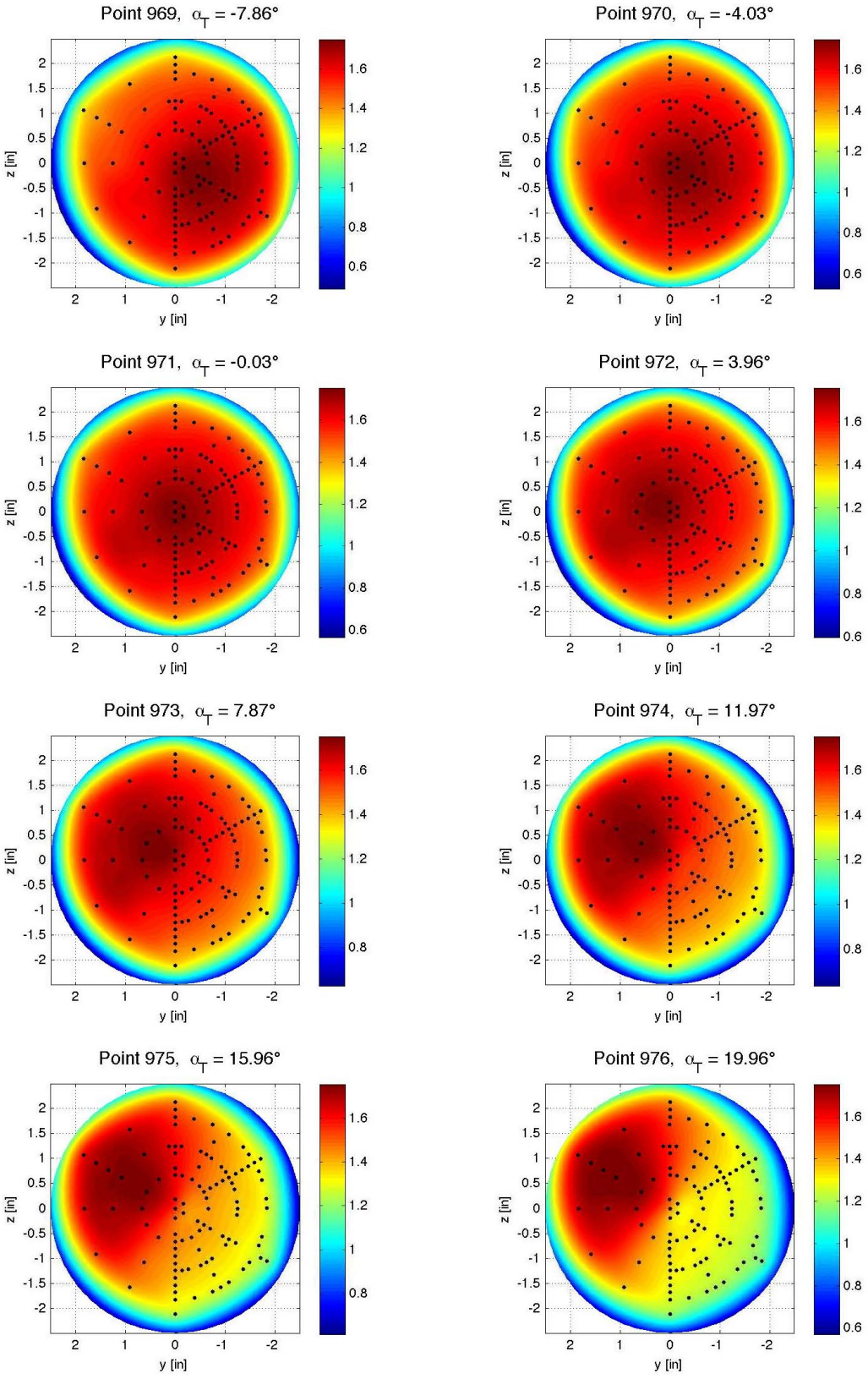

Figure E-50. Baseline configuration, Run 068, M_∞ = 3.5, Re_∞ = 1.0x10^6/ft, ϕ = 119.96°, X_S = 25.16 in, Y_S = –8.00 in, C_T = 0.00.

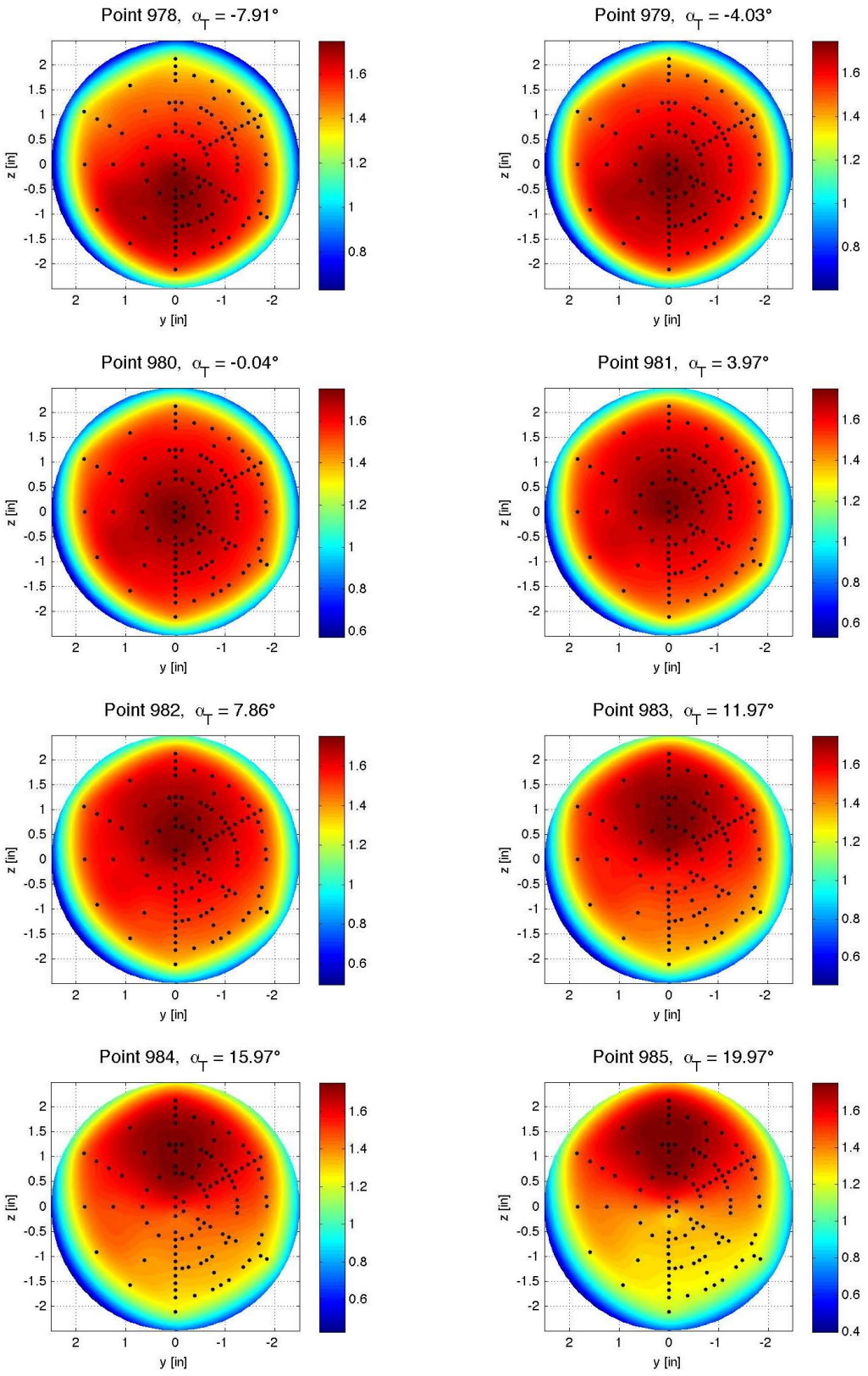

Figure E-51. Baseline configuration, Run 069, M_∞ = 3.5, Re_∞ = 1.0x10^6/ft, ϕ = 179.95°, X_S = 25.16 in, Y_S = –8.00 in, C_T = 0.00.

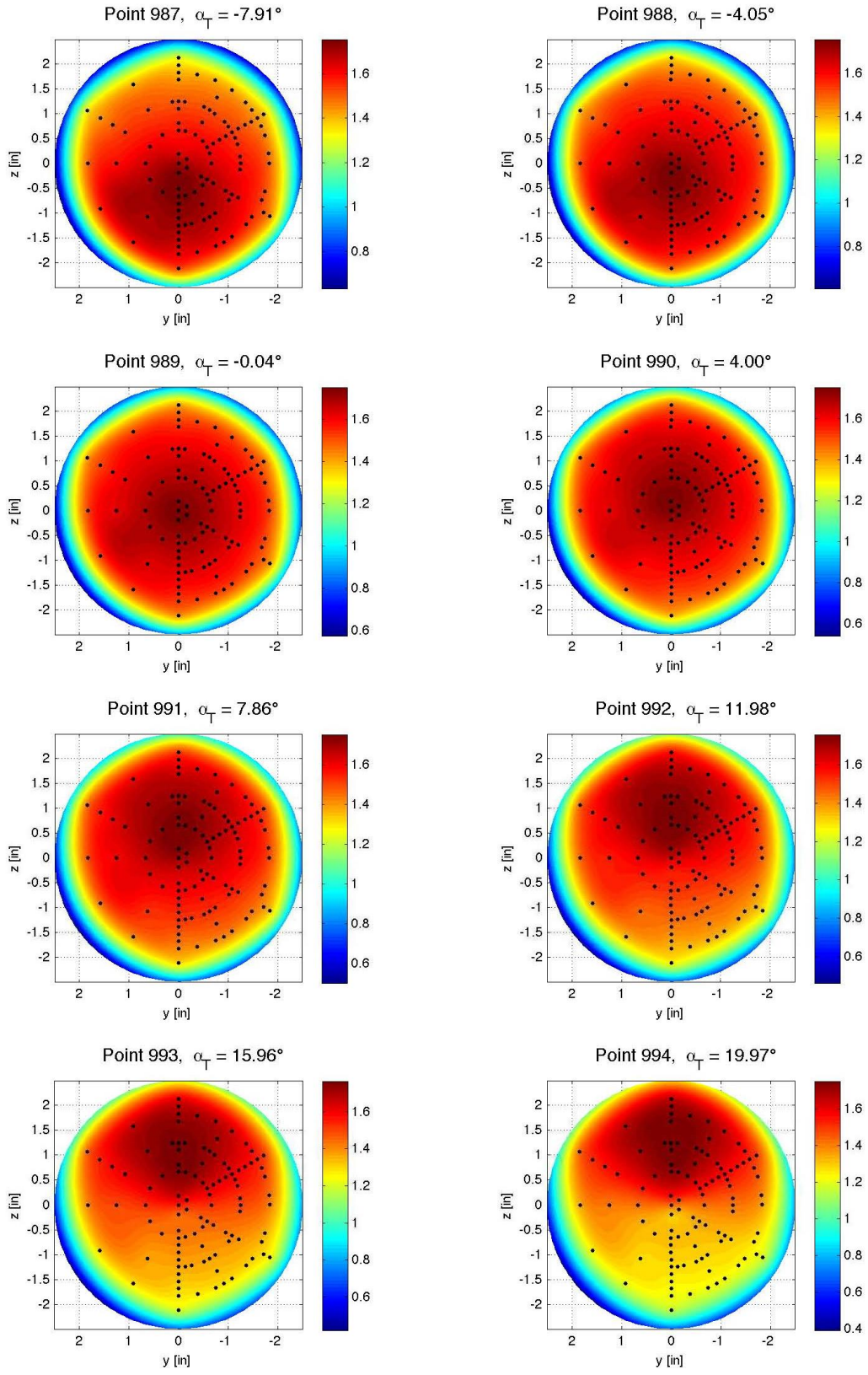

Figure E-52. Baseline configuration, Run 070, M_∞ = 3.5, Re_∞ = 1.0x10^6/ft, ϕ = 179.95°, X_S = 40.16 in, Y_S = –8.00 in, C_T = 0.00.

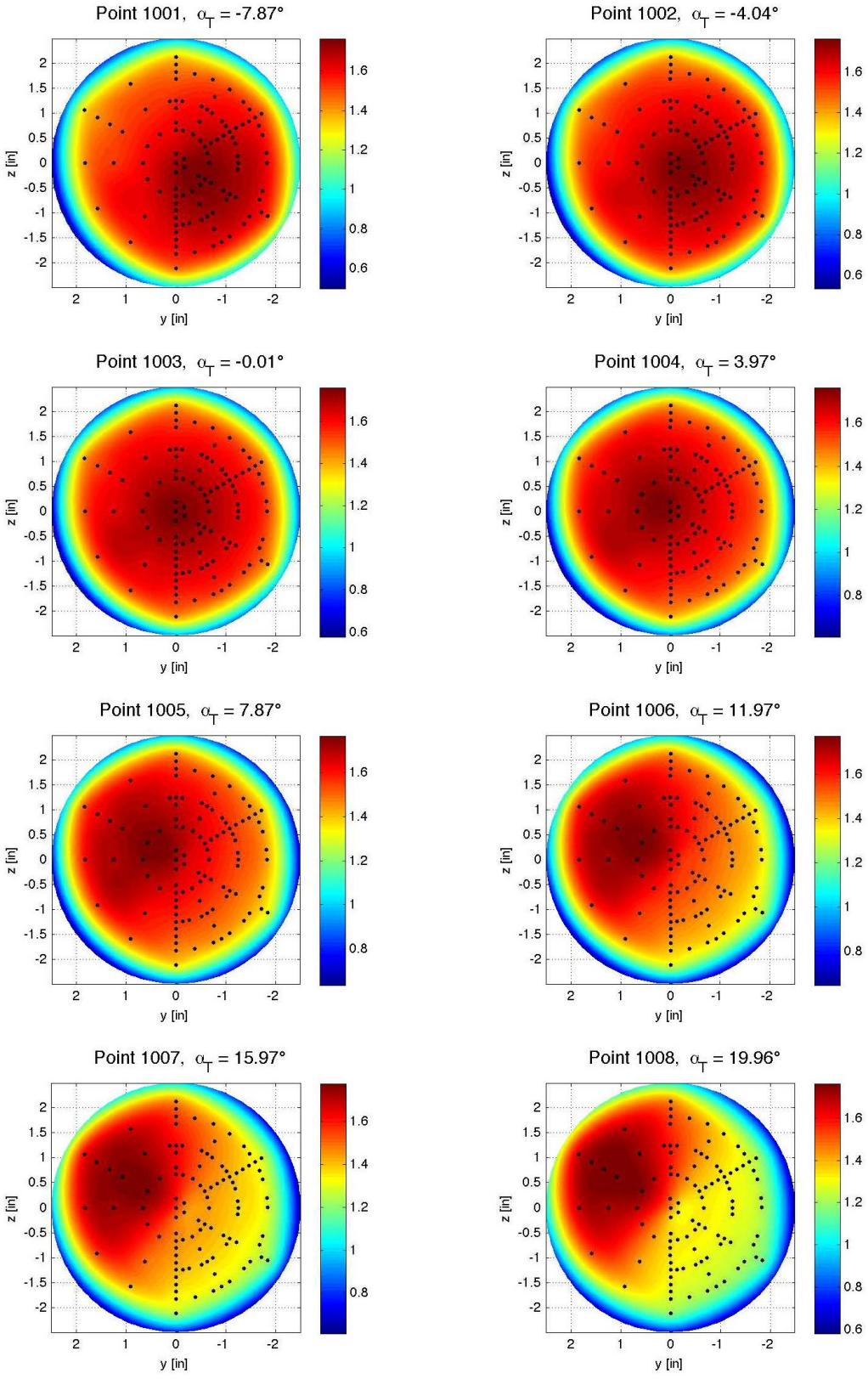

Figure E-53. Baseline configuration, Run 073, M_∞ = 3.5, Re_∞ = 1.0x10^6/ft, ϕ = 119.92°, X_S = 40.18 in, Y_S = –8.00 in, C_T = 0.00.

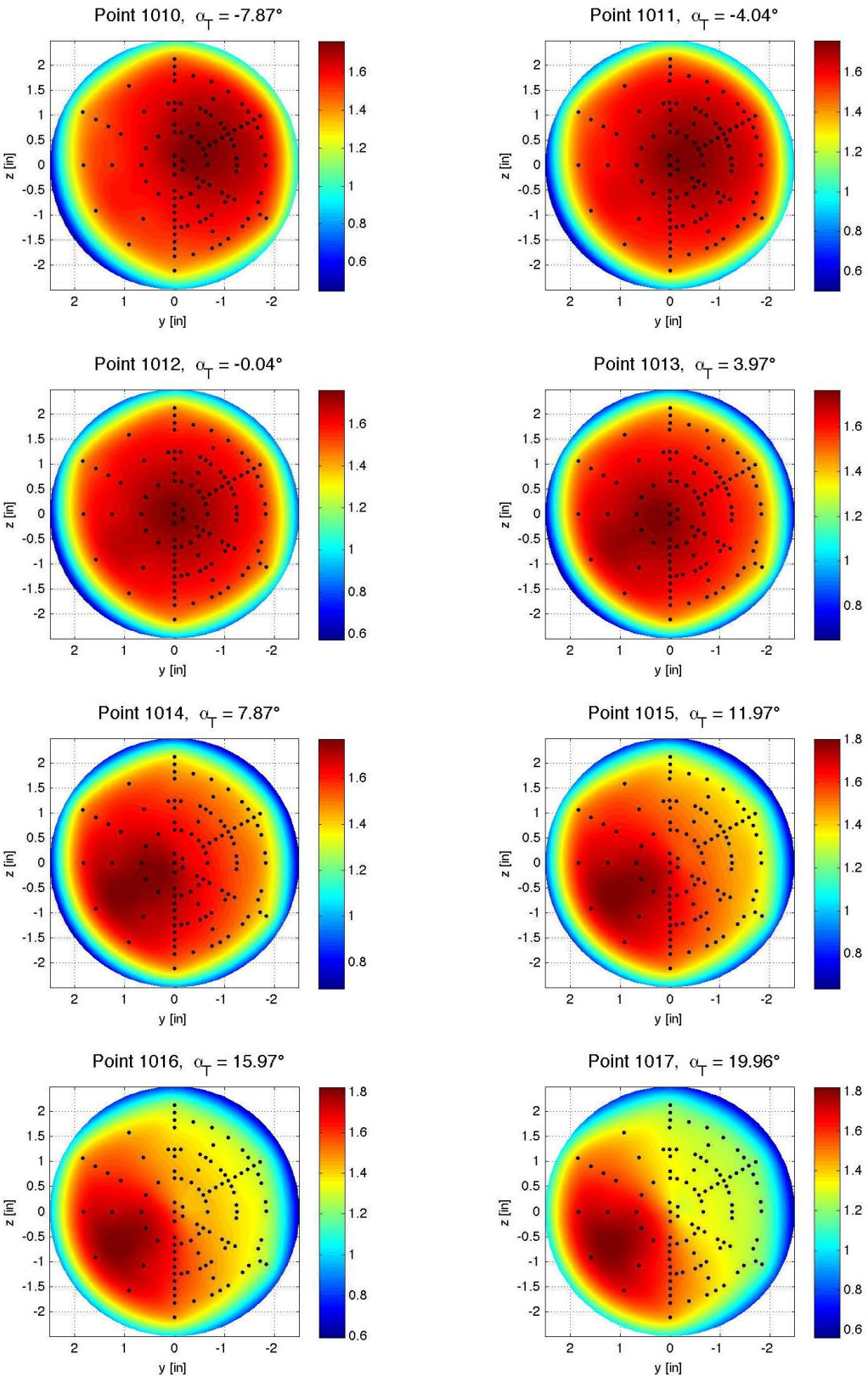

Figure E-54. Baseline configuration, Run 074, M_∞ = 3.5, Re_∞ = 1.0x10^6/ft, ϕ = 60.02°, X_S = 40.18 in, Y_S = –8.00 in, C_T = 0.00.

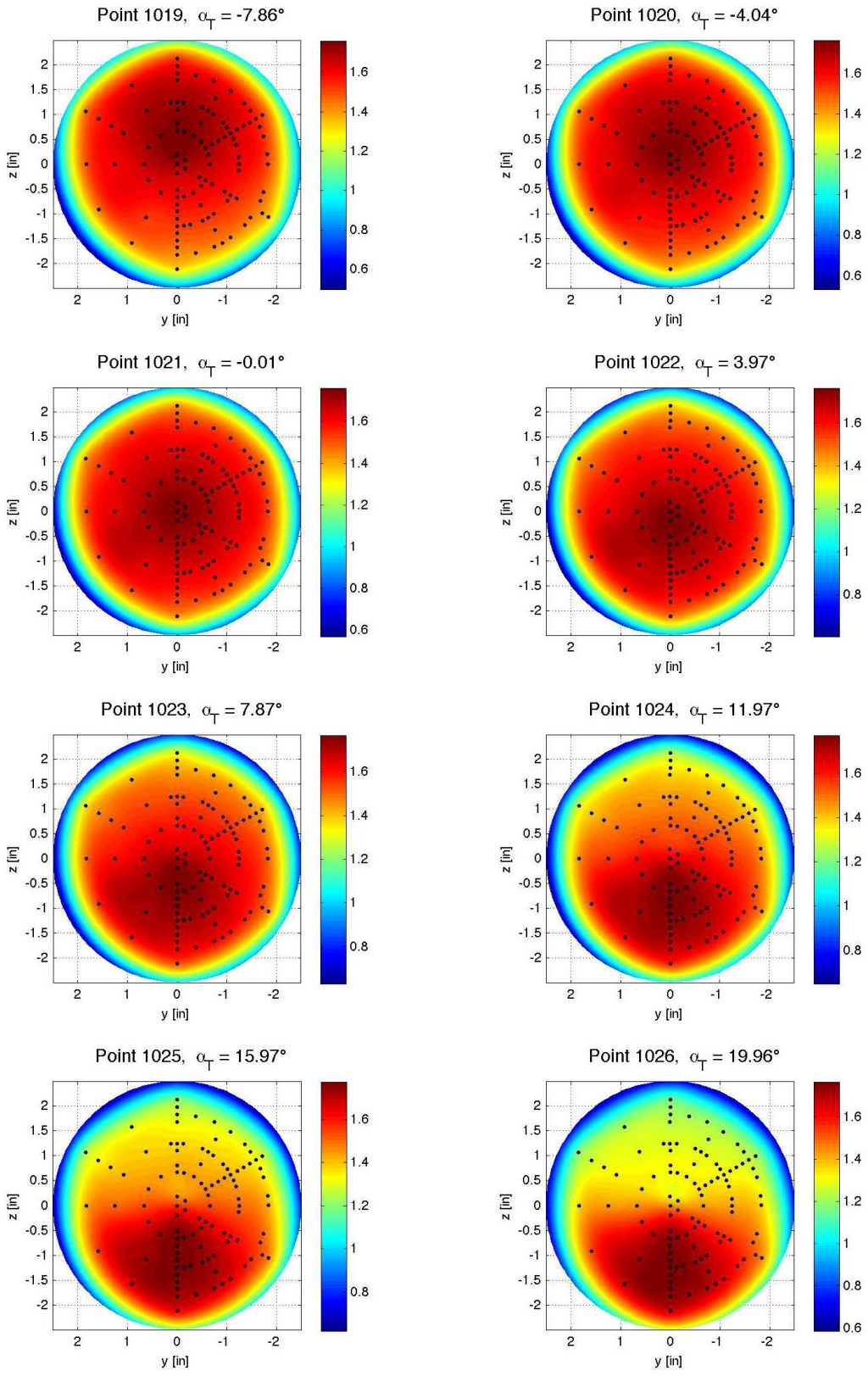

Figure E-55. Baseline configuration, Run 075, M_∞ = 3.5, Re_∞ = 1.0x10^6/ft, ϕ = 0.03°, X_S = 40.18 in, Y_S = –8.00 in, C_T = 0.00.

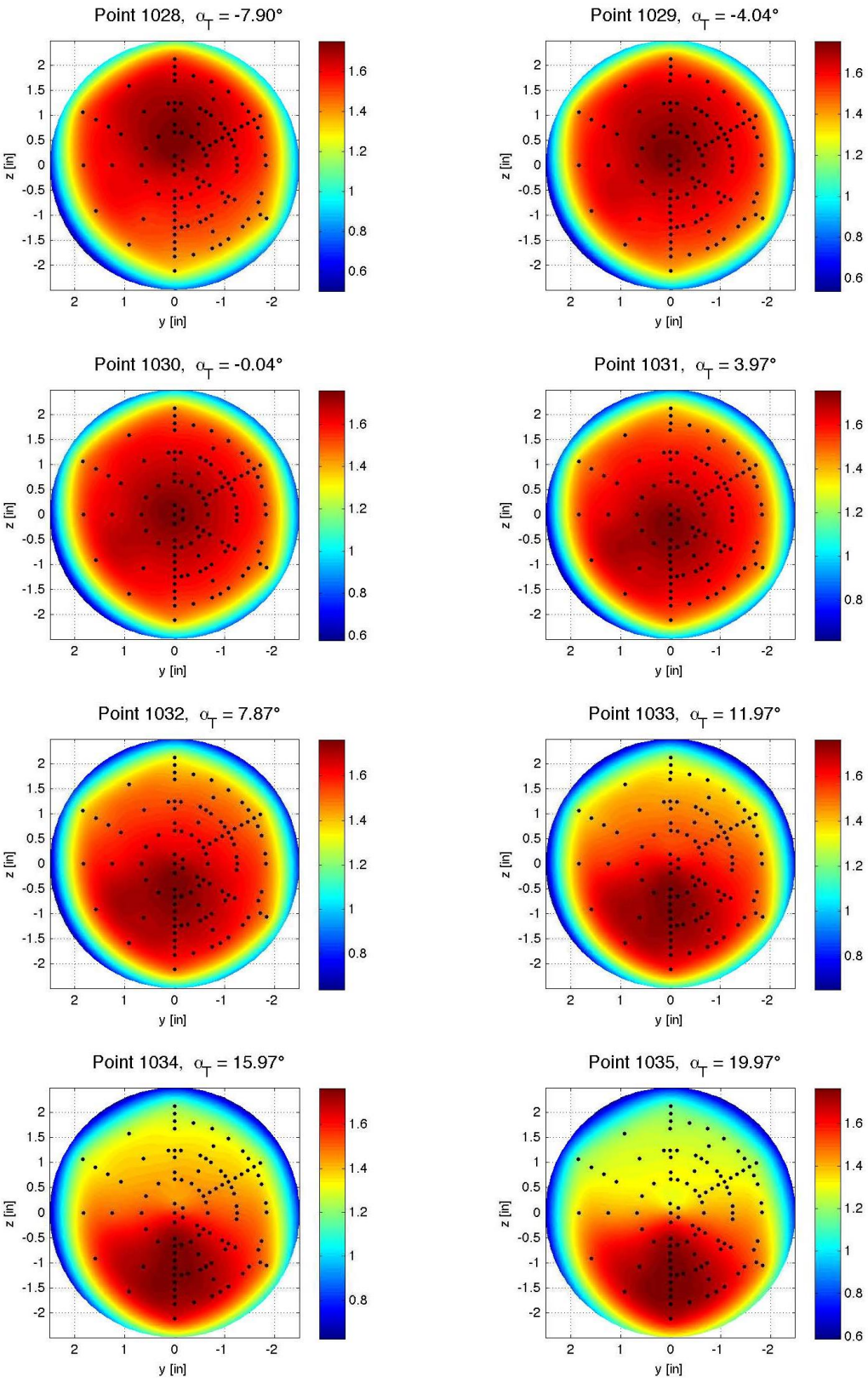

Figure E-56. Baseline configuration, Run 076, M_∞ = 3.5, Re_∞ = 1.0x10^6/ft, ϕ = 0.03°, X_S = 40.18 in, Y_S = 7.99 in, C_T = 0.00.

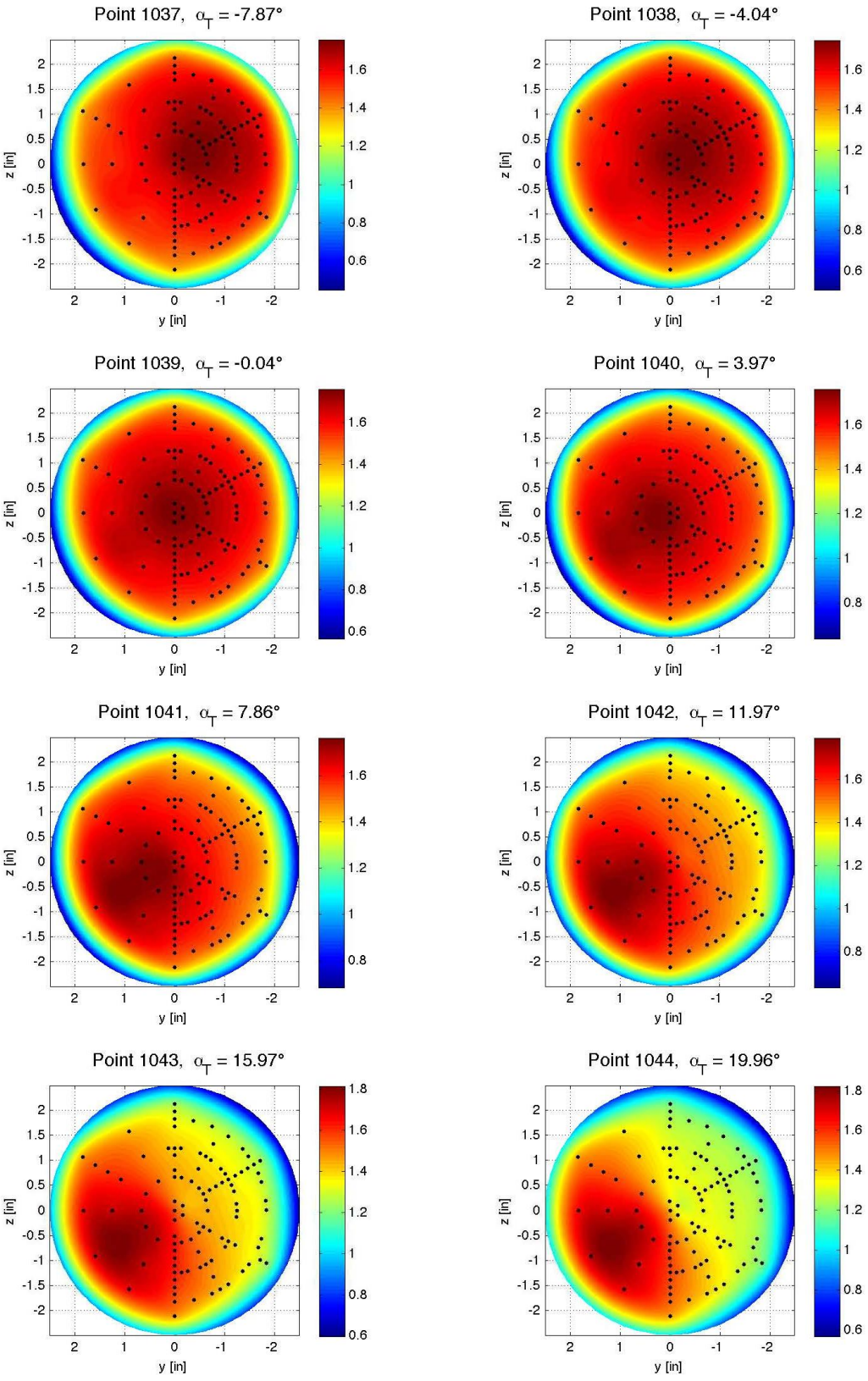

Figure E-57. Baseline configuration, Run 077, M_∞ = 3.5, Re_∞ = 1.0x10^6/ft, ϕ = 59.98°, X_S = 40.16 in, Y_S = 7.99 in, C_T = 0.00.

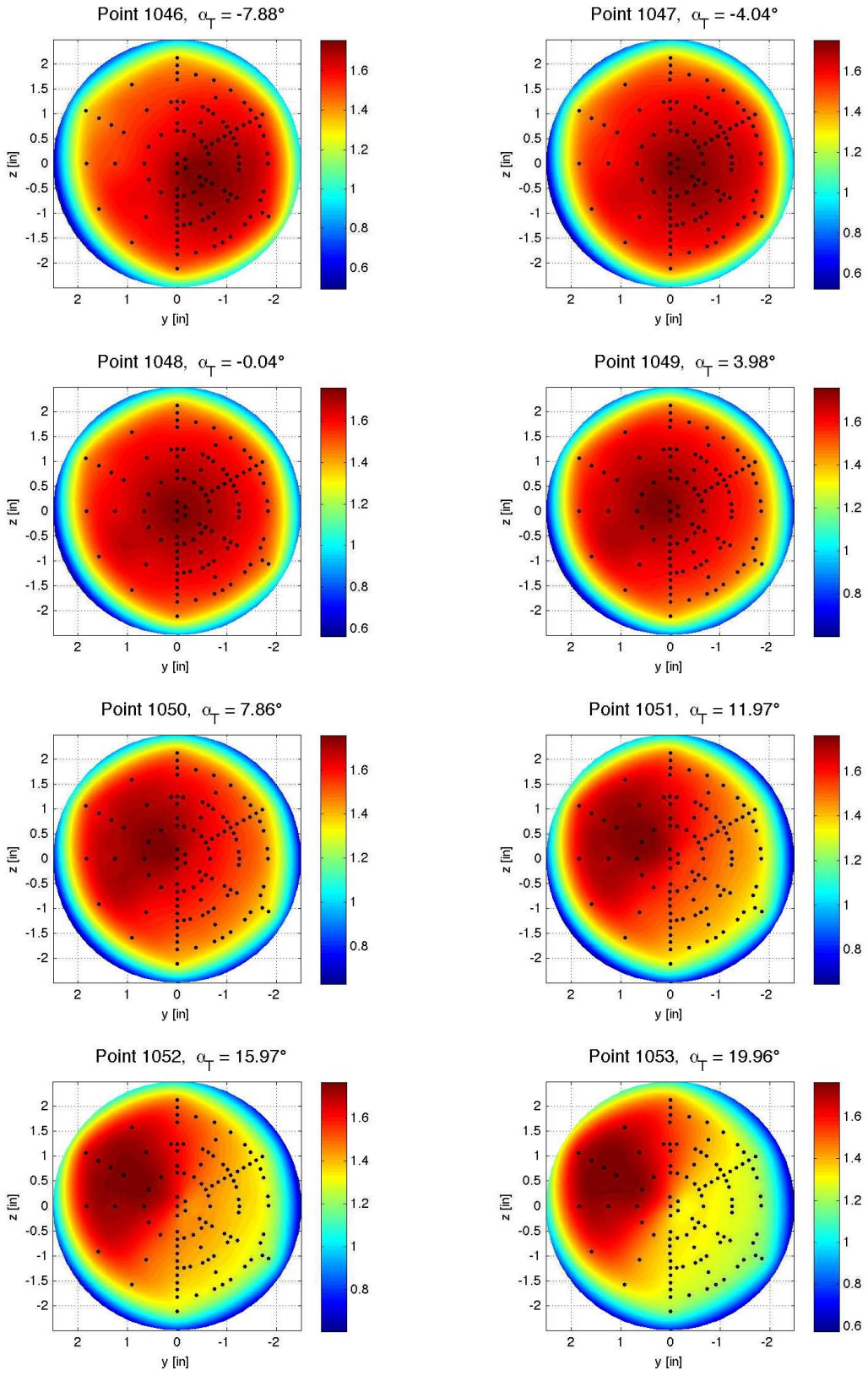

Figure E-58. Baseline configuration, Run 078, M_∞ = 3.5, Re_∞ = 1.0x10^6/ft, ϕ = 119.92°, X_S = 40.16 in, Y_S = 7.95 in, C_T = 0.00.

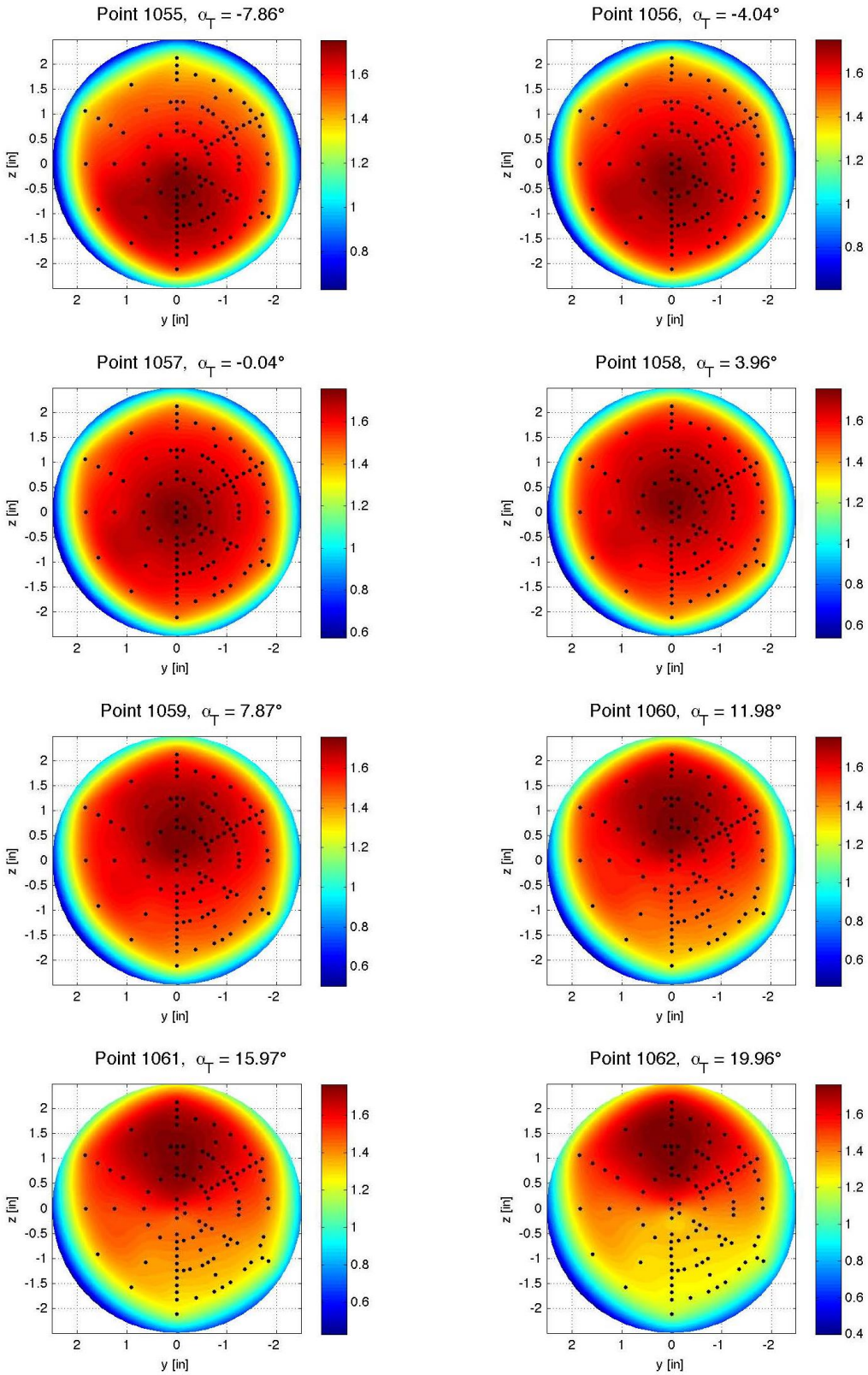

Figure E-59. Baseline configuration, Run 079, M_∞ = 3.5, Re_∞ = 1.0x10^6/ft, ϕ = −179.99°, X_S = 40.16 in, Y_S = 7.95 in, C_T = 0.00.

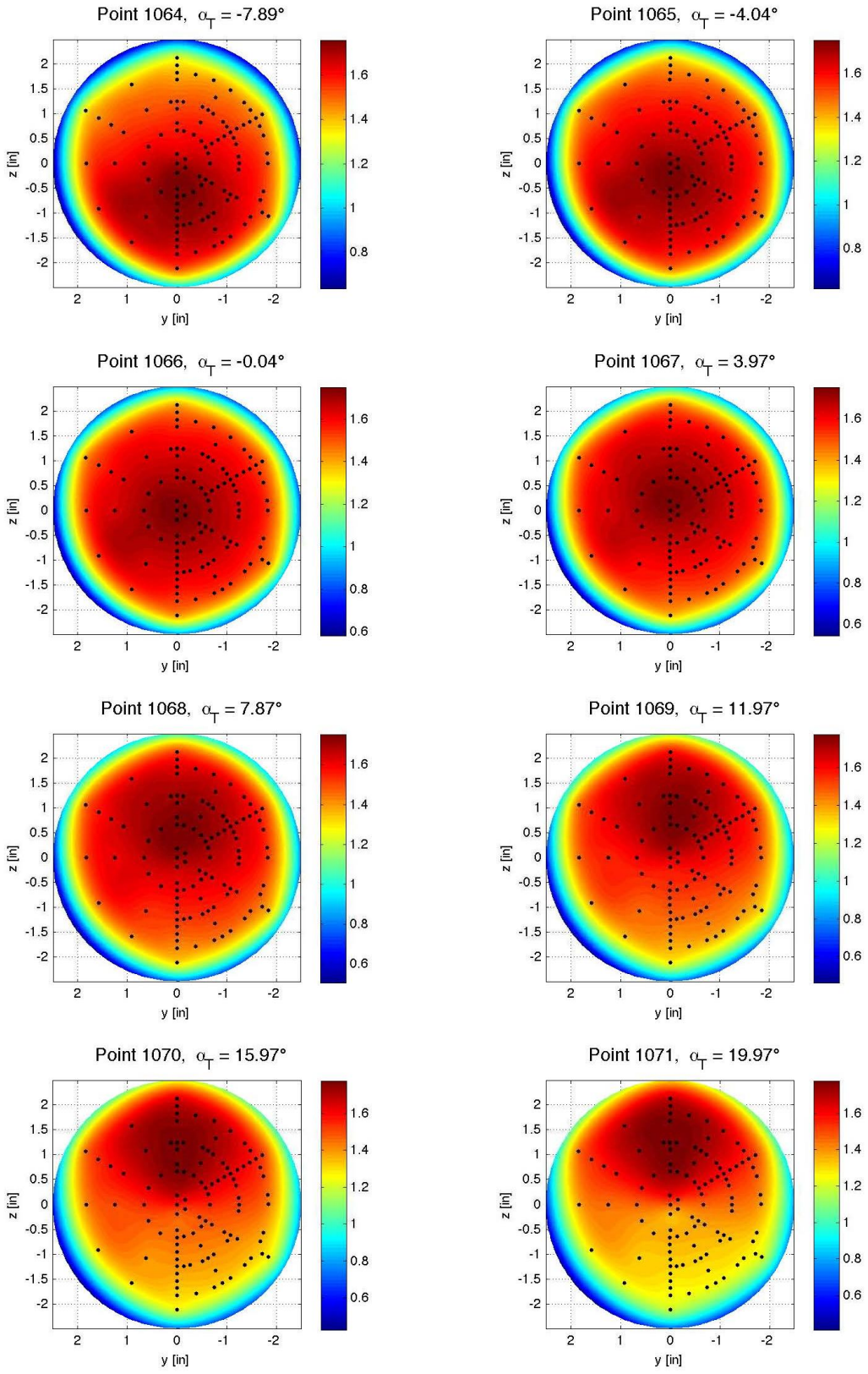

Figure E-60. Baseline configuration, Run 080, M_∞ = 3.5, Re_∞ = 1.0x10^6/ft, ϕ = −179.99°, X_S = 50.15 in, Y_S = 7.95 in, C_T = 0.00.

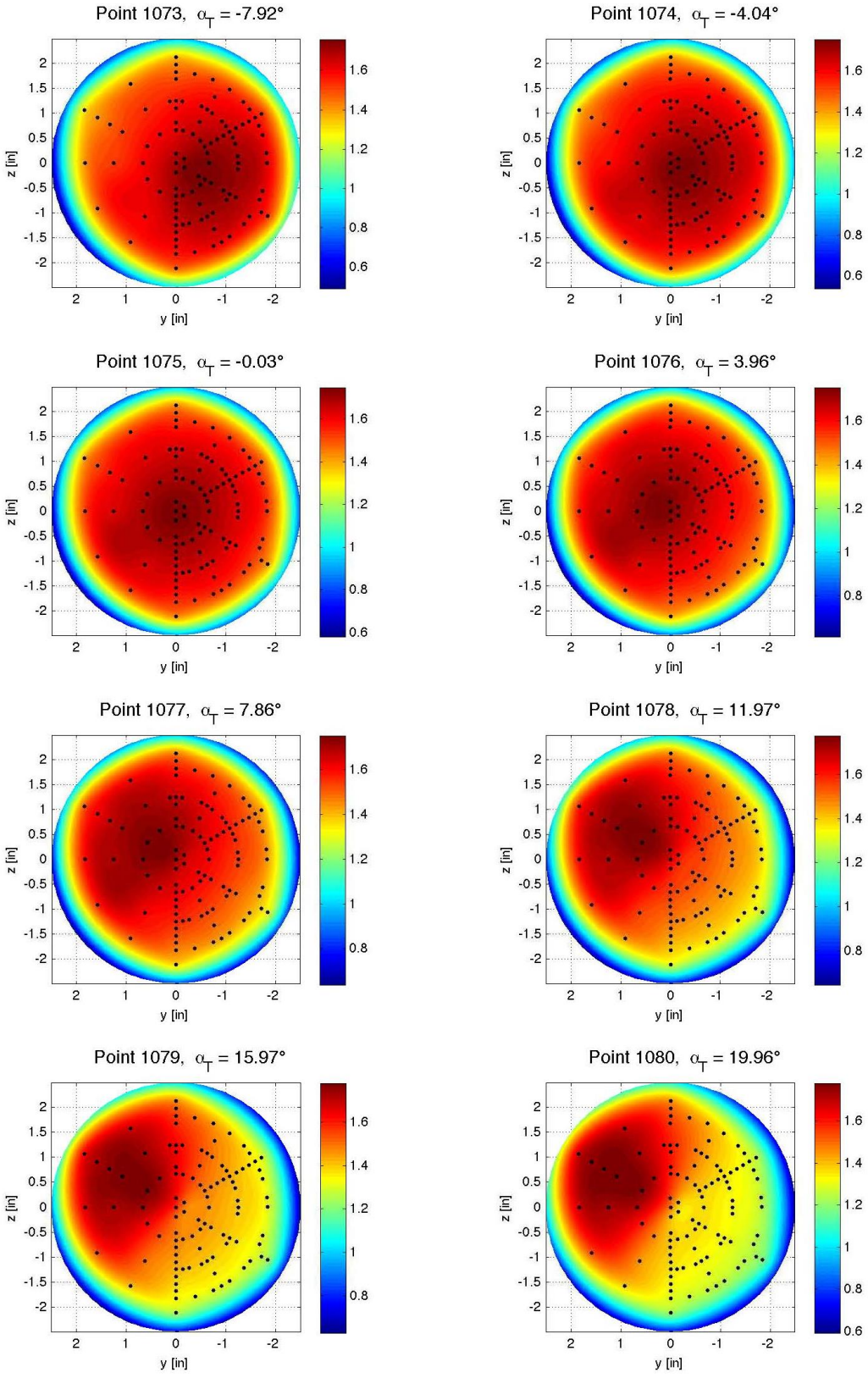

Figure E-61. Baseline configuration, Run 081, M_∞ = 3.5, Re_∞ = 1.0x10^6/ft, ϕ = 119.92°, X_S = 50.15 in, Y_S = 7.95 in, C_T = 0.00.

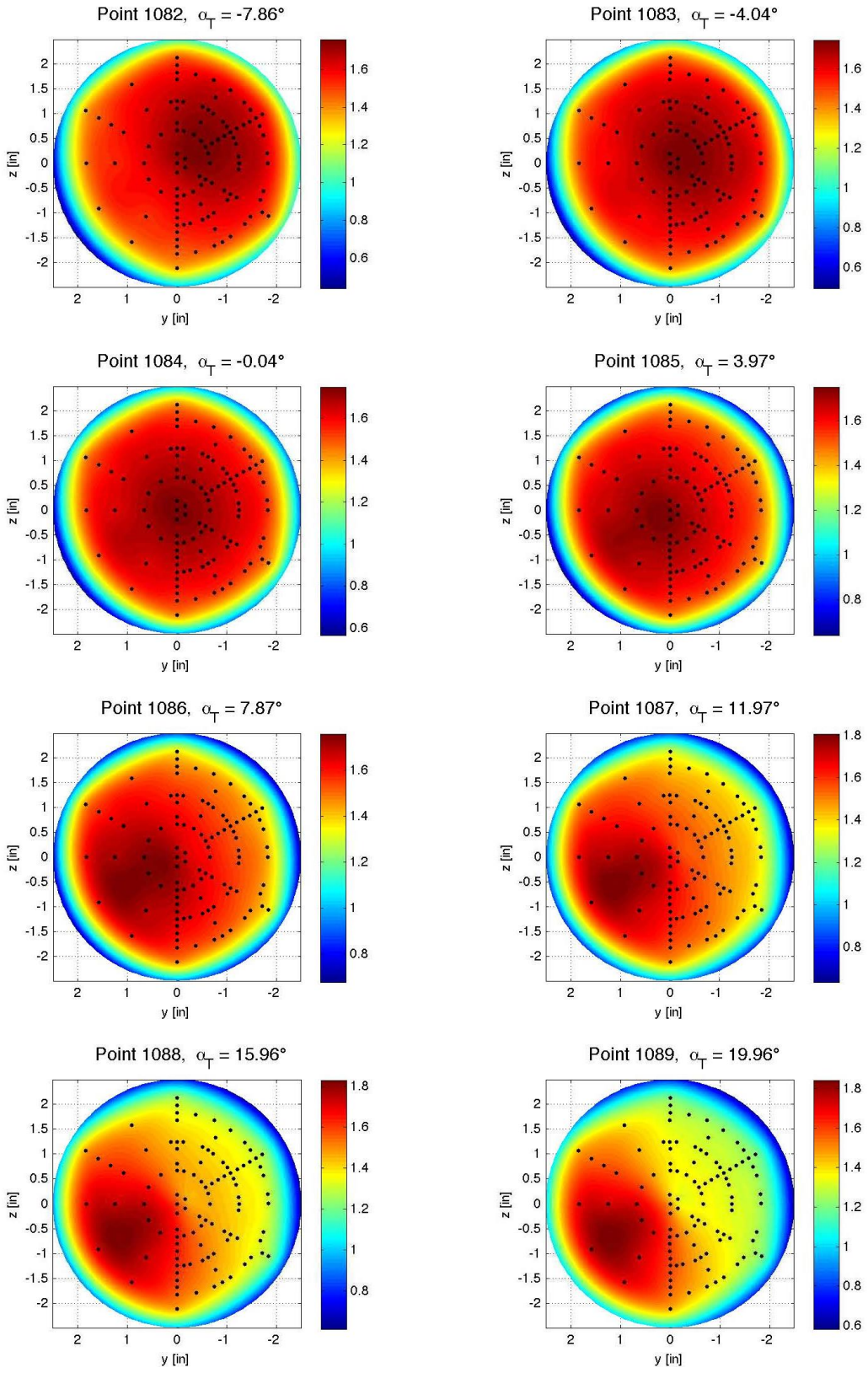

Figure E-62. Baseline configuration, Run 082, M_∞ = 3.5, Re_∞ = 1.0x10^6/ft, ϕ = 60.00°, X_S = 50.15 in, Y_S = 7.95 in, C_T = 0.00.

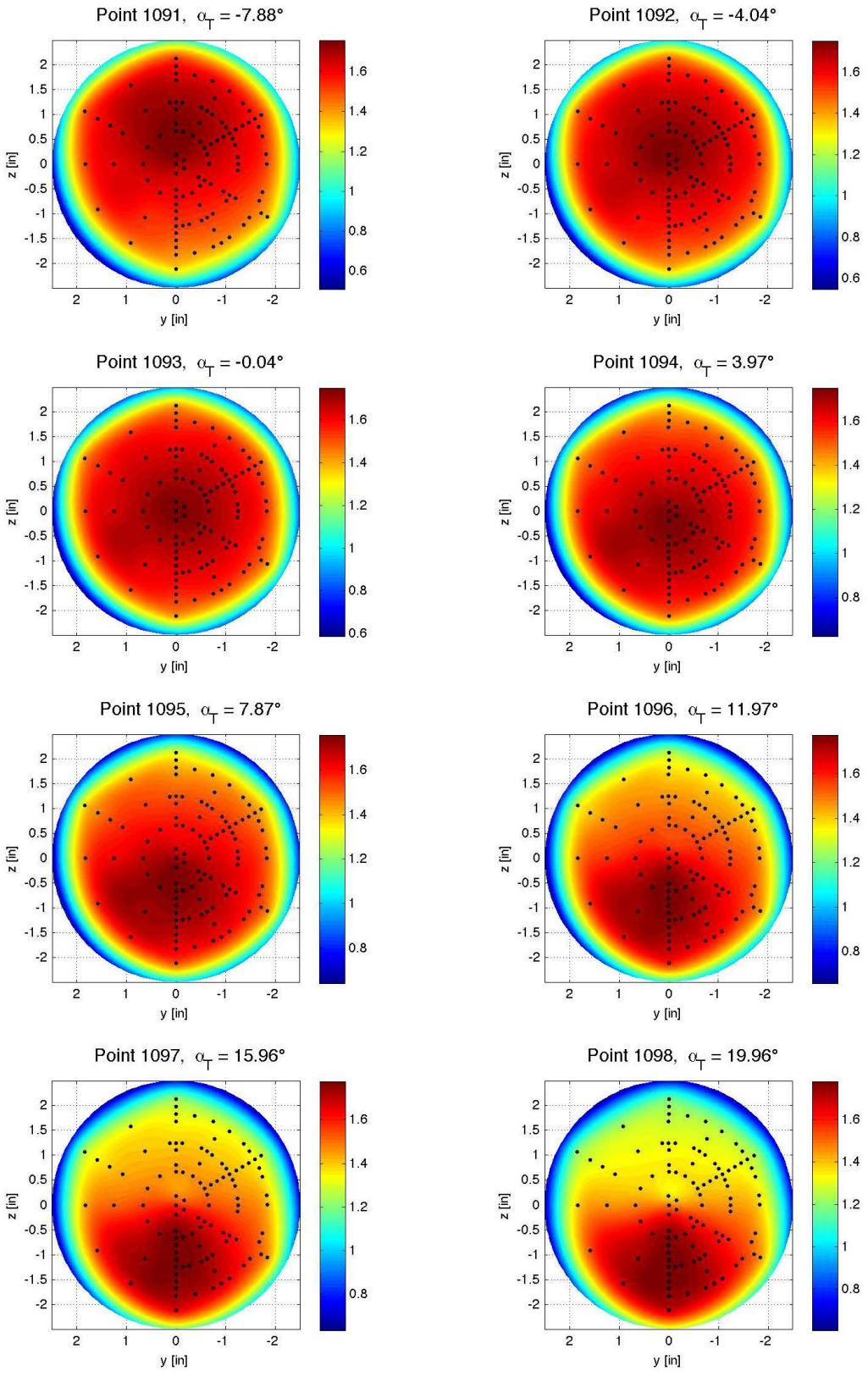

Figure E-63. Baseline configuration, Run 083, M_∞ = 3.5, Re_∞ = 1.0x10^6/ft, ϕ = 0.01°, X_S = 50.15 in, Y_S = 7.95 in, C_T = 0.00.

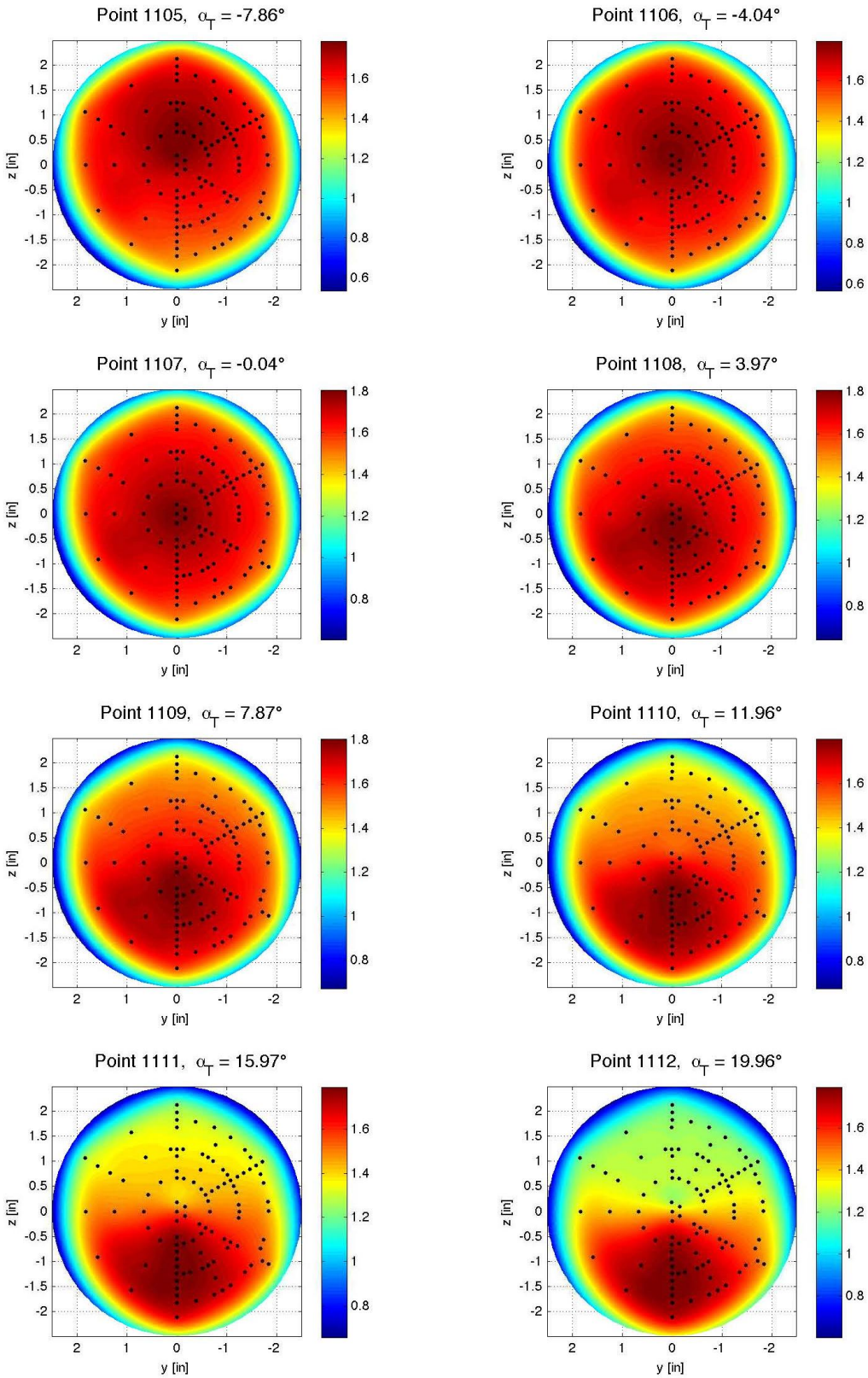

Figure E-64. Baseline configuration, Run 086, M_∞ = 4.6, Re_∞ = 1.1x10^6/ft, ϕ = 0.01°, X_S = 25.17 in, Y_S = 0.00 in, C_T = 0.00.

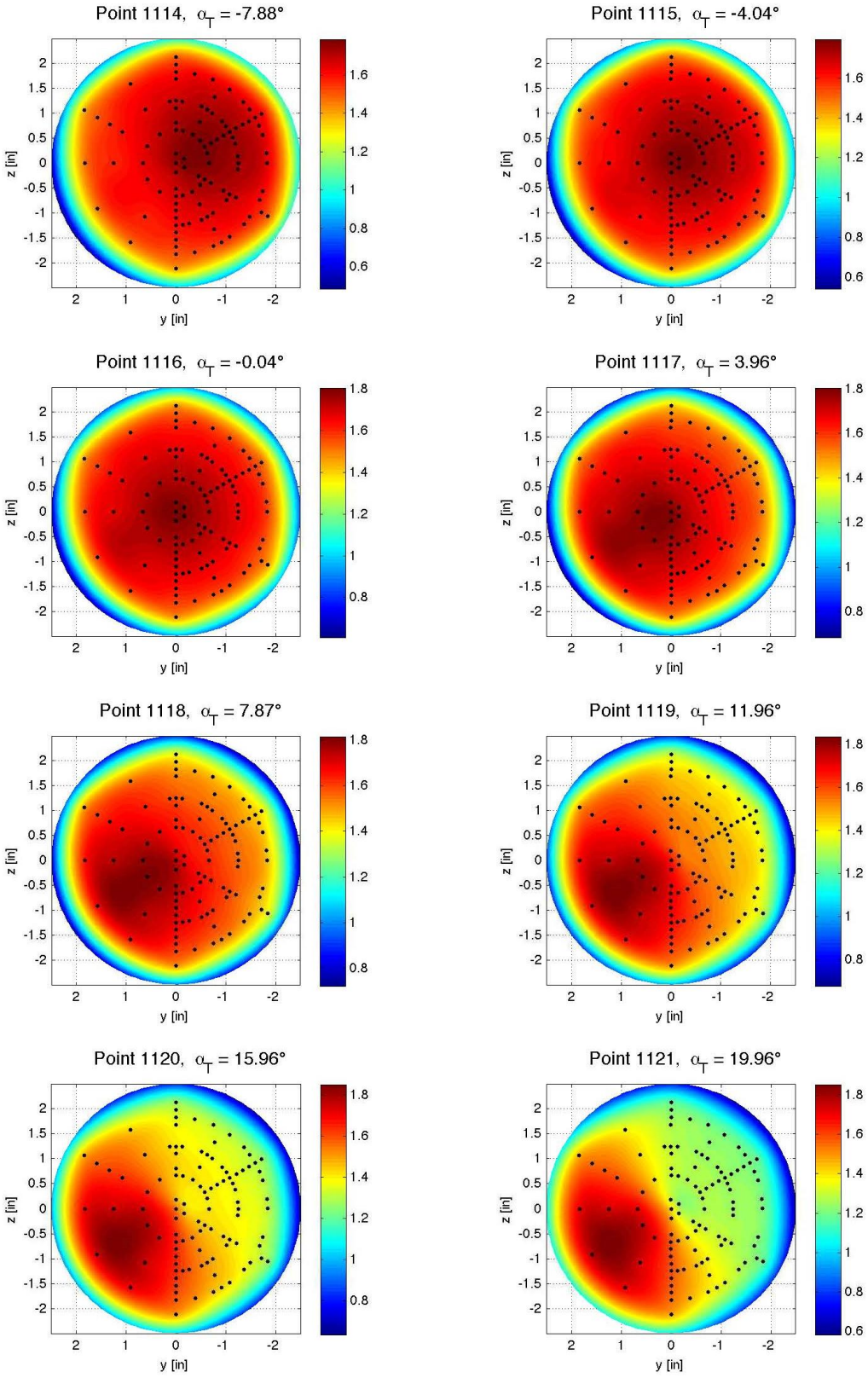

Figure E-65. Baseline configuration, Run 087, M_∞ = 4.6, Re_∞ = 1.1x10^6/ft, ϕ = 60.04°, X_S = 25.17 in, Y_S = 0.00 in, C_T = 0.00.

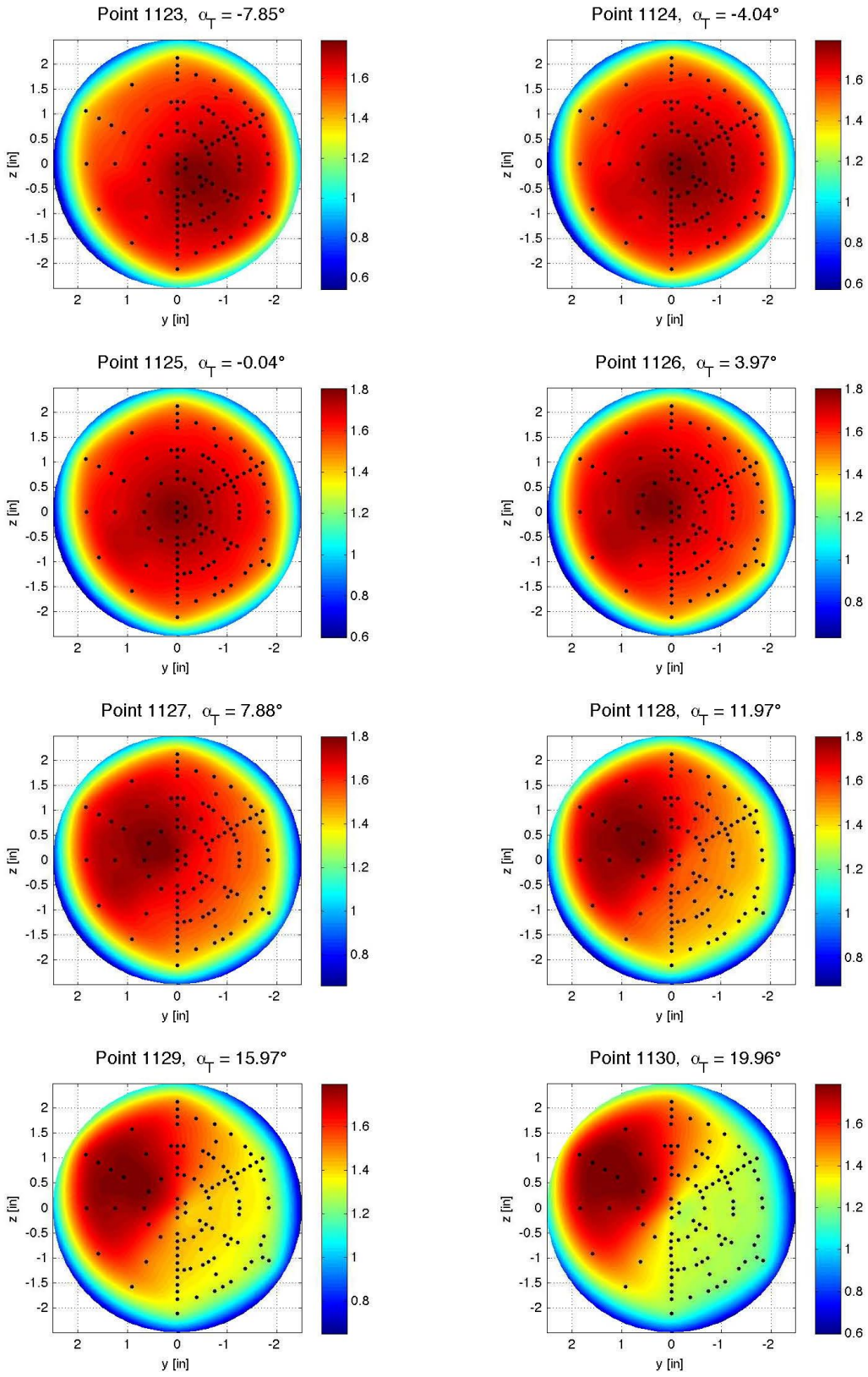

Figure E-66. Baseline configuration, Run 088, M_∞ = 4.6, Re_∞ = 1.1x10^6/ft, ϕ = 119.90°, X_S = 25.17 in, Y_S = 0.00 in, C_T = 0.00.

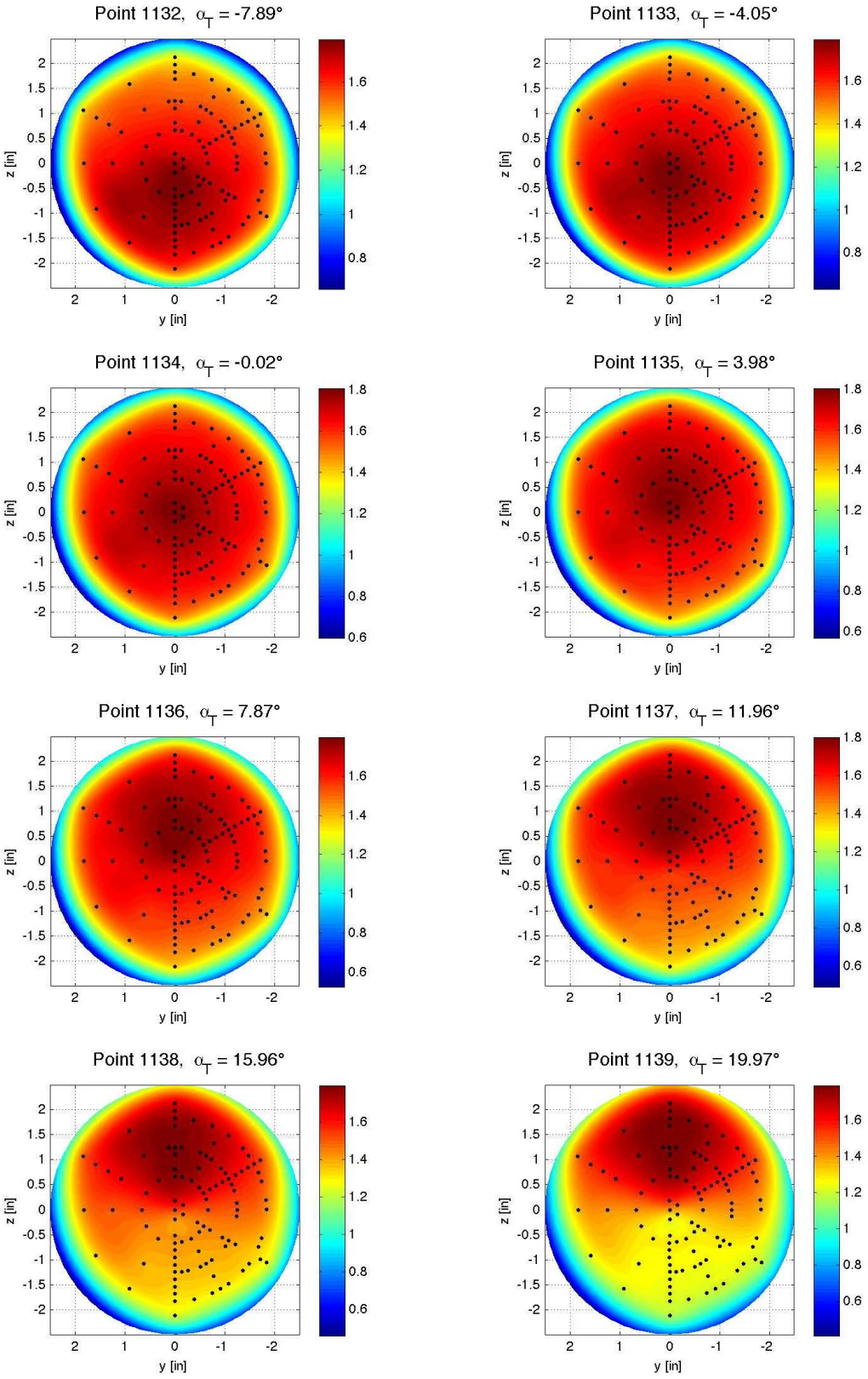

Figure E-67. Baseline configuration, Run 089, M_∞ = 4.6, Re_∞ = 1.1x10^6/ft, ϕ = 179.91°, X_S = 25.17 in, Y_S = 0.00 in, C_T = 0.00.

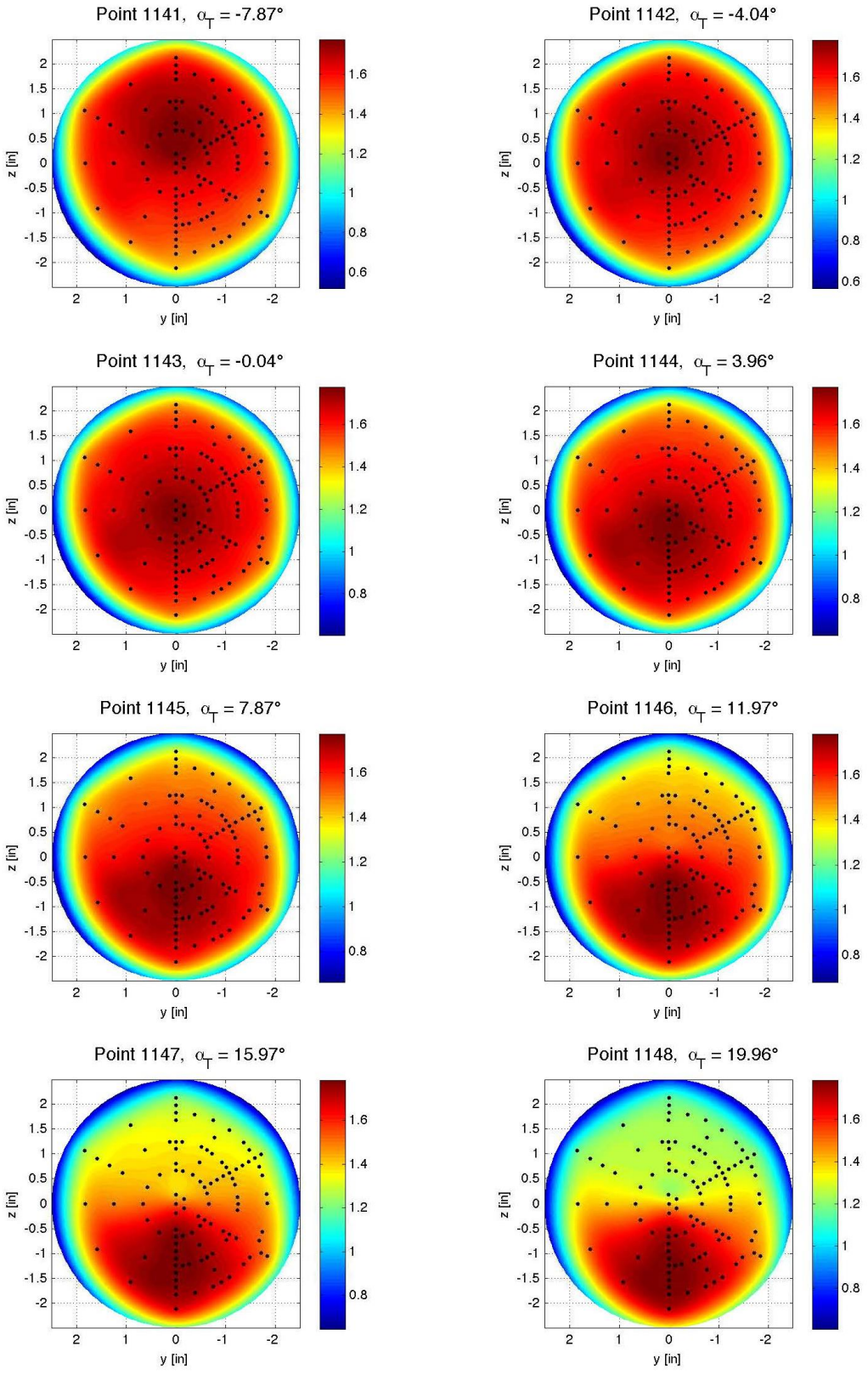

Figure E-68. Baseline configuration, Run 090, M_∞ = 4.6, Re_∞ = 1.1x10^6/ft, ϕ = 0.01°, X_S = 40.15 in, Y_S = 0.00 in, C_T = 0.00.

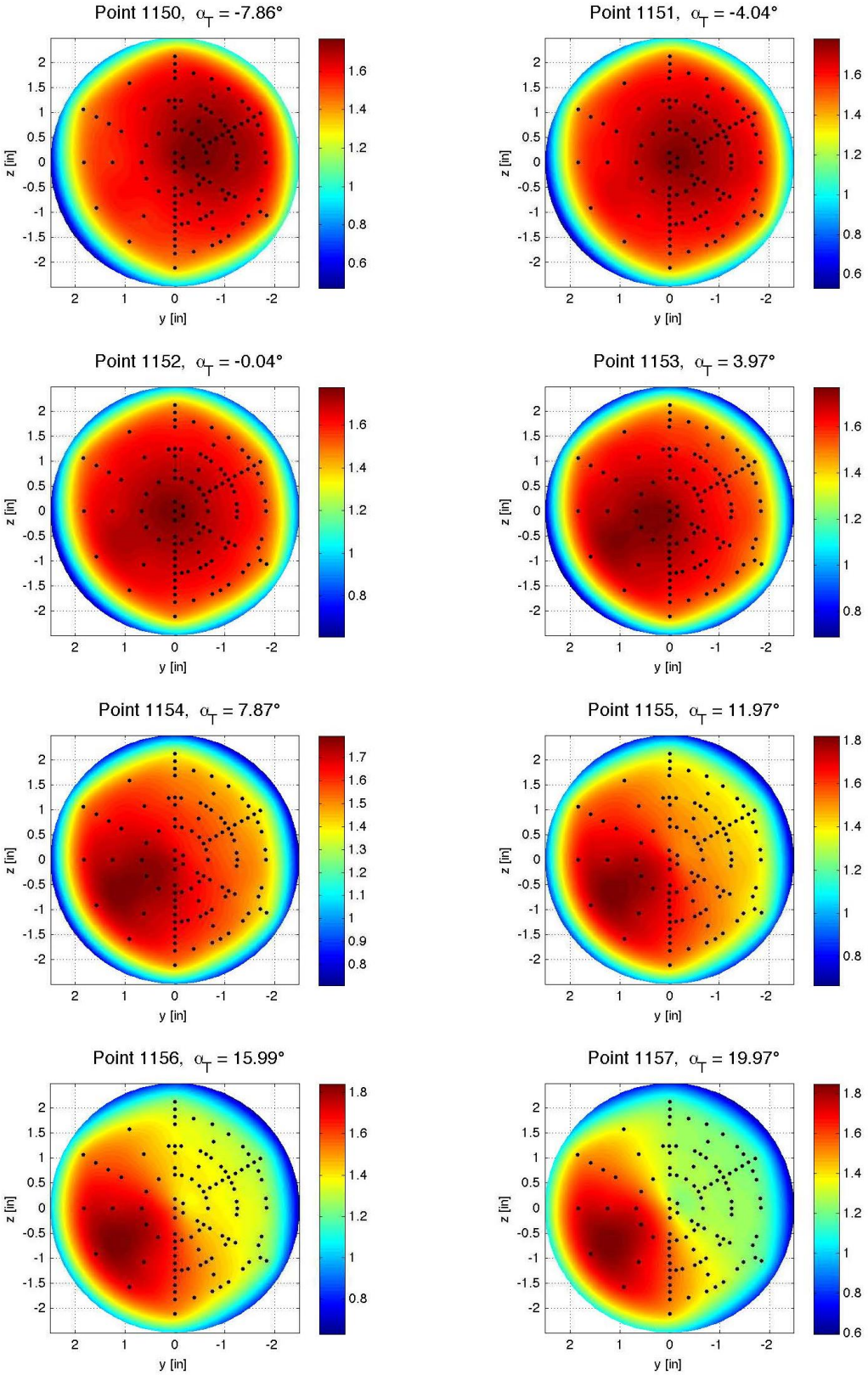

Figure E-69. Baseline configuration, Run 091, M_∞ = 4.6, Re_∞ = 1.1x10^6/ft, ϕ = 60.00°, X_S = 40.18 in, Y_S = 0.00 in, C_T = 0.00.

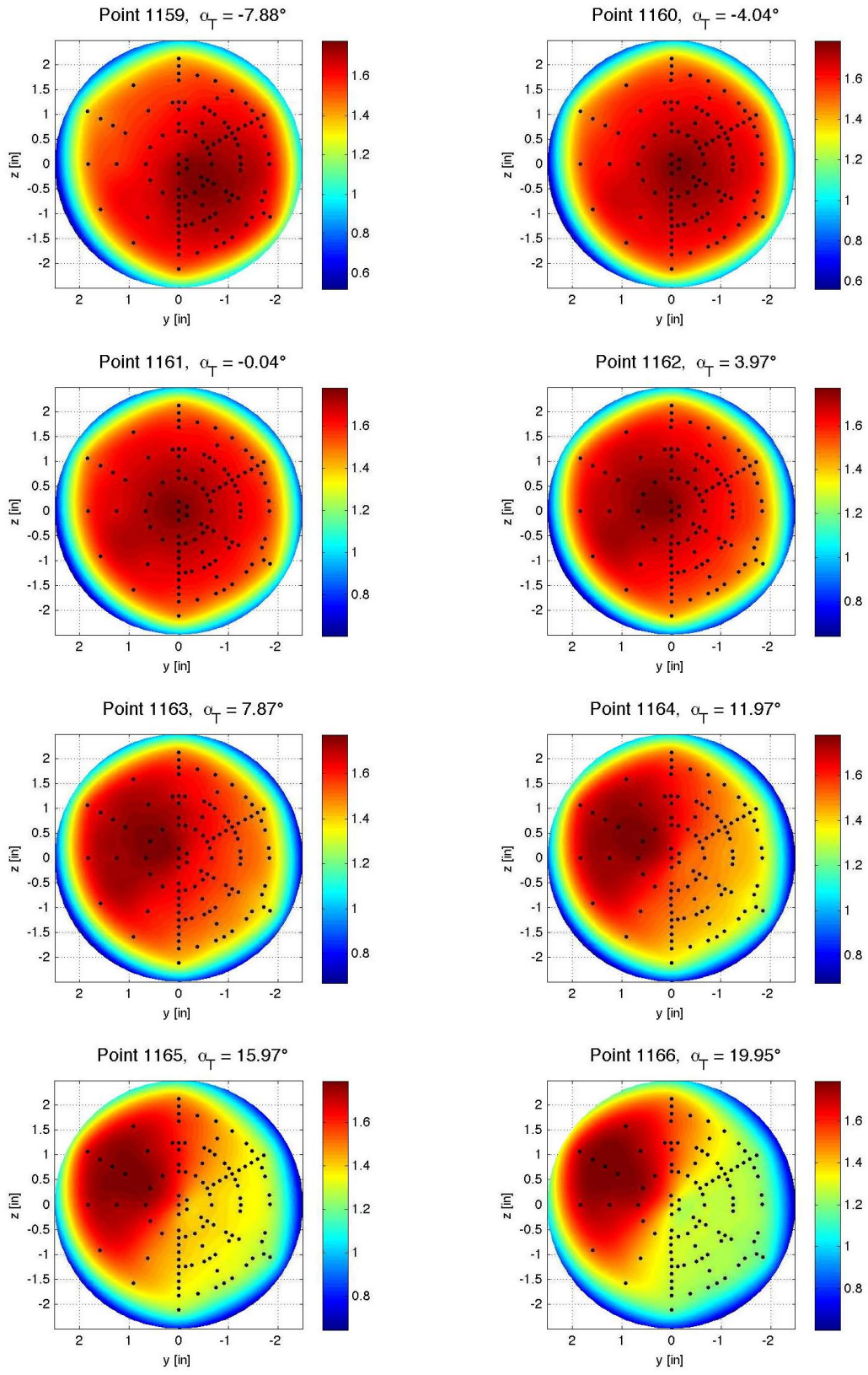

Figure E-70. Baseline configuration, Run 092, M_∞ = 4.6, Re_∞ = 1.1x10^6/ft, ϕ = 119.92°, X_S = 40.18 in, Y_S = 0.00 in, C_T = 0.00.

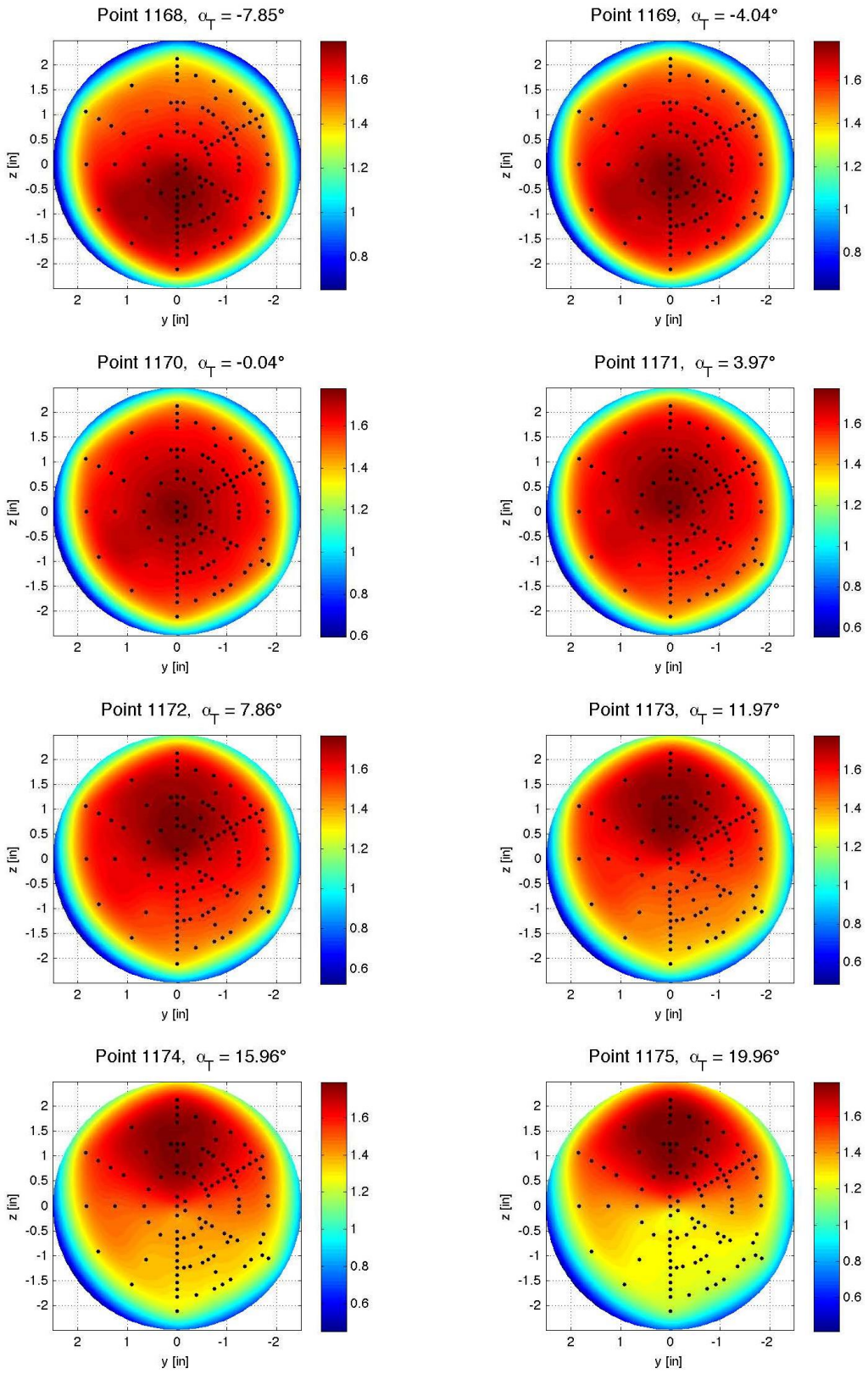

Figure E-71. Baseline configuration, Run 093, M_∞ = 4.6, Re_∞ = 1.1x10^6/ft, ϕ = 179.91°, X_S = 40.18 in, Y_S = 0.00 in, C_T = 0.00.

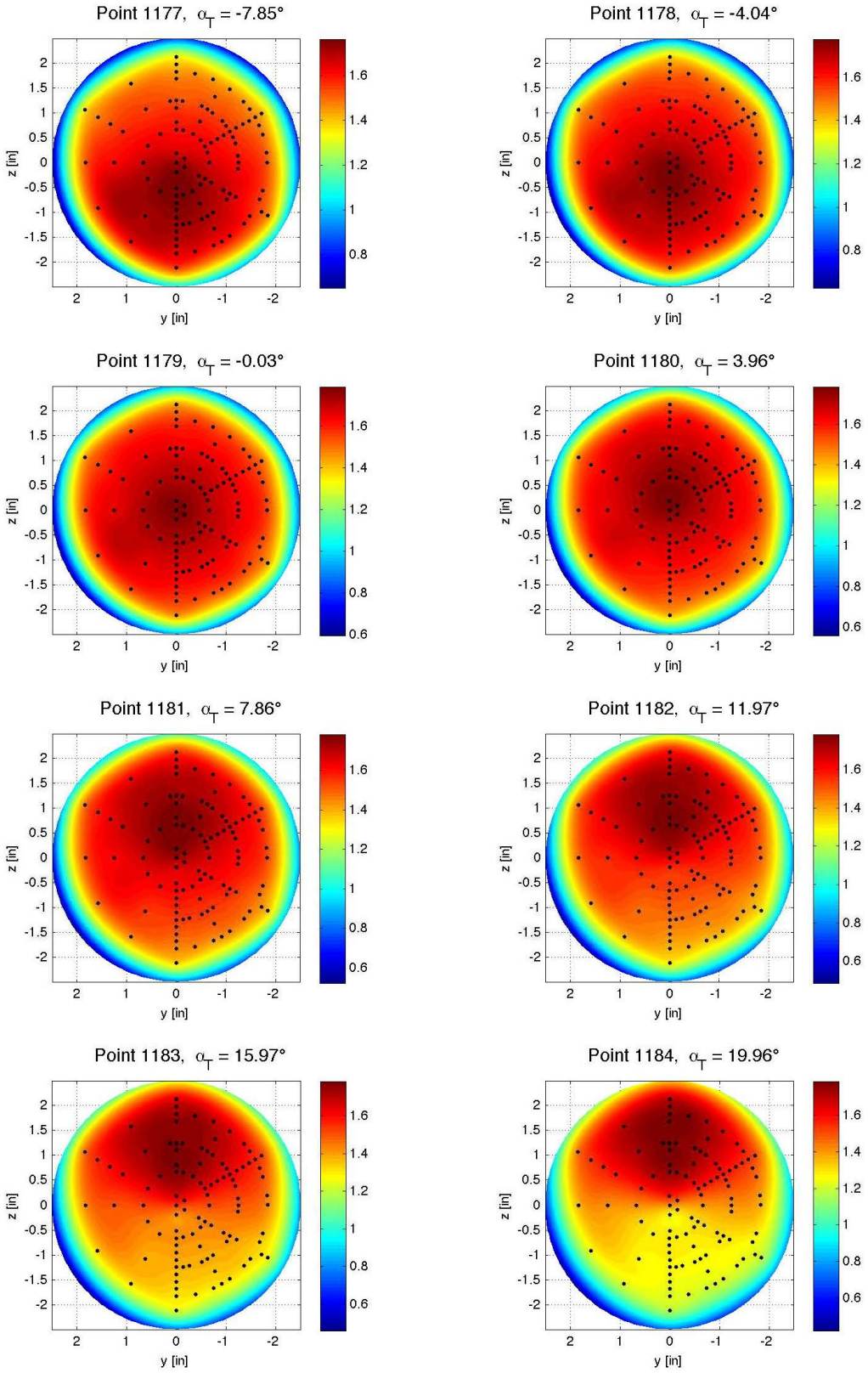

Figure E-72. Baseline configuration, Run 094, M_∞ = 4.6, Re_∞ = 1.1x10^6/ft, ϕ = 179.91°, X_S = 50.14 in, Y_S = 0.00 in, C_T = 0.00.

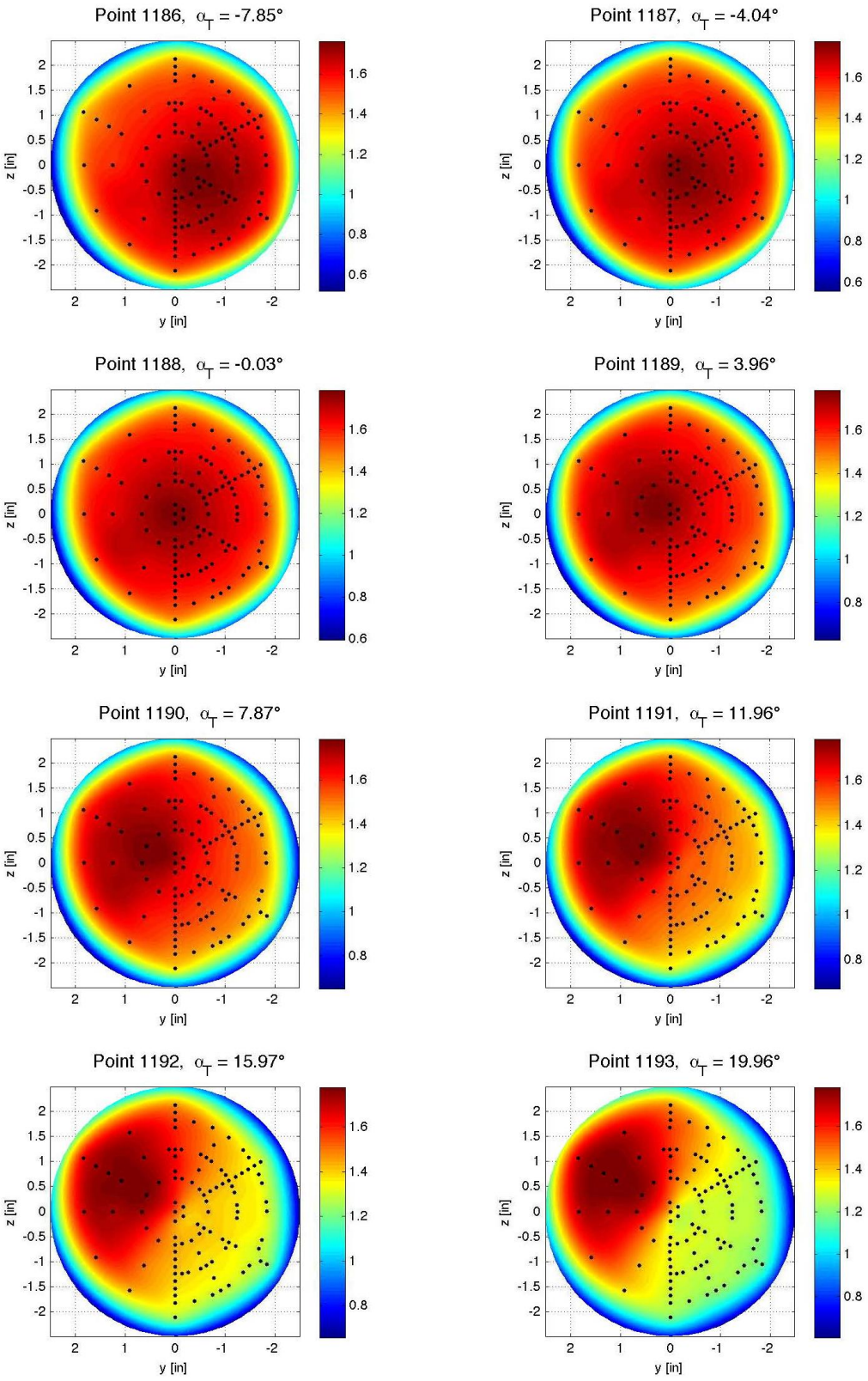

Figure E-73. Baseline configuration, Run 095, M_∞ = 4.6, Re_∞ = 1.1x10^6/ft, ϕ = 119.90°, X_S = 50.14 in, Y_S = 0.00 in, C_T = 0.00.

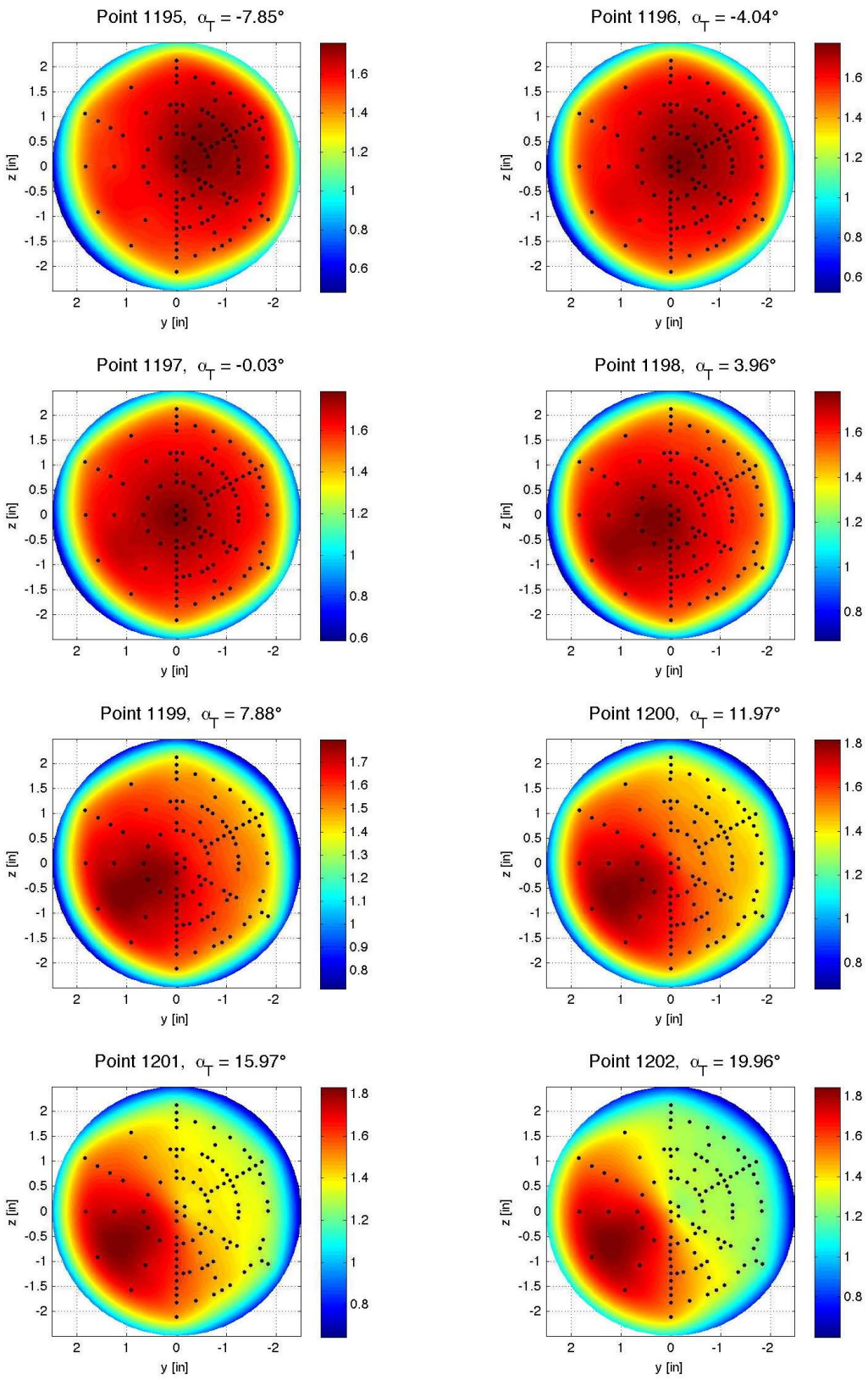

Figure E-74. Baseline configuration, Run 096, M_∞ = 4.6, Re_∞ = 1.1x10^6/ft, ϕ = 59.96°, X_S = 50.14 in, Y_S = 0.00 in, C_T = 0.00.

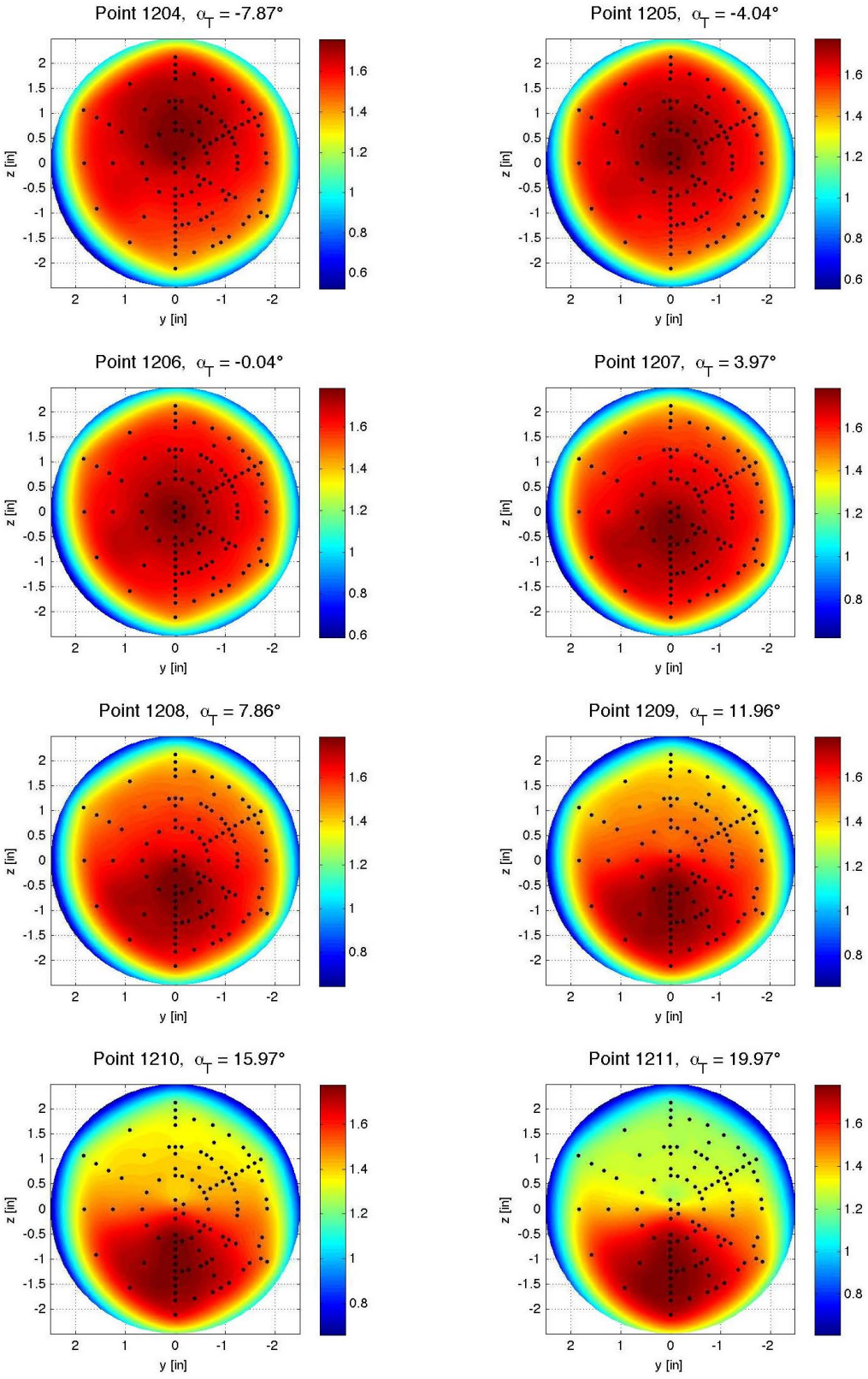

Figure E-75. Baseline configuration, Run 097, M_∞ = 4.6, Re_∞ = 1.1x10^6/ft, ϕ = −0.07°, X_S = 50.14 in, Y_S = 0.00 in, C_T = 0.00.

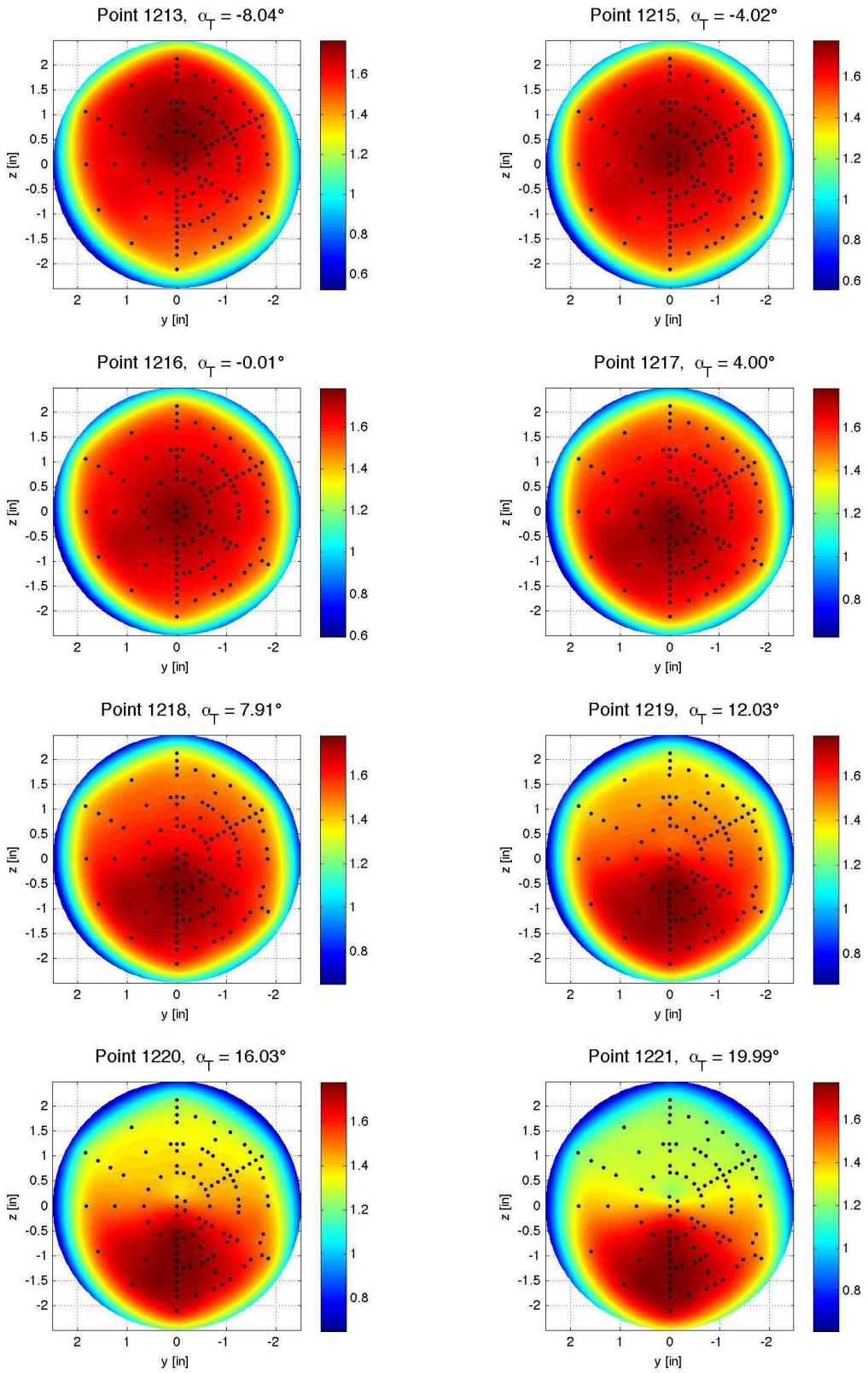

Figure E-76. Baseline configuration, Run 098, M_∞ = 4.6, Re_∞ = 1.1x10^6/ft, ϕ = −0.07°, X_S = 50.14 in, Y_S = 7.99 in, C_T = 0.00.

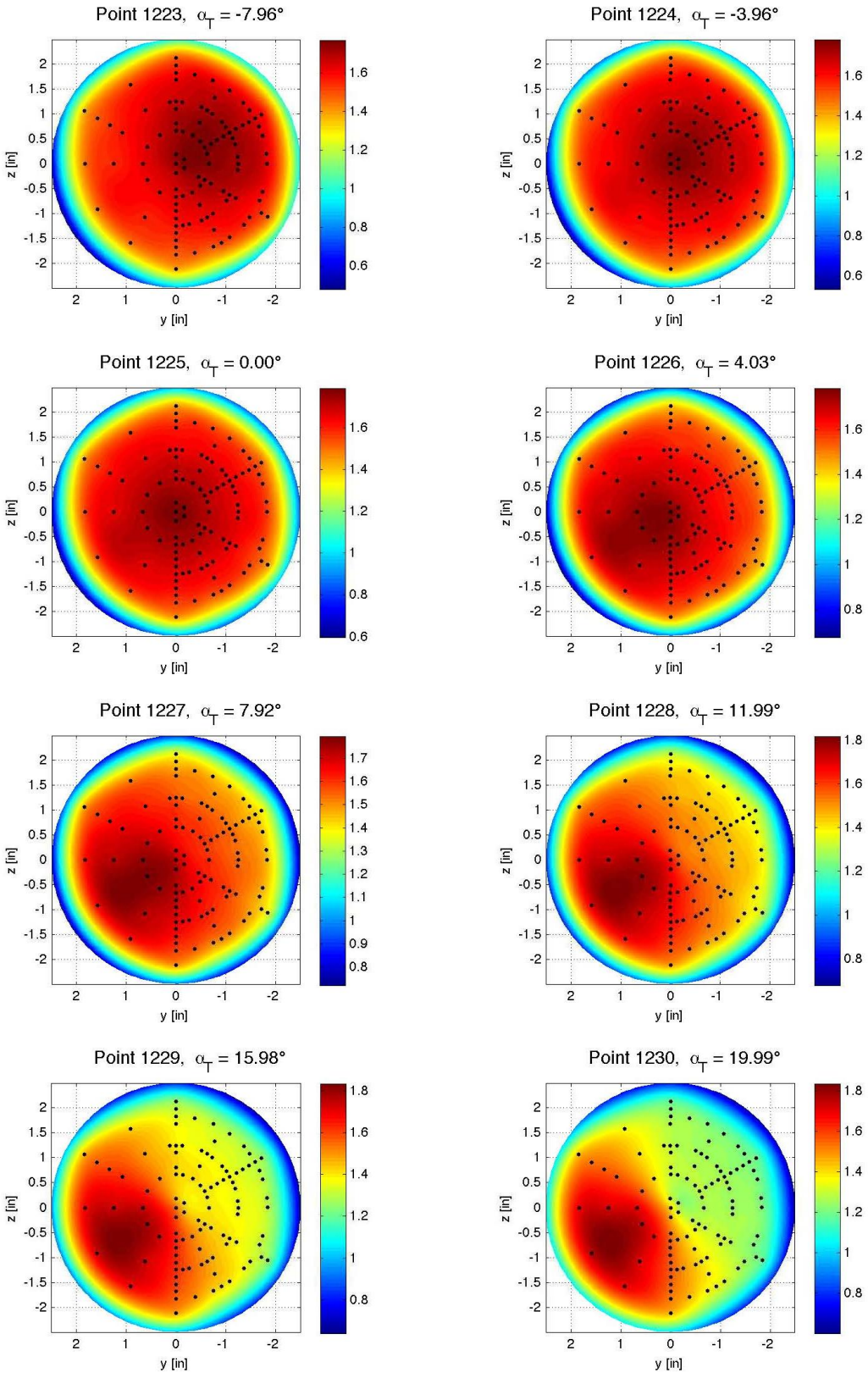

Figure E-77. Baseline configuration, Run 099, M_∞ = 4.6, Re_∞ = 1.1x10^6/ft, ϕ = 59.92°, X_S = 50.14 in, Y_S = 7.99 in, C_T = 0.00.

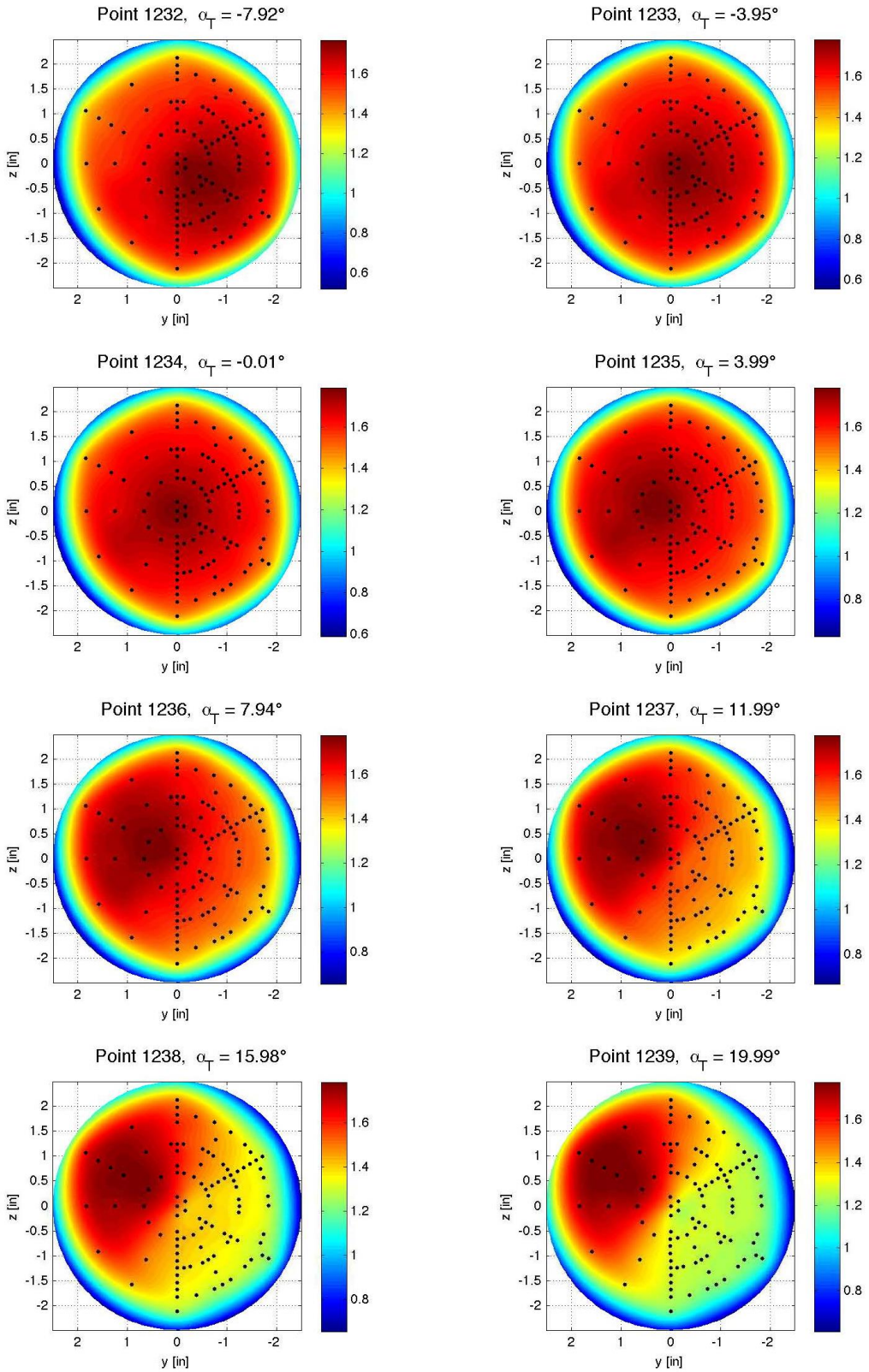

Figure E-78. Baseline configuration, Run 100, M_∞ = 4.6, Re_∞ = 1.1x10^6/ft, ϕ = 120.00°, X_S = 50.14 in, Y_S = 7.99 in, C_T = 0.00.

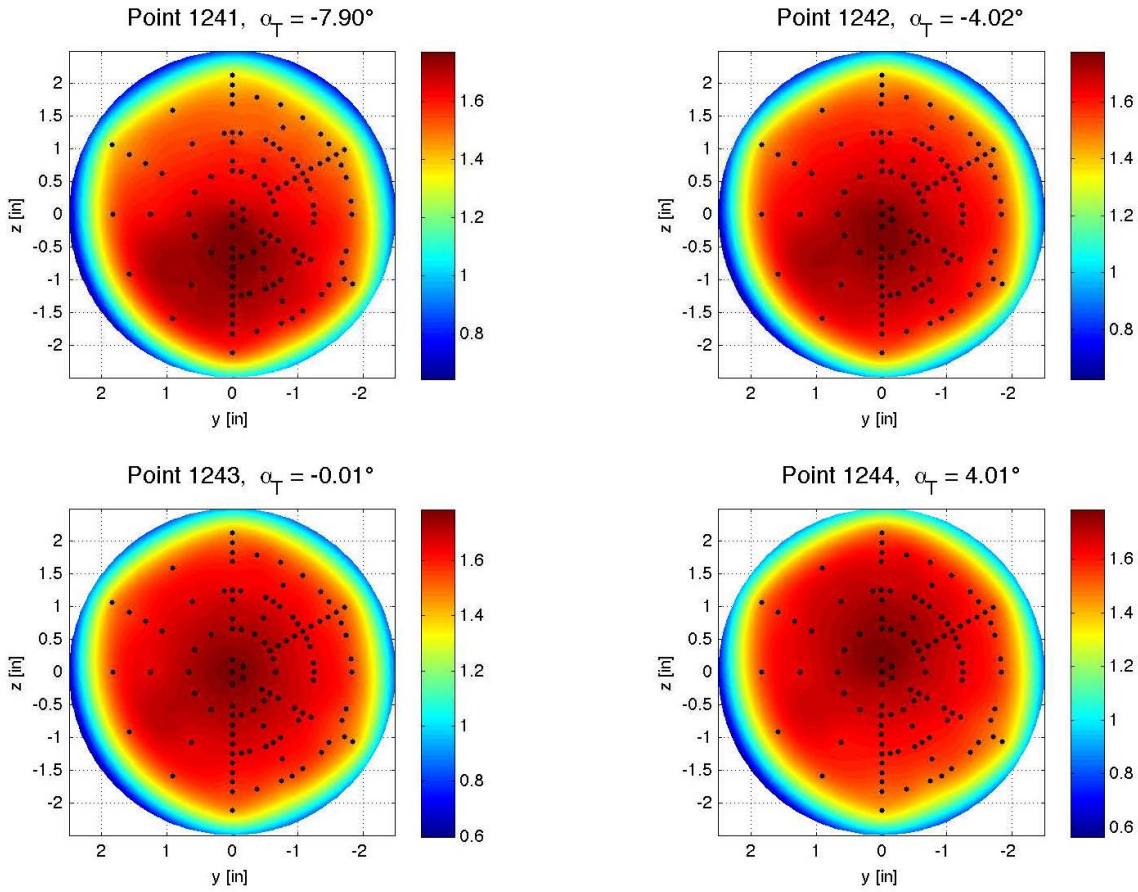

Figure E-79. Baseline configuration, Run 101, $M\infty$ = 4.6, Re_∞ = 1.1x10^6/ft, ϕ = 179.97°, X_S = 50.14 in, Y_S = 7.99 in, C_T = 0.00.

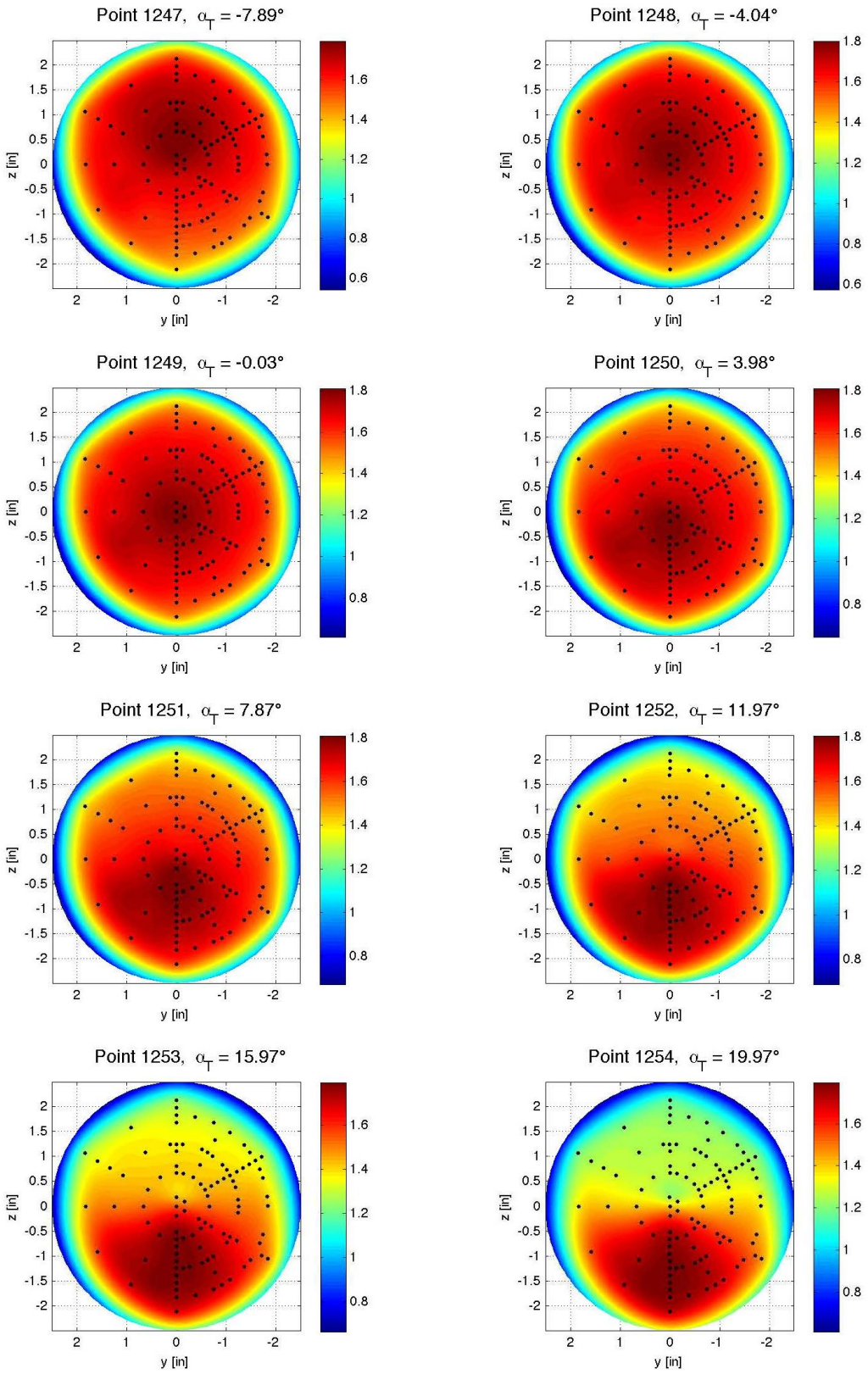

Figure E-80. Baseline configuration, Run 104, M_∞ = 4.6, Re_∞ = 1.5x10^6/ft, ϕ = −0.03°, X_S = 25.19 in, Y_S = 0.00 in, C_T = 0.00.

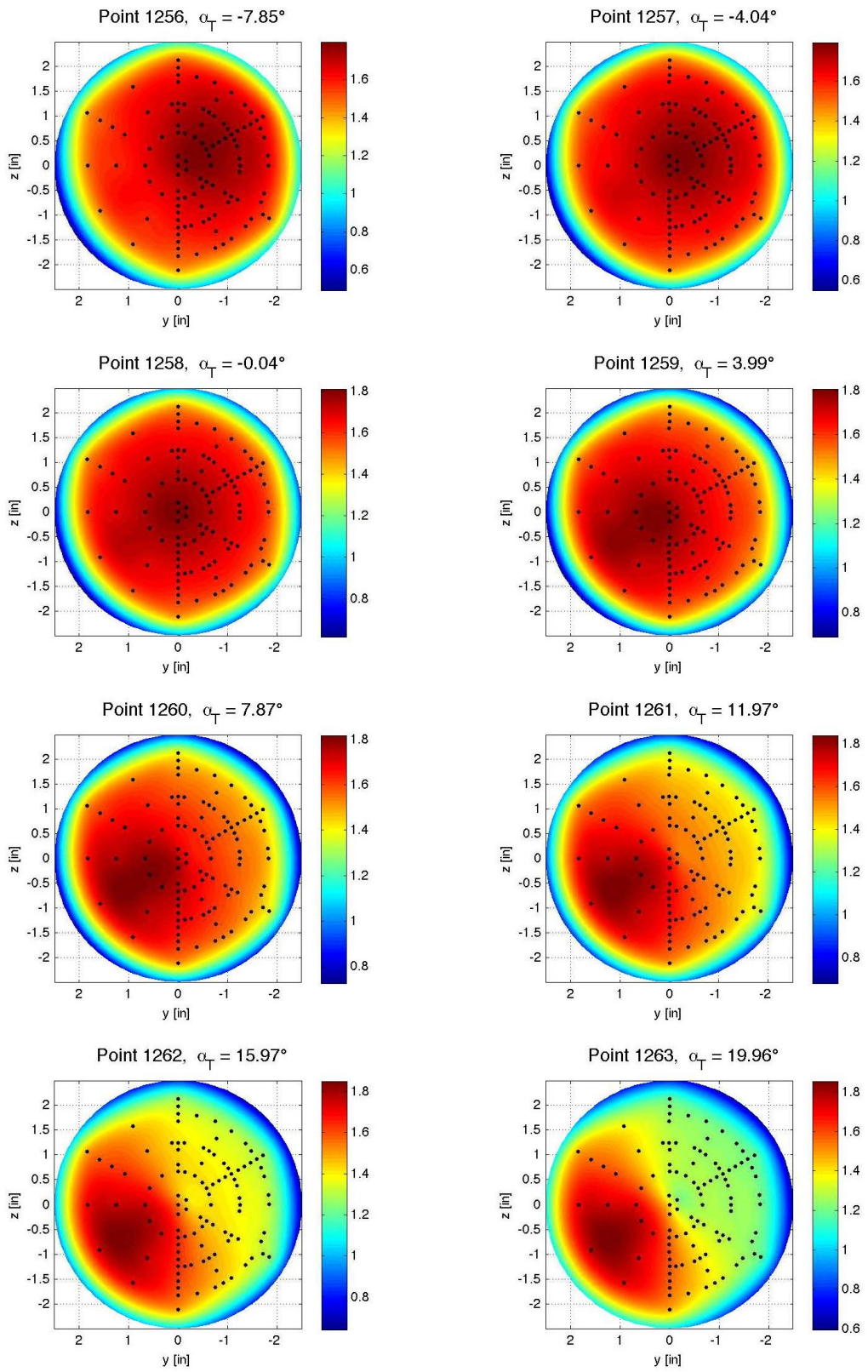

Figure E-81. Baseline configuration, Run 105, M_∞ = 4.6, Re_∞ = 1.5x10^6/ft, ϕ = 60.00°, X_S = 25.19 in, Y_S = 0.00 in, C_T = 0.00.

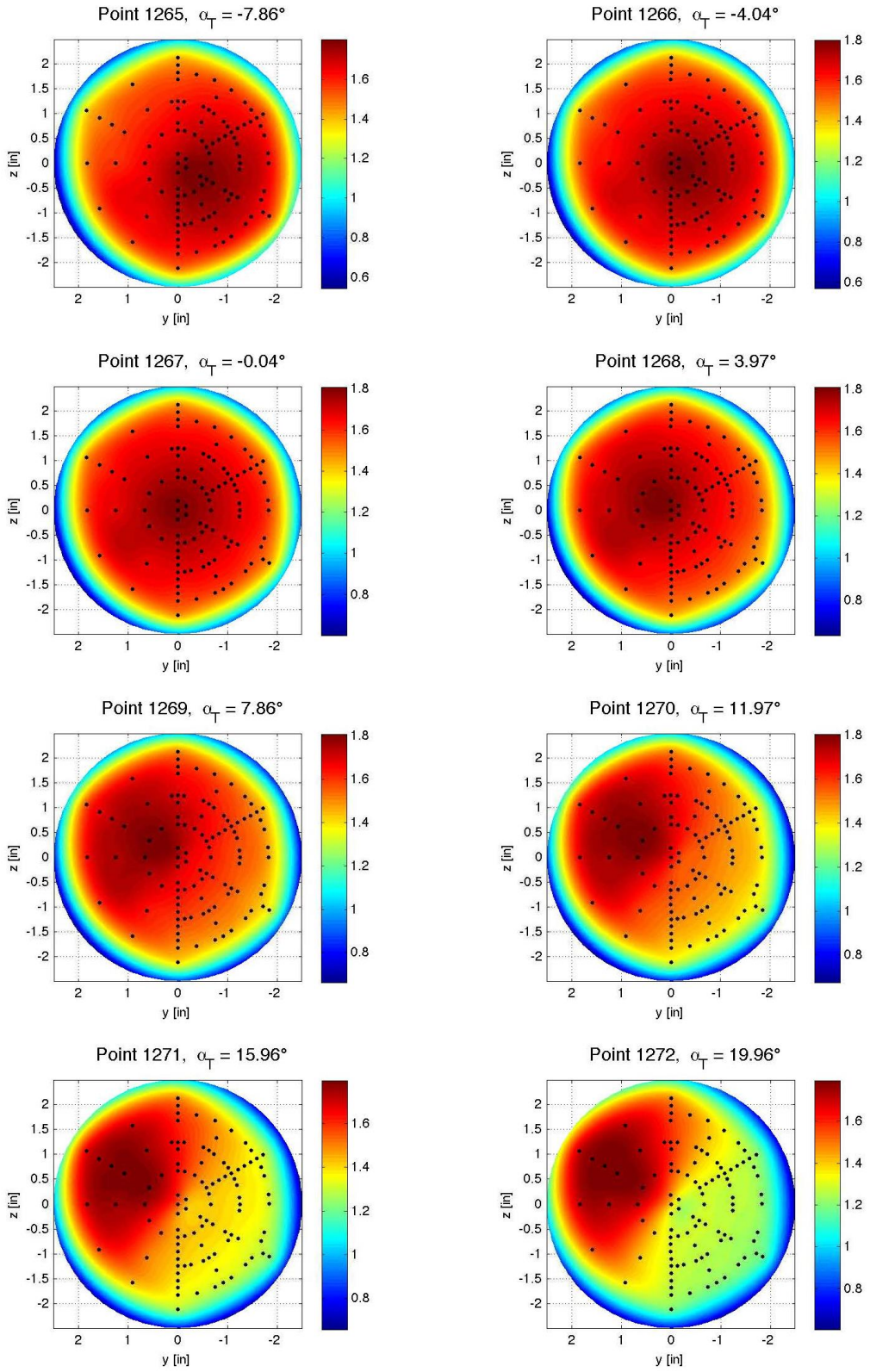

Figure E-82. Baseline configuration, Run 106, M_∞ = 4.6, Re_∞ = 1.5x10^6/ft, ϕ = 119.96°, X_S = 25.19 in, Y_S = 0.00 in, C_T = 0.00.

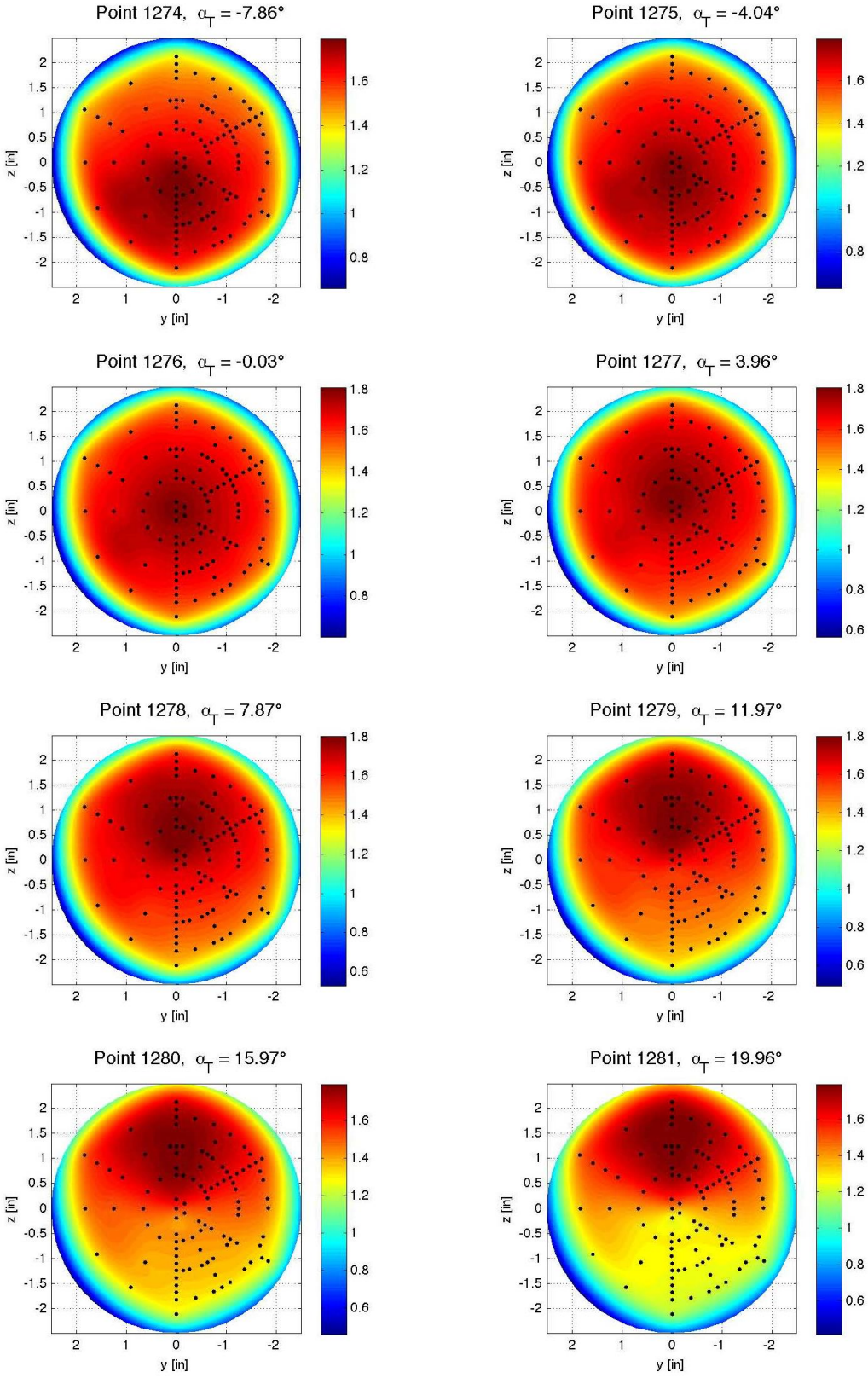

Figure E-83. Baseline configuration, Run 107, M_∞ = 4.6, Re_∞ = 1.5x10^6/ft, ϕ = 179.93°, X_S = 25.19 in, Y_S = 0.00 in, C_T = 0.00.

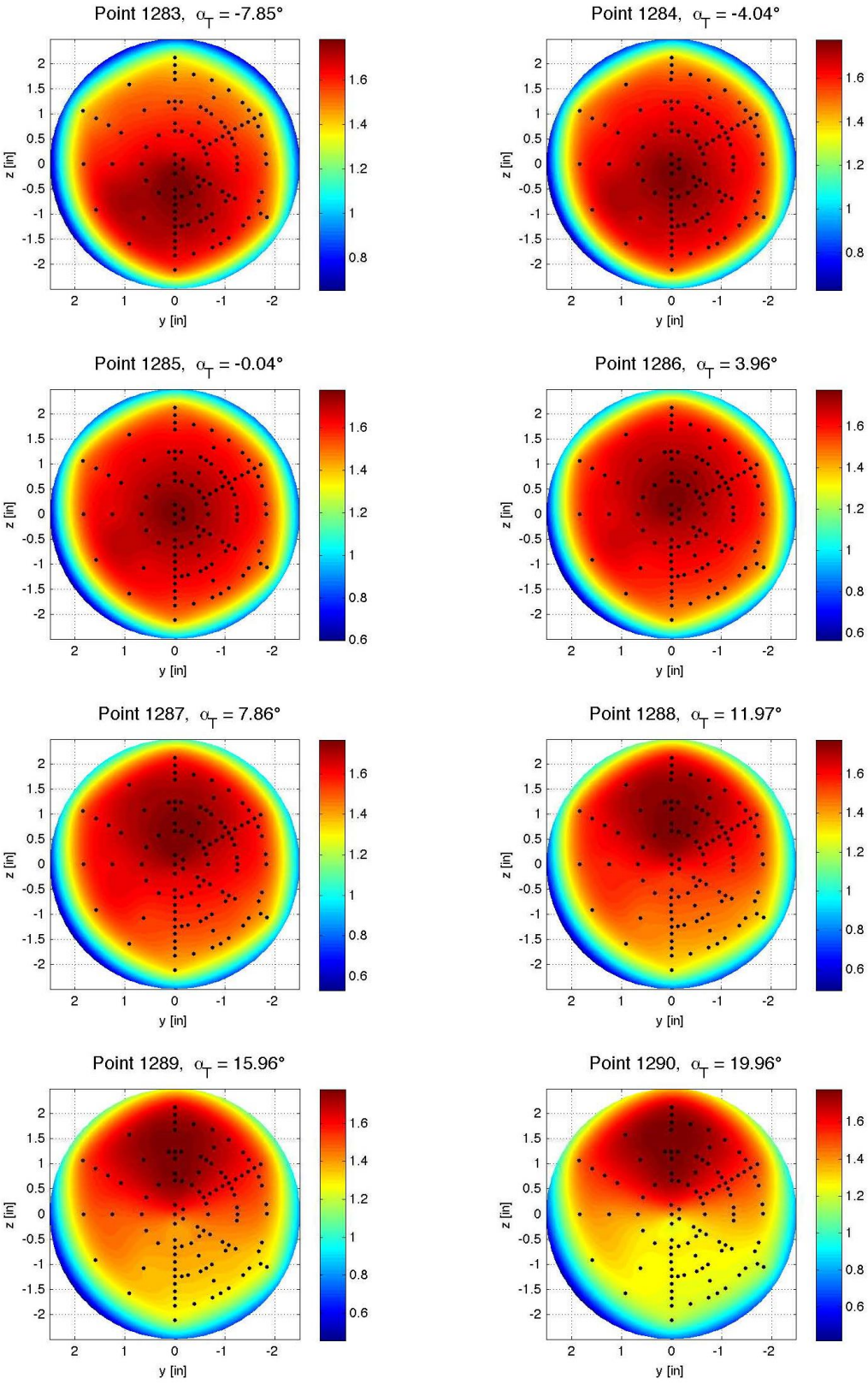

Figure E-84. Baseline configuration, Run 108, M_∞ = 4.6, Re_∞ = 1.5x10^6/ft, ϕ = 179.93°, X_S = 40.15 in, Y_S = 0.00 in, C_T = 0.00.

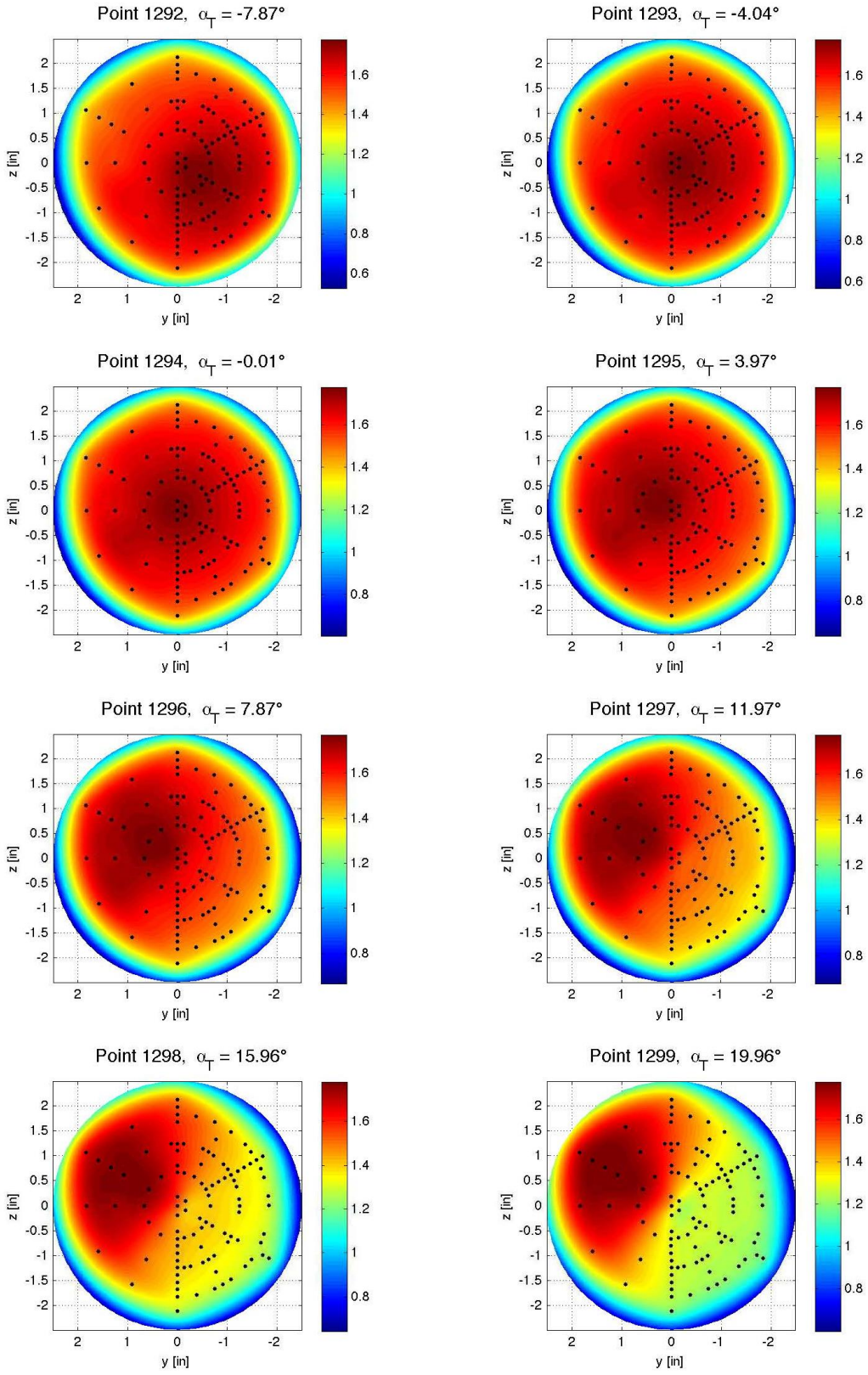

Figure E-85. Baseline configuration, Run 109, M_∞ = 4.6, Re_∞ = 1.5x10^6/ft, ϕ = 119.92°, X_S = 40.15 in, Y_S = 0.00 in, C_T = 0.00.

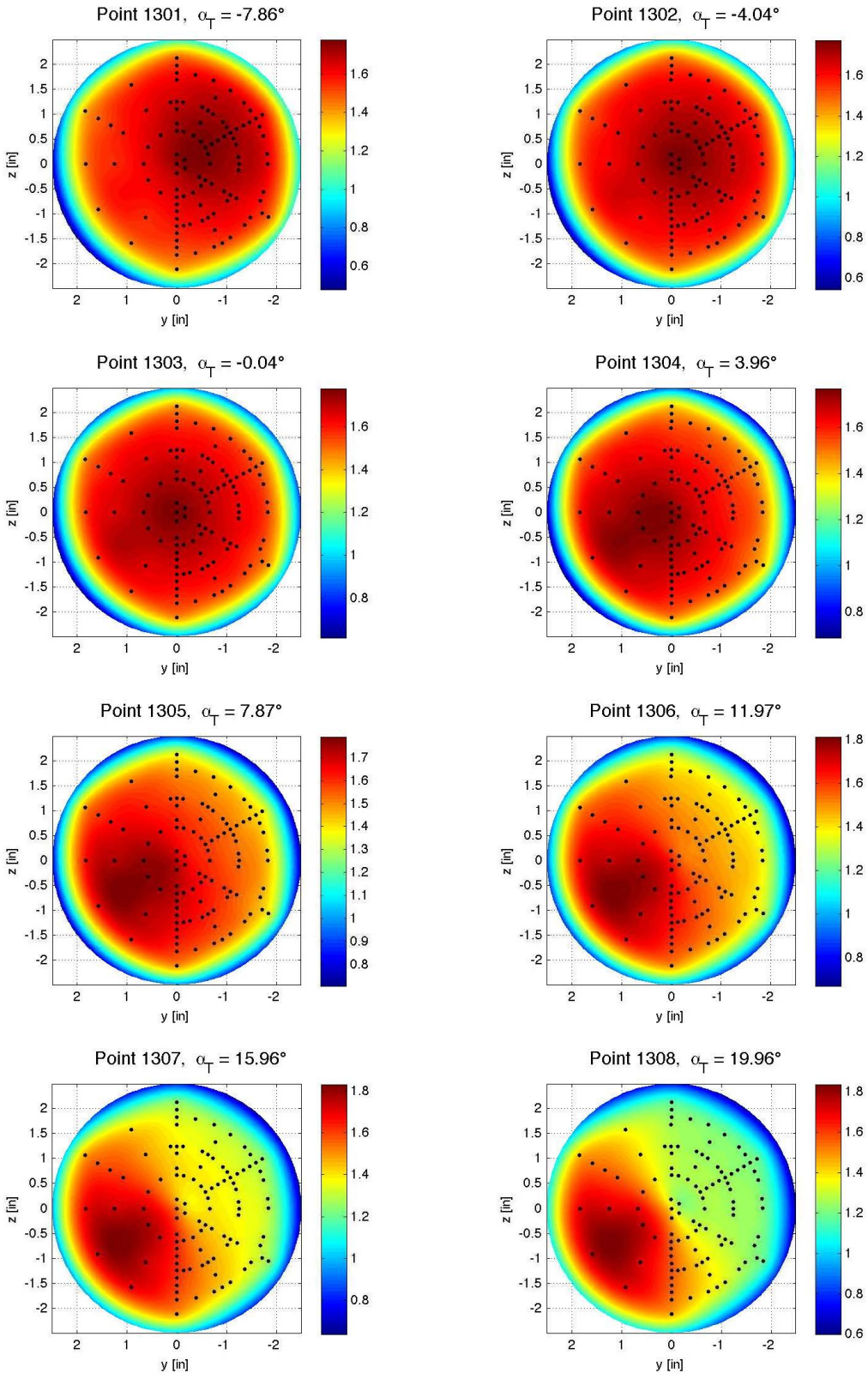

Figure E-86. Baseline configuration, Run 110, M_∞ = 4.6, Re_∞ = 1.5x10^6/ft, ϕ = 59.94°, X_S = 40.15 in, Y_S = 0.00 in, C_T = 0.00.

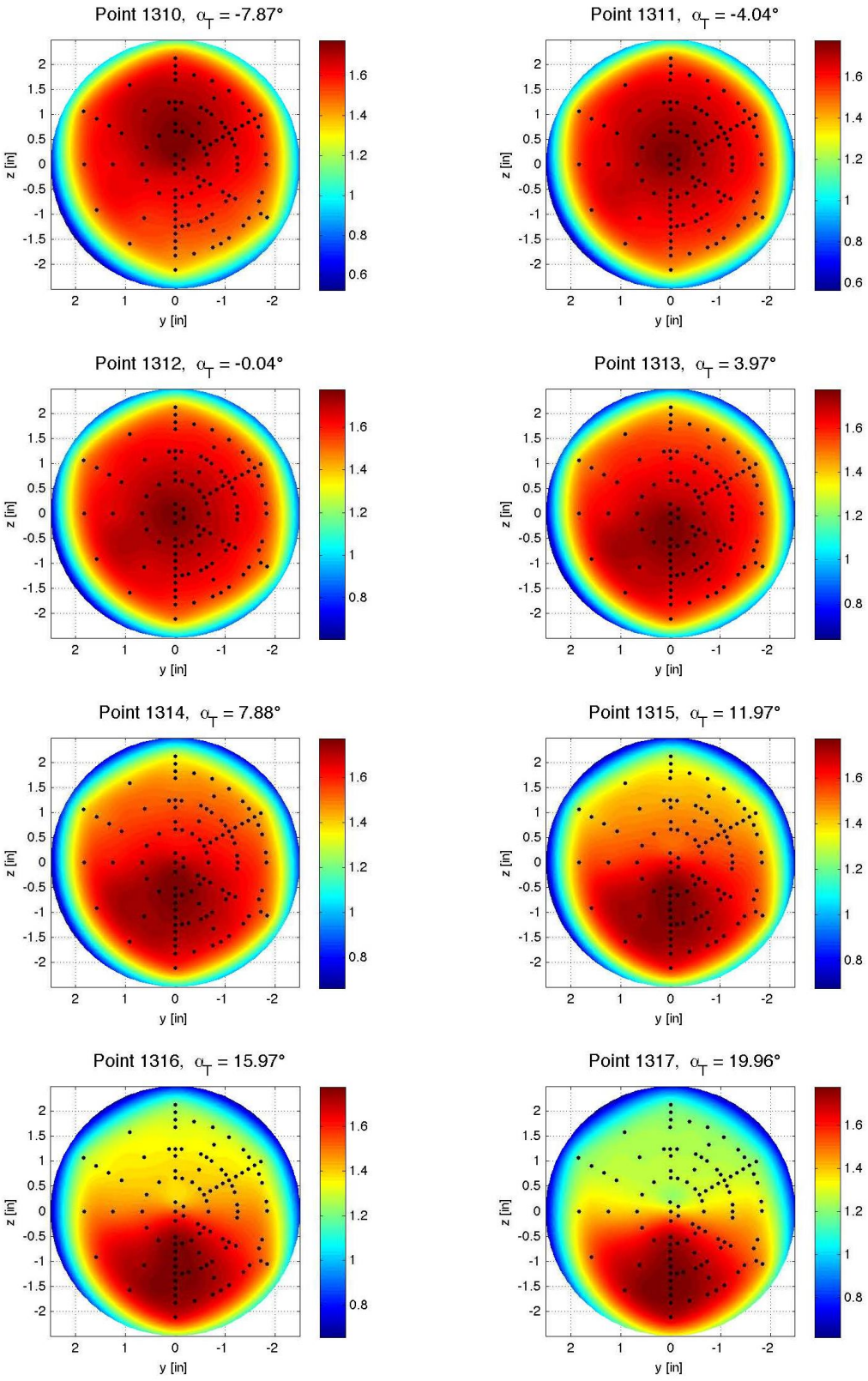

Figure E-87. Baseline configuration, Run 111, M_∞ = 4.6, Re_∞ = 1.5x10^6/ft, ϕ = −0.01°, X_S = 40.09 in, Y_S = 0.00 in, C_T = 0.00.

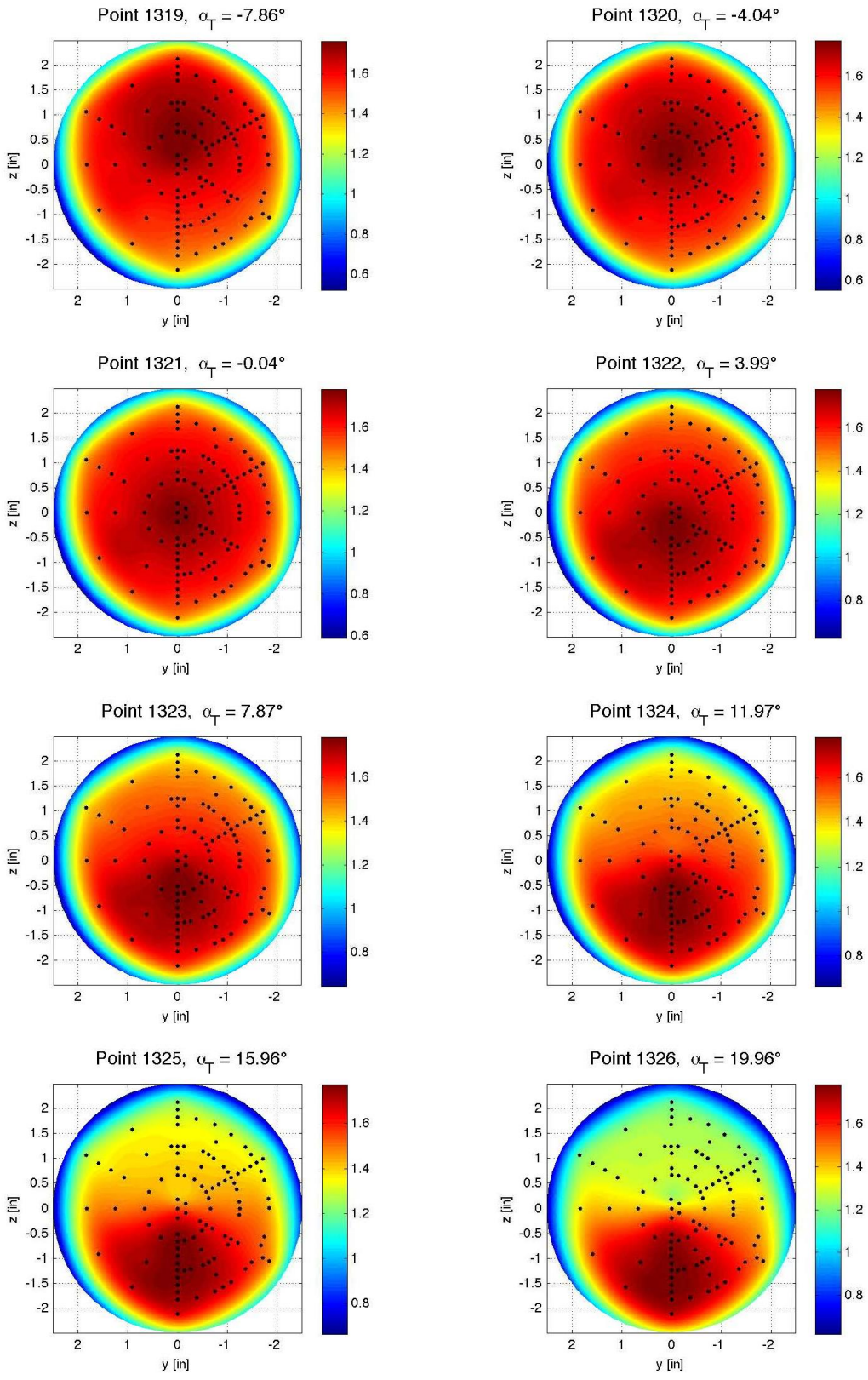

Figure E-88. Baseline configuration, Run 112, M_∞ = 4.6, Re_∞ = 1.5x10^6/ft, ϕ = −0.01°, X_S = 50.19 in, Y_S = 0.00 in, C_T = 0.00.

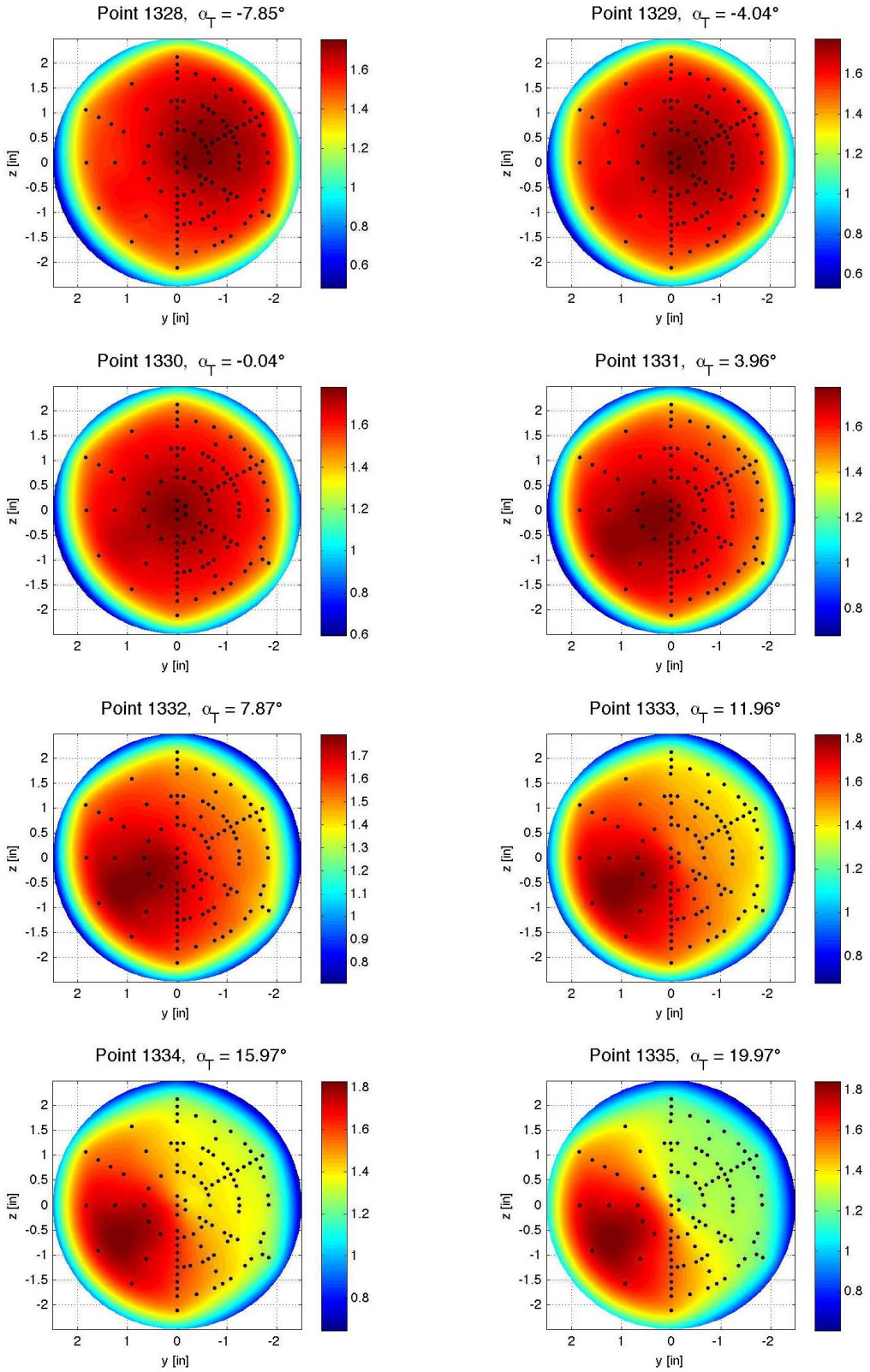

Figure E-89. Baseline configuration, Run 113, M_∞ = 4.6, Re_∞ = 1.5x10^6/ft, ϕ = 60.02°, X_S = 50.19 in, Y_S = 0.00 in, C_T = 0.00.

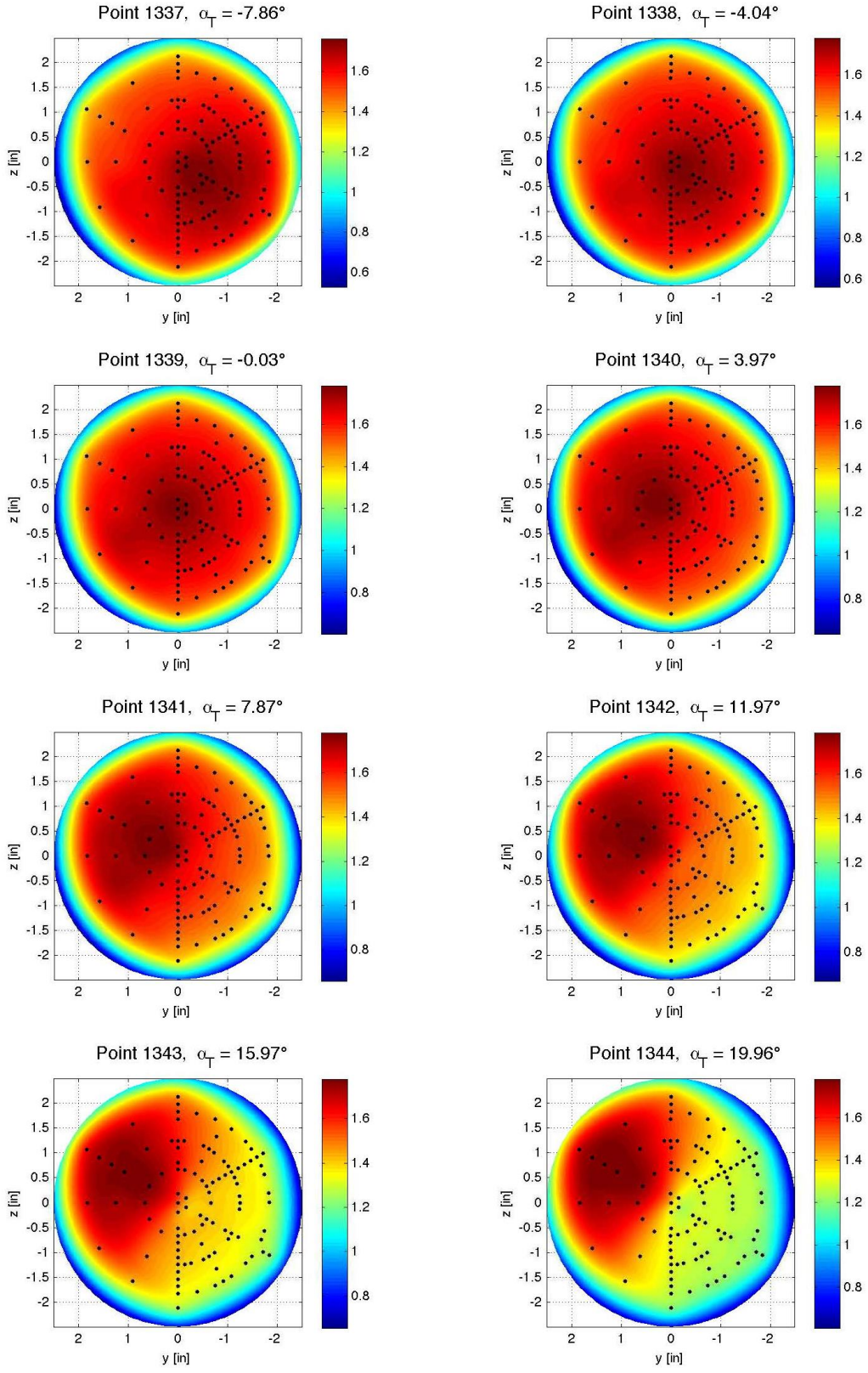

Figure E-90. Baseline configuration, Run 114, M_∞ = 4.6, Re_∞ = 1.5x10^6/ft, ϕ = 120.04°, X_S = 50.19 in, Y_S = 0.00 in, C_T = 0.00.

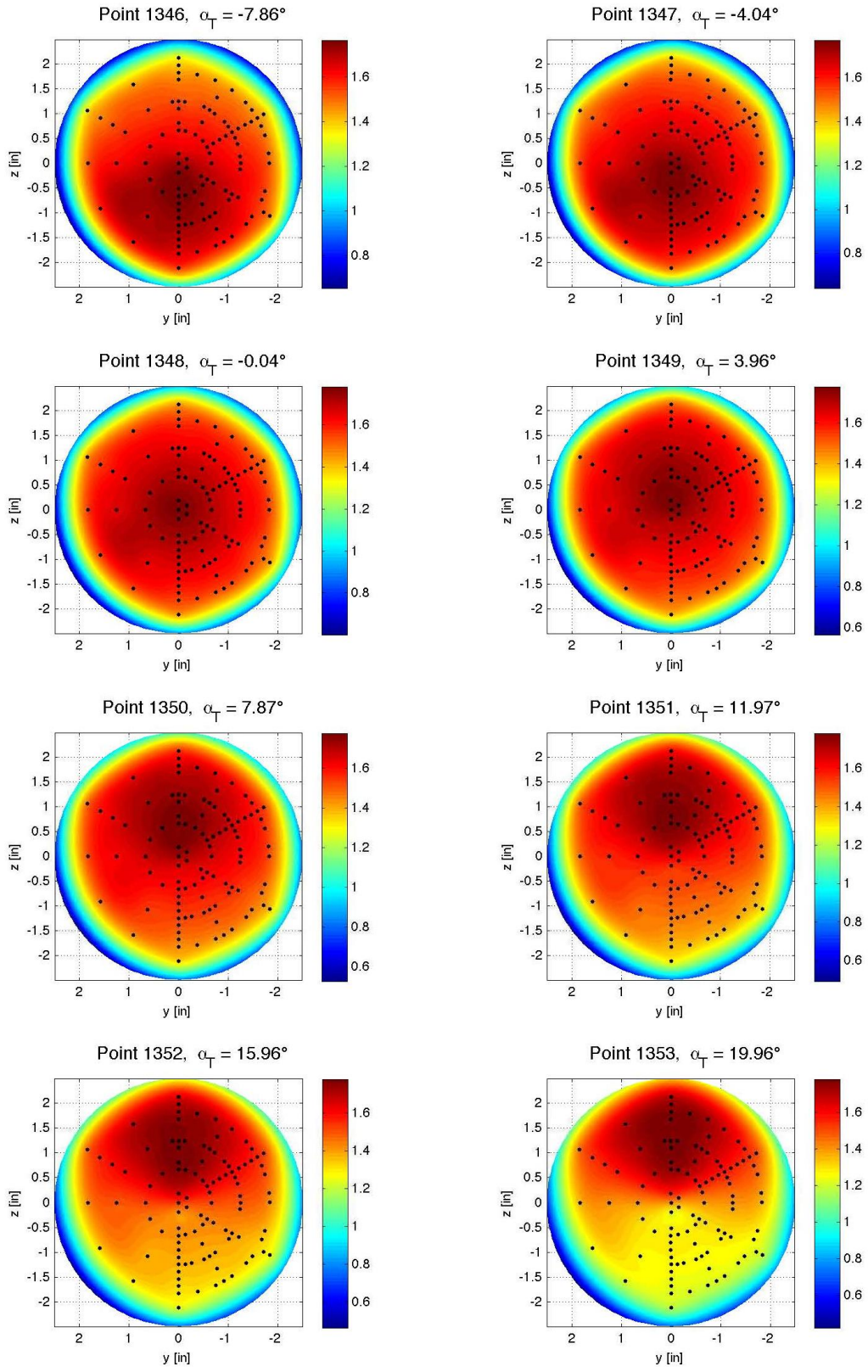

Figure E-91. Baseline configuration, Run 115, M_∞ = 4.6, Re_∞ = 1.5x10^6/ft, ϕ = 179.97°, X_S = 50.19 in, Y_S = 0.00 in, C_T = 0.00.

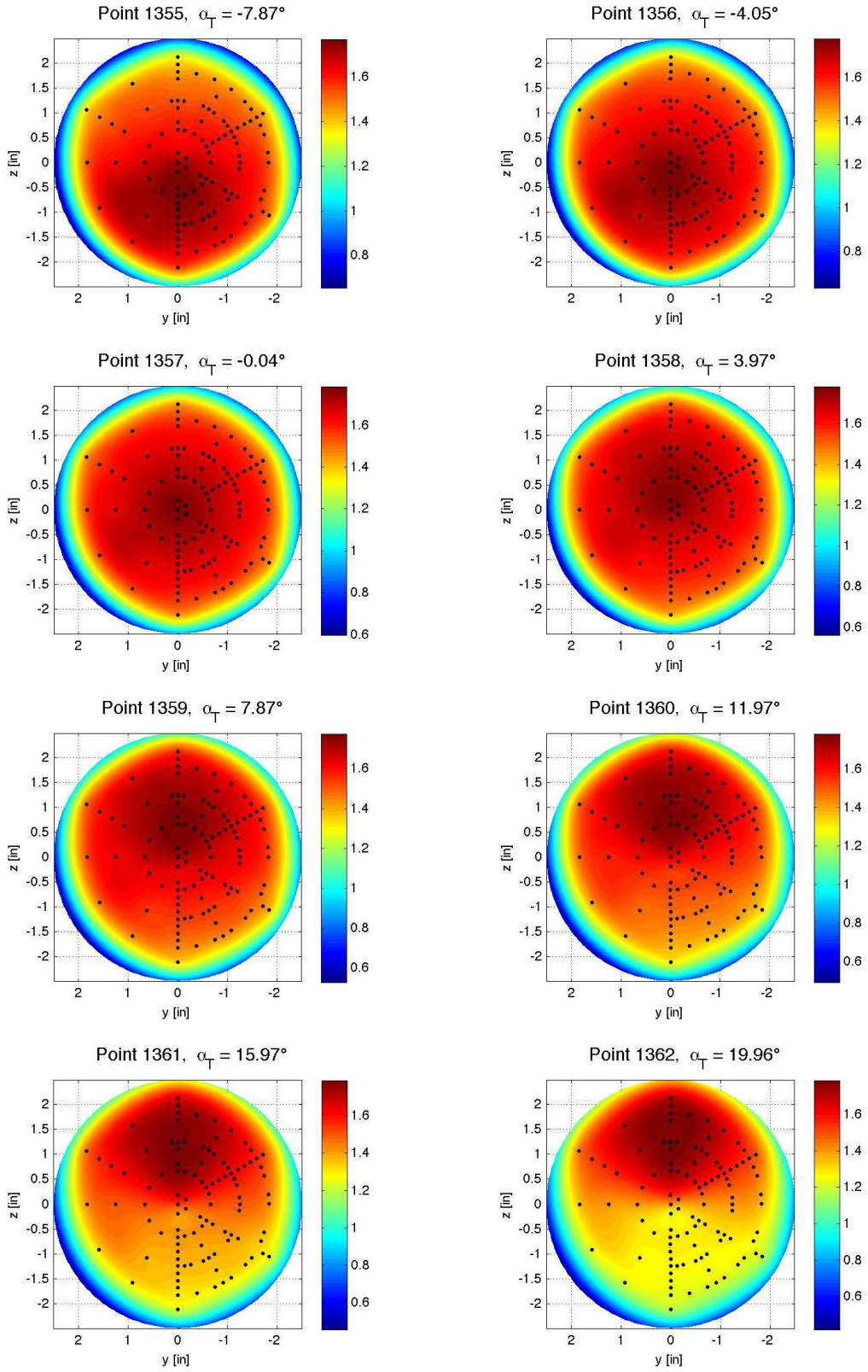

Figure E-92. Baseline configuration, Run 116, M_∞ = 4.6, Re_∞ = 1.5x10^6/ft, ϕ = 179.97°, X_S = 50.19 in, Y_S = 8.00 in, C_T = 0.00.

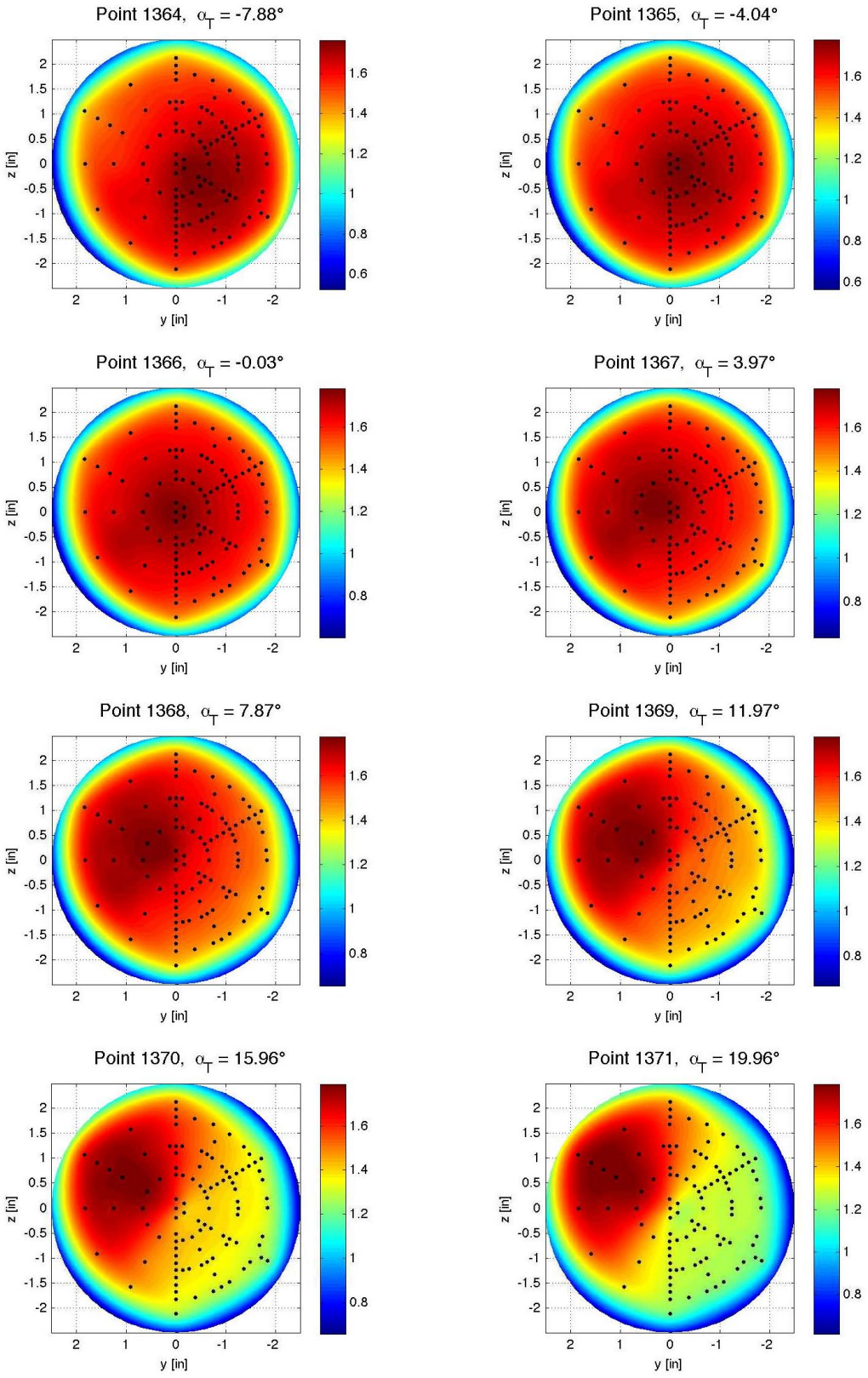

Figure E-93. Baseline configuration, Run 117, M_∞ = 4.6, Re_∞ = 1.5x10^6/ft, ϕ = 119.92°, X_S = 50.19 in, Y_S = 8.00 in, C_T = 0.00.

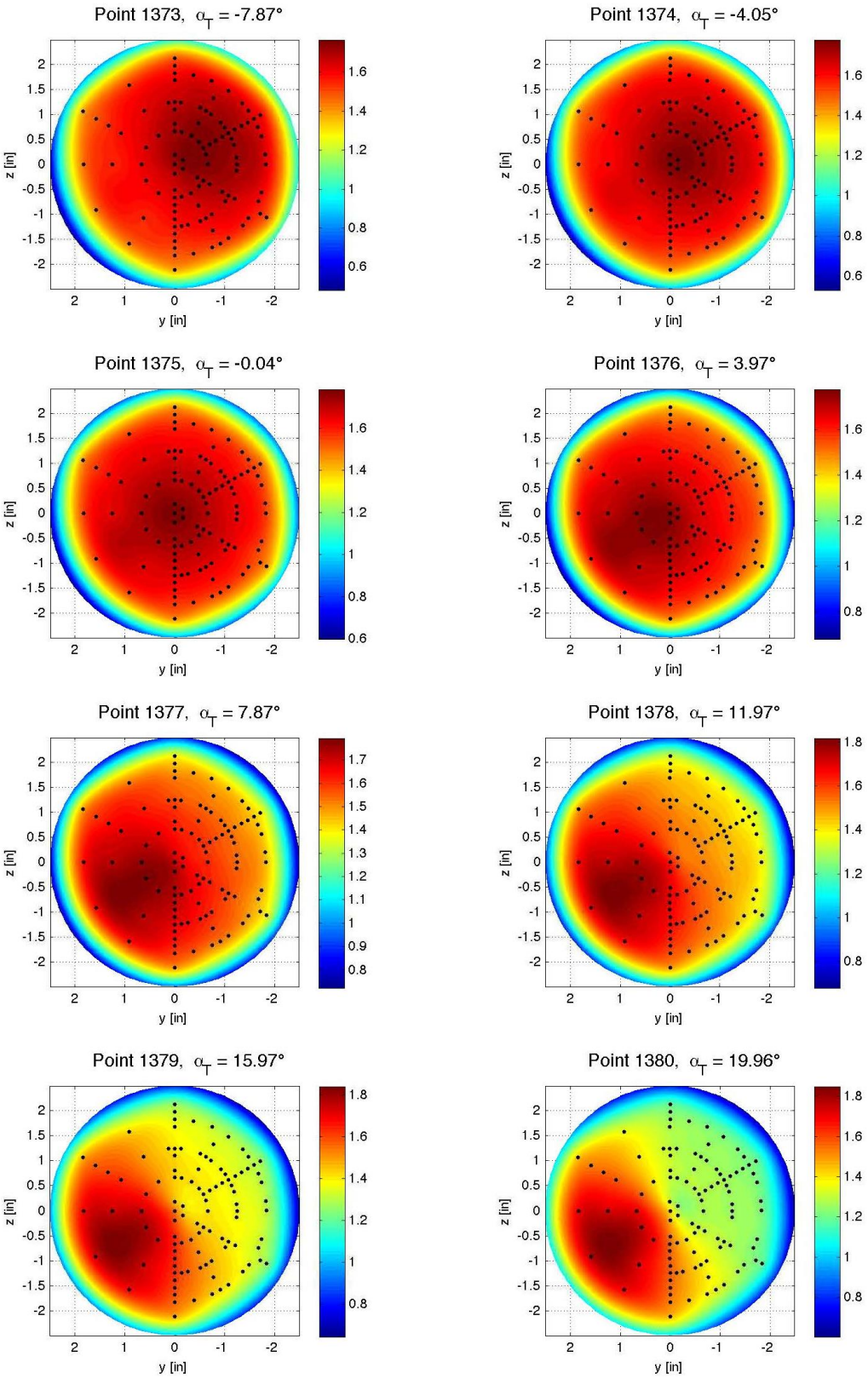

Figure E-94. Baseline configuration, Run 118, M_∞ = 4.6, Re_∞ = 1.5x10^6/ft, ϕ = 59.96°, X_S = 50.19 in, Y_S = 8.00 in, C_T = 0.00.

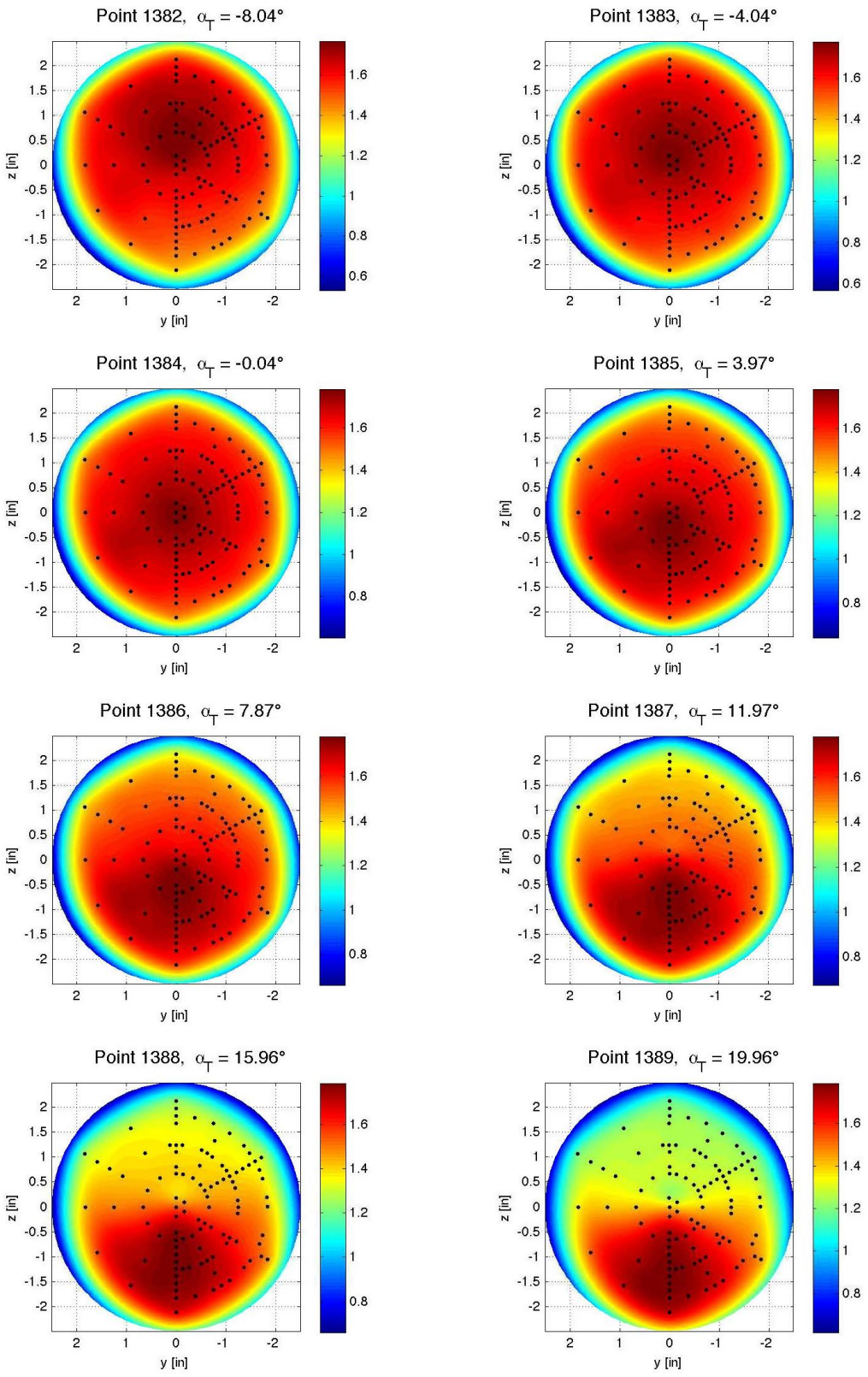

Figure E-95. Baseline configuration, Run 119, M_∞ = 4.6, Re_∞ = 1.5x10^6/ft, ϕ = 0.03°, X_S = 50.19 in, Y_S = 8.00 in, C_T = 0.00.

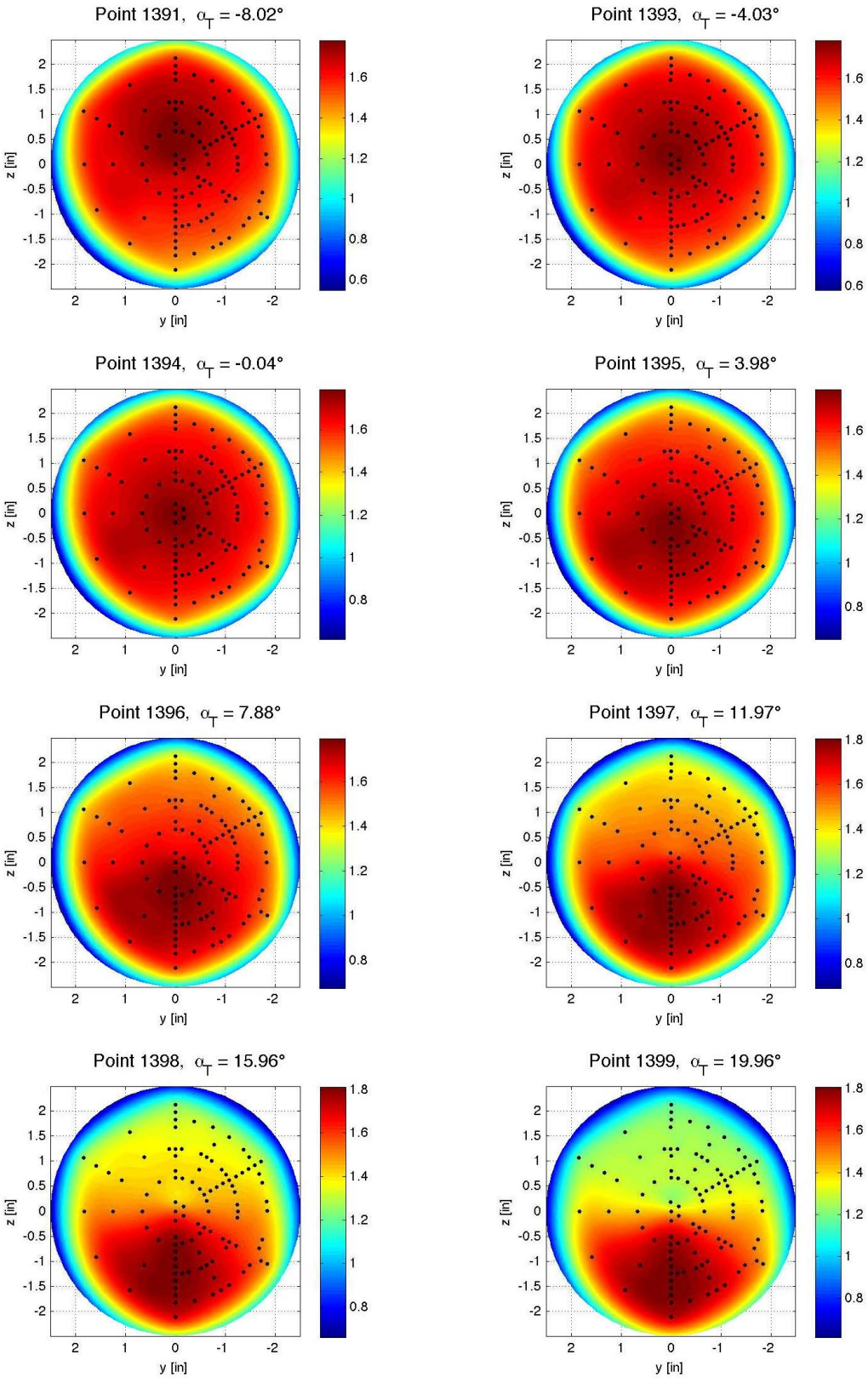

Figure E-96. Baseline configuration, Run 120, M_∞ = 4.6, Re_∞ = 1.5x10^6/ft, ϕ = 0.03°, X_S = 25.16 in, Y_S = –8.00 in, C_T = 0.00.

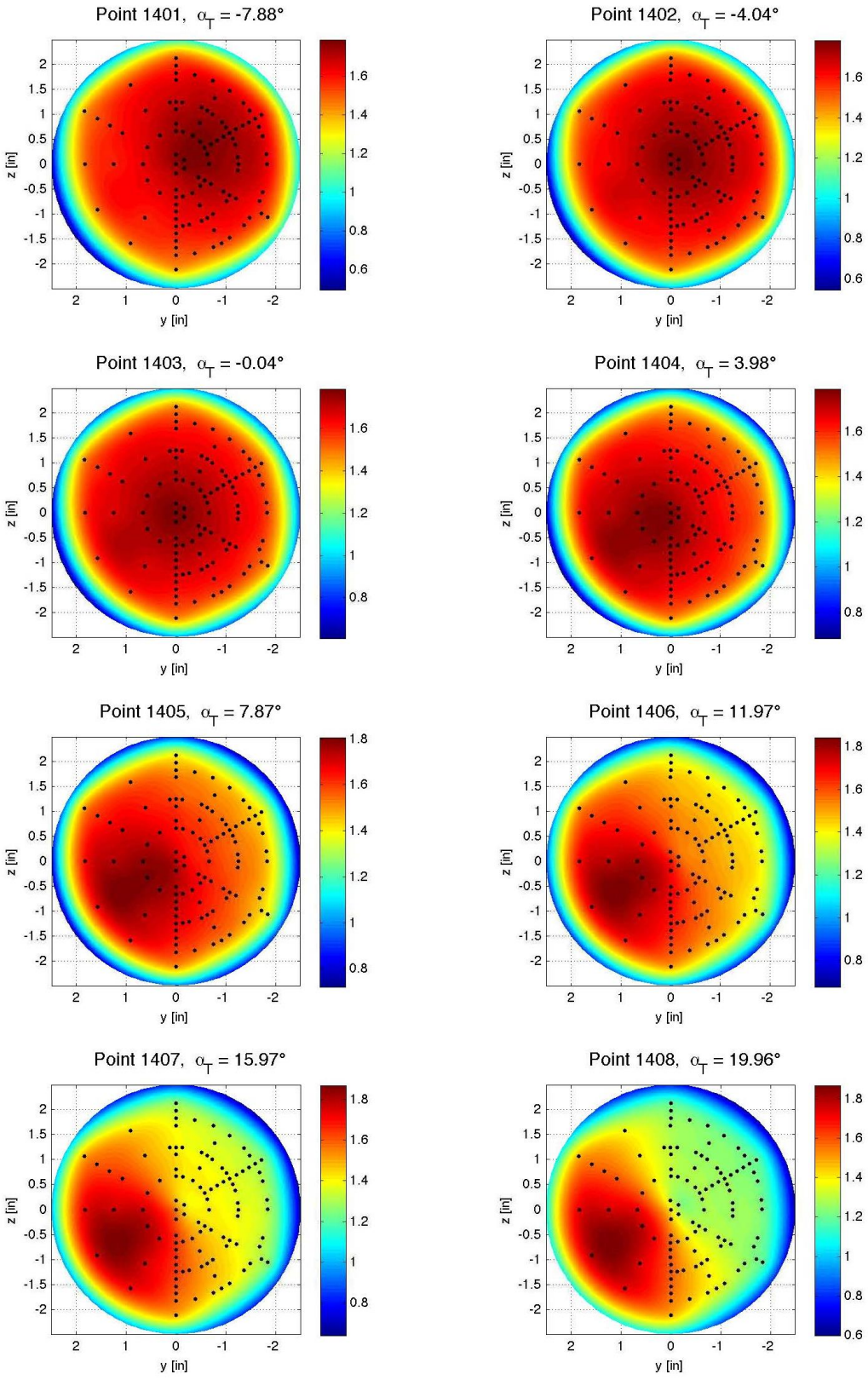

Figure E-97. Baseline configuration, Run 121, M_∞ = 4.6, Re_∞ = 1.5x10^6/ft, ϕ = 60.06°, X_S = 25.16 in, Y_S = –8.00 in, C_T = 0.00.

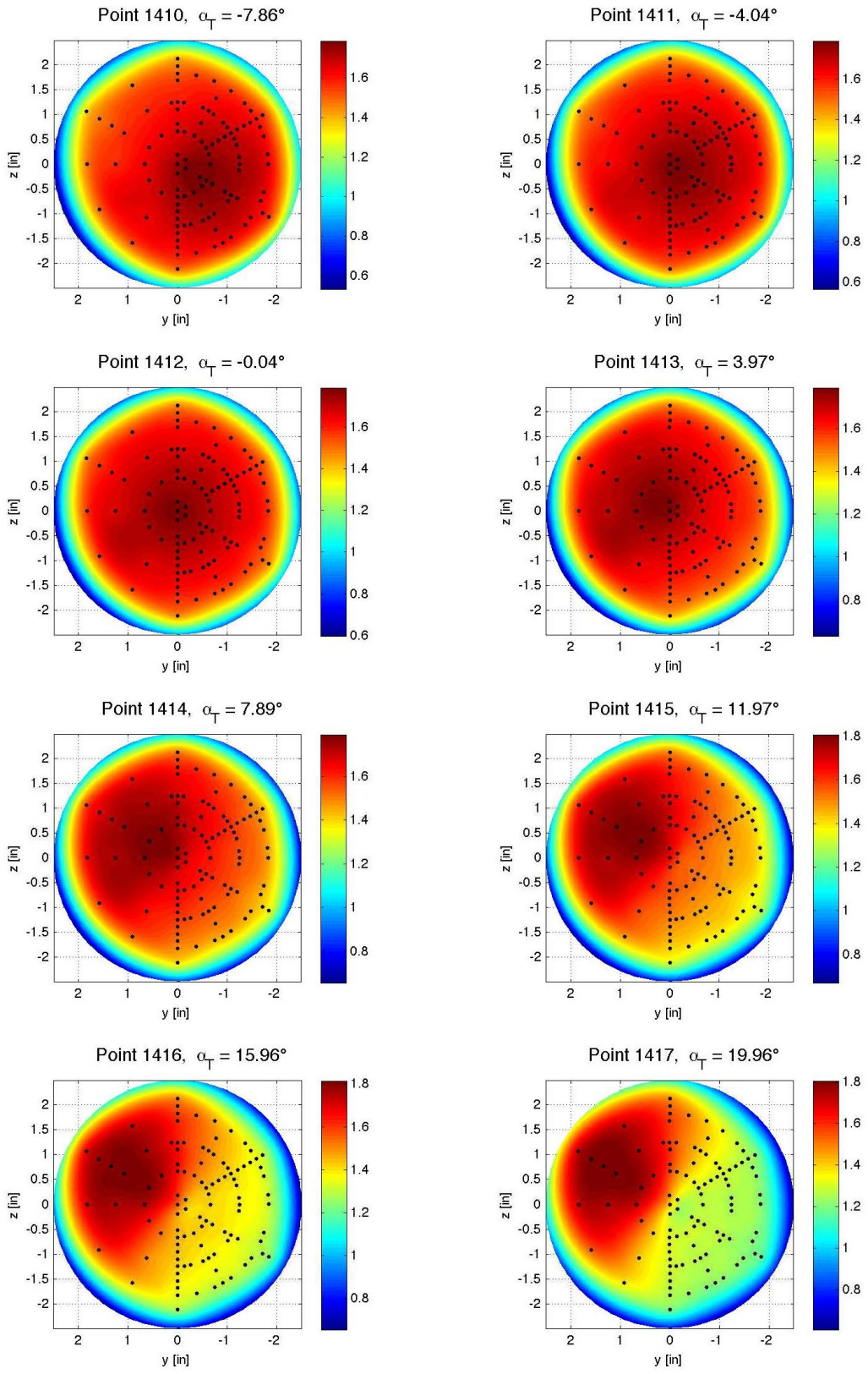

Figure E-98. Baseline configuration, Run 122, M_∞ = 4.6, Re_∞ = 1.5x10^6/ft, ϕ = 120.00°, X_S = 25.16 in, Y_S = –8.00 in, C_T = 0.00.

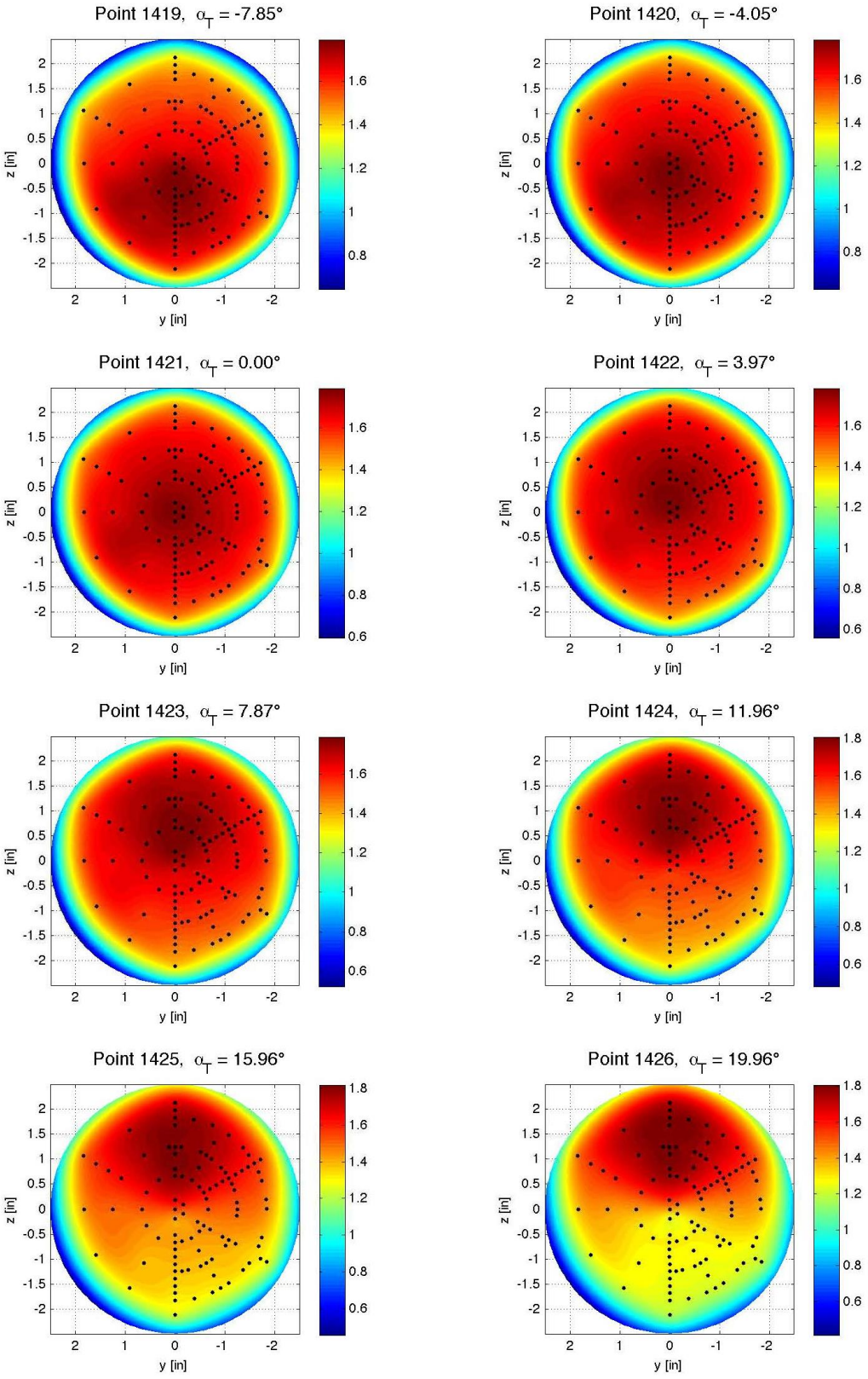

Figure E-99. Baseline configuration, Run 123, $M\infty$ = 4.6, Re_∞ = 1.5x10^6/ft, ϕ = 179.91°, X_S = 25.16 in, Y_S = –8.00 in, C_T = 0.00.

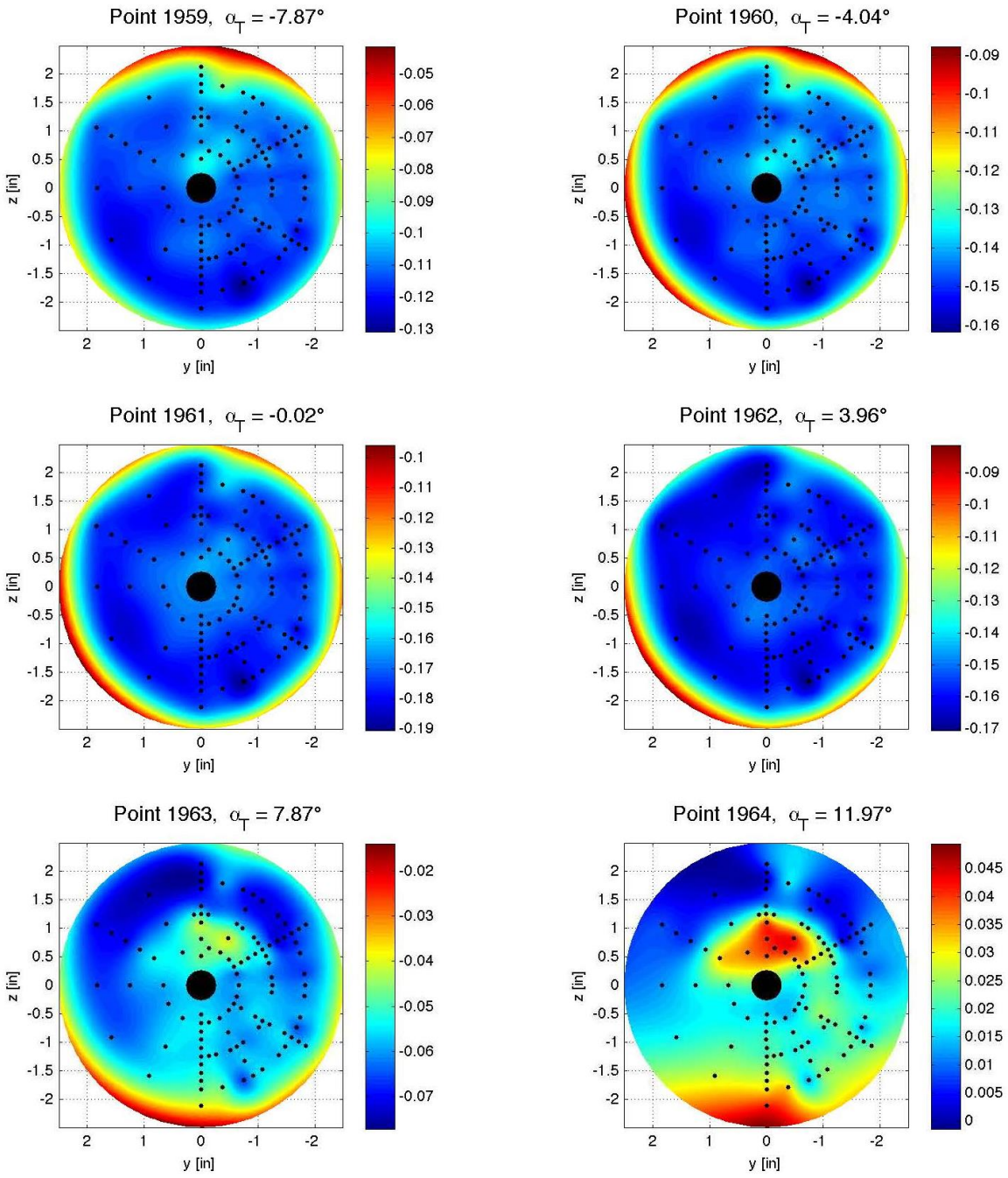

Figure E-100. Center nozzle configuration, Run 136, M_∞ = 2.4, Re_∞ = 1.0x10^6/ft, ϕ = –0.01°, X_S = 40.16 in, Y_S = 0.00 in, C_T = 4.03.

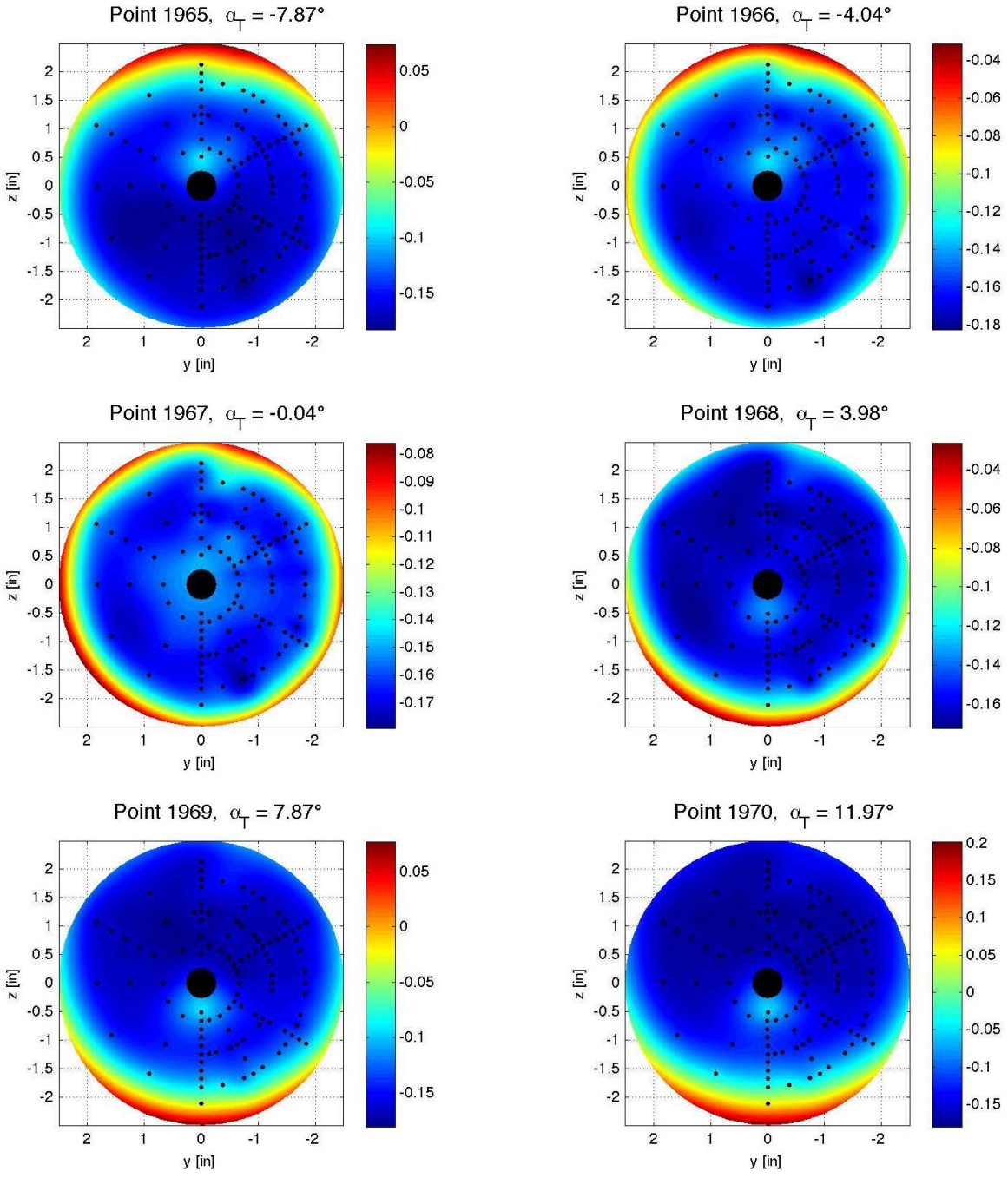

Figure E-101. Center nozzle configuration, Run 137, M_∞ = 2.4, Re_∞ = 1.0x10^6/ft, ϕ = −0.03°, X_S = 40.15 in, Y_S = 0.00 in, C_T = 2.99.

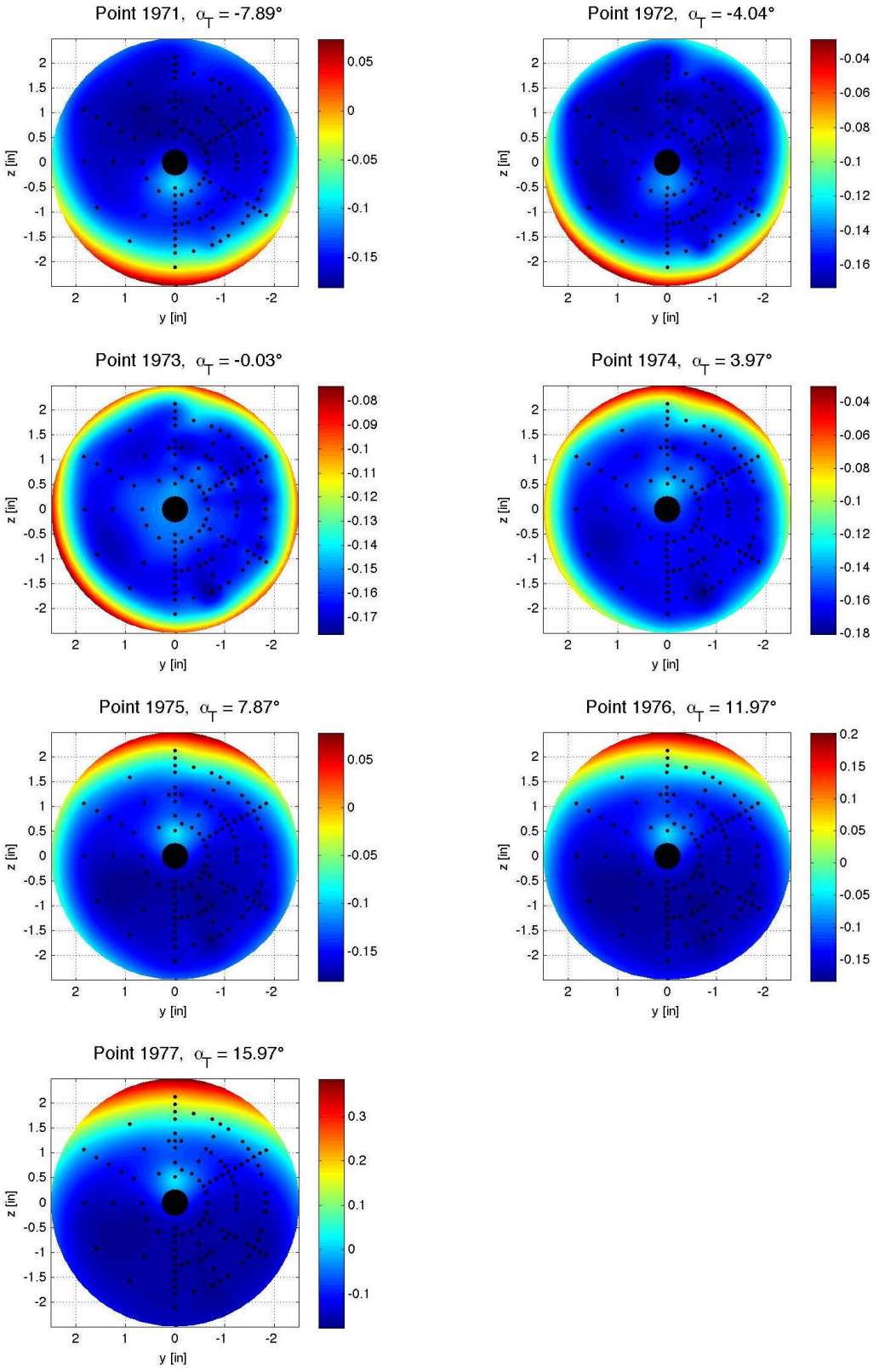

Figure E-102. Center nozzle configuration, Run 138, $M\infty$ = 2.4, Re_∞ = 1.0x10^6/ft, ϕ = 179.97°, X_S = 40.15 in, Y_S = 0.00 in, C_T = 3.01.

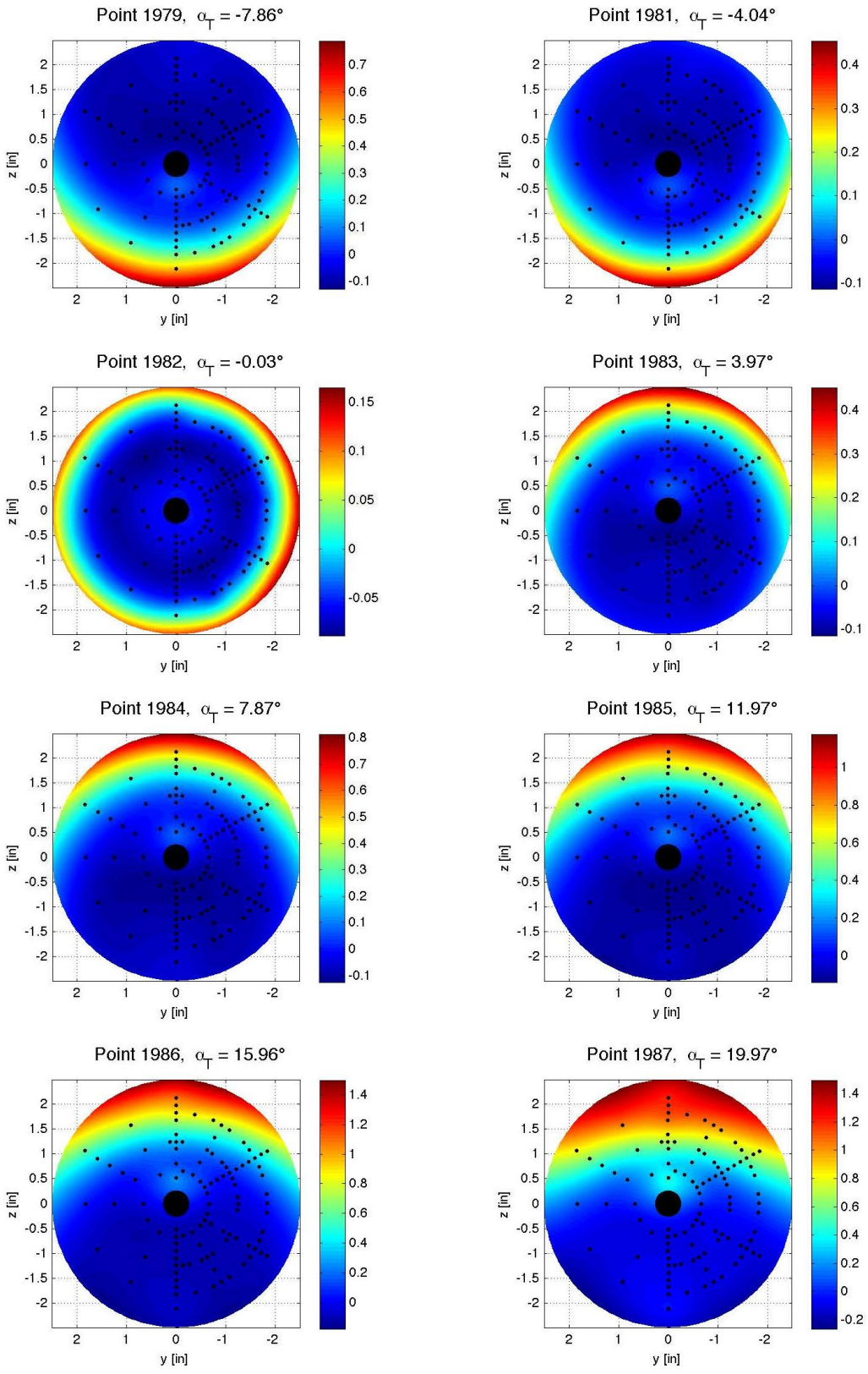

Figure E-103. Center nozzle configuration, Run 139, M_∞ = 2.4, Re_∞ = 1.0x10^6/ft, ϕ = 179.97°, X_S = 40.15 in, Y_S = 0.00 in, C_T = 0.97.

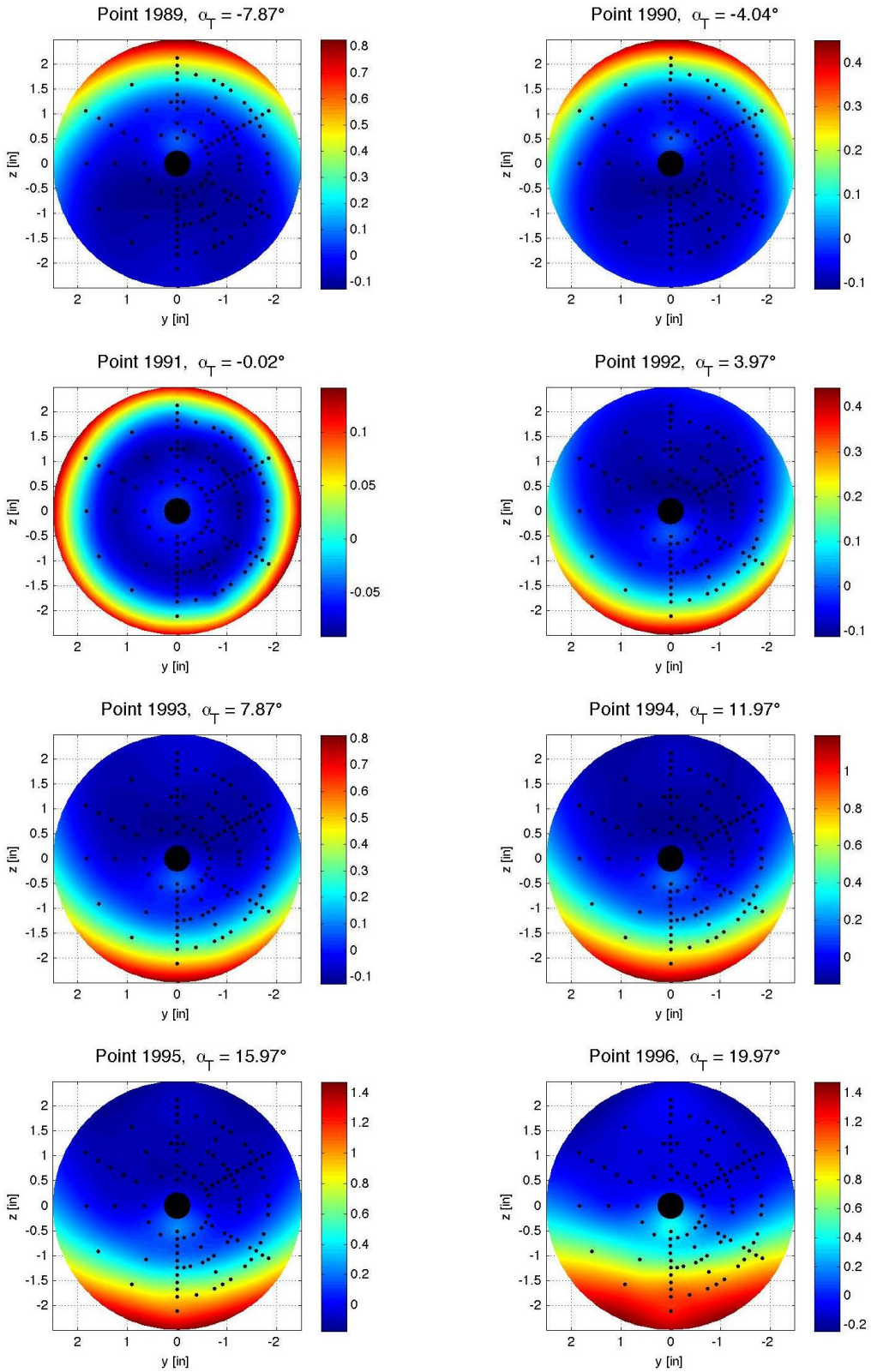

Figure E-104. Center nozzle configuration, Run 140, M_∞ = 2.4, Re_∞ = 1.0x10^6/ft, ϕ = –0.03°, X_S = 40.15 in, Y_S = 0.00 in, C_T = 0.97.

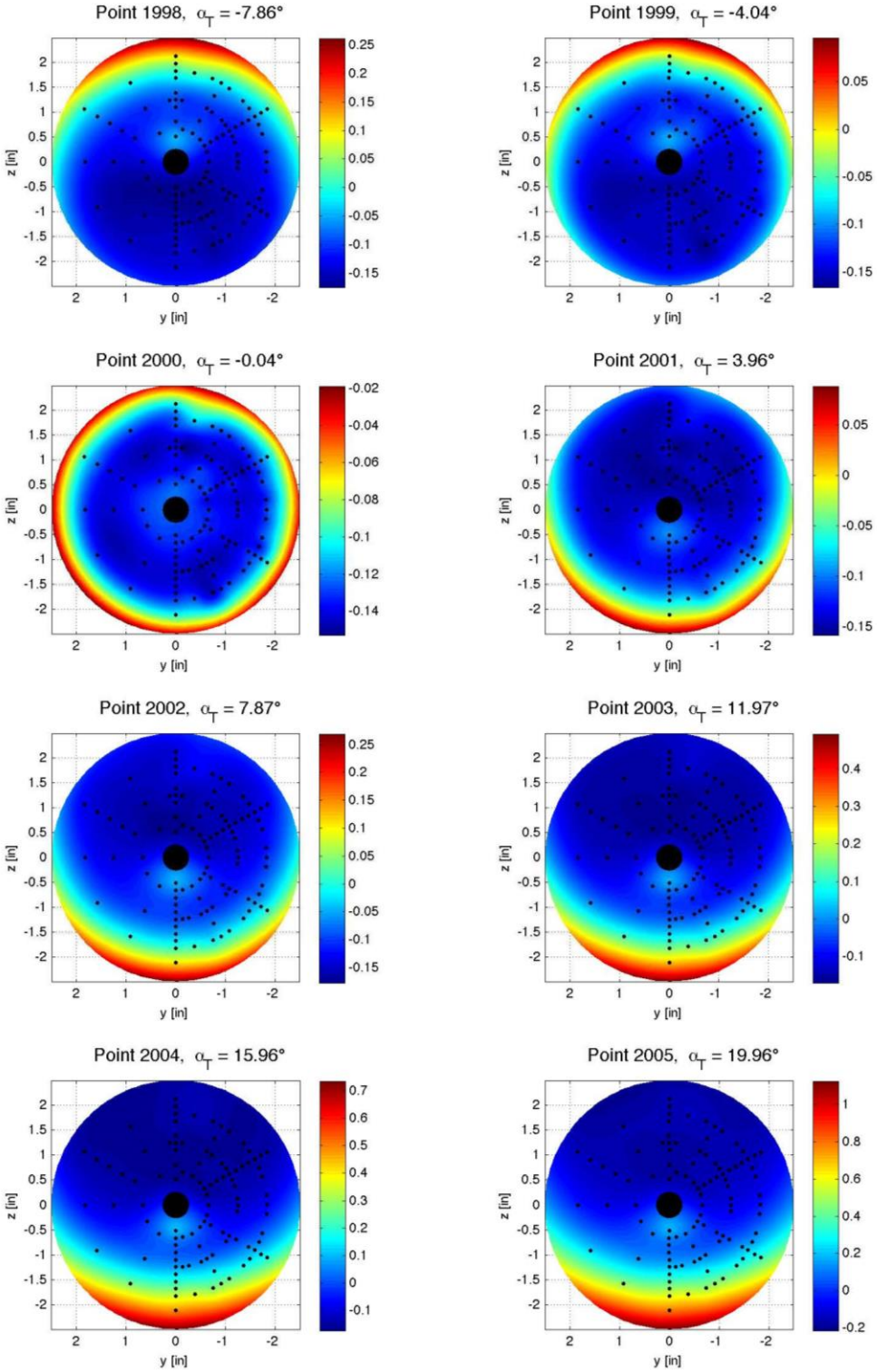

Figure E-105. Center nozzle configuration, Run 141, $M\infty$ = 2.4, Re_∞ = 1.0x10^6/ft, ϕ = −0.03°, X_S = 40.15 in, Y_S = 0.00 in, C_T = 1.98.

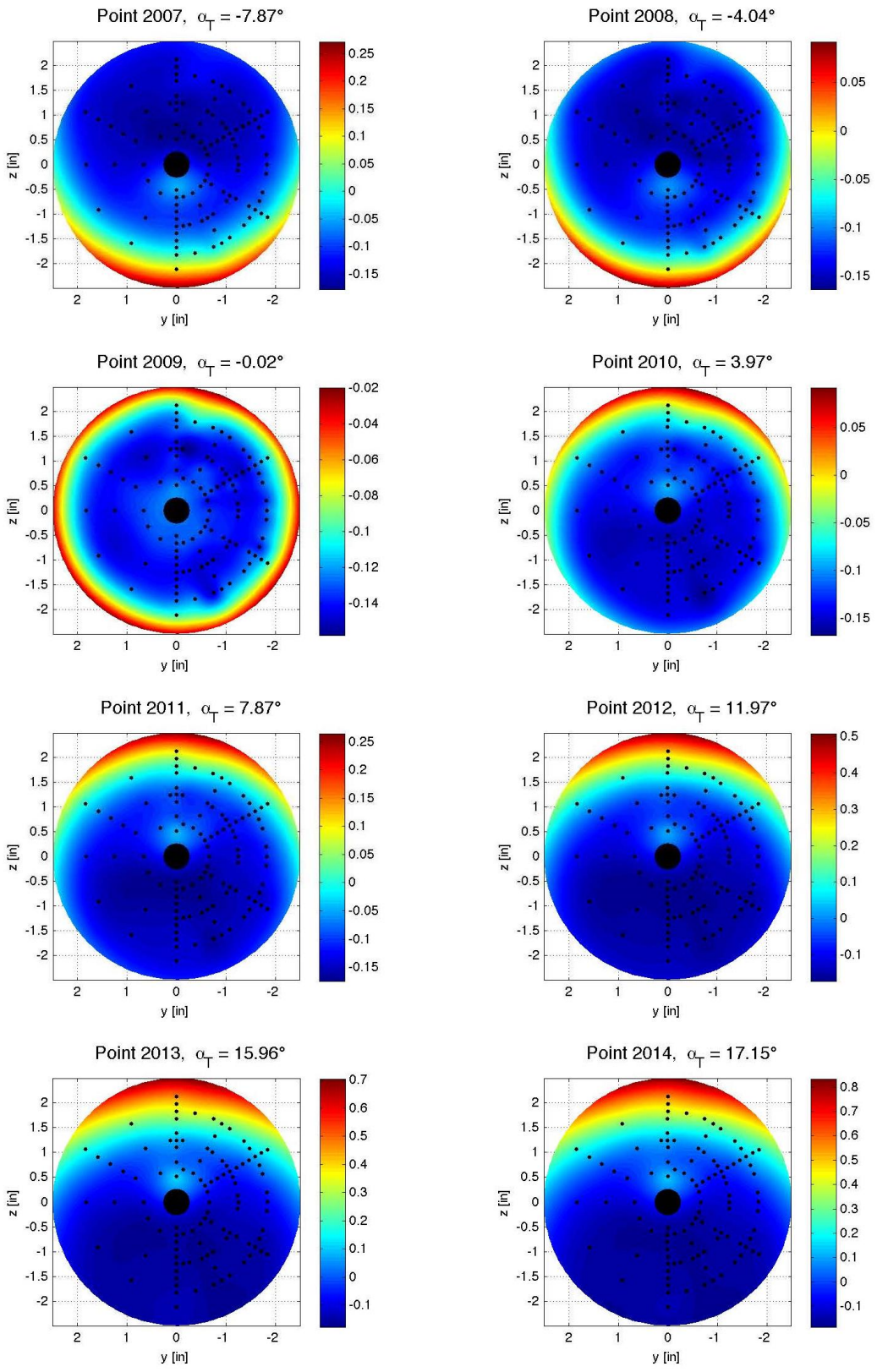

Figure E-106. Center nozzle configuration, Run 142, $M\infty$ = 2.4, Re_∞ = 1.0x10^6/ft, ϕ = −179.91°, X_S = 40.15 in, Y_S = 0.00 in, C_T = 1.99.

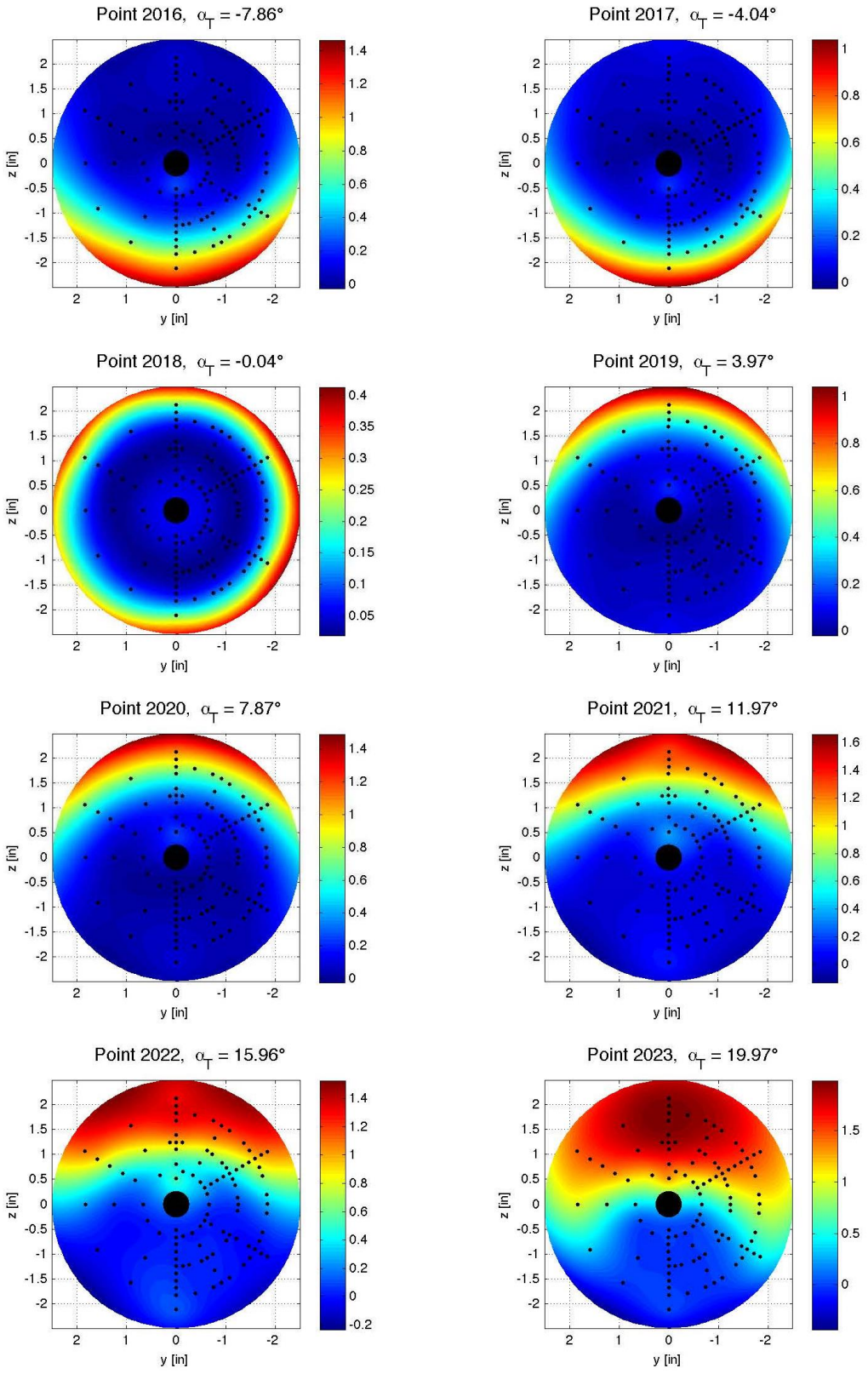

Figure E-107. Center nozzle configuration, Run 143, M_∞ = 2.4, Re_∞ = 1.0x10^6/ft, ϕ = −179.91°, X_S = 40.15 in, Y_S = 0.00 in, C_T = 0.46.

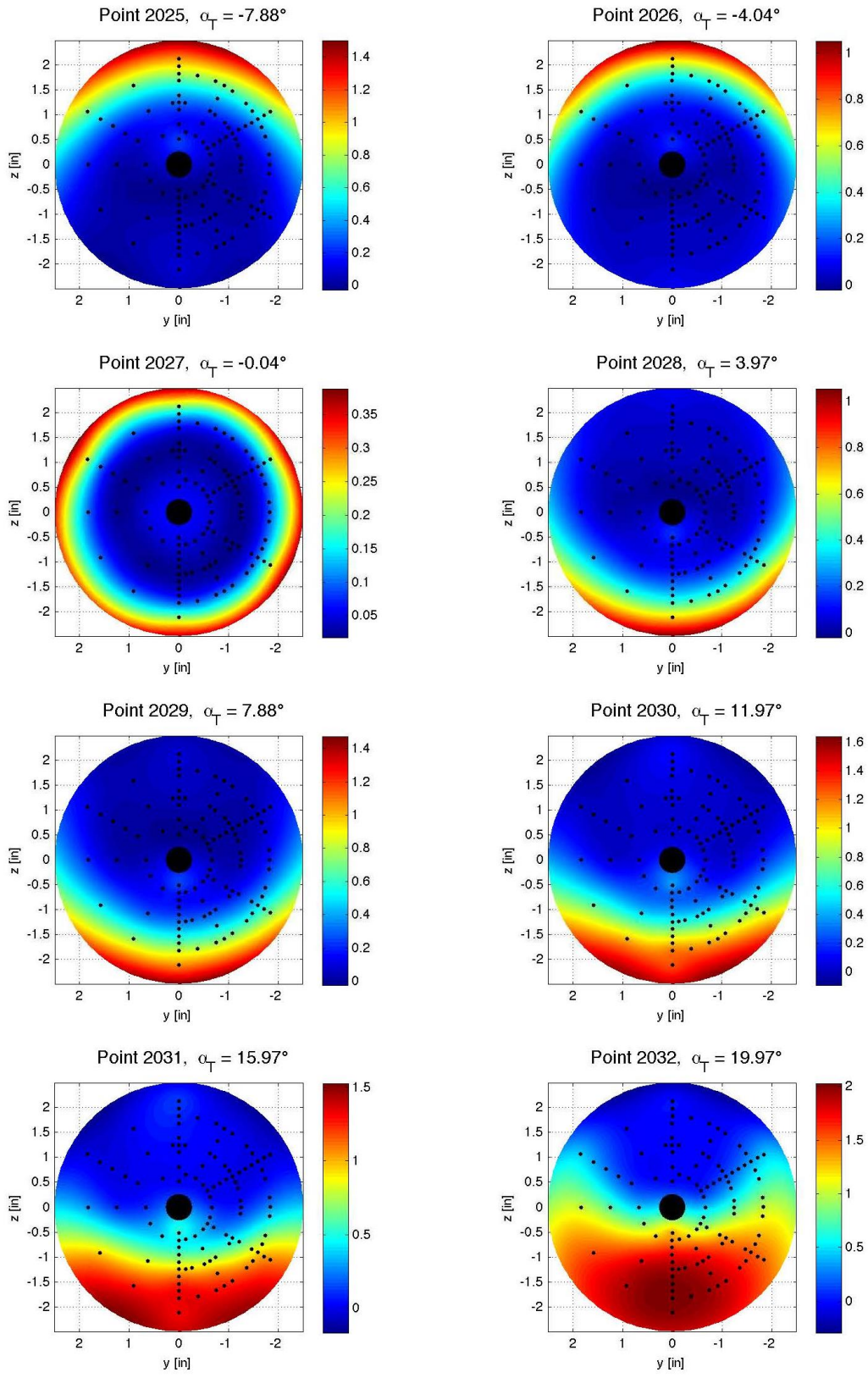

Figure E-108. Center nozzle configuration, Run 144, M_∞ = 2.4, Re_∞ = 1.0x10^6/ft, ϕ = 0.01°, X_S = 40.15 in, Y_S = 0.00 in, C_T = 0.47.

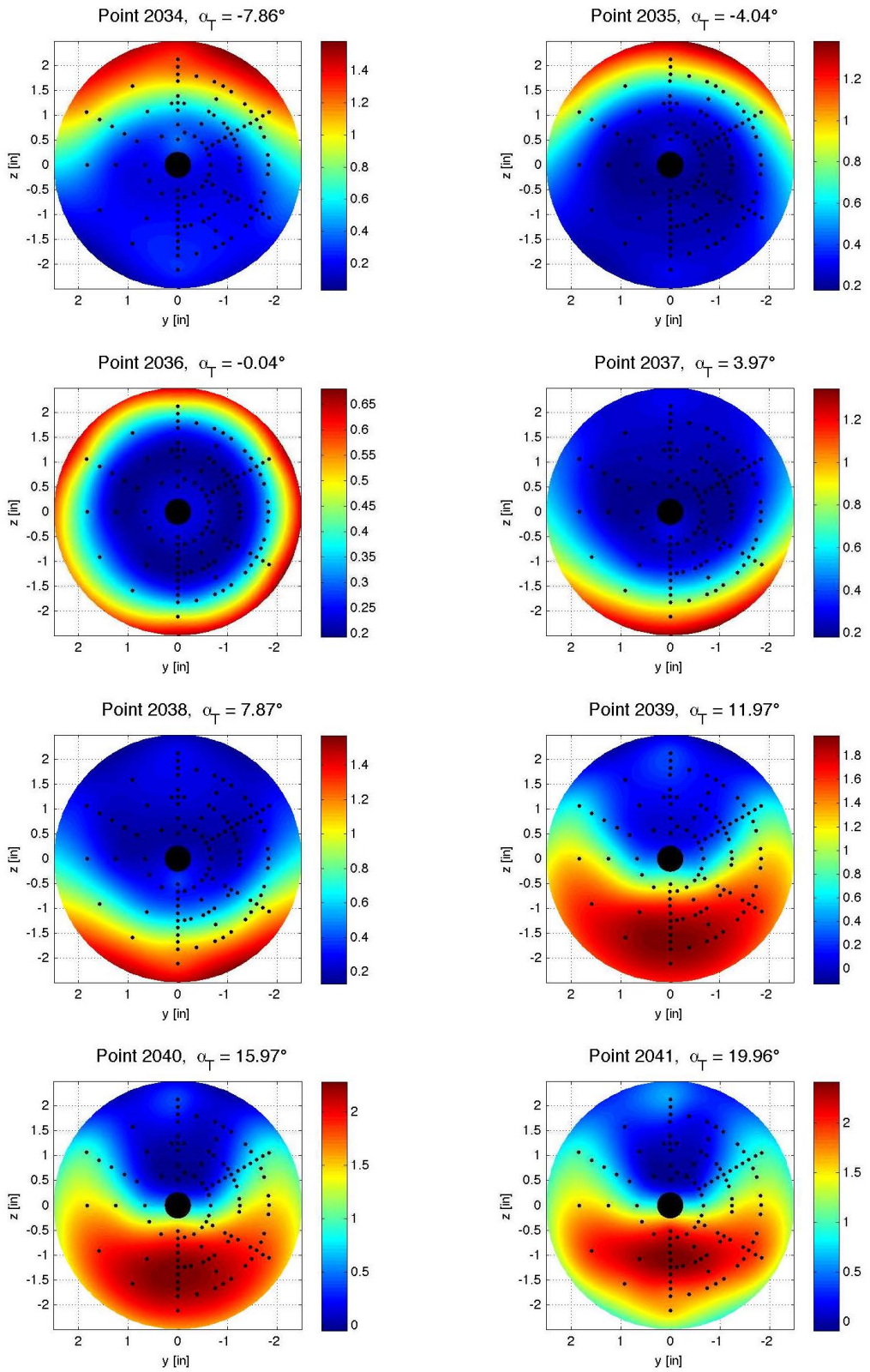

Figure E-109. Center nozzle configuration, Run 145, M_∞ = 2.4, Re_∞ = 1.0x10^6/ft, ϕ = 0.01°, X_S = 40.15 in, Y_S = 0.00 in, C_T = 0.23.

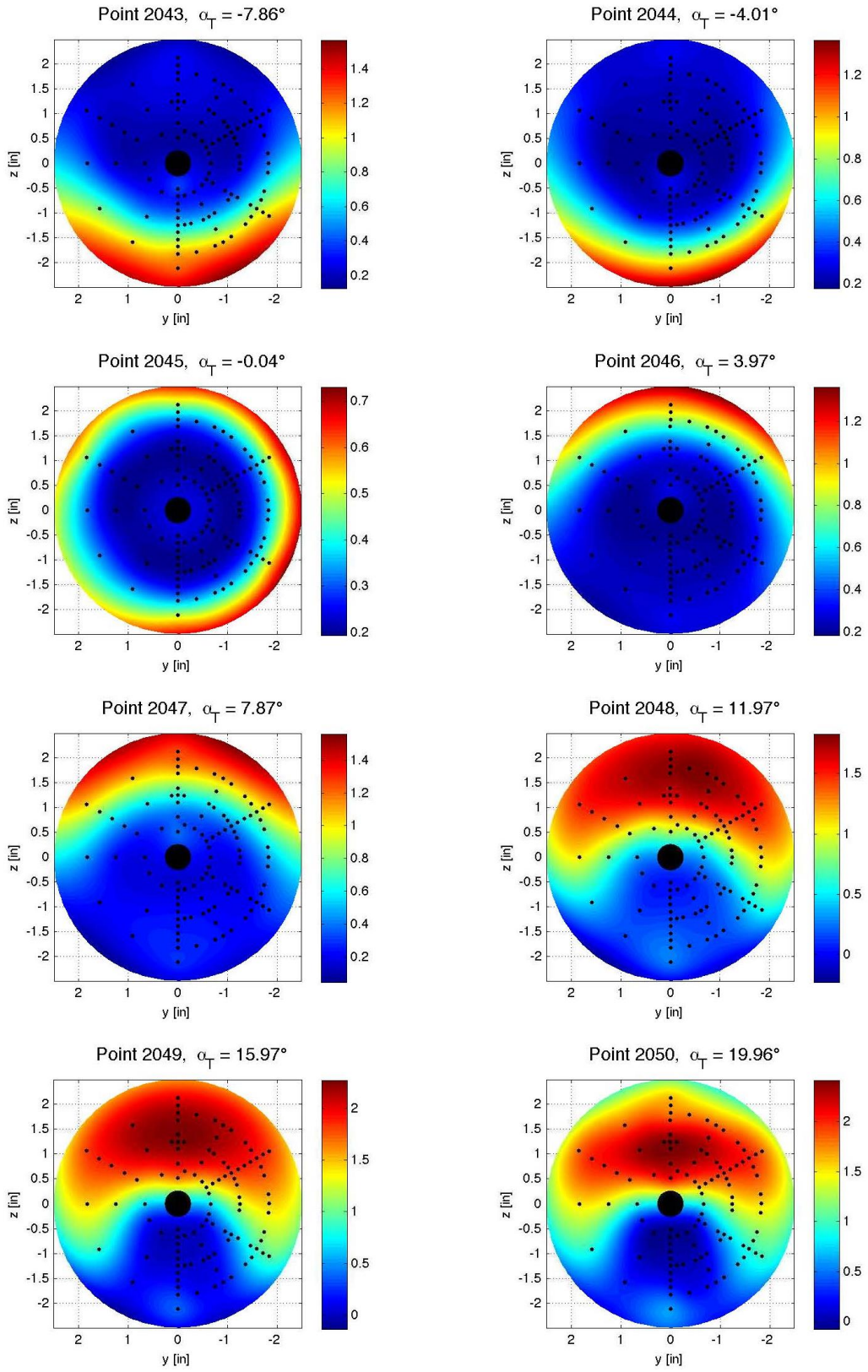

Figure E-110. Center nozzle configuration, Run 146, M_∞ = 2.4, Re_∞ = 1.0x10^6/ft, ϕ = 179.99°, X_S = 40.15 in, Y_S = 0.00 in, C_T = 0.23.

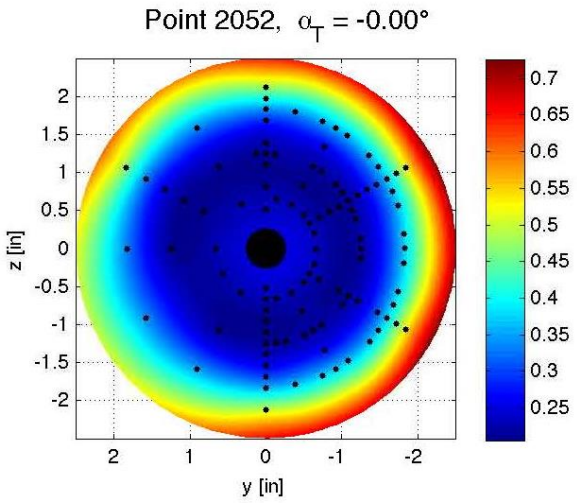

Figure E-111. Center nozzle configuration, Run 147, M_∞ = 2.4, Re_∞ = 1.0x10^6/ft, ϕ = −180.00°, X_S = 40.15 in, Y_S = 0.00 in, C_T = 0.19.

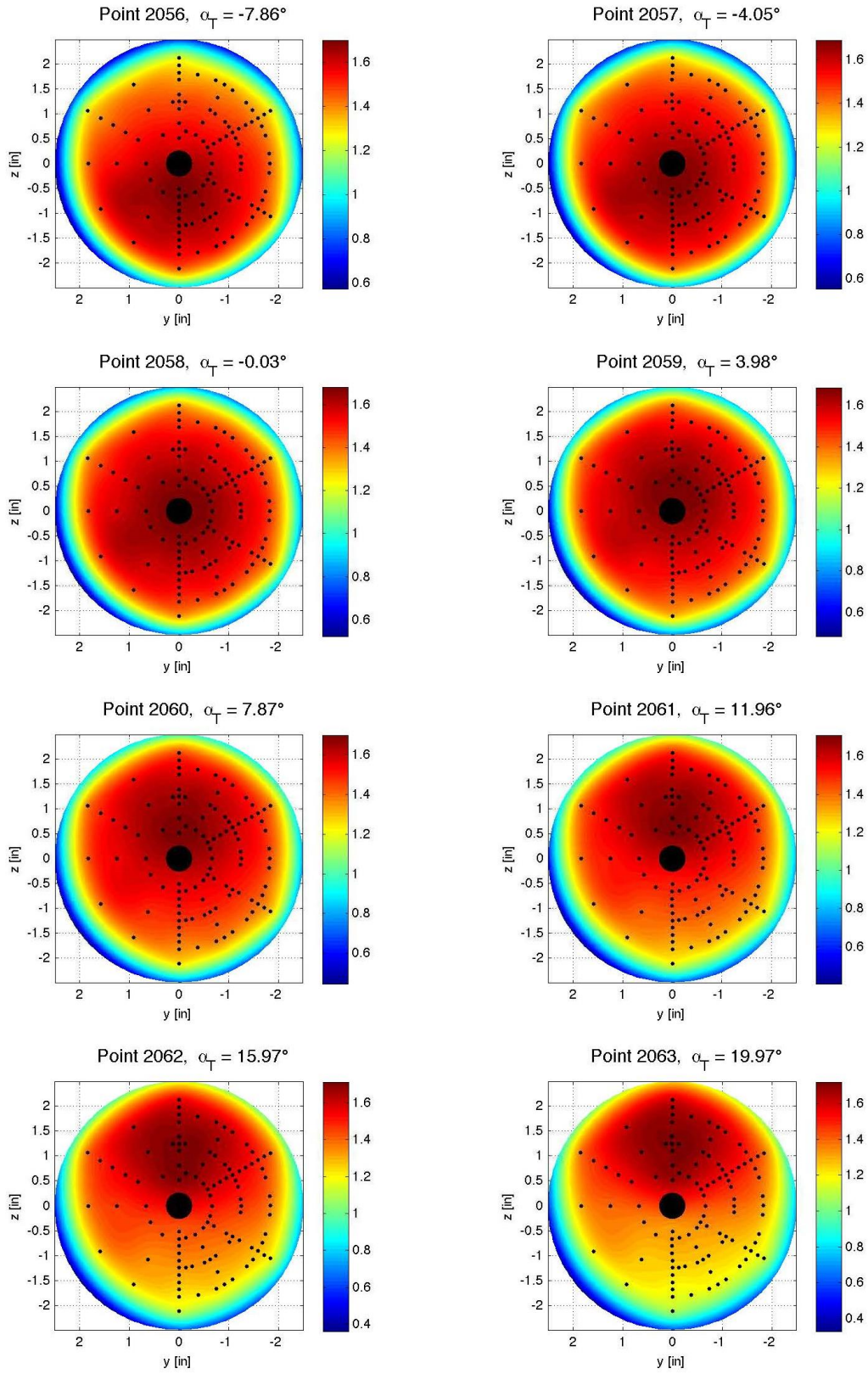

Figure E-112. Center nozzle configuration, Run 148, M_∞ = 2.4, Re_∞ = 1.0x10^6/ft, ϕ = 179.99°, X_S = 40.15 in, Y_S = 0.00 in, C_T = 0.00.

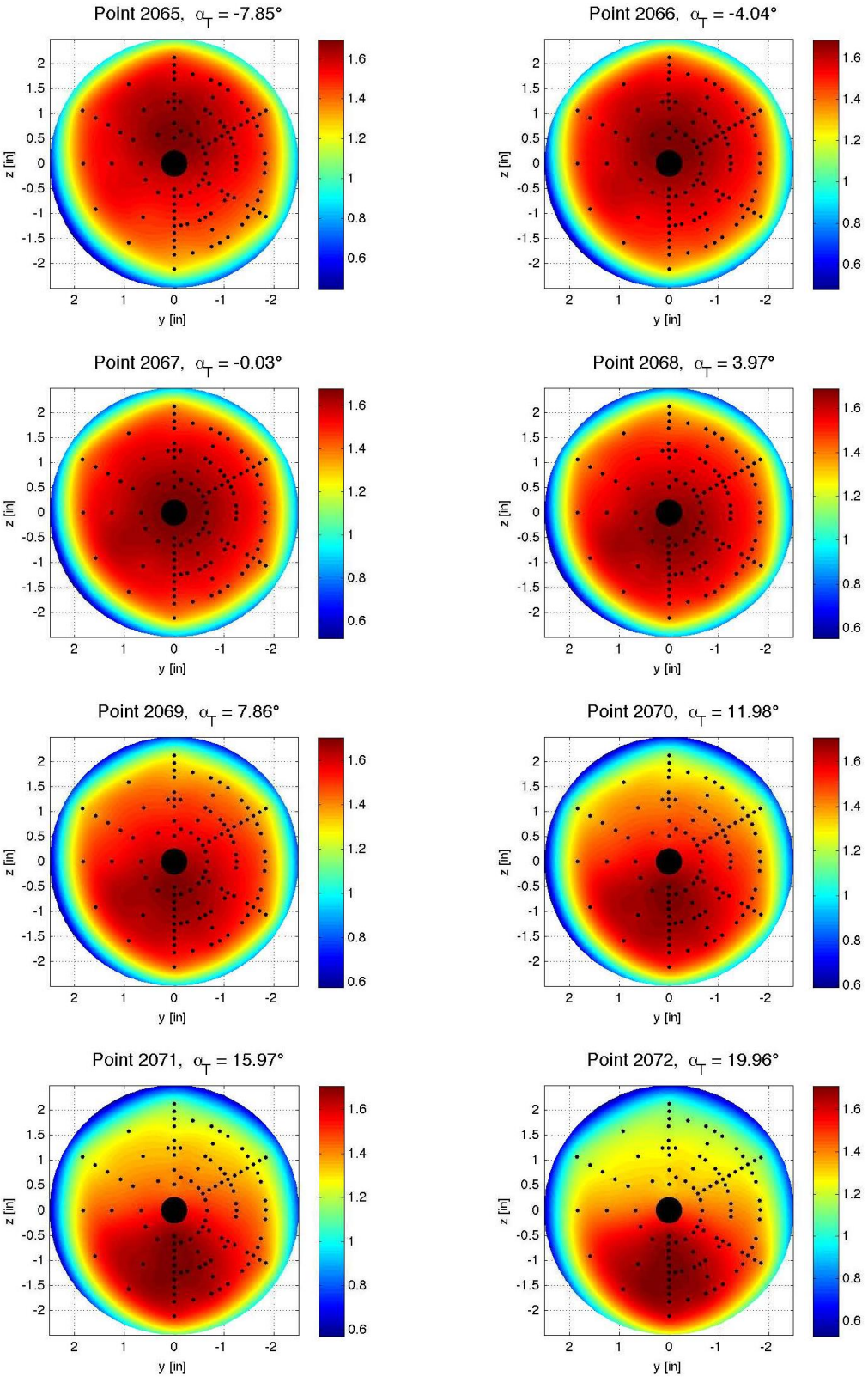

Figure E-113. Center nozzle configuration, Run 149, M_∞ = 2.4, Re_∞ = 1.0x10^6/ft, ϕ = −0.03°, X_S = 40.15 in, Y_S = 0.00 in, C_T = 0.00.

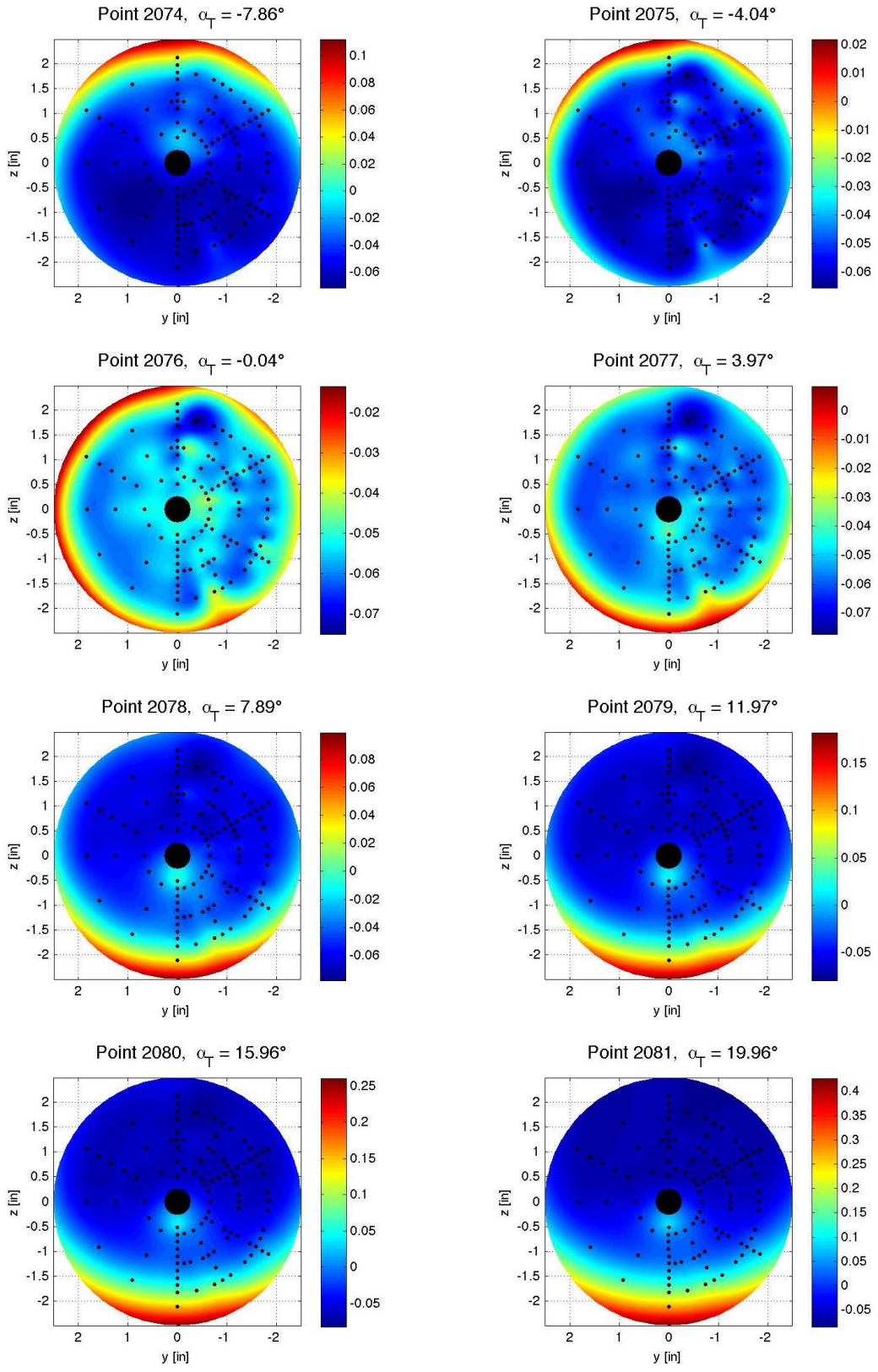

Figure E-114. Center nozzle configuration, Run 150, M_∞ = 3.5, Re_∞ = 1.0x10^6/ft, ϕ = −0.03°, X_S = 40.17 in, Y_S = 0.00 in, C_T = 2.99.

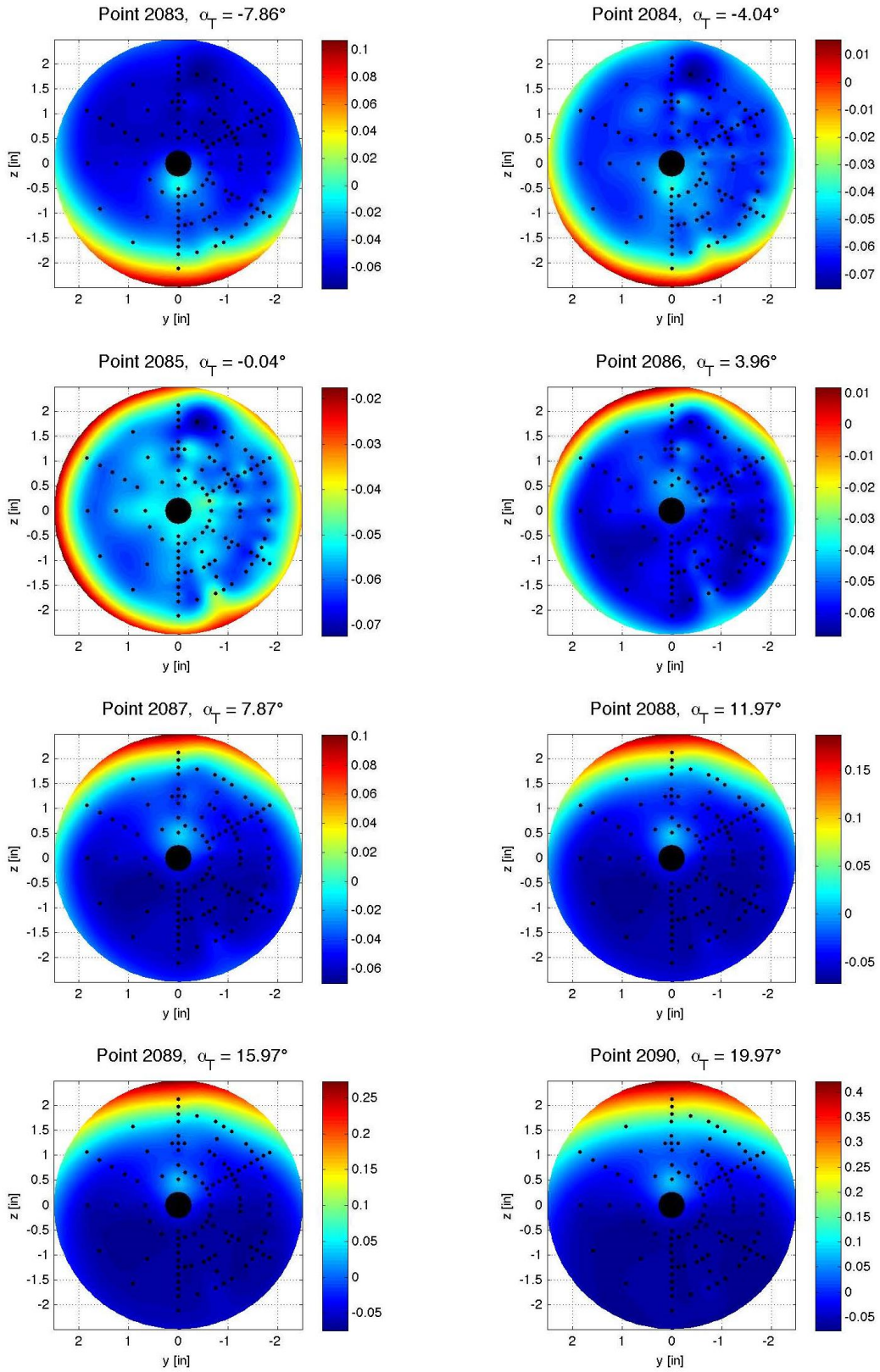

Figure E-115. Center nozzle configuration, Run 151, $M\infty$ = 3.5, Re_∞ = 1.0x10^6/ft, ϕ = −179.97°, X_S = 40.17 in, Y_S = 0.00 in, C_T = 3.01.

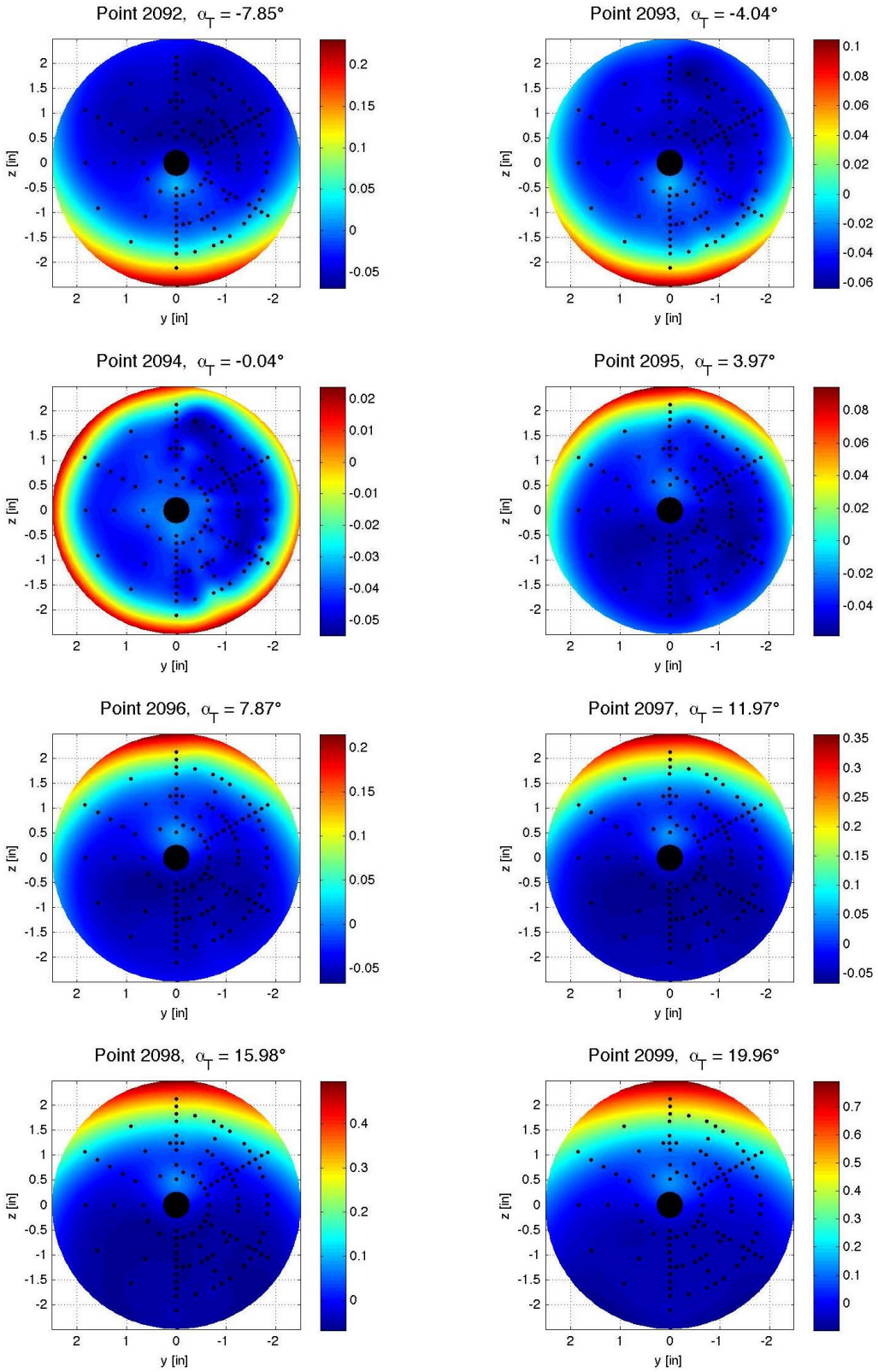

Figure E-116. Center nozzle configuration, Run 152, $M\infty$ = 3.5, Re_∞ = 1.0x10^6/ft, ϕ = −179.97°, X_S = 40.17 in, Y_S = 0.00 in, C_T = 1.95.

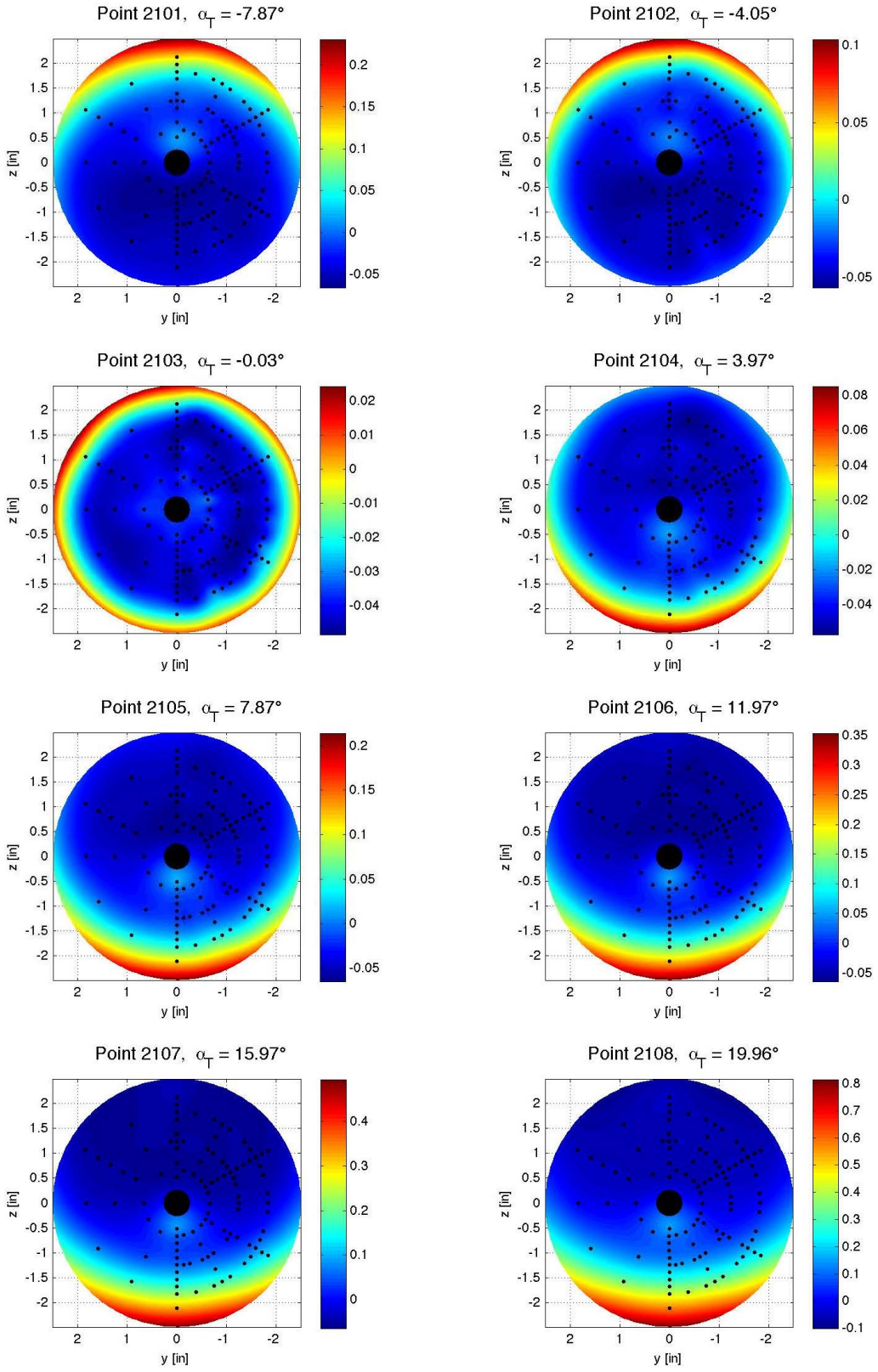

Figure E-117. Center nozzle configuration, Run 153, $M\infty$ = 3.5, Re_∞ = 1.0x10^6/ft, ϕ = −0.09°, X_S = 40.17 in, Y_S = 0.00 in, C_T = 1.96.

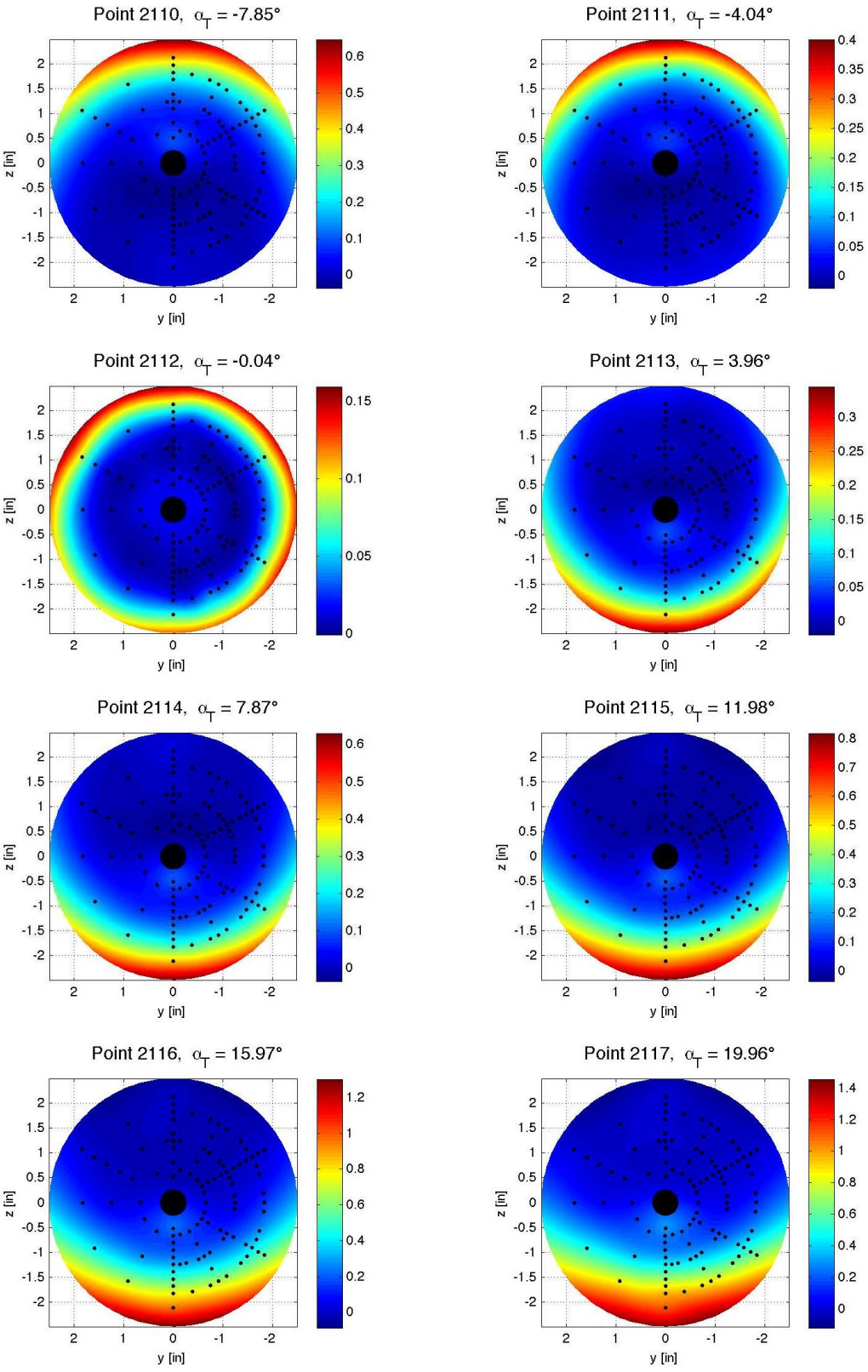

Figure E-118. Center nozzle configuration, Run 154, M_∞ = 3.5, Re_∞ = 1.0x10^6/ft, ϕ = −0.09°, X_S = 40.17 in, Y_S = 0.00 in, C_T = 0.94.

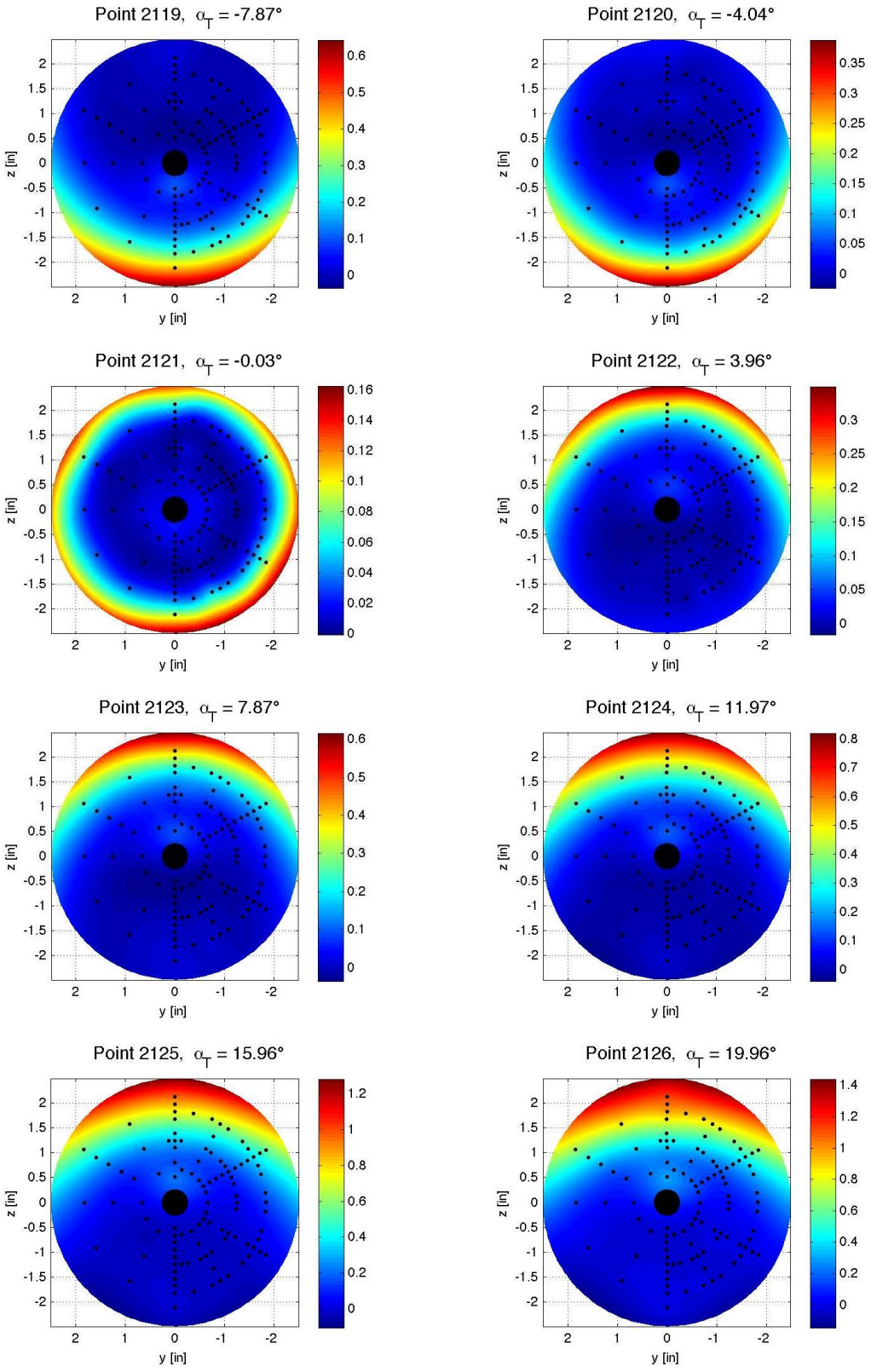

Figure E-119. Center nozzle configuration, Run 155, M_∞ = 3.5, Re_∞ = 1.0x10^6/ft, ϕ = 179.91°, X_S = 40.17 in, Y_S = 0.00 in, C_T = 0.95.

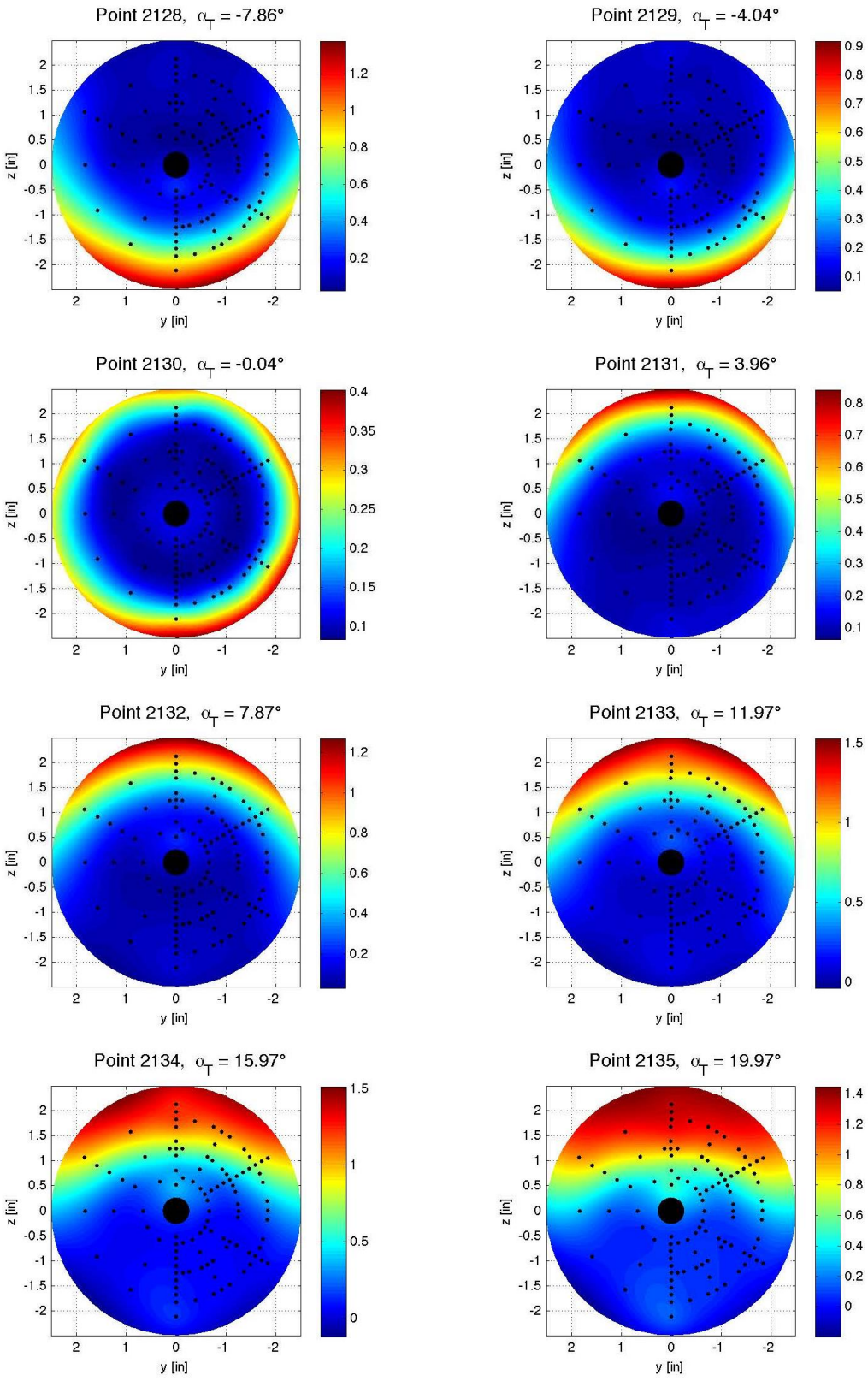

Figure E-120. Center nozzle configuration, Run 156, M_∞ = 3.5, Re_∞ = 1.0x10^6/ft, ϕ = 179.93°, X_S = 40.17 in, Y_S = 0.00 in, C_T = 0.45.

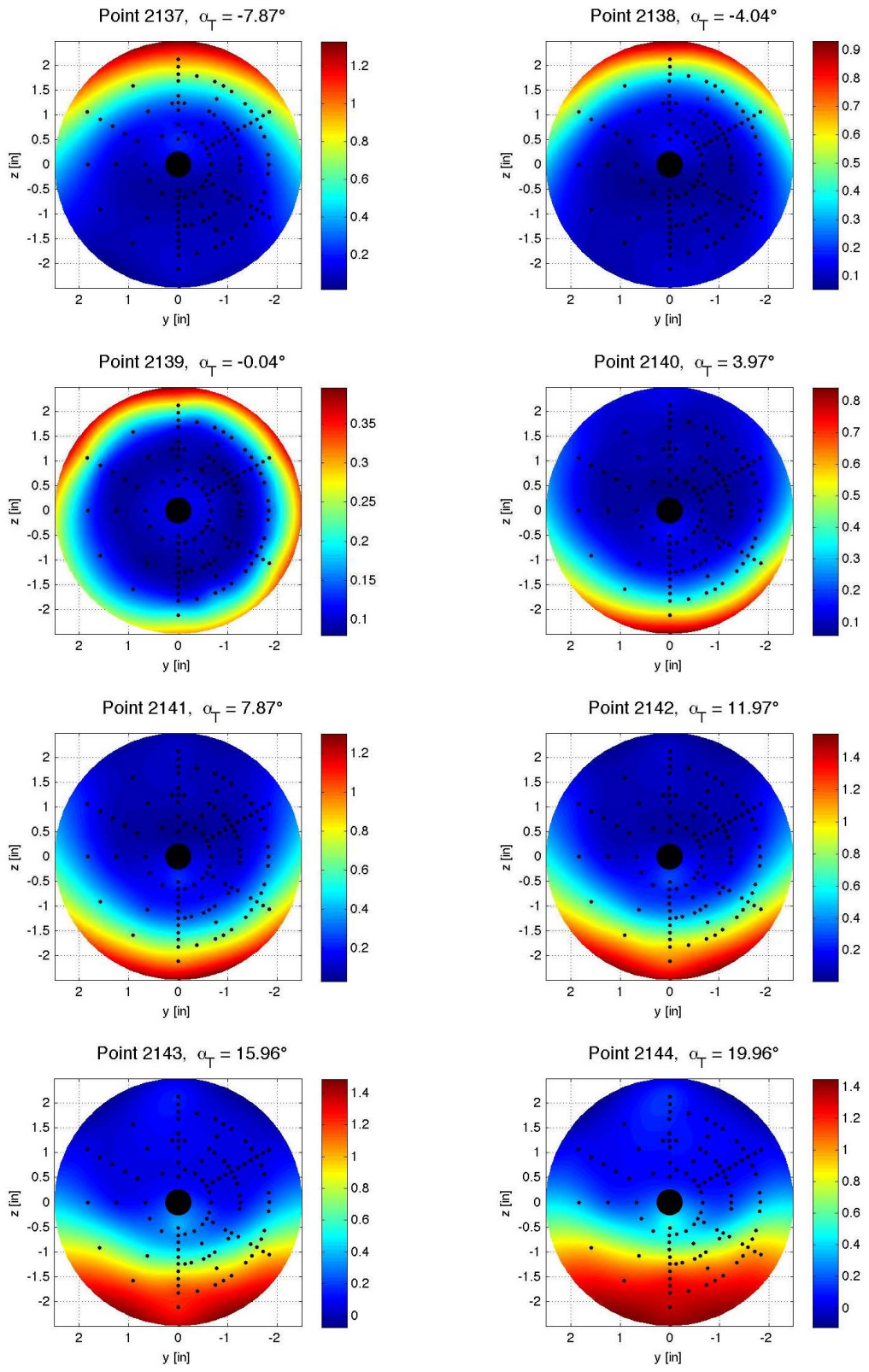

Figure E-121. Center nozzle configuration, Run 157, M_∞ = 3.5, Re_∞ = 1.0x10^6/ft, ϕ = 0.07°, X_S = 40.17 in, Y_S = 0.00 in, C_T = 0.45.

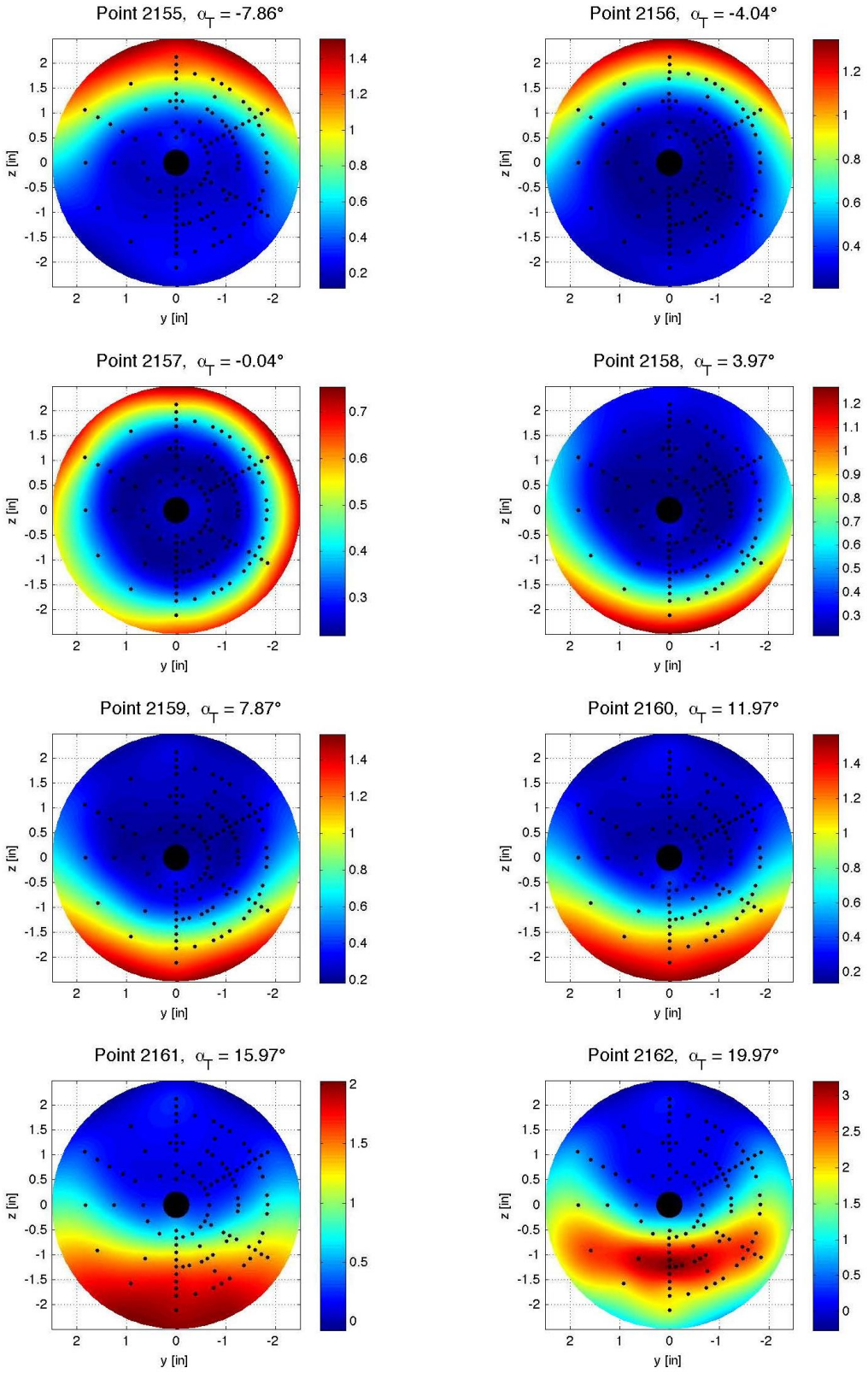

Figure E-122. Center nozzle configuration, Run 159, $M\infty$ = 3.5, Re_∞ = 1.0x10^6/ft, ϕ = −0.01°, X_S = 40.17 in, Y_S = 0.00 in, C_T = 0.21.

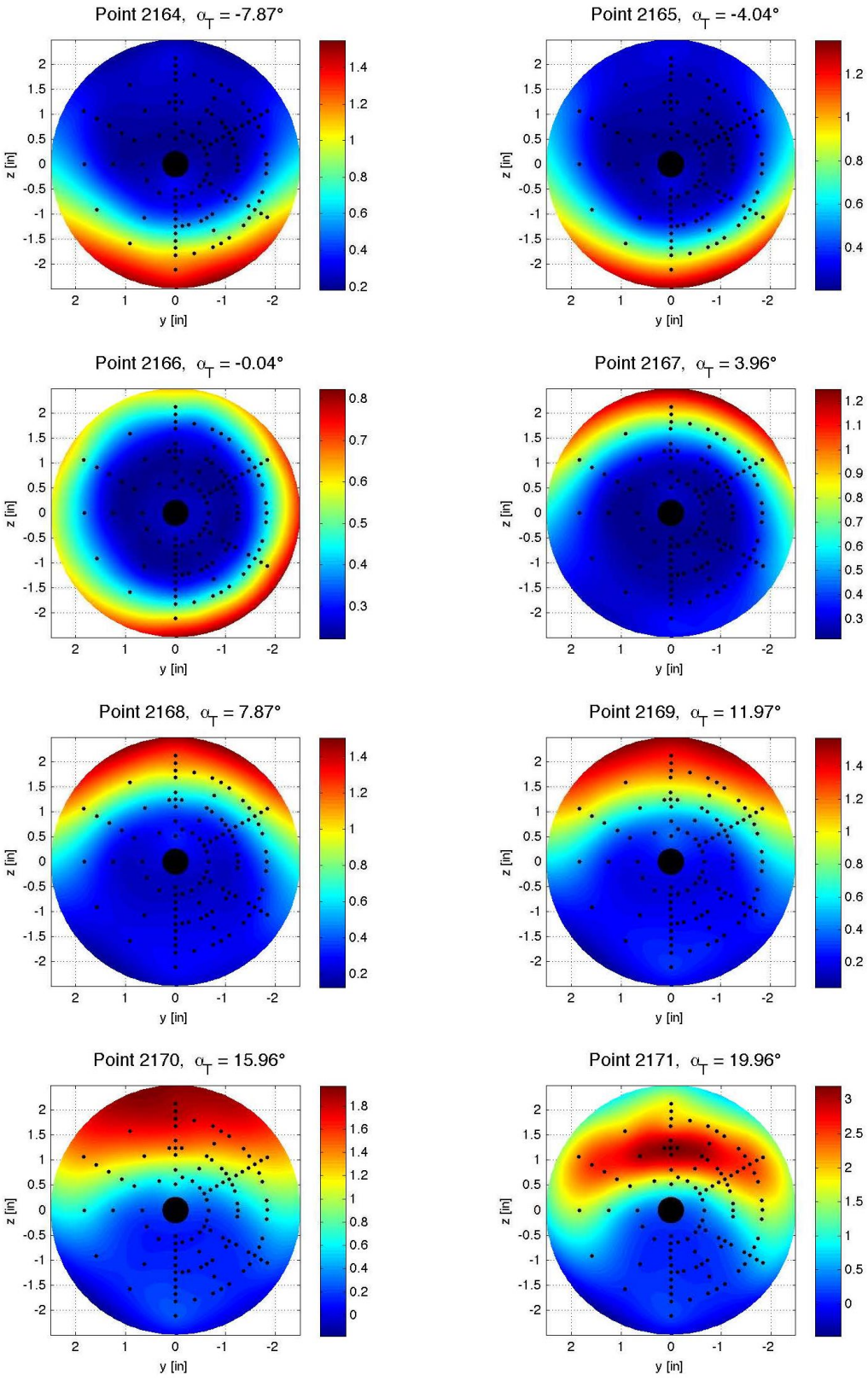

Figure E-123. Center nozzle configuration, Run 160, M_∞ = 3.5, Re_∞ = 1.0x10^6/ft, ϕ = 179.93°, X_S = 40.17 in, Y_S = 0.00 in, C_T = 0.21.

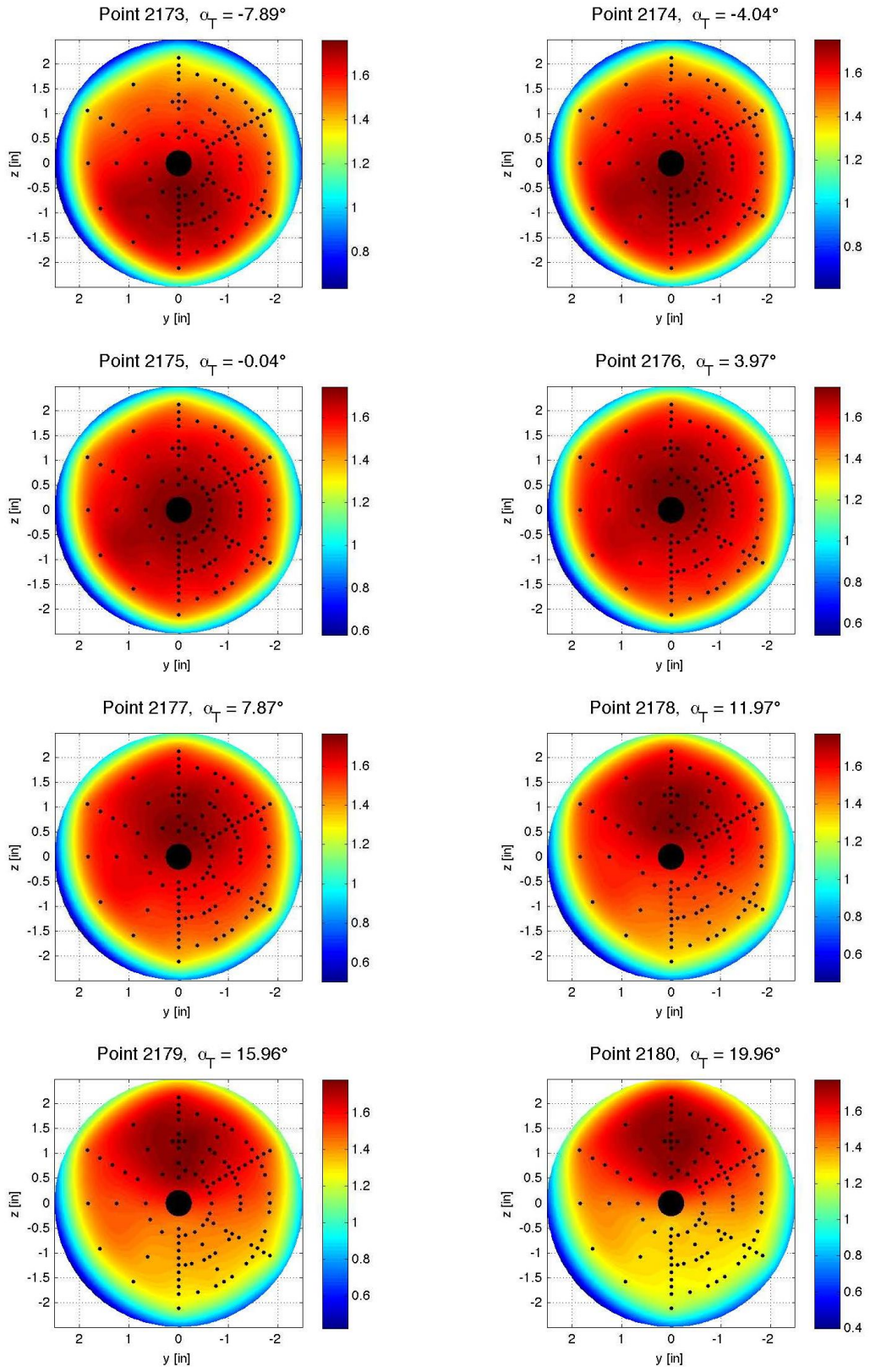

Figure E-124. Center nozzle configuration, Run 161, M_∞ = 3.5, Re_∞ = 1.0x10^6/ft, ϕ = 179.93°, X_S = 40.17 in, Y_S = 0.00 in, C_T = 0.00.

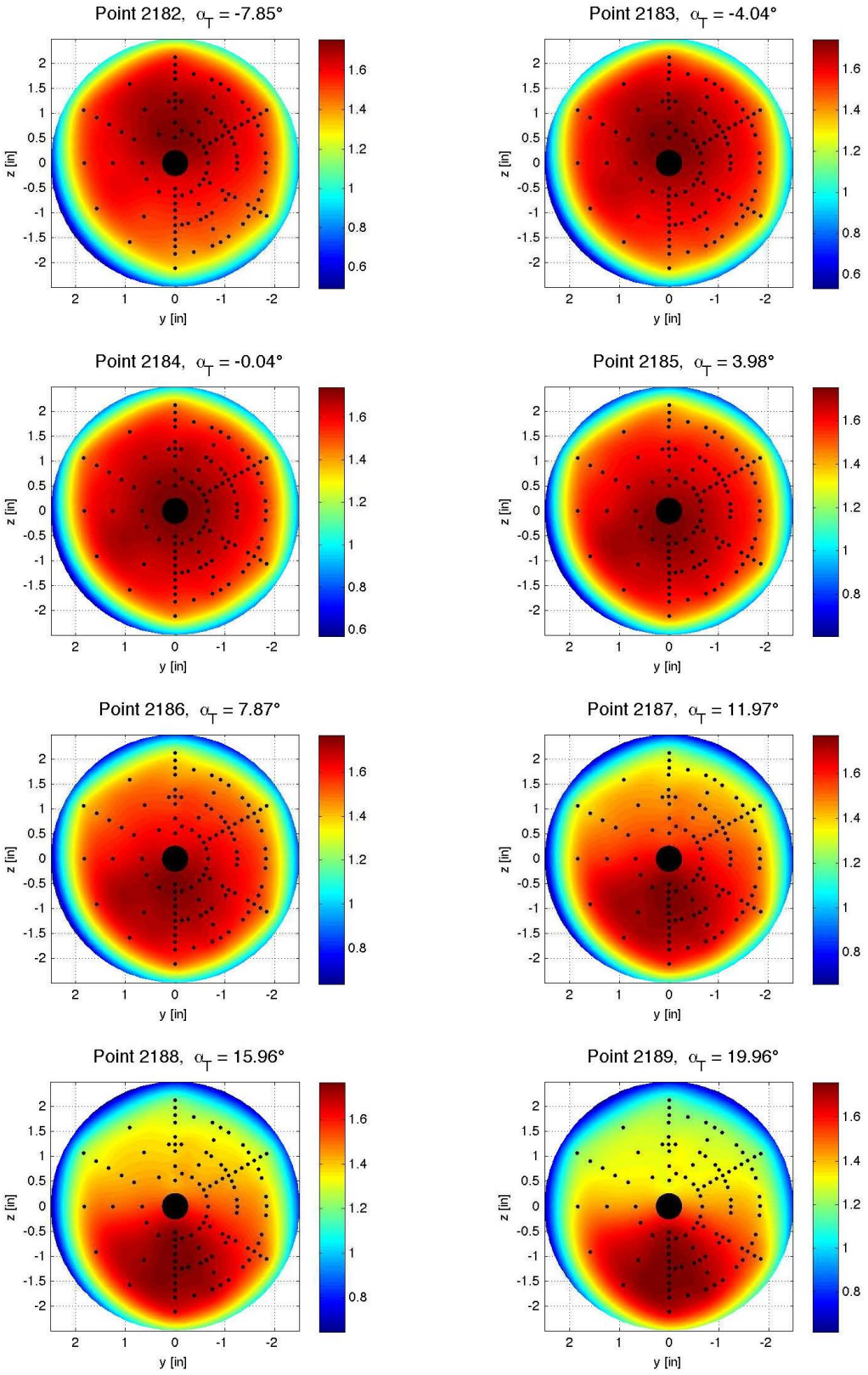

Figure E-125. Center nozzle configuration, Run 162, $M\infty$ = 3.5, Re_∞ = 1.0x10^6/ft, ϕ = 0.03°, X_S = 40.17 in, Y_S = 0.00 in, C_T = 0.00.

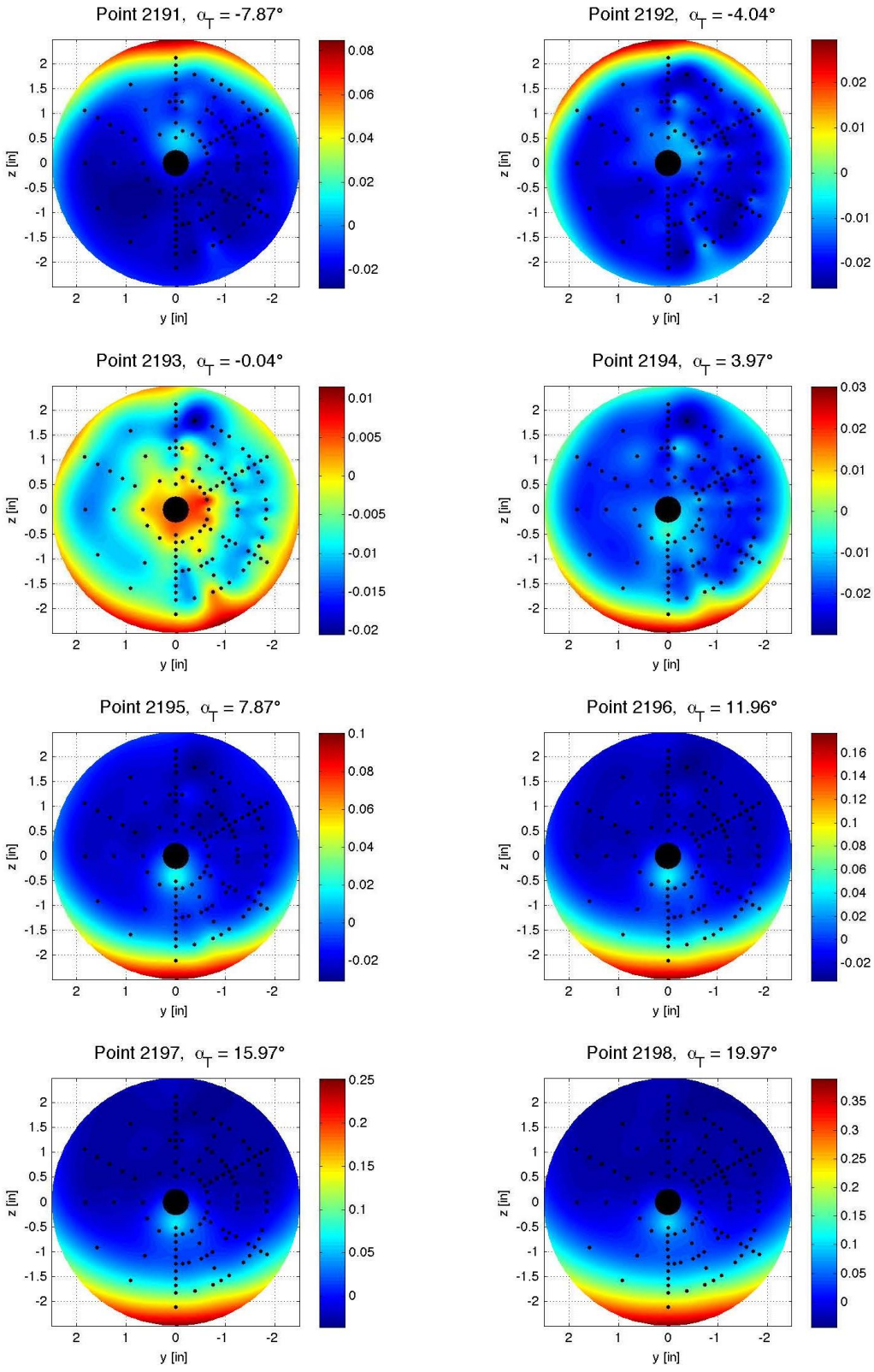

Figure E-126. Center nozzle configuration, Run 163, M_∞ = 4.6, Re_∞ = 1.5x10^6/ft, ϕ = 0.03°, X_S = 40.17 in, Y_S = 0.00 in, C_T = 2.92.

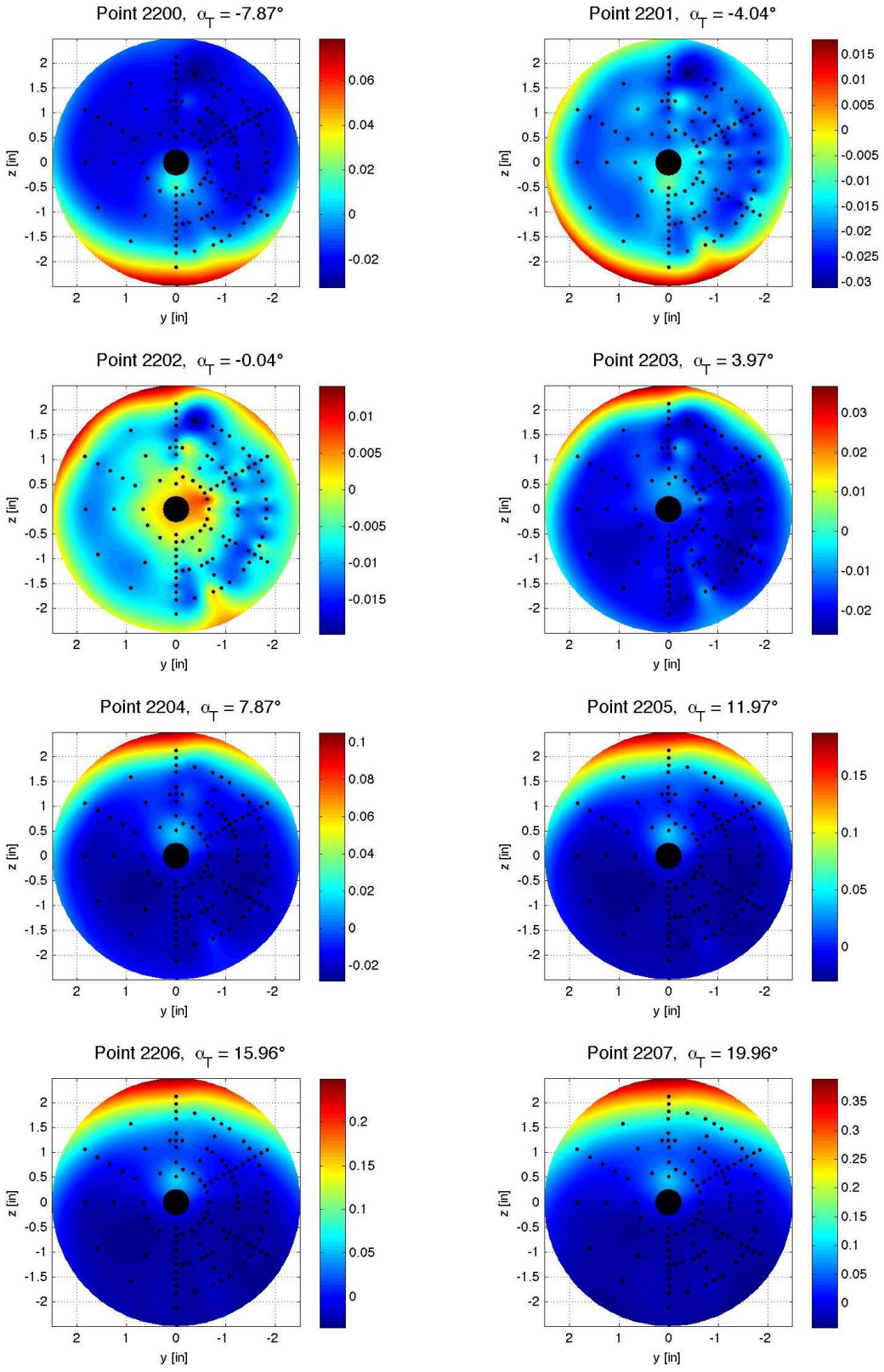

Figure E-127. Center nozzle configuration, Run 164, $M\infty$ = 4.6, Re_∞ = 1.5x10^6/ft, ϕ = 1479.91°, X_S = 40.17 in, Y_S = 0.00 in, C_T = 2.91.

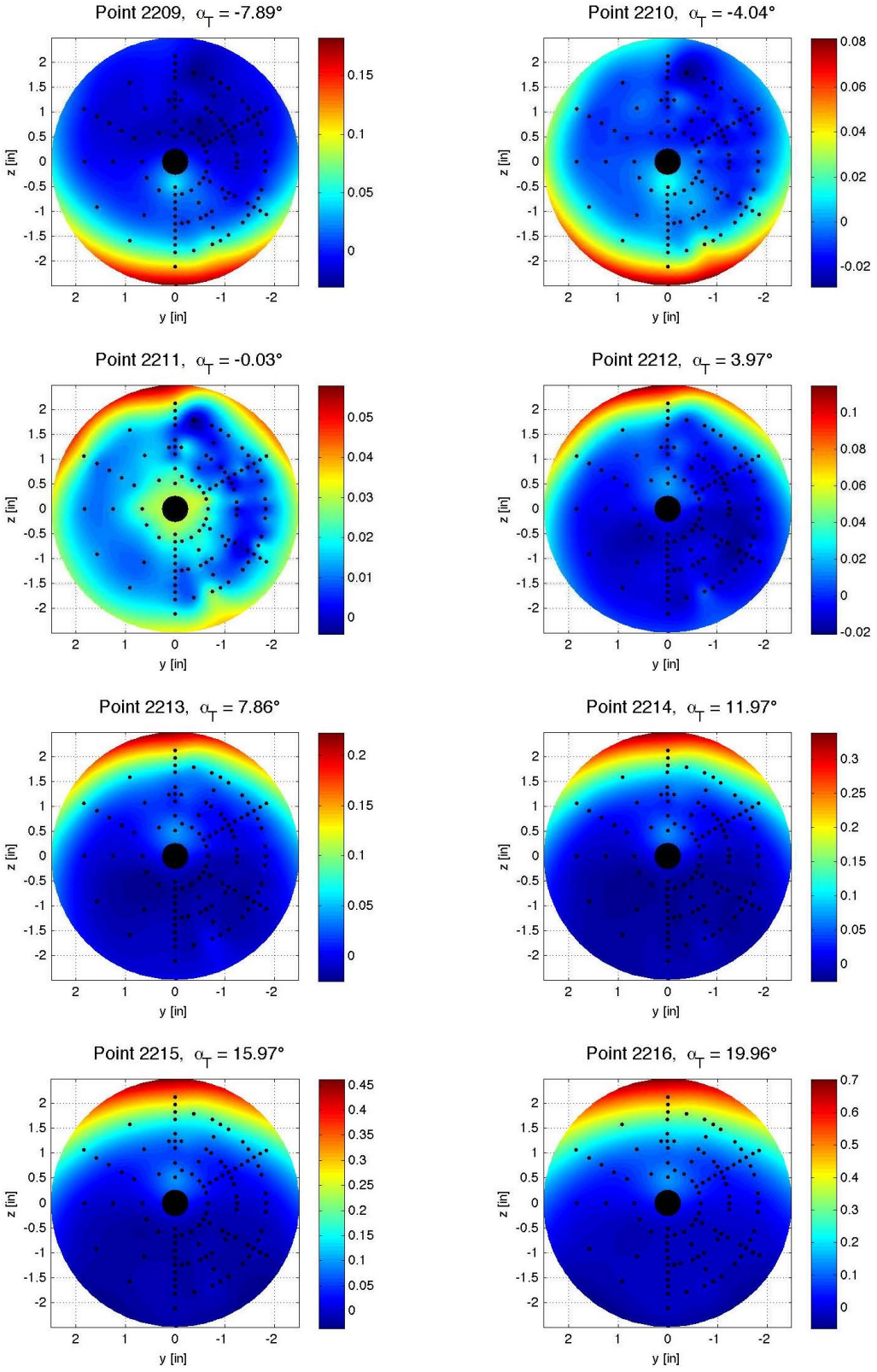

Figure E-128. Center nozzle configuration, Run 165, M_∞ = 4.6, Re_∞ = 1.5x10^6/ft, ϕ = 179.93°, X_S = 40.15 in, Y_S = 0.00 in, C_T = 1.93.

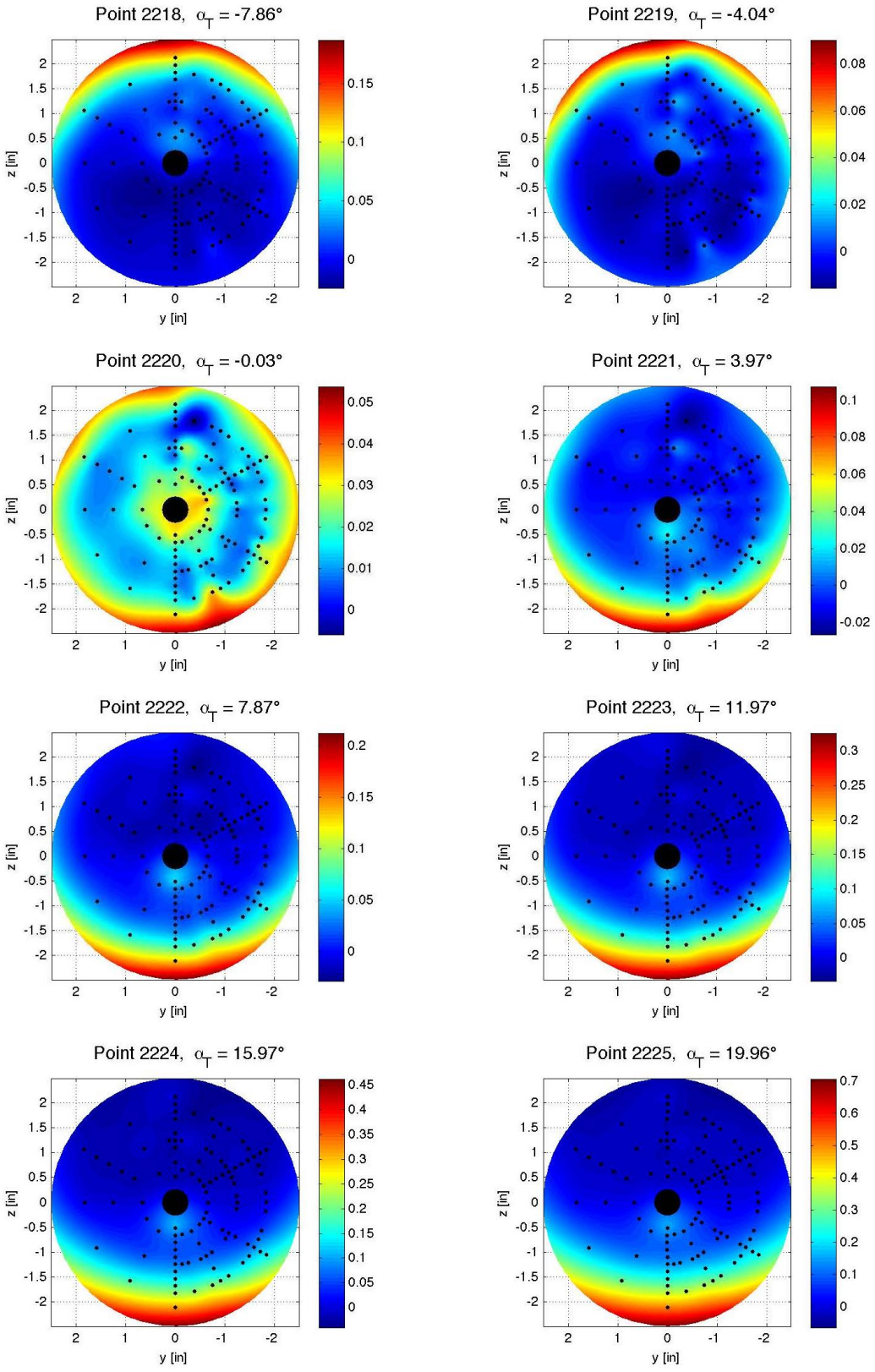

Figure E-129. Center nozzle configuration, Run 166, M_∞ = 4.6, Re_∞ = 1.5x10^6/ft, ϕ = 0.03°, X_S = 40.15 in, Y_S = 0.00 in, C_T = 1.96.

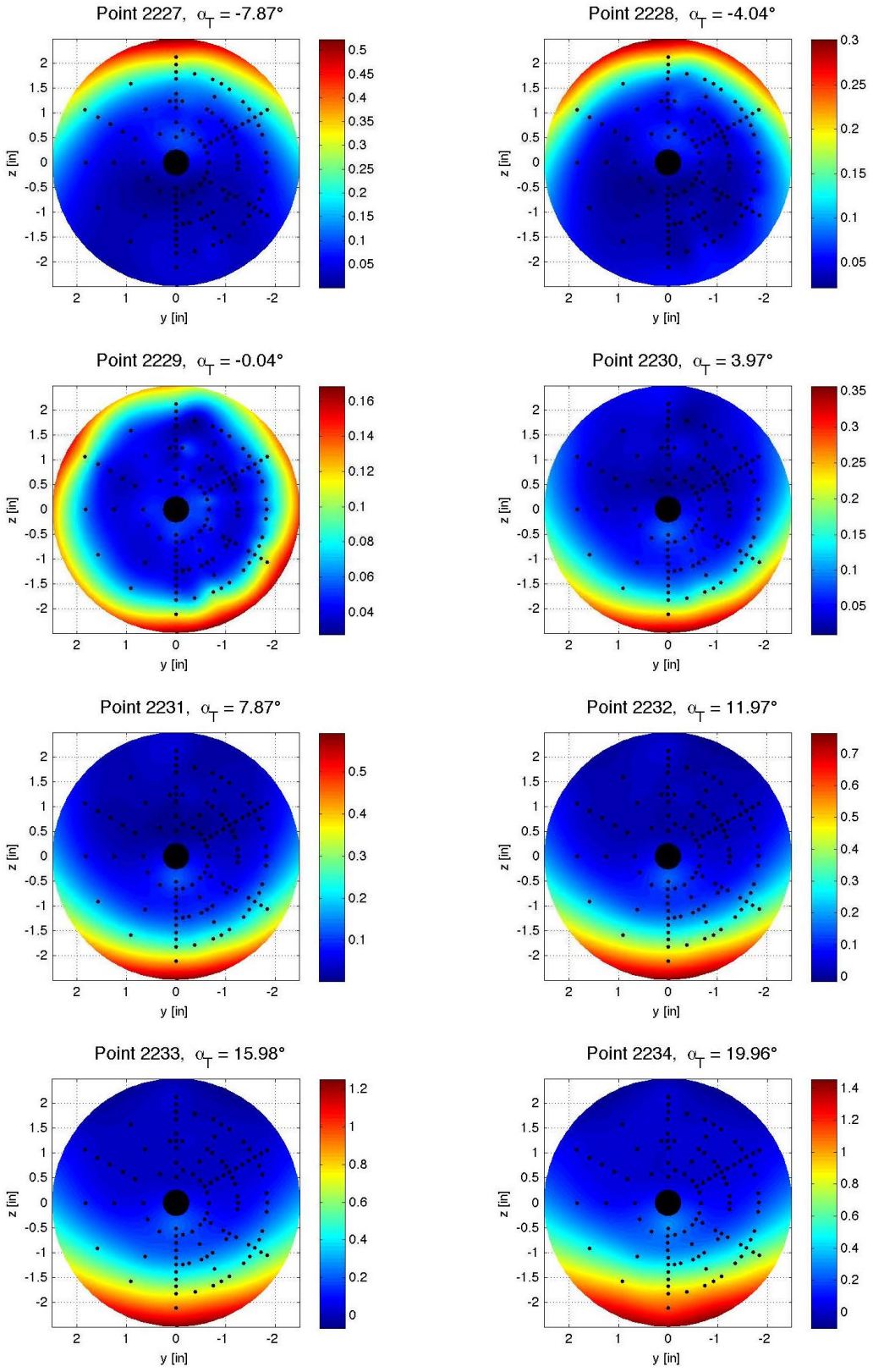

Figure E-130. Center nozzle configuration, Run 167, $M\infty$ = 4.6, Re_∞ = 1.5x10^6/ft, ϕ = 0.03°, X_S = 40.15 in, Y_S = 0.00 in, C_T = 0.94.

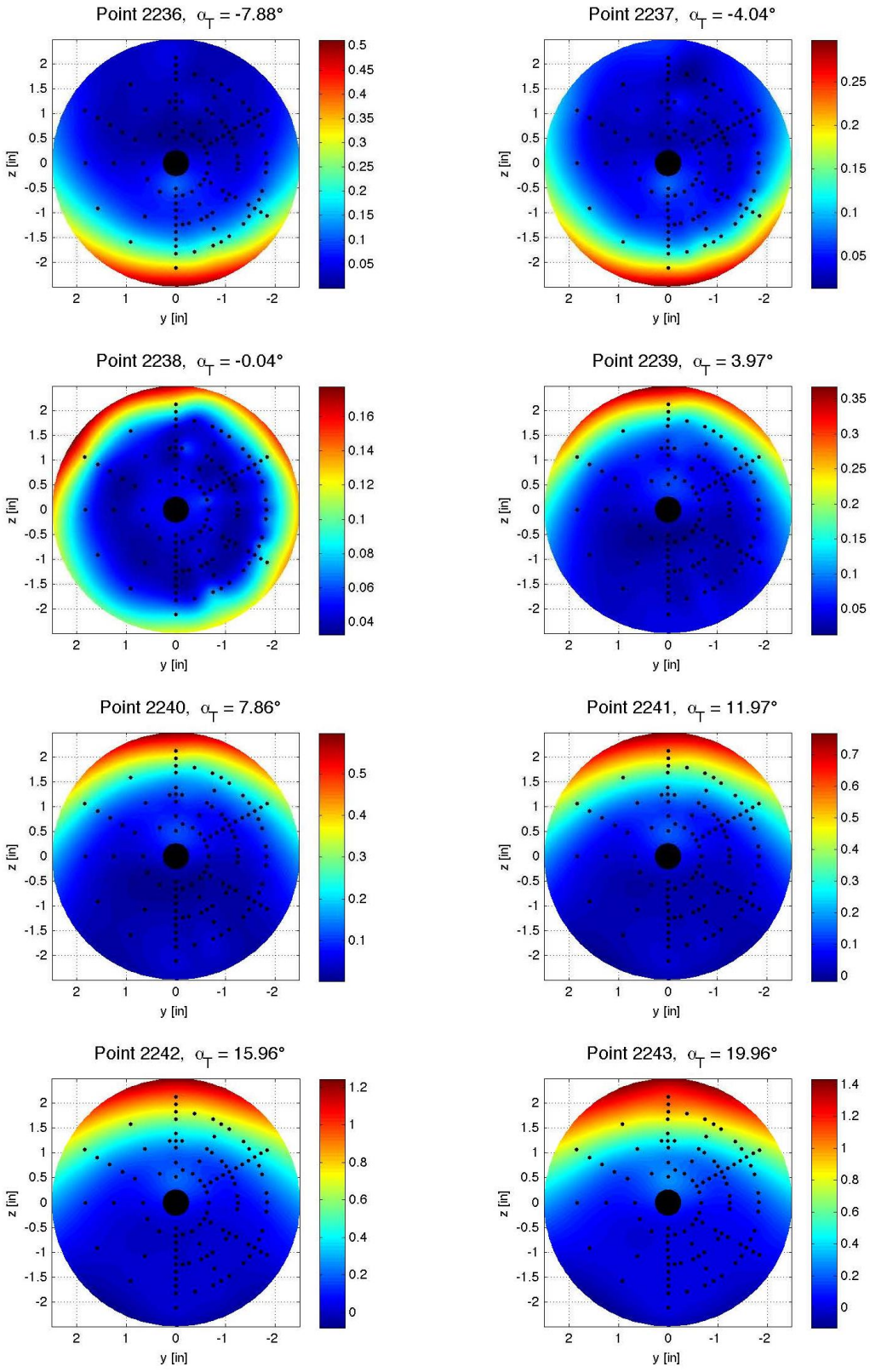

Figure E-131. Center nozzle configuration, Run 168, M_∞ = 4.6, Re_∞ = 1.5x10^6/ft, ϕ = 179.95°, X_S = 40.15 in, Y_S = 0.00 in, C_T = 0.96.

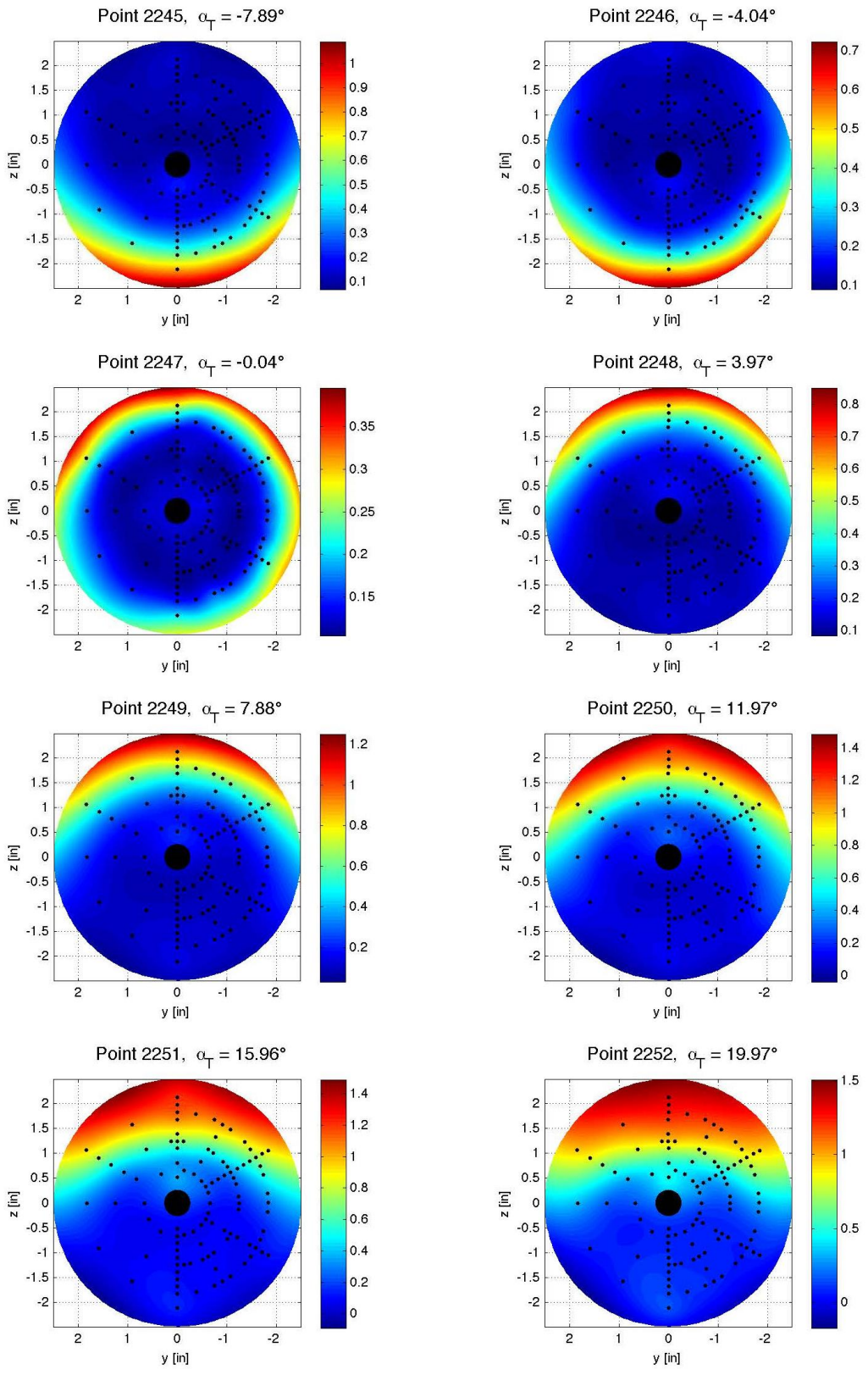

Figure E-132. Center nozzle configuration, Run 169, M_∞ = 4.6, Re_∞ = 1.5x10^6/ft, ϕ = 179.95°, X_S = 40.15 in, Y_S = 0.00 in, C_T = 0.45.

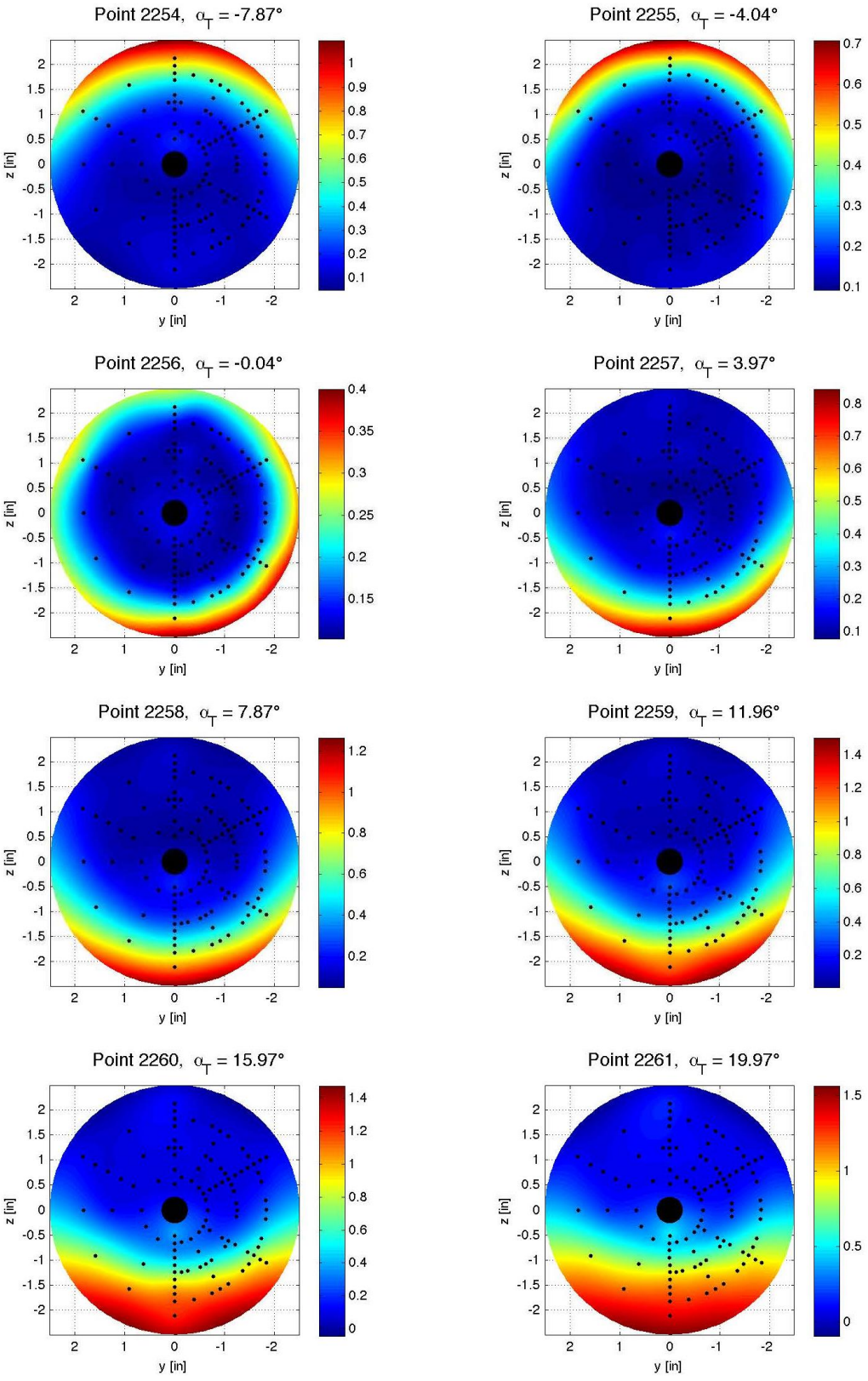

Figure E-133. Center nozzle configuration, Run 170, M_∞ = 4.6, Re_∞ = 1.5x10^6/ft, ϕ = 0.03°, X_S = 40.15 in, Y_S = 0.00 in, C_T = 0.46.

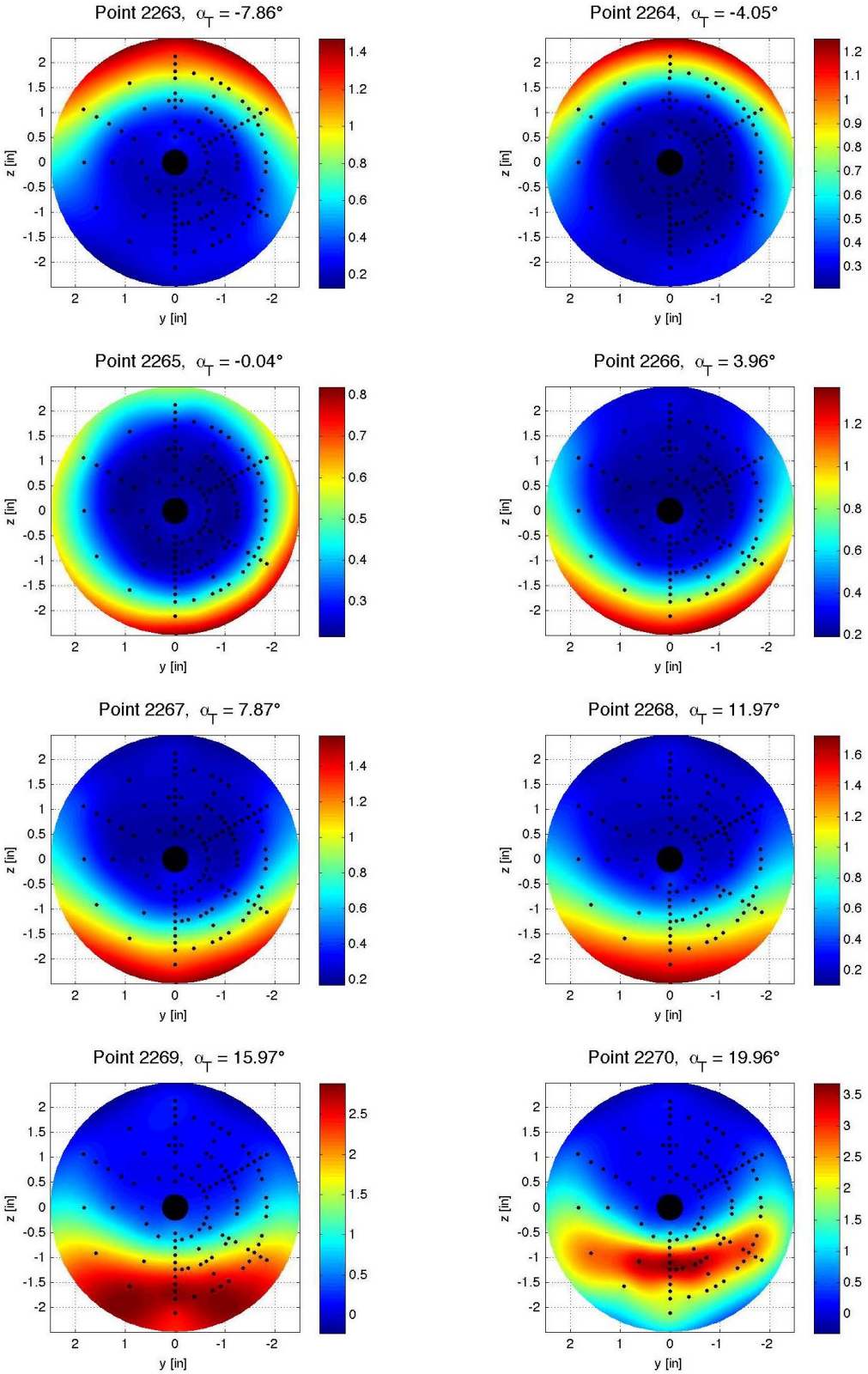

Figure E-134. Center nozzle configuration, Run 171, M_∞ = 4.6, Re_∞ = 1.5x10^6/ft, ϕ = 0.03°, X_S = 40.15 in, Y_S = 0.00 in, C_T = 0.22.

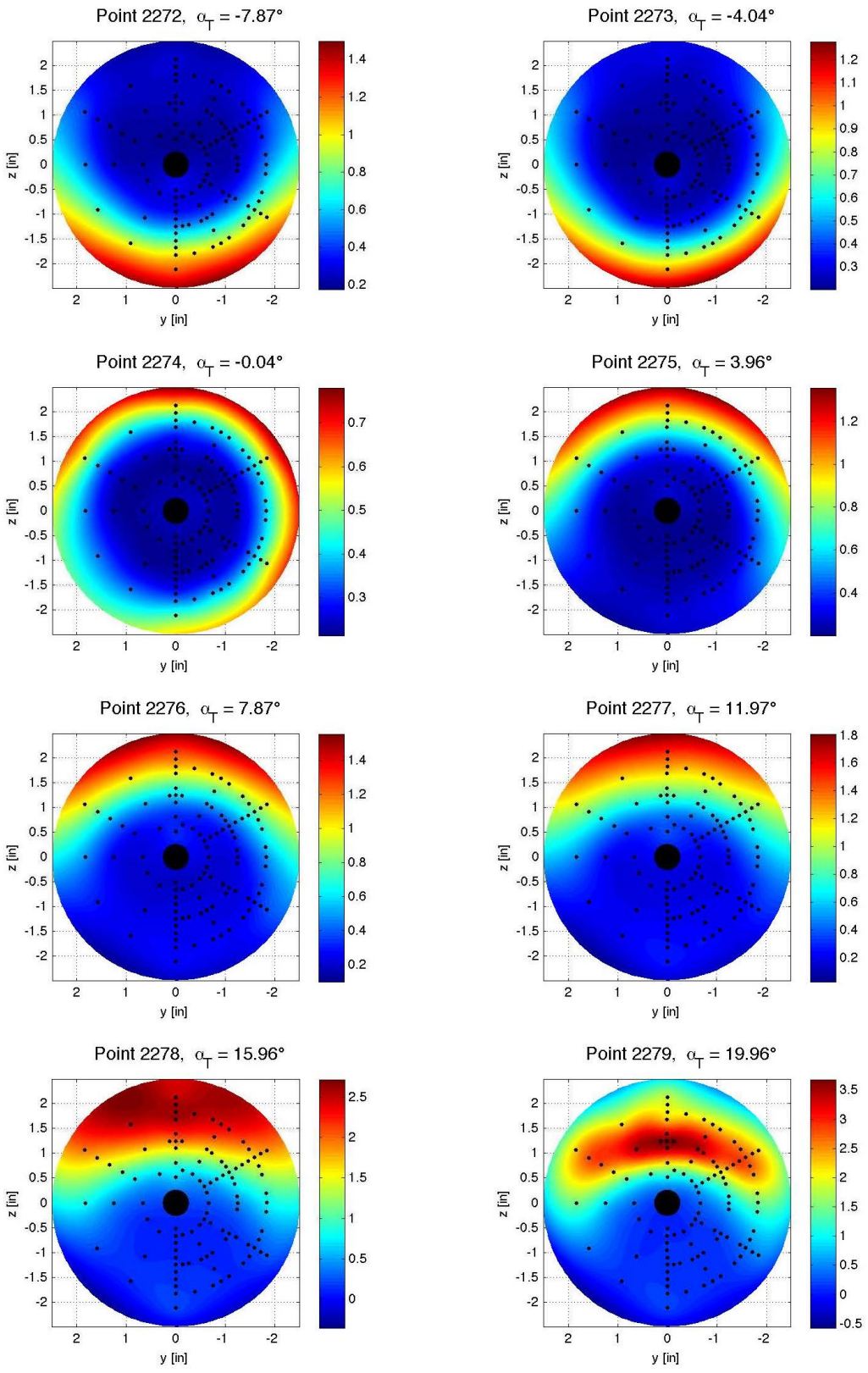

Figure E-135. Center nozzle configuration, Run 172, M_∞ = 4.6, Re_∞ = 1.5x10^6/ft, ϕ = 179.91°, X_S = 40.15 in, Y_S = 0.00 in, C_T = 0.22.

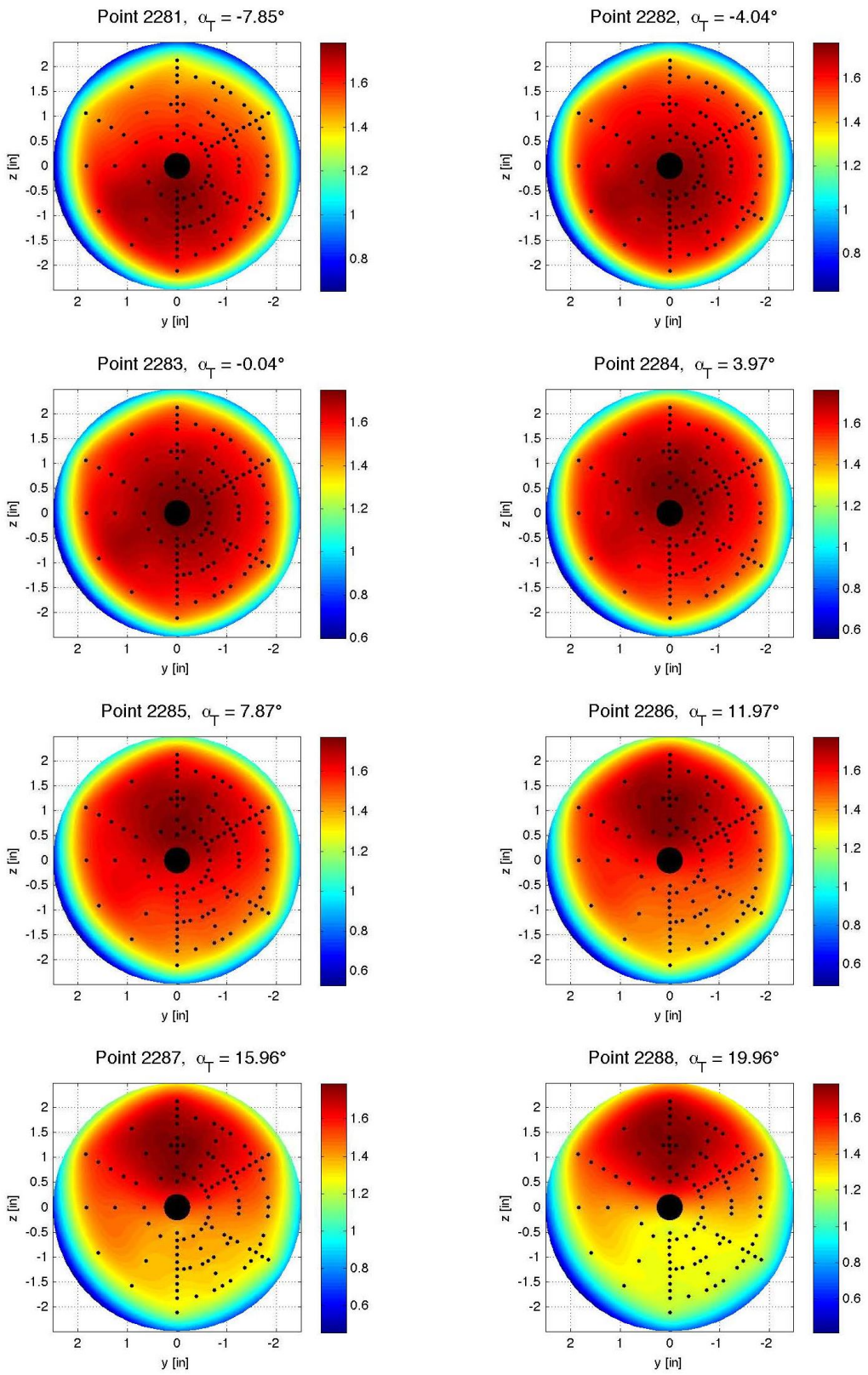

Figure E-136. Center nozzle configuration, Run 173, M_∞ = 4.6, Re_∞ = 1.5x10^6/ft, ϕ = 179.91°, X_S = 40.15 in, Y_S = 0.00 in, C_T = 0.00.

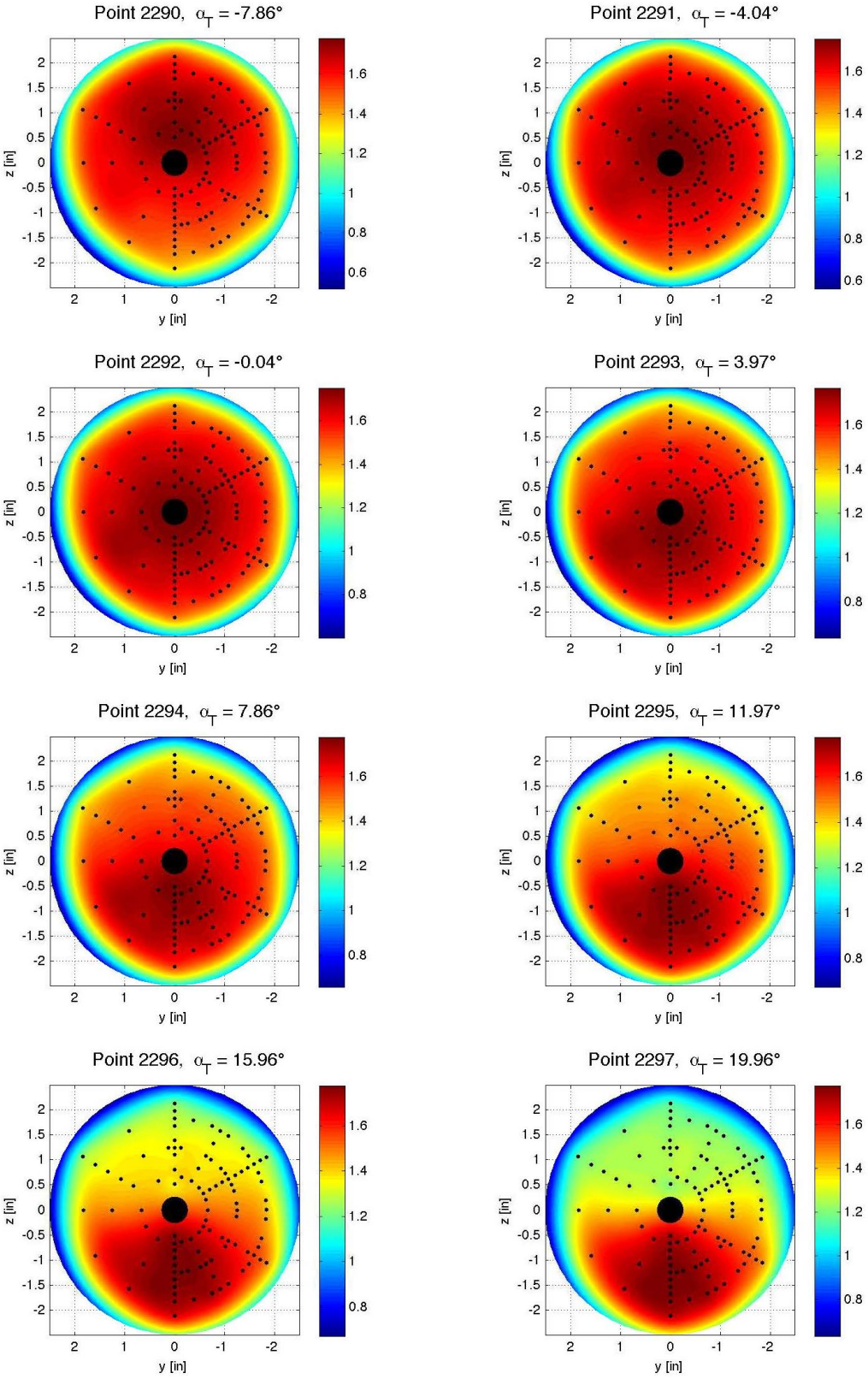

Figure E-137. Center nozzle configuration, Run 174, M_∞ = 4.6, Re_∞ = 1.5x10^6/ft, ϕ = −0.07°, X_S = 40.15 in, Y_S = 0.00 in, C_T = 0.00.

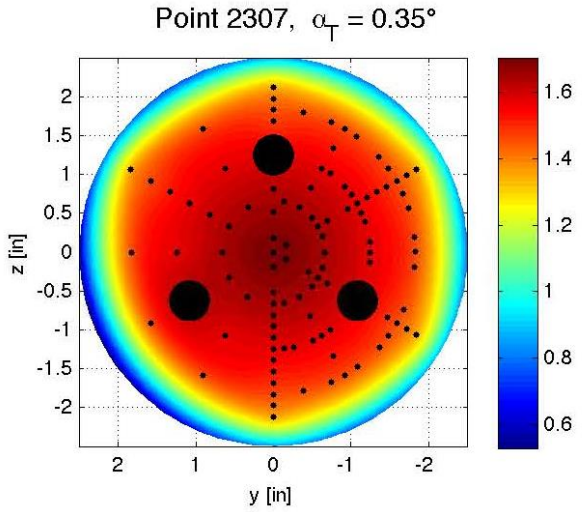

Figure E-138. Tri-nozzle configuration, Run 179, M_∞ = 2.4, Re_∞ = 1.0x10^6/ft, ϕ = 0.09°, X_S = 40.15 in, Y_S = 0.00 in, C_T = 2.95.

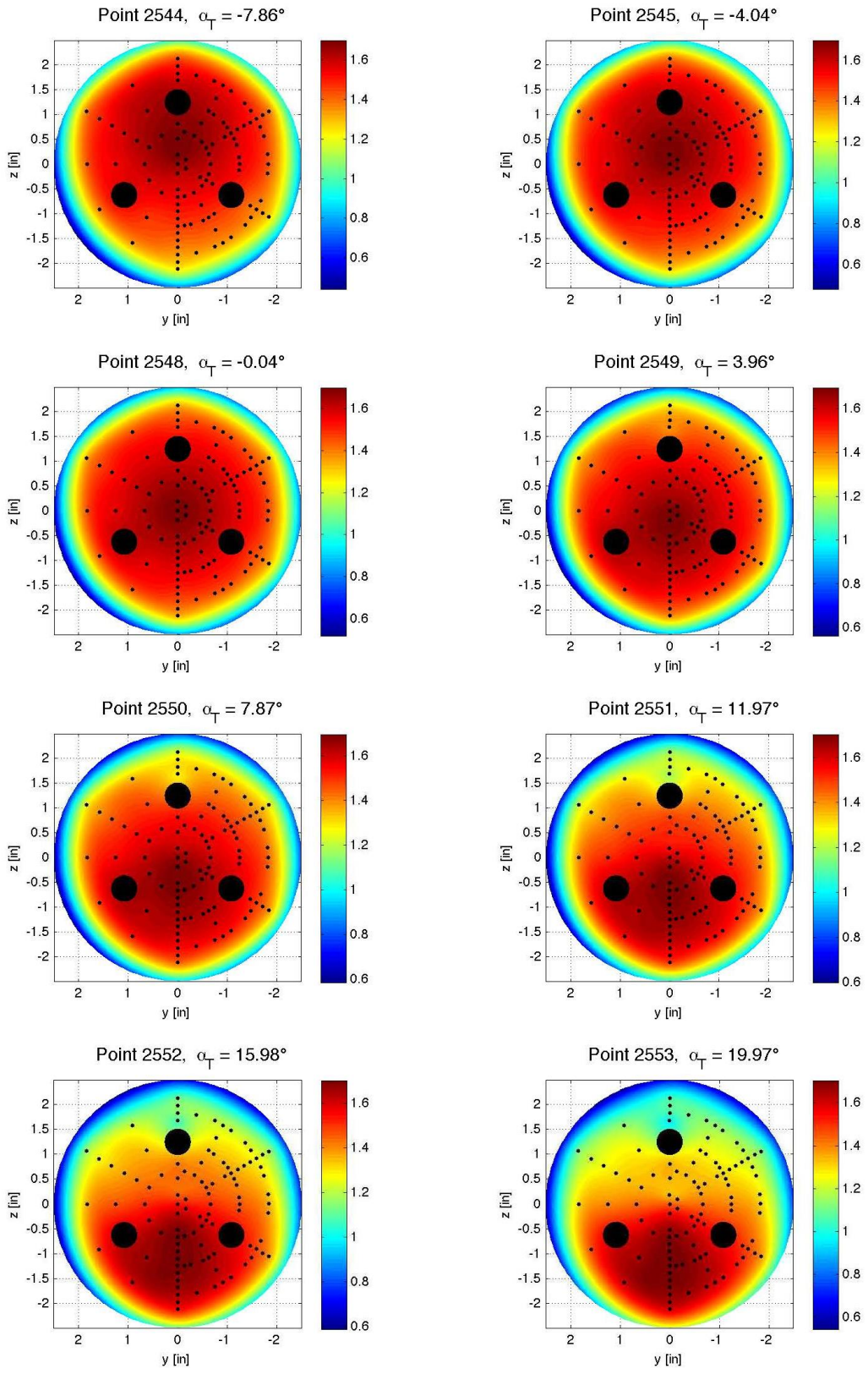

Figure E-139. Tri-nozzle configuration, Run 180, M_∞ = 2.4, Re_∞ = 1.0x10^6/ft, ϕ = −0.01°, X_S = 40.15 in, Y_S = 0.00 in, C_T = 0.00.

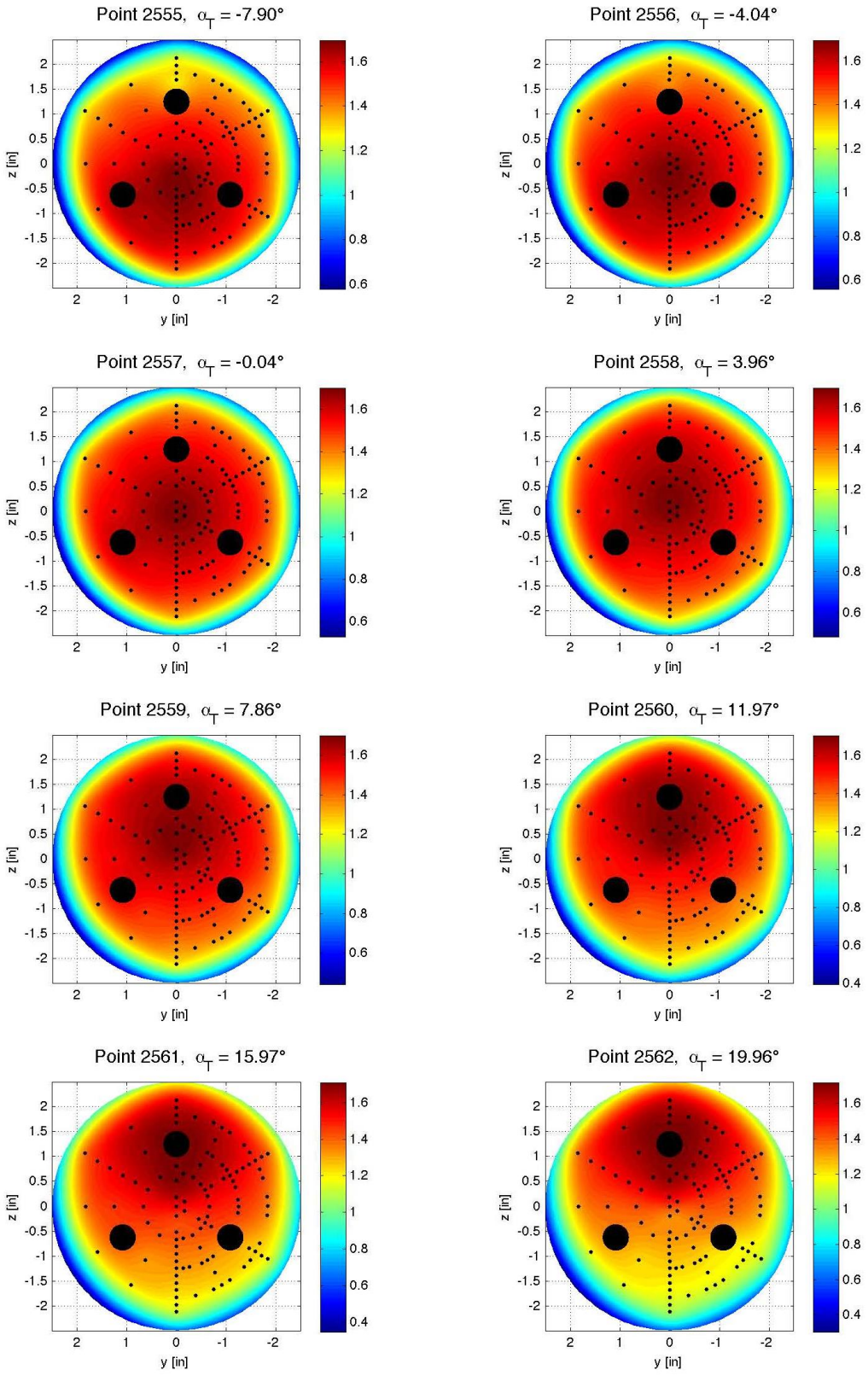

Figure E-140. Tri-nozzle configuration, Run 181, M_∞ = 2.4, Re_∞ = 1.0x10^6/ft, ϕ = 179.97°, X_S = 40.15 in, Y_S = 0.00 in, C_T = 0.00.

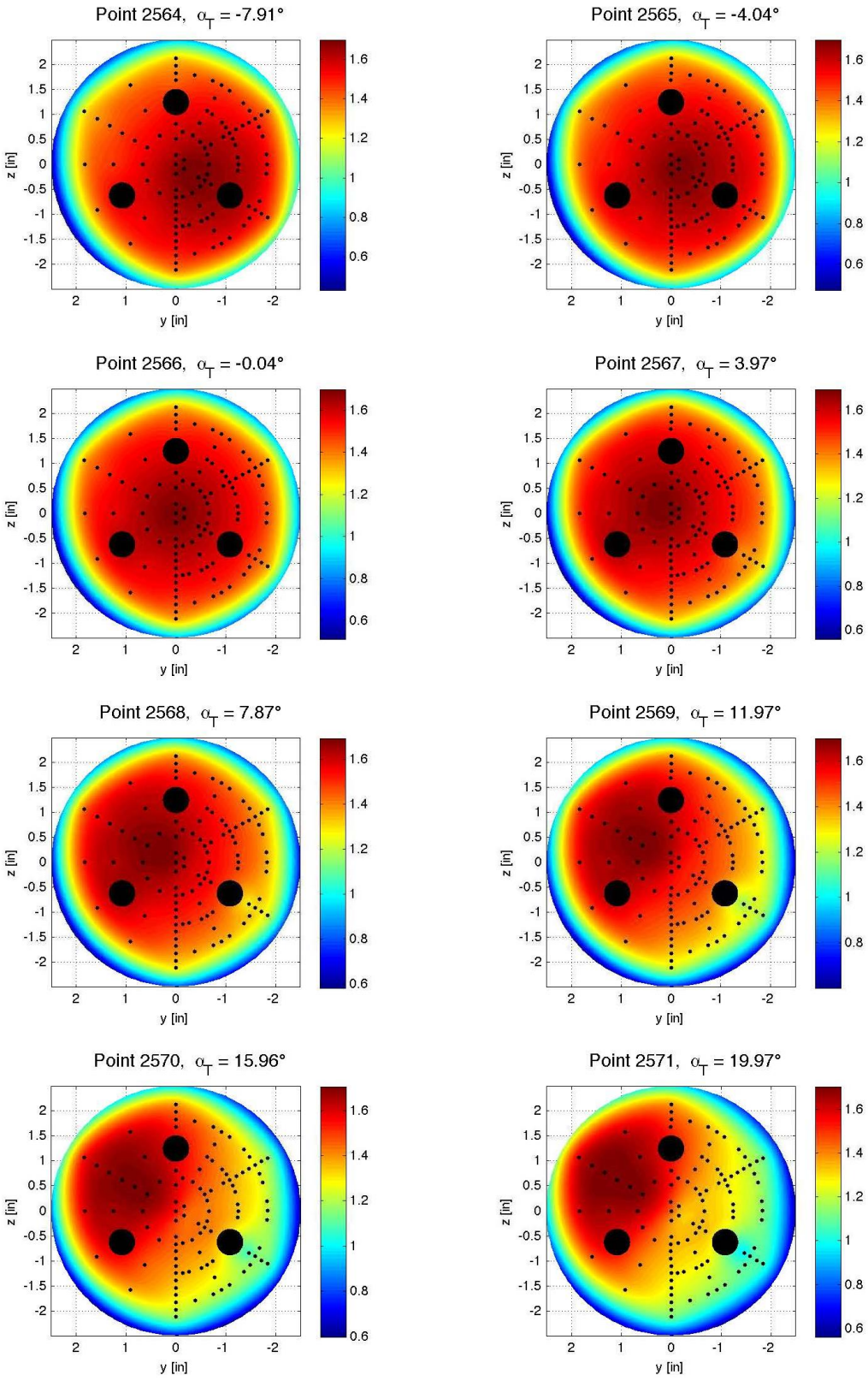

Figure E-141. Tri-nozzle configuration, Run 182, M_∞ = 2.4, Re_∞ = 1.0x10^6/ft, ϕ = 119.96°, X_S = 40.15 in, Y_S = 0.00 in, C_T = 0.00.

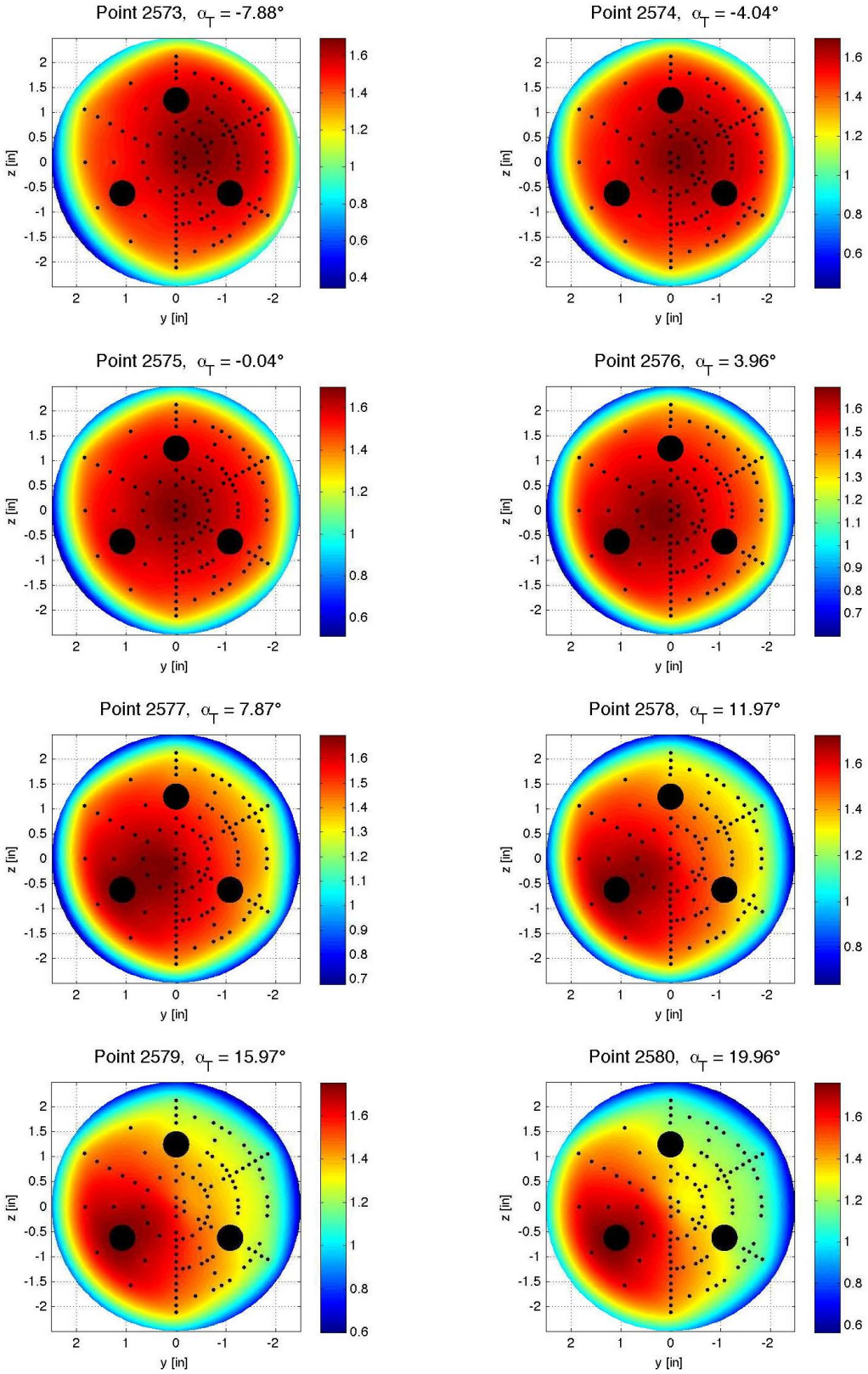

Figure E-142. Tri-nozzle configuration, Run 183, M_∞ = 2.4, Re_∞ = 1.0x10^6/ft, ϕ = 60.04°, X_S = 40.15 in, Y_S = 0.00 in, C_T = 0.00.

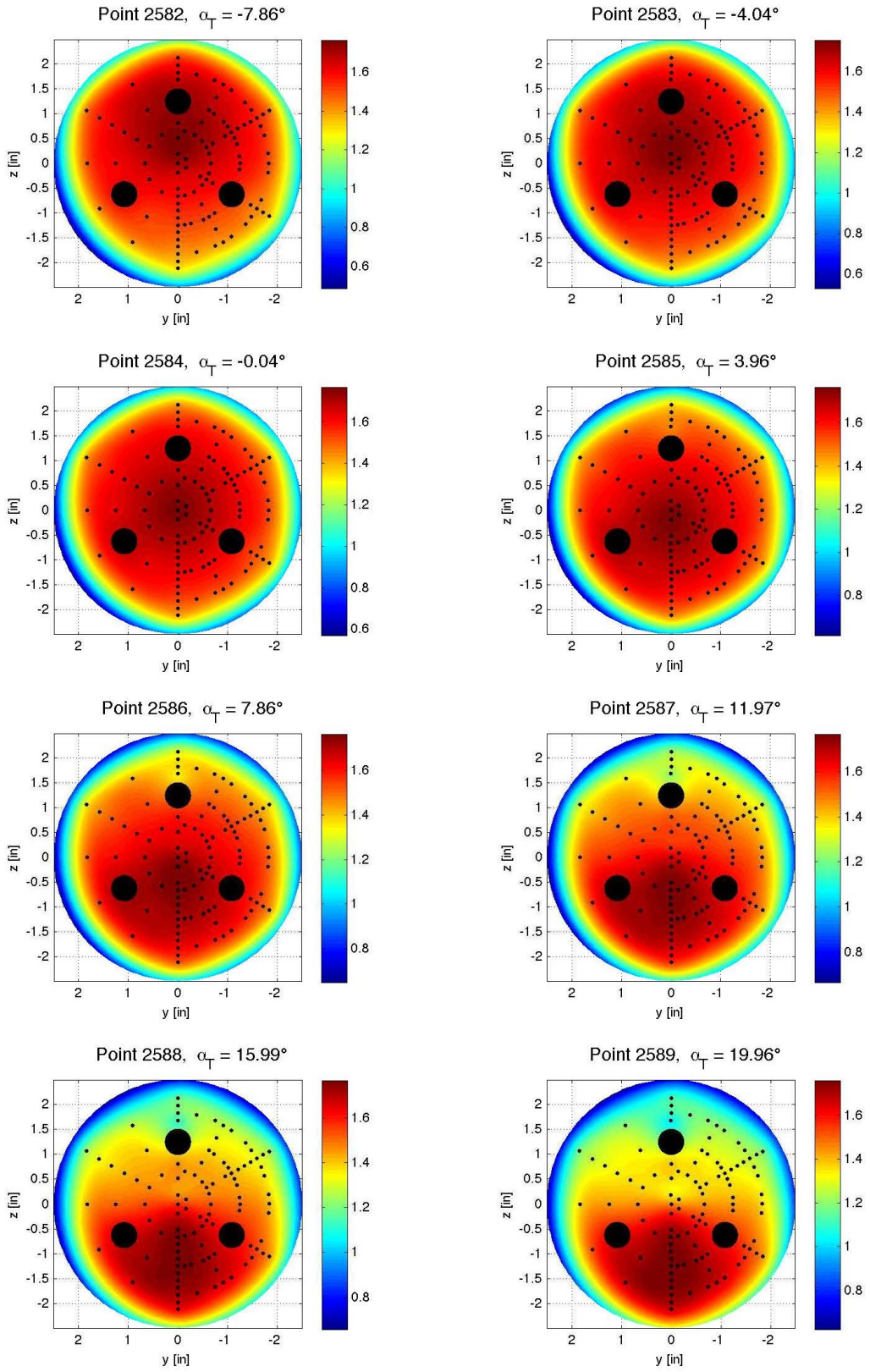

Figure E-143. Tri-nozzle configuration, Run 184, M_∞ = 3.5, Re_∞ = 1.0x10^6/ft, ϕ = 0.05°, X_S = 40.15 in, Y_S = 0.00 in, C_T = 0.00.

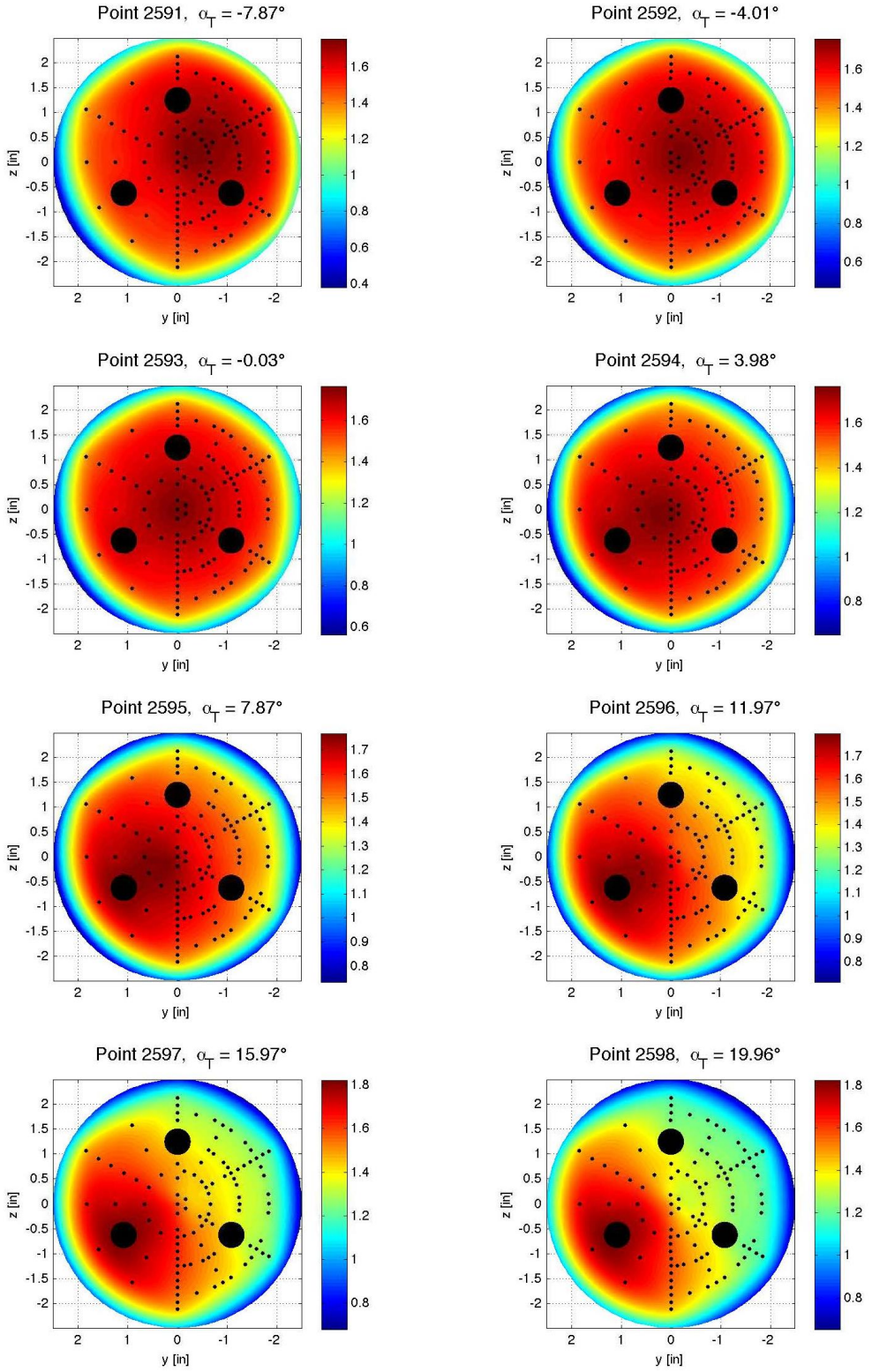

Figure E-144. Tri-nozzle configuration, Run 185, M_∞ = 3.5, Re_∞ = 1.0x10^6/ft, ϕ = 59.94°, X_S = 40.15 in, Y_S = 0.00 in, C_T = 0.00.

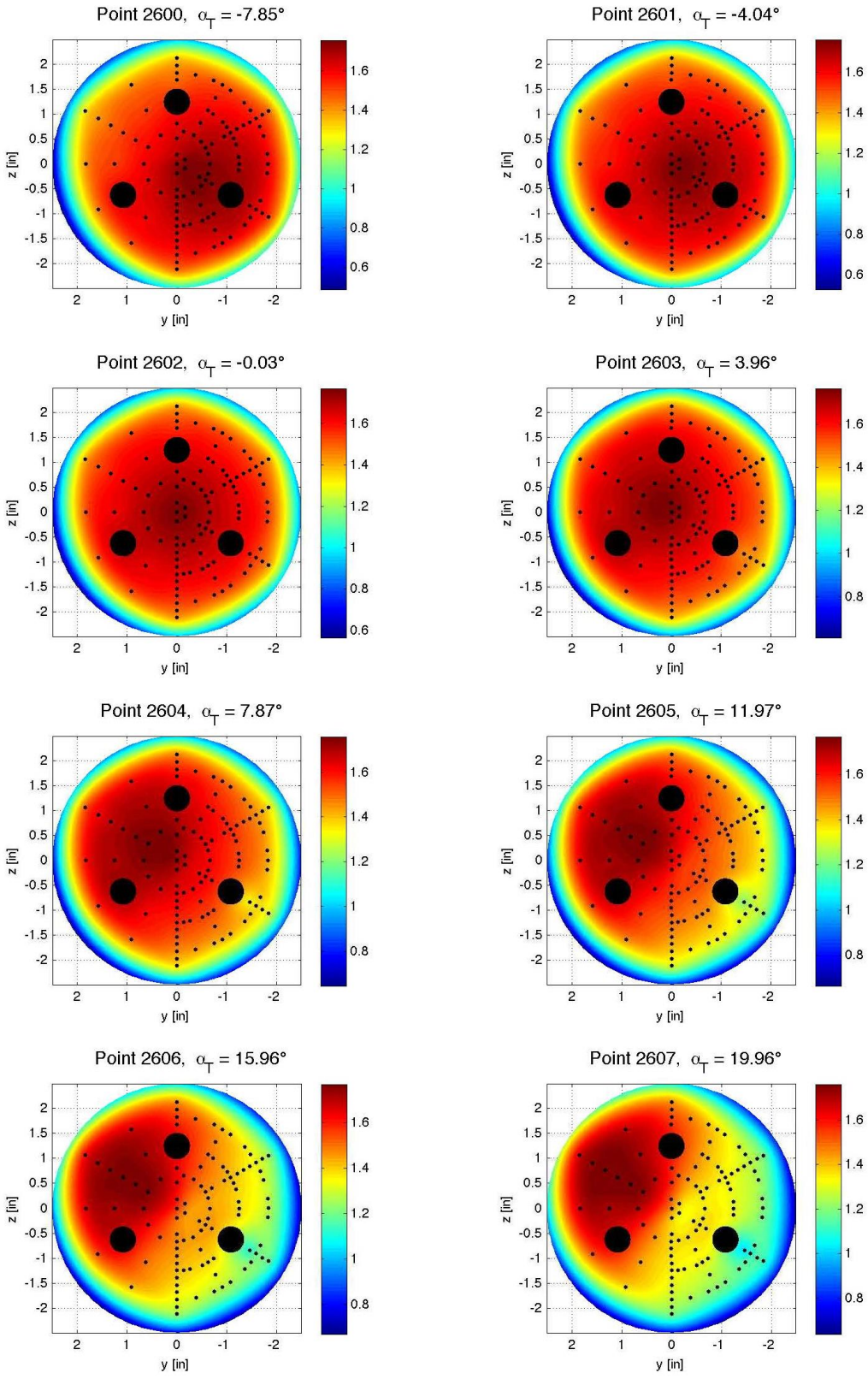

Figure E-145. Tri-nozzle configuration, Run 186, M_∞ = 3.5, Re_∞ = 1.0x10^6/ft, ϕ = 119.94°, X_S = 40.15 in, Y_S = 0.00 in, C_T = 0.00.

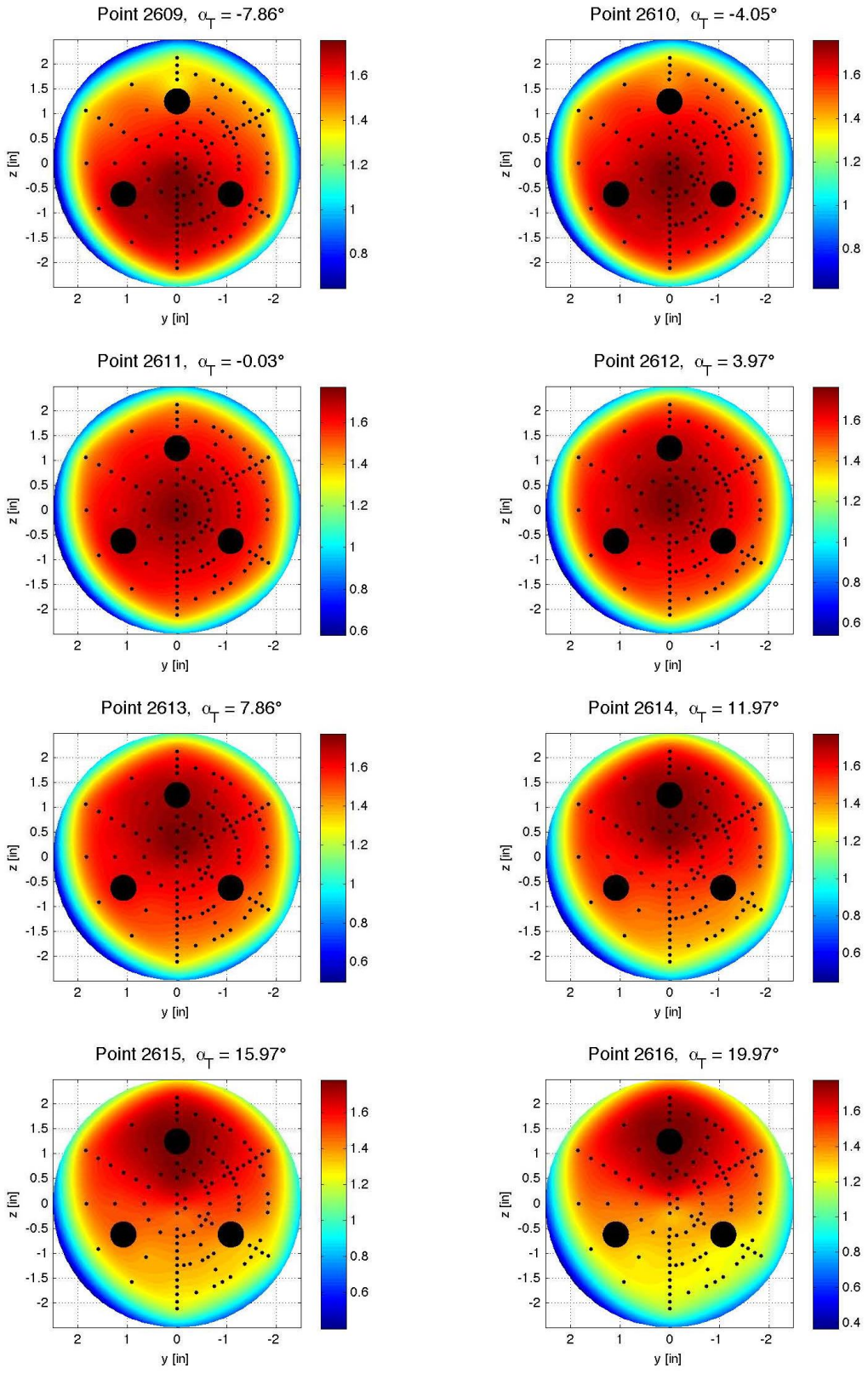

Figure E-146. Tri-nozzle configuration, Run 187, M_∞ = 3.5, Re_∞ = 1.0x10^6/ft, ϕ = 179.97°, X_S = 40.15 in, Y_S = 0.00 in, C_T = 0.00.

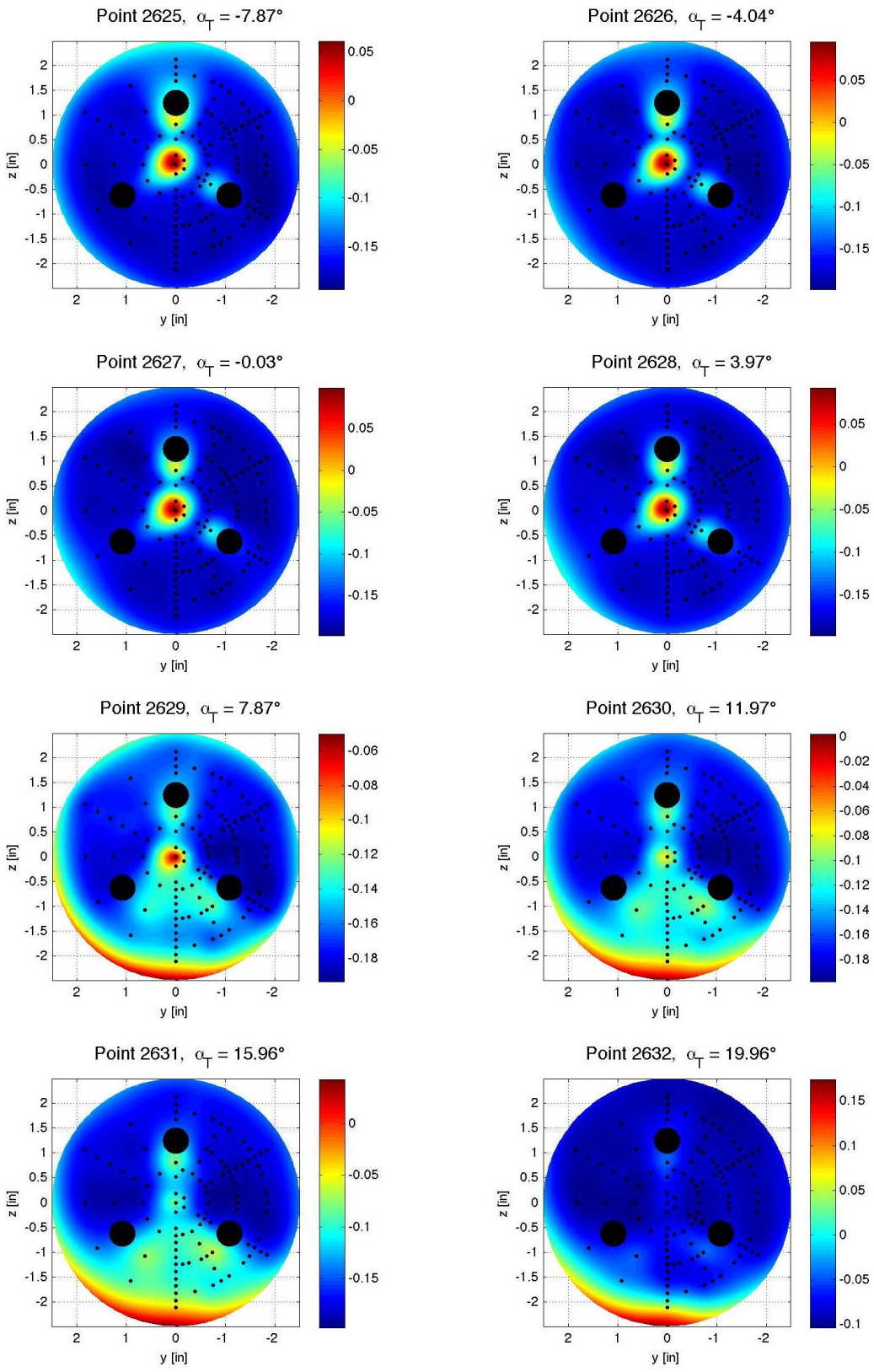

Figure E-147. Tri-nozzle configuration, Run 190, M_∞ = 2.4, Re_∞ = 1.0x10^6/ft, ϕ = −0.03°, X_S = 40.15 in, Y_S = 0.00 in, C_T = 2.95.

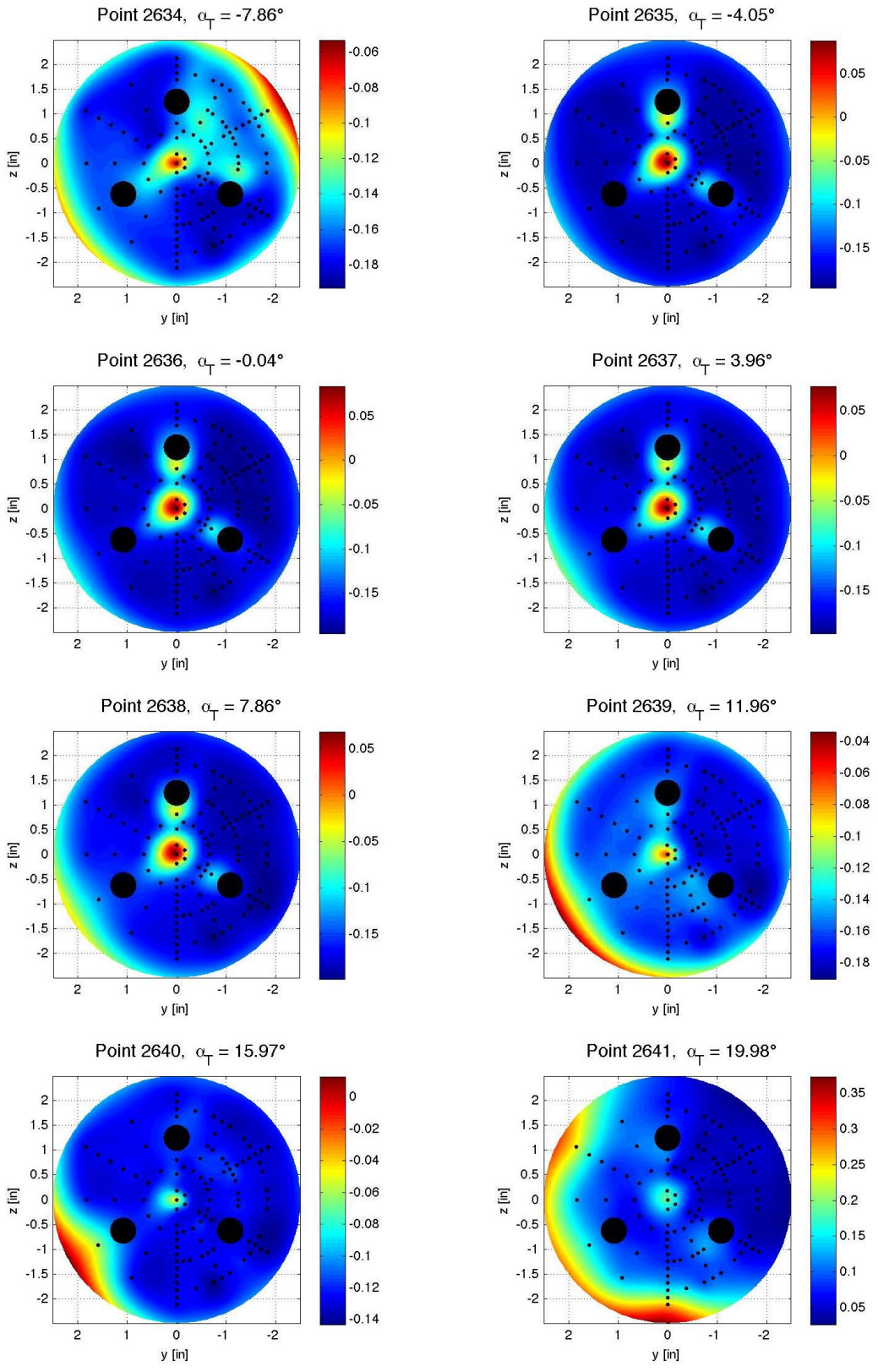

Figure E-148. Tri-nozzle configuration, Run 191, M_∞ = 2.4, Re_∞ = 1.0x10^6/ft, ϕ = 58.37°, X_S = 40.15 in, Y_S = 0.00 in, C_T = 2.95.

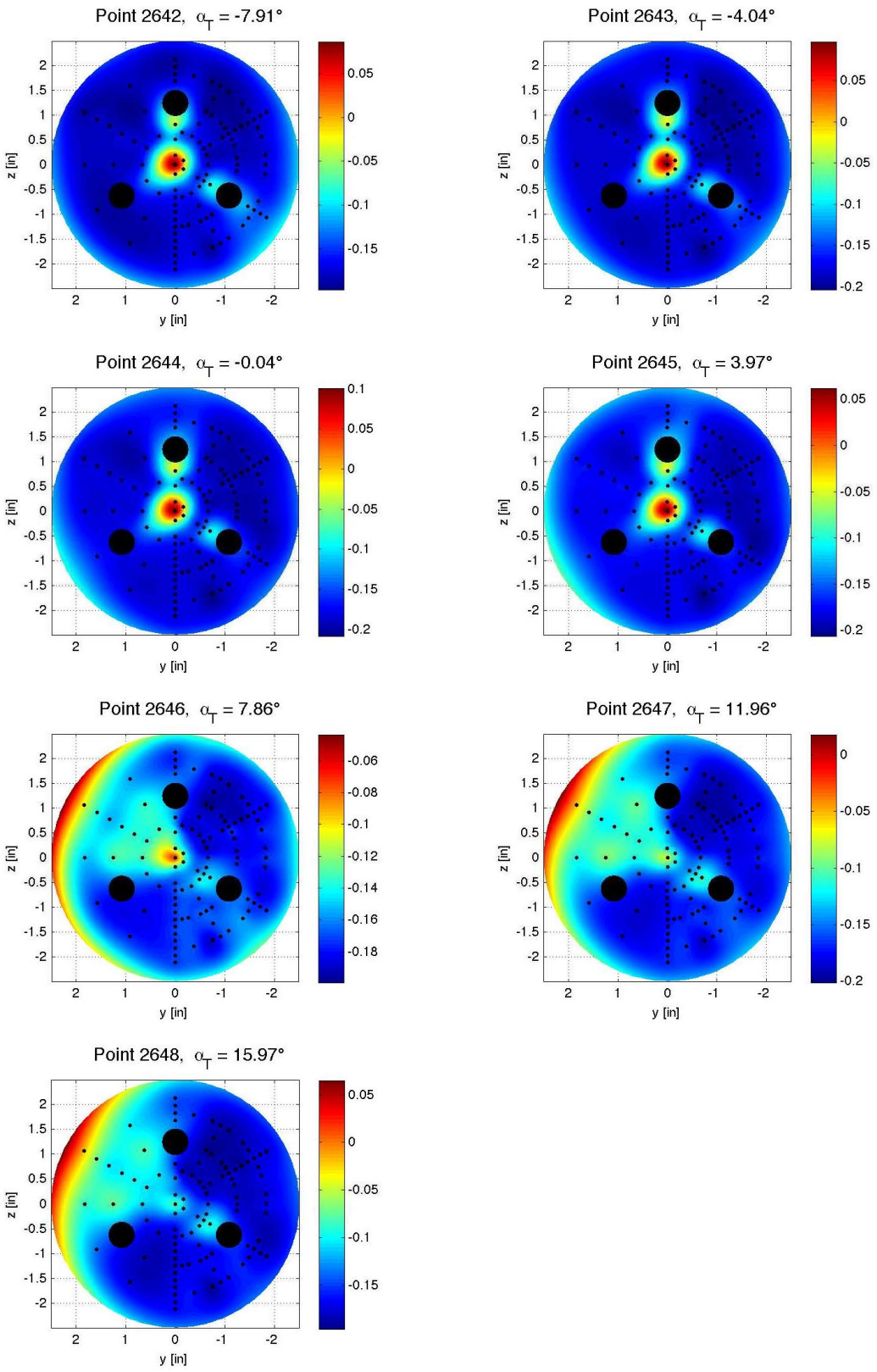

Figure E-149. Tri-nozzle configuration, Run 192, M_∞ = 2.4, Re_∞ = 1.0x10^6/ft, ϕ = 119.94°, X_S = 40.15 in, Y_S = 0.00 in, C_T = 2.93.

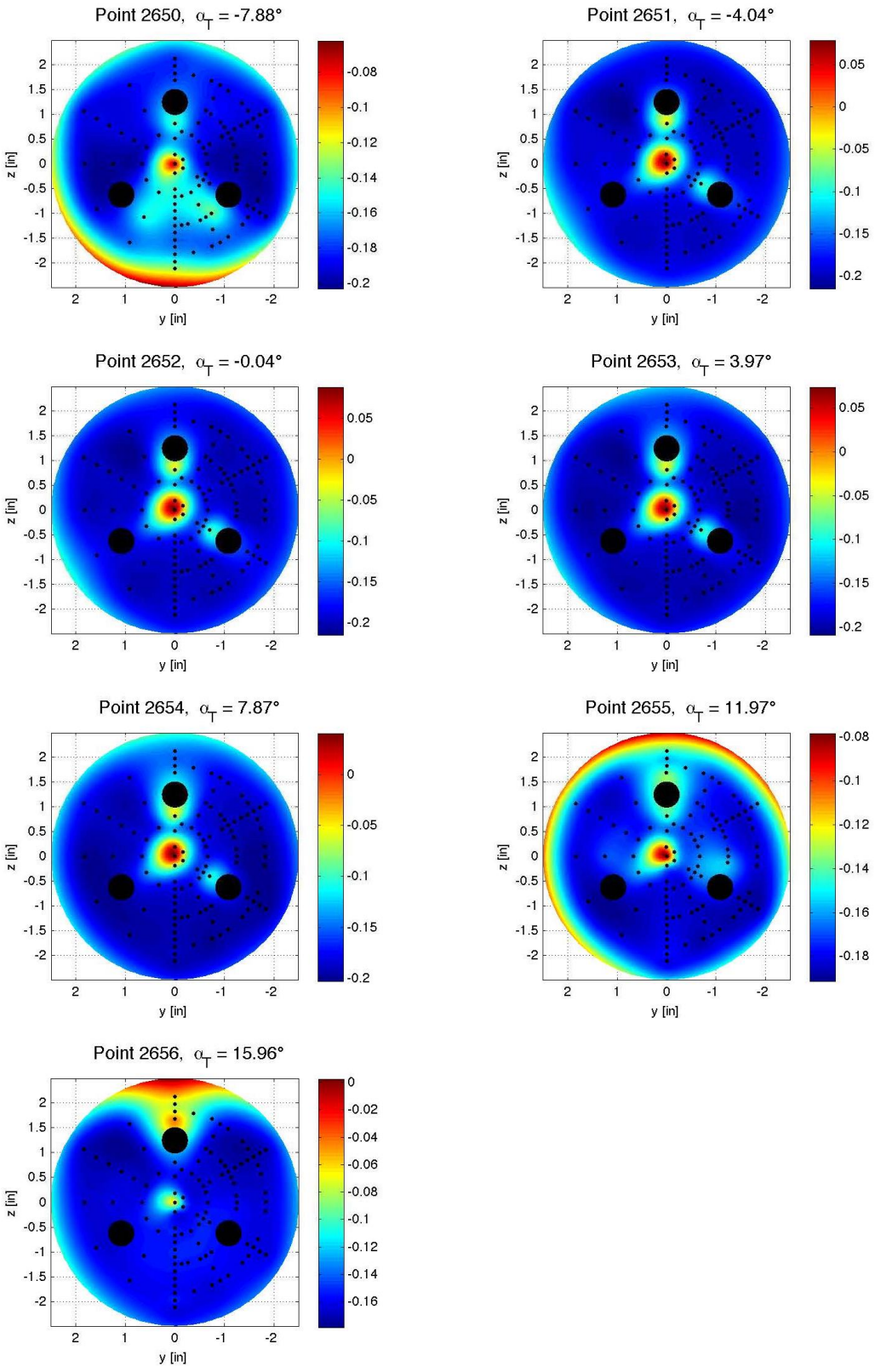

Figure E-150. Tri-nozzle configuration, Run 193, M_∞ = 2.4, Re_∞ = 1.0x10^6/ft, ϕ = −179.97°, X_S = 40.15 in, Y_S = 0.00 in, C_T = 2.95.

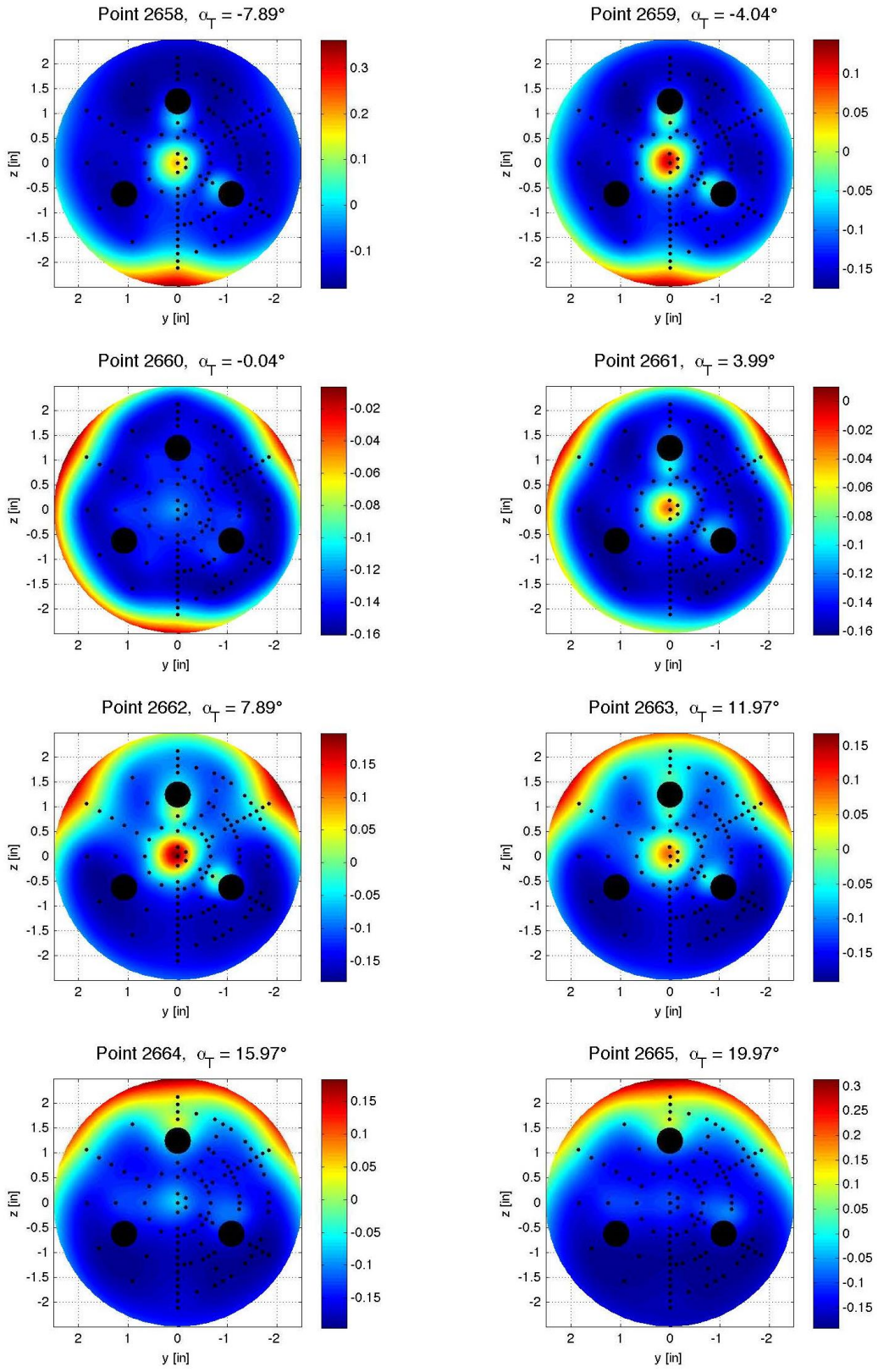

Figure E-151. Tri-nozzle configuration, Run 194, M_∞ = 2.4, Re_∞ = 1.0x10^6/ft, ϕ = −179.97°, X_S = 40.15 in, Y_S = 0.00 in, C_T = 1.94.

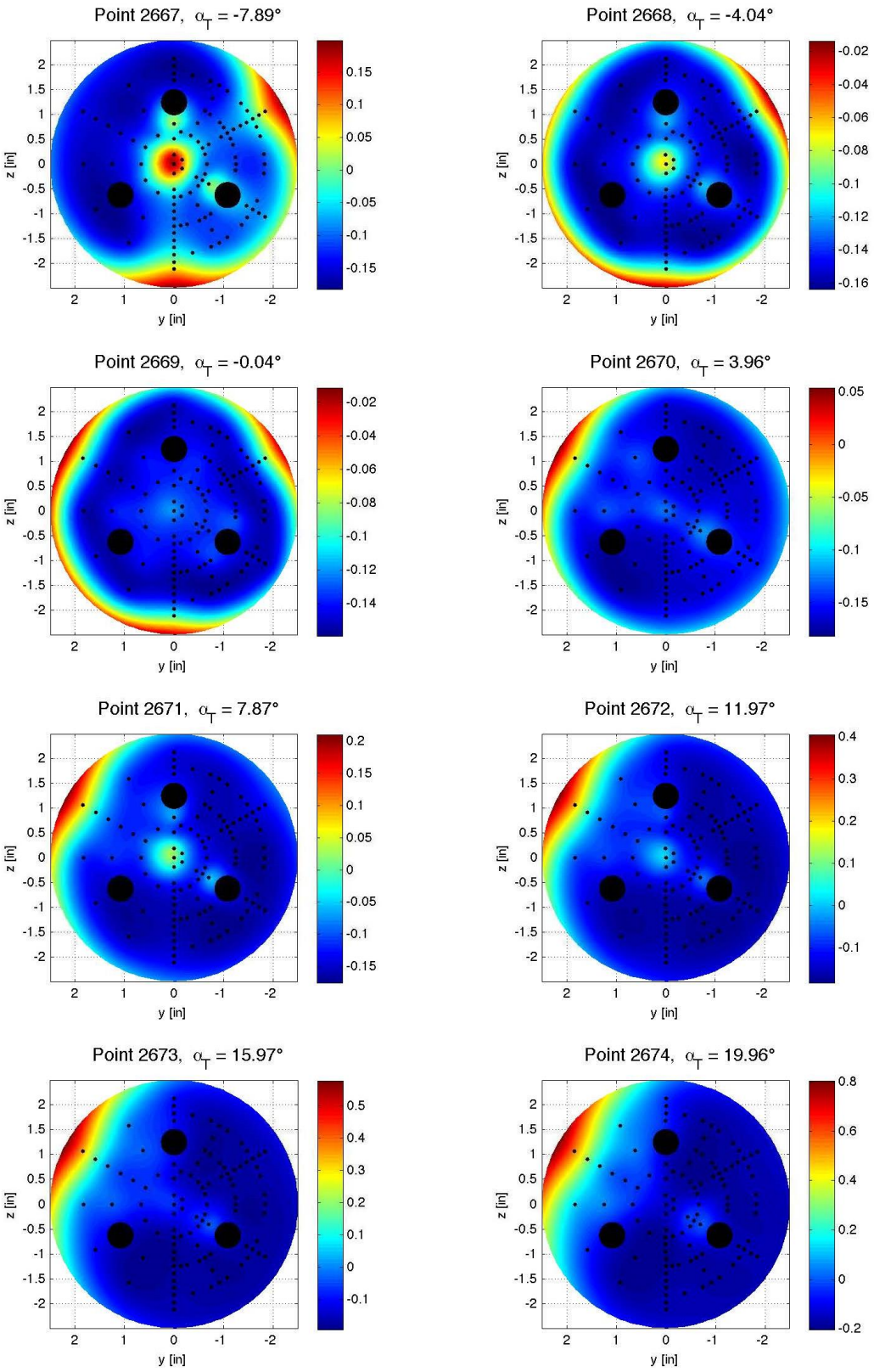

Figure E-152. Tri-nozzle configuration, Run 195, M_∞ = 2.4, Re_∞ = 1.0x10^6/ft, ϕ = 119.96°, X_S = 40.15 in, Y_S = 0.00 in, C_T = 1.93.

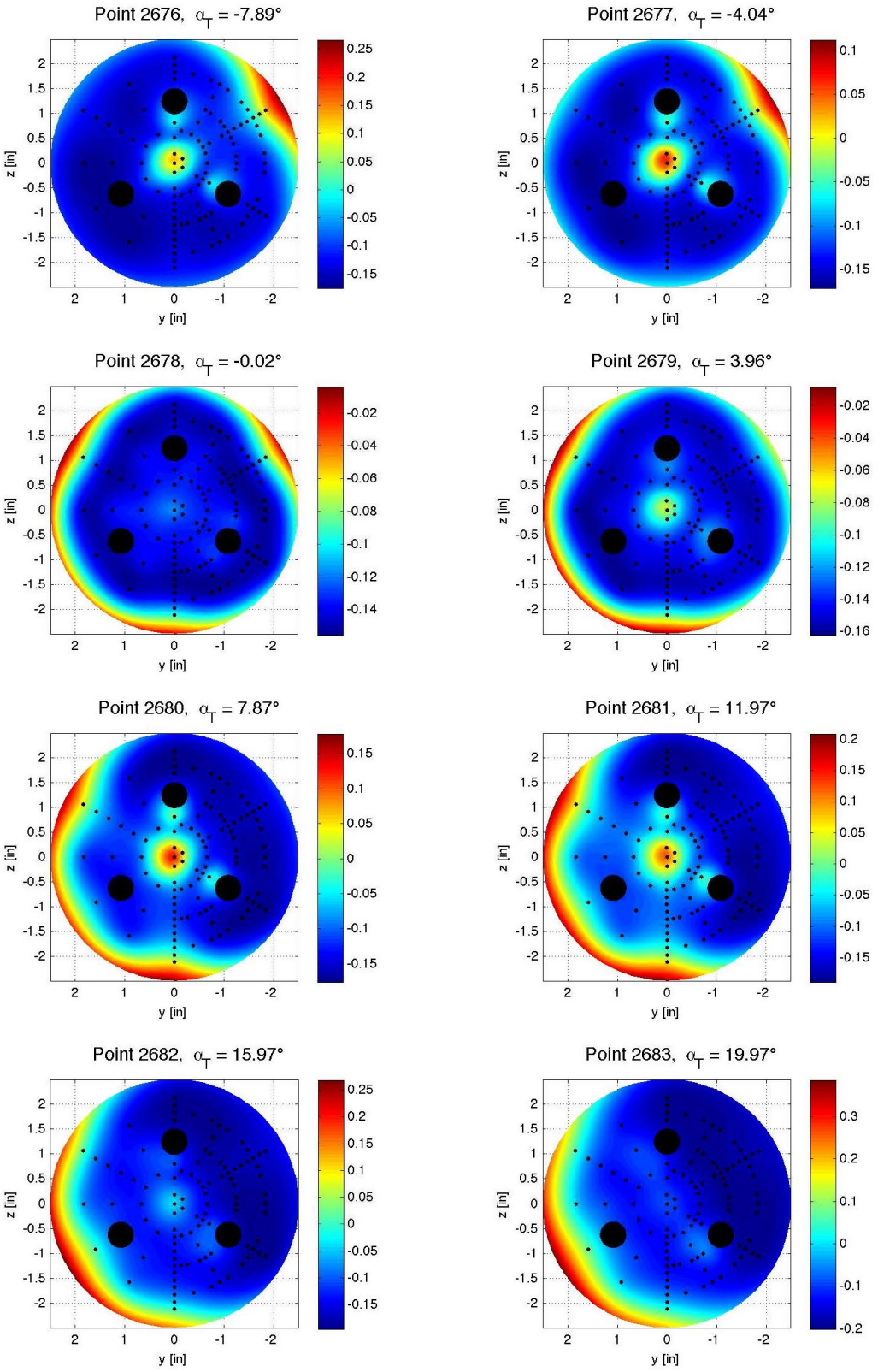

Figure E-153. Tri-nozzle configuration, Run 196, M_∞ = 2.4, Re_∞ = 1.0x10^6/ft, ϕ = 59.94°, X_S = 40.15 in, Y_S = 0.00 in, C_T = 1.93.

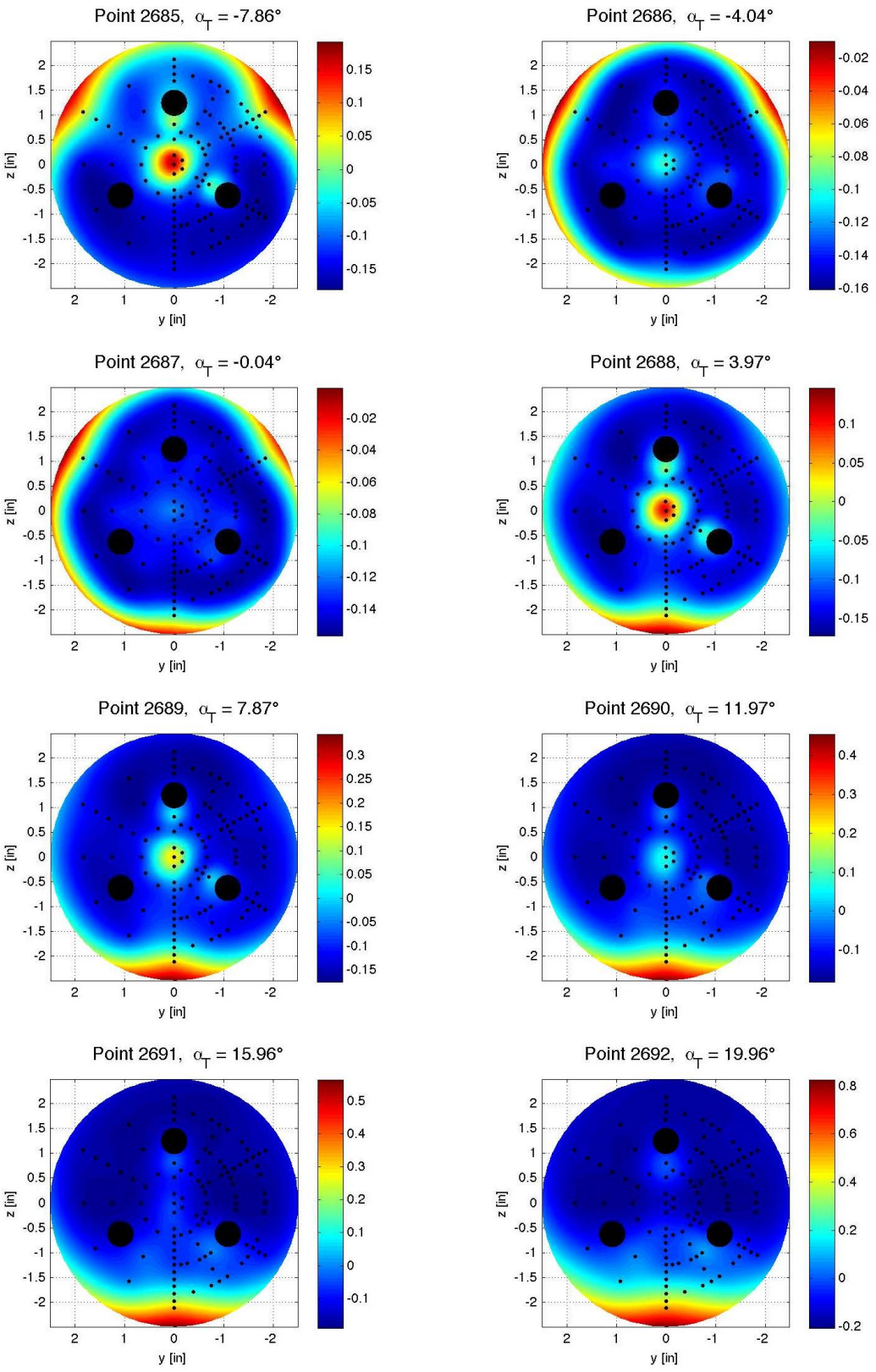

Figure E-154. Tri-nozzle configuration, Run 197, M_∞ = 2.4, Re_∞ = 1.0x10^6/ft, ϕ = −0.01°, X_S = 40.15 in, Y_S = 0.00 in, C_T = 1.93.

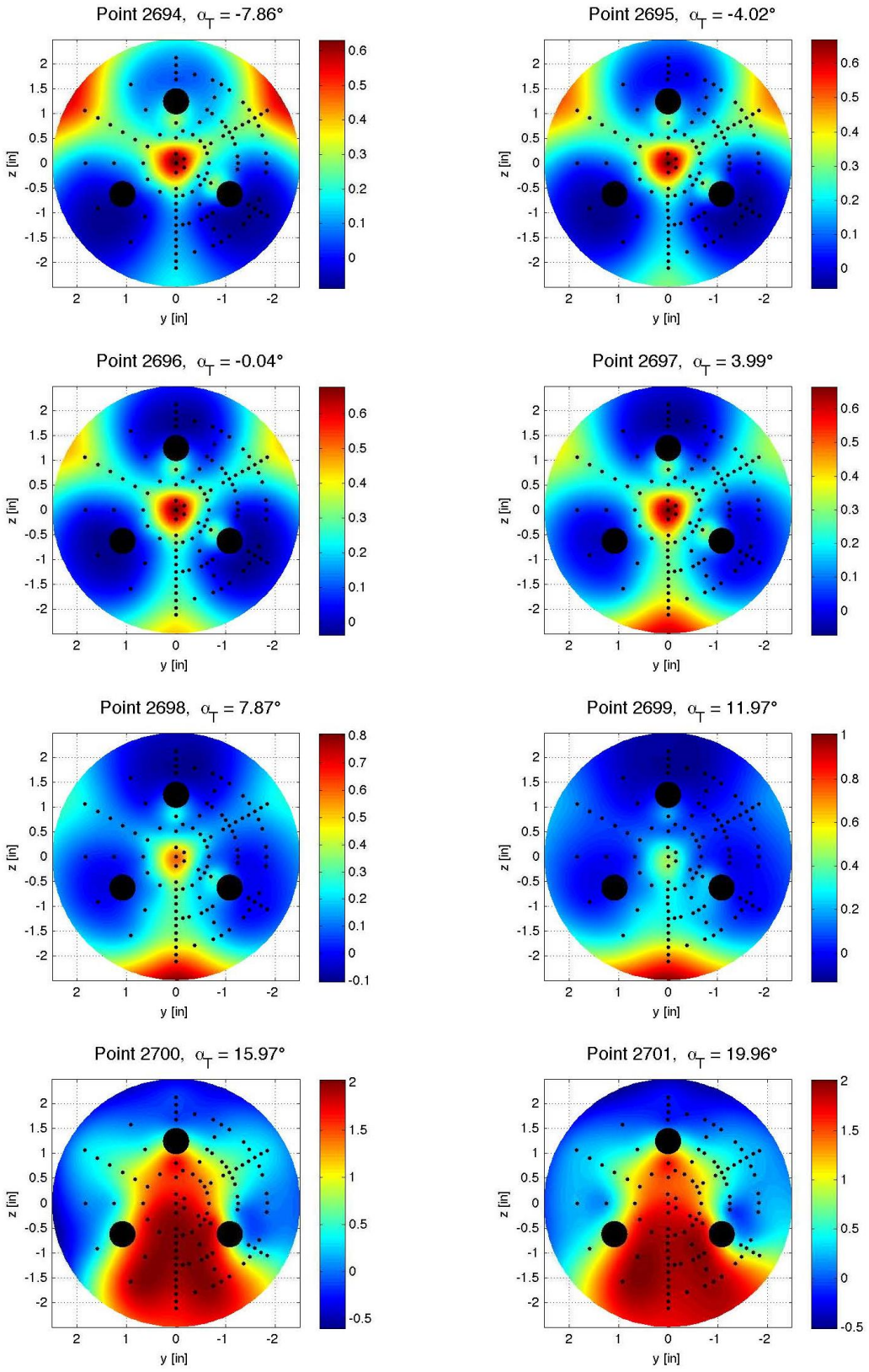

Figure E-155. Tri-nozzle configuration, Run 198, M_∞ = 2.4, Re_∞ = 1.0x10^6/ft, ϕ = −0.01°, X_S = 40.15 in, Y_S = 0.00 in, C_T = 0.95.

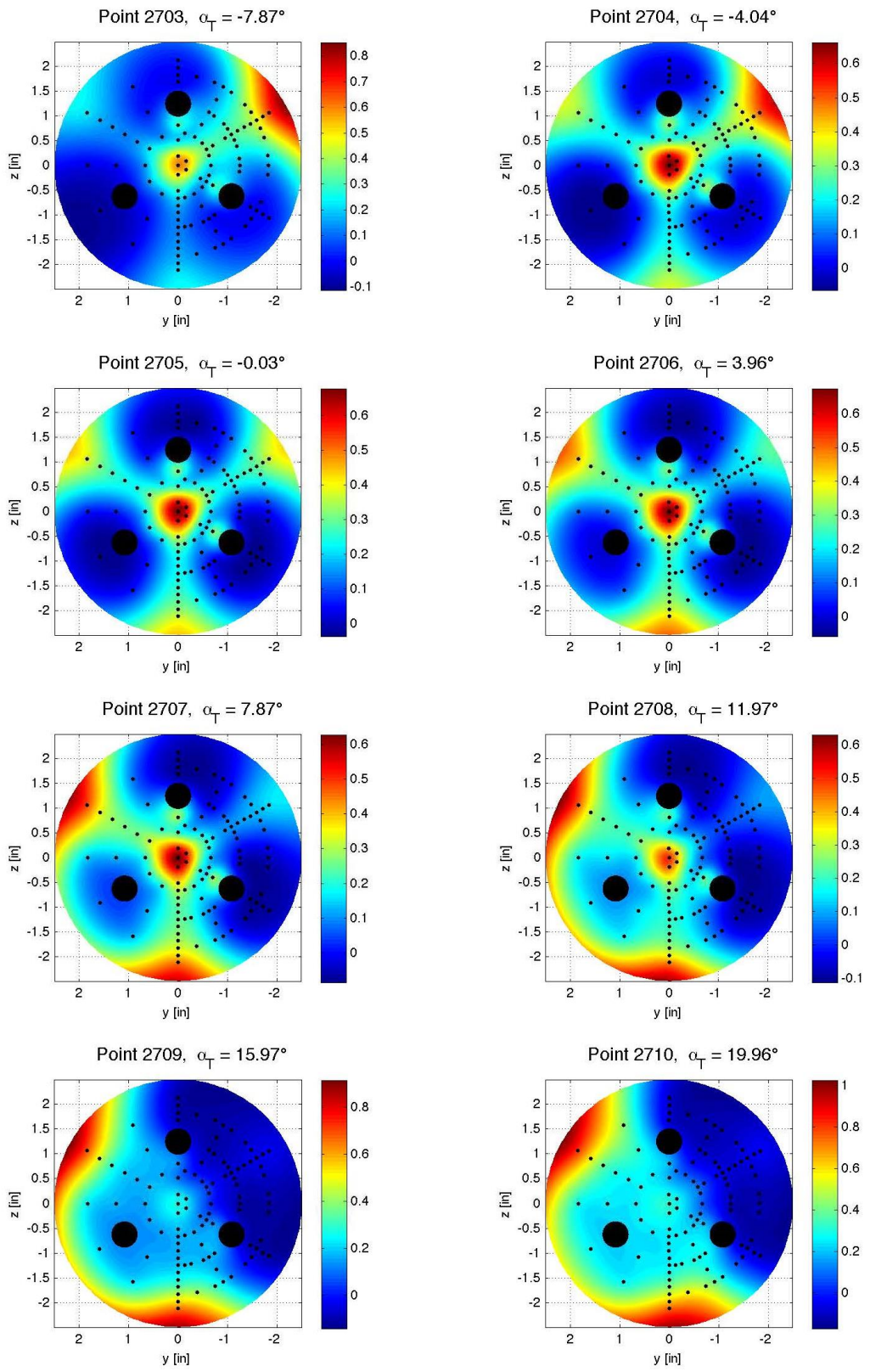

Figure E-156. Tri-nozzle configuration, Run 199, M_∞ = 2.4, Re_∞ = 1.0x10^6/ft, ϕ = 59.98°, X_S = 40.15 in, Y_S = 0.00 in, C_T = 0.94.

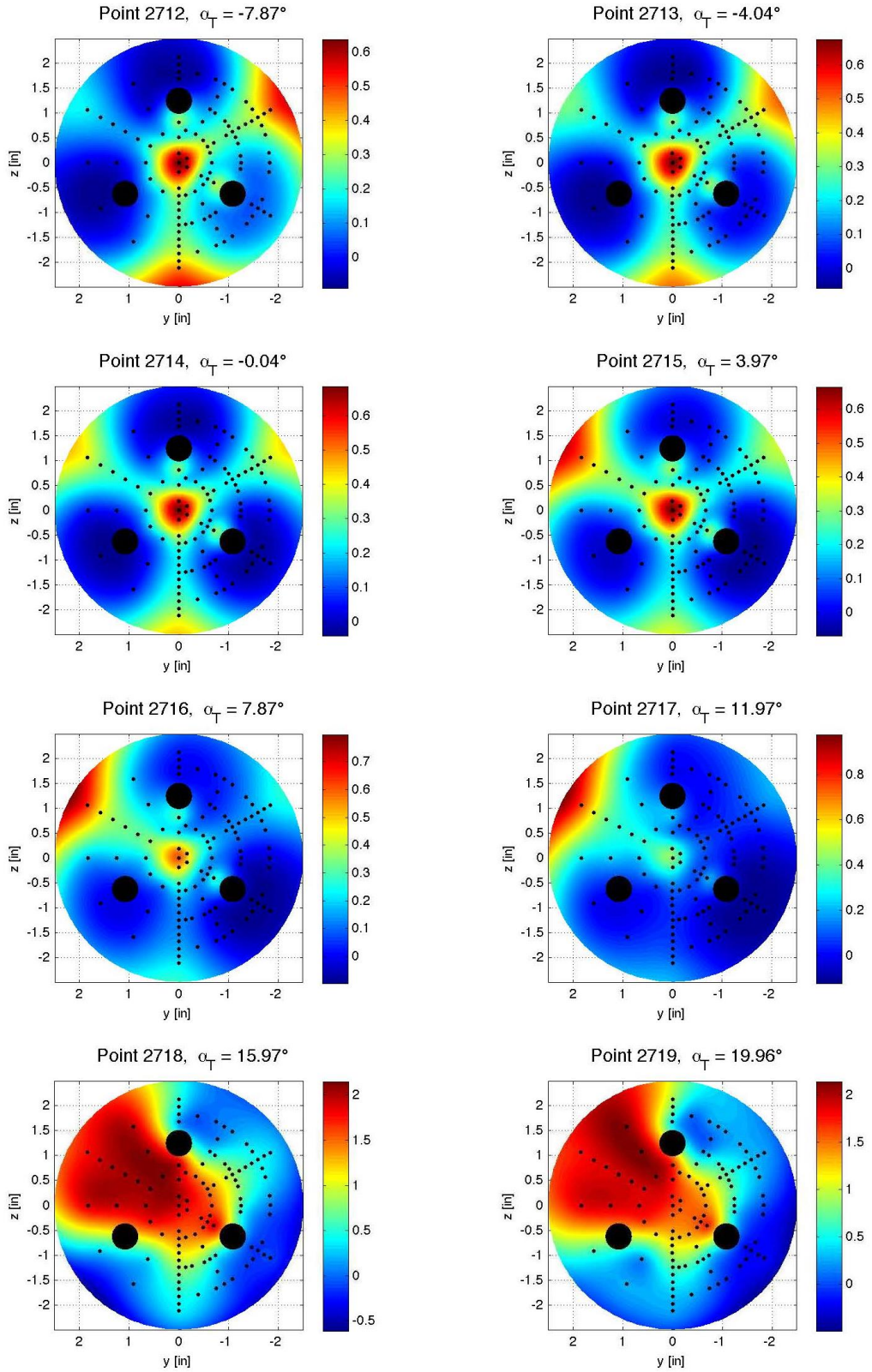

Figure E-157. Tri-nozzle configuration, Run 200, M_∞ = 2.4, Re_∞ = 1.0x10^6/ft, ϕ = 119.94°, X_S = 40.15 in, Y_S = 0.00 in, C_T = 0.94.

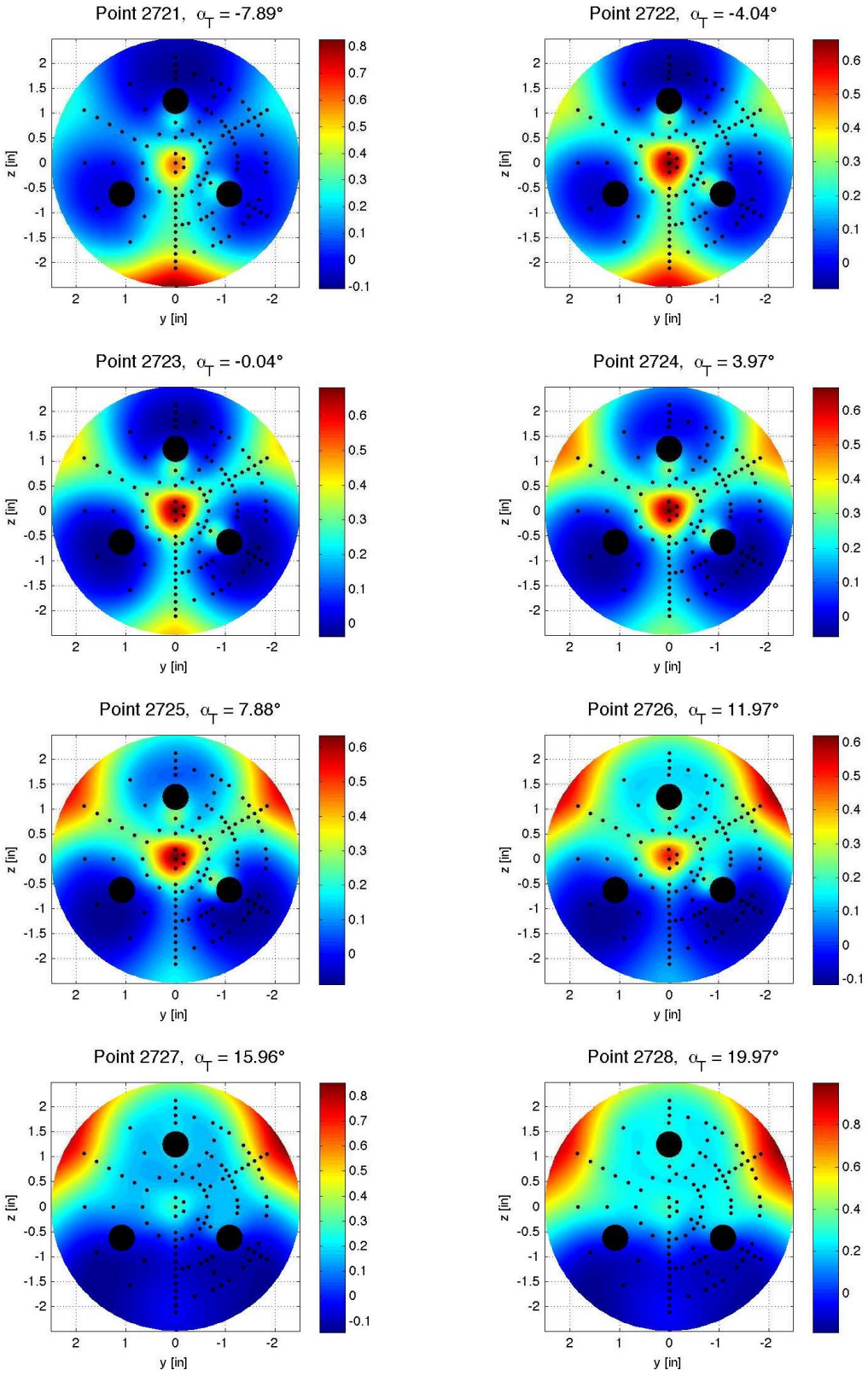

Figure E-158. Tri-nozzle configuration, Run 201, M_∞ = 2.4, Re_∞ = 1.0x10^6/ft, ϕ = 179.99°, X_S = 40.15 in, Y_S = 0.00 in, C_T = 0.94.

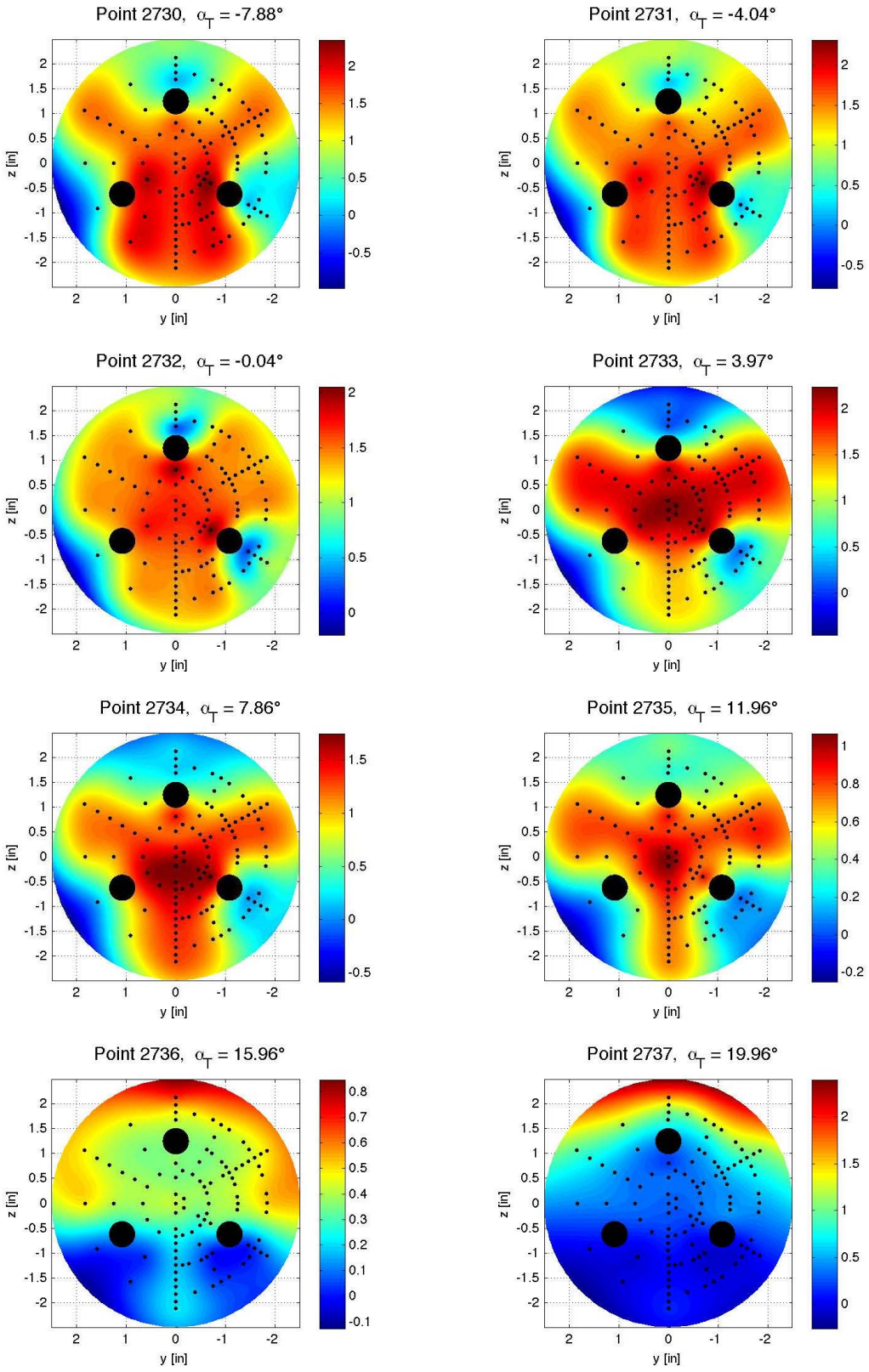

Figure E-159. Tri-nozzle configuration, Run 202, $M\infty$ = 2.4, Re_∞ = 1.0x10^6/ft, ϕ = 179.99°, X_S = 40.15 in, Y_S = 0.00 in, C_T = 0.43.

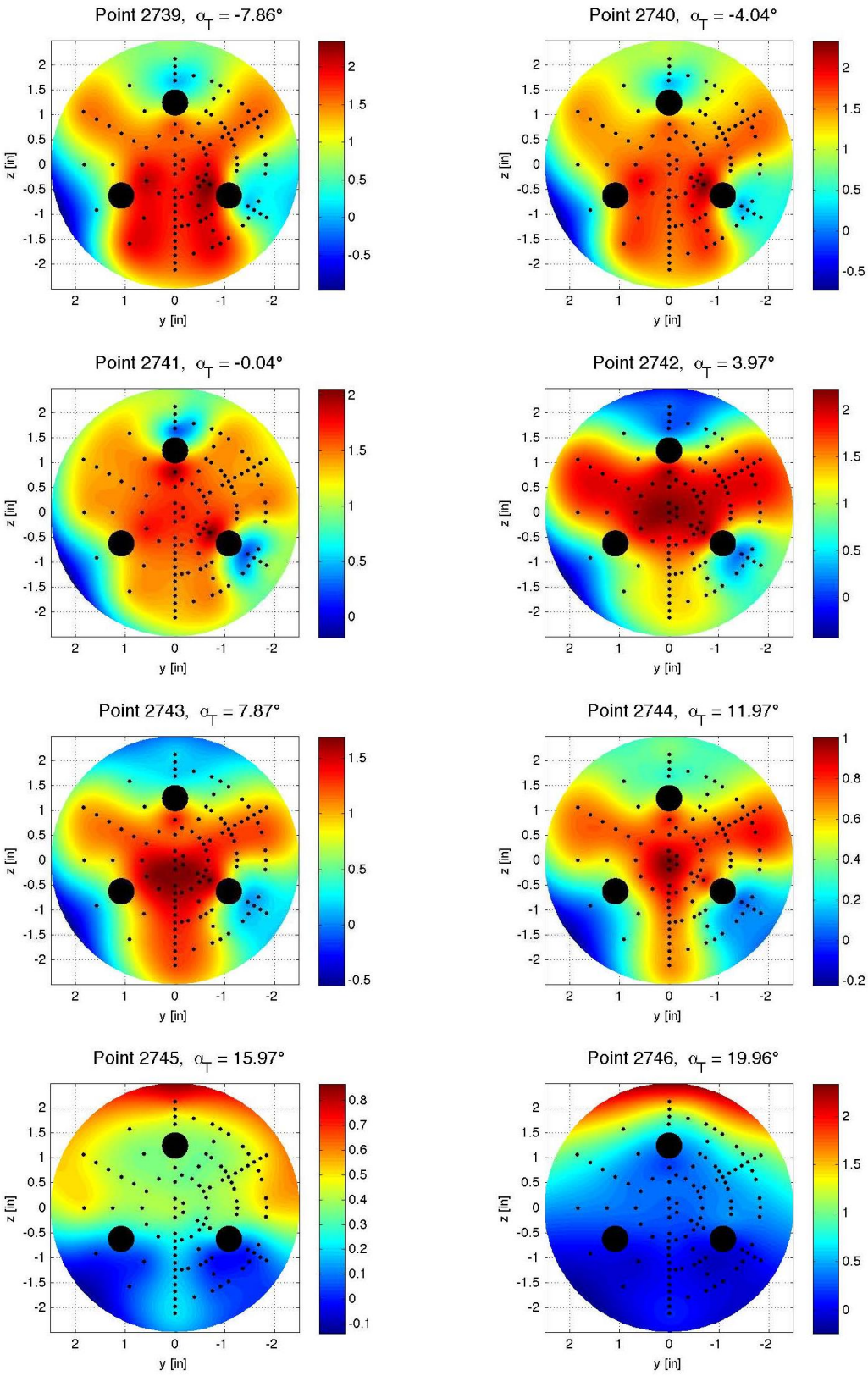

Figure E-160. Tri-nozzle configuration, Run 203, M_∞ = 2.4, Re_∞ = 1.0x10^6/ft, ϕ = −179.97°, X_S = 40.15 in, Y_S = 0.00 in, C_T = 0.44.

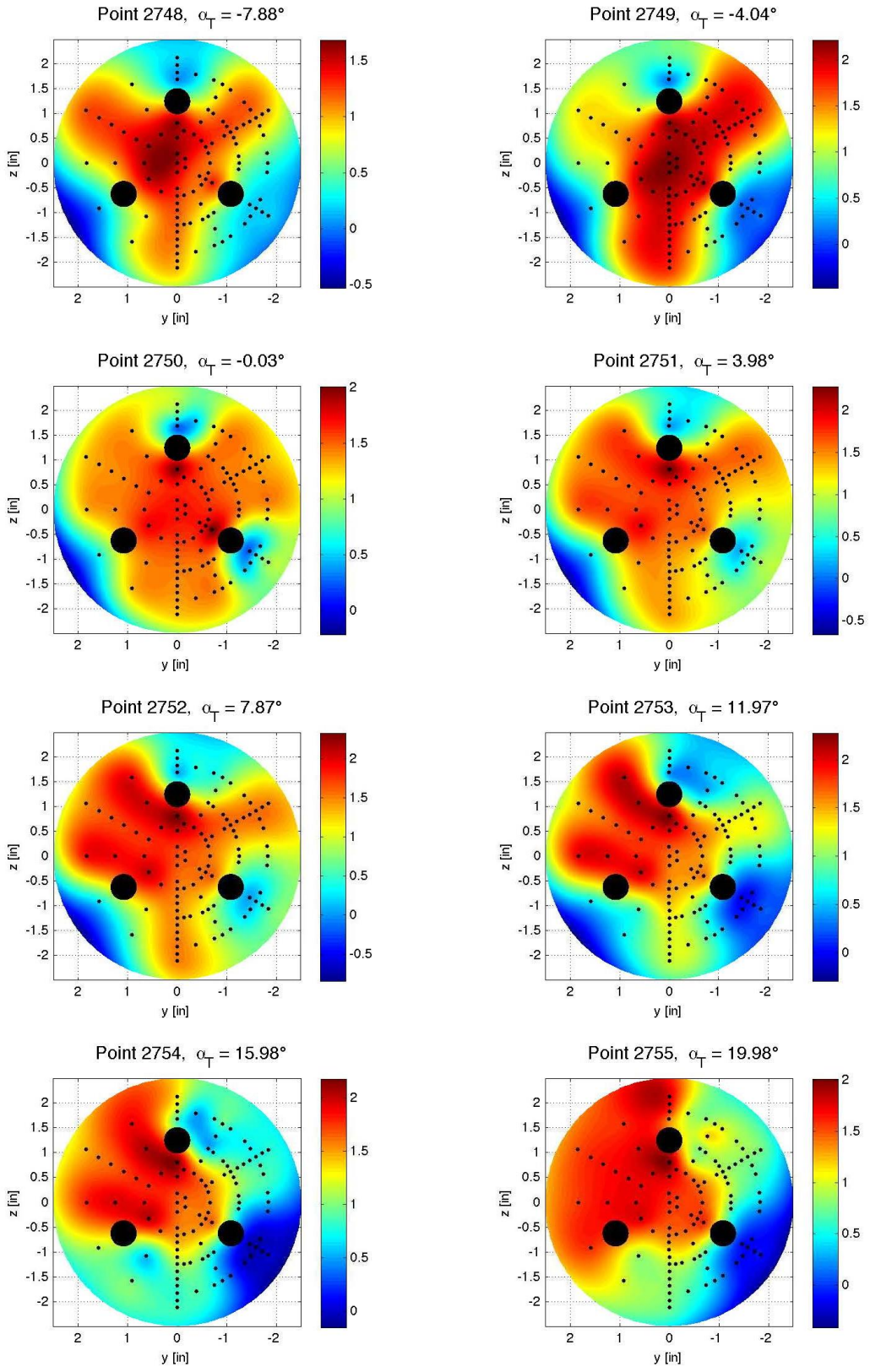

Figure E-161. Tri-nozzle configuration, Run 204, M_∞ = 2.4, Re_∞ = 1.0x10^6/ft, ϕ = 119.98°, X_S = 40.15 in, Y_S = 0.00 in, C_T = 0.44.

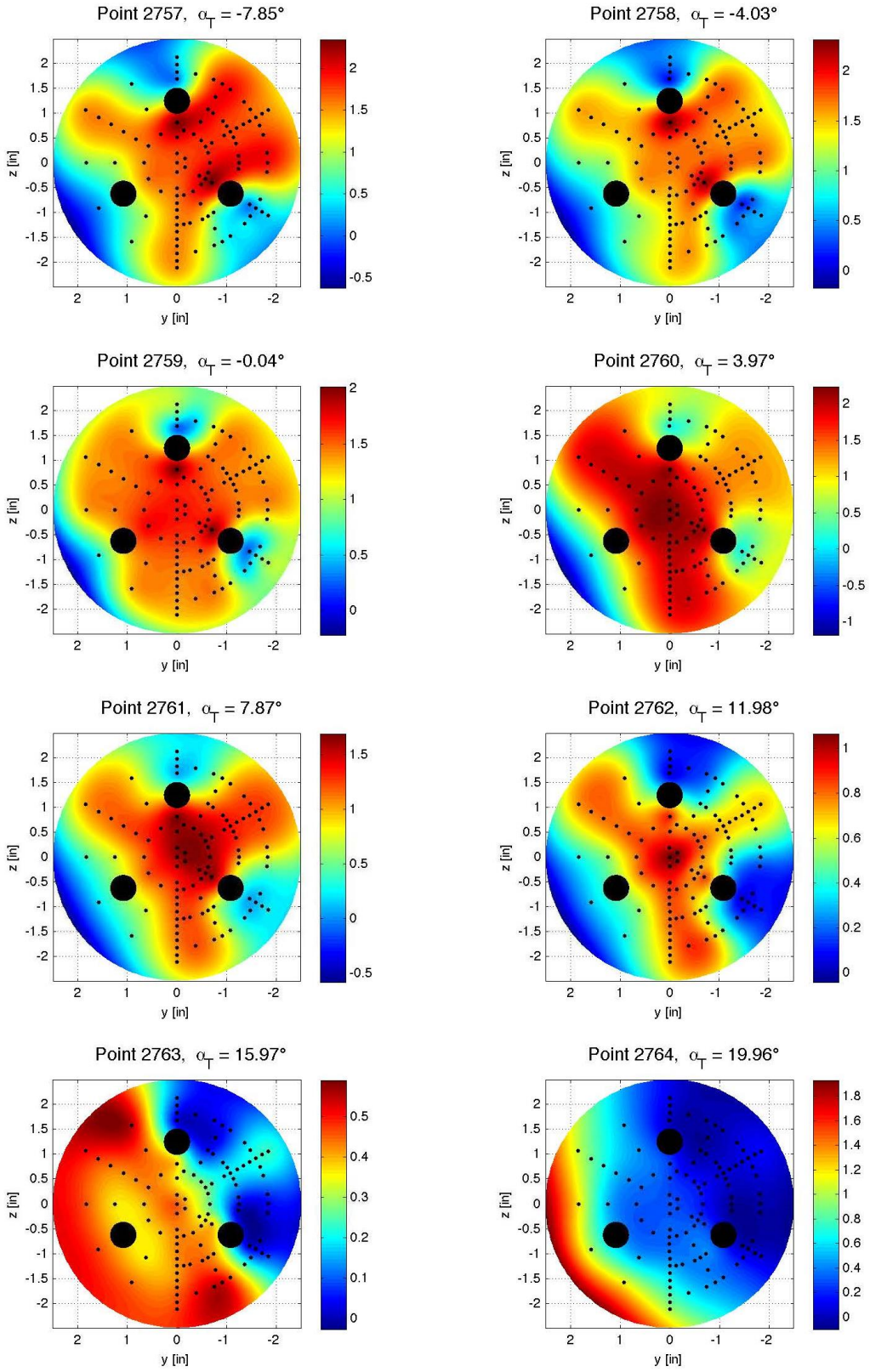

Figure E-162. Tri-nozzle configuration, Run 205, M_∞ = 2.4, Re_∞ = 1.0x10^6/ft, ϕ = 59.94°, X_S = 40.15 in, Y_S = 0.00 in, C_T = 0.43.

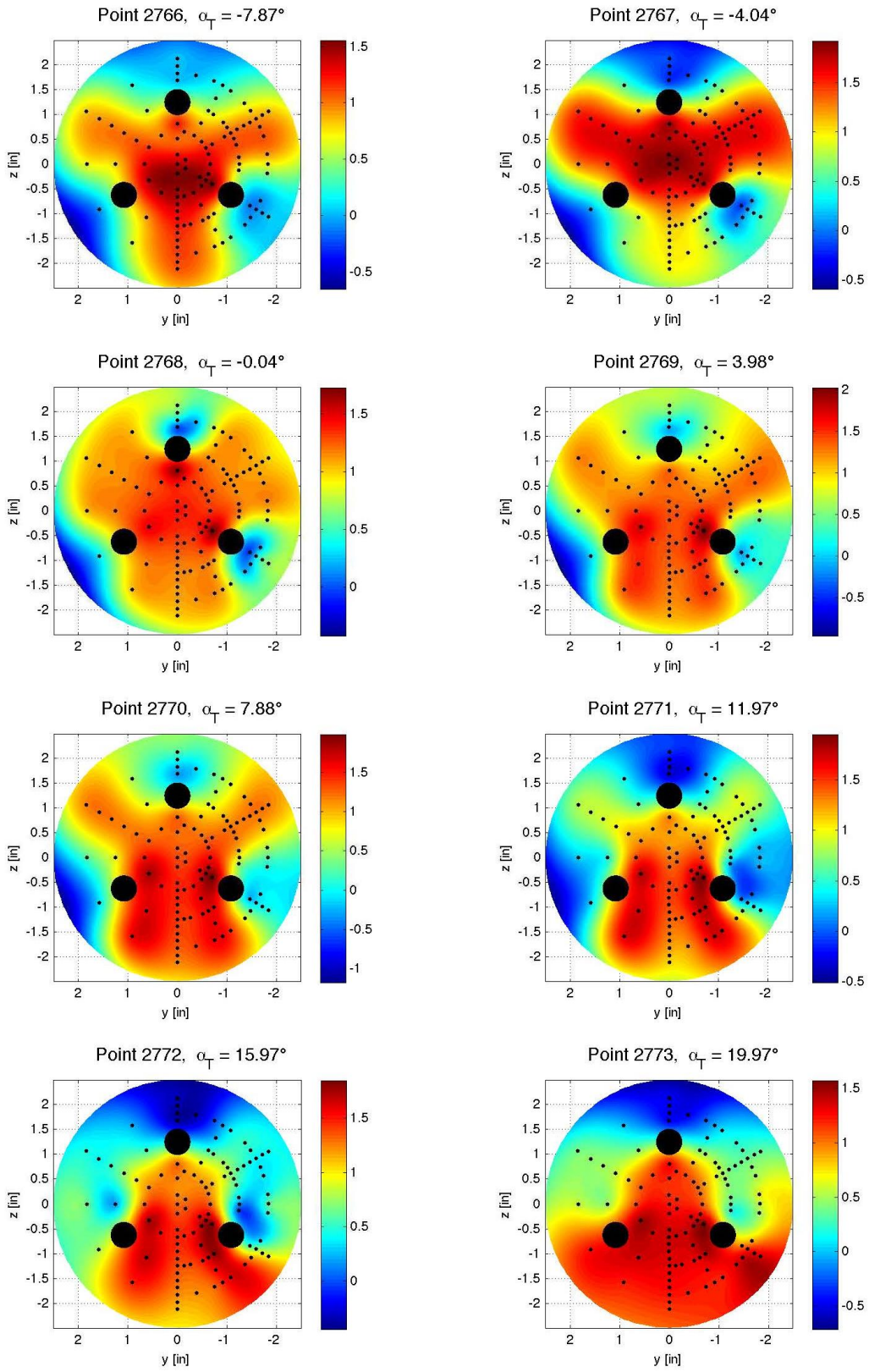

Figure E-163. Tri-nozzle configuration, Run 206, M_∞ = 2.4, Re_∞ = 1.0x10^6/ft, ϕ = −0.05°, X_S = 40.15 in, Y_S = 0.00 in, C_T = 0.43.

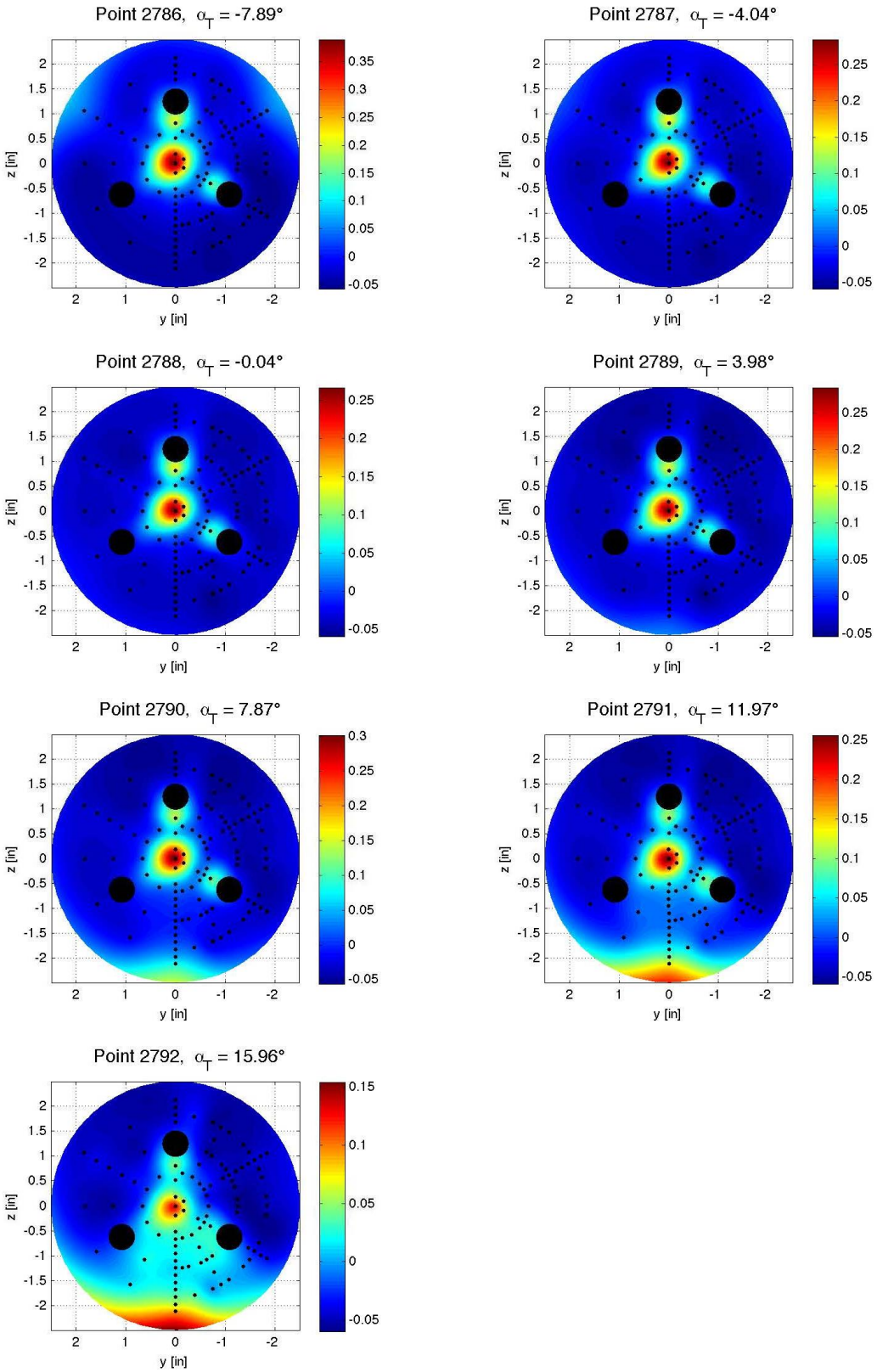

Figure E-164. Tri-nozzle configuration, Run 211, M_∞ = 4.6, Re_∞ = 1.5x10^6/ft, ϕ = −0.03°, X_S = 40.15 in, Y_S = 0.00 in, C_T = 2.94.

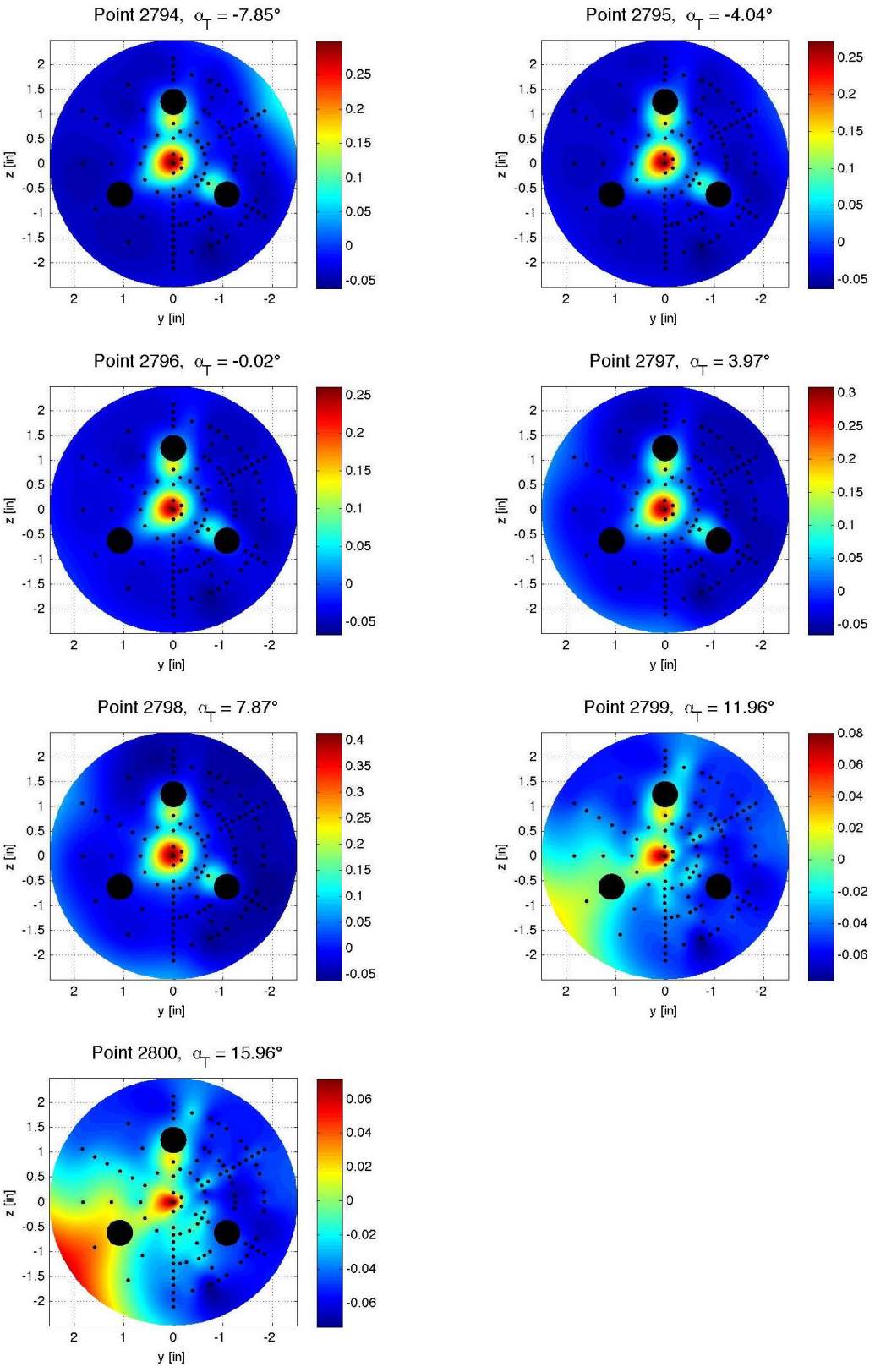

Figure E-165. Tri-nozzle configuration, Run 212, M_∞ = 4.6, Re_∞ = 1.5x10^6/ft, ϕ = 60.02°, X_S = 40.15 in, Y_S = 0.00 in, C_T = 2.93.

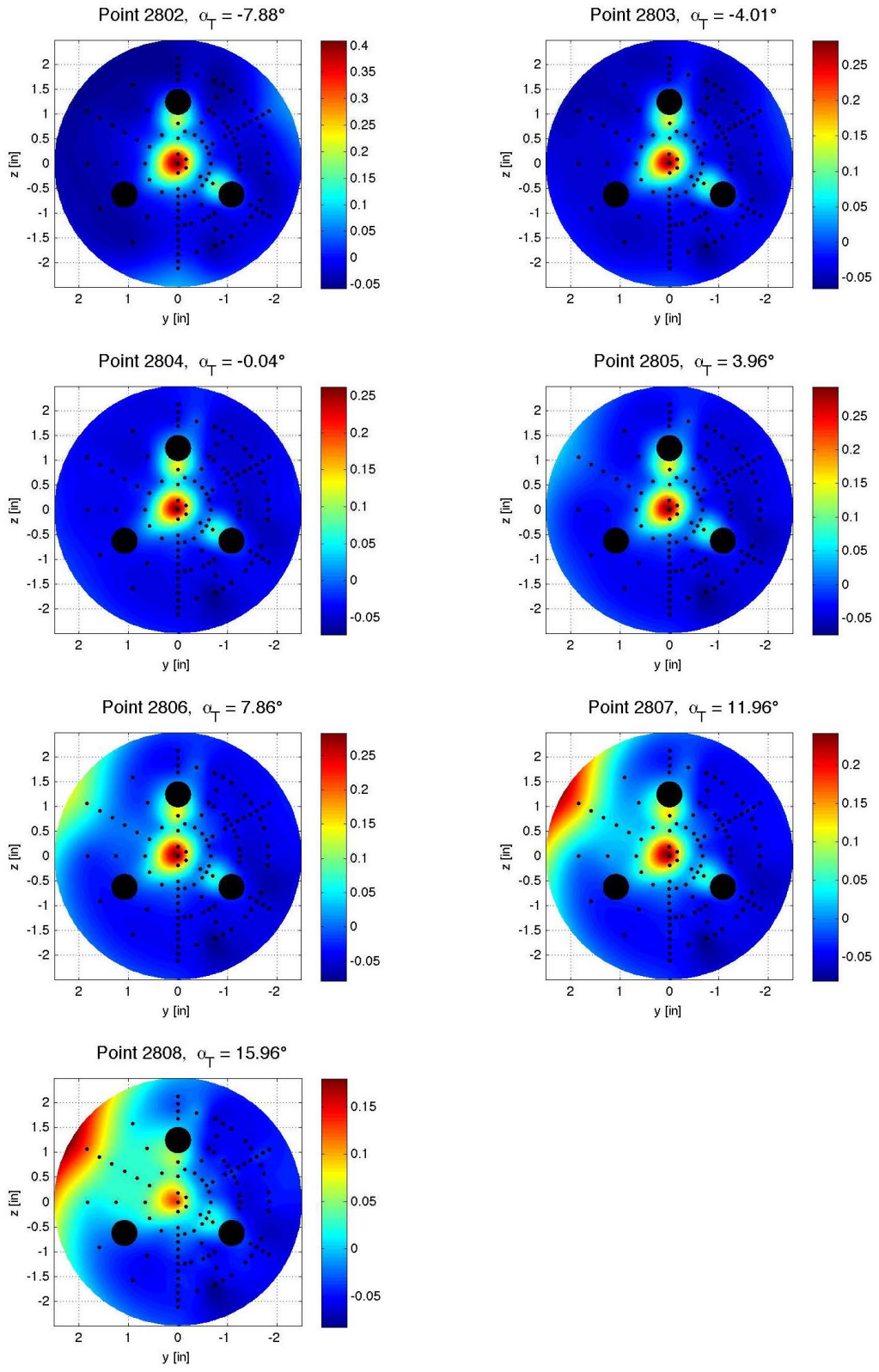

Figure E-166. Tri-nozzle configuration, Run 213, M_∞ = 4.6, Re_∞ = 1.5x10^6/ft, ϕ = 119.98°, X_S = 40.15 in, Y_S = 0.00 in, C_T = 2.95.

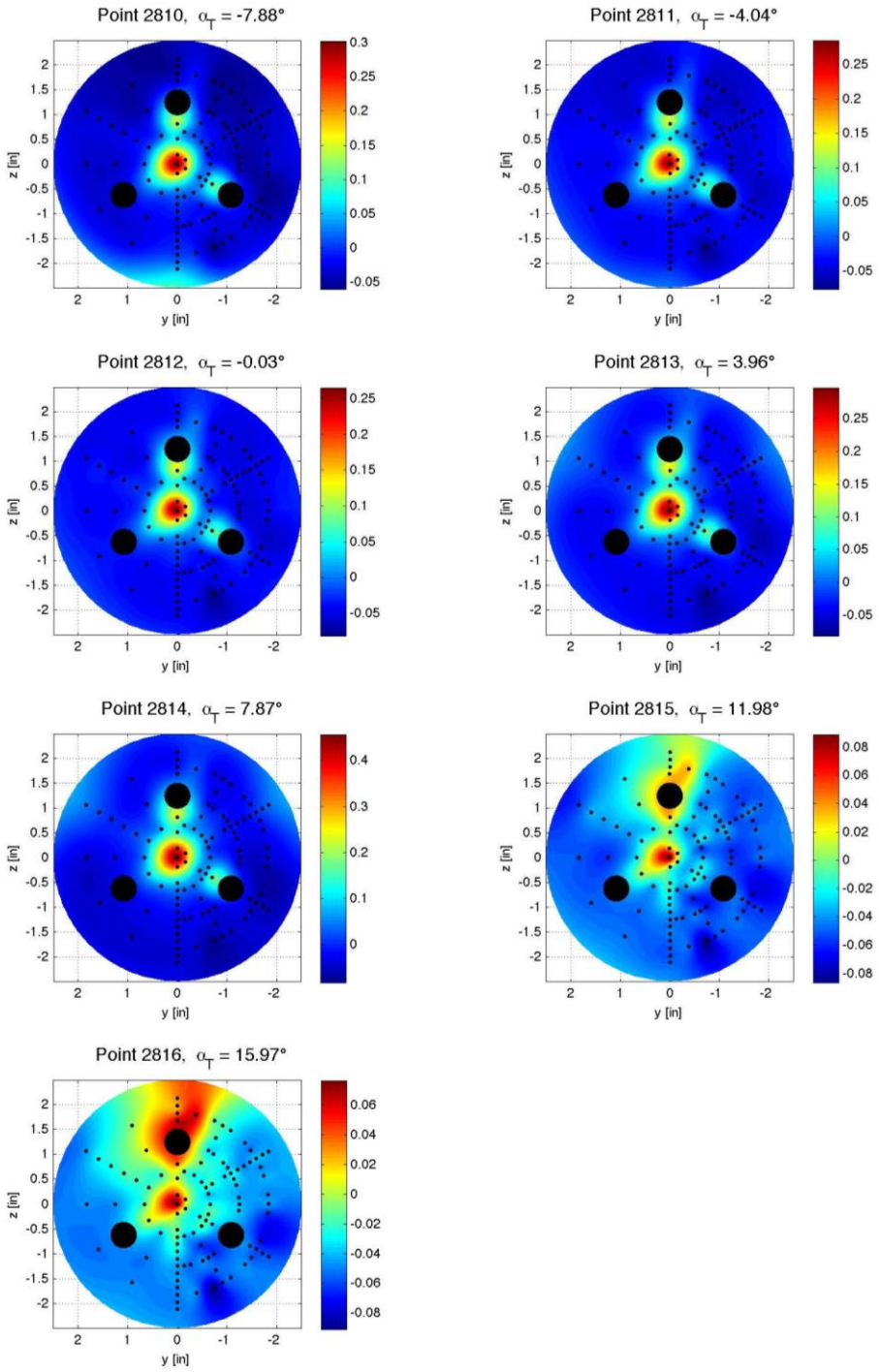

Figure E-167. Tri-nozzle configuration, Run 214, $M\infty$ = 4.6, Re_∞ = 1.5x10^6/ft, ϕ = 179.99°, X_S = 40.15 in, Y_S = 0.00 in, C_T = 2.95.

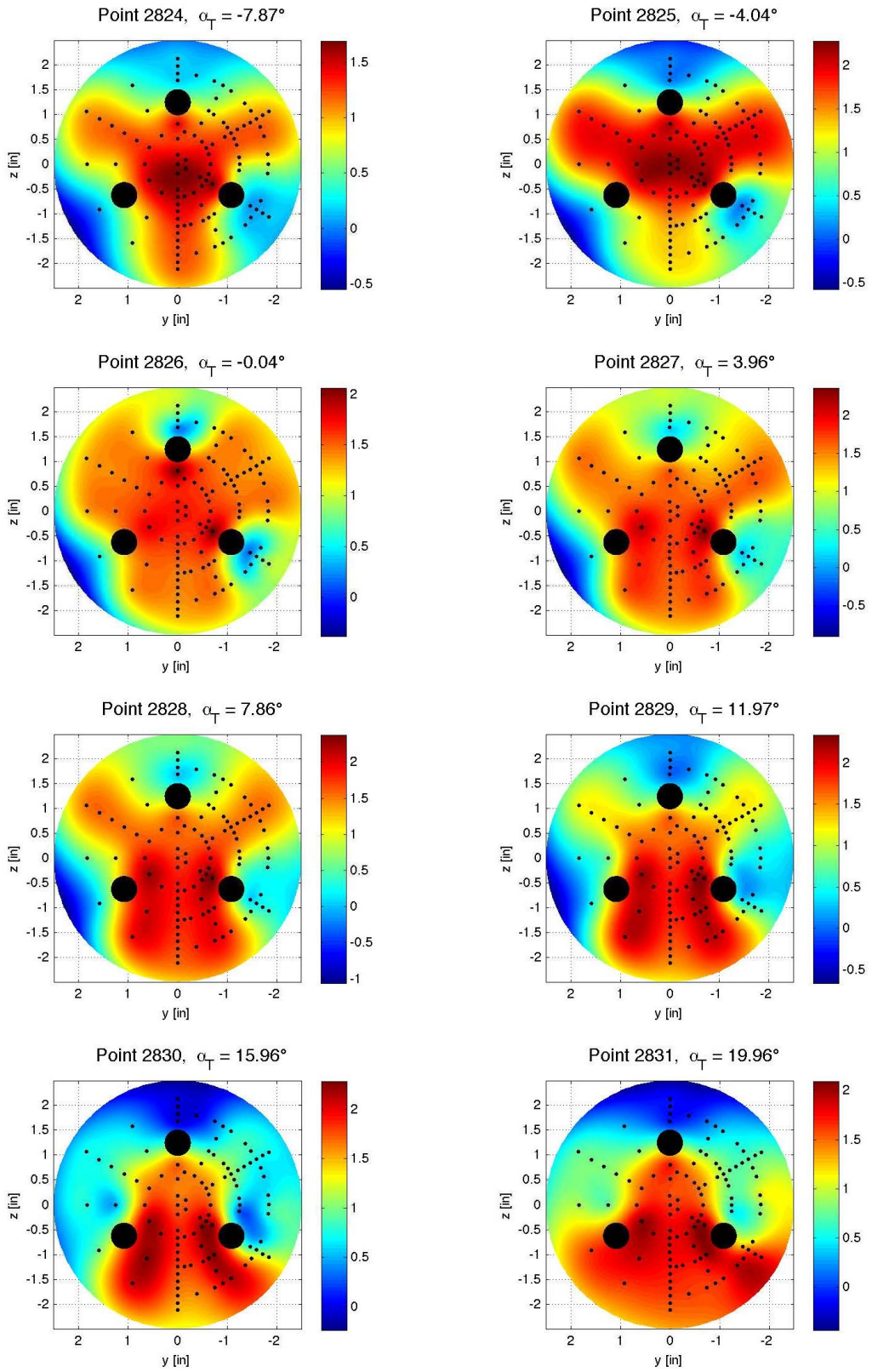

Figure E-168. Tri-nozzle configuration, Run 217, M_∞ = 2.4, Re_∞ = 1.0x10^6/ft, ϕ = −0.03°, X_S = 40.15 in, Y_S = 0.00 in, C_T = 0.48.

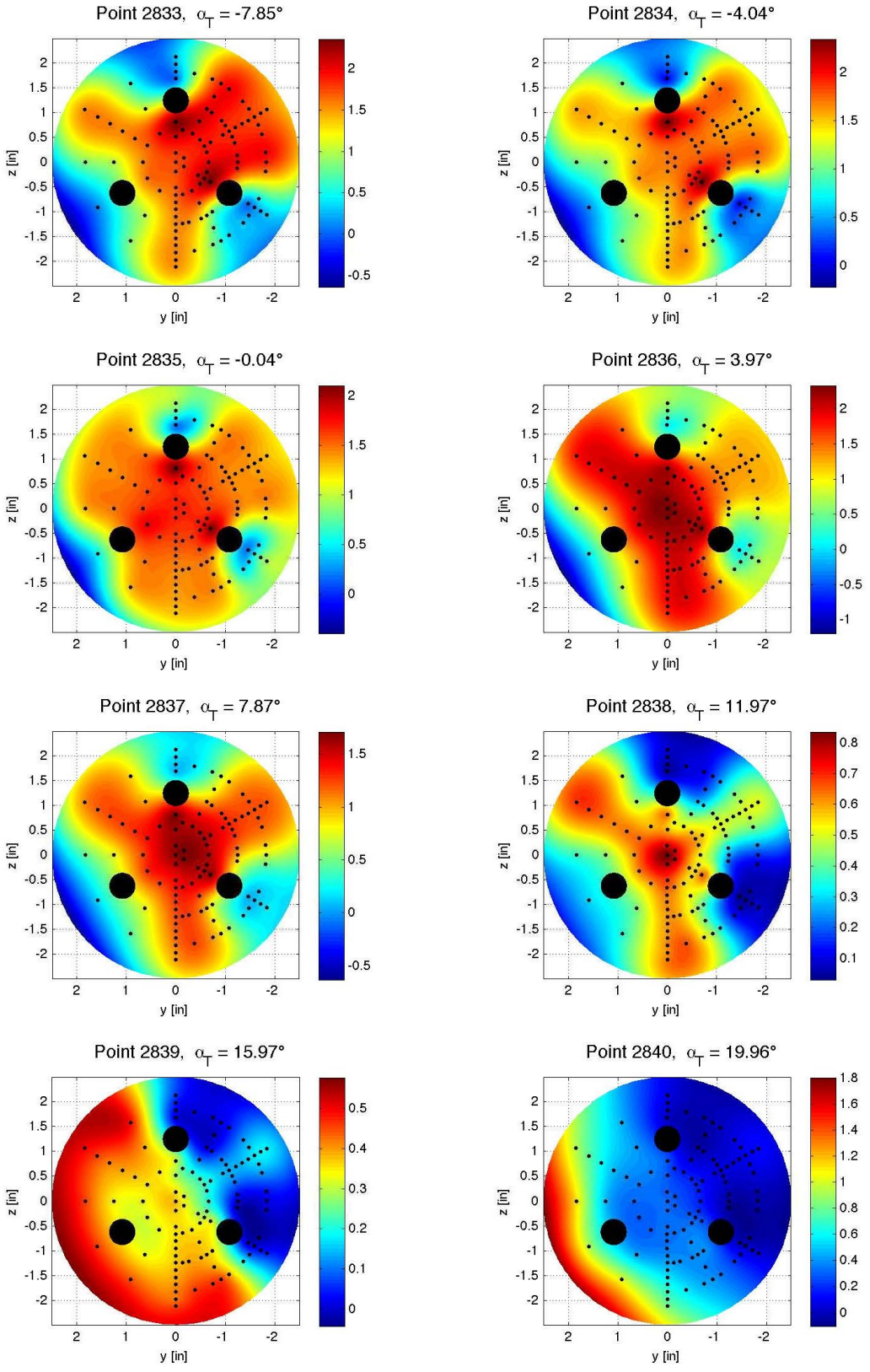

Figure E-169. Tri-nozzle configuration, Run 218, M_∞ = 2.4, Re_∞ = 1.0x10^6/ft, ϕ = 59.94°, X_S = 40.15 in, Y_S = 0.00 in, C_T = 0.48.

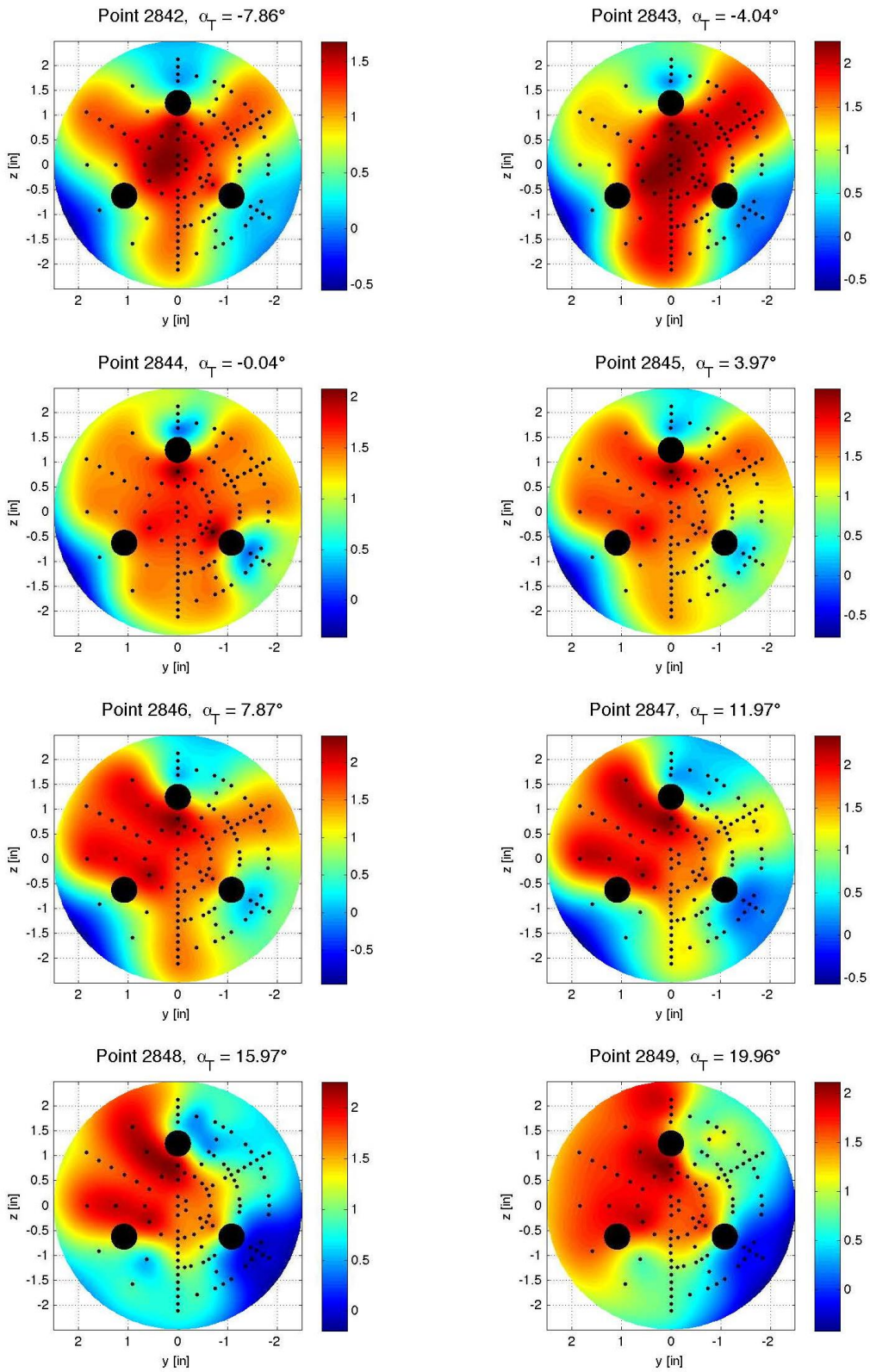

Figure E-170. Tri-nozzle configuration, Run 219, M_∞ = 2.4, Re_∞ = 1.0x10^6/ft, ϕ = 119.96°, X_S = 40.15 in, Y_S = 0.00 in, C_T = 0.48.

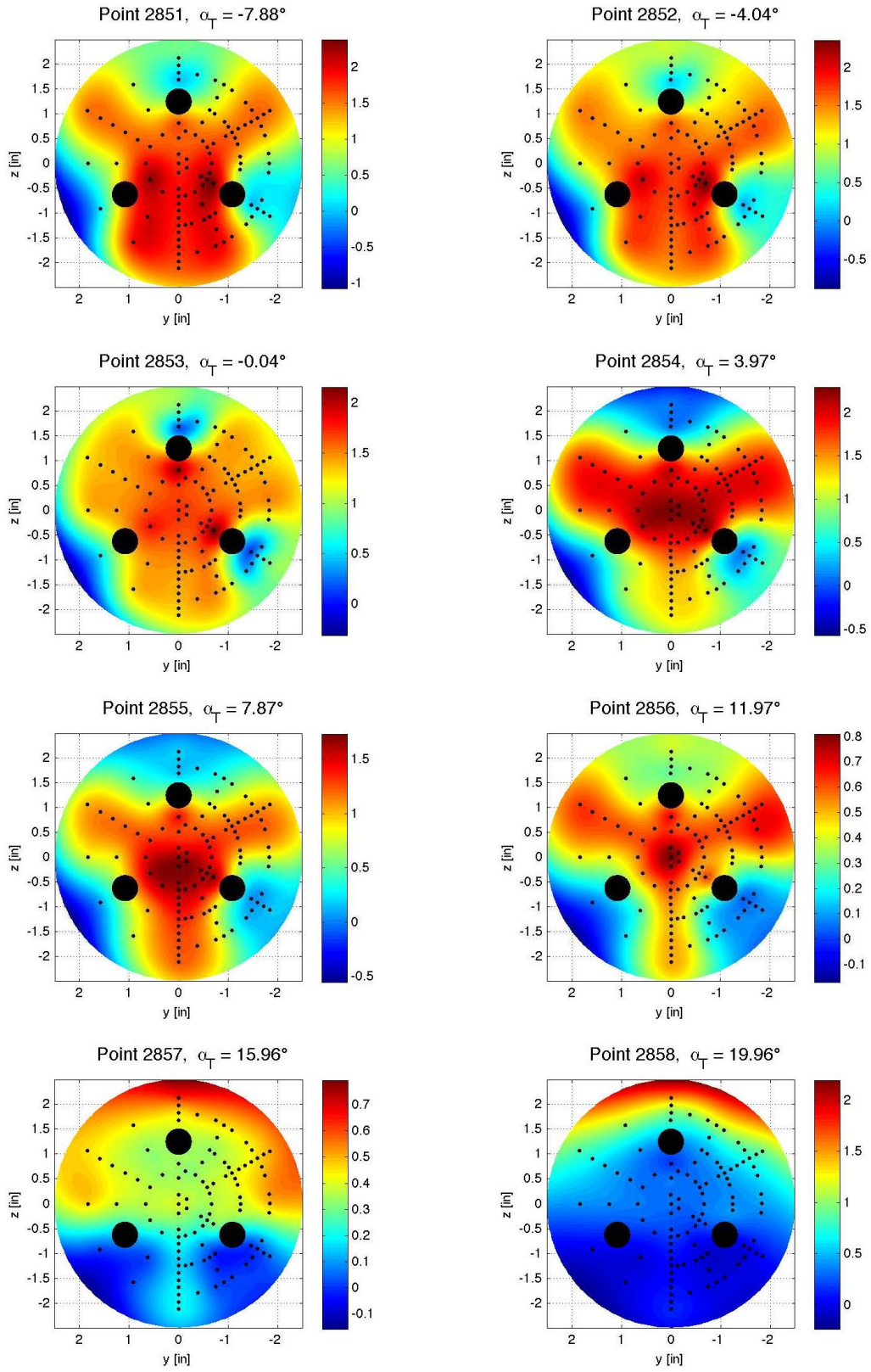

Figure E-171. Tri-nozzle configuration, Run 220, M_∞ = 2.4, Re_∞ = 1.0x10^6/ft, ϕ = 179.95°, X_S = 40.15 in, Y_S = 0.00 in, C_T = 0.48.

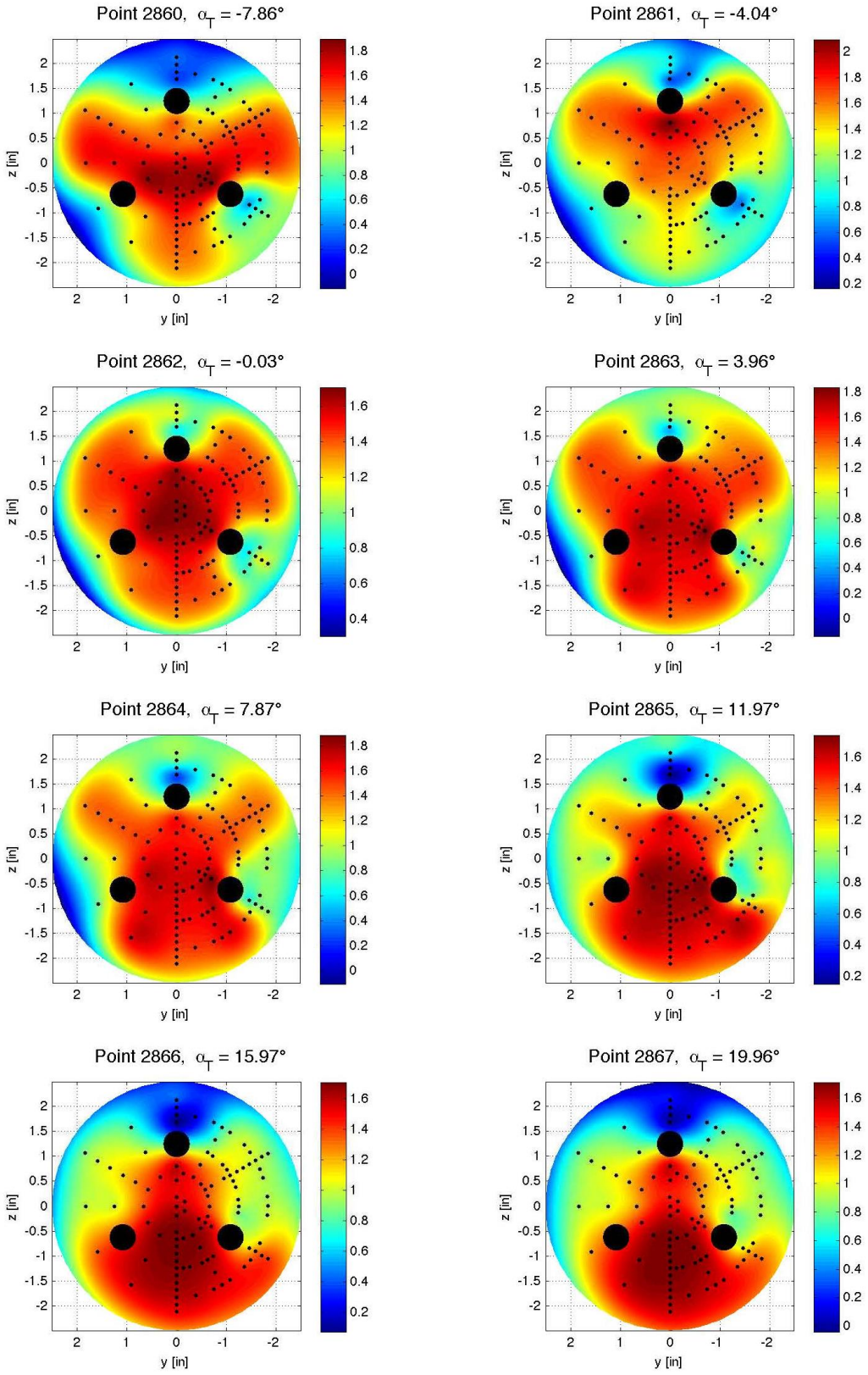

Figure E-172. Tri-nozzle configuration, Run 221, M_∞ = 2.4, Re_∞ = 1.0x10^6/ft, ϕ = −0.01°, X_S = 40.15 in, Y_S = 0.00 in, C_T = 0.23.

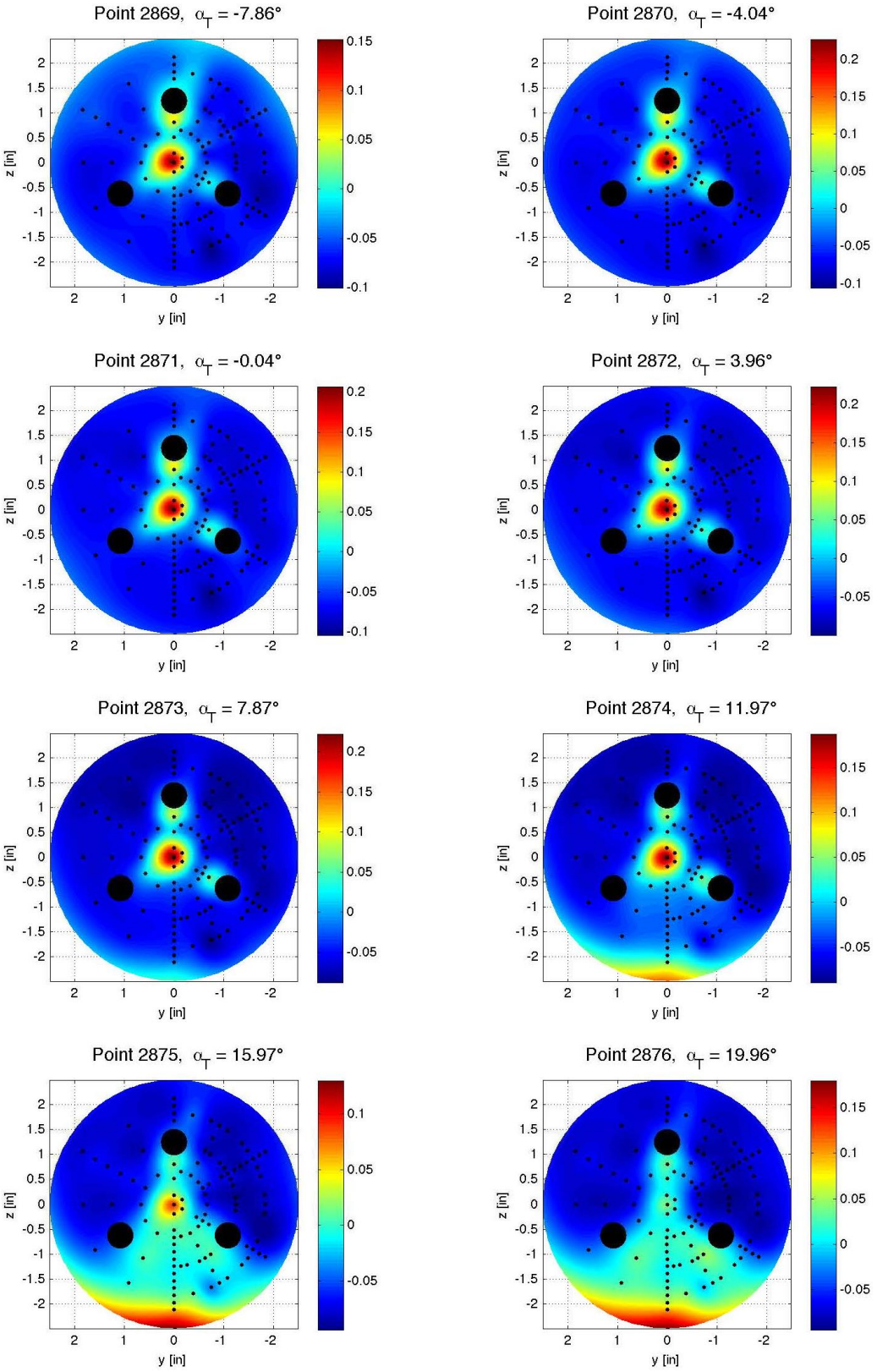

Figure E-173. Tri-nozzle configuration, Run 222, M_∞ = 3.5, Re_∞ = 1.0x10^6/ft, ϕ = −0.01°, X_S = 40.15 in, Y_S = 0.00 in, C_T = 2.95.

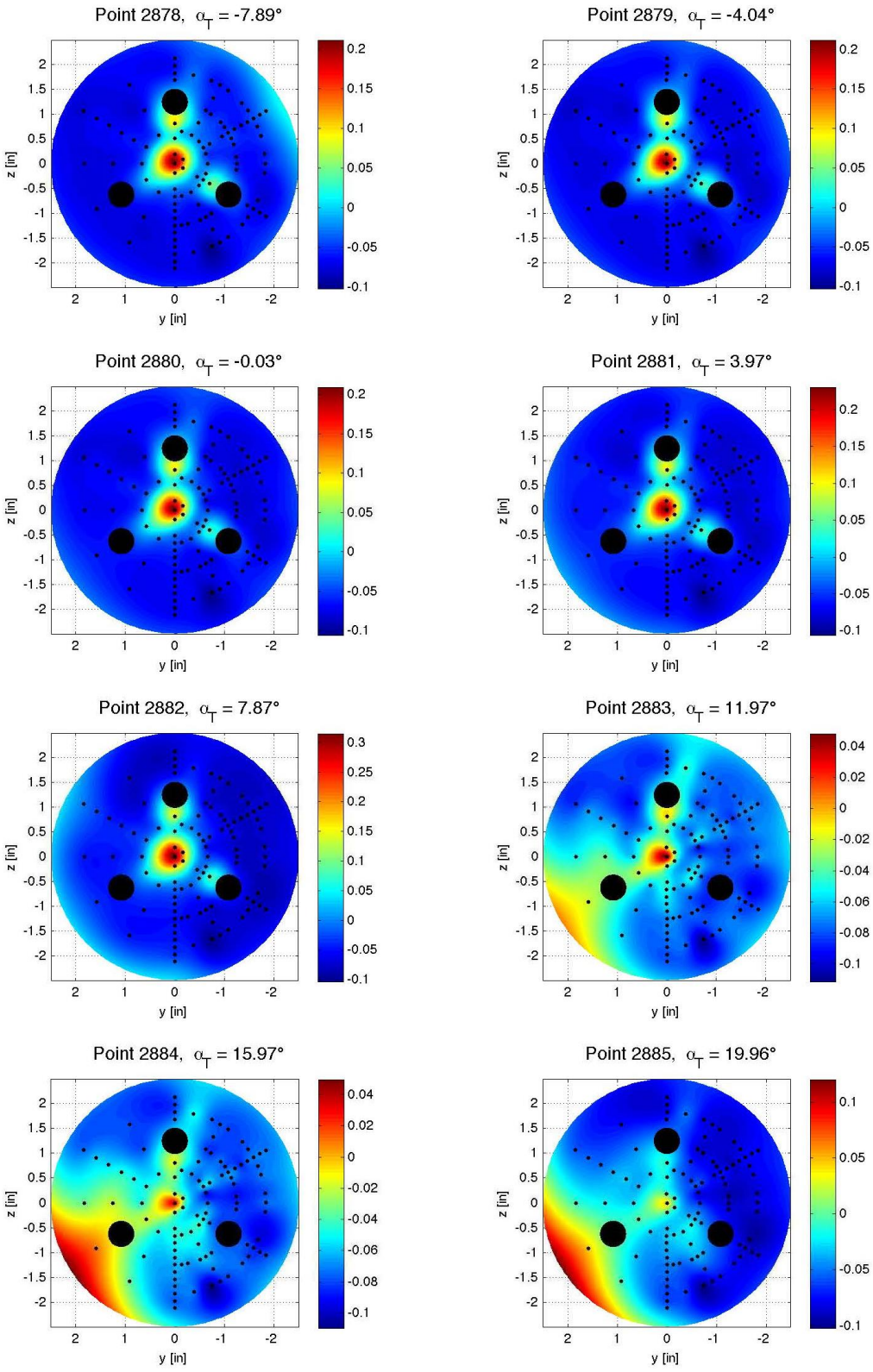

Figure E-174. Tri-nozzle configuration, Run 223, M_∞ = 3.5, Re_∞ = 1.0x10^6/ft, ϕ = 59.96°, X_S = 40.15 in, Y_S = 0.00 in, C_T = 2.94.

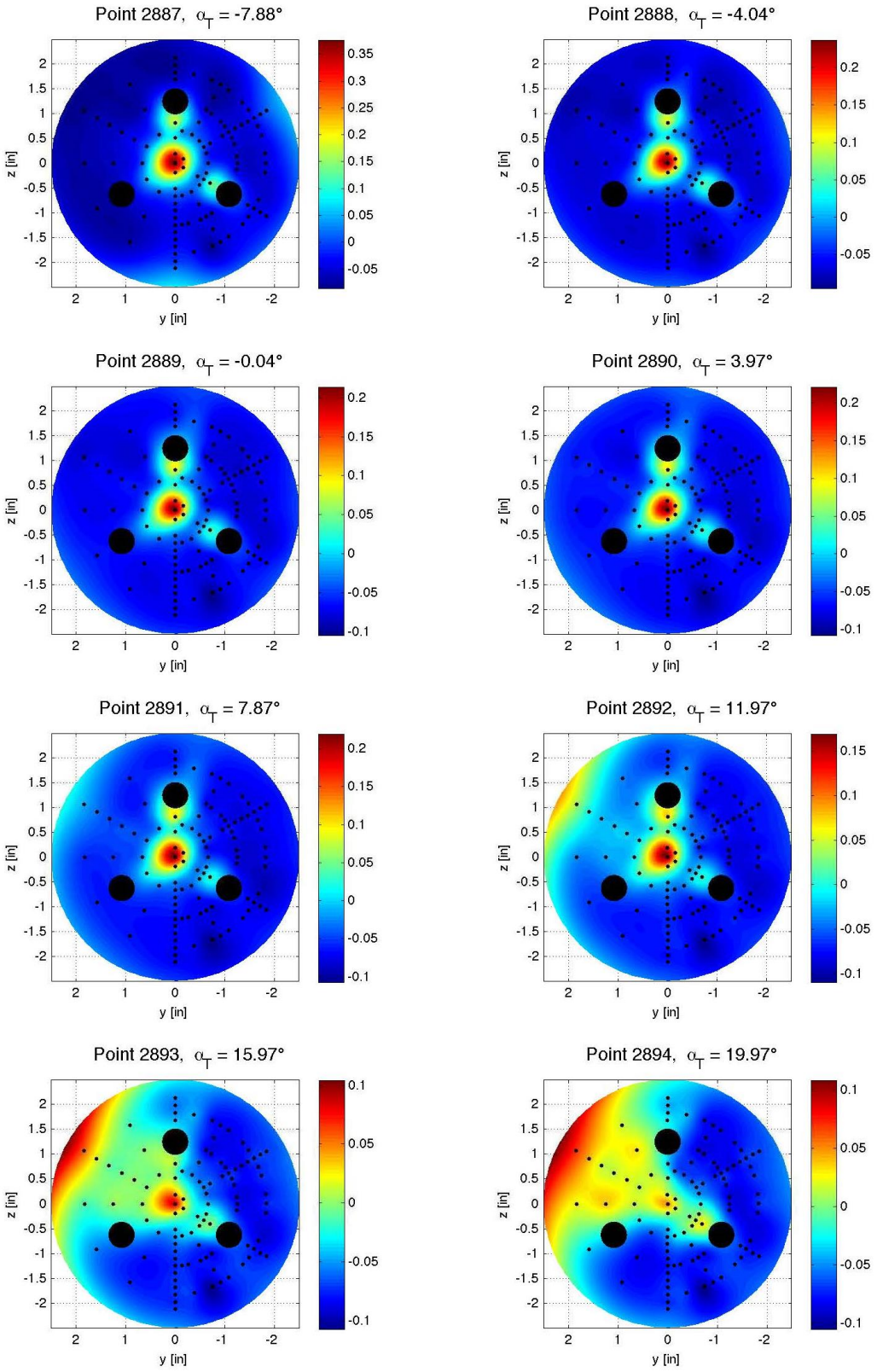

Figure E-175. Tri-nozzle configuration, Run 224, M_∞ = 3.5, Re_∞ = 1.0x10^6/ft, ϕ = 120.00°, X_S = 40.15 in, Y_S = 0.00 in, C_T = 3.00.

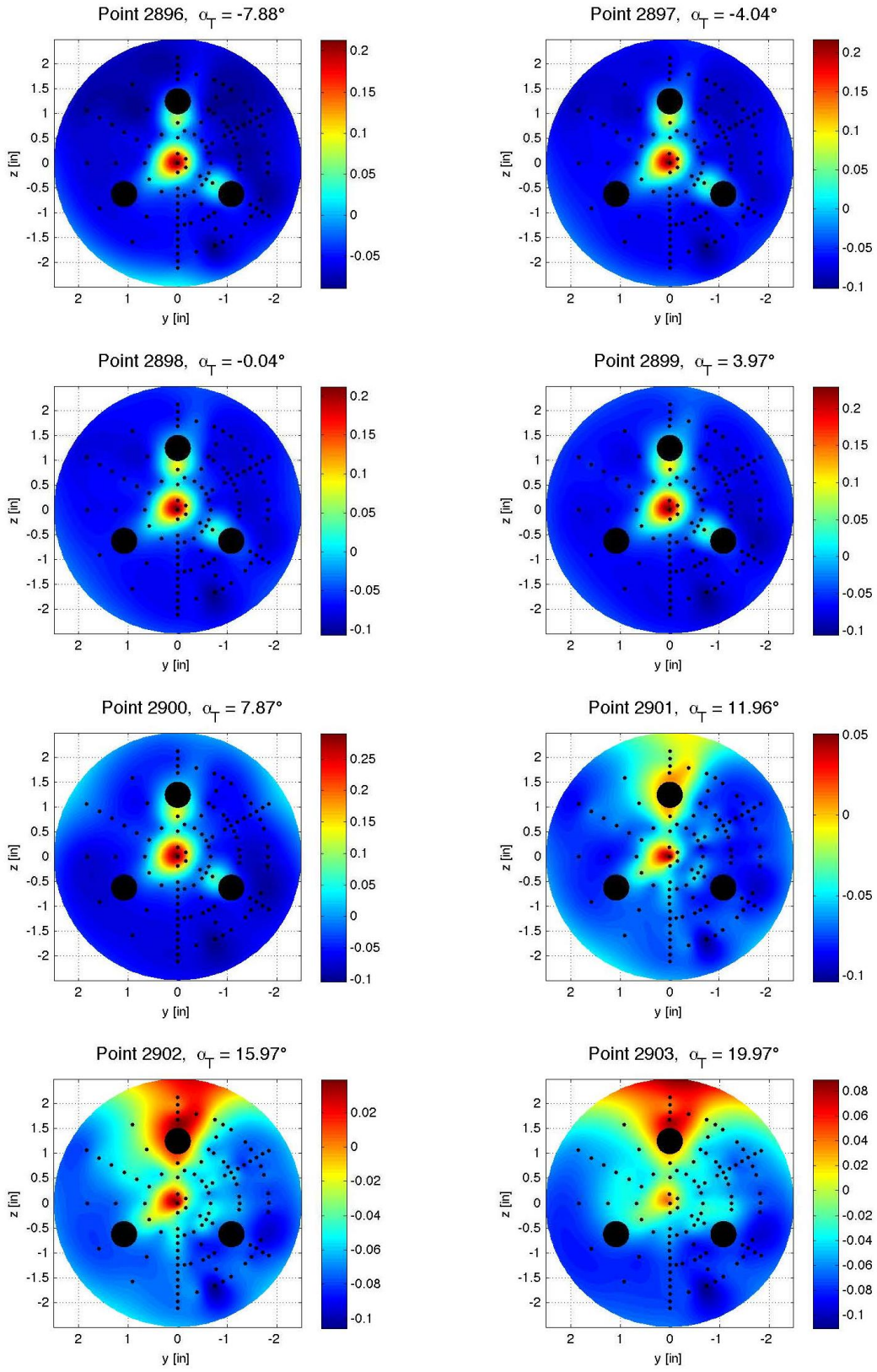

Figure E-176. Tri-nozzle configuration, Run 225, M_∞ = 3.5, Re_∞ = 1.0x10^6/ft, ϕ = 179.97°, X_S = 40.15 in, Y_S = 0.00 in, C_T = 2.98.

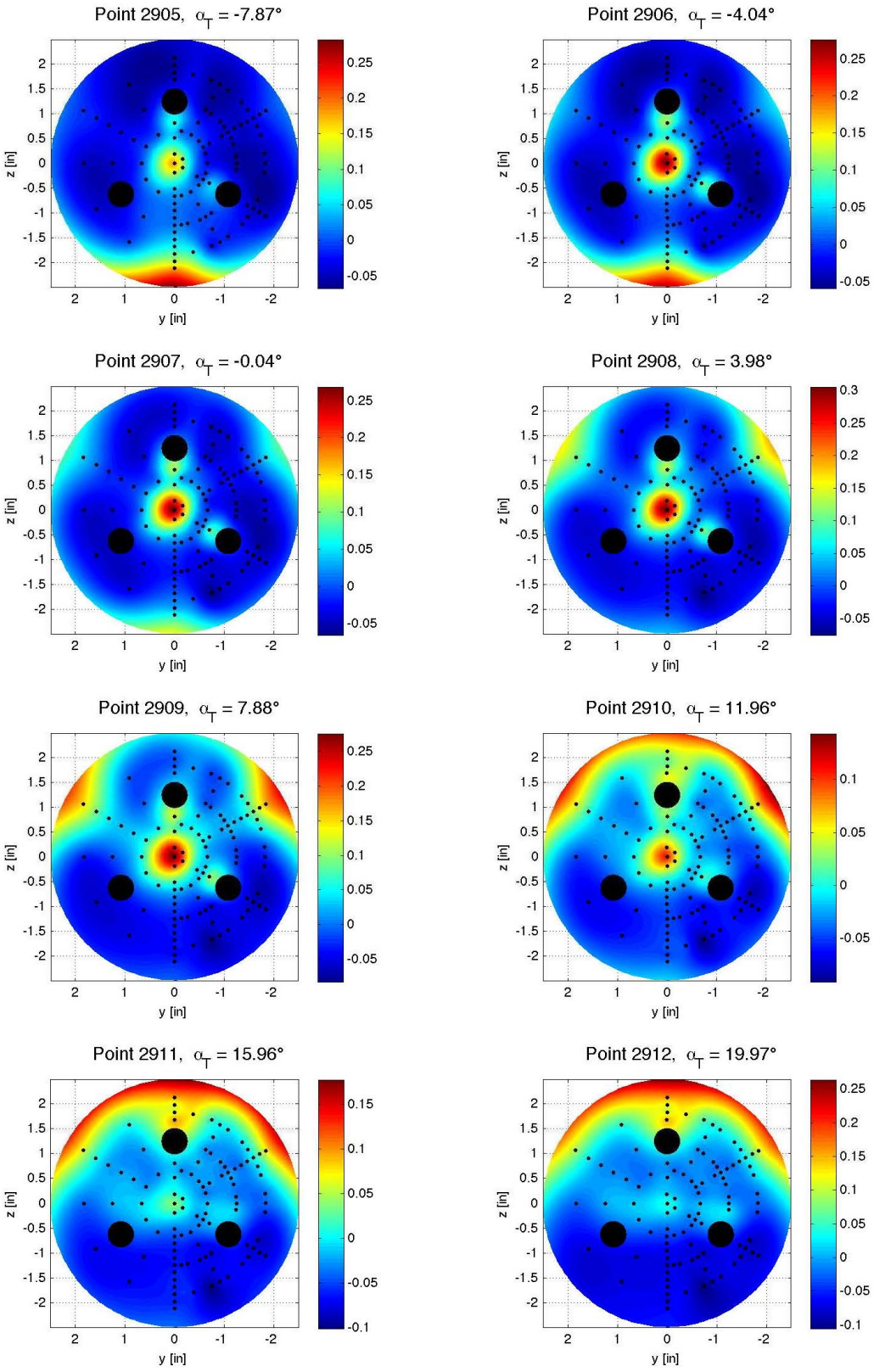

Figure E-177. Tri-nozzle configuration, Run 226, M_∞ = 3.5, Re_∞ = 1.0x10^6/ft, ϕ = 179.97°, X_S = 40.15 in, Y_S = 0.00 in, C_T = 1.96.

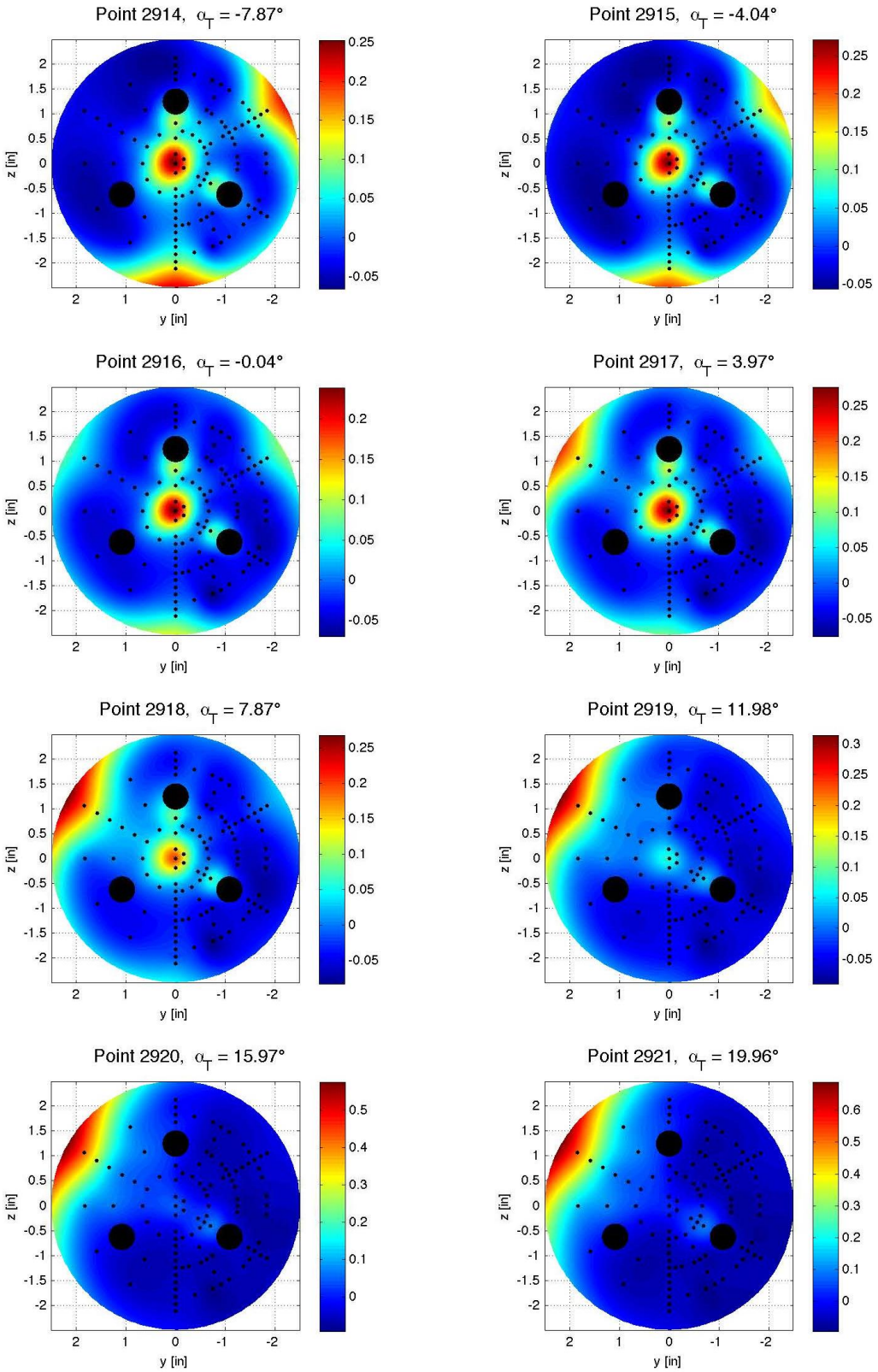

Figure E-178. Tri-nozzle configuration, Run 227, M_∞ = 3.5, Re_∞ = 1.0x10^6/ft, ϕ = 119.98°, X_S = 40.15 in, Y_S = 0.00 in, C_T = 1.94.

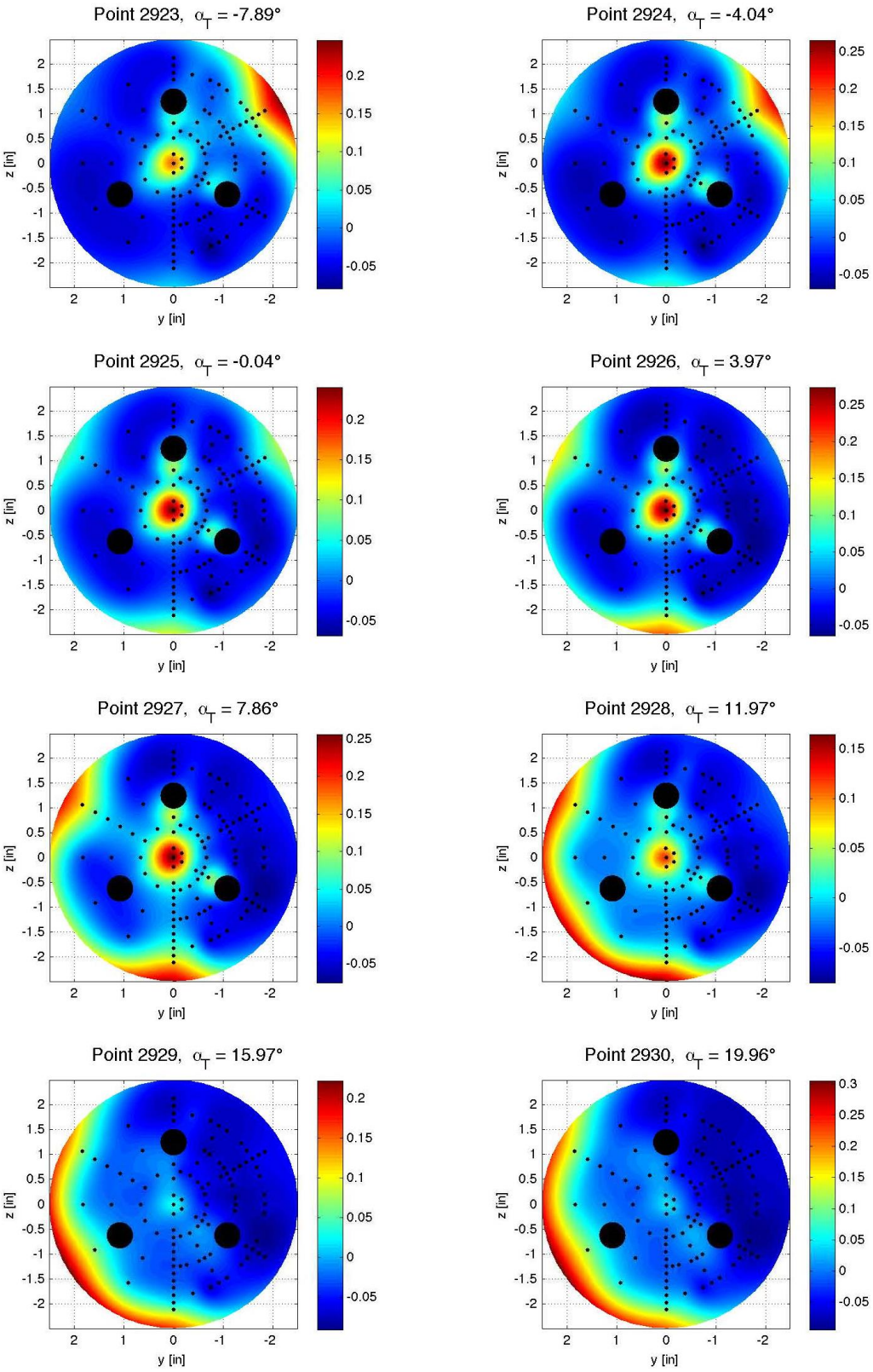

Figure E-179. Tri-nozzle configuration, Run 228, M_∞ = 3.5, Re_∞ = 1.0x10^6/ft, ϕ = 60.02°, X_S = 40.15 in, Y_S = 0.00 in, C_T = 1.94.

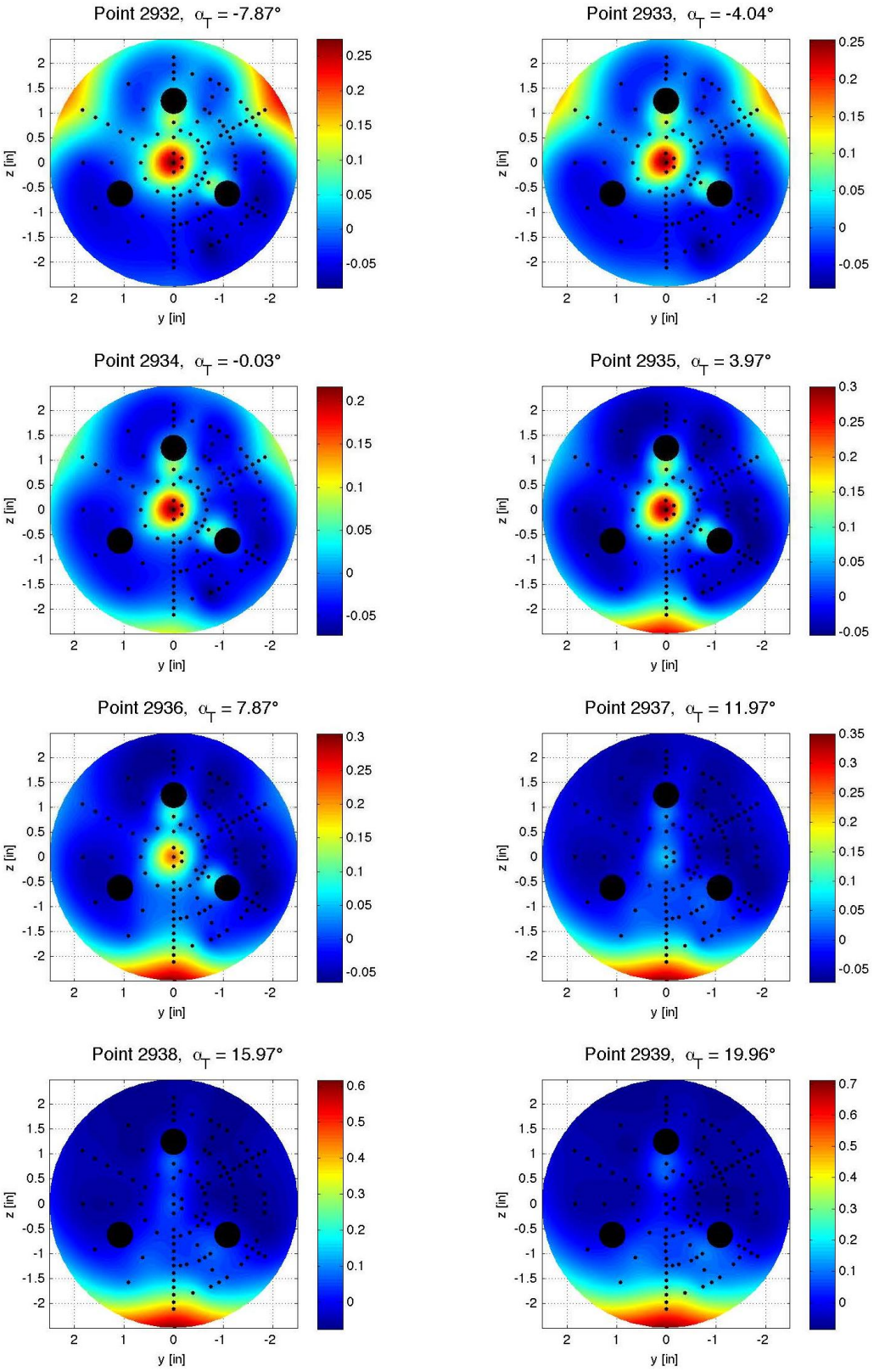

Figure E-180. Tri-nozzle configuration, Run 229, M_∞ = 3.5, Re_∞ = 1.0x10^6/ft, ϕ = −0.03°, X_S = 40.15 in, Y_S = 0.00 in, C_T = 1.95.

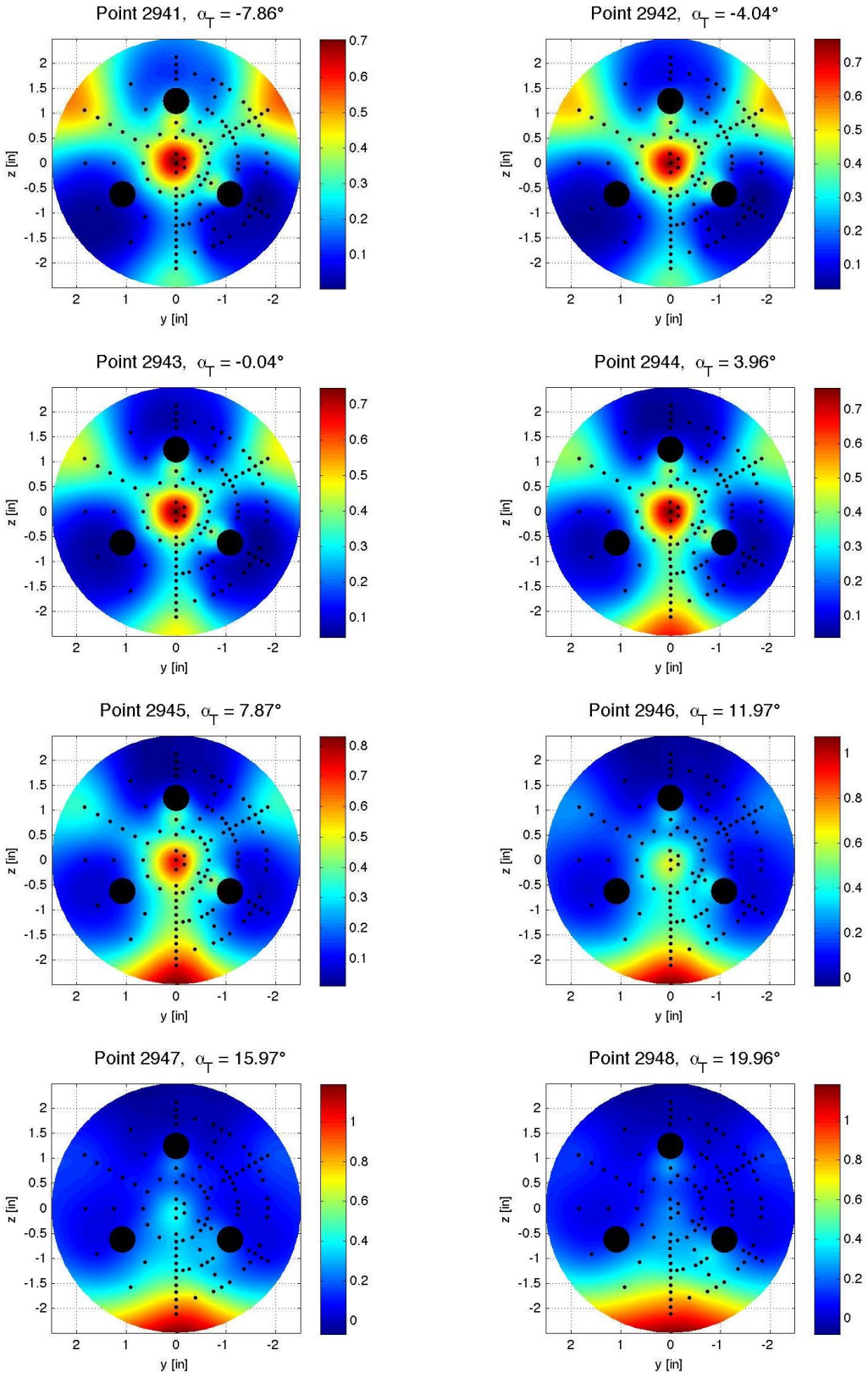

Figure E-181. Tri-nozzle configuration, Run 230, M_∞ = 3.5, Re_∞ = 1.0x10^6/ft, ϕ = −0.03°, X_S = 40.15 in, Y_S = 0.00 in, C_T = 0.97.

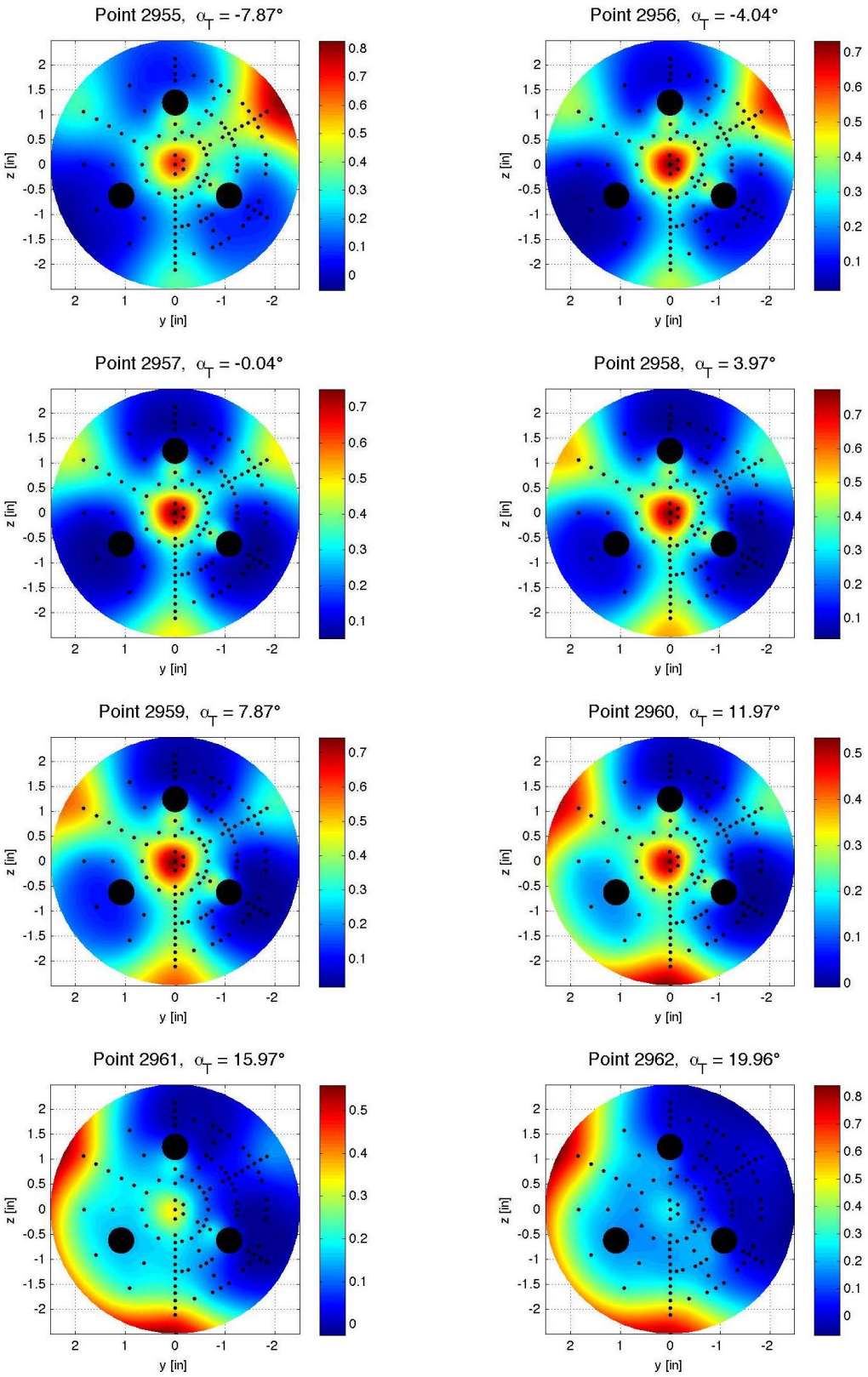

Figure E-182. Tri-nozzle configuration, Run 233, M_∞ = 3.5, Re_∞ = 1.0x10^6/ft, ϕ = 59.96°, X_S = 40.15 in, Y_S = 0.00 in, C_T = 0.96.

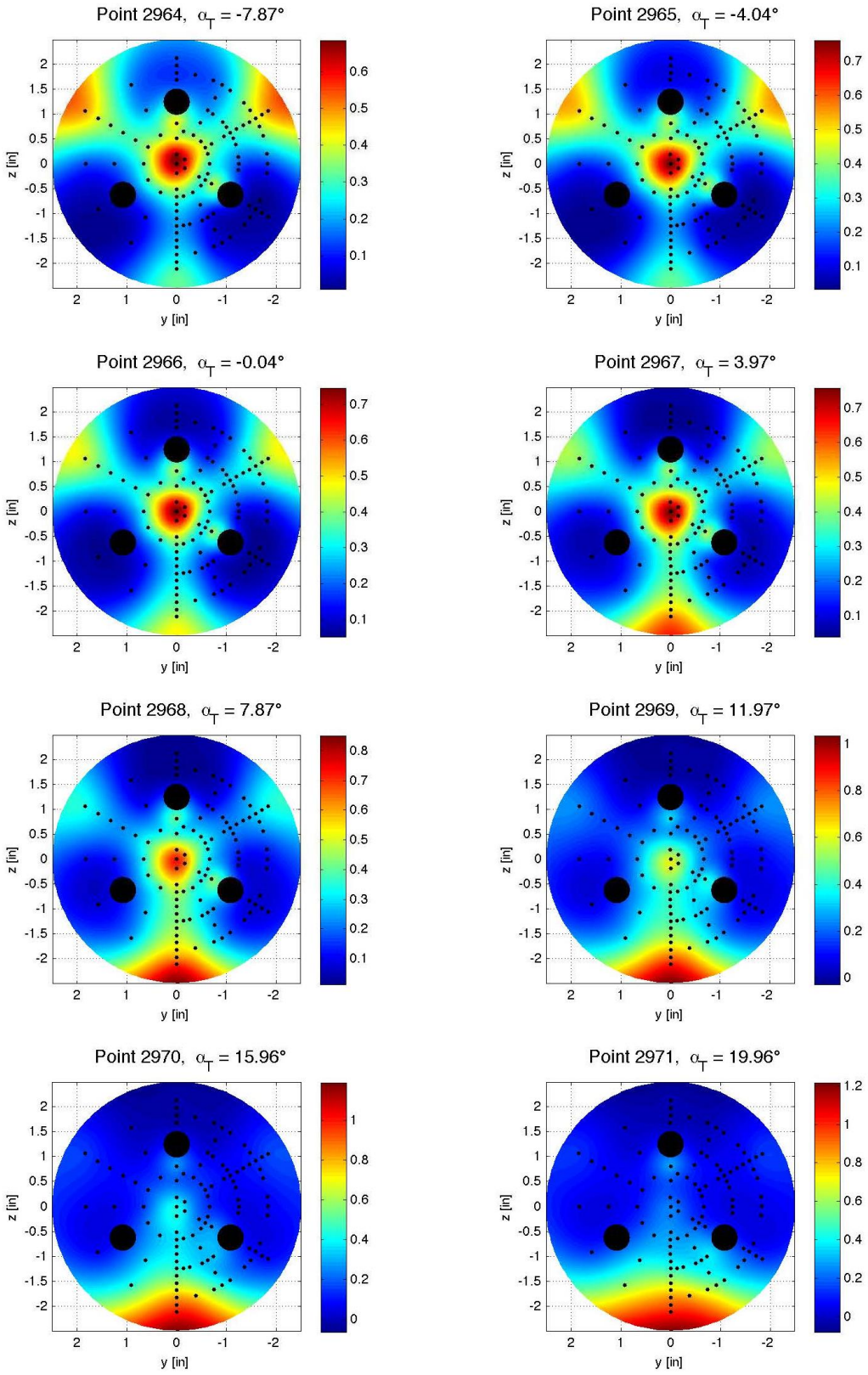

Figure E-183. Tri-nozzle configuration, Run 234, M_∞ = 3.5, Re_∞ = 1.0x10^6/ft, ϕ = −0.05°, X_S = 40.15 in, Y_S = 0.00 in, C_T = 0.97.

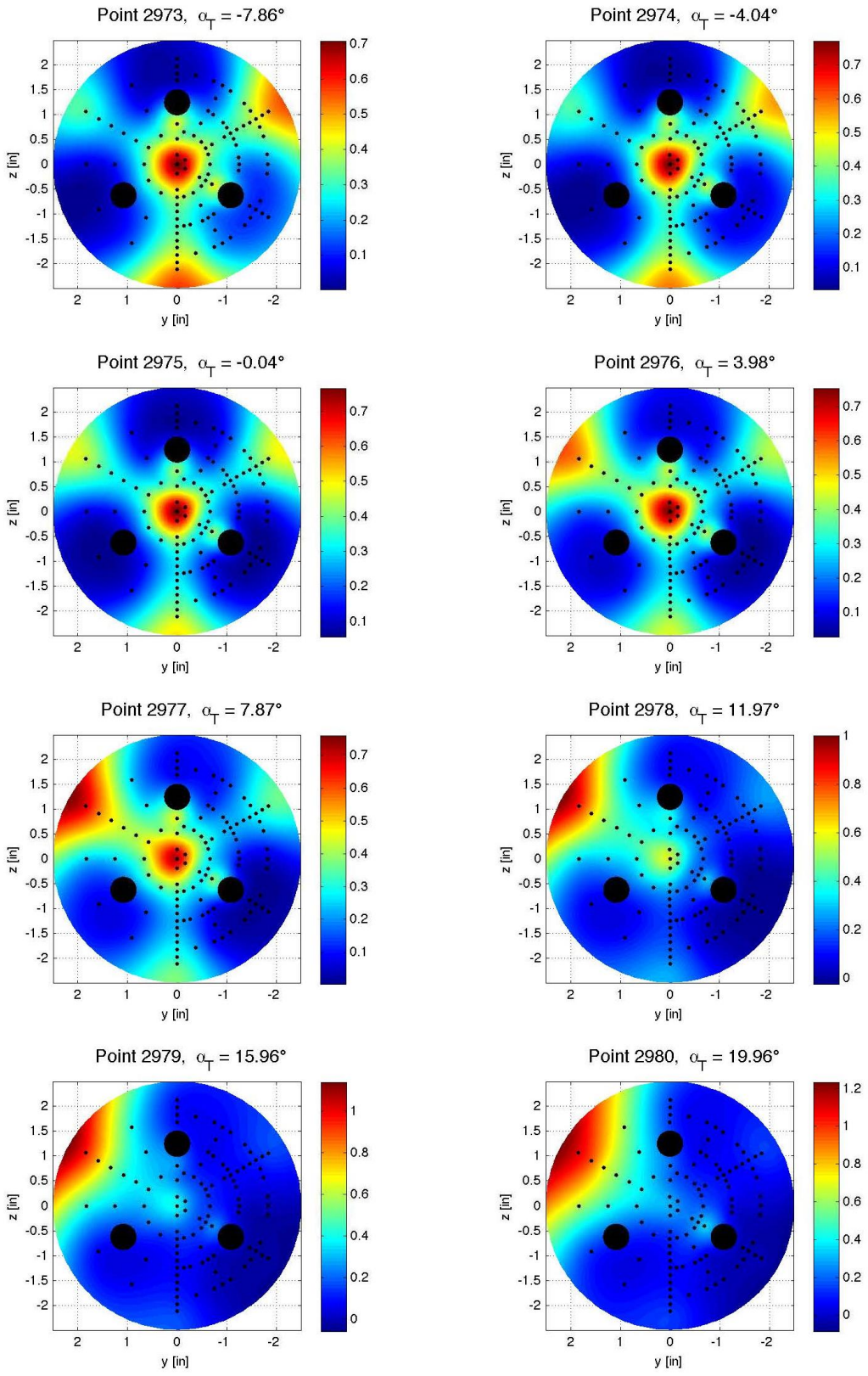

Figure E-184. Tri-nozzle configuration, Run 235, M_∞ = 3.5, Re_∞ = 1.0x10^6/ft, ϕ = 120.00°, X_S = 40.15 in, Y_S = 0.00 in, C_T = 0.96.

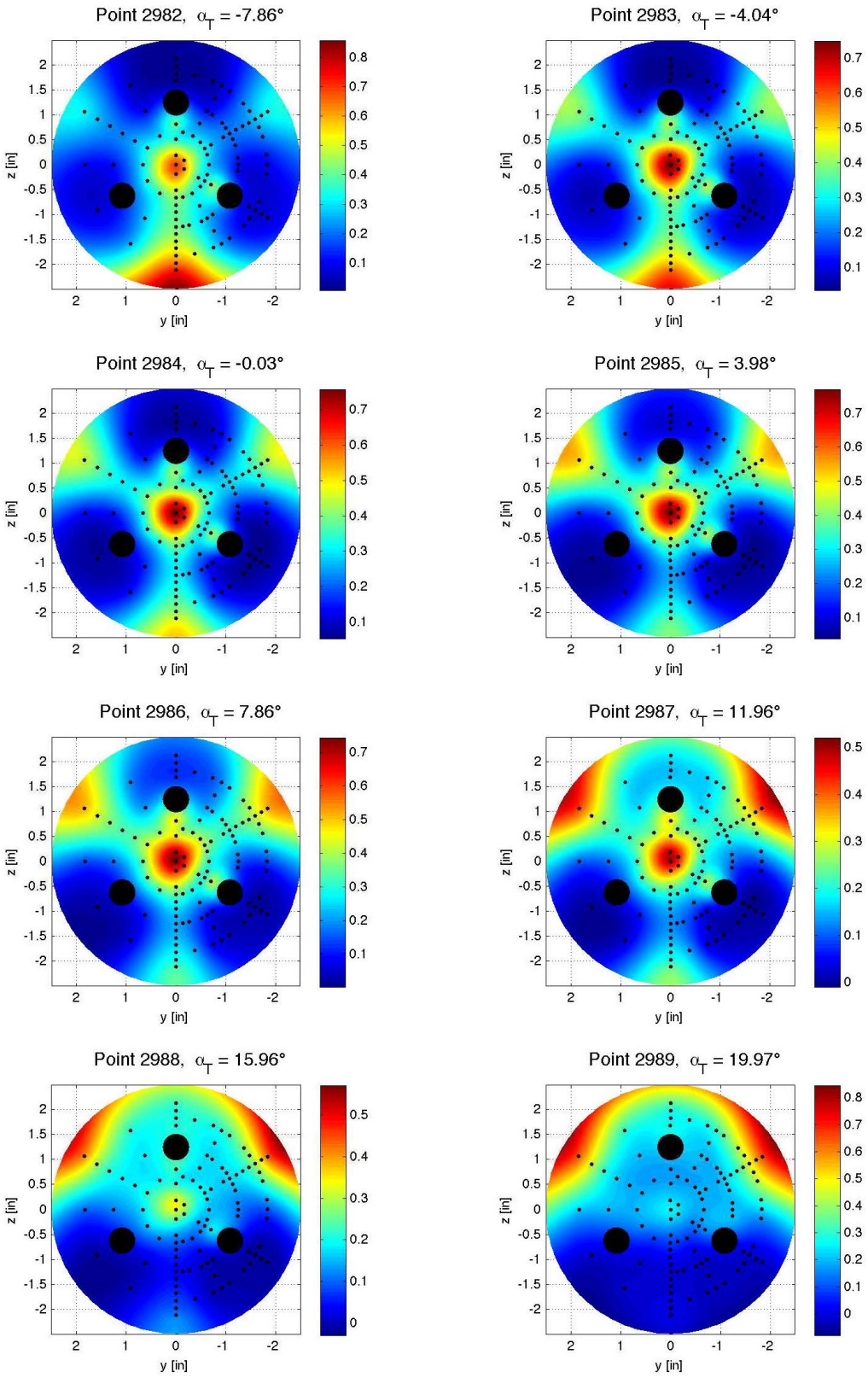

Figure E-185. Tri-nozzle configuration, Run 236, M_∞ = 3.5, Re_∞ = 1.0x10^6/ft, ϕ = 179.95°, X_S = 40.15 in, Y_S = 0.00 in, C_T = 0.96.

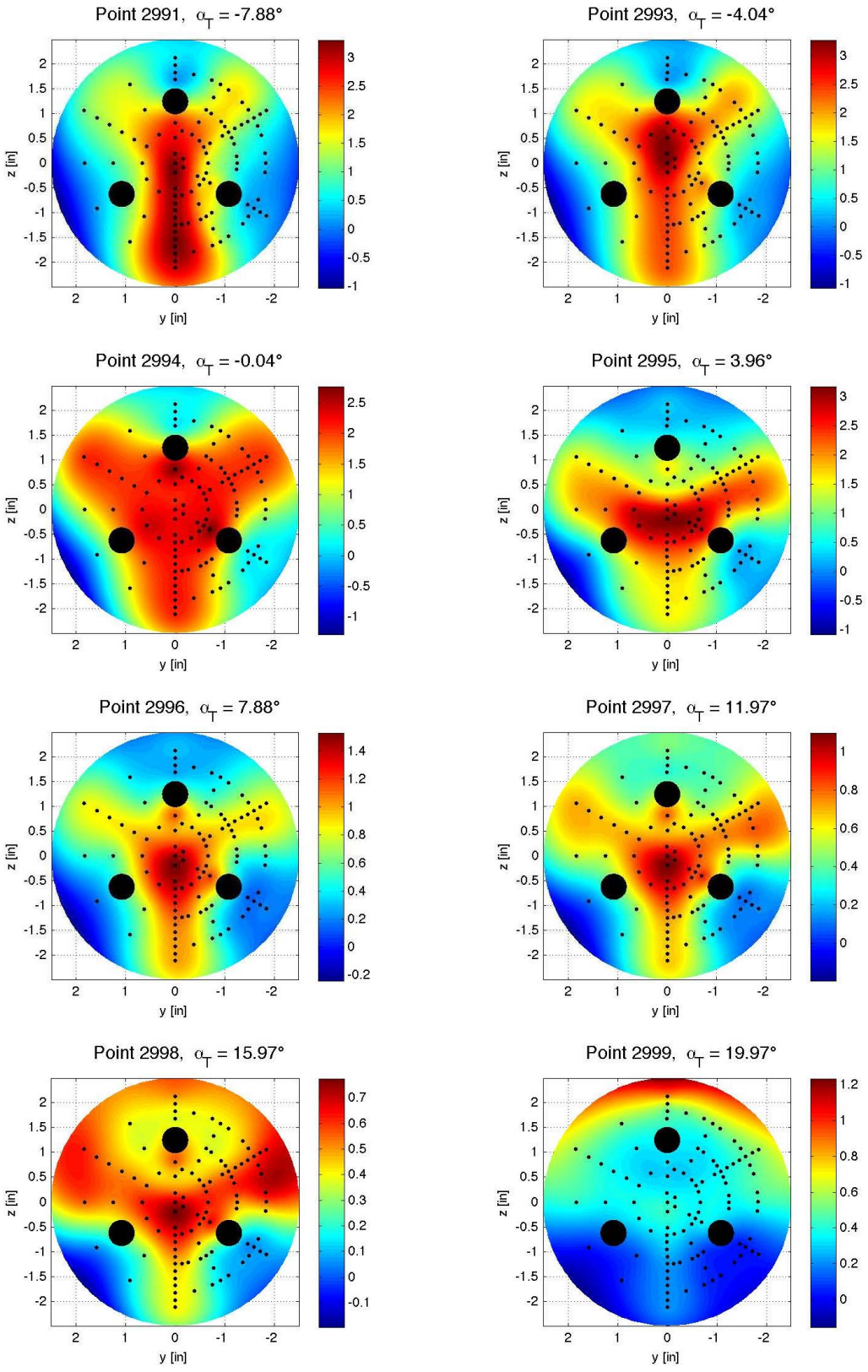

Figure E-186. Tri-nozzle configuration, Run 237, $M\infty$ = 3.5, Re_∞ = 1.0x10^6/ft, ϕ = 179.95°, X_S = 40.15 in, Y_S = 0.00 in, C_T = 0.47.

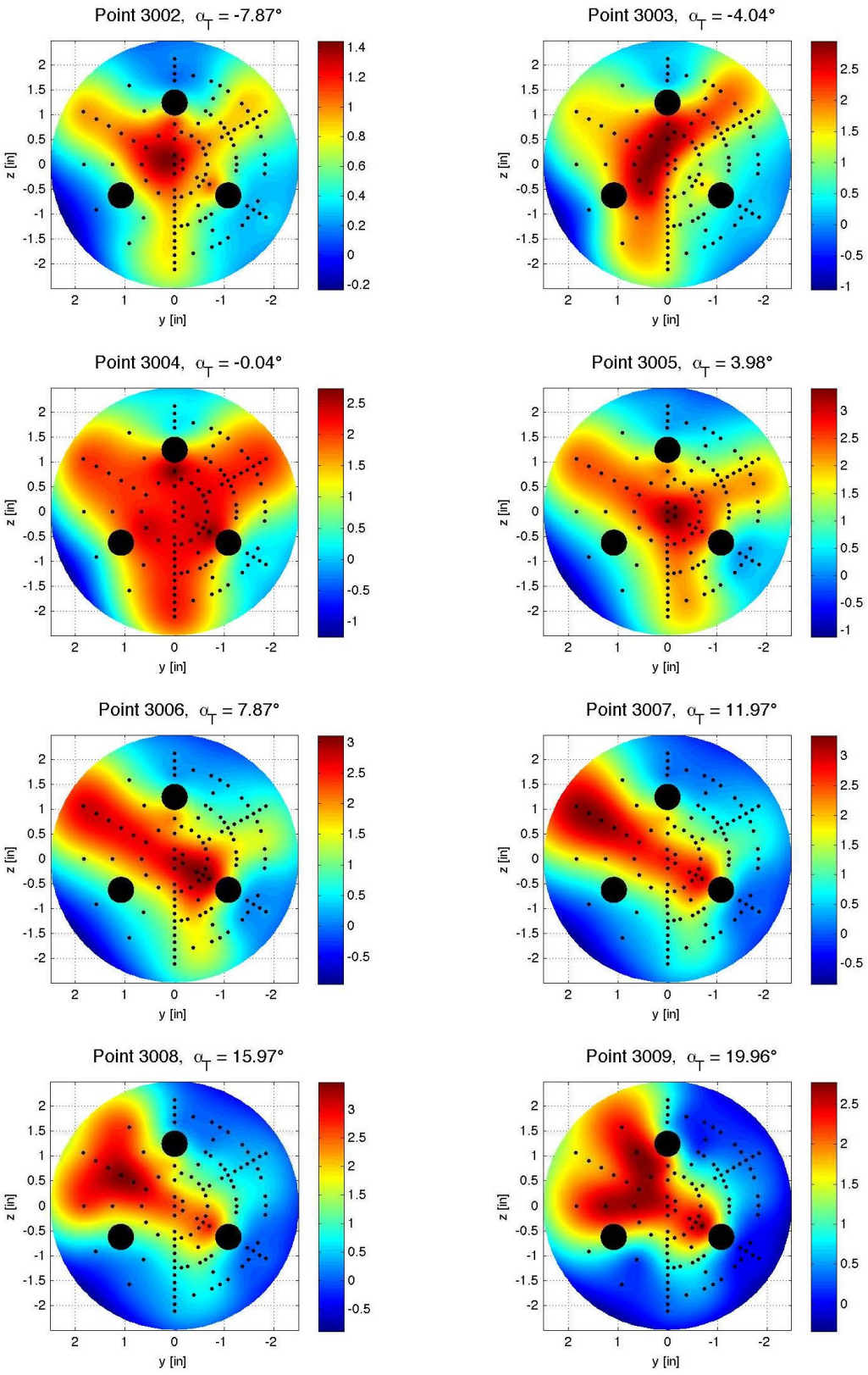

Figure E-187. Tri-nozzle configuration, Run 238, M_∞ = 3.5, Re_∞ = 1.0x10^6/ft, ϕ = 119.94°, X_S = 40.15 in, Y_S = 0.00 in, C_T = 0.47.

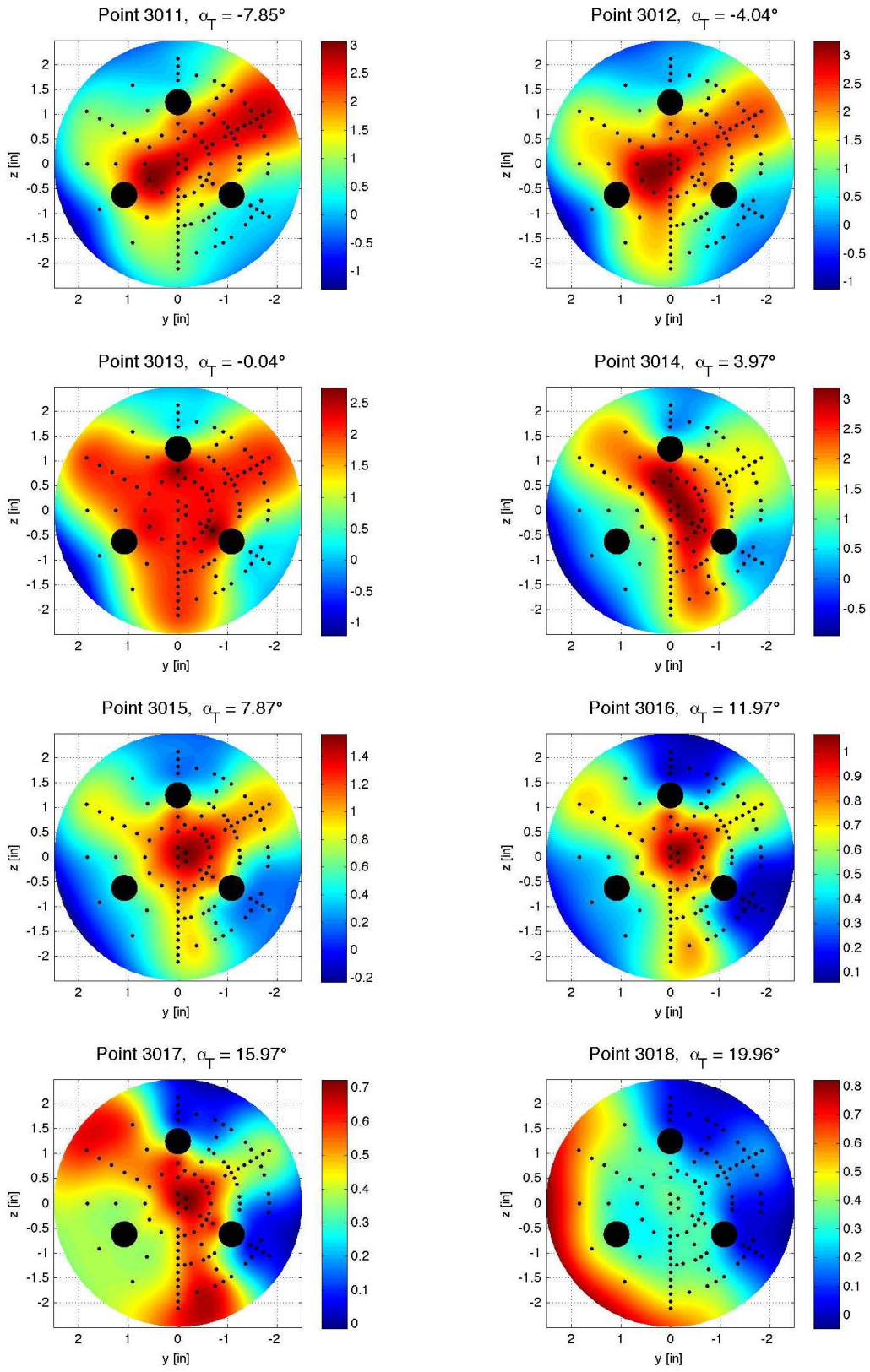

Figure E-188. Tri-nozzle configuration, Run 239, M_∞ = 3.5, Re_∞ = 1.0x10^6/ft, ϕ = 60.00°, X_S = 40.15 in, Y_S = 0.00 in, C_T = 0.00.

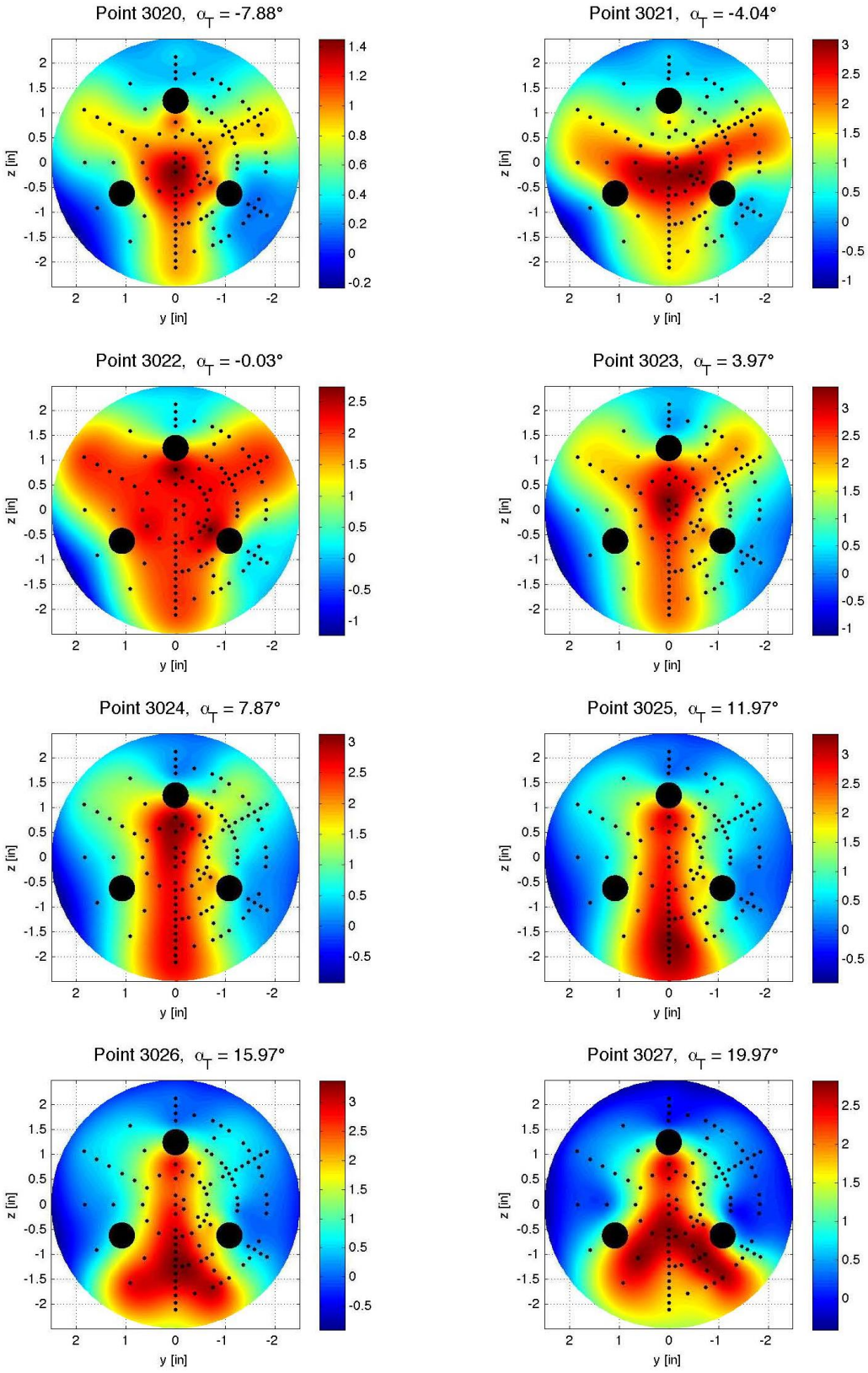

Figure E-189. Tri-nozzle configuration, Run 240, M_∞ = 3.5, Re_∞ = 1.0x10^6/ft, ϕ = −0.05°, X_S = 40.15 in, Y_S = 0.00 in, C_T = 0.46.

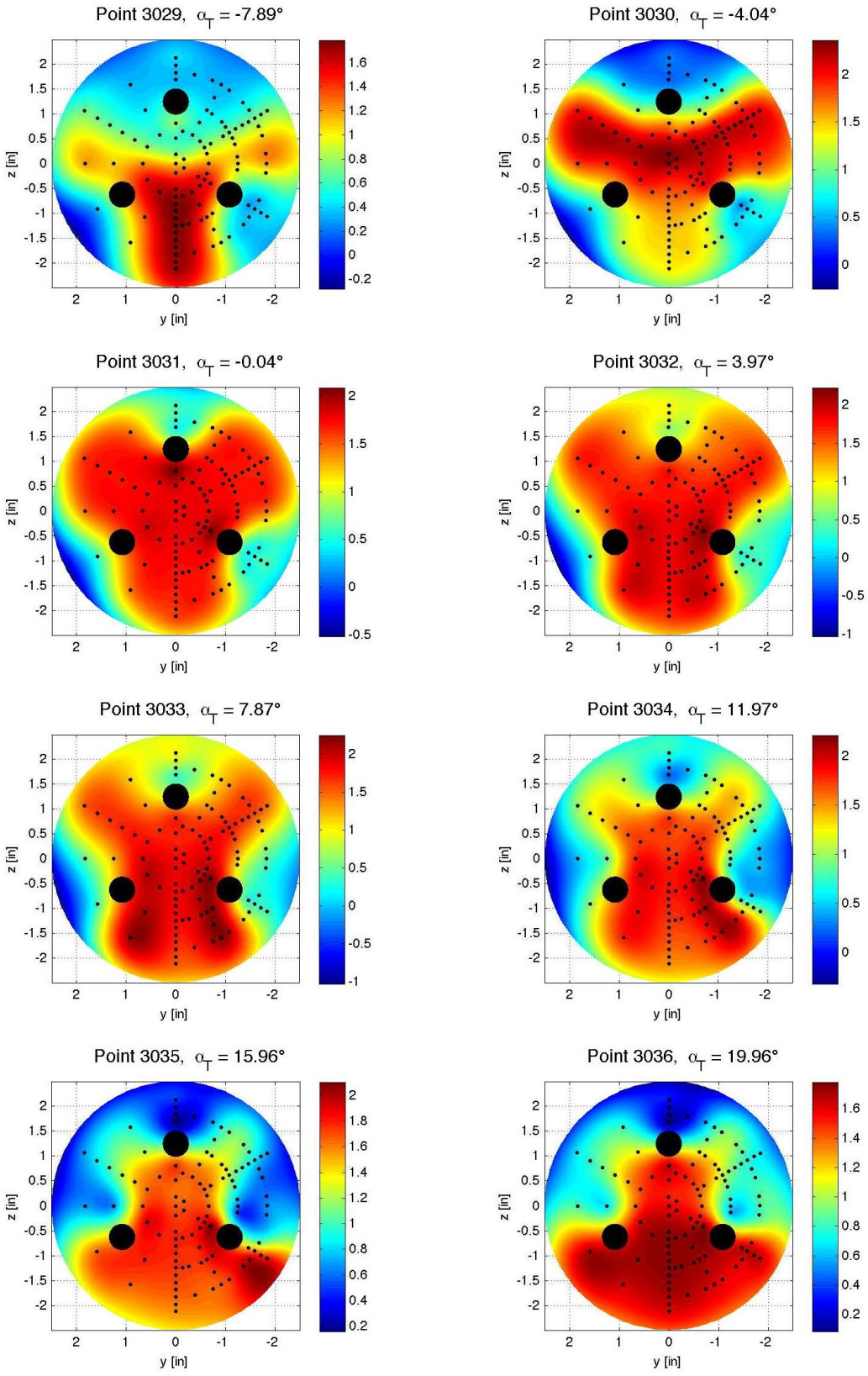

Figure E-190. Tri-nozzle configuration, Run 241, M_∞ = 3.5, Re_∞ = 1.0x10^6/ft, ϕ = −0.05°, X_S = 40.15 in, Y_S = 0.00 in, C_T = 0.22.

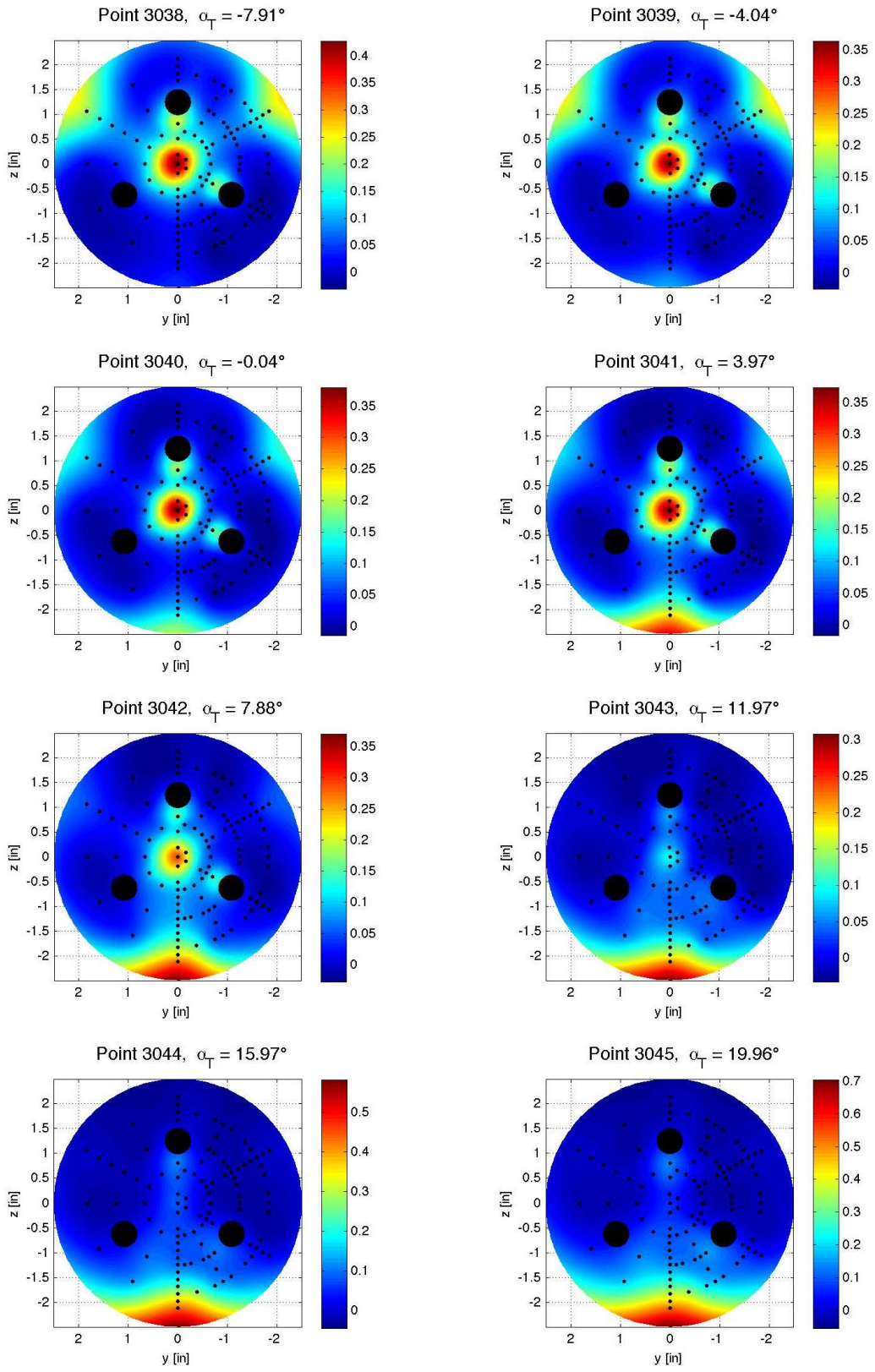

Figure E-191. Tri-nozzle configuration, Run 242, M_∞ = 4.6, Re_∞ = 1.5x10^6/ft, ϕ = −0.05°, X_S = 40.15 in, Y_S = 0.00 in, C_T = 1.96.

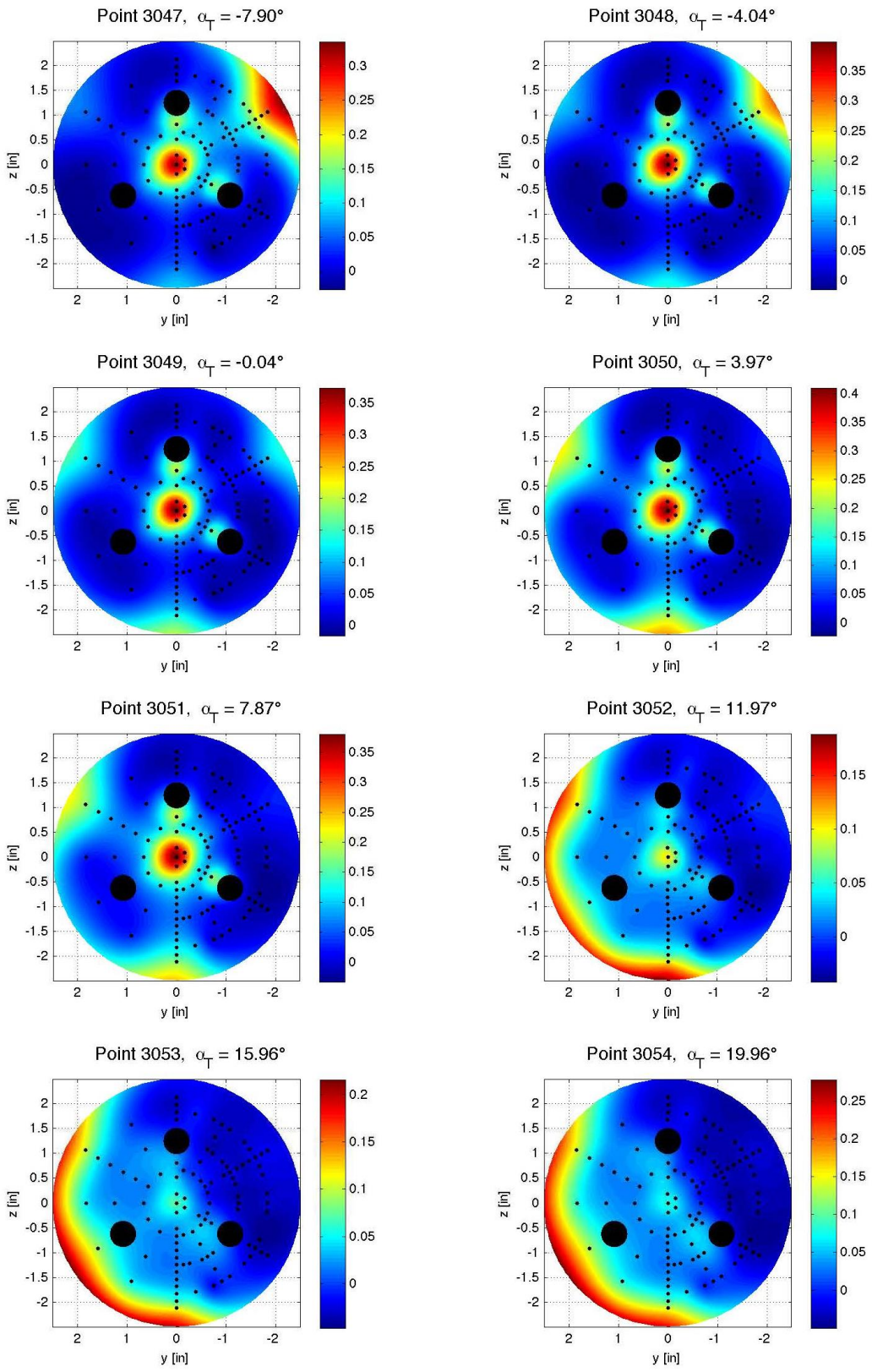

Figure E-192. Tri-nozzle configuration, Run 243, $M\infty$ = 4.6, Re_∞ = 1.5x10^6/ft, ϕ = 60.00°, X_S = 40.15 in, Y_S = 0.00 in, C_T = 1.95.

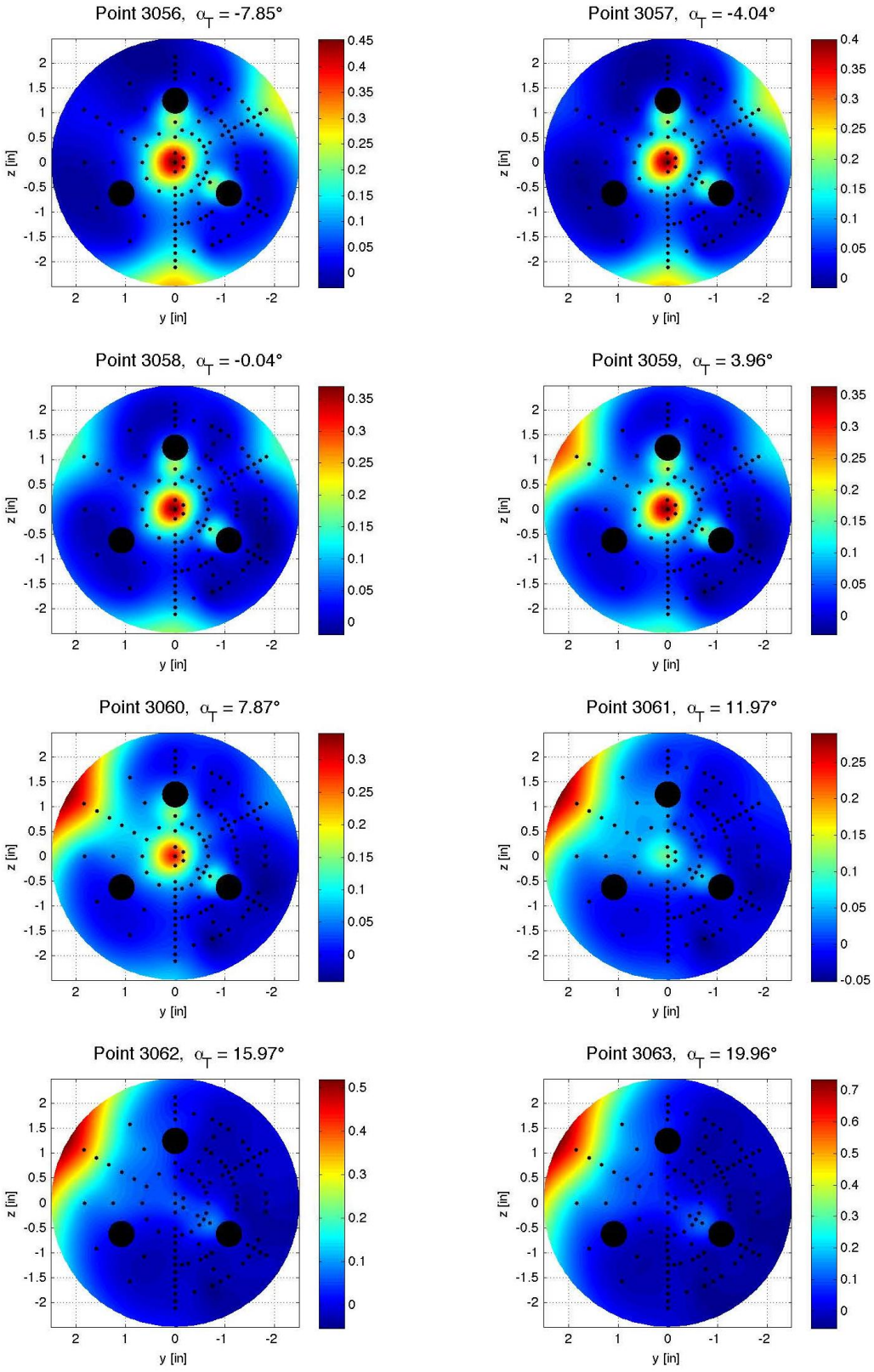

Figure E-193. Tri-nozzle configuration, Run 244, M_∞ = 4.6, Re_∞ = 1.5x10^6/ft, ϕ = 120.00°, X_S = 40.15 in, Y_S = 0.00 in, C_T = 1.96.

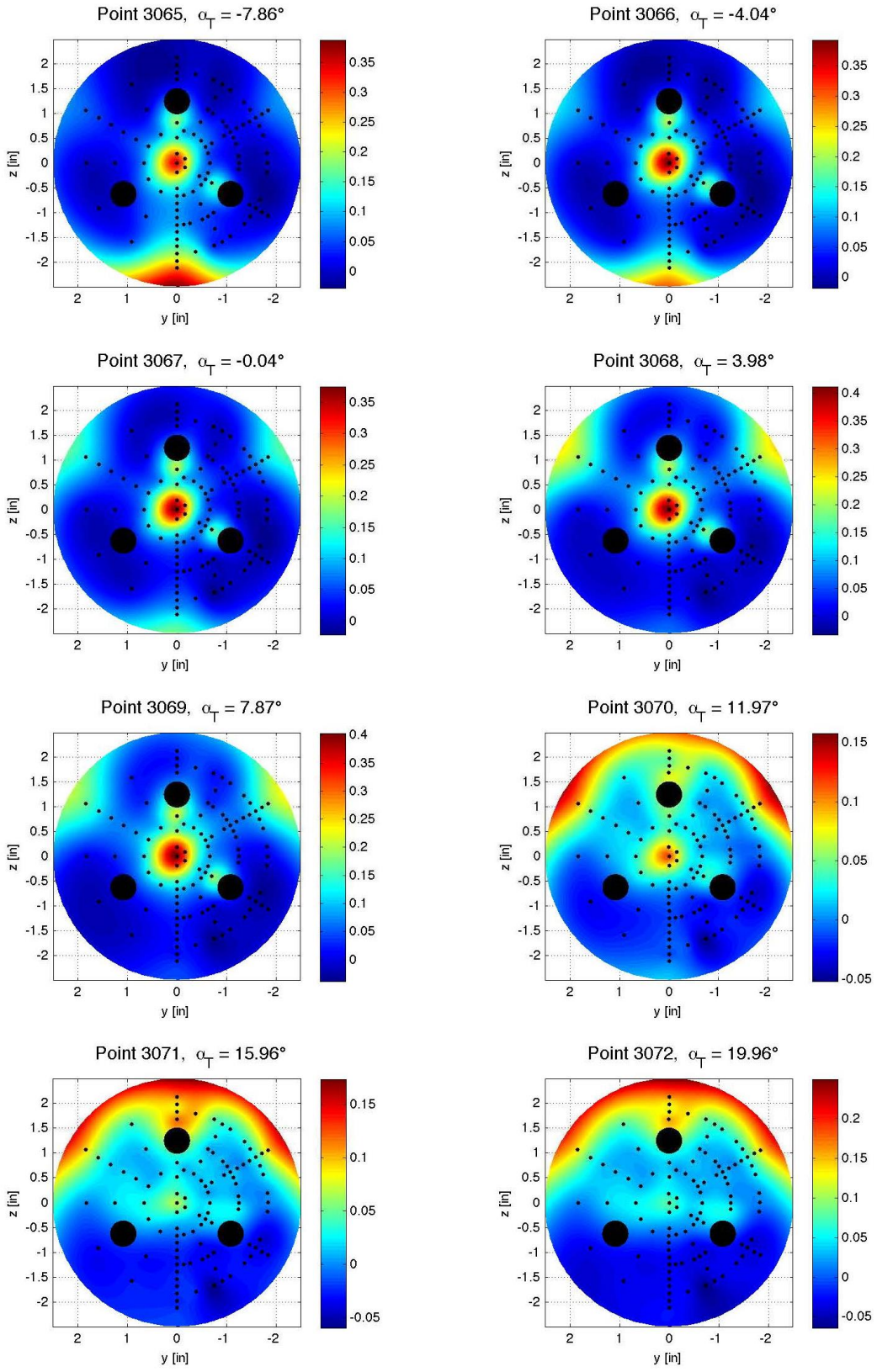

Figure E-194. Tri-nozzle configuration, Run 245, M_∞ = 4.6, Re_∞ = 1.5x10^6/ft, ϕ = −179.99°, X_S = 40.15 in, Y_S = 0.00 in, C_T = 1.97.

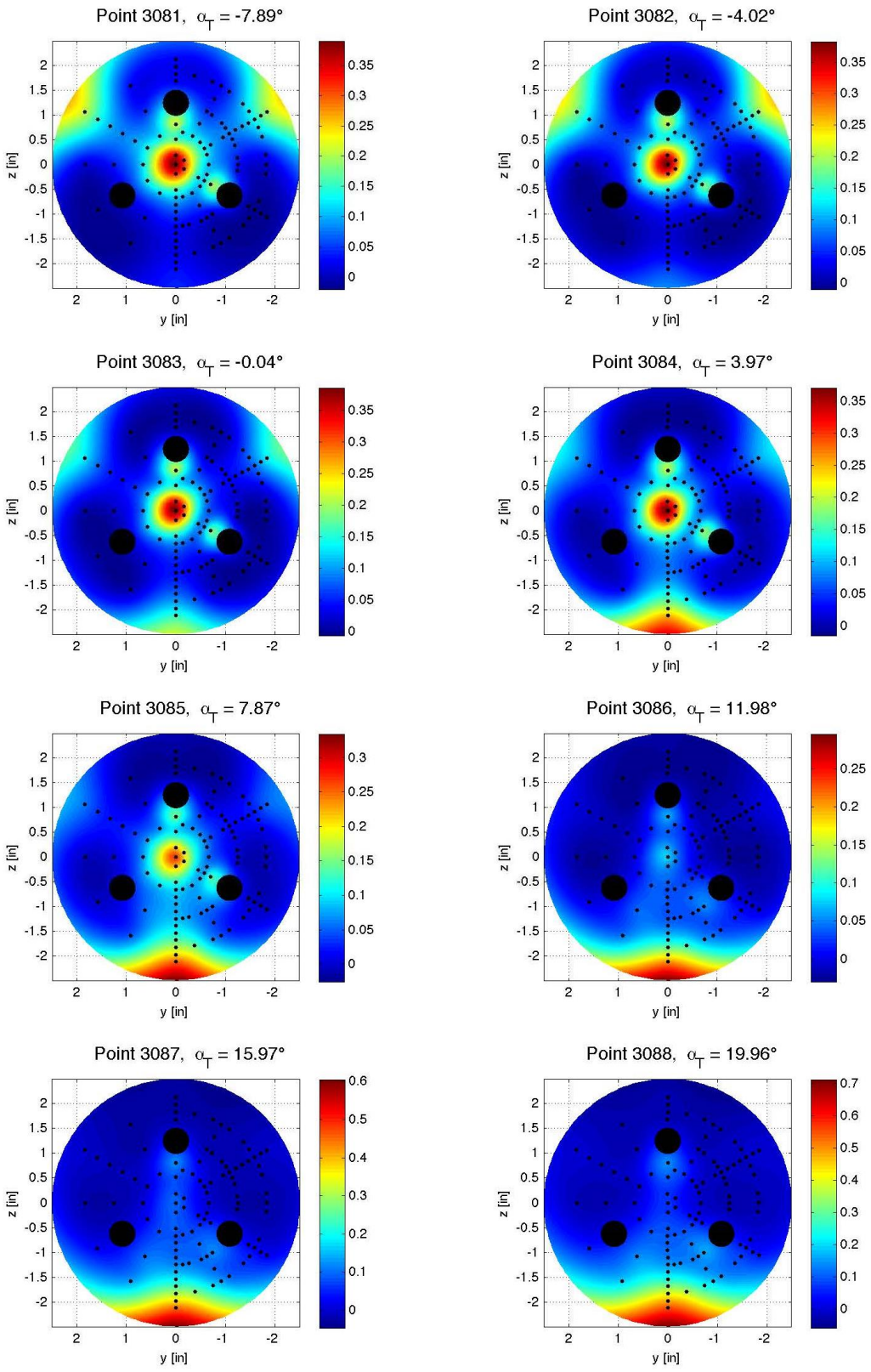

Figure E-195. Tri-nozzle configuration, Run 247, M_∞ = 4.6, Re_∞ = 1.5x10^6/ft, ϕ = −0.03°, X_S = 40.15 in, Y_S = 0.00 in, C_T = 1.92.

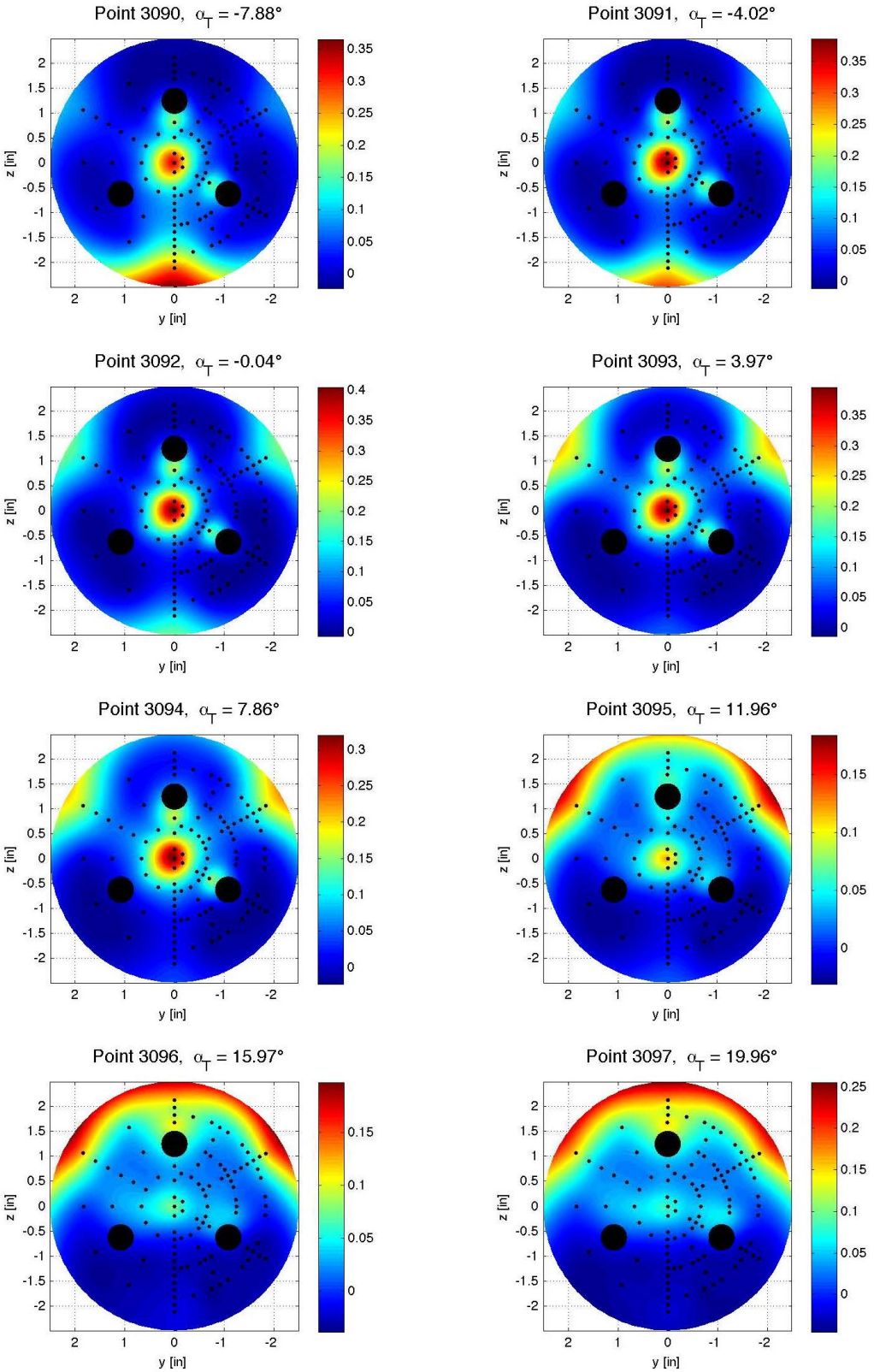

Figure E-196. Tri-nozzle configuration, Run 248, M_∞ = 4.6, Re_∞ = 1.5x10^6/ft, ϕ = 179.99°, X_S = 40.15 in, Y_S = 0.00 in, C_T = 1.93.

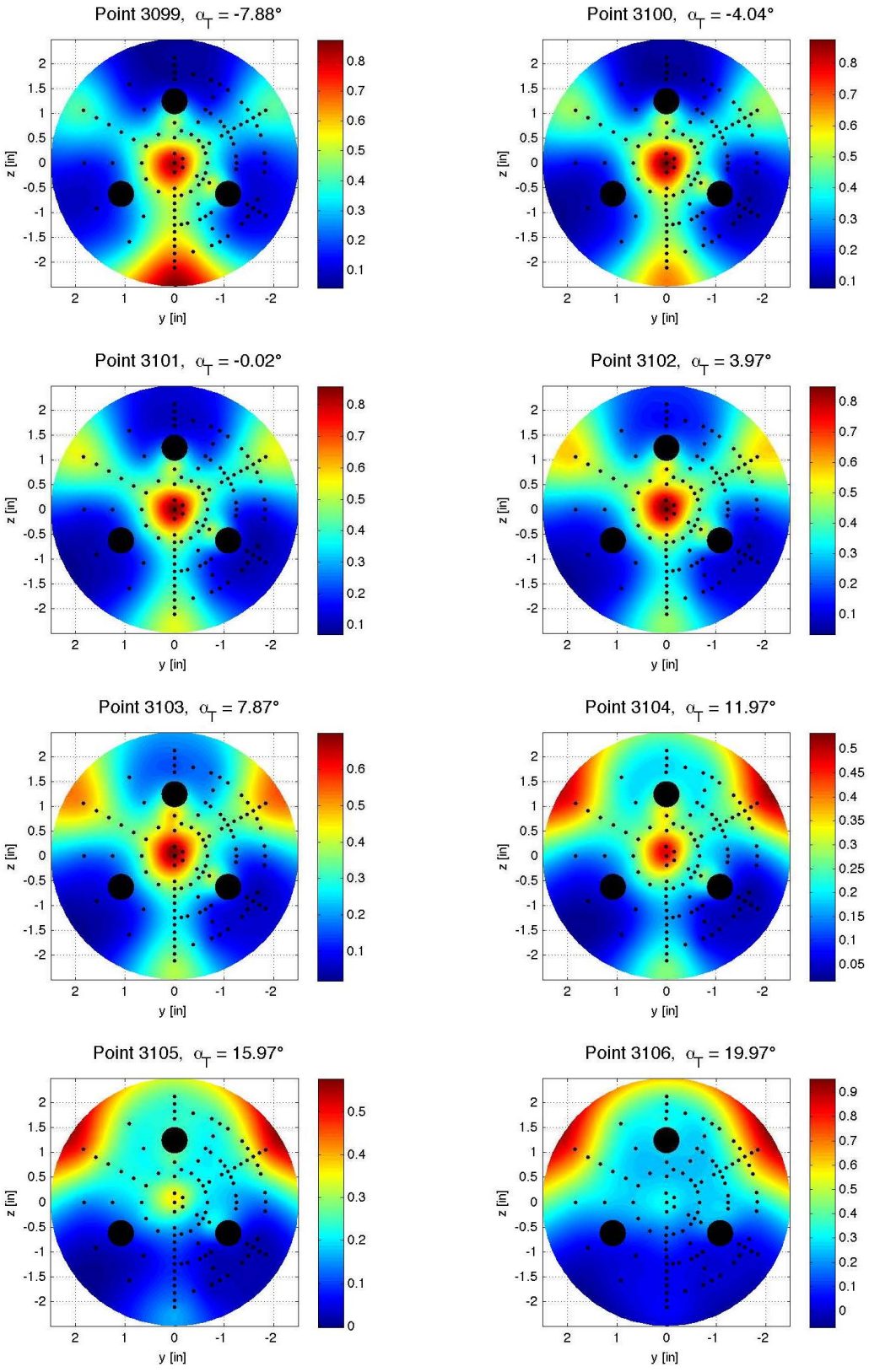

Figure E-197. Tri-nozzle configuration, Run 249, M_∞ = 4.6, Re_∞ = 1.5x10^6/ft, ϕ = 179.99°, X_S = 40.15 in, Y_S = 0.00 in, C_T = 0.90.

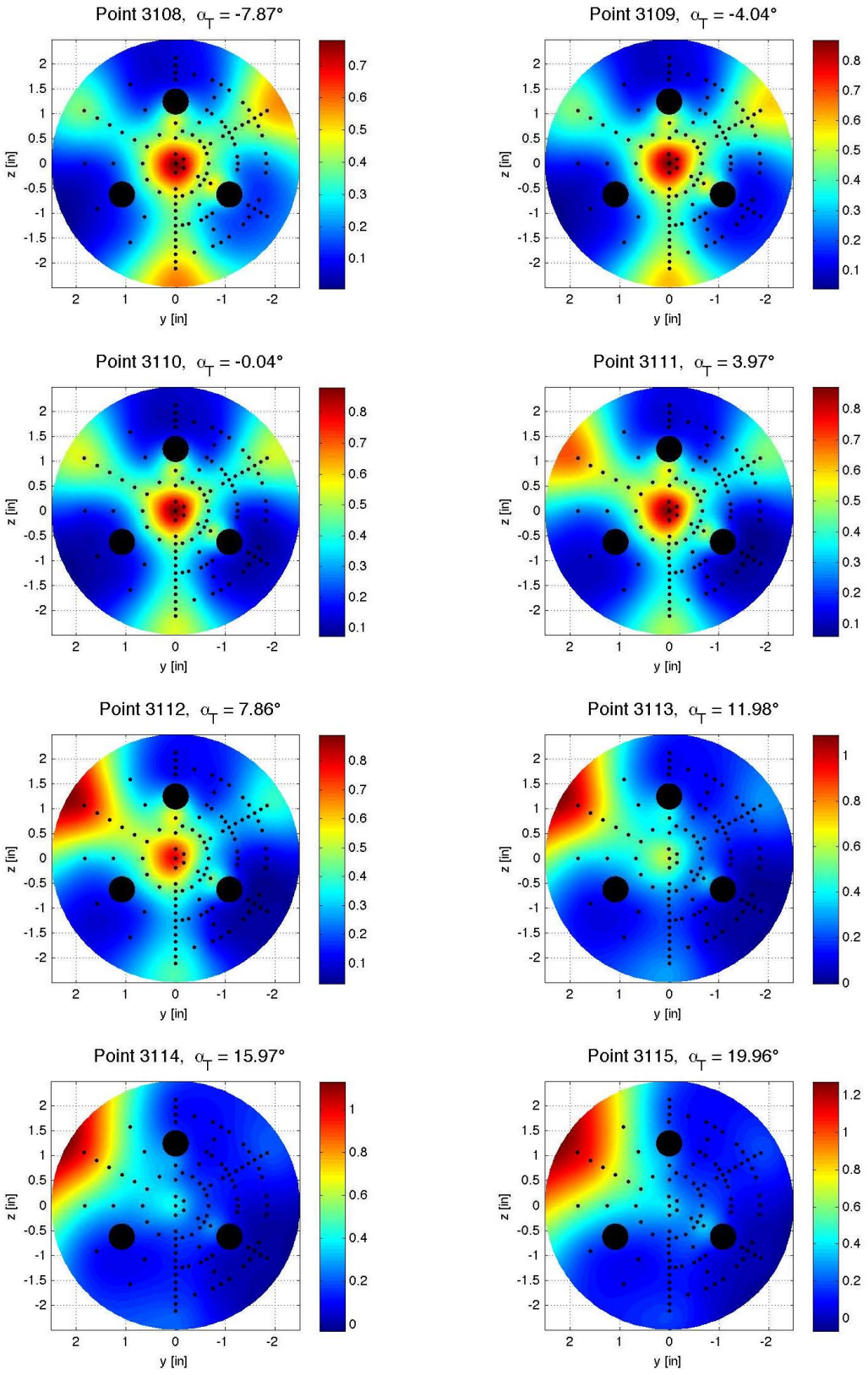

Figure E-198. Tri-nozzle configuration, Run 250, M_∞ = 4.6, Re_∞ = 1.5x10^6/ft, ϕ = 119.96°, X_S = 40.15 in, Y_S = 0.00 in, C_T = 0.90.

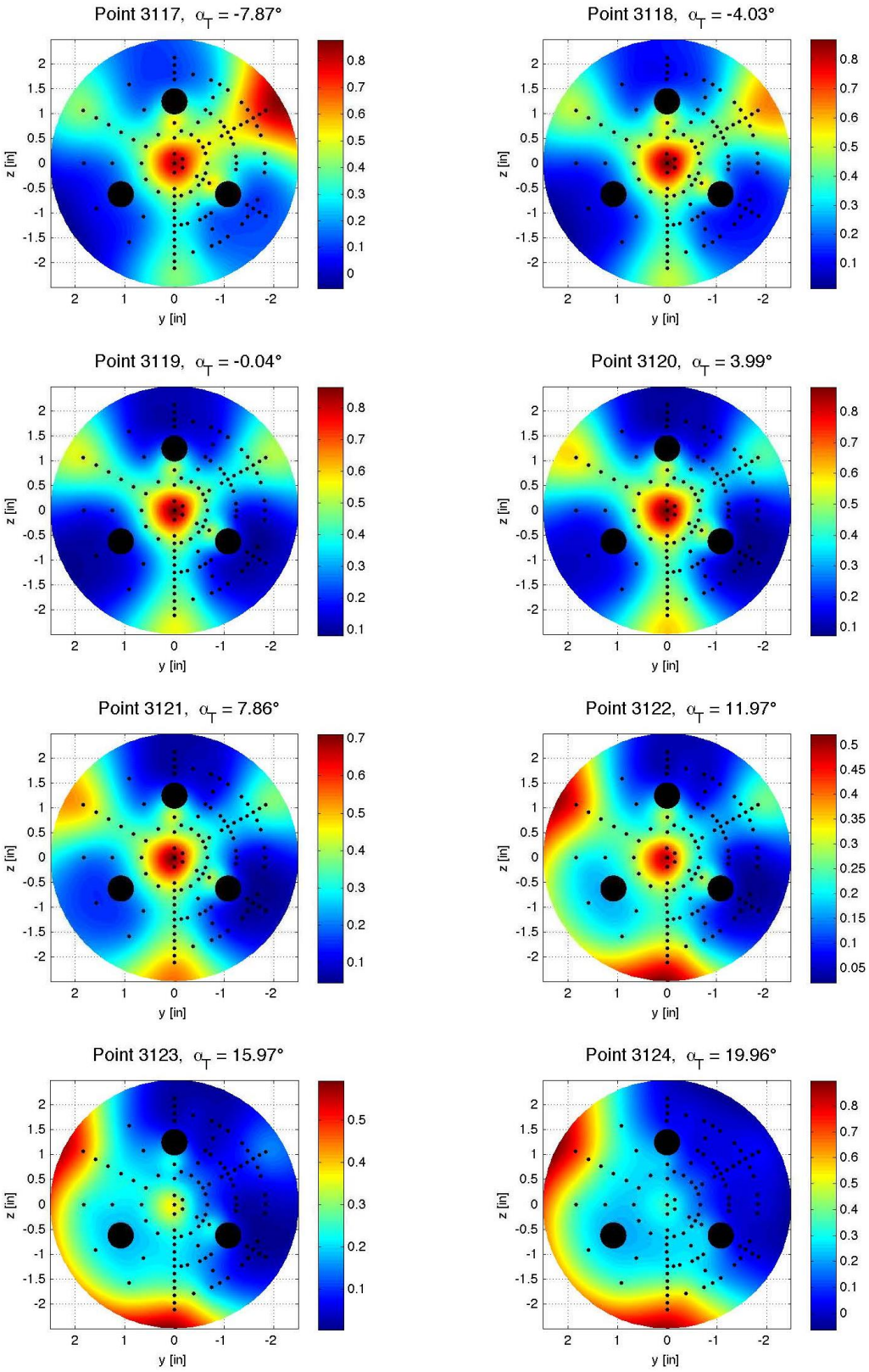

Figure E-199. Tri-nozzle configuration, Run 251, M_∞ = 4.6, Re_∞ = 1.5x10^6/ft, ϕ = 60.04°, X_S = 40.15 in, Y_S = 0.00 in, C_T = 0.90.

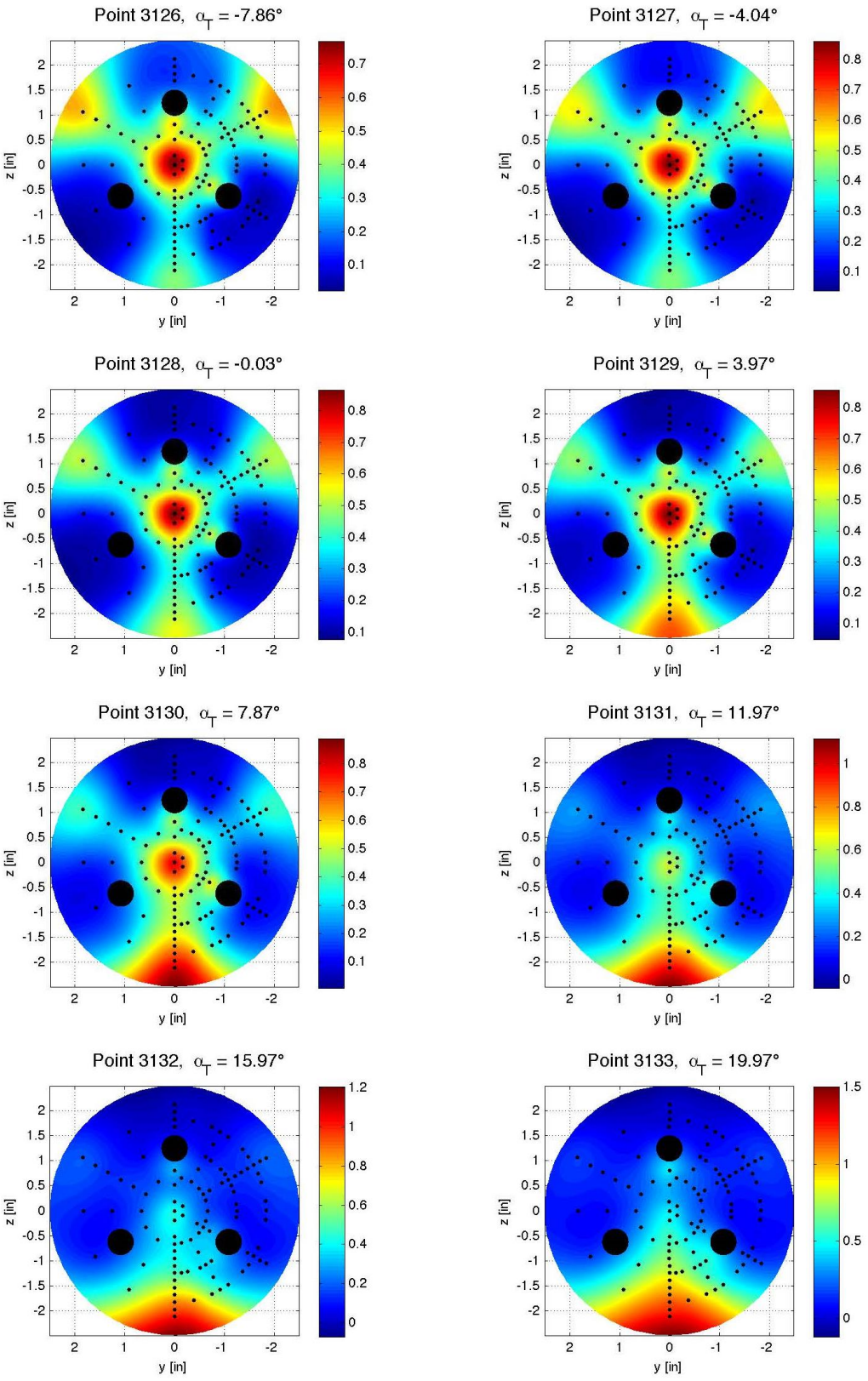

Figure E-200. Tri-nozzle configuration, Run 252, M_∞ = 4.6, Re_∞ = 1.5x10^6/ft, ϕ = −0.03°, X_S = 40.15 in, Y_S = 0.00 in, C_T = 0.90.

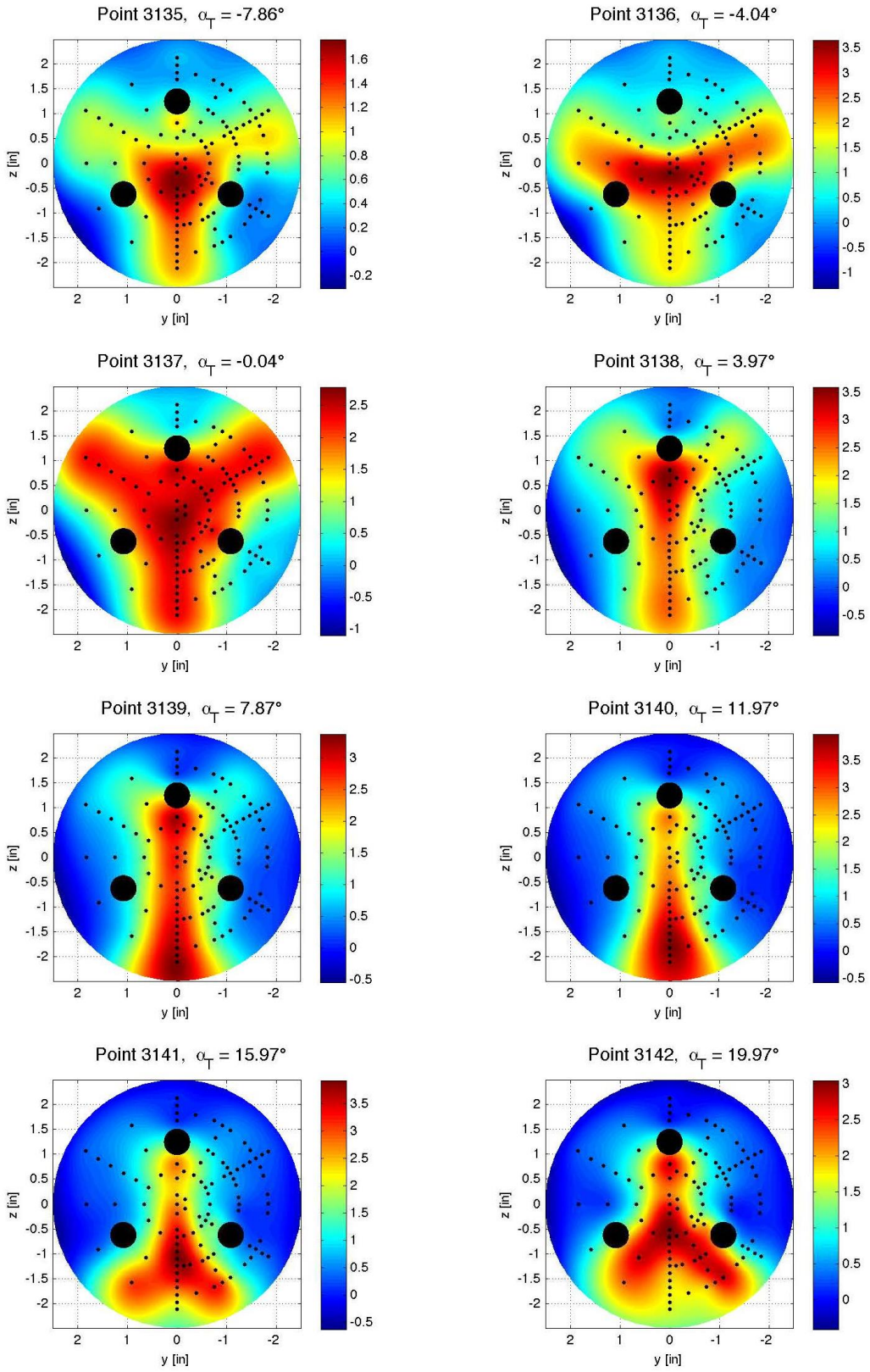

Figure E-201. Tri-nozzle configuration, Run 253, M_∞ = 4.6, Re_∞ = 1.5x10^6/ft, ϕ = −0.03°, X_S = 40.15 in, Y_S = 0.00 in, C_T = 0.42.

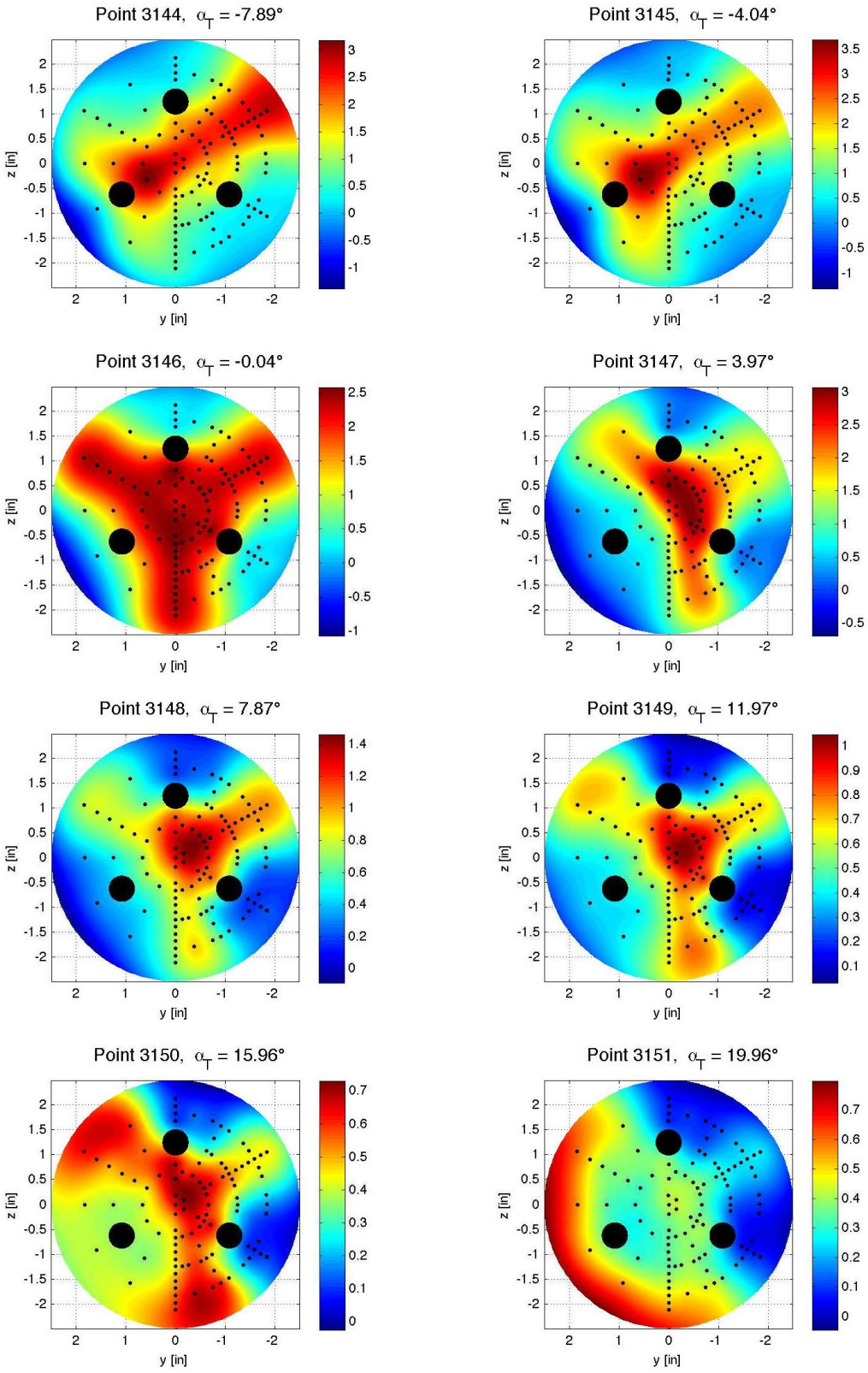

Figure E-202. Tri-nozzle configuration, Run 254, M_∞ = 4.6, Re_∞ = 1.5x10^6/ft, ϕ = 60.00°, X_S = 40.15 in, Y_S = 0.00 in, C_T = 0.42.

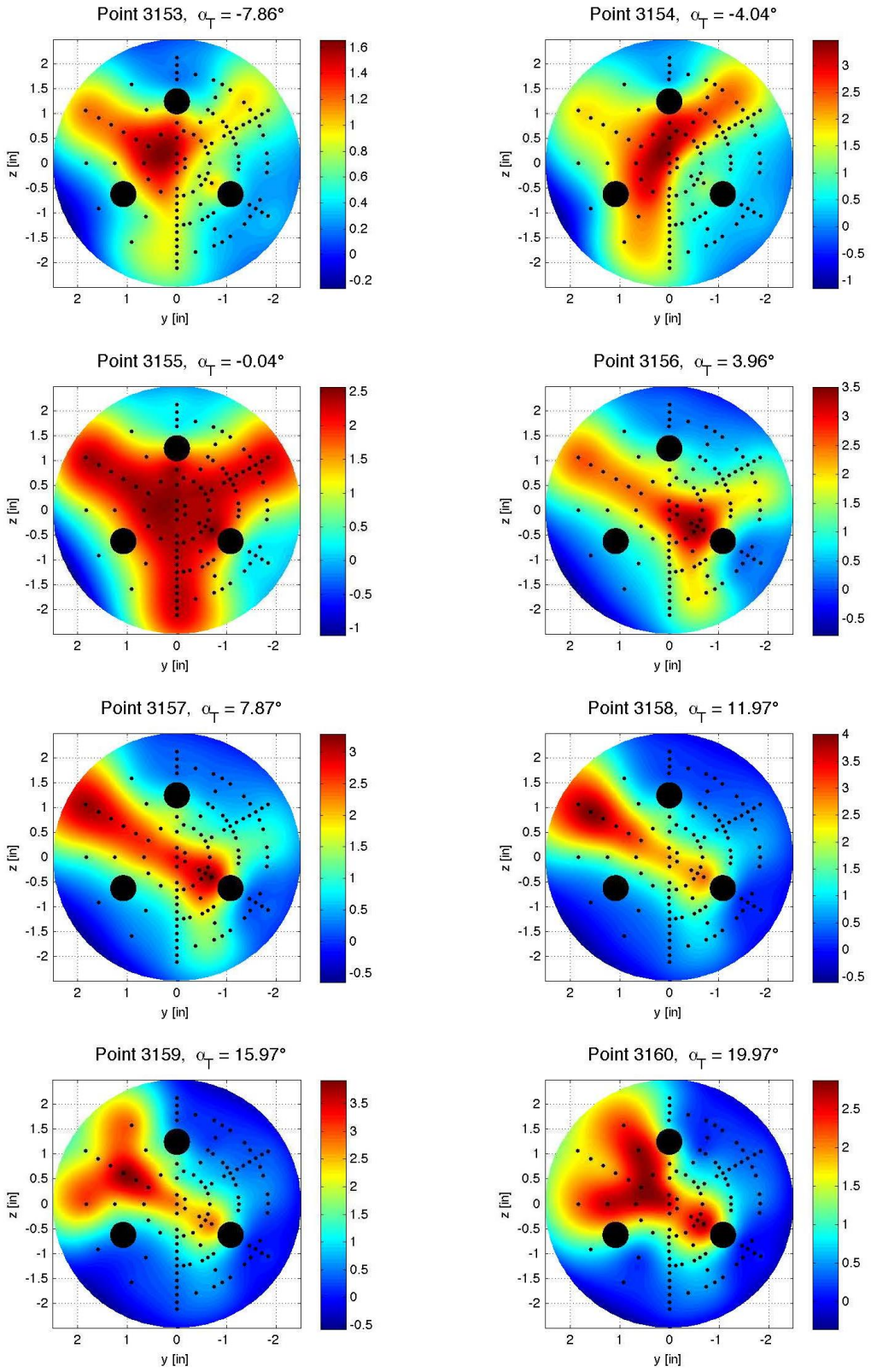

Figure E-203. Tri-nozzle configuration, Run 255, M_∞ = 4.6, Re_∞ = 1.5x10^6/ft, ϕ = 119.96°, X_S = 40.15 in, Y_S = 0.00 in, C_T = 0.42.

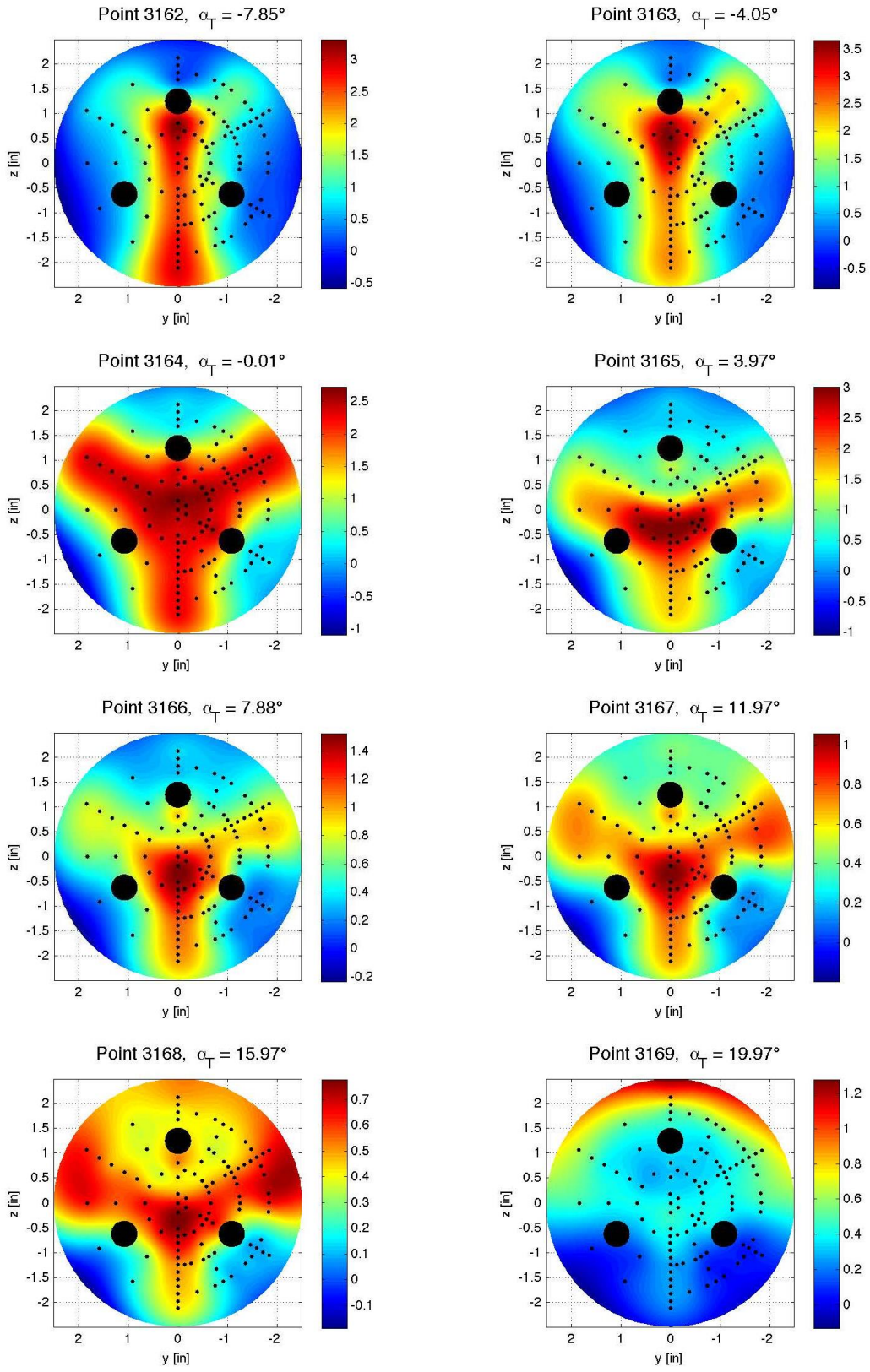

Figure E-204. Tri-nozzle configuration, Run 256, M_∞ = 4.6, Re_∞ = 1.5x10^6/ft, ϕ = 179.95°, X_S = 40.15 in, Y_S = 0.00 in, C_T = 0.43.

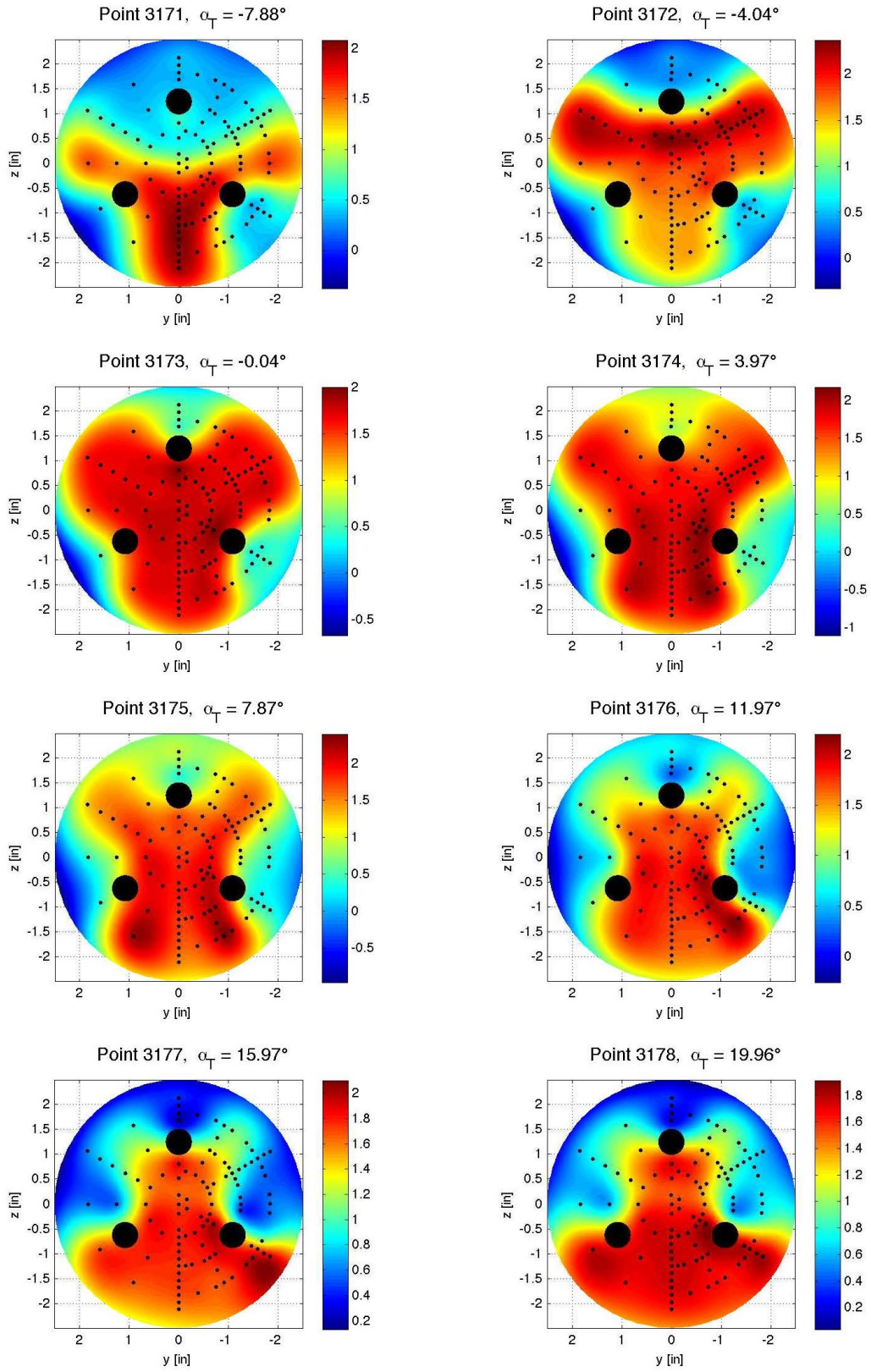

Figure E-205. Tri-nozzle configuration, Run 257, M_∞ = 4.6, Re_∞ = 1.5x10^6/ft, ϕ = −0.03°, X_S = 40.15 in, Y_S = 0.00 in, C_T = 0.20.

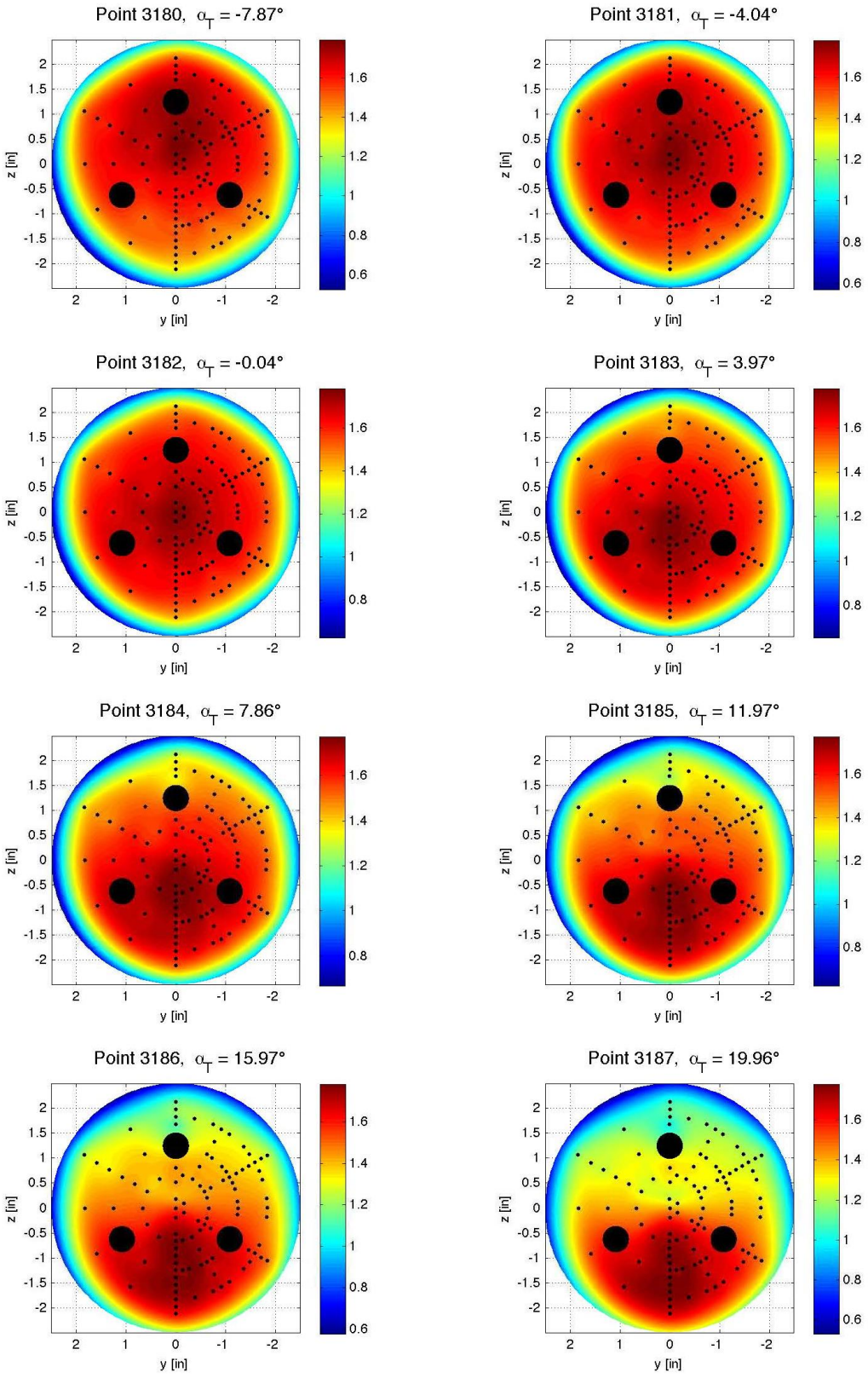

Figure E-206. Tri-nozzle configuration, Run 258, M_∞ = 4.6, Re_∞ = 1.5x10^6/ft, ϕ = −0.03°, X_S = 40.15 in, Y_S = 0.00 in, C_T = 0.00.

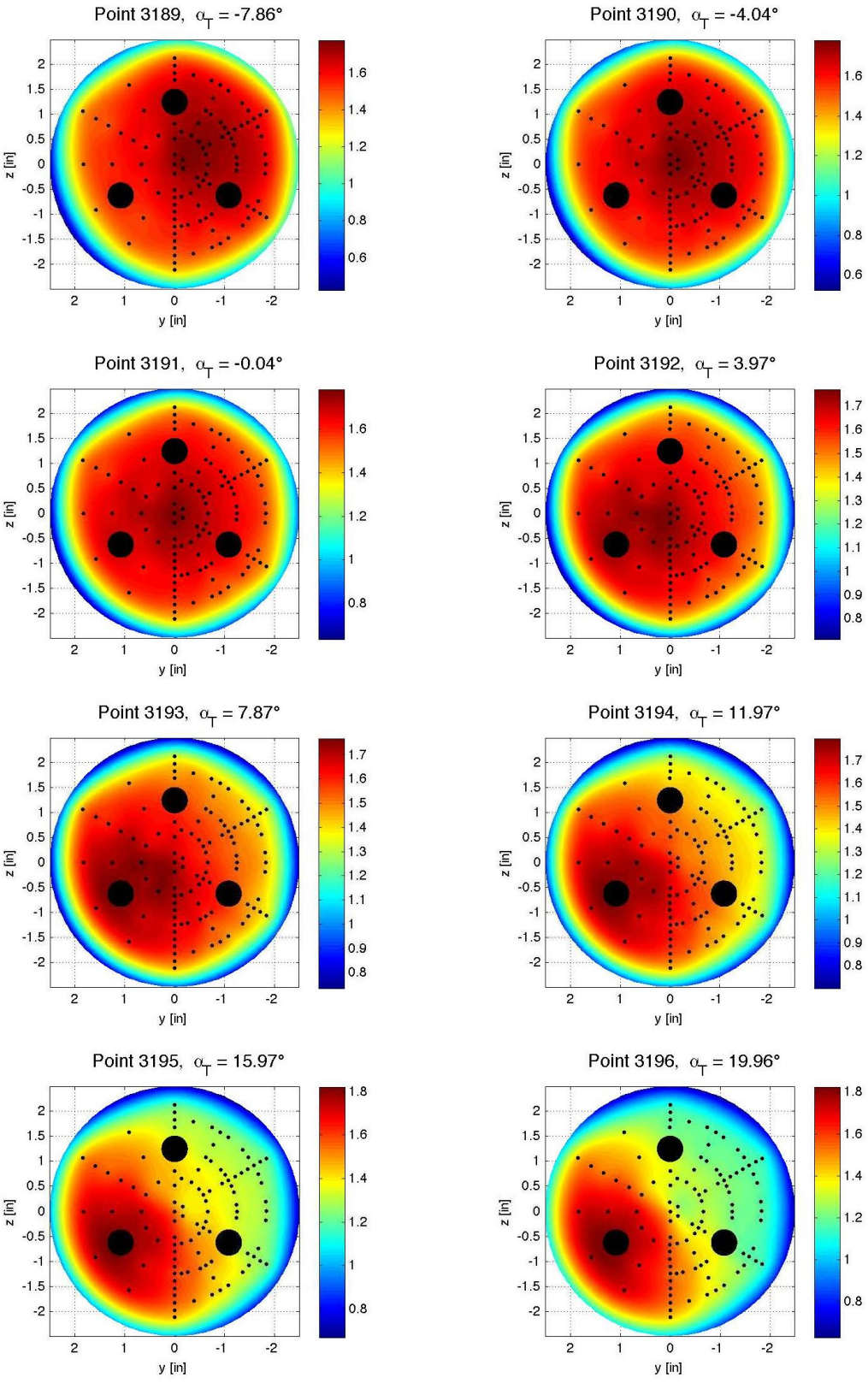

Figure E-207. Tri-nozzle configuration, Run 259, M_∞ = 4.6, Re_∞ = 1.5x10^6/ft, ϕ = 59.96°, X_S = 40.15 in, Y_S = 0.00 in, C_T = 0.00.

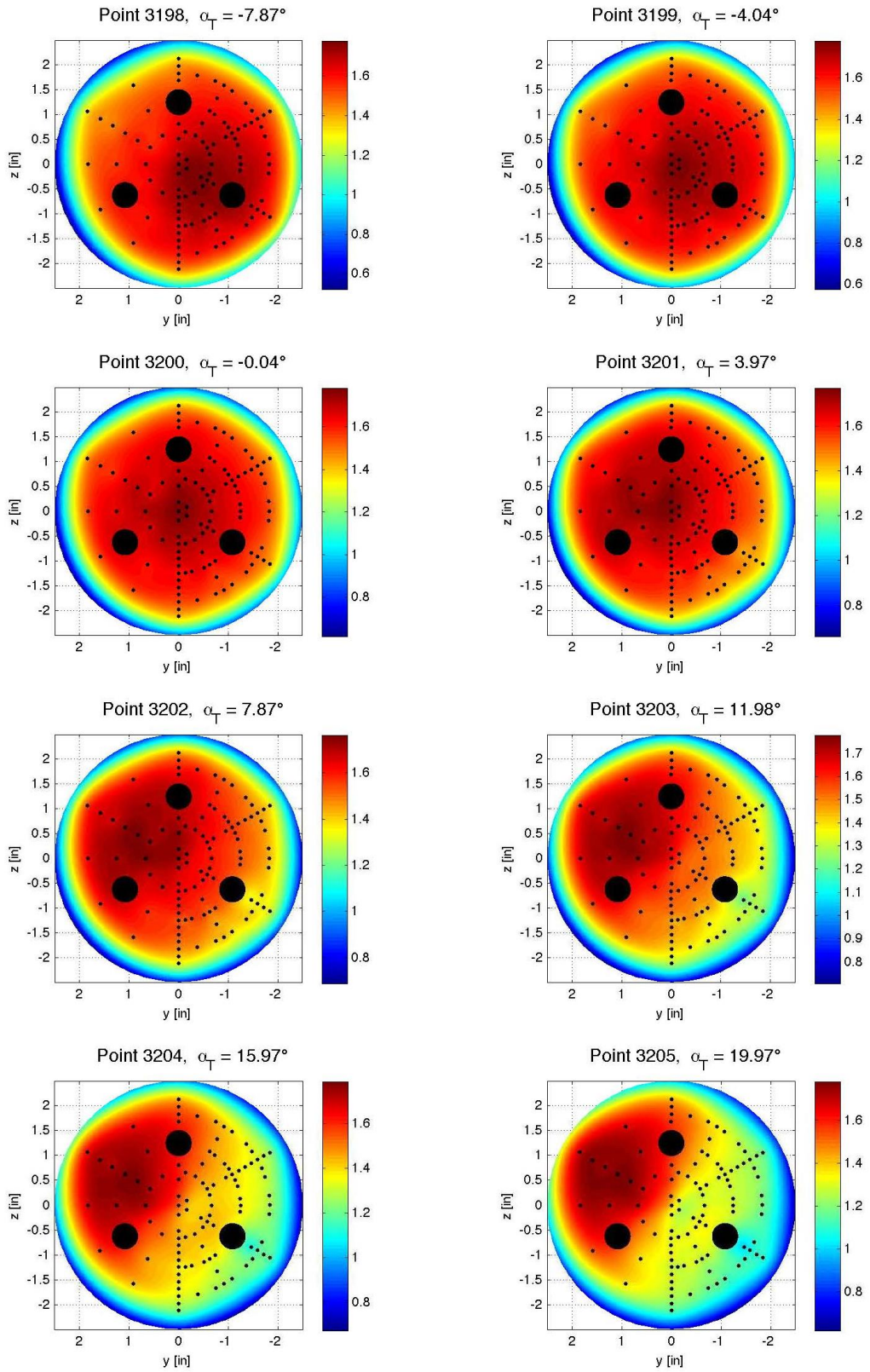

Figure E-208. Tri-nozzle configuration, Run 260, M_∞ = 4.6, Re_∞ = 1.5x10^6/ft, ϕ = 119.94°, X_S = 40.15 in, Y_S = 0.00 in, C_T = 0.00.

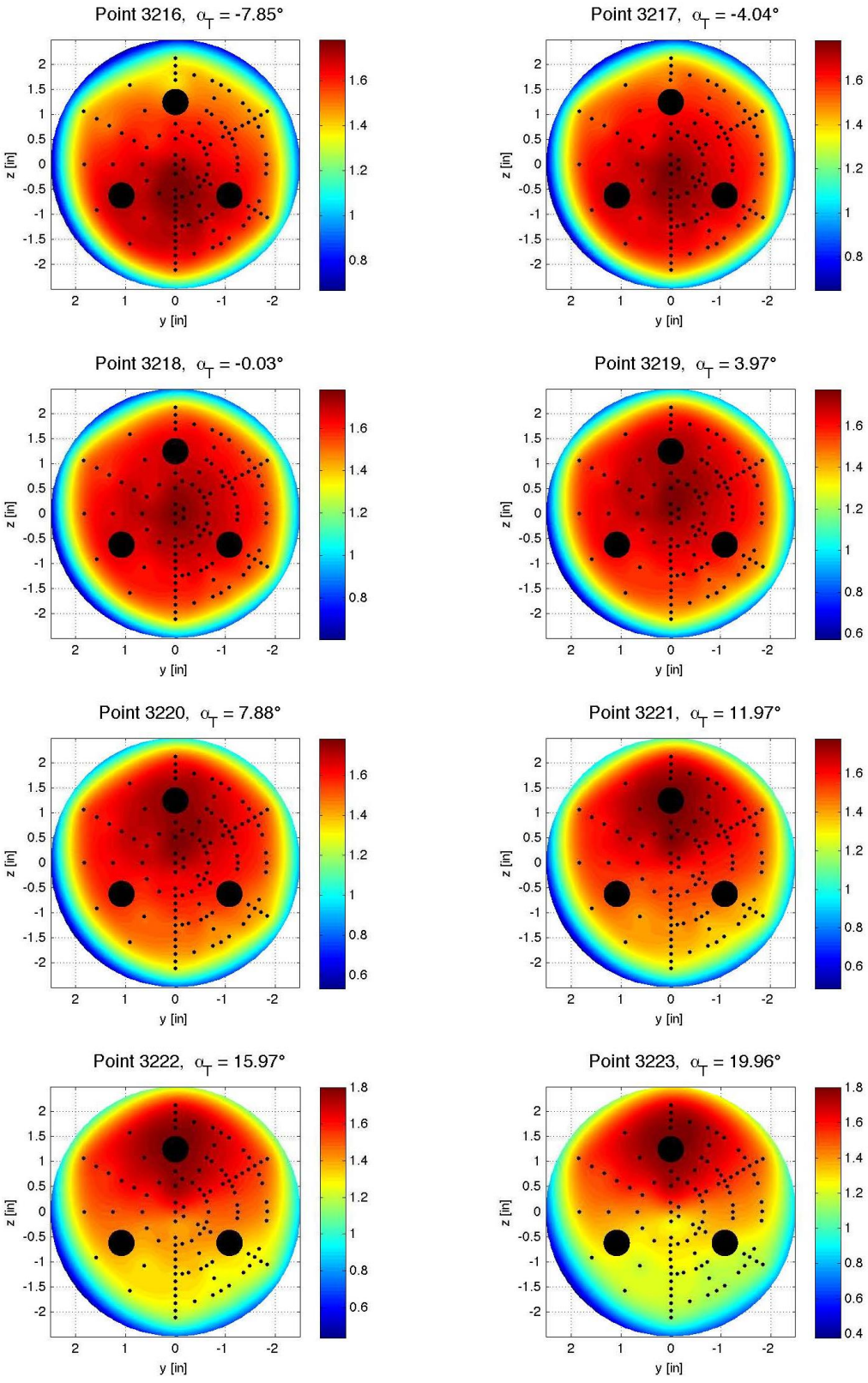

Figure E-209. Tri-nozzle configuration, Run 261, M_∞ = 4.6, Re_∞ = 1.5x10^6/ft, ϕ = 179.95°, X_S = 40.15 in, Y_S = 0.00 in, C_T = 0.00.

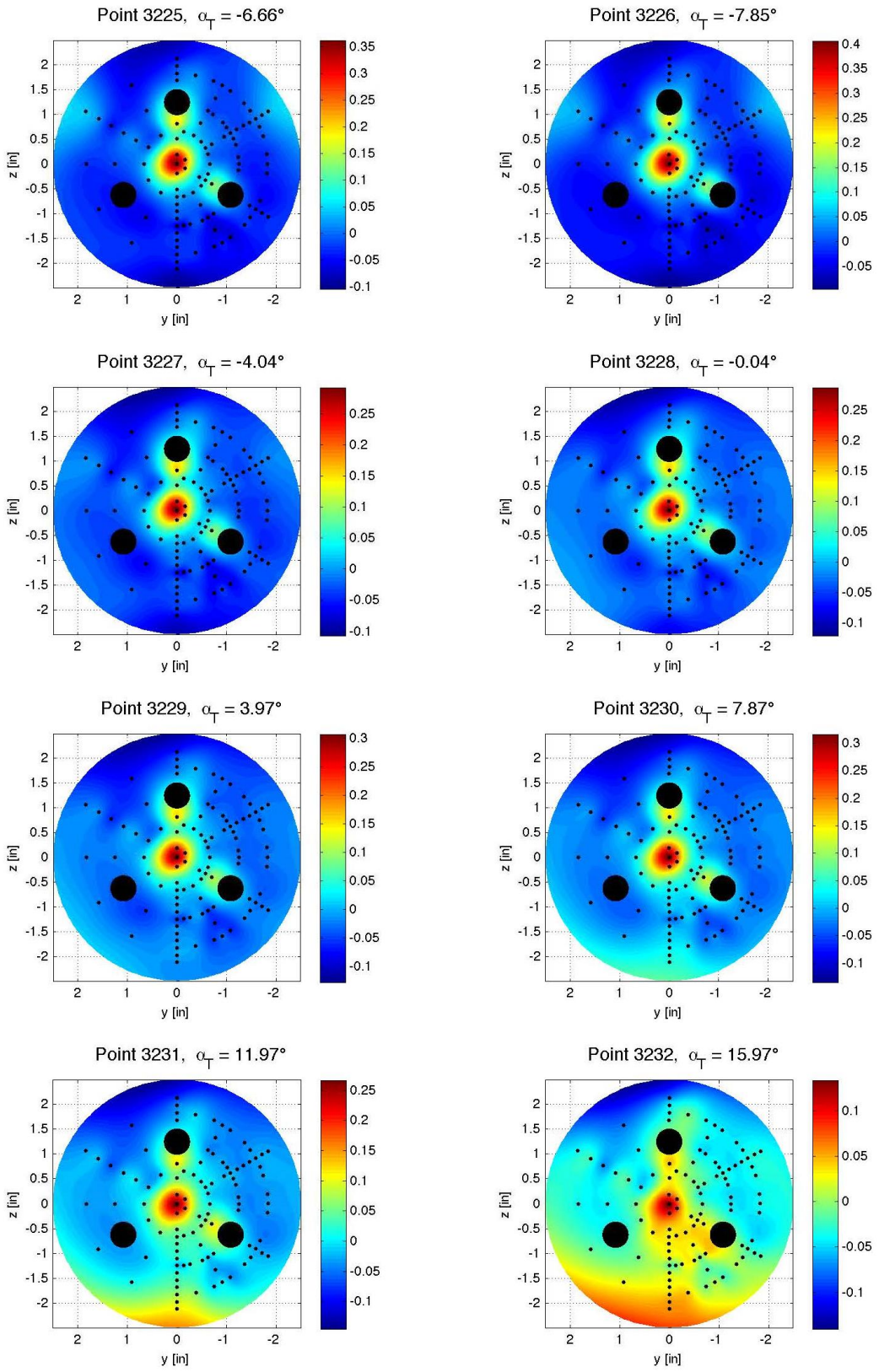

Figure E-210. Tri-nozzle configuration, Run 262, M_∞ = 4.6, Re_∞ = 1.5x10^6/ft, ϕ = 0.01°, X_S = 40.15 in, Y_S = 0.00 in, C_T = 2.94.

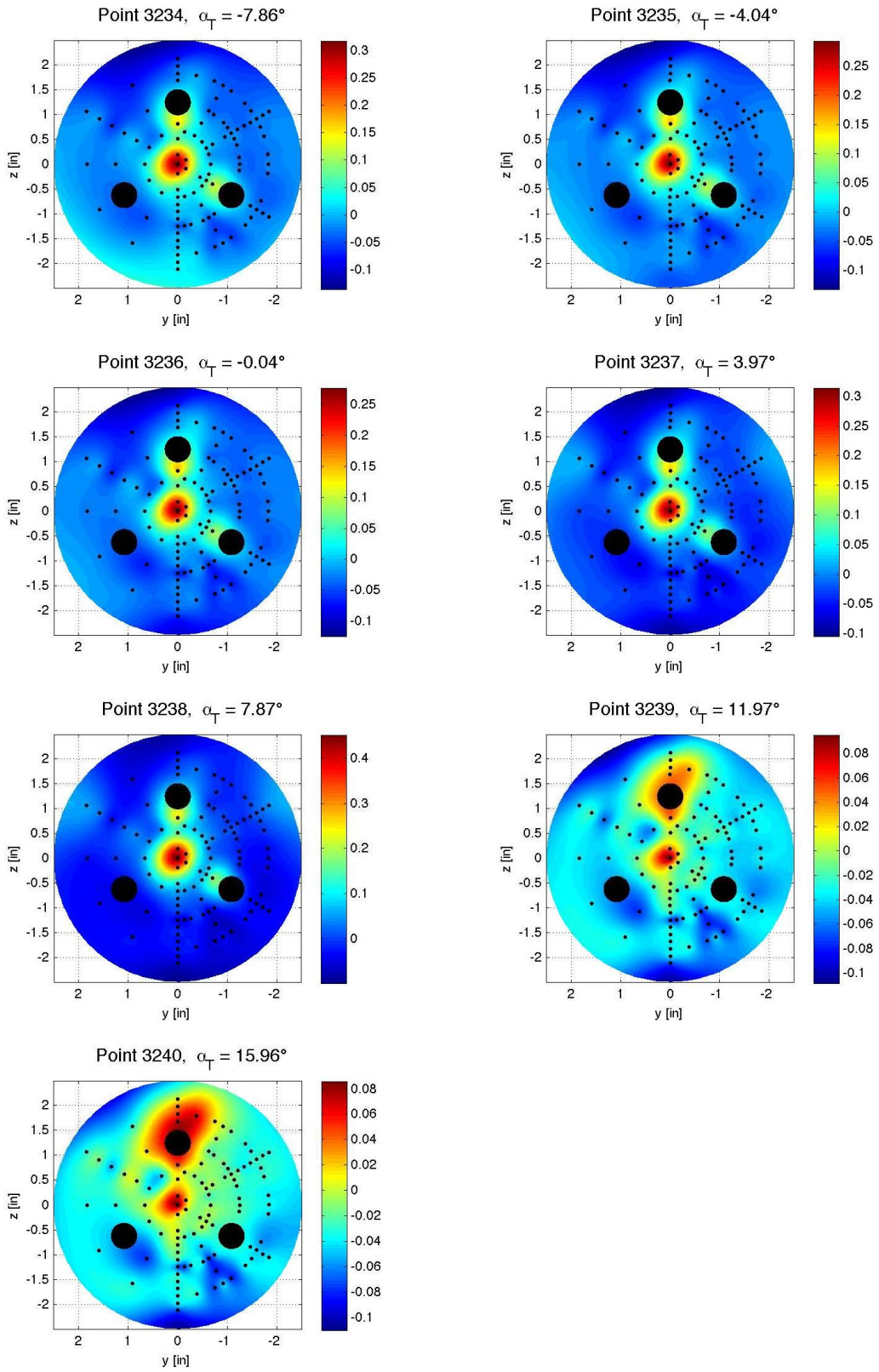

Figure E-211. Tri-nozzle configuration, Run 263, M_∞ = 4.6, Re_∞ = 1.5x10^6/ft, ϕ = −179.99°, X_S = 40.15 in, Y_S = 0.00 in, C_T = 2.93.

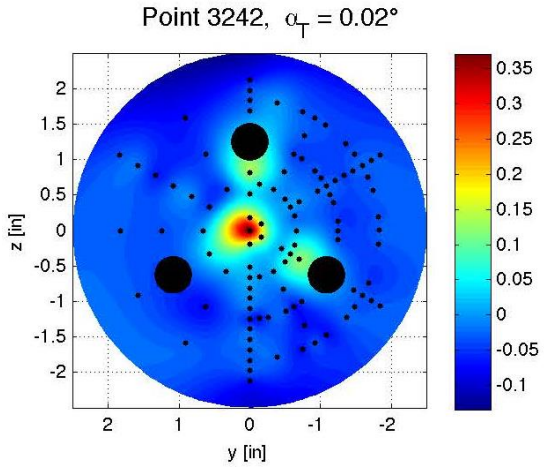

Figure E-212. Tri-nozzle configuration, Run 264, $M\infty$ = 4.6, Re_∞ = 1.5x10^6/ft, ϕ = 179.99°, X_S = 40.15 in, Y_S = 0.00 in, C_T = 5.95.

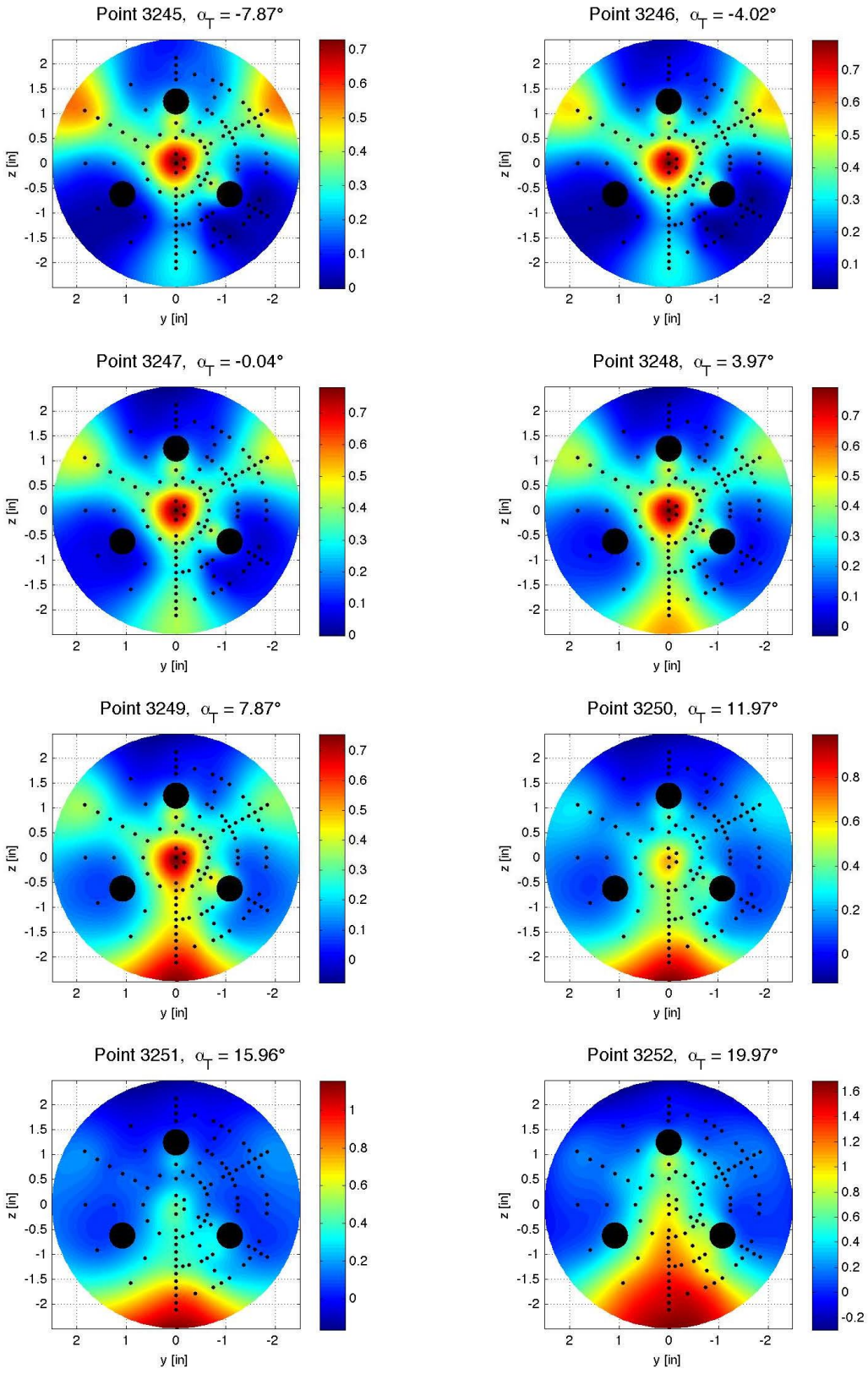

Figure E-213. Tri-nozzle configuration, Run 265, M_∞ = 3.5, Re_∞ = 1.0x10^6/ft, ϕ = −0.05°, X_S = 40.15 in, Y_S = 0.00 in, C_T = 0.91.

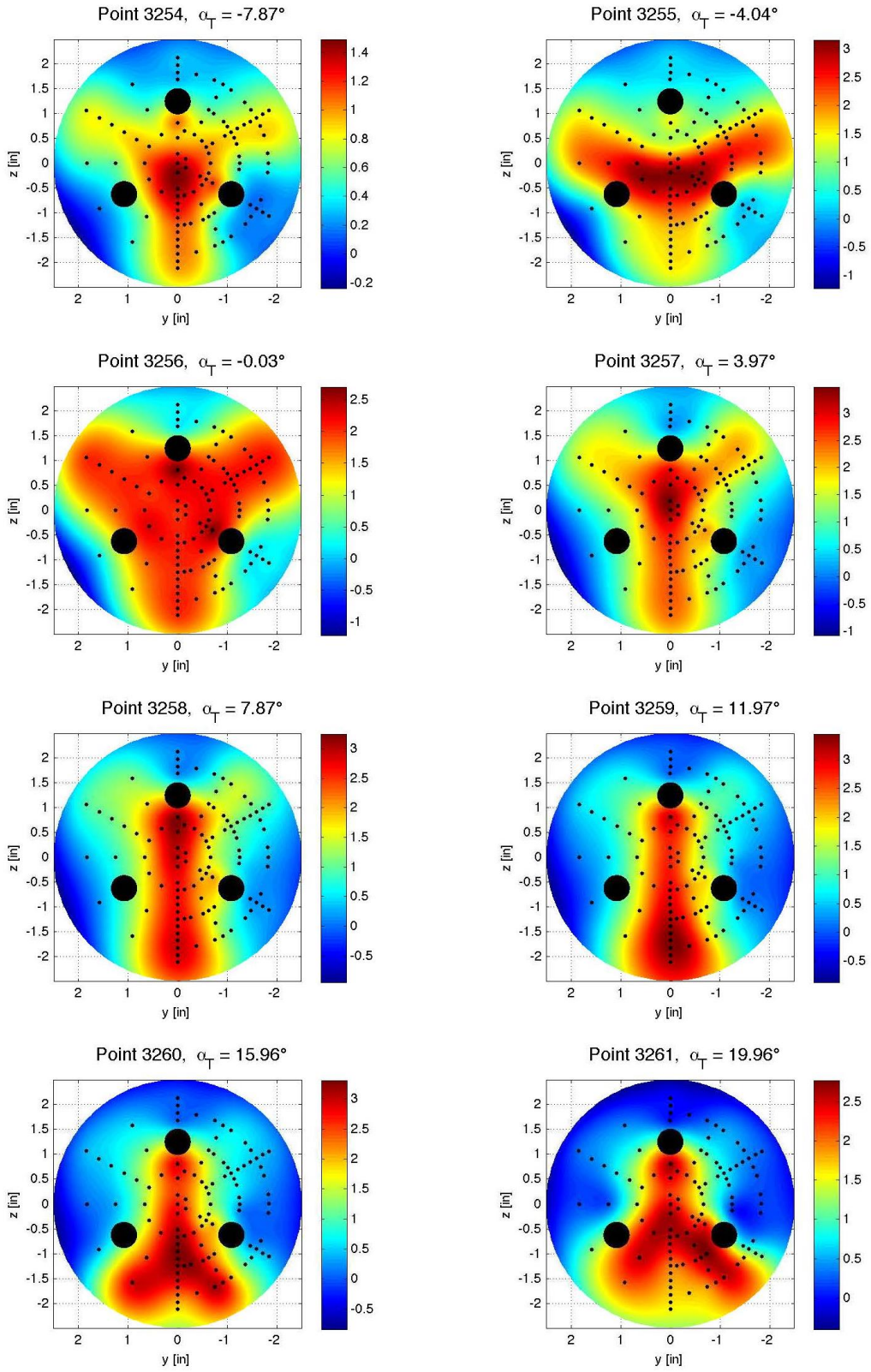

Figure E-214. Tri-nozzle configuration, Run 266, M_∞ = 3.5, Re_∞ = 1.0x10^6/ft, ϕ = −0.05°, X_S = 40.15 in, Y_S = 0.00 in, C_T = 0.45.

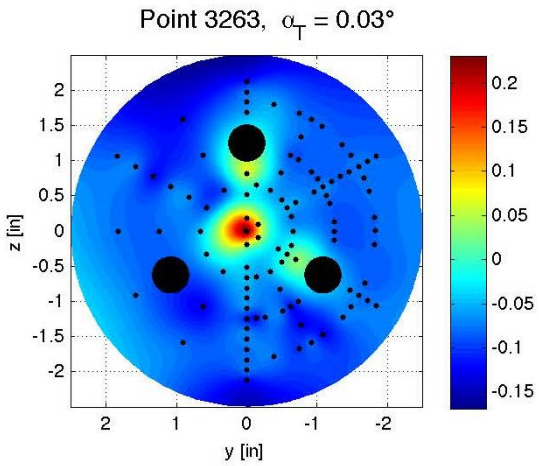

Figure E-215. Tri-nozzle configuration, Run 267, M_∞ = 3.5, Re_∞ = 1.0x10^6/ft, ϕ = −0.05°, X_S = 40.15 in, Y_S = 0.00 in, C_T = 4.95.

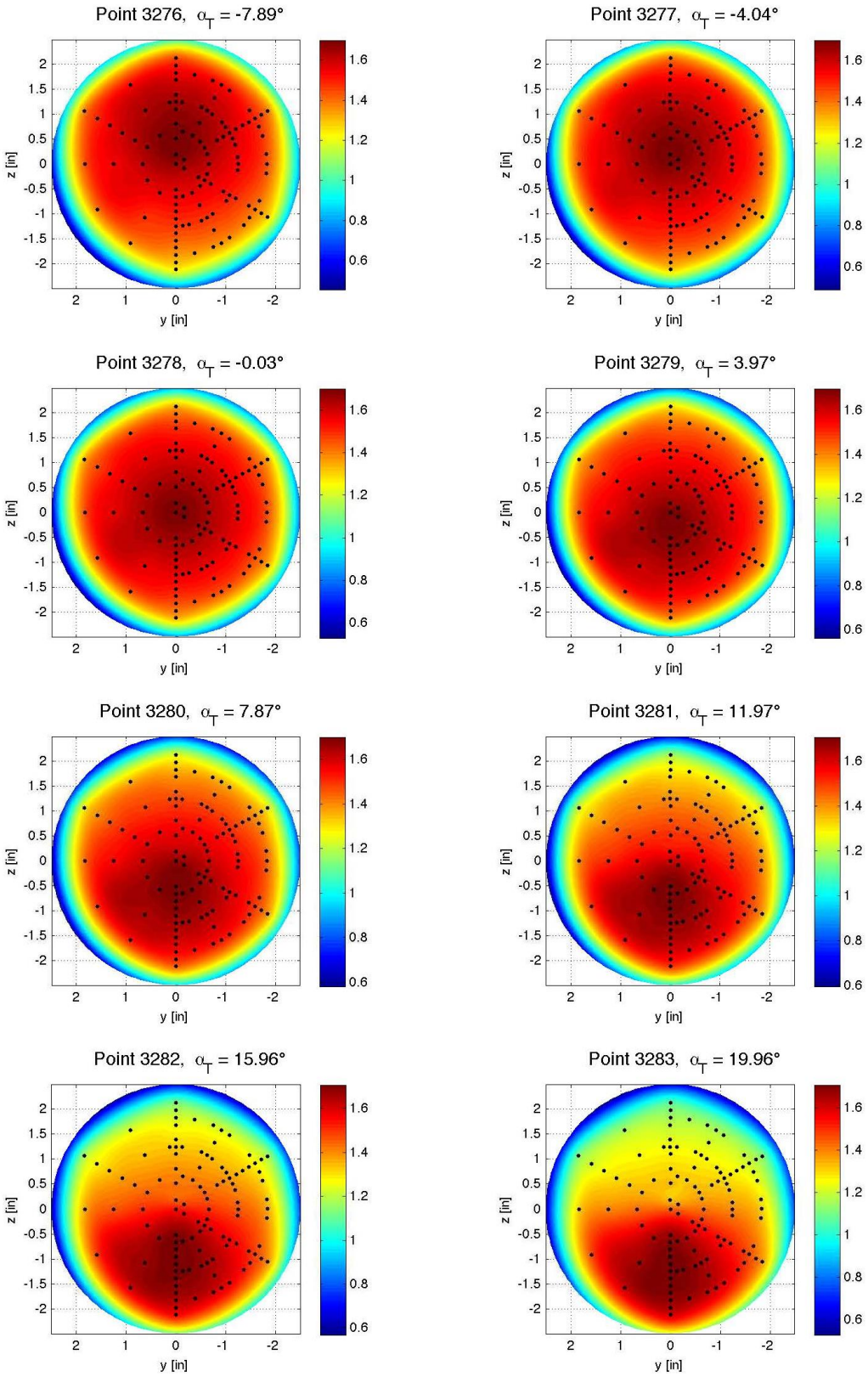

Figure E-216. Baseline configuration, Run 271, $M\infty$ = 2.4, Re_∞ = 1.0x10^6/ft, ϕ = −0.03°, X_S = 40.16 in, Y_S = 0.00 in, C_T = 0.00.

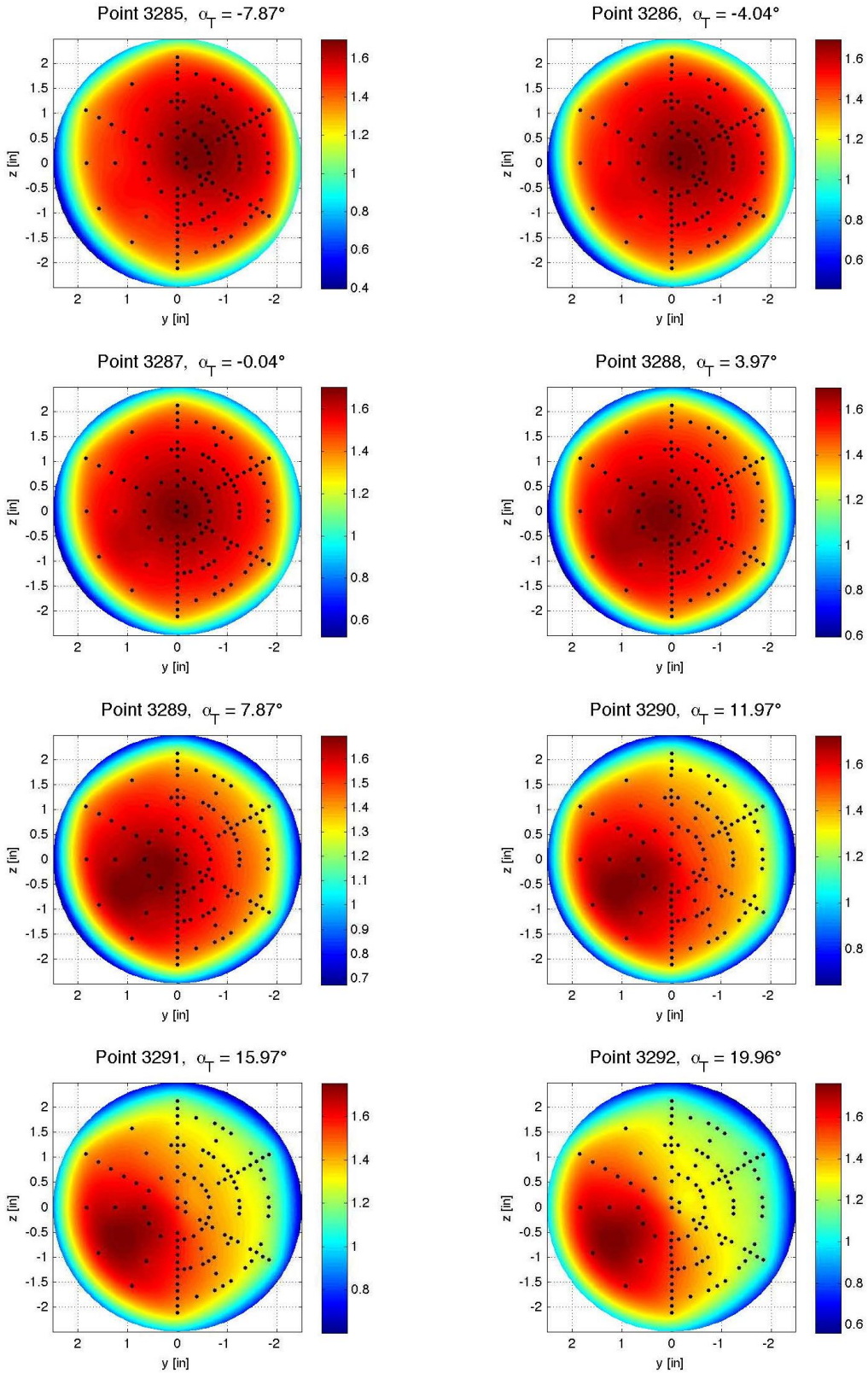

Figure E-217. Baseline configuration, Run 272, $M\infty$ = 2.4, Re_∞ = 1.0x10^6/ft, ϕ = 59.98°, X_S = 40.16 in, Y_S = 0.00 in, C_T = 0.00.

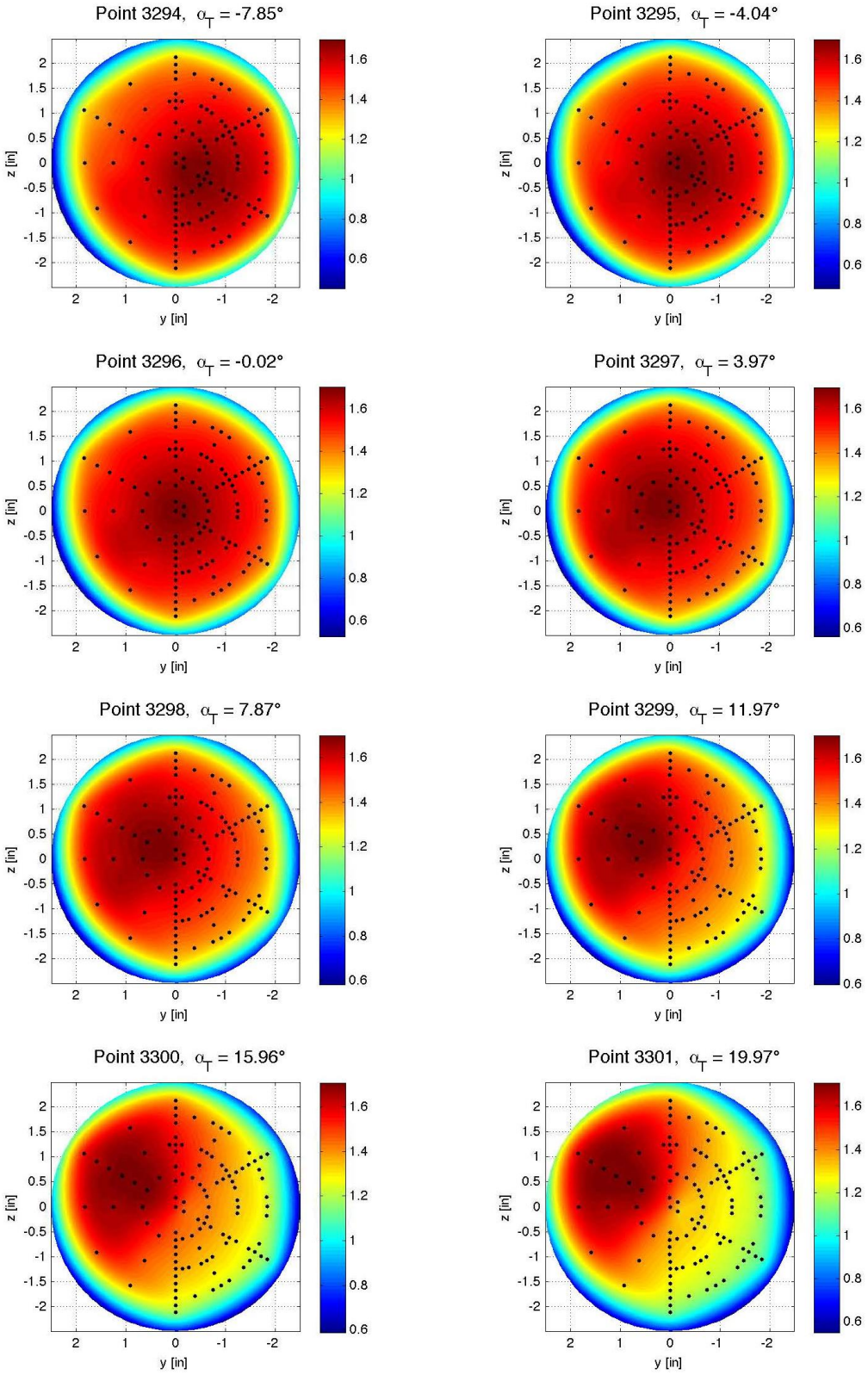

Figure E-218. Baseline configuration, Run 273, $M\infty$ = 2.4, Re_∞ = 1.0x10^6/ft, ϕ = 119.94°, X_S = 40.16 in, Y_S = 0.00 in, C_T = 0.00.

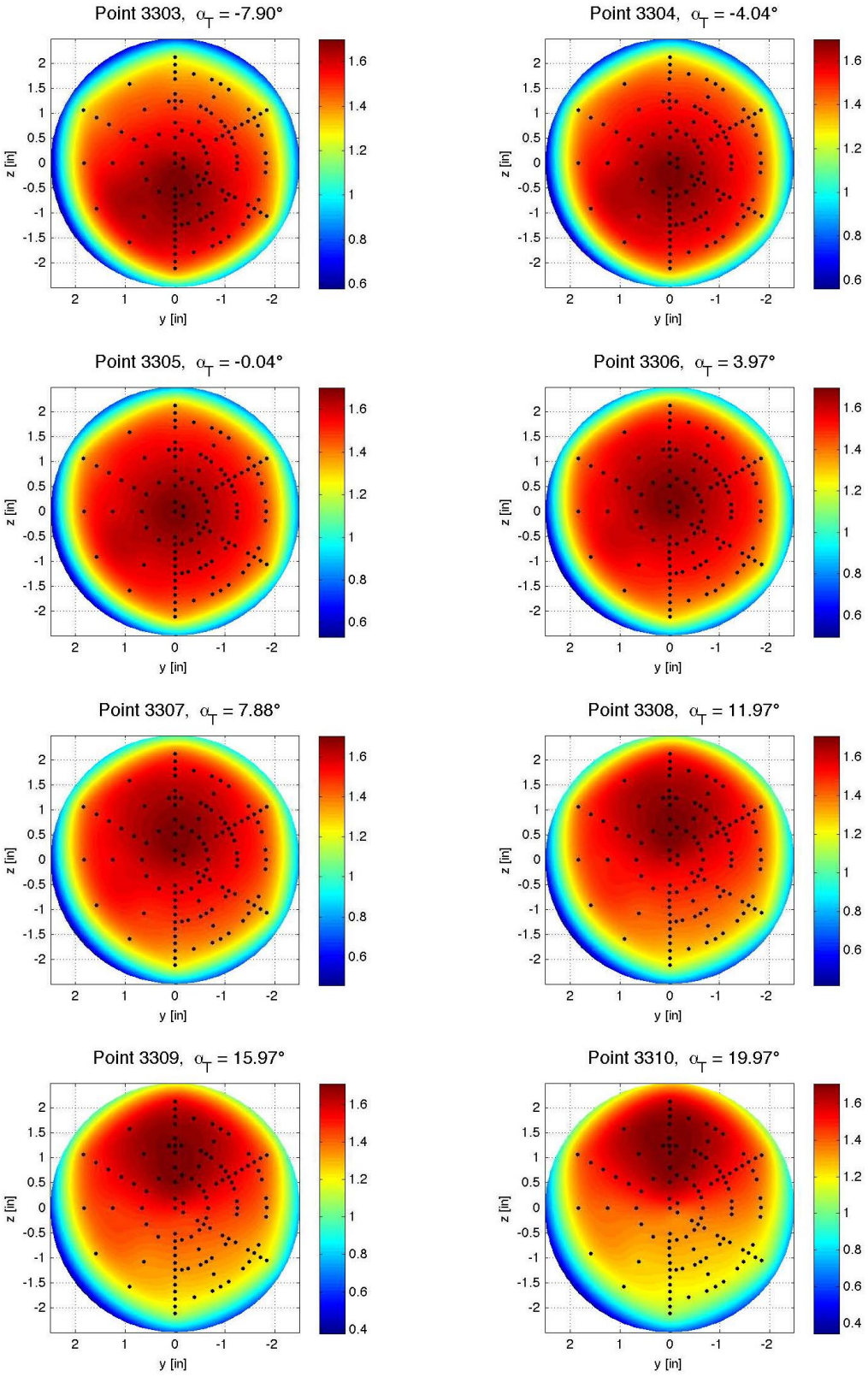

Figure E-219. Baseline configuration, Run 0274, $M\infty$ = 2.4, Re_∞ = 1.0x10^6/ft, ϕ = 179.99°, X_S = 40.16 in, Y_S = 0.00 in, C_T = 0.00.

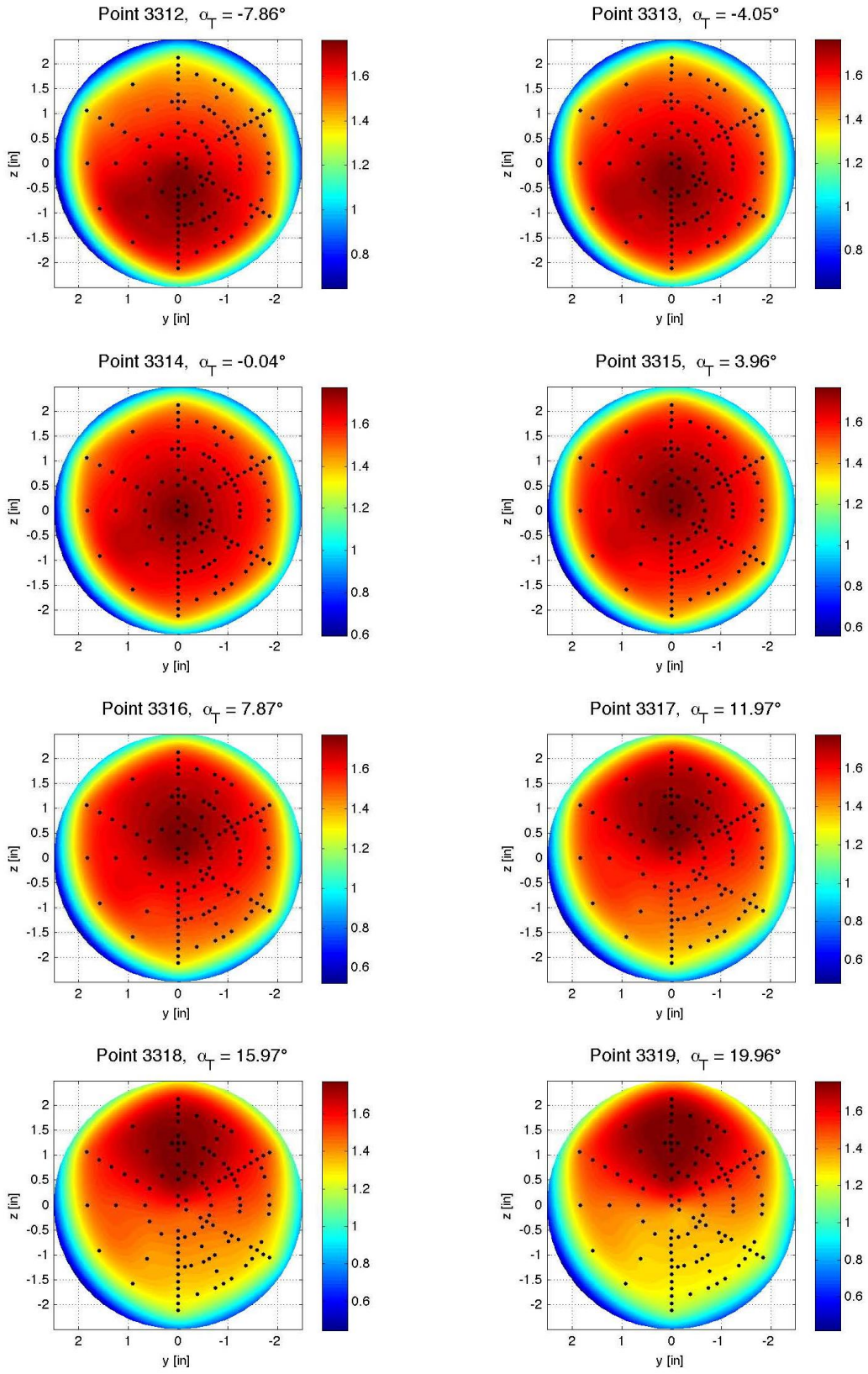

Figure E-220. Baseline configuration, Run 276, $M\infty$ = 3.5, Re_∞ = 1.0x10^6/ft, ϕ = 179.99°, X_S = 40.16 in, Y_S = 0.00 in, C_T = 0.00.

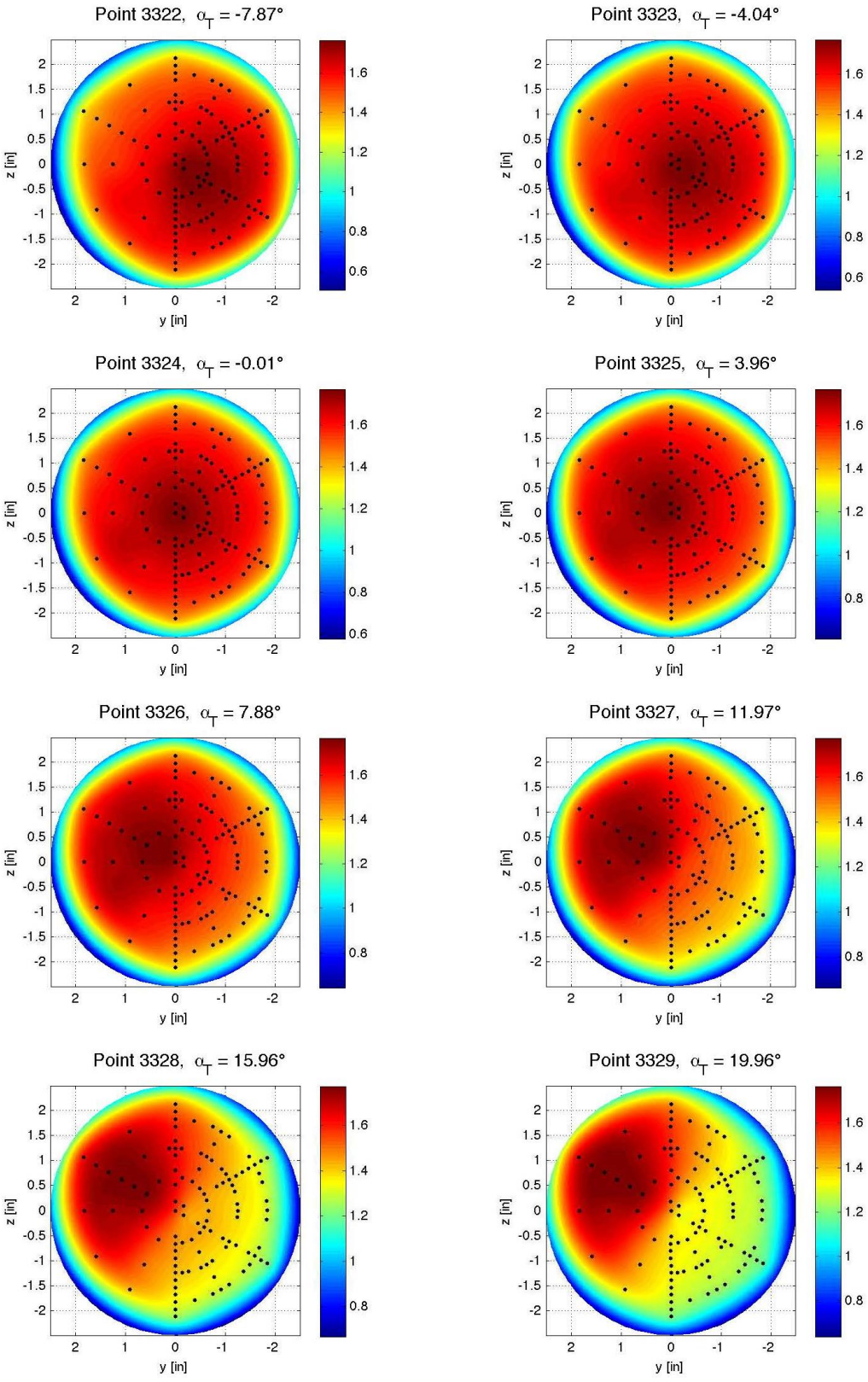

Figure E-221. Baseline configuration, Run 277, $M\infty$ = 3.5, Re_∞ = 1.0x10^6/ft, ϕ = 119.94°, X_S = 40.16 in, Y_S = 0.00 in, C_T = 0.00.

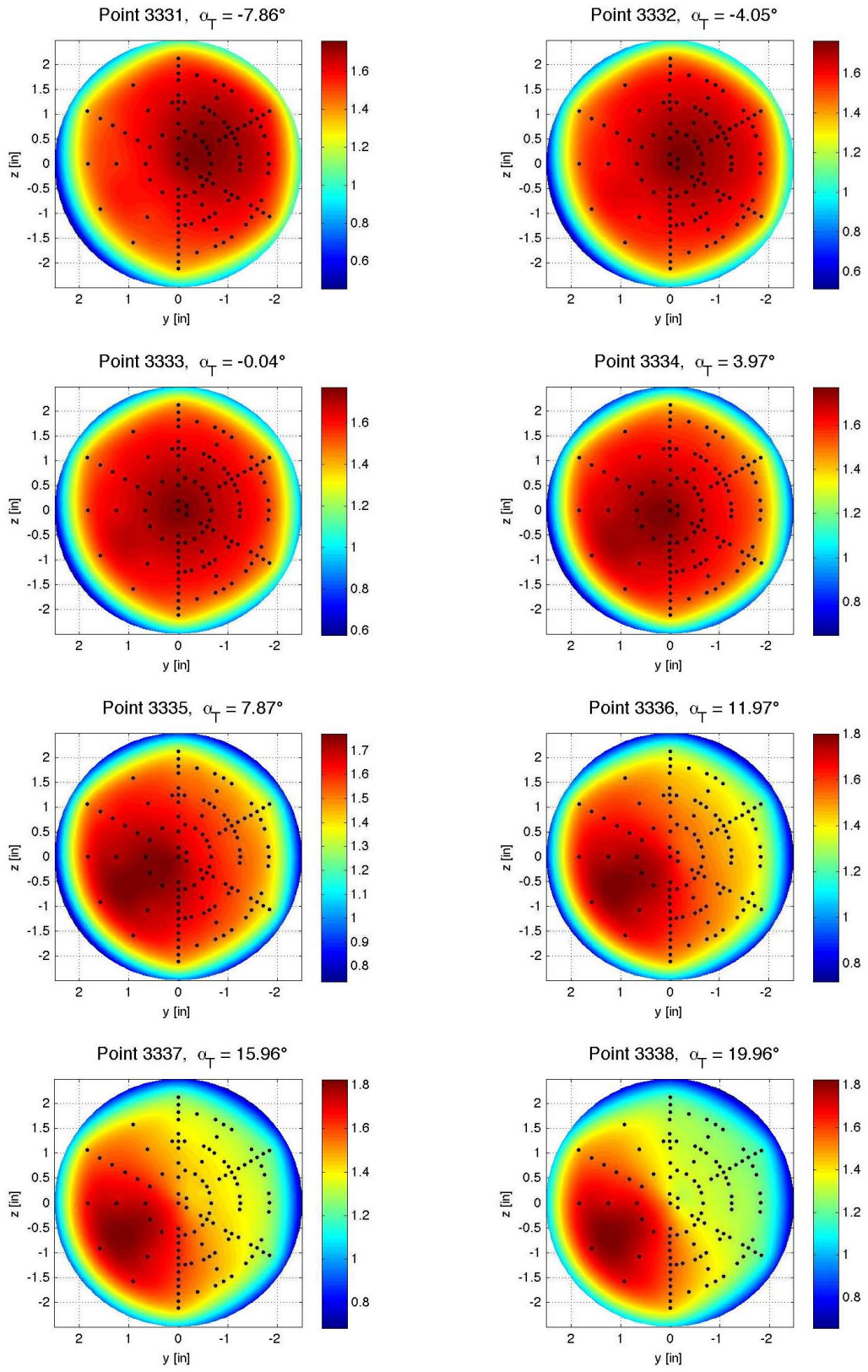

Figure E-222. Baseline configuration, Run 278, $M\infty$ = 3.5, Re_∞ = 1.0x10^6/ft, ϕ = 60.00°, X_S = 40.16 in, Y_S = 0.00 in, C_T = 0.00.

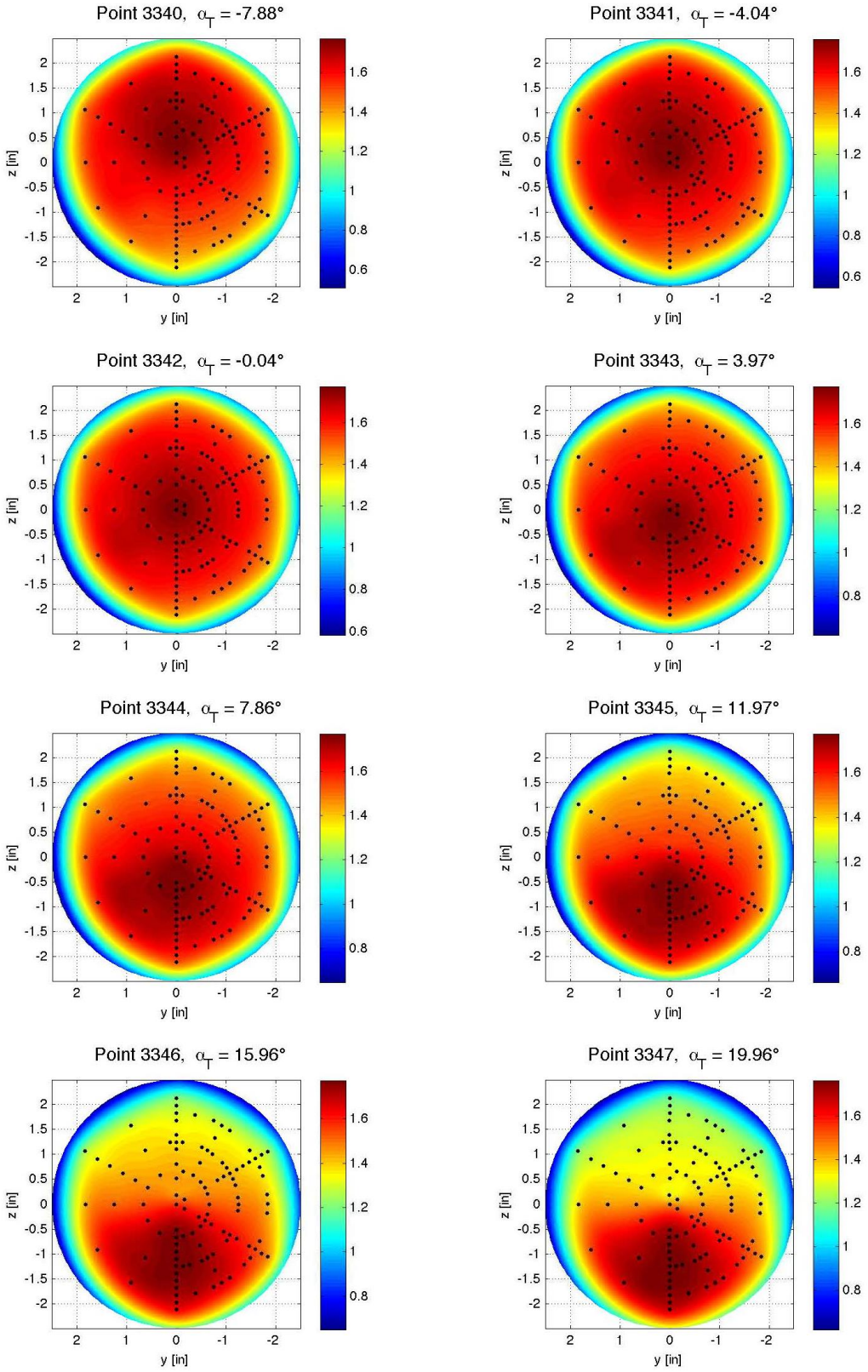

Figure E-223. Baseline configuration, Run 279, $M\infty$ = 3.5, Re_∞ = 1.0x10^6/ft, ϕ = −0.05°, X_S = 40.16 in, Y_S = 0.00 in, C_T = 0.00.

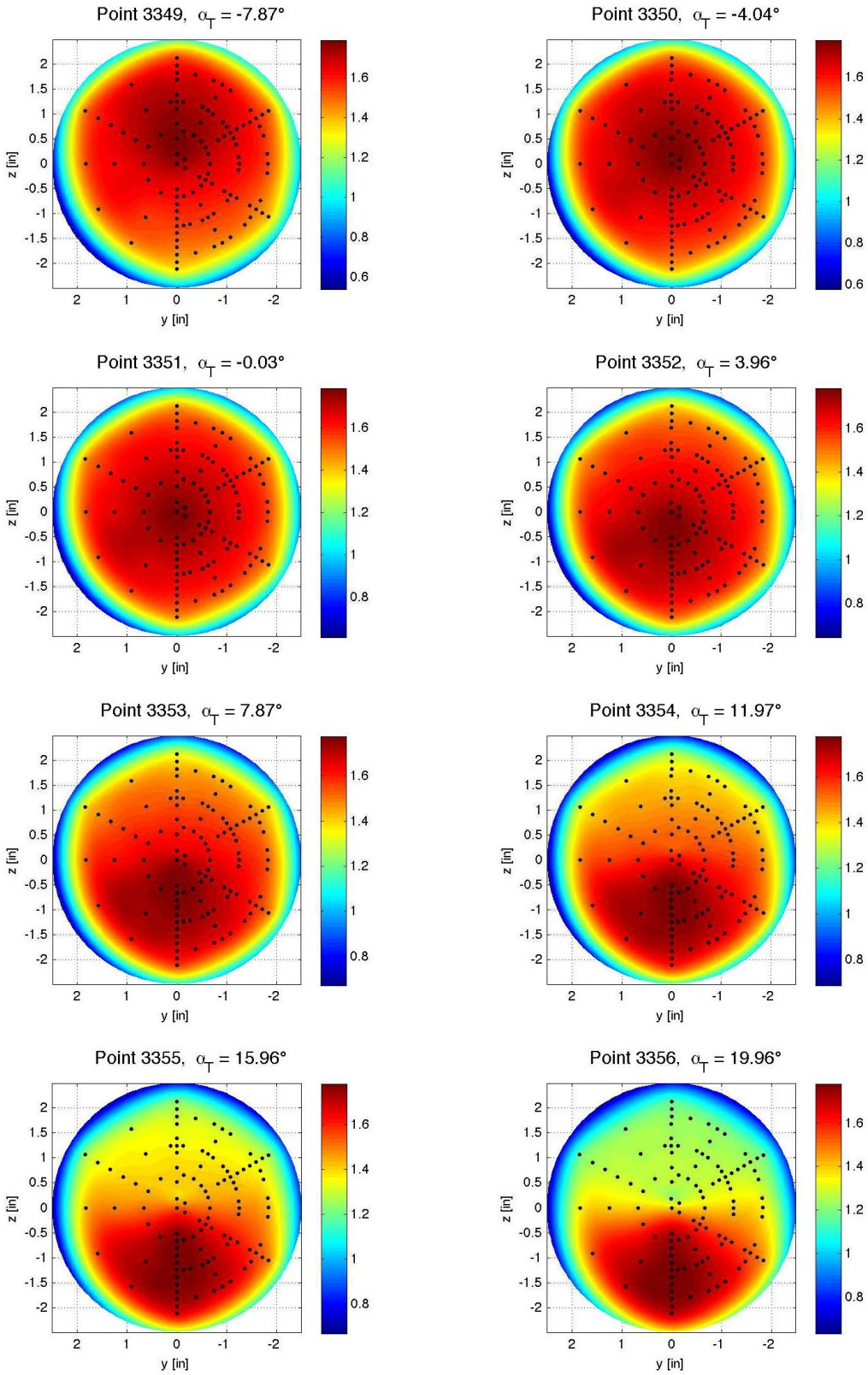

Figure E-224. Baseline configuration, Run 280, $M\infty$ = 4.6, Re_∞ = 1.5x10^6/ft, ϕ = −0.05°, X_S = 40.16 in, Y_S = 0.00 in, C_T = 0.00.

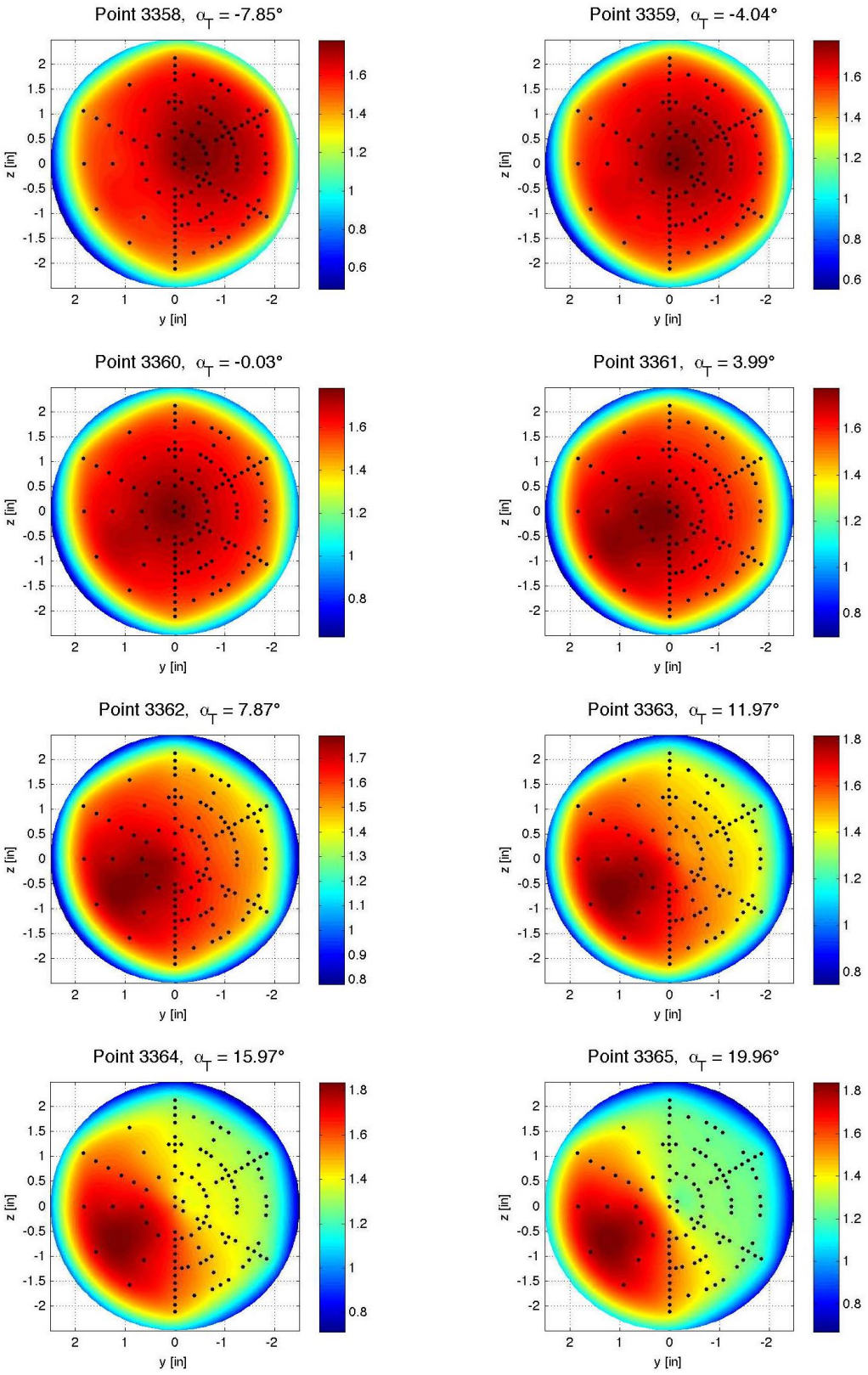

Figure E-225. Baseline configuration, Run 281, $M\infty$ = 4.6, Re_∞ = 1.5x10^6/ft, ϕ = 59.98°, X_S = 40.16 in, Y_S = 0.00 in, C_T = 0.00.

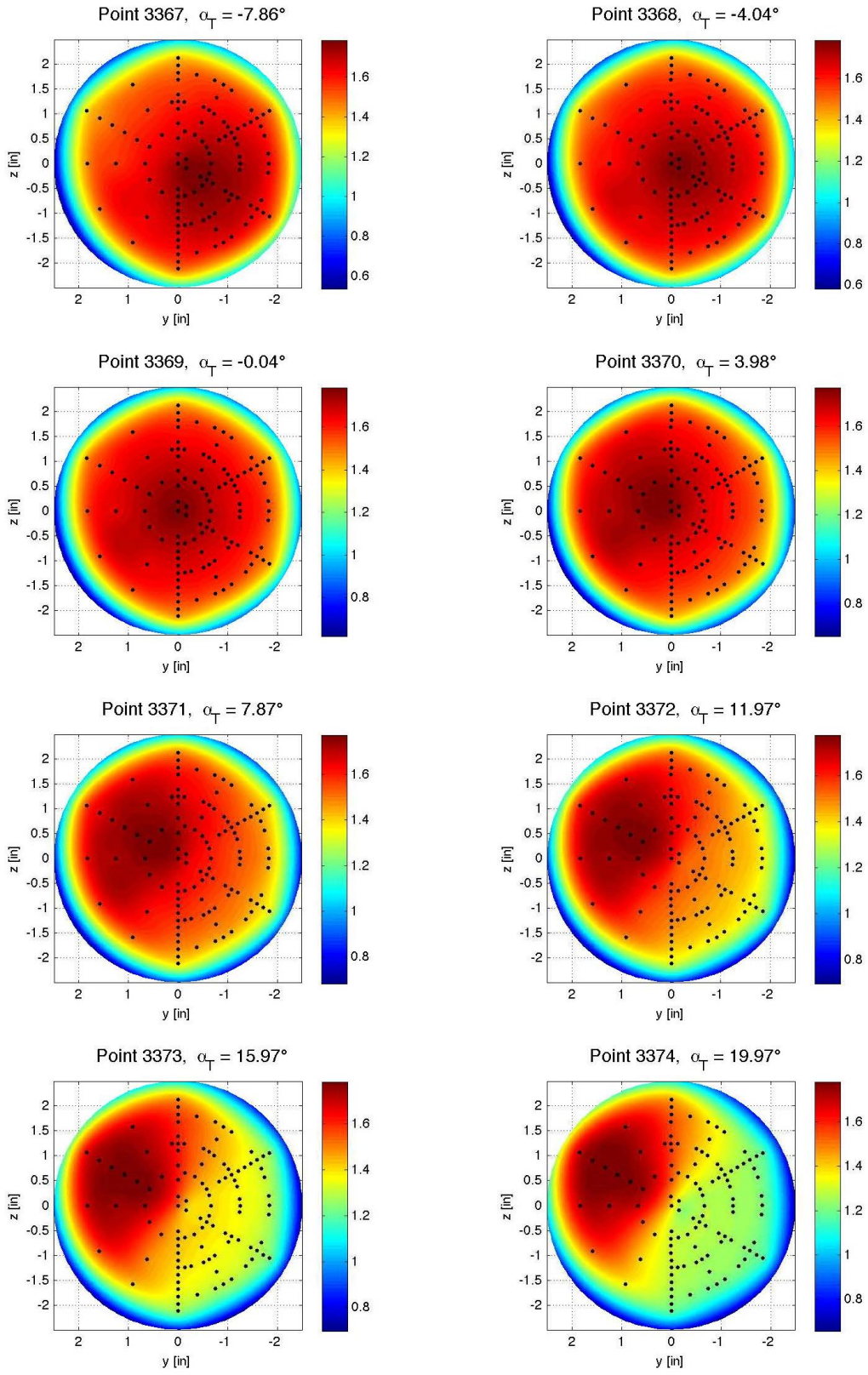

Figure E-226. Baseline configuration, Run 282, $M\infty$ = 4.6, Re_∞ = 1.5x10^6/ft, ϕ = 119.96°, X_S = 40.16 in, Y_S = 0.00 in, C_T = 0.00.

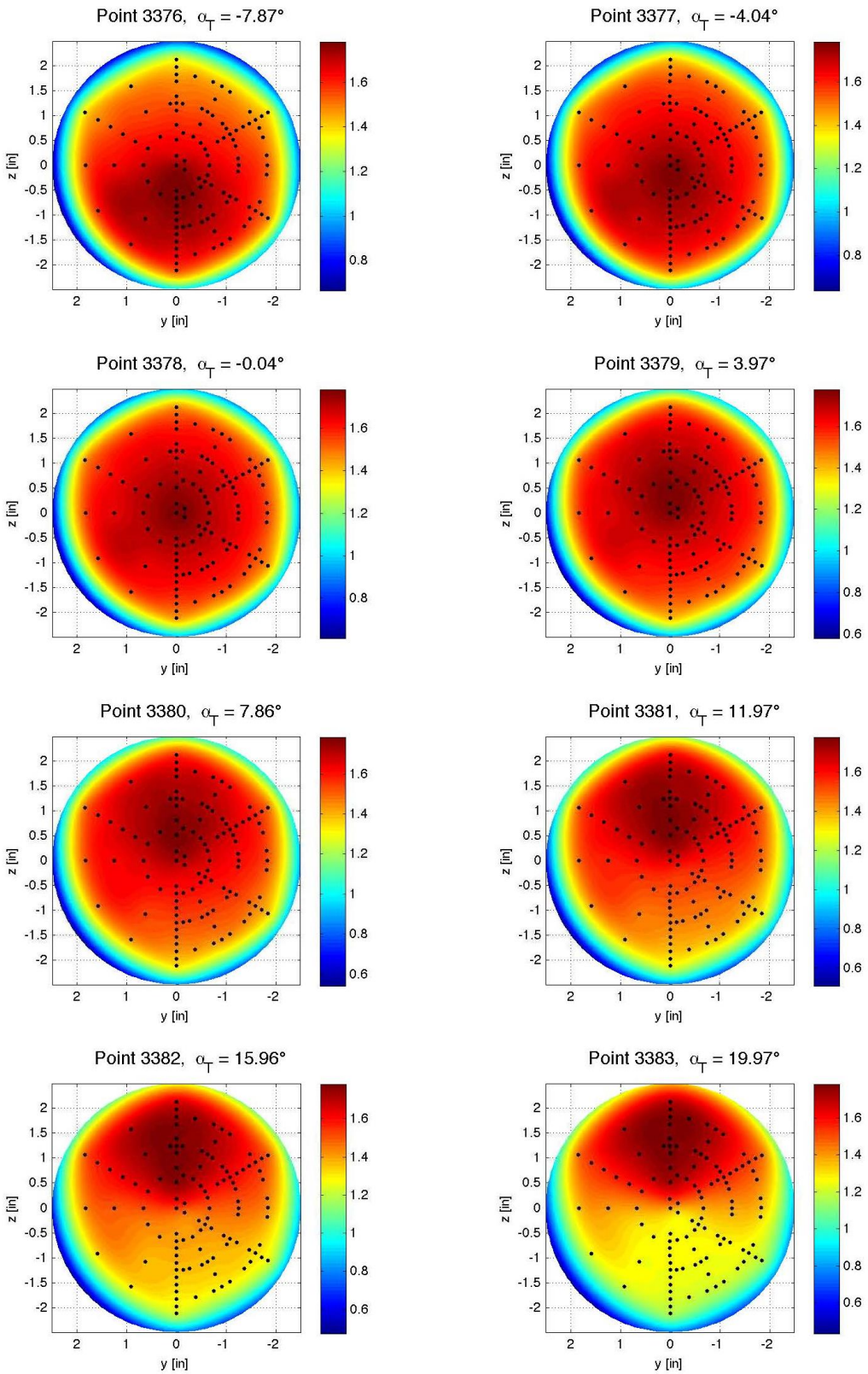

Figure E-227. Baseline configuration, Run 283, $M\infty$ = 4.6, Re_∞ = 1.5x10^6/ft, ϕ = 179.97°, X_S = 40.16 in, Y_S = 0.00 in, C_T = 0.00.

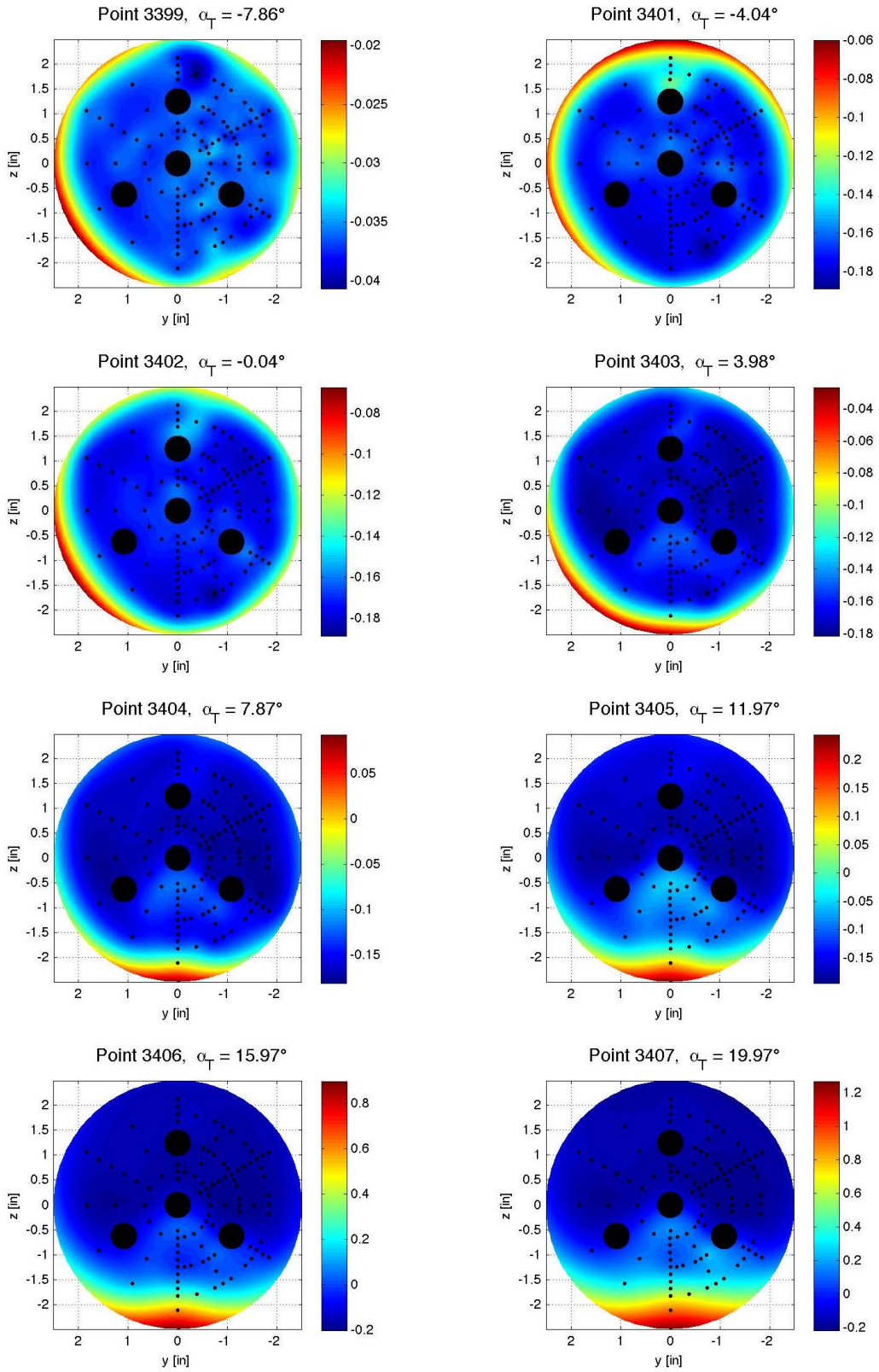

Figure E-228. Quad-nozzle configuration, Run 288, M_∞ = 2.4, Re_∞ = 1.0x10^6/ft, ϕ = −0.03°, X_S = 40.17 in, Y_S = 0.00 in, C_T = 1.92.

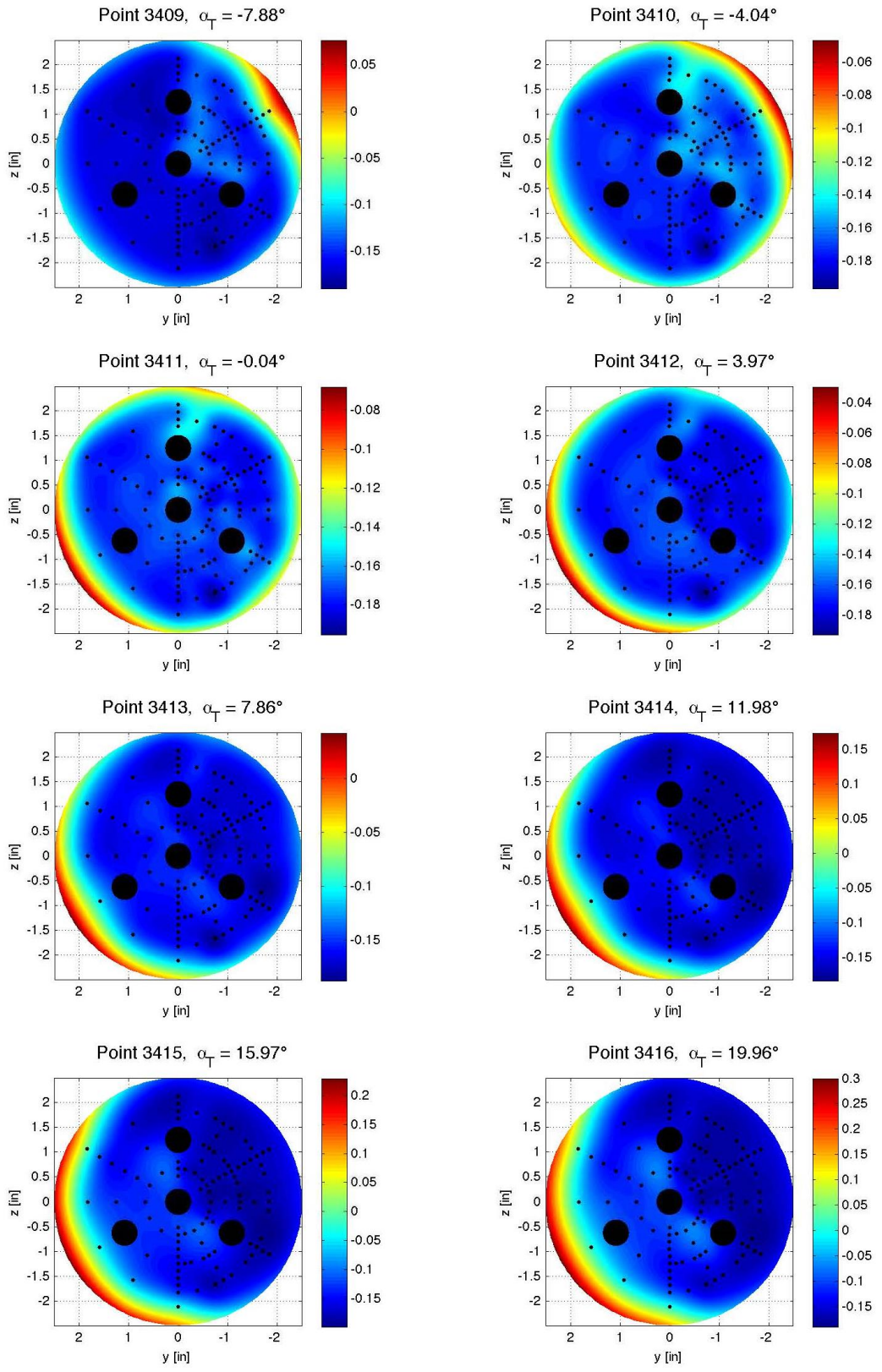

Figure E-229. Quad-nozzle configuration, Run 289, M_∞ = 2.4, Re_∞ = 1.0x10^6/ft, ϕ = 59.98°, X_S = 40.17 in, Y_S = 0.00 in, C_T = 1.93.

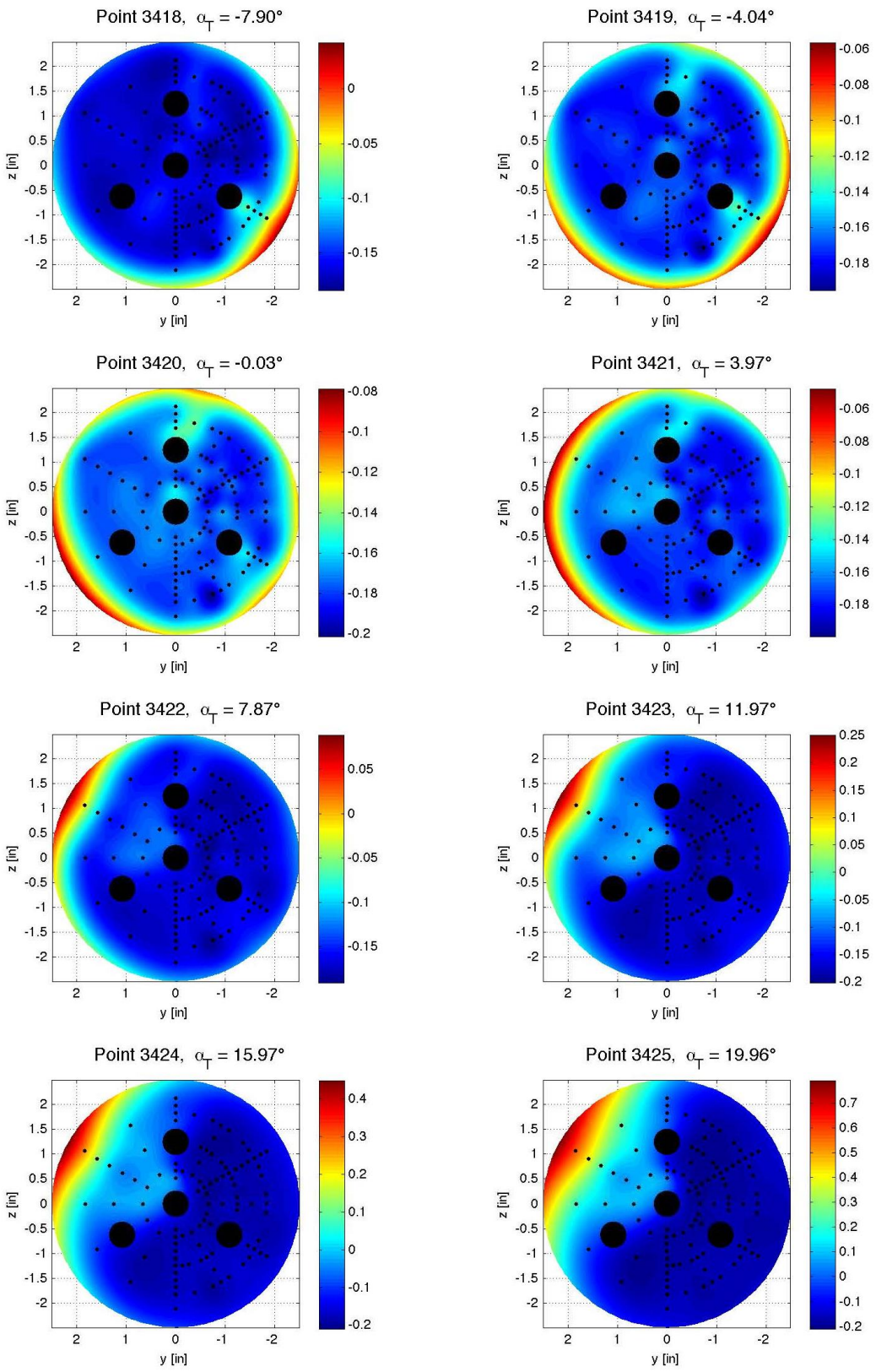

Figure E-230. Quad-nozzle configuration, Run 290, $M\infty$ = 2.4, Re_∞ = 1.0x10^6/ft, ϕ = 119.98°, X_S = 40.17 in, Y_S = 0.00 in, C_T = 1.93.

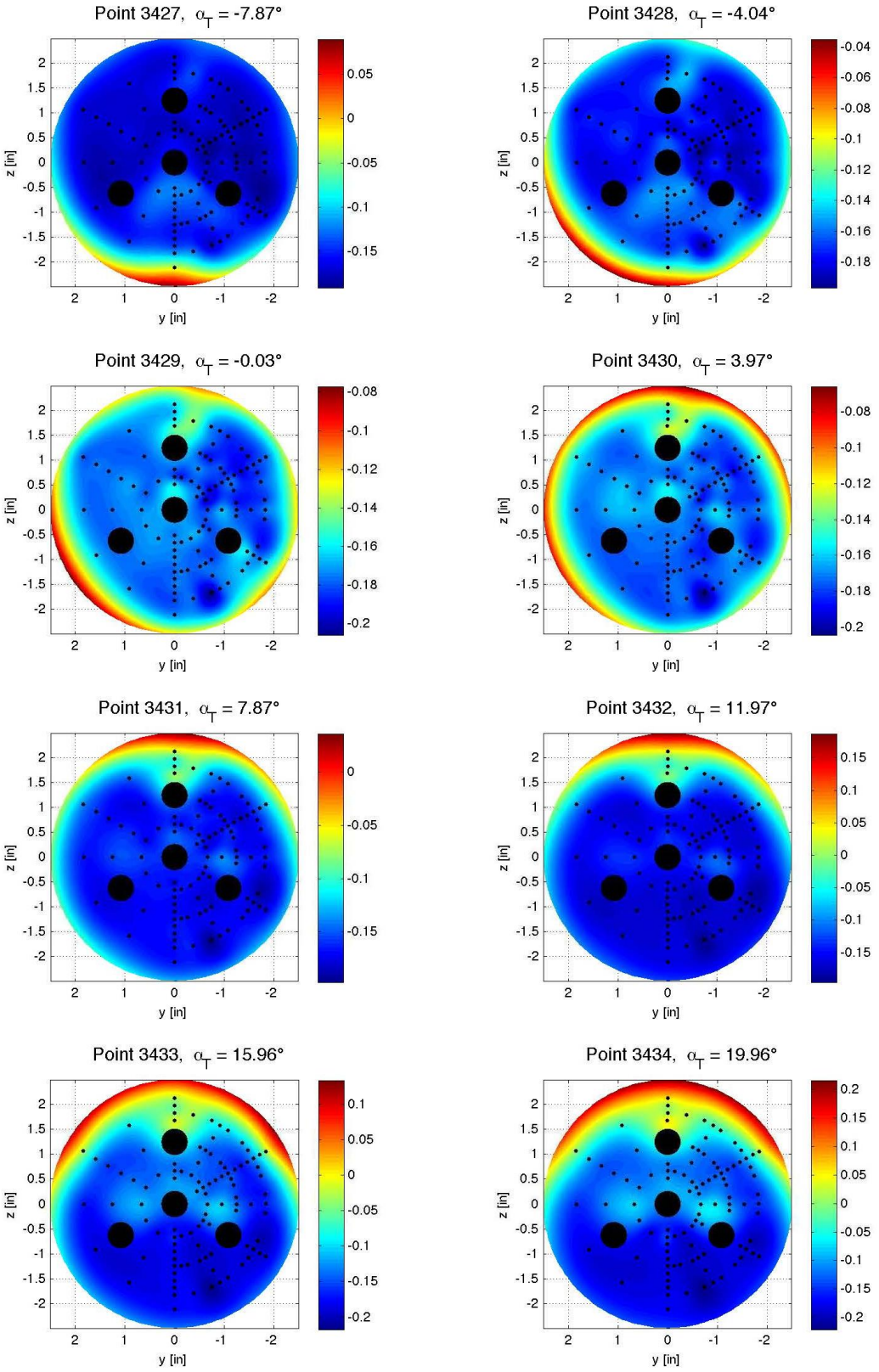

Figure E-231. Quad-nozzle configuration, Run 291, $M\infty$ = 2.4, Re_∞ = 1.0x10^6/ft, ϕ = −179.95°, X_S = 40.17 in, Y_S = 0.00 in, C_T = 1.94.

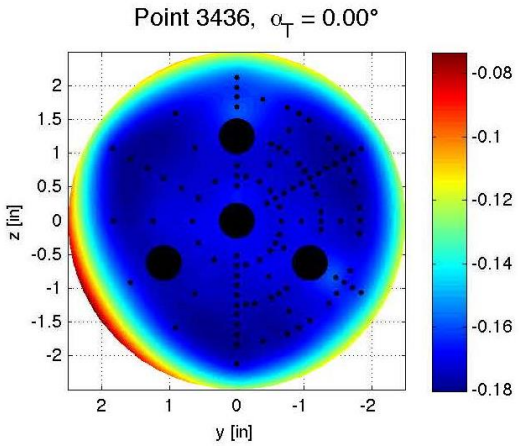

Figure E-232. Quad-nozzle configuration, Run 292, $M\infty$ = 2.4, Re_∞ = 1.0x10^6/ft, ϕ = 149.95°, X_S = 40.16 in, Y_S = 0.00 in, C_T = 1.93.

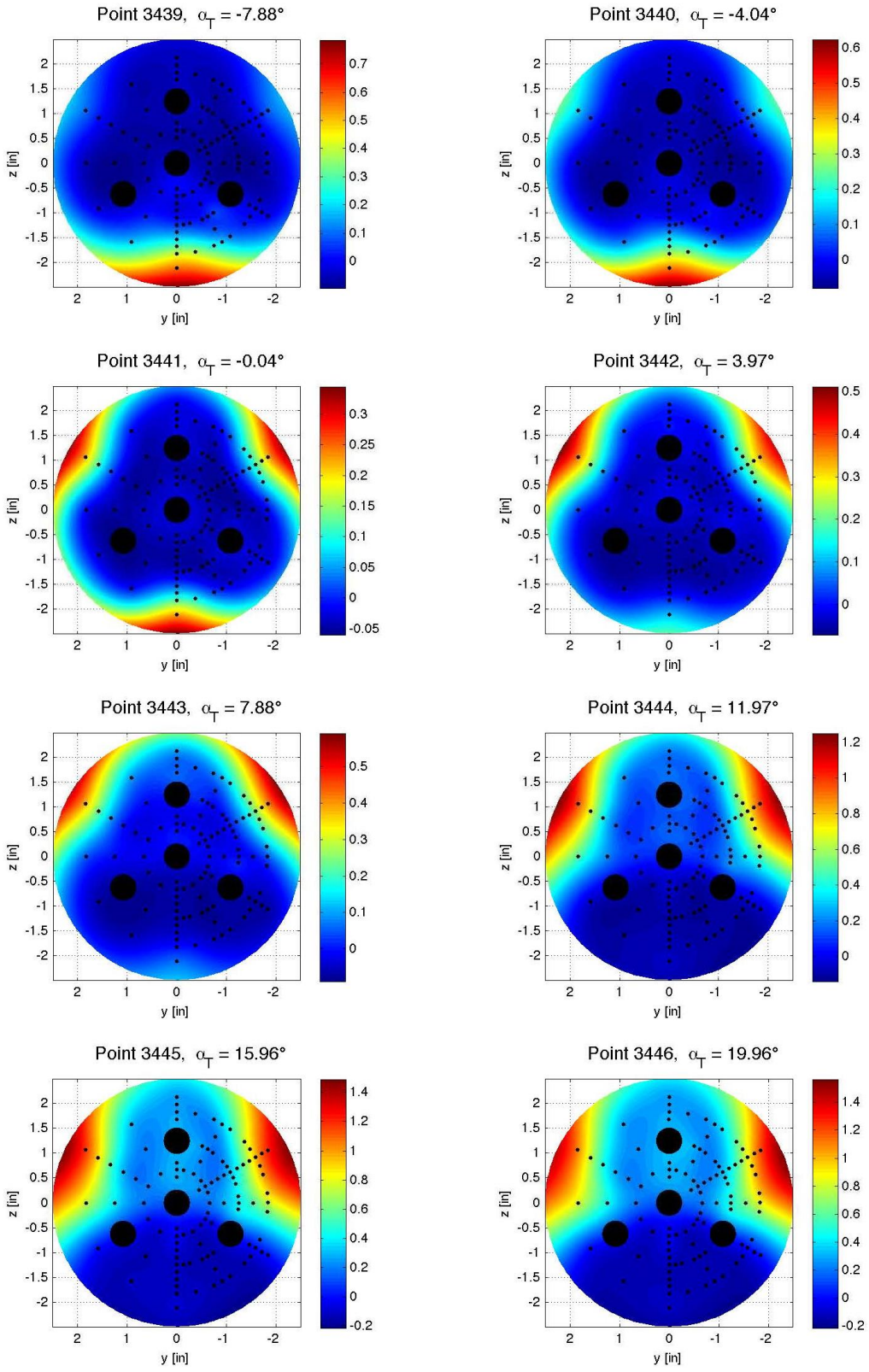

Figure E-233. Quad-nozzle configuration, Run 293, $M\infty$ = 2.4, Re_∞ = 1.0x10^6/ft, ϕ = 179.97°, X_S = 40.16 in, Y_S = 0.00 in, C_T = 0.94.

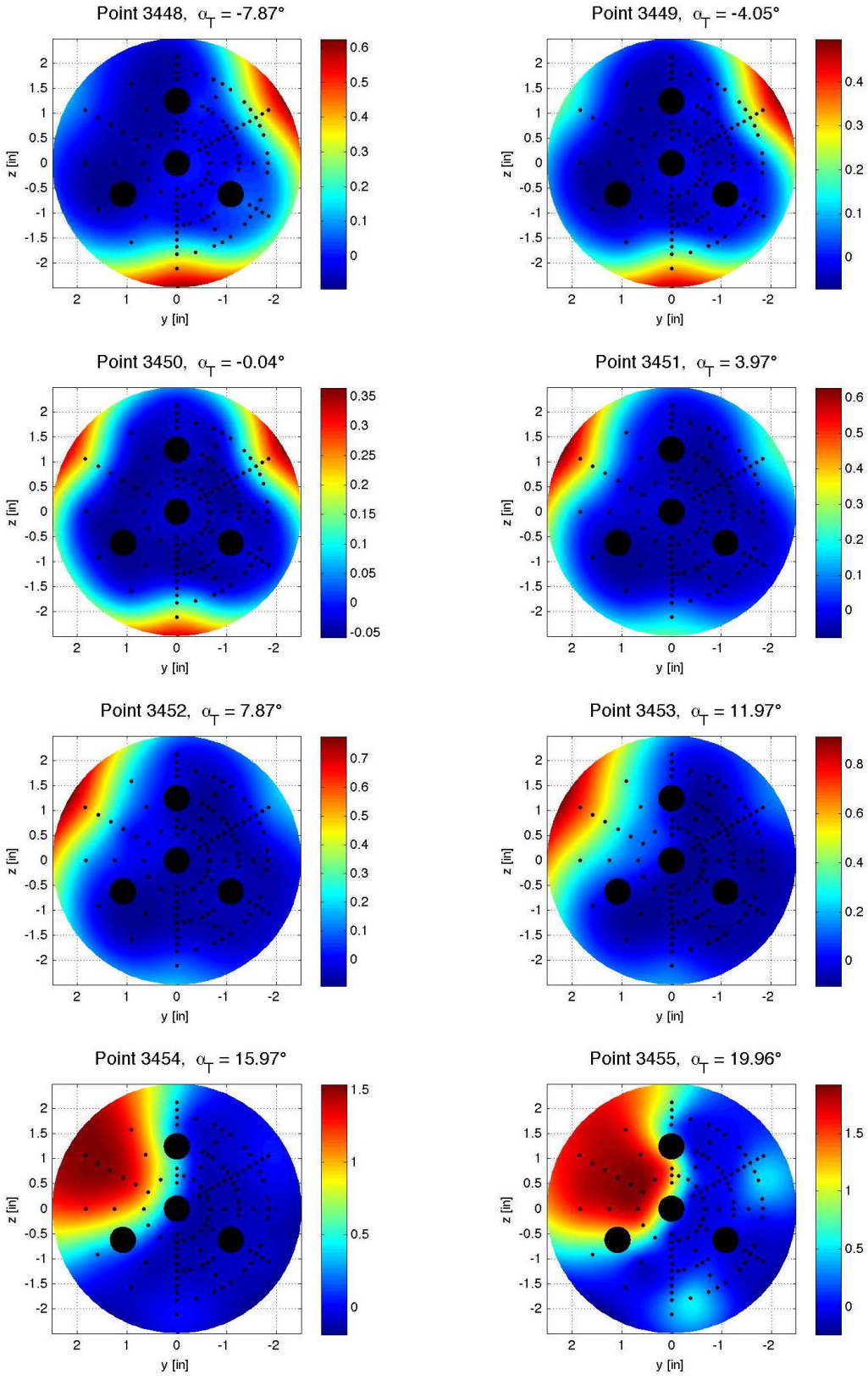

Figure E-234. Quad-nozzle configuration, Run 294, M_∞ = 2.4, Re_∞ = 1.0x10^6/ft, ϕ = 119.96°, X_S = 40.16 in, Y_S = 0.00 in, C_T = 0.95.

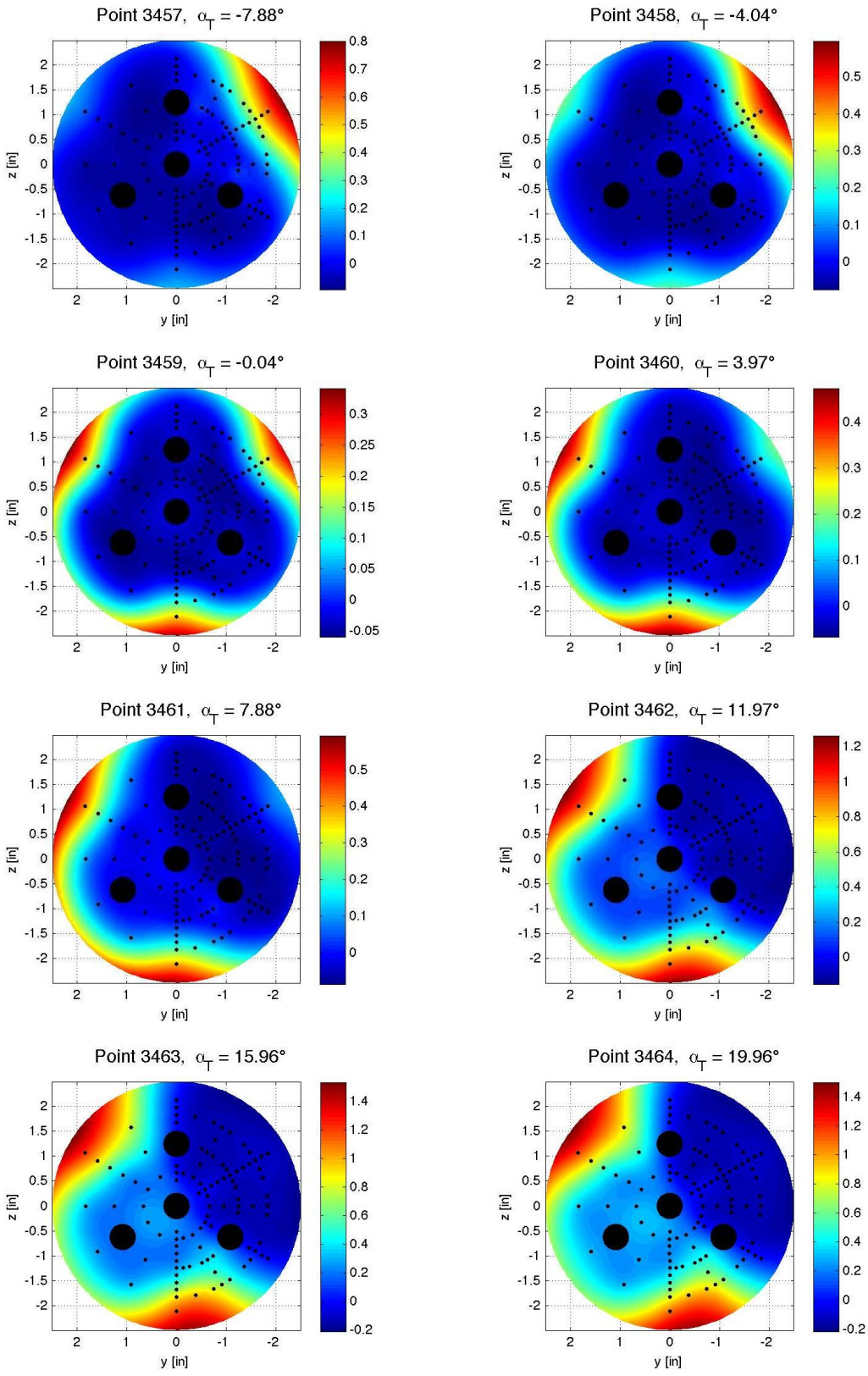

Figure E-235. Quad-nozzle configuration, Run 295, $M\infty$ = 2.4, Re_∞ = 1.0x10^6/ft, ϕ = 60.02°, X_S = 40.16 in, Y_S = 0.00 in, C_T = 0.94.

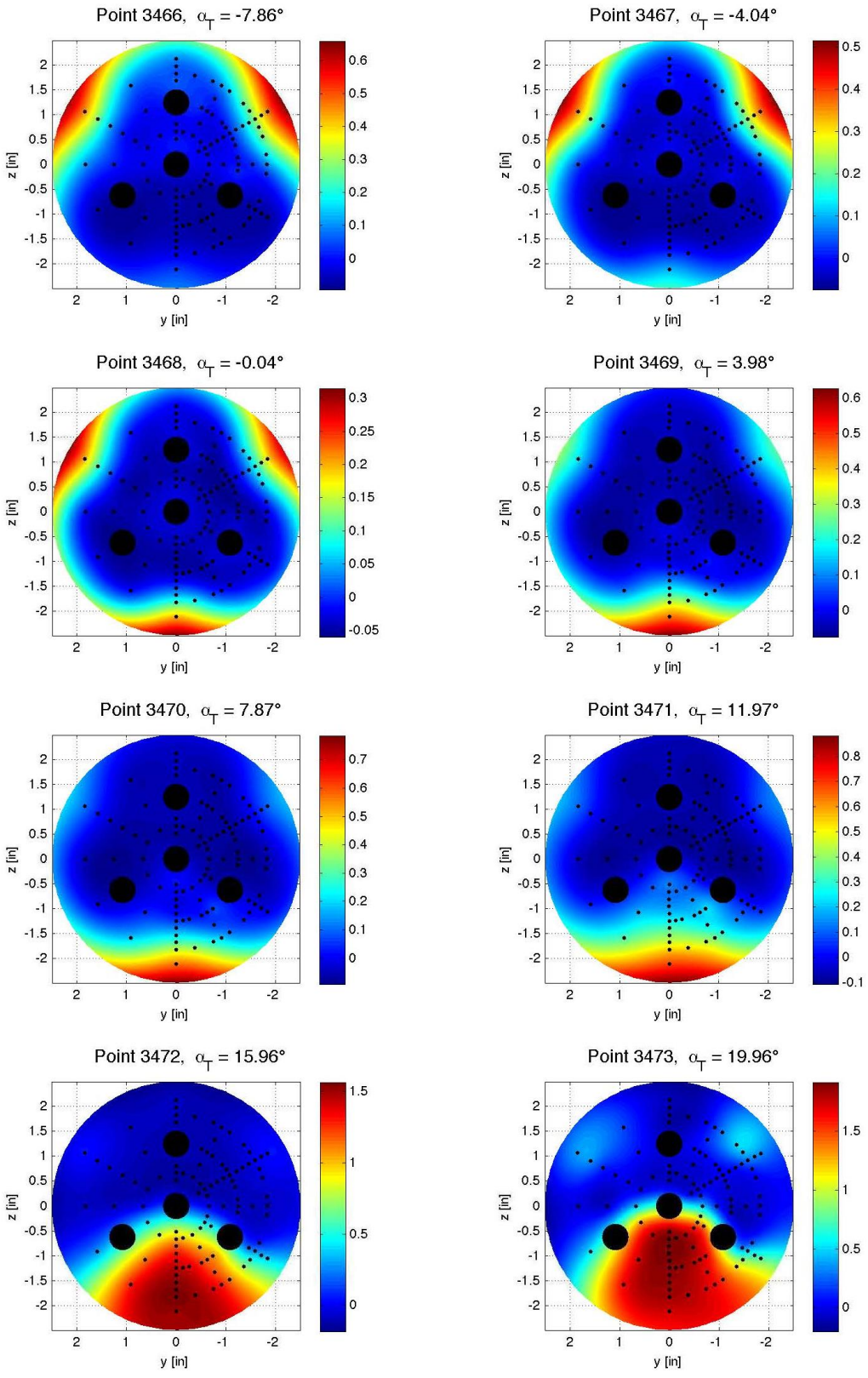

Figure E-236. Quad-nozzle configuration, Run 296, M_∞ = 2.4, Re_∞ = 1.0x10^6/ft, ϕ = −0.05°, X_S = 40.16 in, Y_S = 0.00 in, C_T = 0.95.

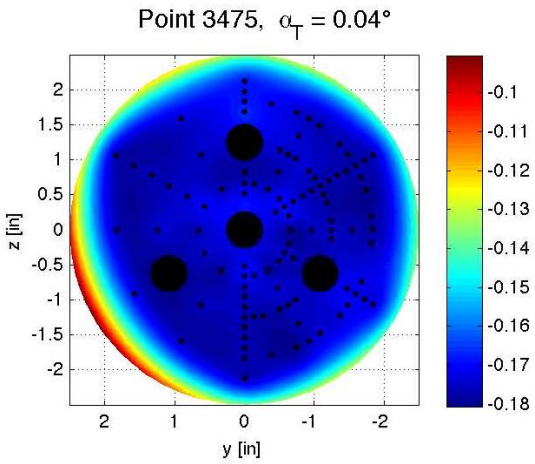

Figure E-237. Quad-nozzle configuration, Run 297, $M\infty$ = 2.4, Re_∞ = 1.0x10^6/ft, ϕ = 30.03°, X_S = 40.15 in, Y_S = 0.00 in, C_T = 2.95.

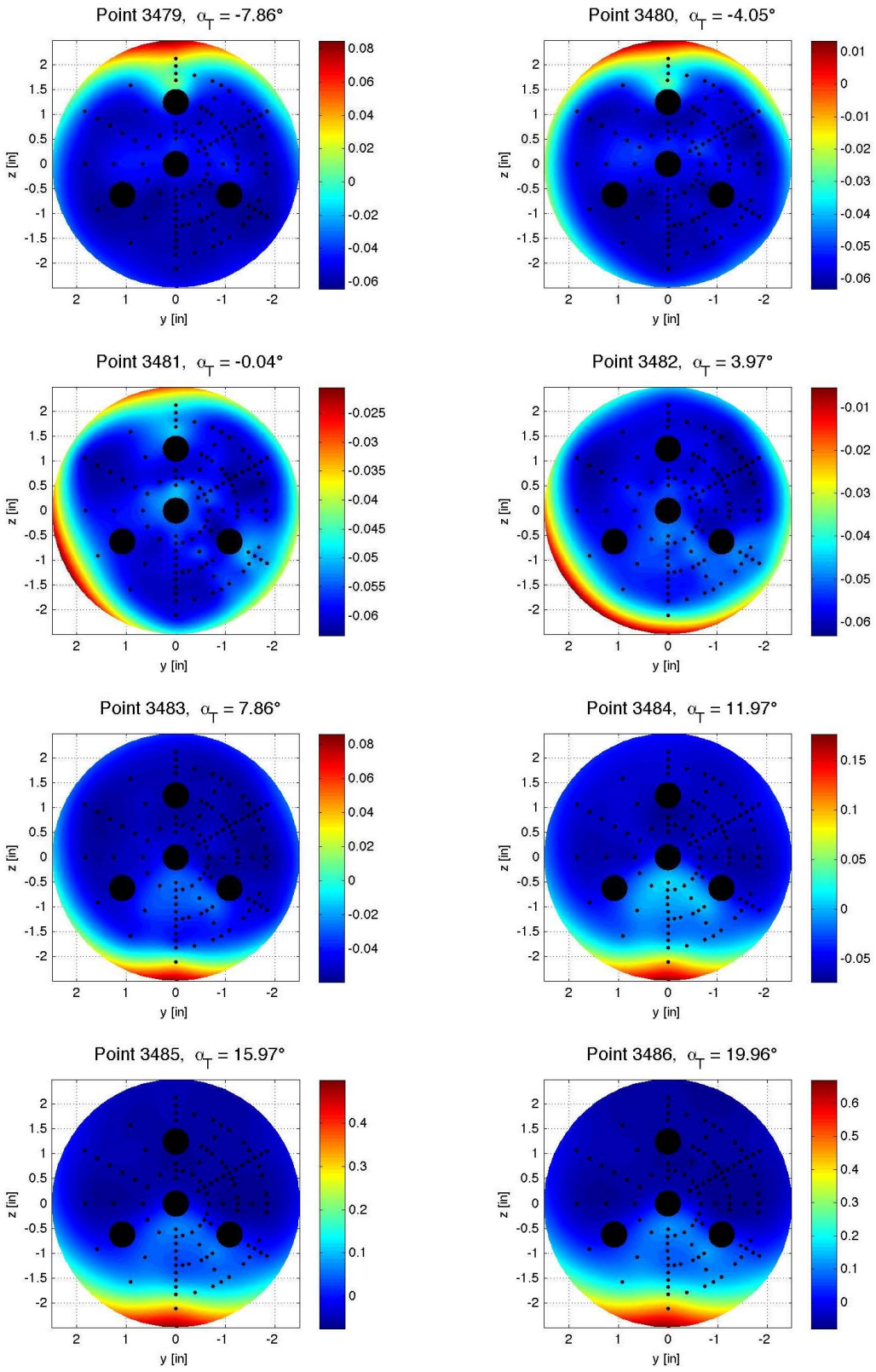

Figure E-238. Quad-nozzle configuration, Run 298, M_∞ = 3.5, Re_∞ = 1.0x10^6/ft, ϕ = 0.01°, X_S = 40.16 in, Y_S = 0.00 in, C_T = 1.91.

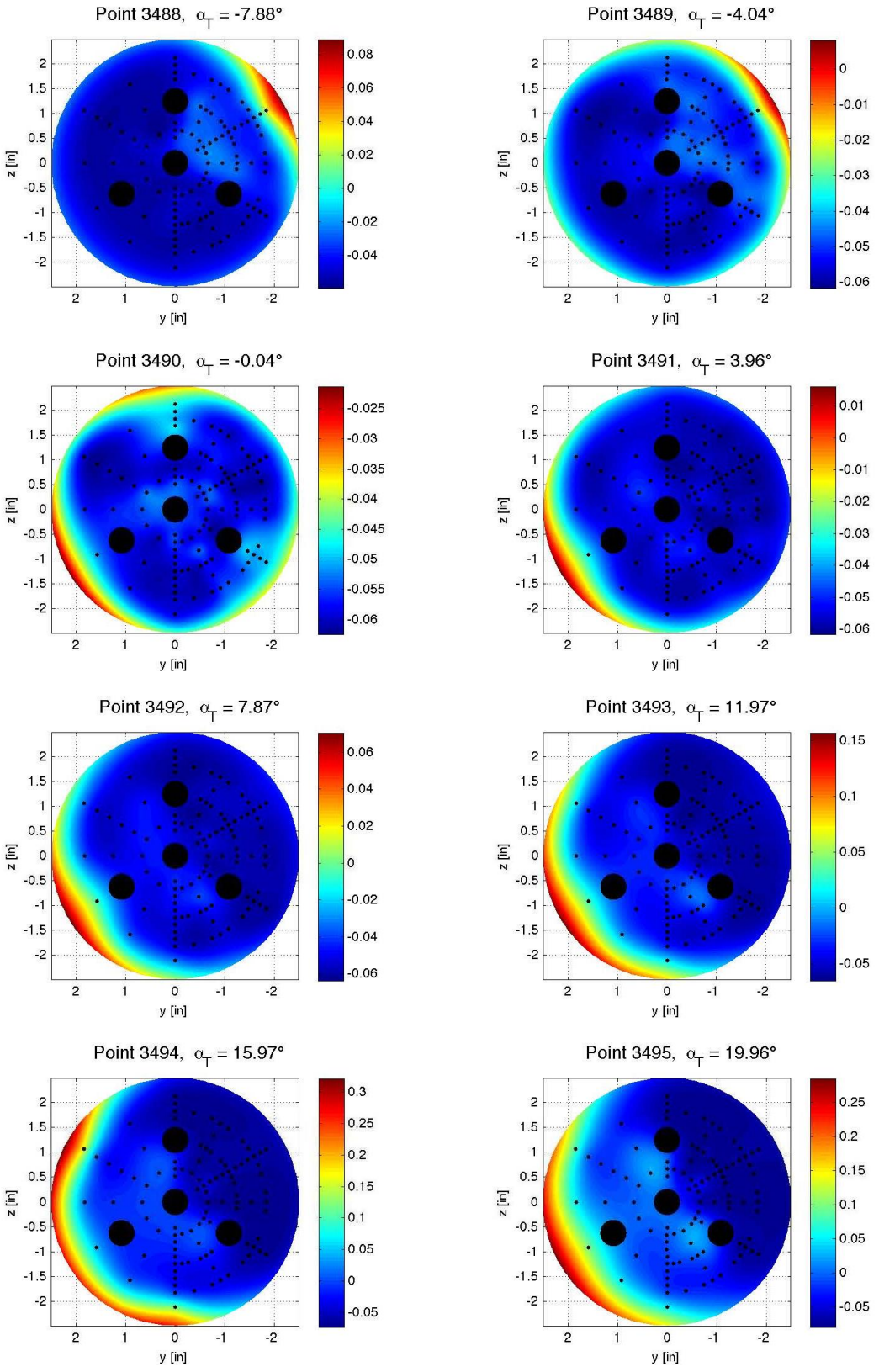

Figure E-239. Quad-nozzle configuration, Run 299, $M\infty$ = 3.5, Re_∞ = 1.0x10^6/ft, ϕ = 59.98°, X_S = 40.16 in, Y_S = 0.00 in, C_T = 1.92.

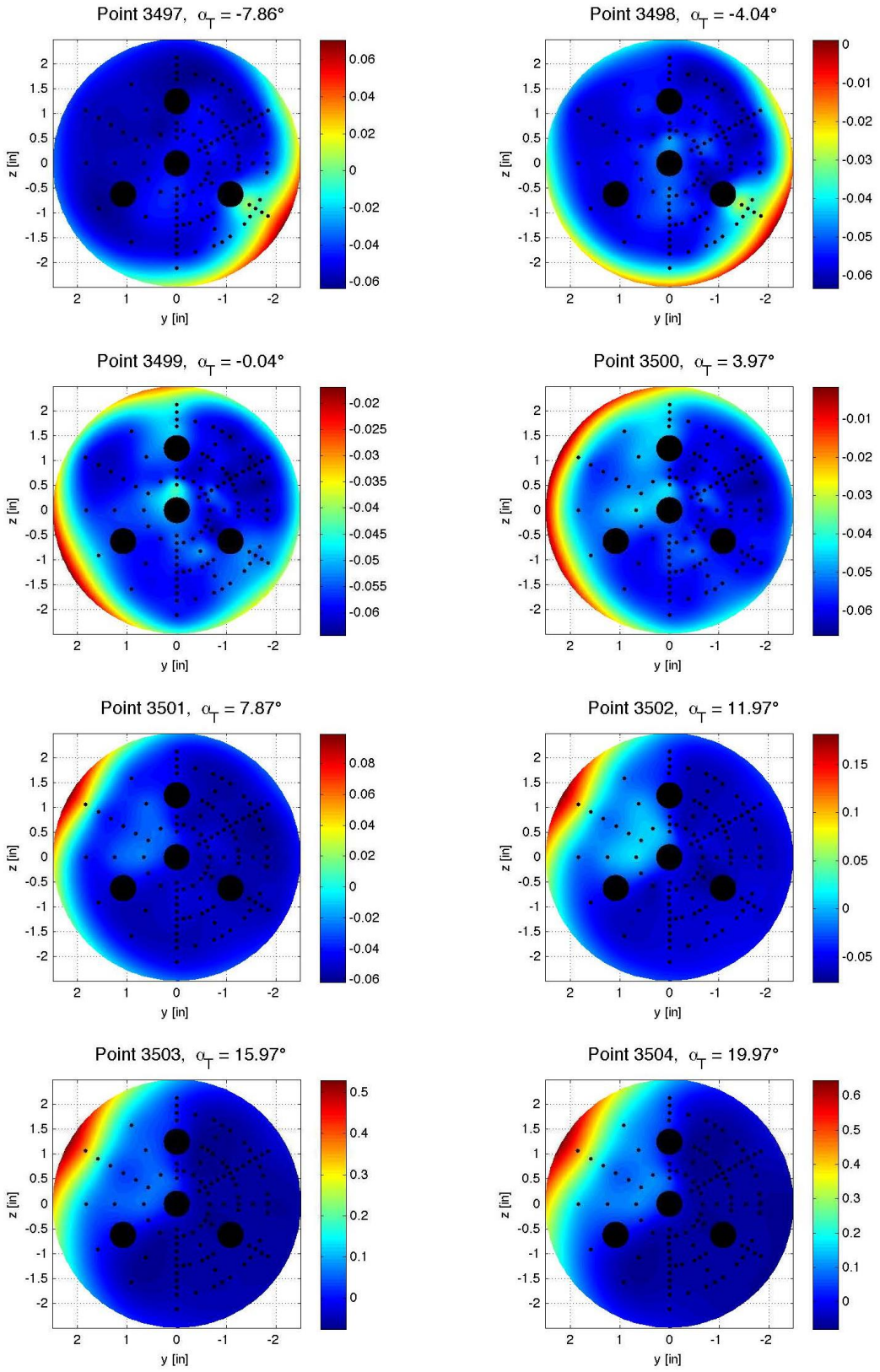

Figure E-240. Quad-nozzle configuration, Run 300, M_∞ = 3.5, Re_∞ = 1.0x10^6/ft, ϕ = 119.96°, X_S = 40.16 in, Y_S = 0.00 in, C_T = 1.92.

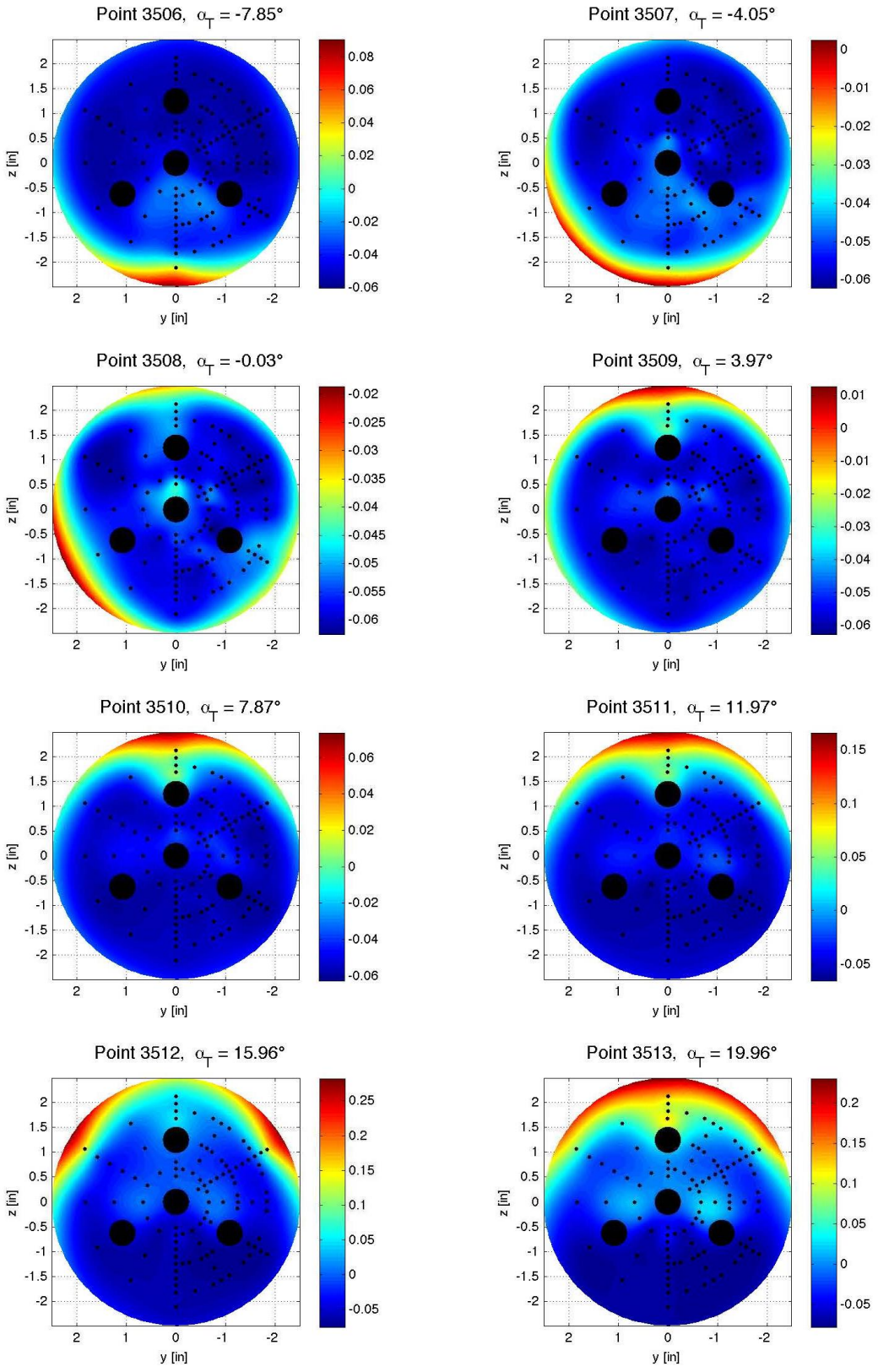

Figure E-241. Quad-nozzle configuration, Run 301, $M\infty$ = 3.5, Re_∞ = 1.0x10^6/ft, ϕ = 179.95°, X_S = 40.16 in, Y_S = 0.00 in, C_T = 1.92.

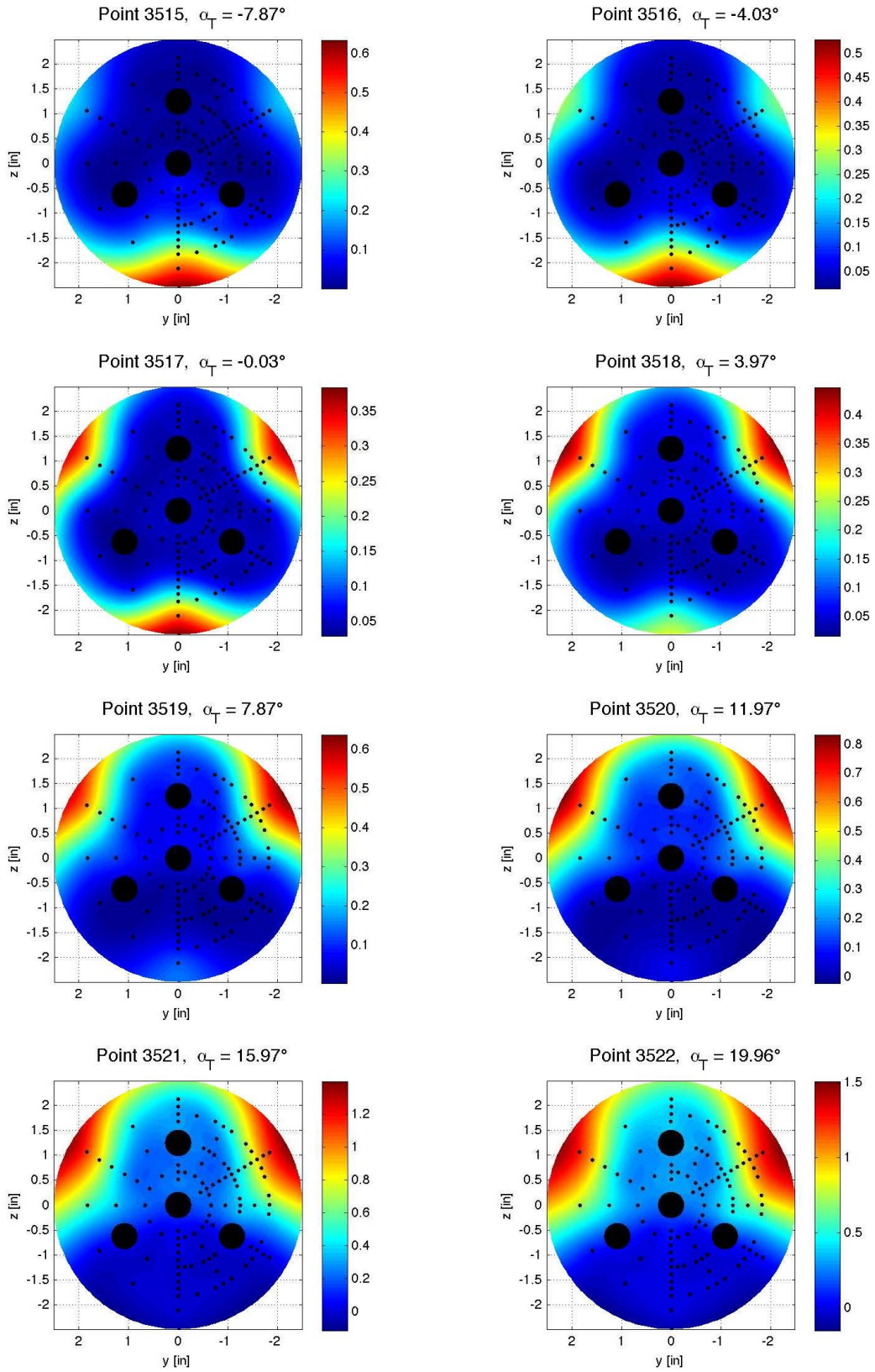

Figure E-242. Quad-nozzle configuration, Run 302, M_∞ = 3.5, Re_∞ = 1.0x10^6/ft, ϕ = 179.95°, X_S = 40.16 in, Y_S = 0.00 in, C_T = 0.90.

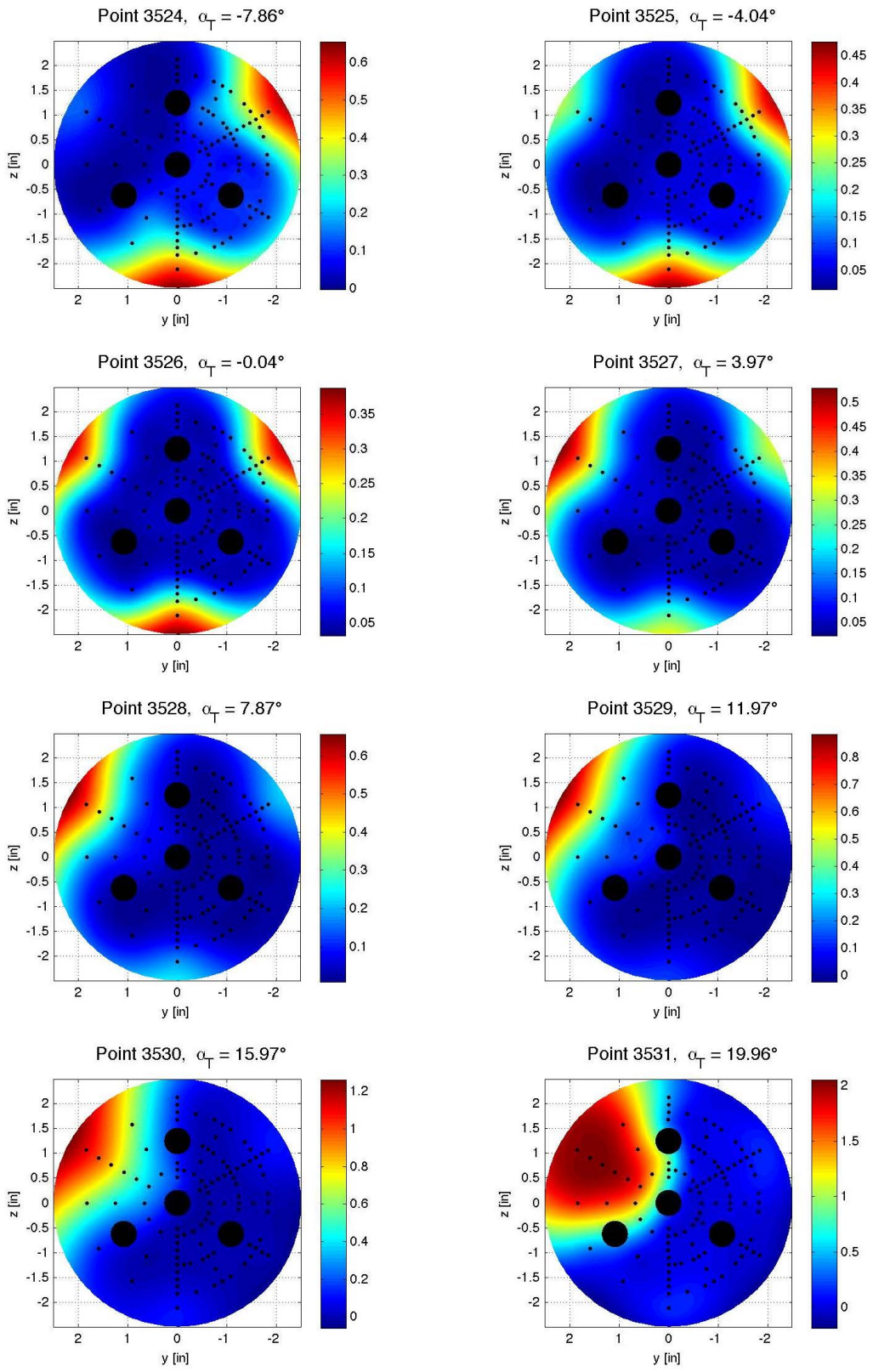

Figure E-243. Quad-nozzle configuration, Run 303, M_∞ = 3.5, Re_∞ = 1.0x10^6/ft, ϕ = 120.02°, X_S = 40.16 in, Y_S = 0.00 in, C_T = 0.89.

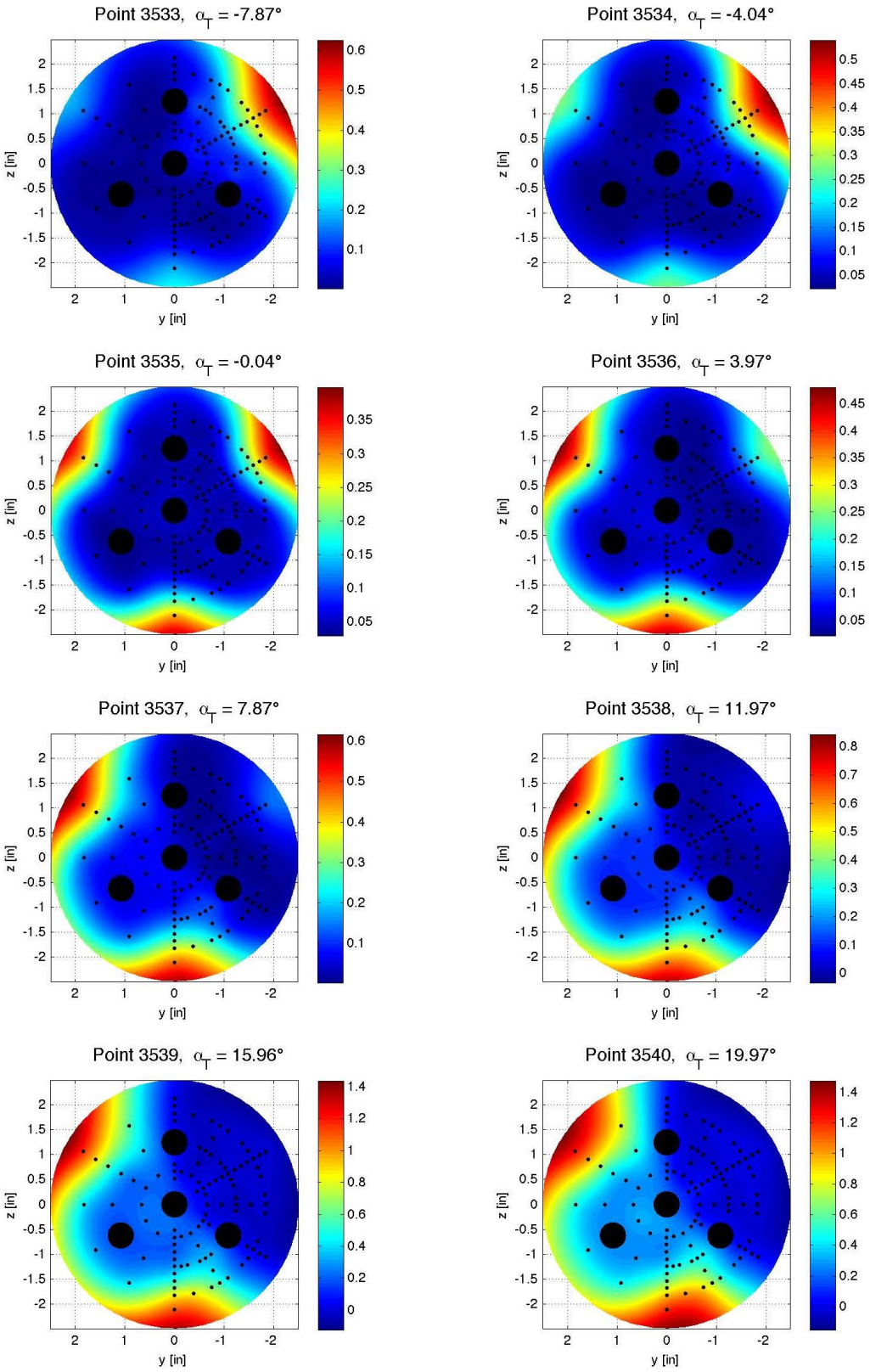

Figure E-244. Quad-nozzle configuration, Run 304, M_∞ = 3.5, Re_∞ = 1.0x10^6/ft, ϕ = 60.00°, X_S = 40.16 in, Y_S = 0.00 in, C_T = 0.90.

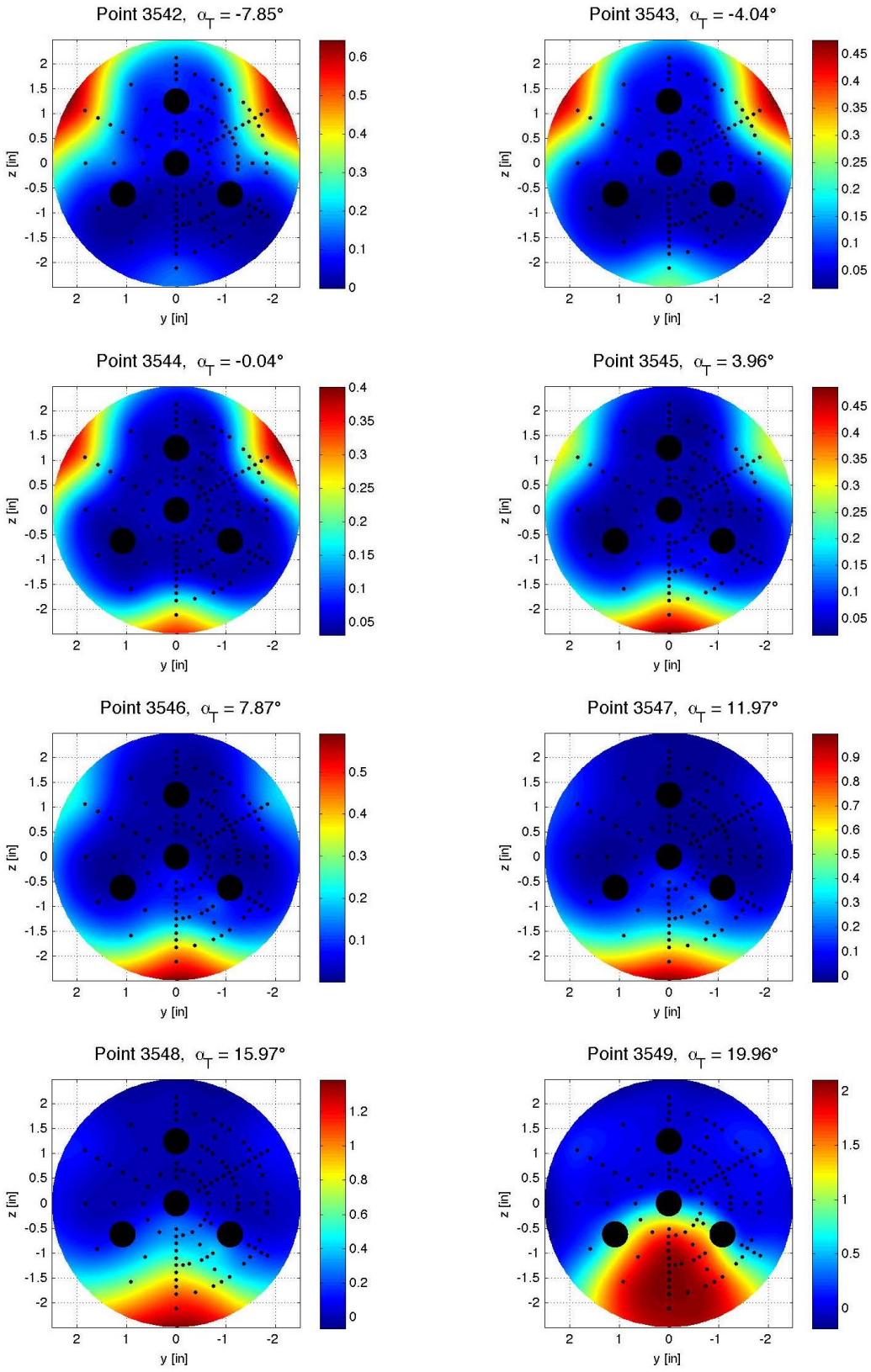

Figure E-245. Quad-nozzle configuration, Run 305, $M\infty$ = 3.5, Re_∞ = 1.0x10^6/ft, ϕ = −0.03°, X_S = 40.16 in, Y_S = 0.00 in, C_T = 0.90.

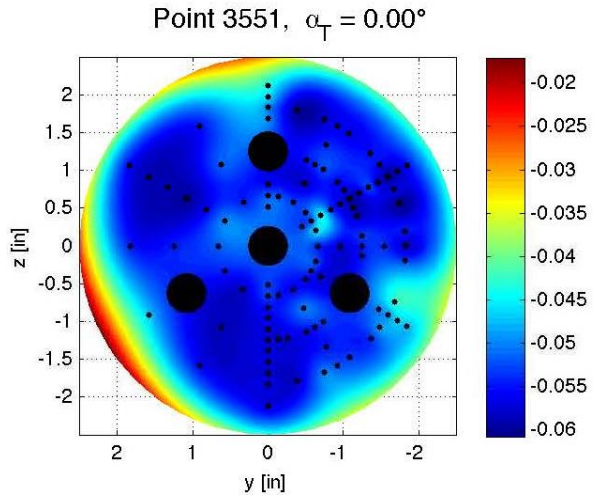

Figure E-246. Quad-nozzle configuration, Run 306, M_∞ = 3.5, Re_∞ = 1.0x10^6/ft, ϕ = 29.99°, X_S = 40.17 in, Y_S = 0.00 in, C_T = 2.92.

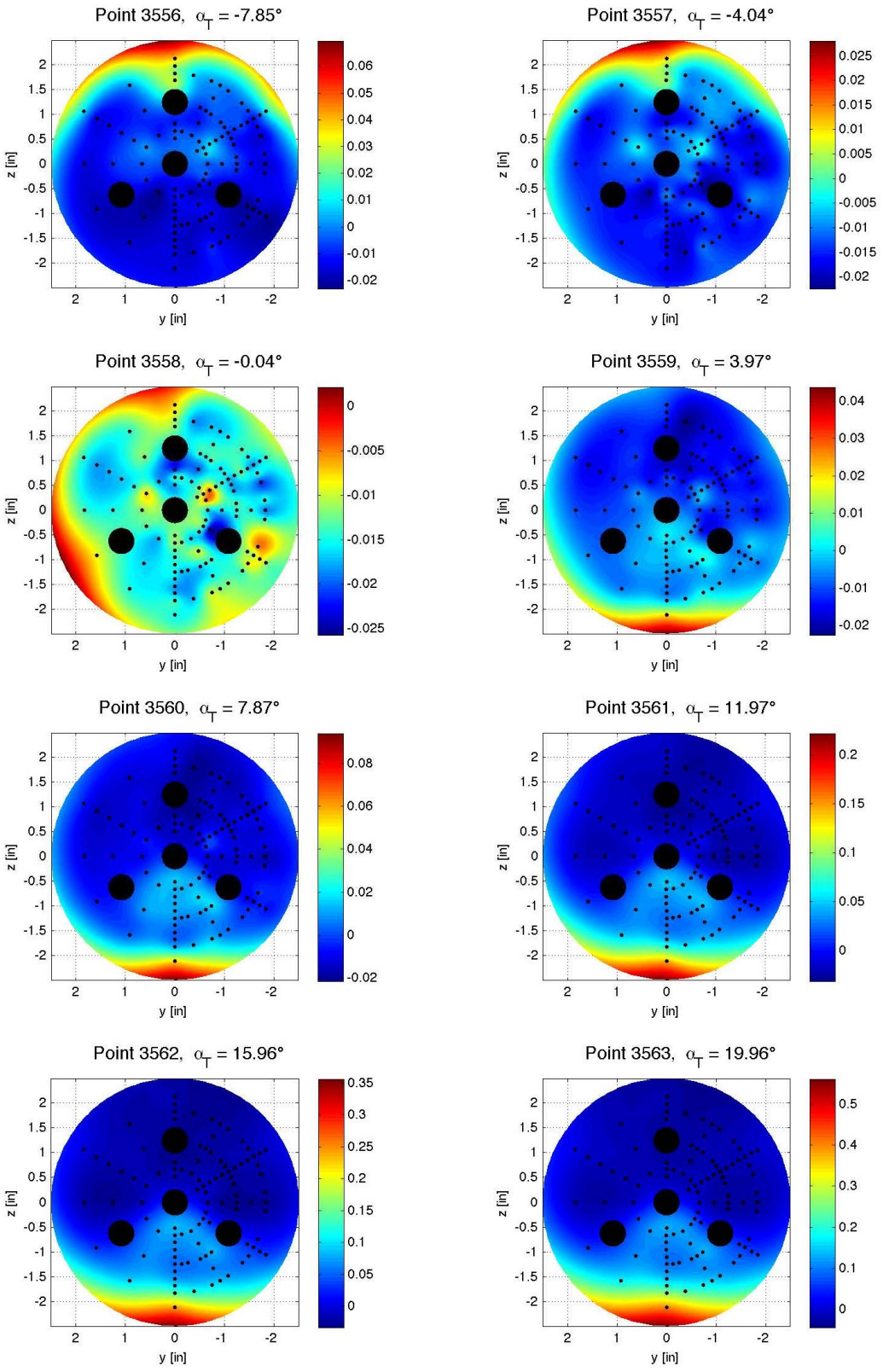

Figure E-247. Quad-nozzle configuration, Run 307, M_∞ = 4.6, Re_∞ = 1.5x10^6/ft, ϕ = 0.05°, X_S = 40.17 in, Y_S = 0.00 in, C_T = 1.93.

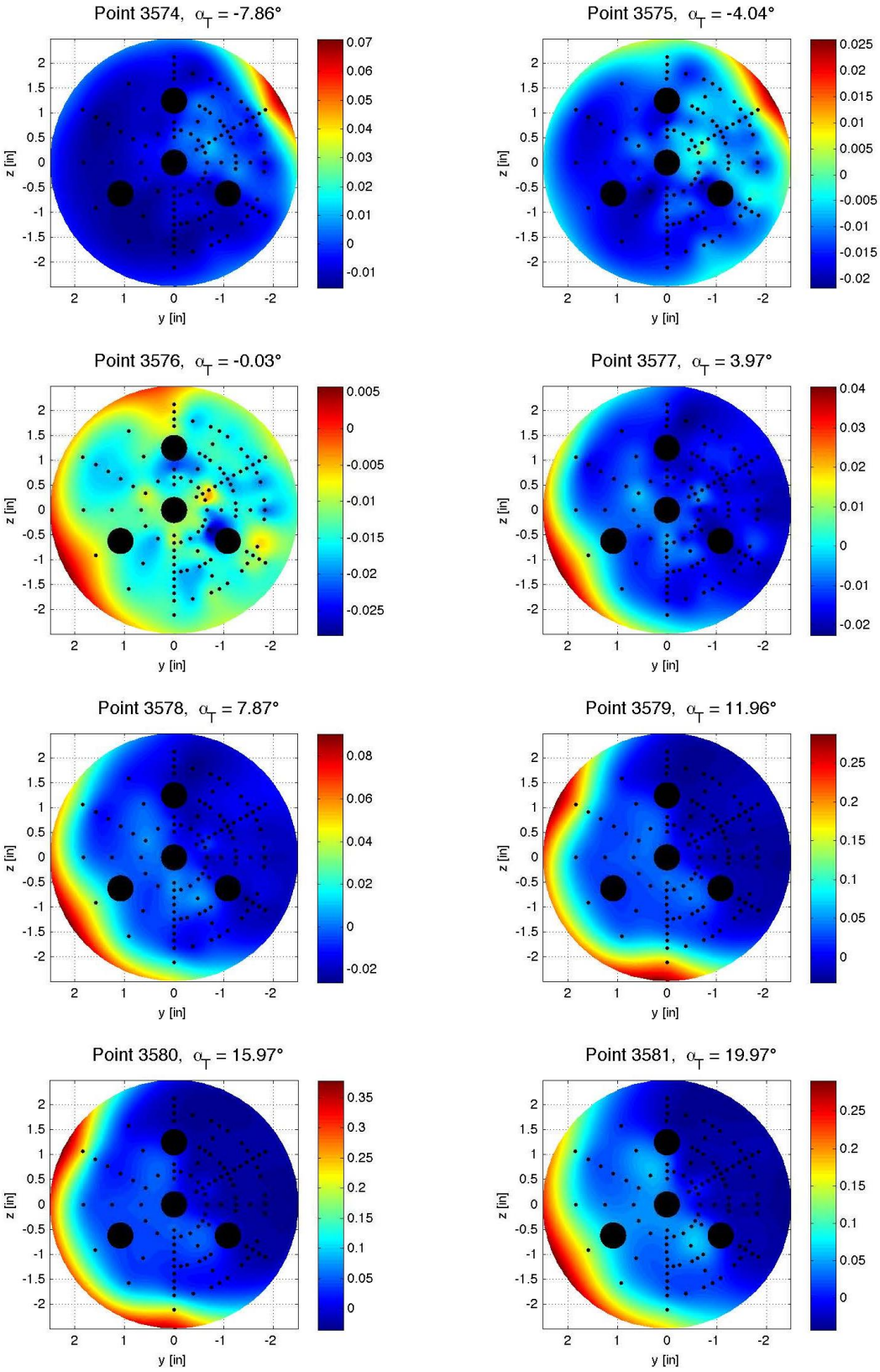

Figure E-248. Quad-nozzle configuration, Run 309, M_∞ = 4.6, Re_∞ = 1.5x10^6/ft, ϕ = 59.94°, X_S = 40.17 in, Y_S = 0.00 in, C_T = 1.92.

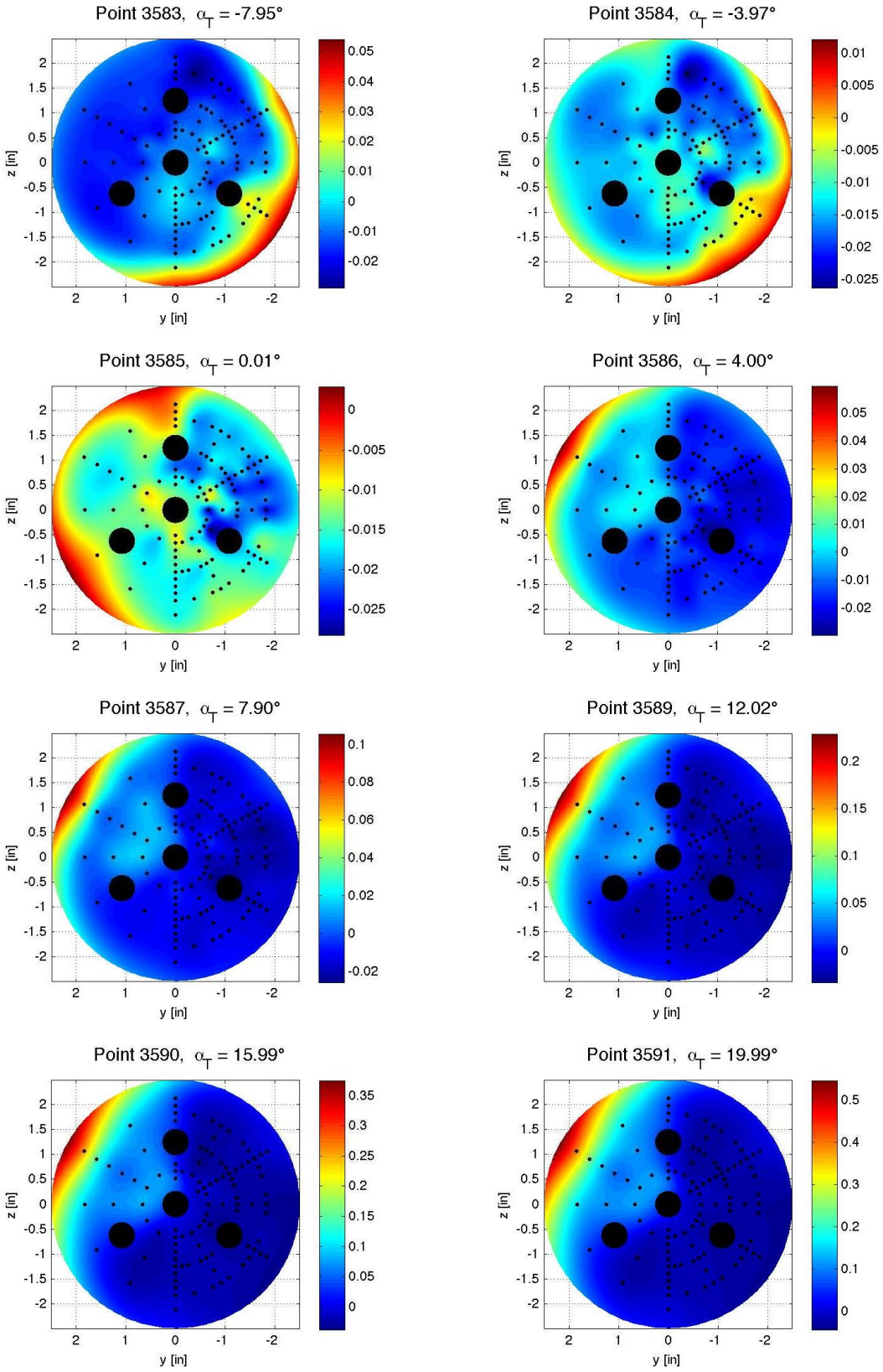

Figure E-249. Quad-nozzle configuration, Run 310, M_∞ = 4.6, Re_∞ = 1.5x10^6/ft, ϕ = 119.96°, X_S = 40.17 in, Y_S = 0.00 in, C_T = 1.92.

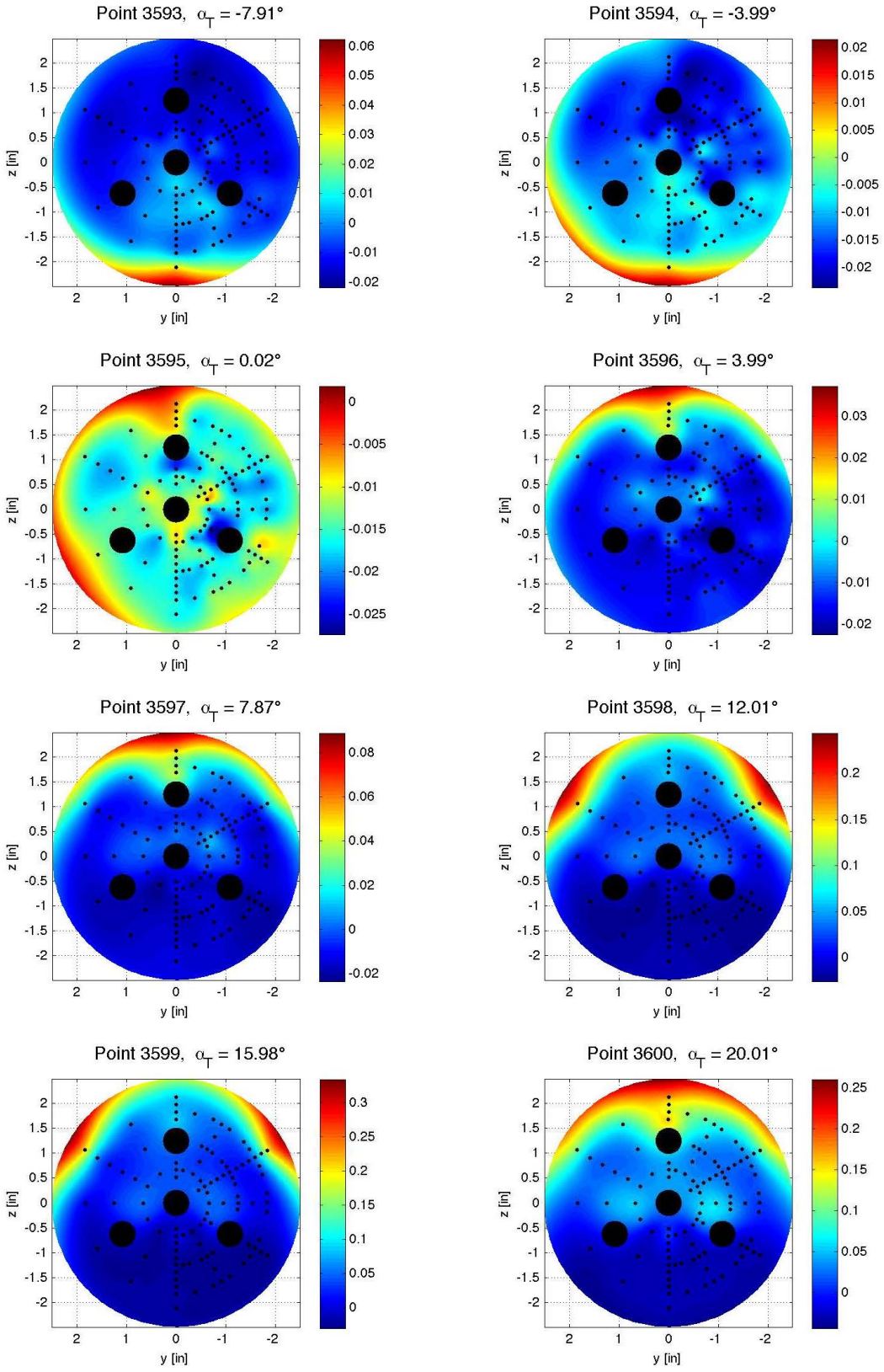

Figure E-250. Quad-nozzle configuration, Run 311, M_∞ = 4.6, Re_∞ = 1.5x10^6/ft, ϕ = −179.97°, X_S = 40.17 in, Y_S = 0.00 in, C_T = 1.92.

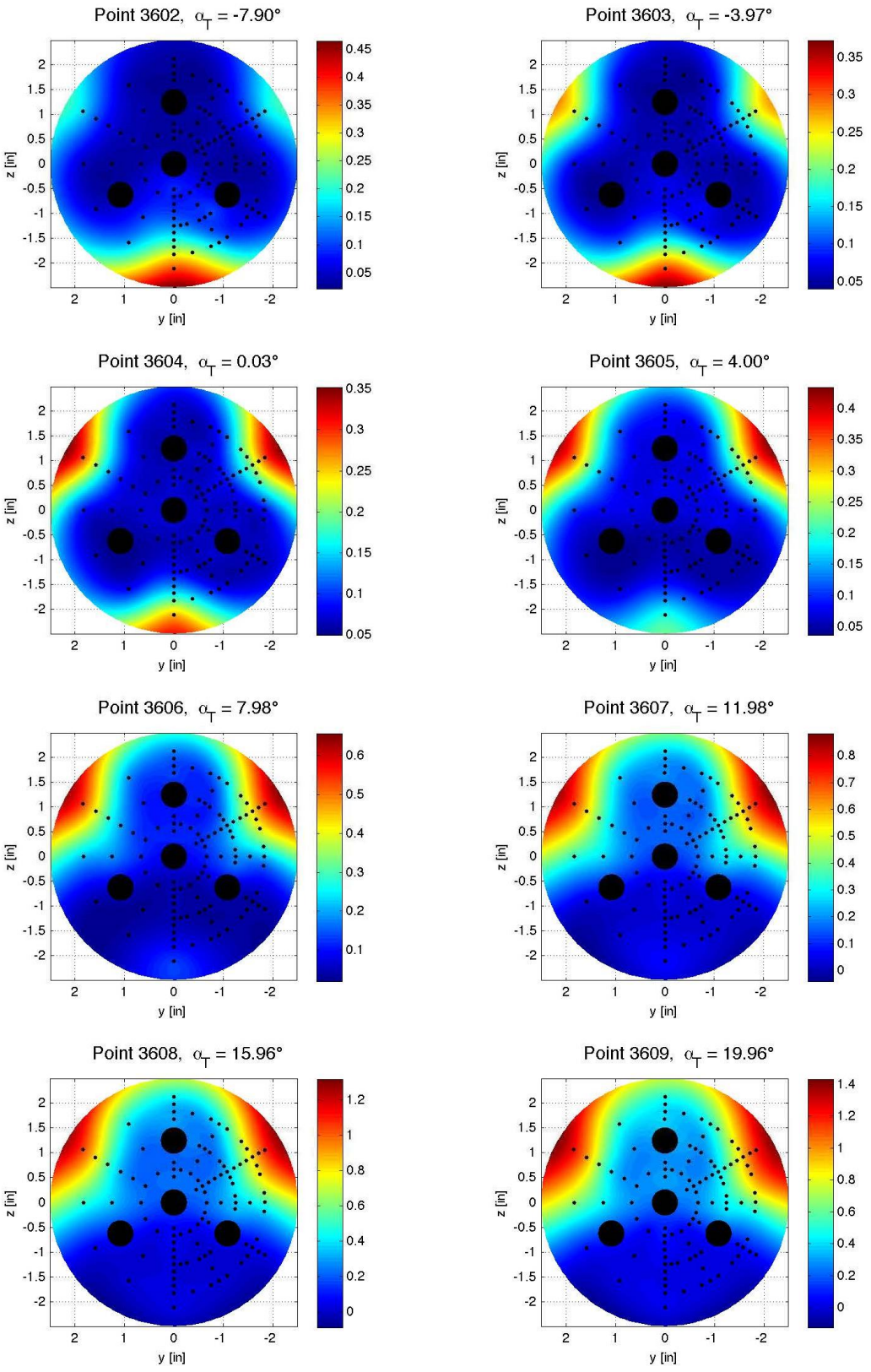

Figure E-251. Quad-nozzle configuration, Run 312, $M\infty$ = 4.6, Re_∞ = 1.5x10^6/ft, ϕ = −179.97°, X_S = 40.17 in, Y_S = 0.00 in, C_T = 0.91.

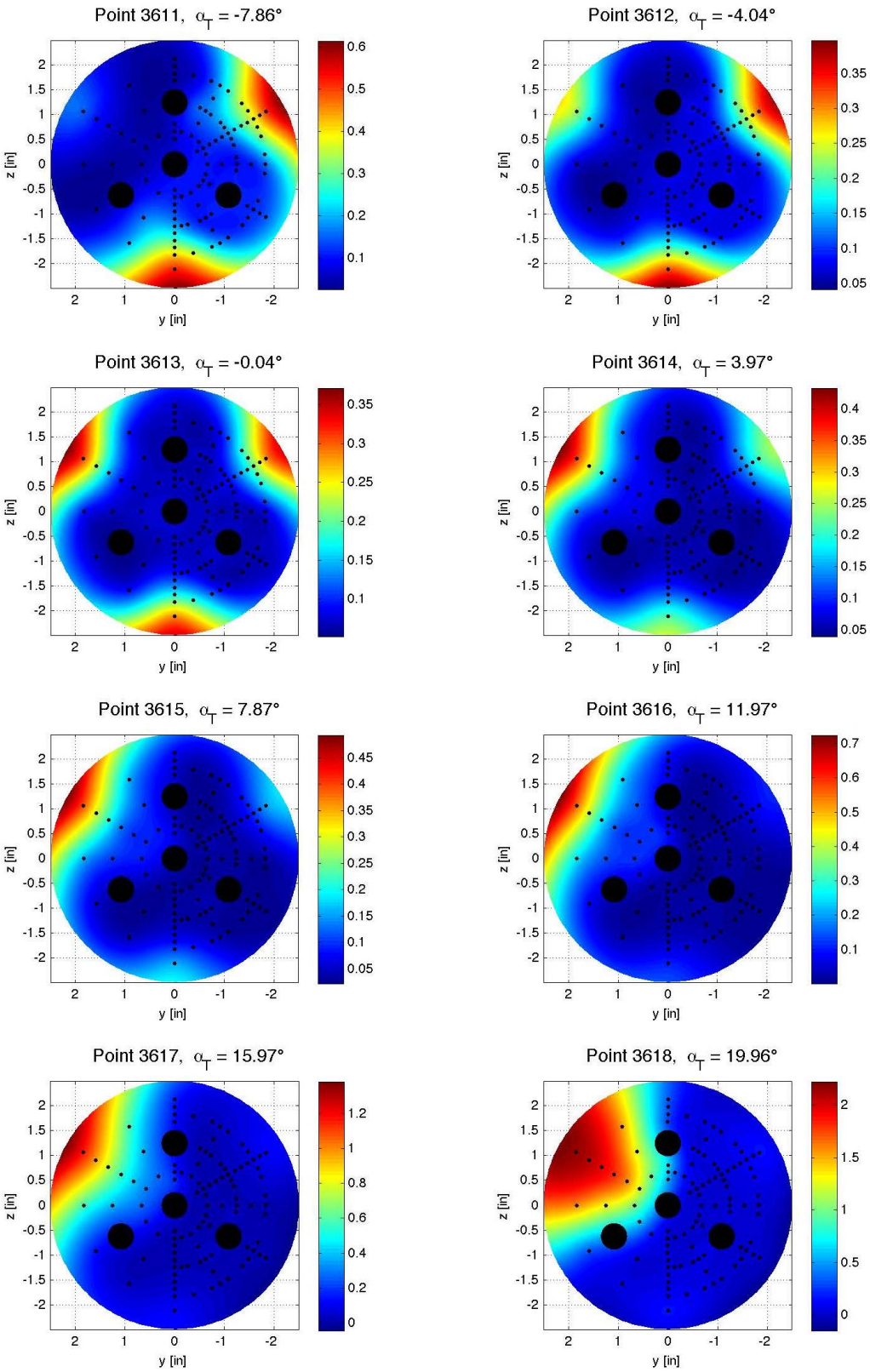

Figure E-252. Quad-nozzle configuration, Run 313, M_∞ = 4.6, Re_∞ = 1.5x10^6/ft, ϕ = 119.98°, X_S = 40.17 in, Y_S = 0.00 in, C_T = 0.92.

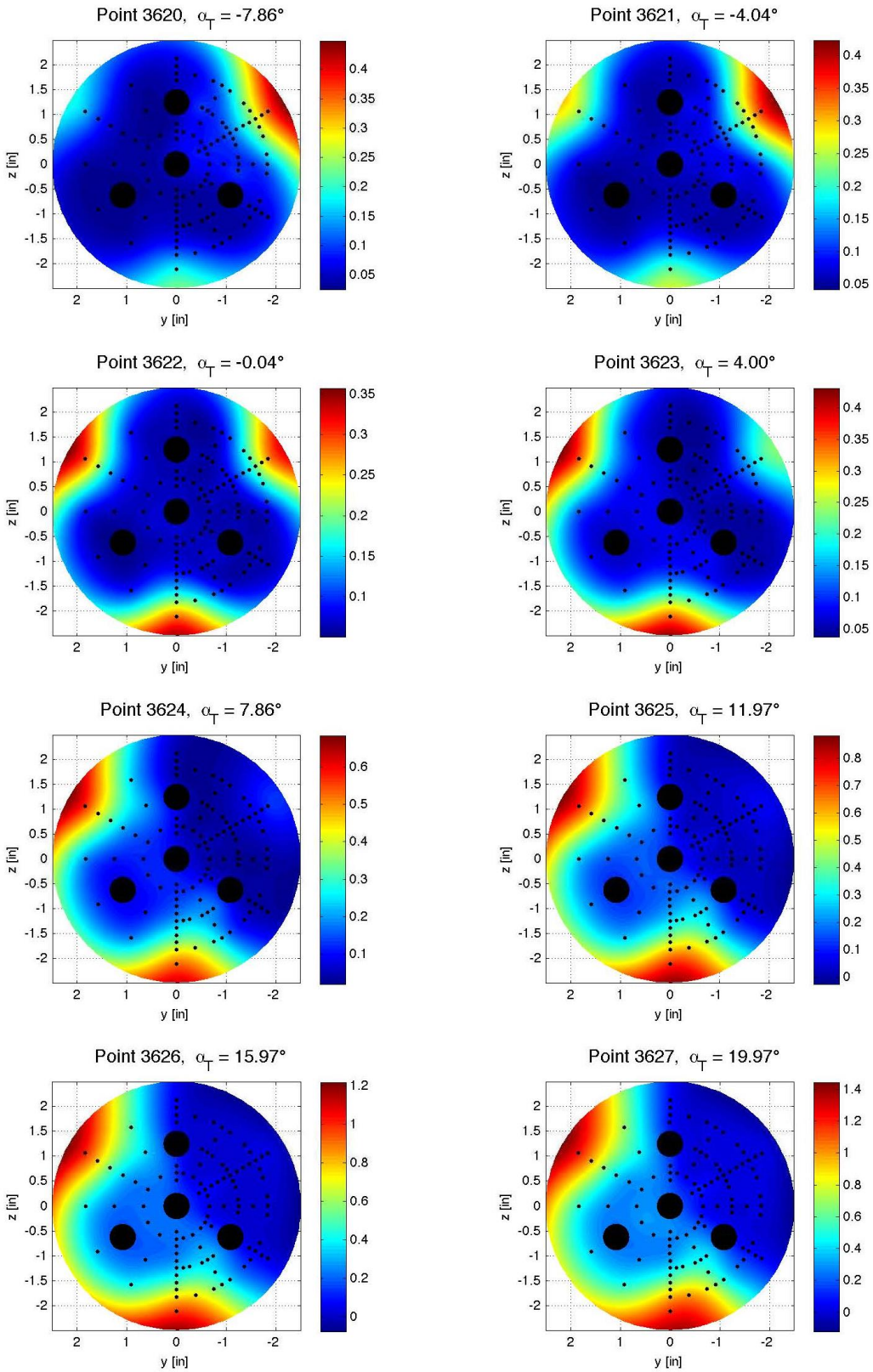

Figure E-253. Quad-nozzle configuration, Run 314, M_∞ = 4.6, Re_∞ = 1.5x10^6/ft, ϕ = 60.04°, X_S = 40.17 in, Y_S = 0.00 in, C_T = 0.91.

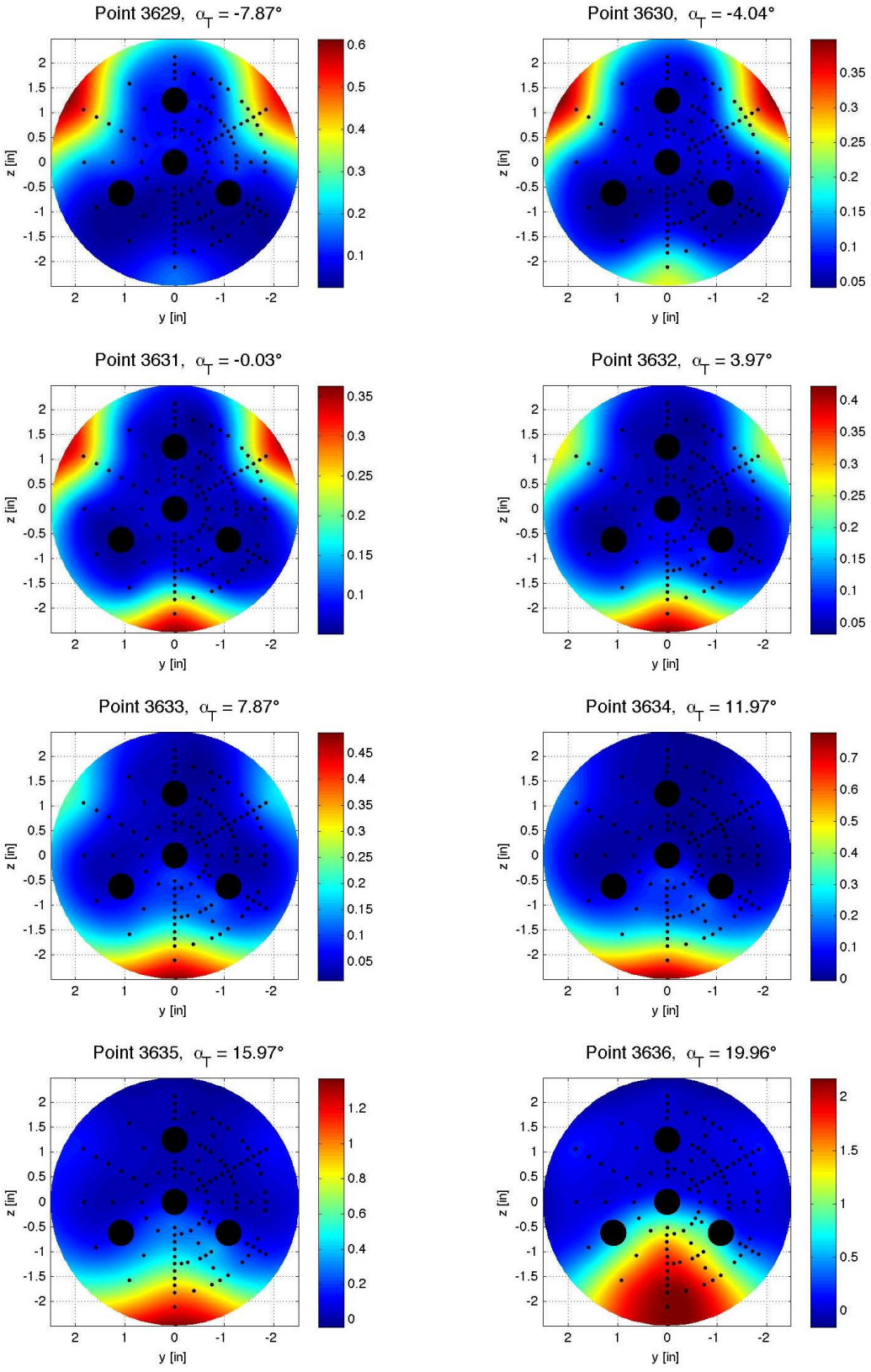

Figure E-254. Quad-nozzle configuration, Run 315, M_∞ = 4.6, Re_∞ = 1.5x10^6/ft, ϕ = 0.05°, X_S = 40.17 in, Y_S = 0.00 in, C_T = 0.92.

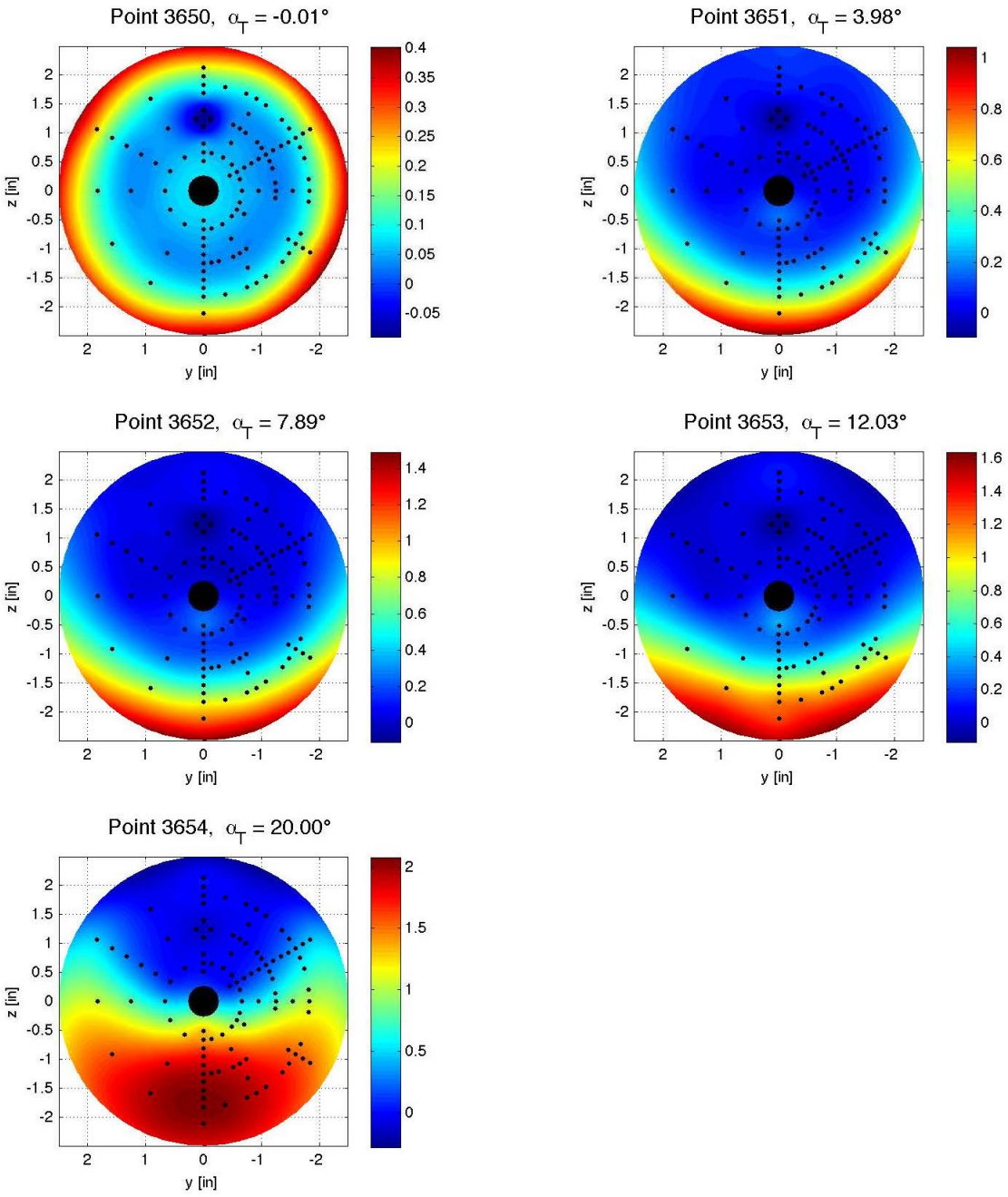

Figure E-255. Center nozzle configuration, Run 319, $M\infty$ = 2.4, Re_∞ = 1.0x10^6/ft, ϕ = 0.01°, X_S = 37.47 in, Y_S = 0.00 in, C_T = 0.45.

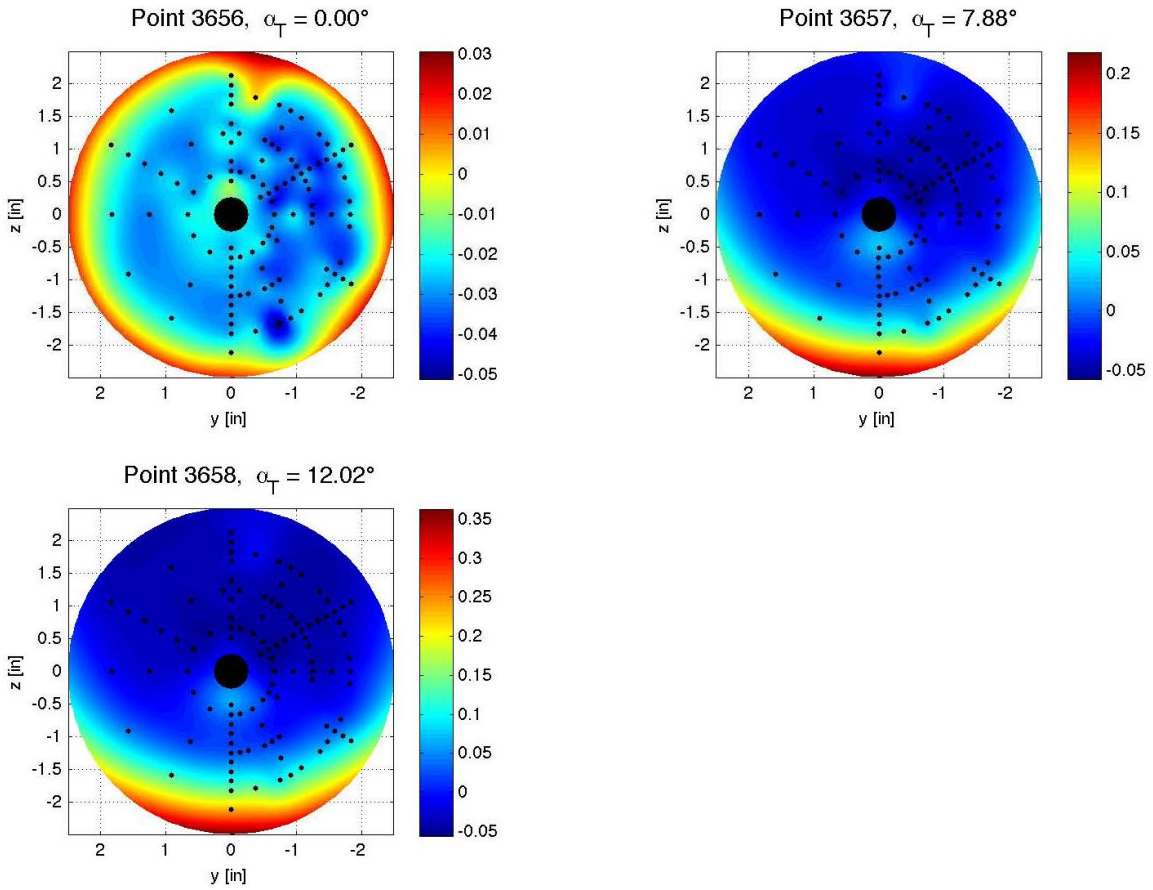

Figure E-256. Center nozzle configuration, Run 320, $M\infty$ = 3.5, Re_∞ = 1.0x10^6/ft, ϕ = 0.01°, X_S = 43.35 in, Y_S = 0.00 in, C_T = 1.96.

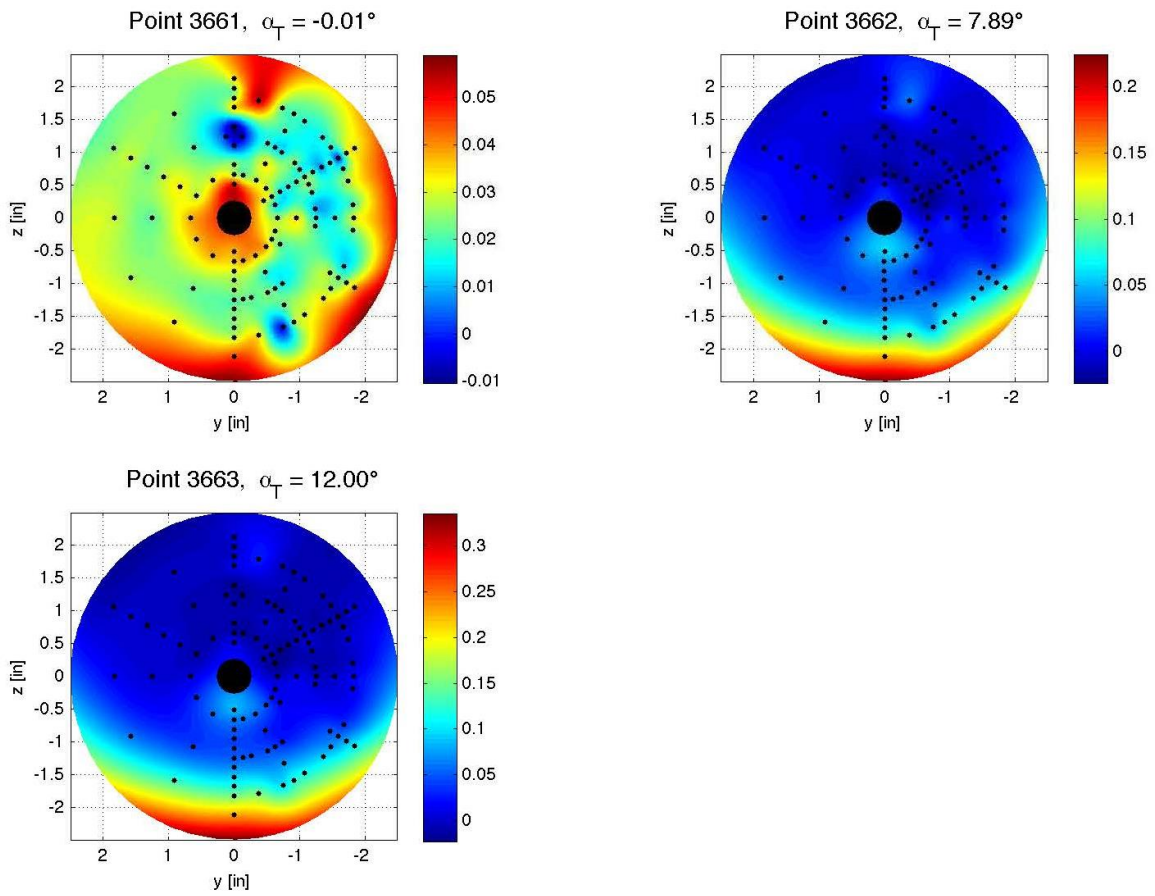

Figure E-257. Center nozzle configuration, Run 321, $M\infty$ = 4.6, Re_∞ = 1.5x10^6/ft, ϕ = 0.01°, X_S = 42.98 in, Y_S = 0.00 in, C_T = 1.96.

REPORT DOCUMENTATION PAGE

Form Approved
OMB No. 0704-0188

The public reporting burden for this collection of information is estimated to average 1 hour per response, including the time for reviewing instructions, searching existing data sources, gathering and maintaining the data needed, and completing and reviewing the collection of information. Send comments regarding this burden estimate or any other aspect of this collection of information, including suggestions for reducing this burden, to Department of Defense, Washington Headquarters Services, Directorate for Information Operations and Reports (0704-0188), 1215 Jefferson Davis Highway, Suite 1204, Arlington, VA 22202-4302. Respondents should be aware that notwithstanding any other provision of law, no person shall be subject to any penalty for failing to comply with a collection of information if it does not display a currently valid OMB control number.
PLEASE DO NOT RETURN YOUR FORM TO THE ABOVE ADDRESS.

1. REPORT DATE *(DD-MM-YYYY)*	2. REPORT TYPE	3. DATES COVERED *(From - To)*
01- 04 - 2014	Technical Publication	

4. TITLE AND SUBTITLE

Supersonic Retropropulsion Test 1853 in NASA LaRC Unitary Plan Wind Tunnel Test Section 2

5a. CONTRACT NUMBER

5b. GRANT NUMBER

5c. PROGRAM ELEMENT NUMBER

6. AUTHOR(S)

Berry, Scott A.; Rhode, Matthew N.

5d. PROJECT NUMBER

5e. TASK NUMBER

5f. WORK UNIT NUMBER

902152.01.07.01

7. PERFORMING ORGANIZATION NAME(S) AND ADDRESS(ES)

NASA Langley Research Center
Hampton, VA 23681-2199

8. PERFORMING ORGANIZATION REPORT NUMBER

L-20392

9. SPONSORING/MONITORING AGENCY NAME(S) AND ADDRESS(ES)

National Aeronautics and Space Administration
Washington, DC 20546-0001

10. SPONSOR/MONITOR'S ACRONYM(S)

NASA

11. SPONSOR/MONITOR'S REPORT NUMBER(S)

NASA/TP-2014-218256

12. DISTRIBUTION/AVAILABILITY STATEMENT

Unclassified - Unlimited
Subject Category 34
Availability: NASA CASI (443) 757-5802

13. SUPPLEMENTARY NOTES

14. ABSTRACT

A supersonic retropropulsion experiment was conducted in the Langley Research Center Unitary Plan Wind Tunnel Test Section 2 at Mach numbers of 2.4, 3.5, and 4.6. Intended as a code validation effort, this study used pretest computations to size and refine the model such that tunnel blockage and internal flow separations were minimized. A 5-in diameter 70 degree sphere-cone forebody, which can accommodate up to four 4:1 area ratio nozzles, followed by a 9.55 inches long cylindrical aft body was selected for this test after computational maturation. The primary measurements for this experiment were high spatial-density surface pressures. In addition, high speed schlieren video and internal pressures and temperatures were acquired. The test included parametric variations in the number of nozzles utilized, thrust coefficients (roughly 0 to 4), and angles of attack (–8 to 20 degrees). The run matrix was developed to also allow quantification of various sources of experimental uncertainty, such as random errors due to run-to-run variations and systematic errors due to flowfield or model misalignments. To accommodate the uncertainty assessment, many runs and replicates were conducted with the model at various locations within the tunnel and with model roll angles of 0, 60, 120, and 180 degrees. This test report provides operational details of the experiment, contains a review of trends, and provides all schlieren and pressure results within appendices.

15. SUBJECT TERMS

Decelerators; Experimental; Retropropulsion; Supersonic

16. SECURITY CLASSIFICATION OF:			17. LIMITATION OF ABSTRACT	18. NUMBER OF PAGES	19a. NAME OF RESPONSIBLE PERSON
a. REPORT	b. ABSTRACT	c. THIS PAGE			STI Help Desk (email: help@sti.nasa.gov)
					19b. TELEPHONE NUMBER *(Include area code)*
U	U	U	UU	1016	(443) 757-5802